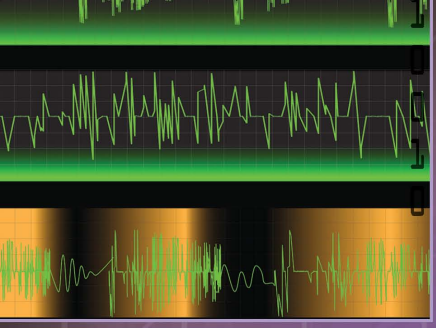

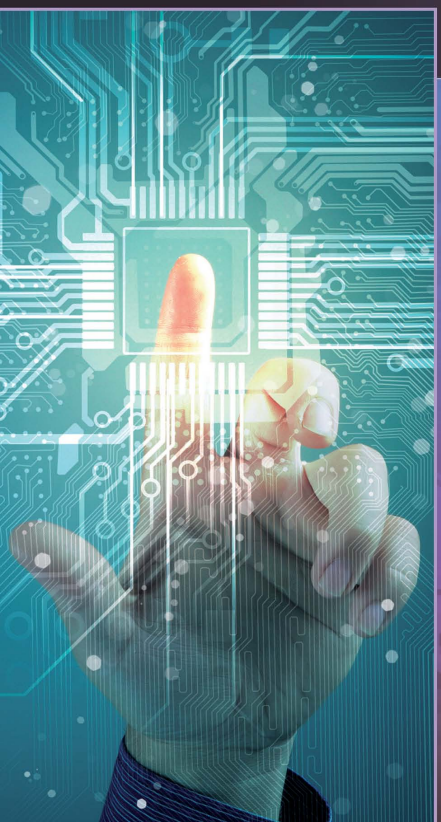

SECOND EDITION

Measurement, Instrumentation, and Sensors Handbook

Spatial, Mechanical, Thermal, and Radiation Measurement

EDITED BY
John G. Webster
Halit Eren

CRC Press
Taylor & Francis Group

SECOND EDITION

Measurement, Instrumentation, and Sensors Handbook

Spatial, Mechanical, Thermal, and Radiation Measurement

SECOND EDITION

Measurement, Instrumentation, and Sensors Handbook

Spatial, Mechanical, Thermal, and Radiation Measurement

EDITED BY
John G. Webster
Halit Eren


CRC Press
Taylor & Francis Group
Boca Raton London New York

CRC Press is an imprint of the
Taylor & Francis Group, an **informa** business

CRC Press
Taylor & Francis Group
6000 Broken Sound Parkway NW, Suite 300
Boca Raton, FL 33487-2742

Version Date: 20130725

International Standard Book Number-13: 978-1-4398-4889-0 (eBook - PDF)

Contents

PART IV Mechanical Variables

PART VII Thermal and Temperature Measurement

PART VIII Radiation

PART IX Wireless Instrumentation

PART X Control and Human Factors

Preface

Introduction

The second edition of *The Measurement, Instrumentation, and Sensors Handbook* comes in two volumes. This edition reflects the current state of the art in measurement, instrumentation, and sensors. In this two-volume set, all chapters have been updated, and 40 new chapters have been included to provide the finest possible reference that is both concise and useful for engineers practicing in industry, scientists and engineers involved in R&D, designers, college and university personnel and students, as well as managers, together with many others who are involved in instrumentation and measurement design and applications.

The handbook covers an extensive range of topics that comprise the subject of measurement, instrumentation, and sensors. It describes the use of instruments and techniques for practical measurements required in engineering, physics, chemistry, environmental science, and the life sciences. It also explains sensors, techniques, hardware, and the associated software. The handbook includes information processing systems, automatic data acquisition, reduction and analysis, operation characteristics, accuracy, errors, calibrations, standards, and their incorporation for control purposes. Emphasis is given on modern intelligent instruments and techniques, wireless network operations, human factors, and modern display methods, as well as virtual instruments.

The chapters include descriptive information for professionals, students, and workers interested in measurement. They include equations to assist engineers and scientists who seek to discover applications and solve problems that arise in fields not in their specialty. They also include specialized information needed by informed specialists who seek to learn advanced applications of the subject, evaluative opinions, and possible areas for future study. Thus, the handbook serves the reference needs of the broadest group of users—from the advanced high-school science student to industrial and university professionals.

Organization

In this edition, the first volume has 10 parts, each having several chapters, for a total of 96 chapters written by experts in their areas. It concentrates on concepts in instrumentation and measurements, spatial variable measurement, displacement measurement, mechanical variable measurement, acoustics, flow and spot velocity, thermal and temperature measurement, and radiation. It reflects recent trends in instrumentation and measurements with the addition of a new part on wireless instrumentation. Concepts in control systems and human factors are given as a separate part.

The second volume has 10 parts, each having several chapters, for a total of 96 chapters written by experts in their areas as in volume 1. It concentrates on sensors and sensor technology, electric variable measurement, electromagnetic variables, time and frequency, optical measurement, chemical variables,

medical, biomedical and health, and environmental measurement. Signal processing, and displays and recorders constitute the last two parts of this volume.

Locating Your Topic

To find out how to measure a given variable, skim the table of contents, turn to that section, and find the chapters that describe different methods of making the measurement. Consider the alternative methods of making the measurement and each of their advantages and disadvantages. Select a method, sensor, and signal processing method. Many chapters list a number of vendors to contact for more information. You can also visit http://www.globalspec.com/ to obtain a list of vendors.

For more detailed information, consult the index, since certain principles of measurement may appear in more than one chapter.

John G. Webster and Halit Eren
Co-Editors

Acknowledgments

We would like to thank all the authors for their valuable contribution toward this two-volume set book. We appreciate the time and effort devoted by all our new authors and those authors who went an extra mile to revise and update their chapters. We are grateful to the CRC Press team for their encouragement to prepare this second edition. The publication of this book would not have been possible without their tireless dedication in putting it together. Last but not least, we would like to thank all our readers in selecting this book for advancing their knowledge and technical skills.

John G. Webster and Halit Eren
Co-Editors

Editors

John G. Webster received his BEE from Cornell University, Ithaca, New York, in 1953, and his MSEE and PhD from the University of Rochester, Rochester, New York, in 1965 and 1967, respectively.

He is professor emeritus of biomedical engineering at the University of Wisconsin–Madison. He is a highly cited researcher at King Abdulaziz University, Jeddah, Saudi Arabia. In the field of medical instrumentation, he teaches undergraduate and graduate courses and does research on intracranial pressure monitors, ECG dry electrodes, and tactile vibrators.

Dr. Webster is the author of *Transducers and Sensors, an IEEE/EAB Individual Learning Program* (Piscataway, NJ: IEEE, 1989). He is the coauthor, with B. Jacobson, of *Medicine and Clinical Engineering* (Englewood Cliffs, NJ: Prentice-Hall, 1977) and, with R. Pallas-Areny, of *Sensors and Signal Conditioning*, Second Edition (New York: Wiley, 2001), and *Analog Signal Conditioning* (New York: Wiley, 1999). He is the editor of *Encyclopedia of Medical Devices and Instrumentation*, Second Edition (New York: Wiley, 2006), *Tactile Sensors for Robotics and Medicine* (New York: Wiley, 1988), *Electrical Impedance Tomography* (Bristol, U.K.: Adam Hilger, 1990), *Teaching Design in Electrical Engineering* (Piscataway, NJ: Educational Activities Board, IEEE, 1990), *Prevention of Pressure Sores: Engineering and Clinical Aspects* (Bristol, U.K.: Adam Hilger, 1991), *Design of Cardiac Pacemakers* (Piscataway, NJ: IEEE Press, 1995), *Design of Pulse Oximeters* (Bristol, U.K.: IOP Publishing, 1997), *Medical Instrumentation: Application and Design*, Fourth Edition (Hoboken NJ: Wiley, 2010), *Encyclopedia of Electrical and Electronics Engineering* (New York, Wiley, 1999), *Minimally Invasive Medical Technology* (Bristol, U.K.: IOP Publishing, 2001), and *Bioinstrumentation* (Hoboken NJ: Wiley, 2004). He is the coeditor, with A. M. Cook, of *Clinical Engineering: Principles and Practices* (Englewood Cliffs, NJ: Prentice-Hall, 1979) and *Therapeutic Medical Devices: Application and Design* (Englewood Cliffs, NJ: Prentice-Hall, 1982), with W. J. Tompkins of *Design of Microcomputer-Based Medical Instrumentation* (Englewood Cliffs, NJ: Prentice-Hall, 1981) and *Interfacing Sensors to the IBM PC* (Englewood Cliffs, NJ: Prentice Hall, 1988), and, with A. M. Cook, W J. Tompkins, and G. C. Vanderheiden, of *Electronic Devices for Rehabilitation* (London, U.K.: Chapman & Hall, 1985).

Dr. Webster has been a member of the IEEE-EMBS Administrative Committee and the NIH Surgery and Bioengineering Study Section. He is a fellow of the Institute of Electrical and Electronics Engineers, the Instrument Society of America, the American Institute of Medical and Biological Engineering, the Biomedical Engineering Society, and the Institute of Physics. He is the recipient of the IEEE EMBS Career Achievement Award.

Halit Eren received his BEng in 1973, MEng in 1975, and PhD in 1978 from the University of Sheffield, United Kingdom. He obtained an MBA from Curtin University in 1999.

After his graduation, Dr. Eren worked in Etibank (a mining and metallurgy company in Turkey) as an instrumentation engineer for two years. He was an assistant professor at Hacettepe University in 1980–1981 and Middle East Technical University in 1982. He has been at Curtin University since

1983, researching and teaching primarily in the areas of control systems, instrumentation, and engineering management.

Dr. Eren was appointed as visiting associate professor at the Polytechnic University in Hong Kong in 2004 and is currently a visiting professor at the University of Wisconsin, USA. He is a senior member of IEEE, taking roles in Region 10 activities, various committees for organizing conferences, and as a member of editorship in transactions. Dr. Eren has over 180 publications in conference proceedings, books, and transactions. He is the author of *Electronic Portable Instruments—Design and Applications* (Boca Raton, FL: CRC Press, 2004) and *Wireless Sensors and Instruments—Networks, Design and Applications* (Boca Raton, FL: CRC Press, 2006). He has coedited, with Bela Liptak, *Instruments Engineers' Handbook—Process Software and Digital Networks*, Vol. 3, edn. 4 (Boca Raton, FL: CRC Press, 2011). He is involved in writing a number of books in the field of instrumentation and measurement. Dr. Eren is active in researching and publishing on intelligent sensors, wireless instrumentation, wireless sensor networks, automation and control systems, and very large control systems.

Contributors

René G. Aarnink
University Hospital Nijmegen
Nijmegen, the Netherlands

Ben A. Abbott
Southwest Research Institute
San Antonio, Texas

Jugal K. Agarwal
TSI, Inc.
Shoreview, Minnesota

Keith Antonelli
Kinetic Sciences, Inc.
Vancouver, British Colombia, Canada

John C. Armitage
Ottawa–Carleton Institute for Physics
Carleton University
Ottawa, Ontario, Canada

Marc J. Assael
Faculty of Chemical Engineering
Department of Chemical Engineering
Aristotle University of Thessaloniki
Thessaloniki, Greece

Viktor P. Astakhov
Astakhov Tool Service
Rochester Hills, Michigan

Manouchehr Bahrami
University of Tabriz
Tabriz, Iran

William E. Baker
Department of Mechanical Engineering
University of New Mexico
Albuquerque, New Mexico

W. John Ballantyne
Department of Systems Engineering
Spar Aerospace Ltd.
Brampton, Ontario, Canada

Amit Bandyopadhyay
Department of Ceramic Science and Engineering
Rutgers University
Piscataway, New Jersey

Partha P. Banerjee
Department of Electrical and Computer Engineering
University of Alabama at Huntsville
Huntsville, Alabama

William H. Bayles, Jr.
The Fredericks Company
Huntington Valley, Pennsylvania

Ben Benhabib
Department of Mechanical and Industrial Engineering
University of Toronto
Toronto, Ontario, Canada

Vikram Bhatia
Virginia Tech
Blacksburg, Virginia

A. Bonen
University of Toronto
Toronto, Ontario, Canada

Howard M. Brady
The Fredericks Company
Huntington Valley, Pennsylvania

John C. Brasunas
Goddard Space Flight Center
National Aeronautics and Space Administration
Greenbelt, Maryland

Detlef Brumbi
Krohne Messtechnik GmbH
Duisburg, Germany

Christophe Bruttin
Rittmeyer Ltd.
Zug, Switzerland

Wolfgang P. Buerner
Los Angeles Scientific Instrumentation Co.
Los Angeles, California

Jim Burns
Burns Engineering, Inc.
Minnetonka, Minnesota

Barrett S. Caldwell
Purdue University
West Lafayette, Indiana

J.P. Carmo
Department of Industrial Electronics
University of Minho
Guimarães, Portugal

Kevin H.L. Chau
Micromachined Products Division
Analog Devices, Inc.
Cambridge, Massachusetts

Adam Chrzanowski
University of New Brunswick
Fredericton, New Brunswick, Canada

Richard O. Claus
Bradley Department of Electrical Engineering
Virginia Tech
Blacksburg, Virginia

J.H. Correria
Department of Industrial Electronics
University of Minho
Guimarães, Portugal

Charles B. Coulbourn
Los Angeles Scientific Instrumentation Co.
Los Angeles, California

Bert M. Coursey
Ionizing Radiation Division
Physics Laboratory
National Institute of Standards and Technology
Gaithersburg, Maryland

Brian Culshaw
Department of Electronic and Electrical Engineering
University of Strathclyde
Glasgow, England

G. Mark Cushman
Goddard Space Flight Center
National Aeronautics and Space Administration
Greenbelt, Maryland

Larry S. Darken
Oxford Instruments, Inc.
Oak Ridge, Tennessee

David Dayton
ILC Data Device Corp.
Bohemia, New York

J.R. deBruyn
University of Western Ontario
DeKalb, Illinois

Ronald H. Dieck
Pratt & Whitney
and
Ron Dieck Associates, Inc.
Palm Beach Gardens, Florida

Thomas E. Diller
Virginia Tech
Blacksburg, Virginia

Madhu S. Dixit
Centre for Research in Particle Physics
Carleton University
Ottawa, Ontario, Canada

Emil Drubetsky
The Fredericks Company
Huntington Valley, Pennsylvania

Jacques Dubeau
Centre for Research in Particle Physics
Carleton University
Ottawa, Ontario, Canada

M.A. Elbestawi
Department of Mechanical Engineering
McMaster University
Hamilton, Ontario, Canada

Halit Eren
Department of Electrical and Computer Engineering
Curtin University
Perth, Western Australia, Australia

Giuseppe Fazio
Department of Electronic Engineering
University of Rome "Tor Vergata"
Rome, Italy

and

Isatel Ltd.
Moscow, Russia

Richard S. Figliola
Department of Mechanical Engineering
Clemson University
Clemson, South Carolina

Frederick Fortson
Solidica, Inc.
Ann Arbor, Michigan

Jacob Fraden
Fraden Corporation
San Diego, California

Randy Frank
Randy Frank & Associates, Ltd
Scottsdale, Arizona

and

Motorola, Inc.
Phoenix, Arizona

Larry A. Franks
Sandia National Laboratories
Livermore, California

Yusaku Fujii
Department of Electronic Engineering
Gunma University
Kiryu, Japan

Ivan J. Garshelis
Magnova, Inc.
Pittsfield, Massachusetts

Manel Gasulla
Universitat Politècnica de Catalunya
Barcelona, Catalonia, Spain

Mauro Giaconi
Department of Electronic Engineering
University of Rome "Tor Vergata"
Rome, Italy

Paolo Giordano
Rittmeyer Ltd.
Zug, Switzerland

Ron Goehner
The Fredericks Company
Huntington Valley, Pennsylvania

Ronald T. Green
Southwest Research Institute
San Antonio, Texas

Steven M. Grimes
Department of Physics and Astronomy
Ohio University
Athens, Ohio

Reinhard Haak
University of Erlangen–Nuernberg
Erlangen, Germany

John R. Hansman, Jr.
Department of Aeronautics and Astronautics
Massachusetts Institute of Technology
Cambridge, Massachusetts

Emil Hazarian
Master of Science Quality Assurance Program
and
Bachelor of Science Quality Assurance Program
California State University, Dominguez Hills
Carson, California

and

ANSI-ASQ National Accreditation Board
ACLASS
Alexandria, Virginia

Michael Healy
University of Limerick
Limerick, Ireland

Sander van Herwaarden
Xensor Integration
Delft, the Netherlands

Thomas Hossle
Rittmeyer Ltd.
Zug, Switzerland

C.H. Houpis
Air Force Institute of Technology
Wright–Patterson Air Force Base, Ohio

Zaki D. Husain
Daniel Flow Products, Inc.
Bellaire, Texas

Alan L. Huston
Naval Research Laboratory
Washington, District of Columbia

Robert M. Hyatt, Jr.
Howell Electric Motors
Plainfield, New Jersey

Elina Iervolino
Xensor Integration

Ralph B. James
Sandia National Laboratories
Livermore, California

Victor F. Janas
Center for Ceramic Research
Rutgers University
Piscataway, New Jersey

Kenneth Johnson
Solidica, Inc.
Ann Arbor, Michigan

Brian L. Justus
Department of Optical Science
Naval Research Laboratory
Washington, District of Columbia

Nils Karlsson
Department of Sensor and EW Systems
Swedish Defence Research Agency
Linköping, Sweden

Sam S. Khalilieh
Department of Electrical Engineering
Earth Tech
Grand Rapids, Michigan

Andrei Kholkine
Rutgers University
Piscataway, New Jersey

John A. Kleppe
Department of Electrical and Biomedical Engineering
University of Nevada, Reno
Reno, Nevada

James Ko
Kinetic Sciences, Inc.
Vancouver, British Columbia, Canada

Herbert Köchner
University of Erlangen–Nuernberg
Erlangen, Germany

M. Kostic
Northern Illinois University
DeKalb, Illinois

Shyan Ku
Kinetic Sciences, Inc.
Vancouver, British Columbia, Canada

Brook Lakew
Goddard Space Flight Center
National Aeronautics and Space Administration
Greenbelt, Maryland

Elfed Lewis
University of Limerick
Limerick, Ireland

Robert Lofthus
Xerox Corporation
Rochester, New York

Oscar Lopez-Lapeña
Universitat Politècnica de Catalunya
Barcelona, Catalonia, Spain

Albert Lozano-Nieto
Penn State University
Lehman, Pennsylvania

Christopher S. Lynch
Department of Mechanical Engineering
Georgia Tech
Atlanta, Georgia

Tolestyn Madaj
Technical University of Gdansk
Gdansk, Poland

Kin F. Man
Jet Propulsion Laboratory
California Institute of Technology
Pasadena, California

Dimitris E. Manolakis
Alexander Technological Education Institute
of Thessaloniki
Thessaloniki, Greece

Wade M. Mattar
The Foxboro Company
Foxboro, Massachusetts

J.R. René Mayer
Department of Mechanical Engineering
Ecole Polytechnique de Montreal
Montreal, Quebec, Canada

John McInroy
Department of Electrical Engineering
University of Wyoming
Laramie, Wyoming

Adrian Melling
University of Erlangen–Nuernberg
Erlangen, Germany

Rajan K. Menon
Laser Velocimetry Products
TSI Inc.
St. Paul, Minnesota

Hans Mes
Centre for Research in Particle Physics
Carleton University
Ottawa, Ontario, Canada

Jaroslaw Mikielewicz
Institute of Fluid Flow Machinery
Gdansk, Poland

Harold M. Miller
Data Industrial Corporation
Mattapoisett, Massachusetts

Mark A. Miller
Naval Research Laboratory
Washington, District of Columbia

Roger Morgan
School of Engineering
Liverpool John Moores University
Liverpool, England

Steven A. Murray
University of San Diego
San Diego, California

Thomas Newe
University of Limerick
Limerick, Ireland

J.V. Nicholas
Temperature Standards Section
Measurement Standards Laboratory of
New Zealand
Lower Hutt, New Zealand

Seiji Nishifuji
Department of Electrical and Electronic
Engineering
Yamaguchi University
Ube, Japan

David S. Nyce
Revolution Sensor Company
Cary, North Carolina

F. Gerald Oakham
Centre for Research in Particle Physics
Carleton University
Ottawa, Ontario, Canada

John G. Olin
Sierra Instruments, Inc.
Monterey, California

Jeffrey D. Onken
Purdue University
West Lafayette, Indiana

M. Pachter
Air Force Institute of Technology
Wright–Patterson Air Force Base, Ohio

Reza Pakdaman Zangabad
Faculty of Engineering and Natural Sciences
Sabanci University
Istanbul, Turkey

Franco Pavese
Thermodynamic Division
National Institute of Meterology Research
Turin, Italy

Ole Pedersen
Department of Science and Technology
Linköping University
Linköping, Sweden

Peder C. Pedersen
Department of Electrical and Computer Engineering
Worcester Polytechnic Institute
Worcester, Massachusetts

Maria Teresa Penella
Urbiotica S.L.
Barcelona, Catalonia, Spain

B.W. Petley
Centre for Basic, Thermal and Length Metrology
National Physical Laboratory
London, England

Rekha Philip-Chandy
School of Engineering
Liverpool John Moores University
Liverpool, England

Charles P. Pinney
Pinney Technologies, Inc.
Albuquerque, New Mexico

David Potter
National Instruments
Austin, Texas

Davide Quatrini
Italcertifer, Inc.
and
Department of Electronic Engineering
University of Rome "Tor Vergata"
Rome, Italy

Per Rasmussen
G.R.A.S. Sound and Vibration
Vedback, Denmark

R.P. Reed
Proteun Services
Albuquerque, New Mexico

Herbert M. Runciman
Pilkington Optronics
Scotland, United Kingdom

Ricardo E. Saad
Harmonics Lightwaves
Sunnyvale, California

Ahmad Safari
Department of Ceramic Science and Engineering
Rutgers University
Piscataway, New Jersey

Adelio Salsano
Italcertifer, Inc.
and
Department of Electronic Engineering
University of Rome "Tor Vergata"
Rome, Italy

Robert J. Sandberg
Department of Mechanical Engineering
University of Wisconsin–Madison
Madison, Wisconsin

Meyer Sapoff
MS Consultants
Princeton, New Jersey

Stuart Schweid
Xerox Corporation
Rochester, New York

Patricia J. Scully
School of Engineering
Liverpool John Moores University
Liverpool, England

R.A. Secco
University of Western Ontario
London, Ontario, Canada

James M. Secord
Department of Geodesy and Geomatics Engineering
University of New Brunswick
Fredericton, New Brunswick, Canada

DeWayne B. Sharp
Shape of Things
San Luis Obispo, California

F. Greg Shinskey
Process Control Consultant
North Sandwich, New Hampshire

K.C. Smith
University of Toronto
Toronto, Ontario, Canada

Jan Stasiek
Department of Mechanical Engineering
Technical University of Gdansk
Gdansk, Poland

Mark A. Stedham
Department of Electrical and Computer Engineering
University of Alabama at Huntsville
Huntsville, Alabama

Peter H. Sydenham
University of South Australia
Mawsons Lakes, South Australia, Australia

Akihiro Takita
Department of Electronic Engineering
Gunma University
Kiryu, Japan

Shogo Tanaka
Department of Electrical and Electronic Engineering
Yamaguchi University
Ube, Japan

Jin Tao
Department of Electronic Engineering
Gunma University
Kiryu, Japan

David B. Thiessen
California Institute of Technology
Pasadena, California

Richard Thorn
School of Engineering
University of Derby
Derby, United Kingdom

Hans-Peter Vaterlaus
Department of Instrument
Rittmeyer Ltd.
Zug, Switzerland

James H. Vignos
The Foxboro Company
Foxboro, Massachusetts

David Wadlow
Sensors Research Consulting, Inc.
Basking Ridge, New Jersey

William A. Wakeham
Department of Chemical Engineering
Imperial College, London
London, England

Anbo Wang
Bradley Department of Electrical Engineering
Virginia Tech
Blacksburg, Virginia

Donald J. Wass
Daniel Flow Products, Inc.
Houston, Texas

Grover C. Wetsel
Erik Jonsson School of Engineering and Computer Science
University of Texas at Dallas
Richardson, Texas

Rod White
Temperature Standards Section
Callaghan Innovation
Measurement Standards Laboratory of New Zealand
Lower Hutt, New Zealand

Hessel Wijkstra
University Hospital Nijmegen
Nijmegen, the Netherlands

Gregory C. Willden
Southwest Research Institute
San Antonio, Texas

Jesse Yoder
Flow Research, Inc.
Wakefield, Massachusetts

and

Automation Research Corporation
Dedham, Massachusetts

Bernhard Günther Zagar
Department of Electrical Engineering
Technical University of Graz
Graz, Austria

I

Instrumentation and Measurement Concepts

1

Measurements, Instrumentation, and Sensors

Halit Eren
Curtin University

1.1 Introduction

Measurement is a process of gathering information from a physical world and comparing this information with agreed standards. As highlighted in this chapter and discussed in detail in this book, measurements are essential activities for observing and testing scientific and technological investigations.

Measurements are carried out by using instruments, which are designed and manufactured to fulfill specific tasks. Sensors are used as the primary elements in instruments to respond to the physical variable under investigation. In this book, a diverse range of sensors and instruments are discussed; the advances and the recent developments in measurements, instrumentation, and sensors are introduced in the proceeding sections and chapters.

In many applications, many sensors and instruments are used to collect information about the process under investigation. These instruments are connected together using wired, optical, or wireless networks. The details of the supporting hardware and software technologies behind these networks are discussed extensively.

1.2 Measurements

If the behavior of the physical variable is known, its performance can be monitored and assessed by means of suitable methods of sensing, signal conditioning, and termination. The applications of instruments range from laboratory conditions to arduous environments such as inside nuclear reactors or remote locations such as satellite systems and spaceships.

The sensor-output signals of the majority of modern instruments are in electric form. This is due to electric signals being easy to process, display, store, and transmit. Once converted to electric forms, the relation between the sensor signals and the physical variations can be expressed in the form of *transfer functions*. The transfer function is a mathematical model between the sensor signal and the physical variable. In a continuous system, the transfer function may be linear or nonlinear. A linear relationship may be expressed by the following equation:

$$y = a + bx \tag{1.1}$$

where

y is the electric signal
x is the physical stimulus
a is the intercept on the y-axis, which gives the output signal for a zero input
b is the slope that is also known as the sensitivity

In ideal cases, this relationship should be consistent without any errors, nonlinearity, or deviation.

However, in measurements, there may be many sources of errors; therefore, it is important to identify these sources and draw up an error budget by considering factors, such as

- Imperfections in electric and mechanical components (e.g., high tolerances and noise or offset voltages)
- Changes in component performances (e.g., shift in gains, changes in chemistry, aging, and drifts in offsets)
- External and ambient influences (e.g., temperature, pressure, and humidity)
- Inherent physical fundamental laws (e.g., thermal and other electric noises, Brownian motion in materials, and radiation)

Once the measurements are made, various forms of data analysis may be used to extract useful information about the measurements and draw conclusions. Data analysis may include statistical methods, curve fitting, selecting or discarding subsets of data, or many other techniques. For example, a typical data analysis tool is the data mining, which aims to discover unforeseen patterns hidden in the data. There is an extensive range of software available for the analysis (e.g., MATLAB®) to suit specific needs of information obtained from experimental or test results. Further information on measurements and analysis can be found throughout this book.

1.3 Instruments

Instruments are man-made devices for determining the value of the quantity/variable. They are designed to maintain prescribed relationships between the parameters being measured and the physical variables under investigation. Instruments can be designed and constructed to be analog, digital, or hybrid.

The construction of an instrument can be broken into smaller elements, as illustrated in Figure 1.1. Typically, an instrument will have a sensor or transducer stage, a signal-conditioning stage, and an output or termination stage. All instruments have some or all of these functional blocks.

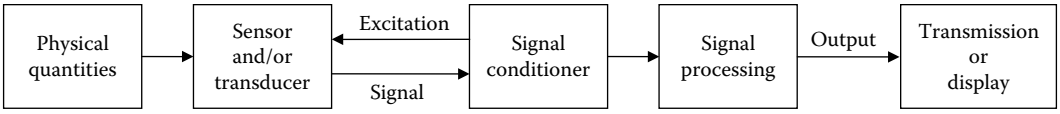

FIGURE 1.1 Construction structure of a typical instrument.

A diverse range of sensors and transducers may be available to meet the measurement requirements of a physical system. The sensors can be categorized in a number of ways depending on the energy input and output, input variables, sensing elements, and electric or physical principles.

In recent years, the rapid growth of the integrated circuit (IC) electronics and the availability of cost-effective processors have led to an impressive progress in instrumentation and measurements in all fields. This coupled with the improvement of mathematical methods, the extensive applications of digital techniques, and the addition of new application areas enabled modern instruments to excel to new heights as discussed in detail in this two-volume *Measurements, Instrumentation, and Sensors Handbook*.

1.3.1 Design of Instruments

Instruments are designed on the basis of existing knowledge, which is gained either from the experiences of people about the physical process or from structured understanding of the process. In any case, ideas conceived about an instrument are translated into hardware and software that can perform well within the expected standards and easily be accepted by the end users.

Usually, the design of instruments requires many multidisciplinary activities. In the wake of a rapidly changing technology, instruments are upgraded often to meet the demands of the marketplace. Depending on the complexity of the proposed instrument, it may take many years to produce an instrument for a relatively short commercial lifetime. In the design and production stages, engineers must consider factors such as simplicity, appearance, ease and flexibility of use, maintenance requirements, production costs, lead time to product, and positioning strategy in the marketplace.

The design process of an instrument may follow well-ordered procedures from ideas to marketing of the final products. The process may be broken down into smaller tasks such as identifying specifications, developing possible solutions for these specifications, modeling, prototyping, installing and testing, making modifications, manufacturing, planning marketing and distribution, evaluating customer feedback, and making design and technological improvements. For example, many different specifications may be considered for particular product, which may include but are not limited to operational requirements, functionality, technological limitations, quality, installation, maintenance, documentation, servicing, and acceptance level usage by customers.

1.3.2 Testing and Use of Instruments

After the instrument is designed and prototyped, various evaluation tests may be conducted. These tests may be made under reference conditions or under simulated environmental conditions. Some examples of reference condition tests are accuracy, response time, drift, and warm-up time. Simulated environmental tests may be compulsory, being regulated by governments and other authorities. Some simulated environment tests include climatic test, drop test, dust test, insulation-resistance test, vibration test, electromagnetic compatibility tests, and safety and health hazard tests. Many of these are strictly regulated by national and international standards.

For maximum efficiency, an appropriate instrument for the measurement must be selected. Users should be fully aware of their application requirements, since instruments that do not fit their purposes will deliver false data resulting in wasted time and effort. For a particular application, users must

carefully study the documents about all the candidates and make comparisons among all options. While selecting the instrument, users must evaluate many factors such as accuracy, frequency response, electric and physical loading effects, sensitivity, response time, calibration intervals, power supply needs, spare parts, technology, and maintenance requirements. They must ensure compatibility with the existing equipment.

When selecting and implementing of instruments, quality becomes an important issue from both quantitative and qualitative perspectives. The quality of an instrument may be viewed differently depending on the people involved. For example, quality in the eyes of designer may be an instrument designed on sound physical principles, whereas from the users' point of view, it may be reliability, maintainability, cost, and availability.

1.3.3 Response and Drift

Instruments respond to physical phenomenon by sensing and generating signals. Depending on the type of instrument used and the physical phenomenon, the signals may be either slow or fast to change and may also contain transients. The response of the instruments to the signals can be analyzed in a number of ways by establishing static and dynamic performance characteristics. Although the static performances are relatively simple, the dynamic performances may be complex. More information on this can be found in Chapters 4, 11, and 12.

1.3.4 Accuracy and Errors

The performance of an instrument depends on its static and dynamic characteristics. The performance may be indicated by its *accuracy*, which may be described as the closeness of measured values to the real values of the variable. The total response is a combination of dynamic and static responses. If the signals generated by the physical variable are changing rapidly, then the dynamic properties of the instrument become important. For slow-varying systems, the dynamic errors may be neglected. Further information on accuracy can be found in Chapter 5.

The performance of an instrument may also be decided by other factors, such as the magnitudes of errors; the *repeatability*, which indicates the closeness of sets of measurements made in the short term; and the *reproducibility* of the instrument. The reproducibility is the closeness of sets of measurements when repeated in similar conditions over a long period of time.

The ideal or perfect instrument would have perfect sensitivity, reliability, and repeatability without any spread of values and would be within the applicable standards. However, in many cases, there will be imprecise and inaccurate results because of internal and external factors. The departure from the expected perfection is called the *error*. Often, sensitivity analyses are conducted to evaluate the effect of individual components that are causing these errors. Sensitivity to the affecting parameter can be obtained by varying that one parameter and keeping the others constant. This can be done practically by using the developed instruments or mathematically by means of appropriate models.

When determining the performance of an instrument, it is essential to appreciate how errors arise. There may be many sources of errors; therefore, it is important to identify these sources and draw up an error budget. In the error budget, there may be many factors, such as (1) imperfections in electric and mechanical components (e.g., high tolerances and noise or offset voltages), (2) changes in component performances (e.g., shift in gains, changes in chemistry, aging, and drifts in offsets), (3) external and ambient influences (e.g., temperature, pressure, and humidity), and (4) inherent physical fundamental laws (e.g., thermal and other electric noises, Brownian motion in materials, and radiation).

In instrumentation systems, errors can be broadly classified as systematic, random, or gross errors. For further information, readers can refer to Chapters 2 and 4.

1.3.5 Error Reduction

Controlling errors is an essential part of measurements and instrumentation. Various techniques are available to achieve this objective. The error control begins in the design stages by choosing the appropriate components, filtering, and bandwidth selection; by reducing the noise; and by eliminating the errors generated by the individual subunits of the complete system. In a good design, the errors of the previous group may be compensated adequately by the following groups.

The accuracy of instruments can be increased by postmeasurement corrections. Various calibration methods may be employed to alter parameters slightly to give correct results. In many cases, calibration graphs, mathematical equations, tables, the experiences of the operators, and the like are used to reduce measurement errors. In recent years, with the application of digital techniques and intelligent instruments, error corrections are made automatically by the computers or the devices themselves. More information is available in Chapters 8 and 9.

In many instrumentation systems, the application of compensation strategy is used to increase static and dynamic performances. In the case of static characteristics, compensations can be made by many methods, including introducing opposing nonlinear elements into the system, using isolation and zero environmental sensitivity, opposing compensating environmental inputs, using differential systems, and employing feedback systems. On the other hand, dynamic compensation can be achieved by applying these techniques as well as by reducing harmonics, using filters, adjusting bandwidth, using feedback compensation techniques, and the like. Further information on dynamic error measurements can be found in Chapter 12.

1.3.6 Calibration of Instruments

The calibration of all instruments is essential for checking their performances against known standards. This provides consistency in readings and reduces errors, thus validating the measurements universally. After an instrument is calibrated, future operation is deemed to be error bound for a given period of time for similar operational conditions. The calibration procedure involves comparison of the instrument against primary or secondary standards. In some cases, it may be sufficient to calibrate a device against another one with a known accuracy.

Many nations and organizations maintain laboratories with the primary functions of calibrating instruments and field measuring systems that are used in everyday operations. Examples of these laboratories are National Association of Testing Authorities (NATA) of Australia and the British Calibration Services (BCS). Detailed information on calibration is available in Chapter 8.

Calibrations may be made under static or dynamic conditions. A typical calibration procedure of a complex process involving many instruments is illustrated in Figure 1.2. In an ideal situation, for

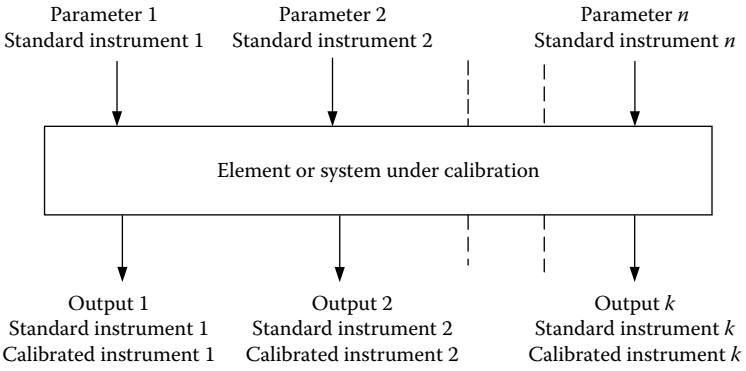

FIGURE 1.2 Instruments need to be frequently calibrated sequentially for all affecting inputs. Calibrations are made under static or dynamic conditions by varying a single input and observing the corresponding output while keeping all the other inputs constant until all inputs are covered.

an instrument that response to a multitude of physical variables, a commonly employed method is by keeping all the inputs constant except one. The input is varied in increments in increasing and decreasing directions over a specified range. The observed output then becomes a function of that single input. The calibration is continued in a similar manner until all other inputs are covered. For better results, this procedure may be repeated by varying the sequences of inputs, thus developing a family of relationships between the inputs and the outputs. As a result of these calibration readings, the input and output relation usually demonstrates statistical characteristics. From these characteristics, appropriate calibration curves can be obtained, and other statistical techniques can be applied.

1.4 Analog and Digital Instruments

Instruments can be analog or digital or a combination of the two. Nowadays, most instruments are produced to be digital because of the advantages they offer. However, the front end of majority of instruments is still analog; that is, most of the sensors and transducers generate analog signals. The signals initially are conditioned by analog circuits before converting into digital form for further signal processing. It is important to mention that nowadays, digital instruments operating purely on digital principles are being developed. For instance, today's smart sensors contain the complete signal condition circuits in a single chip integrated with the sensor itself. The output of smart sensors can be interfaced directly with other digital devices. More information on smart sensors can be found in Chapter 9.

1.4.1 Analog Instruments

Analog instruments are characterized by continuous signals. A purely analog system measures, transmits, displays, and stores data in analog form. The signal conditioning is usually made by integrating many functional blocks such as bridges, amplifiers, filters, oscillators, modulators, offsets and level converters, and buffers, as illustrated in Figure 1.3. Generally, in the initial stages, the signals produced by the sensors and transducers are conditioned mainly by analog electronics, even if they are configured as digital instruments later.

In analog instruments, the changes in amplitudes, phases, or frequencies or a combination of the three convey the useful information in response to physical variables. These signals can be deterministic or nondeterministic. As in the case with all signal-bearing systems, there are useful signals that respond to the physical phenomena and unwanted signal resulting from various forms of noise requiring extensive filtering and other signal processing as explained in the chapters in *Electrical, Optical, Chemical, and Biomedical Measurement*.

Analog signals can also be nondeterministic; that is, the future state of the signal cannot be determined. If the signal varies in a probabilistic manner, its future can be determined only by statistical methods. The mathematical and practical treatment of analog and digital signals, having foreseen, stochastic, and nondeterministic properties, is a very lengthy subject, and a vast body of information can be found in the literature; therefore, they will not be treated here.

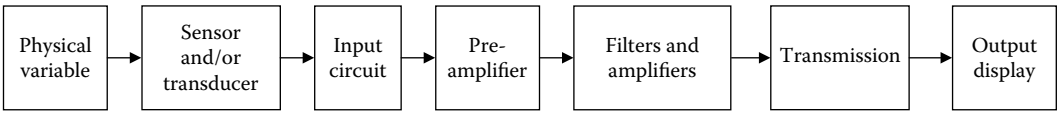

FIGURE 1.3 Analog instruments measure, transmit, display, and store data in analog form. The signal conditioning involves such components as bridges, amplifiers, filters, oscillators, modulators, offsets and level converters, buffers, and so on.

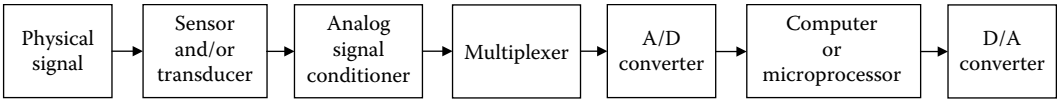

FIGURE 1.4 Digital instruments have more signal-processing components than analog counterparts. However, they have the advantage of data handling, storing, displaying, and transmitting.

1.4.2 Digital Instruments

In modern instruments, the original data acquired from the physical variables are usually in analog form. This analog signal is converted to digital before being passed onto the other parts of the system. For conversion purposes, analog-to-digital (A/D) converters are used together with appropriate sample-and-hold and multiplexing devices. The typical components of a digital instrument are illustrated in Figure 1.4. The digital systems are particularly useful in performing mathematical operations and storing and transmitting data.

A/D conversion involves three stages: sampling, quantization, and encoding. The Nyquist sampling theorem must be observed during sampling; that is, "the number of samples per second must be at least twice the highest frequency present in the continuous signal." As a rule of thumb, depending on the significance of the high frequencies, the sampling must be about 5 to 10 times the highest frequency of the signal. The next stage is the quantization, which determines the resolution of the sampled signals. The quantization error decreases as the number of bits increases. In the encoding stage, the quantized values are converted to binary numbers to be processed digitally. Once in digital form, the data can further be processed by employing various techniques such as FFT analysis, digital filtering, sequential or logical decision making, correlation methods, spectrum analysis, and more.

1.5 Sensors and Transducers

A sensor is a device that responds to a changing phenomenon. A transducer is a device that transfers energy from one form to another.

Sensors and transducers can be categorized in a number of ways depending on factors such as the energy input and output, input variables, sensing elements, and electric or physical principles. From the energy input and output point of view, there are three types: the modifiers, the self-generators, and the modulators.

In modifiers, a particular form of energy is modified rather than converted; therefore, the same form of energy exists in both the input and the output stages. In self-generators, electric signals are produced from nonelectric inputs without the application of external energy. Typical examples are piezoelectric transducers and photovoltaic cells. Modulators, on the other hand, produce electric outputs from nonelectric inputs, but they require an external source of energy. Strain gages are typical examples of such devices. Some examples of sensors and measurements are listed as follows:

- Spatial variables, discussed in Part II of this book
- Displacements, discussed in Part III of this book
- Mechanical variables, discussed in Part IV of this book
- Acoustics, discussed in Part V of this book
- Flow measurements and sensors, discussed in Part VI of this book
- Thermal and temperature, discussed in Part VII of this book
- Radiation, Part VIII of this book
- Electric variables, discussed in Part II of *Electrical, Optical, Chemical, and Biomedical Measurement*
- Electromagnetic variables discussed in Part III of *Electrical, Optical, Chemical, and Biomedical Measurement*

- Time and frequency, discussed in Part IV of *Electrical, Optical, Chemical, and Biomedical Measurement*
- Optical variables, Part V of *Electrical, Optical, Chemical, and Biomedical Measurement*
- Chemical variables, discussed in Part VI of *Electrical, Optical, Chemical, and Biomedical Measurement*
- Medical, biomedical, and health, Part VII of *Electrical, Optical, Chemical, and Biomedical Measurement*
- Environmental sensors and measurements, Part VIII of *Electrical, Optical, Chemical, and Biomedical Measurement*

The present trend in sensor technology has been shifted toward IC sensors in the form of microsystems, intelligent sensors, nanosensors, and others. The usefulness of semiconductor-based IC sensors is enhanced considerably by the integrations of microprocessors, microcontroller, converters, logic circuits, and other digital components in the same chip. Further, micromachining techniques combined with semiconductor processing technology provide a multiple range of sensors all integrated in the same chip for mechanical, optical, magnetic, chemical, biological, and other types of measurements.

IC devices refer to the dimensions of devices in micrometer (10^{-6} m) ranges, whereas nanotechnology refers to the dimensions of devices in nanometer (10^{-9} m) ranges. The microsystems technology (MST) is well established and simply known as the MST. A subset of MST is the *microelectromechanical systems* (MEMS). Another subset of MST is the *microelectro-optical systems* (MEOMs) and *systems-on-chip* (SOC) devices. Most of the sensors manufactured by MEMs and MEOMs are 3D devices with dimensions in the order of few micrometers.

For example, single-chip microsensors and microinstruments are being developed and used extensively for temperature, pressure, and radiation measurements, as well as mechanical, chemical, environmental, biomedical, biological variables, and implantable sensors, and many others. A typical example is illustrated in Figure 1.5, and detailed information on such devices can be found in Part I of *Electrical, Optical, Chemical, and Biomedical Measurement*. This particular single-chip implementation of microinstrumentation system is based on complementary metal–oxide–semiconductors (CMOS) and other technologies. It incorporates voltage, current, and capacitive-sensor interface; a temperature sensor; a 10-channel 12 bit A/D converter; and an 8 bit microcontroller with a 16 bit hardware multiplier and a 40 bit accumulator. This device operates on 3 V power supply drawing 16 mA when fully powered or 850 μA at standby.

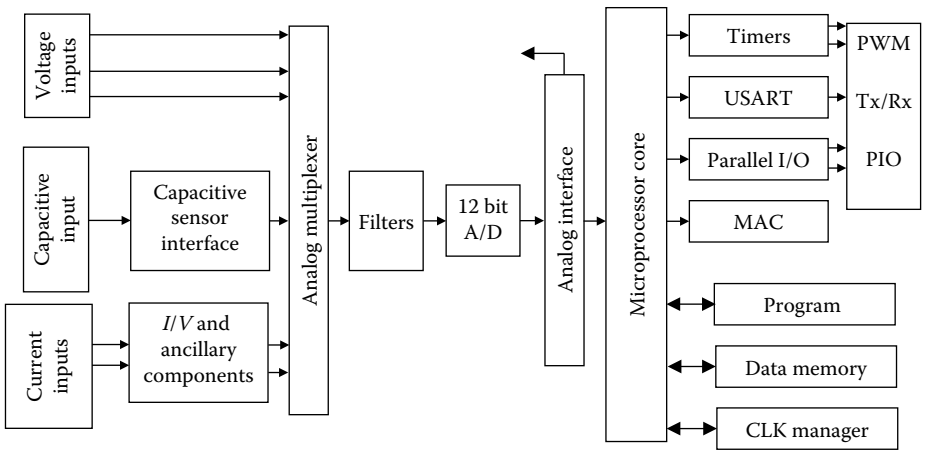

FIGURE 1.5 Block diagram of a typical micro-instrument.

Modern microsensors and microinstruments are fabricated by making full use of properties of semiconductors and their associated technologies. In the manufacturing process, the use of other materials and the deposition of thick and thin films are often required to give the sensing materials useful properties otherwise they would not have. For example, piezoelectric material films applied to silicon wafers provide piezoelectric properties. There are several methods of depositing thin and thick films on substrates or semiconductor wafers. Some of the methods are spin casting, vacuum deposition, sputtering, electroplating, screen printing, etc.

1.5.1 Smart Sensors

A conventional sensor measures physical, biological, or chemical parameters and converts these parameters into electric signals. They require extensive external circuits and components for signal processing and display. The term *smart sensor* was adopted in the mid-1980s to differentiate a new class of sensors from the conventional ones. Smart sensors have intelligence of some form and can convert a raw sensor signal into a level that makes them much more convenient to use. They provide value-added functions, thus increasing the quality of information rather than just passing the raw signal. They can perform functions such as self-identification, self-testing, lookup tables, calibration curves as well as ability to communicate with other devices. These functions are conducted by the integration of sensors with microcontrollers or microprocessor or logic circuits in the same chip. Understandably, the microprocessor contains RAM and ROM and can conveniently be programmed externally. Smart sensors also include signal amplification, conditioning, processing, and A/D conversions.

A variety of smart sensors are manufactured with the neural network and other intelligence techniques programmed and held onboard the chip. These sensors are capable of assimilating a large quantity of data; hence, they are capable of taking autonomous and appropriate actions to achieve goals in any dynamically changing environment. They are adaptable in anticipating events and complexities of the process; therefore, sensing, learning, and self-configurations are the key elements. Intelligent sensors appear in the marketplace as pressure sensors and accelerometers, biosensors, chemical sensors, optical sensors, magnetic sensors, and so on. Intelligent vision systems and parallel processors–based sensors are typical examples of such devices.

1.5.2 Wireless and Autonomous Sensors and Instruments

Sudden growth in the wireless communication technology has prompted the expansion of wireless industry by order of magnitudes. This is largely supported by improvement in digital and RF circuit fabrication methods, advances in signal-processing theory and applications, and emergence of new large-scale wireless-related ICs and other supporting devices. Particularly, the new IC technology makes radio equipment smaller, cheaper, and more reliable. In parallel to industrial expansion, consumer acceptance and need for products permit widespread deployment of the wireless communication systems. Trends will continue at an even greater pace in the coming years.

Wireless technology is used extensively in modern sensors and instrumentation. A typical wireless sensor contains sensing elements, signal-processing circuits, and wireless communication components in the same chip. Several miniaturization techniques are available for wireless sensors, including SOC, MEMS, and ASICs. In a wireless sensor, there are five main components that need to be integrated for a complete system; these components are sensor, signal-processing circuitry, radio, battery, and package. Radio, sensors, and signal-processing circuitry can be reduced in size through hybrid circuits, MEMS, or mixed-signal ASIC design. However, the power supply components must be dealt with separately as explained in Chapter 90 of this book and Chapter 13 of *Electrical, Optical, Chemical, and Biomedical Measurement*.

Wireless instruments consist of five main components—sensors and signal conditioners, programmable digital hardware, memory and storage, input/output and communication components, and others, for

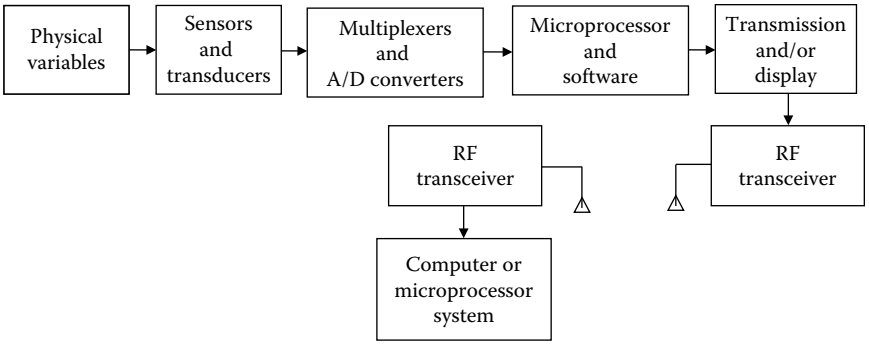

FIGURE 1.6 Components of a wireless instrument.

example, displays, keypads, and power supplies. A typical wireless instrument is illustrated in Figure 1.6. Instruments differ from each other by the way that they handle, transmit, and display information. Further information can be found in Part IX, which is dedicated to wireless technology for instruments and sensors.

Autonomous sensors are self-powered measurement devices that are capable of communicating wirelessly. They serve as the nodes in distributed data acquisition systems and wireless sensor networks (WSN) finding applications such as in health care, aerospace, and environmental monitoring. To increase their autonomy, autonomous sensors seek to reduce their average power consumption by working in low power modes whenever possible. They spend most of the time in *sleep* (standby) mode and only *wake up* to perform specific actions—namely, measurement, processing, and transmission/reception of data.

Autonomous sensors are composed of sensors, signal conditioners, processors, and transceivers. Sensors convert a signal from a physical or chemical quantity to a corresponding signal in the electric domain. Often, commercial transceivers are used for wireless communication. They transmit in the free-licensed ISM bands and can use a proprietary or standard (e.g., IEEE 802.15.4) protocol. Further information on autonomous sensors can be found in Chapter 90.

1.6 Instrumentation and Networks

Networking of hardware and software resources is essential to bring multiple sensors and instruments together for exchange of information, collaborative operations, and sharing of functions of equipment and devices. Networks are made by the collection of devices, the medium that links these devices, and the software that supports the networking of the entire system. A *system* is made from a group of interrelated parts with the focus of establishing an interrelationship between them to improve efficiency, to facilitate integration of the application, and to share the resources.

Due to recent progress in communications technology, sensors and instruments can easily be networked. Many processes require measurements of hundreds and perhaps thousands of parameters employing many instruments. The resulting arrangement for performing the overall measurement in a complex processes is called the *measurement system*. In measurement systems, instruments operate autonomously but in a coordinated manner. Information generated by each instrument may be communicated between the instruments themselves and the controllers or between instruments and other digital devices such as recorders, display units, printers, routers, base stations, or host computer.

Connecting devices together to form networks is not a new concept, and it has been operational for many years in a diverse range of applications. In the earlier networks, almost all the communicating devices were connected by wires; hence, they were largely fixed in space. The devices in modern networks, as discussed in this book, can be configured by using wireless communication technology and related software; hence, they can have mobility in space while still maintaining feasible networks. Therefore, modern networks can be viewed as (1) *wired networks* in which the communication devices are connected by wires, hence largely fixed in space, (2) *wireless networks* in which devices communicate wirelessly,

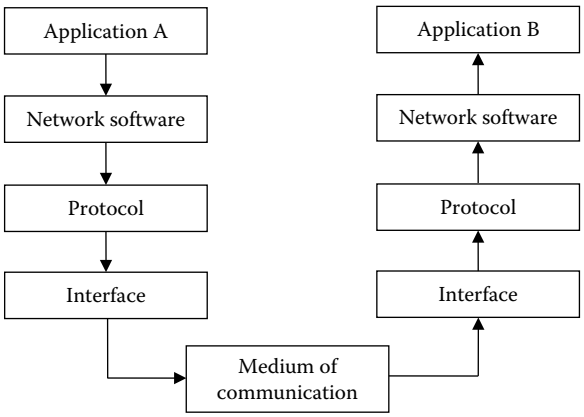

FIGURE 1.7 Process of communication of networked devices.

hence can move in space, and (3) *hybrid networks* in which both wired and wireless techniques are used in combination. At the moment, mobile networks based on wireless techniques provide primarily voice-based services, but they are increasingly handling data and other forms of information. Wireless networks can match similar functions as fixed networks plus they offer many advantages such as the reduction in cost for initial setup and maintenance.

Devices need network software to issue the requests and responses that allow them communicate with each other successfully. A communication process between two devices is illustrated in Figure 1.7. In this case, communication is taking place in simplex form; device A is sending information to device B.

In many networks, communicating devices invoke a layer of codes, which is called *network operating systems* (NOSs). NOSs control the access to network recourses. Examples of common NOSs used in computers are Windows.NET, WindowsXP, Novell's NetWare, etc.

Most network software packages come with modules for logging on and off the network. Logging on and logging off network modules may include considerations such as password security, validation of user access to specific files and software, automatic log-on feature for some devices, help menus, and error messages.

More information on instrument networks can be found in Part IX of this book and Part I of *Electrical, Optical, Chemical, and Biomedical Measurement*.

1.7 Software Support for Sensors and Instruments

The *software* is a term for describing the role of programs, procedures, and documentation in programmable digital devices and computer systems. Software support is an integral part of modern instrumentation system. It can be divided into three major groups: (1) system software, (2) programming software, and (3) application software. All are developed using programming languages, scripting languages, machine languages or assembly codes, or FPGA configurations. Some examples of programming languages are C or C++, Java, and Basic.

The software in instrumentation systems includes

- *Application software* such as Excel, word processors, video games, and Open Office that provides tasks for users.
- *Firmware* is software permanently stored in programmable memory devices on the main boards or other types of integrated hardware carriers.
- *Middleware* controls and coordinates distributed systems.
- *System software* such as operating systems that interface with hardware to provide a coordinated service for applications such as Linux and Microsoft Windows.
- *Web pages* developed by technologies such as HTML, Perl, JSP, XML, PHP.

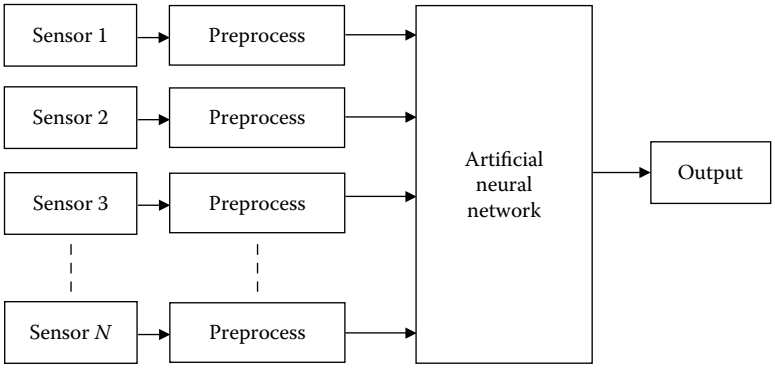

FIGURE 1.8 AI-controlled single-chip multisensor array.

At the lowest level, software consists of a *machine language* specific to an individual processor. A machine language consists of groups of binary values signifying processor instructions that change the state of the computer from its preceding state. Software is an ordered sequence of instructions for changing the state of hardware in a particular sequence. It is usually written in high-level programming languages that are easier and more efficient for humans to use than machine language. High-level languages are compiled or interpreted into machine language object code. Software may also be written in an assembly language that is mnemonic representation of a machine language using a natural language alphabet. Assembly language must be assembled into object code via an assembler.

For example, the microinstrument illustrated in Figure 1.5 is supported by C programming language. It includes hardware support for a single break point and trace event for code debugging. A development system interface provides instructions for halting the processor, single stepping through code, and reading and writing system registers. Single-cycle interrupt response and direct memory access (DMA) allow application of this device in time-critical applications. A clock manager is used to divide the system clock to reduce power, assign a slow clock, or halt the clock to the different sections of the chip until a programmed event occurs.

The integration of sensors with complex analog and digital signal-processing circuits and microprocessors in the same chip has enabled extensive development of the supporting software. The use of digital signal-processing circuits and the integration of intelligent techniques such as the artificial neural networks (ANNs) and other techniques serve as nonlinear signal-processing tools leading to convenient and easy to use devices. The onboard operating system and the additional decision-making software such as artificial intelligence (AI) and complex logic circuits result in much faster and efficient, fault-tolerant and reliable systems. A typical system configuration of an AI-controlled single-chip, multisensor array is shown in Figure 1.8. In *fully integrated decision and control systems*, an ANN performs both sensor enhancement and intelligent control. Fully integrated systems find extensive applications in aerospace, defense, consumer products, and industrial needs.

There are many different software tools to implement applications of sensors and instruments such as the LabWindows and LabVIEW from National Instruments and the VEE from Hewlet-Packard. Further information can be found in Chapter 10.

1.8 Application Examples

Many different instruments are offered to fulfill specific measurement requirements. Here, some examples will be discussed briefly. In this book, detailed information can be found on specific instruments, sensors, and measurements in the proceeding chapters.

In medical technology, there are three basic types of instruments—imaging, physiological measurements, and laboratory analysis. In imaging and physiological measurements, the instruments are closely

linked with patients. Some examples of these instruments are x-ray tomography, magnetic resonance imaging (MRI) and magnetic resonance tomography, ultrasound imaging, thermography, brain and nervous system sensors, and respiratory sensors. Many instruments are based on radiation and sound, force and tactile sensing, electromagnetic sensing, and chemical and bio-analytical sensors.

Power plants are instrumented for maximum availability, operational safety, and environmental planning. Therefore, their measurements must be as accurate as possible and reliable. Instruments are used for temperature, pressure, flow, level, vibration measurements, and water, steam, and gas analysis. For example, gas analysis requires instruments to measure carbon compounds, sulfur and nitrogen compounds, and dust and ash contents.

Environmental monitoring requires a diverse range of instruments for air, water, and biological monitoring. Instruments are used for measuring various forms of radiation, chemical hazards, air pollutants, and organic solvents. Many sophisticated instruments are also developed for remote monitoring via satellites, and they operate on optical, microwave, and RF electromagnetic radiation principles.

Industry uses instruments extensively for online monitoring purposes and off-line analysis. Specific instruments are used commonly for sensing variables such as temperature, pressure, volumetric and mass flow rate, density, weight, displacement, pH levels, color, absorbency, viscosity, material flow, dew point, organic and inorganic components, turbidity, solid and liquid level, humidity, and particle-size distribution.

In automobiles, instruments are used to assist drivers by sensing variables such as cooling, braking, fuel consumption, humidity control, speed, travel route monitoring, and position sensing. Instruments also find applications for safety and security purposes, such as passenger protection and locking and antitheft systems. Recently, with the advent of micromachined sensors, many diverse instruments such as engine control, fuel injection, air regulation, and torque sensing are developed.

The manufacturing industry, especially automated manufacturing, requires a diverse range of instruments. Machine diagnosis and process parameters are made by instruments that are based on force, torque, pressure, speed, temperature, and electric-parameter sensing. Optics, tactile arrays, and acoustic scanning instruments are used for pattern recognition. Distance and displacement measurements are made by many methods (e.g., inductive, capacitive, optical, and acoustic techniques).

Aerospace instrumentation requires an accurate indication of physical variables and the changes in these variables. Instruments are designed to suit specific conditions of operations. Some of the measurements are gas temperature and pressure, fluid flow, aircraft velocity, aircraft icing, thrust and acceleration, load, strain and force, position, altitude sensing, and direction finding.

Bibliography

Bakshi, U. A. and A. V. Bakshi, *Electronic Instrumentation*, Technical Publications, Pune, India, 2008.

Eren, H., *Electronic Portable Instruments—Design and Applications*, CRC Press, LLC, Boca Raton, FL, 2004.

Eren, H., *Wireless Sensors and Instruments—Networks, Design and Applications*, CRC Press, LLC, Boca Raton, FL, 2006.

Kalsi, H. S., *Electronic Instrumentation*, 2nd edn., Tata McGrawhill, New Delhi, India, 2006.

Lazzaroni, M., V. Piuri, and C. Mazerio, Computer security aspects in industrial instrumentation and measurements, *Proceedings of 2010 IEEE International Instrumentation and Measurement Technology Conference, I2MTC 2010*, Austin, TX: pp. 1216–1221, 2010.

Liptak, B. and H. Eren, *Instrument Engineers Handbook: Process Software and Digital Networks*, Vol. 3, 4th edn., CRC Press, LLC, Boca Raton, FL, 2011.

Morris, A. S., *Measurement and Instrumentation Principles*, 3rd edn., Butterworth-Heinemann, Oxford, U.K., 2001.

Northrop, R. B., *Introduction to Instrumentation and Measurement*, 2nd edn., CRC Press, Boca Raton, FL, 2005.

Tanabe, K., M. Hirose, A. Otani, K. Mochizuki, and M. Uchida, Recent topics in instrumentation and measurement, *IEEJ, Transactions on Fundamentals and Materials*, 129(2), 70–74, 2009.

Partial List of Vendors and Suppliers

AMETEK Power Instruments, 255 N. Union St., Rochester, NY 14605, Phone: 585-263-7700, 800-881-4156 (toll free), Fax: 585-262-4777, www.ametekpower.com

Analtech, Inc., 75 Blue Hen Dr., Newark, DE 19713, Phone: 302-737-6960, 800-441-7540 (toll free), Fax: 302-737-7115, www.ichromatography.com

Davis/Inotek, 1236 Mark St. Bensenville, IL 60106, Phone: 410-358-3900, 800-548-9409 (toll free), Fax: 410-358-0252, www.davis.com

Dwyer Instruments, Inc., Hwy. 212 at 12 P.O. Box 373 Michigan City, IN 46361, Phone: 219-879-8000, 800-872-9141 (toll free), Fax: 219-872-9057, www.dwyer-inst.com

Electro-Sensors, Inc., 6111 Blue Circle Dr. Minnetonka, MN 55343-9108, Phone: 952-930-0100, 800-328-6170 (toll free), Fax: 952-930-0130, www.electro-sensors.com

Honeywell Sensing and Control, 1985 Douglas Dr. North, MN10-192B Golden Valley, MN 55422, Phone: 763-954-4818, 800-446-6555 (toll free), sensing.honeywell.com/index.cfm/ci_id/15…

Instrumented Sensor Technology, Inc., 4704 Moore Street Okemos, MI 48864, Phone: 517-349-8487, Fax: 517-349-8469, www.isthq.com

Jewell Instruments, LLC, 850 Perimeter Rd. Manchester, NH 03103, Phone: 603-669-6400, 800-638-3771 (toll free), Fax: 603-669-5962, www.jewellinstruments.com

Macro Sensors, Division of Howard A. Schaevitz Technologies, 7300 US Rte. 130 N. Bldg. 22 Pennsauken, NJ 08110, Phone: 856-662-8000, Fax: 856-317-1005, www.macrosensors.com

Micro Sense, LLC, 70 Industrial Ave. E. Lowell, MA 01852, Phone: 978-843-7673, www.microsense.net

MKS Instruments, Inc., 2 Tech Dr., Suite 201 Andover, MA 01810, Phone: 978-645-5500, 800-227-8766 (toll free), Fax: 978-557-5100, www.mksinst.com

MTI Instruments, Inc., 325 Washington Ave., Extension Albany, NY 12205-5505, Phone: 518-218-2550, Fax: 518-218-2506, www.mtiinstruments.com

OTP Industrial Solutions, 1900 Jetway Blvd. Columbus, OH 43219, Phone: 614-342-6123, Fax: 614-342-6490, www.otpnet.com

PCB Piezotronics, Inc., 3425 Walden Ave. Depew, NY 14043-2417, Phone: 716-684-0001, 800-828-8840 (toll free), Fax: 716-684-0987, www.pcb.com

Piezo Technologies, 8431 Georgetown Rd., Suite 300 Indianapolis, IN 46268, Phone: 317-876-4670, Fax: 317-876-4681, www.piezotechnologies.com

Schneider Electric-Hyde Park, 1875 Founders Dr. Dayton, OH 45420, Phone: 937-514-7207, Fax: 937-258-5830, www.sesensors.com

Silicon Designs, Inc., 1445 NW Mall St. Issaquah, WA 98027, Phone: (425) 391-8329, Fax: (425) 391-0446, www.silicondesigns.com/contact.html

Turck, Inc., 3000 Campus Dr. Plymouth, MN 55441-2619, Phone: 763-553-7300, 800-554-4989 (toll free), Fax: 763-553-0708, www.turck.com

Warren-Knight Instrument Co., 2045 Bennett Dr. Philadelphia, PA 19116-3019, Phone: 215-464-9300, Fax: 215-464-9303, www.warrenind.com

Wilcoxon Research Inc., 20511 Seneca Meadows Pkwy. Germantown, MD 20876, Phone: 301-330-8811, 800-945-2696 (toll free), Fax: 301-330-8873, www.wilcoxon.com

2

Characteristics of Instrumentation

John R. Hansman, Jr.
Massachusetts Institute of Technology

In addressing measurement problems, it is often useful to have a conceptual model of the measurement process. This chapter presents some of the fundamental concepts of measurement in the context of a simple generalized instrument model.

In abstract terms, an *instrument* is a device that transforms a *physical variable* of interest (the *measurand*) into a form that is suitable for recording (the *measurement*). In order for the measurement to have broad and consistent meaning, it is common to employ a standard system of *units* by which the measurement from one instrument can be compared with the measurement of another.

An example of a basic instrument is a ruler. In this case, the measurand is the length of some object, and the measurement is the number of units (meters, inches, etc.) that represent the length.

2.1 Simple Instrument Model

Figure 2.1 presents a generalized model of a simple instrument. The physical process to be measured is in the left of the figure, and the measurand is represented by an observable physical variable $\boldsymbol{X}$. Note that the observable variable $\boldsymbol{X}$ need not necessarily be the measurand but simply related to the measurand in some known way. For example, the mass of an object is often measured by the process of *weighing*, where the measurand is the mass but the physical measurement variable is the downward force the mass exerts in the Earth's gravitational field. There are many possible physical measurement variables. A few are shown in Table 2.1.

The key functional element of the instrument model shown in Figure 2.1 is the *sensor*, which has the function of converting the *physical variable input* into a *signal variable output*. Signal variables have the property that they can be manipulated in a transmission system, such as an electrical or mechanical circuit. Because of this property, the signal variable can be transmitted to an output or recording device that can be remote from the sensor. In electric circuits, voltage is a common signal variable. In mechanical systems, displacement or force is commonly used as a signal variable. Other examples of signal variable are shown in Table 2.1. The signal output from the sensor can be displayed, recorded, or used as an input signal to some secondary device or system. In a basic instrument, the signal is transmitted to a *display* or recording device where the measurement can be read by a human observer. The observed

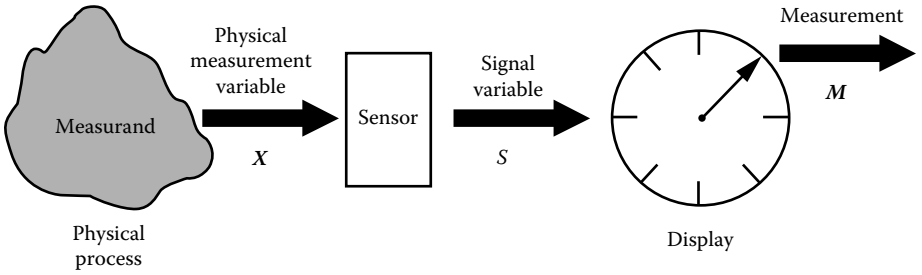

FIGURE 2.1 Simple instrument model.

TABLE 2.1 Examples of Physical Variables and Typical Signal Variables

Common Physical Variables	Typical Signal Variables
Force	Voltage
Length	Displacement
Temperature	Current
Acceleration	Force
Velocity	Pressure
Pressure	Light
Frequency	Frequency
Capacity	—
Resistance	—
Time	—
…	—

output is the measurement ***M***. There are many types of display devices, ranging from simple scales and dial gages to sophisticated computer display systems. The signal can also be used directly by some larger system of which the instrument is a part. For example, the output signal of the sensor may be used as the input signal of a closed-loop control system.

If the signal output from the sensor is small, it is sometimes necessary to amplify the output shown in Figure 2.2. The amplified output can then be transmitted to the display device or recorded, depending on the particular measurement application. In many cases, it is necessary for the instrument to provide a digital signal output so that it can interface with a computer-based data acquisition or communication system. If the sensor does not inherently provide a digital output, then the analog output of the sensor is converted by an analog-to-digital converter (ADC) as shown in Figure 2.2. The digital signal is typically sent to a computer processor that can display, store, or transmit the data as output to some other system, which will use the measurement.

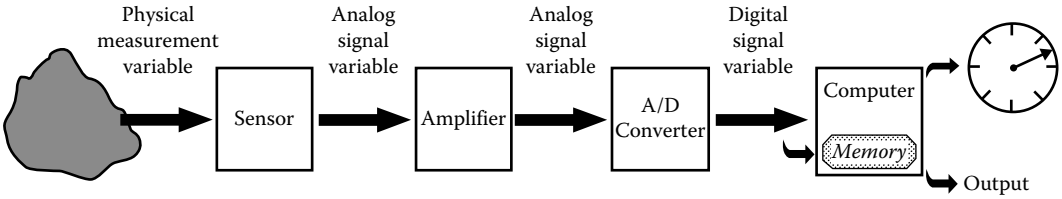

FIGURE 2.2 Instrument model with amplifier, ADC, and computer output.

2.1.1 Passive and Active Sensors

As discussed earlier, sensors convert physical variables to signal variables. Sensors are often transducers in that they are devices that convert input energy of one form into output energy of another form. Sensors can be categorized into two broad classes depending on how they interact with the environment they are measuring. *Passive sensors* do not add energy as part of the measurement process but may remove energy in their operation. One example of a passive sensor is a thermocouple, which converts a physical temperature into a voltage signal. In this case, the temperature gradient in the environment generates a thermoelectric voltage that becomes the signal variable. Another passive transducer is a pressure gage where the pressure being measured exerts a force on a mechanical system (diaphragm, aneroid, or Borden pressure gage) that converts the pressure force into a displacement, which can be used as a signal variable. For example, the displacement of the diaphragm can be transmitted through a mechanical gearing system to the displacement of an indicating needle on the display of the gage.

Active sensors add energy to the measurement environment as part of the measurement process. An example of an active sensor is a radar or sonar system, where the distance to some object is measured by actively sending out a radio (radar) or acoustic (sonar) wave to reflect off of some object and measure its range from the sensor.

2.1.2 Calibration

The relationship between the physical measurement variable input and the signal variable (output) for a specific sensor is known as the *calibration* of the sensor. Typically, a sensor (or an entire instrument system) is calibrated by providing a known physical input to the system and recording the output. The data are plotted on a calibration curve such as the example shown in Figure 2.3. In this example, the sensor has a linear response for values of the physical input less than $\boldsymbol{X}_0$. The *sensitivity* of the device is determined by the slope of the calibration curve. In this example, for values of the physical input greater than $\boldsymbol{X}_0$, the calibration curve becomes less sensitive until it reaches a limiting value of the output signal. This behavior is referred to as *saturation*, and the sensor cannot be used for measurements greater than its saturation value. In some cases, the sensor will not respond to very small values of the physical input variable. The difference between the smallest and the largest physical inputs that can reliably be measured by an instrument determines the *dynamic range* of the device.

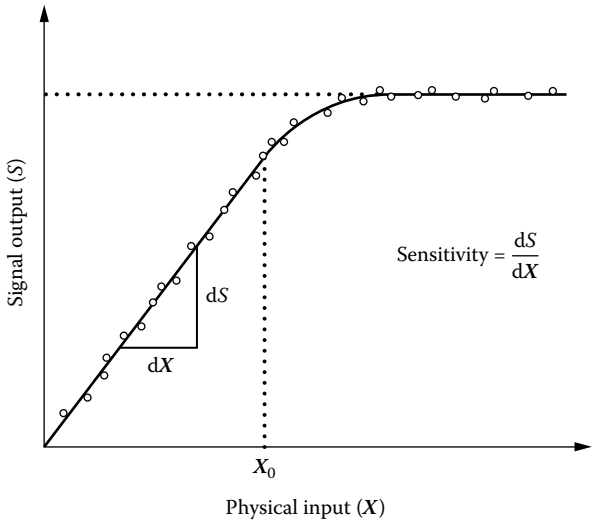

FIGURE 2.3 Calibration curve example.

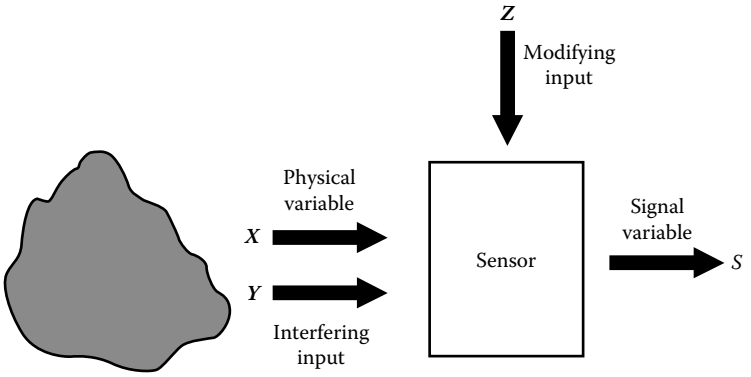

FIGURE 2.4 Interfering inputs.

The accuracy of instruments can be increased by calibration. In many cases, calibration graphs, mathematical equations, tables, and experience of the operators can be utilized. In recent years, with the application of digital techniques and intelligent instruments, error corrections are made automatically by computers or within the devices and sensors themselves.

2.1.3 Modifying and Interfering Inputs

In some cases, the sensor output will be influenced by physical variables other than the intended measurand. In Figure 2.4, ***X*** is the intended measurand, ***Y*** is an *interfering input*, and ***Z*** is a *modifying input*. The interfering input ***Y*** causes the sensor to respond in the same manner as the linear superposition of ***Y*** and the intended measurand ***X***. The measured signal output is therefore a combination of ***X*** and ***Y***, with ***Y*** interfering with the intended measurand ***X***. An example of an interfering input would be a structural vibration within a force measurement system.

Modifying inputs changes the behavior of the sensor or measurement system, thereby modifying the input/output relationship and calibration of the device. This is shown schematically in Figure 2.5. For various values of ***Z*** in Figure 2.5, the slope of the calibration curve changes. Consequently, changing ***Z*** will result in a change of the apparent measurement even if the physical input variable ***X*** remains constant. A common example of a modifying input is temperature; it is for this reason that many devices are calibrated at specified temperatures.

2.1.4 Accuracy and Error

The *accuracy* of an instrument is defined as the difference between the *true value* of the measurand and the *measured value* indicated by the instrument. Typically, the true value is defined in reference to some absolute or agreed upon standard. For any particular measurement, there will be some error due to *systematic* (*bias*) and *random* (*noise*) error sources. The combination of systematic and random error can be visualized by considering the analogy of the target shown in Figure 2.6. The total error in each shot results from both systematic and random errors. The systematic (bias) error results in the grouping of shots being offset from the bulls eye (presumably a misalignment of the gunsight or wind). The size of the grouping is determined by random-error sources and is a measure of the *precision* of the shooting.

2.1.5 Systematic Error Sources (Bias)

There are a variety of factors that can result in systematic measurement errors. One class of cause factors are those that change the input–output response of a sensor resulting in miscalibration. The modifying inputs and interfering inputs discussed earlier can result in sensor miscalibration. For example,

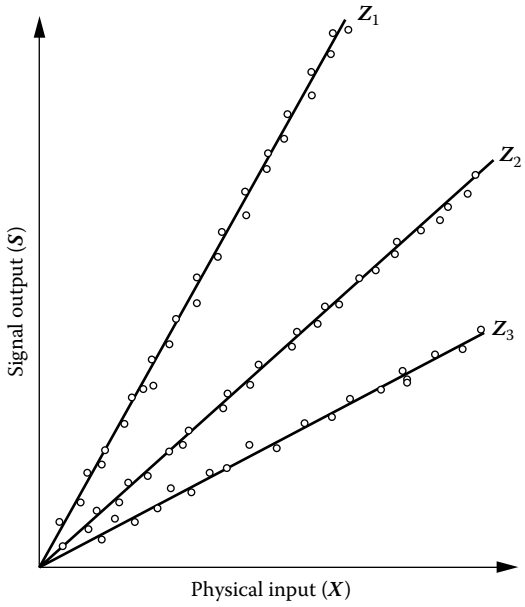

FIGURE 2.5 Illustration of the effect of a modifying input on a calibration curve.

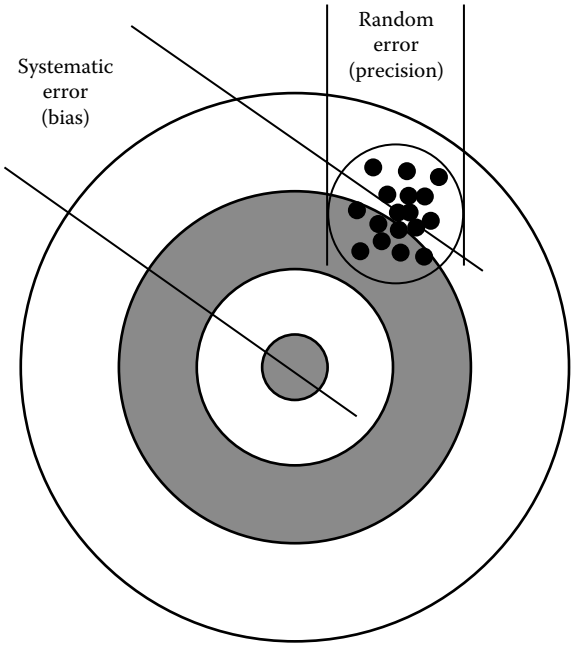

FIGURE 2.6 Target analogy of measurement accuracy.

if temperature is a modifying input, using the sensor at a temperature other than the calibrated temperature will result in a systematic error. In many cases, if the systematic error source is known, it can be corrected for by the use of *compensation methods*.

There are other factors that can also cause a change in sensor calibration resulting in systematic errors. In some sensors, aging of the components will change the sensor response and hence the calibration.

Damage or abuse of the sensor can also change the calibration. In order to prevent these systematic errors, sensors should be periodically recalibrated.

Systematic errors can also be introduced if the measurement process itself changes the intended measurand. This issue, defined as *invasiveness*, is a key concern in many measurement problems. Interaction between measurement and measurement device is always present; however, in many cases, it can be reduced to an insignificant level. For example, in electronic systems, the energy drain of a measuring device can be made negligible by making the input impedance very high. An extreme example of invasiveness would be to use a large warm thermometer to measure the temperature of a small volume of cold fluid. Heat would be transferred from the thermometer and would warm the fluid, resulting in an inaccurate measurement.

Systematic errors can also be introduced in the signal path of the measurement process shown in Figure 2.4. If the signal is modified in some way, the indicated measurement will be different from the sensed value. In physical signal paths such as mechanical systems that transmit force or displacement, friction can modify the propagation of the signal. In electric circuits, resistance or attenuation can also modify the signal, resulting in a systematic error.

Finally, systematic errors or bias can be introduced by human observers when reading the measurement. A common example of observer bias error is *parallax error*. This is the error that results when an observer reads a dial from a non-normal angle. Because the indicating needle is above the dial face, the apparent reading will be shifted from the correct value.

2.1.6 Random-Error Sources (Noise)

If systematic errors can be removed from a measurement, some error will remain due to the random-error sources that define the precision of the measurement. Random error is sometimes referred to as *noise*, which is defined as a signal that carries no useful information. If a measurement with true random error is repeated a large number of times, it will exhibit a *Gaussian distribution*, as demonstrated in the example in Figure 2.7 by plotting the number of times values within specific ranges are measured. The Gaussian distribution is centered on the true value (presuming no systematic errors), so the mean or average of all the measurements will yield a good estimate of the true value.

The precision of the measurement is normally quantified by the standard deviation (σ) that indicates the width of the Gaussian distribution. Given a large number of measurements, a total of 68% of the measurements will fall within $\pm 1\sigma$ of the mean, 95% will fall within $\pm 2\sigma$, and 99.7% will fall within $\pm 3\sigma$.

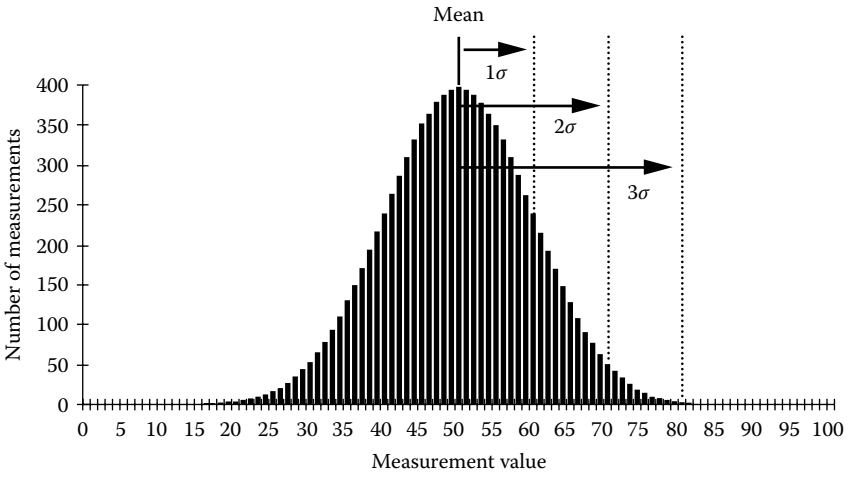

FIGURE 2.7 Example of a Gaussian distribution.

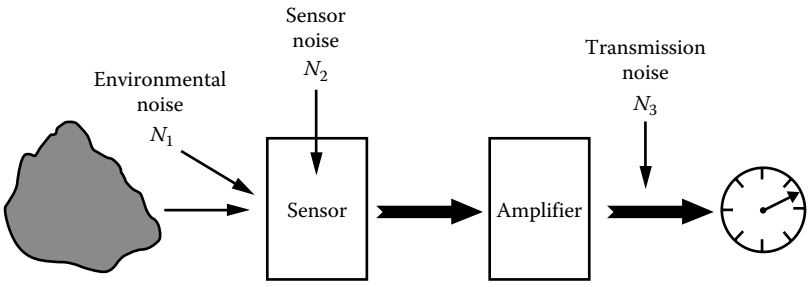

FIGURE 2.8 Instrument model with noise sources.

Smaller standard deviation leads to more precise the measurement. For many applications, it is common to refer to the 2σ value when reporting the precision of a measurement. However, for some applications such as navigation, it is common to report the 3σ value, which defines the limit of likely uncertainty in the measurement.

There are a variety of sources of randomness that can degrade the precision of the measurement—starting with the repeatability of the measurand itself. For example, if the height of a rough surface is to be measured, the measured value will depend on the exact location at which the measurement is taken. Repeated measurements will reflect the randomness of the surface roughness.

Random error generating noise can also be introduced at each stage in the measurement process, as shown schematically in Figure 2.8. Random interfering inputs will result in noise from the measurement environment N_1, which are introduced before the sensor, as shown in the figure. An example would be background noise received by a microphone. Sensor noise N_2 can also be introduced within the sensor. An example of this would be thermal noise within a sensitive transducer, such as an infrared sensor. Random motion of electrons, due to temperature, appears as voltage signals, which are apparently due to the high sensitivity of the device. For very sensitive measurements with transducers of this type (e.g., infrared detectors), it is common to cool the detector to minimize this noise source.

Noise N_3 can also be introduced in the transmission path between the transducer and the amplifier. A common example of transmission noise in the United States is 60 Hz interference from the electric power grid that is introduced if the transmission path is not well grounded or if an inadvertent electric grand loop causes the wiring to act as an antenna.

It is important to note that the noise will be amplified along with the signal as it passes through the amplifier shown in Figure 2.8. As a consequence, the figure of merit when analyzing noise is not the level of the combined noise sources but the level of the *signal-to-noise ratio* (*SNR*), defined as the ratio of the signal power to the power in the combined noise sources. It is common to report SNR in decibel units.

The SNR is ideally much greater than 1 (0 dB). However, it is sometimes possible to interpret a signal that is lower than the noise level if some identifying characteristics of that signal are known and sufficient signal processing power is available. The human ability to hear a voice in a loud noise environment is an example of this signal processing capability.

2.1.7 Error Reduction

Controlling errors is an essential part of instruments and instrumentation systems. Error control begins in the design stages by choosing the appropriate components, filtering, and bandwidth selection and by reducing noise. Minimizing the errors generated by the individual subunits of the complete system will result in lowering the overall error of the instrument.

In many instrumentation systems, the application of compensation strategy is used to increase static and dynamic performances. In the case of static characteristics, compensations can be made by different methods, including the introduction of opposing nonlinear elements into the system; by using isolation and zero environmental sensitivity conditions, opposing compensating environmental inputs; and by

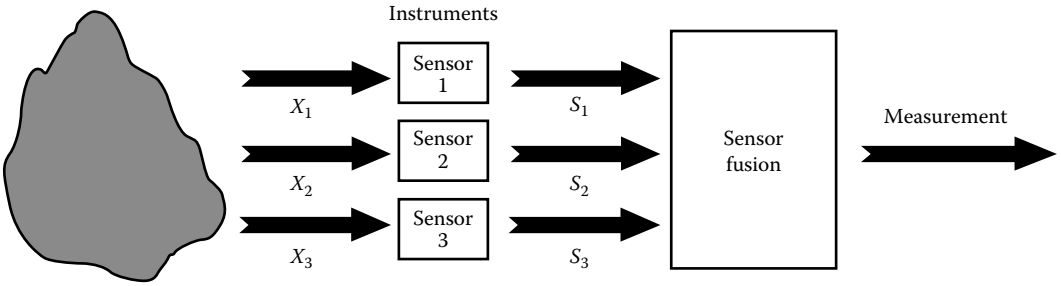

FIGURE 2.9 Example of sensor fusion.

using differential and feedback systems. At the same time, dynamic compensation can be achieved by applying these techniques as well as by taking measures to reduce harmonics, using filters, adjusting bandwidths, using feedback compensation techniques, and so on. Further information can be found in Chapter 1.

2.1.8 Sensor Fusion

The process of *sensor fusion* is modeled in Figure 2.9. In this case, two or more sensors are used to observe the environment, and their output signals are combined in some manner (typically in a processor) to provide a single enhanced measurement. This process frequently allows measurement of phenomena that would otherwise be unobservable. One simple example is thermal compensation of a transducer where a measurement of temperature is made and used to correct the transducer output for modifying effects of temperature on the transducer calibration. Other more sophisticated sensor-fusion applications range to image synthesis where radar, optical, and infrared images can be combined into a single enhanced image. Sensor fusion has become more prevalent with the advent of data bus architectures (such as the Controlled Area Network [CAN] bus) where sensor information can be easily shared between devices through the data bus.

2.1.9 Estimation

With the use of computational power, it is often possible to improve the accuracy of a poor-quality measurement through the use of *estimation techniques*. These methods range from simple-averaging or low-pass filtering to cancel out random fluctuating errors to more sophisticated techniques such as Wiener or Kalman filtering and model-based estimation techniques. The increasing capability and lowering cost of computation makes it increasingly attractive to use lower performance sensors with more sophisticated estimation techniques in many applications.

2.1.10 Testing of Instruments

After the instrument is designed and prototyped, various evaluation tests are conducted. These tests may be made under reference conditions or under simulated environmental conditions. Some examples of reference condition tests are accuracy, response time, drift, and warm-up time. Simulated environmental tests may be compulsory, thus being regulated by the governments and other authorities. Some simulated environment tests include climatic test, drop test, insulation-resistance test, vibration test, electromagnetic compatibility tests, safety and health hazard tests, and ingress progress (IP) tests against water and dust. The IP tests are particularly important for

electronic portable instruments since they are most likely to be used during their operations in unsteady environments containing rain, water, humidity, and dust. Many of these tests are strictly regulated by national and international standards.

Bibliography

Eren, H. *Electronic Portable Instruments—Design and Applications*, CRC Press, LLC, Boca Raton, FL, 2004.

Kalsi, H. S. *Electronic Instrumentation*, 6th edn., McGraw-Hill Companies, Delhi, India, 2006.

Klaassen, K. B. and S. Gee, *Electronic Measurement and Instrumentation*, Cambridge University Press, Cambridge, U.K., Reprint, 2002.

3

Operational Modes of Instrumentation

Richard S. Figliola
Clemson University

3.1 Null Instrument

The null method is one possible mode of operation for a measuring instrument. A null instrument uses the null method for measurement. In this method, the instrument exerts an influence on the measured system so as to oppose the effect of the measurand. The influence and the measurand are balanced until they are equal but opposite in value, yielding a null measurement. Typically, this is accomplished by some type of feedback operation that allows the comparison of the measurand against a known standard value. The key features of a null instrument include an iterative balancing operation using some type of comparator, either a manual or automatic feedback used to achieve balance, and a null deflection at parity.

A null instrument offers certain intrinsic advantages over other modes of operation (e.g., see deflection instruments). By balancing the unknown input against a known standard input, the null method minimizes interaction between the measuring system and the measurand. As each input comes from a separate source, the significance of any measuring influence on the measurand by the measurement process is reduced. In effect, the measured system sees a very high input impedance, thereby minimizing loading errors. This is particularly effective when the measurand is a very small value. Hence, the null operation can achieve a high accuracy for small input values and with a low loading error. In practice, the null instrument will not achieve perfect parity due to the usable resolution of the balance and detection methods, but this is limited only by the state of the art of the circuit or scheme being employed.

A disadvantage of null instruments is that an iterative balancing operation requires more time to execute than simply measuring sensor input. Thus, this method might not offer the fastest measurement possible when high-speed measurements are required. However, the user should weigh achievable accuracy against needed speed of measurement when considering operational modes. Further, the design of the comparator and balance loop can become involved such that highly accurate devices are generally not the lowest cost measuring alternative.

An equal-arm balance scale is a good mechanical example of a manual balance-feedback null instrument, as shown in Figure 3.1. This scale compares the unknown weight of an object on one side against a set of standard or known weights. The known values of weight are added iteratively to one side to

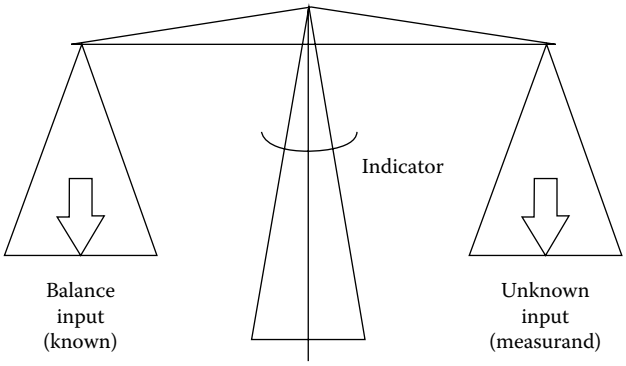

FIGURE 3.1 Measurand and the known quantities balance one another in a null instrument.

exert an influence to oppose the effect of the unknown weight on the opposite side. Until parity, a high or low value is noted by the indicator providing the feedback logic to the operator for adding or removing weights in a balancing iteration. At true parity, the scale indicator is null; that is, it indicates a zero deflection. Then, the unknown input or measurand is deduced to have a value equal to the balance input, the amount of known weights used to balance the scale. Factors influencing the overall measurement accuracy include the accuracy of the standard weights used and resolution of the output indicator and the friction at the fulcrum. Null instruments exist for measurement of most variables. Other common examples include bridge circuits, often employed for highly accurate resistance measurements and found in load cells, temperature-compensated transducers, and voltage-balancing potentiometers used for highly accurate low-voltage measurements.

Within the null instrument, the iteration and feedback mechanism is a loop that can be controlled either manually or automatically. Essential to the null instrument are two inputs: the measurand and the balance input. The null instrument includes a differential comparator, which compares and computes the difference between these two inputs. This is illustrated in Figure 3.2. A nonzero output from the comparator provides the error signal and drives the logic for the feedback correction. Repeated corrections provide for an iteration toward eventual parity between the inputs and the results in the null condition where the measurand is exactly opposed by the balance input. At parity, the error signal is driven to zero by the opposed influence of the balance input, and the indicated deflection is at null, thus lending the name to the method. It is the magnitude of the balance input that drives the output reading in terms of the measurand.

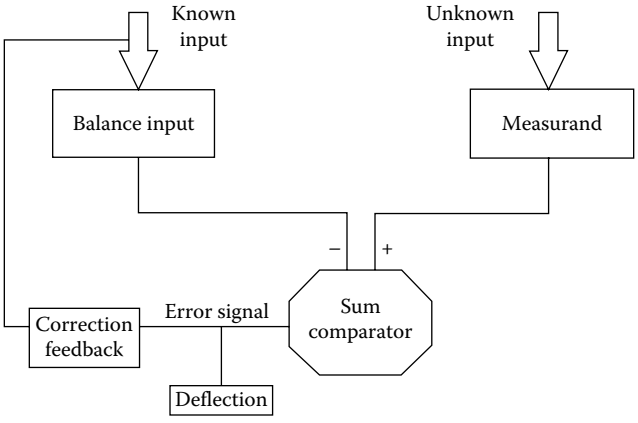

FIGURE 3.2 Null instrument requires input from two sources for comparison.

3.2 Deflection Instrument

The deflection method is one possible mode of operation for a measuring instrument. A deflection instrument uses the deflection method for measurement. A deflection instrument is influenced by the measurand so as to bring about a proportional response within the instrument. This response is an output reading that is a deflection or a deviation from the initial condition of the instrument. In a typical form, the measurand acts directly on a prime element or primary circuit so as to convert its information into a detectable form. The name is derived from a common form of instrument where there is a physical deflection of a prime element that is linked to an output scale, such as a pointer or other type of readout, which deflects to indicate the measured value. The magnitude of the deflection of the prime element brings about a deflection in the output scale that is designed to be proportional in magnitude to the value of the measurand.

Deflection instruments are the most common of measuring instruments. The relationship between the measurand and the prime element or measuring circuit can be a direct one, with no balancing mechanism or comparator circuits used. The proportional response can be manipulated through signal-conditioning methods between the prime element and the output scale so that the output reading is a direct indication of the measurand. Effective designs can achieve a high accuracy, yet sufficient accuracy for less demanding uses can be achieved at moderate costs.

An attractive feature of the deflection instrument is that it can be designed for either static or dynamic measurements or both. An advantage to deflection design for dynamic measurements is in the high dynamic response that can be achieved. A disadvantage of deflection instruments is that by deriving its energy from the measurand, the act of measurement will influence the measurand and change the value of the variable being measured. This change is called a loading error. Hence, the user must ensure that the resulting loading error is acceptable. This usually involves a careful look at the instrument input impedance for the intended measurement.

A spring scale is a good, simple example of a deflection instrument. As shown in Figure 3.3, the input weight or measurand acts on a plate spring. The plate spring serves as a prime element. The original position of the spring is influenced by the applied weight and responds with a translational displacement, a deflection x. The final value of this deflection is a position that is at equilibrium between the downward force of the weight, W, and the upward restoring force of the spring, kx. That is, the input force is balanced against the restoring force. A mechanical coupler is connected directly or by linkage to a pointer. The pointer position is mapped out on a corresponding scale that serves as the readout scale. For example, at equilibrium $W = kx$ or by measuring the deflection of the pointer, the weight is deduced by $x = W/k$.

The flow-diagram logic for a deflection instrument is rather linear, as shown in Figure 3.4. The input signal is sensed by the prime element or primary circuit and thereby deflected from its initial setting. The deflection signal is transmitted to signal conditioners that act to condition the signal into

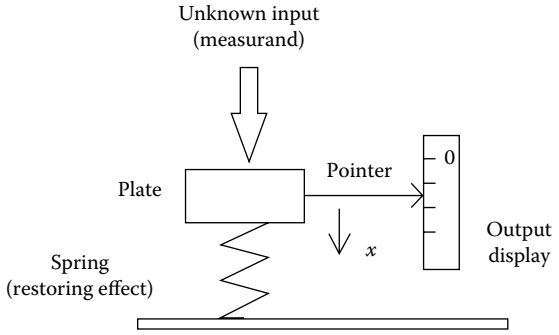

FIGURE 3.3 Deflection instrument requires input from only one source but may introduce a loading error.

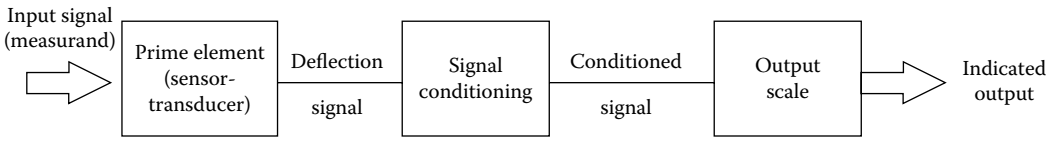

FIGURE 3.4 Logic flowchart for a deflection instrument is straightforward.

a desired form. The examples of signal conditioning are to multiply the deflection signal by some scaler magnitude, such as in amplification or filtering, or to transform the signal by some arithmetic function. The conditioned signal is then transferred to the output scale, which provides the indicated value corresponding to the measurand value.

3.3 Analog and Digital Sensors

Analog sensors provide a signal that is continuous in both its magnitude and its temporal (time) or spatial (space) content. The defining word for analog is "continuous." If a sensor provides a continuous output signal that is directly proportional to the input signal, then it is analog.

Most physical variables, such as current, temperature, displacement, acceleration, speed, pressure, light intensity, and strain, tend to be continuous in nature and are readily measured by an analog sensor and represented by an analog signal. For example, the temperature within a room can take on any value within its range, will vary in a continuous manner in between any two points in the room, and may vary continuously with time at any position within the room. An analog sensor, such as a bulb thermometer or a thermocouple, will continuously respond to such temperature changes. Such a continuous signal is shown in Figure 3.5, where the signal magnitude is analogous to the measured variable (temperature) and the signal is continuous in both magnitude and time.

Digital sensors provide a signal that is a direct digital representation of the measurand. Digital sensors are basically binary ("on" or "off") devices. Essentially, a digital signal exists at only discrete values of time (or space). And within that discrete period, the signal can represent only a discrete number of magnitude values. A common variation is the discrete sampled signal representation, which represents a sensor output in a form that is discrete both in time or space and in magnitude.

Digital sensors use some variation of a binary numbering system to represent and transmit the signal information in digital form. A binary numbering system is a number system using the base 2. The simplest binary signal is a single bit that has only one of two possible values, a 1 or a 0. Bits are like electrical "on–off" switches and are used to convey logical and numerical information. With appropriate input, the value of the bit transmitted is reset corresponding to the behavior of the measured variable. A digital sensor that transmits information one bit at a time uses serial transmission. By combining bits or transmitting bits in groups, it is also possible to define logical commands or integer numbers beyond a 0 or 1. A digital sensor that transmits bits in groups uses parallel transmission. With any digital device, an M-bit signal can express 2^M different numbers. This also provides the limit for the different values that a digital device can discern. For example, a 2 bit device can express 2^2 or 4

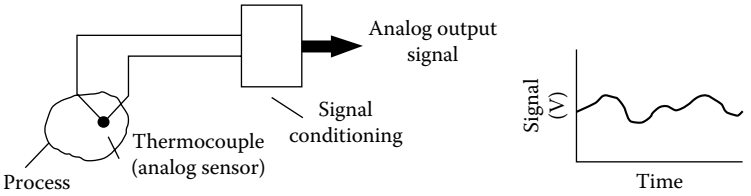

FIGURE 3.5 Thermocouple provides an analog signal for processing.

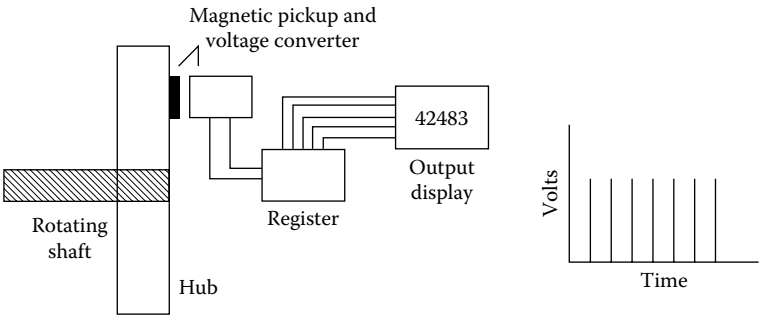

FIGURE 3.6 Rotating shaft with a revolution counter produces a digital signal.

different numbers, 00, 01, 10, and 11, corresponding to the values of 0, 1, 2, and 3, respectively. Thus, the resolution in a magnitude discerned by a digital sensor is inherently limited to 1 part in 2^M.

The concept of a digital sensor is illustrated by the revolution counter in Figure 3.6. Such devices are widely used to sense the revolutions per minute of a rotating shaft. In this example, the sensor is a magnetic pickup/voltage converter that outputs a pulse with each pass of a magnetic stud mounted to a hub on the rotating shaft. The output from the pickup normally is "off" but is momentarily turned "on" by the passing stud. This pulse is a voltage spike sent to a digital register whose value is increased by a single count with each spike. The register can send the information to an output device, such as the digital display shown. The output from the sensor can be viewed in terms of voltage spikes with time. The count rate is related to the rotational speed of the shaft. As seen, the signal is discrete in time. A single stud with pickup will increase the count by one for each full rotation of the shaft. The fractions of a rotation can be resolved by increasing the number of studs on the hub. In this example, the continuous rotation of the shaft is analog but the revolution count is digital. The amplitude of the voltage spike is set to activate the counter and is not related to the shaft rotational speed.

3.4 Analog and Digital Readout Instruments

An analog readout instrument provides an output indication that is continuous and directly analogous to the behavior of the measurand. Typically, this might be the deflection of a pointer or an ink trace on a graduated scale or the intensity of a light beam or a sound wave. This indicated deflection may be driven by changes in voltage or current; or by mechanical, magnetic, or optical means; or combinations of these. The resolution of an analog readout is defined by the smallest usable increment on its readout scale. The span of the readout is defined by the difference between the minimum and the maximum values that it can indicate. Its range specifies the minimum and maximum values that it can indicate.

A digital readout instrument provides an output indication that is a discrete value. The value is directly related to the value of the measurand. The digital readout is typically in the form of a numerical value that is either a fixed number or a number that is updated periodically. One means of displaying a digital number is the seven-segment digital display chip, shown in Figure 3.7, whose output can be updated by altering the grounding inputs A through G. The resolution of a digital readout is given by its least count, the equivalent amount of the smallest change resolved by the least significant digit in the readout. The span and the range are defined as for analog instruments.

Many digital devices combine features of an analog sensor with a digital readout or, in general, convert an analog signal to a discrete signal, which is indicated through a digital output. In such situations, an analog-to-digital converter (ADC) is required. This hybrid device has its analog side specified in terms of its full-scale analog range, E_{FSR}, which defines the analog voltage span over which the device will operate. The digital side is specified in terms of the bit size of its register. An M-bit device will output an M-bit binary number. The resolution of such a device is given by $E_{FSR}/2^M$.

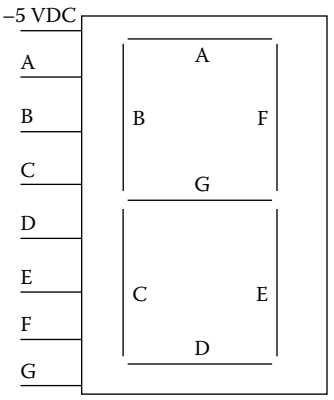

FIGURE 3.7 Seven-segment display chip can display any digit from 0 to 9.

3.5 Input Impedance

In the ideal sense, the very act of measurement should not alter the value of the measured signal. Any such alteration is a loading error. Loading errors can occur at any junction along the signal chain but can be minimized by impedance matching of the source with the measuring instrument. The measuring instrument input impedance controls the energy that is drawn from the source, or measured system, by a measuring instrument. The power loss through the measuring instrument is estimated by $P = E^2/Z_2$ where Z_2 is the input impedance of the measuring instrument and E is the source voltage potential being measured. Thus, to minimize the power loss, the input impedance should be large.

This same logic holds for the two instruments in a signal chain as the subsequent instrument draws energy from the previous instrument in the chain. As a general example, consider the situation in Figure 3.8 in which the output signal from one instrument provides the input signal to a subsequent device in a signal chain. The open circuit potential, E_1, is present at the output terminal of source device 1 having output impedance, Z_1. Device 2 has input impedance Z_2 at its input terminals. Connecting the output terminals of Device 1 to the input terminals of Device 2 creates the equivalent circuit also shown in Figure 3.7. The potential actually sensed by Device 2 will be

$$E_2 = E_1 \frac{1}{1 + Z_1/Z_2}$$

The difference between the actual potential E_1 at the output terminals of Device 1 and the measured potential E_2 is a loading error brought on by the input impedance of measuring Device 2. It is clear that a high input impedance Z_2 relative to Z_1 minimizes this error. A general rule is for the input impedance to be at least 100 times the source impedance to reduce the loading error to 1%.

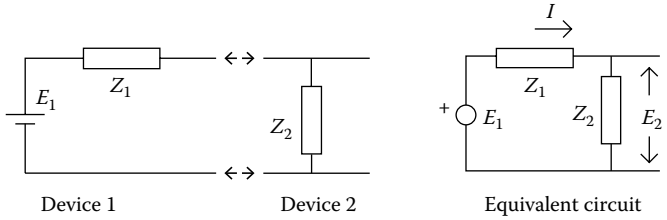

FIGURE 3.8 Equivalent circuit is formed by applying a measuring instrument to the output terminals of an instrument.

In general, null instruments and null methods will minimize loading errors. They provide the equivalent of a very high input impedance to the measurement, minimizing energy drain from the measured system. Deflection instruments and deflection measuring techniques will derive energy from the process being measured and therefore require attention to proper selection of input impedance.

Defining Terms

Analog sensor: Sensors that output a signal that is continuous in both magnitude and time (or space).

Deflection instrument: A measuring device whose output deflects proportional to the magnitude of the measurand.

Digital sensor: Sensors that output a signal that is discrete (noncontinuous) in time and/or magnitude.

Input impedance: The impedance measured across the input terminals of a device.

Loading error: That difference between the measurand and the measuring system output attributed to the act of measuring the measurand.

Measurand: A physical quantity, property, or condition being measured. Often, it is referred to as a measured value.

Null instrument: A measuring device that balances the measurand against a known value, thus achieving a null condition. A null instrument minimizes measurement loading errors.

Readout: This is the display of a measuring system.

Resolution: This is the least count or smallest detectable change in measurand capable.

Sensor: The portion of a measurement system that responds directly to the physical variable being measured.

Further Information

Doebelin, E. O., *Measurement Systems,* 4th edn., New York: McGraw-Hill, 1990.

Figliola, R. S. and D. E. Beasley, *Theory and Design for Mechanical Measurements,* 5th edn., New York: Wiley, 2011.

Northrop, R. B., *Introduction to Instrumentation and Measurement,* Boca Raton, FL: CRC Press, 2005.

Wobschall, D., *Circuit Design for Electronic Instrumentation: Analog and Digital Devices from Sensor to Display,* 2nd edn., New York: McGraw-Hill, 1987.

4

Static and Dynamic Characteristics of Instrumentation

Peter H. Sydenham
University of South Australia

Before we can begin to develop an understanding of the static and time-changing characteristics of measurements, it is necessary to build a framework for understanding the process involved, setting down the main words used to describe concepts as we progress.

Measurement is the process by which relevant information about a system of interest is interpreted using the human thinking ability to define what is believed to be the new knowledge gained. This information may be obtained for purposes of controlling the behavior of the system (as in engineering applications) or for learning more about it (as in scientific investigations).

The basic entity needed to develop the knowledge is called *data*, and it is obtained with physical assemblies known as sensors that are used to observe or sense system variables. The terms *information* and *knowledge* tend to be used interchangeably to describe the entity resulting after data from one or more sensors have been processed to give more meaningful understanding. The individual variables being sensed are called *measurands*.

The most obvious way to make observations is to use the human senses of seeing, feeling, and hearing. This is often quite adequate or may be the only means possible. In many cases, however, sensors are used that have been devised by man to enhance or replace our natural sensors. The number and variety of sensors is very large indeed. Examples of man-made sensors are those used to measure temperature, pressure, or length. The process of sensing is often called *transduction*, being made with transducers. These man-made sensor assemblies, when coupled with the means to process the data into knowledge, are generally known as (measuring) instrumentation.

The degree of perfection of a measurement can only be determined if the goal of the measurement can be defined without error. Furthermore, instrumentation cannot be made to operate perfectly. Because of these two reasons alone, measuring instrumentation cannot give ideal sensing performance, and it must be selected to suit the allowable error in a given situation.

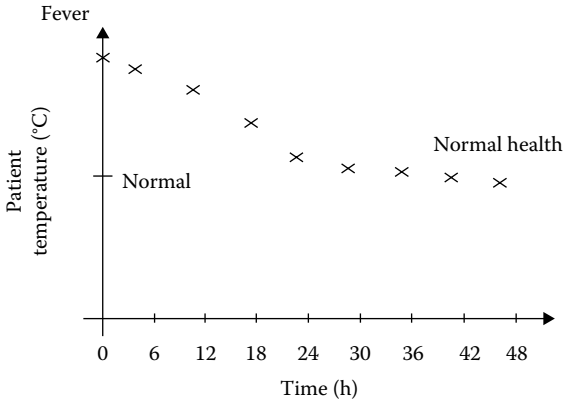

FIGURE 4.1 A patient's temperature chart shows changes taking place over time.

Measurement is a process of mapping actually occurring variables into equivalent values. Deviations from perfect measurement mappings are called *errors*: what we get as the result of measurement is not exactly what is being measured. A certain amount of error is allowable provided it is below the level of uncertainty we can accept in a given situation. As an example, consider two different needs to measure the measurand, time. The uncertainty to which we must measure it for daily purposes of attending a meeting is around a min in 24 h. In orbiting satellite control, the time uncertainty needed must be as small as milliseconds in years. Instrumentation used for the former case costs a few dollars and is the watch we wear; the latter instrumentation costs thousands of dollars and is the size of a suitcase.

We often record measurand values as though they are constant entities, but they usually change in value as time passes. These "dynamic" variations will occur either as changes in the measurand itself or where the measuring instrumentation takes time to follow the changes in the measurand—in which case it may introduce unacceptable error.

For example, when a fever thermometer is used to measure a person's body temperature, we are looking to see if the person is at the normally expected value and if it is not, to then look for changes over time as an indicator of his or her health. Figure 4.1 shows a chart of a patient's temperature. Obviously, if the thermometer gives errors in its use, wrong conclusions could be drawn. It could be in error due to incorrect calibration of the thermometer or because no allowance for the dynamic response of the thermometer itself was made.

Instrumentation, therefore, will only give adequately correct information if we understand the static and dynamic characteristics of both the measurand and the instrumentation. This, in turn, allows us to then decide if the error arising is small enough to accept.

As an example, consider the electronic signal amplifier in a sound system. It will be commonly quoted as having an amplification constant after feedback if applied to the basic amplifier of, say, 10. The actual amplification value is dependent on the frequency of the input signal, usually falling off as the frequency increases. The frequency response of the basic amplifier, before it is configured with feedback that markedly alters the response and lowers the amplification to get a stable operation, is shown as a graph of amplification gain versus input frequency. An example of the open-loop gain of the basic amplifier is given in Figure 4.2. This lack of uniform gain over the frequency range results in error—the sound output is not a true enough representation of the input.

Before we can delve more deeply into the static and dynamic characteristics of instrumentation, it is necessary to understand the difference in meaning between several basic terms used to describe the results of a measurement activity.

The correct terms to use are set down in documents called *standards*. Several standardized metrology terminologies exist, but they are not consistent. It will be found that books on instrumentation and statements of instrument performance often use terms in different ways. Users of measurement information need to be constantly diligent in making sure that the statements made are interpreted correctly.

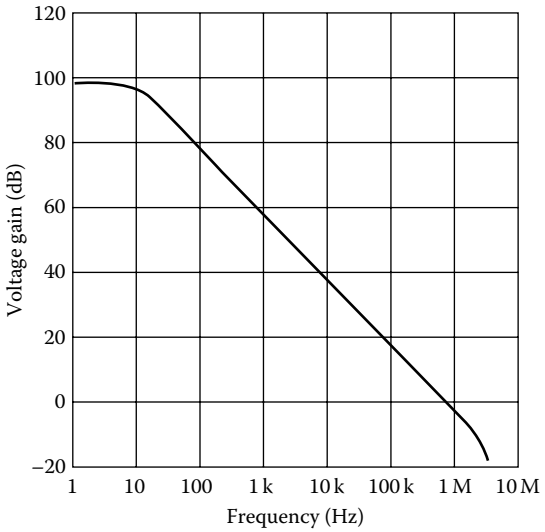

FIGURE 4.2 This graph shows how the amplification of an amplifier changes with input frequency.

The three companion concepts about a measurement that need to be well understood are its *discrimination*, its *precision*, and its *accuracy*. These are too often used interchangeably—which is quite wrong to do because they cover quite different concepts, as will now be explained.

When making a measurement, the smallest increment that can be discerned is called the *discrimination*. (Although now officially declared as wrong to use, the term *resolution* still finds its way into books and reports as meaning discrimination.) The discrimination of a measurement is important to know because it tells if the sensing process is able to sense fine enough changes of the measurand.

Even if the discrimination is satisfactory, the value obtained from a repeated measurement will rarely give exactly the same value each time the same measurement is made under conditions of constant value of measurand. This is because errors arise in real systems. The spread of values obtained indicates the precision of the set of the measurements. The word *precision* is not a word describing a quality of the measurement and is incorrectly used as such. Two terms that should be used here are *repeatability*, which describes the variation for a set of measurements made in a very short period, and the *reproducibility*, which is the same concept but now used for measurements made over a long period. As these terms describe the outcome of a set of values, there is a need to be able to quote a single value to describe the overall result of the set. This is done using statistical methods that provide for calculation of the "mean value" of the set and the associated spread of values, called its *variance*.

The *accuracy* of a measurement is covered in more depth elsewhere, so only an introduction to it is required here. Accuracy is the closeness of a measurement to the value defined to be the true value. This concept will become clearer when the following illustrative example is studied, for it brings together the three terms into a single perspective of a typical measurement.

Consider then the situation of scoring an archer shooting arrows into a target as shown in Figure 4.3a. The target has a central point—the bull's-eye. The objective for a perfect result is to get all arrows into the bull's-eye. The rings around the bull's-eye allow us to set up numeric measures of less-perfect shooting performance.

Discrimination is the distance at which we can just distinguish (i.e., discriminate) the placement of one arrow from another when they are very close. For an arrow, it is the thickness of the hole that decides the discrimination. Two close-by positions of the two arrows in Figure 4.3a cannot be separated easily. Use of thinner arrows would allow finer detail to be decided.

Repeatability is determined by measuring the spread of values of a set of arrows fired into the target over a short period. The smaller the spread, the more precise is the shooter. The shooter in Figure 4.3a is more precise than the shooter in Figure 4.3b.

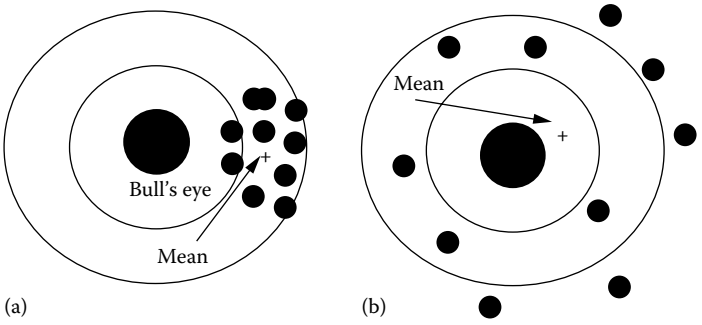

FIGURE 4.3 Two sets of arrow shots fired into a target allow understanding of the measurement concepts of discrimination, precision, and accuracy. (a) The target used for shooting arrows allows investigation of the terms used to describe the measurement result. (b) A different set of placements.

If the shooter returned to shoot each day over a long period, the results may not be the same each time for a shoot made over a short period. The mean and variance of the values are now called the *reproducibility* of the archer's performance.

Accuracy remains to be explained. This number describes how well the mean (the average) value of the shots sits with respect to the bull's-eye position. The set in Figure 4.3b is more accurate than the set in Figure 4.3a because the mean is nearer the bull's-eye (but less precise).

At first sight, it might seem that the three concepts of discrimination, precision, and accuracy have a strict relationship in that a better measurement is always that with all three aspects made as high as is affordable. This is not so. They need to be set up to suit the needs of the application.

We are now in a position to explore the commonly met terms used to describe aspects of the static and the dynamic performance of measuring instrumentation.

4.1 Static Characteristics of Instrument Systems

4.1.1 Output/Input Relationship

Instrument systems are usually built up from a serial linkage of distinguishable building blocks. The actual physical assembly may not appear to be so, but it can be broken down into a representative diagram of connected blocks. Figure 4.4 shows the block diagram representation of a humidity sensor. The sensor is activated by an input physical parameter and provides an output signal to the next block that processes the signal into a more appropriate state.

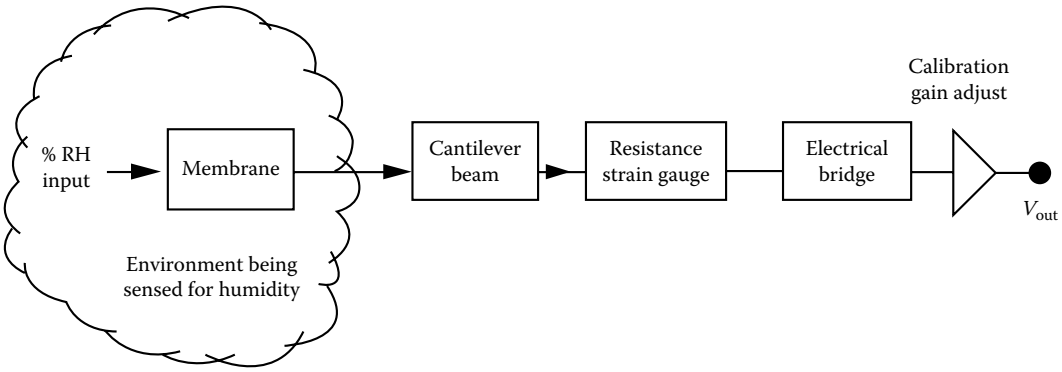

FIGURE 4.4 Instruments are formed from a connection of blocks. Each block can be represented by a conceptual and mathematical model. This example is of one type of humidity sensor.

A key generic entity is, therefore, the relationship between the input and output of the block. As was pointed out earlier, all signals have a time characteristic, so we must consider the behavior of a block in terms of both the static and dynamic states.

The behavior of the static regime alone and the combined static and dynamic regime can be found through use of an appropriate mathematical model of each block. The mathematical description of system responses is easy to set up and use if the elements all act as linear systems and where addition of signals can be carried out in a linear additive manner. If nonlinearity exists in elements, then it becomes considerably more difficult—perhaps even quite impractical—to provide an easy to follow mathematical explanation. Fortunately, general description of instrument systems responses can be usually adequately covered using the linear treatment.

The output/input ratio of the whole cascaded chain of blocks 1, 2, 3, etc. is given as

$$\left[\frac{\text{Output}}{\text{Input}}\right]_{\text{total}} = \left[\frac{\text{Output}}{\text{Input}}\right]_1 \times \left[\frac{\text{Output}}{\text{Input}}\right]_2 \times \left[\frac{\text{Output}}{\text{Input}}\right]_3 \ldots$$

The output/input ratio of a block that includes both the static and dynamic characteristics is called the *transfer function* and is given the symbol *G*.

The equation for *G* can be written as two parts multiplied together. One expresses the static behavior of the block, that is, the value it has after all transient (time-varying) effects have settled to their final state. The other part tells us how that value responds when the block is in its dynamic state. The static part is known as the *transfer characteristic* and is often all that is needed to be known for block description.

The static and dynamic response of the cascade of blocks is simply the multiplication of all individual blocks. As each block has its own part for the static and dynamic behavior, the cascade equations can be rearranged to separate the static from the dynamic parts, and then by multiplying the static set and the dynamic set, we get the overall response in the static and dynamic states. This is shown by the sequence of Equations 4.1 through 4.4:

$$G_{\text{total}} = G_1 \times G_2 \times G_3 \ldots \tag{4.1}$$

$$= [\text{Static} \times \text{Dynamic}]_1 \times [\text{Static} \times \text{Dynamic}]_2 \times [\text{Static} \times \text{Dynamic}]_3 \ldots \tag{4.2}$$

$$= [\text{Static}]_1 \times [\text{Static}]_2 \times [\text{Static}]_3 \ldots \times [\text{Dynamic}]_1 \times [\text{Dynamic}]_2 \times [\text{Dynamic}]_3 \ldots \tag{4.3}$$

$$= [\text{Static}]_{\text{total}} \times [\text{Dynamic}]_{\text{total}} \tag{4.4}$$

An example will clarify this. A mercury-in-glass fever thermometer is placed in a patient's mouth. The indication slowly rises along the glass tube to reach the final value, the body temperature of the person. The slow rise seen in the indication is due to the time it takes for the mercury to heat up and expand up the tube. The static *sensitivity* will be expressed as so many scale divisions per degree and is all that is of interest in this application. The dynamic characteristic will be a time-varying function that settles to unity after the transient effects have settled. This is merely an annoyance in this application but has to be allowed by waiting long enough before taking a reading. The wrong value will be viewed if taken before the transient has settled.

At this stage, we will now consider only the nature of the static characteristics of a chain; dynamic response is examined later.

If a sensor is the first stage of the chain, the static value of the gain for that stage is called the *sensitivity*. Where a sensor is not at the input, it is called the *amplification factor* or *gain*. It can take a value less than unity where it is then called the *attenuation*.

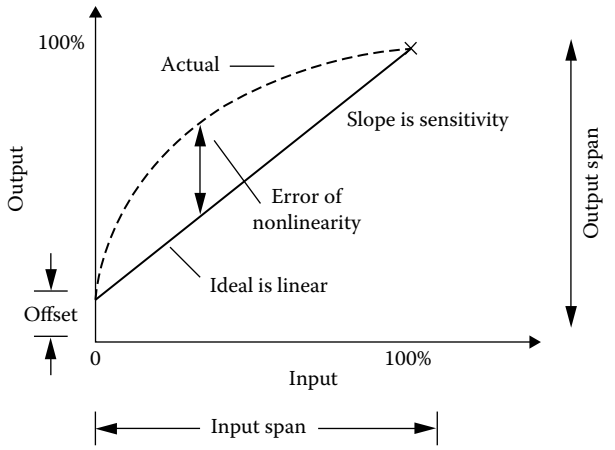

FIGURE 4.5 The graph relating input to output variables for an instrument block shows several distinctive static performance characteristics.

Sometimes, the instantaneous value of the signal is rapidly changing, yet the measurement aspect part is static. This arises when using AC signals in some forms of instrumentation where the amplitude of the waveform, not its frequency, is of interest. Here, the static value is referred to as its *steady-state* transfer characteristic.

Sensitivity may be found from a plot of the input and output signals, wherein it is the slope of the graph. Such a graph (see Figure 4.5) tells much about the static behavior of the block.

The intercept value on the *y-axis* is the *offset* value being the output when the input is set to zero. Offset is not usually a desired situation and is seen as an error quantity. Where it is deliberately set up, it is called the *bias*.

The range on the *x*-axis, from zero to a safe maximum for use, is called the *range* or *span* and is often expressed as the zone between the 0% and 100% points. The ratio of the span that the output will cover for the related input range is known as the *dynamic range*. This can be a confusing term because it does not describe dynamic time behavior. It is particularly useful when describing the capability of such instruments as flow rate sensors—a simple orifice plate type may only be able to handle dynamic ranges of 3–4, whereas the laser Doppler method covers as much as 10^7 variation.

4.1.2 Drift

It is now necessary to consider a major problem of instrument performance called *instrument drift*. This is caused by variations taking place in the parts of the instrumentation over time. Prime sources occur as chemical structural changes and changing mechanical stresses. Drift is a complex phenomenon for which the observed effects are that the sensitivity and offset values vary. It also can alter the accuracy of the instrument differently at the various amplitudes of the signal present.

Detailed description of drift is not at all easy, but it is possible to work satisfactorily with simplified values that give the average of a set of observations, this usually being quoted in a conservative manner. The first graph (*a*) in Figure 4.6 shows typical steady drift of a measuring spring component of a weighing balance. Figure 4.6b shows how an electronic amplifier might settle down after being turned on.

Drift is also caused by variations in environmental parameters such as temperature, pressure, and humidity that operate on the components. These are known as *influence parameters*. An example is the change of the resistance of an electrical resistor, this resistor forming the critical part of an electronic amplifier that sets its gain as its operating temperature changes.

Unfortunately, the observed effects of influence parameter–induced drift often are the same as for time-varying drift. Appropriate testing of blocks such as electronic amplifiers does allow the two to be

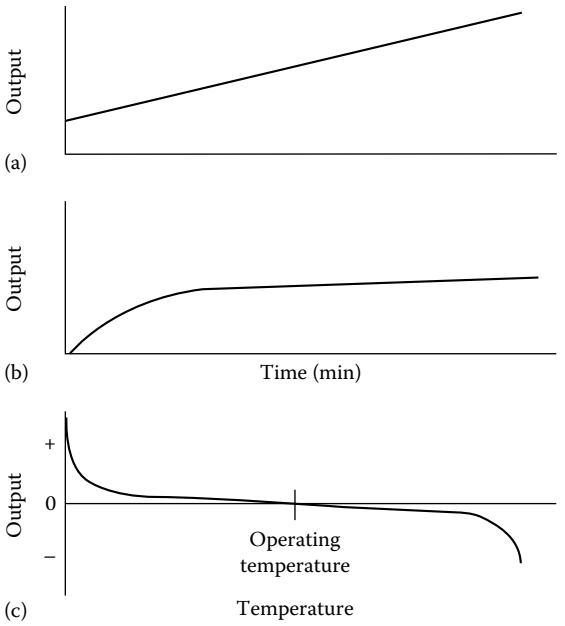

FIGURE 4.6 Drift in the performance of an instrument takes many forms: (a) drift over time for a spring balance, (b) how an electronic amplifier might settle over time to a final value after power is supplied, and (c) drift, due to temperature, of an electronic amplifier varies with the actual temperature of operation.

separated to some extent. For example, altering only the temperature of the amplifier over a short period will quickly show its temperature dependence.

Drift due to influence parameters is graphed in much the same way as for time drift. Figure 4.6c shows the drift of an amplifier as temperature varies. Note that it depends significantly on the temperature of operation, implying that the best designs are built to operate at temperatures where the effect is minimum.

Careful consideration of the time and influence parameter causes of drift shows they are interrelated and often impossible to separate. Instrument designers are usually able to allow for these effects, but the cost of doing this rises sharply as the error level that can be tolerated is reduced.

4.1.3 Hysteresis and Backlash

Careful observation of the output/input relationship of a block will sometimes reveal different results as the signals vary in the direction of the movement. Mechanical systems will often show a small difference in length as the direction of the applied force is reversed. The same effect arises as a magnetic field is reversed in a magnetic material. This characteristic is called *hysteresis*. Figure 4.7 is a generalized plot of the output/input relationship showing that a closed loop occurs. The effect usually gets smaller as the amplitude of successive excursions is reduced, this being one way to tolerate the effect. It is present in most materials. Special materials have been developed that exhibit low hysteresis for their application—transformer iron laminations and clock spring wire being examples.

Where this is caused by a mechanism that gives a sharp change, such as caused by the looseness of a joint in a mechanical joint, it is easy to detect and is known as *backlash*.

4.1.4 Saturation

So far, the discussion has been limited to signal levels that lie within acceptable ranges of amplitude. Real system blocks will sometimes have input signal levels that are larger than allowed. Here, the dominant errors that arise—*saturation* and *crossover distortion*—are investigated.

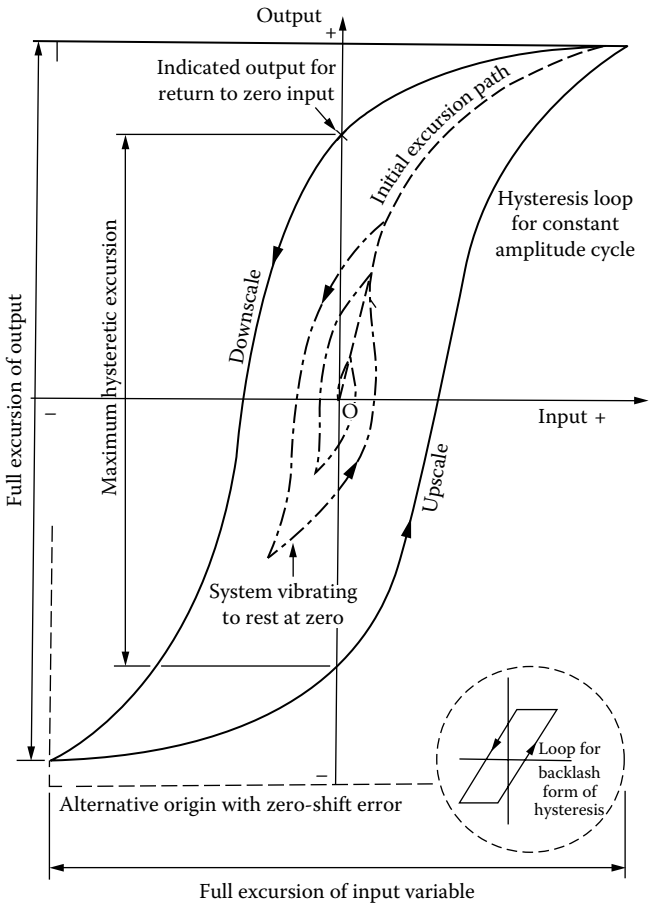

FIGURE 4.7 Generalized graph of output/input relationship where hysteresis is present. (Sydenham, P.H.: *Handbook of Measurement Science, Vol. 2*. 1983. Copyright Wiley-VCH Verlag GmbH & Co. KGaA. Reproduced with permission.)

As mentioned earlier, the information-bearing property of the signal can be carried as the instantaneous value of the signal or be carried as some characteristic of a rapidly varying AC signal. If the signal form is not amplified faithfully, the output will not have the same linearity and characteristics.

The gain of a block will usually fall off with increasing size of signal amplitude. A varying amplitude input signal, such as the steadily rising linear signal shown in Figure 4.8, will be amplified differently according to the gain/amplitude curve of the block. In uncompensated electronic amplifiers, the larger amplitudes are usually less amplified than at the median points.

At very low levels of input signal, two unwanted effects may arise. The first is that small signals are often amplified more than at the median levels. The second error characteristic arises in electronic amplifiers because the semiconductor elements possess a dead zone in which no output occurs until a small threshold is exceeded. This effect causes crossover distortion in amplifiers.

If the signal is an AC waveform (see Figure 4.9) then the different levels of a cycle of the signal may not all be amplified equally. Figure 4.9a shows what occurs because the basic electronic amplifying elements are only able to amplify one polarity of signal. The signal is said to be *rectified*. Figure 4.9b shows the effect when the signal is too large and the top is not amplified. This is called *saturation* or *clipping*. (As with many physical effects, this effect is sometimes deliberately invoked in circuitry, an example being where it is used as a simple means to convert sine-waveform signals into a square waveform.) Crossover distortion is evident in Figure 4.9c as the signal passes from negative to positive polarity.

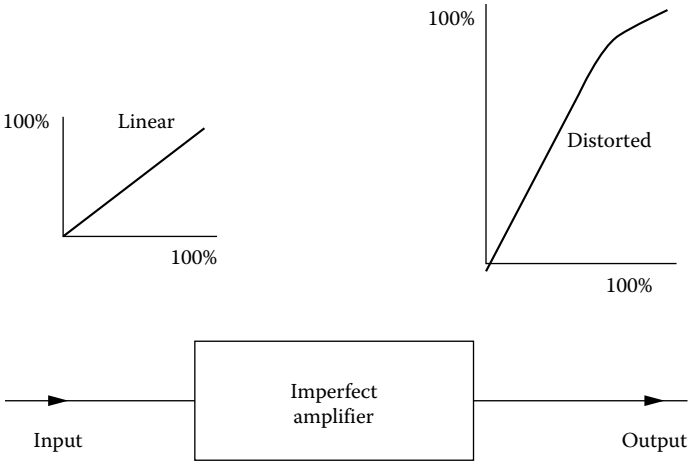

FIGURE 4.8 Nonlinear amplification can give rise to unwanted output distortion.

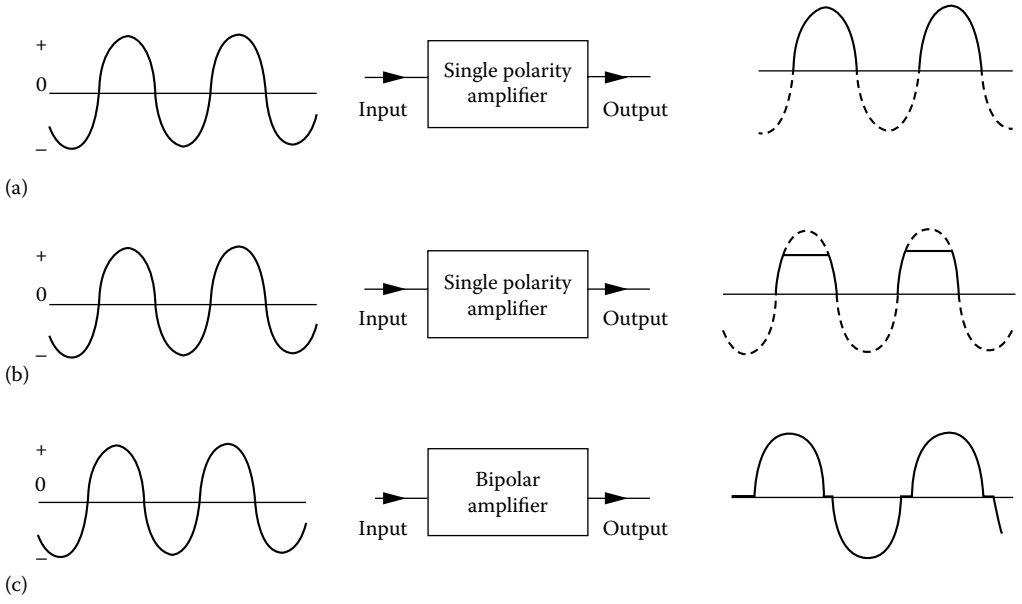

FIGURE 4.9 Blocks can incorrectly alter the shape of waveforms if saturation and crossover effects are not controlled: (a) rectification, (b) saturation, and (c) crossover distortion.

Where input signals are small, such as in sensitive sensor use, the form of analysis called *small signal* behavior is needed to reveal distortions. If the signals are comparatively large, as for digital signal considerations, a *large signal* analysis is used. Design difficulties arise when signals cover a wide dynamic range because it is not easy to allow for all of the various effects in a single design.

4.1.5 Bias

Sometimes, the electronic signal-processing situation calls for the input signal to be processed at a higher average voltage or current than arises normally. Here a DC value is added to the input signal to raise the level to a higher state as shown in Figure 4.10. A need for this is met where only one polarity of signal can be amplified by a single semiconductor element. Raising the level of all of the waveform equally takes all

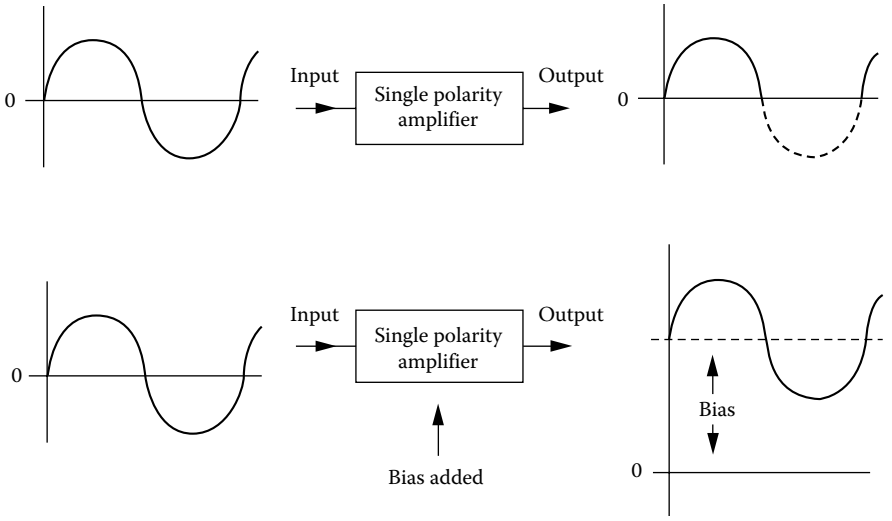

FIGURE 4.10 Bias is where a signal has all of its value raised by an equal amount. Shown here is an AC input waveform biased to be all of positive polarity.

parts into the reasonably linear zone of an amplifier, allowing more faithful replication. If bias were not used here, then the lower half cycle would not be amplified, resulting in only the top half appearing in the output.

4.1.6 Error of Nonlinearity

Ideally, it is often desired that a strictly linear relationship exists between input and output signals in amplifiers. Practical units, however, will always have some degree of nonconformity, which is called the *nonlinearity*. If an instrument block has constant gain for all input signal levels, then the relationship graphing the input against the output will be a straight line; the relationship is then said to be linear. *Linearity* is the general term used to describe how close the actual response is compared with that ideal line. The correct way to describe the error here is as the *error of nonlinearity*. Note, however, that not all responses are required to be linear; another common one follows a logarithmic relationship.

Detailed description of this error is not easy, for that would need a statement of the error values at all points of the plot. Practice has found that a shorthand statement can be made by quoting the maximum departure from the ideal as a ratio formed with the 100% value.

Difficulties arise in expressing error of nonlinearity, for there exist many ways to express this error. Figure 4.11 shows the four cases that usually arise. The difference arises in the way in which the ideal (called the "best fit") straight line can be set up. Figure 4.11a shows the line positioned by the usually calculated statistical averaging method of least squares fit; other forms of line-fitting calculation are also used. This will yield the smallest magnitude of error calculation for the various kinds of line fitting but may not be appropriate for how the stage under assessment is used. Other, possibly more reasonable, options exist. Figure 4.11b constrains the best-fit line to pass through the zero point. Figure 4.11c places the line between the expected 0% and the 100% points. There is still one more option, that where the theoretical line is not necessarily one of the above yet is the ideal placement (Figure 4.11d).

In practice then, instrument systems linearity can be expressed in several ways. Good certification practice requires that the method used to ascertain the error is stated along with the numerical result, but this is often not done. Note also that the error is the worst case and that part of the response may be much more linear.

The description of instrument performance is not a simple task. To accomplish this fully would require very detailed statements recording the performance at each and every point. That is often

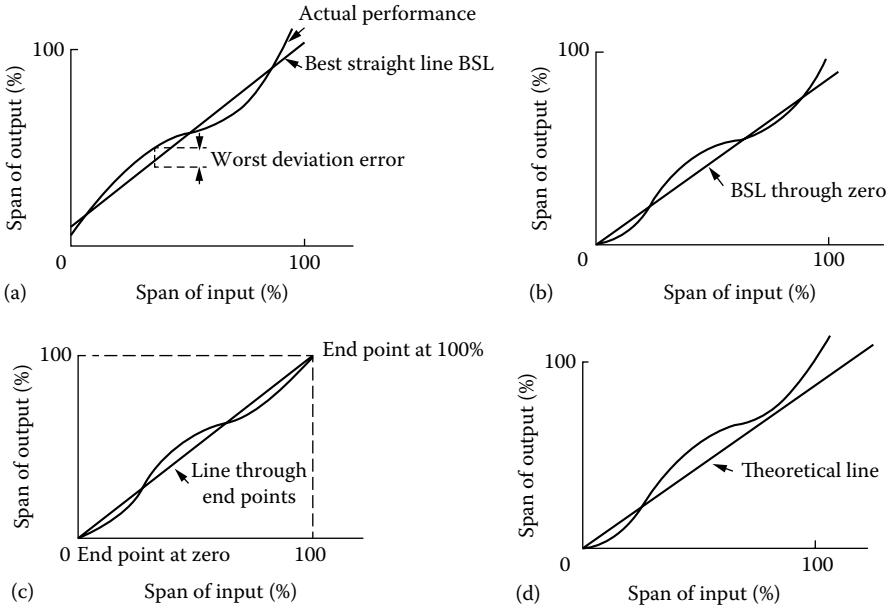

FIGURE 4.11 Error of nonlinearity can be expressed in four different ways: (a) best-fit line (based on selected method used to decide this); (b) best-fit line through zero; (c) line joining 0% and 100% points; and (d) theoretical line. (Sydenham, P.H.: *Handbook of Measurement Science, Vol. 2*. 1983. Copyright Wiley-VCH Verlag GmbH & Co. KGaA. Reproduced with permission.)

too cumbersome, so the instrument industry has developed many short-form statements that provide an adequate guide to the performance. This guide will be seen to be generally a conservative statement.

Many other descriptors exist for the static regime of an instrument. The reader is referred to the many standards documents that exist on instrument terminology; for example, see Ref. [3].

4.2 Dynamic Characteristics of Instrument Systems

4.2.1 Dealing with Dynamic States

Measurement outcomes are rarely static over time. They will possess a dynamic component that must be understood for correct interpretation of the results. For example, a trace made on an ink pen chart recorder will be subject to the speed at which the pen can follow the input signal changes.

To properly appreciate instrumentation design and its use, it is now necessary to develop insight into the most commonly encountered types of dynamic response and to develop the mathematical modeling basis that allows us to make concise statements about responses.

If the transfer relationship for a block follows linear laws of performance, then a generic mathematical method of dynamic description can be used. Unfortunately, simple mathematical methods have not been found that can describe all types of instrument responses in a simplistic and uniform manner. If the behavior is nonlinear, then description with mathematical models becomes very difficult and might be impracticable. The behavior of nonlinear systems can, however, be studied as segments of linear behavior joined end to end. Here, digital computers are effectively used to model systems of any kind provided the user is prepared to spend time setting up an adequate model.

Now the mathematics used to describe linear dynamic systems can be introduced. This gives valuable insight into the expected behavior of instrumentation, and it is usually found that the response can be approximated as linear.

The modeled response at the output of a block G_{result} is obtained by multiplying the mathematical expression for the input signal G_{input} by the transfer function of the block under investigation $G_{response}$, as shown in Equation 4.5:

$$G_{result} = G_{input} \times G_{response} \tag{4.5}$$

To proceed, one needs to understand commonly encountered input functions and the various types of block characteristics. We begin with the former set: the so-called forcing functions.

4.2.2 Forcing Functions

Let us first develop an understanding of the various types of input signals used to perform tests. The most commonly used signals are shown in Figure 4.12. These each possess different valuable test features.

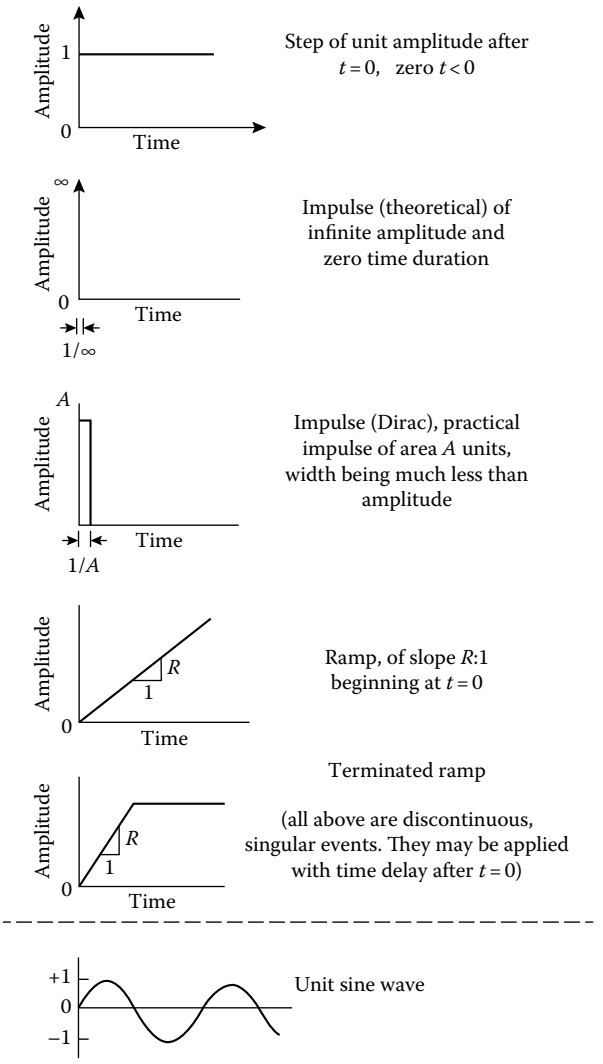

FIGURE 4.12 The dynamic response of a block can be investigated using a range of simple input forcing functions. (Sydenham, P.H.: *Handbook of Measurement Science, Vol. 2*. 1983. Copyright Wiley-VCH Verlag GmbH & Co. KGaA. Reproduced with permission.)

For example, the sine wave is the basis of analysis of all complex wave shapes because they can be formed as a combination of various sine waves, each having individual responses that add to give all other wave shapes. The step function has intuitively obvious uses because input transients of this kind are commonly encountered. The ramp test function is used to present a more realistic input for those systems where it is not possible to obtain instantaneous step input changes, such as attempting to move a large mass by a limited size of force. Forcing functions are also chosen because they can be easily described by a simple mathematical expression, thus making mathematical analysis relatively straightforward.

4.2.3 Characteristic Equation Development

The behavior of a block that exhibits linear behavior is mathematically represented in the general form of expression given as Equation 4.6:

$$\cdots + \frac{a_2 d^2 y}{dt^2} + \frac{a_1 dy}{dt} + a_0 y = x(t) \tag{4.6}$$

Here, the coefficients a_2, a_1, and a_0 are constants dependent on the particular block of interest. The left-hand side of the equation is known as the *characteristic equation*. It is specific to the internal properties of the block and is not altered by the way the block is used.

The specific combination of forcing function input and block characteristic equation collectively decides the combined output response. Connections around the block, such as feedback from the output to the input, can alter the overall behavior significantly: such systems, however, are not dealt with in this section being in the domain of feedback control systems.

Solution of the combined behavior is obtained using Laplace transform methods to obtain the output responses in the time or the complex frequency domain. These mathematical methods might not be familiar to the reader, but this is not a serious difficulty, for the cases most encountered in practice are well documented in terms that are easily comprehended, the mathematical process having been performed to yield results that can be used without the same level of mathematical ability. More depth of explanation can be obtained from Ref. [1] or any one of the many texts on energy systems analysis. Space here only allows an introduction; this account is linked to Ref. [1] of Sydenham, Chapter 17, to allow the reader to access a fuller description where needed.

The next step in understanding block behavior is to investigate the nature of Equation 4.6 as the number of derivative terms in the expression increases (Equations 4.7 through 4.10):

$$\text{Zero order} \quad a_0 y = x(t) \tag{4.7}$$

$$\text{First order} \quad \frac{a_1 dy}{dt} + a_0 y = x(t) \tag{4.8}$$

$$\text{Second order} \quad \frac{a_2 d^2 y}{dt^2} + \frac{a_1 dy}{dt} + a_0 y = x(t) \tag{4.9}$$

$$n\text{th order} \quad \frac{a_n d^n y}{dt^n} + \frac{a_{n-1}\, d^{n-1} y}{dt^{n-1}} + \cdots + a_0 y = x(t) \tag{4.10}$$

Note that specific names have been given to each order. The zero-order situation is not usually dealt with in texts because it has no time-dependent term and is thus seen to be trivial. It is an amplifier (or attenuator) of the forcing function with gain of a_0. It has infinite bandwidth without change in the amplification constant.

The highest order usually necessary to consider in first-cut instrument analysis is the second-order class. Higher-order systems do occur in practice and need analysis that is not easily summarized here. They also need deep expertise in their study. Computer-aided tools for systems analysis can be used to study the responses of systems.

Another step is now to rewrite the equations after Laplace transformation into the frequency domain. We then get the set of output/input (Equations 4.11 through 4.14):

$$\text{Zero order} \quad \frac{Y(s)}{X(s)} = 1 \tag{4.11}$$

$$\text{First order} \quad \frac{Y(s)}{X(s)} = \frac{1}{(\tau s + 1)} \tag{4.12}$$

$$\text{Second order} \quad \frac{Y(s)}{X(s)} = \frac{1}{(\tau_1 s + 1)(\tau_2 s + 1)} \tag{4.13}$$

$$n\text{th order} \quad \frac{Y(s)}{X(s)} = \frac{1}{(\tau_1 s + 1)(\tau_2 s + 2)\ldots(\tau_n s + 1)} \tag{4.14}$$

The terms $\tau_1, \ldots, \tau_n$ are called *time constants*. They are key system performance parameters.

4.2.4 Response of the Different Linear Systems Types

Space restrictions do not allow a detailed study of all of the various options. A selection is presented to show how they are analyzed and reported, leading to how the instrumentation person can use certain standard charts in the study of the characteristics of blocks.

4.2.5 Zero-Order Blocks

To investigate the response of a block, multiply its frequency domain forms of equation for the characteristic equation with that of the chosen forcing function equation.

This is an interesting case because Equation 4.7 shows that the zero-order block has no frequency-dependent term (it has no time derivative term), so the output for all given inputs can only be of the same time form as the input. What can be changed is the amplitude given as the coefficient a_0. A shift in time (phase shift) of the output waveform with the input also does not occur as it can for the higher-order blocks.

This is the response often desired in instruments because it means that the block does not alter the time response. However, this is not always so because, in systems, design blocks are often chosen for their ability to change the time shape of signals in a known manner.

Although somewhat obvious (Figure 4.13), a resistive strain gage is given to illustrate zero-order behavior.

4.2.6 First-Order Blocks

Here, Equation 4.8 is the relevant characteristic equation. There is a time-dependent term, so analysis is needed to see how this type of block behaves under dynamic conditions. The output response is different for each type of forcing function applied. Space limitations only allow the most commonly encountered cases—the step and the sine-wave input—to be introduced here. It is also only possible here to outline the method of analysis and to give the standardized charts that plot generalized behavior.

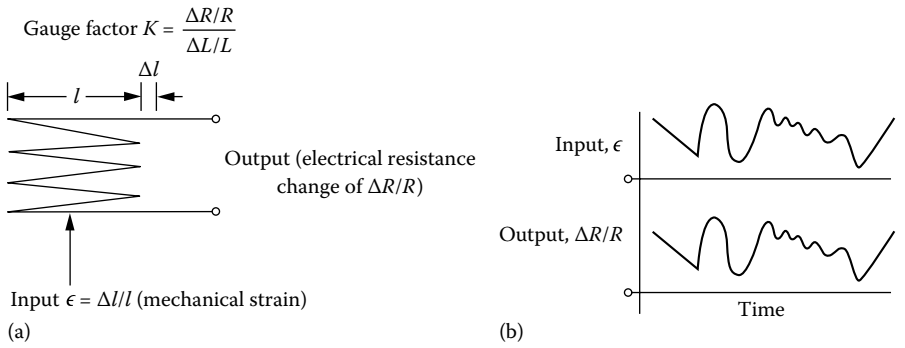

FIGURE 4.13 Input and output responses for a zero-order block: (a) strain gage physical and mathematical model and (b) responses. (Sydenham, P.H.: *Handbook of Measurement Science, Vol. 2*. 1983. Copyright Wiley-VCH Verlag GmbH & Co. KGaA. Reproduced with permission.)

The step response of the first-order system is obtained by multiplying Equation 4.12 by the frequency domain equation for a step of amplitude A. The result is then transformed back into the time domain using Laplace transforms to yield the expression for the output, $y(t)$:

$$y(t) = AK(1 - e^{t/\tau}) \tag{4.15}$$

where

A is the amplitude of the step
K is the static gain of the first-order block
t is the time in consistent units
τ is the time constant associated with the block itself

This is a tidy outcome because Equation 4.15 covers the step response for all first-order blocks, thus allowing it to be graphed in normalized manner, as given in Figure 4.14. The shape of the response is

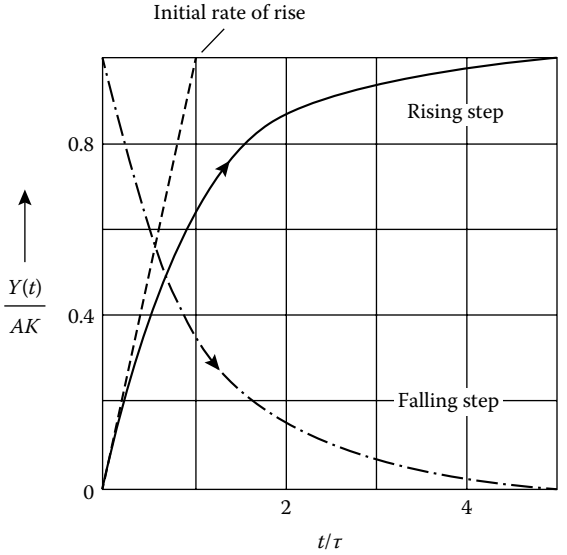

FIGURE 4.14 The step response for all first-order systems is covered by these two normalized graphs. (Sydenham, P.H.: *Handbook of Measurement Science, Vol. 2*. 1983. Copyright Wiley-VCH Verlag GmbH & Co. KGaA. Reproduced with permission.)

always of the same form. This means that the step response of a first-order system can be described as having "a step of AK amplitude with the time constant τ."

If the input is a sine wave, the output response is quite different, but again, it will be found that there is a general solution for all situations of this kind. As before, the input forcing equation is multiplied by the characteristic equation for the first-order block and Laplace transformation is used to get back to the time-domain response. After rearrangement into two parts, this yields

$$y(t) = \left[\frac{AK\tau\omega e^{-t/\tau}}{(\tau^2\omega^2 + 1)}\right] + \left[\frac{AK}{(\tau^2\omega^2 + 1)^{1/2} \cdot \sin(\omega t + \phi)}\right] \tag{4.16}$$

where

ω is the signal frequency in angular radians, $\phi = \tan^{-1}(-\omega t)$
A is the amplitude of the sine-wave input
K is the gain of the first-order block
t is the time in consistent units
τ is the time constant associated with the block

The left side of the right-hand bracketed part is a short-lived, normally ignored, time transient that rapidly decays to zero, leaving a steady-state output that is the parameter of usual interest. Study of the steady-state part is best done by plotting it in a normalized way, as has been done in Figure 4.15.

These plots show that the amplitude of the output is always reduced as the frequency of the input signal rises and that there is always a phase lag action between the input and the output that can range from 0° to 90° but never can be more than 90°. The extent of these effects depends on the particular coefficients of the block and input signal. These effects must be well understood when interpreting measurement results because substantial errors can arise with using first-order systems in an instrument chain.

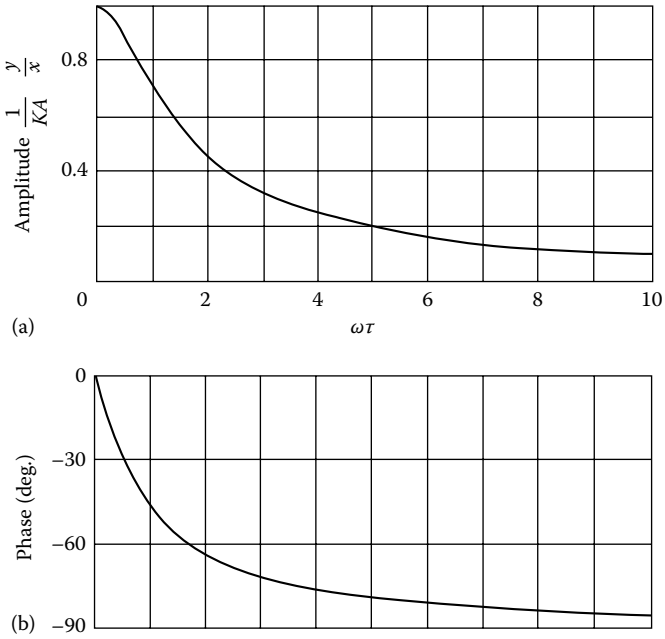

FIGURE 4.15 The amplitude and phase shift of the output of all first-order systems to a sine-wave input is shown by these two normalized curves: (a) amplitude and (b) phase. (Sydenham, P.H.: *Handbook of Measurement Science, Vol. 2*. 1983. Copyright Wiley-VCH Verlag GmbH & Co. KGaA. Reproduced with permission.)

4.2.7 Second-Order Blocks

If the second-order differential term is present, the response of a block is quite different, again responding in quite a spectacular manner with features that can either be wanted or unwanted.

As before, to obtain the output response, the block's characteristic function is multiplied by the chosen forcing function. However, to make the results more meaningful, we first carry out some simple substitution transformations.

The steps begin by transforming the second-order differential Equation 4.6 into its Laplace form to obtain

$$X(s) = a_2 s^2 Y(s) + a_1 s Y(s) + a_0 Y(s) \tag{4.17}$$

This is then rearranged to yield

$$G(s) = \frac{Y(s)}{X(s)} = \frac{1}{a_0} \cdot \frac{1}{\left\{(a_2/a_0)s^2 + (a_1/a_0)s + 1\right\}} \tag{4.18}$$

The coefficients can then be expressed in system performance terms as follows:

$$\text{Angular natural frequency} \quad \omega_n = \left(\frac{a_0}{a_2}\right)^{1/2} \tag{4.19}$$

$$\text{Damping ratio} \quad \zeta = \frac{a_1}{2(a_0 \cdot a_2)^{1/2}} \tag{4.20}$$

$$\text{Static gain} \quad K = \frac{1}{a_0} \tag{4.21}$$

These three variables have practical relevance, as will be seen when the various responses are plotted.

Using these transformed variables, the characteristic equation can be rewritten in two forms ready for investigation of output behavior to step and sine-wave inputs, as

$$G(s) = \frac{K}{\left\{(1/\omega_n^2)s^2 + (2\zeta/\omega_n)s + 1\right\}} \tag{4.22}$$

and then as

$$G(s) = \frac{K}{(\tau^2 s^2 + 2\zeta\tau s + 1)} \tag{4.23}$$

We are now ready to consider the behavior of the second-order system to the various forcing inputs.

First consider the step input. After forming the product of the forcing and characteristic functions, the time-domain form can be plotted as shown in Figure 4.16.

This clearly shows that the response is strongly dependent on the damping ratio ζ, value. If it is less than unity, it exhibits an oscillatory movement settling down to the final value. If the damping value is greater than unity, the response moves to the final value without oscillation. The often preferred state is to use a damping factor of unity, *critical damping*. The choice of response depends strongly on the applications, for all levels of damping ratio have use in practice, ranging from needing an oscillation that never ceases (zero damping) to the other extreme where a very gradual rate of change is desired.

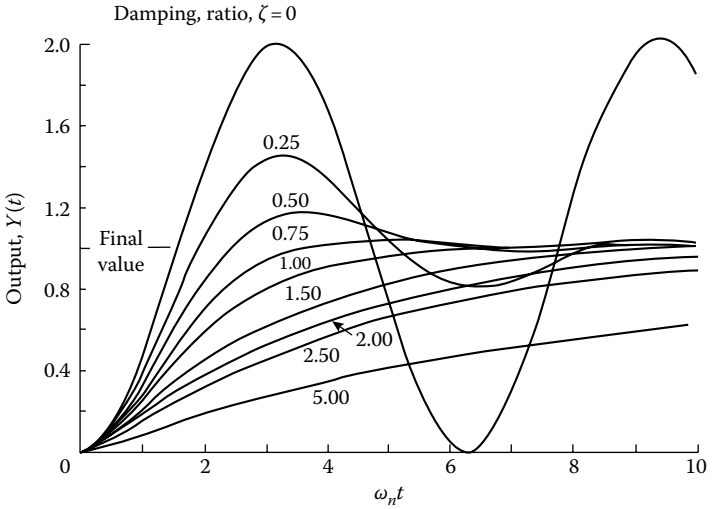

FIGURE 4.16 The response of second-order systems to a step input is seen from this normalized plot. (Sydenham, P.H.: *Handbook of Measurement Science, Vol. 2*. 1983. Copyright Wiley-VCH Verlag GmbH & Co. KGaA. Reproduced with permission.)

A similar analysis is used to see how the second-order system responds to the sine-wave input. The two response plots obtained are shown in Figure 4.17: one for the amplitude response and the other showing how the phase shifts as the frequency changes.

The most unexpected result is seen at the point where the gain rises to infinity for the zero damping state. This is called *resonance* and it occurs at the block's *natural frequency* for the zero damping state. Resonance can be a desirable feature, as in detecting a particular frequency in a radio-frequency detection circuit, or it may be most undesirable, as when a mechanical system resonates, possibly to destruction. It can be seen that it is mostly controlled by the damping ratio. Note also that the phase shift for the second-order system ranges from 0° to 180°. This has important implications if the block is part of a feedback loop because as the frequency rises, the phase shift from the block will pass from stable negative feedback (less than 90°) to positive feedback (greater than 90°), causing unwanted oscillation.

More detail of the various other situations, including how to deal with higher orders, cascaded blocks of similar kind, and ramp inputs are covered elsewhere [1].

4.3 Calibration of Measurements

We have already introduced the concept of accuracy in making a measurement and how the uncertainty inherent in all measurements must be kept sufficiently small. The process and apparatus used to find out if a measurement is accurate enough is called *calibration*. It is achieved by comparing the result of a measurement with a method possessing a measurement performance that is generally agreed to have less uncertainty than that in the result obtained. The error arising within the calibration apparatus and process of comparison must necessarily be less than that required. This means that calibration is often an expensive process. Conducting a good calibration requires specialist expertise.

The method and apparatus for performing measurement instrumentation calibrations vary widely. An illustrative example of the comparison concept underlying them all is given in the calibration of flowmeters, shown diagrammatically in Figure 4.18.

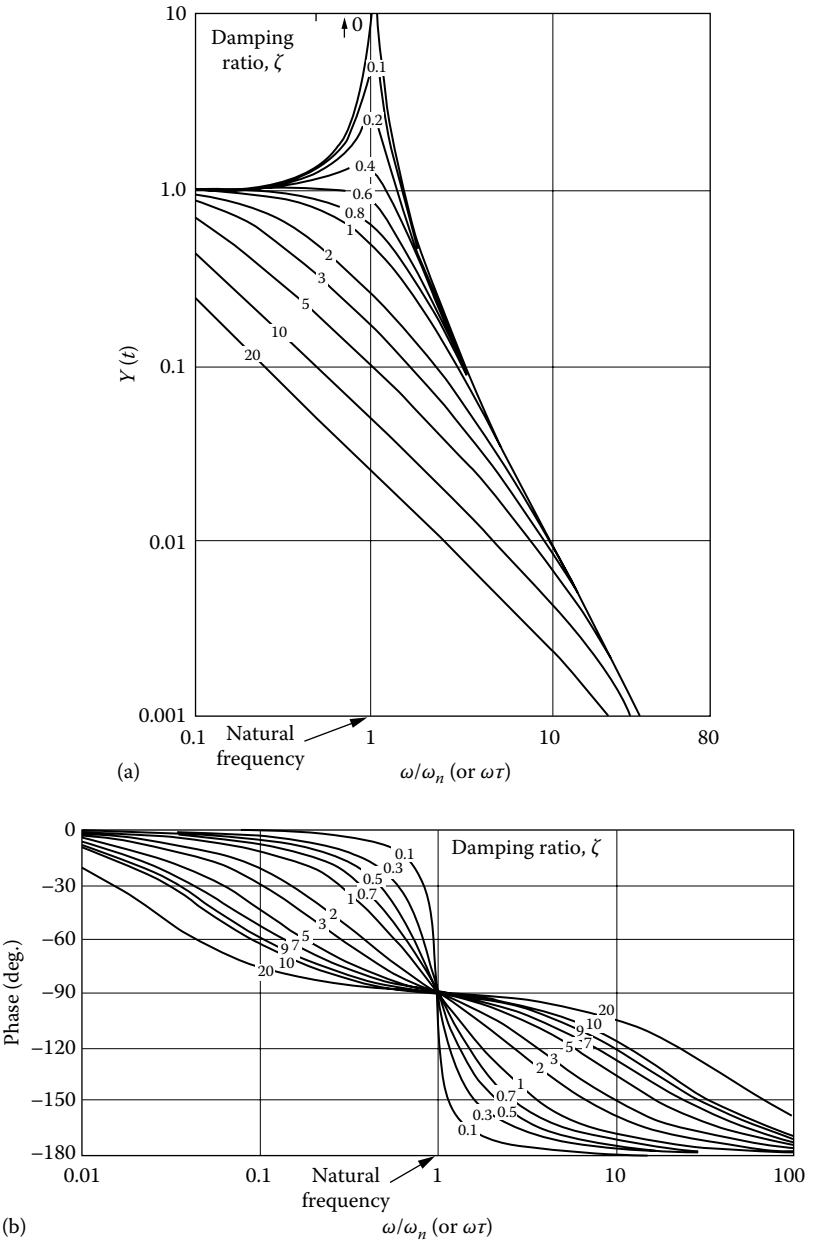

FIGURE 4.17 These two plots allow the behavior of second-order blocks with sine-wave inputs to be ascertained: (a) amplitude and (b) phase. (Sydenham, P.H.: *Handbook of Measurement Science, Vol. 2*. 1983. Copyright Wiley-VCH Verlag GmbH & Co. KGaA. Reproduced with permission.)

By the use of an overflowing vessel, the top tank provides a flow of water that remains constant because it comes from a constant height. The meter to be calibrated is placed in the downstream pipe.

The downstream is either deflected into the weigh tank or back to the supply. To make a measurement, the water is first set to flow to the supply. At the start of a test period, the water is rapidly and precisely deflected into the tank. After a given period, the water is again sent back to the supply.

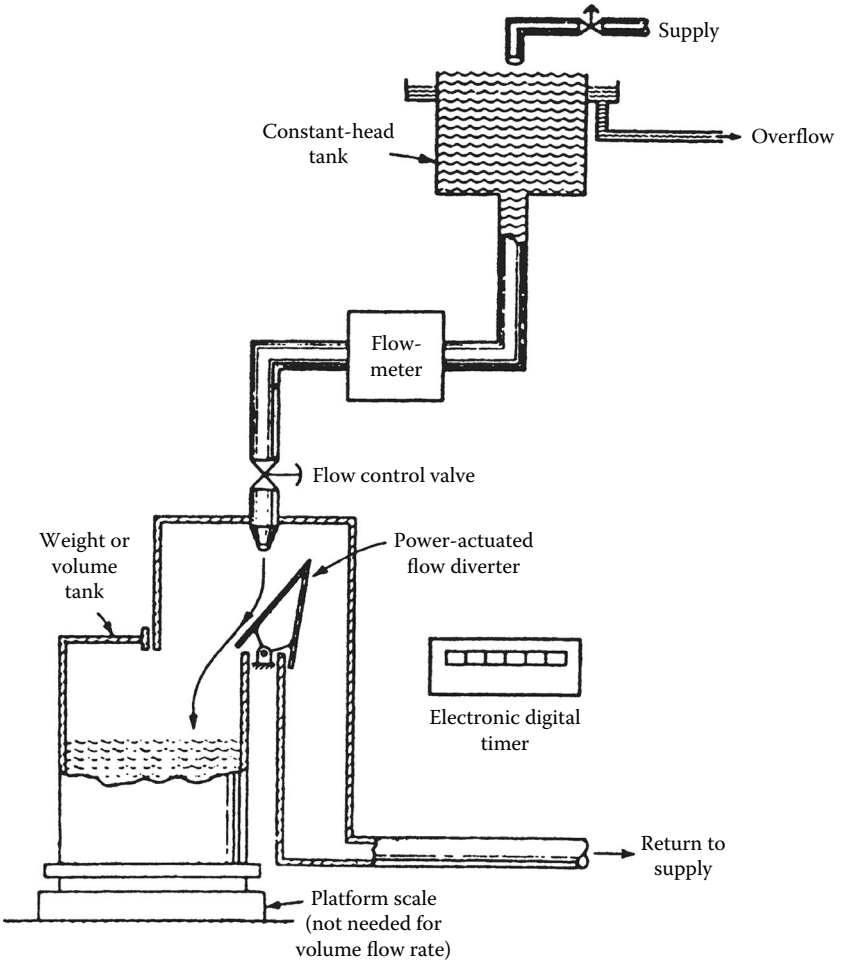

FIGURE 4.18 This practical example illustrates how flowmeters are calibrated by passing a known quantity of fluid through the meter over a given time. (From Sydenham, P. H., *Transducers in Measurement and Control*, Adam Hilger, Bristol, U.K., IOP Publishing, 1980.)

This then has filled the tank with a given amount of water for a given time period of flow. Calculations are then undertaken to work out the quantity of water flowing per unit time period, which is the *flow rate*. The meter was already registering a flow rate as a constant value. This is then compared with the weighed method to yield the error. Some thought will soon reveal many sources of error in the test apparatus, such as that the temperature of the water decides the volume that flows through, and thus this must be allowed for in the calculations.

It will also be clear that this calibration may not be carried out under the same conditions as the measurements are normally used. The art and science and difficulties inherent in carrying out quality calibration for temperature sensors are well exposed [2].

Calibration of instrumentation is a must, for, without it, measurement results may be misleading and lead to costly aftermath situations. Conducting good calibration adds overhead cost to measurement, but it is akin to taking out insurance. If that investment is made properly, it will assist in mitigating later penalties. For example, an incorrectly calibrated automatic cement batcher was used in making concrete for the structural frame of a multistory building. It took several days before concrete strength tests revealed the batcher had been out of calibration for a day with the result that the concrete already

poured for three floors was not of adequate strength. By then, more stories had been poured on top. The defective floors had to be fully replaced at great cost. More resource put into the calibration process would have ensured that the batcher was working properly.

4.3.1 Self-Calibrations

Due to advances in digital systems, most modern instruments have the self-calibrating capabilities. In self-calibrations, postmeasurement corrections are made, and the magnitudes of various errors are stored in the memory to be recalled and used in laboratory and in field applications. Further information on calibrations of instruments can be found in Chapter 8 and Refs. [4–6].

References

1. P. H. Sydenham, *Handbook of Measurement Science*, Vol. 2, Chichester, U.K.: John Wiley & Sons, 1983.
2. J. V. Nicholas and D. R. White, *Traceable Temperatures*, Chichester, U.K.: John Wiley & Sons, 1994.
3. British Standard Institution, *PD 6461: Vocabulary of Metrology*, London, U.K.: BSI, 1995.
4. S. V. Gupta, *Measurement Uncertainties: Physical Parameters and Calibration Instruments*, Berlin, Germany: Springer-Verlag, 2012.
5. Fluke, Calibration and Repair Services, http://www.fluke.com/fluke/usen/service/calibration/default.htm (accessed on March 13, 2013).
6. NIST, Calibrations, http://www.nist.gov/calibrations/ (accessed on March 13, 2013).
7. P. H. Sydenham, *Transducers in Measurement and Control*, Adam Hilger, Bristol, U.K., IOP Publishing, 1980.

5

Measurement Accuracy

Ronald H. Dieck
Ron Dieck Associates, Inc.
Pratt & Whitney

All test measurements are taken so that data that are useful in decision making may be acquired. No tests are run and no measurements made when the "answer" is already known. For data to be useful, it is necessary that their measurement errors be small in comparison to the changes or effect under evaluation. Measurement error is unknown and unknowable. This chapter addresses the techniques used to estimate, with some confidence, the expected limits of the measurement errors.

5.1 Error: The Normal Distribution and the Uniform Distribution

Error is defined as the difference between the measured value and the true value of the measurand [1]. That is,

$$E = (\text{measured}) - (\text{true}) \tag{5.1}$$

where

E is the measurement error
(measured) is the value obtained by a measurement
(true) is the true value of the measurand

It is only possible to estimate, with some confidence, the expected limits of error. The most common method for estimating those limits is to use the *normal distribution* [2]. It is

$$Y = \frac{1}{\sigma\sqrt{2\pi}} e^{-1/2(X-\mu)^2/\sigma^2} \tag{5.2}$$

where

X is the input variable, here the value obtained by a measurement
μ is the average of the population of the X variable
σ is the standard deviation of the population

expressed as

$$\sigma = \sqrt{\frac{\sum_{i=1}^{n} (X_i - \mu)^2}{N}} \tag{5.3}$$

where

X_i is the ith X measurement
N is the number of data points measured from the population

Typically, N, μ, and σ are not known.

Figure 5.1 illustrates this distribution. Here, for an infinite population ($N = \infty$), the standard deviation, σ, would be used to estimate the expected limits of a particular error with some confidence. That is, the average, plus or minus 2σ divided by the square root of the number of data points, would contain the true average, μ, 95% of the time.

However, in test measurements, one typically cannot sample the entire population and must make do with a sample of N data points. The sample standard deviation, S_X, is then used to estimate σ_X, the expected limits of a particular error. (That sample standard deviation divided by the square root of the number of data points is the starting point for the confidence interval estimate on μ.) For a large dataset (defined as having 30 or more degrees of freedom), plus or minus $2S_X$ divided by the square root of the number of data points in the reported average, M, would contain the true average, μ, 95% of the time. That S_X divided by the square root of the number of data points in the reported average is called the standard deviation of the average and is written as

$$S_{\bar{X}} = \frac{\sqrt{\sum_{i=1}^{N} (X_i - \bar{X})^2 \Big/ N-1}}{\sqrt{M}} = S_X / \sqrt{M} \tag{5.4}$$

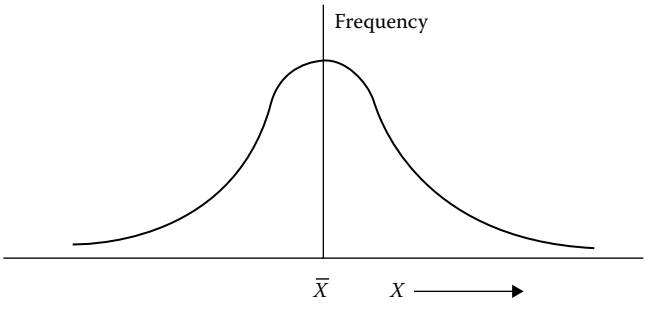

FIGURE 5.1 Normal distribution curve.

where

$S_{\bar{X}}$ is the standard deviation of the average, the sample standard deviation of the data divided by the square root of M

S_X is the sample standard deviation

$\bar{X}$ is the sample average, that is,

$$\bar{X} = \sum_{i=1}^{N}\left(\frac{X_i}{N}\right) \tag{5.5}$$

where

X_i is the ith data point used to calculate the sample standard deviation and the average, $\bar{X}$, from the data

N is the number of data points used to calculate the standard deviation

$(N - 1)$ is the degrees of freedom of S_X and $S_{\bar{X}}$

M is the number of data points in the reported average test result

Note in Equation 5.4 that N does not necessarily equal M. It is possible to obtain S_X from historical data with many degrees of freedom ([$N - 1$] greater than 30) and to run the test only M times. The test result, or average, would therefore be based on M measurements, and the standard deviation of the average would still be calculated with Equation 5.4.

Note that the sample standard deviation, S_X, is simply

$$S_X = \sqrt{\frac{\sum_{i=1}^{N}(X_i - \bar{X})^2}{N-1}} \tag{5.6}$$

In some cases, a particular error distribution may be assumed or known to be *a uniform or rectangular distribution* (Figure 5.2) instead of a normal distribution. For those cases, the sample standard deviation of the data is calculated as

$$S_X = \frac{L}{\sqrt{3}} \tag{5.7}$$

where L is the plus/minus limits of the uniform distribution for a particular error [3].

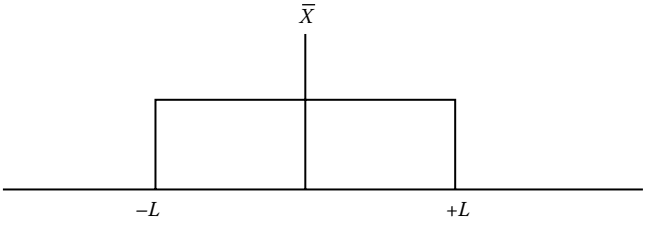

FIGURE 5.2 Uniform distribution curve.

For those cases, the standard deviation of the average is written as

$$S_{\bar{X}} = \frac{L/\sqrt{3}}{\sqrt{M}} \tag{5.8}$$

Although the calculation of the sample standard deviation (or its estimation by some other process) is required for measurement uncertainty analysis, all the analytical work computing the measurement uncertainty uses only the standard deviation of the average for each error source.

5.1.1 Uncertainty (Accuracy)

Since the error for any particular error source is unknown and unknowable, its limits, at a given confidence, must be estimated. This estimate is called the *uncertainty*. Sometimes, the term accuracy is used to describe the quality of test data. This is the positive statement of the expected limits of the data's errors. Uncertainty is the negative statement. Uncertainty is, however, unambiguous. Accuracy is sometimes ambiguous. (For example, what is twice the accuracy of ±2%? ±1% or ±4%?) For this reason, this chapter will use the term *uncertainty* throughout to describe the quality of test data.

5.2 Measurement Uncertainty Model

5.2.1 Purpose

One needs an estimate of the uncertainty of test results to make informed decisions. Ideally, the uncertainty of a well-run experiment will be much less than the change or test result expected. In this way, it will be known, with high confidence, that the change or result observed is real or acceptable and not a result of the errors of the test or measurement process. The limits of those errors are estimated with uncertainty, and those error sources and their limit estimators, the uncertainties, may be grouped into classifications to ease their understanding.

5.2.2 Classifying Error and Uncertainty Sources

There are two classification systems in use. The final expanded uncertainty calculated at a confidence is identical no matter what classification system is used. The two classifications utilized are the *ISO classifications* (International Standards Organization) and the *engineering classifications*. The former groups errors and their uncertainties by type, depending evidently on whether or not there are data available to calculate the sample standard deviation for a particular error and its uncertainty. The latter classification groups errors and their uncertainties by their effect on the experiment or test. That is, the engineering classification groups errors and uncertainties by random and systematic types, with subscripts used to denote whether there are data to calculate a standard deviation or not for a particular error or uncertainty source. For this reason, engineering classification groups usually are comprehensive and therefore more useful and recommended.

5.2.3 ISO Classifications

This error and uncertainty classification system is not recommended in this chapter, but will yield an expanded uncertainty in complete agreement with the recommended classification system—the engineering classification system. In this ISO system, errors and uncertainties are classified as type *A* if there are data available to calculate a sample standard deviation and type *B* if there are not [4]. In the latter case, the sample standard deviation might be obtained from engineering estimates, experience, or manufacturer's specifications, to name three possibilities.

The impact of multiple sources of error is estimated by root-sum-squaring their corresponding elemental uncertainties. The operating equations are as follows.

For Type *A*, data are available for the calculation of the standard deviation:

$$U_A = \left[\sum_{i=1}^{N_A} \left(\theta_i u_{A_i} \right)^2 \right]^{1/2} \tag{5.9}$$

where

u_{A_i} is the standard deviation (based on data) of the average for uncertainty source i of type A each with its own degrees of freedom

U_A is in units of the test or measurement result. It is an $S_{\bar{X}}$

N_A is the number of parameters with a type A uncertainty

θ_i is the sensitivity of the test or measurement result, R, to the ith type A uncertainty. θ_i is the partial derivative of the result with respect to each i^{th} independent measurement

The uncertainty of each error source in units of that source, when multiplied by the sensitivity for that source, converts that uncertainty to result units. Then the effect of several error sources may be estimated by root-sum-squaring their uncertainties as they are now all in the same units. The sensitivities, θ_i, are obtained for a measurement result, R, which is a function of several parameters, P_i. The basic equations are

$$R = f(P_1, P_2, P_3, \ldots P_N) \tag{5.10}$$

where

R is the measurement result

P_i is the measurement parameter i used to calculate the result, R

The sensitivity, θ_i, also called error propagation or uncertainty propagation is found by differentiation as $\partial R/\partial P_i$.

Type *B* (no data for standard deviation) calculation

$$U_B = \left[\sum_{i=1}^{N_B} \left(\theta_i u_{B_i} \right)^2 \right]^{1/2} \tag{5.11}$$

where

u_{B_i} is the standard deviation of the average (based on an estimate, not data) for uncertainty source i of type B

U_B is in units of the test or measurement result, R. It is an $S_{\bar{X}}$

N_B is the number of parameters with a type B uncertainty

θ_i is the sensitivity of the test or measurement result, R, to the i^{th} Type B uncertainty

θ_i is the $\partial R/\partial P_i$

For these uncertainties, it is assumed that the u_{B_i} represent one standard deviation of the average for one uncertainty source with an assumed normal distribution. (They also represent one standard deviation as the square root of the "M" by which they are divided is one, that is, there is only one Type B error sampled from each of these distributions.) The degrees of freedom assumed to apply to this standard deviation (also standard deviation of the average) are assumed to be infinity [5] in the absence of other information.

Note that θ_i, the sensitivity of the test or measurement result to the i^{th} Type *B* uncertainty, is actually the change in the result, *R*, that would result from a change, of the size of the Type *B* uncertainty, in the i^{th} input parameter used to calculate that result.

The degrees of freedom of the u_{A_i} and the u_{B_i} are needed to compute the degrees of freedom of the combined total uncertainty. It is calculated with the Welch–Satterthwaite approximation. The general formula for degrees of freedom [6] is

$$df_R = \nu_R = \frac{\left[\sum_{i=1}^{N}\left(S_{\bar{X}_i}\right)^2\right]^2}{\left[\sum_{i=1}^{N}\left(S_{\bar{X}_i}\right)^4 \Big/ (\nu_i)\right]} \tag{5.12a}$$

where

$df_R = \nu_R$ are the degrees of freedom for the result

ν_i is the degrees of freedom of the i^{th} standard deviation of the average

For the ISO model, Equation 5.11 becomes

$$df_{R,\mathrm{ISO}} = \nu_{R,\mathrm{ISO}} = \frac{\left[\sum_{i=1}^{N_A}(\theta_i u_{A,i})^2 + \sum_{i=1}^{N_B}\left(\theta_i u_{B,i}\right)^2\right]^2}{\left[\sum_{i=1}^{N}\left(\theta_i u_{A,i}\right)^4 \Big/ \nu_i + \sum_{i=1}^{M}\left(\theta_i u_{B,i}\right)^4 \Big/ \nu_i\right]} \tag{5.12b}$$

The degrees of freedom calculated with Equation 5.12 are often a fraction. This may be truncated to the next lower whole number to be conservative [5].

Note that in Equations 5.9, 5.10, and 5.12, N_A and N_B need not be equal. They are only the total number of parameters with uncertainty sources of Types *A* and *B*, respectively.

In computing a total uncertainty, the uncertainties noted by Equations 5.10 and 5.11 are combined. For the ISO model [3], this is calculated as

$$U_{\mathrm{total,ISO}} = \pm\left[(U_A)^2 + (U_B)^2\right]^{1/2} \tag{5.13a}$$

Then the expanded 95% confidence uncertainty is obtained with Equation 5.13b:

$$U_{R,\mathrm{ISO}} = \pm t_{95}\left[(U_A)^2 + (U_B)^2\right]^{1/2} \tag{5.13b}$$

where

t_{95} is the Student's *t* for ν_r, 150 degrees of freedom

Student's *t* is obtained from Table 5.1

Note that alternative confidences are permissible. Ninety-five percent is recommended by the ASME [1], but 99% or 99.7% or any other confidence is obtained by choosing the appropriate Student's *t*. Ninety-five percent confidence is, however, recommended for uncertainty analysis.

In all the aforementioned, the errors were assumed to be independent. Independent sources of error are those that have no relationship to each other. That is, an error in a measurement from one source

TABLE 5.1 Student's *t* Statistic for 95% Confidence, t_{95}, Degrees of Freedom, ν

ν	t_{95}	ν	t_{95}	ν	t_{95}
1	12.706	11	2.201	21	2.080
2	4.303	12	2.179	22	2.074
3	3.182	13	2.160	23	2.069
4	2.776	14	2.145	24	2.064
5	2.571	15	2.131	25	2.060
6	2.447	16	2.120	26	2.056
7	2.365	17	2.110	27	2.052
8	2.306	18	2.101	28	2.048
9	2.262	19	2.093	29	2.045
10	2.228	20	2.086	≥30	2.000

Note: This is frequently written as $t_{95,\nu}$.

cannot be used to predict the magnitude or direction of an error from the other, independent, error source. Nonindependent error sources are related. That is, if it were possible to know the error in a measurement from one source, one could calculate or predict an error magnitude and direction from the other, nonindependent error source. These are sometimes called *dependent error sources*. Their degree of dependence may be estimated with the linear correlation coefficient. If they are nonindependent, whether Type *A* or Type *B*, Equation 5.13 becomes [7]

$$U_{R,\mathrm{ISO}} = \pm\, t_{95}\left\{\sum_{T=A}^{B}\sum_{i=1}^{N_{i,T}}\left[(\theta_i u_{i,T})^2 + \sum_{j=1}^{N_{j,T}}\theta_i\theta_j u_{(i,T),(j,T)}(1-\delta_{i,j})\right]\right\}^{1/2} \tag{5.14}$$

where

$u_{i,T}$ is the i^{th} elemental uncertainty of Type T (can be Type A or B)
$U_{R,\mathrm{ISO}}$ is the total uncertainty of the measurement or test result
θ_i is the sensitivity of the test or measurement result to the i^{th} Type T uncertainty
θ_j is the sensitivity of the test or measurement result to the j^{th} Type T uncertainty
$u_{(i,T),(j,T)}$ is the covariance of $u_{i,T}$ on $u_{j,T}$
$\delta_{i,j}$ is the Kronecker delta. $\delta_{i,j} = 1$ if $i = j$, and $\delta_{i,j} = 0$ if not [7]

$$u_{(i,T)(j,T)} = \sum_{l=1}^{K} u_{i,T}(l)u_{j,T}(l) \tag{5.15}$$

where

l is the index or counter for common uncertainty sources
K is the number of common source pairs of uncertainties
T is the index or counter for the ISO uncertainty Type, A or B
$N_{i,T}$ is the number of error sources for Types A and B

Equation 5.15 equals the sum of the products of the elemental systematic standard uncertainties that arise from a common source (l).

This ISO classification equation will yield the same expanded uncertainty as the engineering classification, but the with ISO classification it is more difficult to gain insight into how to improve an experiment's or test's uncertainty. That is, whether to possibly take more data because the random standard uncertainties are too high or calibrate better because the systematic standard uncertainties are too large. The engineering classification now presented is therefore the preferred approach.

5.2.4 Engineering Classifications

The engineering classification recognizes that experiments and tests have two major types of errors that affect results and whose limits are estimated with uncertainties at some chosen confidence. These error types may be grouped as random and systematic. Their corresponding limit estimators are the random standard uncertainty and systematic standard uncertainties, respectively.

5.2.5 Random

The general expression for random standard uncertainty is the ($1S_{\bar{X}}$) standard deviation of the average [6]:

$$S_{\bar{X},R} = \left[\sum_{T=A}^{B}\sum_{i=1}^{N_{i,T}}\left(\theta_i S_{\bar{X}_{i,T}}\right)^2\right]^{1/2} = \left[\sum_{T=A}^{B}\sum_{i=1}^{N_{i,T}}\left(\frac{\theta_i S_{X_{i,T}}}{\sqrt{M_{i,T}}}\right)^2\right]^{1/2} \tag{5.16}$$

where

$S_{X_{i,T}}$ is the sample standard deviation of the i^{th} random error source of Type T
$S_{\bar{X}_{i,T}}$ is the random standard uncertainty (standard deviation of the average) of the ith parameter random error source of Type T
$S_{\bar{X},R}$ is the random standard uncertainty of the measurement or test result
$N_{i,T}$ is the total number of random standard uncertainties, Types A and B, combined
$M_{i,T}$ is the number of data points averaged for the i^{th} error source, Type A or B
θ_i is the sensitivity of the test or measurement result to the ith random standard uncertainty

Note that $S_{\bar{X},R}$ is in units of the test or measurement result because of the use of the sensitivities, θ_i. Here, the elemental random standard uncertainties have been root-sum-squared with due consideration for their sensitivities or influence coefficients. Since these are all random standard uncertainties, there is, by definition, no correlation in their corresponding error data, so these can always be treated as independent uncertainty sources.

(Note that the term "standard" is inserted to provide harmony with ISO terminology and to indicate that the uncertainties are standard deviations of the average.)

5.2.6 Systematic

The systematic standard uncertainty of the result, b_R, is the root sum square (RSS) of the elemental systematic standard uncertainties with due consideration for those that are correlated [5]. The general equation is

$$b_R = \left\{\sum_{T=A}^{B}\sum_{i=1}^{N_T}\left[(\theta_i b_{i,T})^2 + \sum_{j=1}^{N_T}\theta_i\theta_j b_{(i,T),(j,T)}(1-\delta_{i,j})\right]\right\}^{1/2} \tag{5.17}$$

where

$b_{i,T}$ is the i^{th} parameter elemental systematic standard uncertainty of Type T
b_R is the systematic standard uncertainty of the measurement or test result
N_T is the total number of systematic standard uncertainties
θ_i is the sensitivity of the test or measurement result to the i^{th} systematic standard uncertainty
θ_j is the sensitivity of the test or measurement result to the j^{th} systematic standard uncertainty
$b_{(i,T),(j,T)}$ is the covariance of $b_{i,T}$ on $b_{j,T}$
$\delta_{i,j}$ is the Kronecker delta. $\delta_{i,j} = 1$ if $i = j$, and $\delta_{i,j} = 0$ if not [5]

$$= \sum_{l=1}^{M} b_{i,T}(l) b_{j,T}(l) \tag{5.18}$$

where

l is the index or counter for common uncertainty sources
T is the index or counter for the ISO uncertainty type, A or B

Equation 5.18 equals the sum of the products of the elemental systematic standard uncertainties that arise from a common source (l).

Here, each $b_{i,T}$ and $b_{j,T}$ is estimated as $1S_{\bar{X}}$ for an assumed normal distribution of errors with infinite degrees of freedom [5].

The random standard uncertainty, Equation 5.16, and the systematic standard uncertainty, Equation 5.17, must be combined to obtain a total uncertainty, Equation 5.19a:

$$U_{\text{total,ENG}} = \pm\left[(b_R)^2 + (S_{\bar{X},R})^2\right]^{1/2} \tag{5.19a}$$

Then the expanded 95% confidence uncertainty may be calculated with Equation 5.19b:

$$U_{\text{R,ENG}} = \pm t_{95}\left[(b_R)^2 + (S_{\bar{X},R})^2\right]^{1/2} \tag{5.19b}$$

Note that b_R in units of the test or measurement result is an $S_{\bar{X},R}$.

The degrees of freedom will be needed for the engineering system total and expanded uncertainties. It is accomplished with the Welch–Satterthwaite approximation, the general form of which is Equation 5.10, and the specific formulation here is

$$df_R = \nu_R = \frac{\left\{\sum_{T-A}^{B}\left[\sum_{i=1}^{N}(\theta_i S_{\bar{X},T,i})^2 + \sum_{i=1}^{M}(\theta_i b_{T,i})^2\right]\right\}^2}{\left\{\sum_{T-A}^{B}\left[\sum_{i=1}^{N}(\theta_i S_{\bar{X},T,i})^4 / \nu_{i,T} + \sum_{i=1}^{M}(\theta_i b_{T,i})^4 / \nu_i\right]\right\}} \tag{5.20}$$

where

N is the number of random standard uncertainties of Type T
M is the number of systematic standard uncertainties of Type T
ν_i is the degree of freedom for the i^{th} uncertainty of Type T
$\nu_{i,T}$ is the degree of freedom for the ith uncertainty of type T and is infinity for all systematic standard uncertainties

5.2.7 Symmetrical Systematic Standard Uncertainties

Most times, all elemental uncertainties will be symmetrical. That is, their ± limits about the measured average will be the same. That is, they will be ±3 °C or ±2.05 kPa and the like and not +2.0 °C and −1.0 °C nor +1.5 kPa and −0.55 kPa. The symmetrical measurement uncertainty may therefore be calculated as follows (For an elegant treatment of nonsymmetrical uncertainties, see that section in Ref. [8]).

Note that throughout these uncertainty calculations, all the uncertainties are expressed in engineering units. All the equations will work with relative units as well. However, it is often easier to express all the uncertainties and the uncertainty estimation calculations in engineering units and then, at the end, with the expanded uncertainty, convert the result into relative terms. That is what this section recommends.

5.3 Calculation of Expanded Uncertainty

5.3.1 ISO Total and Expanded Uncertainty

The ISO expanded uncertainty for independent uncertainty sources (the most common) is Equation 5.13b:

$$U_{R,\mathrm{ISO}} = \pm t_{95}\left[(U_A)^2 + (U_B)^2\right]^{1/2} \tag{5.21}$$

where

$U_{R,\mathrm{ISO}}$ is the measurement uncertainty of the result
U_A is the Type *A* uncertainty for the result
U_B is the Type *B* uncertainty for the result
t_{95} is Student's t_{95} is the recommended multiplier to assure 95% confidence

The ISO uncertainty with some nonindependent uncertainty sources is Equation 5.14:

$$U_{R,\mathrm{ISO}} = \pm t_{95}\left\{\sum_{T=A}^{B}\sum_{i=1}^{N_{i,T}}\left[(\theta_i u_{i,T})^2 + \sum_{j=1}^{N_{j,T}}\theta_i\theta_j u_{(i,T),(j,T)}(1-\delta_{i,j})\right]\right\}^{1/2} \tag{5.22}$$

5.3.2 Engineering System Expanded Uncertainty

The engineering system equation for total uncertainty for independent uncertainty sources (the most common) is Equation 5.19b:

$$U_{R,\mathrm{ENG}} = \pm t_{95}\left[(b_R)^2 + (S_{\bar{X},R})^2\right]^{1/2} \tag{5.23}$$

The engineering system equation for uncertainty for nonindependent uncertainty sources (those with correlated systematic standard uncertainties) is also Equation 5.23 but remember to use the full expression for B_R, Equation 5.17:

$$b_R = \left\{\sum_{T=A}^{B}\sum_{i=1}^{N_T}\left[(\theta_i b_{i,T})^2 + \sum_{j=1}^{N_T}\theta_i\theta_j b_{(i,T),(j,T)}(1-\delta_{i,j})\right]\right\}^{1/2} \tag{5.24}$$

The degrees of freedom for Equations 5.21 through 5.23 are calculated with the Welch–Satterthwaite approximation, Equation 5.12b for the ISO system, and Equation 5.20 for the engineering system.

5.3.3 High Degrees of Freedom Approximation

It is often the case that it is assumed that the degrees of freedom are 30 or higher. In these cases, the equations for uncertainty simplify further by setting t_{95} equal to 2.000. This approach is recommended for a first-time user of uncertainty analysis procedures as it is a fast way to get to an approximation of the measurement uncertainty.

5.3.4 Calculation Example

The following calculation example is taken where all the uncertainties are independent and are in the units of the test result—temperature. It is a simple example that illustrates the combination of measurement uncertainties in their most basic case. More detailed examples are given in many of the references cited. Their review may be needed to assure a more comprehensive understanding of uncertainty analysis.

It has been shown [9] that there is no difference in the uncertainties calculated with the different models. The data from Table 5.2 [10] will be used to calculate measurement uncertainty with the two models. These data are all in temperature units and thus the influence coefficients, or sensitivities, are all unity.

Note the use of subscripts "*A*" and "*B*" to denote where data exist to calculate a standard deviation. Note too that in this example, all errors (and therefore uncertainties) are independent and that all degrees of freedom for the systematic standard uncertainties are infinity except for the reference junction whose degrees of freedom are 12.

Each uncertainty model will now be used to derive a measurement uncertainty.

For the U_{ISO} model, one obtains, via Equations 5.13a and b, the expressions

$$U_A = \left[(0.095)^2 + (0.045)^2 + (0.173)^2 + (0.032)^2\right]^{1/2} = 0.21 \tag{5.25}$$

$$U_B = \left[(0.03)^2 + (0.05)^2\right]^{1/2} = 0.058 \tag{5.26}$$

Thus,

$$U_{R,\text{ISO}} = \pm t_{95}\left[(U_A)^2 + (U_B)^2\right]^{1/2} = \pm t_{95}\left[(0.21)^2 + (0.058)^2\right]^{1/2} \tag{5.27}$$

Here, remember that the 0.21 is the RSS of the $1S_{\bar{x}}$ Type *A* uncertainties in Table 5.2 and 0.058 that for the $1S_{\bar{x}}$ Type *B* uncertainties. Also note that in most cases, the Type *B* uncertainties have infinite degrees of freedom and represent an equivalent $1S_X$.

TABLE 5.2 Temperature Measurement Uncertainties, °F

Defined Measurement Process	Systematic Standard Uncertainty, B_i	*df* for b_i	Standard Deviation, $S_{\bar{X},i}$	Number of Data Points N_i	Random Standard Uncertainty, $S_{\bar{X},i}$	Degrees of Freedom, *df*, ν_i
Calibration of *t*c	0.030_B	∞	0.30_A	10	0.095_A	9
Reference junction	0.032_A	12	0.10_A	5	0.045_A	4
Data acquisition	0.050_B	∞	0.60_A	12	0.173_A	11
RSS						

To obtain Student's t_{95}, the degrees of freedom must first be calculated. All the systematic components of type "*B*" have infinite degrees of freedom except for the 0.032, which has 12 degrees of freedom. Also, all the b_i, in Table 5.1, represents an equivalent $1S_X$. All Type *A* uncertainties, whether systematic or random in Table 5.1, have degrees of freedom as noted in the table. The degrees of freedom for U_{ISO} are then

$$\frac{\left[(0.095)^2+(0.045)^2+(0.173)^2+(0.03)^2+(0.032)^2+(0.05)^2\right]^2}{\left[(0.095)^4/9+(0.045)^4/4+(0.173)^4/11+(0.03)^4/\infty+(0.032)^4/12+(0.05)^4/\infty\right]}=22.51\approx 22 \tag{5.28}$$

t_{95} is, therefore, 2.07. $U_{R,ISO}$, the expanded uncertainty, is determined with Equation 5.13b:

$$U_{R,ISO}=\pm 2.07\left[(0.21)^2+(0.058)^2\right]^{1/2}=0.45 \quad \text{for 95\% confidence} \tag{5.29}$$

For a detailed comparison to the engineering system, here denoted as the $U_{R,ENG}$ model, three significant figures are carried so as not to be affected by round-off errors. Then

$$U_{R,ISO}=\pm 2.074\left[(0.205)^2+(0.0583)^2\right]^{1/2}=0.442 \quad \text{for 95\% confidence} \tag{5.30}$$

For the engineering system, $U_{R,ENG}$, model, one obtains the random standard uncertainty with Equation 5.16:

$$S_{\bar{X},R}=\left[(0.095)^2+(0.045)^2+(0.173)^2\right]^{1/2}=0.20 \tag{5.31}$$

The systematic standard uncertainty is obtained with Equation 5.17 greatly simplified as there is no correlated error or uncertainties in this example. Equation 5.17 then becomes

$$b_R=\left[(0.03)^2+(0.032)^2+(0.05)^2\right]^{1/2}=0.065 \tag{5.32}$$

$U_{R,ENG}$, the expanded uncertainty, is then obtained with Equation 5.19b:

$$U_{R,ENG}=\pm t_{95}\left[(0.065)^2+(0.20)^2\right]^{1/2} \tag{5.33}$$

The degrees of freedom need to be calculated just as in Equation 5.28. Therefore, the degrees of freedom were 22 and t_{95} equals 2.07. $U_{R,ENG}$ is then

$$U_{R,ENG}=\pm 2.07\left[(0.065)^2+(0.20)^2\right]^{1/2}=0.44 \quad \text{for 95\% confidence} \tag{5.34}$$

Carrying three significant figures for a comparison to $U_{R,ISO}$ not affected by round-off errors, one obtains

$$U_{R,ENG}=\pm 2.07\left[(0.0665)^2+(0.202)^2\right]^{1/2}=0.442 \quad \text{for 95\% confidence} \tag{5.35}$$

This is identical to $U_{R,ISO}$, Equation 5.30, as predicted.

5.4 Summary

Although these formulae for uncertainty calculations will not handle every conceivable situation, they will provide, for most experimenters, a useful estimate of test or measurement uncertainty. For more detailed treatment or specific applications of these principles, consult the references and the recommended "Further Information" section at the end of this chapter.

Defining Terms

Accuracy: The antithesis of uncertainty. An expression of the maximum possible limit of error at a defined confidence.

Confidence: A statistical expression of percent likelihood.

Correlation: The relationship between two data sets. It is not necessarily evidence of cause and effect.

Degrees of freedom: The amount of room left for error. It may also be expressed as the number of independent opportunities for error contributions to the composite error.

Error: [error] = [measured] − [true]. It is the difference between the measured value and the true value.

Expanded uncertainty: The 95% confidence interval uncertainty. It is the product of the total uncertainty and the appropriate Student's *t*.

Influence coefficient: See Sensitivity.

Measurement uncertainty: The maximum possible error, at a specified confidence, that may reasonably occur. Errors larger than the measurement uncertainty should rarely occur.

Nonsymmetrical uncertainty: An uncertainty for which there is an uneven likelihood that the true value lies on one side of the average or the other.

Propagation of uncertainty: An analytical technique for evaluating the impact of an error source (and its uncertainty) on the test result. It employs the use of influence coefficients.

Random error: An error that causes scatter in the test result.

Random standard uncertainty: An estimate of the limits of random error, one standard deviation of the average.

Sensitivity: An expression of the influence an error source has on a test or measured result. It is the ratio of the change in the result to an incremental change in an input variable or parameter measured.

Standard deviation of the average or mean: The standard deviation of the data divided by the number of measurements in the average.

Systematic error: An error that is constant for the duration of a test or measurement.

Systematic standard uncertainty: An estimate of the limits of systematic error, usually taken as 68% confidence for an assumed normal error distribution and infinite degrees of freedom.

Total uncertainty: The RSS combination of either the Type *A* or *B* uncertainties for the ISO error classifications or the random and systematic standard uncertainties for the engineering error classifications.

True value: The desired result of an experimental measurement.

Welch–Satterthwaite: The approximation method for determining the number of degrees of freedom in a combined uncertainty.

References

1. American National Standards Institute/American Society of Mechanical Engineers (ANSI/ASME) PTC 19.1-2005, *Instruments and Apparatus, Part 1, Test Uncertainty*, 1985, p. 5.
2. E. O. Doebelin, *Measurement Systems, Application and Design*, 4th edn., New York: McGraw-Hill, 1990, 38 ff.

3. International Standards Organization, *Guide to the Expression of Uncertainty Measurement*, Geneva, Switzerland, 1993, p. 16.
4. International Standards Organization, *Guide to the Expression of Uncertainty in Measurement*, Geneva, Switzerland, 1993, pp. 10, 11.
5. International Standards Organization, *Guide to the Expression of Uncertainty in Measurement*, Geneva, Switzerland, 1993, p. 64.
6. R. H. Dieck, *Measurement Uncertainty: Methods and Applications*, Research Triangle Park, NC: ISA, 1992, p. 45.
7. K. K. Brown, H. W. Coleman, W. G. Steele, and R. P. Taylor, Evaluation of correlated bias approximations in experimental uncertainty analysis, *Proceedings of 32nd Aerospace Sciences Meeting & Exhibit*, Reno, NV, AIAA paper no. 94-0772, January 10–13, 1996.
8. American National Standards Institute/American Society of Mechanical Engineers (ANSI/ASME) PTC 19.1-2005, *Instruments and Apparatus, Part 1, Test Uncertainty*, 1985, pp. 33–35.
9. W. T. Strike, III and R. H. Dieck, Rocket impulse uncertainty: An uncertainty model comparison, *Proceedings of 41st International Instrumentation Symposium*, Denver, CO, May 1995.
10. R. H. Dieck, Measurement uncertainty models, *Proceedings of 42nd International Instrumentation Symposium*, San Diego, CA, May 1996.

Further Information

Abernethy, R. B. and B. Ringhiser, The history and statistical development of the New ASME-SAE-AIAA-ISO measurement uncertainty methodology, *Proceedings of AIAA/SAE/ASME/ASME 21st Joint Propulsion Conference*, Monterey, CA, July 8–10, 1985.

Abernethy, R. B. et al., *Handbook-Gas Turbine Measurement Uncertainty*, AEDC, Tullahoma, TN, 1973.

Bevington, P. R. and D. K. Robinson, *Data Reduction and Error Analysis for the Physical Sciences*, New York: McGraw-Hill, 2003.

Dieck, R. H., *Measurement Uncertainty: Methods and Applications*, 4th edn., Research Triangle Park, NC: ISA, 2006.

Grabe, M., *Measurement Uncertainties in Science and Technology*, Berlin, Germany: Springer, 2005.

ICRPG Handbook for Estimating the Uncertainty in Measurements Made with Liquid Propellant Rocket Engine Systems, Chemical Propulsion Information Agency, No. 180, April 30, 1969.

Steele, W. G., R. A. Ferguson, and R. P. Taylor, Comparison of ANSI/ASME and ISO models for calculation of uncertainty, *Proceedings of 40th International Instrumentation Symposium*, Paper Number 94–1014, pp. 410–438, 1994.

6

Development of Standards

Halit Eren
Curtin University

6.1 Introduction

The word "standard" implies comparative evaluations of physical quantities, processes, and procedures.

Standards in instrumentation and measurement are implemented in a number of ways, as

- The fundamental physical standards
- Published standards (or the paper standards) that are published by national and international organizations and they are available for anyone to use
- De facto standards that are followed by convention or popular use
- De jure standards that are part of legally binding contracts, laws, or regulations

The standards and the implementation of standards are highly important in instrumentation and measurement systems. They are important documents that provide textual and illustrative information on what and how the processes and practices should be performed to achieve a particular task, for example, the measurement of temperature. The National Standards Policy Advisory Committee (http://www.nist.gov/) describes a standard as "a prescribed set of rules, conditions, or requirements concerning definitions of terms: classification of components; specification of materials, performance, or operations; delineation of procedures; or measurement of quantity and quality in describing materials, products, systems, services, or practices."

Published standards are necessary for worldwide trading, business practices, production of goods, manufacturing, scientific investigations, and research and development. They ensure consistency in implementation and interpenetration of different technologies in different organizations and sectors. Because of the national and international implications, there are many institutions that are responsible for developing, investigating, and maintaining the relevant standards to support worldwide scientific, commercial, and industrial activities. In this chapter, the published standards relevant to the instruments, instrumentation, and measurements will be explained in detail.

6.2 Standard Organizations

Standards are formulated by standards developing organizations (SDOs). These organizations can be government agencies, societies, international or regional organizations, private companies, professional institutions, and trade associations. World standards organizations can be categorized in four major groups as national, international, consortiums, and industrial and professional organizations, as illustrated in Figure 6.1.

A partial list of national and international standards organizations that deals with published standards is given in Table 6.1.

Each national or international organization has several specialist groups that encompass a broad range of scientific disciplines such as the measurements, measuring instruments, instrumentation and control, process control, safety, installations, electromagnetism, chemical engineering, mechanical engineering, radiation, and optical standards.

Common to all these organizations, the general terminology, vocabulary, and definitions concerning standardization and related activities are determined firstly. This acts as an agent to develop a mutual understanding among the members, development groups, and other concerned parties at the individual,

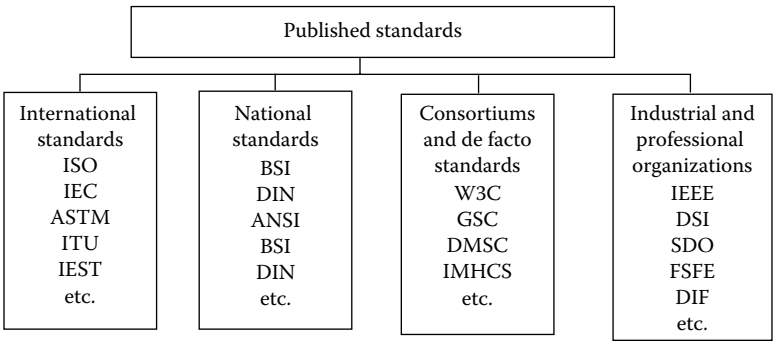

FIGURE 6.1 World standards organizations.

TABLE 6.1 Partial List of National and International Standards Organizations

Acronym	Organization Name and Web Address
ANSI	American National Standards Institute (http://www.ansi.org/)
AFNOR	Association Française de Normalization (http://www.afnor.fr/)
BSI	British Standards Institution (http://www.bsi-global.com/)
CEI	Comitato Elettrotecnico Italiano (http://www.ceiuni.it/)
CEN	Comité Européen de Normalisation (http://www.cenorm.be/)
CENELEC	Comité Européen de Normalisation Electrotechnique (http://www.cenelec.be/)
CSSN	China Standards Information Center (http://www.cssn.net.cn/)
DIN	Deutsches Institut für Normung (http://www2.din.de/)
IEC	International Electrotechnical Commission (http://www.iec.ch/)
ISO	International Organization for Standardization (http://www.iso.org/)
JISC	Japan Industrial Standards Committee (http://www.jisc.go.jp/)
NIST	American National Standards and Technology (http://www.nist.gov/)
SA	Standards Australia (http://www.standards.com.au/)
SCC	Standards Council of Canada (http://www.scc.ca/)
NZS	Standards New Zealand (http://www.standards.co.nz/)
TSE	Türk Standardlari Enstitüsü (http://www.tse.org.tr/)

governmental, and organizational levels. The aim is to prepare standards in such a manner that they can be interpreted, implemented, and referred to easily by all users. To stimulate this, standards organizations have strict guidelines to assist technical groups and committees in drafting and producing the standards. A typical preparation process has two main stages:

- *Preliminary work* that includes overall analysis, identification of the target groups, determination of subject delimitation, finding the relevant sources, determining the affecting concepts, choosing languages, and working out of the schedules.
- *Working procedure* that includes collecting and recording terminological data, establishing the term list, determining the concept fields and concept systems, formulating definitions, establishing and structuring the entries, streamlining the order of entries, indexing, graphic representation, and bibliography.

In many cases, the standards are produced by various bodies sometimes operating totally independent from each other. Hence, there may be different versions for the same subject. However, there are a number of international standards organizations such as the International Organization for Standardization (ISO) and the International Electrotechnical Commission (IEC) representing many member countries. These organizations have multiple internal departments, international committees, subcommittees, and working groups to support their activities.

6.2.1 Relations of Standards Organizations

Standards are important for scientific, research and development activities, and international trade; therefore, there is continuous relation and cooperation between national, regional, and international organizations. For example, in the case of ISO, there are many affiliated standards organizations, which represent member countries. The membership structure is as follows:

1. *Full members* are national bodies that are entitled to participate and exercise full voting rights on any technical committee and policy committee of the ISO.
2. *Correspondent members* that do not take an active part in the technical and policy development, but are entitled to be kept fully informed about their work of interest. These are countries that do not have their own standards organizations.
3. *Subscriber members* that represent the countries with small economies. The membership fees of the subscriber members are reduced but are allowed to be represented in some committees.

Apart from the international standards organizations, such as the ISO, that are structured with voting and nonvoting members, there are also numerous other mechanisms that maintain links between standards institutions and organizations. Examples are

- *The Asia-Pacific Legal Metrology Forum* (APLMF) is a grouping of legal metrology authorities in the Asia-Pacific Economic Cooperation (APEC). The objective of this forum is the development of legal metrology and the promotion of free and open trade in the region through the harmonization and removal of technical or administrative barriers.
- *Bureau International des Poids et Mesures* (BIPM) that ensures worldwide uniformity of measurements and their traceability to the International System of Units (SI).
- *World Trade Organization* (WTO) is an international agency whose purpose is to help trade flow as smoothly as possible in a system based on rules, to settle trade disputes between governments, and to organize related negotiations.
- *Joint technical committees* are formed to deal with the consequences of substantial overlap in areas of standardization and work related to information technology. For example, IEC has formed a joint technical committee known as the ISO/IEC JTC1, which was the first such joint committee and it is still fully functional.

Many standards organizations collaborate as consortiums to develop and implement particular standards, as in the case of fieldbus systems for industrial digital information transmissions and applications. The development of standards is a complex procedure involving many groups at the national, international, and industrial organizational levels. Some examples will be provided in the Section 6.3.

6.3 Development of Standards

SDOs undertake the task of producing relevant standards in their expertise areas. There are many different national and international SDOs; some of these organizations are as follows:

- National Electrical Manufactures Association (NEMA) (http://www.nema.org/)
- National Institute of Standards and Technology (NIST) (http://www.nist.gov/index.html)

At the individual organization level, each organization has its own different way of developing standards, which depends on its size, culture, aims, and structure. In this chapter, the ISO will be given as an example of a typical standardization body. More information can be found on ISO website (http://www.iso.org/) and indeed on the websites of many other organizations.

6.3.1 The International Standards Organization

The ISO plays an important role in development and proliferation of international standards. The organizational and governance structure is illustrated in Figure 6.2. It has worldwide representation having 110 full voting member countries, 43 corresponding members, and 10 subscriber members as it stands today in March 2012. It has 3335 technical bodies comprising 224 technical committees, 513 subcommittees, 2516 working groups, and 82 ad hoc study groups. Although being a nongovernment organization, it can set standards such that many of them become legislated laws either through international treaties or national governments. Therefore, here, further explanation will be provided about the ISO, but more information can be found on their website (http://www.iso.org/).

ISO promulgates worldwide proprietary industrial and commercial standards. It produces international standards as well as publishing technical reports, technical specifications, technical corrigenda, and guides as explained as follows.

One of the products of the ISO is the *technical reports*. Technical reports are produced by the technical committees or subcommittees after having collected substantial data on a particular subject.

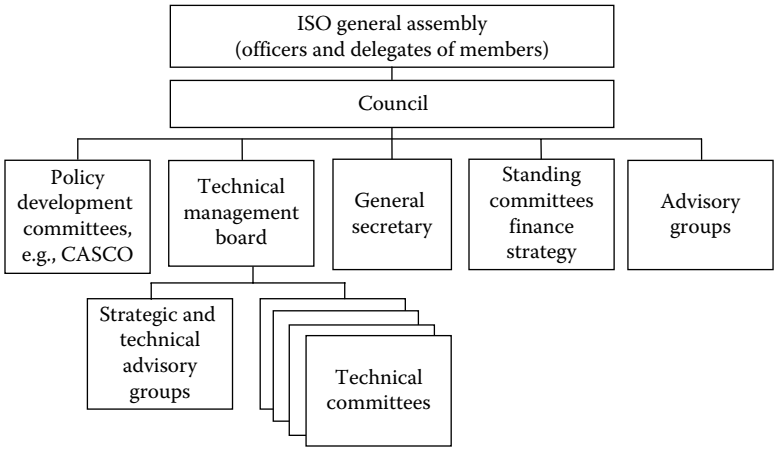

FIGURE 6.2 Branches of ISO.

These reports normally lead to the development of international standards and they are identified with *TR* on their titles. Some examples are

- ISO/TR 19033:2000. Technical product documentation—metadata for construction documentation
- SO/IEC TR 17799:2000. Code of practice for information security management

The ISO publishes *technical specifications* and *publicly available specifications* as intermediate information before the development of full international standard on a particular subject. Technical specifications are identified with *TS*, for example,

- ISO/TS 16952-1:2006. Technical product documentation—reference designation system—Part 1: General application rules
- ISO/PAS 11154:2006. Road vehicles—roof load carriers

ISO also issues *technical corrigendum*, which are amendments to existing standards because of minor technical flaws, improvements, or extend applicability in a limited way. Generally, technical corrigendum is issued with the expectation that the affected standard will be updated or withdrawn at its next review.

ISO *guides* are produced as meta-standards. They cover guides and rules for matters related to international standardization efforts, for example,

- ISO/IEC Guide 2:2004. Standardization and related activities—general vocabulary
- ISO/IEC Guide 65:1996. General requirements for bodies operating product certification

In order to understand how ISO develops standards, it is important to look at its organizational structure more closely.

6.3.2 Structure of ISO

A broad view of the structure of ISO is illustrated in Figure 6.2. Going to the details, it operates with the following committees and groups:

- *Policy development committees* that are established by the general assembly to draft policies. The committees are open to all full member and correspondent members, and they directly report to the council. Policy development committees have several branches such as the Committee on Conformity Assessment and Committee on Consumer Policy
- *Council* that operates the ISO itself. It consists of 18 elected representatives of full members and some permanent officers
- *Council standing committees* that advise the council on policy and strategic matters and raise any related issues
- *Technical management board* that examines proposals, monitors the work of technical committees, and establishes and dissolves technical advisory groups
- *Technical advisory groups* (TAGs) that advise the board on basic, sectoral, and cross-sectoral coordination; coherent planning; and the needs for new work. For example, TAG 4 is responsible for metrology matters
- *Technical committees* that are responsible with a particular area such as TC 12 for quantities, units, symbols, and conversion factors and TC 108 for mechanical vibration and shock
- *Ad hoc advisory groups* that recommend standardizations

The standards are developed according to the following principles:

- *Consensus*: The views of all interest manufacturers, vendors, users, consumer groups, testing laboratories, governments, engineering professions, and research organizations are taken into account.
- *Industry-wide*: Solutions intend to satisfy industries and customers worldwide.
- *Voluntary*: International standardization is market driven and therefore based on voluntary involvement of all interests in the marketplace.

There are three main phases in developing the standards, which can be explained as follows:

1. The need for a standard is usually expressed by an industry sector, which communicates this need to a national member body. The latter proposes the new work item to ISO as a whole. Once the need for an international standard has been recognized and formally agreed, the first phase involves definition of the technical scope of the future standard. This phase is usually carried out in working groups that comprise technical experts from countries interested in the subject matter.
2. Once agreement has been reached on which technical aspects are to be covered in the standard, a second phase is entered during which countries negotiate the detailed specifications within the standard. This is the consensus-building phase.
3. The final phase comprises the formal approval of the resulting draft international standard (DIS) (the acceptance criteria stipulate approval by two-thirds of the ISO members that have participated actively in the standards development process and approval by 75% of all members that have voted), following which the agreed text is published as an ISO international standard.

A normal procedure is that the standards to be internationalized can be brought to the attention of the ISO from a country or industry or business through one or more of the member organizations. The members propose the new work item to the ISO as a whole. If accepted, the work item is assigned to an existing technical committee. The technical committees are composed of experts appointed from industrial, technical, and business sectors. These experts may be joined by others with relevant knowledge, such as representatives of government agencies, testing laboratories, consumer associations, and environmentalists. Generally, the experts are selected from the national delegations nominated by the member institutes of the countries concerned. The ISO rules state that the member institutions are expected to take account of the views of a broad range of interested parties and other stakeholders so that acceptance of the proposal becomes consolidated in a consensus manner.

The national delegations of experts of a technical committee meet to discuss and debate until a consensus is reached on a draft agreement. The draft agreement is then circulated as a DIS to members for comments and balloting. Members are responsible for providing public review procedures for making draft standards known and available to interested parties as well as to the general public. Once the feedback is received from members, the draft standard is formulated in its final form to be voted by the members. If the voting is in favor, the document, with eventual modifications, is circulated to the ISO members as a final draft international standard (FDIS). If that vote is positive again, the document is then published as an international standard.

Most standards require periodic revision as several factors combine to render a standard out of date: technological evolution, new methods and materials, and new quality and safety requirements. To take account of these factors, ISO has established the general rule that all ISO standards should be reviewed at intervals of not more than 5 years. On occasion, it is necessary to revise a standard earlier.

Similar processes take place in other organizations depending on their internal cultures and structures. For example, in the case of IEC, there are seven stages to develop a full standard document (http://www.iec.org/):

1. Proposal stage—new work item proposal (NP).
2. Preparatory stage—working draft(s) (WD).
3. Committee stage—committee drafts (CD).
4. Inquiry stage—inquiry draft (DIS, CDV).
5. Approval stage (FDIS).
6. Publication stage.
7. If FDIS fails, the Technical Report 2 (TR2) is published and revised after 2 years.

TR2 status means publication of work is still under technical development or where for any other reason there is a future but not immediate possibility of agreement.

6.3.3 Obtaining ISO Standards

ISO documents are copyrighted and ISO charges for copies of most. ISO does not charge for most draft copies of documents in electronic format. Although useful, care must be taken using these drafts since there is the possibility of substantial change before it becomes finalized as an international standard. Some standards by ISO and its official U.S. representative (and the IEC via the U.S. National Committee) are made freely available.

Many of the ISO standards are ubiquitous, which has led to common use of "ISO" to describe the actual product that conforms to a standard. Some examples of this are as follows:

- ISO 9660. Standard file system has been adopted by many organizations; hence, the CD images are commonly referred to as "ISOs." Almost all computers with CD-ROM drives can read CDs that use this standard. Some DVD-ROMs also use ISO 9660 file systems.
- ISO 5800:1987. Photographic film's sensitivity to light and its film speed is often referred to as its "ISO number."

6.4 Obtaining and Using Standards

There are several hundred thousand standards and technical regulations in the world containing special requirements for a particular industry, country, or region. Finding relevant information on the specific standards can be a difficult task. Nevertheless, once the standard is identified for a particular application, it can be obtained in paper or electronic forms from various sources. For example, standards can be purchased online from standards institution or other providers using their catalogs. Some of the websites that provide full-text standards are given as follows, but the list is not exhaustive:

- ETSI, European Telecommunications Standards Institute, offers direct access to publicly available ETSI telecommunications standards (http://www.etsi.org/).
- IAEA, International Atomic Energy Agency, offers most recent IAEA publications online (http://www.iaea.org/).
- IEEE Xplore, Institute of Electrical and Electronics Engineers, offers standards for members (http://ieeexplore.ieee.org/).
- NISO, National Information Standards Organization, offers free full-text access to NISO information standards (http://www.niso.org/).
- ANSI, American National Standards Institute, offers a range of standards for purchasing (http://www.ansi.org/).
- Global Engineering Documents offers national and international standards (http://global.ihs.com/).
- Information Handling Services, Englewood, CO (IHS) offers most engineering standards (http://www.ihs.com/).
- World Standards Services Networks (WSSN) offers national and international standards (http://www.wssn.net/).
- National Standards Services Networks (NSSN) offers national and international standards (http://www.nssn.org/).

Standards used in measurement and metrology largely define guidelines for testing methodology, accuracy, data collection, and data dissemination, use and reporting criteria for consistency and accuracy. From guidelines, the necessary instrumentation, procedures, and control processes can be determined and used appropriately for the design, construction, operation, maintenance,

installations, safety, and other related areas. The use of standards in the design and the operations offer many advantages, such as

- Improves the communication between the designers and the operators
- Provides practical application of expert knowledge
- Represents accumulated experience, thus avoiding ground-up starts
- Enhances operability and interoperability thus ensures compatibility
- Ensures consistency, accuracy, and data interpretation
- Sets a benchmark for global applications
- Sets the recognized level of quality
- Increases market access and user acceptance
- Improves communication between peers in industry and other concerned parties
- Provides immediate access to technical resources
- Provides an understanding on the future trends
- Provides consistency in products and traceability
- Facilitates interchangeability of products and quality assurance
- Ensures safety
- Facilitates migration of products for integrated systems

6.5 Examples of Standards

As explained previously, due to the range of standards organizations, interest groups, and diversity on the subject matters, there are many standards available worldwide. This sentiment is summarized on the ISO website with the following information: ISO has developed 19,023 international standards to date on a variety of subjects, and some 1,208 new ISO standards have been published in the year 2011. The full range of technical fields can be seen from the listing international standards. Users can browse that listing to find bibliographic information on each standard and, in many cases, a brief abstract. The online ISO standards listing integrate both the ISO catalog of published standards and the ISO technical program of standards under development (http://www.iso.org/iso/iso_catalogue.htm#).

Some examples of standards relevant to instrumentation and measurement are given in Table 6.2.

6.6 Software Standards

Software is a set of instructions for digital systems, programmable devices, and computers. It describes computer programs, procedures, and documentation. Software is developed by programming languages like assembly language and C++. There are two types of software, being the system software and the application software. The system software enables the computer to execute its own internal operations as well as the application programs such as the word processors. System software includes an operating system to interface with hardware to provide the necessary services for applications.

Software is often regarded as anything except the hardware. Software encompasses a wide range of products and technologies, such as programming languages, FPGA configuration, web pages, HTML, and Microsoft Word, running under operating systems such as Linux and Microsoft Windows.

Software has its own niche industry made up of different entities and people. There are many software companies and programmers in the world specialized in certain areas such as mathematic applications, interfacing, measurements, and data processing. Also, there are many software standard organizations like the W3C and IETF (Internet Engineering Task Force). These organizations are primarily made up of people from large companies like Microsoft and IBM.

TABLE 6.2 Partial List of Standards on Instrumentation, Measurement, and Related Fields

ASTM B896-99	Standard test methods for evaluating connectability characteristics of electrical conductor materials
ASTM D4356	Standard practice for establishing consistent test method tolerances
ASTM E119	Standard test methods for fire tests of building construction and materials
ASTM G138	Standard test method for calibration of a spectroradiometer using a standard source of irradiance
ASTM 167	Standard test method for calibration of a pyranometer using pyrheliometer
ASTM G169	Standard guide for application of basic statistical methods to weathering tests
ASTM G187	Standard test method for measurement of soil resistivity using the two-electrode soil box
DIN1311-4	Vibration; vibrating continua, waves
DIN 12975-4	Thermal solar systems and components—solar collectors—Part 2: Test methods
DIN 19237	Measurement and control; control engineering vocabulary
DIN 43780	Electrical measuring instruments; direct acting indicating electrical measuring instruments and their accessories
DIN 45507	Measuring apparatus for frequency variations in sound recording equipment
DIN 54836	Testing of combustible materials; determination of ignition temperature
EN 10002-1	Method of test at ambient temperature
EN 13146	Railway applications—track—test methods for fastening systems
EN 55011:2000	Industrial, scientific, and medical RF equipment
IEC 60068	Environmental testing
IEC 60331	Test for electric cables under fire conditions
IEC 60601	Medical electric equipment
IEC 60793	Optical fibers
IEC 60801	EMI and RFI immunity
IEC 6095	Maritime navigation and radio communication equipment
IEC 61000	Electromagnetic compatibility (EMC)
IEC 61000-4 P1-30	Testing and measurement techniques
IEC 61043	Sound intensity meters with pairs of microphones
IEC 61326	Electrical equipment for measurement, control, and laboratory use
IEC 61724	Photovoltaic system performance monitoring
IEC 62366	Medical devices—application of usability engineering to medical devices
IEEE 82	Standard test procedure for impulse voltage test on insulated conductors
IEEE 299:1997	Measuring the effectiveness of the shielding enclosure
IEEE 1460	Guide for the measurement of quasi-static magnetic and electric fields
IEEE 1521	Standard for measurement of video jitter and wander
IEEE 1650	Test methods for measurement of electrical properties of carbon nanotubes
IEEE/IEC C57.12.20	Draft standard for nuclear power plants—instrumentation and control important to safety—electric equipment condition monitoring methods—Part 3
IEEE 61588	Standards for precision clock synchronization protocol for networked measurement and control systems
ISO 11:1987	Aircraft—ground pressure testing connections for pressure cabins
ISO ICS 01	Generalities, terminology, standardization, documentation—graphical symbols, technical drawings, info, science
ISO ICS 17	Metrology and measurement, physical phenomena
ISO 10993-4	Selection of tests for interactions with blood
ISO 14644	Clean rooms and associated controlled environment
ISO 15189	Medical laboratories—particular requirements for quality and competence
ISO 15970	Natural gas—measurement properties
ISO 16750	Road vehicles—environmental conditions and testing for electric and electronic equipment
ISO/IEC 19794	Information technology—biometric data interchange formats
ISO 22241-2	Diesel engines—NOx reduction agent AUS 32—test methods
ISO 7700-2:1987	Check of calibration of moisture meters

6.6.1 Types of Software Standards

Software standards are certain terms, concepts, and techniques agreed to by software creators. For instance, HTML, TCP/IP, SMTP, POP, and FTP are standards that all software designers must adhere to, if their software aims to interface within the standards. Complexity of a standard can vary depending on type of the problem and the people involved. Standard is often made to be as simple as possible, maintainable, understandable, and easy to follow.

There are two types of basic software standards:

1. *Closed standards*: In which the specifications are kept secret to prevent interference from third parties. It inhibits third-party software from being installed; it keeps third-party hardware from interoperating with it, and it prevents third-party enhancements from improving the product.
2. *Open standards*: Specifications for hardware or software that are developed by a standards organization or a consortium involved in supporting a standard. Available to the public for developing compliant products, open standards imply "open systems" that an existing component in a system can be replaced with that of another vendor. Although many vendors may have contributed to an open standard and one may have contributed more than others and even have great influence, an open standard is not completely controlled by a single vendor.

Some examples of software standards are given in Table 6.3.

6.6.2 Instrumentation and Measurement Software Standards

The use of software is an integral part of instrumentation and measurements for data collection, data processing, interpretation, and decision making. Therefore, the functional and structural quality of the supporting software bares ultimate importance. The ISO 25000:2005 quality model describes the structure, classification, and terminology of the attributes of the measurement and metric-related software.

TABLE 6.3 Examples of Software Standards

ISO/CDTS8000-1	Data quality—Part 1: Overview, principles, and general requirements
ISO/TS8000-100:2009	Data quality—Part 100: Master data: Overview
ISO8000-102:2009	Data quality—Part 102: Master data: Exchange of characteristic data: Vocabulary
ISO8000-110:2009	Data quality—Part 110: Master data: Exchange of characteristic data: Syntax, semantic encoding, and conformance to data specification
ISO/TS8000-120:2009	Data quality—Part 120: Master data: Exchange of characteristic data: Provenance
ISO/TS8000-130:2009	Data quality—Part 130: Master data: Exchange of characteristic data: Accuracy
ISO/TS8000-140:2009	Data quality—Part 140: Master data—Exchange of characteristic data: Completeness
ISO9506-1:2003	Industrial automation systems—manufacturing message specification—Part 1: Service definition
ISO9506-2:2003	Industrial automation systems—manufacturing message specification—Part 2: Protocol specification
ISO10303-1:1994	Industrial automation systems and integration—product data representation and exchange—Part 1: Overview and fundamental principles
ISO/PRFTS29002-20	Industrial automation systems and integration—exchange of characteristic data—Part 20: Concept dictionary resolution services
ISO/TS29002-31:2009	Industrial automation systems and integration—exchange of characteristic data—Part 31: Query for characteristic data
IEC62264-1:2003	Enterprise-control system integration—Part 1: Models and terminology
IEC62264-2:2004	Enterprise-control system integration—Part 2: Model object attributes
IEC62264-3:2007	Enterprise-control system integration—Part 3: Activity models of manufacturing operations management

The general requirements of the relevant software are reliability, efficiency, security, and maintainability. A number of examples of the existing standards addressing the instrumentation and measurements are given here, but the examples are not exhaustive:

ASTM E2439–09 (Standard Guide for Instrumentation, Sensors and Operating Software Used in Forensic Psychophysiological Detection of Deception [Polygraph] Examinations). This standard covers the minimum requirements for instrumentation (both analog and computerized systems), sensors, and operating software used in the forensic psychophysiological detection of deception (PDD).

IEEE–STD 1057 provides algorithms for fitting parameters of a sine wave to discrete time observations. It covers electronic digitizing waveform recorders, waveform analyzers, and digitizing oscilloscopes with digital outputs. It gives accurate estimation to Gaussian and quantization noise that commonly exists in measurement systems.

ISO 18629 standard is a process specification language (PSL) that can be used to represent manufacturing engineering and business processes including production planning, simulation, process modeling, and project management.

IEC 62304 is a standard that specifies the life cycle for the development of medical software within medical devices. It targets to harmonize the medical equipment produced by European Union and United States so that a benchmark is achieved to comply with regulatory requirements.

Bibliography

Alves, J. G. Developments in standards and other guidance for individual monitoring, *Radiation Measurements*, 43(2–6), 558–564, 2008.

American National Standards Institute (ANSI), http://www.ansi.org/ (accessed on February 5, 2012).

British Standards Institution (BSI), http://www.bsi-global.com/ (accessed on December 10, 2011).

Busch, L., *Recipes for Reality (Infrastructure)*, The MIT Press, Cambridge, MA, 2011.

Eren, H. Standards in process control and automation, *Process Software Digital Networks*, Eds., H. Eren. and B. Liptak, Vol. 3, 4th edn., CRC Press, Boca Raton, FL, pp. 150–157, 2011.

European Committee for Standardization (CEN), http://www.cen.eu/cen/pages/default.aspx (accessed on February 20, 2012).

German Institute for Standardization (DIN), http://www.din.de/cmd?level=tpl-home&languageid=en (accessed on February 5, 2012).

International Bureau of weights and measures, http://en.wikipedia.org/wiki/International_Bureau_of_Weights_and_Measures (accessed on February 10, 2012).

International Electrotechnical Commission (IEC), http://www.iec.org/ (accessed on July 10, 2011).

International Organization for Standardization (ISO), http://www.iso.org/ (accessed on January 26, 2012).

National Standards Services Networks (NSSN), http://www.nssn.org/ (accessed on March 7, 2012).

SIA, Global info store, ISO publications, http://infostore.saiglobal.com/store/Portal.aspx?publisher=ISO&gclid=CMX1sN_P4K4CFeRKpgodXFMKYw (accessed on February 12, 2012).

Techstreet Thomson, standards catalogs, http://www.techstreet.com/ (accessed on February 11, 2012).

Velychko, O. and Gordiyenko, T. The use of metrological terms and SI units in environmental guides and international standards, *Measurement*, 40(2), 202–212, 2007.

World Standards Services Networks (WSSN), http://www.wssn.net/ (accessed on November 18, 2011).

7

Measurement Standards

DeWayne B. Sharp
Shape of Things

Measurement standards are those devices, artifacts, procedures, instruments, systems, protocols, or processes that are used to define (or to realize) measurement units and on which all lower echelon (less accurate) measurements depend. A measurement standard may also be said to store, embody, or otherwise provide a physical quantity that serves as the basis for the measurement of the quantity. Another definition of a standard is the physical embodiment of a measurement unit, by which its assigned value is defined and to which it can be compared for calibration purposes. In general, it is not independent of physical environmental conditions, and it is a true embodiment of the unit only under specified conditions. Another definition of a standard is a unit of known quantity or dimension to which other measurement units can be compared.

7.1 Historical Perspective

Many early standards were based on the human body: the length of man's hand, the width of his thumb, the distance between outstretched fingertips, the length of one's foot, a certain number of paces, etc. In the beginning, while groups were small, such standards were convenient and uniform enough to serve as the basis for measurements.

The logical person to impose a single standard was the ruler of the country—hence, our own 12 in. or other short measuring stick is still called a *ruler*. The establishment of measurement standards thus became the prerogative of the king or emperor, and this right has since been assumed by all governments.

History is replete with examples that show the importance of measurements and standards. In a report to the U.S. Congress in 1821, John Quincy Adams said, "Weights and measures may be ranked among the necessaries to every individual of human society." Our founding fathers thought them so important that the U.S. Constitution expressly gives the Congress the power to fix uniform standards of weights and measures. The need for weights and measures (standards) dates back to earliest recorded history and is even mentioned in the Old Testament of the Bible. Originally, they were locally decreed to

serve the parochial needs of commerce, trade, land division, and taxation. Because the standards were defined by local or regional authorities, differences arose that often caused problems in commerce and early scientific investigation. The rapid growth of science in the late seventeenth century highlighted a number of serious deficiencies in the system of units then in use and, in 1790, led the French National Assembly to direct the French Academy of Sciences to "deduce an invariable standard for all measures and all the weights." The academy proposed a system of units, the metric system, to define the unit of length in terms of the earth's circumference, with the units of volume and mass being derived from the unit of length. Additionally, they proposed that all multiples of each unit be a multiple of 10.

In 1875, the United States and 16 other countries signed the "Treaty of the Meter," establishing a common set of units of measure. It also established an International Bureau of Weights and Measures (called the BIPM). That bureau is located in the Parisian suburb of Sèvres. It serves as the worldwide repository of all the units that maintain our complex international system of weights and measures. It is through this system that compatibility between measurements made thousands of miles apart is currently maintained.

The system of units set up by the BIPM is based on the meter and kilogram instead of the yard and the pound. It is called the Système International d'Unités (SI) or the International System of Units. It is used in almost all scientific work in the United States and is the only system of measurement units in most countries of the world today.

Even a common system of units does not guarantee measurement agreement, however. Therein lies the crux of the problem. We must make measurements, and we must know how accurately (or, to be more correct, with what uncertainty) we made those measurements. In order to know that point, there must be standards. Even more important, everyone must agree on the values of those standards and use the same standards.

As the level of scientific sophistication improved, the basis for the measurement system changed dramatically. The earliest standards were based on the human body, and then attempts were made to base them on "natural" phenomena. At one time, the basis for length was supposed to be a fraction of the circumference of the earth, but it was "maintained" by the use of a platinum/iridium bar. Time was maintained by a pendulum clock but was defined as a fraction of the day and so on. Today, the meter is no longer defined by an artifact. Now, the meter is the distance that light travels in an exactly defined fraction of a second. Since the speed of light in a vacuum is now defined as a constant of nature with a specified numerical value (299,792,458 m/s), the definition of the unit of length is no longer independent of the definition of the unit of time.

Prior to 1960, the second was defined as 1/86,400th of a mean solar day. Between 1960 and 1967, the second was defined in terms of the unit of time implicit in the calculation of the ephemerides: "The second is the fraction 1/31, 556, 925.9747 of the tropical year for January 0 at 12 hours of ephemeris time." With the advent of crystal oscillators and, later, atomic clocks, better ways were found of defining the second. This, in turn, allowed a better understanding of things about natural phenomena that would not have been possible before. For example, it is now known that the earth does not rotate on its axis in a uniform manner. In fact, it is erratically slowing down. Since the second is maintained by atomic clocks, it is necessary to add "leap seconds" periodically so that the solar day does not gradually change with respect to the time used every day. It was decided that a constant frequency standard was preferred over a constant length of the day.

7.2 What Are Standards?

One problem with standards is that there are several kinds. In addition to "measurement standards," there are "standards of practice or protocol standards" that are produced by the various standard bodies such as the International Organization for Standardization (ISO), the International Electrotechnical Commission (IEC), the American National Standards Institute (ANSI), and the Standards Council of Canada (SCC) (see Figure 7.1).

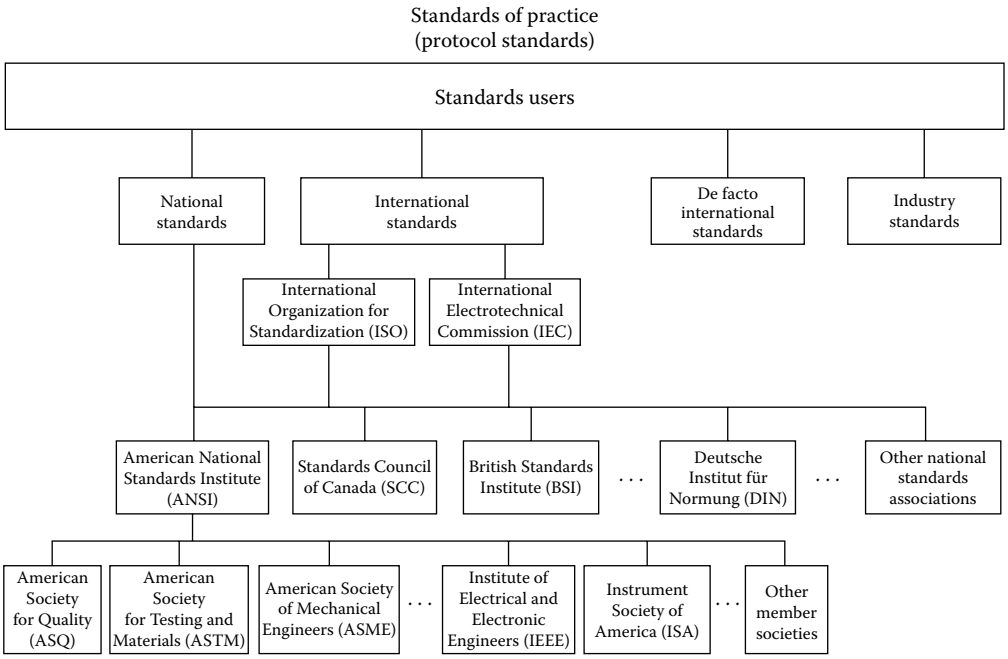

FIGURE 7.1 Standardization organizations and standards structure.

7.2.1 Standards of Practice (Protocol Standards)

These standards define everything from the dimensions and electrical characteristics of a flashlight battery to the shape of the threads on a machine screw and from the size and shape of an IBM punched card to the quality assurance requirements for measuring equipment. Such standards can be defined as documents describing the operations and processes that must be performed in order for a particular end to be achieved. They are called a "protocol" by Europeans to avoid confusion with a physical standard.

7.2.2 Legal Metrology

The application of measurement standards to the control of the daily transactions of trade and commerce is known as legal metrology; within the United States, it is more commonly known as weights and measures. Internationally, coordination among nations on legal metrology matters is, by international agreement, handled by a quasi-official body—the International Organization for Legal Metrology (OIML).

Within the United States, domestic uniformity in legal metrology matters is the responsibility of National Institute of Standards and Technology (NIST) acting through its Office of Weights and Measures. Actual enforcement is the responsibility of each of the 50 states and the various territories. These, in turn, generally delegate the enforcement powers downward to their counties and, in some cases, to large cities.

7.2.3 Forensic Metrology

Forensic metrology is the application of measurements and hence measurement standards to the solution and prevention of crime. It is practiced within the laboratories of law enforcement agencies throughout the world. Worldwide activities in forensic metrology are coordinated by Interpol (*International Police*; the international agency that coordinates the police activities of the member nations). Within the United States, the Federal Bureau of Investigation (FBI), an agency of the Department of Justice, is the focal point for most U.S. forensic metrology activities.

7.2.4 Standard Reference Materials

Another type of standard that should be mentioned here is the Standard Reference Materials (SRMs). SRMs are discrete quantities of substances or minor artifacts that have been certified as to their composition, purity, concentration, or some other characteristics useful in the calibration of the measurement devices and the measurement processes normally used in the process control of those substances. SRMs are the essential calibration standards in stoichiometry (the metrology of chemistry).

In the United States, the NIST, through its SRM program, offers for sale over 1300 SRMs. These range from ores to pure metals and alloys. They also include many types of gases and gas mixtures and many biochemical substances and organic compounds. Among the artifact devices available are optical filters with precise characteristics and standard lamps with known emission characteristics.

7.3 Conceptual Basis of Measurements

Lord Kelvin's oft-quoted statement may bear repeating here:

> I often say that when you can measure what you are speaking about, and can express it in numbers, you know something about it; but when you cannot measure it, cannot express it in numbers, your knowledge is of a meager and unsatisfactory kind; it may be the beginnings of knowledge, but you have scarcely, in your thoughts, advanced to the stage of science, whatever the matter may be. So therefore, if science is measurement, then without metrology there can be no science.
>
> **William Thomson (Lord Kelvin), May 6, 1886**

Lord Kelvin's statement has been quoted so many times that it has almost become trite, but looking at Figure 7.2 will show an interesting hierarchy. In order to achieve quality or "to do things right," it is

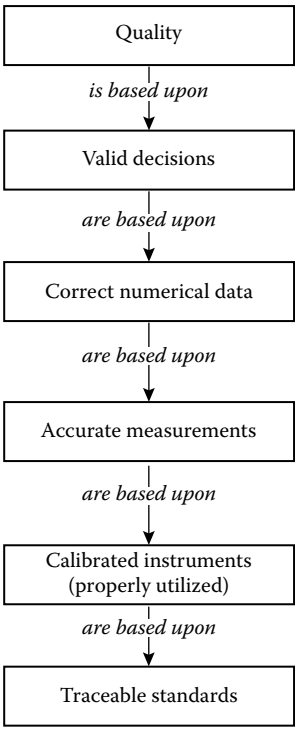

FIGURE 7.2 Decision-making process in applications of standards.

necessary to make some decisions. The correct decisions cannot be made unless there are good numerical data on which to base those decisions. Those numerical data, in turn, must come from measurements, and if "correct" decisions are really needed, they must be based on the "right" numbers. The only way to get "good" numerical data is to make accurate measurements using calibrated instruments that have been properly utilized. Finally, if it is important to compare those measurements to other measurements made at other places and other times, the instruments must be calibrated using traceable standards.

7.4 Need for Standards

Standards define the units and scales in use and allow comparison of measurements made in different times and places. For example, buyers of fuel oil are charged by a unit of liquid volume. In the United States, this would be the gallon, but in most other parts of the world, it would be the liter. It is important for the buyer that the quantity ordered is actually received and the refiner expects to be paid for the quantity shipped. Both parties are interested in accurate measurements of the volume and, therefore, need to agree on the units, conditions, and method(s) of measurement to be used.

Persons needing to measure a mass cannot borrow the primary standard maintained in France or even the national standard from the NIST in the United States. They must use lower-level standards that can be checked against those national or international standards. Everyday measuring devices, such as scales and balances, can be checked (calibrated) against working-level mass standards from time to time to verify their accuracy. These working-level standards are, in turn, calibrated against higher-level mass standards. This chain of calibrations or checking is called "traceability." A proper chain of traceability must include a statement of uncertainty at every step.

7.5 Types of Standards

7.5.1 Basic or Fundamental Standards

In the SI system, there are seven basic measurement units from which all other units are derived. All of the units except one are defined in terms of their unitary value. The one exception is the unit of mass. It is defined as 1000 g or 1 kg. It is also unique in that it is the only unit currently based on an artifact. The U.S. kilogram and hence all other standards of mass are based on one particular platinum/iridium cylinder kept at the BIPM in France. If that International Prototype Kilogram were to change, all other mass standards throughout the world would be wrong.

The seven basic units are listed in Table A.1. Their definitions are listed in Table A.2.

7.5.2 Derived Standards

All of the other units are derived from the seven basic units described in Table A.1. Measurement standards are devices that represent the SI standard unit in a measurement. (For example, one might use a Zener diode together with a reference amplifier and a power source to supply a known voltage to calibrate a digital voltmeter. This could serve as a measurement standard for voltage and be used as a reference in a measurement.)

Table A.3 lists the most common derived SI units, together with the base units that are used to define the derived unit. For example, the unit of frequency is the hertz; it is defined as the reciprocal of time. That is, 1 hertz (1 Hz) is one cycle per second.

7.5.3 Measurement Assurance System

Figure 7.3 illustrates the interrelationship of the various categories of standards throughout the world. While it gives more detail to U.S. structure, similar structures exist in other nations. Indeed, a variety of regional organizations exist that help relate measurements made in different parts of the world to each other.

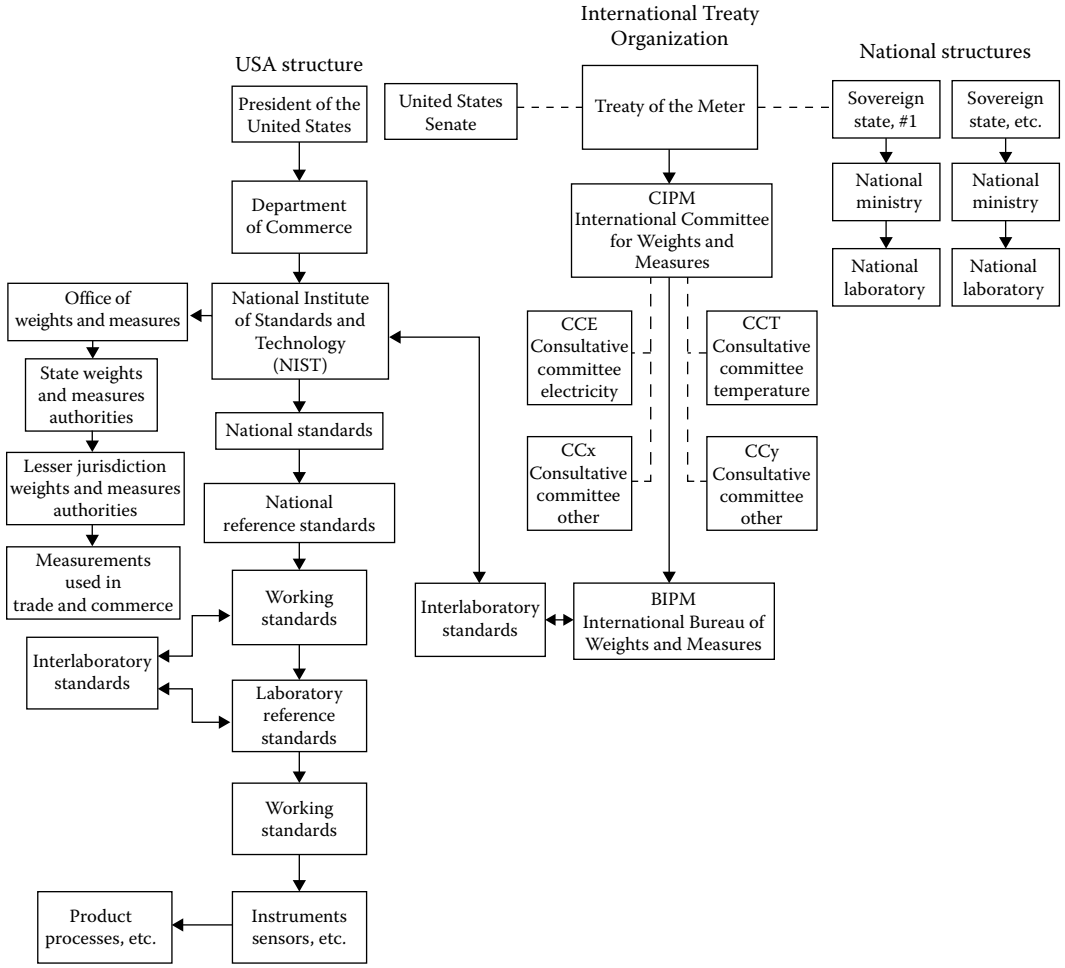

FIGURE 7.3 Measurement assurance systems.

7.6 Numbers, Dimensions, and Units

A measurement is always expressed as a multiple (or submultiple) of some unit quantity. That is, both a numeric value and a unit are required. If electric current were the measured quantity, it might be expressed as some number of milliamperes or even microamperes. It is easy to take for granted the existence of the units used, because their names form an indispensable part of the vocabulary.

7.7 Multiplication Factors

Since it is inconvenient to use whole units in many cases, a set of multiplication factors has been defined that can be used in conjunction with the units to bring a value being measured to a more reasonable size. It would be difficult to have to refer to large distances in terms of the meter; thus, one defines longer distances in terms of kilometers. Short distances are stated in terms of millimeters, micrometers, nanometers, etc. (see Table A.4).

7.8 Conversions of Units

Historically, many different units are involved in different places of the world or even within the same country; the relationships between different units are defined in fixed terms. For example, 1 lb = 453.59237 g. A partial list of conversions can be found in Table A.5. A more comprehensive list can be found in Liptak and Eren (2011).

Further information on standardization and processes can be found in Chapter 6.

7.9 Examples of Defining Terms

Most of the definitions in this listing were taken from the *International Vocabulary of Basic and General Terms in Metrology*, published by the ISO, 1993 (VIM) (ISO, 1993). They are indicated by the inclusion (in brackets) of their number designation in the VIM. The remainder of the definitions is not intended to represent any official agency but is ones widely accepted and is included to help in the understanding of this material. More detailed and rigorous definitions can be found in other works available from ANSI, IEC, ISO, and NIST. Words enclosed in parentheses "(…)" may be omitted from the term if it is unlikely that such omission will cause confusion.

Accuracy of measurement [3.5]: The closeness of the agreement between the result of a measurement and a true value of the measurand.

Notes:

1. *Accuracy* is a qualitative concept.
2. The term *precision* should not be used for *accuracy*. (Precision only implies repeatability.)

Note, that to say an instrument is accurate to 5% (a common way of stating it) is wrong. One would not find such an instrument very useful if it, in fact, were only accurate 5% of the time. What is meant when such a statement is made is that the instrument's inaccuracy is less than 5% and it is accurate to better than 95%. Unfortunately, this statement is almost as imprecise as "accurate to 5%." An instrument would not be useful if it were accurate only 95% of the time; but this is not what is implied by "5% accuracy." What is meant is that, (almost) all of the time, its indication is within 5% of the "true" value.

Calibration [6.11]: A set of operations that establish, under specified conditions, the relationship between values of quantities indicated by a measuring instrument or measuring system, or values represented by a material measure or a reference material, and the corresponding values realized by standards.

Notes:

1. The result of a calibration permits either the assignment of values of measurands to the indicators or the determination of corrections with respect to indications.
2. A calibration can also determine other metrological properties, such as the effect of influence quantities.
3. The result of a calibration can be recorded in a document, sometimes called a *calibration certificate* or a *calibration report*.

Calibration laboratory: A work space, provided with test equipment, controlled environment, and trained personnel, established for the purpose of maintaining proper operation and accuracy of measuring and test equipment. *Calibration laboratories* typically perform many routine calibrations, often on a production-line basis.

Certified reference material (CRM) [6.14]: A *reference material*, accompanied by a certificate, one or more of whose property values are certified by a procedure that established traceability to an accurate realization of the unit in which the property values are expressed and for which each certified value is accompanied by an uncertainty at a stated level of confidence

1. The definition of a *reference material* is given elsewhere in this vocabulary.
2. CRMs are generally prepared in batches for which the property values are determined within stated uncertainty limits by measurements on samples representative of the entire batch.
3. The certified properties of *CRM*s are sometimes conveniently and reliably realized when the material is incorporated into a specifically fabricated device, for example, a substance of known triple-point into a triple-point cell, a glass of known optical density into a transmission filter, and spheres of uniform particle size mounted on a microscope slide. Such devices can also be considered CRMs.
4. All CRMs lie within the definition of "measurement standards" given in the VIM.
5. Some RMs and CRMs have properties that, because they cannot be correlated with an established chemical structure or for other reasons, cannot be determined by exactly defined physical and chemical measurement methods. Such materials include certain biological materials such as vaccines to which an international unit has been assigned by the World Health Organization.

This definition, including the Notes, is taken from ISO Guide 30:1992.

Coherent (derived) unit (of measurement) [1.10]: A derived unit of measurement that may be expressed as a product of powers of base units with the proportionality factor one (1).

Note: Coherency can be determined only with respect to the base units of a particular system. A unit can be coherent with respect to one system but not to another.

Coherent system of units (of measurement) [1.11]: A system of units of measurement in which all of the derived units are coherent.

Conservation of a (measurement) standard [6.12]: A set of operations necessary to preserve the metrological characteristics of a measurement standard within appropriate limits.

Note: The operations commonly include periodic calibration, storage under suitable conditions, and care in use.

Interlaboratory standard: A device that travels between laboratories for the sole purpose of relating the magnitude of the physical unit represented by the standards maintained in the respective laboratories.

International (measurement) standard [6.2]: A standard recognized by an international agreement to serve internationally as the basis for assigning values to other standards of the quantity concerned.

International System of Units (SI) [1.12]: The coherent system of units adopted and recommended by the General Conference on Weights and Measures (CGPM).

Note: The SI is based at present on the following seven base units: meter, kilogram, second, ampere, Kelvin, mole, and candela.

Measurand [2.6]: A particular quantity subject to measurement.

Example: Vapor pressure of a given sample of water at 20 °C.

Note: The specification of a measurand may require statements about quantities such as time, temperature, and pressure.

Measurement [2.1]: A set of operations having the object of determining a value of a quantity.

Note: The operations may be performed automatically.

Method of measurement [2.4]: A logical sequence of operations, described generically, used in the performance of measurements.

Note: Methods of measurement may be qualified in various ways, such as

- Substitution method
- Differential method
- Null method

Metrology [2.2]: The science of measurement.

Note: Metrology includes all aspects, both theoretical and practical, with reference to measurements, whatever their uncertainty and in whatever fields of science or technology they occur.

National (measurement) standard [6.3]: A standard recognized by a national decision to serve, in a country, as the basis for assigning values to other standards of the quantity concerned.

National reference standard: A standard maintained by national laboratories such as the NIST in Gaithersburg, MD; the National Research Council (NRC) located in Ottawa, Canada; the National Physical Laboratory (NPL) in Teddington, U.K.; and the Physikalisch-Technische Bundesanstalt (PTB) at Braunschweig, Germany, which are the legal standards of their respective countries.

NIST: The U.S. national standards laboratory, responsible for maintaining the physical standards upon which measurements in the United States are based.

Primary standard [6.4]: A standard that is designated or widely acknowledged as having the highest metrological qualities and whose value is accepted without reference to other standards of the same quantity.

Note: The concept of primary standard is equally valid for base quantities and derived quantities.

Principle of measurement [2.3]: The scientific base of a measurement.

Examples

- The thermoelectric effect applied to the measurement of temperature
- The Josephson effect applied to the measurement of electric potential difference
- The Doppler effect applied to the measurement of velocity
- The Raman effect applied to the measurement of the wave number of molecular vibrations

Reference standard [6.6]: A standard, generally having the highest metrological quality available at a given location or in a given organization, from which measurements made there are derived.

Reference material [6.13]: A material or substance, one or more of whose property values are sufficiently homogeneous and well established to be used for the calibration of an apparatus, the assessment of a measurement method, or for assigning values to materials.

Note: A reference material can be in the form of a pure or mixed gas, liquid, or solid. Examples are water for the calibration of viscometers, sapphire as a heat-capacity calibrant in calorimetry, and solutions used for calibration in chemical analysis.

This definition, including the Note, is taken from ISO Guide 30:1992.

Repeatability (of results of measurements) [3.6]: The closeness of the agreement between the results of successive measurements of the same measurand carried out under the same conditions of measurement.

Notes:

1. These conditions are called *repeatability conditions*.
2. Repeatability conditions include
   a. The same measurement process
   b. The same observer
   c. The same measuring instrument, used under the same conditions
   d. The same location
   e. Repetition over a short period of time
3. Repeatability can be expressed quantitatively in terms of the dispersion of characteristics of the results.

Reproducibility (of results of measurements) [3.7]: The closeness of the agreement between the results of measurements of the same measurand carried out under changed conditions of measurement.

Notes:

1. A valid statement of reproducibility requires specification of the conditions changed.
2. The changed conditions include
   a. Principle of measurement
   b. Method of measurement
   c. Observer
   d. Measuring instrument
   e. Reference standard
   f. Location
   g. Condition of use
   h. Time
3. Reproducibility can be expressed quantitatively in terms of the dispersion characteristics of the results.
4. Results here are usually understood to be corrected results.

Secondary standard [6.5]: A standard whose value is assigned by comparison with a primary standard of the same quantity.

Standards laboratory: A work space, provided with equipment and standards, a properly controlled environment, and trained personnel, established for the purpose of maintaining traceability of standards and measuring equipment used by the organization it supports. Standard laboratories typically perform fewer, more specialized, and higher accuracy measurements than calibration laboratories.

Tolerance: In metrology, the limits of the range of values (the uncertainty) that apply to a properly functioning measuring instrument.

Traceability [6.10]: The property of the result of a measurement or the value of a standard whereby it can be related to stated references, usually national or international standards, through an unbroken chain of comparisons all having stated uncertainties.

Notes:

1. The concept is often expressed by the adjective *traceable*.
2. The unbroken chain of comparisons is called a *traceability chain*.

Even though the ISO has published (and accepted) the definition listed earlier, many practitioners endeavor to make this term more meaningful. They feel that the definition should introduce the aspect of evidence being presented on a continuing basis, to overcome the idea that if valid traceability is achieved, it could last forever. A definition similar to the following one would meet that requirement.

Traceability is a characteristic of a calibration or a measurement. A traceable measurement or calibration is achieved only when each instrument and standard, in a hierarchy stretching back to the national

(or international) standard, was itself properly calibrated and the results properly documented including statements of uncertainty on a continuing basis. The documentation must provide the information needed to show that all the calibrations in the chain of calibrations were appropriately performed.

Transfer standard [6.8]: A standard used as an intermediary to compare standards.

Notes: The term *transfer device* should be used when the intermediary is not a standard.

Traveling standard [6.9]: A standard, sometimes of special construction, intended for transport between locations.

Example: A portable battery-operated cesium frequency standard.

Uncertainty of measurement [3.9]: A parameter, associated with the result of a measurement that characterizes the dispersion of the values that could reasonably be attributed to the measurand.

Notes:

1. The parameter can be, for example, a standard deviation (or a given multiple of it) or the half-width of an interval having a stated level of confidence.
2. Uncertainty of measurement comprises, in general, many components. Some of these components can be evaluated from the statistical distribution of the results of series of measurements and can be characterized by experimental standard deviations. The other components, which can also be characterized by standard deviations, are evaluated from assumed probability distributions based on experience or other information.
3. It is understood that the result of the measurement is the best estimate of the value of the measurand and that all components of uncertainty (including those arising from systematic effects), such as components associated with corrections and reference standards, contribute to the dispersion.

This definition is that of the *Guide to the Expression of Uncertainty in Measurement*, in which its rationale is detailed (see, in particular, 2.2.4 and annex D) [4].

Value (of a quantity) [1.18]: The magnitude of a particular quantity generally expressed as a unit of measurement multiplied by a number.

Examples

- Length of a rod: 5.34 m or 534 cm
- Mass of a body: 0.152 kg or 152 g
- Amount of substance of a sample of water (H_2O): 0.012 mol or 12 mmol

Notes:

1. The value of a quantity can be positive, negative, or zero.
2. The value of a quantity can be expressed in more than one way.
3. The values of quantities of dimension one are generally expressed as pure numbers.
4. A quantity that cannot be expressed as a unit of measurement multiplied by a number can be expressed by reference to a conventional reference scale or to a measurement procedure or both.

Working standard [6.7]: A standard that is used routinely to calibrated or check material measures, measuring instruments, or reference materials.

Notes:

1. A working standard is usually calibrated against a *reference standard*.
2. A working standard used routinely to ensure that a measurement is being carried out correctly is called a *check standard*.

Bibliography

Alves, J. G., Developments in standards and other guidance for individual monitoring, *Radiation Measurements*, 43(2–6), 558–564, 2008.

Cochrane, R. C., Measures for progress—History of the National Bureau of Standards, United States Department of Commerce, Library of Congress Catalog Card Number: 65-62472, 1966.

JCGM/WG 2 Document N318, *International Vocabulary of Basic and General Concepts and Associated Terms, NIST*, http://www.nist.gov/pml/div688/grp40/upload/International-Vocabulary-of-Metrology.pdf (accessed on March 13, 2013).

Klein, H. A., *The Science of Measurement: A Historical Survey*, New York: Dover Publications, Inc., 1974.

Liptak, B. and H. Eren, *Instrument Engineers Handbook: Process Software and Digital Networks*, Vol. 3, 4th edn., LLC, Boca Raton, FL: CRC Press, pp. 953–961, 2011.

NIST Calibration Program, Calibration services users guide, SP 250 Appendix fee schedule 2011, NIST, http://www.nist.gov/calibrations/upload/feesch-11-2-2.pdf (accessed on March 13, 2013).

Publications, BIPM, http://www.bipm.org/en/publications/ (accessed on March 13, 2013).

Standards, Legistlation, Technical Information, Browse by the subject, SAI Global, http://infostore.saiglobal.com/store/ (accessed on March 13, 2013).

Taylor, B. N., NIST Special Publication 811, *Guide for the Use of the International System of Units* (*SI*), U.S. Department of Commerce, National Institute of Standards and Technology, Gaithersburg, MD, 1995.

Taylor, B. N. and C. E. Kuyatt, Guidelines for evaluating and expressing the uncertainty of NIST measurement results, NIST Technical Note 1297, 1994.

Velychko, O. and T. Gordiyenko, The use of metrological terms and SI units in environmental guides and international standards, *Measurement*, 40(2), 202–212, 2007.

8

Calibrations in Instrumentation and Measurements

Halit Eren
Curtin University

8.1 Introduction

The Oxford English Dictionary explains the meaning and scope of calibration by defining it as follows: "(1) mark (a gauge or instrument) with a standard scale of readings, (2) compare the readings of (an instrument) with those of a standard, and (3) adjust (experimental results) to take external factors into account or to allow comparison with other data." Basically, calibration is the comparison between measurements and it is an essential component of measurements.

The ability of an instrument or a device to measure accurately depends on a number of factors, such as its duration in service, temperature, vibrations, humidity, environmental exposure, corrosion, electronic malfunctioning, drift, and changes in application conditions. Calibration quantifies the change in the measurements, and hence, periodical adjustments on the device become necessary to decrease or eliminate possible errors.

Calibration of instruments assures that the processes are well controlled and the products meet expected specifications since the measurements can drift away from their correct and calibrated values resulting in unreliable readings. For example, if the representation of process variables drifts away from their true range, it can result in costly production downtimes, create adverse safety issues, and lead to inferior quality goods being produced. Today, in our daily lives, we are very much dependent on the correct operations of instruments, for example, when driving vehicles, but we take them for granted with the expectation that they are all functioning well giving us correct readings, which may not be the case.

An important element in calibrations is the relationship between a single measurement and the reference base. The base unit of measurement is Le Système International d'Unités (SI) units maintained in the Bureau International des Poids et Mesures, Paris. These are *kilogram* for mass, *meter* for length, *second* for time, *candela* for luminous intensity, *Kelvin* for thermodynamics, *ampere* for current, and *mole* for amount of substance. Other reference bases such as *Newton* for force and *hertz* for frequency are derived from the base units and maintained by national standards institutions.

8.2 Errors and Uncertainties in Calibrations

Most instruments and sensors are designed to meet certain accuracy specifications; the process of adjusting an instrument to meet those specifications is known as the calibration. The device used to calibrate other instruments is known as a calibrator. Before the calibration is attempted, the calibrator itself must be calibrated to ensure that they themselves are performing error-free. Although calibration and accuracy are performed by the instrument manufacturers, it may also be necessary for the operators to perform a "user calibration." The user calibration includes the equipment settings, test setup, and verification of correct application to validate that the desired levels of precision and accuracy are achieved. The term *calibration standard* is used when an absolute measured value and the reference standards are traceable back to national and international primary standards.

Despite strict rules and procedures, most calibrations are likely to have errors and uncertainties in their final values. These calibration errors and uncertainties can be evaluated by implementing Type A and/or Type B techniques:

1. *Type A*: Evaluation applies to errors, uncertainties, and bias by using statistical techniques. The ISO guidelines, such as ISO 11095, give guidance on how to assess, correct, and calculate errors, uncertainties, and biases.
2. *Type B*: Evaluations can apply to errors, uncertainties, and bias too. The calculation of the uncertainty component is not based on a statistical analysis but on factors such as experience, scientific judgment, scant data, and the use of different laboratory assessments.

However, in many situations, it may be impossible to achieve a perfect calibration because of instrument and measurement biases and uncontrollable random errors. These can mathematically be expressed as

$$\text{Ideal value} = \text{Measured value} + \text{Bias} + \text{Error}$$

Similarly, reference value may be subject to bias and error:

$$\text{Ideal reference value} = \text{Reference value} + \text{Bias} + \text{Error}$$

This leads to a deficiency in the calibration as

$$\text{Deficiency} = \text{Ideal measured value} - \text{Ideal reference value}$$

Due to the randomness of errors, this deficiency may not be zero; therefore, in some cases, the calibration measurements may have to be repeated many times. Then the statistical techniques can be applied to work out the calibration curves, average readings, and standard deviations. The process of collecting data for creating the calibration curve is critical to the success of the calibration program.

8.3 Benefits of Calibrations

Usually, the calibration procedure involves comparison of the instrument against primary or secondary standards. In some cases, it may be sufficient to calibrate a device against another one with a known accuracy. After the calibration of a device or a process, future operation is considered to be error-bound for a period of time under similar operational conditions thus yielding to the following benefits:

- Confidence on the future measurements
- Consistency and compatibility
- Repeatability and reproducibility
- Products meeting their specifications, thus reducing legal liability
- Proper documentation to meet quality standards such as those set by the ISO
- Frequent calibrations can provide graphical view of the equipment uncertainty over time and lead to reliability in performance
- Measurements made within international standards promote global acceptance thus increasing competitiveness
- As the technology changes, the regulations and legislation of test and measuring instruments change continually and calibration helps compliance validity of measurements and processes under changing conditions

8.4 Calibration Procedure and Personnel

A successful calibration process requires hardware and software, special equipment, and skilled personnel. It is a process that assigns values to the response of an instrument relative to reference standards or to a designated process. The aim is to eliminate or reduce the errors, uncertainties, and biases in the measurements relative to the reference standard. In order to achieve this aim, a step-by-step calibration procedure and following this procedure with the detailed instructions are essential. In doing so, the following factors must be considered:

1. The type of calibration process to be employed
2. Calibration equipment and environment setup
3. Calibration cycles
4. Types of records, reports, and report keeping
5. Possible factors that may affect the calibration
6. Mathematical analysis and tools
7. In-house versus outsourced calibration
8. Reference standards to be used
9. Traceability issues
10. ISO 9000 compliance
11. Published standards to be used
12. Handling measurement uncertainties and errors
13. Identification of random and systematic errors

Once these factors have been noted, an appropriate calibration procedure must be followed. Calibrations must be repeatable and mathematically expressible.

Skilled personnel are essential to obtain successful calibrations. The personnel may have appropriate clothing (static-free clothing, gloves, face masks, etc.) for safety as well as to avoid the possibility of contamination. Although fully trained and experienced, it is possible for different operators to produce different results. To overcome this problem, measurements by different operators can be plotted and compared. Another solution may be to employ separate calibration curves by the same operator. This may not be a problem in automated calibrations.

8.5 Calibration Methods

Two basic calibration methods are the static calibration and the dynamic calibration.

8.5.1 Static Calibration

Static calibration aims the tuning of static characteristics of instruments under off-line conditions.

8.5.2 Dynamic Calibration

Dynamic calibration aims tuning of the dynamic characteristics, while the process is taking place. It makes use of multisampling points to dynamically decide stable and accurate operations of the process under different conditions.

In many dynamic applications, calibrated variables have multiple inputs and multiple outputs. In these cases, an input is varied in increments in increasing and decreasing directions over a specified range. The observed outputs then become a function of that single input. This procedure may be repeated by varying other inputs, thus developing a family of relationships between inputs and outputs. In these multivariable situations, the input/output relationship usually demonstrates statistical characteristics. From these characteristics, appropriate calibration curves can be obtained, and statistical techniques can be applied by using various mathematical tools, such as averaging, weighed average, and multi-fixed-range averaging or standard-deviation-range averaging.

8.6 Laboratories and Institutions

In many organizations, calibrations are conducted either on-site or in laboratories or remote locations. Large organizations may have several calibration laboratories dedicated for different instruments and processes. Laboratories are accredited by authorities in accordance with the guidelines such as the ISO Guide 58. Accreditation is a formal recognition that a particular laboratory is competent to conduct specific tests and/or calibrations.

During the calibration process, the readings of the test item are compared with the reference standards such as resistors, length standards, and voltage standards.

A successful laboratory calibration procedure requires the following basic steps:

- Selection of an appropriate reference standard with known values covering the range of interest
- Conducting calibration curves (i.e., least-squares fit) to establish the relationship between the measured and known values of the reference standard
- Correction of measurements by using calibration curves
- Preparation of the appropriate documentation of the calibration procedure, results, analysis, and interpretation of results for the client

Once the procedure is adapted, the calibration relies on the instrument continuing to respond consistently and in the same way during the calibrations. If the system drifts or takes unpredictable deviations, the calibrated values may not be easily corrected for errors and bias, thus degrading the accuracy of the measurements.

Many institutions provide comprehensive calibration services. A typical institution can provide calibration of multitude of variables, such as force, pressure, weight and mass, metrological values, dimensions, temperature, flow, and electronics test and measurement equipment.

Customers of an institution can be from a wide range of industries, such as automotive, aviation, contractor engineering, food and beverage, manufacturing, marine, metal and mining, nuclear, oil and gas, petrochemical and chemical, pharmaceutical, power and energy, and pulp and paper industries.

Some institutions develop, manufacture, and market calibration equipment, software, systems, and services. Their product range includes portable calibrators, workstations, calibration software, accessories, industry-specific solutions, and professional services. They comply with customer requirements for accuracy, versatility, efficiency, ease of use, compatibility, and reliability.

8.6.1 Calibration Records

Calibration history is an important part of knowing data quality. The records can be kept in software environment or in printed formats. Many companies provide software in data file format that enables the sharing of structured data across different information systems. Data fields such as position ID, device ID, location, serial number, and work order number can be transferred from one form to another suitable for engineers to evaluate or the managers to view. In addition, the data can include maximum errors, pass/fail notifications, calibration date and time, calibration frequency, and who carried out the calibration task.

Once calibration is completed, appropriate labeling is used for that instrument to supply information on the applicability of instruments. The labels indicate parameters of instrument, tolerances, and special conditions of use. Calibration labels need to conform to the requirements of ISO/IEC 17025 General Requirements for the Competence of Testing and Calibration Laboratories. ISO 17025 requires that the following conditions be met:

- All measurement equipment shall be securely and durably labeled
- The labels should clearly indicate the name of the calibration laboratory, date of calibration, due date, usage equivalent, and the authorized officer
- Information on label must be legible and durable under reasonable use and storage conditions
- When it is impractical to affix a label directly on an item, the label may be affixed to the instrument container
- Temper resistance seals may be used when necessary
- Functional labels should contain reference standards

8.7 Calibration Software Support

Calibrations are mostly conducted by using computers to capture and analyze data. Once the results are obtained, software packages assist in analyzing the information. Most packages use method of least squares for estimating the coefficients. Some of the packages are capable of performing weighted fit if the errors of the measurements are not constant over the calibration interval. The spreadsheets and software packages provide information such as the coefficients of the calibration curve, standard deviations, residual standard deviation of the fit, and goodness of the fit.

8.7.1 Spreadsheets and Calibration Management Software

A set of spreadsheets are used to perform random-number-driven simulations, including single standard, bracket, calibration curve, and standard addition methods. These simulations include additive and multiplicative interferences (systematic errors) and random errors in both signal and measurements. It is possible to observe how nonlinearity, interferences, and random errors combine and attempt to

optimize precision and accuracy of the measurement. Some of these spreadsheet models are linear fit, nonlinear fit, single standard addition, multiple standard addition, and others.

In addition to spreadsheets, there are many calibration management software (CMS) to schedule calibrations, track usage and locations, maintain histories, generate work orders, issue certificates, and print calibration labels. Most CMS will support web-based access. They support information on short- and long-term effects on the devices and their linearity and stability.

CMS may have automated features. An automated system promotes efficient management of plant assets and field instruments in one database. They generate future calibration schedules and alerts on the past failed calibrations. Most CMS complies with the ISO 17025 requirements. Some examples of the CMS are as follows:

1. *Ape Software* (calibration control): intuitive database program that organizes calibration data for gages and other test equipment
2. *AssetSmart*: web-based asset, calibration, material, and tool maintenance management software
3. *BDR Systems*: preventive calibration system that provides monitoring, tracking, and control of the calibration function
4. *Beamex*: CMS for documenting, planning, analyzing, and optimizing calibration work
5. *CompuCal Software*: online compliant calibration and maintenance management that ensure quality compliance with 21 CFR Part 11, GxP, ISO, and PAT initiatives
6. *CyberMetrics*: GAGEtrak—CMS
7. *Diversified Data Systems* (OpenMETRIC): Calibration and Metrology Data Management and Tracking Software for ISO 17025 and ISO 9000 with 21 CFR Part 11
8. *Honeywell International*: DocuMint automated calibration management system that promotes efficient management of plant assets and field instruments in one database
9. *IBM*: Maximo Calibration—provides all requirements for traceability and reverse traceability, all calibration history data, calibration data sheets, and reporting

8.8 Cost of Calibrations

The cost of calibration depends on what is calibrated and who is calibrating it. In simple cases where a single instrument is involved, the cost can be lower than one hundred dollars, but some complex cases can cost thousands of dollars. Calibration cost depends on where the calibration is carried out whether it takes place in special laboratories or on the plant. The cost of calibration may be dependent on the availability of expert in-house personnel or outsourcing it to third parties. Certification by ISO 10012-1, ISO 9001, MIL-STD 45662A, and MIL-HDBK-52B requires careful calibration of the measuring equipment used in the process. Also, in some cases such as the weighting systems, calibration is a statutory requirement.

One of the major factors for cost is the frequency of calibration. In most cases, a validity period is issued during which calibrated devices can be used without concern for major errors and uncertainties. Some organizations conduct calibrations in regular intervals, while others opt for conservative calibration intervals simply to meet the legal demands. Nevertheless, the use of uncalibrated instruments in an organization can be costly as it may affect the product quality and the quality of downstream operations.

Standards such as MIL-STD 45662A suggest regular and well-organized calibration intervals. As a rule of thumb, 85%–95% of all instruments returned for calibration must meet the calibration limits determined by the probability chart of age and failure data. Usually an instrument must be calibrated if failure rate increases or functionality deteriorates when compared to other standard devices. In this respect, a number of different mathematical techniques, such as the Weibull statistics and renewal equations, can be employed. A range of software, for example, the visualSMITH and Calibration Manager, is available for determining the calibration intervals and the cost analysis.

8.8.1 Obtaining Information

Information on calibration is available from various sources. These are

1. *Manufacturers* supply comprehensive information about calibration requirements of their products
2. *Regulating authorities and standards institutions* supply information about calibration requirements of instruments and devices. Calibration can be statutory particularly where health and safety are important
3. *Calibration services* provide information on calibration processes
4. *Organizations* provide rules and regulations for their equipments for assurance planning
5. *Books* provide information on calibration issues and processes

Many nations and organizations maintain laboratories with the primary functions of calibrating instruments and field measuring systems that are used in everyday operations. Examples of these laboratories are Standards Council of Canada (SCC), National Institute of Standards and Technology (NIST), National Association of Testing Authorities (NATA) of Australia and the British Calibration Services (BCS), and Australian Standards (AS). Some important information on calibration can be found in sources of ISO, IEC, IEEE, and national standards publications. Few of these publications will be briefly explained in the following.

ISO 17025 is an international standard for calibration and testing laboratories. It requires labs to demonstrate that they operate a quality system covering processes, documentation, and quality management. The laboratories need to generate technically valid results accounting of the equipment procedures and personnel. Information on ISO 1705 can be found in many books or ISO publications (http://www.fasor.com/iso25/).

The military standards MIL-STD-45662A is a standard that describes the requirements for creating and maintaining calibration systems for measurement and testing (available at http://store.mil-standards.com/).

8.9 Trends in Calibrations

With the availability of advancing technology, the classical calibration process is changing at least in three fronts, these being

1. Electronic calibrations
2. Intelligent, soft calibrations, and self-calibrations
3. Remote and e-calibrations

These techniques will be explained next and some examples will be given.

8.9.1 Electronic Calibration

Many modern instruments offer features for closed-case calibrations so that electronic calibration can be employed. Electronic calibration is a single connection and one- or two-port calibration technique without tempering the components inside the case. Once the calibrating equipment, for example, computer, is linked with the device under calibration, appropriate software generates the necessary calibration information. Errors due to gains and offsets of the instrument are corrected mathematically within the instrument processor to obtain the correct measured values. Analog corrections can also be made via the adjustment of the parameters of some components such as the digital-to-analog converters. Corrected calibration constants are kept within the nonvolatile memory for permanent use.

As an example of this method, Agilent electronic calibration modules 8719, 8720, and 8722 microwave network analyzers provide a broad frequency range of calibrations from 10.0 MHz to 67.0 GHz

(http://we.home.agilent.com/). Similarly, Fluke offers electronic calibration facilities for multifunction process, pressure, and temperature instruments (http://www.fluke.com/).

8.9.2 Self-Calibration

With the wide applications of digital systems, many intelligent instruments are available and widely used in process industry. Many of these devices have self-calibrating features. In self-calibrations, post-measurement corrections are made, and the magnitudes of various errors are stored in the memory to be recalled and used in laboratory and in field applications.

Apart from the intelligent instruments, many intelligent (smart) sensors are being employed. Particularly, sensors complying with IEEE 1451.4 standards provide comprehensive Transducer Electronic Data Sheets (TEDS) that contain configuration, scaling, and calibration information necessary to make measurement through mixed-mode interface. Many smart sensors are capable of calibrating themselves, scaling the incoming data, computing statistics, and communicating with other digital systems on the network. Most commercially available software permits calibration of smart sensors and uploads the new parameters directly to the circuitry of the sensors. More information can be found on this topic in the chapter dedicated on intelligent instruments in this book.

In an application of smart sensors (e.g., the Atmos SSP14 Sensor Signal Processor family; http://www.sensorsmag.com/), the sensors have memory programmed at the factory with a set of default zero values and span curves defining the relationships with the physical phenomenon. These default curves represent average sensor output adjusted for the most accurate response at the room temperature. Each time calibration is done, an appropriate zero or span curve adjusted in the vicinity of the desired functionality points.

8.9.3 Soft Calibration

Soft calibration is a strategy for constructing a global multivariate calibration model that includes calibration samples measured over time on different days and is used in analysis.

8.9.4 Remote and e-Calibration, iCal

A new trend of calibration is the Internet calibration. Internet calibration technique is supported by web-accessible test procedures and appropriate hardware and software.

As examples of Internet calibration, Fluke, U.K., offer calibration systems for the Fluke 4950 multifunctional instruments (http://www.npl.co.uk/). On the other hand, Anritsu is active in investigating the possibilities of Internet-based calibration by using portable Optical Time Domain Reflectometer (OTDR) MW9076 (http://www.electronicstalk.com/news/anr/anr163.html). The OTDR is controlled via the Internet with the aid of appropriate software. The software can be controlled through a PC via modem, mobile telephone access, or PCI cards. Internet calibration is supported by appropriate software that includes the mathematical models of the interface electronics and optimizes calibration on that basis of this model.

Regular calibration is essential for quality and traceability to national and international standards. One way of achieving traceability is to send the instruments to be calibrated and acquiring certificate and correction values from a National Measurement Institute (NMI). In many cases, the value of settings can be affected by transport leading to uncertainty. This exercise can be costly and time consuming. Also, in many cases of the process industry, some of the equipment is bulky for transport and dynamic calibrations are necessary on-site. A solution to these problems is the e-calibrations through the Internet. This reduces the transportation needs, environmental effects, downtime, cost issues, and the need for in-house expertise.

Internet assists calibrations to take place in a number of ways:

1. Internet acts as a means of exchanging information between two remote sides with human operators at each end using interactive links
2. Remote monitoring of the sensors

Internet calibration consists of the operations to be performed for maintaining the system tuned for properly executing the process tasks in hand. Measurements rely on the available standards and the associated software suitable for the Internet calibrations. Typical requirements are

1. A computer connected to the Internet
2. Appropriate calibration software
3. A login name and password to use the service
4. Understanding of basic calibration principles
5. Understanding of the principles and functionality of the instrument under calibration
6. Understanding of scientific principles

Once a computer has been connected to the measurement system to be calibrated, the computer needs to log on to the calibration service provider. Services that offer online calibrations are known as *Internet Calibration Services* or iCals.

Once connected to the system, iCal instructs the operator, in the correct order, to perform the measurements. Effectively, it provides the operator with a soft procedure to perform the measurements. Once the measurement procedure is completed, the system generates the required final data with uncertainties ascertained from the measured and database information, providing the operator with a certificate if applicable.

During the measurement process, there is potential for the iCal system to provide measurement assistance screens with video or procedural details for specific parts of the process. In addition, it provides the administration with any measurement procedural changes through new international standards and ensures all groups are following common guidelines. The new data and historical records are automatically kept on the websites and they can be accessed and checked by the service users.

8.10 Calibration Examples

There are examples of many other Internet calibration and metrology in the process industry and medical and optical network markets. The optical communications network provides a method of a real standard transfer for wavelength measurements.

One of the first iCal services was developed by the United Kingdom's National Physical Laboratory (NPL). It was combined with the technology of remote monitoring, remote control, and NMI calibration techniques for application in a microwave frequency measurement system called *vector network analyzers* (VNAs).

In this application, the client enters the required measurement parameters and is offered options based on the knowledge that the NMI has about the client's equipment. From this point, the entire measurement process is controlled by NMI. VNAs provide a swept frequency measurement of the transmission and reflection coefficients for an electrical network. Calibration is performed using instrument firmware and a set of standard devices, all of which are assumed to be ideal and are available as standard items from the VNA manufacturer. The correction of the measurement data to that of the NMI comes via precision verification artifacts, air-spaced transmission lines, attenuators, and terminations, whose properties change little over time. Once the calibration is completed, all correction factors are stored in an online database. The standard is returned, all a client needs to do to measure a device with traceability.

A few other calibration examples are given in the following sections.

8.10.1 Flow Calibration

There are many devices available for the measurement of liquid, air, or solid flow. Once the method of measurement is determined by the use of appropriate flowmeter, static or dynamic calibrations can be carried. For example, in the case of static–gravimetric liquid flow, a calibration facility may include a reservoir, pumping system, piping system, flowmeter under test located on the pipeline, collection system, computers and interface, and supporting software. The calibration of flow of fluid through the meter can be determined by collecting prescribed mass of steady fluid flowing over a measured time interval.

The calibrations of flowmeters fall into three distinct categories:

- Factory calibration
- Initial site calibration
- Routine site recalibration

All size flowmeters, large or small, can be calibrated by mobile or static test rigs. Flowmeter calibration is very important in international trade of oil and other bulk fluid movements. Therefore, flowmeters require to be calibrated against accurate reference standards traceable to internationally accepted primary standards.

8.10.2 Sensor Calibration

Sensors may have to be calibrated after having integrated with a signal conditioning system. This process requires an injection of known input signal into the sensor. By observing the output, a correct output scale can be configured for that particular application. If the sensor is used for time-varying inputs, the dynamic calibration becomes necessary. In most cases, transient behavior of sensor top step response may be sufficient to assess the dynamic response of the sensor.

8.10.3 Calibration of Chemical Mixtures

As food contains many chemical substances, the calibration of devices becomes complex. For example, in the case of honey in food processing industry, the following parameters need to be identified by calibrating instruments: fructose, glucose, maltose, moisture level, acidity, etc.

8.10.4 Static Pressure Calibrations

For example, for aircraft pressure transducers, pressure up to 500 psi can be calibrated on computer-controlled automatic test facilities, using gas as the pressure medium. Ranges above 1000 psi can be calibrated manually using hydraulic media. Most calibration standards can have accuracies better than ±0.01%.

In an application, the computer-controlled calibrations are performed at zero and 20% increments of full scale to 100%. Manual calibrations are performed at zero and 25% increments of full scale. For all transducers, the test data are fed into a computer, which calculates the test parameters; plots nonlinearity, thermal zero shift, and thermal sensitivity shift; and prints out the test report. The computer then compares the test data with stored specification limits and accepts or rejects each transducer.

Measurements are first made at zero pressure, then 2 times full scale, then zero, to establish zero shifts after 2 × FSO. Then two complete cycles from zero to full scale and return are performed, measuring output at 20% (or 25%) increments. These data points are used for calculation of nonlinearity, hysteresis, and nonrepeatability.

8.10.5 Dynamic Pressure Calibrations

In some cases, dynamic characteristics can be established from periodic static calibrations. However, in many cases, the accuracy available in dynamic measurements cannot be extrapolated from only static calibrations. Several of the more commonly used methods of dynamic calibration are as follows:

- Comparison pressure calibrations can be performed dynamically with a range of sinusoidal pressure generators.
- Hydraulic pressure generators can be used. They incorporate a compression spring, piston and seismic mass assembly, hydraulic oil-filled chamber, and mounting cavities for the reference standard and test transducers. Sinusoidal vibratory motion applied to the generator housing imparts sinusoidal pressure to oil, which is exposed simultaneously to the sensing surfaces of both transducers providing a direct comparison calibration capability.
- Sinusoidal vibration of a vertically mounted liquid column provides a dynamic pressure that can be applied to a test transducer mounted at the bottom of the tube. By attachment to an electrodynamic vibrator, short liquid columns can be used to provide about 5 psi from about 50 to 2,000 Hz. Low frequency is generally limited by the vibrator and the high frequency is limited by the resonance frequency and damping of the liquid column.
- The inlet modulated pressure generator (IMPG) consists of a wheel with holes drilled through its periphery, which is rotated at high speed. Air is blown through the holes from one side of the wheel and there is a cavity on the opposite side of the wheel in which are located the transducer under test and a reference transducer. The frequency of the signal generated is directly proportional to the speed of rotation. Frequencies of up to 12 kHz can be generated with pressure amplitudes of 1.0 Bar at 1.0 kHz falling to 0.1 Bar at 12.0 kHz. Static mean pressures can be generated.
- The Galton whistle consists of a tube, which is sharp edged at one end and is closed with a moveable piston at the other. Air, which is blown over the edge of the tube, excites the first organ pipe resonance. The resonant frequency is adjusted by the position of the piston within the tube. Mounted in the piston are the reference pressure transducer and the transducer under test.
- Small shock tubes are often used to provide rise time and frequency response characteristics for transducers. Because of difficulties in determining the pressure level in the step, shock tubes are not usually used for pressure sensitivity calibration. Pressure rise times of about 1 μs are practical, which permit transducer characterization to frequencies beyond 100 kHz.

Bibliography

Alessio, C. et al., Quality management issues for PC-controlled calibration systems, *IEEE Instrumentation and Measurement Technology Conference*, *I2MTC*, Singapore, pp. 1610–1615, 2009.

Bucher, J. L., *Quality Calibration Handbook—Developing and Managing a Calibration Program*, ISA Publication, ASQ Quality Press, Milwaukee, WI, 2007.

Busoni, S. et al., Performance evaluation of a full line of medical diagnostic displays and test of a web-based service for remote calibration and quality assurance, *Proceedings of the SPIE—The International Society for Optical Engineering*, 7263, 72630A, 2009.

Commercial Services—National Physical Laboratory, Measurement Services, http://www.npl.co.uk (accessed on February 6, 2012).

Dixson, R. et al., Reference metrology in a research Fab: The NIST clean calibrations thrust, *Proceedings of the SPIE—The International Society for Optical Engineering*, 7272, 727209, 2009.

Eren, H., Calibration in process control, in: *Instruments Engineers' Handbook, The IEH*, Eds., B. Liptak and H. Eren, Vol. 3, 4th edn., Chapter 7, CRC Press, Boca Raton, FL, pp. 141–149, 2011.

Fluke testing and calibration, http://www.fluke.com (accessed on July 8, 2011).

Gupta, S. V., *Measurement Uncertainties: Physical Parameters and Calibration Instruments*, Springer-Verlag, Berlin, Germany, 2012.

Internet Enabled Calibration—Electronics Talk, http://www.electronicstalk.com/news/anr/anr163.html (accessed on December 19, 2011).

ISO/IEC/EN 17025, http://www.fasor.com/iso25 (accessed on February 18, 2012).

Menzies, T. et al., Accurate estimates without calibration? *Making Globally Distributed Software Development a Success Story—International Conference on Software Process, ICSP 2008*, Leipzig, Germany, Vol. 5007, LNCS, pp. 210–221, 2008.

MIL-Standards, Handbooks and specifications, http://store.mil-standards.com (accessed on January 16, 2012).

Technical Articles—Sensors, http://www.sensorsmag.com (accessed on January 24, 2012).

Test management products—Agilent Technologies, http://we.home.agilent.com (accessed on August 20, 2010).

Xuzhang, W. and R. Feng, Research on control methods of calibration program in tele-calibration system, *Proceeding of the International Conference on Networked Computing, INC2010*, Xiang, China, pp. 303–306, 2010.

Zagozdzon, M. and M. Turkowski, Computerization and automation of the water facility for flowmeters calibration, *Przeglad Elektrotechniczny*, 84(5), 195–199, 2008.

Partial List of Calibration Service and Software Providers

American Calibration, Inc., 4410 Rte 176, Suite 14, Crystal Lake, IL 60014, Phone: 815-356-5839, Fax: 815-356-5851, www.americancalibration.com

AMETEK Calibration Instruments, 8600 Somerset Dr., Largo, FL 33773, Phone: 727-536-7831, 800-527-9999 (toll free), Fax: 727-539-6882, www.ametekcalibration.com

Atlantic Instrument & Controls Service, Inc., 168 Old Bulgarmarsh Rd., Tiverton, RI 02878, Phone: 401-625-5778, Fax: 401-625-5730, www.aics-ri.com

Automated Precision, Inc., 15000 John Hopkins Dr., Rockville, MD, Phone: 800-537-2720 (toll free), Fax: 301-990-864820850, www.apisensor.com

Calibrators, Inc., 38 Morning Glory Rd., Cumberland, RI 02864, Phone: 401-769-0333, Fax: 401-769-0335, www.calibratorsinc.com

Cal Lab Co., Inc., 17035 Westview Ave., South Holland, IL 60473-2743, Phone: 708-596-5800, 800-373-1759 (toll free), Fax: 708-596-5802, www.callabco.com

Cal Tec Labs, Inc., 501 Mansfield Ave., Pittsburgh, PA 15205, Phone: 412-919-1377, www.cal-tec.com

CATLab-Accredited Calibration Laboratories, P.O. Box 6598, Williamsburg, VA 23188, Phone: 757-565-4767, Fax: 757-565-4767, catlab.net

CMM Technology, Inc., 1230 Puerta Del Sol, San Clemente, CA 92673, Phone: 949-366-0707, Fax: 949-366-6503, www.cmmtechnology.com

Endress+Hauser, 2350 Endress Place, Greenwood, IN 46143, Phone: 888-363-7377, 888-ENDRESS (toll free), Fax: 317-535-8498, www.us.endress.com

Exact Calibration, Inc., 264 Rancho Santa Fe Rd., Encinitas, CA 92024, Phone: 800-599-1497 (toll free), Fax: 760-753-7959, www.exactcalibration.com

Hayes Instrument Service, Inc., 530 Boston Rd., Billerica, MA 01821, Phone: 978-663-4800, Fax: 978-663-3812, www.hayesinstruments.com

Honeywell Sensing and Control, 1985 Douglas Dr. North, MN10-192B, Golden Valley, MN 55422, Phone: 763-954-4818, 800-446-6555 (toll free), www.sensing.honeywell.com/index.cfm/ci_id/

Indiana Standards Laboratory, 2919 Shelby St., Indianapolis, IN 46203, Phone: 317-787-6578, Fax: 317-787-6580, www.indianastandards.com

Inspec, Inc., 7282 Haggerty Rd., Suite 170, Canton, MI 48187, Phone: 734-451-8740, 800-246-7094 (toll free), Fax: 734-451-8741, www.inspec-inc.com

International Crystal Laboratories, 11 Erie St., Garfield, NJ 07026, Phone: 973-478-8944, Fax: 973-478-4201, www.internationalcrystal.net

Master Metrology, 1041 Cromwell Bridge Rd., Towson, MD 21286, Phone: 410-337-0687, 800-532-8020 (toll free), Fax: 410-337-0787, www.mastermetrology.com

Micro Quality Calibration, Inc., 20743 Marilla St., Chatsworth, CA 91311-4408, Phone: 818-701-4969, Fax: 818-341-9109, www.microqualitycalibration.com

MCMS Metrology, PO Box 232, Lewiston, CA 96052, Phone: 650-521-7678, Fax: 530-623-2289, www.mcmsmetrology.com

Precision Calibration Systems, LLC, 4901 Enka Hwy., Morristown, TN 37813, Phone: 423-278-0946, Fax: 865-281-0604, www.pcsllctn.com

Precision Metrology, 7350 N. Teutonia Ave., Milwaukee, WI 53209, Phone: 414-351-7420, 888-330-3303 (toll free), Fax: 414-351-7429, www.precisionmetrology.com

Restor Metrology, 921 Venture Ave., Leesburg, FL 34748, Phone: 877-220-5554 (toll free), www.restormetrology.com

RS Calibration Services, Inc., 1047 Serpentine Lane, Pleasanton, CA, 94566, Phone: 925-462-4217, www.rscalibration.com

Sears Calibration, 3845 Grader St., Suite A, Garland, TX 75041, Phone: 214-553-6787, 800-736-8830 (toll free), www.searstoolcalibration.com/

Transducer Techniques, Inc., 42480 Rio Nedo, Temecula, CA 92590, Phone: 951-719-3965, 800-344-3965 (toll free), Fax: 951-719-3900, www.transducertechniques.com

Tru Cal International, 401 Country Club Dr., Bensenville, IL 60106, Phone: 630-238-8100, 800-681-5540 (toll free), Fax: 630-238-8101, www.rucal.com/index.lasso

Warren-Knight Instrument Co., 2045 Bennett Dr., Philadelphia, PA 19116-3019, Phone: 215-464-9300, Fax: 215-464-9303, www.warrenknight.com

9

Intelligent Sensors and Instruments

Halit Eren
Curtin University

9.1 Introduction

In measurement and monitoring, there always has been a need to employ devices with the classical requirements, such as the communication capabilities, data processing, fault analysis, configuration guidance, performance tracking and enhancement, calibrations, drift monitoring, convenient access to devices, network management, and security. Most modern intelligent sensors and instruments address these requirements as will be explained in this chapter. Emphasis will be given to intelligent sensors since they represent the state of art of this technology.

Intelligent and smart sensors are devices in a single chip equipped with the necessary digital electronics capable of delivering communications, data processing, and self-health-monitoring features with minimal cost and power overhead on the overall system. Successful integration of these device and their protocols to measurement systems enables a smooth and seamless networking capabilities as well as many additional features. They are capable of interfacing with other devices using agreed protocols such as the IEEE 1451 standards.

Intelligent instruments are computerized devices distinguished from nonintelligent ones by the inclusion of microcontrollers and microprocessor to fulfill the signal processing, communications, data handling, self-calibrations, and decision-making functions. Some examples that intelligent instruments can perform are the correction of the instrument output for biases that are caused by environmental variations (e.g., temperature, humidity) and ability to produce linear outputs and highly nonlinear variables and sensors.

9.2 Intelligent Sensors

A sensor is considered to be intelligent if

- It can provide data, a measure of the quality of the data, and a measure of the health of the sensor possibly based on some intelligent algorithms.
- It embodies specification/identification information as in the embedded form on the physical sensor or virtually on a remote node.
- It can communicate through a network using TCP/IP or similar protocols to support configuration and operation activities.

In order for sensors to integrate into networks successfully, they must embody networking capabilities that provide information flow and control. Currently, there is no defined common digital interface standard on how they should provide information flow. However, there is a strong push in the industry to harmonize the standards that enable networking and data acquisition of sensors.

9.3 The IEEE 1451 Standard

The IEEE-1451 is a set of standards for Smart Sensor Networks to unify the data acquisition control systems across various sensors and transducers [1]. A simplified diagram of this standard is illustrated in Figure 9.1. IEEE 1451 aims for easy connections by using the existing networking technologies, standardized connections, and common software architectures. The standard allows application software, field network, and transducer decisions to be made independently. It also offers flexibility to choose the products and vendors that are most appropriate for a particular application.

At physical connection level, the IEEE-1451 provides standard ways of creating self-describing measurements and control devices. Sensors complying with these standards are expected to have onboard information on the serial numbers, calibration factors, accuracy specifications, and so on. During the installation, location information can also be loaded so that the system can have self-describing properties.

The IEEE P1451 standards come in seven sections:

1. *1451.0-2007* IEEE Standard for a Smart Transducer Interface for Sensors and Actuators—Common Functions, Communication Protocols, and Transducer Electronic Data Sheet (TEDS) Formats
2. *1451.1-1999* IEEE Standard for a Smart Transducer Interface for Sensors and Actuators—Network Capable Application Processor (NCAP) information model
3. *1451.2-1997* IEEE Standard for a Smart Transducer Interface for Sensors and Actuators—Transducer to Microprocessor Communication Protocols and TEDS Formats
4. *1451.3-2003* IEEE Standard for a Smart Transducer Interface for Sensors and Actuators—Digital Communication and TEDS Formats for Distributed Multidrop Systems
5. *1451.4-2004* IEEE Standard for a Smart Transducer Interface for Sensors and Actuators—Mixed-Mode Communication Protocols and TEDS Formats

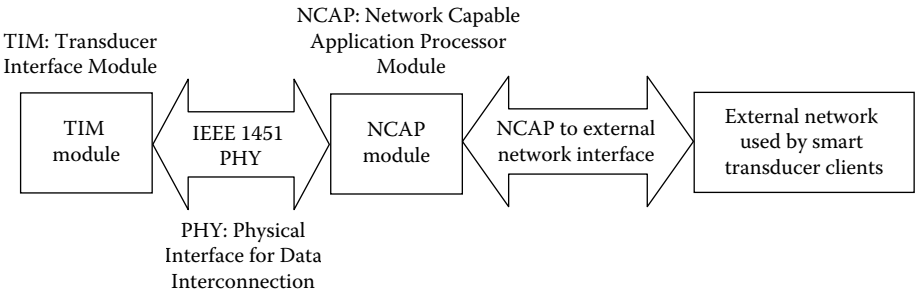

FIGURE 9.1 Simplified functionality of IEEE 1451 standards.

6. *1451.5-2007* IEEE Standard for a Smart Transducer Interface for Sensors and Actuators—Wireless Communication Protocols and TEDS Formats
7. *1451.7-2010* IEEE Standard for a Smart Transducer Interface for Sensors and Actuators—Transducers to Radio Frequency Identification (RFID) Systems Communication Protocols and TEDS Formats

IEEE 1451.1 is termed NCAP information model concerned with the software architecture that moves the intelligence to device level. IEEE 1451.1 uses the benefits of object-oriented technology to create flexible, natural software modules that allow designers to think at the level of real-world systems, not at the level of programming languages. In this way, flexibility can be achieved so that that system can be assembled, reassembled, or modified quickly.

IEEE 1451.2 concerns with the transducers and Microprocessor Communication Protocols and TEDS. It defines the transducer data and electronic interface of digital information direct from the sensors, thus creating a modular architecture to allow embedding of the module to any field networks automatically and transparently.

9.3.1 Transducer Electronic Data Sheet

The heart of IEEE 1451 standard is the definition of the TEDS, the information structure that contains the critical sensor information to enable plug-and-play (PnP) operation. The TEDS, which typically resides in an EEPROM embedded in the sensor, is accessed by the measurement system via a serial interface.

IEEE 1451.4 defines the TEDS structure to be compact yet flexible and extensible to be able to handle a wide range of sensor application requirements. The TEDS has two types of information: (1) the basic information that contains the sensor identification, details of the manufacturer, model number, and the serial number and (2) the standard information containing the specific "data sheet" (e.g., data needed to properly configure the electrical interface and other parameters) and conversion of the measurement data into engineering units. Typical parameters include measurement range, electrical output range, sensitivity, power requirements, and calibration data. IEEE provides standard templates as shown in Table 9.1.

TABLE 9.1 IEEE Standard Templates

Types	Template ID	Name of Template
Transducer templates	25	Accelerometer and force
	26	Charge amplifiers—accelerometer
	27	Microphone preamplifier—built-in
	28	Microphone preamplifier—attached
	29	Capacitive microphones
	30	High-level voltage output sensor
	31	Current loop output sensor
	32	Resistance sensor
	33	Bridge sensor
	34	AC linear/rotary differential transformer
	35	Strain gage
	36	Thermocouple
	37	Resistance temperature detector
	38	Thermistor
	39	Potentiometric voltage divider
	43	Charge amplifier—attached to force transducer
Calibration templates	40	Calibration table
	41	Polynomial calibration curve
	42	Frequency response table

Before installing intelligent sensors supported by Virtual TEDS technology, as an alternative one can configure traditional analog sensors by using binary files. These files can be used to store the information on identification, configuration, and calibration for an individual sensor.

9.3.2 Network Capable Application Processor

Defined in IEEE 1451, each node primarily consists of three fundamental components, which are the NCAP, the smart transducer interface module (STIM), and the physical transducer itself. The NCAP is responsible for providing intelligence and network communication with other nodes in the network. The STIM is responsible for controlling the transducers and their communication with the NCAP. The transducers are connected to the STIM. The NCAP and the STIM together form a networked smart transducer. The sensor nodes thus have the ability to take crucial decisions on their own and communicate more efficiently with other nodes in the network.

The NCAP hosts the processor that makes intelligent control decisions and is responsible for communication with the other NCAPs in the network. It consists of various blocks, namely, functional blocks, transducer blocks, and ports (e.g., application processor client port, publisher port, subscriber port). Each block is in charge of a unique group of functions and manages associated ports. NCAP block is mandatory but other blocks are optional. All of the objects residing in an NCAP process are state based. The blocks in the node would have different states and substates during the life cycle of the node, and only particular set of operations can be performed by a block in a particular state. IEEE 1451.1 defines classes for such blocks and ports. It also lists the operations performed in each class.

The STIM is responsible for housing the transducers and providing the information from the transducers to the NCAP. An STIM acts as an interface between an NCAP and a transducer. It performs the A/D conversion and houses the control unit as well. It usually also contains the TEDS, which provides calibration and other important information about the transducers and the STIM.

9.4 Communications of Intelligent Sensors

IEEE 1451.1 provides the object model of the networked transducer nodes and how they communicate among themselves. IEEE 1451 supports two paradigms of communication among the nodes, which are

1. Multicast publish–subscribe model
2. Point-to-point client–server model

In publish–subscribe communication model, a node publishes a message on a multicast address. This publication message is received by the nodes with subscription to the publication domain specified in the message. By definition for implementation, publish–subscribe messages use User Datagram Protocol (UDP) sockets in order to send and receive messages. This model is primarily used for node discovery and other operations.

Once the nodes are discovered and two nodes have adequate information (such as object tag and object dispatch address) about each other, the two nodes can start client–server communication between each other. Major operations performed by the NCAPs are client–server operations. The communication infrastructure uses TCP/IP for client–server communication.

9.5 Plug-and-Play Capability

A node is PnP if it becomes operational and networked immediately after it is turned on while physically connected to a network. PnP functionality includes self-announcement, self-configuration to a default setting, and acknowledgement to clients/servers of its availability to report sensor readings or to perform actuator functions. PnP capability is not complete unless an application layer communication

language is standardized, which is independent of the network and data link layer communication protocols (e.g., TCP/IP with ZigBee, TCP/IP with 802.11). PnP capability of intelligent sensors has found numerous applications [2,3].

A network becomes dynamic when all the elements in the network have PnP capability and a node is PnP node when it becomes operational and networked immediately after it is turned on and physically connected to a network. Thus, PnP capability plays a very important role in managing a dynamic network. For capability, a node has to

- Announce its presence to other nodes in the network
- Configure itself to the default settings during a start-up
- Acknowledge clients/servers in the network of its availability to report sensor readings or to perform actuator functions

The IEEE 1451.4 standard reduces the time and challenges associated with sensor configuration. The standard establishes a universally accepted method of giving sensors PnP capability, similar to the PnP capability of a USB mouse and personal computers. IEEE 1451.4 defines a mechanism for adding self-describing behavior to sensors with an analog signal interface.

In sensor networks, achievement of PnP provides the following advantages:

- Reduced configuration time by eliminating manual data entry
- Better sensor tracking by storing data sheets electronically
- Improved accuracy by providing detailed calibration information
- Simplified asset management by eliminating paper data sheets
- Reliable sensor location by identifying individual sensors electronically

9.6 Applications and Examples of Intelligent Sensors

Intelligent sensors find many industrial, consumers, and scientific applications, some of which are

- Manufacturing and assembly lines integrated with the machines
- Medicine for dedicated signal processing of the human sensory systems
- Transportation and automotive industries
- Consumer goods

Some examples are as follows.

In consumer industry, SONY has introduced an intelligent presence sensor in their BRAVIA brand televisions. This sensor is based on built-in camera, which detects the body movements and recognizes the facial patterns of up to five viewers (http://esupport.sony.com/docs/imanual/NA/EN/1a/ipsensor_uc_1a.html).

PCB PIEZOTRONICS produces a range of smart sensors. Some examples are 352A56 Series Accelerometers, 481 Series Multichannel Signal Conditioners, TEDS Sensor Interface Kits, and T422 Series In-Line Charge Converters. For instance, Model 352A56 accelerometer conforms to the IEEE 1451.4 standard to define a mixed-mode interface that retains the analog signal but adds a digital link to access TEDS embedded in the sensor for self-identification and self-description. It eliminates the need to manually input sensor parameters such as manufacturer, model number, serial number, calibration fate, and sensitivity when configuring the system (http://www.sensorsportal.com/HTML/SENSORS/TEDS_SensManuf.htm).

The DS2430A 256-bit 1-wire EEPROM produced by Maxim identifies and stores information about the product it is associated. It is capable of storing calibration constants, board identification, and product revision status. This chip finds TEDS compliant applications in smart devices such as piezoelectric force sensors, pressure sensors, and accelerometers. For instance, Model 2801, Smart Remote Charge Converter produced by ENDEVCO, is a TEDS-based low-noise, two-wire single-ended device to be used with nonsmart sensors such as some accelerometers to convert high impedance charge output to low impedance voltages.

9.7 Intelligent Instruments

Intelligent instruments have functionality of learning and adaptation capabilities. They have embedded processing to provide the computational features to perform complex sensing and actuating tasks. A typical structure of intelligent instrument is shown in Figure 9.2.

The functions of an intelligent instrument can be summarized as compensation, information processing, communications, integration, self-calibration, adaptation, and evaluation of the validity of collected data. Information processing encompasses the data-related processing that aims to enhance and interpret the collected data and maximize the efficiency of the system, through signal conditioning, data reduction, event detection, and decision making.

Communications component of intelligent instrument systems incorporates the standardized network protocol, which serves to link the distributed instruments in a coherent manner, enabling efficient communications and fault tolerance. Traditional task-specific instrument systems often contain a number of limitations in terms of complexity, cost, and flexibility. Intelligent instruments aim to overcome these limitations through the utilization of standardized transducer interfaces and communication protocols, resulting in autonomous, distributed, and reconfigurable instrument.

As far as the user is concerned, an intelligent instrument behaves like a black box, and no knowledge of its internal mode of operation is required for normal measurements. These types of instruments offer many advantages over their nonintelligent counterparts, principally because of the improvement in accuracy achieved by processing the output of transducers to correct for errors inherent in the measurement process.

Intelligent instruments usually provide many other functions, such as

1. Signal damping with selectable time constants
2. Switchable ranges (using several primary transducers within the instrument, which each measure over a different range)
3. Switchable output units (e.g., display in imperial or SI units)
4. Diagnostic facilities
5. Remote adjustment and control of instrument options
6. Self-calibrations
7. Various output options, 4–20 mA, Ethernet, Internet, wireless, etc.
8. Self-learning ability

In this chapter, we will not go into the details and intricacies of internal structures and principles of operations of intelligent instruments. Instead, some typical examples will be provided. The underlying technologies are also discussed at various other chapters of this book.

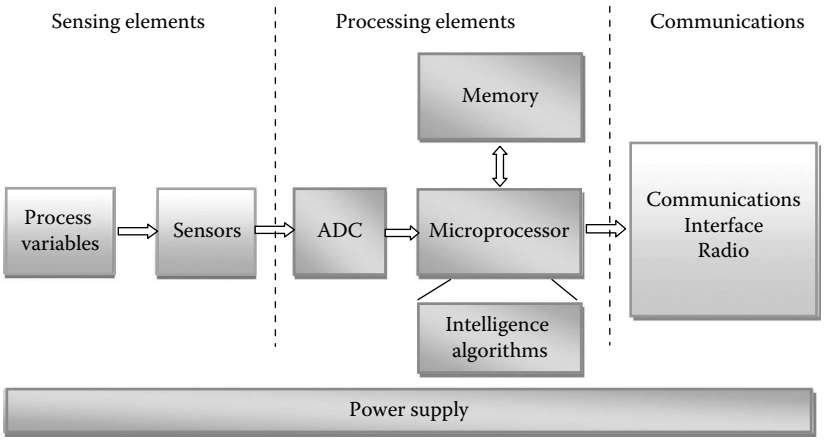

FIGURE 9.2 Architecture of an intelligent instrument.

9.8 Examples of Intelligent Instruments

There are many examples of intelligent instruments. Four typical examples are provided here.

Example 9.1

Intelligent microsurgical instruments [4,5]: They are designed as handheld instruments to be used particularly in microsurgery. Positioning error is inherent in a normal human such as tremor and jerk, which limit the accuracy of the hand motion of the surgeon. Intelligent behavior instruments sense their own motion and distinguish between desired and undesired motions using advanced filtering techniques. They can actively compensate for undesired motions by equal but opposite deflections of their own tips.

Example 9.2

Intelligent temperature transducers [6–8]: A typical intelligent temperature transducer is capable of measuring and controlling temperature. They can use fieldbus protocols to read measured values, set alarm limits, adjust the probes, and read firmware version. For this, appropriate ports are used to set alarm limits, time delays, e-mail addresses, probe description, refresh of www pages, select type of www pages, and set storing interval to history and automatic IP address assignment from a server. In case of alarm creation, warning e-mail message is sent to addresses defined by the user.

Another example of an intelligent temperature transducer is the Ethernet interface-capable temperature sensor. A typical device can sense display and communicate temperature, barometric pressure, relative humidity, dew point temperature, absolute humidity, specific humidity, mixing ratio, and specific enthalpy. Its communication modes are as follows:

- Modbus protocol enables to read measured values, set alarm limits, adjust the probe, and read firmware version.
- www pages: User-selectable design of www pages enabling to display curves of measurement history. User can design the look of www pages and select values to display.
- E-mail: In case of alarm creation, warning e-mail message is sent to addresses defined by the user.

Example 9.3

Intelligent flowmeters [9–13]: There are many intelligent flowmeters commercially available. They are based on different principles for different applications. Some of the intelligent flowmeters are coriolis mass flowmeters, electromagnetic flowmeters, ultrasonic flowmeters, variable area, vortex flowmeters, water flowmeters, oil flowmeters, metal rotameters, steam flowmeters, gas flowmeters, air flowmeters, mass flowmeters, and so on.

As an example, a typical intelligent vortex flowmeter contains four-piece piezoelectric sensors, two of which are used to detect the flow of fluid and the other two for detecting vibration signal of pipe. It can provide temperature and pressure compensation. The meter parameters and meter range can be changed by manual buttons. It provides 4–20 mA current signal output/pulse signal and communicates with Highway Addressable Remote Transducer communication protocol, PROFIBUS and Foundation Fieldbus. Liquid crystal displays can exhibit the instantaneous flow and accumulated flow of measured medium simultaneously.

Another example is the intelligent electromagnetic flowmeter used for high-viscosity uniform medium such as detecting paper pulp, mud, cement slurry, and mortar. It has compensation capability for fluid density, viscosity, temperature, and pressure change. It has double flow direction measurement and double direction quantum accumulating function.

Example 9.4

Intelligent pressure transmitters [14,15]: A typical intelligent pressure transmitter has onboard diagnostics, time-tracking functions, install date, calibration date, time in service, stress monitoring, point value, body temperature meter, as well as general reading functions. All diagnostics automatically run when the transmitter is powered and the information can be fed directly into the plant's digital control system (DCS) and asset management. This information remains in the transmitter for use in troubleshooting, in which it can measure absolute pressure, differential pressure, gage pressure, flange mount, and temperature.

Many other intelligent instruments have similar structure, software support, and functionalities. In some cases, intelligent instruments use artificial intelligence to learn from the past operations and external data.

References

1. IEEE Standard for a Smart Transducer Interface for Sensors and Actuators—Network Capable Application Processor (NCAP) Information Model, IEEE 1451.1 Standard, The Institute of Electrical and Electronics Engineers, Inc., New York.
2. Wall, R.W. and Huska, A., Design platform for plug-and-play IEEE 1451 traffic signal, *31st Annual Conference of the IEEE Industrial Electronics Society*, Montreal, Quebec, Canada, pp. 6–10, 2005.
3. Patra, J.C., Kot, A.C., and Panda, G., An intelligent pressure sensor using neural networks, *IEEE Transactions on Instrumentation and Measurement*, 49(4), 829–835, 2000.
4. Ang, W.T., Khosla, P.K., and Riviere, C.N., An intelligent hand-held microsurgical instrument for improved accuracy, *Proceedings of the 23rd Annual International Conference of the IEEE Engineering in Medicine and Biology Society*, Istanbul, Turkey, Vol. 4, pp. 3450–3453, 2001.
5. Hunter, I.W., Lafontaine, S.R., Brenan, C.J.H., and Jones, L.A., Medical robots and micro machines, *Proceedings of the 6th International Symposium on Micro Machine and Human Science* (*MHS'95*), Nagoya, Japan, pp. 25–30, 1995.
6. Jingwei, Y. et al., The portable temperature and humidity monitor based on intelligent sensor, *1st International Conference on Information Science and Engineering* (*ICISE 2009*), Nanjing, China, pp. 5245–5247, 2009.
7. Xu, J., You, B., and Li, Q., Implementation of an IEEE 1451 smart quartz tuning fork temperature transducer for real-time distributed measurement and control system, *6th World Congress on Intelligent Control and Automation*, Dalian, China, pp. 6, 2006.
8. Zhaochun, L., Yuzhu, C., and Jin, H., Design of smart temperature sensor based on IEEE1451.2 standard, *International Forum on Information Technology and Applications (IFITA)*, Chengdu, China, pp. 312–314, 2009.
9. Yi, Y. and Huifeng, W., An improved intelligent calibration method for vortex flowmeter, *American Control Conference*, New York, pp. 2927–2931, 2007.
10. Yong-hui, H., Intelligent turbine flowmeter based on CAN bus, *Instrument Techniques and Sensor,* 12, 69–70, 2007.
11. Liao, J. and Liu, Y., Distributed flowmeter data acquisition system based on WirelessHART networks, *International Conference on Apperceiving Computing and Intelligence Analysis (ICACIA 2009)*, Chengdu, China, pp. 383–386, 2009.
12. Yuhui, W., A new-type high-speed data sampling circuit based on FPGA and its application in flowmeter, *2nd International Asia Conference on Informatics in Control, Automation and Robotics,* Wuhan, China, Vol. 2, pp. 454–457, 2010.
13. Marshall, R., Facts at your fingertips: Flowmeter selection, *Chemical Engineering,* 113(12), 23, 2006.

14. Hao, J., Li, Q., and Yang, L., Intelligent pressure transmitter based on HART protocol, *Instrument Techniques and Sensor,* 2, 16–22, 2007.
15. Li, Y.-L., Design of tyre pressure intelligence monitoring system based on wireless transmission technology, *Instrument Techniques and Sensor,* 11, 40–47, 2007.

Bibliography

Bhuyan, M., *Intelligent Instrumentation: Principles and Applications*, CRC Press, Boca Raton, FL, 2011.

Bruey, D., *SNMP: Simple Network Management Protocol*, Rane Corporation, RaneNote 161, written December 2005, http://www.rane.com/note161.html (accessed on January 28, 2012).

Casucci, A.T., *Intelligent Components and Instruments for Control Applications*, 2000, IFAC, Pergamon Press, Great Britain, U.K., 2001.

Case, J., Fedor, M., Schoffstall, M., and Davin, J., *RFC1157—Simple Network Management Protocol (SNMP)*, May 1990, http://www.faqs.org/rfcs/rfc1157.html (accessed on March 13, 2013).

Huddleston, C., *Intelligent Sensor Design Using the Microchip dsPIC*, Newness, Oxford, U.K., 2007.

Manufacturers of Plug-and-Play (TEDS) Smart Sensors (IEEE 1451), http://www.sensorsportal.com/HTML/SENSORS/TEDS_SensManuf.htm (accessed on March 24, 2012).

Meijer, G. C., *Smart Sensors Handbook,* Wiley, Chichester, U.K., 2008.

Randy, F., *Understanding Smart Sensors*, 2nd edn., Artech House, Boston, MA, 2000.

Sony Bravia i-Manual online, http://esupport.sony.com/docs/imanual/NA/EN/1a/ipsensor_uc_1a.html (accessed on March 20, 2012).

Partial List of Manufacturers/Suppliers

Cetacea Sound, Inc., 2950 Airways Blvd., Memphis, TN 38116, Phone: 901-363-3856, 800-489-1759 (toll free), Fax: 901-367-1420, www.cetacea.com

Endevco Corp., 30700 Rancho Viejo Rd., San Juan Capistrano, CA 92675-1748, Phone: 800-982-6732, Fax: 949-661-7231, www.endevco.com

Enga Tech, 607 Fairway Woods Dr., Chester, VA 23836, Phone: 888-492-5886 (toll free), Fax: 804-530-9223, www.engatechvision.com

Esensors, Inc., 4240 Ridge Lea Rd Ste 37, Amherst, NY 14226, Phone: 716-837-8719, Fax: 716-837-8740, www.eesensors.com

Fife Corp., P.O. Box 26508, Oklahoma City, OK 73126, Phone: 405-755-1600, 800-639-3433 (toll free), Fax: 405-755-8425, fife.maxcessintl.com

Honeywell Sensing and Control, 1985 Douglas Dr. North, MN10-192B, Golden Valley, MN 55422, Phone: 763-954-4818, 800-446-6555 (toll free), sensing.honeywell.com/index.cfm/ci_id/15…

Kistler North America, 75 John Glenn Dr., Amherst, NY 14228-2119, Phone: 716-691-5100, 888-KISTLER, 888-547-8537 (toll free), Fax: 716-691-5226, www.kistler.com

MAGPOWR, 222 W. Memorial Rd., Oklahoma City, OK 73114, Phone: 405-755-1600, 800-MAGPOWR (toll free), Fax: 405-755-8425, magpowr.maxcessintl.com

Microstrain, Inc., 459 Hurricane Lane, Suite 102, Williston, VT 05495, Phone: 802-862-6629, 800-449-3878 (toll free), Fax: 802-863-4093, www.microstrain.com

Monitor Technologies, LLC, 44W320 Keslinger Rd., Elburn, IL 60119, Phone: 630-365-9403, 800-601-5924 (toll free), Fax: 630-365-5646, www.monitortech.com

National Instruments Corp. 11500 N. Mopac Expwy., Austin, TX 78759-3504, Phone: 512-794-0100, 888-280-7645 (toll free), Fax: 512-683-8411, www.ni.com

PCB Piezotronics, Inc., 3425 Walden Ave., Depew, NY 14043-2417, Phone: 716-684-0001, 800-828-8840 (toll free), Fax: 716-684-0987, www.pcb.com

PICS, Inc., 81 Lancaster Ave., Suite 202, Malvern, PA 19355, Phone: 610-644-7701, Fax: 610-644-9297, www.picscontrols.com

Sensor Platforms, Inc., 1550 Airport Blvd Ste 220, Santa Rosa, CA 95403, Fax: 707-581-7361, www.sensorplatforms.com

Sensors Unlimited, Inc., 3490 Route 1 Bldg 12, Princeton, NJ 08540, Phone: 609-520-0610, Fax: 609-520-1663, www.sensorsinc.com

Sony Manufacturing Systems America, Inc., 20381 Hermana Cir., Lake Forest, CA 92630, Phone: 949-770-8400, Fax: 949-770-8408, www.sonypt.com

Steven Engineering, 230 Ryan Way, South San Francisco, CA 94080, Phone: 888-790-0022 (toll free), Fax: 800-314-0716, 800-314-0716 (toll free), stevenengineering.rtrk.com/?scid=1975164…

Technica-Tool, Inc., 553 Industrial Dr., Hartland, WI 53029, Phone: 262-367-8665, Fax: 262-367-0208, www.techna-tool.com

Turck, Inc., 3000 Campus Dr., Plymouth, MN 55441-2619, Phone: 763-553-7300, 800-554-4989 (toll free), Fax: 763-553-0708, www.turck.com

Unisys Corp., 20 Research Dr., Hampton, VA 23666, Phone: 757-865-0637, www.unisys.com/unisys/

Valin Corp., 555 E. California Ave., Sunnyvale, CA 94086, Phone: 408-370-7444, 800-922-6646 (toll free), Fax: 408-370-1356, www.automationcontrols.com

10

Virtual Instruments

David Potter
National Instruments

Halit Eren
Curtin University

10.1 Introduction

The rapid adoption and technological evolution of the (personal computer) PC in the last 25 years or so catalyzed a revolution in instrumentation for test, measurement, and data acquisition (DAQ). There are at least two substantial developments in this area, being the concept of virtual instrumentation (VI) and the supervisory control and data acquisition (SCADA). In this chapter, primarily virtual instruments will be discussed and SCADA systems will be introduced briefly.

The virtual instruments consist of industry-standard computers or workstations equipped with application software, modular DAQ hardware such as plug-in boards, and driver software. Together, these components replicate the functions of traditional stand-alone instruments. Virtual instruments represent a fundamental shift from traditional hardware-centric instrumentation systems to software-centric systems that exploit the computing power, productivity, display, and connectivity capabilities of popular desktop computers and workstations.

10.2 Virtual Instrument Architecture

VI can be traced back to the birth of the International Business Machines Corporation (IBM) PC (in 1981) and the emergence of general purpose interface bus (GPIB) as a tool that enabled engineers to use a PC to control and communicate with instruments to automate test and measurement tasks. In 1986, National Instruments introduced the LabVIEW graphical development environment, which offered to acquire data, control instruments, and analyze and present data from a PC without sacrificing performance or functionality. Since then, the development and evolution of all aspects of VI—PC processors, memory, bus and networking technologies, software technologies, and DAQ hardware—had a phenomenal growth. As a result, VIs are widely used in everything from simple, low-cost applications, such as environmental temperature monitoring, to large-scale, real-time measurement and control applications, such as the real-time control of over a hundred collimators to help control the particle beam in the world's largest particle accelerator, the Large Hadron Collider (LHC) at CERN.

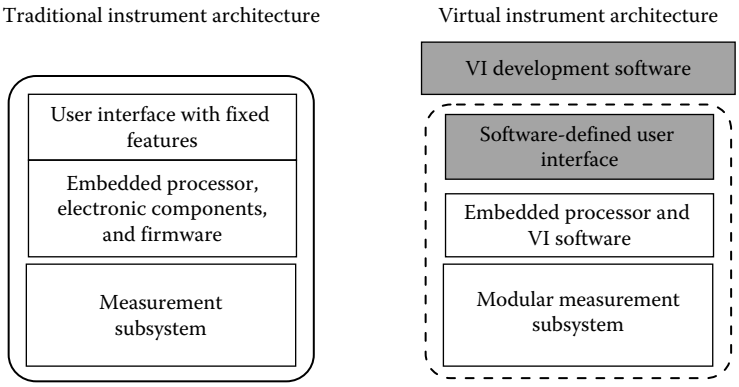

FIGURE 10.1 Traditional versus virtual instruments.

Traditionally, the stand-alone traditional instruments such as oscilloscopes, data recorders, waveform generators, and electronic measuring instruments are designed to perform one or more specific tasks defined by the vendors. While stand-alone traditional instruments can be very powerful, they also can be expensive and generally the users cannot extend or customize the instruments for their needs. The knobs and buttons on the instrument, the built-in circuitry, and the functions available to the user are all configured specifically for the instrument. In addition, special technology and components must be developed to build these instruments, making them expensive and slow to adapt to changing market conditions and the user needs. A comparison of the traditional and VI architecture is given in Figure 10.1.

10.3 Virtual Instrument Software

Virtual instruments are supported by a number of software used for different purposes such as DAQ, device driver, and application software. Some of this supporting software will be explained in Section 10.2.1.

10.3.1 Data Acquisition Software

In today's instruments and instrumentation systems, the software plays an important role as it determines the ultimate success or failure of the system. Nowadays, almost all aspects of modern instrumentation and DAQ system are software driven. This includes configuring and managing the hardware, controlling the flow and storage of the acquired data, processing and analyzing of the data, as well as visually displaying and communicating the data.

Essentially, there are two layers of the DAQ software as shown in Figure 10.2. Firstly, most vendors of DAQ hardware supply some type of device driver software for controlling and accessing the device. The device driver manages the low-level access and manipulation of the hardware, as well as management of the computer and operating system resources, hence simplifying the programming of the DAQ system.

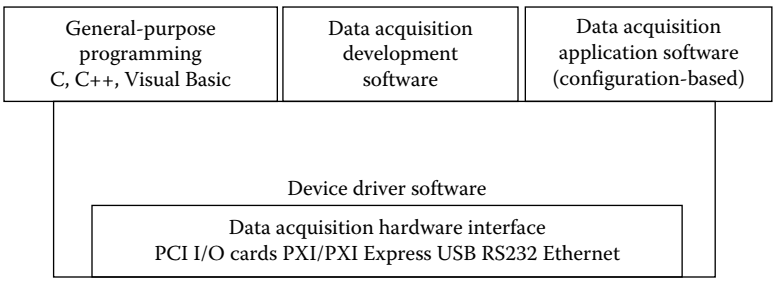

FIGURE 10.2 Levels of DAQ software application.

Secondly, the driver software is used in conjunction with a higher-level program, which may be developed using a general-purpose programming language or specialized DAQ software that includes tools for acquiring, analyzing, and managing the acquired data. DAQ software can further be divided into development software environments, which allow users to fully customize their systems and develop application-specific systems and configuration-based software. These are simpler, easier-to-use software packages designed to perform a fixed set of DAQ and analysis functions.

10.3.2 Device Driver Software

A DAQ device driver is software that allows higher-level computer programs to interact with the DAQ hardware. The driver communicates with the DAQ hardware through a bus or network, essentially coordinating the passing of commands and data to and from the hardware. The higher-level software invokes routines, or functions, in the driver to initiate interaction with the hardware. The collection of these functions and their formats is known as the application programming interface (API). In Microsoft Windows, drivers are usually distributed as dynamic link library (DLL) files that can be accessed by most Windows programming languages, such as Visual Basic, C++, LabVIEW, and C#.

Although driver software works "behind the scenes" and is not as visible as application software, DAQ device drivers can be very complex and critical to the effectiveness of the DAQ systems. Following is a brief description of the main functions and capabilities provided by driver software.

Configuration: Most DAQ and signal conditioning devices support multiple modes of operations and variable settings. Parameters such as A/D sampling rate, amplifier gain, filter settings, trigger mode, and sensor excitation are typically configurable via the driver software. In addition to these hardware settings, configuration of key acquisition and data scaling parameters must be set.

Driver software often includes a software utility, which you can use to easily and interactively set theses parameters, such as the Measurement and Automation Explorer utility shown in Figure 10.3.

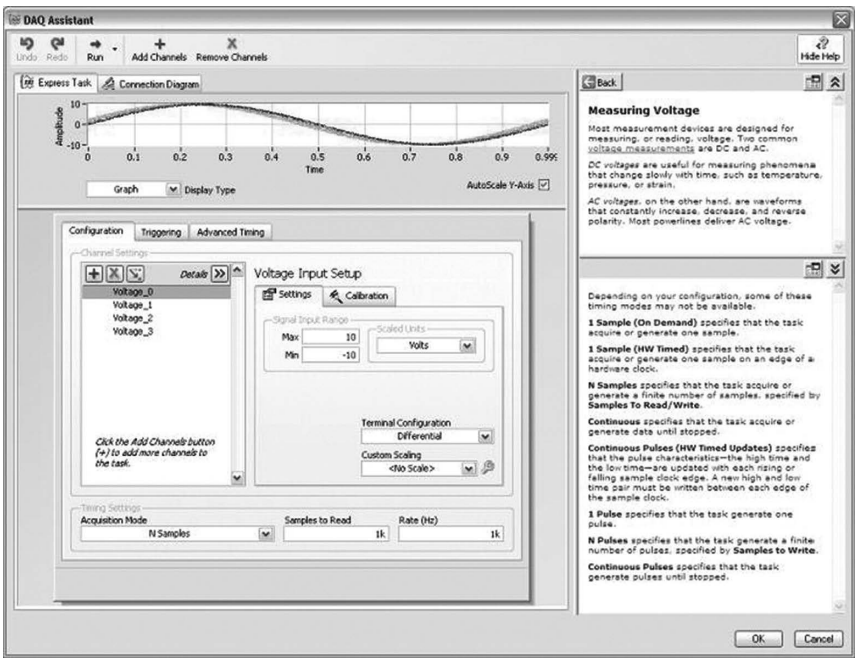

FIGURE 10.3 Example of a software configuration tool for setting up a DAQ system. (Courtesy of National Instruments, http://zone.ni.com/cms/images/devzone/tut/DAQ_Asst_20090321150309.png)

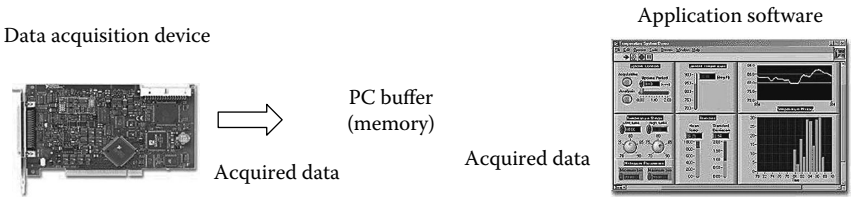

FIGURE 10.4 DAQ software must manage reliable buffering of acquired data.

The settings for the acquisition voltage measurements and the signal conditioning, and a data display or test panel to interactively check the settings. Additionally, many applications require the ability to programmatically set these parameters. For these applications, it is critical that the driver library exposes these configuration settings through its API.

Calibration: Calibration of a DAQ device consists of verifying its measurement accuracy by measuring a known value and adjusting for any measurement error. Modern DAQ devices often include the capability of self-calibration using an onboard reference voltage, which should be very stable and have high precision. A more complete calibration, often referred to as end-to-end calibration, encompasses the entire measurement path, from the sensor all the way through to the ADC. For example, an end-to-end calibration of a thermocouple would involve heating or cooling the thermocouple probe to a controlled, known temperature. By recording the difference in the measurement acquired by the DAQ device and the known temperature at multiple temperatures, this difference can be used in subsequent measurements to compensate for much of the gain and offset errors of the DAQ system.

Data buffering and management: Acquisition of dynamic waveforms can require streaming large amounts of data from the DAQ device to memory on the controller or PC. This PC memory acts as a data buffer to temporarily hold the data until the application software can access and process the data, store it to disk, etc., as shown in Figure 10.4. There are two basic modes of operation that DAQ driver software should handle effectively.

Finite buffered acquisition: The DAQ device is programmed to perform a finite number of A/D conversions and transfer the data into the PC buffer. When finished, the DAQ device is idle until programmed for another task.

Continuous buffered acquisition: With continuous acquisition, the DAQ device is programmed to perform acquisitions indefinitely as shown in flow diagram form in Figure 10.5. Data are streamed continuously to the PC memory buffer. However, because the PC buffer is of a finite size, data must be simultaneously pulled out and transferred to the application software for processing and more permanent storage. This requires that the driver manage the PC buffer as a circular buffer, meaning that when incoming data reach the end of the buffer, storage resumes at the beginning of the buffer. This process can continue indefinitely without losing acquired data as long as data are being simultaneously copied to the application software memory at a rate as fast as the data coming in from the DAQ device.

Advanced driver capabilities: In addition to the basic operations of sending configuration commands to the hardware and managing the transfer and buffering of acquired data, more advanced DAQ drivers also include advanced capabilities that can save significant development time and yield higher-performance systems.

Multithreading: DAQ multithreading is the concept of independently controlling more than one I/O function on the acquisition device. In many DAQ applications, analog output or digital I/O is needed for stimulus or control in addition to analog input measurements. For these applications, it is critical that the drivers support concurrent I/O operations and not limit the programmer to sequential tasks.

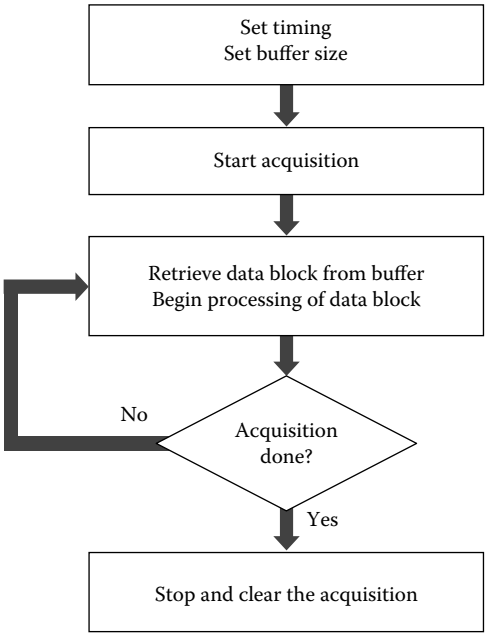

FIGURE 10.5 Flowchart for program for a continuous buffered acquisition.

Intelligent timing, triggering, and synchronization: Many DAQ devices include a number of timing and triggering mechanisms that can be configured in multiple ways. Setting up a synchronized I/O application on multiple devices can become very complex, involving complicated counter timer configurations and low-level signal routing of clock and trigger signals. More advanced drivers automatically handle this lower-level configuration and signal routing, thus simplifying the application program.

Hardware simulation: During development and system integration, the developer of the DAQ system may not always have access to operational DAQ hardware. Therefore, it can be very useful if the driver allows the use of a simulated device, allowing the developer to test and try out his code without having fully operational hardware setup.

Automatic data logging to disk: While most drivers manage the transfer of data to the PC or controller memory, and it is left to the application program to process and store the data to a nonvolatile location, such as the hard disk, more advanced driver software includes built-in functionality to simultaneously transfer data from the PC memory to a file on the hard disk.

10.3.3 Application Software

A real-world DAQ system typically includes much more than the acquisition of data. Systems very often include signal generation, digital I/O, and timing I/O, as well as processing and analysis of data, data visualization, user interfaces, data storage, and communications with distributed systems. Fortunately, developers of integrated DAQ systems do not have to be professional programmers who must code these systems from scratch using general-purpose programming tools such as C++ or Visual Basic. Specialized DAQ software development tools are available to engineers to greatly simplify the integration of DAQ systems.

While there is a wide range of application software packages, it is useful to categorize the options into two general types: (1) application development environments (ADEs) and (2) configuration-based programs.

10.3.3.1 Application Development Environments

ADEs offer the high level of customization and flexibility in developing DAQ systems. DAQ environments are specialized software development environments that integrate functions and tools for DAQ, analysis, visualization, and other functions common in applications. Users develop a DAQ program or script and are able to highly customize the program. Many of today's ADE software packages utilize some form of graphical development, which is generally considered more intuitive and easier to learn for nonprofessional programmers.

For example, the LabVIEW software is a popular development tool for DAQ system, which uses graphical programming language. Figure 10.6 shows a LabVIEW front panel. Execution of the program is determined by the structure of the graphical block diagram in which the programmer connects different icons, or function nodes, by drawing wires. The front panel serves as the user interface, allowing the user/operator to input data, interact with controls, or visualize outputs of the VI. The VIs can be embedded into higher-level programs or other VIs. In these cases, the front panel serves as the programmatic interface for I/O to the embedded VI.

The graphical programming language used in LabVIEW, also referred to as "G," is a dataflow programming language. These wires in the block diagram propagate variables, and any node can execute as soon as all its input data become available. Since this might be the case for multiple nodes simultaneously, G is inherently capable of parallel execution. Figure 10.7 shows a simple program with two parallel programming structures. Because no wires interconnect the two structures, the two loops will run in parallel and the program will automatically execute the two loops on multiple processors.

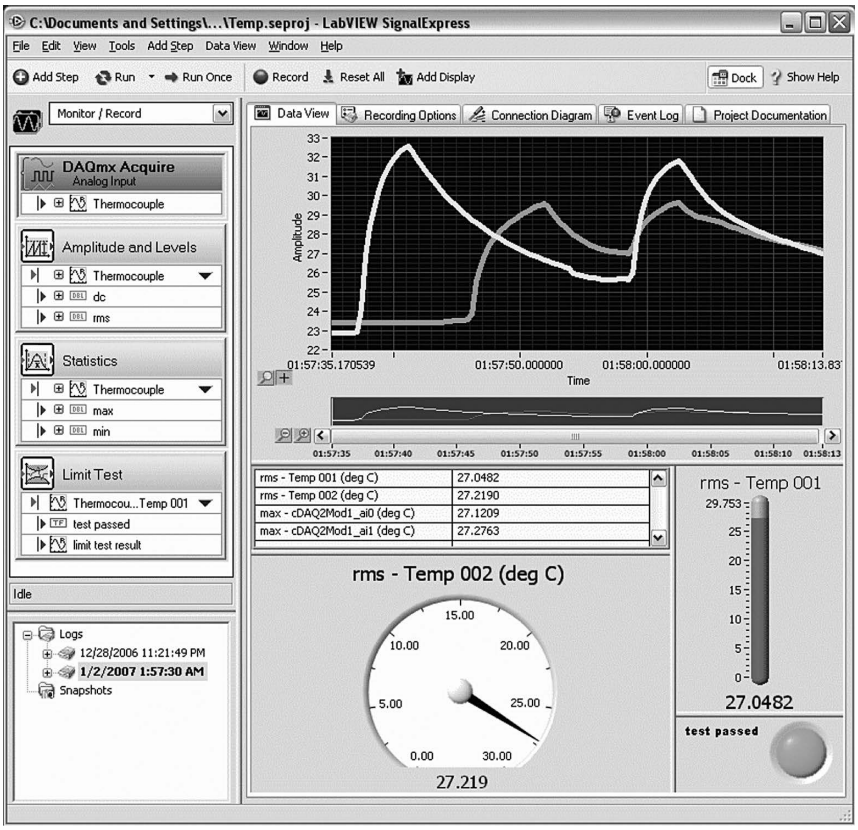

FIGURE 10.6 A typical VI front panel. (Courtesy of National Instruments, http://zone.ni.com/cms/images/devzone/tut/Figure%203.gif)

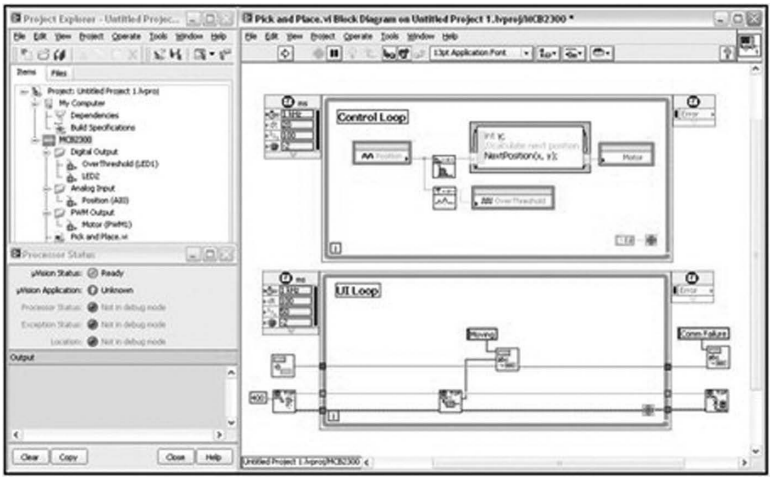

FIGURE 10.7 Graphical dataflow structure of LabVIEW programming. (Courtesy of National Instruments, http://zone.ni.com/cms/images/devzone/pub/arm1.jpg)

10.3.3.2 Configuration-Based Application Software

Graphical development applications can be made flexible. For simpler or smaller scope implementations, a number of application software packages are available for common DAQ tasks, such as acquiring and logging data to disk. These packages require no additional programming and are configured by the user, typically through intuitive menus and software wizards.

Figure 10.8 shows an example of a configure-based software package, LabVIEW SignalExpress. Acquisitions and some limited analysis routines are configured through the menu structure on the left side of the window. The acquired data can be displayed in configurable graphs and charts in real time, as well as stored to disk for later retrieval.

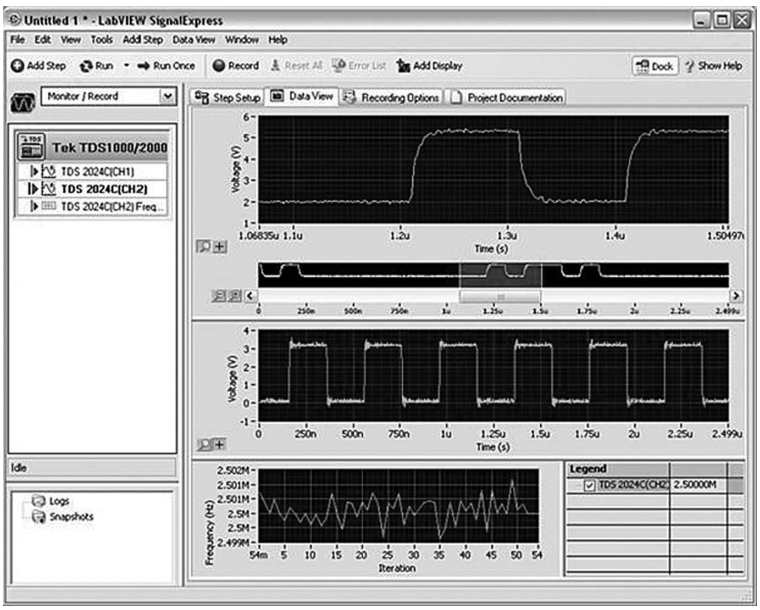

FIGURE 10.8 A configuration-based DAQ application where one can set up DAQ operations without any programming. (From http://www.tek.com/sites/tek.com/files/media/image/A002_8167-L.jpg)

TABLE 10.1 Types of Data Analysis and Processing Functions in Typical DAQ Applications

Measurement Analysis	Signal Processing Routines	Mathematical Processes
Amplitude, level, peak frequency, spectral, noise, distortion, pulse, transition, signal generation, time domain, tone measurements, etc. *Control*: PID, fuzzy control	Digital filters, convolution and correlation, frequency/spectral analysis, joint time-frequency analysis, sampling/resampling, decimation signal generation, transforms, time domain analysis, wavelet and filter bank design, windowing, etc.	Basic math, curve fitting, data modeling, differential equations, interpolation, extrapolation, linear algebra, nonlinear systems, optimization, root finding, statistics, and probability. *Geometry*: (2D, 3D), polynomial functions, etc.

10.3.3.3 Data Analysis and Visualization

The actual acquisition and storage of data are only a part of the DAQ system. In order to extract useful information from those data, make decisions on the process, and obtain results, the data need to be manipulated and analyzed. Therefore, data analysis and visualization are important components of data LabVIEW software systems, and many software packages include routines for data analysis and signal processing. Other packages require the data to be saved to disk or a database and retrieved later for processing using dedicated analysis software.

The type of analysis is, of course, very dependent on the goals of the application. Table 10.1 lists classes of analysis tools that might be integrated into a DAQ and analysis software program. This list is not all inclusive and only includes categories of analysis routines that are relevant for applications.

One key consideration for data analysis is whether the analysis is to be performed *inline* in real time or *offline* at a later time after the data have been stored. Inline analysis is used when decisions have to be made during run time and the results have direct consequences on the process. This is typically the case in control applications. When dealing with inline analysis, it is important to consider the amount of data acquired and the particular analysis routines that are performed on those data, as the processing could easily become computationally intensive and have an adverse effect on the performance of the application. The other key consideration for inline analysis is the use of point-by-point analysis algorithms. Most analysis software has analysis functions geared toward working on waveforms or arrays of data. Point-by-point analysis routines can simplify the program as they tend to more naturally match the flow of incoming data in an inline processing or control application.

Visualization is the ability of the software package to display the data and the results of the analysis in a meaningful way. Information and data may be plotted as graphs, charts, 2D images, and 3D graphs and even incorporate photos, videos, and 3D CAD models. Figures 10.9 is an example of a 3D analysis of a temperature distribution of a surface. Figure 10.10 is an example of LabVIEW application using sensor mapping function to map a 3D model of the analyzed data simultaneously displaying with synchronized sensor data.

10.4 Supervisory Control and Data Acquisition

SCADA is an industrial computer system monitoring and controlling large processes by using graphical user interface (GUI). The SCADA system consists of human machine interface (HMI), remote terminal units (RTUs), programmable logic controllers (PLCs), communications and network infrastructure, computers, embedded and other controllers, and appropriate software support at various levels. The term SCADA usually refers to centralized large systems that monitor and control entire sites or complex processes spread out over large areas. A typical SCADA network is illustrated in Figure 10.11. In this chapter, a brief description of SCADA is introduced.

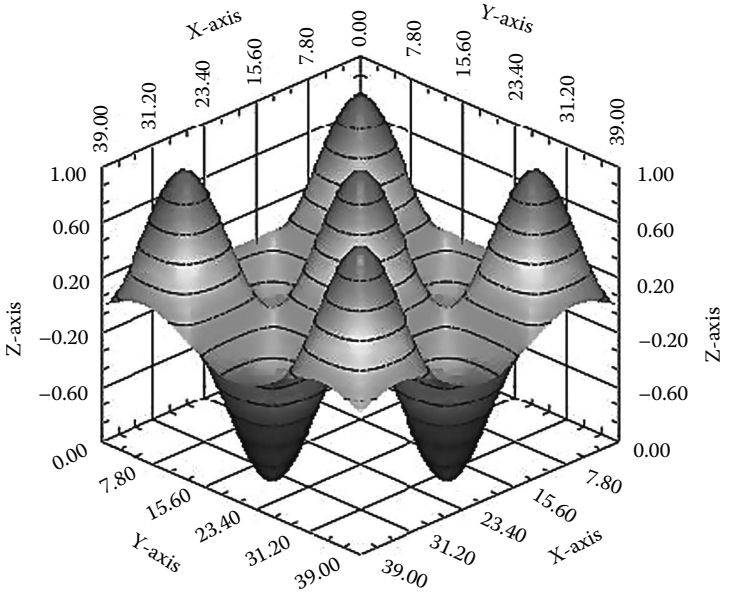

FIGURE 10.9 Example of 3D data graph of temperature distribution in LabVIEW. (Courtesy of National Instruments, http://www.ni.com/images/labview/2010/neutral/ui_3d_surface_graph.jpg)

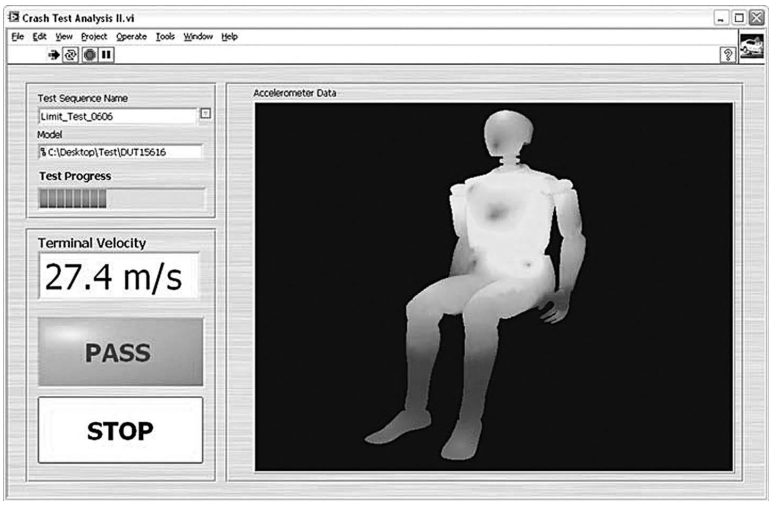

FIGURE 10.10 LabVIEW 3D sensor mapping forms the data analysis. (Courtesy of National Instruments, http://zone.ni.com/cms/images/devzone/tut/LV8.6_CrashTest_Analysis_fp_ss_p.jpg)

10.4.1 Components of SCADA

SCDA is a network of instrumentation systems. It has seven main components:

1. *Field I/O*: Digital and analog I/Os, rack mount with CPUs or networked.
2. *Logic solver*: Rack-mounted or RTU style wall mounted.
3. *Network and network components*: Ethernet and other networks.
4. *CPU, I/O, and network configuration and application development software*: Hardware platforms, such as Rockwell Automation and Allen-Bradley.

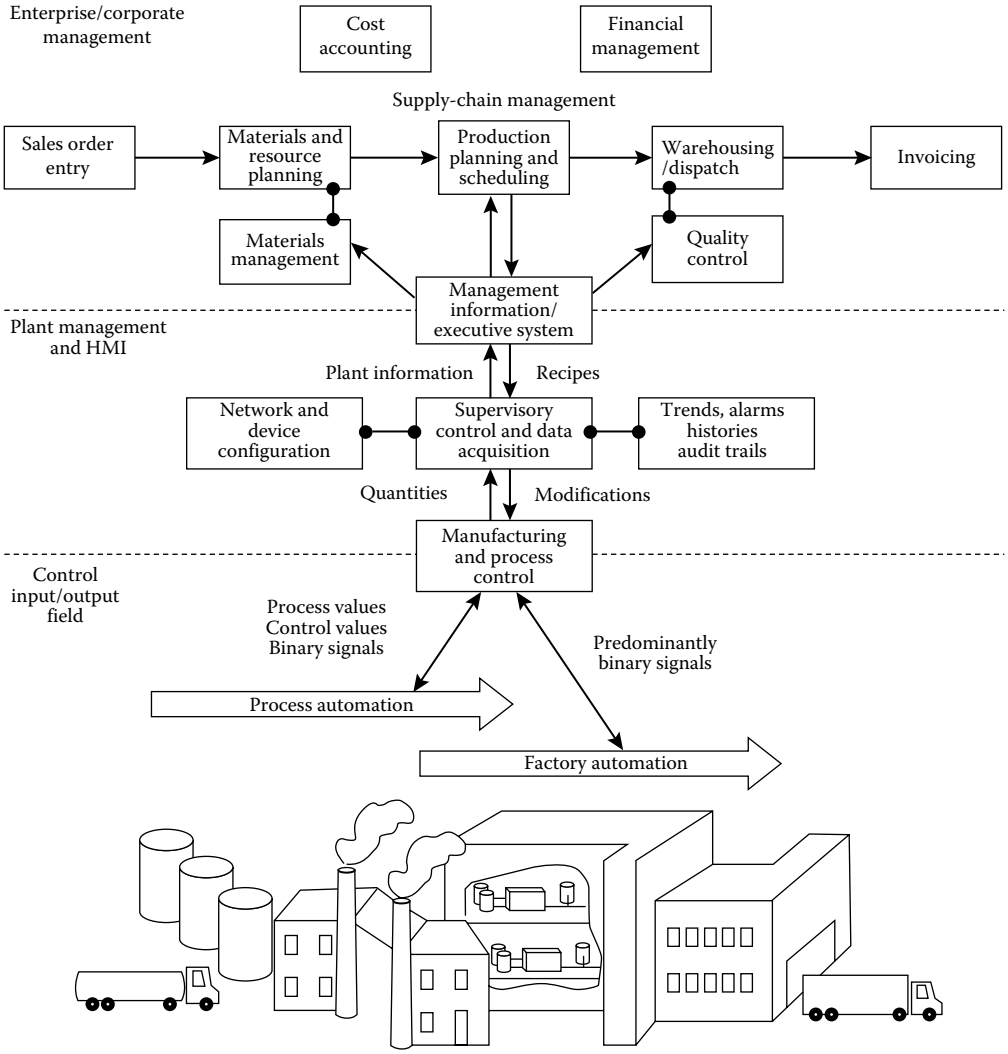

FIGURE 10.11 Typical SCADA network. (From Liptak, B. and Eren, H., *Instrument Engineers Handbook: Process Software and Digital Networks*, Vol. 3, 4th edn., CRC Press, LLC, Boca Raton, FL, 2011.)

5. *HMI hardware*: This can be industrial ruggedized PC hardware such as Versaview from GE Intelligent Platforms (GE-IP).
6. *HMI software*: Software, such as Wonderware, InTouch, or iFix for developing GUI.
7. *Engineering/maintenance workstation*: PC with all development software with the necessary licenses.

10.4.2 SCADA Software

Software support of SCADA is configured in four layers:

- User machine interface
- Process and control
- Communication and memory
- Field drivers

User machine interface indicates the software for HMI and interactivity of operators with the process. The HMI programs can be very large and they are developed by following procedures such as

- HMI concept development—a mutually agreed requirement with the end user based on their existing standard or experience. It needs to define color scheme, navigation scheme, and individual equipment and device animation guidelines
- Preliminary system configuration—defines various nodes and configuration
- Middleware tag definitions and configuration—middleware is used such as object linking and embedding (OLE) for Process Control (OPC) or Modbus for live data
- Tag database loading—depends on completion of logic development because in the course of logic development, several memory tags are defined that may require animation
- Creation of building blocks of the process such as control valves, pumps, blowers, and tanks
- Creation of home screen and process screens by using process blocks and attaching tag names
- Creation of control panels or pop-ups that are detailed screens for operation of equipment
- Creation of setup parameter screens
- Creation of alarm management screen
- Creation of historical trends
- Creation of reports
- Basic navigation tests
- Connecting with controllers
- Testing set of screens with respective controller using forced tag values or jumpers

A simple example of a SCADA control system is illustrated in Figure 10.12a and b. In Figure 10.12a, the status and temperature and alarm condition of an electric motor are examined by calling a dedicated screen display. In Figure 10.12b, the operational characteristics of a substation in a large power distribution system are monitored.

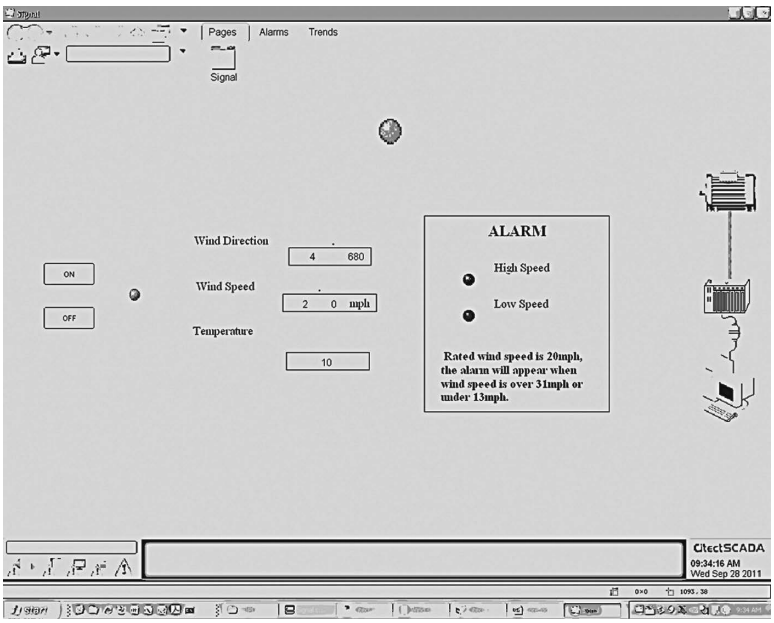

(a)

FIGURE 10.12 SCADA displays for (a) to examine the status of a motor.

(*continued*)

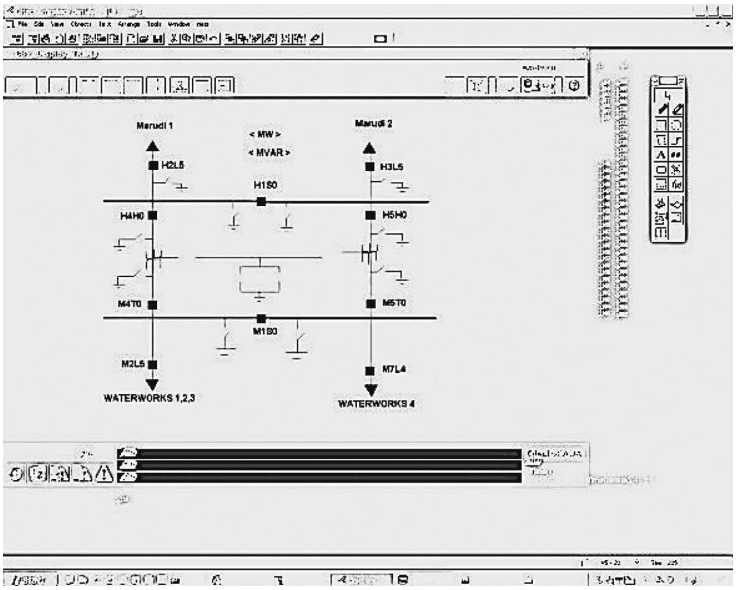

(b)

FIGURE 10.12 (continued) SCADA displays for (b) monitoring a substation. (Developed by author at Curtin University, Bentley, Australia.)

10.5 Conclusions

Over the last few decades, DAQ systems have grown to fill an expanding role in process control, test, measurement, and automation. The wide adoption in particular of PC-based DAQ systems has been fueled by the technological evolution of PC technologies on all fronts. For example, a 65,000-point fast Fourier transform (FFT) would take over 15 min to execute on a commercial circa 1990 PC (Intel 386). On today's 3 GHz processors, equipped with multiple gigabytes of memory, the same FFT takes well under a second to execute. Those 1990 PCs utilized an 8 MHz parallel bus to move data. Today's PCs incorporate PCI Express data paths that can move data at rates up to 4 GB/s. DAQ software has grown to take advantage of the increased memory, speed, and multicore architectures of PCs, evolving into sophisticated graphical engineering tools such as the virtual instruments and SCADA for large systems involving hundreds and thousands of inputs and outputs.

Bibliography

Bentley, J. P., *Principles of Measurement Systems*, 4th edn., Prentice Hall, London, U.K., 2005.

Blume, P. A., *The Labview Style Book,* Prentice Hall, London, U.K., 2005.

Boyer, S. A., *SCADA: Supervisory Control and Data Acquisition*, 2nd edn., ISA, Research Triangle Park, NC, 1999.

Johnson, G. W. and Jennings, R., *Labview Graphical Programming: Practical Applications in Instrumentation and Control*, McGraw-Hill, New York, 2006.

Liptak, B. and Eren, H., *Instrument Engineers Handbook: Process Software and Digital Networks*, Vol. 3, 4th edn., CRC Press, LLC, Boca Raton, FL, 2011.

Mihura, B., *Labview Data Acquisition*, Prentice Hall, Upper Saddle River, London, U.K., 2001.

Potter, D. and Eren, H., Data acquisition fundamentals, *Instruments Engineers' Handbook*, The IEH, Eds., B. Liptak and H. Eren, CRC Press, Boca Raton, FL, Vol. 3, 4th edn., pp. 330–341, 2011.

Travis, J. and Kring, J., *Labview for Everyone—Graphical Programming Made Easy*, 3rd edn., Prentice Hall, London, U.K., 2007.

Partial List of Suppliers

ABB Automation, 2487 S. Commerce Dr., New Berlin, WI 53151, Phone: 262-785-3400, Fax: 262-785-0342, www.abb.us

Agilent Technologies, 140 Green Pond Rd., Rockaway, NJ 07866, Phone: 973-627-6400, Fax: 973-627-0570, www.home.agilent.com/

Alacron, Inc., 71 Spit Brook Rd Ste 200, Nashua, NH 03060, Phone: 603-891-2750, Fax: 603-891-2745, www.alacron.com

National Instruments Corp., 11500 N Mo Pac Expy, Austin, TX 75759, Phone (512) 338-9119, www.ni.com

Rockwell Automation, 1201 South Second Street, Milwaukee, WI USA 53204, Phone: 414-382-2000, Fax: 414-382-4444, http://www.rockwellautomation.com

Schneider Electric, Telemetry&Remote SCADA Solutions, 48 Steacie Dr., Kanata, ON K2K2A9, Phone: 613-591-1943, Fax: 613-591-1022, www.controlmicrosystems.com

Siemens Corp., 300 New Jersey Avenue, N.W., Suite 1000, Washington, DC 20004-2611, Phone: 202-434-4800, 800-SIEMENS (toll free), Fax: 202-347-4015, www.usa.siemens.com/entry/en/

Tektronix, Inc., 14200-T S.W. Karl Braun Dr., P.O. Box 500, Beaverton, OR 97077, Phone: 503-627-7111, 800-833-9200 (toll free), www.tek.com

Test Equipment Depot, 99 Washington St., Melrose, MA 02176-6024, Phone: 781-665-1400, 800-517-8431 (toll free), Fax: 781-665-0780, www.testequipmentdepot.com

Visidaq Solutions, Inc., 1970 Swarthmore Ave., Lakewood, NJ 08701, Phone: 732-901-6100, Fax: 732-901-2288, www.visidaq.com

11

Fail-Safe Instruments and Devices

Davide Quatrini
Italcertifer, Inc.
University of Rome "Tor Vergata"

Giuseppe Fazio
University of Rome "Tor Vergata" & Isatel Ltd.

Mauro Giaconi
University of Rome "Tor Vergata"

Adelio Salsano
University of Rome "Tor Vergata"

11.1 Introduction

Some electronic applications are related to safety-of-life quality services, that is, services that must assure the safety of users or customers lives. Such an important task needs a life-cycle philosophy for the product strongly different from the one used in the development of other simpler commercial applications. For this reason all over the world, norms that describe the mandatory life-cycle management for fail-safe devices exist and must be applied by designers, verifiers, assessors, etc. The aim of this chapter is to provide the basic information needed for understanding how the world of fail-safe electronics is different from the one tied to standard applications in which human life is not involved.

A fail-safe device is essentially a device for which the final status in case of failure is absolutely known. This is a task that is hard to accomplish. Failures in fact can have several origins and several effects and can combine among themselves for producing unpredictable results. If we think, for example, of a railway traffic light, we must assure if we want it to be a real fail-safe device that all possible failures (including electrical and mechanical ones, both internal and external) lead to a situation in which the light is red or off, never green.

In this chapter, we intend to show the key concepts related to fail-safe instrument and device realization and how those concepts assemble to form a complete life cycle for such devices. The concepts are taken from the European norms and railway technical scenario, but they will be treated in a sufficiently generic way to be applied to the majority of devices that need strong safety performance. There are many fields in which the design philosophy here described should be applied (other than the already cited railway scenario): avionics, automotive, medical devices, nuclear plants, etc.

11.2 Fail-Safe Realization: Relevant Features

The first item on which safety is built is quality. The realization of a safe device must be done using the most modern methods and applying the most modern techniques of quality management, methods, and techniques that assure the minimization of human-related errors. Such a task is mainly achieved in a twofold way: a complete and correct documentation that follows the fail-safe device for the entirety of its life cycle and a deep and detailed technical analysis. The documentation, which should be prepared and maintained by a specialized team, should address at least the following issues from the very beginning of device life:

- The description of system architecture, with specific subsets related to the subsystem features
- A detailed description of system interfaces, both for the human user and other systems and also between the subsystems
- A complete tracking of system requirements, both functional and safety ones
- A detailed description of software and hardware functioning, with particular emphasis on their mutual relationships

Note that the software and hardware functioning description must detail also the RAMS parameters of the system, that is, its reliability, availability, maintainability, and safety, from both qualitative and (if possible) quantitative points of view.

The technical analysis, although based on the quality criteria detailed earlier, must be solidly focused on safety. For this reason, the analysis must start with a systematic evaluation of the faults, carried on using both top-down techniques like fault tree analysis (FTA) and bottom-up systems like failure mode effects analysis (FMEA). This approach should lead to a scenario in which the device remains safe if any single random fault occurs or, in other words, it is fail-safe. This goal could be achieved in several ways:

- *Composite fail safety*: The system is designed to be oversized/redundant. Every additional unit must be independent from other units, thus avoiding common-mode failures, and also for taking safety decisions based on a majority vote. An implementation in which the units are functionally equivalent but architecturally different is strongly recommended.
- *Reactive fail safety*: The system is formed by a single unit, but every possible fault of this unit is immediately detected and negated. This task is accomplished by an additional unit that is not functionally equivalent to the first (as in composite fail safety), but instead it is totally focused on the continual testing of the first.
- *Inherent fail safety*: The system is formed by a single unit, but its every possible fault has been analyzed and judged as not hazardous. An example could be a very simple analog hardware–based watchdog, in which all the possible faults, related to its single components, lead to a shutdown of the system (but only if the shutdown is the final, desired, safe status of the system).

It is evident that independently from the chosen approach (which can consist also in a combination of the aforementioned techniques), the practical realization of a fail-safe device requires a deep and complete knowledge of its single components, both software and hardware. Such a knowledge level is very hard to obtain using recent up-to-date VLSI products or powerful programming languages, so very often, the fail-safe designer must be a specialist of the old, well-tested, and completely debugged elements, for example, the microprocessors developed during the 1980s and the 1990s (or their DSP counterparts), the ANSI specification for the C programming language, or also even the assembly approach to software writing. Sometimes the necessity for a tailor-made ASIC could arise, so HDL skills are required. Use of commercial-off-the-shelf (COTS) products must be avoided, if possible, or minimized, and however, its employment is often regulated by strict norms. This choice is not based on technological reasons tied to specific performances (which can be obviously more easily obtained using the most recent multipurpose devices); the reason is always the necessity for the absolute knowledge of the system status in case of failure.

11.2.1 Safety in Communications

When dealing with secure communications, a general problem is detecting changes to raw data.

In this context, changes may be accidental or intentional. In case of accidental modification of data, cyclic redundancy check (CRC) is commonly used; the algorithms rely on cyclic codes and are simple to implement in hardware and very powerful in detecting errors due to noise in digital transmission, especially burst-type errors.

CRC algorithms are based on CRC polynomials of degree k of the variable x, specifically designed to protect messages of various lengths. The messages of n bits are considered polynomials of the variable x, with coefficients given by the values of bits, of degree $n + k - 1$, appending k zeroes at the end of messages. In order to compute the k-bit CRC, the polynomial message is divided by the CRC polynomial, appending at the end of polynomial message the remainder of the division. At the receiver, the division is performed again, verifying the equality of the received and newly calculated remainders.

In case of intentional changes, CRCs are totally useless and more powerful algorithms must be used, for instance, message integrity code (MIC) adopted by IEEE 802.11, based on secret temporal keys and Advanced Encryption Standard (AES).

11.3 Fail-Safe Realization: In-Depth Example

The cited safe systems can be realized in wired logic with electromechanical devices: the diagnostics are implemented using fail-safe relays and are based on the hypothesis that all possible faults could be individuated and the consequence would be to drive the system toward a "safer" state.

In the following, we will instead focus on the usage of programmable circuits in fail-safe systems. Since these systems can be considered as a subset of the self-checking ones, the typical diagnostic procedures of fault tolerance (Hayes and McCluskey 1980) can be used. Such procedures consist of the implementation of structures that must be self-checking as a whole: this goal can be obtained either with single electronic systems (Rennels 1978, Toy 1978) using a suitable redundancy or with two or more identical systems working synchronously whose outputs are compared in real time (Hopkins and Smith 1975). A solution of the second type is described in the following.

This solution consists of a system realized with two microcomputers and an arbitration unit; moreover, the correct flow of the software is controlled with a suitable hardware and software redundancy. A structure as the proposed one has the advantage of a high degree of software transparency with respect to other systems (Rennels 1980). In fact, as the only requirement on the software is some constraints on its flow, the whole system can be considered, from a functional point of view, as equivalent to a normal microcomputer.

11.3.1 General Architecture

The structure of the fail-safe computer is shown in Figure 11.1.

In this figure, the central unit, the input and output (I/O) blocks, and the circuits dedicated to the generation of fail-safe signals are recognizable. The central unit is a fault-tolerant system where the diagnostics are implemented through two identical microprocessor-based subsystems working synchronously. The following assumptions were assumed when developing the design:

- Both hardware and software are intrinsically "unsafe," and therefore, the final aim is to obtain a "fail-safe" system using unsafe instruments.
- The diagnostic signals that indicate a fault can arise anywhere in the system: from any origin, the design must warrant that the safe shutdown procedure would start, driving the system to the programmed safer state. This safer state corresponds to the absence of a secure supply voltage, which is normally generated through the relay R_{FS} of Figure 11.1.

Finally, the control signals and the procedures working in safety must be dynamic, to avoid faults of the "stuck-at" type.

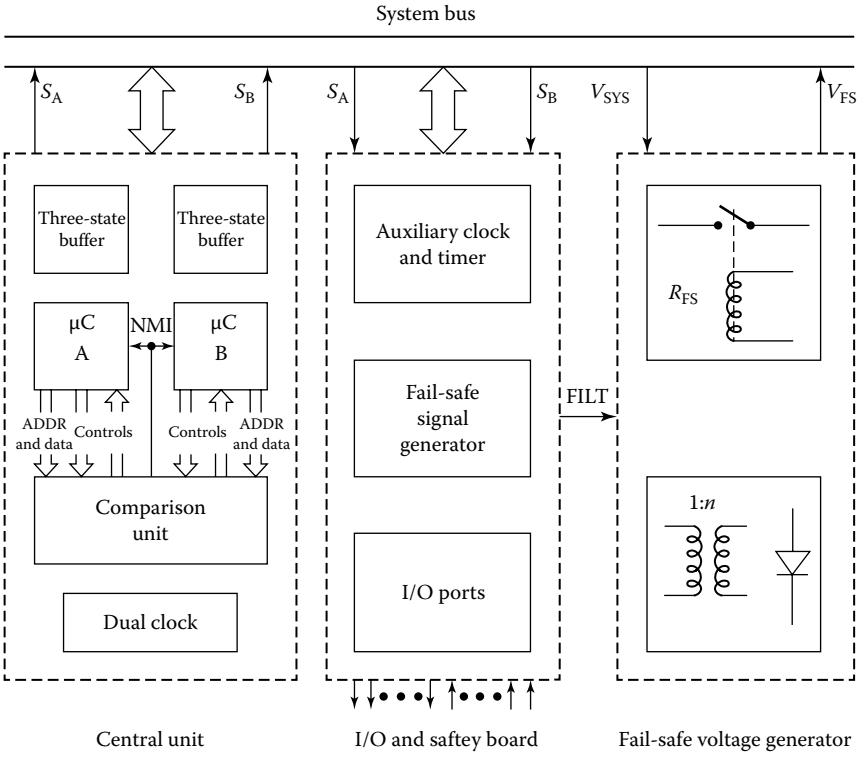

FIGURE 11.1 Structure of the fail-safe computer.

11.3.2 Central Unit

The central unit is realized with two Zilog Z80 CPUs, each with its own ROM and RAM, which run identical programs; output data and address are compared and possible disagreements are shown, causing the de-energization of the relay R_{FS}.

The correct flow of the program is verified by dividing the whole software, both user and system, into a known number of identical length blocks. This total number of blocks and their length are calculated by the "I/O and safety board" (described as follows) and compared with the theoretical ones.

The dual clock indicated in Figure 11.1 corresponds to the possible implementation of a real-time test procedure of the clock frequency, with the possible substitution of the faulty clock.

Finally, a periodic test procedure of the comparators is also implemented, to avoid stuck-at faults. Some different instructions are periodically inserted in the programs of both CPUs, and the outputs of the comparators are tested, looking now for the detection of the disagreement. The de-energization of the relay R_{FS} is correlated to the faulty operation of the comparators.

11.3.3 I/O and Safety Board

Figure 11.2 shows the block diagram of the board dedicated to the I/O and to the fail-safe controls.

This board, connected through the system bus to the central unit board,

- Manages the bidirectional communications with the external world
- Periodically checks the correct operation of the I/O devices
- Tests the duration of the software blocks and the frequency of the main clock
- Controls the energization of the fail-safe relay R_{FS}, dropping it out if some fault is detected, either in the same I/O or in the central unit board

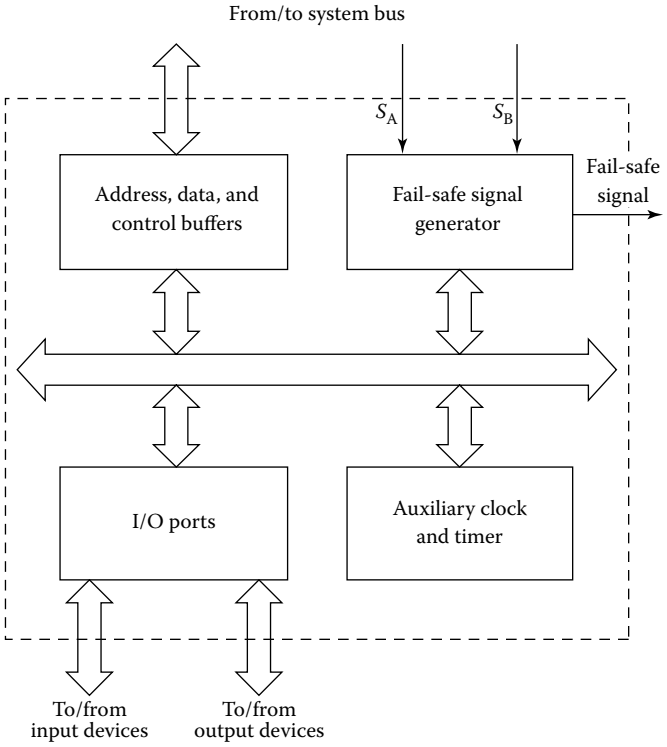

FIGURE 11.2 I/O and safety board.

11.3.4 I/O Ports

The system allows the safe transmission of remote controls and the safe acquisition of telesignals.

Two PIOs are used as shown in Figure 11.3, where Port A of the PIO 1 and the Port B of the PIO 2 are, respectively, dedicated to the output and to the test of the output, while the Port A of the PIO 2 and the Port B of the PIO 1 correspond to the input and to the control of the input. The output works as follows: The remote control signals, issued by the Port A of the PIO 1, drive the power transistors, whose outputs are read by the Port B of the PIO 2, and the system is considered faulty if no correspondence exists between issued and read signals. Moreover, the output is periodically checked to verify its capacity-changing state.

The input section is realized with optoisolators, which allow, varying one resistor, to work with digital signals of various values and protect the system from anomalous voltages. The test of this section is carried out by putting the output buffers in the low-impedance state and driving the input of the optoisolators with test signals issued by the Port B of the PIO 1. If appropriate ratios of R_{IN}/R are used, the signals read by the Port A of the PIO 2 must correspond to the issued ones: when such correspondence does not occur, the safe shutdown procedure will start. This test can be made either periodically or continuously, issuing after each input signal is received or the same signal is denied.

11.3.5 Fail-Safe Signal Generator

The safety characteristics of the whole system are correlated to the generation of a fixed frequency signal FILT, which is switched off when a fault is recognized. The frequency of FILT corresponds to the length of the blocks in which the whole program is divided and its generation is related to both hardware and software procedures.

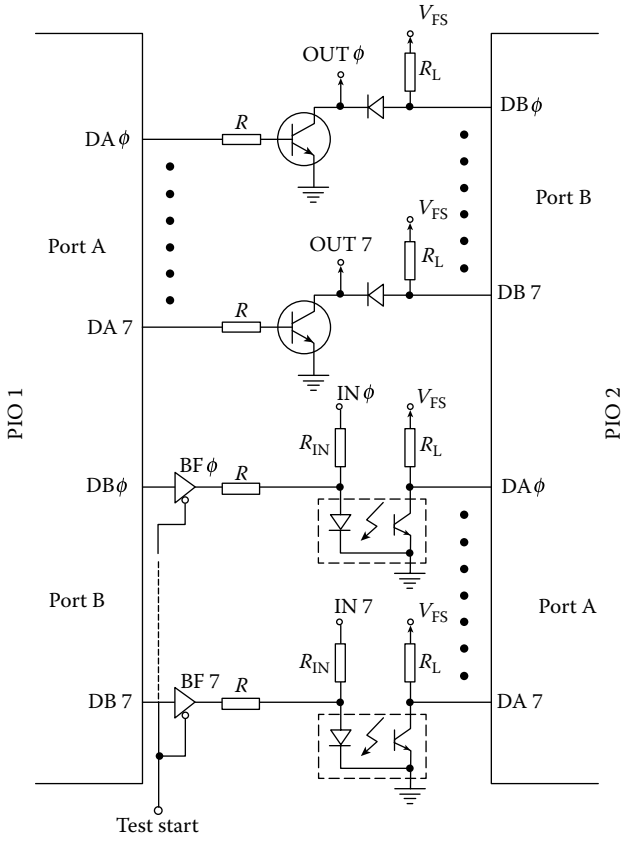

FIGURE 11.3 I/O configuration.

Each software block holds some instructions able to drive a hardware network that generates the basic signal *F*1. The block configuration of the circuit is shown in Figure 11.4. The *S* and *R* inputs of the flip-flop *F* are normally high: they go to zero at the end of each software block, when appropriate words on the address and data are generated by the program through arithmetic and logic operations. The output of the flip-flop *F* is the signal *F*1, while the final fail-safe signal FILT is obtained through SW_A and SW_B that halt the signal if some real-time test gives a wrong result. The control of the frequency of FILT is one of those real-time tests, made on the same I/O and safety board; therefore, the signal FILT outputted toward the fail-safe voltage generator can be the square wave, the correct frequency signal, or a zero-voltage signal, when a fault has occurred.

11.3.6 Auxiliary Clock and Timer Block

The auxiliary clock and timer block carries the appropriate time controls for the whole system. It is realized with a clock independent from the clock subsystem of the central unit and a CTC (or CTC-like circuits), and it calculates the number and the time length of the software blocks in which the program is divided and the frequency of the main clock.

Correct operation causes a signal to be forwarded to the fail-safe signal generator block, and consequently, the absence of this signal halts the signal FILT. This block can be easily duplicated in order to increase the reliability.

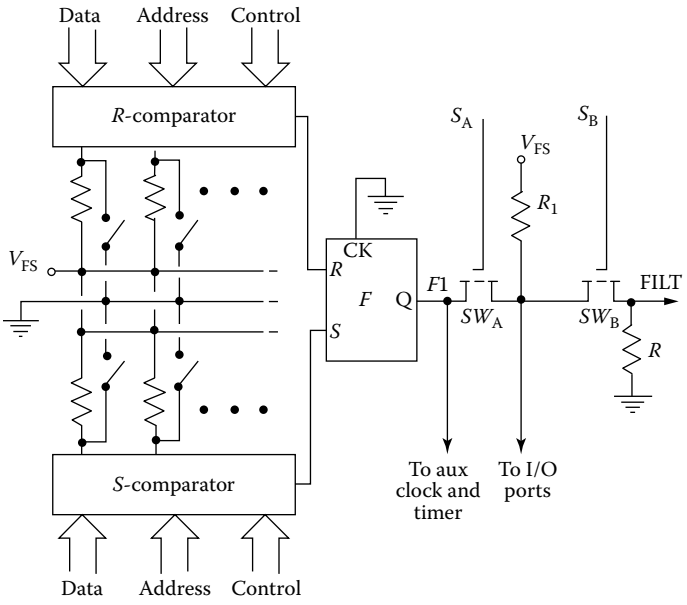

FIGURE 11.4 Fail-safe signal generator.

11.3.7 Fail-Safe Voltage Generator

The subsystem used to generate the fail-safe voltage is shown in Figure 11.5. This configuration prevents the input voltage from reaching the final fail-safe relay in the presence of any foreseeable fault of the transformer, diodes, etc.

The fail-safe voltage V_{FS} is used to supply through the system bus all the circuits, devices, and peripherals that must be halted when a possible fault is recognized, while the other circuits can be supplied directly by the voltage V_{SYS}.

Finally, the start of the system is assured using the fail-safe button B_{FS}, which bypasses the feedback control system of the supply voltage.

11.3.8 Fail-Safe Procedures: Tests and Their Timing

The starting point for the fail-safe operation of the whole system is the fail-safe relay R_{FS} that supplies voltage to all the parts of the system that must operate safely and defines the class of faults that must be

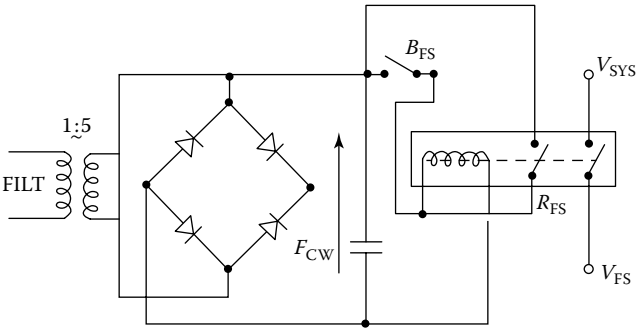

FIGURE 11.5 Subsystem used to generate the fail-safe voltage.

considered as foreseeable during the normal life of the system. To avoid the most common faults, the "stuck-at" faults, the fail-safe voltage generator with the relay R_{FS} is driven by a dynamic signal FILT; every foreseeable fault, both hardware and software, implies either a fixed value of $F1$ or a frequency different from the theoretical one and the consequent halt of the input signal FILT of the voltage generator (Figure 11.4).

The halt of FILT is tied to the correct operation of the switches SW_A and SW_B. The configuration shown in Figure 11.4 allows an easy test of the functionality of the MOS switches oriented to safety. Since the absence of FILT drives the system toward a safer state, the test must warrant against the permanent short circuit of the switches and it is accomplished, when FILT is low, driving both MOS switches to the OFF state. Every fault, either of SW_A and SW_B or of the signals S_A and S_B, will make the I/O Port read a LOW value instead of a HIGH one if an appropriate ratio R_1/R is used.

The tests implemented on the computer are of two types, continuous, or real-time, and periodic.

The continuous tests mainly consist of the comparison of address and output data from the CPUs A and B of Figure 11.1, made by the comparator C. When a disagreement is detected, an NMI signal is generated to both A and B CPUs. The CPUs forward on different lines the signals S_A and S_B that are independently able to drop out the switches SW_A and SW_B (Figure 11.4), and they also signal the I/O tristate buffers of the central unit board to the system bus in the high-impedance state, so halting the whole system.

The first periodic test considered is the test of comparators. Disagreement, which corresponds in this case to the right operation, always generates the NMI signal. But unlike the previous case, the system software prevents the tristate buffers from going into the high-impedance state, it doesn't allow the signals S_A and S_B to reach the MOS switches SW_A and SW_B (Figure 11.4), and it also actively contributes to the generation of the signal FILT. Another periodic test concerns the I/O ports: again when a fault is detected, the central unit board generates the signal S_A and S_B that stops the signal FILT.

Finally, a real-time test is implemented during output operations, in order to verify the agreement between the transmitted output and the signal received by the driven device: a disagreement causes the generation of the previously cited S_A and S_B that stop FILT.

The generation of FILT is obtained, using hardware and software procedures with the maximum possible degree of safety; moreover, each fault that causes, for instance, the absence of the alternating pulses at the inputs of the flip-flop F of Figure 11.5, determines a continuous value of FILT, not valid for the generation of V_{FS}. The frequency of FILT is directly related to the minimum reaction time requested for the safe operation of the whole system.

But all the previously cited test and procedures are useful only if they are "sure" that every fault will cause the de-energization of the relay R_{FS}. Such "sureness" has been reached, to a certain degree, making it possible that every class of faults will operate in different ways for preventing a square-wave signal FILT from reaching R_{FS}, not generating the signal $F1$ and doubling the lines S_A and S_B of Figure 11.1.

11.3.9 Fail-Safe Relays

Another assumption on which this work is based is that the fail-safe relays, if broken, go into a foreseeable state. In effect, if the relays are of the fail-safe type used, for instance, in the railway field, this assumption is commonly accepted and, moreover, contributes to the acceptability of the proposed system in fields connected with safety that are, rightly, very conservative.

However, alternative solutions based on the hypothesis, generally accepted in fault-tolerant systems, which two contemporary faults cannot occur, can be proposed.

An example consists of the use of MOS switches of the appropriate power mounted with a suitable redundancy that uses diagnostic methods for their periodic test. A possible configuration is shown in Figure 11.6, where the relay is replaced with eight MOS switches arranged in two parallel identical paths.

Considering the four driving MOS indicated with MD, the continuous fail-safe voltage is the supply, while the gates are driven by a fail-safe I/O configuration such as the one shown in Figure 11.3.

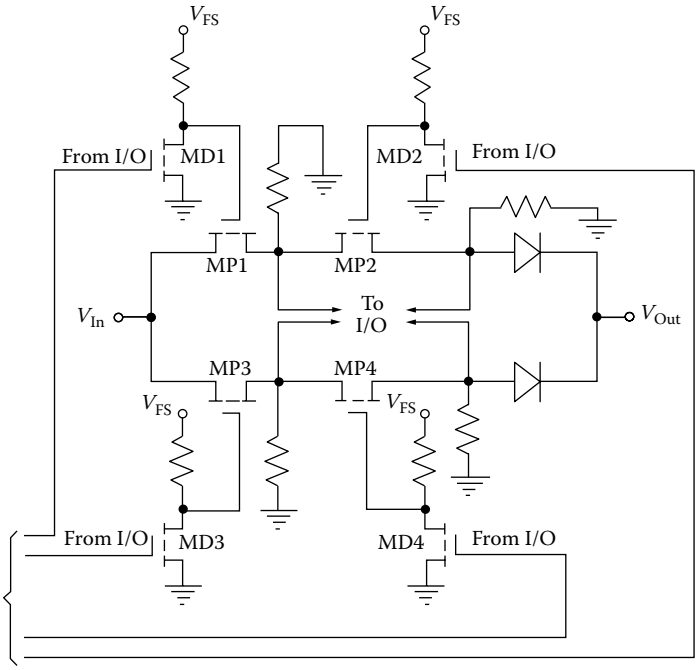

FIGURE 11.6 Solid-state fail-safe relay.

The test is made in sequence on the electronic switches MP, comparing I/O of each MOS, while the connection between the input and the output of the whole relay is assured by an independent test.

11.3.10 Reconfigurability

Although the described system is capable of a single kind of action, it is surely possible to modify it in the way in which its safe outcomes could be different on the basis of some configuration choices. For this reason, most recent fail-safe systems (e.g., European Railway Traffic Management System (ERTMS); see the following) include a configuration file in which parameters can be set at specific values, thus setting the performance of the system. Also for the production of the configuration files, fail-safe design techniques must be used, of course, from both design and communication points of view.

11.4 Case Study: Level 1 ERTMS

The ERTMS is a signaling system capable of maintaining the railway traffic safe in every condition, including the driver's incapacitation or death. Although it is mainly a European product, it is actually spreading all over the world, and its installations exist (or will exist very soon) in Asia, Africa, America, and Oceania. Its system requirement specifications are actually very solid: they are the product of a long effort, a work in which infrastructure managers, railway companies, technological companies, and various suppliers have been involved in for many years. From a very-high-level point of view, the system is formed by two segments: the trackside subsystem (composed of devices installed on the ground) and the onboard subsystem (i.e., installed on trains and called ETCS, i.e., European Train Control System). Both of the subsystems are modular and can be configured for using different technological solutions as substratum: low-frequency dedicated radio transmission, GSM for railway (GSM-R), and also satellite communication are all viable implementations (although the last is actually only at the prototype level). The combination of a specific subset of the system requirements specifications and one (or more) of the

technological solutions makes what is called a "level." ERTMS is, in fact, available in three levels: 1, 2, and 3 (plus Level 0 that is used for indicating ERTMS predisposition or transition from a legacy national train run protection system toward an ERTMS level). In the following paragraphs, a brief description of Level 1 in its simplest implementation is provided, with emphasis added on the practical implementation of the safety concepts shown before.

The trackside subsystem of Level 1 ERTMS is formed of passive devices installed on the railway lines, devices called "Eurobalises." Two types of Eurobalises exist: one with fixed informative content and one with variable informative content. The first is used, for example, for communicating to the onboard subsystem (and so to the driver) the exact position of the train, while the second is used for transmitting the information about the status of the line (e.g., free or occupied by another vehicle). Independent from the type, the transmission of the information is possible only through strict interaction between the trackside subsystem and the onboard subsystem. Eurobalises are passive devices and can transmit only when a certain quantity of energy is given to them by a specific antenna, part of ETCS, installed on trains. When the train passes on a Eurobalise (installed on the "sleepers" between the steel rails), its ETCS antenna, situated on the bottom of the locomotive, transmits electromagnetic energy to the balise itself that, being energized, "answers" sending a proper "telegram" to the same antenna, which is a transmitter/receiver. The "telegram," which is transmitted using a dedicated channel at MHz frequencies, contains the information about position or line status described before (the transmission uses the frequency-shift keying technique, although also amplitude-shift keying is available for retrocompatibility purposes). The telegram received by the ETCS antenna is then converted into a digital string by a specific ETCS module (the BTM, Balise Transmission Module) and then sent to the ETCS logic for elaboration. The elaboration leads to some actions by the ETCS logic, actions that often involve the driver's interaction with the train (usually requiring speed reduction or braking application) or automatic reaction in case of the driver's unavailability. As it is easy to see, the high-level architecture is simple (as always requested for fail-safe applications) but also sufficiently modular to allow a great range on configurability and usability. Let us now see how the fail-safe concepts are taken into account for the implementation of Level 1 ERTMS.

First of all, in Eurobalises, we can see a clear example of inherent fail safety in their design: they are passive (i.e., not connected to any power supply), so leading to a technical analysis that is exhaustive from the fault/failure point of views (for both internal and external causes). Besides, they are designed to transmit both default telegram or no telegram in case of vital/fatal error, leading to a safe reaction by the onboard subsystem (which is often the emergency braking, i.e., the one performed acting directly on the brake commanded by a pneumatic pipe and capable of blocking the train wheels). Also composite fail-safety techniques are used in their deployment: they are always installed in couples, in a full redundant configuration (a configuration called "balise group"). Finally, each Eurobalise, when transmitting its telegram, communicates also to the ETCS the position of the following balise group ("announcing" it): it is easy to imagine the ETCS reaction when an "announced" balise group is not encountered, both for its proper failure (e.g., on the antenna) or for balise fault. It is, of course, emergency braking.

ETCS: For a system that must be capable of "making decisions," that is, a system that has a complex hardware architecture with a software logic embedded and that must perform different actions on the basis of the information transmitted by the balises, inherent fail safety is not, obviously, a viable option, at least from a high-level point of view (it could be a possible design choice for single components, however, as seen in detail in Section 11.3). For this reason, the ETCS system is designed to be fully redundant, both at a system level (which is formed, substantially, by two twin systems installed on the same train-borne rack) and at a single-board level (each fully equipped with redundant logic units), characterizing itself as a composite fail-safe system. In addition, specific modules are built also with a reactive fail-safety approach. The antenna (used, as already said, for energizing the balises), for example, must include a subsystem capable of testing its transmitting/receiving performances at least at the system start-up (several antenna implementations are built having autotesting capabilities active also after the system start-up, however, and the tests are executed very frequently).

Note how the concepts related to fail safety are extensively used in ERTMS. Any single fatal fault or failure, either on the trackside segment or on the train-borne one, leads the system to a safe status (the application of the emergency brake). A task that is accomplished through the use of all the fail-safe design techniques described earlier, using composite systems that are also inherently safe on their low-level architecture or reactively safe because of the presence of external "verifiers."

11.5 Summary

A device is fail-safe only if its final status is always known, despite the kind of failure that may occur. This performance is necessary because human life depends on the safety of the device, and so exceptions are not acceptable. For this reason, the design approach for safety devices is radically different from the one used for not-safety-related applications. A very solid process, which must comply with the strictest quality standards, must be carried on by groups of experts rigidly separated by function (design, engineering, verification and validation, assessment). The components, both software and hardware, must be selected to be simple, fully known and debugged, and not extremely recent. They must be deeply analyzed from both top-down and bottom-up perspectives and combined together using techniques (composite, reactive, and inherent fail safety) capable of assuring the overall safety of the system, also formed by a large number of components or segments.

In this way, the possibility for building trains that guarantee the safety of the users' lives or medical devices that never cause harm to patients surely exists.

References

Hayes, J.P. and E.J. McCluskey, Testability considerations in microprocessor-based design, *Computer* 13: 17–25, 1980.

Hopkins, A.L. and T.B. Smith, The architectural elements of a symmetric fault-tolerant multiprocessor, *IEEE Transactions on Computer* C-24: 498–505, 1975.

Rennels, D.A., Architectures for fault tolerant spacecraft computers. *Proceedings of IEEE* 66: 1255–1268, 1978.

Rennels, D.A., Distributed fault-tolerant computer systems, *Computer* 13: 55–65, 1980.

Toy, W.N., Fault tolerant design of local ESS processors, *Proceedings of IEEE* 66: 1126–1145, 1978.

12

Dynamic Error Measurements of Force Sensors

Akihiro Takita
Gunma University

Jin Tao
Gunma University

Yusaku Fujii
Gunma University

12.1 Introduction

Force sensors are extensively used in various research and industrial fields such as monitoring, testing, and manufacturing. Further, it is extremely important to calibrate the static and dynamic errors of sensors in order to improve their accuracy. However, only static calibration methods are available currently. It is easy to generate static forces precisely by using well-calibrated balance weights. However, this has a significant disadvantage, that is, the absence of a well-established method for generating and measuring dynamic force precisely. If we attempt to measure the dynamic forces acting on a force sensor for calibration, another force sensor with better dynamic properties and more accuracy than the tested sensor becomes necessary, thereby creating infinite loop and somewhat nonsensical situation. In this chapter, we introduce a method for calibrating force sensors without using other force sensors.

12.2 Problems and Solutions of Dynamic Calibrations

Although there are no well-established methods for the dynamic calibration of force sensors, a few researchers have previously attempted to develop them. Prof. Kumme has proposed and developed a method that uses the inertial force of the attached mass shaken by a shaker [1,2], and Prof. Park et al. have used this method to investigate the dynamic characteristics of multicomponent force–moment sensors [3,4]. This method enables the evaluation of the dynamic characteristics of force sensors under a condition in which the force acts as a continuous and single-frequency vibration. Therefore, this method was not suitable for evaluating the dynamic characteristics with impulse responses, which is important for analyzing crash tests.

A few researchers [5,6] have attempted to develop the dynamic calibration method for impulse responses as well; they concluded that the differences between the static and the dynamic characteristics

are explained by the inertial force of a part of the force sensor itself. However, their methods could only evaluate the response after an impact because the force could not be measured during the impact itself; moreover, the reference forces also cannot be measured.

Hence, we developed some methods for dynamic force calibration by using the levitation mass method (LMM). In the LMM, the force acting on the sensor can be measured precisely without using any other force sensors.

12.2.1 Levitation Mass Method

The LMM was proposed and developed by the authors. In this method, a rigid body is made to collide with the measurement object and a dynamic force is applied on it. The velocity of the rigid body during the collision is then measured, and as a result, the force acting on the object can be measured by using the equation of motion, $F = ma$, where F is the instantaneous force; m, the mass of the rigid body; and a, the instantaneous acceleration of the rigid body calculated by the differentiation of the instantaneous velocity of the rigid body. To move the rigid body linearly with little friction, an aerostatic linear bearing is used. Because the velocity and the mass can be measured precisely by using a laser Doppler interferometer and a well-calibrated balance, the force also can be measured precisely. Therefore, the LMM is suitable for calibrating the dynamic error of force sensors. The authors applied this method for dynamic force calibration under impact, oscillating, and step loads [7–11]. In the following section, the dynamic calibration methods using the LMM are reviewed.

The LMM can be applied not only to the dynamic calibration but also to the other force measurement applications. The authors developed evaluating method for material viscoelasticity, material friction, biomechanics, dynamic performances of linear motor, and human body weights under microgravity condition [12–23].

12.3 Evaluation of Dynamic Characteristics of Force Sensors

An example of the calibration and correction method of dynamic force measurements using the LMM is shown here. An S-shaped force sensor was used to measure the impact force with a pulse width of approximately 7 ms full width at half maximum (FWHM).

12.3.1 Structure of S-Shaped Force Sensor

Strain-gage force sensors are the most common force sensors because they are inexpensive but have high sensitivity. Figure 12.1a shows the schematic diagram of an S-shaped strain-gage force sensor. The sensor is formed by two metal blocks and a parallel leaf spring connecting the two blocks. Therefore, the sensor is modeled as a mass spring model, as shown in Figure 12.1b. When the force is acting on the sensing point, the spring is compressed in proportion to the force. The displacement of the sensing point is measured by strain gages and is converted into force by using Hooke's law, $F = -kx$, where F is the force; k, the spring constant; and x, the displacement. In the dynamic force measurements, the metal block, including the sensing point, is in motion, and its velocity is changed by the force acting on the sensing point. In such a case, the force that compresses the spring is not only the force acting on the sensing point but also the inertial force of the block. This inertial force is the primary cause of the error in the dynamic measurements with this type of force sensor.

Figure 12.2 shows a schematic diagram of the experimental setup for measuring the electric and mechanical responses of the force sensors against the impact force. A force sensor, whose rated force capacity is 200 N, was stiffly fixed to a base. The base was heavy and entirely fixed to the floor. An aerostatic linear bearing was used to enable horizontal linear motions with negligible friction. An impact force was generated and applied to the sensor by making the moving part of an aerostatic linear bearing to collide with the sensor. An initial velocity was manually imparted to the moving part. An extension

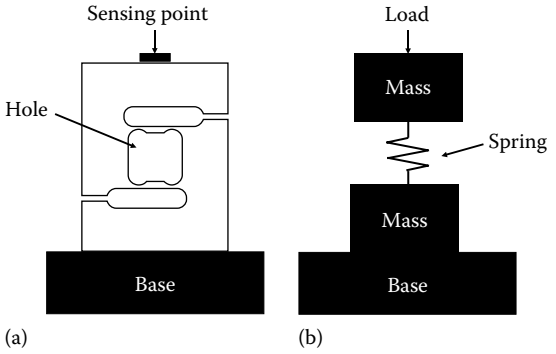

FIGURE 12.1 S-shaped strain-gage force sensor: (a) Schematic diagram, (b) spring mass model.

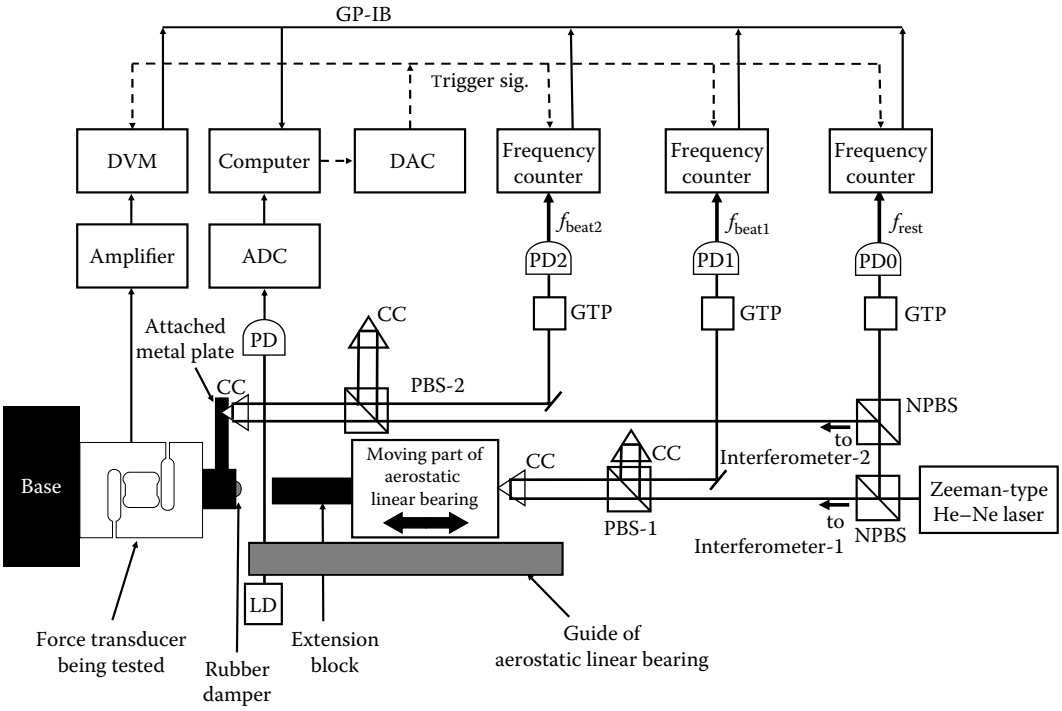

FIGURE 12.2 Experimental setup for calibrating the impact test of force sensors. CC, corner cube; PBS, polarized beam splitter; NPBS, nonpolarizing beam splitter; GTP, Glan–Thompson prism; ADC, analog-to-digital converter; DAC, digital-to-analog converter; DVM, digital voltmeter; PD, photodetector; LD, laser diode.

block for adjusting the collision position as well as a corner cube (CC) prism for turning the laser beam was attached to the moving part. The total mass of the moving part including the extension block and CC, M_1, was 2.653 kg.

The sensor being tested was statically calibrated with the standard uncertainty of approximately 0.2 N, that is, 0.1% against the rated force capacity. The output signal of the sensor was measured by using a digital voltmeter (DVM) (VP5481L, Panasonic Corp.). A CC prism was attached near the sensing point of the force sensor, as shown in Figure 12.2, in order to measure the displacement of the sensing point by an optical interferometer. The mass of the attached metal plate including the CC prism, M_2, was approximately 0.082 kg.

The force acting on the moving part of the linear bearing, F_{mass}, is calculated as a product of its mass and its acceleration, a_1, as follows:

$$F_{mass} = M_1 a_1 \tag{12.1}$$

Because the friction acting on the moving part of the bearing was negligible, the force acting on the moving part can be considered to be equal to the force acting on the force sensor. The acceleration was calculated from the velocity of the moving part. The velocity of the moving part was measured by the optical interferometer.

The instantaneous velocities of the moving part and the sensing point of the force sensor, v_1 and v_2, respectively, were measured by using two optical interferometers. A Zeeman-type two-frequency He–Ne laser was used as the light source. The frequency difference between the two frequencies was $f_{rest} = |f_1 - f_2| = 2.6$ MHz. The velocity was measured as the Doppler shift frequency, $f_{Doppler}$, of the signal beam. The velocity can be expressed as follows:

$$v_1 = \frac{\lambda_{air}(f_{Doppler1})}{2} \tag{12.2}$$

$$f_{Doppler1} = -(f_{beat1} - f_{rest}) \tag{12.3}$$

$$v_2 = \frac{\lambda_{air}(f_{Doppler2})}{2} \tag{12.4}$$

$$f_{Doppler2} = -(f_{beat2} - f_{rest}) \tag{12.5}$$

where

λ_{air} is the wavelength of the signal beam
f_{beat1} is the beat frequency detected by the photodetector (PD)-1
f_{beat2} is the beat frequency detected by the PD-2

Further, the directions of the coordinate system for the force, velocity, and acceleration for the moving part were toward the right (Figure 12.2). Three electric frequency counters (R5363, Advantest Corp.) measured and recorded the beat frequencies 14,000 times with the sampling interval of $T = 400/f$. The sampling rate of the counter was approximately 6.6 kHz for f of 2.6 MHz. The DVM and the three counters were triggered by a signal generated by a computer and initiated by an optical switch comprising an LD and a PD.

Results and Discussions: Figure 12.3 shows the force measured by the force sensor, F_{trans}; the force measured by the optical interferometer-1, F_{mass}; and their difference $F_{diff} = F_{trans} - F_{mass}$; further, the electric response of the force sensor under an impact load can be observed. The difference between F_{trans} and F_{mass} was caused mainly by the difference between the static and the dynamic characteristics of the force sensor, and the root mean square (rms) value of F_{diff} during the collision, 0 ms < t < 14 ms, was approximately equal to 3.97 N. The LMM can be used to obtain this result because its performance is the best among available methods.

Figure 12.4 shows the second-order derivative of the force measured by the force sensor, d^2F_{trans}/dt^2, and F_{diff}. The solid line shows a regression line expressed by $F_{reg} = C(d^2F_{trans}/dt^2) = (-3.33 \times 10^{-7})(d^2F_{trans}/dt^2)$. The coefficient C is obtained by the gradient of the regression line determined by the least-square method.

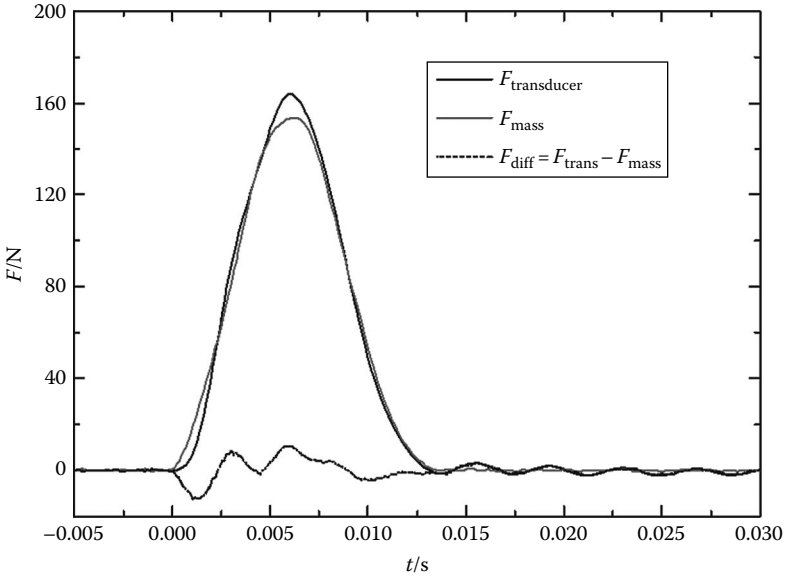

FIGURE 12.3 Force measured by the force sensor, F_{trans}; the force measured by the optical interferometer, F_{mass}; and their difference $F_{diff} = F_{trans} - F_{mass}$.

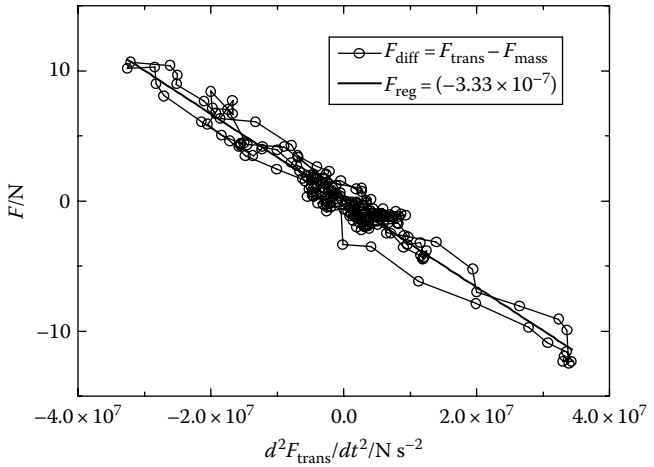

FIGURE 12.4 Relationship between the second-order derivative of the force measured by the force sensor, d^2F_{trans}/dt^2, and F_{diff}.

Figure 12.5 shows the changes in the difference F_{diff} between the forces measured by the force sensor and the optical interferometer and the force regressed by using F_{trans} and F_{reg}, against time. The measurement error F_{diff} is almost identical to the results of the regression analysis, F_{reg}. Therefore, F_{diff} can be represented by $F_{reg} = (-3.33 \times 10^{-7})$ (d^2F_{trans}/dt^2), and the force measured by the force sensor can be corrected using the output signal of the sensor itself by using the following equation:

$$F_{corrected} = F_{trans} - F_{reg} = F_{trans} - C\left(\frac{d^2F_{trans}}{dt^2}\right) \tag{12.6}$$

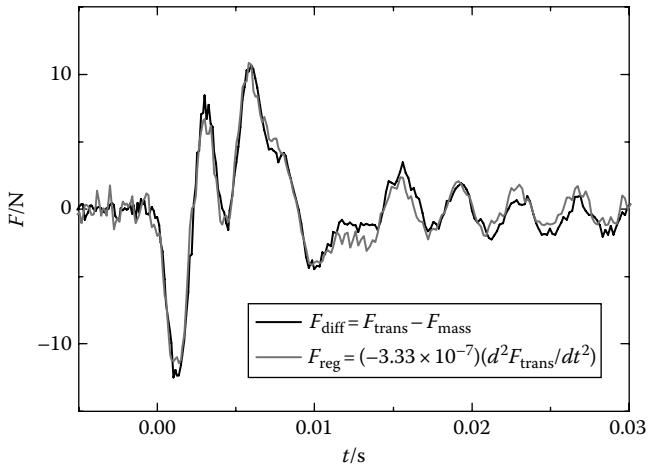

FIGURE 12.5 Changes in F_{diff} and F_{reg} against time.

This is the theory of the self-correction method. Once the coefficient C has been measured for a force sensor by using the LMM, the dynamic force measured by the force sensor can be corrected with output signal of the force sensor itself without the LMM setup.

Figure 12.6 shows the rms value of the errors of the measured force with and without self-correction; the results of the 10 impact tests are plotted. The regression coefficient of the single experiment (shown in Figure 12.4) is used for all the self-corrections. The rms value of the F_{diff} error drastically increases with the peak forces of F_{mass}, $F_{mass,\,max}$. The rms value of $(F_{corrected} - F_{mass})$ also increases with $F_{mass,\,max}$, but the increment is significantly smaller than that of the rms value of the error of F_{diff}. This result shows the efficiency of the self-correction method.

Figure 12.7 shows relationship between the second-order derivative of the force measured by the force sensor, d^2F_{trans}/dt^2, and the acceleration of the sensing point of the force sensor, a_2, measured by the optical interferometer-2. The plotted data are from the same experiment shown in Figure 12.3 through Figure 12.5. It is clear that a_2 is almost proportional to d^2F_{trans}/dt^2. The solid line shows a regression line expressed by $a_2 = (-1.03 \times 10^{-6})\ (d^2F_{trans}/dt^2)$. According to the operational principle of the force sensor,

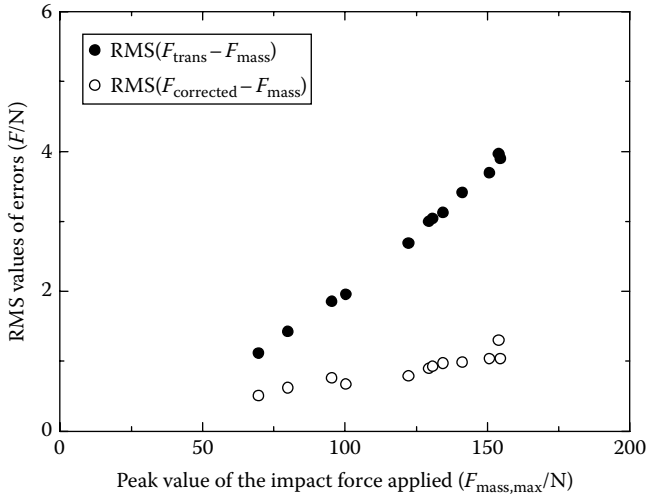

FIGURE 12.6 Rms values of the errors of measured force with and without self-correction.

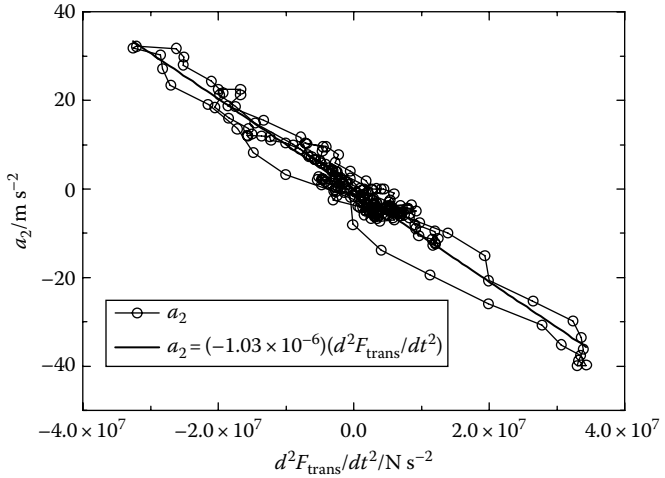

FIGURE 12.7 Relationship between d^2F_{trans}/dt^2 and the acceleration of the sensing point of the force sensor, a_2.

the force measured by the sensor is a product of the spring constant and displacement. Therefore, the acceleration of the sensing part of the force sensor can be obtained by the second time derivative of the F_{trans} as follows:

$$F_{trans} = -kx$$

$$-\frac{1}{k}\frac{d^2F_{trans}}{dt^2} = \frac{d^2x}{dt^2} = a_2$$

The slope of the regression line (-1.03×10^{-6}) is almost identical to $-1/k = -0.95 \times 10^{-6}$, where k is the nominal value of the spring constant of the force sensor. The relationship shown in Figure 12.7 is a validation of the aforementioned equation. Further, the aforementioned results prove that the tested force sensor can be modeled by a mass–spring model, and the primary reason for the dynamic error is the inertial force of the sensing part of the force sensor.

The other application of the LMM for calibrating force sensors is described in the sections as follows.

12.4 Impulse Response

Introduction: The impulse response refers to the response when the force is inputted as a Dirac delta function, and it is the most important dynamic characteristics for analyzing dynamic systems. Because the input of a Dirac delta function cannot be obtained experimentally, a very short pulse is substituted for the Dirac delta input. In our experiment, the FWHM of the pulse duration of approximately 1 ms and a maximum impact force of up to approximately 1 kN could be achieved by using our improved measurement method.

Experimental Setup: Figure 12.8 shows the schematic diagram of the experimental setup for evaluating the impulse responses of force sensors. This setup was roughly the same setup shown in Figure 12.2 except the lack of the second optical interferometer. In order not to prevent the sensor from fast motion, the external weight such as the CC and the metal plate were not attached to the sensor. Further, no damper was used to reduce the steepness of the impulse. The total mass of the moving part of the aerostatic linear bearing, M, is 4.5000 kg.

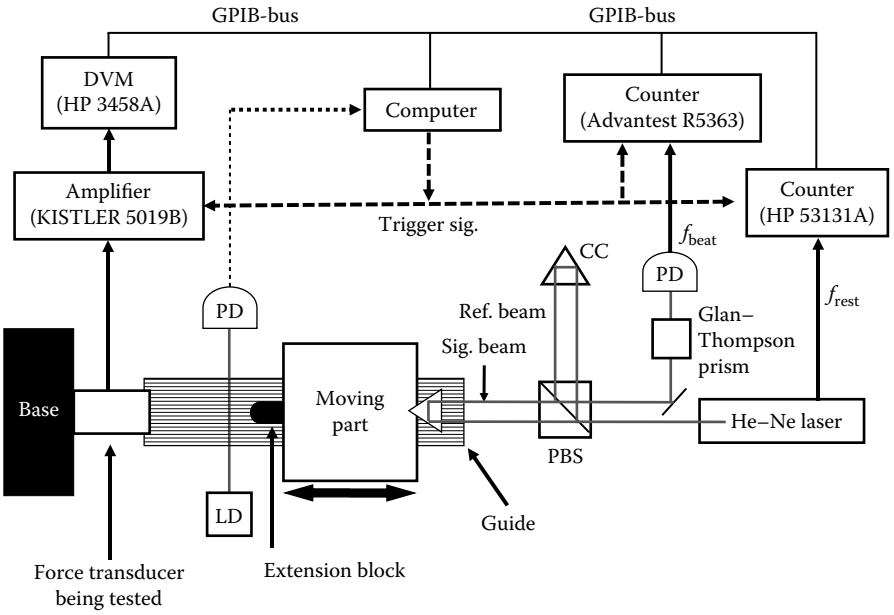

FIGURE 12.8 Experimental setup for evaluating impulse response. CC, corner cube; PBS, polarized beam splitter; PD, photodetector; LD, laser diode.

A piezoelectric force sensor (9213A, Kistler Instrument Corp.) was used for measuring the high-speed responses. The rated force capacity and the characteristic frequency of the sensor were 2.5 kN and approximately 200 kHz. The sensor was statically calibrated with the standard uncertainty of approximately 25 N, that is, 1% against the rated force capacity. The output signal of the sensor was measured by a digital multimeter (HP 3458A, Agilent Technologies Corp.) with the sampling rate of 50 kHz.

The instantaneous velocity of the moving part was measured by using an optical interferometer. A Zeeman-type two-frequency He–Ne laser was used as the light source, and the frequency difference between the two frequencies was $f_{rest} = |f_1 - f_2| = 2.6$ MHz. The velocity was measured using the Doppler shift frequency, $f_{Doppler}$, of the signal beam by using the following equation:

$$v = \lambda_{air} \frac{f_{Doppler}}{2} \tag{12.7}$$

$$f_{Doppler} = -(f_{beat} - f_{rest}) \tag{12.8}$$

where

λ_{air} is the wavelength of the signal beam

f_{beat} is the beat frequency detected by the PD

The directions of the coordinate system for the force, velocity, and acceleration on the moving part were toward the right (Figure 12.8). An electric frequency counter (R5363, Advantest Corp.) was used to measure and record the beat frequency. Another electric counter (HP53131A, Agilent Technologies Corp.) measured f_{rest} by using the trigger signal supplied by a photodiode embedded in the He–Ne laser.

In the experiment, the initial velocity of the moving part, v_1, changed to v_2 after the collision. The impulse responses of the force sensors were determined by comparing the impulse obtained by

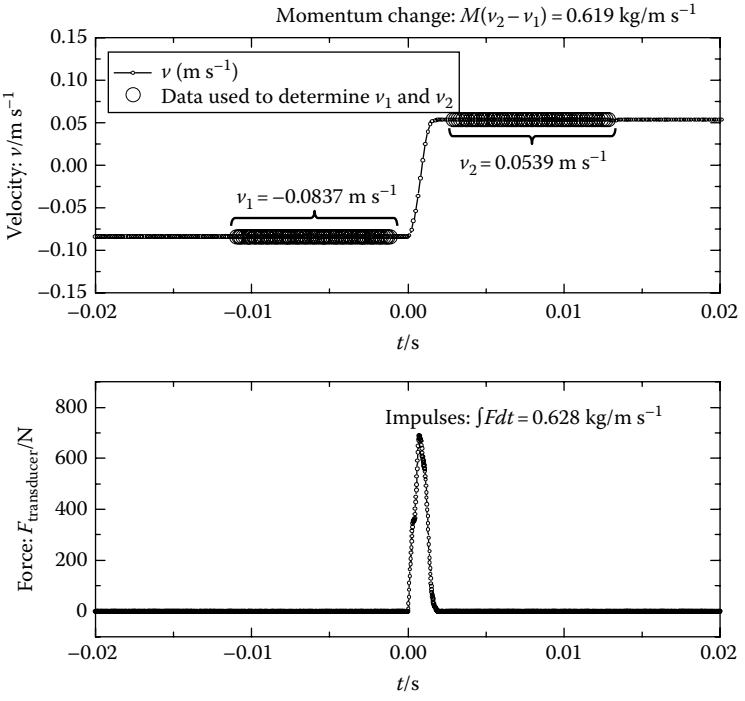

FIGURE 12.9 Changes in the velocity of the moving part and impact force detected by the force sensor.

integrating the output signal of the sensor, F_{sensor}, with the momentum changes of the moving part measured by the optical interferometer, $M(v_2 - v_1)$.

Results and Discussion: Figure 12.9 shows the velocity and force measured by the interferometer and force sensor. The velocities before and after the collision, v_1 and v_2, were measured as mean velocities during 10 ms before and after the collision. In this experiment, v_1 and v_2 were −0.0837 and 0.0539 m/s, respectively. The sample standard deviation of the velocities was $\mu_{v,1} = 4.0 \times 10^{-6}$ m/s and $\mu_{v,2} = 1.9 \times 10^{-5}$ m/s, respectively. The corresponding total velocity changes caused by the collision were 0.003% and 0.014%, respectively. These values are sufficiently smaller than the required uncertainty of 0.1%. The changes in momentum were approximately 0.619 kg m/s.

Figure 12.10 shows the instantaneous values of the impact force measured by the optical interferometer, $F_{inertial}$, and the force sensor, F_{sensor}. $F_{inertial}$ is calculated by using the following equation:

$$F_{inertial} = M\frac{d}{dt}(-f_{beat} + f_{rest}) \tag{12.9}$$

Although the time resolution of $F_{inertial}$ is not sufficient to determine the difference between $F_{inertial}$ and F_{sensor}, the response of F_{sensor} seems to overshoot near the peak of the pulse. The relative difference between the impulse measured by the sensor and the momentum change measured by the interferometer

$$\frac{\int F_{transducer} dt}{M(v_2 - v_1)} - 1 \tag{12.10}$$

is approximately 0.015. This error is mainly from the overshoot of F_{sensor}.

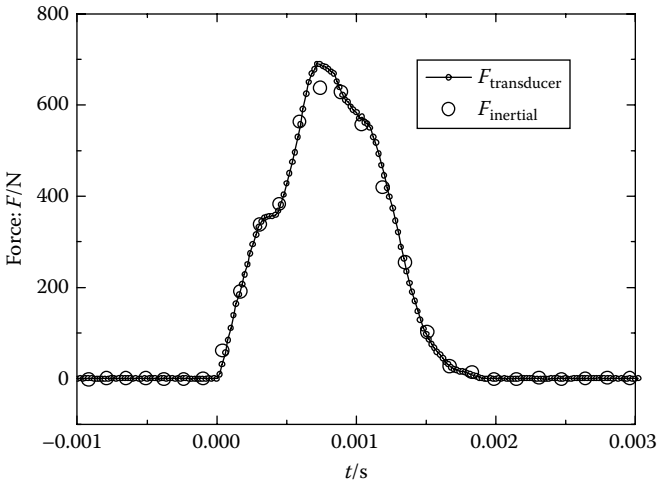

FIGURE 12.10 Instantaneous value of force measured by optical interferometer and force sensor.

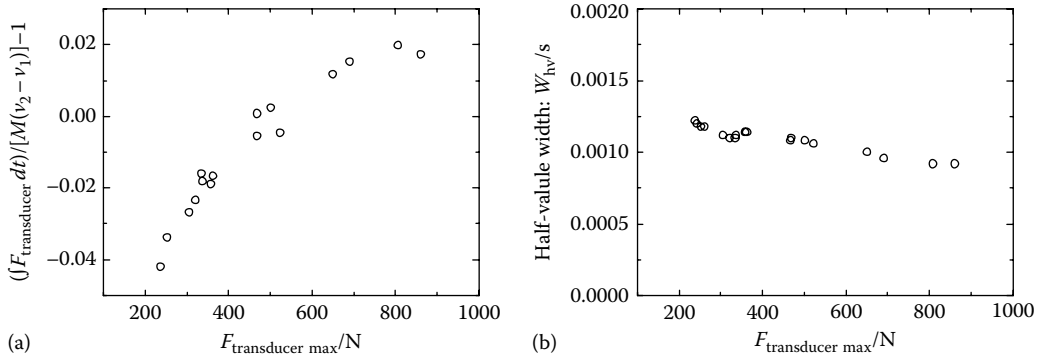

FIGURE 12.11 (a) Relative difference between impulse and change in momentum against the maximum force and (b) FWHM of pulse duration against the maximum force.

Figure 12.11a shows the relative difference between the impulse and the changes in momentum against the peak value of the force measured by the sensor, $F_{\text{sensor\_max}}$. This figure shows a clear relationship between the relative difference and $F_{\text{sensor\_max}}$.

Figure 12.11b shows the pulse duration in FWHM against $F_{\text{sensor\_max}}$. From the results, the pulse width can be estimated at approximately 1 ms in FWHM.

12.5 Oscillation Response

The continuous oscillation response of force sensor is also evaluated by using LMM.

Experimental Setup: Figure 12.12 shows a schematic diagram of the experimental setup for evaluating the oscillation responses of a force sensor. The components of the setup were almost identical to those for evaluating the impulse response. The major difference was that the rigid body—a moving part of an aerostatic linear bearing—was connected to the side of the tested force sensor with a steel spring. The other side of the sensor was fixed to the base. The moving part, the force sensor, and the spring comprised a mass–spring system. The inertial force of the moving part was used as the standard oscillation force and was compared to the output signal of the force sensor when the mass–spring system

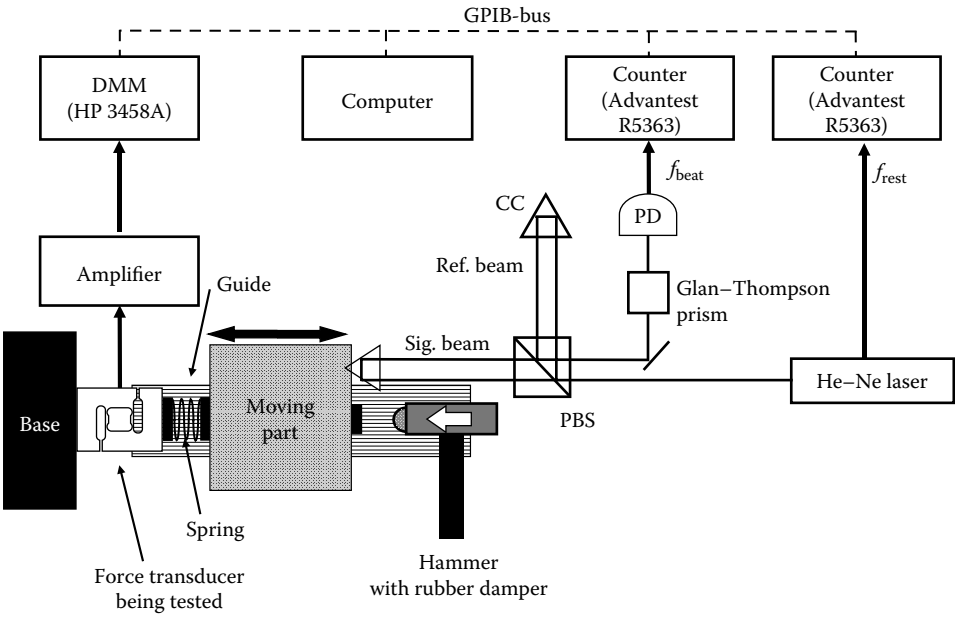

FIGURE 12.12 Experimental setup for evaluating oscillation response. CC, corner cube; PBS, polarized beam splitter; PD, photodetector.

was continuously oscillating. The oscillation was excited by hitting the moving part with a hammer. The inertial force acting on the moving part was measured accurately by measuring the velocity of the moving part with an optical interferometer.

The force acting on the moving part from the sensor, *F*, was equal to the inertial force of the moving part according to the principle of action and reaction if other forces, such as the inertial force of the spring and the friction of the aerostatic bearing, were ignored. In the case of the inertial force of the spring, half the mass of the spring was considered to be the moving part of the bearing, and the other half was considered to be the sensing part of the force sensor; the spring itself was treated as having uniform composition. The mass of the spring was approximately 0.0257 kg. The total mass of the moving part including the half part of the spring was approximately 4.6126 kg.

In this experiment, a conventional S-shaped sensor was used for the test. The rated force capacity was 200 N, and it was statically calibrated with the standard uncertainties of approximately 0.2 N, which corresponded to 0.1% of the rated force capacity. The output signal of the force sensor was measured by using a digital multimeter (HP 3458A, Agilent Technologies Corp.) with a sampling rate of 5 kHz.

The inertial force was measured by using an optical interferometer similar to the procedure described as follows. One of the two-frequency laser lights was modulated by the Doppler effects, and the Doppler frequency was calculated as $-(f_{beat} - f_{rest})$. The frequency difference between the signal beam and reference beam, f_{beat}, and the fundamental frequency difference, f_{rest}, were measured by employing counters (R5363, Advantest). The sample number and the sampling frequency of the counter were 14 k samples and *f*/400 Hz, where *f* is the instantaneous frequency for the measurement. HP3458A and R5363 were triggered by an external synchronizing signal. An aerostatic linear bearing was used so that the rigid body, which is the moving part, can move linearly with less friction.

Results: Figure 12.13 shows the changes in frequency, velocity, acceleration, and force for a set of measurements. At $t = 0.0$ s, an impulse was manually applied to the moving part with a hammer. The frequency of f_{beat} changed immediately. After the impact, f_{beat} began to oscillate at a frequency of approximately 15 Hz. By using the frequency measured from f_{beat}, the velocity, acceleration, and inertial force could be calculated.

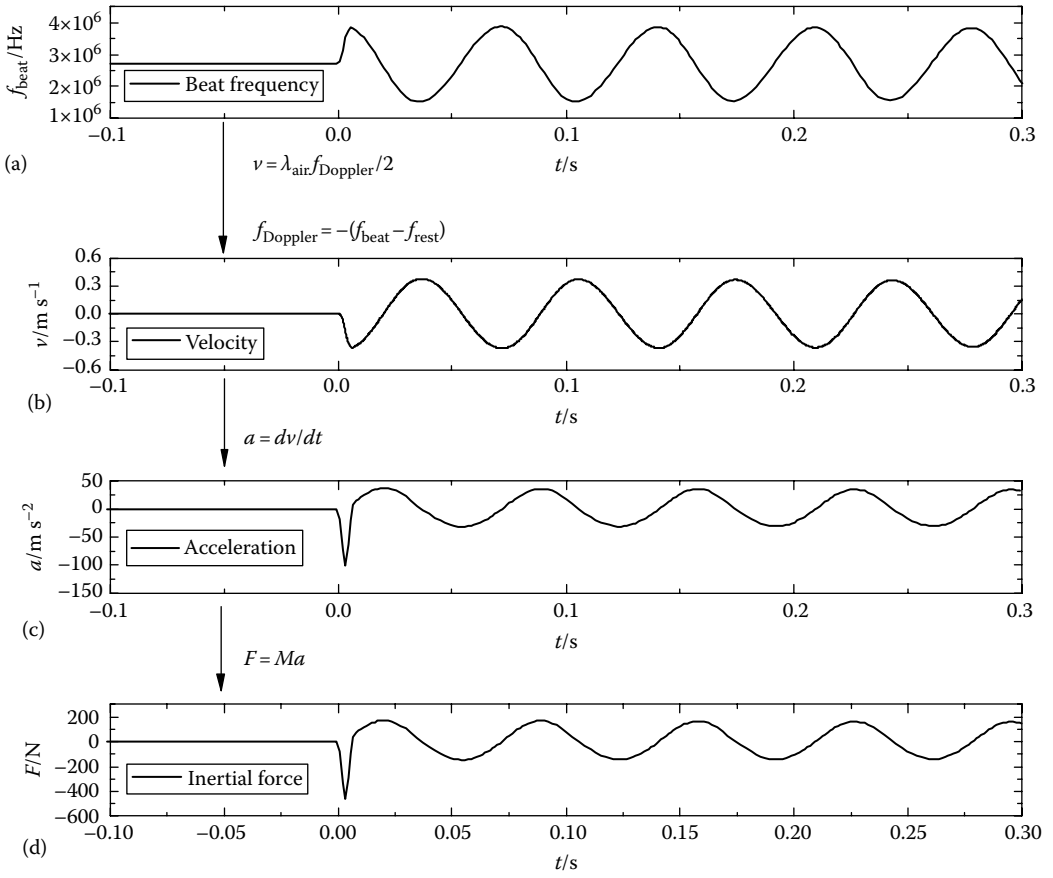

FIGURE 12.13 (a) Frequency, (b) velocity, (c) acceleration, and (d) force measured during oscillation.

Figure 12.14 shows the forces measured by the interferometer, $F_{inertial}$, as shown in Figure 12.13, and by the force sensor, F_{sensor}.

Figure 12.15 shows the details of the same data shown in Figure 12.14 in a different manner. In the first half wave, just after the impulse was manually applied by the hammer, a high-frequency oscillation was superimposed on an oscillation with a frequency of approximately 15 Hz, probably as a result of the vibration of the optical interferometer. The impact force applied by the hammer has a vertical component against the moving direction of the aerostatic linear bearing, and the force including the vertical component is propagated along the base plate on which the optical interferometer is constructed; this force causes the vibration of the optics.

To evaluate the responses of the sensor against the oscillation force, the impulse, that is, the time integration of the oscillation force during half a period, is introduced. "Half a period" is determined as the period from the time at which the oscillation force $f_{inertial}$ crosses the coordinate axis to the time at which $f_{inertial}$ again crosses the coordinate axis in the reverse direction. As schematically shown in Figure 12.15, consecutive numbers have been assigned to all the impulses except the first one because the first impulse includes a sharp impulse applied by the hammer.

Figure 12.16 shows the relative difference between the impulse measured by the sensor, $\int F_{transducer} dt$, and the impulse measured by the optical interferometer, $\int F_{inertial} dt$, against the peak value of $F_{inertial}$ in

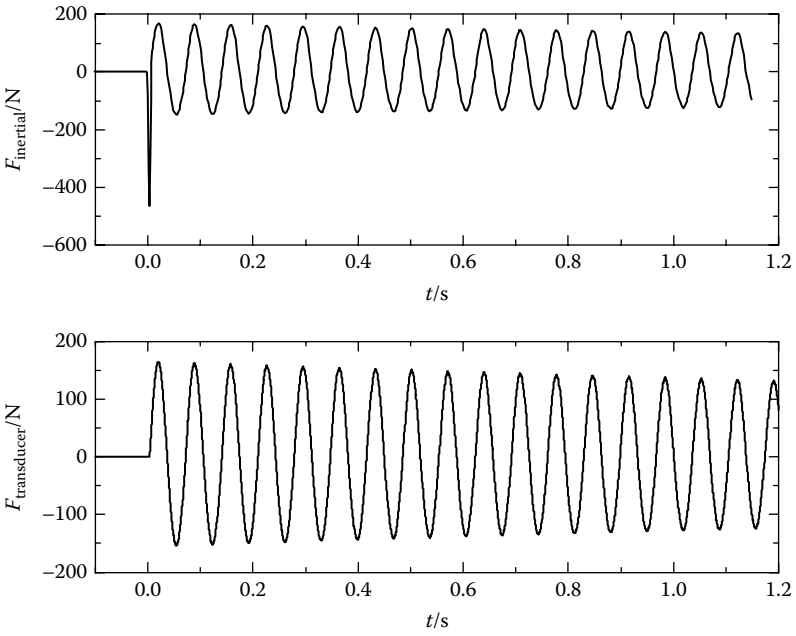

FIGURE 12.14 Oscillating forces measured by the interferometer, $F_{inertial}$, and by the force sensor, F_{sensor}.

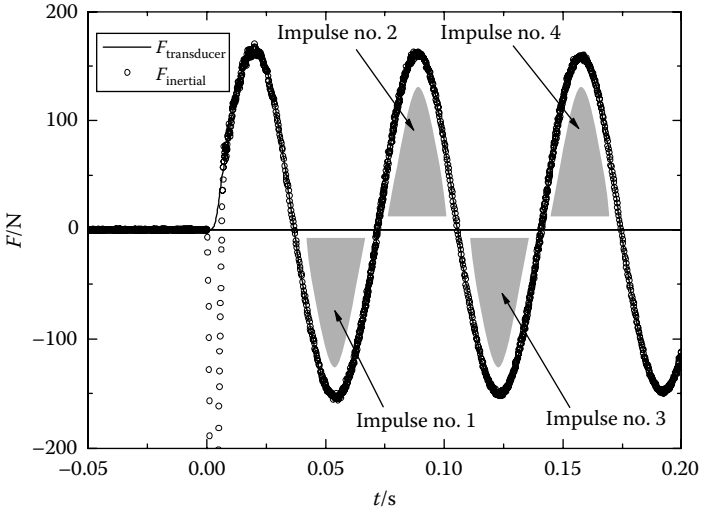

FIGURE 12.15 Changes in $F_{inertial}$ and F_{sensor}.

each sample. In the figure, the results of the 10 impact tests and 30 impulses for each test are plotted. The filled black circles show the data for the first three impulses of each impact test, and the circles show all the other data.

Discussion: As shown in Figures 12.13 through 12.15, because of the asymmetry of the spring constant of the spring, the shapes of the time series of the velocity, acceleration, and force are not perfectly symmetrical. Gradually damping is also observed. In this experiment, only the amplitude of the oscillation could be changed by changing the initial impulse applied by the hammer. For more accurate sensor

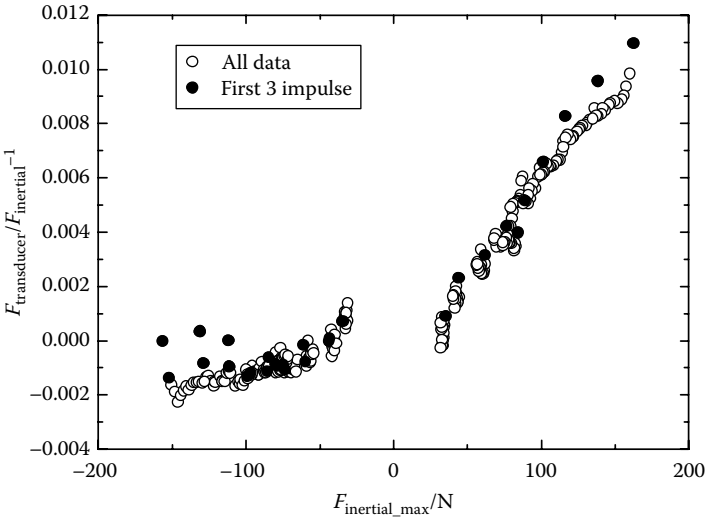

FIGURE 12.16 Relative differences between the impulse measured by the sensor and the impulse measured by the optical interferometer against the peak value of $F_{inertial}$ in each sample.

calibrations, more accurate amplitude controls are required, for example, using a linear actuator to impart a certain amount of the momentum on the hammer. Further, in order to change the oscillation frequency, an elastic body with an appropriate elastic modulus is required. A piezoelectric body, which can be controlled as if it is a perfect elastic body with a certain spring constant, could be suitable for realizing oscillations with a definite frequency and amplitude. However, in general, the control routine may become more sophisticated, and the number of uncertainty sources may increase.

In Figure 12.16, a clear relationship is observed in the case of the relative difference between the impulse measured by the sensor and those measured by the optical interferometer, and this indicates the validity and reproducibility of the method. Although the relative standard uncertainty of the statically calibrated sensor is approximately 0.1%, the relative difference changes by more than 1% along with the peak value of the force. In each test, the tendencies are different for the beginning part and the other parts, and these differences show that the first few impulses are in the transient state.

12.6 Conclusions

In this chapter, we have reviewed a calibration method for force sensors by using the LMM. The dynamic force acting on the force sensor was accurately measured and compared with the force measured by the sensor itself. This calibration method can be applied under other force conditions such as steep impulse and oscillating forces.

References

1. R. Kumme, Investigation of the comparison method for the dynamic calibration of force transducers, *Measurement* 23, 239–245, 1998.
2. R. Kumme and M. Dixon, The results of comparisons between two different dynamic force measurement system, *Measurement* 10, 140–144, 1992.
3. Y.-K. Park, R. Kumme, and D.-I. Kang, Dynamic investigation of a three-component force-moment sensor, *Measurement Science and Technology* 13, 654–659, 2002.
4. Y.-K. Park, R. Kumme, and D.-I. Kang, Dynamic investigation of a binocular six-component force-moment sensor, *Measurement Science and Technology* 13, 1311–1318, 2002.

5. Y. F. Li and X. B. Chen, On the dynamic behavior of a force/torque sensor for robots, *IEEE Transactions on Instrumentation and Measurement* 47(1), 304–308, 1998.
6. K. J. Xu and L. Jia, One-stage identification algorithm and two-step compensation method of Hammerstein model with application to wrist force sensor, *Review of Scientific Instruments* 73(4), 1949–1955, 2002.
7. Y. Fujii, Measurement of steep impulse response of a force transducer, *Measurement Science and Technology* 14, 65–69, 2003.
8. Y. Fujii, A method for calibrating force transducers against oscillation force, *Measurement Science and Technology* 14, 1259–1264, 2003.
9. Y. Fujii, Proposal for a step response evaluation method for force transducers, *Measurement Science and Technology* 14, 1741–1746, 2003.
10. Y. Fujii, Dynamic force calibration method for force transducers, *IEEE Transactions on Instrumentation and Measurement* 58, 2358–2364, 2009.
11. Y. Fujii, Toward dynamic force calibration, *Measurement* 42, 1039–1044, 2009.
12. Y. Fujii and T. Yamaguchi, Method for evaluating material viscoelasticity, *Review of Scientific Instruments* 75, 119–123, 2004.
13. Y. Fujii and T. Yamaguchi, Proposal for material viscoelasticity evaluation method under impact load, *Journal of Materials Science* 40, 4785–4790, 2005.
14. Y. Fujii and D. W. Shu, Impact force measurement of an actuator arm of a hard disk drive, *International Journal of Impact Engineering* 35, 98–108, 2008.
15. Y. Fujii and T. Yamaguchi, Optical method for evaluating material friction, *Measurement Science and Technology* 15, 1971–1976, 2004.
16. Y. Fujii, Method for measuring transient friction coefficients for rubber wiper blades on glass surface, *Tribology International* 41, 17–23, 2008.
17. Y. Fujii, T. Yamaguchi, and J. Valera, Impact response measurement of a human arm, *Experimental Techniques* 30, 64–68, 2006.
18. Y. Fujii and T. Yamaguchi, Method of evaluating the force controllability of human finger, *IEEE Transactions on Instrumentation and Measurement* 55, 1235–1241, 2006.
19. Y. Fujii, K. Maru, and T. Jin, Method for evaluating the electrical and mechanical characteristics of a voice coil actuator, *Precision Engineering* 34, 802–806, 2010.
20. Y. Fujii and K. Shimada, Instrument for measuring the mass of an astronaut, *Measurement Science and Technology* 17, 2705–2710, 2006.
21. Y. Fujii and K. Shimada, The space scale: An instrument for astronaut mass measurement, *Transactions of the Japan Society for Aeronautical and Space Sciences* 50, 251–257, 2008.
22. Y. Fujii, K. Shimada, M. Yokota, S. Hashimoto, Y. Sugita, and H. Ito, Mass measuring instrument for use under microgravity conditions, *Review of Scientific Instruments* 79, 056105, 2008.
23. Y. Fujii, K. Shimada, and K. Maru, Instrument for measuring the body mass of astronauts under microgravity conditions, *Microgravity Science and Technology* 22, 115–121, 2010.

II

Spatial Variables

13

Thickness Measurement

John C. Brasunas
Goddard Space Flight Center

G. Mark Cushman
Goddard Space Flight Center

Brook Lakew
Goddard Space Flight Center

One can measure thickness on many scales. The galaxy is a spiral disk about 100 Em (10^{20} m) thick. The solar system is pancake-like, about 1 Tm (10^{12} m) thick. The rings of Saturn are about 10 km thick. Closer to home, the Earth's atmosphere is a spherical shell about 40 km thick; the weather occurs in the troposphere, about 12 km thick. The outermost shell of the solid Earth is the crust, about 35 km thick. The ocean has a mean depth of 3.9 km. In the Antarctic, the recently discovered objects believed to be microfossils indicative of ancient Martian life are less than 100 nm thick. In terms of the man-made environment, industry must contend with thickness varying from meters, for construction projects, to millimeters on assembly lines and to micrometers and nanometers for the solid-state, optical, and coating industries. Perhaps the most familiar way of measuring thickness is by mechanical means, such as by ruler or caliper. Other means are sometimes called for, either because both sides of an object are not accessible; the dimension is either too big or too small for calipers; the object is too fragile, too hot, or too cold for direct contact; or the object is in motion on an assembly line—it may not even be a solid. Thickness may also be a function of position, as either the object may have originally been made with nonuniform thickness, deliberately or not, or the thickness may have become nonuniform with time due to either corrosion, cracking, or some other deterioration. The thickness may also be changing with time due to deliberate growth or etching, as example for thin films. Thus, it follows that, in more general terms, measuring thickness might require measuring the topography or height profile of two surfaces and taking the difference. Alternatively, the measurement technique may produce a reading directly related to the difference. Table 13.1 lists some of the many techniques suited to determining thickness, together with the range of usefulness and some comments on accuracy and/or precision.

TABLE 13.1 Thickness Measuring Techniques

Technique	Range	Comments
Mechanical		
Caliper gage, micrometer	1 μm–100 mm	±3 μm accuracy
Electronic gages: LVDT	0–1 m	Precision depends on noise level
Pneumatic gaging	50 nm minimum	
Optical/focusing, shadowing, comparing		
Microscope	5 μm minimum	About 1% accuracy
Comparators/projectors	25–250 nm	
Laser caliper	100 μm–100 mm	Precision of 6 μm or better
Weighing	Range depends on area	
Capacitive gaging	From <1 μm to about 1 cm	
Inductive gaging (eddy-current sensing)	0–1.5 mm	Precision of 2.5 μm
Magnetic induction	0–4 mm	10% accuracy
Hall effect gage	0–10 mm	1%–3% accuracy
Far field/time of flight		
Sonar/ultrasound	0.5–250 mm	25 μm accuracy
Radar	0.1 to few hundred km	
Lidar	10 m–5 km	
THz technology		
Far field/resonance		
Resonant ultrasound		
Interferometry: spectral and spatial	1 nm–100 μm	Accuracy about $\lambda/50$
Ellipsometry	0.3 nm–10 μm	0.1 nm accuracy
Far field/absorption, scattering, emission		
Gamma-ray backscatter	Range to 25 mm	0.5% precision
Beta-transmission	2 μm–1 mm	0.2% precision
Beta-backscatter	100 nm–50 μm	3%–20% precision
X-ray fluorescence	0–30 μm	
Infrared absorption	Depends on material	
Scanning techniques: scanning probe microscopy		Precision better than 0.1 nm
Destructive techniques: electrolytic	15 nm–50 μm	

13.1 Descriptions of the Relatively Mature Measuring Techniques

The following descriptions will also refer to some of the relevant vendors, whose addresses are found in Table 13.2. Additional vendor information, with specific price or model number identification, is found in Table 13.3. The words "gage" and "gauge" are used interchangeably.

13.1.1 Mechanical

The fundamental tool for measuring thickness is the line-graduated instrument [1,2]. It is the only mechanical means to make direct measurements. Graduated spacing that represents known distances is used as direct comparisons to the unknown distance. Instruments include bars, rules, and tapes generically called rulers; caliper gages, which employ a positive contact device for improved alignment of the distance boundaries; and micrometers, which typically have greater precision due to a combination of

TABLE 13.2 Vendor Addresses

Vendor	Address
Bomem	Quebec, Canada
Brown & Sharpe	North Kingstown, RI
CMI International	Elk Grove Village, IL
Conductus	Sunnyvale, CA
deFelsko	Ogdensburg, NY
Digilab	Cambridge, MA
Digital Instruments	Santa Barbara, CA
Electromatic	Cedarhurst, NY
Fischer	Windsor, CT
Hewlett Packard	Englewood, CO
Kta-Tator	Pittsburgh, PA
Magnetic Analysis Corp.	Mount Vernon, NY
Mattson	Madison, WI
Measurex	Cupertino, CA
Micro Photonics	Allentown, PA
Midac	Costa Mesa, CA
Mitutoyo	Plymouth, MI
Moore Products Co.	Spring House, PA
NDC Systems	Irwindale, CA
Nicolet	Madison, WI
Ono Sokki	Addison, IL
Oxford Instruments	Concord, MA
Panametrics	Waltham, MA
Park Scientific Instruments	Sunnyvale, CA
Penny + Giles	Attleboro, MA
Perkin-Elmer	Norwalk, CT
Phase-Shift Technology	Tucson, AZ
Rudolf Instruments	Fairfield, NJ
Scantron	Dist. by Micro Photonics
Schaevitz	Pennsauken, NJ
Sentech	Dist. by Micro Photonics
SolveTech	Claymont, DE
Starrett	Athol, MA
Stresstel	Scotts Valley, CA
Transicoil Inc.	Valley Forge, PA
Trans-Tek	Ellington, CT
Willrich Precision Instrument Co.	Cresskill, NJ
J.A. Woollam Co., Inc.	Lincoln, NE
Wyko	Tucson, AZ
Zygo	Middlefield, CT

linear and circumferential scales. Caliper precision can be improved with Vernier scales or linear transducers. Fixed gages are often used to measure objects on a pass/fail basis. An object of fixed geometry (length, tapered bore, thread, etc.) is compared to a test piece typically for part inspection. Variations include the master gage, an object used to represent the nominal dimension of the part; the limit gage, an object used to represent the limit condition for tolerance dimensioning; and gage blocks or Johansson blocks, an object of fixed length used as a dimensional reference standard. Dial indicators are used to

TABLE 13.3 Instruments for Measuring Thickness

Manufacturer	Model Number	Price	Description
KTa-Tator	TI-12	$1,595	General-purpose ultrasonic gage, 0.75–75 mm range
NDC Systems	6100TC	$49,300	Backscatter gamma-gage for 60 in. web, 25 mm range
NDC Systems		$66,600	Transmission beta-gage, for continuous web products
Panametrics	25DL	$2,200–$3,800	Single-element ultrasonic gage, 50 mm range
Panametrics	26DL Plus	$1,400–$2,500	Dual-element ultrasonic gage, 250 mm range
Panametrics	8000	$6,500	Hall effect magnetic gage, for nonferrous materials, 6 mm range
DeFelsko	Positest 1000-N	$1,995	Eddy-current sensor, Apple Newton readout, measure out to 1.5 mm nonferrous, nonconducting coating on conducting substrate
Magnetic Analysis	Various	$1,500–$100,000	Ultrasonic, time-of-flight gages
Fischer	Deltascope MP2C	$1,200	Magnetic induction gage, measure nonmagnetic coating on ferromagnetic substrate
Fischer	IsoScope MP1C	$1,200	Eddy-current gage, measure nonconducting coating on nonferrous conducting substrate
Fischer	Fischerscope MMS	$6,500	Beta-backscatter system to measure coating thickness
Fischer	Fischerscope X-Ray	$34,000	X-ray fluorescence system to measure coating
	1020 video		Thickness
Fischer	Couloscope Sx	$2,500+ accessories	Electrolytic, destructive system to measure coating thickness
J.A. Woollam Co. Inc.	M-44	Application specific	Variable angle, multiwavelength spectroscopic ellipsometer
Rudolf Instruments	431A31WL633	$10,100	Manual, He–Ne wavelength ellipsometer
Rudolf Instruments	444A12	$34,000	Automatic, He–Ne wavelength ellipsometer
Hewlett Packard	HP8712C	$13,500	RF vector network analyzer, measure transmission/reflection frequency response to 1.3 GHz, optional to 3 GHz
Stresstel	T-Mike Programmable	$995	Dual-element ultrasonic system
Stresstel	TM1D	$1,795	Single-element ultrasonic system
Measurex	DMC480	Application specific	High-speed x-ray thickness gage
Bomem	MB series	$20,000 and up	1 cm^{-1} resolution FTR
Park Scientific Instrumens	Autoprobe CP	$65,000	Ambient SPM
Park Scientific Instruments	Autoprobe VP2	$130,000	UHV SPM
Digital Instruments	Nanoscope IIIa/D3000	$90,000	Small-sample SPM

sense displacement from a reference plane and display the deviation thereof. The display can be electronically coupled for amplification and/or display purposes. The range of a measuring instrument may be extended if multiple copies of the object to be measured are available. For example, the thickness of a sheet of paper may be measured by a simple ruler if 500 sheets of paper are stacked (vendors: Brown & Sharpe, Starrett, and Mitutoyo; also see [3]).

13.1.2 Electronic Gages

A linear variable differential transformer (LVDT) utilizes multiple toroidal transformers to sense axial displacement of an iron core that is attached to a measuring contact, either directly or by another joint (such as a lever). The displacement has a direct correlation to the distance that other electronics display. Thus, the LVDT serves as a replacement for a lined ruler or micrometer, incorporating an electrical readout (vendors: Penny + Giles, Schaevitz, Transicoil Inc., and Trans-Tek).

13.1.3 Pneumatic Gaging

Pneumatic gages have pressurized air exiting gage orifices. The air velocity differential or back pressure is a function of the separation of the gage and the part. In the direct or open jet method, the pressurized air experiences back pressure due to the impedances posed by the measured part. The typical scenario is that the gage head and the measured part have similar geometry (i.e., a cylindrical gage in a bored hole). By placing two gages on either side of a flat plate, the thickness may be inferred. In the indirect or contact method, the pressurized air pushes on a contact piece that directly contacts the part. Tolerances as small as 50 nm can be measured (vendors: Willrich Precision Instrument Co. and Moore Products Co.).

13.1.4 Optical: Focusing, Shadowing, and Comparing

This includes microscopes, which can determine thickness either by comparison with a known reference or by focusing on the front and rear surfaces of a sample, noting the difference in focus position. Comparators project onto a screen what might be noted through a microscope. Laser calipers retrieve dimensions by measuring the shadowing of a laser beam (vendors: NDC Systems for laser caliper and Scantron for laser profilometer).

13.1.5 Weighing

Given a plate of material with known density, first, measure the area with some type of calibrated video system. Then, a measurement of weight can be simply converted to an estimate of the thickness. As is common with this technique and most of the following techniques, estimating the thickness requires knowledge of some other property of the material to be measured—in this case, the density.

13.1.6 Capacitive Gaging

Capacitive gaging is realized by inserting a nonmetallic material into a known electric field. Knowing the gage sensor area and the material's dielectric constant, the thickness can be determined. Submicron thickness levels can be achieved (vendors: Ono Sokki and SolveTech).

13.1.7 Inductive Gaging (Eddy-Current Sensing)

The principle here is that AC currents in a coil induce eddy currents in a nearby conducting plate [4,5]. These eddy currents can be sensed by a pickup coil, which may be the exciting coil or a second coil. The presence of the eddy currents manifests itself as a modification of the apparent inductance and/or

the loss of the pickup coil. This technique is appropriate for nonferrous metals and is especially sensitive to thickness variations due to flaws such as cracks or corrosion. There is one particular instance in which it is common to measure thickness rather than variations. That would be the thickness of a nonconducting coating on a nonferrous conducting substrate. The coating thickness creates a gap (liftoff) between the exciting coil and the eddy currents, thereby affecting the eddy-current signal. The range of this technique would be about 1 mm. Fischer has an instrument designed for measuring the thickness of a newly laid road surface coating to a depth of 40 cm, by burying a conductive plate below the road (vendors: Fischer, deFelsko, CMI International).

13.1.8 Magnetic Induction

This technique is also used to measure coating thickness, in this case a nonmagnetic coating on a ferromagnetic substrate. The nonmagnetic coating creates a gap (liftoff) between the ferromagnetic substrate and a probe. One way to measure the gap and thereby the thickness is by measuring the force required to pull away a magnetic probe. Another technique would be to magnetically couple the ferromagnetic substrate to a transformer core, with a gap between the substrate and the core. This technique would have a range of about 4 mm. CMI International has an informative brochure describing the relative merits of measuring coating thickness via eddy current, magnetic induction, beta-backscatter, microresistance, and x-ray fluorescence; the choice of technique depends, among other things, on the material to be tested (vendors: Fischer, CMI International, Electromatic, and deFelsko).

13.1.9 Hall Effect Gage

This sensor measures the thickness of nonferrous materials with 1% accuracy by sandwiching the material being measured between a magnetic probe on one side and a small target steel ball on the other side [6]. It measures up to 10 mm. The Hall effect sensor is used to measure the magnetic field, as a DC measurement; the AC Hall effect measurements can be made more precisely because they eliminate bias and are done with less noise (vendor: Panametrics).

13.1.10 Far Field/Time of Flight: Ultrasound, Radar, and Lidar

Using the 1940s sonar principles and today's microprocessor technology, high-frequency (1–20 MHz) ultrasound waves can be used to measure thickness by sending pulsed sound waves through a material and measuring the transit time of the reflected signal [5,7]. Knowing the sound velocity of the material, the materials from 0.5 to 250 mm can be measured, often as fine as 25 μm. Media include metal, glass, ceramic, liquid, rubber, fiberglass, plastic, and concrete. Ultrasound can also be used to measure living tissues, as is often done in the agricultural and medical fields. The fat layers of cattle and pigs can influence marketability. Skin burn depths can direct treatment procedures. The depth of foreign objects in the body is useful for microsurgery. Ultrasonic thickness determination has expanded to include multidimensional echolocation applications, such as imagery and acoustic microscopes that can resolve in the submicron level. The principles behind ultrasound also apply to electromagnetic waves. In the gigahertz range, this is called radar. Radar can be used to estimate the thickness of atmospheric layers such as cloud layers. The light-wave version of radar, called lidar, can be used to measure the thickness of water vapor layers in the lower atmosphere (ultrasonic vendors: KTa-Tator, deFelsko, Stresstel, Magnetic Analysis Corp., Panametrics, and Electromatic).

13.1.11 Far Field/Resonance: Ultrasound, Interferometry, and Ellipsometry

The idea here is that when waves such as ultrasound impinge on a plane-parallel slab of material, there will be reflected power from both the front and the rear surfaces; depending on whether the

slab thickness is an odd or even number of quarter wavelengths, the reflected beams will be in constructive or destructive interference. If the frequency is swept, the distance in frequency between successive maxima and minima may be related to the slab thickness, if the index of refraction is known. Since the natural, or resonant, modes of an object depend on the properties and dimensions of an object, the knowledge of the properties enables estimation of dimensions from the resonant frequencies. Compared with time-of-flight ultrasound, resonant ultrasound is much less common. It has been used to characterize concrete and is quite sensitive to flaws, as anyone who has heard a cracked bell would know. Resonant techniques are much more common with visible [8], infrared, or microwave [4] radiation. Spectral interferometry would be appropriate to characterize the thickness of transparent substrates with reasonably flat surfaces, sufficiently parallel to one another. A common way to do this would be to measure a transmission spectrum with a spectrometer such as a Fourier transform spectrometer (FTS). The successive maxima and minima are here called the Fabry–Perot effect, and their appearance in a spectrum is called channeling. Thickness can also be measured with spatial interferometry, which is essentially a way of measuring surface topography. An example would be the phenomenon of Newton's rings, which occur when the surface to be tested is in contact with an optical flat. Using a transparent optical flat, transmit monochromatic light such as a mercury lamp through the flat and onto the interface between the flat and the test surfaces. If there are variations in the height of the test surface, then the two return beams from the optical flat and the test surface will alternate between constructive and destructive interferences, producing fringes or rings. The sensitivity is not limited to the scale of the wavelength λ: with sufficient stability and signal to noise, dimensions down to 1/1000 of a fringe can be measured. With sources of longer coherence length, such as lasers, the test surface and the optical flat need not be in direct contact.

Another optical way to measure thickness is with ellipsometry [9], typically used to measure properties of thin, transparent films from a few tenths of nanometers to several hundreds of nanometers thick. This includes metals, as long as the metal is sufficiently thin to be partially transparent. By measuring the change in polarization state for nonnormal incidence light, both the thickness and the refractive index of a thin layer may be inferred. Additional information (e.g., the properties of multiple layers) can be obtained by varying the angle of incidence and by observing at multiple wavelengths. The ability to estimate both thickness and refractive index is an important advantage of this technique, as often the refractive index of a material in thin film form is not the same as the bulk value and indeed may be a property of the deposition conditions. (FTS vendors: Bomem, Digilab, Mattson, Midac, Nicolet, and Perkin-Elmer. FTS system pricing may range from about $15,000 to over $100,000, depending on the application. Spatial interferometer vendors: Zygo, Wyko, and Phase-Shift Technology. Ellipsometer vendors: J.A. Woollam Co., Inc.; Rudolf Instruments; and Sentech. The cost of an ellipsometer may range from $10,000 for a manual, single-wavelength system to $200,000 for an automatic, multiwavelength system. Microwave resonance vendor: Hewlett-Packard.)

13.1.12 Far Field/Absorption, Scattering, and Emission

13.1.12.1 Beta, Gamma, X-Ray, and Infrared

These techniques depend on the extinction (scattering or absorption) or emission of photons or massive particles (electrons, protons, neutrons) when transiting the material to be measured. Typically, the extinction or emission shows an exponential dependence on thickness; the dependence becomes linear if the absorption is sufficiently low. These techniques, in particular gamma-ray backscatter and beta-ray transmission, are used to measure continuously moving web materials (paper, metals, fabrics) on assembly lines. Infrared absorption is also suitable if the moisture content is controlled. Beta-backscatter and x-ray fluorescence [10] are used for measuring coatings. In x-ray fluorescence, upon exposure to x-rays,

certain elements fluoresce (emit) x-rays at characteristic wavelengths. The strength of this emission is related to thickness. These absorption/emission techniques may sometimes be better suited than time-of-flight ultrasound to the dimensional measurement of objects with complex shapes. (Gamma-gage vendor: NDC Systems; x-ray absorption vendor: Measurex; x-ray fluorescence vendors: Fischer, NDC Systems, and CMI International; Beta-backscatter vendor: Fischer, Electromatic, CMI International, and Measurex; Infrared absorption vendor: NDC Systems. The prices for these systems will depend on the application; a typical system could cost $500,000.)

13.1.13 Destructive Techniques

Fischer markets a system that removes a coating into an electrolyte and then electrolytically deposits the removed coating. The electrical charge required for deposition is related to the coating thickness.

13.2 Future Directions in Thickness Measurement

13.2.1 Concerning Techniques Mentioned Earlier

Concerning capacitive sensors, the NASA Langley Research Center is developing sensors based on patterns of conductors sandwiched between insulating layers. The presence of ice over the conductors changes the capacitance, providing a way of sensing ice buildup on aircraft wings. With respect to eddy-current sensing, one limitation is that a nonsuperconducting sense coil responds best to high-frequency excitations and not at all to DC magnetic fields. This limits the technique to fairly high frequencies and thus low penetration depths, since the skin depth becomes shallower with increasing frequency. One possibility is to use a superconducting quantum interference detector (SQUID) as the sensor, since the SQUID is probably the most sensitive sensor of DC and low-frequency magnetic fields. One disadvantage of the SQUID has been the need for liquid helium for cooling for low-temperature superconductors; with the recent availability of high-temperature superconductors (HTS, above 90 K) and now HTS SQUIDS, cooling can be done with liquid nitrogen or single-stage mechanical coolers. In the area of spatial interferometry, the work at Lawrence Livermore National Laboratory replaces the reference surface with a single-mode fiber in a process called phase-shifting diffraction interferometry. A measurement accuracy of 1.44 nm rms is quoted, with a goal of 0.1 nm rms (HTS SQUID vendor: Conductus).

13.2.2 THz Technology

With the availability of femtosecond pulsed lasers, Bell Labs has been investigating a technique using 100 fs pulses to pulse an antenna in the range of 0.1–3.0 THz. The terahertz pulses are sent through the material to be tested and detected, and the received pulse shape is analyzed to extract constituent information. This technique may also provide information on thickness.

13.2.3 Nanoscale Scanning Probe Microscopy

Scanning probe microscopes (SPMs) are used in a wide variety of disciplines, including fundamental surface science, routine surface roughness analysis, and spectacular 3-D imaging—from atoms of silicon to micron-sized protrusions on the surface of a living cell [11]. The SPM is an imaging tool with a vast dynamic range, spanning the realms of optical and electron microscopes. It is also a profiler with unprecedented 3-D resolution. In some cases, SPMs can measure physical properties such as surface conductivity, static charge distribution, localized friction, magnetic fields, and elastic moduli. As a result, the applications of SPMs are very diverse. The scanning tunneling microscope (STM), the progenitor of SPMs, utilizes a sharp conductive tip with a bias voltage applied between the tip and the sample.

When the tip is within 1 nm of the sample, the electrons from the sample begin to tunnel through the 1 nm gap into the tip. If the bias voltage is reversed, the tunneling occurs into the sample. The tunneling current is a function of the separation. Both the tip and the sample must be conductors or semiconductors.

The atomic force microscope (AFM) utilizes a small tip at the end of a cantilever. Forces between the tip and the sample cause a deflection in the cantilever, which is translated into signals. The tip or sample can be scanned covering a large area, producing a topographical map. AFMs can be used on insulators or conductors. AFMs are used in two modes: contact and noncontact. In contact mode, the tip is brought within about 200 pm—about the length of a chemical bond. The electron clouds of the tip and sample atoms interact, netting a repulsive force. For this reason, the contact mode is also called repulsive. The vertical resolution of about 50 pm can be achieved. In noncontact mode, a vibrating cantilever is used in the attractive regime of the van der Waals interactions. The cantilever is typically 2–20 nm away from the sample surface and has low total force. Noncontact AFM is subsequently less sensitive; thus, sensitive AC detection systems must be employed. The low force does have the advantage of not contaminating the sample surface and is preferred for applications involving silicon wafers and soft or elastic tissues. In noncontact mode, the cantilever is resonated with a small amplitude. As the tip comes near the sample surface, the resultant force changes the spring constant, translating into a deviation of the resonance frequency. This change in resonance (or vibrational amplitude) reflects changes in the sample topology.

Intermittent contact mode is a combination of noncontact and contact modes and best suited for soft, adhesive, or fragile samples. Contact mode can damage the tip and the sample due to frictional or shear forces and/or create data artifacts from tip/surface adhesion. Noncontact mode produces lower amplitudes and hence lower resolution. Furthermore, surface monolayers of adsorbed gases such as water vapor can produce erroneous results. Intermittent contact mode avoids these pitfalls by placing the tip in contact with the surface, providing high resolution and then removing the tip to prevent dragging and/or lateral forces. The cantilever is resonated via a piezoelectric crystal (50–500 kHz in ambient, 5–40 kHz in fluids) overcoming the tip/sample adhesion forces.

In magnetic force microscopy (MFM), the noncontact mode is employed using a tip coated with a ferromagnetic film. Both magnetic and van der Walls interactions are present, but at larger tip/sample separations, the magnetic forces dominate. Multiple scans as a function of tip/sample distance allow differentiation of magnetic forces and topographic information. Magnetic domain structures are resolved to 50 nm via this technique. Current applications of MFM include data storage devices, imaging of micromagnetic structures, IC analysis, imaging of magnetotactic bacteria, and magnetic geophysics. Lateral force microscopy (LFM) is used to generate profiles of changes in surface friction and/or height variations. The probe tip is deflected laterally, indicating some sort of twist. Electronics measure the cantilever deflection. To differentiate between the two effects, LFM and AFM images should be obtained simultaneously. Phase detection microscopy or phase imaging is an extension of intermittent contact AFM. It utilizes the phase lag between the driving frequency (cantilever) and the output signal frequency, generating a map of specific mechanical properties such as adhesion, elasticity, and friction. The identification of contaminants, composite materials, and regions of hardness and low surface adhesion can be obtained at the nanometer scale. Additional techniques include force modulation microscopy, where a periodic signal is applied to the cantilever, generating a map of the sample's elastic modulus and/or contaminants; electrostatic force microscopy, where a charged tip is scanned over the sample, revealing the locally charged domains generating a map of the charge-carrier density; scanning capacitance microscopy, where a charged tip, kept at a constant tip/sample distance, generates a map of capacitance correlated information such as dielectric material thickness and subsurface charge-carrier distributions (i.e., dopant profiles of ion-implanted semiconductors); and thermal scanning microscopy, where the tip in noncontact mode and a bimetal cantilever are used to map the thermal conductivity of the sample (vendors: Park Scientific Instruments, Digital Instruments, and Oxford Instruments).

References

1. R. E. Green (ed.), *Machinery's Handbook,* 28th edn., New York: Industrial Press, 2008.
2. M. A. Curtis and F. T. Farago, *Handbook of Dimensional Measurement,* 4th edn., New York: Industrial Press, 2007.
3. T. Busch, *Fundamentals of Dimensional Metrology,* 2nd edn., Albany, NY: Delmar Publishers, 1989.
4. R. C. McMaster, P. McIntire, and M. L. Mester (eds.), *Nondestructive Testing Handbook,* Vol. 4, 2nd edn., Columbus, OH: American Society for Nondestructive Testing, 1986.
5. D. E. Bray and D. McBride, *Nondestructive Testing Techniques*, New York: John Wiley & Sons, 1992.
6. Application Notes, Wall Thickness Gaging in the Blow Molding in Industry, Olympus (http://www.olympus-ims.com/pl/applications/wall-thickness-gaging-blow-molding-industry/347-pos.56.html (accessed on March 14, 2013).
7. A. S. Birks, R. E. Green, and P. McIntire (eds.), *Nondestructive Testing Handbook,* Vol. 7, 2nd edn., Columbus, OH: American Society for Nondestructive Testing, 1991.
8. D. Malacara, *Optical Shop Testing*, New York: John Wiley & Sons, 1978.
9. J. A. Woollam, B. Johs, C. M. Herzinger, J. Hilfiker, R. Synowicki, and C. L. Bungay, "Overview of variable abgle spectroscopy ellipsometry (VASE): Basic theory and typical applications" Reviews of Optical Scinece and Technology (1999), Mendeley, http://www.mendeley.com/research/overview-variable-angle-spectroscopic-ellipsometer-vase-part-i-basic-theory-typical-applications/ (accessed on March 14, 2013).
10. H. H. Behncke, Coating thickness measurement by the X-ray fluorescence method, *Metal Finishing*, 82, 33–39, 1984.
11. R. Howland and L. Benatar, *A Practical Guide to Scanning Probe Microscopy*, Sunnyvale, CA: Park Scientific Instruments, 1993.

Bibliography

Dotson, C. L., *Fundamentals of Dimensional Metrology,* Vol. 5, Clifton Park, NY: Thomson Delmar Learning, 2006.

Moore, P. O., *Non-Destructive Testing Handbook: Infrared and Thermal Testing*, Vol. 3, 3rd edn., Columbus, OH: American Society of Nondestructive Testing, 2001.

de Silva, G. M. S., *Basic Metrology for ISO 9000 Certification*, Oxford, U.K.: Butterworth-Heinermann 2002.

14

Distance Measurement

W. John Ballantyne
Spar Aerospace Ltd.

The tools and techniques of distance measurement are possibly one of humankind's longest-running inventive pursuits. Figure 14.1 illustrates the enormous range of distances that science and engineering have an interest in measuring [1]. This chapter concerns itself with methods to measure a relatively small segment of this range—from centimeters to kilometers. Even within this limited segment, it would hardly be possible to list, much less describe, all of the distance measurement approaches that have been devised. Nevertheless, the small sampling of technologies that are covered here should be of help to a broad range of readers.

Distance measurement, at its most basic, is concerned with determining the length of a unidimensional line joining two points in 3-D space. Oftentimes, a collection of distance measurements is called for, so that the shape, the orientation, or the changes in position of an object can be resolved. Therefore, one must consider not only the measurement of distances but also their spatial and temporal distributions. The terminology "ranging" will be used in reference to systems that perform single sensor-to-target measurements, "range imaging" for systems that collect a dense map or grid of spatially distributed range measurements, and "position tracking" for systems that record the time history of distance measurement to one or several targets.

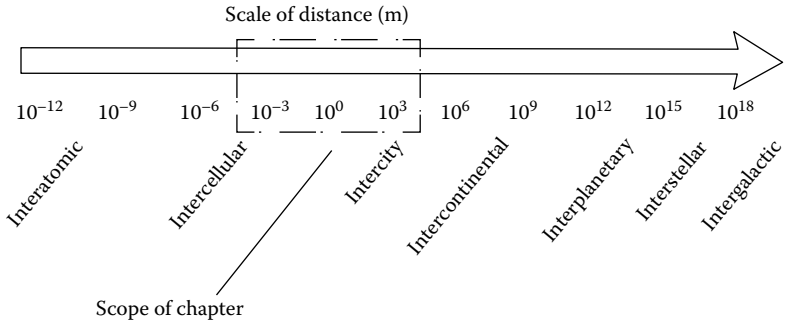

FIGURE 14.1 From the interatomic to the intergalactic, the range of measurable distances spans at least 30 orders of magnitude. The box outline indicates the relatively small segment that concerns this chapter.

14.1 Basic Distinctions between Range Measurement Techniques

Range measurement devices may be classified according to some basic distinctions. Generalization can be made based on these broad classes, thereby facilitating the process of comparison and selection. The following sections identify the fundamental bases for classification.

14.1.1 Contact or Noncontact

A common approach to measuring the distance to a point on an object is through a calibrated mechanical device that simultaneously connects the selected point to a reference position. Any tape measure, feeler gage, or dial gage may be considered an example of a simple contacting measurement device. Mechanical/electronic devices are available that allow a user to "digitize" discrete point positions on a 3-D surface. A gimbaled probe on the end of an *X-Y-Z* positioner or articulated arm is used to touch a specific point, and sensory information of the linear positions or joint articulations provides an accurate position estimate. Mechanical, contact-based methods are widely used in industry and can be extremely accurate. Some coordinate measuring machines (CMMs), for example, can achieve 1 μm repeatability.

The chief disadvantage of mechanical approaches is that they are usually restricted to distances and work volumes up to a few meters at maximum. This is due to fundamental scaling laws for mechanical structures. As the requirement to span larger distances increases, the mass and mechanical tolerancing requirements on the machine make designs impractical. Also, mechanical approaches are too slow to make multiple measurements in rapid succession, as is typically required in range imaging or position tracking, when the measurement involves large sets of spatially or temporally distributed data.

Noncontact techniques for performing ranging, range imaging, and position tracking are many and varied. Besl [2] reviews and compares several of these. In the centimeters to meters range, most do not approach the accuracy of CMMs, but at larger scales and for large quantities of data, they become a practical necessity. The rest of this chapter will review noncontact approaches only.

14.1.2 Active or Passive

Noncontact distance measurement may be divided into *active* or *passive* techniques. Active techniques involve some form of controlled energy (field or wave) linking a known reference location to the unknown target location. The source of energy is typically associated with the reference location, but in some cases the target, or both target and reference, may be active. Passive techniques rely on an externally occurring source of energy (e.g., sunlight or target/background temperature contrast) to make the target detectable.

An active approach can often simplify the distance measurement problem because it allows a greater degree of control over the many factors that can influence a measurement. For example, the choice of the form of energy and the power level of the active source can minimize the effect of uncontrolled variables like ambient illumination, weather, and atmospheric conditions. Furthermore, an active approach provides an opportunity to selectively localize the measurement spatially and temporally, eliminating possible ambiguity about which target point was measured at a given time. In contrast, passive systems (e.g., stereo ranging) sometimes suffer from the so-called correspondence problem, which is concerned with how to determine whether a given target point, detected from two or more viewpoints, or over two or more instants, is in fact the same physical point.

A common use of active approaches is to make range measurements "through" materials that are mechanically or optically impenetrable. Examples include medical imaging, where various forms of directed energy (ultrasound, x-rays) are used to build surface or volumetric maps of organs and bones; sonar, which penetrates water better than light does; and ground-penetrating radar, which can detect objects and their depth beneath ground surface.

Passive approaches, while not offering the same range of control and flexibility of active approaches, offer certain advantages. First, because they emit no energy, their existence cannot be detected by another remote detection system. This feature is very important in military applications. Second, passive systems can often collect multiple point range measurements more quickly because they are not limited by the rate at which they can direct an energy source toward a target point, as is the case with most active systems. For example, a stereo ranging system effectively collects all resolvable target points in its field of view simultaneously, while a scanning laser, radar, or sonar ranging system collects each measured point sequentially. Finally, the absence of a directed energy source is a simplification that can significantly reduce the size, cost, and hardware complexity of a device (although at the expense of increased signal-processing complexity).

14.1.3 Time of Flight, Triangulation, or Field Based

There are many different classes and instances of noncontact ranging devices, but with very few exceptions, they are based on one of the following three basic principles:

1. Energy propagates at a known, finite speed (e.g., the speed of light, the speed of sound in air).
2. Energy propagates in straight lines through a homogeneous medium.
3. Energy fields change in a continuous, monotonically decreasing, and predictable manner with distance from their source.

The techniques associated with these basic phenomena are referred to as time of flight (TOF), triangulation, and field based, respectively.

14.1.4 Time of Flight

TOF systems may be of the "round-trip" (i.e., echo, reflection) type or the "one-way" (i.e., cooperative target, active target) type. Round-trip systems effectively measure the time taken for an emitted energy pattern to travel from a reference source to a partially reflective target and back again. Depending on whether radio frequencies, light frequencies, or sound energy is used, these devices go by names such as RADAR, LIDAR, and SONAR. One-way systems transmit a signal at the reference end and receive it at the target end or vice versa. Some form of synchronizing reference must be available to both ends in order to establish the TOF.

A characteristic of many TOF systems is that their range resolution capability is based solely on the shortest time interval they can resolve and not the absolute range being measured. That is, whether an object is near or far, the error on the measurement is basically constant.

14.1.5 Triangulation

Triangulation techniques were known and practiced by the ancients. Triangulation is based on the idea that if one knows the length of one side of a triangle and two of its angles, the length of the other sides can be calculated. The known side is the "baseline." Lines of detection extend from either end of the baseline to the target point as shown in Figure 14.2. If the angles formed between these lines and the baseline can be determined, the distance is calculated as

$$R = \frac{b \sin \alpha_{\text{left}} \sin \alpha_{\text{right}}}{\sin(\alpha_{\text{right}} - \alpha_{\text{left}})} \tag{14.1}$$

Classical surveying is a passive range-finding technique based on the aforementioned formula. A surveyor uses a precision pointing instrument to sight a target from two positions separated by a known baseline. Reference [3] notes that the distance to a nearby star may be calculated by observing it through a pointing instrument at 6 month intervals and by using the diameter of Earth's solar orbit as the baseline. Stereo ranging, which compares the disparity (parallax) between common features within images from two cameras, is another form of passive triangulation. It is of interest to note that human vision estimates distance using a variety of cues, but two of the most important—stereopsis and motion parallax—are fundamentally triangulation based [4].

Active triangulation techniques use a projected light source, often laser, to create one side of the triangle, and the viewing axis of an optical detection means to create the second side. The separation between the projector and detector is the baseline.

A fundamental issue for all triangulation-based approaches is that their ability to estimate range diminishes with the square of the range being measured. This may be contrasted with TOF approaches, which have essentially constant error over their operating range. Figure 14.3 illustrates how, conceptually, there is a "crossover" distance where TOF techniques become preferable to triangulation techniques.

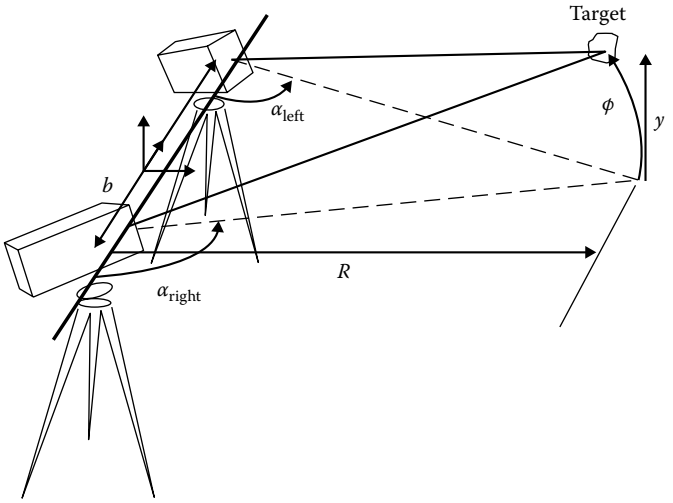

FIGURE 14.2 The basic triangulation geometry as used in classical surveying determines the distance to a remote point by sighting it from two locations separated by a known baseline. The pointing angles α_{left} and α_{right} are measured locally.

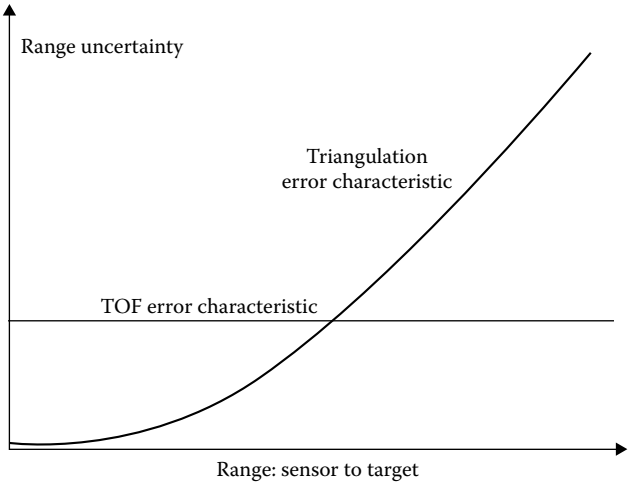

FIGURE 14.3 TOF and active triangulation techniques tend to exhibit error characteristics related to their fundamental principles of operation. The dominant error source in TOF systems is usually the shortest measurable time interval, but this is a detection issue and is essentially independent of distance. Active triangulation systems are typically more accurate at close distances, but geometry considerations dictate that the effects of their error sources will increase with the square of distance.

14.1.6 Field-Based Approaches

Whereas TOF and active triangulation techniques employ the wave propagation phenomena of a particular energy form, *field-based* approaches make use of the spatially distributed nature of an energy form. The intensity of any energy field changes as a function of distance from its source. Moreover, fields often exhibit vector characteristics (i.e., directionality). Therefore, if the location of a field generator is known and the spatial characteristics of the field that it produces are predictable, remote field measurements contain information that may be used to infer distance from the source.

An interesting distinction between field-based approaches and wave-based approaches is that the former, although they employ energy fields, do not rely on the propagation and conversion (and concomitant losses) of energy. That is, they may employ stationary fields, like those generated by a magnet or static charge. Such fields encode position information by their very shape. Sound and light, although having a wave nature, can be exploited in the same manner as stationary fields because of their distance-dependent intensity.

Field-based techniques must confront some basic issues that limit their range of application. First, the characteristics of most practically exploitable fields are typically influenced by objects or materials in the vicinity, and it is not always possible to ensure that these influences will remain constant. Second, the variation of fields through space is highly nonlinear (typically inverse square or inverse cube), implying that the sensitivity of a measurement is strongly affected by proximity to the source. Notwithstanding these concerns, devices have been developed and are available that perform very well in the situations for which they are intended [7].

14.1.7 Form of Energy

As discussed previously, all noncontact, active ranging devices employ some form of energy. This is true whether TOF, triangulation, or field-based principles apply. The following sections describe the various forms of energy employed and some generalizations about the effectiveness of each in various situations.

14.1.8 Sound

Ranging systems based on sound energy are usually of the pulsed-echo TOF type and employ carrier frequencies in the so-called "ultrasonic" (beyond audible) range of frequencies. Besides being inaudible (an obvious benefit), ultrasonic frequencies are more readily focused into directed beams and are practical to generate and detect using piezoelectric transducers. Ultrasonic signals propagate through air, but long-distance transmission is much more effective in liquids, like water, where higher density-to-viscosity ratios result in higher wave velocity and lower attenuation per unit distance. Ultrasonic ranging techniques (or SONAR, for sound navigation and ranging) were first developed for subsea applications, where sound is vastly superior to electromagnetic energy (including light) in terms of achievable underwater transmission distances [5]. Low-cost, portable sonar systems are widely used by sport fisherman as "fish finders" [6].

The frequencies typically used in sonic ranging applications are at a few tens of kilohertz to a few hundred kilohertz. A basic trade-off in the choice of ultrasonic frequency is that while high frequencies can be shaped into narrower beams and therefore higher lateral resolution is achieved, they tend to fade more quickly with distance. It may be noted that beam widths narrow enough for range-imaging applications (less than 10°) are effective in a fluid medium but attenuate too quickly to be practical in air. Interestingly, although sound energy attenuates more rapidly in air than in water, useful short-range signals can be generated in air with relatively low power levels because the much lower density of air requires smaller dynamic forces in the transducer for a given wave amplitude.

When comparing sound energy to electromagnetic energy for TOF-based techniques, one need to remember that sound, unlike light, propagates at not only much lower speeds but also with considerably more speed variation, depending on the type and state of the carrying media. Therefore, factors like air humidity and pressure will affect the accuracy of a TOF ranging device. For underwater applications, salinity and depth influence the measurement. The lower speed of sound has a detrimental impact on the rate at which range samples can be collected. For example, a target 10 m away takes at least 60 ms to measure through an air medium. This may not seem like a long time to wait for a single sample, but it becomes an issue if the application involves multiple sampling, as in motion tracking or collision avoidance sensing.

14.1.9 Stationary Magnetic Fields

Stationary or pseudostationary (i.e., low frequency) magnetic fields are only used in field-based approaches. An advantage of such fields is that they are easily and cheaply produced by either a permanent magnet or electrical coil. Since stationary fields do not transmit energy, the targets cannot be passive—they must actively sense the properties of the field at their particular location. A variety of sensing technologies may be used to make measurements of the direction and intensity of a magnetic field, including flux gate, Hall effect, and magnetostrictive type magnetometers. A comprehensive list of such technologies is given in Ref. [7].

14.1.10 Radio Frequencies

Echo-type TOF ranging systems based on the band of the electromagnetic spectrum between approximately 1 m and 1 mm wavelength are known as RADAR (radio detection and ranging). Radio waves can be used for long-distance detection in a variety of atmospheric conditions. As in the case of sound waves, there are few trade-offs to be addressed in the choice of frequency. Long waves tend to propagate better over long distances, but short waves can be focused into narrow beams capable of better lateral discrimination. An interesting application of short-range radar is ground-penetrating radar, which can be used to locate and image subsurface objects [8]. Here, the frequency versus range trade-off is particularly acute because of the need to balance reasonable imaging capability (narrow beam) with good depth penetration (long wave).

An example of a TOF one-way (active receiver) system that uses radio frequencies is the global positioning system (GPS). The distances between a receiver on land and satellites are determined by each of several orbiting satellites equipped with a transmitter and a very precise Cesium clock for synchronization. A good description of GPS and its use in vehicle navigation is available in Ref. [9].

14.1.11 Light Frequencies

Beyond the radio portion of the electromagnetic spectrum are the infrared, visible, and ultraviolet frequencies. These frequencies can be produced by lasers and detected by solid-state photosensitive devices and are useful for both TOF and active triangulation ranging. Echo-type TOF techniques are known as LIDAR (light detection and ranging), in keeping with the terminology introduced earlier.

While light frequencies attenuate more than radio frequencies through cloud and fog, they can have very narrow beam widths, allowing superior lateral resolution and target selectivity.

14.1.12 Coherent or Noncoherent Detection

Echo-type TOF devices, whether sonar, radar, or lidar, can be further classified according to whether the detection approach measures TOF directly (noncoherent) or exploits an inherent periodicity in the emitted energy to ascertain the flight distance (coherent).

Noncoherent techniques face the problem of timing short intervals. This is not a serious challenge in the case of sound waves, where a meter round trip corresponds to 6 ms, but is somewhat more problematic for light and radio waves, where that distance equates to only 6 ns. Accuracy of noncoherent detection typically relies on the averaging of repeated measurements.

Coherent detection is achieved by combining a portion of the emitted signal with the reflected signal to produce a third signal indicating the amount of phase delay. The signals are continuous wave (CW) as opposed to pulsed. Coherent detection techniques are classified as amplitude modulated (AMCW) or frequency modulated (FMCW).

A basic issue with coherent detection techniques is the inability to distinguish between integral multiples of the basic modulation wavelength. Any coherent detection system must employ techniques to resolve the so-called ambiguity interval. Noncoherent techniques do not face this problem.

14.1.13 Ranging, Range Imaging, or Position Tracking

Ranging devices are typically pointed toward a target to produce a single range reading. A common example of simple ranging is the feedback sensor used in autofocus cameras. There are many active ranging devices currently available based on TOF (i.e., RADAR, SONAR, LIDAR) and active triangulation principles.

Range-imaging devices use the same principles as ranging devices, except that they include some form of scanning that is employed to generate an array of spatially distributed range samples. Sometimes, the scanning action is accomplished by means of intrinsic to the sensor (e.g., spinning and nodding mirrors or phased-array antenna) so that the reference location remains fixed. In this case, the data are recorded in the polar form (range, elevation, azimuth) as shown in Figure 14.4. In other cases, the sensor might scan on only one axis internally, while the second scan dimension is realized by moving the sensor location through some set pattern. It is not uncommon to record the "intensity" or return energy associated with a range sample as well. The intensity map may be presented as a "gray scale" image and, like a black and white photograph, often contains additional information useful in interpreting a scene. Range images can be used to produce 3-D graphic representations of scenes and objects. A common use of range imaging is aerial terrain mapping.

Position-tracking devices are used to measure the change in an object's position and orientation over time. Basic issues in position tracking are the acquiring of, and locking on to, specific target points. These issues can be avoided by employing active targets, and most systems available today are of this type.

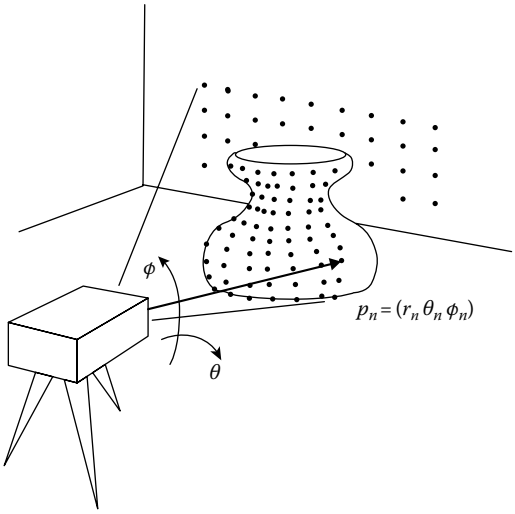

FIGURE 14.4 Range images are typically an array of individual range values sampled while changing the pointing direction (e.g., azimuth and elevation angles) of a ranging device. A digital range image of the polar form shown can be readily transformed into rectangular coordinates if required.

14.2 Performance Limits of Ranging Systems

The performance characteristics of available ranging systems vary widely, as do the requirements of the applications for which they are designed. The following sections review the most basic performance categories and the technical issues of performance limits.

14.2.1 Range Accuracy

As illustrated in Figure 14.3, TOF and active triangulation techniques differ fundamentally in their error versus distance characteristics. Currently available systems based on active triangulation achieve better repeatability and accuracy in the less than 1 m range than do TOF systems but are seldom used at distances of several meters. Hymarc Ltd. and Perceptron Inc. each offer laser triangulation systems with 3σ accuracy of 25 and 50 mm, respectively [10,11].

In principle, TOF systems could achieve accuracy rivaling active triangulation, but the most promising detection technique—a variation of laser interferometry, which solves the ambiguity interval problem [12]—has yet to make its commercial debut.

14.2.2 Depth of Field

Depth of field refers to the interval of distance through which a stationary reference ranging system can measure without resorting to a change in configuration. Large depth of field is often an important characteristic in practical applications. For example, if the distance to the target is poorly known a priori, then a large depth of field is desirable.

Passive optical triangulation approaches like stereography and photogrammetry tend to have restricted depth of field because they rely on camera-type imaging, which is inherently limited by depth of focus. Timed-interval TOF systems have excellent depth of field because they do not rely strongly on optical imaging except to concentrate the collected returned energy on the detector. Some active triangulation systems do rely on optical imaging of the projected laser spot, but the design employed by Hymarc Ltd. regains a large depth of field by tilting the detector array with respect to the lens plane [13].

14.2.3 Maximum Range

Any active ranging, range-imaging, or position-tracking system has a practical maximum distance that it can measure. This is because the controlled energy, whether propagated as a wave or established as a field, must spread before reaching the detector. The spreading inevitably increases with distance and all detectors, no matter what form of energy they measure, require a certain minimum amount to exceed their inherent "noise floor."

The "classical radar range equation" is introduced in many texts on radar (e.g., [14]). Jelalian [15] points out that the equation is equally applicable to lidar, which, after all, just employs a higher frequency version of electromagnetic wave. In fact, the same idea applies to sonar and to active triangulation systems as well. The equation computes the power of the received signal as

$$P_R = \frac{P_T G_T}{4\pi R^2} \times \frac{\rho A}{4\pi R^2} \times \frac{\pi D^2}{4} \times \eta_{atm}\eta_{sys} \tag{14.2}$$

where

P_R is the power at the receiver
P_T is the power transmitted
G_T is the transmitter gain
R is the range to target
ρ is the reflectivity of target
A is the effective area of target
D is the diameter of collecting aperture
η_{atm} is the atmospheric transmission coefficient
η_{sys} is the system transmission coefficient

Equation 14.2 applies when the target area is smaller than the footprint of the incident beam, which is often the case for radar and sonar ranging. However, in the case of laser-based systems, the relatively narrow beam usually means that the laser spot is small compared to the target. For a transmitted beam that spreads with a solid angle θ_T, the illuminated patch area is

$$\sigma_{spot} = \pi R^2 \theta_T^2 \tag{14.3}$$

The definition of transmitter gain is based on the notion of the solid angle beam width as compared to an omnidirectional transmitter:

$$G_T = \frac{4\pi}{\theta_T^2} \tag{14.4}$$

One can substitute for Equation 14.4 for G_T and Equation 14.3 for the variable s in Equation 14.2 to produce the range equation for a small spot size:

$$P_R = \frac{P_T}{R^2} \times \frac{\rho}{4} \times \frac{\pi D^2}{4} \times \eta_{atm}\eta_{sys} \tag{14.5}$$

The importance of this equation is primarily in the $1/R^2$ dependence. Any ranging system that works by bouncing energy off a diffuse reflective target encounters severe signal attenuation with

increasing distance. Given a detector with a fixed noise floor, the only way to improve maximum range is to increase the transmitted power or the collecting area. In practice, there are design constraints that limit both of these measures. For example, laser power must sometimes be limited for eye-safety considerations, and increased collecting area can imply a proportional increase in sensor packaging volume.

14.2.4 Lateral Resolution

In range-imaging applications, it is generally desirable to use the narrowest possible beam width to provide good lateral discrimination of target surface features. Lasers, because of their short wavelength, can be optically collimated to produce much narrower beam widths than are possible with radio sources. However, even lasers cannot produce arbitrarily narrow beams. The interested reader is referred to Ref. [13] for a discussion of Gaussian beam propagation and optimal focusing. There are basically two ways to project laser light. The beam can be "focused down" to produce the smallest possible spot at a particular point inside the measurement range, in which case the beam will diverge as the distance from that point increases, or the beam can be focused at infinity or some very distant point so as to minimize the divergence through the entire measurement range. The former approach provides higher lateral resolution at the focus distance, but by implication restricts the practical depth of field. The latter compromises spot sizes for the increased depth of the field.

14.2.5 Rate of Acquisition

The rate at which a ranging sensor can acquire range samples is important when the target object is changing shape or position or when the required sample density of a range image is very high. There are several potential factors that can limit sample acquisition rate: the amount of time required by the detector to integrate the weak return signal to a sufficient level (integration time), the time constant of any filtering or averaging that must be performed to realize an acceptably "clean" signal (smoothing time), the rate at which samples can be transferred through the signal-processing stages (transfer time), and the velocity limits of mechanical scanning apparatus (scanning bandwidth). Acquisition rates vary widely: from tens of hertz for acoustic ranging devices to tens of kilohertz for some laser-based systems. It is worth noting that, in general, there is a trade-off between rate of acquisition, accuracy, and maximum range. Some systems permit control over basic parameters so that this trade-off may be optimized for a particular application. The reader should be aware that data sheets may not be clear as to whether stated performance figures for these three specifications are valid in combination.

14.3 Selected Examples of Ranging, Range-Imaging, and Motion-Tracking Systems

The following sections review selected examples of some specific ranging, range-imaging, and position-tracking sensor systems. The list is by no means exhaustive but offers a reasonable sampling of available technologies.

14.3.1 Laser-Based Active Triangulation Ranging and Range-Imaging Sensors

14.3.1.1 Active Triangulation Basics

Figure 14.5 illustrates the basic active triangulation geometry. In this so-called "pinhole camera" model, practical aspects like lenses for projection and detection and mirrors for scanning are eliminated

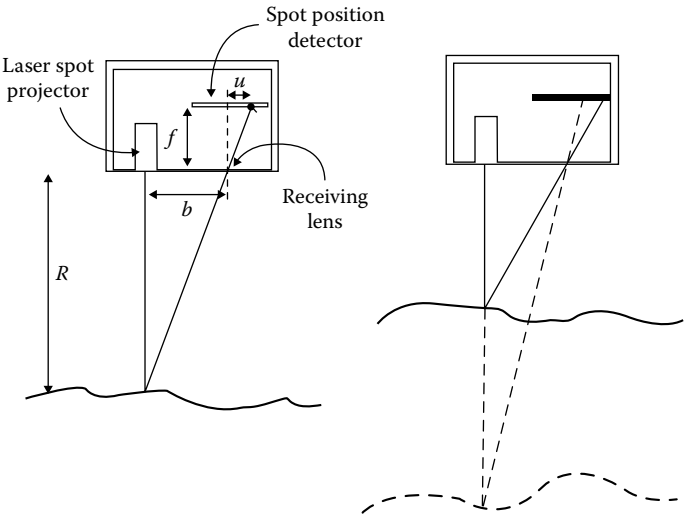

FIGURE 14.5 A simple pinhole camera model illustrates the basic active triangulation principle. As the distance R to the target surface changes, the spot position u on the detector changes, maintaining similarity between the large triangle outside the camera and the small triangle inside. There is an inverse relationship between R and u.

for clarity. It can be shown by means of similar triangles that the range is inversely proportional to the deflection of the imaged spot:

$$R = \frac{bf}{u} \tag{14.6}$$

where
R is the distance to object
b is the baseline distance
f is the lens-to-detector distance
u is the detected spot position in the image plane

The sensitivity of the range measurement, or the incremental change in u with R, is

$$\left|\frac{du}{dR}\right| = \frac{bf}{R^2} \tag{14.7}$$

The significance of Equation 14.7 is that range estimating performance is expected to fall as distance increases. Improvements in accuracy are realized by increasing the baseline or the lens-to-detector distance (i.e., the focal length).

14.3.1.2 Synchronized Scanning Principle

Lateral scanning of an active triangulation ranging sensor is accomplished by an elegant and effective technique developed at Canada's National Research Council and now marketed by Hymarc Ltd. under the name "HYSCAN" [10]. A two-sided oscillating mirror simultaneously steers the outgoing beam on one face and directs the collected light to the spot-imaging optics on the opposite face. By synchronously scanning both the beam and the axis of the detection system, rather than the beam only, as conventionally practiced, significant performance improvements are made. Figure 14.6 is a schematic illustration

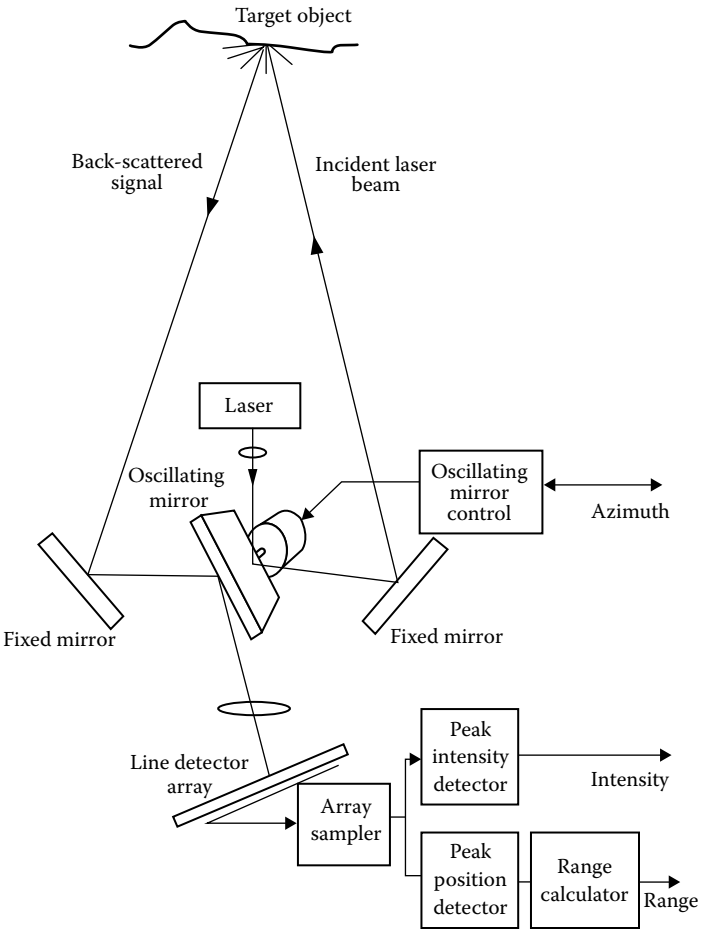

FIGURE 14.6 The Hymarc laser triangulation line scanner uses the synchronized scanning principle. Both sides of an oscillating mirror are used to sweep both the projected beam and the axis of detection over the target. The detector array is tilted to the lens plane to maximize the depth of focus.

of the approach. Note also that the detector plane is tilted with respect to the lens plane. This feature increases the depth of focus so that the ranging performance is maximized over the measuring volume. The HYSCAN sensor produces a single-axis sweep, or so-called line scan. Full-dimension range images are acquired by translating the sensor over a target surface with a controlled motion pattern.

14.3.1.3 Light Plane Principle

Perceptron Inc. offers a similar line-scan system under the name "TriCam" [11]. In this case, the laser is not swept. Instead, the beam is transformed to a focused plane by means of cylindrical lenses. A 2-D detector is used to generate range profiles through the analysis of a deformation of the laser line as the sensor is translated over the object surface.

14.3.2 Laser-Based LIDAR Range-Imaging Sensors

14.3.2.1 AM LIDAR (Phase-Based Detection)

Perceptron Inc. also offers a scanning LIDAR under the name "LASAR" that can produce high-resolution range images through a large measurement volume. The device uses a near-infrared laser that is projected

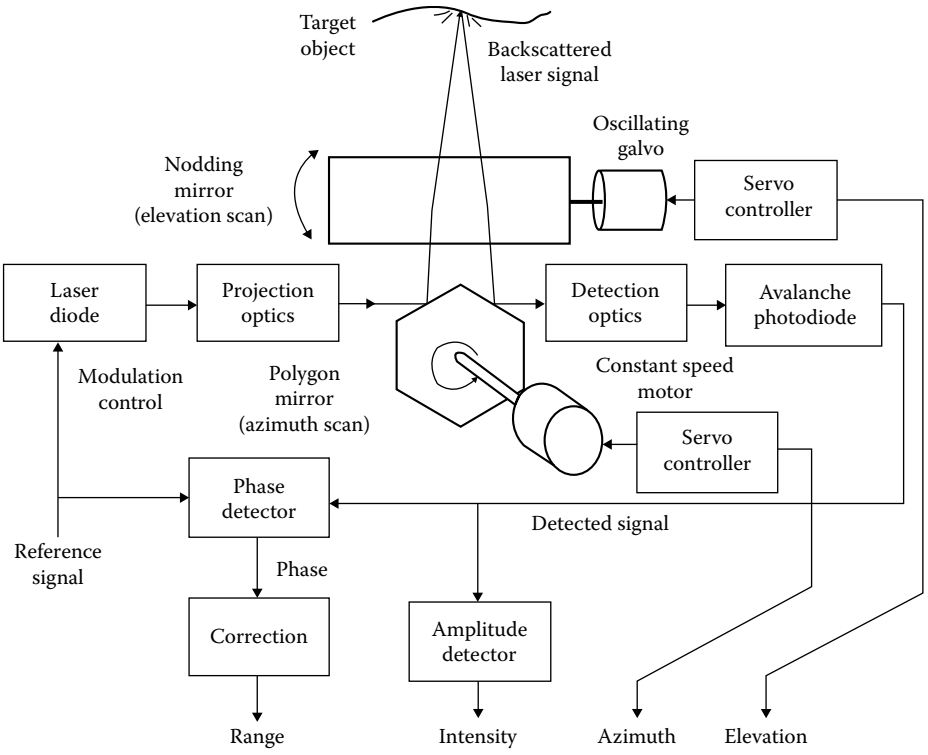

FIGURE 14.7 The Perceptron AM LIDAR system described in U.S. patent 5,006,721 uses a rotating polygon mirror for synchronized scanning. A "nodding mirror" is also added to sweep at a slower rate in the orthogonal direction, producing a raster scan pattern. Range measurement is determined by comparing the phase of the outgoing and returning AM laser signal.

through a collimating telescope to form a spot on the first surface encountered. The spot is swept over a programmable field of view in a raster pattern by means of a spinning polygon mirror and an oscillating "nodding mirror." Some of the backscattered light is collected and directed by means of an adjacent facet of the polygon mirror. The projected laser light is amplitude modulated at a reference frequency by controlling the power to the laser diode source. The return signal, although orders of magnitude weaker than the outgoing signal, is phase-compared to determine the range for a particular azimuth and elevation. The intensity of the return energy is also recorded. The Perceptron sales literature claims a maximum measurement volume of 60° × 72° × 40 m, a range image grid resolution of 1024 × 2048 pixels and a maximum acquisition rate of 360,000 pixels/s. A schematic diagram of the LASAR™ system is shown in Figure 14.7. Details of the Perceptron technical approach may be found in Ref. [16].

14.3.3 Resonating LIDAR (Frequency-Based Detection)

Acuity Research Inc. has developed a laser-based TOF ranging sensor based on a simple but effective idea. The detector controls the laser output such that the absence of a signal drives the laser on and the presence of a signal turns it off. The finite transit time of the light bounce turns this arrangement into a two-state resonator, with the period being proportional to the target distance. Rather than measuring the period, which is extremely short and difficult to time, the frequency is measured using conventional counting techniques for as many cycles as necessary to yield the required accuracy. The AccuRange 4000, as it is named, is also available in a 360° line-scanning arrangement suitable for robotic vehicle navigation applications [17]. Details of the technical approach may be found in Ref. [18].

14.3.4 Position Tracking with Active Targets

Active target approaches are not convenient in some applications, but they are an excellent way to track the changing positions of several target points simultaneously. Active targets are a way of getting around the "correspondence problem" mentioned earlier. The two systems introduced here are interesting to compare. One employs light energy and triangulation; the other uses a magnetic field-based approach. They are both used for real-time tracking and recording of human kinetics, robotics, and other moving objects.

14.3.5 Active Target Triangulation

The "OPTOTRAK" system offered by Northern Digital Ltd. [19] uses infrared light-emitting diodes (LEDs) as targets. The LEDs are multiplexed so that only one at a time can be seen by the camera system, avoiding the correspondence problem. The unique form of stereo ranging is based on three line detectors with lenses that transform the point source LED illumination into a focused line. The simplified triangulating geometry is shown in Figure 14.8. It may be shown from this geometry that the target position (x_p, y_p, z_p) can be determined from the detector outputs u_{left}, u_{right}, and v as follows:

$$x_p = \frac{b(u_{right} + u_{left})}{2(u_{right} - u_{left})} \tag{14.8}$$

$$y_p = \frac{bv}{(u_{right} - u_{left})} \tag{14.9}$$

$$z_p = \frac{fb}{(u_{right} - u_{left})} \tag{14.10}$$

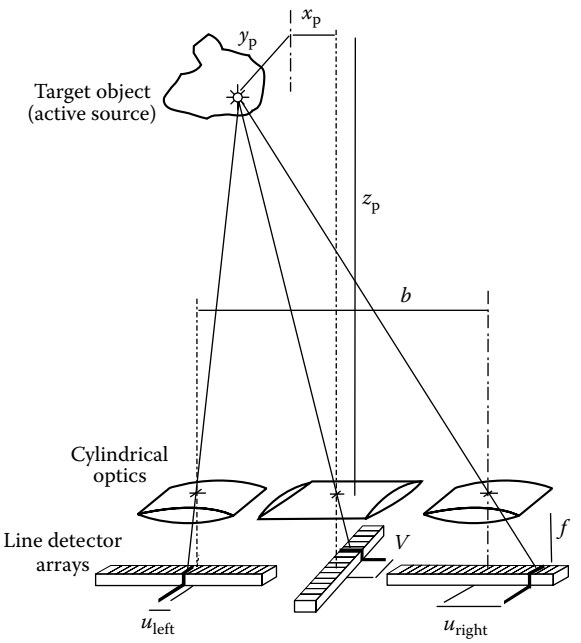

FIGURE 14.8 The OPTOTRAK position-tracking system employs a novel arrangement of cylindrical optics and 1-D detectors to triangulate the 3-D position of an infrared LED target. Up to 255 individual multiplexed targets can be tracked by the system.

where f and b are the lens-to-detector distance and the baseline separation, respectively. In practice, the image space to object space mapping is much more complicated than Equations 14.8 through 14.10 and involves a camera model with more than 60 parameters that are determined through a calibration process.

OPTOTRACK offers high sampling rate, large measurement volume, and high accuracy compared to many other position-tracking systems.

14.3.6 Magnetic Position Tracking

A position/orientation tracking sensor based on a three-axis magnetic dipole transmitter and a three-axis magnetic loop detector has been developed by Polhemus Inc. [20]. The transmitted fields are alternating current for ease of detection (i.e., transformer coupled) and time-multiplexed so that the field due to each axis can be distinguished from the others. Distance between transmitter and detector is determined by exploiting the $1/R^3$ relationship between field strength and distance from the source. Orientation of the detector is determined by exploiting the directionality of magnetic fields and the direction sensitivity of loop detectors.

An issue with respect to the use of ac fields is the distortions in field shape that occur if metal objects are present and the consequent effect on sensor accuracy. These distortions result from eddy currents in the conducting metal. Ascension Technology Corp. has developed a variation on the Polhemus sensor

TABLE 14.1 Ranging, Range-Imaging, and Position-Tracking Products and Vendors

Class	Trade Name	Principle	Features	Contact
Ranging (contact)	MicroScribe-3DX	Instrumented arm	50 in. spherical work volume, 0.3 mm accuracy	Immersion Corp., (408)467–1900, info@immerse.com
Ranging (noncontact)	LASERVISION	TOF, laser	50 m range, 4.9 mm accuracy at 15 m, integrated electronic level	ZIRCON Corp., (408) 866–8600
Range imaging (line scan)	HYSCAN	Active triangulation laser	40 mm depth of field, 70 mm swath, 0.025 mm accuracy, 10,000 points/s	Hymarc Ltd., (613)727–1584, info@hymarc.com
Range imaging (line scan)	TriCam	Active triangulation laser	120 mm depth of field, 60 mm swath, 0.05 mm accuracy	Perceptron Inc., (810) 478–7710, inquiry@perceptron.com
Range imaging (line scan)	ALTM 1020	TOF laser time interval	330–1000 m range, 15 cm accuracy, 20° swath	Optech Inc., (416) 661–5904
Range imaging (area scan)	Rangecam 7000	Laser or strobe triangulation	Uses standard CCD camera and light plane projector	Range Vision Inc., (604)473–9411
Range imaging (area scan)	LASAR	TOF, AM LIDAR	2–40 m range, 60° × 70° max field of view, 360,000 samples/s	Perceptron Inc., (810) 478–7710
Position tracking	OPTOTRAK	Active target triangulation	Up to 255 targets, submillimeter accuracy, 5000 3 DoF samples/s	Northern Digital Inc., (519) 884–5142
Position tracking	Flock of Birds	Magnetic field based	Up to 30 position/orientation targets, approx. 10 mm accuracy, 144 6-DoF samples/s	Ascension Technology Corp., (802) 860–6440

based on dc magnetic fields. The switching transient due to time-multiplexing does produce an eddy current effect, but it is allowed to die out before measurement is made. Details of the dc technique are available in Ref. [21].

An important difference between optical and magnetic tracking technologies is that the former require an unbroken line of sight to the targets while the latter do not. This gives magnetic trackers an advantage in some applications. On the other hand, the $1/R^3$ field distribution characteristic of magnetic tracking implies an extreme sensitivity loss with distance, whereas optical triangulation has a more benign $1/R$ characteristic. This, to some extent, explains why the volume of measurement and accuracy of optical triangulation systems is generally much better than for magnetic systems.

14.4 A Sampling of Commercial Ranging, Range-Imaging, and Motion-Tracking Products

Table 14.1 contains information collected from vendor literature. Be advised when comparing specifications that test conditions, standards, and interpretations can vary significantly. The specifications, therefore, should serve only as a rough guide.

References

1. R. Resnick and D. Halliday, *Physics (Part 1)*. John Wiley & Sons, New York, 1966, Ch. 4.
2. P. J. Besl, *Range Imaging Sensors*. General Motors Research Publication, GMR-6090, General Motors Research Laboratories, Warren, MI, March, 1988.
3. R. Resnick and D. Halliday, *Physics (Part 1)*. John Wiley & Sons, New York, 1966, Ch. 3.
4. D. F. McAllister (ed.), *Stereo Computer Graphics and Other True 3D Technologies*, Princeton University Press, Princeton, NJ, 1993. Ch. 4.
5. L. E. Kinsler and A. R. Frey, *Fundamentals of Acoustics*, 2nd edn., John Wiley & Sons, New York, 1962, Chs. 9, 15.
6. W. Diedrich, Foundations of reading sonar, *The In-Fisherman*, April–May, 42–56, 1996.
7. E. B. Blood, Device for quantitatively measuring the relative position and orientation of two bodies in the presence of metals utilizing direct current magnetic fields, U.S. Patent 4,945,305, July 31, 1990.
8. W. J. Steinway and C. R. Barrett, Development status of a stepped-frequency ground penetrating radar, in *Underground and Obscured Object Imaging and Detection*, *SPIE Proceedings*, Vol. 1942, Orlando, FL, April 1993, pp. 34–43.
9. J. Borenstein, H. R. Everett, and L. Feng, *Where am I? Sensors and Methods for Autonomous Mobile Robot Positioning*, 1995 edn., University of Michigan report for the United States Department of Energy Robotics Technology Development Program, Ann Arbor, MI, 1995. Ch. 3.
10. Hymarc Ltd., *Product Information*, Hyscan 3D Laser Digitizing Systems, Ottawa, Ontario, Canada, 1995.
11. Perceptron Inc., *Product Information*, TriCam Non-Contact Measurement Solutions, Farmington Hills, MI, 1995.
12. F. E. Goodwin, Frequency modulated laser radar, U.S. Patent 4,830,486, May 16, 1989.
13. F. Biais, M. Rioux, and J.-A. Beraldin, Practical considerations for a design of a high precision 3D laser scanner system, SPIE Vol. 959, Optomechanical and Electro-Optical Design of Industrial Systems, 1988.
14. D. K. Barton, *Radar System Analysis*, Prentice-Hall, Englewood Cliffs, NJ, 1964, Ch. 4.
15. A. V. Jelalian, *Laser Radar Systems*, Artech House, Boston, MA, 1992. Ch. 1.
16. E. S. Cameron, R. P. Srumski, and J. K. West, Lidar scanning system, U.S. Patent 5,006,721, April 9, 1991.

17. Acuity Research Inc., *Product Information*, Accurange 4000, Menlo Park, CA, 1995.
18. R. R. Clark, Scanning rangefinder with range to frequency conversion, U.S. Patent 5,309,212, May 3, 1994.
19. Products, Northern Digital Inc., NDI, http://www.ndigital.com/products.php (accessed on March 14, 2013).
20. F. H. Raab, E. B. Blood, T. O. Steiner, and H. R. Jones, Magnetic position and orientation tracking system, *IEEE Transactions on Aerospace Electronic Systems*, AES-15(5), September 1979.

15

Altitude Measurement

Dimitris E. Manolakis
Alexander Technological Education Institute of Thessaloniki

Altitude can be determined via barometric altimeters or it can be measured via electronic radio wave systems. The indication of the first equipment is referred to as pressure altitude, or simply altitude, whereas that of the second category is referred to as geometric height or simply height or true altitude. Pressure altitude is derived onboard, whereas the height can be derived either onboard or in ground stations.

15.1 Pressure Altitude Measurement

Actually, the altitude information is an atmospheric pressure measurement transformed to altitude indication through a formula expressing the pressure/altitude relationship. Thus, a pressure altimeter or barometric altimeter is a barometer that is provided with a nonlinear calibration in order to transform it to altitude indication, through the following form:

$$z = kT \log\left(\frac{P_0}{P}\right) \tag{15.1}$$

where
P is the pressure at altitude z
P_0 is the pressure at sea level
T is the absolute temperature

Constant k expresses the effect of the molar mass of the air and the acceleration of gravity according to a mathematical model defined by the International Standard Atmosphere (ISA). It is important to note that this type of altimeter relies on "density altitude" and consequently can shift its indication by tens or hundreds of meters because of abrupt changes in air pressure although the altitude actually remains the same.

Pressure altimeters are used in aircrafts, meteorological stations, mountain climbers, etc.

15.2 Radar Altimeter

A more direct measurement of the altitude is via onboard radar. The altitude z is derived by measuring the time T that the signal needs to travel from the board to the surface and back after its reflection:

$$z = \frac{Tc}{2} \tag{15.2}$$

where c is the velocity of the signal. Radar altimeters are used in commercial and military aircrafts to measure height above ground level during landing. These altimeters are part of terrain avoidance warning systems as well as and of terrain-following systems permitting fighter aircraft to fly at very low altitude.

15.3 Height Measurement

The altitude information at air traffic control (ATC) centers is based on pressure altitude measurement that is derived onboard, and the aircraft transponder sends it after an appropriate interrogation transmitted by secondary surveillance radar (SSR). When a flight level (FL) is cleared for an aircraft, it actually means that the pilot must keep flying on an isobaric surface. However, the barometric altimetry system may present systematic errors (biases) that are different for each airplane and that significantly affect safety. In addition, the atmospheric conditions rarely match the standard atmosphere, so true and indicated altitudes are not equal. For example, if the temperature is about 10°C colder than standard, then indicated altitude is approximately 4% higher than true altitude. This means an error of 600 ft at 15,000 ft flying level that is a substantial divergence if flying on a cold day. The vertical separation minimum (VSM) at FL lower than 2900 ft (FL290) is 1000 ft, whereas for FL higher than FL290, it is 2000 ft due to the deterioration of the performance of pressure altimeters at high FL. A program started in 1982 from ICAO to assess the feasibility of reducing the VSM from 2000 to 1000 ft for levels between FL290 and FL410. The benefit is the increase of the capacity of the airspace especially at levels where they operate most cost effectively [1]. Thus, the altimetry system performance as well as the aircraft height-keeping performance should be monitored by independent radar systems in order to grant approval to fly at reduced VSM [2]. Between 1997 and 2011, RVSM was implemented all over the world for aircrafts with certified altimeters and autopilots.

Radar or satellite systems determine the position of an object through algorithms that are fed with range, or range difference (RD), or range sum, or range and bearing measurements, and they estimate the object position vector employing appropriate techniques such as triangulation or trilateration. The radar measurements are contaminated by two kinds of errors: random and systematic errors. The effect of random errors can be reduced by the use of appropriate noise rejection filters, such as a Kalman filter. The second kind of error is usually removed by calibrating the instrument if this is possible; otherwise, suitable algorithms must be invented to anticipate it.

The estimation may be derived in ground stations or on board the aircraft according to where the data acquisition and processing is performed. In the latter case, the vertical position estimation has to be downlinked to the appropriate ATC center. Also, the estimation may be performed off-line or on-line. Ground-based methods or systems are the navigation accuracy measurement system (NAMS), the height estimation method with a single ATC radar, the method with one SSR and one omnidirectional radar,

the dual-synchronized autonomous height monitoring system (DAMS), and methods that use multiple SSRs and estimate the height by quadrilateration, or by the use of pseudorange measurements, or by the use of RD measurements. Onboard height measurement methods derive their estimates by trilateration using the distance measuring equipment (DME) or the Global Positioning System (GPS) signals.

15.4 Ground-Based Height Estimation

The radars used to derive the original measurements are either primary or SSR. Primary radar sends a signal and scans for the arrival of its reflection. The range to the object reflecting the signal is derived from the time elapsed between transmission and reception. With secondary radar, the radar sends an interrogation to aircraft—to all aircraft or to a selected one—and the appropriate aircraft sends a reply via its transponder. The range to the aircraft is computed from the time elapsed between the signal transmission and the signal arrival, taking into account the nominal delay time of the transponder. Most of the methods estimating the aircraft height make use of the SSR equipment because it is cost-effective, the transponder reply signal is stronger than that reflected to a primary radar, and the system can operate more reliably in dense traffic areas.

Any systematic errors in the primary radar and in the ground equipment of the SSR can be corrected by calibration. However, the problem encountered with SSR is that it involves the transponder delay time in the range measurement process. Thus, any systematic error in the transponder delay time causes range bias errors that are different for each aircraft, and thus, suitable methods must be used to anticipate for it in the subsequent measurement data processing.

15.4.1 Navigation Accuracy Measurement System

Nagaoka has proposed an off-line height estimation system [3,4]. It is composed of a primary marine radar located under an air lane and measures range R and depression angle β. Figure 15.1 shows the geometry of the system. The antenna rotates about a vertical axis and scans the area above it with rate equal to 1 rotation per 3 s. The principle exploited to derive the height estimate is that the range varies as the aircraft passes through the data acquisition area. The rate of change of range is mainly a function of the flight height z and secondarily of depression angle. It is easily derived from Figure 15.1 that the relation between the aforementioned quantities and the position x along the x-axis at time t is

$$R(t) = \sqrt{x^2(t) + R'(t)^2} = \sqrt{x^2(t) + \frac{z^2}{\cos^2 \beta(t)}} \tag{15.3}$$

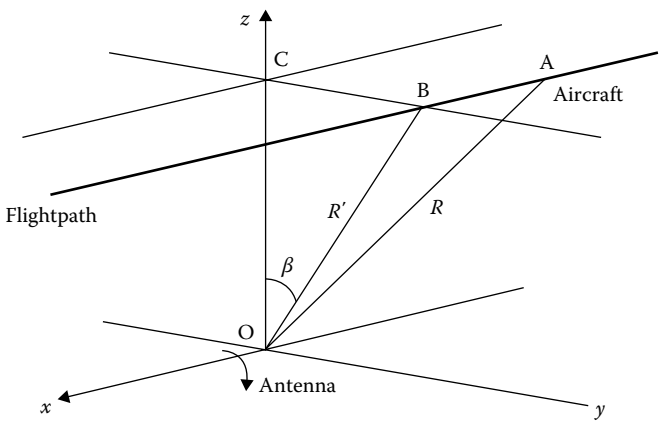

FIGURE 15.1 Geometry of the NAMS. BA = x, CB = y, OC = z, $R' = z/\cos(\beta)$.

Let x_0 denote the position of the aircraft at time t_0. Assuming the aircraft flies in straight and level flight, this means that the velocity V_x, the depression angle, and the height z remain constant during the data collection period. The aforementioned quantities and the range measurement at time t_t are related through Equation 15.4:

$$R_i = \sqrt{[x_0 + V_x(t_i - t_0)]^2 + \frac{z^2}{\cos^2 \beta}} = f(t_i, \beta, q) = f_i(q) \tag{15.4}$$

where $\mathbf{q}$ is the unknown quantities vector, $\mathbf{q} = [x_0, V_x, Z]^T$.

Measurements of R_i and β are collected at times $t_0, t_v, \ldots, t_n$, and their set is briefly expressed as a vector function of the unknown quantities with the following matrix equation:

$$\mathbf{R} = \mathbf{f}(\mathbf{q}) \tag{15.5}$$

where

$$\mathbf{R} = \begin{bmatrix} R_0 \\ R_1 \\ . \\ R_n \end{bmatrix} \quad \mathbf{f} = \begin{bmatrix} f_0 \\ f_1 \\ . \\ f_n \end{bmatrix}$$

Equation 15.5 is nonlinear. Thus, a nonlinear least squares method, such as the Gauss–Newton iterative method, must be used to estimate the unknown vector. Let $\mathbf{q_k}$ be the estimate at the kth iteration. Then, the next estimate is

$$\hat{\mathbf{q}}_{\mathbf{k+1}} = \hat{\mathbf{q}}_{\mathbf{K}} + (\mathbf{F}^{\mathbf{T}}\mathbf{F})^{-1}\mathbf{F}^{\mathbf{T}}[\mathbf{R} - \mathbf{f}(\hat{\mathbf{q}}_{\mathbf{K}})] \tag{15.6}$$

where $\mathbf{F}$ is the partial derivatives (Jacobian) matrix; that is,

$$\mathbf{F} = \frac{\vartheta f}{\vartheta q} = \begin{bmatrix} \frac{\vartheta f_0}{\vartheta x_0} & \frac{\vartheta f_0}{\vartheta V_x} & \frac{\vartheta f_0}{\vartheta z} \\ . & . & . \\ . & . & . \\ \frac{\vartheta f_n}{\vartheta x_0} & \frac{\vartheta f_n}{\vartheta V_x} & \frac{\vartheta f_n}{\vartheta z} \end{bmatrix} \tag{15.7}$$

Assuming typical aircraft velocities and FL and taking into account the antenna fan beam and rotation rate, it is determined that the observation time is approximately 1 min and the number of measurements is approximately 20. The standard deviation (SD) of the height estimation errors is σ_z = 10 m when the SD of the measurement errors of range and depression angle are σ_R = 10 m and σ_β = 0.08°, respectively.

The system has been developed and operates at the Electronic Navigation Institute of Tokyo, Japan. To estimate and anticipate for systematic errors in the depression angle and range measurements, it has been proposed to perform 40 experimental flights above the radar range. The basic assumption of the NAMS system (i.e., that the aircraft flies at constant height) cannot be validated by the NAMS itself. Thus, an SSR is required to confirm that the flight is indeed performed at the same level via the mode C interrogations [4].

15.4.2 Height Estimation with Single Air Traffic Control Radar

Nagaoka at the Electronic Navigation Institute of Tokyo investigated the possibility to derive height estimation with a very simple and inexpensive method [5]. The idea is to use single radar normally used for ATC. The radar antenna rotates around a horizontal axis once every 4 s and measures range R and bearing β, as shown in Figure 15.2.

Let (x, y, z) be the 3-D position of the aircraft. The bearing angle is defined as

$$\beta = \cos^{-1}\left(\frac{y}{\sqrt{x^2 + y^2}}\right) \tag{15.8}$$

Thus, the relation between the measurements and the unknown quantities is

$$R = \left(z^2 + x^2 + y^2\right)^{1/2} = \left(z^2 + \frac{y^2}{\cos^2\beta}\right)^{1/2} \tag{15.9}$$

The measurement principle is similar to that of NMAS, that is, that during the time the aircraft passes through the data acquisition area, the range varies as a function of both the horizontal position and the height. When straight and level flight is assumed, the unknown quantities are the height z, the y-axis initial position y_0, and the velocity V_y. The expression relating the measurements R_i and β_i and the unknown quantities vector $\mathbf{q} = [y_0, V_y, z]^{\mathrm{T}}$ at time t_i is

$$R_i = \left(z^2 + \frac{\left[y_0 + V_y\left(t_i - t_0\right)\right]^2}{\cos^2\beta_i}\right) = f\left(t_i, \beta, \mathbf{q}\right) = f_i(\mathbf{q}) \tag{15.10}$$

The measurements are collected as the aircraft flies close to the radar at a distance of 30 km. Approximately, the data acquisition area is 15 km, the observation time is 1 min, and the total number of scans is 15. The total set of measurements is expressed as a nonlinear matrix function in the form of Equation 15.5; that is, $\mathbf{R} = \mathbf{f}(\mathbf{q})$, where $\mathbf{R}$ denotes the measurement vector. The unknown vector is estimated using a nonlinear least squares method like that of the NAMS system expressed by Equation 15.6.

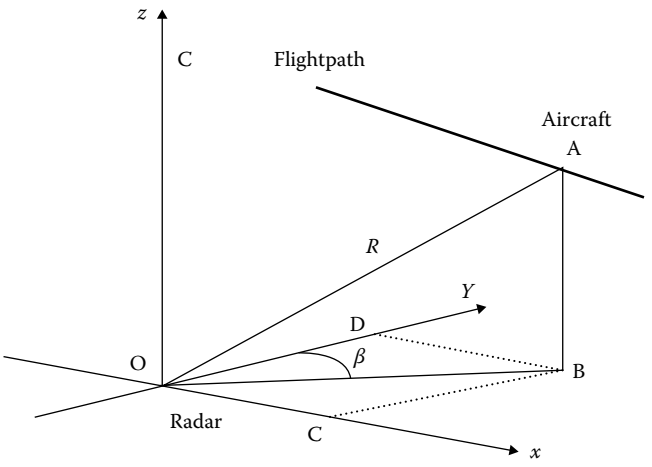

FIGURE 15.2 Geometric configuration of the height measurement system with a single ATC radar. OC = x, OD = y, AB = z, and $\beta = \widehat{\mathrm{BOD}}$.

The system performance is evaluated with Monte Carlo simulations. The best accuracy achieved is σ_z = 100 m under the assumption that the SD errors of range and bearing measurements are σ_R = 100 m and σ_β = 0.06°. The method can use either primary or secondary radar. However, in the latter case, the method has to include systematic delays by the transponder.

15.4.3 Height Estimation with One SSR and One Omniradar

Manolakis et al. investigated the possibility to estimate the aircraft flight height with a system that consists of one standard SSR plus a secondary radar equipped with an omnidirectional antenna located far away from the SSR; hence, this system could be referred to as one SSR and one omnidirectional radar (SSROR) [6]. Figure 15.3 shows a typical geometric configuration of the system. The SSR measures bearing θ and slant range R_s, which is transformed to horizontal range R with correcting lookup tables. The omniradar measures range R_a. Let (x, y, z), (x_a, y_a, z_a), and (0, 0, 0) be the coordinates of aircraft, omniradar, and SSR, respectively. Then, from Figure 15.3, it follows that the theoretical height function is

$$z = f(R_a, x, y) = z_a + [R_a^2 - (x - x_a)^2 - (y - y_a)^2]^{1/2} \tag{15.11}$$

$$x = R\sin\theta \tag{15.12}$$

$$y = R\cos\theta \tag{15.13}$$

However, the height measurement obtained through the preceding formula will be biased because of the transponder delay systematic deviation from its nominal value that affects the range measurements. Since this bias cannot be removed by calibration, a suitable algorithm has to be applied to anticipate for it. The approach proposed is to augment the unknown vector by incorporating the bias term. Let b denote the bias in range measurements. The biased measurements R_b and R_{ab} of R and R_a, respectively, are expressed as

$$R_b = R + b\cos\phi \tag{15.14}$$

$$R_{ab} = R_a + b \tag{15.15}$$

where ϕ is the elevation angle. Let s denote the squared height:

$$s = (z - z_a)^2 \tag{15.16}$$

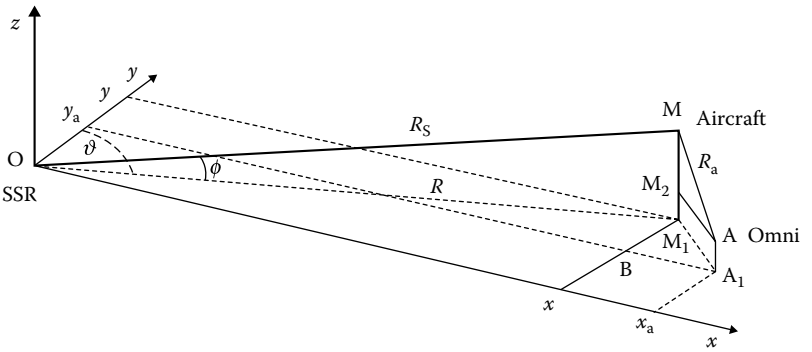

FIGURE 15.3 Geometry of the height estimation system with SSROR. The distance x_a of the radars typically ranges from 80 km up to 160 km. $M_1M = z$.

and s_b denote the corresponding quantity derived from (biased) range measurements. Then, after some manipulations of the preceding equations, the following relation is obtained:

$$s_b = s + ba \tag{15.17}$$

$$a = 2[R_a - \cos\phi(R - x_a \sin\theta - y_a \cos\theta)] \tag{15.18}$$

The term a is the bias multiplying factor determined by the relative geometry of the system. Equation 15.17 is a linear relation between measurement s_b and the unknown quantities s and b. The effect of the bias varies as the aircraft passes through the surveillance area. Its form is mainly determined by the flight height. Consequently, it is possible to estimate both the height and the bias by collecting data during the period the aircraft remains in the surveillance area. The measurement equation at time t_i is

$$s_{bi} = s_i + ba_i + e_i \tag{15.19}$$

where e_i represents the effect of the random measurement errors; hence, it could be referred to as the equation error. Assuming level flight, $s_i = s$, and the set of collected data is expressed with the following linear matrix equation:

$$\mathbf{s_b} = \mathbf{Aq} + \mathbf{e} \tag{15.20}$$

$$\mathbf{s_b} = \begin{bmatrix} s_{b0} \\ s_{b1} \\ . \\ s_{bn} \end{bmatrix} \quad \mathbf{A} = \begin{bmatrix} 1 & a_0 \\ 1 & a_1 \\ . & . \\ 1 & a_n \end{bmatrix} \quad \mathbf{e} = \begin{bmatrix} e_0 \\ e_1 \\ . \\ e_n \end{bmatrix} \quad \mathbf{q} = \begin{bmatrix} s \\ b \end{bmatrix}$$

The best estimate $\hat{\mathbf{q}}$ of $\mathbf{q}$, minimizing the weighted sum of the squared errors $\mathbf{e}^T\mathbf{We}$, is

$$\hat{\mathbf{q}} = (\mathbf{A}^T\mathbf{WA})^{-1}\mathbf{A}^T\mathbf{Ws_b} \tag{15.21}$$

where $\mathbf{W}$ is the weighting matrix defined as the inverse of the equation error covariance matrix:

$$\mathbf{W}^{-1} = \mathrm{E}\left\{\mathbf{ee}^T\right\} \tag{15.22}$$

The notation $E\{\}$ stands for the expected value operation. Thus, the estimate of the geometric height is

$$\hat{z} = \sqrt{\hat{q}_1} = \sqrt{\hat{s}} \tag{15.23}$$

In the case of nonlevel flights, an augmented unknown vector should be used that comprises bias b, initial height Z_0, and vertical velocity V_z. In this case, however, the measurement equation is nonlinear in terms of the unknown quantities; hence, a nonlinear least squares iterative algorithm must be employed.

The system performance is a function of (1) the range and bearing measurement SD errors, σ_R and σ_θ, respectively; (2) the aircraft velocity, which affects the number of scans; (3) the omniradar scan rate; and (4) geometric terms such as the FL and the distance between the radars. By assuming that $\sigma_R = 70$ m and $\sigma_\theta = 0.08°$, the SD of the height estimation error will be between 50 and 100 m when the values of the other factors lie in reasonable ranges.

15.4.4 Dual-Synchronized Autonomous Monitoring System

The research for this system has been conducted in the National Aerospace Laboratory NLR, the Netherlands [7]. The system is composed of two primary marine radars. Each of the radars has a rotating antenna. The antennas scan, with different directions, the same volume—that is an area 3 km × 10 km above the location site. The primary surveillance area is 3 km × 3 km. The two antennas (A and B) are separated by 2.5 m, mechanically synchronized, and scan once every 2.5 s. Their data extractors produce measurements of slant ranges and elevation angles, (R_A, ϕ_A) and (R_B, ϕ_B), respectively, for each radar. The tracking software derives estimation of the aircraft position and trajectory in off-line mode. At each scan, a combination of four measurements $(R_A, \phi_A, R_B, \phi_B)$ is available to be used in the estimation of the unknown vector $\mathbf{q} = [x_0, y_0, z_0, V_x, V_y, V_z]^T$. A local Cartesian frame is used to perform the calculations. Finally, 16 equations are available to be solved for the 6 unknowns with a weighted least squares method. The weight of each measurement is the measured amplitude of the radar pulse. The maths of the tracker is not presented in [7]. However, one approach could be the following. If a coordinate system is defined such that radar A is at the origin (0, 0, 0) and radar B is at $(x_B, 0, 0)$, then the measurements obtained at scan time t_i can be expressed as

$$R_{Ai} = \sqrt{x_i^2 + y_i^2 + z_i^2} = \sqrt{[x_0 + V_x(t_i - t_0)]^2 + [y_0 + V_y(t_i - t_0)]^2 + [z_0 + V_z(t_i - t_0)]^2} \tag{15.24a}$$

$$\phi_{Ai} = \tan^{-1}\left[\frac{z_i}{\sqrt{x_i^2 + y_i^2}}\right] = \tan^{-1}\left[\frac{z_0 + V_z(t - t_i)}{\sqrt{[x_0 + V_x(t - t_i)]^2 + [y_0 + V_y(t - t_i)]^2}}\right] \tag{15.24b}$$

$$\begin{aligned} R_{Bi} &= \sqrt{(x_i - x_B)^2 + y_i^2 + z_i^2} \\ &= \sqrt{[x_0 + V_x(t_i - t_0) - x_B]^2 + [y_0 + V_y(t_i - t_0)]^2 + [z_0 + V_z(t_i - t_0)]^2} \end{aligned} \tag{15.24c}$$

$$\phi_{Bi} = \tan^{-1}\left[\frac{z_i}{\sqrt{(x_i - x_B)^2 + y_i^2}}\right] = \tan^{-1}\left[\frac{z_0 + V_z(t - t_i)}{\sqrt{[x_0 + V_x(t - t_i)]^2 + [y_0 + V_y(t - t_i)]^2}}\right] \tag{15.24d}$$

Notice that x_B has a small value (2.5 m) compared to the magnitude of the other quantities; consequently, it can be neglected. The preceding set of equations at four different times yields 16 equations that can be solved with a nonlinear least squares method such as the Gauss–Newton iterative method presented in Equation 14.6.

The SD of the height estimation error will be less than 15 m in the primary surveillance area and 30 m at the edges of the area when the SD of range and elevation angle measurements are smaller than 10 m and 0.1°, respectively.

15.4.5 Height Measurement by Quadrilateration

Rice proposed a system consisting of four synchronized receiving SSR stations S_i, $i = 0, 1, 2, 3$, that use SSR transmissions from the aircraft transponder and estimate the height by quadrilateration [8]. Figure 15.4 shows a typical configuration of systems composed of N SSRs. One of them is an active station, which means that this station has both an interrogator and a receiver. Let (x, y, z) and (x_i, y_i, z_i) denote the Cartesian coordinates of aircraft and station S_i, respectively. Also let R_i denote the range from station S_i to aircraft, c denote the velocity of the light, and T_s denote the time of signal transmission

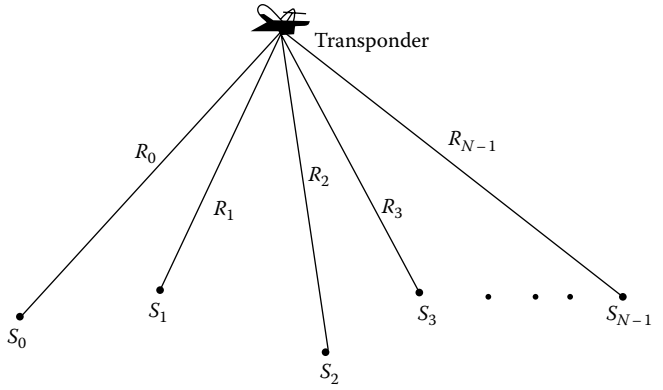

FIGURE 15.4 Typical configuration of the height estimation systems that are based on N SSR stations. One of the stations is active, that is, it both transmits the interrogations and receives the replies, whereas the other stations are receivers only.

from aircraft transponder. The stations measure the time of arrival (TOA) T_i, $i = 0, 1, 2, 3$, of the aircraft transponder signal at each site. The following relations hold:

$$T_i = T_s + \frac{R_i}{c} \quad i = 0, 1, 2, 3 \tag{15.25}$$

$$R_i^2 = (x - x_i)^2 + (y - y_i)^2 + (z - z_i)^2 \quad i = 0, 1, 2, 3 \tag{15.26}$$

The preceding system of eight equations can be solved for the unknown quantities. The unknown quantities used by Rice are $(R_0, R_1, R_2, R_3, x, y, z, T_s)^T$. However, an equivalent approach is to substitute for R_i in Equation 15.25, which becomes

$$T_i = T_s + \frac{1}{c}\sqrt{(x - x_i)^2 + (y - y_i)^2 + (z - z_i)^2} = f_i(\mathbf{q}) \quad i = 0, 1, 2, 3 \tag{15.27}$$

where $\mathbf{q} = [x, y, z, T_s]^T$ is the unknown vector. Thus, there are four nonlinear equations to be solved for $\mathbf{q}$. One suitable method, for example, is the Newton–Raphson method, which iteratively approximates the solution via the following formula:

$$\mathbf{q_{k+1}} = \mathbf{q_k} + \mathbf{F}(\mathbf{q_k})^{-1}[\mathbf{T} - \mathbf{f}(\mathbf{q_k})] \tag{15.28}$$

where $\mathbf{T} = [T_0, T_1, T_2, T_3]^T$ is the measurement vector and $\mathbf{F}$ is the Jacobian matrix:

$$\mathbf{F} = \frac{\vartheta f}{\vartheta q} = \begin{bmatrix} \frac{\vartheta f_0}{\vartheta x} & \frac{\vartheta f_0}{\vartheta y} & \frac{\vartheta f_0}{\vartheta z} & \frac{\vartheta f_0}{\vartheta T_s} \\ . & . & . & . \\ \frac{\vartheta f_3}{\vartheta x} & \frac{\vartheta f_3}{\vartheta y} & \frac{\vartheta f_3}{\vartheta z} & \frac{\vartheta f_3}{\vartheta T_s} \end{bmatrix} \tag{15.29}$$

Notice that the time of interrogation transmission, as well as the transponder nominal delay time, is not involved in the measurements. The measured quantities are only the TOAs at the station sites. Thus, the height estimate is not affected by any transponder bias.

The theoretical and experimental research has been conducted at the GEC-Marconi Research Center, U.K. The optimum station arrangement is to locate the three of them equispaced on a circle and the

fourth in the middle. The typical circle radius is 35 km. The same magnitude holds for the measurement range. The method may be implemented in on-line or off-line mode. In the first case, there must be transmitters at the stations to transmit their measurements of TOA to the height monitoring center. The vertical dilution of precision (VDOP) is a performance index defined by the ratio:

$$\text{VDOP} = \frac{\sigma_z}{c\sigma_{\text{rte}}} \tag{15.30}$$

where σ_{rte} is the SD of the relative timing errors. The VDOP expresses the effect of the relative geometry to system performance. The VDOP of this system achieves a typical value of 3.

15.4.6 Height Estimation with SSRs and Pseudoranges

This approach has been investigated by Nagaoka at Electronic Navigation Institute of Tokyo [9]. The system consists of N SSR receiving stations like the previous system; see again Figure 15.5. Again one of them, say S_0, must be active to transmit interrogations to aircraft. The time of interrogation transmission, T_t, and the time of signal arrivals at the receiving stations T_i, $i = 0, 1, \ldots, N-1$, are measured. Thus, N pseudorange measurements r_i are obtained where $r_i = c(T_i - T_t)$. Let T_D denote the transponder delay and D denote the distance corresponding to this delay, $D = cT_D$. Then, for each pseudorange measurement r_i, the following relation holds:

$$\begin{aligned} r_i &= D + R_i + R_0 + = D + \sqrt{(x-x_i)^2 + (y-y_i)^2 + (z-z_i)^2} + \sqrt{(x-x_0)^2 + (y-y_0)^2 + (z-z_0)^2} \\ &= f_i(\mathbf{q}) \quad i = 0, 1, ..., N-1 \end{aligned} \tag{15.31}$$

where $\mathbf{q} = [x, y, z, D]^T$ is the unknown vector. The set of N measurements $\boldsymbol{\rho} = [\rho_0, \rho_1, \ldots, \rho_{N-1}]^T$, $N \geq 4$, and the unknown vector are related through Equation 15.30:

$$\mathbf{r} = \mathbf{f}(\mathbf{q}) \tag{15.32}$$

The unknown vector $\mathbf{q}$ can be obtained from the solution of Equation 15.32 with a nonlinear weighted least squares method. Thus, the best estimate of $\mathbf{q}$ is iteratively calculated as

$$\hat{\mathbf{q}}_{\mathbf{k}+1} = \hat{\mathbf{q}}_{\mathbf{k}} + (\mathbf{F}^{\mathbf{T}}\mathbf{F})^{-1}\mathbf{F}^{\mathbf{T}}[\mathbf{r} - \mathbf{f}(\hat{\mathbf{q}}_{\mathbf{k}})] \tag{15.33}$$

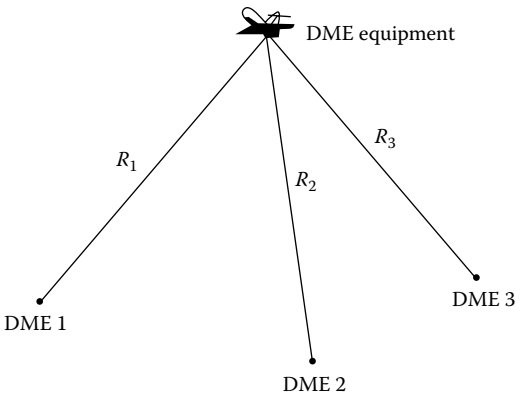

FIGURE 15.5 Configuration of the onboard height estimation system that utilizes the distance measurements derived from the DME.

where **F** is the Jacobian matrix

$$\mathbf{F} = \frac{\vartheta \mathbf{f}}{\vartheta \mathbf{q}} = \begin{bmatrix} \frac{\vartheta f_0}{\vartheta x} & \frac{\vartheta f_0}{\vartheta y} & \frac{\vartheta f_0}{\vartheta z} & \frac{\vartheta f_0}{\vartheta D} \\ . & . & . & . \\ \frac{\vartheta f_{N-1}}{\vartheta x} & \frac{\vartheta f_{N-1}}{\vartheta y} & \frac{\vartheta f_{N-1}}{\vartheta z} & \frac{\vartheta f_{N-1}}{\vartheta D} \end{bmatrix} \tag{15.34}$$

The estimate of **q** is free of the transponder delay systematic error because the estimation is based not on the nominal delay, but on the actual delay time, which is one of the parameters to be estimated, whereas the rest of the parameters are the aircraft 3-D position coordinates x, y, z.

The station arrangement proposed by Nagaoka, when there are four stations, is an equilateral triangle formed by the three stations, whereas the fourth station is located in the center. The VDOP, defined as the ratio σ_z/σ_R (where σ_R is the observation error) has a typical value of 4 when the aircraft is above the center at a height equal to the baseline radius. The VDOP increases as the aircraft flies higher and longer and as the baseline radius becomes smaller.

15.4.7 Height Measurement with SSRs and Range Differences (RDHMU)

This approach has been proposed in [10,11]. The system consists of $N-1$ receiving SSR stations S_i, $i = 1, N-1$, and one station, say S_0, which is both receiver and interrogator, like that in Figure 15.4. The stations receive the reply and the time difference of arrival (TDOA) between a reference station, say S_0, and station S_i is measured. A set of $N-1$ TDOA or, equivalently, RD measurements, is collected at each time the transponder sends a reply signal. The height estimation derived from this set of measurements is not affected by any transponder delay systematic error since this error is inherently subtracted from the measurements used. This system could be referred to as RD height monitoring unit (RDHMU). The systems that derive the position fix based on this kind of measurement are known as TDOA or hyperbolic systems.

Let τ_i denote the TDOA between stations S_i and S_0, and d_i denote the corresponding RD measurement, $d_i = c\tau_i$. The following relation holds:

$$\begin{aligned} d_i &= R_i - R_0 = \sqrt{(x-x_i)^2 + (y-y_i)^2 + (z-z_i)^2} - \sqrt{(x-x_0)^2 + (y-y_0)^2 + (z-z_0)^2} \\ &= f_i(\mathbf{q}) \quad i = 1, 2, ..., N-1 \end{aligned} \tag{15.35}$$

where $\mathbf{q} = [x, y, z]^T$ is the unknown aircraft position vector. The vector of RD measurements $\mathbf{d} = [d_1, d_2, \ldots, d_m)$ is expressed as

$$\mathbf{d} = \mathbf{f}(\mathbf{q}) \tag{15.36}$$

A commonly employed method to solve for **q** in this nonlinear equation is the Taylor series method or equivalently the Gauss–Newton iterative method. The best estimate of **q** is iteratively approximated as

$$\hat{\mathbf{q}}_{\mathbf{k+1}} = \hat{\mathbf{q}}_{\mathbf{k}} + (\mathbf{F}^T\mathbf{F})^{-1}\mathbf{F}^T[\mathbf{d} - \mathbf{f}(\hat{\mathbf{q}}_{\mathbf{k}})] \tag{15.37}$$

where **F** is the Jacobian matrix:

$$\mathbf{F} = \frac{\vartheta \mathbf{f}}{\vartheta \mathbf{q}} = \begin{bmatrix} \frac{\vartheta f_1}{\vartheta x} & \frac{\vartheta f_1}{\vartheta y} & \frac{\vartheta f_1}{\vartheta z} \\ \frac{\vartheta f_{N-1}}{\vartheta x} & \frac{\vartheta f_{N-1}}{\vartheta y} & \frac{\vartheta f_{N-1}}{\vartheta z} \end{bmatrix} \tag{15.38}$$

In the case of four stations, the best arrangement is an equilateral triangle with the fourth station in the center. The SD of height estimation error σ_z will be 15 m when the baseline radius is 6 km, the flying height is 9 km, and σ_{TDOA} is 10 ns.

Work on proof of principles and system development of an HMU based on the concept of TDOA measurement of SSR signals has been conducted by Roke Manor Research Ltd., U.K. [12].

15.5 Onboard–Derived Height Estimation

15.5.1 Height Measurement with Distance Measuring Equipment

With this approach, the geometric height is derived onboard the aircraft using DME [13,14]. Using the DME interrogation equipment, the distance from three DME ground stations is measured onboard (see Figure 15.5). The three stations are located under an airway. The height is then computed from the range measurement vector $\mathbf{R} = [R_1, R_2, R_3]^{\text{T}}$ by trilateration. An exact and efficient solution of the nonlinear measurement equation was derived in [14]. Specifically, the height is computed from the closed form:

$$z = g(\mathbf{R}) = \frac{-b(\mathbf{R}) + \sqrt{d(\mathbf{R})}}{2a} \tag{15.39}$$

where $b(\mathbf{R})$ and $d(\mathbf{R})$ are the following simple polynomial-type functions:

$$b(\mathbf{R}) = b_0 + b_1 R_1^2 + b_2 R_2^2 + b_3 R_3^2 \tag{15.40}$$

$$d(\mathbf{R}) = d_{00} + d_{01}R_1^2 + d_{02}R_2^2 + d_{03}R_3^2 + d_{11}R_1^4 + d_{22}R_2^4 + d_{33}R_3^4 + d_{12}R_1^2R_2^2 + d_{13}R_1^2R_3^2 + d_{23}R_2^2R_3^2 \tag{15.41}$$

The coefficients a, b_i, d_{ij} are analytically defined in the appendix of [15]. An important aspect of these coefficients is that they are completely defined by the ground stations' coordinates (x_i, y_i, z_i), which are fixed. Thus, the coefficients are calculated only once at the moment the aircraft enters the data acquisition area. Then, every time a new set of range measurements is available, the height is computed from the aforementioned equations using the range measurements and the stored coefficients. Define the ratio σ_z/σ_R as the VDOP of this technique, where σ_R is the SD of the ranging error. The VDOP is 1 in the case where the stations form an equilateral triangle inscribed in a circle with 10 km radius and the aircraft is above the triangle center at a height of 8 km.

15.5.2 Estimation of Vertical Position with the Global Positioning System

The height could be also determined with GPS receivers with four or more satellites. However, the vertical position determined using GPS alone is not precise. Thus, an augmentation method is required such as differential GPS. The VDOP, defined as $\sigma_z/\sigma_{\text{D}}$, depends on the geometry that varies continuously, even in the case of a fixed receiver, because the satellites are not geostationary but move in such orbits as to complete a rotation in 12 h. The precision is very bad when all the available satellites happen to be close to the horizon. The world mean value of VDOP is about 2 [15]. However typical VDOP values range from 1.5 to 7, depending on the area of the receiver and on the time of day. The details for position determination with satellite systems such as GPS, GLONASS, and Galileo are presented in a subsequent specific section of this chapter.

15.6 Special Topics

The performance analysis of the various parameter estimation systems is usually restricted to the variance analysis, and the estimation error is usually assumed to have zero mean value. However, it is proven that in all of the aforementioned systems, the estimation error does not have zero mean value due to the nonlinearity of the measurement equation. Another important aspect is that there are cases where it is not possible to obtain a solution due to the relative geometry of aircraft vs. stations that leads to large errors. In these cases, the successive iterations applied to solve the system of nonlinear equations may not converge. Also, even after convergence, the solutions need not necessarily be "the best" or the "correct ones."

15.6.1 Inherent Bias

The nonlinearity of the systems, joined with the measurement random errors, causes inherently biased estimations although the measured quantities are unbiased. For example, take the case of height estimation with DME measurements. The function $g(\mathbf{R})$ in Equation 15.39 determines that the height z is nonlinear. In addition, range measurements will be contaminated by additive zero mean value random errors. Let $\mathbf{R}_m$ denote the noisy measurement vector and z_m denote the height measurement derived from $g(\mathbf{R}_m)$, that is, from the measurement function when it is fed with noisy measurements. Extending $g(\mathbf{R}_m)$ in a Taylor series around the actual values of ranges R_1, R_2, R_3 up to second-order terms and taking the expected values, it is derived that the expected value of z_m will not be the actual value z, but it will differ by an amount b_z, which is called inherent bias. Specifically, for the DME case, the inherent bias is evaluated as

$$b_z = E[z_m] - z = \frac{1}{2}\left[\frac{\partial^2 g}{\partial R_1^2}\sigma_{R_1}^2 + \frac{\partial^2 g}{\partial R_2^2}\sigma_{R_2}^2 + \frac{\partial^2 g}{\partial R_3^2}\sigma_{R_3}^2\right] \tag{15.42}$$

Figure 15.6 shows the inherent bias generated in the case of the DME system. The inherent bias becomes larger as the magnitude of the measurement errors and the system nonlinearity becomes stronger. This bias error is inherently generated in all position estimation algorithms and must be taken into account when precise position estimation is required.

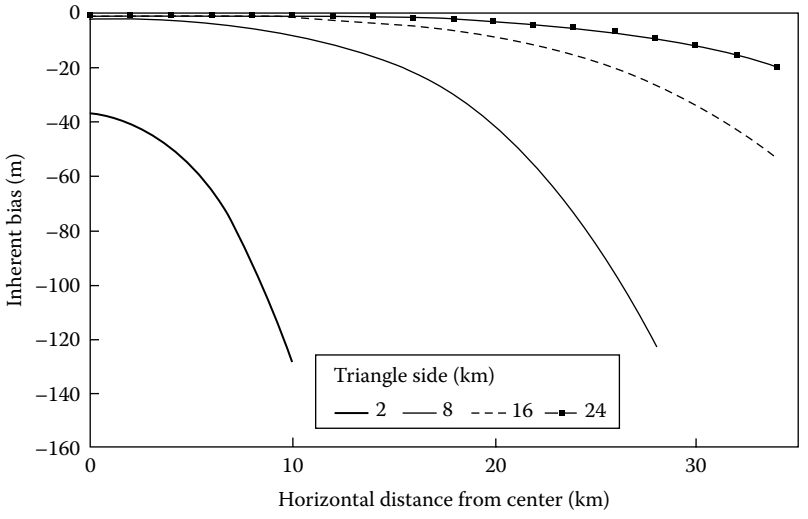

FIGURE 15.6 Bias inherently generated by the height estimation algorithm of the system based on DME measurements. The stations' sites form an equilateral triangle. The inherent bias is shown as function of the horizontal distance from the center for various magnitudes of the triangle side. The flight height is $z = 9$ km, and the SD of the distance measurement error is $s_R = 90$ m.

15.6.2 Existence and Uniqueness of Position Fix

In some systems, there are singular cases for which it is not possible to achieve a position fix. This fact has been reported by Abel and Chafee for the GPS system in [16], where it is shown that for some satellites/aircraft relative geometries, it is not possible to solve the relevant equation or there is more than one solution. Also, for the RDHMU, it has been shown that there are some station arrangements for which it is not possible to derive height estimation when the aircraft is at specific areas [11]. For example, in the case of four stations, when the quadrilateral defined by the stations is inscribed in a circle, it is not possible to estimate the height when the aircraft is above the center. Also, when the quadrilateral is a rectangle or symmetric trapezoid, it is not possible to derive a position fix when the aircraft is above the line that passes from the middle of the parallel sides. From a mathematical point of view, this singularity is expressed by the singularity of the Jacobian matrix; consequently, this matrix cannot be inverted as is required by the relevant position estimation algorithm. The algorithm in this case diverges from the actual height and finally collapses. Notice that height estimation is achieved everywhere except at this singular point. However, when the aircraft is close to the singular region, although a position fix is achieved, it is not actually reliable since it is affected by large errors; for example, the VDOP could be larger than 600 in regions close to the singular region.

Table 15.1 presents the institutes and companies that either investigate and develop prototype height monitoring units or provide relevant systems in the market.

TABLE 15.1 Height Monitoring Systems and Companies/Institutes that Develop and Provide Them

System	Company/Institute	
NAMS	Electronic Navigation Research Institute Ministry of Transport, 6-38-1 Shinkawa, Mitaka, Tokyo, 181, Japan. Tel: +81 422 413171, Fax: 81-422-413176	
DAMS height monitoring unit	National Aerospace Laboratory NLR Anthony Fokkerweg 2, 1059 CM Amsterdam, the Netherlands. Tel: +31 (0)20 511 3113, Fax: +31 (0)20 511 3210	
SSR and quadrilateration technique	GEC-Marconi Electronics Ltd. Marconi Research Laboratories, West Hanningfield Road, Great Baddow, Chelmsford Essex, England	
SSR and TDOA technique (RDHMU)	Roke Manor Research Ltd. Roke Manor, Romsey, Hampshire S051 OZN, U.K. Tel: +44(0)794 833000, Fax: +44(0)794 833433	
GPS providers	Trimble Navigation 585 North Mary Avenue, Sunnyvale, CA 94086. Tel: (408) 730-2900	Trimble Navigation Europe Ltd. 79-81 High Str., West Mailing, Kent ME19 6NA, U.K. Tel: +44(0)732 849242, Fax: +44(0)732 847437
	Rockwell International Digital Communication Division, 4311 Jamboree Road, Newport Beach, CA 92660-3095. Tel: (714) 221-4600, Fax: (714) 221-6375	Rockwell Semiconductor System Berkshire Court, Western Road, Bracknell, Berkshire RG12 IRE, England. Tel: +44(0)1344 48644, Fax: +44(0)1344 48655

References

1. ICAO doc 9574, *Manual on Implementation of a 300 m (1000 ft) Vertical Separation Minimum between FL 290 and FL 410 Inclusive*, 2nd edn., 2002, ICAO, Montreal, retrieved from http://www.skybrary.aero/bookshelf/books/1311.pdf (accessed on March 14, 2013).
2. FAA, Reduced vertical separation minimum (RVSM), http://www.faa.gov/about/office_org/headquarters_offices/ato/service_units/enroute/rvsm/ (accessed on March 14, 2013).
3. S. Nagaoka, E. Yoshioka, and P. T. Muto, A simple radar for navigation accuracy measurements, *J. Navigation*, 34(3), 462–469, 1981.
4. S. Nagaoka, Possibility of detecting a non-level-flight aircraft by the navigation accuracy measurement system (NAMS), *ICAO, Review of the General Concept of Separation Panel, 7th Meeting*, Montreal, Canada, RGCSP-WP/180, October 30, 1990.
5. S. Nagaoka, Height estimation of a cruising aircraft via a radar for air traffic control, *Electronics and Communications in Japan, Part 1 (Communications), USA*, 71(11), 95–105, 1988.
6. D. E. Manolakis, C. C. Lefas, G. S. Stavrakakis, and C. M. Rekkas, Computation of aircraft geometric height under radar surveillance, *IEEE Transactions on Aerospace and Electronic Systems*, 28(1), 241–248, 1992.
7. J. Brugman, J. Verpoorte, and A. I. L. Willekens, DAMS height monitoring unit-phase one, Report CR 92328 C, NLR, the Netherlands, 1992.
8. D. E. Rice, Height measurement by quadrilateration, *The Marconi Review*, XLVI(228), 1–17, 1983.
9. S. Nagaoka, Possibility of geometric height measurement by using secondary surveillance radars, *ICAO, Review of the General Concept of Separation Panel, 7th Meeting*, Montreal, RGCSP-WP/181, October 30, 1990.
10. D. E. Manolakis and C. C. Lefas, Aircraft geometric height computation using secondary surveillance radar range differences, *IEEE Proceedings Radar, Sonar and Navigation*, 141(2), 119–124, 1994.
11. D. E. Manolakis and C. C. Lefas, Station arrangement effects on ground referenced height computation by using time differences, *Navigation*, *Journal of the Institute of Navigation*, 42(2), 409–420, 1995.
12. L. G. Hopkins, D. Sherry, and D. C. Rickard, Geometric Height Monitor Unit (HMU) Programme—Final Report on Phase 1, Proof of Principles, Roke Manor Research Ltd., Report No. 72/91/R161IU, Roke Manor, U.K., 1991.
13. D. E. Manolakis, Efficient solution and performance analysis of 3-D position estimation by trilateration, *IEEE Transactions on Aerospace and Electronic Systems*, 32(4), 1239–1248, 1996.
14. D. E. Manolakis and A. I. Dounis, Advances in aircraft height computation using distance measuring equipment, *IEEE Proceedings Radar, Sonar and Navigation*, 143(1), 47–52, 1996.
15. J. L. Leva, Relationship between navigation vertical error, VDOP, and pseudorange error in GPS, *IEEE Transactions on Aerospace and Electronic Systems*, 30(4), 1138–1142, 1994.
16. J. S. Abel and J. W. Chaffee, Existence and uniqueness of GPS solutions, *IEEE Transactions on Aerospace and Electronic Systems*, 27(6), 952–956, 1991.

16

Attitude Measurement

Mark A. Stedham
University of Alabama at Huntsville

Partha P. Banerjee
University of Alabama at Huntsville

Seiji Nishifuji
Yamaguchi University

Shogo Tanaka
Yamaguchi University

In many practical situations, it is important to determine and measure the attitude of a particular vehicle, such as a ship, an airplane, a piece of mechanical equipment such as a crane lifter, or a spacecraft. For this reason, many attitude sensors have been developed with advanced computer and semiconductor technologies. This section first introduces the various attitude sensors with an explanation of their operating principles and then presents several methodologies for attitude measurement and determination, including ships and crane lifters, aircraft, and spacecraft applications.

16.1 Introduction to Attitude Sensors for Ships, Aircraft, and Crane Lifters

There are many types of gyroscopes that, corresponding to the physical measurement mechanisms used, may be classified as two-axis *freedom gyro* and single-axis freedom gyro using precession, *vibratory gyro* using Coriolis' force, and *optic gyro* using Sagnac effect. Among them, the two-axis freedom gyro has the longest history. It consists of a high-speed rotating rotor around a spin axis supported by two orthogonal axes. This type of gyro is generally classified as either a *free gyro*, a *vertical gyro* (VG), or a *directional gyro* (DG).

The single-axis freedom gyro has only one output axis in addition to the spin axis. Depending on the specifications (in which) the gyro is designed, there are two types of gyros, the *rate gyro* and the *rate-integrating gyro*. Related to these rotating-type gyros is another type of gyro known as the *electrostatic gyro*, which makes use of a high-speed rotating sphere in a vacuum cavity. Because of its resistance-free property, the electrostatic gyro has the highest accuracy among existing gyros. There are also rotorless gyros.

TABLE 16.1 Performance of Different Types of Gyros

Type of the Gyro	Degrees of Freedom	Quantities to Be Detected	Accuracy (° h^{-1})
Free gyro	2	Angle	1
VG	2	Declination from horizontal plane	1
DG	2	Shift from reference direction	1
Rate gyro	1	Angular velocity	10
Rate-integrating gyro	1	Angle	0.001–1
Ring laser gyro	1	Angular velocity	0.003
Fiber-optic gyro	1	Angular velocity	0.01
Electrostatic gyro	2	Angle	0.00001–0.01

The first one is a vibratory gyro that uses Coriolis' force as the measurement principle. The second type is an optical one. Among optical gyros, there are two types: the *ring laser gyro* and the *fiber-optic gyro*. Both rely on the Sagnac effect in their measurement mechanisms. The performance of gyros is evaluated by their drift rates, and the performance of various gyros is shown in Table 16.1, for reference, with their primary usages.

Recently, with the development of computer technology, many types of three-axis gyros have been developed that can measure not only the tilt angles but also the angular velocities and the accelerations along the three axes by combining several gyros and accelerometers. Accelerometers are often coupled with gyros to provide flight and ship navigation systems as well as attitude sensors for dynamic objects such as crane lifters. Examples include the *attitude and heading reference system* (AHRS), *inertial navigation system* (INS), *inertial measurement unit* (IMU), and *gyro compass* (GC), as well as the VGs and DGs discussed previously [1].

The principle of a servo-type accelerometer is explained later (see Figure 16.1). As soon as the shift of the beam caused by the acceleration α is detected by the deflection pickup, the current i is generated by the servo amplifier, which produces a torque to keep the beam at the principal axis of the sensor. Since the torque and the current that generates the torque are proportional to α, the acceleration can be measured using the current. The measurement process forms a closed-loop system, so that the sensor is not only robust to disturbances but also achieves high measurement accuracy (see Table 16.2).

Similarly, an inclinometer is another inertial sensor that measures tilt angle to provide attitude information (see Figure 16.2). The principle of servo-type inclinometers is the same as that of the servo-type accelerometer, except that the beam in the accelerometer is replaced by a pendulum suspended from the supporting point in the sensor. When the sensor is placed on the inclined static inclined surface of tilt

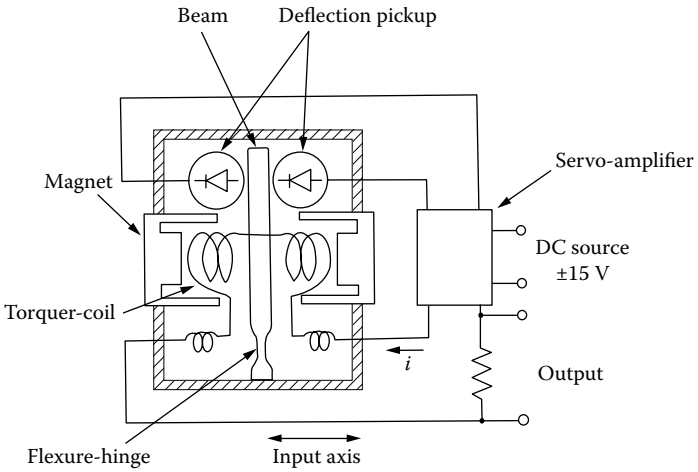

FIGURE 16.1 Servo-type accelerometer.

TABLE 16.2 Specification of a Servo-Type Accelerometer

Measurement range	±5 *g*
Resolution	Less than 5 μ*g* (dc)
Sensitivity	2 V g^{-1}
Output resistance	560 Ω
Torque current	3.5 mA g^{-1}
Case alignment	Less than ±1°
Frequency response	450 Hz (+3 dB)
Temperature range	−25 to +70 °C
Power source	±15 V (DC)
Consumption current	Less than 15 mA
Size	28.4 mm × 24.5 mm
Mass	46 g (including the cable 10 g)

Note: *g*, gravitational acceleration (according to the type TA-25D-05 by TOKIMEC).

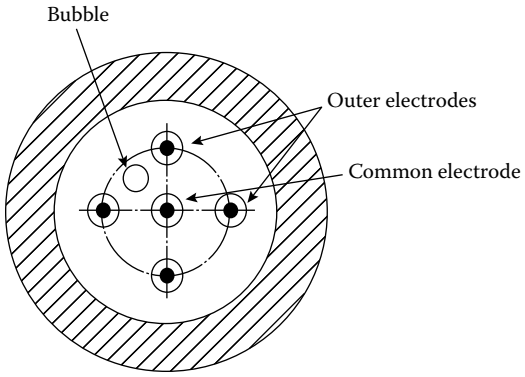

FIGURE 16.2 Dielectric-type inclinometer (front view).

angle β, the pendulum takes the angle β against the principal axis of the sensor, assuming the sensor has no force other than gravity acting on it. The sensor can, however, generate a torque $T_c = mgl\sin\beta \cong mgl\beta$ to keep the pendulum at the principal axis, then the tilt angle β can be accurately measured using the torque (and consequently the current producing the torque), where m and l are the pendulum mass and length of the pendulum to its mass center, respectively. One must note, however, that such a sensor is essentially designed to measure the tilt angles of static inclined surfaces. Thus, when applied to dynamic inclined surfaces, the accelerations will affect the torque, making the sensor unreliable. An intelligent attitude sensing system that overcomes such difficulty will be introduced later. Although application is limited to static inclined surfaces with minute tilt angles, a dielectric-type inclinometer employing electrodes and a bubble kept in an electrolyte can achieve high accuracies on the order of $10^{-4\circ}$.

16.2 Attitude Sensors for Spacecraft Applications

Attitude measurement for spacecraft usually requires two or more sensors for detecting the reference sources needed to satisfy attitude requirements. The choice of which sensors to employ is primarily influenced by the direction the spacecraft is usually pointing as well as the accuracy requirements for attitude determination [2]. Table 16.3 summarizes some performance parameters for these sensors as well as typical manufacturers.

IMUs generally consist of gyroscopes coupled with accelerometers, which together measure both rotational and translational motion. These IMUs may be either gimbal mounted (movement about

TABLE 16.3 Spacecraft Attitude Determination Sensors

Sensor	Accuracy	Mass (kg)	Typical Vendors
IMU	$1–5 \times 10^{-6}\ g$	3–25	Northrop Grumman, Bendix, Kearfott. Honeywell, Hamilton, Standard, Litton, Teledyne
Sun sensor	10^{-2} to 3°	0.5–2	Adcole, TRW, Ball Aerospace
Horizon sensor	10^{-1} to 1°	2–5	Barnes, Ithaco, Lockheed Martin, Lockheed Barnes
Star sensor	10^{-3} to 10^{-2}°	3–7	Ball Aerospace, Bendix, Honeywell, Hughes
Magnetometer	0.5–3°	∼1	Schonstedt, Develco

Source: Adapted from Larson, W. J. and Wertz, J. R., eds., *Space Mission Analysis and Design*, Microcosm, Inc., Torrance, CA, 1992, p. 360.

a gimbal point, independent of the spacecraft) or a strapdown system (rigidly mounted to the spacecraft body), where expansive software is used to convert sensor outputs into reference frame measurements. IMUs tend to suffer gyro drift and other bias errors and, when used for spacecraft attitude measurements, are often used with one or more of the sensors discussed as follows.

Sun sensors detect the visible light from the sun, measuring the angle between the sun's radiation and the detector's photocell. The sun is a commonly chosen attitude reference source since it is by far the visually brightest object in the sky, having a total radiation per unit area of 1353 W m^{-2} at Earth distances [3]. Also, it is generally accepted as a valid point source for most attitude applications, having an angular radius of 0.25° at Earth distances. Increased measurement accuracy can be obtained by determining its centroid. Even though sun sensors are quite accurate (0.01°–3.0°), they do require clear fields of view and sometimes suffer periods of eclipse from both the Earth and the moon [4]. Also, sensitive equipment (such as imaging devices) must be protected from the powerful radiation of direct sunlight. When the sun is available, the angle between it and the sensor's primary axis is referred to as the *sun angle*.

For spacecraft in near-Earth orbits, the Earth is the second brightest object in the sky and covers as much as 40% of the sky. Earth *horizon sensors* detect the interface between the Earth's edge (or limb) and the space background. Horizon sensors can detect either of the Earth's visible limb (albedo sensor), infrared limb, or airglow. The infrared limb is the edge between the warm Earth and the cold space background. The airglow is a region of the atmosphere around the Earth that is visible to the spacecraft when it is on the night side of the Earth. Accuracies for horizon sensors are in the 0.1°–1.0° range. Increased accuracy requires Earth oblate spheroid modeling [4]. Some problems associated with albedo detection include the distortion effects of the Earth's atmosphere, falsely identifying the day/night terminator crossing as the true Earth limb, and the considerable variability of the Earth's albedo in the visible spectrum (varies from land, sea, ice).

Most sensors used to detect the Earth's horizon are scanning sensors with narrow fields of view that measure the time between horizon crossings. In general, two horizon crossings occur per sensor scan period: one crossing when the sensor scans from the space background onto the Earth, followed by a second crossing when the sensor scans from the Earth back to space. The combination of horizon crossing times, scan rate, and spacecraft altitude allows for the computation of the Earth's apparent *angular radius*. The apparent angular radius will be smaller than the real (or physical) angular radius if the spacecraft is tilted away from the Earth nadir vector. The nadir vector is defined as the vector connecting the center of the spacecraft to the center of the Earth. To see this effect, one needs to compute the Earth's physical radius p, which for a given spacecraft altitude h (in kilometers) is given by $\rho = \sin^{-1}[(6371)/(6371 + h)]$.

If the spacecraft horizon sensor is pointing exactly *nadir*, then the apparent angular radius as measured by the sensor will agree with the physical radius given by the aforementioned relation for ρ. However, if the horizon sensor is pointed away from nadir, the horizon crossing times will be smaller than when pointing exactly nadir. This results in an apparent angular radius that is smaller than the physical radius by an amount proportional to the angle between the sensor axis and the nadir vector. This angle is referred to as the *nadir angle*.

Star sensors are used when extreme accuracy requirements are necessary. This high degree of sensor accuracy (0.003°–0.01°) can be attributed mainly to the point source nature and precise fixed location

of stars in space. Star sensors may be categorized as either star trackers or star mappers. A star tracker utilizes a wide field of view in order to search for a given star of specific brightness. A star mapper is similar to a tracker, except that it scans over many stars, recording their relative positions and angular separations. By comparing the recorded data with that from a *star catalog* (database), exact spacecraft orientation can be obtained. The angle between the star line of sight and the sensor's primary axis is referred to as the *star angle*.

The accuracy of star sensors is obtained with higher costs, however. Star sensors are generally heavier and consume more power than other types of attitude sensors. In addition, star sensors are quite sensitive to stray light sources such as sunlight reflected from the spacecraft or the Earth and sunlight scattered from dust particles and jet exhausts [4]. Most rely on optical shielding to reduce the effects of stray light.

Magnetic sensors (called *magnetometers*) measure both the magnitude and direction of the Earth's magnetic field. The difference in orientation between the measured field and the true field translates into attitude determination. Magnetometer accuracies (0.5°–3.0°) are usually less than the other sensor types because of the uncertainty in the Earth's true field, which tends to change or shift over time. In addition, the Earth's magnetic field decreases with increasing altitude and magnetometers are generally limited to altitudes of about 6000 km. For this reason, magnetometers are often used with one of the other sensor types already discussed for improved measurement accuracy [2].

16.3 Automatic On-Line Attitude Measurement for Ships and Crane Lifters

For on-line attitude measurement for ships and crane lifters, the first thing that comes to mind is to use gyros. However, because they often suffer from drifts, accurate attitude measurements might not be achieved using the gyros. Accordingly, one uses on-line attitude measurement systems that do not utilize gyros but servo-type accelerometers and inclinometers. The philosophy of the measurement systems introduced here is to make the best use of the system dynamics of the object and the sensors and to apply Kalman filters or adaptive filters to achieve high measurement accuracy.

16.4 Attitude Measurement for Ships

On-line accurate measurement of a ship's attitude is extremely important in exact search of the seabed patterns with sonars [5,6]. It is also required by high-performance ships like hovercrafts from the viewpoint of suppressing swings by the waves. The measurement of a ship's attitude can usually be reduced to that of the heaving, rolling, and pitching of the ship. For such a measurement, a heave sensor has been used, whose output is given by double integration of the output of an accelerometer vertically directed with a gyroscope. However, since the initial values of heaving displacement and its velocity are unknown, the output will contain a bias that increases with time, and the accuracy of the sensor deteriorates considerably. From this viewpoint, one introduces a strapdown-type on-line measurement system that adequately processes the outputs of the two servo-type inclinometers and one accelerometer mounted on the ship [7].

16.4.1 Location of Sensors and Outputs

The two servo-type inclinometers and one servo-type accelerometer are located on the deck (at the point A) of vertical distance L from O, the intersection of rolling and pitching axes (see Figure 16.3). The two inclinometers are set in such a way that the rolling and the pitching angles are measured respectively. The accelerometer is set upward to the deck to obtain the information on the heaving. Because inclinometers were originally developed for the measurement of the tilt angles of static inclined surfaces, the rigid pendulum inside the sensor is considerably affected by the ship's acceleration other than the gravitational one.

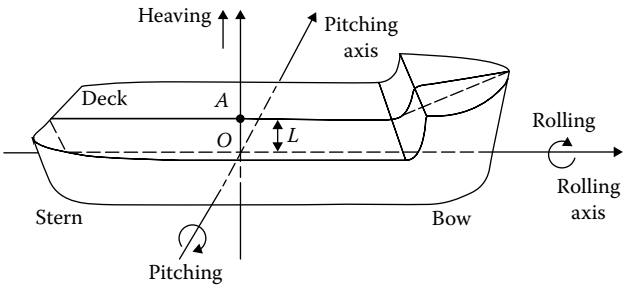

FIGURE 16.3 Location of sensors.

Applying Lagrange's equations of motion [8,9] to rigid pendulums and calculating the torques to keep their deflections from the principal axes almost zero yield the sensor outputs [7]:

$$z_1(t) = \theta(t) - \frac{L}{g}\ddot{\theta}(t) + v_1(t) \tag{16.1}$$

$$z_2(t) = p(t) - \frac{L}{g}\ddot{p}(t) + v_2(t) \tag{16.2}$$

where $z_1(t)$, $z_2(t)$, $\theta(t)$, $p(t)$, and g denote, respectively, the outputs of the two inclinometers, the rolling and the pitching angles, and the gravitational acceleration ($v_1(t)$ and $v_2(t)$: noises of the outputs, including the approximation errors in deriving the outputs).

On the other hand, the accelerometer output is expressed as

$$z_3(t) = (g + \alpha(t))\cos\theta(t)\cos p(t) + v_3(t) \tag{16.3}$$

where $\alpha(t)$ and $v_3(t)$ represent, respectively, the heaving acceleration and the accelerometer noise.

16.4.2 Dynamics of Attitude Signals

It is well known that each of the heaving, rolling, and pitching in inshore seas has two dominant waves in a short interval. That is, a sinusoidal wave of long periodic length (in the range of 6–10 s) and a sinusoidal wave of short periodic length (in the range of 2–3 s) [10–12]. Thus, one models each of the signals in a short interval by a composite wave of the two dominant sinusoidal waves. For the heaving (in a short interval), the displacement is modeled by

$$x(t) = a_1 \sin(\omega_1 t + \phi_1) + a_2 \sin(\omega_2 + \phi_2) \tag{16.4}$$

with the parameters $\{a_i\}$, $\{\phi_i\}$, and $\{\omega_i\}$ unknown. From the 4th-order differential equation satisfied by the $x(t)$, we obtain the linear dynamic equation [7]:

$$\dot{x}(t) = Ax(t), \quad A \equiv \begin{bmatrix} 0 & 1 & 0 & 0 \\ 0 & 0 & 1 & 0 \\ 0 & 0 & 0 & 1 \\ -\omega_1^2\omega_2^2 & 0 & -(\omega_1^2 + \omega_2^2) & 0 \end{bmatrix} \tag{16.5}$$

where $x(t) = (x_1, x_2, x_3, x_4)^{\mathrm{T}}$ ($x_n = d^{n-1}x/dt^{n-1}$ ($n = 1, \ldots, 4$)). On the other hand, the rolling and pitching angles can be modeled by

$$x(t) = a_1 \sin(\omega_1 t + \phi_1) + a_2 \sin(\omega_2 t + \phi_2) + b \tag{16.6}$$

because there are usually some biases associated with them. From the 5th-order differential equation that Equation 16.6 satisfies, we get the similar state variable representation of the model as Equation 16.5. In practice, the heaving, rolling, and pitching signals have many nondominant sinusoidal waves in addition to the dominant ones. Therefore, Equation 16.5 is modified by introducing a white Gaussian noise $w(t)$ with zero mean and adequate variance σ^2 as follows:

$$\dot{x}(t) = Ax(t) + \Gamma w(t) \tag{16.7}$$

where $\Gamma = (0, 1, 0, 0)^{\mathrm{T}}$ for the heaving and $\Gamma = (0, 1, 0, 0, 0)^{\mathrm{T}}$ for the rolling and pitching. The higher the order of the models, the better the measurement accuracy will be. If we consider the on-line measurement of the signals, Equation 16.7 will be sufficient.

16.4.2.1 On-Line Attitude Measurement

The observation Equations 16.1 and 16.2 are expressed using their own state vector $x(t)$. The observation equations in a discretized form are

$$y_k = Hx_k + v_k \tag{16.8}$$

where $H = (1, 0, -L/g, 0, 0)$ and y_k, x_k, and v_k, respectively, denote $y(t)$, $x(t)$, and $v(t)$ of the corresponding signals at the kth sampling instant [7,9]. The discretized form of the dynamic Equation 16.7 is

$$x_{k+1} = Fx_k + w_k \tag{16.9}$$

where

$$F = \Phi(t)\Big|_{t=\Delta T}, \quad \Phi(t) \equiv L^{-1}\{(sI - A)^{-1}\} \tag{16.10}$$

Here, L^{-1} and ΔT, respectively, denote the inverse Laplace transformation and the sampling period. The discretized transition noise w_k becomes a white Gaussian noise with zero mean and covariance:

$$w = \sigma^2 \int_0^{\Delta T} \Phi(\Delta T - \tau)\Gamma\Gamma^{\mathrm{T}}\Phi^{\mathrm{T}}(\Delta T - \tau)d\tau \tag{16.11}$$

The measurement of the rolling and pitching can thus be reduced to the state estimation of the linear discrete dynamic systems (Equations 16.8 and 16.9), if the angular frequencies ω_1 and ω_2 are given and v_k is assumed to have a white Gaussian property. The state estimation is achieved by a Kalman filter [7,13]. However, difficulties in implementing the filter are that the exact values of the two angular frequencies are a priori unknown and also time variant. To overcome the difficulty, adequate candidates $\{(\omega_1^i, \omega_2^i); 1 \le i \le M\}$ for the parameters $\{\omega_1\omega_2\}$ are set and a bank of Kalman filters is used. Then, the final estimate is obtained as the conditional expectation of the state estimate as follows:

$$\hat{x}_{k/k}^0 = \sum_{i=1}^{M} p_k^i \hat{x}_{k/k}^i \tag{16.12}$$

where $\hat{X}_{k/k}^i$ represents the state estimate $\hat{X}_{k/k}$ for the ith candidate $\Omega_i = (\omega_1^i, \omega_2^i)$ and p_k^i denotes the conditional posteriori probability of the ith candidate calculated based on the Bayesian theorem:

$$p_k^i = \frac{p(y_k/\Omega_i, Y^{k-1})p_{k-1}^i}{\sum_{j=1}^{M} p_{k-1}^j p(y_k/\Omega_j), Y^{k-1}} \tag{16.13}$$

Here, $p(y_k/\Omega_i Y^{k-1})$ represents the conditional Gaussian probability density function of y_k under Ω_i and $y^{k-1} = \{y_j; j \le k-1\}$, whose mean and variance are calculated recursively [7].

The proposed measurement system can adaptively and automatically select the most appropriate candidate versus time. It thus enables an accurate on-line measurement of the rolling and pitching whose dominant angular frequencies vary with time. The first, second, and third components of the final estimate $\hat{X}^0_{k/k}$ represent the estimates of the displacement, velocity, and acceleration, respectively. The proposed system thus has an advantage in that it can measure not only the displacements but also the velocities and the accelerations of the three signals. In order to improve the measurement accuracy of the rolling and pitching, one should place the inclinometers near the intersection O of the rolling and the pitching axes.

Finally, the dynamics of the heaving is given by Equation 16.7 similar to that of the rolling and pitching. Substituting the estimates $\hat{\theta}(t)$ and $\hat{p}(t)$ obtained earlier into Equation 16.3 and subtracting the effect of the gravitational acceleration, one can derive a linear observation equation for $\alpha(t)$:

$$\begin{aligned} y_k &= [z_3(t) - g\cos\hat{\theta}(t)\cos\hat{p}(t)]\big|_{t=k\triangle T} \\ &= H_k x_k + \nu_k \end{aligned} \tag{16.14}$$

where

$$H_k = [0, 0, \cos\hat{\theta}(t)\cos\hat{p}(t), 0]\big|_{t=k\triangle T}$$

$$\nu_k = \nu_3(k\Delta T)$$

Thus, the on-line measurement of the heaving is also realized by executing the same procedure as described before. The locations of the rolling and pitching axes were assumed to be known; however, even when they are unknown, the attitude measurement system described previously is effective, if we introduce the candidates on the location of the axes adding to the angular frequencies.

16.5 Attitude Measurement for Crane Lifters

16.5.1 Dynamics of Attitude Signals

An illustrative diagram of a crane lifter system is shown in Figure 16.4. One of the easiest ways to measure the attitude of the lifter is to set up a high-resolution camera on the bottom of the trolley and to track a mark on the top of the lifter. However, it increases the cost and also the difficulty in maintenance. Furthermore, sometimes the scheme does not work because of shadows and light reflection. As previously mentioned, for gyros not offering sufficiently accurate measurement, a high-sensitivity servo-type accelerometer is used to extract the attitude signals. When setting up the sensor on the lifter, however, there is a secondary swing signal adding to the primary one, due to the free suspension of the lifter and the structure of the lifter. Despite its small amplitude, the secondary one has a higher frequency and for this reason has a large magnitude on the sensor output. The important signal for practical applications, such as the attitude control of the lifter, is the primary one, which has larger amplitude with a lower angular frequency of $\omega = \sqrt{g/l}$ (g, the gravitational acceleration; l, the wire length from the primary supporting point to the center of gravity of the pulley). If we try to attenuate the secondary swing signal by passing the output through a low-pass filter, the phase lag is also introduced into the primary swing signal and the signal can no longer be used for the accurate attitude control of the lifter.

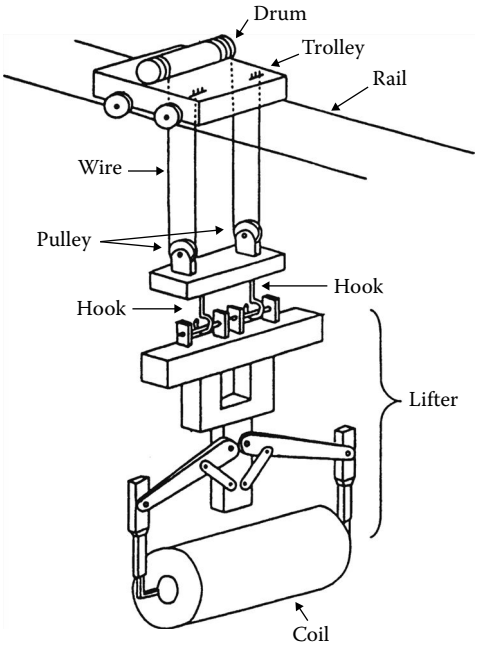

FIGURE 16.4 A crane lifter system.

For the aforementioned reasons, we introduce an autonomous measurement system that measures both the primary and the secondary swings by modeling the lifter system with a double pendulum and applying a Kalman filter to it [14]. The dynamics of the trolley-lifter system is derived using Lagrange's equations of motion [8,9]:

$$\frac{d}{dt}\left(\frac{\partial T}{\partial \dot{x}}\right)-\frac{\partial T}{\partial x}+\frac{\partial V}{\partial x}=u-z\dot{x} \tag{16.15}$$

$$\frac{d}{dt}\left(\frac{\partial T}{\partial \dot{\theta}_1}\right)-\frac{\partial T}{\partial \theta_i}+\frac{\partial V}{\partial \theta_i}=0(i=1,2) \tag{16.16}$$

where

T and V represent, respectively, the kinetic and the potential energies of the trolley-lifter system

θ_1, θ_2 denote, respectively, the angles that the primary and the secondary pendulums take against the vertical line

The other variables x, u, and a represent the location of the trolley, the driving force, and the coefficient of friction between the trolley and the rail, respectively. Considering that θ_i, θ_i, $(1 \le i \le 2)$ are small, the dynamic equation of the trolley-lifter system can be expressed as [14]

$$\dot{x}(t)=Ax(t)+bu(t) \tag{16.17}$$

where $\mathbf{x}(t)$ is the state vector $x(t)=(x, \dot{x}, \theta_1, \dot{\theta}_1, \theta_2, \dot{\theta}_2)^{\mathrm{T}}$. Taking into account the approximation errors in deriving Equation 16.17, air resistance, friction in the wires, and microscopic swings at the other

connection points, it is reasonable to introduce white Gaussian noises $w(t)$ $(1 \leq i \leq 3)$ with zero mean and appropriate variances to the dynamic Equation 16.17 as in Equation 16.5 as follows [14]:

$$\dot{x}(t) = Ax(t) + bu(t) + \Gamma w(t) \tag{16.18a}$$

where

$$\Gamma = \begin{bmatrix} 0 & 1 & 0 & 0 & 0 & 0 \\ 0 & 0 & 0 & 1 & 0 & 0 \\ 0 & 0 & 0 & 0 & 0 & 1 \end{bmatrix}^{\mathrm{T}}, \quad \omega(t) = [\omega_1(t), \omega_2(t), \omega_3(t)]^{\mathrm{T}} \tag{16.18b}$$

16.5.2 Sensor Outputs and On-Line Attitude Measurement

When a servo-type accelerometer is set up on the lifter (in the direction of the swing) at the place of the distance ℓ'_2 from the secondary supporting point, the output of the sensor becomes [14]

$$y(t) \cong -\ddot{x} - \ell'_1 \ddot{\theta}_1 - \ell'_2 \ddot{\theta}_2 - g\theta_2 \tag{16.19}$$

where ℓ'_1 is the distance between the primary and the secondary supporting points (see Figure 16.5). Substitution of Equation 16.17 into Equation 16.19 yields an output expressed in terms of the state vector $\mathbf{x}(t)$, as in Equation 16.8. Using a rotary encoder to measure the location and the velocity of the trolley, and then combining these three sensor outputs with the dynamic Equation 16.18 and applying a Kalman filter, enables the state vector to be estimated on-line. Using this approach, both angular displacement and velocity of the deflections θ_1, θ_2 of the two pendulums can be measured exactly.

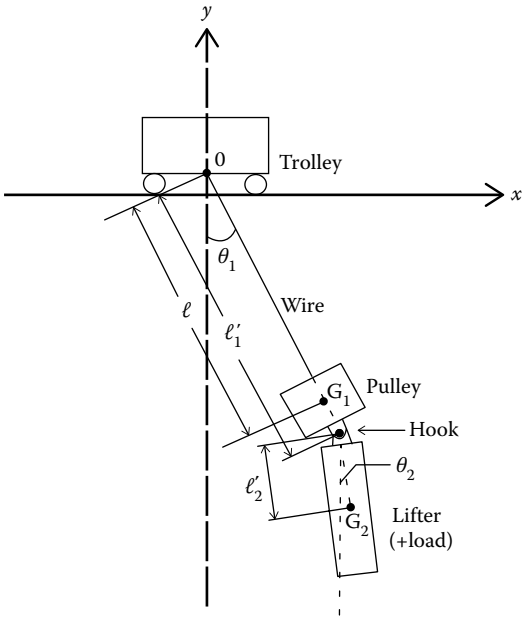

FIGURE 16.5 Dynamics of a trolley-lifter system.

16.6 Aircraft Attitude Determination

The determination of aircraft attitude requires the measurement of angles about three independent body axes. These angles are the roll, pitch, and yaw angles. There are two primary means employed today for measuring these angles; the first method uses VGs to measure the roll and pitch angles and a DG to measure the yaw angle. The second method, more commonly used today, employs an IMU for full three-axis attitude determination coupled with a baro-altimeter to correct for vertical drift errors in the IMU. Both methods are described as follows.

16.6.1 Vertical and Directional Gyro Analysis

A VG is a two degree-of-freedom gyro with its spin axis mounted nominally vertical. It employs two specific force sensors mounted nominally horizontal on the inner gimbal. The two angles measured by the VG—roll and pitch—require nearly identical analyses [1]. Consider the situation shown in Figure 16.6, depicting an aircraft with a roll angle of ϕ with respect to the local vertical. The sensed roll angle ϕ_s is given by the difference in the actual roll angle and the gyro roll drift error ϕ_Δ:

$$\phi_s = \phi - \phi_\Delta \tag{16.20}$$

In order to compensate for this drift error, gyros employ a specific force sensor such as an electrolytic bubble device, which senses drift error. This correction device senses the angular difference between the specific force vector **f** acting on the aircraft roll axis and the gyro axis, as shown in Figure 16.6. Thus,

$$\phi_B = \tan^{-1}\left[\left(\frac{f_\phi}{f_v}\right) - \phi_\Delta\right] \cong \left(\frac{f_\phi}{f_v}\right) - \phi_\Delta \tag{16.21}$$

where

f_ϕ is the side horizontal component of **f**

f_v is the force of gravity is the vertical component

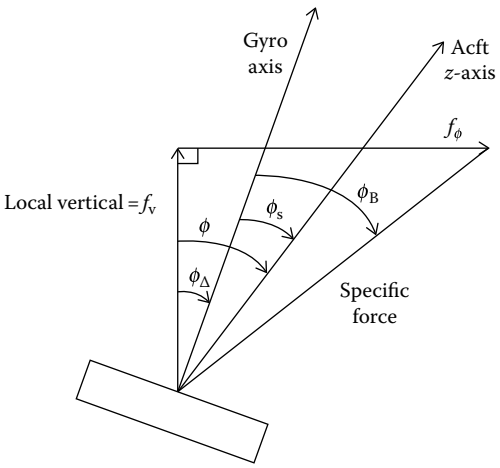

FIGURE 16.6 VG analysis.

A similar analysis for the pitch angle θ yields

$$\theta_s = \theta - \theta_\Delta \tag{16.22}$$

$$\theta_B = \tan^{-1}\left[\frac{f_0}{f_v} - \theta_\Delta\right] \cong \frac{f_\theta}{f_v} - \theta_\Delta \tag{16.23}$$

where f_θ is the back horizontal component of **f**. Next, define the gyro angular momentum vector by

$$H_{VG} = [J_x \dot{\phi}_\Delta, J_y \dot{\theta}_\Delta, -h] \tag{16.24}$$

where

J_x and J_y are the sensor moments of inertia
h is the gyro spin angular momentum

In addition, define the inner gimbal axes angular velocity vector as

$$\omega_{VG} = [\dot{\phi}_\Delta, \dot{\theta}_\Delta, 0] \tag{16.25}$$

Finally, define the gimbal torque vector by

$$Q_{VG} = [Q_{cx} + Q_{dx}, Q_{cy} + Q_{dy}, 0] \tag{16.26}$$

where

$$Q_{cx} = \text{gimbal roll control torque} = -k_c \theta_B \tag{16.27a}$$

$$Q_{cy} = \text{gimbal pitch control torque} = k_c \phi_B \tag{16.27b}$$

$$Q_{dx} = \text{gimbal roll disturbance torque} = -k_d(\dot{\phi}_\Delta - \dot{\phi}) + \text{random torques} \tag{16.27c}$$

$$Q_{dy} = \text{gimbal pitch disturbance torque} = k_d(\dot{\theta}_\Delta - \dot{\theta}) + \text{random torques} \tag{16.27d}$$

and the k_c and k_d are constant scaling factors related to each torque component.

Using the vectors defined in Equations 16.24 through 16.26, the gyro equations of motion are given by

$$\frac{\partial}{\partial t}(H_{VG}) + (\omega_{VG} \times H_{VG}) = Q_{VG} \tag{16.28}$$

Taking the Laplace transform of the expansion of Equation 16.28, with the assumption that $J_x = J_y = J$, yields the following gyro equations of motion in the Laplace domain:

$$\begin{bmatrix} J_x s^2 + k_d s & -(hs + k_c) \\ hs + k_c & J_y s^2 + k_d s \end{bmatrix} \begin{bmatrix} \phi_\Delta(s) \\ \theta_\Delta(s) \end{bmatrix} \equiv \begin{bmatrix} -k_c \theta_B + k_d s\phi(s) + \text{random torques} \\ (k_c/g) f_\phi(s) + k_d s\theta(s) + \text{random torques} \end{bmatrix} \tag{16.29}$$

For normal gyro operation, $J_x \cong J_y \cong 0$ and $k_d/h \ll 1$, so these factors may be ignored in Equation 16.29. Thus, solving for the desired roll and pitch angles under these assumptions gives [1]

$$\phi_s = \begin{cases} \phi & \omega \gg k_c/h \\ \phi - f_\phi/g & \omega \ll k_c/h \end{cases} \tag{16.30}$$

$$\theta_s = \begin{cases} \theta & \omega \gg k_c/h \\ \theta - f_\theta/g & \omega \ll k_c/h \end{cases} \tag{16.31}$$

A DG is a two degree-of-freedom gyro with its spin axis mounted nominally horizontal and pointing in the direction of magnetic north. It employs a single specific force sensor mounted on the inner gimbal [1]. The DG measures the third required aircraft angle, yaw, generally denoted by ψ. The sensed yaw angle ψ_s is given by the difference in the actual yaw angle ψ (angle between the aircraft z-axis and true north) and the gyro heading angle drift error ψ_Δ (angle between the gyro axis and true north):

$$\psi_s = \psi - \psi_\Delta \tag{16.32}$$

Define the gyro angular momentum vector by

$$H_{DG} = [J_y \dot{\theta}_\Delta, J_z \dot{\psi}_\Delta, -h] \tag{16.33}$$

and the inner gimbal axes angular velocity vector as

$$\omega_{DG} = [\dot{\theta}_\Delta, \dot{\psi}_\Delta, -h] \tag{16.34}$$

and the gimbal torque vector as

$$Q_{DG} = [Q_{cy} + Q_{dy}, Q_{cz} + Q_{dz}, 0] \tag{16.35}$$

Here, the torque vector components are given by

$$Q_{cy} = k_c(M_\Delta - \psi_\Delta) \tag{16.36a}$$

$$Q_{cz} = -k_c\theta_B \tag{16.36b}$$

$$Q_{dy} = -k_d(\dot{\theta}_\Delta - \dot{\theta}) + \text{random torques} \tag{16.36c}$$

$$Q_{dz} = -k_d(\dot{\psi}_\Delta - \dot{\psi}) + \text{random torques} \tag{16.36d}$$

where M_Δ = magnetic compass heading error (from true north). Therefore, the DG equations of motion are given in Laplace domain as

$$\begin{bmatrix} J_y s^2 + k_d s & -(hs + k_c) \\ hs + k_c & J_z s^2 + k_d s \end{bmatrix} \begin{bmatrix} \theta_\Delta(s) \\ \psi_\Delta(s) \end{bmatrix} \cong \begin{bmatrix} k_c M_\Delta(s) + k_d s\theta(s) + \text{random torques} \\ -k_c\theta_B + k_d s\psi(s) + \text{random torques} \end{bmatrix} \tag{16.37}$$

The desired yaw angle measurement for the DG is thus given as [1]

$$\Psi_s = \begin{cases} \Psi & \omega \gg k_c/h \\ \Psi - M_\Delta & \omega \ll k_c/h \end{cases} \tag{16.38}$$

As indicated in Table 16.1, the accuracies of both VGs and DGs are approximately 1°. An improvement of over two orders of magnitude can be obtained through the use of IMUs, which are described next.

16.6.2 Inertial Measurement Units

IMUs consist of gyroscopes and accelerometers that together provide full three-axis attitude measurements. Most are mounted on stable gimbaled platforms that remain locally horizontal via torquing devices. An IMU aboard an aircraft cannot measure exactly the local vertical due to the fact that the specific force acting on the aircraft has a horizontal component due to vehicle motion. In addition, since the vehicle is moving with respect to the inertial reference frame, the Earth's magnetic pole cannot be determined precisely [1].

These problems (errors) are minimized by aligning the IMU to be exactly horizontal and north pointing while the aircraft is stationary. Once platform motion begins, the IMU may be constantly realigned by sensing changes in the direction of vertical and north and then applying appropriate torques to the platform to keep it properly aligned. This realignment is accomplished by integrating the two orthogonal accelerometer outputs to determine the components of horizontal velocity. These data, combined with the Earth's rotation rate, yield the desired rates of change in local vertical and true north at the vehicle's current latitude and longitude. Performing a second integration of the sensor outputs yields an estimate of relative position.

Analysis in Bryson [1] has shown that the pitch angle (variation in platform horizontal position) is given by the IMU sensor output as

$$\theta(t) = \frac{-\varepsilon}{\omega_s}\sin(\omega_s t) - \frac{b}{g} \tag{16.39}$$

where

ε is the gyro drift rate error

b is the specific force sensor error

$\omega_s \equiv$ Schuler frequency $= \sqrt{g/R}$, [g = force of gravity, R = Earth's radius]

Thus, the platform root-mean-square (rms) pitch angle becomes

$$\theta_{rms} = \left[\frac{1}{2}\left(\frac{\varepsilon}{\omega_s}\right)^2 + \left(\frac{b}{g}\right)^2\right]^{\frac{1}{2}} \tag{16.40}$$

Using typical values for $\varepsilon(\cong 0.05°\text{h}^{-1})$, $\omega_s \cong (0.71°\text{h}^{-1})$, and $b(\cong 0.01)$ yields an rms pitch angle error of $\theta_{rms} = 0.01°$. Thus, it is apparent that under normal operating conditions, the IMU provides a two order-of-magnitude improvement in sensor accuracy when compared to the VG and DG.

16.7 Spacecraft Attitude Determination

Most spacecraft attitude determination techniques rely upon finding the orientation of a single axis in space (e.g., the spacecraft z-axis) plus the spacecraft rotation about this axis. This provides a full three-axis attitude solution. In order to achieve this, reference sources that are external to the spacecraft must be used. Specifically, full three-axis spacecraft attitude determination requires at least two external vector measurements. Commonly used reference sources for these external vector measurements include the sun, Earth, moon, stars, planets, and the Earth's magnetic field. In addition, IMUs are also used to provide the necessary attitude measurements.

16.7.1 Attitude Determination Methodology

The first step in attitude determination is to determine the angles between the spacecraft's primary axis and the two (or more) attitude reference sources. For example, suppose a particular spacecraft is using the sun and the Earth for attitude reference. The two angles in this case are referred to as the sun angle β_s and the nadir angle Γ_N. Since the orientation of even a single spacecraft axis is unknown at this point, these angles establish two *cones* along which the attitude vector **A** must lie. Since the attitude vector must lie on both cones, it must lie along the intersection between the two cones [4] (see Figure 16.7). The two vectors, notably $\mathbf{A}_1$ and $\mathbf{A}_2$, resulting from the intersection of these two cones may be determined by the following method derived by Grubin [15]. Let **S** represent the sun vector, **E** the spacecraft nadir vector, and **A** the desired attitude vector, each defined in Cartesian space as follows:

$$\mathbf{S} = (\mathbf{s}_x, \mathbf{s}_y, \mathbf{s}_z) \tag{16.41}$$

$$\mathbf{E} = (\mathbf{E}_X, \mathbf{E}_y, \mathbf{E}_z) \tag{16.42}$$

$$\mathbf{A} = (\mathbf{A}_x, \mathbf{A}_y, \mathbf{A}_z) \tag{16.43}$$

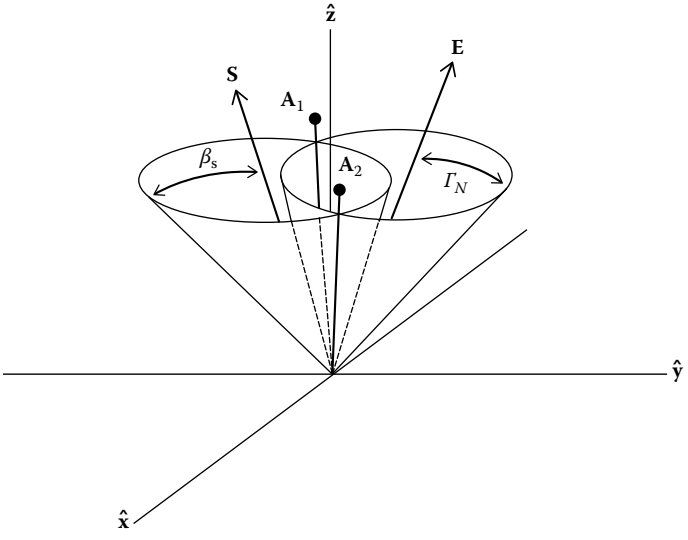

FIGURE 16.7 Relationship between reference vectors and single-axis attitude cones.

Let the vectors **S**, **E**, and **N** define a set of base unit vectors with

$$\mathbf{N} = \frac{\mathbf{S} \times \mathbf{E}}{|\mathbf{S} \times \mathbf{E}|} = (\mathbf{N}_x, \mathbf{N}_y, \mathbf{N}_z) \tag{16.44}$$

If we introduce a proper set of scaling factors as follows:

$$I_x = \frac{[\cos\beta_s - (\mathbf{S} \cdot \mathbf{E})\cos\Gamma_N]}{1 - (\mathbf{S} \cdot \mathbf{E})^2} \tag{16.45a}$$

$$I_y = \frac{[\cos\Gamma_N - (\mathbf{S} \cdot \mathbf{E})\cos\beta_s]}{1 - (\mathbf{S} \cdot \mathbf{E})^2} \tag{16.45b}$$

$$I_z = \sqrt{1 - I_x \cos\beta_s - I_y \cos\Gamma_N} \tag{16.45c}$$

then the two possible attitude vectors **A** and $\mathbf{A}_2$ are found to be

$$\mathbf{A}_{1,2} = [(I_x\mathbf{S}_x + I_y\mathbf{E}_y \pm I_z\mathbf{N}_x), (I_x\mathbf{S}_y + I_y\mathbf{E} \pm I_z\mathbf{N}_y), (I_x\mathbf{S}_z + I_y\mathbf{E}_z \pm I_z\mathbf{N}_z)] \tag{16.46}$$

In Equations 16.44 through 16.46, $\mathbf{S} \times \mathbf{E}$ represents the Cartesian vector product, and $\mathbf{S} \times \mathbf{E}$ represents the Cartesian scalar product. The radicand in Equation 16.45c may be negative, thus producing imaginary values for I_z whenever the two cones do not intersect. Such occurrences are usually attributed to sensor error or random noise fluctuations. In this case, one can add a predetermined sensor bias to both sensors in order to "broaden" the cone angles, thus forcing the cones to intersect.

Note that for most applications involving spacecraft attitude determination, the principal coordinate system used is the *celestial sphere* coordinate system. This coordinate system has the *z*-axis aligned with the Earth's polar axis and the *x*-axis aligned with the intersection of the Earth's equatorial plane and the Earth's orbital plane around the sun (i.e., aligned with the *vernal equinox*). In this coordinate system, all vectors are considered unit vectors and the two principal measurements describing a vector's position are the *right-ascension* and *declination angles*, denoted Ω and Δ, respectively. Thus, the sun vector **s** and the Earth nadir vector **E** used in Equations 16.41 and 16.42 will in general be given as right-ascension and declination angles that can be converted to Cartesian coordinates via the following set of transformations:

$$x = \cos(\Omega)\cos(\Delta); \quad y = \sin(\Omega)\cos(\Delta); \quad z = \sin(\Delta) \tag{16.47a}$$

$$\Omega = \tan^{-1}\left(\frac{y}{x}\right); \quad \Delta = \sin^{-1}(z) \tag{16.47b}$$

The final step in measuring three-axis attitude is to determine which attitude solution is correct, $\mathbf{A}_1$ or $\mathbf{A}_2$, and then measure the rotation about this axis. The two ambiguous attitude solutions may be resolved by comparison with a priori attitude information, if available, or through the use of *trace averaging* [4]. Trace averaging is a method of plotting each attitude solution on a right-ascension versus declination plot and choosing the area of greatest concentration as the correct solution, as demonstrated in Figure 16.8. Since the attitude is assumed to change more slowly than the attitude sensor's sample rate, over short time intervals, the data for the correct solution usually form a "cluster" near the correct attitude; the data for the incorrect solution are usually much more scattered.

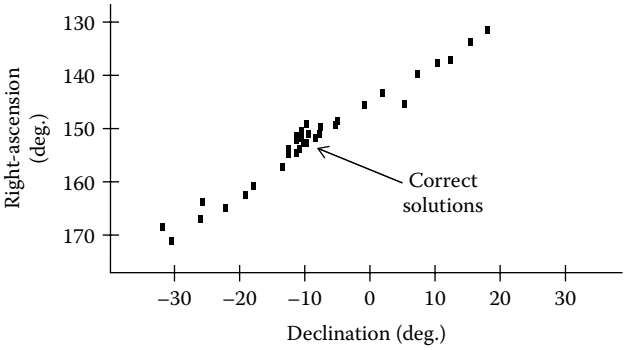

FIGURE 16.8 Method of trace averaging for resolving ambiguous attitude solutions.

Once the correct attitude vector has been obtained, the orientation of the remaining two orthogonal axes may be found by measuring the rotation, or phase angle, of the spacecraft about the preferred axis. Any sensor measurement that provides this phase angle may be used. An example of this technique is provided by the panoramic annular lens attitude determination system (PALADS), described in the next section. This imaging system uses a unique "3D" lens that provides simultaneous detection of two (or more) reference sources [16]. This information, combined with the orientation of the single axis, uniquely determines three-axis attitude.

The three angles derived earlier, which are commonly referred to as *Euler angles*, define the orientation of the three spacecraft axes with respect to the chosen reference frame. A more formal treatment of the attitude solution usually requires specifying the components of the 3×3 attitude matrix **A**. Each component of the attitude matrix defines the angular relationship between a given spacecraft axis and a reference frame axis. Various methods exist for computing the attitude matrix **A** (see Ref. [4]); the preferred method depends on the particular application at hand.

16.8 PALADS

The primary component of PALADS is the panoramic annular lens (PAL), a single-element lens made from a high index of refraction glass with certain portions of the lens coated with a mirrored surface. Hence, it relies on both refraction and reflection in forming an image (Figure 16.9). The lens is unique in that it images a 3D object field onto a 2D image plane, whereas a "normal" lens is capable of only imaging 2D object space onto an image plane. The combination of high index of refraction glass and mirrored surfaces provides the PAL with a field of view extending from approximately 65° to 110° from the optical axis. This 45° field of view covers the entire 360° surrounding the optical axis [17]. Any ray originating from outside the 45° field of view will not form a part of the image. The PAL may be attached to any

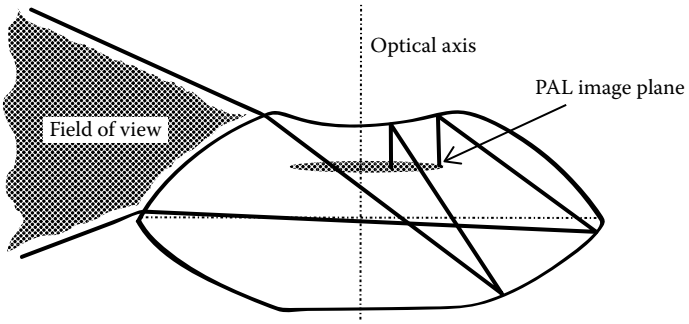

FIGURE 16.9 PAL lens ray diagram.

high-quality imaging system using an appropriate *transfer lens*. As currently configured, the PALADS imaging system utilizes a Sony XC-73 charged-couple device (CCD), a black-and-white video camera coupled to the PAL via a Nikon *f*/1.4 transfer lens.

The hemispherical view provided by PALADS allows for single-sensor detection of multiple attitude reference sources, such as the Earth and the sun or moon. The position of each reference source in the image plane translates into a unique azimuth elevation angle between the PAL's optical axis and the reference source. Since the PAL has a 360° field of view surrounding the optical axis, it may detect several reference sources simultaneously. The data points associated with each source are extracted from the image plane using digital image processing techniques. Thus, it is easy to see how a single image from PALADS (containing two or more reference sources) provides the necessary angle data to determine three-axis spacecraft attitude.

References

1. A. E. Bryson, *Control of Spacecraft and Aircraft*, Chapter 10, Princeton, NJ: Princeton University Press, 1994.
2. W. J. Larson and J. R. Wertz (eds.), *Space Mission Analysis and Design*, Chapter 11, Torrance, CA: Microcosm, Inc., 1992.
3. NASA Technical Memorandum NASA TM X-64757, *Terrestrial Environment (Climatic) Criteria Guidelines for Use in Aerospace Vehicle Development (1973 Revision)*, Marshall Space Flight Center, AL, 1973.
4. J. R. Wertz (ed.), *Spacecraft Attitude Determination and Control*, Chapters 11 and 12, Dordrecht, the Netherlands: Reidel Publishing Company, 1980.
5. R. D. Angelari, A deterministic and random error model for a multibeam hydrographic sonar system, *Proceedings of the OCEANS'78: The Ocean Challenge*, Washington, DC, 1978, pp. 48–53.
6. C. de Moustier, T. Hylas, and J. C. Phillips, Modifications and improvements to the Sea Beam system on board R/V Thomas Washington, *Proceedings of the OCEANS'88: A Partnership of Marine Interests*, Baltimore, MD, 1988, pp. 372–378.
7. S. Tanaka and S. Nishifuji, Automatic on-line measurement of ship's attitude by use of a servo-type accelerometer and inclinometers, *IEEE Trans. Instrum. Meas*., 45, 209–217, 1996.
8. D. G. Shultz and J. L. Melsa, *State Functions and Linear Control Systems*, New York: McGraw-Hill, 1967.
9. Y. Takahashi, M. J. Rabins, and D. M. Auslander, *Control and Dynamic Systems*, Reading, MA: Addison-Wesley, 1971.
10. S. Tanaka and S. Nishifuji, On-line sensing system of dynamic ship's attitude by use of servo-type accelerometers, *IEEE J. Oceanic Eng.*, 20, 339–346, 1995.
11. S. Tanaka, On automatic attitude measurement system for ships using servo-type accelerometers (in Japanese), *Trans. SICE*, 27, 861–869, 1991.
12. D. E. Cartwright and M. S. Longuet-Higgins, The statistical distribution of the maxima of a random function, *Proc. R. Soc. Lond, Ser. A*, 237, 212–232, 1956.
13. R. E. Kaiman, A new approach to linear filtering and prediction problems, *Trans. ASME, J. Basic Eng.*, 82, 35–45, 1960.
14. S. Tanaka, S. Kouno, and H. Hayashi, Automatic measurement and control of attitude for crane lifters (in Japanese), *Trans. SICE*, 32(1), 97–105, 1996.
15. C. Grubin, Simple algorithm for intersecting two conical surfaces, *J. Spacecraft Rockets*, 14(4), 251–252, 1977.
16. M. A. Stedham and P. P. Banerjee, The panoramic annular lens attitude determination system, *SPIE Proceedings, Space Guidance, Control, and Tracking II*, Orlando, FL, April 17–18, pp. 108–117, 1995.
17. J. A. Gilbert, D. R. Matthys, and P. Greguss, Optical measurements through panoramic imaging systems, *Proceedings of the International Conference on Hologram Interferometry and Speckle Metrology*, Baltimore, MD, November 4–7, 1990.

17

Inertial Navigation

Halit Eren
Curtin University

17.1 Principles of Inertial Navigation

The original meaning of the word *navigation* is "ship driving." In ancient times when sailing boats were used, navigation was a process of steering the ship in accordance with some means of directional information, and adjusting the sails to control the speed of the boat. The objective was to bring the vessel from location A to location B safely. At present, navigation is a combination of science and technology. No longer is the term limited to the control of a ship on the sea surface; it is applied to land, air, sea surface, underwater, and space.

The concept of inertial-navigator mechanization was first suggested by Schuler in Germany in 1923. His suggested navigation system was based on an Earth-radius pendulum. However, the first inertial guidance system based on acceleration was suggested by Boykow in 1938. The German A-4 rocket, toward the end of World War II, used an inertial guidance system based on flight instrument type gyroscopes for attitude control and stabilization. In this system, body-mounted gyro-pendulum-integrating accelerometers were used to determine the velocity along the trajectory. The first fully operational inertial autonavigator system in the United States was the XN-1 developed in 1950 to guide C-47 rocket. Presently, inertial navigation systems (INSs) are well developed theoretically and technologically. They find diverse applications, allowing the choice of appropriate navigation devices, depending on cost, accuracy, human interface, global coverage, time delay, and autonomy.

Inertial navigation is a technique using a self-contained system to measure a vehicle's movement and determine how far it has moved from its starting point. Acceleration is a vector quantity involving magnitude and direction. A single accelerometer measures magnitude but not direction. Typically, it measures the component of acceleration along a predetermined line or direction. The direction information is usually supplied by gyroscopes that provide a reference frame for the accelerometers. Unlike other positional methods that rely on external references, an INS is compact and self-contained, as it is not required to communicate to any other stations or other references. This property enables the craft to navigate in an unknown territory.

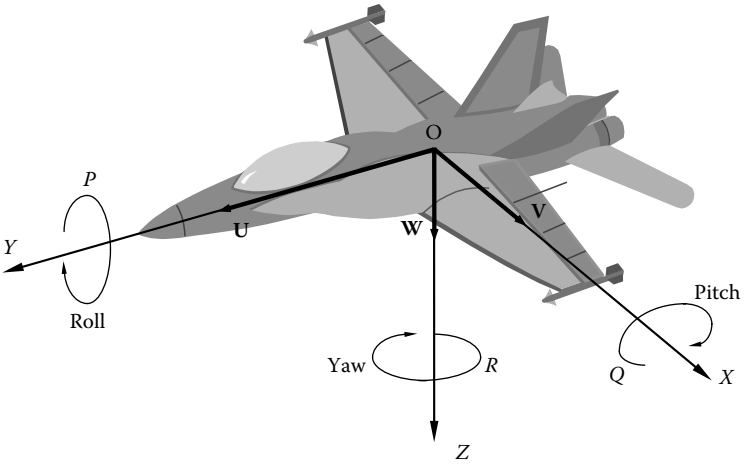

FIGURE 17.1 Inertial navigation is for monitoring the movement of an object such as a vehicle, rocket, ship, aircraft, and robot with respect to a reference axis. Vehicles such as aircrafts and marine vessels have their own local axes, known as the roll, the pitch, and the yaw.

Inertial navigation can also be described as a process of directing the movement of a vehicle, rocket, ship, aircraft, robot, and so on, from one point to another with respect to a reference axis. The vehicle's current position can be determined from "dead reckoning" with respect to a known initial starting reference position. On the Earth's surface, the conventional reference will be north, east, and down. This is referred to as the *Earth's fixed axes*. A vehicle such as an aircraft or a marine vessel will have its own *local axes:* roll, pitch, and yaw, as shown in Figure 17.1.

The inertial sensors of the INS can be mounted in such a way that they stay leveled and pointing in a fixed direction. This system relies on a set of gimbals and sensors attached on three axes to monitor the angles at all times. This type of INS is based on a *navigational platform*. A sketch of a three-axis platform is shown in Figure 17.2. Another type of INS is the *strapdown system* that eliminates the use of gimbals. In this case, the gyros and accelerometers are mounted to the structure of the vehicle. The measurements received are made in reference to the local axes of roll, pitch, and yaw. The gyros measure the movement of angles in the three axes in a short time interval of few milliseconds. The computer then uses this information to resolve the accelerometer outputs into the navigation axes. A schematic block diagram of the strapdown system is shown in Figure 17.3.

The controlling action is based on the sensing components of acceleration of the vehicle in known spatial directions, by instruments that mechanize Newtonian laws of motion. The first and second integrations of the sensed acceleration determine velocity and position, respectively. A typical INS includes a set of gyros, a set of accelerometers, and appropriate signal processing units. Although the principle of the systems may be simple, the fabrication of a practical system demands a sophisticated technological base. The system accuracy is independent of altitude, terrain, and other physical variables but is limited almost purely by the accuracy of its own components. Traditional INSs mainly rely on mechanical gyros and accelerometers, but today there are many different types available, such as optical gyroscopes, piezoelectric vibrating gyroscopes, and active and passive resonating gyroscopes. Also, micromachined gyroscopes and accelerometers are making an important impact on modern INSs. A brief description and operational principles of gyroscopes and accelerometers suitable for inertial navigation are as follows.

Major advances in INS over the years include the development of the *electrostatic gyro* (ESG) and the laser gyro. In ESG, the rotor spins at a speed above 200,000 rpm in a near-vacuum environment. The rotor is suspended by an electrostatic field; thus, it is free from bearing friction and

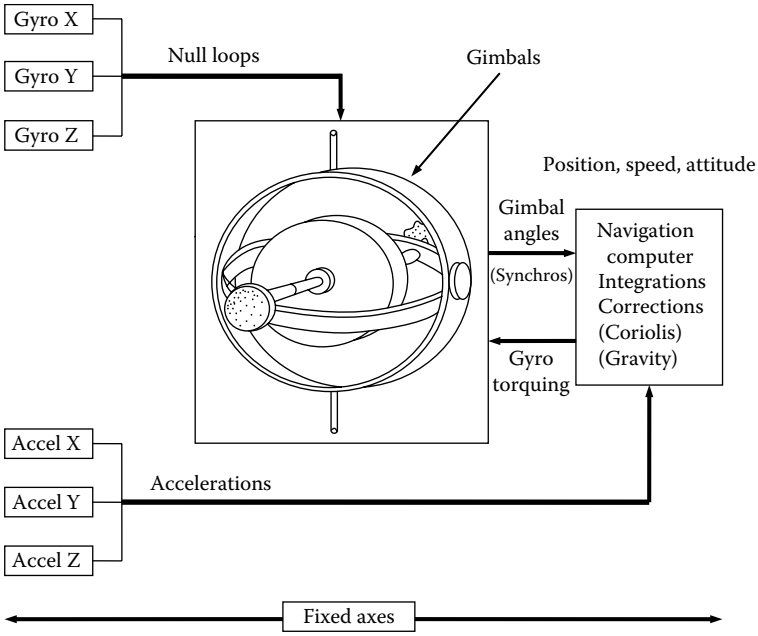

FIGURE 17.2 Some INSs are based on a navigational platform. The sensors are mounted in such a way to stay leveled at all times and pointing in a fixed direction. This system uses a set of gimbals and sensors attached on three axes in the *x*, *y*, and *z* directions to continuously monitor the angles and accelerations. The navigation computer makes corrections for coriolis forces, gravity, and other adverse effects.

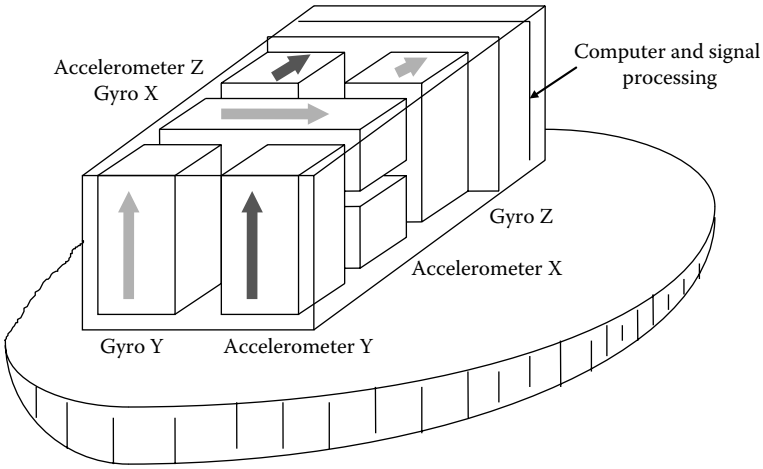

FIGURE 17.3 Strapdown gyros and accelerometers are mounted rigidly on the structure of the vehicle, and the measurements are referenced to the local axes of roll, pitch, and yaw. The gyros measure the movement of angles in the three axes in short time intervals to be processed by the computer. This information is used, together with the accelerometer outputs, for predicting navigation axes, thus eliminating the need for gimbals.

other random torques due to mechanical supports. Hence, its operation results in a superior performance compared to others, closely resembling the performance of a theoretical gyro. Although no system can claim to reach perfection, an ESG requires less frequent updates compared to other mechanical gyros. Gyroscopes are an important element of inertial navigation; therefore, they will be described further.

17.2 Gyroscopes

There are two broad categories: (1) mechanical gyroscopes and (2) optical gyroscopes. Within both of these categories, there are many different types available. Only the few basic types will be described to illustrate the operating principles; detailed information may be found in the references listed at the end of this chapter.

17.2.1 Mechanical Gyroscopes

The first mechanical gyroscope was built by Foucault in 1852, as a gimbaled wheel that stayed fixed in space due to angular momentum while the platform rotated around it. They operate on the basis of *conservation of angular momentum* by sensing the change in direction of an angular momentum. There are many different types, which are the following:

1. *Single-degree-of-freedom gyroscopes* include the rate, rate integrating, a spinning rotor flywheel, electron, and particle gyros.
2. *Two-degree-of-freedom gyroscopes* incorporate the external gimbal types, two-axis-floated, spherical free-rotor and electrically suspended, gas-bearing free-rotor gyros.
3. *Vibrating gyroscopes* include the tuning fork, vibrating string, vibrating shell, hemispherical resonating, and vibrating cylinder gyros.
4. *Continuous-linear-momentum gyroscopes* incorporate a steady stream of fluid, plasma, or electrons, which tends to maintain its established velocity vector as the platform turns. One typical example is based on a differential pair of hot-wire anemometers to detect the apparent lateral displacement of the flowing air column.

The operating principle of all mechanical gyroscopes is based on the conservation of angular momentum, as shown in Figure 17.4. The angular momentum is important since it provides an axis of reference. From Newton's second law, the angular momentum of a body remains unchanged unless it is acted upon by a torque. The rate of change of angular momentum is equal to the magnitude of the torque. It can be expressed, in vectorial form, as

$$T = \frac{\mathrm{d}H}{\mathrm{d}t} \tag{17.1}$$

where H is the angular momentum (=inertia × angular velocity, $I\omega$).

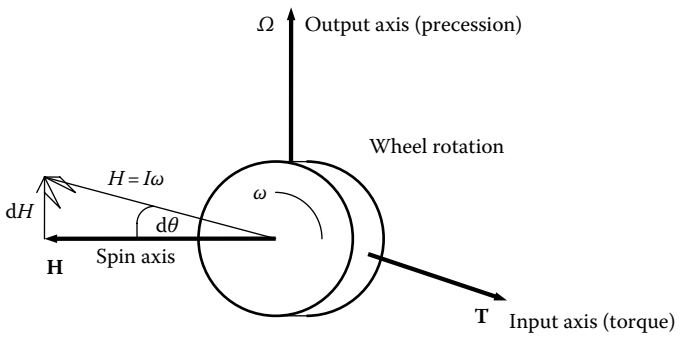

FIGURE 17.4 The operational principle of gyroscopes is based on the angular momentum of a carefully constructed rotating body. The angular momentum stabilizes the system and it remains unchanged unless acted upon by a torque. If the torque is orthogonal to the spin axis, it cannot change the velocity, but it can change the direction in the same direction as the torque. The spin axis always tries to align with the external torque.

If a torque acts about the axis of rotation, it changes the angular velocity by

$$T = \frac{I\mathrm{d}\omega}{\mathrm{d}t} = I\alpha \tag{17.2}$$

where
I is the inertia about the spin axis
α is the angular acceleration

If the torque is orthogonal to the spinning axis, it cannot change the magnitude of the angular velocity vector, but it can change direction in the same direction as torque T; then

$$\mathrm{d}H = H\mathrm{d}\theta \tag{17.3}$$

where θ is the angle of rotation.

Therefore, from Equations 17.1 and 17.4,

$$T = \frac{\mathrm{d}H}{\mathrm{d}t} = \frac{H\mathrm{d}\theta}{\mathrm{d}t} = H\Omega \tag{17.4}$$

where Ω is the precession rate or the angular velocity of the spinning wheel about the axis normal to the plane of the spin and the input torque. Generally, the spin axis tries to align with the external input torque.

These equations can be elaborated to describe the operating principles of mechanical gyros by taking into account the angular momentum in x, y, and z directions, nutation, coriolis accelerations, directions of other influencing torques, and linear forces. Here, the operation of the well-known *flywheel gyroscope* will be described as the basis for further discussions on INSs.

17.2.2 Flywheel Gyroscopes

Flywheel gyroscopes are based on an electrically driven rotor suspended in a pair of precision low-friction bearings at both ends of the rotor axle. An example of a double-axis flywheel gyro is shown in Figure 17.5. The rotor bearings are supported by a circular ring known as an *inner gimbal ring*, which in turn pivots on a second set of bearings that is attached to the *outer gimbal ring*. The pivoting action of the inner gimbal defines the horizontal axis of the gyro, which is perpendicular to the spin axis of the rotor. The outer gimbal ring is attached to the instrument frame by a third set of bearings that defines the vertical axis of the gyro that is perpendicular to both the horizontal axis and the spin axis. This type of suspension has the property of always preserving the predetermined spin-axis direction in inertial space. Equations governing the two-degree-of-freedom gyroscope can be written using Equations 17.1 through 17.4. The torque with respect to an inertial reference frame can be expressed as

$$T = \dot{H}_{\mathrm{t}} \tag{17.5}$$

If the Earth is taken as a moving reference frame, then

$$\dot{H}_{\mathrm{t}} = \dot{H}_{\mathrm{E}} + \omega_{\mathrm{IE}}H \tag{17.6}$$

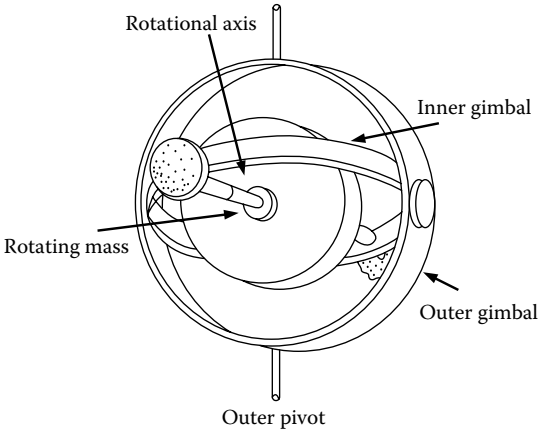

FIGURE 17.5 In a double-axis flywheel gyro, an electrically driven rotor is suspended by a pair of precision low-friction bearings at the rotor axle. The rotor bearings are supported by a circular inner gimbal ring. The inner gimbal ring in turn pivots on a second set of bearings attached to an outer gimbal ring. The pivoting action of the inner gimbal defines the horizontal axis of the gyro, which is perpendicular to the spin axis of the rotor. The outer gimbal ring is attached to the instrument frame by a third set of bearings.

If the gyroscope itself is mounted on a vehicle (e.g., aircraft) that is moving with respect to the Earth, then

$$\dot{H}_E = \dot{H}_B + \omega_{EB} H \tag{17.7}$$

The case of the gyroscope can be mounted on a platform so that it can rotate relative to the platform; then

$$\dot{H}_B = \dot{H}_C + \omega_{BC} H \tag{17.8}$$

Finally, the inner gimbal can rotate relative to the case; hence,

$$\dot{H}_C = \dot{H}_G + \omega_{GC} H \tag{17.9}$$

Substituting Equations 17.7 and 17.9 into Equation 17.4 yields

$$T = \dot{H}_G(\omega_{GC} + \omega_{BC} + \omega_{EB} + \omega_{IE})H \tag{17.10}$$

But

$$(\omega_{GC} + \omega_{BC} + \omega_{EB} + \omega_{IE}) = \omega_{IG} \tag{17.11}$$

Therefore,

$$T = \dot{H}_G + \omega_{IG} H \tag{17.12}$$

By carefully constructing the gyroscope and maintaining the spin velocity of the rotor constant, H_G can be made to be zero. Thus, the law of gyroscopes can be written as

$$T = \omega_{IG} H \tag{17.13}$$

This means that if an external torque T is applied to the gyroscope, the inner gimbal will precess with respect to the inertial frame with a velocity ω such that Equation 17.13 is satisfied.

In most designs (e.g., rate gyros), the gimbal is hermetically sealed in a liquid and liquid is floated in the case, to unload the gimbal bearings and to provide viscous damping. A pick-off senses gimbal deflection by means of position transducers, and it controls a servo system, with a servomotor driving the case to maintain pick-off null.

17.2.3 Optical Gyroscopes

Optical gyroscopes are based on the inertial properties of light instead of Newton's law of motion. They operate on the Sagnac effect, which produces interferometer fringe shift against the rotation rate. In this case, two light waves circulate in opposite directions around a path of radius R, beginning at source S. A typical arrangement for the illustration of operation principles is shown in Figure 17.6. When the gyro is stationary, the two beams arrive at the detector at the same time, and no phase difference will be recorded. Assume that the source is rotating with a velocity CO so that light traveling in the opposite direction to rotation returns to the source sooner than that traveling in the same direction. Thus, any rotation of the system about the spin axis causes the distance covered by the beam traveling in the direction of rotation to lengthen and the distance traveled by the beam in the opposite direction to shorten. The two beams interfere to form a fringe pattern and the fringe position may be recorded, or the phase differences of the two beams may be sensed. This phase difference is directional and proportional to the angular velocity. Usually, photodetectors are used to measure the phase shift.

Optical gyros can be categorized to be either passive or active and resonant or nonresonant. In passive gyrosensors, the Sagnac phase is measured by some external means, whereas in active gyros, the Sagnac phase causes a frequency change internal to the gyro that is directly proportional to the rotation rate.

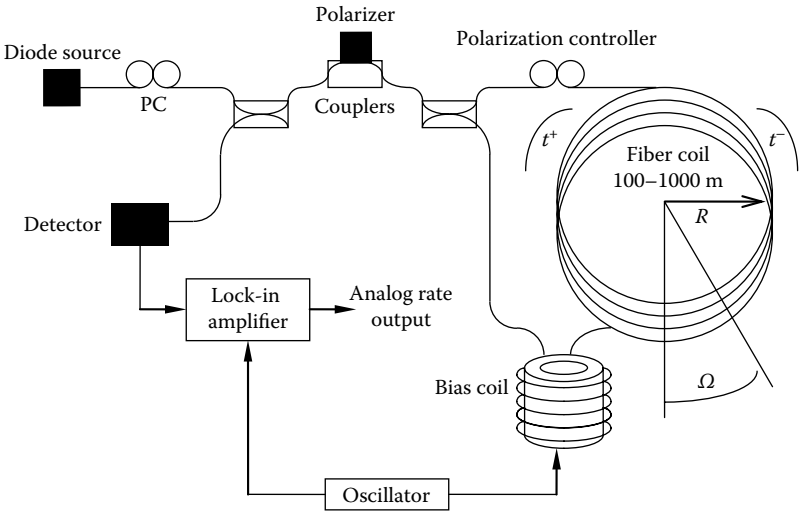

FIGURE 17.6 A typical fiber-optic gyroscope is based on the inertial properties of light, making use of the Sagnac effect. The Sagnac effect describes interferometer fringe shift against rotation rate. Two light waves circulate in opposite directions around a path of radius R, beginning at source S. When the gyro is stationary, the two beams arrive at the detector at the same time, and no phase difference is recorded. If the optical path is rotating with a velocity, the light traveling in the opposite direction to rotation returns to the source sooner than that traveling in the same direction. The two beams interfere to form a fringe pattern and the fringe position may be recorded, or the phase differences of the two beams may be sensed by photodetectors.

The Sagnac interferometer is the basis of the *interferometric fiber-optic gyro* (IFOG). A typical fiber-optic gyroscope is shown in Figure 17.6. However, the most widely used gyro is the active resonant *ring-laser gyro* (RLG), which is applied extensively in aircraft navigation. Two different types of resonant passive gyros, the *resonant fiber-optic gyro* (RFOG) and the *micro-optic gyro* (MOG), are lower-cost devices commonly used and comparable to RLGs.

17.3 Accelerometers

In inertial navigation, the absolute acceleration is measured in terms of three mutually perpendicular components of the total acceleration vector. Integrating these acceleration signals twice gives the displacement from an initial known starting location. Details of the acceleration and accelerometers are given elsewhere in this book (e.g., acceleration, vibration, and shock); therefore, accelerometers as applied to inertial navigations will be discussed here.

Accelerometers are made from three basic elements: proof mass, suspension mechanism, and pick-off mechanism. Some accelerometers require electric or magnetic force generators and appropriate servo loops. Accelerometers measure not only real vehicular acceleration but also respond to gravitational reaction forces. Acceleration due to gravity is a function of position—in particular, latitude and altitude—and is compensated by computers.

The most commonly used accelerometer in navigation systems is based on the pendulous types. They can be classified as

1. Generic pendulous accelerometer
2. Q-flex-type accelerometers
3. Micromachined accelerometers (A typical example of a modern micromachined accelerometer is given in Figure 17.7.)

Accelerations in the three axes are measured by suitably positioned accelerometers. Since accelerometers contain errors, the readings must be compensated by removing fixed biases or by applying scaling factors. The errors may be functions of operating temperature, vibration, or shock. Measurement of time must be precise as it is squared within the integration process for position determination. The Earth's rotation must also be considered, and gravitational effects must be compensated appropriately.

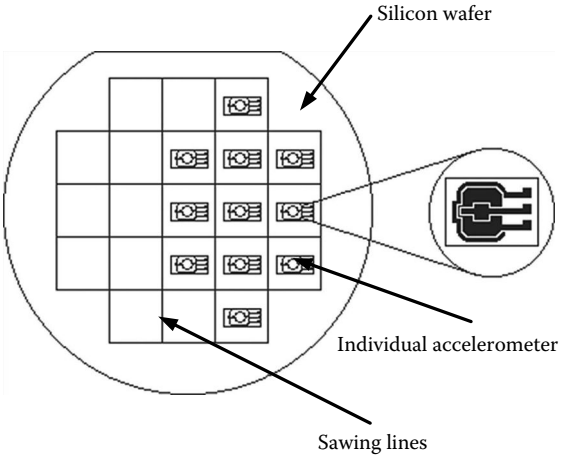

FIGURE 17.7 In modern micromachined accelerometers, multiple accelerometers can be mounted on a single chip to sense accelerations in *x*, *y*, and *z* directions. The primary signal conditioning is also provided in the same chip. The output from the chip is usually read in the digital form.

17.4 Errors and Stabilization in Inertial Navigation Systems

17.4.1 Errors

In general, inertial navigation is an initial value process in which the location of the navigating object is determined by adding distances moved in known directions. Any errors in the system cause misrepresentation of the desired location by being off target. The major disadvantage of an inertial guidance system is that its errors tend to grow with time. These errors in the deduced location are due to a number of reasons, including imperfect knowledge of the starting conditions, errors in computation, and mainly errors generated by gyros and accelerometers.

If the error buildup with time becomes too large, external aids (e.g., the global positioning system [GPS]) may be used to reset or update the system. Optimal use of the data from external aids must account for the geometry of the update and also for the accuracy of the update relative to the accuracy of the inertial system. The Kalman filter, for example, is one of the computational procedures frequently applied for optimally combining data from different sources.

Errors can broadly be classified as

1. *System heading error*: A misalignment angle in the heading of an object traveling with a velocity can cause serious errors. For example, a vehicle traveling with a velocity of 500 km h^{-1} in the same direction with 0.1° initial heading error will be off the target by approximately 873 m at the end of 1 h travel.
2. *Scale error*: Error in scaling can accumulate. In order to minimize scale errors, a scale factor is used. The scale factor is the ratio between changes in the input and output signals. It simply translates the gyro output (counts per second in the case of RLG) into a corresponding angle rotation. Some instruments may have different scale factors for positive and negative inputs, known as *scale factor asymmetry*. (Scale factors are measured in h^{-1}, mA^{-1}, h^{-1} Hz^{-1}, or g Hz^{-1}.)
3. *Nonlinearity and composite errors*: In most cases, scale factors are not constant, but they can have second- or higher-order terms relating the output signals to the input. Statistical techniques can be employed to minimize these errors.
4. *Bias errors*: Zero offset or bias error is due to existence of some level of output signal for a zero input. Bias errors exist in accelerometers, gyros, and tilt misalignments.
5. *Random drift and random walk errors*: In some cases, the outputs of the devices can change due to disturbances inside the sensors, such as ball bearing noise in mechanical gyros. These disturbances may be related to temperature changes, aging, etc. White noise in optical gyros can cause a long-term accumulation in angle error known as the *random walk*.
6. *Dead band*, *threshold*, *resolution*, *and hysteresis errors*: These errors can be related to inherent operation of accelerometers and gyros. They can be due to stiction, minimum input required for an output, minimum measurable outputs, and nonrepeatability of variations in the output versus variations in the input.

Note that this list is by no means exhaustive. For those readers with further interest, the detailed error analysis can be found in the bibliography.

17.4.2 Stabilization

The inertial navigation sensors must maintain angles within specified limits in spite of the disturbances imposed by the moving object. Accuracy requirements demand that the system must provide reliable and stable information in spite of vibrations and other disturbing factors. One way of achieving stabilization is by using a stabilized platform. These platforms are designed to maintain accelerometers and gyros accurately leveled and oriented in the azimuth direction. In some cases, the platform is driven around its axis by servo amplifiers and electric motors. Usually, outputs of doubly integrating

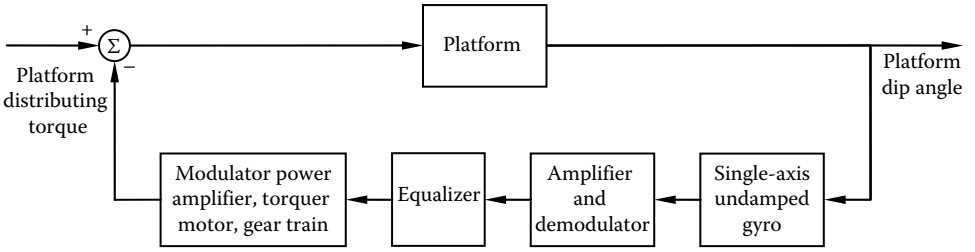

FIGURE 17.8 Stabilization is obtained using platforms designed to maintain accelerometers and gyros leveled accurately and properly oriented in the azimuth direction. In some cases, the platform is driven around its axis by servo amplifiers and electric motors. Sensitive pick-offs on the gyroscopes that fed error signals are used to maintain the desired stability of the platform in the presence of disturbances.

accelerometers are used directly to control the level-axis gyroscope precession rates. Sensitive pick-offs on the gyroscopes that fed error signals are used to maintain a desired stable platform in the face of disturbing torques. The operation of a typical system, in block diagram form, is shown in Figure 17.8.

Unlike platform models, in a strapdown system, gyroscopes and accelerometers are rigidly mounted to the vehicle structure so that they move with the vehicle. The accelerometers and gyroscopes are manufactured to measure accelerations and angles up to the maximum expected values. As the vehicle travels, the measured values are frequently transmitted to a computer. The computer uses these values to resolve the readings into the navigation axis sets and make deductions on the body axis sets.

17.5 Vehicular Inertial Navigation

In modern vehicular navigation, computerized maps and mobile communication equipment are integrated together with inertial and/or other electronic navigation systems. In recent years, in the wake of low-cost GPS systems, the vehicular navigation system has found a wide range of applications from consumer product to self-navigating systems.

Automobile navigation systems are based on dead-reckoning, map-matching, satellite-positioning, and other navigational technologies. Map intelligent systems achieve high relative accuracy by matching dead-reckoned paths with road geometry encoded in a computerized map. This is also used to perform other functions such as vehicle routing and geocoding. Satellite-based navigation systems achieve high absolute accuracy with the support of dead-reckoning augmentation. The capabilities and functions of automobile navigation systems depend on

- Choosing the necessary technology
- Integrating the overall system
- Resolving driver interface
- Providing map data basis
- Coordinating mobile communications

Digital maps and mobile data communications combine together for full usefulness and effectiveness. The navigation systems are greatly enhanced in conjunction with stored digital maps combined with effective communications.

The usefulness of a navigation system is related to the accuracy in position determination. There are a number of methods available with varying accuracy; these include the following:

Dead reckoning: Dead reckoning is the process of determining vehicle location relative to an initial position by integrating measured increments and directions of travel. The devices include the odometer, the differential odometer, and a magnetic compass. Gyros and inertial systems prove to have limited applications in harsh automotive environments. Although dead-reckoning systems suffer from error accumulation,

they are still used in INSs, particularly in robotics and vehicular applications. Even the most precise navigation system requires periodic re-initialization and continuous calibrations by computers.

Most of the dead-reckoning equipment commercially available is sufficiently robust to support map matching when operating in a defined road network. However, a good dead-reckoning accuracy is required to achieve re-initialization through map matching upon returning to the road network after off-road operations.

Radiolocation: In radiolocation, the GPS is used extensively.

Map matching: Artificial intelligence concepts are applied to match dead-reckoned vehicle paths, which are stored in computers. In map matching, sensed mathematical features of the vehicle paths are continuously associated with those encoded in a map database. Thus, a vehicle's dead-reckoned location can be initialized automatically at every turn to prevent accumulation of dead-reckoning errors.

The first application of map-matching technology was in the automatic route control system (ARCS), which used a differential odometer for dead reckoning. In another system, the Etak map-matching system, a solid-state flux gate compass, is used as well as a differential odometer to dead-reckon paths for matching with digitized maps and aerial photographs.

In a map-matching system, as long as the streets and road connectivities are accurately defined, the process identifies position relative to the road network as visually perceived by the automatic system or by the driver of the vehicle.

Proximity beacon: This uses strategically located short-range transmitters, and reception of their location-coded signal infers the receiving vehicle's instantaneous location. There are several variations of the proximity approach; some versions involve two-way communications with the equipped vehicle. Typically, the driver enters the destination code on the vehicle panel, for automatic transmission to the roadside unit, as the vehicle approaches an instrumented intersection. The roadside unit, which can be networked with a traffic management system, analyzes the destination code and transmits route instructions to the display on the vehicle panel.

The approach to the interface between an onboard navigation system and a vehicle operator must take into account ergonomics and safety considerations as well as functional requirements. As a result of intensive research, especially in the aerospace industry, display of information for the operator is a well-developed area. In a well-known European system, Philips' CARiN, a color CRT map display, is used to show vehicle location relative to the surroundings. Many other systems use short visual messages, symbolic graphics, and voice.

Data communications in modern navigation systems provide current updates (road additions, closures, detours, etc.) for onboard map databases. It also provides real-time information on traffic conditions for onboard route generation.

17.6 Applications of Inertial Navigation

17.6.1 Aircraft

The primary navigation aid for civil aircraft flying in the airspace of most of the developed countries is the very-high-frequency omnirange (VOR)/distance-measuring equipment (DME) system. The VOR and the DME enable onboard determination of an aircraft's bearing relative to north at the fixed ground station and slant range from the station, respectively.

Many commercial aircraft are still equipped with precision INSs not only for navigation purposes but also for stabilization of the aircraft at all times. Suitably located gyroscopes and accelerometers give signals to control the stability of the aircraft, as illustrated in Figure 17.9.

Many aircraft INSs utilize a gyro-stabilized platform on which the accelerometers are mounted. The platform is aligned before take-off to the desired orientation. Due to alignment errors and in-flight

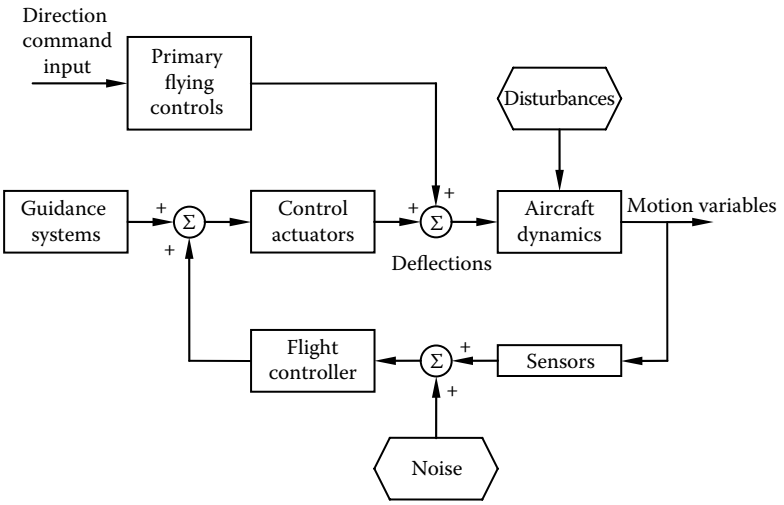

FIGURE 17.9 In many commercial aircraft, suitably located gyroscopes and accelerometers give signals for controlling the stability of the aircraft. Due to various instrumental errors and in-flight random disturbances such as gyro drift, scale factor errors, and accelerometer bias errors, the errors in the desired orientation increase with time. These accumulated errors need to be compensated periodically by information from the GPS systems.

random disturbances such as gyro drift, scale factor errors, and accelerometer bias errors, the errors in the desired orientation increase with time. The errors need to be compensated periodically by external information such as radar and GPS navigation systems.

GPS systems give all vehicles on or near the Earth unprecedented navigation accuracy. Most of the airlines are equipped with confined GPS receivers. Airborne receivers are designed that combine navaids operating in a common radio bands.

17.6.2 Underwater

The Ship's Inertial Navigational System (SINS) was originally developed for precision position finding required by ballistic missile submarines in the late 1950s and the early 1960s. The first deployment was onboard U.S. George Washington in 1960, and SINS are used today in submarines, aircraft carriers, and other surface warships. As the cost and size are continually decreasing, the system is also deployed in naval as well as merchant vessels. Another development of INS for underwater application is in the area of the autonomous underwater vehicle (AUV). In this section, a number of such products are described.

AUVs are used extensively for military and civilian purposes. Application examples are mapping, surveillance, ocean exploration, survey, and mining, all of which require precise position determination. The desired features of such systems are low power, high accuracy, small volume, light weight, and low cost. Two typical examples were given as follows:

KN-6050 underwater navigators are based on Kearfott's Monolithic RLG INS system. It is assisted by a Doppler Velocity Log (DVL) and GPS position inputs. They find applications in AUVs as well as surface unmanned vehicles (SUV) and remotely operated vehicles (RUV). It requires a multitude of inputs, such as depth sensor, position inputs, and speed and sound sensors. Navigation outputs are position, altitude and depth, ground speed, and heading. These devices provide vehicle stabilization and control by monitoring angular rates, linear accelerations, roll, and pitch.

The second example is the HUGIN 1000 AUV, developed by Konsberg, Norway, suitable for military applications as well as ocean research and environmental monitoring. HUGIN 1000 uses hydroacoustic-aided INS, which combines acoustic and inertial positioning principles. It also uses various types of transponders.

17.6.3 Robotics

Autonomous mobile robots also use INS extensively as a self-contained, independent navigation system. Typical applications are mining, unknown terrain exploration, and off-line path planning. There are many commercially available INSs suitable for cost-effective utilization in the navigation of robots. Some of these are gyrocompasses, rate gyros, gyrochip, piezoelectric vibrating gyros, RLGs, interferometric, and other types of fiber-optic gyros.

The Honeywell Modular Azimuth Position System (MAPS): The MAP-H is a typical example of an INS for land-based vehicles. It consists of a dynamic reference unit (DRU) that provides processed information from the inertial sensor assembly, a control display unit (CDU) that is used for human–machine interface, and a vehicle motion sensor (VMS) that monitors the vehicle's directional and distance information. The inertial sensor assembly comprises three Honeywell ring-laser gyros and three accelerometers mounted to measure movements in three local axes. The inertial processor translates the information to the navigation processor that resolves the vehicle movement information from the VMS. The CDU provides mode selection, data display, waypoint information, and general operator interface.

Bibliography

Aggarwall, P., Syed, Z., Noureldin, A., El-Sheimy, N., *MEMS-Based Integrated Navigation*, Artech House, Norwood, MA, 2010.

Bijker, J., Kalman filter configurations for a low-cost loosely, integrated inertial navigation system on an airship, *Control Engineering Practice*, 16(12), 1509–1518, 2008.

Bird, J., Arden, D., Indoor navigation with foot mounted strapdown inertial navigation and magnetic sensors, *IEEE Wireless Communications*, 18(2), 35–42, 2011.

Hablani, H. B., Autonomous inertial relative navigation with sight-line stabilized integrated sensors for spacecraft randevous, *Journal of Guidance, Control, and Dynamics*, 32(1), 172–183, 2009.

Lawrence, A., *Modern Inertial Navigation Technology: Navigation, Guidance, and Control*, 2nd edn., Springer, London, U.K., 1998.

Qin, F. J., Xu, J. N., Jiang, S., A new scheme of gyroscope free inertial navigation system using 9 accelerometers, *2009 International Workshop on Intelligent Systems and Applications*, ISA 2009, Wuhan, China, May 2009.

Sonmez, T., Bingol, H. H., Modelling and simulation of a terrain aided inertial navigation algorithm, for land vehicles, *IEEE Position, Location and Navigation Symposium*, Monterey, Canada, pp. 1046–1052, 2008.

Titterton, D. H., Weston, J. L., *Strapdown Inertial Navigation Technology*, 2nd edn., The Institution of Electrical Engineering, Stevenage, U.K., 2004.

Woodman, O. J., An introduction to inertial navigation, Technical Report No. 696, University of Cambridge, Cambridge, U.K., 2007. Available at http://www.cl.cam.ac.uk/techreports/UCAM-CL-TR-696.pdf (accessed on March 3, 2012).

Partial List of Manufacturers/Suppliers

ACUTRONICUSA, Inc., 700 Waterfront Dr., Pittsburgh, PA 15222-4742, Phone: 412-926-1200, Fax: 412-697-8111, www.acutronic.com

Astronautics Corp. of America, 4115 N. Teutonia Ave., Milwaukee, WI 53209-6731, Phone: 414-449-4000, Fax: 414-447-8231, www.astronautics.com

Automatic Equipment Mfg. Co./BlueOx, 1 Mill Rd, P.O. Box P, Pender, NE 68047, Phone: 402-385-3051, Fax: 402-385-3360, www.aemfg.com

Boeing Co., 1215 N. 2200 W., Salt Lake City, UT 84116-4128, Phone: 801-537-6400, www.boeing.com

Condor Pacific Industries, Inc., 31829 La Tienda Dr., Westlake Village, CA 91362-4011, Phone: 818-865-3000, Fax: 818-865-3010, www.condorpacific.com

Crossbow Technology, Inc., 4145 N. 1st St., San Jose, CA 95134-1504, Phone: 408-965-3300, Fax: 408-324-4840, www.xbow.com

Davis Instruments Corp., 3465 Diablo Ave., Hayward, CA 94545, Phone: 510-732-9229, 800-678-3669 (toll free), Fax: 510-670-0589, www.davisnet.com

Electron Energy Corp., 924 Links Ave., Landisville, PA 17538-1615, Phone: 717-898-2294, 800-824-2735 (toll free), Fax: 717-898-0660, www.electronenergy.com

Frog Navigation Systems, 691 N. Squirrel Rd Ste 115, Auburn Hills, MI 48326, Phone: 248-373-7200, Fax: 248-373-7400, www.frogusa.com

Garmin Corporation, 1200 E. 151st St., Olathe, KS 66062-3426, Phone: 913-397-8200, 800-525-6726 (toll free), Fax: 913-397-8282, www.garmin.com/garmin/cms/site/us

Hitachi Cable America, Inc., Optical Div., 3031 Tisch Way, Ste. 150, San Jose, CA 95128, Phone: 408-260-2630, Fax: 408-260-2756, www.hitachi-cable.com

Honeywell International, Inc., 101 Columbia Rd., Morristown, NJ 07962-1057, Phone: 973-455-2000, 800-707-4555 (toll free), Fax: 973-455-4807, honeywell.com/Pages/Home.aspx

Inertial Labs, 13800 Coppermine Rd., Suite 300, Herndon, VA 20171, Phone: 703-880-4222, Fax: 703-991-5378, www.inertiallabs.com

Jae Electronics, Inc., 142 Technology Dr. W. # 100, Irvine, CA 92618-2430, Phone: 949-753-2600, Fax: 949-753-2699, www.jae.com

Kearfott Guidance & Navigation Corp., 1150 McBride Ave., Little Falls, NJ 07424, Phone: 973-785-6000, Fax: 973-785-5400, www.kearfott.com/

Litton Guidance & Control Systems, 5500 Canoga Ave., Woodland Hills, CA 91367, Phone: 818-715-4040, Fax: 818-715-4467, http://www.littoncorp.com/

Lockheed Martin, 6417 Deere Rd., Syracuse, NY 13206, Phone: 315-456-3660, www.lockheedmartin.com/

Mi-Tech Metals, Inc., 4701 Massachusetts Ave., Indianapolis, IN 46218-3144, Phone: 317-549-4290, 800-624-1895 (toll free), Fax: 317-549-4295, www.mi-techmetals.com

Mil-Spec Industries Corp., 10 Mineola Ave., Roslyn Heights, NY 11577, Phone: 516-625-5787, Fax: 516-625-0988, www.mil-spec-industries.com

Navhouse Co., 10 Loring Drive, Bolton, ON L7E1J9, Phone: 905-857-8102, Fax: 905-857-8104, www.navhouse.com

Navico, Inc., 1010 S.E. Everett Mall Way Ste. 101, Everett, WA 98208, Phone: 603-324-2042, Fax: 603-324-2043, http://www.navico.com/en/

Northrop Grumman Corporation, 755 Dedham St., Canton, MA 02021, Phone: 866-646-2879 (toll free), http://www.northropgrumman.com/

Northstar, 30 Sudbury Rd., Acton, MA 01720, Phone: 978-897-6600, 800-628-4487 (toll free), Fax: 978-897-8264, www.northstarnav.com/

Precision Navigation, Inc., 5464-T Skylane Blvd., Santa Rosa, CA 95403-1084, Phone: 707-566-2260, Fax: 707-566-2260, www.pnicorp.com/

Rockwell International Corp., Aerospace & Defense, Autonetics & Missile Systems Div., 3370-T Miraloma Ave., Anaheim, CA 92803, Phone: 714-762-8111, Fax: 714-762-1243, http://www.rockwellautomation.com/

Select Controls, Inc., 45 Knickerbocker Ave., Bohemia, NY 11716-3110, Phone: 866-929-5312 (toll free), Fax: 631-567-9013, www.select-controls.com

Southern Avionics Company, P.O. Box 5345, Beaumont, TX 77726-5345, Phone: 409-842-1717, 800-648-6158 (toll free), Fax: 409-842-2987, www.southernavionics.com

Systron Donner Inertial, 2700 Systron Dr., Concord, CA 94518, Phone: 925-671-6400, Fax: 925-671-6647, www.systron.com

Trimble Navigation, Ltd., 936 Stewart Dr., Sunnyvale, CA 94088, Phone: 408-481-8000, www.trimble.com

Warren-Knight Instrument Co., 2045 Bennett Dr., Philadelphia, PA 19116-3019, Phone: 215-464-9300, Fax: 215-464-9303, www.warrenknight.com

18

Level Measurement

Detlef Brumbi
Krohne Messtechnik GmbH

Level is defined as the filling height of a liquid or bulk material, for example, in a tank or reservoir. Generally, the position of the surface is measured relative to a reference plane, usually the tank bottom. If the product's surface is not flat (e.g., with foam, waves, turbulences, or with coarse-grained bulk material), level usually is defined as the average height of a bounded area.

Various classic and modern methods exist to measure product level in process and storage tanks in the chemical, petrochemical, pharmaceutical, water, and food industries, in mobile tanks on vehicles and ships, but also in natural reservoirs like seas, dams, lakes, and oceans. Typical tank heights are approximately between 0.5 and 40 m.

Two different tasks can be distinguished: (1) continuous level measurements (level indication, LI) and (2) level switches (LSs) (e.g., to detect an alarm limit to prevent overfilling). Figure 18.1 shows the principal operational modes of level measurement. Every continuous system can also be used as a programmable switch. Many level devices are mounted on top of the tank and measure primarily the distance d between their mounting position and the product's surface. The level L is then calculated, defining the tank height h as constant, as shown in Figure 18.1 and expressed as:

$$L = h - d \tag{18.1}$$

The following examples describe primarily the measurement of liquids, but most of the methods can also be applied to solids (bulk material). The emphasis of this chapter will be general information about the measurement principles. The focus of the descriptions is on the methods most commonly practiced; other principles are mentioned less comprehensively. Readers interested in more detailed discussions may refer to [1–4].

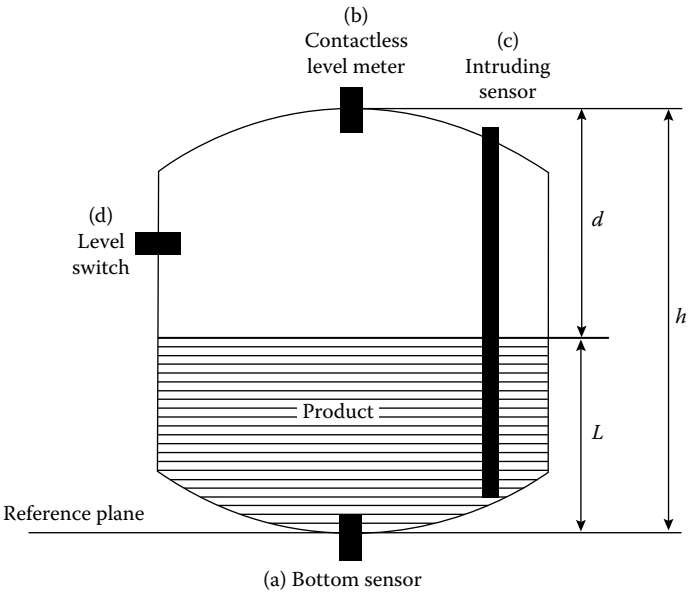

FIGURE 18.1 Representation of a tank with a liquid or solid material (hatched area), the product to be measured. The level sensor can be mounted (a) contacting product at the bottom, (b) as a contactless instrument on top, (c) as an intrusive sensor, or (d) at the sides as an LS.

18.1 Measurements Using the Effects of Density

All methods described in this chapter have in common that the product in the tank has an effect due to its density ρ, (1) producing buoyancy to a solid submerged into the liquid or (2) executing a force due to its weight.

18.1.1 Displacer

Displacers measure the buoyancy of a solid body that is partially submerged in the liquid. The change in weight is measured. Figure 18.2 illustrates the parameters used for these calculations. The cross section A of the body is assumed to be constant over its length b. The weight of force F_G due to gravity g and mass m is

$$F_G = gm = gAb\rho_D \tag{18.2}$$

The buoyant force F_B accounts for the partial length L_d that is submerged with the remainder of the body in the atmosphere:

$$F_B = gAL_d\rho_L + gA(b - L_d)\rho_A \tag{18.3}$$

Combining Equations 18.2 and 18.3 gives the resulting force to be measured by an appropriate method as follows:

$$F_R = F_G - F_B \tag{18.4}$$

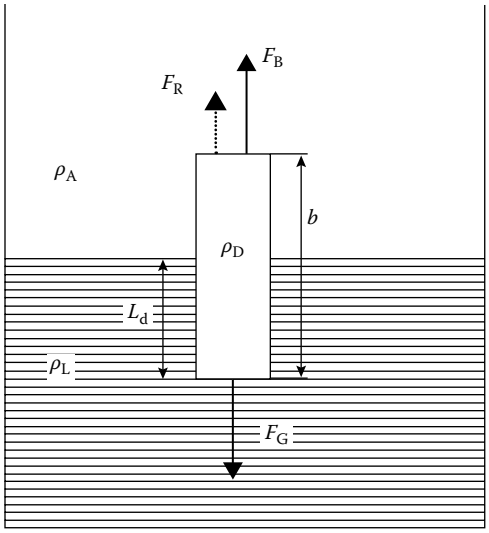

FIGURE 18.2 Quantities of a solid body immersed into a liquid. The forces F can be calculated from Equations 18.2 through 18.4. ρ = density, b = length of the body, and L_d = dipped length.

The result for level L_d, related to the lower edge of the displacer, is

$$L_d = \frac{b(\rho_D - \rho_A) - F_R/gA}{\rho_L - \rho_A} \tag{18.5}$$

The density of the body should be higher than the density of the liquid; otherwise, the measurement operating range is limited (until the displacer floats on the liquid). In another version, a servo gage moves the displacer up and down to detect the interface between the atmosphere and a liquid, or between two different liquids, by measuring the change in buoyancy. Figure 18.3 shows a special configuration, in which a small ball with volume V is mounted to a thin wire driven by a stepping motor and put into resonant vibration. The resulting force F can be measured from the resonating frequency f of the wire between points A and B:

$$F = \rho_w A_w 4 f^2 l^2 \tag{18.6}$$

where

l is the length of the wire between the points A and B
ρ_w is the density of the wire
A_w is the cross-sectional area of the wire

And the surrounding density ρ_L can be calculated as follows:

$$F = gV(\rho_D - \rho_L) \Leftrightarrow \rho_L = \rho_D - \frac{F}{gV} \tag{18.7}$$

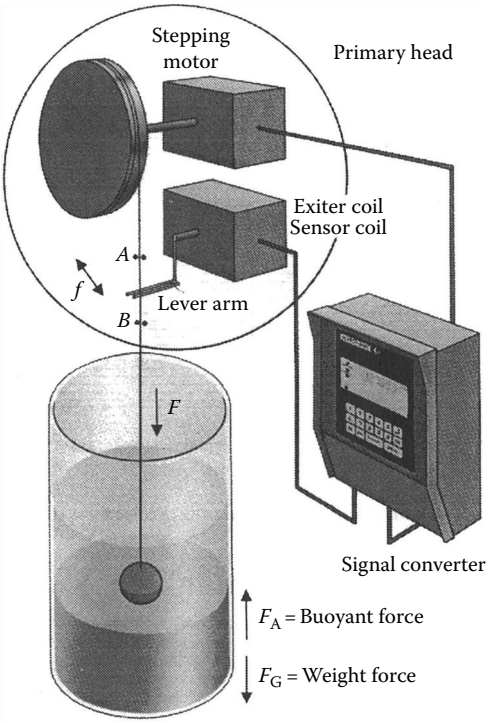

FIGURE 18.3 Level, interface, and density sensor using the effects of buoyancy. A stepping motor drives the small ball attached to the thin wire to different heights in the liquid or to the interfaces. The resulting force F as a difference between weight force and buoyant force is measured from the resonant frequency of the wire-ball system. The lever arm excites the wire into oscillation and a sensor coil coupled to the lever arm measures its frequency. The signal converter controls the stepping motor and calculates the measured values. (From Messtechnik, K., *Technical Data Sheets of Level Measurement Products*, Krohne, Duisburg, Germany, 1996.)

18.1.2 Float

Floats are similar to displacers but are swimming on the liquid's surface due to the buoyancy. Hence, the density of the float must be lower than the density of the liquid. Figure 18.4a shows the principle of operation. The position of the float is (1) observed visually or (2) transferred to an external display or to an angle transmitter. In general, the float is coupled to the transmitter magnetically. Figure 18.4b shows an LS, using a reed relay magnetically coupled with the float. Also, a magnetostrictive linear sensor may determine the position of the float.

If the float is very flat, it is called a "sensing plate." This plate is mechanically guided, for example, by a servo control, on the surface until uplift is detected. For solids, specially shaped perpendicular floats are helpful.

18.1.3 Pressure Gages

A hydrostatic pressure p, caused by the weight of the product, is present at the bottom of a tank, in addition to the atmospheric pressure p_0:

$$p = p_0 + g\rho_L L \Leftrightarrow L = \frac{p - p_0}{g\rho_L} \tag{18.8}$$

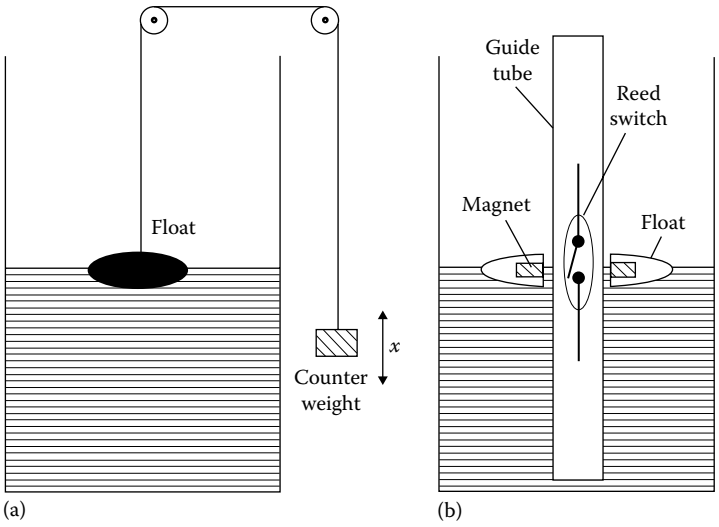

FIGURE 18.4 Principle of operation for float level meters. (a) *A* counterweight balances the float that swims on the liquid's surface. Its position represents the level; (b) the float contains a magnet that contacts a reed switch inside a guide tube. Using a bistable relay, this system is used as an LS. One can also insert multiple relays into the tube to achieve different switching points for quasicontinuous operation.

Pressure gages at the bottom of the tank measure this pressure. In process tanks with varying atmospheric pressure, a differential pressure measurement is achieved by measuring the difference between the pressure at the bottom and that at the top of the tank, above the liquid. Figure 18.5a shows such a configuration with a differential pressure sensor. Because measurement by hydrostatic pressure is proportional to the density, level errors result if density changes; see Equation 18.8. Primary pressure gaging is a mass measurement. Figure 18.5b shows a vertical arrangement with three sensors; the measurements of p_1 and p_2 are used to compensate for the influence of density ρ_L and to calculate the level:

$$\rho_L = \frac{p_2 - p_1}{gl} \Rightarrow L = \frac{p_2 - p_0}{p_2 - p_1} l \tag{18.9}$$

A system of this configuration is often called "hydrostatic tank gaging" (HTG). Figure 18.5c shows a further arrangement, called "bubble tube," in which the bottom pressure is transmitted to the top of the tank. This is often used for level gaging if the sensor cannot be mounted at the bottom of the tank. It requires a tank with pressure equalization due to the steady insertion of inert gas.

18.1.4 Balance Method

Here simply the weight F of the complete tank is measured, dependent on the level L:

$$F = F_0 + gAL\rho_L \tag{18.10}$$

where

F_0 is the weight of the empty tank
A is the cross-sectional area

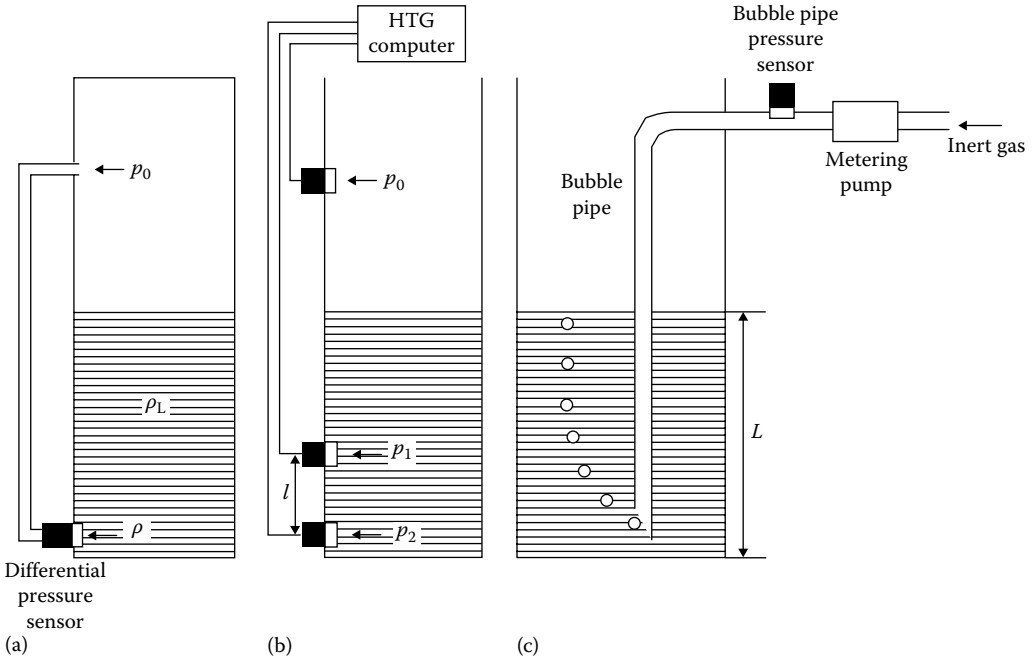

FIGURE 18.5 Level gaging by hydrostatic pressure measurement. The bottom pressure p is proportional to level. (a) The atmospheric pressure p_0 can be taken into consideration by a differential measurement. The low side of the differential pressure sensor is connected via a thin pipe to the top of the tank. (b) A differential measurement within the liquid is called "hydrostatic tank gaging" and can be used to compensate for errors due to density variations of the liquid. The signals from all three sensors are evaluated by a computer. (c) With a so-called bubble tube, the sensor can be mounted on the top of the tank: an inert gas is injected into the tube such that bubbles of gas escape from the end of the tube. The flow rate of the gas is constant, so the head pressure in the system can be measured at the inlet of the pipe.

which is assumed to be constant throughout the tank height. In order to measure the weight force correctly, it is necessary to isolate the complete tank mechanically. For precise measurements, the buoyancy in air must be taken into consideration:

$$F = F_0 + gAL(\rho_L - \rho_A) \Leftrightarrow L = \frac{F - F_0}{gA(\rho_L - \rho_A)} \tag{18.11}$$

This method has severe disadvantages when the tank is not inside a building. Outside, wind forces and the weight of snow and rain can cause errors.

18.2 Time-of-Flight Measurements

An indirect measurement of level is evaluating the time of flight of a wave propagating through the atmosphere above the liquid or solid. This is primarily a distance measurement; the level can then be calculated accordingly. The increasing demand of industry for nonintrusive continuous level gaging systems has been instrumental in accelerating the development of technologies using time-of-flight measurements [5].

18.2.1 Basic Principle

Although different types of physical waves (acoustic or electromagnetic) are applied, the principle of all these methods is the same: a modulated signal is emitted as a wave toward the product, reflected at its surface and received by a sensor, which in many cases is the same (e.g., the ultrasonic piezoelectric transducer or the RADAR antenna). Figure 18.6 demonstrates the principle of operation. The measuring system evaluates the time of flight t of the signal:

$$t = \frac{2d}{v} \tag{18.12}$$

where v is the propagation velocity of the waves.

One can generate an unmodulated pulse, a modulated burst as in Figure 18.6b, or special forms. Table 18.1 lists the main properties of the three preferred types of waves, used for time-of-flight level gaging.

The very short time spans of only a few nanoseconds for RADAR and laser measurement techniques require the use of time expansion by sampling as discussed later.

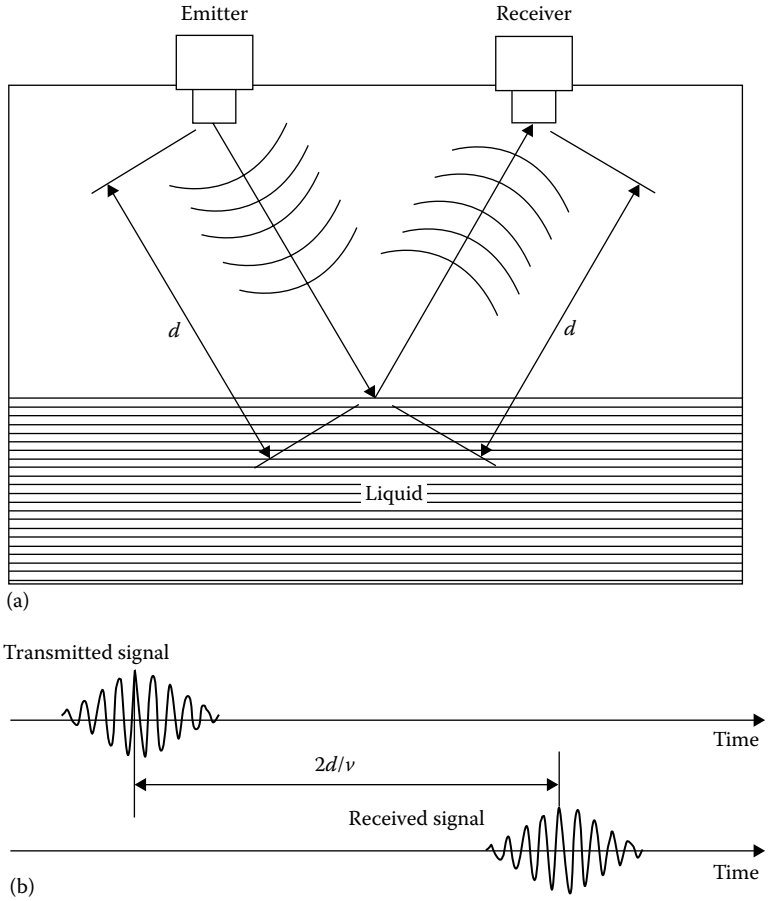

FIGURE 18.6 (a) Representation of time-of-flight measurements. The emitter couples a wave (ultrasonic or electromagnetic) into the atmosphere that propagates the wave toward the liquid. Its surface reflects the wave and a sensor receives it. (b) Due to the propagation velocity v, a time delay is measured between emission and receipt of the signal. This example is characterized by a modulated burst. The time scale is arbitrary.

TABLE 18.1 Properties of the Wave Types for Time-of-Flight Measuring

Principle	Wave Velocity	Avg. Carrier Frequency	Wavelength	Avg. Burst Time
Ultrasonic	340 m s^{-1}	50 kHz	7 mm	1 ms
RADAR	300,000 km s^{-1}	10 GHz	3 cm	1 ns
Laser	300,000 km s^{-1}	300 THz	1 μm	1 ns

18.2.2 Ultrasonic

Ultrasonic waves are longitudinal acoustic waves with frequencies above 20 kHz. Ultrasonic waves need a propagation medium, which for level measurements is the atmosphere above the product being measured. Sound propagates with a velocity of about 340 m s^{-1} in air, but this value is highly dependent on temperature and composition of the gas and also on its pressure. In vacuum, ultrasonic waves cannot propagate. In practice, the reflection ratio is nearly 100% at the product's surface (e.g., at transitions gas/liquid or gas/solid). Piezoelectric transducers are utilized as emitter and detector for ultrasonic waves, a membrane coupling it to the atmosphere. The sensor is installed as in Figure 18.1b, the signal form is as in Figure 18.6b. Level gaging is, in principle, also possible with audible sound 16 Hz–20 kHz or infrasonic waves less than 16 Hz.

Another procedure is to propagate the waves within the liquid by a sensor mounted at the bottom of the tank. The velocity of sound in the liquid must be known, considering the dependence on temperature and type of liquid. This method is similar to an echo sounder on ships for measuring the water depth.

18.2.3 Microwaves

Microwaves are generally understood to be electromagnetic waves with frequencies above 2 GHz and wavelengths of less than 15 cm. For technical purposes, microwave frequencies are used up to a maximum of 120 GHz; in practice, the range around 10 GHz (X-band) is preferred.

The usually applied time-of-flight measurements with microwaves are RADAR based [6,7]. The term "RADAR" is generally understood to mean a method by means of which short electromagnetic waves are used to detect distant objects and determine their location and movement. It is an acronym from radio detection and ranging. Figure 18.7 shows preferred antenna forms. They are usually combined with a compact sensor, as in Figure 18.8. For level measuring systems, a small radiation angle is desirable in order to avoid interfering reflections from the tank wall or tank internals as much as possible. The larger the aperture area, the smaller the radiation angle and the higher the antenna gain. The power balance is given by the general RADAR equation:

$$P_R = \frac{P_T G_T R G_R}{D^2} \tag{18.13}$$

where

P_R is the received power
P_T is the transmitted power
G_T is the transmitting antenna gain
R is the reflection factor of target
G_R is the receiving antenna gain
D^2 is the propagation loss to and from the surface, due to power density decrease and atmospheric influences

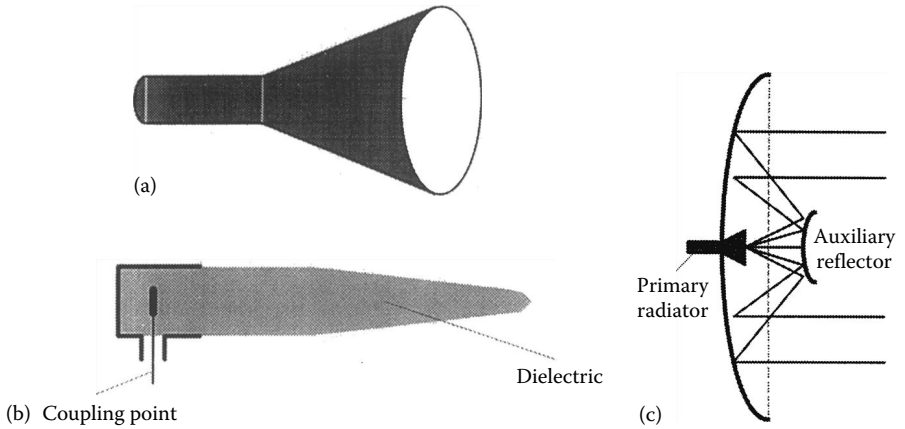

FIGURE 18.7 Practical antenna forms used for RADAR level instruments: (a) conical horn antenna, (b) dielectric rod antenna, and (c) parabolic mirror with a small antenna as primary radiator and an auxiliary reflector giving a very small beam angle (so-called Cassegrain model).

FIGURE 18.8 Design of a compact industrial level RADAR system. The converter above the flange includes the complete microwave circuitry, signal-processing stages, microprocessor control, display, power supply, and output signal. (From Messtechnik, K., *Technical Data Sheets of Level Measurement Products*, Krohne, Duisburg, Germany, 1996.)

The reflection factor R of the product's surface is dependent on the dielectric permittivity ε_r of the liquid or bulk material:

$$R = \frac{\left(\sqrt{\varepsilon_r} - 1\right)^2}{\left(\sqrt{\varepsilon_r} + 1\right)^2} \tag{18.14}$$

In level measurement situations, the reflecting area is so large that it intersects the beam cross section completely; therefore, D^2 is approximately proportional with distance d^2. Thus also, the received power decreases proportionately with d^2, as derived in [6]:

$$P_R \propto \frac{1}{d^2} \tag{18.15}$$

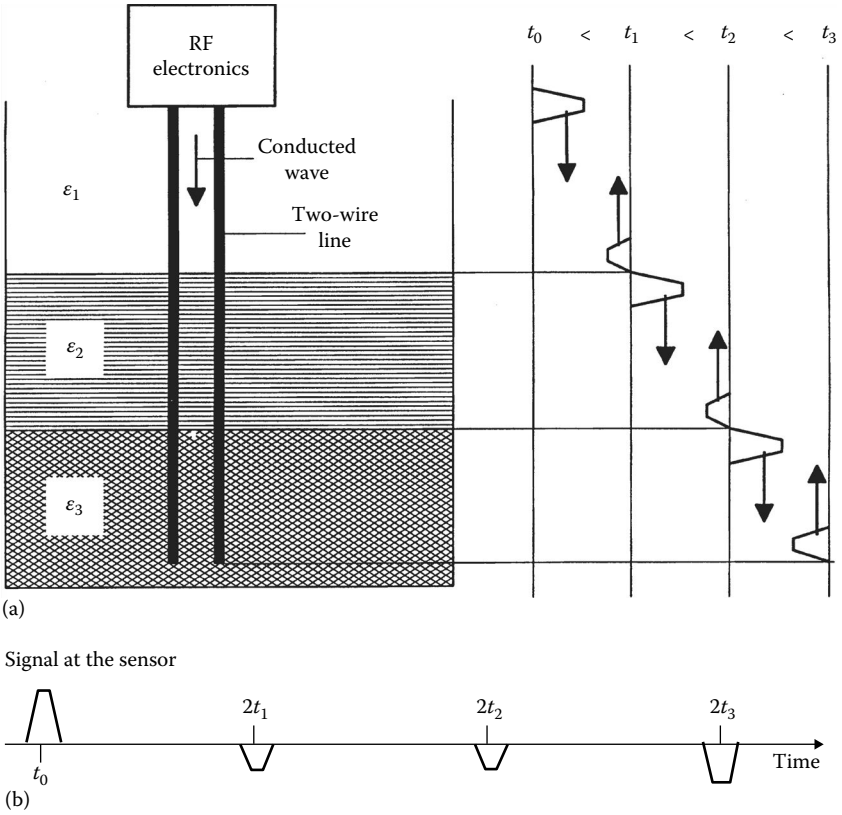

FIGURE 18.9 Principle of operation of a wire-conducting high-frequency level measurement system. (a) An electrical pulse is generated (time t_0) and a two-wire line guides the electromagnetic wave. At every position where the surrounding permittivity e changes, a part of the wave is sharply reflected (time t_1) back to the sensor. The wave propagates along the entire line and is reflected a second time (t_2) at the interface between the two liquids and a third time at the end of the line. (b) The signal delay times ($2t_1$, $2t_2$, and $2t_3$) represent the positions of the interfaces with respect to the end of the line, which can be used as a reference. The signal polarity is inverted due to the reflection from lower to higher permittivity. The time scale is arbitrary.

This is not the case if the waves propagate within an electromagnetic waveguide, like a vertical tube dipping into the liquid, called a stilling well. Here, the propagation is nearly without losses.

An alternative method using electromagnetic waves is to propagate them in a cable. Figure 18.9a illustrates the operation with a cable dipped into the liquid or bulk material. In this case, the dielectric permittivity of the surrounding medium changes; part of the wave is reflected. This method can be applied to interface measurements too. Figure 18.9 shows the signals in an application with a two-phase product. This method is called "time domain reflectometry" (TDR).

18.2.4 Laser/Light

Lasers and light-emitting diodes produce electromagnetic waves of very short wavelength (less than 2 μm), which can also be used for time-of-flight measurements, similar to the described microwave methods. Preferred laser signals are (1) short pulses of less than 1 ns duration or (2) lasers with amplitude-modulated intensity with frequencies of some megahertz. For more details about laser operation and interferometry methods, refer to Section 6.5 of this handbook.

Laser systems are very precise and can achieve accuracies better than 1 mm. Because the laser beam is very narrow, such level measurement systems can be installed without influence of tank internals. Some practical disadvantages of laser level measurement are as follows: (1) It functions as does your eye to see the product's surface and therefore fails if dust, smoke, etc. are present; (2) it is sensitive to dirt on the optical sensors; and (3) the equipment is expensive.

18.3 Commonly Used Evaluation Methods

Due to the great benefits of contactless time-of-flight measurement, some typical methods have been evaluated for level gaging within the last few years, mainly in RADAR techniques [6].

18.3.1 Frequency-Modulated Continuous-Wave RADAR

Because the flight times in typical level applications are very short (a resolution of 1 mm requires a 7 ps time resolution), it is difficult to evaluate information directly in the time domain. By modulation of the microwave signals, the time delay is transformed into the frequency domain, obtaining low-frequency signals.

Therefore, frequency-modulated continuous-wave (FMCW) RADAR has been established as the dominant technique. FMCW RADAR utilizes a linearly frequency-modulated microwave signal; the transmission frequency rises linearly in a time interval T. The frequency difference in this interval is called the frequency sweep F.

Figure 18.10 shows the principle of FMCW RADAR. Due to the time delay during signal propagation, the transmitted frequency changes such that the difference between the momentary transmitted frequency and the received frequency, a low-frequency signal, is obtained. The frequency f of that signal (typically up to a few kilohertz) is proportional to the reflector distance d (see Figure 18.6); in this method, therefore, the delay t is transformed into a frequency f:

$$f = \frac{F}{T}t = \frac{F}{T}\frac{2d}{c} \Leftrightarrow d = \frac{fcT}{2F} \tag{18.16}$$

In Equation 18.16, c is the speed of light and F/T is the sweep velocity; see Figure 18.10.

Figure 18.11 shows a basic circuit block diagram of an FMCW RADAR system. Because the resultant signal frequencies are low, further signal processing is technically simple and very accurate. Normally, evaluation is by means of digital signal processing.

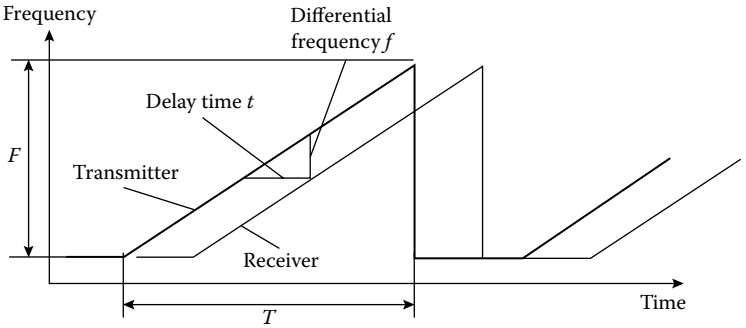

FIGURE 18.10 Operation characteristics of FMCW RADAR. The frequency of the transmitter changes linearly by time in an interval (sweep). The received signal has the same form but is time delayed. At every point of the sweep, the differential frequency is constant and proportional to the time delay. Time and frequency scales are arbitrary.

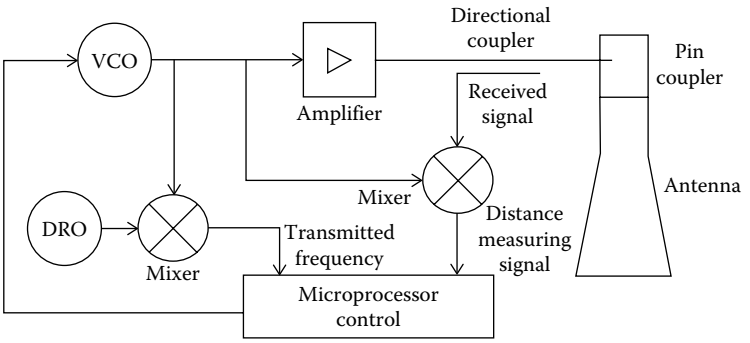

FIGURE 18.11 Basic circuit block diagram of an FMCW RADAR system: a microprocessor controls a voltage-controlled oscillator (VCO), such that the desired frequency sweep is obtained. This signal is amplified and fed into the transmitting antenna. The instantaneous frequency must be measured in order to ensure good sweep linearity. This is accomplished by counting the frequency after it has been mixed with the known frequency of a dielectric resonance oscillator (DRO). A directional coupler decouples the received signal, which is mixed with the transmission signal and processed by the microprocessor.

18.3.2 Time-of-Flight through Product

Alternatively, the propagation time of the waves through a weakly absorbing liquid or bulk material of low permittivity ε_r can be measured, as well as the propagation through the air. In cases where the reflection from the interface between air and the upper surface of the product is poor, part of the signal travels through the liquid and is reflected a second time at the tank bottom or at an interface between two liquids (e.g., oil on water).

Figure 18.12 demonstrates this technique. The evaluation is done in the following four steps:

1. Where microwaves in the tank atmosphere of height d are propagated at the speed of light c, microwaves in the medium (relative permittivity = ε_r, height L) are propagated at a slower velocity v.
2. Hence, the reflection r_2 from the tank bottom appears to be shifted downward, and the apparent tank height h_v is greater than the true height h.
3. The transit time in the medium is $t_1 = L/v$, where for the same distance in an empty tank would be $t_0 = L/c$. The ratio of apparent "thickness layer" ($h_v - d$) to true filling height ($h - d$) therefore corresponds to the ratio of the wave propagation rates:

$$\frac{h_v - d}{h - d} = \frac{c}{v} = \sqrt{\varepsilon_r} \tag{18.17}$$

4. When ε_r, h, and h_v are known, distance d and, from that, filling height L can be calculated exactly as follows:

$$L = h - d = \frac{h_v - h}{\sqrt{\varepsilon_r} - 1} \tag{18.18}$$

By this method, a direct level measurement—not a distance measurement—is attained. It can even be applied when signal r_1 from the surface of the medium is no longer measurable. The evaluation of the tank bottom reflection signal is known as "tank bottom tracing" and is used in the RADAR level system offered by Krohne in Figure 18.8.

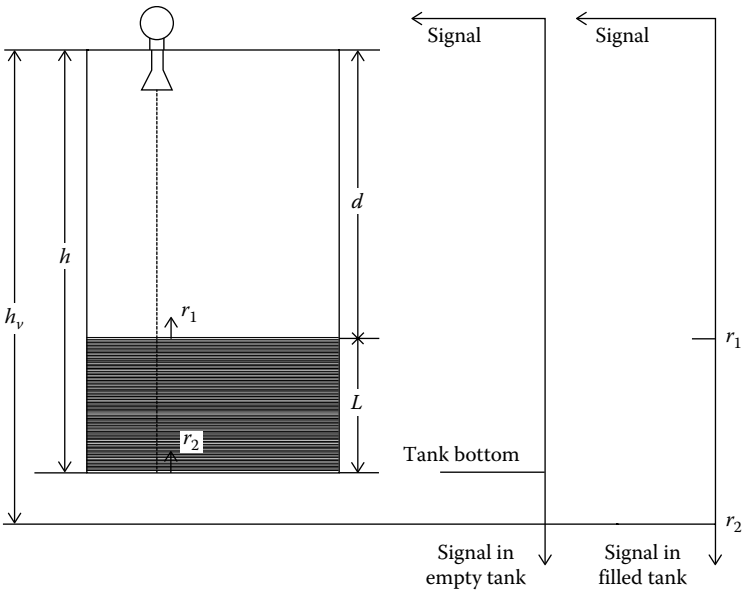

FIGURE 18.12 Representation of time-of-flight measurement through liquid: the wave is reflected once (r_1) at the product's surface and a second time (r_2) at the tank bottom. Due to the reduced wave velocity within the liquid, the reflection r_2 appears below the geometric position of the bottom. From that shift, the level can be calculated; see Equations 18.17 and 18.18.

18.4 Level Measurements by Detecting Physical Properties

To measure level, one can detect physical parameters that are significantly different between the atmosphere and the product; for example, conductivity, viscosity, or attenuation of any type of radiation. Two types are possible: (1) continuous measurement with an integral sensor or (2) switching by a point measurement when the sensor comes in contact with the product.

18.4.1 Electrical Properties

The sensor must be in direct or indirect contact with the product to detect its electrical properties. For continuous measurement, only part of the intrusive sensor must be in contact with the product to detect the difference in dielectric permittivity or conductivity.

18.4.2 Capacitive

In most applications, a rod electrode is arranged vertically in the tank. The electrode can be (1) noninsulated if the liquid is nonconductive or (2) insulated. The metallic vessel acts as a reference electrode.

The result depends on the permittivity ε_2 of the product. Figure 18.13a shows an electrode concentrically mounted on a cylindrical tank. For such a rotationally symmetrical configuration, the capacitance C of an insulated electrode changes with level L according to

$$C = \frac{2\pi\varepsilon_0 L}{1/\varepsilon_1 \ln d_2/d_1 + 1/\varepsilon_2 \ln d_3/d_2} \Leftrightarrow L = \frac{C\left(1/\varepsilon_1 \ln d_2/d_1 + 1/\varepsilon_2 \ln d_3/d_2\right)}{2\pi\varepsilon_0} \tag{18.19}$$

where

ε_0 is the dielectric constant of vacuum (8.85×10^{-12} $V^{-1}m^{-1}$)

ε_1 and ε_2 are the relative permittivities of the insulation material and the liquid, respectively

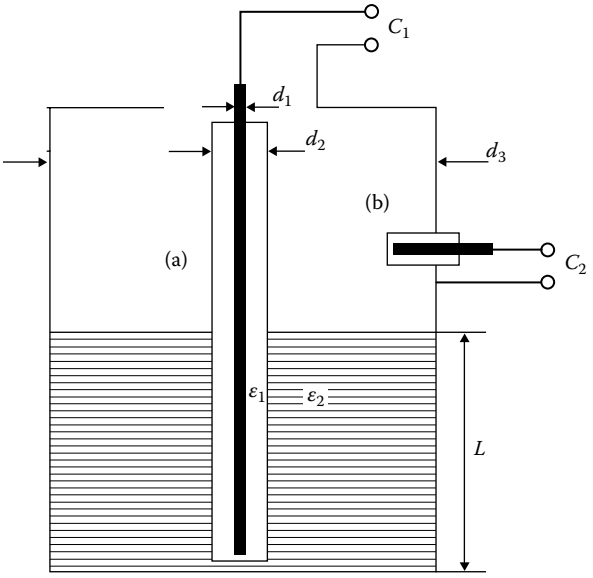

FIGURE 18.13 Principle of operation for a capacitance-type level device. (a) An insulated electrode protrudes into the liquid. The capacitance between the inner conductor and the tank walls is measured. (b) As a capacitance LS, the electrode can be mounted at the appropriate position directly into the tank wall.

If the liquid itself is highly conductive, Equation 18.19 simplifies to

$$C = \frac{2\pi\varepsilon_0\varepsilon_1 L}{\ln d_2/d_1} \Leftrightarrow L = \frac{\ln d_2/d_1}{2\pi\varepsilon_0\varepsilon_1} \tag{18.20}$$

If the electrode is not insulated, the following equation is valid:

$$C = \frac{2\pi\varepsilon_0\varepsilon_2 L}{\ln d_3/d_1} \Leftrightarrow L = \frac{\ln d_3/d_1}{2\pi\varepsilon_0\varepsilon_2} \tag{18.21}$$

When arranged horizontally, as in Figure 18.13b, a capacitive sensor can act as an LS.

For a more precise measurement of conductive liquids, a method measuring the complex impedance is helpful.

18.4.3 Conductive

The resistance of the liquid between two electrodes is measured with (1) a strip line with two parallel electrodes similar to Figure 18.9a or (2) a rod electrode with the metal vessel as the reference electrode, similar to Figure 18.13a without insulator.

18.4.4 Radiation Attenuation

All radiation (e.g., gamma rays, ultrasonic waves, electromagnetic waves) is attenuated to some degree in any medium. In general, attenuation in liquids or bulk materials is higher than in gases. This effect is used to measure level or limits, without direct contact of the sensor.

18.4.5 Radiometric

The intensity I of gamma rays is attenuated by the liquid according to its damping factor α:

$$I = I_0 \exp(-\alpha d) \tag{18.22}$$

The source can be a radioactive material Co-60 or Cs-137, having half-lives of 5.23 years and 29.9 years, respectively. Emitter and sensor may take the form of (1) a point emitting the rays radially in all directions, (2) a rod emitting radially from a line, or (3) an array consisting of several point emitters in a row. Any combination of point/rod/array emitter with point/rod/array detector is possible. Figure 18.14 shows two different configurations. Radiation protection regulations must be considered. A real-time clock in the system must compensate for the decrease of intensity (dose rate) I by time t according to the half-life T_H of the applied material:

$$I = I_0 2^{-t/T_H} \tag{18.23}$$

For more information about radiation detection methods, refer to Chapter 66. Plastic scintillators and counting tubes are preferred for radiometric level gaging. The level–intensity characteristic is nonlinear, so the equipment should be calibrated in place. Mengelkamp [8] describes the radiometric techniques in more detail.

18.4.6 Ultrasonic Switch

A short ultrasonic transmission path can be used to detect products that dampen sonar waves. For instance, this method is applicable for the detection of slurries or to determine the interface between two different liquids. When combined with a servo system, the vertical profile of ultrasonic attenuation can be measured. Another application uses a noncontact sensor mounted on the outside of the vessel. It measures the acoustic impedance through the vessel wall that changes if liquid or gas is present behind the wall.

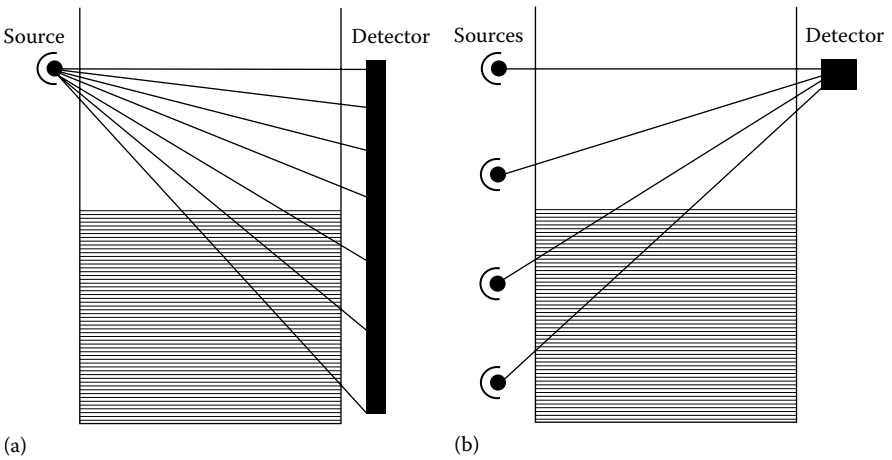

FIGURE 18.14 Representation of a radiometric continuous level gage. The rays are emitted by a radioactive source, propagate through the tank walls, and are damped by the liquid. (a) A point source is combined with a rod detector (e.g., scintillator rod); (b) a source array is combined with a point detector.

18.4.7 Microwave Switch

Liquids and solids dampen microwaves in many cases, sometimes absorbing them completely. A simple unmodulated microwave source and an accompanying receiver are sufficient for level switching.

18.4.8 Photoelectric Barrier

A photoelectric barrier can act as an LS for liquids that are not transparent, as well as most solids. But in closed nontransparent tanks, the coupling of the photoelectric components to the tank will not be possible in most cases.

18.4.9 Thermal and Mechanical

For some special applications, level sensors utilize the different heat dissipation properties and viscosities of the media.

18.4.10 Thermal

A self-heated resistor with a high temperature coefficient is immersed into the liquid. Heat dissipation causes the temperature to drop somewhat in the region where the liquid covers the sensor. Therefore, the resistance change is nearly linear with the level. This method is often used in automotive applications. In some applications, with heated liquids (e.g., chemical reaction vessels), a simple temperature sensor can be used as an LS by emitting a signal when the liquid contacts the sensor and heats it.

18.4.11 Viscosity

The effect of viscosity, which is significantly higher for liquids than for gases, dampens the movement of a body. These level sensors measure the degree of damping of a vibrating fork when dipped in a liquid. Normally, it is only used as a point LS. Figure 18.15 shows such a "tuning fork," named according to the

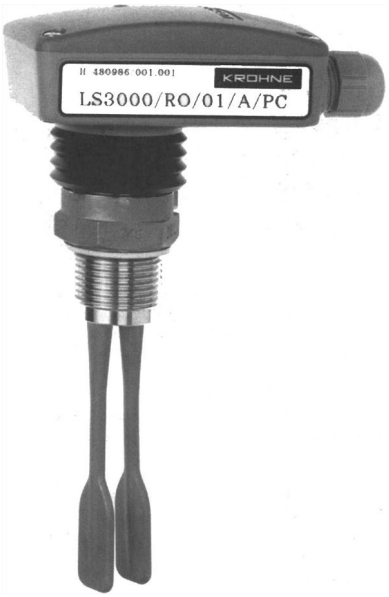

FIGURE 18.15 Design of a vibrating LS. The switch reacts to product viscosity changes, which dampens the vibration of the paddles. (From Messtechnik, K., *Technical Data Sheets of Level Measurement Products*, Krohne, Duisburg, Germany, 1996.)

TABLE 18.2 Priority Level Measurement Techniques and Prices for Industrial Applications

Technique	Application Range	Attainable Accuracy (mm)	Average Price
Displacer/float	Continuous, liquids	1	$2,000
Float	Switch, liquids	10	$500
Pressure	Continuous, liquids	10	$2,000
Ultrasonic	Continuous, liquids, solids	5	$2,500
RADAR	Continuous, liquids, solids	1	$3,000
TDR	Continuous, liquids, solids	3	$2,500
Laser	Continuous, liquids, solids	0.1	$10,000
Radiometric	Continuous, liquids, solids	10	$5,000
Capacitive	Switch, liquids	10	$500
Viscosity	Switch, liquids	10	$500

typical form with two or three vibrating paddles. The integrated electronics evaluate the power loss or the frequency shift of the mechanical resonance system. For solids, a sensor with a rotating paddle that stops when contacting the product is useful.

18.5 Level Measuring Instruments

Table 18.2 lists the most common techniques for level gaging with corresponding application range, accuracy, and average prices. Pricing as shown is for typical industrial applications and can vary widely, depending on materials of construction, measuring range, accuracy, approval requirements, etc. Partial list of manufacturers and suppliers of level instruments is provided at the end of this chapter. Most of these companies manufacture various instruments, using the different technologies shown in Table 18.2. This list is not comprehensive; additionally, some smaller companies provide equipment for specialized level measurements.

References

1. D.M. Considine, *Process Instruments and Control Handbook*, 2nd edn., New York: McGraw-Hill, 1974.
2. E.B. Jones, *Instrument Technology*: *Measurement of Pressure, Level and Temperature*, Vol. 1, London, U.K.: Butterworth & Co., 1974.
3. Verein Deutscher Ingenieure, Verband Deutscher Elektrotechniker (VDI/VDE), *Füllstandmessung von Flüssigkeiten und Feststoffen* (*Level Measurement of Liquids and Solids*), VDI/VDE 3519, Part 1, Berlin, Germany: Beuth, 1984.
4. K.W. Bonfig (ed.), *Technische Füllstandsmessung und Grenzstandskontrolle*, Ehningen, Germany: Expert, 1990.
5. Harold R. Raemer, *Radar System Principles*, Boca Raton, FL: CRC Press, 1997.
6. D. Brumbi, *Fundamentals of Radar Techniques for Level Gauging*, Duisburg, Germany: Krohne, 1995.
7. D. Brumbi, Measuring process and storage tank level with radar technology, *Int. Radar Conf. IEEE*, 256–260, 1995.
8. William L. Wolfe, *Introduction to Radimetry*, Bellingham, Washington, DC: SPIE, 1998.
9. K. Messtechnik, *Technical Data Sheets of Level Measurement Products*, Duisburg, Germany: Krohne, 1996.

Further Readings

Technical Reference-Level Measurement, OMEGA, http://www.omega.com/toc_asp/sectionSC.asp?section=K&book=Green (accessed on June 14, 2012).

Process Instrumentation, Level Measurements with Level Measuring Instruments, SIEMENS, http://www.automation.siemens.com/w1/automation-technology-level-measurement-with-level-measuring-instruments-18693.htm (accessed on July 18, 2012).

Partial List of Manufacturers and Suppliers

Berthold Systems, Inc., 101 Corporation Drive, Aliquippa, PA 15001, Tel: (508) 378–1900

Bindicator, 150 Venture Blvd, Spartanburg, SC 29306, Phone: 864-574-8060, www.bindicator.com

Danfoss Automatic Controls, 7941 Corporate Dr., Baltimore, MD 21236, Phone: 410-931-8250, Fax: 410-931-8256, www.danfoss.com/North_America/

Drexelbrook Engineering Company, 205 Keith Valley Road, Horsham, PA 19044, Tel: (215) 674–1234, www.gilsoneng.com

Dwyer Instruments, Inc., Hwy. 212 at 12, P.O. Box 373, Michigan City, IN 46361, Phone: 219-879-8000, 800-872-9141 (toll free), Fax: 219-872-9057, www.dwyer-inst.com.

Endress & Hauser Instruments, 2350 Endress Place, Greenwood, IN 46143, Tel: (317) 535–7138, www.us.endress.com

The Foxboro Company, 500 N. Bedford St., P.O. Box 500, East Bridgewater, MA 02333, Phone: 508-543-8750, 800-321-0322 (toll free), iom.invensys.com

Honeywell Enraf, 2000 Northfield Ct, Roswell, GA 30076, Phone: 770-475-1900, Fax: 770-475-1717, hpsweb.honeywell.com/Cultures/en-US/Prod…

Krohne America Inc., 7 Dearborn Road, Peabody, MA 01960, Tel: (508) 535–1720, http://krohne.com/

Miltronics LTD-Sherrex Systems Division, 4130-93rd St., Edmonton, AB T6E5P5, www.sherrex.com

MTS Systems Corporation, Sensors Division, 1001 Sheldon Drive, Cary, NC 27513, Tel: (919) 677–0100, www.mts.com

Rosemount, Inc., 21785 Hamburg Ave., Lakeville, MN 55044–9035, Phone: 952-985-6200, 877-985-6221 (toll free), Fax: 952-985-6205, www.rosemount-office.com

Saab Tank Control, 10700 Hammerley Blvd., Houston, TX 7743, Tel: (713) 722–9199, Fax: (713) 722–9115, www.rosemount-tankradar.com/home_index.a…

Siemens Corp., 300 New Jersey Avenue, N.W., Suite 1000, Washington, DC 20004–2611, Phone: 202-434-4800, 800-SIEMENS (toll free), Fax: 202-347-4015, www.usa.siemens.com/entry/en/

TN Technologies, Inc., 2555 North Interstate 35, P.O. Box 800, Round Rock, TX 78680, Tel: (512) 388–9100, www.tn-technologies.com

Yokogawa Filed Instruments Division, 2 Dart Rd., Newnan, GA 30265, Phone: 770-254-0400

Fax: 770-254-4913, www.yokogawa.com/us/ia/fieldinstruments/…

19

Area Measurement

Charles B. Coulbourn
Los Angeles Scientific Instrumentation Co.

Wolfgang P. Buerner
Los Angeles Scientific Instrumentation Co.

One must often measure the area of enclosed regions on plan-size drawings. These areas might be either regular or irregular in shape and describe one of the following:

- Areas enclosed by map contours
- Cross section of the diastolic and systolic volumes of heart cavities
- Farmland or forestland shown in aerial photographs
- Cross sections of proposed and existing roads
- Quantities of materials used in clothing manufacture
- Scientific measurements
- Swimming pools
- Quantities of ground cover

The tools for this type of measurement include planimeters, digitizer–computer setups, digitizers with built-in area measuring capability, and grid overlay transparencies.

19.1 Theory

19.1.1 Planimeter

A planimeter is a mechanical integrator that consists of a bar (tracer arm), a measuring wheel with its axis parallel to the bar, and a mechanism that constrains the movement of one end of the bar to a fixed track (Figure 19.1). The opposite end of the bar is equipped with a pointer for tracing the outline of an area. The measuring wheel (Figure 19.2) is calibrated with 1000 or more equal divisions per revolution. Each division equals one count. It accumulates counts, P, according to

$$P = \frac{K}{\pi D} \int \sin\phi \, ds \tag{19.1}$$

where

K is the number of counts per revolution of the measuring wheel
D is the diameter of the measuring wheel
ϕ is the angle between the measuring wheel axis and the direction of travel
s is the traced path

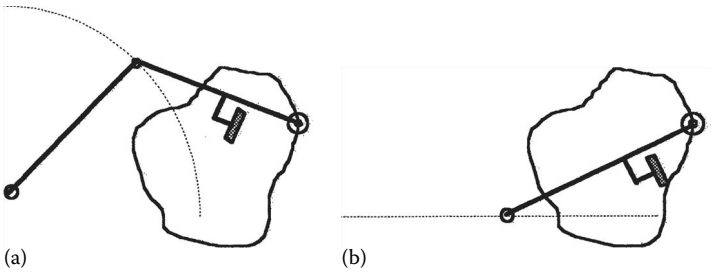

FIGURE 19.1 Constrained end of a polar planimeter (a) follows a circular path; the constrained end of a linear planimeter (b) follows a straight line path.

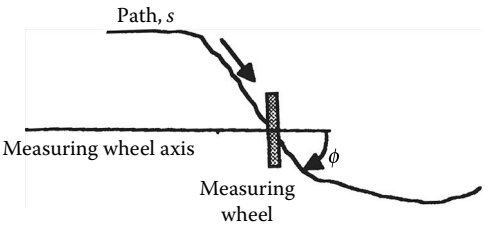

FIGURE 19.2 Rotation of a measuring wheel is proportional to the product of distance moved and the sine of the angle between the wheel axis and the direction of travel.

The size of an area, A, traced is

$$A = \frac{P}{K} \times \pi D \times L \tag{19.2}$$

where

L is the length of bar

P is the accumulated counts (Equation 19.1)

Figure 19.3 shows how a basic wheel and bar mechanism determines the area of a parallelogram. The traced path is along the sloped line; however, the wheel registers an amount that is a function of the product of the distance traveled and the sine of the angle between the direction of travel and the axis of the measuring wheel (Equation 19.1). This is the altitude of the parallelogram. The product of the altitude (wheel reading converted to distance) and base (bar length) is the area.

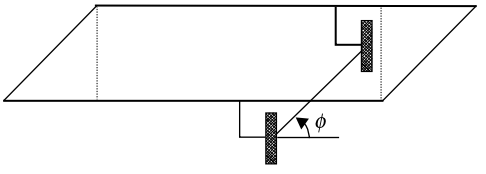

FIGURE 19.3 Area of this parallelogram is proportional to the product of tracer arm length and measuring wheel revolutions.

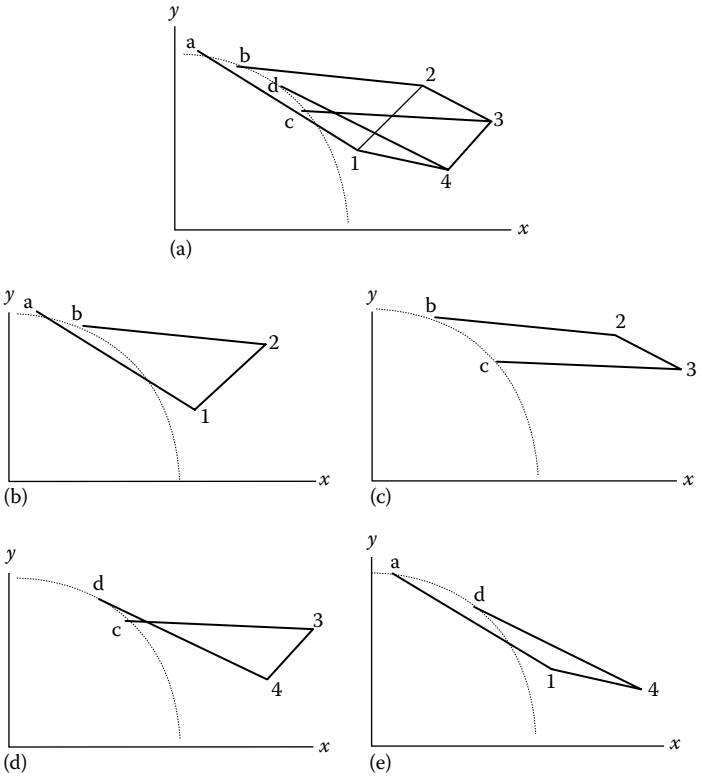

FIGURE 19.4 This schematic shows a planimeter pointing to each junction of a four-sided figure being traced in (a) and at the ends of each of the segments in (b) through (e). The constrained end of the tracer arm follows a circle.

Figure 19.4a illustrates the operation of a planimeter when the area of a four-sided figure is measured. Figure 19.4b–e shows the initial and final positions of the bar as each side of the figure is traced. Applying the general expression for the area under a curve, $A = \int f(x)dx$, for each of these partial areas gives

$$A_a = \left(\int_a^1 + \int_1^2 + \int_2^b + \int_b^a \right) f(x)dx \tag{19.3}$$

$$A_b = \left(\int_b^2 + \int_2^3 + \int_3^c + \int_c^b \right) f(x)dx \tag{19.4}$$

$$A_c = \left(\int_c^3 + \int_3^4 + \int_4^d + \int_d^c \right) f(x)dx \tag{19.5}$$

$$A_d = \left(\int_d^4 + \int_4^1 + \int_1^a + \int_a^d \right) f(x)dx \tag{19.6}$$

where A_a, A_b, A_c, and A_d are the four partial areas.

The total area of the figure is the sum of the four partial areas. Combining the terms of these partial areas and rearranging them so that those defining the area traced by the left end of the bar are in one group, those defining the area traced by the other end of the bar are in a second group, and those remaining are in a third group, results in the following:

$$A = \left\{ \left[\int_{b}^{a} + \int_{c}^{b} + \int_{d}^{c} + \int_{a}^{d} \right] f(x)dx + \left[\int_{a}^{1} + \int_{2}^{b} + \int_{b}^{2} + \int_{3}^{c} + \int_{c}^{3} + \int_{\mathbf{4}}^{d} + \int_{d}^{4} + \int_{1}^{a} \right] f(x)dx \right.$$
$$\left. + \left[\int_{1}^{2} + \int_{2}^{3} + \int_{3}^{4} + \int_{4}^{1} \right] f(x)dx \right\} \tag{19.7}$$

The first four integrals describe the area traced by the left end of the bar. Since this end runs along an arc, it necessarily encloses an area equal to zero. The final four integrals describe the area traced by the right end of the bar. This is the four-sided figure. The remaining eight integrals cancel out since $\int_{a}^{1} + \int_{1}^{a} = 0$, etc. Thus, the total area equals the area traced by the right end of the bar. Note that the same reasoning applies to figures of any number of sides and of any shape.

19.1.2 Digitizer

A digitizer converts a physical location on a map to digital code representing the (x, y) coordinates of the location. The digital code is normally converted to a standard ASCII or binary format and transmitted to a computer where computations are made to determine such things as area or length. Certain digitizers can also compute areas and lengths without the use of a computer.

Area, A, can be computed using the coordinate pairs that define the area boundary:

$$A = \frac{1}{2}(y_1 + y_2)(x_2 - x_1) + \frac{1}{2}(y_2 + y_3)(x_3 - x_2) + \cdots + \frac{1}{2}(y_{n-1} + y_n)(x_n - x_{n-1})$$
$$+ \frac{1}{2}(y_n + y_1)(x_1 - x_n) \tag{19.8}$$

where

x_1, x_2, x_3, etc., are the sequentially measured x-coordinates along the boundary
y_1, y_2, y_3, etc., are the corresponding y-coordinates

All digitized coordinate pairs must be used in the computations since the Δx intervals of these data are typically unequal.

In Equation 19.8, the final term deserves special consideration because it contains both the first and the last coordinate pairs of the series. When computations are performed from the data stored in a computer, the information is available for computing the final term so that no special actions are necessary. However, when the computations are performed by an embedded microprocessor with limited memory, normally each term is computed as the coordinates are read. In this case, one of the two actions must be taken. First, the first coordinate pair is saved, and then, once the measurement has been completed, a key is pressed to initiate computation of the final term. This is called "closing the area." Second, if the first coordinate pair is not saved, to prevent an error, the final point digitized must coincide with the first point digitized so that $x_n = x_1$, $y_n = y_1$, and the final term is zero.

The popular types of digitizers in use today are tablets, sonic digitizers, and arm digitizers. Probably the most popular type is the tablet.

19.1.3 Tablet Digitizer

Tablet digitizers consist of a pointer and a work surface containing embedded wires configured as a grid. The horizontal wires are parallel and spaced by about 12 mm. The vertical wires are also parallel and spaced the same. Different sensing techniques are used to locate the pointer position relative to the grid wires.

One sensing technique employs grid wires made from magnetostrictive material that has the property of changing shape very rapidly when subjected to a magnetic field. Each set of grid wires, the horizontal and the vertical, is independently energized by a send wire that lies perpendicular to that set of wires [1]. A pulse transmitted over the send wire has a magnetic field that changes the shape of each magnetostrictive wire, causing a strain wave to propagate down the wire. Coincidentally, the pulse starts a counter. A coil in the pointer senses the strain wave and sends a signal to stop the counter. The counter reading is thus proportional to the propagation time of the strain wave. The product of the propagation time and velocity of the strain wave equals the physical distance between send line and pointer detector. The velocity of the strain waves is slow enough so that any errors in time measurement can be made acceptable.

A second sensing technique uses a grid made of conductive wires and a pointer that emits a signal on the order of 57.6 kHz. The vertical grid wires are sensed to determine the amplitude distribution of signal induced in each wire. The point of maximum signal strength determines the location of the pointer along the horizontal axis. The horizontal grid wires are likewise sensed to find the point of maximum signal strength that determines the pointer location along the vertical axis. Coupling between the pointer and the grid can be by either electromagnetic or electrostatic means.

Signals can also be applied to the grid wires and the pointer used as a receiver. In this case, the signal to each grid wire must be coded or else applied sequentially, first to one set of grid wires and then to the other. The amplitude profiles of the signals received by the pointer are determined to locate the pointer along each axis.

19.1.4 Sonic Digitizers

Sonic digitizers consist of a pointer and two or more microphones. The pointer, used to identify the point to be digitized, typically contains a spark gap that periodically emits a pulse of sonic energy [2]. The microphones in certain cases are mounted in a bar that is located along the top of the drawing area. In other cases, they are mounted in an L frame and located along the top and one side of the drawing area.

The microphones receive the sonic pulse emitted by the pointer. The time taken for the pulse to travel from the transmitter to each receiver is measured, and the slant distance is computed from the product of this elapsed time and the sonic velocity. The x- and y-coordinates of the pointer are computed from the slant ranges and the locations of the microphones.

Ambiguities exist since a single set of slant ranges describe two points; however, the ambiguities can be resolved either by using additional microphones or by ensuring that the ambiguous points are outside the work area. With the microphones aligned along the top of the work area, the ambiguous points are outside the work area; with them aligned along the top and the side, the ambiguities have to be resolved with additional microphones.

The sound-wave velocity is slow enough so that errors in time measurements can be made acceptable.

19.1.5 Arm Digitizer

An arm digitizer consists of a base, two arms, two rotary encoders, and a pointer. The *base* must be anchored at a point removed from the work area, normally at the top of the user's desk. One end of the arm, called the *base arm*, swivels about a vertical axis at the base. The other end of the base arm

hinges to one end of a second arm, called the *tracer arm*, about a vertical axis. On the other end of the tracer arm is the *pointer*. One of the encoders, the *base encoder*, detects the angle between the base and the base arm. The other encoder, the *arm encoder*, detects the angle between the base arm and the tracer arm.

To simplify implementation, each arm is made the same length, and for sufficient accuracy, each encoder provides in excess of 36,000 counts per revolution. The encoder output signals consist of dual square waves with a 90° phase relationship. The leading and trailing edges of each square wave are counted and the 90° phase relationship provides count direction.

Since each encoder is a relative rather than absolute counting device, the count registers of each encoder must be initialized at a known angle. The count register of the arm encoder is set to the angle that results when the pointer is moved to a precisely known location. This location is called "home." The count register for the base encoder is initialized when the rotation of the *x*–*y*-coordinate system is set. Thereafter, the encoders add to or subtract from their count registers as the pointer is moved.

With the arm lengths and the angles precisely known, the x and y positions of the pointer can be computed. However, x and y are relative to a coordinate system whose origin is at the axis of the base and whose rotation is unknown. The user must therefore select an origin, usually near the lower left corner of the drawing area, and the direction of the x-axis, usually parallel to the bottom edge of the drawing area. This information is sufficient for the processor to compute the correct translation and rotation or the coordinate system.

19.1.6 Grid Overlay

A grid overlay is simply a transparent sheet onto which a grid has been drawn. To use it, place it atop the drawing or photo of the area to be measured (Figure 19.5). Then count the number of squares that lie within the boundary of the area. Squares that are at least half enclosed should be counted. The unknown area equals the product of the number of blocks counted and the area of each block. The accuracy achieved is dependent on grid size, precision of the grid dimensions, and counting accuracy.

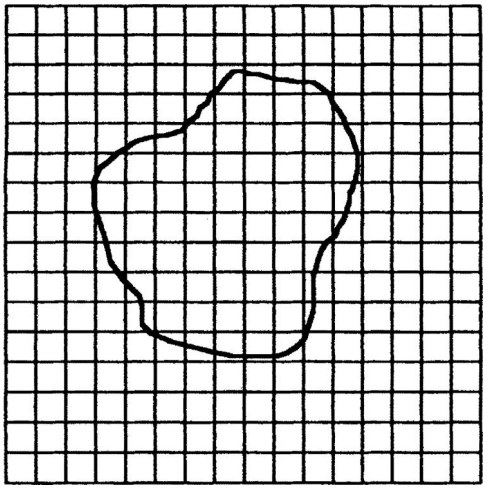

FIGURE 19.5 Grid overlays offer a simple and readily available method for measuring areas.

19.2 Equipment and Experiment

Many different types of planimeters and digitizers are manufactured in the United States, Europe, and Japan. A representative sample of these instruments is described in this section.

One of the simplest and least costly area measuring devices is the manual polar planimeter (Figure 19.6). It consists of a weight, two arms, a measuring wheel, and a pointer. The *weight* secures one end of a pole arm, allowing the other end to rotate along a fixed arc. The rotating end of the pole arm attaches to one end of a *tracer arm* and constrains its movement to the arc. At the other end of the tracer arm is a *pointer* used for tracing the periphery of an unknown area. The *measuring wheel* is located in the box at one end of the tracer arm. The location of the measuring wheel is not critical; however, its axle must be parallel to the tracer arm.

The length of both arms of the planimeter shown in Figure 19.6 can be adjusted. The length of the pole arm has absolutely no effect on measurement accuracy and is adjustable only for convenience. The effective length of the tracer arm directly affects the reading; a shorter arm results in a larger reading. By adjusting the tracer arm length, one can achieve a very limited range of scaling; however, this is usually not done. Rather, the arm length is adjusted according to the general size of areas to be measured: a shorter arm for smaller areas and a longer arm for larger areas. A shorter arm results in a greater number of counts per unit area, which is needed for smaller areas. Scaling is usually done by multiplying the result by an appropriate value.

One zeros the measuring wheel of the planimeter shown in Figure 19.6 by turning a small knurled wheel attached to the measuring wheel axle. On other models, one pushes a plunger to zero the wheel. The latter method is easier but is sensitive to misalignment.

A planimeter pointer is usually a lens with a small circle engraved in the center, although some planimeter models use a needle as the pointer. The best type of pointer is a matter of personal preference although lens pointers are much more popular.

Figure 19.7 shows two electronic planimeters with digital readouts. With these planimeters, one can measure length as well as area. To measure length, snap out the measuring wheel housing, attach an auxiliary handle, and roll the wheel along the line to be measured. Extremely high accuracy can be achieved.

The upper planimeter in Figure 19.7 is a polar type. It consists of the same parts as the model in Figure 19.6, except that the measuring wheel is attached to a small optical encoder and the weight is packaged in the digital readout. The encoder provides two square-wave outputs that are in phase quadrature, that is, one is 90° out of phase with the other. Both outputs are fed to a processor that counts the pulses and uses the phase difference to determine count direction.

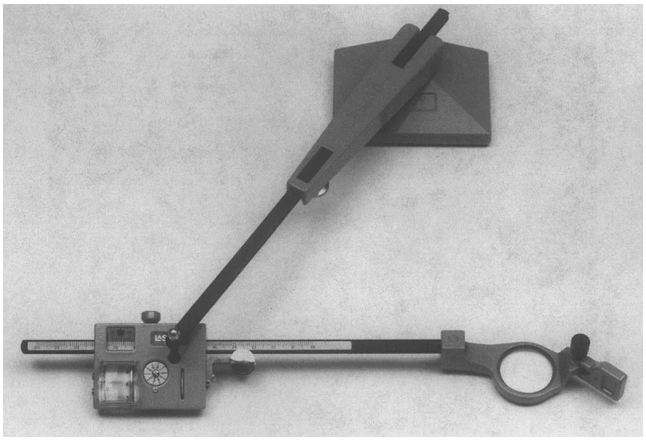

FIGURE 19.6 Mechanical planimeters are normally preferred when occasional use is required.

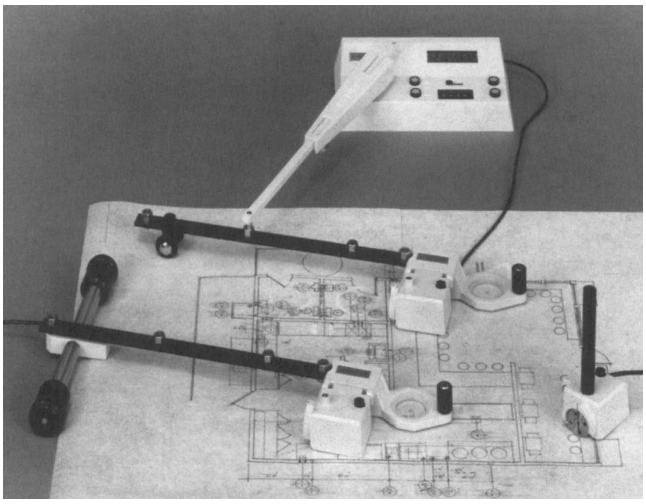

FIGURE 19.7 Electronic planimeters are easier to use and read and are preferred especially when frequently used.

The processor has an electronic scale feature that translates the planimeter reading to real measurement units such as square feet, square meters, acres, or hectares. One can transmit processor data to a computer using an auxiliary interface unit (not shown).

The planimeter at the bottom of Figure 19.7 is a linear model since the path traveled by the constrained end of the tracer arm is a straight line. The straight line path is maintained by a rigid connection between the two carriage wheels and their axle. Other linear planimeters use an actual rail to guide the constrained end of the tracer arm along a straight line path.

The polar planimeter shown at the top of Figure 19.8 and the linear planimeter shown at the bottom of Figure 19.8 are both compact battery-operated models. The measuring wheel is built into the processor, which is attached to the pole arm of the planimeter. The effective length of the tracer arm for both instruments extends from the axis of the constrained end to the pointer, which for these instruments is a small circle engraved in the center of a lens. These planimeters provide electronic scaling and averaging of multiple readings. They cannot be used to measure length.

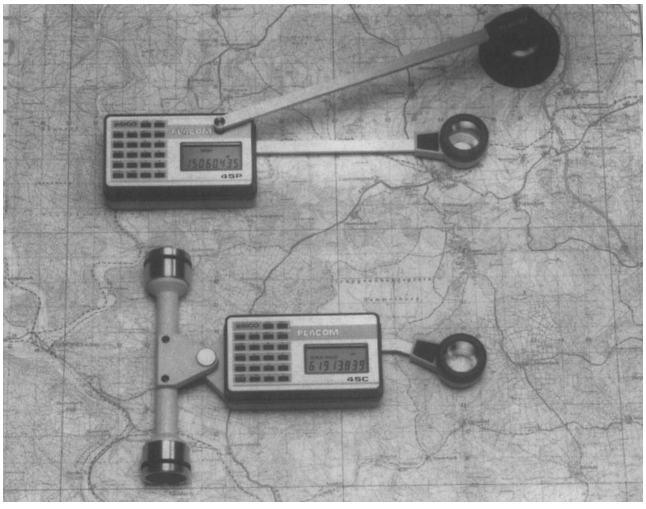

FIGURE 19.8 Battery-operated planimeters have the advantages of electronic planimeters and are portable.

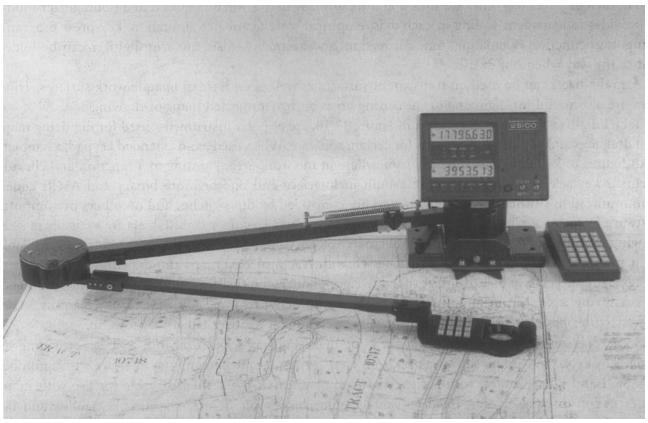

FIGURE 19.9 Arm digitizer lets one measure area, length, and coordinates and transmits the displayed data to a computer; it requires minimum desk space.

Figure 19.9 shows an arm digitizer that can be used either as a stand-alone area and length measuring device or to digitize a map or drawing. When operating as a digitizer, the arm digitizer displays the (x, y) coordinates as well as transmits them to a computer. The digitizer has a built-in interface and can transmit using any of over 24 different ASCII and binary codes, each with a choice of parameters. It can be set to measure x- and y-coordinates in either English or metric units.

Three other modes, in addition to the digitizer mode, are available for computing and displaying either area and length and area and item count or item count and length. Measurements can also be made in either English or metric units. Any displayed item can be transmitted to a computer through the built-in interface.

The arm digitizer has other features that are especially useful when it is used in a nondigitizer mode. It provides independent scaling in each axis, empirical scale factor determination, key-press programming, four-function calculating, unit conversion, and averaging. Also, the arm digitizer can be folded out of the way when not in use.

Arm digitizers can be used on transparent surfaces as well as on normal opaque work surfaces. Thus, they are also useful for digitizing or measuring areas on rear-projected maps or drawings.

Tablet digitizers, like the one shown in Figure 19.10, are popular instruments used for digitizing maps and drawings and as extended keypads for certain software. When used as an extended keypad, a template with figures of key functions is placed somewhere in the work area. Pointing to a function

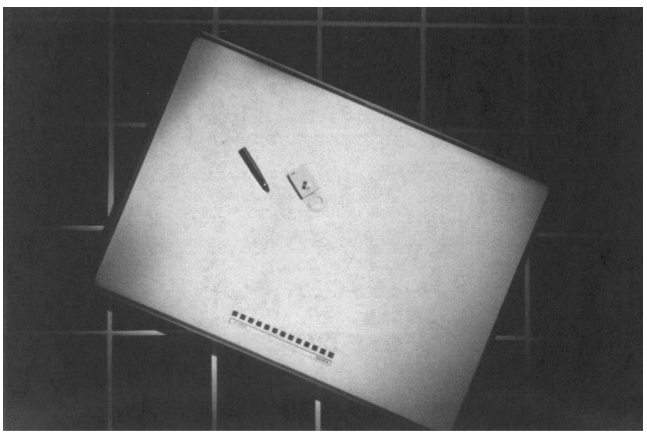

FIGURE 19.10 Popular pad digitizer includes a lightweight puck or pen-type pointer for selecting points whose coordinates are transmitted to a computer for processing.

TABLE 19.1 Companies That Make Planimeters

Gebruder Haff Gmbh Tiroler Strasse 5, D-87459 Pfronten, Germany, Tel: 49-8363-9122-0
Koizumi Sokki Mfg. Co., Ltd. 1–132, Midori-Cho, Nagaoka-Shi, Niigata 940–21, Japan, Tel: (0)258-27-1102
Lasico Inc. 2451 Riverside Drive, Los Angeles, CA 90039, Tel: (213) 662–2128
Sokkia Corporation 9111 Barton St., Overland Park, KS, P.O. Box 2934, Tel: (800) 476–5542

TABLE 19.2 Companies That Make Digitizers

Altek Corporation 12210 Plum Orchard St., Silver Spring, MD 20904, Tel: (301) 572–2555
Calcomp Technology Inc. 2411 West La Palma Ave., Anaheim, CA 92801-2589, Tel: (800) 445–6515
GTCO Corporation 7125 Riverwood Drive, Columbia, MD 21046, Tel: (800) 344–4723
Lasico Inc. 2451 Riverside Drive, Los Angeles, CA 90039, Tel: (213) 662–2128
Numonics Corporation 101 Commerce Drive, Box 1005, Montgomeryville, PA 18936, Tel: (215) 362–2766
Wacom Technology Corporation 501 S.E. Columbia Shores Blvd., Suite 300, Vancouver, WA 98661, Tel: (360) 750–8882

and clicking a cursor key selects it. Tablets feature a built-in interface and one or more binary and ASCII codes. Communication parameters on some tablets are controlled by dip switches and on others by computer software. Pointers are lightweight and include between 1 and 16 cursor keys. Tablets are available in sizes ranging from that of a notebook up to 122 cm × 168 cm (48 in. × 66 in.) or more. Models are available with transparent work surfaces and can be used with rear-projected maps and drawings.

Tablet digitizers have the advantage of lightweight pointers, but the larger tablets have the disadvantages of occupying a significant amount of floor space and being relatively difficult to move around. One manufacturer has overcome this disadvantage by designing a digitizer tablet that rolls up.

Sonic digitizers, like tablets, are intended for digitizing maps and drawings and for providing an extended keypad for certain software packages. They feature a built-in computer interface with a number of ASCII and binary codes, with a choice of parameters, which make them suitable for use with many different software packages. A major advantage enjoyed by sonic digitizers is their portability and the fact that they operate well with a transparent work surface required for rear-projected drawings and maps.

Table 19.1 provides a list of manufacturers of planimeters, and Table 19.2 lists many of the manufacturers of graphic digitizers.

19.3 Evaluation

Each of the area measuring devices described in this section is excellent and has been thoroughly proven by use. However, some of the devices are more suited to certain tasks and operating environments than others.

To measure an area that is smaller than an equivalent circle of about 2 cm in diameter, a digitizer is probably the best choice. For areas of this magnitude, the resolution element of planimeters starts to become a significant portion of the total area. The resolution element of most digitizers is significantly less than that of a planimeter, and any measurement is always plus or minus a resolution element.

For measuring areas that are equivalent to a circle between 2 and 55 cm in diameter, either a planimeter or a digitizer will provide excellent results.

When measuring areas larger than an equivalent circle of about 55 cm in diameter, one can still use a planimeter; however, one must subdivide the large area into smaller areas and then individually measure each of the smaller areas. A digitizer can measure significantly larger areas, but at some point, it too will reach a limit. Then, one can use the same technique of subdividing the large area into smaller areas that the digitizer can handle.

Area measuring instruments of the future will undoubtedly make even greater use of microprocessors to provide more features such as incorporation of slope and tilt correction, statistical operations, and determination of centroids, moment, etc. The instruments should become mechanically simpler and more reliable. Features such as conservation of office space and portability will be emphasized. The ultimate area measuring device will consist of a detached cursor for pointing and a small calculator-like device for operating on the results, displaying them, storing them, and sending them to a computer.

Scanners and associated software will also impact the field of area measurement, particularly as their coverage increases and their price decreases.

Defining Terms

Digitizer: A device to convert data or an image to digital form. The digitizers discussed here convert images to digital form and are categorized as graphic digitizers.

Linear planimeter: A planimeter with a tracer arm whose constrained end follows a straight line.

Measuring wheel: The planimeter wheel whose degree of rotation is directly proportional to the area.

Planimeter: A mechanical integrator used for measuring the area of enclosed regions on maps, plans, etc.

Pointer: The part of a planimeter or digitizer that is used to follow the line being traced.

Pole arm: One of the two bars comprising a polar planimeter. One end of the pole arm is fixed and the other end is free to rotate. The length of the pole arm has no effect on the planimeter reading.

Polar planimeter: A planimeter with a tracer arm whose constrained end follows a circle.

Resolution element: The smallest elemental area that can be discerned. When referred to in connection with area measurement, it is an area with a value of 1.

Tracer arm: The bar of a planimeter that is attached to the measuring wheel. One end of the tracer arm is constrained to a fixed path, while the other end traces the perimeter of an enclosed region whose area is being measured. The length of the pole arm is indirectly proportional to the planimeter reading.

References

1. P. A. Santi, J. Fryhofer, and G. Hansen, Electronic planimetry, *Byte*, 5(3), 113–122, March 1980.
2. D. Dayton Reuter, *Computer Graphics for Architects, Engineers, and Environmental Designers*, New York: Allworth Press, 2002.

Further Information

Sullivan, N., *Area, Distance and Volume*, Marshall Cavendish Corporation, New York, 2007.
Willers, F. A., *Mathematische Instrumente*, Munchen und Berlin, Germany: Verlag von R. Oldenbourg, 1943.

20

Volume Measurement

René G. Aarnink
University Hospital Nijmegen

Hessel Wijkstra
University Hospital Nijmegen

For simple geometric shapes, volume measurements can be performed analytically by measuring the dimensions of the object in question and using the appropriate formula for that shape. Volume formulae are found in geometry and calculus textbooks as well as in reference books such as CRC Press's *Handbook of Mathematical Science* or other references.

Volume can also be measured by fluid displacement. The object whose volume is to be measured is placed in a container filled with fluid, and the initial and final volumes are measured. The object's volume is equal to the final volume minus the initial volume. This technique is especially useful for irregularly shaped objects.

Fluids can also be used to measure volume of cavities within objects by filling the cavity entirely with a fluid and then measuring the volume of the fluid after it is removed from the cavity.

The remainder of this chapter is dedicated to the more specific problem of volume measurements in medical applications.

Quantitative volume information can be of importance to the clinician in the diagnosis of a variety of diseases or abnormalities. It can also improve the understanding of the physiology of the patient. Information on volume may be used in various applications such as cardiac monitoring, diagnosis of prostate diseases, follow-up during organ transplantation, surgery for tumor resection, blood flow measurements, plastic surgery, follow-up of preterm infants, and sports performance analysis. Because of this wide spectrum of applications, various techniques for volume measurements have been developed, some of which are useful in determining the amount of blood flow to the organ (dynamic), while others are used to obtain the size of the object (static). The techniques can be invasive or noninvasive and are based on either direct or indirect measurements. Each technique has its own advantages and disadvantages, and the application determines the selection of volume measurement method.

One of the earliest techniques to measure (changes of) body volume was *plethysmography*, originally developed by Glisson (1622) and Swammerdam (1737) to demonstrate isovolumetric contraction of

isolated muscle. The measuring technique consists of surrounding the organ or tissue with a rigid box filled with water or air. The displacement of the fluid or the change in air pressure indicates the volume changes of the tissue due to arterial inflow. Two major types of plethysmography exist, and these can be distinguished by the technique used to measure the volume change. These are *volume plethysmography* (direct-measurement displacement plethysmography including water and air types) and *electrical plethysmography* (strain-gage, inductive, and impedance plethysmographs). The physical condition in which the measurements should be performed determines the plethysmographic method chosen.

Advances in medical imaging have provided new possibilities for noninvasively extracting quantitatively useful diagnostic information. Images are constructed on a grid of small picture elements (pixels) that reflect the intensity of the image in the array occupied by the pixel. Most medical images represent a 2D projection of a 3D object.

Currently, the most commonly used medical imaging modalities are ultrasound, nuclear magnetic resonance imaging, x-rays, and x-ray computer tomography. *Ultrasound imaging* is based on the transmission and reflection of high-frequency acoustic waves. Waves whose frequencies lie well above the hearing range can be transmitted through biological tissue and will be reflected if they cross a boundary between media of different acoustic properties. These reflected signals can be reconverted to electrical signals and displayed to obtain a 2D section. *Magnetic resonance imaging* is based on the involvement of the interaction between magnetic moment (or spin) of nuclei and a magnetic field. The proton spins are excited by an external radio-frequency signal and the return to an equilibrium distribution is used to construct cross-sectional images. *Computer tomography* or *CT scanning* uses a rotating source of x-rays. The x-ray source and detector are scanned across a section of the object of interest, and the transmission measurements are used to reconstruct an image of the object.

These imaging techniques display cross sections of views that can be used to estimate the size of specific components. One way to estimate the volume of internal objects is to make certain assumptions concerning the shape and to apply formulae to estimate the volume with dimensions of the object such as length, height, and width. A more accurate technique is *step-section planimetry*, a clinical application of numerical integration. During this procedure, cross sections of the object are recorded with a certain (fixed) interval. The area of the object is determined in every section, and the total volume is calculated by multiplying the contribution of each section with the interval and summarizing all contributions.

The volume of a fluid-filled region can be calculated if a known quantity of indicator is added to the fluid and the concentration measured after it has been dispersed uniformly throughout the fluid. The selection of the indicator used to measure the volume depends on the application and can be based on temperature, color, or radioactivity.

Finally, volume (changes) can also be performed directly using *water displacement volumetry*, a sensitive but time-consuming method to measure the volume of an extremity. This method is not suitable for patients in the immediate postoperative period.

20.1 Plethysmography Theory

Fluid inflow can be measured by blocking the outflow and then measuring the change in volume due to the inflow over a defined time interval. Plethysmography enables the volume change to be determined in a reasonably accurate manner. A direct-volume displacement plethysmograph uses a rigid chamber usually filled with water, into which the limb or limb segment is placed. This type of plethysmograph, sometimes called *chamber plethysmography*, can be used in two ways. It can be used to measure the sequence of pulsations proportional to the individual volume changes with each heartbeat (arterial plethysmography or rheography). Also, the total amount of blood flowing into the limb or digit can be measured by venous occlusion: by inflating the occluding cuff placed upstream of the limb or digit just above the venous pressure 5–8 kPa (40–60 mm Hg), arterial blood can enter the region but venous blood is unable to leave. The result is that the limb or digit increases its volume with each heartbeat by the volume entering during that beat.

20.1.1 Air/Water Plethysmography or Chamber Plethysmography

Air plethysmography uses the relation between the volume change of a gas in a closed system and the corresponding pressure and temperature [1]. The relation between pressure and volume is described by Boyle's law, which can be written as

$$P_i V_i = P_f V_f \tag{20.1}$$

where P_i and V_i are the initial pressure and volume, respectively, and P_f and V_f are the final pressure and volume, respectively.

Measured at constant temperature, the displacement of the fluid or the compressing of the air is a direct measure of the blood flow or original volume. The air plethysmograph uses the change in pressure that occurs in a cuff wrapped around the segment of interest due to the change in volume. By inflating the cuff to about 60 mm Hg, the arterial inflow causes small increases in pressure. These small changes in pressure over the cardiac cycle can be monitored (see Figure 20.1). The measurement of blood flow is achieved by comparing the pressure changes to changes caused by removing known amounts of air from the system. The second measurement uses volume changes at various pressures between systolic and diastolic pressures, and the peak deflection is compared with the deflection caused by removal of known amounts of air from the system. In segmental plethysmography, two cuffs are used to measure the volume changes in a segment of a limb. Venous occlusion is established by the first cuff, while the second is inflated to a pressure that will exclude blood flow from those parts that should not be included in the measurement.

The technique can also be used for whole-body plethysmography [2], a common technique used to measure residual volume, functional residual capacity (FRC), and total lung volume, the parameters usually determined during pulmonary function testing [3]. In body plethysmography, the patient sits inside an airtight box and inhales or exhales to a particular volume (usually the FRC, the volume that remains after a normal exhalation). Then, a shutter closes the breathing tube, while the subject tries to breathe through the closed tube. This causes the chest volume to expand and decompress the air in the lungs. The increase in chest volume slightly reduces the air volume of the box, thereby increasing the pressure. First, the change in volume of the chest is quantified using Boyle's law with the initial pressure and volume of the box and the pressure in the box after expansion. The change in volume of the box is

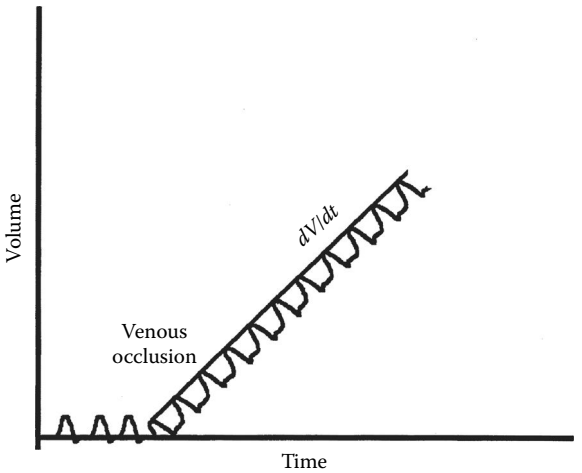

FIGURE 20.1 Typical recording from air plethysmograph during venous occlusion, revealing the changes in volume over time caused by arterial inflow.

equal to the change in volume of the chest. A second measurement method is based on the initial volume of the chest (unknown) and the initial pressure at the mouth, and the inspiratory volume (the unknown chest volume and the change in volume obtained in the first measurement) together with the pressure at the mouth during the inspiratory effort. By solving Boyle's law for the unknown volume, the original volume of gas present in the lungs when the shutter was closed is obtained, which is normally the volume present at the end of a normal exhalation or FRC.

Alternative methods for measurement of volume changes with plethysmography have been introduced to overcome the disadvantages of chamber plethysmography such as cost, complexity, and awkwardness of use. Important alternatives are elastic-resistance strain-gage plethysmography, impedance plethysmography, inductive plethysmography, and photoelectric plethysmography.

20.1.2 Electrical Plethysmography

20.1.2.1 Strain-Gage Plethysmography

In 1953, Whitney described the elastic-resistance strain-gage plethysmograph [4]. The strain-gage instrument quantifies the change in resistance of the gage as it is stretched due to the enlargement of the object (e.g., limb segment). The gage is typically a small elastic tube filled with mercury or an electrolyte or conductive paste. The ends of the tube are sealed with copper plugs or electrodes that make contact with the conductive column. These plugs are connected to a Wheatstone bridge circuit.

To illustrate the principle of the strain-gage method, a strain gage of length l_0 is placed around the limb segment, a circular cross section with radius r_0. The length of the strain gage can thus also be expressed as $l_0 = 2\pi r_0$. Expansion of the limb gives a new length $l_1 = 2\pi r_1$, with r_1 the new radius of the limb. The increase in length of the strain gage is thus $\delta l = 2\pi(r_1 - r_0)$, while the change in cross-sectional area of the limb δA is $\pi(r_1^2 - r_0^2)$. This can also be expressed as

$$\delta A = \pi[2r_0(r_1 - r_0) + (r_1 - r_0)^2] \tag{20.2}$$

Since $r_1 - r_0$ is usually small, $(r_1 - r_0)^2$ can be neglected. Consequently, δA can be written as $2\pi r_0(r_1 - r_0)$, which, on dividing by $A = \pi(r_0)^2$, gives

$$\frac{\delta A}{A} = 2\left(\frac{r_1 - r_0}{r_0}\right) \tag{20.3}$$

But since $\delta V/V = \delta A/A$ and $\delta l/l = \delta r/r$,

$$\frac{\delta V}{V} = 2\left(\frac{l_1 - l_0}{l_0}\right) \tag{20.4}$$

Thus, the percentage increase in volume can be obtained by measuring the initial gage length and the change in length. In practice, this change in length of the strain gage is recorded over a relatively short period to overcome the problem of back pressure that builds up in the limb or digit because of the venous occlusion, and the measurement is usually expressed as milliliters per minute per 100 g of tissue or volume flow rate = $2(\delta l/l_0) \times (100/t)$, where δl is the increase in gage length during time t. To measure $\delta l/t$, the gage must be calibrated by removing it from the limb and stretching it on a measuring jig until the recorder returns to the zero level; this is the length l_0. The gage can then be stretched accurately by typical amounts, to calibrate the output and calculate the volume flow rate.

20.1.2.2 Impedance Plethysmography

The physical principle of impedance plethysmography is the variation in electrical impedance of a tissue segment over the cardiac cycle due to a changing conductance. The change is caused by arterial inflow to the segment while the venous drainage is occluded.

If a segment of limb is assumed to be cylindrical and of length l and volume V, the impedance Z of that part can be written as

$$z = \frac{\rho l^2}{V} \tag{20.5}$$

where ρ is the specific resistivity of the tissue forming the cylinder.

Blood entering the tissue segment during the cardiac cycle introduces a parallel impedance Z_b described as $Z_b = Z_0 Z_1/(Z_0 - Z_1)$ with Z_0 the initial impedance and Z_1 the new value. A small change in volume δV is related to a small change in resistance δZ, such that

$$\delta Z = Z_0 - Z_1 = \rho l^2 \left(\frac{1}{V_0} - \frac{1}{V_1} \right) = \rho l^2 \frac{(V_1 - V_0)}{V_1\ V_0} \approx -\rho l^2 \frac{\delta V}{V^2} = -Z \frac{\delta V}{V} \tag{20.6}$$

when very small changes in volume are assumed [5]. Thus, δV can be written as

$$\delta V = \rho \left(\frac{1}{Z_0^2} \right) \delta Z \tag{20.7}$$

and these parameters Z_0 and δZ can be obtained from the impedance plethysmogram. If it is assumed that $\rho = 150\ \Omega$ cm, being the specific resistivity of soft tissue, the change in volume can be determined.

Two major techniques have been used to measure tissue impedance. One method uses two electrodes to measure both the voltage drop across the electrodes and the current flow. The main disadvantage of this technique is that the current distribution in the vicinity of the electrodes is not known, meaning the exact volume of the interrogated tissue is also unknown. In 1974, Kubicek et al. [6] described the use of four electrodes to measure tissue impedance: the outer electrodes supply a small-amplitude, high-frequency AC signal, while the inner two are used to measure the potential difference between two points on the same surface (see Figures 20.2 and 20.3).

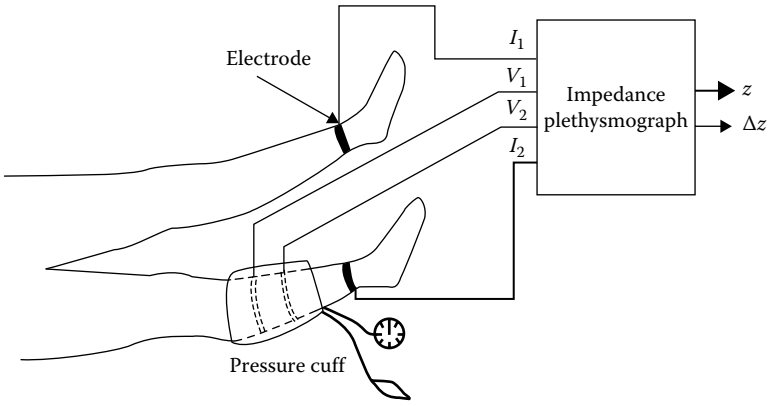

FIGURE 20.2 Electrode positioning for impedance plethysmography used for early detection of peripheral atherosclerosis: the outer two supply current, while the inner two measure voltage. The combination of these two is used to obtain the changes in impedance, and these changes are then used to obtain the changes in volume of the leg. (From Shankar, R. and Webster, J. G., *IEEE Trans. Biomed. Eng.*, 38, 62, 1993. With permission.)

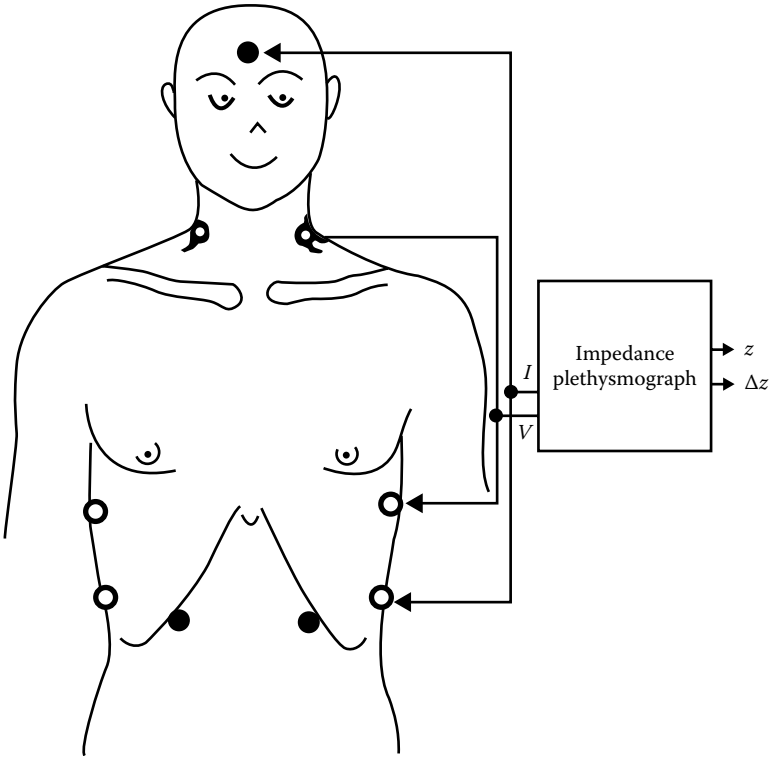

FIGURE 20.3 A second example of electrode positioning for impedance plethysmography here used to estimate stroke volume: the outer two supply current, while the inner two measure voltage. (From Verschoor, N. et al., *Physiol. Meas.*, 17, 29, 1996. With permission.)

20.1.2.3 Inductive Plethysmography

For measurement of volume changes during respiration, a system based on inductive plethysmography has been developed; the respiratory inductive plethysmograph was introduced in 1978. During inductive plethysmography, two coils are attached—one placed around the rib cage (RC) and the other around the abdomen. During respiration, the cross-sectional diameter of the coils changes, leading to a change in the inductances of the coils. By converting these inductances into proportional voltages, a measure for the changes in volume during respiration can be obtained. The conversion is achieved by using oscillators whose frequencies depend on a fixed internal capacitor and the inductance of each coil. These oscillator frequencies are converted to proportional voltages, voltages that are then recorded. After calibration on the patient, the system can be used for respiratory volume measurement [9].

Two general methods have been introduced for calibration of the respiratory inductive plethysmograph. These calibration methods are based on the following equation:

$$V_T = V_{RC} + V_{AB} \tag{20.8}$$

where V_{RC} and V_{AB} are the contributions of the RC and abdominal compartments (AB) to the tidal volume V_T. Calibration can be performed by determining the calibration constant in an isovolume measurement or by regression methods of differences in inductance changes due to a different body position or a different state of sleep [10]. Once it is calibrated, the respiratory inductive plethysmograph can be used for noninvasive monitoring of changes of thoracic volume and respiratory patterns.

20.2 Numerical Integration with Imaging

For diagnostic purposes in health care, a number of imaging modalities are currently in use. Webb nicely reviewed the scientific basis and physical principles of medical imaging [11].

With medical imaging modalities, diameters of objects can be determined in a noninvasive manner. By applying these diameters in an appropriate formula for volume calculation, the size of the object can be estimated. For example, in a clinical setting, the prostate volume V_p can be approximated with an ellipsoid volume calculation:

$$V_p = \frac{\pi}{6} HWL \tag{20.9}$$

where

H is the height

W is the width

L is the length of the prostate as illustrated in Figure 20.4

Variations have been introduced to find the best formulae to estimate the prostate volume [12,13]. Also, for the determination of ventricular volumes, formulae have been derived, based on the following variation of the formula for prostate volume measurements: (1) The volume is obtained with the same formula as for prostate volume measurements, (2) the two short axes are equal, (3) the long axis is twice the short axis, and (4) the internal diameter is used for all axes.

By displaying cross-sectional images of a 3D object (e.g., an organ), volume calculations can also be performed by integrating areas of the organ over a sequence of medical images as illustrated in Figure 20.5. For ultrasound images, applications have been reported in the literature on prostate, heart, bladder, and kidney volume. The application of integration techniques involves the application of segmentation algorithms on sequences of images, either in transverse direction with fixed intersection distance or in the radial with images at a fixed intersection angle.

For a volume defined by the function $f(x, y, z)$, the volume can be calculated from

$$V = \int_{x=x_1}^{x_2} \int_{y=y_1}^{y_2} \int_{z=z_1}^{z_2} f(x,y,z)dzdydx \tag{20.10}$$

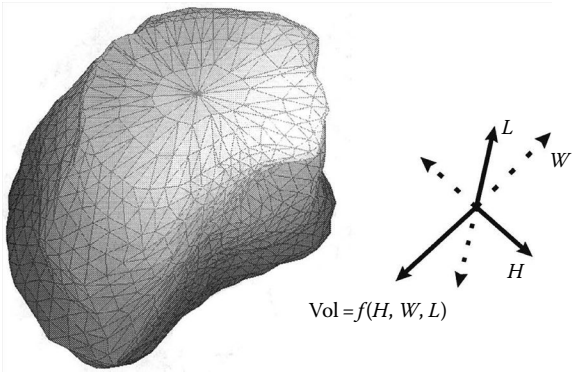

FIGURE 20.4 Volume estimate of a prostate, obtained from 3D reconstruction of cross-sectional images, using the dimensions in three planes: the length, height, and width in a volume formula describing an ellipsoid shape.

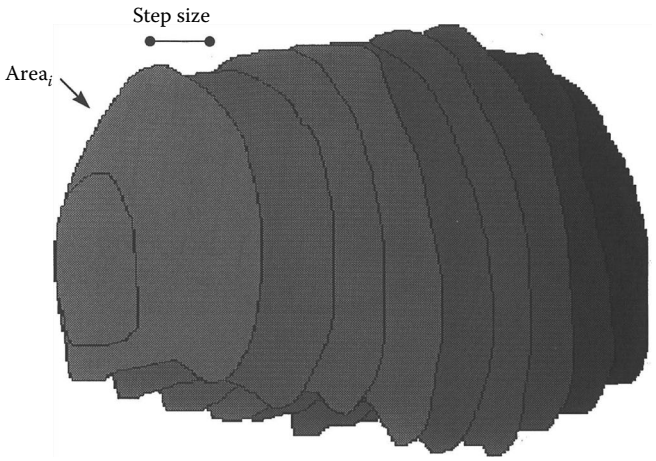

FIGURE 20.5 Outlines of cross-sectional images of the prostate used for planimetric volumetry of the prostate: transverse cross sections obtained with a step size of 4 mm have been outlined by an expert observer, and the contribution of each section to the total volume is obtained by determining the area enclosed by the prostate contour.

By applying numerical integration, the volume calculation using an integral is approximated by a linear combination of the values of the integrand. For reasons of simplicity, this approximation is first illustrated for a 1D case:

$$\int_{x=a}^{b} f(x)dx \approx w_1 f(x_1) + w_2 f(x_2) + \cdots + w_{nf} f(x_n) \tag{20.11}$$

In this equation, $x_1, x_2, \ldots, x_n$ are n points chosen in the interval of integration $[a, b]$, and the numbers $w_1, w_2, \ldots, w_n$ are n weights corresponding to these points. This approximation can also be expressed in the so-called Riemann sum:

$$\int_{x=a}^{b} f(x)dx \approx w_1 f(x_1) + w_2 f(x_2) + \cdots + w_n f(x_n) = \sum_{i=1}^{n} f(\xi_i)(x_i - x_{i-1}) \tag{20.12}$$

For volume calculation, the Riemann sum needs to be extended to a 3D case:

$$V = \int_{x=x_1}^{x_2} \int_{y=y_1}^{y_2} \int_{z=z_1}^{z_2} f(x,y,z)dzdydx \approx \sum f(p_{ijk})(x_{i+1} - x_i)(y_{j+1} - y_j)(z_{k+1} - z_k) \tag{20.13}$$

This 3D case can be reduced by assuming that $(x_{i+1} - x_i)(y_{i+1} - y_i)f(P_{ijk})$ represents the surface S_k of a 2D section at position z_k, while $(z_{k+1} - z_k)$ is constant for every k and equals h, the intersection distance:

The volume is then determined by summarizing all contributions after multiplying them with the step size:

$$V \approx h \sum S(z_k) = h \sum_{k=0}^{n-1} S(a + kh) \tag{20.14}$$

where

a represents the position of the first section

n is the number of sections

h is the step size, given by $h = (b - a)/n$, where b is the position of the last section

In general, three different forms of the approximation can be described, depending on the position of the section. The first form is known as the rectangular rule and is presented in Equation 20.14. The midpoint rule is described by

$$V \approx h\sum S(z_k) = h\sum_{k=0}^{n-1} S\left[a + \left(k + \frac{1}{2}h\right)\right] \tag{20.15}$$

The trapezoidal rule is similar to the rectangular rule, except that it uses the average of the right-hand and left-hand Riemann sum:

$$T_n(f) = h\left[\frac{f(a)}{2} + f(a+h) + f(a+2h) + \cdots + f(a+(n-1)h) + \frac{f(b)}{2}\right] \tag{20.16}$$

The trapezoidal and midpoint rules are exact for a linear function and converge at least as fast as n^{-2}, if the integrand has a continuous second derivative [14].

A number of parameters are associated with the accuracy of the approximation of the volume integral with a Riemann sum; first of all, the number of cross sections n is important as the sum converges with n^{-2}: the more sections, the more accurate the results. Furthermore, the selection of the position of the first section is important. While the interval of integration is mostly well defined in theoretical analyses, for in vivo measurements, the first section is often less well defined. This means not only that the selection of this first section is random with the first possible section and this section increased with the step size but also that sections can be missed. The last effect that may influence the numerical results is the effect of taking oblique sections, cross sections that are not taken perpendicular to the axis along which the intersection distance is measured. All the aforementioned assume that every section S_k can be exactly determined.

The influence of the parameters associated with these kinds of measurements can be tested in a theoretical model. In a mathematical model with known exact volume or surface, the parameters—including step size, selection of the first section, and the scan angle—can be tested. Figure 20.6 shows a model used to model the prostate in two dimensions. It consists of a spheroid function with a length of the long axis of 50 mm and a length of the short axis of 40 mm. In mathematical form, this function can be described as

$$y = f(x) = y_m \pm y_0\sqrt{1 - \left(\frac{x - x_m}{x_0}\right)^2} \tag{20.17}$$

where

x_0 is half the diameter of the ellipse in x-direction (25 mm)
y_0 is half the diameter of the ellipse in y-direction (20 mm)
(x_m, y_m) is the center point of the ellipse

The analytical solution of the integral to obtain the surface of this model is $\pi x_0 y_0$.

Figure 20.6 also reveals the possible influence of the parameters h and α. Figure 20.7 shows the results for varying the step size h between 4 and 16 mm corresponding to between 13 and

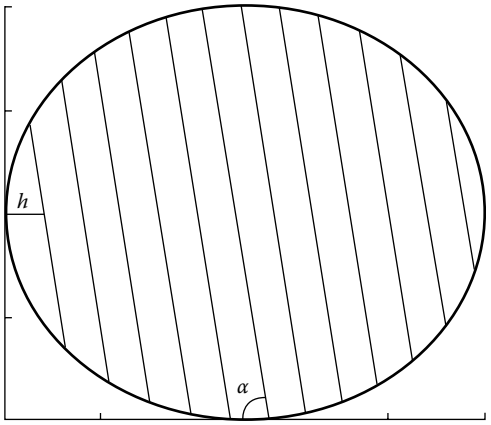

FIGURE 20.6 An ellipsoid-shaped model of the prostate that was used for theoretical analysis of planimetric volumetry. Indicated are the intersection distance h and the scan angle α with the axis of the probe. (From Aarnink, R.G. et al., *Physiol. Meas*., 16, 141, 1995. With permission.)

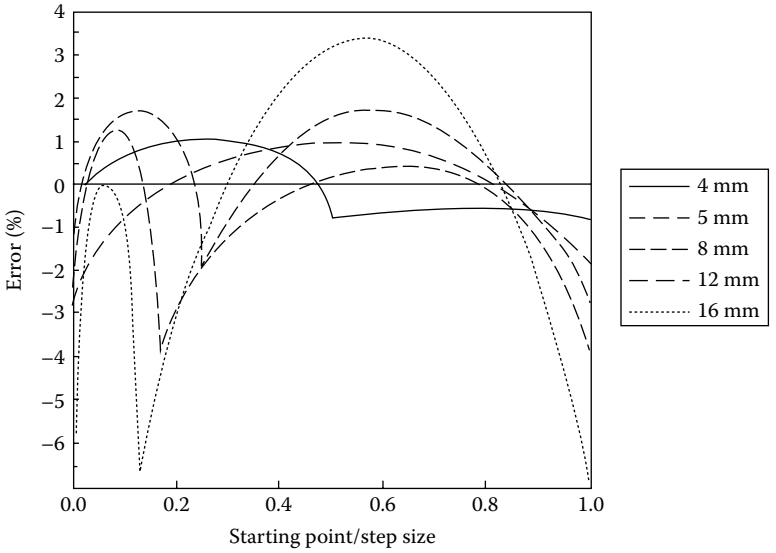

FIGURE 20.7 The errors in surface estimates by numerical integration for different step sizes h presented as percentage of the exact solution, as a function of the position of the first section, located between 0 and h. (From Aarnink, R.G. et al., *Physiol Meas*., 16, 141, 1995. With permission.)

3 sections used for numerical integration as a function of the position of the first section. The first section is selected (at random) between the first coordinate of the function and this coordinate plus the step size h. The sections were taken perpendicular to the long axis. From this study, which is fully described by Aarnink et al. [15], it was concluded that if the ratio of step size to the longest diameter is 6 or more, then the error in volume estimation is less than 5%. Although clinical application might introduce additional errors such as movement artifacts, this rule provides a good indication of the intersection distance that should be used for good approximations with numerical integration.

20.3 Indicator Dilution Methods

The principle of the indicator dilution theory to determine gas or fluid volume was originally developed by Stewart and Hamilton. It is based on the following concept: if the concentration of an indicator that is uniformly dispersed in an unknown volume is determined, and the volume of the indicator is known, the unknown volume can be determined. Assuming a single inflow and single outflow model, all input will eventually emerge through the output channel, and the volumetric flow rate can be used to identify the volume flow. It can be described with two equations, of which the second is used to determine the volume using the result of the first equation [16]:

$$F = \frac{I_i}{\int_0^\infty C(t)dt} \tag{20.18}$$

$$\text{Vol} = Ft_m \tag{20.19}$$

where

F is the flow rate
I_i is the total quantity of injected indicator
$C(t)$ is the concentration of the contrast as function of time
Vol is the volume flow
t_m is the mean transit time

The integrated value of the concentration over time can be obtained from the concentration-time curve (Figure 20.8) using planimetry and an approximation described by the Riemann sum expression (Equation 20.13). Care must be taken to remove the influence of the effect of recirculation of the indicator. An indicator is suitable for use in the dilution method if it can be detected and measured and remains within the circulation during at least its first circuit, without doing harm to the object. Subsequent removal from the circulation is an advantage. Dyes such as Coomassie blue and indocyanine green were initially used, using the peak spectral absorption at certain wavelengths to detect the indicator. Also, radioisotopes such as *I*-labeled human serum albumin have been used. Currently, the use of cooled saline has become routine in measurement of cardiac output in the intensive care unit.

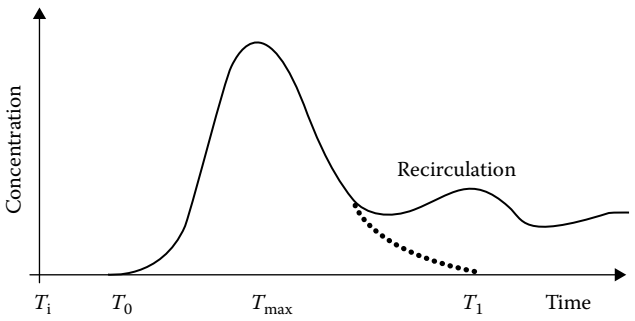

FIGURE 20.8 The time–concentration curve of the indicator is used to obtain the unknown volume of the fluid. The area under the time–concentration curve is needed to estimate the volumetric flow rate, and this flow rate can be used to estimate the volume flow. For accurate determination of the flow rate, it is necessary to extrapolate the first-pass response before the area under the curve is estimated.

20.3.1 Thermodilution

To perform cardiac output measurements, a cold bolus (with a temperature gradient of at least 10 K) is injected into the right atrium, and the resulting change in temperature of the blood in the pulmonary artery is detected using a rapidly responding thermistor. After recording the temperature–time curve, the blood flow is calculated using a modified Stewart–Hamilton equation. This equation can be described as follows [17]:

$$V_i SW_i SH_i (T_b - T_i) = F \int T_b(dt) SW_b SH_b \tag{20.20}$$

The terms on the left represent the cooling of the blood (with temperature T_b), as caused by the injection of a cold bolus with volume V_i, temperature T_i, specific weight SW_i, and specific heat SH_i. The same amount of "indicator" must appear in the blood (with specific weight and heat SW_b and SH_b, respectively) downstream to the point of injection, where it is detected in terms of the time course of the temperature T_b in the flow F by means of a thermistor. The flow can be described as

$$F = \frac{T_b - T_i}{\int T_b(dt)} K \tag{20.21}$$

where K (the so-called calculation constant) is described as

$$K = V_i \frac{SW_i - SH_i}{SW_b - SH_b} C \tag{20.22}$$

This constant is introduced to the computer by the user. T_i is usually measured at the proximal end of the injection line; therefore, a "correction factor" C must be introduced to correct for the estimated losses of cold saline in the catheter, due to the dead space volume. Furthermore, the warming effect of the injected fluid during passing through the blood must be corrected; this warming effect depends on the speed of injection, the length of immersion of the catheter, and the temperature gradient. This warming effect reduces the actual amount of injected fluid, so the correction factor C is less than 1 [17].

20.3.2 Radionuclide Techniques

Radionuclide imaging is a common noninvasive technique used in the evaluation of cardiac function and disease. It can be compared to x-ray radiology, but now the radiation emanating from inside the human body is used to construct the image. Radionuclide imaging has proven useful to obtain ejection fraction (EF) and left ventricular volume. As in thermodilution, a small volume of indicator is injected peripherally; in this case, radioisotopes (normally indicated as radiopharmaceuticals) are used. The radioactive decay of radioisotopes leads to the emission of alpha, beta, gamma, and x-radiation, depending on the radionuclide used. For in vivo imaging, only gamma or x-radiation can be detected with detectors external to the body, while the minimal amount of energy of the emitted photons should be greater than 50 keV. Using a photon counter such as a gamma camera, equipped with a collimator, the radioactivity can be recorded. Two techniques are commonly used: the first-pass method and the dynamic recording method [11].

20.3.3 First-Pass Method

To inject a radionuclide bolus into the blood system, a catheter is inserted in a vein, for example, an external jugular or an antecubital vein. The camera used to detect the radioactive bolus is usually positioned in the left anterior oblique position to obtain optimal right and left ventricular separation and is tilted slightly in an attempt to separate left atrial activity from that of the left ventricle. First, the background radiation is obtained by counting the background emissions. Then, a region of interest is determined

over the left ventricle and a time–activity curve is generated by counting the photon emissions over time. The radioactivity count over time usually reveals peaks at different moments; the first peak occurs when the radioactivity in the right ventricle is counted, the second peak is attributed to left ventricular activity. More peaks can occur during recirculation of the radioactivity. After correction for background emissions, the time–intensity curve is evaluated to determine the EF of the heart, which is given by

$$\mathrm{EF} = \frac{c_\mathrm{d} - c_\mathrm{s}}{c_\mathrm{d} - c_\mathrm{b}} \tag{20.23}$$

where

c_d is the end diastolic count
c_s is the end systolic count
c_b is the background count [18]

Using a dynamic cardiac phantom, the accuracy of the EF measurement and LV volume estimation by radionuclide imaging has been determined [18]. The count-based method was found to give accurate results for evaluating cardiac EF and volume measurements.

20.3.4 Dynamic Recording Method

During dynamic recording, the data acquisition is triggered by another signal, usually the ECG, to obtain the gated activity during ventricular systole and diastole. The contraction of the left ventricle of the heart is used to align the acquisition data from different cardiac cycles. During dynamic recording, information about the cardiac function is averaged over many heartbeats during a period when the radiopharmaceuticals are uniformly distributed in the blood pool. Estimations of end systolic and end diastolic volumes are made and the EF is calculated (see preceding text). Also, other parameters can be obtained, for example, the amplitude and phase of the ejection from the left ventricle. These parameters may show malfunction in the cardiac cycle. These dynamic recordings may also be applied to the brain, lungs, liver, kidney, and vascular systems, and they can be important to judge the function of these organs (e.g., after kidney transplantation).

20.3.5 Gas Dilution

Gas dilution is a method to determine lung volumes because standard techniques for lung measurements measure only the inhaled or exhaled air as a function of time (spirometry) and cannot be used to assess the absolute lung volume. The subject is connected to a spirometer that contains a known concentration of gas (e.g., helium). The subject is then asked to breathe for several minutes, to equalize the concentration of helium in the lung and the spirometer. Using the law of conservation of matter, the volume of the lung can be calculated. Since the total amount of helium is the same before and after measurement, the fractional concentration times the volume before equals the fractional concentration times the volume after: $C_1, \times V_1, = C_2 \times (V_1, + V_2)$. The volume after the measurement can be extracted from this equation, and by subtracting the volume of the spirometer, the lung volume is calculated.

20.4 Water Displacement Volumetry

The measurement of the volume of an extremity such as arm or leg can be measured using a water tank, which is illustrated schematically in Figure 20.9. The advantage of water displacement volumetry is the possibility for direct measurement of objects with an irregular form. In the clinical situation, volume determination of the leg can be valuable for monitoring the severity of edema or hematoma after surgery or trauma. A setup for water displacement can be developed by the user, and an example of such a system is described by Kaulesar Sukul et al. [19]. A special tank for water displacement volumetry of

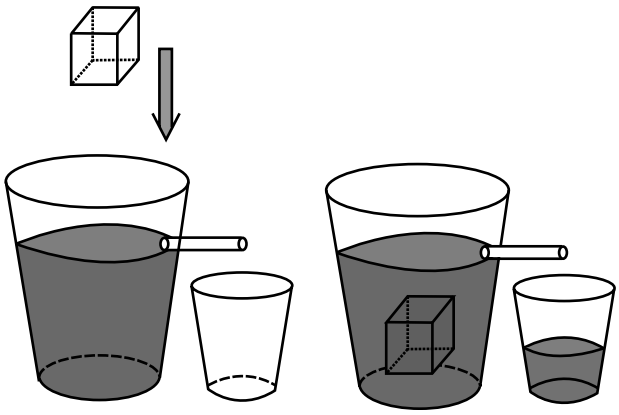

FIGURE 20.9 A schematic overview of a volume-measuring method using water displacement: the desired volume of the object is represented by the overflow volume in the small tank after lowering the object into the large tank. This technique is especially useful for irregular-shaped objects.

the leg was constructed consisting of two overflow tubes. The tank was filled to the lower overflow tube, and the overflow tube was subsequently closed. The patient was then asked to lower his leg into the tank, and the amount of overflow of the upper tube was measured. The total volume was then calculated by measuring the fluid volume delivered to the upper tube and the volume difference between the lower and upper overflow tube, the so-called reserve volume. The volume of ankle and foot was then measured by filling the tank to the upper overflow tube and measuring the amount of water in the cylinder when the foot and ankle were immersed in the water.

Disadvantages of water displacement volumetry are hygiene problems; it is time-consuming and not suitable for measurements of the volume of extremities of patients in the immediate postoperative period. Therefore, alternatives have been sought, with the disk model method as a promising one. The calculation of the volume of the leg is performed by dividing the leg into disks of thickness h (e.g., 3 cm) as illustrated in Figure 20.10. The total volume is equal to the sum of the individual disk volumes:

$$V = \sum_{i=1}^{n} \frac{C_i^2}{4\pi} h = \sum_{i=1}^{n} \pi r_i^2 h = h \sum_{i=1}^{n} \pi r_i^2 \tag{20.24}$$

where C_i is the circumference of the disk at position i with assumed radius of r_i.

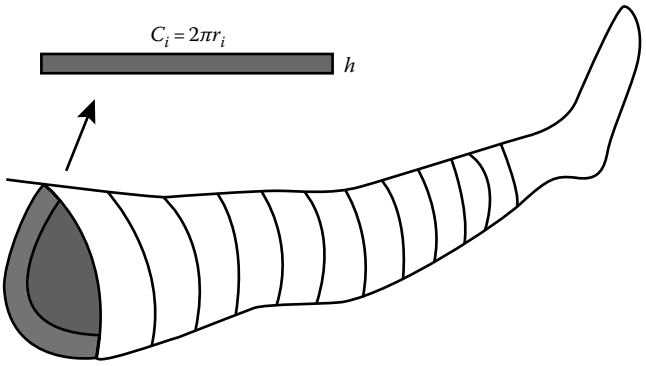

FIGURE 20.10 Illustration of the disk model to measure leg volume. The leg is divided in different sections with a fixed intersection distance; the circumference of each section is obtained. This circumference is then used to describe the leg as perfect circles with an assumed radius calculated from the circumference. This radius is then used to calculate the contribution of that section to the volume and the total volume is obtained by summation.

A study to compare water displacement volumetry with the results of the disk model method indicated that both methods give similar results. Consequently, because of the ease of application, the disk model method is the method of choice to measure volumes of extremities. Assuming the length of a leg to be 75 cm, a ratio between length and step size (3 cm was proposed in [19]) of 25 is obtained. According to a study by Aarnink et al. [15], this ratio can be reduced while still obtaining an accuracy of >95%. A disk height of 10 cm will be sufficient to measure the leg volume with an accuracy of at least 95%. However, it might be necessary to use a small interdisk section to obtain a higher accuracy, which might be needed to accurately monitor the edema changes in volume.

20.5 Equipment and Experiments

Table 20.1 summarizes the different methods for volume measurement and their applications. The table serves as a starting point to evaluate the available equipment for volume measurement.

20.6 Evaluation

Plethysmography is an easy and noninvasive method to obtain knowledge for assessing vascular diseases, cardiac output disorders, or pulmonary dysfunctions. Systems for direct measurement of volume changes have been developed, but physical properties have also been introduced as an indirect measure of the change in volume. Each system has its own advantages and disadvantages.

For *chamber plethysmography*, the water-filled type is more stable with respect to temperature change, but thermal problems may occur if the water temperature is significantly different from that of the limb segment. Furthermore, the hydrostatic effect of the water may alter the blood flow. Also, the rubber sleeve between the limb segment and the water may influence the release of sweat. It is a cumbersome measurement that is not very useful during or after exercise. The *air displacement* type introduces problems of drift because of its high coefficient of expansion, although self-compensating systems

TABLE 20.1 Volume-Measuring Techniques, Applications, and Equipment for Different Applications

Technique	Application	Companies	Products	Price (U.S.$)
Spirometry	Lung volume	Nellcor Puritan Bennett	Renaissance	
		Morgan Science Spirometrics		
		CDX Corporation	Spiro 110S	
Whole-body plethysmography	Lung volume	Morgan Science ACI Medical Inc.		25,000.00
Gas dilution	Lung volume	Equilibrated Biosystems Inc. Melville		
Thermodilution	Heart	Abbott Critical Care System Baxter		
		American Edwards Laboratories		
Strain-gage plethysmography	Cardiac output	Parks Medical Electronics		
Impedance plethysmography	Perfusion studies	Ambulatory monitoring systems Vitalog		
		RJL systems Detroit Codman and Shurtleff Inc. Randolph		
		Electrodiagnostic Instrument Inc. Burbank		
Inductive Plethysmograph	Lung volume	SensorMedics BV	RespiTrace plus SomnoStar PT	15,000.00
Radionuclide imaging	Heart, peripheral organs	Schering		

have been proposed. Also, the thermal behavior of the body plethysmograph may produce variations in pressure inside the airtight box. Two sources of temperature variation can be mentioned: the chest volume variation induced by breathing produces heat and a temperature gradient may exist between the patient and the internal temperature of the box [20].

In *impedance plethysmography*, the changes in impedance in tissue are used, which are primarily due to changes in the conductivity of the current path with each pulsation of blood. Several theories attempt to explain the actual cause of these changes in tissue impedance. One explanation is that blood filling of a segment of the body lowers the impedance of that segment. A second theory is that the increase in diameter due to additional blood in a segment of the body increases the cross-sectional area of the segment's conductivity path and thereby lowers the resistance of the path. A third explanation is based on the principle of pressure changes on the electrodes that occur with each blood pulsation and uses the changes in the impedance of the skin–electrode interface. The main difficulty with the procedure is the problem of relating the output resistance to any absolute volume measurement. Detection of the presence of arterial pulsations, measurement of pulse rate, and determination of time of arrival of a pulse at any given point in the peripheral circulation can all be satisfactorily handled by impedance plethysmography. Also, the impedance plethysmograph can measure time-variant changes in blood volume. A problem with impedance plethysmography may be the sensitivity to movement of the object. Research is being conducted to reduce the influences of these movement artifacts, either by different electrode configuration, electrode location, or using multiple sensors or different frequencies [21].

A low-cost *inductive plethysmograph* was designed by Cohen et al. to obtain a noninvasive measure of lung ventilation [22]. This plethysmograph indirectly monitors ventilation by measuring the cross-sectional area of the chest and abdomen. They attached commercially available elastic bands containing wire around the chest and abdomen and determined their inductances by measuring the frequency of an inductive-controlled oscillator.

New devices for plethysmographic measurements are under development, using different properties to obtain the quantitative knowledge required. For example, *acoustic plethysmography* measures body volume by determining changes in the resonant frequency of a Helmholtz resonator. A Helmholtz resonator consists of an enclosed volume of gas connected to its surroundings through a single opening. The gas can be forced to resonate acoustically by imposing periodic pressure fluctuations of the opening. The resonator frequency is inversely proportional to the square root of the volume of air in the resonator. An object placed in the resonator reduces the volume of air remaining in the resonator by its own volume, causing an increase in the resonator frequency. From a study to obtain density values of preterm infants, it was concluded that the acoustic plethysmograph can be used to measure total body volume of preterm infants [23].

In addition, volume measurements with diagnostic imaging modalities are well established in the clinical environment, for example, prostate ultrasonography or echocardiography. Besides important parameters such as step size and first step selection, accurate determination of the surface in different sections is important. While predominantly performed manually now, several attempts for automated detection of the surface have been reported [24–27]. Automatic detection of the surface in each section should be possible and would enable a system for automated measurement of the prostate, heart, liver, etc. Further research will indicate the usefulness of such a system in a clinical setting.

References

1. A. J. Comerota, R. N. Harada, A. R. Eze, and M. L. Katz, Air plethysmography: A clinical review, *Int. Angiol.*, 14, 45–52, 1995.
2. A. B. Dubois, S. J. Botello, G. N. Beddell, R. Marshall, and J. H. Comroe, A rapid plethysmographic method for measuring thoracic gas volume: A comparison with a nitrogen washout method for measuring functional residual capacity in normal subjects, *J. Clin. Invest.*, 35, 322–326, 1956.
3. J. B. West, *Respiratory Physiology—The Essentials*, Baltimore, MD: Williams and Wilkins, 1987.

4. J. R. Whitney, The measurement of volume changes in human limbs, *J. Physiol*., 121, 1–27, 1953.
5. J. Nyboer, S. Bagno, and L. F. Nims, The impedance plethysmograph: An electrical volume recorder, National Research Council, Committee on Aviation Medicine, Report No. 149, Washington, DC, 1943.
6. W. G. Kubicek, F. J. Kottke, M. V. Ramos, R. P. Patterson, D. A. Witsoe, J. W. Labree, W. Remole, T. E. Layman, H. Schoening, and J. T. Garamala, The Minnesota impedance cardiograph—Theory and applications, *Biomed. Eng*., 9, 410–416, 1974.
7. R. Shankar and J. G. Webster, Noninvasive measurement of compliance of human leg arteries, *IEEE Trans. Biomed. Eng*., 38, 62–67, 1993.
8. N. Verschoor, H. H. Woltjer, B. J. M. van der Meer, and P. M. J. M. de Vries, The lowering of stroke volume measured by means of impedance cardiography during endexpiratory breath holding, *Physiol. Meas*., 17, 29–35, 1996.
9. M. A. Cohn, H. Watson, R. Weisshaut, F. Stott, and M. A. Sackner, A transducer for non-invasive monitoring of respiration, in *ISAM 1977, Proceedings of Second International Symposium on Ambulatory Monitoring*, London, U.K.: Academic Press, 1978, pp. 119–128.
10. J. A. Adams, Respiratory inductive plethysmography, in J. Stocks, P. D. Sly, R. S. Tepper, and W. J. Morgan (eds.), *Infant Respiratory Function Testing*, New York: Wiley-Liss, 1996, pp. 139–164.
11. S. Webb, *The Physics of Medical Imaging*, Bristol, U.K.: IOP Publishing, 1988, pp. 204–221.
12. M. K. Terris and T. A. Stamey, Determination of prostate volume by transrectal ultrasound, *J. Urol*., 145, 984–987, 1991.
13. R. G. Aarnink, J. J. M. C. H. de la Rosette, F. M. J. Debruyne, and H. Wijkstra, Formula-derived prostate volume determination, *Eur. Urol*., 29, 399–402, 1996.
14. P. J. Davis and P. Rabinowitz, *Methods of Numerical Integration*, San Diego, CA: Academic Press, 1975, pp. 40–43.
15. R. G. Aarnink, R. J. B. Giesen, J. J. M. C. H. de la Rosette, A. L. Huynen, F. M. J. Debruyne, and H. Wijkstra, Planimetric volumetry of the prostate: How accurate is it? *Physiol. Meas*., 16, 141–150, 1995.
16. E. D. Trautman and R. S. Newbower, The development of indicator-dilution techniques, *IEEE Trans. Biomed. Eng*., 31, 800–807, 1984.
17. A. Rubini, D. Del Monte, V. Catena, I. Ittar, M. Cesaro, D. Soranzo, G. Rattazzi, and G. L. Alatti, Cardiac output measurement by the thermodilution method: An in vitro test of accuracy of three commercially available automatic cardiac output computers, *Intensive Care Med*., 21, 154–158, 1995.
18. S. Jang, R. J. Jaszczak, F. Li, J. F. Debatin, S. N. Nadel, A. J. Evans, K. L. Greer, and R. E. Coleman, Cardiac ejection fraction and volume measurements using dynamic cardiac phantoms and radionuclide imaging, *IEEE Trans. Nucl. Sci*., 41, 2845–2849, 1994.
19. D. M. K. S. Kaulesar Sukul, P. T. den Hoed, E. J. Johannes, R. van Dolder, and E. Benda, Direct and indirect methods for the quantification of leg volume: Comparison between water displacement volumetry, the disk model method and the frustum sign model method, using the correlation coefficient and the limits of agreement, *J. Biomed. Eng*., 15, 477–480, 1993.
20. P. Saucez, M. Remy, C. Renotte, and M. Mauroy, Thermal behavior of the constant volume body plethysmograph, *IEEE Trans. Biomed. Eng*., 42, 269–277, 1995.
21. J. Rosell, K. P. Cohen, and J. G. Webster, Reduction of motion artifacts using a two-frequency impedance plethysmograph and adaptive filtering, *IEEE Trans Biomed. Eng*., 42, 1044–1048, 1995.
22. K. P. Cohen, D. Panescu, J. H. Booske, J. G. Webster, and W. L. Tompkins, Design of an inductive plethysmograph for ventilation measurement, *Physiol. Meas*., 15, 217–229, 1994.
23. O. S. Valerio Jimenez, J. K. Moon, C. L. Jensen, F. A. Vohra, and H. P. Sheng, Pre-term infant volume measurements by acoustic plethysmography, *J. Biomed. Eng*., 15, 91–98, 1993.
24. R. G. Aarnink, R. J. B. Giesen, A. L. Huynen, J. J. M. C. H. de la Rosette, F. M. J. Debruyne, and H. Wijkstra, A practical clinical method for contour determination in ultrasonographic prostate images, *Ultrasound Med. Biol*., 20, 705–717, 1994.

25. C. H. Chu, E. J. Delp, and A. J. Buda, Detecting left ventricular endocardial and epicardial boundaries by digital two-dimensional echocardiography, *IEEE Trans. Med. Imag.*, 7, 81–90 1988.
26. J. Feng, W. C. Lin, and C. T. Chen, Epicardial boundary detection using fuzzy reasoning, *IEEE Trans. Med. Int.*, 10, 187–199, 1991.
27. S. Lobregt and M. A. Viergever, A discrete contour model, *IEEE Trans. Med. Imag.*, 14, 12–24, 1995.

Further Information

Anonymous, AARC clinical practice guideline: Static lung volume, *Respir. Care*, 39, 830–836, 1994.
Anonymous, AARC clinical practice guideline: Body plethysmography, *Respir. Care*, 39, 1184–1190, 1994.
Bernstein, E. F. (ed.), *Noninvasive Diagnostic Techniques in Vascular Disease*, 3rd edn., St. Louis, MO: Mosby, 1985.
Davis, P. J. and Rabinowitz, P., *Methods of Numerical Integration*, London, U.K.: Academic Press, 1975.
Feigenbaum, H., *Echocardiography*, 5th edn., Philadelphia, PA: Lee & Febiger, 1993.
McDicken, W. N., *Diagnostic Ultrasonics: Principles and Use of Instruments*, 3rd edn., London, U.K.: Crosby Lockwood Staples, 1991.
Nyboer, J., *Electrical Impedance Plethysmography*, Springfield, IL: Charles Thomas, 1959.
The Science Notebook, *Exploring Measurement Volume*, http://science-notebook.com/measure02-vol.html, accessed on August 6, 2012.
Webb, S., *The Physics of Medical Imaging*, Bristol, U.K.: IOP Publishing, 1988.
West, J. B., *Respiratory Physiology—The Essentials*, Baltimore, MD: Williams and Wilkins, 1987.

Partial List of Manufacturers and Suppliers

BrandTech Scientific, Inc., 11 Bokum Rd., Essex, CT 06426, Phone: 860-767-2562, Fax: 860-767-2563, www.brandtech.com
Emerson Process Management, 310 E. University Dr., McKinney, TX 75069, Phone: 972-548-3574, 800-558-5853 (toll free), Fax: 972-542-6433, www2.emersonprocess.com/en-US/brands/fis…
Floyd Bell, Inc., 720 Dearborn Park Lane, Columbus, OH 43085, Phone: 614-294-4000, 888-356-9323 (toll free), Fax: 614-291-0823, www.floydbell.com
Fluid Metering, Inc., 5 Aerial Way, Suite 500, Syosset, NY 11791, Phone: 516-922-6050, 800-747-5858 (toll free), Fax: 516-624-8261, www.fmipump.com/
Seraphin Test Measure/Pemberton, 30 Indel Ave., Rancocas, NJ 08073-0227, Phone: 609-267-0922, 800-573-6322 (toll free), Fax: 609-261-2546, 800-373-6322 (toll free), www.seraphinusa.com
Sick, Inc., 6900 W. 110th St., Bloomington, MN 55438, Phone: 952-941-6780, 800-325-7425 (toll free), Fax: 952-941-9287, www.sick.com/us/en-us/home/Pages/Homepag…
Simtech, USA, 47-A Runway Rd., Bristol Industrial Park, Levittown, PA 19057, Phone: 215-547-0444, 877-777-2467 (toll free), Fax: 215-547-9129, www.simtechusa.com
Vindum Engineering. Inc., 1 Woodview Court, San Ramon, CA 94582, Phone: 925-275-0633, Fax: 925-275-9697, www.vindum.com

21

Tilt Measurement

Adam Chrzanowski
University of New Brunswick

James M. Secord
University of New Brunswick

If the relative position of two points is described by the 3D orientation of a line joining them, then, in general, *tilt* is the angular amount that the orientation has changed, in a vertical plane, from a previous direction or from a reference direction. If the original or reference orientation is nearly horizontal, then the term "tilt" is usually used. If it is nearly vertical, then the change is often regarded as "inclination." Here, "tilt" will refer to either. The two points can be separated by a discernable amount, the base, or the tilt can be measured at a point with the reference orientation being defined by the direction of the force of gravity at that point. Thus, the same instrument that measures tilt at a point can be called either a *tiltmeter* or an *inclinometer* (or clinometer), depending on the interpretation of the results. The instrument used to measure a series of tilts along any vertical orientation is often called an inclinometer (e.g., [1]).

Angular tilt is directly related to the linear amount of change subtending the length of the base. Consequently, angular tilt does not have to be measured directly but can be derived from the mechanical or other measurement of this linear change if the length of the base is known.
Therefore, the following discussion has been subdivided into

1. Tiltmeters or inclinometers (angular tilt at a point or over a limited, relatively small base length)
2. Geodetic leveling (tilt derived from a height difference over an extended base of virtually limitless length)
3. Hydrostatic leveling (tilt derived from a height difference over an extended base of limited length)
4. Suspended and inverted pendula or plumb lines (inclination from a difference in horizontal relative position over a vertical base or height difference)

21.1 Tiltmeters or Inclinometers

Considering the basic principle of operation, tiltmeters may be divided into liquid (including spirit bubble type), vertical pendulum, or horizontal pendulum. Dunnicliff [1] provides a comprehensive review of tiltmeters and inclinometers according to the method in which the tilt is sensed (i.e., mechanical, with accelerometer transducer, with vibrating wire transducer, or with electrolytic transducer).

The sensitivity of tilt falls into two distinct groups: geodetic or geophysical special tiltmeters with a resolution of 10^{-8} rad (0.002 in.) or even 10^{-9} rad and engineering tiltmeters with resolutions from 0.1 in. to several seconds of arc, depending on the required range of tilt to be measured.

The first group includes instruments that are used mainly for geophysical studies of Earth tide phenomena and tectonic movements, for example, the Verbaander–Melchior [2] and the Zöllner [3,4] horizontal pendulum tiltmeters and the Rockwell Model TM-1 [5] liquid-bubble type. This category of instrument requires extremely stable mounting and a controlled environment. There are very few engineering projects where such sensitive instruments are required. However, deformation measurements of underground excavations for the storage of nuclear waste may be one of the few possible applications. An example is a mercury tiltmeter (Model 300) developed for that purpose by the Auckland Nuclear Accessory Co. Ltd. in New Zealand. In this instrument, the change in capacitance between electrodes and a mercury surface is proportional to the tilt. This tiltmeter, with a total range of 15 in., is claimed to give a resolution of 10^{-9} rad (0.0002 in.), which corresponds to a relative vertical displacement of only 6×10^{-7} mm over its base length of 587 mm.

In the second group, there are many models of liquid or pendulum tiltmeters of reasonable price ($2000–$5000) that satisfy most needs in engineering studies. Apart from a spirit level or level vial by itself, the simplest form of tiltmeter is a base that is tens of centimeters long and leveled by centering the bubble in the vial by direct viewing or by an optical coincidence viewing of the two ends of the bubble. Direct viewing gives a resolution of 1/5 of a vial division (usually 2 mm), which typically has a sensitivity of 10–30 in. per division. Coincidence viewing increases the setting accuracy to 0.03 of the sensitivity of the vial. The discrepancy from horizontal between the two measurement points can be determined by a dial gage or micrometer that has a resolution of 0.0005 in. or 0.02 mm. Huggenberger AG claims a sensitivity of 0.3 in. over a range of ±21 ft for their clinometer with a 100 mm base and coincidence centering of the bubble in the level vial. The clinometer can be attached to 1 m bases for either horizontal or vertical measurements.

If the vial is filled with an electrolytic liquid, the centering of the bubble can be done electrically. An example is the Electrolevel (by the British Aircraft Corp.), which uses the spirit bubble principle [6] and in which the movement of the bubble is sensed by three electrodes. A tilt produces a change in differential resistivity between the electrodes that is measured by means of a Wheatstone bridge. A resolution of 0.25 in. is obtained over a total range of a few minutes of arc. Many other liquid types of tiltmeters with various ranges (up to 30°) are available from various companies. Holzhausen [7] and Egan and Holzhausen [8] discuss the application of electrolytic tiltmeters (resolution of 2 in. over a range of ±1°, manufactured by Applied Geomechanics) in the monitoring of various hydroelectric power dams in the United States.

The Rank Organization in the United Kingdom [9] makes a liquid-dampened pendulum-type electronic level, the Talyvel, which gives an accuracy of ±0.5 in. over a total range of ±8 ft. A similar transducer of the pendulum type is used in the Niveltronic tiltmeter (range of ±150 in. with an accuracy of ±0.2 in.) produced by TESA S.A. in Switzerland. Of particular popularity are servo-accelerometer tiltmeters with horizontal pendula. They offer ruggedness and durability and can operate in low temperatures. The output voltage is proportional to the sine of the angle of tilt. Schaevitz Engineering produces such a servo-accelerometer that employs a small-mass horizontal paddle (pendulum), which tries to move in the direction of tilt, due to the force of gravity. Any resultant motion is converted by position sensors to a signal input to the electronic amplifier whose current output is applied to the torque motor. This develops a torque that is equal and opposite to the original. The torque motor current produces a voltage output that is proportional to the sine of the angle of tilt.

The typical output voltage range for tiltmeters is ±5 V, which corresponds to the maximum range of tilt and readily allows for serial interfacing. The angular resolution of a tiltmeter depends on its range of tilt since a larger range would result in more angular tilt per unit voltage so a higher-resolution tiltmeter would have a smaller range of measurable tilt. Typically, the resolution is 0.02% of the range (volts) [10].

There are many factors affecting the accuracy of tilt sensing, not just the resolution of the readout. A temperature change produces dimensional changes in the mechanical components and changes in the viscosity of the liquid in electrolytic tiltmeters and of the dampening oil in pendulum-type tiltmeters.

Also, electric characteristics can alter with temperature changes. Drifts in tilt indications and fluctuations of the readout may also occur. Compensation for the effects of temperature changes can be incorporated in the construction of an instrument but at an increased cost. An alternative is to design a linear reaction by the instrument to the effects of temperature and to apply simple calibration corrections.

In less expensive models, compensation for the aforementioned sources of error is not very sophisticated, and such tiltmeters may show nonlinear output in reaction to changes in temperature and erratic drifts or other behavior that would be difficult to predict without testing. Consequently, very thorough testing and calibration are required even when the accuracy requirement is not very high [11]. Testing should investigate, at least, the linearity of output in reaction to induced tilts over the instrument's full range (±) and to changes in temperature. Some suggestions for testing and calibrating inclinometers, among other instruments, are given in Dunnicliff [1]. It is further emphasized that regular and up-to-date calibration is important in order to ensure continuity in the fidelity of the data being gathered. In most cases, the behavior being investigated changes with time and incorrect data cannot be recaptured.

Compensators for vertical circle readings in precision theodolites work on the same principle as some engineering tiltmeters. The liquid compensator of the Kern E2 electronic theodolite [12] gave a repeatability of better than 0.3 in. over a range of ±150 in. and was incorporated in their tiltmeter, NIVEL 20, in 1989. The same compensation system has been used in the currently available Leica TC2002 precision electronic total station [13]. Consequently, the theodolite may also be used as a tiltmeter, in some applications, giving the same accuracy as the Electrolevel, for example.

Tiltmeters have a wide range of applications. A series of tiltmeters, if arranged along a terrain profile in a mining area, may replace geodetic leveling in the determination of ground subsidence [11] as shown in Figure 21.1. For example, the subsidence (i.e., the variation from the previous or original profile) of point 4 (Δh_4) with respect to point 1 may be estimated from the observed changes in tilt, from a base or original position, (α_i in radians) and known distances between the points as

$$\delta h_4 = s_1 \frac{(\alpha_1 + \alpha_2)}{2} + s_2 \frac{(\alpha_2 + \alpha_3)}{2} + s_3 \frac{(\alpha_3 + \alpha_4)}{2} \tag{21.1}$$

The fidelity of this method depends on the density of tilt measurements along the profile and the continuity of the profile (a constant slope of the terrain between measurement points is assumed). Similarly, deformation profiles of tall buildings may be determined by placing a series of tiltmeters at different levels of the structure [14]. Also, changes in borehole profiles can be created in a similar manner. The absolute profile of a borehole can be generated by considering the horizontal displacement in the direction of the orientation of the inclinometer (usually controlled by guide grooves in the borehole casing) for the *i*th position, as it traverses a borehole with observation of α_i at a depth s_i. However, this would require calibration of the inclinometer to correct its output to show zero in its vertical position since the α_i are tilts from the vertical rather than angular changes from an original inclination.

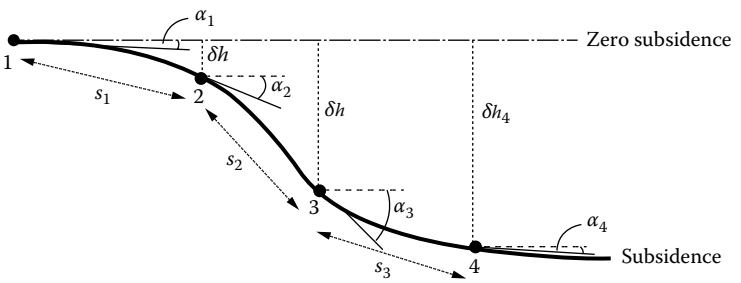

FIGURE 21.1 Ground subsidence derived from tilt measurements.

In geomechanical engineering, the most popular application of tiltmeters and borehole inclinometers is in slope stability studies and in monitoring earth-fill dams. Torpedo-shaped biaxial inclinometers are used to scan boreholes drilled to the depth of expected stable strata in the slope. By lowering the inclinometer on a cable with marked intervals and taking readings of the inclinometer at those intervals, a full profile of the borehole and its changes may be determined through repeated surveys, as mentioned earlier. Slope Indicator Co. (SINCO) and other producers of tiltmeters provide special borehole inclinometers (50 cm or 2 ft long) with guide wheels to control the orientation of the inclinometer. A special borehole casing (plastic or aluminum) with guiding grooves for the wheels is available. Usually, servo-accelerometer-type inclinometers are used with various ranges of inclination measurements, for example, ±6°, ±53°, or even ±90°. A 40 m deep borehole, if measured every 50 cm with an inclinometer having an accuracy of only ±100 in., should allow for the determination of linear lateral displacement of the collar of the borehole with an accuracy of ±2 mm.

In cases where there is difficult access to the monitored area or a need for continuous data acquisition or both, tiltmeters or borehole inclinometers can be left in place at the observing station with a telemetry monitoring system allowing for communication to the processing location. One example of a station setup of a telemetric monitoring of ground subsidence in a mining area near Sparwood, British Columbia, Canada, used a telemetry system developed for the Canadian Centre for Mining and Energy Technology (CANMET) by the University of New Brunswick [11,15]. Terra Technology biaxial servo-accelerometer tiltmeters of ±1° range were used in the study. The telemetry system could work with up to 256 field stations. Each station accepted up to six sensors (not only tiltmeters but any type of instrument with electric output, e.g., temperature, power level, or voltage). Another example is a fully automated borehole scanning system with a SINCO inclinometer and telemetric data acquisition that was also developed at the University of New Brunswick [16]. It has been used successfully in monitoring highwall stability at the Syncrude Canada Limited tar sand mining operation in northern Alberta.

21.2 Geodetic Leveling

Geodetic or differential leveling measures the height difference between two points using precision tilting levels, or precision automatic levels with compensators, with parallel plate micrometers and calibrated invar leveling staves or rods. Recent technology has provided digital automatic levels that use a CCD sensor in the instrument and bar codes, rather than linear graduations, on the staves [17]. Their ease of use and comparable precision have quickly made them rivals to the traditional optical instruments. In a single setup of the level, the height difference is the backsight rod reading minus the foresight rod reading. Any number of setup height differences can be combined to determine the height difference between two points of interest; however, the errors involved accumulate with the number of setups. With sight lengths limited to no more than 20 m, geodetic leveling can produce height differences with a precision of ±0.1 mm per setup, which is equivalent to a precision of ±0.5 in. in tilt. Although geodetic leveling is traditionally used to determine elevations, it is often used not only to monitor the settlement of sensitive structures but also to describe the tilt of components of a structure by determining the tilt between appropriate pairs of benchmarks (monumented in or on the structure) [18]. Since the level reference is created by an optical line of sight through a telescope (magnification up to 40×), a major source of systematic error is the effect of vertical atmospheric refraction. A vertical temperature gradient of 1°C m^{-1} across the line of sight would bend the line of sight to be in error by 0.4 mm at 30 m. Gradients of this magnitude are commonly encountered in industrial settings and are usually even more evident outdoors. Less effect is realized if the sight lengths are kept short, but this must be weighted against the accumulation of random error with each additional setup (shorter sight lengths would require more setups to traverse the same height difference). The errors that seem to be insignificant in a single setup (or in a few setups) become magnified in height differences involving a large number of setups (e.g., rod scale error and settlement of the instrument or rods). Such errors have become quite noticeable in the

monitoring of tectonic plate movement, and undetected systematic effects can be misleading. Further discussion on precision leveling and sources of error is available in Vanicek et al. [19] and in Schomacker and Berry [20].

Having the elevations or heights, h_1 and h_2, of two points or having measured, or determined, the height difference between them, $\Delta h_{12^t} = h_2 - h_1$, at a time t, means that, if $\delta\Delta h = \Delta h_{12^{t2}} - \Delta h_{12^{t1}}$, the tilt, T_{12}, can be calculated if the horizontal separation s_{12} is known, since $T_{12} = \delta\Delta h/s_{12}$. The separation does not have to be known as precisely as the height difference since the total random error is $\sigma_{T^2} = \sigma_{\delta\Delta h^2}/s^2 + \sigma_{s^2}(\delta\Delta h^2/s^4)$. As an example, for two points that are 60 m apart with a height difference of 0.5 m (extreme in most structural cases) with the height difference known to ±50 (μm ($\sigma_{\delta\Delta h}$) and the distance known to ±0.01 m (σ_s), the tilt would have a precision (σ_T) of ±0.3 in. Further, neither the measurement of the height difference nor the determination of the separation has to be done directly between the two points. The leveling can be done along whatever route is convenient and the separation can be obtained in a variety of ways, for example, inversing from coordinated values for the points [21].

21.3 Hydrostatic Leveling

If two connected containers (Figure 21.2) are partially filled with a liquid, then the heights h_1 and h_2 are related through the hydrostatic equation (Bernoulli's equation, as given in [22]):

$$h_1 + \frac{P_1}{(g_1\rho_1)} = h_2 + \frac{P_2}{(g_2\rho_2)} = c \tag{21.2}$$

where

P is the barometric pressure
g is the force of gravity
ρ is the density of the liquid, which is a function of temperature
c is a constant

The previously mentioned relationship has been employed in hydrostatic leveling, as shown schematically in Figure 21.3. The air tube connecting the two containers eliminates possible error due to different air pressures at two stations. The temperature of the liquid should also be maintained constant

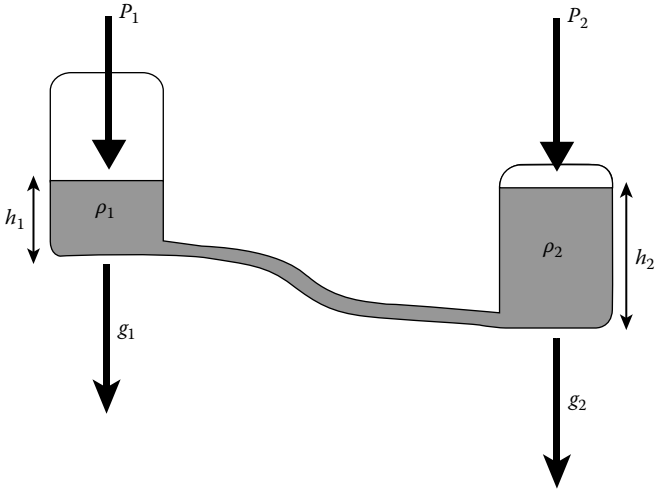

FIGURE 21.2 Hydrostatic equilibrium in connected vessels.

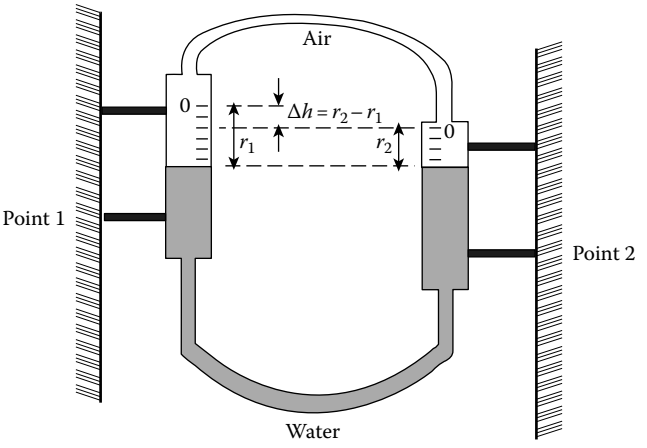

FIGURE 21.3 Hydrostatic leveling ($\Delta h_{12} = r_2 - r_1$).

because, for example, a difference of 1.2 °C between two containers may cause an error of 0.05 mm in a Δh determination for an average $h = 0.2$ m and $t = 20$ °C. Huggett et al. [23] devised a two-fluid tiltmeter to overcome the temperature effect by using two liquids with different temperature coefficients and claim a resolution of 10^{-8}–10^{-9} rad over a separation of up to 1 km. In a discussion of liquid level gages, Dunnicliff [1] emphasizes that care should be exercised to ensure that there is no discontinuity in the liquid since any gas (usually air, often entering when filling the tubing) in the liquid line will introduce an error in the level difference, especially in a vertical, more than in a horizontal, portion of tubing. He also mentions that the behavior of the liquid is influenced by the inside diameter and capillary effects of the tubing, while the outside diameter is likely what is quoted by manufacturers. Dunnicliff [1] also provides a comprehensive summary of the variety of liquid level gages.

Two examples of typical hydrostatic instruments used in precision leveling will be mentioned here. The ELWAAG 001, developed in Germany [24], is a fully automatic instrument with a traveling (by means of an electric stepping motor) sensor pin that closes the electric circuit on touching the surface of the liquid. A standard deviation of ±0.03 mm is claimed over distances of 40 m between the instruments [22]. Another automatic system, the Nivomatic Telenivelling System, is available from Telemac or Roctest Ltd. The Nivomatic uses inductance transducers that translate the up and down movements of its floats into electric signals (frequency changes in a resonant circuit). An accuracy of ±0.1 mm is claimed over a 24 m length. P & S Enterprises, Ltd. produces a Pellissier model H5 portable hydrostatic level/tiltmeter, for which they claim an accuracy of ±5 μm over a tube length of 14 m, for engineering and Earth tide measurements.

Hydrostatic levels may be used in a network formation of permanently installed instruments to monitor tilts in large structures. Robotti and Rossini [25] report on a DAG (automatic measuring device of levels and inclinations) network monitoring system available from SIS Geotecnica (Italy) that offers an accuracy of about ±0.01 mm using inductive transducers in the measurement of liquid levels. Various systems of double liquid (e.g., water and mercury) settlement gages based on the principle of hydrostatic leveling are used for monitoring power dams [26] with extended networks of connecting tubing.

Instruments with direct measurement of liquid levels are limited in their vertical range by the height of their containers. This problem may be overcome if liquid pressures are measured instead of the changes in elevation of the liquid levels. Pneumatic pressure cells or pressure transducer cells may be used. Both Dunnicliff [1] and Hanna [26] give numerous examples of various settlement gages based on that principle. Meier [27] mentions the application of a differential pressure tiltmeter in the monitoring of a concrete dam.

21.4 Suspended and Inverted Plumb Lines

Two types of mechanical plumbing are used in monitoring the stability of vertical structures:

1. Suspended pendula or plumb lines (Figure 21.4a)
2. Floating pendula or inverted, or reversed, plumb lines (Figure 21.4b)

Typical applications are in the monitoring of power dams and of the stability of reference survey pillars. Suspended pendula are also commonly used in mine orientation surveys and in monitoring the stability of mine shafts. Tilt, or inclination, is derived from differences in horizontal relative position combined with vertical separation in the same way as tilt is derived from geodetic leveling. So, similarly, the vertical separation between two reading tables or between a reading table and anchor point does not have to be known as precisely as the change in relative position. Two table readings, each ±0.02 mm, with a relative position difference of 100 mm and a vertical separation of 10 m, known to ±0.01 m, would result in a tilt precision of ±2 in.

Inverted plumb lines have become standard instrumentation in large dams (e.g., Hydro-Quebec uses them routinely). Their advantage over suspended plumb lines is in the possibility of monitoring the absolute displacements of structures with respect to deeply anchored points in the foundation rock, which may be considered as stable. In power dams, the depth of anchors must be 30 m or even more below the foundation in order to obtain absolute displacements of the surface points. The main problem with inverted plumb lines is the drilling of vertical boreholes so that the vertical wire of the plumb line would have freedom to remain straight and vertical. A special technique for drilling vertical holes has been developed at Hydro-Quebec [28].

Several types of recording devices that measure displacements of structural points with respect to vertical plumb lines are produced by different companies. The simplest are mechanical or electromechanical micrometers with which the plumb wire can be positioned with respect to reference lines of a recording (coordinating) table with an accuracy of ±0.2 mm or better. Traveling microscopes may give the same accuracy. Automatic sensing and recording is possible with a Telecoordinator from

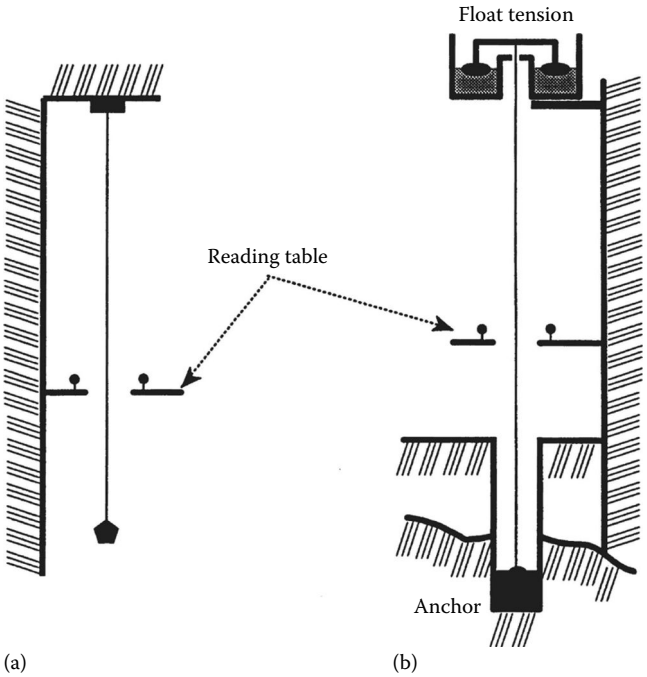

FIGURE 21.4 Inclination measurements with plumb lines. (a) Suspended pendulum, (b) Inverted pendulum.

Huggenberger AG in Switzerland. Telemac Co. (France) developed a system, Telependulum (marketed by Roctest), for continuous sensing of the position of the wire with remote reading and recording. A rigidly mounted reading table supports two pairs of induction-type proximity sensors arranged on two mutually perpendicular axes. A hollow cylinder is fixed on the pendulum wire at the appropriate level, passing through the center of the table and between the sensors. Changes in the width of the gap between the target cylinder and the sensors are detected by the corresponding changes in the induction effect. The system has a resolution of ±0.01 mm.

An interesting Automated Vision System has been developed by Spectron Engineering (Denver, Colorado). The system uses solid-state electronic cameras to image the plumb line with a resolution of about 3 μm over a range of about 75 mm. Several plumb lines at Glen Canyon dam and at Monticello dam, near Sacramento, California, have been using the system since 1982 [29].

Two sources of error, which may be often underestimated by the user, may strongly affect plumb line measurements:

1. The influence of air currents
2. The spiral shape of the wire

If the wire of a plumb line (Figure 21.5a), with pendulum mass Q, is exposed along a length h to an air current of speed v at a distance H from the anchor point, then the plumb line is deflected by an amount [30]:

$$e = f_o h \frac{H}{Q} \tag{21.3}$$

where f_o is the acting force of air current per unit length of the wire. The value of f_o may be calculated approximately from [30]:

$$f_o = 0.08 \frac{dv^2}{Q} \tag{21.4}$$

where

d is the diameter of the wire in millimeters
v is in meters per second
Q is in kilograms

As an example, if $H = 50$ m, $h = 5$ m, $d = 1$ mm, $Q = 20$ kg, and $v = 1$ m s^{-1} (only 3.6 km h^{-1}), then $e = 1$ mm.

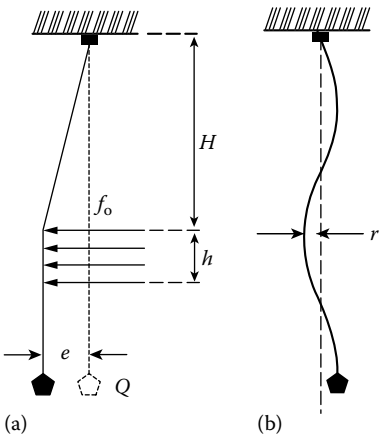

FIGURE 21.5 (a) Influence of air currents on a suspended plumb line. (b) Horizontal error due to the spiral shape of the wire.

The second source of error, which is usually underestimated in practice, is that the spiral shape (annealing) of the wire (Figure 21.5b) affects all wires unless they are specially straightened or suspended for a prolonged time (on the order of several months). If the wire changes its position (rotates) between two campaigns of measurements, then the recorded displacements could have a maximum error of 2*r*. The value of *r* can be calculated from [30]:

$$r = \frac{(\pi d^4 E)}{(64\ RQ)} \tag{21.5}$$

where

E is Young's modulus of elasticity (about 2×10^{11} Pa for steel)
R is the radius of the free spirals of the unloaded wire that, typically, is about 15 cm for wires up to 1.5 mm diameter
d and *Q* are as mentioned previously

For a plumb wire with $d = 1$ mm, $R = 15$ cm, and $Q = 196$ N (i.e., 20 kg), $r = 0.3$ mm.

If one plumb line cannot be established through all levels of a monitored structure, then a combination of suspended and inverted plumb lines may be used as long as they overlap at least at one level of the structure. At Hydro-Quebec, the drill holes of the plumb lines are also used for monitoring height changes (vertical extension) by installing tensioned invar wires [31].

21.5 Integration of Observations

The earlier discussion has considered using individual instruments. Because many investigations, using other instrumentation as well as the measurement of tilt, involve the repetition of measurements, often over a long term, the fidelity of the measurements and their being referenced to the original or initial observation are vital to the investigation. It is risky to expect consistent behavior of instrumentation, particularly in environments with dramatic variations (especially in temperature), and over a long period of time. Any conclusion relating to the behavior of a structure is only as good as the data used in the analysis of the behavior. Two ways to ensure reliability are possible. One is to make regular testing and calibration of a component of the observation regimen. The other is to analyze the observations as they are accumulated either each observable as a temporal series of repeated measurements or observations of different locations or types together in an integrated analysis. The analytical tools for integrated analyses, as well as for calibration testing and temporal series analysis, have been developed [21,32] and successfully implemented in several projects [15,18,33]. Proper calibration testing and correction, rigorous statistical analysis of trend in temporal series, and integrated analysis have proven to be valuable tools in the analysis of deformations and serve to enhance the monitoring of sensitive structures.

References

1. J. Dunnicliff, *Geotechnical Instrumentation for Monitoring Field Performance*, John Wiley & Sons, New York, 1988.
2. P. Melchior, *The Tides of the Planet Earth*, 2nd edn., Pergammon Press, Oxford, U.K., 1983.
3. W. Torge, *Geodesy*, Walter de Gruyter, New York, 1991.
4. M. van Ruymbeke, Sur un pendule horizontal équipé d'un capteur de déplacement a capacité variable, *Bull. Géodesique*, 50, 281–290, 1976.
5. G. L. Cooper and W. T. Schmars, Selected applications of a biaxial tiltmeter in the ground motion environment, *J. Spacecraft Rockets*, 11, 530–535, 1974.
6. M. A. R. Cooper, *Modern Theodolites and Levels*, Crosby Lockwood, London, U.K., 1971.
7. G. R. Holzhausen, *Low-Cost, Automated Detection of Precursors to Dam Failure: Coolidge Dam, Arizona*; *8th Annual Conference on Association of State Dam Safety Officials*, San Diego, CA, 1991.

8. N. H. Egan and G. R. Holzhausen, Evaluating structures using tilt (rotation) measurements, *Sensors Expo West Proceedings*, San Diego, CA, 1991.
9. W. Caspary and A. Geiger, Untersuchungen zur Leistungsfähigkeit elektronischer Neigungsmesser, *Schriftenreihe, Vermessungswesen HSBW*, 3, München, Germany, 1978.
10. A. Chrzanowski, Geotechnical and other non-geodetic methods in deformation measurements, in Y. Bock (ed.), *Proceedings of Deformation Measurements Workshop*, Massachusetts Institute of Technology, Boston, MA, 1986, pp. 112–153.
11. A. Chrzanowski, W. Faig, B. Kurz, and A. Makosinski, Development, installation and operation of a subsidence monitoring and telemetry system, Contract report submitted to CANMET, Calgary, Canada, November 1980.
12. Kern & Co. Ltd., E2 Instruction Manual, Kern & Co. Ltd., Aarau, Germany, 1984.
13. Leica AG, *Wild TC2002 User Manual*, Leica AG, Heerbrugg, Germany, 1993.
14. H. Kahmen, *Elektronische Messverfahren in der Geodäsie*, Herbert Wichmann, Karlsruhe, Germany, 1978.
15. A. Chrzanowski and M. Y. Fisekci, Application of tiltmeters with a remote data acquisition in monitoring mining subsidence, *Proceedings of 4th Canadian Symposium on Mine Surveying*, Banff, Alberta, Canada, June 1982.
16. A. Chrzanowski, A. Makosinski, A. Zielinski, and W. Faig, Highwall monitoring system, Contract report to Syncrude Canada Limited, Canada, April 1988.
17. H. Ingensand, Wild NA2002, NA3000, Technical paper digital levels, Leica AG, Heerbrugg, Germany, 1993.
18. A. Chrzanowski and J. M. Secord, The 1989 Integrated analysis of deformation measurements at the Mactaquac generating station, Contract Report to N.B. Power, May 1990.
19. P. Vanicek, R. O. Castle, and E. I. Balazs, Geodetic leveling and its applications, *Rev. Geophys. Space Phys*., 18(2), 505–524, 1980.
20. M. C. Schomaker and R. M. Berry, *Geodetic Levelling*, NOAA Manual NOS NGS 3, U.S. Department of Commerce, National Oceanic and Atmospheric Administration, National Ocean Survey, Rockville, MD, 1981.
21. J. M. Secord, Development of the automatic data management and the analysis of integrated deformation measurements, Ph.D. dissertation, Department of Geodesy and Geomatics Engineering Technical Report 176, University of New Brunswick, Fredericton, New Brunswick, Canada, 1995.
22. K. Schnädelbach, Neuere Verfahren zur präzisen Längen-und Höhenmessung, *Algemeine Vermessungs-Nachrichten*, 1980.
23. G. R. Huggett, L. E. Slater, and G. Pavlis, Precision leveling with a two-fluid tiltmeter, *Geophys. Res. Lett*., 3(12), 754–756, 1976.
24. H. Thierbach and W. Barth, Eine neue automatische Präzisionsschlauchwaage, *Z. Vermessungswesen*, 100, 470–478, 1976.
25. F. Robotti and T. Rossini, Analysis of differential settlements on monumental structures by means of the DAG automatic measuring device of levels and inclinations, in *Land Subsidence*, IAHA Publication No. 151, International Association of Hydrological Sciences, IAHS, Wallingford, Oxfordshire, UK, 1984.
26. T. H. Hanna, *Field Instrumentation in Geotechnical Engineering*, Trans Tech Publications, Clausthal-Zellerfeld, Germany1985.
27. E. Meier, A differential pressure tiltmeter for large-scale ground monitoring, *Water Power & Dam Constr*., 43(1), 38–40, 1991.
28. L. Dubreuil and R. Hamelin, Le forage vertical des trous de pendules inversés, *Proceedings of 2nd Canadian Symposium on Mining Surveying Rock Deformation Measurements*, Kingston, Ontario, Canada, 1974.
29. G. Kanegis, Automated vision system installed at Glen Canyon Dam, Spectron Engineering, n.d. [circa 1983].

30. A. Chrzanowski, E. Derenyi, and P. Wilson, Underground survey measurements—Research for progress, *Can. Min. Metall. Bull.*, June 1967.
31. B. Boyer and R. Hamelin, Monitoring survey: Recent developments in the use of inverted pendula, Report No. 4, Question 56, *15th Congress International Commission Large Dams,* Lausanne, Switzerland, 1985.
32. A. Chrzanowski, Y. Q. Chen, P. Romero, and J. Secord, Integration of geodetic and geotechnical deformation surveys in the geosciences, *Tectonophysics*, 130, 369–383, 1986.
33. A. Chrzanowski, Y. Q. Chen, J. Secord, and A. Szostak-Chrzanowski, Problems and solutions in the integrated monitoring and analysis of dam deformations, *CISM J. ACSGC*, 45(4), 547–560, 1991.

Further Readings

Leavitt, J., Sideris, A., and Bobrow, J. E., High bandwidth tilt measurement using low-cost sensors, *IEEE/ASME Trans. Mechatron*., 11(3), 320–327, 2006.

Miskam, A., Korakkotil, S., Zaidi, M., and Sidck, O., Development of a tilt measurement unit using micro-electromechanical system accelerometer, *J. Appl. Sci*., 9(13), 2451–2456, 2009.

Wang, J., Zhou, W., Lim, L. E. N., and Asundi, A. K., Strain and tilt measurement using multi-point diffraction strain sensor, *Opt. Laser Technol*., 40(8), 1099–1103, 2008.

Yang, J., Zhao, Y., Yang, S. Y., Xu, Y., and Zhao, Y., Novel tilt measurement method based on self-demodulated FBG sensor and pendulum clinometer, *Proc. SPIE Int. Soc. Opt. Eng*., 5634(1), 533–540, 2005.

Zhu, R., and Zheng, W., Tilt measurement research based on Moire fringe technique of SLR digital camera, *Appl. Mech. Mater*., 90–93, 2840–2843, 2011.

Partial List of Vendors and Suppliers

Applied Geomechanics Inc.
1336 Brommer Street, Santa Cruz, CA 95062

Eastman Whipstock GmbH
Gutenbergstrasse 3, 3005 Hannover-Westerfeld,
West Germany

Huggenberger AG
Hohlstrasse 176, CH-8040 Zürich, Switzerland

Leica AG
CH-9435 Heerbrugg, Switzerland

Maihak AG
Semperstrasse 38, D-2000 Hamburg 60, West Germany

RST Instruments Ltd.
1780 McLean Avenue, Port Coquitlam, B.C., Canada V3C 4K9

Serata Geomechanics, Inc.
4124 Lakeside Drive, Richmond, CA 94806

Soil Instruments Ltd.
Bell Lane, Uckfield, East Sussex TN22 1Q1, England

Solinst Canada Ltd.
2440 Industrial St., Burlington, Ontario, Canada L7P 1A5

Spectron Engineering
800 West 9th Avenue, Denver, CO 80204

Telemac
2 Rue Auguste Thomas, 92600 Asnieres, France

P & S Enterprises, Ltd.
240 South Monaco Pkwy, # 302, Denver, CO 80224

Auckland Nuclear Accessory Company Ltd.
P.O. Box 16066, Auckland, 3, New Zealand

Geotechnical Instruments Ltd.
Station House, Old Warwick Road, Leamington Spa,
Warwickshire CV31 3HR, England

IRAD GAGE
Etna Road, Lebanon, NH 03766

Measurement Devices Limited
11211 Richmond Avenue, Suite 106, Building B,
Houston, TX 77082

Roctest Ltée Ltd.
665 Pine, Montreal, P.Q., Canada J4P 2P4

Schaevitz Engineering
P.O. Box 505, Camden, NJ 08101

SINCO
3668 Albion Place N., Seattle, WA 98103

Solexperts AG
Postfach 274, CH-8034 Zürich, Switzerland

SIS Geotecnica
Via Roma, 15, 20090 Segrate (Mi), Italy

Spectron Glass and Electronics Inc.
595 Old Willets Path, Hauppauge, NY 11788

TerraMetrics
16027 West 5th Avenue, Golden, CO 80401

Edi Meier & Partner
8408 Winterthur, Switzerland

22

Proximity Sensing for Robotics

Ricardo E. Saad
Harmonics Lightwaves

Ben Benhabib
University of Toronto

A. Bonen
University of Toronto

K.C. Smith
University of Toronto

The objective of this chapter is to review the state of the art in proximity-sensing technologies for robotics. Special attention is paid to the sensing needs of robotic manipulators for grasping applications, in contrast to the needs of mobile robots for navigation purposes. For a review of the application of proximity sensing to mobile robots, the reader is referred to [1].

Robotic sensors can be categorized into three groups: medium-range (object recognition and gross position/orientation estimation) sensors, short-range (proximity) sensors, and contact sensors. Recent literature [2–6] suggests that robotic end effectors should be equipped with both short-range proximity and contact sensors.

Proximity sensors should be able to measure the position and orientation (pose) of an object's surface. The range must be sufficiently large to compensate for uncertainties in the medium-range pose-estimation process while maintaining sufficient accuracy to permit effective grasping of the object.

Transducers used by current proximity sensors vary in sophistication. Despite their great variety, however, these transducers and their accompanying electronic interface circuits (together comprising proximity sensor) cannot presently meet the stringent robustness requirements of most industrial robotic applications. Novel sensing algorithms and techniques still must be developed in order to improve on their current characteristics and, furthermore, to control both the sensing and grasping processes.

22.1 Proximity Definition

The term "proximity," quantified by "pose" in this chapter, refers to three geometrical parameters x, u, and v as shown in Figure 22.1, where

x is the translation from the origin of the sensor's reference coordinate frame, F_p, to a target point on the surface of the object measured along X_p. This target point defines the origin of the surface frame, F_r.

u is the *vertical* orientation of the object's surface, defined as a rotation around Y_p (of the translated frame), thereby specifying the new Z_r.

v is the *horizontal* orientation of the object's surface, defined as a rotation around Z_r, thereby specifying Y_r.

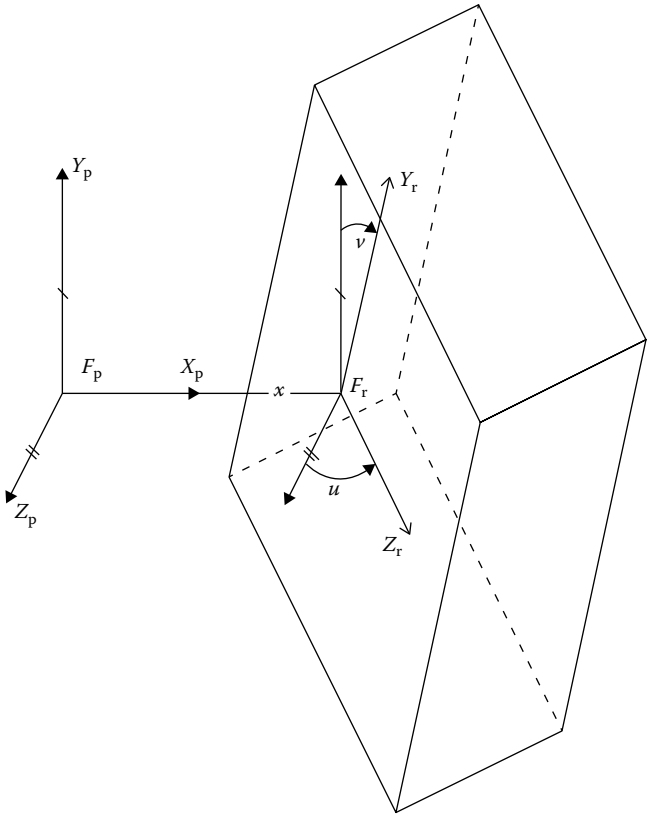

FIGURE 22.1 Proximity parameters.

22.2 Typical Sensor Characteristics

Conventionally, proximity sensors should be capable of measuring distances of up to 50 mm and two degree-of-freedom orientations equivalent to an overall inclination of up to ±30°. The intended principal application of the sensor is to act as a guide for the robot. Thus, it would be desirable to have higher sensitivity and accuracy as the gripper approaches the object, namely, when both the relative orientation and the distance approach near-zero values.

The signals received by the electronic interface circuit should be processed without limiting the required operating range of the sensor. The interface circuit should also minimize the effect of interference from the surroundings. It should therefore employ solutions to reduce background-noise interference and dynamic-range limitations.

The operation of the robot should not be slowed down by the sensor. Namely, a pose of the object should normally be estimated in 1–10 ms.

22.3 Technologies for Proximity Sensing

Proximity sensors have employed various transduction media, including sound waves, magnetic fields, electric fields, and light. Presently, electro-optical techniques seem to be the most appropriate for robotic-grasping applications. Such sensors are relatively small in size, have a large range of operation, and impose almost no restrictions on the object's material. However, recently, some new ultrasonic and capacitive proximity sensors have been fabricated directly as ICs, also showing the possibility of very-small-size proximity sensors based on these technologies [7,8].

Brief descriptions of the principles of the primary technologies used by proximity sensors are given in the following, with the main emphasis being on optical transducers. A survey of commercial proximity sensors capable of measuring distances can be found in [6].

22.3.1 Electro-Optical Sensors

Many proximity sensors use light, directly scattered from a target surface, to determine the distance and orientation of the target object from the gripper. The mechanism by which light is reflected can be explained by a model that specifies four different reflection phenomena. According to this model, light reflects from the surface primarily as a result of one or more of the following interactions:

1. *Single-surface reflection*: Light waves that reflect specularly a single time off a planar microfacet, whose dimensions are significantly larger than the wavelength
2. *Multiple-surface reflection*: Light waves that reflect specularly at least twice between multiple microfacets
3. *Reflection after penetration*: Light waves that penetrate into the material, refract, and then reflect back out as diffused light
4. *Corner reflection*: Light waves that diffract from interfaces with surface details about the same size or smaller than the wavelength (such as from corners of microfacets)

The primary phenomenon (1) usually exists in both dielectrics and metal. However, due to the high conductivity of metal surfaces, most of the light reflects specularly off the interface between the metal and the air, while the portion that penetrates into the metal surface is absorbed. Accordingly, the reflection intensity originating from internal refraction in metals is practically zero. In dielectrics, however, a large portion of the light penetrates into the surface and then reflects back out as diffused light (3). The secondary phenomena (2) and (4) exist both in metals and dielectrics and add to the diffused reflectance.

Common measurement techniques used in optical proximity sensing utilize one or more of the reflected components to determine the pose of the object in relation to the transducer.

22.3.2 Phase Modulation

A phase-modulated (PM) proximity sensor usually consists of two light sources and one or more photodetectors. The light sources are driven by modulated sinusoidal signals having a 90° phase relationship (Figure 22.2).

The emitter control voltages of the emitters, V_{em1} and V_{em2}, have amplitudes of a and b, respectively:

$$V_{em1}(t) = a \cdot \cos \omega t \tag{22.1}$$

$$V_{em2}(t) = b \cdot \sin \omega t \tag{22.2}$$

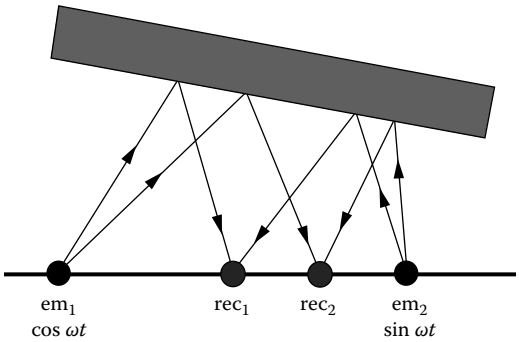

FIGURE 22.2 Basic PM proximity-sensor configuration.

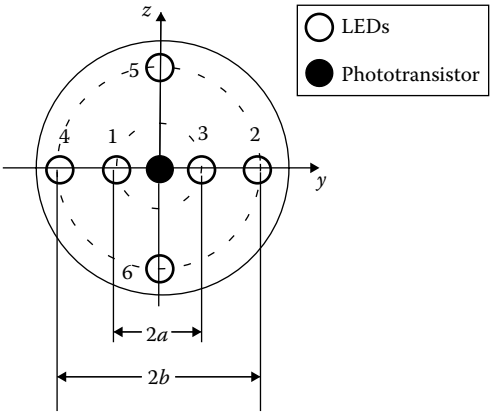

FIGURE 22.3 Sensor head reported in [9].

The signal detected by the receiver is a superposition of the two reflected signals, having corresponding attenuations of A and B:

$$V_{\text{rec}}(t) = A \cdot V_{\text{em1}} + B \cdot V_{\text{em2}} \tag{22.3}$$

The signal attenuation is a function of the geometrical and electrical parameters of the sensor, the reflectivity characteristics of the object's surface, and the surface's distance and orientation with respect to the sensor. The combined signal at the receiver is therefore

$$V_{\text{rec}}(t) = M \cdot \sin(\omega t + \phi) \tag{22.4}$$

where

M is the combined attenuation function
ϕ is the combined phase shift

Usually, only the phase information ϕ is used, and the amplitude is completely neglected or used only for verifying the likelihood of error and its potential magnitude.

A proximity sensor that uses this technique has been reported in [9]. Figure 22.3 shows a *sensor head*; it comprises six light sources (LEDs) and a photodetector (phototransistor). This sensor can measure the distance from the sensor's coordinate frame to the target point on the surface of the object (x), as well as the horizontal and vertical orientation of the object surface (u, v).

A simple model for the sensor was developed assuming that the light sources (LEDs) have low directivity, the photodetector (phototransistor) has high directivity, and the surface has diffused reflectivity. Figure 22.4 shows the basic configuration for the measurement of distance (x) and orientation (u and v). Table 22.1 shows the combinations of the driving signals in each LED needed for the measurement of distance and orientation.

For the measurement of the distance x, LED1 and LED3 are modulated by $K_1 \sin\omega t$ and LED2 and LED4 by $K_2 \cos\omega t$, respectively. The brightness detected by the photodetector can be calculated (using Lambert's law) to be

$$L_P = C\left(G_1 \frac{\cos(\alpha - v)}{a^2 + x^2}\right) + G_2 \frac{\cos(\beta - v)}{b^2 + x^2} + G_3 \frac{\cos(\alpha + v)}{a^2 + x^2} + G_4 \frac{\cos(\beta + v)}{b^2 + x^2} \tag{22.5}$$

where

G_i (i = 1, 2, 3, 4) are the intensities of the light sources
C is the reflection factor of the surface at point P

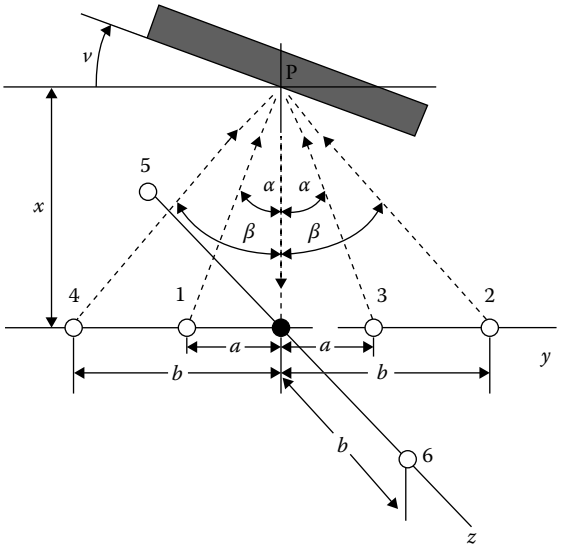

FIGURE 22.4 Measurement parameters for the sensor reported in [9].

TABLE 22.1 Combinations of the LED Driving Signals

Mode	LED1	LED2	LED3	LED4	LED5	LED6
Distance (x)	$\sin \omega t$	$\cos \omega t$	$\sin \omega t$	$\cos \omega t$	—	—
Orientation (u)	—	$\cos \omega t$	—	$\sin \omega t$	—	—
Orientation (v)	—	—	—	—	$\cos \omega t$	$\sin \omega t$

Considering that for this case $G_1 = G_3 = K_1 \sin\omega t$, $G_2 = G_4 = K_2 \cos\omega t$, $\cos\alpha = x/\sqrt{a^2 + x^2}$ and $\cos\beta = x/\sqrt{b^2 + x^2}$, Equation 22.5 can be rewritten as

$$L_P = 2Cx\left\{\frac{K_1}{(a^2 + x^2)^{3/2}}\sin\omega t + \frac{K_2}{(b^2 + x^2)^{3/2}}\cos\omega t\right\}\cos v = M\sin(\omega t + \phi_x) \tag{22.6}$$

The amplitude M and the phase shift ϕ_x are given by

$$M = 2Cx\left\{\frac{K_1^2}{(a^2 + x^2)^3} + \frac{K_2^2}{(b^2 + x^2)^3}\right\}^{1/2}\cos v \tag{22.7}$$

$$\phi_x = \tan^{-1}\left[\frac{K_2(a^2 + x^2)^{3/2}}{K_1(b^2 + x^2)^{3/2}}\right] \tag{22.8}$$

From Equation 22.8, it can be observed that the distance (x) can be obtained from ϕ_x. It is important to note that, in theory, the calculation is not affected by the reflection factor (C) of the surface.

Similarly, the orientation angles u and v can be obtained by driving the LEDs as indicated in Table 22.1. For example, v can be determined by modulating LED4 and LED2 by the signals $K_1\sin\omega t$ and $K_2\cos\omega t$, respectively. For this case, the phase shift associated with the brightness of the object at point P is given by

$$\phi_v = \tan^{-1}\left[\frac{K_2(x - b\tan v)}{K_1(x + b\tan v)}\right] \tag{22.9}$$

Note that, in order to recover v from Equation 22.9, x must be known. Accordingly, the distance x must be determined first. Correspondingly, the orientation angle (v) can be calculated from the new phase shift ϕ_v. The angle u can be calculated by modulating LED6 and LED5 with $K_1 \sin\omega t$ and $K_2 \cos\omega t$, respectively, and then determining the corresponding phase shift of the associate brightness at point P.

The pose-estimation results using this sensor were quite satisfactory and showed a good agreement between theory and experiment.

In [10], an experimental setup of a PM distance sensor, similar to the one in [9], was reported for investigating the effect of the geometrical and electronic parameters on the performance of the sensor. Optimal parameters were obtained for some targeted sensor-operation characteristics.

22.3.3 Amplitude Modulation

In amplitude-modulated (AM) sensors, the magnitude of the light reflected from a surface is utilized to determine the pose of the object.

AM transducers usually consist of one light source and several photodetectors (Figure 22.5). They were redesigned and optimized several times over the past decade to yield better measurement accuracy [11–14].

Many AM proximity sensors utilize optical fibers to illuminate and collect light from the surfaces of objects. The use of optical fibers, in a Y-guide configuration (Figure 22.6), facilitates the operation of sensitive low-noise circuitry in a shielded environment appropriately remote from the robot's electromagnetic interference sources.

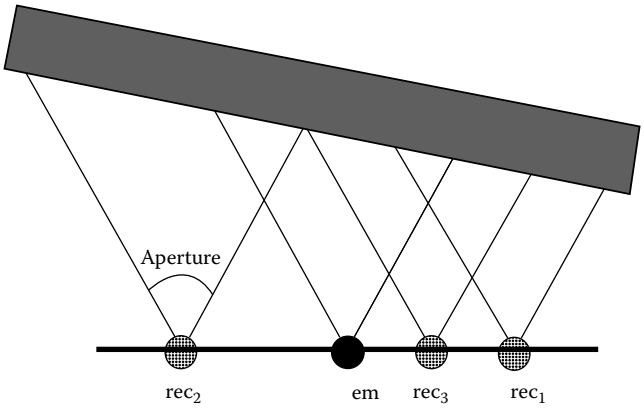

FIGURE 22.5 Bask AM proximity-sensor configuration.

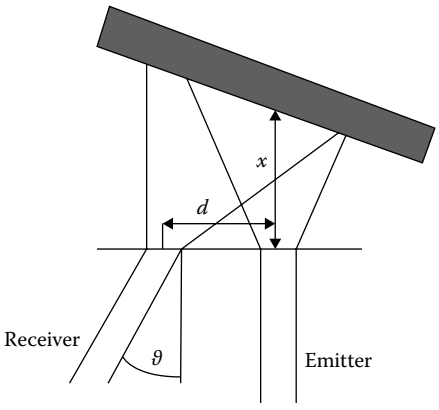

FIGURE 22.6 Y-guide transducer.

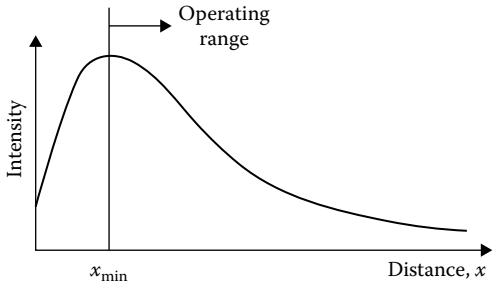

FIGURE 22.7 *Y*-guide response for distance measurement.

AM transducers primarily use variations of the basic *Y*-guide transducer. Two important parameters can be varied in the design of *Y*-guides: the distance, d, between the emitting and receiving fibers (referred to hereafter as the emitter and the receiver, respectively) and the inclination angle, ϑ, of the receiver fiber with respect to the transducer's surface. The emitter is usually placed perpendicular to the transducer's surface, due to symmetry requirements, as will be explained later in this section.

The collection of a sufficient amount of reflected light requires the use of relatively wide-diameter fibers, typically having a 0.3–2 mm core size. This requirement demands the use of relatively low-grade plastic fibers. Although attenuations of up to 1 dB m^{-1} are common in such plastic fibers, this loss rate is relatively insignificant for *Y*-guide applications because of the short length of the cables normally used. The numerical aperture (NA) of the plastic fibers, on the other hand, is an important parameter in the transducer design, since lenses are rarely used in conjunction with AM-type transducers. In particular, the acceptance angle of the fiber is fixed and given by $\alpha = 2\sin^{-1}$ NA.

For a *Y*-guide, the intensity of the light reflected from the surface is not monotonic function of the distance. Thus, the minimum operating distance of the transducer (x_{min}) is usually limited to a value that will guarantee monotonic response (Figure 22.7).

For the measurement of surface orientation, a symmetrical three-fiber constellation (Figure 22.8) can be used. In this *Y*-guide configuration, the emitter is at the center and the two receivers are positioned symmetrically on either side [12]. The light intensities detected by the receivers, for the transducer shown in Figure 22.8, are illustrated in Figure 22.9 as a function of the surface orientation.

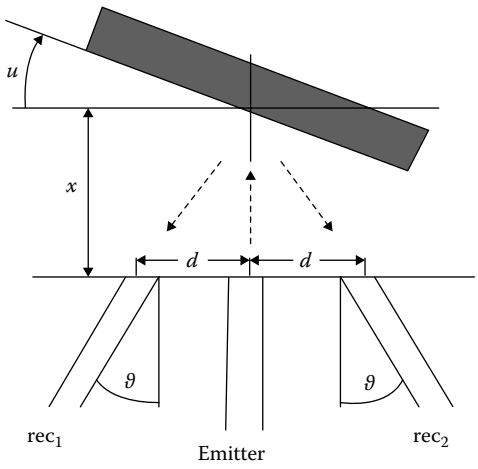

FIGURE 22.8 Typical receiver-pair constellation for orientation measurements.

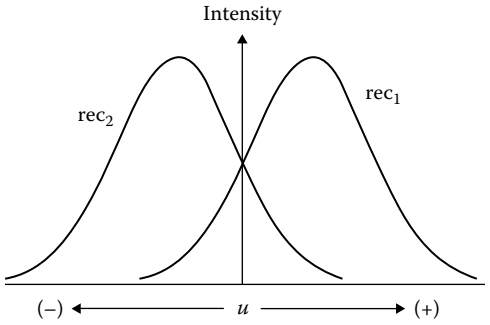

FIGURE 22.9 Light intensity detected by each receiver as a function of the surface orientation (u).

In the usual operating range of an AM transducer, the intensity of the light at the receiver is inversely related to the distance squared. As a result, it is conceptually possible to configure a transducer such that its sensitivity and accuracy will increase as the gripper nears the contact point, at which both the distance and the orientation of the object's surface are zero [10,12]. However, in practice, because of the limited dynamic range of the electronic transducer interface, a trade-off exists between the desired maximum accuracy near contact and the maximum range of operation. These and other considerations must be taken into account when establishing the geometrical features of the transducer.

Another important factor to take into account in the design of an AM sensor is the need to reduce, as much as possible, the effect of the variation in the emitting power of the light source, P_0, on the transducer's measurements. This normally leads to the employment of a pair of receivers. A normalized differential voltage (DV) estimation scheme, such as the following, is then applied to the pair of measurements:

$$\mathrm{DV} = \frac{V_{\mathrm{rec1}} - V_{\mathrm{rec2}}}{V_{\mathrm{rec1}} + V_{\mathrm{rec2}}} \tag{22.10}$$

where V_{rec1}, V_{rec2} are the voltages measured by receivers 1 and 2. However, in order to eliminate the effect of P_0 on DV, each receiver must linearly convert the light intensity to a corresponding voltage measurement.

In order to use a DV scheme for the measurement of distance, an asymmetrical transducer configuration can be used (Figure 22.10). However, one must note that, although orientation measurements are not affected by variations in distance, distance measurements are significantly affected by the orientation of the surface, for example [15].

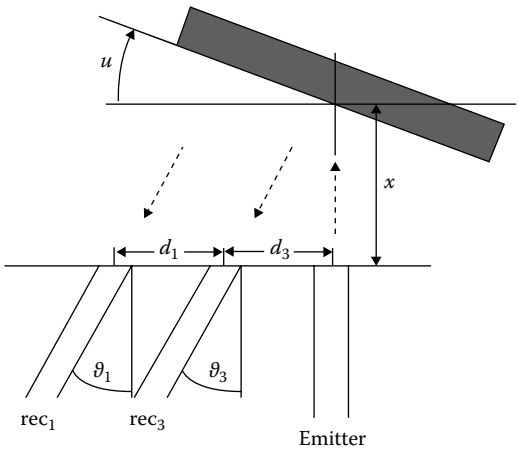

FIGURE 22.10 Asymmetrical receiver-pair constellation for distance measurements.

Accordingly, in using an AM proximity sensor with a DV scheme, the orientation is first approximated, and subsequently the distance is determined. The accuracies of the measured distance and orientation angle can be further improved by an iterative process.

Based on the earlier issues and observations, the outputs of the three receivers of the basic AM proximity sensor (Figure 22.5) can be paired for measuring both distance and orientation: the pair rec_1–rec_2 can be used for orientation measurement, while the pair rec_1–rec_3 can be used for distance measurement.

An experimental AM proximity sensor, capable of estimating the pose of an object with high accuracy, was reported in [14,16,17]. The transducer consists of one emitter, placed perpendicularly to the sensor head, and eight inclined receiver elements (Figure 22.11). The receivers of this transducer were paired for the specific measurements of distance, as well as of the vertical or horizontal orientation. However, the pose of the surface was determined with higher accuracy by using a polynomial fit technique (as opposed to the DV scheme described earlier) that provided relationships between the individual estimated parameters (x, u, and v) and all eight signals received.

The sensor presented in [14], and shown in Figure 22.11, operates in the range of 0–50 mm and ±20°. It can achieve an accuracy of 6.25 μm in distance and an accuracy of 0.02° in angular measurements in the near-contact region (0–6 mm range), using a general calibration-per-group strategy for different material groupings. This implies that the measured object's material belongs to a calibration group, which includes similar object surface characteristics, for example, machined metals. Better accuracies can be achieved using a calibration-per-surface strategy.

A similar configuration to the one shown in Figure 22.11 was reported earlier in [18] for the measurement of distances, where the orientations of each receiver pair relative to the emitter ϑ_1 and ϑ_3 were set at 10°. However, in this case, the apertures of the emitter and receiver were severely restricted by a collimating graded index (GRIN) lens. The emitter diameter was larger than that of the receivers in order

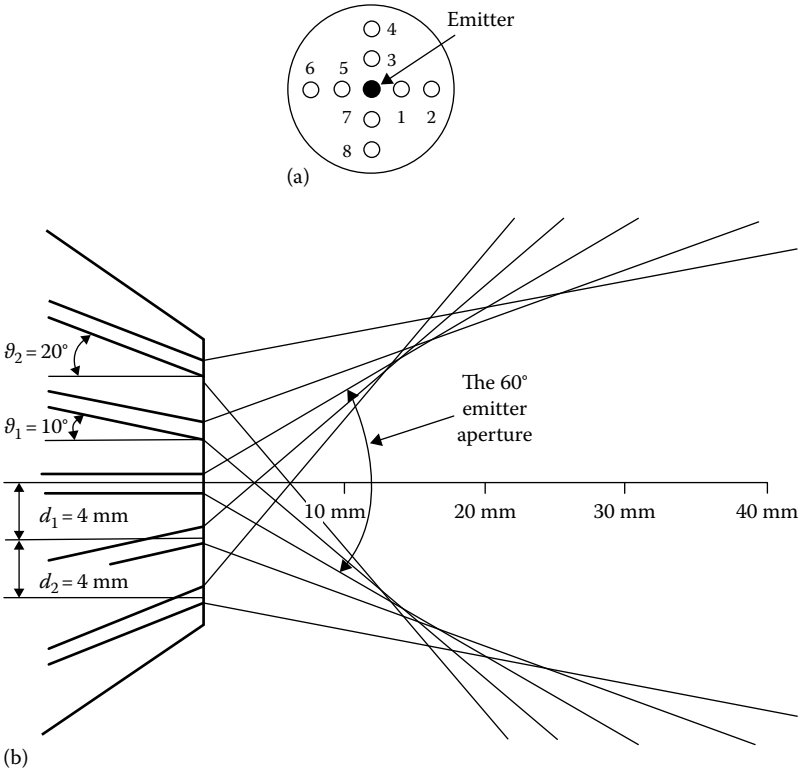

FIGURE 22.11 AM transducer design for the sensor reported in [14]: (a) top view, (b) front view.

to transmit more light. The measurements of the transducer were then processed in two phases: (1) The DVs of all the receiver pairs were processed independently to provide four distance estimations, and (2) the four distance estimations were then averaged to provide a more accurate estimate, eliminating adverse effects due to variations in surface orientation.

22.3.4 Geometrical Techniques

Proximity sensors based on geometrical techniques determine the pose of the object by examining the geometrical attributes of the reflected and incident light beams. Two of these techniques, one based on triangulation and the other based on the Gaussian lens law, are presented here.

Figure 22.12 shows the basic configuration of a proximity transducer for measuring distance (x) based on the triangulation technique [19,20]. The sensor head consists of a laser light source and a linear array of photodetectors (R_i with $i = 1, 2, \ldots, n$). A narrow light beam illuminates point P, and the receivers detect the reflected light from the illuminated point through a transmitting slit. The geometry of the ray trajectory provides the basic information for the estimation of the distance (x). While the light source illuminates the surface of the object, the photodetector array is scanned to detect the light path used for making the output signal maximum. The light path obtained by this scanning is called the effective light path [19]. This light path is the one indicated in Figure 22.12. The distance (x) can be determined by accurately detecting the position (y_i) and precisely measuring the dimensions (h) and (y_o):

$$\frac{x}{x+h} = \frac{y_o}{y_i} \tag{22.11}$$

or

$$x = \frac{y_o h}{y_i - y_o} \tag{22.12}$$

In [26], it is claimed that such a sensor has the following properties: (1) The influence of irregularities, reflectivity, and orientation of the object is negligible; (2) the distance measurement is not affected by illumination from the environment and luminance of the object (their influence is eliminated by comparison of two sensor signals obtained in successive on-and-off states of the light source); and (3) the sensor head is sufficiently small to be used in a robot hand.

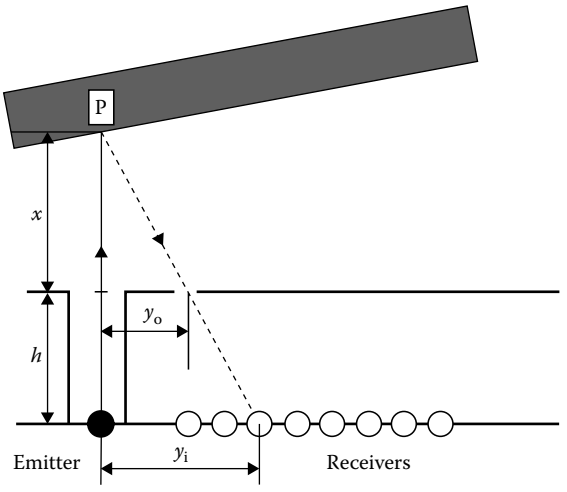

FIGURE 22.12 Basic principle of a proximity sensor for measuring distance based on triangulation.

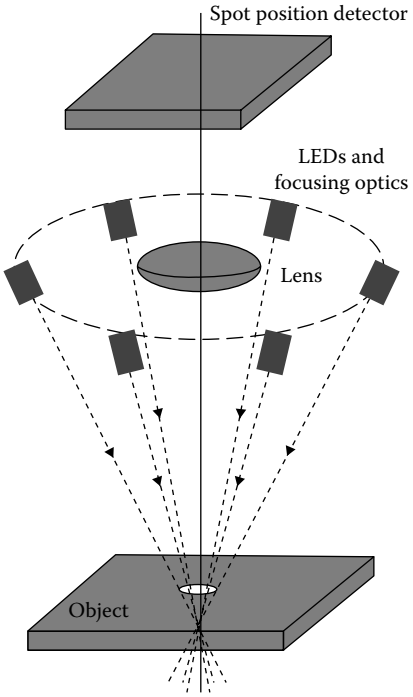

FIGURE 22.13 Multilight source proximity sensor reported in [21].

An experimental proximity-sensor configuration, based on triangulation and capable of measuring both distance and orientation, is shown in Figure 22.13 [21]. The sensor uses six infrared LEDs as light sources, an objective lens, and an area-array detector chip for detecting spot positions. The directions of the beams are aligned to form a fixed cone of light. This sensor is of a type called scanning emitter since each LED is sequentially pulsed to perform the measurements. As each LED is sequentially pulsed, the sensor IC detects the position of the spot projected by the reflected light beam from the object's surface. Knowledge of the spot's position, together with the camera's optics and the trajectory of each light beam, can be used to perform a triangulation to determine the 3D coordinates of each light spot on the target surface. A set of six 3D points are obtained for the six LEDs. Then, by fitting a plane to those points, the distance and orientation of the object's surface are approximated.

Another scanning-emitter-type proximity sensor was reported in [22]. In this case, a mechanical scanning system was utilized. One notes that inherent problems with sensors that use mechanical scanning devices include lower reliability and increased overall size.

Some recently reported triangulation sensors are sufficiently small in size to be mounted on a gripper [5]. However, they are still susceptible to errors due to distortion and separation of the light beam's reflection caused by surface irregularity and can also have blind spots as a result of discontinuities associated with the shape of the sensed object.

Another group of geometrical electro-optical proximity sensors are those based on the Gaussian lens law [23,24]. The basic configuration of such a transducer is shown in Figure 22.14. A light beam, collinear to the optical axis, forms a spot on the target's surface. The light scattered from the spot is collected by the lens. In Figure 22.14, PN represents the limiting ray that can be collected by the lens. The target distance (x) can be calculated in terms of the focal length of the lens (f) and the image position (w). Applying the Gaussian lens law, the distance x can be calculated as

$$x = \frac{fw}{w - f} \tag{22.13}$$

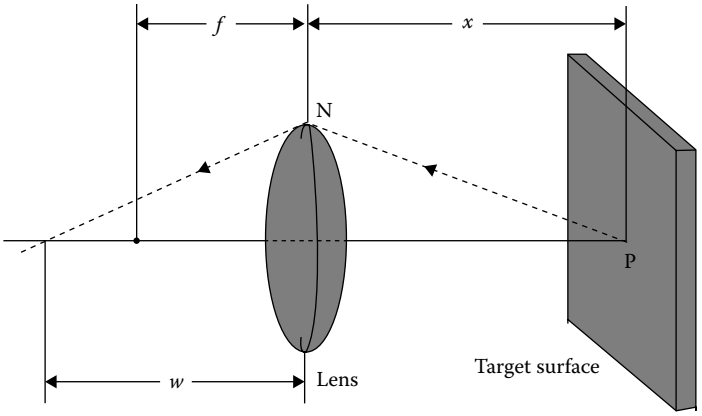

FIGURE 22.14 The principle of proximity sensing based on the Gaussian lens law reported in [7].

A proximity sensor (the HexEye) based on this lens principle is shown in Figure 22.15 [23,24]. The sensor consists of seven identical "sensing units" arranged in a hexagonal pattern. Each sensing unit in turn comprises four main parts: an objective lens, a conical mirror, six linear receiver arrays, and a laser diode light source.

The light beam generated by a light source forms a spot on the target surface, and the light flux scattered from the spot is collected by the objective lens and projected onto the receiver arrays in each sensing unit. The target distance is determined by the position, size, and shape of an image formed on individual receiver arrays of the unit.

The sensor operates in two modes, either distance or orientation. In the distance measurement mode, the seven light sources are activated one at a time to generate a light spot on the target surface, while all the sensing units receive the light flux scattered from the same light spot. The active unit determines the distance using the principle of the Gaussian lens law, while the nonactive units determine the distance based on triangulation. For the orientation measurement mode, the seven sensing units are grouped into orientation measurement units (OMUs). Each OMU comprises three neighboring sensing units around the center, resulting in a total of six possible OMUs. The local orientation of the surface is estimated by integrating the six orientation measurements.

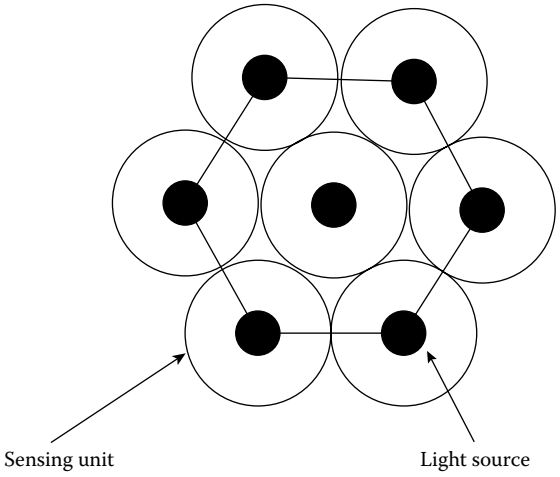

FIGURE 22.15 Configuration of HexEye (top view).

The mapping between the light distribution on the arrays of light detectors and the target distance is obtained through calibration. Using the light distribution (instead of light intensity as in the case of AM sensors), it is intended that the mapping be independent of surface properties such as color, material, diffusion, and reflectance factors. However, it has been shown that the mapping may be corrupted by "noise" from several sources, including reflection patterns and ambient light.

Using the Gaussian lens law has the following advantages over the triangulation principle: (1) The light source can be located at the center of the objective lens, allowing not only the sensor to be compact but also the amount of light flux input to the lens to be maximized, and (2) the sensitivity can be optimized for a certain range of measurement distance by controlling *f*.

22.3.5 Time of Flight

Time-of-flight-measuring electro-optical sensors are radar-type systems. However, unlike regular radar, which transmits a pulse of radio-frequency energy, these sensors normally use a modulated light beam. The distance to the target is extracted from the measured phase shift of the reflected light. Two problems associated with such sensors are difficulty in measuring short distances (which requires a very high modulation frequency) and the need for a mechanical scanning/switching system to get additional information (such as orientation) [5,25].

22.3.6 Photothermal Effect

The photothermal effect transducer uses a strong light beam directed toward the object's surface. The distance to the object is extracted from measurements of the thermal wave generated by the light absorbed by the object. The detection scheme and signal processing are similar to those used in an AM sensor. Since the shape of the thermal wave generated at the surface is surface texture independent, the photothermal sensor does not suffer from the surface robustness problem associated with AM sensors. However, the photothermal sensor is rather slow and limited to highly absorbing surfaces [26].

22.3.7 Capacitive Sensors

Capacitive sensors generate and measure changes in an electric field caused by either a dielectric or conducting object in their proximity.

There are basically two types of capacitive proximity sensor. One type uses the principle of a parallel plate capacitors, and the other uses the principle of fringing capacitances [8,27,28]. For the parallel plate-type proximity sensor, the transducer forms one plate and the object measured forms the other plate. The structure of a parallel plate-type proximity sensor and its typical response are shown in Figure 22.16 [8].

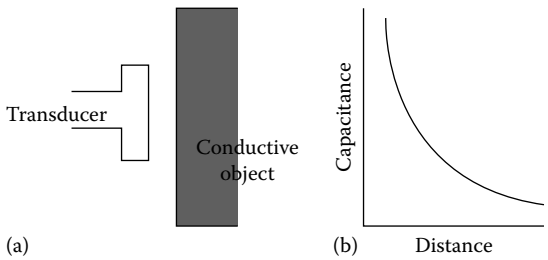

FIGURE 22.16 Capacitive proximity sensor based on the principle of parallel plates: (a) structure and (b) sensor response.

The parallel plate-type proximity sensor is widely applied in industry. However, this type of a sensor has three major limitations: (1) The object being measured must be conductive, (2) the inverse gap–capacitance relationship is highly nonlinear, and (3) the sensitivity drops significantly in the case of large gaps.

The second type of capacitive proximity sensor uses the principle of fringing capacitance [8]. The sensor has two "live" electrodes and the object being measured does not need to be part of the sensor system. The target object could be either conductive or nonconductive. However, the measurement of distances is affected by the type of object material. Therefore, separate calibrations must be carried out for different materials.

In [29], an innovative capacitive microsensor was presented. Using micromachining technology, the electrode thickness can be significantly reduced and the fringing effect increased when compared with other capacitive sensors. Consequently, this sensor yields a better sensitivity. An array of such transducers can be implemented to measure the distance and orientation of an object.

Proximity capacitive sensors have the following general advantages: (1) low energy consumption and (2) simple structure. The major disadvantages, however, are that they are influenced by external signals and a calibration-per-surface technique must be carried out, since their operation directly depends on the object's material.

22.3.8 Ultrasonic Sensors

The basic principle underlying ultrasonic ranging sensors is the measurement of the time required for a sound wave to travel from the emitter to the object's surface and return to the detector. By using several such emitters and detectors, one can obtain information about the distance and orientation of the surface.

In [19], a novel method is proposed to measure the orientation angles of an object's surface using the phase differences of reflected echoes. Figure 22.17a shows the configuration of a planar sensor head with n receivers, which are equally spaced and located on a circle of radius R around the transmitter T. A linear relationship exists between the difference in lengths, δ, of two reflecting paths for an adjacent pair of receivers and the object inclinations.

In Figure 22.17b, the relationship between the inclination of the target surface and δ is shown. It can be observed that the measuring range of the sensor can be enlarged with an increase in the number of receivers. In [30], it is also shown that the measuring range can be enlarged by reducing R. However, it was noted that measurements carried out with a small sensor are potentially less accurate.

Experimental results using a transducer with six (R = 30 mm) and eight (R = 20 mm) receivers were reported in [30]. With the six-receiver transducer, the measuring range of the orientation angles was ±15°,

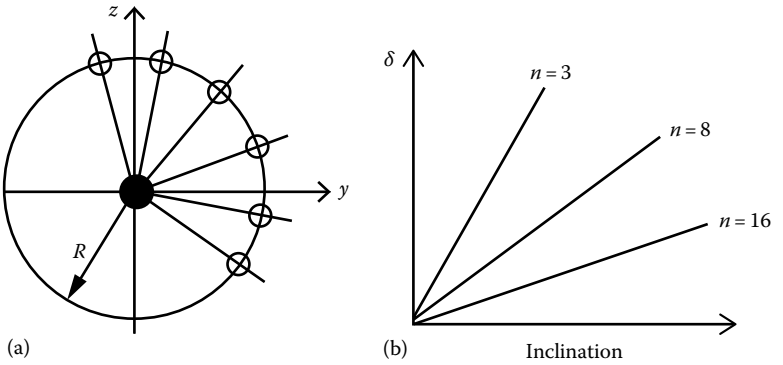

FIGURE 22.17 (a) Configuration of the ultrasonic sensor and (b) surface inclination versus δ.

while for the eight-receiver transducer, the maximum measuring range was ±30°. With the six-receiver transducer, the orientation angle could be determined with an accuracy of 0.5°, in the measuring range of ±15°, and 0.2° when the range was restricted to ±5°.

One of the major disadvantages of ultrasonic proximity sensors is that they are relatively large in size. However, implementing these sensors using micromachining could solve this problem. In [7], the generation and detection of ultrasound, for proximity sensing, were investigated using micromachined resonant membrane structures.

22.3.9 Magnetic Sensors

A magnetic-type sensor creates an alternating magnetic field, whose variation provides information about the object's position.

The simplest magnetic sensors are reed microswitches or Hall effect switches. However, the most commonly used sensors in robotics are based on the electromagnetic inductive principle, emphasizing eddy current generation. The basic principle consists of creating a magnetic field using appropriate coils around a core with high permeability and an oscillator with a frequency excitation high enough to minimize the penetration of the field inside a conductive material. The main problems with magnetic sensors are their high size/range ratio and difficulty in providing reliable distance measurements in varying magnetic environments.

Acknowledgments

The authors would like to thank Martin Bonert for careful review and critique of this chapter. They also acknowledge the financial support of the Natural Sciences and Engineering Research Council of Canada.

References

1. H. R. Everett, *Sensors for Mobile Robots: Theory and Application*, Natick, MA: A. K. Peters, Ltd., 1995.
2. B. Espiau, An overview of local environment sensing in robotics applications, *Sensors and Sensory Systems for Advanced Robots, NATO ASI Series*, F43, 125–151, 1988.
3. W. D. Koenigsberg, Noncontact distance sensor technology, *SPIE*, *Intelligent Robots*, 449, 519–531, 1988.
4. Å. Wernersson, B. Boberg, B. Nilsson, J. Nygårds, and T. Rydberg, On sensor feedback for gripping an object within prescribed posture tolerances, *Proceedings of IEEE, International Conference on Robotics and Automation*, Nice, France, 1992, pp. 1654–1660.
5. A. Bradshaw, Sensors for mobile robots, *Measurement and Control*, 23(2), 48–52, 1990.
6. R. Volpe and R. Ivlev, A survey and experimental evaluation of proximity sensors for space robotics, *Proceedings of IEEE International Conference on Robotics and Automation*, Vol. 4, San Diego, CA, 1994, pp. 3466–3473.
7. O. Brand, H. Baltes, and U. Baldenweg, Ultrasound-transducer using membrane resonators realized with bipolar IC technology, *Proceedings of IEEE Conference on Micro Electro Mechanical Systems*, Oiso, Japan, 1994, pp. 33–38.
8. R. C. Luo and Z. Chen, Modeling and implementation of an innovative micro proximity sensor using micromachining technology, *Proceedings of IEEE/RSJ International Conference on Intelligent Robots and Systems*, Yokohama, Japan, 1993, pp. 1709–1716.
9. R. Masuda, Multifunctional optical proximity sensor using phase modulation, *Journal of Robotic Systems*, 3(2), 137–147, 1986.
10. O. Partaatmadja, B. Benhabib, and A. A. Goldenberg, Analysis and design of a robotic distance sensor, *Journal of Robotic Systems*, 10, 427–445, 1993.

11. O. Partaatmadja, B. Benhabib, A. Sun, and A. A. Goldenberg, An electrooptical orientation sensor for robotics, *Proceedings of IEEE Transactions on Robotics and Automation*, 8, 111–119, 1992.
12. O. Partaatmadja, B. Benhabib, E. Kaizerman, and M. Q. Dai, A two-dimensional orientation sensor, *Journal of Robotic Systems*, 9, 365–383, 1992.
13. P. P. L. Regtien, Accurate optical proximity detector, *Proceedings of IEEE Conference on Instrumentation and Measurement Technology*, San Jose, CA, 1990, pp. 141–143.
14. A. Bonen, R. E. Saad, K. C. Smith, and B. Benhabib, Active-sensing via a novel robotic proximity sensor, *Proceedings of International Conference on Recent Advances in Mechatronics (ICRAM'95)*, Istanbul, Turkey, 1995, pp. 1053–1058.
15. Y. F. Li, Characteristics and signal processing of a proximity sensor, *Robotica*, 12, 335–341, 1994.
16. A. Bonen, R. E. Saad, K. C. Smith, and B. Benhabib, A novel calibration technique for electro-optical proximity sensors, *Proceedings of International Conference on Industrial Electronics, Control and Instrumentation (IECON'95)*, Orlando, FL, 1995, pp. 1190–1195.
17. A. Bonen, R. E. Saad, K. C. Smith, and B. Benhabib, A novel optoelectronic interface-circuit design for sensing applications, *IEEE Transactions on Instrumentation and Measurement*, 45, 580–584, 1996.
18. H. Bukow, Fiber optic distance sensor for robotic applications, *Proceedings of SME Conference, Sensors*, Detroit, MI, 1986, pp. MS86–MS938.
19. T. Okada, Development of an optical distance sensor for robots, *International Journal of Robotics Research*, 1, 3–14, 1982.
20. M. A. Kujoory, Real-time range and elevation finder, *Proceedings of IEEE*, 72(12), 1821–1822, 1984.
21. M. Fuhrman and T. Kanade, Optical proximity sensor using multiple cones of light for measuring surface shape, *Optical Engineering*, 23, 546–553, 1984.
22. T. Okada and U. Rembold, Proximity sensor using a spiral-shaped light-emitting mechanism, *IEEE Transactions on Robotics and Automation*, 7, 798–805, 1991.
23. S. Lee, Distributed optical proximity sensor system: HexEYE, *Proceedings of IEEE International Conference on Robotics and Automation*, Vol. 2, Nice, France, 1992, pp. 1567–1572.
24. S. Lee and J. Desai, Implementation and evaluation of HexEye: A distributed optical proximity sensor system, *Proceedings of IEEE International Conference on Robotics and Automation*, Vol. 3, Nagoya, Aichi, Japan, 1995, pp. 2353–2360.
25. S. Shinohara et al., Compact and high precision range finder with wide dynamic range using one sensor head, *Proceedings of IEEE Conference on Instrumentation and Measurement Technology,* Atlanta, GA, 1991, pp. 126–130.
26. M. Ito, K. Hane, F. Matsuda, and T. Goto, Proximity sensing technique using the photothermal effect, *Journal of the Japan Society of Precision Engineering*, 58, 139–144, 1992.
27. B. E. Noltingk, A novel proximity gauge, *Journal of Scientific Instruments, Series 2*, 2, 356–360, 1969.
28. B. E. Noltingk, A. E. T. Nye, and H. J. Turner, Theory and application of a proximity gauge using fringing capacitance, *Proceedings of ACTA IMEKO*, London, UK, 29, 537–549, 1976.
29. A. Moldoveanu, Inductive proximity sensors, fundamentals and standards, *Sensors*, 10(6), 11–14, 1993.
30. S. Nakajima and Y. Takahashi, An ultrasonic orientation sensor with distributed receivers, *Advanced Robotics*, 4, 151–168, 1990.

Further Readings

Everitt, B. S., Landau, S., Leese, M., and Stahl, D., *Measurement of Proximity*, Wiley Online library, http://onlinelibrary.wiley.com/doi/10.1002/9780470977811.ch3/summary, Published Online: January 25, 2011.

Hornung, M. R. and Brand, O., *Micromachined Ultrasound-Based Proximity Sensor*, Kluwer Academic Publisher, Boston, MA, 1999.

Mechanical Engineering Design Guide—Engineer's Handbook, *Sensors: Proximity, Mechanical Components*, http://engineershandbook.com/Components/proximitysensors.htm (accessed on June 24, 2012).

Partial List of Vendors and Suppliers

Autonics USA, 1353 Armour Blvd., Mundelein, IL 60060, Phone: 847-680-8160, 866-862-2602 (toll free), Fax: 847-680-8155, www.autonicsonline.com

Gems Sensors and Control, 1 Cowles Rd., Plainville, CT 06062-1198, Phone: 860-747-3000, 800-378-1600 (toll free), Fax: 860-747-4244, www.gemssensors.com

IFM Efector, Inc., 782 Springdale Dr., Exton, PA 19341-2843, Phone: 610-524-2000, 800-441-8246 (toll free), Fax: 800-329-0436, www.ifm.com/ifmus/web/home.htm

Kinequip. Inc., 365 Old Niagara Falls Blvd., Buffalo, NY 14228, Phone: 716-694-5000, 800-982-8894 (toll free), Fax: 716-694-5097, www.kinequip.com

Madison Co., 27 Business Park Dr., Branford, CT 06405, Phone: 203-488-4477, 800-466-5383 (toll free), Fax: 203-481-5036, madisonco.com/

Measurement Specialties, Inc., 1000 Lucas Way, Hampton, VA 23666, Phone: 757-766-1500, 800-745-8008 (toll free), Fax: 757-766-4297, www.meas-spec.com

Micro-Epsilon America, 8120 Brownleigh Dr., Raleigh, NC 27617, Phone: 919-787-9707, Fax: 919-787-9706, www.micro-epsilon.us

Schneider Electric, 1875 Founders Dr., Dayton, OH 45420, Phone: 937-514-7207, Fax: 937-258-5830, www.tesensors.com

Smith Systems, Inc., 6 Mill Creek Center, P.O. Box 667, Brevard, NC 28712, Phone: 828-884-3490, Fax: 828-877-3100, www.smith-systems-inc.com

III

Displacement

23

Resistive Displacement Sensors

Keith Antonelli
Kinetic Sciences, Inc.

James Ko
Kinetic Sciences, Inc.

Shyan Ku
Kinetic Sciences, Inc.

Resistive displacement sensors are commonly termed potentiometers or "pots." A pot is an electromechanical device containing an electrically conductive *wiper* that slides against a fixed *resistive element* according to the position or angle of an external shaft (see Figure 23.1). Electrically, the resistive element is "divided" at the point of wiper contact. To measure displacement, a pot is typically wired in a "voltage divider" configuration, as shown in Figure 23.2. The circuit's output, a function of the position of the wiper, is an analog voltage available for direct use or digitization. Calibration maps the output voltage to units of displacement.

Table 23.1 lists some attributes inherent to pots. This chapter describes the different types of pots available, their electrical and mechanical characteristics, and practical approaches to using them for precision measurement. Sources and typical prices are also discussed. Versatile, inexpensive, and easy-to-use pots are a popular choice for precision measurement.

23.1 Precision Potentiometers

Pots are available in great variety, with specific kinds optimized for specific applications. Position measurement requires a high-quality pot designed for extended operation. Avoid pots classified as trimmers, rheostats, attenuators, volume controls, panel controls, etc. Instead, look for *precision potentiometers*.

23.1.1 Types of Precision Potentiometers

Precision pots are available in *rotary, linear-motion*, and *string pot* forms. String pots—also called *cable pots*, *yo-yo pots*, *cable extension transducers*, and *draw wire transducers*—measure the extended length of a spring-loaded cable. Rotary pots are available with single- or multiturn abilities: commonly 3, 5, or 10 turns. Linear-motion pots are available with maximum strokes ranging from roughly 5 mm to over 4 m [1,2]. String pots are available with maximum extensions exceeding 50 m [3]. Pot manufacturers

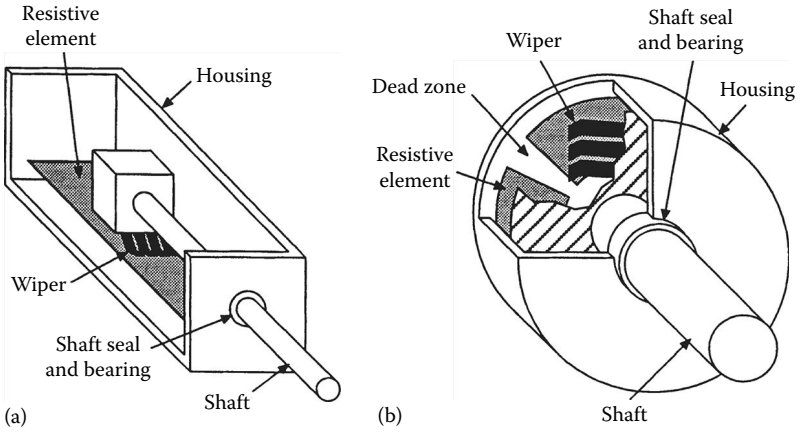

FIGURE 23.1 Representative cutaways of (a) linear-motion and (b) rotary potentiometers.

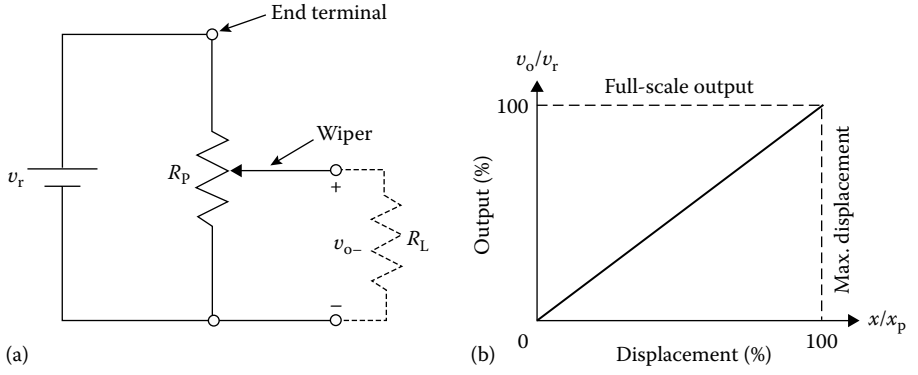

FIGURE 23.2 (a) Schematic diagrams depict a potentiometer as a resistor with an arrow representing the wiper. This schematic shows a pot used as a variable voltage divider—the preferred configuration for precision measurement. R_P is the total resistance of the pot, R_L is the load resistance, v_r is the reference or supply voltage, and v_o is the output voltage. (b) Shows an ideal linear output function where x represents the wiper position and x_p is its maximum position.

TABLE 23.1 Fundamental Potentiometer Characteristics

Advantages	Disadvantages
Easy to use	Limited bandwidth
Low cost	Frictional loading
Nonelectronic	Inertial loading
High-amplitude output signal	Wear
Proven technology	

usually specify a pot's type, dimensions, resistive element composition, electrical and mechanical parameters, and mounting method.

23.1.2 Resistive Element

Broadly, a pot's resistive element can be classified as either *wirewound* or *nonwirewound*. Wirewound elements contain tight coils of resistive wire that quantize measurement in steplike increments.

TABLE 23.2 Characteristics of Conductive Plastic, Wirewound, and Hybrid Resistive Elements

	Conductive Plastic	Wirewound	Hybrid
Resolution	Infinitesimal	Quantized	Infinitesimal
Power rating	Low	High	Low
Temperature stability	Poor	Excellent	Very good
Noise	Very low	Low, but degrades with time	Low
Life	10^6–10^8 cycles	10^5–10^6 cycles	10^6–10^7 cycles

In contrast, nonwirewound elements present a continuous sheet of resistive material capable of essentially unlimited measurement resolution.

Wirewound elements offer excellent temperature stability and high power dissipation abilities. The coils quantize measurement according to wire size and spacing. Providing the resolution limits are acceptable, wirewound elements can be a satisfactory choice for precision measurement; however, conductive plastic or hybrid elements will usually perform better and for considerably more cycles. These and other popular nonwirewound elements are described in more detail in the following.

Conductive plastic elements feature a smooth film with unlimited resolution, low friction, low noise, and long operational life. They are sensitive to temperature and other environmental factors and their power dissipation abilities are low; however, they are an excellent choice for most precision measurement applications.

Hybrid elements feature a wirewound core with a conductive plastic coating, combining wirewound and conductive plastic technologies to realize some of the more desirable attributes of both. The plastic limits power dissipation abilities in exchange for low noise, long life, and unlimited resolution. Like wirewounds, hybrids offer excellent temperature stability. They make an excellent choice for precision measurement.

Cermet elements made from a ceramic–metal alloy offer unlimited resolution and reasonable noise levels. Their advantages include high power dissipation abilities and excellent stability in adverse conditions. Cermet elements are rarely applied to precision measurement because conductive plastic elements offer lower noise, lower friction, and longer life.

Carbon composition elements, molded under pressure from a carbon–plastic mixture, are inexpensive and very popular for general use, but not for precision measurement. They offer unlimited resolution and low noise but are sensitive to environmental stresses (e.g., temperature, humidity) and are subject to wear.

Table 23.2 summarizes the distinguishing characteristics of the preferred resistive elements for precision measurement.

23.1.3 Electrical Characteristics

Before selecting a pot and integrating it into a measurement system, the following electrical characteristics should be considered.

23.1.3.1 Terminals and Taps

Table 23.3 shows the conventional markings found on the pot housing [4,5]; CW and CCW indicate clockwise and counterclockwise rotation as seen from the front end. Soldering studs and eyelets, integral connectors, and flying leads are common means for electrical connection. In addition to the wiper and end terminals, a pot may possess one or more terminals for *taps*. A tap enables an electrical connection to be made with a particular point along the resistive element. Sometimes, a *shunt resistor* is connected to a tap in order to modify the output function. End terminations and taps can exhibit different electrical characteristics depending on how they are manufactured (see Ref. [2] for more details).

TABLE 23.3 Potentiometer Terminal Markings

Terminal	Possible	Color	Codings	Rotary Pot	Linear-Motion Pot
1	Yellow	Red	Black	CCW limit	Fully retracted limit
2	Red	Green	White	Wiper	Wiper
3	Green	Black	Red	CW limit	Fully extended limit

23.1.3.2 Taper

Pots are available in a variety of different tapers that determine the shape of the output function. With a linear-taper pot, the output varies linearly with wiper motion, as shown in Figure 23.2. (Note that a pot with a linear taper should not be confused with a linear-motion pot, which is sometimes called a "linear pot.") Linear-taper pots are the most commonly available and are widely used in sensing and control applications. Pots with nonlinear tapers (e.g., logarithmic, sine, cosine, tangent, square, and cube) can also be useful, especially where computer control is not involved. Nonstandard tapers can be custom manufactured or alternatively, certain types of output functions can be produced using shunt resistors, by combining outputs from ganged pots or by other means (refer to Refs. [6,7] for more details). Of course, if a computer is involved, the output function can always be altered through a software lookup table or mapping function.

23.1.3.3 Electrical Travel

Figure 23.2 shows how the ideal output of a pot changes with wiper position. In practice, there is a small region at both ends where output remains constant until the wiper hits a mechanical stop. *Mechanical travel* is the total motion range of the wiper, and *electrical travel* is the slightly smaller motion range over which the electrical output is "valid." Thus, when using a pot as a sensor, it is important to ensure that the wiper motion falls within the electrical travel limits.

23.1.3.4 Linearity

Linearity is the maximum deviation of the output function from an ideal straight line. *Independent linearity* is commonly specified, where the straight line is defined as the line that minimizes the linearity error over a series of sampled points, not necessarily measured over the full range of the pot (see Figure 23.3). Other linearity metrics, such as *terminal-based linearity*, *absolute linearity*, and *zero-based linearity*, are also sometimes used (refer to Ref. [8] for more details). Pots are commonly available with independent linearities ranging from under 0.1% to 1%. When dealing with nonlinear output functions, *conformity* is specified since it is the more general term used to describe deviation from any ideal function. Conformity and linearity are usually expressed as a percentage of full-scale output (FSO).

23.1.3.5 Electrical Loading

Loading can significantly affect the linearity of measurements, regardless of a pot's quality and construction. Consider an ideal linear pot connected to an infinite load impedance (i.e., as in Figure 23.2). Since no current flows through the load, the output changes perfectly linear as the wiper travels along the length of the pot. However, if the load impedance is finite, the load draws some current, thereby affecting the output as illustrated in Figure 23.4. Circuit analysis shows that

$$\frac{v_o}{v_r} = \frac{(x/x_P)(R_L/R_P)}{(R_L/R_P)+(x/x_P)-(x/x_P)^2} \tag{23.1}$$

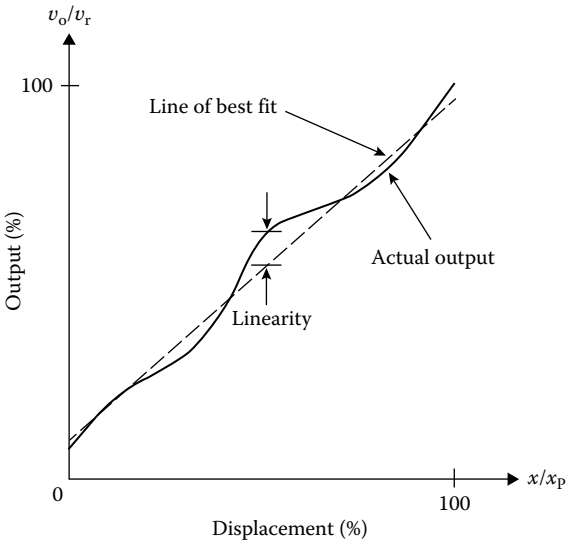

FIGURE 23.3 Independent linearity is the maximum amount by which the actual output function deviates from a line of best fit.

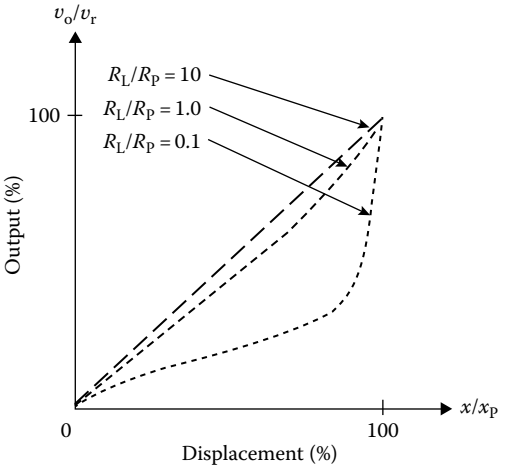

FIGURE 23.4 Linearity can be greatly influenced by the ratio of load resistance, R_L, to potentiometer resistance, R_P.

Therefore, R_L/R_P should be maximized to reduce loading effects (this also involves other trade-offs, to be discussed). A minimum R_L/R_P value of 10 is sometimes used as a guideline since loading error is then limited to less than 1% of FSO. Also, some manufacturers recommend a minimum load impedance or maximum wiper current in order to minimize loading effects and prevent damage to the wiper contacts. The following are some additional strategies that can be taken:

- Use a regulated voltage source whose output is stable with load variations.
- Use high-input-impedance signal-conditioning or data acquisition circuitry.
- Use only a portion of the pot's full travel.

23.1.3.6 Resolution

Resolution defines the smallest possible change in output that can be produced and detected. In wire-wound pots, the motion of the wiper over the coil generates a quantized response. Therefore, the best

attainable resolution is $r = (1/N) \times 100\%$, where N is the number of turns in the coil. Nonwirewound pots produce a smooth response with essentially unlimited resolution. Hybrid pots also fall into this category. In practice, resolution is always limited by factors such as

- Electrical noise, usually specified as *noise* for wirewound pots and *smoothness* for nonwirewound pots, both expressed as a percentage of FSO [10]
- Stability of the voltage supply, which can introduce additional noise into the measurement signal
- Analog-to-digital converter (ADC) resolution, usually expressed in "bits" (e.g., 10 mm travel digitized using a 12 bit ADC results in 10 mm/4096 = 0.0024 mm resolution at best)
- Mechanical effects such as stiction

23.1.3.7 Power Rating

The power dissipated by a pot is $P = v_r^2/R_P$; therefore, power rating determines the maximum voltage that can be applied to the pot at a given temperature. With greater voltage supplied to the pot, greater output (and noise) is produced but more power is dissipated, leading to greater thermal effects. In general, wirewound and cermet pots are better able to dissipate heat and thus have the highest power ratings.

23.1.3.8 Temperature Coefficient

As temperature increases, pot resistance also increases. However, a pot connected as shown in Figure 23.2 will divide the voltage equally well, regardless of its total resistance. Thus, temperature effects are not usually a major concern as long as the changes in resistance are uniform and the pot operates within its ratings. However, an increase in pot resistance also increases loading nonlinearities. Therefore, temperature coefficients can become an important consideration. The temperature coefficient, typically specified in ppm°C^{-1}, can be expressed as $\alpha = (\Delta R_P/R_P)/\Delta t$, where Δt is the change in temperature and ΔR_P is the corresponding change in total resistance. In general, wirewound pots possess the lowest temperature coefficients. Temperature-compensating signal-conditioning circuitry can also be used.

23.1.3.9 Resistance

Since a pot divides voltage equally well regardless of its total resistance, resistance tolerance is not usually a major concern. However, total resistance can have a great impact on loading effects. If resistance is large, less current flows through the pot, thus reducing temperature effects but also increasing loading.

23.1.3.10 AC Excitation

Pots can operate using either a DC or an AC voltage source. However, wirewound pots are susceptible to capacitive and inductive effects that can be substantial at moderate to high frequencies.

23.1.4 Mechanical Characteristics

The following mechanical characteristics influence measurement quality and system reliability and thus should be considered when selecting a pot.

23.1.4.1 Mechanical Loading

A pot adds inertia and friction to the moving parts of the system that it is measuring. As a result, it increases the force required to move these parts. This effect is referred to as *mechanical loading*.

To quantify mechanical loading, rotary pot manufacturers commonly list three values: the equivalent *mass moment of inertia* of the pot's rotating parts, the *dynamic* (or *running*) *torque* required to maintain rotation in a pot shaft, and the *starting torque* required to initiate shaft rotation. For linear-motion pots, the three analogous loading terms are *mass*, *starting force*, and *dynamic* (or *running*) *force*.

In extreme cases, mechanical loading can adversely affect the operating characteristics of a system. When including a pot in a design, ensure that the inertia added to the system is insignificant or that the inertia is considered when analyzing the data from the pot. The starting and running force or torque values might also be considered, although they are generally small due to the use of bearings and low-friction resistive elements.

23.1.4.2 Mechanical Travel

Distinguished from electrical travel, *mechanical travel* is the wiper's total motion range. A mechanical stop delimits mechanical travel at each end of the wiper's range of motion. Stops can withstand small loads only and therefore should not be used as mechanical limits for the system. Manufacturers list maximum loads as the *static stopping strength* (for static loads) and the *dynamic stopping strength* (for moving loads).

Rotary pots are also available without mechanical stops. The shaft of such an "unlimited travel" pot can be rotated continuously in either direction; however, electrical travel is always less than 360° due to the discontinuity or "dead zone" where the resistive element begins and ends (see Figure 23.1). Multiple revolutions can be measured with an unlimited travel pot in conjunction with a counter: the counter maintains the number of full revolutions, while the pot measures subrevolution angular displacement.

23.1.4.3 Operating Temperature

When operated within its specified temperature range, a pot maintains good electrical linearity and mechanical integrity. Depending on construction, pots can operate at temperatures from as low as −65 °C to as high as 150 °C. Operating outside specified limits can cause material failure, either directly from temperature or from thermally induced misalignment.

23.1.4.4 Vibration, Shock, and Acceleration

Vibration, shock, and acceleration are all potential sources of contact discontinuities between the wiper and the resistive element. In general, a contact failure is considered to be a discontinuity equal to or greater than 0.1 ms [2]. The values quoted in specification sheets are in *g*s and depend greatly on the particular laboratory test. Some characterization tests use sinusoidal vibration, random vibration, sinusoidal shock, sawtooth shock, or acceleration to excite the pot. Manufacturers use mechanical design strategies to eliminate weaknesses in a pot's dynamic response. For example, one technique minimizes vibration-induced contact discontinuities using multiple wipers of differing resonant frequencies.

23.1.4.5 Speed

Exceeding a pot's specified maximum speed can cause premature wear or discontinuous values through effects such as wiper bounce. As a general rule, the slower the shaft motion, the longer the unit will last (in total number of cycles). Speed limitations depend on the materials involved. For rotary pots, wirewound models have preferred maximum speeds on the order of 100 rpm, while conductive plastic models have allowable speeds as high as 2000 rpm. Linear-motion pots have preferred maximum velocities up to 10 m s^{-1}.

23.1.4.6 Life

Despite constant mechanical wear, a pot's expected lifetime is on the order of a million cycles when used under proper conditions. A quality film pot can last hundreds of millions of cycles. Of wirewound, hybrid, and conductive plastic pots, the uneven surface of a wirewound resistive element inherently experiences the most wear and thus has the shortest expected operating life. Hybrids improve on this by using a wirewound construction in combination with a smooth conductive film coating. Conductive plastic pots generally have the longest life expectancy due to the smooth surface of their resistive element.

23.1.4.7 Contamination and Seals

Foreign material contaminating pots can promote wear and increase friction between the wiper and the resistive element. Consequences range from increased mechanical loading to outright failure (e.g., seizing, contact discontinuity). Fortunately, sealed pots are available from most manufacturers for industrial applications where dirt and liquids are often unavoidable. To aid selection, specifications often include the type of *case sealing* (i.e., mechanisms and materials) and the *seal resistance* to cleaning solvents and other commonly encountered fluids.

23.1.4.8 Misalignment

Shaft misalignment in a pot can prematurely wear its bearing surfaces and increase its mechanical loading effects. A good design minimizes misalignment (see *Implementation* in the following). Manufacturers list a number of alignment tolerances. In linear-motion pots, *shaft misalignment* is the maximum amount a shaft can deviate from its axis. The degree to which a shaft can rotate around its axis is listed under *shaft rotation*. In rotary pots, *shaft end play* and *shaft radial play* both describe the amount of shaft deflection due to a radial load. *Shaft runout* denotes the shaft diameter eccentricity when a shaft is rotated under a radial load.

23.1.5 Mechanical Mounting Methods

Hardware features on a pot's housing determine the mounting method. Options vary with manufacturer and among rotary, linear-motion, and string pots. Offerings include custom bases, holes, tabs, flanges, and brackets—all of which secure with machine screws—and threaded studs, which secure with nuts. Linear-motion pots are available with rod or slider actuation, some with internal or external return springs. Mounting is typically accomplished by movable clamps, often supplied by the pot manufacturer. Other linear-motion pots mount via a threaded housing. For rotary pots, the two most popular mounting methods are the *bushing mount* and the *servo mount* (see Figure 23.5).

23.1.5.1 Bushing Mount

The pot provides a shaft-concentric, threaded sleeve that invades a hole in a mounting fixture and secures with a nut and lock washer. An off-axis tab or pin prevents housing rotation. Implementing a bushing mount requires little more than drilling a hole; however, limited rotational freedom and considerable play before tightening complicate precise setup.

23.1.5.2 Servo Mount

The pot provides a flanged, shaft-concentric, precision-machined rim that slips into a precision-bored hole in a mounting fixture. The flange secures with symmetrically arranged, quick-releasing *servo mount clamps*, available from Timber-Top, Inc. [9] and also from the sources listed in Table 23.4. (These

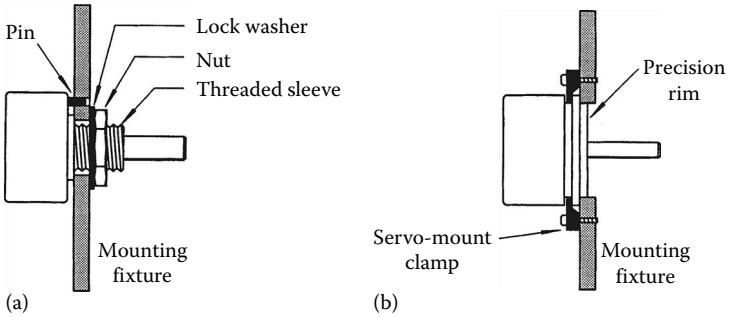

FIGURE 23.5 The two most common rotary pot mounts are (a) the bushing mount and (b) the servo mount.

TABLE 23.4 Sources of Small Mechanical Components

PIC Design, 86 Benson Road, P.O. Box 1004, Middlebury, CT 06762-1004, Tel: (800) 243-6125, (203) 758-8272; Fax: (203) 758-8271, http://www.pic-design.com/
Stock Drive Products/Sterling Instrument, 2101 Jericho Turnpike, Box 5416
New Hyde Park, NY 11042-5416, Tel: (516) 328-3300; Fax: (800) 737-7436, (516) 326-8827, http://www.sdp-si.com/
W.M. Berg, Inc., 499 Ocean Ave., East Rockaway, NY 11518, Tel: (800) 232-2374, (516) 599-5010; Fax: (800) 455-2374, (516) 599-3274, http://www.wmberg.com/

clamps are also called *synchro mount clamps* and *motor mount cleats*, since servo-mounting synchros and stepper motors are also available.) Servo mounts are precise and easy to adjust but entail the expense of precision machining.

23.2 Measurement Techniques

To measure displacement, a pot must attach to mechanical fixtures and components. The housing typically mounts to a stationary reference frame, while the shaft couples to a moving element. The *input motion* (i.e., the motion of interest) can couple directly or indirectly to the pot's shaft. A direct connection, although straightforward, carries certain limitations:

- The input motion maps 1:1 to the shaft motion.
- The input motion cannot exceed the pot's mechanical travel limits.
- Angle measurement requires a rotary pot; position measurement requires a linear-motion pot.
- The pot must mount close to the motion source.
- The input motion must be near-perfectly collinear or coaxial with the shaft axis.

Figure 23.6 shows ways to overcome these limitations. Mechanisms with a mechanical advantage scale motion and adjust travel limits. Mechanisms that convert between linear and rotary motion enable any type of pot to measure any kind of motion. Transmission mechanisms distance a pot from the measured motion. Compliant mechanisms compensate for misalignment. Examples and more details follow. Most of the described mechanisms can be realized with components available from the sources in Table 23.4.

Gears scale the mapping between input and pot shaft motions according to gear ratio. They also displace rotation axes to a parallel or perpendicular plane according to type of gear (e.g., spur vs. bevel). Gears introduce backlash. Friction rollers are a variation on the gear theme, immune to backlash but prone to slippage. The ratio of roller diameters scales the mapping between input and pot shaft motions.

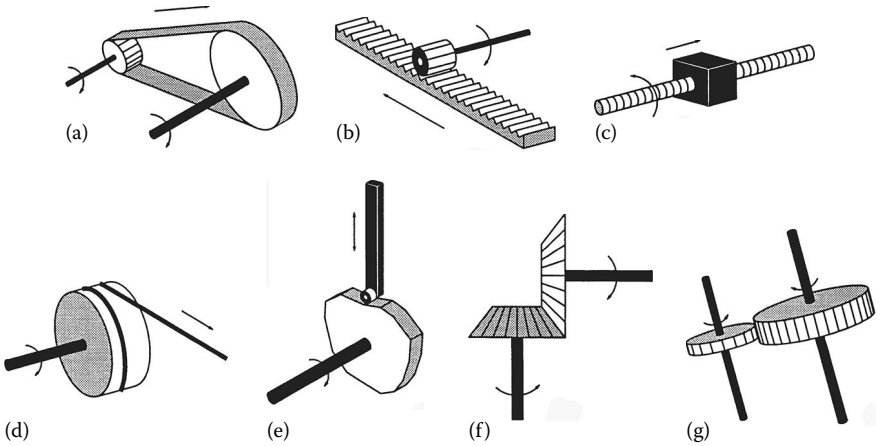

FIGURE 23.6 Mechanisms that extend a precision potentiometer's capabilities include (a) belts and pulleys, (b) rack and pinions, (c) lead screws, (d) cabled drums, (e) cams, (f) bevel gears, and (g) spur gears.

Rack-and-pinion mechanisms convert between linear and rotary motion. Mapping is determined by the rack's *linear pitch* (i.e., tooth-to-tooth spacing) compared to the number of teeth on the pinion. Backlash is inevitable.

Lead screws convert rotary motion to linear motion via the screw principle. Certain low-friction types (e.g., ball screws) are also capable of the reverse transformation (i.e., linear to rotary). Either way, mapping is controlled by the screw's *lead*—the distance the nut travels in one revolution. Lead screws are subject to backlash.

Cabled drums convert between linear and rotary motion according to the drum circumference, since one turn of diameter D wraps or unwraps a length πD of cable. An external force (e.g., supplied by a spring or a weight) might be necessary to maintain cable tension.

Pulleys can direct a string pot's cable over a complex path to a motion source. Mapping is 1:1 unless the routing provides a mechanical advantage.

Pulleys and *belts* transmit rotary motion scaled according to relative pulley diameters. The belt converts between linear and rotary motion (see Figure 23.6a). The empty area between pulleys provides a convenient passageway for other components. Sprocket wheels and chain have similar characteristics. Matched pulley–belt systems are available that operate with negligible slip, backlash, and stretch.

Cams map rotary motion into linear motion according to the function "programmed" into the cam profile (see Ref. [10] for more information).

Linkages can be designed to convert, scale, and transmit motion. Design and analysis can be quite complex and mapping characteristics tend to be highly nonlinear (see Ref. [11] for details).

Flexible shafts transmit rotary motion between two nonparallel axes with a 1:1 mapping, subject to torsional windup and hysteresis if the motion reverses.

Conduit, like a bicycle brake cable or *Bowden cable*, can route a cable over an arbitrary path to connect a pot to a remote motion source. The conduit should be incompressible and fixed at both ends. Mapping is 1:1 with some mechanical slop. Lubrication helps mitigate friction.

A mechanism's mapping characteristics impact measurement resolution and accuracy. Consider a stepper motor turning a lead screw to translate a nut. A linear-motion pot could measure the nut's position directly to some resolution. Alternatively, a rotary pot linked to the lead screw could measure the position with increased resolution if the mechanism mapped the same amount of nut travel to considerably more wiper travel. Weighing the resolution increase against the uncertainty due to backlash would determine which approach was more accurate.

23.3 Implementation

Integrating a pot into a measurement system requires consideration of various design issues, including the impact of the pot's physical characteristics, error sources, space restrictions, and wire routing. The pot's shaft type and bearings must be taken into consideration and protected against excessive loading. A good design will

- Give the pot mount the ability to accommodate minor misalignment
- Protect the shaft from thrust, side, and bending loads (i.e., not use the pot as a bearing)
- Provide hard limit stops within the pot's travel range (i.e., not use the pot's limit stops)
- Protect the pot from contaminants
- Strain relieve the pot's electrical connections

A thorough treatment of precision design issues appears in Ref. [12].

23.3.1 Coupling to the Pot

Successful implementation also requires practical techniques for mechanical attachment. A string pot's cable terminator usually fastens to other components with a screw. For other types of pots, coupling technique is partly influenced by the nature of the shaft. Rotary shafts come with various endings, including plain, single-flatted, double-flatted, slotted, and knurled. Linear-motion shafts usually terminate in threads but are also available with roller ends (to follow surfaces) or with spherical bearing ends (to accommodate misalignment). With care, a shaft can be cut, drilled, filed, threaded, etc.

In a typical measurement application, the pot shaft couples to a mechanical component (e.g., a gear, a pulley) or to another shaft of the same or different diameter. Successful couplings provide a positive link to the shaft without stressing the pot's mechanics. Satisfying these objectives with rotary and linear-motion pots requires a balance between careful alignment and compliant couplings. Alignment is not as critical with a string pot. Useful coupling methods include the following.

Compliant couplings: It is generally wise to put a compliant coupling between a pot's shaft and any other shafting. A compliant coupling joins two misaligned shafts of the same or different diameter. Offerings from the companies in Table 23.4 include bellow couplings, flex couplings, spring couplings, spider couplings, Oldham couplings, wafer spring couplings, flexible shafts, and universal joints. Each type has idiosyncrasies that impact measurement error; manufacturer catalogs provide details.

Sleeve couplings: Less expensive than a compliant coupling, a rigid sleeve coupling joins two shafts of the same or different diameter with the requirement that the shafts be perfectly aligned. Perfect alignment is difficult to achieve initially and impossible to maintain as the system ages. Imperfect alignment accelerates wear and risks damaging the pot. Sleeve couplings are available from the companies listed in Table 23.4.

Press fits: A press fit is particularly convenient when the bore of a small plastic part is nominally the same as the shaft diameter. Carefully force the part onto the shaft. Friction holds the part in place, but repeated reassembly will compromise the fit.

Shrink fits: Components with a bore slightly under the shaft diameter can be heated to expand sufficiently to slip over the shaft. A firm grip results as the part cools and the bore contracts.

Pinning: Small hubbed components can be pinned to a shaft. The pin should extend through the hub partway into the shaft, and the component should fit on the shaft without play. Use roll pins or spiral pins combined with a thread-locking compound (e.g., Loctite 242).

Setscrews: Small components are available with hubs that secure with setscrews. The component should fit on the shaft without play. For best results, use two setscrews against a shaft with perpendicular flats.

Dimple a plain shaft using the component's screw hole(s) as a drill guide. Apply a thread-locking compound (e.g., Loctite 242) to prevent the setscrews from working loose.

Clamping: Small components are also available with split hubs that grip a shaft when squeezed by a matching hub clamp. Clamping results in a secure fit without marring the shaft.

Adhesives: Retaining compounds (e.g., Loctite 609) can secure small components to a shaft. Follow manufacturer's instructions for best results.
Spring-loaded contact: A spring-loaded shaft will maintain positive contact against a surface that moves at reasonable speeds and without sudden acceleration.

23.4 Costs and Sources

Precision pots are inexpensive compared to other displacement measurement technologies. Table 23.5 lists approximate costs for off-the-shelf units in single quantity. Higher quality generally commands a higher price; however, excellent pots are often available at bargain prices due to volume production or surplus conditions. Electronic supply houses offer low-cost pots (i.e., under $20) that can suffice for short-term projects. Regardless of price, always check the manufacturer's specifications to confirm a pot's suitability for a given application.

Table 23.6 lists several sources of precision pots. Most manufacturers publish catalogs, and many have websites. In addition to a standard product line, most manufacturers will custom-build pots for high-volume applications.

23.5 Evaluation

Precision pots are a mature technology, effectively static except for occasional developments in materials, packaging, manufacturing, etc. Recent potentiometric innovations—including momentary-contact membrane pots [13] and solid-state digital pots [14]—are unavailing to precision measurement.

The variable voltage divider is the traditional configuration for precision measurement. The circuit's output, a high-amplitude DC voltage, is independent of variations in the pot's total resistance and is highly compatible with other circuits and systems. Other forms of output are possible with a precision pot configured as a variable resistor. For example, paired with a capacitor, a pot could supply a position-dependent *RC* time constant to modulate an oscillator's output frequency or duty cycle. In this setup, the pot's stability and AC characteristics would be important.

An alternative resistive displacement sensing technology is the *magnetoresistive potentiometer*, available in rotary and linear-motion forms. Magnetoresistive pots incorporate a noncontacting, permanent magnet "wiper" that rides above a pair of magnetoresistive elements. The elements, configured as a voltage divider, change their resistances according to the strength of the applied magnetic field and thus divide the voltage as a function of the magnet's position. The output is approximately linear over a limited range of motion (e.g., 90° in rotary models). Magnetoresistive pots offer unlimited resolution and exceptionally long life but may require temperature compensation circuitry (see Ref. [15] for more information).

TABLE 23.5 Typical Single-Quantity Prices ($US) for Commercially Available Pots

Potentiometer Type	Approximate Price Range
Rotary	$10–$350
Linear motion	$20–$2000
String	$250–$1000

TABLE 23.6 Sources of Precision Pots

Company	Potentiometer Types
Betatronix, Inc. 110 Nicon Court Hauppauge, NY 11788, Tel: (516) 582-6740; Fax: (516) 582-6038, http://www.betatronix.com/	Exotic linear motion, rotary
BI Technologies Corp. 4200 Bonita Place, Fullerton, CA 92635, Tel: (714) 447-2345; Fax: (714) 447-2500, http://www.bitechnologies.com/index.htm	Rotary
Bourns, Inc. Sensors & Controls Division, 2533 N. 1500 W., Ogden, UT 84404, Tel: (801) 786-6200; Fax: (801) 786-6203, http://www.bourns.com/	Mostly rotary, some linear motion
Celesco Transducer Products, Inc. 7800 Deering Avenue, Canoga Park, CA 91309, Tel: (800) 423-5483, (818) 884-6860, Fax: (818)340-1175, http://www.celesco.com/	String
Honeywell Data Instruments, Inc. 100 Discovery Way, Acton, MA 01720-3648, Tel: (800) 333-3282, (978) 264-9550, Fax: (978) 263-0630, http://sensing.honeywell.com/	Linear motion, rotary
BEI Sensors, Duncan Electronics Division BEI Sensors & Systems Company, 15771 Red Hill Avenue, Tustin, CA 92680, Tel: (714) 258-7500; Fax: (714) 258-8120, http://www.beiduncan.com/index.php	Linear motion, rotary
Dynamation Transducers Corp. 348 Marshall Street, Holliston, MA 01746-1441, Tel: (508) 429-8440; Fax: (508) 429-1317, http://www.dynamationtransducers.com/	Linear motion, rotary
JDK Controls, Inc. 424 Crown Pt. Circle, Grass Valley, CA 95945, Tel: (530) 273-4608; Fax: (530) 273-0769, http://www.jdkcontrols.com	Rotary, "do-it-yourself" rotor/wiper assemblies
Midori America Corp. 2555 E. Chapman Ave, Suite 400, Fullerton, CA 92631, Tel: (714) 449-0997; Fax: (714) 449-0139, http://www.midoriamerica.com/	Linear motion, rotary, string; also magnetoresistive
New England Instrument 245 Railroad Street, Woonsocket, RI 02895-1129, Tel: (401) 769-0703; Fax: (401) 769-0037, http://www.newenglandinstrument.com/	Linear motion, rotary, resistive elements
Novotechnik U.S., Inc. 237 Cedar Hill Street, Marlborough, MA 01752, Tel: (800) 667-7492, (508) 485-2244, Fax: (508) 485-2430, http://www.novotechnik.com/	Linear motion, rotary
Servo Systems, Co. 115 Main Road, PO Box 97, Montville, NJ 07045-0097, Tel: (800) 922-1103, (973) 335-1007, Fax: (973) 335-1661, http://www.servosystems.com/	Linear motion, rotary (surplus)
SpaceAge Control, Inc. 38850 20th Street East, Palmdale, CA 93550, Tel: (805) 273-3000; Fax: (805) 273-4240, http://spaceagecontrol.com/	String
UniMeasure, Inc. 501 S.W. 2nd Street, Corvallis, OR 97333, Tel: (541) 757-3158, Fax: (541) 757-0858, http://www.unimeasure.com/	String
Axsys Technologies, Inc. Vernitron Sensor Systems Division, Precision Potentiometer Division, 2800 Anvil Street North, St. Petersburg, FL 33710, Tel: (813) 347-2181; Fax: (813) 347-7520, http://www.axsys.com	Linear motion, rotary

References

1. Bourns, Inc., *Electronic Components RC4 Solutions Guide*, New York, 1995, p. 304.
2. Vernitron Motion Control Group, *Precision Potentiometers*, Catalog #752, New York, 1993.
3. Products, *Linear Position Transducers*, Unimeasure, Inc., http://unimeasure.com/ (accessed on March 24, 2013).
4. Instrument Society of America, *ISA-S37.12–1977* (*R1982*) *Specifications and Tests for Potentiometric Displacement Transducers*, Research Triangle Park, NC, 1982.
5. E. C. Jordan (Ed.), *Reference Data for Engineers: Radio, Electronics, Computer, and Communications*, 7th edn., Indianapolis, IN: H.W. Sams, 1985, pp. 5–16.
6. D. C. Greenwood, *Manual of Electromechanical Devices*, New York: McGraw-Hill, 1965, pp. 297–299.
7. E. S. Charkey, *Electromechanical System Components*, New York: Wiley-Interscience, 1972, pp. 302–303.
8. Variable Resistive Components Institute, *VRCI-P-100A Standard for Wirewound and Nonwirewound Precision Potentiometers*, Vista, CA, 1988.
9. Timber-Top, Inc., P.O. Box 517, Watertown, CT 06795, Tel: (860)-274–6706; Fax (860)-274–8041.
10. J. Angeles and C. S. López-Cajún, *Optimization of Cam Mechanisms*, Dordrecht, the Netherlands: Kluwer Academic, 1991.
11. P. W. Jensen, *Classical and Modern Mechanisms for Engineers and Inventors*, New York: Marcel Dekker, 1991.
12. A. H. Slocum, *Precision Machine Design*, Englewood Cliffs, NJ: Prentice Hall, 1992.
13. Spectra Symbol Inc., data sheet: *SoftPot*® (*Membrane Potentiometer*), Salt Lake City, UT, 1996.
14. Dallas Semiconductor Corp., *Digital Potentiometer Overview*, web page: www.dalsemi.com/Prod_info/Dig_Pots/, December 1997.
15. Midori America Corp., *Midori Position Sensors 1995 Catalog*, Fullerton, CA, 1995.

24

Inductive Displacement Sensors

Halit Eren
Curtin University

24.1 Theory

Inductive sensors are widely used in industry in many diverse applications. They are robust and compact and are less affected by environmental factors (e.g., humidity, dust) in comparison to their capacitive counterparts.

Inductive sensors are based on the principles of magnetic circuits. They can be classified as self-generating sensors or passive sensors. The self-generating types utilize an electrical generator principle; that is, when there is a relative motion between a conductor and a magnetic field, a voltage is induced in the conductor. Or a varying magnetic field linking a stationary conductor produces voltage in the conductor. In instrumentation applications, the magnetic field may be varying with some frequency, and the conductor may also be moving at the same time. In inductive sensors, the relative motion between field and conductor is supplied by changes in the measurand, usually by means of some mechanical motion. On the other hand, the passive transducer requires an external source of power. In this case, the action of the transducer is simply the modulation of the excitation signal.

Inductive displacement sensors can be divided into two major types:

1. Air core sensors
2. Magnetic core sensors

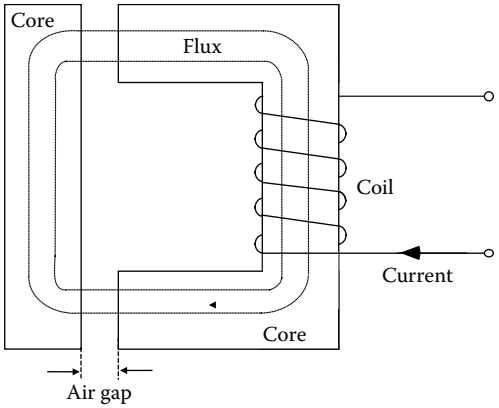

FIGURE 24.1 A basic inductive sensor consists of a magnetic circuit made from a ferromagnetic core with a coil wound on it. The coil acts as a source of mmf that drives the flux through the magnetic circuit through the core and the air gap. The presence of the air gap causes a large increase in circuit reluctance and a corresponding decrease in the flux. Hence, small variations in the air gap result in measurable changes in inductance.

Although air core sensors are used in some applications, they tend to have a lower sensitivity when compared to magnetic core sensors. Therefore, in this article, more emphasis will be given on magnetic core sensors. The basic principles are the same in both types.

A simple magnetic circuit is shown in Figure 24.1 to explain the basic principles of inductive sensors. In this figure, the magnetic circuit consists of a core, made from a ferromagnetic material together with a coil having n number of turns wound on it. The coil acts as a source of magnetomotive force (mmf), which drives the flux Φ through the magnetic circuit. If one assumes that the air gap is zero, the equation for the magnetic circuit can be expressed as

$$\text{mmf} = \text{Flux} \times \text{Reluctance} = \Phi \times \Re \text{ A-turns} \tag{24.1}$$

such that the reluctance $\Re$ limits the flux in a magnetic circuit similar to a resistance that limits the current in an electric circuit. By writing the mmf in terms of current, the magnetic flux may be expressed as

$$\Phi = \frac{ni}{\Re} \text{ weber} \tag{24.2}$$

In Figure 24.1, the flux linking a single turn is expressed by Equation 24.2, but for the total flux linking the entire n number of the turns of the coil, the equation becomes

$$\Psi = n\Phi = \frac{n^2 i}{\Re} \text{ weber} \tag{24.3}$$

Equation 24.3 leads to self-inductance L of the coil, which is described as the total flux (ψ weber) per unit current for that particular coil; that is

$$L = \frac{\Psi}{I} = \frac{n^2}{\Re} \tag{24.4}$$

This indicates that the self-inductance of an inductive element can be calculated by magnetic circuit properties. Expressing $\Re$ in terms of dimensions as

$$\Re = \frac{l}{\mu\mu_0 A} \tag{24.5}$$

where

l is the total length of the flux path
μ is the relative permeability of the magnetic circuit material
μ_0 is the permeability of free space ($=4\pi \times 10^{-7}$ H/m)
A is the cross-sectional area of the flux path

The arrangement illustrated in Figure 24.1 becomes a basic inductive sensor if the air gap is allowed to vary. In this case, the ferromagnetic core is separated into two parts by the air gap. The total reluctance of the circuit now is the addition of the reluctance of core and the reluctance of air gap. The relative permeability of air is close to unity, and the relative permeability of the ferromagnetic material can be of the order of a few thousand, indicating that the presence of the air gap causes a large increase in circuit reluctance and a corresponding decrease in the flux. Hence, as one would expect, a small variation in the air gap causes a measurable change in the inductance. Most of the inductive transducers are based on these principles and are discussed in the following in greater detail.

24.2 Linear and Rotary Variable-Reluctance Transducer

The variable-reluctance transducers are based on changes in the reluctance of a magnetic flux path. This type of transducer finds application particularly in acceleration measurements. However, they can be constructed in a suitable manner for sensing displacements as well as velocities. They come in many different forms, as described in the following.

24.2.1 Single-Coil Linear-Variable-Reluctance Sensor

A typical single-coil variable-reluctance displacement sensor is illustrated in Figure 24.2. The sensor consists of three elements: a ferromagnetic core in the shape of a semicircular ring, a variable air gap, and a ferromagnetic plate. The total reluctance of the magnetic circuit is the sum of the individual reluctances:

$$\Re_T = \Re_C + \Re_G + \Re_A \tag{24.6}$$

where $\Re_C$, $\Re_G$, and $\Re_A$ are the reluctances of the core, air gap, and armature, respectively.

Each one of these reluctances can be determined by using the properties of materials involved, as in Equation 24.5. In this particular case, the reluctance $\Re_T$ can be approximated as

$$\Re_T = \frac{R}{\mu_C \mu_0 r^2} + \frac{2d}{\mu_0 \pi r^2} + \frac{R}{\mu_A \mu_0 rt} \tag{24.7}$$

In obtaining Equation 24.7, the length of flux path in the core is taken as πR. The cross-sectional area is assumed to be uniform, with a value of πr^2. The total length of the flux path in air is $2d$, and it is assumed that there is no fringing or bending of the flux through the air gap, such that the cross-sectional area of the flux path in air will be close to that of the cross-sectional area of the core. The length of an average

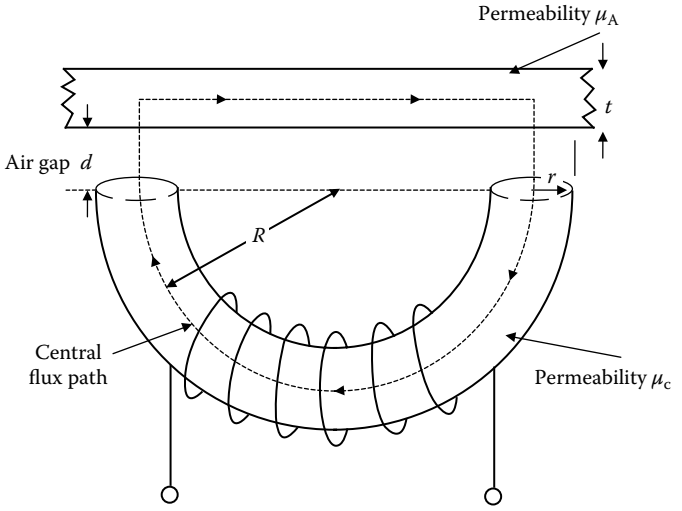

FIGURE 24.2 A typical single-coil, variable-reluctance displacement sensor. The sensor consists of three elements: a ferromagnetic core in the shape of a semicircular ring, a variable air gap, and a ferromagnetic plate. The reluctance of the coil is dependent on the single variable. The nonlinearly reluctance increases with the increasing air gap.

central flux path in the armature is $2R$. The calculation of the appropriate cross-sectional area of the armature is difficult, but it may be approximated to $2rt$, where t is the thickness of the armature.

In Equation 24.7, all of the parameters are fixed except for the one independent variable—the air gap. Hence, it can be simplified as

$$\Re_T = \Re_0 + kd \tag{24.8}$$

where

$$\Re_0 = \frac{R}{\mu_0 r}[1/\mu_C r + 1/\mu_A t]$$

$$k = \frac{2}{\mu_0 \pi r^2}$$

Using Equations 24.4 and 24.8, the inductance can be written as

$$L = \frac{n^2}{\Re_0 + kd} = \frac{L_0}{1 + \alpha d} \tag{24.9}$$

where

L_0 is the inductance at zero air gap

$\alpha = k/\Re_0$

The values of L_0 and α can be determined mathematically: they both depend on the core geometry and permeability, as explained earlier. From Equation 24.9, it can be seen that the relationship between L and α is nonlinear. Despite this nonlinearity, these types of single-coil sensors find applications in a number

of areas, such as force measurements and telemetry. In force measurements, the resultant change in inductance can be made to be a measure of the magnitude of the applied force. The coil usually forms one of the components of an *LC* oscillator, for which the output frequency varies with the applied force. Hence, the coil modulates the frequency of the local oscillator.

24.2.2 Variable-Differential Reluctance Sensor

The problem of the nonlinearity explained earlier can be eliminated by modifying the single-coil system into a variable-differential reluctance sensor (also known as push–pull sensor), as shown in Figure 24.3. This sensor consists of an armature moving between two identical cores and separated by a fixed distance of 2*d*. Now, Equation 24.9 can be written for both coils as

$$L_1 = \frac{L_{01}}{1+\alpha(d-x)}, \quad L_2 = \frac{L_{02}}{1+\alpha(d+x)} \tag{24.10}$$

Although the relationship between L_1 and L_2 is still nonlinear, the sensor can be incorporated into an ac deflection bridge to give a linear output for small movements. The hysteresis errors of these transducers are almost entirely limited to the mechanical components. These sensors respond to both static and dynamic measurements. They have continuous resolution and high outputs, but they may give erratic performance in response to presence of external magnetic fields. A typical sensor of this type has an input span of 1 cm, a coil inductance of 25 mH, and a coil resistance of 75 Ω. The resistance of the coil must carefully be considered when designing oscillator circuits. In many cases, the maximum nonlinearity is about 0.5%.

A typical commercially available variable-differential sensor is shown in Figure 24.4. The iron core is located halfway between the two E-shaped frames. The flux generated by primary coils depends on

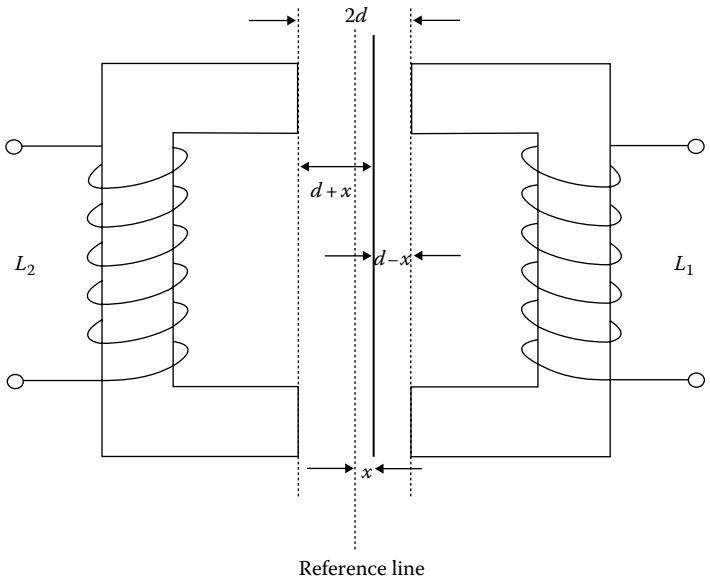

FIGURE 24.3 A variable-differential reluctance sensor consists of an armature moving between two identical cores separated by a fixed distance. The armature moves in the air gap in response to a mechanical input. This movement alters the reluctance of coils 1 and 2, thus altering their inductive properties. This arrangement overcomes the problem of nonlinearity inherent in single-coil sensors.

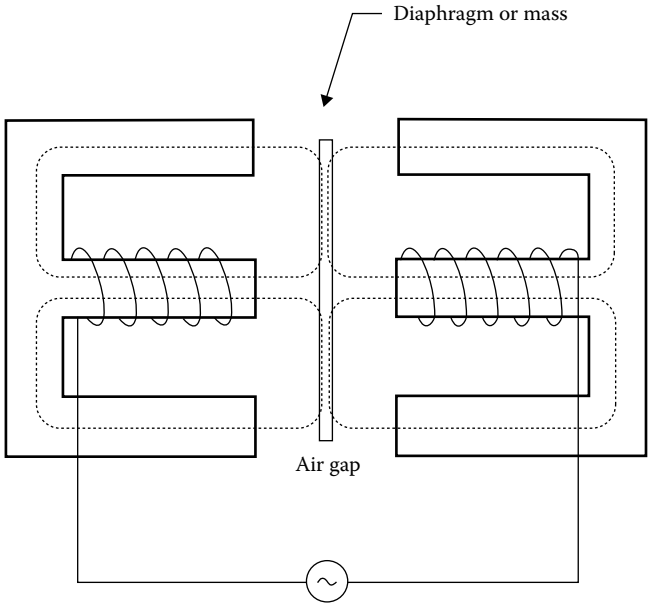

FIGURE 24.4 A typical commercial variable-differential sensor. The iron core is located halfway between the two E frames. Motion of the core increases the air gap for one of the E frames while decreasing the other side. This causes reluctances to change, thus inducing more voltage on one side than on the other. Motion in the other direction reverses the action, with a 180° phase shift occurring at null. The output voltage can be processed, depending on the requirements, by means of rectification, demodulation, or filtering. The full-scale motion may be extremely small, on the order of few thousandths of a centimeter.

the reluctance of the magnetic path, the main reluctance being the air gap. Any motion of the core increases the air gap on one side and decreases it on the other side, thus causing reluctance to change, in accordance with the principles explained earlier, and thereby inducing more voltage on one of the coils than on the other. Motion in the other direction reverses the action with a 180° phase shift occurring at null. The output voltage can be modified, depending on the requirements in signal processing, by means of rectification, demodulation, or filtering. In these instruments, full-scale motion may be extremely small—on the order of few thousandths of a centimeter.

In general, variable-reluctance transducers have small ranges and are used in specialized applications such as pressure transducers. Magnetic forces imposed on the armature can be quite large, and this severely limits their application. Nevertheless, the armature can be constructed as a diaphragm; hence, they become suitable for pressure measurements.

24.2.3 Variable-Reluctance Tachogenerators

Another example of a variable-reluctance sensor is shown in Figure 24.5. These sensors are based on Faraday's law of electromagnetic induction; therefore, they may also be referred to as electromagnetic sensors. Basically, the induced emf in the sensor depends on the linear or angular velocity of the motion.

The variable-reluctance tachogenerator consists of a ferromagnetic, toothed wheel attached to a rotating shaft and a coil wound onto a permanent magnet, extended by a soft iron pole piece. The wheel moves in close proximity to the pole piece, causing the flux linked by the coil to change, thus inducing an emf in the coil. The reluctance of the circuit depends on the width of the air gap between the rotating wheel and the pole piece. When the tooth is close to the pole piece, the reluctance is at

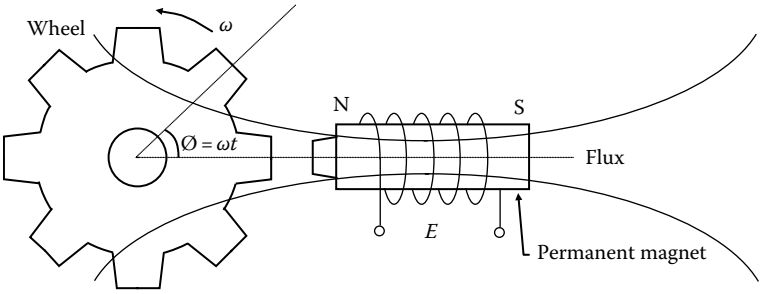

FIGURE 24.5 A variable-reluctance tachogenerator is a sensor that is based on Faraday's law of electromagnetic induction. It consists of a ferromagnetic toothed wheel attached to the rotating shaft and a coil wound onto a permanent magnet extended by a soft iron pole piece. The wheel rotates in close proximity to the pole piece, thus causing the flux linked by the coil to change. The change in flux causes an output in the coil similar to a square waveform whose frequency depends on the speed of the rotation of the wheel and the number of teeth.

its minimum, and it increases as the tooth moves away from the pole. When the wheel rotates with a velocity ω, the flux mathematically may be expressed as

$$\Psi(\theta) = A + B\cos m\theta \tag{24.11}$$

where
A is the mean flux
B is the amplitude of the flux variation
m is the number of teeth

The induced emf is given by

$$E = \frac{-d\Psi(\theta)}{dt} = -\left(\frac{d\Psi(\theta)}{d\theta}\right) \times \frac{d\theta}{dt} \tag{24.12}$$

or

$$E = bm\omega \sin m\omega t \tag{24.13}$$

Both amplitude and frequency of the generated voltage at the coil are proportional to the angular velocity of the wheel. In principle, the angular velocity ω can be found from either the amplitude or the frequency of the signal. In practice, the amplitude measured may be influenced by loading effects and electrical interference. In signal processing, the frequency is the preferred option because it can be converted into digital signals easily.

The variable-reluctance tachogenerators are most suitable for measuring angular velocities. They are also used in the volume flow rate measurements and the total volume flow determination of fluids.

24.3 Microsyn

Another commonly used example of variable-reluctance transducer is the Microsyn, as illustrated in Figure 24.6. In this arrangement, the coils are connected in such a manner that at the null position of the rotary element, the voltages induced in coils 1 and 3 are balanced by the voltages induced in coils 2 and 4.

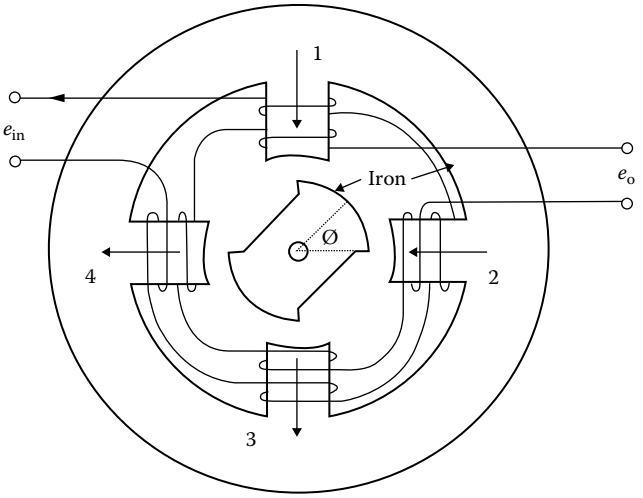

FIGURE 24.6 A Microsyn is a variable-reluctance transducer that consists of a ferromagnetic rotor and a stator carrying four coils. The stator coils are connected such that at the null position, the voltages induced in coils 1 and 3 are balanced by voltages induced in coils 2 and 4. The motion of the rotor in one direction increases the reluctance of two opposite coils while decreasing the reluctance in others, resulting in a net output voltage e_o. The movement in the opposite direction reverses this effect with a 180° phase shift.

The motion of the rotor in the clockwise direction increases the reluctance of coils 1 and 3 while decreasing the reluctance of coils 2 and 4, thus giving a net output voltage e_o. The movement in the counterclockwise direction causes a similar effect in coils 2 and 4 with a 180° phase shift. A direction-sensitive output can be obtained by using phase-sensitive demodulators, as explained in Section 24.6.

Microsyn transducers are used extensively in applications involving gyroscopes. By the use of microsyns, very small motions can be detected, giving output signals as low as 0.01° of changes in angles. The sensitivity of the device can be made as high as 5 V/degree of rotation. The nonlinearity may vary from 0.5% to 1.0% at full scale. The main advantage of these transducers is that the rotor does not have windings and slip-rings. Another advantage is that the magnetic reaction torque is also negligible.

24.4 Synchros

The term *synchro* is associated with another family of electromechanical devices that can be discussed under different headings. They are used primarily in angle measurements and are commonly applied in control engineering as parts of servomechanisms, machine tools, and antennas.

The construction of synchros is similar to that of wound-rotor induction motors, as shown in Figure 24.7. The rotation of the motor changes the mutual inductance between the rotor coil and the three stator coils. The three voltage signals from these coils define the angular position of the rotor. Synchros are used in connection with a variety of devices, including control transformers, Scott T transformers, resolvers, phase-sensitive demodulators, and analog-to-digital converters.

In some cases, a control transformer is attached to the outputs of the stator coils such that the output of the transformer produces a resultant mmf aligned in the same direction as that of the rotor of the synchro. In other words, the synchro rotor acts as a search coil in detecting the direction of the stator field of the control transformer. When the axis of this coil is aligned with the field, the maximum voltage is supplied to the transformer.

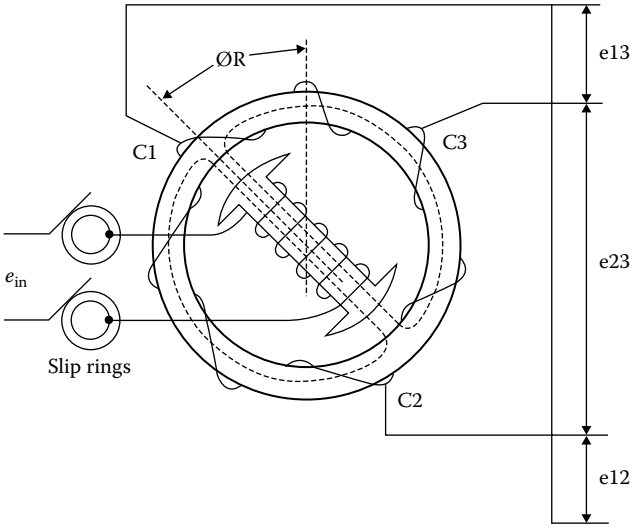

FIGURE 24.7 A synchro is similar to a wound-rotor induction motor. The rotation of the rotor changes the mutual inductance between the rotor coil and the stator coils. The voltages from these coils define the angular position of the rotor. They are primarily used in angle measurements and are commonly applied in control engineering as parts of servomechanisms, machine tools, and antennas.

In other cases, ac signals from the synchros are first applied to a Scott T transformer, which produces ac voltages with amplitudes proportional to the sine and cosine of the synchro's shaft angle. It is also possible to use phase-sensitive demodulations to convert the output signals to make suitable for the purpose of digital signal processing.

24.5 Moving-Coil Inductive Displacement Sensors

When the coil of the sensor rotates with a stable speed, it can pick up non-varying magnetic fields, but still comply with Faraday's Law of Induction. In some cases, the coil is made vibrate rather than rotate. Due to possibility of high-frequency vibrations, it is possible to make very small sensors with good geometric resolutions. Moving-coil inductive displacement sensors find limited applications in digital fluxmeters along with other sensors such as Hall and fluxgate sensors.

24.5.1 Linear-Variable Inductor

Mathematically, the principles of linear-variable inductors are very similar to the variable-reluctance type of transducer as explained at the beginning of the chapter. Also, in physical construction, there is a little distinction between variable-reluctance and variable-inductance transducers. The main difference is the way that the signals are picked up rather than the principles of operations. A typical linear-variable inductor consists of a movable iron core that provides the mechanical inputs and two coils forming two legs of an electrical bridge network. A typical example of such a transducer is the variable-coupling transducer, which is discussed next.

24.5.2 Variable-Coupling Transducers

These transducers consist of a former holding, a center-tapped coil, and a ferromagnetic plunger, as shown in Figure 24.8.

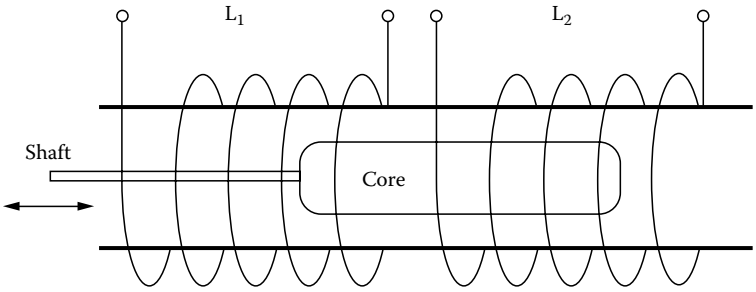

FIGURE 24.8 A typical linear-variable inductor consists of a movable iron core inside a former holding a center-tapped coil. The core and both of the coils have the same length L. When the core is in the reference position, each coil will have equal inductances of value L. As the core moves by δl, changes in inductances $+\delta L$ and $-\delta L$ create voltage outputs from the coils.

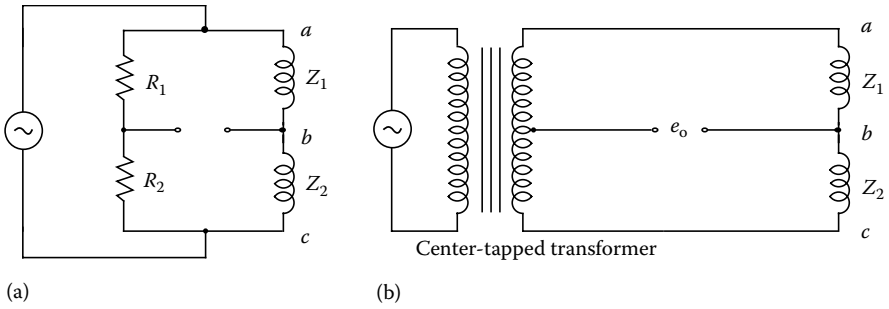

FIGURE 24.9 The two coils of a linear-variable inductor are usually placed to form two arms of a bridge circuit, also having two equal balancing resistors as in circuit (a). The bridge is excited with ac of 5–25 V with a frequency of 50 Hz–5 kHz. At a selected excitation frequency, the total transducer impedance at null conditions is set in the 100–1000 Ω range. By careful construction of the bridge, the output voltage can be made a linear function displacement of the core within a limited range. In some cases, in order to reduce power losses due to heating of resistors, center-tapped transformers may be used as a part of the bridge network (b).

The plunger and the two coils have the same length L. As the plunger moves, the inductances of the coils change. The two inductances are usually placed to form two arms of a bridge circuit with two equal balancing resistors, as shown in Figure 24.9a. The bridge is excited with ac of 5–25 V with a frequency of 50 Hz–5 kHz. At the selected excitation frequency, the total transducer impedance at null conditions is set in the 100–1000 Ω range. The resistors are set to have about the same value as transducer impedances. The load for the bridge output must be at least 10 times the resistance, R, value. When the plunger is in the reference position, each coil will have equal inductances of value L. As the plunger moves by δl, changes in inductances $+\delta L$ and $-\delta L$ creates a voltage output from the bridge. By constructing the bridge carefully, the output voltage can be made as a linear function displacement of the moving plunger within a rated range.

In some transducers, in order to reduce power losses due to heating of resistors, center-tapped transformers can be used as a part of the bridge network, as shown in Figure 24.9b. In this case, the circuit becomes more inductive and extra care must be taken to avoid the mutual coupling between the transformer and the transducer.

It is particularly easy to construct transducers of this type, by simply winding a center-tapped coil on a suitable former. The variable-inductance transducers are commercially available in strokes from

about 2 mm to 500 cm. The sensitivity ranges between 1.0% full scale to 0.02% in long stroke special constructions. These devices are also known as linear displacement transducers or LDTs, and they are available in various shape and sizes.

Apart from linear-variable inductors, there are rotary types available too. Their cores are specially shaped for rotational applications. Their nonlinearity can vary from 0.5% to 1.0% full scale over a range of 90° rotation. Their sensitivity can be up to 100 mV/degree of rotation.

24.5.3 Induction Potentiometer

One version of a rotary type linear inductor sensor is the induction potentiometer, shown in Figure 24.10. Two concentrated windings are wound on the stator and the rotor. The rotor winding is excited with an ac, thus inducing voltage in the stator windings. The amplitude of the output voltage is dependent on the mutual inductance between the two coils, where mutual inductance itself is dependent on the angle of rotation. For concentrated coil type induction potentiometers, the variation of the amplitude is sinusoidal, but linearity is restricted in the region of the null position. A linear distribution over an angle of 180° can be obtained by the construction of carefully designed distributed coils.

Standard commercial induction pots operate in a 50–400 Hz frequency range. They are small in size, from 1 to 6 cm, and their sensitivity can be in the order of 1 V/degree of rotation. Although the ranges of induction potentiometers are limited to less than 60° of rotation, it is possible to measure displacements in angles from 0° to full rotation by suitable arrangement of a number of induction pots. As in the case of many inductive sensors, the output of an induction pot may need phase-sensitive demodulators and suitable filters. In most cases, additional dummy coils are used to improve linearity and accuracy.

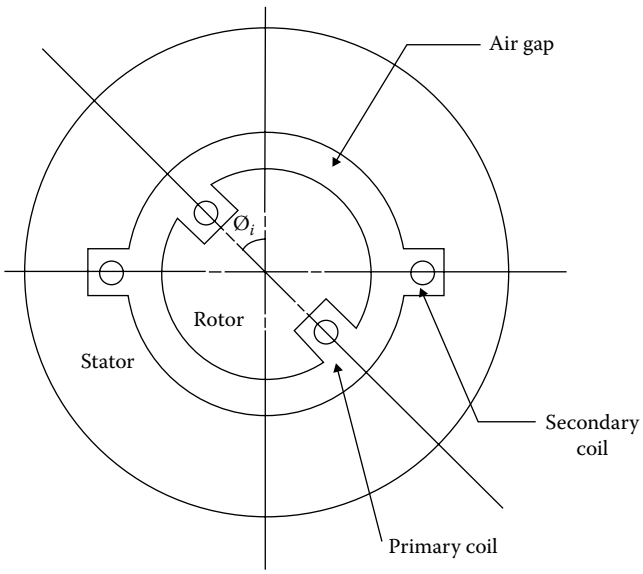

FIGURE 24.10 An induction potentiometer is a linear-variable inductor with two concentrated windings wound on the stator and on the rotor. The rotor winding is excited with ac, inducing voltage in the stator windings. The amplitude of the output voltage is dependent on the relative positions of the coils, as determined by the angle of rotation. For concentrated coils, the variation of the amplitude is sinusoidal, but linearity is restricted in the region of the null position. Different variations of induction potentiometers are available with distributed coils that give linear voltages over an angle of 180° of rotation.

24.6 Linear-Variable-Differential Transformer

The linear-variable-differential transformer (LVDT) is a passive inductive transducer. They find diverse range of applications. An LVDT consists of a single primary winding positioned between two identical secondary windings wound on a tubular ferromagnetic former, as shown in Figure 24.11. The primary winding is energized by a high frequency from 50 Hz to 20 kHz ac voltage. The two secondary windings are made identical by having an equal number of turns and similar geometry. They are connected in series opposition so that the induced output voltages oppose each other.

In many applications, the outputs are connected in opposing form, as shown in Figure 24.12a. The output voltages of individual secondaries v_1 and v_2 at null position are illustrated in Figure 24.12b. However, in opposing connection, any displacement in the core position x from the null point causes amplitude of the voltage output v_o and the phase difference α to change. The output waveform v_o in relation to core position is shown in Figure 24.12c. When the core is positioned in the middle, there is an equal coupling between the primary and secondary windings, thus giving a null point or reference point of the sensor. As long as the core remains near the center of the coil arrangement, output is linear. The linear ranges of commercial differential transformers are clearly specified, and the devices are seldom used outside this linear range.

The ferromagnetic core or plunger moves freely inside the former, thus altering the mutual inductance between the primary and secondaries. With the core in the center, or at the reference position, the induced emfs in the secondaries are equal, and since they oppose each other, the output voltage is zero. When the core moves, say to the left, from the center, more magnetic flux links with the left-hand coil than with the right-hand coil. The voltage induced in the left-hand coil is therefore larger than the induced voltage on the right-hand coil. The magnitude of the output voltage is then larger than at the null position and is equal to the difference between the two secondary voltages. The net output voltage is in phase with the voltage of the left-hand coil. The output of the device is then an indication of the displacement of the core. Similarly, movement in the opposite direction to the right from the center reverses this effect, and the output voltage is now in phase with the emf of the right-hand coil.

For mathematical analysis of the operation of LVDTs, Figure 24.12a can be used. The voltages induced in the secondary coils are dependent on the mutual inductance between the primary and

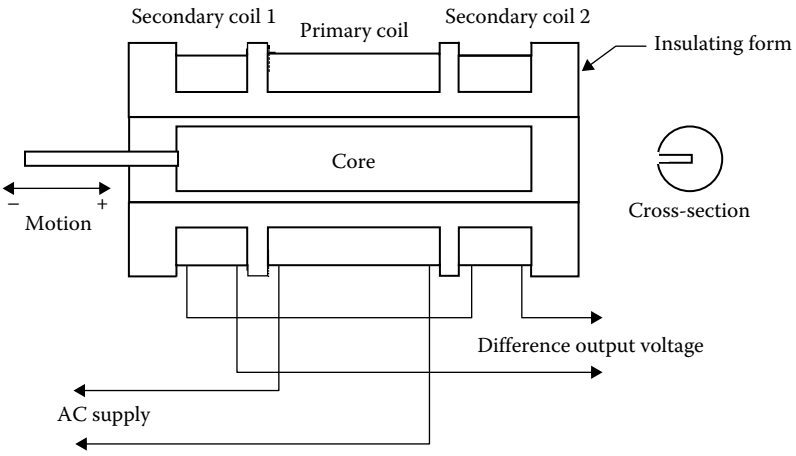

FIGURE 24.11 A LVDT is a passive inductive transducer consisting of a single primary winding positioned between two identical secondary windings wound on a tubular ferromagnetic former. As the core inside the former moves, the magnetic paths between primary and secondaries change, thus giving secondary outputs proportional to the movement. The two secondaries are made as identical as possible by ensuring equal sizes, shapes, and number of turns.

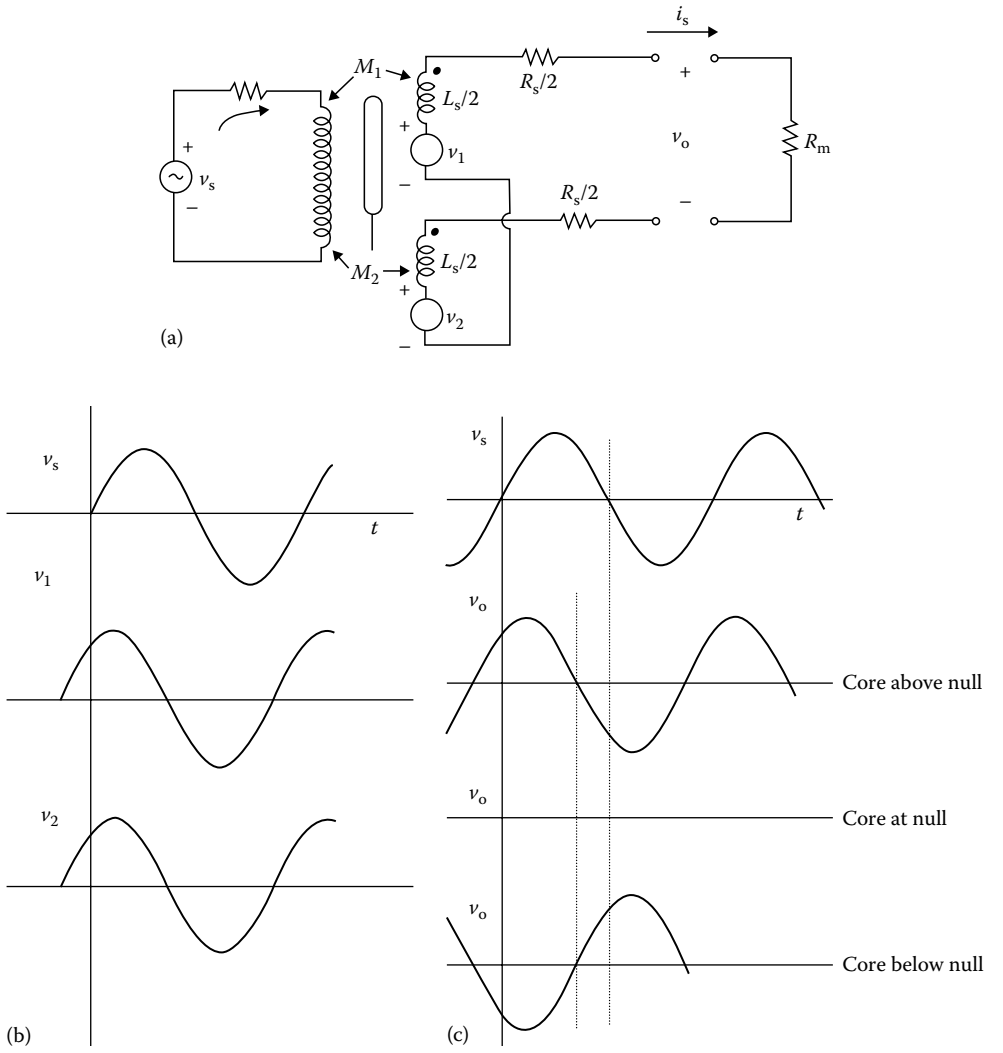

FIGURE 24.12 The voltages induced in the secondaries of an LVDT (a) may be processed in a number of ways. The output voltages of individual secondaries v_1 and v_2 at null position are illustrated in (b). In this case, the voltages of individual coils are equal and in phase with each other. Sometimes, the outputs are connected opposing each other, and the output waveform v_o becomes a function of core position x and phase angle α, as in (c). Note the phase shift of 180° as the core position changes above and below the null position.

individual secondary coils. Assuming that there is no cross coupling between the secondaries, the induced voltages may be written as

$$v_1 = M_1 s i_p \quad \text{and} \quad v_2 = M_2 s i_p \tag{24.14}$$

where

M_1 and M_2 are the mutual inductances between primary and secondary coils for a fixed core position
s is the Laplace operator
i_p is the primary current

In the case of opposing connection, no load output voltage v_o without any secondary current may be expressed as

$$v_o = v_1 - v_2 = (M_1 - M_2)si_p \tag{24.15}$$

writing

$$v_s = i_p(R + sL_p) \tag{24.16}$$

Substituting i_p in Equation 24.15 gives the transfer function of the transducer as

$$\frac{v_o}{v_s} = \frac{(M_1 - M_2)s}{R + sL_p} \tag{24.17}$$

However, if there is a current due to output signal processing, then describing equations may be modified as

$$v_o = R_m i_s \tag{24.18}$$

where

$$i_s = \frac{(M_1 - M_2)si_p}{R_s + R_m + sL_s}$$

and

$$v_s = i_p(R + sL_p) - (M_1 - M_2)si_s \tag{24.19}$$

Eliminating i_p and i_s from Equations 24.19 and 24.20 results in a transfer function:

$$\frac{v_o}{v_s} = \frac{R_m(M_1 - M_2)s}{[(M_1 - M_2)^2 + L_sL_p]s^2 + [L_p(R + R_m) + RL_s]s + (R_s + R_m) + R} \tag{24.20}$$

This is a second-order system, which indicates that due to the effect of the numerator of Equation 24.20, the phase angle of the system changes from +90° at low frequencies to −90° at high frequencies. In practical applications, the supply frequency is selected such that at the null position of the core, the phase angle of the system is 0°.

The amplitudes of the output voltages of secondary coils are dependent on the position of the core. These outputs may directly be processed from each individual secondary coil for slow movements of the core and when the direction of the movement of the core does not bear any importance. However, for fast movements of the core, the signals can be converted to dc and the direction of the movement from the null position can be detected. There are many options to do this; however, a *phase-sensitive demodulator* and filter arrangement are commonly used, as shown in Figure 24.13a. A typical output of the phase-sensitive demodulator is illustrated in Figure 24.13b, in relation to output voltage v_o, displacement x, and phase angle α.

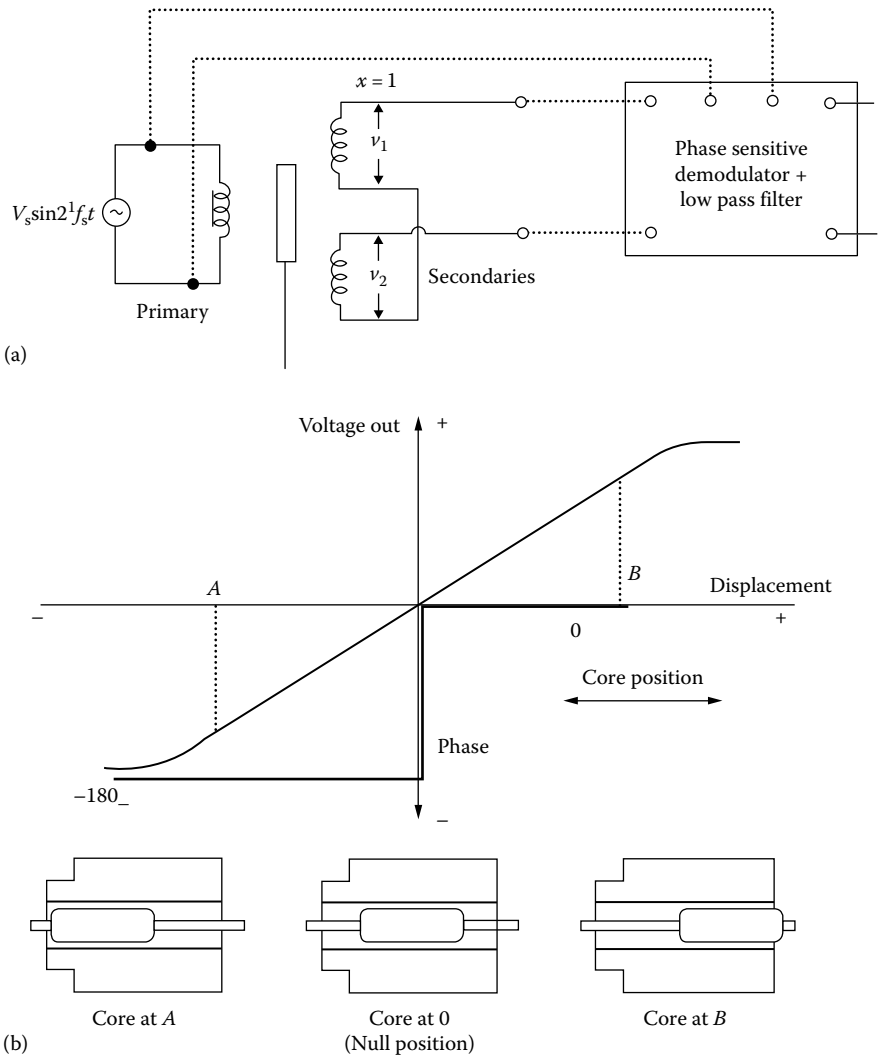

FIGURE 24.13 Phase-sensitive demodulator and (a) are commonly used to obtain displacement proportional signals from LVDTs and other differential-type inductive sensors. They convert the ac outputs from the sensors into dc values and also indicate the direction of movement of the core from the null position. A typical output of the phase-sensitive demodulator is shown in (b). The relationship between output voltage v_o and phase angle α is also shown against core position x.

The phase-sensitive demodulators are used extensively in differential-type inductive sensors. They basically convert the ac outputs to dc values and also indicate the direction of movement of the core from the null position. A typical phase-sensitive demodulation circuit may be constructed, based on diodes shown in Figure 24.14a. This arrangement is useful for very slow displacements, usually less than 1 or 2 Hz. In this figure, bridge 1 acts as a rectification circuit for secondary 1, and bridge 2 acts as a rectifier for secondary 2. The net output voltage is the difference between the outputs of two bridges, as in Figure 24.14b. The position of the core can be determined from the amplitude of the dc output, and the direction of the movement of the core can be determined from the polarity of the dc voltage. For rapid movements of the core, the outputs of the diode bridges need to be filtered, wherein only the frequencies of the movement of the core pass through and all the other frequencies produced by the modulation process are filtered. For this purpose, a suitably designed simple *RC* filter may be sufficient.

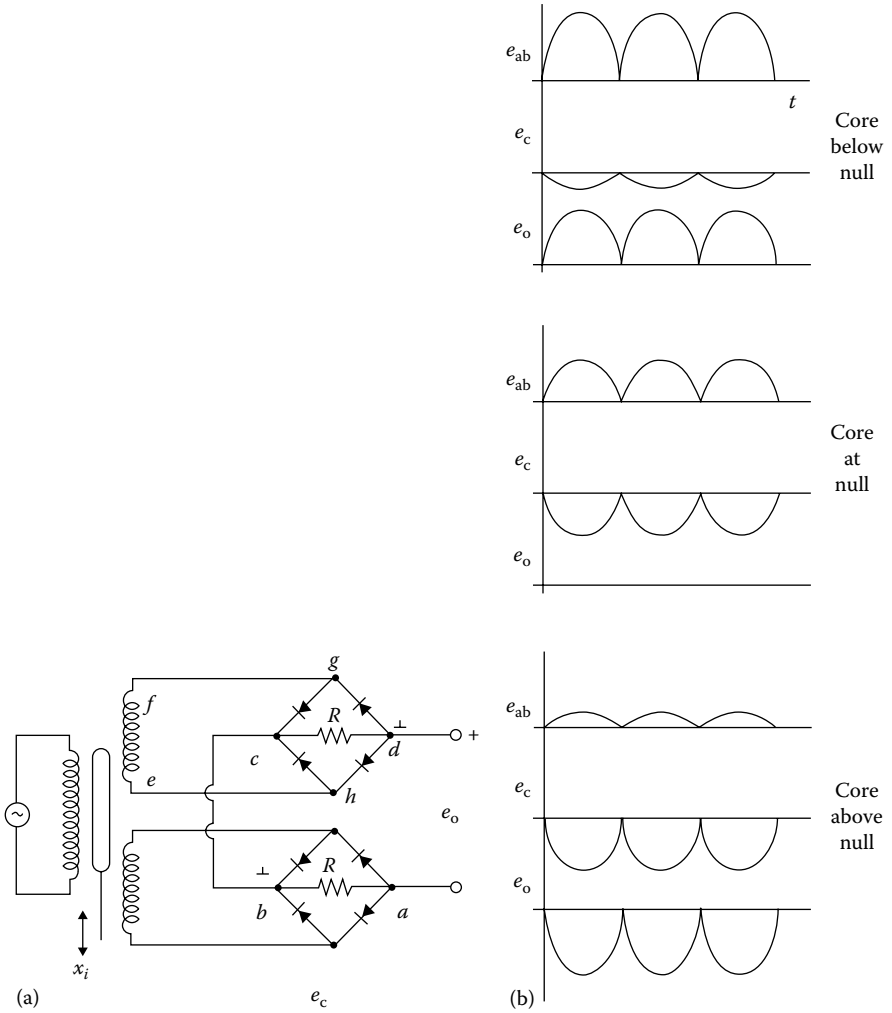

FIGURE 24.14 A typical phase-sensitive demodulation circuit based on diode bridges as in (a). Bridge 1 acts as a rectification circuit for secondary 1, and bridge 2 acts as a rectifier for secondary 2 where the net output voltage is the difference between the two bridges, as in (b). The position of the core can be determined from the amplitude of the dc output, and the direction of the movement of the core can be determined from the polarity of the voltage. For rapid movements of the core, the output of the diode bridges must be filtered; for this, a suitably designed simple *RC* filter may be sufficient.

There are phase-sensitive demodulator chips available in the marketplace, such as AD630 offered by Analog Devices Inc. These chips are highly versatile and flexible to use to suit particular application requirements. These chips offer many advantages over conventional phase-sensitive demodulation devices; for example, frequency off excitation may be adjusted to any value between 20 Hz and 20 kHz by connecting an external capacitor between two pins. The amplitude of the excitation voltage can be set up to 24 V. The internal filters may be set to required values by external capacitors. Connections to analog-to-digital converters are easily made by converting the bipolar output to unipolar scale.

The frequency response of LVDTs is primarily limited by the inertia characteristics of the device. In general, the frequency of the applied voltage should be 10 times the desired frequency response. Commercial LVDTs are available in a broad range of sizes, and they are widely used for displacement measurements in a variety of applications. These displacement sensors are available to cover ranges

from ±0.25 mm to ±7.5 cm. They are sensitive enough to be used to respond to displacements well below 0.0005 mm. They have operational temperature ranges from –265 °C to 600 °C. They are also available in radiation-resistant designs for operation in nuclear reactors. For a typical sensor of ±25 mm range, the recommended supply voltage is 4–6 V, with a nominal frequency of 5 kHz and a maximum nonlinearity of 1% full scale. Several commercial models are available that can produce a voltage output of 300 mV for 1 mm displacement of the core.

One important advantage of the LVDT is that there is no physical contact between the core and the coil form and hence no friction or wear. Nevertheless, there are radial and longitudinal magnetic forces on the core at all times. These magnetic forces may be regarded as magnetic springs that try to displace the core to its null position. This may be a critical factor in some applications.

A problem with LVDTs is that it may not be easy to make the two halves of the secondary identical; their inductance, resistance, and capacitance may be different, causing a large unwanted quadrature output in the balance position. Precision coil winding equipment may be required to reduce this problem to an acceptable value.

Another problem is associated with null position adjustments. The harmonics in the supply voltage and stray capacitances result in small null voltages. The null voltage may be reduced by proper grounding, which reduces the capacitive effects and center-tapped voltage source arrangements. In center-tapped supplies, a potentiometer may be used to obtain a minimum null reading.

The LVDTs have a variety of applications, including control for jet engines in close proximity to exhaust gases and measuring roll positions in the thickness of materials in hot-slab steel mills. Force and pressure measurements may also be made by LVDTs after some mechanical modifications.

24.7 Rotary-Variable-Differential Transformer

A variation from the LVDT is the rotary core differential transformer shown in Figures 24.15a and b. Here, the primary winding is wound on the center leg of an E core, and the secondary windings are wound on the outer legs of the core. The armature is rotated by an externally applied force about a pivot point above the center leg of the core. When the armature is displaced from its reference, the reluctance of the magnetic circuit through one of the secondary coils decreases and, simultaneously, increases the reluctance through the other coil. The induced emfs in the secondary windings, which are equal in the reference position of the armature, are now different in magnitude and phase as a result of the applied displacement. The induced emfs in the secondary coils are made to oppose each other, and the transformer operates in the same manner as an LVDT. The rotating variable transformers may be sensitive to vibrations. If a dc output is required, a demodulator network can be used, as in the case of LVDTs.

In most rotary LVDTs, the rotor mass is very small, usually less than 5 g. The nonlinearity in the output ranges between ±1% and ±3%, depending on the angle of rotation. The motion in the radial direction produces a small output signal that can affect the overall sensitivity. However, this transverse sensitivity is usually kept below 1% of the longitudinal sensitivity.

24.8 Eddy Current Proximity Sensors

Inductive transducers based on eddy currents are mainly probe types, containing two coils as shown in Figure 24.16. One of the coils, known as the active coil, is influenced by the presence of the conducting target. The second coil, known as the balance coil, serves to complete the bridge circuit and provides temperature compensation. The magnetic flux from the active coil passes into the conductive target by means of a probe. When the probe is brought close to the target, the flux from the probe links with the target produces eddy currents within the target.

The eddy current density is greatest at the target surface and becomes negligibly small at about three skin depths below the surface. The skin depth depends on the type of material used and the excitation frequency. While thinner targets can be used, a minimum of three skin depths is often necessary to

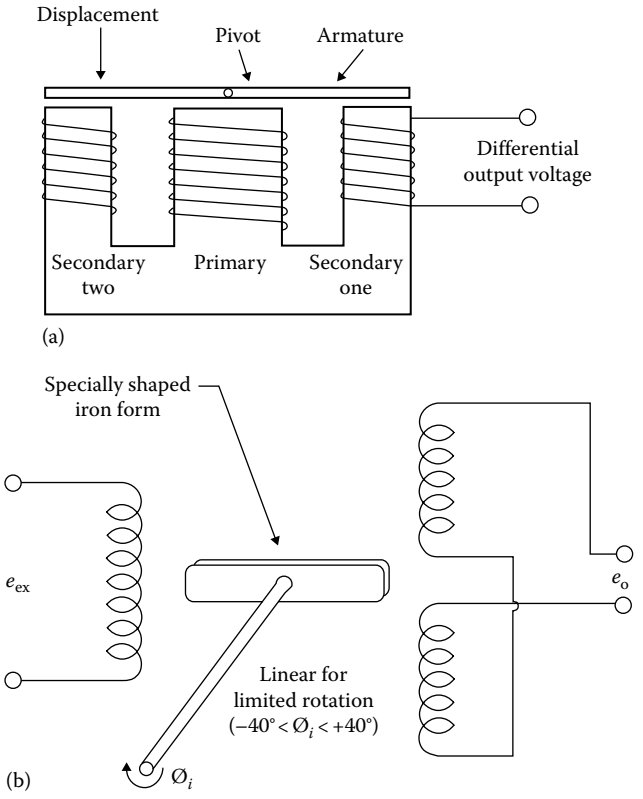

FIGURE 24.15 A rotary core differential transformer has an E-shaped core, carrying the primary winding on the center leg and the two secondaries on the outer legs, as in (a). The armature is rotated by an externally applied force about a pivot point above the center leg of the core (b). When the armature is displaced from its reference or balance position, the reluctance of the magnetic circuit through one secondary coil is decreased, increasing the reluctance through the other coil. The induced emfs in the secondary windings are different in magnitude and phase as a result of the applied displacement.

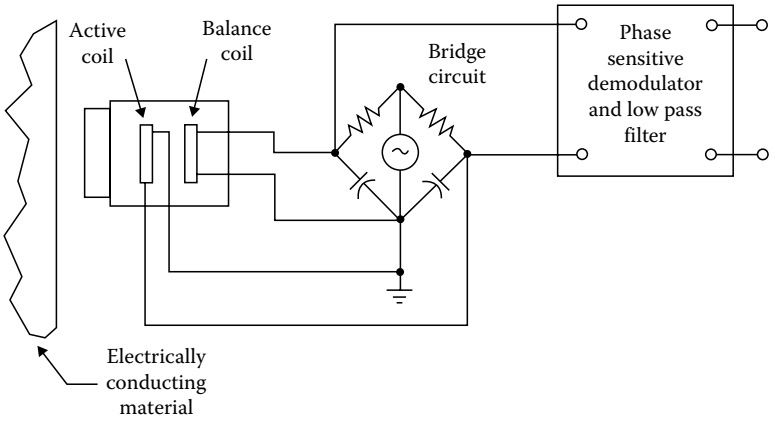

FIGURE 24.16 Eddy current transducers are inductive transducers using probes. The probes contain one active and one balance coil. The active coil responds to the presence of a conducting target, while the balance coil completes a bridge circuit and provides temperature compensation. When the probe is brought close the target, the flux from the probe links with the target, producing eddy currents within the target that alter the inductance of the active coil. This change in inductance is detected by a bridge circuit.

minimize the temperature effects. As the target comes closer to the probe, the eddy currents become stronger, causing the impedance of the active coil to change and thus altering the balance of the bridge in relation to the target position. This unbalance voltage of the bridge may be demodulated, filtered, and linearized to produce a dc output proportional to target displacement. The bridge oscillation may be as high as 1 MHz. High frequencies allow the use of thin targets and provide a good system frequency response.

Probes are commercially available with full-scale diameter ranging from 0.25 mm to 30 mm with a nonlinearity of 0.5% and a maximum resolution of 0.0001 mm. Targets are usually supplied by the clients, involving noncontact measurements of machine parts. For nonconductive targets, conductive materials of sufficient thickness must be attached to the surface by means of commercially available adhesives. Since the target material, shape, etc., influence the output, it is necessary to calibrate the system statistically for a specific target. The recommended measuring range of a given probe begins at a standoff distance equal to about 20% of the stated range of the probe. In some cases, a standoff distance of 10% is recommended for which the system is calibrated as standard. A distance greater than 10% of the measuring range can be used as long as the calibrated range is reduced by the same amount.

Flat targets must be of the same diameter as the probe or larger. If the target diameter is smaller than the probe diameter, the output drops considerably, thus becoming unreliable. Curved-surface targets can behave similar to flat surfaces if the diameter exceeds about three or four times the diameter of the probe. In this case, the target essentially becomes an infinite plane. This also allows some cross-axis movement without affecting the system output. Target diameters comparable to the sensor could result in detrimental effects in measurements due to cross-axis movements.

For curved or irregular-shaped targets, the system must be calibrated using the exact target that is seen in the operation. This tends to eliminate any errors caused by the curved surfaces during application. However, special multiprobe systems are available for orbital motions of rotating shafts. If the curved (shaft) target is about 10 times larger than the sensor diameter, it acts as an infinite plane and does not need special calibration. Care must be exercised to deal with electrical runout due to factors such as inhomogeneities in hardness, particularly valid for ferrous targets. However, nonferrous targets are free from electrical runout concerns.

24.9 Gradiometer-Inductive Displacement Sensors

Gradiometer sensors are used when the external magnetic field is generated by a large distant source. If, for example, two identical coils are placed in a uniform magnetic field, both will sense the same magnetic field. When both coils are connected differentially, the influence of the external (ambient) field will be eliminated. At the same time, if there is a smaller magnetic field due to a second source, the magnetic coil placed nearer the second source will be subjected larger field; hence, the differential output will change. This differential change can be processed suitably to detect the local source relative to the larger one. Gradiometer sensors can be made to detect variations in magnetic field of few femtotesla in the presence of few millitesla uniform ambient fields.

24.10 Miniature-Inductive Displacement Sensors

Recent developments in microchip technology allow the formation of inductive displacement sensors at the chip level. A typical configuration consists of multiple-coil system as illustrated in Figure 24.17. A structure with three excitation and three coils allows the corrections for the angular misalignments and lateral displacements. A typical application is in the implantable sensors to monitor activities in humans. They can achieve a sensitivity 5 μV/10 mm displacements. They can be as small as 1 mm in diameter 4 mm in length.

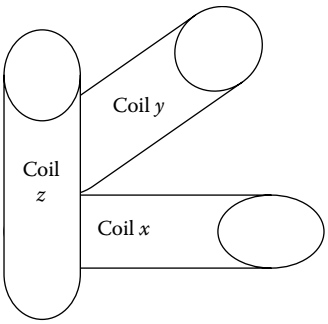

FIGURE 24.17 An implantable three-coil inductive sensor. A typical system consists of transmitter coil, which generates magnetic field and sensing coil that measures the field amplitude that depends on the distance and the mutual position between the coils.

24.11 Shielding and Sensitivity of Inductive Sensors to Electromagnetic Interference

Magnetic fields are produced by currents in wires and more strongly by the coils. The fields due to coils are important due to magnetic coupling, particularly when there are two or more coils in the circuit. The magnetic coupling between coils may be controlled by large spacing between coils, orientation of coils, and the shape of the coils and by shielding.

Inductive sensors come in different shapes and sizes. While some sensors have closed cores such as toroidal shapes, others have open cores and air gaps between cores and coils. Closed cores can have practically zero external fields, except for small leakage fluxes. Even if the sensors do not have closed cores, most variable inductor sensors have rather limited external fields, due to two neighboring sets of coils connected in opposite directions that minimize the external fields.

Inductive sensors are made from closed conductors. This implies that if the conductor moves in a magnetic field, a current will flow. Alternatively, a magnetic change produces current in a stationary closed conductor. Unless adequate measures are taken, there may be external magnetic fields linking (interference) with the sensor coils, thus producing currents and unwanted responses.

Due to inherent operations, inductive sensors are designed to have high sensitivity to magnetic flux changes. External electromagnetic interference and external fields can seriously affect the performance of the sensors. It is known that moderate magnetic fields are found near power transformers, electrical motors, and power lines. These small fields produce current in the inductive sensor elements. One way of eliminating external effects is accomplished by magnetic shielding of the sensors and by grounding appropriately. In magnetic shielding, one or more shells of high-permeability magnetic materials surround the part to be shielded. Multiple shells may be used to obtain very complete shielding. The ends of each individual shell are separated by insulation so that the shell does not act as a single shorted turn, thus accommodating high current flows. Similarly, in the case of multiple shielding, shells are isolated from each other by proper insulation.

Alternating magnetic fields are also screened by interposing highly conductive metal sheets such as copper or aluminum on the path of the magnetic flux. The eddy currents induced in the shield give a counter mmf that tends to cancel the interfering magnetic field. This type of shielding is particularly effective at high frequencies. Nevertheless, appropriate grounding must still be observed.

In many inductive sensors, stray capacitances can be a problem, especially at the null position of the moving core. If the capacitive effect is greater than a certain value, say 1% of the full-scale output, this effect may be reduced by the use of center-tapped supply and appropriate grounding.

Bibliography

Bentley, J. P., *Principles of Measurement Systems*, 2nd edn., Longman Scientific and Technical, Essex, U.K., 1988.

Chunhong, H. and Zhenghong, Q., Application of magnetic sensors in automation control, *J. Phys.: Conf. Ser.*, 263, 012003, 2011.

Gatzen, H. H., Anreeva, E., and Iswahjudi, H., Eddy-current microsensors based on thin film technology, *IEEE Trans. Magn.*, 38, 3368–3370, 2002.

Doebelin, E. O., *Measurement Systems: Application and Design*, 4th edn., McGraw-Hill, Singapore, 1990.

Duc, N. H. and Giang, D. T. H., Magnetic sensors based on piezoelectric-magnetostrictive composites, *J. Alloys Compd.*, 449(1–2), 214–218, 2008.

Holman, J. P., *Experimental Methods for Engineers*, 5th edn., McGraw-Hill, Singapore, 1989.

Magnes, W. and Diaz-Michelana, M., Future directions for magnetic sensors for space applications, *IEEE Trans. Magn.*, 45(10), 4493–4498, 2009.

Nippon Steel Technical Report, A survey method using magnetic sensors to detect the contact locations of other metal structures on pipelines, Nippon Steel Corp., No. 92, 2005, pp. 95–96.

Ripka, P., *Induction Sensors Magnetic Sensors and Magnetometers*, Artech House, Boston, MA, 2001, pp, 47–74.

Ripka, P. and Janosek, M., Advances in magnetic sensors, *Proceedings of the IEEE Sensors 2008*, Piscataway, NJ, 2008, pp. 1–4.

Partial List of Manufacturers and Suppliers

American Aerospace Controls, Inc. (AAC), 570A Smith St., Farmingdale, NY 11735, Phone: 631-694-5100, 888-873-8559 (toll free), Fax: 631-694-6739, www.a-a-c.com

AutomationDirect.com (AutomationDirect), 3505 Hutchinson Rd., Cumming, GA 30040-5860, Phone: 770-889-2858, 800-633-0405 (toll free), Fax: 770-889-7876, www.automationdirect.com

Automation Products Group, Inc. (APGSENSORS), 1025 W. 1700 N., Logan, UT 84321, Phone: 435-753-7300, 888-525-7300 (toll free), Fax: 435-753-7490, www.apgsensors.com

Autonics USA, 1353 Armour Blvd., Mundelein, IL 60060, Phone: 847-680-8160, 866-862-2602 (toll free), Fax: 847-680-8155, www.autonicsonline.com

Banner Engineering Corp., 9714 Tenth Ave. N., Minneapolis, MN 55440, Phone: 763-544-3164, 877-581-1749 (toll free), Fax: 763-544-3213, www.bannerengineering.com/en-US/

Baumer Ltd., 122 Spring St. Suite C-6, Southington, CT 06489-1534, Phone: 860-621-2121, 800-937-9336 (toll free), Fax: 860-628-6280, www.baumerelectric.com

Fargo Controls, Inc., P.O. Box 539, Eatontown, NJ 07724, Phone: 732-389-3376, 800-241-3755 (toll free), Fax: 732-542-3553, www.fargocontrols.com

Honeywell Sensing and Control, 1985 Douglas Dr., North, MN 10-192B Golden Valley, MN 55422, Phone: 763-954-4818, 800-446-6555 (toll free), www.honeywell.com/

IFM Efector, Inc., 782 Springdale Dr., Exton, PA 19341-2843, Phone: 610-524-2000, 800-441-8246 (toll free), Fax: 800-329-0436, www.ifm.com/ifmus/web/home.htm

ISSC-Kanson Electronics, Inc., 245 Forrest Ave., Hohenwald, TN 38462, Phone: 931-796-3050, 800-233-9354 (toll free), Fax: 931-796-3956, www.issc-kanson.com/

Leuze Electronic, Inc., 55395 Lyon Industrial Dr., New Hudson, MI 48165, Phone: 248-486-4466 Fax: 248-486-6699, www.leuzeusa.com

Macro Sensors, Division of Howard A. Schaevitz Technologies, 7300 US Rte. 130 N. Bldg. 22, Pennsauken, NJ 08110, Phone: 856-662-8000, Fax: 856-317-1005, www.macrosensors.com

MTI Instruments, Inc., 325 Washington Ave., Extension Albany, NY 12205-5505, Phone: 518-218-2550, Fax: 518-218-2506, www.mtiinstruments.com

OTP Industrial Solutions, 1900 Jetway Blvd., Columbus, OH 43219, Phone: 614-342-6123, Fax: 614-342-6490, www.otpnet.com/

Pilz Automation Safety L.P., 7150 Commerce Blvd., Canton, MI 48187, Phone: 866-889-1726 (toll free), Fax: 734-354-3355, www.pilz.us/index.jsp

Schneider Electric-Hyde Park, 1875 Founders Dr., Dayton, OH 45420, Phone: 937-514-7207, Fax: 937-258-5830, www.sesensors.com

SICK, Inc., 6900 W. 110th St., Bloomington, MN 55438, Phone: 952-941-6780, 800-325-7425 (toll free), Fax: 952-941-9287, www.sick.com/us/en-us/home/Pages/Homepag…

Smith Systems, Inc., 6 Mill Creek Center, P.O. Box 667, Brevard, NC 28712, Phone: 828-884-3490, Fax: 828-877-3100, www.smith-systems-inc.com

SoftNoze USA, Inc., 2216 Broad St., Frankfort, NY 13340-5100, Phone: 315-732-2726, Fax: 315-732-2963, www.softnoze.com

Spectec, 9 Polaris Way, P.O. Box 360, Emigrant, MT 59027, Phone: 406-333-4967, 800-735-9373 (toll free), Fax: 406-333-4259, www.spectecsensors.com

Turck, Inc., 3000 Campus Dr., Plymouth, MN 55441-2619, Phone: 763-553-7300, 800-554-4989 (toll free), Fax: 763-553-0708, www.turck.com

25

Capacitive Sensors: Displacement, Humidity, Force

Halit Eren
Curtin University

25.1 Introduction

Capacitive sensors are based on changes in capacitance in response to physical variations. Capacitive displacement sensors are noncontact devices yielding high-resolution measurements of the position and/or change of position. They are used in a wide variety of applications such as assembly of equipment, disk drives, thickness measurements, machine tools, semiconductor devices, machining, and in some cases in density measurements. In some cases, the basic operational and sensing principles are common in dissimilar applications, and in other cases, different principles can be used for the same applications. For example, capacitive microphones are based on variations of spacing between plates in response to acoustical pressure, thus turning audio signals to variations in capacitance. On the other hand, a capacitive level indicator makes use of the changes in the relative permittivity between the plates.

However, capacitive sensors are best known to be applicable with displacement measurements for rotational or translational motions, as will be described in this chapter. Other applications of capacitance sensors such as humidity and moisture will also be discussed.

25.1.1 Basic Principles of Capacitive Displacement Sensors

The measurement of distances or displacements is an important aspect of many industrial, scientific, and engineering systems. The displacement is basically the vector representing a change in the position of a body or point with respect to a reference point. Capacitive displacement sensors satisfy the requirements of many applications where high linearity and wide ranges (from a few centimeters to a couple of nanometers) are needed.

The basic sensing element of a typical displacement sensor consists of two parallel electrodes with capacitance C. The capacitance is a function of the distance d (cm) between the electrodes, the surface area A (cm^2) of the electrodes, and the permittivity ε (8.85×10^{-12} F m^{-1} for air) of the dielectric between the electrodes; therefore,

$$C = f(d, A, \varepsilon) \tag{25.1}$$

There are three basic methods for realizing a capacitive displacement sensor, that is, by varying d, or A, or ε, as discussed in the following.

25.2 Variable Distance Displacement Sensors

A capacitor displacement sensor, made from two flat coplanar plates with a variable distance x apart, is illustrated in Figure 25.1. Ignoring fringe effects, the capacitance of this arrangement can be expressed by

$$C(x) = \frac{\varepsilon A}{x} = \frac{\varepsilon_r \varepsilon_0 A}{x} \tag{25.2}$$

where

ε is the dielectric constant or permittivity
ε_r is the relative dielectric constant (in air and vacuum $\varepsilon_r \approx 1$)
ε_0 is 8.854188×10^{-12} F m^{-1}, the dielectric constant of vacuum
x is the distance of the plates in m
A is the effective area of the plates in m^2

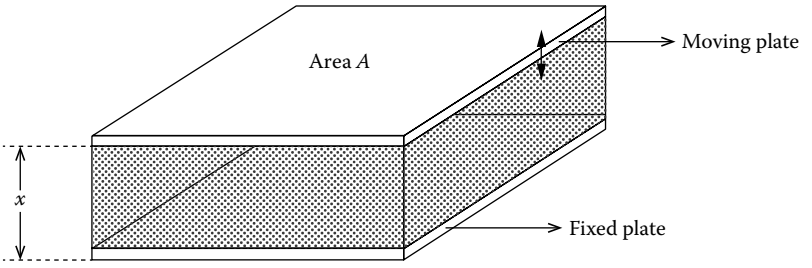

FIGURE 25.1 A variable distance capacitive displacement sensor. One of the plates of the capacitor moves to vary the distance between plates in response to changes in a physical variable. Generally, the outputs of these sensors are nonlinear with respect to displacement of an x having a hyperbolic transfer function characteristic. Appropriate signal processing must be employed for linearization.

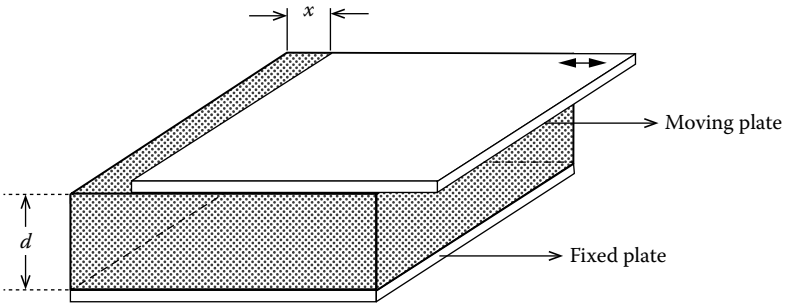

FIGURE 25.2 A variable area capacitive displacement sensor. The sensor operates on the variation in the effective area between plates of a flat-plate capacitor. The transducer output is linear with respect to displacement x. This type of sensor is normally implemented as a rotating capacitor for measuring angular displacements.

The capacitance of this transducer is nonlinear with respect to distance x, having a hyperbolic transfer function characteristic. The sensitivity of capacitance to changes in plate separation is

$$\frac{dC}{dx} = \frac{-\varepsilon_r \varepsilon_0 A}{x^2} \tag{25.3}$$

Equation 25.3 indicates that the sensitivity increases as x decreases. Nevertheless, from Equations 25.2 and 25.3, it follows that the percent change in C is proportional to the percent change in x. This can be expressed as

$$\frac{dC}{C} = \frac{-dx}{x} \tag{25.4}$$

This type of sensor is often used for measuring small incremental displacements without making contact with the object.

25.3 Variable Area Displacement Sensors

Alternatively, the displacements may be sensed by varying the surface area of the electrodes of a flat-plate capacitor, as illustrated in Figure 25.2. In this case, the capacitance would be

$$C = \frac{\varepsilon_r \varepsilon_0 (A - wx)}{d} \tag{25.5}$$

where

w is the width

wx is the reduction in the area due to movement of the plate

Then, the transducer output is linear with displacement x. This type of sensor is normally implemented as a rotating capacitor for measuring angular displacement. The rotating capacitor structures are also used as an output transducer for measuring electric voltages as capacitive voltmeters.

25.4 Variable Dielectric Displacement Sensors

In some cases, the displacement may be sensed by the relative movement of the dielectric material between the plates, as shown in Figure 25.3. The corresponding equations would be

$$C = \varepsilon_0 w[\varepsilon_2 l - (\varepsilon_2 - \varepsilon_1)x] \tag{25.6}$$

where

ε_1 is the relative permittivity of the dielectric material

ε_2 is the permittivity of the displacing material (e.g., liquid)

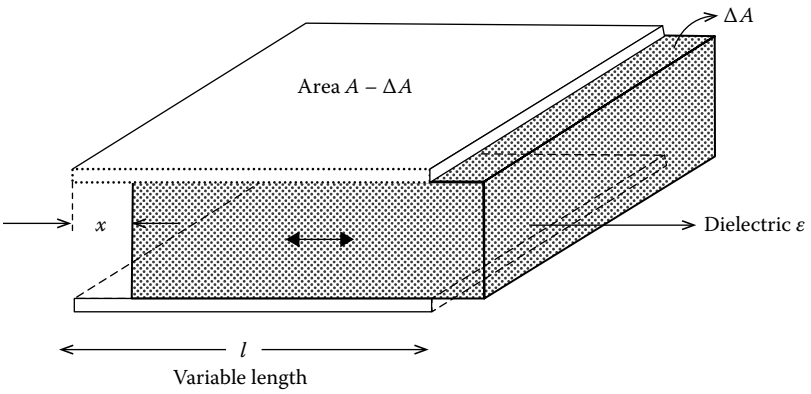

FIGURE 25.3 A variable dielectric capacitive displacement sensor. The dielectric material between the two parallel plate capacitors moves, varying the effective dielectric constant. The output of the sensor is linear.

In this case, the output of the transducer is also linear. This type of transducer is predominantly used in the form of two concentric cylinders for measuring the level of fluids in tanks. A nonconducting fluid forms the dielectric material. Further discussion will be included in the level measurements section.

25.5 Differential Capacitive Displacement Sensors

Some of the nonlinearity in capacitive sensors can be eliminated using differential capacitive arrangements. These sensors are three-terminal capacitors, as shown in Figure 25.4. Slight variations in the construction of these sensors find many different applications, including differential pressure measurements. In some versions, the central plate moves in response to physical variables with respect to the fixed plates. In others, the central plate is fixed and outer plates are allowed to move. The output from the center plate is zero at the central position and increases as it moves left or right. The range is equal to twice the separation d. For a displacement d, one obtains

$$2\delta C = C_1 - C_2 = \frac{\varepsilon_r \varepsilon_0 lw}{d - \delta d} - \frac{\varepsilon_r \varepsilon_0 lw}{d + \delta d} = \frac{2\varepsilon_r \varepsilon_0 lw \delta d}{d^2 + \delta d^2} \tag{25.7}$$

and

$$C_1 + C_2 = 2C = \frac{\varepsilon_r \varepsilon_0 lw}{d - \delta d} + \frac{\varepsilon_r \varepsilon_0 lw}{d + \delta d} = \frac{2\varepsilon_r \varepsilon_0 lwd}{d^2 + \delta d^2} \tag{25.8}$$

giving approximately

$$\frac{\delta C}{C} = \frac{\delta d}{d} \tag{25.9}$$

This indicates that the response of the device is linear compared to the response of the two-plate counterparts. However, in practice, some nonlinearity is still observed due to structural defects. Therefore, the outputs of these types of sensors still need to be treated carefully, as explained in the Section 25.11.

In some differential capacitive sensors, the two spherical depressions are ground into glass disks; then, these are gold plated to form the fixed plates of a differential capacitor. A thin, stainless-steel diaphragm is clamped between the disks and serves as a movable plate. With equal pressure applied to both ports,

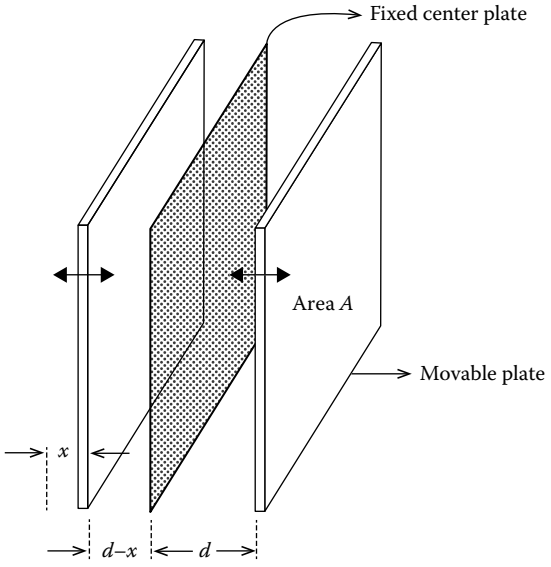

FIGURE 25.4 A differential capacitive sensor. They are essentially three-terminal capacitors with one fixed center plate and two outer plates. The response to physical variables is linear. In some versions, the central plate moves in response to physical variable with respect to two outer plates, and in others, the central plate is fixed and the outer plates are allowed to move.

the diaphragm is then in neutral position and the output is balanced at an electrical bridge. If the pressure on one side is greater than on the other side, the diaphragm deflects proportionally, thus giving an output due to the pressure difference. For the reverse pressure difference, there is a phase change of 180°. A direction-sensitive DC output voltage can be obtained by conventional phase-sensitive demodulation and appropriate filtering. Details of signal processing are given at the end of this chapter. In general, the differential capacitors exhibit better linearity than the single-capacitor types as explained earlier.

25.6 Integrated Circuit Smart Capacitive Displacement Sensors

Figure 25.5 shows a typical microstructure capacitive displacement sensor. The sensor consists of two electrodes with capacitance, C_x. Since the system is simple, the determination of the capacitance between the two electrodes is straightforward. The smaller electrode is surrounded by a guard electrode to make C_x

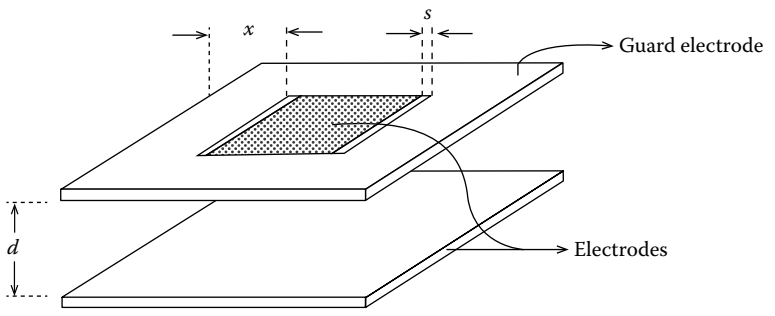

FIGURE 25.5 A typical smart capacitive position sensor. This type of microstructure position sensor contains three electrodes, two of which are fixed and the third electrode moves infinitesimally relative to the others. Although the response is highly nonlinear, the integrated chip contains linearization circuits. They feature a 0–1 mm measuring range with 1 μm accuracy.

independent of lateral and rotational movements of the system parallel to the electrode surface. However, the use of a guard electrode introduces relative deviations in the capacitance C_x between the two electrodes. This is partially true if the size of the guard electrode is smaller than

$$\delta < \exp\left(\frac{-\pi x}{d}\right) \tag{25.10}$$

where

x is the width of the guard
d is the distance between the electrodes

Since this deviation introduces nonlinearity, δ is required to be less than 100 part per million (ppm). Another form of deviation also exists between the small electrode and the surrounding guard, particularly for gaps:

$$\delta < \exp\left(\frac{-\pi d}{s}\right) \tag{25.11}$$

where s is the width of the gap. When the gap width, s, is less than 1/3 of the distance between electrodes, this deviation is negligible.

For signal processing, the system uses the three-signal concept. The capacitor C_x is connected to an inverting operational amplifier and oscillator. If the external movements are linear, by taking into account the parasitic capacitors and offsetting effects, the following equation can be written as

$$M_x = mC_x + M_{\text{off}} \tag{25.12}$$

where

m is the unknown gain
M_{off} is the unknown offset

By performing the measurement of a reference C_{ref}, by measuring the offset, M_{off}, and by making $m = 0$, the parameters m and M_{off} can be eliminated. The final measurement result for the position, P_{os}, can be defined as

$$P_{\text{os}} = \frac{M_{\text{ref}} - M_{\text{off}}}{M_x - M_{\text{off}}} \tag{25.13}$$

In this case, the sensor capacitance C_x can be simplified to

$$C_x = \frac{\varepsilon A_x}{d_0 + \Delta d} \tag{25.14}$$

where

A_x is the area of the electrode
d_0 is the initial distance between them
ε is the dielectric constant
Δd is the displacement to be measured

For the reference electrodes, the reference capacitance may be determined by

$$C_{\text{ref}} = \frac{\varepsilon A_{\text{ref}}}{d_{\text{ref}}} \tag{25.15}$$

with A_{ref} the area and d_{ref} the distance. Substitution of Equations 25.14 and 25.15 into Equations 25.12 and 25.13 yields

$$P_{\text{os}} = \frac{A_{\text{ref}}(d_0 + \Delta d)}{A_x d_{\text{ref}}} = a_1 \frac{\Delta d}{d_{\text{ref}}} + a_0 \tag{25.16}$$

P_{os} is a value representing the position if the stable constants a_1 and a_0 are unknown. The constant $a_1 = A_{\text{ref}}/A_x$ becomes a stable constant so long as there is good mechanical matching between the electrode areas. The constant $a_0 = (A_{\text{ref}}d_0)/(A_x d_{\text{ref}})$ is also a stable constant for fixed d_0 and d_{ref}. These constants are usually determined by calibrating repeatedly over a certain time span. In many applications, these calibrations are omitted if the displacement sensor is part of a larger system where an overall calibration is necessary. This overall calibration usually eliminates the requirement for a separate determination of a_1 and a_0.

The accuracy of this type of system could be as small as 1 μm over a 1 mm range. The total measuring time is better than 0.1 s. The capacitance range is from 1 pF to 50 fF.

25.7 Capacitive Pressure Sensors

A commonly used two-plate capacitive pressure sensor is made from one fixed metal plate and one flexible diaphragm, as shown in Figure 25.6. The flat circular diaphragm is clamped around its circumference and bent into a curved shape by an applied pressure *P*. The vertical displacement *y* of this system at any radius *r* is given by

$$y = \frac{3(1-\nu^2)(a^2 - r^2)\,P}{16\,Et^3} \tag{25.17}$$

where

a is the radius of diaphragm
t is the thickness of diaphragm
E is Young's modulus
ν is Poisson's ratio

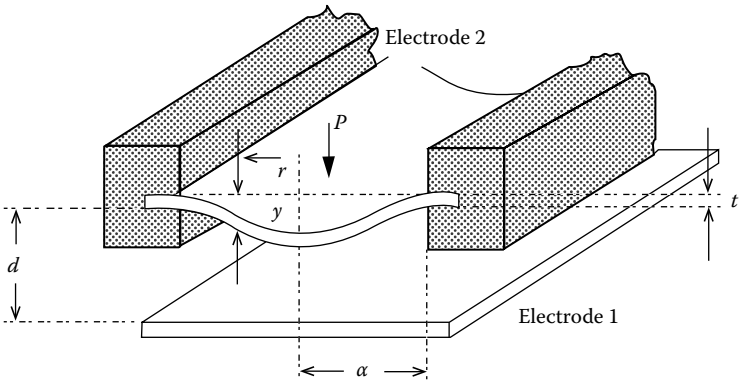

FIGURE 25.6 A capacitive pressure sensor. These pressure sensors are made from a fixed metal plate and a flexible diaphragm. The flat flexible diaphragm is clamped around its circumference. The bending of the flexible plate is proportional to the applied pressure *P*. The deformation of the diaphragm results in changes in capacitance.

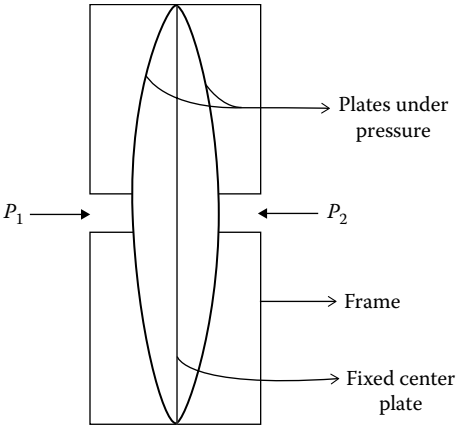

FIGURE 25.7 A differential capacitive pressure sensor. The capacitances C_1 and C_2 of the sensors change due to deformation of the outer plates, with respect to the fixed central plate, in response to the applied pressures P_1 and P_2.

Deformation of the diaphragm means that the average separation of the plates is reduced. Hence, the resulting increase in the capacitance ΔC can be calculated by

$$\frac{\Delta C}{C} = \frac{(1-\nu^2)a^4 P}{16Et^3} \tag{25.18}$$

where
d is the initial separation of the plates
C is the capacitance at zero pressure

Another type of sensor is the differential capacitance pressure sensor shown in Figure 25.7. The capacitances C_1 and C_2 of the sensor change with respect to the fixed central plate in response to the applied pressures P_1 and P_2. Hence, the output of the sensor is proportional to $(P_1 - P_2)$. The signals are processed using one of the techniques described in Section 25.11.

25.8 Capacitive Accelerometers and Force Transducers

Acceleration is the rate of change in velocity and the velocity is the rate or change in distance. As explained earlier, capacitive devices are commonly used in displacement measurements, and hence, they can be configured for acceleration measurement too. In recent years, capacitive-type micromachined accelerometers, as illustrated in Figure 25.8, are commonly used. These accelerometers are arranged such that a proof mass forms one of the plates of the capacitor and the other plate fixed as the base. When the sensor is accelerated, the proof mass moves altering the distance between itself and the base plate; thus, the capacitance changes. This change in capacitance corresponds to the applied acceleration.

In Figure 25.8, let $F(x)$ be the positive force in the direction in which x increases. Neglecting all losses (due to friction, resistance, etc.), the energy balance of the system can be written for an infinitesimally small displacement dx, electrical energy dE_e, and field energy dE_f of the electrical field between the electrodes as

$$dE_m + dE_c = dE_f \tag{25.19}$$

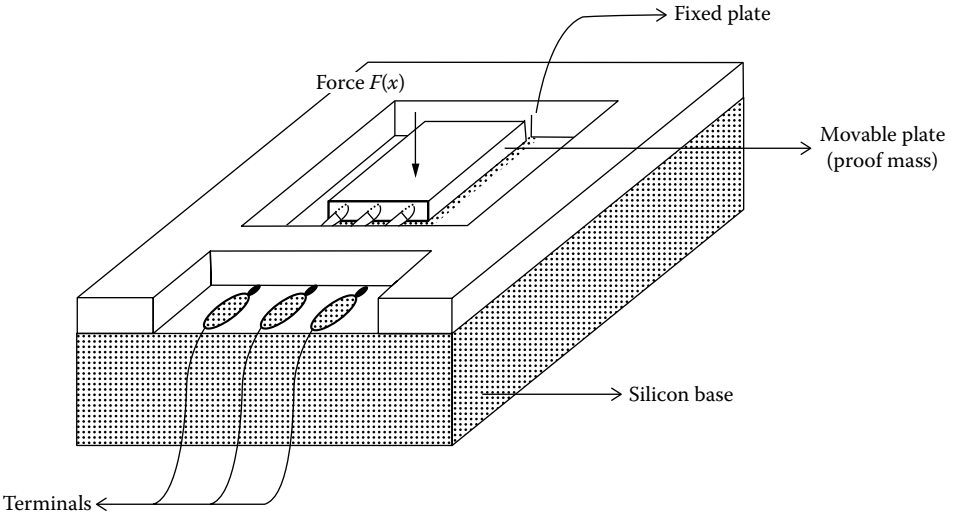

FIGURE 25.8 A capacitive force transducer. A typical capacitive micromachined accelerometer has one of the plates as the proof mass. The other plate is fixed, thus forming the base. When the sensor is accelerated, the proof mass tends to move, thus varying the distance between the two plates and altering the voltage across the capacitor. This change in voltage can be made directly proportional to the applied acceleration.

in which

$$dE_m = F(x)\ dx \tag{25.20}$$

Also,

$$dE_m = d(QV) = Q\ dV + V\ dQ \tag{25.21}$$

If the supply voltage V across the capacitor is kept constant, it follows that $dV = 0$. Since $Q = VC(x)$, the Coulomb force is given by

$$F(x) = -V^2 \frac{dC(x)}{dx} \tag{25.22}$$

Thus, if the movable electrode has complete freedom of motion, it will have assumed a position in which the capacitance is maximal; also, if C is a linear function of x, the force $F(x)$ becomes independent of x.

Capacitive silicon accelerometers are available in a wide range of specifications. A typical lightweight sensor will have a frequency range of 0–1000 Hz and a dynamic range of acceleration of ±2 g to ±500 g.

25.9 Capacitive Liquid-Level Measurement

The level of a nonconducting liquid can be determined by capacitive techniques. The method is generally based on the difference between the dielectric constant of the liquid and that of the gas or air above it. This is similar to variable dielectric displacement sensors as explained earlier. In capacitive liquid-level measurements, two concentric metal cylinders are used, as shown in Figure 25.9. The height of the liquid, h, is measured relative to the total height, l. An appropriate provision is made to ensure that the space between the cylindrical electrodes is filled by the liquid to the same height as the rest of the container.

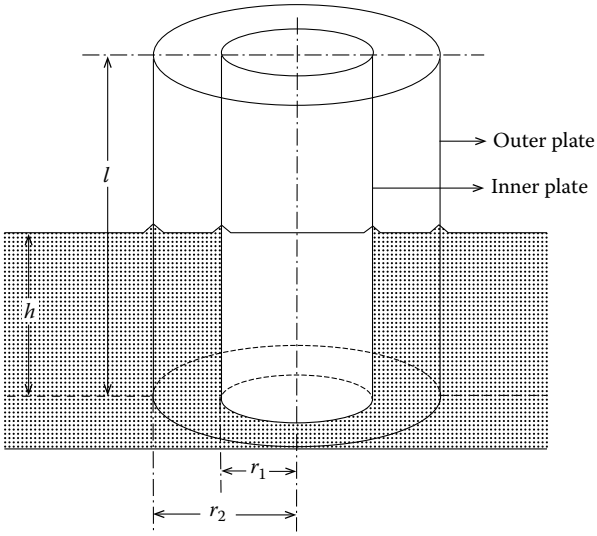

FIGURE 25.9 A capacitive liquid-level sensor. Two concentric metal cylinders are used as electrodes of a capacitor. The value of the capacitance depends on the permittivity of the liquid and that of the gas or air above it. The total permittivity changes depending on the liquid level. These devices are usually applied in nonconducting liquid applications.

The usual operational conditions dictate that the spacing between the electrodes, $s = r_2 - r_1$, should be much less than the radius of the inner electrode, r_1. Furthermore, the tank height should be much greater than r_2. When these conditions apply, the capacitance can be approximated by

$$C = \frac{\varepsilon_1(1) + \varepsilon_g(h-1)}{4.6\log\left[1-(s/r)\right]} \tag{25.23}$$

where ε_1 and ε_g are the dielectric constants of the liquid and gas (or air), respectively. The denominator of the earlier equation contains only terms that relate to the fixed system. Therefore, they become a single constant. A typical application is the measurement of the amount of gasoline in a tank in airplanes. The dielectric constant for most compounds commonly found in gasoline is approximately equal to 2, while that of air is approximately unity. A linear change in capacitance with gasoline level is expected for this situation. Quite high accuracy can be achieved if the denominator is kept quite small, thus accentuating the level differences. These sensors often incorporate an AC deflection bridge for signal processing.

25.10 Capacitive Humidity and Moisture Sensors

Capacitive humidity and moisture sensors are mostly based on the changes in the permittivity of the dielectric material, in principle, similar to variable dielectric displacement sensors explained previously. The permittivity of atmospheric air, some gases, and many solid materials are functions of their moisture contents and their temperature. The main disadvantage of this type of sensor is that a relatively small change in humidity results in a large change in capacitance sufficient enough for a sensitive detection.

Capacitive humidity sensors enjoy wide dynamic ranges, from 0.1 ppm to saturation points. They can function in saturated environments for long periods of time, a characteristic that would adversely affect many other humidity sensors. Their ability to function accurately and reliably extends over a wide range

of temperatures and pressures. Capacitive humidity sensors also exhibit low hysteresis and high stability with minimal maintenance requirements. These features make them viable for many specific operating conditions and ideally suitable for a system where uncertainty of unaccounted conditions exists during operations.

There are many types of capacitive humidity sensors. In here, aluminum, tantalum, silicon, and polymer types are introduced.

25.10.1 Aluminum Capacitive Humidity Sensors

The majority of capacitive humidity sensors are based on aluminum oxide-type dielectric material. In these types of sensors, high-purity aluminum is chemically oxidized to produce a prefilled insulating layer of partially hydrated aluminum oxide, which acts as the dielectric. A water-permeable but conductive gold film is deposited onto the oxide layer, usually by vacuum deposition, which forms the second electrode of the capacitor.

In another type, the aluminum–aluminum oxide sensor has a pore structure as illustrated in Figure 25.10. The oxide, with its pore structure, forms the active sensing material. Moisture in the air reaching the pores reduces the resistance and increases the capacitance. The decreased resistance can be thought of as being due to an increase in the conduction through the oxide. An increase in capacitance can be viewed due to an increase in the dielectric constant. The quantity measured can be either resistance or capacitance or impedance. High humidity is best measured by capacitance because resistance changes are vanishingly small at high levels.

In addition to the kind of transducer design illustrated in Figure 25.10, there are many others available with a number of substantial modifications due to their particular properties, such as the increased

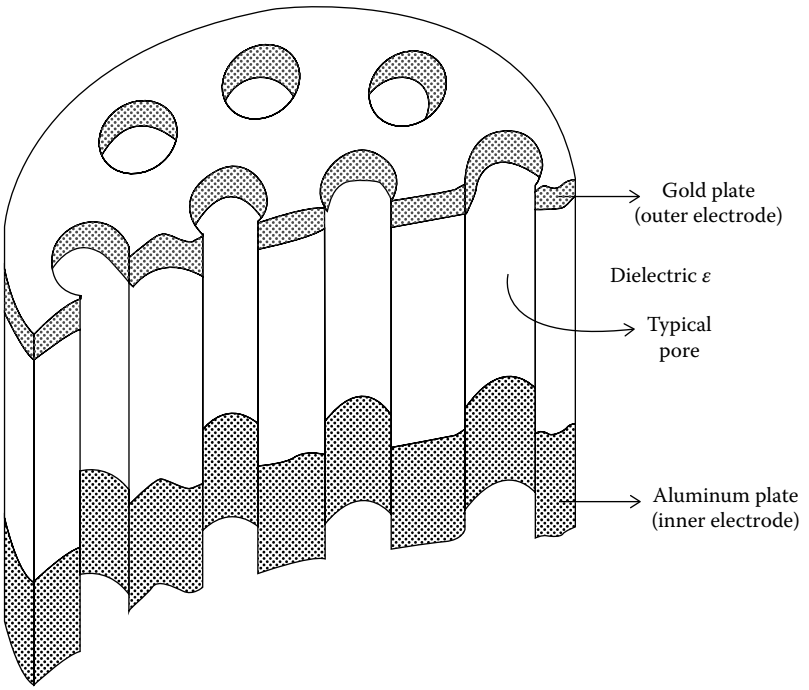

FIGURE 25.10 A typical capacitive humidity sensor. The sensors have pore or cracked mosaic structure for the moisture in air or gas to reach the dielectric material. The characteristics of the dielectric material change with the amount of water absorbed, thus reducing the resistance and increasing the capacitance. The quantity measured can be either the resistance or the capacitance or the impedance.

sensitivity and/or the faster response. Although most of these modifications can result in a change in physical dimensions or appearance, the basic sensing material—the aluminum oxide—remains the same.

In some versions, the oxide layer is formed by parallel tubular pores that are hexagonally packed and perpendicular to the plane of the base layer. These pores stop just before the aluminum layer, forming a very thin pore base. Water absorbed in these tubules is directly related to the moisture content of the gas in contact with it. The porous nature of the oxide layer produces a large area for the absorption of water vapor. At low humidity, the capacitance is due entirely to the mixed dielectric formed between the oxide, water vapor, and air. However, at higher humidity, parallel conductance paths through the absorbed water are formed down the pore surfaces. Near saturation, this pore surface resistance becomes negligible, implying that the measured capacitance is virtually in between the very thin pore base and the aluminum core.

25.10.2 Tantalum Capacitive Humidity Sensors

In some versions of capacitive humidity sensors, one of the capacitor plates consists of a layer of tantalum deposited on a glass substrate. A layer of polymer dielectric is then added, followed by a second plate made from a thin layer of chromium. The chromium layer is under high tensile stress such that it cracks into a fine mosaic structure that allows water molecules to penetrate inside the dielectric material. The stress in the chromium also causes the polymer to crack into a mosaic structure. A sensor of this type has an input range of 0%–100% relative humidity (RH). The capacitance is 375 pF at 0% RH and a linear sensitivity of 1.7 pF per% RH. The error is usually less than 2% due to nonlinearity and 1% due to hysteresis.

25.10.3 Silicon Capacitive Humidity Sensors

In some capacitive humidity sensors, silicon is used as the dielectric. The structure and operation of silicon humidity sensors are very similar to the aluminum oxide types. Some silicon-type humidity sensors also use the aluminum base and a thin-film gold layer as the two electrodes. The silicon dielectric has a very large surface area, which means that the sensitivity is still relatively large even if the sensing area is very small. This is an important feature with the increasing chances of miniaturization. Both sensor types are now typically found as extremely small wafer-shaped elements, placed on a mechanical mount with connecting lead wires. The formation of porous silicon is a very simple anodization process, and since no elaborate equipment is needed, devices can be made relatively at low costs. Also, by controlling the formation conditions, the structure of the porous silicon can easily be modified so devices can be tailored to suit particular applications.

In both the silicon and the aluminum oxide capacitive humidity sensors, the radii of the pores in the dielectric are such that they are specifically suited for water molecules. Most possible contaminants are too large in size to pollute the dielectric. However, contaminants can block the flow of water vapor into the sensor material, thus affecting the accuracy of the sensor. For example, in dust-contaminated streams, it may be possible to provide a simple physical barrier such as a sintered metal or plastic hood for the sensor heads. Many sensors come with specially designed casings to provide protection.

25.10.4 Polymer Capacitive Humidity Sensors

In some sensors, the dielectric consists of a polymer material that can absorb water molecules. The absorption of water vapor of the material results in changes in the dielectric constant of the capacitor. By careful design, the capacitance can be made directly proportional to percentage RH of the surrounding gas or atmosphere.

In general, an important key feature of capacitive humidity sensors is the chemical stability. Often, humidity sensing is required in an air sample that contains vapor contaminants (e.g., carbon monoxide) or the measurements are performed on a gas sample other than air (e.g., vaporized benzene). The performance of these sensors, and in particular the silicon types, is not affected by many of these gases. Hydrocarbons, carbon dioxide, carbon monoxide, and CFCs do not cause interference. However, the ionic nature of the aluminum oxide dielectric makes it susceptible to certain highly polar, corrosive gases such as ammonia, sulfur trioxide, and chlorine. Silicon is inert; its stable nature means that these polar gases affect the sensor element to a far lesser degree.

25.10.5 Capacitive Moisture Sensors

Capacitive moisture measurements are based on the changes in the permittivity of granular- or powder-type dielectric materials such as wheat and other grains containing water. Usually, the sensor consists of a large cylindrical chamber (e.g., 150 mm deep and 100 mm in diameter), as shown in Figure 25.11. The chamber is filled with samples under test. The variations in capacitance with respect to water content are processed. The capacitor is incorporated into an oscillatory circuit operating at a suitable frequency.

Capacitive moisture sensors must be calibrated if the samples are made from different materials, as the materials themselves demonstrate different permittivity and other properties. Accurate temperature is necessary as the dielectric constant may be highly dependent on temperature. Most of these devices are built to operate at temperature ranges of 0 °C–50 °C, supported by tight temperature compensation circuits. Once calibrated for a specific application, they are suitable for measuring moisture in the range of 0%–40%.

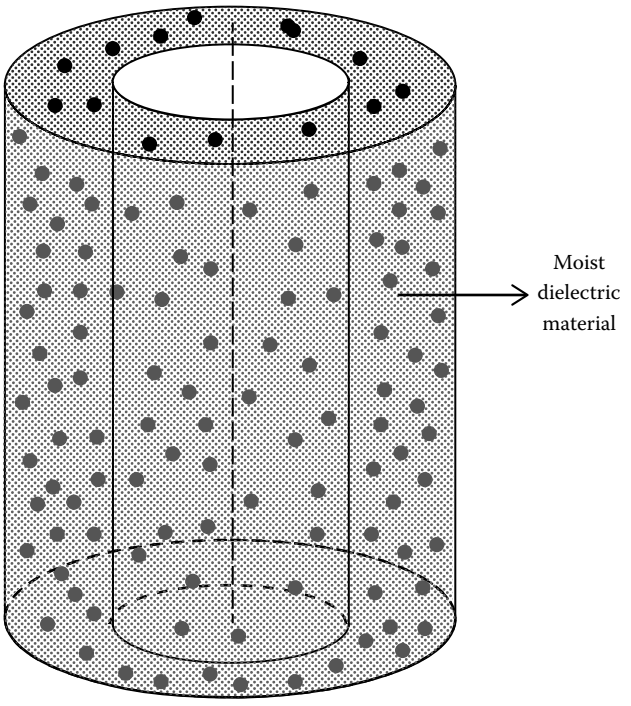

FIGURE 25.11 A capacitive moisture sensor. The permittivity of material between two cylindrical or parallel plates with fixed dimensions changes, depending on the moisture level of the material in the chamber. The variations in capacitance values with respect to water content are processed. The capacitor is incorporated as a part of an oscillatory circuit operating at a suitable frequency, usually at radio frequencies.

25.11 Signal Processing

Signal processing for capacitive sensors requires relatively complex circuitry in comparison to many other sensor types, but they have the advantage of mechanical simplicity. They have good sensitivity and range, exhibiting minimum mechanical loading effects. Capacitive sensors are usually incorporated either in some form of AC deflection bridges or oscillator circuits. In practice, capacitive sensors are not pure capacitances but have associated resistances representing losses in the dielectric. This can have an important influence in the design of the associated circuits, particularly in oscillator circuits. A number of the signal processing circuits are discussed in the following.

25.11.1 Operational Amplifier and Charge Amplifier-Based Circuits

An effective method of eliminating the nonlinearity of the relationship between the physical variable (e.g., two-plate displacement sensors) and capacitance, C, is by the use of operational amplifiers. An example of such circuits is illustrated in Figure 25.12. In this circuit, if the input impedance of the operational amplifier is high, the output is not saturated, and the input voltage is small, it is possible to write

$$\frac{1}{C_f} = \int i_f \, dt = e_{ex} - e_{ai} = e_{ex} \tag{25.24}$$

$$\frac{1}{C_x} = \int i_x \, dt = e_0 - e_{ai} = e_0 \tag{25.25}$$

$$i_f + i_x - i_{ai} = 0 = i_f + i_x \tag{25.26}$$

Manipulation of these equations yields to

$$e_0 = \frac{-C_f e_{ex}}{C_x} \tag{25.27}$$

Substituting the value of C_x gives

$$e_0 = \frac{-C_f x e_{ex}}{\varepsilon A} \tag{25.28}$$

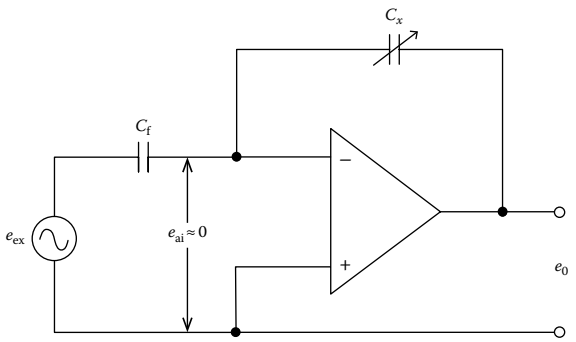

FIGURE 25.12 An operational amplifier signal processor. This method is useful to eliminate the nonlinearity in the signals generated by capacitive sensors. By this type of arrangement, the output voltage can be made directly proportional to variations in the signal representing the nonlinear operation of the device.

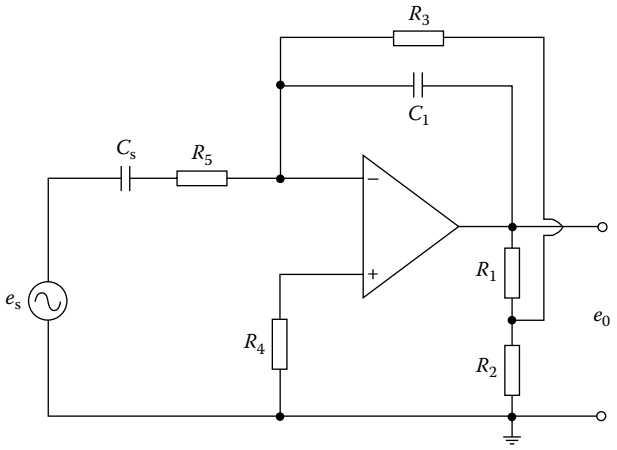

FIGURE 25.13 A practical charge amplifier. The effective feedback resistance is a function of other resistances. It is possible to reduce the output drift substantially by selecting the resistors suitably. The accuracy of this circuit can be improved further by cascading two or more amplifiers, thereby substantially improving the signal-to-noise ratio.

Equation 25.28 shows that the output voltage is directly proportional to the plate separation x, thus resulting in the linearity for all variations in the motion under measurement.

However, a practical circuit requires a resistance across C_f to limit drift in the output. The value of this resistance must be greater than the impedance of C_f at the lowest frequency of interest. Also, because the sensor impedance is assumed to be purely capacitive, the effective gain becomes independent of the frequency.

A practical charge amplifier circuit is depicted in Figure 25.13. In this case, the effective feedback resistance R_{ef} is given by

$$R_{ef} = \frac{R_3(R_1 + R_2)}{R_2} \tag{25.29}$$

It is possible to reduce the output drift substantially by the suitable selection of the resistors. The accuracy of this circuit can be improved substantially by cascading two or more amplifiers. In this way, a good improvement in the signal-to-noise ratio can be achieved. In the inverting input, the use of resistor R_4 is necessary because of the bias currents.

25.11.2 Pulse Width Modulation

As in the case of some capacitive vibration and displacement sensors, the output voltage may be in amplitude-modulated waveform, as shown in Figure 25.14. When rectified, the average value of this wave gives the mean separation between the plates. The vibration amplitude around this mean may be extracted by the use of a demodulator and a low-pass filter circuit. Then the output of the low-pass filter becomes a direct indication of the vibration, and the waveform can also be viewed on an oscilloscope.

25.11.3 Square-Wave Linearization

Another linearization technique applied in capacitive pressure sensors and accelerometers is the pulse width modulation. The sensor consists of two differential capacitors as shown in Figure 25.15. The voltages of these capacitors, e_1 and e_2, switch back and forth with a high excitation frequency (e.g., 400 kHz) between excitation voltage and ground. The system is arranged in such a way that the output voltage is

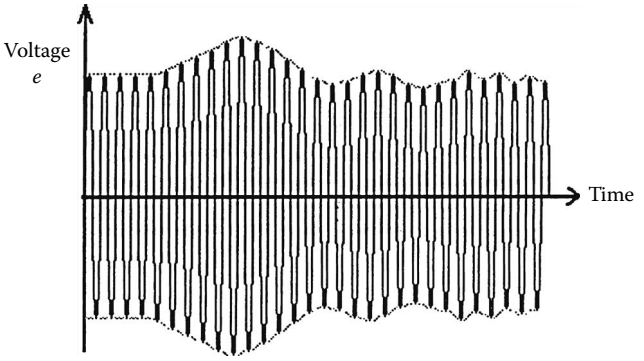

FIGURE 25.14 An amplitude-modulated signal. It is possible to configure some sensors to give amplitude-modulated signals, as in the case of capacitive vibration displacement sensors. When rectified, the average value of this wave gives the mean separation of the plates. The vibration amplitude around this mean position can be extracted by a demodulator and low-pass filter circuit. The output of the low-pass filter is a direct indication of the vibrations.

the average voltage difference between e_1 and e_2. At null position, $e_1 = e_2$, the output is a symmetrical square wave with zero average value. As the relative positions of the plates change, due to vibration, the average value of the output voltage shifts from the zero average value and becomes positive or negative depending on the direction of the displacement. The output voltage can be expressed by

$$e_o = \frac{e_{ex}(C_1 - C_2)}{C_1 + C_2} \tag{25.30}$$

Substituting

$$C_1 = \frac{C_0 x_0}{x_0 - x_i} \quad \text{and} \quad C_2 = \frac{C_0 x_0}{x_0 + x_i}$$

yields

$$e_o = \frac{e_{ex} x_i}{x_0} \tag{25.31}$$

Thus, the output is directly proportional to the variable x_i.

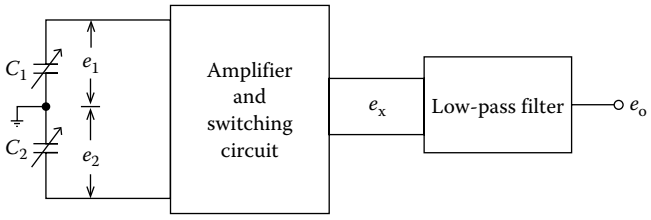

FIGURE 25.15 Block diagram of a square-wave linearization circuit. This is particularly useful for differential capacitance-type sensors. The voltages of these two capacitors are made to switch back and forth with a high excitation frequency between excitation voltage and ground. As the relative positions of the plates change due to vibration, the average value of the output voltage becomes positive or negative, depending on the direction of the displacement.

25.11.4 Feedback Linearization

Linearization of a capacitive sensor can also be obtained using a feedback system that adjusts capacitor current amplitude so that it stays constant at a reference value for all displacements. This is accomplished by obtaining a DC signal proportional to capacitor current from a demodulator, comparing this current with the reference current, and adjusting the voltage amplitude of the system excitation oscillator until the two currents agree. If the capacitor current is kept constant irrespective of the motion, then the voltage amplitude is linearly related to x as

$$e = Kx_i \tag{25.32}$$

where

$$K = \frac{|i_c|}{\omega C_0 x_0} \tag{25.33}$$

25.11.5 Oscillator Circuits

In many applications, the resultant changes in the capacitance of capacitive transducers can be measured with a suitable AC bridge such as Wein bridge or Schering bridge. However, in majority of cases, improvised versions of bridges are used as oscillator circuits for signal processing. The transducer is configured as a part of the oscillatory circuit that causes changes in the frequency of the oscillations. This change in frequency is scaled to be a measure of the magnitude of the physical variable.

As part of the oscillator circuits, the capacitive transducer has excellent frequency response and can measure both static and dynamic phenomena. Its disadvantages include sensitivity to temperature variations and the possibility of erratic or distorted signals due to long length of connection leads. Also, the receiving instrumentation may be large and complex, and it often includes a second fixed-frequency oscillator for heterodyning purposes. The difference frequency thus produced can be read by an appropriate output device such as an electronic counter.

Bibliography

Capacitive sensors—An overview, LION PRECISION, http://www.lionprecision.com/capacitive-sensors/index.html (accessed on September 9, 2011).

Capacitive sensors for noncontact position and displacement measurements and nano-positioning, ChenYang Technologies GmbH & Co. KG, http://www.chenyang-ism.com/CapaSensorPosi.htm (accessed on September 6, 2011).

Doebelin, E. O., *Measurement Systems: Application and Design*, 4th edn., New York, McGraw-Hill, 1990.

Eren, H., Displacement and angle sensors performance and selection, In *Handbook of Measuring and System Design*, P. Sydenham and R. Thorn (eds.), Wiley Online Library, 2005, http://onlinelibrary.wiley.com/book/10.1002/0471497398/homepage/EditorsContributors.html (accessed on September 4, 2011).

Hongshen, Ma., Capacitive displacement sensing for the nanogate, http://www.media.mit.edu/resenv/pubs/theses/HongMa-MSThesis.pdf (accessed on September 9, 2011).

Rhead, P. M., Patel, J., Atherton, P. D., Hicks, T. R., and McConnell, M., Capacitive displacement sensor—Design characterization of a long range, low noise non-contact, QUEENSGATE INTRUMENTS, http://www.azonano.com/article.aspx?ArticleID=1465 (accessed on August 30, 2011).

Xiaohui, H. and Wuqiang, Y., Planar capacitive sensors—Designs and applications, *Sensor Review*, 30(3), 24–39, 2010.

Yusof, N. B., Soin, N., and Dawal, S. Z. M., Capacitive interfacing for MEMS humidity and accelerometer sensors, *Proceedings of the IEEE International Conference for Technical Postgraduates*, Kuala Lumpur, Malaysia, Article 5412067, 2009.

Partial List of Manufacturers and Suppliers

AutomationDirect.com (AutomationDirect), 3505 Hutchinson Rd., Cumming, GA 30040-5860, Phone: 770-889-2858, 800-633-0405 (toll free), Fax: 770-889-7876, www.automationdirect.com

Automation Products Group, Inc. (APGSENSORS), 1025 W. 1700 N., Logan, UT 84321, Phone: 435-753-7300, 888-525-7300 (toll free), Fax: 435-753-7490, www.apgsensors.com

Autonics USA, 1353 Armour Blvd., Mundelein, IL 60060, Phone: 847-680-8160, 866-862-2602 (toll free), Fax: 847-680-8155, www.autonicsonline.com

Balluff, Inc., 8125 Holton Dr., Florence, KY 41042-0937, Phone: 859-727-2200, 800-543-8390 (toll free), Fax: 859-727-4823, www.balluff.com

Baumer Ltd., 122 Spring St., Suite C-6 Southington, CT 06489-1534, Phone: 860-621-2121, 800-937-9336 (toll free), Fax: 860-628-6280, www.baumerelectric.com

Capacitec, Inc., 87 Fitchburg Rd., P.O. Box 819 Ayer, MA 01432, Phone: 978-772-6033 Fax: 978-772-6036, www.capacitec.com

Custom Sensors & Technologies (CST), 14401 Princeton Ave., Moorpark, CA 93021-9707, Phone: 805-552-3599, Fax: 805-552-3577, www.cstsensors.com

Davis/Inotek, 1236 Mark St., Bensenville, IL 60106, Phone: 410-358-3900, 800-548-9409 (toll free), Fax: 410-358-0252, www.davis.com

EMRA Controls, Inc., 1502 Pike St., N.W. Suite 4B Auburn, WA 98001, Phone: 253-351-0292, 800-351-0293 (toll free), Fax: 253-804-2678, www.emracontrols.com

Fargo Controls, Inc., P.O. Box 539, Eatontown, NJ 07724, Phone: 732-389-3376, 800-241-3755 (toll free), Fax: 732-542-3553, www.fargocontrols.com

Honeywell Sensing and Control, 1985 Douglas Dr. North, MN10-192B Golden Valley, MN 55422, Phone: 763-954-4818, 800-446-6555 (toll free), www.honeywell.com/

IFM Efector, Inc., 782 Springdale Dr., Exton, PA 19341-2843, Phone: 610-524-2000, 800-441-8246 (toll free), Fax: 800-329-0436, www.ifm.com/ifmus/web/home.htm

Horizon Systems, Inc., 1101 Horizon Dr., Lawrence, KS 66046, Phone: 785-842-1299, Fax: 785-842-0181, www.horizonsystemsinc.com

ISSC-Kanson Electronics, Inc., 245 Forrest Ave., Hohenwald, TN 38462, Phone: 931-796-3050, 800-233-9354 (toll free), Fax: 931-796-3956, www.issc-kanson.com/

Leuze Electronic, Inc., 55395 Lyon Industrial Dr., New Hudson, MI 48165, Phone: 248-486-4466, Fax: 248-486-6699, www.leuzeusa.com

Lion Precision, Inc., 563 Shoreview Park Rd., Saint Paul, MN 55126-7014, Phone: 651-484-6544, 800-250-9297 (toll free), Fax: 651-484-6824, www.lionprecision.com

MicroSense, LLC, 70 Industrial Ave. E., Lowell, MA 01852, Phone: 978-843-7673, www.microsense.net

Maxcess, 2305 S.E. 8th Ave., Camas, WA 98607, Phone: 360-834-2345, Fax: 360-834-5865, www. maxcessintl.com

Measurement Specialties, Inc., 1000 Lucas Way, Hampton, VA 23666, Phone: 757-766-1500, 800-745-8008 (toll free), Fax: 757-766-4297, www.meas-spec.com

MicroEpsilon, 3200-110 Glen Royal Rd., Raleigh, NC 27617-7419, Phone: 919-787-9707, Fax: 919-787-9708, www.micro-epsilon.com

MKS Instruments, Inc., 2 Tech Dr., Suite 201 Andover, MA 01810, Phone: 978-645-5500, 800-227-8766 (toll free), Fax: 978-557-5100, www.mksinst.com

MTI Instruments, Inc., 325 Washington Ave., Extension Albany, NY 12205-5505, Phone: 518-218-2550, Fax: 518-218-2506, www.mtiinstruments.com

Pilz Automation Safety L.P., 7150 Commerce Blvd., Canton, MI 48187, Phone: 866-889-1726 (toll free), Fax: 734-354-3355, www.pilz.us/index.jsp

RDP Electrosense, Inc., 2216 Pottstown Pike, Pottstown, PA 19465, Phone: 610-469-0850, 800-334-5838 (toll free), Fax: 610-469-0852, www.rdpe.com

Schneider Electric-Hyde Park, 1875 Founders Dr., Dayton, OH 45420, Phone: 937-514-7207, Fax: 937-258-5830, www.sesensors.com

SICK, Inc., 6900 W. 110th St., Bloomington, MN 55438, Phone: 952-941-6780, 800-325-7425 (toll free), Fax: 952-941-9287, www.sick.com/us/en-us/home/Pages/Homepag…

TR Electronic, P.O. Box 2543, Station B, London, ON N6A4G9, Phone: 800-265-9483 (toll free), Fax: 519-452-1177, www.trelectronic.com

Turck, Inc., 3000 Campus Dr., Plymouth, MN 55441-2619, Phone: 763-553-7300, 800-554-4989 (toll free), Fax: 763-553-0708, www.turck.com

Vaisala, Inc., 10-D Gill St., Woburn, MA 01801-1068, Phone: 781-933-4500, 888-824-7252 (toll free), Fax: 781-933-8029, www.vaisala.com/en/lifesciencehightech/p…

26

Piezoelectric Sensors and Transducers

Ahmad Safari
Rutgers University

Victor F. Janas
Rutgers University

Amit Bandyopadhyay
Rutgers University

Andrei Kholkine
Rutgers University

Piezoelectricity, discovered in Rochelle salt in 1880 by Jacques and Pierre Curie, is the term used to describe the ability of certain materials to develop an electric charge that is proportional to a direct applied mechanical stress. These materials also show the converse effect; that is, they will deform (strain) proportionally to an applied electric field. Some crystalline materials show piezoelectric behavior due to their unique crystal structure. The lattice structure of a crystal is described by the Bravais unit cell [1]. There are 230 microscopic symmetry types (space groups) in nature, based on the several symmetry elements such as translation, inversion center, mirror plane, or rotation axes. The combinations of these symmetry elements yield the macroscopic symmetry known as point groups. All natural crystals can be grouped into 32 different classes (point groups) based on their symmetry elements. The 32 point groups can be further classified into two subgroups: (1) crystals with a center of symmetry and (2) crystals with no center of symmetry. The 11 centrosymmetric subgroups do not show piezoelectricity. Of the 21 non-centrosymmetric groups, 20 show the piezoelectric effect along unique directional axes. An important class of piezoelectric materials includes ferroelectrics, in which the piezoelectric effect is closely related to the ferroelectric polarization that can be reversed by the application of sufficiently high electric field [2,3]. To induce piezoelectric properties in ferroelectric materials, a poling procedure is often required, which consists of the temporary application of a strong electric field. Poling is analogous to the magnetizing of a permanent magnet.

26.1 Governing Equations and Coefficients

The phenomenological master equation describing the deformations of an insulating crystal subject to both elastic and electric stresses is given by

$$x_{ij} = si_{ijkl}X_{kl} + d_{mij}E_m + M_{mnij}E_mE_n \tag{26.1}$$

where

x_{ij} are the components of elastic strain
s_{ijkl} is the elastic compliance tensor
X_{kl} are the stress components
d_{mij} are the piezoelectric tensor components
M_{mnij} is the electrostrictive tensor
E_m and E_n are the components of the electric field

Neglecting the second-order effects (electrostriction) and assuming that the material is under no stress ($X_{kl} = 0$), the elastic strain is given by

$$x_{ij} = d_{mij}E_m \tag{26.2}$$

Equation 26.2 is the mathematical definition of the converse piezoelectric effect, where induced strain is directly proportional to the first power of the field. The thermodynamically equivalent direct piezoelectric effect is given by

$$P_m = d_{mij}X_{ij} \tag{26.3}$$

where P_m is the component of electric polarization. The difference between the direct and the converse piezoelectric effect is shown schematically in Figure 26.1. The converse effect describes the actuating function of a piezoelectric, where a controlled electric field accurately changes the shape of a piezoelectric material. The sensing function of a piezoelectric is described by the direct effect, where a controlled stress on a piezoelectric material yields a charge proportional to the stress.

The third-rank tensor d_{mij} may be simplified using matrix notation [1] to d_{ij}, a second-rank tensor. In this form, d_{ij} is simply known as the piezoelectric charge coefficient, with units of coulombs per newton (C N^{-1}) or meters per volt (m V^{-1}). Another set of moduli that may be used to characterize piezoelectric materials are the piezoelectric voltage coefficients, g_{ij}, defined in matrix notation as

$$E_i = g_{ij}X_j \tag{26.4}$$

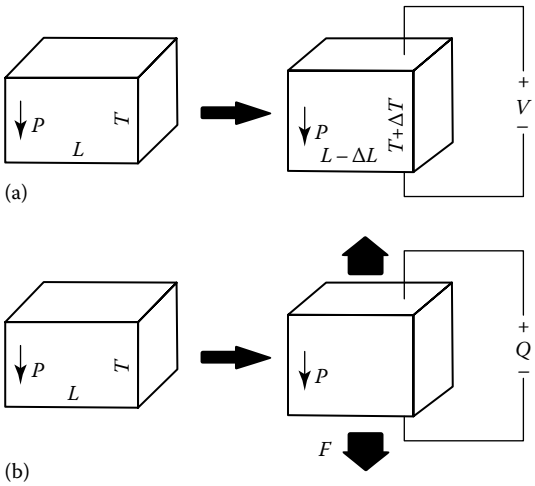

FIGURE 26.1 Schematic representations of the direct and converse piezoelectric effect: (a) An electric field applied to the material changes its shape, (b) a stress on the material yields a surface charge.

where E_i is the component of electric field arising due to the stress X_j. The d_{ij} and g_{ij} coefficients are related by

$$g_{ij} = \frac{d_{ij}}{\varepsilon_0 \varepsilon_{ii}} \tag{26.5}$$

where
ε_{ii} is the dielectric constant (relative permittivity)
ε_0 is the permittivity of free space (8.854×10^{-12} F m^{-1})

Another key property of piezoelectric materials is their electromechanical coupling coefficient k, defined as

$$k^2 = \frac{\text{Resulting mechanical energy}}{\text{Input electrical energy}} \tag{26.6}$$

or

$$k^2 = \frac{\text{Resulting electrical energy}}{\text{Input mechanical energy}} \tag{26.7}$$

The value of k represents the efficiency of the piezoelectric in converting one form of energy to another. Since energy conversion is never complete, the value of k^2 is always less than unity, so k is always less than 1.

Two final important parameters for piezoelectric (ferroelectric) materials are their Curie point (T_0) and Curie temperature (T_c). The Curie point is the temperature above which the material loses its ferroelectric and piezoelectric behavior. The Curie temperature is defined by the Curie–Weiss law:

$$\varepsilon = \varepsilon_0 + \frac{C}{T - T_c} \quad \text{for } T > T_c \tag{26.8}$$

where
ε is the dielectric constant of the material
C is the Curie–Weiss constant
T is the temperature

It represents the temperature where the material tends to have its highest dielectric constant. The Curie temperature is always lower (often within 10 °C) than the Curie point.

26.2 Piezoelectric Materials

26.2.1 Single Crystals

A number of single-crystal materials have demonstrated piezoelectricity. These materials dominate certain applications, such as frequency-stabilized oscillators in watches and radars and surface acoustic wave devices in television filters and analog signal correlators. A list of single-crystal piezoelectric materials includes quartz, lithium niobate and lithium tantalate, ammonium dihydrogen sulfate,

lithium sulfate monohydrate, and Rochelle salt. Recently, it was discovered that some relaxor-based ferroelectric single crystals of lead zinc niobate and lead magnesium niobate (PMN) and their solid solutions with lead titanate possess superior piezoelectric properties when compared to other piezoelectric materials.

Quartz, which is crystalline SiO_2, has a low value of d_{11} (12.3×10^{-12} C N^{-1}) [1]. The right-handed quartz develops a positive charge when put under compression and a negative charge when put under tension. The coupling coefficient k for quartz is also very low, typically around 0.1 [4]. In addition, the dielectric constant ε for quartz is small (~4) [5]. The Curie point, however, is relatively high ($T_0 \sim 573$ °C) [5], so quartz is stable for high-temperature applications. Despite the low piezoelectric properties, quartz is very abundant and inexpensive and has found a strong position in low-cost or high-temperature applications.

Piezoelectric behavior in lithium niobate ($LiNbO_3$) and lithium tantalate ($LiTaO_3$) was first studied in the mid-1960s [2]. Under shear, the d_{15} of $LiNbO_3$ and $LiTaO_3$ is 73 and 26 ($\times 10^{-12}$ C N^{-1}), respectively. Both have ε values of approximately 40. If cut correctly, they have coupling coefficient (k) values of 0.65 and 0.4, respectively. In addition, the Curie points for both are extremely high ($T_0 \sim 1210$ °C for $LiNbO_3$ and 620 °C for $LiTaO_3$). Both $LiNbO_3$ and $LiTaO_3$ are commonly used in infrared detectors.

Rochelle salt ($KNaC_4H_4O_6\ H_2O$) was first found to be piezoelectric in 1880 [2]. The d_{31} and k_{31} are 275×10^{-12} C N^{-1} and 0.65, respectively. The relative dielectric constant is approximately 350. Rochelle salt has two Curie points (lower $T_0 \sim 18$ °C and upper $T_0 \sim 24$ °C). It is highly soluble in water and is still extensively used in electroacoustic transducers.

Lead zinc niobate, $Pb(Zn_{1/3}Nb_{2/3})O_3$, and PMN, $Pb(Mg_{1/3}Nb_{2/3})O_3$, are typical relaxor materials characterized by the broad frequency-dependent maximum of dielectric constant versus temperature. The solid solutions of these materials with lead titanate, $PbTiO_3$, were shown to possess excellent piezoelectric properties when oriented along the [001] direction [6]. The piezoelectric charge coefficient d_{33} of 25×10^{-10} C N^{-1}, coupling coefficient k of more than 0.9, and the ultrahigh strain of 1.7% were achieved in $Pb(Zn_{1/3}Nb_{2/3})O_3$–$PbTiO_3$ solid solution. These single-crystal relaxor materials are now being intensively investigated and show great promise for future generations of piezoelectric transducers and sensors.

Other types of piezoelectric materials dominate the market for transducers. These materials include piezoelectric ceramics, piezoelectric polymers, and composites of piezoelectric ceramic with inactive polymers. The focus of the remainder of this chapter will be on non-single-crystal piezoelectric materials.

26.2.2 Piezoelectric Ceramics

In polycrystalline ceramics with polar grains, the randomness of the grains, as shown schematically in Figure 26.2a, yields a nonpiezoelectric material. The piezoelectric behavior is induced by "poling" the ceramic. By applying a strong dc electric field at a temperature just below the Curie temperature, the spontaneous

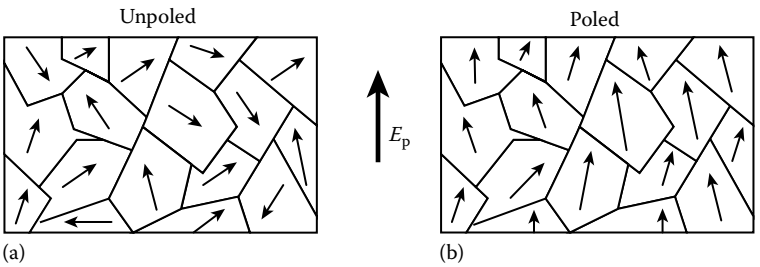

FIGURE 26.2 Schematic of the poling process in piezoelectric ceramics: (a) In the absence of an electric field, the domains have random orientation of polarization, (b) the polarization within the domains is aligned in the direction of the electric field.

polarization in each grain gets oriented toward the direction of the applied field. This is schematically shown in Figure 26.2b. Although all of the domains in a ceramic can never be fully aligned along the poling axis due to symmetry limitations, the ceramic ends up with a net polarization along the poling axis.

The largest class of piezoelectric ceramics is made up of mixed oxides containing corner-sharing octahedra of O^{2-} ions. The largest structure type, built with corner-shared oxygen octahedra, is the perovskite family, which is discussed in the following section.

26.2.3 Perovskites

Perovskite is the name given to a group of materials with general formula ABO_3 having the same structure as the mineral calcium titanate ($CaTiO_3$). Piezoelectric ceramics having this structure include barium titanate ($BaTiO_3$), lead titanate ($PbTiO_3$), lead zirconate titanate ($PbZr_xTi_{1-x}O_3$, or PZT), lead lanthanum zirconate titanate ($Pb_{1-x}La_x(Zr_yT_{1-y})_{1-x/4}O_3$, or PLZT), and PMN ($PbMg_{1/3}Nb_{2/3}O_3$). Several of these ceramics are discussed as follows.

The piezoelectric effect in $BaTiO_3$ was discovered in the 1940s [4], and it became the first piezoelectric ceramic developed. It replaced Rochelle salt because it is more stable, has a wider temperature range of operation, and is easily manufacturable. The Curie point, T_0, is about 130 °C. Above 130 °C, a nonpiezoelectric cubic phase is stable, where the center of positive charge (Ba^{2+} and Ti^{4+}) coincides with the center of the negative charge (O^{2-}) (Figure 26.3a). When cooled below the Curie point, a tetragonal structure (shown in Figure 26.3b) develops where the center of positive charge is displaced relative to the O^{2-} ions, leading to the formation of electric dipoles. Barium titanate has a relative dielectric constant ε_{33} of 1400 when unpoled and 1900 when poled [2,4]. The d_{15} and d_{33} coefficients of $BaTiO_3$ are 270 and 191 × 10^{-12} C N^{-1}, respectively. The k for $BaTiO_3$ is approximately 0.5. The large room temperature dielectric constant in barium titanate has led to its wide use in multilayer capacitor applications.

Lead titanate, $PbTiO_3$, first reported to be ferroelectric in 1950 [4], has a similar structure to $BaTiO_3$ but with a significantly higher Curie point (T_0 = 490 °C). Pure lead titanate is difficult to fabricate in bulk form. When cooled through the Curie point, the grains go through a cubic to tetragonal phase change, leading to large strain and ceramic fracturing. This spontaneous strain can be decreased by the addition of dopants such as Ca, Sr, Ba, Sn, and W. The calcium-doped $PbTiO_3$ [7] has a relative dielectric constant ε_{33} of 200, a d_{33} of 65 × 10^{-12} C N^{-1}, and a k of approximately 0.5. The addition of calcium results in a lowering of the Curie point to 225 °C. The main applications of lead titanate are hydrophones and sonobuoys.

PZT is a binary solid solution of $PbZrO_3$ (an antiferroelectric orthorhombic structure) and $PbTiO_3$ (a ferroelectric tetragonal perovskite structure) [2–4]. It has a perovskite structure, with the Zr^{4+} and Ti^{4+} ions occupying the B site of the ABO_3 structure at random. At the morphotropic phase

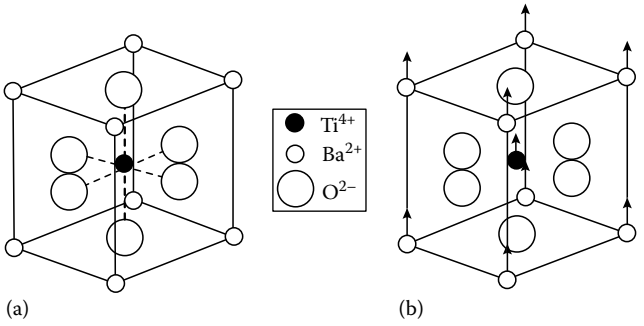

FIGURE 26.3 Crystal structure of $BaTiO_3$: (a) Above the Curie point, the cell is cubic; (b) below the Curie point, the cell is tetragonal with Ba^{2+} and Ti^{4+} ions displaced relative to O^{2-} ions.

boundary (MPB) separating the tetragonal and orthorhombic phases, PZT shows excellent piezoelectric properties. At room temperature, the MPB is at a Zr/Ti ratio of 52/48, resulting in a piezoelectric ceramic that is extremely easy to pole. Piezoelectric PZT at the MPB is usually doped by a variety of ions to form what are known as "hard" and "soft" PZTs. Hard PZT is doped with acceptor ions, such as K^+ or Na^+ at the A site or Fe^{3+}, Al^{3+}, or Mn^{3+} at the B site. This doping lowers the piezoelectric properties and makes the PZT more difficult to pole or de-pole. The typical piezoelectric properties of hard PZT include [5,7] a Curie point, T_0, of 365 °C; a ε_{33} of 1700–1750 (poled); a piezoelectric charge coefficient d_{33} of 360 to 370 × 10^{-12} C N^{-1}; and a coupling coefficient of about 0.7. Soft PZT is doped with donor ions such as La^{3+} at the A site or Nb^{5+} or Sb^{5+} at the B site. It has very high piezoelectric properties and is easy to pole or de-pole. The typical piezoelectric properties of soft PZT include [5,7] a Curie point, T_0, of 210 °C; a relative dielectric constant ε_{33} of 3200–3400 (poled); a d_{33} of 580 to 600 × 10^{-12} C N^{-1}; and a coupling coefficient k_{33} of 0.7.

26.2.4 Processing of Piezoelectric Ceramics

The electromechanical properties of piezoelectric ceramics are largely influenced by their processing conditions. Each step of the process must be carefully controlled to yield the best product. Figure 26.4 is a flowchart of a typical oxide manufacturing process for piezoelectric ceramics. The high-purity raw materials are accurately weighed according to their desired ratio and mechanically or chemically mixed. During the calcination step, the solid phases react to yield the piezoelectric phase. After calcining, the solid mixture is ground into fine particles by milling. Shaping is accomplished by a variety of ceramic processing techniques, including powder compaction, tape casting, slip casting, or extrusion. During the shaping operation, organic materials are typically added to the ceramic powder to improve its flow and binding characteristics. These organics are removed in a low-temperature (500 °C –600 °C) binder burn-off step.

After burnout, the ceramic structure is sintered to an optimum density at an elevated temperature. For the lead-containing piezoelectric ceramics ($PbTiO_3$, PZT, PLZT), sintering is performed in sealed crucibles with an optimized PbO atmosphere. This is because lead loss occurs in these ceramics above 800 °C. As mentioned earlier (Figure 26.2), the randomness of the ceramic grains yields a nonpiezoelectric material. By electroding the ceramic and applying a strong dc electric field at high temperature, the ceramic is poled. At this point, the piezoelectric ceramic is ready for final finishing and characterization.

26.2.5 Piezoelectric Polymers

The piezoelectric behavior of polymers was first reported in 1969 [8]. The behavior results from the crystalline regions formed in these polymers during solidification from the melt. When the polymer is drawn, or stretched, the regions become polar and can be poled by applying a high electric field. The most widely known piezoelectric polymers are polyvinylidene fluoride [9,10], also known as PVDF, PVDF—trifluoroethylene copolymer or P(VDF–TrFE) [9,10], and odd-number nylons, such as Nylon-11 [11].

The electromechanical properties of piezoelectric polymers are significantly lower than those of piezoelectric ceramics. The d_{33} values for PVDF and P(VDF–TrFE) are approximately 33 (× 10^{-12} C N^{-1}), and

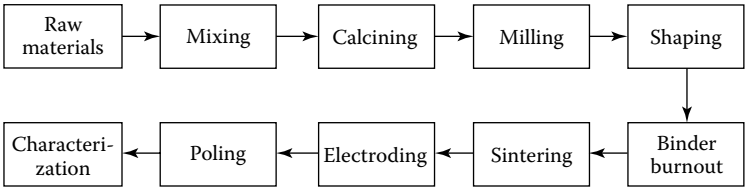

FIGURE 26.4 Flowchart for the processing of piezoelectric ceramics.

TABLE 26.1 Advantages (+) and Disadvantages (–) of Piezoelectric Ceramics, Polymers, and Composites

Parameter	Ceramic	Polymer	Ceramic/Polymer Composite
Acoustic impedance	High (–)	Low (+)	Low (+)
Coupling factor	High (+)	Low (–)	High (+)
Spurious modes	Many (–)	Few (+)	Few (+)
Dielectric constant	High (+)	Low (–)	Medium (+)
Flexibility	Stiff (–)	Flexible (+)	Flexible (+)
Cost	Cheap (+)	Expensive (–)	Medium (+)

Source: Adapted from Gururaja, T. R., *Am. Ceram. Soc. Bull.*, 73, 50, 1994.

the dielectric constant ε is in the range 6–12 [12,13]. They both have a coupling coefficient (k) of 0.20 and a Curie point (T_0) of approximately 100 °C. For Nylon-11, ε is around 2 [11], while k is approximately 0.11.

26.2.6 Piezoelectric Ceramic/Polymer Composites

As mentioned earlier, a number of single-crystal, ceramic, and polymer materials exhibit piezoelectric behavior. In addition to the monolithic materials, the composites of piezoelectric ceramics with polymers have also been formed. Table 26.1 [14] summarizes the advantages and disadvantages of each type of material. Ceramics are less expensive and easier to fabricate than polymers or composites. They also have relatively high dielectric constants and good electromechanical coupling. However, they have high acoustic impedance and are therefore a poor acoustic match to water, the media through which it is typically transmitting or receiving a signal. Also, since they are stiff and brittle, monolithic ceramics cannot be formed onto curved surfaces, limiting design flexibility in the transducer. Finally, they have a high degree of noise associated with their resonant modes. Piezoelectric polymers are acoustically well matched to water, are very flexible, and have few spurious modes. However, the applications for these polymers are limited by their low electromechanical coupling, low dielectric constant, and high cost of fabrication. Piezoelectric ceramic/polymer composites have shown superior properties when compared to single-phase materials. As shown in Table 26.1, they combine high coupling, low impedance, few spurious modes, and an intermediate dielectric constant. In addition, they are flexible and moderately priced.

26.3 Measurements of Piezoelectric Effect

Different means have been proposed to characterize the piezoelectric properties of materials. The resonance technique involves the measurement of the characteristic frequencies when the suitably shaped specimen (usually ceramic) is driven by a sinusoidally varying electric field. To a first approximation, the behavior of a piezoelectric sample close to its fundamental resonance frequency can be represented by an equivalent circuit as shown in Figure 26.5a. The schematic behavior of the reactance of the sample as a function of frequency is represented in Figure 26.5b. By measuring the characteristic frequencies of the sample, the material constants including piezoelectric coefficients can be calculated. The equations used for the calculations of the electromechanical properties are described in the IEEE Standard on piezoelectricity [15]. The simplest example of piezoelectric measurements by resonance technique relates to a piezoelectric ceramic rod (typically 6 mm in diameter and 15 mm long) poled along its length. It can be shown that the coupling coefficient k_{33} is expressed as a function of the series and parallel resonance frequencies, f_s and f_p, respectively:

$$k_{33}^2 = \frac{\pi}{2}\frac{f_s}{f_p}\tan\left(\frac{\pi}{2}\frac{f_p - f_s}{f_p}\right) \tag{26.9}$$

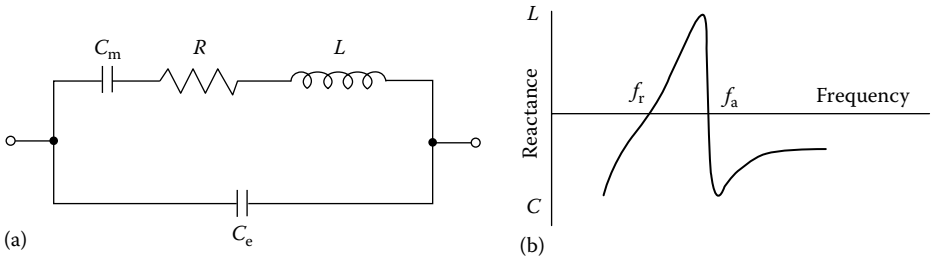

FIGURE 26.5 (a) Equivalent circuit of the piezoelectric sample near its fundamental electromechanical resonance (top branch represents the mechanical part and bottom branch represents the electric part of the circuit) and (b) electric reactance of the sample as a function of frequency.

The longitudinal piezoelectric coefficient d_{33} is calculated using k_{33}, elastic compliance s_{33}^E, and low-frequency dielectric constant ε_{33}^X:

$$d_{33} = k_{33}\left(\varepsilon_{33}^X s_{33}^E\right)^{1/2} \tag{26.10a}$$

Similarly, other electromechanical coupling coefficients and piezoelectric moduli can be derived using different vibration modes of the sample. The disadvantage of the resonance technique is that measurements are limited to the specific frequencies determined by the electromechanical resonance. It is used mostly for the rapid evaluation of the piezoelectric properties of ceramic samples whose dimensions can be easily adjusted for specific resonance conditions.

Subresonance techniques are frequently used to evaluate piezoelectric properties of materials at frequencies much lower than the fundamental resonance frequency of the sample. They include both the measurement of piezoelectric charge under the action of external mechanical force (direct effect) and the measurement of electric field–induced displacements (converse effect). In the latter case, the displacements are much smaller than in resonance; however, they still can be measured by using strain gages, capacitive sensors, linear variable differential transformer (LVDT) sensors, or optical interferometry [16,17].

A direct method is widely used to evaluate the sensor capabilities of piezoelectric materials at sufficiently low frequency. The mechanical deformations can be applied in different modes such as thickness expansion, transverse expansion, thickness shear, and face shear to obtain different components of the piezoelectric tensor. In the simplest case, the metal electrodes are placed onto the major surfaces of the piezoelectric transducer normal to its poling direction (direction of ferroelectric polarization), and the mechanical force is applied along this direction (Figure 26.1b). Thus, the charge is produced on the electrode plates under mechanical loading, which is proportional to the longitudinal piezoelectric coefficient d_{33} of the material. To relate the output voltage of the transducer to the piezoelectric charge, it is necessary to consider the equivalent circuit (Figure 26.6a). A circuit includes the charge generator, $Q = d_{33}F$; the leakage resistor of the transducer, R_s; the transducer capacitance, C_s; the capacitance of the connecting cables, C_c; and the input resistance and capacitance of the amplifier, R_a and C_a, respectively. Here, F denotes the force applied to the transducer (tensile or compressive). All the resistances and capacitances shown in Figure 26.6a can be combined, as shown in Figure 26.6b. A charge generator can be converted to a current generator, I, according to

$$I = \frac{dQ}{dt} = d_{33}\frac{dF}{dt} \tag{26.10b}$$

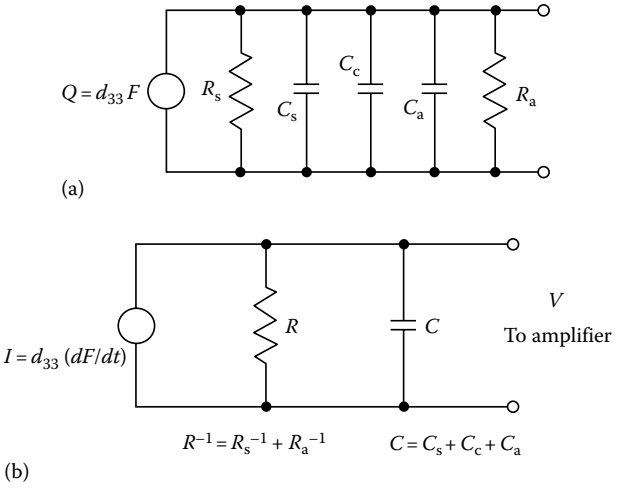

FIGURE 26.6 (a) Full and (b) simplified equivalent electric circuits of the piezoelectric sensor connected to the voltage amplifier.

Assuming that the amplifier does not draw any current, the output voltage V at a given frequency ω can be calculated:

$$V = \frac{d_{33}F}{C}\frac{j\omega\tau}{1+j\omega\tau} \tag{26.11}$$

where $\tau = RC$ is the time constant that depends on all resistances and capacitances of the circuit. For sufficiently high frequency, the measured response is frequency independent, and d_{33} can be easily evaluated from Equation 26.11 if the equivalent capacitance C is known. Since C is determined by the parallel capacitances of the sample, connecting cables, and amplifier (typically not exactly known), the standard capacitance is often added to the circuit, which is much greater than all the capacitances involved. However, according to Equation 26.11, the sensitivity of the circuit is greatly reduced with decreasing C. If τ is not large enough, the low-frequency cutoff does not allow piezoelectric measurements in quasistatic or low-frequency conditions.

To overcome the difficulties of using voltage amplifiers for piezoelectric measurements, a so-called charge amplifier was proposed. The idealized circuit of a charge amplifier connected to the piezoelectric transducer is shown in Figure 26.7. Note that an FET-input operational amplifier is used with a capacitor

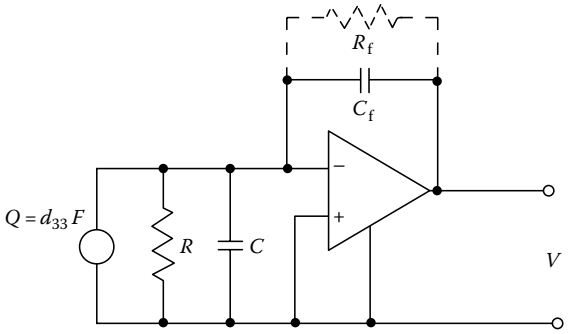

FIGURE 26.7 Equivalent electric circuit of the piezoelectric sensor connected to the charge amplifier.

C_f in the feedback loop. Assuming that the input current and the voltage of the operational amplifier are negligible, one can relate the charge on the transducer with the output voltage:

$$V = \frac{-Q}{C_f} = -d_{33}\frac{F}{C_f} \tag{26.12}$$

Equation 26.12 gives frequency-independent response where the output voltage is determined only by the piezoelectric coefficient d_{33} and the known capacitance C_f. Unfortunately, this advantage is difficult to realize since even a small input current of the amplifier will charge the feedback capacitor, leading to saturation of the amplifier. Therefore, a shunt resistor R_f is added to the circuit (dotted line in Figure 26.7), which prevents such charging. If one takes into account the *RC* circuit of the feedback loop, the output voltage will have the form of Equation 26.11, that is, becomes frequency dependent. In this case, the time constant τ is determined by the parameters of the feedback loop and does not depend on the capacitance of the transducer, connecting cables, or the input capacitance of the amplifier. This gives an important advantage to the charge amplifier when it is compared to the ordinary voltage amplifier.

26.4 Applications

The direct and converse piezoelectric effects in a number of materials have led to their use in electromechanical transducers. Electromechanical transducers convert electric energy to mechanical energy, and vice versa. These transducers have found applications where they are used in either passive or active modes. In the passive (sensor) mode, the transducer only receives signals. Here, the direct piezoelectric properties of the material are being exploited to obtain a voltage from an external stress. The applications in the passive mode include hydrophones, or underwater listening devices; microphones; phonograph pickups; gas igniters; dynamic strain gages; and vibrational sensors. In the active (actuator) mode, the transducer, using the converse piezoelectric properties of the material, changes its dimensions and sends an acoustic signal into a medium. The active-mode applications include nondestructive evaluation, fish/depth finders, ink-jet printers, micropositioners, micropumps, and medical ultrasonic imaging. Often, the same transducer is used for both sensor and actuator functions.

Two examples of piezoelectric sensors are given as follows. The first example is the ceramic transducer, which relates the deformation of the piezoelectric sensor to the output voltage via direct piezoelectric effect. Piezoceramics have high Young's moduli; therefore, large forces are required to generate strains in the transducer to produce measurable electric response. The compliance of the piezoelectric sensor can be greatly enhanced by making long strips or thin plates of the material and mounting them as cantilevers or diaphragms. The displacement of the cantilever end will result in a beam bending, leading to the mechanical stress in the piezoelectric material and the electric charge on the electrodes. A common configuration of the piezoelectric bender is shown in Figure 26.8a. Two beams poled in opposite directions are cemented together with one common electrode in the middle and two electrodes on the outer surfaces. The bending of such a bimorph will cause the upper beam to stretch and the lower beam to compress, resulting in a piezoelectric charge of the same polarity for two beams connected in series. To the first approximation, the charge Q appearing on the electrodes is proportional to the displacement Δl of the end of the bimorph via Equation 26.13 [18]:

$$Q = \frac{3}{8}\frac{Hw}{L}e_{31}\Delta l \tag{26.13}$$

where

H, w, and L are the thickness, the width, and the length of the bimorph, respectively

e_{31} is the transverse piezoelectric coefficient relating electric polarization and strain in a deformed piezoelectric material

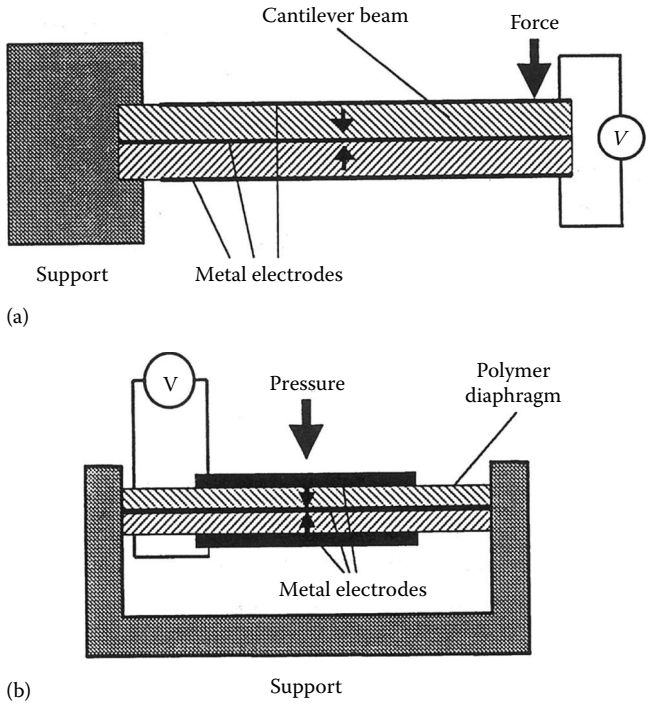

FIGURE 26.8 Schematic designs of the displacement sensor based on piezoelectric ceramic (a) and of the pressure sensor based on piezoelectric polymer film (b). The arrows indicate the directions of ferroelectric polarization in the piezoelectric material.

The charge can be measured either by the voltage amplifier (Figure 26.6) or by the charge amplifier (Figure 26.7).

In certain applications, the parameters of piezoelectric sensors can be improved by using ferroelectric polymers instead of single crystals and piezoceramics. Although the electromechanical properties of polymers are inferior to those of piezoelectric ceramics, their low dielectric constant offers the higher voltage response since they possess higher *g* piezoelectric coefficients. Also, the polymers are more mechanically robust and can be made in the form of thin layers (down to several micrometers). An example using the polymer bimorph as a pressure sensor is shown in Figure 26.8b. A circular diaphragm composed of two oppositely poled polymer films is clamped along its edges to a rigid surround, forming a microphone. The voltage appearing on the electrodes is proportional to the applied pressure *p* by Equation 26.14 [19]:

$$V = \frac{3}{16}\frac{d_{31}}{\varepsilon_{33}}\frac{D^2}{h}(1-\nu)p \tag{26.14}$$

where

D and h are the diameter and the thickness of the diaphragm, respectively

ν is the Poisson ratio

The high d_{31}/ε_{33} value for polymer sensors is advantageous to obtain higher voltage response. According to Equation 26.11, this advantage can be realized only if the high-input-impedance amplifier is used in close proximity to the transducer to reduce the influence of the connecting cables.

TABLE 26.2 Suppliers of Piezoelectric Materials and Sensors

Name	Address	Ceramic	Polymer	Composite
AMP Sensors	950 Fore Ave., Morristown, PA 19403, Phone: (610) 650-1500, Fax: (610) 650-1509		X	
Krautkramer Branson	50 Industrial Park Rd., Lewistown, PA 17044, Phone: (717) 242-0327, Fax: (717) 242-2606			X
Materials Systems, Inc.	531 Great Road, Littleton, MA 01460, Phone: (508) 486-0404, Fax: (508) 486-0706, http://www.materialsystems.com/			X
Morgan Matroc, Inc.	232 Forbes Rd., Bedford, OH 44146, Phone: (216) 232-8600, Fax: (216) 232-8731 http://www.morganelectroceramics.com/	X		
Sensor Technology Ltd.	20 Stewart Rd., P.O. Box 97, Collingwood, Ontario, Canada, Phone: +1 (705) 444-1440, Fax: +1 (705) 444-6787, http://www.sensortech.ca/site/index.cfm	X		
Staveley Sensors, Inc.	91 Prestige Park Circle, East Hartford, CT 06108, Phone: (860) 289-5428, Fax:(860) 289-3189, http://www.sensortech.ca/site/index.cfm			X
CTS Valpey Corporation	Hopkinton, MA 01748, Phone: (508) 435-6831, Fax: (508) 435-5289, http://www.ctsvalpey.com/		X	
Vermon USA	6288 SR 103 North Bldg. 37, Lewistown, PA 17044, Phone: (717) 248-6838, Fax:(717) 248-7066	X		
TRS Ceramics, Inc.	2820 E. College Ave., State College, PA 16801, Phone: (814) 238-7485, Fax: (814) 238-7539 http://www.trstechnologies.com/Products/piezoelectric_ceramics.php	X		

26.4.1 Suppliers of Piezoelectric Materials

Table 26.2 lists a number of the suppliers of piezoelectric materials, their addresses, and whether they supply piezoelectric ceramic, polymers, or composites. Most of them tailor the material to specific applications.

Defining Terms

Charge amplifier: An operational amplifier used to convert the input charge into output voltage by means of the capacitor in the feedback loop

Coupling coefficients: The materials constants that describe an ability of piezoelectric materials to convert electric energy into mechanical energy and vice versa

Ferroelectrics: A subgroup of piezoelectric materials possessing a net dipole moment (ferroelectric polarization) that can be reversed by the application of sufficiently high electric field

Piezoelectric coefficients: The materials constants that are used to describe the linear coupling between electric and mechanical parameters of the piezoelectric

Piezoelectric composites: The materials containing two or more components with different piezoelectric properties

Piezoelectric transducer: A device that converts the input electric energy into mechanical energy and vice versa via piezoelectric effect

Poling: The process of aligning the ferroelectric polarization along a unique (poling) direction

References

1. J. F. Nye, *Physical Properties of Crystals*, Oxford, U.K.: Oxford University Press, 1985.
2. Y. Xu, *Ferroelectric Materials and Their Applications*, Amsterdam, the Netherlands: North-Holland, 1991.
3. L. E. Cross, Ferroelectric ceramics: Tailoring properties for specific applications, In N. Setter and E. L. Colla (eds.), *Ferroelectric Ceramics: Tutorial Reviews, Theory, Processing, and Applications*, Basel, Germany: Birkhauser, 1993.
4. B. Jaffe, W. R. Cook, Jr., and H. Jaffe, *Piezoelectric Ceramics*, Marietta, OH: R.A.N., 1971.
5. *The User's Guide to Ultrasound & Optical Products*, Hopkinton, MA: Valpey-Fisher Corporation, 1996.
6. S.-E. Park and T. R. Shrout, Relaxor based ferroelectric single crystals with high piezoelectric performance, *Proceedings of the 8th US–Japan Seminar on Dielectric and Piezoelectric Ceramics*, October 15–18, Plymouth, MA, 1997, p. 235.
7. *Piezoelectric Products*, Collingwood, Ontario, Canada: Sensor Technology Limited, 1991.
8. H. Kawai, The piezoelectricity of poly(vinylidene fluoride), *Jpn. J. Appl. Phys.*, 8, 975, 1969.
9. L. F. Brown, Ferroelectric polymers: Current and future ultrasonic applications, *Proceedings of the 1992 IEEE Ultrasonics Symposium*, New York, 1992, p. 539.
10. T. Furukawa, Recent advances in ferroelectric polymers, *Ferroelectrics*, 104, 229, 1990.
11. L. F. Brown, J. I. Scheinbeim, and B. A. Newman, High frequency dielectric and electromechanical properties of ferroelectric nylons, *Proceedings of the 1994 IEEE Ultrasonics Symposium*, New York, 1995, p. 337.
12. *Properties of Raytheon Polyvinylidene Fluoride (PVDF)*, Raytheon Research Division, Lexington, MA, 1990.
13. *Standard and Custom Piezo Film Components*, Valley Forge, PA: Atochem Sensors, Inc., 1991.
14. T. R. Gururaja, Piezoelectric transducers for medical ultrasonic imaging, *Am. Ceram. Soc. Bull.*, 73, 50, 1994.
15. IEEE standards on piezoelectricity, *IEEE Std.* 176, 1978.
16. W. Y. Pan and L. E. Cross, A sensitive double beam laser interferometer for studying high-frequency piezoelectric and electrostrictive strains, *Rev. Sci. Instrum.*, 60, 2701, 1989.
17. A. L. Kholkin, Ch. Wuethrich, D. V. Taylor, and N. Setter, Interferometric measurements of electric field-induced displacements in piezoelectric thin films, *Rev. Sci. Instrum.*, 67, 1935, 1996.
18. A. J. Moulson and J. M. Herbert, *Electroceramics: Materials, Properties, Applications*, London, U.K.: Chapman and Hall, 1990.
19. J. M. Herbert, *Ferroelectric Transducers and Sensors*, New York: Gordon and Breach, 1982.

Further Readings

Achenbach, J. D., *Reciprocity for Piezoelectric System*, Cambridge, U.K.: Cambridge University Press, Online publication, December 2009, http://ebooks.cambridge.org/chapter.jsf?bid=CBO9780511550485&cid=CBO9780511550485A122 (accessed on June 25, 2012).

Arnau, A., *Piezoelectric Transducers and Applications*, Berlin, Germany: Springer, 2004.

Tichy, J., J. Erhart, E. Kittinger, and J. Privratska, *Fundamentals of Piezoelectric Sensorics*, Berlin, Germany: Springer, 2010.

Wolfbeis, O.S., C. Steinem, and A. Janshoff, *Piezoelectric Sensors*, Berlin, Germany: Springer, 2007.

27

Laser Interferometer Displacement Sensor

Bernhard Günther Zagar
Technical University of Graz

27.1 Introduction

In the past few years, very high precision, numerically controlled machine tools have been developed. To achieve the potential precision of these tools, length and displacement measurements whose resolution exceeds the least significant digit of the tool must be made. The measurement equipment typically would not rely on mechanical scales.

Laser interferometers compare the changes in optical path length to the wavelength of light, which can be chosen from atomic constants that can be determined with very little uncertainty.

In 1983, there was a redefinition of the meter [1] that was previously defined in 1960. The old definition was based on the wavelength of a certain radiation (the krypton-86 standard) that could not be realized to better than four parts in 10^9. The new definition, being based on frequency but not related to any particular radiation, opened the way to significant improvements in the precision with which the meter can be realized. As recommended in resolution 2 for the practical realization of the meter, the wavelength in vacuum λ_v of a plane electromagnetic wave of frequency f is $\lambda_v = c/f$, where c is the speed of light in vacuum, $c = 299,792,458$ m s^{-1} exactly. This way, the wavelength is related to *frequency* and *time*, which can be measured with the highest precision of all units within the Système International (SI).

In order to be independent of any environmental parameters, the meter is defined using the speed of light in a vacuum. However, interferometers usually must operate in ambient air.

Thus, environmental parameters that influence the speed of light in a particular medium (air) will affect and degrade the precision of the measurement.

Three major factors limit the absolute accuracy attainable with laser interferometers operating in ambient air: (1) the uncertainties of the vacuum wavelength, λ_v, of the laser source; (2) the uncertainty of the refractive index of the ambient air; and (3) the least-count resolution of the interferometer.

This chapter section is organized as follows. First, some basic laser principles are detailed, including ways to stabilize the vacuum wavelength of the laser. The effect most often used to stabilize lasers in commercial interferometers is the Zeeman effect, which yields relative uncertainties of 10^{-8}.

Second, the refractive index of air as another major factor limiting the attainable accuracy of laser interferometers operated in air is addressed. It is shown that it cannot be determined currently with uncertainty better than 5×10^{-8}.

And finally, the chapter section describes the most widely used Michelson interferometer and two of its variants for long-travel length measurement and gives their resolution.

27.2 Helium–Neon Laser

In order to attain the best possible accuracy, great care must be taken to ensure the highest wavelength stability of the light source. Almost all interferometric dimensional gages utilize a helium–neon laser because it has proven reliable, its emitted wavelength is in the visible range at about 633 nm, and it can be stabilized sufficiently well utilizing the Zeeman effect and to an even higher degree with the use of a very well-defined iodine absorption line also at ≈633 nm [1,2].

The helium–neon laser consists of a discharge tube as shown in Figure 27.1 [3] filled with the single-isotope gases helium (He^3) at a partial pressure of ≈105 Pa and neon (Ne^{20}) with a partial pressure of ≈13 Pa. It is pumped electrically using a voltage on the order of kilovolts with a current of a few milliamperes to excite both helium and neon atoms. Since the helium gas is the major component, it dominates the discharge properties of the laser tube. Neutral helium atoms collide with free electrons that are accelerated by the axial voltage and become excited and remain in two rather long-lived metastable states. These are close enough to the energy levels of certain excited states of neon atoms so that collisional energy transfer can take place between these two groups of atoms. Excited helium atoms may drop down to the ground state, while simultaneously neon atoms take up almost exactly the same amount of energy. Therefore, helium only serves to excite neon atoms; they do not contribute to the emission of light. The excited neon atoms remain in the excited state for a rather long period of time (on the order of 10^{-3} s). They return to lower energetic levels by stimulated emission of highly coherent light. This stimulated emission comes into effect when the light emitted by some neon atoms also prompts other atoms to emit. The mirrors of the laser cavity,

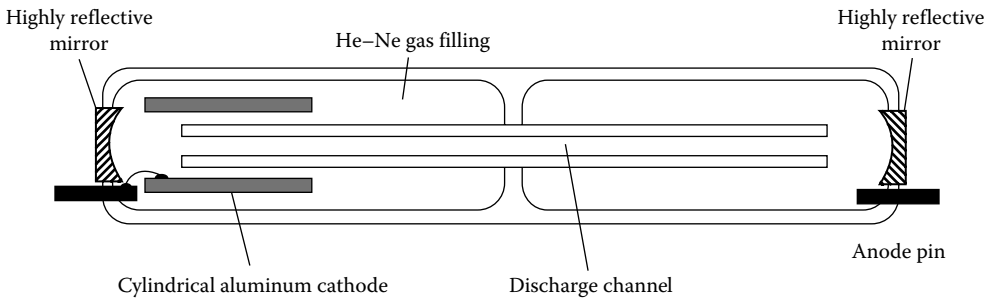

FIGURE 27.1 Schematics of the helium–neon laser. (Reprinted with permission from Siegman, A. E., *Lasers*, University Science Books, Mill Valley, CA.)

by reflecting most of the incident light, cause the light to traverse multiple paths through the active laser volume, thereby greatly amplifying the light if the cavity length L is an integer multiple m of half the wavelength λ:

$$L = m\frac{\lambda}{2} \tag{27.1}$$

The emitted light is fairly monochromatic but still has some finite spectral line width determined by the random emissions of Ne^{20}.

Brewster-angle [4] end windows of the discharge tube transmit light of the proper linear polarization if desired. The end mirrors have to be carefully polished. Their curvature radii have to satisfy the condition for stability. They have wavelength-selective dielectric coatings of very high reflectivity sometimes exceeding 99%.

Unless special precautions are taken, a He–Ne laser will emit several axial modes as shown schematically in Figure 27.1, resulting in a beat frequency that limits the temporal coherence and renders the laser unsuitable for interferometric purposes. Also, due to thermal expansion of the laser tube, the end mirrors will change their relative distance, thereby effectively tuning the wavelength within the line width of the gain curve.

Another important property of a high-quality He–Ne laser is its Gaussian cross-sectional profile, which is maintained along a propagating wave, that is, fundamental lateral mode. It is also a necessary condition for the wave fronts to remain quasiplanar.

27.2.1 Frequency Stabilization of He–Ne Lasers

The resonant frequency (and the wavelength λ) of the laser is determined in part by the distance between the two end mirrors and also by the refractive index n_M of the active medium (the He–Ne mixture). Since the line width of the gain profile of the active medium is usually in the gigahertz range, multiple axial modes can resonate in the cavity as is shown in Figure 27.2. The frequency difference Δf between two adjacent longitudinal modes is the *free spectral range* (FSR), which is given by Equation 27.2 and depends only on the cavity length, L; the refractive index of the active medium, n_M; and the speed of light in vacuum, c:

$$\Delta f = \frac{c}{2n_M L} \tag{27.2}$$

Due to thermal expansion of the laser cavity and/or thermally induced change in refractive index of the active medium, all resonating laser modes will move within the envelope of the gain profile. The effort undertaken in stabilizing the laser wavelength or equivalently stabilizing its frequency is aimed at locking the modes with respect to the gain profile and reducing the number of modes resonating simultaneously.

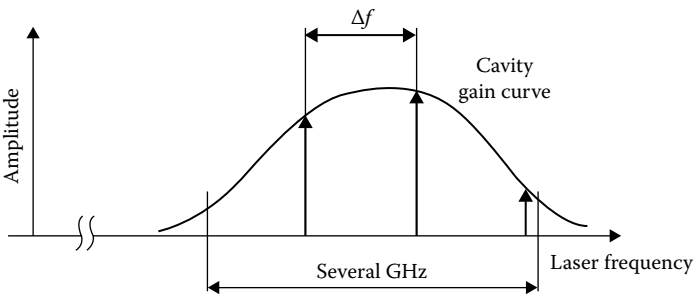

FIGURE 27.2 He–Ne laser can have multiple resonating modes (shown for ≈20 cm cavity length). (Reprinted with permission from Siegman, A. E., *Lasers*, University Science Books, Mill Valley, CA.).

27.2.2 Longitudinal Zeeman Effect

One of the most often used effects in stabilizing the frequency of a He–Ne laser for distance measurements is the Zeeman effect [3,5].

The tube of the laser whose frequency is to be stabilized is mounted inside an axial permanent magnet as shown in Figure 27.3. Because of a short cavity length chosen, the FSR Δf of the laser is large. Therefore, the laser emission appears as a single longitudinal mode when the cavity length is properly controlled. An externally applied magnetic field in longitudinal direction causes the transition frequencies of the neon atoms to split symmetrically to the nominal frequency, the separation in frequency being proportional to the magnetic field strength. This phenomenon is called the *longitudinal Zeeman effect*.

With the applied field strength, the single longitudinal laser mode of the He–Ne laser is split into right and left circularly polarized modes with a frequency difference of typically 1.5 MHz. The frequency difference depends on the laser frequency and exhibits an extreme value when the laser frequency matches exactly the atomic transition frequency. Frequency stabilization is accomplished with control of the cavity length so that the frequency is locked to the extreme value corresponding to the nominal frequency of the laser. In order to determine the actual laser frequency within the gain profile, the cavity length is periodically modulated with a piezoelectric actuator as shown in Figure 27.3. The frequency difference is constantly monitored at the minimum and maximum elongation of the modulation cycle. In the case when the extremal values are identical, the difference frequency will assume a maximum, and thus, the nominal value of the laser frequency is attained. This is achieved by controlling the length of the laser cavity. The cavity length is controlled both by using the thermal expansion of the laser tube, which is in close proximity to an electric heater whose operating current can be varied on a less dynamic scale, and on a very short time basis with a piezoelectric actuator attached to one of the end faces of the cavity [5].

This fast actuator allows for only limited amplitude, typically on the order of less than a wavelength. Therefore, the thermal expansion must be used to attain greater modulation amplitude. To obtain the highest possible stability of the laser frequency, the frequency differences are measured within a very short time interval, and the determined deviations from the nominal value are fed back in a closed control loop to the electromechanical and thermal positioning devices.

The short- and long-term frequency stability $\Delta f/f$ of such a stabilized laser can be as high as 2×10^{-8}, depending also on the parameters of the feedback loop.

Another phenomenon that exceeds the stabilization attainable with the Zeeman effect by far uses a particular absorption line of an iodine isotope ($^{127}I_2$, transition 11–5, R(127), component *i*) and locks the He–Ne laser [2,6] in that very well-defined frequency. Its wavelength $\lambda_1 = 632.9913981$ nm is very

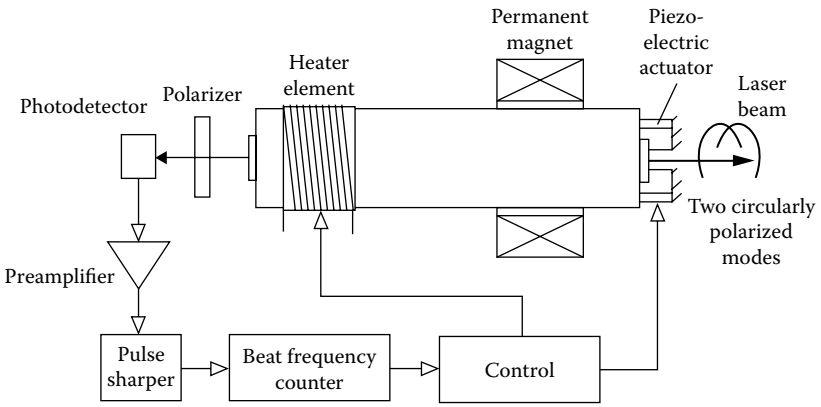

FIGURE 27.3 Laser wavelengths can be stabilized by utilizing the Zeeman effect. (Courtesy of Spindler & Hoyer, Inc., Milford, MA.)

close to one of the nominal wavelengths of the He–Ne laser, so this can easily be accomplished; however, the necessary equipment including the sophisticated electronics is rather involved [2]. For this reason, iodine-stabilized He–Ne lasers are only used where very high precision is required.

The overall estimated relative uncertainty of such a stabilized laser is $\pm 10^{-9}$ (which results from an estimated relative standard deviation of 3.4×10^{-10} [1]), which makes it suitable for the practical realization of the definition of primary and secondary standards.

27.3 Refractive Index of Air

The length scale of a displacement interferometer that is operated in ambient air is given by $\lambda_A = \lambda_V / n_A$, where λ_A is the wavelength of the source in air, λ_v is the wavelength in vacuum, and n_A is the refractive index of air. The vacuum wavelength λ_v is related to the speed of light by $\lambda_v = c/f_0$. The constant c, the speed of light in vacuum, was redefined in 1983 [1]. It is now defined to be exactly $c = 299{,}792{,}458$ m s^{-1}.

Thus, in order to measure distances interferometrically, it is essential to know the refractive index of air with an accuracy that is not less than the stability and the degree of certainty of the vacuum wavelength of the light source.

According to Edlén [7,8] and Owens [9], the refractive index is a function of the atmospheric pressure P, the temperature T, the relative humidity H, or alternatively the partial pressure of the water vapor in air e_s and the carbon dioxide concentration by volume D. The standard composition by volume of dry air is given by 78.03% N_2, 20.99% O_2, 0.933% Ar, 0.035% CO_2, and some other trace components, mainly noble gases [10]. The only component of the aforementioned list that might have variability is CO_2, which follows a long-term increasing behavior presumably associated with the combustion of fossil fuel [11]. The current value is ≈350 ppm by volume and is increasing by ≈1.4 ppm/year. The CO_2 concentration in air can also change in an industrial environment due to CO_2 emitters and can therefore show significant local variations.

More recently, the dependencies of the refractive index on nonnatural gaseous compounds like hydrocarbons in the air have been published [12] as well as corrections to Edlén's formulations [13–15]. Corrections to the refractive index due to those compounds may be necessary for very high-precision measurements in an industrial environment where chemical solvents or oils are in use. In Table 27.1, some nonnatural compounds, their maximum workplace concentrations (MWCs), and their effect on the refractive index if present at the location of the interferometer are listed.

TABLE 27.1 Refractive Indices n of Various Gaseous Compounds, Their MWC, and the Change in Refractive Index Caused by That Particular Concentration (for $T = 20$ °C, $P = 101.315$ hPa, $\lambda = 633$ nm)

Gas	Refractive Index $(n-1)10^4$	Concentration for $\Delta n/n = 10^{-7}$ in Air (ppm)	MWC (mg m^{-3})	$\Delta n/n \times 10^7$ due to MWC
Air	2.72			
Propane	10.3	130	1800	8
Butane	12.9	98	2350	10
Ethanol	8.1	190	1900	5
Ethyl acetate	13.0	97	1400	4
Dimethylketone	10.2	130	2400	9
Octane	23	50	2350	10
Chlorofluorocarbons (e.g., R12)	10.3	130	5000	7

Source: Reprinted with permission of VDI Verein Deutscher Ingenieure, G. Wilkening, Kompensation der Luftbrechzahl.

Jones [16] combined a precise determination of the density of moist air with Edlén's formulation to yield a somewhat simpler representation. For a typical iodine-stabilized He–Ne laser that has a vacuum wavelength of λ_v = 632.9913 nm, the Jones formulation is given by [17]

$$n(P,T,H,D) = 1 + A - B \tag{27.3}$$

where

$$\begin{aligned} A &= 78.603\left[1 + 0.540(D - 0.0003)\right]\frac{P}{TZ} \times 10^{-8} \\ B &= \left(0.00042066\, f_E e_s H\right) \times 10^{-8} \end{aligned} \tag{27.4}$$

where

P is the atmospheric pressure in pascals
T is the absolute temperature in kelvin
H is the relative humidity in %
D is the concentration of CO_2 in percent by volume

There are three additional factors in Jones' formulation that take the nonideal behavior of moist air as compared to an ideal gas into account. They are Z, a compressibility factor that reflects the nonideality of the air–water vapor mixture and that, for air containing reasonable amounts of CO_2 at a temperature between 15 °C and 28 °C and pressure of between 7×10^4 and 11×10^4 Pa, lies in the range between 0.99949 and 0.99979. f_E is an enhancement factor that expresses the fact that the effective saturation vapor pressure of water in air is greater than the saturation vapor pressure e_s. For the pressure and temperature ranges given earlier, f_E is bounded between 1.0030 and 1.0046 [16]. e_s is the saturation vapor pressure over a plane surface of pure liquid water and according to Jones is about 1705 Pa at a temperature of 15.0 °C and about 3,779 Pa for 28.0 °C. In the tables of Z, f_E and e_s are included in the Appendix of Jones' paper [16].

Table 27.2 gives an overview of the changes in environmental parameters that would cause a relative index change of 10^{-7}.

Edlén [8] and Jones [16] estimate that their empirical expressions for the dependency of the refractive index of air on the listed parameters have an absolute uncertainty of 5×10^{-8}.

Besides this fundamental limitation, there are some practical considerations that must be taken into account regarding the precision with which the environmental parameters can be measured. Estler [17] states that atmospheric pressure P can currently be determined with an uncertainty of ≈2.7 Pa, which can be assumed to be constant for the entire optical path of the interferometer if it is oriented horizontally.

TABLE 27.2 Parameters of Standard Air and Their Deviation to Cause a $\Delta n/n$ of 10^{-7}

Parameter	Standard Value	Variation for $\Delta n/n = +1 \times 10^{-7}$
Pressure P	101.3 kPa	+37.3 Pa
Temperature T	20.0°C	−0.1°C
Humidity H	40%	−10.0%
CO_2 concentration	350 ppm	+670 ppm

Source: Reprinted with permission of Estler, W. T., *J. Appl. Opt.*, 24(6), 808, 1985.

Please note that at sea level, the pressure gradient is ≈−13 Pa m^{-1}, resulting in a pressure-induced change in n_A of 3.4×10^{-8} m^{-1} if the measuring equipment is not kept level.

In an exceptionally well-controlled laboratory environment where special care is devoted to keep temperature gradients from affecting the refractive index along the optical path as much as possible, uncertainties of the temperature measurement can be as low as 0.01 °C according to [17]. Humidity measured with high-accuracy dew-point hygrometers can have uncertainties down to 0.5%. Changes in carbon dioxide concentrations have to be very significant (20% of the natural concentration) to cause a $\Delta n/n$ of 10^{-8}.

27.3.1 Other Sources of Error in Interferometers

Although the variation of the index of refraction of air is the most obvious source of error in typical interferometer applications, there are some often overlooked additional sources that are being discussed here briefly (from [18]):

- Cosine error results from the angular misalignment between the measurement axis and the axis of motion. Magnitude: $L[1 - \cos(\delta)]$ for $\delta = 0.1$ mrad and $L = 1$ m gives ≈ 4 nm in total.
- Optical alignment or better optical misalignment of the measurement beam with reference to the axis of motion can be visualized by observing the return beam of the measurement beam with respect to the reference beam. As the mechanical stage is moved, the reference signal will remain fixed, and any angular error (cosine error) of the measurement beam shows up as a runout in the beam overlap decreasing optical output level and thus increasing noise and uncertainty.
- *Target nonuniformity*: The target mirror must be flat to fractions of a wavelength λ in applications that require multiple axes of travel. A target mirror with a surface figure of $\lambda/10$ can contribute up to 63 (= $\lambda/10$) nm (for He–Ne lasers) of error as the stage travels along the axis parallel to the clear aperture of the mirror. In a measurement configuration where the beam reflects from the same location on the target mirror, this error source will be zero.
- Opposite axis error is often present in mechanical measuring systems. An opposite axis error is caused when perpendicular axes are not truly orthogonal to each other.
- Abbé error occurs when the axis of measurement is offset from the axis of interest. As first described by Dr. Ernst Abbé of Zeiss, "If errors of parallax are to be avoided, the measuring systems must be placed coaxially to the line in which displacement is to be measured on the workpiece."
- The mechanical stability or stiffness of the mechanical assembly is critical. If the physical relationship between the target optic and the point of interest changes during the measurement time, this is indistinguishable from actual motion. Vibration effects can be minimized by taking several measurements at one position and averaging them together.
- *Data age uncertainty*: Data age is defined as the difference in the time between when the object of interest is measured and when the user control system gets the position information. Data age uncertainty is defined as the maximum variation in the data age in a multi-axis system, due primarily to process variation in the electronics. Having minimum data age and data age uncertainty is critical for multi-axis high-velocity applications.

27.4 Michelson Interferometer

The basis for most interferometers used in interferometric dimensional gages is the classical Michelson interferometer [4] that is shown in Figure 27.4. The coherent monochromatic light of a wavelength-stabilized He–Ne laser is incident onto a beam splitter that splits the light into two equally intense beams (1) and (2).

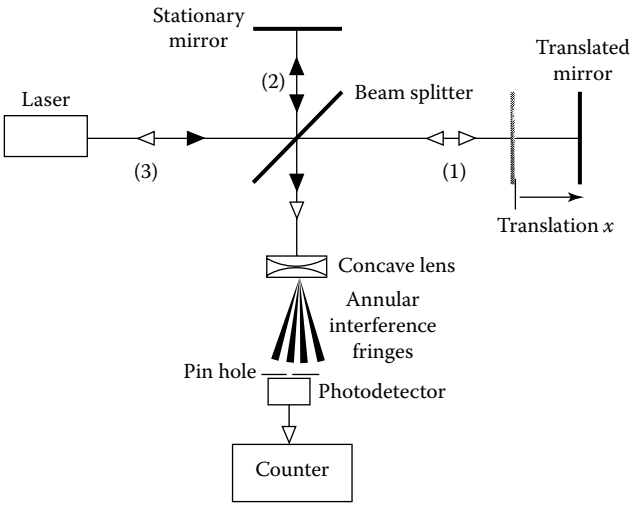

FIGURE 27.4 Schematics of the basic Michelson interferometer.

They are reflected off of both the stationary and the translatable mirror whose displacement x is to be measured and recombined at the splitter, where they are redirected toward a concave lens. Due to the coherence of the laser light, the wave fronts have a well-defined phase relation with respect to each other. This phase is determined by the difference between the optical path lengths of the two beams in arms 1 and 2. If this path difference is continuously changed by translating one of the mirrors, a sinusoidal

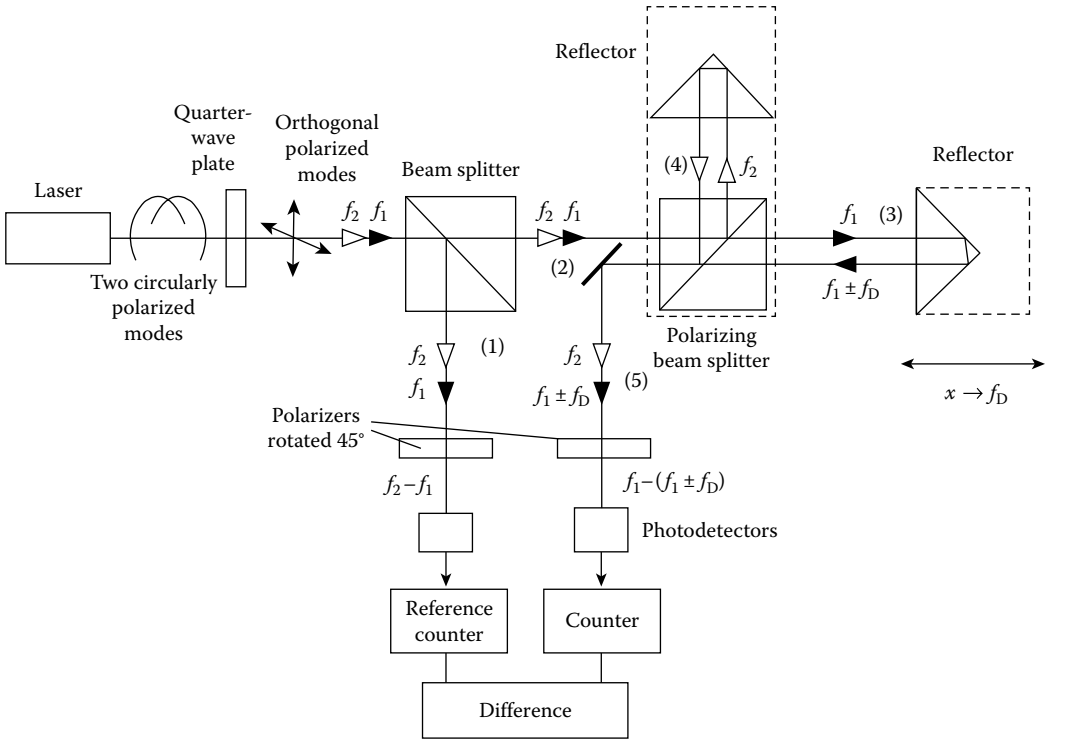

FIGURE 27.5 Two-frequency heterodyne interferometer. (Courtesy of Spindler & Hoyer, Inc., Milford, MA.)

intensity variation can be observed at a fixed location in space behind the lens used to introduce a beam divergence, resulting in an annular fringe pattern. The pinhole is used to define an exact location of observation, and the photodetector picks up the varying intensity for further processing. In the most basic signal processing setup, a number of bright and dark cycles are fed into a counter, which then counts changes in optical path length in integer multiples of $\lambda_A/2$. More sophisticated signal processing not only counts cycles but also determines relative phase changes in the sinusoidal varying intensity so that resolutions of $\lambda_A/512$ can ultimately be achieved.

When moving the mirror, one must guarantee a smooth motion without backward jitter of the mirror carriage to avoid double counts of interference fringes. Very high-quality linear bearings (such as air bearings) are necessary to accomplish just that.

As can be seen in Figure 27.4, the light reflected off both mirrors essentially retraces its own path and is at least partially incident onto the active volume of the laser source (3), thereby forming an external laser resonator that is able to detune the laser, effectively modulating its output power as well as its wavelength. To avoid this effect, commercial versions of Michelson interferometers employ corner-cube reflectors instead of plane mirrors as well as optical isolators, as shown in Figures 27.5 and 27.6. Some authors, however, report using optical arrangements that utilize this effect in conjunction with laser diodes to realize low-cost, short-travel displacement sensors [19,20]. These setups will not be discussed here, however.

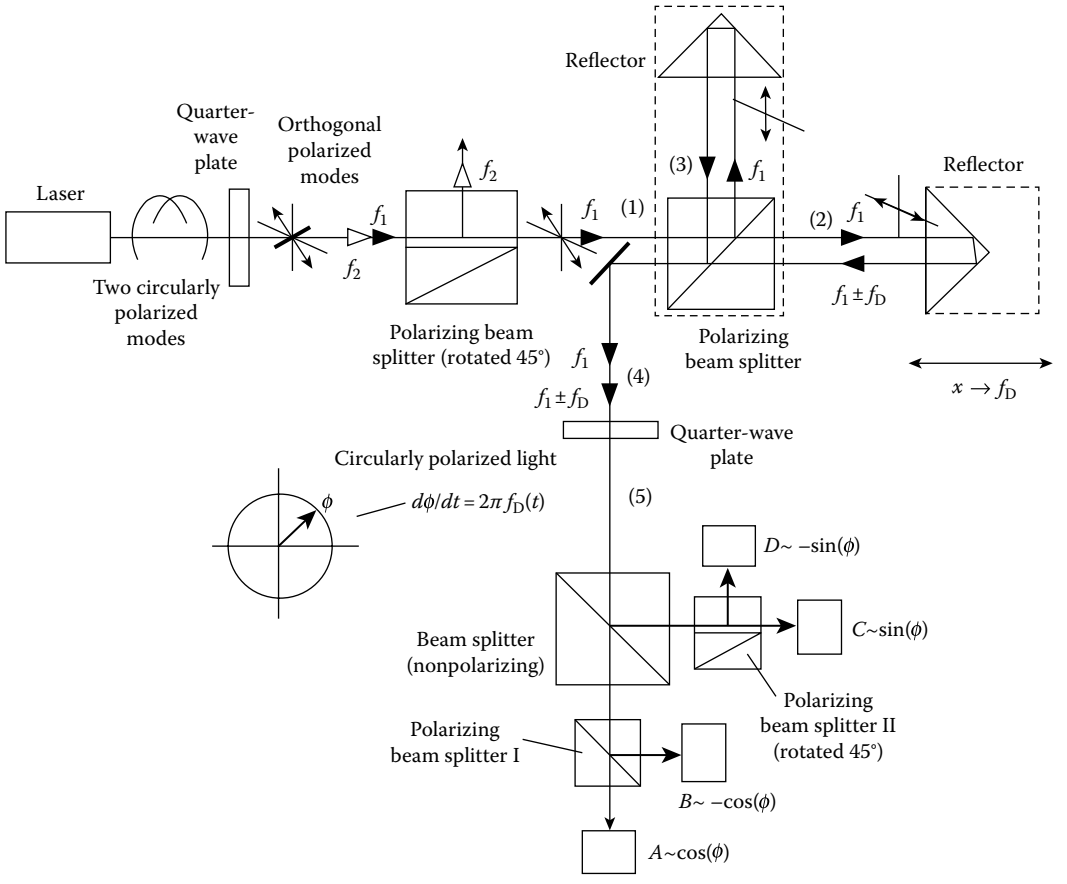

FIGURE 27.6 Single-mode homodyne interferometer. (Courtesy of Spindler & Hoyer, Inc., Milford, MA.)

27.5 Two-Frequency Heterodyne Interferometer

Figure 27.5 shows the commercially available two-frequency Michelson interferometer operating with a Zeeman-stabilized He–Ne laser source. This laser emits two longitudinal modes with frequencies f_1 and f_2 that are both circularly polarized in opposite directions. By passing the modes through a quarter-wave plate, two orthogonal linearly polarized waves are generated. Both are split by a nonpolarizing beam splitter. There is a polarizer located in arm 1 of that splitter, which is rotated by 45° with respect to both polarized waves impinging on it, thus effectively allowing them to interfere behind it yielding a difference frequency of $f_2 - f_1$ that is picked up by a photodetector and counted by a reference counter (frequency difference typically 1.5 MHz).

The orthogonal polarized waves in 2 are further split by a polarizing splitter. Spectral component $f_1 < f_2$ is transmitted into measuring arm 3, and frequency component f_2 is reflected into reference arm 4 of the interferometer. Due to the velocity v of the reflector in arm 3 resulting in a displacement x, the frequency f_1 is Doppler shifted by f_D (Equation 27.5). The movement of the reflector toward the interferometer results in a positive Doppler frequency $f_D > 0$. After recombining both waves from 3 and 4 in the beam splitter again, they are sent through a polarizer in arm 5 that also is rotated by 45° with respect to the direction of polarization of both recombined waves, thereby allowing them to interfere, yielding a difference frequency of $f_2 - f_1 - f_D$ at the location of the photodetector, which is counted by a second counter. By continuously forming the difference of both counts, the measurand (the displacement of x in multiples of $\lambda_A/2$) is calculated.

With this type of interferometer, the direction of motion is given by the sign of the resulting count. One disadvantage of the two-mode heterodyne interferometer is its limited dynamic range for the velocity v of the reflector moving toward the interferometer, since the Doppler frequency f_D, given by

$$f_D = \frac{2}{\lambda_A} v \tag{27.5}$$

is bound to be less than the initial frequency difference between f_2 and f_1 for stationary reflectors. Given a typical Zeeman effect–induced frequency difference f_z of 1.5 MHz, the velocity v is therefore bound to be less than

$$v < \frac{f_z}{2} \lambda_A = 0.474 \text{ m s}^{-1} \tag{27.6}$$

There is no such bound if the reflector is traveling away from the interferometer. By electronically interpolating the output signal of the photodetector, subwavelength resolution can be obtained [21].

27.6 Single-Mode Homodyne Interferometer

An interferometer setup that has no limitation on the maximum velocity in the aforementioned sense is the single-mode homodyne interferometer shown in Figure 27.6.

As in the two-frequency heterodyne interferometer, a Zeeman effect–stabilized laser source that emits two-frequency-displaced circularly polarized axial modes is usually used. After passing through a quarter-wave plate, two orthogonal polarized waves are generated, only one of which (f_1) is further used. The other (f_2) is reflected out of the optical path by an appropriately oriented polarizing beam splitter. The plane of polarization in arm 1 of the interferometer is tilted by 45° with respect to the plane defined by the two arms 2 and 3. The second polarizing beam splitter will transmit one horizontally oriented component into the measuring arm 2 and reflect a vertically oriented component into the reference arm 3 of the interferometer. The two arms of the interferometer maintain their orthogonal polarizations.

The frequency of the wave front in arm 2 is shifted by the Doppler effect (Equation 27.5) due to the motion of the reflector. The light reflected by the two triple mirrors is recombined in the polarizing beam splitter and redirected by a mirror. Since in this particular optical setup, the polarization states of the two beams in the two arms of the interferometer are orthogonal, there is no interference after the redirecting mirror in arm 4 as was the case with the basic Michelson interferometer setup (Figure 27.4). After passing a quarter-wave plate at 45°, two opposite circular polarized waves (one with frequency f_1, the other with frequency $f_1 \pm f_D$) are generated and can be described by a rotating phasor (characterized by $\Phi(t)$) with constant amplitude whose rate of rotation is dependent on the Doppler frequency (in arm 5). Amplitude fluctuations can be observed at the photodetectors A–D after this phasor has passed polarizers, which it does after being split by a nonpolarizing beam splitter.

The output of an interferometer has the general form

$$I(t) = I_o(t)\frac{1}{2}[1+\cos(\Phi(t))] \tag{27.7}$$

It is desired to infer $\Phi(t)$ from observation of $I(t)$. Note that $I_o(t)$, which is the intensity of the laser, can also fluctuate with time. The problems encountered with this are (1) the ambiguity in the sign of $\Phi(t)$ and (2) the dependence of the calculated phase on the intensity fluctuations due to the aging of the laser and optical components. The first problem stems from the fact that arccos(…) yields two solutions to Equation 27.7:

$$\Phi(t) = \pm\arccos\left[\frac{2I(t)}{I_o(t)} - 1\right] \tag{27.8}$$

The sign ambiguity can be resolved by also generating a $\sin(\Phi(t))$ yielding quadrature signals. In order to do so, a second output of the interferometer of the form

$$I_2(t) = I_o(t)\frac{1}{2}\left[1+\sin\left(\Phi(t)\right)\right] \tag{27.9}$$

is sought. Equations 27.7 and 27.9 will determine $\Phi(t)$ unambiguously only in the region $[0,2\pi)$, but there is still an ambiguity modulo 2π. The second problem can be dealt with by adding two more outputs of the form

$$I_3(t) = I_o(t)\frac{1}{2}\left[1-\cos\left(\Phi(t)\right)\right] \tag{27.10}$$

$$I_4(t) = I_o(t)\frac{1}{2}\left[1-\sin\left(\Phi(t)\right)\right] \tag{27.11}$$

Taking Equations 27.7 through 27.10 and 27.9 through 27.11, it is possible to obtain a zero crossing at the linear most sensitive point of inflection of the fringe where the effect of intensity fluctuations on the phase measurement is minimal. The setup of Figure 27.6 attempts to obtain these four outputs. Signal A represents the intensity variations as given in Equation 27.7, and signal B due to the nature of the splitting action is shifted with respect to A by 180° (Equation 27.10). There is another arm to the right of the nonpolarizing beam splitter incorporating the polarizing beam splitter II, which is rotated by 45° with respect to beam splitter I so that the attached detectors C and D are generating the signals defined by Equations 27.9 and 27.11.

Since the Doppler frequency is time dependent according to the velocity v of the measuring reflector, the distance, x, traveled by the reflector up to time T is given by Equation 27.12:

$$x = \int_0^T v(t)dt = \int_0^T f_D(t)\frac{\lambda_A}{2}dt = \int_0^T \frac{\partial \Phi(t)}{\partial t}\frac{\lambda_A}{4\pi}dt \tag{27.12}$$

It should be noted that the resolution of this interferometer is limited to $\lambda_A/4$ if no special hardware is used to interpolate between interference fringes.

This particular interferometer is not limited with respect to a maximum unambiguous Doppler frequency.

27.7 Displacement Sensor Based on a Fabry–Pérot Interferometer

The classical Michelson interferometer as detailed in the section earlier clearly is the system of choice for larger distances to be measured and if there is sufficient space to place the optical components in. In case there is a little available space to place a sensor but still there is the requirement for high precision measurements, a Fabry–Pérot-type sensor, as shown in Figure 27.7a, might be a good choice. A Fabry–Pérot interferometer is typically made of a resonator with two reflecting surfaces causing the light waves to multiply and bounce back and forth thus resulting in transmittance functions exhibiting steep transmission peaks dependent on the wavelength of the light source and the reflectivity of the surfaces as measured by the so-called finesse [20].

If a fixed laser wavelength λ is used and the finesse is kept rather small by using the nonpolished surface of the object as retroreflector (actually scatterer) and the end face of the monomode optical fiber as the second surface, one still obtains a Fabry–Pérot cavity if a collimating lens is properly placed between the fiber and the object. The optical output intensity is now varying as the distance x between the sensor (actually the fiber end face) and the retroreflecting surface is changed. This change in intensity $I_R(x)$ as a function of distance is shown in Figure 27.7b.

One can identify regions that allow for a large sensitivity (the steep slopes of the curve) but also regions (encircled) that do not show changes in output intensity if x is varied. To overcome this restricting drawback, the wavelength λ is periodically modulated (f in the kHz range) in the time domain by $\Delta\lambda$. In analyzing the systems response to this modulation, one can show [22] that the λ modulation results in an output signal whose modulation component is 90° phase shifted (yielding a quadrature component $\delta I_R(x)$) to the main signal, thus allowing to evaluate also in the flat and insensitive part of the Fabry–Pérot characteristic.

This extra feature not only overrules the usual Fabry Pérot blind spot limitations but also allows the sensing of displacement direction. Therefore, it paves the way toward ultrahigh resolution displacement sensing on the overall mirror displacement range. Moreover, by means of a special engineering technique, the fiber probe allows a tilt of ±0:4° at a 100 mm range, thus allowing a plug-and-measure application of the sensor without the need for prior careful alignment. The attainable measurement range is on the order of $x_{min} < x < 100$ mm with a repeatability of better than 10 nm combined with a maximum displacement velocity of 25 mm s^{-1}.

27.8 Interferometer Signal Processing

At the photodetectors ends the optical path of the interferometers. Since the photodetectors are sensitive to light intensity values, only the sinusoidal signal caused by the motion of the reflector will be superimposed onto a pedestal signal proportional to the mean intensity overtime or displacement, respectively. The electronics attached to the photodetectors is aimed to reliably detect zero crossings of the sinusoidal

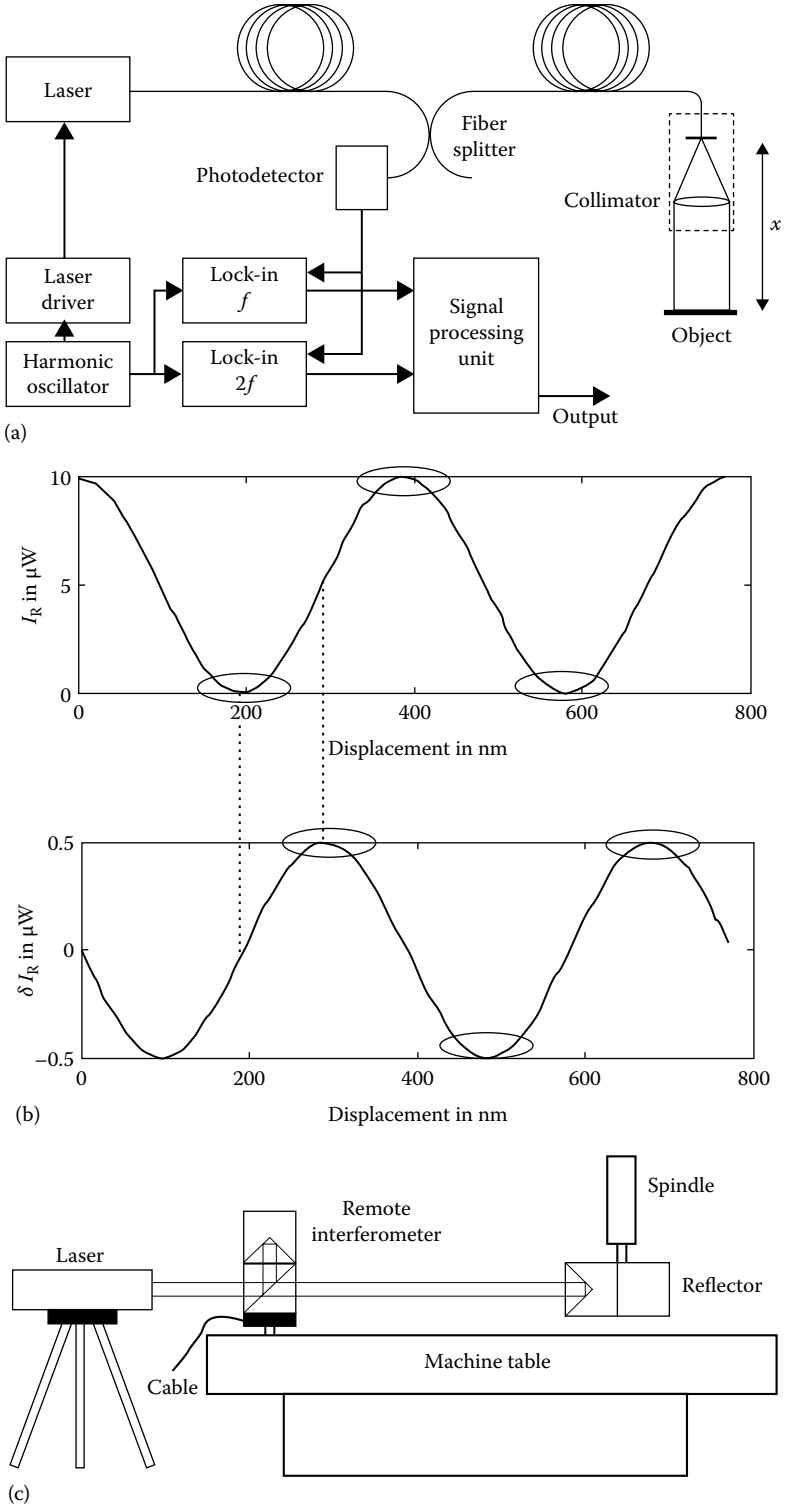

FIGURE 27.7 Displacement sensor based on a Fabry–Pérot interferometer: (a) a Fabry–Pérot-type sensor, (b) change in intensity as a function of distance, and (c) an experimental set up.

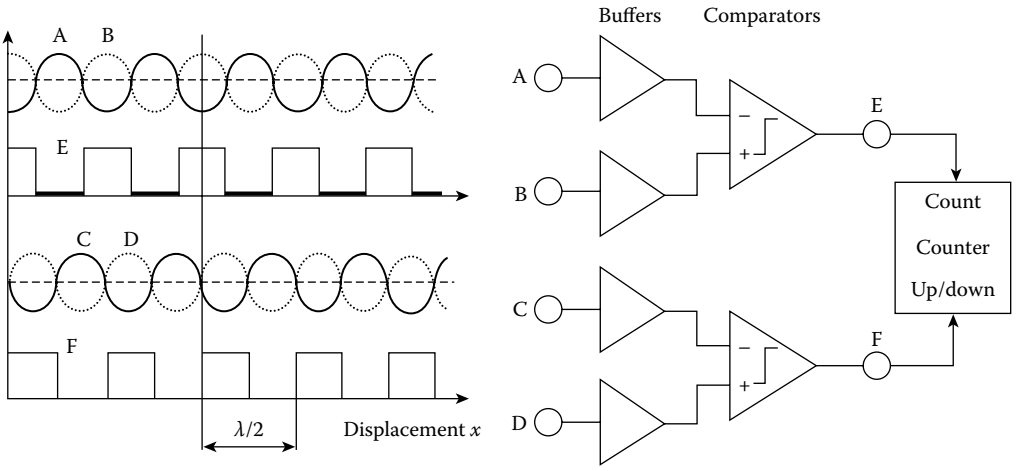

FIGURE 27.8 Simple signal conditioning circuit yielding quadrature signals E and F.

component of the signals (A through D) even under low-contrast conditions by subtracting out the pedestal signal component in the comparators. Low fringe contrast can be the result of small reflector tilt and/or vibration during periods of reflector movement, nonideal interferometer alignment, and imperfections in optical components like unequal splitting of the beam in beam splitters. Figure 27.8 shows a simple conditioning unit.

The main purpose of that setup is to produce digital quadrature signals (E and F in Figure 27.8) that can most easily be used to perform signal interpolation digitally [23,24] and also allow for the determination of the direction of movement by using, for example, signal E as count signal and F as an up/down indicator.

Both comparators compare sinusoidal components having a possibly slowly time-varying dc pedestal amplified by buffer amplifiers. All photodetector signals A through D will be affected by this dc pedestal so that forming their difference in the comparator will yield zero-crossing signals independent of the pedestal. The two comparator units are necessary to generate quadrature signals for direction detection. Furthermore, this electronics allows easily for a fringe interpolation by a factor of 4, bringing the least-count resolution of the interferometer down to $1 \approx 60$ nm. This interpolation can be done if instead of feeding the signal E into the count input, the exored signal E⊕F is used. In this case, the up/down terminal of the counter circuit needs to connect to the signal E&F. If an even higher resolution is sought, the digital interpolation of these quadrature signals can be performed [21,23,24].

27.9 Typical Interferometer Applications

Interferometers are typically used in calibration procedures for machine tools or coordinate-measuring machines (CMMs). A typical so-called remote interferometer optics arrangement is shown in Figure 27.7c. The advantage of the arrangement is twofold. Firstly, as compared to the interferometer optics directly attached to the laser, any vibrations between the laser head and the machine table do not influence (to a first degree) the measurement accuracy, and secondly, any heat dissipated by the laser is kept away from the interferometer optics, the optical paths, and clearly also from the machine under test. The last point is especially important since typical helium–neon lasers do dissipate on the order of 5–10 W; thus, they have the potential to cause significant warming of the high-accuracy machines resulting in a degradation of accuracy at the micron level.

Providing thermal drift has been eliminated this way; the accuracy of the linear laser measurement depends primarily on the performance of the weather station used to correct for air humidity, temperature, and pressure.

27.10 Conclusions

Using laser interferometers operating with highly stabilized laser sources, relative uncertainties in length measurements as low as 5×10^{-8} can be realized, which makes these kinds of equipment suitable to convey primary and secondary length standards into industrial measurement labs. Since, for practical purposes, these interferometers need to be operated in ambient air, the uncertainty in the refractive index of air gives the largest single factor limiting the overall precision. Decreasing the uncertainty stemming from that source necessitates the determination of environmental parameters such as relative humidity, temperature along the optical path, and atmospheric pressure with very little error. Laser refractometers able to determine the refractive index of air directly, on the other hand, allow for the direct measurement and compensation of the refractive index. Zeeman effect–stabilized laser sources can reach a relative uncertainty of less than 10^{-8} and thus contribute only a small portion of the overall error. The interferometer itself, depending on the signal processing involved, will have at least-count resolution of $\lambda_A/4$ without any optical or electronic interpolation and can have an order of magnitude less uncertainty if high-performance phase meters are used to subdivide the wavelength λ_A. The very high-quality air bearings and a very well-controlled measurement environment are necessary to reach these goals.

27.A Appendix

In Table 27.A.1, some companies are listed that manufacture either complete interferometer systems or major components thereof, such as beam splitters, retroreflectors, refractometers, and wavemeters. This list is by no means exhaustive. Furthermore, no price information is included because the system cost is too much dependent on the particular choice of system components.

TABLE 27.A.1 Companies that Produce Interferometers or Components

Manufacturer	Components	Complete Systems
Agilent Technologies, Inc., 5301 Stevens Creek Blvd, Santa Clara, CA 95051, (877) 424 4536	*	*
AttoCube Systems, Koeniginstr. 11, D-80539 Munich, Germany, +49 89 2877 809—19	*	*
Lasertex Sp., ul.Radzionkowska 17, 51-506 Warsaw, Poland, +48 509 495 023	*	—
CVI Melles Griot, Inc., 200 Dorado Place SE, Albuquerque, NM 87123, (505) 296 9541	*	—
Polytec PI, Inc., Auburn, MA 01501, (508) 832 3456	*	—
Renishaw plc New Mills, Wotton-under-Edge, Gloucestershire, GL12 8JR, United Kingdom, +44 1453 524524	—	*
SIOS Messtechnik GmbH, Am Vogelherd 46, D-98693 Ilmenau, Germany, +49 3677 64470	*	*
Zygo Corporation, Middlefield, CT 06455-0448, (860) 347 8506	*	*

Defining Terms

Heterodyne technique: The superposition of two harmonic signals with frequencies f_1 and f_2 in a nonlinear device that results in a signal containing both sum and differences frequencies. For interferometric purposes where each individual frequency is in the 10^{14} Hz range, the frequency difference might be low enough to be registered by photodetectors. They also serve as nonlinear devices because their response is to light intensity only, which is proportional to the light amplitude squared.

Interference: A phenomenon that strikingly illustrates the wave nature of light. It occurs when radiation follows more than one path from its source to the point of detection. It may be described as the local departures of the resultant intensity from the law of addition as the point of detection is moved, for the intensity oscillates about the sum of the separate intensities.

Laser: The acronym of *l*ight *a*mplification by *s*timulated *e*mission of *r*adiation. It was originally used to describe light amplification but has more recently come to mean an optical oscillator.

Refractive index: A number specifying the ratio of the propagation velocities of light in vacuum c to that in a medium. The refractive index for any medium is always somewhat larger than 1. Its value is dependent on the composition of the medium and the wavelength of the incident radiation.

Zeeman effect: An effect that is observed if excited atoms emit their radiation in the presence of a magnetic field. The longitudinal Zeeman effect causes a single emission line to split symmetrically into right and left circularly polarized lines.

References

1. Documents concerning the new definition of the metre, *Metrologia*, 19, 163–177, 1984.
2. E. Jaatinen and N. Brown, A simple external iodine stabilizer applied to 633 nm, 612 nm, and 543 nm He-Ne lasers, *Metrologia*, 32, 95–101, 1995.
3. A. E. Siegman, *Lasers*, Mill Valley, CA: University Science Books, 1986.
4. W. R. Steel, *Interferometry*, 2nd edn. (Cambridge studies in modern optics), Cambridge, U.K.: Cambridge University Press, 1985.
5. W. R. C. Rowley, The performance of a longitudinal Zeeman-stabilized He–Ne laser (633 nm) with thermal modulation and control, *Meas. Sci. Technol.*, 1, 348–351, 1990.
6. W. Demtröder, *Laser Spectroscopy: Basic Concepts and Instrumentation*, 2nd edn., Berlin, Germany: Springer, 1996.
7. B. Edlén, The dispersion of standard air, *J. Opt. Soc. Am.*, 43(5), 339–344, 1953.
8. B. Edlén, The refractive index of air, *Metrologia*, 2(2), 71–80, 1966.
9. J. C. Owens, Optical refractive index of air: Dependence on pressure, temperature and composition, *Appl. Opt.*, 6(1), 51–59, 1967.
10. H. D. Baehr, *Thermodynamik*, 6th edn., Berlin, Germany: Springer, 1988.
11. R. Revelle, Carbon dioxide and world climate, *Sci. Am.*, 247(2), 35, 1982.
12. K. P. Birch, F. Reinboth, R. W. Ward, and G. Wilkening, Evaluation of the effect of variations in the refractive index of air upon the uncertainty of industrial length measurement, *Metrologia*, 30(1), 7–14, 1993.
13. K. P. Birch and M. J. Downs, An updated Edlén equation for the refractive index of air, *Metrologia*, 30, 155–162, 1993.
14. K. P. Birch and M. J. Downs, Corrections to the updated Edlén equation for the refractive index of air, *Metrologia*, 31, 315–316, 1994.
15. P. E. Ciddor, Refractive index of air: new equations for the visible and near infrared, *Appl. Opt.*, 35(9), 1566–1573, 1996.
16. F. E. Jones, The refractivity of air, *J. Natl. Bur. Stand.*, 86(1), 27–32, 1981.

17. W. T. Estler, High-accuracy displacement interferometry in air, *J. Appl. Opt.*, 24(6), 808–815, 1985.
18. Zygo Corporation, Error sources in displacement measuring interferometry, see http://www.zygo.com/library/papers/ZMI_Error_Sources.pdf (accessed on March 14, 2013).
19. J. A. Smith, U. W. Rathe, and C. P. Burger, Lasers with optical feedback as displacement sensors, *Opt. Eng.*, 34(9), 2802–2810, 1995.
20. N. Takahashi, S. Kakuma, and R. Ohaba, Active heterodyne interferometric displacement measurement using optical feedback effects of laser diodes, *Opt. Eng.*, 35, 802–907, 1996.
21. J. A. Smith and C. P. Burger, Digital phase demodulation in heterodyne sensors, *Opt. Eng.*, 34, 2793–2801, 1995.
22. K. Karrai, Device for position detection, Patent No. U.S.2010/0259760 A1, October 14, 2010.
23. K. Oka, M. Tsukada, and Y. Ohtsuka, Real-time phase demodulator for optical heterodyne detection processes, *Meas. Sci. Technol.*, 2, 106–110, 1991.
24. J. Waller, X. H. Shi, N. C. Altoveros, J. Howard, B. D. Blackwell, and G. B. Warr, Digital interface for quadrature demodulation of interferometer signals, *Rev. Sci. Instrum.*, 66, 1171–1174, 1995.

28

Bore-Gaging Displacement Sensors

Viktor P. Astakhov
Astakhov Tool Service

28.1 Introduction

Holes, also known as bores, in general are one of the most common features of mechanical component. In precision applications, eccentricity and diameter of the holes directly relate to the performance and even service life of the component. Deviation from the permissible tolerances can impede operation and result in premature failure of the system, It is thus important to inspect and validate the dimensional accuracy, such as the diameter, shape, and position (e.g., eccentricity) of the holes. To do these, many state-of-the-art hole inspection gages are available.

Bore gaging, already a significant factor in manufacturing, has become increasingly important in metrology because of the growing concern for total quality assurance (TQA). Compared with outside-diameter (OD) measurement, bore gaging creates more engineering challenges by the very nature of its special role in QA. This is especially true when measuring difficult-to-assess internal features such as splines, threads, and deep bores.

As machine capability increases, so does the demand for dimensional gaging to cope with tighter limits on tolerances and greater complexity of component parts. Manufacturers are concerned not only with making the component to a specific tolerance band but also with size variation from component to component because it gives them better control of their process. To meet this demand, the gage they use must be able to discriminate size variation better than before. Moreover, many manufacturers now require that any in-process or post-process gage record and send the measured size of a component to a statistical process control (SPC) or data-collection system. This chapter is to familiarize manufacturing professionals with the basic concepts of bore gaging.

Dimensions are a part of the total specification assigned to parts designed by engineering. However, the engineer in industry is constantly faced with the fact that no two objects in the material world can

ever be made exactly the same. The small variations that occur in repetitive production must be considered in the design. To inform the workman how much variation from exact size is permissible, the designer uses a tolerance or limit dimension technique. A *tolerance* is defined as the total permissible variation of size, or the difference between the limits of size. *Limit dimensions* are the maximum and minimum permissible dimensions. Proper tolerancing practice ensures that the finished product functions in its intended manner and operates for its expected life.

28.2 Bore Tolerancing

All bore dimensions applied to the drawing, except those specifically labeled as basic, gage, reference, maximum, or minimum, will have an exact tolerance, either applied directly to the dimension or indicated by means of general tolerance notes. For any directly tolerated decimal dimension, the tolerance has the same number of decimal places as the decimal portion of the dimension [1].

Engineering tolerances may broadly be divided into three groups: (1) *size tolerances* assigned to dimensions such as length, diameter, and angle; (2) *geometric tolerances* used to control a hole shape in the longitudinal and transverse directions; and (3) *positional tolerances* used to control the relative position of mating features. Interested readers may refer to [1,2].

The ISO system of limits and fits (ISO 286-2:2010 "Geometrical product specifications (GPS)—ISO code system for tolerances on linear sizes—Part 2: Tables of standard tolerance classes and limit deviations for holes and shafts") covers standard tolerances and deviations for sizes up to 3150 mm. The system is based on a series of tolerances graded to suit all classes of work from the finest to the coarsest, along with different types of fits that range from coarse clearance to heavy interference. Here, *fit* is the general term used to signify the range of tightness that may result from the application of a specific combination of tolerances in the design of mating parts.

There are 18 tolerance grades intended to meet the requirements of different classes of parts. These tolerance grades are referred to as ITs and range from IT 01, IT 02 (reserved for the future), and IT 1 to IT 16 (for today's use). In each grade, the tolerance values increase with size according to a formula that relates the value of a given constant to the mean diameter of a particular size range. The system provides 27 different fundamental deviations for sizes up to and including 500 mm and 14 for larger sizes to give different type of fits ranging from coarse clearance to heavy interference. Interested readers may refer to standard ISO/TS 14253-4:2010 Geometrical product specifications (GPS)—Inspection by measurement of workpieces and measuring equipment—Part 4: Background on functional limits and specification limits in decision rules.

28.3 Components of Gage Accuracy

The accuracy of a gage is determined by three factors:

- *Resolution*: For a gage to accurately determine whether or not a component is in tolerance, the general rule is that the gage resolution should be near 10% of the tolerance.
- Reproducibility and repeatability (R&R).
- *Linear accuracy*: This is the value of maximum deviation from the true size a gage will be capable of measuring across its entire working range. As this figure is intrinsically linked to the range of the gage, it means nothing unless considering both the value of deviation and the range together. Many manufacturers mistakenly use the 10% rule that establishes an appropriate resolution and apply it to linear accuracy. This is incorrect, because it does not take into account the range of the gage.

28.4 Bore-Gage Classification and Specification

To measure the aforementioned tolerances, modern manufacturing requires the use of gages. A *gage* is defined as a device for investigating the dimensional fitness of a part for specific function. *Gaging* is defined by ANSI as a process of measuring manufactured materials to assure the specified uniformity

of size and contour required by industries. Gaging thereby assures the proper functioning and interchangeability of parts; that is, one part will fit in the same place as any similar part and perform the same function, whether the part is for the original assembly or replacement in service [3].

Bore gages may be classified as follows:

1. Master gages
2. Inspection gages
3. Manufacturer's gages
4. Gages that control dimensions
5. Gages that control various parameters of bore geometry
6. Fixed-limit working gages
7. Variable-indicating gages
8. Post-process gages
9. In-process gages

Master gages are made to their basic dimensions as accurately as possible and are used for reference, such as for checking or setting inspection of manufacturer's gages. *Inspection gages* are used by inspectors to check the manufactured products. *Manufacturer's gages* are used for inspection of parts during production.

Post-process gages are used for inspecting parts after being manufactured. Basically, this kind of gage accomplishes two things: (1) it controls the dimensions of a product within the prescribed limitations, and (2) it segregates or rejects products that are outside these limits. Post-process gaging with feedback is a technique to improve part accuracy by using the results of part inspection to compensate for repeatable errors in the bore manufacturing operations. The process is normally applied to CNC (computer numerically controlled) machines using inspection data to modify the part program and on tracer machines using the same data to modify the part template.

In-process gages are used for inspecting parts during the machining cycle. In today's manufacturing strategy, in-process gages and data-collection software provide faster feedback on quality. Indeed, the data-collection and distribution aspect of 100% inspection has become as important as the gaging technology itself. Software specifically designed to capture information from multiple gages, measure dozens of products types and sizes, and make it available to both roving inspectors and supervising quality personnel as needed is quickly becoming part of quality control strategies as an integral part of the measurement systems analysis (MSA). In conjunction with CNC units, in-process gaging can automatically compensate for workpiece misalignment, tool length variations, and errors due to tool wear.

28.5 Bore-Gage Types

In choosing a bore gage, one should first eliminate those types of bore gages that are least appropriate for the application. For example, for a production environment, noncontact measurement techniques, including optical and laser methods, tend to be bulky, relatively expensive, and inflexible when measuring special internal features. Such gaging requires the part to be taken to the gage. Not all types of noncontact systems are suitable for a production environment, and many entail high maintenance costs.

Gages that control dimensions are used to control bore diameter [3]. These gages can be either post-process or in-process gages. Further, these gages can be either *fixed-limit gages* or *variable-indicating gages*. These cages are classified as (1) plug/pin gages, (2) needle gages, (3) chamfer gages, countersink gages, (4) dial caliper gages, (5) dial bore gages, (6) electronic bore gages, (7) hole micrometers/ingages, and (8) telescopic gages.

28.5.1 Fixed-Limit Gages

A *plug (pin) gage* is a fixed-limit working bore gage [3]. These inexpensive gages do not actually measure dimensions or geometry. They simply tell the operator whether the bore is oversized or undersized.

FIGURE 28.1 Typical plug gages: (a) double end (left go, right no-go) and (b) progressive.

The actual design of most plug gages is standard, being covered by American Gage Design (AGD) standards. A plug gage is usually made up of two members. One member is called the go end and the other the no-go or not-go end. The gage commonly has two parts: the gaging members, and a handle with the sign, go or no go, and the gage maker's tolerance marked on it. In today's manufacturing, three types of AGD standard plug/pin gages are used. The first is the double end (Figure 28.1a); the second is the progressive gage in which the go and no-go parts follow each other (Figure 28.1b); and the third is the pin gage (Figure 28.2) that comes with the set of pins of various bore sizes. Pin gages became the most popular in the automotive industry due to their versatility and fast interchangeability of pins. Plug gages are used not only to inspect round holes but also to inspect hole of any shape. For example, Figure 28.3 shows a plug gage for threaded holes. Interested readers may refer to [3].

Fixed-limit gage tolerance is generally determined from the amount of workpiece tolerance. A 10% rule is generally used for determining the amount of gage tolerance for fixed, limit-type gages. Four classes of gage makers' tolerances have been established by the American Gage Design Committee and are in general use [3]. These four classes establish maximum variation for any designed gage size. The degree of accuracy needed determines the class of gage to be used. Table 28.1 shows these four classes of gage makers' tolerances. Referring to Table 28.1, class XX gages are used primarily as master gages and for final close tolerance inspection. Class X gages are used for some types of master gage work and as close tolerance inspection and working gages. Class Y gages are used as inspection and working gages.

FIGURE 28.2 Typical pin gage and set of pins.

FIGURE 28.3 Plug thread gage.

TABLE 28.1 Standard Gage Makers' Tolerances (ANSI/ASME B89.1.5)

Diameter	XXX	XX	X	Y	Z	ZZ
Above-Including						
Inches						
0.010–0.825	0.000010	0.000020	0.000040	0.000070	0.0001	0.0002
0.825–1.1510	0.000015	0.000030	0.000060	0.000090	0.00012	0.00024
1.510–2.510	0.000020	0.000040	0.000080	0.00012	0.00016	0.00032
2.510–4.510	0.000025	0.000050	0.0001	0.00015	0.0002	0.0004
4.510–6.510	0.000033	0.000065	0.00013	0.00019	0.00025	0.0005
6.510–9.010	0.000040	0.000080	0.00016	0.00024	0.00032	0.00064
9.010–12.010	0.000050	0.0001	0.00002	0.0003	0.0004	0.0008
Millimeters						
0.254–20.96	0.00025	0.00051	0.00102	0.00178	0.00254	0.00508
20.96–38.35	0.00038	0.00076	0.00152	0.00229	0.00305	0.00610
38.35–63.75	0.00051	0.00102	0.00203	0.00305	0.00406	0.00813
63.75–114.55	0.00064	0.00127	0.00254	0.00381	0.00508	0.01016
114.55–165.35	0.00084	0.00165	0.00330	0.00483	0.00635	0.01217
165.35–228.85	0.00102	0.00203	0.00406	0.00610	0.00813	0.01626
228.85–305.05	0.00127	0.00254	0.00508	0.00762	0.01016	0.02032

TABLE 28.2 Class X MG-25 Series Pin Gage Sets by Meyer Gage Company, Inc.

	Nominal Size Range		
Gage Set No.	English (in.)	Metric (mm)	Set Price USD
MG1-25	0.0110–0.0609	0.28–1.55	240.79
MG2-25	0.0610–0.2509	1.55–6.37	119.79
MG3-25	0.2510–0.5009	6.38–12.72	138.10
MG4-25	0.5010–0.7499	12.73–19.05	190.58
MG5-25	0.7500–0.8129	19.05–20.65	266.82

Class Z gages are used as working gages where part tolerances are large. Table 28.2 shows the diameter ranges of pin gage sets manufactured by Meyer Gage Company, Inc.

28.5.2 Variable-Indicating Gages: Two- and Three-Point Bore-Gage Options

Two- and three-point contact measurement is a popular solution as a production gage and provides many options. The gage is typically calibrated to a reference master, such as a setting ring, which means that only the setting ring itself must be calibrated regularly. Depending on the type chosen, gages under this description can have a wide working range. Moreover, they offer the best flexibility for adaptation to special feature measurement. Both two- and three-point contact methods can measure deep into bores, have lower initial and maintenance costs, and are portable. Digital versions can interface with SPC systems.

Cylinder bore gage was originally developed to measure cylinder bores in the automotive industry. It is a two-point contact measuring system for use on components that may be subject to ovality problems. The design includes a mechanism to centralize the measuring head in the bore. It is a cost-effective solution for simple bore measurement and can be easily adapted to measure deep bores up to 6 ft (approx. 1.8 m) deep. Cylinder bore gages are not easily adapted to measure special features

FIGURE 28.4 Self-centering two-point bore gage.

and require multiple setting masters. Analog versions require the operator to decide when he has established the minimum value, which can introduce variability from operator to operator. Unless a definite tendency toward ovality exists in the manufacturing process, a three-point system is a better solution.

A mechanical self-centering two-point bore gage shown in Figure 28.4 is made for comparative measurements of bores along with their form errors. This self-centering tool can be used with dial indicators, precision comparator indicators, and electrical or digital probes. The bore gage will accept both 8 mm and 3/8 in. diameter stems, virtually any dial indicator, right off the shelf, even indicators that one may already have in the shop. No special housing is required. By using indicators reading in 0.0001 in. or 0.002 mm, one can have a bore gage that measures both metric and inch. Table 28.3 shows the diameter ranges and prices of self-centering two-point bore gages manufactured by TESA Co.

Micrometer bore gages come in a wide variety. The simplest micrometer bore gage is shown in Figure 28.5. The traditional internal micrometer has many advantages because of its flexibility, offering a choice of two- or three-point systems, a large working range on each measuring head, and adaptability to measuring special features. Depending on which design is chosen, it is possible to find systems that can measure from 0.040 in. (1 mm) to 12 in. (300 mm) as a standard range. Both analog (Figure 28.5) and digital (Figure 28.6) versions are available, with the digital available as either mechanical or electronic. Basic parameters of bore-gage micrometers by Bowers Metrology UK are presented in Table 28.4. Only the electronic versions have the ability to send data to an SPC system, printer, or data collector.

TABLE 28.3 TESA Veribor Bore Gages

Range	Veribor Number	Order Number	Sale Price (USD)
0.7–1.4 in. 18–35 mm	05790090	29457	437.00
1.4–2.5 in. 35–63 mm	05790091	29458	426.00
2–6 in. 50–152 mm	05790092	29459	491.00
0.7–6 in. 18–152 mm	05790093	29479	833.00

FIGURE 28.5 Simplest bore-gage micrometer.

FIGURE 28.6 Bore-gage micrometer with a digital readout by Bowers Metrology UK.

For example, Marposs Corp. developed a new wireless bore gage called iWave (Figure 28.7). It is composed of a standard MBG plug gage directly connected to a special handle housing the wireless (*Bluetooth*® wireless technology) transmitter and the power supply batteries. By pushing a button, real-time measurement values are displayed on the receiving electronic unit, with the possibility to store the measurement data. The robust and reliable StarLock system allows gage head changeover in just few seconds, without the need of any tool accommodating various mechanical gage heads such as (a) Marposs M1 Star MBG plug heads and any existing plug head on the market, (b) Marposs M3 Star snap heads and rings, (c) depth gages, (d) sweep gages, and (e) gages for chamfers, spot facings, and countersinks. A dedicated computer (Merlin™) that receives the signal is capable of statistical analysis with graphic display (histogram, control charts, value chart, etc.), numeric summary (e.g., spread and average), and data segregation (by machine, product batch, and analysis purposes), and measured part counters local and remote data storage and access.

TABLE 28.4 Parameters of Bore-Gage Micrometers by Bowers Metrology UK

Product Code (mm)	Range (mm)	Product Code (mm)	Range (mm)	Accuracy		Measuring Depth		Setting Ring	
				mm	in.	mm	in.	mm	in.
XTD6M	6–8	XTD6i	1/4–5/16	0.003	0.0001	58	2.28	8	0.312
XTD8M	8–10	XTD8i	5/16–3/8	0.003	0.0001	58	2.28	8	0.312
XTD10M	10–12.5	XTD10i	3/8–1/2	0.003	0.0001	58	2.28	12.5	0.500
XTD12M	12.5–16	XTD12i	1/2–5/8	0.003	0.0001	62	2.44	12.5	0.500
XTD16M	16–20	XTD16i	5/8–3/4	0.003	0.0001	62	2.44	20	0.750
XTD20M	20–25	XTD20i	3/4–1	0.003	0.00015	66	2.62	20	0.750
XTD25M	25–35	XTD25i	1–1 3/8	0.003	0.00015	66	2.62	35	1.375
XTD35M	35–50	XTD35i	1 3/8–2	0.003	0.00015	80	3.15	35	1.375
XTD50M	50–65	XTD50i	2–2 5/8	0.004	0.00015	80	3.15	65.0	2.625
XTD65M	65–80	XTD65i	2 5/8–3 1/4	0.004	0.00015	80	3.15	65.0	2.625
XTD80M	80–100	XTD80i	3 1/4–4	0.004	0.00015	100	3.94	80.0	3.250
XTD100M	100–125	XTD100i	4–5	0.005	0.0002	115	4.53	125	5.000
XTD125M	125–150	XTD125i	5–6	0.005	0.0002	115	4.53	125	5.000
XTD150M	150–175	XTD150i	6–7	0.005	0.0002	115	4.53	175	7.000
XTD175M	175–200	XTD175i	7–8	0.005	0.0002	115	4.53	175	7.000

FIGURE 28.7 iWave wireless bore gage by Marposs Corp.

Pistol-grip bore gages (Figure 28.8) offer all the advantages of the traditional internal micrometer, and also allow a fast, single-handed operation. The fact that there is a constant gaging force, independent of operator "feel," with the pistol-grip bore gage, facilitates good gage repeatability and reproducibility results. It is very adaptable to measuring special features such as spline pitch diameter, ball races, and ball nuts.

FIGURE 28.8 Pistol-grip bore gage and its use.

Multipoint contact bore gages shown in Figure 28.9 are still the most popular for high-precision inspections. This line of bore gages has been the industry standard for more than 60 years. Its features are as follows: (1) Comfortable and ergonomic well-balanced handle can be removed to gain clearance in restricted areas; (2) precision-machined aluminum dial unit housing, stainless steel bore-gage extension tubing in wide variety of standard and special lengths; (3) thermally insulated high-impact resistant shield protects extension tubing, replicable contacts available in steel, carbide, or diamond. Proven bell crank transfer is accurate and linear over its entire range; (4) precisely machined cast-phosphor-bronze gaging head for sensitivity and durability; and (5) all bore-gage sizes utilize the same dial unit housing for extreme versatility.

Air gages are used in the measurement of multiple features of precision bores. Air gage sensors measure the backpressure created when an air nozzle is brought in close proximity to the workpiece. Figure 28.10 shows the principle of air gaging: the air gage readout measures this pressure and displays the dimensional change in the air gap. The following features of air gages should be pointed out: (a) *Noncontact*—the air nozzle throttles the air at the point where the air exits the jet hole, thus the average height of a spot on the surface opposite the jet hole is sensed by the air readout. Since the nozzle does not contact the workpiece, wear does not directly affect the accuracy of the gage; moreover, the pressure of the air has a self-cleaning effect on the workpieces, making air gages perform exceptionally well in shop-floor environments. (b) *Sensor size*—air nozzles can be made with jet holes from 0.010 to 0.100 in. (0.25–2.54 mm),

FIGURE 28.9 Multipoint contact bore gages.

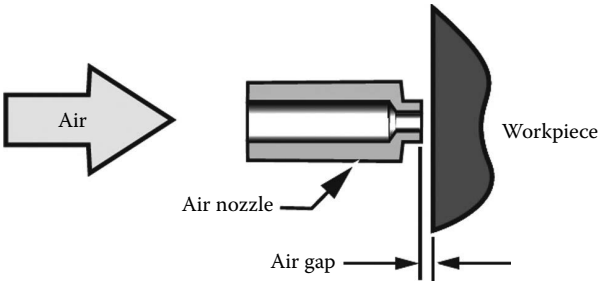

FIGURE 28.10 Principle of air gaging.

with 0.050 in. (1.25 mm) being preferred for most applications. (c) *Gaging ranges*—air gages have relatively limited ranges. For good linearity, the gaging range of air gage member must be less than 8% of the jet hole size. For most applications, practical limits on air flow limit jet sizes to 0.079 in. (2 mm) and gaging ranges to 0.006 in. (0.1 mm) or less. Furthermore, applications requiring exceptionally high accuracies, such as diametrical tolerance limits of 0.00008 in. (0.002 mm), are best measured by air gage members designed for ranges 0.0006 in. (0.015 mm) or less. (d) *Response time* depends on the volume of the air circuit and the size of the gaging nozzles. Response times can vary from less than 100 ms to several seconds; except for gages with very small jet sizes, typical response times will be less than 2 s. (e) *Cost*—air gage nozzles are less expensive than electromagnetic gaging cartridges. For applications that require the summing of inputs from two or more sensors, they are significantly less expensive than electromagnetic gaging.

Figure 28.11 shows the construction of a typical air probe. The probe comprises a hardened steel body in which air passages are drilled to two or more gaging nozzles. The body is precision ground to slip into

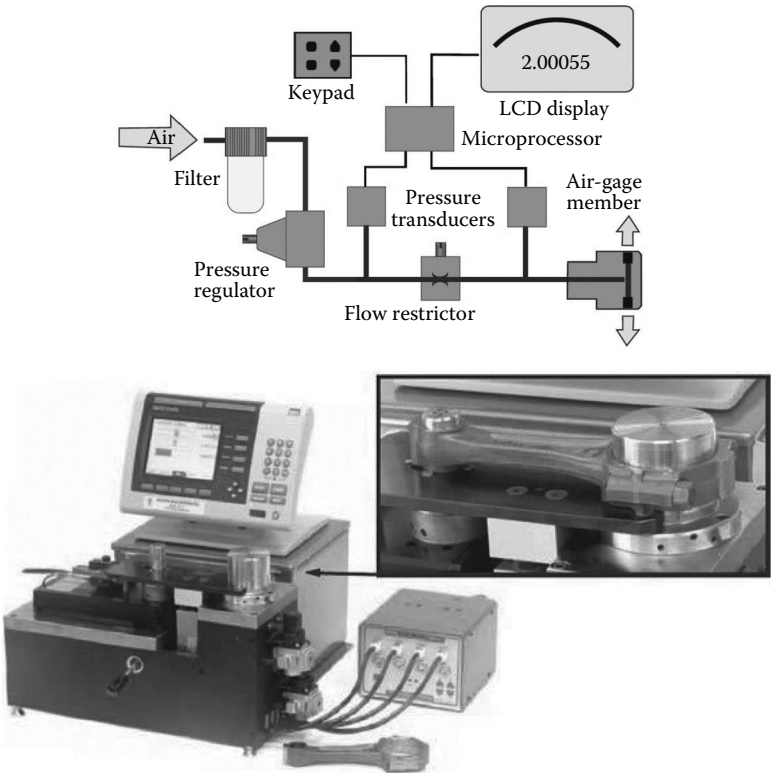

FIGURE 28.11 Electronic air gage by Western Gage Corp.

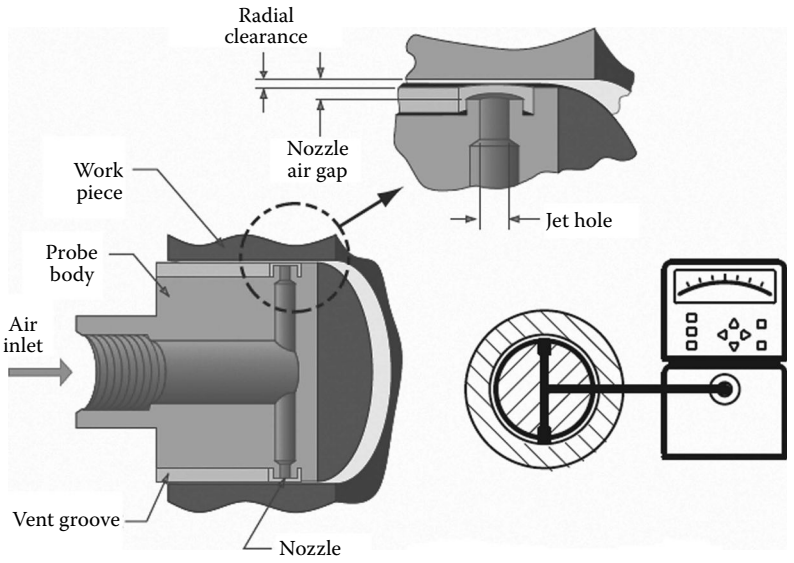

FIGURE 28.12 Air probe features.

the bore at the low limit of the product tolerance; Figure 28.12 shows the nozzle tips are recessed a small amount below the probe body as shown in the magnified view of the air gage nozzle. By recessing the air nozzles below the probe body, the measurement is made noncontact so that wear does not directly affect the accuracy of the gage. The air flow purges the gaging surface of contaminants, thus making air gage measurements highly reliable. The opposed nozzle design of the probe creates a "differential" type of measurement that is independent of how the probe is positioned radially within the test bore, that is, radial movement causing an increase in air flow in one nozzle is offset by a corresponding decrease in flow in the opposing nozzle. These features are key factors in attaining fast accurate gaging with unskilled operators.

28.6 Form-Measuring Instruments

Most modern form-measuring instruments stage the part on a turntable and provide a means to position a gage head against the part (Figure 28.13). As the turntable rotates, the gage head measures deviation from the true circle. Those gages where the gage heads are supported by a simple, rigid, manual, or motorized stand that does not provide precise control over positioning are capable of performing the following measurements: roundness, concentricity, circular runout, circular flatness, perpendicularity, plane runout, top and bottom face runout, circular parallelism, and coaxiality. Modern fully automatic machines are the most sophisticated measuring instruments. Normally, they are equipped with a Windows™-based, PC-compatible graphical user interface to perform real-time data acquisition and processing.

Mitutoyo/MTI Corp. produces a wide range of these machines. Basic characteristics of machines from Series 211—roundness/cylindricity measuring system—are shown in Table 28.5. The RA-2200 round tester (Figure 28.14) provides high accuracy, high speed, and high performance in roundness measurement. The fully automatic or a DAT (digital adjustment table) function aided manual workpiece centering and leveling turns what used to be a difficult and finicky task into one that is simple enough for even untrained users to measure with high accuracy. This facilitates substantial reductions in overall measurement time. The RA-2200 system comes complete with powerful data analysis software ROUNDPAK, which requires only simple manipulation using a mouse and icon, achieving enhanced functionality and ease of operation.

See Table 28.6 for a list of companies that make bore gages.

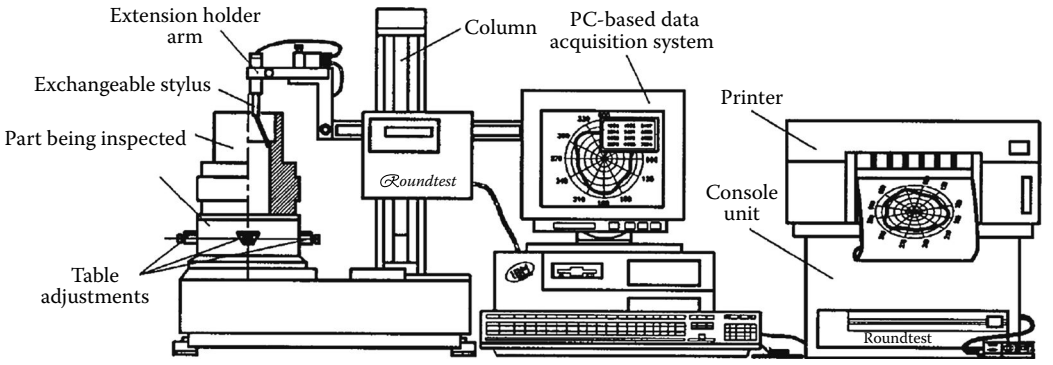

FIGURE 28.13 Form-measuring machine.

TABLE 28.5 Specification of Mitutoyo Round Tester Series 211

Model No.	RA-2200AS	RA-2200DS	RA-2200AH	RA-2200DH
Order No.	211–511A (mm/in.)	211–514A (in.)	211–512A (mm/in.)	211–515A (mm/in.)
Effective table diameter	9.25 in. (235 mm)	8 in. (200 mm)	9.25 in. (235 mm)	8 in. (200 mm)
Centering/leveling adjustment	Automatic centering/leveling turntable	Digital adjustment table	Automatic centering/ leveling turntable	Digital adjustment table
Centering range	±0.118 in. (±3 mm)	±0.197 in. (±5 mm)	±0.118 in. (±3 mm)	±0.197 in. (±5 mm)
Column travel	12 in. (300 mm) (standard column)		20 in. (500 mm) (high column)	
Basic unit mass	396 lb (180 kg)		440 lb (200 kg)	

FIGURE 28.14 Round test RA-2200AS/DS/AH/DH by Mitutoyo.

TABLE 28.6 Companies That Make Bore Gages

Company	Products
Bowers Metrology UK, Unit 15, Bordon Trading Estate, Bordon, Hampshire GU35 9HH, Tel.: 08708 50 90 50, Fax: 08708 50 90 60, http://www.bowers.co.uk/	Wide choice of cost-effective, quality measuring instruments from simple calipers to wireless data transmission gages
Western Gage Corporation, 3316 A Maya Linda Camarillo, CA 93012-8059, Tel: (800) 423-5062 (805) 445-1410 Fax: (805) 445-7530, http://www.westerngage.com/index.htm	Custom manufacturer of *gages*. Types of *gages* include air probe, air ring, plug, comparator, and master *gages*
Meyer Gage Company, Inc., 230 Burnham St., South Windsor, CT 06074, Tel.: 1-888-Pin-Gage (1-888-746-4243), Fax: 1-860-528-1428, http://www.meyergage.com/	Manufacturer of plug gages, pin gages, trilock, and taperlock gages
Marposs S.p.A., Company with a sole shareholder, Via Saliceto, 13-40010 Bentivoglio (BO), Italy; 3300 Cross Creek Pkwy., Auburn Hills, MI 48326, Tel.: 248-370-0404, 888-627-7677, Fax: 248-370-0621, http://www.marposs.com/	Leading global supplier of precision gaging equipment for shop-floor inspection, measurement, and process control solutions
The L. S. Starrett Company, 121 Crescent Street, Athol, MA 01 331, Tel.: 010 1 978-249-3551, Main Fax: 010 1 978-249-8495, http://www.starrett.com/	Manufactures more than 5000 variations of precision tools, gages, measuring instruments, and saw blades for industrial, professional, and consumer markets
Mitutoyo America Corporation, 965 Corporate Blvd., Aurora, IL 60502, Tel.: 630-820-9666, Fax: 630-978-3501, http://www.mitutoyo.com/	Offers the widest array of precision measuring products in the world, as well as the infrastructure and expertise to support them. It includes Mitutoyo hardware and software and Mitutoyo Engineered Systems expertise.
Brown & Sharpe, brand of, Hexagon Metrology, Inc., 250 Circuit Drive, North Kingstown, RI 02852, Tel.: 800-343-7933, 401-886-2000, http://brownandsharpe.com/	Offers a complete line of dimensional metrology products. Brown & Sharpe and TESA-branded precision hand tools and 1D to 3D measuring instruments, the TESAStar CMM probing system
Mahr GmbH, Carl Mahr Str.1, D-37073 Göttingen, Germany, Tel.: +49(0)551-70730, http://www.mahr.com	The Mahr Group is the world's third largest manufacturer of a complete range of production dimensional measuring technology. Mahr measuring instruments range from calipers to optical coordinate measuring systems.
Dyer Company, 1500 McGovernville Rd., P.O. Box 4966, Lancaster, PA 17604, Tel.: 1-800-631-3333, http://www.dyergage.com/	Production gages for precision bores, groves, minimum wall thickness, and special applications
Flexbar Machine Corporation, 250 Gibbs Road, Islandia, NY 11749, Tel.: 800.879.7575, Fax: 631.582.8487, http://www.flexbar.com/	Offers a wide variety of precision measuring instruments, machine tool accessories, machine safety guards, hardness testers, surface roughness gages, and optical and video inspection systems
Taylor Hobson Ltd, PO Box 36, 2 New Star Road, Leicester LE4 9JQ, United Kingdom, Tel.: +44 (0) 116 276 3771, Fax: +44 (0) 116 246 0579, http://www.taylor-hobson.com	Taylor Hobson is a high precision technology company, operating at the highest levels of accuracy within the field of surface, roundness, and form measurement. We provide contact and noncontact metrology solutions for the most demanding applications, with a worldwide infrastructure to support our clients on a global basis.

28.7 Gage Repeatability and Reproducibility

28.7.1 Understanding the Terms

Repeatability is the variability of the measurements obtained by one person while measuring the same item repeatedly. This is also known as the inherent precision of the measurement equipment (gage). Consider the probability density functions shown in Figure 28.15. The density functions were constructed from measurements of the bore diameter with gage A and gage B. The density functions demonstrate that gage B is more repeatable than gage A.

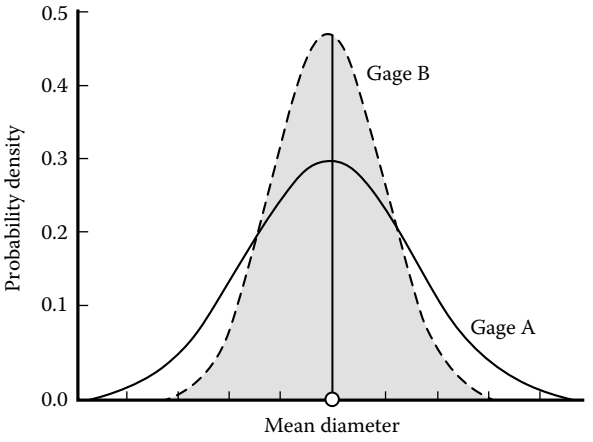

FIGURE 28.15 Probability density functions.

Reproducibility is the variability of the measurement system caused by differences in operator behavior. Mathematically, it is the variability of the average values obtained by several operators while measuring the same item. Figure 28.16 displays the probability density functions of the measurements for three operators. The variability of the individual operators is the same, but because each operator has a different bias, the total variability of the measurement system is higher when three operators are used than when one operator is used. Figure 28.16a also displays the probability density functions of the measurements for three operators using the same scale as Figure 28.16a. Notice that there is more difference in the means of the measurements shown in Figure 28.16b than those shown in Figure 28.16a. Therefore, the reproducibility of the system shown in Figure 28.16b is higher than the reproducibility of the system shown in Figure 28.16a.

Gage R&R methodology was developed in the 1960s to address the estimation of measurement system variation as applied to manufacturing. It was developed by ASTM for raw materials testing. Later on, the automotive industry developed the MSA as one of the core components of the Six Sigma approach to quality control. It was found that many problems encountered with SPC and design of experiments (DOE) is caused by problems with measurement systems. As a result, the MSA (gage R&R studies) became a core component of the QS9000/TS16949 Automotive Quality System Requirements. The standard is supported by manuals published by the Automotive Industry Action Group (AIAG).

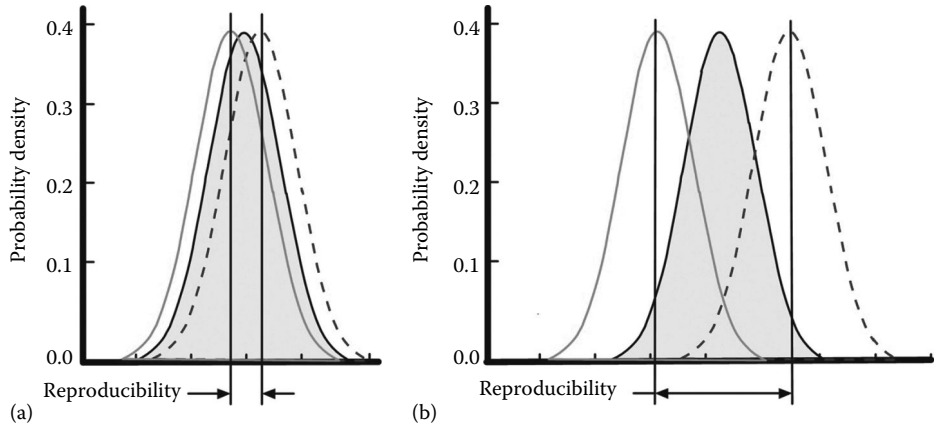

FIGURE 28.16 Reproducibility demonstration based on the results of measurements: (a) High reproducibility, and (b) low reproducibility.

The MSA standard is described in the third edition of the Measurement Systems Analysis Manual AIAG MSA-3 published in May 2003.

28.7.2 Application Notes

The role of reproducibility in gage R&R methodology is to define the variation among operator averages. Here, the term operator, or appraiser, refers to the person who uses the gage. Operator averages are thought to vary from person to person, and R&R is attempting to estimate the variance due to operator differences in practice. The statistical model in gage R&R methodology (without interaction) is as follows (Equation 28.1):

$$y_{ijk} = \chi_i + \alpha_j + \varepsilon_{ijk} \tag{28.1}$$

where

y_{ijk} is the kth repeat measurement of the ith part by the jth operator
χ_i component is the true value of the ith part dimension
α_j component is the reproducibility effect associated with operator j
ε_{ijk} is the random repeatability error that occurs with each measurement

Each measurement, y, is composed of these three components. The reproducibility term (α) may be thought of as a kind of personal bias associated with an operator, that is, each operator measures the various parts somewhat differently than the true value x, and this is the individual's α-effect. When several operators are involved in a gage R&R study, they effectively pick of a random sample (of operators) from a potentially infinite universe of all such possible operators. The α-terms are assumed to have a mean of 0 and an unknown variance θ^2.

The total variance of all measurements, y, has a variance equal to the sum of the individual variance components as in Equation 28.2:

$$\text{var}(y) = \nu^2 + \theta^2 + \sigma^2 \tag{28.2}$$

A gage R&R study is a designed experiment used to estimate the individual variance components. Typically, θ^2 and σ^2 are the main components of interest. The method, based on sample ranges, has enjoyed continued popularity, particularly for small to modest sample sizes, for many years. Today, many computer packages perform gage R&R using the analysis of variance (or ANOVA) technique [4]. The measurement study (classic) typically utilizes one to three appraisers for one measuring instrument that is measuring a single characteristic. Each appraiser measures five to ten units selected from a process two or three times (replications). Before proceeding with the analysis of the study, the ranges for the replications of the measurements made by each appraiser on each part are determined and used to calculate control limits for the range chart. Then each range is checked to determine if it falls inside the limits. Those measurements that result in a range outside the limits should be excluded from further analysis or should be redone. Operative assumptions include the following:

1. The measuring instrument stays in calibration (central location does not change)
2. Appraisers use the same method of measurement
3. Parts are measured in the same place (if the assumption that the parts are measured in the same place is incorrect, the possibility of within-part variation will need to be considered)

Among the many known methods, "average and range" and "ANOVA" methods are mostly used today. However, "ANOVA" method has a more widespread usage as it constitutes the basis of a number of modern commercial software packages to analyze gage R&R (e.g., GAGE). In the selection of a software package suitable for a given application, the first and foremost requirement to any gage R&R

software package is that it should directly follow the recommendations specified in AIAG's third edition of the MSA manual and help your organization conform to ISO/TS 16949-2002, ISO 9000 Section 4.11, FDA 21 CRF11.1, and other critical gage calibration standards.

References

1. Gooldy, G., *Dimensioning, Tolerancing, and Gaging Applied*: Ref. ASME Y14.5M-1994 ANSI B4.4 (B89.3.6) AMD ISO 1101, Prentice Hall, Upper Saddle River, NJ, 1998.
2. Smith, G. T., *Industrial Metrology: Surfaces and Roundness*, Springer, London, U.K., 2002.
3. Nee, J., *Fundamentals of Tool Design*, 6th edn., SME, Deborn, MI, 2010.
4. Burdick, R. K., Borror, C. M., and Montgomery, D. C., Design and analysis of gauge R&R studies: Making decisions with confidence intervals in random and mixed ANOVA models, ASA-SIAM Series on Statistics and Applied Probability, Alexandria, VA, 2003.

Further Information

Evans, J. R. and Lindsay, W. M., *The Management and Control of Quality*, Thomson South-Western, Mason, OH, 2008—provides a reader the strength and proven experience of well-known authors. Presents the fundamental principles and historical foundations of total quality.

Figliola, R. S. and Beasley, D. E., *Theory and Design for Mechanical Measurements*, 4th edn., Wiley, New York, 2005—provides a fundamental treatment for developing, operating, and analyzing measurements systems and for reporting results.

Meadows, G. D., *Geometric Dimensioning and Tolerancing Handbook: Applications, Analysis & Measurement*, James D. Meadows & Associates, Inc., Hendersonville, TN, 2009—explains the new ASME Y14.5-2009 standard. This is one of the most comprehensive GD&T volumes ever written and has the unprecedented ability to cover almost every facet of dimensioning and tolerancing. It includes step-by-step procedures for dimensioning and tolerancing parts and assemblies.

Pyzdek, T. and Keller, P. A., *The Six Sigma Handbook*, 3rd edn., McGraw Hill, New York, 2009—provides comprehensive reference to make Six Sigma strategy and operations, as well as successful project management of quality assurance.

29

Ultrasonic Displacement Sensors

Nils Karlsson
Swedish Defense Research Agency

Ole Pedersen
Linköping University

Ultrasound is an acoustic wave with a frequency higher than the audible range of the human ear, which is 20 kHz. Ultrasound can be within the audible range for some animals, like dogs, bats, or dolphins. Around 1883, Sir Francis Galton performed the first known experiments with whistles generating ultrasound. Many decades later, people started to find ultrasound applications in engineering, medicine, and daily life. The basic principle for the use of ultrasound as a measurement tool is the *time-of-flight technique*. The pulse-echo method is one example. In the pulse-echo method, a pulse of ultrasound is transmitted in a medium. When the pulse reaches another medium, it is totally or partially reflected, and the elapsed time from emission to detection of the reflected pulse is measured. This time depends on the distance and the velocity of the sound. When sound travels with a known velocity c, the time t elapsed between the outgoing signal and its incoming echo is a measure of the distance d to the object causing the echo:

$$d = \frac{ct}{2} \tag{29.1}$$

Figure 29.1 shows a simple pulse-echo system. The transmitter and the receiver could be the same device, but they are separated for clarity in this figure.

The oscillator generates an electric signal with a typical frequency of 40 kHz. This electric signal is transformed into mechanical vibrations of the same frequency in the transmitter. These vibrations generate sound waves that are reflected by the object. The reflected sound echo causes an electric signal in the receiver. For precise measurements, the speed of sound is a crucial parameter. A typical value in air at 1 atm pressure and room temperature is 343 m s^{-1}, but the speed of sound is influenced by air pressure, air temperature, and the chemical composition of air (water, CO_2, etc.). For example, the speed of sound is proportional to the square root of absolute temperature. Measuring distances in an environment with large temperature gradients can result in erroneously calculated distances. As an advantage, ultrasound waves are robust against other disturbances such as light, smoke, and electromagnetic interference [1–9].

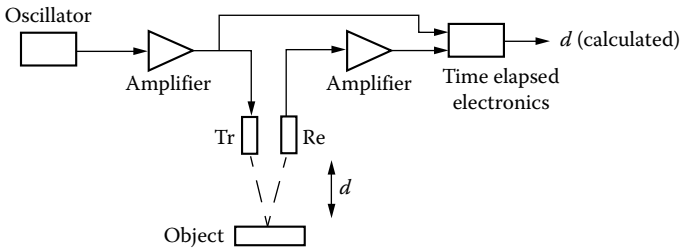

FIGURE 29.1 Principle of a pulse-echo ultrasound system for distance measurements (Tr, transmitter; Re, receiver).

29.1 Physical Characteristics of Sound Waves

Sound is a vibration in matter. It propagates as a longitudinal wave, i.e., the displacement in the material is in the direction of the sound propagation.

The velocity of sound depends on the medium in which it propagates. In a homogeneous and isotropic solid, the velocity depends on the density, ρ, and the modulus of elasticity, E, according to following equation:

$$c = \sqrt{\frac{E}{\rho}} \tag{29.2}$$

In a liquid, the velocity depends on the density and the adiabatic compressibility κ; Equation 29.2 can be expressed as

$$c = \sqrt{\frac{1}{\kappa \cdot \rho}} \tag{29.3}$$

In gases, the velocity of sound is described by equation. Here g represents the ratio of the specific heat constant at constant pressure (c_p) to the specific heat constant at constant volume (c_v), p is pressure, R is the universal gas constant, T is the absolute temperature, and M is the molecular weight:

$$c = \sqrt{\frac{gRT}{M}} = \sqrt{\frac{c_p}{c_v}\frac{p}{\rho}} \tag{29.4}$$

The energy of a sound wave passing a point in the medium consists of alternatively the kinetic energy of particles in motion and the potential energy due to pressure differences. The energy passing a unit surface area per a unit of time is the intensity, I. If this intensity propagates from a point source equally in all directions, the intensity at a distance R is spread over the area of a sphere of radius R. The intensity at a distance R is then proportional to $1/R^2$. The sound wave is also attenuated due to friction and absorption. The attenuation increases with higher frequencies. The signal also decreases due to scattering. The sound beam from a transmitting transducer concentrates the energy to a fraction of the area of the sphere, but the $1/R^2$ dependence still remains. The directivity of a transducer increases with its size and signal frequency. To get a narrow beam, the transmitter membrane diameter must be large with respect to the wavelength. High-frequency ultrasound cannot be the general solution as ultrasound of a high frequency is absorbed faster than ultrasound of a lower frequency.

An important quantity is the acoustic impedance. In the far field, it can be treated as the characteristic impedance R_a, which is the product of the density of the medium, ρ, and the sound of speed, c:

$$R_a = \rho c \tag{29.5}$$

When the acoustic wave reaches the boundary of two different mediums, they have different acoustic impedance. This will cause a reflection of the wave. With the increase in difference in impedance, a larger portion of the sound is reflected. The acoustic impedance of a target to detect shall differ significantly from the medium in which the sound propagates, while the medium for propagation should be as uniform as possible:

$$\text{Reflection coefficient} = \frac{I_{\text{reflected}}}{I_{\text{incident}}} = \frac{(R_1 - R_2)^2}{(R_1 + R_2)^2} \tag{29.6}$$

The reflection of a target also depends on its size and shape. This can be expressed as the effective scattering area or the "equivalent cross section." The target is when compared with a sphere and what size this sphere must have to give the same reflection. In the case when this reflection is received by a receiver at distance R at the same place as the transmitter, the intensity spreading due range is $1/R^2$ again. This gives total range dependence for the received echo of $1/R^4$ [1–9].

The practical importance of the acoustic impedance is realized when the ultrasonic pulse-echo system shown in Figure 29.1 is considered. First, the electric energy is converted into mechanical vibrations of a membrane in the transmitter. Second, the vibrations (the sound wave) have to pass through the boundary between the membrane (usually a solid material) and free air. Because the transmitter membrane and the free air have different characteristic impedances, much of the acoustic intensity is reflected (Figure 29.2).

The transmitted ultrasound in free air will first propagate in a parallel beam (near field of the transducer), but after a distance L, the beam diverges (the far field of the transducer). See Equation 29.7 and Figure 29.3:

$$L \approx \frac{D^2}{4\lambda} \tag{29.7}$$

where

D is the diameter of the circular transmitter

λ is the wavelength of the ultrasound

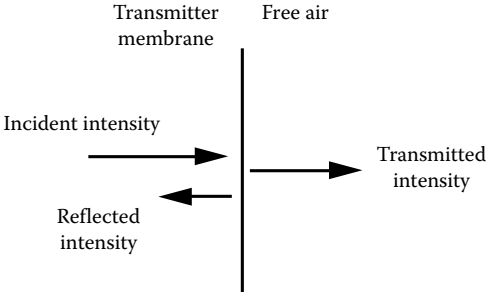

FIGURE 29.2 Reflection and transmission of a sound wave at the interface between media of different characteristic impedances.

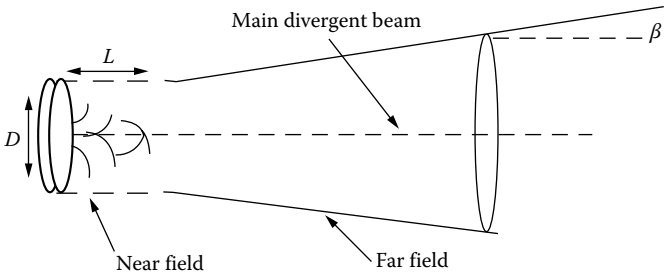

FIGURE 29.3 Illustration of the ultrasound beam in the near field and the far field of the transducer.

The sound intensity in the near field is complicated due to interference effects of sound originating from different parts of the transducer membrane. In the far field, the intensity is approximately uniform and the beam spread follows:

$$\sin\beta = 1.22\frac{\lambda}{D} \tag{29.8}$$

where β is the half lobe angle.

To get a narrow beam, the transmitter membrane diameter must be large with respect to the wavelength. High-frequency ultrasound cannot be the general solution as ultrasound of a high frequency is absorbed faster than ultrasound of a low frequency.

29.2 Ultrasound Transducer

Ultrasonic transducers can be based on different techniques. The most common types of in-air transducers are

- Mechanical
- Electromagnetic
- Piezoelectric
- Electrostatic
- Magnetostrictive

The simplest type, mechanical transducers such as whistles and sirens are used up to approximately 50 kHz. This type only works as a transmitter. Electromagnetic transducers such as loudspeakers and microphones can be used, but they are mainly suited for lower frequencies. The piezoelectric transducer is more suitable for ultrasonic frequencies and is quite common. Piezoelectric crystals change dimensions when they are exposed to an electric field. When an alternating voltage is applied over the piezoelectric material, it changes its dimensions with the frequency of the voltage. The transducer is mainly suited for use at frequencies near the mechanical resonance frequency of the crystal. The piezoelectric transducer works as both a transmitter and a receiver. When a piezoelectric material is forced to vibrate by a sound pulse, it generates a voltage. Some natural crystals, such as quartz, are piezoelectric. Ceramics and some polymers, like PVDF (polyvinylidene fluoride) can be polarized to become piezoelectric. Polymers are suitable as transducers in air since their acoustic impedance is low compared to other standard piezoelectric materials.

The electrostatic transducer (Figure 29.4) is a plate capacitor with one plate fixed and the other free to vibrate as a membrane. When a voltage is applied between the plates, the electrostatic forces tend to attract or repel the plates relative to each other depending on the polarity of the voltage. This transducer can be used as both a transmitter and a receiver. The magnetostrictive transducer is based on the

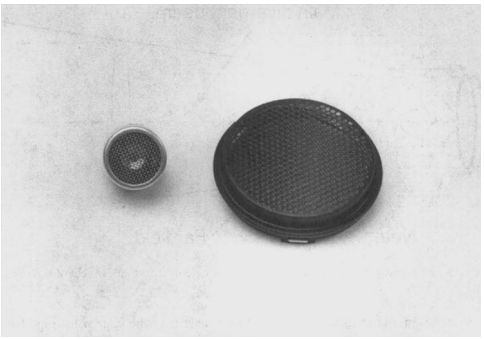

FIGURE 29.4 Ultrasonic transducers: piezoelectric (left) and electrostatic (right).

phenomenon of magnetostriction, which means that the dimensions of a ferromagnetic rod change due to the changes of an externally applied magnetic field. This transducer can also act as both a transmitter and a receiver [10–16].

Transducers are often integrated with electronics to a complete system for the measurement.

29.3 Principles of Time-of-Flight Systems

There are several techniques for ultrasonic range measurements. They are all based on the principle of measuring the time difference between transmitted and received ultrasound signal as shown in Figure 29.5.

The *pulse-echo method* is the simplest one. Usually, this method has a low signal-to-noise ratio (SNR) because of the low transmitted energy due to the short duration of the pulse. Multireflections are detectable.

In the *phase-angle method*, the phase angle is measured between the continuous transmitted signal and the continuous received signal and is used to measure the distance. The method is relatively insensitive to disturbances. Multireflections are not detected in a meaningful way. When the distance is longer than one wavelength, another method must be used to monitor the distance.

The *frequency-modulation method* uses transmitted signals that are linearly frequency modulated. Thus, detected signals are a delayed replica of the transmitted signal at an earlier frequency. The frequency shift is proportional to the time of flight. The method is robust against disturbing signals and multireflections are detectable.

The *correlation method* determines the cross-correlation function between transmitted and received signals. When the transmitted signal is a random sequence, the cross-correlation function estimates the

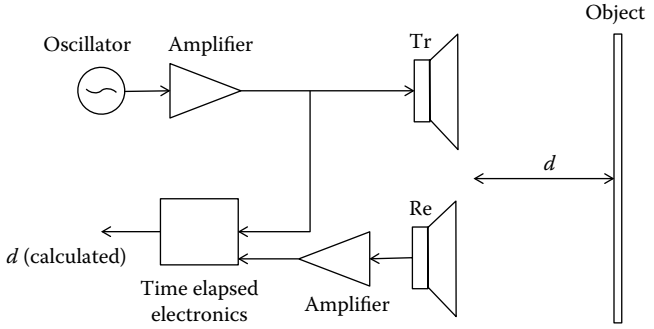

FIGURE 29.5 Principle of an ultrasonic distance measurement system.

impulse response of the system, which in turn is a good indicator of all possible time delays. The method is robust against disturbances, and multireflections are detectable [17–21].

Industrial acoustic noise can affect the received signals in an ultrasound time-of-flight system. The noise can be generated from leaking compressed air pipes, noisy machines, or other ultrasonic systems. This external noise is not correlated with the relevant echo signals of the transmitted noise and can therefore be eliminated by the use of correlation methods. Disturbances correlated with the relevant echo signal (e.g., unwanted reflections) will not be eliminated by the use of correlation methods.

The impulse response $h(t, t_0)$ is used as a sensitive indicator of time delay between transmitted signal at time t_0 and received signal at time t. The impulse response is given by

$$h(t, t_0) = F^{-1}\left[\frac{S_{xy}}{S_{xx}}\right] \tag{29.9}$$

where

F^{-1} is the inverse Fourier transform
x is the transmitted signal
y is the received signal
$S_{xy}(f)$ is the cross-spectral density function [the Fourier transform of the cross-correlation function of the transmitted signal $x(t)$ and the received signal $y(t)$]
S_{xx} is the power density function (the Fourier transform of the autocorrelation function of the transmitted signal)

To analyze the transfer channel by data acquisition requires a high sampling rate, theoretically at least two times the highest frequency component in the received signal (and in practice as high as 10 times the highest frequency). One way to reduce the sampling rate is to first convert the signal from its band-pass characteristics around a center frequency f_0 (approx. 50 kHz) to low-pass characteristics from dc to $B/2$, where B is the appropriate bandwidth. The accuracy of the range estimate, and hence the time interval $t - t_0$, can be improved by processing the estimate of the impulse response $h(t - t_0)$ with a curve-fitting (least square) method and digital filtering in a computer. A correlation-based time-of-flight system is described in Ref. [18].

Table 29.1 lists some advantages and drawbacks of the described time-of-flight methods.

29.3.1 Suppliers and Vendors

There are many manufacturers and vendors of ultrasonic sensors for displacement measurements. There are several types of sensors depending on physical principle of the sensor, mounting, and capsuling.

TABLE 29.1 Advantages and Disadvantages of Time-of-Flight Methods

Method	Main Advantage	Main Disadvantage
Pulse-echo method	Simple	Low SNR
Phase-angle method	Rather insensitive to disturbances	Cannot be used directly at distances longer than the wavelength of the ultrasound
Frequency-modulation method	Robust against disturbances; multireflections detectable	Can give ambiguous results in long distance measurements, but can give similar results as phase-angle method in short distance measurements
Correlation method	Very robust against disturbances	Make relatively high demands on hardware and/or computations

The sensor is often integrated with electronics for distance measurements including more or less advanced intelligence, handling unwanted phenomena, and also prepared with an interface to other systems. A partial list of vendors and suppliers is given at the end of this chapter.

References

1. J. Blitz, *Elements of Acoustics*, London, U.K.: Butterworth, 1964.
2. L. E. Kinsler, A. R. Frey, A. B. Coppens, and t. V. Sanders, *Fundamentals of Acoustics*, 3rd edn., New York: John Wiley & Sons, 1982.
3. G. Lindstedt, Borrowing the bat's ear for automation. Ultrasonic measurements in an industrial environment, Department of Industrial Electrical Engineering and Automation, Lund Institute of Technology, Lund, Sweden, 1996.
4. G. S. Kino, *Acoustic Waves: Devices, Imaging and Analog Signal Processing*, Englewood Cliffs, NJ: Prentice Hall, 1987.
5. J. Burczynski, Introduction to the use of sonar systems for estimating fish biomass, FAO Fisheries Technical Paper No. 191, Revision 1, Food and Agriculture Organization of the United Nations, Rome, Italy, 1982.
6. F. Widmann, Parking aid with a wheel sensor, United States Patent No. 5,602,542, February 1997.
7. V. Mágori, Ultrasonic sensors in air, pp 471–481, *Proceedings of the IEEE Ultrasonic Symposium*, New York, 1994.
8. D. P. Massa, Choosing an ultrasonic sensor for proximity or distance measurement part 1: Acoustic considerations, *Sensors*, 16/2 (3), 1999. Available online at Acoustic/Ultrasound, http://www.sensorsmag.com/sensors/acoustic-ultrasound/choosing-ultrasonic-sensor-proximity-or-distance-measurement-825 (accessed on March 14, 2013).
9. D. P. Massa, Choosing an ultrasonic sensor for proximity or distance measurement part 2: Optimizing sensor selection, 16/3 (10), 1999. Available online at Acoustic/Ultrasound, http://www.sensorsmag.com/sensors/acoustic-ultrasound/choosing-ultrasonic-sensor-proximity-or-distance-measurement-838 (accessed on March 14, 2013).
10. S. R. Ruocco, *Robot Sensors and Transducers*, New York: John Wiley & Sons 1987.
11. P. H. Sydenham and R. Thorn, *Handbook of Measurement Science*, Vol. 3, *Elements of Change*, New York: John Wiley & Sons, 1992.
12. J. Fraden, *Handbook of Modern Sensors, Physics, Design and Applications*, 4th edn., New York: Springer, 2010.
13. H. R. Gallantree, Review of transducer application of polyvinylidene fluoride, *IEEE Proceedings*, 130, 219–224, 1983.
14. T. T. Wang and J. M. Herbert, *The Applications of Ferroelectric Polymers*, London, U.K.: Chapman & Hall, 1988.
15. C. Z. Rosen, B. V. Hiremath, and R. Newham, *Piezoelectricity*, New York: American Institute of Physics, 1992.
16. P. Mattila, F. Tsuzuki, H. Väätäjä, and K. Sasaki, Electroacoustic model for electrostatic ultrasonic transducers with V-grooved backplates, *IEEE Transactions on Ultrasonics, Ferroelectrics and Frequency Control*, 42(1), 1–7, 1995.
17. J. A. Kleppe, *Engineering Applications of Acoustics*, Boston, MA: Artech House Publishers, 1989.
18. P. Holmberg, Robust ultrasonic range finder—An FFT analysis, *Measurement Science and Technology*, 3, 1025–1037, 1992.
19. T. Kimura, S. Wadaka, K. Misu, T. Nagatsuka, T. Tajime, and M. Koike, A high resolution range measurement method using double frequencies and phase detection, pp. 737–741, *Proceedings of the IEEE Ultrasonic Symposium*, Seattle, WA, 1995.

20. M. M. Saad, C. J. Bleakley, and S. Dobson, Robust high-accuracy ultrasonic range measurement system, *IEEE Transactions on Instrumentation and Measurement*, 60, 3334–3341, 2011.
21. M. Parilla, J. J. Anaya, and C. Fritsch, Digital signal processing techniques for high accuracy ultrasonic range measurements, *IEEE Transactions on Instrumentation and Measurement*, 40(4), 759–763, 1991.

Partial List of Vendors and Suppliers

Advanced Sonic Processing Systems, 324 Christian St., Oxford, CT 06478-1023, Phone: 203-266-4440, Fax: 203-266-4441, www.advancedsonics.com

Banner Engineering Corp, 9714 Tenth Ave. N., Minneapolis, MN 55440, Phone: 763-544-3164, 877-581-1749 (toll free), Fax: 763-544-3213, www.bannerengineering.com/en-US/

Blue Wave Ultrasonics, Inc., P.O. Box 4347, Davenport, IA 52808-4347, Phone: 563-322-0144, 800-373-0144 (toll free), Fax: 563-322-7180, www.bluewaveinc.com

DeFelsko Corp., 802 Proctor Ave., Ogdensburg, NY 13669, Phone: 315-393-4450, 800-448-3835 (toll free), Fax: 315-393-8471, www.defelsko.com

Olympus NDT, 48 Woerd Ave., Waltham, MA 02453, Phone: 781-419-3900, 800-225-8330 (toll free), Fax: 781-419-3980, www.olympus-ims.com/?apd=1

Senix Corp, 52 Maple St., Bristol, VT 05443, Phone: 866-919-2671 (toll free), Fax: 802-453-2549, www.senix.com

Sonic and Materials, Inc., 53 Church Hill Rd., Newtown, CT 06470, Phone: 203-270-4600, 800-745-1105 (toll free), Fax: 203-270-4610, www.sonics.com

Ultrasonic Power Corp., 239 E. Stephenson St., Freeport, IL 61032, Phone: 815-235-6020, 800-575-0168 (toll free), Fax: 815-232-2150, www.upcorp.com

Transducers Direct, 12115 Ellington Court, Cincinnati, OH 45249, Phone: 513-583-9491, Fax: 513-583-9476, www.transducersdirect.com

30

Optical Encoder Displacement Sensors

J.R. René Mayer
Ecole Polytechnique de Montreal

The detection of angular and linear motion is a key function in a multitude of systems such as machine tools, industrial robots, a variety of instruments, and computer mice. Although they are one of the many techniques capable of such measurements, the ease with which they are interfaced to digital systems has made them very popular.

Optical encoders are used to measure either angular or linear positions. Those used for angular detection are commonly called rotary or shaft encoders, since they usually detect the rotation of a shaft. Optical encoders encompass a variety of devices, all of which use light as the means to transform movement into electrical signals. All devices have two basic building blocks: a main grating and a detection system. It is the position of one with respect to the other that is detected. The main grating represents the measurement standard. For linear measurements, the main grating, commonly called the scale, is one or more sets of parallel lines of constant or specially coded pitch supported by a substrate. Similarly, a rotary encoder has a grating with radial lines on a disk.

Both linear and rotary encoders can, in principle, be absolute or incremental, although in practice, linear absolute encoders employing optical principles are quite uncommon and have drastically limited performance characteristics (accuracy, resolution, and/or maximum operating speed). Figure 30.1 shows a simplified classification of optical encoders. This classification refers to the nature of the information generated. The incremental encoder detects movement relative to a reference point. As a result, some form of reference signal is usually supplied by the encoder at a fixed position in order to define a reference position. The current position is then incremented (or decremented) as appropriate. Multiple reference marks can also be used, where the distance between successive marks is unique so that as soon as two successive marks have been detected, it becomes possible to establish absolute position from then on. The reference point can also be mechanical. Should power be lost or a signal transmission error occur, then the absolute position is lost and the encoder must return to one or more reference points in order to reset its counters. Unfortunately, a loss of count may not be detected until a reference point is reaccessed. Furthermore, reading errors may accumulate. On the other hand, absolute encoders

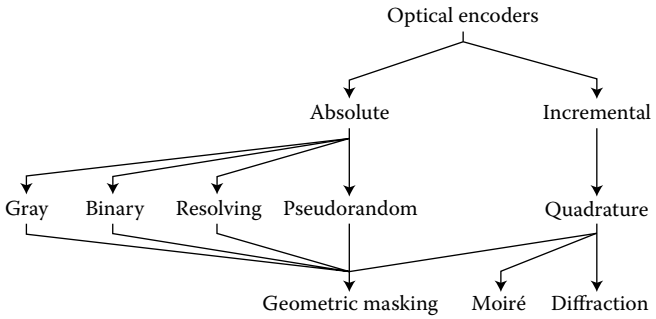

FIGURE 30.1 Classifications of optical encoders based on (1) the nature of the final information provided, (2) the type of signals generated, and (3) the technology used to generate the signals.

produce a set of binary signals from which the absolute position can be deduced without the knowledge of the previous motion history. The current position is known right from powering on. In the case of absolute rotary encoders, single and multiturn devices are available. Multiturn devices use an internal mechanical transmission system to drive a second grating that serves as a turn counter.

Most incremental encoders use quadrature signals as output to carry the motion information. Some encoders use one square-wave signal, which is used for position in one direction only. Also, this single square wave can be fed into either a PLC (programmable logic controller) or another electronic interface that converts this signal to a rate or revolution per minute (RPM) for speed indication. However, whenever bidirectional operation is required, quadrature signals are necessary. Quadrature signals come in analog or digital form. The analog form consists simply of a sine and a cosine signal. The number of sinusoidal cycles per unit change of the measured variable (a revolution or 360° for a rotary encoder) determines the basic resolution of the encoder prior to interpolation. The digital form consists of two square-wave trains, 90° (often called electrical degree) out of phase. The 90° phase lag is indispensable in detecting the motion direction and hence increment or decrement of the position counter accordingly. The main optical techniques to generate the quadrature signals are geometric masking, Moiré fringes, and diffraction based. For linear encoders, the basic resolution is related to the distance traveled by the grating in order for the encoder to produce one full quadrature cycle. For rotary encoders, the basic resolution is usually described as the number of quadrature cycles per turn. The resolution of an encoder system can be increased by electronic means. With analog quadrature signals, it is possible to interpolate within each quadrature cycle. The limit of the interpolation factor depends on the quality (mark space, quadrature separation, and jitter) of the basic signals. With square-wave signals, multiplication by a factor of two or four is easily achieved. Increasing the resolution in this manner does not, however, improve the trueness, often called accuracy (or linearity) of the measurement.

Absolute encoders are classified according to the type of code used. The main four codes are Gray, binary (usually read by vee-scan detection), optical resolving, and pseudorandom. All absolute encoders use geometric masking to generate the code.

30.1 Encoder Signals and Processing Circuitry

30.1.1 Absolute Encoders

30.1.1.1 Direct Binary

Figure 30.2a illustrates the concept of an absolute linear optical encoder using a direct binary-encoded scale. The fixed scale has n tracks (here n is 4), each providing one bit of a direct binary number. The lowest track (first track from the center of the disk for a rotary encoder) is the most significant digit and has a weight, 2^{n-1} (here 2^3), while the upper track is the least significant digit with a weight 2^0. The track providing the least significant digit has 2^{n-1} cycles of light and dark records, while the most significant

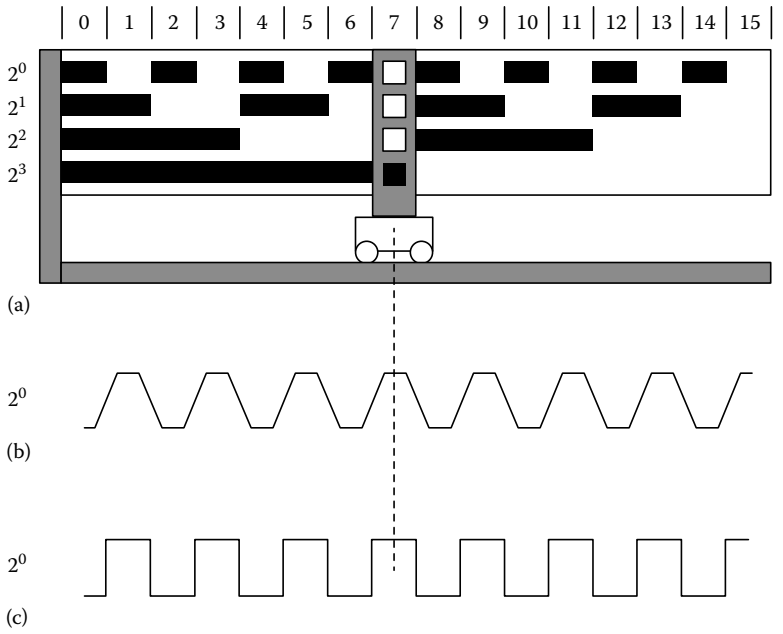

FIGURE 30.2 (a) Absolute encoders using a natural binary code of four digits. Four tracks are required. The moving read head has four apertures and is shown in position 7 along the scale. (b) The output of the read-head aperture corresponding to the least significant track. It represents the proportion of light area covering the aperture. (c) The binary digit obtained after squaring the raw output signal.

track has 2^0 or 1 such cycle. For each track, the moving read head has a readout unit consisting of a light source, a mask, and a photodetector. Figure 30.2b shows the output from the photodetector, which represents the total intensity of light reaching its surface. As the mask passes over a clear region of the grating, the photodetector output increases and then decreases. In theory, a truncated triangular wave is obtained, which can easily be converted to a square wave (Figure 30.2c) by a suitably chosen threshold level. The result is a high or 1 for a light record and a low or 0 for a dark one. The position, in base 10, corresponding to the reading head position in Figure 30.2 is

$$1\times 2^0 + 1\times 2^1 + 1\times 2^2 + 0\times 2^3 = 7 \tag{30.1}$$

The code configuration just described is not suitable for practical use because some transitions require that two or more bit values change simultaneously. For example, from positions 7 to 8, all bits change values. Unless the change is simultaneous, incorrect position readout results at some position. This would require that the scale is geometrically perfect, that the read head be perfectly aligned with the scale, and that the electronics are perfectly adjusted and stable over time. This problem is solved either by the use of a vee-scan detection method or by the use of a unit-distance code such as the Gray code.

30.1.1.2 Vee-Scan

The vee-scan method uses a V-shape pattern of readout units that removes the potential reading ambiguity of direct binary scales. Stephens and Davies [1] indicate the read points at which transitions are detected in Figure 30.3a. They also describe the conversion of the threshold output signals to binary code using combinational logic. The primary advantage is that the location tolerance of the transition point of each reading unit need only be ±1/8 of the cycle length for that particular track. For example, ±45° is for the most significant track of a rotary encoder disk. Figure 30.3b shows a direct binary word obtained through logic combinations of the vee-scan readings.

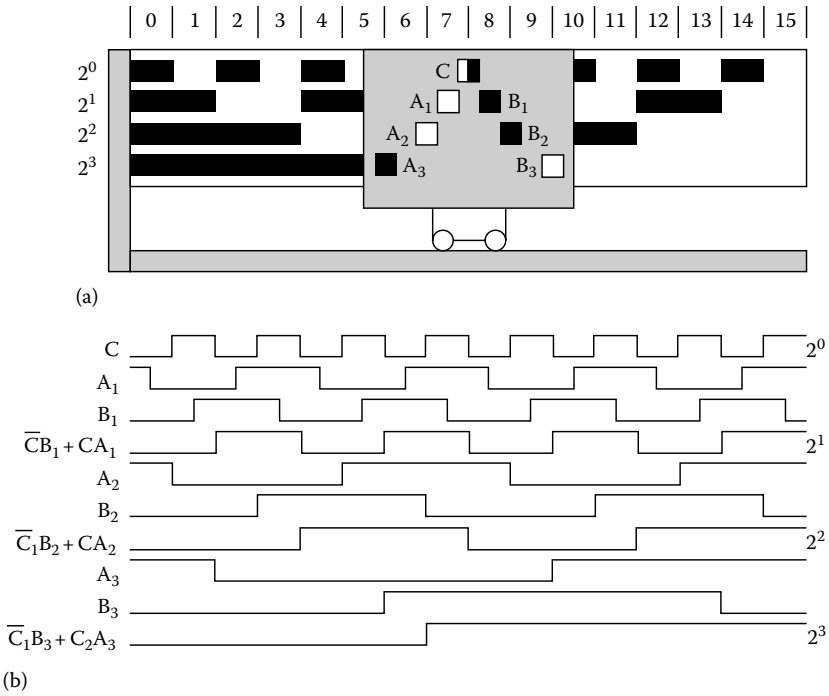

FIGURE 30.3 Vee-scan configuration of reading units in (a) removes the ambiguity associated with a natural binary scale. Simple combinational logic is then used to generate the natural binary readout in (b).

30.1.1.3 Gray Code

The use of vee-scan requires additional reading heads as well as processing electronics. The Gray code is a unit-distance code, and so only one bit of data changes between representations of two consecutive numbers or successive positions. This removes the possibility of ambiguous readout. It has the following advantages: (1) It is easily converted to direct binary code, and (2) the finest tracks are twice the width of equivalent direct binary code tracks. Figure 30.4a shows a Gray code linear scale. Figure 30.4b shows a scheme for the conversion from Gray code to binary code and proceeds as follows: (1) The most significant bit (msb) of the binary code equals the msb of the Gray-coded number, (2) add (modulo 2) the msb of the binary number to the next significant bit of the Gray-coded number to obtain the next binary bit, and (3) repeat step (2) until all bits of the Gray-coded number have been added modulo 2. The resultant number is the binary equivalent of the Gray-coded number. The modulo-2 addition is equivalent to the action of an exclusive OR. Figure 30.4c shows a simple circuit using combinational logic to perform Gray to binary conversion. Sente and Buyse [2] suggest the use of an external ROM to convert the code where the input-coded word is the address and the output-coded word is the data. Using a 16-bit ROM for a 12-bit code, Sente and Buyse [2] suggest using the remaining 4 bits to implement a direction signal. Stephens et al. [1] describe the use of vee-scan with a Gray code scale for even better robustness.

30.1.1.4 Pseudorandom Code

Pseudorandom encoding allows the use of only two tracks, and more recently only one, to produce an absolute encoder. One track contains the pattern used to identify the current position, while the other is used to synchronize the reading of the encoded track and remove ambiguity problems. A pseudorandom binary sequence (PRBS) is a series of binary records or numbers, generated in such a way that any consecutive series of n digits is unique. Such code is called chain code, and it has the property that the first $n - 1$ digits of an

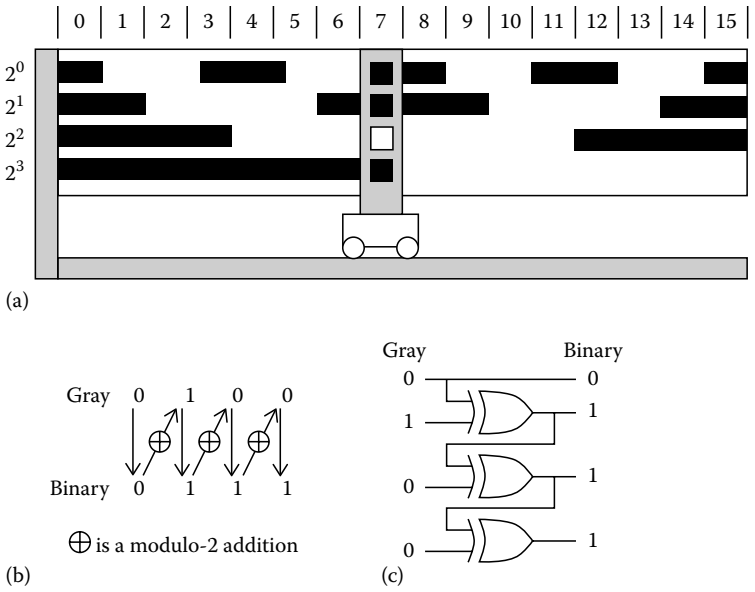

FIGURE 30.4 (a) Gray code allows a transition on only one track between each successive position so that no ambiguity arises. A scheme based on modulo-2 additions converts the Gray code to natural binary code in (b). Exclusive ORs implement the conversion in (c).

n-bit word are identical to the last $n - 1$ digits of the previous code word. This allows their partial overlapping on a single track. A PRBS of length $2^n - 1$ is defined by

$$XN(j)\Big|j = 0, 1, ..., 2^{n-1} \tag{30.2}$$

The code can be generated by reading the *n*th stage of a feedback shift register after *j* shifts. The register must be initialized so that at least one of the registers is nonzero and the feedback connection implements the formula

$$X(0) = X(n) \oplus c(n-1)X(n-1) \oplus \cdots \oplus c(1)X(1) \tag{30.3}$$

where the *c* coefficients are 0 or 1. The feedback registers for which *c* is 1 are listed in Table 30.1 for values of *n* from 4 to 14. The following is a PRBS for $n = 4$ with the pseudocode obtained using all registers set to 1 initially, 111101011001000. For a rotary encoder disk, the 15 sectors would have a 24° width.

Petriu [3,4] describes a possible configuration of a PRBS disk that uses a PRBS track and a synchronization track (Figure 30.5), together with the processing method to reconstitute the position in natural binary. Table 30.1 gives the reverse feedback configuration. The shift register is initially loaded with the current *n*-tuple. Then the reverse logic is applied recurrently until the initial sequence of the PRBS is reached. At this point, the *n*-bit counter represents the value of *j*. For a rotary encoder, $(j * 360)/(2^n - 1)$ is the current angular position, whereas for a linear encoder, the position is $j * P$ where *P* is the scale record length or pitch. Petriu [4] suggests that in order to allow nonambiguous bidirectional reading, $n + 1$ heads are used on the PRBS track. The synchronization track has a series of 0s and 1s in records of the same width as the PRBS track and in phase. There is a *P*/2 shift, where *P* is the record's length between the A head on the synchronization track and the $n + 1$ read heads on the PRBS track. The $n + 1$ records are updated on a trigger from the A signal. This ensures that the $n + 1$ heads are closely aligned with the PRBS record mid-position. A second read head called *B* on the synchronization track is shifted by *P/2* relative to *A*. *A* and *B* are in quadrature, which allows their simultaneous use to generate a motion direction signal. The correct *n*-tuple, i.e., the lower or upper subset, is selected on the basis of the moving direction and is then converted to natural binary by reverse feedback. Petriu [4] also suggests a simple means of increasing the

TABLE 30.1 Shift-Register Feedback Connections for Generating Pseudorandom Binary Sequences

N	Length	Direct Sequence	Reverse Sequence
4	15	1, 4	3, 4
5	31	2, 5	3, 5
6	63	1, 6	5, 6
7	127	3, 7	4, 7
8	255	2, 3, 4, 8	4, 5, 6, 8
9	511	4, 9	5, 9
10	1023	3, 10	7, 10
11	2047	2, 11	9, 11
12	4095	1, 4, 6, 12	6, 8, 11, 12
13	8191	1, 3, 4, 13	9, 10, 12, 13
14	16,383	1, 6, 10, 14	4, 8, 13, 14

resolution by a factor of 2 using some additional electronics. He also proposes a scheme to use an arbitrary (not $2^n - 1$) number of sectors, but this requires a third track and some additional correction electronics to handle the last $n - 1$ records of a disk, since these are no longer PRBS patterns. Tomlinson [5] proposes another method for truncation of the PRBS sequence that does not require a third track. Instead, particular codes were removed by applying additional logic in the direct and reverse feedback logic.

Ross and Taylor [6] and Arsic and Denic [7] suggest ways of reducing the number of reading heads by accumulating readings into a shift register so that a minimum of two heads are sufficient to read the PRBS track. However, on a start-up, the correct position is not known until the encoder has moved so that all registers have been updated. This type of encoder is therefore not completely absolute because it does not indicate its correct position on the start-up. Finally, Arazi [8] mentions the use of a ROM that stores the translation table, as an alternative to a logic circuit.

30.1.1.5 Optical Resolving

Renishaw Inc. now commercializes a range of single-track absolute linear and rotary encoders that use a track consisting of a long non-repeated binary pattern akin to a barcode. A camera takes a picture of the current visible track portion, which has embedded absolute position code and phase information in a single track of graduations that appear as a long, non-repeating bar code with a 30 μm pitch, and decodes it into an absolute position, claiming a resolution of 1 nm, even at speeds up to 100 m/s. The photo image includes redundancy, so only about a quarter of the code captured in the image needs to be correct, providing good immunity to dirt and contamination. A high-speed digital signal processor (DSP) is used to process the position determination and checking algorithms and answer the position request in less than 15 μs. The system is capable of processing and answering up to 25,000 position requests per second. The encoder is primarily linear but is also used for rotary applications by putting the scale on the outer perimeter of a disk.

This method has similarities with its electromagnetic counterpart and depends on the generation of a sine and a cosine signal pair per encoder shaft revolution. The resolution and accuracy of this encoder depend on its ability to generate signals that conform to their ideal waveforms and the resolving power of the electronic circuit responsible for performing the rectangular to polar conversion to produce angular output data. The methods for accomplishing this conversion are similar to those described in the sections on analog quadrature signal interpolation. The code disk of such a device does not incorporate a series of parallel lines of constant pitch, but rather depends on special code tracks having analog profile signal outputs. These can be affected by changing the code tracks' cross sections or by graduating their optical density around the revolution. In the latter case, a masking reticle need not be employed.

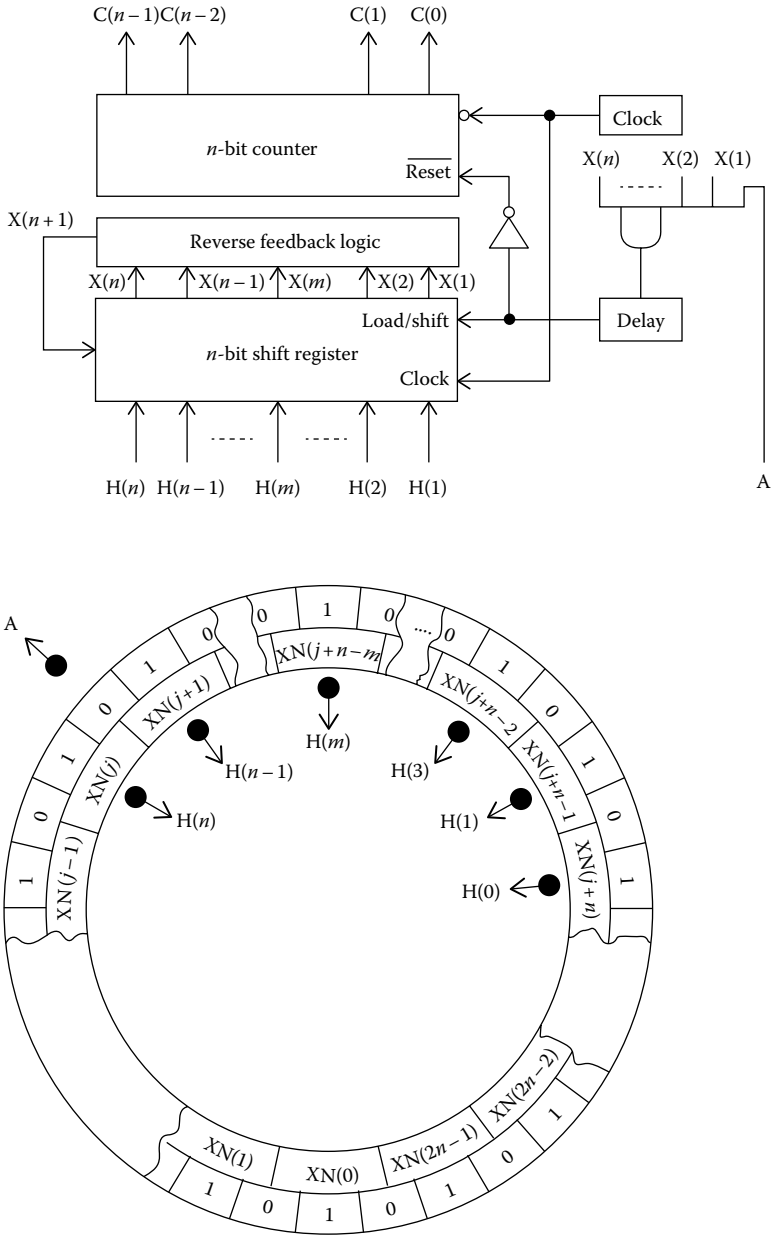

FIGURE 30.5 Pseudorandom shaft encoder with a simple synchronization track to validate the readout from the n-tuple read by the reading heads $H(i)$, $i = n, \ldots, 1$. The circuit is a simplified code conversion to binary based on the reverse feedback logic. The counter counts the number of steps required to return to the initial sequence.

30.2 Incremental Encoder Quadrature Signals

30.2.1 Digital Quadrature Signals

Figure 30.6 illustrates the concept of an incremental rotary optical encoder. The shaft-mounted disk has a series of alternating dark and light sectors of equal length and in equal numbers. The dark and light code is detected by a stationary mask with two apertures, *A* and *B*, displaced one quarter of a cycle from

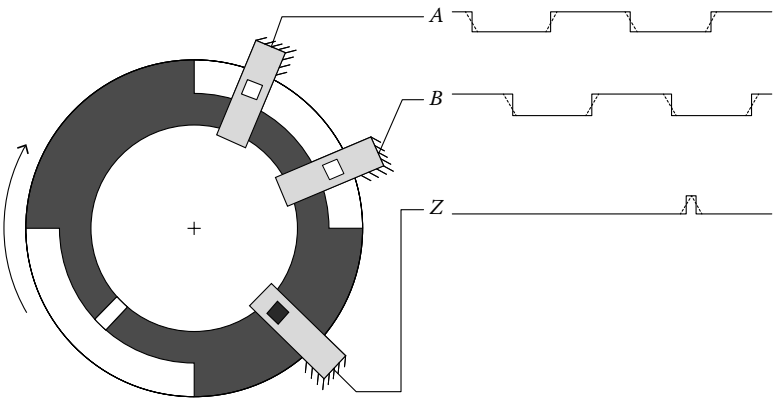

FIGURE 30.6 The lowest possible resolution for a rotary incremental encoder. The outer track provides $n = 2$ cycles of the alternating black and clear records. Two heads *A* and *B* displaced by 90° give, after squaring, two square waves in quadrature.

each other. When a light sector covers a window, a 1 signal is produced, and a 0 results from a dark sector. At a transition, a rising or falling signal occurs. These signals require some pretreatment to square the signals and avoid problems associated with slow movement at the transition positions, resulting in slow rise time and fall time, in the presence of low noise. The resulting cleaned *A* and *B* signals are two square waves 90° out of phase and are called quadrature signals. Since the *A* and *B* signals have only four possible states, they clearly do not provide a means of distinguishing more than four different locations. As a result, absolute position discrimination is only possible within one quadrature cycle. Instead, the quadrature signals are used to increment or decrement a counter that gives the actual position. The counter is initialized (usually reset) on a *z*-phase signal produced on a separate track, the innermost track in Figure 30.6. It is also possible to have a number of *z*-phase signals over the encoder range with a distance-coded variation between the *z*-phase markers. The code can be used to initialize the counter at nonzero positions.

Figure 30.7a shows a simple circuit from Conner [9] to provide one count per cycle of the quadrature signal. The direction information necessary to decide whether to increment or decrement the counters is also produced. Note that Schmitt triggers provide some amount of hysteresis and redress the falling and rising edges from the encoder. Further circuitry is required to increase the amount of hysteresis in very noisy environments. Additional treatment may be required before feeding these signals to counters. The reason is that if, following a count, there is a small movement in the opposite direction without a reverse count signal being issued followed by a forward motion, then the forward motion produces a second count at the same position. Kuzdrall [10] proposes a more reliable circuit in Figure 30.7b. The circuit drives a 74HC193 counter with a down clock and an up clock. Both flip-flops are normally in the high state. Whenever one of them switches to a low state, it is soon reset by the use of that output as a set signal. That low output is only possible when phase *B* is low and there is a transition on *A*. Depending on the direction of that transition, one of the flip-flops produces the brief low state, causing an appropriate up or down count. The problem associated with small oscillations around a position is reduced since the up and down counts occur at the same encoder position. Venugopal [11] proposes a circuit, in Figure 30.7c, which produces a similar effect. A count can only occur when *B* is low and there is a transition on *A*. Depending on the transition direction, one of two the monostables triggers and effectively allows the count at the appropriate input of the 74LS193 counter.

In cases where a noisy environment is present, Holle [12] describes a digital filter to clean the *A* and *B* signals further, a filter that uses a small number of logic gates to form a 4-bit delay filter. Wigmore [13] proposes other circuits for count and direction detection.

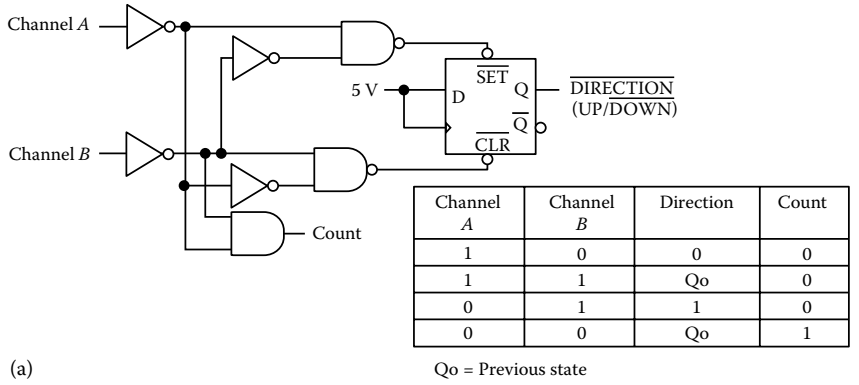

Channel *A*	Channel *B*	Direction	Count
1	0	0	0
1	1	Qo	0
0	1	1	0
0	0	Qo	1

Qo = Previous state

(a)

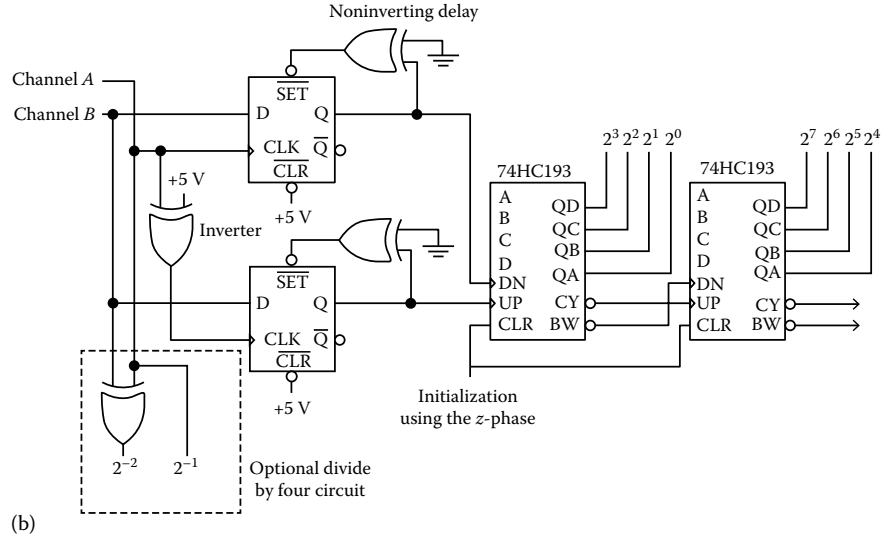

(b)

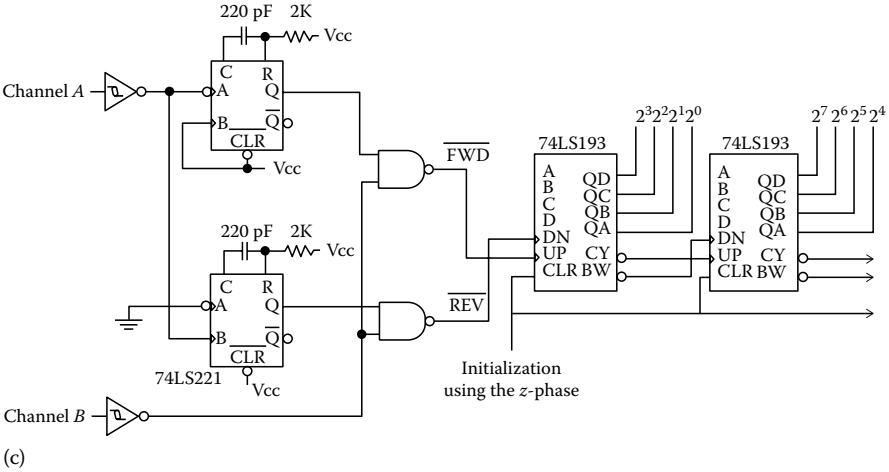

(c)

FIGURE 30.7 Circuit producing a direction and a count signal. (From Conner, D., *EDN*, 35(9), 57, 1990.) (a) Caution must be exercised when using this circuit for counting purposes since multiple counts are possible when the encoder oscillates around the $A = 0$ and $B = 0$ and the $A = 0$ and $B = 1$ states. (From Kuzdrall, J.A., *Electron. Des.*, 17, 81, 1992.) (b) Counts up and down at the same states transition but depending on the direction of movement.

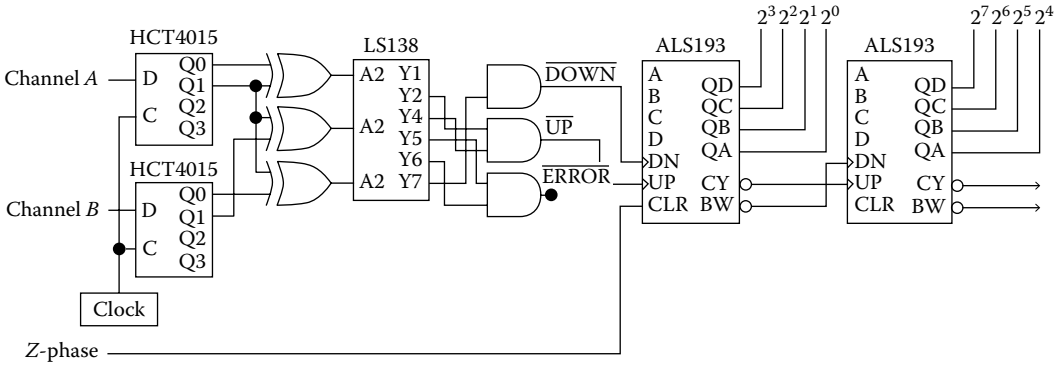

FIGURE 30.8 Divide-by-four circuit producing four counts per cycle of the quadrature signals. Based on except for the LS138 demultiplexer that replaces the suggested 4051 multiplexer because of the latter's unequal fall time and rise time. The clocked shift registers generate a 4-bit code to the demultiplexer for each clock cycle. The clock frequency should be eight times the maximum frequency of the quadrature signals. (From Butler, M.M., *Electronics*, 20, 128, 1980.)

Tables 30.6 and 30.7 list commercial chips and their suppliers' details. Some chips produce count and direction signals or up and down clocking signals. Others also include counters.

The aforementioned circuits do not fully exploit the information contained in the quadrature signals since only one of the four edges (or states) within one quadrature cycle is used to count. Figure 30.8 shows a slightly modified version of a divide-by-four counter circuit proposed by Butler [14]. Two 4-bit shift registers, three exclusive OR gates, and an 8-channel demultiplexer derive the up and down count signals. The clocked shift registers generate a 4-bit code to the demultiplexer for each clock cycle. To ensure that no encoder transitions are missed, the clock frequency should be at least 8 *NS*, where *N* is the number of cycles produced by the encoder for each shaft revolutions and *S* is the maximum speed in revolutions per second. The up and down signals can be fed to cascaded 74ALS193 counters. This circuit analyzes the current and previous states of the *A* and *B* channels to either count up, count down, or issue an error flag when an improper sequence occurs.

Kuzdrall [10] proposes to view a quadrature signal cycle as a Gray code so that the two least significant bits of the count are obtained by a Gray code to binary code conversion as in Figure 30.7b. Phase *A* generates bit 1 of the natural binary position, and phase *B* is exclusive ORed with phase A to produce the least significant bit. The counter provides the remaining bits of the natural binary position. Marty [15] proposes a state machine that stores both the actual *A* and *B* values and the previous values using *D*-type flip-flops (in a similar way to Butler) to form a hexadecimal number. In all, eight different hex digits are generated, four for each direction of motion. A 4-line to 16-line decoder then feeds into two 4-input NAND gates to produce an up or down count signal. As for Butler, this last circuit is not dependent on propagation delays as with Kuzdrall's circuit.

30.2.2 Analog Quadrature Signals

30.2.2.1 Interpolation by Resistor Network

Some optical encoders deliver analog quadrature signals in the form of a $\sin(\theta)$ signal, *A*, and a $\cos(\theta)$ signal, *B*, where θ is the phase (electrical degree) within one cycle of the quadrature signal. θ does not equal shaft angle but is related to it: 360 electrical degrees of θ corresponds to $360/N$ mechanical degrees, where *N* is the number of analog quadrature signal cycles per shaft revolution. Indeed, θ still exists for linear encoders of this type. Although these signals can be squared and fed to a divide-by-four counter, they can also be processed directly to generate a finer resolution. The main techniques are (1) multiple phase-shifted signals, (2) lookup table, and (3) arctangent processor.

The multiple phase-shifted signals method relies solely on electronics to increase the frequency of the final digital quadrature signals by an integer amount. Benzaid and Bird [16] propose the circuit of Figure 30.9a, which has been designed in this particular case for a fourfold frequency increase. This can then be followed by a digital divide-by-four circuit (not shown). The A and B signals are combined to produce an additional six phase-shifted signals, three of which are shifted by $\pi/8$, $\pi/4$, and $\pi/8$, respectively, from the A signal and three others that are shifted similarly from the B signal. The result is a total of eight available sinusoidal signals, phase shifted by $\alpha = i\,\pi/8$ with $i = 0, 1, \ldots, 7$. This can be generalized, saying that for an m-fold increase in resolution, $2m$ signals that are phase shifted by $\alpha i\,\pi/2m$ with $i = 0, 1, \ldots, 2m - 1$ are required. The phase-shifted sinusoidal signals are then squared using TTL

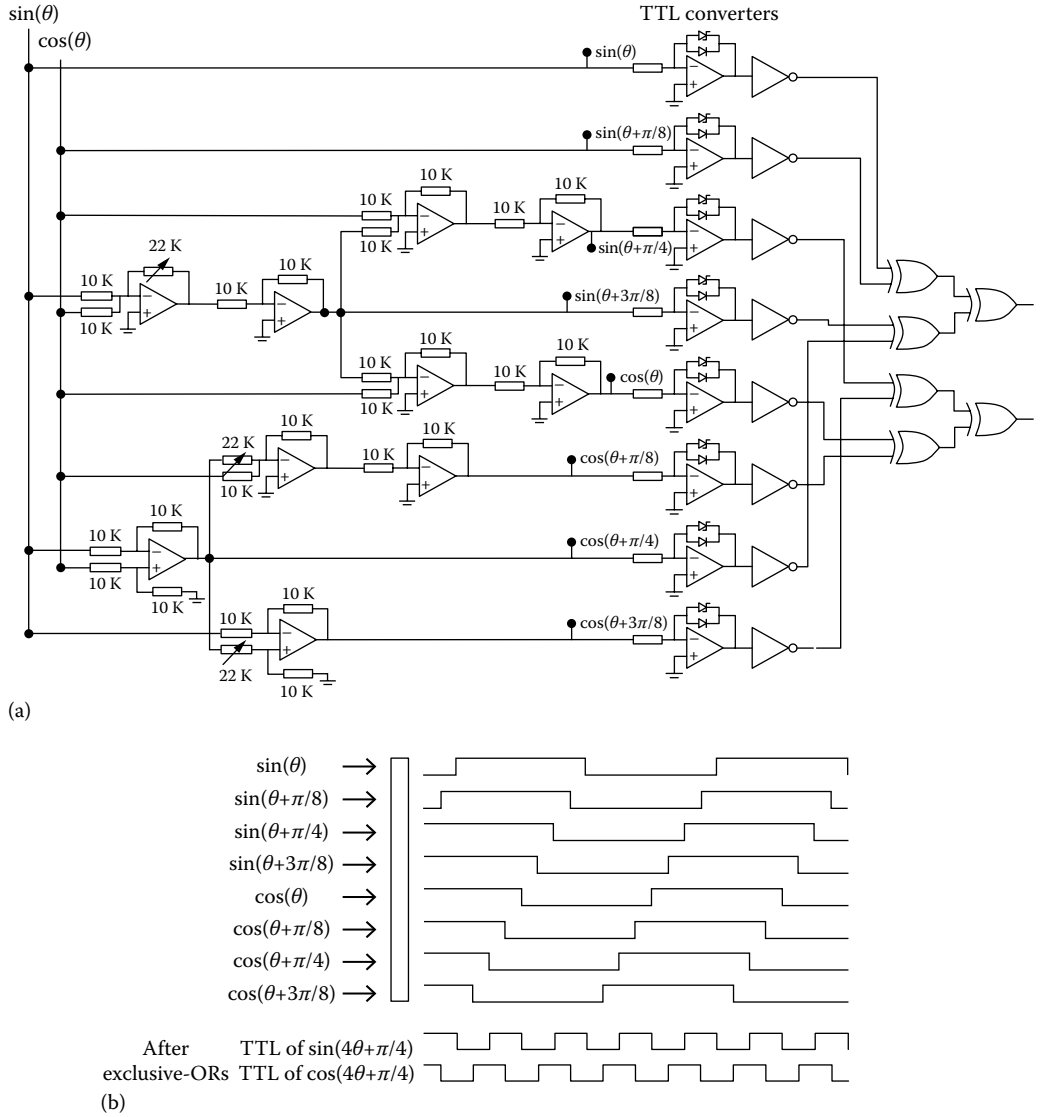

FIGURE 30.9 Interpolation circuit. The sine and cosine signals from the encoder are vector combined in (a) to produce various phase-shifted signals. Following TTL conversion, they are exclusive ORed. The squared phase-shifted signals and the final result are in (b). (From Benzaid, O. and Bird, B.M., Interpolation techniques for incremental encoders, *Proceedings of 23rd International Conference on Intelligent Motion*, June 22–24, pp. 165–172, 1993.)

converters. Figure 30.9b shows the resulting square waves. The addition, modulo 2, of the signals for even values of i gives A' and similarly for the signals with odd values of i gives B'. The modulo-2 sum is performed via exclusive ORs.

The vector additions of the initial A and B signals result in phase-shifted signals. The weights of A and B are calculated from the trigonometric relations:

$$\sin(\theta+\alpha)=\cos(\alpha)\sin(\theta)+\sin(\alpha)\cos(\theta) \tag{30.4}$$

and

$$\cos(\theta+\alpha)=-\sin(\alpha)\sin(\theta)+\cos(\alpha)\cos(\theta) \tag{30.5}$$

where $\sin(\theta) = A$ and $\cos(\theta) = B$.

Thus,

$$\sin(\theta+\alpha)=\cos(\alpha)\ A+\sin(\alpha)\ B \tag{30.6}$$

and

$$\cos(\theta+\alpha)=-\sin(\alpha)\ A+\cos(\alpha)\ B \tag{30.7}$$

Note that the amplitudes of the phase-shifted signals are not critical, since it is their zero-crossing points that produce the square-wave transition. Also, in the circuit of Figure 30.9a, the weights were slightly modified to simplify the implementation, which results in a small variation of the duty cycle of A' and B'.

The phase-shifted signals can alternatively be produced using voltage dividers and Schmitt triggers, where the divider resistors are in the ratio $\tan(\alpha)$ [17]. As m increases, the precision of the weights becomes more stringent, and the speed of the electronics processing the high-frequency square signals might limit the upper value of m possible with this method.

30.2.2.2 Interpolation by Sampling and Numerical Processing

A number of methods digitize the analog quadrature signals in order to perform a digital interpolation within one cycle of the quadrature signals. These techniques permit an even higher interpolation. The signals are periodically sampled in sample-and-hold circuitry and digitized by an analog-to-digital converter (ADC). One technique uses an interpolation table, while the other performs arctangent calculations.

Hagiwara [18] uses an m-bit ADC to digitize the analog A and B signals into the binary numbers Da and Db. Figure 30.10a shows how these binary numbers are used as the addresses of a grid, here built for $m = 3$ as a 2^m by 2^m grid. Hagiwara then associates a phase angle with the center of each cell of the matrix using simple arctangent calculations. The angle is calculated with respect to the center of the grid. This phase angle is then associated with one of $2^n - 1$ phase codes using

$$\text{Phase code} = \text{ integer part of } \left(2^n \frac{\theta}{2\pi}\right) \tag{30.8}$$

as shown in Figure 30.10b.

The proposed circuit includes the means of performing the accumulation of interpolated values to deliver the encoder absolute position. A modification to this circuit is also proposed that can compensate the phase code for known inaccuracies in the encoder signals with respect to the actual encoder position.

For the highest possible level of interpolation, Mayer [19] describes an arctangent calculator method. It uses a microprocessor to perform high-level trigonometric calculations on the digitized analog signals. As this process is performed, the analog signals are continuously squared and fed to a

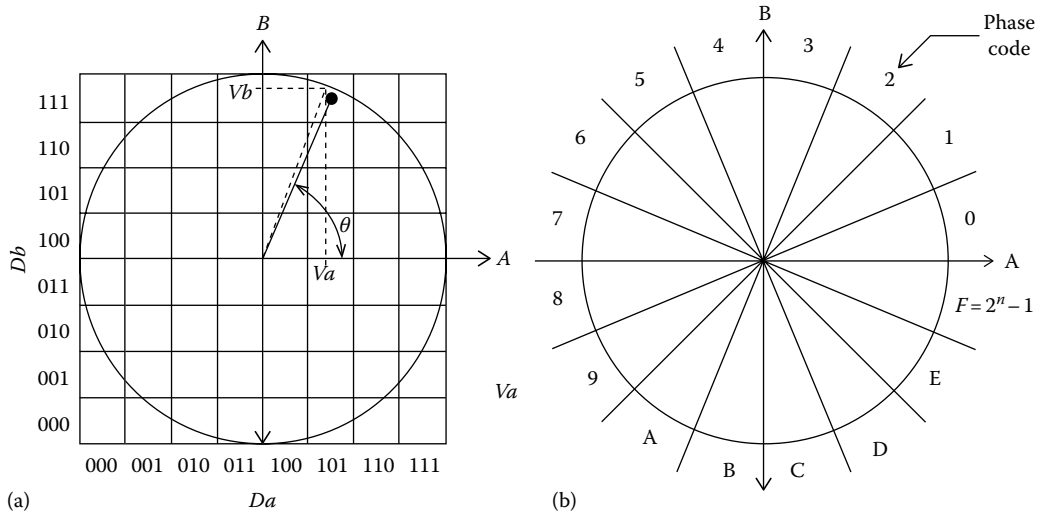

FIGURE 30.10 Hagiwara proposes a 2D lookup table that associates a quantized phase value to a set of digitized values of the quadrature signals. The phase code associated with a grid address may be adjusted to compensate for known errors in the quadrature signals: (a) the use of binary numbers for addressing a grid, and (b) calculation of angles with respect to the center of the grid. (From Hagiwara, N., *IEEE Trans. Instrum. Meas.*, 41(1), 98, 1992.)

divide-by-four counter. The two information sources are combined to produce the encoder's position with a very high level of resolution. Note, however, that although the resulting theoretical resolution is limited only by the ADC, in practice, it is the quality of the analog signals in relation to the physical position being measured that will limit the precision obtained.

30.3 Encoding Principles

Optical encoders use one of three techniques to generate the electrical signals from the relative movement of the grating and the reading heads. They are (1) geometric masking, (2) Moiré effects, and (3) laser interference. Note that absolute encoders mainly use geometric masking. Geometric masking relies on geometric optics theory and considers light as traveling in a straight line. However, as the grating period reduces and the resolution of the encoder increases, Moiré fringe effects are observed and used to produce the signals. Although diffraction effects then become nonnegligible, their influence can be controlled by careful design. Finally, for very high resolution, diffraction effects are directly exploited to perform the measurements.

30.3.1 Geometric Masking

Geometric masking is applied to absolute and incremental encoders. The electromagnetic field associated with the propagation of visible light is characterized by very rapid oscillations (frequencies of the order of 10^{14} s^{-1}). It may therefore be expected that a good first-order approximation to the propagation laws of light is obtained by neglecting the wavelength of light. In this case, diffraction phenomena may be ignored, and light may be thought to propagate in a straight line. Geometry can then be used to analyze the behavior of light. The approximation is valid whenever light rays propagate through an encoder grating with fairly coarse pitch (say, more than 10 μm). Figure 30.11 shows a portion of an encoder scale being scanned by a reading head with multiple slits in order to send more light onto the photosensitive area. The light source is collimated (rays are made parallel to each other after having been emitted in multiple directions from a small source), passes through the stationary grating or index grating, and propagates through the moving grating. In the case of an incremental encoder, a second head would read from the same moving grating but

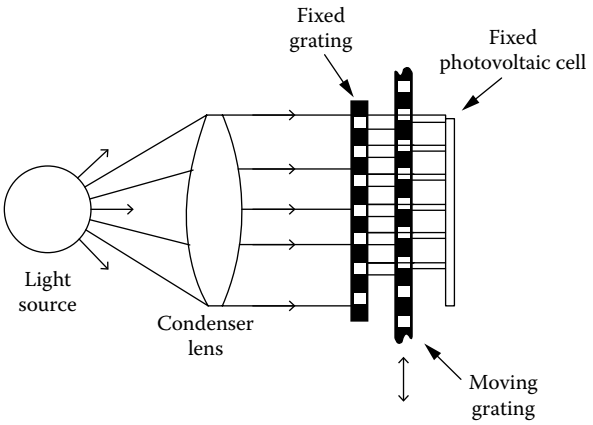

FIGURE 30.11 The reading head contains a light source that can be an incandescent bulb or a light-emitting diode. The light may require a condenser in order to collimate it. This redirects the light rays from the source so that they travel perpendicular to the gratings. The stationary index grating structures the light beam into bands that then cross the moving grating. Depending on the relative position of the fixed and the moving gratings, more or less light reaches the photodetector. The detector produces a signal proportional to the total amount of light on its sensitive surface.

be displaced by n + 1/4 pitch in order to produce a second signal with a phase of 90°. When the slits of the two gratings are aligned, a maximum amount of light reaches the detector. Similarly, a minimum amount of light is transmitted when the gratings are out of phase by 180°. Depending on the design of the grating, such as the duty cycle of the transmitting and opaque sectors, various cyclic signal patterns are obtained. Generally, it is noteworthy that optical encoders can also be used as a reflective as opposed to transmissive design. Also, in some absolute optical encoders, the encoding principle does not rely on a primary grating, per se, or the detection system does not necessarily incorporate any masking element.

30.3.2 Moiré Fringes

Moiré fringe methods are primarily associated with incremental encoders. Moiré fringes are observed when light passes through two similar periodic patterns brought close to each other and with their line pattern nearly parallel. Figure 30.12 shows linear and radial gratings producing Moiré fringes. Take a linear grating with sinusoidal amplitude transmittance as proposed by Gasvik [20]:

$$f(x,y) = a + a\cos\left(\frac{2\pi x}{P}\right) \tag{30.9}$$

where

P is the grating period
a is the amplitude
x is measured perpendicularly to the grating lines

It is also possible to represent a square-wave-type grating using a Fourier series in the case of a radial grating and a Fourier integral for a linear grating. When two linear gratings, a and b, are laid in contact, the resulting transmittance, f_c, is the product of their individual transmittances f_a and f_b:

$$f_c = f_a \times f_b \tag{30.10}$$

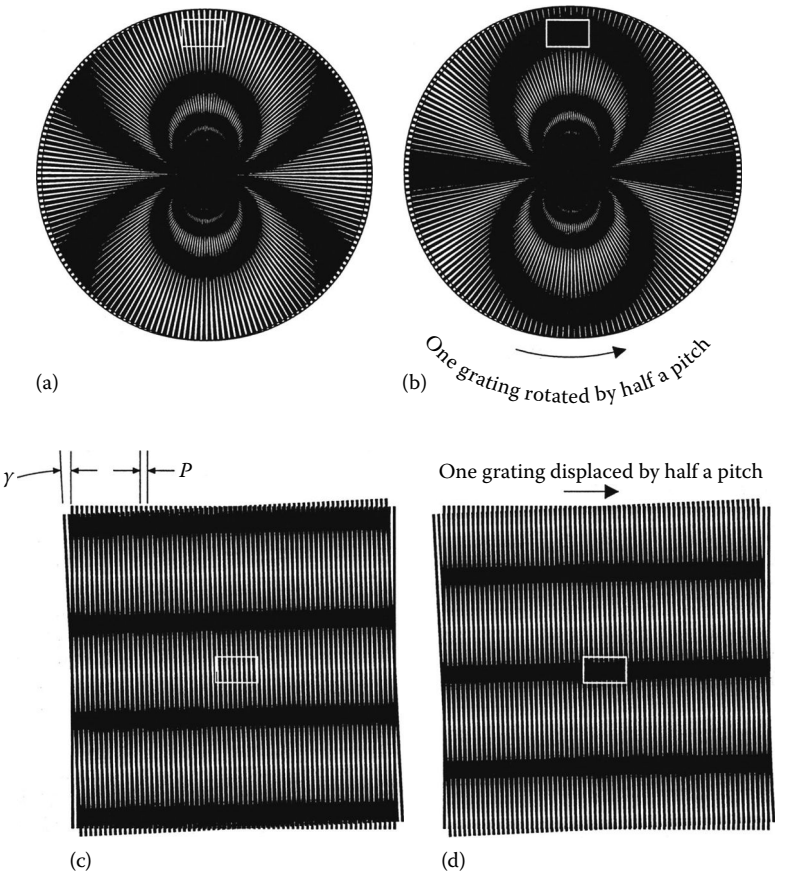

FIGURE 30.12 Moiré fringes produced when two gratings of equal pitch are overimposed. In (a), two radial gratings with 180 cycles have their centers displaced horizontally by approximately half of the grating pitch (as measured on the perimeter). This could be due to encoder-assembly errors. The fringes are always circular and pass by the two centers. In (b), the same displacement was followed by a rotation of half a pitch as a result of the normal movement of the encoder disk. This causes a phase change of 180° of the fringe pattern at any fixed observation point, as represented by the rectangular observation region. The width of the fringes depends on the offset displacement between the two grating centers. If they coincide, the whole pattern changes from a dark to a relatively bright fringe. In (c), two linear gratings are rotated by one-tenth (in radian) of their grating pitch. This could be due to encoder assembly or mounting errors. As a result, Moiré fringes occur at 90° to the grating and with a period 10 times larger. The normal displacement of one grating by half of the grating pitch causes a phase change of 180° of the Moiré fringe pattern at any fixed observation point, as represented by the rectangular observation region. (From Ditchburn, R.W., *Light*, Vol. 1, Academic Press, New York, 1976.)

In the case when a misalignment γ exists between the two gratings, the separation of the Moiré fringe is d with

$$d = \frac{P}{2\sin(\gamma/2)} \tag{30.11}$$

and for small γ,

$$d = \frac{P}{\gamma} \tag{30.12}$$

It follows that when the two gratings are moved relative to each other by a distance x' in the direction perpendicular to their lines, then the phase $\phi(x')$ of the Moiré fringes at a stationary location changes by

$$\phi(x') = \frac{2\pi x'}{P} \tag{30.13}$$

In effect, every time x' equals P, the entire Moiré fringe pattern undergoes one complete cycle of fluctuation. If the two gratings are adjusted to near parallelism, then the fringes are "fluffed out" (see Burch [21]) to an infinite width. Under such conditions, there is no fringe motion to be observed, and the entire region simply goes from brightness to darkness. These effects are mathematically predicted using a convolution integral:

$$f_c(x') = \frac{\int_{x_1}^{x_2} f_a(x) f_b(x - x')}{dx} \tag{30.14}$$

where x_1 to x_2 represents the region covered by the photodetector. If $g_a(k)$ and $g_b(k)$ are the exponential Fourier transforms of f_a *and* f_b, then the photodetector response f_c will have the Fourier transform $g_c(k)$:

$$g_c(k) = g_a(k) g_b(-k) \tag{30.15}$$

Moiré effects can be obtained by transmission or by reflection at the grating.

It must be kept in mind, however, which as the grating pitch reduces, diffraction effects become significant; careful design and adjustment of the gap between the stationary and the moving grating and also lighting and detection arrangements become critical. Since a large number of lines of the gratings are used to generate the photodetector response, small local imperfections of the grating pitch are averaged out, resulting in improved measurement accuracy.

30.3.3 Diffraction-Based Encoders

Diffraction-based encoders are used for the highest levels of precision. They successfully exploit diffraction effects and are referred to as physical optics encoders as opposed to geometrical optics encoders. Figure 30.13 shows diffraction effects observed when coherent light encounters a pattern of slits [20]. The slit is a few wavelengths wide, so strong diffraction effects are observed. Each slit may be thought of as acting as a coherent light source producing circular wave fronts. Along certain directions, the portions of these wave fronts are in phase with each other. These directions are given by

$$\sin\theta_m = \frac{m\lambda}{P} \tag{30.16}$$

where

m is the positive or negative integer and is the order of diffraction
P is the diffraction grating period

Suppose now that the slits are moving by a distance x as shown in Figure 30.13. Then the phase of the wave front at a stationary location will increase for m positive and decrease for m negative by $2\pi mx/P$.

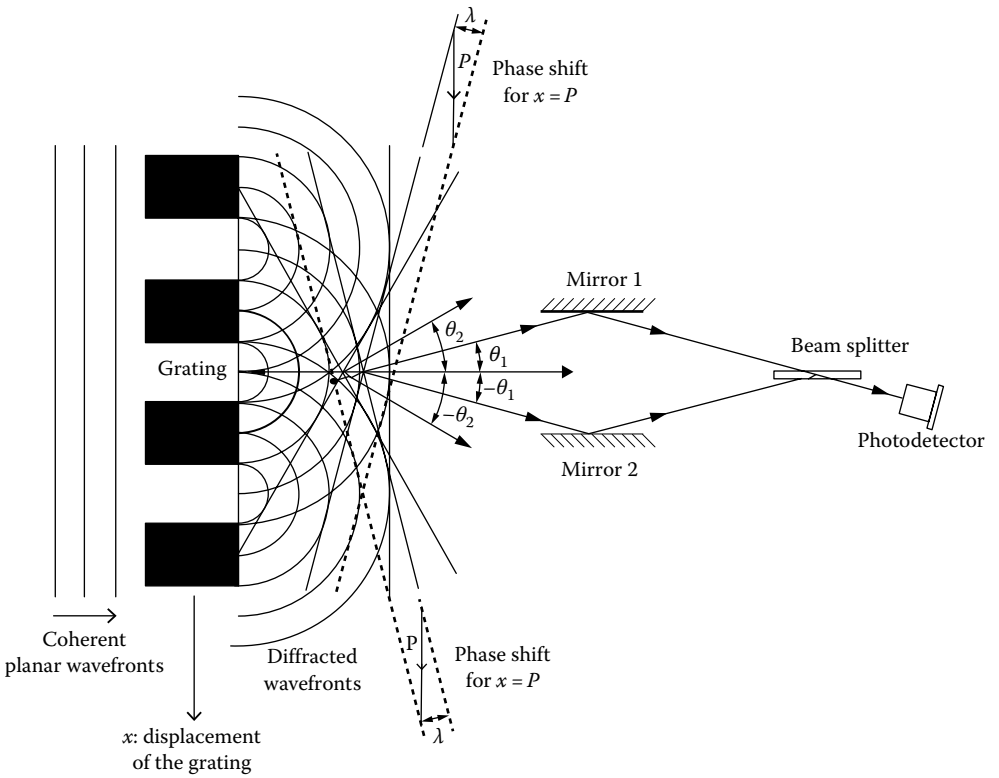

FIGURE 30.13 The grating diffracts the coherent planar wave front coming from the left into a series of circular wave fronts. The coherent circular wave fronts are in phase along certain directions resulting in diffracted planar wave fronts. These planar wave fronts correspond to the common tangents of the circles. For example, the third innermost circle of the uppermost slit is in phase with the fourth innermost circle of the middle slit and also with the fifth innermost circle of the lowest slit. This diffracted wave front corresponds to the first-order diffraction ($m = 1$) and makes an angle θ_1, with the initial planar wave-front direction. A similar order wave front ($m = -1$) has a direction $-\theta_1$. These two wave fronts are initially in phase. A displacement of the grating downward by x causes the $m = 1$ wave front to move by a distance $x\lambda/P$ and the $m = -1$ wave front by $-x\lambda/P$, thus causing a relative phase shift between the two wave fronts of $2x\lambda/P$. This relative phase shift produces a movement of interference fringes at the photodetector.

When the slit pattern has moved by one pattern cycle, then the two wave fronts will have developed a relative phase change of $2m$ cycles. The two phase-shifted wave fronts may be recombined to produce interference fringes.

30.3.4 Rotary Encoders

The Canon laser rotary encoder uses an optical configuration that generates four cycles of interference fringes per cycle of the diffraction grating. This is achieved by splitting the original wave front in two and interrogating the grating at two diametrically opposed locations. Reflecting both diffracted beams back through the grating results in a further doubling of the resolution. The two beams are finally recombined for interference fringe counting. Furthermore, as explained by Nishimura and Ishizuka [22], using diametrically opposed portions of the disk attenuates the effect of eccentricity. An encoder with an external diameter of 36 mm produces 81,000 analog quadrature cycles/revolution. The grating has a pitch of approximately 5 μm and the laser light has a wavelength of 780 nm.

A grating motion by P causes four fringe cycles.

30.3.5 Linear Encoders

Sony markets a laser linear encoder with a volume hologram grating of 0.55 μm pitch [23]. Figure 30.14 gives some insight into the principle of operation of this type of encoder. In theory, for maximum intensity of the reflected light beam through the hologram grating, the path length difference from successive plane mirrors must be equal to λ [20]. The Sony Laserscale encoder uses a semiconductor laser as the coherent light source. The beam splitter produces two beams to interrogate the grating at two separate locations. The beams are then diffracted by the hologram grating, followed by a reflection at the mirrors and pass a second time through the grating. They are finally recombined at the photodetector to produce interference fringes. Because the two beams are diffracted by the grating in opposite directions, and because they pass twice through the grating, four signal cycles are obtained when the grating moves by one pitch.

The Heidenhain Company produces both linear and rotary encoders of very high resolution, also using the principles of diffraction. Their approach, unlike those previously mentioned, uses an index grating and a reflecting scale grating [17,24].

The Renishaw Company uses a fine reflective grating of 20 μm pitch that diffuses the light from an infrared light-emitting diode. In order to avoid the problems caused by diffraction effects, the index grating of a conventional Moiré approach would require a very small gap between the index and

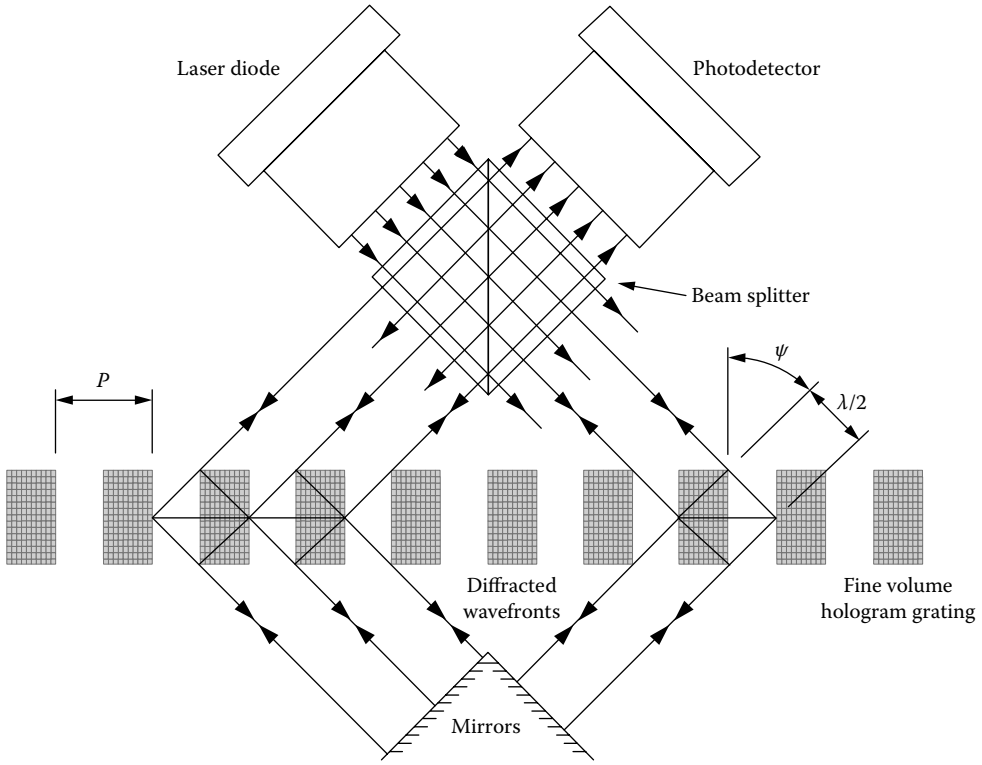

FIGURE 30.14 The coherent planar wave front of the laser diode is split into two at the beam splitter. Both beams can be regarded as being partially reflected at the grating by minute mirrors separated by a pitch, *P*. Maximum reflection is achieved when $2P \sin \psi = \lambda$. Each reflected portion of the incident beam is phase shifted by one λ with respect to that reflected by an adjacent mirror so that the reflected wave front remains coherent. The reflected wave fronts are truly reflected at the orthogonal mirrors for a second pass through the grating, after which they are recombined by the splitter to interfere at the photodetector. A displacement of the grating by x along its axis causes one beam path to be shortened by $2x\lambda/P$, while the other is lengthened by the same amount.

the main gratings. Instead, the index grating is located at a distance of 2.5 mm. The index grating is then able to diffract the diffused light from the main grating and to image it 2.5 mm further. There, a fringe pattern of the Moiré type is produced and photoelectrically analyzed [25].

30.4 Components and Technology

The choice of an encoder demands careful consideration of a number of factors, such as (1) the required resolution, repeatability, and accuracy (linearity); (2) the maximum and minimum operating speeds; (3) the environmental conditions (temperature range, relative humidity (condensing or not condensing), contaminants such as dust, water, and oil); (4) the minimum friction torque (or force) acceptable; (5) the maximum inertia acceptable; (6) the available space; (7) the position to be known immediately after a power loss; (8) the range in degrees (or mm); (9) the mounting and shaft loading; and (10) the price.

Rotary encoders also sometimes employ reflective tapes attached to, or markings directly etched into, the surface of a drum or spindle to be read from the side. In special cases, tapes or engravings of this type can be made to conform to the surface of an elliptical cross-sectional cam or other irregular contour. Cylindrical primary gratings employing transmissive readout have also been produced.

The main gratings (scale) come in a wide variety of materials, both for the substrate and for the marking. Flexible scales based on a metal tape substrate are also available from Renishaw, allowing very long (tens of meters) continuous reading of linear motion. Tables 30.2 through 30.4 give a partial list of encoders currently available on the market. The list is not exhaustive in terms of suppliers and does not cover all the models of the suppliers listed. Table 30.5 gives the address and telephone numbers of the suppliers. Tables 30.6 and 30.7 list some suppliers of quadrature-decoding circuits.

TABLE 30.2 Commercial Optical Rotary Incremental Encoders

Manufacturer	Model No.	Output Type	Counts[a]	Resolution[b]	Price[c]
BEI	H25	Square wave	2,540	50,800	$340
Canon	Kl	Sine wave	81,000	1,296,000	$2,700
Canon	X-1M	Sine wave	225,000	18,000,000	$14,000
Dynamics	25	Sine wave	3,000	60,000	$290
Dynamics	35	Sine wave	9,000	360,000	$1,150
Gurley	911	Square wave	1,800	144,000	$1,300
Gurley	920	Square wave	4,500	144,000	$500
Gurley	835	Square wave	11,250	360,000	$1,500
Heidenhain	ROD 426	Square wave	50–10,000	200–40,000	$370
Heidenhain	ROD 905	Analog	36,000	0.035 arcsec	$12,600
Lucas Ledex	LD20	Square wave	100	—	$180
Lucas Ledex	LD20	Square wave	1,000	—	$195
Lucas Ledex	DG60L	Square wave	5,000	—	$245
Renco	RM21	Square wave	2,048	—	$176
TR Electronic	IE58	Square wave	10,000	—	$428

[a] Number of quadrature cycles per revolution without electronic divide-by-four or interpolation.

[b] Unless otherwise specified, is the number of counts per revolution with electronic interpolation, either internal or external to the encoder, supplied by the manufacturer as an option.

[c] Based on orders of one unit. Must not be used to compare products since many other characteristics, not listed in this table, determine the price.

TABLE 30.3 Commercial Optical Rotary Absolute Encoders

Manufacturer	Model No.	Steps per Turn	No. of Turn	Price[a]
BEI	M25	65,536	1	$2130
BEI	MT40	512	16	$1240
BEI	MT40	65,530	512	$5000
Gurley	25/04S	131,072	1	$1900
Heidenhain	ROC 424	4,096	4096	
Lucas Ledex	AG60E	360 or 512	1	$486
Lucas Ledex	AG661	4,096	4096	$1260
TR Electronic	CE65[b]	8,192	4096	$1408

[a] Based on orders of one unit. Must not be used to compare products since many other characteristics, not listed in this table, determine the price.

[b] Programmable output.

TABLE 30.4 Commercial Optical Linear Incremental Encoders

Manufacturer	Model No.	Output Type	Pitch[a] (μm)	Resolution[b] (μm)	Length (mm)	Price[c] (Length)
Canon	ML-16+	Sine wave	1.6	0.4	To 300	$1525 (50 mm)
Canon	ML-08+	Sine wave	0.8	0.2	To 150	$3100
Gurley	LE18	Square wave	20	0.1	To 1500	$750 (1000 mm)
Gurley	LE25	Square wave	20	0.1	To 3000	$800 (1000 mm)
Heidenhain	LS603	Sine wave	20	5	To 3040	$932 (1020 mm)
Heidenhain	LIP401	Sine wave	2	0.005	To 420	$4000 (100 mm)
Renishaw	RG2	RS422A	20	0.5	To 60,000	$640 + $360/1000 mm
Sony	BS75A-30NS	Square wave	0.14	0.05	30	$2628

[a] Period of the quadrature cycle without electronic divide-by-four or interpolation.

[b] With electronic interpolation supplied by the manufacturer.

[c] Based on orders of one unit. Must not be used to compare products since many other characteristics, not listed in this table, determine the price.

TABLE 30.5 Companies That Make Optical Encoders

BEI Sensors and Motion Systems Company
Encoder Systems Division, 13100 Telfair Avenue, Sylmar, CA. Tel.: (848) 341-6161, http://www.beisensors.com/index.html

Canon USA Inc.
Components Division, New York Headquarters, One Canon Plaza, Lake Success, NY 11042, Tel.: (516) 488-6700, http://www.usa.canon.com/cusa/home

Dr. Johannes Heidenhain GmbH
DR.-Johannes-Heidenhain-Strasse 5, D83301 Traunreut, Deutschland, Tel.: (08669)31-0,

Gurley Precision Instruments Inc.
514 Fulton Street, Troy, NY 12181-0088, Tel.: (518) 272-6300, http://www.gurley.com/

Ledex Products
Lucas Control Systems Products, 801 Scholz Drive, P.O. Box 427, Vandalia, OH 45377-0427, Tel.: (513) 454-2345, http://www.ledex.com/

Renco Encoders Inc.
26 Coromar Drive, Goleta, CA 93117, Tel.: (805) 968-1525, http://www.renco.com/

Renishaw plc,
Transducer Systems Division, Old Town, Wotton-under-Edge, Gloucestershire GL12 7DH, U.K., Tel.: +44 1453 844302, http://www.renishaw.com/en/renishaw-enhancing-efficiency-in-manufacturing-and-healthcare—1030

TR Electronic GmbH
Eglishalde 6, Postfach 1552, D-7218 Trossingen, Germany, Tel.: 0 74 25/228-0, http://www.tr-electronic.de/trgroup/index.html

Sony Magnescale Inc.
Toyo Building, 9-17, Nishigotanda 3-chome, Shinagawa-ku, Tokyo, 141 Japan, Tel.: (03)-3490-9481, http://www.magnescale.com/mgs/index.html

TABLE 30.6 Commercial Digital Quadrature Signal Decoder Circuits

Manufacturer	Model No.	Output	Decoding Factor	Counter	Price
Hewlett-Packard	HCTL-2000	Count	12 bits	x4	$12.75
Hewlett-Packard	HCTL-2016	Count	16 bits	x4	$12.75
Hewlett-Packard	HCTL-2020	Count	16 bits and cascade o/p	x4	$14.55
U.S. Digital Corp.	LS7083	Up and down clock		xl or x4	$3.05
U.S. Digital Corp.	LS7084	Count and direction		xl or x4	$3.60

TABLE 30.7 Companies That Make Divide-by-Four Decoders

U.S. Digital Corporation
3800 N.E. 68th Street, Suite A3, Vancouver, WA 98661-1353, Tel.: (360) 696-2468

Hewlett-Packard Company
Direct Marketing Organization
5301 Stevens Creek Boulevard, P.O. Box 58059, MS 51LSJ, Santa Clara, CA 95052-8059, Tel.: (408) 246-4300

References

1. P. E. Stephens and G. G. Davies, New developments in optical shaft-angle encoder design, *Marconi Rev.*, 46(228), 26–42, 1983.
2. P. Sente and H. Buyse, From smart sensors to smart actuators: Application of digital encoders for position and speed measurements in numerical control systems, *Measurement*, 15(1), 25–32, 1995.
3. E. M. Petriu, Absolute-type position transducers using a pseudorandom encoding, *IEEE Trans. Instrum. Meas.*, IM-36, 950–955, 1987.
4. E. M. Petriu, Scanning method for absolute pseudorandom position encoders, *Electron. Lett.*, 24, 1236–1237, 1988.
5. G. H. Tomlinson, Absolute-type shaft encoder using shift register sequences, *Electron. Lett.*, 23, 398–400, 1987.
6. J. N. Ross and P. A. Taylor, Incremental digital position encoder with error detection and correction, *Electron. Lett.*, 25, 1436–1437, 1989.
7. M. Arsic and D. Denic, New pseudorandom code reading method applied to position encoders, *Electron. Lett.*, 29, 893–894, 1993.
8. B. Arazi, Position recovery using binary sequences, *Electron. Lett.*, 20, 61–62, 1984.
9. D. Conner, Long-lived devices offer high resolution, *EDN*, 35(9), 57–64, 1990.
10. J. A. Kuzdrall, Build an error-free encoder interface, *Electron. Design*, September 17, 81–86, 1992.
11. P. Venugopal, Reflective optical SMT module reduces encoder size, *Power Conver. Intell. Motion*, 21(5), 60–62, 1995.
12. S. Holle, Incremental encoder basics, *Sensors*, 7(4), 22–30, 1990.
13. T. Wigmore, Optical shaft encoder from sharp, *Elektor Electron.*, 15(169), 60–62, 1989.
14. M. M. Butler, Simplified multiplier improves standard shaft encoder, *Electronics*, November 20, 128–129, 1980.
15. B. Marty, Design a robust quadrature encoder, *Electron. Design*, June 24, 71–72, 74, 76, 1993.
16. O. Benzaid and B. M. Bird, Interpolation techniques for incremental encoders, *Proceedings of 23rd International Conference on Intelligent Motion*, June 22–24, pp. 165–172, 1993.
17. Heidenhain General Catalog, Dr. Johannes Heidenhain GmbH, DR.-Johannes-Heidenhain-Strasse 5, D83301 Traunreut, Deutschland, November 1993, 8.
18. N. Hagiwara, Y. Suzuki, and H. Murase, A method of improving the resolution and accuracy of rotary encoders using a code compensation technique, *IEEE Trans. Instrum. Meas.*, 41(1), 98–101, 1992.

19. J. R. R. Mayer, High-resolution of rotary encoder analog quadrature signals, *IEEE Trans. Instrum. Meas*., 43(3), 494–498, 1994.
20. K. J. Gasvik, *Optical Metrology*, New York: John Wiley & Sons, 1987.
21. J. M. Burch, The metrological applications of diffraction gratings, in E. Wolf (Ed.), *Progress in Optics,* Vol. II, Amsterdam, the Netherlands: North-Holland Publishing, 1963.
22. T. Nishimura and K. Ishizuka (From Canon, Inc., Tokyo), Laser Rotary Encoders, Motion: Official Journal of the Electronic Motion Control Association, September/October 1986, Reprint obtained from Canon.
23. Anonymous from Sony Magnescale America Inc., Hologram technology goes to work, *Mach. Des*., January 12, 32, 1995.
24. Anonymous from Heidenhain, Encoding systems Vorsprung durch Heidenhain, *Eng. Mater. Des*., September 1989, 53–54.
25. Jim Henshaw of Renishaw, Linear encoder offers superior flexibility, *Des. Eng*., September 1995.
26. R. W. Ditchburn, *Light*, Vol. 1, New York: Academic Press, 1976.

Further Readings

Latest Encoder News, BEI Sensors. http://www.beiied.com/news/BEI_industrial-encoders_for-dummies.html, (accessed on June 10, 2012).

Linear and Rotary Encoders, National Instruments. http://www.magnescale.com/mgs/index.html (accessed on March 25, 2012).

O. Solgaard, *Photonic Microsystems: Micro and Nanotechnology Applied to Optical devices and Systems*, Berlin, Germany: Springer Science, 2009.

31

Magnetic Displacement Sensors

David S. Nyce
Revolution Sensor Company

31.1 Introduction

Several types of linear and angular displacement measuring devices rely on electromagnetic fields, and the magnetic properties of materials, in the operation of their basic sensing elements. Some may not commonly be referred to as magnetic sensors but are instead named according to their specific sensing technique. The magnetic sensors presented here use either a permanent magnet, an AC- or DC-powered electromagnet, or a coiled conductor. Together with various components and materials used to sense the magnetic field, the combination is arranged to obtain a response indicating angular or linear displacement or position. Either the sensor is caused to operate by a magnetic field or the properties of the sensor are derived from the use of a magnetic field. Types of magnetic sensors presented in this section include magnetostrictive, distributed impedance, magnetoresistive, Hall effect, and magnetic encoders. Some versions of synchro/resolvers and related sensors loosely meet the characteristics listed earlier but are included in another section of this handbook and thus will not be included in this section. Linear variable differential transformers (LVDTs) and inductive proximity sensors are types of magnetic displacement sensors, but measure displacement over a limited range, and are also covered in another section of this handbook.

An important aspect of magnetic sensors is that they utilize a noncontact sensing element. There is no mechanical connection or linkage between the stationary members and the movable members of the sensor. In some devices that sense a position magnet or core, the sensor can even be designed to allow removal of the magnet or core from the sensitive element, when readings are not required. Noncontact implies that the lifetime of the sensing element is not limited to a finite number of cycles by friction-induced wear. This is important in some industrial machinery and in many applications requiring high reliability. All of the sensors presented in this chapter utilize noncontact sensing techniques.

Displacement refers to a change in position, or the amount by which an object has been displaced, rather than to a single, absolute position. In common industrial practice and by many sensor manufacturers, however, the terms displacement sensor and position sensor are commonly confused, and displacement sensors are typically labeled as either incremental or absolute. Nonetheless, a displacement

sensor indicates the amount of change between the present location and a previous location by providing a magnitude and direction of change with respect to the previously reported location. For example, with a rotation sensor, the indication may be a number of counts clockwise from the previously recorded location, where the number of counts is the magnitude and clockwise is the direction. If the information that describes the current location is lost, due to power loss or other disturbance, the system must be reset, re-zeroed, or "homed." During the reset, the sensor must be in a reference, or zero, location or can be moved to a "homing" position where the absolute location is known. Magnetic encoders can be designed as either incremental or absolute reading (i.e., displacement or position, respectively). Optical encoders, inductosyns, and synchro/resolvers are types of displacement and position sensors that can be designed as either incremental or absolute reading but are covered in other chapters of this handbook.

Most sensors described in this section are absolute reading. They supply a reading of distance or angle from a fixed datum, rather than from a previous position. Consecutive readings can be subtracted to give an incremental indication, thus emulating a displacement sensor. Such emulation can be useful when replacing an incremental encoder in the field with an absolute-reading type of sensor. An absolute sensor indicates the current position without the need for knowledge of the previous position. It never needs to be reset to a reference location or homed in order to derive the measured location. As mentioned earlier, such absolute-reading sensors are called *position sensors*.

Magnetic sensor types will be described here based on the technology employed, rather than the application. Relative usefulness for making linear or angular measurements will be indicated for each type of sensor.

Noncontact magnetic sensor technology described here for position or displacement measurement includes magnetostrictive, distributed impedance, magnetoresistive, Hall effect, and magnetic encoders.

31.2 Magnetic Field Terminology: Defining Terms

Magnetic field intensity (H) or magnetizing force: The force that drives the generation of magnetic flux in a material. H is measured in A m^{-1} (where A is for amperes and m is for meters).

Magnetic flux density (B): The amount of magnetic flux resulting from the applied magnetizing force. B is measured in N/(A · m) (where N is for Newton).

Magnetic permeability (μ): The ability of a material to support magnetic lines of flux. The μ of a material (pronounced myoo) is the product of the relative permeability of that material and the permeability of free space. The relative permeability of most nonferrous materials is near unity. In free space, magnetic flux density is related to magnetic field intensity by the formula:

$$B = \mu_0 H \tag{31.1}$$

where μ_0 is the permeability of free space, having the value $4\pi \times 10^{-7}$ H m^{-1} (where H is for henries). In other materials, the magnetic flux density at a point is related to the magnetic intensity at the same point by

$$B = \mu H \tag{31.2}$$

where

$$\mu = \mu_0 \mu_r \tag{31.3}$$

and μ_r is the relative permeability [1].

See Table 31.1 for a list of materials with approximate relative magnetic permeabilities.

Hysteresis: A phenomenon in which the state of a system does not reversibly follow changes in an external parameter [2]. In a displacement sensor, it is the difference in output readings obtained at a given point when approaching that point repeatedly from upscale and downscale readings. Figure 31.1 is a typical output versus input graph.

TABLE 31.1 Various Materials and Their Relative Permeabilities

Material	Approximate Relative Permeability
Vacuum	1
Air	1
Water	1
Aluminum	1
Copper	1
316 stainless steel (annealed)	1
Cold rolled steel	180
Nickel	600
Iron	5,000
Permalloy	8,000
Mu metal	20,000

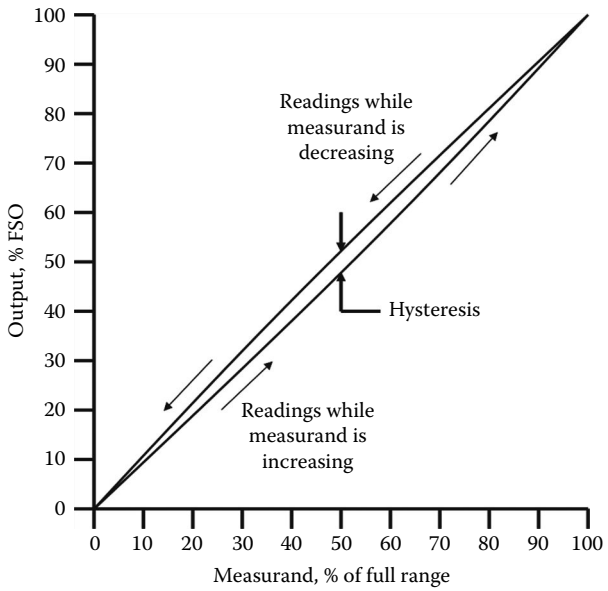

FIGURE 31.1 Hysteresis: output versus input. FSO, full scale output.

Magnetic hysteresis: Depicted in the hysteresis loop, Figure 31.2. When a ferromagnetic material is placed in an alternating magnetic field, the flux density (B) lags behind the magnetizing force (H) that causes it. The area under the hysteresis loop is the hysteresis loss per cycle and is high for permanent magnets and low for high permeability, low-loss magnetic materials [3].

Magnetic saturation: The upper limit to the ability of ferromagnetic materials to carry magnetic flux.

Magnetization curve: Shows the amount of magnetizing force needed for a ferromagnetic material to become saturated. It is a graph with B as the ordinate and H as the abscissa (also known as the B–H curve). A magnetization curve for a specific material would look the same as Figure 31.2, with the addition of calibration marks and the curve adjusted to describe the characteristic of that material.

Permittivity: Is a measure of the resistance encountered regarding the formation of an electric field in a medium or how much an electric field affects a dielectric medium (a dielectric material is a nonconductor of electricity). Permittivity quantifies the degree to which a material is able to "permit" an

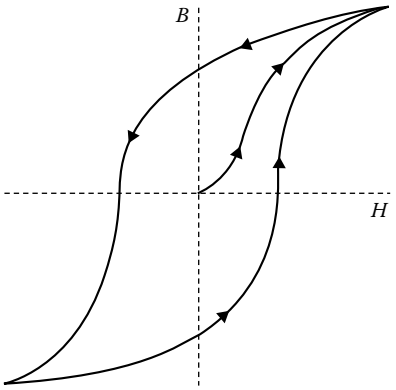

FIGURE 31.2 Magnetic hysteresis.

electric field to be formed, rather than polarizing the material (polarizing a material would reduce the magnitude of electric field to be formed within the material). Whereas permeability is measured in henries per meter, absolute permittivity, ε_0, is measured in farads per meter. In many calculations, relative permittivity, ε_r, is used, which assumes that the relative permittivity of vacuum is 1. Then the relative permittivity of a material is the ratio of its permittivity to that of vacuum. Air has a relative permittivity of approximately 1.

See Table 31.2 for a list of materials with approximate relative magnetic permeabilities.

Field propagation velocities: The higher the relative permeability of a material, the slower a magnetic field will travel, and the larger will be the inductance of a coil wound on this material, having a given size and turns count [4]. Likewise, the higher the relative permittivity of a material, the slower an electric field will travel, and the larger will be the capacitance of a given size and spacing of parallel plates [4]. The absolute speed, c_0, of propagation of an electromagnetic wave is given by

$$c_0 = \frac{1}{\left(\varepsilon_0 \mu_0\right)^{1/2}} \tag{31.4}$$

This relationship also describes the speed of light.

TABLE 31.2 Various Materials and Their Relative Permittivities

Material	Approximate Relative Permittivity
Vacuum	1
Air	1
Water	1
Gasoline	2
Methanol	30
Ethylene glycol	37
Paper	3.5
PTFE	2.1
Polyethylene	2.3
Polypropylene	2.3
Concrete	4.5

31.3 Magnetostrictive Sensors

A magnetostrictive sensor is commonly used to measure displacement, although fundamentally being an absolute position sensor. It uses a ferromagnetic element to detect the location of a position magnet that is displaced along its length. The position magnet is attached to a member whose position is to be sensed, and the sensor body remains stationary (see Figure 31.3). The position magnet moves along the measuring length without contacting the sensing element.

Ferromagnetic materials such as iron and nickel display the property called *magnetostriction*. Application of a magnetic field to these materials causes a strain in the crystal structure, resulting in a change in the size and shape of the material. A material exhibiting positive magnetostriction will expand when magnetized. Conversely, with negative magnetostriction, the material contracts when magnetized [5].

The ferromagnetic materials used in magnetostrictive displacement sensors are transition metals, such as iron, nickel, and cobalt. In these metals, the 3*d* electron shell is not completely filled, which allows the formation of a magnetic moment (i.e., the shells closer to the nucleus are complete, and they do not contribute to the magnetic moment). As electron spins are rotated by a magnetic field, coupling between the electron spin and the electron orbit causes electron energies to change. The crystal strains so that electrons at the surface can relax to states of lower energy [6].

This physical response of a ferromagnetic material is due to the presence of magnetic moments and can be understood by considering the material as a collection of tiny permanent magnets, called *domains*. Each domain consists of many atoms. When a material is not magnetized, the domains are randomly arranged. However, when the material is magnetized, the domains are oriented with their axes approximately parallel to each other. Interaction of an external magnetic field with the domains causes the magnetostrictive effect (see Figure 31.4). This effect can be optimized by controlling the ordering of domains through alloy selection, thermal annealing, cold working, and magnetic field strength.

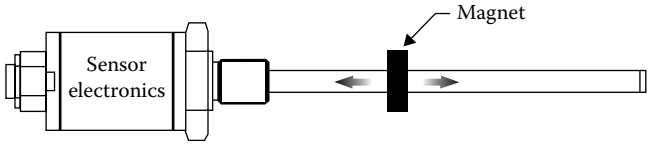

FIGURE 31.3 Magnetostrictive sensor with position magnet.

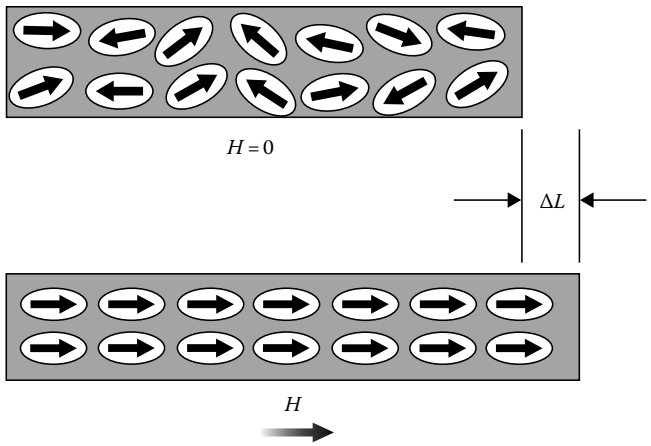

FIGURE 31.4 Magnetic domains: alignment with magnetic field, "*H*," causes dimensional changes.

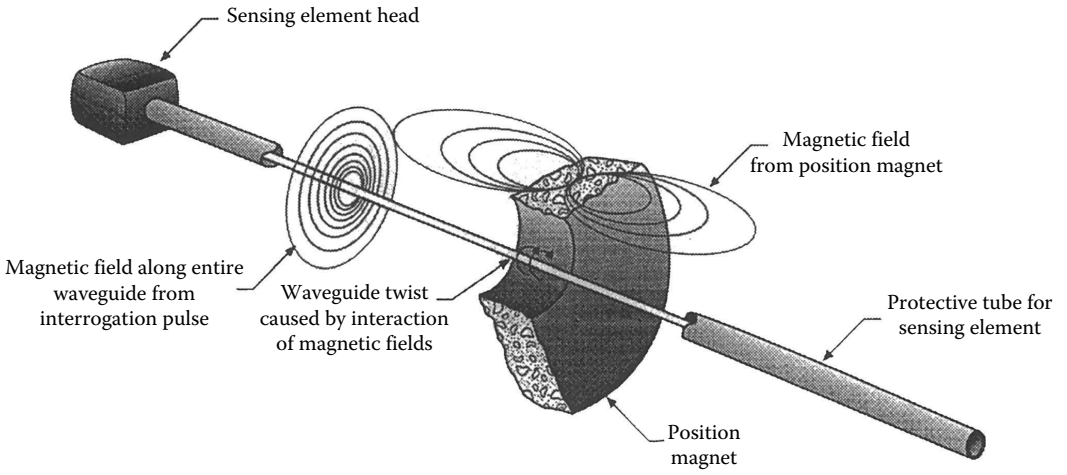

FIGURE 31.5 Operation of magnetostrictive position sensor.

While application of a magnetic field causes the physical strain, as described earlier, the reverse is also true: exerting stress causes the magnetic properties (i.e., permeability, susceptibility) to change. This is called the *Villari effect*.

In magnetostrictive sensors, uniform distortions of length, as shown in Figure 31.4, offer limited usefulness. Usually, the magnetization is rotated with a small field to induce a local distortion, described as the *Wiedemann effect*. This is a mechanical torsion that occurs at a point along a magnetostrictive wire or tube when an electric current is passed through the wire or tube while it is subjected to an axial magnetic field. The torsion occurs at the location of the axial magnetic field, which is usually provided by a small permanent magnet called the position magnet.

In a position (or displacement) sensor, a ferromagnetic wire or tube, called the waveguide, is used as the sensing element (see Figure 31.5). The sensor measures the distance between the position magnet and the pickup. To start a measurement, a current pulse I (called the interrogation pulse) is applied to the waveguide. This causes a magnetic field to instantly surround the waveguide along its full length.

In a magnetostrictive position sensor, the current is a pulse of approximately 1–2 μs duration. A torsional mechanical wave is formed at the location of the position magnet due to the Wiedemann effect. Portions of this wave travel from the position magnet both toward and away from the pickup. The wave traveling along the waveguide toward the pickup is detected when it arrives at the pickup. The time measurement between application of the current pulse (forming of the torsional wave at the position magnet) and its detection by the pickup is indicative of the distance between the position magnet and the pickup. The speed of the wave is typically in a range of about 2500–3000 m s^{-1}. The portion of the wave traveling away from the pickup could act as an interfering signal after it is reflected from the waveguide tip. So instead, it is damped by a damping element when it reaches the end of the waveguide opposite the pickup. Damping is usually accomplished by attaching one of various configurations of elastomeric materials to the end of the waveguide. The end of the waveguide within the damping element is unusable for position determination and therefore called the "dead zone." In cases where the waveguide is interrogated infrequently, the reflected wave is eventually attenuated without using a damping element, and therefore a damping element may not be needed.

The time measurement can be buffered and used directly as the sensor output, or it can be conditioned inside the sensor to provide various output types, including analog voltage or current, pulse width modulation, controller area network (CAN) bus, synchronous serial interface (SSI), highway addressable remote transducer (HART), and PROFIBUS. Magnetostrictive position sensors can be made as short as 1 cm long or up to more than 30 m long. Resolution of some magnetostrictive position sensors can be as fine as 1 μm. Temperature coefficients of 2–5 ppm $°C^{-1}$ can be achieved, depending on the material selected for the waveguide. The sensors are inherently stable, since the

measurement mainly relies on the physical properties of the waveguide material, rather than the stability of electronic circuits. Longer sensors become very cost effective because the same electronics package can drive sensors of varying length; only the waveguide and its packaging are increased in length to make the sensor longer, and sometimes the waveguide drive pulse may be modified.

The magnetostrictive wire can be straight for a linear sensor or shaped to provide curved or rotary measurements. Curved sensors are sometimes used to measure angular or nonlinear motion in industrial applications, although rotary magnetostrictive sensors are not yet very popular.

31.3.1 Distributed Impedance Sensors

Inductive sensors have long been used, in which a magnetically permeable target is allowed to move in the vicinity of a coil and in which the coil inductance varies with movement of the target. This type of sensor and the related LVDT have been included in another chapter of this handbook. A new type of magnetic sensor that responds to changes in an electromagnetic field is called the distributed impedance sensor. In this patented technology, a linear or rotary sensor is formed of a sensing element and driving electronics. The sensing element comprises inductance, capacitance, and resistance, all of which are distributed along the length of the sensing element, rather than treated as a lump inductance as would be done with an inductive sensor (in an inductive sensor, the capacitance is considered to be negligible) or a lump capacitance as would be done with a capacitive sensor (in which the inductance would be negligible). A configuration of the sensing element that is preferred for high performance and high manufacturability is that of a flat conductor wrapped in a helical pattern around a temperature stable rod or tube. Two such helices form an approximate double helix, with the helices wound in opposite phase from one another. This configuration can be seen in Figure 31.6, a photo of a typical position sensor.

The sensing element is driven in antiphase mode by an oscillator circuit operating at a frequency where the capacitive reactance is nonnegligible as compared with the inductive reactance. A surface wave travels along the sensing element, providing a time delay depending upon the position of a target tube. The target tube is formed of an electrically conductive material and covers various portions of the sensing element, depending on the position to be measured. The time delay can be directly measured or can be converted into a frequency that varies with position, thereby providing a signal that is simple to interface with digital circuits.

Separating the series inductances along a sensing axis by parallel capacitances provides distributed impedance whereby both the inductances and capacitances are distributed along the length of the sensing axis. This enables shaping of the electromagnetic field along the sensing element so that the magnetic field penetrates into a measured material (such as the target tube) but is concentrated in a volume close to the sensing element in order to avoid sensing unwanted conductive materials that may be nearby [7].

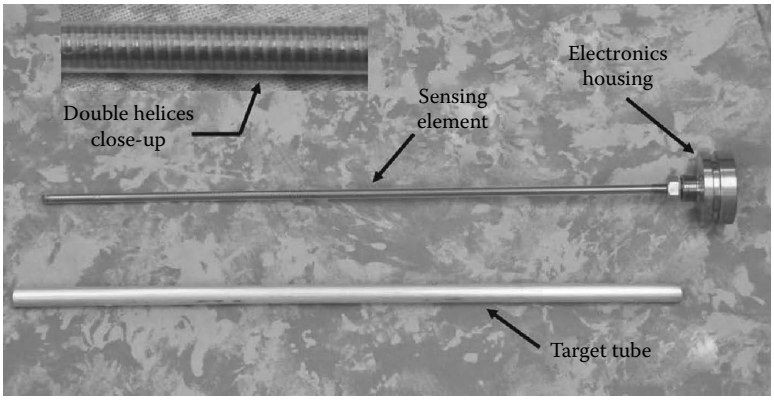

FIGURE 31.6 A distributed impedance sensor with target tube and a close-up view of the helices that are inside of the sensing element. (Photo courtesy of Nyce, D.S., Revolution Sensor Company, Apex, NC.)

The target tube can be formed of any electrically conductive material and does not need to be of high magnetic permeability. Because of this, a tube, which is already a part of the measured assembly, can serve as the target, such as part of the rod or cylinder in a suspension strut or hydraulic cylinder. This means that the target does not need to be changed to nonmagnetic stainless steel, as is needed with a magnetostrictive sensor and as sometimes needed with other magnetic or inductive sensors. It also does not require a position magnet as with a magnetostrictive sensor.

This technology has been trademarked as NyceWave™ by the Revolution Sensor Company. Typical sensors are available with analog and digital outputs including voltages (0–5 V, 0.5–4.5 V, 1–5 V, 0–10 V, etc.), currents (0–20 mA, 4–20 mA), SSI, and CAN bus.

The solid construction of a distributed impedance position sensor provides a very robust product that can operate over a wide temperature range. Typical industrial products can operate over a range of −40 °C to 150 °C, including the sensing element as well as the electronics head. This positions the distributed impedance sensor as a technology that is well suited for high-reliability applications, such as in aircraft, space vehicles, vehicle suspensions, mobile hydraulics, and others. Rotary sensors are also available.

31.3.2 Magnetoresistive Sensors

In most magnetic materials, electrical resistance decreases when a magnetic field is applied and the magnetization is *perpendicular* to the current flow (a current will be flowing any time electrical resistance is measured) (see Figure 31.7). The resistance decreases as the magnetic flux density increases, until the material reaches magnetic saturation.

The rate of resistance decrease is less as the magnetic material nears saturation. The amount of resistance change is on the order of about 1% at room temperature (0.3% in iron, 2% in nickel). When the magnetic field is *parallel* to the current, the resistance increases with increasing magnetic field strength. Sensitivity is greatest when the magnetic field is perpendicular to the current flow. These are properties of the phenomenon called *magnetoresistance* (MR). The MR effect is due to the combination of two component parts. These are a reduction in forward carrier velocity as a result of the carriers being forced to move sideways as well as forward and a reduction in the effective cross-sectional area of the conductor as a result of the carriers being crowded to one side [8].

When a position magnet is brought close to a single MR sensing element, the resistance change is at its maximum as the magnet passes over the approximate center of the element and then reduces until the magnet is past the element. The resistance changes according to

$$\text{Resistivity} = \frac{\text{Voltage}}{(\text{Carrier density} \times \text{Carrier velocity})} \tag{31.5}$$

By using multiple MR elements arranged along a line, a longer displacement measuring device can be fashioned. The signals from the string of sensors are decoded to find which elements are being affected by the magnet. Then the individual readings are used to determine the magnet position more precisely. Relatively high-performance sensors can be manufactured. Temperature sensitivity of the MR elements needs to be compensated, and longer sensors contain many individual sensing elements. Because of this, longer sensors become more difficult to manufacture and are expensive.

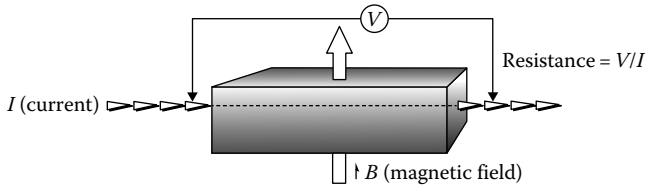

FIGURE 31.7 Magnetoresistance.

Anisotropic MR materials are capable of resistance changes in the range of 1%–2%. The MR of a conductor body can be increased by making it a composite of two or more layers of materials having different levels of MR. Multilayered structures of exotic materials (sometimes more than 10 layers) have enabled development of materials that exhibit much greater magnetoresistive effect and saturate at larger applied fields. This has been named giant magnetoresistance (GMR). Some commercial sensors based on GMR are currently available. The GMR elements can be arranged in a four-element bridge connection for greater sensitivity. In this arrangement, two of the elements are shielded from the applied magnetic field. The other two elements are sensitive to the applied field. Sensitivity can also be increased by incorporating flux concentrators on the sensitive elements. In a bridge connection, the output voltage can vary by more than 5% of the supply voltage [9]. Rotary sensors can be constructed by attaching a pole piece to a rotating shaft. One or more permanent magnets and the pole piece are arranged to cause the magnetic field around the MR element to change with angular displacement.

Further research is being conducted on MR materials to improve the sensitivity by lowering the strength of magnetic field needed and increasing the amount of resistance change. The next higher level of MR performance is called colossal magnetoresistance (CMR). CMR is not yet practical for industrial sensors because of severe limitations on the operating temperature range.

Although MR, GMR, and CMR are limited for use in displacement sensors at this time by cost, temperature, and fabrication constraints, much research is in progress. Maybe humongous magnetoresistance (HMR) is next?

31.4 Hall Effect Sensors

The Hall effect is a property exhibited in a conductor affected by a magnetic field. A voltage potential V_H, called the Hall voltage, appears across the conductor when a magnetic field is applied at right angles to the current flow. Its direction is perpendicular to both the magnetic field and the current. The magnitude of the Hall voltage is proportional to both the magnetic flux density and the current. The magnetic field causes a gradient of carrier concentration across the conductor. The larger number of carriers on one side of the conductor, compared to the other side, causes the voltage potential V_{H}. A pictorial representation is shown in Figure 31.8. The amplitude of the voltage varies with the current and magnetic field according to [10]

$$V_{\mathrm{H}} = K_{\mathrm{H}}\left(\frac{\beta I}{z}\right) \tag{31.6}$$

where

V_{H} is the Hall voltage
K_{H} is the Hall constant
β is the magnetic flux density
I is the current flowing through the conductor
z is the thickness of the conductor

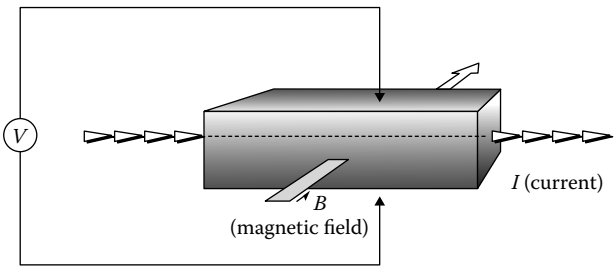

FIGURE 31.8 Hall effect.

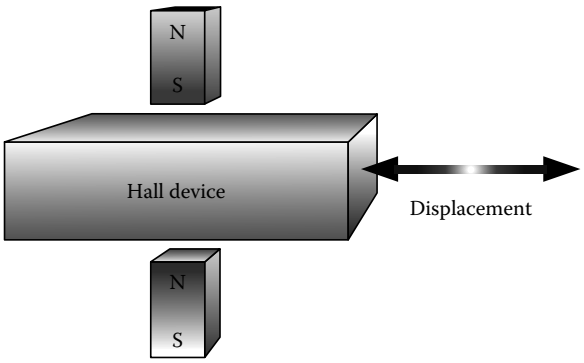

FIGURE 31.9 Two-magnet Hall effect sensors.

Sensors utilizing the Hall effect typically are constructed of semiconductor material, giving the advantage of allowing conditioning electronics to be deposited right onto the same material. Either *p*- or *n*-type semiconductor material can be used, with the associated polarity of current flow. The greatest output is achieved with a large Hall constant, which requires high carrier mobility. Low resistivity will limit thermal noise voltage, for a more useful signal-to-noise ratio (SNR). These conditions are optimized using an *n*-type semiconductor [7].

A displacement sensor can be made with a Hall sensing element and a movable magnet, with an output proportional to the distance between the two. Two magnets can be arranged with one Hall sensor as in Figure 31.9 to yield a near-zero field intensity when the sensor is equidistant between the magnets.

These single Hall effect device configurations have a very limited linear range. Longer range displacement sensors can be built by using multiple Hall sensors spaced along a carrier substrate. A magnet is moved along in close proximity to the carrier. As the magnet approaches and then moves away from each Hall element, the respective sensors will have increasing or decreasing outputs, respectively. The output from the battery of sensors is derived by reading the individual outputs of the sensors closest to the magnet and also decoding the locations of those particular sensors being read. This method can produce relatively high-performance displacement sensors of up to several meters long. Longer sensors become increasingly more difficult to produce and are expensive because of the large number of sensors being multiplexed. Rotary, as well as linear, sensors can be produced by mechanical arrangement of the sensing elements to cause magnetic field variation with the desired angular or linear input.

31.5 Magnetic Encoders

Magnetic encoders use a strip or disk of magnetic media onto which digital information is stored. This information is recorded at the location it describes and is in the form of a collection of magnetized and nonmagnetized areas. A magnetic encoder includes this sensing element, as well as one or more read heads, electronics, and a mechanical enclosure with input shaft and bushings. The input shaft moves in and out for a linear sensor. It has wipes to prevent ingestion of foreign material and bushings designed to accept sideloading. An angular sensor has a shaft that rotates and includes bushings to withstand thrust and sideloading. The encoded media is implemented as either a strip in a linear sensor or as a disk in an angular sensor.

As a read head passes above the encoded area, it picks up the magnetic variations and reads the position information. The information, digital ones and zeroes, will usually be encoded in several parallel tracks to represent the binary digits of the position information. A standard binary code presents a problem for encoders in that some numbers require the changing of several of the bits at one time to indicate a single increment of the number represented. If all the changing bits are not perfectly aligned

TABLE 31.3 Gray Code, as Used in Some Encoders

$Base_{10}$ Number	"Natural" Binary	Gray Code	Binary Coded Decimal (BCD) Tens Units	Hexadecimal (HEX)
0	0000	0000	0000 0000	0
1	0001	0001	0000 0001	1
2	0010	0011	0000 0010	2
3	0011	0010	0000 0011	3
4	0100	0110	0000 0100	4
5	0101	0111	0000 0101	5
6	0110	0101	0000 0110	6
7	0111	0100	0000 0111	7
8	1000	1100	0000 1000	8
9	1001	1101	0000 1001	9
10	1010	1111	0001 0000	A
11	1011	1110	0001 0001	B
12	1100	1010	0001 0010	C
13	1101	1011	0001 0011	D
14	1110	1001	0001 0100	E
15	1111	1000	0001 0101	F

with each other, instantaneous erroneous readings will result. To avoid this problem, a special adaptation of the binary code called "Gray code" is used (see Table 31.3). A single increment of the number represented causes a change of only 1 bit in the Gray code.

The read head incorporates a ferromagnetic core wound with input and output windings. A read pulse is applied to the input winding, and information is read on the output winding. If the core is above a magnetized area of the magnetic media, the core becomes saturated, no output pulse is generated, and a logic 0 results [11]. If the core is above a nonmagnetized area when the read pulse is applied, an output pulse occurs and produces a logic 1. Another arrangement that is practical for angular, but not linear, encoders uses a ring-shaped multipole permanent magnet. The magnet is rotated past a pair of sensors to yield an incremental reading with sine and cosine outputs (called "quadrature" output, see Figure 31.10).

The waveforms can be square, sinusoidal, or triangular. *A* and *B* outputs are used to indicate the displacement and the direction of the displacement. The number of transitions or "counts" is proportional to the displacement magnitude. The direction of displacement (i.e., + or –) can be found by comparing the two phases. For example, in Figure 31.10, at the time the *A* changes from a logic 0 to a logic 1, the status of the *B* will indicate the direction of travel. A logic 0 on the *B* could equal the positive direction; a logic 1 could equal the negative direction.

Magnetic encoders can be incremental or absolute (i.e., indicating displacement or position). In an incremental configuration, equally spaced pulses encoded on the magnetic media are read from one or more tracks. The pulses are collected by an up/down counter, and the counter output

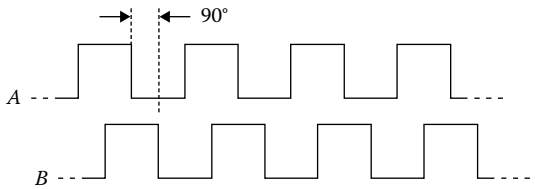

FIGURE 31.10 Quadrature output.

TABLE 31.4 Sensors and Manufacturers

Technology	Manufacturers	Description	Price
Magnetostrictive	MTS Systems Corp., Balluff Inc.	Lengths to 20 m, 2 μm resolution, analog/digital outputs	$100–$3,000
Magnetoresistive	Nonvolatile Electronics, Midori America	Linear GMR, rotary MR, linear MR up to 30 mm	<$10 up to $500
Distributed impedance	LRT Sensors, Alliance Sensors	Lengths to 2 m, infinite resolution, inaccuracy to 0.02%	$50–$350
Hall effect	Optec Technology, Spectec	Standard and custom sensors	Approximately $10–$100
Magnetic encoder	Heidenhain, Sony Precision Technology	Rotary and linear encoders	$100–$2,000

represents the position. Quadrature outputs can be coded to tell the direction of displacement, as described earlier. The zero position is set by resetting the counter.

Absolute magnetic encoders have the digital code representing the position encoded directly at that position. No counter is needed. The Gray code can be interpreted to yield the position in engineering units. Nonlinear coding, such as sine or cosine, is sometimes used.

31.6 Conclusion

Some technologies, such as magnetostrictive, can provide very low inaccuracies over a long measurement range. Other technologies, such as distributed impedance, can provide a very high level of reliability and resistance to shock and vibration. The cost of sensors varies widely by technology and application. Accordingly, several sensor technologies should be considered for a given application, before choosing the best overall match combining the requirements for performance, reliability, and cost. Table 31.4 provides a list of sensors and some manufacturers.

References

1. O. Esbach, *Handbook of Engineering Fundamentals*, New York: John Wiley & Sons, 1975, p. 957.
2. R. Lerner and G. Trigg, *Encyclopedia of Physics*, New York: VCH Publishers, 1990, p. 529.
3. P. Neelakanta, *Handbook of Electromagnetic Materials*, Boca Raton, FL: CRC Press, 1995, p. 333.
4. D. S. Nyce, *Linear Position Sensors, Theory & Application*, Hoboken, NJ: John Wiley & Sons, 2004, pp. 66, 84.
5. D. S. Nyce, Magnetostriction-based linear position sensors, *Sensors Magazine*, 11(4), 22, 1994.
6. R. Philippe, *Electrical and Magnetic Properties of Materials*, Norwood, MA: Artech House, 1988.
7. H. Burke, *Handbook of Magnetic Phenomena*, New York: Van Nostrand Reinhold, 1986.
8. D. S. Nyce, *Distributed Impedance Sensor*, U.S. Patent # 7,340,951, March 11, 2008.
9. Nonvolatile Electronics Inc. NVSB series datasheet. March 1996.
10. J. R. Carstens, *Electrical Sensors and Transducers*, Englewood Cliffs, NJ: Regents/Prentice-Hall, 1992, p. 125.
11. H. Norton, *Handbook of Transducers*, Englewood Cliffs, NJ: Prentice-Hall, 1989, pp. 106–112.

Further Information

Askeland, D., *The Science and Engineering of Materials*, Boston, MA: PWS-Kent Publishing, 1989.
Boll, R., *Soft Magnetic Materials*, London, U.K.: Heyden & Son, 1977.
Craik, D., *Magnetism Principles and Applications*, New York: John Wiley & Sons, 1995.
Cullity, B. D., *Introduction to Magnetic Materials*, Reading, MA: Addison-Wesley, 1972.
Herceg, E., *Handbook of Measurement and Control*, Pennsauken, NJ: Schaevitz Engineering, 1976.

Jiles, D., *Introduction to Magnetism and Magnetic Materials*, London, U.K.: Chapman and Hall, 1991.
Lorrain, P. and Corson, D., *Electromagnetic Fields and Waves*, San Francisco, CA: WH. Freeman, 1962.
Mazda, F., *Electronics Engineer's Reference Book*, 6th edn., London, U.K.: Butterworth, 1989.
Nyce, D., Magnetostrictive Linear Position Sensors, *Sensors Magazine*, November 1999, also available at http://archives.sensorsmag.com/articles/1199/38_1199/index.htm (accessed on March 4, 2013).
Olson, H., *Dynamical Analogies*, New York: D. Van Nostrand, 1943.
Rose, R., Shepard, L., and Wulff, J., *The Structure and Properties of Materials*, New York: John Wiley & Sons, 1966.
Shackelford, J., *Introduction to Materials Science for Engineers*, New York: Macmillan, 1985.

32

Synchro/Resolver Displacement Sensors

Robert M. Hyatt, Jr.
Howell Electric Motors

David Dayton
ILC Data Device Corp.

Most electromagnetic position transducers are based on transformer technology. Transformers work by exciting the primary winding with a continuously changing voltage and inducing a voltage in the secondary winding by subjecting it to the changing magnetic field set up by the primary. They are ac-only devices, which make all electromagnetically coupled position sensors ac transformer coupled. They are inductive by nature, consisting of wound coils. By varying the amount of coupling from the primary (excited) winding of a transformer to the secondary (coupled) winding with respect to either linear or rotary displacement, an analog signal can be generated that represents the displacement. This coupling variation is accomplished by moving either one of the windings or a core element that provides a flux path between the two windings.

One of the simplest forms of electromagnetic position transducers is the LVDT, which is described in the section on inductive sensors. If the displacement of the core in an LVDT-type unit is changed from linear to rotary, the device becomes an RVDT (rotary variable differential transformer).

32.1 Induction Potentiometers

The component designer can "boost" the output, increase accuracy, and achieve a slightly greater angular range if windings are placed on the rotor as shown in Figure 32.1. The disadvantages to this method are (1) additional windings, (2) more physical space required, (3) greater variations over temperature, and (4) greater phase shift due to the additional windings.

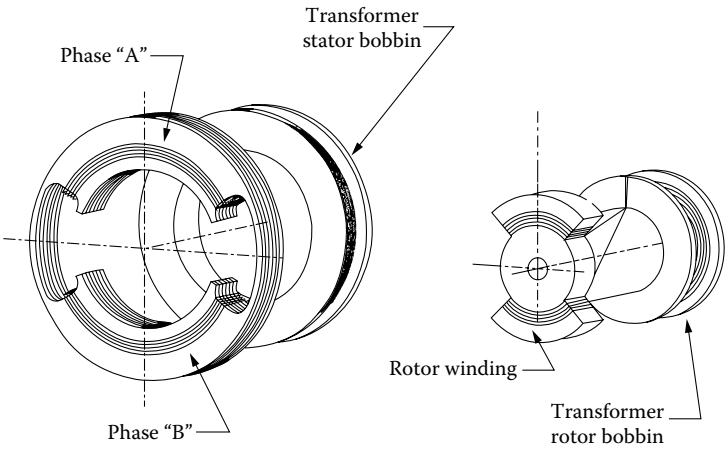

FIGURE 32.1 The induction potentiometer has windings on the rotor and the stator.

The advantage of the induction pot design is greater sensitivity (more volts per degree), resulting in better signal to noise and higher accuracy in most cases.

32.2 Resolvers

If the two-slot lamination in the stator stack shown in Figure 32.1 is replaced by a multislot lamination (see Figure 32.2), and two sets of windings are designed in concentric coil sets and distributed in each quadrant of the laminated stack, a close approximation to a sine wave can be generated on one of the secondary windings, and a close approximation to a cosine wave can be generated on the other set of windings. Rotary transformers of this design are called *resolvers*. Using a multislot rotor lamination and distributing the windings in the rotor, the sine–cosine waveforms can be improved even further.

A resolver effectively amplitude-modulates the ac excitation signal placed on the rotor windings in proportion to the sine and the cosine of the angle of mechanical rotation. This sine–cosine electrical output information measured across the stator windings may be used for position and velocity data. In this manner, the resolver is an analog trigonometric function generator. Most resolvers have two primary windings that are located at right angles to each other in the stator, and two secondary windings also at right angles to each other, located on the rotor (see Figure 32.3).

If the rotor winding (R1–R3) is excited with the rated input voltage (see Figure 32.4), the amplitude of the output winding of the stator (S2–S4) will be proportional to the sine of the rotor angle θ,

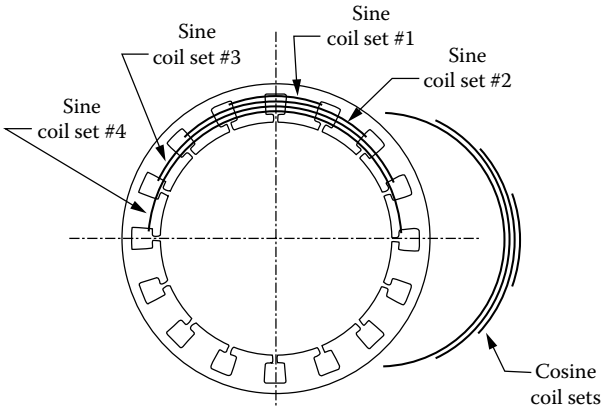

FIGURE 32.2 The resolver stator has distributed coil windings on a 16-slot lamination to generate a sine wave.

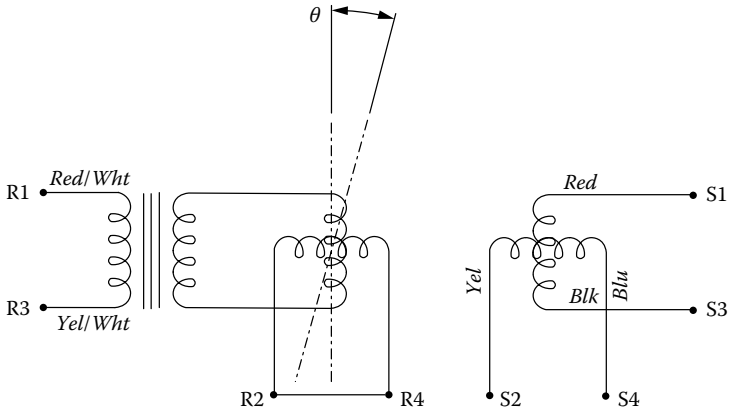

FIGURE 32.3 A brushless resolver modulates the ac excitation on the rotor by the rotation angle.

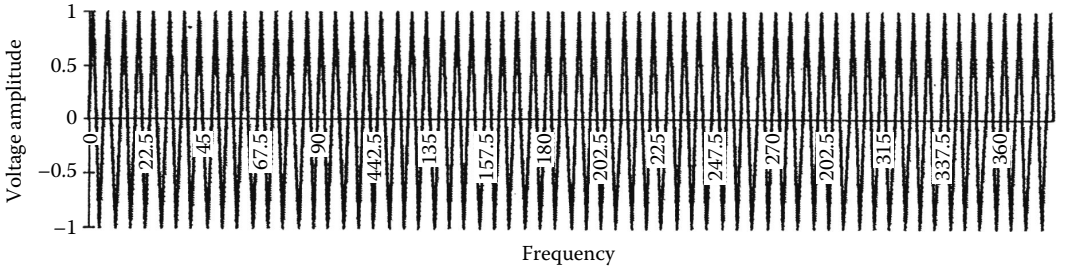

FIGURE 32.4 The resolver rotor winding is excited with the rated input voltage.

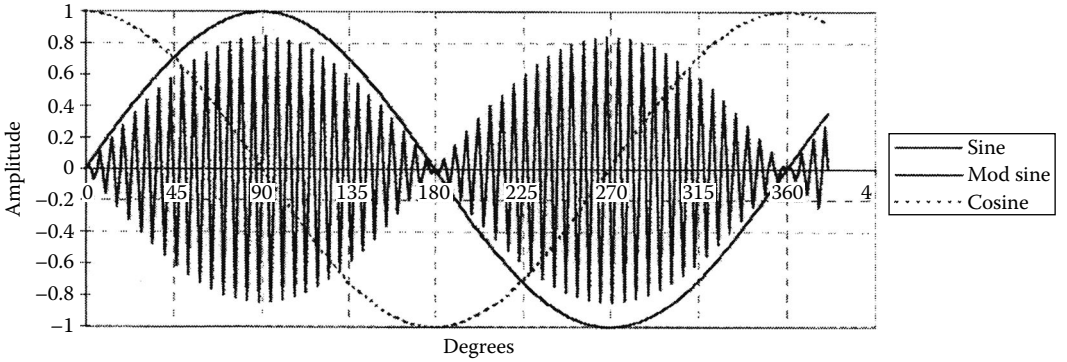

FIGURE 32.5 The single-speed resolver stator output is the sine or cosine of the angle.

and the amplitude of the output of the second stator winding (S1–S3) will be proportional to cosine θ (see Figure 32.5). This is commonly called the "control transmitter" mode and is used with most "state-of-the-art" resolver-to-digital converters.

In the control transmitter mode, electrical zero may be defined as the position of the rotor with respect to the stator at which there is minimum voltage across S2–S4 when the rotor winding R1–R3 is excited with rated voltage. Nulls will occur across S2–S4 at the 0° and 180° positions and will occur across SI–S3 at the 90° and 270° positions.

If the stator winding SI–S3 is excited with the rated input voltage and stator winding S2–S4 is excited with the rated input voltage electrically shifted by exactly 90°, then the output sensed on the rotor winding R1–R3 does not vary with rotor rotation in amplitude or frequency from the input reference signal.

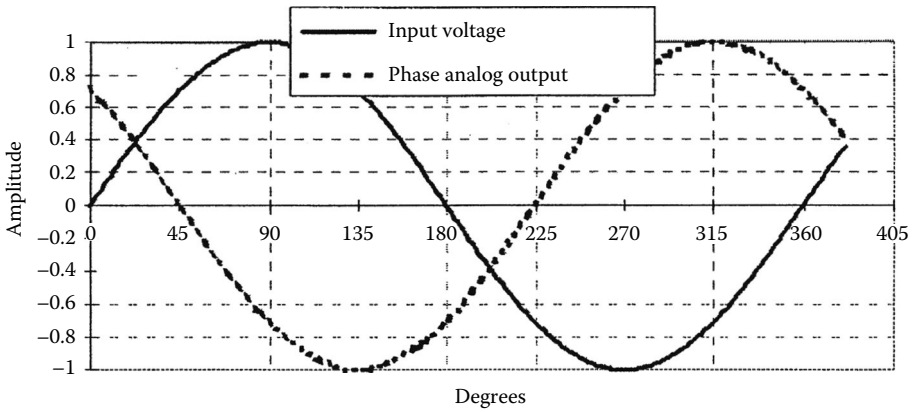

FIGURE 32.6 Resolver stator windings excited at 0° and 90° yield a phase shift with rotor rotation. Phase analog output at 225° versus input voltage.

It is the sum of both inputs. It does, however, vary in time phase from the rated input by the angle of the shaft from a referenced "zero" point (see Figure 32.6). This is a "phase analog" output and the device is termed a "control transformer." By measuring the time difference between the zero crossing of the reference voltage waveform and the output voltage waveform, the phase angle (which is the physical angular displacement of the output shaft) can be calculated.

Because the resolver is an analog device and the outputs are continuous through 360°, the theoretical resolution of a resolver is infinite. There are, however, ambiguities in output voltages caused by inherent variations in the transformation of the voltage from primary to secondary through 360° of rotation. These ambiguities result in inaccuracy when determining the true angular position. The types of error signals that are found in resolvers are shown in Figure 32.7.

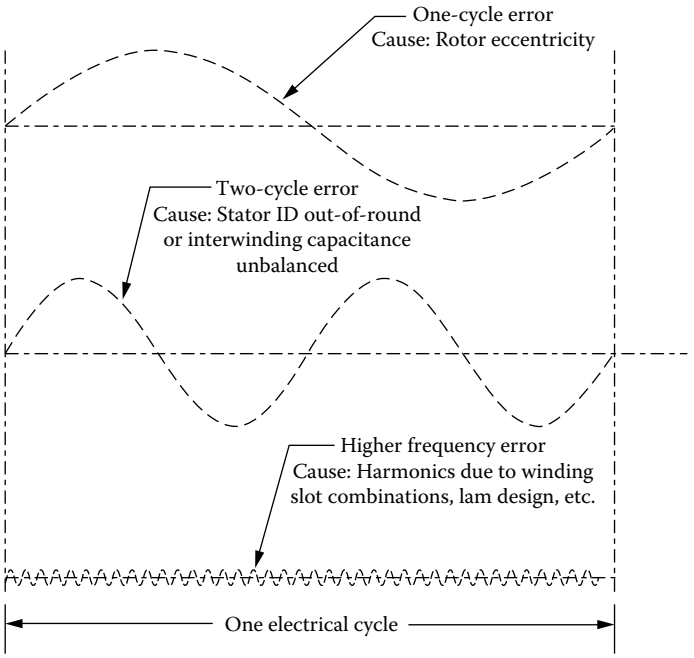

FIGURE 32.7 There are several causes of errors in resolvers and synchros.

As a rule, larger diameter stator laminations lead to a better accuracy and higher absolute resolution of the device. This is a function of the number of magnetic poles that can be fit into the device, which is a direct function of the number of slots in the stator and rotor laminations. With multispeed units (see the section on multispeed as follows), the resolution increases as a multiple of the speeds. For most angular excursions, the multispeed resolver can exceed the positioning accuracy capability of any other component in its size, weight, and price range.

32.3 Operating Parameters and Specifications for Resolvers

There are seven functional parameters that define the operation of a resolver in the analog mode. These are (1) accuracy, (2) operating voltage amplitude, (3) operating frequency, (4) phase shift of the output voltage from the referenced input voltage, (5) maximum allowable current draw, (6) transformation ratio of output voltage over input voltage, and (7) null voltage. Although impedance controls the functional parameters, it is transparent to the user. The lamination and coil design are usually developed to minimize null voltage and input current, and the impedance is the direct fallout of the inherent design of the resolver. The following procedure can be used to measure the seven values for most resolvers.

32.4 Equipment Needed for Testing Resolvers

A mechanical index stand that can position the shaft of the resolver to an angular accuracy that is an order of magnitude greater than the specified accuracy of the resolver
An ac signal generator capable of up to 24 V rms at 10 kHz
A phase angle voltmeter (PAV) capable of measuring "in phase" and "quadrature" voltage components for determining the transformation ratio and the null voltage as well as the phase angle between the output voltage and the reference input voltage
A 1 Ω resistor used to measure input current with the PAV

An angle position indicator (API) used in conjunction with the index stand to measure the accuracy of the resolver

1. Using the aforementioned equipment with the index stand in the 0° position, mount the resolver on the index stand and lock the resolver shaft in place.
2. Place the 1 Ω resistor in series with the R1 (red/wht) lead of the resolver.
3. Connect the resolver rotor leads, R1 (red/wht) and R3 (yel/wht) (see Figure 32.3) to the sine wave signal generator and set the voltage and frequency to the designed values for the resolver.
4. Connect the terminals from the sine wave signal generator to the reference input of the PAV.
5. Connect the resolver output leads S2 (yel) and S4 (blu) to the PAV input terminals and place the PAV in the total output voltage mode.
6. Rotate the index stand to the 0° position.
7. Turn the resolver housing while monitoring the total output voltage on the PAV until a minimum voltage reading is obtained on the PAV. Record this value. This is the *null voltage* of the resolver.
8. Turn the index stand to the 90° position.
9. Change the output display on the PAV to show the *phase angle* between the reference voltage and the voltage on leads S2–S4. Record this phase angle reading.
10. Change the output display on the PAV to show the *total output voltage* of the resolver.
11. Record this voltage.
12. Calculate the *transformation ratio* by dividing the reading in step 11 by the input reference voltage amplitude.
13. Connect the input leads of the PAV across the 1 Ω resistor and record the total voltage on the PAV display. Since this reading is across a 1 Ω resistor, it is also the *total current*.

14. Disconnect the resolver and the signal generator from the PAV.
15. Connect the terminals from the sine wave signal generator to the reference input of the API.
16. Connect the stator leads S1 (red), S3 (blk), S2 (yel), and S4 (blu) to the API S1, S3, S2, and S4 inputs, respectively.
17. Check the *accuracy* of the resolver by recording the display on the API every 20°–360° of mechanical rotation on the index stand. Record all values.

32.5 Resolver Benefits

Designers of motion control systems today have a variety of technologies from which to choose feedback devices. The popularity of brushless dc motors has emphasized the need for rotor position information to commutate windings as a key application in sensor products. Encoders are widely used due to the ease of interface with today's drivers but have some inherent performance limitations in temperature range, shock and vibration handling, and contamination resistance. The resolver is a much more rugged device due to its construction and materials and can be mated with modular R to D converters that will meet all performance requirements and work reliably in the roughest of industrial and aerospace environments.

The excitation signal E_x into the resolver is converted by transformer coupling into sine and cosine (quadrature) outputs that equal $E_x \sin\theta$ and $E_x \cos\theta$. The resolver-to-digital converter (shown in Figure 32.10) calculates the angle:

$$\Theta = \arctan\left(\frac{E_x \sin\Theta}{E_x \cos\Theta}\right) \tag{32.1}$$

In this ratiometric format, the output of the sine winding is divided by the output of the cosine winding, and any injected noise whose magnitude is approximately equivalent on both windings is canceled. This provides an inherent noise rejection feature that is beneficial to the resolver user. This feature also results in a large degree of temperature compensation.

32.5.1 Multispeed Units

The relationship for multispeeds is that the speed (2×, 3×, etc.) designates how many full sinusoidal cycles the resolver output electrically completes in 360° of mechanical rotation. The 2× electrical output is such that the full sinusoidal cycle for a 2× resolver occurs in 180° instead of 360°. A 2× resolver output is shown in Figure 32.8. A full 3× cycle is completed in 120°. The number of speeds selected for use is a function of the system requirements. Increasing the number of magnetic poles in the rotor and stator creates multispeed units. Each speed has several winding and slot combinations. The optimum combination is selected by the resolver designer based on system demands.

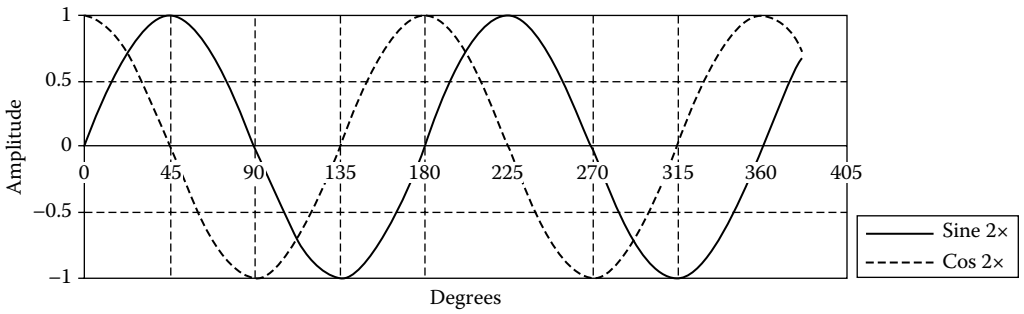

FIGURE 32.8 A two-speed resolver yields two electrical cycles for one rotation.

32.5.2 Applications

Resolvers are often used in conjunction with motors, and because of their inherent similarity of design (copper windings on iron lamination stacks), their environmental resistance is quite similar. They are ideal to design into industrial applications where dust and airborne liquids can obscure optical encoder signals. NC machines, coil winders, presses, and positioning tables are uses where resolvers excel. The resolver's inherent resistance to shock and vibration makes it uniquely suited to moving platforms, and their reliability under these conditions lends a welcome hand to the designers of robots, gantries, and automotive transfer lines.

Heat sensitivity is always a problem for motion control systems designers. Resolvers used for sensing the position of valves in high-temperature applications such as aircraft engines, petrochemical refining, and chemical processing have continually proven their reliability.

Moving devices to precise positions with smooth and accurate control can be a real challenge in the electromagnetic noise environment of the modern industrial facility. Emitted and conducted EMI from adjacent equipment and input voltage variations with unwanted current spikes on input power lines can rob digital systems of their signal integrity. The analog resolver continues to function without information loss or signal interruption. Digitizing the signal can be done at a remote interface under more controlled conditions than on the factory floor. Only robust materials can perform well in harsh environments.

32.6 Synchros

As long ago as World War II, synchros were used in analog positioning systems to provide data and to control the physical position of mechanical devices such as radar antennae, indicator needles on instrumentation, and fire control mechanisms in military equipment. The term "synchro" defines an electromagnetic position transducer that has a set of three-phase output windings that are electrically and mechanically spaced by 120° instead of the 90° spacing found in a resolver. In the rotor primary mode, the synchro is excited by a single-phase ac signal on the rotor. As the rotor moves 360°, the three amplitude-modulated sine waves on the three phases of the output have a discrete set of amplitudes for each angular position. By interpreting these amplitudes, a table can be established to decode the exact rotary position. In most applications, resolvers have replaced synchros because of the sophistication of the resolver-to-digital converters that are commercially available. Working with a sine and cosine is simpler and requires less conversion and decoding than using three 120°-spaced signals. If conversion of a synchro output is desired in resolver format, a device known as a Scott "T" transformer can be used for conversion. In most synchro-to-digital processors, the first step is to convert the signal to a resolver format with a Scott "T" device.

32.7 Modular Solution

The brushless resolver is a self-contained feedback device that, unlike optical encoders, provides an analog signal with infinite resolution. Not only can the output signal be converted to precise digital position information, but it also provides an accurate velocity signal, thus eliminating the need for using a separate tachometer. Reliability is enhanced using the same resolver for speed feedback and commutation. Piece part count can be reduced and the complexity of using Hall-effect devices for timing signals for commutation can be eliminated.

A modular approach allows the designer to easily select a single or multispeed resolver and appropriate electronics that will meet almost any desired level of resolution and accuracy. The resolvers are designed in the most commonly used frame sizes: 8, 11, 15, and 21. Housed models feature high-quality, motor-grade ball bearings. Heavy-duty industrial grade units are enclosed in rugged black-painted aluminum housings with flange, face, or servo-type mounting and utilize MS-style connectors.

32.8 Sensible Design Alternative for Shaft Angle Encoding

The requirement for velocity and position feedback plays an important role in today's motion control systems. With the development of low-cost monolithic resolver-to-digital converters, a resolver-based system provides design engineers with the building blocks to handle a wide variety of applications. A resolver's small size, rugged design, and the ability to provide a very high degree of accuracy under severe conditions make this the ideal transducer for absolute position sensing. These devices are also well suited for use in extremely hostile environments such as continuous mechanical shock and vibration, humidity, oil mist, coolants, and solvents. Absolute position sensing vs. incremental position sensing is a necessity when working in an environment where there is the possibility of power loss. Whenever power is supplied to an absolute system, it is capable of reading its position immediately; this eliminates the need for a "go home" or reference starting point.

32.8.1 Resolver-to-Digital Converters

A monolithic resolver-to-digital converter requires only six external passive components to set the bandwidth and maximum tracking rate. The bandwidth controls how quickly the converter will react to a large change in position on the resolver output. The converter can also be programmed to provide 10, 12, 14, or 16 bits of parallel data. A resolver-based system can provide high dynamic capability and high resolution for today's motion control systems where precision feedback for both position and velocity is required.

32.8.2 Closed-Loop Feedback

In a typical closed-loop servo model as in Figure 32.9, the position sensor plays an important role by constantly updating the position and velocity information. Selection of a machine control strategy will often be based on performance, total application cost, and technology comfort.

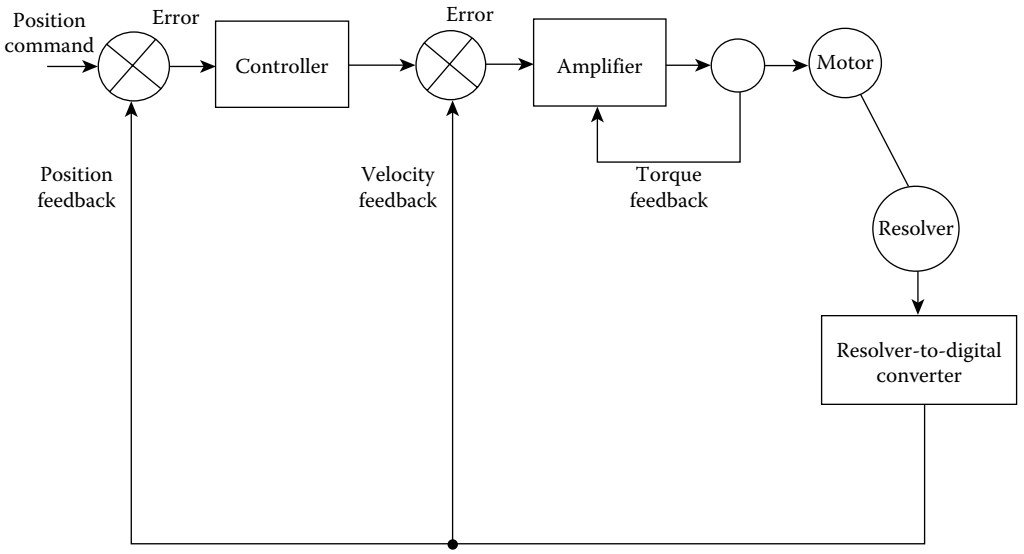

FIGURE 32.9 A closed-loop servo model uses a resolver-to-digital converter.

The accuracy of the system is determined by the smallest resolution of the position-sensing device. A resolver-to-digital converter in the 16-bit mode has 2^{16} (65,536) counts per revolution, which is equivalent to a resolution of 20 arcs. The overall accuracy of the resolver-to-digital converter is ±2.3 arcmin. An accuracy specification defines the maximum error in achieving a desired position. System accuracy must be smaller than the tolerance on the desired measurement. An important feature of the resolver-to-digital converter is repeatability. With a repeatability specification of ±1 LSB (least significant bit) in the 16-bit mode, this provides an accurate measurement when determining position from point to point. For example, moving from point A to point B and back to point A, the converter in the 16-bit mode will be accurate within 20 arcs of the original position. The error curve of a resolver-to-digital converter is repeatable within ±1 LSB. The combination of high-precision resolvers (±20 arcs) with a resolver-to-digital converter provides accurate absolute position information for precision feedback for motion control.

32.9 Type II Servo Loop

The motor speed is monitored using the velocity output signal generated by the resolver-to-digital converter. This signal is a dc voltage proportional to the rate of speed, positive for increasing angles and negative for decreasing angles, with a typical linearity specification of 0.25% and a typical reversal error of 0.75%. The error processing is performed using the industry standard technique for type II tracking, resolver-to-digital converters (see Figure 32.10).

The dc error is integrated, yielding a velocity voltage that drives a voltage-controlled oscillator (VCO). This VCO is an incremental integrator (constant voltage input to position rate output) that together with the velocity integrator forms a type II critically damped, servo feedback loop. This information allows the motor to maintain constant speeds under varying loads when it is interfaced with a programmable logic controller (PLC). The PLC-based architecture is used for integration of the motion (I/O) intensive control applications. The PLC provides a low-cost option for those developers familiar with its ladder logic programming language. I/O operator's interface and communication are usually supported through additional cards that are plugged into the backplane.

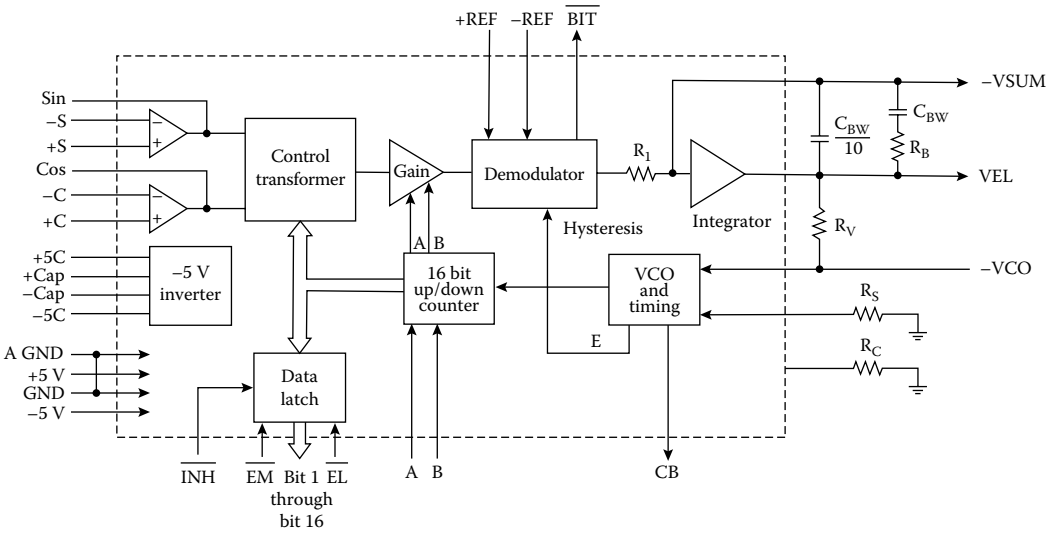

FIGURE 32.10 Error processing uses type II tracking resolver-to-digital converters.

32.10 Applications

Specific applications require unique profiles to control the speed and acceleration of the motor to perform the task at hand. By reducing the accelerations and decelerations that occur during each operation, it is possible to lower the cost and use more efficient motors. Industrial applications include the following:

- Ball-screw positioning
- Motor commutation
- Robotics positioning
- Machine vision systems
- *X*–*Y* tables
- Component insertion
- Remote video controls
- Web guides
- Pick and place machines

32.10.1 Resolver-to-Digital Conversion

For a resolver-to-digital converter, the resolver information is presented to a solid-state resolver conditioner that reduces the signal amplitude to 2 V rms sine and cosine, the amplitude of one being proportional to the sine of θ (the angle to be digitized) and the amplitude of the other being proportional to the cosine of θ. (The amplitudes referred to are, of course, the carrier amplitudes at the reference frequency, i.e., the cosine wave is actually $\cos\theta \cos\omega t$, but the carrier term, $\cos\omega t$, will be ignored in this discussion because it will be removed in the demodulator and at any rate contains no data.) A quadrant selector circuit in the control transformer enables selection of the quadrant in which θ lies and automatically sets the polarities of the $\sin\theta$ and $\cos\theta$ appropriately, for computational significance. The $\sin\theta$ and $\cos\theta$ outputs of the quadrant selector are then fed to the sine and cosine multipliers, also contained in the control transformer. These multipliers are digitally programmed resistive networks. The transfer function of each of these networks is determined by a digital input (which switches in proportioned resistors), so that the instantaneous value of the output is the product of the instantaneous value of the analog input and the sine (or cosine) of the digitally encoded angle. If the instantaneous value of the analog input of the sine multiplier is $\cos\theta$, and the digitally encoded "word" presented to the sine multiplier is ϕ, then the output code is $\cos\theta \sin\phi$. Thus, the two outputs of the multipliers are

$$\text{From the sine multiplier: } \cos\theta\sin\phi$$

$$\text{From the cosine multiplier: } \sin\theta\cos\phi$$

These outputs are fed to an operational subtractor, at the differencing junction shown, so that the input fed to the demodulator is

$$\sin\theta\cos\phi - \cos\theta\sin\phi = \sin(\theta - \phi) \tag{32.2}$$

The right-hand side of this trigonometric identity indicates that the differencing-junction output represents a carrier-frequency sine wave with an amplitude proportional to the sine of the difference between θ (the angle to be digitized) and ϕ (the angle stored in digital form in the up/down counter).

This point is the ac error signal brought out as (e). The demodulator is also presented with the reference voltage, which has been isolated from the reference source, and appropriately scaled, by the reference conditioner. The output of the demodulator is then, an analog dc level, proportional to sin ($\theta - \phi$), in other words, to the sine of the "error" between the actual angular position of the resolver and the digitally encoded angle, ϕ, which is the output of the counter. This point dc error is sometimes brought out as (D), while an addition of a threshold detector will give a built-in-test (BIT) flag. When the ac error signal exceeds 100 LSBs, the BIT flag will indicate a tracking error. This angular error signal is then fed into the error processor and VCO. This circuit consists essentially of an analog integrator whose output (the time integral to the error) controls the frequency of a VCO. The VCO produces clock pulses that are counted by the up/down counter. The "sense" of the error (ϕ too high or ϕ too low) is determined by the polarity of (ϕ) and is used to generate a control counter signal (U), which determines whether the counter increments upward or downward. Finally, note that the up/down counter, like any counter, is functionally an incremental integrator; therefore, the tracking converter constitutes in itself a closed-loop servomechanism (continuously attempting to null the error to zero) with two integrators in series. This called a "type II" servo loop, which has decided advantages over type 1 or type 0 loops. In order to appreciate the value of a type II servo behavior of this tracking converter, consider first the shaft is not moving. Ignoring inaccuracies, drifts, and the inevitable quantizing error, the error should be zero ($\theta = \phi$) and the digital output represents the true shaft angle of the resolver. Now, start the resolver shaft moving, and allow it to accelerate uniformly, from $d\theta/dt = 0$ to $d\theta/dt = V$. During the acceleration, an error will develop because the converter cannot instantaneously respond to the change of angular velocity. However, since the VCO is controlled by an integrator, the output of which is the integral of the error, the greater the lag (between θ and ϕ), the faster the counter will be called on to catch up. When the velocity becomes constant at V, the VCO will have settled to a rate of counting that exactly corresponds to the rate of change in θ per unit time and instantaneously $\theta = \phi$. Therefore, $d\phi/dt$ will always track $d\theta/dt$ without a velocity or position error, the only error will be momentary (transient) error, during acceleration or deceleration. Furthermore, the information produced by the tracking converter is always "fresh," being continually updated, and always available at the output of the counter. Since $d\theta/dt$ tracks the input velocity, it can be brought out as velocity, a dc voltage proportional to the rate of rotation, which is of sufficient linearity in modern converters to eliminate the need for a tachometer in many systems.

32.10.2 Bandwidth Optimization

When using a low-cost monolithic converter for position and velocity feedback, it is important to understand the dynamic response for a changing input. When considering what bandwidth to set the converter, several parameters must be taken into consideration. The ability to track step responses and accelerations will determine what bandwidth to select. The lower the bandwidth of the resolver-to-digital converter, the greater the noise immunity; high-frequency noise will be rejected. The relationship between the maximum tracking rate and bandwidth determines the settling time for small and large steps. For a small step input, the bandwidth determines the converter settling time. When one has a large step, the maximum velocity slew rate and bandwidth together determine the settling time.

32.10.3 Encoder Emulation

Today's resolver-to-digital converters also have the ability to emulate the output of an optical incremental encoder. By providing the outputs A, B, and zero index, the encoder can be replaced with a resolver and resolver-to-digital converter without changing the existing interface hardware.

32.10.4 Determining Position Lag Error Due to Acceleration

As the bandwidth and the maximum tracking rate are varied, one can determine the acceleration constant (K_a) and large step settling time.

Example 32.1

Resolution: 16 bit
Bandwidth: 100 Hz
Reference: 1000 Hz
Max tracking: 10 rps

$$\text{BW} = \frac{\sqrt{2}A}{\pi} \tag{32.3}$$

If the bandwidth = 100 Hz
$A = 222$
$K_a = A^2$
$K_a = 49{,}284° \text{ s}^{-2}$
The lag in degrees during acceleration is

$$\frac{\text{Acceleration}}{K_a} \tag{32.4}$$

Example 32.2

Acceleration = $19{,}000° \text{ s}^{-2}$
$K_a = 49{,}284° \text{ s}^{-2}$
LAG = 19,000/49,284 = 0.38°
In 16 bit 1 LSB = 0.0055°
Acceleration (1 LSB lag) = $K_a \times 0.0055$ (16 bit)
$49{,}284 \times 0.0055 = 270° \text{ s}^{-2}$

32.10.5 Large Step Settling Time

To determine the settling time for a large step response (179°), one must take into account the maximum tracking rate and bandwidth.

Example 32.3

A 179° step with 100 Hz BW and 10 rps max tracking
Max tracking at 10 rps = $3600° \text{ s}^{-1}$
179/3600 = 49 ms

Then one must add the settling time due to bandwidth limitations; this is approximately 11 time constants (16-bit mode).

Time Constants

Resolution	Number of Counts/Rotation	Number of Time Constants
10	1,024	7
12	4,096	8
14	16,384	10
16	65,536	11

Time constant = $1/A$
$A = 222$
$1/A = 4.5$ ms
11 time constants = 45 ms

Therefore, the approximate settling time for a large step would be 94 ms. This is an approximation. Synchros and resolvers are used in a wide variety of dynamic conditions. Understanding how the converter reacts to these input changes will allow one to optimize the bandwidth and maximum tracking rate for each application. Table 32.1 provides a list of resolver and synchro suppliers.

TABLE 32.1 List of Resolver and Synchro Suppliers

Company	Location, Phone Number	Types of Resolvers
API Harowe	West Chester, PA, (800) 566-5274, http://www.servosystems.com/harowe_resolvers.htm	Brushless frameless, housed, and heavy-duty units
Admotec, Inc.	Norwich, VT, (802) 649-5800, http://www.admotec.com/	Rotasyn solid rotor resolvers
Neotech, Inc.	Hatfield, PA, (215) 822-5520, http://neotechsystems.com/	Housed brush and brushless units
Vernitron Corp.	San Diego, CA, (800) 777-3393	Brushless, segment, brushed, housed units
Servo Systems	Montville, NJ, (973)335-1007, http://www.servosystems.com/	Brushed 8c brushless units
American Electronics	Fullerton, CA (714)871-3020	Housed units
Computer Conversions, Corp.	East Northport, NY, (516) 261-3300, http://www.computerconversions.com/index.html	Explosion proof 8c specialty units
Poltron Corp.	Gaithersburg, MD, (301)208-6597	Resolvers
Tamagawa Seiki Co., Ltd.	Tokyo, Japan, 011-81-37-383-175, http://www.tamagawa-seiki.co.jp/english/index.html	Brushless frameless 8c housed units
MPC Products	Skokie, IL, (800) 323-4302	Housed resolvers
Transicoil, Inc.	Trooper, PA, (800)323-7115, http://www.isensors.com/nav/manuf.asp?vid=35	Housed brushless 8c brushed resolvers
Litton Poly-Scientific	Blacksburg, VA, (800)336-2112	Brushed and brushless resolvers
Kearfott Guidance & Navigation Corp.	Wayne, NJ, (973) 785-6000, http://www.kearfott.com/	Brushed 8c brushless resolvers
Novatronics, Inc.	Stratford, Ontario, Canada, (519) 271-3880, http://www.novatronicsinc.com/	Resolvers
Muirhead Vactric	Lake Zurich, IL, (847) 726-0270, http://www.muirheadaerospace.com/	Resolvers

Further Readings

Analog Devices, Inc., *Analog-Digital Conversion Handbook*, 3rd edn., Englewood Cliffs, NJ: Prentice-Hall, 1986.

Moog Components, Components Groop. http://www.scribd.com/doc/68820721/Synchro-and-Resolver-Hand-Book (accessed on June 26, 2012).

Synchro & Resolver Conversion, East Molesey, U.K.: Memory Devices Ltd., 1980.

Synchro/Resolver Conversion Handbook, 4th edn., Bohemia, NY: ILC Data Device Corp., 1994.

Synchro resolver, Otomation. http://www.globalspec.com/Industrial-Directory/synchro_resolver (accessed on June 28, 2012).

Welbun, R. D., *Self corrected synchro/resolver*. http://www.devileye.net/catalog/manufacturing_metallosilicates/self-corrected_synchro_resolver.html (accessed July 1, 2012).

33

Optical Fiber Displacement Sensors

Richard O. Claus
Virginia Tech

Vikram Bhatia
Virginia Tech

Anbo Wang
Virginia Tech

The objective of this chapter is to present a rigorous theoretical and experimental analysis of short gage length optical fiber sensors for measurement of cyclical strain on or in materials. Four different types of sensors are evaluated systematically on the basis of various performance criteria such as strain resolution, dynamic range, cross sensitivity to other ambient perturbations, simplicity of fabrication, and complexity of demodulation process. The sensing methods that would be investigated include well-established technologies (e.g., fiber Bragg gratings (FBGs)) and rapidly evolving measurement techniques such as long-period gratings. Other than the grating-based sensors, two popular versions of Fabry–Perot interferometric sensors (intrinsic and extrinsic) will be evaluated for their suitability. A theoretical study of the cross sensitivities of these sensors to an arbitrary combination of strain vectors and temperature, similar to that proposed by Sirkis in his SPIE paper in 1991 [1], will be developed.

The outline of this chapter is as follows. The principle of operation and fabrication process of each of the four sensors is discussed separately. Sensitivity to strain and other simultaneous perturbations such as temperature are analyzed. The overall cost and the performance of a sensing technique depend heavily on the signal demodulation process. The detection schemes for all four sensors are discussed and compared on the basis of their complexity. Finally, a theoretical analysis of the cross sensitivities of the four sensing schemes is presented and their performances are compared.

Strain measurements using optical fiber sensors in both embedded and surface-mounted configurations have been reported by researchers in the past [2]. Fiber-optic sensors are small in size and immune to electromagnetic interference and can be easily integrated with existing optical fiber communication links. Such sensors can typically be easily multiplexed, resulting in distributed networks that can be used for health monitoring of integrated, high-performance materials and structures. Optical fiber sensors for strain measurements should possess certain important characteristics. These sensors should either be insensitive to ambient fluctuations in temperature and pressure or should have demodulation techniques

that compensate for changes in the output signal due to the undesired perturbations. In the embedded configuration, the sensors for axial strain measurements should have minimum cross sensitivity to other strain states. The sensor signal should itself be simple and easy to demodulate. Nonlinearities in the output demand expensive decoding procedures or require precalibrating the sensor. The sensor should ideally provide an absolute and real-time strain measurement in a form that can be easily processed. For environments where large strain magnitudes are expected, the sensor should have a large dynamic range while at the same time maintaining the desired sensitivity. A discussion of each of the four sensing schemes individually, along with their relative merits and demerits, follows.

33.1 Extrinsic Fabry–Perot Interferometric Sensor

The extrinsic Fabry–Perot interferometric (EFPI) sensor, proposed by Murphy et al., is one of the most popular fiber-optic sensors used for applications in health monitoring of smart materials and structures [3]. As the name suggests, the EFPI is an interferometric sensor in which the detected intensity is modulated by the parameter under measurement. The simplest configuration of an EFPI is shown in Figure 33.1.

The EFPI system consists of a single-mode laser diode that illuminates a Fabry–Perot cavity through a fused biconical tapered coupler. The cavity is formed between an input single-mode fiber and a reflecting single-mode or multimode fiber. Since the cavity is external to the lead-in/lead-out fiber, the EFPI sensor is independent of transverse strain and small ambient temperature fluctuations. The input fiber and the reflecting fiber are aligned using a hollow-core silica fiber. For uncoated fiber ends, a 4% Fresnel reflection results at both ends. The first reflection, R_1, called the reference reflection, is independent of the applied perturbation. The second reflection, R_2, termed the sensing reflection, is dependent on the length of the cavity, d, which in turn is modulated by the applied perturbation. These two reflections interfere (provided $2d < L_c$, the laser diode's coherence length), and the intensity I at the detector varies as a function of the cavity length:

$$I = I_0 \cos\left(\frac{4\pi}{\lambda} d\right) \tag{33.1}$$

where

I_0 is the maximum value of the output intensity
λ is the laser diode center wavelength

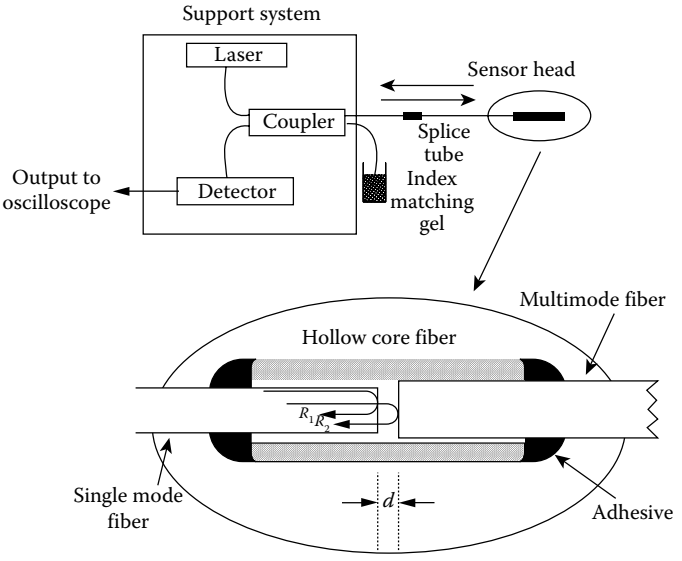

FIGURE 33.1 Simple configuration of an EFPI sensing system.

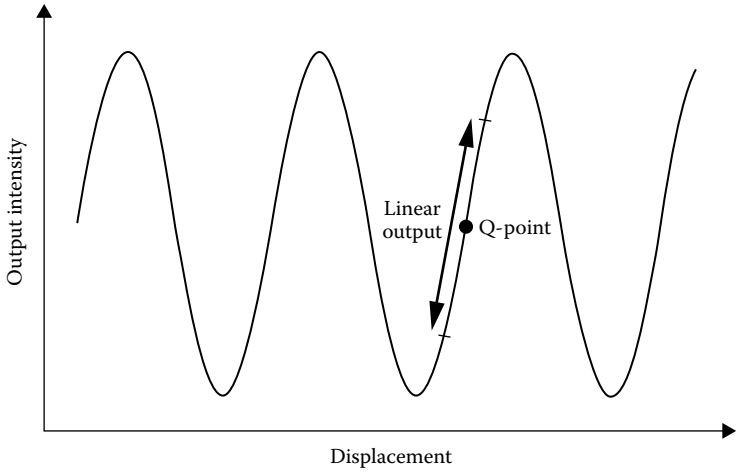

FIGURE 33.2 Typical EFPI transfer function curve.

The typical EFPI transfer function curve is shown in Figure 33.2. Small perturbations that result in operation around the quiescent-point or Q-point of the sensor lead to a linear variation in output intensity. A fringe in the output signal is defined as the change in intensity from a maximum to a maximum or from a minimum to a minimum. Each fringe corresponds to a change in the cavity length by one-half of the operating wavelength, λ. The change in the cavity length, Δd, is then employed to calculate the strain ε using the expression

$$\varepsilon = \frac{\Delta d}{L} \tag{33.2}$$

where L is defined as the gage length of the sensor and is typically the distance between two points where the input and the reflecting fibers are bonded to the hollow-core fiber. Matching of the two reflection signal amplitudes allows good fringe visibility in the output signal.

The EFPI sensor has been extensively used for measuring fatigue loading on F-15 aircraft wings, detection of crack formation and propagation in civil structures, and cure and lifetime monitoring in concrete and composite specimens [2,4]. The temperature insensitivity of this sensor makes it attractive for a large number of applications. The EFPI sensor is capable of measuring sub-angstrom displacements with strain resolution better than 1 microstrain and a dynamic range greater than 10,000 $\mu\varepsilon$. Although the change in output intensity of the EFPI is nonlinear corresponding to the magnitude of the parameter being measured, for small perturbations, its operation can be limited to that around the Q-point of the transfer function curve. Moreover, the large bandwidth available with this sensor simplifies the measurement of highly cyclical strain. The EFPI sensor is capable of providing single-ended operation and is hence suitable for applications where access to the test area is limited. The sensor requires simple and inexpensive fabrication equipment and an assembly time of less than 10 min. Additionally, since the cavity is external to the fibers, transverse strain components that tend to influence intrinsic sensors through the Poisson's effect have negligible effect on the EFPI sensor output. The sensitivity to only axial strain and the insensitivity to input polarization state have made the EFPI sensor the most preferred fiber-optic sensor for embedded applications [1]. Thus, overall, the EFPI sensing system is very well suited to measurement of small magnitudes of cyclical strain.

Although a version of the EFPI sensor that provides absolute output has been demonstrated, it lacks the bandwidth typically desired during the measurement of cyclical strain [5]. We have also recently proposed a small-cavity-length/high-finesse EFPI sensor for measurement of small perturbations [6]. This configuration has a simple output that can be demodulated using an optical filter/photodetector combination.

33.2 Intrinsic Fabry–Perot Interferometric Sensor

The intrinsic Fabry–Perot interferometric (IFPI) sensor is similar in operation to its extrinsic counterpart, but significant differences exist in the configurations of the two sensors [7]. The basic IFPI sensor is shown in Figure 33.3. An optically isolated laser diode is used as the optical source to one of the input arms of a bidirectional 2 × 2 coupler. The Fabry–Perot cavity is formed by fusing a small length of a single-mode fiber to one of the output legs of the coupler. As shown in Figure 33.3, the reference (R) and sensing (S) reflections interfere at the detector face to provide a sinusoidal intensity variation. The cavity can also be obtained by introducing two Fresnel reflectors—discontinuities in refractive index—along the length of a single fiber. Photosensitivity in germanosilicate fibers has been used in the past to fabricate broadband reflectors that enclose an IFPI cavity [8]. Since the cavity is formed within an optical fiber, changes in the refractive index of the fiber due to the applied perturbation can significantly alter the phase of the sensing signal, S. Thus, the intrinsic cavity results in the sensor being sensitive to ambient temperature fluctuations and all states of strain.

The IFPI sensor, like all other interferometric signals, has a nonlinear output that complicates the measurement of large magnitude strain. This can again be overcome by operating the sensor in the linear regime around the Q-point of the sinusoidal transfer function curve. The main limitation of the IFPI strain sensor is that the photoelastic effect–induced change in index of refraction results in a nonlinear relationship between the applied perturbation and the change in cavity length. In fact, for most IFPI sensors, the change in propagation constant of the fundamental mode dominates the change in cavity length. Thus, IFPIs are highly susceptible to temperature changes and transverse strain components [1]. In embedded applications, the sensitivity to all the strain components can result in erroneous outputs. The fabrication process of an IFPI strain sensor is more complicated than that of the EFPI sensor since the sensing cavity must be formed within the optical fiber by some special procedure. The strain resolution of the IFPIs is also expected to be around 110 $\mu\varepsilon$ with an operating range greater than 10,000 $\mu\varepsilon$. IFPI sensors also suffer from drift in the output signal due to variations in the polarization state of the input light.

Thus, the preliminary analysis shows that the extrinsic version of the Fabry–Perot optical fiber sensor seems to have an overall advantage over its intrinsic version. The extrinsic sensor has negligible cross sensitivity to temperature and transverse strain. Although the strain sensitivity, dynamic range, and bandwidth of the two sensors are comparable, the IFPIs can be expensive and cumbersome to fabricate due to the intrinsic nature of the sensing cavity.

The EFPI and the IFPI sensors possess nonlinear sinusoidal outputs that complicate the signal processing at the detection end. Although intensity-based sensors have a simple output variation, they suffer from limited sensitivity to strain or other perturbations of interest. Grating-based sensors have recently become popular as transducers that provide wavelength-encoded output signals that can typically be easily demodulated to derive information about the perturbation under investigation. The advantages and drawbacks of Bragg-grating sensing technology are discussed first. The basic operating mechanism of the Bragg-grating-based strain sensor is elucidated, and the expressions for strain resolution are obtained. These sensors are then compared to the recently developed long-period gratings in terms of fabrication process, cross sensitivity to other parameters, and simplicity of signal demodulation.

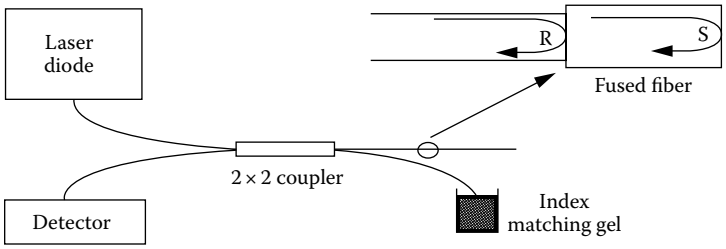

FIGURE 33.3 Intrinsic Fabry–Perot interferometric (IFPI) sensor.

33.3 Fiber Bragg-Grating Sensor

The phenomenon of photosensitivity in optical fibers was discovered by Hill and coworkers in 1978 [9]. It was found that permanent refractive index changes could be induced in fibers by exposing the germanium-doped core to intense light at 488 or 514 nm. The sinusoidal modulation of index of refraction in the core due to the spatial variation in the writing beam gives rise to a refractive index grating that can be used to couple the energy in the fundamental guided mode to various guided and lossy modes. Later, Meltz et al. proposed that photosensitivity is more efficient if the fiber is side exposed to fringe pattern at wavelengths close to the absorption wavelength (242 nm) of the germanium defects in the fiber [10]. The side-writing process simplified the fabrication of Bragg gratings, and these devices have recently emerged as highly versatile components for communication and sensing systems. Recently, loading the fibers with hydrogen has been reported to result in two orders of magnitude higher index change in germanosilicate fibers [11].

33.3.1 Principle of Operation

Bragg gratings are based on the phase-matching condition between spatial modes propagating in optical fibers. This phase-matching condition is given by

$$k_g + k_c = k_B \tag{33.3}$$

where k_g, k_c, and k_B are, respectively, the wave vectors of the coupled guided mode, the resulting coupling mode, and the grating. For a first-order interaction, $k_B = 2\pi/\Lambda$, where Λ is the grating periodicity. Since it is customary to use propagation constants while dealing with optical fiber modes, this condition reduces to the widely used equation for mode coupling due to a periodic perturbation:

$$\Delta\beta = \frac{2\pi}{\Lambda} \tag{33.4}$$

where $\Delta\beta$ is the difference in the propagation constants of the two modes involved in mode coupling (both assumed to travel in the same direction).

FBGs involve the coupling of the forward-propagating fundamental LP_{01} optical fiber waveguide propagation mode to the reverse-propagating LP_{01} mode [12]. Consider a single-mode fiber with β_{01} and $-\beta_{01}$ as the propagation constant of the forward- and reverse-propagating fundamental LP_{01} modes. To satisfy the phase-matching condition,

$$\Delta\beta = \beta_{01} - (-\beta_{01}) = \frac{2\pi}{\Lambda} \tag{33.5}$$

where $\beta_{01} = 2\pi n_{eff}/\lambda$ (n_{eff} is the effective index of the fundamental mode and λ is the free-space wavelength). Equation 33.5 reduces to [12]

$$\lambda_B = 2\Lambda n_{eff} \tag{33.6}$$

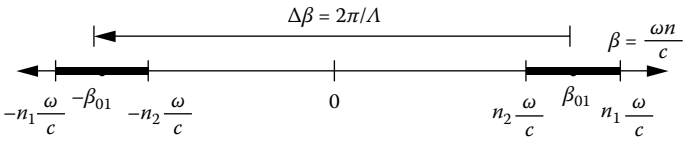

FIGURE 33.4 Mode-coupling mechanism in an FBG.

where λ_B is termed the Bragg wavelength. The Bragg wavelength is the wavelength at which the forward-propagating LP_{01} mode couples to the reverse-propagating LP_{01} mode. This coupling is wavelength dependent since the propagation constants of the two modes are a function of the wavelength. Hence, if an FBG is interrogated by a broadband optical source, the wavelength at which phase-matching occurs is found to be reflected back. This wavelength is a function of the grating periodicity (Λ) and the effective index (n_{eff}) of the fundamental mode (Equation 33.6). Since strain and temperature effects can modulate both these parameters, the Bragg wavelength shifts with these external perturbations. This spectral shift is utilized to fabricate FBGs for sensing applications.

Figure 33.4 shows the mode-coupling mechanism in FBGs using the β-plot. Since the difference in propagation constants ($\Delta\beta$) between the modes involved in coupling is large, Equation 33.4 reveals that only a small value of periodicity, Λ, is needed to induce this mode coupling. Typically for telecommunication applications, the value of λ_B is around 1.5 μm. From Equation 33.6, Λ is determined to be 0.5 μm (for $n_{eff} = 1.5$). Due to the small periodicities (of the order of 1 μm), FBGs are classified as short-period gratings.

33.3.2 Fabrication Techniques

FBGs have commonly been manufactured using two side-exposure techniques: the interferometric method and the phase-mask method. The interferometric method, depicted in Figure 33.5, comprises a UV beam at 244 or 248 nm spilt in two equal parts by a beam splitter [10]. The two beams are then focused on a portion of Ge-doped fiber (whose protective coating has been removed) using cylindrical lenses, and the periodicity of the resulting interference pattern and, hence, the Bragg wavelength are varied by altering the mutual angle, θ. The limitation of this method is that any relative vibration of the pairs of mirrors and lenses can lead to the degradation of the quality of the final grating and, hence, the entire system has a stringent stability requirement. To overcome

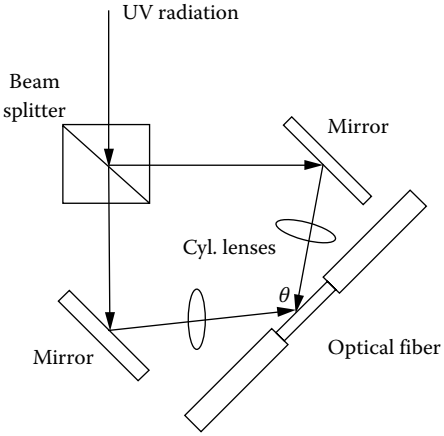

FIGURE 33.5 Interferometric FBG.

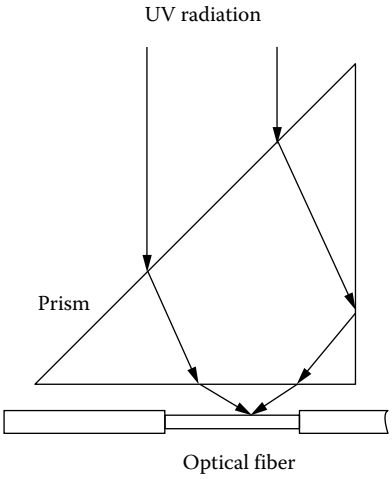

FIGURE 33.6 Novel interferometer technique.

this drawback, Kashyap et al. have proposed the novel interferometer technique where the path difference between the interfering UV beams is produced by the propagation through a right-angled prism (Figure 33.6) [12]. This technique is inherently stable because both beams are perturbed similarly by any prism vibration.

The phase-mask technique has recently gained popularity as an efficient holographic side-writing procedure for grating fabrication [13]. In this method, as shown in Figure 33.7, an incident UV beam is diffracted into –1, 0, and +1 orders by a relief grating generated on a silica plate by *e*-beam exposure and plasma etching. The two first diffraction orders undergo total internal reflection at the glass/air interface of a rectangular prism and interfere on the bare fiber surface placed directly behind the mask. This technique is wavelength specific since the periodicity of the resulting two-beam interference pattern is uniquely determined by the diffraction angle of –1 and +1 orders and, thus, the properties of the phase mask. Obviously, different phase masks are required for fabrication of gratings at different Bragg wavelengths. The setup for actively monitoring the growth of the grating in transmission during fabrication is shown in Figure 33.8.

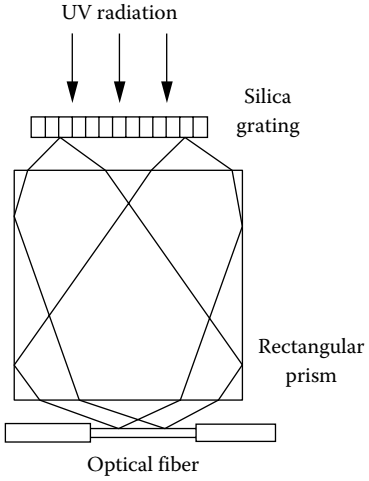

FIGURE 33.7 Phase-mask technique for grating fabrication.

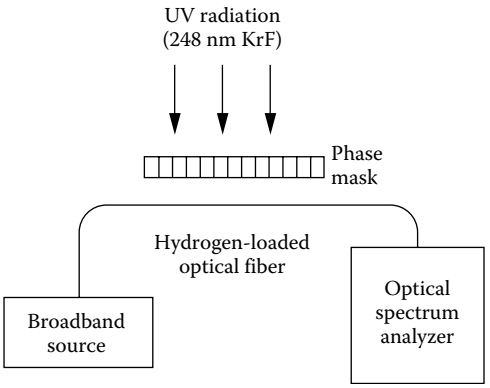

FIGURE 33.8 Diagram of the setup for monitoring the growth of the grating in transmission during fabrication.

33.3.3 Bragg-Grating Sensors

From Equation 33.6, we see that a change in the value of n_{eff} and/or Λ can cause the Bragg wavelength, λ, to shift. This fractional change in the resonance wavelength, $\Delta\lambda/\lambda$, is given by the expression

$$\frac{\Delta\lambda}{\lambda} = \frac{\Delta\Lambda}{\Lambda} + \frac{\Delta n_{\text{eff}}}{n_{\text{eff}}} \tag{33.7}$$

where $\Delta\Lambda/\Lambda$ and $\Delta n_{\text{eff}}/n_{\text{eff}}$ are the fractional changes in the periodicity and the effective index, respectively. The relative magnitudes of the two changes depend on the type of perturbation the grating is subjected to; for most applications, the effect due to change in effective index is the dominating mechanism.

Any axial strain, ε, applied to the grating changes the periodicity and the effective index and results in a shift in the Bragg wavelength, given by

$$\frac{1}{\lambda}\frac{\Delta\lambda}{\varepsilon} = \frac{1}{\Lambda}\frac{\Delta\Lambda}{\varepsilon} + \frac{1}{n_{\text{eff}}}\frac{\Delta n_{\text{eff}}}{\varepsilon} \tag{33.8}$$

The first term on the right-hand side is unity, while the second term has its origin in the photoelastic effect. An axial strain on the fiber serves to change the refractive index of both the core and the cladding. This results in the variation in the value of the effective index of glass. The photoelastic or strain-optic coefficient that relates the change in index of refraction due to mechanical displacement is about −0.27. Thus, the variations in n_{eff} and Λ due to strain have contrasting effects on the Bragg peak. The fractional change in the Bragg wavelength due to axial strain is 0.73 ε or 73% of the applied strain. At 1550 and 1300 nm, the shifts in the resonance wavelength are 11 nm $\%\varepsilon^{-1}$ and 9 nm $\%\varepsilon^{-1}$, respectively. With temperature, an FBG at 1500 nm shifts by 1.6 nm for every 100 °C rise in temperature [9].

33.3.4 Limitations of Bragg-Grating Strain Sensors

The major limitation of Bragg-grating sensors is the complex and expensive fabrication technique. Although side writing is commonly used to manufacture these gratings, the requirement of expensive phase masks increases the cost of the sensing system. In the interferometric technique, stability of the setup is a critical factor in obtaining high-quality gratings. Since index changes of the order of 10^{-3} are required to fabricate these gratings, laser pulses of high energy levels are necessary. This might reduce laser operating lifetime and lead to increased maintenance expense. Additionally, introducing hydrogen or deuterium into the fiber allows increased index modulation as a result of the irradiation process.

The second major limitation of Bragg gratings is their limited bandwidth. The typical value of the full width at half maximum (FWHM) is between 0.1 and 1 nm. Although higher bandwidths potentially can be obtained by chirping the index or periodicity along the grating length, this adds to the cost of the grating fabrication. The limited bandwidth requires high-resolution spectrum analyzers to monitor the grating spectrum. Kersey et al. have proposed an unbalanced Mach–Zehnder interferometer to detect the perturbation-induced wavelength shift [14]. Two unequal arms of the Mach–Zehnder interferometer are excited by the back reflection from a Bragg-grating sensor element. Any change in the input optical wavelength modulates the phase difference between the two arms and results in a time-varying sinusoidal intensity at the output. This interference signal can be related to the shift in the Bragg peak, and hence, the magnitude of the perturbation can be obtained. Recently, modal interferometers have also been proposed to demodulate the output of a Bragg-grating sensor [15]. The unbalanced interferometers are also susceptible to external perturbations and hence need to be isolated from the parameter under investigation. Moreover, the nonlinear output might require fringe counting equipment, which can be complex and expensive. Additionally, a change in the perturbation polarity at the maxima or minima of the transfer function curve will not be detected by this demodulation scheme. To overcome this limitation, two unbalanced interferometers can be employed for dynamic measurements.

The cross sensitivity to temperature fluctuations leads to erroneous strain measurements in applications where the ambient temperature has a temporal variation. Thus, a reference grating that measures the temperature change must be utilized to compensate for the output of the strain sensor. Recently, temperature-independent sensing has been demonstrated using chirped gratings written in tapered optical fibers [16].

Last, the sensitivity of FBG strain sensors might not be adequate for certain applications. This sensitivity of the sensor depends on the minimum detectable wavelength shift at the detection end. Although excellent wavelength resolution can be obtained with unbalanced interferometric detection techniques, standard spectrum analyzers typically provide a resolution of 0.1 nm. At 1300 nm, this minimum detectable change in wavelength corresponds to a strain resolution of 111 $\mu\varepsilon$. Hence, in applications where strain smaller than 100 $\mu\varepsilon$ is anticipated, Bragg-grating sensors might not be practical. The dynamic range of strain measurement can be as much as 15,000 $\mu\varepsilon$.

33.4 Long-Period Grating Sensor

This section discusses the use of novel long-period gratings as strain sensing devices. The principle of operation of these gratings and their fabrication process, preliminary strain tests, demodulation process, and cross sensitivity to ambient temperature are analyzed.

33.4.1 Principle of Operation

Long-period gratings that couple the fundamental guided mode to different guided modes have been demonstrated in the past [17,18]. Gratings with longer periodicities that involve coupling of a guided mode to forward-propagating cladding modes were recently proposed by Vengsarkar et al. [19,20]. As stated previously, fiber gratings satisfy the Bragg phase-matching condition between the guided and the cladding or radiation modes or another guided mode. This wavelength-dependent phase-matching condition is given by

$$\beta_{01} - \beta = \Delta\beta = \frac{2\pi}{\Lambda} \tag{33.9}$$

where

Λ is the periodicity of the grating

β_{01} and β are the propagation constants of the fundamental guided mode and the mode to which coupling occurs, respectively

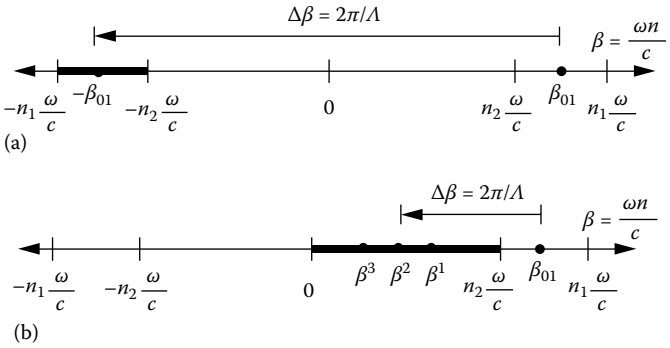

FIGURE 33.9 Blazed and unblazed cladding mode periodicities.

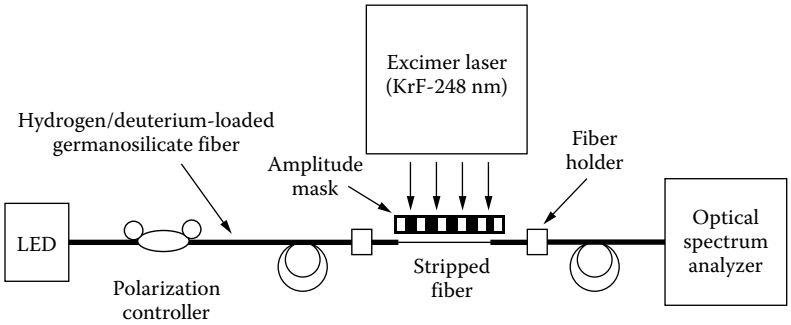

FIGURE 33.10 Setup used to fabricate long-period gratings.

For conventional FBGs, the coupling of the forward-propagating LP_{01} mode occurs to the reverse-propagating LP_{01} mode ($\beta = -\beta_{01}$). Since $\Delta\beta$ is large in this case (Figure 33.9a), the grating periodicity is small, typically of the order of 1 μm. Unblazed long-period gratings having index variations parallel to the long axis of the fiber couple the fundamental mode to the discrete and circularly symmetric, forward-propagating cladding modes ($\beta = \beta^n$), resulting in smaller values of $\Delta\beta$ (Figure 33.9b) and hence periodicities ranging in hundreds of micrometers [19]. The cladding modes attenuate rapidly as they propagate along the length of the fiber due to the lossy cladding-coating interface and bends in the fiber. Since $\Delta\beta$ is discrete and function of the wavelength, this coupling to the cladding modes is highly selective, leading to a wavelength-dependent loss. As a result, any modulation of the core and cladding guiding properties modifies the spectral response of long-period gratings, and this phenomenon can be utilized for sensing purposes. Moreover, since the cladding modes interact with the fiber jacket or any other material surrounding the cladding, changes in the properties of these ambient materials can also be detected. A typical example of such setup is illustrated in Figure 33.10.

33.4.2 Fabrication Procedure

To fabricate long-period gratings, hydrogen-loaded (3.4 mol%) germanosilicate fibers are exposed to 248 nm UV radiation from a KrF excimer laser, through a chrome-plated amplitude mask possessing a periodic rectangular transmittance function. Figure 33.10 shows the setup used to fabricate the gratings. The laser was pulsed at 20 Hz with an 8 ns pulse duration. The typical writing times for energy of 100 mJ cm^{-2} $pulse^{-1}$ and a 2.5 cm exposed length vary between 6 and 15 min for different fibers. The coupling wavelength, λ_p, shifts to higher values during exposure, due to the photoinduced enhancement of the refractive index of the fiber core and the resulting increase in β_{01}. After writing, the gratings

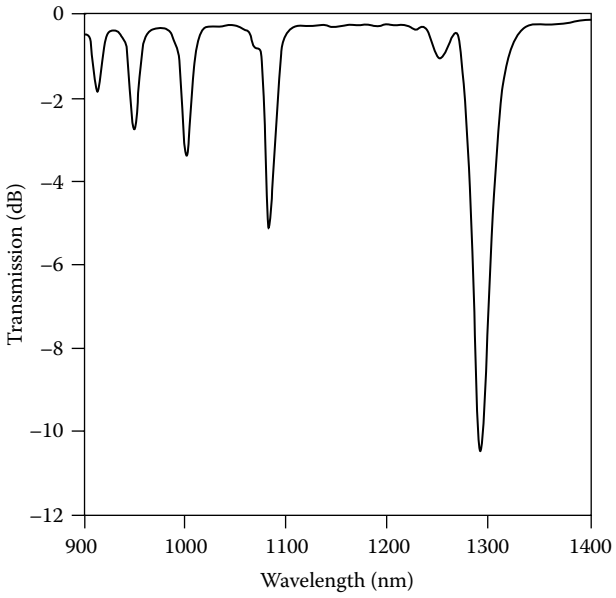

FIGURE 33.11 Typical transmission of a grating.

are annealed at 150 °C for 10 h to remove the unreacted hydrogen. This high-temperature annealing causes λ_p to move to shorter wavelengths due to the decay of UV-induced defects and diffusion of molecular hydrogen from the fiber. Figure 33.11 depicts the typical transmittance of a grating. Various attenuation bands correspond to coupling to discrete cladding modes of different orders. A number of gratings can be fabricated at the same time by placing more than one fiber behind the amplitude mask. Moreover, the stability requirements during the writing process are not as severe as those for short-period Bragg gratings.

For coupling to the highest-order cladding mode, the maximum isolation (loss in transmission intensity) is typically in the 5–20 dB range on wavelengths, depending on fiber parameters, duration of UV exposure, and mask periodicity. The desired fundamental coupling wavelength can easily be varied using inexpensive amplitude masks of different periodicities. The insertion loss, the polarization-mode dispersion, the back reflection, and the polarization-dependent loss of a typical grating are 0.2 dB, 0.01 ps, −80 dB, and 0.02 dB, respectively. The negligible polarization sensitivity and the back reflection of these devices eliminate the need for expensive polarizers and isolators.

Preliminary experiments were performed to examine the strain sensitivity of long-period gratings written in different fibers [21,22]. Gratings were fabricated in four different types of fibers: standard dispersion-shifted fiber (DSF), standard 1550 nm fiber, and conventional 980 and 1050 nm single-mode fibers, which for the sake of brevity are referred to as fibers A, B, C, and D, respectively. The strain sensitivity of gratings written in different fibers was determined by axially straining the gratings between two longitudinally separated translation stages. The shift in the peak loss wavelength of the grating in fiber D as a function of the applied strain is depicted in Figure 33.12, along with that for a Bragg grating (about 9 nm $\%\varepsilon^{-1}$, at 1300 nm) [9]. The strain coefficients of wavelength shift (β) for fibers A, B, C, and D are shown in Table 33.1. Fiber D has a coefficient 15.2 nm $\%\varepsilon^{-1}$ that gives it a strain-induced shift that is 50% larger than that for a conventional Bragg grating. The strain resolution of this fiber for a 0.1 nm detectable wavelength shift is 65.75 $\mu\varepsilon$.

The demodulation scheme of a sensor determines the overall simplicity and sensitivity of the sensing system. Short-period Bragg-grating sensors were shown to possess signal processing techniques that are complex and expensive to implement. A simple demodulation method to extract

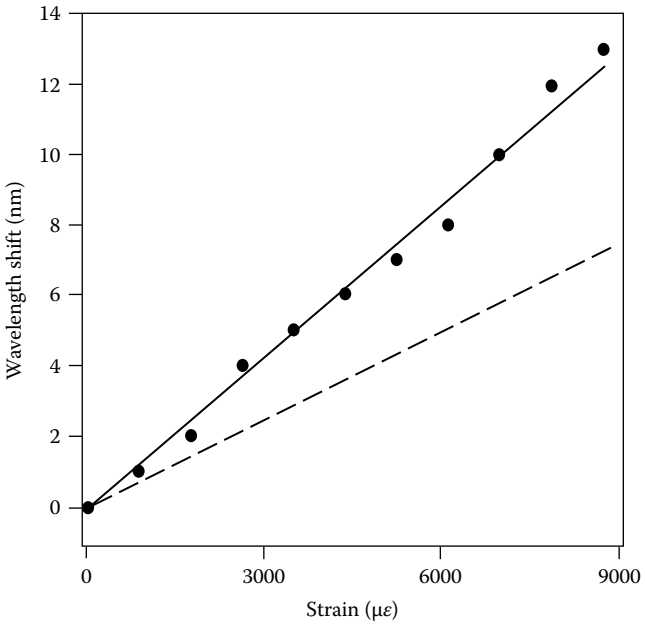

FIGURE 33.12 Shift in peak loss wavelength as a function of the applied strain.

TABLE 33.1 Strain Sensitivity of Long-Period Gratings Written in Four Different Types of Fibers

Type of Fiber	Strain Sensitivity (nm% ε^{-1})
A—DSF	−7.27
B—Standard 1550 nm communication fiber	4.73
C—Conventional 980 nm single-mode fiber	4.29
D—Conventional 1060 nm single-mode fiber	15.21

Note: The values correspond to the shift in the highest-order resonance wavelength.

information from long-period gratings is possible. The wide bandwidth of the resonance bands enables the wavelength shift due to the external perturbation to be converted into an intensity variation that can be easily detected.

Figure 33.13 shows the shift induced by strain in a grating written in fiber C. The increase in the loss at 1317 nm is about 1.6 dB. A laser diode centered at 1317 nm was used as the optical source, and the change in transmitted intensity was monitored as a function of applied strain. The transmitted intensity is plotted in Figure 33.14 for three different trials. The repeatability of the experiment demonstrates the feasibility of using this simple scheme to utilize the high sensitivity of long-period gratings. The transmission of a laser diode centered on the slope of the grating spectrum on either side of the resonance wavelength can be used as a measure of the applied perturbation. A simple detector and amplifier combination at the output can be used to determine the transmission through the detector. On the other hand, a broadband source can also be used to interrogate the grating. At the output, an optical band-pass filter can be used to transmit only a fixed bandwidth of the signal to the detector. The band-pass filter should again be centered on either side of the peak loss band of the resonance band. These schemes are easy to implement, and unlike conventional Bragg gratings, the requirement of complex and expensive interferometric demodulation schemes is not necessary [22].

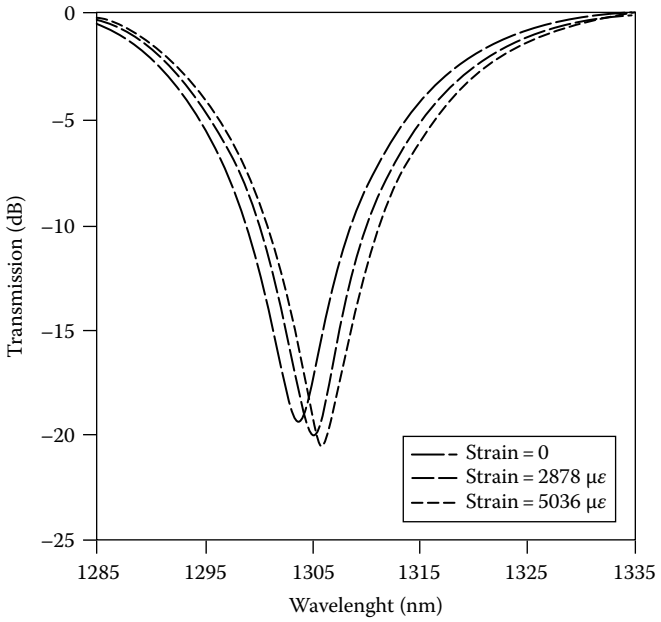

FIGURE 33.13 Shift induced by strain in a grating written in fiber C.

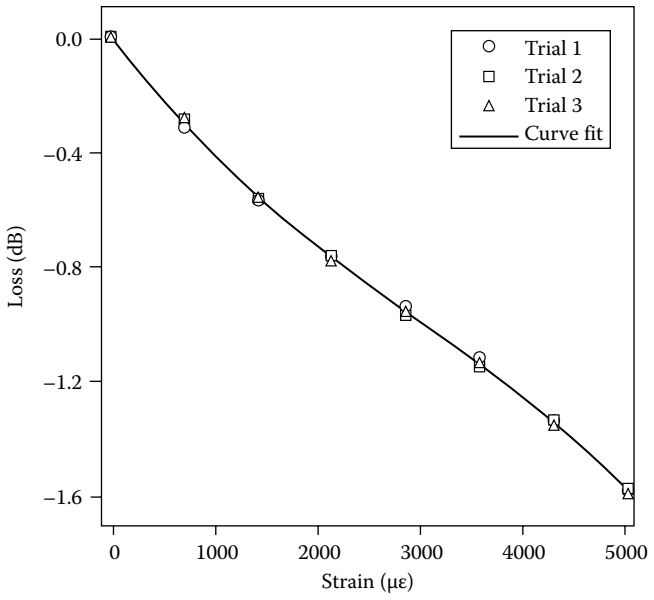

FIGURE 33.14 Plot of the change in transmitted intensity as a function of strain, for three different trials.

33.4.3 Temperature Sensitivity of Long-Period Gratings

Gratings written in different fibers were also tested for their cross sensitivity to temperature [22]. The temperature coefficients of wavelength shift for different fibers are shown in Table 33.2. The temperature sensitivity of an FBG is 0.014 nm °C^{-1}. Hence, the temperature sensitivity of a long-period grating is typically an order of magnitude higher than that of a Bragg grating. This large cross sensitivity to ambient temperature can degrade the strain sensing performance of the system unless the output signal

TABLE 33.2 Temperature Sensitivity of Long-Period Gratings Written in Four Different Types of Fibers

Type of Fiber	Temperature Sensitivity (nm °C^{-1})
A—DSF	0.062
B—Standard 1550 nm communication fiber	0.058
C—Conventional 980 nm single-mode fiber	0.154
D—Conventional 1060 nm single-mode fiber	0.111

Note: The values correspond to the shift in the highest-order resonance wavelength.

is adequately compensated. Multiparameter sensing using long-period gratings has been proposed to obtain precise strain measurements in environments with temperature fluctuations [21].

In summary, long-period grating sensors are highly versatile. These sensors can easily be used in conjunction with simple and inexpensive detection techniques. Experimental results prove that these methods can be used effectively without sacrificing the enhanced resolution of the sensors. Long-period grating sensors are insensitive to the input polarization and do not require coherent optical sources. The cross sensitivity to temperature is a major concern while using these gratings for strain measurements.

33.5 Comparison of Sensing Schemes

Based on the aforementioned results, the interferometric sensors have a high sensitivity and bandwidth but are limited by the nonlinearity in their output signals. Conversely, intrinsic sensors are susceptible to ambient temperature changes, while the grating-based sensors are simpler to multiplex. Each may be used in specific applications.

33.6 Conclusion

We have investigated the performance of four different interferometric and grating-based sensors. This analysis was based on the sensor-head fabrication and cost, signal processing, cross sensitivity to temperature, resolution, and operating range. The relative merits and demerits of the various sensing schemes were also discussed.

References

1. J. Sirkis, Phase-strain-temperature model for structurally embedded interferometric optical fiber strain sensors with applications, *Fiber Optic Smart Structures and Skins IV*, Boston, MA, *Proc. SPIE*, 1588, 26–43, 1991.
2. R. O. Claus, M. F. Gunther, A. Wang, and K. A. Murphy, Extrinsic Fabry-Perot sensor for strain and crack opening displacement measurements from −200 to 900°C, *J. Smart Mater. Struct.*, 1, 237–242, 1992.
3. K. A. Murphy, M. F. Gunther, A. M. Vengsarkar, and R. O. Claus, Fabry-Perot fiber optic sensors in full-scale fatigue testing on an F-15 aircraft, *Appl. Opt.*, 31, 431–433, 1991.
4. V. Bhatia, C. A. Schmid, K. A. Murphy, R. O. Claus, T. A. Tran, J. A. Greene, and M. S. Miller, Optical fiber sensing technique for edge-induced and internal delamination detection in composites, *J. Smart Mater. Struct.*, 4, 164–169, 1995.
5. V. Bhatia, M. J. de Vries, K. A. Murphy, R. O. Claus, T. A. Tran, and J. A. Greene, Extrinsic Fabry-Perot interferometers for absolute measurements, *Fiberopt. Prod. News*, 9(December), 12–13, 1994.
6. V. Bhatia, M. B. Sen, K. A. Murphy, and R. O. Claus, Wavelength-tracked white light interferometry for highly sensitive strain and temperature measurements, *Electron. Lett.*, 32, 247–249, 1996.

7. C. E. Lee and H. F. Taylor, Fiber-optic Fabry-Perot temperature sensor using a low-coherence light source, *J. Lightwave Technol.*, 9, 129–134, 1991.
8. J. A. Greene, T. A. Tran, K. A. Murphy, A. J. Plante, V. Bhatia, M. B. Sen, and R. O. Claus, Photoinduced Fresnel reflectors for point-wise and distributed sensing applications, *Proceedings of the Conference on Smart Structures and Materials, SPIE'95*, San Jose, CA, paper 2444-05, February 1995.
9. K. O. Hill, Y. Fuijii, D. C. Johnson, and B. S. Kawasaki, Photosensitivity in optical fiber waveguides: Applications to reflection filter fabrication, *Appl. Phys. Lett.*, 32, 647, 1978.
10. G. Meltz, W. W. Morey, and W. H. Glenn, Formation of Bragg gratings in optical fibers by transverse holographic method, *Opt. Lett.*, 14, 823, 1989.
11. P. J. Lemaire, A. M. Vengsarkar, W. A. Reed, V. Mizrahi, and K. S. Kranz, Refractive index changes in optical fibers sensitized with molecular hydrogen, *Proceedings of the Conference on Optical Fiber Communications, OFC'94*, San Jose, CA, Technical Digest, paper TuLl, 47, 1994.
12. R. Kashyap, Photosensitive optical fibers: Devices and applications, *Opt. Fiber Technol.*, 1, 17–34, 1994.
13. D. Z. Anderson, V. Mizrahi, T. Ergodan, and A. E. White, Phase-mask method for volume manufacturing of fiber phase gratings, *Proceedings of the Conference on Optical Fiber Communication*, San Jose, CA, post-deadline paper PD16, 1993, p. 68.
14. A. D. Kersey and T. A. Berkoff, Fiber-optic Bragg-grating differential-temperature sensor, *IEEE Photonics Technol. Lett.*, 4, 1183–1185, 1992.
15. V. Bhatia, M. B. Sen, K. A. Murphy, A. Wang, R. O. Claus, M. E. Jones, J. L. Grace, and J. A. Greene, Demodulation of wavelength-encoded optical fiber sensor signals using fiber modal interferometers, *SPIE Photonics East*, Philadelphia, PA, paper 2594-09, October 1995.
16. M. G. Xu, L. Dong, L. Reekie, J. A. Tucknott, and J. L. Cruz, Chirped fiber gratings for temperature-independent strain sensing, *Proceedings of the. First OSA Topical Meeting, Photosensitivity and Quadratic Non-linearity in Glass Waveguides: Fundamentals and Applications*, Monterey, CA, paper PMB2, 1995.
17. K. O. Hill, B. Malo, K. Vineberg, F. Bilodeau, D. Johnson, and I. Skinner, Efficient mode-conversion in telecommunication fiber using externally written gratings, *Electron. Lett.*, 26, 1270–1272, 1990.
18. F. Bilodeau, K. O. Hill, B. Malo, D. Johnson, and I. Skinner, Efficient narrowband $LP_{01} \leftrightarrow LP_{02}$ mode convertors fabricated in photosensitive fiber: Spectral response, *Electron. Lett.*, 27, 682–684, 1991.
19. A. M. Vengsarkar, P. J. Lemaire, J. B. Judkins, V. Bhatia, J. E. Sipe, and T. E. Ergodan, Long-period fiber gratings as band-rejection filters, *Proceedings of the Conference on Optical Fiber Communications, OFC '95*, Washington, DC, post-deadline paper, PD4-2, 1995.
20. A. M. Vengsarkar, P. J. Lemaire, J. B. Judkins, V. Bhatia, J. E. Sipe, and T. E. Ergodan, Long-period fiber gratings as band-rejection filters, *J. Lightwave Technol.*, 14, 58–65, 1996.
21. V. Bhatia, M. B. Burford, K. A. Murphy, and A. M. Vengsarkar, Long-period fiber grating sensors, *Proceedings of the Conference on Optical Fiber Communication*, San Jose, CA, paper ThPl, February 1996.
22. V. Bhatia and A. M. Vengsarkar, Optical fiber long-period grating sensors, *Opt. Lett.*, 21, 692–694, 1996.
23. C. D. Butter and G. B. Hocker, Fiber optics strain gage, *Appl. Opt.*, 17, 2867–2869, 1978.
24. J. S. Sirkis and H. W. Haslach, Interferometric strain measurement by arbitrarily configured, surface mounted, optical fiber, *J. Lightwave Technol.*, 8, 1497–1503, 1990.

Further Readings

Crisp, J. and Elliott, B., *Introduction to Fiber Optics*, 3rd edn., Elsevier, Oxford, U.K., 2005.

Downing, J. N., *Fiber Optic Communication*, Thomson Delmar, Clifton Park, NY, 2005.

Elsevier, Recent optical fiber technology articles. http://www.journals.elsevier.com/optical-fiber-technology/recent-articles/ (accessed on August 2, 2012).

Hecht, J., *Understanding of Fiber Optics*, 5th edn., Prentice Hall, Upper Saddle Drive, NJ, 2005.

34

Optical Beam Deflection Sensors

Grover C. Wetsel
University of Texas at Dallas

Measurements of the intensity of the light reflected and transmitted by a sample have been sources of information concerning the structure of matter for over a century. In recent decades, it has been found that measurement of the position of an optical beam that has scattered from a sample is an important and versatile means of characterizing materials and the motion of devices. Surely, the availability of a well-collimated beam from a laser has been crucial in the development of techniques and applications of *optical beam deflection* (OBD) sensing; however, the development and ready availability of various types of *position-sensing detectors* (PSDs) have also been important factors. OBD may be caused, for example, by propagation of a laser beam through a refractive-index gradient or by reflection from a displaced surface. A PSD provides an electronic signal that is a function of the laser beam position on the detector.

In this section, applications of OBD sensing are reviewed, the theories of operation of the three most common types of OBD sensors are developed, and typical operational characteristics of the devices are presented. The advantages and disadvantages of the various PSDs are also discussed.

A schematic diagram of the basic OBD sensing configuration is illustrated in Figure 34.1. In this case, the displacement, u, of the surface causes the position of the reflected beam on the PSD to move from point P to point P′; the positional change produces a change in the output voltage of the PSD. The output voltage, V, of the PSD electronics can be calibrated in terms of the actual displacement, u, by measuring V versus u for known displacements.

OBD sensing has been used in a variety of applications, including photothermal optical beam deflection (PTOBD) spectroscopy [1], absolute measurement of optical attenuation [2], PTOBD imaging of surface and subsurface structure [3], photothermal displacement spectroscopy [4], atomic-force microscopy [5], and materials characterization [6]. It has also been used as an uncomplicated, sensitive, and accurate method of measurement of surface motion for scanning tunneling microscope scanner transducers [7] and ultrasonic transducer imaging [8].

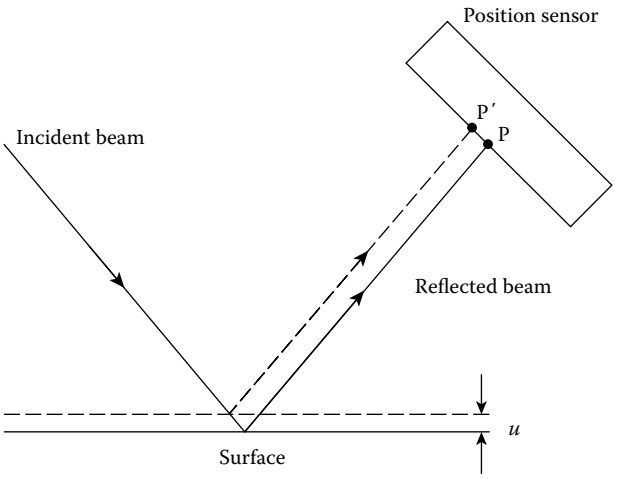

FIGURE 34.1 A schematic diagram of the basic OBD sensing configuration.

34.1 Theory

The three basic types of devices for OBD sensing are (1) a photodetector behind a sharply edged screen (a knife edge), (2) a small array of photodetectors separated by relatively small, insensitive areas (bicell, quadcell), and (3) a continuous solid-state position sensor (1-D or 2-D). Sensing characteristics of a device are determined by the effect of optical beam displacement on the photodetector power distribution. Since laser beams are commonly used in OBD sensing, the analysis involves the assumption that the spatial distribution of the intensity (I) in the plane perpendicular to the direction of wave propagation is axially symmetric with a Gaussian radial variation.

34.1.1 Knife-Edge Photodetector

The essential features of a PSD are represented by a photodetector shadowed by a semi-infinite knife edge, $y < 0$, as illustrated in Figure 34.2. As can be anticipated from the symmetry of the arrangement and proved mathematically, the maximal deflection sensitivity occurs when the undeflected beam is centered on the knife edge. The intensity of the light reaching the photodetector due to the displacement (u) of the center of the beam is given in the reference frame of the displaced beam by

$$I(r') = \frac{aP}{\pi} e^{-ar'^2} \tag{34.1}$$

where

P is the total incident beam power
$a = 2/r_1^2$
r_1 is the Gaussian beam radius
$r'^2 = x'^2 + y'^2$

In terms of the coordinates (x, y) of the undeflected beam, the rectangular coordinates of the deflected beam are $x' = x$ and $y' = y - u$. The power (P_d) on the detector is thus given by

$$P_d = \frac{aP}{\pi} \int_0^\infty e^{-a(y-u)^2} dy \int_{-\infty}^{\infty} e^{-ax^2} dx = \frac{P}{2}\left[1 + erf\left(\sqrt{2}\,\frac{u}{r_1}\right)\right] \tag{34.2}$$

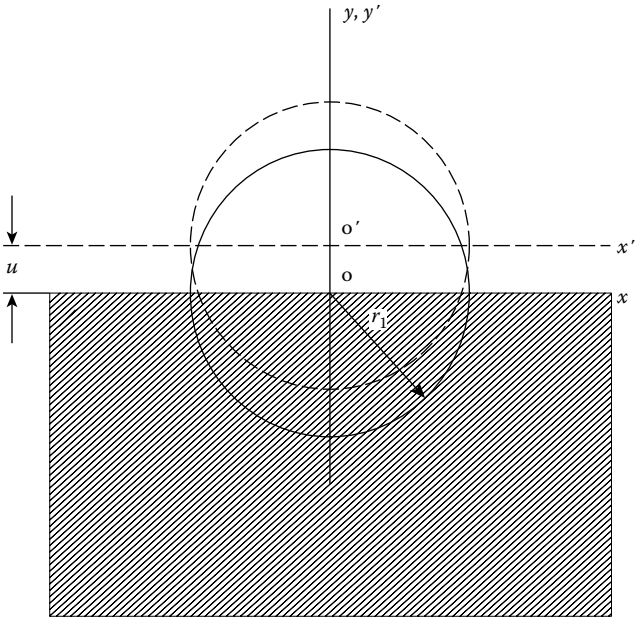

FIGURE 34.2 Essential features of a position-sending detector (PSD), as represented by a photodetector shadowed by a semi-infinite knife edge.

where *erf* is the error function. One can see by inspection of Equation 34.2 that the essential characteristics of this position sensor are determined by u/r_1. The normalized response, P_d/P, is shown in Figure 34.3 as a function of u/r_1. When $u = r_1$, then $P_d = 97.7\%\ P$.

The deflection sensitivity is given by the slope of Equation 34.2:

$$\frac{dP_d}{du} = \sqrt{\frac{2}{\pi}}\frac{P}{r_1}e^{-2(u/r_1)^2},\ \text{with}\left(\frac{dP_d}{du}\right)_{max} = \left(\frac{dP_d}{du}\right)_{u=0} = \sqrt{\frac{2}{\pi}}\frac{P}{r_1} \tag{34.3}$$

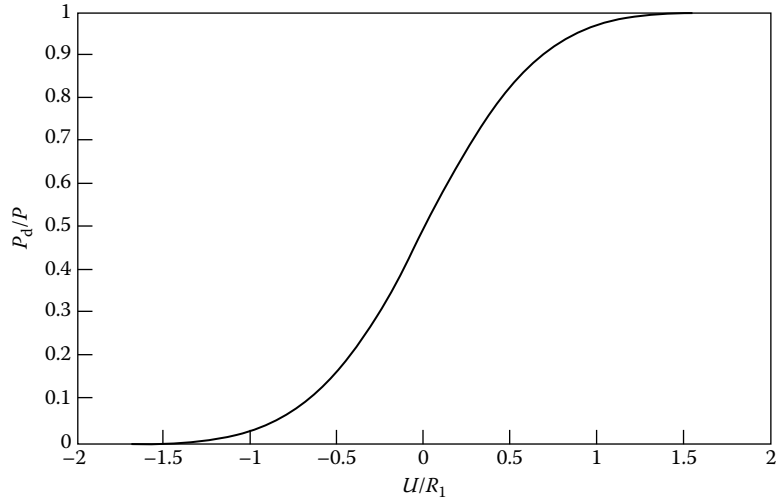

FIGURE 34.3 The normalized response P_d/P as a function of u/r_1. u, displacement of center of beam; r_1, Gaussian beam radius; P_d, power on the detector; P, total incident beam power.

Define the small-signal position sensor sensitivity (units of m^{-1}):

$$\alpha_{KE} \equiv \frac{1}{P}\left(\frac{dP_d}{du}\right)_{u=0} = \frac{1}{r_1}\sqrt{\frac{2}{\pi}} \tag{34.4}$$

The optical power reaching the photodetector for small signals is then given by

$$P_d \cong \frac{P}{2} + \left(\frac{dP_d}{du}\right)_{u=0} u = \frac{P}{2} + \alpha u P = \frac{P}{2}[1 + 2\alpha u] \tag{34.5}$$

The photodetector signal will be linear in displacement if $u \leq 0.387 r_1$.

The photocurrent is

$$I = KP_d \cong \frac{KP}{2}[1 + 2\alpha u] \tag{34.6}$$

where K is the photodetector responsivity in A W^{-1}. The position sensor voltage is obtained using a transimpedance amplifier with gain Z:

$$V = KZP_d \cong \frac{KZP}{2}[1 + 2\alpha u] \tag{34.7}$$

34.1.2 Bicell Detector

The deflection of a Gaussian beam initially centered in the insensitive gap of a bicell detector is illustrated in Figure 34.4. The power incident on the upper half of the bicell is given by

$$P_2 = \frac{aP}{\pi}\int_{y_2}^{\infty} e^{-a(y-u)^2} dy \int_{-\infty}^{\infty} e^{-ax^2} dx = \frac{P}{2}\left[1 - erf\left(\frac{\sqrt{2}}{r_1}(y_2 - u)\right)\right] \tag{34.8}$$

The power incident on the lower half of the bicell is given by

$$P_1 = \frac{aP}{\pi}\int_{-\infty}^{-y_1} e^{-a(y-u)^2} dy \int_{-\infty}^{\infty} e^{-ax^2} dx = \frac{P}{2}\left[1 - erf\left(\frac{\sqrt{2}}{r_1}(y_1 + u)\right)\right] \tag{34.9}$$

The photocurrent from each detector of the bicell is converted to voltage by identical transimpedance amplifiers: $V_2 = KZP_2$ and $V_1 = KZP_1$; a difference amplifier is then used to obtain the bicell signal voltage:

$$V = V_2 - V_1 = KZ(P_2 - P_1) = \frac{KZP}{2}\left[erf\left(\frac{\sqrt{2}}{r_1}(y_1 + u)\right) - erf\left(\frac{\sqrt{2}}{r_1}(y_2 - u)\right)\right] \tag{34.10}$$

The normalized response, $2V/(KZP)$, is shown in Figure 34.5 as a function of u/r_1 for $y_1 = y_2 = r_1/10$.

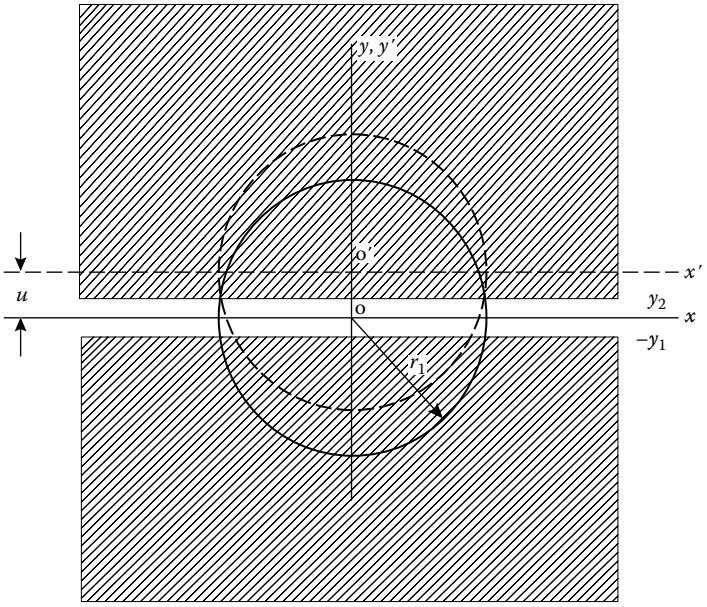

FIGURE 34.4 Deflection of a Gaussian beam initially centered in the insensitive gap of a bicell detector.

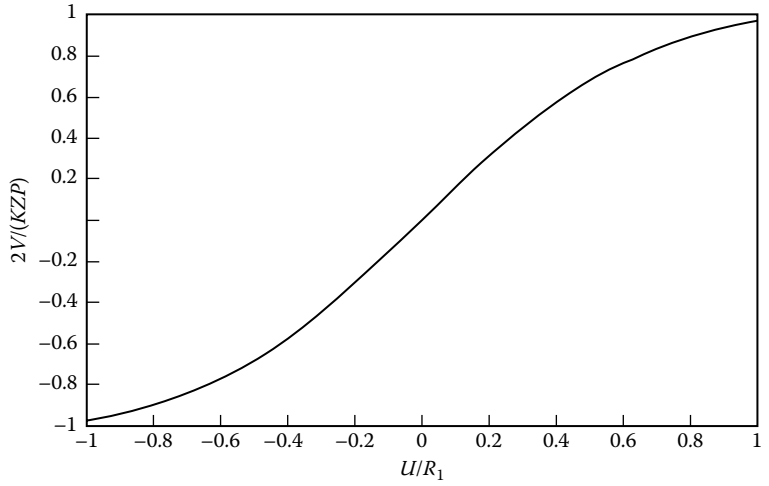

FIGURE 34.5 The normalized response $2V/KZP$ in a bicell detector as a function of u/r_1 for $y_1 = y_2 = r_1/10$.

Suppose that the beam is centered in the gap, $y_1 = y_2$; then, for small displacements, one obtains

$$V \cong 2\sqrt{\frac{2}{\pi}}\frac{KZPu}{r_1}e^{-2(y_1/r_1)^2} \tag{34.11}$$

The small-signal sensitivity is

$$\alpha_{BC} \equiv \frac{1}{KZP}\left(\frac{dV}{du}\right)_{u=0} = 2\sqrt{\frac{2}{\pi}}\frac{e^{-2(y_1/r_1)^2}}{r_1} \tag{34.12}$$

This quantity is optimized when $r_1 = 2y_1$ and the optimal sensitivity is $0.484/y_1$.

34.1.3 Continuous Position Sensor

The position information in a continuous position sensor (also known as a lateral-effect photodiode) is derived from the divided path taken by photon-generated electrons to two back electrodes on the device. For a homogeneous device, the current to an electrode depends only on the distance of the centroid of the light beam from that electrode; the currents would be equal in an ideal device when the beam is located at its electrical center.

Consider the analysis of a 1-D continuous PSD. The current signal from each electrode is converted to a voltage signal by a transimpedance amplifier with gain, Z. Operational amplifiers are then used to provide the sum signal, $V_s = KPZA_s$, and the difference signal, $V_d = KPZA_d\alpha u$, where A_s and A_d are the sum and difference amplifier gains, respectively. The position sensor sensitivity, α, is then given by

$$\alpha \equiv \frac{V_d A_s}{u V_s A_d} \tag{34.13}$$

which is determined by measuring V_d and V_s as a function of u.

34.2 Characterization of PSDs

The PSD characteristics presented here were measured by mounting the device to a translation stage with an optical encoder driven by a piezoelectric motor [9]; the position accuracy was ±0.1 μm. An appropriately attenuated He–Ne laser beam was directed at normal incidence to the PSD as it was translated past the beam. The PSD sum and difference voltages were measured with GP–IB digital voltmeters as a function of displacement, and the PSD displacements and voltage measurements were computer controlled.

The operation of a knife-edge PSD can be evaluated using the signal from one side of a bicell as well as from a photodetector behind a knife edge. The transimpedance amplifier output voltage corresponding to the current signal from one cell of a United Detector Technology [10] (UDT) SPOT2D bicell is shown as a function of displacement in Figure 34.6. The data are plotted as normalized cell voltage as a function of u/r_1. Since the signal from one cell of a bicell is equivalent to a knife-edge photodetector, the data can be compared with Figure 34.3. The data are in reasonable agreement for $u/r_1 < 1$, and a best fit allows the inference of $r_1 = 0.4$ mm; the disagreement for $u/r_1 \geq 1$ corresponds to the laser beam partially moving off the outside edge of the cell.

The operation of a bicell PSD is evaluated by the data of Figure 34.7, which shows the difference voltage as a function of displacement for the UDT SPOT2D. The deviations from the theoretical curve of

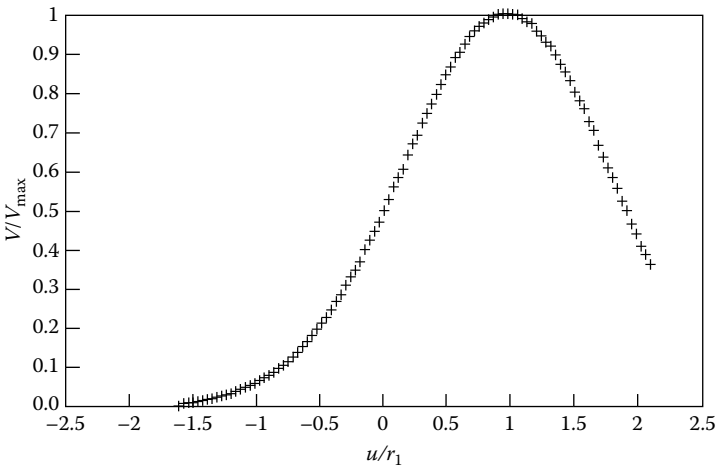

FIGURE 34.6 Transimpedance amplifier output voltage corresponding to the current signal from one cell of a UDT SPOT2D bicell as a function of displacement. Data are plotted as normalized cell voltage versus u/r_1.

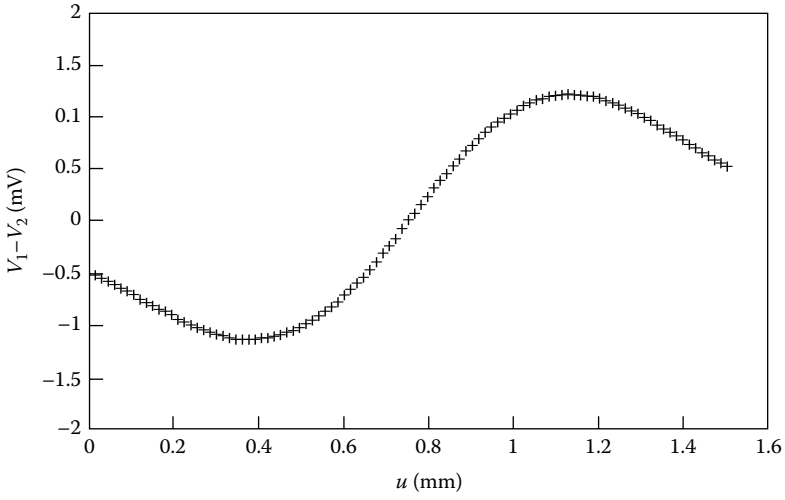

FIGURE 34.7 Difference voltage as a function of displacement for the UDT SPOT2D bicell.

Figure 34.5 for $u \leq 0.4$ mm and $u \geq 1.1$ mm are due to the beam moving off the outside edges of the bicell. The linear region of the PSD is centered at the optimal quiescent point ($V_1 - V_2 = 0$); a least-squares fit of a straight line gives a slope of $A_{12} = 4.88$ mV μm^{-1} for this device. For the data of Figures 34.6 and 34.7, $P = 0.37$ mW and $Z = 5$ kΩ; thus, the experimental value of the responsivity is determined to be $K_{exp} = 0.65$ A W^{-1}. The nominal gap size of the SPOT2D bicell is such that $y_1 = 63.5$ μm; thus, using this value of y_1 and $r_1 = 0.4$ mm in Equation 34.12, the calculated bicell sensitivity is 3.8×10^3 m^{-1}. The experimental value of sensitivity is calculated from A_{12}, K_{exp}, P, and Z to be 4.1×10^3 m^{-1}.

Evaluation of the operation of the x-axis of a UDT SC10 two-axis continuous PSD is illustrated in Figures 34.8 through 34.10. The PSD was oriented such that the y-axis was vertical; thus, ideally, V_{dy} is constant as the PSD is translated, except near the edges of the 10 mm × 10 mm device. As shown in Figure 34.8, V_{sx} is virtually constant except near the edges of the device; this means that the optical responsivity (K) does not greatly vary with the laser beam position on this detector. Variation of V_{dx} with displacement is shown in Figure 34.9; this PSD has a broad linear range. The linearity of continuous PSDs can often be improved by using the ratio, V_{dx}/V_{sx}, as shown in Figure 34.10; the sensitivity of this PSD is determined from a least-squares fit of the linear part of this characteristic to be 183 m^{-1}.

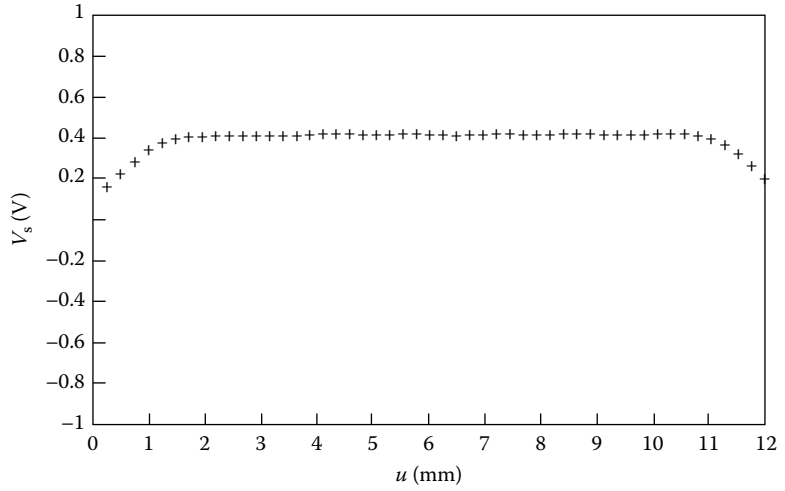

FIGURE 34.8 Sum voltage versus displacement for x-axis of UDT SCIO continuous PSD.

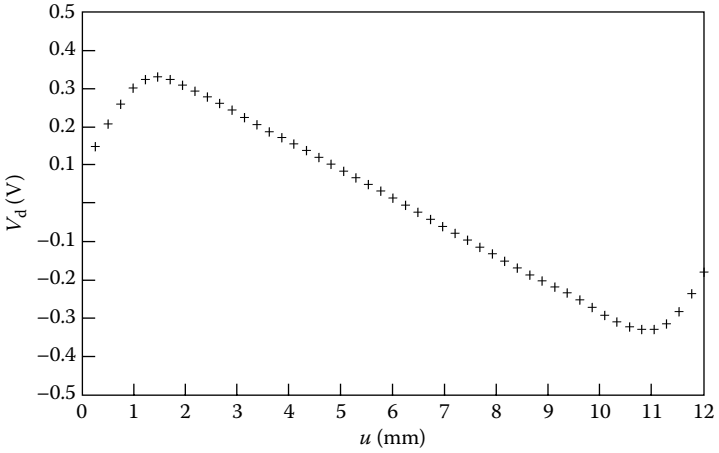

FIGURE 34.9 Difference voltage versus displacement for x-axis of UDT SCIO continuous PSD.

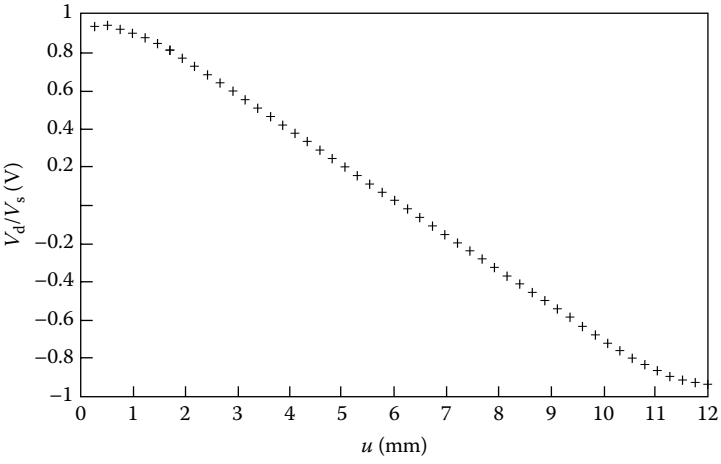

FIGURE 34.10 Ratio of difference voltage to sum voltage versus displacement for x-axis of UDT SCIO continuous PSD.

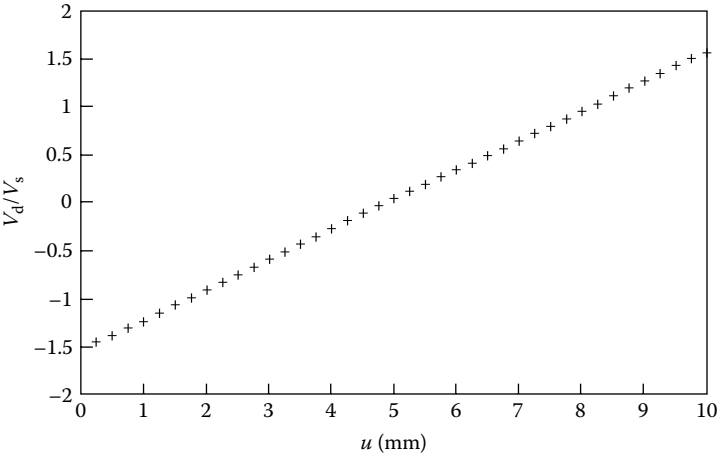

FIGURE 34.11 Ratio of difference voltage to sum voltage versus displacement for SiTek 1L10 continuous PSD.

A newer class of PSDs is represented by the SiTek [11] 1L10 single-axis continuous PSD, which is typically more linear. An example of the V_d/V_s versus u characteristic is shown in Figure 34.11. The sensitivity is determined from a least-squares fit of the linear part of the characteristic to be 307 m^{-1}.

34.3 Summary

A PSD composed of a knife-edge photodetector is simple, has a sensitivity that depends only on the radius of the laser beam, and has a response time determined by the photodetector. Thus, for fast rise-time detection of small displacements, this type of PSD is to be preferred.

The maximal sensitivity of a bicell is about 20% greater than that of a knife-edge photodetector. It has the advantages of small size and economy. The nominal risetime of the UDT SPOT2D is of the order of 10 ns. Furthermore, two-axis detection can be readily obtained with a quadcell, with an increase in risetime due to the increased capacitance of the detector.

The disadvantages due to small laser beam sizes and small displacements are overcome by the continuous PSDs. Since these devices are typically much larger (available in several-inch diameters), they typically have longer risetimes than the other PSDs. However, the Sitek 1L10, with a 10 mm linear active range, has a measured upper half-power frequency of 3 MHz.

In applications where the output signal from a PSD must be linearly proportional to the displacement of the beam, analog-divider operational amplifiers to obtain V_d/V_s in real time are used to extend the range of linearity of the device. Unfortunately, the frequency response of these amplifiers is often the frequency-response-limiting factors of the PSD system. In cases where high-frequency response is important, V_d alone can often be used if care is taken to operate in the linear range of the device. For large static displacements that are of the order of the size of the detector, V_d and V_s can be recorded with computer-controlled data acquisition, the calibration characteristic numerically fitted to a polynomial, and then any voltage from the detector can be related to beam position.

The noise limitations in OBD sensing are due to the laser, the nature of the reflecting surface, and the PSD. Lasers with good amplitude stability are to be preferred, but this is not an important contribution to noise when V_d/V_s is used to infer displacement. Laser beam-pointing stability, on the other hand, is important. If the reflecting surface is that of a typical solid, then negligible noise is introduced on reflection; this may not be true for a reflector such as a pellicle, where Brownian motion of the surface may be significant. The noise limitations of the PSD are the usual ones associated with the photodetector and the amplifiers.

References

1. A. C. Boccara, D. Fournier, and J. Badoz, *Appl. Phys. Lett.*, 30, 933, 1983.
2. G. C. Wetsel, Jr. and S. A. Stotts, *Appl. Phys. Lett.*, 42, 931, 1983.
3. D. Fournier and A. C. Boccara, In *Scanned Image Microscopy*, E. A. Ash (Ed.), London, U.K.: Academic Press, 1980, pp. 347–351; J. C. Murphy and L. C. Aaamodt, *Appl. Phys. Lett.*, 39, 519, 1981; G. C. Wetsel, Jr. and F. A. McDonald, *Appl. Phys. Lett.*, 41, 926, 1982.
4. M. A. Olmstead, S. Kohn, N. M. Amer, D. Fournier, and A. C. Boccara, *Appl. Phys. A*, 132, 68, 1983.
5. G. Meyer and N. M. Amer, *Appl. Phys. Lett.*, 53, 1045, 1988.
6. J. C. Murphy and G. C. Wetsel, Jr., *Mater. Eval.*, 44, 1224, 1986.
7. G. C. Wetsel, Jr., S. E. McBride, R. J. Warmack, and B. Van de Sande, *Appl. Phys. Lett.*, 55, 528, 1989.
8. S. E. McBride and G. C. Wetsel, Jr., Surface-displacement imaging using optical beam deflection, In *Review of Progress in Quantitative Nondestructive Evaluation*, Vol. 9A, D. O. Thompson and D. E. Chimenti (Eds.), New York: Plenum, 1990, pp. 909–916.
9. Burleigh Instruments, Inc., Fishers, NY.
10. United Detector Technology, Hawthorne, CA.
11. On-Trak Photonics, Inc., Lake Forest, CA.

Further Readings

Alwyn, V., *Fiber-Optic Technologies*, Cisco Press, Indianapolis, IN, April 2004. http://www.ciscopress.com/articles/article.asp?p=170740 (accessed on July 22, 2012).

Crisp, J. and Elliott, B., *Introduction to Fiber Optics*, 3rd edn., Elsevier, Oxford, U.K., 2005.

Elsevier, Recent optical fiber technology articles. http://www.journals.elsevier.com/optical-fiber-technology/recent-articles/ (accessed on August 2, 2012).

Hecht, J., *Understanding of Fiber Optics*, 5th edn., Prentice Hall, Upper Saddle Drive, NJ, 2005.

Oliver, B., An introduction to fiber optic technology, Ezine Articles. http://ezinearticles.com/?An-Introduction-to-Fiber-Optic-Technology&id=1363984 (accessed on July 23, 2012).

35

Velocity Measurement

Charles P. Pinney
Pinney Technologies, Inc.

William E. Baker
University of New Mexico

35.1 Introduction

The *linear velocity* of an object, or more correctly a particle, is defined as the time rate of change of position of the object. It is a vector quantity, meaning it has a direction as well as a magnitude, and the direction is associated with the direction of the change in position. The magnitude of velocity is called the speed (or pace), and it quantifies how fast an object is moving. This is what the speedometer in a car tells you; thus, the speedometer is well named. Linear velocity is always measured in terms of, or from, some reference object. Thus, the speedometer of a car tells how fast one is moving relative to the earth. Usually, linear velocity is identified using only the term "velocity." Common units for velocity include meters per second and miles per hour, but any similar combination of units of length per unit of time is correct.

The *rotational velocity* (or angular velocity) of an object is defined as the time rate of change of angular position, and it is a measure of how fast an object is turning. It is completely analogous to linear velocity but for angular motion. Common units are revolutions per minute, but any angular unit of measurement per unit of time can be used. Rotational velocity is a vector quantity also, with the direction of the vector being the same as the direction of the axis about which object is turning. For example, with a car stopped at a stop light with the motor running, the rotational velocity of the crankshaft of the motor is given by a magnitude (rotational speed), say, 800 rpm (rev/min), and a direction associated with the direction in which the crankshaft is pointing. The axis of rotation of the object may be moving, rather than fixed as when the car is turning a corner. The roll, yaw, or pitch velocity of an airplane would be given in terms of rotational speeds about each of the turning axes in the same manner as for a crankshaft.

Usually, the reference from which linear or rotational velocity is given is understood from the context of the problem. It is often not stated explicitly. The measurement method used defines the reference.

Applications for velocity measurement include the following:

1. Controlling the speed at which metal stock is fed into a machine tool. If the metal is fed too quickly, the result could be premature tool wear or it could even lead to machine failure. Feeding the material too slowly will reduce the yield of the machine tool.
2. Measuring the approach speed of a robotic tool onto its target.
3. Monitoring the speed of a generator in an electric power station.
4. An airport radar system measuring the speed of an approaching aircraft using the Doppler effect.
5. Measuring an automobile's wheel speed in order to provide feedback to an antilock brake system.

35.2 Measurement of Linear Velocity

The problem of velocity measurement is somewhat different from that of measurement of other quantities in that there are not a large number of transducer types and transducer manufacturers from which to choose for a given problem. Frequently, the problem is such that the person must use his/her knowledge of measurement of other quantities and ingenuity to develop a velocity measurement method suitable for the problem at hand. Velocity is often obtained by differentiation of displacement or integration of acceleration. As background information for this, the necessary equations are given later.

Figure 35.1 shows a graph that represents the position of an object as a function of time as it moves along a straight, vertical path (y direction). The quantity to be measured could be an average velocity, and its magnitude would then be defined as follows:

$$\text{Average speed} = V_{\text{avg}} = \frac{y_2 - y_1}{t_2 - t_1} = \frac{\Delta y}{\Delta t} \tag{35.1}$$

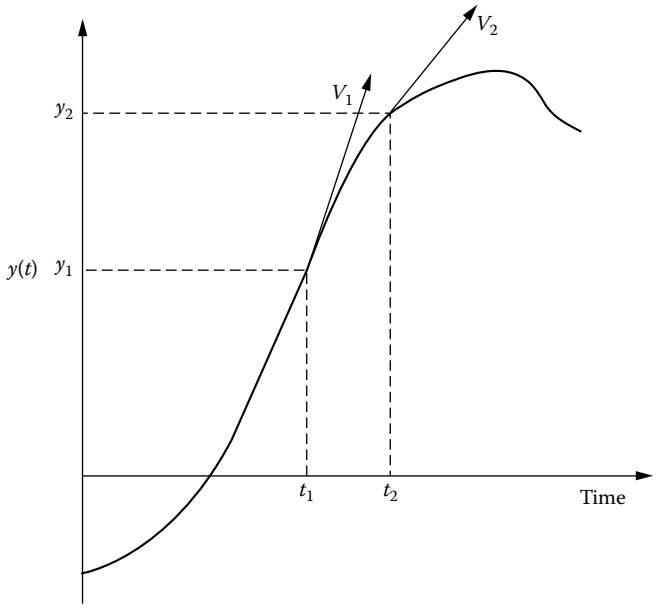

FIGURE 35.1 Position–time function for an object moving on a straight path.

for the time interval t_1 to t_2. As the time interval becomes small, the average speed becomes the instantaneous speed V_y, and the definition becomes

$$V_y = \lim_{\Delta t \to 0} \frac{\Delta y}{\Delta t} = \frac{dy}{dt} \tag{35.2}$$

which is the slope of the position–time curve. The subscript indicates the y component. This speed, when associated with the known direction, becomes the velocity.

Since acceleration is defined as the time rate of change of velocity, the speed of an object may also be given by

$$V_y(t) = V_i - \int_{t_i}^{t} a_y(t)dt \tag{35.3}$$

where

$a_y(t)$ is the acceleration in the y direction (for Figure 35.1)
V_i is the speed at time t_i

Each of the preceding equations can be used as a basis for making a velocity measurement. Note that for motion in more than one dimension, there would be more than one component, and there would be corresponding equations for the other dimensions (x and y). However, velocity measurements are always done by individual component.

It is convenient in the discussion of techniques of measuring velocity to divide the methods into two categories: one will be called "reference-based methods" and the other "seismic or inertial referenced transducers." Reference-based methods refer to measurements made for which the instrumentation has component(s) on both the moving object and the reference frame for the measurement. The seismic transducers do not require contact with the reference frame. However, they give a speed relative to the transducer speed at the start of the test. The initial motion must be determined from other considerations in the test setup and added to the relative speed.

35.3 Reference-Based Linear Velocity Measurement

Using Equation 35.1, one value of the average speed in a given direction of an object can be determined from the distance traveled in that direction and the time required. Determining the muzzle speed of a projectile is an example. Having two pickups spaced at known distance apart, and recording the time for the projectile edge to pass between them, is a common way of doing this. Typical pickups would include proximity transducers (see displacement measurement), laser or collimated light beams with diode sensors, and electric contacts closed (or opened) by the moving object. Measuring the time interval can be done with an electronic counter or displaying the output of the pickups on an oscilloscope. In designing such a system, care must be exercised to minimize or eliminate the effect to the object passing through the window on the positions of the sensors and their response. For example, pressure from a muzzle blast can move the sensors on their supports. This could distort the distance between them during the measurement, but afterward, the appearance of the setup could be unchanged, so the experimenter would be unaware of the error.

Using a series of equally spaced pickups can determine the average speed for a sequence of positions. For some applications, illumination of the path of motion of the object with a stroboscope flashing at a known rate and use of time exposure photography can give a single picture of the object at a sequence of positions. With knowledge of the length scale and the flash rate, the average speed at a sequence of

positions can be calculated. If the plane of motion is the same as the plane of the photograph, then two components of the velocity can be determined. A variation of this method is to use video recording of the motion and the time base of the video for measurement of time increments. Availability of high-speed video cameras, to 12,000 frames/s, extends the range of applicable velocities, and digital recording can enhance the ease and accuracy of making the distance measurements.

Another variation of this method is to use some type of position transducer to record the position–time function of the moving object and then differentiate this function to get speed–time. Displacement transducers were discussed in an earlier chapter, and the selection of an acceptable transducer is important. Range, resolution, and mass loading are important parameters. Because differentiation of experimental data is a noise-generating process, particular care must be exercised to reduce the electric noise in the displacement data to a minimum. Also, the calculated speed–time function might require some smoothing to reduce the numerically introduced noise.

One type of velocity transducer is based on a linear generator. When a coil cuts the magnetic field lines around a magnet, a voltage is induced in the coil, and this voltage is dependent on the following relation:

$$e_i \propto BLV \tag{35.4}$$

where

e_i is the induced voltage
B is the magnetic field strength
L is the length of wire in the coil
V is the speed of the coil relative to the magnet

This relation is used as the basis for linear velocity transducers, called LVTs, and a schematic is shown in Figure 35.2. Manufacturers of these transducers include Trans-Tek, Inc., of Ellington, CN; Robinson-Halpern Products of Valley Forge, PA; and the Macro Sensors, Div. of Howard A. Schaevitz Technologies, Inc., of Pennsauken, NJ. The working displacement ranges are from 0.5 to 24 in., and typical sensitivities are from 40 mV/ips (inches per second) to 600 mV/ips.

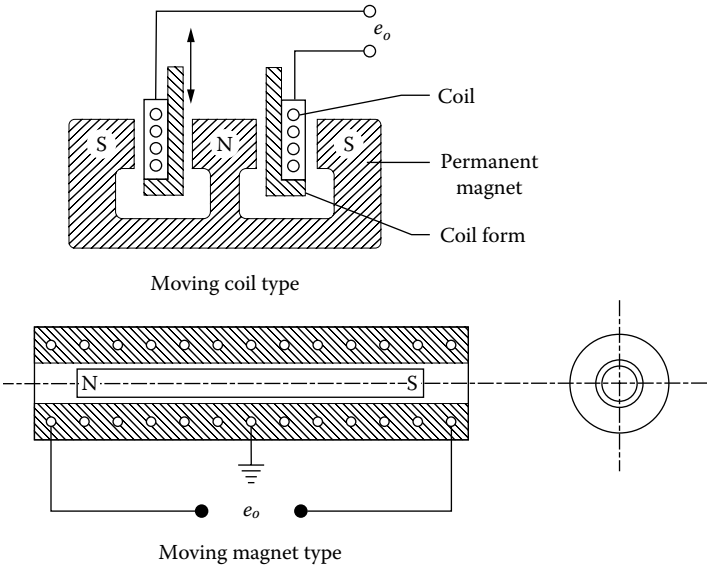

FIGURE 35.2 Velocity transducers (LVT).

35.3.1 Conversion of Linear to Rotational Velocity

A rotational dc generator (discussed in the next section) can also be used to measure linear velocities by placing a rack on the moving object and having the rack drive the generator through a pinion gear. This is the same principle by which a speedometer converts the linear velocity of an automobile to an angular velocity gage on the dashboard of a car.

35.3.2 Doppler Shift

The Doppler shift is an apparent change in the frequency of waves occurring when the source and observer are in motion relative to each other. This phenomenon is applicable to waves in general, for example, sound, light, and microwaves. It was first observed for sound waves, and it is named after the Austrian mathematician and physicist Christian Doppler (1803–1853) who first published a paper on it for light waves in 1842. The frequency will increase when the source and observer approach each other (red shift) and decrease when they move apart (blue shift). This phenomenon was illustrated by having people listen to the pitch of an oncoming train. The high-pitched whistle would transition to a lower pitch as the train passed the observer.

Radar, which is named for radio detection and ranging, is another technique for detecting the position, motion, and nature of a remote object by means of radio waves reflected from its surface. Pulse radar systems use a single directional antenna to transmit and receive the waves. They transmit pulses of electromagnetic waves (usually microwaves), some of which are reflected by objects in the path of the beam. Reflections are received by the radar unit, processed electronically, and converted into images on a cathode-ray tube. The antenna must be connected only to the transmitter when sending and only to the receiver while receiving; this is accomplished by switching from one to the other and back again in the fraction of a microsecond between pulses. The distance of the object from the radar source is determined by measuring the time required for the radar signal to reach the target and return. The direction of the object with respect to the radar unit is determined from the direction in which the pulses were transmitted. In most units, the beam of pulses is continuously rotated at a constant speed, or it is scanned (swung back and forth) over a sector at a constant rate. Pulse radar is used primarily for aircraft and naval navigation and for military applications. In Doppler radar, or continuous-wave radar, two antennas are used—one to transmit and the other to receive. Because the time a continuous-wave signal takes to reach the target and return cannot be measured, Doppler radar cannot determine distance. The velocity of the object is determined using the Doppler effect. If the object is approaching the radar unit, the frequency of the returned signal is greater than the frequency of the transmitted signal. If the object is receding, the returned frequency is less, and if the object is not moving relative to the radar unit, the frequency of the returned signal is the same as the frequency of the transmitted signal.

One value of this Doppler technology is shown on the evening weather broadcast. Radar can measure wind rotation inside a thunderstorm and identify possible tornadoes. The VORAD system by Eaton is an onboard system for vehicle safety. It detects when a dangerous approach to another vehicle is taking place. It will automatically apply the brakes in an emergency situation.

35.4 Light Interference Methods for Linear Velocity Measurement

Velocity measurements can be made using light interference principles. Figure 35.3 shows the setup used by Michelson in the 1890s to demonstrate light interference. A beam of monochromatic light is split into two beams. One beam is directed onto a stationary mirror. The other beam is directed onto a moving target. The observer sees the superposition of the two beams. As the mirror moves in one direction, summation of the waves of the two beams will alternately reinforce and cancel each other. The amount of motion for one cycle of light intensity variation is the wavelength of the light being used.

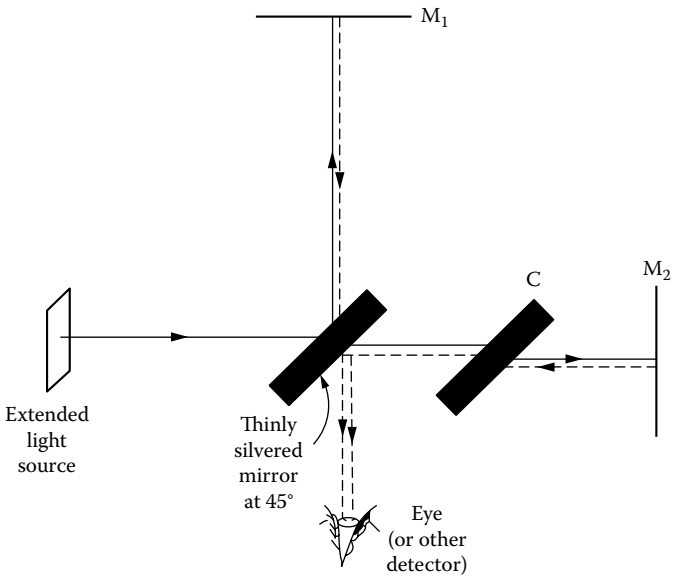

FIGURE 35.3 Basic components of a Michelson interferometer. The clear glass slab C is called a compensating plate. It has the same dimensions and orientation as the 45° mirror in order to make the light paths in glass equal along the two arms, a condition necessary when a white-light source is used. (From Hudson, A. and Nelson, R., *University Physics*, Harcourt Brace Jovanovich, New York, 1982. With permission.)

The frequency of these light-to-dark transitions is proportional to the velocity of the moving target. Highly accurate measurements are available with interferometer techniques. For example, 1 m is 1,650,763.73 fringe counts for the orange light emitted by krypton-86.

Refinements of this principle are needed for convenience of use. Lasers are used as the light source, for example. One commercial supplier of this type of device, commonly called a laser Doppler vibrometer, is Polytec PI, Inc., of Costa Mesa, CA. The basic principle gives velocity parallel to the laser beam, but Polytec PI also has a unit that utilizes scattered laser light that permits measurement of the in-plane velocity. It is called a laser surface velocimeter.

35.4.1 VISAR System

Another application of interferometry to the measurement of velocity–time profiles is a device called VISAR, for "velocity interference system for any reflector." Earlier interferometer systems had required that the target have a highly polished reflecting surface and that there be very little surface tilt during a test. The VISAR system functions with either specularly or diffusely reflecting surfaces and is quite insensitive to tilting of the target. It was developed for shock wave research work and is useful for measurement of very high speeds. Reference [3] gives a detailed description of the principles of operation.

The signal from the VISAR is generated with a photodiode or other light-sensitive device and is basically a measure of the rate of fringe variation. Additional data reduction is required to obtain speeds. The sensitivities of the devices are specified in "fringes per meter per second." Typical sensitivities are in the range of 100–4000 m/s per fringe.

The first VISARs were laboratory devices, individually assembled from the needed optical components. Commercial units are now available. Valyn International of Albuquerque, NM, makes VISARs and components. Figure 35.4 shows a schematic of a test setup. The standard measurement range, given as depth of field, of the VISAR is 12 mm, but systems measuring over 10 m have been used.

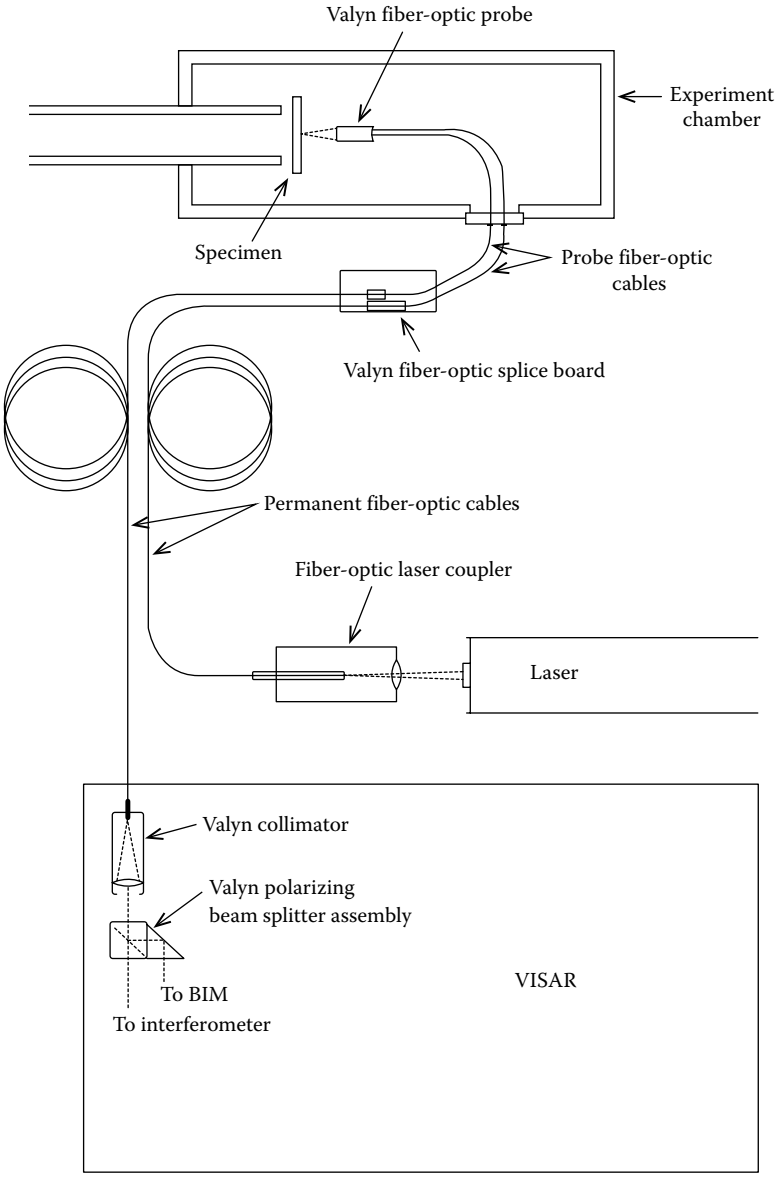

FIGURE 35.4 Schematic diagram showing how fiber-optic components, available from Valyn, can transport laser light to and from a shock experiment, minimizing any laser light beam hazards. (Courtesy of Valyn International, Albuquerque, NM.)

Applications for the VISAR include the following:

In-bore projectile velocity
Flyer plate velocity
Flying foil velocity
Hugoniot equation of state
Structural response to shock loading

35.5 Seismic Devices for Linear Velocity

The devices discussed in the previous section required a link of some type between the reference and the moving object. Seismic devices do not have this requirement. A seismic device refers to a transducer, which is based on a mass attached to the transducer base, usually with a linear spring. The base is attached to the surface whose motion is desired, and the motion of the seismic mass relative to the base is recorded with a motion transducer. Figure 35.5 shows the principal components of this transducer type. Use of the governing equation of motion for the seismic mass permits the determination of the motion of the base from the relative motion function.

If the motion transducer in the seismic instrument measures the displacement of the mass relative to the base, the output of the transducer is proportional to the acceleration of the transducer base for a specific frequency range, and the device is called an *accelerometer*. Acceleration measurement using this type of device (or with other types of accelerometers) permits the determination of the velocity–time function by integration through the application of Equation 35.3. In this equation, $a_y(t)$ would be determined from the output of the accelerometer.

The simplicity of this concept is evident, and because integration is a smoothing process, the numerically introduced noise encountered with a "differentiation of displacement" method of speed measurement does not occur. However, other errors can be introduced. First, any error in the acceleration measurement will be carried over. However, additional precautions are necessary to obtain good results for speed measurement. The problem areas include the following:

- The initial speed, V_i, must be known at the beginning of the time of interest. Because this quantity is added to the change in speed, an error in it will be a constant on each value.
- A bias, or zero shifts, in the accelerometer signal will be included as a constant acceleration, and thus introduce a linearly increasing error in the calculated values throughout the time interval of interest.

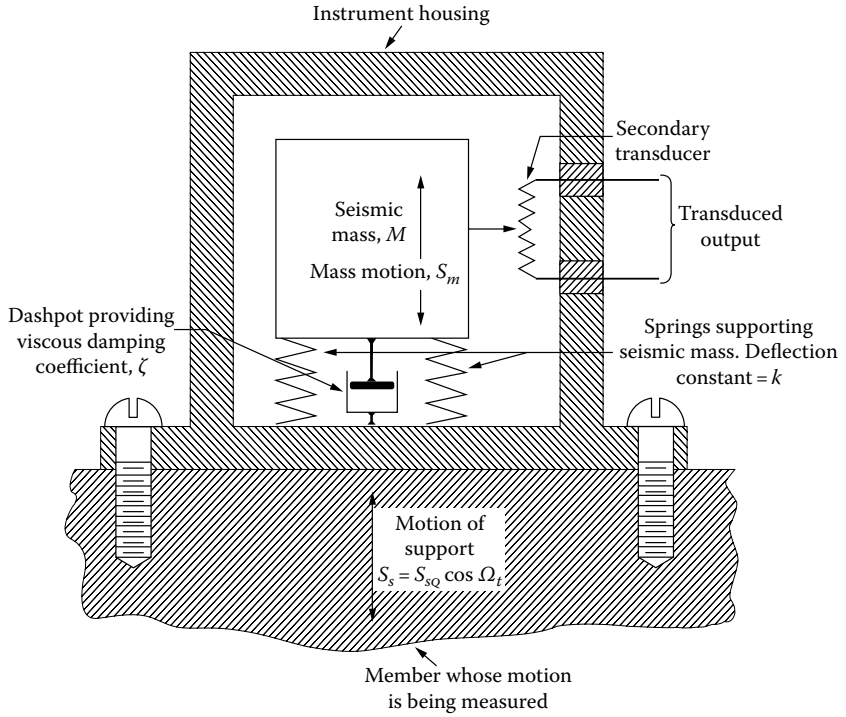

FIGURE 35.5 Seismic type of motion-measuring instrument. (From Beckwith, T. et al., *Mechanical Measurements*, 4th edn., Addison-Wesley, Reading, MA. With permission.)

This bias may be introduced from electrical or thermal characteristics of the circuit or, in the case of measurement of accelerations during impact after a free fall, by the 1 *g* acceleration of gravity.
- If the frequency content of the acceleration falls outside the usable bandwidth of the accelerometer and recording circuit, errors in acceleration occur. The low-frequency cutoff depends on the recording equipment and circuit, and the high-frequency cutoff depends on the natural frequency and damping of the accelerometer, as well as the bandwidth of each piece of equipment in the recording circuit.
- Accelerometer theory is based on harmonic excitation of the system. For many velocity measurement applications, the input is a transient. Combination of these two factors can result in inaccurate accelerometer data; for example, ringing may occur and cause errors in the calculated speeds. This problem is accentuated for lightly damped accelerometers.

When this method of speed measurement must be used, a series of check tests should be conducted to evaluate the accuracy of the method for that particular system.

A variation of the aforementioned method is to put an integrating circuit in the accelerometer and perform the integration with an analog circuit. Then, the output of the "velocity" transducer is proportional to the change in speed. This type of device is subject to all of the potential error sources discussed previously. A manufacturer of this type of transducer is Wilcoxon Research of Gaithersburg, MD.

It can be shown that if the electromechanical transducer in a seismic instrument gives an output that is proportional to the speed on one end relative to the other end, then the output of the seismic transducer is proportional to the speed of the transducer in an inertial reference frame, that is, relative to the earth, for input motion frequencies well above the natural period of the seismic mass. Thus, use of a linear velocity transducer as the motion measurement transducer in a seismic instrument makes it a "seismic velocity transducer." This type of device is called several different names, including seismometer, geophone, and vibrometer, as well as velocity transducer.

The natural frequency and damping in these instruments are selected to match the application. As with an accelerometer, the usable bandwidth depends on these two characteristics. The low-frequency limit for this type of transducer is dependent on the accuracy required in the measurement. The governing equation is given in Doebelin [3]. As an example, it can be used to show that if an accuracy of 5% is required, the lowest data frequency must be 4.6 times the natural frequency of the transducer and that the upper data frequency is not limited. In fact, the higher the upper frequency is, the more accurate the results.

Seismometers are used for recording and studying motion from earthquakes, and these devices can be quite large. Natural periods can be in the range of 10–50 s, and damping is normally selected as 0.7 of critical to extend the frequency range as much as possible. Geophones are commonly used for oil well logging and related work. Their natural periods are in the vicinity of 10 s. Manufacturers of these devices include Teledyne Brown Engineering and GeoSpace Corporation of Houston, TX.

35.6 Angular Velocity Measurement

Measurement of angular velocity is often applied to rotating machinery such as pumps, engines, and generators. The most familiar unit of measurement in rotating machinery applications is revolutions per minute (rpm). In most cases, the measurement of rpm involves the generation of a pulse train or sine wave whose frequency is proportional to angular velocity. The measuring technologies using pulse trains and waves include ac and dc generator tachometers, optical sensors, variable reluctance sensors, rotating magnet sensors, Wiegand effect sensors, and stroboscopy.

These types of measurements are taken with respect to the base of the item being measured. They are relative measurements because one is measuring the motion between two bodies.

Another class of measurement problem is that of moving or inertial bodies. In this case, a measurement of absolute motion is performed. Some fixed reference must be stated or implied. This reference is often the Earth. A universal reference is sometimes required for celestial measurements. These inertial measurements are typically taken with gyroscope-type devices.

35.7 Relative Angular Sensors

35.7.1 Electrical (dc and ac) Tachometer Generator

A rotating generator produces a voltage signal proportional to the rotational velocity of the input shaft. A dc generator produces a voltage level proportional to speed, as in Figure 35.6. The ac generator produces an ac voltage output with a frequency proportional to rotational speed, as shown in Figure 35.7. In a simple two-phase motor, the ac voltage is applied to one phase of the motor and the measurement is taken off the other. Typical operating frequencies are 60 and 400 Hz. This carrier frequency should be 5–10 times the required frequency response of the ac generator tachometer. The direction of travel is determined by the phase of the signal with opposite directions being 180° out of phase. The basic dc generator is shown in Figure 35.8.

Sources of tachometer generators include the GE Company of Fairfield, CT; Kollmorgen Motion Technologies Group of Radford, VA; Sierracin/Magnedyne of Vista, CA; and MicroMo Electronics of Clearwater, FL.

35.7.2 Counter Types

An entire class of angular velocity measuring techniques exists that uses pulses generated by electromechanical interaction. The common thread is a pulse-to-voltage converter giving a voltage output proportional to velocity.

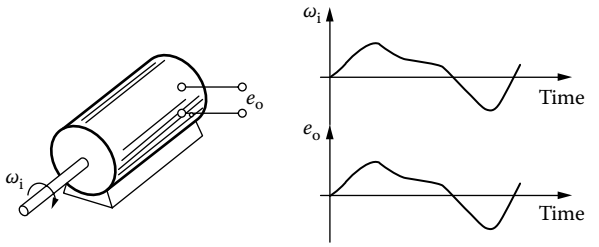

FIGURE 35.6 Permanent-magnet dc tachogenerator. (With permission.)

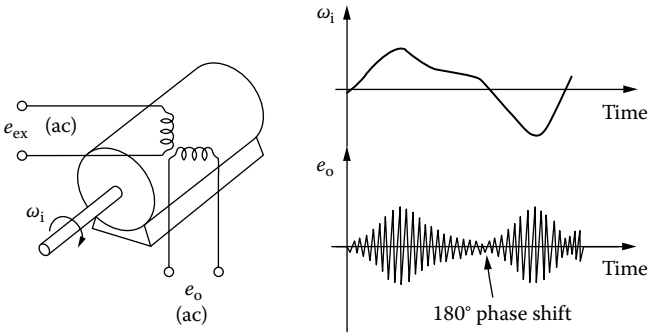

FIGURE 35.7 Ac tachogenerator. (With permission.)

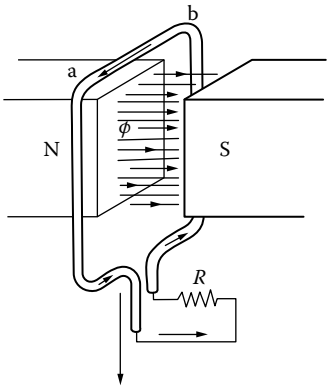

FIGURE 35.8 Generated electromotive force. Moving conductor. (From Loew, E.A., *Direct and Alternating Currents: Theory and Machinery*, McGraw-Hill, New York, 1946. With permission.)

Rotating magnet sensors: Passive speed sensors convert mechanical motions to ac voltages without the need for an external power source. These self-contained magnetic sensors produce a magnetic field that, when in the proximity of ferrous objects in motion, generates a voltage.

When a magnetic sensor is mounted in the proximity of a ferrous target, such as gear teeth on a rotating shaft, the voltage output frequency is directly proportional to the rotational speed of the target. A frequency-to-voltage converter can then convert the signal to a voltage. An engineering unit conversion from voltage to velocity then provides an actual velocity measurement.

Typical applications for these types of sensors include the following:

Transmission speed
Engine rpm
Over/under speed
Wheel speed
Pump shaft speed
Multiple engine synchronization
Feedback for speed control
Crankshaft position/engine timing
Computer peripheral speeds

The typical specifications for magnetic speed sensors are given by a graph of output voltage vs. surface speed in inches per second, as in Figure 35.9.

Sources for magnetic sensors include Smith Systems of Brevard, NC; Optek Technology of Carrolton, TX; AlliedSignal of Morristown, NJ; and Baluff of Florence, KY.

35.7.3 Optical Sensors

Optical methods of angular velocity detection employ a light emitter and a light detector. A light-emitting diode (LED) paired with a light-sensitive diode is the most common arrangement.

A slotted disk is placed in the axis of a rotating shaft. Each slot or slit will allow the light to pass through the disk. Figure 35.10 shows a typical arrangement. The detector will generate a pulse train with a rate proportional to the angular velocity.

The effects of external light sources must be considered in the application of optical sensors.

Sources of optical sensor systems include Scientific Technologies of Fremont, CA; Banner Engineering Corp. of Minneapolis, MN; and Aromat Corp. of New Providence, NJ.

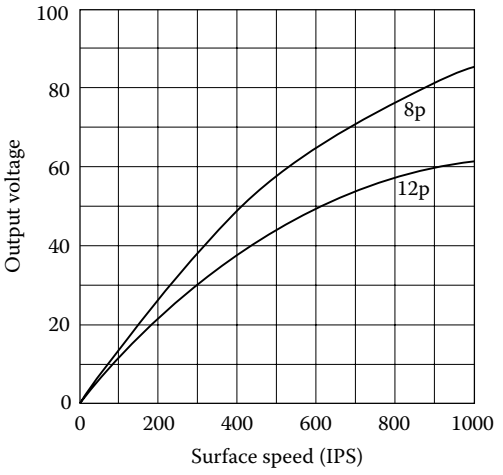

FIGURE 35.9 Magnetic speed sensor output voltage vs. speed. (Courtesy of Smith Systems, Inc., Brevard, NC.)

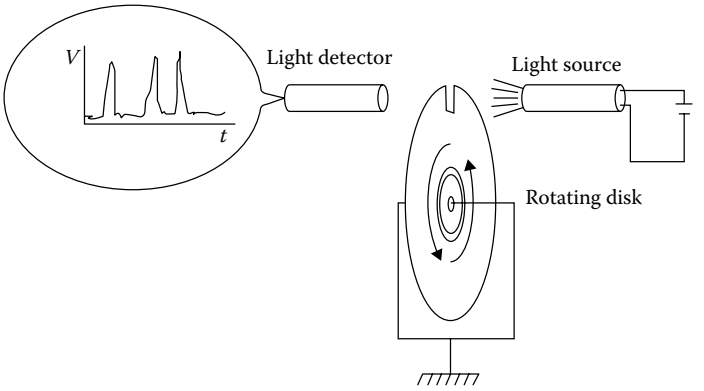

FIGURE 35.10 A slotted disk provides one pulse output for each rotation.

35.7.4 Hall Effect

The Hall effect describes the potential difference that develops across the width of a current-carrying conductor. E.H. Hall first used this effect in 1879 to determine the sign of current carriers in conductors. Hall-effect devices are finding their way into many sensing applications. A typical Hall-effect sensor application is the wheel speed sensor for antilock braking systems in automobiles. The Allegro ATS632LSC gear-tooth sensor, shown in Figure 35.11, is an optimized Hall-effect IC/magnet combination. The sensor consists of a high-temperature plastic shell that holds together a compound samarium–cobalt magnet, a single-element self-calibrating Hall-effect IC, and a voltage regulator. The operation of this circuit is shown in Figure 35.12.

35.7.5 Wiegand Effect

The Wiegand effect is useful for proximity sensing, tachometry, rotary shaft encoding, and speed sensing in applications such as

Electronic indexing for water, gas, and electric meters and remote metering systems
Measuring shaft speed in engines and other machinery
Tachometers, speedometers, and other rotational counting devices

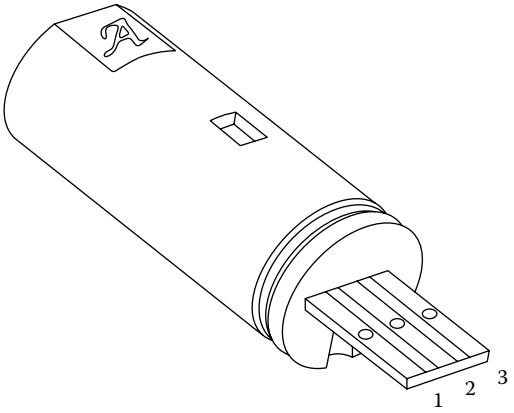

FIGURE 35.11 Hall-effect gear-tooth sensor. *Note*: 1, supply; 2, output; 3, ground. (Courtesy of Allegro Microsystems, Inc., Worcester, MA.)

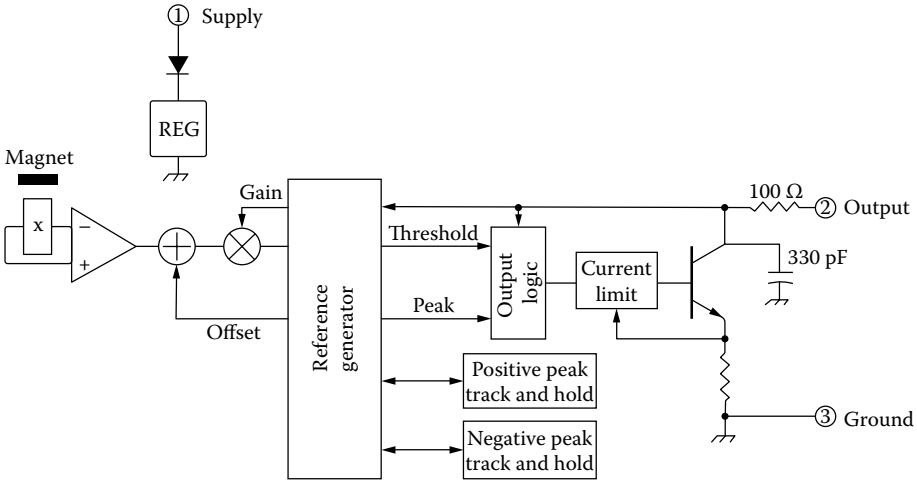

FIGURE 35.12 Functional block diagram of Hall-effect sensor circuit in a gear-tooth application. (Courtesy of Allegro Microsystems, Inc., Worcester, MA.)

Wiegand effect technology employs unique magnetic properties of specially processed, small-diameter ferromagnetic wire. By causing the magnetic field of this wire to suddenly reverse, a sharp, uniform voltage pulse is generated. This pulse is referred to as a Wiegand pulse. Sensors utilizing this effect require only a few simple components to produce sharply defined voltage pulses in response to changes in the applied magnetic field. These sensors consist of a short length of Wiegand wire, a sensing coil, and alternating magnetic fields that generally are derived from small permanent magnets.

The major advantages of the Wiegand effect–based sensors are

No external power requirement
Two-wire operation
Noncontact with no wear
20 kHz pulse rate
High-level voltage output pulse
Wide operating temperature range (e.g., −40 °C to +125 °C)

When an alternating magnetic field of proper strength is applied to the Wiegand wire, the magnetic field of the core switches polarity and then reverses, causing the Wiegand pulse to be generated, as shown in

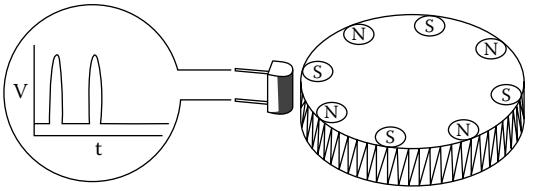

FIGURE 35.13 Small magnets cause sudden reversal in the ferromagnetic wire in a Wiegand sensor. (Courtesy of HID Corporation, North Haven, CT.)

Figure 35.13. The magnetic switching action of the Wiegand wire induces a voltage across the pickup coil of approximately 10 μs duration. These alternating magnetic fields are typically produced by magnets that are affixed to the rotating or moving equipment, by a stationary read head and moving Wiegand wires or by an ac-generated field.

35.8 Absolute Angular Velocity Sensors

35.8.1 Gyroscopes

Many absolute angular rate-measuring devices fall under the designation of gyroscope. A mechanical gyroscope is a device consisting of a spinning mass, typically a disk or wheel, mounted on a base so that its axis can turn freely in one or more directions and thereby maintain its orientation regardless of any movement of the base. It is important to make an initial distinction between angular velocity gyros and rate-integrating gyros. Angular velocity gyros are used to measure motion and as signal inputs to stabilization systems. Rate-integrating gyros are used as the basis for highly accurate inertial navigation systems. They allow a stable platform to maintain a fixed attitude with reference. These devices can be very complex. Three gyros are often teamed with three double-integrated accelerometers to provide an accurate measurement of absolute vehicle motion.

Ricardo Dao of Humphrey Inc. provided an excellent comparison of angular rate sensors in an article in *Measurements & Control* [14]. The five different technologies are summarized as follows.

Spinning mass: The traditional gyro consists of a spinning wheel in a gimbaled frame. The principle of conservation of angular momentum provides the measurement tool.

Fluidic: A stream of helium gas flows past two thin tungsten wires [14]. The tungsten wires act as two arms of a Wheatstone bridge. At rest, the gas flow cools the sensing wires equally and the transducer bridge is balanced with zero output. When angular motion is applied to the sensor, one sensor wire will be subjected to increased flow while the other will see less flow. The resistance of the two wires will change, and the bridge will be unbalanced. The sensor will produce a voltage output proportional to the angular velocity.

A pump is used to circulate the helium gas. This pump is a piezoelectric crystal circular disk that is excited with an external circuit. The pump produces a laminar flow of relatively high-velocity gas across the two parallel sensing wires.

Piezoelectric vibration: A number of angular velocity sensors have been developed that use micromachined quartz elements. A number of shapes are used, but the operating principle is similar for each. The quartz element vibrates at its natural frequency. Angular motion causes a secondary vibration that, when demodulated, is proportional to angular vibration. A description of one design follows.

The QRS and GyroChip™ family products use vibrating quartz tuning fork to sense angular velocity [15,16]. Using the Coriolis effect, a rotational motion about the sensor's longitudinal axis produces a dc voltage proportional to the rate of rotation. Figure 35.14 shows that the sensor consists of a microminiature double-ended quartz tuning fork and supporting structure, all fabricated chemically from a single wafer of monocrystalline piezoelectric quartz (similar to quartz watch crystals).

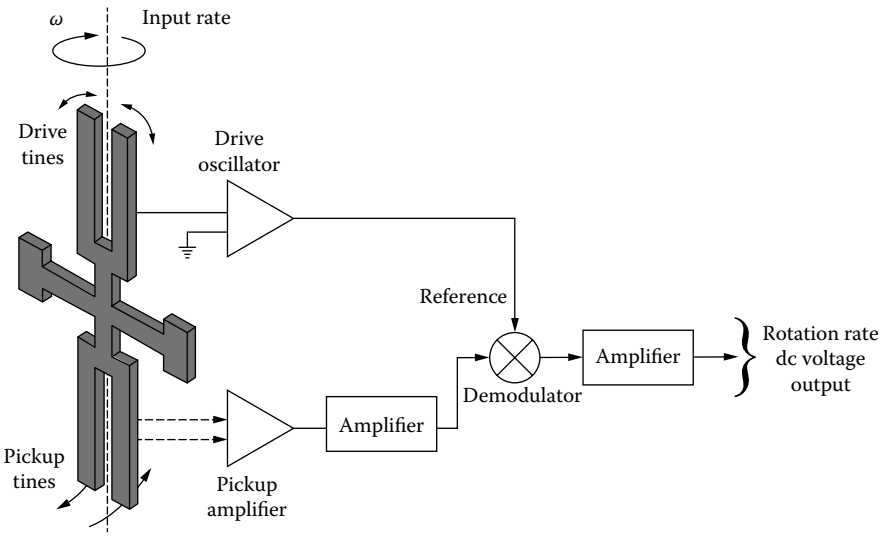

FIGURE 35.14 A vibrating quartz tuning fork uses the Coriolis effect to sense angular velocity. (Courtesy of BEI Sensors and Systems Co., Concord, CA.)

Use of piezoelectric quartz material simplifies the active element, resulting in exceptional stability over temperature and time. The drive tines, being the active portion of the sensor, are driven by an oscillator circuit at precise amplitude, causing the tines to move toward and away from each another at a high frequency.

Each tine will have Coriolis force acting on it of: $\{F = 2m\ W_i \times V_r\}$ where the tine mass is m, the instantaneous radial velocity is V_r, and the input rate is W_i. This force is perpendicular to both the input rate and the instantaneous radial velocity.

The two drive tines move in opposite directions, and the resultant forces are perpendicular to the plane of the fork assembly and in opposite directions. This produces a torque that is proportional to the input rotational rate. Since the radial velocity is sinusoidal, the torque produced is also sinusoidal at the same frequency of the drive tines and in-phase with the radial velocity of the tine.

The pickup tines, being the sensing portion of the sensor, respond to the oscillating torque by moving in and out of plane, producing a signal at the pickup amplifier. After amplification, those signals are demodulated into a dc signal that is proportional to the rotation of the sensor.

The output signal of the GyroChip™ reverses sign with the reversal of the input rate since the oscillating torque produced by the Coriolis effect reverses phase when the direction of rotation reverses. The GyroChip™ will generate a signal only with rotation about the axis of symmetry of the fork, that is, the only motion that will, by Coriolis sensing, produce an oscillating torque at the frequency of the drive tines. This also means that the GyroChip™ can truly sense a zero rate input.

MHD effect: The magnetohydrodynamic angular rate sensor is used to measure angular vibrations in the frequency range of 1–1000 Hz. It is used where there is a high-shock environment and a high rate of angular motion such as 10–250 rad s^{-1}. It does not measure a constant or dc velocity. It is used to measure impacts shorter than 1 s duration and vibrations between 1 and 1000 Hz.

The principle of operation is illustrated in Figure 35.15 [17,18]. A permanent magnet is attached to the outer case of the sensor. When the case turns, a moving magnetic field is produced (B). There is also a conductive fluid inside the sensor. When the sensor case turns, the fluid tends to stay in one place, according to Newton's first law. This produces a relative motion (U) between a magnetic field and conductor. This motion will produce a voltage (E) across the conductor proportional to relative velocity according to Faraday's law.

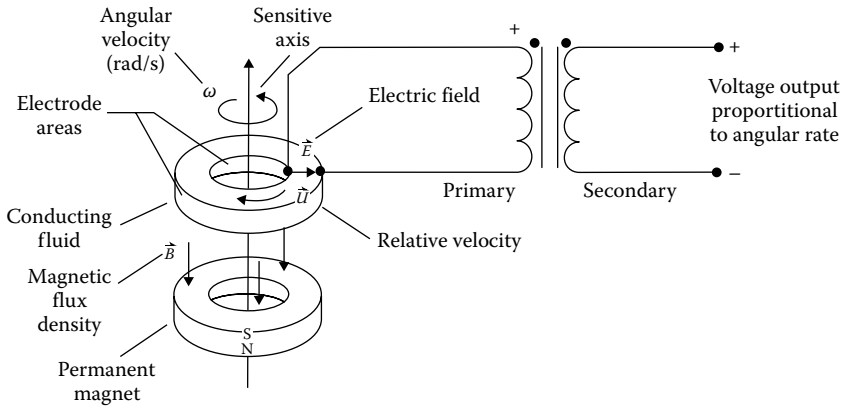

FIGURE 35.15 Magnetohydrodynamic angular rate sensor. (Courtesy of ATA Sensors, Albuquerque, NM.)

Since the fluid is constrained to move in an angular path, the voltage signal will be proportional to angular velocity about the center axis of the sensor. Due to this constraint, the sensor is insensitive to linear motion. The voltage signal is amplified through a transformer or an amplifier for output to a measuring device.

Fiber optic/laser: A beam of light is directed around the axis of rotation. A phase shift of the optical or laser beam is detected to measure angular velocity. The principle of operation is similar to the Doppler shift.

Differenced and integrated accelerometers: An array of accelerometers can be used to measure angular motion. The output of the accelerometers is differenced when they are aligned or summed when they are mounted in opposite directions. This differencing will eliminate the linear component of motion. As shown in Figure 35.16, the magnitude of the differenced signals, a_1, and a_2, is divided by the distance between the two sensors, l. This gives a measure of angular acceleration. The angular acceleration is integrated over time to give angular velocity. It is important to address the same concerns in this process as when integration was discussed in the linear section. It is assumed that there is a rigid mounting structure between the two accelerometers.

This technique is commonly applied to crash testing of anthropomorphic test devices (ATDs). The ATDs are used in automotive crash testing and aerospace egress system testing.

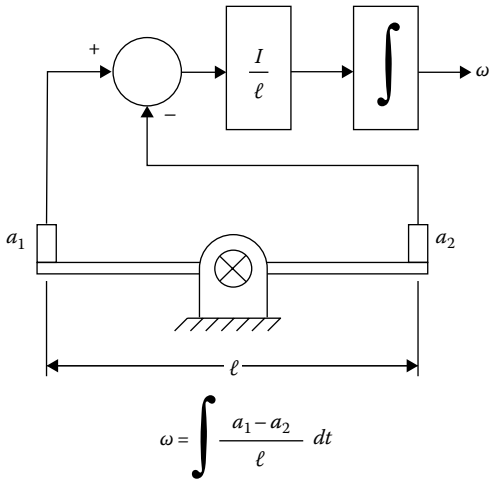

FIGURE 35.16 Angular acceleration by differencing accelerometers and integration.

35.9 Conclusion

But alas, as Poincaré [20] stated, there is no way to determine absolute velocity.

References

1. J. W. Dally, W. F. Riley, and K. G. McConnell, *Instrumentation for Engineering Measurements*, New York: John Wiley & Sons, 1984.
2. A. Hudson and R. Nelson, *University Physics*, New York: Harcourt Brace Jovanovitch, 1982.
3. E. O. Doebelin, *Measurement Systems,* 4th edn., New York: McGraw-Hill, 1990.
4. Trans-Tek, Inc., [Online], 1998. Available at: http://transtekinc.com/lvt.htm (accessed on March 15, 2013).
5. L. M. Barker and R. E. Hollenbach, Laser interferometer for measuring high velocities of any reflecting surface, *J. Appl. Phys*., 43(11), 4669–4675, 1972.
6. Valyn International, [Online], 1998. Available at: www.valynvisar.com (accessed on March 15, 2013).
7. L. C. Rodman, J. H. Bell, and R. D. Mehta, A 3-component laser-Doppler velocimeter data acquisition and reduction system, NASA contractor report; NASA CR-177390.
8. E. A. Loew, *Direct and Alternating Currents,* 3rd edn., New York: McGraw-Hill, 1946.
9. P. Emerald, Low duty cycle operation of hall effect sensors for circuit power conservation, *Sensors*, 15(3), 38, 1998.
10. Allegro MicroSystems, Inc., [Online], 1998. Available at: http://www.allegromicro.com/ (accessed on March 15, 2013).
11. Electronic Tutorials, Tutorial 6, Hall Effect Sensors, http://www.electronics-tutorials.ws/electromagnetism/hall-effect.html (accessed on March 15, 2014).
12. J. B. Scarborough, *The Gyroscope: Theory and Applications*, New York: Interscience, 1958.
13. R. F. Deimel, *Mechanics of the Gyroscope: The Dynamics of Rotation*, New York: Dover Publications, 1950.
14. E. Dao, Fluidic angular rate sensors, *Measurements & Control*, February 1994, Vol. 16, No. 1, 126–131.
15. Systron Donner Inertial Division, [Online], 1998. Available at: http://www.systron.com (accessed on March 15, 2013).
16. S. Orloski and B. Zimmerman, Dead reckoning in an emergency vehicle location system using a quartz rotation sensor and GPS, *Proceedings of Sensor Expo*, Chicago, IL, September 1995, pp. 103–109, Peterborough, NH: Helmers Publishing, 1995.
17. G. Kulikovskiy and G. A. Lyubimov, *Magnetohydrodynamics*, Reading, MA: Addison-Wesley, 1965.
18. Applied Technology Associates, [Online], 1998. Available at: http://www.aptec.com/ (accessed on March 15, 2013).
19. G. Unger et al., NASA's first in-space optical gyroscope: A technology experiment on the X-ray timing Explorer spacecraft, NASA technical memorandum; 109242.
20. R.P. Feynman, R.B. Leighton, and M. Sands, *The Feynman Lectures on Physics*, Reading, MA: Addison-Wesley, 1963, p. 15-5.

Further Readings

Gu, J. H., Song, C. H., and Lee, S. Y., A new velocity measurement method using linear type Hall-effect sensor for an electro-mechanical fin actuator, *SICE '07. 46th SICE Annual Conference*, Takamatsu, Japan, pp. 2179–2183, 2007.

Limin, Y., A current statistical model adopted velocity measurement, *International Conference on Computer Science and Service System (CSSS)*, Nanjing, China, pp. 1914–1917, 2011.

Liu, L., Hu, J., He, Z., Han, C., Li, H., and Li, J., A velocity measurement method based on scaling parameter estimation of a chaotic system, *Metrology and Measurement Systems*, 18(2), 275–281, 2011.

Ma, C. and Xu, X., A novel technique for accurate velocity measurement using LFM radar, *Proceedings of the SPIE—The International Society for Optical Engineering*, 8186, 81860L (11 pp.), 2011.

Nabavi, M. and Siddiqui, K., A critical review on advanced velocity measurement techniques in pulsating flows, *Measurement Science & Technology*, 21(4), 042002 (19 pp.), April 2010.

Partial List of Vendors and Suppliers

Apex instruments, Inc., 204 Technology Park Lane, Fuquay Varina, NC 27526, Phone: 919-557-7300, 800-882-3214 (toll free), Fax: 919-557-7110, www.apexinst.com

Archangel Systems, Inc., 1635 Pumphrey Ave., Auburn, AL 36832, Phone: 334-826-8008, Fax: 334-826-8038, www.archangel.com

Davis/Inotek, 1236 Mark St., Bensenville, IL 60106, Phone: 410-358-3900, 800-548-9409 (toll free), Fax: 410-358-0252, www.davis.com

Furness Controls, 2020 Younts Rd., Indian Trail, NC 28079, Phone: 704-882-3311, 800-898-5325 (toll free), Fax: 704-882-3811, www.furnesscontrols.com/

Neal system Inc., 122 Terry Dr., Newtown, PA 18940, Phone: 215-968-7577, Fax: 215-968-6480, www.nealsystems.com/newsite/

Siemens Corp, 300 New Jersey Avenue, N.W., Suite 1000, Washington, DC 20004-2611, Phone: 202-434-4800, 800-SIEMENS (toll free), Fax: 202-347-4015, www.usa.siemens.com/entry/en/

Wilcoxon research Inc., 20511 Seneca Meadows Pkwy., Germantown, MD 20876, Phone: 301-330-8811, 800-945-2696 (toll free), Fax: 301-330-8873, www.wilcoxon.com

Zemarc Corp., 6431 Flotilla St., Los Angeles, CA 90040, Phone: 323-721-5598, 800-275-8698 (toll free), Fax: 323-722-2220, www.zemarc.com

IV

Mechanical Variables

36

Acceleration, Vibration, and Shock Measurement

Halit Eren
Curtin University

Acceleration is an important parameter for general-purpose absolute motion measurements and vibration and shock sensing. Acceleration is measured accelerometers, which are commercially available in a wide variety, types, and shapes to meet the requirements of diverse range applications. They are manufactured in small sizes, light in weight, rugged, and robust to be able to operate in harsh environment. They can be configured as active or passive sensors. An active accelerometer (e.g., piezoelectric) gives an output without the need for an external power supply, while a passive accelerometer only changes its electric properties (e.g., capacitance) and requires an external electrical

power source. In applications, the selection of active- or passive-type accelerometer is important, since active sensors cannot measure static or DC mode operations. In applications where static measurements are involved, passive sensors must be used. In general, accelerometers are preferred over displacement and velocity sensors for the following reasons:

1. They have a wide frequency range from zero to very high values. Steady accelerations can easily be measured.
2. Acceleration is more frequently needed since destructive forces are often related to acceleration rather than to velocity or displacement.
3. Measurement of transients and shocks can readily be made, easier than displacement or velocity sensing.
4. Displacement and velocity can be obtained by simple integration of acceleration by electronic circuitry. Integration is preferred over differentiation.

Accelerometers can be classified in a number of ways, such as *deflection* or *null-balance* types, mechanical or electrical types, and dynamic or kinematic types. The majority of industrial accelerometers can be classified as either deflection or null-balance type. Those used in vibration and shock measurements are usually the deflection types, whereas those used for measurements of motions of vehicles, aircraft, etc., for navigation purposes may be either type. In general, null-balance types are used when extreme accuracy is needed.

A large number of practical accelerometers are of the deflection type; a general configuration is shown in Figure 36.1. There are many different deflection-type accelerometers. Although their principles of operation are similar, they only differ in minor details, such as the spring elements used, types of damping provided, and types of relative motion transducers employed. These types of accelerometers behave as second-order systems; the detailed mathematical analysis will be given in this chapter in the following.

Accelerometers can be classified as *dynamic*, meaning that the operation is based on measuring the force required to constrain a seismic mass to track the motion of the accelerated base, such as spring-constrained slug types. Another type is the *kinematic* accelerometer, which is based on timing of the passage of an unconstrained proof mass from spaced points marked on the accelerated base. These types of accelerometers are used in highly specific applications such as interspace spacecrafts and gravimetric measurements.

For practical purposes, accelerometers can also be classified as *mechanical* or *electrical*, depending on whether the restoring force or other measuring mechanism is based on mechanical properties (e.g., the law of motion, distortion of a spring or fluid dynamics, etc.) or on electrical or magnetic forces.

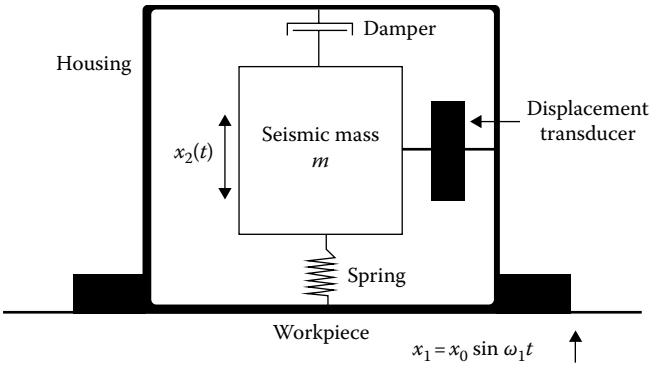

FIGURE 36.1 A typical deflection-type seismic accelerometer. In this basic accelerometer, the seismic mass is suspended by a spring or cantilever inside a rigid frame. The frame is connected to the vibrating structure; as vibration takes place, the mass tends to remain fixed such that the relative displacements can be picked up. They are manufactured in many different types and sizes and they exhibit diverse characteristics.

The calibration of accelerometers is very important and necessary in acceleration, vibration, and shock sensing applications. The calibration methods can broadly be classified to be *static* or *dynamic*. Static calibration is conducted at one or several levels of constant acceleration. For example, if a tilting table calibration method is selected, the vertical component of the free fall is used without a choice of magnitude. On the other hand, if a centrifuge is selected, it produces a constant acceleration as a function of the speed of rotation, and the magnitudes can be selected in a wide range from 0 to well over 50,000 *g*. The dynamic calibration is usually done using an electrodynamics shaker. The electrodynamics shaker is designed to oscillate in a sinusoidal motion with variable frequencies and amplitudes. They are stabilized at selected levels of calibration. This is an absolute method that consists of measuring the displacement with a laser interferometer and a precise frequency meter for accurate frequency measurements. The shaker must be driven by a power amplifier, thus giving a sinusoidal output with minimal distortion. The National Bureau of Standards uses this method as a reference standard. Precision accelerometers, mostly of the piezoelectric type, are calibrated by the absolute method and then used as the working standard. A preferred method is back-to-back calibration, where the test specimen is directly mounted on the working standard that, in turn, is mounted on an electrodynamics shaker.

Before providing details of different types of accelerometers, the common features such as accelerometer dynamics, velocity, distance, and shock frequency responses will be introduced next.

36.1 Accelerometer Dynamics: Frequency Response, Damping, Damping Ratio, and Linearity

This section concerns the physical properties of acceleration, vibration, and shock measurements in which accelerometers are commonly used. A full understanding of accelerometer dynamics is necessary in relation to characteristics of acceleration, vibration, and shock. For instance, the vibrations can be periodic, stationary random, nonstationary random, or transient, all of which affect the operational nature of the accelerometers and the arrangements to be made for correct measurements.

36.1.1 Periodic Vibrations

In periodic vibrations, the motion of an object repeats itself in an oscillatory manner. This can be represented by a sinusoidal waveform:

$$x(t) = X_{\text{peak}} \sin(\omega t) \tag{36.1}$$

where

$x(t)$ is the time-dependent displacement
$\omega = 2\pi ft$ is the angular frequency
X_{peak} is the maximum displacement from a reference point

The velocity of the object is the time rate of change of displacement:

$$u(t) = \frac{dx}{dt} = \omega X_{\text{peak}} \cos(\omega t) = U_{\text{peak}} \sin\left(\omega t + \frac{\pi}{2}\right) \tag{36.2}$$

where

$u(t)$ is the time-dependent velocity
$U_{\text{peak}} = \omega X_{\text{peak}}$ is the maximum velocity

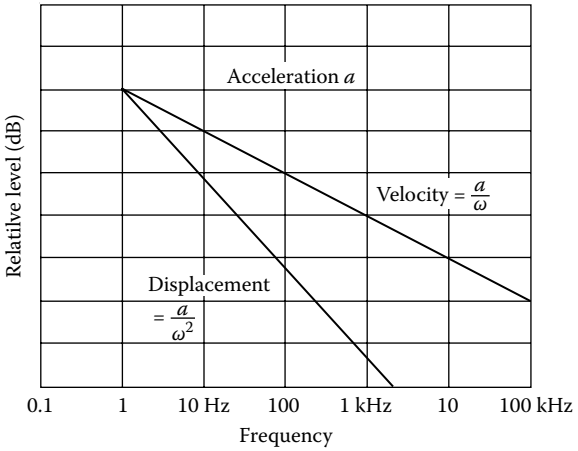

FIGURE 36.2 The logarithmic relationship between acceleration, velocity, and displacement. Velocity at a particular frequency can be obtained by dividing acceleration by a factor proportional to frequency. For displacement, acceleration must be divided by another factor proportional to the square of the frequency. Phase angles need to be determined separately, but they can be neglected in measurements in which time averages are involved.

Then the acceleration of the object is the time rate change of the velocity:

$$a(t) = \frac{du}{dt} = \frac{d^2u}{dt^2} = -\omega^2 X_{\text{peak}} \sin(\omega t) = A_{\text{peak}} \sin(\omega t + \pi) \tag{36.3}$$

where

$a(t)$ is the time-dependent acceleration

$A_{\text{peak}} = \omega^2 X_{\text{peak}} = \omega U_{\text{peak}}$ is the maximum acceleration

From the earlier equations, it can be seen that the basic form and the period of vibration remain the same in the case of acceleration, velocity, and displacement. But velocity leads displacement by a phase angle of 90° and acceleration leads velocity by another 90°. The amplitudes of the three quantities are related as a function of frequency, as shown in Figure 36.2.

In nature, vibrations are often periodic but not necessarily sinusoidal. If they are periodic but non-sinusoidal, they can be expressed as a combination of a number of pure sinusoidal signals that can be described by Fourier analysis as

$$x(t) = X_0 + X_1 \sin(\omega_1 t + \phi_1) + X_2 \sin(\omega_2 t + \phi_2) + \cdots X_n \sin(\omega_n t + \phi_n) \tag{36.4}$$

Where

$\omega_1, \omega_2, \ldots, \omega_n$ are the frequencies (rad s^{-1})

$X_0, X_1, \ldots, X_n$ are the maximum amplitudes of respective frequencies

$\phi_1, \phi_2, \ldots, \phi_n$ are the phase angles

The number of terms may be infinite: the higher the number of terms, the better the approximation. These terms constitute the *frequency spectrum*. This indicates that the vibrations can be represented in time domain or frequency domain, both of which are extremely useful in the analysis. As an example, in Figure 36.3, the time response of the seismic mass of an accelerometer is given against a rectangular pattern of excitation of the base.

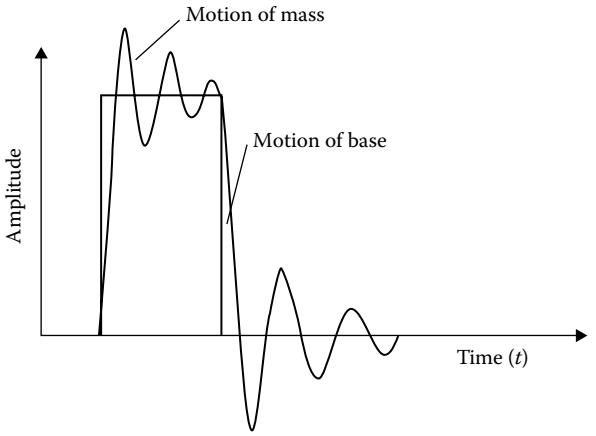

FIGURE 36.3 Time response of a shock excitation of a single degree-of-freedom system. As the duration of the shock pulse increases, sustained oscillations get shorter in time but become larger in amplitude. The maximum system response may be as high as twice the magnitude of the shock pulse.

36.1.2 Stationary Random Vibrations

Random vibrations are often met in nature where they constitute irregular cycles of motions that never repeat themselves exactly. Theoretically, an infinitely long time record is necessary to obtain a complete description of these vibrations. However, statistical methods and probability theory can be used for mathematical analysis by taking representative samples. Tools such as probability distributions, probability densities, frequency spectra, cross-correlation, autocorrelations, digital Fourier transforms (DFT), fast Fourier transforms (FFT), autospectral analysis, RMS values, and digital filter analysis are some of the techniques that are commonly employed.

36.1.3 Transients and Shocks

Often, short-duration and sudden-occurrence vibrations need to be measured. Shock and transient vibrations may be described in terms of force, acceleration, velocity, or displacement. As in the case of random transients and shocks, statistical methods and Fourier transforms are frequently used in the analysis.

36.1.4 Nonstationary Random Vibrations

In this case, the statistical properties of vibrations vary in time. Methods such as time averaging and other statistical techniques can be employed. A majority of accelerometers described here can be viewed and analyzed as seismic instruments consisting of a mass, a spring, and a damper arrangement, as shown in Figure 36.1. Taking only the mass–spring system, if the system behaves linearly in a time invariant manner, the basic second-order differential equation for the motion of the mass alone under the influence of a force can be written as

$$f(t) = \frac{md^2x}{dt^2} + c\frac{dx}{dt} + kx \tag{36.5}$$

where
$f(t)$ is the force
m is the mass
c is the velocity constant
k is the spring constant

Nevertheless, in seismic accelerometers, the base of the arrangement is also in motion. Therefore, Equation 36.5 can be generalized by taking the effect motion into account. Then, it can be expressed as

$$\frac{md^2z}{dt^2} + c\frac{dz}{dt} + kz = mg\cos(\theta) - \frac{md^2x_1}{dt^2} \tag{36.6}$$

where

$z = x_2 - x_1$ is the relative motion between the mass and the base
x_1 is the displacement of the base
x_2 is the displacement of the mass
θ is the angle between sense axis and gravity

In order to lay a background for further analysis, taking the simple case, the complete solution to Equation 36.5 can be obtained by applying the superposition principle. The superposition principle states that if there are simultaneously superimposed actions on a body, the total effect can be obtained by summing the effects of each individual action.

Equation 36.5 describes essentially a second-order system that can be expressed in Laplace transform as

$$\frac{X(s)}{F(s)} = \frac{1}{ms^2} + cs + k \tag{36.7}$$

or

$$\frac{X(s)}{F(s)} = \frac{K}{s^2/\omega_n^2 + 2\zeta s/\omega_n + 1} \tag{36.8}$$

where

s is the Laplace operator
$K = 1/\underline{k}$ is the static sensitivity
$\omega_n = \sqrt{k/m}$ is the undamped critical frequency, rad/s
$\zeta = c/2\sqrt{km}$ is the damping ratio

As can be seen, in the performance of accelerometers, important parameters are the static sensitivity, the natural frequency, and the damping ratio, which are functions of mass, velocity, and spring constants. Accelerometers are designed to have different performance characteristics by suitable selection of these parameters.

Once the response is expressed in the form of Equations 36.7 and 36.8, analysis can be taken further, either in the time domain or in the frequency domain. The time response of a typical second-order system for a unit-step input is given in Figure 36.4. The Bode plot gain phase responses are depicted in Figure 36.5. Detailed discussions about frequency response, damping, damping ratio, and linearity are made in relevant sections.

Systems in which a single structure moves in more than one direction are termed *multidegree-of-freedom systems*. In this case, the accelerations become functions of dimensions as d^2x/dt^2, d^2y/dt^2, and d^2z/dt^2. Hence, in multichannel vibration tests, multiple transducers must be used to create uniaxial, biaxial, or triaxial sensing points for measurements. Mathematically, a linear multidegree-of-freedom system can be described by a set of coupled second-order linear differential equations, and when the frequency response is plotted, it normally shows one resonance peak per degree of freedom.

Frequently, acceleration and vibration measurements of thin plates or small masses are required. Attaching an accelerometer with a comparable mass onto a thin plate or a small test piece can cause "mass loading." Since acceleration is dependent on the mass, the vibration characteristics of the loaded

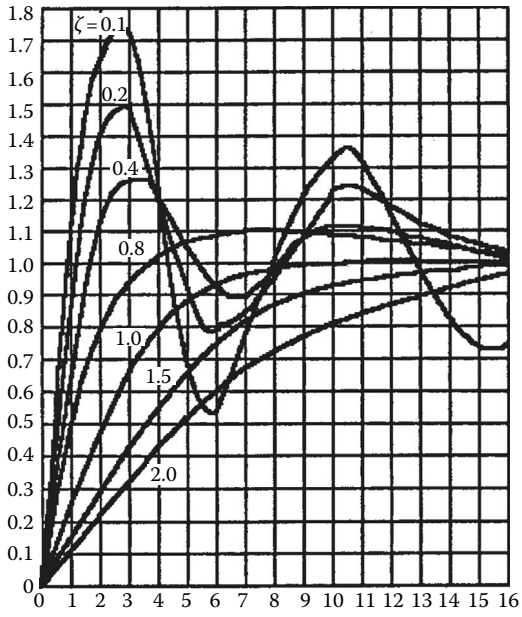

FIGURE 36.4 Unit-step time responses of a second-order system with various damping ratios. The maximum overshoot, delay, rise, settling times, and frequency of oscillations depend on the damping ratio. Smaller damping ratios give faster response but larger overshoot. In many applications, a damping ratio of 0.707 is preferred.

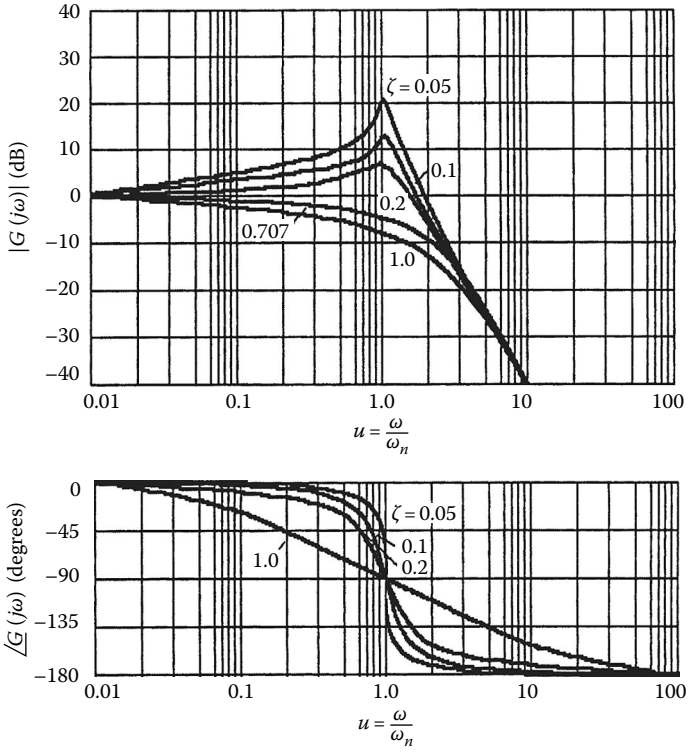

FIGURE 36.5 Bode plots of gains and phase angles against frequency of a second-order system. Curves are functions of frequencies as well as damping ratios. These plots can be obtained theoretically or by practical tests conducted in specified frequency ranges.

test piece could be altered, thus yielding wrong measurements. In such cases, a correct interpretation of the results of the measuring instruments must be made. Some experimental techniques are also available for the correction of the test results by performing repetitive tests conducted by sequentially adding small known masses and by observing the differences.

The following sections discuss different types of accelerometers.

36.2 Electromechanical Force-Balance (Servo) Accelerometers

Electromechanical accelerometers, essentially servo- or null-balance types, rely on the principle of feedback. In these devices, an acceleration-sensitive mass is kept very close at a neutral position or zero displacement point by sensing the displacement and feeding back this displacement. A proportional magnetic force is generated to oppose the motion of the mass displaced from the neutral, thus restoring neutral position—just as a mechanical spring in a conventional accelerometer would do. The advantages of this approach are (1) better linearity and (2) elimination of hysteresis effects when compared to mechanical spring countertypes. Also, in some cases, an electric damping can be provided so that the system becomes less sensitive to variations in temperature.

One very important feature of null-balance types is the capability of testing the static and dynamic performances of the devices by introducing electrically excited test forces into the system. This self-checking feature can be quite convenient in complex and expensive tests where it is extremely critical that the system operates correctly before the test commences. They are also useful in acceleration control systems, since the reference value of acceleration can be introduced by means of a proportional current from an external source. They are usually used for general-purpose motion measurements and monitoring low-frequency vibrations. They are specifically used in applications requiring better accuracy than achieved by those accelerometers based on mechanical springs used as force-to-displacement transducers.

There are a number of different types of electromechanical accelerometers: coil and magnetic types and induction types.

36.2.1 Coil- and Magnetic-Type Accelerometers

These accelerometers are based on Ampere's law; that is, "a current carrying conductor disposed within a magnetic field experiences a force proportional to the current, the length of the conductor within the field, the intensity of the magnetic field, and the sine of the angle between the conductor and the field."

Figure 36.6 illustrates one form of accelerometer making use of the earlier principle. The coil is located within the cylindrical gap defined by a permanent magnet and a cylindrical soft iron flux return path. It is mounted by means of an arm situated on a minimum friction bearing so as to constitute an acceleration-sensitive seismic mass. A pick-off mechanism senses the displacement of the coil under acceleration and causes the coil to be supplied with a direct current via a suitable servo controller to restore or maintain a null condition.

Assuming a downward acceleration with the field being radial (90°) and using Ampere's law, the force experienced by the coil may be written as

$$F = ma = ilB \tag{36.9}$$

or the current

$$i = \frac{ma}{lB} \tag{36.10}$$

where

B is the effective flux density

l is the total effective length of the conductor in the magnetic field

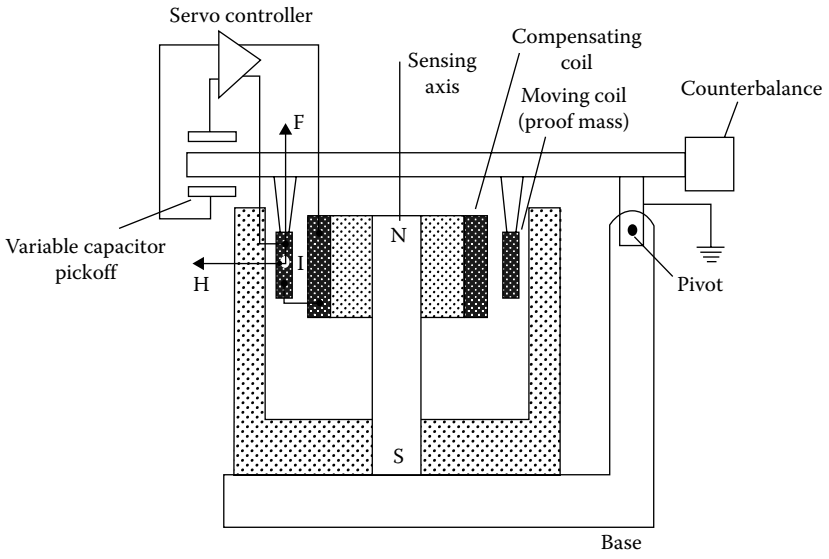

FIGURE 36.6 A basic coil and permanent magnet accelerometer. The coil is supported by an arm with minimum friction bearings to form a proof mass in a magnetic field. Displacement of the coil due to acceleration induces an electric potential in the coil to be sensed and processed. A servo system maintains the coil in a null position.

Current in the restoring circuit is linearly proportional to acceleration, if (1) the armature reaction effects are negligible and fully neutralized by the compensating coil in opposition to the moving coil and (2) the gain of the servo system is large enough to prevent displacement of the coil from the region in which the magnetic field is constant.

In these accelerometers, the magnetic structure must be shielded adequately to make the system insensitive to external disturbances and Earth's magnetic field. Also, in the presence of acceleration, there will be a temperature rise due to i^2R losses. The effects of these i^2R losses are determined by the appropriate thermal design and the heat transfer properties of the accelerometer. In many applications, special care must be exercised in choosing an appropriate accelerometer such that the temperature rises caused by unexpected accelerations cannot affect excessively the scale factors or the bias conditions.

A simplified version of another type of servo accelerometer is given in Figure 36.7. The acceleration a of the instrument case causes an inertial force F on the sensitive mass m, tending to make it pivot in its bearings or flexure mount. The rotation θ from neutral is sensed by an inductive pickup to be amplified, demodulated, and filtered to produce a current i_a, which is directly proportional to the motion from the null. This current is passed through a precision stable resistor R to give an output voltage signal and is applied to a coil suspended in a magnetic field. The current through the coil produces magnetic torque on the coil, which takes action to return the mass to neutral. The current required to produce magnetic torque that just balances the inertial torque due to acceleration is directly proportional to acceleration a. Therefore, the output voltage e_o becomes a measure of acceleration a. Since a nonzero displacement θ is necessary to produce the current i_a, the mass is not exactly returned to null but becomes very close to zero because of the high-gain amplifier. Analysis of the block diagram reveals that

$$\frac{e_o}{R} = \left(mra - \frac{e_o K_c}{R} \right) \times \left(\frac{K_p K_a / K_s}{s^2/\omega_{nl}^2 + 2\zeta_1 s/\omega_{nl} + 1} \right) \tag{36.11}$$

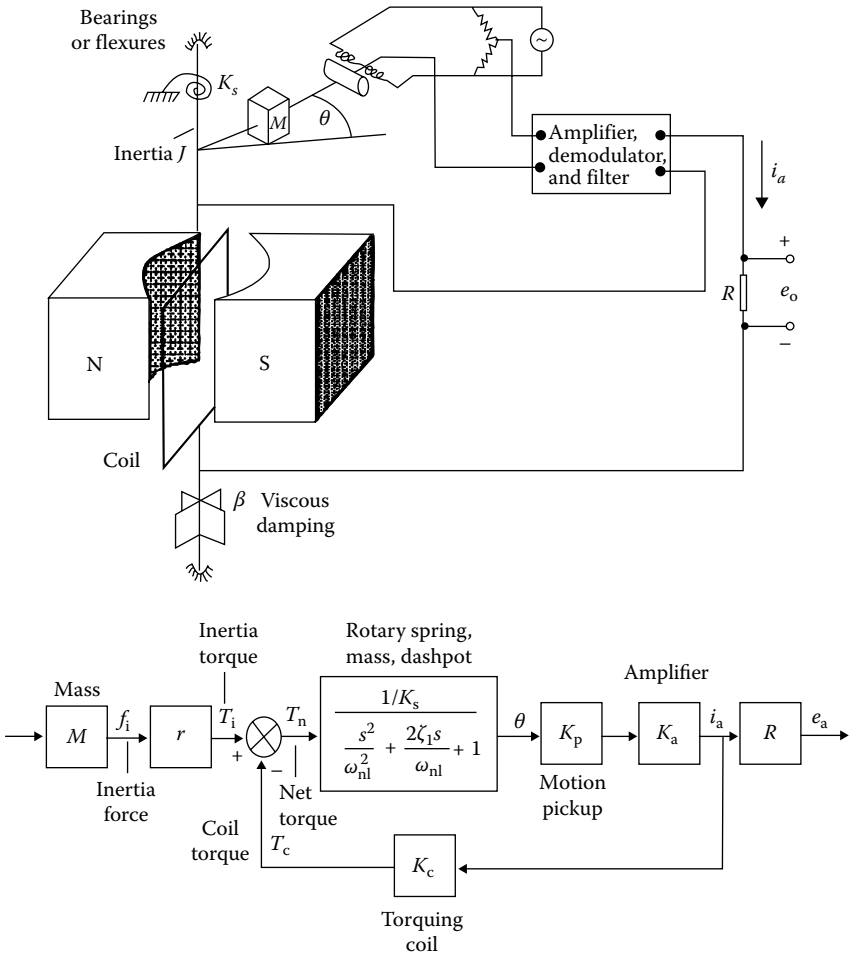

FIGURE 36.7 A simplified version of a rotational-type servo accelerometer. Acceleration of the instrument case causes an inertial force on the sensitive mass, tending to make it pivot in its bearings or flexure mounts. The rotation from neutral is sensed by inductive sensing and amplified, demodulated, and filtered to produce an electric current that is directly proportional to the motion from the null. The block diagram representation is useful in analysis.

Rearranging this expression gives

$$\frac{mrRK_pK_aa}{K_s} = \frac{s^2}{\omega_{nl}^2} + \frac{2\zeta_1 s}{\omega_{nl}} + 1 + \left(\frac{K_cK_pK_aa}{K_s}\right) e_o \tag{36.12}$$

By designing the amplifier gain, K_a is made large enough so that $K_cK_pK_aa/K_s \gg 1.0$; then

$$\frac{e_o}{a(s)} = \frac{K}{(s^2/\omega_{nl}^2 + 2\zeta_1 s/\omega_{nl} + 1 + K_cK_pK_aa/K_s)e_o} \tag{36.13}$$

where

$$K \equiv \frac{MrR}{K_c}, \quad (\text{V m}^{-1}\text{s}^{-2}) \tag{36.14}$$

$$\omega_n \cong \omega_{nl}\sqrt{\frac{K_c K_p K_a}{K_s}} \text{ rad/s} \tag{36.15}$$

$$\zeta \equiv \frac{\zeta_1}{\sqrt{K_c K_p K_a / K_s}} \tag{36.16}$$

Equation 36.14 shows that the sensitivity depends on the values of m, r, R, and K_c, all of which can be made constant. In this case, a high-gain feedback is useful in shifting the requirements for accuracy and stability from mechanical components to a selected few parameters where the requirements can easily be met. As in all feedback systems, the gain cannot be made arbitrarily high because of dynamic instability; however, a sufficiently high gain can be achieved to obtain good performance. An excellent comprehensive treatment of this topic is given by Doebelin (1990), and the detail of the book is given in the bibliography.

36.2.2 Induction-Type Accelerometers

The cross-product relationship of current, magnetic field, and force gives the basis for induction-type electromagnetic accelerometers, which are essentially generators rather than motors. One type of instrument, cup and magnet, includes a pendulous element with a pick-off and a servo controller driving a tachometer coupling and a permanent magnet and a flux return ring, closely spaced with respect to an electrically conductive cylinder attached to the pendulous element. A rate proportional drag force is obtained by electromagnetic induction effects between magnet and conductor. The pick-off senses pendulum deflection under acceleration and causes the servo controller to turn the rotor in a sense to drag the pendulous element toward null. Under steady-state conditions, motor speed is a measure of the acceleration acting on the instrument. Stable servo operation is achieved employing a time-lead network to compensate the inertial time lag of the motor and magnet combination. The accuracy of servo-type accelerometers is ultimately limited by consistency and stability of the scale factors of coupling devices and magnet and cup as a function of time and temperature.

Another accelerometer based on induction types is the *eddy current induction torque generation*. It was noted that the force-generating mechanism of an induction accelerometer consists of a stable magnetic field, usually supplied by a permanent magnet, which penetrates orthogonally through a uniform conduction sheet. The movement of the conducting sheet relative to the magnetic field in response to an acceleration results in a generated electromotive potential in each circuit in the conductor. This action is in accordance with Faraday's law induction. In these accelerometers, the induced eddy currents are confined to the conductor sheets, making the system essentially a drag coupling.

A typical commercial instrument based on the servo-accelerometer principle might have a micromachined quartz flexure suspension, differential capacitance angle pick-off, and air squeeze film, plus servo lead compensation for system damping. Of the various available models, a 30 *g* range unit has threshold and resolution of 1 μ*g*, frequency response flat within 0.05% at 10 Hz and 2% at 100 Hz, natural frequency 500 Hz, damping ratio 0.3–0.8, and transverse or cross-axis sensitivity 0.1%. If the output current is about 1.3 mA g^{-1}, then a 250 Ω readout resistor would give about ±10 V full scale at 30 *g*. These accelerometers are good with respect to precision and are used in many applications, such as aircrafts, missiles, measurement of tilt angles, and axle angular bending in weight and balance systems.

36.3 Piezoelectric Accelerometers

Piezoelectric accelerometers are very popular and are used extensively for general-purpose acceleration, shock, and vibration measurements. They are based on the piezoelectric properties of some materials. When a physical force is exerted on the piezoelectric material, it generates a voltage proportional to the force.

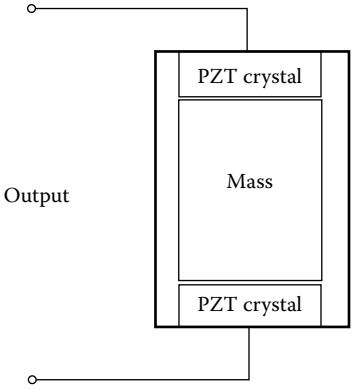

FIGURE 36.8 A compression-type piezoelectric accelerometer. The crystals are under compression at all times, either by a mass or mass and spring arrangement. Acceleration causes a deformation of the crystal, thus producing a proportional electric signal. They are small in size and are widely used. They demonstrate poor performance at low frequencies.

Piezoelectric accelerometers are basically motion transducers with large output signals and comparatively small sizes. They are available with very high natural frequencies and are therefore suitable for a wide range of applications.

These devices utilize a mass in direct contact with the piezoelectric component or crystal, as shown in Figure 36.8. When a varying motion is applied to the accelerometer, the crystal experiences a varying force excitation ($F = ma$), causing a proportional electric charge q to be developed across it:

$$q = d_{ij}F = d_{ij}ma \tag{36.17}$$

where

q is the charge developed

d_{ij} is the material's piezoelectric coefficient

As Equation 36.17 shows, the output from the piezoelectric material is dependent on its mechanical properties, d_{ij}. Two commonly used piezoelectric crystals are lead–zirconate–titanate ceramic (PZT) and quartz. They are both self-generating materials and produce a large electric charge compared to their sizes. The piezoelectric strain constant of PZT is about 150 times that of quartz. As a result, PZTs are much more sensitive and smaller in size than their quartz counterparts. In accelerometers, the mechanical spring constants for the piezoelectric components are high, and the inertial masses attached to them are small. Therefore, these accelerometers are useful for high-frequency applications. Figure 36.9 illustrates a typical frequency response for a PZT device. Since piezoelectric accelerometers have comparatively low mechanical impedances, their effects on the motion of most structures are negligible. They are also manufactured to be rugged and they have outputs that are stable with time and environment.

Mathematically, their transfer function approximates to a third-order system as

$$\frac{e_o(s)}{a(s)} = \frac{(K_q/C\omega_n{}^2)\tau s}{[(\tau s+1)(s^2/\omega_n{}^2 + 2\zeta s/\omega_n + 1)]} \tag{36.18}$$

where

K_q is the piezoelectric constant related to charge (Coulomb cm)

τ is the time constant of the crystal

It is worth noting that the crystal itself does not have a time constant τ, but the time constant is observed when the accelerometer is connected into an electric circuit (e.g., an *RC* circuit).

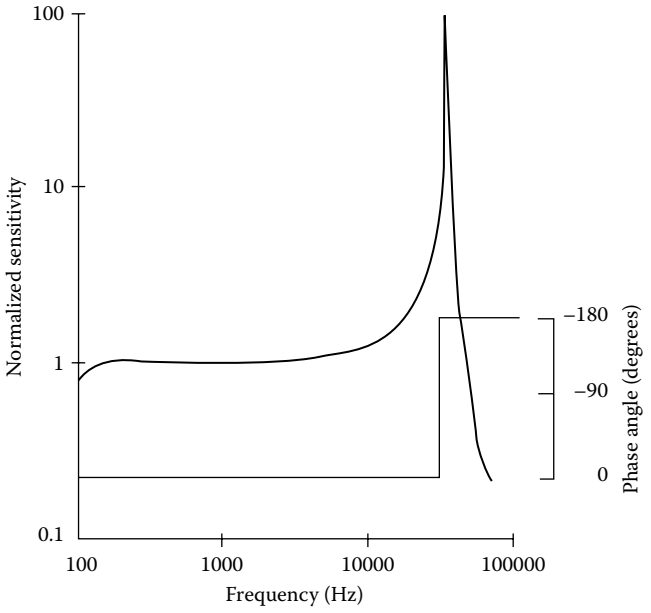

FIGURE 36.9 Frequency response of a typical piezoelectric accelerometer. Measurements are normally confined to the linear portion of the response curve. The upper frequency of the accelerometer is limited by the resonance of the PZT crystal. The phase angle is constant up to the resonance frequency.

The low-frequency response is limited by the piezoelectric characteristic $\tau s/(\tau s + 1)$, while the high-frequency response is related to mechanical response. The damping factor ζ is very small, usually less than 0.01 or near zero. Accurate low-frequency response requires large τ, which is usually achieved by the use of high-impedance voltage amplifiers. At very low frequencies, thermal effects can have severe influences on the operation characteristics.

In piezoelectric accelerometers, two basic design configurations are used: compression types and shear stress types. In compression types, the crystal is held in compression by a preload element; therefore, the vibration varies the stress in compressed mode. In the shear accelerometer, vibration simply deforms the crystal in shear mode. The compression type has a relatively good mass/sensitivity ratio and hence exhibits better performance. But, since the housing acts as an integral part of the spring mass system, it may produce spurious interfaces in the accelerometer output, if excited in its proper natural frequency.

Microelectronic circuits have allowed the design of piezoelectric accelerometers with charge amplifiers and other signal-conditioning circuits built into the instrument housing. This arrangement allows greater sensitivity, high-frequency response, and smaller-size accelerometers, thus lowering the initial and implementation costs.

Piezoelectric accelerometers are available in a wide range of specifications and are offered by many manufacturers. For example, the specifications of a shock accelerometer may have 0.004 pC g^{-1} sensitivity and a natural frequency of up to 250,000 Hz, while a unit designed for low-level seismic measurements might have 1,000 pC g^{-1} in sensitivity and with only 7,000 Hz natural frequency. They are manufactured as small as 3 × 3 mm in dimensions with about 0.5 g in mass, including cables. They have excellent temperature ranges, and some of them are designed to survive intensive radiation environment of nuclear reactors. However, piezoelectric accelerometers tend to have larger cross-axis sensitivity than other types, about 2%–4%. In some cases, large cross-axis sensitivity can be used during installation for the correct orientation of the device. These accelerometers can be mounted with threaded studs, with cement or wax adhesives, or with magnetic holders.

36.4 Piezoresistive Accelerometers

Piezoresistive accelerometers are essentially semiconductor strain gages with large gage factors. High gage factors are obtained because the material resistivity is dependent primarily on the stress, not only on dimensions. The increased sensitivity is critical in vibration measurement because it allows the miniaturization of the accelerometer. Most piezoresistive accelerometers use two or four active gages arranged in a Wheatstone bridge. Extraprecision resistors are used, as part of the circuit, in series with the input to control the sensitivity, balancing, and offsetting temperature effects. The mechanical construction of a piezoresistive accelerometer is shown in Figure 36.10.

In some applications, overload stops are necessary to protect the gages from high-amplitude inputs. These instruments are useful for acquiring vibration information at low frequencies (e.g., below 1 Hz). In fact, the piezoresistive sensors are inherently true static acceleration measurement devices. Typical characteristics of piezoresistive accelerometers are 100 mV g^{-1} in sensitivity, 0–750 Hz in frequency range, 2500 Hz in resonance frequency, 25 *g* in amplitude range, 2000 *g* in shock rating, and 0 °C–95 °C in temperature range and has a total mass of about 25 g.

36.5 Differential-Capacitance Accelerometers

Differential-capacitance accelerometers are based on the principle of change of capacitance in proportion to applied acceleration. These accelerometers come in different shapes and sizes. In one type, the seismic mass of the accelerometer is made as the movable element of an electrical oscillator as shown in Figure 36.11. The seismic mass is supported by a resilient parallel-motion beam arrangement from the base. The system is characterized to have a certain defined nominal frequency when undisturbed. If the device is accelerated, the frequency varies above and below the nominal value, depending on the direction of the acceleration.

The seismic mass carries an electrode located in opposition to a number of base-fixed electrodes that define variable capacitors. The base-fixed electrodes are resistance coupled in the feedback path of a wideband, phase-inverting amplifier. The gain of the amplifier is made of such a value to ensure

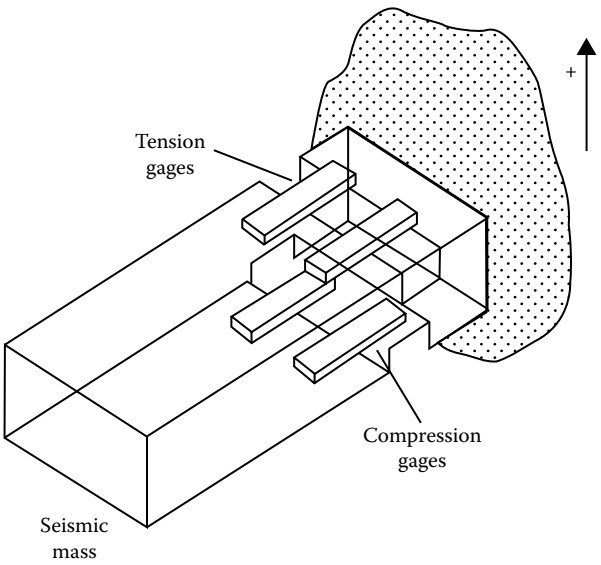

FIGURE 36.10 Bonding of piezoelectric and piezoresistive elements onto an inertial system. As the inertial member vibrates, deformation of the tension and compression gages causes the resistance to change. The change in resistance is picked up and processed further. Accelerometers based on PZTs are particularly useful in medium- to high-frequency applications.

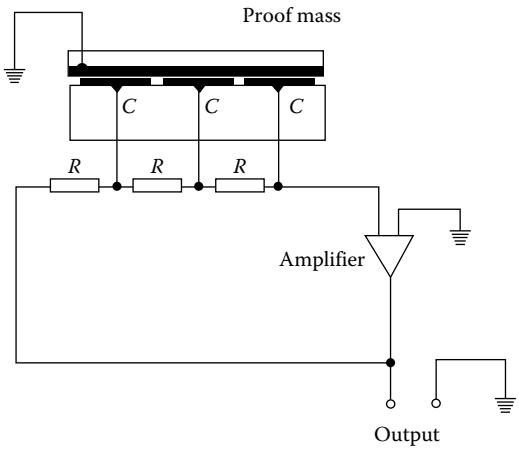

FIGURE 36.11 A typical differential capacitive accelerometer. The proof mass is constrained in its null position by a spring. Under acceleration, variable frequencies are obtained in the electric circuit. In a slightly different version, the proof mass may be constrained by an electrostatic feedback force, thus resulting in a convenient mechanical simplicity.

maintenance of oscillations over the range of variation of capacitance determined by the applied acceleration. The value of the capacitance C for each of the variable capacitor is given by

$$C = \frac{\varepsilon k S}{h} \tag{36.19}$$

where
- k is the dielectric constant
- ε is the permittivity of free space
- S is the area of electrode
- h is the variable gap

Denoting the magnitude of the gap for zero acceleration as h_0, the value of h in the presence of acceleration a may be written as

$$h = h_0 + \frac{ma}{K} \tag{36.20}$$

where m is the value of the proof mass and K is the spring constant. Thus,

$$C = \frac{\varepsilon k S}{(h_0 + ma/K)} \tag{36.21}$$

If the frequency of oscillation of the resistance-capacitance-type circuit is given by the expression, then

$$f = \frac{\sqrt{6}}{2\pi RC} \tag{36.22}$$

Substituting this value of C in Equation 36.21 gives

$$f = \left(h_0 + \frac{ma}{K}\right) \frac{\sqrt{6}}{2\pi R\varepsilon kS} \tag{36.23}$$

Denoting the constant quantity $(\sqrt{6}/2\pi R\varepsilon kS)$ as B and rewriting Equation 36.23 give

$$f = Bh_0 + \left(\frac{Bma}{K}\right) \tag{36.24}$$

The first term on the right-hand side expresses the fixed bias frequency f_0, and the second term denotes the change in frequency resulting from acceleration, so that the expression may be written as

$$f = f_0 + f_a \tag{36.25}$$

If the output frequency is compared with an independent source of constant frequency f_0, f_a can be determined.

A commonly used example of a capacitive-type accelerometer is based on a thin diaphragm with spiral flexures that provide the spring, proof mass, and moving plate necessary for the differential capacitor, as shown in Figure 36.12. Plate motion between the electrodes pumps air parallel to the plate surface and through holes in the plate to provide squeeze film damping. Since air viscosity is less temperature sensitive than oil, the desired damping ratio of 0.7 hardly changes more than 15%. A family of such instruments is readily available, having full-scale ranges from ±0.2 *g* (4 Hz flat response) to ±1000 *g* (3000 Hz), cross-axis sensitivity less than 1%, and full-scale output of ±1.5 V. The size of a typical device is about 25 mm^3 with a mass of 50 g.

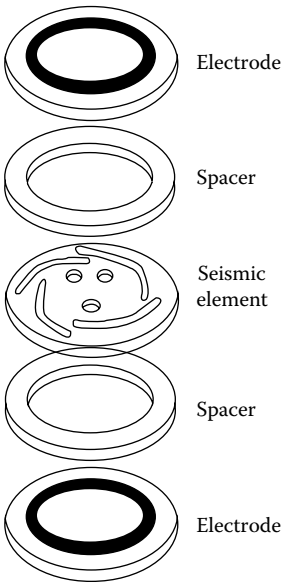

FIGURE 36.12 A diaphragm-type capacitive accelerometer. The seismic element is cushioned between the electrodes. Motion of the mass between the electrodes causes air movement through the holes, which provides a squeeze film damping. In some cases, oil can be used as the damping element.

36.6 Strain-Gage Accelerometers

Strain-gage accelerometers are based on resistance properties of electrical conductors. If a conductor is stretched or compressed, its resistance alters due to two reasons: dimensional changes and the changes in the fundamental property of material called *piezoresistance*. This indicates that the resistivity ρ of the conductor depends on the mechanical strain applied onto it. The dependence is expressed as the gage factor:

$$\left(\frac{dR/R}{dL/L}\right) = 1 + 2\nu + \left(\frac{d\rho/\rho}{dL/L}\right) \tag{36.26}$$

where

1 is the resistance change due to length
2ν is the resistance change due to area
$(d\rho/\rho)/(dL/L)$ is the resistance change due to piezoresistivity

In acceleration measurements, the resistance strain gages can be selected from different types, including unbonded metal-wire gages, bonded metal-wire gages, bonded metal-foil gages, vacuum-deposited thin-metal-film gages, bonded semiconductor gages, and diffused semiconductor gages. However, usually, bonded and unbonded metal-wire gages find wider applications in accelerometers. Occasionally, bonded semiconductor gages, known as piezoresistive transducers, are used but suffer from high-temperature sensitivities, nonlinearity, and some mounting difficulties. Nevertheless, in recent years, they have found new application areas with the development of micromachine transducer technology, which is discussed in detail in Section 36.14.3.

Unbonded strain-gage accelerometers use the strain wires as the spring element and as the motion transducer, using similar arrangements as in Figure 36.10. They are useful for general-purpose motion and vibration measurements from low to medium frequencies. They are available in wide ranges and characteristics, typically ±5–±200 *g* full scale, natural frequency 17–800 Hz, 10 V excitation voltage AC or DC, full-scale output ±20–±50 mV, resolution less than 0.1%, inaccuracy less than 1% full scale, and cross-axis sensitivity less than 2%. Their damping ratio (using silicone oil damping) is 0.6–0.8 at room temperature. These instruments are small and lightweight, usually with a mass of less than 25 g.

Bonded strain-gage accelerometers generally use a mass supported by a thin flexure beam. The strain gages are cemented onto the beam to achieve maximum sensitivity, temperature compensation, and a good sensitivity to both cross-axis and angular accelerations. Their characteristics are similar to unbonded strain-gage accelerometers but have larger sizes and weights. Often, silicone oil is used for damping. Semiconductor strain gages are widely used as strain sensors in cantilever beam/mass types of accelerometers. They allow high outputs (0.2–0.5 V full scale). Typically, a ±25 *g* acceleration unit has a flat response from 0 to 750 Hz, a damping ratio of 0.7, a mass of 28 g, and an operational temperature of −18 °C to +93 °C. A triaxial ±20,000 *g* model has a flat response from 0 to 15 kHz, a damping ratio 0.01, a compensation temperature range of 0°C–45°C, 13 × 10 × 13 mm in size, and 10 g in mass.

36.7 Seismic Accelerometers

These accelerometers make use of a seismic mass that is suspended by a spring or a lever inside a rigid frame. The schematic diagram of a typical instrument is shown in Figure 36.1. The frame carrying the seismic mass is connected firmly to the vibrating source whose characteristics are to be measured. As the system vibrates, the mass tends to remain fixed in its position so that the motion can be registered as a relative displacement between the mass and the frame. This displacement is sensed by an appropriate transducer and the output signal is processed further. Nevertheless, the seismic mass does not remain absolutely steady, but for selected frequencies, it can satisfactorily act as a reference position.

By proper selection of mass, spring, and damper combinations, the seismic instruments may be used for either acceleration or displacement measurements. In general, a large mass and soft spring are suitable for vibrations and displacements, while a relatively small mass and stiff spring are used in accelerometers.

The following equation may be written by using Newton's second law of motion to describe the response of seismic arrangements similar to what is shown in Figure 36.1:

$$\frac{md^2x_2}{dt^2} + \frac{cdx_2}{dt} + kx_2 = \frac{cdx_1}{dt} + kx_1 + mg\ \cos(\theta) \tag{36.27}$$

where

x_1 is the displacement of the vibration frame
x_2 is the displacement of the seismic mass
c is the velocity constant
k is the spring constant

Taking md^2x_1/dt^2 from both sides of the equation and rearranging give

$$m\frac{d^2z}{dt^2} + c\frac{dz}{dt} + kz = mg\ \cos(\theta) - m\frac{d^2x_1}{dt^2} \tag{36.28}$$

where

$z = x_2 - x_1$ is the relative motion between the mass and the base
θ is the angle between sense axis and gravity

In Equation 36.27, it is assumed that the damping force on the seismic mass is proportional to velocity only. If a harmonic vibratory motion is impressed on the instrument such that:

$$x_1 = x_0 \sin \omega_1 t \tag{36.29}$$

where ω_1 is the frequency of vibration, in rad s^{-1}.

Writing

$$\frac{md^2x_1}{dt^2} = mx_0{\omega_1}^2 \sin\omega_1 t$$

modifies Equation 36.28 as

$$m\frac{d^2z}{dt^2} + c\frac{dz}{dt} + kz = mg\cos(\theta) + ma_1 \sin\omega_1 t \tag{36.30}$$

where $a_1 = mx_0\omega_1^2$.

Equation 36.30 will have transient and steady-state solutions. The steady-state solution of the differential Equation 36.30 can be determined as

$$z = \left(\frac{mg\cos(\theta)}{k}\right) + \left(\frac{ma_1 \sin\omega_1 t}{(k - m{\omega_1}^2 + jc\omega_1)}\right) \tag{36.31}$$

Rearranging Equation 36.31 results in

$$z = \left(\frac{mg\cos(\theta)}{\omega_n}\right) + \left\{\frac{a_1 \sin(\omega_1 - \phi)}{[\omega_n{}^2(1-r^2)^2 + (2\zeta r)^2]^{1/2}}\right\} \tag{36.32}$$

where

$\omega_n = \sqrt{k/m}$ is the natural frequency of the seismic mass
$\zeta = c/2\sqrt{km}$ is the damping ratio and also can be written in terms of critical damping ratio as $\zeta = c/c_c$, where $\left(c_c = 2\sqrt{km}\right)$
$\phi = \tan^{-1}(c\omega_1/(k - m\omega_1^2))$ is the phase angle
$r = \omega_1/\omega_n$ is the frequency ratio

A plot of Equation 36.32, $(x_1 - x_2)_0/x_0$ against frequency ratio ω_1/ω_n, is illustrated in Figure 36.13. This figure shows that the output amplitude is equal to the input amplitude when $c/c_c = 0.7$ and $\omega_1/\omega_n > 2$. The output becomes essentially a linear function of the input at high-frequency ratios. For satisfactory system performance, the instrument constant c/c_c and ω_n should carefully be calculated or obtained from calibrations. In this way, the anticipated accuracy of measurement can be predicted for frequencies of interest.

If the seismic instrument has a low natural frequency and a displacement sensor is used to measure the relative motion z, then the output is proportional to the displacement of the transducer case. If the velocity sensor is used to measure the relative motion, the signal is proportional to the velocity of the transducer. This is valid for frequencies significantly above the natural frequency of the transducer. However, if the instrument has a high natural frequency and the displacement sensor is used, the measured output is proportional to the acceleration:

$$kz = \frac{m\, d^2x_1}{dt^2} \tag{36.33}$$

This equation is true since displacement x_2 becomes negligible in comparison to x_1.

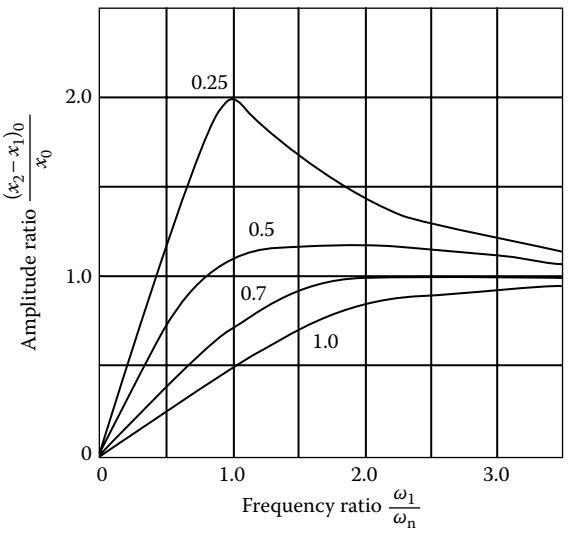

FIGURE 36.13 A typical displacement of a seismic instrument. Amplitude becomes large at low damping ratios. The instrument constants should be selected such that, in measurements, the frequency of vibration is much higher than the natural frequency (e.g., greater than by a factor of 2). Optimum results are obtained when the value of instrument constant c/c_c is about 0.7.

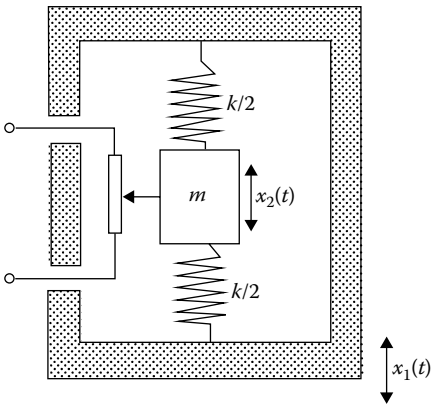

FIGURE 36.14 A potentiometer accelerometer. The relative displacement of the seismic mass is sensed by a potentiometer arrangement. The potentiometer adds extra weight, making these accelerometers relatively heavier. Suitable liquids filling the frame can be used as damping elements. These accelerometers are mainly used in low-frequency applications.

In these instruments, the input acceleration a_0 can be calculated by simply measuring $(x_1 - x_2)_0$. Generally, in acceleration measurements, unsatisfactory performance is observed at frequency ratios above 0.4. Thus, in such applications, the frequency of acceleration must be kept well below the natural frequency of the instrument. This can be accomplished by constructing the instrument to have a low natural frequency by selecting soft springs and large masses.

Seismic instruments are constructed in a variety of ways. Figure 36.14 illustrates the use of a voltage divider potentiometer for sensing the relative displacement between the frame and the seismic mass. In the majority of potentiometric instruments, the device is filled with a viscous liquid that interacts continuously with the frame and the seismic mass to provide damping. These accelerometers have low frequency of operation (less than 100 Hz) and are mainly intended for slow varying acceleration and low-frequency vibrations. A typical family of such instrument offers many different models, covering the range of ±1 to ±50 *g* full scale. The natural frequency ranges from 12 to 89 Hz, and the damping ratio ζ can be kept between 0.5 and 0.8, by using a temperature-compensated liquid damping arrangement. Potentiometer resistance can be selected in the range of 1,000–10,000 Ω, with a corresponding resolution of 0.45%–0.25% of full scale. The cross-axis sensitivity is less than ±1%. The overall accuracy is ±1% of full scale or less at room temperatures. The size is about 50 mm^3, with a mass of about 1/2 kg.

Linear variable differential transformers (LVDTs) offer another convenient means to measure the relative displacement between the seismic mass and the accelerometer housing. These devices have higher natural frequencies than potentiometer devices, up to 300 Hz. Since the LVDT has lower resistance to the motion, hence, it offers much better resolution. A typical family of liquid-damped differential-transformer accelerometers exhibits the following characteristics: full-scale range from ±2 to ±700 *g*, natural frequency from 35 to 620 Hz, nonlinearity 1% of full scale, the full-scale output about 1 V with an LVDT excitation of 10 V at 2000 Hz, damping ratio 0.6–0.7, residual voltage at null less than 1%, and hysteresis less than 1% full scale; the size is 50 mm^3, with a mass of about 120 g.

Electric resistance strain gages are also used for displacement sensing of the seismic mass as shown in Figure 36.15. In this case, the seismic mass is mounted on a cantilever beam rather than on springs. Resistance strain gages are bonded on each side of the beam to sense the strain in the beam resulting from the vibrational displacement of the mass. Damping for the system is provided by a viscous liquid that entirely fills the housing. The output of the strain gages is connected to an appropriate electric

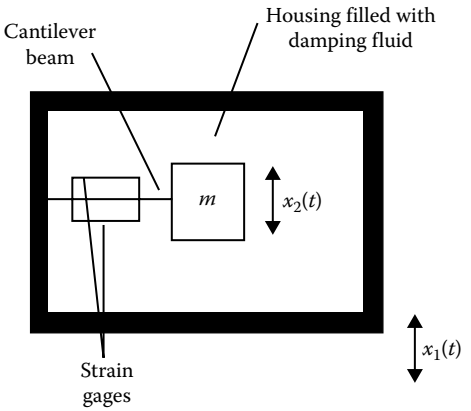

FIGURE 36.15 A strain-gage seismic instrument. The displacement of the proof mass is sensed by piezoresistive strain gages. The natural frequency of the system is low, due to the need of a long lever beam to accommodate the strain gages. The signal is processed by bridge circuits.

bridge circuit. The natural frequency of such a system is about 300 Hz. The low natural frequency is due to the need for a sufficiently large cantilever beam to accommodate the mounting of the strain gages. Other types of seismic instruments using piezoelectric transducers and seismic masses are discussed in detail in the section dedicated to piezoelectric-type accelerometers.

Seismic vibration instruments are affected seriously by the temperature changes. Devices employing variable resistance displacement sensors require correction factors to account for resistance change due to temperature. The damping of the instrument may also be affected by changes in the viscosity of the fluid due to temperature. For example, the viscosity of silicone oil, often used in these instruments, is strongly dependent on temperature. One way of eliminating the temperature effect is by using an electrical resistance heater in the fluid to maintain the temperature at a constant value regardless of surrounding temperatures.

36.8 Inertial Types, Cantilever, and Suspended-Mass Configuration

There are a number of different inertial accelerometers, including gyropendulum, reaction rotor, vibrating string, and centrifugal-force-balance types. In many of them, the force required to constrain the mass in the presence of the acceleration is supplied by an inertial system.

A vibrating string-type instrument, Figure 36.16, makes use of proof mass supported longitudinally by a pair of tensioned, transversely vibrating strings with uniform cross section and having equal lengths and masses. The frequency of vibration of the strings is set to several thousand cycles per second. The proof mass is supported radially in such a way that the acceleration normal to strings does not affect the tension of the string. In the presence of acceleration along the sensing axis, a differential tension exists on the two strings, thus altering the frequency of vibration. From the second law of motion, the frequencies can be written as

$$f_1^2 = \frac{T_1}{4m_s l} \quad \text{and} \quad f_2^2 = \frac{T_2}{4m_s l} \tag{36.34}$$

where

T is the tension

m_s and l are the masses and lengths of strings, respectively

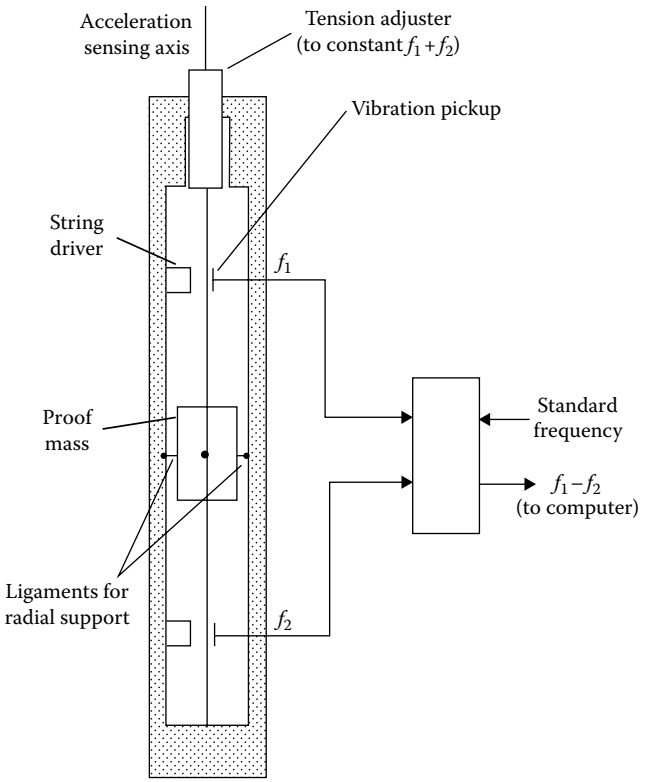

FIGURE 36.16 A vibrating string accelerometer. A proof mass is attached to two strings of equal mass and length and supported radially by suitable bearings. The vibration frequencies of strings are dependent on the tension imposed by the acceleration of the system in the direction of the sensing axis.

Quantity $(T_1 - T_2)$ is proportional to ma, where a is the acceleration along the axis of the strings. An expression for the difference of the frequency-squared terms may be written as

$$f_1^2 - f_2^2 = \left(\frac{T_1 - T_2}{4ml_s}\right) = \left(\frac{ma}{4m_s l}\right) \tag{36.35}$$

Hence,

$$f_1 - f_2 = \frac{ma}{\left[(f_1 + f_2)4m_s l\right]} \tag{36.36}$$

The sum of frequencies $(f_1 + f_2)$ can be held constant by servoing the tension in the strings with reference to the frequency of a standard oscillator. Then, the difference between the frequencies becomes linearly proportional to acceleration. In some versions, the beam-like property of the vibratory elements is used by gripping them at nodal points corresponding to the fundamental mode of vibration of the beam. Improved versions of these devices lead to cantilever-type accelerometers, as discussed next.

In cantilever-type accelerometers, a small cantilever beam mounted on the block is placed against the vibrating surface, and an appropriate mechanism is provided for varying the beam length. The beam length is adjusted such that its natural frequency is equal to the frequency of the vibrating surface—hence the resonance condition obtained. Slight variations of cantilever beam-type arrangements are finding new applications in microaccelerometers.

In a different type of suspended-mass configuration, a pendulum is used that is pivoted to a shaft rotating about a vertical axis. The pick-off is provided for the pendulum and the shaft speed. The system is servo controlled to maintain it at null position. Gravitational acceleration is balanced by the centrifugal acceleration. Shaft speed is proportional to the square root of the local value of the acceleration.

All inertial force accelerometers described earlier have the property of absolute instruments. That is, their scale factors can be predetermined solely by establishing mass, length, and time quantities, as distinguished from voltage, and spring stiffness.

36.9 Electrostatic Force Feedback Accelerometers

Electrostatic accelerometers are based on Coulomb's law between two charged electrodes. They measure the voltage in terms of force required to sustain a movable electrode of known area, mass, and separation from an affixed electrode. The field between the electrodes is given by

$$E = \frac{Q}{\varepsilon k S} \tag{36.37}$$

where

E is the intensity or potential gradient (dV/dx)
Q is the charge
S is the area of the conductor
k is the dielectric constant of the space outside the conductor

Using this expression, it can be shown that the force per unit area of the charged conductor (in N m^{-2}) is given by

$$\frac{F}{S} = \frac{Q^2}{2\varepsilon k S^2} = \frac{\varepsilon k E^2}{2} \tag{36.38}$$

In an electrostatic force feedback-type accelerometer (similar in structure to that in Figure 36.10), an electrode of mass m and area S is mounted on a light pivoted arm for moving relative to the fixed electrodes. The nominal gap, h, between the pivoted and fixed electrodes is maintained by means of a force balancing servo system capable of varying the electrode potential in response to signals from a pick-off that senses relative changes in the gaps.

Considering one movable electrode and one stationary electrode and assuming that the movable electrode is maintained at a bias potential V_1 and the stationary one at a potential V_2, the electrical intensity E in the gap can be expressed as

$$E_1 = \frac{(V_1 - V_2)}{h} \tag{36.39}$$

so that the force of attraction may be found as

$$F_1 = \frac{\varepsilon k E^2 S}{(2h^2)} = \frac{\varepsilon k (V_1 - V_2)^2 S}{(2h^2)} \tag{36.40}$$

In the presence of acceleration, if V_2 is adjusted to restrain the movable electrode to null position, the expression relating acceleration and electrical potential may be given by

$$a = \frac{F_1}{m} = \frac{\varepsilon k (V_1 - V_2)^2 S}{(2h^2 m)} \tag{36.41}$$

The device thus far described can measure acceleration in one direction only, and the output is of quadratic character; that is,

$$(V_1 - V_2) = D\sqrt{a} \tag{36.42}$$

where D is the constant of proportionality.

The output can be linearized in a number of ways, for example, by quarter-square method. If the servo controller applies a potential $-V_2$ to other fixed electrode, the force of attraction between this electrode and the movable electrode becomes

$$a = \frac{F_1}{m} = \frac{\varepsilon k(V_1 + V_2)^2 S}{(2h^2 m)} \tag{36.43}$$

and the force-balance equation of the movable electrode when the instrument experiences a downward acceleration a is

$$ma = F_1 - F_2 = \frac{[(V_1 + V_2)^2 - (V_1 - V_2)^2]\varepsilon kS}{(2h^2 m)}$$

or

$$= \frac{\varepsilon kS(4V_1V_2)}{(2h^2 m)} \tag{36.44}$$

Hence, if the bias potential V_1 is held constant and the gain of the control loop is high so that variations in the gap are negligible, the acceleration becomes a linear function of the controller output voltage V_2 as

$$a = V_2\left[\frac{\varepsilon kS(2V_1)}{(h^2 m)}\right] \tag{36.45}$$

The principal difficulty in mechanizing the electrostatic force accelerometer is the relatively high electric field intensity required to obtain adequate force. Also, extremely good bearings are necessary. Damping can be provided electrically or by viscosity of gaseous atmosphere in the interelectrode space if the gap h is sufficiently small.

The main advantages of the electrostatic accelerometers include extreme mechanical simplicity, low-power requirements, absence of inherent sources of hysteresis errors, zero temperature coefficients, and ease of shielding from stray fields.

36.10 Microaccelerometers

By the end of the 1970s, it became apparent that the essentially planar processing IC (integrated circuit) technology could be modified to fabricate 3D electromechanical structures, called micromachining. Accelerometers and pressure sensors were among the first IC sensors and today they are produced in large numbers by a diverse range of manufacturers. The first accelerometer was developed in 1979. Since then, technology has been progressing rapidly to the point where an extremely diverse range of accelerometers are cost-effectively available for mass consumption. Most sensors use

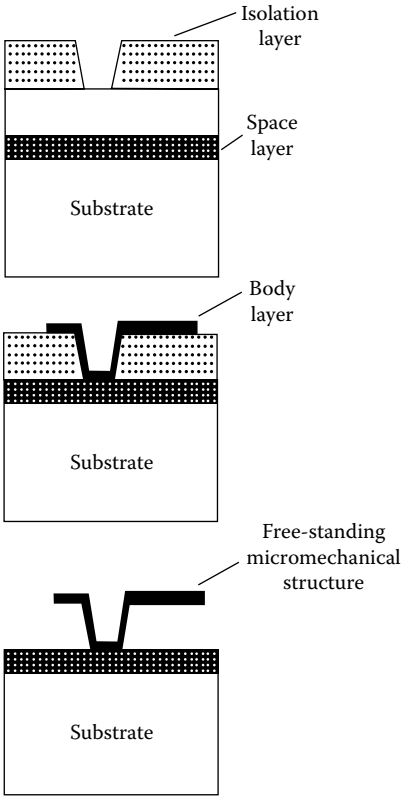

FIGURE 36.17 Steps of surface micromachining. The acceleration-sensitive, 3D structure is formed on a substrate and a sacrificial element. The sacrificial element is etched to leave a free-standing structure. The spacing between the structure and the substrate is about 2 μm.

bulk micromachining rather than surface micromachining techniques. In bulk micromachining, the flexures, resonant beams, and all other critical components of the accelerometer are made from bulk silicon in order to exploit the full mechanical properties of single-crystal silicon. With proper design and film process techniques, the bulk micromachining yields in manufacturing of extremely stable and robust accelerometers.

The selective etching of multiple layers of deposited thin films, or surface micromachining, allows movable microstructures to be fabricated on silicon wafers. With surface micromachining, layers of structure material are disposed and patterned, as shown in Figure 36.17. These structures are formed by polysilicon and a sacrificial material such as silicon dioxide. The sacrificial material acts as an intermediate spacer layer and is etched away to produce a free-standing structure. Surface machining technology also allows smaller and more complex structures to be built in multiple layers on a single substrate.

The operational principles of microaccelerometers are very similar to capacitive force-balance-type accelerometers or vibrating beam types, as discussed earlier. Nevertheless, manufacturing techniques may change from one manufacturer to another. In general, the vibrating beam accelerometers are preferred because of better air-gap properties and improved bias performance characteristics.

The vibrating beam accelerometers, also called resonant beam force transducers, are made in such a way that the acceleration along a positive input axis places the vibrating beam in tension. Thus, the resonant

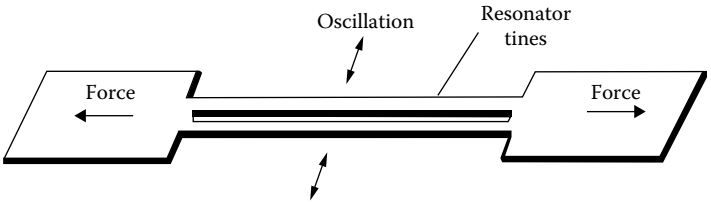

FIGURE 36.18 A DETF acceleration sensor. Two beams are vibrated 180° out of phase to eliminate reaction forces at the beam ends. The resonant frequency of the beam is altered by the acceleration. The signal processing circuits are also integrated in the same chip.

frequencies of the vibrating beam increase or decrease with the applied acceleration. Another version known as the mechanically coupled beam structure, also known as a double-ended tuning fork (DETF), is shown in Figure 36.18.

In DETF, an electronic oscillator capacitively couples energy into two vibrating beams to keep them oscillating at their resonant frequency. The beams vibrate 180° out of phase to cancel reaction forces at the ends. The dynamic cancellation effect of the DETF design prevents energy from being lost through the ends of the beam. Hence, the dynamically balanced DETF resonator has a high Q factor, which leads to a stable oscillator circuit. The acceleration signal is an output from the oscillator as a frequency-modulated square wave that can be used for digital interface.

The frequency of resonance of the system must be much higher than any input acceleration, and this limits the measurable range. In a typical military micromachine accelerometer, the following characteristics are given: range ±1,200 g, sensitivity 1.11 Hz g^{-1}, bandwidth 2,500 Hz, unloaded DETF frequency 9,952 Hz, frequency at +1,200 g 11,221 Hz, frequency at –1,200 g 8,544 Hz, and temperature sensitivity 5 mg°C^{-1}. Accelerometer size is 6 mm diameter × 4.3 mm length, with a mass of about 9 g, and it has a turn on time less than 60 s. The accelerometer is powered with +9 to +16 V DC and the nominal output is a 9000 Hz square wave.

Surface micromachining has also been used to manufacture specific application accelerometers, such as air-bag applications in automotive industry. In one type, a three-layer differential capacitor is created by alternate layers of polysilicon and phosphosilicate glass (PSG) on a 0.38 mm thick and 100 mm long wafer. A silicon wafer serves as the substrate for the mechanical structure. The trampoline-shaped middle layer is suspended by four supporting arms. This movable structure is the seismic mass for the accelerometer. The upper and lower polysilicon layers are fixed plates for the differential capacitors. The glass is sacrificially etched by hydrofluoric acid.

36.10.1 3D Accelerometers

Micromachined IC accelerometers are produced in a single chip for measuring accelerations in three dimensions: X, Y, and Z axes. They offer integrated features including multiple analog to digital converters (ADCs), digital low-pass filters, and other signal processors. They have selectable sensitivity ranges, typically ±2, ±4, ±8, or ±16 g. Many of these devices can be configured to detect motion pulses as single taps, double taps, and 0 g (free fall) conditions on any or all axes. They also can be integrated with devices such as gyroscopes and temperature sensors that require sensitive signal processing techniques. They are small and can be housed in 3 × 3 × 1 mm packages.

36.11 Cross-Axis Sensitivity

A vibrational structure may have been subjected to different forms of vibrations, such as compressional, torsional, and transverse, or a combination of all these vibrations may take place simultaneously, which makes the analysis and measurements difficult and complex. It was discussed

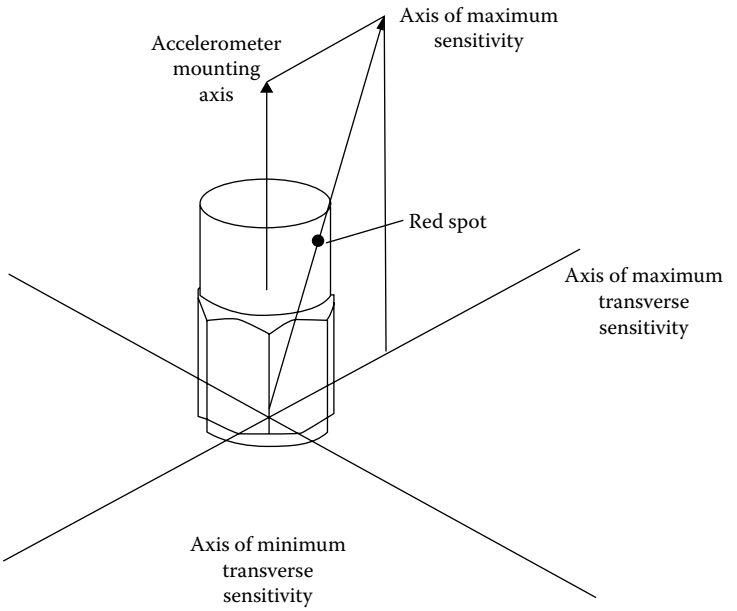

FIGURE 36.19 Vectorial illustration of cross-axis sensitivity. Accelerometers may sense vibrations not only in the direction of main axis but also perpendicular to the main axis. These cross-axis responses are minimized in many accelerometers to a value less than 1%. Sometimes, this sensitivity is used to determine the correct orientation of the device.

earlier that the differential equations governing the vibrational motion of a structure were dependent on the number of degrees of freedom, which can be described as a function of the space coordinates $f(x, y, z, t)$. For example, the transverse vibrations of structures may be a fourth-order differential equation.

Fortunately, most common acceleration and vibration measurements are simple in nature, being either compressional or torsional types. They can easily be expressed as second-order differential equations, as explained in the frequency response section. However, during measurements, most accelerometers are affected by transverse vibrations and their sensitivity can play a major role in the accuracy of the measurements.

The transverse, also known as cross-axis sensitivity, of an accelerometer is its response to acceleration in a plane perpendicular to the main accelerometer axis, as shown in Figure 36.19. The cross-axis sensitivity is normally expressed in percent of the main axis sensitivity and should be as low as possible. There is not a single value of cross-axis sensitivity, but it varies depending on the direction. The direction of minimum sensitivity is usually supplied by the manufacturer.

The measurement of the maximum cross-axis sensitivity is part of the individual calibration procedure and should always be less than 3%–4%. If high levels of transverse vibration are present, this may result in erroneous overall results. In this case, separate arrangements should be made to establish the level and frequency contents of the cross-axis vibrations. Cross-axis sensitivities of typical accelerometers are mentioned in the relevant sections: 2%–3% for piezoelectric types and less than 1% in most others.

36.12 Selection, Full-Scale Range, and Overload Capability

Ultimate care must be exercised for the selection of the correct accelerometer to meet the requirements of a particular application. At first glance, there may seem to be a confusingly large repertoire of accelerometers available; however, they can be classified into two main groups. The first group is

the general-purpose accelerometers offered in various sensitivity, frequency, full-scale range, and overload capabilities together with different mechanical and electrical connection options. The second group of accelerometers is the special types that have characteristics targeted toward a particular application.

In deciding the application type (e.g., general purpose or special) and the accelerometer to be employed, the following characteristics need to be considered: transient response or cross-axis sensitivity; frequency range; sensitivity, mass, and dynamic range; cross-axis response; and environmental conditions such as temperature and cable noise. Some useful hints about these characteristics are given in the following.

36.12.1 Frequency Range

Acceleration measurements are normally confined to using the linear portion of the response curve. The response is limited at the low frequencies as well as at the high frequencies by their natural resonances. As a rule of thumb, the upper frequency limit for the measurement can be set to one-third of the accelerometer's resonance frequency such that the vibrations measured will be less than 1 dB in linearity. It should be noted that an accelerometer's useful frequency range can significantly be higher, that is, to 1/2 or 2/3 of its resonant frequency. The measurement frequencies may be set to higher values in applications where lower linearity (e.g., 3 dB) may be acceptable, as in the case of monitoring internal conditions of machines since the reputability is more important than the linearity. The lower measuring frequency limit is determined by two factors. The first is the low-frequency cut-off of the associated preamplifiers. The second is the effect of ambient temperature fluctuations that an accelerometer could be sensitive to.

36.13 Selection, Full-Scale Range, and Overload Capability (Frequency Range): Sensitivity, Mass, and Dynamic Range

Ideally, the higher the transducer sensitivity, the better, but compromises might have to be made for sensitivity versus frequency, range, overload capacity, and size.

Accelerometer mass becomes important when using it on small and light test objects. The accelerometer should not load the structural member, since additional mass can significantly change the levels and frequency presence at measuring points and invalidate the results. As a general rule, the accelerometer mass should not be greater than one-tenth the effective mass of the part or the structure that it is mounted onto for measurements.

The dynamic range of the accelerometer should match the high or low acceleration levels of the measured objects. General-purpose accelerometers can be linear up to 5,000 *g*–10,000 *g*, which is well into the range of most mechanical shocks. Special accelerometers can measure up to 100,000 *g*.

An important point in the practical application of accelerometers is that if mechanical damping is a problem, air damping is preferable to oil damping, since oil damping is extremely sensitive to viscosity changes. If the elements are temperature stable, electronic damping may be sufficient.

36.13.1 Transient Response

Shocks are characterized as sudden releases of energy in the form of short-duration pulses exhibiting various shapes and rise times. They have high magnitudes and wide frequency contents. In applications where transients and shock measurements are involved, the overall linearity of the measuring system may be limited to high and low frequencies by phenomena known as *zero shift*

and *ringing*, respectively. The zero shift is caused by both the phase nonlinearity in the preamplifiers and the accelerometer not returning to steady-state operating conditions after being subjected to high shocks. Ringing is caused by high-frequency components of the excitation near resonance frequency preventing the accelerometer to return to its steady state. To avoid measuring errors due to these effects, the operational frequency of the measuring system should be limited to the linear range.

36.13.2 Full-Scale Range and Overload Capability

Most accelerometers are able to measure acceleration in both positive and negative directions. They are also designed to be able to accommodate overload capacity. Appropriate discussions are made on full-scale range and overload capacity of accelerometers in the relevant sections. Manufacturers usually supply information on these characteristics.

36.13.3 Environmental Conditions

In the selection and implementation of accelerometers, environmental conditions such as temperature ranges, temperature transients, cable noise, magnetic field effects, humidity, and acoustic noise need to be considered. Manufacturers also supply information on the environmental conditions for effective usage.

36.14 Signal Conditioning

Most of the common signal conditioners are appropriate to use for interfacing accelerometers to computers or other instruments. Particular caution needs to be exercised to provide appropriate electric loads when self-generating accelerometers are used. Generally, the generated raw signals are amplified and filtered suitably by the circuits within the accelerometer casing supplied by the manufacturers. Nevertheless, piezoelectric and piezoresistive sensors require special signal conditioners with certain characteristics, as will be discussed in Sections 36.14.1 and 36.14.2. Examples of signal-conditioning circuits are also given for microaccelerometers.

36.14.1 Signal-Conditioning Piezoelectric Accelerometers

The piezoelectric accelerometers supply very small energy to the signal conditioners. They have high capacitive source impedances. The equivalent circuit of a piezoelectric accelerometer can be regarded as an active capacitor that charges itself when loaded mechanically. The configuration of external signal-conditioning elements is dependent on the equivalent circuit selected. The charge amplifier design of the conditioning circuit is the most common approach since the system gain and low-frequency responses are well defined. The performance of the circuit is independent of cable length and capacitance of the accelerometer.

A charge amplifier consists of a charge converter output voltage that occurs as a result of the charge input signal returning through the feedback capacitor to maintain the input voltage at the input level close to zero, as shown in Figure 36.20. An important point about charge amplifiers is that their sensitivities can be standardized. They basically convert the input charge to voltage first and then amplify this voltage. With the help of basic operational-type feedback, the amplifier input is maintained essentially at zero volts; therefore, it looks like a short circuit to the input. The charge converter output voltage that occurs as a result of a charge input signal is returned through

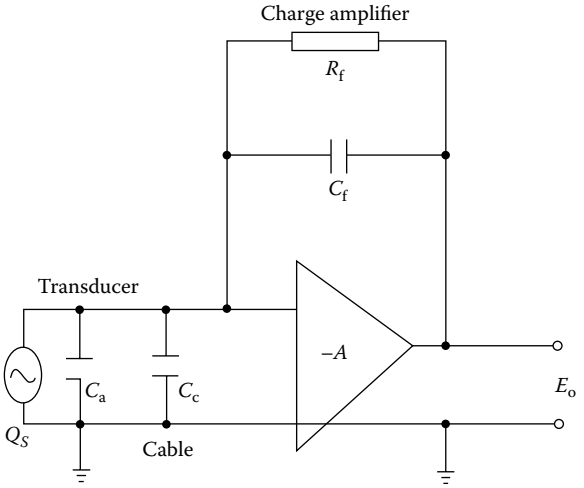

FIGURE 36.20 A typical charge amplifier. The transducer charge, proportional to acceleration, is first converted to voltage form so that it can be amplified. The output voltage is a function of the input charge. The response of the amplifier can be approximated by a first-order system. In PZT transducers, the preamplifier is integrated within the same casing.

the feedback capacitor to maintain the voltage at the input level near zero. Thus, the charge input is stored in the feedback capacitor, producing a voltage across it, that is, equal to the value of the charge input divided by the capacitance of the feedback capacitor. The complete transfer function of the circuit describing the relationship between the output voltage and the input acceleration magnitude can be determined by

$$\frac{E_o}{a_0} = \frac{S_a jR_f C_f \omega}{\left\{1 + jR_f C_f \left[1 + (C_a + C_c)/(1+G) \times C_f\right]\omega\right\}} \tag{36.46}$$

where

E_o is the charge converter output (V)
a_0 is the magnitude of acceleration (m s^{-2})
S_a is the accelerometer sensitivity (mV g^{-1})
C_a is the accelerometer capacitance (F)
C_c is the cable capacitance (F)
C_f is the feedback capacitance (F)
R_f is the feedback loop resistance
G is the amplifier open loop gain

In most applications, since C_f is selected to be large compared to $(C_a + C_c)/(1+G)$, the system gain becomes independent of the cable length. In this case, the denominator of the equation can be simplified to give a first-order system with roll-off at

$$f_{-3\,\mathrm{dB}} = \frac{1}{(2\pi R_f C_f)} \tag{36.47}$$

with a slope of 20 dB per decade. For practical purposes, the low-frequency response of this system is a function of well-defined electronic components and does not vary with cable length. This is an important feature when measuring low-frequency vibrations.

Many accelerometers are manufactured with preamplifiers and other signal-conditioning circuits integrated with the transducer enclosed in the same casing. Some accelerometer preamplifiers include integrators to convert the acceleration proportional outputs to either velocity or displacement proportional signals. To attenuate noise and vibration signals that lie outside the frequency range of interest, most preamplifiers are equipped with a range of high-pass and low-pass filters. This avoids interference from electric noise or signals inside the linear portion of the accelerometer frequency range. Nevertheless, it is worth mentioning that these devices usually have two time constants, external and internal. The mixture of these two time constants can lead to problems, particularly at low frequencies. The internal time constant is usually fixed by the manufacturer in design and construction. Special care must be observed to take care of the effect of external time constants by mainly observing strict impedance matching.

36.14.2 Signal Conditioning of Piezoresistive Transducers

Piezoresistive sensors have high-amplitude outputs, low output impedances, and low intrinsic noise. Most of them are designed for constant voltage excitations. They are usually calibrated for constant current excitations to minimize external influences. Many piezoresistive accelerometers are configured as part of a full bridge. In some cases, all four arms of the bridge are made from the sensors, as shown in Figure 36.21.

36.14.3 Microaccelerometers

In microaccelerometers, signal-conditioning circuitry is integrated within the same chip with the sensor as shown in Figure 36.22. A typical example of the signal-conditioning circuitry is given in Figure 36.23 in block diagram form. In this type of accelerometer, the electronic system is essentially a crystal-controlled oscillator circuit and the output signal of the oscillator is a frequency-modulated acceleration signal. Some circuits provide a buffered square-wave output that can directly be interfaced digitally. In this case, the need for analog to digital conversion is eliminated, thus removing one of the major sources of error. In other types of accelerometers, signal-conditioning circuits such as ADCs are retained within the chip.

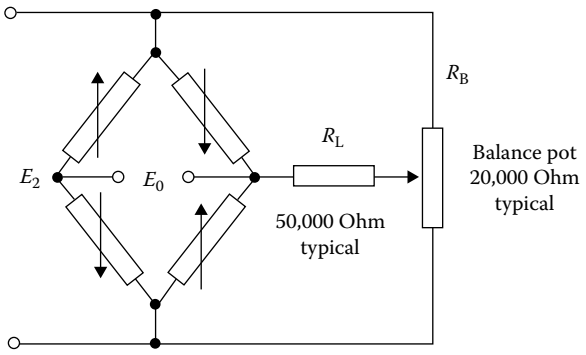

FIGURE 36.21 Bridge circuit for piezoresistive and strain-gage accelerometers. The strain gages form the four arms of the bridge. The two extra resistors are used for balancing and for the purpose of precision adjustment. This type of arrangement reduces temperature effects.

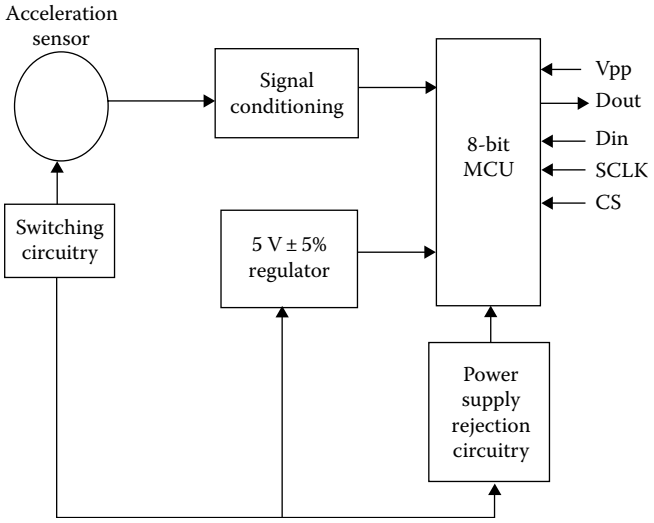

FIGURE 36.22 A block diagram of an accelerometer combined with MCU. The signal-conditioning, switching, and power supply circuits are integrated to form a microaccelerometer. The device can directly be interfaced with a digital signal processor or a computer. In some cases, ADCs and memory are also integrated within the chip.

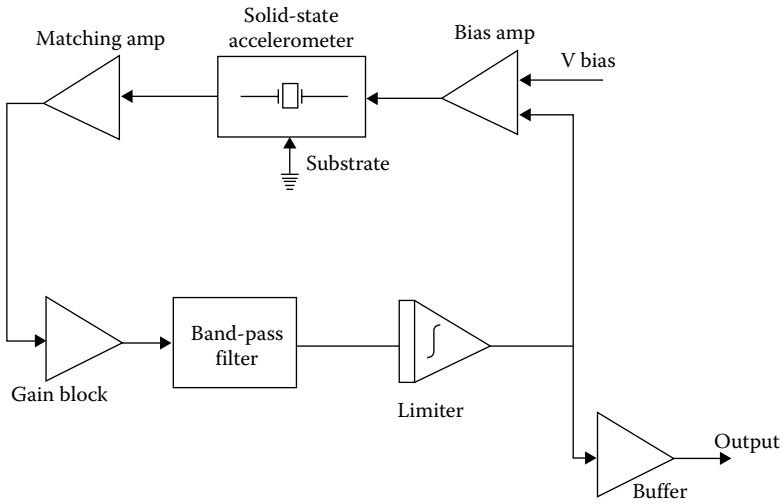

FIGURE 36.23 Block diagram of a signal-conditioning circuit of a microaccelerometer. The output signal of the oscillator is a frequency-modulated acceleration signal. The circuit provides a buffered square wave so that the output can directly be read into a digital device.

Bibliography

Bernstein, J., An overview of MEMS inertial sensing technology. http://www.sensorsmag.com/sensors/acceleration-vibration/an-overview-mems-inertial-sensing-technology-970 (accessed on September 9, 2011).

Connolly, C., Vibration isolation theory and practice, In: Conneely, K. (ed.), *Assembly Automation*, Emerald Publisher, U.K., Vol. 29, No. 1, pp. 8–13, 2009.

Doebelin, E. O., *Measurement Systems: Application and Design*, 4th edn., New York: McGraw-Hill, 1990.

Fleming, W. E., Overview of automotive sensors, *IEEE Sensors Journal*, 1(4), 296–308, 2001.

Hong, J. and Park, K., Design and control of six degree-of-freedom active vibration isolation table, *Review of Scientific Instruments*, American Institute of Physics, Vol. 81, No. 3, Article number 035106, 2010.

McConnell, K. G., *Vibration Testing: Theory and Practice*, New York: John Wiley & Sons, 1995.

Omega Engineering, Inc., Force Acceleration and Torque. http://www.omega.com/literature/transactions/volume3/force2.html (accessed on September 9, 2011).

Ripper, G. P., Dias, R. S., and Garcia, G. A., Primary accelerometer calibration problems due to vibration exciters, *Measurement*, 42(9), 1363–1369, 2009.

Silicon Design Inc., MEMS Accelerometers. http://www.silicondesigns.com/tech.html (accessed on September 15, 2011).

Stauffer, J. M., Dutoit, B., and Arbab, B., Standard MEMS sensor technologies for harsh environment, *Institution of Engineering and Technology Seminar on MEMS Sensors and Actuators*, London, U.K., pp. 93–96, 2006.

Partial List of Vendors and Suppliers

Allied International, 7 Hill St. Bedford Hills, NY 10507-1811, Phone: 914-241-6900, Fax: 914-241-6985, www.alliedinter.com

Allied Signal Aerospace, 15001-T N.E. 36th St. Redmond, WA 98073-9701, Phone: 425-885-3711, Fax: 425-885-8866, www.alliedinter.com

Automation Products Group, Inc.(APGSENSORS), 1025 W. 1700 N. Logan, UT 84321, Phone: 435-753-7300, 888-525-7300 (toll free), Fax: 435-753-7490, www.apgsensors.com

CEC Vibration Products Inc., 746 Arrow Grand Circle Covina, CA 91722, Phone: 626-468-1345, 800-468-1345 (toll free), Fax: 626-938-0202, www.cecvp.com

Davis/Inotek, 300 Garden Oaks Houston, TX 77018, Phone: 800-548-9409, Fax: 410-358-0252, www.davis.com

Electro-Sensors, Inc., 6111 Blue Circle Dr. Minnetonka, MN 55343-9108, Phone: 952-930-0100, 800-328-6170 (toll free), Fax: 952-930-0130, www.electro-sensors.com

Honeywell Sensing and Control, 1985 Douglas Dr. North, MN10-192B Golden Valley, MN 55422, Phone: 763-954-4818, 800-446-6555 (toll free), sensing.honeywell.com/index.cfm/ci_id/15…

Inertia Switch, Inc., 70 S. Greenbush Rd. Orangeburg, NY 10962, Phone: 845-359-8300, Fax: 845-359-6227, www.inertiaswitch.com

Instrumented Sensor Technology, Inc., 4704 Moore Street Okemos, MI 48864, Phone: +1 517 349-8487, Fax: +1 517 349-8469, www.isthq.com

Integrated Dynamics Engineering, Inc., 377 T-University Ave Westwood, MA 02090, Phone: 781-326-5700, Fax: 781-326-3004, www.ideworld.com

Jewell Instruments, LLC, 850 Perimeter Rd. Manchester, NH 03103, Phone: 603-669-6400, 800-638-3771 (toll free), Fax: 603-669-5962, www.jewellinstruments.com

Kearfott Guidance & Navigation, US Hwy. 70 Black Mountain, NC 28711, Phone: 828-686-3811, Fax: 828-686-3567, www.kearfott.com

Kinetic Ceramics, Inc., 26242 Industrial Blvd. Hayward, CA 94545-5012, Phone: 510-264-2140, 800-806-6016 (toll free), Fax: 510-264-2159, www.kineticceramics.com

Kistler North America, 75 John Glenn Dr. Amherst, NY 14228-2119, Phone: 716-691-5100, 888-KISTLER, 888-547-8537 (toll free), Fax: 716-691-5226, www.kistler.com

Measurement Specialties, Inc., 1000 Lucas Way Hampton, VA 23666, Phone: 757-766-1500, 800-745-8008 (toll free), Fax: 757-766-4297, www.meas-spec.com

Motion Sensors, Inc., 786 Pitts Chapel Rd. Elizabeth City, NC 27909, Phone: 252-331-2080, Fax: 252-331-1666, www.motionsensors.com

MTI Instruments, Inc., 325 Washington Ave., Extension Albany, NY 12205-5505, Phone: 518-218-2550, Fax: 518-218-2506, www.mtiinstruments.com

PCB Piezotronics, Inc., 3425 Walden Ave. Depew, NY 14043-2417, Phone: 716-684-0001, 800-828-8840 (toll free), Fax: 716-684-0987, www.pcb.com

Piezo Technologies, 8431 Georgetown Rd., Suite 300 Indianapolis, IN 46268, Phone: 317-876-4670, Fax: 317-876-4681, www.piezotechnologies.com

Schneider Electric-Hyde Park, 1875 Founders Dr. Dayton, OH 45420, Phone: 937-514-7207, Fax: 937-258-5830, www.sesensors.com

Select Controls, Inc., 45 Knickerbocker Ave. Bohemia, NY 11716-3110, Phone: 866-929-5312 (toll free), Fax: 631-567-9013, www.select-controls.com

Shock Watch, 1111 W. Mockingbird Lane, Suite 1050 Dallas, TX 75247, Phone: 214-630-9625, 800-527-9497 (toll free), Fax: 214-638-4512, www.shockwatch.com/

Silicon Designs, Inc., 1445 NW Mall St. Issaquah, WA 98027, Phone: (425) 391-8329, Fax: (425) 391-0446, www.silicondesigns.com/contact.html

Spectrum Sensors & Controls, 3939 West Ridge Rd. Suite A—108 Erie, PA 16505, Phone: 814-474-1571, www.specsensors.com

Vitec, Inc., 24755 Highpoint Rd. Cleveland, OH 44122-5915, Phone: 216-464-4670, 800-321-6384 (toll free), Fax: 216-464-5324, www.vitec-inc.com

Warren-Knight Instrument Co., 2045 Bennett Dr. Philadelphia, PA 19116-3019, Phone: 215-464-9300, Fax: 215-464-9303, www.warrenind.com

Wilcoxon Research, Inc., 20511 Seneca Meadows Pkwy. Germantown, MD 20876, Phone: 301-330-8811, 800-945-2696 (toll free), Fax: 301-330-8873, www.wilcoxon.com

37

Strain Measurement

Christopher S. Lynch
Georgia Tech

This chapter begins with a review of the fundamental definitions of strain and ways it can be measured. This is followed by a review of the many types of strain sensors and their application and sources for strain sensors and signal conditioners. Next, a more detailed look is taken at operating principles of various strain measurement techniques and the associated signal conditioning.

37.1 Fundamental Definitions of Strain

Stress and strain are defined in many elementary textbooks about the mechanics of deformable bodies [1,2]. The terms *stress* and *strain* are used to describe loads on and deformations of solid materials. The simplest types of solids to describe are homogeneous and isotropic. *Homogeneous* means the material properties are the same at different locations and *isotropic* means the material properties are independent of direction in the material. An annealed steel bar is homogeneous and isotropic, whereas a human femur is not homogeneous because the marrow has very different properties from the bone, and it is not isotropic because its properties are different along the length and along the cross section.

The concepts of stress and strain are introduced in the context of a long homogeneous isotropic bar subjected to a tensile load (Figure 37.1). The stress σ is the applied force F, divided by the cross-sectional area A. The resulting strain ε is the length change ΔL, divided by the initial length L. The bar elongates in the direction the force is pulling (longitudinal strain ε_L) and contracts in the direction perpendicular to the force (transverse strain ε_t).

When the strain is not too large, many solid materials behave like linear springs; that is, the displacement is proportional to the applied force. If the same force is applied to a thicker piece of material, the spring is stiffer and the displacement is smaller. This leads to a relation between force and displacement that depends on the dimensions of the material. Material properties, such as the density and specific heat, must be defined in a manner that is independent of the shape and size of the specimen. Elastic material properties are defined in terms of stress and strain. In the linear range of material response, the stress is proportional to the strain (Figure 37.2). The ratio of stress to strain for the bar under tension is an elastic constant called the Young's modulus E. The negative ratio of the transverse strain to longitudinal strain is the Poisson's ratio ν.

Forces can be applied to a material in a manner that will cause distortion rather than elongation (Figure 37.3). A force applied tangent to a surface divided by the cross-sectional area is described as a shear stress τ. The distortion can be measured by the angle change produced. This is the shear strain γ

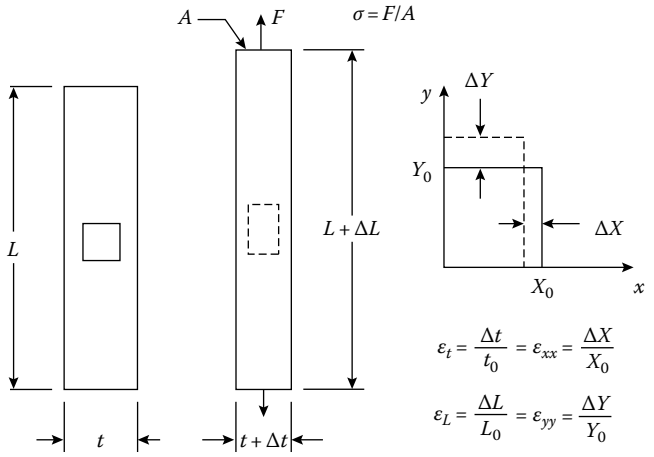

FIGURE 37.1 When a homogeneous isotropic bar is stretched by a uniaxial force, it elongates in the direction of the force and contracts perpendicular to the force. The relative elongation and contraction are defined as the longitudinal and transverse strains, respectively.

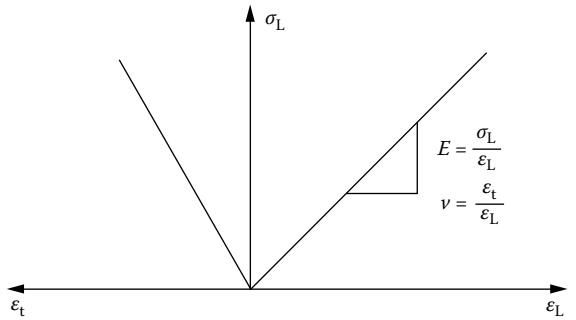

FIGURE 37.2 The uniaxial force shown in Figure 37.1 produces uniaxial stress in the bar. When the material response is linear, the slope of the stress versus strain curve is the Young's modulus. The negative ratio of the transverse to longitudinal strain is the Poisson's ratio.

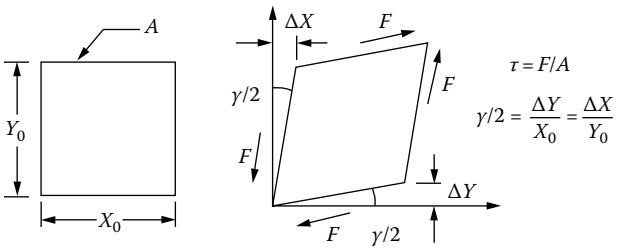

FIGURE 37.3 When a block of material is subjected to forces parallel to the sides as shown, it distorts. The force per unit area is the shear stress τ, and the angle change is the shear strain γ.

when the angle change is small. When the relation between shear stress and shear strain is linear, the ratio of the shear stress to shear strain is the shear modulus G.

Temperature change also induces strain. This is thermal expansion. In most materials, thermal strain increases with temperature. Over a limited temperature range, the relationship between thermal strain and temperature is linear. In this case, the strain divided by the temperature change is the thermal expansion coefficient α. In isotropic materials, thermal expansion only produces elongation strain, no shear strain.

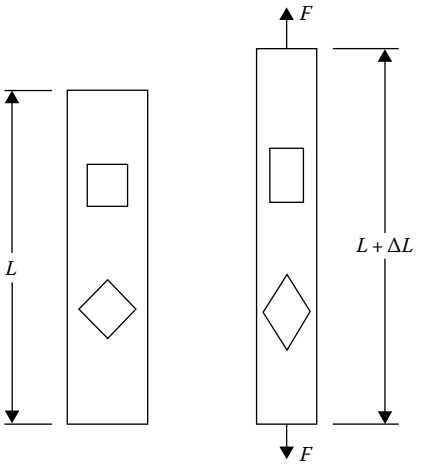

FIGURE 37.4 Some elements of a bar under uniaxial tension undergo elongation and contraction. These elements lie in principal directions. Other elements undergo distortion as well.

Principal directions in a material are directions that undergo elongation but no shear. On any particular surface of a solid, there are always at least two principal directions in which the strain is purely elongation. This is seen if two squares are drawn on the bar under uniform tension (Figure 37.4). When the bar is stretched, the square aligned with the load is elongated, whereas the square at 45° is distorted (angles have changed) and elongated. If the principal directions are known, as with the bar under tension, then strain gages can be applied in these directions. If the principal directions are not known, such as near a hole or notch, in an anisotropic specimen, or in a structure with complicated geometry, then additional strain gages are needed to fully characterize the strain state.

The elastic and thermal properties can be combined to give Hooke's law, Equations 37.1 through 37.6:

$$\varepsilon_{xx} = \frac{\sigma_{xx}}{E} - \frac{\nu}{E}(\sigma_{yy} + \sigma_{zz}) \tag{37.1}$$

$$\varepsilon_{yy} = \frac{\sigma_{yy}}{E} - \frac{\nu}{E}(\sigma_{xx} + \sigma_{zz}) \tag{37.2}$$

$$\varepsilon_{xx} = \frac{\sigma_{zz}}{E} - \frac{\nu}{E}(\sigma_{xx} + \sigma_{yy}) \tag{37.3}$$

$$\gamma_{xy} = \frac{\tau_{xy}}{G} \tag{37.4}$$

$$\gamma_{xz} = \frac{\tau_{xz}}{G} \tag{37.5}$$

$$\gamma_{yz} = \frac{\tau_{yz}}{G} \tag{37.6}$$

Several types of sensors are used to measure strain. These include piezoresistive gages (foil or wire strain gages and semiconductor strain gages), piezoelectric gages (polyvinylidene fluoride [PVDF] film and quartz), fiber-optic gages, birefringent films and materials, and moiré grids. Each type of sensor requires its own specialized signal conditioning. Selection of the best strain sensor for a given measurement is based on many factors, including specimen geometry, temperature, strain rate, frequency, magnitude, as well as cost, complexity, accuracy, spatial resolution, time resolution, sensitivity to transverse strain, sensitivity to temperature, and complexity of signal conditioning. Table 37.1 describes typical

TABLE 37.1 Comparison of Strain Sensors

Description	Longitudinal Strain Sensitivity	Transverse Strain Sensitivity	Temperature Sensitivity	Strain Resolution	Spatial Resolution	Time Resolution (μs)	Measurable Strain Range (%)
Piezoresistive constantan foil	$\Delta R/R/\Delta\varepsilon_L = 2.1$	$\Delta R/R/\Delta\varepsilon_t = <0.02$	$\Delta R/R/\Delta T = 2 \times 10^{-6}\ °C^{-1}$	<1 μstrain[a]	5–100 mm[b]	<1[c]	0–3
Annealed constantan foil[d]	$\Delta R/R/\Delta\varepsilon_L = 2.1$	$\Delta R/R/\Delta\varepsilon_t = <0.02$	$\Delta R/R/\Delta T = 2 \times 10^{-6}\ °C^{-1}$	<11 μstrain	5–100 mm	<1	0–10
Piezoresistive semiconductor	$\Delta R/R/\Delta\varepsilon_L = 150$	$\Delta R/R/\Delta\varepsilon_t = ???$	$\Delta R/R/\Delta T = 1.7 \times 10^{-3}\ °C^{-1}$	<0.1 μstrain	1–15 mm	<1	0–0.1
Piezoelectric PVDF	$\Delta Q/A/\Delta\varepsilon_L = 120\ nC/m^2/\mu\varepsilon$	$\Delta Q/A/\Delta\varepsilon_t = 60\ nC/m^2/\mu\varepsilon$	$\Delta Q/A/\Delta T = -27\ \mu C\ m^{-2}\ °C^{-1}$	1–10 μstrain	Gage size	<1	0–30
Piezoelectric quartz	$\Delta Q/A/\Delta\varepsilon_L = 150\ nC/m^2/\mu\varepsilon$ bonded to steel		$\Delta Q/A/\Delta T = 0$	<0.01 μstrain 20 mm gage	Gage size	<10	0–0.1
Fiber-optic Fabry–Perot	2–1000 μstrain V^{-1}	Near zero		<1 μstrain	2–10 mm	<20	
Birefringent film	K[e] = 0.15–0.002				0.5 mm[f]	<5	0.05–5
Moiré	1 fringe order/417 nm displ.	1 fringe order/417 nm displ.	Not defined	41.7 $\mu\varepsilon$ over 10 mm	Full fields[g]	Limited by signal conditioning	0.005–5

[a] With good signal conditioning.
[b] Equal to grid area.
[c] Gage response is within 100 ns. Most signal conditioning limits response time to far less than this.
[d] Annealed foil has a low yield stress and a large strain to failure. It also has hysteresis in the unload and a zero shift under cyclic load.
[e] This technique measures a difference in principal strains. $\varepsilon_2 - \varepsilon_1, = N\lambda/2tK$.
[f] Approximately the film thickness.
[g] The spatial strain resolution depends on the strain level. This is a displacement measurement technique.

TABLE 37.2 Sources and Prices of Strain Sensors

Supplier	Address	Sensor Types	Sensor Cost	Signal Conditioning	Cost
Micro-Measurements	P.O. Box 27777, Raleigh, NC 27611	Piezoresistive foil	From $5.00	Wheatstone bridge	From $500
		Birefringent film	From $10.00	Polariscope	$5,000–10,000
Texas Measurements	P.O. Box 2618, College Station, TX 77841	Piezoresistive foil and wire Load cells	From $5.00		
Omega Engineering	P.O. Box 4047, Stamford, CT 06907-0047	Piezoresistive foil	From $5.00	Strain meter Wheatstone bridge	From $550 From $2700
Dynasen, Inc.	20 Arnold Pl., Goleta, CA 93117	Piezoresistive foil	From $55.00	2-Channel pulsed	$5000
		Specialty gages for shock wave measurements	From $55.00	Wheatstone bridge	$250.00
		Piezoelectric PVDF (calibrated)		Passive charge integrator	
Entran Sensors and Electronics, Entran Devices, Inc.	10 Washington Ave., Fairfield, NJ 07004-3877	Piezoresistive semiconductor	From $15.00		
Amp, Inc.	Piezo Film Sensors P.O. Box 799, Valley Forge, PA 19482	Piezoelectric PVDF (not calibrated)	From $5.00		
Kistler Instrument Corp.	Amherst, NY 14228-2171	Piezoelectric quartz		Electrometer Charge amplifier	
F&S, Inc.	Fiber and Sensor Technologies P.O. Box 11704, Blacksburg, VA 24062-1704	Fabry–Perot strain sensors	From $75	Electronics	From $3500.00
Photomechanics, Inc.	512 Princeton Dr., Vestal, NY 13850-2912	Moiré interferometer			$60,000

characteristics of several sensors. Table 37.2 lists some manufacturers and the approximate cost of the sensors and associated signal conditioning electronics.

The data in Table 37.1 are to be taken as illustrative and by no means complete. The sensor description section describes only the type of sensor, not the many sizes and shapes. The longitudinal strain sensitivity is given as sensor output per unit longitudinal strain in the sensor direction. If the signal conditioning is included, the sensitivities can all be given in volts out per unit strain [3,4], but this is a function of amplification and the quality of the signal conditioner. The temperature sensitivity is given as output change due to a temperature change. In many cases, higher strain resolution can be achieved, but resolving smaller strain is more difficult and may require vibration and thermal isolation. For the moiré technique, the strain resolution is a function of the length of the viewing area. This technique can resolve a displacement of 100 nm (1/4 fringe order). This is divided by the viewing length to obtain the strain resolution. The spatial resolution corresponds to the gage length for most of the sensor types. The measurable strain range listed is the upper limit for the various sensors. Accuracy and reliability are usually reduced when sensors are used at the upper limit of their capability.

Manufacturers of the various sensors provide technical information that includes details of using the sensors, complete calibration or characterization data, and details of signal conditioning. The extensive

technical notes and technical tips provided by Measurements Group, Inc. address such issues as thermal effects [5], transverse sensitivity corrections [6], soldering techniques [7], rosettes [8], and gage fatigue [9]. Strain gage catalogs include information about gage materials, sizes, and selection. Manufacturers of other sensors provide similar information.

37.2 Principles of Operation of Strain Sensors

37.2.1 Piezoresistive Foil Gages

Piezoresistive foil and wire gages comprise a thin insulating substrate (usually polyimide film), a foil or wire grid (usually constantan) bonded to the substrate, lead wires to connect the grid to a resistance measuring circuit, and often an insulating encapsulation (another sheet of polyimide film) (Figure 37.5). The grid is laid out in a single direction so that strain will stretch the legs of the grid in the length direction. The gages are designed so that strain in the width or transverse direction separates the legs of the grid without straining them. This makes the gage sensitive to strain only along its length. There is always some sensitivity to transverse strain and almost no sensitivity to shear strain. In most cases, the transverse sensitivity can be neglected.

When piezoresistive foil or wire strain gages are bonded to a specimen and the specimen is strained, the gage strains as well. The resistance change is related to the strain by a gage factor, Equation 37.7:

$$\frac{\Delta R}{R} = G_L \varepsilon_L \tag{37.7}$$

where

$\Delta R/R$ is the relative resistance change
G is the gage factor
ε is the strain

These gages respond to the average strain over the area covered by the grid [10]. The resistance change is also sensitive to temperature. If the temperature changes during the measurement period, a correction must be made to distinguish the strain response from the thermal response. The gage response to longitudinal strain, transverse strain, and temperature change is given by Equation 37.8:

$$\frac{\Delta R}{R} = G_L \varepsilon_L + G_t \varepsilon_t + G_T \Delta T \tag{37.8}$$

where G_L, G_t, and G_T are the longitudinal, transverse, and temperature sensitivity, respectively. Micro-Measurements, Inc., uses a different notation. Their gage data are provided as $G_L = F_G$, $G_t = K_t F_G$, $G_T = \beta_g$.

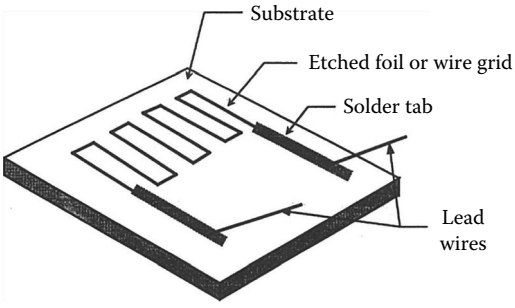

FIGURE 37.5 Gage construction of a foil or wire piezoresistive gage.

When a strain gage is bonded to a specimen and the temperature changes, the strain used in Equation 37.8 is the total strain, thermal plus stress induced, as given by Equation 37.7.

The temperature contribution to gage output must be removed if the gages are used in tests where the temperature changes. A scheme referred to as self-temperature compensation (STC) can be used. This is accomplished by selecting a piezoresistive material whose thermal output can be canceled by the strain induced by thermal expansion of the test specimen. Gage manufacturers specify STC numbers that match the thermal expansion coefficients of common specimen materials.

Strain of piezoresistive materials produces a relative resistance change. The resistance change is the result of changes in resistivity and dimensional changes. Consider a single leg of the grid of a strain gage with a rectangular cross section (Figure 37.6). The resistance is given by Equation 37.9:

$$R = \rho \frac{L}{A} \tag{37.9}$$

where

R is the resistance
ρ is the resistivity
L is the length
A is the area of the cross section

A small change in resistance is given by the first-order terms of a Taylor's series expansion, Equation 37.10:

$$\Delta R = \frac{\partial R}{\partial \rho}\Delta\rho + \frac{\partial R}{\partial L}\Delta L + \frac{\partial R}{\partial A}\Delta A \tag{37.10}$$

Differentiating Equation 37.9 to obtain each term of Equation 37.10 and then dividing by the initial resistance lead to Equation 37.11:

$$\frac{\Delta R}{R_0} = \frac{\Delta\rho}{\rho_0} + \frac{\Delta L}{L_0} - \frac{\Delta A}{A_0} \tag{37.11}$$

The relative resistance change is due to a change in resistivity, a change in length strain, and a change in area strain.

The strain gage is a composite material. The metal in a strain gage is like a metal fiber in a polymer matrix. When the polymer matrix is deformed, the metal is dragged along in the length direction, but in the width and thickness directions, the strain is not passed to the metal. This results in a stress state called uniaxial stress. This state was discussed in the examples earlier. The mathematical details involve an inclusion problem [11,12]. Accepting that the stress state is uniaxial, the relationship between the area change and the length change in Equation 37.11 is found from the Poisson's ratio. The area strain is the sum of the width and thickness strain, Equation 37.12:

$$\frac{\Delta A}{A_0} = \frac{\Delta w}{w_0} + \frac{\Delta t}{t_0} \tag{37.12}$$

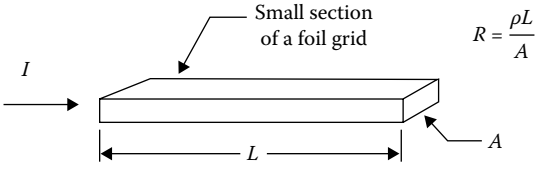

FIGURE 37.6 A single leg of a piezoresistive gage is used to explain the source of the relative resistance change that occurs in response to strain.

The definition of the Poisson's ratio gives Equation 37.13:

$$\frac{\Delta A}{A_0} = -2\nu\frac{\Delta L}{L_0} \tag{37.13}$$

where

$\Delta w/w$ is the width strain

$\Delta t/t$ is the thickness strain

Substitution of Equation 37.13 into 37.11 gives Equation 37.14 for the relative resistance change:

$$\frac{\Delta R}{R_0} = \frac{\Delta\rho}{\rho_0} + \frac{\Delta L}{L_0}(1+2\nu) \tag{37.14}$$

The relative resistivity changes in response to stress. The resistivity is a second-order tensor [13], and the contribution to the overall resistance change can be found in terms of strain using the elastic constitutive law [14]. The results lead to an elastic gage factor just over 2 for constantan gages. If the strain is large, the foil or wire in the gage will experience plastic deformation. When the deformation is plastic, the resistivity change is negligible and the dimensional change dominates. In this case, Poisson's ratio is 0.5 and the gage factor is 2. This effect is utilized in manufacturing gages for measuring strains larger than 1.5%. In this case, annealed foil is used. The annealed foil undergoes plastic deformation without failure. These gages are capable of measuring strain in excess of 10%. When metals undergo plastic deformation, they do not unload to the initial strain. This shows up as hysteresis in the gage response, that is, on unload, the resistance does not return to its initial value.

Foil and wire strain gages can be obtained in several configurations. They can be constructed with different backing materials and left open faced or fully encapsulated. Backing materials include polyimide and glass fiber-reinforced phenolic resin. Gages can be obtained with solder tabs for attaching lead wires or with lead wires attached. They come in many sizes and in multiple gage configurations called rosettes.

Strain gages are mounted to test specimens with adhesives using a procedure that is suitable for bonding most types of strain sensors. This is accomplished in a step-by-step procedure [15] that starts with surface preparation. An overview of the procedure is briefly described. To successfully mount strain gages, the surface is first degreased. The surface is abraded with a fine emery cloth or 400 grit paper to remove any loose paint, rust, or deposits. Gage layout lines are drawn (not scribed) on the surface in a cross pattern with pen or pencil, one line in the grid direction and one in the transverse direction. The surface is then cleaned with isopropyl alcohol. This can be done with an ultrasonic cleaner or with wipes. If wiped, the paper or gauze wipe should be folded and a small amount of alcohol applied. The surface should be wiped with one pass and the wipe discarded. This should be repeated, wiping in the other direction. The final step is to neutralize the surface, bringing the alkalinity to a pH of 7–7.5. A surface neutralizer is available from most adhesive suppliers. The final step is to apply the gage.

Gage application is accomplished with cellophane tape, quick-set glue, and a catalyst. The gage is placed on a clean glass or plastic surface with bonding side down, using tweezers. (Never touch the gage. Oils from skin prevent proper adhesion.) The gage is then taped down with a 100 mm piece of cellophane tape. The tape is then peeled up with the gage attached. The gage can now be taped onto its desired location on the test specimen. Once the gage has been properly aligned, the tape is peeled back from one side, lifting the gage from the surface. The tape should remain adhered to the surface about 1 cm from the gage. Note that one side of the tape is still attached to the specimen so that the gage can be easily returned to its desired position. A thin coating of catalyst is applied to the exposed gage surface. A drop of glue is placed at the joint of the tape and the specimen. Holding the tape at about a 30° angle from the surface, the tape can be slowly wiped down onto the surface. This moves the glue line forward.

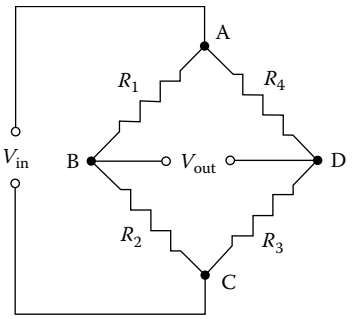

FIGURE 37.7 The Wheatstone bridge is used to measure the relative resistance change of piezoresistive strain gages.

After the glue line has passed the gage, the gage should be pressed in place and held for approximately 1 min. The tape can now be peeled back to expose the gage, and lead wires can be attached.

The relative resistance change of piezoresistive gages is usually measured using a Wheatstone bridge [16]. This allows a small change of resistance to be measured relative to an initial zero value, rather than relative to a large resistance value, with a corresponding increase in sensitivity and resolution. The Wheatstone bridge is a combination of four resistors and a voltage source (Figure 37.7). One to four of the resistors in the bridge can be strain gages. The output of the bridge is the difference between the voltage at points B and D. Paths ABC and ADC are voltage dividers so that V_B and V_D are given by Equations 37.15a and 37.15b:

$$V_B = V_{in}\frac{R_2}{R_1 + R_2} \tag{37.15a}$$

$$V_D = V_{in}\frac{R_3}{R_3 + R_4} \tag{37.15b}$$

The bridge output, Equation 37.16, is zero when the balance condition, Equation 37.17, is met:

$$V_{out} = V_B - V_D \tag{37.16}$$

$$R_1R_3 = R_2R_4 \tag{37.17}$$

Wheatstone bridge signal conditioners are constructed with a way to "balance" the bridge by adjusting the ratio of the resistances so that the bridge output is initially zero.

The balance condition is no longer met if the resistance values undergo small changes ΔR_1, ΔR_2, ΔR_3, ΔR_4. If the values $R_1 + \Delta R_1$ are substituted into Equation 37.15, the results substituted into Equation 37.16, condition (37.17) used, and the higher-order terms neglected, the result is Equation 37.18 for the bridge output:

$$V_{out} = V_{in}\frac{R_1R_3}{(R_1 + R_2)(R_3 + R_4)}\left(-\frac{\Delta R_1}{R_1} + \frac{\Delta R_2}{R_2} - \frac{\Delta R_3}{R_3} + \frac{\Delta R_4}{R_4}\right) \tag{37.18}$$

The Wheatstone bridge can be used to directly cancel the effect of thermal drift. If R_1 is a strain gage bonded to a specimen and R_2 is a strain gage held onto a specimen with heat sink compound (a thermally conductive grease available at any electronics store), then R_1 will respond to strain plus temperature, and R_2 will only respond to temperature. Since the bridge subtracts the output of R_1 from that of R_2, the temperature effect cancels.

The sensitivity of a measuring system is the output per unit change in the quantity to be measured. If the resistance change is from a strain gage, the sensitivity of the Wheatstone bridge system is proportional to the input voltage. Increasing the voltage increases the sensitivity. There is a practical limitation to increasing the voltage to large values. The power dissipated (heat) in the gage is $P = I^2R$, where I, the current through the gage, can be found from the input voltage and the bridge resistances. This heat must go somewhere or the temperature of the gage will continuously rise and the resistance will change due to heating. If the gage is mounted on a good thermal conductor, more power can be conducted away than if the gage is mounted on an insulator. The specimen must act as a heat sink.

Heat sinking ability is proportional to the thermal conductivity of the specimen material. A reasonable temperature gradient to allow the gage to induce in a material is 40 °C m^{-1} (about 1 °C per 25 mm). For thick specimens (thickness several times the largest gage dimension), this can be conducted away to the grips or convected to the surrounding atmosphere. If the four bridge resistances are approximately equal, the power to the gage in terms of the bridge voltage is given by Equation 37.19:

$$P_g = \frac{V_{in}^2}{4R} \tag{37.19}$$

The power per unit grid area, A_g, or power density to the gage can be equated to the thermal conductivity of the specimen and the allowable temperature gradient in the specimen by Equation 37.20:

$$\frac{P_g}{A_g} = \frac{V_{in}^2}{4\ RA_g} = K\nabla T \tag{37.20}$$

Thermal conductivities of most materials can be found in tables or on the web. Some typical values are Al, K = 204 W m^{-1} °C^{-1}; steel, K = 20–70 W m^{-1} °C^{-1}; and glass, K = 0.78 W m^{-1} °C^{-1} [17].

The acceptable bridge voltage can be calculated from Equation 37.21:

$$V_{in} = \sqrt{K\nabla T 4RA_g} \tag{37.21}$$

A sample calculation shows that for a 0.010 m × 0.010 m 120 Ω grid bonded to a thick piece of aluminum with a thermal conductivity of 204 W m^{-1} °C^{-1} and an acceptable temperature gradient of 40 °C m^{-1}, the maximum bridge voltage is 19 V. If thin specimens are used, the allowable temperature gradient will be smaller. If smaller gages are used for better spatial resolution, the bridge excitation voltage must be reduced with a corresponding reduction in sensitivity.

A considerably higher bridge voltage can be used if the bridge voltage is pulsed for a short duration. This dissipates substantially less energy in the gage and thus increases the sensitivity by a factor of 10–100. Wheatstone bridge pulse power supplies with variable pulse width from 10 μs and excitation of 350 V are commercially available [18].

The strain measurement required is often in a complex loading situation where the directions of principal strain are not known. In this case, three strain gages must be bonded to the test specimen at three angles. This is called a strain rosette. The angle between the rosette and the principal directions, as well as the magnitude of the principal strains, can be determined from the output of the rosette gages. This is most easily accomplished using the construct of a Mohr's circle (Figure 37.8).

A common rosette is the 0°–45°–90° pattern. The rosette is bonded to the specimen with relative rotations of 0°, 45°, and 90°. These will be referred to as the x, x', and y directions. The principal directions are labeled the 1 and 2 directions. The unknown angle between the x direction and the 1 direction is labeled θ. The Mohr's circle is drawn with the elongational strain on the horizontal axis and the shear strain on the vertical axis. The center of the circle is labeled C and the radius R. The principal directions correspond to zero shear strain. The principal values are given by Equations 37.22 and 37.23:

$$\varepsilon_1 = C + R \tag{37.22}$$

$$\varepsilon_2 = C - R \tag{37.23}$$

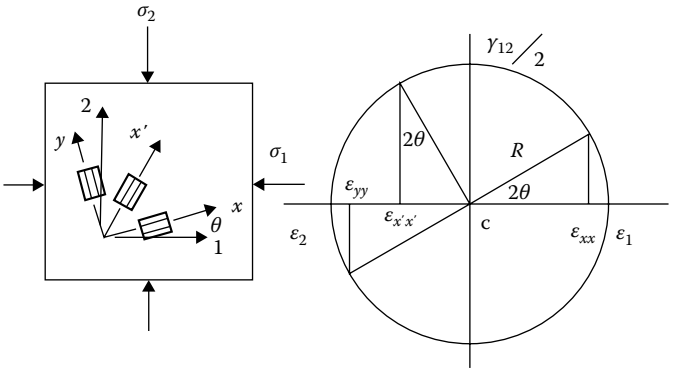

FIGURE 37.8 A three-element rosette is used to measure strain when the principal directions are not known. The Mohr's circle is used to find the principal directions and the principal strain values.

A rotation through an angle 2θ on the Mohr's circle corresponds to a rotation of the rosette of θ relative to the principal directions. The center of the circle is given by Equation 37.24 and the output of the strain gages is given by Equations 37.25 through 37.27:

$$C = \frac{\varepsilon_{xx} + \varepsilon_{yy}}{2} \tag{37.24}$$

$$\varepsilon_{xx} - C = R\cos 2\theta \tag{37.25}$$

$$\varepsilon_{x'x'} - C = -R\sin 2\theta \tag{37.26}$$

$$\varepsilon_{yy} - C = -R\cos 2\theta \tag{37.27}$$

Dividing Equation 37.25 by Equation 37.26 leads to θ and then to R, Equations 37.28 and 37.29:

$$R^2 = (\varepsilon_{xx} - C)^2 + (\varepsilon_{x'x'} - C)^2 \tag{37.28}$$

$$\tan 2\theta = \frac{C - \varepsilon_{x'x'}}{\varepsilon_{xx} - C} \tag{37.29}$$

The principal directions and principal strain values have been found from the output of the three rosette gages.

37.2.2 Piezoresistive Semiconducting Gages

Piezoresistive semiconductor strain gages, like piezoresistive foil and wire gages, undergo a resistance change in response to strain but with nearly an order of magnitude larger gage factor [19]. The coupling between resistance change and temperature is very large, so these gages have to be temperature compensated. The change of resistance with a small temperature change can be an order of magnitude larger than that induced by strain. Semiconductor strain gages are typically used to manufacture transducers such as load cells. They are fragile and require great care in their application.

37.2.3 Piezoelectric Gages

Piezoelectric strain gages are, effectively, parallel plate capacitors whose dielectric changes polarization in response to strain [14]. When the polarization changes, a charge proportional to the strain is produced on the electrodes. PVDF film strain gages are inexpensive, but not very accurate and subject

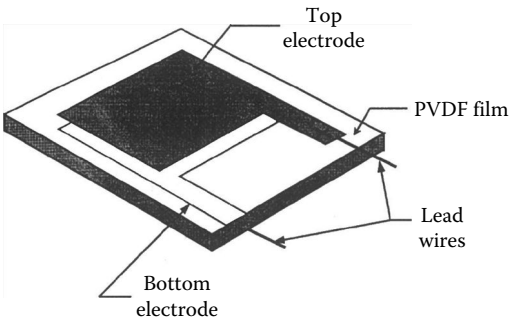

FIGURE 37.9 Typical gage construction of a piezoelectric gage.

to depoling by moderate temperature. They make good sensors for dynamic measurements such as frequency and logarithm decrement, but not for quantitative measurements of strain. When used for quasistatic measurements, the charge tends to drain through the measuring instrument. This causes the signal to decay with a time constant dependent on the input impedance of the measuring instrument. Quartz gages are very accurate but also lose charge through the measuring instrument. Time constants can be relatively long (seconds to hours) with electrometers or charge amplifiers.

The PVDF gage consists of a thin piezoelectric film with metal electrodes (Figure 37.9). Lead wires connect the electrodes to a charge measuring circuit. Gages can be obtained with the electrodes encapsulated between insulating layers of polyimide.

The gage output can be described in terms of a net dipole moment per unit volume. If the net dipole moment is the total charge, Q, on the electrodes multiplied by spacing, d, between the electrodes, then the polarization is given by Equation 37.30:

$$P = \frac{Qd}{V} \tag{37.30}$$

From Equation 37.30, it is seen that the polarization P (approximately equal to the electric displacement D) is the charge per unit electrode area (Figure 37.10).

A Taylor's series expansion of Equation 37.30 gives Equation 37.31:

$$\Delta P = \frac{\partial P}{\partial V}\Delta V + \frac{\partial P}{\partial (Qd)}\Delta Q d, \tag{37.31}$$

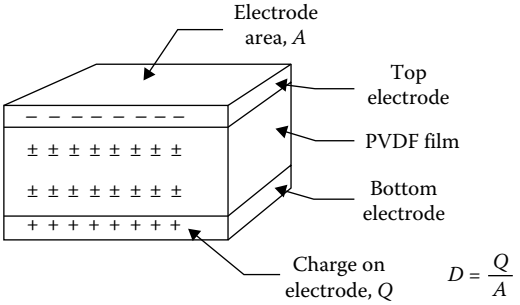

FIGURE 37.10 A representative cross section of a piezoelectric material formed into a parallel plate capacitor. The piezoelectric material is polarized. This results in charge on the electrodes. When the material is strained, the polarization changes and charge flows.

which, after differentiating Equation 37.30 and substituting in Equation 37.31, gives

$$\Delta P = \frac{\Delta Q d}{V_0} - \frac{\Delta V}{V_0} P_0 \tag{37.32}$$

For PVDF film, the second term in Equation 37.32 dominates. The output is proportional to the remanent polarization P_0. The remanent polarization slowly decays with time, has a strong dependence on temperature, and decays rapidly at temperatures around 50 °C. This makes accuracy a problem. If the sensors are kept at low temperature, accuracy can be maintained within ±3%.

Strain sensors can also be constructed from piezoelectric ceramics like lead zirconate titanate (PZT) or barium titanate. Ceramics are brittle and can be depoled by strain so should only be used at strains less than 200 μstrain. PZT loses some of its polarization with time and thus has accuracy problems but remains polar to temperatures of 150 °C or higher. "Hard" PZT (usually iron doped) is the best composition for polarization stability and low hysteresis. Quartz has the best accuracy. It is not polar but polarization is induced by strain. Quartz has excellent resolution and accuracy over a broad temperature range but is limited to low strain levels. It is also brittle and so is limited to small strain.

Two circuits are commonly used for piezoelectric signal conditioning: the electrometer and the charge amplifier (Figure 37.11). In the electrometer circuit, the piezoelectric sensor is connected to a capacitor with a capacitance value C, at least 1000 times that of the sensor C_g. There is always some resistance in the cable that connects the sensor to the capacitor. The circuit is simply two capacitors in parallel connected by a resistance. The charge equilibrates with a time constant given by $R_g C_g$. This time constant limits the fastest risetime that can be resolved to about 50 ns, effectively instantaneous for most applications. The charge is measured by measuring the voltage on the capacitor, then using Equation 37.33:

$$Q = CV \tag{37.33}$$

The difficulty is that measuring devices drain the charge, causing a time decay with a time constant RC. This causes the signal to be lost rapidly if conventional op amps are used. FET input op amps have very high input impedance and can extend this time constant to many hours. The charge amplifier is another circuit used to measure charge. This is usually an FET input op amp with a capacitor feedback. This does not really amplify charge but produces a voltage proportional to the input charge. Again, the time constant can be many hours, allowing use of piezoelectric sensors for near static measurements.

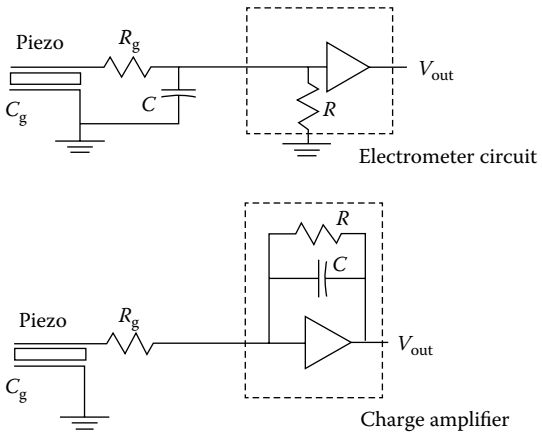

FIGURE 37.11 The electrometer and charge amplifier are the most common circuits used to measure charge from piezoelectric transducers.

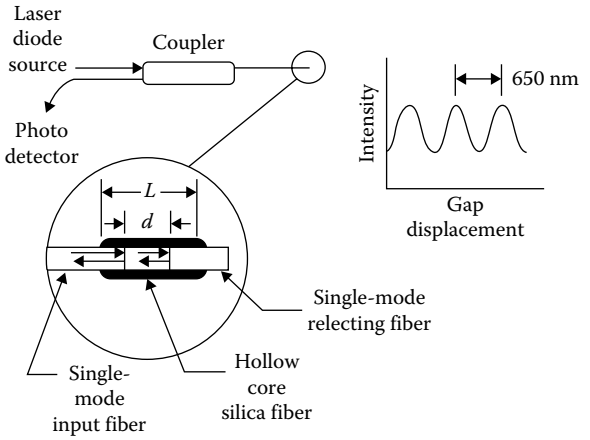

FIGURE 37.12 A schematic of the Fabry–Perot fiber-optic strain gage. When the cavity elongates, alternating constructive and destructive interferences occur.

High input impedance electrometer and charge amplifier signal conditioners for near static measurements are commercially available [20] as well as low-cost capacitive terminators for high-frequency (high kilohertz to megahertz) measurements [18]. An advantage of piezoelectric sensors is that they are active sensors that do not require any external energy source.

37.2.4 Fiber-Optic Strain Gages

Fiber-optic strain gages are miniature interferometers [21,22]. Many commercially available sensors are based on the Fabry–Perot interferometer. The Fabry–Perot interferometer measures the change in the size of a very small cavity.

Fabry–Perot strain sensors (Figure 37.12) comprise a laser light source, single-mode optical fibers, a coupler (the fiber-optic equivalent of a beam splitter), a cavity that senses strain, and a photodetector. Light leaves the laser diode. It passes down the fiber, through the coupler, and to the cavity. The end of the fiber is the equivalent of a partially silvered mirror. Some of the light is reflected back up the fiber and some is transmitted. The transmitted light crosses the cavity and then is reflected from the opposite end back into the fiber where it recombines with the first reflected beam. The two beams have a phase difference related to twice the cavity length. The recombined beam passes through the coupler to the photodetector. If the two reflected beams are in phase, there will be constructive interference. If the two beams are out of phase, there will be destructive interference. The cavity is bonded to a specimen. When the specimen is strained, the cavity stretches. This results in a phase change of the cavity beam, causing a cycling between constructive and destructive interference. For a 1.3 μm light source, each peak in output corresponds to a 650 nm gap displacement. The gap displacement divided by the gap length gives the strain. The output is continuous between peaks so that a 3 mm gage can resolve 1 μstrain.

37.2.5 Birefringent Film Strain Sensing

Birefringent film strain sensors give a full field measurement of strain. A nice demonstration of this effect can be achieved with two sheets of inexpensive Polaroid film, a 6 mm thick, 25 mm × 200 mm bar of Plexiglas (polymethylmethacrylate or PMMA), and an overhead projector. Place the two Polaroid sheets at 90° to one another so that the light is blocked. Place the PMMA between the Polaroid sheets. Apply a bending moment to the bar and color fringes will appear. Birefringent materials have a different

speed of light in different directions. This means that if light is polarized in a particular direction and passed through a birefringent specimen, if the fast direction is aligned with the electric field vector, the light passes through faster than if the slow direction is aligned with the electric field vector. This effect can be used to produce optical interference. In some materials, birefringence is induced by strain. The fast and slow directions correspond to the directions of principal strain, and the amount of birefringence corresponds to the magnitude of the strain. One component of the electric field vector travels through the specimen faster than the other. They emerge with a phase difference. This changes the relative amplitude and thus rotates the polarization of the light. If there is no birefringence, no light passes through the second polarizer. As the birefringence increases with strain, light passes through. As it further increases, the polarization rotation will be a full 180°, and again no light will pass through. This produces a fringe that corresponds to a constant difference in principal strains. The difference in principal strains is given by Equation 37.34:

$$\varepsilon_2 - \varepsilon_1 = \frac{N\lambda}{tK} \tag{37.34}$$

where

ε_1, ε_2 are the principal strains
N is the fringe order
λ is the wavelength
t is the specimen thickness
K is the strain-optical coefficient of the photoelastic material

A similar technique can be used with a birefringent plastic film with a silvered backing laminated to the surface of a specimen. Polarized light is passed through the film; it reflects from the backing, passes back through the film, and through the second polarizer. In this case, because light passes twice through the film, the equation governing the difference in principal strains is Equation 37.35:

$$\varepsilon_2 - \varepsilon_1 = \frac{N\lambda}{2tK} \tag{37.35}$$

If the polarizers align with principal strain directions, no birefringence is observed. Rotation of both polarizers allows the principal directions to be found at various locations on the test specimen. If a full view of the fringes is desired, quarter-wave plates are used (Figure 37.13). In this arrangement, light is passed through the first polarizer, resulting in plane polarization; through the quarter-wave plate, resulting in circular polarization; through the test specimen, resulting in phase changes; through the second quarter-wave plate to return to plane polarization; and then through the final polarizer.

The optical systems for viewing birefringence are commercially available as "polariscopes" [23]. Optical components to construct custom systems are available from many optical component suppliers.

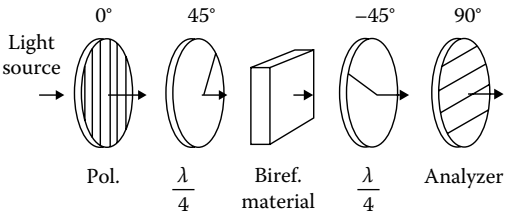

FIGURE 37.13 A schematic of the polariscope, a system for measuring birefringence. This technique gives a full field measure of the difference in principal strains.

37.2.6 Moiré Strain Sensing

Moiré interference is another technique that gives a full field measurement, but it measures displacement rather than strain. The strain field must be computed from the displacement field. This technique is based on the interference obtained when two transparent plates are covered with equally spaced stripes. If the plates are held over one another, they can be aligned so that no light will pass through or so that all light will pass through. If one of the plates is stretched, the spacing of the lines is wider on the stretched plate. Now, if one plate is placed over the other, in some regions light will pass through and in some regions it will not (Figure 37.14). The dark and light bands produced give information about the displacement field.

Moiré is defined as a series of broad dark and light patterns formed by the superposition of two regular gratings [24]. The dark or light regions are called fringes. Examples of pure extension and pure rotation are shown. In both cases, some of the light that would emerge from the first grating is obstructed by the superimposed grating. At the centers of the dark fringes, the bar of one grating covers the space of the other and no light comes through. The emergent intensity, I, is zero. Proceeding from there toward the next dark fringe, the amount of obstruction diminishes linearly and the amount of light increases linearly until the bar of one grating falls above the bar of the other. There, the maximum amount of light passes through the gratings.

Both geometric interference and optical interference are used. This discussion is restricted to geometric interference. Geometric moiré takes advantage of the interference of two gratings to determine displacements and rotations in the plane of view. In-plane moiré is typically conducted with two gratings, one applied to the specimen (specimen grating) and the other put in contact with the specimen grating (reference grating). When the specimen is strained, interference patterns or fringes occur. N is the moiré fringe order. Each fringe corresponds to an increase or decrease of specimen displacement by one grating pitch. The relationship between displacement and fringes is $\delta = gN$,

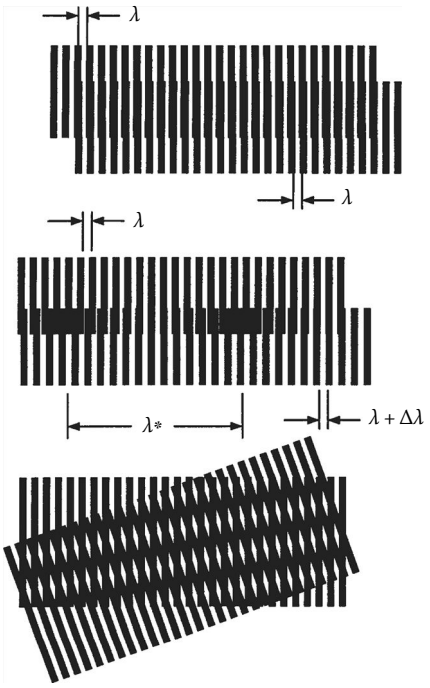

FIGURE 37.14 A demonstration of moiré fringes formed by overlapping gratings. The fringes are the result of stretching and relative rotation of the gratings. The fringe patterns are used to determine displacement fields.

where δ is the component of the displacement perpendicular to the reference grating lines, g is the reference grating pitch, and N is the fringe order.

For convenience, a zero-order fringe is designated assuming the displacement there is zero. With the reference grating at 0° and 90°, the fringe orders N_x and N_y are obtained. The displacements in x, y directions are then obtained from Equations 37.36 and 37.37:

$$u_x(x,y) = gN_x(x,y) \tag{37.36}$$

$$u_y(x,y) = gN_y(x,y) \tag{37.37}$$

Differentiation of Equations 37.36 and 37.37 gives the strains, Equations 37.38 through 37.40:

$$\varepsilon_x = \frac{\partial u_x}{\partial x} = g\frac{\partial N_x}{\partial x} \tag{37.38}$$

$$\varepsilon_{xy} = \frac{1}{2}\left(\frac{\partial u_y}{\partial x} + \frac{\partial u_x}{\partial y}\right) = \frac{1}{2}\left(g\frac{\partial N_y}{\partial x} + g\frac{\partial N_x}{\partial y}\right) \tag{37.39}$$

$$\varepsilon_y = \frac{\partial u_y}{\partial_y} = g\frac{\partial N_y}{\partial y} \tag{37.40}$$

In most cases, the sensitivity of geometric moiré is not adequate for determination of strain distributions. Strain analysis should be conducted with high-sensitivity measurement of displacement using moiré interferometry [24,25]. Moiré interferometers are commercially available [26]. Out-of-plane measurement can be conducted with one grating (the reference grating). The reference grating is made to interfere with either its reflection or its shadow [27,28].

References

1. N. E. Dowling, *Mechanical Behavior of Materials*, Englewood Cliffs, NJ: Prentice-Hall, 1993, pp. 99–108.
2. R. C. Craig, *Mechanics of Materials*, New York: John Wiley & Sons, 1996.
3. A. Vengsarkar, Fiber optic sensors: A comparative evaluation, In *The Photonics Design and Applications Handbook*, Pittsfield, MA: Laurin Publ., 1991, pp. 114–116.
4. H. U. Eisenhut, Force measurement on presses with piezoelectric strain transducers and their static calibration up to 5 MN, *New Industrial Applications of the Piezoelectric Measurement Principle*, July 1992, pp. 1–16.
5. TN-501-4, Strain gauge temperature effects, Measurements Group, Inc., Raleigh, NC.
6. TN-509, Transverse sensitivity errors, Measurements Group, Inc., Raleigh, NC.
7. TT-609, Soldering techniques, Measurements Group, Inc., Raleigh, NC.
8. TN-515, Strain gage rosettes, Measurements Group, Inc., Raleigh, NC.
9. TN-08-1, Fatigue of strain gages, Measurements Group, Inc., Raleigh, NC.
10. C. C. Perry and H. R. Lissner, *The Strain Gage Primer*, New York: McGraw-Hill, 1962.
11. J. B. Aidun and Y. M. Gupta, Analysis of Lagrangian gauge measurements of simple and nonsimple plain waves, *J. Appl. Phys.*, 69, 6998–7014, 1991.
12. Y. M. Gupta, Stress measurement using piezoresistance gauges: Modeling the gauge as an elastic-plastic inclusion, *J. Appl. Phys.*, 54, 6256–6266, 1983.
13. D. Y. Chen, Y. M. Gupta, and M. H. Miles, Quasistatic experiments to determine material constants for the piezoresistance foils used in shock wave experiments, *J. Appl. Phys.*, 55, 3984, 1984.

14. C. S. Lynch, Strain compensated thin film stress gauges for stress wave measurements in the presence of lateral strain, *Rev. Set. Instrum*., 66(11), 1–8, 1995.
15. B-129-7 M-Line Accessories Instruction Bulletin, Measurements Group, Inc., Raleigh, NC.
16. J. W. Dally, W. F. Riley, and K. G. McConnell, *Instrumentation for Engineering Measurements*, 2nd edn., New York: John Wiley & Sons, 1993.
17. J. P. Holman, *Heat Transfer*, 7th edn., New York: McGraw Hill, 1990.
18. Dynasen, Inc., 20 Arnold Pl., Goleta, CA 93117.
19. M. Dean (Ed.) and R. D. Douglas (assoc. Ed.), *Semiconductor and Conventional Strain Gages*, New York: Academic Press, 1962.
20. Kistler, Instruments Corp., Amhurst, NY, 14228–2171.
21. J. S. Sirkis, Unified approach to phase strain temperature models for smart structure interferometric optical fiber sensors. 1. Development, *Opt. Eng*., 32(4), 752–761, 1993.
22. J. S. Sirkis, Unified approach to phase strain temperature models for smart structure interferometric optical fiber sensors. 2. Applications, *Opt. Eng*., 32(4), 762–773, 1993.
23. Photoelastic Division, Measurements Group, Inc., P.O. Box 27777, Raleigh, NC 27611.
24. T. Valis, D. Hogg, and R. M. Measures, Composite material embedded fiber-optic Fabry-Perot strain rosette, *SPIE*, 1370, 154–161, 1990.
25. D. Post, B. Han, and P. Lfju, *High Sensitivity Moiré*, New York: Springer-Verlag, 1994.
26. V. J. Parks, Geometric Moiré, In *Handbook on Experimental Mechanics*, A. S. Kobayashi (ed.), New York: VCH Publisher, Inc., 1993.
27. Photomechanics, Inc., 512 Princeton Dr. Vestal, NY, 13850–2912.
28. T. Y. Kao and F. P. Chiang, Family of grating techniques of slope and curvature measurements for static and dynamic flexure of plates, *Opt. Eng*., 21, 721–742, 1982.
29. D. R. Andrews, Shadow moiré contouring of impact craters, *Opt. Eng*., 21, 650–654, 1982.

38

Tactile Sensing

Ricardo E. Saad
Harmonics Lightwaves

A. Bonen
University of Toronto

K.C. Smith
University of Toronto

Ben Benhabib
University of Toronto

Robots in industrial settings perform repetitive tasks, such as machine loading, parts assembly, painting, and welding. Only in rare instances can these autonomous manipulators modify their actions based on sensory information. Although, thus far, a vast majority of research work in the area of robot sensing has concentrated on computer vision, contact sensing is an equally important feature for robots and has received some attention as well. Without tactile-perception capability, a robot cannot be expected to effectively grasp objects. In this context, robotic-tactile sensing is the focus of this chapter.

38.1 Sensing Classification

Robotic sensing can be classified as either of the noncontact or of the contact type [1]. *Noncontact sensing* involves interaction between the robot and its environment by some physical phenomenon, such as acoustic or electromagnetic waves that interact without contact. The most important types of robotic sensors of the noncontact type are vision and proximity sensors. *Contact sensing*, on the other hand, implies the measurement of the general interaction that takes place when the robot's end effector is brought into contact with an object. Contact sensing is further classified into force and tactile sensing.

Force sensing is defined as the measurement of the global mechanical effects of contact, while *tactile sensing* implies the detection of a wide range of local parameters affected by contact. Most significant among those contact-based effects are contact stresses, slippage, heat transfer, and hardness.

The properties of a grasped object that can be derived from tactile sensing can be classified into geometric and dynamometric types [2]. Among the geometric properties are presence, location in relation to the end effector, shape and dimensions, and surface condition [3–7]. Among the dynamometric parameters associated with grasping are force distribution, slippage, elasticity and hardness, and friction [8–12].

Tactile sensing requires sophisticated transducers; yet the availability of these transducers alone is not a sufficient condition for successful tactile sensing. It is also necessary to accurately control the modalities through which the tactile sensor interacts with the explored objects (including contact forces, as well as end-effector position and orientation) [13–15]. This leads to active tactile sensing, which requires a high degree of complexity in the acquisition and processing of the tactile data [16].

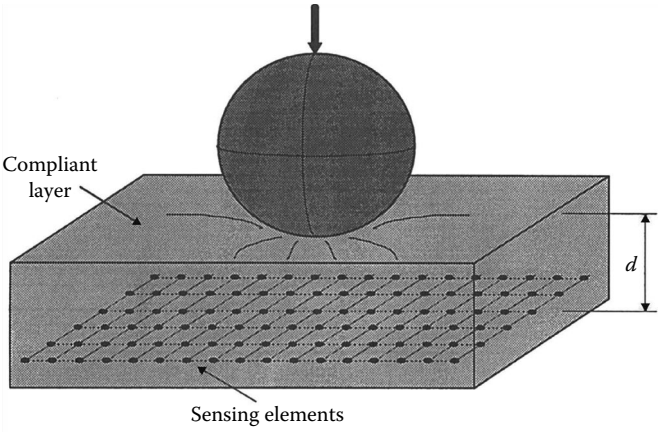

FIGURE 38.1 Object indenting a compliant layer, where an array of force-sensing elements is placed at a distance *d* from the surface.

38.2 Mechanical Effects of Contact

Tactile sensing normally involves a rigid object indenting the compliant cover layer of a tactile sensor array [17] (Figure 38.1). The indentation of a compliant layer due to contact can be analyzed from two conceptually different points of view [1]. The first one is the measurement of the actual contact stresses (force distribution) in the layer, which is usually relevant to controlling manipulation tasks. The second one is the deflection profile of the layer, which is usually important for recognizing geometric object features. Depending on the approach adopted, different processing and control algorithms must be utilized.

There exists a definite relationship between the local shape of a contacting body and a set of subsurface strains (or displacements); however, this relationship is quite complex. Thus, it requires the use of the theory of elasticity and contact mechanics to model sensor–object interaction [18] and the use of finite element analysis (FEA) as a practical tool for obtaining a more representative model of the sensor [19].

In general, the study of tactile sensors comprises two steps: (1) the *forward analysis*, related to the acquisition of data from the sensor (changes on the stress or strains, induced by the indentation of an object on the compliant surface of the transducer), and (2) the *inverse problem*, normally related to the recovery of force distribution or, in some cases, the recovery of the indentor's shape.

38.3 Theory for Tactile Sensing

For simplicity, the general 2D tactile problem is reduced herein to a 1D one. Figure 38.2 shows a 1D transducer that consists of a compliant, homogeneous, isotropic, and linear layer subjected to a normal stress $q_v(x)$ created by the indentation of an object.

For modeling purposes, it is assumed that the compliant layer is an elastic half-space. This simplification yields closed-form equations for the analysis and avoids the formation of a more complex problem, in which the effect of the boundary conditions at x_{min} and x_{max} must be taken into account. It has been proven that the modeling of the sensor by an elastic half-space represents a reasonable approximation to the real case [18]. Under these conditions, it can be shown that the normal strain, at a depth $y = d$, due to the normal stress $q_v(y)$ is given by [20]

$$\varepsilon_z(x) = \int_{-\infty}^{\infty} q_v(x - x_0) h_z(x_0, d) dx_0 \tag{38.1}$$

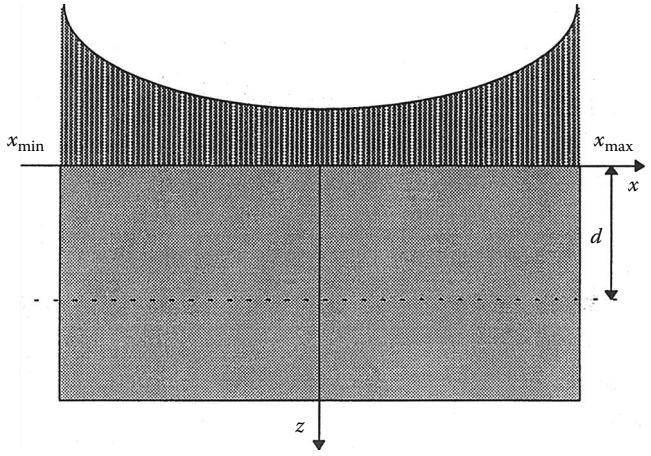

FIGURE 38.2 Ideal 1D transducer subjected to a normal stress.

where

ε_z is the strain at x

$z = d$ due to the normal stress on the surface

$$h_z(x) = -\frac{2d(1+\nu)[d^2(1-\nu) - \nu x^2]}{\pi r E(x^2 + d^2)^2} \tag{38.2}$$

E and ν are, respectively, the modulus of elasticity and the Poisson's coefficient of the compliant layer. In obtaining Equation 38.2, it is assumed that the analysis is performed under *planar strain* conditions. It should be noted that a similar analysis can be performed for tangential contact stresses or strains.

The normal displacement at the surface, w, is given by

$$w(x) = \int_{-\infty}^{\infty} q_v(x - x_0)k(x_0)dx_0 \tag{38.3}$$

where

$$k(x) = \frac{-2(1-\nu^2)}{\pi E}\log\left|\frac{x}{x_a}\right| \tag{38.4}$$

The singularity at $x = 0$ is expected due to the singularity of stress at that point. Note that $k(x)$ is the deformation of the surface when a singular load of 1 N is applied at $x = 0$. The constant x_a should be chosen such that at $x = x_a$, the deformation is zero. In this case, zero deformation should occur at $x \to \infty$ (note that it has been assumed that the sensor is modeled by an elastic half-space), namely, $x_a \to \infty$. This problem is associated with the 2D deformation of an elastic half-space. To eliminate this difficulty, the boundary conditions of the transducer must be taken into account (i.e., a finite transducer must be analyzed), which requires, in general, the use of FEA.

Since measurements of strain (or stress) are usually done by a discrete number of sensing elements, Equation 38.2 must be discretized (Figure 38.3). Correspondingly, the force distribution must be reconstructed at discrete positions as shown in Figure 38.3. Let Δx_q be the distance between points, where the force distribution must be reconstructed from strain (or stress) measurements carried out by strain (or stress) sensing elements uniformly distributed at intervals Δx_p, at $z = d$. Also assume, even though it is

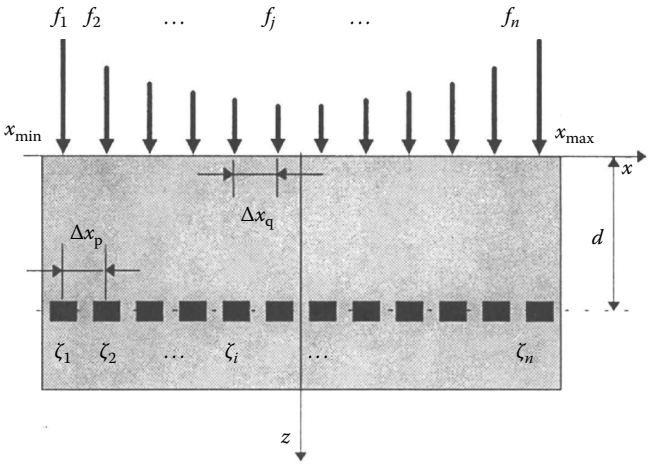

FIGURE 38.3 1D transducer with discrete-sensing elements located at $z = d$.

not necessary, that $\Delta x_q = \Delta x_p = \Delta x$ and that the forces are applied at positions immediately above the sensor elements. One can now define the strain (stress)-sample vector, ζ, whose components are given by $\zeta_i = \varepsilon_x(x_i)$, $i = 1, 2, \ldots, n$, and the force distribution vector, **F**, whose components are given by $f_i = q_v(x_j)$, $j = 1, 2, \ldots, n$. Then, the discrete form of Equation 38.1 is given by

$$\zeta = \mathbf{TF} \tag{38.5}$$

where the elements of the matrix **T** are given by $T_{ij} = k_v(x_i - x_j)$, $i = 1, 2, \ldots, n$, and $j = 1, 2, \ldots, n$ [23]. A similar relation to Equation 38.5 can be obtained discretizing Equation 38.3 in the general case, where $\Delta x_q \neq \Delta x_p$ and **T** is not square. Furthermore, in the general case, the vector **F** comprises both vertical and tangential components.

Equations 38.1 and 38.3 represent the regular *forward problem*, while Equation 38.5 represents the discretized version of the forward problem. The *inverse problem*, in most cases, consists of recovering the applied force profile from the measurements of strain, stress, or deflection. (Note that the surface displacement can also be used to recover the indentor's shape.)

In [20], it was shown that the inverse problem is ill posed because the operators h and k, of Equations 38.1 and 38.3, respectively, are ill conditioned. Consequently, the inverse problem is susceptible to noise. To solve this problem, regularization techniques must be utilized [20].

It has been proven that in order to avoid aliasing in determining the continuous strain (stress) at a depth d using a discretized transducer, the elements have to be separated by one-tenth of the compliant layer's thickness. However, good results were obtained, without much aliasing, by separating the sensing elements by a distance equal to the sensor's depth [18].

38.4 Requirements for Tactile Sensors

In 1980, Harmon conducted a survey to determine general specifications for tactile sensors [21]. Those specifications have been used subsequently as guidelines by many tactile sensor designers:

1. Spatial resolution of 1–2 mm
2. Array sizes of 5×10 to 10×20 points
3. Sensitivity of 0.5×10^{-2} to 1×10^{-2} N for each force-sensing element (tactel)
4. Dynamic range of 1000:1
5. Stable behavior and with no hysteresis

6. Sampling rate of 100 Hz–1 kHz
7. Monotonic response, though not necessarily linear
8. Compliant interface, rugged and inexpensive

While properties (5), (7), and (8) earlier should apply to any practical sensor, the others are merely suggestions, particularly with respect to the number of array elements and spatial resolution.

Developments on tactile sensing following [21] have identified additional desirable qualities, namely, reliability, modularity, speed, and availability of multisensor support [16].

38.5 Technologies for Tactile Sensing

The technologies associated with tactile sensing are quite diverse: extensive surveys of the state of the art of robotic-tactile-transduction technologies have been presented in [2,3,16,17]. Some of these technologies will be briefly discussed.

38.5.1 Resistive

The transduction method that has received the most attention in tactile sensor design is concerned with the change in resistance of a conductive material under applied pressure. A basic configuration of a resistive transducer is shown in Figure 38.4. Each resistor, whose value changes with the magnitude of the force, represents a resistive cell of the transducer. Different materials have been utilized to manufacture the basic cell.

Conductive elastomers were among the first resistive materials used for the development of tactile sensors. They are insulating, natural, or silicone-based rubbers made conductive by adding particles of conductive or semiconductive materials (e.g., silver or carbon). The changes in resistivity of the elastomers under pressure are produced basically by two different physical mechanisms. In the first approach, the change in resistivity of the elastomer under pressure is associated with deformation that alters the particle density within it. Two typical designs of this kind are given in [22,23]. In the second approach, while the bulk resistance of the elastomer changes slightly when it is compressed, the design allows the

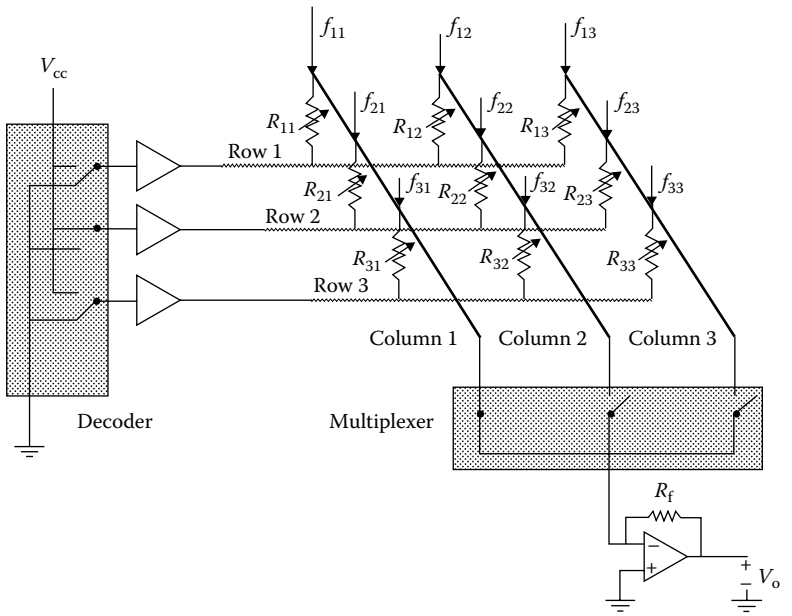

FIGURE 38.4 General configuration of a resistive transducer.

increase of the area of contact between the elastomer and an electrode and correspondingly a change in the contact resistance. A typical design of this kind is given in [24]. In [25], a newer tactile sensor is reported with both three-axis force-sensing and slippage-sensing functions. In the former case, the pressure-sensing function is achieved utilizing arrays of pressure transducers that measure a change in contact resistance between a specially treated polyimide film and a resistive substrate.

Piezoresistive elements have also been used in several tactile sensors. This technology is specifically attractive at present because, with micromachining, the piezoresistive elements can be integrated together with the signal-processing circuits in a single chip [26]. A 32 × 32-element silicon pressure sensor array incorporating CMOS processing circuits for the detection of a high-resolution pressure distribution was reported in [8]. The sensor array consists of an *x*–*y*-matrix-organized array of pressure cells with a cell spacing of 250 μm. CMOS processing circuits are formed around the array on the same chip. The fabrication of the sensor array was carried out using a 3 mm CMOS process combined with silicon micromachining techniques. The associated diaphragm size is 50 μm × 50 μm. The overall sensor-array chip size is 10 mm × 10 mm.

In Figure 38.4, a circuit topology, to scan a 3 × 3 array of piezoresistive elements, is shown. The basic idea was originally proposed in [24] and adapted on several occasions by different researchers. Using this method, the changes in resistance are converted into voltages at the output. With the connections as shown in Figure 38.4, the resistance R_{21} can be determined from

$$V_o = \frac{R_f}{R_{21}} V_{cc} \tag{38.6}$$

where

V_o is the output voltage
V_{cc} is the bias voltage
R_f is the feedback resistance of the output amplifier stage

One problem with the configuration shown in Figure 38.4 is the difficulty in detecting small changes in resistance due to the internal resistance of the multiplexer as well as changes in the voltage of power source, which have a great influence at the output. Other methods utilized to scan resistive transducer arrays are summarized in [3].

When piezoresistors and circuits are fabricated on the same silicon substrate, the sensor array can be equipped with a complex switching circuit, next to the sensing elements, which allows a better resolution in the measurements [9].

38.5.2 Capacitive

Tactile sensors within this category are concerned with measuring capacitance, which varies under applied load. The capacitance of a parallel-plate capacitor depends on the separation of the plates and their areas. A sensor using an elastomeric separator between the plates provides compliance such that the capacitance will vary according to the applied normal load (Figure 38.5a).

Figure 38.5b shows the basic configuration of a capacitive tactile sensor. The intersections of rows and columns of conductor strips form the capacitors. Each individual capacitance can be determined by measuring the corresponding output voltage at the selected row and column. To reduce cross talk and electromagnetic interference, the rows and columns that are not connected are grounded. Figure 38.5c shows an equivalent circuit when the sensor is configured to measure the capacitance formed at the intersection of rows *i* and *j*, C_{ij}. R_d is the input resistance of the detector, and C_d represents the effects of the stray capacitances, including the detector–amplifier input capacitance, the stray capacitance due to the unselected rows and columns, and the capacitance contributed by the cable that connects the transducer to the detector. Since the stray capacitance due to the unselected rows and columns changes with the applied forces, the stray capacitance due to the cable is designed to be predominant [18].

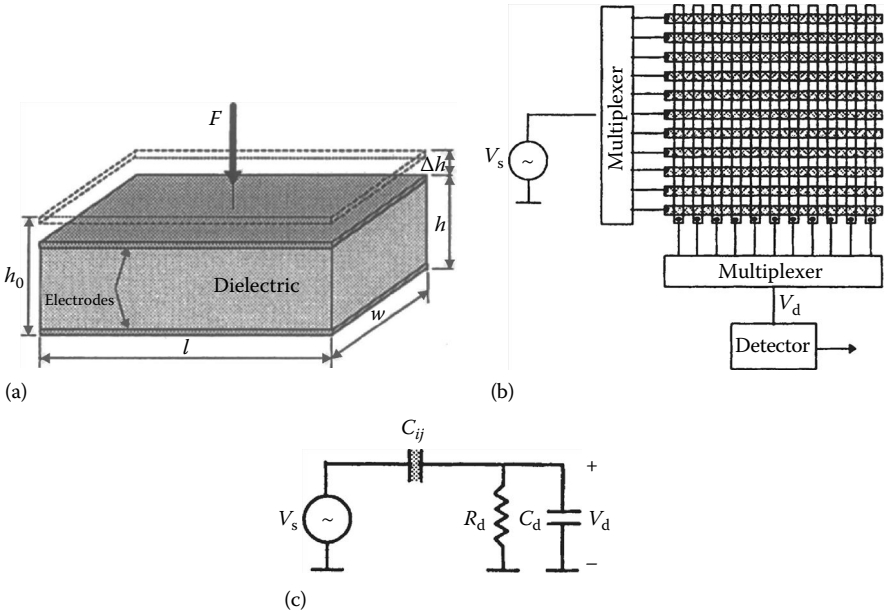

FIGURE 38.5 (a) Basic cell of a capacitor tactile sensor. (b) Typical configuration of a capacitive tactile sensor. (c) Equivalent circuit for the measurement of the capacitance C_{ij}.

The magnitude of voltage at the input of the detector, $|V_d|$, is given by

$$|V_d| = \frac{C_{ij} R_d \omega}{\sqrt{1 + [\omega R_d (C_{ij} + C_d)]^2}} |V_s| \tag{38.7}$$

Assuming that $C_d \gg C_{ij}$ and ω is sufficiently large,

$$|V_d| \cong \frac{C_{ij}}{C_d} |V_s| \tag{38.8}$$

When a load is applied to the transducer, the capacitor is deformed as shown in Figure 38.5a. For modeling purposes, it is assumed that the plate capacitor is only under compression. When no load is applied, the capacitance due to the element in the *i*th row and the *j*th column, C_{ij}^0, is given by

$$C_{ij}^0 = \varepsilon \frac{wl}{h_0} \tag{38.9}$$

where

ε is the permittivity of the dielectric
w and l are the width and the length of the plate capacitor, respectively
h_0 is the distance between plates when no load is applied

The voltage at the input of the detector for this particular case is indicated by V_{d0}; then from Equation 38.8, one obtains

$$|V_{d0}| \cong \frac{C_{ij}^0}{C_d} |V_s| \tag{38.10}$$

When a load is applied, the capacitor is under compression and the capacitance is given by

$$C_{ij} = \varepsilon \frac{wl}{h_0 - \Delta h} \tag{38.11}$$

The strain in this case is given by

$$\zeta_z \cong \frac{\Delta h}{h_0} \tag{38.12}$$

where

Δh is the displacement of the top metal plate
$\Delta h \ll h_0$

The strain can be measured by

$$\frac{|V_d| - |V_{d0}|}{|V_d|} = \frac{(C_{ij}/C_d) - (C_{ij}^0/C_d)}{C_{ij}/C_d} = 1 - \frac{C_{ij}^0}{C_{ij}} = 1 - \frac{h_0 - \Delta h}{h_0} = \frac{\Delta h}{h_0} = \frac{\Delta h}{h_0} \cong \zeta_z \tag{38.13}$$

Consequently, the strain at each tactel can be determined by measuring the magnitudes of V_d and V_{d0} for each element.

Note that the presence of a tangential force would offset the plates tangentially and change the effective area of the capacitor plates. An ideal capacitive pressure sensor can quantify basic aspects of touch by sensing normal forces and can detect slippage by measuring tangential forces. However, distinguishing between the two forces at the output of a single sensing element is a difficult task and requires a more complex transducer than the one presented in Figure 38.5a [27].

Micromachined, silicon-based capacitive devices are especially attractive due to their potential for high accuracy and low drift. A sensor with 1024 elements and a spatial resolution of 0.5 mm was reported in [28]. Several possible structures for implementing capacitive high-density tactile transducers in silicon have been reported in [29]. A cylindrical finger-shaped transducer was reported in [18].

The advantages of capacitive transducers include wide dynamic range, linear response, and robustness. Their major disadvantages are susceptibility to noise, sensitivity to temperature, and the fact that capacitance decreases with physical size, ultimately limiting the spatial resolution. Research is progressing toward the development of electronic processing circuits for the measurement of small capacitances using charge amplifiers [30] and the development of new capacitive structures [29].

38.5.3 Piezoelectric

A material is called piezoelectric if, when subjected to a stress or deformation, it produces electricity. Longitudinal piezoelectric effect occurs when the electricity is produced in the same direction of the stress (Figure 38.6). In Figure 38.6a, a normal stress σ (=F/A) is applied along the direction 3, and the charges are generated on the surfaces perpendicular to direction 3. A transversal piezoelectric effect occurs when the electricity is produced in the direction perpendicular to the stress.

The voltage V generated across the electrodes by the stress σ is given by

$$V = d_{33} \frac{h}{\varepsilon} \sigma \tag{38.14}$$

where

d_{33} is the piezoelectric constant associated with the longitudinal piezoelectric effect
ε is the permittivity
h is the thickness of the piezoelectric material

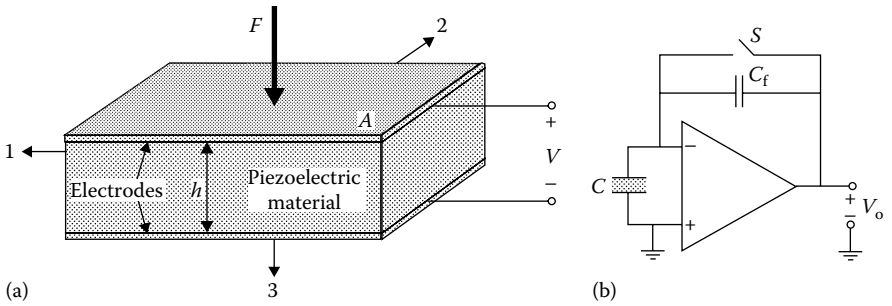

FIGURE 38.6 (a) Basic cell of a piezoelectric transducer. (b) Charge amplifier utilized for the measurement of the applied force.

Since piezoelectric materials are insulators, the transducer shown in Figure 38.6a can be considered as a capacitor, from an electric point of view. Consequently,

$$V = \frac{Q}{C} = \frac{Q}{\varepsilon A} h \tag{38.15}$$

where

Q is the charge induced by the stress σ
C is the capacitance of the parallel capacitor
A is the area of each electrode

A comparison of Equations 38.14 and 38.15 leads to

$$Q = d_{33} A \sigma \tag{38.16}$$

It is concluded that the force applied to the photoelastic material can be determined by finding the charge Q. Charge amplifiers are usually utilized for determining Q. The basic configuration of a charge amplifier is shown in Figure 38.6b. The charge generated in the transducer is transferred to the capacitor C_f, and the output voltage, V_0, is given by

$$V_0 = -\frac{Q}{C_f} \tag{38.17}$$

The circuit must periodically discharge the feedback capacitor C_f to avoid saturation of the amplifier by stray charges generated by the offset voltages and currents of the operational amplifier. This is achieved by a switch as shown in Figure 38.6b or by a resistor parallel to C_f.

The piezoelectric material most widely used in the implementation of tactile transducers is PVF2. It shows the largest piezoelectric effect of any known material. Its flexibility, small size, sensitivity, and large electric output offer many advantages for sensor applications in general and tactile sensors in particular. The examples of tactile sensors implemented with this technology can be found in [1,31].

The major advantages of the piezoelectric technology are its wide dynamic range and durability. Unfortunately, the response of available materials does not extend down to dc, and therefore, steady loads cannot be measured directly. Also, the PVF2 material produces a charge output that is prone to electric interference and is temperature dependent.

The possibility of measuring transient phenomenon using piezoelectric material has recently encouraged some researchers to use the piezoelectric effect for detecting vibrations that indicate incipient slip, occurrence of contact, local change in skin curvature, and estimating friction and hardness of

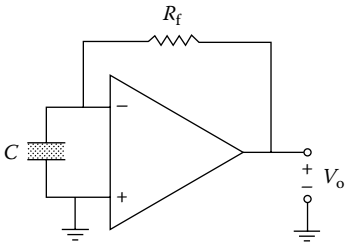

FIGURE 38.7 Current-to-voltage converter.

the object [7,10,11]. If the piezoelectric transducer shown in Figure 38.6a is connected to an FET-input operational amplifier configured as a current-to-voltage converter as shown in Figure 38.7, the output voltage is given by

$$V_o = \frac{dQ}{dt} R_f = AR_f d_{33} \frac{d\sigma}{dt} \tag{38.18}$$

where R_f is the feedback resistor. Correspondingly, the circuit configuration provides the mean to measure of changes in the contact stress. A detailed explanation of the behavior of this sensor can be found in [7].

38.5.4 Optical

Recent developments in fiber-optic technology and solid-state cameras have led to numerous novel tactile sensor designs [32,33]. Some of these designs employ flexible membranes incorporating a reflecting surface (Figure 38.8). Light is introduced into the sensor via a fiber-optic cable. A wide cone of light propagates out of the fiber, reflects back from the membrane, and is collected by a second fiber. When an external force is applied onto the elastomer, it shortens the distance between the reflective side of the membrane and the fibers, h. Consequently, the light gathered by the receiving fiber changes as a function of h (Figure 38.8b). To recover univocally the distance from the light intensity, a monotonic function

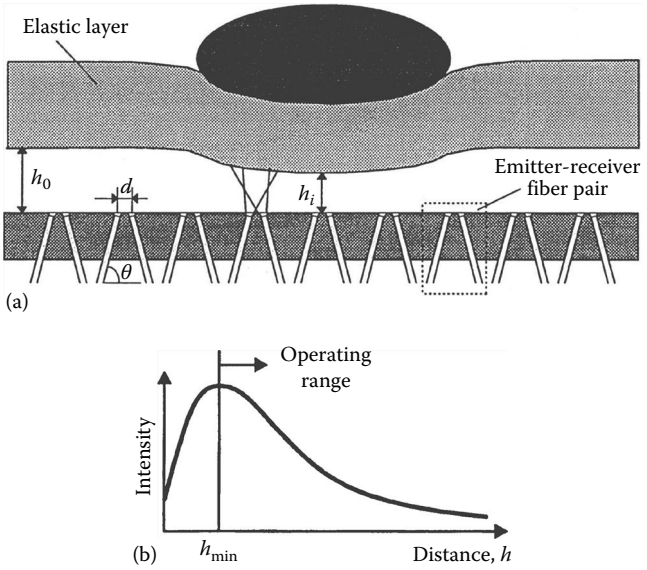

FIGURE 38.8 (a) Reflective transducer. (b) Light intensity as a function of the distance h.

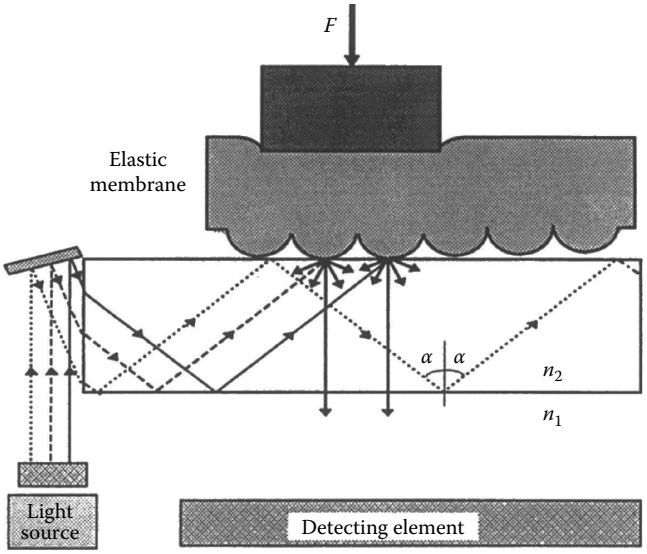

FIGURE 38.9 Tactile transducer based on the principle of internal reflection.

is needed. This can be achieved by designing the transducer such it operates for $h > h_{min}$, where h_{min} is indicated in Figure 38.8b. (The region $h > h_{min}$ is preferred to the $h < h_{min}$ for dynamic range reasons.)

Another optical effect that can be used is that of frustrated total internal reflection [5,34]. With this technique, an elastic rubber membrane covers, without touching, a glass plate (waveguide); light entering the side edge of the glass is totally reflected by the top and bottom surfaces and propagates along it (Figure 38.9).

The condition for total internal reflection occurs when

$$n_2 \sin\alpha \leq n_1 \tag{38.19}$$

where

n_1 is the index of refraction of the medium surrounding the waveguide (in this case air, $n_1 \cong 1$)
n_2 is the index of refraction of the waveguide
α is the angle of incidence at the interface glass–air

Objects in contact with the elastic membrane deform it and induce contact between the bottom part of the membrane and the top surface of the waveguide, disrupting the total internal reflection. Consequently, the light in the waveguide is scattered at the contact location. Light that escapes through the bottom surface of the waveguide can be detected by an array of photodiodes and a solid-state sensor or, alternatively, transported away from the transducer by fibers [3]. The detected imaged is stored in a computer for further analysis. A rubber membrane with a flat surface yields a high-resolution binary (contact or noncontact) image [5]. If the rubber sheet is molded with a textured surface (Figure 38.9), then an output proportional to the area of contact is obtained and, consequently, the applied forces can be detected [3]. Shear forces can also be detected using special designs [35]. Sensors based on frustrated internal reflection can be molded into a finger shape [5] and are capable of forming very high-resolution tactile images. Such sensors are commercially available. An improved miniaturized version of a similar sensor was proposed in [34].

Other types of optical transducers use "occluder" devices. One of the few commercially available tactile sensors uses this kind of transducer [36]. In one of the two available designs, the transducer's surface is made of a compliant material, which has on its underside a grid of elongated pins. When force is applied to the compliant surface, the pins on the underside undergo a mechanical motion normal to

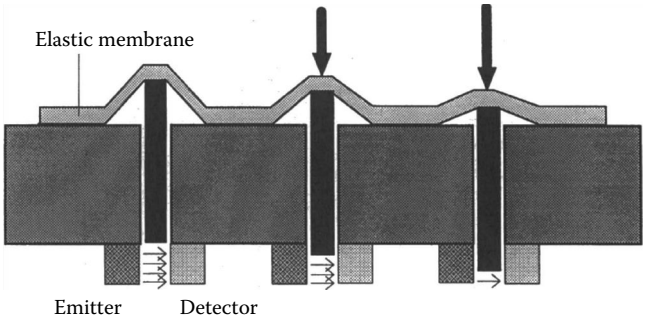

FIGURE 38.10 Principle of operation of an occluder–transducer.

the surface, blocking the light path of a photoemitter–detector pair. The amount of movement determines the amount of light reaching the photoreceiver. Correspondingly, the more force applied, the less amount of light is collected by the photoreceiver (Figure 38.10). The major problems with this specific device are associated with creep, hysteresis, and temperature variation. This scheme also requires individual calibration of each photoemitter–photodetector pair.

Fibers have also been used directly as transducers in the design of tactile sensors. Their use is based on two properties of fiber-optic cables: (1) If a fiber is subjected to a significant amount of bending, then the angle of incidence at the fiber wall can be reduced sufficiently for light to leave the core [37], and (2) if two fibers pass close to one another and both have roughened surfaces, then light can pass between the fibers. Light coupling between adjacent fibers is a function of their separation [3].

An example of an optical fiber tactile sensor, whose sensing mechanism is based on the increase of light attenuation due to the microbend in the optical fibers, is shown in Figure 38.11 [37]. The transducer consists of a four-layer, 2D fiber-optic array constructed by using two layers of optical fibers as a corrugation structure, through which microbends are induced in two orthogonal layers of active fibers. Each active fiber uses LED as the emitter and PIN photodiode as a detector. When an object is forced into contact with the transducer, a light distribution is detected at each detector. This light distribution is related to the applied force and the shape of the object. Using complex algorithms and active sensing (moving the object in relation to the transducer), the object position, orientation, size, and contour information can be retrieved [37]. However, the recovery of the applied force profiles was not reported in [37].

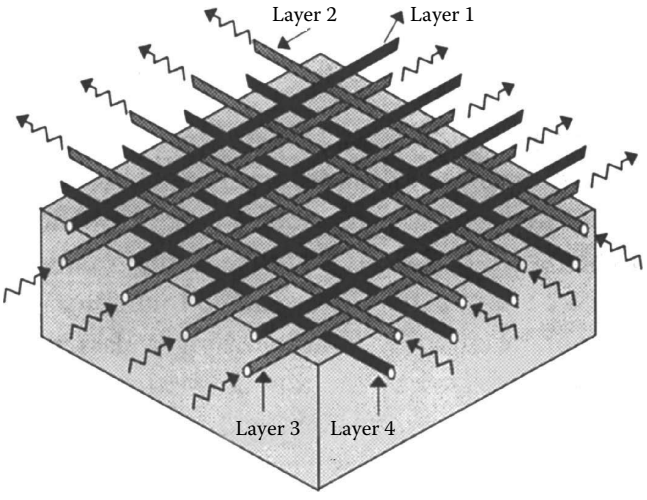

FIGURE 38.11 Four-layer tactile transducer.

38.5.5 Photoelastic

An emerging technology in optical tactile sensing is the development of photoelastic transducers. When a light ray propagates into an optically anisotropic medium, it splits into two rays that are linearly polarized at right angles to each other and propagate at different velocities. This splitting of a ray into two rays that have mutually perpendicular polarizations results from a physical property of crystalline material that is called *optical birefringence* or simply *birefringence*. The direction in which light propagates with the higher velocity is called the *fast axis*, and the one in which it propagates more slowly is called the *slow axis*. Some optically isotropic materials—such as glass, celluloid, bakelite, and transparent plastics in general—become birefringent when they are subjected to a stress field. The birefringent effect lasts only during the application of loads. Thus, this phenomenon is called *temporary* or *artificial birefringence* or, more commonly, the *photoelastic phenomenon*.

Figure 38.12a shows a photoelastic transducer proposed in [38]. It consists of a fully supported two-layer beam with a mirrored surface sandwiched in between. Normal line forces are applied to the top

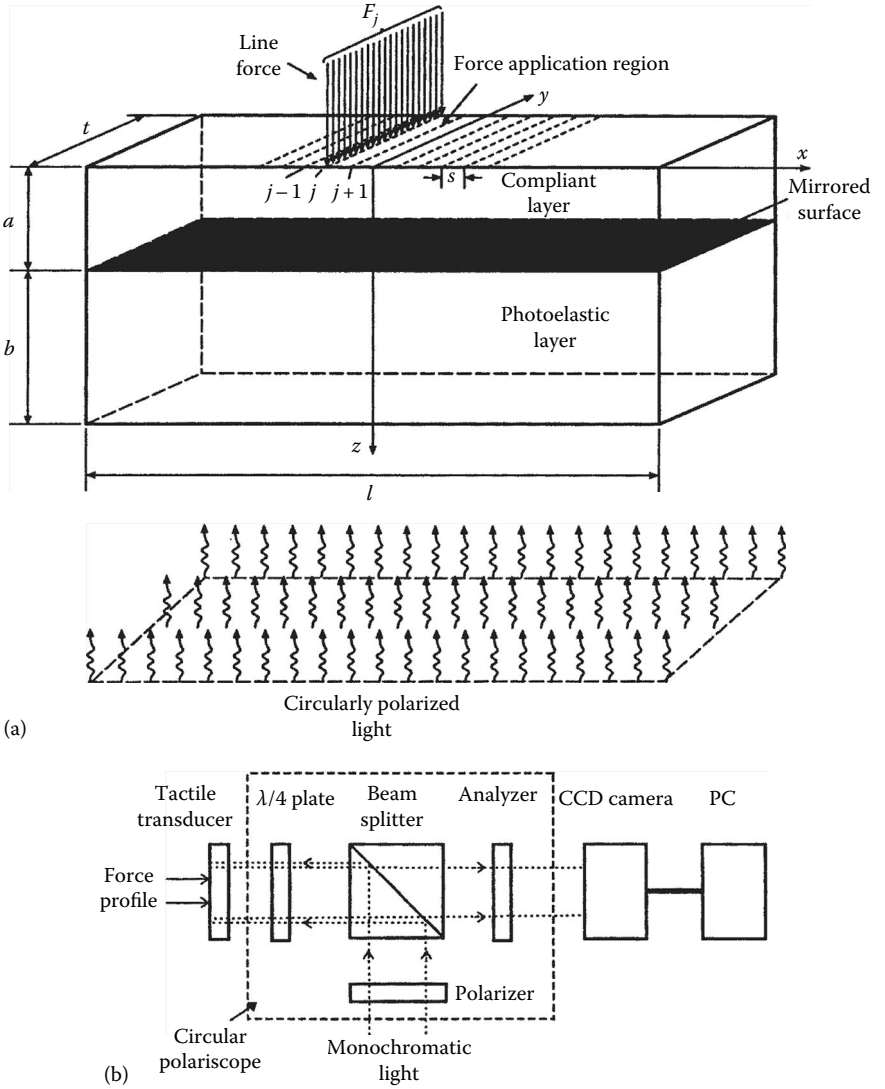

FIGURE 38.12 (a) Photoelastic transducer. (b) Circular reflective polariscope.

surface of the beam at discrete tactels, separated by equal distances, *s*, along the beam. The upper compliant layer is for the protection of the mirror, while the lower one is the photoelastic layer.

Circularly polarized monochromatic light, incident along the *z*-axis, illuminates the bottom surface of the transducer. The light propagates parallel to the *z*-axis, passes through the photoelastic layer, and then reflects back from the mirror. If no force is applied to the transducer, the returning light is circularly polarized because unstressed photoelastic material is isotropic. If force is applied, stresses are induced in the photoelastic layer, making the material birefringent. This introduces a certain phase difference between the components of the electric field associated with the light-wave propagation. The two directions of polarization are in the plane perpendicular to the direction of propagation (in this case, the *x*–*y* plane). As a consequence of this effect, the output light is elliptically polarized, creating a phase difference distribution, *p*, between the input light and the output light at each point in the *x*–*y* plane. The phase difference distribution carries the information of the force distribution applied to the transducer.

A *polariscope* is a practical method to observe the spatial variation on light intensity (fringes) due to the effect of induced phase difference distribution. Polariscopes can be either linear or circular, depending on the required polarization of the light. They can also be characterized as a reflective or a transparent type, depending on whether the photoelastic transducer reflects or transmits the light.

A circular, reflective polariscope, shown in Figure 38.12b, is utilized to illuminate the transducer shown in Figure 38.12a. The input light is linearly polarized and is directed toward the photoelastic transducer by a beam splitter. Before reaching the transducer, the light is circularly polarized by a quarter-wave plate. The output light is elliptically polarized when a force is applied. This light is directed toward a detector passing through the quarter-wave plate, the beam splitter, and an analyzer. Finally, it is detected by a camera linked to a frame grabber connected to a PC, for further data processing. The light that illuminates the camera consists of a set of fringes from where the force distribution applied to the transducer must be recovered. A technique for the recovery of the forces from the fringes is described in [38]. A model of the transducer using FEA is reported in [39].

One of the earlier applications of photoelasticity to tactile sensing dates back to the era of development phase of the Utah/MIT dextrous hand [40]. The researchers proposed the use of the photoelastic phenomenon as a transduction method for the recovery of the force profile applied to the fingers of the hand. They limited their application to the development of a single-touch transducer, although they claimed that an array of such devices could be implemented. However, the construction of a large array of their devices would be difficult. To overcome this difficulty, another research group proposed a different transducer [41]. Although an analytical model was developed for the sensor, a systematic method for recovering the 2D force profile from the light intensity distribution was not reported. Thus, the sensor was used mainly for the study of the forward analysis, namely, observing the light intensity distribution for different touching objects brought into contact with the sensor. This sensor could eventually be used for determining some simple geometric properties of a touching object.

A tactile sensor reported in [42] is capable of detecting slippage. The output light intensity (the fringe pattern) is captured by a camera interfaced to a PC. The light intensity distribution changes when an object moves across the surface of the transducer. A direct analysis of the fringes is used to detect movement of the grasped object; a special technique was reported to optimize the comparison process for detecting differences between two fringe patterns occurring due to the slippage of the object in contact with the sensor [42]. It is important to note that such an analysis of the fringes does not require the recovery of the applied force profile.

Photoelasticity offers several attractive properties for the development of tactile sensors: good linearity, compatibility with vision-base sensing technologies, and high spatial resolution associated with the latter that could lead to the development of high-resolution tactile imagers needed for object recognition and fine manipulation. Also, photoelastic sensors are compatible with fiber-optic technology that allows remote location of electronic processing devices and avoidance of interference problems.

Other technologies for tactile sensing include acoustic, magnetic, and microcavity vacuum sensors [43,44].

References

1. P. Dario, Contact sensing for robot active touch, in *Robotic Science*, M. Brady (ed.), Cambridge, MA: MIT Press, 1989, Chapter 3, pp. 138–163.
2. P. P. L. Regtien, Tactile imaging, *Sens. Actuat. A*, 31, 83–89, 1992.
3. R. A. Russell, *Robot Tactile Sensing*, Brunswick, Victoria, Australia: Prentice Hall, 1990.
4. A. D. Berger and P. K. Khosla, Using tactile data for real-time feedback, *Int. J. Rob. Res.*, 10(2), 88–102, 1991.
5. S. Begej, Planar and finger-shaped optical tactile sensors for robotic applications, *IEEE J. Rob. Autom.*, 4, 472–484, 1988.
6. R. A. Russell and S. Parkinson, Sensing surface shape by touch, *Proceedings of the IEEE International Conference on Robotics Automation*, Atlanta, GA, 1993, pp. 423–428.
7. R. D. Howe, A tactile stress rate sensor for perception of fine surface features, *Proceedings of the IEEE International Conference on Solid-State Sensors Actuators*, San Francisco, CA, 1991, pp. 864–867.
8. S. Sugiyama, K. Kawahata, H. Funabashi, M. Takigawa, and I. Igarashi, A 32 × 32 (1K)-element silicon pressure-sensor array with CMOS processing circuits, *Electron. Commun. Jpn.*, 75(1), 64–76, 1992.
9. J. S. Son, E. A. Monteverde, and R. D. Howe, A tactile sensor for localizing transient events in manipulation, *Proceedings of the IEEE International Conference on Robotics Automation*, San Diego, CA, 1994, pp. 471–476.
10. M. R. Tremblay and M. R. Cutkosky, Estimating friction using incipient slip sensing during manipulation task, *Proceedings of the IEEE International Conference on Robotics Automation*, Atlanta, GA, 1993, pp. 429–434.
11. S. Omata and Y. Terubuna, New tactile sensor like the human hand and its applications, *Sens. Actuat. A*, 35, 9–15, 1992.
12. R. Bayrleithner and K. Komoriya, Static friction coefficient determination by force sensing and its applications, *IROS'94*, Munich, Germany, 1994, pp. 1639–1646.
13. M. A. Abidi and R. C. Gonzales, The use of multisensor data for robotic applications, *IEEE Trans. Rob. Autom.*, 6, 159–177, 1990.
14. A. A. Cole, P. Hsu, and S. S. Sastry, Dynamic control of sliding by robot hands for regrasping, *IEEE Trans. Rob. Autom.*, 8, 42–52, 1992.
15. P. K. Allen and P. Michelman, Acquisition and interpretation of 3-D sensor data from touch, *IEEE Trans. Rob. Autom.*, 6, 397–404, 1990.
16. H. R. Nicholls (ed.), *Advanced Tactile Sensing for Robotics*, Singapore: World Scientific Publishing, 1992.
17. J. G. Webster (ed.), *Tactile Sensors for Robotics and Medicine*, New York: John Wiley & Sons, 1988.
18. R. S. Fearing, Tactile sensing mechanism, *Int. J. Rob. Res.*, 9(3), 3–23, 1990.
19. T. H. Speeter, Three-dimensional finite element analysis of elastic continua for tactile sensing, *Int. J. Rob. Res.*, 11(1), 1–19, 1992.
20. Y. C. Pati, R. S. Krishnaprasad, and M. C. Peckerar, An analog neural network solution to the inverse problem of early taction, *IEEE Trans. Rob. Autom.*, 8(2), 196–212, 1992.
21. L. D. Harmon, Automated tactile sensing, *Int. J. Rob. Res.*, 1(2), 3–32, 1982.
22. W. E. Snyder and J. St. Clair, Conductive elastomers as a sensor for industrial parts handling equipment, *IEEE Trans. Instrum. Meas.*, 27(1), 94–99, 1991.
23. M. Shimojo, M. Ishikawa, and K. Kanaya, A flexible high resolution tactile imager with video signal output, *Proceedings of the IEEE International Conference on Robotics Automation*, Sacramento, CA, 1991, pp. 384–391
24. W. D. Hillis, A high resolution imaging touch sensor, *Int. J. Rob. Res.*, 1(2), 33–44, 1982.
25. Y. Yamada and M. R. Cutkosky, Tactile sensor with 3-axis force and vibration sensing functions and its applications to detect rotational slip, *Proceedings of the IEEE International Conference on Robotics Automation*, San Diego, CA, 1994, pp. 3550–3557.
26. K. Njafi and C. H. Mastrangelo, Solid-state microsensors and smart structure, *Ultrasonic Symposium*, Baltimore, MD, 1993, pp. 341–350.

27. F. Zhu and J. W. Spronck, A capacitive tactile sensor for shear and normal force measurements, *Sens. Actuat. A*, 31, 115–120, 1992.
28. K. Suzuki, K. Najafi, and K. D. Wise, A 1024-element high-performance silicon tactile imager, *IEEE Trans. Electron Devices*, 17(8), 1852–1860, 1990.
29. M. R. Wolffenbuttel and P. L. Regtien, The accurate measurement of a micromechanical force using force-sensitive capacitances, *Conference on Precision Electromagnetic Measurement*, Boulder, CO, 1994, pp. 180–181.
30. M. R. Wolffenbuttel, R. F. Wolffenbuttel, and P. P. L. Regtien, An integrated charge amplifier for a smart tactile sensor, *Sens. Actuat. A*, 31, 101–109, 1992.
31. E. D. Kolesar, Jr. and C. S. Dyson, Object imaging with piezoelectric robotic tactile sensor, *J. Microelectromech. Syst*., 4(2), 87–96, 1995.
32. J. L. Scheiter and T. B. Sheridan, An optical tactile sensor for manipulators, *J. Rob. Comput. Integr. Manuf*., 1, 65–71, 1989.
33. R. Ristic, B. Benhabib, and A. A. Goldenberg, Analysis and design of a modular electrooptical tactile sensor, *IEEE Trans. Rob. Autom*., 5(3), 362–368, 1989.
34. H. Maekawa, K. K. Tanie, K. Komoriya, M. Kaneko, C. Horiguchi, and T. Sugawara, Development of a finger shaped tactile sensor and it evaluation by active touch, *Proceedings of the IEEE International Conference on Robotics Automation*, Nice, France, 1992, pp. 1327–1334.
35. M. Ohka, Y. Mitsurya, S. Takeuchi, and O. Kamekawa, A three-axis optical tactile sensor (fern contact analyses and sensing experiments using a large-sized tactile sensor), *Proceedings of the IEEE International Conference on Robotics Automation*, Nagoya, Aichi, Japan, 1995, pp. 817–824.
36. J. Rebman and K. A. Morris, A tactile sensor with electro-optical transduction, in *Robots Sensors, Tactile and Non-Vision*, Vol. 2, A. Pugh (ed.), Berlin, Germany: EFS Publications, 1986, pp. 145–155.
37. S. R. Emge and C. L. Chen, Two dimensional contour imaging with a fiber optic microbend tactile sensor array, *Sens. Actuat. B*, 3, 31–42, 1991.
38. R. E. Saad, A. Bonen, K. C. Smith, and B. Benhabib, Distributed-force recovery for a planar photoelastic tactile sensor, *IEEE Trans. Instrum. Meas*., 45, 541–546, 1996.
39. R. E. Saad, A. Bonen, K. C. Smith, and B. Benhabib, Finite-element analysis for photoelastic tactile sensors, *Proceedings of the IEEE International Conference on Industrial Electronics, Control, and Instrumentation*, Orlando, FL, 1995, pp. 1202–1207.
40. S. C. Jacobsen, J. E. Wood, D. F. Knutti, and B. Biggers, The Utah/MIT dexterous hand: Work in progress, in *Robotics Research: The First International Symposium*, M. Brady and R. Paul (eds.), Cambridge, MA: MIT Press, 1983, pp. 601–653.
41. A. Cameron, R. Daniel, and H. Durrant-Whyte, Touch and motion, *Proceedings of the IEEE International Conference on Robotics Automation*, Philadelphia, PA, 1988, pp. 1062–1067.
42. S. H. Hopkins, F. Eghtedari, and D. T. Pham, Algorithms for processing data from a photoelastic slip sensor, *Mechatronics*, 2(1), 15–28, 1992.
43. S. Ando and H. Shinoda, Ultrasonic emission tactile sensing, *IEEE Trans. Control Syst*., 15(1), 61–69, 1996.
44. J. C. Jiang, V. Faynberg, and R. C. White, Fabrication of micromachined silicon tip transducer for tactile sensing, *J. Vac. Sci. Technol. B*, 11, 1962–1967, 1993.

Further Readings

Amazeen, C. A. and Bishop, S. S., Triaxial tactile sensor, http://www.devileye.net/catalog/motor-vehicle_seat_headrest/triaxial_tactile_sensor.html (accessed on June 22, 2012).

Dahiya, R. S. and Valle, M., *Robotic Tactile Sensing*, Dordrecht, the Netherlands: Springer, 2013. Online version available http://www.springerlink.com/content/978-94-007-0579-1#section=1102532&page=1&locus=71 (accessed August 10, 2012).

Najarian, S., Dargahi, J., and Mehrizi, A., *Artificial Tactile Sensing in Biomedical Engineering*, New York: McGraw-Hill, 2009,

Tiwana, M. I., Redmond, S. J., and Lovell, N. H., A review of tactile sensing technologies with applications in biomedical engineering, *Sens. Actuat*., 179, 17–31, 2012. Also available at http://www.sciencedirect.com/science/article/pii/S0924424712001641 (accessed on July 24, 2012).

Partial List of Vendors and Suppliers

Beijer Electronics, Inc., 2212 South West Temple No. 50, Salt Lake City, UT 84115, Phone: 801-466-8770, 866-648-3767 (toll free), Fax: 801-466-8792, www.beijerelectronicsinc.com/?cid=ndc~th…

Densitron Corp, 2330 Pomona Rincon Rd., Corona, CA 92880, Phone: 951-284-7600, Fax: 951-284-7699, www.densitron.com

Ercon, Inc., 7 Kendrick Rd., Wareham, MA 02571, Phone: 508-291-1400, Fax: 508-291-2400, www.erconinc.com

Honeywell Sensing and Control, 1985 Douglas Dr. North, MN10-192B, Golden Valley, MN 55422, Phone: 763-954-4818, 800-446-6555 (toll free), sensing.honeywell.com/index.cfm/ci_id/15…

IFM Efector, Inc., 782 Springdale Dr., Exton, PA 19341-2843, Phone: 610-524-2000, 800-441-8246 (toll free), Fax: 800-329-0436, www.ifm.com/ifmus/web/home.htm

Kanson Electronics, 245 Forrest Ave., Hohenwald, TN 38462, Phone: 931-796-3050, Fax: 931-796-3956, www.issc-kanson.com

Microstrain, Inc., 459 Hurricane Lane, Suite 102, Williston, VT 05495, Phone: 802-862-6629, 800-449-3878 (toll free), Fax: 802-863-4093, www.microstrain.com

PICS INC, 81 Lancaster Ave., Suite 202, Malvern, PA 19355, Phone: 610-644-7701, Fax: 610-644-9297, www.picscontrols.com

Steven Engineering, 230 Ryan Way, South San Francisco, CA 94080, Phone: 888-790-0022 (toll free), Fax: 800-314-0716, 800-314-0716 (toll free), stevenengineering.rtrk.com/?scid=1975164…

Tekscan, 307 W. First St., South Boston, MA 02127, Phone: 617-464-4500, 800-248-3669 (toll free), Fax: 617-464-4266, www.tekscan.com

39

Pressure Measurement

Kevin H.L. Chau
Analog Devices, Inc.

39.1 Basic Definitions

Pressure is defined as the normal force per unit area exerted by a fluid (liquid or gas) on any surface. The surface can be either a solid boundary in contact with the fluid or, for purposes of analysis, an imaginary plane drawn through the fluid. Only the component of the force normal to the surface needs to be considered for the determination of pressure. Tangential forces that give rise to shear and fluid motion will not be a relevant subject of discussion here. In the limit that the surface area approaches zero, the ratio of the differential normal force to the differential area represents the pressure at a point on the surface. Furthermore, if there is no shear in the fluid, the pressure at any point can be shown to be independent of the orientation of the imaginary surface under consideration. Finally, it should be noted that pressure is not defined as a vector quantity and is therefore nondirectional.

Three types of pressure measurements are commonly performed:

Absolute pressure is the same as the pressure defined earlier. It represents the pressure difference between the point of measurement and a perfect vacuum where pressure is zero.

Gage pressure is the pressure difference between the point of measurement and the ambient. In reality, the ambient (atmospheric) pressure can vary, but only the pressure difference is of interest in gage pressure measurements.

Differential pressure is the pressure difference between two points, one of which is chosen to be the reference. In reality, both pressures can vary, but only the pressure difference is of interest here.

39.1.1 Units of Pressure and Conversion

The SI unit of pressure is the *pascal* (Pa), which is defined as the newton per square meter (N/m); 1 Pa is a very small unit of pressure. Hence, decimal multiples of the pascal (e.g., kilopascals [kPa] and megapascals [MPa]) are often used for expressing higher pressures. In weather reports, the hectopascal (1 hPa = 100 Pa) has been adopted by many countries to replace the millibar (1 bar = 10^5 Pa; hence, 1 millibar = 10^{-3} bar = 1 hPa) as the unit for atmospheric pressure. In the United States, pressure is commonly expressed in pound force per square inch (psi), which is about 6.90 kPa. In addition, the absolute,

TABLE 39.1 Pressure Unit Conversion Table

Key
1. kPa = kilopascal
2. psi = pound force per square inch
3. in. H_2O = inch of water at 4 °C
4. cm H_2O = centimeter of water at 4 °C
5. in. Hg = inch of mercury at 0 °C
6. mm Hg = millimeter of mercury at 0 °C
7. mbar = millibar

gage, and differential pressures are further specified as psia, psig, and psid, respectively. However, no such distinction is made in any pressure units other than the psi. There is another class of units, for example, millimeter of mercury at 0 °C (mm Hg, also known as the *torr*) or inch of water at 4 °C (in H_2O), which expresses pressure in terms of the height of a static liquid column. The actual pressure p referred to is one that will be developed at the base of the liquid column due to its weight, which is given by Equation 39.1:

$$p = \rho g h \tag{39.1}$$

where
- ρ is the density of the liquid
- g is the acceleration due to gravity
- h is the height of the liquid column

A conversion table for the most popular pressure units is provided in Table 39.1.

39.2 Sensing Principles

39.2.1 Sensing Elements

Since pressure is defined as the force per unit area, the most direct way of measuring pressure is to isolate an area on an elastic mechanical element for the force to act on. The deformation of the sensing element produces displacements and strains that can be precisely sensed to give a calibrated measurement of the pressure. This forms the basis for essentially all commercially available pressure sensors today. Specifically, the basic requirements for a pressure-sensing element are a means to isolate two fluidic pressures (one to be measured and the other one as the reference) and an elastic portion to convert the pressure difference into a deformation of the sensing element. Many types of pressure-sensing elements are currently in use. These can be grouped as diaphragms, capsules, bellows, and tubes, as illustrated in Figure 39.1. Diaphragms are by far the most widely used of all sensing elements. A special form of tube, known as the *Bourdon tube*, is curved or twisted along its length and has an oval cross section. The tube is sealed at one end and tends to unwind or straighten when it is subjected to a pressure applied to the inside. In general, Bourdon tubes are designed for measuring high pressures, while capsules and bellows are usually for measuring low pressures. A detailed description of these sensing elements can be found in [1].

39.2.2 Detection Methods

A detection means is required to convert the deformation of the sensing element into pressure readout. In the simplest approach, the displacements of a sensing element can be amplified mechanically by lever and flexure linkages to drive a pointer over a graduated scale, for example, in the moving pointer barometers. Some of the earliest pressure sensors employed a Bourdon tube to drive the wiper arm over a potentiometric resistance element. In *linear-variable differential-transformer* (LVDT) pressure sensors, the displacement of a Bourdon tube or capsule is used to move a magnetic core inside a coil assembly

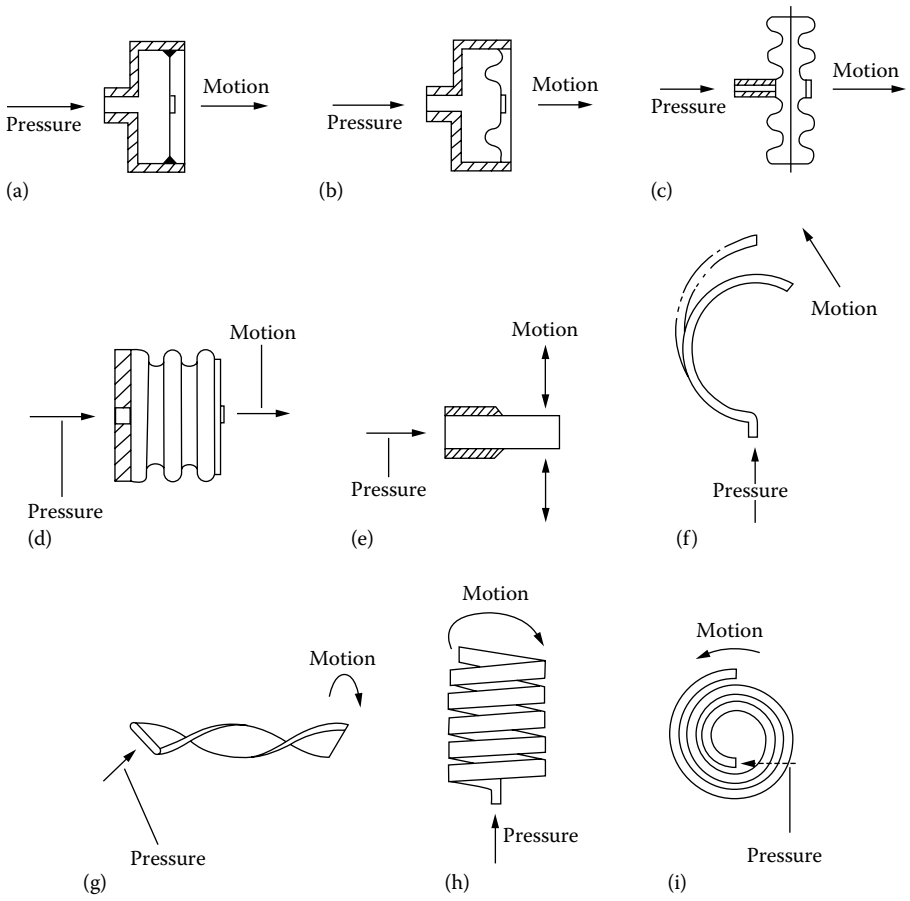

FIGURE 39.1 Pressure-sensing elements: (a) flat diaphragm, (b) corrugated diaphragm, (c) capsule, (d) bellows, (e) straight tube, (f) C-shaped Bourdon tube, (g) twisted Bourdon tube, (h) helical Bourdon tube, and (i) spiral Bourdon tube. (From Norton, H.N., *Handbook of Transducers*, Prentice Hall, Englewood Cliffs, NJ, 1989. Reprinted with permission.)

to vary its inductance. In *piezoelectric* pressure sensors, the strains associated with the deformation of a sensing element are converted into an electric charge output by a piezoelectric crystal. Piezoelectric pressure sensors are useful for measuring high-pressure transient events, for example, explosive pressures. In *vibrating-wire* pressure sensors, a metal wire (typically tungsten) is stretched between a fixed anchor and the center of a diaphragm. The wire is located near a permanent magnet and is set into vibration at its resonant frequency by an ac current excitation. A pressure-induced displacement of the diaphragm changes the tension and therefore the resonant frequency of the wire, which is measured by the readout electronics. A detailed description of these and other types of detection methods can be found in [1].

39.2.2.1 Capacitive Pressure Sensors

Many highly accurate (better than 0.1%) pressure sensors in use today have been developed using the capacitive detection approach. Capacitive pressure sensors can be designed to cover an extremely wide pressure range. Both high-pressure sensors with full-scale pressures above 10^7 Pa (a few thousand psi) and vacuum sensors (commonly referred to as capacitive *manometers*) usable for pressure measurements below 10^{-3} Pa (10^{-5} torr) are commercially available. The principle of *capacitive pressure sensors* is illustrated in Figure 39.2. A metal or silicon diaphragm serves as the pressure-sensing element and

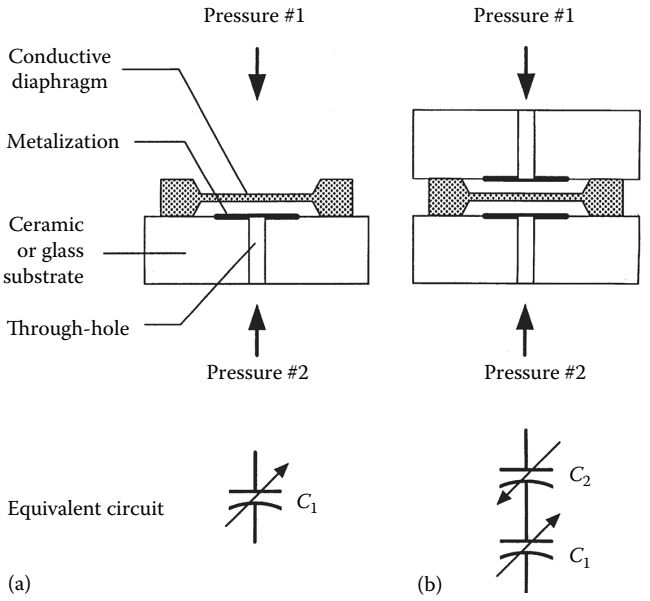

FIGURE 39.2 Operating principle of capacitive pressure sensors, (a) single capacitor design and (b) differential capacitor design.

constitutes one electrode of a capacitor. The other electrode, which is stationary, is typically formed by a deposited metal layer on a ceramic or glass substrate. An applied pressure deflects the diaphragm, which in turn changes the gap spacing and the capacitance [2]. In the differential capacitor design, the sensing diaphragm is located in between two stationary electrodes. An applied pressure will cause one capacitance to increase and the other one to decrease, thus resulting in twice the signal while canceling many undesirable common-mode effects. Figure 39.3 shows a practical design of a differential capacitive sensing cell that uses two isolating diaphragms and an oil fill to transmit the differential pressure to the

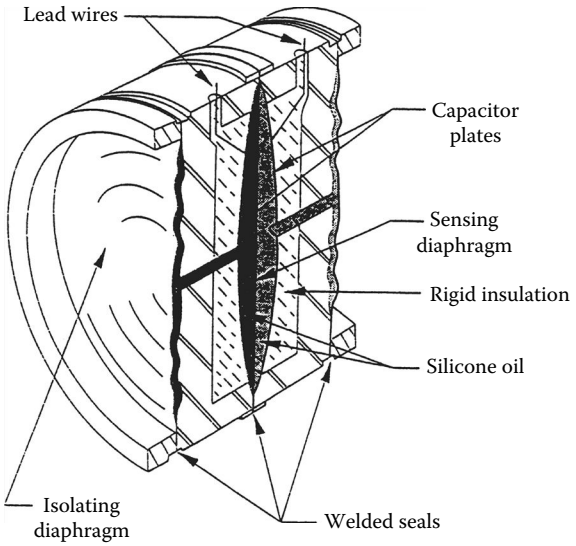

FIGURE 39.3 Differential capacitive sensing cell that is equipped with isolating diaphragms and silicone oil transfer fluid suitable for measuring pressure in corrosive media. (Courtesy of Rosemount, Inc., Eden Prairie, MN.)

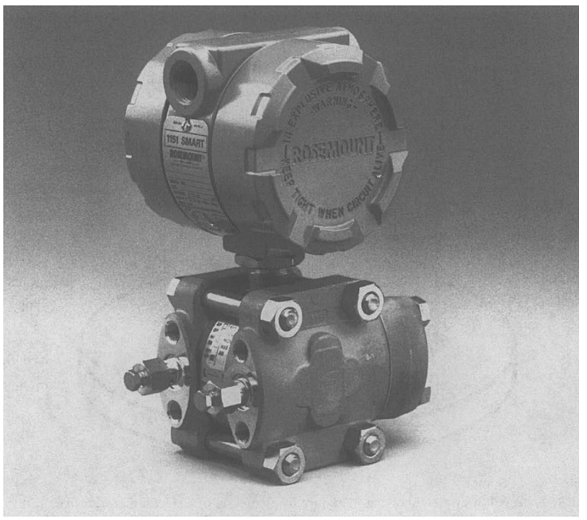

FIGURE 39.4 Rugged capacitive pressure sensor product for industrial applications. It incorporates the sensing cell shown in Figure 39.3. Readout electronics are contained in the housing at the top. (Courtesy of Rosemount, Inc., Eden Prairie, MN.)

sensing diaphragm. The isolating diaphragms are made of special metal alloys that enable them to handle corrosive fluids. The oil is chosen to set a predictable dielectric constant for the capacitor gaps while providing adequate damping to reduce shock and vibration effects. Figure 39.4 shows a rugged capacitive pressure sensor for industrial applications based on the capacitive sensing cell shown in Figure 39.3. The capacitor electrodes are connected to the readout electronics housing at the top. In general, with today's sophisticated electronics and special considerations to minimize stray capacitances (which can degrade the accuracy of measurements), a capacitance change of 10 aF (10^{-18} F) provided by a diaphragm deflection of only a fraction of a nanometer is resolvable.

39.2.2.2 Piezoresistive Pressure Sensors

Piezoresistive sensors (also known as *strain-gage* sensors) are the most common type of pressure sensor in use today. *Piezoresistive effect* refers to a change in the electric resistance of a material when stresses or strains are applied. Piezoresistive materials can be used to realize strain gages that, when incorporated into diaphragms, are well suited for sensing the induced strains as the diaphragm is deflected by an applied pressure. The sensitivity of a strain gage is expressed by its *gage factor*, which is defined as the fractional change in resistance, $\Delta R/R$, per unit strain:

$$\text{Gage factor} = \frac{\Delta R/R}{\varepsilon} \tag{39.2}$$

where strain ε is defined as $\Delta L/L$, or the extension per unit length. It is essential to distinguish between two different cases in which (1) the strain is parallel to the direction of the current flow (along which the resistance change is to be monitored) and (2) the strain is perpendicular to the direction of the current flow. The gage factors associated with these two cases are known as the *longitudinal gage factor* and the *transverse gage factor*, respectively. The two gage factors are generally different in magnitude and often opposite in sign. Typical longitudinal gage factors are ~2 for many useful metals, 10–35 for polycrystalline silicon (polysilicon), and 50–150 for single-crystalline silicon [3–5]. Because of its large piezoresistive effect, silicon has become the most commonly used material for strain gages. There are several ways to incorporate strain gages into pressure-sensing diaphragms. For example, strain gages can be

directly bonded onto a metal diaphragm. However, hysteresis and creep of the bonding agent are potential issues. Alternatively, the strain-gage material can be deposited as a thin film on the diaphragm. The adhesion results from strong molecular forces that will not creep, and no additional bonding agent is required. Today, the majority of piezoresistive pressure sensors are realized by integrating the strain gages into the silicon diaphragm using integrated circuit fabrication technology. This important class of silicon pressure sensors will be discussed in detail in the next section.

39.3 Silicon Micromachined Pressure Sensors

Silicon micromachined pressure sensors refer to a class of pressure sensors that employ integrated circuit batch processing techniques to realize a thinned-out diaphragm sensing element on a silicon chip. Strain gages made of silicon diffused resistors are typically integrated on the diaphragm to convert the pressure-induced diaphragm deflection into an electric resistance change. Over the past 20 years, silicon micromachined pressure sensors have gradually replaced their mechanical counterparts and have captured over 80% of the pressure sensor market. There are several unique advantages that silicon offers. Silicon is an ideal mechanical material that does not display any hysteresis or yield and is elastic up to the fracture limit. It is stronger than steel in yield strength and comparable in Young's modulus [6]. As mentioned in the previous section, the piezoresistive effect in single-crystalline silicon is almost two orders of magnitude larger than that of metal strain gages. Silicon has been widely used in integrated circuit manufacturing for which reliable batch fabrication technology and high-precision dimension control techniques have been well developed. A typical silicon wafer yields hundreds of identical pressure sensor chips at very low cost. Further, the necessary signal-conditioning circuitry can be integrated on the same sensor chip no more than a few millimeters in size [7]. All these are key factors that contributed to the success of silicon micromachined pressure sensors.

Figure 39.5 shows a typical construction of a silicon piezoresistive pressure sensor. An array of square or rectangular diaphragms is "micromachined" out of an (100) oriented single-crystalline silicon wafer by selectively removing material from the back. An anisotropic silicon etchant (e.g., potassium hydroxide) is typically employed; it etches fastest on (100) surfaces and much slower on (111) surfaces. The result is a pit formed on the backside of the wafer bounded by (111) surfaces and a thinned-out diaphragm section on the front at every sensor site. The diaphragm thickness is controlled by a timed etch or by using suitable etch-stop techniques [6,8]. To realize strain gages, a *p*-type dopant, typically boron, is diffused into the front of the *n*-type silicon diaphragm at stress-sensitive

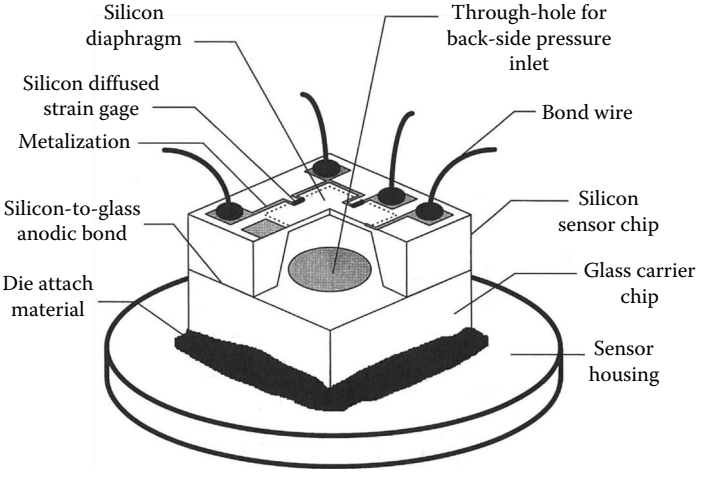

FIGURE 39.5 Cutaway view showing the typical construction of a silicon piezoresistive pressure sensor.

FIGURE 39.6 Examples of commercially available packages for silicon pressure sensors. Shown in the photo are surface-mount units, dual-in-line (DIP) units, TO-8 metal cans, and stainless steel units with isolating diaphragms. (Courtesy of EG&G IC Sensors, Eden Prairie, MN.)

locations to form resistors that are electrically isolated from the diaphragm and from each other by reverse biased p–n junctions. The strain gages, the diaphragm, and the rest of the supporting sensor chip all belong to the same single-crystalline silicon. The result is a superb mechanical structure that is free from creep, hysteresis, and thermal expansion coefficient mismatches. However, the sensor die must still be mounted to a sensor housing, which typically has mechanical properties different from that of silicon. It is crucial to ensure a high degree of stress isolation between the sensor housing and the sensing diaphragm that may otherwise lead to long-term mechanical drifts and undesirable temperature behavior. A common practice is to bond a glass wafer or a second silicon wafer to the back of the sensor wafer to reinforce the overall composite sensor die. This way, the interface stresses generated by the die mount will also be sufficiently remote from the sensing diaphragm and will not seriously affect its stress characteristics. For gage or differential pressure sensing, holes must be provided through the carrier wafer prior to bonding that are aligned to the etch pits of the sensor wafer leading to the back of the sensing diaphragms. No through holes are necessary for absolute pressure sensing. The wafer-to-wafer bonding is performed in a vacuum to achieve a sealed reference vacuum inside the etch pit [6,9]. Today's silicon pressure sensors are available in a large variety of plastic, ceramic, metal can, and stainless steel packages (some examples are shown in Figure 39.6). Many are suited for printed circuit board mounting. Others have isolating diaphragms and transfer fluids for handling corrosive media. They can be readily designed for a wide range of industrial, medical, automotive, aerospace, and military applications.

39.3.1 Silicon Piezoresistive Pressure Sensor Limitations

Despite the relatively large piezoresistive effects in silicon strain gages, the full-scale resistance change is typically only 1%–2% of the resistance of the strain gage (which yields an unamplified voltage output of 10–20 mV/V). To achieve an overall accuracy of 0.1% of full scale, for example, the combined effects of mechanical and electric repeatability, hysteresis, linearity, and stability must be controlled or compensated to within a few parts per million (ppm) of the gage resistance. Furthermore, silicon strain gages are also very temperature sensitive and require careful compensations. There are two primary sources of temperature drifts: (1) the temperature coefficient of resistance of the strain gages (from 0.06%/°C to 0.24%/°C) and (2) the temperature coefficient of the gage factors (from −0.06%/°C to −0.24%/°C), which will cause

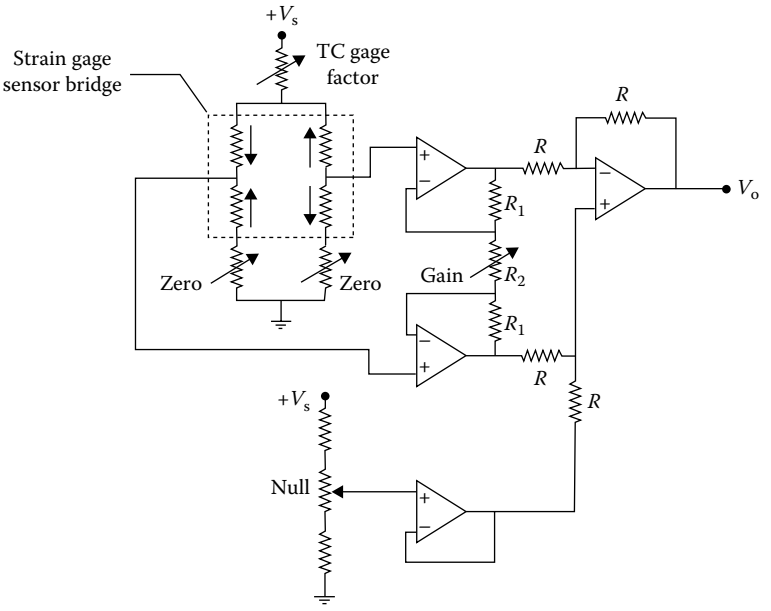

FIGURE 39.7 Signal-conditioning circuit for silicon piezoresistive pressure sensor.

a decrease in pressure sensitivity as the temperature rises. Figure 39.7 shows a circuit configuration that can be used to achieve offset (resulting from gage resistance mismatch) and temperature compensations as well as providing signal amplification to give a high-level output. Four strain gages that are closely matched in both their resistances and temperature coefficients of resistance are employed to form the four active arms of a Wheatstone bridge. Their resistor geometry on the sensing diaphragm is aligned with the principal strain directions so that two strain gages will produce a resistance increase and the other two a resistance decrease on a given diaphragm deflection. These two pairs of strain gages are configured in the Wheatstone bridge such that an applied pressure will produce a bridge resistance imbalance while the temperature coefficient of resistance will only cause a common-mode resistance change in all four gages, keeping the bridge balanced. As for the temperature coefficient of the gage factor, because it is always negative, it is possible (e.g., with the voltage divider circuit in Figure 39.7) to utilize the positive temperature coefficient of the bridge resistance to increase the bridge supply voltage, compensating for the loss in pressure sensitivity as temperature rises. Another major limitation in silicon pressure sensors is the nonlinearity in the pressure response that usually arises from the slight nonlinear behavior in the diaphragm mechanical and the silicon piezoresistive characteristics. The nonlinearity in the pressure response can be compensated by using analog circuit components. However, for the most accurate silicon pressure sensors, digital compensation using a microprocessor with correction coefficients stored in memory is often employed to compensate for all the predictable temperature and nonlinear characteristics. The best silicon pressure sensors today can achieve an accuracy of 0.08% of full scale and a long-term stability of 0.1% of full scale per year. Typical compensated temperature range is from −40 °C to 85 °C, with the errors of compensation on span and offset both around 1% of full scale. Commercial products are currently available for full-scale pressure ranges from 10 kPa to 70 MPa (1.5–10,000 psi). The 1998 prices are U.S. $5–$20 for the most basic uncompensated sensors, $10–$50 for the compensated (with additional laser-trimmed resistors integrated either on a chip or on a ceramic substrate) or signal-conditioned (compensated with amplified output) sensors, and $60–$300 for sensors with isolating diaphragms in stainless steel housings. Table 39.2 provides contact information for selected companies making pressure sensors.

TABLE 39.2 Selected Companies That Make Pressure Sensors and Pressure Calibration Systems

1. Silicon micromachined piezoresistive pressure sensor
   Druck, Inc., 4 Dunham Drive, New Fairfield, CT 06812, Tel: (203) 746-0400, http://www.druck.com
   EG&G IC Sensors, 1701 McCarthy Blvd., Milpitas, CA 95035-7416, Tel: (408) 432-1800
   Foxboro ICT, 199 River Oaks Pkwy., San Jose, CA 95134-1996, Tel: (408) 432-1010, http://www.foxboro-eckardt.com/company/company_en.html
   Honeywell, Inc., Micro Switch Div., 11 W. Spring St., Freeport, IL 61032-4353, Tel: (815) 235-5500, http://www.honeywell.com/sensing
   Lucas NovaSensor, 1055 Mission Ct., Fremont, CA 94539, Tel: (800) 962-7364, http://www.novasensor.com
   Motorola, Inc., Sensor Products Div., 5005 E. McDowell Rd., Phoenix, AZ 85008, Tel: (602) 244-3381, http://mot-sps.com/senseon
   SenSym, Inc., 1804 McCarthy Blvd., Milpitas, CA 95035, Tel: (408) 954-1100, http://www.sensym.com
2. Bonded strain-gage pressure sensors
   Gefran, Inc., 122 Terry Dr., Newtown, PA 18940, Tel: (215) 968-6238, http://www.gefran.it
3. Capacitive pressure sensors
   Kavlico Corp., 14501 Los Angeles Ave., Moorpark, CA 93021, Tel: (805) 523-2000, http://www.kavlico.com/
   Rosemount, Inc., Measurement Div., 12001 Technology Drive, Eden Prairie, MN 55344, Tel: (800) 999-9307, http://www.rosemount.com
4. Pressure calibration systems
   Mensor Corp., 2230 IH-35 South, San Marcos, TX 78666-5917, Tel: (512) 396-4200, http://www.mensor.com
   Ruska Instruments, 10311 Westpark Drive, Houston, TX 77042, Tel: (713) 975-0547, http://www.ruska.com

Note: This is not intended to be an exhaustive list of all manufacturers.

References

1. H. N. Norton, *Handbook of Transducers*, Englewood Cliffs, NJ: Prentice Hall, 1989, pp. 294–330.
2. W. H. Ko, Solid-state capacitive pressure transducers, *Sens. Actuat*., 10, 303–320, 1986.
3. C. S. Smith, Piezoresistance effect in germanium and silicon, *Phys. Rev*., 94, 42–49, 1954.
4. O. N. Tufte and E. L. Stelzer, Piezoresistive properties of silicon diffused layers, *J. Appl. Phys*., 34, 313–318, 1963.
5. D. Schubert, W. Jenschke, T. Uhlig, and F. M. Schmidt, Piezoresistive properties of polycrystalline and crystalline silicon films, *Sens. Actuat*., 11, 145–155, 1987.
6. K. E. Petersen, Silicon as a mechanical material, *IEEE Proc*., 70, 420–457, 1982.
7. R. F. Wolffenbuttel (ed.), *Silicon Sensors and Circuits: On-Chip Compatibility*, London, U.K.: Chapman & Hall, 1996, pp. 171–210.
8. H. Seidel, The mechanism of anisotropic silicon etching and its relevance for micromachining, Tech. Dig., *Transducers '87*, Tokyo, Japan, June 1987, pp. 120–125.
9. E. P. Shankland, Piezoresistive silicon pressure sensors, *Sensors*, 22, 22–26, 1991.

Further Information

ISA Directory of Instrumentation On-Line (http://www.isa.org) from the Instrument Society of America maintains a list of product categories and active links to many sensor manufacturers.

Muller, R. S., Howe, R. T., Senturia, S. D., Smith, R. L., and White, R. M. (eds.), *Microsensors*, New York: IEEE Press, 1991, provides an excellent collection of papers on silicon microsensors and silicon micromachining technologies.

Pressure Measurement Glossary, Sensors One, http://www.sensorsone.co.uk/pressure-measurement-glossary.html (accessed on June 25, 2012).

Pressure Measurements, National Instruments, http://www.ni.com/pressure/ (accessed on June 2, 2012).

Van Nostrand, J., Pressure measurement in industrial applications, Intech, http://www.isa.org/InTechTemplate.cfm?Section=Automation_Basics&template=/ContentManagement/ContentDisplay.cfm&ContentID=82299 (accessed on June 23, 2012).

Wolffenbuttel, R. F. (ed.), *Silicon Sensors and Circuits: On-Chip Compatibility*, London, U.K.: Chapman & Hall, 1996, provides a thorough discussion on sensor and circuit integration.

40

Vacuum Measurement

Ron Goehner
The Fredericks Company

Emil Drubetsky
The Fredericks Company

Howard M. Brady
The Fredericks Company

William H. Bayles, Jr.
The Fredericks Company

40.1 Background and History of Vacuum Gages

To make measurements in the vacuum region, one must possess knowledge of the expected pressure range required by the processes taking place in the vacuum chamber as well as the accuracy and/or repeatability of the measurement required for the process. Typical vacuum systems require that many orders of magnitude of pressures must be measured. In many applications, the pressure range may be eight orders of magnitude or from atmospheric 1.01×10^5 Pa (760 torr) to 1×10^{-3} Pa (7.5×10^{-6} torr).

For semiconductor lithography, high-energy physics experiments, and surface chemistry, ultimate vacuum of 7.5×10^{-9} torr and much lower is required (a range of 11 orders of magnitude below atmospheric pressure). One gage will not give reasonable measurements over such large pressure ranges. Over the past 50 years, vacuum measuring instruments (commonly called gages) have been developed that used transducers (or sensors) that can be classified as either direct reading (usually mechanical) or indirect reading [1] (usually electronic). Figure 40.1 shows vacuum gages typically in current use. When a force on a surface is used to measure pressure, the gages are mechanical and are called *direct reading* gages, whereas when any property of the gas that changes with density is measured by electronic means, they are called *indirect reading* gages. Figure 40.2 shows the range of operating pressure for various types of vacuum gages.

40.2 Direct Reading Gages

A subdivision of direct reading gages can be made by dividing them into those that utilize a liquid wall and those that utilize a solid wall. The force exerted on a surface from the pressure of thermally agitated molecules and atoms is used to measure the pressure.

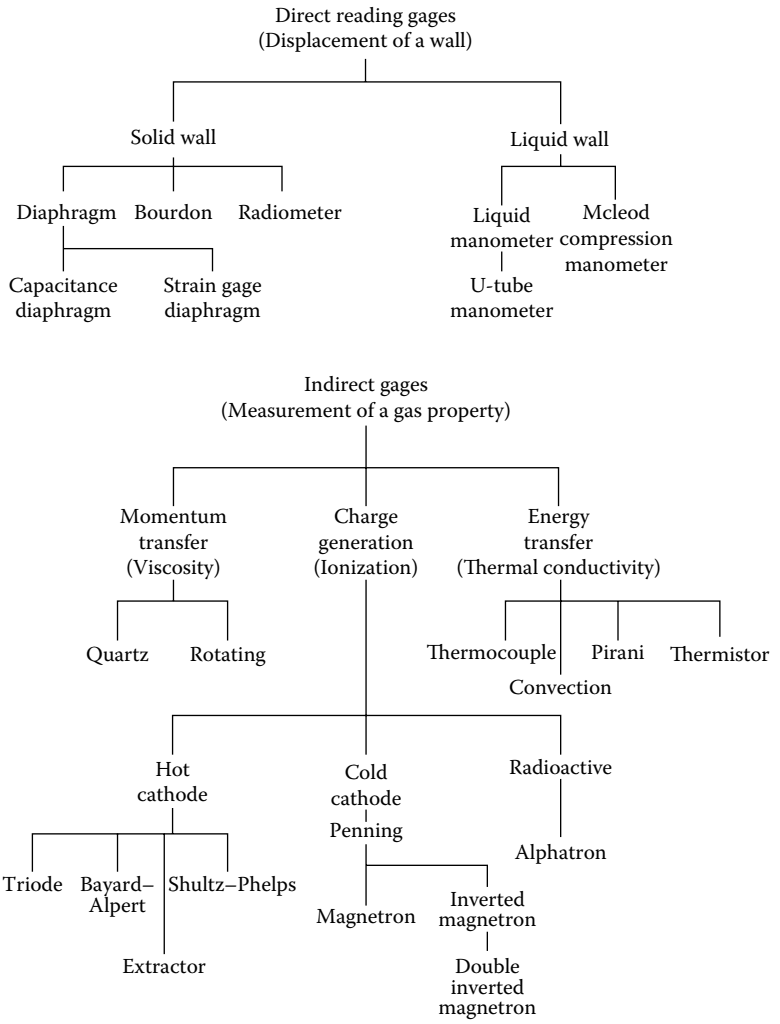

FIGURE 40.1 Classification of pressure gages. (From Hoffman, D.M. et al., *The Handbook of Vacuum Science and Technology*, Academic Press, Orlando, FL, 1998. With permission.)

40.2.1 Liquid Wall Gages

The two common gages that use a liquid wall are the manometer and the McLeod gage. The liquid column *manometer* is the simplest type of vacuum gage. It consists of a straight or U-shaped glass tube evacuated and sealed at one end and filled partly with mercury or a low vapor pressure liquid such as diffusion pump oil (see Figure 40.3). In the straight tube manometer, as the space above the mercury is evacuated, the length of the mercury column decreases. In the case of the U-tube, as the free end is evacuated, the two columns approach equal height. The pressure at the open end is measured by the difference in height of the liquid columns. If the liquid is mercury, the pressure is directly measured in mm of Hg (torr). The manometer is limited to pressures equal to or greater than ~1 torr (133 Pa). If the liquid is a low-density oil, the U-tube is capable of measuring a pressure as low as ~0.1 torr. This is an absolute, direct reading gage, but the use of mercury or low-density oils that will in time contaminate the vacuum system precludes its use as a permanent vacuum gage.

Due to the pressure limitation of the manometer, the McLeod gage [2,3] was developed to significantly extend the range of vacuum measurement (see Figure 40.4). This device is essentially a mercury

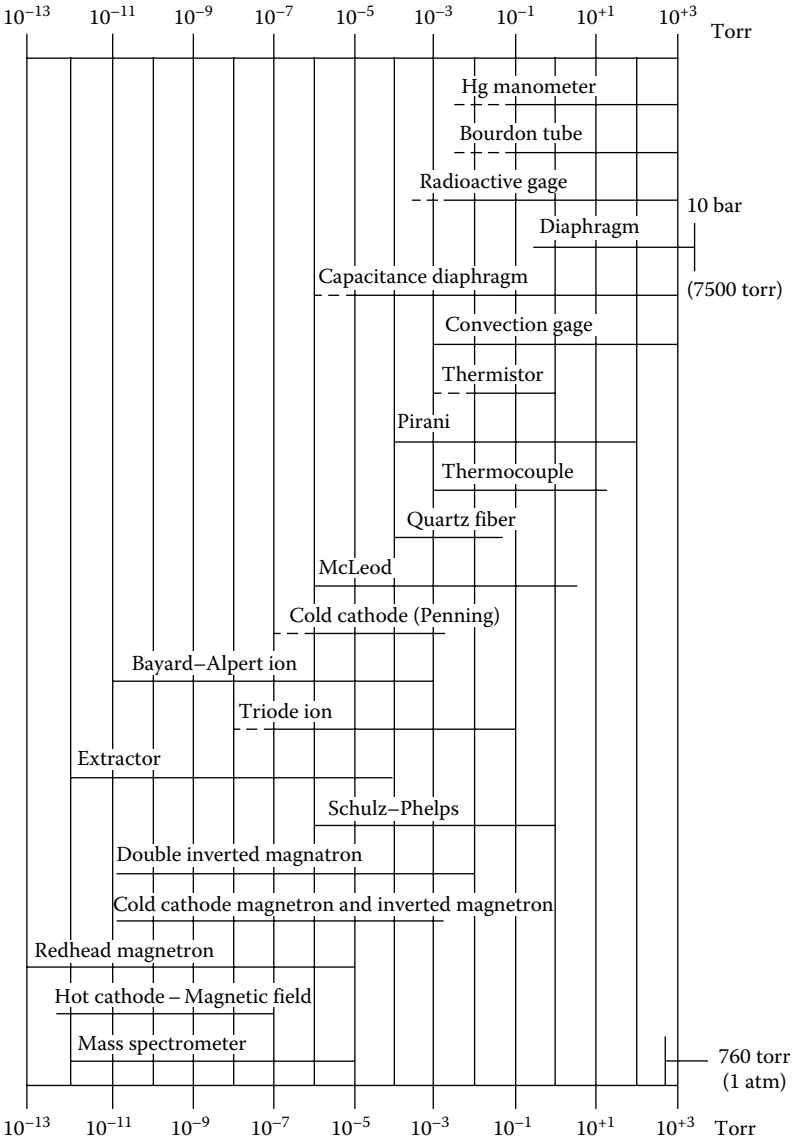

FIGURE 40.2 Pressure ranges for various gages. (From Hoffman, D.M. et al., *The Handbook of Vacuum Science and Technology*, Academic Press, Orlando, FL, 1998. With permission.)

manometer in which a volume of gas is compressed before measurement. This can be used as a primary standard device when a liquid nitrogen trap is used on the vacuum system. Figure 40.4 shows gas at 10^{-6} torr and a compression ratio of 10^{7}. In this example, the difference of the columns will be 10 mm. Extreme care must be taken not to break the glass and expose the surroundings to the mercury. The McLeod gage is an inexpensive standard but should only be used by skilled and careful technicians. The gage will give a false low reading unless precautions are taken to ensure that any condensable vapors present are removed by liquid nitrogen trapping.

40.2.2 Solid Wall Gages

There are two major mechanical solid wall gage types: capsule and diaphragm.

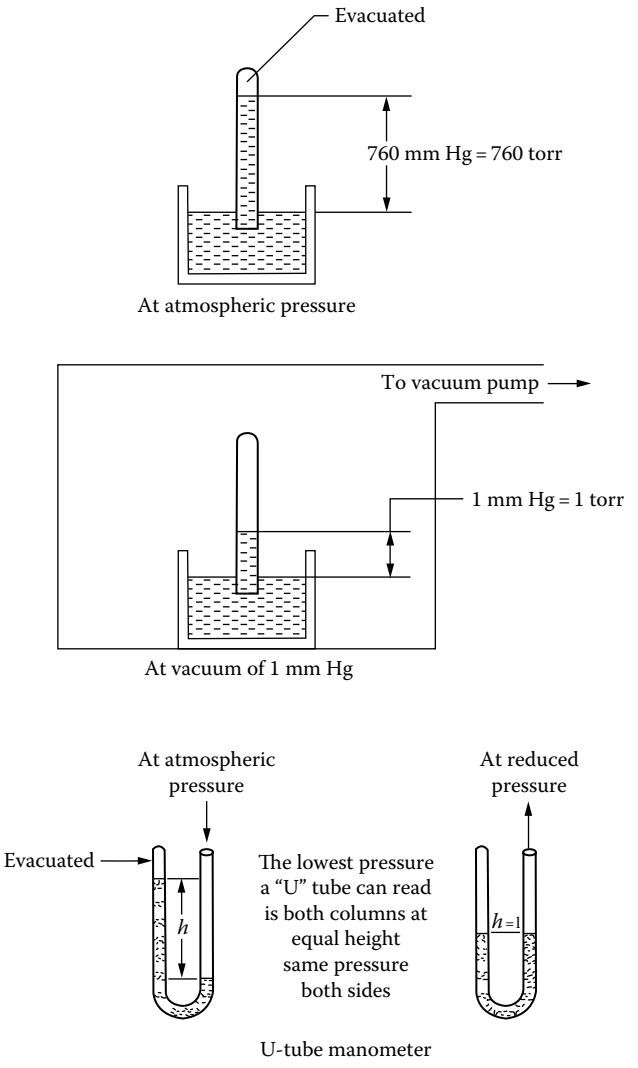

FIGURE 40.3 Mercury manometers. (From Bayles, W.H. Jr., *Ind. Heat.*, 1992. With permission.)

40.2.2.1 Bourdon Gages

The capsule-type gages depend on the deformation of the capsule with changing pressure and the resultant deflection of an indicator. Pressure gages using this principle measure pressures above atmospheric to several thousand psi and are commonly used on compressed gas systems. This type of gage is also used at pressures below atmospheric, but the sensitivity is low. The Bourdon gage (Figure 40.5) is used as a moderate vacuum gage. In this case, the capsule is in the form of a thin-walled tube bent in a circle, with the open end attached to the vacuum system with a mechanism and a pointer attached to the other end. The atmospheric pressure deforms the tube; a linear indication of the pressure is given that is independent of the nature of the gas. Certain manufacturers supply capsule gages capable of measuring pressures as low as 1 torr. These gages are rugged, inexpensive, and simple to use and can be made of materials inert to corrosive vapors. Since changing atmospheric pressure causes inaccuracies in the readings, compensated versions of the capsule and Bourdon gage have been developed that improve the accuracy [4].

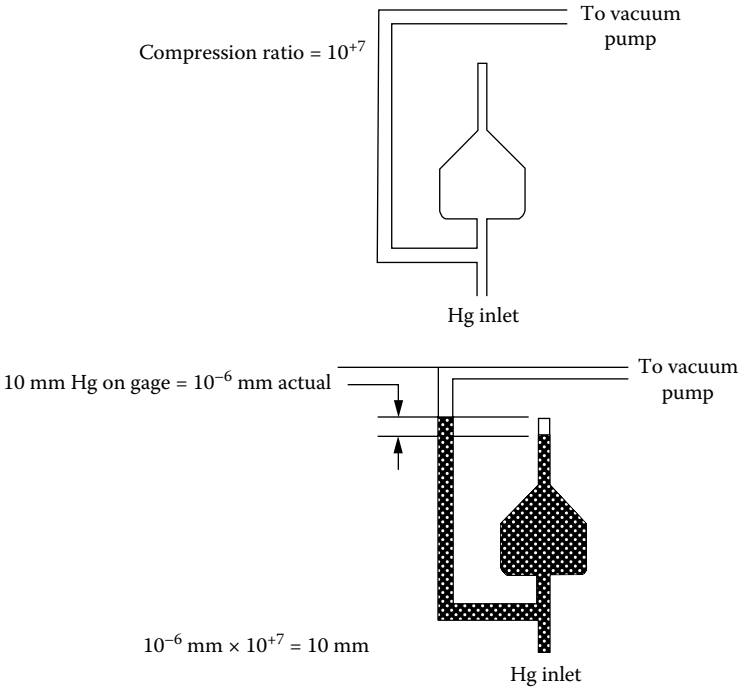

FIGURE 40.4 McLeod gage. (From Hoffman, D.M. et al., *The Handbook of Vacuum Science and Technology*, Academic Press, Orlando, FL, 1998. With permission.)

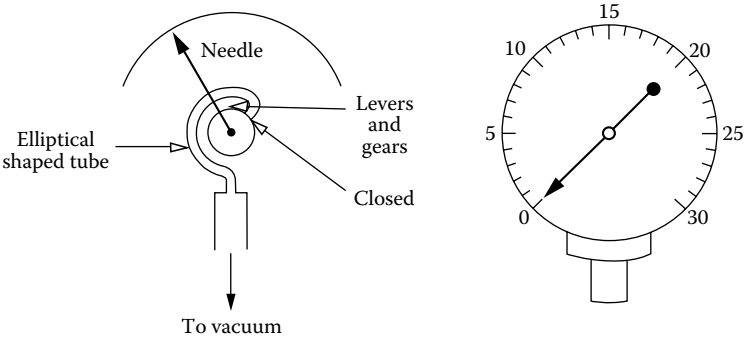

FIGURE 40.5 Bourdon gage. (From Varian Associates, *Basic Vacuum Practice*, Varian Associates, Inc., Lexington, MA, 02173, 1992. With permission.)

40.2.2.2 Diaphragm Gages

If compensated capsule or diaphragm mechanisms are combined with sensitive and stable electronic measuring circuits, performance is improved. One such gage is the capacitance diaphragm gage (also referred to as the capacitance manometer).

The capacitance diaphragm gage is shown in Figure 40.6. A flexible diaphragm forms one plate of a capacitor and a fixed probe the other. The flexible diaphragm deforms due to even slight changes in pressure, resulting in a change in the capacitance. The capacitance is converted to a pressure reading. The sensitivity, repeatability, and simplicity of this gage enables this type of direct reading gage to be a standard from 10^{-6} torr to atmospheric pressure, provided multiple heads designed for each pressure range are used. A single head can have a dynamic range of 4 or 5 orders of magnitude [5].

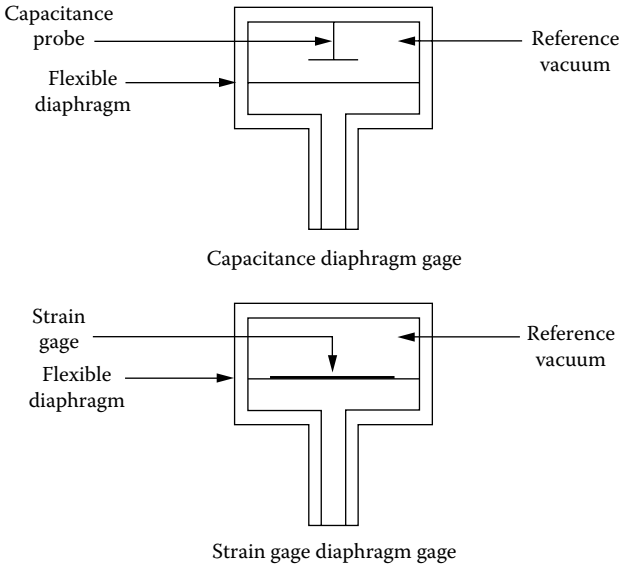

FIGURE 40.6 Diaphragm gage. (From Bayles, W.H. Jr., *Ind. Heat.*, 1992. With permission.)

The strain-gage type of diaphragm gage is shown in Figure 40.6. In this case, the deformation of the diaphragm causes a proportional output from the attached strain gage. Sensitivities and dynamic range tend to be less than those of the capacitance diaphragm gage, but the price of the strain-gage-type diaphragm gage is usually lower.

Both of these gages are prone to errors caused by small temperature changes due to the inherent high sensitivity of this gage type. Temperature-controlled heads or correction tables built into the electronics have been used to minimize this problem. Other sources of error in all solid wall gages are hysteresis and metal fatigue.

40.3 Indirect Reading Gages

Indirect reading gages measure some property of the gas that changes with the density of the gas and usually produces an electric output. Electronic devices amplify and compensate this output to provide a pressure reading.

40.3.1 Thermal Conductivity Gages

Thermal conductivity gages utilize the property of gases in which reduced thermal conductivity corresponds to decreasing density (pressure). The thermal conductivity decreases from a nearly constant value above ~1 torr to essentially 0 at pressures below 10^{-2} torr. The gage controllers are designed to work with a specific sensor tube, and substitutions are limited to those that are truly functionally identical. Heat transfer at various pressures is related to the Knudsen number, as is shown in Figure 40.7 for various heat transfer regimes. The Knudsen number can then be related to pressure through the geometry of the sensor, providing a relationship of heat transfer to pressure for a particular design thermal conductivity gage.

40.3.1.1 Pirani Gages

The Pirani gage is perhaps the oldest indirect gage that is still used today. In operation, a sensing filament carrying current and producing heat is surrounded by the gas to be measured. As the pressure changes, the thermal conductivity changes with it too, thus altering the temperature of the sensing filament.

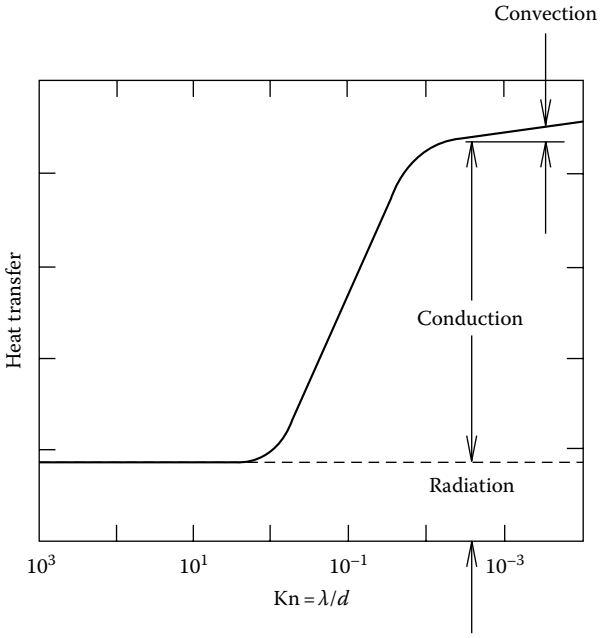

FIGURE 40.7 Heat transfer regimes in a thermal conductivity gage. (From O'Hanlon, J.F., *A User's Guide to Vacuum Technology*, John Wiley & Sons, Hoboken, NJ, 1980.)

The temperature change causes a change in the resistance of the sensing filament. The sensing filament is usually one leg of a Wheatstone bridge. The bridge can be operated so that the voltage is varied to keep the bridge balanced; that is, the resistance of the sensing filament is kept constant.

This method is called the constant-temperature method and is deemed the fastest, most sensitive, and most accurate. To reduce the effect of changing ambient temperature, an identical filament sealed off at very low pressure is placed in the leg adjacent to the sensing filament as a balancing resistor. Because of its high thermal resistance coefficient, the filament material is usually a thin tungsten wire. It has been demonstrated that a 10 W light bulb works quite well [6] (Figure 40.8).

A properly designed, compensated Pirani gage with sensitive circuitry is capable of measuring upto 10^{-4} torr. However, the thermal conductivity of gases varies with the gas being measured, causing a

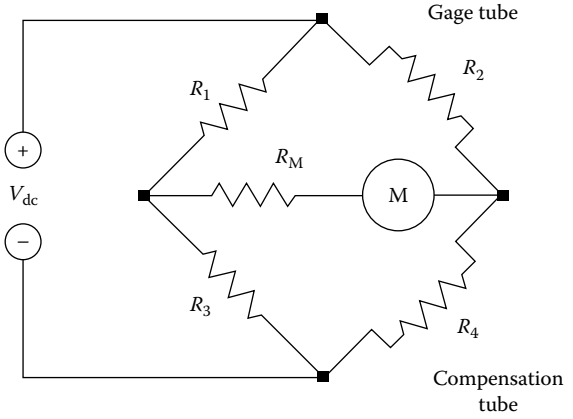

FIGURE 40.8 Pirani gage. (From O'Hanlon, J.F., *A User's Guide to Vacuum Technology*, John Wiley & Sons, Hoboken, NJ, 1980.)

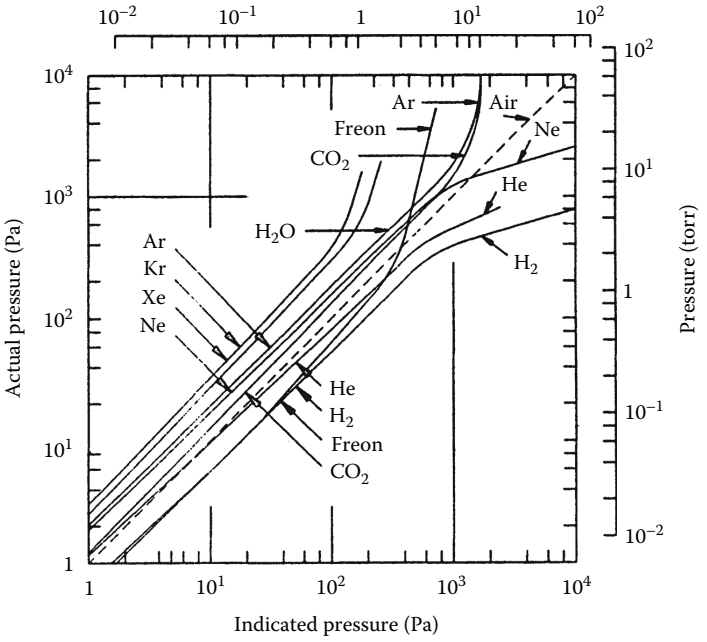

FIGURE 40.9 Calibration curves for the Pirani gage. (Reprinted with permission from Leybold-Herqeus GMblt, Köhn, Germany.)

variation in gage response. These variations can be as large as a factor of 5 at low pressures and as high as 10 at high pressures (see Figure 40.9). The correction for these variations can be made on the calibration curves supplied by the manufacturer if the composition of the gas is known. The operation in the presence of high partial pressures of organic molecules such as oils is not recommended.

40.3.1.2 Thermistor Gages

In the thermistor gage, a thermistor is used as one leg of a bridge circuit. The inverse resistive characteristics of the thermistor element unbalance the bridge as the pressure changes, causing a corresponding change in current. Sensitive electronics measure the current and are calibrated in pressure units. The thermistor gage measures approximately the same pressure range as the thermocouple. The exact calibration depends on the gas measured. In a well-designed bridge circuit, the plot of current vs. pressure is practically linear in the range 10^{-3} to 1 torr [7]. Modern thermistor gages use constant-temperature techniques.

40.3.1.3 Thermocouple Gages

Another example of an indirect reading thermal conductivity gage is the thermocouple gage. This is a relatively inexpensive device with proven reliability and a wide range of applications. In the thermocouple gage, a filament of resistance alloy is heated by the passage of a constant current (see Figure 40.10). A thermocouple is welded to the midpoint of the filament or preferably to a conduction bridge at the center of the heated filament. This provides a means of directly measuring the temperature. With a constant current through the filament, the temperature increases as the pressure decreases as there are fewer molecules surrounding the filament to carry the heat away. The thermocouple output voltage increases as a result of the increased temperature and varies inversely with the pressure. The thermocouple gage can also be operated in the constant-temperature mode.

Gas composition effects apply to all thermal conductivity gages. The calibration curves for a typical thermocouple gage are shown in Figure 40.11. The thermocouple gage can be optimized for operation

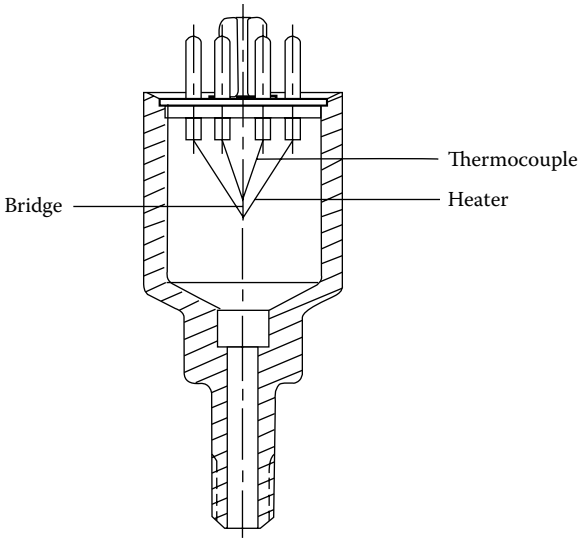

FIGURE 40.10 Thermocouple gage. (Reprinted with permission from Engleman and Televac Division, The Fredericks Co., Huntingdon Valley, PA.)

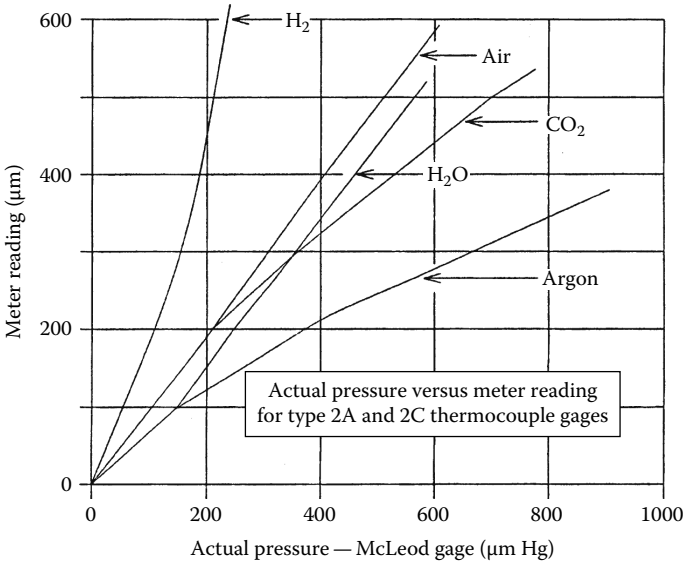

FIGURE 40.11 Calibration curves for the thermocouple gage. (Reprinted with permission from Engleman and Televac Division, The Fredericks Co., Huntingdon Valley, PA.)

in various pressure ranges. The operation of the thermocouple gage in high partial pressures of organic molecules such as oils should be avoided. One manufacturer pre-oxidizes the thermocouple sensor for stability in "dirty" environments and for greater interchangeability in clean environments.

40.3.1.4 Convection Gages

Below 1 torr, a significant change in thermal conductivity occurs as the pressure changes. Thus, the thermal conductivity gage is normally limited to 1 torr.

At pressures above 1 torr, there is, in most gages, a small contribution to heat transfer caused by convection. Manufacturers have developed gages that utilize this convection effect to extend the usable range

to atmospheric pressure and slightly above [8–12]. The orientation of a convection gage is critical because this convection heat transfer is highly dependent on the orientation of the elements within the gage.

The Convectron™ uses the basic structure of the Pirani with special features to enhance convection cooling in the high-pressure region [13]. To utilize the gage above 1 torr (133 Pa), the sensor tube must be mounted with its major axis in a horizontal position. If the only area of interest is below 1 torr, the tube can be mounted in any position. As mentioned earlier, the gage controller is designed to be used with a specific model sensor tube; because extensive use is made of calibration curves and lookup tables stored in the controller, no substitution is recommended.

The Televac convection gage uses the basic structure of the thermocouple gage except that two thermocouples are used [14]. As in any thermocouple gage, the convection gage measures the pressure by determining the heat loss from a fine wire maintained at constant temperature. The response of the sensor depends on the gas type. A pair of thermocouples is mounted a fixed distance from each other (see Figure 40.12). The one mounted lower is heated to a constant temperature by

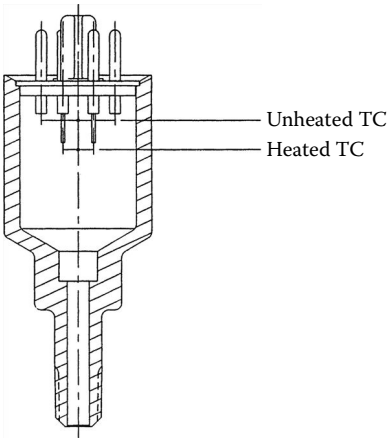

FIGURE 40.12 Convection gage. (Reprinted with permission from Engleman and Televac Division, The Fredericks Co., Huntingdon Valley, PA.)

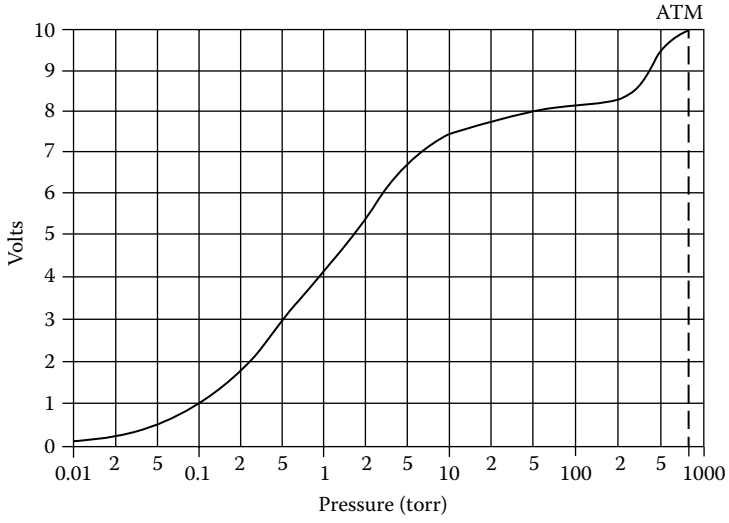

FIGURE 40.13 Output curve for the convection gage. (Reprinted with permission from Engleman and Televac Division, The Fredericks Co., Huntingdon Valley, PA.)

a variable current power supply. Power is pulsed to this lower thermocouple and the temperature is measured between heating pulses. The second (upper) thermocouple measures convection effects and also compensates for ambient temperature. At pressures below ~2 torr (270 Pa), the temperature in the upper thermocouple is negligible. The gage tube operates as a typical thermocouple in the constant-temperature mode. Above 2 torr, convective heat transfer causes heating of the upper thermocouple. The voltage output is subtracted from that of the lower thermocouple, thus requiring more current to maintain the wire temperature. Consequently, the range of pressure that can be measured (via current change) is extended to atmospheric pressure (see Figure 40.13). The orientation of the sensor is with the axis vertical.

The use of convection gages with process control electronics allows for automatic pump down with the assurance that the system will neither open under vacuum nor be subject to overpressure during backfill to atmospheric pressure. These gages, with their controllers, are relatively inexpensive. In oil-free systems, they afford long life and reproducible results.

40.4 Cathode Ionization Gages

40.4.1 Hot Cathode Ionization Gages

Hot cathode ionization gage designs consist of triode gages, Bayard–Alpert gages, and others.

40.4.1.1 Triode Hot Cathode Ionization Gages

For over 80 years, the triode electron tube has been used as an indirect way to measure vacuum [15,16]. A typical triode connection is as an amplifier, as shown in Figure 40.14. A brief description of its operation is given here, but more rigorous treatment of triode performance is given in [17–20]. However, if the triode is connected as in Figure 40.15 so that the grid is positive and the plate is negative with respect to the filament, then the ion current collected by the plate for the same electron current to the grid is greatly increased [21].

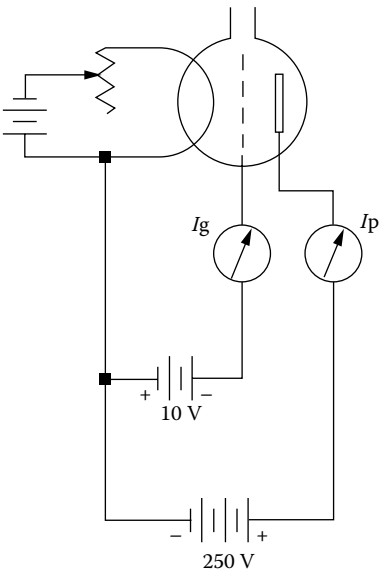

FIGURE 40.14 Typical triode connection.

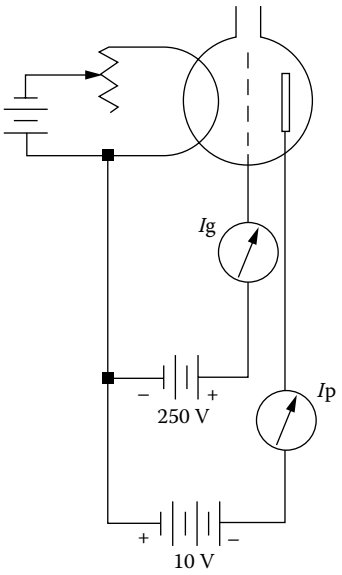

FIGURE 40.15 Alternative triode connection.

Today, the triode gage is used in this higher sensitivity mode. Many investigators have shown that a linear change in molecular density (pressure) results in a linear change in ion current [15,21,22]. This linearity allows a sensitivity factor *S* to be defined such that

$$I_i = S \times I_e \times P \tag{40.1}$$

where

I_i is the ion current (A)
I_e is the electron current (A)
P is the pressure
S is the sensitivity (in units of reciprocal pressure)

Additional details are found in [23–25]. In nearly all cases, except at relatively high pressures, the triode gage has been replaced by the Bayard–Alpert gage.

40.4.1.2 Bayard–Alpert Hot Cathode Ionization Gages

It became apparent that the pressure barrier observed at 10^{-8} torr was caused by a failure in measurement rather than pumping [26,27]. A solution to this problem was proposed by Bayard and Alpert [28] that is now the most widely used gage for general UHV measurement.

The Bayard–Alpert gage is similar to a triode gage but has been redesigned so that only a small quantity of the internally generated x-rays strike the collector. The primary features of the Bayard–Alpert gage and its associated circuit are shown in Figures 40.16 and 40.17. The cathode has been replaced by a thin collector located at the center of the grid, and the cathode filament is now outside and several millimeters away from the grid. The Bayard–Alpert design utilizes the same controller as the triode gage, with corrections for sensitivity differences between the gage designs. When a hot filament gage is exposed to high pressures, burnout of the tungsten filaments often occurs. To prevent this, platinum metals were coated with refractory oxides to allow the gage to withstand sudden exposure to atmosphere with the filament hot [29,30]. Typical materials include either thoria or yttria coatings on iridium. Bayard–Alpert and triode gages of identical structure and dimensions but with different filaments

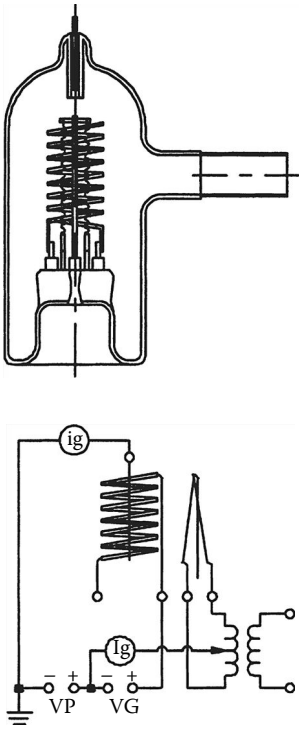

FIGURE 40.16 Bayard–Alpert hot cathode ionization gage.

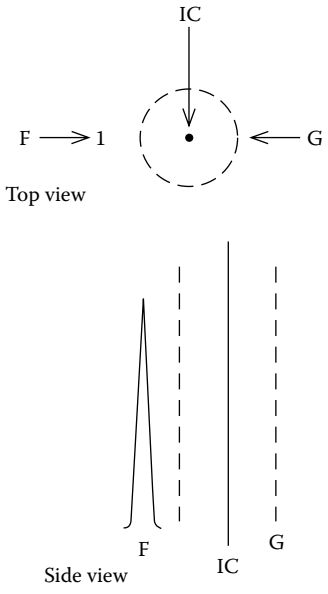

FIGURE 40.17 Bayard–Alpert gage configuration. F, filament; G, grid; IC, ion collector.

(i.e., tungsten vs. thoria iridium) were observed to have different sensitivities, with the tungsten filament versions being 20%–40% more sensitive than the iridium of the same construction.

The lowest pressure that can be measured is limited by low-energy x-rays striking the ion collector and emitting electrons. Several methods to reduce this x-ray limit were developed. Gage designs with

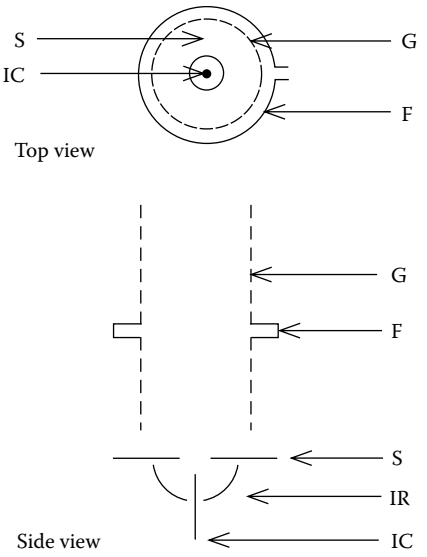

FIGURE 40.18 Extractor ionization gage. F, filament; G, grid; S, shield; IR, iron reflector; and IC, ion collector.

very small diameter collectors have been made that extend the high vacuum range down to 10^{-12} torr, but accuracy was lost at the high pressures [31,32].

The modulated gage was designed by Redhead [33] with an extra electrode near the ion collector. In this configuration, the x-ray current could be subtracted by measuring the ion current at two modulator potentials, thus increasing the range to 5×10^{-12}. Other gages use suppressor electrodes in front of the ion collector [34,35].

The extractor gage (Figure 40.18) is the most widely used UHV hot cathode gage for those who need to measure 10^{-2} torr [36]. In this gage, the ions are extracted out of the ionizing volume and deflected or focused onto a small collector. More recent designs have been developed [37,38]. The use of a channel electron multiplier [39] has reduced the low pressure limit to 10^{-15} torr.

The Bayard–Alpert gage suffers from some problems, however. The ion current is geometry dependent. Investigators have reported on the sensitivity variations, inaccuracy, and instability of Bayard–Alpert gages with widely differing results [40–49]. Investigators have developed ways to reduce or eliminate some of these problems [50,51].

40.4.2 Cold Cathode Ionization Gages

To measure pressures below 10^{-3} torr, Penning [52] developed the cold cathode discharge gage. Below 10^{-3} torr, the mean free path is so high that little ionization takes place. The probability of ionization was increased by placing a magnetic field parallel to the paths of ions and electrons to force these particles into helical trajectory.

This gage consists of two parallel cathodes and an anode, which is placed midway between them (see Figure 40.19). The anode is a circular or rectangular loop of metal wire whose plane is parallel to that of the cathodes. A few kilovolts potential difference is maintained between the anode and the cathodes. Furthermore, a magnetic field is applied between the cathodes by a permanent magnet usually external to the gage body. Electrons emitted from either of the two cathodes must travel in helical paths due to the magnetic field eventually reaching the anode, which carries a high positive charge. During the travel along this long path, many electrons collide with the molecules of the gas, thus creating positive ions

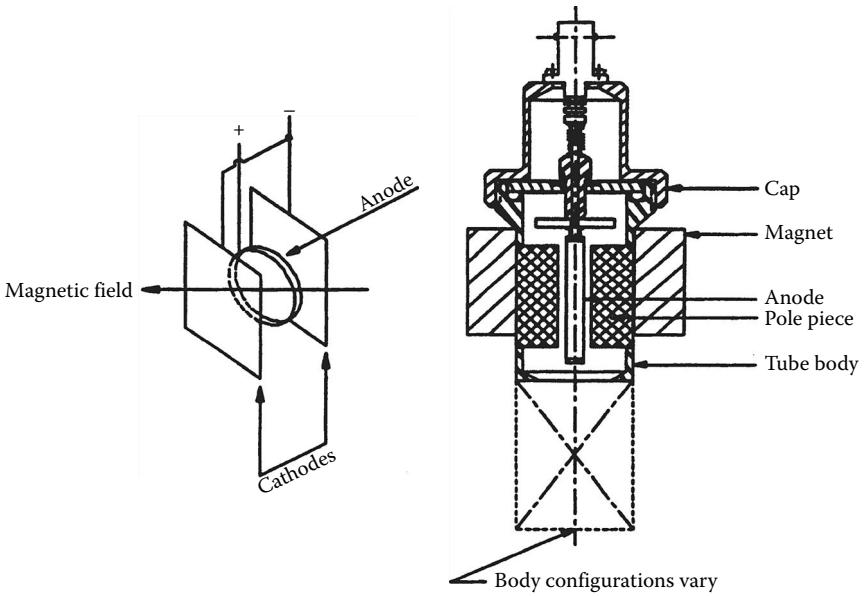

FIGURE 40.19 Penning gages. (a) Basic arrangement. (From O'Hanlon, J.F., *A User's Guide to Vacuum Technology*, John Wiley & Sons, Hoboken, NJ, 1980.) (b) Complex assembly. (Reprinted with permission from Engleman and Televac Division, The Fredericks Co., Huntingdon Valley, PA.)

that travel more directly to the cathodes. The ionization current thus produced is read out on a sensitive current meter as pressure.

This is a rugged gage used for industrial applications such as in leak detectors, vacuum furnaces, electron beam welders, and other industrial processes. The Penning gage is rugged, simple, and inexpensive. Its range is typically 10^{-3}–10^{-6} torr, and some instability and lack of accuracy has been observed [53]. The magnetron design [54] and the inverted magnetron design [55] extended the low pressure range to 10^{-12} torr [56] or better. These improvements produced a better gage, but instability, hysteresis, and starting problems remain [57,58]. Magnetrons currently in use are simpler and do not use an auxiliary cathode.

More recently, a double inverted magnetron was introduced [59]. This gage has greater sensitivity (amp/torr) than the other types (see Figure 40.20). It has been operated successfully at $\sim 1 \times 10^{-11}$ torr. The gage consists of two axially magnetized, annular-shaped magnets (1) placed around a cylinder (2) so that the north pole of one magnet faces the north pole of the other one. A nonmagnetic spacer (3) is placed between the two magnets, and thin shims (4) are used to focus the magnetic fields. This gage has been operated to date at 10^{-11} torr and stays ignited and reignites quickly when power is restored at this pressure. Essentially instantaneous reignition has been demonstrated by the use of radioactive triggering [60].

40.5 Resonance Gages

One example of a resonance-type vacuum gage is the quartz friction vacuum gage [61]. A quartz oscillator can be built to measure pressure by a shift in resonance frequency caused by static pressure of the surrounding gas or by the increased power required to maintain constant amplitude. Its range is from near atmospheric pressure to about 0.1 torr. A second method is to measure the resonant electric impedance of a tuning fork oscillator. Test results for this device show accuracy within ±10% for pressure from 10^{-3} to 10^{3} torr. There is little commercial use to date for these devices.

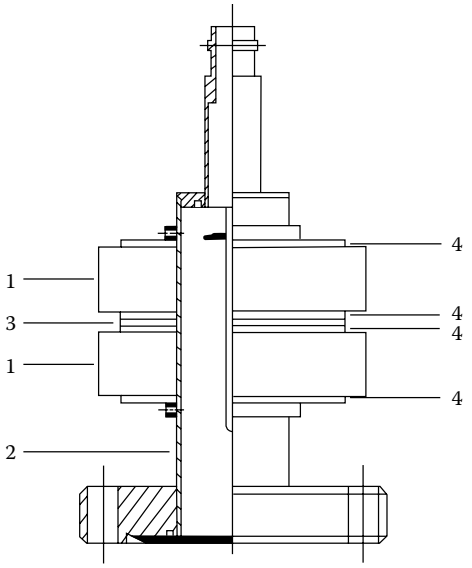

FIGURE 40.20 Double inverted magnetron. (Reprinted with permission from Engleman and Televac Division, The Fredericks Co., Huntingdon Valley, PA.)

40.6 Molecular Drag (Spinning Rotor) Gages

Meyer [62] and Maxwell [63] introduced the idea of measuring pressure by means of the molecular drag of rotating devices in 1875. The rotors of these devices were tethered to a wire or thin filament. The gage was further enhanced by Holmes [64], who introduced the concept of the magnetic rotor suspension, leading to the spinning rotor gage. Nearly 10 years later, Beams et al. [65] disclosed the use of a magnetically levitated, rotating steel ball to measure pressure at high vacuum. Fremerey [66] reported on the historical development of this gage.

The molecular drag gage (MDG), often referred to as the spinning rotor gage, received wider acceptance after its commercial introduction in 1982 [67]. It is claimed to be more stable than other gages at lower pressures [68].

The principle of operation of the modern MDG is based on the fact that the rate of change of the angular velocity of a freely spinning ball is proportional to the gas pressure and inversely proportional to the mean molecular velocity. When the driving force is removed, the angular velocity is determined by measuring the ac voltage induced in the pickup coils by the magnetic moment of the ball (see Figure 40.21).

In current practice, a small rotor (steel ball bearing) about 4.5 mm in diameter is magnetically levitated and spun up to about 400 Hz by induction. The ball, enclosed in a thimble connected to the vacuum system, is allowed to coast by turning off the inductive drive. Then, the time of a revolution of the ball is measured by timing the signal induced in a set of pickup coils by the rotational component of the ball's magnetic moment. Gas molecules will exert a drag on the ball, slowing it at a rate set by the pressure P, its molecular mass m, the temperature T, and the coefficient of momentum transfer σ, between the gas and the ball. A perfectly smooth ball would have a value of unity. There is also a pressure-independent residual drag (RD) caused by eddy current losses in the ball and surrounding structure. There will also be temperature effects that will cause the ball diameter and moment of inertia to change.

The pressure in the region of molecular flow is given by

$$P = \frac{\pi \rho a \bar{c}}{10\sigma_{\text{eff}}}\left(\frac{-\omega' - \text{RD} - 2\alpha T'}{\omega}\right) \tag{40.2}$$

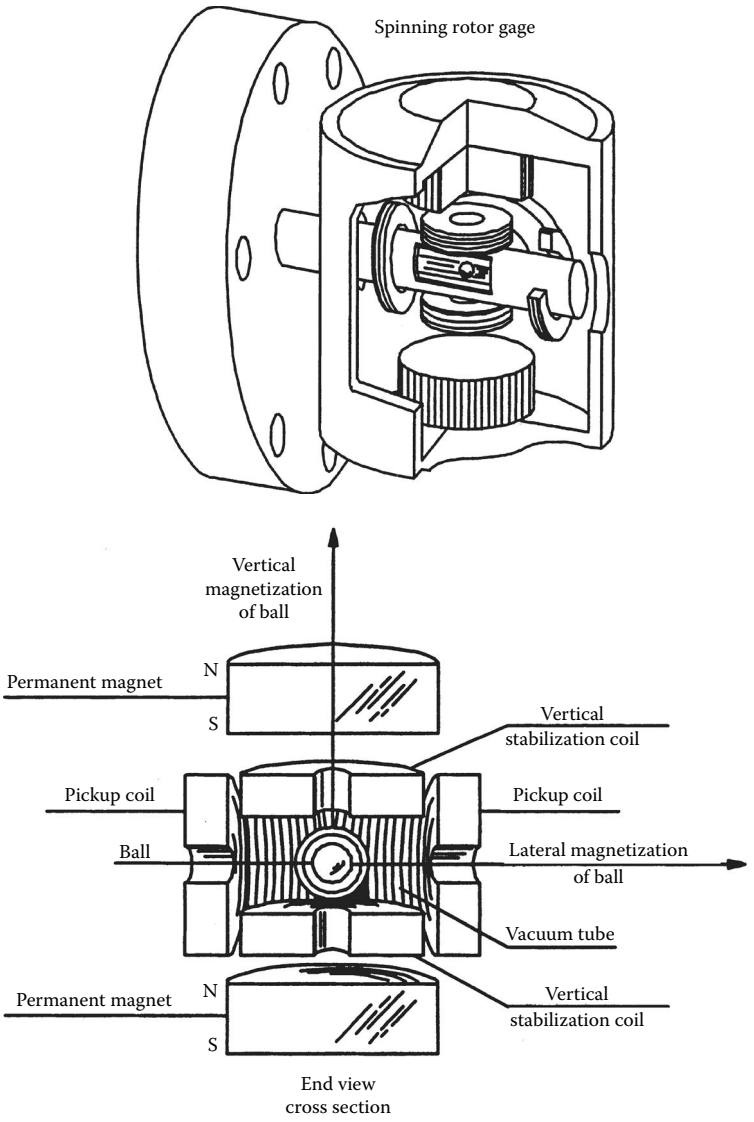

FIGURE 40.21 MDG (spinning rotor).

Note: Some sources include the term

$$\frac{(8kT')}{(\pi m)}$$

where

ρ is the density of the rotor
a is the radius of the rotor
ω'/ω is the fractional rate of slowing of the rotor
$\bar{c}$ is the mean gas molecular velocity
α is the linear coefficient of expansion of the ball
T' is the rate of change of the ball's temperature

All of the terms in the first part of the equation can be readily determined except for the accommodation coefficient σ, which depends on the surface of the ball and the molecular adhesion between the gas and the surface of the ball. The accommodation coefficient σ must be determined by calibration of the MDG against a known pressure standard or if repeatability is more important than the highest accuracy, by assuming a value of 1 for σ. Measurements of σ on many balls over several years have been repeatedly performed by Dittman et al. [68]. The values obtained ranged from 0.97 to 1.06 for 68 visually smooth balls, so using a value of 1 for σ would not introduce a large error and would allow the MDG to be considered a primary standard (Fremerey [66]).

The controller [68] contains the electronics to power and regulate the suspension and drive, detect and amplify the signal from the pickup coils, and then time the rotation of the ball. It also contains a data processor that stores the calibration data and computes the pressure.

The MDG is perhaps the best available transfer standard for the pressure range of 10^{-2}–10^{-7} torr (1–10^{-5} Pa) because it is designed for laboratory use in controlled relatively vibration-free environments [69,70].

40.7 Partial Pressure Measurements and Mass Spectrometers

The theory and the practical applications of partial pressure measurements and mass spectrometers are discussed in detail in the literature [71]; however, an overview is presented herein [72].

A simple device for measuring the partial pressure of nitrogen as well as the total pressure in a vacuum system is the residual nitrogen analyzer (RNA). Operating in high vacuum, it is used to detect leaks in a vacuum system. It is effective because various gases are pumped at different rates and nitrogen is readily pumped, leaving a much lower percentage than is present at atmospheric pressure. Thus, the presence of a significant percentage of nitrogen at high vacuum indicates an air leak. The RNA consists of a cold cathode gage with an optical filter and a photomultiplier tube. Since ionization in the cold cathode tube produces light and the color is determined by the gases present, the RNA filters out all except for that corresponding to nitrogen and is calibrated to give the partial pressure of nitrogen.

A more complex device to measure the partial pressure of many gases in a vacuum chamber is the mass spectrometer–type residual gas analyzer (RGA). This device comes in many forms and several sizes. The quadrupole mass spectrometer is shown in Figure 40.22. The sensing head consists of an ion source, a quadrupole mass filter, and a Faraday cup collector. The quadrupole mass filter consists of two pairs of parallel rods having equal and opposite RF and dc voltages. For each combination of voltages, only ions of a specific mass will pass through the filter. The mass filter is tuned to pass only ions of a specific mass-to-charge ratio at a given time. As the tuning is changed to represent increasing mass numbers, a display such as Figure 40.23 is produced, showing the relative intensity of the signal vs. the mass number. This display can then be compared electronically with similar displays for known gases to determine the composition of the gases in the vacuum chamber.

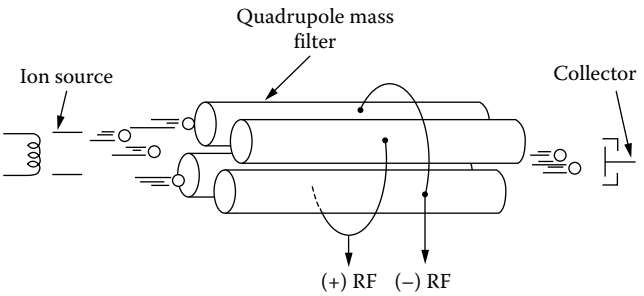

FIGURE 40.22 Quadrupole mass spectrometer. (From Varian Associates, *Basic Vacuum Practice*, Varian Associates, Inc., Lexington, MA, 1992. With permission.)

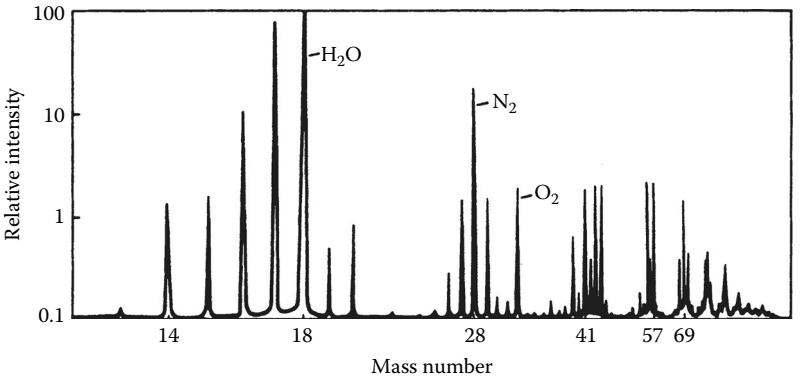

FIGURE 40.23 Relative intensity versus mass number. (From Varian Associates, *Basic Vacuum Practice*, Varian Associates, Inc., Lexington, MA, 1992. With permission.)

The head can operate only at high vacuum. However, by maintaining the head at high vacuum and using a sampling technique, the partial pressures of gases at higher pressures can be determined.

The calibration of mass spectrometers can be accomplished by equating the integral (the total area under all the peaks, taking into account the scale factors) to the overall pressure as measured by another gage (cold cathode, BA, or MDG). Once calibrated, the mass spectrometer can be used as a sensitive monitor of system pressure. It is also important when monitoring system pressure to know what gases are present. Most gages have vastly different sensitivities to different gas species.

Additional references on the details of the MDG and other types of gages available and on calibration are found in the literature [69–71,73,75–77]. The material in this chapter was summarized from an article on the fundamentals of vacuum measurement, calibration, and certification [78] from the authors' contribution to *The Handbook of Vacuum Technology* [71] and from other referenced sources.

References

1. J.F. O'Hanlon, *A User's Guide to Vacuum Technology*, New York: John Wiley & Sons, 1980, p. 47.
2. H. McLeod, *Phil. Mag.*, 47, 110, 1874.
3. C. Engleman and Televac Div. The Fredericks Co., Huntingdon Valley, PA, 19006, private communication.
4. Wallace and Tiernan Div., High Precision Gages, Pennwalt Corp., Bellville, NJ, http://www.wallaceandtiernan-usa.com/ (accessed on March 15, 2013).
5. R.W. Hyland and R.L. Shaffer, *J. Vac. Sci. Tech. A*, 9(6), 2843, 1991.
6. K.R. Spangenberg, *Vacuum Tubes*, New York: McGraw-Hill, 1948, p. 766.
7. S. Dushman, *Scientific Foundations of Vacuum Technique*, 2nd edn., J.M. Lafferty (ed.), New York: John Wiley & Sons, 1962.
8. W. Steckelmacher and B. Fletcher, *J. Physics E.*, 5, 405, 1972.
9. W. Steckelmacher, *Vacuum*, 23, 307, 1973.
10. A. Beiman, *Total Pressure Measurement in Vacuum Technology*, Orlando, FL: Academic Press, 1985.
11. Granville-Phillips, Boulder CO, 80303.
12. Televac Div., The Fredericks Co., Huntingdon Valley, PA, 19006.
13. Granville-Phillips, Boulder CO, Data Sheet 360127, 3/95.
14. Televac U.S. Patent No. 5351551.
15. O.E. Buckley, *Proc. Natl. Acad. Sci.*, 2, 683, 1916.
16. M.D. Sarbey, *Electronics,* 2, 594, 1931.

17. R. Champeix, *Physics and Techniques of Electron Tubes*, Vol. 1, New York: Pergamon Press, 1961, pp. 154–156.
18. N. Morgulis, *Physik Z. Sowjetunion*, 5, 407, 1934.
19. N.B. Reynolds, *Physics*, 1, 182, 1931.
20. J.H. Leck, *Pressure Measurement in Vacuum Systems*, London, U.K.: Chapman & Hall, 1957, pp. 70–74.
21. S. Dushman and C.G. Found, *Phys. Rev*., 17, 7, 1921.
22. E.K. Jaycock and H.W. Weinhart, *Rev. Sci. Instr*., 2, 401, 1931.
23. G.J. Schulz and A.V. Phelps, *Rev. Sci. Instr*., 28, 1051, 1957.
24. Japanese Industrial Standard (JIS-Z-8570), Method of Calibration for Vacuum Gages.
25. J.W. Leck, op. cit., 69.
26. W.B. Nottingham, *Proceedings of 7th Annual Conference on Physical Electronics*, MIT Press, Cambridge, MA, 1947.
27. H.A. Steinhertz and P.A. Redhead, *Sci. Am*., 206, 78, 1962.
28. R.T. Bayard and D. Alpert, *Rev. Sci. Instr*., 21, 571, 1950.
29. O.A. Weinreich, *Phys. Rev*., 82, 573, 1951.
30. O.A. Weinreich and H. Bleecher, *Rev. Sci. Instr*., 23, 56, 1952.
31. H.C. Hseuh and C. Lanni, *J. Vac. Sci. Technol*., A5, 3244, 1987.
32. T.S. Chou and Z.Q. Tang, *J. Vac. Sci. Technol*., A4, 2280, 1986.
33. P.A. Redhead, *Rev. Sci. Instr*., 31, 343, 1960.
34. G.H. Metson, *Br. J. Appl. Phys*., 2, 46, 1951.
35. J.J. Lander, *Rev. Sci. Inst*., 21, 672, 1950.
36. P.A. Redhead, *J. Vac. Sci. Technol*., 3, 173, 1966.
37. J. Groszkowski, *Le Vide*, 136, 240, 1968.
38. L.G. Pittaway, *Philips Res. Rept*., 29, 283, 1974.
39. D. Blechshmidt, *J. Vac. Sci. Technol*., 10, 376, 1973.
40. P.A. Redhead, *J. Vac. Sci. Technol*., 6, 848, 1969.
41. S.D. Wood and C.R. Tilford, *J. Vac. Sci. Technol*., A3, 542, 1985.
42. C.R. Tilford, *J. Vac. Sci. Technol*., A3, 546, 1985.
43. P.C. Arnold and D.G. Bills, *J. Vac. Sci. Technol*., A2, 159, 1984.
44. P.C. Arnold and J. Borichevsky, *J. Vac. Sci. Technol*., A12, 568, 1994.
45. D.G. Bills, *J. Vac. Sci. Technol*., A12, 574, 1994.
46. C.R. Tilford, A.R. Filippelli, et al., *J. Vac. Sci. Technol*., A13, 485, 1995.
47. T.A. Flaim and P.D. Owenby, *J. Vac. Sci. Technol*., 8, 661, 1971.
48. J.F. O'Hanlon, op. cit., 65.
49. N. Ohsako, *J. Vac. Sci. Technol*., 20, 1153, 1982.
50. P.C. Arnold, D.G. Bills et al., *J. Vac. Sci. Technol*., A12, 580, 1994.
51. ETI Division of the Fredericks Co., Huntingdon Valley, PA, Gage Type 8184.
52. F.M. Penning, *Physica*, 4, 71, 1937.
53. F.M. Penning and K. Nienhauis, *Philips Tech. Rev*., 11, 116, 1949.
54. P.A. Redhead, *Can. J. Phys*., 36, 255, 1958.
55. J.P. Hobson and P.A. Readhead, *Can. J. Phys*., 33, 271, 1958.
56. NRC type 552 data sheet.
57. D. Pelz and G. Newton, *J. Vac. Sci. Technol*., 4, 239, 1967.
58. R.N. Peacock, N.T. Peacock, and D.S. Hauschulz, *J. Vac. Sci. Technol*., A9, 1977 1991.
59. E. Drubetsky, D.R. Taylor, and W.H. Bayles, Jr., *Am. Vac. Soc., New Engl. Chapter, 1993 Symp*.
60. B.R. Kendall and E. Drubetsky, *J. Vac. Sci. Technol*., A14, 1292, 1996.
61. M. Ono, K. Hirata, et al., *J. Vac. Sci. Technol*., A4, 1728, 1986.
62. O.E. Meyer, *Pogg. Ann*., 125, 177, 1865.
63. J.C. Maxwell, *Phil. Trans. R. Soc*., 157, 249, 1866.

64. F.T. Holmes, *Rev. Sci. Instru.*, 8, 444, 1937.
65. J.W. Beams, J.L. Young, and J.W. Moore, *J. Appl. Phys.*, 17, 886, 1946.
66. J.K. Fremery, *Vacuum*, 32, 685, 1946.
67. NIST, Vacuum calibrations using the molecular drag gage, Course Notes, April 15–17, 1996.
68. S. Dittman, B.E. Lindenau, and C.R. Tilford, *J. Vac. Sci. Technol.*, A7, 3356, 1989.
69. K.E. McCulloh, S.D. Wood, and C.R. Tilford, *J. Vac. Sci. Technol.*, A3, 1738, 1985.
70. G. Cosma, J.K. Fremerey, B. Lindenau, G. Messer, and P. Rohl, *J. Vac. Sci. Technol.*, 17, 642, 1980.
71. D.M. Hoffman, B. Singh, and J.H. Thomas, III (eds.), *The Handbook of Vacuum Science and Technology*, Orlando, FL: Academic Press, 1998.
72. Varian Associates, *Basic Vacuum Practice*, Lexington, MA: Varian Associates, Inc., p. 02173, 1992.
73. C.R. Tilford, S. Dittman, and K.E. McCulloh, *J. Vac. Sci. Technol.*, A6, 2855, 1988.
74. M. Hirata, M. Ono, H. Hojo, and K. Nakayama, Calibration of secondary standard ionization gauges, *J. Vac. Sci. Technol.*, 20(4), 1159, 1982.
75. S. Dittman, NIST Special Publication 250–34, 1989.
76. National Conference of Standards Laboratories, Boulder, CO.
77. H. Gantsch, J. Tewes, and G. Messer, *Vacuum*, 35(3), 137, 1985.
78. W.H. Bayles, Jr., Fundamentals of vacuum measurement, calibration and certification, *Ind. Heat.*, October 1992.

Further Readings

Barbour, E., How Vacuum Tubes Work, http://www.vacuumtubes.net/How_Vacuum_Tubes_Work.htm (accessed on July 11, 2012).

O'Hanlon, J. F., *A User Guide to Vacuum Technology*, 3rd edn., Hoboken, NJ: John Wiley & Sons, 2003.

Hoffman, D. M., Bawa S., and Thomas, J. H., *Handbook of Vacuum Science and Technology*, San Diego, CA: Academic Press, 1998.

Partial List of Vendors and Suppliers

9scale Vacuum Products, Inc., 192 Anawan St., Box 1B, Fall River, MA 02721, Phone: 508-646-9352, 800-565-6911 (toll free), Fax: 508-646-9597, www.systemsfab.com

Airserco, 7555 Tyler Blvd., Mentor, OH 44060, Phone: 440-946-2700, 800-473-1754 (toll free), Fax: 440-946-8188, www.airserco.com

McGrath, E., Inc., 35 Osborne St., Salem, MA 01970-2529, Phone: 978-744-3546, 877-744-3546 (toll free), Fax: 978-741-4020, www.emcgrath.com

Precision Metrology, 7350 N. Teutonia Ave., Milwaukee, WI 53209, Phone: 414-351-7420, 888-330-3303 (toll free), Fax: 414-351-7429, www.precisionmetrology.com

TM Limited, P.O. Box 1438, Middleboro, MA 02346, Phone: 508-946-4533, 800-910-2352 (toll free), Fax: 508-947-4686, www.tmlimited.com

Vacuubrand, Inc., 11 Bokum Rd., Essex, CT 06426-1506, Phone: 860-767-5341, 888-882-6730 (toll free), Fax: 860-767-2563, www.vacuubrand.com

41

Force Measurement

M.A. Elbestawi
McMaster University

Force, which is a vector quantity, can be defined as an action that will cause acceleration or a certain reaction of a body. This chapter will outline the methods that can be employed to determine the magnitude of these forces.

41.1 General Considerations

The determination or measurement of forces must yield to the following considerations: If the forces acting on a body do not produce any acceleration, they must form a *system of forces in equilibrium*. The system is then considered to be in static equilibrium. The forces experienced by a body can be classified into two categories: internal, where the individual particles of a body act on each other, and external, otherwise. If a body is supported by other bodies while subject to the action of forces, deformations and/or displacements will be produced at the points of support or contact. The internal forces will be distributed throughout the body until equilibrium is established, and then the body is said to be in a state of tension, compression, or shear. In considering a body at a definite section, it is evident that all the internal forces act in pairs, the two forces being equal and opposite, whereas the external forces act singly.

41.2 Hooke's Law

The basis for force measurement results from the physical behavior of a body under external forces. Therefore, it is useful to review briefly the mechanical behavior of materials. When a metal is loaded in uniaxial tension, uniaxial compression, or simple shear (Figure 41.1), it will behave elastically until a critical value of normal stress (S) or shear stress (τ) is reached, and then it will deform plastically [1]. In the elastic region, the atoms are temporarily displaced but return to their equilibrium positions when the load is removed. Stress (S or τ) and strain (e or γ) in the elastic region are defined as indicated in Figure 41.2.

$$\nu = -\frac{e_2}{e_1} \tag{41.1}$$

Poisson's ratio (ν) is the ratio of transverse (e_2) to direct (e_1) strain in tension or compression. In the elastic region, ν is between 1/4 and 1/3 for metals. The relation between stress and strain in the elastic region is given by Hooke's law:

$$S = Ee \text{ (tension or compression)} \tag{41.2}$$

$$\tau = G\gamma \text{ (simple shear)} \tag{41.3}$$

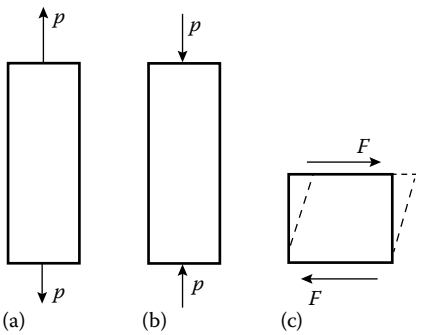

FIGURE 41.1 When a metal is loaded in uniaxial tension (a), uniaxial compression (b), or simple shear (c), it will behave elastically until a critical value of normal stress or shear stress is reached.

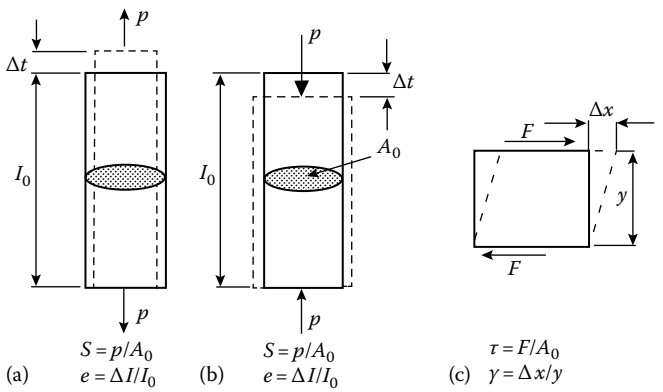

FIGURE 41.2 Elastic stress and strain for (a) uniaxial tension, (b) uniaxial compression, and (c) simple shear. (From Shaw, M.C., *Metal Cutting Principles*, Oxford Science Publications: Clarendon Press, Oxford, U.K., 1989.)

where E and G are the Young's and shear moduli of elasticity, respectively. A small change in specific volume (ΔVol/Vol) can be related to the elastic deformation, which is shown to be as follows for an isotropic material (same properties in all directions):

$$\frac{\Delta \text{Vol}}{\text{Vol}} = e_1(1-2\nu) \tag{41.4}$$

The bulk modulus (K = reciprocal of compressibility) is defined as follows:

$$K = \frac{\Delta p}{\Delta \text{Vol}/\text{Vol}} \tag{41.5}$$

where Δp is the pressure acting at a particular point. For an elastic solid loaded in uniaxial compression (S),

$$K = \frac{S}{\Delta \text{Vol}/\text{Vol}} = \frac{S}{e_1(1-2\nu)} = \frac{E}{1-2\nu} \tag{41.6}$$

Thus, an elastic solid is compressible as long as ν is less than 1/2, which is normally the case for metals. Hooke's law (Equation 41.2) for uniaxial tension can be generalized for a 3D elastic condition.

The theory of elasticity is well established and is used as a basis for force-measuring techniques. Note that the measurement of forces in separate engineering applications is very application specific and care must be taken in the selection of the measuring techniques outlined as follows.

41.2.1 Basic Methods of Force Measurement

An unknown force may be measured by the following means:

1. Balancing the unknown force against a standard mass through a system of levers
2. Measuring the acceleration of a known mass
3. Equalizing it to a magnetic force generated by the interaction of a current-carrying coil and a magnet
4. Distributing the force on a specific area to generate pressure and then measuring the pressure
5. Converting the applied force into the deformation of an elastic element

The aforementioned methods used for measuring forces yield a variety of designs of measuring equipment. The challenge involved with the task of measuring force resides primarily in sensor design. The basics of sensor design can be resolved into two problems:

1. Primary geometric or physical constraints, governed by the application of the force sensor device
2. The means by which the force can be converted into a workable signal form (such as electronic signals or graduated displacements)

The remaining sections will discuss the types of devices used for force to signal conversion and finally illustrate some examples of applications of these devices for measuring forces.

41.3 Force Sensors

Force sensors are required for a basic understanding of the response of a system. For example, cutting forces generated by a machining process can be monitored to detect a tool failure or to diagnose the causes of this failure in controlling the process parameters and in evaluating the quality of the surface produced. Force sensors are used to monitor impact forces in the automotive industry. Robotic handling and assembly tasks are controlled by detecting the forces generated at the end effector. Direct measurement of forces is useful in controlling many mechanical systems.

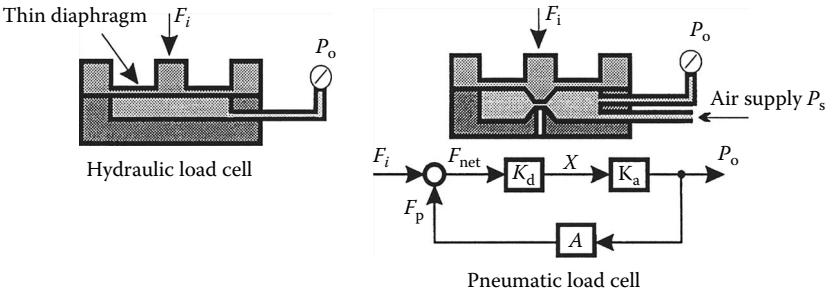

FIGURE 41.3 Different types of load cells. (From Doebelin, E.O., *Measurement Systems, Application and Design*, 4th edn., McGraw-Hill, New York, 1990.)

Some types of force sensors are based on measuring a deflection caused by the force. Relatively high deflections (typically, several micrometers) would be necessary for this technique to be feasible. The excellent elastic properties of helical springs make it possible to apply them successfully as force sensors that transform the load to be measured into a deflection. The relation between force and deflection in the elastic region is demonstrated by Hooke's law. Force sensors that employ strain-gage elements or piezoelectric (quartz) crystals with built-in microelectronics are common. Both impulsive forces and slowly varying forces can be monitored using these sensors.

Of the available force-measuring techniques, a general subgroup can be defined as that of load cells. Load cells are comprised generally of a rigid outer structure, some medium that is used for measuring the applied force, and the measuring gage. Load cells are used for sensing large, static, or slowly varying forces with little deflection and are a relatively accurate means of sensing forces. Typical accuracies are of the order of 0.1% of the full-scale readings. Various strategies can be employed for measuring forces that are strongly dependent on the design of the load cell. For example, Figure 41.3 illustrates different types of load cells that can be employed in sensing large forces for relatively little cost. The hydraulic load cell employs a very stiff outer structure with an internal cavity filled with a fluid. The application of a load increases the oil pressure, which can be read off an accurate gage.

Other sensing techniques can be utilized to monitor forces, such as piezoelectric transducers for quicker response of varying loads, pneumatic methods, and strain gages. The proper sensing technique needs special consideration based on the conditions required for monitoring.

41.4 Strain-Gage Load Cell

The strain-gage load cell consists of a structure that elastically deforms when subjected to a force and a strain-gage network that produces an electric signal proportional to this deformation. Examples of this are beam and ring types of load cells.

41.4.1 Strain Gages

Strain gages use a length of gage wire to produce the desired resistance (which is usually about 120 Ω in the form of a flat coil). This coil is then cemented (bonded) between two thin insulating sheets of paper or plastic. Such a gage cannot be used directly to measure deflection. It has to be first fixed properly to a member to be strained. After bonding the gage to the member, they are baked at about 195 °F (90 °C) to remove moisture. Coating the unit with wax or resin will provide some mechanical protection. The resistance between the member under test and the gage itself must be at least 50 MΩ. The total area of all conductors must remain small so that the cement can easily transmit the force necessary to deform the wire. As the member is stressed, the resulting strain deforms the strain gage and the cross-sectional area diminishes. This causes an increase in resistivity of the gage that is easily determined. In order to

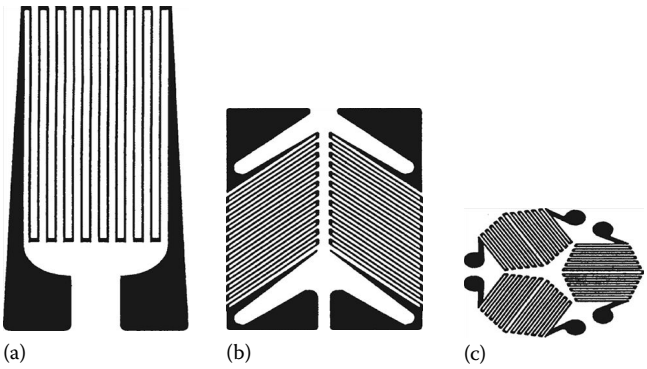

FIGURE 41.4 Configuration of metal-foil resistance strain gages: (a) single element, (b) two elements, and (c) three elements.

measure very small strains, it is necessary to measure small changes of the resistance per unit resistance ($\Delta R/R$). The change in the resistance of a bonded strain gage is usually less than 0.5%. A wide variety of gage sizes and grid shapes are available, and typical examples are shown in Figure 41.4.

The use of strain gages to measure force requires careful consideration with respect to rigidity and environment. By virtue of their design, strain gages of shorter length generally possess higher response frequencies (examples: 660 kHz for a gage of 0.2 mm and 20 kHz for a gage of 60 mm in length). The environmental considerations focus mainly on the temperature of the gage. It is well known that resistance is a function of temperature and, thus, strain gages are susceptible to variations in temperature. Thus, if it is known that the temperature of the gage will vary due to any influence, temperature compensation is required in order to ensure that the force measurement is accurate.

A Wheatstone bridge (Figure 41.5) is usually used to measure this small order of magnitude. In Figure 41.5, no current will flow through the galvanometer (G) if the four resistances satisfy a certain condition. In order to demonstrate how a Wheatstone bridge operates [3], a voltage scale has been drawn at points C and D of Figure 41.5. Assume that R_1 is a bonded gage represented by R_g and that initially Equation 41.7 is satisfied. If R_1 is now stretched so that its resistance increases by one unit ($+\Delta R$), the voltage at point D will be increased from zero to plus one unit of voltage ($+\Delta V$), and there will be a voltage difference of one unit between C and D that will give rise to a current through C. If R_4 is also a bonded gage and at the same time, R_1 changes by $+\Delta R$ and R_4 changes by $-\Delta R$, the voltage at D will move to $+2\Delta V$. Also, if at the same time, R_2 changes by $-\Delta R$ and R_3 changes by $+\Delta R$, then the voltage of point C will move to $-2\Delta V$ and the voltage difference between C and D will now be $4\Delta V$. It is then apparent that although a single gage can be used, the sensitivity can be increased fourfold if two gages are used in tension while two others are used in compression. Similarly, the bridge becomes unbalanced in proportion to the difference in strain when gages are located on

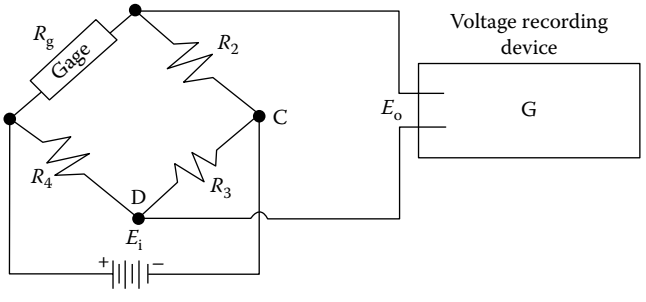

FIGURE 41.5 Wheatstone bridge.

the adjacent leg. The strain gage arrangement determines the relationship between the output and the type of strain being measured for axial, shear, bending, and torsional strains.

$$\frac{R_1}{R_4} = \frac{R_2}{R_3} \tag{41.7}$$

The grid configuration of the metal-foil resistance strain gages is formed by a photo-etching process. The shortest gage available is 0.20 mm; the longest is 102 mm. Standard gage resistance is 120 and 350 Ω. A strain gage exhibits a resistance change $\Delta R/R$ that is related to the strain in the direction of the grid lines by the expression in Equation 41.8 (where S_g is the gage factor or calibration constant for the gage).

$$\frac{\Delta R}{R} = S_g \varepsilon \tag{41.8}$$

41.4.2 Beam-Type Load Cell

Beam-type load cells are commonly employed for measuring low-level loads [3]. A simple cantilever beam (see Figure 41.6a) with four strain gages, two on the top surface and two on the bottom surface (all oriented along the axis of the beam), is used as the elastic member (sensor) for the load cell. The gages are wired into a Wheatstone bridge as shown in Figure 41.6b. The load P produces a moment $M = Px$ at the gage location (x) that results in the following strains:

$$\varepsilon_1 = -\varepsilon_2 = \varepsilon_3 = -\varepsilon_4 = \frac{6M}{Ebh^2} = \frac{6Px}{Ebh^2} \tag{41.9}$$

where

b is the width of the cross section of the beam
h is the height of the cross section of the beam

Thus, the response of the strain gages is obtained from Equation 41.10:

$$\frac{\Delta R_1}{R_1} = -\frac{\Delta R_2}{R_2} = \frac{\Delta R_3}{R_3} = -\frac{\Delta R_4}{R_4} = \frac{6S_g Px}{Ebh^2} \tag{41.10}$$

The output voltage E_o from the Wheatstone bridge, resulting from application of the load P, is obtained from Equation 41.11. If the four strain gages on the beam are assumed to be identical, then Equation 41.11 holds:

$$E_o = \frac{6S_g PxE_1}{Ebh^2} \tag{41.11}$$

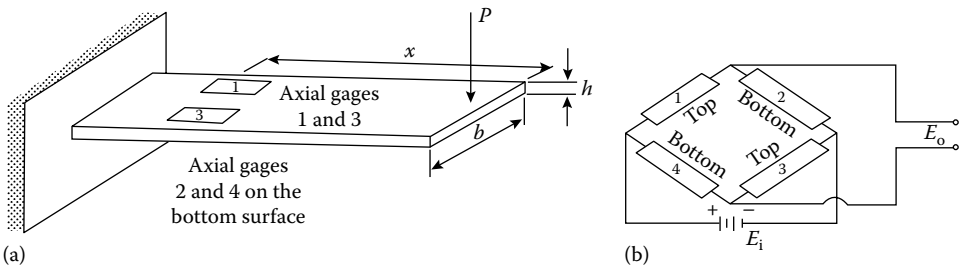

FIGURE 41.6 Beam-type load cells: (a) a selection of beam-type load cells (elastic element with strain gages) and (b) gage positions in the Wheatstone bridge. (From Dally, J.W. et al., *Instrumentation for Engineering Measurements*, John Wiley & Sons, New York, 1984.)

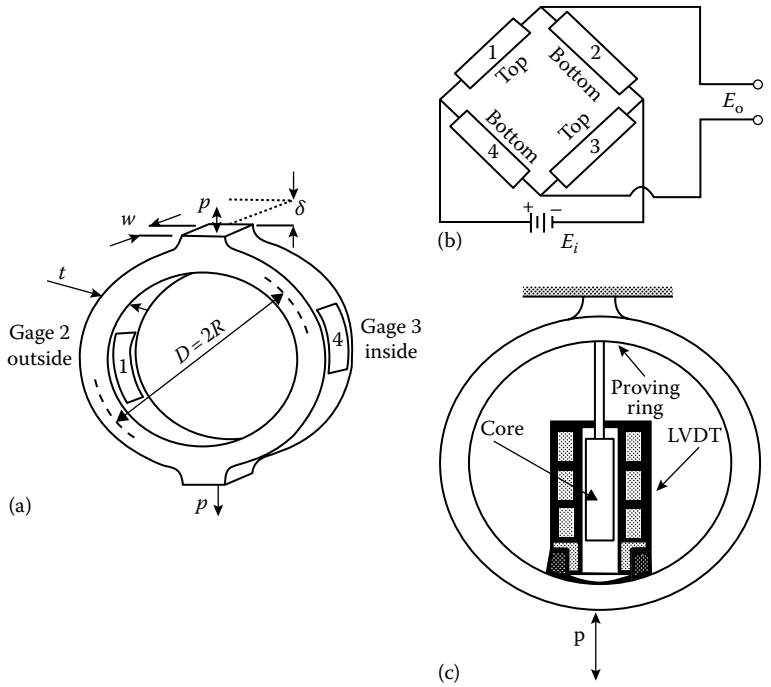

FIGURE 41.7 Ring-type load cells: (a) elastic element with strain-gage sensors, (b) gage positions in the Wheatstone bridge, and (c) elastic element with an LVDT sensor. (From Dally, J.W. et al., *Instrumentation for Engineering Measurements*, John Wiley & Sons, New York, 1984.)

The range and sensitivity of a beam-type load cell depends on the shape of the cross section of the beam, the location of the point of application of the load, and the fatigue strength of the material from which the beam is fabricated.

41.4.3 Ring-Type Load Cell

Ring-type load cells incorporate a proving ring (see Figure 41.7) as the elastic element. The ring element can be designed to cover a very wide range of loads by varying the diameter D, the thickness t, or the depth w of the ring. Either strain gages or linear variable differential transformer (LVDT) can be used as the sensor.

The load P is linearly proportional to the output voltage E_o. The sensitivity of the ring-type load cell with an LVDT sensor depends on the geometry of the ring (R, t, and w), the material from which the ring is fabricated (E), and the characteristics of the LVDT (S and E_i). The range of a ring-type load cell is controlled by the strength of the material used in fabricating the ring.

41.5 Piezoelectric Methods

A piezoelectric material exhibits a phenomenon known as the *piezoelectric effect*. This effect states that when asymmetrical, elastic crystals are deformed by a force, an electric potential will be developed within the distorted crystal lattice. This effect is reversible. That is, if a potential is applied between the surfaces of the crystal, it will change its physical dimensions [4]. Elements exhibiting piezoelectric qualities are sometimes known as electrorestrictive elements.

The magnitude and the polarity of the induced surface charges are proportional to the magnitude and direction of the applied force [4]:

$$Q = dF \tag{41.12}$$

where d is the charge sensitivity (a constant for a given crystal) of the crystal in C/N. The force F causes a thickness variation Δt meters of the crystal:

$$F = \frac{aY}{t}\Delta t \tag{41.13}$$

where
a is area of crystal
t is thickness of crystal
Y is Young's modulus

$$Y = \frac{\text{stress}}{\text{strain}} = \frac{Ft}{a\Delta t} \tag{41.14}$$

The charge at the electrodes gives rise to a voltage $E_o = Q/C$, where C is capacitance in farads between the electrodes and $C = \varepsilon a/t$ where ε is the absolute permittivity:

$$E_o = \frac{dF}{C} = \frac{d}{\varepsilon}\frac{tF}{a} \tag{41.15}$$

The voltage sensitivity = $g = d/\varepsilon$ in volt m/N can be obtained as

$$E_o = g\frac{t}{a}F = gtP \tag{41.16}$$

The piezoelectric materials used are quartz, tourmaline, Rochelle salt, ammonium dihydrogen phosphate (ADP), lithium sulfate, barium titanate, and lead zirconate titanate (PZT) [4]. Quartz and other earthly piezoelectric crystals are naturally polarized. However, synthetic piezoelectric materials, such as barium titanate ceramic, are made by baking small crystallites under pressure and then placing the resultant material in a strong dc electric field [4]. After that, the crystal is polarized, along the axis on which the force will be applied, to exhibit piezoelectric properties. Artificial piezoelectric elements are free from the limitations imposed by the crystal structure and can be molded into any size and shape. The direction of polarization is designated during their production process.

The different modes of operation of a piezoelectric device for a simple plate are shown in Figure 41.8 [4]. By adhering two crystals together so that their electric axes are perpendicular,

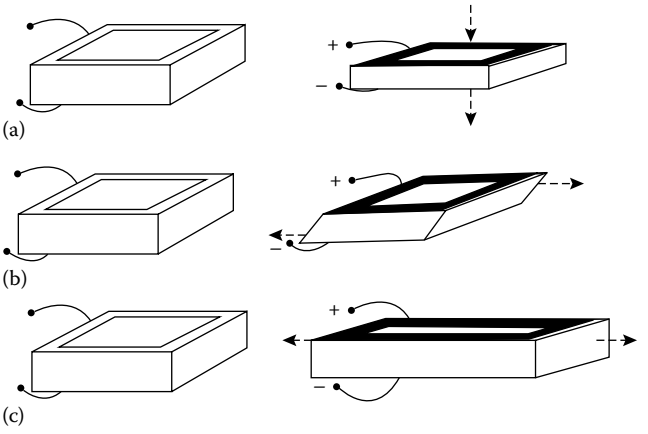

FIGURE 41.8 Modes of operation for a simple plate as a piezoelectric device: (a) Perpendicular force, (b) shear force, and (c) horizontal force. (From Mansfield, P.H., *Electrical Transducers for Industrial Measurement*, The Butterworth Group, London, U.K., 1973.)

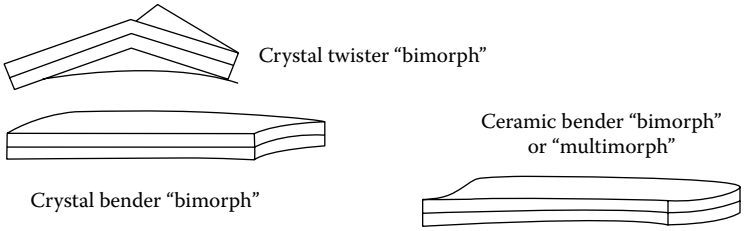

FIGURE 41.9 Curvature of "twister" and "bender" piezoelectric transducers when voltage applied. (From Mansfield, P.H., *Electrical Transducers for Industrial Measurement*, The Butterworth Group, London, U.K., 1973.)

bending moments or torque can be applied to the piezoelectric transducer and a voltage output can be produced (Figure 41.9) [4]. The ranges of forces that can be measured using piezoelectric transducers are from 1 to 200 kN and at a ratio of 2×10^5.

Piezoelectric crystals can also be used in measuring an instantaneous change in the force (dynamic forces). A thin plate of quartz can be used as an electronic oscillator. The frequency of these oscillations will be dominated by the natural frequency of the thin plate. Any distortion in the shape of the plate caused by an external force alters the oscillation frequency. Hence, a dynamic force can be measured by the change in frequency of the oscillator.

41.5.1 Resistive Method

The resistive method employs the fact that when the multiple contact area between semiconducting particles (usually carbon) and the distance between the particles are changed, the total resistance is altered. The design of such transducers yields a very small displacement when a force is applied. A transducer might consist of 2–60 thin carbon disks mounted between a fixed and a movable electrode. When a force is applied to the movable electrode and the carbon disks move together by 5–250 μm per interface, the transfer function of their resistance against the applied force is approximately hyperbolic, that is, highly nonlinear. The device is also subject to large hysteresis and drift together with a high transverse sensitivity.

In order to reduce hysteresis and drift, rings are used instead of disks. The rings are mounted on an insulated rigid core and prestressed. This almost completely eliminates any transverse sensitivity error. The core's resonant frequency is high and can occur at a frequency as high as 10 kHz. The possible measuring range of such a transducer is from 0.1 to 10 kg. The accuracy and linear sensitivity of this transducer is very poor.

41.5.2 Inductive Method

The inductive method utilizes the fact that a change in mechanical stress of a ferromagnetic material causes its permeability to alter. The changes in magnetic flux are converted into induced voltages in the pickup coils as the movement takes place. This phenomenon is known as the *Villari effect* or *magnetostriction*. It is known to be particularly strong in nickel–iron alloys.

Transducers utilizing the Villari effect consist of a coil wound on a core of magnetostrictive material. The force to be measured is applied on this core, stressing it and causing a change in its permeability and inductance. This change can be monitored and used for determining the force.

The applicable range for this type of transducer is a function of the cross-sectional area of the core. The accuracy of the device is determined by a calibration process. This transducer has poor linearity and is subject to hysteresis. The permeability of a magnetostrictive material increases when it is subjected to pure torsion, regardless of direction. A flat frequency response is obtained over a wide range from 150 to 15,000 Hz.

41.5.3 Piezotransistor Method

Devices that utilize *anisotropic stress effects* are described as piezotransistors. In this effect, if the upper surface of a *p–n* diode is subjected to a localized stress, a significant reversible change occurs in the current across the junction. These transistors are usually silicon nonplanar type, with an emitter-base junction. This junction is mechanically connected to a diaphragm positioned on the upper surface of a typical TO-type can [4]. When a pressure or a force is applied to the diaphragm, an electronic charge is produced. It is advisable to use these force-measuring devices at a constant temperature by virtue of the fact that semiconducting materials also change their electric properties with temperature variations. The attractive characteristic of piezotransistors is that they can withstand a 500% overload.

41.5.4 Multicomponent Dynamometers Using Quartz Crystals as Sensing Elements

41.5.4.1 Piezoelectric Effects in Quartz

For force measurements, the *direct piezoelectric effect* is utilized. The direct longitudinal effect measures compressive force; the direct shear effect measures shear force in one direction. For example, if a disk of crystalline quartz (SiO_2) cut normally to the crystallographic *x*-axis is loaded by a compression force, it will yield an electric charge, nominally 2.26 pC/N. If a disk of crystalline quartz is cut normally to the crystallographic *y*-axis, it will yield an electric charge (4.52 pC/N) if loaded by a shear force in one specific direction. Forces applied in the other directions will not generate any output [5].

A charge amplifier is used to convert the charge yielded by a quartz crystal element into a proportional voltage. The range of a charge amplifier with respect to its conversion factor is determined by a feedback capacitor. Adjustment to mechanical units is obtained by additional operational amplifiers with variable gain.

41.5.4.2 Design of Quartz Multicomponent Dynamometers

The main element for designing multicomponent dynamometers is the three-component force transducer (Figure 41.10). It contains a pair of *X*-cut quartz disks for the normal force component and a pair of *Y*-cut quartz disks (shear sensitive) for each shear force component.

Three-component dynamometers can be used for measuring cutting forces during machining. Four three-component force transducers sandwiched between a baseplate and a top plate are shown in Figure 41.10. The force transducer is subjected to a preload as shear forces are transmitted by friction. The four force transducers experience a drastic change in their load, depending on the type and position of force application. An overhanging introduction of the force develops a tensile force for some

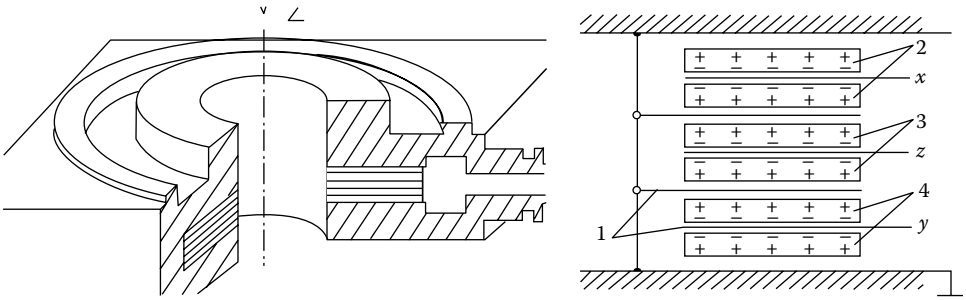

FIGURE 41.10 Three-component force transducer.

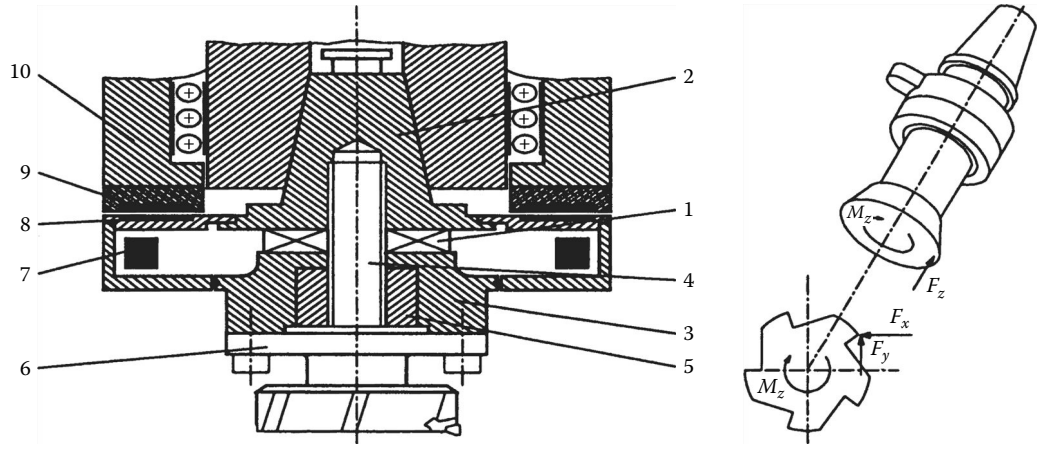

FIGURE 41.11 Force-measuring system to determine the tool-related cutting forces in five-axis milling. (From Spur, G. et al., Measuring the cutting force in five-axis milling, Translated paper "Zerpankraftmessung bei der funfachsigen Frasbearbeitung," Zeitschrift fur wirtschaftliche Fertigung und Automatisierung 9/93 Carl Hanser, Munchen, Kistler Piezo-Instrumentation, 20.162e 9.94.)

transducers, thus reducing the preload. The bending of the top plate of the dynamometer causes bending and shearing stresses. The measuring ranges of a dynamometer depend not only on the individual forces but also on the individual bending stresses.

41.5.4.3 Measuring Signals Transmitted by Telemetry

Figure 41.11 shows the newly designed force-measuring system rotating cutting force dynamometer (RCD). A ring-shaped sensor (1) is fitted in a steep-angle taper socket (2) and a base ring (3) allowing sensing of the three force components F_x, F_y, and F_z at the cutting edge as well as the moment M_z. The physical operating principle of this measuring cell is based on the piezoelectric effect in quartz plates. The quartz plates incorporated in the sensor are aligned so that the maximum cross sensitivity between the force components is 1%. As a result of the rigid design of the sensor, the resonant frequencies of the force-measuring system range from 1200 to 3000 Hz, and the measuring ranges cover a maximum of 10 kN [6].

Force-proportional charges produced at the surfaces of the quartz plates are converted into voltages by four miniature charge amplifiers (7) in hybrid construction. These signals are then filtered by specific electric circuitry to prevent aliasing effects and digitized with 8-bit resolution using a high sampling rate (pulse-code modulation). The digitized signals are transmitted by a telemetric unit consisting of a receiver and transmitter module, an antenna at the top of the rotating force-measuring system (8), as well as a fixed antenna (9) on the splash cover of the two-axis milling head (10). The electric components, the charge amplifier, and the transmitter module are mounted on the circumference of the force-measuring system [6].

The cutting forces and the moment measured are digitized with the force-measuring system described earlier. They are modulated on an FM carrier and transmitted by the rotating transmitter to the stationary receiver. The signals transmitted are fed to an external measured-variable conditioning unit.

41.5.4.4 Measuring Dynamic Forces

Any mechanical system can be considered in the first approximation as a weakly damped oscillator consisting of a spring and a mass. If a mechanical system has more than one resonant frequency, the lowest one must be taken into consideration. As long as the test frequency remains below 10% of the resonant

frequency of the reference transducer (used for calibration), the difference between the dynamic sensitivity obtained and the static calibration will be less than 1%. The aforementioned considerations assume a sinusoidal force signal. The static calibration of a reference transducer is also valid for dynamic calibration purposes if the test frequency is much lower (at least 10 times lower) than the resonant frequency of the system.

41.6 Capacitive Force Transducer

A transducer that uses capacitance variation can be used to measure force. The force is directed onto a membrane whose elastic deflection is detected by a capacitance variation. A highly sensitive force transducer can be constructed because the capacitive transducer senses very small deflections accurately. An electronic circuit converts the capacitance variations into dc-voltage variations [7].

The capacitance sensor illustrated in Figure 41.12 consists of two metal plates separated by an air gap. The capacitance C between terminals is given by the expression

$$C = \varepsilon_0 \varepsilon_r \frac{A}{h} \tag{41.17}$$

where

C is the capacitance in farads (F)
ε_0 is the dielectric constant of free space
ε_r is the relative dielectric constant of the insulator
A is the overlapping area for the two plates
h is the thickness of the gap between the two plates

The sensitivity of capacitance-type sensors is inherently low. Theoretically, decreasing the gap h should increase the sensitivity; however, there are practical electric and mechanical conditions that preclude high sensitivities. One of the main advantages of the capacitive transducer is that moving of one of its plates relative to the other requires an extremely small force to be applied. A second advantage is stability, and the sensitivity of the sensor is not influenced by pressure or temperature of the environment.

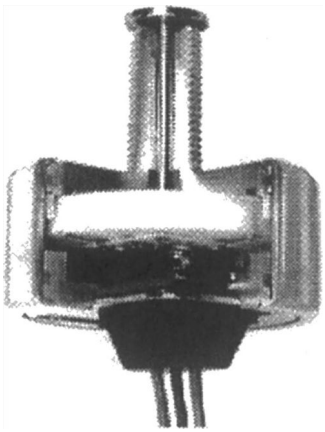

FIGURE 41.12 Capacitive force transducer. (From Nachtigal, C.L., *Instrumentation and Control, Fundamentals and Applications*, John Wiley & Sons, New York, 1990.)

41.7 Force-Sensing Resistors (Conductive Polymers)

Force-sensing resistors (FSRs) utilize the fact that certain polymer thick-film devices exhibit decreasing resistance with the increase of an applied force. An FSR is made up of two parts. The first is a resistive material applied to a film. The second is a set of digitizing contacts applied to another film. Figure 41.13 shows this configuration. The resistive material completes the electric circuit between the two sets of conductors on the other film. When a force is applied to this sensor, a better connection is made between the contacts; hence, the conductivity is increased. Over a wide range of forces, it turns out that the conductivity is approximately a linear function of force. Figure 41.14 shows the resistance of the sensor as a function of force. It is important to note that there are three possible regions for the sensor to operate. The first abrupt transition occurs somewhere in the vicinity of 10g of force. In this region, the resistance changes very rapidly. This behavior is useful when one is designing switches using FSRs.

FSRs should not be used for accurate measurements of force because sensor parts may exhibit 15%–25% variation in resistance between each other. However, FSRs exhibit little hysteresis and are considered far less costly than other sensing devices. Compared to piezofilm, the FSR is far less sensitive to vibration and heat.

41.7.1 Magnetoresistive Force Sensors

The principle of *magnetoresistive force sensors* is based on the fact that metals, when cooled to low temperatures, show a change of resistivity when subjected to an applied magnetic field. Bismuth, in particular, is quite sensitive in this respect. In practice, these devices are severely limited because of their high sensitivity to ambient temperature changes.

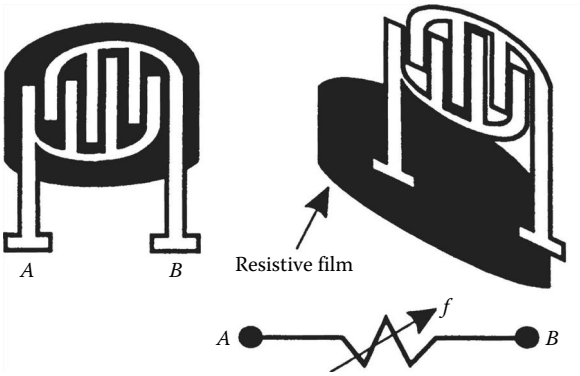

FIGURE 41.13 Diagram of a typical FSR.

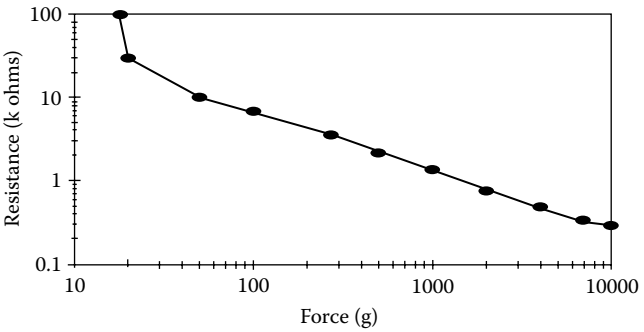

FIGURE 41.14 Resistance as a function of force for a typical FSR.

41.8 Magnetoelastic Force Sensors

Magnetoelastic transducer devices operate based on the Joule effect; that is, a ferromagnetic material is dimensionally altered when subjected to a magnetic field. The principle of operation is as follows: Initially, a current pulse is applied to the conductor within the waveguide. This sets up a magnetic field circumference wise around the waveguide over its entire length. There is another magnetic field generated by the permanent magnet that exists only where the magnet is located. This field has a longitudinal component. These two fields join vectorally to form a helical field near the magnet that, in turn, causes the waveguide to experience a minute torsional strain or twist only at the location of the magnet. This twist effect is known as the *Wiedemann effect* [8].

Magnetoelastic force transducers have a high frequency response (on the order of 20 kHz). Some of the materials that exhibit magnetoelastic include Monel metal, Permalloy, Cekas, Alfer, and a number of nickel–iron alloys. The disadvantages of these transducers include (1) the fact that excessive stress and aging may cause permanent changes, (2) zero drift and sensitivity changes due to temperature sensitivity, and (3) hysteresis errors.

41.9 Torsional Balances

Balancing devices that utilize the deflection of a spring may also be used to determine forces. *Torsional balances* are equal arm scale force-measuring devices. They are comprised of horizontal steel bands instead of pivots and bearings. The principle of operation is based on force application on one of the arms that will deflect the torsional spring (within its design limits) in proportion to the applied force. This type of instrument is susceptible to hysteresis and temperature errors and therefore is not used for precise measurements.

41.10 Tactile Sensors

Tactile sensors are usually interpreted as a touch sensing technique. Tactile sensors cannot be considered as simple touch sensors, where very few discrete force measurements are made. In tactile sensing, a force "distribution" is measured using a closely spaced array of force sensors.

Tactile sensing is important in both grasping and objects identification operations. Grasping an object must be done in a stable manner so that the object is not allowed to slip or damaged. Object identification includes recognizing the shape, location, and orientation of a product, as well as identifying surface properties and defects. Ideally, these tasks would require two types of sensing [9]:

1. Continuous sensing of contact forces
2. Sensing of the surface deformation profile

These two types of data are generally related through stress–strain relations of the tactile sensor. As a result, almost continuous variable sensing of tactile forces (the sensing of the tactile deflection profile) is achieved.

41.10.1 Tactile Sensor Requirements

Significant advances in tactile sensing are taking place in the robotics area. Applications include automated inspection of surface profiles, material handling or parts transfer, parts assembly, and parts identification and gaging in manufacturing applications and fine manipulation tasks. Some of these applications may need only simple touch (force–torque) sensing if the parts being grasped are properly oriented and if adequate information about the process is already available.

Naturally, the main design objective for tactile sensing devices has been to mimic the capabilities of human fingers [9]. Typical specifications for an industrial tactile sensor include

1. Spatial resolution of about 2 mm
2. Force resolution (sensitivity) of about 2 g
3. Maximum touch force of about 1 kg
4. Low response time of 5 ms
5. Low hysteresis
6. Durability under extremely difficult working conditions
7. Insensitivity to change in environmental conditions (temperature, dust, humidity, vibration, etc.)
8. Ability to monitor slip

41.10.2 Tactile Array Sensor

Tactile array sensors (Figure 41.15) consist of a regular pattern of sensing elements to measure the distribution of pressure across the fingertip of a robot. The 8 × 8 array of elements at 2 mm spacing in each direction provides 64 force-sensitive elements. Table 41.1 outlines some of the characteristics of early tactile array sensors. The sensor is composed of two crossed layers of copper strips separated by strips of thin silicone rubber. The sensor forms a thin, compliant layer that can be easily attached to a variety of fingertip shapes and sizes. The entire array is sampled by computer.

A typical tactile sensor array can consist of several sensing elements. Each element or taxel (Figure 41.16) is used to sense the forces present. Since tactile sensors are implemented in applications where sensitivity providing semblance to human touch is desired, an elastomer is utilized to mimic the human skin. The elastomer is generally a conductive material whose electric conductivity changes locally when pressure is applied. The sensor itself consists of three layers: a protective covering, a sheet of conductive elastomer, and a printed circuit board. The printed circuit board consists of two rows of two "bull's-eyes," each with conductive inner and outer rings that compromise the taxels of the sensor.

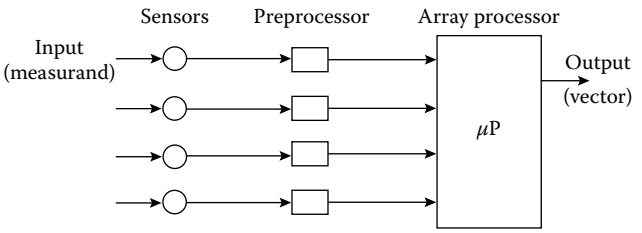

FIGURE 41.15 Tactile array sensor.

TABLE 41.1 Summary of Some of the Characteristics of Early Tactile Array Sensors

	Size of Array		
Device Parameter	(4 × 4)	(8 × 8)	(16 × 6)
Cell spacing (mm)	4.00	2.00	1.00
Zero-pressure capacitance (fF)	6.48	1.62	0.40
Rupture force (N)	18.90	1.88	0.19
Max. linear capacitance (fF)	4.80	1.20	0.30
Max. output voltage (V)	1.20	0.60	0.30
Max. resolution (bit)	9.00	8.00	8.00
Readout (access) time (μs)	—	<20	—

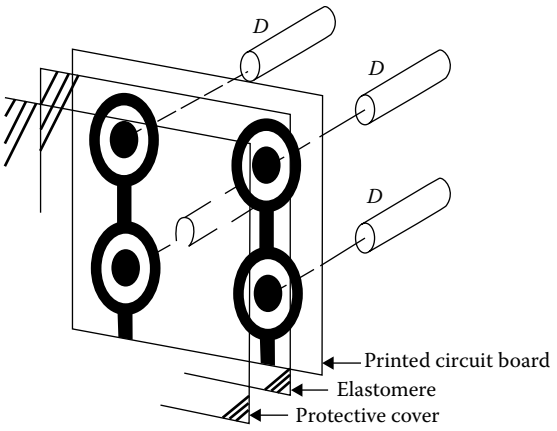

FIGURE 41.16 Typical taxel sensor array.

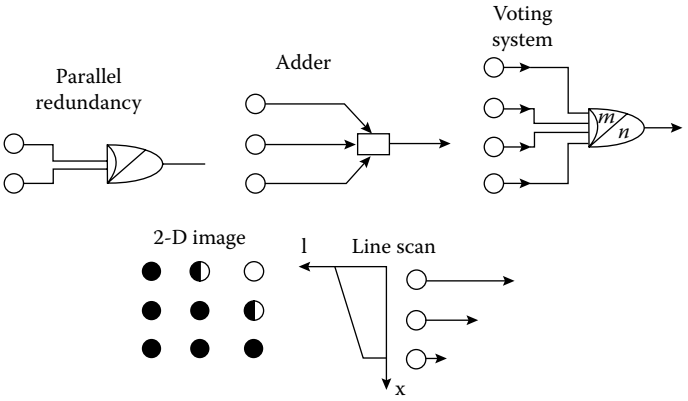

FIGURE 41.17 General arrangement of an intelligent sensor array system. (From Gardner, J.W., *Microsensors Principles and Applications*, John Wiley & Sons, New York, 1995.)

The outer rings are connected together and to a column-select transistor. The inner rings are connected to diodes (D) in Figure 41.16. Once the column in the array is selected, the current flows through the diodes, through the elastomer, and thence through a transistor to ground. As such, it is generally not possible to excite just one taxel because the pressure applied causes a local deformation in neighboring taxels. This situation is called *cross talk* and is eliminated by the diodes [10].

Tactile array sensor signals are used to provide information about the contact kinematics. Several feature parameters, such as contact location, object shape, and pressure distribution, can be obtained. The general layout of a sensor array system can be seen in Figure 41.17. An example of this is a contact and force-sensing finger. This tactile finger has four contact sensors made of piezoelectric polymer strips on the surface of the fingertip that provide dynamic contact information. A strain-gage force sensor provides static grasp force information.

References

1. M. C. Shaw, *Metal Cutting Principles*, Oxford, U.K.: Oxford Science Publications, Clarendon Press, 1989.
2. E. O. Doebelin, *Measurement Systems, Application and Design*, 4th edn., New York: McGraw-Hill, 1990.
3. J. W. Dally, W. F. Riley, and K. G. McConnel, *Instrumentation for Engineering Measurements*, New York: John Wiley & Sons, 1984.

4. P. H. Mansfield, *Electrical Transducers for Industrial Measurement*, London, U.K.: The Butterworth Group, 1973.
5. K. H. Martini, Multicomponent dynamometers using quartz crystals as sensing elements, *ISA Trans*., 22(1), 35–46, 1983.
6. G. Spur, S. J. Al-Badrawy, and J. Stirnimann, Measuring the cutting force in five-axis milling, Translated paper "Zerpankraftmessung bei der funfachsigen Frasbearbeitung," Zeitschrift fur wirtschaftliche Fertigung und Automatisierung 9/93 Carl Hanser, Munchen, Kistler Piezo-Instrumentation, 20.162e 9.94.
7. C. L. Nachtigal, *Instrumentation and Control, Fundamentals and Applications*, Wiley Series in Mechanical Engineering Practice, New York: Wiley Interscience, John Wiley & Sons, 1990.
8. C. W. DeSilva, *Control Sensors and Actuators*, Englewood Cliffs, NJ: Prentice Hall, 1989.
9. J. W. Gardner, *Microsensors Principles and Applications*, New York: John Wiley & Sons, 1995.
10. W. Stadler, *Analytical Robotics and Mechatronics*, New York: McGraw-Hill, 1995.

Further Information

Lindberg, B. and B. Lindstrom, Measurements of the segmentation frequency in the chip formation process, *Ann. CIRP*, 32(1), 17–20, 1983.

Mechanical measurements and Metrology VIDEO LECTURES, Ebookee, Online on 17-02-2011, http://ebookee.org/Mechanical-Measurements-and-Metrology-VIDEO-LECTURES_1056871.html (accessed on July 25, 2012).

Norton, H. N. *Sensor and Analyzer Handbook*, Englewood Cliffs, NJ: Prentice Hall, 1982.

Dan Mihai Stefanescu, *Handbook of Force Transducers: Principles and Components*, Springer, Berlin, Germany, 2011

Sze, S. M. *Semiconductor Sensors*, New York: John Wiley & Sons, 1994.

Tlusty, J. and G. C Andrews, A critical review of sensors for unmanned machining, *Ann. CIRP*, 32(2), 563–572, 1983.

Wright, C. P. *Applied Measurement Engineering: How to Design Effective Mechanical Measurement Systems*, Englewood Cliffs, NJ: Prentice Hall, 1995.

Partial List of Vendors and Suppliers

Kistler North America, 75 John Glenn Dr., Amherst, NY 14228-2119, Phone: 716-691-5100, 888-KISTLER, 888-547-8537 (toll free), Fax: 716-691-5226, www.kistler.com

Mark-10 Corp, 11 Dixon Ave., Copiague, NY 11726, Phone: 631-842-9200, 888-627-5836 (toll free), 888-MARKTEN (toll free), Fax: 631-842-9201, www.Mark-10.com

PCB Piezotronics, Inc., 3425 Walden Ave., Depew, NY 14043-2417, Phone: 716-684-0001, 800-828-8840 (toll free), Fax: 716-684-0987, www.pcb.com

Strainsert Co., 12 Union Hill Rd., West Conshohocken, PA 19428, Phone: 610-825-3310, 800-529-1502 (toll free), Fax: 610-825-1734, www.strainsert.com

Transducer Techniques, Inc., 42480 Rio Nedo, Temecula, CA 92590, Phone: 951-719-3965, 800-344-3965 (toll free), Fax: 951-719-3900, www.transducertechniques.com

Tekscan, 307 W. First St., South Boston, MA 02127, Phone: 617-464-4500, 800-248-3669 (toll free), Fax: 617-464-4266, www.tekscan.com

42

Angle Measurement

Robert J. Sandberg
University of Wisconsin–Madison

An *angle* is defined as the figure formed by two lines or planes that intersect one another. Such lines or planes may be real, such as the edges and surfaces of an object, or they may be defined, such as lines from an observer to two distant stars.

The units of measurement of angle are degrees (°) (1° is defined as 1/360 of a circle) and radians (rad) (1 rad is defined as $1/(2\pi)$ of a circle). One radian is equal to 57.29578°, and small angles may be expressed in the unit of milliradians (1×10^{-3} rad). A degree of angle is further divided into 60′ (min), and 1′ of angle is divided into 60″ (s). One second of angle, being 1/1,296,000 of a circle, is a very small unit of measurement when related to manufactured parts but is a significant unit when related to much larger dimensions such as the Earth (1″ of angle equals approximately 30 m of a great circle) or in space travel (an included angle of 1″ represents about 9 km on the surface of the moon when it is observed from the Earth during its closest approach to Earth.)

Many terms are used to describe angles in many different fields of expertise. Table 42.1 lists some of these terms, along with very basic definitions.

Many devices and instruments are used to measure or set angles. The following paragraphs describe the variety of equipment involved. See Table 42.2 for a partial list of manufacturers and suppliers of this equipment. See Table 42.3 for a partial list of specific models and approximate prices of angle measurement devices and systems.

42.1 Angle Gage Blocks

Angle gage blocks are right triangle-shaped, hardened, and ground steel; flat; and about 7 mm thick and 60 mm long. They are supplied in sets that include blocks with one of the acute angles equal to 1°, 2°, 3°, 4°, 5°, 6°, 7°, 8°, 9°, 10°, 15°, 20°, or 30°. These blocks can be used in combination to set work pieces or measure objects in 1° increments. Other sets include blocks with as small as 1″ steps. Special angle gage blocks can be made to any acute angle with the aid of a sine bar and thickness gage blocks.

Angle gage blocks provide a durable, simple, and inexpensive method for measuring and setting angles, for example, positioning work pieces in a vice or fixture prior to a machining operation such as milling, drilling, or grinding.

Because they are not adjustable and made of hardened steel, their accuracy can be assumed by simple observation of their physical condition. Look for indications of wear, nicks, or dents before using.

TABLE 42.1 Defining Terms Relating to Angles

Term	Definition
Angle	A figure formed by two lines or planes that intersect one another
Acute angle	An angle less than 90°
Azimuth	The horizontal angle measured along the Earth's horizon, between a fixed reference (usually due south) and an object
Bank	A lateral inclination
Circle	A closed plane curve where all of its points are the same distance from its center point
Declination = declivity	A negative slope
Degree	Equal to 1/360 of a circle
Goniometer	An instrument for measuring angles (from the Greek word *gonio*)
Incline = slope = bias = slant = gradient = grade	The deviation, plus or minus, from horizontal as defined by gravity
Latitude	An angle measured north or south from the equator on a meridian to a point on the earth
Lean = List = Tilt	The deviation from vertical as defined by gravity
Longitude	The angle between the prime meridian (through Greenwich, England) and the meridian of a given place on Earth. This angle is defined as positive moving west
Milliradian	An angle equal to 1/1000 rad
Minute	An angle equal to 1/60°
Oblique angle	An obtuse or acute angle
Obtuse angle	An angle greater than 90°
Quadrant	One quarter of a circle (90°)
Radian	The angle subtended by an arc of a circle equal to the radius of that circle. One radian is equal to 57.29578°.
Rake	Equals the deviation in degrees from being perpendicular (90°) to a line or a plane
Right angle	An angle of 90°
Rise	A positive incline
Second	An angle equal to 1/60′ (1/3600°)
Straight	An angle equal to 180°
Taper	The change in diameter or thickness per unit length of axis
Twist	The angle of turn per unit length of axis, as in a gun barrel or a screw thread

TABLE 42.2 A Partial List of Manufacturers and Supplies of Angle Measurement Equipment

Company	Address
Flexbar Machine Corporation (Representative for Erich Preissr & Co., West Germany)	250 Gibbs Road, Islandia, NY 11722–2697, Tel: (800) 879–7575
Fred V. Fowler Co., Inc.	66 Rowe Street, P.O. Box 299, Newton, MA 02166, Tel: (617) 332–7004
L. S. Starrett Company	121 Crescent Street, Athol, MA 01331, Tel: See local distributor
Brown & Sharpe Mfg. Co.	931 Oakton Street, Elk Grove Village, IL 60007, Tel: (312) 593–5950
Swiss Precision Instruments, Inc., SPI	2206 Lively Blvd, Elk Grove Village, IL 60007, Tel: (708) 981–1300
Edmund Scientific Co.	101 East Gloucester Pike, Barrington, NJ 08007–1380, Tel: (609) 573–6250

TABLE 42.3 Instruments and Devices Used to Measure or Indicate Angles

Type	Manufacturer	Model	Description	Approx. Price
Sine bar	Flexbar	16292	5 in. × 15/16 in. wide	$130.00
		16293	10 in. × 1 in. wide	
		16294	5 in. × 2 in. wide	
		12202	5 in. × 1 in. wide, economy	$30.00
	Fowler	52-455-010	5 in. center to center, 15/16 in. wide	
		52-455-015	10 in. C. to C., 1 in. wide	
		52-455-030	2.5 in. C. to C., 1 in. wide	
	SPI	30-712-4	10 in. C. to C., universal bench center	$3048.00
		98-379-1	5 in. C. to C., 1 in. wide, accuracy between rolls = 0.0003 in.	$31.00
		30-091-3	10 in. C. to C., 1 in. wide, accuracy between rolls = 0.0001 in.	$203.00
	Brown & Sharpe	598-291-121-1	5 in. C. to C., 1 in. wide	
		598-293-121-1	10 in. C. to C., 1 1/8 in. wide	
Sine plate	Flexbar	14612	5 in. C. to C., 6 in. × 3 in. × 2 in.	$320.00
		14615	10 in. C. to C., 12 in. × 6 in. × 2 5/8 in.	$1000.00
	Fowler	57-374-001	5 in. C. to C., 6 in. × 3 in. × 2 in.	
		57-374-004	10 in. C. to C., 12 in. × 6 in. × 2 5/8 in.	
	SPI	77-026-3	10 in. C. to C., 12 in. × 6 in. × 2 5/8 in.	$872.00
	Brown & Sharpe	599-925-10	10 in. C. to C., 12 in. × 6 in. × 2 3/8 in.	
Compound sine plate	Flexbar	14616	5 in. C. to C., 6 in. × 6 in. × 3 1/8 in.	$1100.00
	Fowler	57-375-001	5 in. C. to C., 6 in. × 6 in. × 3 1/8 in.	
	SPI	7-072-7	5 in. C. to C., 6 in. × 6 in. × 3 1/8 in.	$926.00
	Brown & Sharpe	599-926-5	5 in. C. to C., 6 in. × 6 in. × 3 1/2 in.	
Angle computer	Flexbar	19860	3-axis with vernier protractors	$3750.00
Protractor—direct	Flexbar	16337	Rectangular head, 0°–180°	$25.00
	Starrett	RP1224W	Head only. To fit 12, 18, and 24 in. blades	
		C183	Rectangular head, 0°–180° 6 in. blade	
	SPI	30-393-3	Rectangular head, 0°–180°	$23.00
		31-804-8	Head only. To fit 12 in., 18 in., and 24 in. blades	$39.00
Protractor—vernier	Flexbar	16339	360° range, 1′ reading with magnifier, 12 in. and 6 in. blades incl.	$400.00
		16338	360° range, 5′ reading	$75.00
	Starrett	C364DZ	12 in. blade, 0°–90° range through 360°, 5′ graduations	
	SPI	30-395-8	6 in. blade, 0°–90° range through 360°, 5′ graduations	$65.00
		30-390-9	6 in. and 12 in. blades, 0°–90° range through 360°, 1′ graduations with magnifier	$540.00
	Brown & Sharpe	599-490-8	8 in. blade, 0°–90° range through 360°, magnifier optional	

(*continued*)

TABLE 42.3 (continued) Instruments and Devices Used to Measure or Indicate Angles

Type	Manufacturer	Model	Description	Approx. Price
Protractor, digital (inclinometer)	Flexbar	17557	±45° range, ±0.1° resolution	$260.00
		17556	±60° range, ±0.01° resolution, SPC output	$450.00
	Fowler	54-635-600	±45° range, ±0.01° resolution, RS232 output available	
	SPI	31-040-9	±45° range, resolution: ±0.01° (0 to ±10°), 0.1° (10° to 90°)	$329.00
Protractor, dial bevel		30-150-7	8 in. blade, 1 3/8 in. diameter dial, geared to direct read to 5′	$527.30
	Brown & Sharpe	599-4977-8	8 in. blade, dial read degrees and 5′	
Square—reference	SPI	30-392-5	90° fixed angle	$55.00
Optical comparator (projector)	Fowler	53-912-000	12 in. screen diameter, 10× , 20× , 25× lens available, horizontal beam, with separate light source for surface illumination	
	Starrett	HB350	14 in. screen diameter, 10× , 20× , 25×, 31.25× , 50× , 100× lens available, horizontal beam	
		VB300	12 in. screen diameter, 10× through 100× lens available, vertical beam	
		HS1000	40 in. screen diameter, 10× through 100× lens available, horizontal beam	
	SPI	40-350-1	14 in. screen diameter, 10, 20× , 50× lens available, horizontal beam	$2995.00
Optical comparator (handheld)	SPI	40-145-3	10× magnification, pocket style	$57.50
			Additional reticles	$11.00
		40-140-6	7× magnification, pocket style with illuminator	$62.50
			Additional reticles	$10.50
	Edmund Scientific	A2046	6× magnification, pocket style, 360° protractor reticle, 1° increments	$58.75
Angle plate	Fowler	52-456-000	Set of 2, 9/32 in. thick, steel, 30° × 60° × 90°, 45° × 45° × 90°	
	SPI	98-463	Set of 2, 5/16 in. thick, steel, 30° × 60° × 90°, 45° × 45° × 90°	$32.00
Angle positioning Block	SPI	70-997-2	0° to 60°, 10′ vernier (for setting work piece in a vice)	$122.00
Angle gage	Fowler	52-470-180	18 leaves, spring steel, 1°–10°, 14°, 14.5°, 15°, 20°, 25°, 30°, 35°, and 45°	
	SPI	31-375-9	18 gage set, 5°–90° in 5° steps, 5′ accuracy	$49.60
Angle gage blocks	Starrett	Ag18.TR	18 block set, use in combination for steps of l″, 1″ accuracy	
	Starrett AG16.LM		16 block set, use in combination for steps of l″, 1/4″ accuracy	
	SPI	30-140-8	10 block set, 1°, 2°, 3°, 4°, 5°, 10°, 15°, 20°, 25°, 30°, accuracy = ±0.000l″/in.	$170.00
			1/4° and 1/2° blocks optional (each)	$18.00

42.2 Clinometers

A *clinometer* is an electronic device that measures vertical angle with respect to gravitational level. It is rectangular, with each side being 90° to its adjacent sides. With a range of readings of at least ±45°, this shape allows measurements up to a full 360°. Floating zero can be set anywhere and resolutions of ±0.01° are obtainable. Some models will convert readings to inches per foot, percentage of grade, and millimeters per meter (mm m^{-1}).

A clinometer can be used wherever the angle of a surface with respect to gravity or another surface needs to be measured. High accuracy and resolution are obtainable, but calibration should be checked periodically with respect to a known level surface and a known angle. Surfaces that are remote to one another or have an intervening obstruction pose no problem for a clinometer.

42.3 Optical Comparator

An *optical comparator* measures angles, along with other dimensions or profiles, by referencing a visual image (usually magnified) of an object to a reticule that is calibrated in the measurement units desired. A handheld optical comparator is placed directly over the object to be measured, and the operator's eye is moved to the proper distance above the comparator for good focus of the magnified image. Some models contain a battery- or line-powered light source. Reticules for these handheld devices are generally graduated in 1° increments.

Projection-type optical comparators are available as bench or floor models and are made for either horizontal or vertical beam viewing. They use a high-intensity light source and magnifying optics to display an image of an object onto a rear projection, frosted glass screen that is inscribed with angular as well as linear markings. The image displayed is the result of light being projected past the object, referred to as a shadow graph, or of light being reflected off the surface of the object. The method used is determined by the shape of the viewed object and its surface quality.

Magnification of the optical system in these devices can range from 10× by 100×, with screen diameters ranging from 0.3 to 1 m.

These instruments are useful for measuring profiles of parts after final matching for the purpose of quality control or duplication.

As the name implies, the image that is projected can be superimposed on a mask or outline drawing placed directly on the view screen so that any deviations from the required shape can easily be determined. Optical comparators are heavy, nonportable devices that require a fairly high amount of maintenance and are best used in a fairly dark room.

42.4 Protractor

A *protractor* is an instrument used for measuring and constructing angles. A direct-reading protractor usually is graduated in 1° increments and can be semicircular or circular in shape. The simplest models are of one-piece construction and made from metal or plastic. Other models include a blade or pointer pivoted in the center of the graduated circle.

More precise protractors are equipped with a vernier scale that allows an angle to be indicated to 5′ of arc. See Figure 42.1 for an explanation of how to read such a vernier scale.

42.5 Sine Bar

A *sine bar* is a device used to accurately measure angles or to position work pieces prior to grinding and other machining procedures. It is constructed from precisely hardened and ground steel rectangular bar to which two hardened and ground steel cylindrical rods of the same diameter are attached. The axis of each rod is very accurately positioned parallel to the other and to the top surface of the bar.

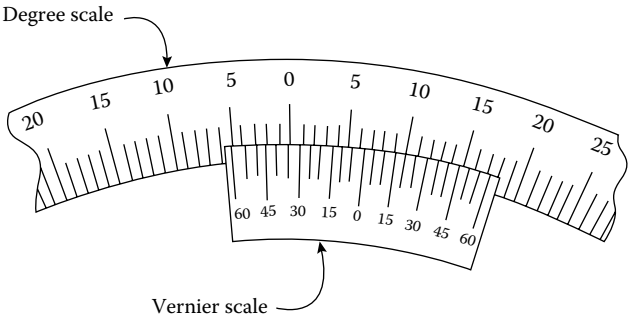

FIGURE 42.1 Vernier protractor. If the zero mark on the vernier scale is to the right of the zero mark on the main scale, as shown in this drawing, then the right side of the vernier scale must be used. Look for the mark on the vernier scale that best aligns with one of the marks of the protractor degree scale. Count the number of marks on the vernier scale from the zero mark to this mark. Each mark thus counted is, in this example, equal to 5′ of arc, and, therefore, the number of minutes to be added to the number of degrees indicated is 5 times the vernier marks counted. (In this example, the fourth mark aligns the best with the main scale indicating 20′). The number of degree indicated is the degree mark just to the left of the zero mark on the vernier scale. The left side of the vernier is similarly used when the indicated angle is to the left of the zero mark on the degree scale.

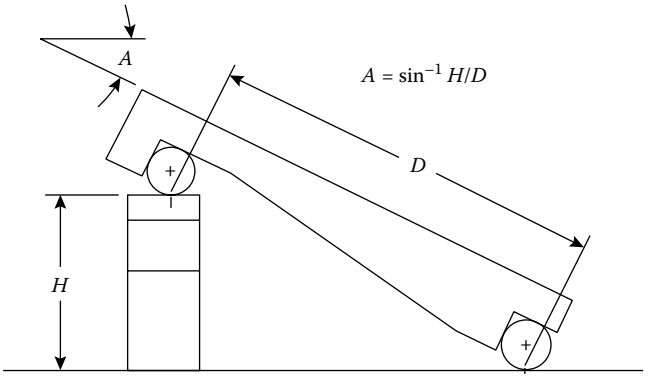

FIGURE 42.2 Sine bar. A sine bar is used in conjunction with precision gage blocks that are placed under one of the cylindrical rods, raising that end a distance, *H*, equal to the sine of the desired angle times the distance, *D*, between the two rods.

A sine bar is used in conjunction with precision gage blocks that are placed under one of the two cylindrical rods to raise that rod above the other rod a distance *H* (see Figure 42.2) equal to the sine of the angle desired, times the distance *D* between the two rods. The standard distance between the rods is 250 mm (5 in.) or 500 mm (10 in.). The governing equation in using a sine bar is $\sin A = H/D$.

A work piece positioned using a sine bar is usually secured with the use of a precision vice. The vice may clamp directly to the work piece or, when using a sine bar that has tapped holes on its top surface, to the sine bar sides with the work piece bolted to the top of the sine bar.

42.6 Sine Plate

A variation of the sine bar is the *sine plate*. A sine plate consists of the three elements of a sine bar plus a bottom plate and side straps used to lock the plate in the desired position. In addition, one of the ground steel rods is arranged to form a hinge between the top and bottom plates. When using a sine plate, a work piece is secured to the top plate using bolts or clamps, and the bottom plate is secured to a machine tool table using clamps or a magnetic chuck.

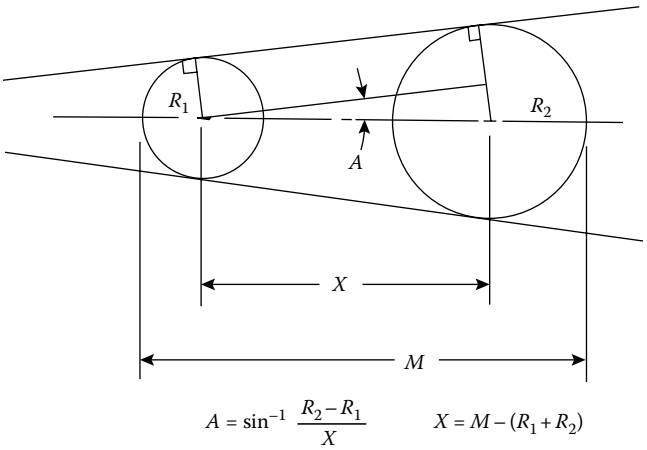

FIGURE 42.3 Measuring tapers. Two balls (for holes) or gage pins (for slots) should be selected to fit the hole size to be measured. The distance between the balls or pins should be as large as possible to allow for the best accuracy of measurement. The position of the balls can be determined and the equations shown in this figure applied to be determined the angle of the taper.

Compound sine plates are bidirectional, allowing angles to be measured and set in each of two orthogonal planes (true compound angles).

42.7 Taper

An accurate method that can be used to measure a tapered hole is described in Figure 42.3. In this method, one uses a pair of steel balls of proper diameters to match the hole size and angle of taper. This method can also be used to measure the angle between two adjacent planes, using either balls or gage pins.

Further Information

Further information on this subject can be found in company catalogs in both print and Internet formats. An additional reference is *Machinery's Handbook*, 25th edn., Industrial Press Inc., 200 Madison Avenue, New York, 10016–4078, 1996.

43

Mass, Weights, and Instrumentation

Emil Hazarian
California State University

43.1 Introduction

The determination of mass is one of the oldest and most engaged activities of the mankind. Ancient primitive forms of trade as well as today's complex global trade exchanges are employing mass measurements to a high extent. Nevertheless, the physical notion of mass is still not completely clear when considering its triple use in atomic models (microstructures), regular size objects and astronomic models (macrostructures).

Weighing technology today permits detection of differences between 1 kg weights, smaller than 1 μg (microgram) with an uncertainty of 10^{-16} kg.

The unit of mass is materialized in weights. The instruments used to determine the mass are called scales, balances, and mass comparators.

43.2 Etymology

The word *mass* comes from the Latin word *massa* meaning bulge of shapeless material that in turn comes from the Greek *massein* or *maza*. Other older and different meanings may be assumed including the religious meanings of the word; also new meanings are used today such as mass media or mass production.

43.3 Definitions of Terms

Measurement accuracy (accuracy of measurement, accuracy): Closeness of agreement between a measured quantity value and a true quantity value of a measurand [4].

Apparent mass: See conventional mass.

Balance: A measuring device designed to evaluate the mass of the objects; in everyday vocabulary, a balance is used to determine the weight of an object. A balance is usually of higher precision.

Buoyancy: A force that acts on any body located in a liquid or gas by operating in a direction opposed to the force of gravity and thus causes an apparent reduction of weight. According to the Archimedean principle, the buoyancy of a body is equal to the weight force of the amount of gas or liquid displaced.

Air buoyancy varies in the United States from 0.98 mg/cm^3 to 1.21 g/cm^3; air is less dense at higher altitude.

Calibration: The set of operations that establish, under specified conditions, the relationship between values indicated by measuring instrument or measuring system, or values represented by a material measure, and the corresponding known value of measurand. Sometimes implies the adjustment of the measurand.

Conventional mass: Sometimes called mass in air, or apparent mass; this is the value of the mass required to balance the object in conventionally chosen conditions of air density of 1.2 kg/m^3, temperature of 20 °C, and atmospheric pressure of 760 mmHg [7].

If the mass required to balance the object is made out of brass with a conventional density of 8390.94 kg/m^3 at 20 °C, we obtain the conventional mass (or apparent mass) versus brass of that object.

If the mass required to balance the object is made out of stainless steel with a conventional density of 8000 kg/m^3 at 20 °C, we obtain the conventional mass (or apparent mass) versus stainless steel of that object.

(See also true mass)

Correction: The value that added algebraically to the uncorrected results of a measurement compensates for an assumed systematic error. **Note**: The correction is equal to the assumed systematic error but has opposite sign.

Drift: The slow variation with time of a metrological characteristic of a measuring instrument. In the case of a balance or scale, it is the change of the indications while the load remains constant.

Mass: The state scalar physical quantity expressing both the inertial property of the matter and the property of the matter to generate a field of attraction forces (gravitational field). This is also called true mass or mass in vacuum.

Numerically the mass is expressed as the ratio between a force and a material object and its resulting acceleration.

Mass comparator: A weighing device used only as an intermediary between weights with a known value (standards) and weights with unknown value with the purpose of determining the unknown value. **Note**: any scale or balance may be used as a mass comparator.

Scale division: The part of a scale between any two successive scale marks.

Scale interval: The difference between the scale values corresponding to two successive scale marks.

Scale spacing: The distance between any two successive scale marks measured along the same line as the scale length (expressed in units of length).

Sensitivity: The change in the response of a measuring instrument divided by the corresponding change in the stimulus.

Tolerance: The maximum permissible variation or limits allowed a quantity or parameter from a specified value.

True mass: The mass of an object determined in vacuum. The true mass of an object can be calculated from the conventional mass, by applying the buoyancy correction. True mass value is usually determined for special applications such as in nuclear field and biotechnology; it implies weights of ASTM class 1.

True value (*of a quantity*): The value that characterizes a quantity perfectly defined, in the conditions that exist when the quantity is considered. **Note**: The true value is an ideal concept and in general cannot be known exactly.

Uncertainty of measurement: An estimate characterizing the range of values within which the true value of a measurand lies. **Note**: Uncertainty of measurement comprises, in general, many components; some of these components may be estimated on the basis of the statistical distribution of the results of series of measurements and can be characterized by experimental standard deviations; estimates of other components can only be based on scientific judgment, experience, or other information.

Universality (replaceability): The quality of a measuring instrument (e.g., scale) is replaceable by another measuring instrument having the same characteristics.

43.4 Theory

Mass is one of the base quantities in classical mechanics. The concept of mass constitutes a universal characteristic of bodies. As a physical quantity, the mass could be determined in relationship with other physical quantities. Such relationships are given by Newton's second law of motion and the law of universal gravitation.

The mathematical expression of Newton's second law of motion is

$$\Sigma F = ma \tag{43.1}$$

where

ΣF is the summation of all the external forces applied to the particle
a is the acceleration of the particle
m is the mass of the particle

From the preceding equation we can write

$$m = \frac{F}{a} \tag{43.2}$$

The mass is numerically determined by the ratio between force and acceleration.

Newton's law of gravitation, published in 1686, may be stated: Every particle of matter in the universe attracts every other particle with a force that is directly proportional to the product of

the masses of the particles and inversely proportional to the square of the distance between them. Or in a mathematical form

$$F = k\frac{m_1 m_2}{r^2} \tag{43.3}$$

where

F is the attraction force between the two bodies m_1 and m_2
m_1, m_2 is the masses of the two bodies
r is the distance between the centers of the two bodies
k is the gravitational constant ($k = 6.670 \times 10^{-11}$ N m^2 kg^{-2})

An immediate application of the universal attraction to be observed on earth is the weight of the bodies. The force with which an object is attracted to the earth is called its weight. Weight is different from mass, which is a measure of the inertia an object displays. Although they are different physical quantities, mass and weight are closely related.

The weight of an object is the force that causes it to be accelerated when it is dropped. All objects in free fall near the earth surface have a downward acceleration of g, the acceleration of gravity. The value of g varies in different locations of the earth surface, due to the distance to the center of the earth. One value used in common calculations is 9.8 ms^{-2}. If the object's mass is m, then the downward force on it, which is the weight w, can be found from the second law of motion, where $F = W$ and $a = g$.

Evidently we have

$$W = mg \tag{43.4}$$

The weight of any object is equal to its mass multiplied by the acceleration of gravity. Since, for practical purposes, g is a constant near the earth's surface, the weight w of an object is always directly proportional to its mass m: a large mass is heavier than a small one. For more accurate applications, the determination of the gravitational acceleration at the very location of the experiment is required.

The mass of an object is a more fundamental property than its weight, because its mass when at rest is constant and is the same everywhere in the universe whereas the gravitational force on it depends upon its position relative to the earth or to some other astronomical body (at the earth's poles $g = 9.831$ ms^{-2}, which is the maximum value, and at the equator $g = 9.781$ ms^{-2}, which is the minimum value).

Mass remains a constant quantity only in classical mechanics. The modern physics, particularly the theory of relativity, shows that the mass of a body increases with the increase of its velocity. The variation of mass with velocity follows the formula:

$$m = \frac{m_0}{\sqrt{1-(v^2/c^2)}} \tag{43.5}$$

The symbols have the following meanings:

m_0 is the mass measured when object is at rest ("rest mass")
m is the mass measured when the object is in relative motion
v is the velocity of relative motion
c is the velocity of light

Relativistic mass increases only at velocities approaching that of light. For velocities smaller than 10^6 m/s, the difference between m and m_0 is insignificant.

43.4.1 Quantities Derived From Mass

Here are some selected quantities derived from mass:

- Density
- Force
- Pressure
- Electric current
- Voltage
- Electric resistance

43.5 Test Instrumentation

43.5.1 Classification of Weighing Devices (Scales, Balances, and Mass Comparators)

Weighing devices are the measuring devices exclusively designed to determine the mass of an object.

The classification of weighing devices could be accomplished according to the following criteria [2]:

- The mass measuring technique
- The extent of operator participation in the weighing process
- Installation
- The method of obtaining the equilibrium position
- The type of the load-receiving element: pan, platform, bucket, rail, hook, conveyer belt, etc.

43.5.2 Mass Measuring Technique

According to this criterion, we have direct weighing devices and indirect weighing devices.

The devices determining directly the mass of an object are those devices employing levers in their construction. The mass is determined by the equality between the moments created by the measurand and the standard weight. This type of weighing devices is called *balances* if they have a single lever, with equal or unequal arms. If they employ multiple levers, they are called *scales* and are used for weighing voluminous and heavy objects (i.e., 50,000 lb).

The weighing devices determining indirectly the mass are based on one the following principles:

- Elastic element (flexure, torsion, compression, traction, etc.)
- Hydraulic element (variation of a liquid pressure)
- Electronic

43.5.2.1 Operator Participation in the Weighing Process

According to this criterion, we have manual, semiautomated, and automated weighing devices.

A manual weighing device is that type where the operator does all three main operations, loading, weighing, and unloading. Examples are equal arm balances, platform scales, and truck scales.

A semiautomated weighing device is loaded and unloaded manually, but the weighing operation is automated. The most common are those scales with dial indicator.

An automated weighing device has all three operations loading, weighing, and unloading completed without the operator intervention.

Examples are the belt conveyer scale and new generation of electronic balances.

43.5.2.2 Installation

According to this criterion, weighing devices are classified into

- Portable
- Stationary (stable)

43.5.2.3 Method of Obtaining the Equilibrium Position

Based on this criterion, we have two types of weighing devices:

- With constant equilibrium position (i.e., two indicators, one fix and one mobile, and two mobile indicators)
- With variable equilibrium position (i.e., the indicator moves in front of a graduated scale, semi-automated weighing devices)

43.5.3 Equal Arm Balance

The equal arm balance is frequently used for precision mass measurements or weighing. To visualize its operation, let us consider for a moment the beam of Figure 43.1, supported at its center by the fulcrum (A). If the system is to be in equilibrium, the sum of all the forces must equal zero.

If the weight of the beam and its load (w_1 and w_2) are considered as the force acting downward, they must be supported by an equal lifting force provided by the fulcrum (A). Thus, there is no rotation.

If the length of the beam on each side of the fulcrum is assumed equal, then

$$x_1 = x_2 \tag{43.6}$$

Furthermore, if the system is in equilibrium, then the torques (forces momentum) about point A must be equal; therefore,

$$w_1 x_1 = w_2 x_2 \tag{43.7}$$

Since the lengths of the arms are assumed equal, then at equilibrium,

$$w_1 = w_2 \tag{43.8}$$

If one of the weights is known (standard), value may be assigned to the other (unknown) weight. This is the basic operating principle of the equal arm balance. Even though the arms of the balance are not exactly equal, precision weighing procedures are available that account for any small inequality.

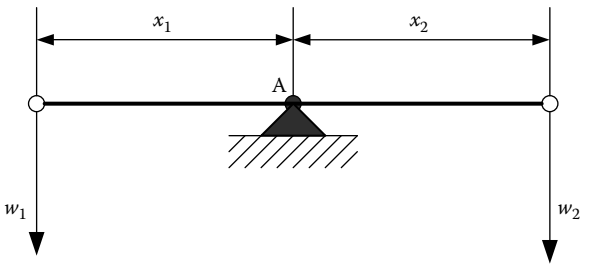

FIGURE 43.1 Beam in equilibrium state.

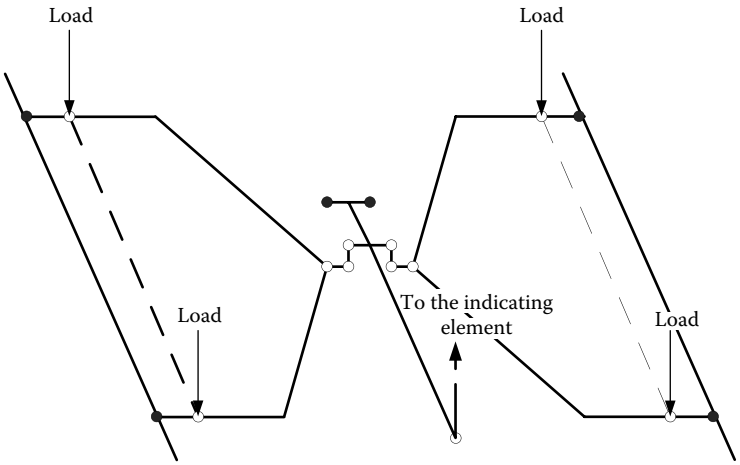

FIGURE 43.2 Typical platform scale lever system. (From Hazarian, E., Some characteristics of weighing devices, Technical paper at *Measurement Science Conference*, 1992, Anaheim, CA.)

43.5.4 Scales

Weighing devices employing multiple levers in their design are called scales. There are a large variety of scales, from which we choose to mention the following categories: platform scales, either portable or built on the floor; vehicle scales; and railroad scales.

The design of scales changed very much from levers and knife-edge joints to levers with flexure joints and lately levers with load cells or just loads cells [1, p. 54]. Nowadays, a scale has three general components: the load-receiving element, the load cell, and an indicating device. Large-capacity scales with load cell elements are achieving higher accuracy than traditional scales employing beams. A typical platform scale lever system is shown in Figure 43.2.

43.5.5 Balances and Mass Comparators

For over three thousand years, the design of balances did not change significantly, mainly because the requirements were unchanged. The last half of the twentieth century changed the situation, and new balances and mass comparators based on electromagnetic force compensation emerged to satisfy new technologies, such as computers, biotechnology and drug manufacturing, and sophisticated accurate weaponry.

43.5.5.1 Top-Loading and Analytical Balances [8, p. 6]

These balances have a single-pan or top-pan load-receiving element [10].

43.5.5.2 Electromagnetic Force Compensation Mass Comparators [10]

These weighing devices are called mass comparators as they perform a comparison between a known weight piece (standard weight) and an unknown weight piece (unknown) in order to determine the mass of the latter. Such devices are designated for high-accuracy mass determinations in the national and primary calibration laboratories.

These weighing devices employ flexure joints in their design, replacing the knife-edge joints. There are no moving parts making these devices practically maintenance-free. Although the electromagnetic force compensation principle was known well before, it is the last generation of mass comparators, created in the last decade, that achieved the accuracy of former equal arm balances combined with electro-optical systems. Another significant advantage of the new mass comparators is the possibility of computer interfacing. Using the computer to record data eliminates one of the writing sources of errors and gives the possibility of instantaneous statistical analysis of real-time data, so critical for making the right decisions.

43.6 Weighing Methods

Selecting the weighing method for your application depends on a series of factors such as

- Required level of accuracy and precision
- Available equipment
- Available trained operators
- Cost-effectiveness

Sometimes a "lower"-level procedure may be sufficient for a specific application, rather than a laborious state-of-the-art intercomparison. Having handy the entire palette of weighing methods will offer a better opportunity for selecting the most appropriate one.

43.6.1 Direct Reading on an Equal Arm Balance

Using an equal arm balance for simple weighing could be accomplished by loading one pan with the measurand (unit to be measured or unknown weight) and the other pan with the necessary weights, until the balance is brought in a normal equilibrium position. This is a lower-level weighing method, for applications that do not require special care with regard to accuracy. In this case, the *mass of the measurand is equal with the total mass of the added weights*.

Same method may proffer a higher accuracy and could be used in industrial laboratories in which case the balance equilibrium position is not approximated but rather determined by reading the balance indicator elongations and by calculation. Bringing the balance in the equilibrium position is a meticulous task, if not impossible. Moreover, it could be considered useless, as soon as we can determine the mass of the measurand even in an intermediate position, close to what is called the normal equilibrium position.

Let us consider the case of an equal arm balance (Figure 43.3) with its beam in horizontal position; therefore, the balance is in a normal equilibrium position (*a*). The second case is when mass Q is heavier than Q_1; therefore, the balance will stop in an inclined position (*b*). The equilibrium equations applied for both situations will give

$$Q_1 \times l = P \times l' \tag{43.9}$$

or

$$m_{Q_1} \times g \times l = m_P \times g \times l' \tag{43.10}$$

We also may write

$$Q \times l \cos\alpha = P \times l' \cos\alpha + G \times a \sin\alpha \tag{43.11}$$

$$m_Q \times g \times l \cos\alpha = m_P \times g \times l' \cos\alpha + m_g \times g \times a \sin\alpha \tag{43.12}$$

If we divide the two equations by g and $g\cos\alpha$, respectively, and consider

$$m_Q - m_{Q_1} = e$$

$$tg\alpha = \frac{d \times n}{l}$$

where

d is the one division on the graduated scale
n is the number of divisions the indicator moved due to the addition to mass m_Q not balanced by m_P
l is the length of the indicator

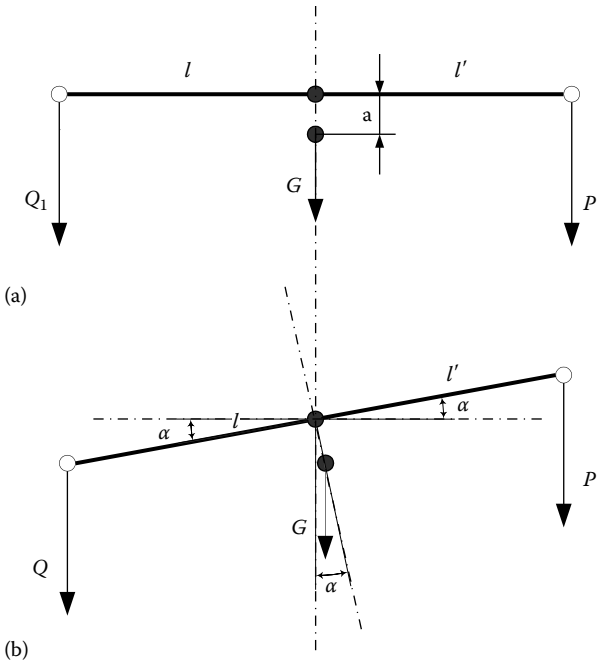

FIGURE 43.3 Direct reading on an equal arm balance: (a) Balance in equilibrium, (b) balance out of equilibrium.

we have

$$m_Q = m_P + S_P \times n \tag{43.13}$$

where

m_Q is the mass of the measurand (unknown)

m_P is the mass of the weights

n is the number of divisions (elongation) of the indicator

$$S_P = m_G \frac{a \times d}{l \times i}, \text{sensitivity}$$

From the preceding equation, we can state that the *mass of the measurand (m_Q) is equal to the algebraic sum of the mass of the weights (m_p) and the product between sensitivity (S_P) and the number of divisions (n), the indicator moved.*

Practically we determine n for every weighing, whereas S_P is determined once for several weighing.

In order to calculate n and S_P, we have to calculate first the equilibrium position L, for which we read the turning points e_i (i = 1, 2, 3) of the balance indicator:

$$L = \frac{e_1 + 2e_2 + e_3}{4} \tag{43.14}$$

The turning point readings (Figure 43.4) are all positive, if the zero graduation is placed at the left end of the graduated scale (unilateral scale). If the zero graduation is placed in the middle of the graduated scale (bilateral scale), the readings will be both positive and negative.

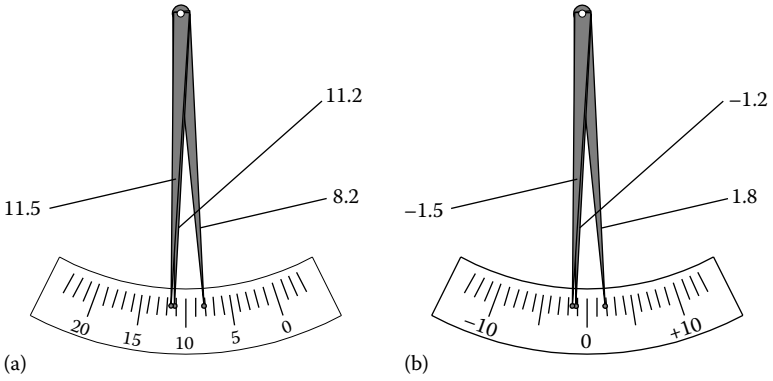

FIGURE 43.4 Example of turning point readings: (a) Unilateral scale, (b) bilateral scale.

Example

The following readings were made on a balance having unilateral scale, the most usual case:

e_1 = 11.5 div.
e_2 = 8.2 div.
e_3 = 11.2 div.

Therefore, $L = (11.5 + 2 \times 8.2 + 11.2)/4 = 9.78$ div.

If the same balance has a bilateral scale, the readings will be

e_1 = −1.5 div.
e_2 = +1.8 div.
e_3 = −1.2 div.

Thus,

$$L = \frac{[(-1.5) + 2(+1.8) + (-1.2)]}{4} = +0.22 \text{ div.}$$

Notice that the two values obtained, 9.78 div. and 0.22 div., are representing the same equilibrium position placed at 0.2 div. to the right of the middle graduation.

Direct reading on an equal arm balance is generally adequate at the industrial laboratories level, a lower level than standard laboratories; however, we still need to have confidence in our measurements. It also requires accuracy and traceability.

$$L = \frac{e_1 + 3e_2 + 3e_3 + e_4}{8} \tag{43.15}$$

43.6.2 Direct Reading on Single-Pan Optical-Mechanical and Electronic Balances

The value of the measurand, in our case the unknown mass, is determined by placing it on the pan of the balance, releasing the pan and read the value of the mass on the balance display. Certainly, we have to verify if the display shows "zero" when the balance is unloaded.

Single-pan optical-mechanical scales provide apparent mass value, depending on balance adjustment. Both single-pan optical-mechanical and electronic scales rely on internal weights of the balance. For that reason, the internal weights should be tested periodically. Also the optical scale should be tested for the same reason.

43.6.3 Substitution Method

The substitution method (Figure 43.5), known also as the Borda method, eliminates the systematic error induced in the weighing process by the unequal arms of the balance beam.

The substitution method consists in the following:

The measurand is placed on the left pan of the balance, while on the right pan, we place tare weights until the balance remains in the normal equilibrium position or close to this position. We replace then the measurand with known weights, adding them until obtaining the same equilibrium position as previously. The mass m_X of the measurand is equal with m_P, the mass of the known weights. In order to demonstrate this, we have to write the equality of the two moments of forces created in the two situations:

$$X\,l = T\,l'$$

$$P\,l = T'\,l$$

also

$$m_X l = m_T l'$$

$$m_P = m_T l'$$

resulting in

$$m_X = m_P \tag{43.16}$$

In practice, the balance may be in equilibrium in any intermediate position, the aforementioned particular case being chosen for convenience purpose only.

The substitution method is largely employed in most of the laboratories performing mass measurements.

1. Single substitution
   In the single substitution method the sequence is as follows:
   a. Standard, S, observation O1
   b. Unknown, X, observation O2
   c. Unknown plus sensitivity, X + sw, observation O3
2. Double substitution
   The measurement sequence in double substitution is as follows:
   a. Standard, S, observation O1
   b. Unknown, X, observation O2
   c. Unknown plus sensitivity, X + sw, observation O3
   d. Standard plus sensitivity, S + sw, observation O4

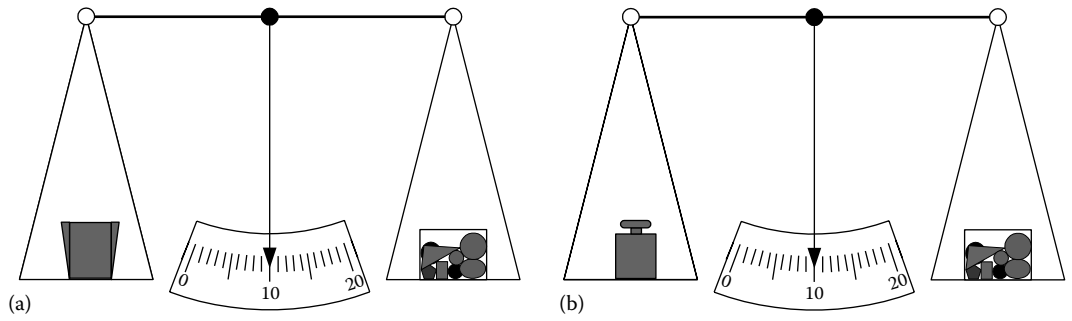

FIGURE 43.5 Substitution method: (a) With measurand, (b) with standard weights.

43.6.4 Transposition Method

The transposition method or Gauss method, after the German mathematician and astronomer Carl Friedrich Gauss (1777–1855), consists of the following:

- The measurand is placed on the left pan of the balance, while on the right pan, we place known weights (standard) until the balance remains in the normal equilibrium position or close to this position (observation O1).
- We permute the measurand and the standard, adding known weights (standards) to the left pan, while the measurand is placed on the right pan (observation O2).
- A sensitivity weight is added to the left pan (observation O3).

43.7 Calibration Standards

Calibration standards for mass measures, called (improperly) weights, represent in the International System of Units (SI), the materialization of the mass unit, the kilogram, its decimal multiples and submultiples, and also their half and double values. The pound unit, in the pound–inch system, derives its value from the kilogram, since there is no international pound mass standard.

Both the SI and pound–inch systems are using the following denominations for weights: 5321, 5221, and 52111. Denominations of weights are selected in order to cover the most possible nominal values with a minimum number of weights. This is particularly important when someone needs to calibrate customary weights using metric standards; in this case because of the conversion factors, the equivalent number of weights composing the standard is larger than initially designed; therefore, the uncertainty of the calibration will be larger versus a one-to-one calibration.

There are three major classifications of weights in use in the United States concentrated in documents generated by three organizations:

1. National Institute of Standards and Technology (NIST), formerly National Bureau of Standards, with the following documents:
   a. Circular 547, Section 1, 1954
      "Precision Laboratory Standards of Mass and Laboratory Weights"
      Note: This classification was withdrawn.
   b. Circular 3, 1918
      "Design and Test of Standard of Mass"
      Note: This classification was withdrawn.
   c. NIST Handbook 105-1, Revised 1990
      "Specifications and Tolerances for Reference Standards and Field Standards Weights and Measures"
   d. Specifications and Tolerances for Filed Standards Weights (NIST Class F),
      Note: The NIST, Weights and Measures Division currently use this classification, for the States Laboratory Program, in Legal Metrology.
2. American Society for Testing Materials, with the following document.
   ASTM E617-97(2008) "Standard Specification for Laboratory Weights and Precision Mass Standards"
3. International Organization for Legal Metrology
   a. OIML R111: 2004
      "Weights of classes E1, E2, F1, F2, M1, M2, M3"

43.7.1 Materials

The following materials are mostly used in the manufacturing of weights:

- Platinum–Iridium (90% Pt, 10% Ir) used for manufacturing the international prototype and national standards. Density: 21.5 g/cm^3
- Stainless steel, density 8.0 g/cm^3
- Tantalum, density 16.0 g/cm^3
- Aluminum, density 2.7 g/cm^3
- Brass, density 8.4 g/cm^3
- Cast iron, density 7.8 g/cm^3

43.7.2 Design

Weights design varies with the nominal value and application. Small weights, from 1 to 500 mg, are leaf shaped with a vertical lip to accommodate handling using fine-tip nonmetallic tweezers.

Fractional pounds (i.e., 0.005 lb) may be shaped as a dish.

Larger weights, up to 50 kg and 100 lb, are usually of cylindrical or rectangular shape with or without adjusting cavity. The adjusting cavity is sealed either with a threaded screw and aluminum seal or a threaded knob.

43.7.3 Maximum Permissible Error

Each weight within a class is assigned a maximum permissible error (MPE) (or tolerance). Unless it is specified otherwise, the maximum permissible error is assigned both plus and minus sign.

Example: ASTM class 6, 1 kg weight has 6 100 mg MPE, meaning the weight value may be anywhere between 1 kg – 100 mg and 1 kg + 100 mg values.

43.7.4 Handling, Storage, Packing, and Shipping

- Weights of ASTM classes 5 or smaller should not be handled with bare hands, due to possible contamination that will change the mass. There are special nonmetallic, nonmagnetic tweezers to handle small and big weights up cca. 100 g. Special lifters are used for bigger weights with cushion material at the point of contact. Chains with soft material sleeves or high-density nylon belts are used for lifting large weights.
- Weights are usually offered as a set. Precision weights are provided in cases made of wood or plastic material with seats for each weight. All weights need to be stored in places free of dust or any other contamination with temperature and humidity not to exceed the prescribed limits. In general, a temperature of 20 °C (68 °F) is considered acceptable for storage.
- Weights of small denomination are packed in their cases in such a way that they are not loosened and lost in transportation. Precision weights are wrapped individually with dry, wax-free paper and placed in their case seats. Cases are wrapped individually with one inch thick foam or other similar wrapping material and placed in cardboard boxes. Weights up to 10 kg or 25 lb are wrapped individually and should not touch each other. Large weights are packed in specially made wooden boxes with 1 in. thick cushion material inside.
- It is preferable that precision weights are hand carried. In general, boxes containing weights should be treated similar with fragile materials and sensitive equipment, for transportation.

43.8 Range and Accuracy

All measuring devices, including weighing devices, have to meet certain requirements and specifications. These requirements are built in what are commonly known as technical characteristics such as range, stability, inertia, replaceability, and metrological characteristics such as accuracy, repeatability, reproducibility, sensitivity, and traceability.

43.8.1 Range

Mass measures or weights have each a nominal value. Usually the weights are presented in sets. The range of a weight set is the difference between the largest and smallest weights in the set.

Example: A set of 21 weights from 1 mg to 100 g has a range of

$$100\ \text{g} - 1\ \text{mg} = 100\ \text{g} - 0.001\ \text{g} = 99.999\ \text{g}$$

Weight value may vary from

- 1 mg (milligram) to 5000 kg (kilogram)
- 0.00001–10,000 lb and 0.0001–12 oz

Scales range is defined as the difference between the highest and smallest indicated mass values on the scale display.

Example: A floor scale with digital indicator has the value of division (smallest indication) of 1 lb and the highest 1000 lb. The scale range will be

$$1000 - 1\ \text{lb} = 999\ \text{lb}$$

Scales ranges may vary from few grams to 50,000 kg or up to 100,000 lb or higher.

43.8.2 Stability

For weights, stability is defined as the capability of the weight piece to retain its mass value unchanged for a longer period of time.

Note: The considered mass value has an uncertainty associated with it. As long as the mass value and its uncertainty are still in statistical control, the weight piece may be considered stable.

For a weighing device, stability is defined as the device capability to restore its equilibrium state. If we consider an unloaded equal arm balance and we initiate an oscillation, the balance beam will oscillate until the state of stable equilibrium is restored. In the case of an electronic scale, the damping process and equilibrium restoration are very fast, almost instantaneous.

43.8.3 Inertia

The inertia describes how the weighing devices are responding to different variations occurring during their operation. It is quantifying the reaction time between changing the mass on the receiving element and the indication on the reading element.

43.8.4 Replaceability

Replaceability applies to both weights and weighing devices; it is the technical characteristic that permits replacing a weight or a weighing device with an identical weight or weighing device, for similar measurements.

43.8.5 Accuracy (Also Trueness or Justness)

The accuracy or justness of a weight is the closeness between the weight calibrated value and the nominal value indicated on the weight.

Accuracy of a scale—the capability of a scale to indicate values closer to the corrected value of a mass (weight) placed on the scale-receiving element. Sometimes, instead of the corrected value, the nominal value of the mass (weight) may be considered. The closer the scale indication, the more accurate it is.

43.8.6 Linearity of a Scale

A balance design and manufacturing target is to obtain a direct proportional relation, graphically represented by a straight line, between the load and the scale reading. That is, if we represent graphically the different readings on scale when we apply increasing different masses (weights), we should obtain a straight line for a perfect linear scale. Again we may consider either the corrected masses (weights) or their nominal values.

Discussion: A scale must be accurate to the same degree in every point of its range, in order to obtain a valid representation of its linearity. If the balance is not accurate in a particular point, the graphic will show a deviation from the straight line. In that point, we have a nonlinearity caused by inaccuracy.

43.8.7 Sensitivity of a Scale

The magnitude of the variation of the scale reading is caused by the variation in the scale load. The smaller the load that creates a perceptible variation of the scale reading, the more sensitive the scale is considered.

The sensitivity of a scale may have different magnitudes at different levels of load.

Here is a discussion of the three parameters: accuracy, linearity, and sensitivity.

Scale is accurate, linear, and sensitive: Good. This is a scale showing values close to the masses' (weights') values we put on, is doing that along the entire range, and is very receptive when we add a small mass (weight) anywhere in the range, that is. It detects better the imperfections (errors) of the masses placed on it.

Scale is not accurate, but is linear and sensitive: Not possible. Inaccuracy generates nonlinearity regardless if the scale is sensitive.

Scale is not accurate, not linear but sensitive: Not good. Who needs a scale not reading close to the value of mass (weight) we put on it, doesn't do that along the entire range, but shows changes in readings when we add a small mass (weight) to the load anywhere in the scale range.

Scale is not accurate, not linear, and not sensitive: Not good.

Scale is accurate, not linear, and sensitive: Not good. It may have segments of linearity along its range, but we don't know where, and it is less probable we would know the law of variation.

Scale is accurate, not linear, and not sensitive: Not good and worst than the aforementioned.

Scale is accurate, linear, but not sensitive: Partially good, for the scale is showing values close to the mass values we put on and is doing that along the entire range, but is not receptive when we add a small mass anywhere in the range, that is, is not detecting the imperfections (errors) of the masses placed on it.

An example will be shipping scales were tolerances are large.

Discussion of the two concepts

- Scale is both accurate and linear: good
- Scale is not accurate but it is linear: not possible
- Scale is accurate, but is not linear: not good (possibly good if we can find the law of variation)
- Scale is not accurate and is not linear: not good, buy a new scale

Measurement repeatability: The measurement precision under a set of repeatability conditions of measurement. VIM 2.21 (3.6)

It is the closeness in the agreement of the results of successive weighing of the same weights that carried out subject to all of the following conditions:

- The same method of weighing
- The same observer
- The same weighing device
- The same location
- The same condition of use
- Repetition over a short period of time

Note:

1. Repeatability may be expressed quantitatively in terms of the dispersion of the results. *Measurement reproducibility*: The measurement precision under reproducibility conditions of measurement. VIM 2.25 (3.7)

Reproducibility is the closeness of the agreement between the results of weighing of the same weights, where individual measurements are carried out changing conditions such as

- Method of weighing
- Observer
- Weighing device
- Location
- Condition of use
- Time

Notes:

- A valid statement of reproducibility requires specification of the conditions changed.
- Repeatability may be expressed quantitatively in terms of the dispersion of the results.

43.8.8 Mass Traceability

Metrological traceability: The property of a measurement result whereby the result can be related to a reference through a documented unbroken chain of calibrations each contributing to the measurement uncertainty. VIM 2.41 (6.10)

Mass traceability—the property of a result of a mass measurement whereby it can be related to appropriate standard weights, generally international or national standards, through an unbroken chain of comparisons each contributing to the measurement uncertainty.

43.8.9 Safety Precautions in Mass Measurement

Safety measures and precautions in mass measurement are related to the following activities:

- Usage of cleaning solvents such as ethylic alcohol and acetone. These substances will be monitored and kept under control. Personnel using these substances need to have appropriate training for storage, usage, disposal, and first aid in case of an accident.
- Usage of paint removal substances, paint thinner, and paint. Wearing adequate protective equipment including mask respirators is mandatory.
- Manipulating metal such as lead and brass. Wearing gloves to avoid direct contact with metallic surface and metallic oxides.
- Manipulating weights to prevent dropping them.
- Manipulating large and very large weights up to 2500 kg and 5000 lb using electrical or compressed air–powered lifting devices (i.e., hoist, forklift) needs to be done by authorized personnel only, wearing adequate protective equipment including hard shoes.

43.9 Units of Measurement

The metric unit of mass is the kilogram. Mass is one of the seven independent base quantities of the International System and is the only base quantity having its measuring unit, the kilogram, defined as an artifact and not based on a natural or physical law.

In the customary (British) system, the unit of mass is the *slug* and the unit of force is the *pound* (lb).

Note: The abbreviation "lb" for pound arrives from the Latin *libra*, which was used in the ancient Roman Empire for balance, scale, or pound.

A body with a mass of 1 slug experiences an acceleration of 1 ft/s^2 when a force of 1 lb works on it. Accordingly, 1 lb = 1 slug · ft/s^2.

The slug is not a familiar unit because in the everyday life, weights rather than masses are specified in the customary system. We are asking for 8 lb of oranges, not for 1/4 slug of oranges.

In the metric system, we normally indicate masses in kilograms not in newtons. To avoid the general misconception, the following stipulations should be taken into consideration:

1. In the metric system
   a. The unit for mass is called kilogram.
   b. The unit for force is called newton.
2. In the pound–inch system
   a. The unit for mass is called slug.
   b. The unit for force is called pound.

Customary and erroneously, when pound–inch system is employed, people are using the unit pound to designate the mass of an object.

Customary and erroneously, the term weight is used to designate the mass of an object (i.e., we say "the weight of the watermelon was…" or "the person's weight is…").

43.9.1 Definition: The Unit of Mass (Kilogram)

The first CGPM (1889) sanctioned the international prototype of the kilogram and declared: this prototype shall henceforth be considered to be the unit of mass.

The third CGPM (1901), in a declaration intended to end the ambiguity that existed as to the meaning of the word "weight" in popular usage, confirmed that the kilogram is the unit of mass; it is equal to the mass of the international prototype of the kilogram.

This international prototype is kept at the International Bureau of Weights and Measures (BIPM) at the Pavillon de Breteuil, Sevres, near Paris. It is made of platinum–iridium alloy.

The same conference adopted the conventional value for the standard acceleration due to gravity that is g_n = 9.806 65 m/s^2.

The United States is in possession of two national prototype kilograms identified as K20 and K4, made of the same alloy of 90% platinum and 10% iridium, as the international prototype. Also the international prototypes as well as the national prototypes are right circular cylinders having the height equal to the diameter and equal to 39 mm (1.535 ft). The material density is 21.5 g/cm^3.

The national prototype kilograms are kept at NIST, located in Gaithersburg, Maryland, near Washington DC.

43.9.2 Conversion Factors

The terms avoirdupois, apothecary, and troy describe units of mass within customary system. The avoirdupois units are extensively used in commerce and trade in the United States.

The following are some conversion factors [6]. Bold face figures are exact.

1 pound avoirdupois (lb avdp) = 0.453 592 37 kilograms (kg)
= 7 000 grains
= 1.215 troy or apothecary pounds

1 ounce avoirdupois (oz avdp) = 28.350 grams (g)
= 437.5 grains
= 0.911 troy or apothecaries ounces

1 pound troy or apothecary (lb t or lb ape) = 373.242 grams (g)
= 5 760 grains
= 0.823 avoirdupois pound

1 ounce troy or apothecaries (oz t or oz ap) = 31.103 grams (g)
= 480 grains
= 1.097 avoirdupois ounces

1 kilogram (kg) = 2.205 pounds

1 carat (c) = 200 milligrams (mg)
= 3.086 grains

1 gram (g) = 0.035 avoirdupois ounce
= 15.432 grains

1 grain = 64.798 91 milligrams (mg)

1 metric ton (t) = 2 204.623 pounds
= 1.102 net tons

1 ton (net or short) = 2000 pounds
= 0.907 metric ton

1 slug = 14.6 kilograms (kg)

References

1. Bucher, J., *The Metrology Handbook*, 2004, ASQ Quality Press, Milwaukee, WI.
2. Hazarian, E., *Techniques of Mass Measurement Workbook*, 1994, Los Angeles, CA.
3. Hazarian, E., Some characteristics of weighing devices, Technical paper at *Measurement Science Conference*, 1992, Anaheim, CA.
4. International Bureau of Weights and Measures, Joint Committee for Guides in Metrology (JCGM) 200:2012, *International Vocabulary of Metrology—Basic and General Concepts and Associated Terms* (VIM), 3rd edition, 2008 version with minor corrections.
5. Jones, F. E., Schoonover, R. M., *Handbook of Mass Measurement*, 2002, CRC Press, Washington, DC.
6. Kochsiek, M., Gläser, M. (eds.), *Comprehensive Mass Metrology*, 2000, Wiley-VCH, Berlin, Germany.
7. Mettler, T., *Glossary of Weighing Terms, A Practical Guide to the Terminology of Weighing*, With the assistance of Prof. Dr. M. Kochsiek, Physikalisch-Technische Bundesanstalt, PTB, English Translation by J. Penton, Zurich, 1997, Berlin, Germany.
8. NBS Metric Information, Letter Circular LC 1071, Factors for High-Precision Conversion, 1976, Gaithersburg, MD.
9. Hazarian, E., Mass measurement techniques IV: Scales uncertainty, *Measurement Science Conference*, Tutorial, 2002, Anaheim, CA.
10. Hazarian, E., *Elements of Measurement Techniques*, California State University Dominguez Hills, MSQA Program, QAS 516 Measurement and Testing Techniques, Supplement, 2000.

44

Torque and Power Measurement

Ivan J. Garshelis
Magnova, Inc.

Torque, speed, and power are the defining parameters of rotating machinery. The ability to accurately measure these quantities is essential for determining a machine's efficiency and to establish operating regimes that are safe and conducive to long and reliable service. On-line measurements of these quantities enable real-time control, help to ensure consistency in product quality, and can provide early indications of impending problems. Torque and power measurements are used in testing new designs of engines, motors, pumps, and other rotating machines and in the development of new machine components. Torque measurements are used routinely for controlling and verifying the tightness of threaded fasteners. Starting from basic concepts, this chapter describes the various methods and devices currently employed for the measurement of torque and power; the measurement of speed, or more precisely, angular velocity, is discussed elsewhere in this handbook [1].

44.1 Fundamental Concepts

44.1.1 Angular Displacement, Velocity, and Acceleration

The concept of *rotational* motion is readily formalized: All points within a rotating rigid body move in parallel or coincident planes while remaining at fixed distances from a line called the *axis*. In a perfectly rigid body, all points also remain at fixed distances from each other. Rotation is perceived as a change in the angular position of a reference point on the body, that is, as its *angular displacement*, $\Delta\theta$, over some time interval, Δt. The motion of that point, and therefore of the whole body, is characterized by its

clockwise (CW) or counterclockwise (CCW) *direction* and by its *angular velocity*, $\omega = \Delta\theta/\Delta t$. If during a time interval Δt, the velocity changes by $\Delta\omega$, the body is undergoing an *angular acceleration*, $\alpha = \Delta\omega/\Delta t$. With angles measured in radians and time in seconds, units of ω become radians per second (rad/s) and of α, radians per second per second (rad/s^2). Angular velocity is often referred to as *rotational speed* and measured in numbers of complete revolutions per minute (rpm) or revolutions per second (rps).

44.1.2 Force, Torque, and Equilibrium

Rotational motion, as with motion in general, is controlled by *forces* in accordance with Newton's laws. Since a force directly affects only that component of motion in its line of action, forces or components of forces acting in any plane that includes the axis produce no tendency for rotation about that axis. Rotation can be initiated, altered in velocity, or terminated only by a *tangential force* F_t acting at a finite radial distance l from the axis. The effectiveness of such forces increases with both F_t and l; hence, their product, called a "moment," is the activating quantity for rotational motion. A moment about the rotational axis constitutes a *torque*. Figure 44.1a shows a force F acting at an angle β to the tangent at a point P, distant l (called the "moment arm") from the axis. The torque T is found from the *tangential component* of F as

$$T = F_t l = (F\cos\beta)l. \tag{44.1}$$

The combined effect, known as the *resultant*, of any number of torques acting on a body is found from their *algebraic* sum, wherein opposite signs are assigned to torques tending to cause rotation in CW and CCW directions. Forces, hence torques, arise from physical contact with other solid bodies or motional interaction with fluids or via gravitational (including inertial), electric, or magnetic force fields. The *source* of each such torque is subjected to an equal, but oppositely directed, *reaction* torque. With force measured in newtons and distance in meters, Equation 44.1 shows the unit of torque to be a "newton meter" (Nm, sometimes N·m).

A nonzero resultant torque will cause the body to undergo a proportional angular acceleration, found, by application of Newton's second law, from

$$T_r = I\alpha, \tag{44.2}$$

where I, having units of kilogram meter^2 (kg m^2), is the moment of inertia of the body around the axis (i.e., its *polar* moment of inertia). Equation 44.2 is applicable to anybody regardless of its state of motion. When $\alpha = 0$, Equation 44.2 shows that T_r is also zero; the body is said to be in *equilibrium*. For a body to be in equilibrium, there must be either more than one *applied* torque or none at all.

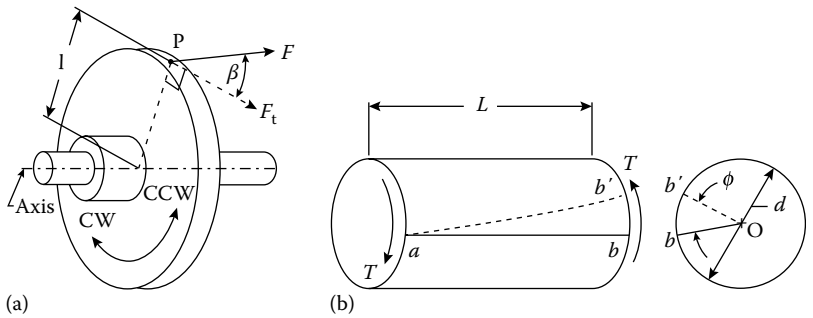

FIGURE 44.1 (a) Off-axis force F at P produces a torque $T = (F\cos\beta)l$ tending to rotate the body in the CW direction. (b) Transmitting torque T over length L twists the shaft through angle ϕ.

44.1.3 Stress, Rigidity, and Strain

Any portion of a rigid body in equilibrium is also in equilibrium; hence, as a condition for equilibrium of the portion, any torques applied thereto from *external* sources must be balanced by equal and directionally opposite *internal* torques from adjoining portions of the body. Torque is *transmitted* internally between adjoining portions by the collective action of *stresses* over their common cross sections. In a solid homogeneous body having a round cross section, for example, a typical shaft, and within a material-dependent upper limit, the *shear stress* τ varies linearly from zero at the axis to a maximum value, τ_m, at the surface. For a shaft of diameter d, transmitting a torque T, τ_m, is found from

$$\tau_m = \frac{16T}{\pi d^3}. \tag{44.3}$$

Real materials are not *perfectly* rigid but have instead a *modulus of rigidity*, G, which expresses the finite ratio between τ and *shear strain*, γ. The maximum strain therefore also exists at the shaft surface and can be found from

$$\gamma_m = \frac{\tau_m}{G} = \frac{16T}{\pi d^3 G}. \tag{44.4}$$

Figure 44.1b shows the manifestation of shear strain as an angular displacement between axially separated cross sections. Over the length L, the solid round shaft shown will be *twisted* by the torque through an angle φ (for small angles, $\varphi = \tan\varphi$) found from

$$\phi = \frac{2L\gamma_m}{d} = \frac{32LT}{\pi d^4 G}. \tag{44.5}$$

44.1.4 Work, Energy, and Power

If during the time of application of a torque T, the body rotates through some angle, θ, mechanical work

$$W = T\theta \tag{44.6}$$

is performed. If the torque acts in the same CW or CCW sense as the displacement, the work is said to be done *on* the body; else, it is done by the body. If the work being done on the body exceeds that being done by the body, the body accelerates; the net work appears as an increase in *kinetic energy* (KE = $I\omega^2/2$). The net work done by the body causes deceleration, with a corresponding decrease in kinetic energy. If the body is not accelerating, any work done on it at one location must be done by it at another location. Work and energy are each measured in units called a joule (J). Equation 44.6 shows that 1 J is equivalent to 1 Nm rad, which is, since a radian is a dimensionless ratio, ≡ 1 Nm. To avoid confusion with torque, it is preferable to quantify mechanical work in units of mN or, better still, in J.

The *rate* at which work is performed is termed *power*, P. If a torque T acts over a small interval of time Δt, during which there is an angular displacement $\Delta\theta$, work equal to $T\Delta\theta$ is performed at the rate $T\Delta\theta/\Delta t$. Replacing $\Delta\theta/\Delta t$ by ω, power is found simply as

$$P = T\omega. \tag{44.7}$$

The unit of power follows from its definition and is given the special name watt (W). 1 W = 1 J/s = 1 m · N/s. Historically, power has also been measured in horsepower (Hp), where 1 Hp = 746 W. Rotating bodies effectively transmit power between locations where torques from external sources are applied.

44.2 Arrangement of Apparatus for Torque and Power Measurement

Equations 44.1 through 44.7 express the physical bases for torque and power measurement. Figure 44.2 illustrates a generalized measurement arrangement, the actual apparatus being selected to fulfill specific measurement purposes. In general, a driving torque originating within a device at one location (B in Figure 44.2) is resisted by an opposing torque developed by a different device at another location (F). The driving torque (from, e.g., an electric motor, a gasoline engine, a steam turbine, a muscular effort) is coupled through connecting members C, transmitting region D, and additional couplings E, to the driven device (an electric generator, a pump, a machine tool, a mated threaded fastener, etc.) within which the resisting torque is met at F. The torque at B or F is the quantity to be measured. They may be *indirectly* determined from a correlated physical quantity, for example, an electric current or fluid pressure associated with the operation of the driving or driven device, or more directly determined by measuring either the *reaction* torque at A or G or the torque *transmitted* through D.

To the extent that the frames of the driving and driven devices and their mountings to the "earth" are *perfectly* rigid, the reaction at A will *at every instant* equal the torque at B, as will the reaction at G equal the torque at F. Under equilibrium conditions, these equalities are independent of the compliance of any member. Also under equilibrium conditions, and except for usually minor *parasitic* torques (due, e.g., to bearing friction and air drag over rapidly moving surfaces), the driving torque at B will equal the resisting torque at F.

Torque is often determined from measurements of reaction forces at dimensionally known locations, for example, mounting feet at A or G, using Equation 44.1. Transmitted torque is determined from measurements, on a suitable member within region D, of τ_m, γ_m, or φ and applying Equations 44.3 through 44.5 (or analogous expressions for members having other than solid round cross sections [2]). *Calibration*, that is, measurement of the stress, strain, or twist angle resulting from the application of *known* torques (within the range of interest), makes knowledge of details about the member within D unnecessary. When $\alpha \neq 0$, and is measurable with suitable accuracy, T may be determined from Equation 44.2. Requiring only noninvasive, observational measurements, this method is especially useful for determining transitory torques, for example, those associated with firing events in multicylinder internal combustion engines [3].

Equations 44.6 and 44.7 are applicable *only* during rotation since in the absence of motion, no work is done and power transfer is zero. Equation 44.6 may be used to determine *average* torque from calorimetric measurements of the heat generated (equal to the mechanical work W) during a totalized number of revolutions ($\equiv\theta/2\pi$). Equation 44.7 is routinely applied in power measurement, wherein T is determined by methods based on Equations 44.1, 44.3, 44.4, or 44.5 and ω is measured by any suitable means [4].

F, T, and φ are sometimes measured by simple mechanical methods. For example, a "torque wrench" is often used for the controlled tightening of threaded fasteners. In one such device, torque is indicated

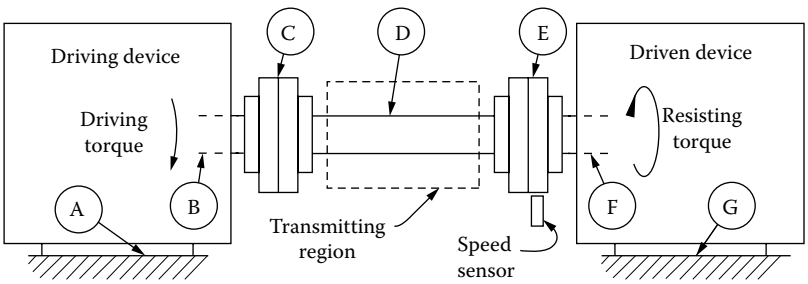

FIGURE 44.2 Schematic arrangement of devices used for the measurement of torque and power.

by the position of a "needle" moving over a calibrated curved scale in response to the deflection of an elastic member, in the simplest case, the bending (as a beam) of the wrench handle [5]. More generally, instruments, variously called *sensors* or *transducers*, are used to convert the torque being measured into a linearly proportional electric signal, typically a voltage or a frequency. The determination of P usually involves multiplication of the two signals from separate T and ω sensors. A transducer wherein the power transmitted by a rotating shaft is indicated by the amplitude of a *single* signal has also been described [6].

44.3 Torque Transducer Technologies

Various physical interactions serve to convert F, τ, γ, or φ into proportional electric signals. Each requires that some axial portion of the shaft be dedicated to the torque sensing function. Figure 44.3 shows typical configurations of the functional parts needed to apply the technologies most often utilized in present-day torque transducers.

44.3.1 Surface Strain

Figure 44.3a illustrates a sensing region configured to convert surface shear strain (γ_m) into an electric signal proportional to the transmitted torque. Surface strain became the key basis for measuring both force and torque following the invention of bonded wire strain gages by E. E. Simmons Jr. and Arthur C. Ruge in 1938 [7]. A modern strain gage consists of an elongated electric conductor (or semiconductor), generally in the form of a thin foil or film in a serpentine pattern, enclosed within a thin insulating carrier. The carrier is securely attached, usually with a thin adhesive layer, to the surface of the torque-carrying member. Strain is sensed as a change in gage resistance. Since these changes are generally too small (e.g., ~0.1%) to be accurately measured directly, it is common practice to employ multiple gages arranged in "half" (two gages) or "full" (four gages) Wheatstone bridge circuits. A four-gage bridge, comprised of two diametrically opposite pairs of matched strain gages, each aligned along a *principal strain* direction, provides independence from axial and bending loads as well as some temperature compensation. Limiting strains, as determined from Equation 44.4 (with τ_m equal to the shear proportional limit of the shaft material), rarely exceed a few parts in 10^3. Measurement sensitivity is maximized by choosing the shaft diameter in the sensing region to attain the limiting strain at the highest value of torque to be measured.

Torque transducers utilizing strain gages based on surface acoustic wave (SAW) technology [8] have been more recently introduced. In one configuration, illustrated in Figure 44.3b, piezoelectric "resonators," aligned with each of the principal strain directions, are attached to the transducer shaft. Under torque, the spacing between those "Interdigital Electrodes" is subjected to compressive strain decrease. The resonant frequencies of SAWs generated on the two substrates by electromagnetically coupled voltages applied to the electrodes of each resonator thereby decrease and increase, respectively. The difference between these two frequencies is thus a measure of the strain, hence (from Equation 44.4) of torque.

44.3.2 Twist Angle

If the shaft is *slender* enough, for example, $L > 5d$, φ, at limiting values of τ_m for typical shaft materials, can exceed 1°, enough to be resolved with sufficient accuracy for practical torque measurements. (φ at τ_m can be found by manipulating Equations 44.3 through 44.5.) Figure 44.3c shows a common arrangement wherein torque is determined from the difference in tooth-space phasing between two identical (and initially aligned for $T = 0$) "toothed" wheels attached at opposite ends of a compliant "torsion bar." The phase displacement of the periodic electric signals from the two "pickups" is proportional to the peripheral displacement of "teeth" or other salient features on the two wheels, hence to the twist angle

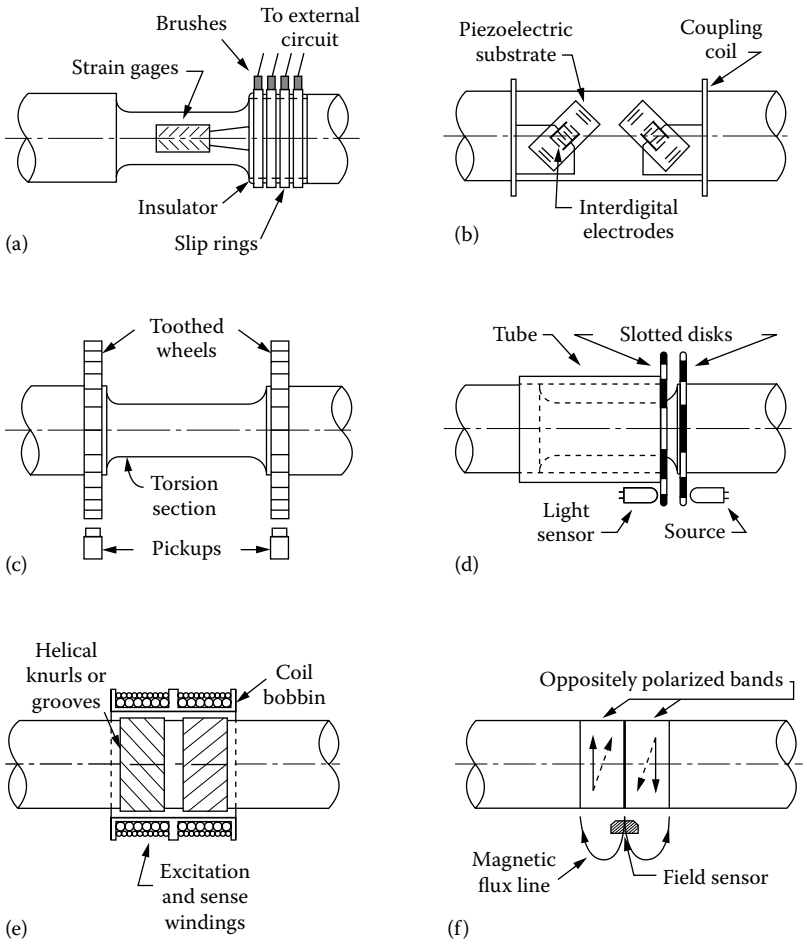

FIGURE 44.3 Six techniques in present use for measuring transmitted torque. (a) Torsional strain in the shaft upsets the balance of the Wheatstone bridge (comprised of four strain gages, two not seen). In the embodiment shown, external connections to the bridge are made through slip rings and brushes. (b) Torsional strain alters the frequencies of the two SAW resonators, increasing one and decreasing the other. Power is inductively coupled to the resonators. (c) Twist of the torsion section causes angular displacement of the surface features on the toothed wheels. This creates a phase difference in the signals from the two pickups. (d) Twist of the shaft section inside the tube causes angular displacement of the two slotted disks, thereby allowing more or less light from the source to reach the sensor. (e) The permeability of the two grooved regions of the shaft changes oppositely with torsional stress. This is sensed as a difference in the output voltages of the two sense windings. (f) Torsional stress causes the initially circumferential magnetizations in the bands (solid arrows) to tilt (dashed arrows). Magnetic poles thereby appear at the band ends and at their interface. The resulting magnetic field is sensed by the field sensor.

of the torsion bar and thus to the torque. These features are designed to enable sensing by one or other noncontacting magnetic, optical, or capacitive techniques. A rigid tube is sometimes used to bring the angular position of an axially remote part of the shaft close to the axial location of one of the sensors. This facilitates the alignment of the two pickups and simplifies associated wiring. It also allows for the use of a wider range of position measurement devices, especially those based on optical techniques as illustrated in Figure 44.3d and those in which the relative angular position of the two wheels (or disks) appears as the amplitude of a *single* electric signal, thus providing for the measurement of torque even on a stationary shaft.

44.3.3 Stress

In addition to elastic strain, the stresses by which torque is transmitted also affect the magnetization orientation in ferromagnetic shaft materials. Unlike strain, this "magnetoelastic interaction" [9] is detectable without contacting the shaft. Two types of magnetoelastic (sometimes called "magnetostrictive") torque transducers are in present use: Type 1 derives output signals from torque-induced variations in permeability; type 2 "measures" magnetic fields created in response to the torque. Type 1 transducers typically employ "branch," "cross," or "solenoidal" constructions [10]. In branch and cross designs, torque is detected as an imbalance in the permeabilities of the shaft surface material along the principal stress directions (orthogonal 45° helical paths). In solenoidal constructions, torque is detected by differences in the *axial* permeabilities of two adjacent surface regions, pre-endowed with symmetrical magnetic "easy" axes (typically in the principal stress directions). A unique variation of this basic construction utilizing copper-plated "V"-shaped stripes has more recently been developed [11]. While branch- and cross-type sensors are readily miniaturized [12], local variations in magnetic properties of typical shaft surfaces compromise their attainable accuracy. Solenoidal designs, illustrated in Figure 44.3e, avoid this pitfall by effectively averaging these local variations.

As indicated by the solid arrows in Figure 44.3f, the sensing region in type 2 transducers consists of (usually 2) remanently magnetized (in, respectively, opposite circumferential directions) adjacent bands. These "polarized" bands are instilled directly either into the near-surface regions of the shaft itself or in a ring of magnetoelastically active material affixed to the shaft [13]. When torque is applied, the magnetizations tilt into helical directions (dashed arrows) causing magnetic poles to develop at the band interface and, with opposite polarity, at their outer ends. Torque is determined from the output signal of one or more magnetic field sensors (e.g., Hall effect, magnetoresistive, or fluxgate devices) located to sense the intensity and polarity of the magnetic field that thereby arises in the space near the ring or band.

44.4 Torque Transducer Constructions, Operation, and Application

Although the application (automotive, aerospace) often requires that a torque sensing region should be created directly on an existing shaft, it is more usual to install a preassembled and calibrated, *modular* torque transducer into the driveline. Standard models with capacities from 0.001 to 300,000 Nm are obtainable from more than 50 manufacturers, worldwide [14]. At least one unit having a 2 MNm measuring range for wind turbine application has been made.

The descriptions of the measuring technology as well as installation and operating instructions can be found in the literature or on the websites of many manufacturers. The patent literature [15] often reveals key construction features in a product line of any one manufacturer.

Trade names generally identify families of transducers, from a single manufacturer, based on a specific operating principle, or possessing a collection of unique features; for example, *Torductor®-S* [11] identifies a unique and proprietary type of type 1 magnetoelastic transducer, *Torquetronic* [16] is a class of transducers using wrap-around twist angle sensors, *TorqSense* identifies a family of SAW-based transducers [17], and *smarttorque®* refers to a bearingless, flange-type, strain-gage-based "intelligent measuring system" [18]. A sampling of other well-known manufacturers is listed in [19–25]. Many of these devices show generic similarities that transcend both their specific sensing technology and torque range. Figure 44.4 identifies these common features in a classical torque transducer construction wherein a shaft having a sensing region is supported on bearings within a housing that encloses ancillary components. In recent times, these often include various types of signal conditioning and signal transmitting (e.g., wireless) electronics. Figure 44.5 illustrates the generic features of a relatively newer, bearingless construction, commonly called a "torque flange." All presently available torque flanges

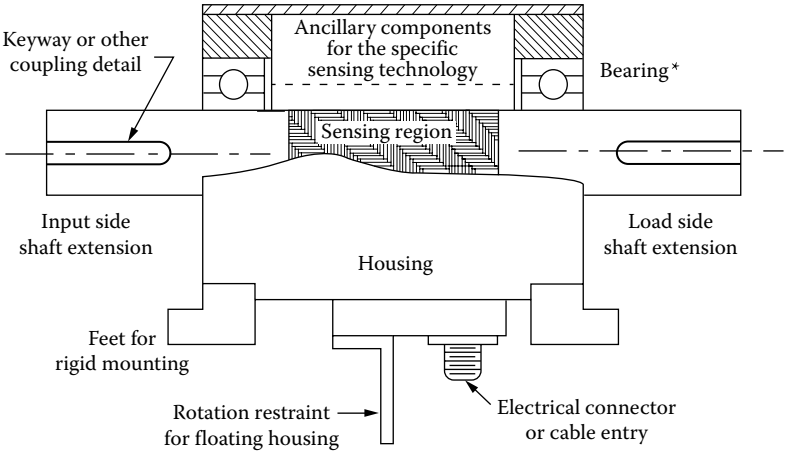

FIGURE 44.4 Generic features of a modular torque transducer. Bearings* are used only if the shaft is to rotate. One, but not both shaft extensions, can be rigidly connected to the driving or driven machine; the coupling at the other end must possess sufficient angular, radial, and axial flexibilities to suit the application. Rigid mounting of the housing requires flexible couplings at both shaft ends. Axially short, dual flange constructions have no bearings (see Figure 44.5).

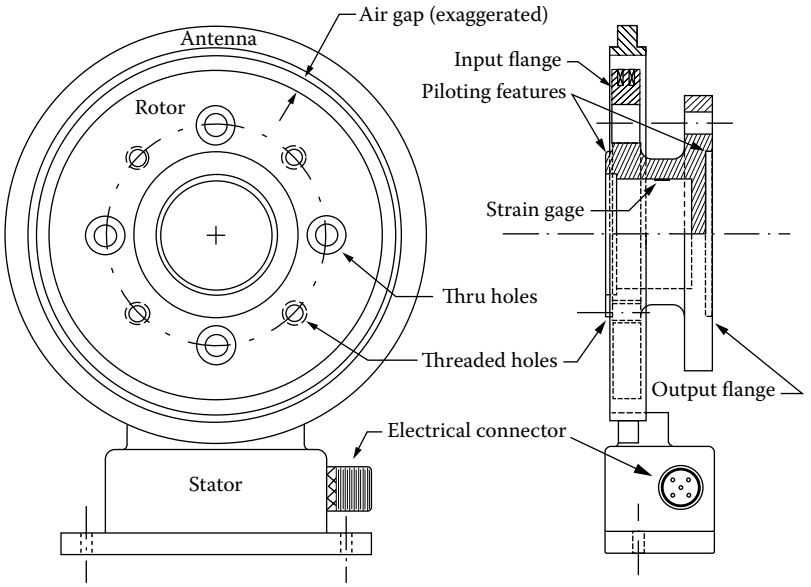

FIGURE 44.5 "Torque-flange" type of torque transducer. "Antennas" through which power and signal are coupled between the rotor and the stator vary greatly in configuration and angular extent between manufacturers and among models of any one manufacturer. Rotors contain a significant amount of electronic circuitry. Some rotors include encoder details for speed measurement. Rotor temperature measurement is sometimes available. Digital and analog telemetries often coexist. A common feature is the use of threaded holes on the input flange and thru holes on the output flange. This allows fastening bolts to both flanges to be installed from the same side.

utilize resistive strain-gage technology, either in torsional strain configurations or, for minimizing the axial width, to sense bending stresses in spokes that connect the concentric input and output flanges.

It is sometimes the case that the torque to be measured has a relatively large constant or slowly varying component, on top of which there are small rapidly varying components. This occurs with many types of motors, pumps, and geared machines. Transducers that respond to the rate of change of

torque (dT/dt) rather than T can more sensitively measure this type of dynamic component. Devices for this purpose typically employ either piezoelectric [26] or magnetoelastic [27] sensing elements that, by their nature, are well suited for such use.

44.4.1 Mechanical Considerations

Maximum operating speeds vary widely; upper limits depend upon the size, operating principle, type of bearings, lubrication, and dynamic balance of the rotating assembly. Ball bearings, lubricated by grease, oil, or oil mist, are typical. Parasitic torques associated with bearing lubricants and seals limit the accuracy of low-end torque measurements. (Minute capacity units have no bearings [23].) Forced lubrication allows operation up to 80,000 rpm [16]. Ceramic races and/or balls allow even higher speeds (120,000 rpm [16]). For any given torque range, flange-type transducers have higher maximum speed ratings than those with bearings. High-speed operation requires consideration of the effects of centrifugal stresses on the sensed quantity as well as of critical (vibration inducing) speed ranges. Torsional oscillations associated with resonances of the shaft elasticity with the rotational inertia of coupled masses can corrupt the measurement, damage the transducer by dynamic excursions above its rated overload torque, and *even be physically dangerous*.

Housings either *float* on the shaft bearings or are *rigidly mounted*. Free-floating housings are restrained from rotating by such "soft" means as a cable, spring, or compliant bracket or by an eccentric external feature simply resting against a fixed surface. In free-floating installations, the axes of the driving and driven shafts must be carefully aligned. Torsionally rigid "flexible" couplings at each shaft end are used to accommodate small angular and/or radial misalignments. Alternatively, the use of dual flexible couplings at one end will allow direct coupling of the other end. Rigidly mounted housings are equipped with mounting feet or lugs similar to those found on the frames of electric motors. Free-floating models are sometimes rigidly mounted using adapter plates fastened to the housing. Rigid mountings are preferred when it is difficult or impractical to align the driving and driven shafts, as, for example, when driving or driven machines are changed often. Rigidly mounted housings *require* the use of dual flexible couplings at *both* shaft ends.

Having neither bearings nor slip rings, torque flanges are completely wear-free. When mounted into an existing drive train, they require no more consideration than if mounting a spacer. One flange is directly connected (usually) to the loaded machine and the other, through universal joints, multiple disk, or similar couplings, is connected to the driving machine.

Transducers designed for zero or limited rotation applications have no need for bearings or noncontact constructions. To ensure that *all* of the torque applied at the ends is sensed, it is important in such "reaction"-type torque transducers that the housing be attached to the "shaft" at only one side of the sensing region. Whether rotating or stationary, the external shaft ends generally include such torque coupling details as flats, keyways, splines, tapers, flanges, and male/female square drives.

44.4.2 Electric Considerations

By their nature, transducers require some electric input power or *excitation*. The "raw" output signal of the actual sensing device also generally requires "conditioning" into a level and format appropriate for display on a digital or analog meter or to meet the requirements of data acquisition equipment. Excitation and signal conditioning are supplied by electronic circuits designed to match the characteristics of the specific sensing technology. For example, strain-gage bridges are typically powered with 10–20 V (dc or ac) and have rated load outputs in the range of 1.5–3.0 mV/V of excitation. Raising these millivolt signals to more usable levels requires amplifiers having gains of 100 or more. With ac excitation, oscillators and demodulators (or rectifiers) are also needed. Circuit elements of these types are normal when inductive elements are used, either as a vital part of the sensor or simply to implement a contactless construction.

Strain gages, differential transformers, and related sensing technologies obviously require that electric components be mounted *on* the torqued member. Various methods are employed to bring electric power to, and signals from, these components on rotating shafts. The most direct and common approach is to use conductive means wherein brushes (typically of silver graphite) bear against (silver) slip rings. Useful life is extended by providing means to lift the brushes off the rotating rings when measurements are not being made. Several "noncontacting" methods are also used. For example, power may be supplied via inductive coupling between stationary and rotating transformer windings [18–25], by the illumination of shaft-mounted photovoltaic cells or even by batteries strapped to the shaft [28] (limited by centrifugal force to relatively low speeds). Output signals are coupled off the shaft through rotary transformers, by frequency-modulated (infrared) LEDs [21] or by radio-frequency (FM) telemetry [28]. Inductive and telemetric components are incorporated into the associated torque flanges. Where shaft rotation is limited to no more than a few full rotations, as in steering gear, valve actuators, or oscillating mechanisms, hard wiring both power and signal circuits is often suitable. Flexible cabling minimizes incidental torques and makes for a long and reliable service life. All such wiring considerations are avoided when noncontact technologies or constructions are used.

44.4.3 Costs and Options

Prices of torque transducers reflect the wide range of available capacities, performance ratings, types, styles, optional features, and accessories. In general, prices of any one type increase with increasing capacity. Reaction types cost about half of similarly rated rotating units. A typical foot mounted, 500 N·m capacity, strain-gage transducer with either slip rings or rotary transformers and integral speed sensor, specified nonlinearity and hysteresis each within ±0.1%, costs about $4000. Compatible accessories providing transducer excitation signal conditioning and analog output with digital display of torque and speed add about $2000. A comparable magnetoelastic transducer with ±0.5% accuracy costs about $1300. Low-range, 1% accuracy magnetoelastic units cost under $500. High-capacity transducers for extreme speed service with appropriate lubrication options can cost well over $50,000. Price ranges for standard units are often posted on manufacturer's web pages. Cost estimates for mass produced torque transducers for use in automotive power steering applications are in the range of $20.

44.5 Apparatus for Power Measurement

Rotating machinery exists in specific types without limit and may operate at power levels from fractions of a watt to some tens of megawatts, a range spanning more than 10^8. Apparatus for power measurement exists in a similarly wide range of types and sizes. Mechanical power flows from a *driver* to a *load*. This power can be determined *directly* by application of Equation 44.7, simply by measuring, in addition to ω, the output torque of the driver or the input torque to the load, whichever is the device under test (DUT). When the DUT is a driver, measurements are usually required over its full service range of speed and torque. The test apparatus therefore must act as a controllable load and be able to *absorb* the delivered power. Similarly, when the DUT is a pump or fan or other type of load, or one whose function is simply to alter speed and torque, for example, a gearbox, the test apparatus must include a *driver* capable of supplying power over the DUT's full rated range of torque and speed. Mechanical power can also be determined *indirectly* by conversion into (or from) another form of energy, for example, heat or electricity, and measuring the relevant calorimetric or electric quantities. In view of the wide range of readily available methods and apparatus for accurately measuring both torque and speed, indirect methods need only be considered when special circumstances make direct methods difficult.

Dynamometer is the special name given to power measuring apparatus that includes absorbing or/and driving means and wherein torque is determined by the reaction forces on a stationary part (the *stator*). An effective dynamometer is conveniently assembled by mounting the DUT in such a manner as to allow measurement of the reaction torque on its frame. Figure 44.6 shows a device

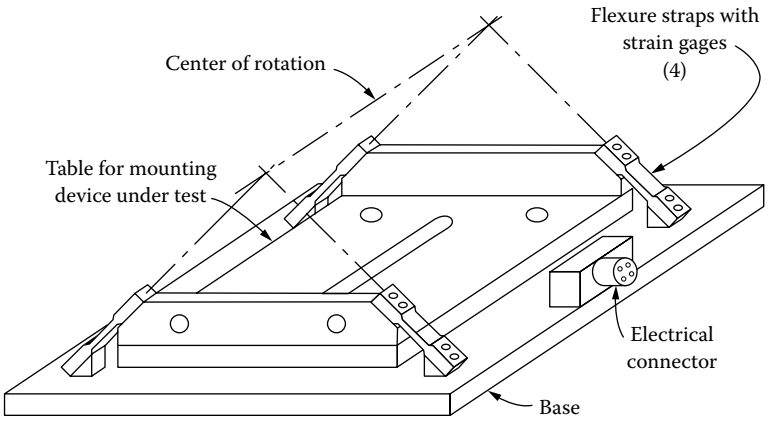

FIGURE 44.6 Support system for measuring the reaction torque of a rotating machine. The axis of the machine must be accurately set on the "center of rotation." The holes and the keyway in the table facilitate machine mounting and alignment. Holes in the front upright provide for attaching a lever arm from which calibrating weights may be hung. (From Supplement to ASME performance test codes, *Measurement of Shaft Power*, ANSI/ASME PTC 19.7-1980 (Reaffirmed 1988); Lebow Products (Honeywell Sensors), 1728 Maplelawn Road, Troy, MI 48099, https://measurementsensors.honeywell.com/pages/ProductInfo.aspx.)

designed to facilitate such measurements. Commercial models (Torque Table® [20]) rated to support DUTs weighing 222–4900 N are available with torque capacities from 1.3 to 226 N·m. "Torque tubes" [4] or other DUT mounting arrangements are also used. Other than for possible rotational/elastic resonances, these systems have no speed limitations. More generally, and especially for large machinery, dynamometers include a specialized driving or absorbing machine. Such dynamometers are classified according to their function as *absorbing* or *driving* (sometimes *motoring*). A *universal* dynamometer can function as either a driver or an absorber.

44.5.1 Absorption Dynamometers

Absorption dynamometers, oftentimes called *brakes* since their operation depends on the creation of a controllable *drag* torque, convert mechanical work into heat. A drag torque, as distinguished from an active torque, can act only to restrain and not to initiate rotational motion. Temperature rise within a dynamometer is controlled by carrying away the heat energy, usually by transfer to a moving fluid, typically air or water. Drag torque is created by inherently dissipative processes such as friction between rubbing surfaces, shear or turbulence of viscous liquids, flow of electric current, or magnetic hysteresis. Gaspard Riche de Prony (1755–1839), in 1821 [29], invented a highly useful form of a friction brake to meet the needs for testing the steam engines that were then becoming prevalent. Brakes of this type are rarely used with modern prime movers, their main use being for instructional purposes, since they embody all of the underlying principles and major operating considerations for all types of absorption dynamometers. Figure 44.7 shows the basic form and constructional features of a *prony brake*. The power that would normally be delivered by the shaft of the driving engine to the driven load is (for measurement purposes) converted instead into heat via the work done by the frictional forces between the friction blocks and the flywheel rim. Adjusting the tightness of the clamping bolts varies the frictional drag torque as required. Heat is removed from the inside surface of the rim by arrangements (not shown) utilizing either a continuous flow or evaporation of water. There is no need to know the magnitude of the frictional forces nor even the radius of the flywheel (facts recognized by Prony), since, while the drag torque tends to rotate the clamped-on apparatus, it is held stationary by the equal but opposite reaction torque Fr. F at the end of the torque arm of radius r (a fixed dimension of the apparatus) is monitored by a scale or load cell. The power is found from Equations 44.1 and 44.7 as $P = Fr\omega = Fr2\pi N/60$ where N is in rpm.

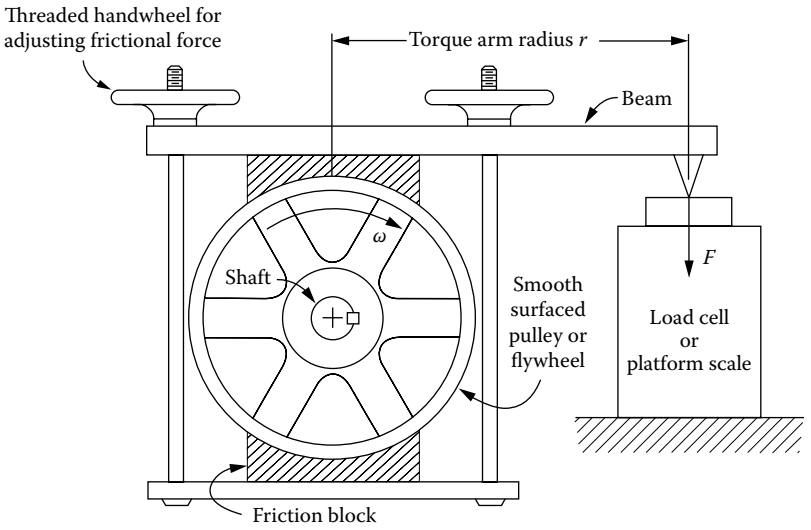

FIGURE 44.7 Classical prony brake. This brake embodies the defining features of all absorbing dynamometers: conversion of mechanical work into heat and determination of power from measured values of reaction torque and rotational velocity.

Uneven retarding forces associated with fluctuating coefficients of friction generally make rubbing friction a poor way to generate drag torque. Nevertheless, because they may be easily constructed, ad hoc variations of prony brakes, often using only bare ropes or wooden cleats connected by ropes or straps, find use in the laboratory or wherever undemanding or infrequent power measurements are to be made. More sophisticated prony brake constructions are used in stand-alone dynamometers with self-contained cooling water tanks in sizes up to 746 kW (1000 Hp) for operation up to 3600 rpm with torques to 5400 N·m [30]. Available in stationary and mobile models, they find use in testing large electric motors as well as engines and transmissions on agricultural vehicles. Prony brakes allow full drag torque to be imposed down to zero speed.

William Froude (1810–1879) [31] invented a *water brake* (1877) that does not depend on rubbing friction. Drag torque within a *Froude brake* is developed between the rotor and the stator by the momentum imparted by the rotor to water contained within the brake casing. Rotor rotation forces the water to circulate between cuplike pockets cast into facing surfaces of both rotor and stator. The rotor is supported in the stator by bearings that also fix its axial position. Labyrinth-type seals prevent water leakage while minimizing frictional drag and wear. The stator casing is supported in the dynamometer frame in cradle fashion by *trunnion* bearings. The torque that prevents rotation of the stator is measured by reaction forces in much the same manner as with the prony brake. Drag torque is adjusted by a valve, controlling either the back pressure in the water outlet piping [32] or the inlet flow rate or sometimes (to allow very rapid torque changes) with two valves controlling both [34]. In any case, the absorbed energy is carried away by the continuous water flow. Other types of cradle-mounted water brakes, while externally similar, have substantially different internal constructions and depend on other principles for developing the drag torque; for example, smooth rotors develop viscous drag by shearing and turbulence. Nevertheless, all *hydraulic dynamometers* purposefully function as *inefficient* centrifugal pumps. Regardless of internal design and valve settings, maximum drag torque is low at low speeds (zero at standstill) but can rise rapidly, typically varying with the square of rotational speed. The irreducible presence of some water, as well as windage, places a speed-dependent lower limit on the *controllable* drag torque. In any one design, wear and vibration caused by cavitation place upper limits on the speed and power level. Hydraulic dynamometers are available in a wide range of capacities between 300 and 25,000 kW with some portable units having capacities as low as 75 kW [33]. The largest ever built [34], absorbing up to about 75,000 kW (100,000 Hp), has been used to test propulsion systems

for nuclear submarines. Maximum speeds match the operating speeds of the prime movers that they are built to test and therefore generally decrease with increasing capacity. High-speed gas turbine and aerospace engine test equipment may operate as high as 30,000 rpm [32].

In 1855, Jean B. L. Foucault (1819–1868) [29] demonstrated the conversion of mechanical work into heat by rotating a copper disk between the poles of an electromagnet. This simple means of developing drag torque, based on *eddy currents*, has, since *ca*. 1935, been widely exploited in dynamometers. Figure 44.8 shows the essential features of this type of brake. Rotation of a toothed or spoked steel rotor through a spatially uniform magnetic field, created by direct current through coils in the stator, induces locally circulating (eddy) currents in electrically conductive (copper) portions of the stator. Electromagnetic forces between the rotor, which is magnetized by the uniform field, and the field arising from the eddy currents create the drag torque. This torque and hence the mechanical input power are controlled by adjusting the *excitation* current in the stator coils. Electric input power is less than 1% of the rated capacity. The dynamometer is effectively an internally short-circuited generator since the power associated with the resistive losses from the generated eddy currents is dissipated *within* the machine. Being heated by the flow of these currents, the stator must be cooled, sometimes (in smaller-capacity machines) by air supplied by blowers [30], more often by the continuous flow of water [32,34,35]. In *dry-gap* eddy current brakes (the type shown in Figure 44.7), water flow is limited to passages within the stator. Larger machines are often of the *water in gap* type wherein water also circulates around the rotor [35]. Water in contact with the moving rotor effectively acts as in a water brake adding a non-electromagnetic component to the total drag torque, thereby placing a lower limit to the controllable torque. Windage limits the minimum value of controllable torque in dry-gap types. Since drag torque is developed by the motion of the rotor, it is zero at standstill for any value of excitation current. Initially rising rapidly, approximately linearly, with speed, torque eventually approaches a current limited saturation value. As in other cradled machines, the torque required to prevent rotation of the stator is measured by the reaction force acting at a fixed known distance from the rotation axis. Standard model eddy current brakes have capacities from less than 1 kW [30,36] to more than 2,000 kW [34,35] with maximum speeds from 12,000 rpm in the smaller-capacity units to 3,600 rpm in the largest units. Special units with capacities of 3,000 Hp (2,238 kW) at speeds to 25,000 rpm have been built [35].

Hysteresis brakes [36] develop drag torque via magnetic attractive/repulsive forces between the magnetic poles established in a reticulated stator structure by a current through the field coil and those created in a "drag-cup" rotor by the stator field gradients. The rotation of the special steel rotor, through the spatial field pattern established by the stator, results in a cyclical reversal of the polarity

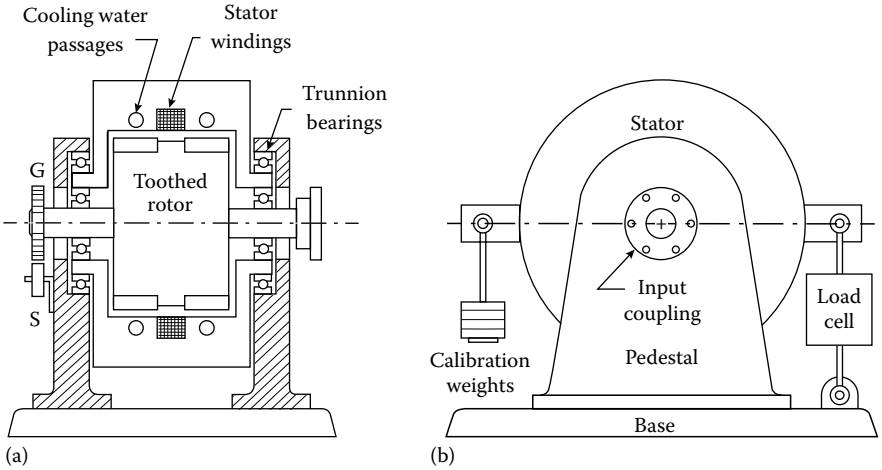

FIGURE 44.8 (a) Cross section and (b) front view of an eddy current dynamometer. G is a gear wheel and S is a speed sensor. Hoses carrying cooling water and cable carrying electric power to the stator are not shown.

of its local magnetizations. The energy associated with these reversals (proportional to the area of the hysteresis loop of the rotor material) is converted into heat within the drag cup. Temperature rise is controlled by forced air cooling from a blower or compressed air source. As with eddy current brakes, the drag torque of these devices is controlled by the excitation current. In contrast with eddy current brakes, rated drag torque is available down to zero speed. (Eddy current effects typically add only 1% to the drag torque for each 1000 rpm.) As a result of their smooth-surfaced rotating parts, hysteresis brakes exhibit low parasitic torques and hence cover a dynamic range as high as 200–1. Standard models are available having continuous power capacities up to 6 kW (12 kW with two brakes in tandem cooled by two blowers). Intermittent capacities per unit (for 5 min or less) are 7 kW. Some low-capacity units are convection cooled; the smallest has a continuous rating of just 7 W (35 W for 5 min). Maximum speeds range from 30,000 rpm for the smallest to 10,000 rpm for the largest units. Torque is measured by a strain-gage bridge on a moment arm supporting the machine stator.

44.5.2 Driving and Universal Dynamometers

Electric generators, both ac and dc, offer another means for developing a controllable drag torque, and they are readily adapted for dynamometer service by cradle mounting their stator structures. Moreover, electric machines of these types can also operate in a motoring mode wherein they can deliver controllable *active* torque. When configured to operate selectively in either driving or absorbing modes, the machine serves as a universal dynamometer. With dc machines in the absorbing mode, the generated power is typically dissipated in a convection-cooled resistor bank. Air cooling the machine with blowers is usually adequate, since *most* of the mechanical power input is dissipated externally. Nevertheless, *all* of the mechanical input power is accounted for by the product of the reaction torque and the rotational speed. In the motoring mode, torque and speed are controlled by adjustment of both field and armature currents. Modern ac machines utilize regenerative input power converters to allow braking power to be returned to the utility power line. In the motoring mode, speed is controlled by high-power, solid-state, adjustable-frequency inverters. Internal construction is that of a simple three-phase induction motor, having neither brushes, slip rings, nor commutators. The absence of rotor windings allows for higher-speed operation than dc machines. Universal dynamometers are "four-quadrant" machines, a term denoting their ability to produce torque in the same or opposite direction as their rotational velocity. This unique ability allows the effective drag torque to be reduced to zero at any speed. Universal dynamometers [32,35] are available in a relatively limited range of capacities (56–450 kW), with commensurate torque (110–1900 N · m) and speed (4,500–13,500 rpm) ranges, reflecting their principal application in automotive engine development. Special dynamometers for testing transmissions and other vehicular drive train components insert the DUT between a diesel engine or electric motor prime mover and a hydraulic or eddy current brake [37].

44.5.3 Foursquare Dynamometers

It is often desirable to perform endurance tests of the various load-carrying parts (shafts, gears, bearings, lubricants, etc.) of the rotating machinery or of the entire assemblies such as automotive or helicopter transmissions or even the gearboxes used in modern wind turbines. This requires that the particular DUT be operated under full torque (or full range of torque variation) at full rated speed for hundreds, sometimes for thousands of hours. To do this with any of the previously described dynamometers could obviously require the expenditure of enormous quantities of energy. Apparatus such as a "foursquare dynamometer" provides a simple means of circulating large (and adjustable) amounts of power while utilizing only the amount of external power required to overcome the static and dynamic friction associated with its operation. Due to the wide range of torques, speeds, and devices to be tested, there are few suppliers of "standard" models of foursquare dynamometers [38], although the principle is often applied in the construction of specialized units for specific applications [39].

44.5.4 Measurement Accuracy

Accuracy of power measurement (see discussion in [4]) is generally limited by the torque measurement (±0.25% to ±1%) since rotational speed can be measured with almost any desired accuracy. Torque errors can arise from the application of extraneous (i.e., not indicated) torques from hose and cable connections, from windage of external parts, and from miscalibration of the load cell. Undetected friction in the trunnion bearings of cradled dynamometers may compromise the torque measurement accuracy. Ideally, well-lubricated antifriction bearings should make no significant contribution to the restraining torque. In practice, however, the unchanging contact region of the balls or other rolling elements on the bearing races makes them prone to brinelling (a form of denting) from forces arising from vibration and unsupported weight of attached devices or even inadvertently during the alignment of connected machinery. The problem can be alleviated by periodic rotation of the (primarily outer) bearing races. In some bearing-in-bearing constructions, the central races are continuously rotated at low speeds by an electric motor, while still others avoid the problem by supporting the stator on hydrostatic oil lift bearings [35].

44.5.5 Costs

The wide range of torque, speed, and power levels, together with the variation in sophistication of associated instrumentation, is reflected in the very wide range of dynamometer prices. Suspension systems of the type illustrated in Figure 44.6 (for which the user must supply the rotating machine) cost $4000–$6000, increasing with capacity [20]. A 100 Hp (74.6 kW) *portable* water brake equipped with a strain-gage load cell and a digital readout instrument for torque, speed, and power cost $5000–$15,000 depending on the sophistication of the data acquisition equipment [33]. Stationary (and some *transportable* [30]) hydraulic dynamometers cost from $125/kW in the smaller sizes [32] down to $40 kW for the very largest [34]. Transportation, installation, and instrumentation can add significantly to these costs. Eddy current dynamometers cost from as little as $65/kW to nearly $800/kW depending on the rated capacity, type of control system, and instrumentation [32,34,35]. Hysteresis brakes with integral speed sensors cost from $4,000 to $20,000 according to capacity [36]. Compatible controllers, from manual to fully programmable for PC test control and data acquisition via an IEEE-488 or other standard interface, vary in price from $700 to $5000. The flexibility and high performance of ac universal dynamometers is reflected in their comparatively high prices of $670–$2200/kW [32,35]. Prices for a wide range of dynamometers, from $13,000 to $1,200,000, are quoted on at least one manufacturer's website [37].

References

1. C. P. Pinney and W. E. Baker, Velocity measurement, In *The Measurement, Instrumentation and Sensors Handbook*, Webster, J. G., ed., Boca Raton, FL: CRC Press, 1999.
2. S. Timoshenko, *Strength of Materials*, 3rd edn., New York: Robert E. Kreiger, 1956, Part I, pp. 281–290, Part II, pp. 235–250.
3. S. J. Citron, On-line engine torque and torque fluctuation measurement for engine control utilizing crankshaft speed fluctuations, U.S. Patent No. 4,697,561, 1987.
4. Supplement to ASME performance test codes, Measurement of shaft power, ANSI/ASME PTC 19.7-1980 (Reaffirmed 1988).
5. See for example the catalog of torque wrench products of Consolidated Devices, Inc., 19220 San Jose Ave., City of Industry, CA 91748, http://www.cditorque.com (accessed on March 16, 2013).
6. I. J. Garshelis, C. R. Conto, and W. S. Fiegel, A single transducer for non-contact measurement of the power, torque and speed of a rotating shaft, SAE Paper No. 950536, 1995.
7. C. C. Perry and H. R. Lissner, *The Strain Gage Primer*, 2nd edn., New York: McGraw-Hill, 1962, p. 9. (This book covers all phases of strain gage technology.)
8. A. Lonsdale, Dynamic rotary torque measurement using surface acoustic waves, *Sensors*, 18, 51–55, 2001.

9. B. D. Cullity, *Introduction to Magnetic Materials*, Reading, MA: Addison-Wesley, 1972, Section 8.5, pp. 266–274.
10. W. J. Fleming, Magnetostrictive torque sensors—Comparison of branch, cross and solenoidal designs, SAE Paper No. 900264, 1990.
11. Torductor®-S, ABB Torque Measurement http://www05.abb.com/global/scot/scot264.nsf/veritydisplay/eef8846525950f25c1257380003623c6/$file/3bse022227r0101_-001.pdf (accessed on March 16, 2013).
12. Y. Nonomura, J. Sugiyama, K. Tsukada, M. Takeuchi, K. Itoh, and T. Konomi, Measurements of engine torque with the intra-bearing torque sensor, SAE Paper No. 870472, 1987.
13. I. J. Garshelis, Circularly magnetized non-contact torque sensor and method for measuring torque using same, U.S. Patent 5,351,555, 1994 and 5,520,059, 1996.
14. Directories of torque transducer (torque sensor) manufacturers can be found at: http://www.thomasnet.com/prodsearch.html?cov=NA&which=prod&what=torque+measurement, http://www.globalspec.com/SpecSearch/Suppliers?Comp=11&ShowAll=true (accessed on March 16, 2013).
15. Search existing U.S. Patents at: http://www.uspto.gov/patents/process/search/index.jsp (accessed on March 16, 2013).
16. Torquemeters Ltd., Ravensthorpe, Northampton NN6 8EH, England/(In USA: Torquetronics, Inc., P.O. Box 100, Allegany, NY 14707), http://www.torquemeters.com (accessed on March 16, 2013).
17. Sensor Technology Ltd., P.O. Box 36, Banbury, Oxon OX15 6JB, UK, http://www.sensors.co.uk/torqsense/ (accessed on March 16, 2013).
18. HBM, Inc., 19 Bartlett St., Marlborough, MA 01752, http://www.hbm.com (accessed on March 16, 2013).
19. S. Himmelstein & Co., 2490 Pembroke, Hoffman Estates, IL 60195, http://www.himmelstein.com (accessed on March 16, 2013).
20. Lebow Products (Honeywell Sensors), 1728 Maplelawn Road, Troy, MI 48099, https://measurementsensors.honeywell.com/pages/ProductInfo.aspx (accessed on March 16, 2013).
21. Sensor Developments, Inc., P.O. Box 290, Lake Orion, MI 48361-0290, http://www.sendev.com (accessed on March 16, 2013).
22. Futek Advanced Sensor Technology, Inc., 10 Thomas, Irvine, CA 92618, http://www.futek.com (accessed on March 16, 2013).
23. Schlenker Enterprises Ltd., P.O. Box 9277, Lombard, IL 60148-9277, http://www.schlenkent.com/torque_transducers.htm (accessed on March 16, 2013).
24. Vibrac Corporation, 16 Columbia Drive, Amherst, NH 03031, http://www.vibrac.com (accessed on March 16, 2013).
25. Kistler North America, 30 Hudson Drive, Novi, MI 48377, http://www.kistler.com (accessed on March 16, 2013).
26. J. Neely et al., Torque ripple sensor and mitigation mechanism, U.S. Patent No. 7,117,754, October 10, 2006.
27. I. J. Garshelis, R. J. Kari, and S. P. L. Tollens, Devices and methods for detecting rates of change of torque, U.S. Patent No. 7,832,289 B2, November 10, 2010.
28. Binsfield Engineering, Inc., 4571 W. MacFarlane, Maple City, MI 49664, http://www.binsfield.com (accessed on March 16, 2013).
29. C. C. Gillispie (ed.), *Dictionary of Scientific Biography*, Vol. XI, New York: Charles Scribner's Sons, 1975.
30. AW Dynamometer, Inc., 10001 W. North Pontiac, IL 61764, http://www.awdynamometer.com (accessed on March 16, 2013).
31. R. Porter (ed.), *The Biographical Dictionary of Scientists*, 2nd edn., New York: Oxford University Press, 1994.
32. Froude Hoffman, Inc., 45225 Polaris Court, Plymouth, MI 48170, http://www.froudehoffman.com (accessed on March 16, 2013).

33. Dyne Systems, Inc. W209 N17391 Industrial Drive, Jackson WI 53037, http://www.dynesystems.com (accessed on March 16, 2013).
34. Taylor Dynamometer, 3602 West Wheelhouse Road, Milwaukee, WI 53208, http://www.taylordyno.com (accessed on March 16, 2013).
35. Drive Source International, Inc., 7900 Durand Ave., Sturtevant, WI, http://www.drivesourceusa.com (accessed on March 16, 2013).
36. Magtrol, Inc., 70 Gardenville Parkway, Buffalo, NY 14224-1322. http://www.magtrol.com (accessed on March 16, 2013).
37. Land and Sea, Inc., 25 Henniker Street, Concord, NH 03301-8528, http://www.land-and-sea.com (accessed on March 16, 2013).
38. MTS, 1400 Technology Drive, Eden Prairie, MN 55344, http://www.mts.com/en/about/news/DEV_002528 (accessed on March 16, 2013).
39. J. Schmitt, Performance and analysis of a dynamic loading four square machine for crawler tractor power train development, SAE Technical Paper 821028, 1982.

45

Density Measurement

Halit Eren
Curtin University

45.1 Introduction

Density measurements are significant part of instrumentation. Density measurements are made for at least two important reasons: (1) for the determination of the mass and the volume of products and (2) for the quality of the products. In many industrial applications, density measurement ascertains the quality and the value of the products.

Density is defined as the mass of a given volume of a substance under fixed physical conditions. However, ultimate care must be exercised in the measurements since the density varies with pressure and temperature. This variation is much greater and significant in gases.

In many modern applications, the densities of the products are obtained by the sampling techniques. In industrial operations, there are two basic concepts: *static density measurements* and *dynamic (online) density measurements*. Within each concept, there are many different methods that can be employed. These methods are based on different physical principles. In many cases, the application itself and the characteristics of the process determine the best suitable method to be used. Generally, static methods are well developed, are lower in cost, and tend to be more accurate. Dynamic density measurements can be expensive, may require high degree of automation, and use microprocessor and computer-based signal-processing devices. Nevertheless, nowadays, many static methods are also computerized, offering easy-to-use, flexible, and self-calibrating features.

There is no single universally applicable density measurement technique that can be applied to all types of measurements due to different characteristics of materials.

In many cases, density is normalized under reference conditions and the density of a substance is determined by dividing the density of that substance by the density of a standard substance obtained

under the same conditions. This dimensionless ratio is called the *specific gravity* (SG), also termed the *relative density*. The specific gravities of liquid and gases under reference conditions are given by

$$\text{Liquid SG} = \frac{\text{Density of liquid}}{\text{Density of water}} \tag{45.1}$$

$$\text{Gas SG} = \frac{\text{Density of gas}}{\text{Density of air}} \tag{45.2}$$

Commonly accepted sets of conditions are *normal temperature and pressure* (NTP) and *standard temperature and pressure* (STP). NTP is usually taken as the temperature of 0.00 °C and a pressure of 760 mmHg. The NTP is accepted as 15.56 °C at a pressure of 101.325 kPa.

45.2 Solid Density

If the uniformity is maintained, the determination of density of solids is a simple task. Once the volume of the solid and its mass are known, the density can be found using the basic ratio: density = mass/volume (kg m^{-3}).

However, in many applications, solids have different constituents and materials having different ratios of mixture. Their volumes can also change often. In these cases, dynamic methods are employed, such as radioactive absorption types, ultrasonic, or other techniques. Some of these methods are described in detail later in this chapter.

45.3 Fluid Density

The measurement of fluid density is much more complex than the solids and there are many different available techniques. This complexity is mainly due to the nature in processes, the variations in fluid densities, and the diverse characteristics of processes as well as characteristics of fluids themselves. Some of these methods are custom designed and applicable to only situations they are designed for. Others are very similar in principles and technology, and they may be applicable on different types of fluids. At present, apart from conventional methods, there are many novel and unusual techniques that are undertaken in research and development efforts. For example, densitometers based on electromagnetic principles can be only small part of an intelligent instrumentation system.

Fluids can be divided to liquids and gases. Extra care and further considerations are necessary in gas density measurements. For example, perfect gases contain an equal number of molecules under the same conditions and volumes. Therefore, molecular weights can be used in the density measurements.

Depending on the applications, fluid densities can be measured in either *static* or *dynamic* forms. In general, static density measurements of fluids are well developed, precise, and have greater resolution and accuracy than most dynamic techniques. Pycnometers and buoyancy are examples of static techniques that can be adapted to cover small density ranges with a high resolution and precision. Nowadays, many manufacturers offer dynamic instruments previously known to be static. Also, many static density measurement devices are computerized and come with appropriate hardware and software. In general, static-type measurements are employed in laboratory conditions, and dynamic methods are employed in real-time measurements where the properties of a fluid can vary from time to time.

In this chapter, the discussion will concentrate on the commonly applied, modern density measuring devices, which include

1. Pycnometric densitometers
2. Buoyancy-type densitometers
3. Hydrometers

4. Hydrostatic weighing densitometers
5. Balance-type densitometers
6. Column-type densitometers
7. Vibrating element densitometers
8. Radioactive densitometers
9. Refractometer and index of reflection densitometers
10. Coriolis densitometers
11. Absorption-type densitometers

45.3.1 Pycnometric Densitometers

Pycnometers are static devices. They are manufactured as fixed-volume vessels that can be filled with the sample liquid. The density of the fluid is measured by weighing the sample. The simplest version consists of a vessel in the shape of a bottle with a long stopper containing a capillary hole, as shown in Figure 45.1. The capillary is used to determine the exact volume of the liquid, thus giving high resolution when filling the pycnometer. The bottle is first weighed empty and then with distilled–aerated water to determine the volume of the bottle. The bottle is then filled with the process fluid and weighed again. The density is determined by dividing the mass by the volume. The SG of the liquid is found by the ratio of the fluid mass to water mass. When pycnometers are used, for good precision, ultimate care must be exercised during the measurements; that is, the bottle must be cleaned after each measurement, the temperature must be kept constant, and precision balances must be used. In some cases, to ensure filling of the pycnometer, twin capillary tubes are used. The two capillaries, made of glass, are positioned such that the fluid can be driven into the vessel under vacuum conditions. Accurate filling to graduation marks on the capillary is then made.

The pycnometers have to be lightweight, strong enough to contain samples, and they need to be nonmagnetic for accurate weighing to eliminate possible ambient magnetic effects. Very high-resolution balances must be used to detect small differences in weights of gases and liquids. Although many

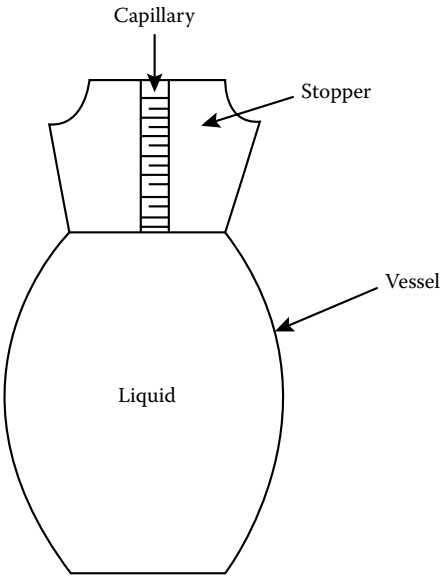

FIGURE 45.1 A pycnometer. A fixed-volume container is filled with liquid and weighed accurately; the capillary is used to determine the exact volume of the liquid.

pycnometers are made of glass, they can also be made from metals to give enough strength for the density measurements of gases and liquids at extreme high pressures. In many cases, metal pycnometers are necessary for taking samples from the line of some rugged processes.

Pycnometers have advantages and disadvantages. Advantages are that if used correctly, they are accurate, and they can be used for both density and SG measurements. The disadvantages include

1. Great care must be exercised for accurate results.
2. The sample must be taken off-line, with consequent time lag in results. This creates problems of relating samples to the materials that exist in the actual process.
3. High-precision pycnometers are expensive. They require precision weighing scales and controlled laboratory conditions. Specialized techniques must be employed to take samples in high-pressure processes and hostile conditions, such as offshore installations.
4. Their good performances might depend on the skill of the operator.

45.3.2 Buoyancy-Type Densitometers

The buoyancy method basically uses Archimedes principle. A suspended sinker, with a known mass and volume attached to a fine wire, is totally immersed in the sample liquid. A precision force balance is used to measure the force to support the sinker. Once the mass, volume, and supporting weight of the sinker are known, the density of the liquid can be calculated. However, some corrections need to be made for surface tension on the suspension wire, the cubicle expansion coefficient of the sinker, and the temperature of process. Buoyancy-type densitometers give accurate results and are used for the calibration of the other liquid density transducers.

One advanced version of the buoyancy technique is the magnetic suspension system. The sinker is fully enclosed in a pressure vessel, thus eliminating surface tension errors. Their uses can also be extended to applications such as the SG measurements under low vapor pressures and density measurements of hazardous fluids.

45.3.3 Hydrometers

Hydrometers are the most commonly used devices for measurement of the density of liquids. They are so commonly used that their specifications and procedure of use are described by national and international standards, such as ISO 387. The buoyancy principle is used as the main technique of operation. The volume of fixed mass is converted to a linear distance by a sealed bulb-shaped glass tube containing a long-stem measurement scale, shown in Figure 45.2. The bulb is ballasted with a lead shot and pitch, the mass of which depends on the density range of the liquid to be measured. The bulb is simply placed into the liquid and the density is read from the scale. The scale is graduated in density units such as kg m^{-3}. However, many alternative scales are offered by manufacturers, such as SG, American Petroleum Institute (API) gravity, Brix, and Brine. Hydrometers can be calibrated for different ranges for surface tensions and temperatures. Temperature corrections can be made for set temperature such as 15°C, 20°C, or 25°C. ISO 387 covers a density range of 600–2000 kg m^{-3}. Hydrometers have a number of advantages and disadvantages. The advantages include

1. Relatively low cost and easy to use
2. Good resolution for small range
3. Traceable to national and international standards

The disadvantages include

1. They have small span; therefore, a number of meters are required to cover a significant range.
2. They are made from glass and fragile. Metal and plastic versions are not as accurate.

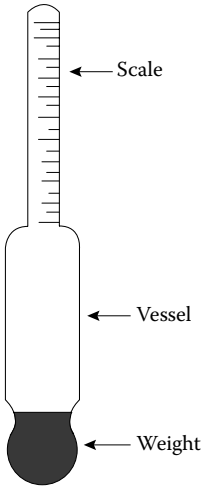

FIGURE 45.2 A hydrometer. A fixed-weight and fixed-volume bulb is placed into the liquid. The bulb sinks in the liquid, depending on its density. The density is read directly from the scale. Temperature correction is necessary.

3. The fluid needs to be an off-line sample, not representing the exact conditions of the process. There are pressure hydrometers for low vapor pressure hydrocarbons, but this adds a need for accurately determining the pressure too.
4. If good precision is required, they are difficult to use, needing surface tension and temperature corrections. Further corrections could be required for opaque fluids.

45.3.4 Hydrostatic Weighing Densitometers

The most common device using a hydrostatic weighing method consists of a U-tube that is pivoted on flexible end couplings. A typical example is shown in Figure 45.3. The total weight of the tube changes, depending on the density of fluid flowing through it. The change in the weight needs to be measured accurately, and there are a number of methods employed to do this. The most common commercial

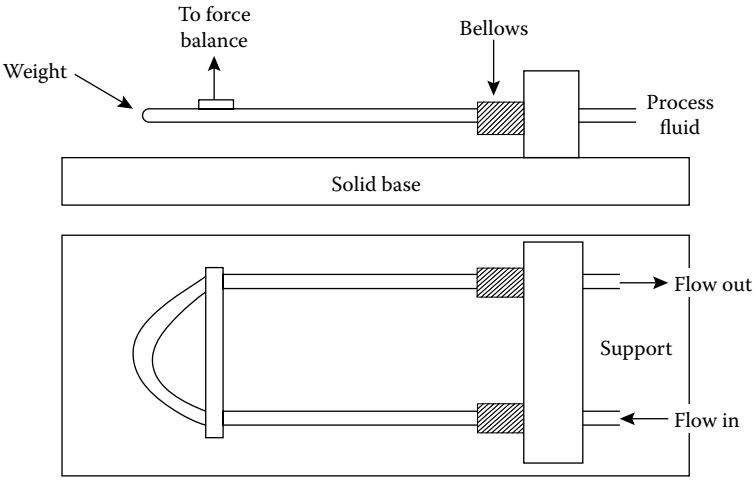

FIGURE 45.3 Hydrostatic weighing. The total weight of a fixed-volume tube containing liquid is determined accurately. The density is calculated using mass-to-volume ratio.

meters use a force balance system. The connectors are stainless steel bellows. In some cases, rubber or PTFE are used, depending on the process fluid characteristics and the accuracy required. There are temperature and pressure limitations due to bellows and the structure of the system may lead to a reading offset. The meter must be securely mounted on a horizontal plane for optimal accuracy.

The advantages of this method include

1. They give continuous reading and can be calibrated accurately.
2. They are rugged and can be used for two-phase liquids such as slurries, sugar solutions, and powders.

The disadvantages of these meters include

1. They must be installed horizontally on a solid base. These meters are not flexible enough to adapt to any process; thus, the process must be designed around it.
2. They are bulky and cumbersome to use.
3. They are unsuitable for gas density measurements.

45.3.5 Balance-Type Densitometers

Balance-type densitometers are suitable for liquid and gas density measurements. There are many different types; four of the most commonly used ones are discussed in the following.

45.3.6 Balanced-Flow Vessel

A fixed-volume vessel, shown in Figure 45.4, is employed for the density measurements. While the liquid is flowing continuously through the vessel, it is weighed automatically by a sensitive scale by means of a spring balance system or a pneumatic force balance transmitter. Because the volume and the weight of the liquid are known, the density or SG can easily be calculated and scaled in respective units. In the design process, extra care must be exercised for the flexible end connections.

45.3.7 Chain-Balanced Float Densitometers

In chain-balanced float densitometers, a self-centering, fixed-volume, submerged plummet is used, as illustrated in Figure 45.5. The plummet is located entirely under the liquid surface. At balance, the plummet operates without friction and is not affected by surface contamination. Under steady-state

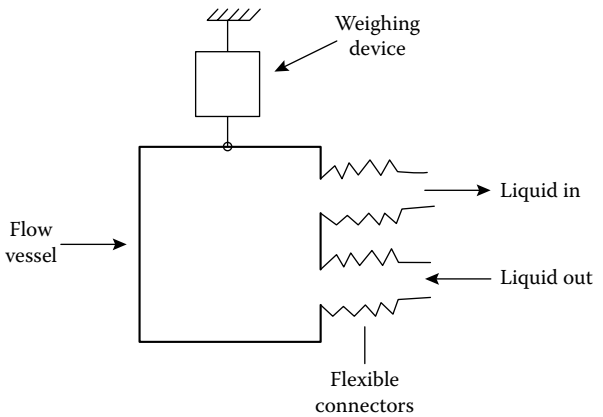

FIGURE 45.4 A balanced-flow vessel. An accurate spring balance or force balance system is used to weigh the vessel as the liquid flows through it.

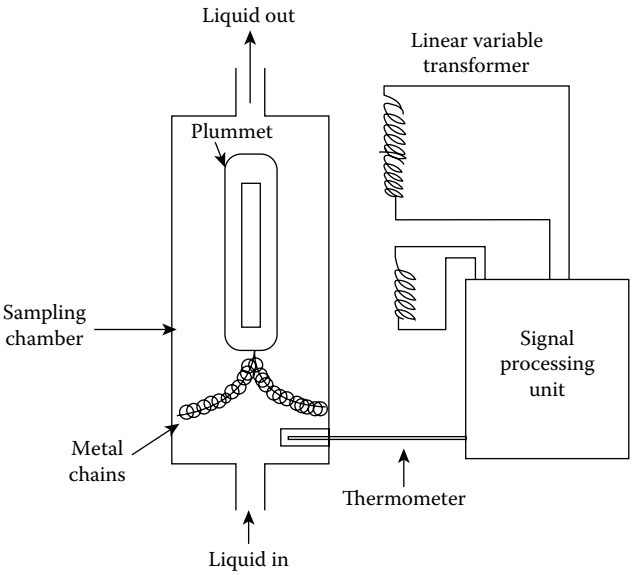

FIGURE 45.5 Chain-balanced float. The fixed-volume and fixed-weight plummet totally suspended in the liquid assumes equilibrium position, depending on the density. The force exerted by the chains on the plummet is a function of plummet position; hence, the measured force is proportional to the density of the liquid.

conditions, the plummet assumes a stable position. The effective weight of the chain on the plummet varies, depending on the position of the plummet, which in turn is a function of the density of the liquid. The plummet contains a metallic transformer core that transmits changes in the position to be measured by a pickup coil. The voltage differential, a function of plummet displacement, is calibrated as a measure of variations in SG. A resistance thermometer bridge is used for the compensation of the effects of temperature on the density.

45.3.8 Gas Specific Gravity Balance

A tall column of gas is weighed by the floating bottom of the vessel. This weight is translated into the motion of an indicating pointer, which moves over a scale graduated in units of density or SG. This method can be employed for the density measurement of gases.

45.3.9 Buoyancy Gas Balance

In this instrument, a displacer is mounted on a balance beam in a vessel, as shown in Figure 45.6. The displacer is balanced for air, and the manometer reading is noted at the exact balance pressure. The air is then displaced by gas, and the pressure is adjusted until the same balance is restored. The ratio of the pressure of air to the pressure of gas is then the density of the gas relative to air. This method is commonly applied under laboratory conditions and is not suitable for continuous measurements.

45.3.10 Column-Type Densitometers

There are a number of different versions of column methods. As a typical example, a reference column method is illustrated in Figure 45.7. A known head of sample liquid and water from the respective bubbler pipes is used. A differential pressure-measuring device compares the pressure differences, proportional to relative densities of the liquid and the water. By varying the depth of immersion of the pipes,

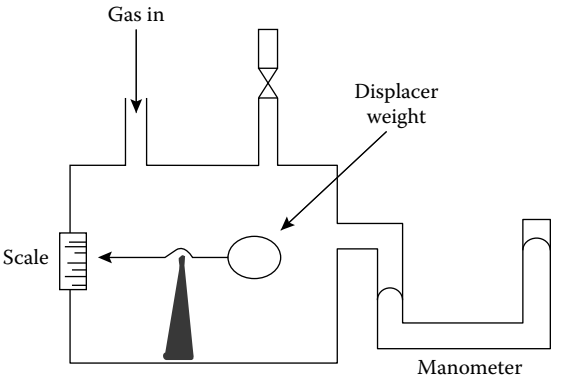

FIGURE 45.6 Buoyancy gas balance. The position of the balance beam is adjusted by a set pressure air. The air is then displaced by gas of unknown density having the same pressure. The difference in the reading of the balance beam gives the SG of the gas. The pressures are read on the manometer.

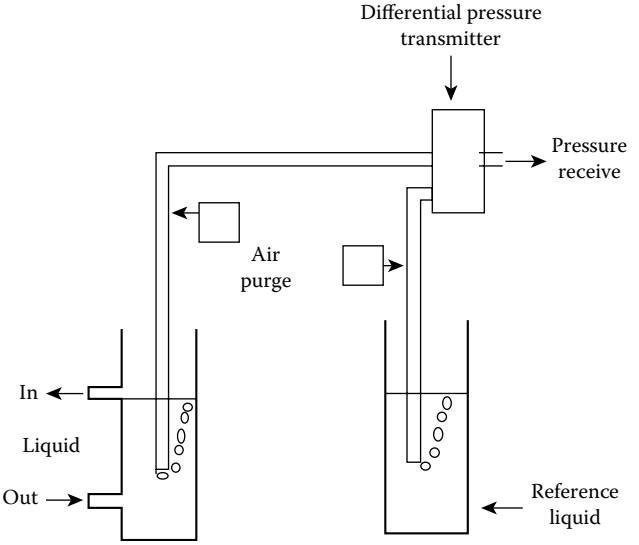

FIGURE 45.7 A reference column densitometer. Two identical tubes, having the same distance from the surface, are placed in water and liquid. Water with known density characteristics is used as the reference. The pressure necessary to displace the fluid inside the tubes is proportional to the density of the fluid. The pressure difference at the differential pressure transmitter is translated into relative densities.

a wide range of measurements can be obtained. Both columns must be maintained at the same temperature to avoid the necessity for corrections due to possible temperature effects.

A simpler and more widely used method of density measurement is achieved by the installation of two bubbler tubes as illustrated in Figure 45.8. The tubes are located in the sample fluid such that the end of one tube is higher than that of the other. The pressure required to bubble air into the fluid from both tubes is equal to the pressure of the fluid at the end of the bubbler tubes. The outlet of one of the tubes is higher than the other one. The distances of the openings of the tubes are fixed; hence, the difference in the pressure is the same as the weight of a column of liquid between the ends. Therefore, the differential pressure measurement is equivalent to the weight of the constant volume of the liquid, and calibrations can be made such that they have a direct relationship to the density of the liquid. This method is accurate to within 0.1%–1% SG. It must be used with liquids that do not crystallize or settle in the measuring chamber during measurements.

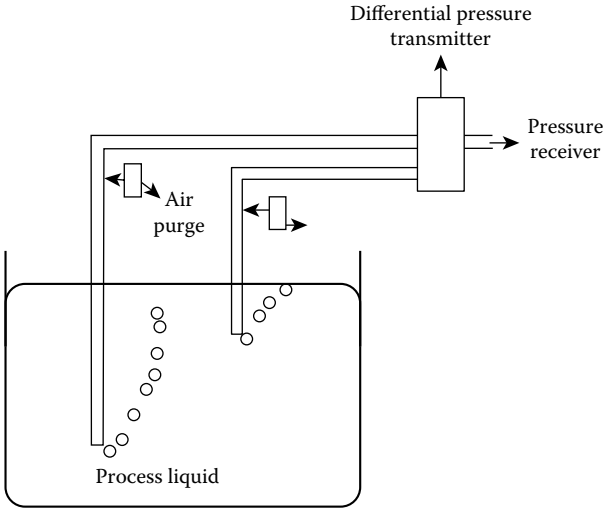

FIGURE 45.8 A two-tube column densitometer. The pressure difference at the differential pressure transmitter depends on the relative positions of the openings of the pipes and the density of liquid. Once the relative positions are fixed, the pressure difference can be related to the equivalent weight of the liquid column at the openings of the pipes, hence the density of the liquid.

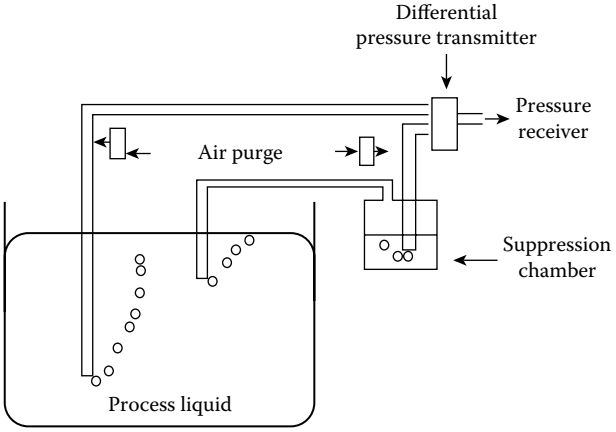

FIGURE 45.9 Suppression-type, two-tube column densitometer. Operation principle is the same as in densitometers in Figures 45.7 and 45.8. In this case, the suppression chamber gives greater accuracy in readings.

Another version is the range suppression type, which has an additional constant pressure drop chamber as shown in Figure 45.9. This chamber is in series with the low-pressure side to give advantages in scaling and accurate readings of densities.

45.3.11 Vibrating Element Densitometers

If a body containing or surrounded by a fluid is set to resonance at its natural frequency, then the frequency of oscillation of the body will vary with the properties of the fluid. The natural frequency is directly proportional to the stiffness of the body and inversely proportional to the combined mass of the body and the fluid. Vibrations are also dependent on the shape, size, and elasticity of the material,

induced stress, mass, and mass distribution of the body. Basically, the vibration of the body can be equated to motion of a mass attached to a mechanical spring. Hence, an expression for the frequency can be written as

$$\text{Resonant frequency} = \text{SQRT}\frac{K}{M + k\rho} \tag{45.3}$$

where
K is the system stiffness
M is the transducer mass
k is the system constant
ρ is the fluid density

A factor common to all types of vibrating element densitometers is the problem of setting the element in vibration and maintaining its natural resonance. There are two drives for the purpose.

45.3.12 Magnetic Drives

Magnetic drives of the vibrating element and the pickup sensors of vibrations are usually achieved using small coil assemblies. Signals picked up by the sensors are amplified and fed back as a drive to maintain the disturbing forces on the vibrating body of the meter.

In order to achieve steady drives, the vibrating element sensor can be made from nonmagnetic materials. In this case, small magnetic armatures are attached.

The main advantage of magnetic drive and pickup systems is that they are noncontact methods. They use conventional copper windings and they are reliable within a wide temperature range of –200 °C to +200 °C.

45.3.13 Piezoelectric Drives

A selective range of piezoelectric materials are available to meet the requirements of driving vibrating elements. These materials demonstrate good temperature characteristics as do magnetic drive types. They also have the advantage of being low in cost. They have high impedances thus making the signal conditioning circuitry relatively easy. They do not require magnetic sensors.

The piezoelectric drives are mechanically fixed on the vibrating element by adhesives. Therefore, attention must be paid to the careful placement of the mount in order to reduce the strain experienced by the piezo element due to thermal and pressure stresses while the instrument is in service.

A number of different types of densitometers have been developed that utilize this phenomenon. The three main commercial types are introduced here.

45.3.14 Vibrating Tube Densitometers

Vibrating tube densitometers are suitable for applications in highly viscous liquids and slurries. The mode of operation of vibration tube meters is based on the transverse vibration of tubes as shown in Figure 45.10. The tube and the driving mechanisms are constrained to vibrate in a single plane. As the liquid moves inside the tube, the density of the entire liquid is measured. The tube length is set to approximately 20 times longer than the tube diameter.

A major design problem with the vibrating tube method is the conflict of limiting the vibrating element to a finite length and fixing the nodes accurately. Special attention must be paid to avoid any exchange of vibration energy outside the sensory tube. In one type, a single tube is used and it has one important disadvantage of presenting obstruction to the flow, thus experiencing some pressure losses. In another type, a twin tube is used, which offers a very small blockage (Figure 45.11), and it can easily

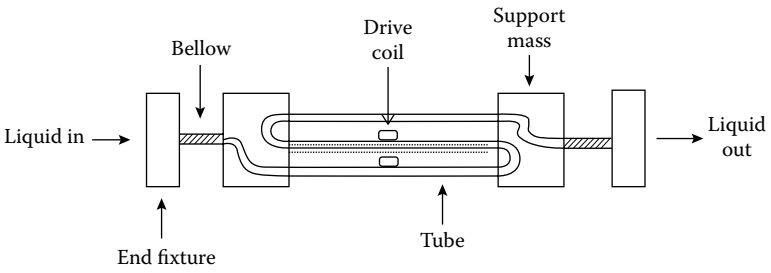

FIGURE 45.10 A vibrating tube densitometer. Tube containing fluid is vibrated at resonant frequency by an electromagnetic vibrator. The resonant frequency, which is a function of the density of the fluid, can be measured accurately. The tube is isolated from the fixtures by carefully designed bellows.

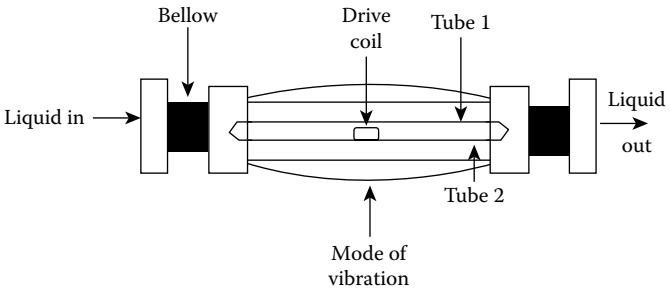

FIGURE 45.11 Two-tube vibrating densitometer. The two tubes are vibrated in antiphase for greater accuracy. Twin-tube densitometers are compact in size and easy to use.

be inspected and cleaned. The twin-tube types are compact size, hence offering another distinct advantage. Often, the twin tubes are designed to achieve a good dynamic balance, with the tubes vibrating in antiphase. Their nodes are fixed at the ends, hence demonstrating maximum sensitivity to installation defects, clamping, and mass loading.

The main design problems of the vibrating tube sensors are in minimizing the influence of end padding and overcoming the effects of pressure and temperature. Bellows are used at both ends of the sensor tubes to isolate the sensors from external vibrations. Bellows also minimize the end loadings due to differential expansions and installation stresses.

The fluid runs through the tubes; therefore, no pressure balance is required. Nevertheless, in some applications, the pressure stresses the tubes, resulting in changes in stiffness. Some manufacturers modify the tubes to minimize the pressure effects. In these cases, corrections are necessary only when high accuracy is mandatory. The changes in the Young's modulus with temperature can be reduced to near zero by using materials such as Ni-span-C compounds whenever corrosive properties of fluids permit. Usually, manufacturers provide pressure and temperature correction coefficients for their products.

It is customary to calibrate each vibration element densitometer against others as a transfer of standards. Often, the buoyancy method is used for calibration purposes. The temperature and pressure coefficients are normally found by exercising the transducer over a range of temperatures and pressures on a liquid with well-known properties. Prior to calibration, the vibration tube densitometers are subjected to a programmed burn-in cycle to stabilize them against temperature and pressure fluctuations.

45.3.15 Vibrating Cylinder Densitometers

A thin-walled cylinder, with a 3:1 length to diameter ratio, is fixed with stiff ends. The thickness of the cylinder wall varies from 25 to 300 μm, depending on the density range and type of fluid used. The cylinder can be excited to vibrate in a hoop mode by magnetic drives mounted either in or outside the cylinder.

For good magnetic properties, the cylinder is made of corrosion-resistant magnetic materials. Steel such as FV520 is often used for this purpose. Such materials have good corrosion-resistance characteristics; unfortunately, due to their poor thermoelastic properties, they need extensive corrections for temperature. Nickel–iron alloys such as Ni-span-C are often used to minimize the effects of temperature. Once correctly treated, the Ni-span-C alloy has near-zero Young's modulus properties. Because the cylinder is completely immersed in the fluid, there are no pressure coefficients.

The change in the resonant frequency is determined by the local mass loading of the fluid in contact with the cylinder. The curve of frequency against density is nonlinear and has a parabolic shape, thus requiring linearization to obtain practical outputs. The resonant frequency varies from 2 to 5 kHz, depending on the density range of the instrument. The cylinders need precision manufacturing and thus are very expensive to construct. Each meter needs to be calibrated individually for different temperatures and densities to suit specific applications. In the case of gas density applications, gases with well-known properties (e.g., pure argon or nitrogen) are used for calibrations. In this case, the meters are subjected to a gas environment with controlled temperature and pressure. The calibration curves are achieved by repetitions to suit the requirements of individual customer for a particular application. In the case of liquids, the meters are calibrated with liquids of known densities, or they are calibrated against another standard (e.g., pycnometer or buoyancy-type densitometers).

Vibration cylinder-type densitometers have zero pressure coefficients and they are ideal for liquefied gas products or refined liquids. Due to relatively small clearances between cylinder and housing, they require regular cleaning. They are not suitable for liquids or slurries with high viscous properties.

45.3.16 Tuning Fork Densitometers

These densitometers make use of the natural frequency of low-mass tuning forks, shown in Figure 45.12. In some cases, the fluid is taken into a small chamber in which the electromechanically driven forks are situated. In other cases, the fork is inserted directly into the liquid. Calibration is necessary in each application. The advantages of vibrating element meters include

1. They are suitable for both liquids and gases with reasonable accuracy.
2. They can be designed for real-time measurements.
3. They can easily be interfaced because they operate on frequencies and they are inherently digital.
4. They are relatively robust and easy to install.
5. Programmable and computerized versions are commonly available. Programmed versions make all the corrections automatically. They provide the output of live density, density at reference conditions, relative density, SG, concentration, solid contents, etc.

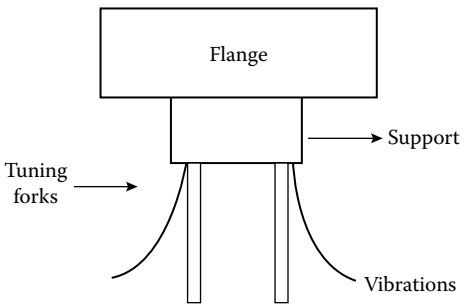

FIGURE 45.12 The tuning fork densitometer. Twin forks are inserted into the fluid, and the natural frequencies are measured accurately. The natural frequency of the forks is a function of the density of the fluid.

The disadvantages include

1. They do not relate directly to primary measurements; therefore, they must be calibrated.
2. They all have problems in measuring multiphase liquids.

45.3.17 Radioactive Densitometers

As radioactive isotopes decay, they emit radiation in the form of particles or waves. This physicalphenomenon can be used for the purposes of density measurement. For example, γ rays can be passed through the samples and their rate of arrivals, which is dependent on the density of the materials in between, can be determined using ion- or scintillation-based detectors. Generally, γ-ray mass absorption rate is independent of material composition; hence, they can be programmed for wide-range applications. Densitometers based on radiation methods can provide accuracy up to +0.0001 g mL^{-1}. Many of these devices have self-diagnostic capabilities and are able to compensate for drifts caused by the decay of the source, thus pinpointing any signaling problems.

If γ rays of intensity J_0 penetrate a material of a density ρ and thickness d, then the intensity of the radiation after passing through the material can be expressed by

$$J = J_0 \exp(n\rho d) \tag{45.4}$$

where n is the mass absorption coefficient.

The accuracy of the density measurement depends on the accuracy of the measurement of the intensity of the radiation and the path length d. A longer path length through the material gives a stronger signal to be detected.

For accurate operations, there are many arrangements for relative locations of transmitters and detectors, some of which are illustrated in Figures 45.13 and 45.14. Generally, the source is mounted in a lead container clamped onto the pipe or the container wall. In many applications, the detector is also clamped onto the wall.

The advantages of using radioactive methods include

1. The sensor does not touch the sample; hence, there is no blockage to the path of the liquid.
2. Multiphase liquids can be measured.
3. They come in programmable forms and are easy to interface.
4. They are most suitable in difficult applications, such as mining, chemical, metallurgical, and other heavy process industries.

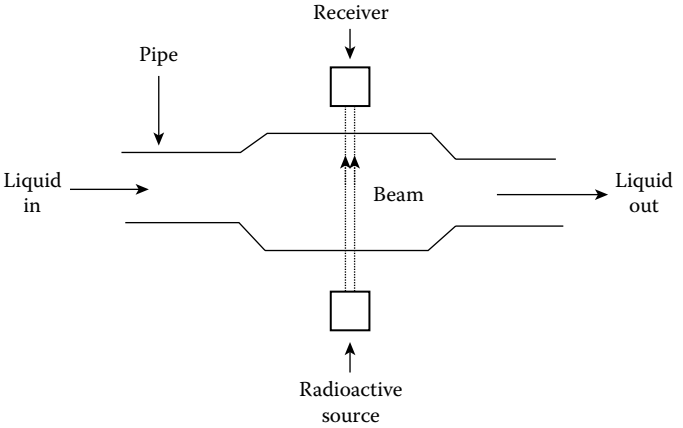

FIGURE 45.13 Fixing radioactive densitometer on an enlarged pipe. The pipe is enlarged to give longer beam length through the liquid and hence better attenuation of the radioactive energy.

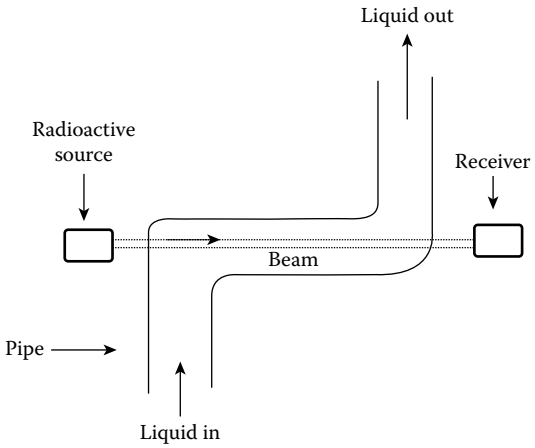

FIGURE 45.14 Fixing radioactive densitometer on an elongated pipe. Elongated path yields a longer path length of the radioactive energy through the liquid, hence a stronger attenuation.

The disadvantages include

1. A radioactive source is needed; hence, there is difficulty in handling.
2. For reasonable accuracy, a minimum path length is required.
3. There could be long time constants, making them unsuitable in some applications.
4. They are suitable only for solid and liquid density measurements.

45.3.18 Refractometer and Index of Refraction Densitometers

Refractometers are essentially optical instruments operating on the principles of refraction of light traveling in liquid media. Depending on the characteristics of the samples, measurement of refractive index can be made in a variety of ways (e.g., critical angle, collimation, and displacement techniques). Usually, an in-line sensing head is employed, whereby a sensing window (commonly known as a prism) is wetted by the product to be measured. In some versions, the sensing probes must be installed inside the pipelines or in tanks and vessels. They are most effective in reaction-type process applications where blending and mixing of liquids take place. For example, refractometers can be used to measure the contents of the dissolved soluble solids accurately.

Infrared diodes, lasers, and other lights may be used as the light sources. However, this measurement technique is not recommended in processes containing suspended solids, high turbidity, entrained air, heavy colors, and poor transparency or opacity, or substances having extremely high flow rates. The readings are automatically corrected for variations in process temperature. The processing circuitry can include signal outputs adjustable in both the frequency and the duration.

Another version of a refractometer is the index of refraction-type densitometer. For example, in the case of position-sensitive detectors, the index of refraction of liquid under test is determined by measuring the lateral displacement of a laser beam. When the laser beam impinges on the cell at an angle of incidence, as in Figure 45.15, the axis of the emerging beam is displaced by the cell wall and by the inner liquid. The lateral displacement can accurately be determined by position-sensitive detectors. For maximum sensitivity, the devices need to be calibrated with the help of interferometers.

Refractometers are often used for the control of adulteration of liquids of common use (e.g., edible oils, wines, and gasoline). They also find application in pulp and paper, food and beverage, sugar, dairy, and other chemical industries.

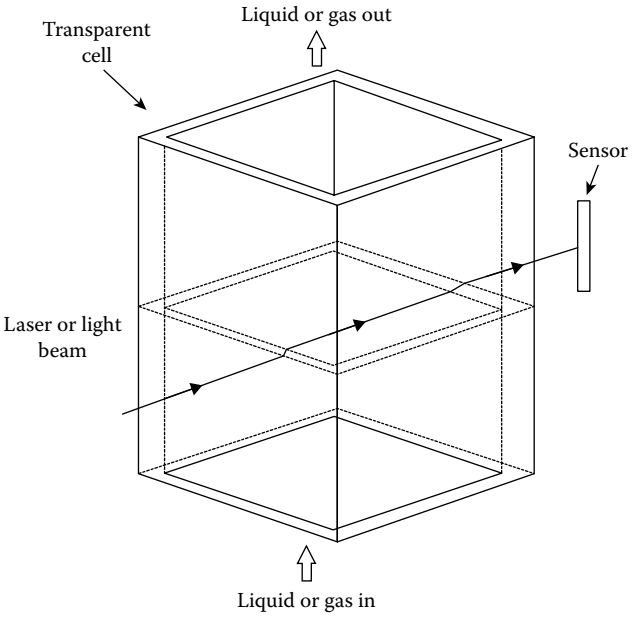

FIGURE 45.15 The index of refraction-type densitometer. The angle of refraction of the beam depends on the shape, size, and thickness of the container and the density of fluid in the container. Because the container has the fixed characteristics, the position of the beam can be related to density of the fluid. Accurate measurement of the position of the beam is necessary.

45.3.19 Coriolis Densitometers

The Coriolis density metering systems employ similar principles as vibrating tube densitometers with slight variations in the design. Often, they contain a number of sensors and signal-processing transmitters. Each sensor consists of one or two flow tubes enclosed in the sensor housing. They are manufactured in various shapes and sizes. The sensor tubes are securely anchored at the fluid inlet and outlet points and force is vibrated at the free end, as shown in Figure 45.16. The sensor operates by applying Newton's second law of motion ($F = ma$).

Inside the housing, the tubes are vibrated in their natural frequencies using drive coils and related feedback circuits. This resonant frequency of the assembly is a function of the geometry of the vibrating element, the material of construction, and the mass of the tube assembly. The tube mass comprises two parts: the mass of the tube itself and the mass of the fluid inside the tube. The mass of the tube is fixed for a given sensor. The mass of fluid in the tube is equal to the fluid density multiplied by the volume.

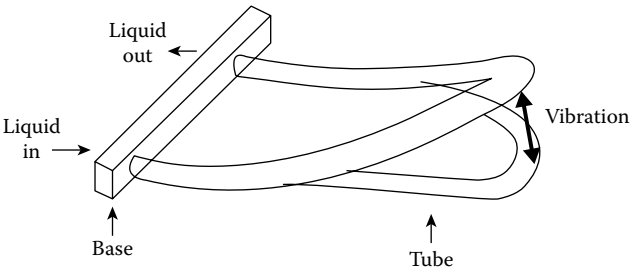

FIGURE 45.16 Coriolis densitometer. Vibration of the tube is detected and related to the mass and flow rate of the fluid. Further calibrations and calculations must be made to determine the densities of fluids in the pipes.

Because the tube volume is constant, the frequency of oscillation can be related directly to the fluid density. Therefore, for a given geometry of tube and the material of the construction, the density of the fluid can be determined by measuring the resonant frequency of the vibration. Temperature sensors are used for overcoming the effects of changes in modulus of elasticity of the tube. The fluid density is calculated using a linear relationship between the density and the tube period and the calibration constants.

Special peripherals, based on microprocessors, are offered by various manufacturers for a variety of measurements. However, all density peripherals employ the natural frequency of the sensor coupled with the sensor temperature to calculate online density of the process fluid. Optional communication, interfacing facilities, and appropriate software are also additional features of these densitometers.

45.3.20 Absorption-Type Densitometers

Absorption techniques are also used for density measurements in some custom-designed and custom-specific applications. X-rays, visible light, UV light, and sonic absorptions are typical examples of this method. Essentially, attenuation and phase shift of a generated beam going through the sample is sensed to be related to the density of the sample. Most absorption-type densitometers are carefully designed for applications having particular characteristics. Two typical examples are (1) UV absorption or x-ray absorptions that are used for determining the local densities of mercury deposits in arc discharge lamps and (2) ultrasonic density sensors that are used in difficult density measurements (e.g., density measurement of slurries). The lime slurry, for example, is a very difficult material to handle. It has a strong tendency to settle out and coat all equipment with which it comes in contact with. An ultrasonic density control sensor can fully be emerged into the agitated slurry, thus avoiding the problems of coating and clogging. Inasmuch as the attenuation of the ultrasonic beam is proportional to the suspended solids, the resultant electronic signal is proportional to the SG of the slurry. Such devices can give accuracy up to 0.01%. The ultrasonic device measures the percentage of the suspended solids in the slurry by providing a close approximation of the SG.

Bibliography

Boiten, W., *Hydrometry: A Comprehensive Introduction to the Measurement of Flow in Open Channels*, CRC Press, Boca Raton, FL, 2008.

Davis, R. S., *Measurement of Mass and Density*, Encyclopedia of Applied Physics, Wiley On-Line Library. http://onlinelibrary.wiley.com/doi/10.1002/3527600434.eap220.pub2/abstract (accessed on July 2, 2012).

Density, New world encyclopedia. http://www.newworldencyclopedia.org/entry/Density (accessed on October 2, 2011).

Density Measurement, Technical data sheet, Emerson process. http://www.emersonprocess.com/rosemount/document/tds/3208_00q.pdf (accessed on July 3, 2012).

Fujii, K., Precision density measurements of solid materials and hydrostatic weighing, *Measurement and Science Technology*, 17, 2551–2559, 2006.

Grimes, C. A., Kouzoudis, D., and Mungle, C., Simultaneous measurement of liquid density and viscosity using remote query magnetoelastic sensors, *Review of Scientific Instruments*, 71(10), 3822–3824, 2000.

Gupta, S. V., *Practical Density Measurements and Hydrometer*, Taylor & Francis Group, Boca Raton, FL, 2002.

Mass and Related Quantities Capabilities, National Measurement Institute, Australia http://www.measurement.gov.au/Services/calibrationtesting/Pages/Massandrelatedquantities.aspx (accessed on August 3, 2012).

Pendrill, L. R., Refractometry and gas density, *Metrologia*, 41(2), l, 2004.

Wiederseiner, S., Andreini, N., Epely-Chauvin, G., and Ancey, C., Refractive-index and density matching in concentrated particle suspensions: A review, *Experiments in Fluids*, 50(5), 1183–1206, 2011.

Partial List of Manufacturers and Suppliers

ABB Automation, Inc.—TOTALFLOW® Products Group, 3010 Briarpark, Houston, TX 77042, Phone: 713-821-8128, 866-365-8299 (toll free), Fax: 713-821-3530, www.totalflow.com

AMETEK Power Instruments, 255 N. Union St., Rochester, NY 14605, Phone: 585-263-7700, 800-881-4156 (toll free), Fax: 585-262-4777, www.ametekpower.com

Analtech, Inc., 75 Blue Hen Dr., Newark, DE 19713, Phone: 302-737-6960, 800-441-7540 (toll free), Fax: 302-737-7115, www.ichromatography.com/

Analytical Process, Inc., 3311 Richmond Ave., Suite 110, Houston, TX 77098, Phone: 713-526-6552, Fax: 713-522-1563, www.processanalytical.com

Automation Products, Inc., 3030 Max Roy St., Houston, TX 77008, Phone: 713-869-0361, 800-231-2062 (toll free), Fax: 713-869-7332, www.dynatrolusa.com

CCSI, 221 Beaver St., Akron, OH 44301, Phone: 330-376-3600, Fax: 330-376-8500, www.ccsi-inc.com

Central States Group, 8720 S. 137th Circle, Omaha, NE 68138-6198, Phone: 402-894-1003, 800-383-2747 (toll free), Fax: 402-894-1339, www.centralstatesgroup.com

Density Analytics LLC, 12 Grand Banks Circle, Marlton, NJ 08053, Phone: 856-797-1449, www.densityanalytics.com/

Dynatrol® Div., Automation Products, Inc., 3030 Maxroy St., Houston, TX 77008, Phone: 713-869-0361, 800-231-2062 (toll free), Fax: 713-869-7332, www.dynatrolusa.com

Eagle Eye Power Solutions LLC, 4230 N. Oakland Ave. #176, Milwaukee, WI 53211, Phone: 414-962-3377, 877-805-3377 (toll free), Fax: 414-962-3660, eepowersolutions.com/

Flexial Corp., Edge Welded Metal Bellows, P.O. Box 3105, Cookeville, TN 38502-3105, Phone: 931-432-1853, Fax: 931-432-1889, www.flexial.com

FMC Technologies-Material Handling Solutions, P.O. Box 1370, Tupelo, MS 38802, Phone: 662-869-5711, Fax: 662-869-7401, www.fmctechnologies.com

Graham Optical Systems, 9530 Topanga Canyon Blvd., Chatsworth, CA 91311, Phone: 818-700-1263, Fax: 818-700-1627, www.grahamoptical.com

Grainger Industrial Supply, 100 Grainger Pkwy., Lake Forest, IL 60045, Phone: 847-535-1000, 888-361-8649 (toll free), Fax: 847-535-9123, www.grainger.com/thomasnet

Honeywell Sensing and Control, 1985 Douglas Dr. North, MN10-192B, Golden Valley, MN 55422, Phone: 763-954-4818, 800-446-6555 (toll free), sensing.honeywell.com/index.cfm/ci_id/15…

ITT Barton, 800 S. Turnbull Canyon Rd., City of Industry, CA 91745, Phone: 626-961-2547, 800-291-3550 (toll free), Fax: 800-408-2168

Ives Equipment Corp., 601 Croton Rd., King of Prussia, PA 19406-3111, Phone: 610-265-3071, 877-768-1600 (toll free), Fax: 610-768-1605, www.ivesequipment.com

KROHNE, Inc., 7 Dearborn Rd., Peabody, MA 01960, Phone: 978-535-6060, 800-356-9464 (toll free), Fax: 978-535-1720, www.krohne.com/index.php?id=12076

LND, Inc., 3230 Lawson Blvd., Oceanside, NY 11572, Phone: 516-678-6141, Fax: 516-678-6704, www.lndinc.com

Mettler-Toledo, Inc., 5 Barr Rd., Ithaca, NY 14850-9117, Phone: 607-257-6000, 800-836-0836 (toll free), Fax: 607-257-5232, us.mt.com/us/en/home.html

Micromeritics Instruments Corp., 4356 Communications Dr., Norcross, GA 30093, Phone: 770-662-3633, Fax: 770-662-3696, www.micromeritics.com

Micro Motion, a Division of Emerson Process Management, 7070 Winchester Circle, Boulder, CO 80301, Phone: 303-530-8400, 800-760-8119 (toll free), Fax: 503-530-8459, www2.emersonprocess.com/en-us/brands/mic…

MPE-Modern Process Equipment, Inc., 3125 S. Kolin Ave., Chicago, IL 60623-4831, Phone: 773-254-3929, Fax: 773-254-3935, www.mpechicago.com

MC Schroeder Co., 3625 Denver Dr., Denver, NC 28037, Phone: 704-489-6171, 800-333-3830 (toll free), Fax: 704-489-6175, www.mcschroeder.com/

NDS Products, Inc., 111 Anderson St., Pasadena, TX 77506, Phone: 713-475-2986, 800-413-4750 (toll free), Fax: 713-477-6741

PICSINC, 81 Lancaster Ave., Suite 202, Malvern, PA 19355, Phone: 610-644-7701, Fax: 610-644-9297, www.picscontrols.com

Princo Instruments, Inc., 1020 Industrial Blvd., Southampton, PA 18966-4095, Phone: 800-221-9237 (toll free), Fax: 215-355-1500, www.princolevelcontrols.com/

Sargent-Welch Scientific Co., Industrial-Collegiate Div., 911 Commerce Court, Buffalo Grove, IL 60089, Phone: 847-677-0600, Fax: 847-677-4869

SC Controls, Inc., 1366 Heritage Ct. Escondido, CA 92027, Phone: 760-480-0473, Fax: 760-480-8309

Schneider Electric-Hyde Park, 1875 Founders Dr., Dayton, OH 45420, Phone: 937-514-7207, Fax: 937-258-5830, www.sesensors.com

Sentinel, 6765 Langley Dr., Baton Rouge, LA 70809, Phone: 225-751-5893, Fax: 225-756-0365, www.sentinelndt.com/

Sierra Monitor Corp., 1991 Tarob Court, Milpitas, CA 95035, Phone: 408-262-6611, 800-727-4377 (toll free), Fax: 408-262-9042, www.sierramonitor.com

Solartron Mobrey, 19408-T Park Row, Suite 320, Houston, TX 77084, Phone: 281-398-7890, 888-696-0706 (toll free), Fax: 281-398-7891, www.solartronmobrey.com

Terriss Consolidated Industries, Inc., 807 Summerfield Ave., Asbury Park, NJ 07712, Phone: 732-988-0909, 800-342-1611 (toll free), Fax: 732-502-0526

Thermo Fisher Scientific, 81 Wyman St., Waltham, MA 02451-1105, Phone: 781-622-1000, 800-678-5599 (toll free), Fax: 781-622-1207, www.thermofisher.com/global/en/home.asp

Toshiba International Corp., 13131 W. Little York Rd., Houston, TX 77041, Phone: 713-466-0277, Fax: 713-466-8773, www.toshiba.com/ind/

Warren-Knight Instrument Co., 2045 Bennett Dr., Philadelphia, PA 19116-3019, Phone: 215-464-9300, Fax: 215-464-9303, www.warrenind.com

46

Fluid Viscosity Measurement

R.A. Secco
University of Western Ontario

M. Kostic
Northern Illinois University

J.R. deBruyn
University of Western Ontario

46.1 Shear Viscosity

An important mechanical property of fluids is *viscosity*. Physical systems and applications as diverse as fluid flow in pipes, the flow of blood, lubrication of engine parts, the dynamics of raindrops, volcanic eruptions, and planetary and stellar magnetic field generation, to name just a few, all involve fluid flow and are controlled to some degree by fluid viscosity. *Viscosity* is the tendency of a fluid to resist flow and can be thought of as the internal friction of a fluid. Microscopically, viscosity is related to molecular diffusion and depends on the interactions between molecules or, in complex fluids, larger-scale flow units. Diffusion tends to transfer momentum from regions of high momentum to regions of low momentum, thus smoothing out variations in flow velocity. In this sense, the internal friction of a fluid is analogous to the macroscopic mechanical friction, which causes an object sliding across a planar surface to slow down. In the mechanical system, energy must be supplied to sustain the motion of the object over the plane, while in a fluid, energy must be supplied to sustain a flow. Since viscosity is related to the diffusive transport of momentum, the viscous response of a fluid is called a *momentum transport process*. The flow velocity within a fluid will vary, depending on location. Consider a viscous fluid at constant pressure between two closely spaced parallel plates as shown in Figure 46.1. A force, *F*, applied to the

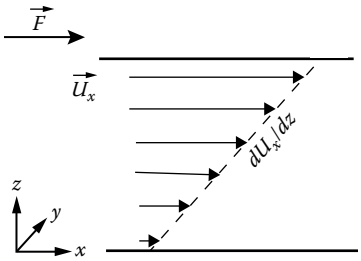

FIGURE 46.1 System for defining Newtonian viscosity. When the upper plate is subjected to a force, the fluid between the plates is dragged in the direction of the force with a velocity of each layer that diminishes away from the upper plate. The reducing velocity eventually reaches zero at the lower plate boundary.

top plate causes the fluid adjacent to the upper plate to move in the direction of $\vec{F}$. The fluid adjacent to the top plate is constrained by the no-slip boundary condition to move at the same speed as the plate. Similarly, the fluid next to the stationary bottom plate must be stationary. The motion of the top plate thus causes the fluid to flow with a velocity profile across the liquid that decreases linearly from the upper to the lower plate, as shown in Figure 46.1. This arrangement is referred to as *simple shear*. The applied force is called a *shear*, and the force per unit area a *shear stress*. The resulting deformation rate of the fluid, or equivalently the *velocity gradient* dU_x/dz, is called the *shear strain rate*, $\dot{\gamma}_{zx}$. The mathematical expression describing the viscous response of the system to the shear stress is simply

$$\tau_{zx} = \frac{\eta dU_x}{dz} = \eta \dot{\gamma}_{zx} \tag{46.1}$$

where

τ_{zx}, the shear stress, is the force per unit area exerted on the upper plate in the x-direction (and hence is equal to the force per unit area exerted by the fluid on the upper plate in the negative x-direction)

dU_x/dz is the gradient of the x-velocity in the z-direction in the fluid, that is, the shear strain rate

η is the *coefficient of viscosity*

Note that in general, the shear strain rate is a more complex function of the fluid velocity-gradient tensor. In this case, because one is concerned with a shear force that produces the fluid motion, η is more specifically called the *shear dynamic viscosity*. In fluid mechanics, where the motion of a fluid is considered without reference to force, it is common to define the *kinematic viscosity*, ν, which is simply given by

$$\nu = \frac{\eta}{\rho} \tag{46.2}$$

where ρ is the mass density of the fluid.

The viscosity defined by Equation 46.1 is relevant only for *laminar* (i.e., layered or sheetlike) or streamline flow as depicted in Figure 46.1, and it refers to the molecular viscosity or *intrinsic viscosity*. The molecular viscosity is a property of the material that depends microscopically on interactions between individual molecules and is manifested macroscopically as the fluid's resistance to flow. When the flow is turbulent, small-scale turbulent vortices can contribute to the overall diffusion of momentum, resulting in an effective viscosity, sometimes called the *eddy viscosity*, that, depending on the Reynolds number, can be as much as 10^6 times larger than the intrinsic viscosity.

Molecular viscosity is separated into *shear viscosity* and bulk or *volume viscosity*, η_v, depending on the type of strain involved. Shear viscosity is a measure of resistance to isochoric flow in a shear field, whereas volume viscosity is a measure of resistance to volumetric flow in a 3D stress field.

For most liquids, including hydrogen bonded weakly associated or unassociated, and polymeric liquids as well as liquid metals, $\eta/\eta_v \approx 1$, suggesting that shear and structural viscous mechanisms are closely related [1].

The shear viscosity of most liquids decreases with temperature, which is opposite to what occurs in gases. Under most conditions, including those relevant in engineering applications, viscosity can be considered to be independent of pressure, as temperature effects are very much larger. In the context of planetary interiors, however, the effects of high pressure cannot be ignored as viscosity normally increases as pressure increases. However, depending on composition, pressure can cause fundamental changes in the molecular structure of the fluid that can result in an anomalous viscosity decrease with increasing pressure [2].

46.2 Newtonian and Non-Newtonian Fluids

Equation 46.1 is known as Newton's law of viscosity. If the viscosity throughout the fluid is independent of strain rate, then the fluid is said to be a *Newtonian fluid*. The constant of proportionality is called the coefficient of viscosity, and a plot of stress versus strain rate for Newtonian fluids yields a straight line with a slope of η, as shown by the solid line flow curve in Figure 46.2. Examples of Newtonian fluids are pure, single-phase, unassociated gases; liquids; and solutions of low molecular weight such as water. There is, however, a large group of fluids for which the viscosity is dependent on the strain rate. Such fluids are said to be non-Newtonian and their study is called *rheology*. In differentiating between Newtonian and non-Newtonian behavior, it is helpful to consider the time scale (as well as the normal stress differences and phase shift in dynamic testing) involved in the process of a liquid responding to a shear perturbation. In general, the shear strain rate $\dot{\gamma}$ is a more complex function of the second invariant of the fluid velocity-gradient tensor; however, in a simple shear flow, like on Figure 46.1, it reduces to the velocity gradient, dU_x/dz. Therefore, the time scale related to the applied shear perturbation about the equilibrium state is t_s, where $t_s = \dot{\gamma}^{-1}$. A second time scale, t_r, called the *relaxation time*, characterizes the rate at which the relaxation of the strain in the fluid can be accomplished and is related to the time it takes for a typical flow unit to move a distance equivalent to its mean diameter. For Newtonian water, $t_r \sim 10^{-12}$ s, and, because shear rates greater than 10^6 s^{-1} are rare in practice, the time required for the fluid to respond to the strain perturbation in water is much less than the time scale of the perturbation itself (i.e., $t_r \ll t_s$). However, for non-Newtonian macromolecular liquids like polymeric liquids, for colloidal and fiber suspensions, and for pastes and emulsions, the long response times of large viscous flow units (e.g., polymer molecules or aggregates of interacting particles) can easily make $t_r > t_s$. An example

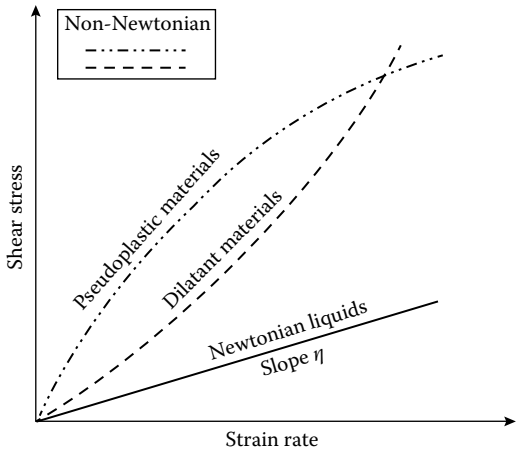

FIGURE 46.2 Flow curves illustrating Newtonian and non-Newtonian fluid behavior.

of a non-Newtonian fluid is liquid elemental sulfur, in which long chains (polymers) of up to 100,000 sulfur atoms form flow units that are easily entangled, which bind the liquid in a "rigid-like" network. Another example of a well-known non-Newtonian fluid is tomato ketchup.

With reference to Figure 46.2, Equation 46.1 can be written in a more general form:

$$\tau_{xy}(\dot{\gamma}) = \tau_{xy}(0) + \frac{\dot{\gamma}\partial\tau_{xy}(0)}{\partial\dot{\gamma}} + O(\dot{\gamma}^2) \tag{46.3}$$

Here $\tau_{xy}(0)$ is a yield stress required for flow to start, the term proportional to $\dot{\gamma}$ is the usual linear Newtonian term in the limit of small strain rates, and the nonlinear term $O(\dot{\gamma}^2)$ accounts for the nonlinear viscous response of some materials.

For a Newtonian fluid, the initial stress at zero shear rate and the nonlinear function $O(\dot{\gamma}^2)$ are both negligible (zero), so Equation 46.3 reduces to Equation 46.1, since $\partial\tau_{xy}(0)/\partial\dot{\gamma}$ then equals η. For a non-Newtonian fluid, $\tau_{xy}(0)$ may be zero but the nonlinear term $O(\dot{\gamma}^2)$ is nonzero. This characterizes fluids in which shear stress varies nonlinearly with strain rate, as shown by the dashed-dotted and dashed flow curves in Figure 46.2. The former type of fluid behavior is known as *shear thickening* or dilatancy, and an example is a concentrated suspension of cornstarch in water. The latter, much more common type of fluid behavior is known as *shear thinning* or pseudoplasticity; cream, blood, most polymers, and liquid cement are all examples. Both behaviors result from particle or molecular reorientations or rearrangements in the fluid that increase or decrease, respectively, the internal friction to shear. Non-Newtonian behavior can also arise in fluids whose viscosity changes with time of applied shear stress. Fluids whose viscosity increases over time when a shear stress is applied are called *rheopectic*. Conversely, liquids whose viscosity decreases with time are called *thixotropic fluids*. Nondrip paint, which will not flow until a shear stress is applied by the paint brush for a sufficiently long time, is a common example of a thixotropic fluid.

Fluid deformation that is not recoverable after removal of the stress is typical of the purely viscous response. The other extreme response to an external stress is purely elastic and is characterized by an equilibrium deformation that is fully recovered on removal of the stress. There are an infinite number of intermediate or combined viscous/elastic responses to external stress, which are grouped under the behavior known as *viscoelasticity*. Fluids that behave elastically in some stress range require a limiting or yield stress before they will flow as a viscous fluid. A simple, empirical, constitutive equation often used for this type of rheological behavior is of the form

$$\tau_{yx} = \tau_y + \dot{\gamma}^n \eta_p \tag{46.4}$$

where τ_y is the *yield stress*, η_p is an *apparent viscosity* called the plastic viscosity, and the exponent n allows for a range of non-Newtonian responses: $n = 1$ describes pseudo-Newtonian behavior and is called a *Bingham fluid*; $n < 1$ describes shear thinning behavior; and $n > 1$ describes shear thickening behavior. Interested readers should consult [3–9] for further information on applied rheology.

46.2.1 Dimensions and Units of Viscosity

From Equation 43.1, the dimensions of dynamic viscosity are $M\,L^{-1}\,T^{-1}$, and the basic SI unit is the Pascal second (Pa · s), where 1 Pa · s = 1 N s m^{-2}. The c.g.s. unit of dyn s cm^{-2} is the poise (P). The dimensions of kinematic viscosity, from Equation 46.2, are $L^2\,T^{-1}$, and the SI unit is $m^2\,s^{-1}$. For most practical situations, this is usually too large and so the c.g.s. unit of $cm^2\,s^{-1}$, or the stoke (St), is preferred. Table 46.1 lists some common fluids and their shear dynamic viscosities at atmospheric pressure and 20 °C.

TABLE 46.1 Shear Dynamic Viscosity of Some Common Fluids at 20 °C and 1 atm

Fluid	Shear Dynamic Viscosity (Pa·s)
Air	1.8×10^{-4}
Water	1.0×10^{-3}
Mercury	1.6×10^{-3}
Automotive engine oil (SAE 10W30)	1.3×10^{-1}
Dish soap	4.0×10^{-1}
Corn syrup	6.0

46.3 Viscometer Types

46.3.1 Rheometer

A viscometer (also called viscosimeter) is an instrument used to measure the viscosity of a fluid. For liquids with viscosities that vary with flow conditions, an instrument called a rheometer is used. Viscometers only measure under one flow condition. The instruments for viscosity measurements are designed to determine "a fluid's resistance to flow," a fluid property defined earlier as viscosity. The fluid flow in a given instrument geometry defines the strain rates, and the corresponding stresses are the measure of resistance to flow. If strain rate or stress is set and controlled, then the other one will, everything else being the same, depend on the fluid viscosity. If the flow is simple (one dimensional, if possible) such that the strain rate and stress can be determined accurately from the measured quantities, the absolute dynamic viscosity can be determined; otherwise, the relative viscosity will be established. For example, the fluid flow can be set by dragging the fluid with a sliding or rotating surface, or a body falling through the fluid, or by forcing the fluid (by external pressure or gravity) to flow through a fixed geometry, such as a capillary tube, annulus, a slit (between two parallel plates), or orifice. The corresponding resistance to flow is measured as the boundary force or torque or pressure drop. The flow rate or efflux time represents the fluid flow for a set flow resistance, like pressure drop or gravity force. The viscometers are classified, depending on how the flow is initiated or maintained, as in Table 46.2.

The basic principle of all viscometers is to provide as simple flow kinematics as possible, preferably 1D (*isometric*) *flow*, in order to determine the shear strain rate accurately, easily, and independent of fluid type. The resistance to such flow is measured, and thereby the shearing stress is determined. The shear viscosity is then easily found as the ratio between the shearing stress and the corresponding shear strain rate. Practically, it is never possible to achieve desired 1D flow or ideal geometry, and a number of errors, listed in Table 46.3, can occur and need to be accounted for [4–8]. A sample list of manufacturers/distributors of commercial viscometers/rheometers is given in Table 46.4. There is no implied endorsement of any manufacturer on this list.

46.3.2 Rotational Methods/Concentric Cylinders

The main advantage of the rotational viscometer as compared to many other viscometers is its ability to operate continuously at a given shear rate, so that other steady-state measurements can be conveniently performed. That way, time dependency, if any, can be detected and determined. Also, subsequent measurements can be made with the same instrument and sampled at different shear rates, temperature, etc. For these and other reasons, *rotational viscometers* are among the most widely used class of instruments for rheological measurements.

TABLE 46.2 Viscometer/Rheometer Classification and Basic Characteristics

Type/Geometry	Basic Characteristics/Comments
Drag flow types: Flow set by motion of instrument boundary/surface using external or gravity force	
Rotating concentric cylinders (Couette)	Good for low viscosity, high shear rates; for $R_2/R_1 \cong 1$, see Figure 46.3; difficult to clean thick fluids
Rotating cone and plate	Homogeneous shear, best for non-Newtonian fluids and normal stresses; need good alignment, problems with loading and evaporation
Rotating parallel disks	Similar to cone and plate but inhomogeneous shear; shear varies with gap height, easy sample loading
Sliding parallel plates	Homogeneous shear, simple design, good for high viscosity; difficult loading and gap control
Falling body (ball, cylinder)	Very simple, good for high temperature and pressure; need density and special sensors for opaque fluids, not good for viscoelastic fluids
Rising bubble oscillating body	Similar to falling body viscometer; for transparent fluids
Oscillating body	Needs instrument constant, good for low-viscous liquid metals
Pressure flow types: Fluid set in motion in fixed instrument geometry by external or gravity pressure	
Long capillary (Poiseuille flow)	Simple, very high shears and range but very inhomogeneous shear, variable time dependency, and is time consuming
Orifice/cup (short capillary)	Very simple, reliable but not for absolute viscosity and non-Newtonian fluids
Slit (parallel plates) pressure flow	Similar to capillary but difficult to clean
Axial annulus pressure flow	Similar to capillary, better shear uniformity but more complex, eccentricity problem and difficult to clean
Others/miscellaneous	
Ultrasonic	Good for high-viscosity fluids, small sample volume, gives shear and volume viscosity, and elastic property data; problems with surface finish and alignment, complicated data reduction

Source: Adapted from Macosko, C. W., *Rheology: Principles*, *Measurements*, *and Applications*, VCH, New York, 1994.

TABLE 46.3 Typical Causes of Viscometer/Rheometer Errors

Error/Effect	Cause/Comment
End/edge effect	Energy losses at the fluid entrance and exit of main test geometry
Kinetic energy losses	Loss of pressure to kinetic energy
Secondary flow	Energy loss due to unwanted secondary flow, vortices, etc.; increases with Reynolds number
Nonideal geometry	Deviations from ideal shape, alignment, and finish
Shear rate nonuniformity	Important for non-Newtonian fluids
Temperature variation and viscous heating	Variation in temperature, in time, and in space, influences the measured viscosity
Turbulence	Partial and/or local turbulence often develops even at low Reynolds numbers
Surface tension	Difference in interfacial tensions
Elastic effects	Structural and fluid elastic effects
Miscellaneous effects	Depend on test specimen, melt fracture, thixotropy, rheopexy

TABLE 46.4 Viscometer/Rheometer Manufacturers and Distributors (for measurement at 1 atm)

A&D Engineering Co. Ltd	Hydramotion	Perten
Ametek	Kinematica AG	Physica Messtechnik GmbH
Ankersmid Lab	Kittiwake	REL
Anton Parr	Koehler Inst. Co., Inc.	Reologica Instr.
ATS	Lamy Rheology	Rheometric Scientific, Inc.
Avenisense	Lauda	Rheotec
Bartec	Lemis	Santam Eng. Energy Co. Ltd
Brookfield Eng. Labs, Inc.	Malvern	SI Analytics
BYK Instr.	Marimex	So Fraser
Cannon Inst. Co.	Micro Motion	Stanhope-Seta
Ceramic Instr.	Nametre Co.	T.A. Instruments, Inc.
Cole-Palmer Inst. Co.	Norcross	Tanaka
Dong Jin Inst. Corp.	Orion	Thermo Scientific
Fungilab	Paar Physica USA, Inc.	TMI
Galvanic Applied Sciences, Inc.	PAC	Toyo Seiki Seisaku-Sho Ltd.
Gottfert Werkstorf-Prufmaschinen GmbH	Parker	Weschler Instr.

Note: All the above-mentioned manufacturers/distributors can be found on the Internet, along with their most recent contact information, product description, and, in some cases, pricing. A variety of products using different viscosity measuring methods are available from this list. There is no implied endorsement of any manufacturer on this list.

Concentric cylinder-type viscometers/rheometers are usually employed when absolute viscosity is required, which in turn requires knowledge of well-defined shear rate and shear stress. Such instruments are available in different configurations and can be used for almost any fluid. There are models for low and high shear rates. More complete discussion on concentric cylinder viscometers/rheometers is given elsewhere [4–9]. In the *Couette-type viscometer*, the rotation of the outer cylinder, or cup, minimizes centrifugal forces, which cause Taylor vortices. The latter can be present in the *Searle-type viscometer* when the inner cylinder, or bob, rotates.

Usually, the torque on the stationary cylinder and rotational velocity of the other cylinder are measured for determination of the shear stress and shear rate, respectively, which is needed for viscosity calculation. Once the torque, T, is measured, it is simple to describe the fluid shear stress $\tau_{r\theta}(r)$ at any point with radius r between the two cylinders, as shown in Figure 46.3:

$$\tau_{r\theta}(r) = \frac{T}{2\pi r^2 L_e} \tag{46.5}$$

In Equation 46.5, $L_e = (L + L_c)$ is the effective length of the cylinder at which the torque is measured. In addition to the cylinder's length L, it takes into account the end-effect correction L_c [4–8].

For a narrow gap between the cylinders ($\beta = R_2/R_1 \cong 1$), regardless of the fluid type, the velocity profile can be approximated as linear, and the shear rate, $\dot{\gamma}(r)$, within the gap will be uniform:

$$\dot{\gamma}(r) \cong \frac{\Omega \bar{R}}{(R_2 - R_1)} \tag{46.6}$$

where

$\Omega = (\omega_2 - \omega_1)$ is the relative rotational speed

$\bar{R} = (R_1 + R_2)/2$ is the mean radius of the inner (1) and outer (2) cylinders

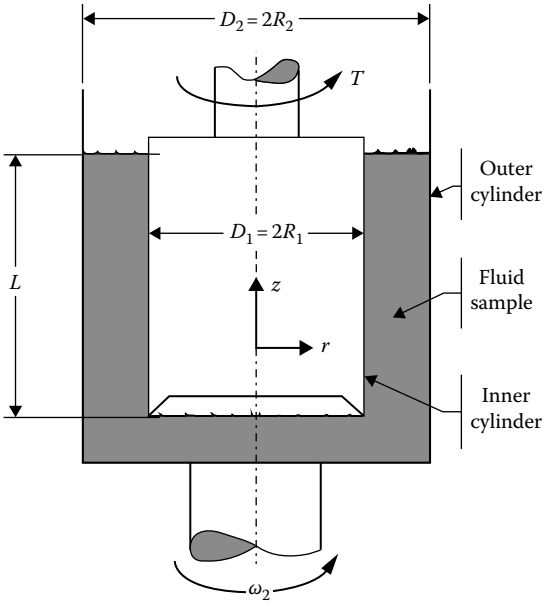

FIGURE 46.3 Concentric cylinder viscometer geometry.

Actually, the shear rate profile across the gap between the cylinders depends on the relative rotational speed, radii, and the unknown fluid properties, which seems an "open-ended" enigma. The solution of this complex problem is given elsewhere [4–8] in the form of an infinite series and requires the slope of a logarithmic plot of T as a function of Ω in the range of interest. Note that for a stationary inner cylinder ($\omega_1 = 0$), which is the usual case in practice, Ω becomes equal to ω_2. However, there is a simpler procedure [10] that has also been established by German standards [11]. For any fluid, including non-Newtonian fluids, there is a radius at which the shear rate is virtually independent of the fluid type for a given Ω. This radius, being a function of geometry only, is called the *representative radius*, R_R, and is determined as the location corresponding to the so-called representative shear stress, $\tau_R = (\tau_1 + \tau_2)/2$, the average of the stresses at the outer and inner cylinder interfaces with the fluid, that is,

$$R_R = R_1 \left\{ \frac{[2\beta^2]}{[1+\beta^2]} \right\}^{1/2} = R_2 \left\{ \frac{2}{[1+\beta^2]} \right\}^{1/2} \tag{46.7}$$

Since the shear rate at the representative radius is virtually independent on the fluid type (whether Newtonian or non-Newtonian), the representative shear rate is simply calculated for Newtonian fluid ($n = 1$) and $r = R_R$, according to [10]:

$$\dot{\gamma}_R = \dot{\gamma}_{r=R_R} = \omega_2 \left\{ \frac{[\beta^2+1]}{[\beta^2-1]} \right\} \tag{46.8}$$

The accuracy of the representative parameters depends on the geometry of the cylinders (β) and fluid type (n).

It is shown in [10] that, for an unrealistically wide range of fluid types ($0.35 < n < 3.5$) and cylinder geometries ($\beta = 1$–1.2), the maximum errors are less than 1%. Therefore, the error associated with the representative parameter concept is virtually negligible for practical measurements.

Finally, the (apparent) fluid viscosity is determined as the ratio between the shear stress and corresponding shear rate using Equations 46.5 through 46.8, as

$$\eta = \eta_R = \frac{\tau_R}{\dot{\gamma}_R} = \left\{\frac{[\beta^2 - 1]}{[4\pi\beta^2 R_1^2 L_e]}\right\}\frac{T}{\omega_2} = \left\{\frac{[\beta^2 - 1]}{[4\pi R_2^2 L_e]}\right\}\frac{T}{\omega_2} \tag{46.9}$$

For a given cylinder geometry (β, R_2, and L_e), the viscosity can be determined from Equation 46.9 by measuring T and ω_2.

As already mentioned, in Couette-type viscometers, the Taylor vortices within the gap are virtually eliminated. However, vortices at the bottom can be present, and their influence becomes important when the Reynolds number reaches the value of unity [10,11]. Furthermore, flow instability and turbulence will develop when the Reynolds number reaches values of 10^3–10^4. The Reynolds number, Re, for the flow between concentric cylinders is defined [11] as

$$\mathrm{Re} = \left\{\frac{[\rho\omega_2 R_1^2]}{2\eta}\right\}[\beta^2 - 1] \tag{46.10}$$

46.3.3 Cone-and-Plate Viscometers

The simple cone-and-plate viscometer geometry provides a uniform rate of shear and direct measurements of the first normal stress difference. It is the most popular instrument for measurement of non-Newtonian fluid properties. The working shear stress and shear strain rate equations can be easily derived in spherical coordinates, as indicated by the geometry in Figure 46.4, and are, respectively,

$$\tau_{\theta\phi} = \frac{3T}{[2\pi R^3]} \tag{46.11}$$

and

$$\dot{\gamma} = \frac{\Omega}{\theta_0} \tag{46.12}$$

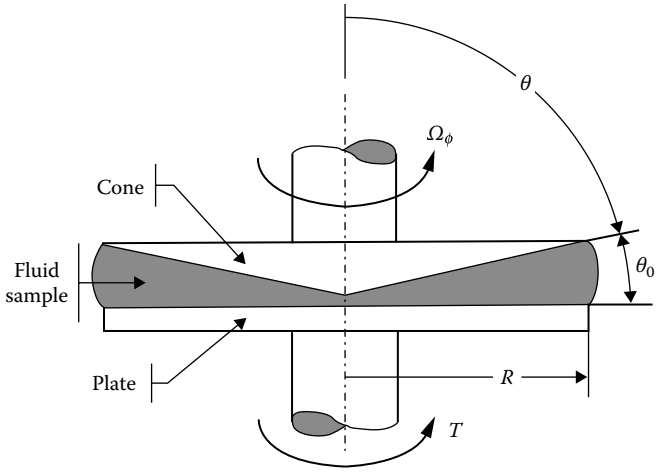

FIGURE 46.4 Cone-and-plate viscometer geometry.

where R and $\theta_0 < 0.1$ rad (≈6°) are the cone radius and angle, respectively. The viscosity is then easily calculated as

$$\eta = \frac{\tau_{\theta\phi}}{\dot{\gamma}} = \frac{[3T\theta_0]}{2\pi\Omega R^3} \tag{46.13}$$

Inertia and secondary flow increase, while shear heating decreases the measured torque (T_m). For more details, see [4,5]. The torque correction is given as

$$\frac{T_m}{T} = 1 + 6 \cdot 10^{-4}\,\mathrm{Re}^2 \tag{46.14}$$

where

$$\mathrm{Re} = \frac{\left\{\rho[\Omega\theta_0 R]^2\right\}}{\eta} \tag{46.15}$$

46.3.4 Parallel Disks

This geometry (Figure 46.5), which consists of a disk rotating in a cylindrical cavity, is similar to the cone-and-plate geometry, and many instruments permit the use of either one. However, the shear rate is no longer uniform but depends on radial distance from the axis of rotation and on the gap h, that is,

$$\dot{\gamma}(r) = \frac{r\Omega}{h} \tag{46.16}$$

For Newtonian fluids, after integration over the disk area, the torque can be expressed as a function of viscosity, so that the latter can be determined as

$$\eta = \frac{2Th}{[\pi\Omega R^4]} \tag{46.17}$$

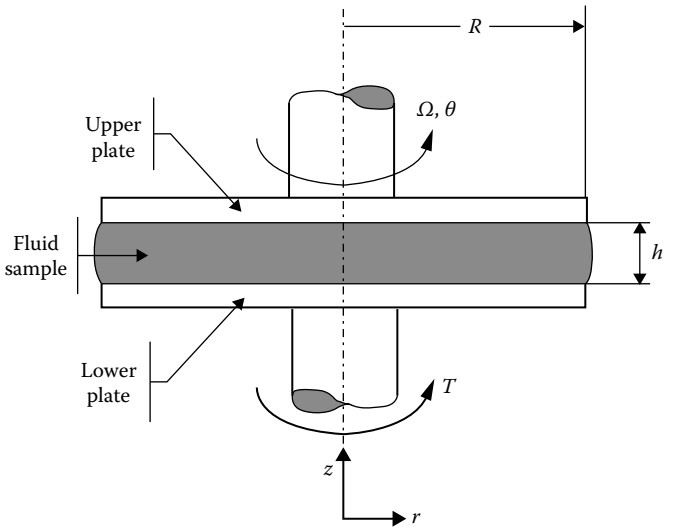

FIGURE 46.5 Parallel disks viscometer geometry.

46.4 Pressure and Gravity Flow Methods

46.4.1 Capillary Viscometers

The *capillary viscometer* is based on the fully developed laminar tube flow theory (*Hagen–Poiseuille flow*) and is shown in Figure 46.6. The capillary tube length is many times larger than its small diameter, so that entrance flow is neglected or accounted for in more accurate measurement or for shorter tubes. The expression for the shear stress at the wall is

$$\tau_w = \left[\frac{\Delta P}{L}\right] \cdot \left[\frac{D}{4}\right] \tag{46.18}$$

and

$$\Delta P = (P_1 - P_2) + (z_1 - z_2) - \frac{[C\rho V^2]}{2} \tag{46.19}$$

where $C \cong 1.1$, P, z, $V = 4Q/[\pi D^2]$, and Q are correction factor, pressure, elevation, the mean flow velocity, and the fluid volume flow rate, respectively. The subscripts 1 and 2 refer to the inlet and outlet, respectively.

The expression for the shear rate at the wall is

$$\dot{\gamma} = \left\{\frac{[3n+1]}{4n}\right\} \cdot \left\{\frac{8V}{D}\right\} \tag{46.20}$$

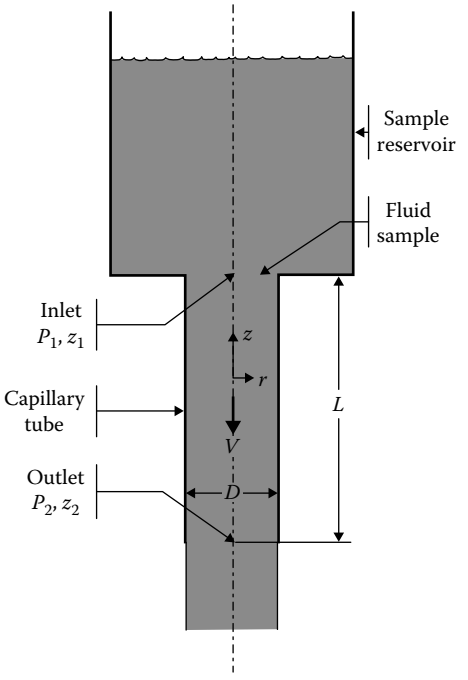

FIGURE 46.6 Capillary viscometer geometry.

where $n = d[\log\tau_w]/d[\log(8V/D)]$ is the slope of the measured $\log(\tau_w) - \log(8V/D)$ curve. Then, the viscosity is simply calculated as

$$\eta = \frac{\tau_w}{\dot{\gamma}} = \left\{\frac{4n}{[3n+1]}\right\} \cdot \left\{\frac{\Delta PD^2}{[32LV]}\right\} = \left\{\frac{4n}{[3n+1]}\right\} \cdot \left\{\frac{[\Delta PD^4\pi]}{[128QL]}\right\} \tag{46.21}$$

Note that $n = 1$ for a Newtonian fluid, so the first term $[4n/(3n + 1)]$ becomes unity and disappears from the earlier equations. The advantages of capillary over rotational viscometers are low cost, high accuracy (particularly with longer tubes), and the ability to achieve very high shear rates, even with high-viscosity samples. The main disadvantages are high residence time and variation of shear across the flow, which can change the structure of complex test fluids, as well as shear heating with high-viscosity samples.

46.4.2 Glass Capillary Viscometers

Glass capillary viscometers are very simple and inexpensive. Their geometry resembles a U-tube with at least two reservoir bulbs connected to a capillary tube passage with inner diameter D. The fluid is drawn up into one bulb reservoir of known volume, V_0, between etched marks. The efflux time, Δt, is measured for that volume to flow through the capillary under gravity.

From Equation 46.21 and taking into account that $V_0 = (\Delta t)VD^2\pi/4$ and $\Delta P = \rho g(z_1 - z_2)$, the kinematic viscosity can be expressed as a function of the efflux time only, with the last term, $K/\Delta t$, added to account for error correction, where K is a constant [7], that is,

$$\nu = \frac{\eta}{\rho} = \left\{\left[\frac{4n}{(3n+1)}\right] \cdot \frac{[\pi g(z_1 - z_2)D^4]}{128LV_o}\right\}(\Delta t - K\Delta t) \tag{46.22}$$

Note that for a given capillary viscometer and $n \cong 1$, the curl-bracketed term is a constant. The last correction term is negligible for a large capillary tube ratio, L/D, where kinematic viscosity becomes linearly proportional to measured efflux time. Various kinds of commercial glass capillary viscometers, like Cannon–Fenske type or similar, can be purchased from scientific and/or supply stores. They are the modified original *Ostwald viscometer* design in order to minimize certain undesirable effects, to increase the viscosity range, or to meet specific requirements of the tested fluids, like opacity. Glass capillary viscometers are often used for low-viscosity fluids.

46.4.3 Orifice/Cup, Short Capillary: Saybolt Viscometer

The principle of these viscometers is similar to that of glass capillary viscometers, except that the flow through a short capillary ($L/D \ll 10$) does not satisfy or even approximate the Hagen–Poiseuille, fully developed, pipe flow. The influences of entrance end effect and changing hydrostatic heads are considerable. The efflux time reading, Δt, represents relative viscosity for comparison purposes and is expressed as "viscometer seconds," like the *Saybolt seconds* or *Engler seconds* or degrees. Although the conversion formula, similar to glass capillary viscometers, is used, the constants k and K in Equation 46.23 are purely empirical and dependent on fluid types:

$$\nu = \frac{\eta}{\rho} = k\Delta t - \frac{K}{\Delta t} \tag{46.23}$$

where k = 0.00226, 0.0216, 0.073 and K = 1.95, 0.60, 0.0631, for Saybolt universal ($\Delta t < 100$ s), Saybolt Furol ($\Delta t > 40$ s), and Engler viscometers, respectively [12,13]. Due to their simplicity, reliability, and low cost, these viscometers are widely used for Newtonian fluids, in the oil and other industries, where simple correlations between the relative properties and desired results are needed. However, these viscometers are not suitable for absolute viscosity measurement nor for non-Newtonian fluids.

46.5 Falling Body Methods

46.5.1 Falling Sphere

The falling sphere viscometer is one of the earliest and simplest methods to determine the absolute shear viscosity of a Newtonian fluid. In this method, a sphere is allowed to fall freely a measured distance through a viscous liquid medium, and its velocity is determined. The viscous drag of the falling sphere results in the creation of a restraining force, *F*, described by Stokes' law:

$$F = 6\pi\eta r_s U_t \tag{46.24}$$

where

r_s is the radius of the sphere
U_t is the *terminal velocity* of the falling body

If a sphere of density ρ_2 is falling through a fluid of density ρ_1 in a container of infinite extent, then by balancing Equation 46.24 with the net force of gravity and buoyancy exerted on a solid sphere, the resulting equation of absolute viscosity is

$$\eta = 2gr_s^2 \frac{(\rho_2 - \rho_1)}{9U_t} \tag{46.25}$$

Equation 46.25 shows the relation between the viscosity of a fluid and the terminal velocity of a sphere falling within it. Having a finite container volume necessitates the modification of Equation 46.25 to correct for effects on the velocity of the sphere due to its interaction with container walls (*W*) and ends (*E*). Considering a cylindrical container of radius *r* and height *H*, the corrected form of Equation 46.25 can be written as

$$\eta = 2gr_s^2 \frac{(\rho_2 - \rho_1)W}{(9U_t E)} \tag{46.26}$$

where

$$W = 1 - 2.104\left(\frac{r_s}{r}\right) + 2.09\left(\frac{r_s}{r}\right)^3 - 0.95\left(\frac{r_s}{r}\right)^5 \tag{46.27}$$

$$E = 1 + 3.3\left(\frac{r_s}{H}\right) \tag{46.28}$$

The wall correction was empirically derived [14,15] and is valid for $0.16 \leq r_s/r \leq 0.32$. Beyond this range, the effects of container walls significantly impair the terminal velocity of the sphere, thus giving rise to a false high-viscosity value.

Figure 46.7 is a schematic diagram of the falling sphere method and demonstrates the attraction of this method—its simplicity of design. The simplest and most cost-effective approach in applying this method to transparent liquids would be to use a sufficiently large graduated cylinder filled with the liquid. With a distance marked on the cylinder near the axial and radial center (the region least influenced by the container walls and ends), a sphere (such as a ball bearing or a material that is nonreactive with the liquid) with a known density and sized to within the bounds of the container correction free falls the

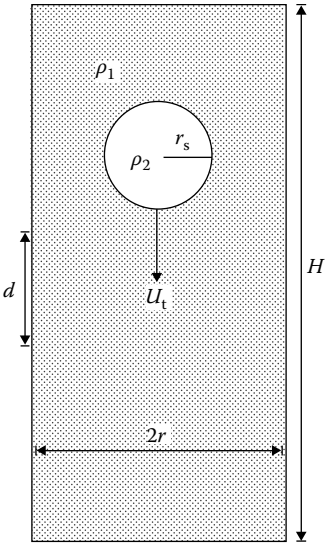

FIGURE 46.7 Schematic diagram of the falling sphere viscometer. Visual observations of the time taken for the sphere to traverse the distance d are used to determine a velocity of the sphere. The calculated velocity is then used in Equation 46.24 to determine a shear viscosity.

length of the cylinder. As the sphere passes through the marked region of length d at its terminal velocity, a measure of the time taken to traverse this distance allows the velocity of the sphere to be calculated. Using Equation 46.26, the shear viscosity of the liquid can be determined.

This method is useful for liquids with viscosities between 10^{-3} and 10^{5} Pa·s.

46.5.2 Falling Cylinder

The *falling cylinder method* is similar in concept to the falling sphere method except that a flat-ended, solid circular cylinder freely falls vertically in the direction of its longitudinal axis through a liquid sample within a cylindrical container. A schematic diagram of the configuration is shown in Figure 46.8. Taking an infinitely long cylinder of density ρ_2 and radius r_c falling through a Newtonian fluid of density ρ_1 with infinite extent, the resulting shear viscosity of the fluid is given as

$$\eta = g r_c^2 \frac{(\rho_2 - \rho_1)}{2U_t} \tag{46.29}$$

Just as with the falling sphere, a finite container volume necessitates modifying Equation 46.29 to account for the effects of container walls and ends. A correction for container wall effects can be analytically deduced by balancing the buoyancy and gravitational forces on the cylinder, of length L, with the shear force on the sides and the compressional force on the cylinder's leading end and the tensile force on the cylinder's trailing end. The resulting correction term, or geometrical factor, $G(k)$ (where $k = r_c/r$), depends on the cylinder radius and the container radius, r, and is given by

$$G(k) = \frac{[k^2(1 - \ln k) - (1 + \ln k)]}{(1 + k^2)} \tag{46.30}$$

Unlike the fluid flow around a falling sphere, the fluid motion around a falling flat-ended cylinder is very complex. The effects of container ends are minimized by creating a small gap between the

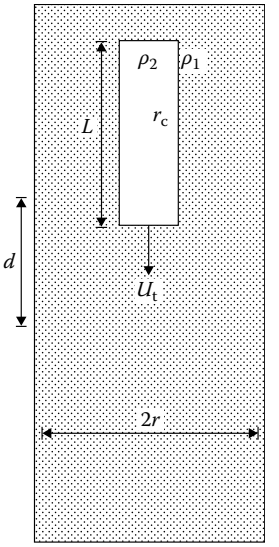

FIGURE 46.8 Schematic diagram of the falling cylinder viscometer. Using the same principle as the falling sphere, the velocity of the cylinder is obtained, which is needed to determine the shear viscosity of the fluid.

cylinder and the container wall. If a long cylinder (here, a cylinder is considered long if $\psi \geq 10$, where $\psi = L/r$) with a radius nearly as large as the radius of the container is used, then the effects of the walls would dominate, thereby reducing the end effects to a second-order effect. A major drawback with this approach is, however, if the cylinder and container are not concentric, the resulting inhomogeneous wall shear force would cause the downward motion of the cylinder to become eccentric. The potential for misalignment motivated the recently obtained analytical solution to the fluid flow about the cylinder ends [16]. An analytical expression for the end correction factor (ECF) was then deduced [17] and is given as

$$\frac{1}{\text{ECF}} = 1 + \left(\frac{8k}{\pi C_w}\right)\left(\frac{\text{G}(k)}{\psi}\right) \tag{46.31}$$

where $C_w = 1.003852 - 1.961019k + 0.9570952k^2$. C_w was derived semi-empirically [17] as a disk wall correction factor. This is based on the idea that the drag force on the ends of the cylinder can be described by the drag force on a disk. Equation 46.31 is valid for $\psi \leq 30$ and agrees with the empirically derived correction [16] to within 0.6%.

With wall and end effects taken into consideration, the working formula to determine the shear viscosity of a Newtonian fluid from a falling cylinder viscometer is

$$\eta = \frac{[gr_c^2(\rho_2 - \rho_1)\,\text{G}(k)]}{(2U_t/\text{ECF})} \tag{46.32}$$

In the past, this method was primarily used as a method to determine relative viscosities between transparent fluids. It has only been since the introduction of the ECF [16,17] that this method could be rigorously used as an absolute viscosity method. With a properly designed container and cylinder, this method is now able to provide accurate absolute viscosities from 10^{-3} to 10^{7} Pa·s.

46.5.3 Falling Methods in Opaque Liquids

The falling body methods described earlier have been extensively applied to transparent liquids where optical (often visual) observation of the falling body is possible. For *opaque liquids*, however, falling body methods require the use of some sensing technique to determine, often in situ, the position of the falling body with respect to time. Techniques have varied, but they all have in common the ability to detect the body as it moves past the sensor. A recent study at high pressure [18] demonstrated that the contrast in electric conductivity between a sphere and opaque liquid could be exploited to dynamically sense the moving sphere if suitably placed electrodes penetrated the container walls as shown in the schematic diagram in Figure 46.9. References to other similar in situ techniques are given in [18].

46.5.4 Rising Bubble/Droplet

For many industrial processes, the rising bubble viscometer has been used as a method of comparing the relative viscosities of transparent liquids (such as varnish, lacquer, and beer) for decades. Although its use was widespread, the actual behavior of the bubble in a viscous liquid was not well understood until long after the method was introduced [19]. The rising bubble method has been thought of as a derivative of the falling sphere method; however, there are fundamental physical differences between the two. The major physical differences are as follows: (1) The density of the bubble is less that of the surrounding liquid, the compressibility of the bubble leads to a change in bubble volume depending on its rise position in the fluid column, and (2) the bubble itself has some unique viscosity. Each of these differences

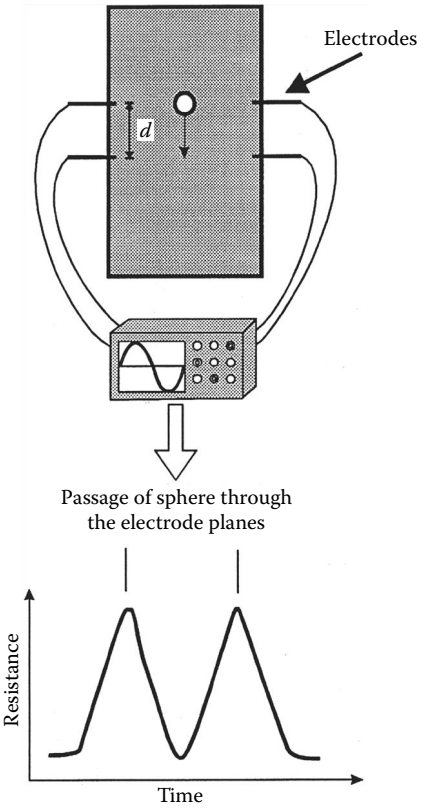

FIGURE 46.9 Diagram of one type of apparatus used to determine the viscosity of opaque liquids in situ. The electrical signal from the passage of the falling sphere indicates the time to traverse a known distance (d) between the two sensors.

can, and do, lead to significant and extremely complex rheological problems that have yet to be fully explained. If a bubble of gas or droplet of liquid with a radius, r_b, and density, ρ', is freely rising in some enclosing viscous liquid of density ρ, then the shear viscosity of the enclosing liquid is determined by

$$\eta = \left(\frac{1}{\varepsilon}\right)\frac{[2gr_b^2(\rho - \rho')]}{9U_t} \tag{46.33}$$

where

$$\varepsilon = \frac{(2\eta + 3\eta')}{3(\eta + \eta')} \tag{46.34}$$

where η' is the viscosity of the bubble. It must be noted that when $\eta' \gg \eta$, ε (as for solid spheres in a fluid), $\varepsilon = 1$, which reduces Equation 46.33 to 46.25. For $\eta' \ll \eta$ (as for gas bubbles in a fluid), ε becomes 2/3, and the viscosity calculated by Equation 46.33 is 1.5 times greater than the viscosity calculated by Equation 46.25.

During the rise, great care must be taken to avoid contamination of the bubble and its surface with impurities in the surrounding liquid. Impurities can diffuse through the surface of the bubble and combine with the fluid inside. Because the bubble has a low viscosity, the upward motion in a viscous medium induces a drag on the bubble that is responsible for generating a circulatory motion within it. This motion can efficiently distribute impurities throughout the whole of the bubble, thereby changing its viscosity and density. Impurities left on the surface of the bubble can form a "skin" that can significantly affect the rise of the bubble, as the skin layer has its own density and viscosity that are not included in Equation 46.33. These surface impurities also make a significant contribution to the inhomogeneous distribution of interfacial tension forces. A balance of these forces is crucial for the formation of a spherical bubble. The simplest method to minimize the earlier effects is to employ minute bubbles by introducing a specific volume of fluid (gas or liquid), with a syringe or other similar device, at the lower end of the cylindrical container. Very small bubbles behave like solid spheres, which make interfacial tension forces and internal fluid motion negligible.

In all rising bubble viscometers, the bubble is assumed to be spherical. Experimental studies of the shapes of freely rising gas bubbles in a container of finite extent [20] have shown that (to 1% accuracy) a bubble will form and retain a spherical shape if the ratio of the radius of the bubble to the radius of the confining cylindrical container is less than 0.2. These studies have also demonstrated that the effect of the wall on the terminal velocity of a rising spherical bubble is to cause a large decrease (up to 39%) in the observed velocity compared to the velocity measured within an unbounded medium. This implies that the walls of the container influence the velocity of the rising bubble more significantly than its geometry. In this method, end effects are known to be large. However, a rigorous, analytically or empirically derived correction factor has not yet appeared. To circumvent this, the ratio of container length to sphere diameter must be in the range of 10–100. As in other Stokesian methods, this allows the bubble's velocity to be measured at locations that experience negligible end effects.

Considering all of the earlier complications, the use of minute bubbles is the best approach to ensure a viscosity measurement that is least affected by both the liquid to be investigated and the container geometry.

46.6 Oscillation Methods

Oscillation methods are based on the measurement of viscous damping of oscillation within a fluid sample. Either the sample itself can be the wave carrying medium (acoustic method) or a separate oscillator can be used in forced oscillation or free decay mode (vibrating wire, transducer, or tuning fork methods). If a liquid is contained within a vessel suspended by some torsional system that is set

in oscillation about its vertical axis, then the motion of the vessel will experience a gradual damping. In an ideal situation, the damping of the motion of the vessel arises purely as a result of the *viscous coupling* of the liquid to the vessel and the viscous coupling between annular layers in the liquid. In any practical situation, there are also frictional losses within the mechanical components of the suspension system that contribute to damping and must be accounted for in the analysis of the measurements. From observations of the amplitudes and time periods of the resulting oscillations, a viscosity of the liquid can be calculated. A schematic diagram of the basic setup of the method is shown in Figure 46.10. Following initial oscillatory excitation, a light source (such as a low-intensity laser) can be used to measure the amplitudes and periods of the resulting oscillations by reflection of the mirror attached to the suspension rod to give an accurate measure of the logarithmic decrement of the oscillations (δ) and the periods (T).

Various working formulae have been derived that associate the oscillatory motion of a vessel of radius r to the absolute viscosity of the liquid. The most reliable formula is the following equation for a cylindrical vessel [21]:

$$\eta = \left[\frac{I\delta}{(\pi r^3 HZ)}\right]^2 \left[\frac{1}{\pi\rho T}\right] \tag{46.35}$$

where

$$Z = \left(\frac{1+r}{4H}\right)a_0 - \frac{[(3/2)+(4r/\pi\mathrm{H})]1}{p} + \frac{[(3/8)+(9r/4\mathrm{H})]a_2}{2p^2} \tag{46.36}$$

$$p = \left(\frac{\pi\rho}{\eta T}\right)^{1/2} r \tag{46.37}$$

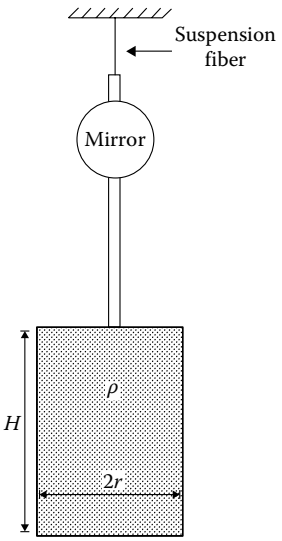

FIGURE 46.10 Schematic diagram of the oscillating cup viscometer. Measurement of the logarithmic damping of the amplitude and period of vessel oscillation is used to determine the absolute shear viscosity of the liquid.

$$a_0 = 1 - \left(\frac{\delta}{4\pi}\right) - \left(\frac{3\delta^2}{32\pi^2}\right) \tag{46.38}$$

$$a_2 = 1 + \left(\frac{\delta}{4\pi}\right) + \left(\frac{\delta^2}{32\pi^2}\right) \tag{46.39}$$

where

I is the mass moment of inertia of the suspended system

ρ is the density of the liquid

A more practical expression of Equation 46.35 is obtained by introducing a number of simplifications. First, it is a reasonable assumption to consider δ to be small (in the order of 10^{-2}–10^{-3}). This reduces a_0 and a_2 to values of 1 and −1, respectively. Second, the effects of friction from the suspension system and the surrounding atmosphere can be experimentally determined and contained within a single parameter or instrument constant, δ_0. This must then be subtracted from the measured δ. A common method of obtaining δ_0 is to observe the logarithmic decrement of the system with an empty sample vessel and subtract that value from the measured value of δ. With these modifications, Equation 46.35 becomes

$$\frac{(\delta - \delta_0)}{\rho} = \left[A\left(\frac{\eta}{\rho}\right)^{1/2} - B\left(\frac{\eta}{\rho}\right) + C\left(\frac{\eta}{\rho}\right)^{3/2} \right] \tag{46.40}$$

where

$$A = \left(\frac{\pi^{3/2}}{I}\right)\left[1 + \left(\frac{r}{4H}\right) Hr^3 T^{1/2}\right] \tag{46.41}$$

$$B = \left(\frac{\pi}{I}\right)\left[\left(\frac{3}{2}\right) + \frac{4r}{\pi H}\right] Hr^2 T \tag{46.42}$$

$$C = \left(\frac{\pi^{1/2}}{2I}\right)\left[\left(\frac{3}{8}\right) + \frac{9r}{4H}\right] HrT^{3/2} \tag{46.43}$$

It has been noted [22] that the analytical form of Equation 46.40 needs an empirically derived, instrument-constant correction factor (ζ) in order to agree with experimentally measured values of η. The discrepancy between the analytical form and the measured value arises as a result of the earlier assumptions. However, these assumptions are required as solutions of the differential equations of motion of this system are nontrivial. The correction factor is dependent on the materials, dimensions, and densities of each individual system but generally lies between the values of 1.0 and 1.08. The correction factor is obtained by comparing viscosity values of calibration materials determined by an individual system (with Equation 46.35) and viscosity values obtained by another reliable method such as the capillary method.

With the earlier considerations taken into account, the final working Roscoe's formula for the absolute shear viscosity is

$$\frac{(\delta - \delta_0)}{\rho} = \zeta\left[A\left(\frac{\eta}{\rho}\right)^{1/2} - B\left(\frac{\eta}{\rho}\right) + C\left(\frac{\eta}{\rho}\right)^{3/2} \right] \tag{46.44}$$

The *oscillating cup method* has been used and is best suited for use with low values of viscosity within the range of 10^{-5}–10^{-2} Pa·s. Its simple closed design and use at high temperatures have made this method very popular for viscosity measurement of liquid metals.

Perhaps the simplest version of the oscillation type of instrument is the vibrating-wire viscometer. Vibrating-wire viscometers are typically quite small and so require small quantities of fluid. They provide accurate measurements but may require calibration using a known fluid. They can be used in quite extreme conditions: the vibrating-wire viscometer was first used to measure the viscosity of liquid helium at temperatures around 2 K [23,24]. Related instruments have been used at pressures in the GPa range [25]. A viscometer based on a vibrating tuning fork, which is capable of accurate measurements over a wide viscosity range (A & D Engineering), is available commercially.

The theory of operation of the vibrating-wire viscometer has been described in detail in the literature [26]. It is based on the phenomenon of resonance. A wire (or more generally a thin beam) fixed at both ends will have a natural vibration frequency ω_0 determined by its length, physical properties, and tension. The vibration amplitude of the wire will be strongly peaked at that resonance frequency, and the height and width of the resonant peak depending on the magnitude of the forces that damp the wire's motion. For a vibrating wire immersed in a fluid, the width of the peak $\Delta\omega$ or equivalently the quality factor $Q = \omega_0/\Delta\omega$ thus depends on viscosity, with higher viscosity leading to a smaller, broader peak and a lower Q. In a typical instrument, the vibrating wire sits in a uniform magnetic field produced by permanent magnets. A small alternating current of angular frequency ω is passed through the wire, and the resulting Lorentz forces cause the wire to vibrate at the same frequency. The voltage across the wire will consist of a constant contribution due to the electrical impedance of the system plus an induced emf that is proportional to the amplitude of the vibration. Vibrating-wire viscometers can operate in a forced mode, in which the wire is driven over a range of frequencies and the resonant peak measured directly, or in a transient mode, in which Q is determined from measurements of the decay rate of the oscillations following a short pulse of the driving current. In some configurations, the tension on the vibrating wire is applied by a mass suspended in the fluid. In this case, the instrument can be used to simultaneously measure fluid density, since the tension and so the resonant frequency will depend on the buoyant force acting on the mass.

Several recent publications describe miniaturized versions of vibrating-object viscometers. Such instruments are of interest in applications ranging from the need for simple bedside measurements of the viscosity of blood, in which the quantity of fluid used must be minimized, to in situ measurement of viscosity in oil field reservoirs, in which the viscometer must withstand high temperatures and pressures. Very small vibrating beam and vibrating plate viscometers have been fabricated using microelectromechanical system (MEMS) technology [27,28]. Smith et al. [29] describe a MEMS oscillating plate viscometer for human blood measurements. Dehestru et al. [30] discuss a vibrating-wire viscometer designed for oil field use. It has an internal volume of a few μL and is accurate to ±10% at pressures up to 24 MPa and temperatures up to 175 °C.

46.7 Acoustic Methods

Viscosity plays an important role in the absorption of energy of an *acoustic wave* traveling through a liquid. By using ultrasonic waves (10^4 Hz < f < 10^8 Hz), the elastic, viscoelastic, and viscous response of a liquid can be measured down to times as short as 10 ns. When the viscosity of the fluid is low, the resulting time scale for structural relaxation is shorter than the ultrasonic wave period, and the fluid is probed in the relaxed state. High-viscosity fluids subjected to ultrasonic wave trains respond as a stiff fluid because structural equilibration due to the acoustic perturbation does not go to completion before the next wave cycle. Consequently, the fluid is said to be in an unrelaxed state that is characterized by dispersion (frequency-dependent wave velocity) and elastic moduli that reflect a much stiffer liquid. The frequency dependence of the viscosity relative to some reference viscosity (η_0) at low frequency, η/η_0, and of the absorption per wavelength, $\alpha\lambda$, where α is the absorption coefficient of the liquid and λ is the wavelength of the compressional

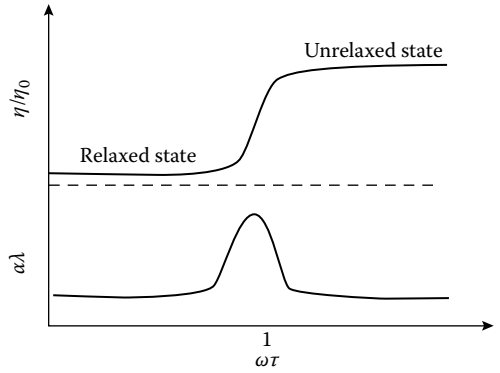

FIGURE 46.11 Effects of liquid relaxation (relaxation frequency corresponds to $\omega\tau = 1$ where $\omega = 2\pi f$) on relative viscosity (upper) and absorption per wavelength (lower) in the relaxed elastic ($\omega\tau < 1$) and unrelaxed viscoelastic ($\omega\tau > 1$) regimes.

wave, for a liquid with a single relaxation time, *t*, is shown in Figure 46.11. The maximum absorption per wavelength occurs at the *relaxation frequency* when $\omega\tau = 1$ and is accompanied by a step in η/η_0, as well as in other properties such as velocity and compressibility. Depending on the application of the measured properties, it is important to determine if the liquid is in a relaxed or unrelaxed state.

A schematic diagram of a typical apparatus for measuring viscosity by the ultrasonic method is shown in Figure 46.12. Mechanical vibrations in a *piezoelectric* transducer travel down one of the buffer rods (BR-1 in Figure 46.12) and into the liquid sample and are received by a similar transducer mounted on the other buffer rod, BR-2. In the fixed buffer rod configuration, once steady-state conditions have been reached, the applied signal is turned off quickly. The decay rate of the received and amplified signal,

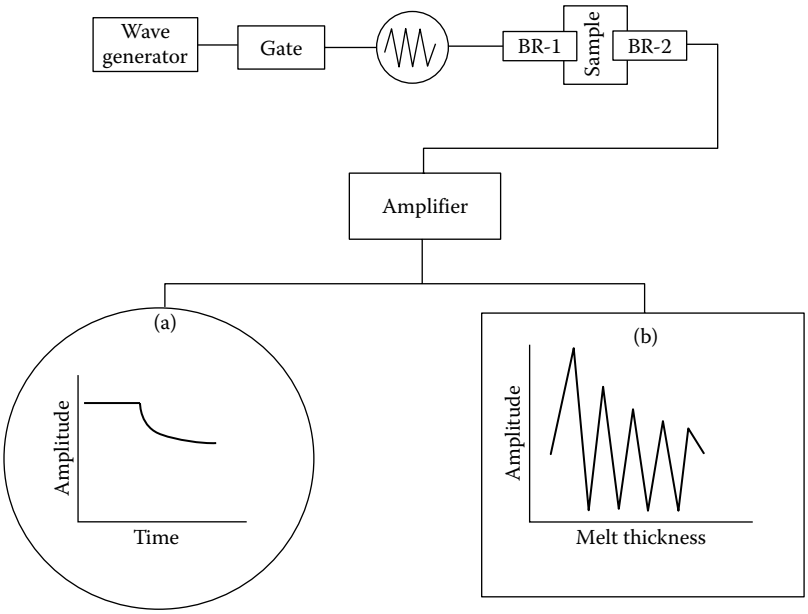

FIGURE 46.12 Schematic diagram of apparatus for liquid shear and volume viscosity determination by ultrasonic wave attenuation measurement showing the received signal amplitude through the exit buffer rod (BR-2) using (a) a fixed buffer rod (BR-2) configuration and (b) an interferometric technique with moveable buffer rod.

displayed on an oscilloscope on an amplitude versus time plot as shown in Figure 46.12a, gives a measure of α. The received amplitude decays as

$$A = A_0 e^{-(b+\alpha c)t'} \tag{46.45}$$

where
- A is the received decaying amplitude
- A_0 is the input amplitude
- b is an apparatus constant that depends on other losses in the system such as due to the transducer and container that can be evaluated by measuring the attenuation in a standard liquid
- c is the compressional wave velocity of the liquid
- t' is the time

At low frequencies, the absorption coefficient is expressed in terms of volume and shear viscosity:

$$\left(\eta_v + \frac{4\eta}{3}\right) = \frac{\alpha\rho c^3}{2\pi^2 f^2} \tag{46.46}$$

One of the earliest ultrasonic methods of measuring attenuation in liquids is based on *acoustic interferometry* [31]. Apart from the instrumentation needed to move and determine the position of one of the buffer rods accurately, the experimental apparatus is essentially the same as for the fixed buffer rod configuration [32]. The measurement, however, depends on the continuous acoustic wave interference of transmitted and reflected waves within the sample melt as one of the buffer rods is moved away from the other rod. The attenuation is characterized by the decay of the maxima amplitude as a function of melt thickness as shown on the interferogram in Figure 46.12b. Determining α from the observed amplitude decrement involves numerical solution to a system of equations characterizing complex wave propagation [33]. The ideal conditions represented in the theory do not account for conditions such as wave front curvature, buffer rod end nonparallelism, surface roughness, and misalignment. These problems can be addressed in the amplitude fitting stage, but they can be difficult to overcome. The interested reader is referred to [33] for further details.

Ultrasonic methods have not been and are not likely to become the mainstay of fluid viscosity determination simply because they are more technically complicated than conventional viscometry techniques. And although ultrasonic viscometry supplies additional related elastic property data, its niche in viscometry is its capability of providing volume viscosity data. Since there is no other viscometer to measure η_v, ultrasonic absorption measurements play a unique role in the study of volume viscosity.

46.8 Microrheology

On the microscopic scale, viscosity is related to the phenomenon of diffusion. A small (i.e., micron sized) particle suspended in a viscous fluid such as water undergoes random motion as a result of thermal fluctuations in the forces acting on it. This is the well-known Brownian motion. Einstein showed in a famous 1905 [34] paper that the mean squared displacement $\langle r^2 \rangle$ of a particle undergoing Brownian motion is given by

$$\left\langle r^2(\tau) \right\rangle = 2dD\tau, \tag{46.47}$$

where
- τ is the time
- d is the dimensionality of the motion
- The angle brackets indicate an average over an ensemble of particles

D is the diffusion constant, which is related to the viscosity η of the fluid by the Stokes–Einstein equation:

$$D = \frac{k_B T}{6\pi\eta a} \tag{46.48}$$

Here
k_B is the Boltzmann constant
T is the absolute temperature

If the radius a of the diffusing particles is known, these equations can be used to determine the viscosity from measurements of their mean squared displacement. In a viscoelastic fluid, the effects of elasticity make the mean squared displacement grow more slowly than linearly. In this case, Equations 46.47 and 46.48 can be generalized to relate the frequency-dependent viscous and elastic moduli to $\langle r^2 \rangle$. This is discussed in detail in Refs. [35–39].

Several techniques collectively referred to as microrheology have been developed to make use of this relationship to measure viscosity or, more generally, the viscoelastic properties of fluids. The most commonly used of these will be discussed briefly in the following. The development and application of microrheological techniques have been discussed in a number of review papers [35,40]. Microrheology can be used to measure the properties of very small quantities of fluid and so is useful for characterizing expensive or scarce fluids. On the other hand, while at least one commercial instrument is available, microrheology is still largely a research laboratory technique. For quantitative measurements of the bulk viscous and elastic moduli, the fluids being tested must be homogeneous on the scale of the particle motion, since, if the fluid has small-scale structure, the local viscoelastic properties felt by the tracer particles can differ dramatically from the bulk properties. This is not an issue for most Newtonian fluids, but it can be for many complex fluids such as suspensions and gels.

46.8.1 Particle-Tracking Microrheology

Particle-tracking microrheology is based on direct imaging of small tracer particles undergoing Brownian motion in a fluid. This limits its application to fluids that are transparent or at least sufficiently so that the positions of the tracer particles can be detected. The maximum viscosity that can be measured with particle tracking is limited by the requirement that the motion of the tracers must be large enough to be detectable. This limit depends on the optical resolution of the microscope and image analysis procedure, as well as on the size of the tracers. For a typical experimental system, this limit is on the order of tens of Pa · s.

Particle-tracking microrheology is done using a high-quality microscope fitted with a video camera interfaced to a computer. Tracer particles are suspended in the fluid of interest, which is placed in a sample holder and mounted on the stage of the microscope. Sample holders can be fabricated to contain any volume of fluid, but 10–100 μL is typical. The microscope must be focused on the center of the holder to avoid any influence of the walls on the motion of the tracer particles. The video camera records images of the tracer particles at a set frame rate, which are stored on the computer, and image analysis software is later used to reconstruct the particles' trajectories and to calculate the mean squared displacement. To obtain good statistics in the data, the trajectories of many particles are tracked simultaneously, and the concentration of tracers in the fluid is typically chosen to give about 50 particles in the microscope's field of view.

The implementation details are discussed more fully elsewhere [35,40], but several points are worth mentioning. The tracer particles should be close in density to the fluid of interest so that they do not settle over the course of the measurement. Polystyrene latex spheres with a density of 1.05 g cm^{-3} can be obtained in a range of sizes and with a variety of chemical coatings and are typically used for aqueous solutions. It is important to ensure that the tracer particles do not interact chemically or

electrostatically with the fluid being tested. Using bright-field microscopy, particles down to 0.5 μm in diameter can be tracked, while fluorescence microscopy can be used to track fluorescently dyed particles as small as 0.1 μm in size. The shortest time over which the mean squared displacement can be measured is limited by the video frame rate and the longest time by computer memory or the stability of the fluid.

The stored video images of the diffusing particles must be analyzed to extract the trajectory of each particle and ultimately the mean squared displacement of the ensemble of particles. Several software packages can be used to do this analysis. Particle-tracking software by Crocker and Grier [41] that uses the interactive data language (IDL)® programming language (Excelis Inc.) is freely available [42] and has been used extensively. This package has also been translated into MATLAB®, and other image analysis software such as ImageJ could also be used. The image analysis involves filtering the images to remove background intensity variations, identifying candidate particles by thresholding the images, determining their positions to subpixel accuracy from the centroid of their brightness distribution, and finally reconstructing particle trajectories by matching particles from one image to the next. Once the trajectories of all recorded particles have been determined, their squared displacements are calculated and averaged. The viscosity, or the viscous and elastic moduli in the case of a non-Newtonian fluid, can then be calculated. Typically measurement uncertainties limit the observable mean squared displacement to about 10^{-4} μm^2.

An individual tracer particle moving in a viscoelastic fluid interacts hydrodynamically with other tracer particles. Two-particle microrheology exploits this fact by using correlations between the motions of pairs of particles to obtain viscoelastic properties of the fluid on the scale of the separation between the particles [43]. Two-particle microrheology gives moduli that are independent of the interactions between the tracer particles and the material under study [43] and so gives the bulk properties even in microscopically inhomogeneous fluids. Two-particle microrheology requires the same equipment as described earlier. The difference comes in the data analysis, which, since it involves analyzing the motion of pairs of particles, requires much more data than in single-particle measurements. This technique has been used to study length-scale-dependent rheology in inhomogeneous materials such as actin networks [43], but for now it remains a research tool rather than a practical technique for routine measurements of material properties.

46.8.2 Dynamic Light Scattering

A second microrheological technique uses dynamic light scattering to measure the mean squared displacement of tracer particles in the fluid. In this technique, incident laser light is scattered by particles suspended in the fluid of interest. A photomultiplier mounted at an angle θ with respect to the incident beam measures the scattered light intensity, which fluctuates in time due to the random motion of the scattering particles. A digital correlator calculates the autocorrelation function of the scattered intensity, $g_2(\tau)$, where τ is the time and g_2 is related to g_1, the autocorrelation function of the scattered electric field, which decays in time as

$$g_1(\tau) = e^{-(q^2/6)\langle r^2(\tau)\rangle}, \tag{46.49}$$

where $q = (4\pi n/\lambda)\sin(\theta/2)$, n is the refractive index of the fluid, and λ is the wavelength of the laser light. The decay rate of $g_1(\tau)$ thus gives the mean squared displacement of the tracer particles, from which the viscosity or viscous and elastic moduli can be calculated using Equations 46.47 and 46.48, as shown earlier. An example of data obtained using this technique is shown in Figure 46.13, where the mean squared displacement is plotted as a function of time for 110 nm polystyrene spheres in water.

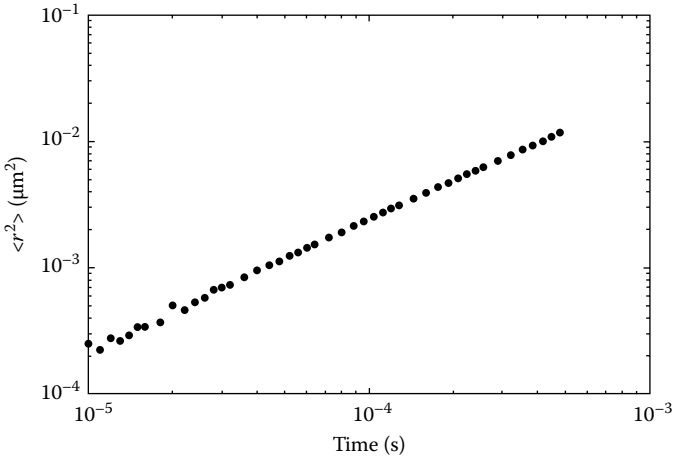

FIGURE 46.13 Mean squared displacement of 100 nm polystyrene sphere diffusion in water, measured using dynamic light scattering. These data can be used to obtain the diffusion constant, from which the viscosity of the fluid can be determined. (From Yang, N. and deBruyn, J.R., unpublished.)

A range of light scattering instruments, including laser, photodetector, and correlator, are available commercially, although many "black-box" scattering systems are intended for particle size determination assuming a known viscosity. The tracer particles must again be neutrally buoyant in the fluid under study, and their concentration must be low enough that the laser light is scattered at most once as it passes through the sample holder. Typically a few milliliters of fluid is required, and the sample must again be transparent. Light scattering microrheology measures the viscoelastic properties of fluids at much higher frequencies than particle tracking, which is useful for characterizing complex fluids such as polymer solutions.

A related microrheological technique uses diffusing-wave spectroscopy. This is also a light scattering technique but requires the light to be scattered many times in the sample, so that the light effectively diffuses through it. This requires a higher concentration of tracer particles. As shown earlier, the decay rate of the electric field autocorrelation function is related to the mean squared displacement of the tracer particles, although the equations involved are slightly more complicated. Details are given in a number of references. Diffusing-wave spectroscopy allows measurements at even higher frequencies than the single-scattering technique. An instrument that does microrheological measurements based on this technique is available commercially.

46.9 High-Pressure Rheology

Measurement of viscosity of fluids at high pressures began with Bridgman [45]. His primary interest was to investigate liquids that would remain fluid at high pressures so they could be used as hydrostatic pressure-transmitting media in his experiments. Since that time, continued development of high-pressure viscometry methods remained in the scientific research realm until recently. Over the past decade, there has been increasing commercial and industrial interest in the application of high-pressure technology in the processing of fluids. A wide range of foods, for example, is now being processed using high-pressure technology principally as a nonthermal alternative for extending shelf life. The technology also provides the food industry with a variety of new product development opportunities able to exploit the functional properties of ingredients such as hydrocolloids and proteins. High-pressure technology is proving increasingly attractive and beneficial in the destruction of microorganisms; activation and deactivation of enzymes; inactivation kinetics of both vegetative

and pathogenic microorganisms; change of functional properties of biopolymers such as proteins and polysaccharides used in foams, gels, and emulsions; and the control of phase change such as fat solidification and ice melting point. The rheology of these fluids and soft solids is important to control process function and speed. In other applications such as in the automotive industry, understanding the high-pressure rheology of petroleum-based fuels is critical for the safe and efficient design and performance of engines. High-pressure rheology has also been recognized as vital information for studies of planetary interiors, where fluids of mainly silicate or metallic composition play significant roles in heat and mass flow and therefore fluid rheology is a pivotal parameter in controlling planetary evolution.

46.9.1 High-Pressure Rheometry

Rheometry methods employed at high pressure are mainly based on traditional methods and can be grouped into four categories: concentric cylinder, capillary, oscillatory, and falling/rolling body. The theoretical treatment given earlier for each of these methods applies, but additional corrections may be required for the container geometry effects due to the limited sample volumes imposed by the high-pressure environment. The approaches to measure motion or stress in situ are often applied outside the high-pressure environment because of the high loads required and can involve detailed experimental setups. Also, depending on the pressure range, the equipment required to generate high pressure can be much more elaborate than the equipment required to measure viscosity. Although there are several high-pressure viscometers commercially available for use below a pressure of 1 GPa and examples are listed in Table 46.5, measurement of viscosity at pressures above 1 GPa is carried out mainly in the research laboratory. There is no implied endorsement of any manufacturer listed in Table 46.5.

Recent reviews of high-pressure viscosity measurement have appeared [46,47] and describe in detail the pressure devices and methods used up to ~1 GPa. This appears to be the pressure limit of the concentric cylinder method because of the engineering challenges presented by the friction effects in rotating high-pressure seals and the difficulties in precise measurement of torque when parts are subjected to high mechanical loads. Most high-pressure rotating systems use the Searle principle with a rotating inner cylinder and stationary outer cylinder. Methods of measuring the resulting shear stress include elastic torsion tubes, magnetic or inductive coupling, strain gauge load cell, or variable torque induction motor. The capillary method is based on pressure-driven flow. The pressure drop along the capillary is normally measured with pressure transducers, which must detect small pressure differences along the capillary on top of a large pressure signal arising from the static high-pressure environment. High-pressure oscillation methods are based on the measurement of viscous damping of an oscillator located within a pressurized fluid sample. Piezoelectric quartz crystals, which can operate at pressures exceeding 1 GPa, show a shift in the

TABLE 46.5 High-Pressure Viscometer/Rheometer Manufacturers

Manufacturers	Maximum Pressure (Bars)	Method
PSL Systemtechnik	1200	Rotational
Cambridge Viscosity, Inc.	1379	Oscillating piston/EM
PAC	2040	Oscillating piston/EM
Chandler Engineering	2721	Rotational
Stony Brook Scientific, Inc.	4082	Falling needle/magnetic
F5 Technologie	5000	Torsional oscillation

Note: All the above-mentioned manufacturers/distributors can be found on the Internet, along with their most recent contact information, product description, and, in some cases, pricing. There is no implied endorsement of any manufacturer listed in this table.

crystal resonant frequency reflecting the mechanical shear impedance of the sample. A second way to measure fluid viscosity is by observation of the free decay of a disk or wire-shaped oscillator. A third way to measure viscosity using the oscillation method at high pressure is by passage of transducer-generated and transducer-detected ultrasonic waves through the pressurized fluid. The viscosity is calculated via the wave absorption coefficient of the sample, which is measured by signal attenuation at the receiving transducer.

At pressures above 1 GPa, the falling/rolling body method is the preferred method although at least one study of a capillary method employed to 6 GPa has been reported [48]. The simplicity and reliability of construction of components for the Stokesian method make it capable of providing viscosity measurements at the highest pressures, where the sample fluid volume ranges from $\sim 10^{-2}$ mm^3 to a few mm^3. In principle, viscosity can be measured with this method at pressures up to several 10's of GPa using the diamond anvil cell high-pressure device. At such high pressures, high temperature is also required in order to melt the pressure-frozen liquid or because this range of pressures is mainly of interest to the Earth and planetary sciences and the relevant materials to be studied have melting temperatures in excess of 1500 °C. Such high temperatures require judicious selection of the material for the falling/rolling body to ensure solid-phase stability of the body at the test conditions, chemical inertness of the body in the fluid, appropriate density contrast of the body and fluid, and ease of fabrication of the desired geometry. The velocimetry method used depends on the body and fluid and on the observational access to the pressurized sample region. Since the diamond anvil cell has the great advantage of optical access through the diamond anvils, this is the method of choice for velocimetry of the moving body between two fiducial points. In large-volume presses, which contain optically opaque components (usually ceramics and metals) in the pressure cell, there are two main approaches to measuring the speed of the moving body. The first involves allowing the body to move for a measured time in the pressurized fluid and then quenching the temperature to freeze the fluid, thereby capturing the body in position. Follow-up measurement of the body position is made by sectioning the recovered sample and measuring the distance the body has moved. This is an effective method for measuring viscosities in the range of approximately 10^{-1}–10^5 Pa s if the density contrast of the body and fluid is chosen appropriately. A technique for tailoring the density of a probe sphere, by cladding a metallic core sphere with a refractory mantle to make a composite sphere [49], allows for adjustment of the fall time of the body to within acceptable ranges considering the fluid density and its expected viscosity. However, for measuring much lower viscosities, the control on quenching the temperature and accurate determination of the body start/stop position are inadequate, and therefore, in situ velocimetry methods are required. Many in situ velocimetry methods have been devised based on the following with either in situ or ex situ components for detection: electromagnetic induction using a two-coil external arrangement and an electrically conducting body in a nonconducting fluid, detecting passage of an insulating body moving through two electrodes placed in a metallic fluid by measuring electrical resistance of the fluid, detecting passage of a weakly radioactive body such as a ^{60}Co sphere sensed by an external scintillation counter, and x-ray radiographic imaging of a body with sufficient absorption x-ray contrast with the fluid. Over the last decade, the last method has become the method of choice for accurate high-pressure viscometry at pressures above 1 GPa [50] on low-viscosity fluids and is described in further detail.

Experiments to measure the viscosity of a fluid at high temperatures and at pressures above 1 GPa are frequently carried out using the x-ray radiography imaging technique in real time at a synchrotron facility. The high photon flux at a synchrotron is needed in order to produce images of sufficient quality and at high enough frequency (or ideally a movie) at various positions during travel of the body in order to derive a velocity. The x-ray radiographic technique images the pressurized region according to the relative x-ray attenuation coefficients of the experimental materials. A diagram of the experimental imaging setup for a high-pressure Stokesian viscometry measurement using synchrotron x-ray radiography, the resultant sequence of time lapse images, and the sphere displacement and velocity data for a falling composite sphere is shown in Figure 46.14.

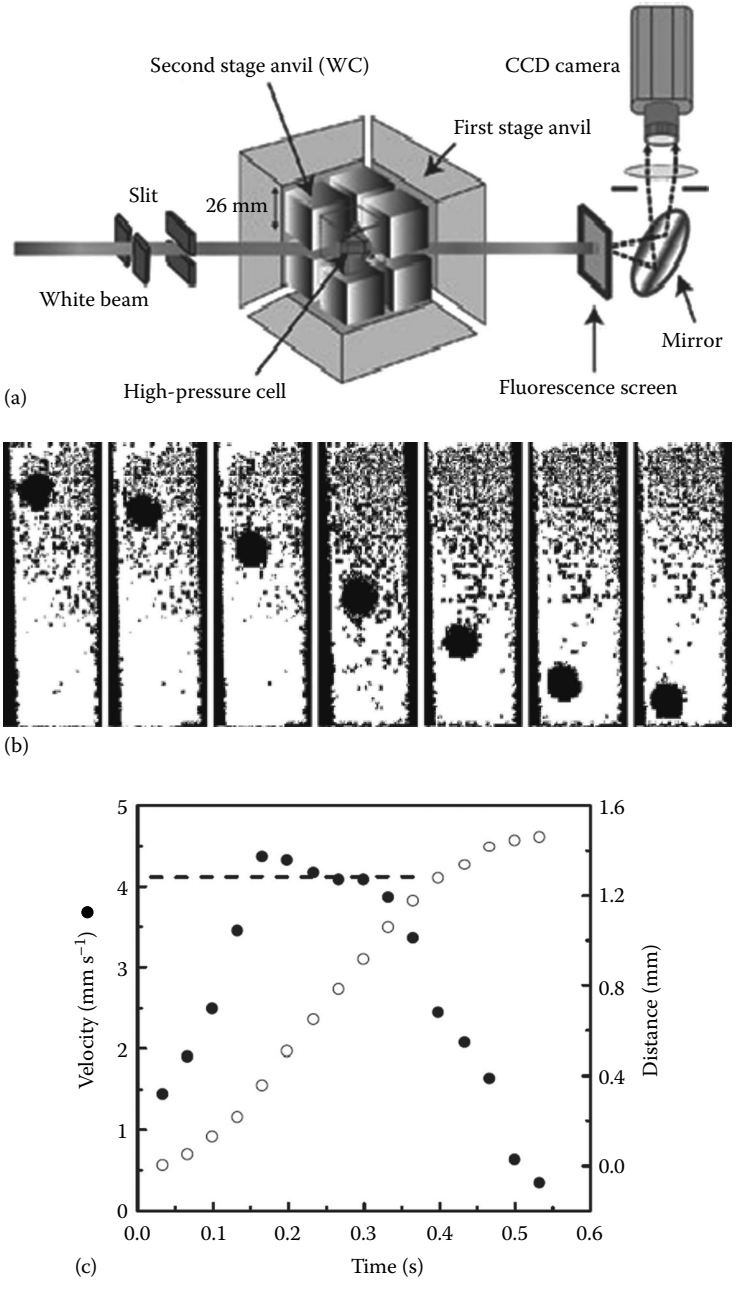

FIGURE 46.14 (a) Synchrotron x-ray radiography setup for a high-pressure Stokesian viscometry measurement [51]. (b) Synchrotron radiographic images of a Pt core—ruby mantle composite sphere falling in liquid Fe–29 wt% S at 2.6 GPa and 1373 K. Images are separated in time by 62 ms [52]. (c) Distance and velocity of falling composite sphere versus time in Fe–29 wt% S liquid, at 2.6 GPa and 1373 K. Dashed line is terminal velocity [52].

References

1. T. A. Litovitz and C. M. Davis, Structural and shear relaxation in liquids: In: W. P. Mason (Ed.), *Physical Acoustics: Principles and Methods*, Vol. II, Part A, *Properties of Gases, Liquids and Solutions*, New York: Academic Press, 1965, pp. 281–349.
2. Y. Bottinga and P. Richet, Silicate melts: The "anomalous" pressure dependence of the viscosity, *Geochim. Cosmochim. Acta*, 59, 2725–2731, 1995.
3. J. Ferguson and Z. Kemblowski, *Applied Fluid Rheology*, New York: Elsevier, 1991.
4. R. W. Whorlow, *Rheological Techniques*, 2nd edn., New York: Ellis Horwood, 1992.
5. K. Walters, *Rheometry*, London: Chapman and Hall, 1975.
6. J. M. Dealy, *Rheometers for Molten Plastics*, New York: Van Nostrand Reinhold, 1982.
7. J. R. Van Wazer, J. W. Lyons, K. Y. Kim, and R. E. Colwell, *Viscosity and Flow Measurement*, New York: Interscience, 1963.
8. C. W. Macosko, *Rheology: Principles, Measurements, and Applications*, New York: VCH, 1994.
9. W. A. Wakeham, A. Nagashima, and J. V. Sengers (Eds.), *Measurement of the Transport Properties of Fluids*, Oxford, U.K.: Blackwell Scientific, 1991.
10. J. A. Himenez and M. Kostic, A novel computerized viscometer/rheometer, *Rev. Sci. Instrum.*, 65(1), 229–241, 1994.
11. DIN 53018 (Parts 1 and 2), 53019, German National Standards.
12. Marks' *Standard Handbooks for Mechanical Engineers*, New York: McGraw-Hill, 1978.
13. ASTM D445-10, Standard Test Method for Kinematic Viscosity of Transparent and Opaque Liquids (and Calculation of Dynamic Viscosity), available at http://enterprise.astm.org/filtrexx40.cgi?HISTORICAL/D445-10.htm (accessed on March 15, 2013).
14. W. D. Kingery, *Viscosity in Property Measurements at High Temperatures*, New York: John Wiley & Sons, 1959.
15. H. Faxen, Die Bewegung einer Starren Kugel Langs der Achsee eines mit Zaher Flussigkeit Gefullten Rohres: Arkiv for Matematik, *Astronomi och Fysik*, 27(17), 1–28, 1923.
16. F. Gui and T. F. Irvine, Jr., Theoretical and experimental study of the falling cylinder viscometer, *Int. J. Heat Mass Transfer*, 37(1), 41–50, 1994.
17. N. A. Park and T. F. Irvine, Jr., Falling cylinder viscometer end correction factor, *Rev. Sci. Instrum.*, 66(7), 3982–3984, 1995.
18. G. E. LeBlanc and R. A. Secco, High pressure stokes' viscometry: A new *in-situ* technique for sphere velocity determination, *Rev. Sci. Instrum.*, 66(10), 5015–5018, 1995.
19. R. Clift, J. R. Grace, and M. E. Weber, *Bubbles, Drops, and Particles*, San Diego: Academic Press, 1978.
20. M. Coutanceau and P. Thizon, Wall effect on the bubble behavior in highly viscous liquids, *J. Fluid Mech.*, 107, 339–373, 1981.
21. R. Roscoe, Viscosity determination by the oscillating vessel method I: Theoretical considerations, *Proc. Phys. Soc.*, 72, 576–584, 1958.
22. T. Iida and R. I. L. Guthrie, *The Physical Properties of Liquid Metals*, Oxford, UK: Clarendon Press, 1988.
23. J. T. Tough, W. D. McCormick, and J. G. Dash, Viscosity of liquid He II, *Phys. Rev.*, 132, 2373–2378, 1963.
24. J. T. Tough, W. D. McCormick, and J. G. Dash, Vibrating wire viscometer, *Rev. Sci. Instrum.*, 35, 1345–1348, 1964.
25. P. S. vander Gulik, R. Mostert, and H. R. vanden Berg, The viscosity of methane at 273 K up to 1 GPa, *Fluid Phase Equil.*, 79, 301–311, 1992.
26. T. Retsina, S. M. Richardson, and W. A. Wakeham, The theory of a vibrating-rod viscometer *Appl. Sci. Res.*, 43, 325–346, 1987.
27. C. Riesch, E. K. Reichel, A. Jachimowicz, J. Schalko, P. Hudek, B. Jakoby, and F. Keplinger, A suspended plate viscosity sensor featuring in-plane vibration and piezoresistive readout, *J. Micromech. Microeng.*, 19, 075010 1–10, 2009.

28. Y. Zhao, S. Li, A. Davidson, B. Yang, Q. Wang, and Q. Lin, A MEMS viscometric sensor for continuous glucose monitoring, *J. Micromech. Microeng.*, 17, 2528–2537, 2007.
29. P. D. Smith, R. C. D. Young, and C. R. Chatwin, A MEMS viscometer for unadulterated human blood, *Measurement*, 43, 144–151, 2010.
30. G. Dehestru, M. Leman, J. Jundt, P. Dryden, M. Sullivan, and C. Harrison, A microfluidic vibrating wire viscometer for operation at high pressure and high temperature, *Rev. Sci. Instrum.*, 82, 035113 1–5, 2011.
31. H. J. McSkimin, Ultrasonic methods for measuring the mechanical properties of liquids and solids, In: W. P. Mason (Ed.), *Physical Acoustics: Principles and Methods*, Vol. I, Part A, *Properties of Gases, Liquids and Solutions*, New York: Academic Press, 1964, pp. 271–334.
32. P. Nasch, M. H. Manghnani, and R. A. Secco, A modified ultrasonic interferometer for sound velocity measurements in molten metals and alloys, *Rev. Sci. Instrum.*, 65, 682–688, 1994.
33. K. W. Katahara, C. S. Rai, M. H. Manghnani, and J. Balogh, An interferometric technique for measuring velocity and attenuation in molten rocks, *J. Geophys. Res.*, 86, 11779–11786, 1981.
34. A. Einstein, Ueberdievondermolekularkinetis chentheoriederwaermegefordertebewegung voninruhendenfluessigkeitensuspendiertenteilchen, *Ann. Phys.*, 17, 549–560, 1905.
35. M. L. Gardel, M. T. Valentine, and D. A. Weitz, Microrheology, In: K. Breuer (Ed.), *Microscale Diagnostic Techniques*, New York: Springer, 2005.
36. T. G. Mason and D. A. Weitz, Optical measurements of frequency-dependent linear viscoelastic moduli of complex fluids, *Phys. Rev. Lett.*, 74, 1250–1253, 1995.
37. T. G. Mason, Estimating the viscoelastic moduli of complex fluids using the generalized Stokes–Einstein equation, *Rheol. Acta.*, 39, 371–378, 2000.
38. A. J. Levine and T. C. Lubensky, One- and two-particle microrheology, *Phys. Rev. Lett.*, 85, 1774–1777, 2000.
39. A. J. Levine and T. C. Lubensky, Response function of a sphere in a viscoelastic two-fluid medium, *Phys. Rev. E*, 63, 041510 1–12, 2001.
40. T. A. Waigh, Microrheology of complex fluids, *Rep. Prog. Phys.*, 68, 685–742, 2005.
41. J. Crocker and D. G. Grier, Methods of digital video microscopy for colloidal studies, *J. Colloid Interface Sci.*, 179, 298–310, 1996.
42. J. Crocker and E. Weeks, Particle tracking using IDL, 1996, http://www.physics.emory.edu/~weeks/idl/
43. J. C. Crocker, M. T. Valentine, E. R. Weeks, T. Gisler, P. D. Kaplan, A. G. Yodh, and D. A. Weitz, Two-point microrheology of inhomogeneous soft materials, *Phys. Rev. Lett.*, 85, 888–891, 2000.
44. N. Yang and J. R. deBruyn, unpublished.
45. P. W. Bridgman, The viscosity of liquids under pressure, *Proc. Natl. Acad. Sci.*, 11, 603–606, 1925.
46. L. Kulisiewicz and A. Delgado, High pressure rheological measurement methods: A review, *Appl. Rheol.*, 20, 13018, 2010.
47. C. J. Schaschke, High pressure viscosity measurement with falling body type viscometers, *Int. Rev. Chem. Eng.*, 2, 564–576, 2010.
48. J. D. Barnett and C. D. Bosco, Viscosity measurements on liquids to pressures of 60 kbar, *J. Appl. Phys.*, 40, 3144–3150, 1969.
49. R. A. Secco, R. F. Tucker, S. P. Balog, and M. D. Rutter, Tailoring sphere density for high pressure physical property measurements on liquids, *Rev. Sci. Instrum.*, 71, 2114–2116, 2001.
50. T. Uchida, Y. Wang, M. L. Rivers, S. R. Sutton, D. J. Weidner, M. T. Vaughan, J. Chen, B. Li, R. A. Secco, M. D. Rutter, and H. Liu, A large-volume press facility at the Advanced Photon Source: Diffraction and imaging studies on materials relevant to the cores of planetary bodies, *J. Phys. Condens. Matter.*, 14, 11517–11523, 2002.
51. K. Funakoshi, A. Suzuki, and H. Terasaki, In situ viscosity measurements of albite melt under high pressure, *J. Phys. Condens. Matter.*, 14, 11343–11347, 2002.
52. R. A. Secco, M. D. Rutter, S. P. Balog, H. Liu, D. C. Rubie, T. Uchida, D. Frost, Y. Wang, M. Rivers, and S. R. Sutton, Viscosity and density of Fe–S liquids at high pressures, *J. Phys. Condens. Matter.*, 14, 11325–11330, 2002.

Further Information

Brooks, R. F., Dinsdale, A. T., and Quested, P. N., The measurement of viscosity of alloys—A review of methods, data and models, *Meas. Sci. Technol.*, 16, 354–362, 2005, a review of methods used to measure viscosity of liquid metals including methods adaptable to "in plant" measurement of fluid flow in metallurgical industrial processes.

Hou, Y. Y. and Kassim, H. O., Instrument techniques for rheometry, *Rev. Sci. Instrum.*, 76. 101101, 2005, a review of some of the latest advances in rheology measuring techniques including new approaches to conventional velocimetry (e.g., nuclear magnetic resonance, ultrasound pulse Doppler mapping) as well as other techniques that are important for industrial processes (e.g., extensional rheometry and interfacial rheometry).

O'Neill, M. E. and Chorlton, F., *Viscous and Compressible Fluid Dynamics*, Chichester, U.K.: Ellis Horwood, 1989, mathematical methods and techniques and theoretical description of flows of Newtonian incompressible and ideal compressible fluids.

Ryan, M. P. and Blevins, J. Y. K., The viscosity of synthetic and natural silicate melts and glasses at high temperatures and 1 bar (10^5 Pascals) pressure and at higher pressures, *U.S. Geological Survey Bulletin* 1764, Denver, CO, 1987, p. 563, an extensive compilation of viscosity data in tabular and graphic format and the main techniques used to measure shear viscosity.

Van Wazer, J. R., Lyons, J. W., Kim, K. Y., and Colwell, R. E., *Viscosity and Flow Measurement: A Laboratory Handbook of Rheology*, New York: Interscience Publishers, Division of John Wiley & Sons, 1963, A comprehensive overview of viscometer types and simple laboratory measurements of viscosity for liquids.

47

Surface Tension Measurement

David B. Thiessen
California Institute of Technology

Kin F. Man
California Institute of Technology

The effect of surface tension is observed in many everyday situations. For example, a slowly leaking faucet drips because the force of surface tension allows the water to cling to it until a sufficient mass of water is accumulated to break free. Surface tension can cause a steel needle to "float" on the surface of water although its density is much higher than that of water. The surface of a liquid can be thought of as having a skin that is under tension. A liquid droplet is somewhat analogous to a balloon filled with air. The elastic skin of the balloon contains the air inside at a slightly higher pressure than the surrounding air. The surface of a liquid droplet likewise contains the liquid in the droplet at a pressure that is slightly higher than ambient. A clean liquid surface, however, is not elastic like a rubber skin. The tension in a piece of rubber increases as it is stretched and will eventually rupture. A clean liquid surface can be expanded indefinitely without changing the surface tension.

The mechanical model of the liquid surface is that of a skin under tension. Any given patch of the surface thus experiences an outward force tangential to the surface everywhere on the perimeter. The force per unit length of the perimeter acting perpendicular to the perimeter is defined as the *surface tension*, γ. Molecules in the interfacial region have a higher potential energy than molecules in the bulk phases because of an imbalance of intermolecular attractive forces. This will result in an excess free energy per unit area associated with the surface that is numerically equivalent to the surface tension, as shown later. Consider a flat rectangular patch of fluid interface of width W and length L. In order to expand the length to $L + \Delta L$, an amount of work $\gamma W \Delta L$ must be done at the boundary. The product $W\Delta L$ is just the change in area ΔA of the surface. The work done to increase the area is thus $\Delta A\gamma$, which corresponds to the increase in surface free energy. Thus, the surface tension γ is seen to be equivalent to the surface free energy per unit area. Room-temperature organic liquids typically have surface tensions in the range of 20–40 mN m^{-1},

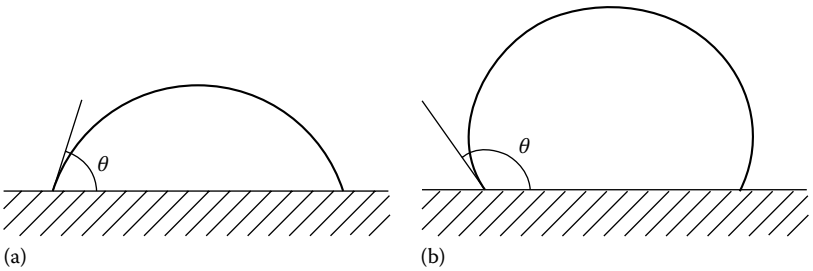

FIGURE 47.1 Illustration of contact angles and wetting. The liquid in (a) wets the solid better than that in (b).

while pure water has a value of 72 mN m^{-1} at 25 °C. The interface between two immiscible liquids, such as oil and water, also has a tension associated with it, which is generally referred to as the *interfacial tension*.

The surface energy concept is useful for understanding the shapes adopted by liquid surfaces. An isolated system in equilibrium is in a state of minimum free energy. Because the surface free energy contributes to the total free energy of a multiphase system, the surface free energy is minimized at equilibrium subject to certain constraints. Also, because the surface free energy is directly proportional to the surface area, surface area is also minimized. In the absence of gravity, a free-floating liquid droplet assumes a spherical shape because, for a given volume of liquid, the sphere has the least surface area. However, a droplet suspended from a needle tip on Earth does not form a perfect sphere because the minimum free energy configuration involves a trade-off between a reduction of the surface energy and a reduction of the gravitational potential. The droplet elongates to reduce its gravitational potential energy.

The surface energy concept is also useful for understanding the behavior of so-called surface active agents or *surfactants*. A two-component liquid mixture in thermodynamic equilibrium exhibits preferential adsorption of one component at the surface if the adsorption causes a decrease in the surface energy. The term surfactant is reserved for molecular species that strongly adsorb at the surface even when their concentration in the bulk liquid is very low. Surfactants are common in natural waters and are very important in many biological and industrial processes.

The interface between a solid and a fluid also has a surface free energy associated with it. Figure 47.1a shows a liquid droplet at rest on a solid surface surrounded by air. This system contains three different types of interfaces: solid–gas, solid–liquid, and liquid–gas, each with a characteristic surface free energy per unit area. The state of minimum free energy for the system then involves trade-offs in the surface area for the various interfaces. The region of contact between the gas, liquid, and solid is termed the *contact line*. The liquid–gas surface meets the solid surface with an angle θ measured through the liquid, which is known as the *contact angle*. The contact angle attains a value that minimizes the free energy of the system and is thus a characteristic of a particular solid–liquid–gas system. The system shown in Figure 47.1a has a smaller contact angle than that shown in Figure 47.1b. The smaller the contact angle, the better the liquid is said to wet the solid surface. For $\theta = 0$, the liquid is said to be perfectly wetting.

Measurement of surface tension is important in many fields of science and engineering, as well as in medicine. A number of standard methods exist for its measurement. In many systems of interest, the surface tension changes with time, perhaps, for example, because of adsorption of surfactants. Several standard methods can be used to measure dynamic surface tension if it changes slowly with time. Special techniques have been developed to measure dynamic surface tensions for systems that evolve very rapidly.

47.1 Mechanics of Fluid Surfaces

Some methods of measuring surface tension depend on the mechanics at the line of contact between a solid, liquid, and gas. When the system is in static mechanical equilibrium, the contact line is motionless, meaning that the net force on the line is zero. Forces acting on the contact line

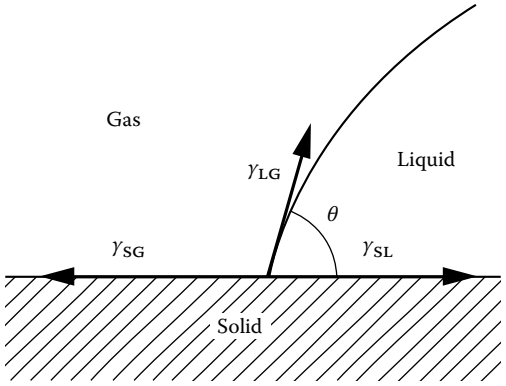

FIGURE 47.2 Surface tension forces acting on the contact line.

arise from the surface tensions of the converging solid–gas, solid–liquid, and liquid–gas interfaces, denoted by γ_{SG}, γ_{SL}, and γ_{LG}, respectively (Figure 47.2). The condition of zero net force along the direction tangent to the solid surface gives the following relationship between the surface tensions and contact angle θ:

$$\gamma_{SG} = \gamma_{SL} + \gamma_{LG}\cos\theta \tag{47.1}$$

This is known as *Young's equation*. The contact angle is thus seen to be dependent on the surface tensions between the various phases present in the system and is therefore an intrinsic property of the system.

As discussed in the introduction, the surface tension of a droplet causes an increase in pressure in the droplet. This can be understood by considering the forces acting on a curved section of surface as illustrated in Figure 47.3a. Because of the curvature, the surface tension forces pull the surface toward the concave side of the surface. For mechanical equilibrium, the pressure must then be greater on the concave side of the surface. Figure 47.3b shows a saddle-shaped section of surface in which surface tension forces oppose each other, thus reducing or eliminating the required pressure difference across the surface. The mean curvature of a 2D surface is specified in terms of the two principal radii of curvature, R_1 and R_2, which are measured in perpendicular directions. A detailed mechanical analysis of curved

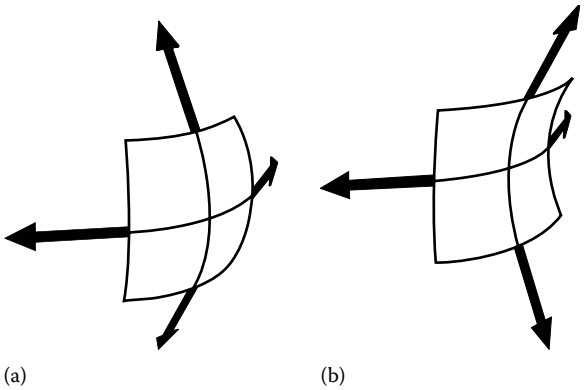

FIGURE 47.3 Mechanics of curved surfaces that have principal radii of curvature of (a) the same sign and (b) the opposite sign.

tensile surfaces shows that the pressure change across the surface is directly proportional to the surface tension and to the mean curvature of the surface:

$$P_A - P_B = \gamma\left(\frac{1}{R_1} + \frac{1}{R_2}\right) \tag{47.2}$$

where γ is the surface tension and the quantity in brackets is twice the mean curvature. The sign of the radius of curvature is positive if its center of curvature lies in phase A and negative if it lies in phase B. Equation 47.2 is known as the *Young–Laplace equation*, and the pressure change across the interface is termed the *Laplace pressure*. Measurement of the Laplace pressure for a surface of known curvature then allows a determination of the surface tension.

Several methods of surface tension measurement are based on the measurement of the static shape of an axisymmetric drop or bubble or on the point of mechanical instability of such drops or bubbles. In a gravitational field, a drop or bubble that is attached to a solid support assumes a nonspherical shape. Figure 47.4a shows the shape of a hanging droplet, also known as a pendant drop, and Figure 47.4b shows a so-called sessile drop. Axisymmetric air bubbles in water attain the same shapes as water drops in air, except that they are inverted. A bubble supported from below is thus called a hanging or pendant bubble, and a bubble supported from above is called a captive or sessile bubble. The reason for the deviation of the shape from that of a sphere can be understood from Equation 47.2. The hydrostatic pressure changes with depth more rapidly in a liquid than in a gas. The pressure difference across the surface of a pendant drop in air therefore increases from top to bottom, requiring an increase in the mean curvature of the surface according to Equation 47.2. The drop in Figure 47.4a has a neck at the top, which means that the two principal radii of curvature have opposite signs and cancel to some extent. At the bottom of the drop, the radii of curvature have the same sign, thus making the mean curvature larger. The Young–Laplace equation can be

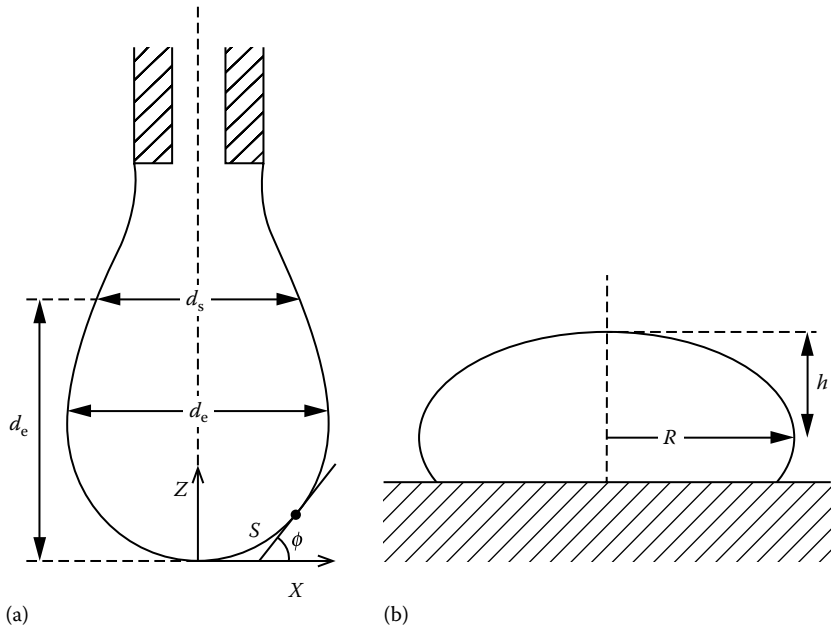

FIGURE 47.4 (a) A pendant drop showing the characteristic dimensions, d_e and d_s, and the coordinates used in the Young–Laplace equation. (b) A sessile drop showing the characteristic dimensions R and h.

written as coupled first-order differential equations in terms of the coordinates of the interface for an axisymmetric surface in a gravitational field as

$$\frac{dx}{ds} = \cos\phi$$
$$\frac{dz}{ds} = \sin\phi \tag{47.3}$$
$$\frac{d\phi}{ds} = \frac{2}{b} + \left(\frac{\Delta\rho g}{\gamma}\right) z - \frac{\sin\phi}{x}$$
$$x(0) = z(0) = \phi(0) = 0$$

where

x and z are the horizontal and vertical coordinates, respectively, with the origin at the drop apex
s is the arc length along the drop surface measured from the drop apex
ϕ is the angle between the surface tangent and the horizontal (Figure 47.4a)
The parameter b is the radius of curvature at the apex of the drop or bubble
$\Delta\rho$ is the density difference between the two fluid phases
g is the acceleration of gravity

Numerical integration of Equation 47.3 allows one to compute the shape of an axisymmetric fluid interface. Comparison of computed shapes with experimentally measured shapes of drops or bubbles is a useful method of measuring surface tension. If all lengths in Equation 47.3 are made dimensionless by dividing them by b, the resulting equation contains only one parameter, $\beta = \Delta\rho g b^2/\gamma$, which is called the Bond number (or shape factor). The shape of an axisymmetric drop, bubble, or meniscus depends only on this one dimensionless parameter. The Bond number can also be written as $\beta = 2b^2/a^2$ where $a = \sqrt{2\gamma/\Delta\rho g}$ is known as the capillary constant and has units of length.

Several dynamic methods of measuring surface tension are based on capillary waves. Capillary waves result from oscillations of the liquid surface for which surface tension is the restoring force. The frequency of the surface oscillation is thus dependent on the surface tension and wavelength. Very low amplitude capillary waves with a broad range of frequencies are always present on liquid surfaces owing to thermal fluctuations. Larger-amplitude capillary waves can be excited by purposely perturbing the surface.

47.2 Standard Methods and Instrumentation

A number of commonly used methods of measuring surface tension exist. The choice of a method depends on the system to be studied, the degree of accuracy required, and possibly on the ability to automate the measurements. In the discussion that follows, these methods are grouped according to the kind of instruments used in the measurements. Because the information presented for each method is necessarily brief, readers who are interested in constructing their own apparatus should consult the more detailed treatises in [1–4]. A list of commercially available instruments is given in Table 47.1, together with manufacturer names and approximate prices. Vendors can be contacted at the addresses given in Table 47.2.

TABLE 47.1 Commercially Available Instruments

Method	Instrument Type	Manufacturer/Product Name	Approximate Price (Range)
Capillary rise	Manual	Fisher	$79
Wilhelmy plate/du Noüy ring	Manual, mechanical balance	CSC, Fisher, Kahl	$2,000–$4,000
Wilhelmy plate/du Noüy ring	Manual, electrobalance	KSV, Lauda, NIMA	$4,000–$11,000
Wilhelmy plate/du Noüy ring	Automatic, electrobalance	Cahn, Krüss, KSV, NIMA	$9,000–$24,000
Maximum bubble pressure	Automatic	Krüss, Lauda, Sensa Dyne	$5,000–$23,000
Pendant/sessile drop	Manual	Krüss, Rame-Hart	$7,000–$10,000
Pendant/sessile drop	Automatic	ADSA, AST, FTA, Krüss, Rame-Hart, Temco	$10,000–$100,000
Drop weight/volume	Automatic	Krüss, Lauda	$16,000–$21,000
Spinning drop	Manual	Krüss	$20,100

Note: Price ranges reflect differences in degree of automation, the number of accessories included, or variation in price between manufacturers.

TABLE 47.2 Manufacturers and Suppliers of Instruments for Surface Tension Measurement

AST Products, 9 Linnell Circle, Billerica, MA 01821-3902, Tel.: (508) 663-7652, http://www.astp.com/

Applied Surface Thermodynamics Research Associates (ASTRA), 15 Brendan Rd., Toronto, Ontario, Canada M4G 2W9, Tel.: (416) 978-3601

Brinkmann Instruments, Inc. (distributor for Lauda tensiometers), One Catiaque Road, P.O. Box 1019, Westbury, NY 11590-0207, Tel.: (800) 645-3050

Cahn Instruments, 5225 Verona Rd., Bldg. 1, Madison, WI 53711, Tel.: (800) 244-6305

CSC Scientific Company, Inc., 8315 Lee Highway, Fairfax, VA 22031, Tel.: (800) 458-2558, http://www.cscscientific.com/

CTC Technologies, Inc. (distributor for NIMA tensiometers), 7925-A North Oracle Road, Suite 364, Tucson, AZ 85704-6356, Tel.: (800) 282-8325, http://www.ctctechnologies.com/

First Ten Angstroms (FTA), 465 Dinwiddie Street, Portsmouth, VA 23704, Tel.: (800) 949-4110, http://firsttenangstroms.com/

Fisher Scientific, 711 Forbes Ave., Pittsburgh, PA 15219-4785, Tel.: (800) 766-7000, http://www.fishersci.com/ecomm/servlet/home?storeId=10652

Kahl Scientific Instrument Corp., P.O. Box 1166, El Cajon, CA 92022-1166, Tel.: (619) 444-2158

Krüss USA., 9305-B Monroe Road, Charlotte, NC 28270-1488, Tel.: (704) 847-8933, http://www.kruss.de/en/contact/kruess-worldwide/usa.html

KSV Instruments USA, P.O. Box 192, Monroe, CT 06468, Tel.: (800) 280-6216

Rame-Hart, Inc., 8 Morris Ave., Mountain Lakes, NJ 07046, Tel.: (201) 335-0560, http://ramehart.com/

Sensa Dyne Instrument Div., Chem-Dyne Research Corp., P.O. Box 30430, Mesa, AZ 85275-0430, Tel.: (602) 924-1744, http://www.sensadyne.com/

Temco, Inc., 4616 North Mingo, Tulsa, OK 74117-5901, Tel.: (918) 834-2337

47.2.1 Capillary Rise Method

If a glass capillary tube is brought into contact with a liquid surface, and if the liquid wets the glass with a contact angle of less than 90°, then the liquid is drawn up into the tube as shown in Figure 47.5a. The surface tension is directly proportional to the height of rise, h, of the liquid in the tube relative to the flat liquid surface in the larger container. By applying Equation 47.2 to the meniscus in the capillary tube, the following relationship is obtained:

$$\Delta\rho g h = \frac{2\gamma}{b} \tag{47.4}$$

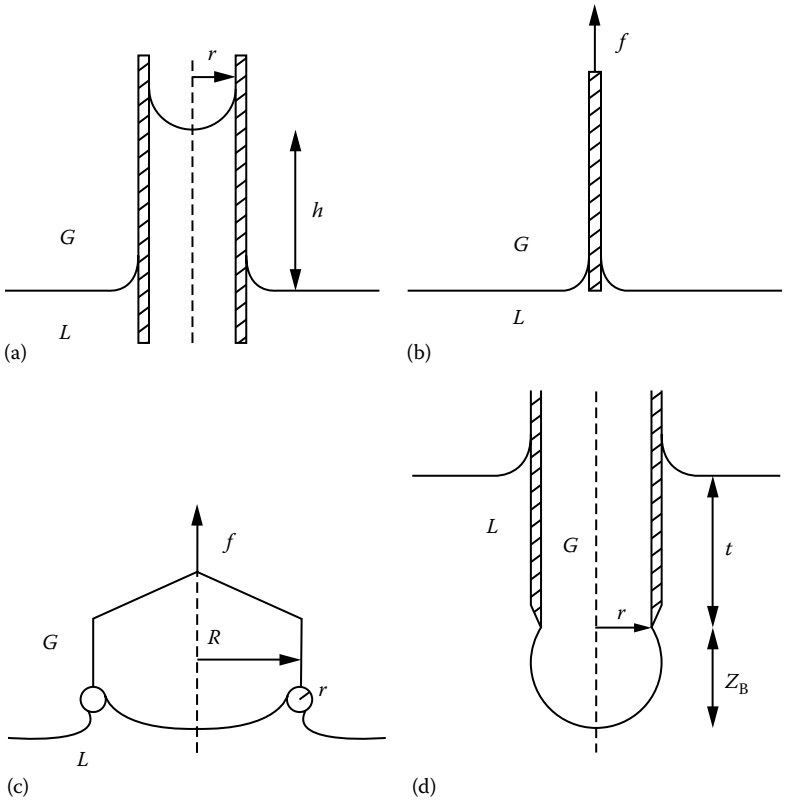

FIGURE 47.5 Geometries for (a) capillary rise method, (b) Wilhelmy plate method, (c) du Noüy ring method, and (d) maximum bubble pressure method.

where

b is the radius of curvature at the center of the meniscus

$\Delta\rho$ is the density difference between liquid and gas

For small capillary tubes, b is well approximated by the radius of the tube itself, assuming that the contact angle of the liquid on the tube is zero. For larger tubes or for increased accuracy, the value of b must be corrected for gravitational deformation of the meniscus (p. 12 of [1]). Obtaining accurate results with the capillary rise method requires using a thoroughly clean glass capillary tube with a very uniform diameter of less than 1 mm. The container for the liquid should be at least 8 cm in diameter, and the liquid must wet the capillary tube with a contact angle of zero. This method is primarily useful for pure liquids and is capable of high accuracy at relatively low cost.

47.2.2 Wilhelmy Plate and du Noüy Ring Methods

Measurement of the pull of a liquid surface directly on a solid object is the basis for two of the standard methods discussed here. In the Wilhelmy plate method, the solid object is a flat, thin plate that the test liquid should wet with a zero contact angle. The plate is suspended vertically from a delicate balance that is zeroed with the plate suspended in air. The test liquid is brought into contact with the bottom of the plate, causing the plate to be pulled down into the liquid by the surface tension force. The force applied to the plate from above is then increased to bring the bottom edge of the plate level with the flat surface

of the liquid (Figure 47.5b). This avoids the necessity to make buoyancy corrections to the measurement. The surface tension is computed from the force measurement, f, using

$$\gamma = \frac{f\cos\theta}{\left[2(l+t)\right]} \tag{47.5}$$

where
l is the length of the plate
t is its thickness

The contact angle θ is often assumed to be zero for common liquids on clean glass or platinum plates, but one should be aware of the error caused by a nonzero contact angle. No other correction factors are necessary for this method, and the fluid density does not need to be known.

The du Noüy ring method is known as a maximum pull method, of which there are several variations. The technique is to contact the liquid surface with a ring and then measure the force continuously as the surface is lowered until a maximum force, f_{max}, is recorded. The maximum force typically occurs just before the ring detaches from the surface. The surface tension is obtained from the formula

$$\gamma = \left(\frac{f_{max}}{4\pi R}\right)\left[F\left(\frac{R^3}{V}, \frac{R}{r}\right)\right] \tag{47.6}$$

where
R and r are the radii of the ring and wire, respectively, as indicated in Figure 47.5c
V is the volume of liquid raised by the ring
F is a correction factor (F is tabulated in Table 5, p. 132 of [4])

The du Noüy ring method requires knowledge of the liquid density, ρ_L, in order to determine V from $V = f_{max}/\rho_L$. This method requires the liquid to wet the ring with zero contact angles, and it is not suitable for solutions that attain surface equilibrium slowly.

A single instrument is normally capable of performing either Wilhelmy plate or du Noüy ring measurements. Some commercially available instruments can perform the complete measurement procedure automatically. Computer interfacing with a Wilhelmy plate instrument allows automatic data logging that can be used to follow changes in surface tension with time in surfactant solutions.

47.2.3 Maximum Bubble Pressure Method

The *maximum bubble pressure method* (MBPM) involves direct measurement of the pressure in a bubble to determine the surface tension. A tube is lowered to a depth t in the test liquid, and gas is injected to form a bubble of height Z_B at the tip of the tube as shown in Figure 47.5d. The increase in bubble pressure, P_b, over ambient pressure, P_a, arising from the interface is given by the sum of a hydrostatic pressure and Laplace pressure:

$$\delta p = P_b - P_a - \Delta\rho g t = \Delta\rho g Z_B + \frac{2\gamma}{b} \tag{47.7}$$

As a new bubble begins to form, Z_B increases while b, the radius of curvature at the bubble apex, decreases, resulting in an increase in pressure in the bubble. Ultimately, b increases as the bubble

grows larger, thus reducing the pressure. The pressure in the bubble thus reaches a maximum when δp reaches a maximum, which in turn can be theoretically related to the surface tension. For $\delta p = \delta p_{max}$, Equation 47.7 can be rewritten in dimensionless form as follows:

$$\frac{r}{X} = \frac{r}{b} + \frac{r}{a}\frac{Z_B}{b}\left(\frac{\beta}{2}\right)^{1/2} \tag{47.8}$$

where

r is the tube radius
X is a length defined as $X = 2\gamma/\delta p_{max}$
a is the capillary constant
β is the Bond number

The dimensionless quantity rlX depends only on r/a, the relationship being determined by Equation 47.8 combined with numerical solutions of Equation 47.3. Tabulations of this relationship are used to calculate the surface tension by an iterative procedure (p. 18 of [1]). The standard MBPM requires knowledge of the fluid densities, tube radius, and depth of immersion of the tube.

A differential MBPM uses two tubes of different diameters immersed to the same depth. The difference in the maximum bubble pressure for the two tubes, ΔP, is measured, eliminating the need to know the immersion depth and making the method less sensitive to errors in the knowledge of the liquid density. For the differential MBPM, surface tension is computed from the following (see [5]):

$$\gamma = A\Delta P\left[1 + \left(\frac{0.69 r_2 \rho_L}{\Delta P}\right)\right] \tag{47.9}$$

where

r_2 is the radius of the larger tube
ρ_L is the liquid density
A is an apparatus-dependent constant that is determined by calibration with several standard liquids [6]

Automated MBPM units are commercially available (see Table 47.1). Sensa Dyne manufactures differential MBPM units that allow for online process measurements under conditions of varying temperature and pressure.

47.2.4 Pendant Drop and Sessile Drop Methods

The shape of an axisymmetric pendant or sessile drop (Figure 47.4) depends on only a single parameter, the Bond number, as discussed previously. The Bond number is a measure of the relative importance of gravity to surface tension in determining the shape of the drop. For Bond numbers near zero, surface tension dominates and the drop is nearly spherical. For larger Bond numbers, the drop becomes significantly deformed by gravity. In principle, the method involves obtaining an image of the drop and comparing its shape and size to theoretical profiles obtained by integrating Equation 47.3 for various values of β and b. Once β and b have been determined from shape and size comparison, the surface tension is calculated from

$$\gamma = \frac{\Delta\rho g b^2}{\beta} \tag{47.10}$$

In practice, the drop shape and size have traditionally been determined by the manual measurement of several characteristic dimensions (see Figure 47.4) of the drop from a photographic print. For pendant drops, the ratio d_s/d_e is correlated to a shape factor H from which surface tension is calculated ([3, p. 27; 7]) according to

$$\gamma = \frac{\Delta\rho g d_e^2}{H} \tag{47.11}$$

For sessile drops, various analytical formulae are available for computation of surface tension directly from the characteristic dimensions (p. 36 of [3]). Drop shape methods based on characteristic dimensions require very accurate measurement of the dimensions for good results. For more accurate results, methods that fit the entire shape of the edge of the drop to the Laplace equation are recommended.

In recent years, the entire procedure has been automated using digital imaging and computer image analysis [8,9]. Typically, several hundred coordinates on the edge of the drop are located with subpixel resolution by computer analysis of the digital image. The size, shape, and horizontal and vertical offsets of the theoretical profile given by Equation 47.3 are varied by varying four parameters: b, β, and the pixel coordinates of the drop apex, x_0 and z_0. A best fit of the theoretical profile to the measured edge coordinates is obtained by minimizing an objective function. A digital image of a pendant drop can be analyzed for surface tension on a desktop computer in 1 or 2 s [10]. The speed of algorithms for pendant drop analysis on modern desktop computers has allowed this method to be used to track changes in surface tension for surfactant-covered surfaces by analyzing a sequence of images. The algorithms can simultaneously track the surface area and volume of the drop or bubble. Both soluble and insoluble surfactants have been studied using the pendant drop, sessile drop, pendant bubble, and captive bubble configurations [11–13]. Table 47.1 lists several manufacturers that can provide software for automated analysis of surface tension from drops or bubbles in pendant or sessile configurations. The increased accuracy and simplicity of the automated pendant drop procedure makes it a very flexible method that has been applied to measure ultralow interfacial tensions, pressure, temperature, and time dependence of interfacial tension, relaxation of adsorption layers, measurement of line tensions, and film-balance measurements [14].

47.2.5 Drop Weight or Volume Method

A pendant drop will become unstable and detach from its support if it grows too large. The weight of the detached portion is related to the surface tension of the fluid by

$$\gamma = \left(\frac{mg}{r}\right)\left[F\left(\frac{r}{V^{1/3}}\right)\right] \tag{47.12}$$

where

mg is the weight of the detached drop
r is the radius of the tip from which the drop hangs
V is the volume of the detached drop

An empirical correction factor, F, is tabulated as a function of $r/V^{1/3}$ (p. 50 of [3]). For Equation 47.12 to apply, drops must be formed slowly. Measurements typically involve weighing the accumulated liquid from a large number of drops to determine the average weight per drop. The density of the fluid must be known in order to determine the drop volume and then obtain the factor F. Another method involves

measuring the volumetric flow rate of liquid to the tip while counting the drops. The density of the fluid must be known in order to determine the drop weight. The latter method allows for automation of measurements [15].

47.2.6 Spinning Drop Method

The spinning drop method is a shape-measurement method similar to the pendant and sessile drop methods. However, the deformation of the drop in this case is caused by radial pressure gradients in a rapidly spinning tube. This method is normally used for measuring interfacial tensions between immiscible liquids. A horizontal glass tube with sealed ends is filled with the more dense liquid through a filling port. The tube is then spun about its axis, while a drop of the lower-density liquid is injected into the tube. The pressure in the outer liquid increases from the center of the tube toward the walls as a result of the spinning motion. The pressure gradient forces the drop to move to the center of the tube and causes it to elongate, while surface tension opposes elongation. Measurement of the maximum drop diameter, $2r_{max}$, and length, $2h_{max}$, together with the angular velocity of rotation, Ω, allows for calculation of the surface tension according to

$$\gamma = \frac{1}{2}\left(\frac{r_{max}}{r^{\star}_{max}}\right)^3 \Delta\rho\Omega^2 \tag{47.13}$$

where $r^{\star}_{max}$ is correlated to the aspect ratio r_{max}/h_{max} [16]. The spinning drop method is particularly suited for measuring ultralow interfacial tensions (10^{-2} to 10^{-4} mN m^{-1}).

47.3 Specialized Methods

47.3.1 Dynamic Surface Tension

In an aqueous solution of soluble surfactant, the surface tension decreases following creation of new surface area because of adsorption of surfactant molecules. Surfactant adsorption kinetics can be studied by measuring the change in surface tension with time. For a dilute solution, the rate of change of surface tension is often slow enough that automated versions of static methods such as the Wilhelmy plate or pendant drop [17] methods can be used to follow the changes in surface tension. In concentrated solutions in which large changes in surface tension can occur within a fraction of a second following surface creation, a dynamic method must be used. A liquid jet emerging from an elliptical orifice has stationary waves on its surface, the wavelengths of which are related to the surface tension. The oscillating jet method has been used to measure surface tension for surface ages as low as 0.6 ms [18]. A dynamic version of the MBPM has been used to measure dynamic surface tension at surface ages down to 0.1 ms [19].

47.3.2 Surface Viscoelasticity

A liquid surface covered by a monolayer of surfactant exhibits viscoelastic behavior. In addition to surface tension, the surface rheology is characterized in terms of dilatational and shear elasticities as well as dilatational and shear viscosities. The dilatational properties in particular are important in a variety of situations from foam stability to the functioning of the human lung. The surface dilatational modulus is proportional to the change in surface tension for a given change in surface area. This modulus depends on the rate of change of surface area for both soluble and insoluble surfactant monolayers, which indicates that relaxation processes are active. These relaxation processes give rise to the surface dilatational viscosity. For the case of soluble surfactants, one of the relaxation processes

is the adsorption or desorption of molecules at the surface. The equilibrium dilatational elasticity of an insoluble monolayer can be measured by slowly expanding or compressing the monolayer in a Langmuir trough while monitoring the surface tension with a Wilhelmy plate apparatus [20]. Studies of surface rheology at high rates of surface expansion or compression are of interest for both soluble and insoluble surfactants.

Surface tension relaxation following sudden expansion or compression of the surface for a soluble surfactant has been studied by the automated pendant drop method [21]. A method known as oscillating bubble tensiometry has been applied to measure the kinetics of adsorption and desorption for soluble surfactants [22,23]. Other methods for studying dynamic dilatational viscoelastic properties are reviewed in [24], including transverse and longitudinal capillary wave methods, a modified MBPM, and an oscillating bubble method.

47.3.3 Measurements at Extremes of Temperature and Pressure

Several of the standard methods described in this chapter can be adapted to make surface or interfacial tension measurements at extreme temperatures and/or pressures. The most common methods used to measure the surface tension of high-temperature molten metals, alloys, and semiconductors are the MBPM [25] and the pendant or sessile drop method [26–28]. Measurement of the interfacial tension between oil and a second immiscible phase at high pressure and elevated temperature is of interest for understanding aspects of enhanced oil recovery. The pendant drop method has been applied under pressures of 82 MPa at 449 K [29], while a capillary wave method has been applied at 136 MPa and 473 K [30]. A pendant drop apparatus capable of measurements to 10,000 psi (69 MPa) and 350 °F (450 K) is commercially available from Temco Inc. (Table 47.2).

47.3.4 Interfacial Tension

Measurement of the interfacial tension between two immiscible liquids can present special difficulties. Measurement by the capillary rise, du Noüy ring, or Wilhelmy plate method is problematic in that the contact angle is often nonzero. The pendant drop [7] and drop weight [31] methods can both be applied, provided the densities of the two liquids are sufficiently different. The pendant drop method, in particular, is widely used for interfacial tension measurement. Interfacial tension can be measured by a modified MBPM in which one measures the maximum pressure in a liquid drop injected into a second immiscible liquid [32]. The modified MBPM [32] and a liquid bridge method [33] have been used to measure interfacial tension between two liquids of equal density. Ultralow values of interfacial tension can be measured by the spinning drop [34], pendant drop [35], and capillary wave methods [34].

Defining Terms

Surface tension: A force per unit length that acts tangential to a liquid surface and perpendicular to any line that lies within the surface.

Surface energy: The excess free energy per unit area associated with a surface between two phases. For a liquid–fluid surface, the surface energy is numerically equivalent to the surface tension.

Acknowledgments

During the preparation of this chapter, one of us (DBT) was supported in part by the National Aeronautics and Space Administration (NASA) and by the Office of Naval Research. The work by one of us (KFM) was performed at the Jet Propulsion Laboratory, California Institute of Technology, under contract with NASA.

References

1. A. W. Adamson, *Physical Chemistry of Surfaces*, 5th edn., New York: John Wiley & Sons, 1990.
2. A. E. Alexander and J. B. Hayter, Determination of surface and interfacial tension. In: A. Weissberger and B. W. Rossiter (Eds.), *Physical Methods of Chemistry*, Part V, 4th edn., New York: John Wiley & Sons, 1971.
3. A. Couper, Surface tension and its measurement, In: B. W. Rossiter and R. C. Baetzold (Eds.), *Physical Methods of Chemistry*, Vol. 9A, 2nd edn., New York: John Wiley & Sons, 1993.
4. J. F. Padday, Surface tension. II. The measurement of surface tension. In: E. Matijevic (Ed.), *Surface and Colloid Science*, Vol. 1, New York: John Wiley & Sons, 1969.
5. S. Sugden, The determination of surface tension from the maximum pressure in bubbles. Part II, *J. Chem. Soc.*, 125, 27–31, 1924.
6. ASTM Standard D3825-90, Standard test method for dynamic surface tension by the fast-bubble technique, *1996 Annual Book of ASTM Standards*, Vol. 05.02, West Conshohocken, PA: ASTM, 1996, pp. 575–579.
7. D. S. Ambwani and T. Fort, Jr., Pendant drop technique for measuring liquid boundary tensions. In: R. J. Good and R. R. Stromberg (Eds.), *Surface and Colloid Science*, Vol. 11, New York: Plenum Press, 1979.
8. Y. Rotenberg, L. Boruvka, and A. W. Neumann, Determination of surface tension and contact angle from the shapes of axisymmetric fluid interfaces, *J. Colloid Interface Sci.*, 93, 169–183, 1983.
9. P. Cheng, D. Li, L. Boruvka, Y. Rotenberg, and A. W. Neumann, Automation of axisymmetric drop shape analysis for measurements of interfacial tensions and contact angles, *Colloids Surf.*, 43, 151–167, 1990.
10. D. B. Thiessen, D. J. Chione, C. B. McCreary, and W. B. Krantz, Robust digital image analysis of pendant drop shapes, *J. Colloid Interface Sci.*, 177, 658–665, 1996.
11. S. Lin, K. McKeigue, and C. Maldarelli, Diffusion-controlled surfactant adsorption studied by pendant drop digitization, *AIChE J.*, 36, 1785–1795, 1990.
12. D. Y. Kwok, D. Vollhardt, R. Miller, D. Li, and A. W. Neumann, Axisymmetric drop shape analysis as a film balance, *Colloids Surf. A*, 88, 51–58, 1994.
13. W. M. Schoel, S. Schurch, and J. Goerke, The captive bubble method for the evaluation of pulmonary surfactant: Surface tension, area, and volume calculations, *Biochim. Biophys. Acta*, 1200, 281–290, 1994.
14. S. Lahooti, O. I. Del Rio, P. Cheng, and A. W. Neumann, Axisymmetric drop shape analysis (ADSA). In: A. W. Neumann and J. K. Spelt (Eds.), *Applied Surface Thermodynamics*, New York: Marcel Dekker, 1996.
15. M. L. Alexander and M. J. Matteson, The automation of an interfacial tensiometer, *Colloids Surf.*, 27, 201–217, 1987.
16. J. C. Slattery and J. Chen, Alternative solution for spinning drop interfacial tensiometer, *J. Colloid Interface Sci.*, 64, 371–373, 1978.
17. D. Y. Kwok, M. A. Cabrerizo-Vilchez, Y. Gomez, S. S. Susnar, O. Del Rio, D. Vollhardt, R. Miller, and A. W. Neumann, Axisymmetric drop shape analysis as a method to study dynamic interfacial tensions. In: V. Pillai and D. O. Shah (Eds.), *Dynamic Properties of Interfaces and Association Structures*, Champaign, IL: AOCS Press, 1996.
18. W. D. E. Thomas and L. Potter, Solution/air interfaces. I. An oscillating jet relative method for determining dynamic surface tensions, *J. Colloid Interface Sci.*, 50, 397–412, 1975.
19. V. B. Fainerman and R. Miller, Dynamic surface tension measurements in the sub-millisecond range, *J. Colloid Interface Sci.*, 175, 118–121, 1995.
20. G. L. Gaines Jr., *Insoluble Monolayers at Liquid-Gas Interfaces*, New York: John Wiley & Sons, 1966, 44.
21. R. Miller, R. Sedev, K.-H. Schano, C. Ng, and A. W. Neumann, Relaxation of adsorption layers at solution/air interfaces using axisymmetric drop-shape analysis, *Colloids Surf.*, 69, 209–216, 1993.

22. D. O. Johnson and K. J. Stebe, Oscillating bubble tensiometry: A method for measuring the surfactant adsorptive-desorptive kinetics and the surface dilatational viscosity, *J. Colloid Interface Sci*., 168, 21–31, 1994.
23. D. O. Johnson and K. J. Stebe, Experimental confirmation of the oscillating bubble technique with comparison to the pendant bubble method: The adsorption dynamics of 1-decanol, *J. Colloid Interface Sci*., 182, 526–538, 1996.
24. D. A. Edwards, H. Brenner, and D. T. Wasan, *Interfacial Transport Processes and Rheology*, Boston, MA: Butter worth-Heinemann, 1991.
25. C. Garcia-Cordovilla, E. Louis, and A. Pamies, The surface tension of liquid pure aluminium and aluminium-magnesium alloy, *J. Mater. Sci*., 21, 2787–2792, 1986.
26. B. C. Allen, The surface tension of liquid transition metals at their melting points, *Trans. Metall. Soc. AIME*, 227, 1175–1183, 1963.
27. D. B. Thiessen and K. F. Man, A quasi-containerless pendant drop method for surface tension measurements on molten metals and alloys, *Int. J. Thermophys*., 16, 245–255, 1995.
28. S. C. Hardy, The surface tension of liquid silicon, *J. Cryst. Growth*, 69, 456–460, 1984.
29. V. Schoettle and H. Y. Jennings, Jr., High-pressure high-temperature visual cell for interfacial tension measurement, *Rev. Sci. Instrum*., 39, 386–388, 1968.
30. R. Simon and R. L. Schmidt, A system for determining fluid properties up to 136 MPa and 473 K, *Fluid Phase Equilib*., 10, 233–248, 1983.
31. K. Hool and B. Schuchardt, A new instrument for the measurement of liquid-liquid interfacial tension and the dynamics of interfacial tension reduction, *Meas. Sci. Technol*., 3, 451–457, 1992.
32. A. Passerone, L. Liggieri, N. Rando, F. Ravera, and E. Ricci, A new experimental method for the measurement of the interfacial tension between immiscible fluids at zero Bond number, *J. Colloid Interface Sci*., 146, 152–162, 1991.
33. G. Pétré and G. Wozniak, Measurement of the variation of interfacial tension with temperature between immiscible liquids of equal density, *Acta Astronaut*., 13, 669–672, 1986.
34. D. Chatenay, D. Langevin, J. Meunier, D. Bourbon, P. Lalanne, and A. M. Bellocq, Measurement of low interfacial tension, comparison between a light scattering technique and the spinning drop technique, *J. Dispersion Sci. Technol*., 3, 245–260, 1982.
35. D. Y. Kwok, P. Chiefalo, B. Khorshiddoust, S. Lahooti, M. A. Cabrerizo-Vilchez, O. Del Rio, and A. W. Neumann, Determination of ultralow interfacial tension by axisymmetric drop shape analysis. In: R. Sharma (Ed.), *Surfactant Adsorption and Surface Solubilization* (*ACS Symp. Ser. 615*), Washington, DC: ACS, 1995, pp. 374–386.

Further Readings

Hartland, S., *Surface and Interfacial Tension: Measurement Theory and Applications*, New York: Marcel Dekker, 2005.

Miller, R., Pison, U., and Kazakov, V. N., *Dynamic Surface Tensiometry in Medicine*, New York: Elsevier Science Ltd., 2000.

Physical and chemistry Resources, Surface tension. http://physicalchemistryresources.com/Book2_sections_graphicfiles_08142009/htm_PPGLS_Surface%20Tension.htm (accessed on August 8, 2012).

Research and Articles, Surface tension. http://www.bookrags.com/research/surface-tension-wop/ (accessed August 1, 2012).

V

Acoustics

48

Acoustic Measurement

Per Rasmussen
G.R.A.S. Sound and Vibration

Sound is normally defined as vibration of a solid, liquid, or gaseous medium in the frequency range of the human ear, that is, between about 20 Hz and 20 kHz. Here, the definition is further limited and only vibrations in liquid and gaseous media are considered. In contrast to solid media, a liquid or gaseous medium cannot transmit shear forces, so sound waves are always longitudinal waves, in which the particles move in the direction of propagation of the wave. The wave propagation in gaseous and liquid media can be described by the three variables: the pressure p, the particle velocity u, and the density ρ. The relation between these is described by the wave equation [1], and this can be derived from three basic equations: the Euler equation (this is essentially Newton's second law applied to a fluid), the continuity equation, and the state equation. Although the wave equation, in principle, can be used to describe and calculate all sound waves in all situations, it will in practice often be impossible to perform the necessary calculations. In some special cases, it is possible to get analytical results directly from the wave equation, and these cases are therefore of special interest. The cases most often encountered in acoustics are the *free field*, the *diffuse* (or reverberant) *field*, and the *closed coupler*. The free field is, in principle, an infinite, empty (except for the medium and the source) space, with no reflections. Here, the waves are allowed to radiate freely in all directions without reflections. In practice, the free field is implemented in anechoic chambers, where all walls have been made nearly 100% absorptive. The diffuse field is obtained in a reverberation room where all walls have been made, in principle, 100% reflective. At the same time, the walls are made nonparallel and the result is a sound field with sound waves in all directions. The closed coupler is a small chamber, with dimensions small compared to the wavelength of the sound. A special case of this is the standing wave tube. This is a tube with a diameter smaller than the wavelength and with a sound source in one end. With a suitable loudspeaker as a source, the wave propagation in the tube can be assumed to be 1-D. This simplifies the mathematical description so that it is possible to calculate the sound field.

In practice, almost the only parameter measured directly in acoustics is the sound pressure, and all other parameters like sound power, particle velocity, reverberation time, and directivity are derived from pressure measurements. These are performed with measurement microphones in gaseous media and hydrophones in liquid media. The measurement microphones are all of the condenser type to ensure precision, long-term stability, and sensitivity. Hydrophones are usually made with a rubber coating over a sensitive element of piezoelectric material.

The traditional frequency range from 20 Hz to 20 kHz for acoustic measurements is selected because this is the range audible to the human ear. Sound waves exist outside this range in the form of infrasound (below 20 Hz) and ultrasound (above 20 kHz). As the basic equations (the wave equation) and measurement principles are the same for both infrasound and ultrasound, many of the principles from the frequency range from 20 Hz to 20 kHz can be extended to these ranges.

48.1 Wave Equation

Sound wave propagation cannot take place in a vacuum, but is always associated with some kind of medium. For simplicity, assume that this medium is air, although the same equations are valid also for all gaseous and fluid media. In this medium, the concept of an air particle can be introduced. An *air particle* is a small volume of air in which the acoustic parameters like pressure and density can be considered constant. On the other hand, the air volume must be large enough to include a very large number of air molecules, so that the air volume can be considered to be a continuous medium and not a collection of molecules. The *Euler equation* for such an air particle is given by

$$-\text{grad}\, p = \rho_0 \left(\frac{\partial \bar{v}}{\partial t} \right) \tag{48.1}$$

where

p is the pressure
ρ_0 is the density
$\bar{v}$ is the particle velocity

This equation can be considered as Newton's second law ($F = ma$) applied to a fluid. Here, the gradient of the pressure equals the force F acting on the air particle, the density equals the mass m, and the time differentiated particle velocity $\partial v/\partial t$ equals the acceleration.

The second equation necessary to derive the wave equation is the *continuity equation*. This simply states that if you have a small volume of air and you bring in some extra air, the density (or the mass) will increase. Mathematically, this can be formulated as

$$\text{div}\, \bar{v} = -\frac{1}{\rho_0} \cdot \frac{\partial \rho}{\partial t} \tag{48.2}$$

where c is the sound velocity. The sound velocity depends on the composition of the air and the temperature. For normal air at 0 °C, the velocity is 314 m s^{-1}, while at 20 °C, the velocity is 340 m s^{-1}.

The third equation is the *state equation*, which relates pressure changes to changes in the density, that is, if a small volume of air is compressed, the density will increase:

$$\frac{\partial \rho}{\partial t} = \frac{1}{c^2} \times \frac{\partial p}{\partial t} \tag{48.3}$$

Now we have three equations relating the three variables: pressure, particle velocity, and density. By eliminating the particle velocity and the density, we obtain one differential equation for the sound pressure:

$$\nabla^2 p = \frac{1}{c^2} \frac{\partial^2 p}{\partial t^2} \tag{48.4}$$

This is the *wave equation* for acoustic waves in gaseous and fluid media. In principle, this allows one to calculate the sound pressure anywhere in a sound field, if some suitable boundary conditions are given. In practice, however, it is only possible to find solutions in a few simple cases.

48.2 Plane Sound Waves

In a free space, at great distance from the sound source, sound waves are approximately plane waves. This means that the wave equation only depends on one of the coordinates in the wave equation. If the direction of propagation of the wave fronts is in the x-direction, the solution to the wave equation reduces to

$$p = A\cos[(\omega t - k)(x + \varphi_a)] \tag{48.5}$$

where ω is the frequency. Similarly, the particle velocity in the free field is given by

$$v = \frac{A}{\rho c}\cos[(\omega t - k)(x + \varphi_a)] = \frac{p}{\rho c} \tag{48.6}$$

This means that in a plane wave, the particle velocity is equal to the pressure divided by the constant ρc and the pressure and particle velocity are inphase. The constant ρc is the *acoustic impedance*, and for air at 20 °C, the density is 1.29 kg m^{-3} and the sound velocity is 340 m s^{-1}, giving an acoustic impedance of 438.6 kg m^{-2} s^{-1}.

The plane wave transmits energy in the direction of propagation. The power transmitted per unit area is the intensity in the direction of the propagation (in many older textbooks, terms like "the intensity of the sound" were mistakenly used for the magnitude of the sound pressure). In general, the intensity is given by the product of the sound pressure and the sound velocity; thus, in the case of the plane wave, the intensity (I) can be calculated from Equations 48.5 and 48.6:

$$I = vp = \frac{p^2}{\rho c} \tag{48.7}$$

Thus, in the plane wave, the intensity transmitted by the wave can be calculated from the sound pressure, and, as the sound power is the intensity per unit area, the sound power can be calculated by multiplying the intensity by the area.

48.3 Spherical Waves

Another simple solution to the wave equation can be found for the radiation from a point source into free space. The point source is an infinitely small sphere whose surface is pulsating radially. In practice, for small sound sources (i.e., where the dimensions of the sound source are small compared to the wavelength of the sound), the point source is a good approximation for the real physical source that makes the spherical wave solution of special interest.

The wave equation in Equation 48.5 is transformed into the spherical coordinates r, θ, and ψ. As the point source radiates equally in all directions, the solution depends only on the distances r from the center of the point source:

$$p = \frac{P_0}{r}\cos(\omega t - kr) \tag{48.8}$$

It can be seen that the sound pressure is inversely proportional to the distance from the sound source. The particle velocity can be divided into a near-field contribution v_n and a far-field contribution v_f:

$$v_f = \frac{P_0}{r\rho c}\cos(\omega t - kr) \tag{48.9}$$

$$v_n = \frac{P_0}{\omega\rho r^2}\sin(\omega t - kr) \tag{48.10}$$

The far-field contribution in Equation 48.9 can be seen to be inphase with the pressure in Equation 48.8, and also the particle velocity is inversely proportional to the distance r from the point source. The near-field contribution is inversely proportional to the square of the distance to the source and therefore dies away rapidly as the distance to the source increases.

As in the case of the plane wave, the intensity in the spherical wave is the product of the pressure and particle velocity. For the near-field contribution, one obtains

$$I = v_n p = \frac{P_0}{\omega\rho r^2}\sin(\omega t - kr)\frac{P_0}{r}\cos(\omega t - kr) = 0 \tag{48.11}$$

That is, the near-field part of the particle velocity does not contribute to the radiated power as the particle velocity is 90° out of phase with the pressure.

The far-field contribution is given by

$$I = v_f p = \frac{P_0}{r\rho c}\cos(\omega t - kr)\frac{P_0}{r}\cos(\omega t - kr) = \frac{P_0^2}{r^2\rho c}\cos^2(\omega t - kr) \tag{48.12}$$

It can be seen that the intensity decreases with the square of the distance to the source and by combining Equations 48.8 and 48.12, one obtains

$$I = \frac{P_0^2}{r^2\rho c}\cos^2(\omega t - kr) = \frac{p^2}{\rho c} \tag{48.13}$$

which is identical to Equation 48.7 for the plane wave. Thus, as for the plane progressive wave, the intensity in the spherical wave can be calculated from the pressure.

48.4 Acoustic Measurements

As can be seen from the wave equation, the full acoustic field can in principle be described from only pressure measurements. This means that all other acoustic parameters can be derived from pressure measurements, and, in practice, pressure is often the only parameter measured. There have been a few attempts to make transducers for particle velocity measurements based on, for example, transmission of ultrasonic waves, but the absolute dominating transducers for acoustic measurements are the condenser-type microphones, as shown in Figure 48.1. These have proven to be superior with respect to temperature stability, long-term stability, and insensitivity to rough handling. While measurement microphones are designed and produced to ensure well-defined and accurate measurements, a wide range of other microphones are available for other purposes. These can, for example, be for incorporation in telephones, where price is a very decisive factor, or for studio recordings, where a subjective evaluation is more important than the objective performance.

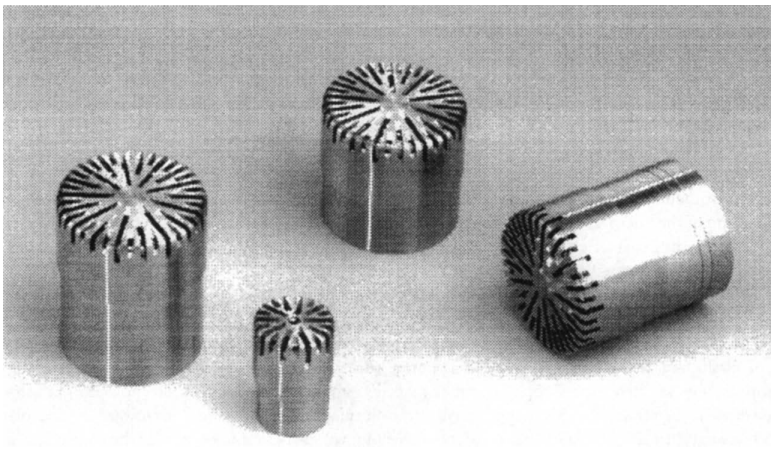

FIGURE 48.1 Measurement microphones: ½ and ¼ in.

48.4.1 Condenser Microphones

The condenser microphone consists basically of five elements: protection grid, microphone casing, diaphragm, backplate, and insulator; see Figure 48.2. The diaphragm and the backplate form the parallel plates of an air capacitor. This capacitor is polarized with a charge from an external voltage supply (externally polarized type) or by an electric charge injected directly into an insulating material on the backplate (prepolarized type). When the sound pressure in the sound field fluctuates, the distances between the diaphragm and the backplate will change and consequently change the capacitance of the diaphragm/backplate capacitor. As the charge on the capacitor is kept constant, the change in capacitance will generate an output voltage on the output terminal of the microphone. The acoustic performance of a microphone is determined by the physical dimensions such as diaphragm area, the distance between the diaphragm and the backplate, the stiffness and mass of the suspended diaphragm, and the internal volume of the microphone casing. These factors will determine the frequency range of the microphone, the sensitivity, and the dynamic range. The sensitivity of the microphone is described as the output voltage of the microphone for a given sound pressure excitation, and is in itself of little interest for the operation of the microphone, except for calibration purposes. However, the sensitivity of the

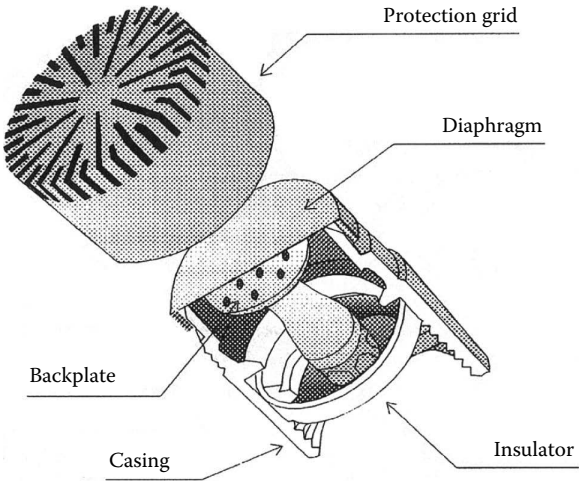

FIGURE 48.2 Basic elements of a measurement microphone.

microphone (together with the electric impedance of the cartridge) also determines the lowest sound pressure level that can be measured with the microphone. For example, with a microphone with a sensitivity of 2.5 mV Pa^{-1}, the lowest level that can be measured is around 40 dB (re. 20 μPa), while a microphone with a sensitivity of 50 mV Pa^{-1} can measure levels down to approximately 15 dB (re. 20 μPa).

The size of the microphone is the first parameter determining the sensitivity of the microphone. In general, the larger the diaphragm diameter, the more sensitive the microphone will be. There are, however, limits to how sensitive the microphone can be made by simply making it larger. The polarization voltage between the diaphragm and the backplate will attract the diaphragm and deflect this toward the backplate. As the size of the microphone is increased, the deflection will increase and eventually the diaphragm will be deflected so much that it will touch the backplate. To avoid this, the distance between the diaphragm and the backplate can be increased or the polarization voltage can be decreased. Both of these actions will, however, decrease the sensitivity, so that the optimum size of a practical measurement microphone for use up to 20 kHz is very close to ½ in. (12.6 mm).

As the size of the microphone is decreased, the useful frequency range of the microphone is increased. The frequency range, which can be obtained, is determined in part by the size of the microphone. At high frequencies, when the wavelength of the sound waves becomes much smaller than the diameter of the diaphragm, the diaphragm will stop behaving like a rigid piston (the diaphragm "breaks up"—this is not a destructive phenomenon). Different parts of the diaphragm will start to move with different magnitude and phase, and the frequency response of the microphone will change. To avoid this, the upper limiting frequency is placed so that the sensitivity of the microphone drops off before the diaphragm starts to break up. This gives, for a typical 0.5 in. microphone, an upper limiting frequency in the range from 20 to 40 kHz, depending on the diaphragm tension. If the diaphragm is tensioned so that it becomes stiffer, the resonance frequency of the diaphragm will be higher; on the other hand, the sensitivity of the microphone will be reduced as the diaphragm deflection by a certain sound pressure level decreases.

The frequency response of the microphone is determined by the diaphragm tension, the diaphragm mass, and the acoustic damping in the air gap between the diaphragm and the backplate. This system can be represented by the mechanical analogy of a simple mass–spring–damper system as in Figure 48.3. The mass in the analogy represents the mass of the diaphragm, and the spring represents the tension in the diaphragm. Thus, if the diaphragm is tensioned to become stiffer, the corresponding spring will become stiffer. The damping element in the analogy represents the acoustic damping between the diaphragm and the backplate. This can be adjusted by, for example, drilling holes in the backplate. This will make it easier for the air to move away from the air gap when the diaphragm is deflected, and therefore decrease damping.

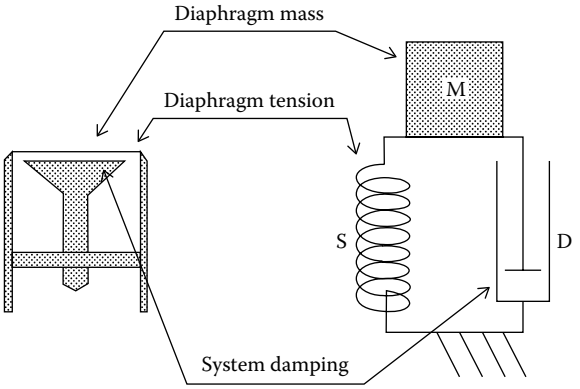

FIGURE 48.3 Mechanical analogy of a microphone.

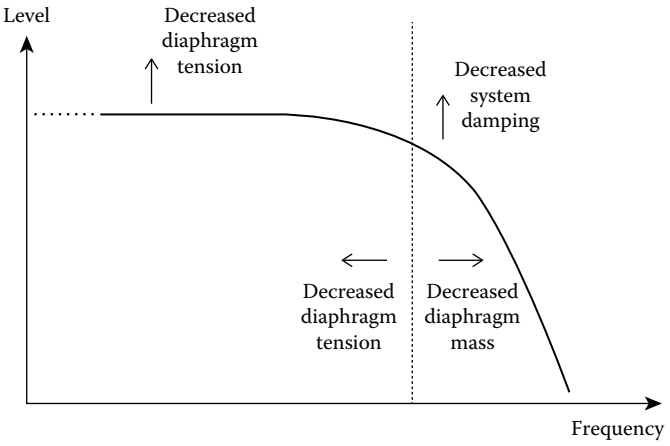

FIGURE 48.4 Influence of microphone parameters on frequency response.

The frequency response of the simple mechanical model of the microphone is given in Figure 48.4, together with the influence of the different parameters. At low frequencies (below the resonant frequency), the response of the microphone is determined by the diaphragm tension, and as described previously, the sensitivity will increase if the tension is decreased. The resonant frequency is determined by the diaphragm tension and the diaphragm mass, with an increased tension giving an increased resonant frequency and an increased mass giving a decreased resonant frequency. The response around the resonant frequency is determined by the acoustic damping, where an increase in the damping will decrease the response.

Although the material selection and assembling techniques have changed during the last few years, the basic types of microphones remain unchanged. The basic types are the free-field microphones, the pressure microphones, and the random incidence microphones. They have been constructed with different frequency characteristics, corresponding to the different requirements.

The *pressure microphone* is meant to measure the actual sound pressure as it exists on the diaphragm. A typical application could be the measurement of the sound pressure in a closed coupler or as in Figure 48.5,

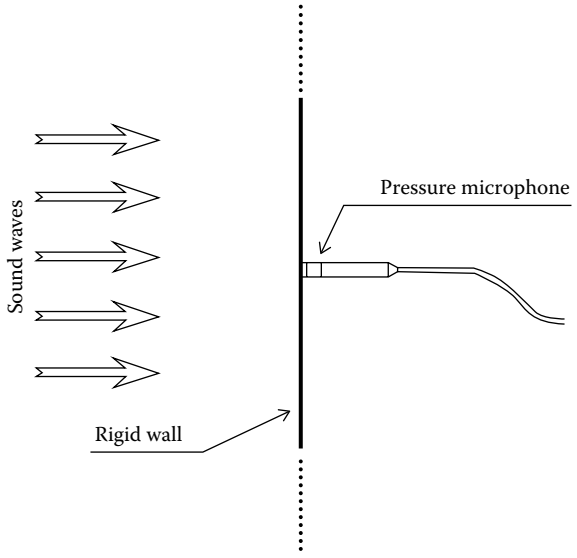

FIGURE 48.5 Application of pressure microphones.

the measurement of the sound pressure at a boundary. In this case, the microphone forms part of the wall and measures the sound pressure on the wall itself. The frequency response of this microphone should be flat in a frequency range as wide as possible, taking into account that the sensitivity will decrease as the frequency range is increased. The acoustic damping in the air gap between the diaphragm and the backplate is adjusted so that the frequency response is flat up to and a little beyond the resonant frequency.

The *free-field microphone* is designed to essentially measure the sound pressure as it existed before the microphone was introduced into the sound field. At higher frequencies, the presence of the microphone itself in the sound field will change the sound pressure. In general, the sound pressure around the microphone cartridge will increase due to reflections and diffraction. The free-field microphone is designed so that the frequency characteristics compensate for this pressure increase. The resulting output of the free-field microphone is a signal proportional to the sound pressure as it existed before the microphone was introduced into the sound field. The free-field microphone should always be pointed toward the sound source (0° incidence), as in Figure 48.6. In this situation, the presence of the microphone diaphragm in the sound field will result in a pressure increase in front of the diaphragm (see Figure 48.7a,) depending on the wavelength of the sound waves and the microphone diameter. For a typical ½ in. microphone, the maximum pressure increase will occur at 26.9 kHz, where the wavelength of the sound ($\lambda = 342$ m s^{-1}/26.9 kHz $\approx$ 12.7 mm $\approx$ 0.5 in.) coincides with the diameter of the microphone. The microphone is then designed so that the sensitivity of the microphone decreases by the same amount as the acoustic pressure increases in front of the diaphragm. This is obtained by increasing the internal acoustic damping in the microphone cartridge, to obtain a frequency response as in Figure 48.7b. The result is an output from the microphone, Figure 48.7c, which is proportional to the sound pressure as it existed before the microphone was introduced into the sound field. The curve in Figure 48.7a is also called the "free-field correction curve" for the microphone, as this is the curve that must be added to the frequency response of the microphone cartridge to obtain the acoustic characteristic of the microphone in the free field.

The free-field microphone is required in principle, to be pointed toward the sound source and that the sound waves travel in essentially one direction. In some cases, (e.g., when measuring in a reverberation room or other highly reflecting surroundings), the sound waves will not have a well-defined propagation direction, but will arrive at the microphone from all directions simultaneously. The sound waves arriving at the microphone from the front will cause a pressure increase, as described for the free-field microphone, while the waves arriving from the back of the microphone will be decreased to a certain extent due to the shadowing effects of the microphone cartridge. The combined influence of the waves coming from different directions therefore depends on the distribution of sound waves from different directions. For measurement microphones, a standard distribution has been defined, based on statistical considerations, resulting in a standardized random incidence microphone.

As mentioned previously, measurement microphones can be of either the externally polarized type or the prepolarized type. The externally polarized types are by far the most stable and accurate

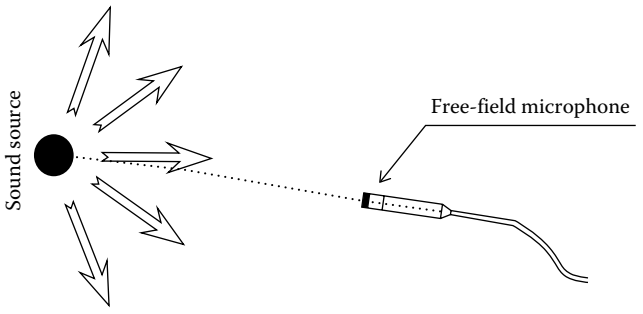

FIGURE 48.6 Application of a free-field microphone.

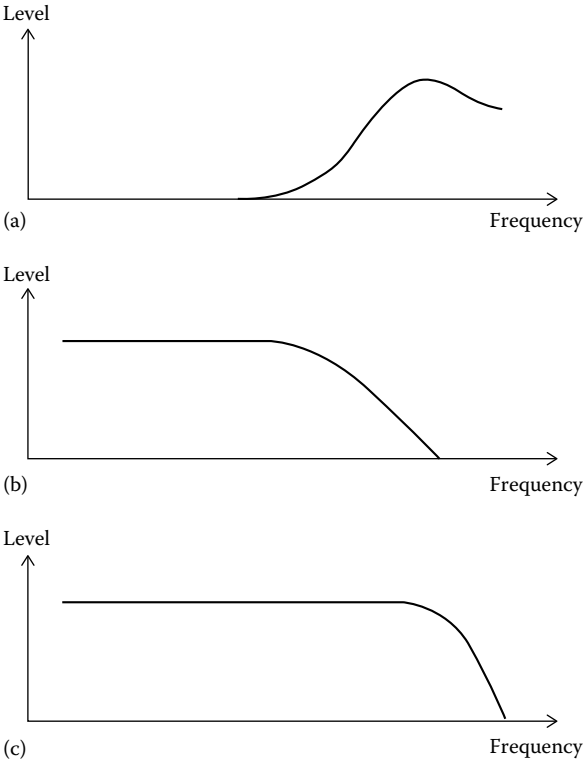

FIGURE 48.7 Frequency response of free-field microphone: (a) pressure increase in front of diaphragm, (b) microphone pressure response, and (c) resulting microphone output.

microphones and should be preferred for precision measurements. The prepolarized microphones are, however, preferred in some cases, in that they do not require the external polarization voltage source. This is typically the case when the microphone will be used on small handheld devices like sound level meters, where a power supply for polarization voltage would add excessively to cost, weight, and battery consumption. Still, it should be realized that prepolarized microphones in general are much less stable to environmental changes than externally polarized microphones.

48.5 Sound Pressure Level Measurements

The human ear basically hears the sound pressure, but the sensitivity varies with the frequency. The human ear is most sensitive to sound in the frequency range from 1 to 5 kHz, while the sensitivity drops at higher and lower frequencies. This has led to the development of several frequency weighting functions, which attempt to replicate the sensitivity of the human ear. Also, the response of the human ear to time-varying signals and impulses has led to the development of instruments with well-defined time weighting functions. The resulting measurement instrumentation is the *sound level meter*, as defined in for example by the IEC International Standard 651, "Sound Level Meters" [2]. The standard defines four classes of sound level meters for different accuracies (Table 48.1). Type 0 is the most accurate, intended for precision laboratory measurements, while type 1 is most widely used for general-purpose measurements; see Figure 48.8. Type 2 is used where low price is of importance, while type 3 is not used in practice because of the wide tolerances, making the results too unreliable. The output of the sound level meter is, in principle, assumed to be an approximate measure of the impression perceived by the human ear.

TABLE 48.1 IEC 651 Sound Level Meter Requirements

Frequency (Hz)	Type 0 (dB)	Type 1 (dB)	Type 2 (dB)	Type 3 (dB)
10	+2; −∞	+3; −∞	+5; −∞	+5; −∞
12.5	+2; −∞	+3; −∞	+5; −∞	+5; −∞
16	+2; −∞	+3; −∞	+5; −∞	+5; −∞
20	±2	±3	±3	+5; −∞
25	±1.5	±2	±3	+5; −∞
31.5	±1	±1.5	±3	±4
40	±1	±1.5	±2	±4
50	±1	±1.5	±2	±3
63	±1	±1.5	±2	±3
80	±1	±1.5	±2	±3
100	±0.7	±1	±1.5	±3
125	±0.7	±1	±1.5	±2
160	±0.7	±1	±1.5	±2
200	±0.7	±1	±1.5	±2
250	±0.7	±1	±1.5	±2
315	±0.7	±1	±1.5	±2
400	±0.7	±1	±1.5	±2
500	±0.7	±1	±1.5	±2
630	±0.7	±1	±1.5	±2
800	±0.7	±1	±1.5	±2
1,000	±0.7	±1	±1.5	±2
1,250	±0.7	±1	±1.5	±2.5
1,600	±0.7	±1	±2	±3
2,000	±0.7	±1	±2	±3
2,500	±0.7	±1	±2.5	±4
3,125	±0.7	±1	±2.5	±4.5
4,000	±0.7	±1	±3	±5
5,000	±1	±1.5	±3.5	±6
6,300	+1; −1.5	+1.5; −2	±4.5	±6
8,000	+1; −2	+1.5; −3	±5	±6
10,000	+2; −3	+2; −4	+5; −∞	+6; −∞
12,500	+2; −3	+3; −6	+5; −∞	+6; −∞
16,000	+2; −3	+3; −∞	+5; −∞	+6; −∞
16,000	+2; −3	+3; −∞	+5; −∞	+6; −∞

The sound level meter can be functionally divided into four parts: microphone and preamplifier, A-weighting filter, rms detector, and display (Figure 48.9). The microphone should ensure the correct measurement of the sound pressure within the frequency range for the given class. Also, the standard gives requirements for the directionality of the microphone. The frequency response of the instrument, including the weighting filter, is given for sound waves arriving at the microphone along the reference direction. For sound waves arriving from other directions, the standard allows wider tolerances at higher frequencies, taking into account the inevitable reflections and diffraction occurring at higher frequencies.

The preamplifier converts the high-impedance output signal from the microphone to a low-impedance signal, but has in itself no or even negative voltage amplification. The signal from the preamplifier is then passed through an A-weighting filter. This is a standardized filter that, in principle, resembles the sensitivity of the human ear, so that a measurement utilizing this filter will give a result that correlates with

FIGURE 48.8 Modern type 1 sound level meter with built-in frequency analyzer.

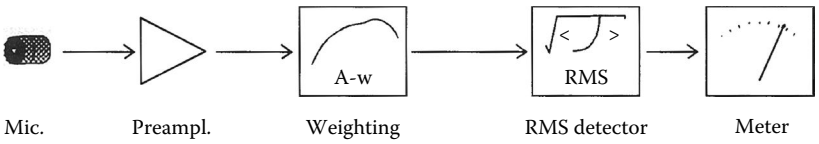

FIGURE 48.9 Functional parts of a sound level meter.

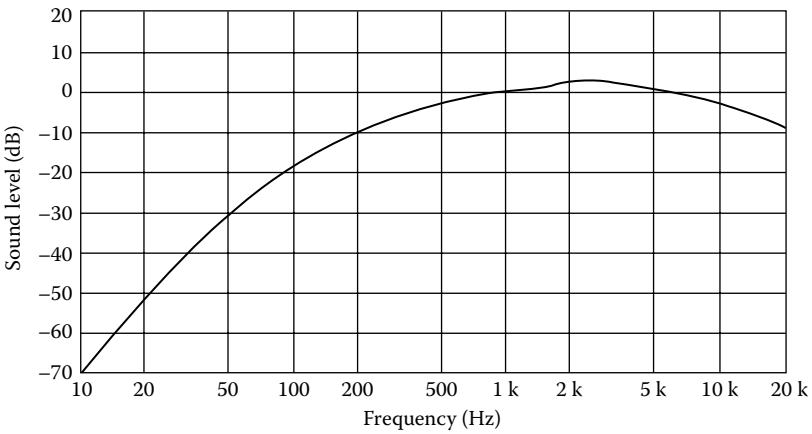

FIGURE 48.10 A-weighting curve in dB vs. Hz.

the subjective response of an average listener. The filter, with the filter characteristic as in Figure 48.10, attenuates low and high frequencies and slightly amplifies frequencies in the mid-frequency range from 1 to 5 kHz. There are a number of other weighting curves, denoted B-weighting, C-weighting, and D-weighting, which may give better correlation with subjective responses in special cases, such as for very high or very low levels or for aircraft noise.

The signal from the A-weighting filter is subsequently passed through an exponential rms detector, with a time constant of either 125 ms ("fast") or 1 s ("slow"). These time constants simulate the behavior of the human ear when subjected to time-varying signals. Especially when the duration of the sound stimuli to the human ear becomes short (e.g., around 200 ms), the sound is subjectively judged as being lower compared to the same sound heard continuously. The same effect is obtained using the "fast" averaging time. This will however give a higher statistical uncertainty on the level estimate than when using the time constant "slow," so this should be chosen if the sound signal is continuously. Other standards describe special sound level meters such as integrating sound level meters or impulse sound level meters intended for special purposes.

48.6 Frequency Analyzers

While the sound level meter gives a single reading for the sound level in the frequency range from 20 Hz to 20 kHz, it is often desirable to have more detailed information about the frequency content of the signal. Two types of frequency analyzers are commonly used in acoustic measurements: FFT analyzers and real-time filter analyzers. The *FFT analyzers*, with very-high-frequency resolutions, can give a wealth of frequency information and make it possible to separate closely space harmonics (e.g., from a gearbox). In contrast to this, the *real-time filter analyzers* (Figure 48.11) use a much broader frequency resolution, usually in one-third-octave bands. The frequency analysis is performed by a bank of filters (nowadays mostly digital filters) with well-defined frequency and time responses. The filter responses have been internationally standardized, with the center frequencies and passbands as shown in Table 48.2. In the frequency range from 20 Hz to 20 kHz, the one-third-octave filter bank consists of 31 filters, simultaneously measuring the input signal. The resulting one-third-octave spectrum resembles the subjective response of the human ear.

48.7 Pressure-Based Measurements

The result of sound pressure measurements will be influenced by many factors: source, source operating conditions, surroundings, measurement position, etc. Depending on the goal of the measurement, these parameters can be controlled in different manners. If the goal of the measurement is to quantify the noise exposure to an operator's ear in a noisy environment, it is important that the microphone is in the same position as the operator's ear would normally be in and that the environment is equal to the normal

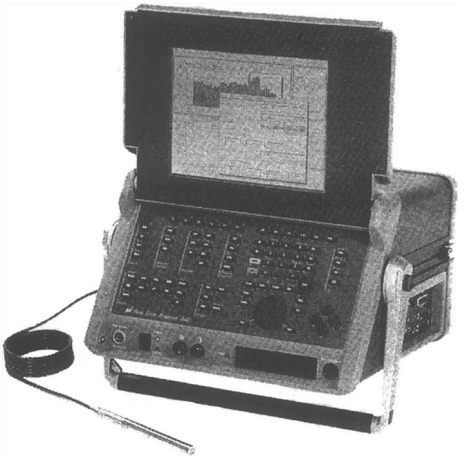

FIGURE 48.11 Real-time frequency analyzer for acoustic measurements.

TABLE 48.2 One-Third-Octave Analysis Frequencies

Nominal Center Frequency (Hz)	Exact Center Frequency (Hz)	Passband (Hz)
20	19.95	17.8–22.4
25	25.12	22.4–28.2
31.5	31.62	28.2–35.5
40	39.81	35.5–44.7
50	50.12	44.7–56.2
63	63.1	56.2–70.8
80	79.43	70.8–89.1
100	100.0	89.1–112
125	125.89	112–141
160	158.49	141–178
200	199.53	178–224
250	251.19	224–282
315	316.23	282–355
400	398.11	355–447
500	501.19	447–562
630	630.96	562–708
800	794.33	708–891
1,000	1,000.0	891–1,120
1,250	1,258.9	1,120–1,410
1,600	1,584.9	1,410–1,780
2,000	1,995.3	1,780–2,240
2,500	2,511.9	2,240–2,820
3,150	3,162.3	2,820–3,550
4,000	3,981.1	3,550–4,470
5,000	5,011.9	4,470–5,620
6,300	6,309.6	5,620–7,080
8,000	7,943.3	7,080–8,910
10,000	10,000.0	8,910–11,200
12,500	12,589.3	11,200–14,100
16,000	15,848.9	14,100–17,800
20,000	19,952.6	17,800–22,400

operating environment. If, on the other hand, the task is to describe the sound source as a noise-emitting machine, it is important to minimize the influence of the environment on the measurement result.

If the aim is to describe the measuring object as a noise source, it is customary to state the radiated sound power for the source. This is a global parameter quantifying the total noise radiation from the source and to a certain extent independent of the environment. The sound power can be measured in a number of different ways: in a free field, in a reverberation room, using a substitution technique, or using sound intensity technique. A free field is a sound field in which the sound is radiated freely in all directions, with no restricting walls or reflections. This is most often obtained in a semi-anechoic chamber, where all walls and ceiling have been covered by nearly 100% absorptive material, with only the floor made of reflecting material. When the sound source is placed in the semi-anechoic chamber, the emitted sound waves will radiate freely away from the source and, in the far field, the waves can be considered to be plane waves or spherical waves. Therefore, the sound intensity can be calculated from pressure measurements using Equation 48.7.

As real sound sources seldom radiate equally in all directions, a number of measurements around the test object are averaged. ISO Standard 3745 "Acoustics—Determination of sound power levels of noise sources—Precision method for anechoic and semi-anechoic rooms" [3] specifies an array of microphone

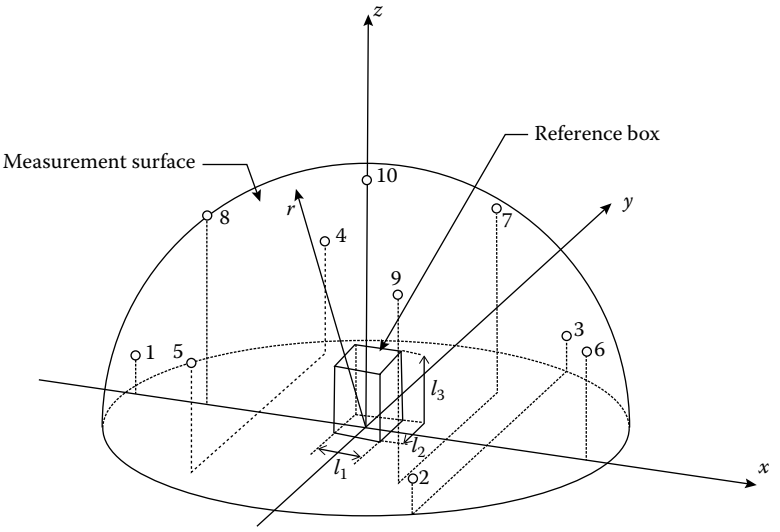

FIGURE 48.12 Measurement points for sound power determination.

TABLE 48.3 Coordinates of Measurement Points for Hemisphere with Radius *r*

Measurement Point No.	*x*/*r*	*y*/*r*	*z*/*r*
1	−0.99	0	0.15
2	0.5	−0.86	0.15
3	0.5	0.86	0.15
4	−0.45	0.77	0.45
5	−0.45	−0.77	0.45
6	0.89	0	0.45
7	0.33	0.57	0.75
8	−0.66	0	0.75
9	0.33	−0.57	0.75
10	0	0	1.0

positions on a hemisphere over the test object, as in Figure 48.12, with the coordinates as in Table 48.3. As all points are associated with the same area and as the sound power is intensity times the area, the total radiated sound power can be calculated as

$$P = A\sum I_n = \frac{2\pi r}{\rho c}\sum p_n^2 \tag{48.14}$$

where

A is the area of the test hemisphere with radius r

p_n is the pressure measured in point number n

48.8 Sound Intensity Measurements

The calculation in Equation 48.14 of the sound power from sound pressure measurements is based on Equation 48.7. This equation, which gives the intensity based on a pressure measurement, is however only valid in a free field, in the direction of propagation. In general, in the presence of background noise

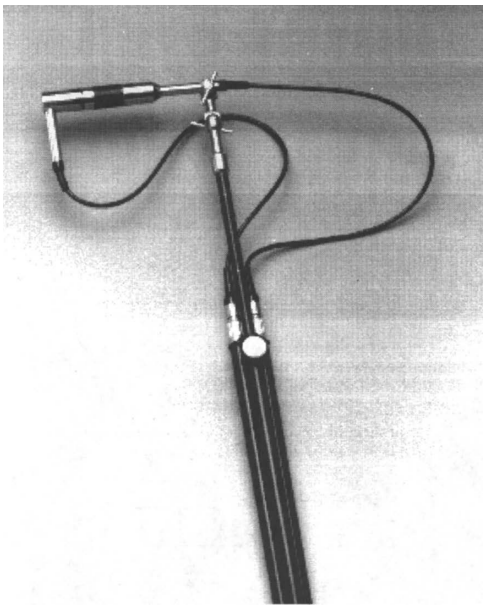

FIGURE 48.13 Two-microphone sound intensity probe.

or with reflections (e.g., from walls), it is not possible to calculate the sound intensity from a single pressure measurement. In these cases, it is, however, possible to measure directly the sound intensity with a two-microphone intensity probe, Figure 48.13.

Sound intensity I is the product of the pressure and the particle velocity:

$$I = pv \tag{48.15}$$

While the pressure p is a scalar and independent of the direction, the particle velocity is a vector quantity and is directionally dependent. When the particle velocity is stated as in Equation 48.15, it is implicit that the velocity is in a certain direction and that the resulting intensity is calculated in the same direction. For example, the particle velocity v in the direction of propagation (Figure 48.14a) gives the intensity radiation away from the point source, while the particle velocity perpendicular to the propagation direction (Figure 48.14b) is zero. The intensity calculated from Equation 48.15 will therefore be zero in the direction perpendicular to the propagation direction even though the sound pressure is the same. This means that the sound energy flows away radially from the point source and no energy is flowing tangentially.

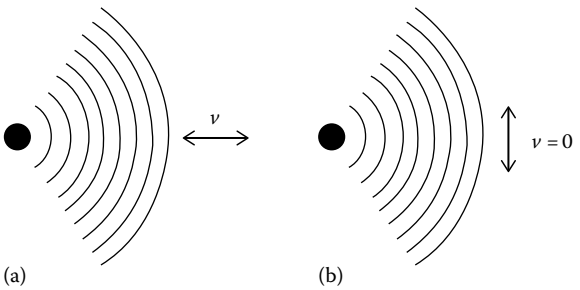

FIGURE 48.14 Particle velocity (a) along direction of propagation and (b) perpendicular to direction of propagation.

The measurement of the sound intensity according to Equation 48.15 requires the measurement of the sound pressure and the particle velocity. With the two-microphone intensity probe, the pressure in a position in between the two microphones is calculated as the mean pressure measured by the two microphones:

$$p = \frac{p_1 + p_2}{2} \tag{48.16}$$

The air particle velocity v, in the direction of the intensity probe, can be calculated from the pressure differences between the two microphone measurements:

$$v = \int \frac{(p_2 - p_1)}{\rho \Delta r} \partial \tau \tag{48.17}$$

where

ρ is the density of the air

Δr is the distance between the microphones

The intensity I is then obtained by multiplying the pressure and the velocity:

$$I = pv = \frac{p_1 + p_2}{2} \int \frac{(p_2 - p_1)}{\rho \Delta r} \partial \tau \tag{48.18}$$

The intensity measurement technique is a powerful tool to localize acoustic noise source and to determine the sound power radiated from a sound source, even in the presence of other strong sound sources.

48.9 Near-Field Acoustic Holography Measurements

The term *acoustic holography* comes from the analogy to optical holographs. It is well known how holography, as opposed to a normal photo, enables one to reconstruct the full image of an object. This is obtained by "recording" information about both the magnitude and the phase of the light, while a normal photo only "records" the magnitude of the light. Similarly, with *acoustic holography*, both the magnitude and the phase of the sound field are measured over a plane surface. These measurements result in a complete description of the sound field where both magnitude and phase are known at all points. It is then possible to calculate acoustic quantities, including sound intensity distribution, particle velocity, sound power, and radiation pattern.

The basic assumption behind *near-field acoustic holography* (NAH) is that the sound field can be decomposed into two simple wave types: plane waves and evanescent waves. The *plane waves* describe the part of the sound field that is propagated away from the near field toward the far field, and the *evanescent waves* describe the complicated sound field existing in the near field. Any sound field can be described as a combination of plane waves and evanescent waves with different magnitude and directions. The magnitude and direction of the individual waves can be described by their spatial frequencies or wave numbers. For a simple plane wave propagating in a certain direction, this can be described in terms of its temporal frequency as well as by its spatial frequency. The temporal frequency (Figure 48.15a), is obtained by looking at the pressure changes with time at a certain point in the sound field. This gives the temporal frequency in hertz or radians per second. Similarly, the spatial frequency (Figure 48.15b) is obtained by looking at the pressure changes at a certain time. At that instant in time, the pressure will be different in different positions in space. If one moves in a certain direction in space, one will see a certain change in the pressure, corresponding to a spatial frequency, measured with the unit cycles per meter or radians per meter. As the temporal frequency gives information about how often the pressure changes with time at a certain point, the spatial frequency gives information about how often the

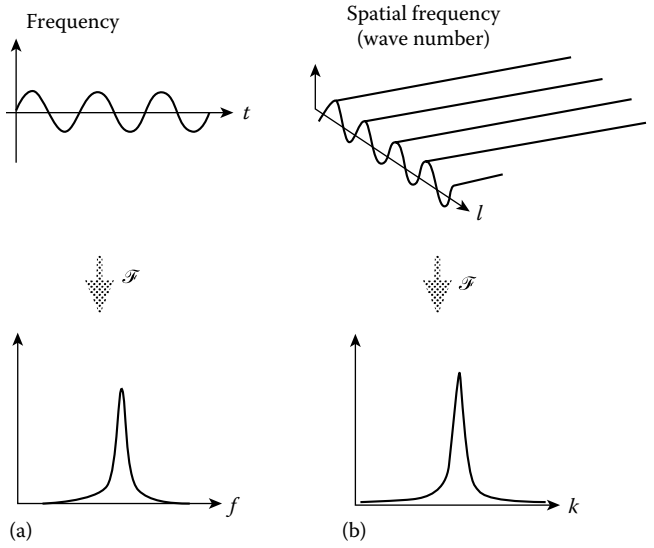

FIGURE 48.15 Spatial and temporal frequency characteristics of plane waves: (a) temporal and (b) spatial.

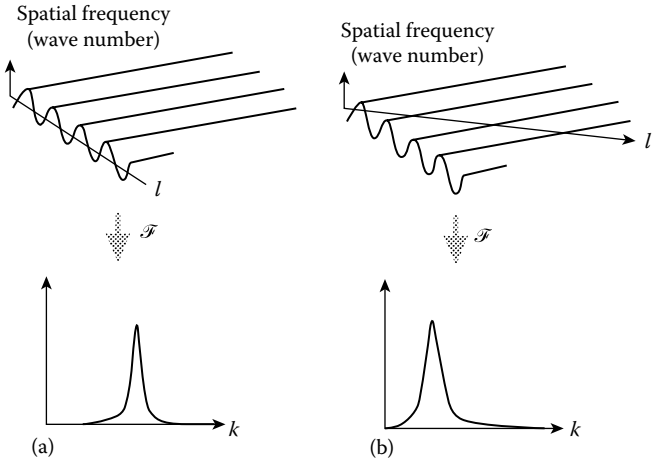

FIGURE 48.16 Spatial frequencies of waves propagating in different directions: (a) measured spatial frequency in the direction of propagation and (b) measured spatial frequency in different direction of propagation.

pressure changes with position at a certain time. In the example of Figure 48.15b, the propagation direction of the plane wave was identical to the direction of the axis along which the spatial frequency was measured. In this case, shown again in Figure 48.16a, the relationship between the spatial frequency k_0 (i.e., the wave number) and the temporal frequency f is given by the speed of sound c:

$$k_0 = \frac{2\pi f}{c} = \frac{\omega}{c} = \frac{2\pi}{\lambda} \tag{48.19}$$

where λ is the wavelength. If, however, the axis along which the spatial frequency is measured is not the same as the propagation direction (see the example in Figure 48.16b), this simple relationship is not valid. In this case, although the temporal frequency is the same as in Figure 48.16a, the spatial frequency is lower. For one particular temporal frequency, the spatial frequencies will thus give information about

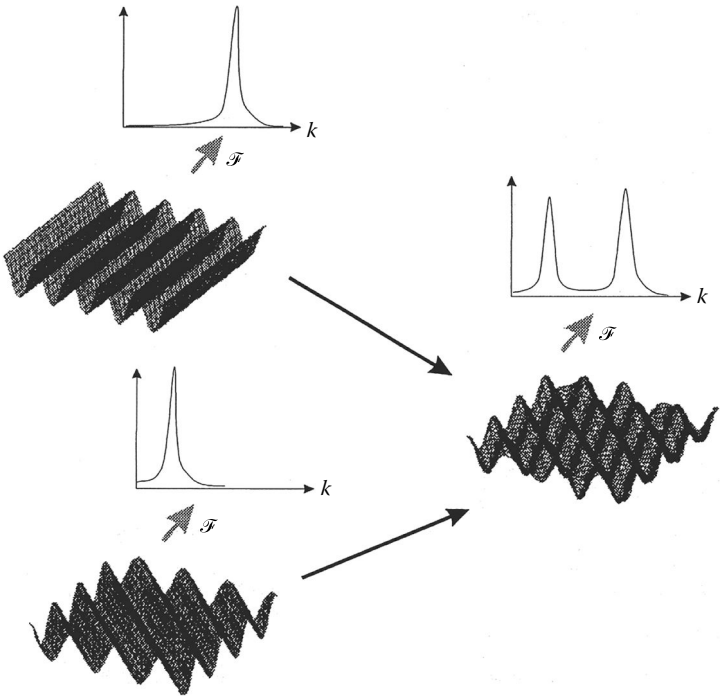

FIGURE 48.17 Spatial spectrum of two waves propagating in different directions.

the propagation directions. Therefore, if the sound field is made up of several plane waves with the same temporal frequency, but with different propagation directions, this will be shown in the spatial spectrum as several spatial frequency components. If, for example, the sound field is a sum of two waves (Figure 48.17) where one wave is traveling along the axis of measurement and the other at an angle of 45° relative to the first wave, the spatial spectrum will contain two spatial frequencies. One spatial frequency will be k, corresponding to a wave in the direction along the axis, and the other frequency will be k^* cos (45°). Thus far, the spatial frequencies have been defined along a single axis corresponding to a 1-D Fourier transformation. In the NAH technique, the sound field is sampled not only along a single axis, but over a plane. Therefore, a 2-D Fourier transformation is used instead. This gives as a result a 2-D spatial frequency spectrum, but otherwise the information is the same as before, namely, information about the direction and magnitude of the simple wave types.

The sound field from a point source cannot be explained by simple plane waves such as those in Figures 48.16 and 48.17, as the amplitude decreases with the distance from the origin. The plane waves retain the same magnitude over the full plane. Thus, to describe the near-field phenomenon, one must introduce evanescent waves. In the 1-D Fourier spectrum, the evanescent waves can be identified as spatial frequencies higher than $k_0 = 2\pi f/c$. Similarly, in the 2-D spatial frequency spectrum, the evanescent waves can be identified as having spatial frequencies or wave numbers higher than k_0.

The individual spatial frequencies in the 2-D spatial frequency spectrum correspond to simple plane waves or evanescent waves in the scan plane (i.e., the measurement plane). For each of these simple wave types, it is easy to calculate the pressure in other planes, see Figure 48.18. For the plane waves, a simple phase shift of the wave is required to calculate the result in a new plane. For the evanescent waves, the changes in amplitude must be taken into account, but in principle, this is also a simple transfer function applied to the 2-D spatial frequency spectrum. In this way, the 2-D spatial frequency spectrum in a new plane can be calculated from the original data by applying simple transfer function operations. The new 2-D spatial frequency spectrum is then an inverse Fourier transform (in two dimensions) to get the sound field in the new plane.

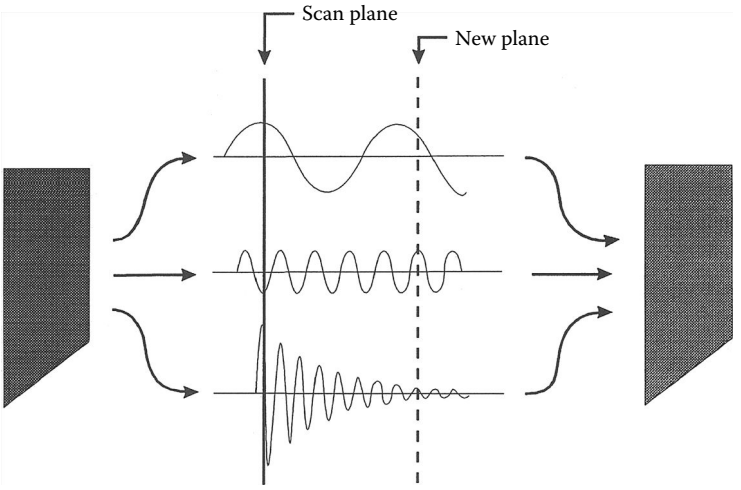

FIGURE 48.18 Transformation of simple wave types in a spatial spectrum, from one measurement plane to another plane.

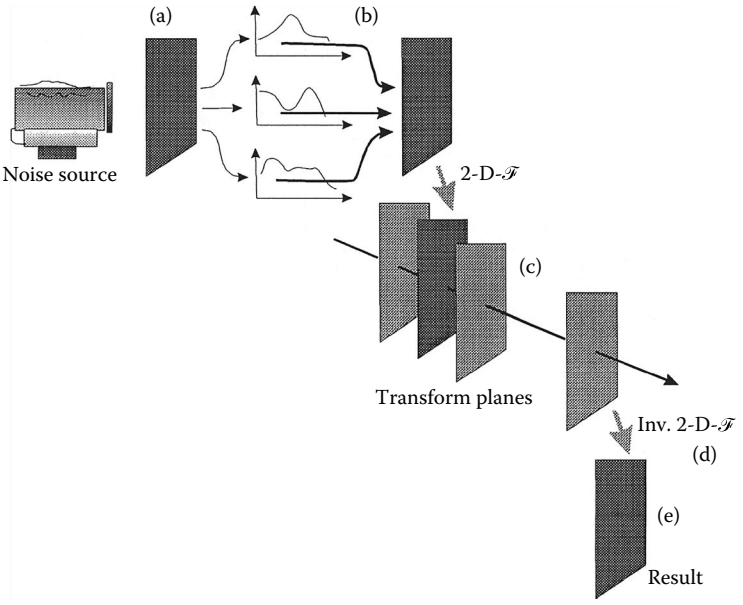

FIGURE 48.19 Overall principle of NAH: (a) measurement of cross spectra in the scan plane, (b) calculation for one temporal frequency at a time; (c) 2-D spatial Fourier transformation, (d) transformation of simple wave types, and (e) inverse 2-D transformation.

The overall principle of NAH can be simplified as in Figure 48.19. The sound field is scanned in a plane close to the measuring object. This gives an array of temporal spectra, one for each scan position. Looking at one temporal frequency at a time, one takes out the information from each of the spectra corresponding to the actual frequency of interest. This generates a new array with information about only one temporal frequency. A Fourier transform (in two dimensions) is then applied to the array to generate a 2-D spatial frequency spectrum. This can then be transformed to new planes using simple transfer function operations. When the 2-D spatial frequency spectrum in the new plane has been calculated, an inverse Fourier transform is used to obtain the new pressure distribution

in the new plane. In principle, the NAH technique requires that all cross spectra between all the scan positions are given; that is, in each of the scan positions, all the cross spectra to all other scan positions must be determined. A simple scan of a sound field with 2,540 scan positions, defining $N = 1{,}000$ scan positions, would result in $\frac{1}{2}N(N+1) = 500{,}500$ cross spectra. Instead of measuring all these cross spectra, the system uses a set of reference transducers to reduce the amount of cross spectra. The number of necessary reference transducers to give a complete description of the sound field without measuring the full amount of data is determined by the complexity of the sound field. A measurement with, for example, four reference transducers and 2540 scan positions will then be reduced to $4N = 4000$ cross spectrum measurements.

48.10 Calibration

In order to make accurate and reliable measurements, the microphone and connected instruments must be properly calibrated. The calibration of measurement microphones can be divided into two parts: a level calibration and a frequency response calibration. The *level calibration* establishes the output signal of the microphone for a given acoustic input signal at a given frequency, while the *frequency response* gives the output at other frequencies relative to the level calibration frequency. The level calibration can be performed by a number of different methods with different accuracies.

The most accurate method is the *reciprocity calibration method*. This method utilizes the fact that a condenser microphone is a reciprocal transducer; that is, it can be used as a microphone (to convert an acoustic signal to a voltage signal) and as a loudspeaker (to convert a voltage signal into an acoustic signal). By measuring the relationship between three test microphones driven as both transmitters and receivers, one obtains a set of three equations with the three microphone sensitivities as the unknowns. By solving these three equations, one obtains the sensitivity of the three microphones. The reciprocity calibration method is very accurate but rather tedious and requires well-controlled environmental conditions and is therefore seldom used in practical situations.

The comparison or substitution methods are essentially identical in that they are based on measuring the differences between the test microphone and a reference microphone with known sensitivity. In this case, the reference microphone is often calibrated at an accredited national acoustic laboratory like NIST, NPL, or PTB, whereby the traceability is ensured. In the substitution method, the acoustic output of a sound source is measured with the reference microphone. Afterward, the reference microphone is replaced with a test microphone and the output is measured again. Provided that the sound source has been stable, the sensitivity of the test microphone can then be calculated. The comparison method is similar to the substitution method, except that the reference microphone and the test microphone are subjected to the same sound pressure simultaneously and therefore the requirements to the sound source stability are less important.

An often-used method for microphone calibration is the *pistonphone method*. The pistonphone, Figure 48.20, is a very stable sound source, which produces a well-defined sound pressure level inside a closed coupler. It works by volume displacements, Figure 48.21, with a well-defined velocity, usually at 250 Hz. As the piston is moving in and out, the volume of the closed coupler is changed and this will result in pressure variations. The actual pressure level obtained in the pistonphone depends on the volume of the coupler, the volume displacement of the pistons, the barometric pressure, and—to a lesser degree—on other factors such as humidity and heat dissipation. As the pistonphone is based on a relatively simple mechanical system, it is very reliable and easy to use in practice, with an accuracy around 0.1 dB. Also, the pistonphone is often used as the stable sound source for calibrations using comparisons or substitution methods.

A *sound pressure calibrator* is basically a small self-contained comparison calibration device. The test microphone is inserted into a small, closed volume and a small loudspeaker produces a single

FIGURE 48.20 Pistonphone for microphone calibration.

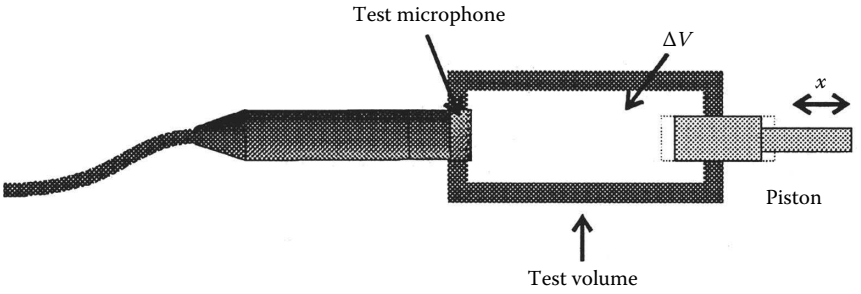

FIGURE 48.21 Principle of a pistonphone.

frequency signal, usually at 1 kHz. The output level of the loudspeaker is controlled in a feedback system with a signal from a reference microphone. Provided that the reference microphone and the feedback gain are stable, the sound level at the test microphone will be well-defined and the sensitivity can be determined. The sound level calibrators are normally not used to make accurate microphone calibrations, but rather to make field checks of the integrity of a complete measurement system.

The frequency response of a microphone is most often determined by the *electrostatic actuator method*. A conducting grid is placed close to and parallel to the microphone diaphragm. An electric field is established between the actuator and the diaphragm by applying 800 V dc to the actuator. A test signal of 50–150 V ac is superimposed on the dc signal, and the electrostatic forces will push and pull the diaphragm, similar to a sound pressure of 1–10 Pa. By sweeping the test signal through the frequencies of interest, the pressure response of the test microphone can be recorded. The electrostatic actuator technique is widely used as a convenient and accurate test method, both during production and final calibration of measurement microphones.

Available instrumentation and manufacturers are given in Tables 48.4 and 48.5.

TABLE 48.4 List of Instrumentation Types, Prices, and Manufacturers

Instrumentation	Types Available	Approximate Price	Manufacturers
Meas. microphones	½ in. free field ½ in. pressure ¼ in. free field ¼ in. pressure	$750–$825	G.R.A.S. Sound & Vibration ACO Pacific B&K The Modal Shop Larson Davies
Preamplifiers	½ and ¼ in.	$600–$850	G.R.A.S. Sound & Vibration ACO Pacific B&K The Modal Shop Larson Davies
Sound level meters	Simple type 1 SLM	$800–$2,000	Rion CEL B&K
	Advanced SLM with freq. analysis and data storage	$2,000–$10,000	Rion CEL Larson Davies B&K
Frequency analyzers	Real-time frequency analyzers/FFT	$5,000–$50,000	Hewlett-Packard Norsonic Data Physics 01 dB
NAH	Complete system with 16–64 channel acquisition and post-processing	$100,000–$200,000	LMS B&K

TABLE 48.5 Companies That Make Acoustic Measurement Instruments

G.R.A.S. Sound & Vibration, Skelstedet 10B, 2950 Vedbaek, Denmark, Tel.: +45 45 66 40 46, http://www.gras.dk/

LMS International, Interleuvenlaan 68, B-3001 Leuven, Belgium, Tel.: +32 16 384 571, http://www.lmsintl.com/

Hewlett-Packard Co., P.O. Box 95052-8059, Santa Clara, CA 95052, Tel.: (206) 335 2000, http://www8.hp.com

Norsonic AS, P.O. Box 24, N-3420 Lierskogen, Norway, Tel.: +47 32 85 20 80, http://www.norsonic.com/

The Modal Shop Inc., 1776 Mentor Avenue, Suite 170, Cincinnati, OH 45212-3521, Tel.: (513) 351 9919, http://www.modalshop.com/

01 dB, 111 rue du 1er Mars, F69100 Villeurbanne, France, Tel.: + 33 4 78 53 96 96

Larson Davies, Inc., 1681 West 820 North, Provo, UT 84601, Tel.: (801) 375 0177, http://www.larsondavis.com/

Brüel & Kjær. Spectris Technologies, Inc., 2364 Park Central Blvd., Decatur, GA 30035-3987, Tel.: (800) 332 2040, http://bksv.com/

Rion, Scantek, Inc., 916 Gist Avenue, Silver Springs, MD 20910, Tel.: (301) 495 7738, http://www.scantekinc.com/

ACO Pacific, Inc., 2604 Read Avenue, Belmont, CA 94002, Tel.: (415) 595 8588, http://acopacific.com/

CEL Instruments, 1 Westchester Drive, Milford, NH 03055, Tel.: (800) 366 2966

References

1. E. Skudrzyk, *The Foundation of Acoustics*, New York: Springer-Verlag, 1971.
2. International Electrotechnical Commission, *Publication 651: Sound Level Meters*, Genève, Switzerland: IEC, 1971.
3. International Organization for Standardization, Standard 3745, Acoustics—Determination of sound power levels of noise sources—Precision method for anechoic and semi-anechoic rooms, Genève, Switzerland, ISO, 1981.

Further Readings

Fraden, J., *Handbook of Modern Sensors*, Berlin, Germany: Springer, 2010.
Iniewski, K., *Optical, Acoustic, Magnetic, and Mechanical Sensor Technologies*, Boca Raton, FL: CRC Press, 2012.
Morgan, D., *Surface Acoustic Wave Filters*, Oxford, U.K.: Elsevier, 2007.
Xiao, Y., *Underwater Acoustic Sensor Networks*, Boca Raton, FL: CRC Press, 2010.

49

Ultrasound Measurement

Peder C. Pedersen
Worcester Polytechnic Institute

49.1 Applications of Ultrasound

49.1.1 Medical

Ultrasound has a broad range of applications in medicine, where it is referred to as *medical ultrasound*. It is widely used in obstetrics to follow the development of the fetus during pregnancy, in cardiology where images can display the dynamics of blood flow and the motion of tissue structures (referred to as

real-time imaging), and for locating tumors and cysts. 3-D imaging, surgical applications, imaging from within arteries (intravascular ultrasound), and contrast imaging are among the newer developments.

49.1.2 Industrial

In industry, ultrasound is utilized for examining critical structures, such as pipes and aircraft fuselages, for cracks and fatigue. Manufactured parts can likewise be examined for voids, flaws, and inclusions. Ultrasound has also widespread use in process control. The applications are collectively called *nondestructive testing* (NDT) or *nondestructive evaluation* (NDE). In addition, *acoustic microscopy* refers to microscopic examinations of internal structures that cannot be studied with a light microscope, such as an integrated circuit or biological tissue.

49.1.3 Underwater

Ultrasound is likewise an important tool for locating structures in the ocean, such as wrecks, mines, submarines, or schools of fish; the term SONAR (sound navigation and ranging) is applied to these applications.

There are many other usages of ultrasound that lie outside the scope of this handbook: ultrasound welding, ultrasound cleaning, ultrasound hyperthermia, and ultrasound destruction of kidney stones (lithotripsy).

49.2 Basic Ultrasound Parameters

Ultrasound refers to acoustic waves of frequencies higher than 20,000 cycles per second (20 kHz), equal to the assumed upper limit for sound frequencies detectable by the human ear. As acoustic waves fundamentally are mechanical vibrations, a medium (e.g., water, air, or steel) is required for the waves to travel, or propagate, in. Hence, acoustic waves cannot exist in vacuum, such as outer space. If a single-frequency sound wave is produced, also termed a *continuous wave* (CW), the fundamental relationship between frequency, f, in Hz, the sound speed of the medium, c_0, in m s^{-1}, and the wavelength, λ, in meters is given as

$$\lambda = \frac{c_0}{f} \tag{49.1}$$

The wavelength λ describes the length, in the direction of propagation, of one period of the sound wave. The wavelength determines, or influences, the behavior of many acoustic functions: The sound field emitted from an acoustic radiator (e.g., a transducer or loudspeaker) is determined by the radiator's size measured in wavelengths; the ability to differentiate between closely spaced reflectors is a function of the separation measured in wavelengths. Even when a sound pulse, rather than a CW sound, is transmitted, the wavelength concept is still useful, as the pulse typically contains a dominant frequency.

The vibrational activity on the surface of the sound source transfers the acoustic energy into the medium. If one were able to observe a very small volume, referred to as a *particle*, of the medium during transmission of sound energy, one would see the particle moving back and forth around a fixed position. Associated with the particle motion is an acoustic pressure, which refers to the pressure variation around the mean pressure (which is typically the atmospheric pressure). This allows the introduction of two important—and closely related—acoustic quantities: the *particle velocity*, $\vec{\mathbf{u}}(\vec{\mathbf{r}}, \mathrm{t})$, and the *acoustic pressure*, $p(\vec{\mathbf{r}}, t)$. In this notation, the arrow above a symbol in bold indicates a vector. The symbol $\vec{\mathbf{r}}$ represents the position vector, which simply defines a specific location in space. Thus, both particle velocity and pressure are functions of three spatial variables, x, y, and z, and the time variable, t.

To characterize a medium acoustically, the most important parameter is the *specific acoustic impedance, z*. For a lossless medium, z is given as follows:

$$z = \rho_0 c_0 \tag{49.2}$$

In Equation 49.2, ρ_0 is the density of the medium, measured in kg m^{-3}. When a medium absorbs acoustic energy (which all media do to a greater or smaller extent), the expression for acoustic impedance also contains a small imaginary term; this will be ignored in the discussions presented in this chapter. The acoustic impedance relates the particle velocity to the acoustic pressure:

$$z = \frac{p(\vec{\mathbf{r}}, t)}{u(\vec{\mathbf{r}}, t)} \tag{49.3}$$

Note that the relationship in Equation 49.3 uses the scalar value of the particle velocity (a scalar is a quantity, such as temperature, that does not have a direction associated with it). Equation 49.3 is exact for plane wave fields and a very good approximation for arbitrary acoustic fields. In a plane wave, all points in a plane normal to (i.e., which forms a 90° angle with respect to) the direction of propagation have the same pressure and particle velocity.

The acoustic impedances on either side of an interface (boundary between different media) determine the acoustic pressure reflected from the interface. Let a plane wave traveling in a medium with the acoustic impedance z_1 encounter a planar, smooth interface with another medium having the acoustic impedance z_2. Assume that the plane wave propagates directly toward the interface; this is commonly referred to as insonification under normal incidence. In this case, the pressure and the intensity reflection coefficients, R_p and R_i, respectively, are as follows:

$$R_p = \frac{p_r}{p_i} = \frac{z_2 - z_1}{z_2 + z_1} \tag{49.4}$$

$$R_i = \frac{I_r}{I_i} = \left(\frac{z_2 - z_1}{z_2 + z_1}\right)^2$$

Intensity is a measure of the mean power transmitted through unit area and is measured in watts per square meter. The corresponding pressure and intensity transmission coefficients, T_p and T_i, Ti respectively, are

$$T_p = \frac{p_t}{p_i} = \frac{2z_2}{z_2 + z_1} \tag{49.5}$$

$$T_i = \frac{I_t}{I_i} = \frac{4z_1 z_2}{(z_2 + z_1)^2}$$

The subscripts "i," "r," and "t" in Equations 49.4 and 49.5 refer to incident, reflected, and transmitted, respectively. The expressions in these two equations can be considered approximately valid for nonplanar waves under near-normal incidence. However, when the incident angle (angle between direction of propagation and the normal to the surface) becomes large, the reflection and transmission coefficients can change dramatically. In addition, the reflected and transmitted signals will also change if the surface is rough to the extent that the root mean square (rms) height exceeds a few percent of the wavelength.

The wave propagation can take several forms. In fluids and gases, only *longitudinal* (or *compressional*) waves exist, meaning that the direction of wave propagation is equal to the direction of the particle velocity vector. In solids, both longitudinal and *shear* waves exist that propagate in different directions and with different sound speeds. Transverse waves can exist on strings where the particle

motion is normal to the direction of propagation. (Strictly speaking, shear waves can propagate a short distance in liquids [fluids] if the viscosity is sufficiently high.)

49.3 Conceptual Description of Ultrasound Imaging and Measurements

Most ultrasound measurements are based on the generation of a short ultrasound pulse that propagates in a specified direction and is partly reflected wherever there is an abrupt change in the acoustic properties of the medium and detection of the resulting echoes (pulse-echo ultrasound). A change in properties can be due to a cyst in liver tissue, a crack in a high-pressure pipe, or a reflection from layers in the sea bottom. The degree to which a pulse is reflected at an interface is determined by the change in acoustic impedance as described in Equation 49.4. An image is formed by mapping echo strength vs. travel time (proportional to distance) and beam direction, as illustrated in Figure 49.1. This is referred to as *B-mode* imaging (brightness mode). Further signal processing can be applied to compensate for attenuation (the damping out of the pressure pulse as it propagates) of the medium or to control focusing. Signal processing can also be applied to analyze echoes for information about the structure of materials or about the surface characteristics of rough surfaces.

A block diagram of a simplified pulse-echo ultrasound measurement system is shown in Figure 49.2. The pulser circuit can generate a large voltage spike for exciting the transducer in B-mode applications, or the arbitrary function source can produce a short burst for Doppler measurements, or a coded

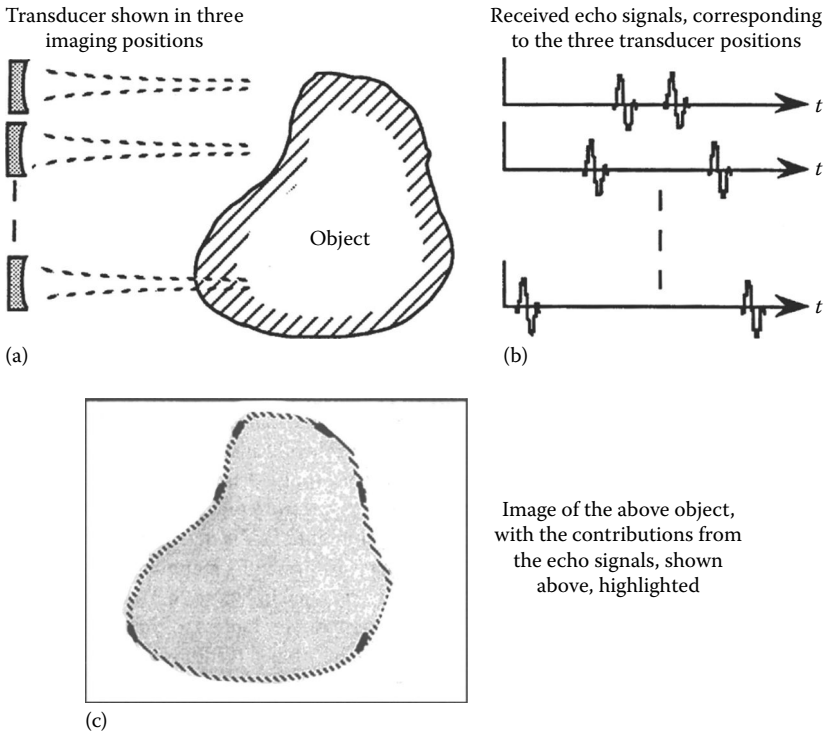

FIGURE 49.1 (a) A focused transducer insonifies the irregular object from different positions out of which only three are shown. The different transducer positions can readily be obtained by the use of an array transducer (to be described later). (b) Received echoes from the front and back of the object are displayed vs. travel time. It is here assumed that the structure is only weakly reflecting and that the attenuation has only a minimal effect. (c) An image is formed, based on the echo strengths and the echo arrival times.

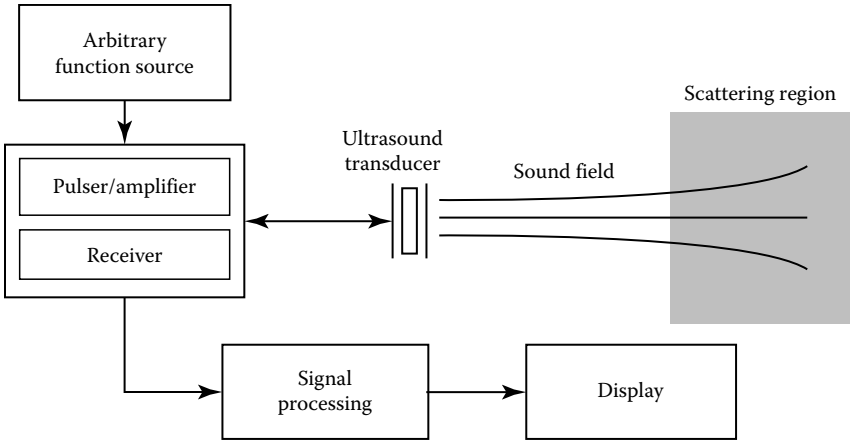

FIGURE 49.2 Simplified block diagram of a pulse-echo ultrasound system.

waveform, such as a linear sweep. The amplifier brings the driving voltage to a level where the transducer can generate an adequate amount of acoustic energy.

The transducer is made from a piezoelectric ceramic that has the property of producing mechanical vibrations in response to an applied voltage pulse and generating a voltage when subjected to mechanical stress. When an image is required, the transducer can be a mechanical sector probe that produces a fan-shaped image by means of a single, mechanically steered, focused transducer element. Alternatively, the transducer can be a linear array transducer (described later) that produces a rectangular image. In the case of an array transducer, the pulser/amplifier must contain a driving circuit for each element in the array, in addition to delay control. To achieve a short pulse and good sensitivity, the transducer is equipped with backing material and matching layers (to be discussed later).

The receiver block contains a low-noise amplifier with time-varying gain to correct for medium attenuation and often a circuit for logarithmic compression. In the case of array transducers, the receiver circuitry is a complex system of amplifiers, time-varying delay elements, and summing circuits. The signal-processing block can be partly analog and partly digital. The echo signals are envelope detected and digitized; the *envelope* of a signal is a curve that follows the amplitude of the received signal. A scan converter changes the signal into a format suitable for display on a grayscale monitor. Information about ultrasound pulser–receiver instrumentation for NDE measurements can be found in [1] and for medical imaging in [2].

Not all ultrasound measurement systems are based on the pulse-echo concept. For material characterization, *transmission measurements* are frequently used, as illustrated in Figure 49.3. The main difference between the pulse-echo system and the transmission system is that two transducers are used

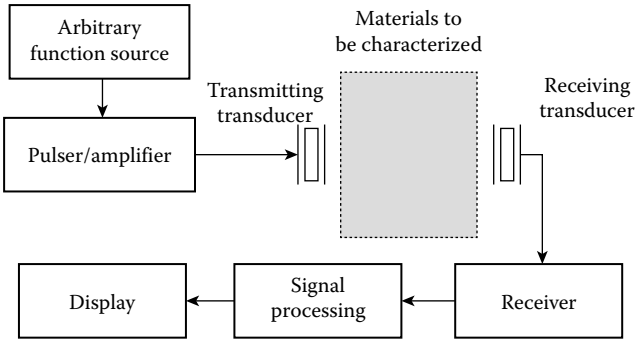

FIGURE 49.3 Simplified block diagram of an ultrasound transmission system.

in the transmission system; the description of the individual blocks for the pulse-echo system applies generally here also. Imaging is generally not possible, although tomographic imaging of either attenuation or velocity has been attempted. If the two transducers are moved together, voids and inclusions located in the transmission path can be detected.

Transmission measurements require, of course, that the structure or the medium of interest is accessible from opposite sides. This system allows accurate characterization of the attenuation and the sound speed of the medium from which a variety of material properties can be derived. Flow in a pipe or a channel can also be determined with a transmission system, by determining the difference between upstream and downstream propagation times.

49.4 Single-Element and Array Transducers

The device that converts electric energy into acoustic energy and vice versa is termed the *transducer* or, more specifically, the ultrasound transducer. Piezoelectric ceramics can be used for all frequencies in the ultrasound range; however, for ultrasound frequencies in the 20–200 kHz range, magnetostrictive devices are occasionally used, which are based on materials that exhibit mechanical deformation in response to an applied magnetic field. Ultrasound transducers are commercially available for many applications over a wide range of frequencies.

Single-element transducers are used for basic measurements and material characterization, while array transducers with many individual transducer elements are used for imaging purposes. The former type costs from a few hundreds of dollars and up, whereas the latter type costs in the thousands of dollars and requires extensive electronics for beam control and signal processing. A third alternative is the mechanical sector scanner where a single transducer is mechanically rotated over a specified angle. A single-element transducer consists of a piezoelectric element, a backing material that enables the transducer to respond to a fairly wide range of frequencies (but with reduced sensitivity), and a matching layer and faceplate that provide improved coupling into the medium and protect the transducer.

Although broadband transducers are very desirable, the energy conversion characteristics of the practical transducer correspond to that of a bandpass filter, that is, the ultrasound pulse has most of its energy distributed around one frequency. This is the frequency referred to when, for example, one orders a 3.5 MHz transducer. The 6 dB bandwidth can be from 50% to 100% of the transducer frequency; the 6 dB bandwidth is the frequency range over which the transducer can produce an acoustic pressure that is at least 50% of the acoustic pressure at the most efficient frequency. The radiation characteristics of transducers are determined by their geometry (square, circular, plane, focused, etc.) and dimensions measured in wavelengths. Hence, a 10 MHz transducer tends to be smaller than a 5 MHz transducer. Focusing can also be achieved by means of an acoustic lens.

Array transducers exist in three main categories: phased arrays, linear arrays, and annular arrays. A fourth category could exist commercially in a few years: the 2-D array or a sparse 2-D array. Common for these array transducers is the fact that *during transmission*, the excitation time and excitation signal amplitude for each transducer element are controlled independently. This allows the beam to be steered in a given direction, as well as focused at a given point in space. *During reception*, an independently controlled time delay—which may be time varying—can be applied to each element before summation with the signal from other elements. The delay control permits the transducer to have maximal sensitivity to an echo from a specified range and, moreover, to shift this point in space away from the transducer as echoes from structures further away are received. A limitation of the phased and linear arrays is that beam steering and focusing can only take place within the image plane. In the direction normal to the image plane, a fixed focus is produced by the physical shape of the array elements.

The phased array transducer consists of a fairly small number of elements, such as 16–32. Both beam steering and focusing is carried out, producing a pie-shaped image. The phased array is most suitable when only a narrow observation window exists, as is the case when imaging the heart from the space between the ribs. The linear array transducer has far more elements, typically between 128 and 256.

It activates only a subset of all the elements for a given measurement and produces focusing, but generally not beam steering, so that the beam direction is normal to the array surface. Consider a linear array transducer with 128 elements, labeled 1–128. If one assumes that the first pulse-echo measurement is made with elements 1–16, the next measurement with elements 2–17, etc., the beam will have been *linearly* translated along the long dimension of the linear array (hence the name), producing a rectangular image format. The annular array transducer consists of a series of concentric rings. As such, it cannot steer the beam, but can focus both in transmit and receive mode, just as the phased and linear arrays. Thus, the annular array transducer is not suitable for imaging unless the transducer is moved mechanically. Its specific advantage is uniform focusing.

49.5 Selection Criteria for Ultrasound Frequencies

The discussion so far has often mentioned *frequency* as an important variable, without providing any guidance as to what ultrasound frequencies should be used. There is generally no technological limitation with respect to choice of ultrasound frequency, as frequencies even in the gigahertz (GHz, 10^9 Hz) range can be produced. The higher the frequency, the better is the control over the direction and the width of the ultrasound beam, leading to improved axial and lateral resolution. However, the attenuation increases with higher frequency. For many media, the attenuation varies with the frequency squared, while for biological soft tissue, the attenuation varies nearly linearly with frequency.

Generally, the ultrasound frequency is chosen as high as possible while still allowing a satisfactory signal-to-noise ratio (SNR) of the received signal. This rule does not always hold; for example, for grain size estimation in metals and for rough surface characterization, the optimal frequency has a specific relationship to the mean grain dimension or the rms roughness.

49.6 Basic Parameters in Ultrasound Measurements

Ultrasound technology today has led to a very wide range of applications, and the following overview mentions only the basic parameters. For an in-depth review, see [3]. A discussion of applications is given at the end of Section 49.7.

49.6.1 Reflection (or Transmission) Detected or Not

The most basic measurement consists of determining whether a reflected or transmitted signal is received or not. This can be used to monitor liquid level where the absence of liquid prevents ultrasound transmission from taking place or to detect the existence of bubbles in a liquid (e.g., for dialysis purposes, where the bubbles are the reflectors) or for counting objects, such as bottles, on a conveyer belt.

49.6.2 Travel Time

Travel time is the elapsed time from transmission of an ultrasound pulse to the detection of a received pulse in either a pulse-echo or a transmission system. If the sound speed is known, the thickness of an object can be found from the time difference between the front surface echo and the back surface echo. Conversely, sound speed can be determined when the thickness is known. By measuring with a broadband pulse (a short pulse containing a broad range of frequencies), velocity dispersion (frequency dependence of velocity) can be found, which has applications for materials characterization. Elastic parameters can also be found from velocity measurements. Imaging applications are generally made based on the assumption of a known, constant velocity; thus, round-trip travel times from the transducer to the reflecting structures and back in a known direction give the basis for the image formation.

49.6.3 Attenuation

The attenuation and its frequency dependence are important materials parameters, as they can be used to differentiate between normal and pathological biological tissue, measure porosity of ceramics, the grain size of metals, and the structure of composite materials. Attenuation can be found by means of transmission measurements by determining the signal amplitude with the test object first absent and then present; here, transmission losses must also be considered, as quantified in Equation 49.5. Attenuation can be obtained from pulse-echo measurements, by comparing the strength of echoes from the front and back surfaces of the specimen under test. Diffraction effects (described later in Section 49.9) might need to be considered. Attenuation can be considered as a bulk parameter for the medium as a whole, or it can be determined for small regions of the medium.

49.6.4 Reflection Coefficient

The strength of a reflection at an interface between two media is determined by the change in acoustic impedance across the interface, as shown in Equation 49.4. This allows, at least in principle, the impedance of one medium to be determined from the measured reflection coefficient and the impedance of the other medium. In fact, the term *impediography* refers to the determination of the impedance profile of a layered medium by means of this concept. In practice, the measurement is not easy to carry out, as the transducer must be aligned very accurately at normal incidence to the medium surface. By measuring the reflection coefficient vs. incident angle at a planar, smooth surface, a velocity estimate of the reflecting medium can be made; in an alternative application, reflection measurements vs. frequency permit the evaluation of rough surface parameters.

49.6.5 Parameters Obtained through Signal Processing

A number of object parameters can be obtained from analysis of the received signals. Material properties can be extracted from speckle analysis (analysis of statistical fluctuations in the image) and other forms of statistical analysis. Recognition of objects with complex shapes can, in some cases, be done by extracting specific features of the received signals. Doppler processing for velocity estimation is another example of information that is only attainable by means of signal processing. By combining several "stacked" images, 3-D reconstruction is possible, from which volume estimation and rate of change of volume are possible, such as for determining the dynamics of the left ventricle of the heart.

49.7 Ultrasound Theory and Applications

49.7.1 Sound Velocity

The propagation speed, c_0, is generally determined by the density and the elastic properties of the medium. For an ideal gas, c_0 may be expressed as [4]

$$c_0 = \sqrt{\gamma \frac{P_0}{\rho_0}} = \sqrt{\gamma r T_K} \tag{49.6}$$

where

$\gamma = C_P/C_V$ is the ratio of specific heats and for air, $\gamma = 1.402$
P_0 is the static pressure of the gas, which at 1 atm is 1.013×10^5 N m^{-2}
ρ_0 is the specific density of the gas, equal to 1.293 kg m^{-3} for air at 1 atm and 0 °C
The constant r is the ratio of the universal gas constant and the molecular weight of the gas
T_K is the temperature in Kelvin

Substituting the values for air into the first equation in Equation 49.6 gives $c_0 = 331.6$ m s^{-1} at 0 °C. As the ratio P_0/ρ_0 is constant for varying pressure but constant temperature, c_0 is likewise pressure independent. (For a real gas, c_0 exhibits, in fact, a small dependence on pressure.)

The temperature dependence of an ideal gas can be obtained by rewriting the second expression in Equation 49.6 as follows:

$$c_0 = c_{\text{ref}}\sqrt{1+\frac{T}{273}} \tag{49.7}$$

where

c_{ref} is the sound speed at 0 °C
T is the temperature in °C

In liquids, the expression for c_0 is given as

$$c_0 = \sqrt{\frac{K_s}{\rho_0}} \tag{49.8}$$

where K_s is the adiabatic bulk modulus. Expressions for actual liquids as a function of temperature and pressure are not easily derived and are often empirically determined. For pure water, the sound speed as a function of temperature and pressure can be given as

$$c_{\text{H}_2\text{O}} = 1402.4 + 5.01T - 0.055T^2 + 0.00022T^3 + 1.6\times10^{-6}P_0 \tag{49.9}$$

where

T is the temperature in °C
P_0 is the static pressure in N m^{-2}

The expression is valid for a pressure range from 1 to 100 atm.

Finally, for solids, the sound speed for longitudinal waves, c_{L}, is [5]

$$c_{\text{L}} = \left(\frac{c_{11}}{\rho_0}\right)^{1/2} = \left(\frac{\lambda+2\mu}{\rho_0}\right)^{1/2} \tag{49.10}$$

where c_{ij} is the the elastic stiffness constant, such that c_{11} refers to longitudinal stress over longitudinal strain, and $\lambda = c_{12}$ and $\mu = c_{44}$ are the Lamé elastic constants.

49.7.2 Wave Propagation in Homogeneous Media

In order to effectively use ultrasound for measurement purposes, it is essential to be able to describe the behavior of acoustic fields. This includes the general behavior, and maybe even a detailed understanding, of the radiated field from ultrasound transducers; the transmission, reflection, and refraction of an acoustic field at boundaries and layers; and the diffraction of acoustic field at finite-sized reflectors.

The wave equation is a differential equation that formulates how an acoustic disturbance (acoustic pressure or particle velocity) propagates through a homogeneous medium. For an arbitrary wave field, the wave equation takes the following general form:

$$\nabla^2 p = \frac{1}{c^2}\frac{\partial^2 p}{\partial t^2} \tag{49.11}$$

where ∇^2 is the Laplace operator. Equation 49.11 is also valid when particle velocity is substituted for pressure. If the condition of a plane wave field at a single frequency (also called a harmonic plane wave field) is imposed, the solution to Equation 49.11 is

$$p(\vec{\mathrm{r}}, t) = A\exp\left[j(\omega t - \vec{\mathrm{k}}\times\vec{\mathrm{r}})\right] + B\exp\left[j(\omega t + \vec{\mathrm{k}}\times\vec{\mathrm{r}})\right] \tag{49.12}$$

In Equation 49.12, $p(\vec{\mathbf{r}}, t)$ consists of a plane wave propagating in the direction defined by the propagation vector $\vec{\mathbf{k}}$ and a plane wave in the direction $-\vec{\mathbf{k}}$. As before, $\vec{\mathbf{r}}$ is a position vector that, in a Cartesian coordinate system, can be expressed as $\vec{\mathbf{r}} = x\hat{x} + y\hat{y} + z\hat{z}$ where $\hat{x}$, $\hat{y}$ and $\hat{z}$ are unit vectors. The magnitude of $\vec{\mathbf{k}}$ is called the wave number:

$$k = \frac{\omega}{c_0} = \frac{2\pi}{\lambda} \tag{49.13}$$

Expressing $\vec{\mathbf{k}}$ in the Cartesian coordinate system gives

$$\vec{\mathbf{k}} = k_x\hat{x} + k_y\hat{y} + k_z\hat{z} \tag{49.14}$$

When k, k_x, and k_y are specified, k_z is defined as well:

$$k_z = \sqrt{\left(\left(\frac{\omega}{c_0}\right)^2 - k_x^2 - k_y^2\right)} \tag{49.15}$$

Applying the expressions for $\vec{\mathbf{r}}$ and $\vec{\mathbf{k}}$ to Equation 49.12 and considering only the plane wave in the direction of $+\vec{\mathbf{k}}$ gives

$$p(\vec{\mathbf{r}}, t) = A\ \exp[j(\omega t - (k_x x + k_y y + k_z z))] \tag{49.16}$$

From Equation 49.16, one sees that the amplitude of a plane wave is constant and equal to A but that the phase varies with both time and space. When the direction of $\vec{\mathbf{k}}$ is specified, k_x, k_y, and k_z are found from projection onto the coordinate axes.

Solving Equation 49.11 under the assumption of spherical waves at a single frequency, with the source placed at the origin of the coordinate system, gives

$$p(r, t) = \frac{A}{r}\exp[j(\omega t - kr)] + \frac{B}{r}\exp[j(\omega t + kr)] \tag{49.17}$$

The first term is a diverging spherical wave, and the second term is a converging spherical wave. The reason that the vector dot product does not appear in Equation 49.17 is that $\vec{\mathbf{k}}$ and $\vec{\mathbf{r}}$ always point in the

same direction for spherical waves. While Equation 49.17 gives the complete solution, in most cases only a diverging spherical wave exists. If spherical waves are produced by a spherical source of radius a, then

$$p(r,t) = \frac{A}{r}\exp[j(\omega t - kr)], \quad r > a \tag{49.18}$$

49.7.3 Acoustic Intensity and Sound Levels

The acoustic intensity, I, describes the mean power transported through a unit area normal to the direction of propagation. A general expression for I for a CW pressure function is

$$I = \frac{1}{T}\int_0^T p(t)u(t)dt \tag{49.19}$$

where

T is the one full cycle of the pressure function
$u(t)$ is the particle velocity function

For a plane wave, the intensity is

$$I = \frac{p^2}{2\rho_0 c_0} = \frac{1}{2}PU \tag{49.20}$$

where P and U are the magnitudes of the pressure and the particle velocity functions, respectively. The expression for I in Equation 49.20 can also be used as an approximation for nonplanar waves, such as spherical waves, as long as (kr) is large.

The intensity levels for pulse-echo measurements are often described by the *spatial peak, temporal average* (SPTA) value, which therefore refers to the mean intensity at the point in space where the intensity is the highest. Although the guidelines for exposure levels for medical imaging, set by the FDA, vary for different parts of the body, a general upper limit is 100 mW cm^{-2}. Given that the duty cycle (pulse duration/pulse interval) is typically in the order of 0.0001 for ultrasound imaging, the temporal peak intensity is much higher and is even approaching the level where nonlinear effects can begin to be observed. Intensity levels used for NDE are application dependent but are generally in the same range as in medical ultrasound.

Sound levels are logarithmic expressions (expressions in dB) of the pressure level or the intensity level. The term SPL stands for sound pressure level and is given as

$$\text{SPL} = 20\log\left(\frac{P_e}{P_{\text{ref}}}\right)[\text{dB}] \tag{49.21}$$

where

P_e is the effective pressure of the acoustic wave
P_{ref} is the reference effective pressure

Correspondingly, IL is the intensity level defined as

$$\text{IL} = 10\log\left(\frac{I}{I_{\text{ref}}}\right)[\text{dB}] \tag{49.22}$$

where I_{ref} is the reference acoustic intensity.

Several reference levels are commonly used [6]. In air, $P_{ref} = 20$ μPa and $I_{ref} = 10^{-12}$ W m^{-2} are nearly equivalent reference levels. For water, typical pressure reference levels are $P_{ref} = 1$ μPa, $P_{ref} = 20$ μPa, or $P_{ref} = 1$ μbar = 0.1 Pa, with corresponding intensity reference levels of $I_{ref} = 6.76 \times 10^{-19}$ W m^{-2}, $I_{ref} = 2.70 \times 10^{-16}$ W m^{-2}, and $I_{ref} = 6.76 \times 10^{-9}$ W m^{-2}.

49.7.4 Wave Propagation across Layers and Boundaries

The reflection and transmission coefficients for a plane wave impinging at normal incidence on the interface between two half spaces were given in Equations 49.4 and 49.5. It is also important to consider the transmission and reflection of waves at non-normal incidence and across a layer.

When a longitudinal wave impinges at a liquid–liquid interface, both the transmitted and the reflected waves are longitudinal waves, as illustrated in Figure 49.4a. However, when a longitudinal wave propagating in a liquid medium encounters a liquid–solid interface under oblique incidence, both a longitudinal and a shear transmitted wave and a longitudinal reflected wave will result, as shown in Figure 49.4b. The change of direction of the transmitted waves relative to the incident wave is referred to as *refraction*, which is caused by the difference in sound speed between the two media.

The magnitude and direction of the reflected and transmitted waves are determined by two simple boundary conditions: (1) The *pressure* on both sides of the boundary must be equal at all times, and (2) the *normal particle velocity* on both sides of the boundary must be equal at all times; the normal particle velocity refers to the component of the particle velocity that is normal to the boundary.

The boundary conditions lead to the following two relationships:

$$\sin\theta_i = \sin\theta_r; \quad \frac{\sin\theta_i}{c_1} = \frac{\sin\theta_t}{c_2} \tag{49.23}$$

where

c_1 and c_2 are the sound speeds of the two media

θ_i, θ_r, and θ_t are the incident, reflected, and transmitted angles, respectively

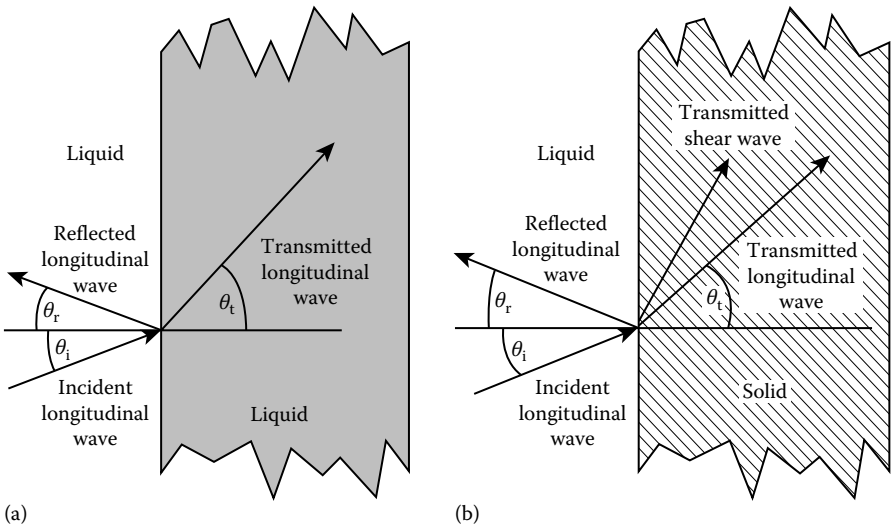

FIGURE 49.4 (a) An incident longitudinal wave at a liquid–liquid interface produces a reflected and a transmitted longitudinal wave. (b) An incident longitudinal wave at a liquid–solid interface produces a reflected longitudinal wave and transmitted longitudinal and shear waves. The incident, reflected, and transmitted angles are indicated.

From Equation 49.23, one sees that

$$\theta_r = \theta_i; \quad \theta_t = \arcsin\left(\frac{c_2}{c_1}\sin\theta_i\right) \tag{49.24}$$

The second expression in Equation 49.24 is referred to as Snell's law and quantifies the degree of refraction. Refraction affects the quality of ultrasound imaging because image formation is based on the assumption that the ultrasound beam travels in a straight path through all layers and inhomogeneities and that the sound speed is constant throughout the medium. When the actual beam travels along a path that deviates to some extent from a straight path and passes through some parts of the medium faster than it does other parts, the resulting image is a distorted depiction of reality. Correcting this distortion is a very complex problem and, in the near future, one should only expect image improvement in the simplest cases.

It can be seen from Equation 49.24 that angle θ_t is not defined if the argument to the arcsine function exceeds unity. This defines a critical incident angle as follows:

$$\sin\theta_c = \frac{c_1}{c_2} \tag{49.25}$$

at or above which the reflection coefficient is 1 and the transmission coefficient is 0. A critical angle only exists when $c_1 < c_2$. The transmitted shear and longitudinal velocities each correspond to a different critical angle of incidence.

From the boundary conditions, the reflection coefficient as a function of incident angle can be determined [7]:

$$R(\theta_i) = \frac{(z_2/z_1) - (\cos\theta_t/\cos\theta_i)}{(z_2/z_1) + (\cos\theta_t/\cos\theta_i)}, \quad \text{where } \cos\theta_t = \sqrt{1-(c_2/c_1)^2\,\sin^2\theta_i} \tag{49.26}$$

The result in Equation 49.26 is referred to as the Rayleigh reflection coefficient.

The transmission of plane waves under normal incidence through a single layer is often of interest. The dimensions and the medium parameters are defined in Figure 49.5.

By applying the boundary conditions to both interfaces of the layer, both reflection and transmission coefficients are obtained [7], as given in Equations 49.27 and 49.28:

$$R = \frac{p_r}{p_i} = \frac{(1 - z_1/z_3)\cos k_2 L + j(z_2/z_3 - z_1/z_2)\sin k_2 L}{(1 + z_1/z_3)\cos k_2 L + j(z_2/z_3 + z_1/z_2)\sin k_2 L} \tag{49.27}$$

$$T = \frac{p_t}{p_i} = \frac{2}{(1 + z_1/z_3)\cos k_2 L + j(z_2/z_3 + z_1/z_2)\sin k_2 L} \tag{49.28}$$

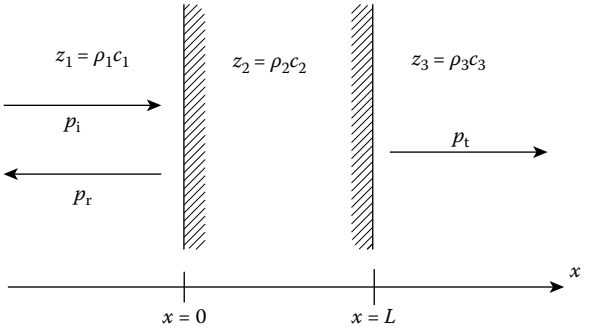

FIGURE 49.5 A pressure wave is incident on a layer of thickness L and with acoustic impedance $z_2 = \rho_2 c_2$.

A number of special conditions for Equation 49.27 can be considered, such as (1) $z_1 = z_3$, which simplifies the numerator in Equation 49.27, and (2) the layer thickness is only a small fraction of a wavelength, that is, $k_2L \ll 1$ which makes $\cos k_2L \approx 1$ and $\sin k_2L \approx k_2L$. One case is of particular interest: the choice of thickness and acoustic impedance for the layer that makes $R = 0$ and therefore gives 100% energy transmission. This is fulfilled for

$$k_2L = \pi/2 + n\pi; \quad z_2 = \sqrt{z_1 z_3} \tag{49.29}$$

The result in Equation 49.29 states that the layer must be a quarter of a wavelength thick (plus an integer number of half wavelengths) and must have acoustic impedance that is the geometric mean of the impedances of the media on either side. Among several applications of the *quarter wavelength impedance matching* is the impedance matching between a transducer and the medium, such as water. A drawback with a single matching layer is that it only works effectively over a narrow frequency range, while the actual acoustic pulse contains a fairly broad spectrum of frequencies. A better matching is achieved by using more than one matching layer, and it has been shown that a matching layer that has continuously varying acoustic impedance across the layer provides broadband impedance matching.

49.7.5 Attenuation: Its Origin, Measurement, and Applications

Attenuation refers to the damping of a signal, here specifically an acoustic signal, with travel time or with travel distance. Attenuation is typically expressed in dB, that is, on a logarithmic scale. Attenuation is an important parameter to measure in many types of materials characterization but also the parameter that sets an upper limit for the ultrasound frequency that can be used for a given measurement. In NDE, attenuation is used for grain size estimation [8,9], for characterization of composite materials, and for determination of porosity [10]. In medical ultrasound, attenuation can be used for tissue characterization [11], such as differentiating between normal and cirrhotic liver tissue, and for classification of malignancies. In flowmeters, attenuation caused by vortices can be used to measure the frequency at which they are shed; this frequency is proportional to the flow velocity.

Attenuation represents the combined effect of *absorption* and *scattering*, where absorption refers to the conversion of acoustic energy into heat due to the viscosity of the medium and scattering refers to the spreading of acoustic energy into other directions due to inhomogeneities in the medium. The absorption can, in part, be due to *classical absorption*, which varies with frequency squared, and *relaxation absorption*, which can result in a complicated frequency dependence of absorption. Gases (except for noble gases), liquids, and biological tissue exhibit mainly relaxation absorption, whereas classical absorption is most prominent in solids, which can also have a significant amount of scattering attenuation.

In general, absorption dominates in homogeneous media (e.g., liquids, gases, fine-grained metals, polymers), whereas scattering dominates in heterogeneous media (e.g., composites, porous ceramics, large-grained materials, bone). The actual attenuation and its frequency dependence can be specified fairly unambiguously for gases and liquids, while for solids it is very dependent on the manufacturing process, which determines the microstructure of the material, such as the grain structure.

Measurement of attenuation can be carried out for at least two purposes: (1) to measure the *bulk attenuation* of a given homogeneous medium and (2) to measure the *spatial distribution of attenuation* over a plane in an inhomogeneous medium. The former approach is most common in materials characterization, whereas the latter approach is found mainly in medical ultrasound. Bulk attenuation can be performed either with transmission measurements or with pulse-echo measurements, as illustrated in Figure 49.6a and b, respectively.

For the measurement of attenuation, in dB/cm, of a medium of thickness d, by transmission measurements, define $v_1(t)$ as the received signal without medium present and $v_2(t)$ as the received signal with

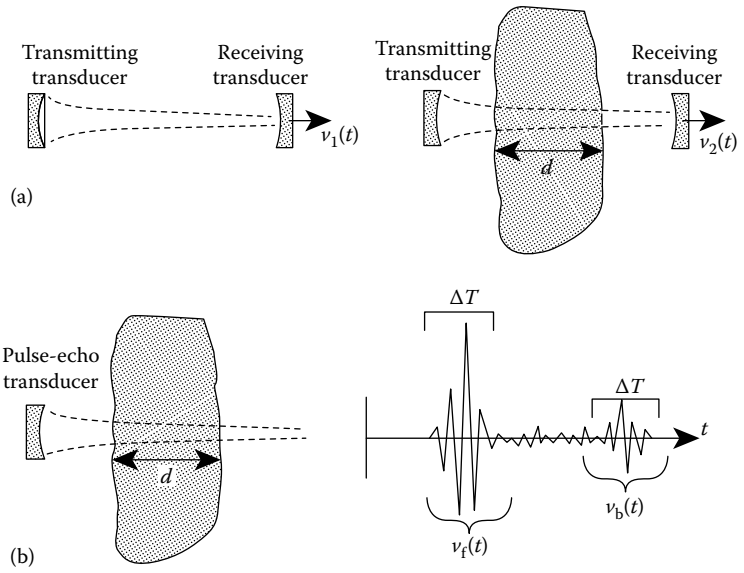

FIGURE 49.6 Measurement of bulk attenuation. (a) Measurement of attenuation by transmission measurement. (b) Measurement of attenuation by pulse-echo measurements.

medium present, as shown in Figure 49.6a. The attenuation is then determined from the ratio of the energies of the two signals, corrected for the transmission losses, as

$$\text{Att [dB/cm]} = \frac{1}{d} 10 \log \left\{ \frac{\int_0^\infty [v_1(t)]^2 dt}{\int_0^\infty [v_2(t)]^2 dt} \right\} - 20 \log \left\{ \frac{4 z_1 z_2}{(z_1 + z_2)^2} \right\} \tag{49.30}$$

Correction for transmission losses (second term) can be avoided by alternatively measuring the incremental attenuation due to an incremental thickness increase.

For the measurement of attenuation by *pulse-echo measurements*, the front and the back wall echoes are termed $v_f(t)$ and $v_b(t)$, respectively. Based on an a priori knowledge of the pulse duration, a time window ΔT is defined. The attenuation is most accurately measured when based on the energies of $v_f(t)$ and $v_b(t)$ but may alternatively be based on the amplitudes of $v_f(t)$ and $v_b(t)$, as stated in Equation 49.31:

$$\text{Att [dB/cm]} = \frac{1}{2d} 10 \log \left\{ \frac{\int_0^{\Delta t} [v_f(t)]^2 dt}{\int_0^{\Delta t} [v_b(t)]^2 dt} \right\} \cong \frac{1}{2d} 20 \log \left\{ \frac{\text{peak ampl., } v_f(t)}{\text{peak ampl., } v_b(t)} \right\} \tag{49.31}$$

Accurate attenuation measurements require attention to several potential pitfalls: (1) diffraction effects (even in the absence of attenuation, echoes from different ranges vary in amplitude, due to beam spreading); (2) misalignment effects (if the reflecting surface is not normal to the transducer axis, there is a reduction in detected signal amplitude, due to phase cancellation at the transducer surface); and (3) transmission losses whose magnitude it is not always easy to determine.

The spatial distribution of attenuation must be measured with pulse-echo measurements, where it is assumed that a backscatter signal of sufficient amplitude can be received from all regions of the medium.

Use is made of the frequency dependence of attenuation, which has the effect that the shift in mean frequency of a given received echo relative to the mean frequency of the transmitted signal varies proportional to the total absorption. The *rate of shift* in mean frequency is thus proportional to the local attenuation.

49.7.6 CW Fields from Planar Piston Sources

In discussing the acoustic fields generated by acoustic radiators (transducers), a clear distinction must be made between fields due to CW excitation and due to pulse excitation. Although the overall field patterns for these two cases are quite similar, the detailed field structure is very different. In this section, only CW fields are discussed.

When a CW excitation voltage is applied to a planar piston transducer, the resulting acoustic field can be divided into a *near-field* region and a *far-field* region. This division is particularly distinct when the transducer has a circular geometry. A piston transducer simply refers to a transducer with the same velocity amplitude at all points on the surface. The length of the near field, NF, is given as

$$\mathrm{NF} = \frac{a^2}{\lambda} \tag{49.32}$$

where

a is the radius of the transducer

λ is the wavelength

As shown in Figure 49.7a, the near field is approximately confined, while the far field is diverging. The angle of divergence, θ, is approximately

$$\theta = \arcsin\left(0.61\frac{\lambda}{a}\right) \tag{49.33}$$

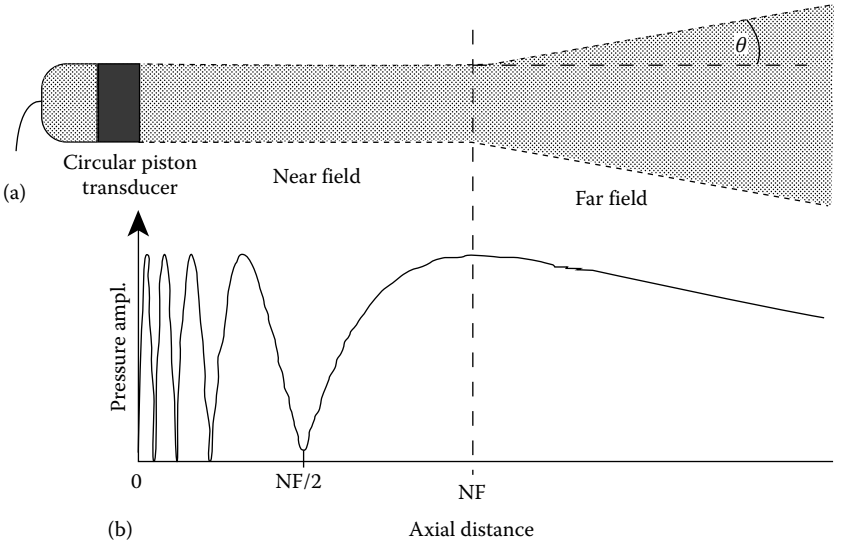

FIGURE 49.7 Pressure fields from a circular planar piston transducer operating with CW excitation. NF = near field. (a) Approximate field distribution in near field and far field. (b) Axial pressure in near field and far field for $(ka) = 31.4$.

Additional comments to the simplified representation in Figure 49.7a are in order:

1. The actual field has no sharp boundaries, in contrast to what is shown in Figure 49.7.
2. While the beam diameter is roughly constant in the near field, it is not as regular as shown, and at the same time, the near-field structure is very complex.
3. The angle of divergence, θ, is only clearly established well into the far field.
4. The depiction of the far field shows only the main lobe; in addition, there are side lobes, which are directions of significant pressure amplitude, separated by *nulls* (i.e., directions with zero-pressure amplitude).

In general, analytical expressions do not exist for the pressure magnitude at an arbitrary field point in the near field, and the pressure must instead be calculated by numerical techniques. However, an exact expression exists for the axial pressure amplitude, P_{ax}, valid in both near and far field [12].

$$P_{ax}(x) = 2\rho_0 c_0 U_0 \left| \sin\left(0.5ka\left[\sqrt{\frac{x^2}{a^2}+1} - \left(\frac{x}{a}\right)\right]\right)\right| \tag{49.34}$$

In Equation 49.34, U_0 is the amplitude of the velocity function on the surface of the transducer. The expression is derived for a baffled planar piston transducer where the term "baffled" means that the transducer is mounted in a large rigid surface, called a baffle. Figure 49.7b shows the amplitude of the axial field for a planar piston transducer for which $(ka) = 31.4$. For field points located more than 3–4 near-field distances away from the transducer, a general expression for the pressure amplitude can be derived [12]:

$$P(r,\theta) = \frac{\rho_0 c_0}{2} U_0 ka\left(\frac{a}{r}\right)\left[\frac{2J_1(ka\,\sin\theta)}{ka\,\sin\theta}\right] \tag{49.35}$$

where

$J_1(\cdot)$ is the Bessel function of the first order
The variable r is the length of the position vector defining the field point
Angle θ is the angle that the position vector makes with the x-axis

Of interest in evaluating transducers in the far field is the *directivity*, D, defined as follows:

$$D(x) = \frac{I_{ax}(x)[\text{given source}]}{I_{ax}(x)[\text{simple source}]} \tag{49.36}$$

Thus, the directivity gives the factor with which the axial intensity of the given source is increased over that of a simple source (omnidirectional radiator), radiating the same total energy. For a baffled, circular planar piston transducer, the directivity in the far field can be calculated to be [12]

$$D = \frac{(ka)^3}{ka - J_1(2ka)} \tag{49.37}$$

When $(2ka) \gg 1$, Equation 49.37 can be approximated to $D = (ka)^2$. Directivity values in the 1000s are common. For example, a 3.5 MHz transducer with 1 cm diameter radiating into water has a (ka) value of 73.3 and a directivity of 5373.

Often, focused transducers are used where the focusing is either created by the curvature of the piezoelectric element or by an acoustic lens in front of the transducer. The degree of focusing is determined by the (ka) value of the transducer.

49.7.7 Generation of Ultrasound: Piezoelectric and Magnetostrictive Phenomena

Ultrasound transducers today are available over a wide frequency range, in many sizes and shapes, and for a wide variety of applications. The behavior of the ultrasound transducer is determined by several parameters: the transduction material, the backing material, the matching layer(s), and the geometry and dimension of the transducer. A good overview of ultrasound transducers is available in [13].

The transduction material is most commonly a piezoelectric material but can, for some applications, be a magnetostrictive material instead. These materials are inherently narrowband, meaning that they work efficiently only over a narrow frequency range. This is advantageous for CW applications such as ultrasound welding and ultrasound hyperthermia, but is a problem for imaging applications, as impulse excitation will produce a long pulse with poor resolving abilities. To overcome this deficiency, a *backing material* is tightly coupled to the back side of the transducer for the purpose of damping the transducer and shortening the pulse. However, the backing material also reduces the sensitivity of the transducer. Some of this reduced sensitivity can be regained by the use of a *matching layer*, specifically selected for the medium of interest. As seen in Equation 49.29, a quarter wavelength matching layer can provide 100% efficient coupling to a medium, albeit only at one frequency. A combination of several matching layers can provide a more broadband impedance matching. The field is determined by both the geometry (planar, focused, etc.) of the transducer and by the frequency content of the velocity function of the surface of the transducer. In this section, unique aspects of the transduction material itself are described.

49.7.7.1 Piezoelectric Materials

A piezoelectric material exhibits a mechanical strain (relative deformation) due to the presence of an electric field and generates an electric field when subjected to a mechanical stress. A detailed review of piezoelectricity is given in [14]. Piezoelectric materials can either be (1) natural material such as quartz, (2) man-made ceramics (e.g., barium titanate [BaTi], lead zirconate titanate [PZT], or lead meta-niobate), and (3) man-made polymers (e.g., polyvinylidene fluoride [PVDF]). The piezoelectric ceramics are the most commonly used materials for ultrasound transducers. These ceramics are made piezoelectric by poling process in which the material is subjected to a strong electric field while at the same time heating it to above the material's Curie temperature.

Several material constants determine the behavior of a given piezoelectric material, the most important of which are listed in Table 49.1 and defined as follows. An extensive list of parameter values for various piezoelectric materials is available in [15].

TABLE 49.1 List of Most Significant Piezoelectric Parameters for Common Piezoelectric Materials

Parameter	Barium Titanate ($BaTiO_3$)	Lead Zirconate Titanate, PZT-5	Lead Meta-Niobate, $PbNb_2O_6$	Polyvinylidene Fluoride (PVDF)
d_{33}	149 (10^{-12} m/V)	374 (10^{-12} m/V)	75 (10^{-12} m/V)	22 (10^{-12} m/V)
g_{33}	14 (10^{-3} Vm/N)	25 (10^{-3} Vm/N)	35 (10^{-3} Vm/N)	339 (10^{-3} Vm/N)
k_{33}	0.50	0.70	0.38	$k_{31} = 0.12$
k_T	0.38	0.68	0.40	0.11
Q_M	600	75	5	19

d_{33}, Transmission constant; g_{33}, Receiving constant; k_{33}, Piezoelectric coupling coefficient; k_T, Piezoelectric coupling coefficient for a transverse clamped material; Q_M, Mechanical Q.

The transmission constant, d_{33}, gives the mechanical deformation of piezoelectric materials for frequencies well below the resonance frequency. A transducer with a large d_{33} value will therefore become an efficient transmitter. If an electric field, E_3, is applied in the polarized direction of a piezoelectric rod or disk, the strain, S_3, in that direction is approximately

$$S_3 = d_{33}E_3 = d_{33}\frac{V_{\text{appl}}}{l} \tag{49.38}$$

where

V_{appl} is the applied voltage
l is the thickness

The total deformation, Δl, becomes

$$\Delta l = d_{33}V_{\text{appl}} \tag{49.39}$$

The receiving constant, g_{33}, defines the sensitivity of a transducer element as a receiver when the frequency of the applied pressure is well below the resonance frequency of the transducer. If the applied stress (force/area) in the direction of polarization is T_3, the output voltage from a rod or disk is approximately

$$v_{\text{out}} = g_{33}T_3 l \tag{49.40}$$

The coupling coefficient describes the power conversion efficiency of a piezoelectric transducer, *operating at or near resonance*. Specifically, k_{33} is the coupling coefficient for an undamped rod; that is, the rod is allowed to deform in the directions orthogonal to the direction of applied force or voltage. In contrast, k_T is the coupling coefficient for a *clamped* disk. Finally, Q_M gives the mechanical Q, which is a measure for how narrowband the transducer material inherently is.

Whereas expressions of the type given in Equations 49.38 through 49.40 are adequate for describing static or low-frequency behavior, the behavior near resonance where most transducers operate requires more complex models, which are beyond the scope of this chapter. The Mason model is adequate for narrowband modeling of transducers, whereas the KLM or Redwood models better describe the transducers for broadband applications [13,15].

49.7.7.2 Magnetostrictive Materials

The magnetostrictive phenomenon refers to a magnetically induced contraction or expansion in ferroelectric media, such as in nickel or alfenol, and was discovered by Joule in 1847. Magnetostrictive materials are generally used for ultrasound frequencies below 100 kHz and are therefore relevant mainly for underwater applications. Eddy current losses influence the performance of magnetostrictive materials, but the losses can be reduced by constructing the magnetostrictive transducer from thin laminations.

49.7.7.3 Transducer Specifications

Ultrasound transducers are generally specified by their diameter, center frequency, focal distance, and type of focusing (if applicable). The transducer can be designed as a contact transducer, a submersible transducer, an air transducer, etc.; in addition, the type of connector or cabling can be specified. In many cases, measurement data for the actual transducer can be supplied by the vendor in the form of a measured pressure pulse and the corresponding frequency spectrum, recorded with a hydrophone at a specific field point. Similarly, the beam profile can be measured in the form of pulse amplitude or pulse energy as a function of lateral position.

Detailed information about the acoustic field from a radiating transducer can be obtained with either the Schlieren technique or the optical interferometric technique. Such instruments are quite expensive, falling in the $50–$120 K range.

49.7.8 Display Formats for Pulse-Echo Measurements

The basic description of ultrasound imaging was presented earlier in this chapter. Based on the information presented so far in this section, more specific aspects of pulse-echo ultrasound imaging will now be described. Different display formats are used; the simplest of these is the *A-mode* display.

49.7.8.1 A-Mode Display

When a pulse-echo transducer has emitted a pulse in a given direction and has been switched to receive mode, an output signal from the transducer is produced based on detected echoes from different ranges, as illustrated conceptually in Figure 49.1a. In this signal, distance to the reflecting structure has been converted into time from the start of signal. This signal is often referred to as the RF signal. Demodulating this signal (i.e., generating the envelope of the signal) produces the A-mode (amplitude mode) display or the A-line signal. This signal can be the basis for range measurements, attenuation measurements, and measurement of reflection coefficient.

49.7.8.2 M-Mode Display

If the A-mode signal from a transducer in a fixed position is used to *intensity* modulate a cathode-ray tube (CRT), such as a monitor or oscilloscope, along a straight vertical line, a line of dots with brightness according to echo strengths would appear on the screen. Moving the display electronically across the screen will result in a set of straight horizontal lines. Now consider the case where the reflecting structures are moving in a direction toward or away from the transducer while pulse-echo measurements were being performed. This gives in variations in the arrival time of echoes in the A-line signal, and the resulting lines across the screen are no longer straight, but curved, as determined by their velocity. Such a display is called *M-mode*, or motion mode, display. An application for this would be measurement of the diameter variation of a flexible tube, or blood vessel, due to a varying pressure inside the tube.

49.7.8.3 B-Mode Display

If pulse-echo measurements are repeatedly being performed, while the transducer scans the objects of interest, an image of the object can be generated, as illustrated in Figure 49.1. Specifically, each A-line signal is used to intensity modulate a line on a CRT corresponding to the location of ultrasound beam, which produces an image that maps the reflectivity of the structures in the object. The resulting image is called a *B-mode* (or brightness mode) image. If the transducer is moved linearly, a rectangular image is produced, whereas a rotated transducer generates a pie-shaped or sector image. This motion is typically done electronically or electromechanically, as described earlier under single-element and array transducers. When the scanning is done rapidly (say, 30 scans/s), the result is a real-time image.

Many forms of signal processing and image enhancement can be applied in the process of generating the B-mode image. Echoes from deeper lying structures will generally be of smaller amplitude, due to the attenuation of the overlying layers of the medium. Attenuation correction is made especially in medical imaging, so that echoes are displayed approximately with their true strength. This correction consists of a time-varying gain, called *time-gain control*, or TGC, such that the early arriving echoes experience only a low gain and later echoes from deeper lying structures experience a much higher gain. Various forms for signal compressions or nonlinear signal transfer function can selectively enhance the weaker or the stronger echoes.

49.7.8.4 C-Mode Display

In a C-mode display, only echoes from a specific depth will be imaged. To generate a complete image, the transducer must therefore be moved in a raster scan fashion over a plane. C-scan imaging is slow and cannot be used for real-time imaging but has several applications in NDE for examining a given layer, or interface, in a composite structure, or the inner surface of a pipe.

49.7.9 Flow Measurements by Doppler Signal Processing

Flow velocity can be obtained by various ultrasonic methods, for example, by measuring the Doppler frequency or Doppler spectrum. The Doppler frequency is the difference between the frequency (and pitch) of a moving sound source, as measured by a *stationary* observer, and the actual frequency of the sound source. The change in frequency is determined by the speed and direction of the moving source. The classical example is a moving locomotive with its whistle blowing; the pitch is increased when the train moves toward the observer and vice versa. With respect to ultrasound measurements, only the reflecting (or scattering) gas, fluid, or structure is moving and not the sound source, yet the Doppler phenomenon is present here as well. In order for ultrasound Doppler to function, the gas or fluid must contain scatterers that can reflect some of the ultrasound energy back to the receiver. The Doppler frequency, f_d, is given as follows:

$$f_d = \frac{2v}{c_0}\cos\theta \tag{49.41}$$

where

v is the velocity of the moving scatterers

θ is the angle between the velocity vector and the direction of the ultrasound beam

Doppler flowmeters require only access to the moving gas, fluid, or object from one side. For industrial use, when the fluids or gases often do not contain scatterers, *transmission* methods are preferred; these methods, however, are not based on the Doppler principle.

Two main categories of Doppler systems exist: the CW Doppler system and the PW (pulsed wave) Doppler system. The CW Doppler system transmits a continuous signal and does not detect the distance to the moving structure. It is therefore only applicable when there is just one moving structure or cluster of scatterers in the acoustic field. For example, a CW Doppler is appropriate for assessing the pulsatility and nature of blood flow in an arm or leg. CW Doppler systems are small and relatively inexpensive.

The PW Doppler system transmits a short burst at precise time intervals; it is therefore inherently a sampled system, and, as such, is subject to aliasing. It measures changes from one transmitted pulse to the next in the received signal from moving structures at one or several selected ranges and is able to determine both velocity and range. Assuming that the ultrasound beam is narrow and thus very directional, the PW Doppler can create a *flow image*; that is, it can indicate the magnitude and direction of flow over an image plane. Commonly, color and color saturation are used to indicate direction and speed in a flow image, respectively. In contrast to CW Doppler systems, the PW Doppler systems require much signal processing and are therefore typically expensive and often part of a complete imaging system. When a distribution of velocities, rather than a single velocity, is encountered, as is often the case with fluid flow, a Doppler spectrum rather than a Doppler frequency is determined. A fast Fourier transform (FFT) routine is then used to reveal the Doppler frequencies and thus the velocity components present.

49.8 Review of Common Applications of Ultrasound and Their Instrumentation

49.8.1 Range Measurements, Air

Ultrasound range measurements are used in cameras, in robotics, for determining dimensions of rooms, etc. Measurement frequencies are typically around 50–60 kHz. The measurement concept is pulse echo but with burst excitation rather than pulse excitation. Special electronic circuitry and a thin low-acoustic-impedance air transducer are the most commonly used. Rugged solid or composite piezoelectric-based transducers, however, can also be used, sometimes up to about 500 kHz.

49.8.2 Thickness Measurement for Testing and Process Control

Measurement of thickness is a widely used application of ultrasound. The measurements can be done with direct coupling between the transducer and the object of interest or—if good surface contact is difficult to establish—with a liquid or another coupling agent between the transducer and the object. Ultrasound measurements of thickness have applications in process control, quality control, measuring buildup of ice on an aircraft wing, detecting wall thickness in pipes, as well as medical applications. The instrumentation involves a broadband transducer, pulser–receiver, and display or, alternatively, echo-detecting circuitry and numerical display.

49.8.3 Detection of Defects, Such as Flaws, Voids, and Debonds

The main ultrasound application in NDE is inspection for the localization of voids, crack, flaws, debonding, etc. [3]. Such defects can exist immediately after manufacturing or were formed due to stresses, corrosion, etc. Various types of standard or specialized flaw detection equipment are available from ultrasound NDE vendors.

49.8.4 Doppler Flow Measurements

The flow velocity of a liquid or a moving surface can be determined through Doppler measurements, provided that the liquid or the surface scatters ultrasound back in the direction of the transducer and that the angle between the flow direction and the ultrasound beam is known. Further details are given in the section about Doppler processing. CW and PW Doppler instruments are commercially available, with CW instrumentation being by far the least expensive.

49.8.5 Upstream/Downstream Volume Flow Measurements

When flow velocity is measured in a pipe with access to one or both sides, an ultrasound transmission technique can be used in which transducers are placed on the same or opposite sides of the pipe, with one transducer placed further upstream than the other transducer. From the measured *difference* in travel time between the upstream direction and the downstream direction, and knowledge about the pipe geometry, the volume flow can be determined. Special clamp-on transducers and instrumentation are available. An overview of flow applications in NDE is given in [16].

49.8.6 Elastic Properties of Solids

Since bulk sound speed varies with the elastic stiffness of the object, as given in Equation 49.11, sound speed measurements can be used to estimate elastic properties of solids under different load conditions and during solidification processes. Such measurements can also be used for measurement of product uniformity and for quality assurance. The measurements can be performed on bulk specimens or on thin rods, using either pulse-echo or transmission instrumentation [17]. Alternatively, measurements of the material's own resonance frequencies can be performed for which commercial instruments, such as the *Grindo-sonics*, are available.

49.8.7 Porosity and Grain Size Estimation

Measurement of ultrasound attenuation can reveal several materials parameters. By observing the attenuation in metals as a function of frequency, the grain size and grain size distribution can be estimated. Attenuation has been used for estimating porosity in composites. In medical ultrasound, attenuation is

widely used for tissue characterization, that is, for differentiating between normal and pathological tissues. Pulse-echo instrumentation interfaced with a digitizer and a computer for data analysis is required.

49.8.8 Acoustic Microscopy

The measurement approaches utilized in acoustic microscopy are similar to other ultrasound techniques, in that A-scan, B-scan, and C-scan formats are used. It is in the applications and the frequency ranges where acoustic microscopy differs from conventional pulse-echo techniques. Although acoustic microscopes have been made with transducer frequencies up to 1 GHz, the typical frequency range is 20–100 MHz, giving spatial resolutions in the range from 100 to 25 μm. Acoustic microscopy is used for component failure analysis, electronic component packaging, and internal delaminations and disbonds in materials, and several types of acoustic microscopes are commercially available.

49.8.9 Medical Ultrasound

Medical imaging is a large and diverse application area of ultrasound, especially in obstetrics, cardiology, and vascular studies and for detecting lesions and abnormalities in organs. The display format is either B-mode, using grayscale image, or a combination of Doppler and B-mode, with flow presented in color and stationary structures in grayscale. A wide variety of instruments and scanners for medical ultrasound are available.

49.8.10 Selected Manufacturers of Ultrasound Products

Table 49.2 contains a representative list of ultrasound equipment and manufacturers.

TABLE 49.2 List of Products for and Manufacturers of Ultrasound Measurements

Product Type	Manufacturer
Ultrasound transducers	GE Panametrics, 221 Crescent St., Waltham, MA 02154. (800) 225-8330 http://www.rshydro.co.uk/GE-Panametrics-mid-3.html
Ultrasound transducers	Krautkramer Branson Inc., 50 Industrial Park Rd., Lewistown, PA 17044. (717) 242-0327, http://www.krautkramer.com.au/
Range measurements, air	Polaroid Corporation, Ultrasonics Components Group, 119 Windsor Street, Cambridge, MA 02139. (800) 225-1618, http://www.polaroid.com/en/stream
Pulser–receivers	Panametrics, 221 Crescent St., Waltham, MA 02154. (800) 225-8330
Pulser–receivers	JSR Ultrasonics, 3800 Monroe Ave., Pittsfield, NY 14534. (716) 264-0480, http://jsrultrasonics.com/
Ultrasound power ampl.	Amplifier Research, 160 School House Rd., Souderton, PA 18964. (800) 254-2677, http://www.amp-research.com/
Ultrasound power ampl.	Ritec, 60 Alhambra Rd., Suite 5, Warwick, RI 02886. (401) 738-3660, http://www.ritec.com/
NDE instrumentation	Panametrics, 221 Crescent St., Waltham, MA 02154. (800) 225-8330
NDE instrumentation	Krautkramer Branson Inc., 50 Industrial Park Rd., Lewistown, PA 17044. (717) 242-0327
Acoustic microscopy	Sonoscan, 530 E. Green St., Bensenville, IL 60106. (708) 766-4603, http://www.sonoscan.com/
Medical imaging	Hewlett Packard, Andover, MA; ATL, Bothell, WA; Diasonics, Milpitas, CA; Siemens Ultrasound, Issaquah, WA.
Schlieren-based imaging of acoustic fields	Optison, 568 Weddell Drive, Suite 6, Sunnyvale, CA 94089. (408) 745-0383
Optical-based imaging of acoustic fields	UltraOptec, 27 de Lauzon, Boucherville, Quebec, Canada J4B 1E7. (514) 449-2096

49.9 Advanced Topics in Ultrasound

49.9.1 Overview of Diffraction

The ultrasound theory presented thus far has emphasized basic concepts, and the applications that have been discussed tacitly assume that the field from the transducer is a plane wave field. This simplifying assumption is acceptable for applications such as basic imaging and measurements based on travel time. However, the plane wave assumption introduces errors when materials parameters (e.g., attenuation, surface roughness, and object shape) are sought to be measured with ultrasound. Therefore, to use ultrasound as a quantitative tool, an understanding is needed of the structure of the radiated acoustic field from a given transducer with a given excitation and—equally important—the ability to calculate the actual radiated field. This leads to the topic of diffraction, which is the effect that accounts for the complex structure of both radiated and scattered fields. Not surprisingly, there are direct parallels between optical diffraction and acoustic diffraction. (As a separate issue, it should be noted that the ultrasound theory presented here assumes that the wave amplitudes [pressure, displacement] are small enough so that nonlinear effects can be disregarded.)

Diffraction is basically an edge effect. Whereas a plane wave incident on a large planar interface is reflected in a specific direction, the plane wave incident on an edge results in waves scattered in many directions. Similar considerations hold for the field produced by a transducer: The surface of the transducer produces a so-called *geometric wave* that has the shape of the transducer itself; the edge of the transducer, however, generates an *edge wave* with the shape of an expanding torus. The actual pressure field is a combination of the two wave fields. Very close to a large transducer, the geometric wave dominates, and diffraction effects might not need to be considered. Over small regions far away from the transducer, the field can be approximated by a plane wave field, and diffraction does not need to be considered. However, in many practical cases, diffraction must be considered if detailed information about the pressure field is desired, and numerical methods must be employed for the calculations.

The structure of the axial field, shown in Figure 49.7b, is a direct result of diffraction. Numerical evaluation of the diffracted field from a transducer can be done in several ways: (1) use of the Fresnel or Fraunhofer integrals (not applicable close to the transducer) to calculate the field at a single frequency at a specified plane normal to the transducer axis; (2) calculation of the pressure function at any point of interest in space, based on a specified velocity function, $u(t)$, on the surface of the transducer, using Rayleigh integral; (3) decomposing the velocity field in the plane of the transducer into its plane wave components, using a 2-D Fourier transform technique, followed by a forward propagation of the plane waves to the plane of interest and an inverse Fourier transform to give the diffracted field; or (4) use of finite element methods to calculate the diffracted field at any point or plane of interest. In the following, methods (1) and (2) will be described.

49.9.2 Fresnel and Fraunhofer Diffraction

Let the velocity function on the surface of the transducer, $u(x, y)$, be specified for a particular frequency, ω. Assume that the transducer is located in the $(x, y, 0)$ plane and that one is interested in the pressure field in the (x_0, y_0, z) plane. The Fresnel diffraction formulation [18] assumes that the paraxial approximation is fulfilled; requiring z to be at least five times greater than the transducer radius, in which case the *Fresnel diffraction integral* applies:

$$p(x_0, y_0, z, \omega) = \frac{A_0}{\lambda_z} \iint_s u(x, y, \omega) \exp\left[-jk\frac{x^2 + y^2}{2z}\right] \exp\left[jk\frac{x_0 x + y_0 y}{z}\right] dx\,dy \tag{49.42}$$

where

s is the surface of the transducer

A_0 is a constant

If one defines the two first terms of the integrand as some complex spatial function, $\Gamma(x, y)$, then Equation 49.42 is a scaled Fourier transform of $\Gamma(x, y)$.

If $k(x^2 + y^2)/2z \ll 1$, or, equivalently, $z > 10\, a^2/\lambda$, the second term in Equation 49.42 can be ignored, and the resulting equation is called the *Fraunhofer diffraction integral:*

$$p(x_0, y_0, z, \omega) = \frac{A_0}{\lambda z} \iint_s u(x, y, \omega) \exp\left[jk \frac{x_0 x + y_0 y}{z} \right] dx dy \tag{49.43}$$

Thus, one can only use the Fraunhofer integral for calculating the far-field diffraction. From Equation 49.43, one can make the interesting observation that the far field of a transducer is a scaled version of the Fourier transform of the source.

49.9.3 Pressure Function at a Given Field Point, Based on Rayleigh Integral

While the Fresnel and Fraunhofer diffraction methods are CW methods, calculation of pressure from the Rayleigh integral is fundamentally an impulse technique and is as such better suited for analysis of pulse-echo measurements. The basis for the calculation is the *velocity potential impulse response*, $h(\vec{\mathbf{r}}, t)$, obtained from the Rayleigh integral:

$$h(\vec{\mathrm{r}}, t) = \frac{1}{2\pi} \iint_s \frac{\delta(t - r'/c)}{r'}\, dS \tag{49.44}$$

In Equation 49.44, r' is the distance from dS on the surface of the transducer to the field point, defined by the position vector $\vec{\mathbf{r}}$, and $\delta(t)$ is the Dirac delta function. As can be seen, $h(\vec{\mathbf{r}}, t)$ is the result of an impulsive velocity excitation on the surface of the transducer and is a function of both time and a spatial location. It is important to note that $h(\vec{\mathbf{r}}, t)$ exists in analytical form for several transducer geometries and, by extension, for annular and linear array transducers [19].

For the case of an arbitrary velocity function, $u(t)$, on the transducer surface, the corresponding velocity potential, $\phi(\vec{\mathbf{r}}, t)$, is obtained as

$$\phi(\vec{\mathbf{r}}, t) = u(t) \otimes h(\vec{\mathbf{r}}, t) \tag{49.45}$$

where $\otimes$ refers to time domain convolution. Both particle velocity, $u(\vec{\mathbf{r}}, t)$, and pressure, $p(\vec{\mathbf{r}}, t)$, can be found from $\phi(\vec{\mathbf{r}}, t)$, as follows:

$$u(\vec{\mathbf{r}}, t) = \nabla \phi(\vec{\mathbf{r}}, t) \tag{49.46}$$

$$p(\vec{\mathbf{r}}, t) = -\rho_0 \frac{\partial}{\partial t} \phi(\vec{\mathbf{r}}, t) \tag{49.47}$$

where ∇ is the gradient operator.

Thus, from the preceding expressions, the pressure can be calculated for any field point, $\vec{\mathbf{r}}$, when $u(t)$ and the transducer geometry are defined. In this calculation, all diffraction effects are included. However, given the high frequency content in $h(\vec{\mathbf{r}}, t)$ and in particular in the time derivative of $h(\vec{\mathbf{r}}, t)$, care must be taken to avoid aliasing errors, as described in [19].

49.9.3.1 Received Signal in Pulse-Echo Ultrasound

The expression in Equation 49.47 allows for quantitative evaluation of the pressure field for an arbitrary point, line, or plane. However, it does not describe the calculation of the received signal in a pulse-echo system.

Consider a small planar reflector, placed in a homogeneous medium, and referred to as *dR*. The reflector has the area *dA*. The dimensions of *dR* must be small with respect to the shortest wavelength in the insonifying pulse. The location and the orientation of the planar reflector is given by $\vec{\mathbf{r}}$ and $\vec{\mathbf{n}}$, respectively, where $\hat{\mathbf{n}}$ is a unit normal vector to the small reflector.

The voltage from the receiving transducer in a pulse-echo system due to *dR* is termed $dv(\vec{\mathbf{r}}, t)$ and can be determined when $u(t)$ is specified. The electroacoustic transfer function for both the transmitting and the receiving transducer is assumed to be unity for all frequencies. For the case when the acoustic impedance of *dR* is much higher than that of the medium, $dv(\vec{\mathbf{r}}, t)$ is given as [20]:

$$dv(\vec{\mathbf{r}}, t) = A_0 \rho_0 \frac{\cos[\psi(\vec{\mathbf{r}})]}{c_0} \left[h(\vec{\mathbf{r}}, t) \otimes h(\vec{\mathbf{r}}, t) \otimes \frac{\partial^2}{\partial t^2} u(t) \right] dA$$

$$= A_0 \cos[\psi(\vec{\mathbf{r}})]\ u(t) \otimes \frac{\rho_0}{c_0} \left[\frac{\partial^2}{\partial t^2} (h(\vec{\mathbf{r}}, t) \otimes h(\vec{\mathbf{r}}, t)) \right] dA \tag{49.48}$$

where

A_0 is determined by the reflection coefficient of the reflector
The term $\cos[\psi(\vec{\mathbf{r}})]$ is a correction term (obliquity factor)
$\psi(\vec{\mathbf{r}})$ is the angle between $\hat{\mathbf{n}}$ and the propagation direction of the wave field at $\vec{\mathbf{r}}$

For an extended surface, the received voltage can be found by decomposing the surface into small reflectors and calculating the total received signal as the sum of the contributions from all the small reflectors. An efficient numerical technique for this type of integration has been developed [21].

References

1. C. M. Fortunko and D. W. Fitting, Appropriate ultrasonic system components for NDE of thick polymer-composites, in D. O. Thompson and D. E. Chimenti, *Review of Progress in Quantitative Nondestructive Evaluation, Vol. 10B*. New York: Plenum Press, 1991, pp. 2105–2112.
2. C. R. Hill, Medical imaging and pulse-echo imaging and measurement, in C. R. Hill (ed.), *Physical Principles of Medical Ultrasound*, New York: Halsted Press, 1986, Chapters 7 and 8, pp. 262–304.
3. L. C. Lynnworth, *Ultrasonic Measurements for Process Control*, San Diego, CA: Academic Press, 1989, pp. 53–89.
4. L. E. Kinsler, A. R. Frey, A. B. Coppens, and J. V. Sanders, *Fundamentals of Acoustics*, 3rd edn., New York: John Wiley & Sons, 1982, p. 106.
5. J. D. Achenbach, *Wave Propagation in Elastic Solids*, 1st edn., New York: Elsevier Science, 1975, p. 123.
6. L. E. Kinsler, A. R. Frey, A. B. Coppens, and J. V. Sanders, *Fundamentals of Acoustics*, 3rd edn., New York: John Wiley & Sons, 1982, pp. 115–117.
7. L. E. Kinsler, A. R. Frey, A. B. Coppens, and J. V. Sanders, *Fundamentals of Acoustics*, 3rd edn., New York: John Wiley & Sons, 1982, pp. 127–133.
8. J. Saniie and N. M. Bilgutay, Quantitative grain size evaluation using ultrasonic backscattered echoes, *J. Acoust. Soc. Am*., 80, 1816–1824, 1986.
9. E. P. Papadakis, Scattering in polycrystalline media, in P. D. Edmonds (ed.), *Ultrasonics*, New York: Academic Press, 1981, pp. 237–298.
10. S. M. Handley, M. S. Hughes, J. G. Miller, and E. I. Madaras, Characterization of porosity in graphite/epoxy laminates with polar backscatter and frequency dependent attenuation, *1987 Ultrasonics Symposium*., Denver, CO, 1987, pp. 827–830.
11. J. C. Bamber, Attenuation and absorption, in C. R. Hill (ed.), *Physical Principles of Medical Ultrasound*, New York: Halsted Press, 1986, pp. 118–199.

12. L. E. Kinsler, A. R. Frey, A. B. Coppens, and J. V. Sanders, *Fundamentals of Acoustics*, 3rd edn., New York: John Wiley & Sons, 1982, pp. 176–185.
13. M. O'Donnell, L. J. Busse, and J. G. Miller, Piezoelectric transducers, in P. D. Edmonds (ed.), *Ultrasonics*, New York: Academic Press, 1981, pp. 29–65.
14. Collaboration, An American National Standard—IEEE standard on piezoelectricity, IEEE Transactions on Sonic and Ultrasonic, v SU-31, n 2, pp. 1–55, March 1984.
15. G. S. Kino, *Acoustic Waves*, Englewood Cliffs, NJ: Prentice-Hall, 1987, pp. 17–83 and 554–557.
16. L. C. Lynnworth, *Ultrasonic Measurements for Process Control*, San Diego, CA: Academic Press, 1989, pp. 245–368.
17. L. C. Lynnworth, *Ultrasonic Measurements for Process Control*, San Diego, CA: Academic Press, 1989, pp. 537–557.
18. V. M. Ristic, *Principles of Acoustic Devices*, New York: John Wiley & Sons, 1983, pp. 316–320.
19. D. P. Orofino and P. C. Pedersen, Multirate digital signal processing algorithm to calculate complex acoustic pressure fields, *J. Acoust. Soc. Am*., 92, 563–582, 1992.
20. A. Lhemery, Impulse-response method to predict echo responses from targets of complex geometry. I. Theory, *J. Acoust. Soc. Am*., 90, 2799–2807, 1991.
21. S. K. Jespersen, P. C. Pedersen, and J. E. Wilhjelm, The diffraction response interpolation method, *IEEE Trans. Ultrason. Ferroelectr. Freq. Control*, 45, 1485–1496, November 1998.

Further Information

Edmonds, P. D. (ed.), *Ultrasonics*, (Vol. 19 in the series: *Methods of Experimental Physics*). New York: Academic Press, 1981, in-depth description of ultrasound interaction with many types of materials, along with discussion of ultrasound measurement approaches.

Ensminger, D. and Bond, L. J., *Ultrasonics: Fundamental, Technologies, and Applications*, 3rd edn., Boca Raton, FL: CRC Press, 2012.

Ensminger, D. and Stulen, F. B., *Ultrasonics: Data, Equations and Their Practical Uses*, Boca Raton, FL: CRC Press, 2009.

Jensen, J. A., *Estimation of Blood Velocities Using Ultrasound*, Cambridge, U.K.: Cambridge University Press, 1996, a very up-to-date book about ultrasound Doppler measurement of flow and the associated signal processing.

Kinsler, L. E., Frey, A. R., Coppens, A. B., and Sanders, J. V., *Fundamentals of Acoustics*, 3rd edn., New York: John Wiley & Sons, 1982, a very readable introduction to acoustics.

Kremkau, F. W., *Diagnostic Ultrasound: Principles and Instruments*, 5th edn., Philadelphia, PA: W. B. Saunders Co., 1998, a very readable and up-to-date introduction to medical ultrasound.

Papadakis, E. P. (ed.), *Ultrasonic Instruments and Devices: Reference for Modern Instrumentations, Techniques, and Technology*, *in the series Physical Acoustics*, Vol. 40, New York: Academic Press, 1998.

Rose, J. L., *Ultrasonic Waves in Solid Media*, Cambridge, U.K.: Cambridge University Press, 1999.

Ultrasonic Scientific, Principles of the Ultrasonic Measurement. http://www.ultrasonic-scientific.com/Technology/Technology%20-%20principles.htm (accessed on July 27, 2012).

VI

Flow and Spot Velocity

50

Capillary-Type Mass Flow Meter

Reza Pakdaman Zangabad
Sabanci University

Manouchehr Bahrami
University of Tabriz

In many processes, mass flow rate, rather than volume flow rate, is the desired parameter because volumetric flow measurements are less reliable than are mass flow measurements. Since changes in gas temperature and pressure will affect the density of a fixed volume of gas, thermal mass flow meters and controllers, unlike rotameters, turbine meters, and other volumetric flow devices, are relatively immune to changes in inlet temperature and pressure. Because these instruments directly measure molecular flow, they provide the most reliable, repeatable, and accurate method for delivering material from a supply volume to a process at a desired rate. Features, such as direct electronic readout, fast response, exceptional sensitivity at low flow rate, negligible pressure drop, no moving parts, simple installation, unobstructed straight through flow path, absence of temperature or pressure corrections, and superior retain accuracy over a wide range of flow rates, make thermal mass flow meters a superior alternative to conventional flow meters in many important applications. Some other advantages of this type of flow meter are accuracy in a 2% range, low flow sensitivity, reliability, and long life with advances in electronic technology; in a sense, these flow meters are getting smarter and more capable with microprocessor computing power, thus expanding the range of their usage.

The technology of the thermal mass flow meter was initially inspired by the space program's need for a reliable, low-power device to measure airflow in an astronaut's space suit. In recent years, they have become the most important instruments for gas flow measurement in the process industry, offering considerably lower cost than the Coriolis alternative. The only requirement for use of this type of flow meter is that the fluid being metered should be very clean and free from solid or liquid particles that may block the sensor passage. One of the big companies fabricating these sensors is "Sierra Instrumentation" [1]. Today, thermal mass flow meters are used to measure the flow of gases in a growing range of applications particularly in the electronic and chemical industries. The addition of an electromagnetic control valve turns the mass flow meter into a mass flow controller (MFC). Thermal mass flow meters are also employed for monitoring or controlling mass-related processes such as chemical reactions that depend on the relative masses of unreacted ingredients. They are thus widely used in automotive industry, utility services, petroleum and gas industries, HVAC, R & D, raw material industries, and food processing.

In short, thermal MFCs and mass flow meters for gases are among the standard instruments used in industrial laboratory and production processes.

Heat transfer is defined as the movement of energy due to a difference in temperature. It is characterized by the three mechanisms of conduction, convention, and radiation. Heat conduction takes place through different mechanisms in different media. Theoretically, it takes place in a gas through collisions of the molecules, in a fluid through oscillations of each molecule in a "cage" formed by its nearest neighbors, in metals mainly by electrons carrying heat, and in other solids by molecular motion that in crystals take the form of lattice vibrations. Typical for heat conduction is that the heat flux is proportional to the temperature gradient. Heat convection takes place through the net displacement of a fluid, which transports the heat content in a fluid through the fluid's own velocity. The term convection is also used for the heat dissipation from a solid surface to a fluid, where the heat transfer coefficient and the temperature difference across a fictitious film describe the flux. It is worthwhile to mention that both types measure fluid mass flow rate by means of the heat convected from a heated surface to the flowing fluid. The principles of operation of the two types are both thermal in nature but are so substantially different that two separate standards are required. Additionally, their applications are much different. Thermal dispersion flow meters are commonly used for general industrial gas flow applications in pipes and ducts, whereas capillary types are primarily used for smaller flows of clean gases or liquids in tubes.

50.1 Principles of Thermal Mass Flow Meters

The heat transfer scenario in the sensor tube consists of heat generation in the heating wire or over the tube wall, conduction along the tube wall, convection into the gas, and heat loss to the surroundings by natural convection, all the phenomena occurring simultaneously.

In general, there are three categories of thermal mass flow meters: insertion type, calorimetric sensors, and time-of-flight sensors. Thermal mass flow meters that measure the effect of the flowing fluid on a hot body are usually called insertion-type thermal mass flow meters. Those that measure the passage time of a heat pulse over a known distance are usually identified as time-of-flight sensors. Thermal mass flow meters that measure the displacement of temperature profile around the heater and also are modulated by the fluid flow are called calorimetric sensors.

Figure 50.1 shows the basic schematic of insertion type. As the figure demonstrates, a heater inside the pipeline heats the fluid to specific temperature that depends on the size of the pipeline. After reaching the desired temperature, the heating power is turned off, and consequently, the temperature will start to decrease. According to the speed of temperature decreasing in temperature profile diagram, the velocity of fluid can be realized. By this approach, the more rapid decrease, for the example, is due to the higher fluid velocity; the slower decrease correspondingly is due to lower fluid velocity.

In the time-of-flight type one, the working principle is as follows: by bringing the heater to a desired temperature and keeping it constant, fluid rate can be measured through sensing the temperature at a known distance away from heater. In this case, the high sensed temperature is due to the low fluid velocity, and the low sensed temperature is the result of high fluid velocity.

As Figure 50.2 depicts, by increasing fluid velocity, sensed temperature will be decreased. The applied heat power to heater is determined by characteristics of conduit and fluid. For example, increasing the temperature can result in better accuracy in conduits with bigger diameter.

50.2 Capillary-Type Thermal Mass Flow Meter

This type of mass flow meter can be classified as calorimetric sensors. In the capillary-type thermal mass flow meter, the sensor is a small diameter stainless steel or constantan capillary, heated by an electric current. The heat is supplied either at the central point or over the whole length of the tube. In the absence of gas flow, the temperature profile is symmetric about the midpoint. Gas flow through the capillary tube cools the entry section while heating the exit. Cooling and heating introduce an asymmetry

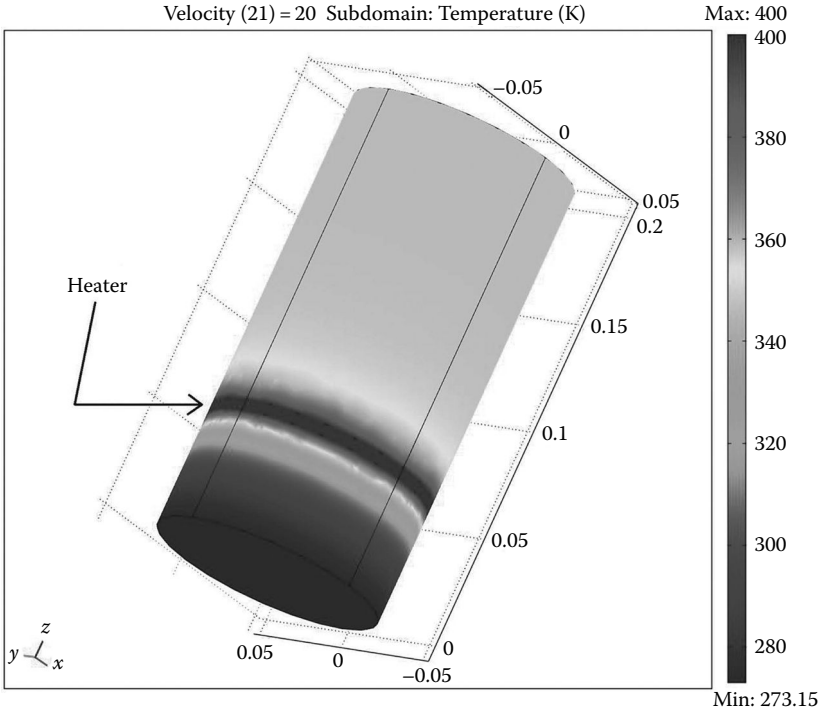

FIGURE 50.1 Basic schematic of thermal mass flow meter. Evenly heat distribution makes a linear relation between temperature and fluid velocity.

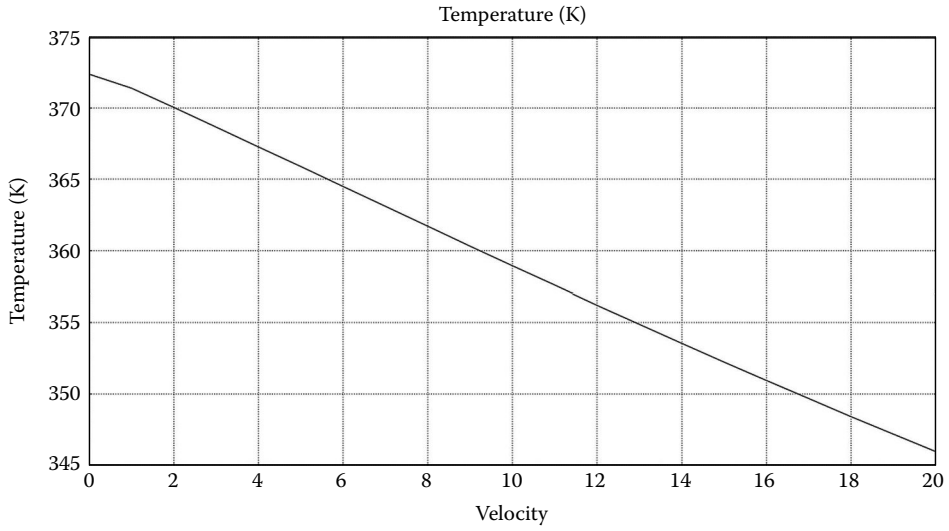

FIGURE 50.2 Linearly varying between sensed temperature and fluid velocity.

in the temperature profile, which is a measure of the fluid flow rate. The asymmetry is measured in terms of difference of temperature between two points on the capillary tube equidistant from the mid-point. A fluid flow shunt (bypass line) is added in parallel to the sensor tube to increase the range of the meter by several orders of magnitude. Flow through both the capillary and the bypass line is required to be laminar, often limited to the Reynolds number of 50–100 in the sensor (capillary) and 500–1500

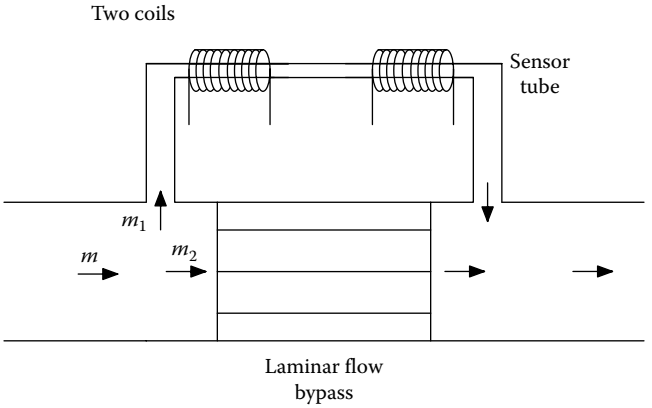

FIGURE 50.3 Structure of basic capillary thermal mass flow meter.

in the bypass line. By maintaining laminar flow within each portion, the split ratio between the sensor and the bypass flow element is maintained independent of the Reynolds number, and the total flow rate can be measured through the sensor path.

As gas from the source adding to the inlet of capillary mass flow meter, it goes through four stages and conditioning that eliminates all effects of flow disturbances and nonuniformities. Accurately achieving laminar flow is the key to assuring either linearity or accuracy. The laminar flow element (LFE) generates a small pressure drop, forcing a very small portion of gas flow through the stainless steel capillary tube where measurement occurs. Figure 50.3 shows a basic schematic of a capillary tube. The LFE plays an important role in capillary flow meter. It must be designed so that the process gas maintains a smooth, uniform flow profile called laminar flow (in other words, the gas has a Reynolds number below 2000). As a result, the small fraction of the total flow measured in the sensor tube (m_1) remains in direct proportion to the gas flowing through the LFE bypass (m_2). If we can measure the flow in the sensor tube, we can calculate the total mass flow rate m. Both m and m_1 are in mass flow rate units of g/s or kg/s:

$$m = m_1 + m_2 \tag{50.1}$$

$$m = m_1\left(1 + \frac{m_2}{m_1}\right) = km_1 \tag{50.2}$$

The sensor tube is precisely wrapped around with two platinum wire coils and heated to form pair resistance temperature detectors known as RTDs, and because they are on the outside of the tube, this sensing technology is noninvasive. When no gas flows, the capillary-tube temperature profile is symmetric around midpoint. It is hotter in the middle and cooler in the ends (Figure 50.4). As gas flows through the heated capillary tube, the gas molecules are also heated and carry the heat downstream; consequently, the temperature profile shifts downstream. This variation in the temperature profile affects the coil resistance. The two identical RTD coils are equally heated by connecting onto an electronic circuit. This method provides an easy method to measure any change in temperature by measuring the change in voltage of the circuit created by the RTD coils. The relative cooling of the upstream coil and the relative heating of downstream coil create a difference in the resistance of two RTDs. This difference in resistance is measured by electronics circuits and converted to the mass flow signal. This signal is directly proportional to the total mass flow.

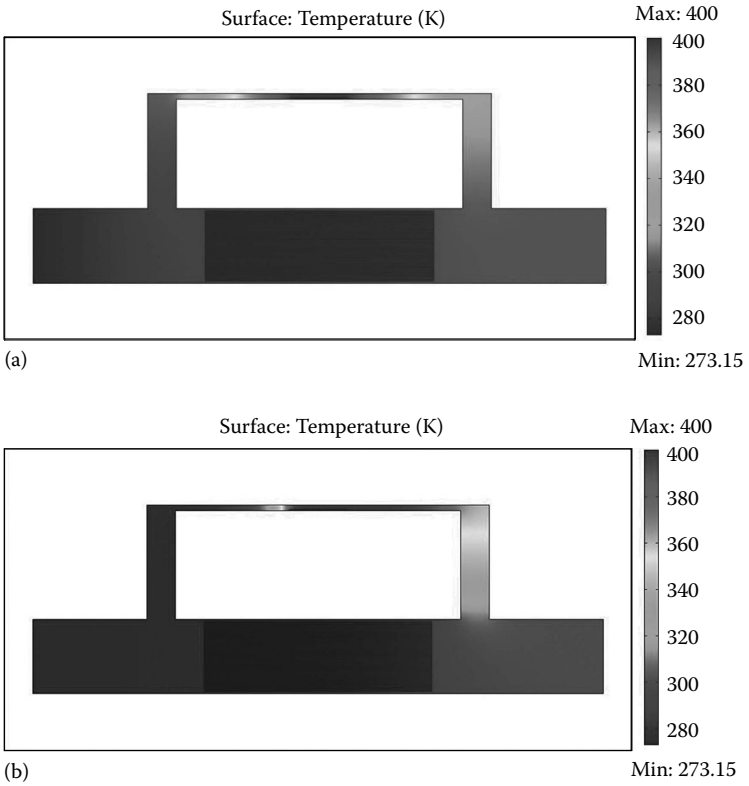

FIGURE 50.4 (a) Temperature profile of capillary zone while there is no fluid. (b) Temperature profile of capillary zone while a fluid passes through it.

Figure 50.4a offers a temperature profile when no fluid passes through the capillary tube and it demonstrates the midpoint's symmetry; Figure 50.4b depicts an exaggeration temperature profile, while a fluid passes through capillary and eventuates in shifting in the profile and creates asymmetric profiles [2].

As we know, heat transfer follows the first law of thermodynamics, commonly referred to as the principle of conservation of energy. Since the internal energy (***U***) is not a common quantity to measure, the basic law is usually rewritten in the term of temperature (***T***). So, the resulting heat equation used for measuring and simulating is written as

$$\rho C_p\left(\frac{\delta T}{\delta t}+(\mathbf{u}\cdot\nabla)T\right)=-(\nabla\cdot\mathbf{q})+\tau:\mathbf{S}-\frac{T}{\rho}\frac{\delta\rho}{\delta T}\bigg|_p\left(\frac{\delta p}{\delta t}+(\mathbf{u}\cdot\nabla)p\right)+Q \tag{50.3}$$

where

ρ is the density (kg/m^3)
C_p is the specific heat capacity at constant pressure (J/(kg·K))
T is absolute temperature (K)
u is the velocity vector (m/s)
q is the heat flux by conduction (W/m^2)
p is pressure (Pa)

S is the strain rate tensor (1/s) that defines as $\mathbf{S} = \frac{1}{2}\left(\nabla\mathbf{u} + (\nabla\mathbf{u})^{\mathrm{T}}\right)$, τ is the viscous stress tensor (Pa) and represents as $\tau = \eta(2\mathbf{s} - (2/3)(\nabla \cdot \mathbf{u})I)$ with viscosity η (Pa·s), and I denotes the identity tensor. In Equation 50.3, Q contains heat sources other than viscous heating (W/m^3).

It is often appropriate to assume that the fluid density is almost constant, i.e., the given fluid is incompressible.

$$\rho\frac{\delta u}{\delta t} - \nabla\cdot\left[\eta\left(\nabla u + (\nabla u)^{\mathrm{T}}\right)\right] + \rho(u\cdot\nabla)u + \nabla p = F \tag{50.4}$$

$$\nabla\cdot\mathbf{u} = 0 \tag{50.5}$$

Equations 50.4 and 50.5 depict momentum equation and continuity condition for incompressible fluids, respectively. In the aforementioned equations, F is volume force and other variables are the same as defined previously.

Another important part of sensor that must be designed carefully in order to fulfill our expectations about achieving laminar flow and all the aforementioned characteristics is LFE. The flow sensor is made of a long, thin capillary tube; therefore, the flow through this sensor will be laminar. If the flow through the LFE is also laminar, then the ratio between the two flows can be considered constant for all flow rates. Therefore, the flow measured by the flow sensor is a ratio of the flow through the flow meter. Changing the capacity of the flow element will change the capacity of a flow meter. An example of such a flow element is given in Figure 50.5. The flow is forced through numerous tiny channels, which have a typical capacity of 10 mL$_n$/min (of air) at 35 mbar. The capacity of the flow element (and consequently of the flow meter) can be set by choosing the number of flow elements, each containing a specified number of channels. In this way, flow instruments can be manufactured from 10 mL$_n$/min up to 1000 L$_n$/min and even higher using single types of sensors.

Making the sensor tube very small will eventuate in restricting the mass flow rate through the tube (m_1); so by carefully designing of the LFE bypass, then we limit the solution of these equations to a

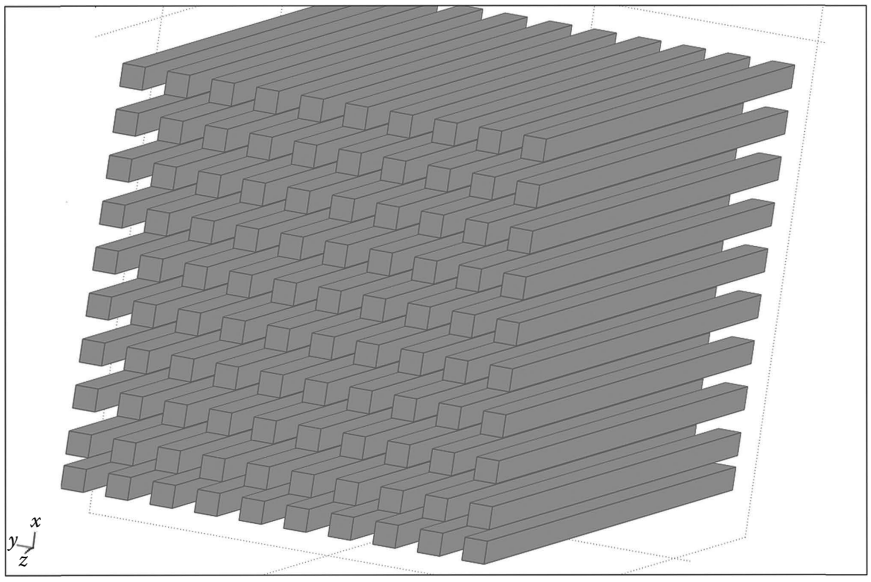

FIGURE 50.5 Basic structure of LFE in capillary-type thermal mass flow meter.

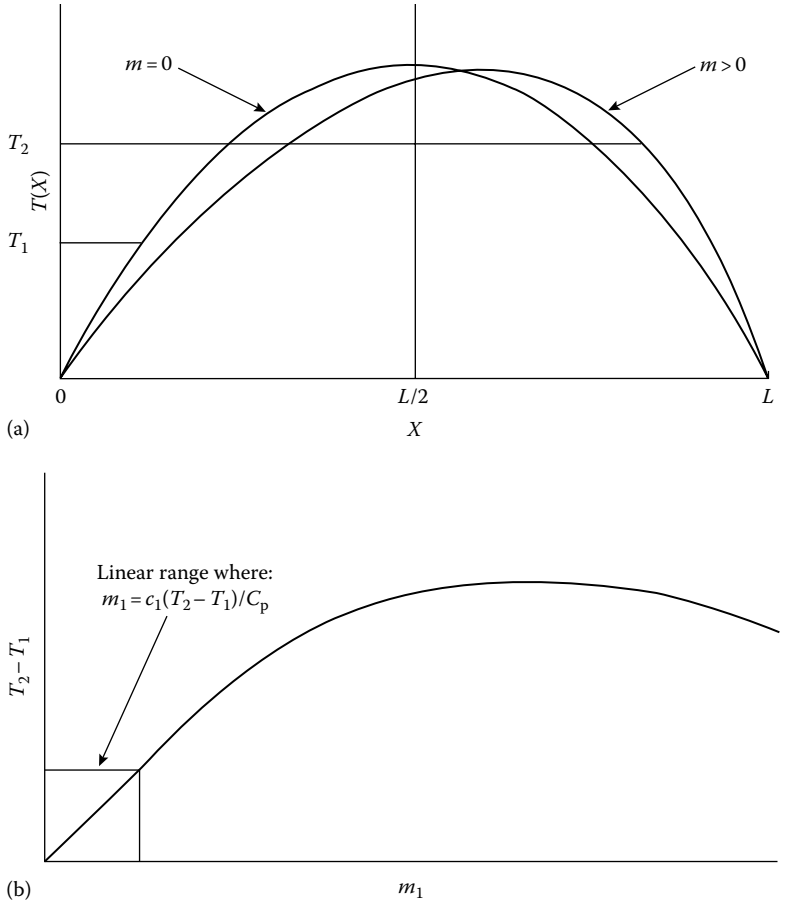

FIGURE 50.6 (a) Capillary-tube zone temperature distribution. (b) Capillary-tube sensor linear range for a given gas.

narrow range over which m_1 is directly proportional to $T_2 - T_1$, the difference in the average temperatures of the downstream coil (T_2) and the upstream coil (T_1).

In the linear range shown earlier in Figure 50.6a, we have for any given gas

$$m_1 C_p = C_1(T_2 - T_1) \tag{50.6}$$

where C_p and C_1 are the coefficient of specific heat for the given gas and a constant for the sensor applicable to all gases (in the linear range only), respectively.

From Figure 50.3, we have derived $m = km_1$. Substituting this into Equation 50.6 earlier, we get

$$mC_p = C(T_2 - T_1) \tag{50.7}$$

where $C = kC_1$, that is again a constant for sensor but applicable to all gases.

Equation 50.7 illustrates how the only parameter required in order to enable us to measure flow is temperature. Consequently, by measuring the upstream and downstream temperature, we will reach to our goal.

Based on the aforementioned discussion, the sensor was designed and simulated using COMSOL Multiphysics in order to verify the theory. Figure 50.7a shows the temperature distribution of sensor in capillary zone and Figure 50.7b shows the temperature profile.

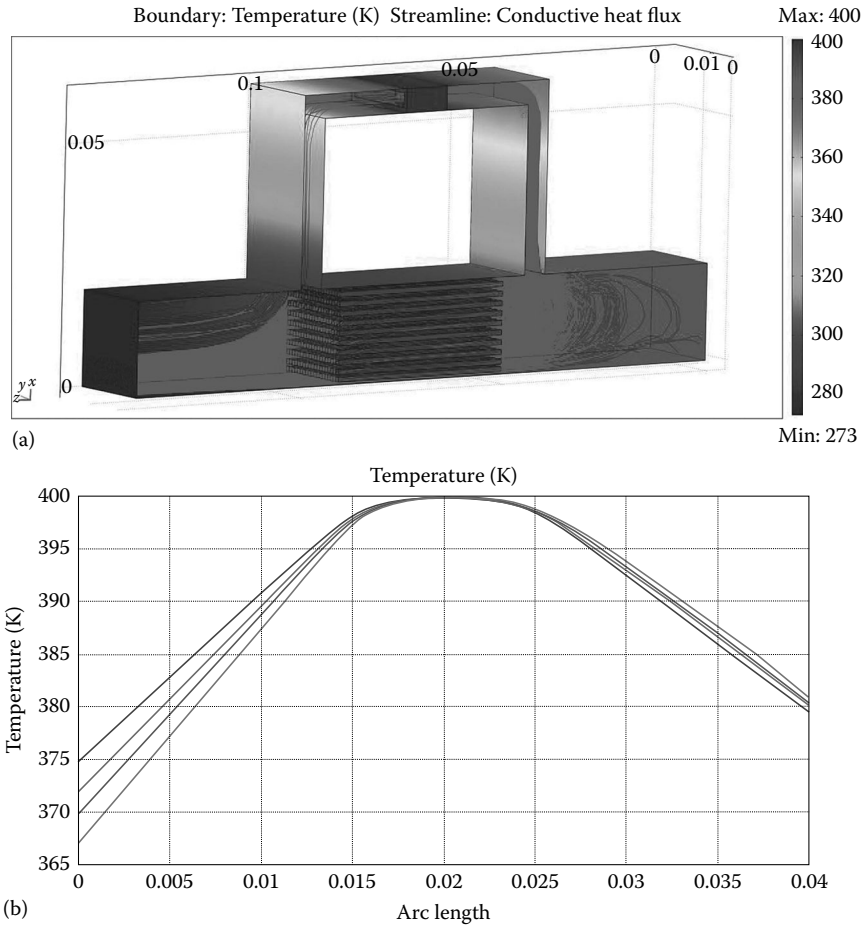

FIGURE 50.7 (a) Simulation result of temperature distribution over capillary zone in the sensor. (b) Simulated profile temperature for capillary-type thermal mass flow meter.

Figure 50.4a demonstrates the effect of LFE in order to have both laminar flows through the capillary and temperature distribution of capillary tube. As it appears, the temperature profile was shifted downstream (right-hand side), and consequently, the downstream temperature is a little higher than that of upstream. The temperature sensor that is located at those two points thus can measure the temperature. The basic and simple circuit for such sensing principle is the Wheatstone bridge, where in this sensing process, the temperature values are changed to resistor and then voltage values.

50.3 Electronic Readout Circuit

A major positive feature of the thermal flow meter is the electrical voltage output and direct digital readout proportional to the mass flow rate through the sensor that is ensured by providing an appropriate electronic circuitry. All the electronic components can be mounted on a PCB that is attached to the body of the flow meter. The main functions of the electronic circuitry are

a. To provide heating current to the sensor
b. To sense, amplify, and display the thermocouple output voltage

Figure 50.8 shows a block diagram of the electric circuit for sensing part.

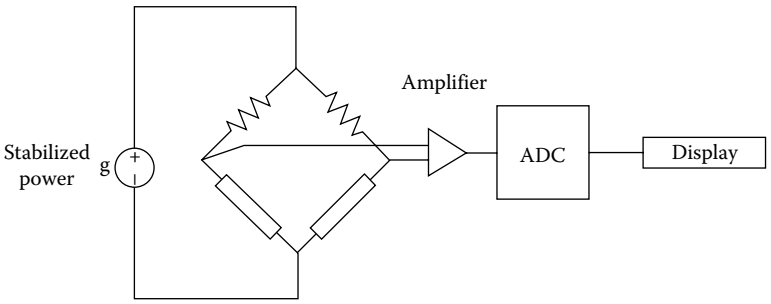

FIGURE 50.8 Basic schematic of electronic readout circuit.

The main sections of the electronic circuit are as follows:

1. DC power supply
2. Current source
3. Sensor assembly
4. Instrumentation amplifier (AD522)
5. Analog-to-digital converter (ADC) and display

50.3.1 Power Supply

For example, the power supply circuit (Figure 50.9) can be designed for an input voltage of 24 ± 10% V that is stabilized to 18 V DC. It can be built using an IC 7818–type voltage regulator, a few capacitors, and the diodes. The IC LM7818 is a three-terminal voltage regulator, which holds the load voltage constant even if the load current and the source voltage change. It needs a minimum input-to-output difference of 2 V, i.e., $(V_i - V_o) \geq 2$ V. For obtaining a regulated output of 18 V, the IC needs an input voltage between 20 and 37 V. A diode is used at the input for protection against accidental polarity reversal.

We have used a 1N4007 diode with a forward bias voltage drop of 0.7 V. Thus, 20.7 V is the minimum input voltage at which the regulator maintains 18 V at the output. We have specified the input voltage to be 24 ± 10% V, i.e., 21.6 to 26.4 V. The maximum output current of the IC is 500 mA. Actual dissipation in the proposed circuits has been estimated to be less than 200 mA. A small heat sink appropriate to the current requirement has been fitted with the IC. The power supply unit is fabricated on the same PCB.

50.3.2 Current Source

A high-frequency current source is used for heating the sensor tube. The heating element (sensor tube) is of very low resistance (50 mΩ) (taking into consideration that the two halves of the capillary tube come in parallel across the heating current source). An equivalent electric circuit of the sensor tube is shown in Figure 50.10.

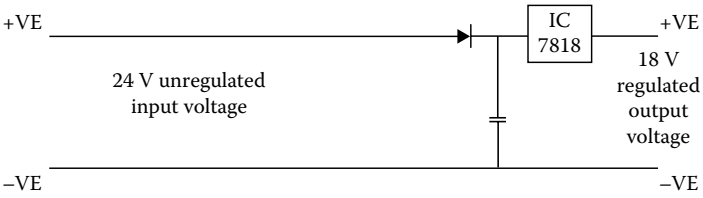

FIGURE 50.9 Circuit diagram of a regulated power supply.

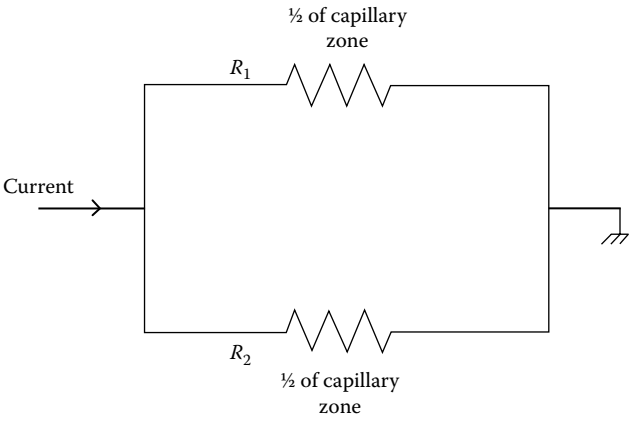

FIGURE 50.10 Equivalent electric circuit of the sensor tube.

For delivering a steady power of approximately 0.25 W, either alternating current (AC) or direct current (DC) could be used. But if a DC voltage is applied, it will be indistinguishable from the thermocouple voltage generated and therefore impossible to measure the temperature asymmetry over the sensor tube. Therefore, the solution to this problem is application of an AC voltage as the heating current so that its remnants can easily filter out from the thermal *emf* during measurement. The applied frequency depends on the transformer size and frequency-handling capability of the active devices (IC, transistor, etc.). In this case, one device can be PWM IC SG3525 as the oscillator with 10% dead time between commutations, as shown in Figure 50.11. A ferrite-ring transformer can be used to convert the power into low voltage and high current (e.g., 0.15 V RMS, 3A). This transformer also provides isolated voltage supply for other sections (amplifier, ADC, and display) through auxiliary windings and rectifiers. IC SG3525 is a pulse-width modulator (PWM) designed for use with switched-mode power supply (SMPS). Another useful feature of this chip is its control over the dead time. When a high frequency is used, self-impedance of the coil is high; hence, the device draws a rather small amount of current from the power supply.

By using high frequency, the audible noise effects from the transformer due to magnetostriction are also eliminated. At higher frequencies, the transformer size becomes smaller for the same power output, but at the same time, the electronic devices in the circuit consume more power. The two-phase output of the IC is buffered (isolated from the following circuits) through transistors (BC 547, BEL 187, BEL 188) to drive the primary winding of the toroidal transformer (ferrite core). The prime output of the transformer in the thick secondary winding is 0.15 V RMS and can provide 3 A of current. This output is used to heat the sensor. Two more auxiliary windings provide isolated voltages of ±5 and 9 V for the amplifier and meter sections.

50.3.3 Sensor Assembly

The heating current source is connected to the center of the capillary tube, and the return path of the current is through the brass body of the sensor assembly (see Figure 50.12). Thus, the sensor tube is split into two equal parts, and the current through each half of the tube becomes half of the current supplied by the source. The potential difference between the points A and B (which are located at equal distance from the midpoint C) vanishes all the time, and the thermal emf generated by temperature asymmetry can be comfortably measured. The small alternating potential difference caused by fabrication errors and resulting current asymmetry can be easily filtered.

Constantan wires are brazed at optimized locations (A and B) to make the constantan-SS constantan differential thermocouple. Connections (*Va*, *Vb*, and *Vc*) from the thermocouples and the midpoint are terminated on a small PCB at the base of the sensor body.

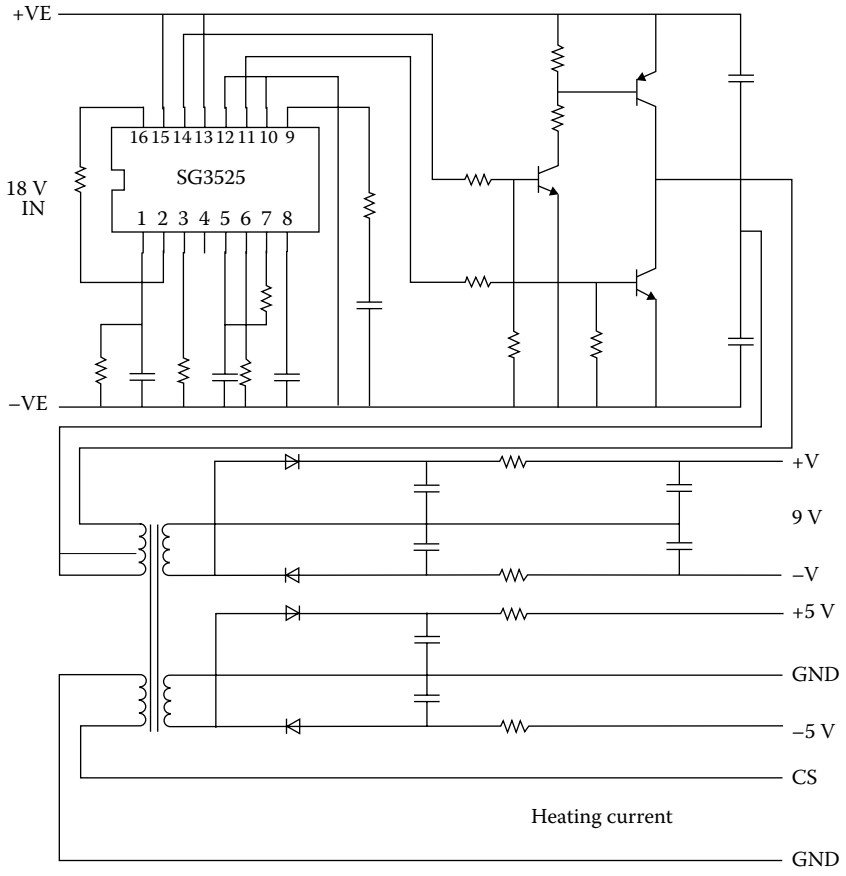

FIGURE 50.11 Proposed current source and power supply.

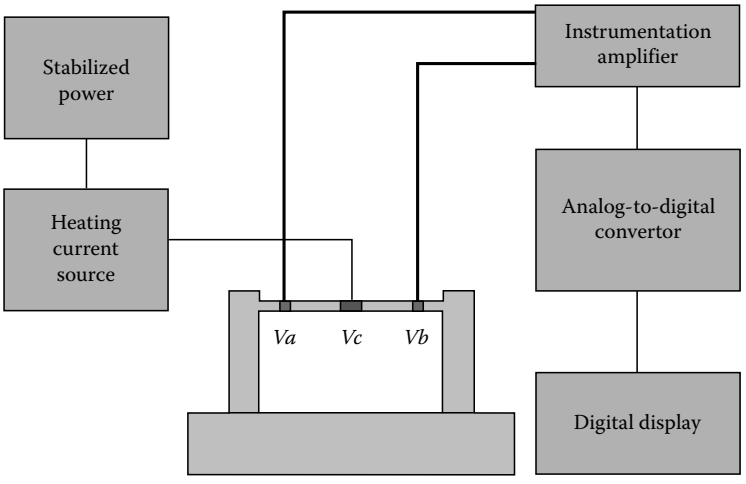

FIGURE 50.12 Basic topology of sensor assembling.

50.3.4 Instrumentation Amplifier (AD522)

The AD522 is a precision IC instrumentation amplifier designed for data acquisition applications requiring high accuracy under worst-case operating conditions. An outstanding combination of high linearity, high common-mode rejection, low voltage drift, and low noise makes the AD522 suitable for use in many 12-bit data acquisition systems. An instrumentation amplifier is usually employed as a bridge amplifier for resistance transducers (thermistors, strain gages, etc.) found in process control, instrumentation, data processing, and medical testing. The operating environment is frequently characterized by low signal-to-noise levels, fluctuating temperatures, imbalanced input impedances, and remote location, all of which hinder recalibration.

50.3.5 Analog-to-Digital Converter and Display

An ADC must be used to convert the analog output of the differential thermocouple into a more sophisticated and easily readable digital display. An inbuilt three-and-half-digit LCD panel meter is one of the devices to cover both ADC and display.

The input sensitivity of the meter is 200 mV DC. The output display gives a direct readout for the flow rate. The digital display cannot exceed the three-and-half digits 1999. Hence, it can read a maximum flow rate of 19.99 slpm. If the flow rate exceeds 19.99 slpm, the rightmost three digits will be blank and only the left hand "1" will appear on the display, indicating an "over-range" condition. After the over-range condition has been removed, it may take several seconds for the flow meter to recover and resume normal operation. This will not harm the instrument.

50.4 Accuracy

The following method is designed to determine the precision and accuracy of the prototype thermal mass flow meter. The experimental setup is employed in series with a known mass flow meter. After the installation of the experimental unit and covering the electronic warm-up period, test loop is purged with clean, dry nitrogen gas for a minimum of 5 min. The flow rate is maintained at the full-scale reading of the prototype flow meter. Once the setup is ready, the flow rate is varied over full range of the instrument in discrete steps in both increasing and decreasing orders. The readings on the test and standard instruments are noted down and analyzed for precision and accuracy.

The bias in a set of readings is defined as the average difference between the readings of the prototype flow meter and a standard flow meter:

$$B = \frac{\sum_{i=1}^{n} (m_i - m_{s,i})}{n} \tag{50.8}$$

where

m_i is flow rate reading in the prototype flow meter
$m_{s,i}$ is flow rate reading in the standard flow meter

The precision of a reading is usually defined in terms of the standard deviation of a set of readings corresponding to the same true value. Extending the concept a little further, the precision is defined in terms of the standard deviation of the difference in readings between the prototype and the standard flow meter. In other words,

$$P = \sqrt{\frac{\sum_{i=1}^{n} \left[(m_i - m_{s,i}) - B\right]^2}{n}} \tag{50.9}$$

where n is total number of readings at flow rates close to the specified value.

Accuracy is defined in terms of bias B and precision P as

$$A = \left(P + |B|\right)\frac{B}{|B|} \tag{50.10}$$

Accuracy has the same sign as bias B and is larger than B by the value of precision P.

50.5 Summary

The capillary-type thermal mass flow meter has been studied in the beginning of this chapter in the discussion of the basic and various parts of a sensor and, more importantly, how these parts affect the sensor characteristics. Then a very basic readout circuit is introduced in order to measure the mass flow; at the end, measuring the accuracy of prototype sensor is introduced.

According to Equation 50.2, by measuring the amount of flow that passes through the capillary zone, the entire flow can be measured. According to the temperature profile of a capillary tube that depicts the shift in the profile according to flow velocity variation, the temperature is measured from two points of upstream and downstream; consequently, Equation 50.6 will supply the amount of total mass flow rate. Here, the most critical factor is measuring the temperature, which is discussed earlier. As mentioned previously, the constants of k, C_1, and C are related to sensors and can be found while measuring the accuracy of prototype sensor.

After precisely measuring the mass flow rate, the accurately control of the mass flow rate is required in most applications. A unit known as mass flow controller consists of a valve in which the data come from the capillary mass flow meter and control the valve in order to achieve a desired mass flow rate.

References

1. Products, SIERRA Instruments, http://www.sierrainstruments.com/ (accessed on March 15, 2013).
2. Pakdaman Zangabad, R., Bahrami, M., Chamanian, S., et al., Design and simulation of a novel capillary-type thermal mass flow meter, *Proceedings of 2012 IEEE Sensors Applications Symposium, SAS 2012*, Brescia, Italy, pp. 6–9, 2012.

51

Differential Pressure Flowmeters

Richard Thorn
University of Derby

Flow measurement is an everyday event. Whether you are filling up a car with petrol (gasoline) or wanting to know how much water the garden sprinkler is consuming, a flowmeter is required. Similarly, it is also difficult to think of a sector of industry in which a flowmeter of one type or another does not play a part. The world market in flowmeters is expected to grow steadily for the foreseeable future. The value of product being measured by these meters is also very large. For example, in the United Kingdom alone, it was estimated that in 1994, the value of crude oil produced was worth $15 billion.

Given the size of the flowmeter market, and the value of product being measured, it is somewhat surprising that both the accuracy and the capability of many flowmeters are poor in comparison to those instruments used for measurement of other common process variables such as pressure and temperature. For example, the orifice plate flowmeter, which was first used commercially in the early 1900s and has a typical accuracy of ±2% of reading, is still the only flowmeter approved by most countries for the fiscal measurement of natural gas. Although newer techniques such as Coriolis flowmeters have become increasingly popular in recent years, the flow measurement industry is by nature conservative and still dominated by traditional measurement techniques. For a review of recent flowmeter developments, refer to [1].

Over 40% of all liquid, gas, and steam measurements made in industry are still accomplished using common types of *differential pressure flowmeters*, such as the orifice plate, venturi tube, and nozzle. The operation of these flowmeters is based on the observation made by Bernoulli that if an annular restriction is placed in a pipeline, then the velocity of the fluid through the restriction is increased. The increase in velocity at the restriction causes the static pressure to decrease at this section, and a pressure difference is created across the element. The difference between the pressure upstream and the pressure downstream of this obstruction is related to the rate of fluid flowing through the restriction and therefore through the pipe. A differential pressure flowmeter consists of two basic elements: an

obstruction to cause a pressure drop in the flow (a *differential producer*) and a method of measuring the pressure drop across this obstruction (a *differential pressure transducer*).

One of the major advantages of the orifice plate, venturi tube, or nozzle is that the measurement uncertainty can be predicted without the need for calibration, if it is manufactured and installed in accordance with one of the international standards covering these devices. In addition, this type of differential pressure flowmeter is simple, has no moving parts, and is therefore reliable. The main disadvantages of these devices are their limited range (typically 3:1), the permanent pressure drop they produce in the pipeline (which can result in higher pumping costs), and their sensitivity to installation effects (which can be minimized using straight lengths of pipe before and after the flowmeter). The combined advantages of this type of flowmeter are still quite hard to beat, and although it has limitations, these have been well investigated and can be compensated for in most circumstances. Unless very high accuracy is required, or unless the application makes a nonintrusive device essential, the differential flowmeter should be considered. Despite the predictions of its demise, there is a little doubt that the differential pressure flowmeter will remain a common method of flow measurement for many years to come.

51.1 Important Principles of Fluid Flow in Pipes

There are a number of important principles relating to the flow of fluid in a pipe that should be understood before a differential pressure flowmeter can be used with confidence. The principles are as follows: the difference between laminar and turbulent flows, the meaning of Reynolds number, and the importance of the flow's velocity profile.

Fluid motion in a pipe can be characterized as one of the three types: laminar, transitional, or turbulent. In *laminar flow*, the fluid travels as parallel layers (known as streamlines) that do not mix as they move in the direction of the flow. If the flow is turbulent, the fluid does not travel in parallel layers, but moves in a haphazard manner with only the average motion of the fluid being parallel to the axis of the pipe. If the flow is *transitional*, then both types may be present at different points along the pipeline, or the flow may switch between the two.

In 1883, Osborne Reynolds performed a classic set of experiments at the University of Manchester that showed that the flow characteristic can be predicted using a dimensionless number, now known as the Reynolds number. The Reynolds number Re is the ratio of the inertia forces in the flow ($\rho\bar{v}D$) to the viscous forces in the flow (η) and can be calculated using

$$\mathrm{Re} = \frac{\rho\bar{v}D}{\eta} \tag{51.1}$$

where

ρ is the density of the fluid
$\bar{v}$ is the mean velocity of the fluid
D is the pipe diameter
η is the dynamic viscosity of the fluid

If Re is less than 2000, viscous forces in the flow dominate and the flow will be laminar. If Re is greater than 4000, inertia forces in the flow dominate and the flow will be turbulent. If Re is between 2000 and 4000, the flow is transitional and either mode can be present. The Reynolds number is calculated using mainly properties of the fluid and does not take into account factors such as pipe roughness, bends, and valves that also affect the flow characteristic. Nevertheless, the Reynolds number is a good guide to the type of flow that can be expected in most situations.

The fluid velocity across a pipe cross section is not constant and depends on the type of flow present. In laminar flow, the velocity profile is parabolic since the large viscous forces present cause the fluid to move more slowly near the pipe walls. Under these conditions, the velocity at the center of the pipe is twice the

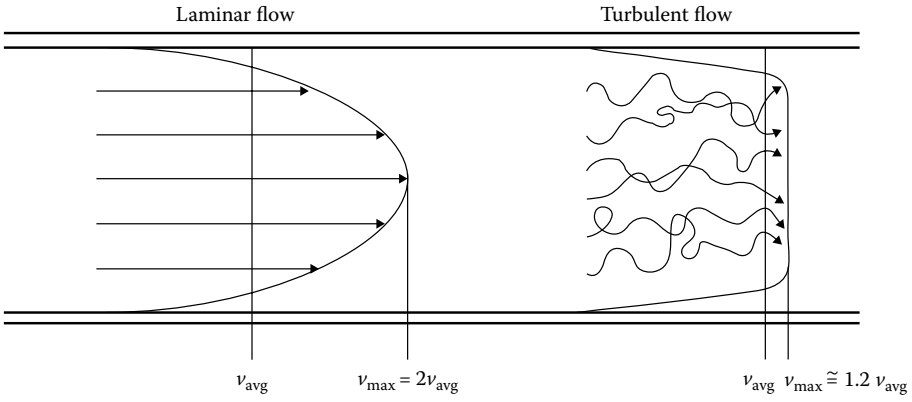

FIGURE 51.1 Velocity profiles in laminar and turbulent flow.

average velocity across the pipe cross section. The laminar-flow profile is unaffected by the roughness of the pipe wall. In turbulent flow, inertia forces dominate, pipe wall effects are less, and flow's velocity profile is flatter, with the velocity at the center being about 1.2 times the mean velocity. The exact flow profile in a turbulent flow depends on pipe wall roughness and Reynolds number. Figure 51.1 shows the "fully developed" flow profiles for laminar and turbulent flow. These are the flow profiles that would be obtained at the end of a very long pipe, thus ensuring that any changes to the flow profile due to pipe bends and fittings are no longer present. To have confidence in the performance of a differential pressure flowmeter, both the characteristic and the velocity profile of the flow passing through the flowmeter should be stable and known.

51.1.1 Bernoulli's Equation

The Bernoulli's equation defines the relationship between fluid velocity (v), fluid pressure (p), and height (h) above some fixed point for a fluid flowing through a pipe of varying cross section and is the starting point for understanding the principle of the differential pressure flowmeter. For the inclined, tapered pipe shown in Figure 51.2, Bernoulli's equation states that

$$\frac{p_1}{\rho g} + \frac{v_1^2}{2g} + h_1 = \frac{p_2}{\rho g} + \frac{v_2^2}{2g} + h_2 \tag{51.2}$$

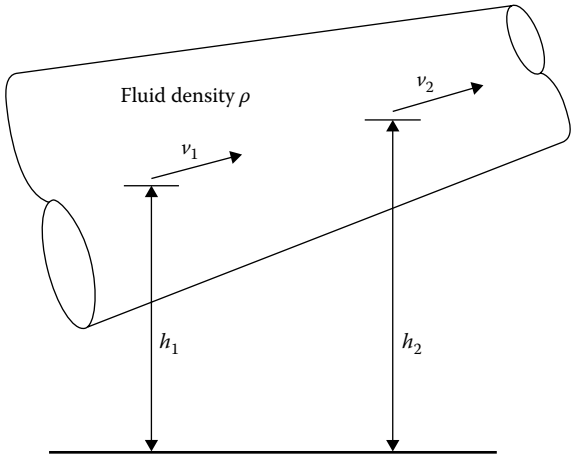

FIGURE 51.2 Flow through an inclined, tapered pipe.

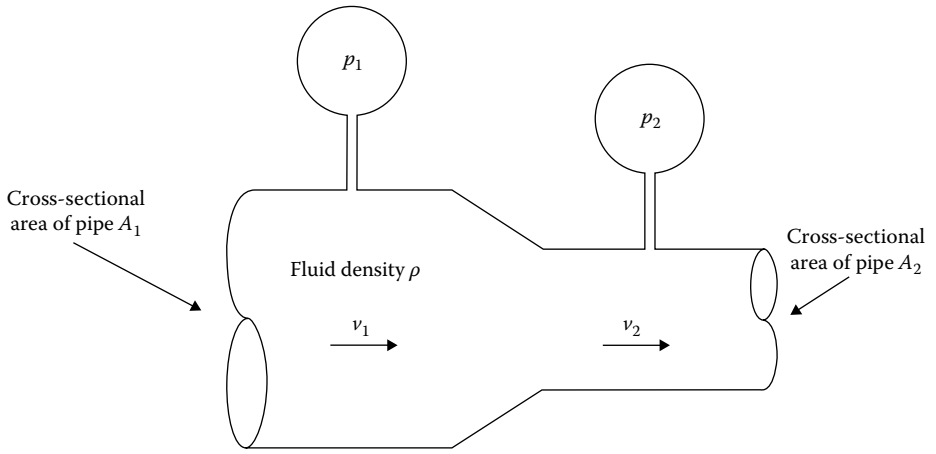

FIGURE 51.3 Using a restriction in a pipe to measure fluid flow rate.

Thus, the sum of the pressure head ($p/\rho g$), the velocity head ($v/2g$), and the potential head (h) is constant along a flow streamline. The term "head" is commonly used because each of these terms has the unit of meters. Equation 51.2 assumes that the fluid is frictionless (zero viscosity) and of constant density (incompressible). Further details on the derivation and significance of Bernoulli's equation can be found in most undergraduate fluid dynamics textbooks (e.g., [2]).

Bernoulli's equation can be used to show how a restriction in a pipe can be used to measure flow rate. Consider the pipe section shown in Figure 51.3. Since the pipe is horizontal, $h_1 = h_2$, and Equation 51.2 reduces to

$$\frac{p_1 - p_2}{\rho} = \frac{v_1^2 - v_2^2}{2} \tag{51.3}$$

The conservation of mass principle requires that

$$v_1 A_1 \rho = v_2 A_2 \rho \tag{51.4}$$

Rearranging Equation 51.4 and substituting for v_2 in Equation 51.3 gives

$$Q = v_1 A_1 = \frac{A_2}{\sqrt{1 - (A_2/A_1)^2}} \sqrt{\frac{2(p_1 - p_2)}{\rho}} \tag{51.5}$$

This shows that the volumetric flow rate of fluid Q can be determined by measuring the drop in pressure ($p_1 - p_2$) across the restriction in the pipeline—the basic principle of all differential pressure flowmeters. Equation 51.5 has limitations, the main ones being that it is assumed that the fluid is incompressible (a reasonable assumption for most liquids) and that the fluid has no viscosity (resulting in a flat velocity profile). These assumptions need to be compensated for when Equation 51.5 is used for practical flow measurement.

51.2 Common Differential Pressure Flowmeters

51.2.1 Orifice Plate

The orifice plate is the simplest and cheapest type of differential pressure flowmeter. It is simply a plate with a hole of specified size and position cut in it, which can then be clamped between flanges in a pipeline (Figure 51.4). The increase that occurs in the velocity of a fluid as it passes through the hole in

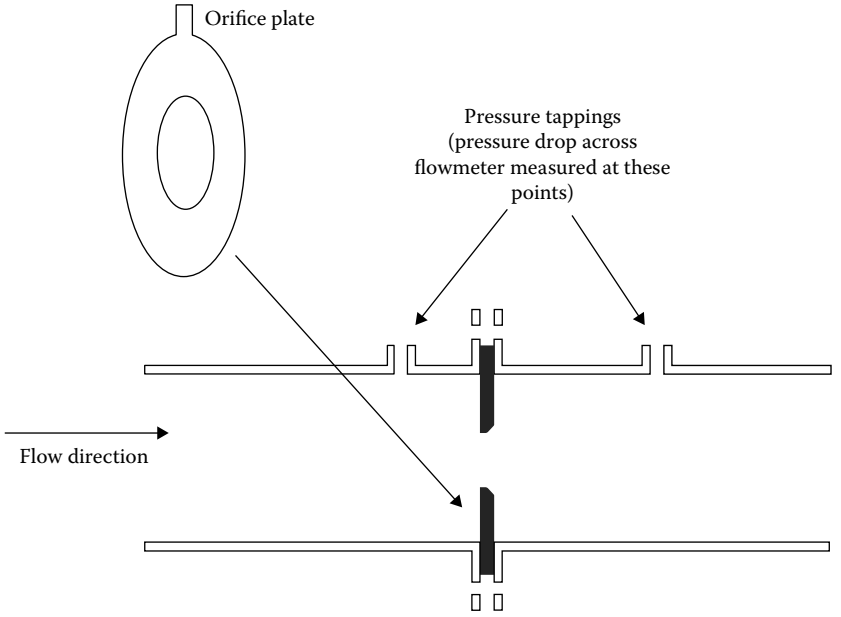

FIGURE 51.4 Square-edged orifice plate flowmeter.

the plate results in a pressure drop being developed across the plate. After passing through this restriction, the fluid flow jet continues to contract until a minimum diameter known as the vena contracta is reached. If Equation 51.5 is used to calculate volumetric flow rate from a measurement of the pressure drop across the orifice plate, then an error would result. This is because A_2 should strictly be the area of the vena contracta, which of course is unknown. In addition, turbulence between the vena contracta and the pipe wall results in an energy loss that is not accounted for in this equation.

To overcome the problems caused by the practical application of Equation 51.5, two empirically determined correction factors are added. After some reorganization, Equation 51.5 can be written as

$$Q = \frac{C}{\sqrt{1-\beta^4}} \varepsilon \frac{\pi}{4} d^2 \sqrt{\frac{2(p_1 - p_2)}{\rho}} \tag{51.6}$$

where

ρ is the density of the fluid upstream of the orifice plate
d is the diameter of the hole in the orifice plate
β = is the diameter ratio d/D, where D is the upstream internal pipe diameter

The two empirically determined correction factors are C the discharge coefficient and ε the expansibility factor. C is affected by the changes in the diameter ratio, the Reynolds number, the pipe roughness, the sharpness of the leading edge of the orifice, and the points at which the differential pressure across the plate is measured. However, for a fixed geometry, it has been shown that C is only dependent on Reynolds number, and so this coefficient can be determined for a particular application; ε is used to account for the compressibility of the fluid being monitored. Both C and ε can be determined from equations and tables in a number of internationally recognized documents known as standards. These standards specify not only C and ε but also the geometry and installation conditions for the square-edged orifice plate, venturi tube, and nozzle and are essentially a design guide for the use of the most commonly used types of differential pressure flowmeter. Installation recommendations are intended

to ensure that fully developed turbulent flow conditions exist within the measurement section of the flowmeter. The most commonly used standard in Europe is ISO 5167-1 [3], while in the United States, API 2530 is the most popular [4]. There are differences between some of the recommendations in these two standards (e.g., the minimum recommended length of straight pipe upstream of the flowmeter), but work is under way to resolve these.

Equation 51.6 illustrates perhaps the greatest strength of the orifice plate, which is that measurement performance can be confidently predicted without the need for calibration if the device is manufactured, installed, and operated in accordance with one of the international standards. In addition, the device is cheap to manufacture, has no moving parts, is reliable, and can be used for metering most clean gases, liquids, and steam.

The major disadvantages of the orifice plate are its limited range and sensitivity to flow disturbances. The fact that fluid flow rate is proportional to the square root of the measured differential pressure limits the range of a one-plate/one-differential-pressure transmitter combination to about 3:1. The required diameter ratio (also known as beta ratio) of the plate depends on the maximum flow rate to be measured and the range of the differential pressure transducer available. Sizing of the orifice plate is covered in most of the books in the further reading list, and nowadays, computer programs are also available to help perform this task. The flow measurement range can be increased by switching; the ways in which this may be achieved are described in [5]. Equation 51.6 assumes a fully developed and stable flow profile, and so installation of the device is critical, particularly the need for sufficient straight pipework upstream of the meter. Wear of the leading edge of the orifice plate can severely alter measurement accuracy; thus, this device is normally only used with clean fluids.

Only one type of orifice plate, the square-edged concentric, is covered by the standards. However, other types exist, having been designed for specific applications. One example is the eccentric orifice plate, which is suited for use with dirty fluids. The details of these other types of orifice plate can be found in [6].

51.2.2 Venturi Tube

The classical or Herschel venturi tube is the oldest type of differential pressure flowmeter, having first been used in 1887. As Figure 51.5 shows, a restriction is introduced into the flow in a more gradual way than for the orifice plate. The resulting flow through a venturi tube is closer to that predicted in theory by Equation 51.5, and so the discharge coefficient C is much nearer unity, being typically 0.95. In addition, the permanent pressure loss caused by the venturi tube is lower, but the differential pressure is also lower than for an orifice plate of the same diameter ratio. The smooth design of the venturi tube means that it is less sensitive to erosion than the orifice plate and thus more suitable for use with dirty gases or liquids. The venturi tube is also less sensitive to upstream disturbances and therefore needs shorter lengths of straight pipework upstream of the meter than the equivalent orifice plate or nozzle. Like the orifice plate and nozzle, the design, installation, and use of the venturi tube is covered by a number of international standards.

The major disadvantages of the venturi tube flowmeter are its size and cost. It is more difficult and therefore more expensive to manufacture than the orifice plate. Since a venturi tube can be typically 6

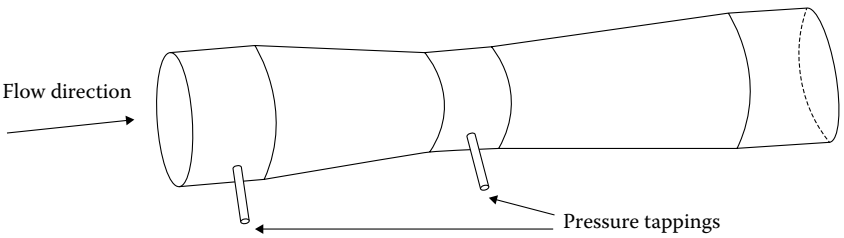

FIGURE 51.5 Venturi tube flowmeter.

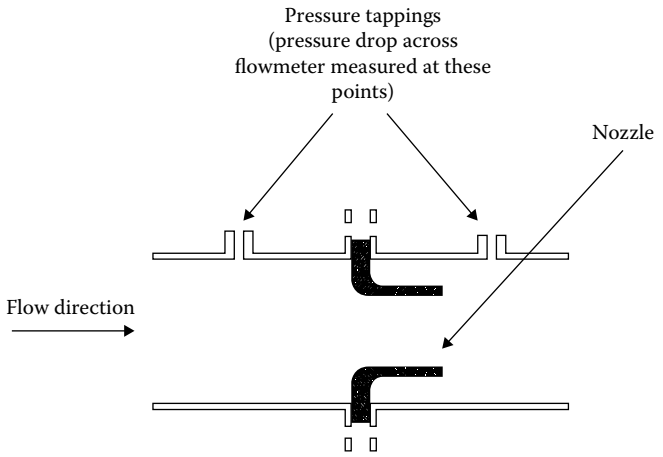

FIGURE 51.6 Nozzle flowmeter.

diameters long, it can become cumbersome to use with larger pipe sizes, with associated maintenance of upstream and downstream pipe lengths also becoming a problem.

51.2.3 Nozzle

The nozzle (Figure 51.6) combines some of the best features of the orifice plate and venturi tube. It is compact and yet, because of its curved inlet, has a discharge coefficient close to unity. There are a number of designs of nozzle, but one of the most commonly used in Europe is the ISA-1932 nozzle, while in the United States, the ASME long-radius nozzle is more popular. Both of these nozzles are covered by international standards.

The smooth inlet of the nozzle means that it is more expensive to manufacture than the orifice plate as the curvature of the inlet changes with diameter ratio, although it is cheaper than the venturi tube. The device has no sharp edges to erode and causes changes in calibration and thus is well suited for use with dirty and abrasive fluids. The nozzle is also commonly used for high-velocity, high-temperature applications such as steam metering.

A variation of the nozzle is the sonic (or critical flow venturi) nozzle, which has been used both as a calibration standard for testing gas meters and as a transfer standard in interlaboratory comparisons [7].

51.3 Other Differential Pressure Flowmeters

There are many other types of differential pressure flowmeter, including the segmental wedge, V-cone, elbow, and Dall tube. Each of these has advantages over the orifice plate, venturi tube, and nozzle for specific applications. For example, the segmental wedge can be used with flows having a low Reynolds number, and a Dall tube has a lower permanent pressure loss than a venturi tube. However, none of these instruments are yet covered by international standards, and thus, calibration is needed to determine their accuracy. Further information on these, and other less-common types of differential pressure flowmeter, can be found in [8].

51.4 Performance and Applications

Table 51.1 shows the performance characteristics and main application areas of the square-edged orifice plate, venturi tube, and nozzle flowmeters. Compared to other types of flowmeters on the market, these differential pressure flowmeters only have moderate accuracy, typically ±2% of reading; but of course,

TABLE 51.1 Performance and Application Areas of Common Differential Pressure Flowmeters

	Performance					Applications				
	Typical Uncalibrated Accuracy (%)	Typical Range	Typical Pipe Diameter (mm)	Permanent Pressure Loss	Comparative Cost	Clean Gas	Dirty Gas	Clean Liquid	Slurry	Steam
Orifice plate	±2	3:1	10–1000	High	Low	Yes	No	Yes	No	Yes
Venturi tube	±2	3:1	25–500	Low	High	Yes	Maybe	Yes	Maybe	Maybe
Nozzle	±2	3:1	25–250	High	Medium	Yes	Maybe	Yes	No	Yes

this can be improved if the device is calibrated after installation. Although in some circumstances, these flowmeters can be used with dirty gases or liquids, usually only small amounts of a second component can be tolerated before large measurement errors occur. When calculating the cost and performance of a differential flowmeter, both the primary element and the differential pressure transducer should be taken into account. Although the orifice plate is the cheapest of the primary elements, the cost of the fitting needed to mount it in the pipeline, particularly if online removal is required, can be significant.

Choosing which flowmeter is best for a particular application can be very difficult. The main factors that influence this choice are the required performance, the properties of the fluid to be metered, the installation requirements, the environment in which the instrument is to be used, and, of course, the cost. There are two standards that can be used to help select a flowmeter: BS 1042 (Section 1.4), which is a guide to the use of the standard differential pressure flowmeters [9], and BS 7405, which is concerned with the wider principles of flowmeter selection [10].

Because all three flowmeters have similar accuracy, one strategy for selecting the most appropriate instrument is to decide if there are any good reasons for not using the cheapest flowmeter that can be used over the widest range of pipe sizes: the orifice plate. Where permanent pressure loss is important, the venturi tube should be considered, although the high cost of this meter can only usually be justified where large quantities of fluid are being metered. For high-temperature or high-velocity applications, the nozzle should be considered because under these conditions, it is more predictable than the orifice plate. For metering dirty fluids, either the venturi tube or the nozzle should be considered in preference to the orifice plate, the choice between the two depending on cost and pressure loss requirements. Table 51.2 lists some suppliers of differential pressure flowmeters.

51.4.1 Installation

Correct installation is essential for successful use of a differential pressure flowmeter because the predicted uncertainty in the flow rate/differential pressure relationship in Equation 51.6 assumes a steady flow, with a fully developed turbulent velocity profile, which is passing through the flowmeter. Standards contain detailed recommendations for the minimum straight lengths of pipe required before and after the flowmeter, in order to ensure a fully developed flow profile. Straight lengths of pipe are required after the flowmeter because disturbances caused by a valve or bend can travel upstream and thus also affect the installed flowmeter. Table 51.3 gives examples of installation requirements taken from ISO 5167-1. If it is not possible to fit the recommended lengths of straight pipe before and after the flowmeter, then the flowmeter must be calibrated once it has been installed.

The other major problem one faces during installation is the presence of a rotating flow or swirl. This condition distorts the flow velocity profile in a very unpredictable way and is obviously not desirable. Situations that create swirl, such as two 90° bends in different planes, should preferably be avoided. However, if this is not possible, then swirl can be removed by placing a flow conditioner (also known as a flow straightener) between the source of the swirl and the flowmeter. There are a wide range of flow conditioner designs, some of which can be used to both remove swirl and correct a distorted velocity

TABLE 51.2 Selection of Companies That Supply Differential Pressure Flowmeters

ABB Kent-Taylor
Oldens Lane, Stonehouse
Gloucestershire, GL10 3TA
England
Tel.: +44 1453 826661
Fax: +44 1453 826358

Daniel Industries Inc.
9720 Katy Road
P.O. Box 19097
Houston, TX 77224
Tel.: (713) 467-6000
Fax: (713) 827-3880

Hartmann & Braun (U.K.) Ltd.
Bush Beach Engineering Division
Stanley Green Trading Estate, Cheadle Hulme
Cheshire SK8 6RN
England
Tel.: +44 161 4858151
Fax: +44 161 4884048

ISA Controls Ltd.
Hackworth Industrial Park
Shildon
County Durham DL4 1LH
England
Tel.: +44 1388 773065
Fax: +44 1388 774888

Perry Equipment Corporation
Wolters Industrial Park
P.O. Box 640
Mineral Wells, TX 76067
Tel.: (817) 325-2575
Fax: (817) 325-4622

TABLE 51.3 Minimum Straight Lengths of Pipe Required between Various Fittings and an Orifice Plate or Venturi Tube (as Recommended in ISO 5167-1) to Ensure That a Fully Developed Flow Profile Exists in the Measurement Section

	Upstream of the Flowmeter				Downstream of the Flowmeter
Diameter Ratio β	Single 90° Bend	Two 90° Bends in the Same Plane	Two 90° Bends in Different Planes	Globe Valve Fully Open	For Any of the Fittings Shown to the Left
0.2	10	14	34	18	4
0.4	14	18	36	20	6
0.6	18	26	48	26	7
0.8	46	50	80	44	8

Note: All lengths are multiples of the pipe diameter.

profile [11]. Because they obstruct the flow, all flow conditioners produce an unrecoverable pressure loss, which in general increases with their capability (and complexity).

51.4.2 Differential Pressure Measurement

Apart from the differential producer, the other main element of a differential pressure flowmeter is the *transducer* needed to measure the pressure drop across the producer. The correct selection and installation of the differential pressure transducer plays an important part in determining the accuracy of the flow rate measurement.

The main factors that should be considered when choosing a differential pressure transducer for a flow measurement application are the differential pressure range to be covered, the accuracy required, the maximum pipeline pressure, and the type and temperature range of the fluid being metered.

Most modern differential pressure transducers consist of a pressure capsule in which either capacitance, strain gage, or resonant wire techniques are used to detect the movement of a diaphragm.

Using these techniques, a typical accuracy of ±0.1% of full scale is possible. The transducer is usually part of a unit known as a transmitter, which converts differential pressure, static pressure, and ambient temperature measurements into a standardized analog or digital output signal. "Smart" transmitters use a local, dedicated microprocessor to condition signals from the individual sensors and compute volumetric or mass flow rate. These devices can be remotely configured, and a wide range of diagnostic and maintenance functions are possible using their built-in "intelligence."

As far as installation is concerned, the transmitter should be located as close to the differential producer as possible. This helps to ensure a fast dynamic response and reduces problems caused by vibration of the connecting tubes. The position of the pressure tappings is also important. If the liquid flow in a horizontal pipe is being measured, then the pressure tappings should be located at the side of the pipe so that they cannot be blocked with dirt or filled with air bubbles. For horizontal gas flows, if the gas is clean, the pressure tappings should be vertical; if steam or dirty gas is being metered, then the tappings should be located at the side of the pipe. These general guidelines show that considerable care must be taken with the installation of the differential pressure transmitter if large measurement errors are to be avoided. For further details on the installation of differential pressure transmitters, see ISO 2186 [12].

51.4.3 Standards

International standards that specify the design, installation, and use of the orifice plate, venturi tube, and nozzle and allow their accuracy to be calculated without the need for calibration are probably the main reason for the continuing use of this type of flowmeter. Table 51.4 gives details of the most common standards related to differential pressure flowmeters. There are still inconsistencies in the various standards. For example, ISO 5167-1 states that any flow conditioner should be preceded by at least 22 diameters of straight pipe and followed by at least 20 diameters of

TABLE 51.4 Standards Related to Differential Pressure Flow Measurement

American National Standards Institute, New York	
ANSI/ASHRAE 41.8	Standard methods of measurement of flow of liquids in pipes using orifice flowmeters
ANSI/ASME MFC-7M	Measurement of gas flow by means of critical flow venturi nozzles
ANSI/ASME MFC-14M	Measurement of fluid flow using small-bore precision orifice meters
American Petroleum Institute, Washington, DC	
API 2530	Manual of Petroleum Measurement Standards, Chapter 14—Natural gas fluids measurement, Section 3—Orifice metering of natural gas and other related hydrocarbon fluids
American Society of Mechanical Engineers, New York	
ASME MFC-3M	Measurement of fluid flow in pipes using orifice, nozzle, and venturi
ASME MFG-8M	Fluid flow in closed conduits—connections for pressure signal transmissions between primary and secondary devices
British Standards Institution, London	
BS 1042	Measurement of fluid flow in closed conduits
International Organization for Standardization, Geneva	
ISO 2186	Fluid flow in closed conduits—connections for pressure transmissions between primary and secondary elements
ISO TR 3313	Measurement of pulsating fluid flow in a pipe by means of orifice plates, nozzles, or venturi tubes
ISO 5167-1	Measurement of fluid flow by means of pressure differential devices
ISO 9300	Measurement of gas flow by means of critical flow venturi nozzles

straight pipe. This would seem to contradict one application of a flow conditioner, which is to reduce the length of straight pipe required upstream of a flowmeter.

Despite the occasional inconsistency and difference between the standards, they are the internationally accepted rules for the installation and use of the square-edged orifice plate, venturi tube, and nozzle.

51.5 Future Developments

In spite of the vast amount of published data available on differential pressure flowmeters, continued research is needed to improve the understanding of the effect of flow conditions, and flowmeter geometry, on the uncalibrated accuracy of these devices. For example, work has been recently undertaken to derive an improved equation for the discharge coefficient of an orifice plate [13].

The metering of multiphase flow is an area of increasing importance. In addition to developing new measurement techniques, many people are investigating ways in which traditional flowmeters can be used to meter multiphase flows. A good review of the use of differential pressure flowmeters for multiphase flow measurement can be found in [14].

The development of "smart" differential pressure transmitters has overcome the limitations of differential pressure flowmeters in some applications. For example, these devices are being used to linearize and extend the range of differential pressure flowmeters.

The aforementioned developments should help to ensure the continued popularity of the differential pressure flowmeter for the foreseeable future, despite increasing competition from newer types of instrument.

Defining Terms

Differential pressure flowmeter: A flowmeter in which the pressure drop across an annular restriction placed in the pipeline is used to measure fluid flow rate. The most common types use an orifice plate, venturi tube, or nozzle as the primary device.

Differential pressure transmitter: Secondary device that measures the differential pressure across the primary device and converts it into an electrical signal.

Nozzle: Primary device consisting of a convergent inlet connected to a cylindrical section.

Orifice plate: Primary device consisting of a thin plate in which a circular aperture has been cut.

Venturi tube: Primary device consisting of a converging inlet, cylindrical mid-section, and diverging outlet.

References

1. R. A. Furness, Flowmetering: evolution or revolution, *Meas. Control*, 27 (8), 15–18, 1994.
2. B. S. Massey, *Mechanics of Fluids*, 6th ed., London, U.K.: Chapman and Hall, 1989.
3. International Organization for Standardization, ISO 5167-1, *Measurement of Fluid Flow by Means of Pressure Differential Devices—Part 1 Orifice Plates, Nozzles and Venturi Tubes Inserted in Circular Cross-Section Conduits Running Full*, Geneva, Switzerland: International Organization for Standardization, 1991.
4. American Petroleum Institute, API 2530, *Manual of Petroleum Measurement Standards Chapter 14—Natural Gas Fluids Measurement, Section 3—Orifice Metering of Natural Gas and Other Related Hydrocarbon Fluids*, Washington, DC: American Petroleum Institute, 1985.
5. E. L. Upp, *Fluid Flow Measurement*, Houston, TX: Gulf Publishing, 1993.
6. H. S. Bean, *Fluid Meters Their Theory and Application*, 6th ed., New York: American Society of Mechanical Engineers, 1983.

7. P. H. Wright, The application of sonic (critical flow) nozzles in the gas industry, *Flow Meas. Instrum.*, 4 (2), 67–71, 1993.
8. D. W. Spitzer, *Industrial Flow Measurement*, 2nd ed., Research Triangle Park, NC: ISA, 1990.
9. British Standards Institution, BS 1042, *Measurement of Fluid Flow in Closed Conduits—Part 1 Pressure Differential Devices—Section 1.4 Guide to the Use of Devices specified in Sections 1.1 and 1.2*, London, U.K.: British Standards Institution, 1992.
10. British Standards Institution, BS7405, *Guide to the Selection and Application of Flowmeters for Measurement of Fluid Flow in Closed Conduits*, London, U.K.: British Standards Institution, 1991.
11. E. M. Laws and A. K. Ouazzane, Compact installations for differential pressure flow measurement, *Flow Meas. Instrum.*, 5 (2), 79–85, 1994.
12. International Organization for Standardization, ISO 2186, *Fluid Flow in Closed Conduits—Connections for Pressure Signal Transmissions between Primary and Secondary Elements*, Geneva, Switzerland: International Organization for Standardization, 1973.
13. M. J. Reader-Harris, J. A. Slattery, and E. P. Spearman, The orifice plate discharge coefficient equation—further work, *Flow. Meas. Instrum.*, 6 (2), 101–114, 1995.
14. F. C. Kinghorn, Two-phase flow measurement using differential pressure meters, *Multi-Phase Flow Measurement Short Course*, London, U.K., June 17–18, 1985.

Further Information

Baker, R. C., *An Introductory Guide to Flow Measurement*, London, U.K.: Mechanical Engineering Publications, 1989, a good pocket sized guide on the choice and use of flowmeters commonly used in industry.

OMEGA Complete Flow and Level Measurement handbook and Encyclopedia, OMEGA Press, 1995. Also available at http://www.omega.com/literature/transactions/volume4/T9904-07-DIFF.html (accessed on June 27, 2012).

Flow Measurement and Instrumentation, Editor-in-Chief: J. Delsing, Oxford, U.K.: Butterworth-Heinemann, a quarterly journal covering all aspects of flowmeters and their applications. A good source of information on current research activity.

Hayward, T. J., *Flowmeters—A Basic Guide and Source-Book for Users*, London, U.K.: Macmillan, 1979, an overview of the important areas of flow measurement which is a joy to read.

Miller, R. W., *Flow Measurement Engineering Handbook*, 3rd ed., New York: McGraw-Hill, 1996, a thorough reference book particularly on differential pressure flowmeters, covers European and U.S. standards with calculations using both U.S. and SI units.

Spitzer, D. W., *Flow Measurement: Practical Guides for Measurement and Control*, Research Triangle Park, NC: ISA, 1991, intended for practicing engineers, this book covers most aspects of industrial flow measurement.

Upp, E. L., *Fluid Flow Measurement*, Houston, TX: Gulf Publishing, 1993, contains a lot of practical advice on the use of differential pressure flowmeters.

Universal Flow Monitors, Differential pressure flowmeter, Hazel Park, MI. http://www.flowmeters.com/ufm/index.cfm?task=differential_pressure (accessed on June 21, 2012).

Partial List of Vendors and Suppliers

Furness Controls, 2020 Younts Rd., Indian Trail, NC 28079, Phone: 704-882-3311, 800-898-5325 (toll free), Fax: 704-882-3811, www.furnesscontrols.com/

Lambda Square, Inc., 71 Deer Park Ave., Babylon, NY 11702, Phone: 631-587-1000, 800-587-5423 (toll free), Fax: 631-587-1011, www.lambdasquare.com

Orange Research, Inc., 140 Cascade Blvd., Milford, CT 06460, Phone: 203-877-5657, 800-989-5657 (toll free), Fax: 203-783-9546, www.orangeresearch.com

Paragon Controls, Inc., 2371 Circadian Way, Santa Rosa, CA 95407, Phone: 707-579-1424, Fax: 707-579-8480, www.paragoncontrols.com

Sensocon, Inc., PO Box 518, Highland City, FL 33846, Phone: 863-248-2800, Fax: 863-248-2798, www.ensocon.com

Sierra Instruments, 5 Harris Ct., Bldg. L, Monterey, CA 93940, Phone: 831-373-0200, 800-866-0200 (toll free), Fax: 831-373-4402, www.sierrainstruments.com

52

Variable Area Flowmeters

Adrian Melling
University of Erlangen–Nuernberg

Herbert Köchner
University of Erlangen–Nuernberg

Reinhard Haak
University of Erlangen–Nuernberg

The term *variable area flowmeters* refers to those meters in which the minimum cross-sectional area available to the flow through the meter varies with the flow rate. Meters of this type that are discussed in this section include the rotameter and the movable vane meter used in pipe flows and the weir or flume used in open-channel flows. The measure of the flow rate is a geometrical quantity such as the height of a bob in the rotameter, the angle of the vane, or the change in height of the free surface of the liquid flowing over the weir or through the flume.

Most of the discussion here is devoted to the rotameter, firstly because the number of installed rotameters and movable vane meters is large relative to the number of weirs and flumes and secondly because the movable vane is often used simply as a flow indicator rather than as a meter.

The following section includes basic information describing the main constructional features and applications of each type of meter. In the third section, the principles of measurement and the design of rotameters and open-channel meters are described in some detail; the movable vane meter is not considered further because most design aspects are similar to those of rotameters. Then, the contribution of modern computational and experimental methods of fluid mechanics to flowmeter design is discussed, using the results of a detailed investigation of the internal flow.

The details of rotameters and movable vane meters, together with approximate costs of these meters, are tabulated in Tables 52.1 and Table 52.2. A partial list of manufacturers and suppliers is provided at the end of this chapter.

52.1 General Description of Variable Area Flowmeters

52.1.1 Rotameter

The *rotameter* is a robust and simple flowmeter for gases and liquids and holds a large share of the market for pipe diameters smaller than about 100 mm. In its basic form, the rotameter consists of a conical transparent vertical glass tube containing a "bob" (Figure 52.1), which rises in the tube with increasing flow rate until a balance is reached between gravitational, buoyancy, and drag forces on the bob. Within

TABLE 52.1 Approximate Rotameter Prices

Type	Size	Price (Plastic)	Price (Stainless Steel, Borosilicate Glass)
Glass	<1/2 in. (12.7 mm)	$50	$200
Plastic	1/2 in. (12.7 mm)	$50	$200
	1 in. (25.4 mm)	$70	$150
	2 in. (50.8 mm)	$200	$500
Metal	1/2 in. (12.7 mm)		$500
	1 in. (25.4 mm)		$600
	2 in. (50.8 mm)		$700
	3 in. (76.2 mm)		$1100
	4 in. (101.6 mm)		$1400
Additional costs			
Electric limit switch	$100		
Current transducer	$500		
Pneumatic	$1200		

TABLE 52.2 Approximate Movable Vane Meter Prices

Type	Price
Plastic versions (small scale)	From $10
Direct-coupled pointer versions incl. electric flow switch: metal, screw connections 1/2 in. (12.7 mm) to 2 in. (50.8 mm)	$400 (brass) to $600 (Stainless steel)
Flanged versions	Add $200 (1/2 in., 12.7 mm) to $400 (2 in., 50.8 mm)
Magnetic-coupled indicator, stainless steel	$1200 (1/2 in., 12.7 mm) to $2100 (8 in., 203 mm)

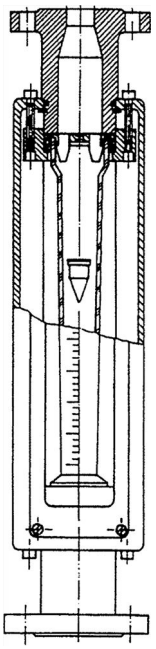

FIGURE 52.1 Cross section of a rotameter. The level of the bob rises linearly with increasing flow rate.

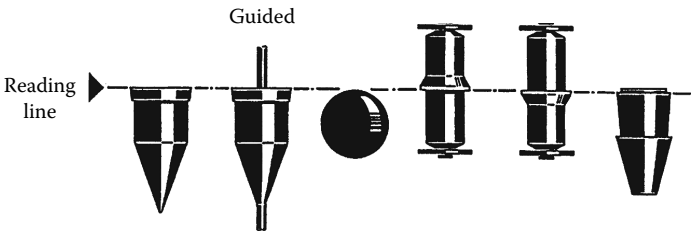

FIGURE 52.2 Typical rotameter bob geometries.

the range of a particular flowmeter (depending on the bob shape and density, the tube shape, and the fluid density and viscosity), the flow rate is linearly proportional to the height of the bob in the tube and is determined simply by reading the level of the upper edge of the bob. The rotameter is also known as "floating element flowmeter," although the buoyancy force on the "floating element" is not sufficient to make it float.

The bob is commonly formed of a combination of cylindrical and conical sections, but a spherical bob is often used in small diameter tubes (see Figures 52.2). More complicated bob geometries can reduce the sensitivity to viscosity of the fluid. Frequently, the bob has several shallow inclined grooves around the upper rim that induce a slow rotation (frequency about 1 Hz) of the bob, which helps to maintain a stable position of the bob. In larger rotameters where the additional friction is acceptable, the bob can be allowed to slide up and down a rod on the tube axis to prevent any sideways motion.

Various tube geometries are in use. The basic requirement for an increase in the cross-sectional area up the height of the tube leads to the conical tube. An alternative form uses three ribs arranged circumferentially around the tube to guide the bob; the flow area between the ribs increases along the tube height. For spherical bobs, a triangular tube in which the bob remains in contact with three surfaces over the whole height of the tube prevents lateral movement of the bob with minimum friction. Commonly, the tube is made of glass to facilitate the reading of the flow rate from a scale engraved on the tube. For general-purpose applications, the scale can be marked in millimeters; the flow rate is then determined by a conversion factor depending on the tube dimensions, the mass of the bob, the pressure and temperature, and the properties of the fluid. For specific application to a single fluid under controlled conditions, it is more convenient to have the flow rate directly marked on the tube.

For laboratory use, medical equipment, and other applications with small flow rates, the glass tube is almost universal. Laboratory meters are often equipped with a flow valve that allows direct-flow setting and reading. For many small rotameters, integrated flow controllers are offered; these hold the pressure drop and the flow setting constant, even with changing upstream or downstream pressure.

For most rotameters, electric limit switches or analog electric signal transducers are available. For glass and plastic meters, inductive or optical switches are used that can be positioned to the desired level of the bob. While some units just detect the bob within their active area, other switches have bistable operation, wherein the switch is toggled by the float passing the switch.

For industrial applications, the metering of corrosive fluids or fluids at high temperature or pressure leads to the use of stainless steel tubes or a wide range of other materials chosen to suit the application requirements (e.g., temperature, pressure, corrosion). Most metal rotameters use a permanent magnetic coupling between the float and the pointer of the indicator, enabling a direct analog flow reading without electric supply. Electric switches can, however, be added to the indicator, and electric and pneumatic transmitters for the flow reading are offered by most producers. Some units are equipped with options such as flow totalizers, mass flow calculation units for gas applications in conjunction with temperature and pressure sensors, or energy calculation units. Due to the frequent application of the rotameter in the chemical and petrochemical industry, electric options are often designed for use in hazardous areas.

The rotameter is characterized by

- Simple and robust construction
- High reliability
- Low pressure drop

Applicable to a wide variety of gases and liquids
Flow range typically 0.04 L h^{-1}–150 m^3 h^{-1} for water
Flow range typically 0.5 L h^{-1}–3000 m^3 h^{-1} for air
10:1 flow range for given bob-tube combination
Uncertainty 0.4%–4% of maximum flow
Insensitivity to nonuniformity in the inflow (no upstream straight piping needed)
Typical maximum temperature 400 °C
Typical maximum pressure 4 MPa (40 bar)

- Low investment cost
- Low installation cost

52.1.2 Movable Vane Meter

The movable vane meter is a robust device suitable for the measurement of high flow rates where only moderate requirements on the measurement accuracy are made. Dirty fluids can also be metered. It contains a flap that at zero flow is held closed by a weight or a spring (Figure 52.3). A flow forces the vane open until the dynamic force of the flow is in balance with the restoring force of the weight or the spring. The angle of the vane is thus a measure of the flow rate, which can be directly indicated by a pointer attached to the shaft of the vane on a calibrated scale. The resistance provided by the vane depends on the vane position and hence on the flow rate or Reynolds number; a recalibration is therefore necessary when the fluid is changed. An important application is the metering of the airflow in automotive engines with fuel injection.

In low-cost flow indicators, a glass or plastic window allows a direct view of the flap (Figure 52.4). Sometimes, optical or reed switches in combination with a permanent magnet attached to the flap are used as electric flow switches. All-metal units use a magnetic coupling between the vane and the pointer of the indicator, thus avoiding most of the friction and material selection problems. Many applications

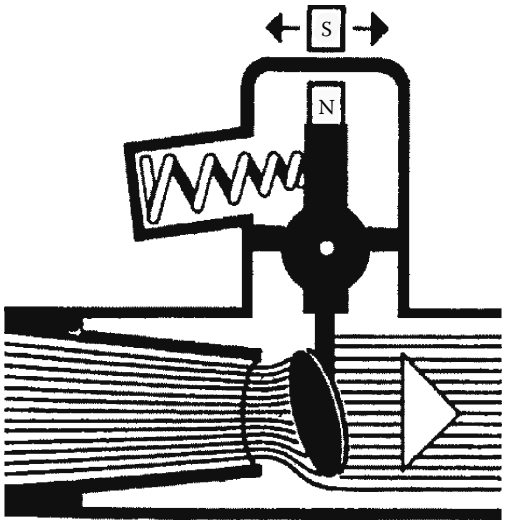

FIGURE 52.3 Movable vane meter. The magnet (N,S) transmits the vane position to an indicator.

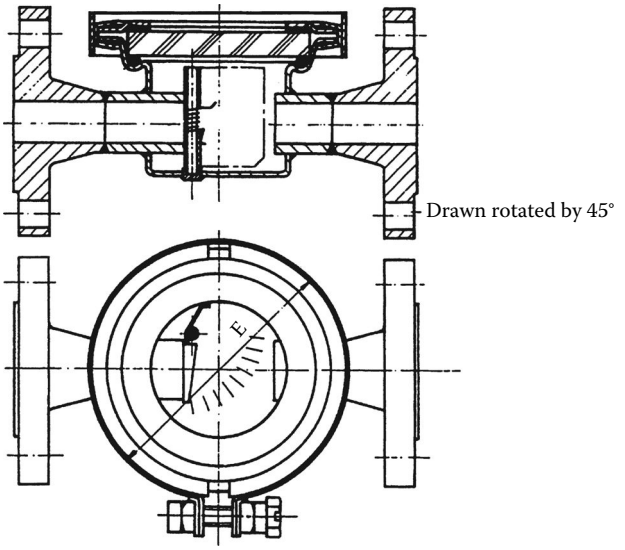

FIGURE 52.4 Flow indicator. The angle of the vane provides a measure of the flow rate.

use the movable vane meter as a flow switch with appropriate mechanical, magnetic, inductive, or optical switches. The setting of the switch is done once for all during the installation. Since a continuous flow indication is not needed, flow reading uncertainties are not of concern.

Most aspects of design and application of rotameters can be applied to movable vane meters, although the latter are characterized by a higher uncertainty of the flow reading. The general features of both types of variable area flowmeter are summarized, for example, in Ref. [1]. Since the basic construction of the two meter types is very similar, the unit costs also lie in the same range.

52.1.3 Weir and Flume

Of the methods available for the metering of a liquid (generally water) in open-channel flow, the weir and the flume fall within the scope of this discussion on variable area flowmeters. In each case, the flowmetering depends on measurement of the difference in height h of the water surface over an obstruction across the channel and the surface sufficiently far upstream. There is a wide variety of geometries in use (see Ref. [2]), but most of these can be described as variants of three basic types. In the sharp-crested weir, also known as the thin-plate weir (Figure 52.5), the sill or crest is only about 1–2 mm thick. The sheet of liquid flowing over the weir, called the nappe or vein, separates from the weir body after passing over the crest. An air-filled zone at atmospheric pressure is formed underneath the outflowing jet, and the streamlines above the weir are strongly curved. When the width of the weir is less than that of the upstream channel (Figures 52.6 and 52.7), the term "notch" is frequently used. A broad-crested weir (Figure 52.8) has a sill that is long enough for straight, parallel streamlines to form above the crest. In this review, the term "weir" is applied generally to both the weir and the notch.

The resistance to flow introduced by the weir causes the water-level upstream to rise. If it is assumed that the flow velocity, some distance upstream of the weir, is zero, then a simple measure of the upstream water level suffices to determine the discharge over a weir of known geometry. As in the case of an orifice in pipe flow, there will be a contraction of the nappe and a frictional resistance at the sides as water flows over a weir. The actual discharge is less than the theoretical discharge according to an empirically determined coefficient of discharge C_d. In the analysis of rectangular notches and weirs, it is frequently

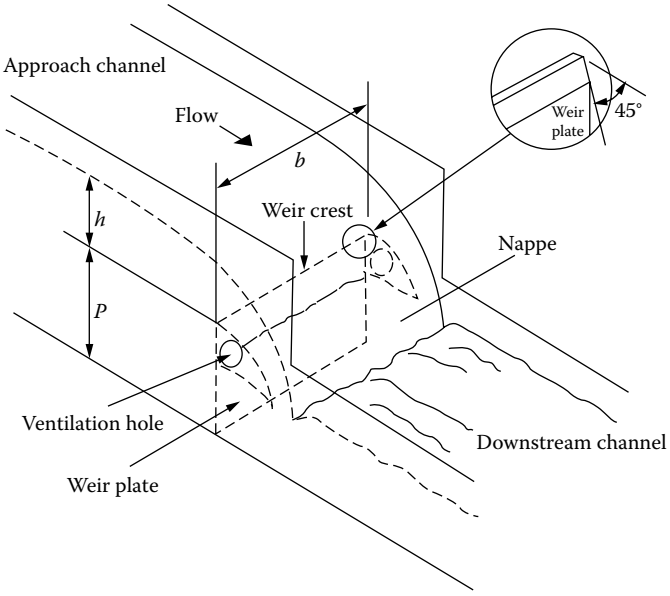

FIGURE 52.5 Full-width thin-plate weir. Flow rate $\dot{Q}$ varies with water level h above the weir crest ($\dot{Q} - h^{3/2}$) and with a flow-dependent discharge coefficient C_d.

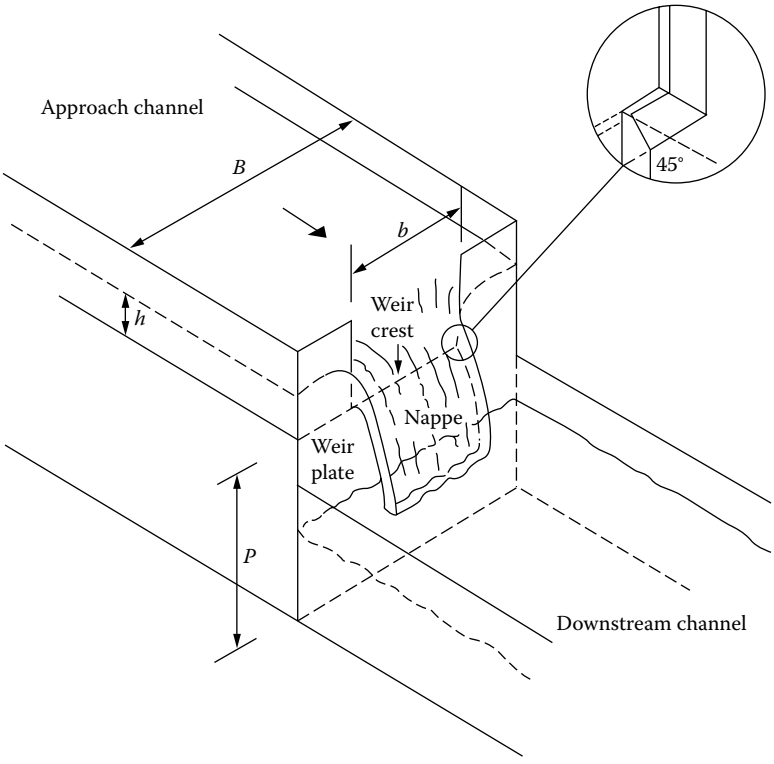

FIGURE 52.6 Thin-plate rectangular notch weir: discharge coefficient C_d is flow dependent.

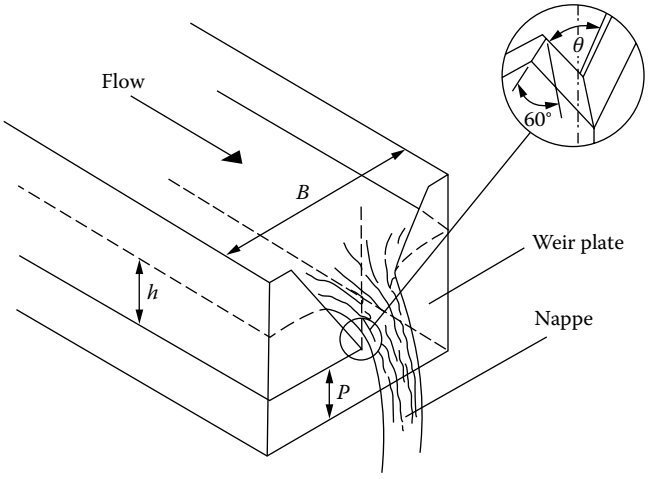

FIGURE 52.7 Thin-plate V-notch weir: discharge coefficient C_d is almost independent of the flow.

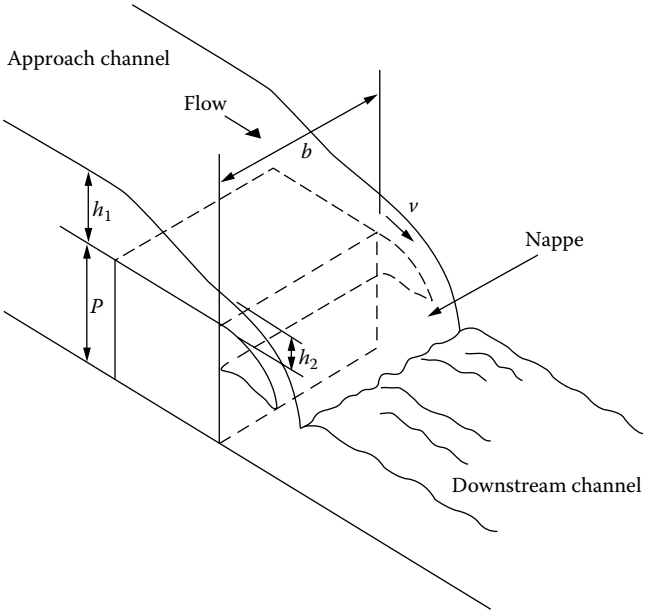

FIGURE 52.8 Broad-crested weir: maximum discharge when $h_2 = 2h_1/3$.

assumed that the channel width remains constant so that a contraction of the nappe occurs only in the vertical direction as the water accelerates over the obstacle. When the weir is narrower than the upstream channel, there is an additional horizontal contraction. The effect of a significant upstream velocity is accounted for empirically.

As an alternative to the weir, the flume (Figure 52.9) provides a method for flowmetering with relatively low pressure loss. By restricting the channel width, analogous to the venturi tube used in pipe flow, the flow velocity in the narrow portion of the channel is increased and the water level sinks accordingly. Most of the head of water is recovered in the diffusing section of the weir. The water levels upstream and in the throat of the weir can be determined by simple floats and recorded on a chart by pens driven mechanically from the floats. For remote monitoring, the use of echo sounders is advantageous.

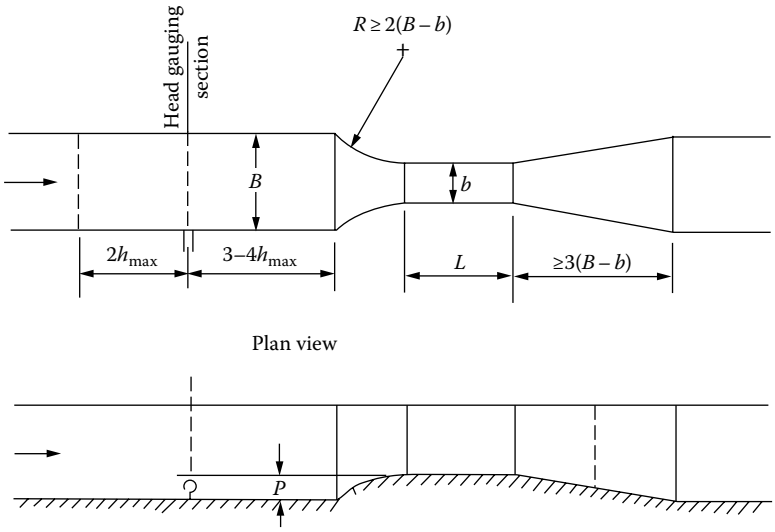

FIGURE 52.9 Venturi flume: maximum discharge when throat depth = 2/3 × total head.

The weir is preferentially used in natural riverbeds and the flume in canalized water courses. The flume must be used in streams with sediment transport to avoid the accumulation of deposits that would occur at the approach to a weir. Weirs and flumes are characterized by

- Simple measurement of the water level
- Simple maintenance
- Reliable measurement of large flow rates at low stream velocity
- Limited measurement accuracy (at best about 2%)
- High installation costs, particularly for flumes

Recommendations for installation of weirs and flumes, for the location of the head measuring station upstream, and for determining the discharge from the measured head are given, for example, in [2, 3] as well as in appropriate standards (e.g., [4–6]).

52.2 Measuring Principles of Variable Area Flowmeters

52.2.1 Rotameter

52.2.1.1 Flow Rate Analysis

The forces acting on the bob lead to equilibrium between the weight of the bob $\rho_b g V_b$ acting downward and the buoyancy force $\rho g V_b$ and the drag force F_d acting upward, where V_b is the volume and ρ_b is the density of the bob, ρ is the density of the fluid, and g is the gravitational acceleration:

$$\rho_b g V_b = \rho g V_b + F_d \tag{52.1}$$

The drag force results from the flow field surrounding the bob and particularly from the wake of the bob. In flow analyses based on similarity principles, these influences are accounted for by empirical coefficient C_L or C_T in the drag law for

$$\text{Laminar flow } F_d = C_L \mu D_b U \tag{52.2}$$

$$\text{Turbulent flow } F_d = C_T \rho D_b^2 U^2 \tag{52.3}$$

where
μ is the fluid viscosity
D_b is the maximum bob diameter
U is the velocity in the annular gap around the bob at the minimum cross section

The volume flow rate through the rotameter is

$$\dot{Q} = \frac{\pi}{4}(D^2 - D_b^2)U \tag{52.4}$$

or

$$\dot{Q} = m\frac{\pi}{4}D_b^2 U \tag{52.5}$$

where m is the open area ratio, defined as

$$m = \frac{D^2 - D_b^2}{D_b^2} \tag{52.6}$$

and D is the tube diameter at the height of the bob.

Combining Equations 52.1, 52.2, and 52.4 for laminar flow gives

$$\dot{Q}_L = \alpha D_b^4 \frac{(\rho_b - \rho)g}{\mu} \tag{52.7}$$

where the parameter α is defined in terms of a constant $K = V_b/D_b^3$ characteristic of the shape of the bob

$$\alpha = \frac{\pi m K}{4C_L} \tag{52.8}$$

Using Equation 52.3 instead of Equation 52.2 yields for turbulent flow

$$\dot{Q}_T = \beta D_b^{5/2}\sqrt{\frac{(\rho_b - \rho)g}{\rho}} \tag{52.9}$$

where

$$\beta = \frac{\pi m}{4}\sqrt{\frac{K}{C_T}} \tag{52.10}$$

With either laminar or turbulent flow through the rotameter, it is clear from Equations 52.7 and 52.9 that the flow rate is proportional to m. If the cross-sectional area of the tube is made to increase linearly with length, that is,

$$D = D_b(1 + h\tan\phi) \tag{52.11}$$

then since the cone angle ϕ of the tube is small, Equation 52.6 can be written as

$$m = 2h\tan\phi \tag{52.12}$$

and the flow rate is directly proportional to the height h of the bob.

52.2.1.2 Similarity Analysis

In early studies of floating element flowmeters, Ruppel and Umpfenbach [7] proposed the introduction of characteristic dimensionless quantities, to permit the use of experimentally determined flow coefficients in flowmeter analysis. Lutz [8] extended these ideas by showing that the transfer of flow coefficients from one flowmeter to another is possible if geometrical similarity exists. More recent works [9–12] have used these principles to produce graphical or computer-based design schemes and have proposed general guidelines for laying out practical flowmetering systems.

The basic scaling parameter for flow is the Reynolds number, defined as

$$\mathrm{Re} = \frac{\rho U_{\mathrm{IN}} D_{\mathrm{b}}}{\mu} \tag{52.13}$$

where U_{IN} is the velocity at the rotameter inlet and the tube diameter D is represented by its value at the inlet, equal to the bob diameter D_{b}. Through the Reynolds number, regimes of laminar or turbulent flow, and particularly important for the rotameter flow regimes with strong or weak viscosity dependence, can be distinguished. Originating in the work [7], it has been found to be practical for rotameters to use an alternative characteristic number, the Ruppel number, defined as

$$\mathrm{Ru} = \frac{\mu}{\sqrt{m_{\mathrm{b}} g \rho (1 - \rho/\rho_{\mathrm{b}})}} \tag{52.14}$$

where $m_{\mathrm{b}} = \rho_{\mathrm{b}} D_{\mathrm{b}}^3$ is the mass of the bob. By combining Equations 52.9, 52.10, and 52.14, the mass flow $\dot{m}$ through the rotameter can be written as

$$\dot{m} = \frac{\pi}{4} \frac{m D_{\mathrm{b}} \mu}{\sqrt{C_{\mathrm{T}}}\,\mathrm{Ru}} \tag{52.15}$$

Alternatively, from the definition

$$\dot{m} = \rho \dot{Q} = \rho U_{\mathrm{IN}} \frac{\pi}{4} D_{\mathrm{b}}^2 \tag{52.16}$$

and Equation 52.13, the flow rate is

$$\dot{m} = \frac{\pi}{4} D_{\mathrm{b}} \mu \mathrm{Re} \tag{52.17}$$

Equations 52.15 and 52.17 give the following relationship between the Ruppel number and the Reynolds number:

$$\mathrm{Ru} = \frac{m}{\sqrt{C_{\mathrm{T}} \mathrm{Re}}} \tag{52.18}$$

An analysis for laminar flow leads to the relationship

$$\mathrm{Ru} = \sqrt{\frac{m}{C_{\mathrm{L}} \mathrm{Re}}} \tag{52.19}$$

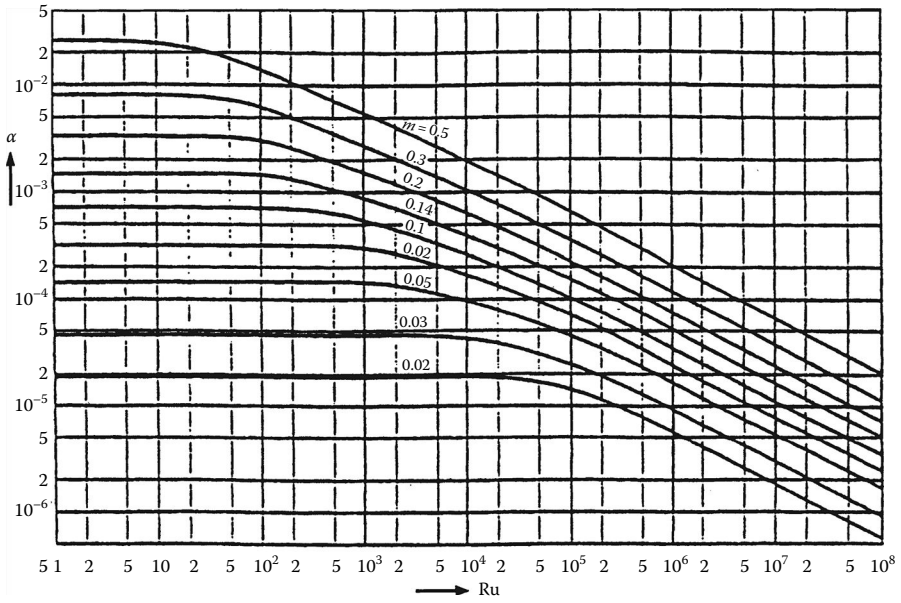

FIGURE 52.10 Rotameter flow coefficient α as a function of Ruppel number Ru and open area ratio m. For a given geometry, α is constant for low Ru (laminar flow).

The advantage of the Ruppel number is its independence of the flow rate. Since the Ruppel number contains only fluid properties and the mass and the density of the bob, it is a constant for a particular instrument.

At low Ruppel numbers, the linear resistance law assumed in Equation 52.2 applies and α is a constant for given m, as shown in Figure 52.10. At higher Ruppel numbers, the flow is transitional or turbulent, and log α decreases linearly with log Ru. In Figure 52.11, curves for β against Ruppel number show a linear increase of log β with log Ru in the laminar region, followed by a gradual transition to horizontal curves in fully turbulent flow.

Similarity analysis of rotameters allows the easy calculation of the flow reading with changing density and viscosity of the fluid. For lower viscosities, only the density effect has to be taken into account; hence, for most gas measurements, simple conversion factors can be used. With higher viscosity, manufacturers offer either Ruppel number–related conversion factors or 2D tables of conversion factors to be applied to different heights of the bob. Some manufacturers offer recalibration services, allowing the user to order new scales for instruments to be used in changed applications and environments. For large-order users, simple computer programs are available from some manufacturers for scale calculations.

Theories based on similarity considerations can predict the variation of the flow coefficient with the Ruppel number in the laminar and turbulent flow regimes but not in laminar–turbulent transitional flow. Detailed experimental and computational studies can assist the flow analysis of floating element flowmeters. An example is given in the section "Rotameter Internal Flow Analysis."

52.2.2 Weir and Flume

52.2.2.1 Flow Rate Analysis for Weirs

Although the determination of the discharge across a weir or a flume generally requires the knowledge of one or more empirical coefficients, the basic equations describing the head-discharge characteristics of the various geometrical forms are readily derived from simple fluid mechanics considerations.

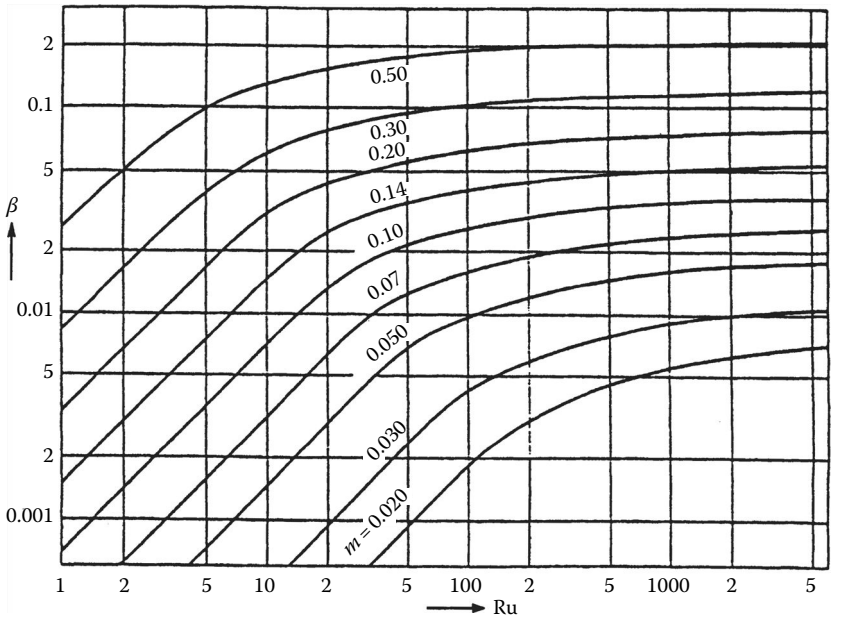

FIGURE 52.11 Rotameter flow coefficient β as a function of Ruppel number Ru and open area ratio m. For a given geometry, β is constant for high Ru (turbulent flow).

The discharge over a sharp-crested weir of width b (Figure 52.5) when the water level over the sill is h is analyzed by considering a horizontal strip of water of thickness δy at a depth y below the water surface. Since the velocity of the water through this strip is $\sqrt{2gy}$, the discharge is

$$\delta\dot{Q} = b\delta y\sqrt{2gy} \tag{52.20}$$

The total discharge is obtained by integration, introducing a coefficient of discharge C_d:

$$\dot{Q} = C_d\sqrt{2gb}\int_0^h \sqrt{y}dy \tag{52.21}$$

$$\dot{Q} = \frac{2}{3}C_d\sqrt{2g}bh^{3/2} \tag{52.22}$$

Empirical corrections to Equation 52.22 to account for the weir height p are given, for example, in [3], but provided h/p does not exceed 0.5, it is adequate to use Equation 52.22 with a discharge coefficient of 0.63 to achieve a flow rate tolerance of 3%.

For the rectangular notch, Equation 52.22 also applies with a discharge coefficient of 0.59 and a flow rate tolerance of 3%. Since in practice, the discharge coefficient varies slightly with the head of water for both weirs and notches, it is sometimes preferred to replace Equation 52.22 by $\dot{Q} = Kbh^n$, where K and n are determined by calibration.

The triangular notch (Figure 52.7) offers the advantage that the length of the wetted edge varies with the head of water, in contrast with the rectangular notch where it is constant. Consequently, the discharge coefficient of the triangular notch is constant for all heads. Furthermore, the achievable range (ratio of maximum to minimum flow rates) is higher for the triangular geometry. If h is the height of the

water surface and θ is the angle of the notch, then a horizontal strip of the notch of thickness δy at depth y has a width $2(h - y)\tan(\theta/2)$. The discharge through this strip is

$$\delta\dot{Q} = 2(h-y)\tan\frac{\theta}{2}\delta y\sqrt{2gy}C_{\mathrm{d}} \tag{52.23}$$

giving a total discharge through the notch

$$\dot{Q} = 2C_{\mathrm{d}}\sqrt{2g}\tan\frac{\theta}{2}\int_0^h (h-y)\sqrt{y}\,dy \tag{52.24}$$

$$\dot{Q} = \frac{8}{15}C_{\mathrm{d}}\sqrt{2g}\tan\frac{\theta}{2}h^{5/2} \tag{52.25}$$

The discharge coefficient is about 0.58.
Commonly used notch angles are 90° (tan $\theta/2 = 1$, $C_{\mathrm{d}} = 0.578$), 53.13° (tan $\theta/2 = 0.5$, $C_{\mathrm{d}} = 0.577$), and 28.07° (tan $\theta/2 = 0.25$, $C_{\mathrm{d}} = 0.587$). Notches with $\theta = 53.13°$ and $\theta = 28.07°$ deliver, respectively, one-half and one-quarter of the discharge of the 90° notch at the same head.

The aforementioned derivations assume that the water is discharging from a reservoir with cross-sectional area far exceeding the flow area at the weir, so that the velocity upstream is negligible. When the weir is built into a channel of cross-sectional area A, the water will have a finite velocity of approach $v_1 = \dot{Q}/A$. As a first approximation, $\dot{Q}$ is obtained from Equation 52.22 assuming zero velocity of approach. Assuming further that v_1 is uniform over the weir, there will be additional head $v_1^2/2g$ acting over the entire weir. Referring to Figure 52.5, the total discharge is then

$$\dot{Q} = C_{\mathrm{d}}\sqrt{2gb}\int_{v_1^2/2g}^{h+v_1^2/2g}\sqrt{y}\,dy \tag{52.26}$$

$$\dot{Q} = \frac{2}{3}C_{\mathrm{d}}\sqrt{2gb}\left[(h+v_1^2/2g)^{3/2} - (v_1^2/2g)^{3/2}\right] \tag{52.27}$$

From Equation 52.27, a corrected value of v_1 can be determined. Further iterations converge rapidly to the final value of the discharge $\dot{Q}$. Equation 52.27 can be written as

$$\dot{Q} = \frac{2}{3}C_{\mathrm{v}}C_{\mathrm{d}}\sqrt{2g}bh^{3/2} \tag{52.28}$$

where

$$C_{\mathrm{v}} = \left(1+\frac{v_1^2}{2gh}\right)^{3/2} - \left(\frac{v_1^2}{2gh}\right)^{3/2} \tag{52.29}$$

is the coefficient of velocity, which is frequently determined empirically.

Over a broad-crested weir (Figure 52.8), the discharge depends on the head h_1, the width b, and the length l of the sill. There is also a dependence on the roughness of the sill surface and the viscosity. Consequently, there is a loss of head as the water flows over the sill. It is assumed that the sill is of suf-

ficient length to allow the velocity to be uniform at a value v throughout the depth h_2 of the water at the downstream edge of the sill. Neglecting losses,

$$v = \sqrt{2g(h_1 - h_2)}$$

and the discharge is

$$\dot{Q} = C_d b h_2 v = C_d b \sqrt{2g\left(h_1 h_2^2 - h_2^3\right)} \tag{52.30}$$

From Equation 52.30, the discharge is a maximum when $(h_1 h_2^2 - h_2^3)$ reaches a maximum, that is, when $h_2 = 2h_1/3$. This discharge is then

$$\dot{Q} = \left(\frac{2}{3}\right)^{3/2} C_d b \sqrt{g} h_1^{3/2} \tag{52.31}$$

The stable condition of the weir lies at the maximum discharge.

52.2.2.3 Flow Rate Analysis for Flumes

The discharge through a flume depends on the water level h, the channel width b, and the velocity v at each of the stations 1 (upstream) and 2 (at the minimum cross section) in Figure 52.9. Applying Bernoulli's equation to the inlet and the throat and neglecting all losses, one obtains

$$\rho g H = \rho g h_1 + \frac{1}{2}\rho v_1^2 = \rho g h_2 + \frac{1}{2}\rho v_2^2 \tag{52.32}$$

where H is the total head. The analysis is then formally the same as that for the broad-crested weir, giving the same expression for the discharge as in Equation 52.31. The flow through the flume is a maximum when the depth at the throat is two-thirds of the total head. Normally, a coefficient of velocity is introduced so that the discharge equation is

$$\dot{Q} = \left(\frac{2}{3}\right)^{3/2} C_v C_d b \sqrt{g} h_1^{3/2} \tag{52.33}$$

The combined coefficient is determined empirically. In [3], a value $C_v C_d = 1.061 \pm 0.085$ is quoted.

The validity of the empirical coefficients quoted earlier, or of other coefficients given in the various standards for metering of open-channel flows, can only be guaranteed with a given confidence level for meter installations satisfying certain geometrical constraints. Limits on quantities such as b, h, and h/b are given in [3] and the standards.

52.2.3 Rotameter: Internal Flow Analysis

52.2.3.1 Computation of Internal Flow

The improvement of rotameter design could be assisted by detailed knowledge of the internal flow field, which is characterized by steep velocity gradients and regions of separated flow. The measurements of the internal flow field are complicated by the small dimensions of the gap around the bob and the strongly curved glass tube. Bückle et al. [13] successfully used laser Doppler anemometry [14] for velocity measurements in a rotameter. The working fluid was a glycerin solution with an index of refraction (1.455) close to that of glass (1.476). Problems with refraction of the laser beams at the curved tube wall were thus avoided, but the high viscosity of glycerin restricted the experiments to laminar flow at Reynolds numbers $\mathrm{Re} = \rho U_{IN} D_b/\mu < 400$.

The application of computational fluid dynamics to the flow in a rotameter [13] involves the finite volume solution of the conservation equations for mass and momentum. For a 2D laminar flow, these equations can be written in a cylindrical polar coordinate system as

$$\frac{\partial \rho}{\partial t} + \frac{\partial(\rho u)}{\partial z} + \frac{1}{r}\frac{\partial(\rho r v)}{\partial r} = 0 \tag{52.34}$$

$$\frac{\partial(\rho u)}{\partial t} + \frac{\partial}{\partial z}\left(\rho uu - 2\mu\frac{\partial u}{\partial z}\right) + \frac{1}{r}\frac{\partial}{\partial r}\left(\rho ruv - \mu r\left(\frac{\partial u}{\partial r} + \frac{\partial v}{\partial z}\right)\right) = -\frac{\partial p}{\partial z} \tag{52.35}$$

$$\frac{\partial(\rho v)}{\partial t} + \frac{\partial}{\partial z}\left(\rho uv - \mu r\left(\frac{\partial u}{\partial r} + \frac{\partial v}{\partial z}\right)\right) + \frac{1}{r}\frac{\partial}{\partial r}\left(\rho rvv - 2\mu r\frac{\partial v}{\partial r}\right) = -\frac{\partial p}{\partial r} \tag{52.36}$$

where

μ is the density
u, v and r, and z are the velocity components and coordinate directions in the axial and radial directions, respectively
μ is the dynamic viscosity
p is the pressure

For the numerical solution, the governing equations for a generalized transport variable ϕ (i.e., u or v) are formally integrated over each control volume (CV) of the computational grid. The resulting flux-balance equation can in turn be discretized as an algebraic equation for ϕ at the center P of each CV in terms of the values ϕ_{nb} at the four nearest neighbors of point P and known functions A:

$$A_{p\phi p} + \sum_{nb} A_{nb}\phi_{nb} = S_{\phi} \tag{52.37}$$

For the whole solution domain, a system of equations results that can be solved by a suitable algorithm (e.g., [15]).

For a rotameter, the symmetry of the problem allows the computational solution domain to be chosen as one-half diametral plane of the rotameter. The boundary conditions are

$$u = v = 0 \tag{52.38}$$

along the walls and

$$\frac{\partial u}{\partial r} = v = 0 \tag{52.39}$$

along the axis of symmetry. At the input boundary, the initial profile for the u velocity is taken from the experiment. At the outlet boundary, zero gradients are assumed for all dependent variables.

52.2.3.2 Computed Flow Field

Representative calculations for Reynolds number 220 are shown as velocity vectors (Figure 52.12) and streamlines (Figure 52.13). Experimental and computed velocity profiles over a radius of the flowmeter tube are shown in Figure 52.14.

At $z = 45$ mm, the computations indicate a stagnation point at the bob tip, but the measurements show a low but finite axial velocity. The deviation from zero is attributable to slight unsteadiness in the position of the bob and to smearing of the steep radial velocity gradient along the measuring volume. This

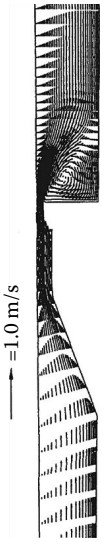

FIGURE 52.12 Computed velocity vectors for laminar flow through a rotameter. Computations in a half diametral plane for axisymmetric flow at Reynolds number 220.

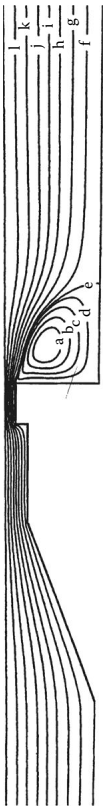

FIGURE 52.13 Computed streamlines for laminar flow through a rotameter (Reynolds number 220).

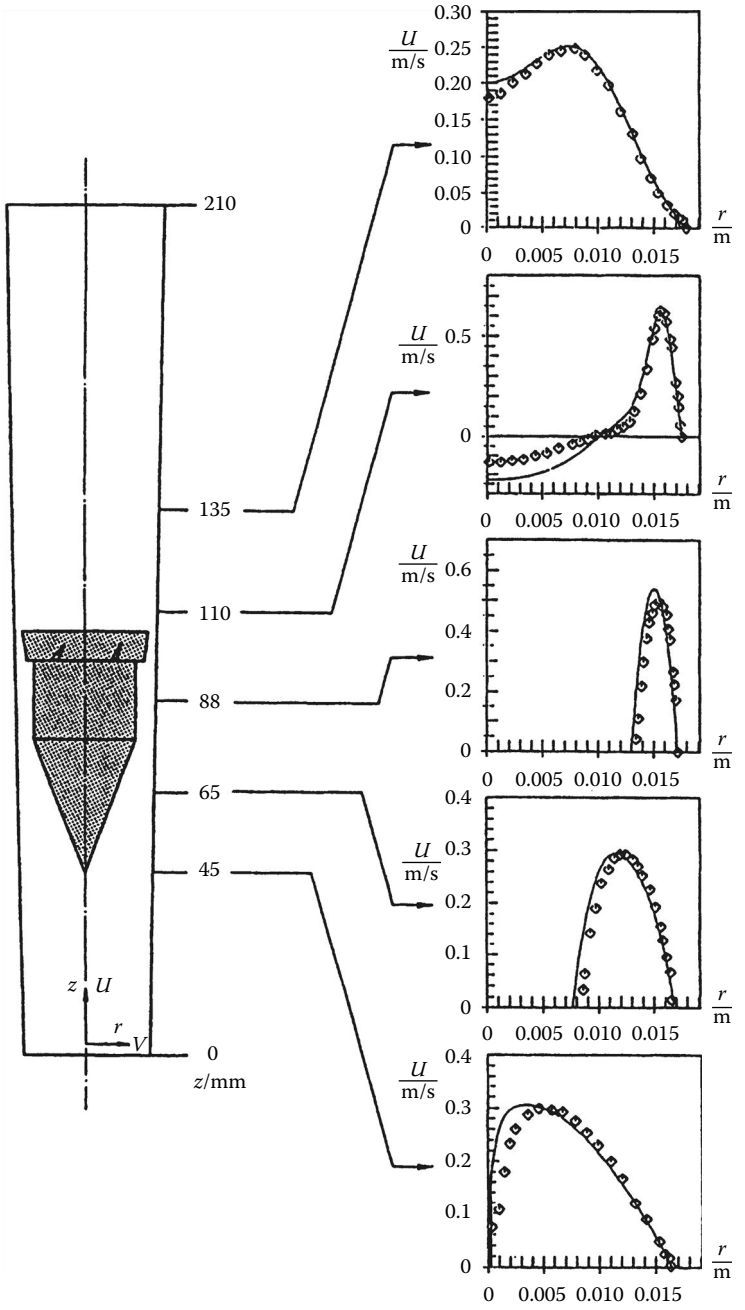

FIGURE 52.14 Comparison of measured and computed velocity profiles for laminar flow through a rotameter (Reynolds number 220). U = axial component (m/s), z = axial position (mm), and r = radial position (m).

effect is also apparent at radii up to about 5 mm, where the computations show a notably steeper velocity gradient than the measurements. The measured and computed peak velocities agree well, although the measured peak is located at a larger radius.

In the strongly converging annulus between the bob and the tube wall (z = 65 mm) and in the plane z = 88 mm, the computations reproduce well the trend of the measured results, particularly near the flowmeter wall. Discrepancies in the region adjacent to the bob are attributable to asymmetry in measured profiles arising from the piping upstream of the rotameter tube.

Above the bob (z = 110 mm), there is a strong upward flow in an annular region near the tube wall and a recirculation region around the axis occupying almost half the tube cross section. The forward velocities show a good match between computations and measurements, but there is a very marked discrepancy in the recirculation zone. At z = 135 mm, the recirculation zone is finished, but the wake of the bob is still very evident. Except for a discrepancy of about 10% on the axis, the results from the two methods agree remarkably well.

The effect of rotation of the bob on the flow field was considered by computations, including an equation for the azimuthal velocity component w:

$$\frac{\partial(\rho w)}{\partial t} + \frac{\partial}{\partial z}\left(\rho uw - \mu\frac{\partial w}{\partial z}\right) + \frac{1}{r}\frac{\partial}{\partial r}\left(\rho rvw - \mu r\frac{\partial w}{\partial r}\right) = -\rho\frac{vw}{r} - \mu\frac{w}{r^2} \tag{52.40}$$

Calculations for 1 Hz rotation frequency showed the highest swirl velocities close to the axis above the bob. There was no observable influence of the rotation on the u- and v-velocity components [16].

52.3 Summary

For pipe flows, variable area flowmeters are most suitable for low flow rates of gases or liquids at moderate temperatures and pressures. Favorable features include rugged construction, high reliability, low pressure drop, easy installation, and low cost. Disadvantages include measurement uncertainty of 1% or more, limited range (10:1), slow response, and restrictions on the meter orientation. A generally good price/performance ratio has led to widespread use of these meters in numerous scientific and medical instruments and in many industrial applications for flow monitoring.

Variable area flowmeters in open-channel flows have applications for flow measurements in wastewater plants, waterworks, rivers and streams, irrigation, and drainage canals. Hydrological applications of weirs with adjustable sill or crest height include flow regulation, flow measurement, upstream water-level control, and discharge of excess flow in streams, rivers, and canals. Ruggedness, simplicity, and low maintenance costs are favorable characteristics for field applications of these meters.

References

1. R. A. Furness, BS7045: the principles of flowmeter selection, *Flow Meas. Instrum.*, 2, 233–242, 1991.
2. W. Boiten, Flow-measuring structures, *Flow Meas. Instrum.*, 4, 17–24, 1993.
3. R. Hershey, General purpose flow measurement equations for flumes and thin plate weirs, *Flow Meas. Instrum.*, 6, 283–293, 1995.
4. ISO 1438, *Thin Plate Weirs*, International Standards Organisation, Geneva, Switzerland, 1980.
5. ISO 4359, *Rectangular, Trapezoidal and U-Shaped Flumes*, International Standards Organisation, Geneva, Switzerland, 1983.
6. ISO 8368, *Guidelines for the Selection of Flow Gauging Structures*, International Standards Organisation, Geneva, Switzerland, 1985.

7. G. Ruppel and K. J. Umpfenbach, Stromungstechnische Untersuchungen an Schwimmermessern, *Technische Mechanik und Thermodynamik*, 1, 225–233, 257–267, 290–296, 1930.
8. K. Lutz, Die Berechnung des Schwebekörper-Durchfluβmessers, *Regelungstechnik*, 10, 355–360, 1959.
9. D. Bender, Ähnlichkeitsparameter und Durchfluβgleichungen für Schwebekörperdurchfluβmesser, *ATM-Archiv für Technisches Messen*, 391, 97–102, 1968.
10. VDE/VDI-Fachgruppe Meβtechnik 3513, *Schwebekörperdurchfiu*βmesser, Berechnungsverfahren, VDE/VDI 3513, 1971.
11. H. Nikolaus, Berechnungsverfahren für Schwebekörperdurchfluβmesser, theoretische Grundlagen und Aufbereitung für die Datenverarbeitungsanlage, *ATM-Archiv für Technisches Messen*, 435, 49–55, 1972.
12. H. Nikolaus and M. Feck, Graphische Verfahren zur Bestimmung von Durchfluβkennlinien für Schwebekörperdurchfluβmeβgeräte, *ATM-Archiv für Technisches Messen*, 1247–5, 171–176, 1974.
13. U. Bückle, F. Durst, B. Howe, and A. Melling, Investigation of a floating element flow meter, *Flow Meas. Instrum*., 3, 215–225, 1992.
14. F. Durst, A. Melling, and J. H. Whitelaw, *Principles and Practice of Laser-Doppler Anemometry*, 2nd ed., Academic Press, London, U.K., 1981.
15. M. Perić, M. Schäfer, and E. Schreck, Computation of fluid flow with a parallel multigrid solver, *Proc. Conf. Parallel Computational Fluid Dynamics*, Stuttgart, 1991.
16. U. Bückle, F. Durst, H. Köchner, and A. Melling, Further investigation of a floating element flowmeter, *Flow Meas. Instrum*., 6, 75–78, 1995.

Further Readings

BES Flowmeters, MPB Variable Area Flowmeters for Air & Water. http://www.besflowmeters.com.au/mpb/mpb.html (accessed on July 27, 2012).

Flow Meter Directory, Variable Area Flowmeter Principles, On Line 22/05/2007. http://www.flowmeterdirectory.com/flowmeter_artc_07052201.html (accessed on July 26, 2012).

Lake Monitors, Variable Area Flow Meters. http://www.lakemonitors.com/variable_area.htm (accessed on July 25, 2012).

Partial List of Vendors and Suppliers

Bailey Fischer & Porter Co., County Line Rd., Warminster, PA 18974, Tel.: (215) 674-6000, Fax: (215) 674-7183,

Bopp & Reuther Heinrichs Messtechnik GmbH, Stolberger Str. 393, D-50933 Köln, Germany, Tel.: +49-221-49708-0, Fax: +49-221-497088

Brooks Instrument Division, 407 W. Vine St., Hatfield, PA 19440, Tel.: (215) 362-3500, Fax: (215) 362-3745, http://www.brooksinstrument.com/

CT Platon, Jays Close, Viables, Basingstoke, Hampshire RG22 4BS, Great Britain, Tel.: +44-1256-470456, Fax: +44-1256-363345

ERDCO Engineering Corp., 721 Custer Ave.8, P.O. Box 6318, Evanston, IL 60204–6318, Tel.: 847-328-0550, 800-553-0550 (toll free), Fax: 847-328-3535, www.erdco.com

Erdman Corp., 1900 W. Muhammad Ali Blvd., Louisville, KY 40203, Tel.: 502-584-1271, 800-523-0420 (toll free), Fax: 502-584-3611, www.erdmanncorp.com

KDG-Mobrey Ltd., Crompton Way, Crawley, West Sussex RH10 2YZ, Great Britain, Tel.: +44-1293-518632, Fax: +44-1293-533095

Kobold Messring GmbH, Nordring 22-24, D-65719 Hofheim/Taunus, Germany, Tel.: +49 6192 2990, Fax: +49 6192 23398, http://kobold.com/

Krohne America Inc., 7 Dearborn Rd., Peabody, MA 01960, Tel.: (508) 535-6060, (800) 356-9464, Fax: (508) 535-1720,

Orange Research, Inc., 140 Cascade Blvd., Milford, CT 06460, Tel.: 203-877-5657, 800-989-5657 (toll free), Fax: 203-783-9546, www.orangeresearch.com

Porter Instrument Div., parker Hannifin Corp., 245 Township Line Rd., P.O. Box 907-TR, Hatfield, PA 19440, Tel.: 215-723-4000, 800-457-2001 (toll free), Fax: 215-723-2199, www.porterinstrument.com

Rota Yokogawa GmbH & Co. KG, Rheinstrasse 8, D-79664 Wehr, Germany, Tel.: +49-7761-567-0, Fax: +49-7761-567-126

Ryan Herco Flow Solutions, 3010 N. San Fernando Blvd., Burbank, CA 91504, Tel.: 818-841-1141, 800-848-1141 (toll free), Fax: 818-973-2650, www.rhfs.com

Tokyo Keiso Co. Ltd., Shiba Toho Building, 1–7–24, Shibakoen, Minato-ku, Tokyo 105, Japan, Tel.: +81-3-3431-1625, Fax: +81-3-3433-4922, http://www.tokyokeiso.co.jp/english/index.html

Wallace & Tiernan, Inc., 25 Main St., St. Belleville, NJ 07109, Tel.: (201) 759-8000, Fax: (201) 759-9333, http://www.wallaceandtiernan-usa.com/

Webster Instruments USA, 1290 E. Waterford Ave., Milwaukee, WI 53235, Tel.: 414-769-6400, 800-932-8378 (toll free), Fax: 414-769-6591, 866-356-9637 (toll free), www.webster-inst.com/

53

Positive Displacement Flowmeters

Zaki D. Husain
Daniel Flow Products, Inc.

Donald J. Wass
Daniel Flow Products, Inc.

A *positive displacement flowmeter*, commonly called a PD meter, measures the volume flow rate of a continuous flow stream by momentarily entrapping a segment of the fluid into a chamber of known volume and releasing that fluid back into the flow stream on the discharge side of the meter. By monitoring the number of entrapments for a known period of time or number of entrapments per unit time, the total volume of flow or the flow rate of the stream can be ascertained. The total volume and the flow rate can then be displayed locally or transmitted to a remote monitoring station.

The PD flowmeter has been in use for many decades to measure both liquid and gas flows. A PD meter can be viewed as a hydraulic motor with high volumetric efficiency that generally absorbs a small amount of energy from the flowing fluid. The energy absorption is primarily to overcome the internal resistance of the moving parts of the meter and its accessories. This loss of energy is observed as the pressure drop across the meter. The differential pressure across the meter is the driving force for the internals of the PD meter.

53.1 Design and Construction

A PD meter has three basic components: an outer housing, the internal mechanism that creates the dividing chamber through its repetitive motion, and the display or counter accessories that determine the number of entrapments of fluid in the dividing chamber and infer the flow rate and the total volume of flow through the meter.

The external housing acts as the holding chamber of the flowing fluid before and after the entrapments by the internals. For low line pressures, the housing is usually single walled, while for higher operating pressures, the housing is double walled where the inner wall is the containment wall for the entrapment chamber and the outer wall is the pressure vessel. For the double-walled housing, the entrapment chamber walls are subjected to the differential pressure across the meter, while the external

housing is subjected to the total line pressure. This allows fabrication of a thin-walled inner chamber that can retain its precise shape and dimensions independent of line pressure.

The measuring mechanism consists of precise metering elements that require tight tolerances on the mating parts. The metering elements consist of the containment wall of the metering chamber and the moving components of the meter that form the entrapment volume of the flowing fluid by cyclic or repetitive motion of those elements. The most common types of PD meters are the oscillating-piston, nutating-disk, oval-gear, sliding-vane, birotor, trirotor, and diaphragm designs.

The counter or output mechanism converts the motion of the internal measuring chamber of a PD meter and displays the flow rate or total flow by correlating the number of entrapments and each entrapped volume. Many PD meters have a mechanical gear train that requires seals and packing glands to transmit the motion of the inner mechanism to the outside counters. This type of display requires more driving power to overcome resistance of the moving parts and the seals, which results in an additional pressure drop for the meter. Many PD meters transmit the motion of the inner mechanism to the counters through switch output utilizing electromechanical, magnetic, optical, or purely electronic techniques in counting the entrapments and displaying the flow rate and total flow volume. The latter processing techniques normally have less pressure drop than the all-mechanical or partly mechanical transmission methods. All-mechanical drive counters do not require external power and, through proper selection of gear train, can display the actual flow volume or the flow rate. Thus, meters can be installed at remote locations devoid of any external power source. Meters with mechanical display cannot easily correct for the changes in volume due to thermal expansion or contraction of the measuring chamber due to flow temperature variation and, in the case of single-walled housing, the changes in the entrapment volume due to variations of the line pressure. An electronically processed output device could monitor both the pressure and the temperature of the meter and provide necessary corrections to the meter output. With constantly changing and improving electronics technology, many PD meters are now installed with solar- or battery-powered electronic output for installations at remote locations with no external power source. Many electronic displays allow access to meter data from a central monitoring station via radio or satellite communication.

53.2 Some Commercially Available PD Meter Designs

Commercially available PD meters have many noticeably different working mechanisms, and a few designs are unique and proprietary. Although each design and working mechanism can be noticeably different from another, all PD meters have a stationary fluid retaining wall and a mechanism that momentarily entraps inlet fluid into a partitioned chamber before releasing it to the downstream side of the meter. This entrapment and release of the flowing fluid occur with such repetitive and sweeping motion that, for most practical purposes, the flow rate appears to be uniform and steady, even though, in reality, the exit flow does have some pulsation. The flow pulsation out of the meter may be more pronounced for some designs of PD meters than others. These flow pulsations are more pronounced at the lower flow rates for all designs. Some designs are more suitable for either liquid or gas flows, while some designs can measure both gas and liquid. For liquid applications, PD meters work best for liquids with heavy viscosities. Almost all PD meters require precisely machined, high-tolerance mating parts; thus, measured fluid must be clean for longevity of the meter and to maintain the measurement precision.

53.2.1 Sliding-Vane-Type PD Meter

Figure 53.1 shows a working cycle of a sliding-vane-type PD meter where vanes are designed to move in and out of the rotating inner mechanism. The position of each sliding vane relative to specific angular rotation of the rotor is usually maintained by a mechanical cam. In the design shown in Figure 53.1,

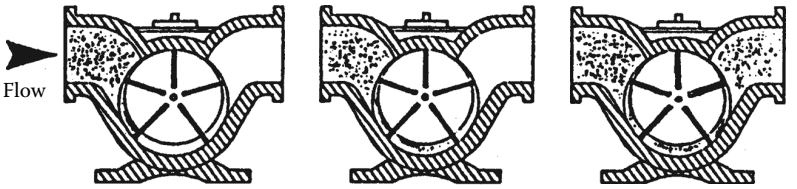

FIGURE 53.1 Sliding-vane-type PD meter. (Courtesy of Daniel Industries, Inc., Houston, TX.)

FIGURE 53.2 Trirotor-type PD meter. (Courtesy of Liquid Controls LLC, Lake Bluff, IL.)

each blade is independently retained in the slots. There are designs with even numbers of blades where diametrically opposite blades are one integral unit. High-pressure application would utilize dual-wall construction.

53.2.2 Trirotor-Type PD Meter

This design has three rotating parts that entrap fluid between the rotors and an outer wall. The working cycle of this type of meter is shown in Figure 53.2. In this design, for one rotation of the top mechanism, two blades rotate twice. The driving mechanism and rotation of each blade with respect to the others is maintained by a three-gear assembly where each rotating blade shaft is connected to one gear of the three-gear assembly to maintain relative rotational speed. This design is used to measure liquid flows.

53.2.3 Birotor PD Meter

The measuring unit of the birotor PD meter has two spiral-type rotors kept in perfect timing by a set of precision gears and is used to measure liquid flows. Flow can enter the meter either perpendicular or parallel to the axis of rotation of the mating rotors, as shown in Figure 53.3. The axial design birotor is identical to the standard model in component parts and in principle; however, it utilizes a measuring unit mounted parallel, rather than perpendicular, to flow. Meter output is registered mechanically through a gear train located outside the measuring chamber or, electronically, using a pickup assembly mounted with a timing gear. Axial orientation results in compact installation, improved accuracy, and low pressure loss. The axial design is ideal for high-flow-rate applications.

53.2.4 Piston-Type PD Meter

A typical design of a piston-type PD meter is shown in Figure 53.4. A centrally located rotating part generates the reciprocating motion for each of the four pistons of the meter. The reciprocating motion of each of the piston is timed such that the discharge from an individual piston–cylinder occurs in a cycle to generate a semicontinuous discharge from the meter. These PD meters are used for very low flow rates of liquid flows. A piston–cylinder design can withstand large differential pressures across the meter, so highly viscous liquids can be measured by this type of meters, and measurements are very precise. Mechanical components of this type of meter require very precise mechanical tolerances, which increase the product cost.

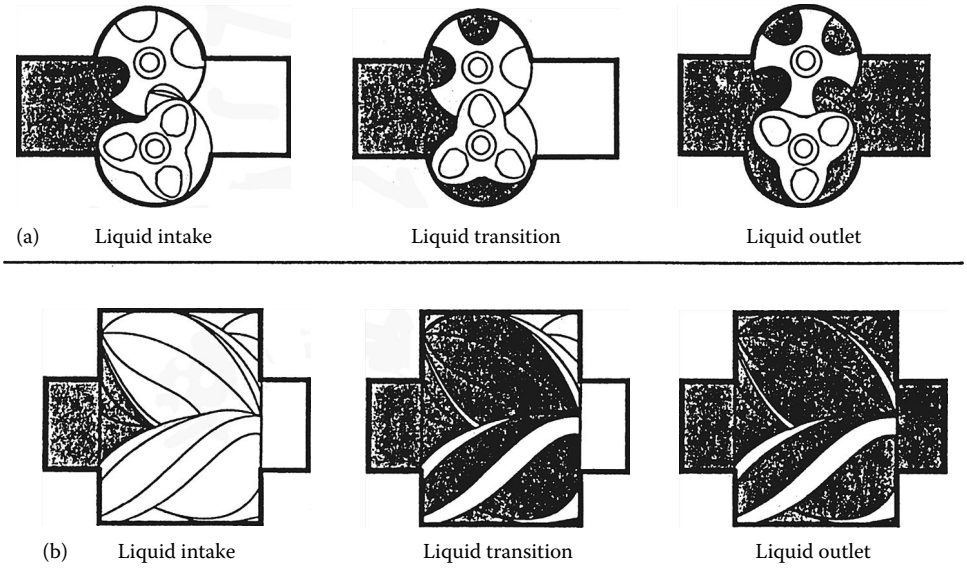

FIGURE 53.3 Birotor-type PD meter. (a) The standard birotor principle and (b) the axial flow principle. (Courtesy of Brooks Instruments Division, Emerson Electric Company, Hatfield, PA.)

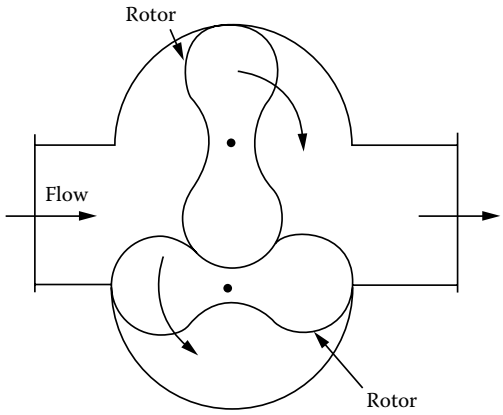

FIGURE 53.4 Piston-type PD meter. (Courtesy of Pierburg Instruments, Inc., Auburn Hills, MI.)

53.2.5 Oval-Gear PD Meter

The measurement of volumetric flow of an oval-gear meter is obtained by separating partial volumes formed between the oval gears and the measuring chamber wall, as shown in Figure 53.5. The rotation of the oval gears results from the differential pressure across the flowmeter. During one revolution of the oval gears, four partial volumes are transferred. The rotation of the gears is transmitted from the measuring chamber to the output shaft directly with mechanical seals or via a magnetic coupling. This type of meter is used to measure liquids having a wide range of viscosity.

FIGURE 53.5 Oval-gear meter. (Courtesy of Daniel Industries, Inc., Houston, TX.)

53.2.6 Nutating-Disk-Type PD Meters

A disk placed within the confines of a boundary wall at a specific orientation can induce a flow instability that can generate a wobbling or nutating motion to the disk. The operating cycle of one such design is shown in Figure 53.6. The entrapment and discharge of the fluid to and from the two chambers occur during different phases of the repetitive cycle of the nutating disk. This type of meter is used to measure liquids. The design provides economic flow measurement where accuracy is not of great importance and is often used in water meters.

Meter designs described hereafter are for gas flows. PD meters for gas flows require very tight tolerances of the moving parts to reduce leak paths, and therefore, the gas must be clean because the meters are less tolerant to solid particles.

53.2.7 Roots PD Meter

The roots meter design is shown in Figure 53.7. This is the most commonly used PD meter to measure gas flows. This is one of the oldest designs of a PD meter. The mechanical clearance between the rotors and the housing requires precisely machined parts. Roots meters are adversely affected if inlet flow to the meter has a relatively high level of pulsation. The main disadvantage of this meter is that it introduces cyclic pulsations into the flow. This meter cannot tolerate dirt and requires filtering upstream of

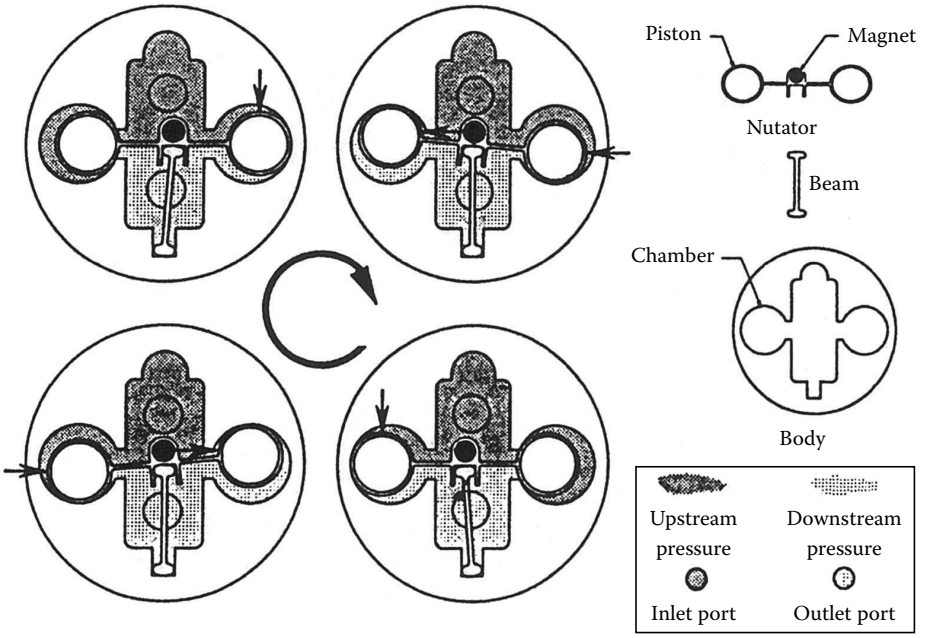

FIGURE 53.6 Nutating-disk-type PD meter. (Courtesy of DEA Engineering Company, Mission Viejo, CA.)

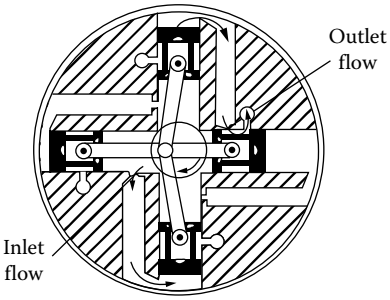

FIGURE 53.7 Schematic diagram of roots meter.

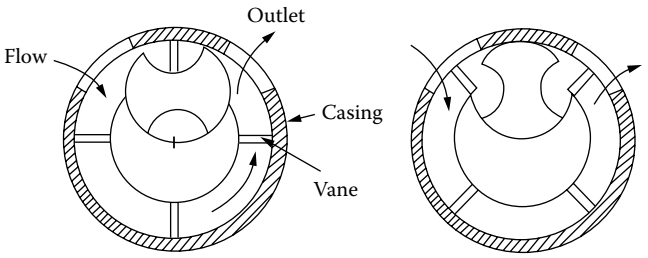

FIGURE 53.8 Operation of CVM meter.

the meter. A roots meter in single-case design is used at near-ambient line pressures. This meter design is very widely used in the low-pressure transmission and distribution market of natural gas. If this meter ever seizes up at any position, the flow is completely blocked.

53.2.8 CVM Meter

The CVM meter (Figure 53.8) is a proprietary design of a PD meter used to measure gas flows. This meter has a set of four vanes rotating in an annular space about the center of the circular housing. A gate similar in shape to the centerpiece of the trirotor design (Figure 53.2) allows the vanes to pass—but not the gas. The measurement accuracy of the CVM meter is similar to the roots meter, but the amplitude of exit pulsation is lower than the roots meter for similar meter size and flow rate. This design is also not as sensitive to inlet flow fluctuations and is widely used in the low-pressure, natural gas distribution market in Europe.

53.2.9 Diaphragm Meter

The diaphragm meter, also known as a bellows-type meter, is simple and relatively inexpensive, has reliable metering accuracy, and is widely used as a domestic gas meter. This design, shown in Figure 53.9,

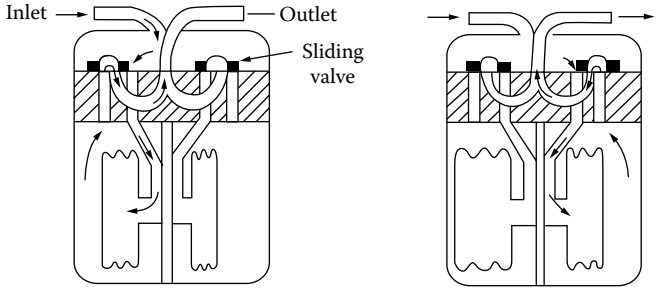

FIGURE 53.9 Operation of a diaphragm meter.

acts like a reciprocating piston meter where the bellows behave as pistons. The operation is controlled by a double-slide valve. In one position, the slide valve connects the inlet to the inside of the bellow, while the outside of the bellow is open to the outlet. In the other position, the outside is connected to the inlet, while the inside of the bellow is open to the outlet. This design can measure extremely low flow rates (e.g., pilot light of a gas burner).

53.3 Advantages and Disadvantages of PD Meters

High-quality PD meters will measure with high accuracy over a wide range of flow rates and are very reliable over long periods. Unlike most flowmeters, a PD meter is insensitive to inlet flow profile distortions. Thus, PD meters can be installed in close proximity to any upstream or downstream piping installations without any loss of accuracy. In general, PD meters have minimal pressure drop across the meter; hence, they can be installed in a pipeline with very low line pressures. Until the introduction of electronic correctors and flow controls on other types of meters, PD meters were most widely used in batch loading and dispensing applications. All-mechanical units can be installed in remote locations.

PD meters are generally bulky, especially in the larger sizes. Due to the tight clearance necessary between mating parts, the fluid must be clean for measurement accuracy and longevity of the meter. More accurate PD meters are quite expensive. If a PD meter ever seizes up, it would completely block the flow. Many PD meters have high inertia of the moving parts; therefore, a sudden change in the flow rate can damage the meter. PD meters are normally suitable over only limited ranges of pressure and temperature. Some designs will introduce noticeably high pulsations into the flow. Most PD meters require a good maintenance schedule and are high-repair and high-maintenance meters. Recurring costs in maintaining a PD flowmeter can be a significant factor in overall flowmeter cost.

53.4 Applications

Liquid PD meters are capable of measuring fluids with a wide range of viscosity and density. Minor changes in viscosity of the fluid have minimal influence on the accuracy of a PD meter. However, no one specific design of PD meter is capable of such a broad application range. The physical properties of the fluid, especially the fluid viscosity, must be reviewed for proper selection of a meter for the application. Many PD meter designs accurately measure flow velocities over a wide range.

Careful dimensional control is required to produce well-regulated clearances around the moving parts of the PD meter. The clearances provide a leakage path around the flow measurement mechanism, and the amount of leakage depends on the relative velocity of the moving parts, the viscosity of the fluid, and the clearances between parts. In general, the leakage flow rate follows the Poiseuille equation; that is, leakage is directly proportional to the differential pressure and inversely proportional to the absolute viscosity and the length of the leakage path.

The leakage flow, in percentage of the total flow rate, is useful information for error measurement. At low flow rates, percent leakage error can be significant, while with modest flow rates, leakage can be insignificant. However, the differential pressure across the PD meter increases exponentially with increasing flow rates. Therefore, at very high flow rates, leakage flow can again be a significant portion of the total flow. As a result, PD meters tend to dispense more fluid than is indicated by the register at the very low and very high flow rates. The amount of error due to leakage depends on the meter design and on the viscosity of the fluid.

PD meters are driven by the differential pressure across the meter. The primary losses within the meter can be attributed to the friction losses and the viscous drag of the fluid on the moving parts. At very low flow rates, the bearing losses are predominant, while at high flow rates, the viscous drags predominate.

The viscous drag is directly proportional to the fluid viscosity and the relative velocity of the moving parts and inversely proportional to the clearance. Within each design, the differential pressure is limited to a predetermined value. Excessive differential pressures can damage the meter. High differential pressure can be avoided by limiting the maximum flow rate, lowering viscosity by heating the fluid, increasing clearances, or various combinations of these techniques. In general, if the differential pressure limit can be addressed, PD meters measuring high-viscosity fluids have less measurement error over a wide flow-rate range.

The viscosity of most gases is too low to cause application problems relating to viscous drag of the form discussed for liquid PD meters. Gas PD meters utilize smaller clearances than liquid PD meters; therefore, gas must be very clean. Even small particles of foreign material can damage gas PD meters. PD meters used in gas flow measurement are primarily in the low line pressure application.

53.4.1 Accessories

Many accessories are available for PD meters. Among the most common and useful accessories for liquid PD meters are the automatic air eliminator and the direct-coupled shutoff valve for batch loading operations. The automatic air eliminator consists of a pressure-containing case surrounding a float valve. When gas in the liquid flow enters the chamber, the float descends by gravity and allows the float valve to open and purge the gas. An air eliminator improves the precision of flow measurement in many applications and is an absolute necessity in applications where air or gas is trapped in the flow stream. The direct-coupled shutoff valve is directly linked to the mechanical register. A predetermined fluid quantity can be entered into the register. When the dispensed amount equals the amount entered in the register, the mechanical linkage closes the valve. Two-stage shutoff valves are often used to avoid line shock in high-flow-rate dispensing applications. Similarly, all-electronic units can control batch operations. The all-electronic units provide great convenience in the handling of data. However, the register-driven mechanical valves have advantages in simplicity of design, field maintenance or repair, and initial cost.

Gas PD meters can be equipped with mechanical registers that correct the totals for pressure and temperature. The pressure and temperature compensation range is limited in the mechanical units but with appropriate application; the range limitation is not a problem. Electronic totalizers for gas PD meters can correct for broad ranges of temperature and pressure. Electronic accessories can provide various data storage, logging, and remote data access capabilities.

53.4.2 Price and Performance

In general, the accuracy of the PD meter is reflected in the sales price. However, several additional factors influence the cost. The intended application, the materials of construction, and the pressure rating have a strong influence on the cost. Although they provide excellent accuracy, small PD meters for residential water or residential natural gas service are very inexpensive. Meters produced for the general industrial market provide good accuracy at a reasonable cost, and meters manufactured for the pipeline or petrochemical markets provide excellent accuracy and are expensive.

Very inexpensive PD meters are available with plastic cases or plastic internal mechanisms. Aluminum, brass, ductile-iron, or cast-iron PD meters are moderately priced. Steel PD meters are relatively expensive, especially for high-pressure applications. If stainless steel or unusual materials are necessary for corrosive fluids or special service requirements, the costs are very high. PD meters are manufactured in a wide range of sizes, pressure ratings, and materials, with a multitude of flow-rate ranges and with an accuracy to match most requirements. The cost is directly related to the performance requirements.

Further Information

API, Measurement of liquid hydrocarbons by displacement meters, *Manual of Petroleum Measurement Standard*, Chapter 5.2, Washington, DC: American Petroleum Institute, 1992.

Bean, H. S., *Fluid Meters: Their Theory and Application*, 6th ed., Report of ASME Research Committee on Fluid Meters, New York: American Society of Mechanical Engineers, 1971.

Mechanical Flowmeters, Flow and Level Measurement. http://www.omega.com/literature/transactions/volume4/T9904–08-MECH.html (accessed on June 23, 2012).

Miller, R. W., *Flow Measurement Engineering Handbook*, New York: McGraw-Hill, 1989.

SmartMeasurement, Positive displacement. http://www.smartmeasurement.com/en/documents/flowmeter/PositiveDisplacement.asp (accessed on June 21, 2012).

Spitzer, D. W. (Ed.), *Flow Measurement: Practical Guides for Measurement and Control*, Research Triangle Park, NC: ISA, 1991.

Streeter, V. L., *Fluid Mechanics*, 4th ed., New York: McGraw-Hill, 1966.

Streeter, V. L., *Handbook of Fluid Dynamics*, New York: McGraw-Hill, 1961.

Universal Flow Monitors, Positive displacement flowmeters. http://www.flowmeters.com/ufm/index.cfm?task=positive_displacement (accessed on June 11, 2012).

Partial List of Vendors and Suppliers

Controls Warehouse, 356 Cypress Rd., Ocala, FL 34472, Phone: 888-212-5531 (toll free), Fax: 352-687-8925, www.controlswarehouse.com

GPI Meters, P.O. Box 1008, Sparta, NJ 07871, Phone: 888-722-3569 (toll free), Fax: 973-940-1651, www.gpimeters.com/

Great Plains Industries, 5252 E. 36th St. N., Wichita, KS 67220-3205, Phone: 316-686-7361, 800-835-0113 (toll free), Fax: 316-686-6746, www.gpi.net

Imac Systems, Inc., 90 Main St., Tullytown, PA 19007, Phone: 215-946-2200, 800-955-4427 (toll free), 800-955-4GAS (toll free), Fax: 215-943-2984, www.imacsystems.com

Ives Equipment Corp., 601 Croton Rd., King of Prussia, PA 19406-3111, Phone: 610-265-3071, 877-768-1600 (toll free), Fax: 610-768-1605, www.ivesequipment.com

Keco Engineering Controls, 1200 River Ave., Bldg. 3A, Lakewood, NJ 08701-5657, Phone: 732-901-5900, Fax: 732-901-5904, www.kecocontrols.com

54

Turbine and Vane Flowmeters

David Wadlow
Sensors Research Consulting, Inc.

This section describes a range of closed-conduit flowmeters that utilize rotating vaned transduction elements, with particular emphasis on axial turbine flowmeters. The various vaned flowmeters used for open channel and free-field flow measurement along with single jet and insertion tangential turbines, also known as paddle wheel flowmeters, are not included in this section.

54.1 Axial Turbine Flowmeters

The modern axial turbine flowmeter, when properly installed and calibrated, is a reliable device capable of providing the highest accuracies attainable for both liquid and gas volumetric flow measurement. It is the product of decades of intensive innovation and refinements to the original axial vaned flowmeter principle first credited to Woltman in 1790 and at that time applied to measuring water flow. The initial impetus for the modern development activity was largely the increasing needs of the U.S. natural gas industry in the late 1940s and 1950s for a means to accurately measure the flow in large-diameter, high-pressure, interstate natural gas lines. Today, due to the tremendous success of this principle, axial turbine flowmeters of different and often proprietary designs are used for a variety of applications where accuracy, reliability, and rangeability are required in numerous major industries besides water and natural gas, including oil, petrochemical, chemical process, cryogenics, milk and beverage, aerospace, and biomedical.

Figure 54.1 is a schematic longitudinal section through the axis of symmetry depicting the key components of a typical meter. As one can see, the meter is an in-line sensor comprising a single turbine rotor, concentrically mounted on a shaft within a cylindrical housing through which the flow passes. The shaft or shaft bearings are located by end supports inside suspended upstream and downstream aerodynamic structures called diffusers, stators, or simply cones. The flow thus passes through an annular

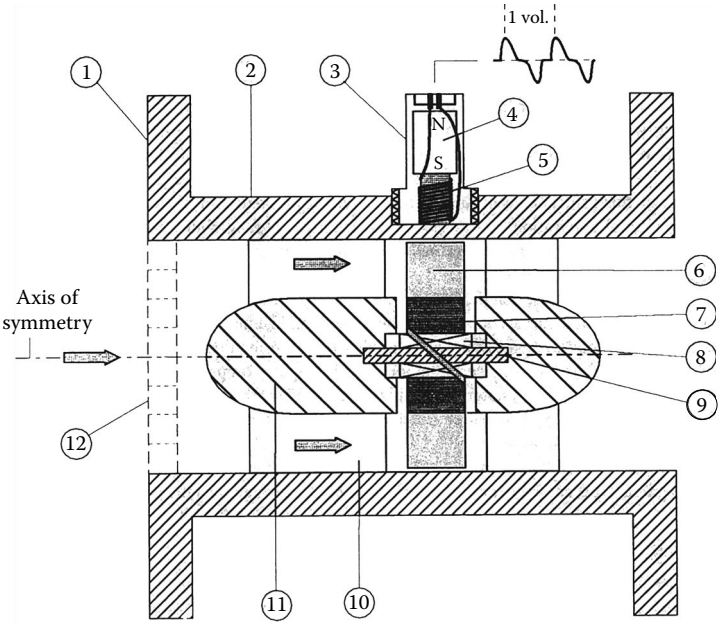

FIGURE 54.1 Longitudinal section of an axial turbine flowmeter depicting the key components. The flowmeter body is usually a magnetically transparent stainless steel such as 304. Common end fittings include face flanges (depicted), various threaded fittings, and tri-clover fittings. The upstream and downstream diffusers are the same in bidirectional meters and generally supported by three or more flat plates or sometimes tubular structures, aligned with the body, which also act as flow straighteners. The relative size of the annular flow passage at the rotor varies among different designs. Journal rotor bearings are frequently used for liquids, while ball bearings are often used for gases. Magnetic reluctance pickups (depicted) are frequently used. Others types include mechanical and modulated carrier pickups. (1) End fitting—flange shown; (2) flowmeter body; (3) rotation pickup—magnetic, reluctance type shown; (4) permanent magnet; (5) pickup cold wound on pole piece; (6) rotor blade; (7) rotor hub; (8) rotor shaft bearing—journal type shown; (9) rotor shaft; (10) diffuser support and flow straightener; (11) diffuser; (12) flow conditioning plate (dotted)—optional with some meters.

region occupied by the rotor blades. The blades, which are usually flat but can be slightly twisted, are inclined at an angle to the incident flow velocity and hence experience a torque that drives the rotor. The rate of rotation, which can be up to several $\times 10^4$ rpm for smaller meters, is detected by a pickup, which is usually a magnetic type, and registration of each rotor blade passing infers the passage of a fixed volume of fluid.

54.1.1 General Performance Characteristics

Axial turbines perform best when measuring clean, conditioned, steady flows of gases and liquids with low kinematic viscosities (below about 10^{-5} m^2 s^{-1}, 10 cSt, although they are used up to 10^{-4} m^2 s^{-1}, 100 cSt) and are linear for subsonic, turbulent flows. Under these conditions, the inherent mechanical stability of the meter design gives rise to excellent repeatability performance. Not including the special case of water meters, which are described later, the main performance characteristics are

- Sizes (internal diameter) range from 6 to 760 mm (1/4 to 30 in.).
- Maximum measurement capacities range from 0.025 to 25,500 Am^3 h^{-1} (0.015–15,000 ACFM), for gases, and 0.036–13,000 m^3 h^{-1} (0.16–57,000 gpm or 82,000 barrels per hour), for liquids, where A denotes actual.

- Typical measurement repeatability is ±0.1% of reading for liquids and ±0.25% for gases with up to ±0.02% for high-accuracy meters. Typical linearities (before electronic linearization) are between ±0.25% and ±0.5% of reading for liquids and ±0.5% and ±1.0% for gases. High-accuracy meters have linearities of ±0.15% for liquids and ±0.25% for gases, usually specified over a 10:1 dynamic range below maximum rated flow. Traceability to National Institute of Standards and Technology (NIST) is frequently available, allowing one to estimate the overall absolute accuracy performance of a flowmeter under specified conditions. Under ideal conditions, absolute accuracies for optimum designs and installations can come close to the accuracy capabilities at the NIST, which are stated as ±0.13% for liquid flows and ±0.25% for air.
- Rangeability, when defined as the ratio of flow rates over which the linearity specification applies, is typically between 10:1 and 100:1.
- Operating temperature ranges span –270 °C to 650 °C (–450 °F to 1200 °F).
- Operating pressure ranges span coarse vacuum to 414 MPa (60,000 psi).
- Pressure drop at the maximum rated flow rate ranges from around 0.3 kPa (0.05 psi) for gases to in the region of 70 kPa (10 psi) for liquids.

54.1.2 Theory

There are two approaches described in the current literature for analyzing axial turbine performance. The first approach describes the fluid driving torque in terms of momentum exchange, while the second describes it in terms of aerodynamic lift via airfoil theory. The former approach has the advantage that it readily produces analytical results describing basic operation, some of which have not appeared via airfoil analysis. The latter approach has the advantage that it allows more complete descriptions using fewer approximations. However, it is mathematically intensive and leads rapidly into computer-generated solutions. One prominent pioneer of the momentum approach is Lee (Lee and Evans 1965), who, using this approach, later went on to invent one of the few, currently successful, dual-rotor turbine flowmeters, while Thompson and Grey (1970) later provided a comprehensive model using the airfoil approach, which, for example, took into account blade interference effects. Stoltenkamp (2007) reviewed the theory in detail and also extended the airfoil model of Thompson and Grey. In the following, the momentum exchange approach is used to highlight the basic concepts of the axial turbine flowmeter.

In a hypothetical situation, where there are no forces acting to slow down the rotor, it will rotate at a speed that exactly maintains the fluid flow velocity vector at the blade surfaces. Figure 54.2 is a vector diagram for a flat-bladed rotor with a blade pitch angle equal to β. Assuming that the rotor blades are flat and that the velocity is everywhere uniform and parallel to the rotor axis, then referring to Figure 54.2, one obtains

$$r\omega_i = V \tan\beta \tag{54.1}$$

When one introduces the total flow rate, this becomes

$$\frac{\omega_i}{Q} = \frac{\tan\beta}{\bar{r}A} \tag{54.2}$$

where

ω_i is the "ideal" rotational speed
Q is the volumetric flow rate
A is the area of the annular flow cross section
$\bar{r}$ is the root mean square of the inner and outer blade radii (R,a)

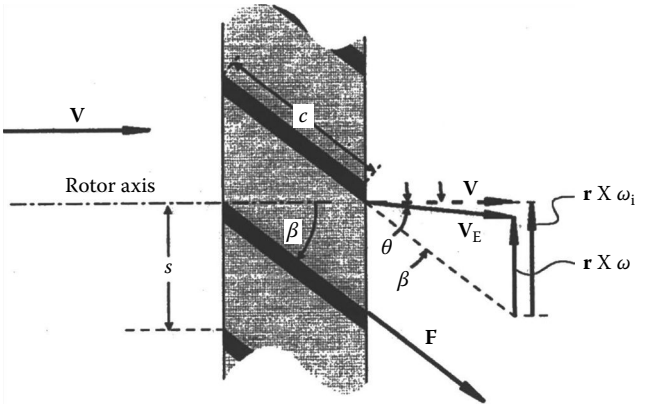

FIGURE 54.2 Vector diagram for a flat-bladed axial turbine rotor. The difference between the ideal (subscript i) and actual tangential velocity vectors is the rotor slip velocity and is caused by the net effect of the rotor retarding torques. This gives rise to linearity errors and creates swirl in the exit flow. **V**, incident fluid velocity vector; $\mathbf{V}_E$, exit fluid velocity vector; θ, exit flow swirl angle due to rotor retarding torques; β, blade pitch angle, same as angle of attack for parallel flow; ω, rotor angular velocity vector; **r**, rotor radius vector; **F**, flow-induced drag force acting on each blade surface; c, blade chord; s, blade spacing along the hub; c/s, rotor solidity factor.

Eliminating the time dimension from the left-hand-side quantity reduces it to the number of rotor rotations per unit fluid volume, which is essentially the flowmeter K factor specified by most manufacturers. Hence, according to Equation 54.2, in the ideal situation, the meter response is perfectly linear and determined only by geometry. (In some flowmeter designs, the rotor blades are helically twisted to improve efficiency. This is especially true of blades with large radius ratios (R/a). If the flow velocity profile is assumed to be flat, then the blade angle in this case can be described by $\tan\beta$ = constant × r. This is sometimes called the "ideal" helical blade.) In practice, there is instead a number of rotor retarding torques of varying relative magnitudes. Under steady flow, the rotor assumes a speed that satisfies the following equilibrium:

$$\begin{aligned}\text{Fluid driving torque} = {}& \text{rotor blade surfaces fluid drag torque} + \text{rotor hub} \\ & \text{and blade tip clearance fluid drag torque} + \text{rotation} \\ & \text{sensor drag torque} + \text{bearing friction retarding torque}\end{aligned} \tag{54.3}$$

Referring again to Figure 54.2, the difference between the actual rotor speed, $r\omega$, and the ideal rotor speed, $r\omega_i$, is the rotor slip velocity due to the combined effect of all the rotor retarding torques as described in Equation 54.3, and as a result of which, the fluid velocity vector is deflected through an exit or swirl angle, θ. Denoting the radius variable by r and equating the total rate of change of angular momentum of the fluid passing through the rotor to the retarding torque, one obtains

$$\int_a^R \frac{\rho Q 2\pi r^2 (r\omega_i - r\omega)}{\pi(R^2 - a^2)} dr = N_T, \tag{54.4}$$

which yields

$$\bar{r}^2 \rho Q(\omega_i - \omega) = N_T \tag{54.5}$$

where ρ is the fluid density and N_T is the total retarding torque. Combining Equations 54.1 and 54.5 and rearranging yield

$$\frac{\omega}{Q} = \frac{\tan\beta}{\bar{r}A} - \frac{N_T}{\bar{r}^2 \rho Q^2} \tag{54.6}$$

The trends evident in Equation 54.6 reflect the characteristic decline in meter response at very low flows and why lower friction bearings and lower drag pickups tend to be used in gas versus liquid applications and small-diameter meters. In most flowmeter designs, especially for liquids, the latter three of the four retarding torques described in Equation 54.3 are small under normal operating conditions compared with the torque due to induced drag across the blade surfaces. As shown in Figure 54.2, the force, *F*, due to this effect acts in a direction along the blade surface and has a magnitude given by

$$F = \frac{\rho V^2}{2} C_D S \tag{54.7}$$

where C_D is the drag coefficient and *S* is the blade surface area per side. Using the expression for drag coefficient corresponding to turbulent flow, as described by Pate et al. (1984) and others, this force can be estimated by

$$F = \rho V^2 0.074 \,\mathrm{Re}^{-0.2} S \tag{54.8}$$

where Re is the flow Reynolds number based on the blade chord shown as dimension *c* in Figure 54.2. Assuming θ is small compared with β, then after integration, the magnitude of the retarding torque due to the induced drag along the blade surfaces of a rotor with *n* blades is found to be

$$N_D = n(R+a)\rho V^2 0.037 \,\mathrm{Re}^{-0.2} S \sin\beta \tag{54.9}$$

Combining Equations 54.9 and 54.6 and rearranging yield

$$\frac{\omega}{Q} = \frac{\tan\beta}{\bar{r}A} - \frac{0.036 n(R+a) S A^2 \,\mathrm{Re}^{-0.2} \sin\beta}{\bar{r}^2} \tag{54.10}$$

Equation 54.10 is an approximate expression for the *K* factor because it neglects the effects of several of the rotor retarding torques and a number of important detailed meter design and aerodynamic factors, such as rotor solidity and flow velocity profile. Nevertheless, it reveals that linearity variations under normal, specified operating conditions are a function of certain basic geometric factors and Reynolds number. These results reflect general trends that influence design and calibration. Additionally, the marked departure from an approximate ρV^2 (actually $\rho^{0.8} V^{1.8} \mu^{-0.2}$ via Equation 54.8) dependence of the fluid drag retarding torque on flow properties under turbulent flow, to other relationships under transitional and laminar flow, gives rise to major variations in the *K* factor versus flow rate and media properties for low-flow Reynolds numbers. This is the key reason why axial turbine flowmeters are generally recommended for turbulent flow measurement.

54.1.3 Calibration, Installation, and Maintenance

Axial turbine flowmeters have a working dynamic range of at least 10:1 over which the linearity is specified. The maximum flow rate is determined by design factors related to size versus maximum pressure drop and maximum rotor speed. The minimum of the range is determined by the linearity specification itself. Due to small, unavoidable, manufacturing variances, linearity error curves are unique to

individual meters and are normally provided by the manufacturer. However, although recommended where possible, the conditions of the application cannot usually and need not necessarily duplicate those of the initial or even subsequent calibrations. This has pivotal importance in applications where actual operating conditions are extreme or the medium is expensive or difficult to handle. Figure 54.3 depicts a typically shaped calibration curve of linearity versus flow rate expressed in terms of multiple alternative measures, various combinations of which can be found in current use. The vertical axis thus represents either the linearity error as a percentage of flow rates, a *K* factor expressed in terms of the number of pulses from the rotation sensor output per volume of fluid, or the deviation from 100% registration; the latter only applies to flowmeters with mechanical pickups. The horizontal axis can be expressed in terms of flow rate in volume units/time, Reynolds number (Re), or pulse frequency (from the rotation sensor for nonmechanical) divided by kinematic viscosity, (f/ν), in units of Hz per $m^2\ s^{-1}$ (Hz/cSt or Hz/SSU; $10^{-6}\ m^2\ s^{-1}$ = 1 centistoke = 31.0 s, Saybolt Universal), where kinematic viscosity is the ratio of absolute viscosity (μ) to density. Calibrations are preferably expressed versus Re or f/ν, which is proportional to Re. The hump shown in the curve is a characteristic frequently observed at lower Re and is due to velocity profile effects. *K* factor versus f/ν calibration curves are specifically called universal viscosity curves (UVC) and, for most meters, are available from the manufacturer for an extra charge. A key utility of UVC is that where media type and properties differ significantly from those of the original calibration, accuracies much greater than the overall linearity error can still readily be obtained via the flowmeter UVC if the kinematic viscosity of the application is known. An alternative calibration technique (Olivier and Ruffner 1992) is to provide response in terms of Strouhal number versus Re or Roshko number.

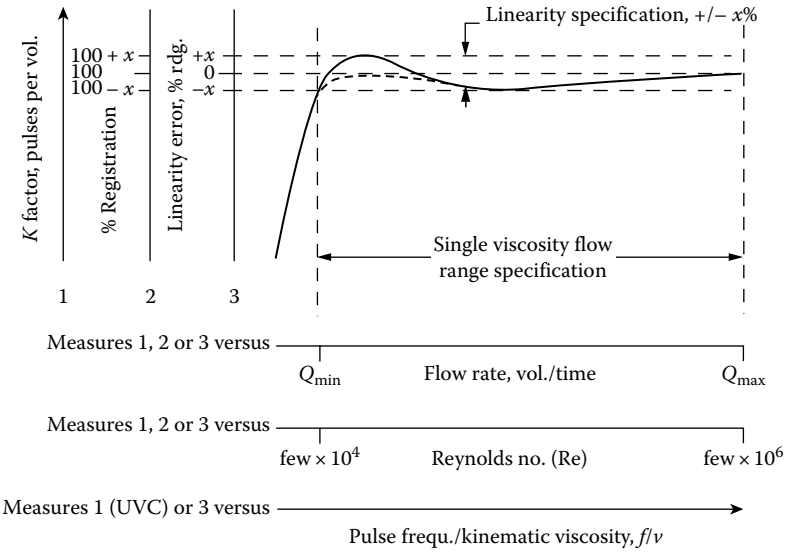

FIGURE 54.3 A typical single-rotor axial turbine linearity error, or calibration, curve for a low-viscosity fluid showing the main alternative presentations in current use. Higher-accuracy specifications usually correspond to a 10:1 flow range down from Q_{max}, while extended operating ranges usually correspond to reduced accuracies. The hump in the depicted curve is a characteristic feature caused by flow velocity profile changes as Re approaches the laminar region. This feature varies in magnitude between meters. Sensitivity and repeatability performance degrade at low Re. Percent registration is only used with meters that have mechanical pickups. All other meters have a *K* factor. UVC and Re calibrations remain in effect at different known media viscosities provided Re or f/ν stays within the specified range. Re is referenced to the connecting conduit diameter and is less within the flowmeter. The Re range shown is therefore approximate and can vary by an order of magnitude, depending on the meter. Linearity error can also be expressed in terms of Strouhal number (fD/V) versus Re (VD/υ) or Roshko number (fD^2/υ), when instead *D* is a flowmeter reference diameter [4]. UVC, the effect of a rotor shroud in a viscosity compensated flowmeter.

This approach is particularly relevant to high-accuracy and extreme temperature applications because it further allows correct compensation for flowmeter thermal expansion errors.

The accuracy of axial turbine flowmeters is reduced by unconditioned flow, especially swirl. An installation incorporating flow conditioners along with specific upstream and downstream straight pipe lengths is generally recommended. See for instance ISA-RP 31.1, 1977. Some axial turbine flowmeters can be purchased with additional large flow straighteners that mount directly ahead of the flowmeter body or conditioning plates that are integral to the body. The manufacturer is the first source of information regarding installation. Errors due to flow velocity pulsations are another concern, particularly in natural gas installations. Flow pulsation errors tend to be positive because turbine rotors tend to speed up faster than they slow down. However, although the problem of flow pulsation-induced errors has been carefully studied, no standard technique for effectively counteracting this source of error has yet been adopted (Jungowski and Weiss 1996, Laurantzon et al. 2012). Periodic maintenance, testing, and recalibration are required because the calibration will shift over time due to wear, damage, or contamination. For certain applications, especially those involving custody transfers of oil and natural gas, national standards, international standards, and other recommendations exist that specify the minimum requirements for turbine meters with respect to these aspects. A number of these are identified separately in the reference section.

54.1.4 Design and Construction

There are numerous, often proprietary, designs incorporating variations in rotors, bearings, pickups, and other components in format and materials that are tailored to different applications. Meter bodies are available with a wide range of standard end fittings. Within application constraints, the primary objective is usually to optimize the overall mechanical stability and fit in order to achieve good repeatability performance. Design requirements for performance, application, and manufacture considerations impacts every internal component but most of all the rotor with respect to blade shape and pitch; blade count; balance and rigidity versus drag, stress, and inertia; bearings with respect to precision versus friction, speed rating, and durability; and rotation pickup versus performance and drag.

Most low-radius ratio blades are machined flat, while high-ratio blades tend to be twisted. The blade count varies from about 6 to 20 or more, depending on the pitch angle and blade radius ratio so that the required rotor solidity is achieved. Rotor solidity is a measure of the "openness" to the flow such that higher solidity rotors are more highly coupled to the flow and achieve a better dynamic range. The pitch angle, which primarily determines the rotor speed, is typically 30°–45° but can be lower in flowmeters designed for low-density gas applications. Rotor assemblies are usually a close fit to the inside of the housing. In large-diameter meters, the rotor often incorporates a shroud around the outer perimeter for enhanced stability. Also, since large meters are often used for heavy petroleum products, via selection of a suitable wall clearance, the fluid drag resulting from this clearance gap is often designed to offset the tendency at high media viscosities for the meter to speed up at lower Reynolds numbers. The materials of construction range from nonmagnetic to magnetic steels to plastics.

Stainless steel ball bearings are traditionally used for gas meters and low-lubricity liquids, while hybrid and full ceramic ball bearings may be preferred for corrosive and cryogenics applications. Combination of tungsten carbide, graphite, ceramic, and sometimes Teflon journal and thrust bearings are also available for many liquid meters with material selection depending on the medium lubricity and corrosiveness. Fluid bearings (sometimes called "bearingless" designs) are often used in conjunction with the latter, but also sometimes with gases, for reducing the drag. They operate by various designs that use flow-induced forces to balance the rotor away from the shaft ends. Either bearing lubrication is derived from the metered medium or an internal or external system is provided. The more fragile, jeweled pivot bearings are also used in certain gas applications and small meters. Sanitary meters can incorporate flush holes in the bearing assembly to meet 3A crack and crevice standards.

The most common types of rotation sensor are magnetic, modulated carrier, and mechanical, while optical, capacitive, and electric resistance is also used. In research, a modulated nuclear radiation flux rotation sensor for use in certain nuclear reactors has also been reported (Van Der Hagen 1993, Termaat et al. 1995). Mechanical pickups, which sometimes incorporate a magnetic coupling, are traditional in some applications and can have high resolution; one advantage is that they require no electric power. However, the pickup drag tends to be high. The magnetic and modulated carrier types utilize at least a coil in a pickup assembly that screws into the meter housing near the rotor. In magnetic inductance types, which are now less common, the blades or shroud carries magnetized inserts, and signals are induced in the coil by the traversing magnetic fields. In the more prevalent magnetic reluctance type, an example of which is schematically depicted in Figure 54.1, the coil is wrapped around a permanent magnet or magnet pole piece in the pickup assembly, which is mounted next to a high magnetic permeability bladed rotor (or machined shroud). The latter is then typically made of a magnetic grade of stainless steel such as 416, 430, or 17–4Ph. As the rotor turns, the reluctance of the magnetic circuit varies, producing signals at the coil. In the more expensive modulated carrier types, the rotor need only be electrically conductive. The coil is part of a radio-frequency (RF) oscillator circuit, and the proximity of the rotor blades changes the circuit impedance, giving rise to modulation at a lower frequency that is recovered. The RF types have much lower drag, have higher signal levels at low flow, and can operate at temperatures above the Curie point of typical ferromagnetic materials. They are preferred for wide dynamic range and high-temperature applications. Bidirectional flowmeters usually have two magnetic pickups to determine flow direction. This is useful, for example, in the monitoring of container filling and emptying operations often encountered in sanitary applications. Multiple magnetic pickups are also used in some designs to provide increased measurement resolution. Regarding output, various pulse amplifiers, totalizers, and flow computers, for instance gas pressure and temperature correction, along with 4–20 mA and other standard interface protocols, are available to suit particular applications. As an example of advanced transmitters, at least one manufacturer (FTI Flow Technology, Inc.) provides a real-time, miniature, reprogrammable transmitter that is integrated into the pickup housing along with a meter body temperature sensor, for full viscosity compensation and UVC linearization. These are sometimes used in dedicated applications, such as airborne fuel management, where the medium viscosity–temperature relationship is known.

Certain applications have uniquely different design requirements and solutions. Three important variations are discussed in the following.

54.1.5 Propeller Meters

Propeller meters are used in municipal, irrigation, and wastewater measurement, although there is increasing competition in those applications from electromagnetic flowmeters. In some designs, propeller and turbine meters look almost identical and operate on the same axial rotor principle. However, this type of flowmeter is currently commercially and officially [AWWA C704] distinguished as a separate category distinct from the axial turbine. Diameters up to 2440 mm (96 in.) are available. The flow rate capacity of a 1800 mm (72 in.) diameter propeller meter is up to about 25,000 $m^3\ h^{-1}$ (110,000 gpm). Typical accuracies are ±2% of reading. A primary requirement is ruggedness, and it is in the designs most suited to harsh environments that the formats are most distinctive. Rotor and pickup assemblies are generally flanged to the housing and removable. The rotors have large clearances, are often cantilevered into the flow, and are supported via a sealed bearing without stators. The rotors are typically made of plastic or rubber and carry as few as three highly twisted, high-radius ratio blades. Pickups are always mechanical and frequently have magnetic couplings.

54.1.6 Helical Turbine Meters

Instead of a flat or slightly twisted multibladed rotor, these meters incorporate a helical, high-radius ratio, two-bladed rotor. This design provides greater accuracy when used to meter higher-viscosity liquids compared with that of the more conventional turbine. Dynamic range is also improved. The reason

for this general improvement is discussed by Mitchell (2010). These meters are sold as helical turbine meters for use in liquid media, and accuracies can be as high as ±0.15%. Applications include the custody transfer of crude oil. Where viscosity can vary, accuracy can be maintained by means of a separate real-time viscosity measurement, flow computer, and UVC correction. When used to meter crude oil, this design has the added advantage of being less susceptible to fouling by wax and other filamentary debris often found in crude oil. The meters are also used for metering chemicals such as ammonia, ethylene, propylene, and acids.

54.1.7 Swirl-Type Axial Turbine Meters

This description is solely due to the author and is in order to distinguish this design. A number of companies manufacture swirl-type axial turbine flowmeters, and the design departs significantly from that of the traditional axial turbine. In these devices, a fixed upstream stator intentionally imparts a high degree of azimuthal velocity or swirl to the flow. Immediately downstream of the stator is an axially mounted rotor where the blades are flat and parallel to the axis. The rotor is driven into rotation by the swirling flow and at a rate that is proportional to the volumetric flow rate. Upstream flow conditioning is typically absent, and two-bladed rotor variants of this design find application as the sensor in diagnostic spirometers where such a conditioning requirement would otherwise be restrictive. Diagnostic spirometers are used to monitor the degree and nature of respiration. With these, a clinician can determine patient respiratory condition by various measures and clinical maneuvers. Low cost, light weight, speed of response, and patient safety are major considerations. Measurement capabilities include the gas volume of a single exhalation and also the peak expiratory flow, measured in liters and liters per second, respectively. A number of manufacturers also provide small, portable diagnostic spirometers for personal use by patients at home. The spirometry market is large and competitive, and other flow sensing technologies are also used in spirometry. However, (swirl-type) axial turbine-based diagnostic spirometers command a significant market share. The devices typically utilize an infrared, optical pickup and have a microprocessor-controlled display. Rotors and housings tend to be plastic, and the entire turbine element may also be disposable. The meters are typically accurate to ± a few percent of reading. In the United States, spirometers are designated as class 2 medical devices, and as such certain FDA approvals are required concerning manufacture and marketing. In the EU, they are class IIb medical devices under a different system, and other approvals are required.

One manufacturer (Equflow BV) makes a range of subinch diameter (swirl-type) axial turbines for single or multiple use liquid applications ranging from fuel consumption measurement and biotechnology applications to corrosive liquids with accuracies in the region of 1% of reading. In these particular devices, the rotor has six blades. Housings and wetted parts may be perfluoroalkoxy (PFA)/Teflon®, polyvinylidene difluoride (PVDF), or in combination with stainless steel, while all models feature ruby bearings. The pickup is infrared where instead the pulse signal is obtained via reflection from a region at the tip of each blade as it passes the sensor. By this means, the flow of opaque liquids can also be monitored.

54.1.8 Dual-Rotor Axial Turbines

Dual-rotor axial turbines have performance features not found in single-rotor designs. In 1981, Lee et al. were issued a U.S. patent for a self-correcting, self-checking dual-rotor turbine flowmeter that is currently manufactured exclusively by Sensus Metering Systems and sold as the Auto-Adjust. This is a high-accuracy flowmeter primarily intended for use on large natural gas lines where even small undetected flow measurement errors can be costly. It incorporates two closely coupled turbine rotors that rotate in the same direction. The upstream rotor is the main rotor, and the second rotor, which has a much shallower blade angle, is the sensor rotor. Continuous and automatic correction of measurement errors due to varying bearing friction is achieved by calculating the flow rate based on the

difference between the rotor speeds. As shown in Figure 54.2 and discussed in the theory section, the flow exit angle is due to the net rotor retarding torque. If this torque increases in the main rotor, thereby reducing its speed, the exit angle increases and the speed of the sensor rotor is then also reduced. The meter is also insensitive to inlet swirl angle because the swirl affects both rotor speeds in the same sense and the effect is then subtracted in the flow calculation. The meter also checks itself for wear and faults by monitoring the ratio of the two rotor speeds and comparing this number with the installation value (Lee et al. 1982).

A dual-rotor liquid flowmeter, invented by Ruffner and Olivier (1997), is manufactured and sold by Exact Flow. It is a high-accuracy flowmeter (up to ±0.25% accuracy and ±0.02% repeatability), which has an extraordinarily wide dynamic range of 500:1 with a single-viscosity liquid. The meter comprises two, closely and hydraulically coupled helical rotors that rotate in opposite directions. Due to the exit angle generated by the first rotor, the second rotor continues to rotate to much lower flow rates compared with the first. Flow conditioning is not essential since swirl impacts both rotors. However, if the flow is conditioned, then changes in the ratio of the two rotor speeds provide a useful bearing diagnostic. This flowmeter is intended for liquid measurement only, in particular fuel and other measurements in aerospace applications.

54.2 Insertion Axial Turbine Flowmeters

These flowmeters comprise a small axial rotor mounted on a stem that is inserted radially through the conduit wall, often through a shutoff valve. They measure the flow velocity at the rotor position from which the volumetric flow rate is inferred. They are an economical solution to flow measurement problems where pipe diameters are high and accuracy requirements are moderate and also may be technically preferred where negligible pressure drop is an advantage, as in high-speed flows. They are typically more linear than insertion tangential turbine flowmeters and compete also with magnetic and vortex shedding insertion flowmeters. They are available for the measurement of a range of liquids and gases, including steam, similar to the media range of full-bore axial turbines, and have a similarly linear response. The rotors, which are usually metal but can be plastic, typically have diameters of 25–51 mm (1–2 in.). They can be inserted into pipes with diameters ranging from 51 to 2032 mm (2–80 in.). Velocity measurement ranges cover 0.04691 ms^{-1} (9–18,000 fpm) for gases and 0.03–30 ms^{-1} (6–6,000 fpm) for liquids. Dynamic ranges vary between 10:1 and 100:1. The maximum flow rate measurement capacity in a 1,836 mm (72 in.) diameter pipe can be as high as nearly 56,500 $m^3 h^{-1}$ (about 250,000 gpm). Since these devices are local velocity sensors, calculating the volumetric flow rate requires knowledge of the area velocity profile and the actual flow area. Flow conditioning is therefore particularly important for accurate volumetric measurements, while radial positioning, which is a further responsibility of the user, must be according to the manufacturer's recommendation, which can either be centerline, one-third of the diameter, 12% of the diameter, or determined by "profiling." Quick (1996) discussed operations and installations for natural gas measurements. Although linearities or "accuracies" can be quoted up to ±1% of velocity, achieving the same accuracy for the volumetric flow rate, although possible, can be difficult or impractical. In this respect, a unique dual-rotor design, exclusive to Onicon, Inc., and primarily used for chilled-water flow measurement in HVAC systems, requires less flow conditioning than single-rotor designs. An Onicon dual-rotor turbine assembly is depicted in Figure 54.4. It comprises two rotors that rotate in opposite directions. The output is based on the average rotor speed. Any flow swirl present due to poor flow conditioning changes the speed of rotation of each rotor by the same but opposite amounts. Swirl-induced error is thus virtually absent in the averaged output. Also, flow profile sampling is improved over that of a single rotor. The devices are calibrated using a volumetric prover, and the specified accuracy of ±2% of reading is for volumetric flow rate rather than velocity. This is the total error and includes an allowance for dimensional variations in industry standard pipes.

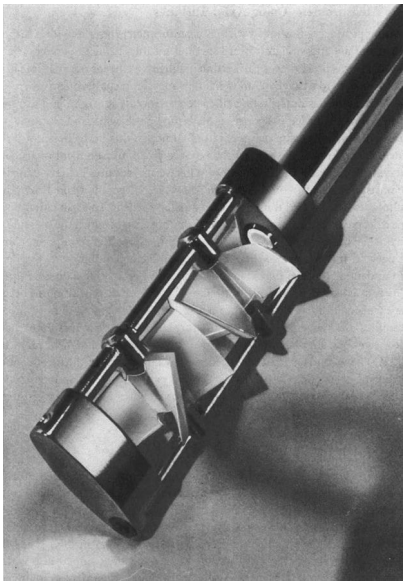

FIGURE 54.4 The rotor assembly of a dual-rotor, insertion axial turbine flowmeter for water flow measurement. This patented design renders the flowmeter insensitive to errors due to flow swirl; an important source of potential error in single-rotor axial turbine flowmeters. The rotations are sensed by two separate, electric impedance sensors. (Courtesy of Onicon Incorporated.)

54.3 Angular Momentum Flowmeters

These are accurate, linear, liquid mass flowmeters that utilize vaned components and are used in aerospace applications. They are currently the instrument of choice for airborne, jet engine fuel flow measurement for large commercial aircraft and some military aircraft for afterburner applications. They are more expensive than the equivalent turbine flowmeters for this application, but they provide mass flow rate measurements directly and are unaffected by fuel density variations. Typical accuracies lie between ±0.5% and ±1.0% over a 40:1 or greater dynamic range. Measurement ranges are available for fuel flows from about 0.01 to 6 kg s^{-1} (70–46,000 PPH).

The principle of operation is long established and based on imparting angular momentum to the fluid flow using a driven, flat-bladed impeller. The force required to drive the impeller at constant speed is monitored as a proportional indication of mass flow rate as this quantity varies. Some designs use an electric motor to drive the impeller. However, the current trend in design is motorless. In such a device, a constant driving speed in the region of 100–200 rpm is provided by one or more turbine rotors driven by the flow. A variable shunt metering valve assembly adjacent to the turbine rotor mechanically opens and closes in response to flow dynamic pressure and thereby automatically maintains a constant speed of rotation provided that the flow rate is above the minimum of the range. The driven impeller carries vanes that are parallel to the flow and resides on a common axis with the turbine rotor. A flow straightener ensures parallel flow past the impeller. There is a carefully engineered constant rate spring connection between the turbine shaft and the impeller so that the angular deflection between the two is proportional to the applied torque, and this quantity is directly proportional to the mass flow rate. Two pickup coils sense the rotations of the turbine and the vaned impeller, and only the time difference between the pulses in these two signals is measured and used to calculate the flow rate. Chiles et al. (1977) provide a detailed illustration and explanation of the intricate mechanism.

54.4 Multijet Turbine Flowmeters

These are linear, volumetric flowmeters designed for liquid measurements and comprise a single, radial vaned impeller, vertically mounted on a shaft bearing within a vertically divided flow chamber, sometimes called a distributor. The impeller is often plastic and can even be neutrally buoyant in water. There are various designs, but typically, both chambers access a series of radially distributed and angled jets. The lower chamber jets connect to the flowmeter input port and distribute the flow tangentially onto the lower region of the impeller blades, while the upper series, which are angled oppositely, allow the flow to exit. The flow pattern within the flow chamber is thus a vertical spiral, and the dynamic pressure drives the impeller to track the flow. This design gives the meters good sensitivity at low flow rates. Due to the distribution principle, the meters are also insensitive to upstream flow condition. Impeller rotation pickups are always mechanical, often magnetically coupled, and frequently also connect with electric contact transmitters. They are primarily used in water measurement, including potable water measurement for domestic and business billing purposes and in conjunction with energy management systems such as hot water building or district heating, in water flood projects for secondary oil recovery, and to a lesser extent in some chemical and pharmaceutical industries for dosing and filling systems involving solvents, refrigerants, acids, and alkalis with absolute viscosities less than 4.5 MPa s (0.045 Poise). Available sizes range from 15 to 50 mm. Dynamic ranges lie between 25:1 and 130:1, and flow measurement ranges cover 0.03–30 $m^3 h^{-1}$ (0.13–130 gpm). Measurement linearities range between ±1% and ±2%, with typical repeatabilities of ±0.3%. Operating temperatures range from normal to 90 °C (200°F), and maximum operating pressures are available up to 6.9 MPa (1000 psi). A number of potable water measurement systems come with sophisticated telemetry options that allow remote interrogation by radio or telephone. For potable water applications in the United States, these meters normally comply with the applicable American Water Works Association (AWWA) standard, while in Europe other national standards apply.

54.5 Cylindrical Rotor Flowmeter

Instead of coupling to a turbulent flow using the fluid dynamic pressure or momentum flux, as in most turbine flowmeters, a demonstrated research device due to Wadlow and Layden (1994) provides a linear, volumetric, low gas flow rate measurement using a single, low-inertia, smooth cylindrical tangential rotor that couples to a laminar flow via surface friction. The geometry is conceptually that of a single-surfaced rotating vane. A plane Poiseuille flow is created that passes azimuthally over most of the curved rotor surface in a narrow annular passage between the rotor and a concentric housing. The rotor is motor driven via a feedback control loop connected to an error signal producing differential pressure sensor connected across the gas ports so as to maintain the meter pressure drop equal to zero. Under this condition, the response, as indicated by motor shaft speed, is exactly linear, determined only by geometry, and is independent of gas density and viscosity. The demonstration device reported has a 40 mm diameter rotor and 15 mm diameter gas ports. It measures up to a maximum of 25 Lpm bidirectionally, has a linear dynamic range greater than 100:1, is insensitive to upstream flow condition, and has a $1/e$ step response time of 42 ms, limited only by the external motor torque and combined motor and rotor inertia.

54.6 Manufacturers

There is significant and dynamic competition among the numerous manufacturers of the different types of flowmeters described in this section. In all flowmeter types, most manufacturers have exclusive patent rights concerning one or more detailed design aspects that make their products perform differently

from those of the competition. Every few years, one or more major turbine flowmeter company can be identified that has changed ownership and name or formed a new partnership. Identifying the competition and selecting the manufacturer are important and sometimes time-consuming parts of the flowmeter selection and specification process. To assist with this, Table 54.1 gives a few selected examples from different manufacturers, of all the different flowmeter types described in this section. Table 54.2 gives the corresponding contact information for those selected manufacturers, along with the general types offered by each.

TABLE 54.1 Examples of Turbine and Vaned Flowmeters

Type	Size(s), in.	Description	Example Application(s)	Manufacturer	Approx. Price Range
Axial	0.5	FT 4–8, with SIL smart transmitter	Helicopters—fuel	EG&G Flow Technology	$2,500
Axial	1	6700 series, type 60	Raw milk, deionized water	Flow Automation	$1,500
Axial	16	Parity series	Custody transfer oil	Fisher-Rosemount Petroleum	$30,000–$38,000
Axial dual rotor	12	Auto-Adjust Turbo-Meter	Custody transfer gas	Equimeter	$42,000
Axial dual rotor	0.25–2	DR Series	Fuel—large jet engine test stands	Exact Flow	$1,300–$1,800
Propeller	48	FM182 (150 PSI)	Municipal water	Sparling	$6,500
Propeller	6	FM102 (150 PSI)	Irrigation	Sparling	$850
Special tangential	—	Wright Mark 8	Monitoring spirometer	Ferraris Medical	$800
Axial	—	MS03/MS04 MicroPlus	Diagnostic spirometer	Micro Medical	$600
Axial	4	WTX802	Chemical dosing for water treatment	Seametrics	$450–$550
Axial insertion	1.5–10	TX101	Municipal water, water—HVAC	Seametrics	$450
Axial insertion	2+	VTS-300	High-pressure steam	Flow Automation	$2,900
Axial insertion	3+	VL-150-LP	Flare stack control	Flow Automation	$2,500
Axial insertion dual rotor	2.5–72	F-1200	Water—HVAC	Onicon	$900
Angular momentum	—	Model 9–217 True Mass Fuel Flowmeter	Large jet aircraft, for example, Airbus A320, A321	Eldec	Not available
Multijet	1	1720	Domestic water	ABB Kent Messtechnik	$170
Multijet	1.5	AMD3000	Chemical liquid filling and dosing	Aquametro AG	$950
Multijet axial	9/32	DFS-2W	Pharmaceutical filling lines, kidney dialysis dialyte, beverage dispensers, OEM	Digiflow Systems	$42 or less, transducer; $235 electronics

TABLE 54.2 Manufacturer Contact Information

Manufacturer	Relevant Types
FTI Flow Technology Inc. 8930 South Beck Ave Suite #107 Tempe, AZ 85284 (480) 240 3400	Axial turbines—liquid and gas, including sanitary
Daniel Measurement and Control Emerson Process Measurements 11100 Brittmoore Park Drive Houston, TX 77041 (713) 467 6000	Axial turbines—liquid and gas
Liquid Controls Sponsler, Inc. A Unit of IDEX Corporation. 105 Albrecht Drive Lake Bluff, IL 60044 (847) 295 1050	Axial turbines—liquid and gas, including sanitary Insertion axial turbines—liquid and gas
McCrometer 3255 West Stetson Ave. Hemet, CA 92545 (951) 652 6811	Propeller meters
FMC Technologies, Inc. 500 N. Sam Houston Pkwy West Suite 100 Houston, TX 77067 (281) 260 2190	Axial turbines—liquid and gas, including sanitary Helical turbine meters
Sensus Metering Systems 8601 Six Forks Road Suites 300 and 700 Raleigh, NC 27615 (800) 375 8875	Axial turbines—gas Dual-rotor axial turbines—gas
Exact Flow 15555 North 79th Place Scottsdale, AZ 85260 (480) 948–3789	Dual-rotor axial turbines—liquid
Seametrics Inc. P.O. Box 1589 Kent, WA 98035 (800).975.8153	Axial turbines—water Insertion axial turbines—water Multijet turbines
InFlow, Inc. 1525 Skyline Lane. Longmont, CO 80501 (303) 652 0444	Insertion axial turbines—liquid and gas
Onicon, Inc. 1500 N. Belcher Road Clearwater, FL 33765 (727) 447–6140	Axial turbines—liquid Insertion axial turbines, single and dual rotor—liquid

TABLE 54.2 (continued) Manufacturer Contact Information

Manufacturer		Relevant Types
Eldec, A Crane Company 16700 13th Avenue W. Lynnwood, WA 98037 (800) 464 0261		Angular momentum flowmeters
Blancett (Div. Racine Federated, Inc.) 8635 Washington Avenue Racine, WI 53406 (800) 235 1638		Axial turbines—liquid and gas, including sanitary Multijet turbines
Zenner Performance P.O. Box 895 Banning, CA 92220 (951) 849 8822		Multijet turbines
Equflow B.V. Postbus 35 5370 AA Ravenstein Langakker 5F 5371 EV Ravenstein The Netherlands (31) 24 3792666	In the United States Clark Solutions 10 Brent Drive Hudson, MA 01749 (978) 568 3400 HP-NA High Purity Unit #4, 25 Thurber Blvd. Smithfield, RI 02917 (401) 349 4477	Swirl-type axial turbines—liquid
MIR Medical International Research S.r.l. via del Maggiolino, 125 00155 Rome, Italy (+39) 0622754777	MIR Medical International Research Inc. 1900 Pewaukee Road Suite O Waukesha, WI 53188 (262)565-6797	Swirl-type axial turbines—diagnostic spirometers (Use a disposable turbine)

References

Chiles, W. E., Vetsch, L. E., and Peterson, J. V., Shrouded flowmeter turbine and improved fluid flowmeter using the same, U.S. Patent No. 4,012,957, 1977.

ISA-RP 31.1, *Specification, Installation and Calibration of Turbine Flowmeters*, Research Triangle Park, NC: ISA, 1977.

Jungowski, W. M. and Weiss, M. H., Effects of flow pulsation on a single-rotor turbine meter, *Trans. ASME J. Fluids Eng.*, 118(1), 198–201, 1996.

Laurantzon, F., Orlu, R., Tillmark, N. et al., Response of common flowmeters to unsteady flow, *Technical Report in Flow Measurements Related to Gas Exchange*, pp. 135–166, Royal Inst. Techn., KTH Mechanics, SE-100 44 Stockholm, Sweden, 2012.

Lee, W. F. Z. and Evans, H. J., Density effect and Reynolds number effect on gas turbine flowmeters, *Trans. ASME J. Basic Eng.*, 87(4), 1043–1057, 1965.

Lee, W. F. Z., White, R. V., Sciulli, F. M. et al., Self-correcting self-checking turbine meter, U.S. Patent No. 4,305,281, 1981.

Lee, W. F. Z., Blakeslee, D. C., and White R. V., A self-correcting and self-checking gas turbine meter, *Trans. ASME J. Fluids Eng.*, 104, 143–149, 1982.

Mitchell, P. R., Helical turbine meters for liquid measurement, *Proc. 85th International School of Hydrocarbon Measurement*, 2010.

Olivier P. D. and Ruffner, D., Improved turbine meter accuracy by utilization of dimensionless data, *Proc. 1992 National Conf. Standards Labs*. (NCSL) Workshop and Symp., Boulder, CO: NCSL, 1992, pp. 595–607.

Pate, M. B., Myklebust, A., and Cole, J. H., A computer simulation of the turbine flow meter rotor as a drag body, *Proc. Int. Comput. in Eng. Conf. and Exhibit 1984*, pp. 184–191, Las Vegas, New York: ASME, 1984.

Quick, L. A., Gas measurement by insertion turbine meter, *Proc. 71st Int. School Hydrocarbon Meas*., 1996.

Stoltenkamp, P. W., Dynamics of turbine flow meters, PhD Thesis, Eindhoven University of Technology, Eindhoven, the Netherlands, 2007.

Termaat, K., Oosterkamp, W. J., and Nissen, W., Nuclear turbine coolant flow meter, U.S. Patent No. 5,425,064, 1995.

Thompson, R. E. and Grey, J., Turbine flowmeter performance model, *Trans. ASME J. Basic Eng*., 92(4), 712–723, 1970.

Van Der Hagen, T. H. J. J., Proof of principle of a nuclear turbine flowmeter, *Nucl. Technol*., 102(2), 167–176, 1993.

Wadlow, D. and Layden, L. M., Controlled flow volumetric flowmeter, U.S. Patent No. 5,284,053, 1994.

Standards and Recommendations Applicable in the United States

AGA Rep. No. 7, *Measurement of Natural Gas by Turbine Meter*, Arlington, VA: AGA (Amer. Gas Assoc.), 2006.

API MPM, *Measurement of Liquid Hydrocarbons by Turbine Meters*, 5th ed., Washington, D.C.: API (Amer. Petroleum Inst.), 2005, Chapter 5.3.

API MPMS, Manual of Petroleum Measurement Standards, *Electronic Liquid Volume Measurement Using Positive Displacement and Turbine Meters*, 1st ed., Washington, D.C.: API (Amer. Petroleum Inst.), 1998, Chapter 21.2. (Reaffirmed 2004).

ASME MFC-4M, *Measurement of Gas Flow by Turbine Meters*, 1986. (Reaffirmed 2008).

ATS, Standardization of spirometry, 1994 update, *Am. J. Respir. Care Med*., 152, 1107–1136, 1995 (is the latest version of the official U.S. guideline for spirometry generated by the American Thoracic Society).

AWWA C701-12, *Cold Water Meters—Turbine Type, for Customer Service*, Denver, CO: Amer. Water Works Assoc., 2012.

AWWA C704-08, *Propeller-Type Meters for Waterworks Applications*, Denver, CO: Amer. Water Works Assoc., 2008.

AWWA C708-11, *Cold-Water Meters, Multi-Jet-Type*, Denver, CO: Amer. Water Works Assoc., 2011.

Int. Recommendation OIML R 137-1, *Gas Meters*, Paris, France: Int. Organization of Legal Metrology, Edition 2006 (E).

Int. Recommendation OIML R 117-1, *Dynamic Measuring Systems for Liquids Other Than Water*, Edition 2007 (E).

ISO 4064:2005, *Measurement of Water Flow in Fully Charged Closed Conduits—Meters for Cold Potable Water and Hot Water*, Geneva, Switzerland: Int. Organization for Standardization.

ISO 9951:1993, *Measurement of Gas Flow in Closed Conduits—Turbine Meters*, Geneva, Switzerland: Int. Organization for Standardization, (also available ANSI), 1993.

NIST Handbook 44, 2012 Edition. Specifications, Tolerances, and Other Technical Requirements for Weighing and Measuring Devices, Section 3, National Institute of Standards and Technology, Office of Weights and Measures, Gaithersburg, MD.

55

Impeller Flowmeters

Harold M. Miller
Data Industrial Corporation

55.1 Introduction

Impeller flowmeters, sometimes called *paddle wheel* meters, are one of the most commonly used flowmeter variety. The impeller flow sensor is a direct offshoot of the old-fashioned undershot waterwheel. They are a cost-effective alternative to turbine meters and can be used in applications that are difficult to handle with other types of flow metering instruments. In their mechanical construction, they are usually very simple, with any sophistication residing in the electronics used to detect the rotation rate of the impeller and in the choice of materials of construction for chemical corrosion attributes of the metered fluids. They are related to turbine meters in that both types use a rotating mechanical element to produce the output signal. They differ in the fact that the impeller meter has its rotary axis transverse to the flow stream, as opposed to the turbine meter axis, which is parallel thereto.

These devices are available in two basic types. The insertion style is the most common (see Figures 55.1b and 55.2). The sensor is directly installed into a hole in a pipe, with saddle or welded fitting installed at the entry to seal the sensor to the pipe. The sensor can also be preinstalled in appropriate tees in the pipeline. Most suppliers have designs that can be installed in operating pipe systems, with little, if any, loss of the fluid during the installation process. The impeller design is also supplied in in-line (through-flow) sensors for those applications where such use is desirable (Figures 55.1a). The in-line meters are commonly of somewhat higher accuracy than the insertion style.

In-line meters are *linear, inferential, volumetric* flowmeters for measuring *liquid and gas flows* and are more *sensitive at lower flow rates* compared with, for example, axial turbine flowmeters. (This is of course because the flow blade incidence angle is much greater.) Insertion impeller flowmeters instead measure the flow velocity in a small region within a flow conduit.

Impeller flowmeters are generally suited to much lower flow rate ranges than the same size axial turbines and hence often find applications where axial turbines cannot be used. This and a tendency for lower cost and high reliability are key strengths. Competition with in-line axial turbines can only occur in overlapping design flow ranges.

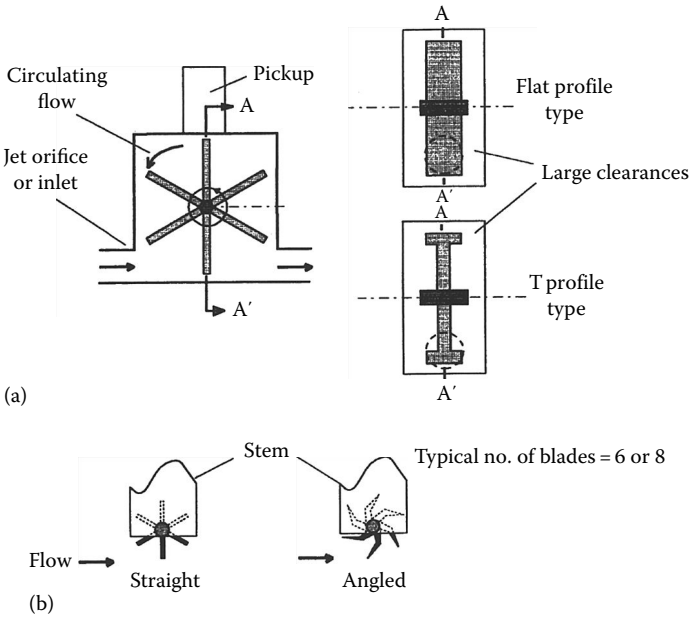

FIGURE 55.1 Impeller flowmeter rotor design variations: (a) in-line meters and (b) insertion meters. (Courtesy of David Wadlow.)

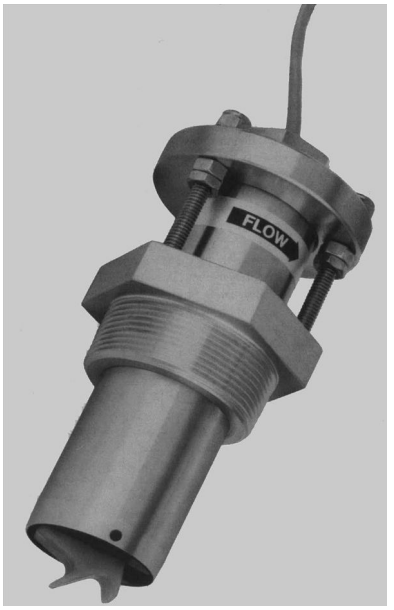

FIGURE 55.2 A typical insertion-type impeller flowmeter.

Some in-line meters have interchangeable orifice sizes, allowing the same body to be used over different flow ranges. The orificed in-line meters are typically insensitive to flow condition. Insertion meters are, of course, very sensitive to flow condition if volumetric measurements are inferred. This is an important distinction and can extend to differences between requirements for specific in-line versions. Installation is important. It affects the user when he or she is designing an installation, selecting a flowmeter, and deciding on how much confidence to place in the measurement reading.

Paddle wheel flowmeters are *never* used in liquid hydrocarbon custody transfer applications. The flow measurement capacity is insufficient to compete in monitoring large volume transfers, and accuracy is not sufficient for valuable fluids.

These meters go by a variety of names, depending on which name the manufacturer selects and also the application. One often-quoted, historical root is also the impulse turbine invented by Pelton in the nineteenth century and has given rise to the "Pelton wheel turbine" description currently used by some suppliers. A device like this was originally used to drive milling wheels directly about the vertical axis, rather than through a right angle gear as in the "undershot" wheel described. Another common name, besides paddle wheel and impeller type, based at least on suppliers' descriptions for the in-line variety, is single-jet tangential, or simply tangential, turbine. The former description distinguishes this design from that of multijet tangential turbine flowmeters and therefore deserves mention. There are thus a confusing variety of names in current use, all relating to essentially the same impeller-like, vaned flowmetering principle:

1. Impeller type: insertion and in-line
2. Paddle wheel type: insertion and in-line
3. Pelton turbine wheel type: in-line
4. Tangential turbine flowmeter: insertion and in-line
5. Single-jet tangential turbine flowmeter: in-line
6. Impulse turbine flowmeter: in-line

Historically, the impeller sensor is based on early electronic speedometers used in pleasure boating. Signet, followed quickly by Data Industrial, moved to modify the basic design of such marine instruments to meet the significantly more demanding service life requirements of industrial flow measurement. The resulting flowmeters, and their descendants, have been widely used since 1975. Significant engineering efforts have resulted in highly reliable instruments used in many extremely demanding applications.

55.2 Sensing Principles

All impeller flow sensors must detect the rotation of the impeller and in their usual form transmit a pulse train, at a frequency related to the rotational velocity of the impeller. Being essentially a digital output, impeller sensors can typically transmit signals over quite long distances, up to 1 km when so required. Detection principles used include

1. One or more magnets retained in the impeller or mechanically connected thereto, using the zero crossing of an induced AC field to generate the pulse train.
2. One or more coupling devices contained within the impeller, modulating a transmitted frequency that is processed to produce the pulse train.
3. One or more metallic targets installed within the sensor, sensed by any of the proximity pickup techniques commercially available, to produce output pulses.
4. One or more magnets retained in the impeller, used to switch a Hall effect device, producing the output pulse train.
5. Optical devices, both transmissive and reflective, have been used to sense the passage of the impeller blades to produce the output pulse train.
6. Measurement of the change in electric reactance due to the passage of impeller vanes through the measurement field area, conditioned to produce the output pulse train.

Any given supplier can produce several types of impeller flowmeter, each type using a different detection method depending on market requirements. Since the impeller can operate to rotational velocities of 4000 rpm or higher, output frequencies can be as high as 500 Hz. At low flow rates, the frequencies can be as low as 0.2 Hz. This factor should be addressed early in the selection procedure because the chosen output device must be capable of the frequency output range of the sensor.

Most sensor manufacturers can either supply or specify an appropriate meter to relate sensor output to flow rate in engineering units, either U.S. customary or SI. These meters are usually capable of displaying both flow rate and accumulated flow for the sensor to which they are connected. Additional outputs are available, either stand-alone or in combination with the meter, providing periodic pulse outputs at definable flow increments or analog outputs scaled to flow rate. In addition, certain control functions, alarms, and other special features required by the various markets served are often incorporated in these meters.

55.3 Flow Ranges

The insertion style of impeller meter, even when Tee installed, is a local sensing device, measuring the flow velocity in only a part of the flow stream. The manufacturer calibrates the meter for average flow across the entire cross section of the pipe. The paddle wheel location is usually close to the inner diameter of the pipe in a region of flow with a velocity significantly below the average flow velocity in the pipe. Proper calibration practices by the manufacturer make the meters effective at flow rates as low as 10 cm s^{-1} average velocity in spite of the low local velocities at the impeller. Generally speaking, flows at Reynolds numbers as low as 5000 can be run with no requirement for special calibration, and frequently lower numbers can be handled with no difficulty. The usual range specification is a flow rate equivalent to 0.3–10 m s^{-1} average flow velocity. The diversity of products available allows operation to velocities considerably lower than the 0.3 m s^{-1} range, indeed to as low as 0.07 m s^{-1} in certain specialty impeller flowmeters.

55.4 Installation and Applications

55.4.1 Pipe Sizes

Pipe sizes in which these sensors have been installed run the gamut from small-bore tubing to 2.3 m outside diameter. The larger pipe sizes are those that show the greatest installed cost savings over alternative metering systems. The impeller meter, in fact, can be cost-effective in any flowmeter application that is consistent with the accuracy of the instrument, particularly if the application involves pump or valve control.

55.4.2 Piping System Restrictions

Most suppliers require at least 10 pipe diameter lengths of straight pipe upstream of the installed meter and 5 downstream. These conditions are required to minimize the asymmetry of the flow stream in the neighborhood of the impeller, in the installed piping, which can be caused by elbows, tees, and valves. More is better; no supplier is likely to complain that there is too great a straight pipe length upstream. Less can adversely affect the calibration of the sensor due to the local variations of velocity resulting from flow disturbances.

55.4.3 Operating Pressure

Manufacturers' standard offerings are usually consistent with the pressure limitations of the materials of construction of the piping system with plastic piping systems and are commonly as high as 2.7 MPa with steel or brass piping. Higher pressures are available but are usually somewhat more expensive. Pressure drop generated by the installed flowmeter is usually low. Manufacturers can usually supply information on the anticipated pressure drop.

55.4.4 Calibration

Calibration of the sensors is usually specified by the manufacturer. Some manufacturers provide a calibration factor in terms of gallons per pulse or in pulses per gallon. Others, such as Data Industrial, provide data relating frequency to flow rate in GPM or other volumetric rate units. For insertion-style sensors, any such instrument must be field calibratable to accommodate the variation in the relation of impeller rotational velocity with average flow rate with pipe-size variation.

55.4.5 Accuracy

Accuracies for in-line impeller flowmeters vary considerably but can be high, ranging from ±0.2% reading for liquids for one manufacturer to several percent of full scale for several others. The difference between accuracies specified as % full scale and % reading should be particularly noted. Manufacturers use both, particularly with this class of meter. A ±1% full-scale device is often far less accurate than, for example, a ±2% reading device. For example, it is in error by 10% at the minimum of its flow range if the turndown is 10:1, whereas the ±2% reading device is still only in error by ±2%.

Output accuracy is usually specified as ±1% of full rated flow. This specification is broad enough to handle the dimensional and frictional variations in the sensors as manufactured. Some producers will custom calibrate the sensors to meet special needs, but this task should be performed only when the mating pipe entry and exit can be shipped to, and accommodated by, the manufacturer. Alternatively, the manufacturer can usually provide new calibration values if the meter used is identified, the meter reading is known, and the actual flow is known for at least two points on the flow curve. When calibration in place is required, the anticipated accuracy is in the range of ±0.5% of full scale or 1% of indicated flow, whichever is greater.

Repeatability of readings is usually on the order of 0.5%. Linearity, except at the extremes of the flow range, is also expected to be no worse than 0.5% and, over the full design range of the meter, is normally accurate within the ±1% of full rated flow.

To achieve the accuracies noted earlier, careful attention must be paid to proper installation, particularly with regard to insertion depth.

55.4.6 Design Features

These flow sensors are offered in materials of construction compatible with a broad range of aqueous solutions, of both high and low pH and with deionized water. For this latter service, the history of the sensor, particularly for particle generation, should be reviewed. Flow streams with high concentrations of solids, and particularly of fibrous solids, should be carefully reviewed when the impeller sensor is under consideration. Construction is reasonably forgiving with particulates, but caution in such applications is warranted. Heat transfer fluids are also compatible with sensors from at least two of the suppliers. Basic application limits should be discussed with the supplier, who should have a broad history of successful applications to back up recommendations, as well as sensor materials with test results specific to the measured fluid. The so-called "hot tap" or "wet tap" versions are available for installation in operating pipelines and in-line or on-line service. A submersible version capable of metering in flooded well pits for extended periods of time is available from some suppliers. At least two manufacturers provide "intrinsically safe" sensors for application in hazardous environments.

55.4.7 Areas of Application

Impeller flow sensors are widely used in the following fields with considerable success:

- Agricultural and horticultural irrigation
- Deionized water systems, including silicon wafer fabrication
- Heating, ventilating, and air conditioning and energy management
- Industrial waste treatment
- Industrial filtration systems
- Chemical reagent metering and batching
- Municipal water systems (potable water)

The sensors can be supplied with analog output for control applications, if desired.

Some suppliers have developed specialty impeller meters adapted to provide long life, ruggedness, and maintainability required in more demanding applications. The history of acceptable operation in applications similar to that proposed for the metering system should be reviewed with the supplier. Custodial transfer applications are normally unsuitable for the impeller sensor.

55.5 Manufacturers

The following is a selection of U.S. manufacturers. Their locations and phone numbers are listed in Table 55.1.

55.5.1 Data Industrial

In-line and insertion meters: 0.07–18 m s^{-1} (0.25–60 fps) fluid velocity. Available materials to accommodate most industrial fluids. Temperatures from –29 °C to 152 °C (–20 °F to 305 °F). Energy monitoring. Digital and/or analog meter outputs. NEMA 4, 4X, and 6P constructions. FM, CSA Approvals.

55.5.2 G. Fischer (Signet)

In-line and insertion meters: 0.1–7 m s^{-1} (0.3–20 fps) fluid velocity. Available materials to accommodate most industrial fluids. Temperatures to 149 °C (300 °F). Energy monitoring. Digital and/or analog meter outputs. NEMA 4, 4X constructions. FM, CE Approvals (http://www.gfsignet.com/go/45C24DDB1999 3E1D34D4906307B08581).

55.5.3 Seametrics

In-line meter. Sizes 3/8–2 in. Plastic, brass. Clean water applications. Flows from 0.05 to 40.0 GPM. Accuracy ±1% of full scale (FS). Insertion. Range of IP probes. Plastic, brass, stainless. Sapphire bearings and carbide shafts. Up to 250°F. 0.3–30 fps. Accuracy ±1% to ±2% FS (http://products.seametrics.com/).

55.5.4 Roper Flow Technology

In-line meters: Omni flow®, liquids and gases, highly precise, range 7.6–5677 mL min^{-1} (liquid), 0.0025–0.68 Am^3 h^{-1} (gases). Cryogenics to 593 °C, pressure to 60,000 psi, viscosity compensated.

Optiflo®, plastic construction for liquids only with some reduction in performance capabilities.

55.5.5 Hoffer

MF series (Miniflow). High-performance, in-line low flowmeters using a "Pelton rotor" for liquids and gases. Liquid flow ranges from 57 mL min^{-1} to 11.5 rpm. Linearity ±1% reading over 10:1 range.

TABLE 55.1 U.S. Manufacturers of Impeller Flowmeters

Manufacturer	City, State	Phone Number
Data Industrial Corp.	Mattapoisett, MA	(508) 758-6390
G. Fischer (Signet)	Tustin, CA	(714) 731-8800
Seametrics	Kent, WA	(206) 872-0284
Roper Flow Technology, Inc.	Phoenix, AZ	(602) 437-1315
Blancett	Altus, OK	(405) 482-0036
Hoffer Flow Controls, Inc.	Elizabeth City, NC	(800) 628-4584, (919) 331
McMillan Co.	Georgetown, TX	(512) 863-0231
Flowmetrics, Inc.	Canoga Park, CA	(818) 346-4492
Proteus Industries, Inc.	Mountain View, CA	(415) 964-4163

Repeatability ±0.1% typical. Gas flow ranges depending on density from 0.02 to 1.0 ACFM. Linearity ±1.5% reading. Repeatability ±0.2%. Various bearings available. Ball bearings used for high-accuracy applications. UVC curves available. "Smart" transmitter available for temperature–viscosity correction + linearization (http://hofferflow.com/).

55.5.6 McMillan

Low-viscosity liquids: In-line meters. Ranges from 13 mL min^{-1} to 10 L min^{-1}. Accuracies ±1%–±3% FS. IR rotation sensors. Have a Teflon version for corrosives.

Gases: Teflon version for chlorine, fluorine, etc. Accuracy ±3% FS. Ranges: 25–5 AmL min^{-1}.

55.5.7 Flowmetrics

Series 600: Stainless steel, in-line tangential turbine for gases and liquids. Ranges: 0.001–2.0 GPM liquids; 0.001–2.0 ACFM gases. Linearities vary according to range from ±1% to ±5% FS. Repeatabilities ± 0.05%, traceable NIST (http://www.flometrics.com/).

55.5.8 Proteus

In-line paddle wheel flowmeters and flow switches—liquids only. Typically used for water cooling lines on electrical or vacuum equipment. Quoted for use with liquids up to 120 cSt. Media include water, treated water, deionized water, ethylene glycol, and light oils. Range 0.08–60 GPM. Accuracies vary between models in the ±3% to ±4% FS range. Meter bodies can incorporate optional integral temperature and pressure transducers. These meters are also available with a FluidTek™ computer interface protocol and PC software for constructing embedded control systems for flow, temperature, and pressure (http://proteuseng.com.au/).

Bibliography

Bean, H. S. (ed.), *Fluid Meters*, 6th ed., New York: American Society of Mechanical Engineers, 1971, p. 99.

Cheremisinoff, N. P., *Applied Fluid Flow Measurement*, New York: Marcel Dekker, 1979, 106.

Impeller Flowmeter, Geophysics done right. http://www.enviroscan.com/html/impeller_flowmeter.html (accessed on July 25, 2012).

Products, Impeller meters, Veris Industries, http://www.veris.com/Category/Flow/Impeller-spcMeters.aspx (accessed on March 15, 2013).

Products, Positive displacement meters, FMC Technologies, http://www.fmctechnologies.com/en/MeasurementSolutions/Technologies/LiquidProducts/PDMeters.aspx (accessed on March 15, 2013).

Kjelstrom, L. C., Methods of measuring pumpage through closed conduit irrigation systems, *J. Irrig. Drain. Eng. ASCE*, 117, 748–757, 1991.

56

Electromagnetic Flowmeters

Halit Eren
Curtin University

Electromagnetic flowmeters have been widely used in industry for many decades. Unlike many other types of flowmeters, they offer true noninvasive measurements. They can easily be installed in the processes. These flowmeters can be used to monitor the reverse flows and are insensitive to viscosity, density, turbulences, and other flow disturbances. *Electromagnetic flowmeters* can rapidly respond to flow changes and exhibit linear characteristics for a wide measurement range. In recent years, technological refinements have resulted in the production and usage of much more economical, accurate, and smaller instruments than the previous versions.

As in the case of many electric devices, the underlying principle of the electromagnetic flowmeter is the Faraday's law of induction. The induced voltages in an electromagnetic flowmeter are linearly proportional to the mean velocity of liquids or to the volumetric flow rates. As is the case in many applications, if the pipe walls are made from nonconducting elements, then the induced voltage is largely independent of the properties of the fluid.

The accuracy of these meters can be as low as 0.25%, and in most cases, an accuracy of 1% is used. At worst, 5% accuracy is obtained in some difficult applications where impurities of liquids and the contact resistances of the electrodes are inferior as in the case of low-purity sodium liquid solutions.

56.1 Faraday's Law of Induction

Faraday's law of induction states that if a conductor of length l (m) is moving with a velocity v (m s^{-1}) perpendicular to a magnetic field of flux density B (Tesla), then the induced voltage e across the ends of conductor can be expressed by

$$e = Blv \tag{56.1}$$

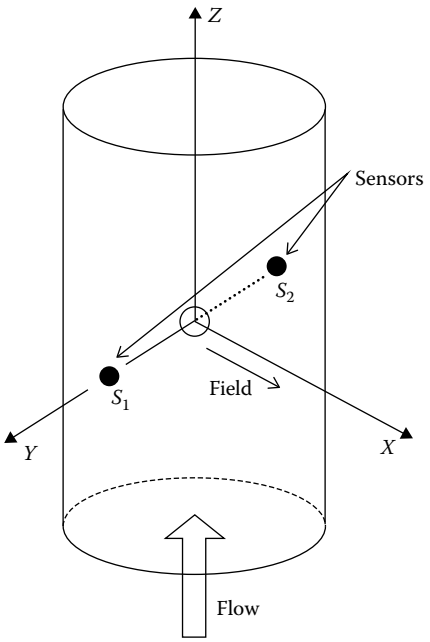

FIGURE 56.1 Operational principles of electromagnetic flowmeters. Faraday's law states that a voltage is induced in a conductor moving in a magnetic field. In electromagnetic flowmeters, the direction of movement of the conductor, the magnetic field, and the induced emf are perpendicular to each other on *x*-, *y*-, and *z*-axes. Sensors S_1 and S_2 experience a virtual conductor due to the flow of conductive fluid in the pipe.

The principle of application of Faraday's law to an electromagnetic flowmeter is given in Figure 56.1. The magnetic field, the direction of the movement of the conductor, and the induced electromotive force (emf) are all perpendicular to each other.

Figure 56.2 illustrates a simplified electromagnetic flowmeter in greater detail. By using externally located electromagnets, a homogeneous magnetic field that passes through the pipe and the liquid inside it is created. When a conducting flowing liquid inside the pipe cuts through the magnetic field, a voltage is induced along the liquid path between the two electrodes positioned on the opposite sides of the pipe.

In the case of electromagnetic flowmeters, the conductor is the liquid flowing through the pipe, and the length of the conductor is the distance between the two electrodes, which is equal to the tube diameter. The velocity of the conductor is proportional to the mean flow velocity of the liquid. Hence, the induced voltage becomes

$$e = BDv \tag{56.2}$$

where D (m) is the diameter of pipe.

If the magnetic field is constant and the diameter of the pipe is fixed, the magnitude of the induced voltage will only be dependent on the velocity of the liquid. If the ends of the conductor, in this case the sensors, are connected to an external circuit, the induced voltage causes a current, i, to flow, which can be processed suitably as a measure of the flow rate.

Electromagnetic flowmeters are often calibrated to determine the volumetric flow of the liquid. The volume of liquid flow, Q (L/s), can be related to the average fluid velocity as

$$Q = Av \tag{56.3}$$

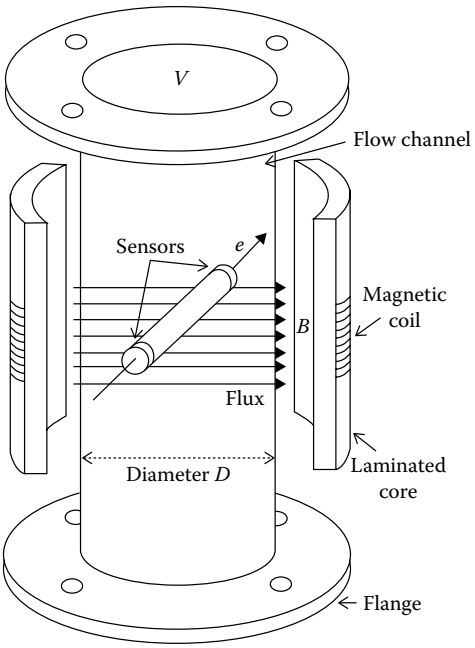

FIGURE 56.2 Construction of practical flowmeters. External electromagnets create a homogeneous magnetic field that passes through the pipe and the liquid inside. Sensors are located 90° to the magnetic field and to the direction of the fluid flow. Sensors are insulated from the pipe walls. Flanges are provided for fixing the flowmeter to external pipes. Usually, manufacturers supply information about the minimum lengths of the straight portions of external pipes.

Writing the area, A (m^2), of the pipe as

$$A = \frac{\pi D^2}{4} \tag{56.4}$$

gives the induced voltage as a function of the flow rate:

$$e = \frac{4BQ}{\pi D} \tag{56.5}$$

Equation 56.5 indicates that in a carefully designed flowmeter, if all other parameters are kept constant, then the induced voltage can be expressed to be linearly proportional to the volume of the liquid flowing through the pipe.

There are many different types of electromagnetic flowmeters available, such as AC, DC, and permanent magnets. The two most commonly used ones are the AC and DC types. This section concentrates mainly on AC- and DC-type flowmeters.

Although the induced voltage is directly proportional to the mean value of the liquid flow, the main difficulty in the use of electromagnetic flowmeters is that the amplitude of the induced voltage is small relative to extraneous voltages and noise. Noise sources include

- Stray voltage in the process liquid
- Capacitive coupling between signal and power circuits
- Capacitive coupling in connection leads
- Electromechanical emf induced in the electrodes and the process fluid
- Inductive coupling of the magnets within the flowmeter

56.2 Construction and Operation of Electromagnetic Flowmeters

Common to both AC and DC electromagnetic flowmeters, the magnetic coils create a magnetic field that passes through the flow tube and process fluid. As the conductive fluid flows through the flowmeter, a voltage is induced between the electrodes in contact with the process liquid. The electrodes are placed at positions where maximum potential differences occur. The electrodes are electrically isolated from the pipe walls by nonconductive liners to prevent short-circuiting of electrode signals. The liner also serves as protection to the flow tube to eliminate galvanic action and possible corrosion due to metal contacts. Electrodes are held in place by holders that also act as sealing.

The resistance of the moving conductor R can be expressed as $R = \rho D/a^2$ where ρ is the resistivity of the fluid and a is the effective area of the sensor. If surfaces of electrodes are not insulated, there will be an associated leakage current due to conductivity of the fluid.

Dimensionally, magnetic flowmeters are manufactured from 2 mm in diameter to 1.2 m. In a particular application, the determination of the size of the flowmeter is a matter of selecting the one that can handle the anticipated liquid velocities. The anticipated velocity of the liquid must be within the linear range of the device. As an example of a typical guide for selection, the capacity of various size flowmeters is given in Figure 56.3.

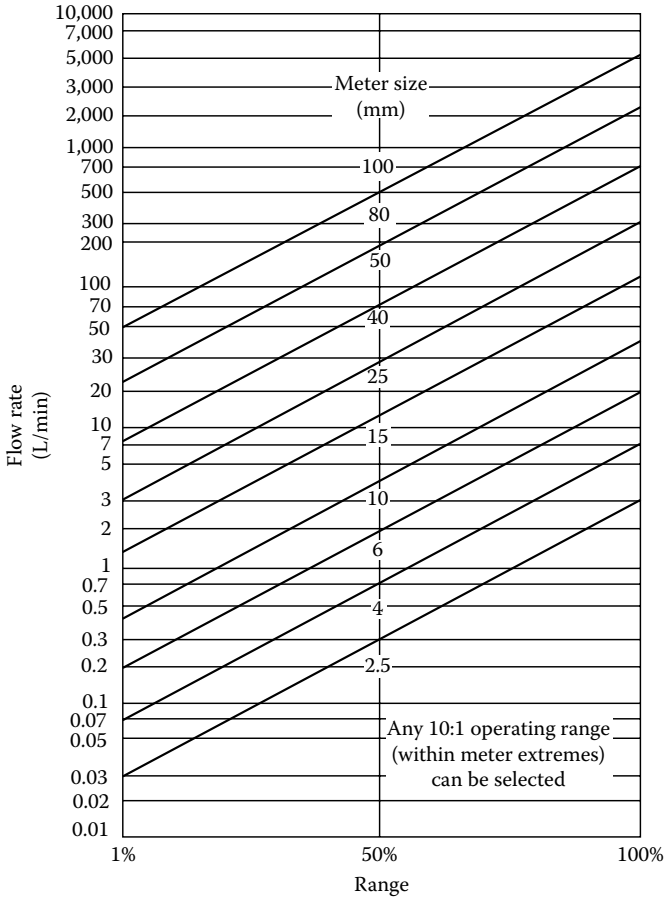

FIGURE 56.3 Selection of flowmeters. In the selection of a suitable flowmeter for a particular application, care must be exercised in handling the anticipated liquid velocities. The velocity of liquid must be within the linear range of the device. For example, a flowmeter with 100 mm internal diameter can handle flows between 50 and 4000 L min^{-1}. An optimum operation will be achieved typically at a flow rate of 500 L min^{-1}.

Some electromagnetic flowmeters are made from replaceable flow tubes, whereby the field coils are located external to the tubes. In these flowmeters, the flanges are located far apart from each other in order to reduce their adverse effects on the accuracy of the measurements; hence, they are relatively larger in dimensions. In other cases, the field coils are integrated with the flow tube itself. In these cases, the flanges are located closer to the magnets and the electrodes, thus yielding to relatively smaller dimensions. On the other hand, miniature and electrodeless magnetic flowmeters are also available, compact enough to allow them to be installed between two closely spaced flanges.

The wetted parts of a magnetic flowmeter include the liners, electrodes, and electrode holders. Many different materials such as rubber, Teflon, polyurethane, and polyethylene are used in the construction of these flowmeters to suit the process corrosion properties, the abrasiveness, and the temperature constraints. The main body and the electrodes are manufactured from stainless steel, tantalum, titanium, and various other alloys. Liners are selected mainly to withstand the abrasive and corrosive properties of the liquid. The electrodes must be selected such that they cannot be coated with the insulating deposits of the process liquid during long time periods of operations.

The pipe between the electromagnets of a flowmeter must be made from nonmagnetic materials to allow the field to penetrate the fluid without any distortion. Therefore, the flow tubes are usually constructed using stainless steel or plastics. The use of steel is a better option because it adds strength to the construction. Flanges are protected with appropriate liners and not allowed to make contact with the process fluid.

In some electromagnetic flowmeters, electrodes are cleaned continuously or periodically by ultrasonic or electric means. Ultrasonic cleaning methods are suitable for both AC- and DC-type magnetic flowmeters when frequent severe insulating coating is expected to be deposited on the electrodes, which might cause the flowmeter to cease to operate in an anticipated manner.

The operation of a magnetic flowmeter is generally limited by factors such as linear characteristics, pressure ratings of flanges, and temperatures of the process fluids. The maximum temperature limit is largely dependent on the liner material selection and usually is set to around 200°C. For example, ceramic liners can withstand high temperatures but are subject to cracking in the cases of sudden changes in temperatures of the process fluid.

During the selection of electromagnetic flowmeters, the velocity constraints should be evaluated carefully to secure accurate performance over the expected range. The full-scale (FS) velocity of the flowmeter is typically 0.3–10 m s^{-1}. Some flowmeters can measure lower velocities with somewhat poorer accuracy. Generally, employment of electromagnetic flowmeters over a velocity of 5 m s^{-1} should be considered carefully because erosion of the pipe and damages to liners can be significant.

The accuracy of a conventional magnetic flowmeter is usually expressed as a function of FS, typically 0.5%–1% FS. However, DC flowmeters have a well-defined zero due to automatic zeroing capabilities; therefore, they have a percentage rate of accuracy better than AC types, typically 0.5%–2%.

56.3 Types of Electromagnetic Flowmeters

56.3.1 AC-Type Electromagnetic Flowmeters

In many commercial electromagnetic flowmeters, an alternating current of 50–60 Hz in coils creates the magnetic field to excite the liquid flowing within the pipe. A voltage is induced in the liquid due to Faraday's law of induction, as explained earlier. A typical value of the induced emf in an AC flowmeter fixed on a 50 mm internal diameter pipe carrying 500 L min^{-1} is about 2.5 mV.

Historically, AC magnetic flowmeters were the most commonly used types because they reduced polarization effects at the electrodes. They are less affected by the flow profiles of the liquid inside the pipes. They allow the use of high Z_{in} amplifiers with low-drift and high-pass filters to eliminate slow and spurious voltage drifts emanating mainly from thermocouple and galvanic actions. These flowmeters

find many applications as diverse as the blood flow measurements in living specimens. Miniaturized sensors allow measurements on pipes and vessels as small as 2 mm in diameter. In these applications, the excitation frequencies are higher than industrial types, 200–1000 Hz.

A major disadvantage of the AC flowmeter is that the powerful AC field induces spurious AC signals in the measurement circuits. This necessitates periodic adjustment of zero output at zero velocity conditions—more frequently than for DC counterparts. Also, in some harsh industrial applications, currents in the magnetic field can vary due to voltage fluctuations and frequency variations in the power lines. The effect of fluctuations in the magnetic fields can be minimized by the use of a reference voltage proportional to the strength of the magnetic field to compensate for these variations. To avoid the effects of noise and fluctuations, special cabling and proper calibration practices recommended by the manufacturers must be followed to ensure accurate operation. Usually, the use of two conduits is required—one for the signal transmission and one for the power supply. The cable lengths should also be set to certain levels to minimize noise and sensitivity problems.

AC flowmeters operating at 50, 60, or 400 Hz are readily available. AC flowmeters can operate from 10 to 5000 Hz. High frequencies are preferred in determining the instantaneous behavior of transients and pulsating flows. Nevertheless, in applications where extremely good conducting fluids and liquid metals are used, the frequency must be kept low to avoid skin effects. On the other hand, if the fluid is a poor conductor, the frequency must not be so high such that dielectric relaxation is not instantaneous.

56.3.2 DC-Type Electromagnetic Flowmeters

Unlike AC magnetic flowmeters, direct current or pulsed magnetic flowmeters excite the flowing liquid with a field operating at 3–8 Hz. As the current to the magnet is turned on, a DC voltage is induced at the electrodes. The signals observed at the electrodes represent the sum of the induced voltage and the noise, as illustrated in Figure 56.4. When the current in the magnetic coils is turned off, the signal represents only the noise. The effect of noise can be eliminated by subtracting the signals of the flowmeter when no current flows through from the signals when the current flows through.

If the magnetic field coils are energized by normal direct current, then several problems can occur: polarization, which is the formation of a layer of gas around the measured electrodes, as well as electrochemical and electromechanical effects. Some of these problems can be overcome by energizing the field coils at higher frequencies or AC. However, higher frequencies and AC generate transformer action in the connectors and the fluid path. Therefore, the coils are excited by DC pulses at low repetition rates to eliminate the transformer action. In some flowmeters, by appropriate sampling and digital signal processing techniques, the zero errors and the noise can be rejected substantially.

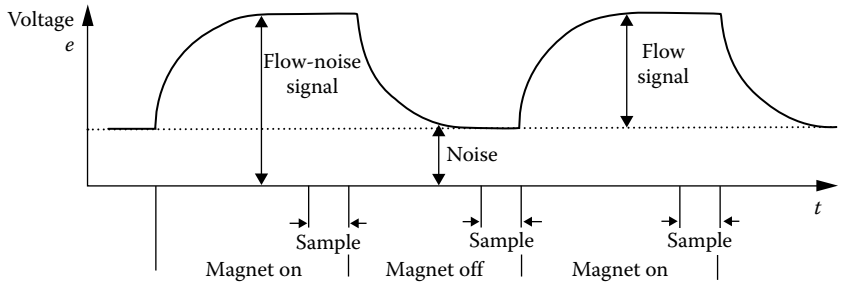

FIGURE 56.4 The signals observed at the electrodes represent the sum of the induced voltage and the noise. When the current in the magnetic coils is turned off, the signal across the electrodes represents only the noise. Subtracting the signal of the flowmeter when there is no current flow through the magnet from the measurement when current flows through the magnet, effectively cancels out the effect of noise.

The zero compensation inherent in DC magnetic flowmeters eliminates the necessity of zero adjustment. This allows the extraction of flow signals regardless of zero shifts due to spurious noise or electrode coating. Unlike AC flowmeters, a larger insulating electrode coating can be tolerated that could shift the effective conductivity significantly without affecting performance. If the effective conductivity remains high enough, a DC flowmeter will operate satisfactorily. Therefore, DC flowmeters are less susceptible to drifts, electrode coatings, and changes in process conditions in comparison to conventional AC flowmeters.

DC magnetic flowmeters do not have good response times due to the slow pulsed nature of operations. However, as long as there are not rapid variations in the flow patterns, zero to FS response times of a few seconds do not create problems in the majority of applications. Power requirements are also much less as the magnet is energized part of the time. This gives an advantage in power saving of up to 75%.

If the DC current to the magnet is constant, the proportional magnetic field can be kept steady. Therefore, the amplitudes of the DC voltages generated at the electrodes will be linearly proportional to the flow. However, in practice, the current to the magnet varies slightly due to line voltage and frequency variations. As in the case of AC flowmeters, voltage and frequency variations could necessitate the use of a reference voltage. Because the effect of noise can be eliminated better, the cabling requirements are not as stringent.

To avoid electrolytic polarization of the electrodes, bipolar pulsed DC flowmeters have been designed. Also, modification of DC flowmeters led to the development of miniature DC magnetic flowmeters with wafer design for a limited range of applications. The wafer design reduces the weights as well as the power requirements.

56.4 Installations and Practical Applications

Conventional AC and DC magnetic flowmeters have flanges at the inlet and the outlet that need to be bolted to the flanges of the pipe. Face-to-face dimensions of magnetic flowmeters differ between manufacturers; therefore, once the flowmeter is installed, new piping arrangements could be necessary if a flowmeter is replaced by one from a different manufacturer.

Upstream and downstream straight piping requirements can vary from one flowmeter to another, depending on the manufacturer's specifications. As a rule of thumb, the straight portion of the pipe should be at least 5D/2D from the electrodes and 5D/5D from the face of the flowmeter in upstream and downstream directions, respectively. For good accuracy, one should adhere carefully to the recommendations of manufacturers for piping requirements. In some magnetic flowmeters, coils are used in such a way that the magnetic field is distributed in the coil to minimize the piping effect.

For accurate measurements, magnetic flowmeters must be kept full of liquid at all times. If the liquid does not contact the electrodes, measurements cannot be taken. Figure 56.5 illustrates this point. If the measurements are made in other than vertical flows, the electrodes should be located in horizontal directions to eliminate the possible adverse effect of the air bubbles, because the air bubbles tend to concentrate on the top vertical part of the liquid.

In the selection of magnetic flowmeters, a number of considerations must be taken into account, as

- Cost, simplicity, precision, and reproducibility
- Metallurgical aspects
- Velocity profiles and upstream disturbances

Most processes employ circular piping that adds simplicity to the construction of the system. The flowmeters connected to circular pipes give relatively better results compared to rectangular- or square-shaped pipes, and velocity profiles of the liquid are not affected by the asymmetry. However, in circular pipes, the fringing of the magnetic field can be significant, making it necessary to employ empirical calibrations.

Selection of materials for constructing the channel of the magnetic flowmeter demands care. If the fluid is nonmetallic, a nonconducting or an insulated channel should be sufficient. In this case, wetted

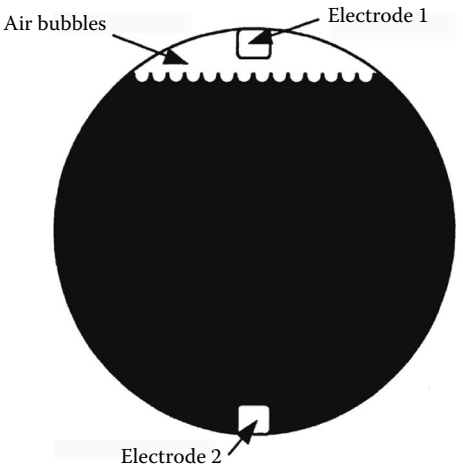

FIGURE 56.5 The pipes of electromagnetic flowmeters must be full of liquid at all times for accurate measurement. If the liquid does not make full contact with electrodes, the high impedance prevents the current flow; hence, measurements cannot be taken. Also, if the pipe is not full, even if the contact is maintained between the liquid and electrodes, the empty portions of the pipe will lead to miscalculated flow rates.

electrodes must be used. Electrodes must be designed to have sufficiently large dimensions to keep the output impedance at acceptable levels. Also, careful handling of electrode signals must be observed because, in many cases, malfunctioning of reference signal electronics is the main cause of flowmeter failure.

Magnetic flowmeters do not require continuous maintenance, except for periodic calibrations. Nevertheless, electrode coating, damage to the liners, and electronic failures can occur. Any modification or repair must be treated carefully because, when installed again, some accuracy can be lost. After each modification or repair, recalibration will be necessary.

Often, magnetic flowmeter liners are damaged by the presence of debris and solids in the process liquid. Also, the use of incompatible liquid with the liners, wear due to abrasion, excess temperature, and installation and removals can contribute to the damage of liners. The corrosion in the electrodes can also be a contributing factor for the damage. In some cases, magnetic flowmeters can be repaired onsite even if severe damage occurs; in other cases, they must be shipped to the manufacturer for repairs. Usually, manufacturers supply spare parts for electrodes, liners, flow tubes, and electronic components.

Calibration of electromagnetic flowmeters is achieved with a magnetic flowmeter calibrator or by electronic means. The magnetic flowmeter calibrators are precision instruments that inject simulated output signals of the primary flowmeter into the transmitter. Effectively, this signal is used to check correct operation of electronic components and make adjustments to the electronic circuits. Alternatively, calibrations can also be made by injecting suitable test signals to discrete electronic components. In some cases, empirical calibrations must be performed at zero flow while the flowmeter is filled with the stationary process liquid.

Application of magnetic flowmeters can only be realized with conductive liquids such as acids, bases, slurries, foods, dyes, polymers, emulsions, and suitable mixtures that have conductivities greater than the minimum conductivity requirements. Generally, magnetic flowmeters are not suitable for liquids containing organic materials and hydrocarbons. As a rule of thumb, magnetic flowmeters can be applied if the process liquids constitute a minimum of about 10% conductive liquid in the mixture.

The lack of any direct Reynolds number constraints and the obstructionless design of magnetic flowmeters make it practical for applications that involve conductive liquids that have high viscosity, which could plug other flowmeters. They also measure bidirectional flows.

Despite the contrary belief, magnetic flowmeters demonstrate a certain degree of sensitivity to flow profiles. Another important aspect is the negative effect of the turbulence. Unfortunately, there is very

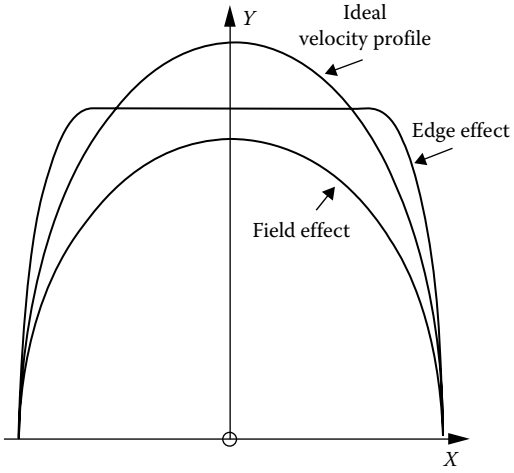

FIGURE 56.6 Flow profiles in the pipes. Magnetic flowmeters demonstrate a certain degree of sensitivity to flow profiles. The ideal velocity profile can be distorted due to edge effects and also field effects known as magnetohydrodynamics. In some applications, the velocity perturbation due to the magnetohydrodynamic effect can be serious enough to severely influence the accuracy of operations.

little information available on the behavior of turbulent flows when they are in transverse magnetic fields. Figure 56.6 shows an example of flow profile in which the velocity profile is perturbed. The fluid is being retarded near the center of the channel and accelerated at the top and bottom near the electrodes.

An important point in electromagnetic flowmeters is the effect of magnetohydrodynamics, especially prominent in fluids with magnetic properties. Hydrodynamics is the ability of a magnetic field to modify the flow pattern. In some applications, the velocity perturbation due to the magnetohydrodynamic effect can be serious enough to influence the accuracy of operations, as in the case of liquid sodium and its solutions.

56.4.1 Effects of Electric Conductivity of Fluid

For electromagnetic flowmeters to operate accurately, the process liquid must have minimum conductivity of 1–5 μS cm^{-1}. Most common applications involve liquids with conductivities greater than 5 μS cm^{-1}. Nevertheless, for accurate operation, the requirement for the minimum conductivity of liquid can be affected by length of leads from sensors to the electronic signal processors.

AC flowmeters are sensitive to the nonconductive coating of the electrodes, which may result in calibration shift or complete loss of signals. The DC flowmeters, on the other hand, should not be affected by nonconductive coating to such a great extent, unless the conductivity between electrodes is less than the minimum required value. In some flowmeters, electrodes can be replaced easily, while in others, electrodes can be cleaned by suitable methods. If coating is a continual problem, ultrasonic and other cleaning methods should be considered.

Zero adjustment of AC magnetic flowmeters requires compensation for noise. If the zero adjustment is performed with any fluid other than the process fluid, serious errors can result because of possible differences in conductivities. Similarly, if the electrodes are coated with an insulating substance, the effective conductivity of the electrodes can be altered, thereby causing a calibration shift. If the coating changes in time, the flowmeter can continually require calibration for repeatable readings.

The resistance between electrodes can be expressed by $R = D/\delta\pi r^2$, where D is the pipe diameter, δ is the fluid conductivity, and r is the electrode radius. For tap water, δ = 200 μS cm^{-1}; for gasoline, δ = 0.01 μS cm^{-1}; and for alcohol, δ = 0.2 μS cm^{-1}. A typical electrode with a 0.74 cm diameter in contact with tap water results in a resistance of 6756 Ω.

56.5 Signal Pickup and Demodulation Techniques

Electromagnetic flowmeters are four-wire devices that require an external power source for operations. Particularly in AC magnetic flowmeters, the high-voltage power cables and low-voltage signal cables must run separately, preferably in different conduits, whereas in DC magnetic flowmeters, the power and signal cables can be in one conduit. This is because in DC-type magnetic flowmeters, the voltage and the frequency of excitation of the electromagnets are relatively much lower. Some manufacturers supply special cables along with their flowmeters.

In AC flowmeters, the electrode signals can be amplified much more readily compared to their DC counterparts. That is the reason why AC flowmeters have been used successfully to measure very low flow rates, as well as the flow of very weakly conducting fluids. Nevertheless, AC flowmeters tend to be more complicated, bulky, and expensive, and they require electromagnets with laminated yokes together with stabilized power supplies. In some magnetic flowmeters, it is feasible to obtain sufficiently large flow signal outputs without the use of a yoke by means of producing a magnetic field by naked coils. In this case, the transformer action to the connecting leads can be reduced considerably.

One of the main drawbacks of AC-type flowmeters is that it is difficult to eliminate the signals due to transformer action from the useful signals. The separation of the two signals is achieved by exploiting the fact that the flow-dependent signal and the transformer signal are in quadrature. That is, the useful signal is proportional to the field strength, and the transformer action is proportional to the time derivative of the field strength. The total voltage v_T can be expressed as

$$v_T = v_F + v_t = V_F \sin(\omega t) + V_t \cos(\omega t) \tag{56.6}$$

where

$v_F = e$ is the induced voltage due to liquid flow

v_t is the voltage due to transformer action on wires

Phase-sensitive demodulation techniques can be employed to eliminate the transformer action voltage. The coil magnetizing current, $i_m = I_m \sin(\omega t)$, is sensed and multiplied by the total voltage v_T, giving

$$v_T i_m = [V_F \sin(\omega t) + V_t \cos(\omega t)]\, I_m \sin(\omega t) \tag{56.7}$$

Integration of Equation 56.7 over one period between 0 and 2π eliminates the transformer voltage, yielding only the voltage that is proportional to the flow:

$$V_f = V_F I_m \pi \tag{56.8}$$

where V_f is the voltage after integration like its DC value once the sinusoidal part is eliminated. This voltage is proportional to the induced voltage modified by constants I_m and π.

In reality, this situation can be much more complicated because of phase shift due to eddy currents in nearby solids and conductors. Other reasons for complexity include the harmonics because of nonlinearity such as hysteresis and capacitive pickup.

A good electrical grounding of magnetic flowmeters, as illustrated in Figure 56.7, is required to isolate relatively high common-mode potential. The sources of ground potential can be in the liquid or in the pipes. In practice, if the pipe is conductive and makes contact with the liquid, the flowmeter should be grounded to the pipe. If the pipe is made from nonconductive materials, the ground rings should be installed to maintain contact with the process liquid.

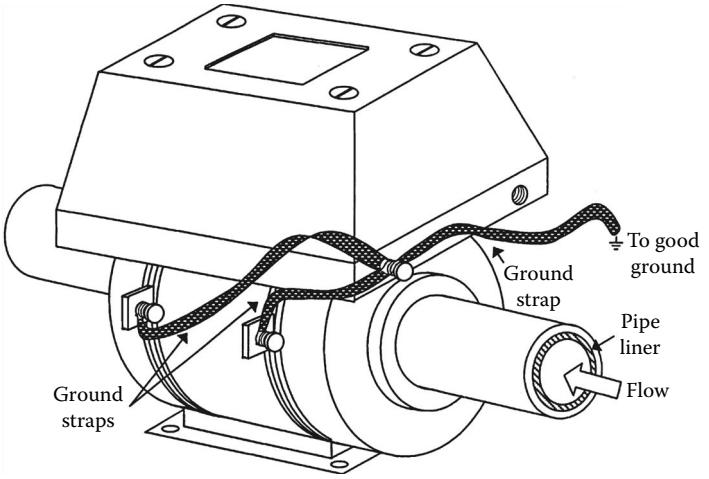

FIGURE 56.7 Grounding of electromagnetic flowmeters. A good grounding is absolutely essential to isolate noise and high common-mode potential. If the pipe is conductive and makes contact with the liquid, the flowmeter should be grounded to the pipe. If the pipe is made from nonconductive materials, ground rings should be installed to maintain contact with the process liquid. Improper grounding results in excessive common-mode voltages that can severely limit the accuracy and also damage the processing electronics.

If the flowmeter is not grounded carefully relative to the potential of the fluid in the pipe, then the flowmeter electrodes could be exposed to excessive common-mode voltages that can severely limit the accuracy. Excessive ground potential can damage the electronic circuits because the least-resistance path to the ground for any stray voltage in the liquid would be via the electrodes.

Some commercial magnetic flowmeters that can operate on sawtooth or square waveforms have been developed. Universally standardized magnetic flowmeters and generalized calibration procedures still do not exist, and manufacturers use their own particular design of flow channels, electromagnets, coils, and signal processors. Most manufacturers provide their own calibration data.

Bibliography

Baker, R. C., *Flow Measurement Handbook*, Cambridge, U.K.: Cambridge University Press, 2000.

Bates, C. J. and Frankilin, B., The performance characteristics of a novel multi-electrode electromagnetic flowmeter, *Measurement*, London, U.K.: Elsevier, Vol. 35, No. 4, pp. 399–408, 2004.

Bates, C. J. and Turner, R. B., Fluid flow studies associated with a new electromagnetic flowmeter, *Measurement*, London, U.K.: Elsevier, Vol. 33, No. 1, pp. 85–94, 2003.

Committee report: Magnetic inductive flowmeters, *Journal of American Water Works Association*, 99(6), 154–160, 2007.

Consumer Guide to Magnetic Flowmeters, Flowmeter Directory. http://www.flowmeterdirectory.com/flowmeter_artc_03112701.html (accessed on September 7, 2011).

Digiacomo, R. W., Understanding electromagnetic flow meters, *Chemical Engineering Progress*, Los Angeles, CA: American Institute of Chemical Engineers, Vol. 106, No. 5, pp. 42–47, 2010.

Doebelin, E. O., *Measurement Systems: Application and Design*, 4th edn., New York: McGraw-Hill, 1990.

Magnetic Flowmeters. Measuring Principle, Rockwell Automation. http://www.instrumentacionycontrol.net/ (accessed on September 2, 2011).

Magnetic Flowmeters, Instrumart. http://www.instrumart.com/Content.aspx?ContentID=223 (accessed on September 5, 2011).

Miller, R. W., *Flow Measurement Engineering Handbook*, Boston, MA: McGraw-Hill, 1996.

Omega Engineering, Introduction to Magnetic Flowmeters. http://www.omega.com/prodinfo/magmeter.html (accessed on September 5, 2011).

Sanderson, M. L., Factors affecting the dynamic performance of electromagnetic flow meters, *Measurement and Control*, London, U.K.: Institute of Measurement Control, Vol. 36, No. 9, pp. 270–274, 2003.

Partial List of Manufacturers and Suppliers

ABB, Inc., 125 E. County Line Rd. Warminster, PA 18974, Phone: 215-674-6580, 800-829-6001 (toll free), Fax: 215-674-7180, www.abb.us/instrumentation

Accu-Chek, Inc., 8385 State Rd. 64 Georgetown, IN 47122, Phone: 877-891-8830 (toll free), Fax: 812-951-2262, aciquality.rtrk.com/?scid=2091472&rl_alt…

American Controls, Inc., 20764 Whitlock Farmington Hills, MI 48336-5168, Phone: 248-476-7782, 800-470-3441 (toll free), Fax: 248-476-3390, www.americancontrolsinc.com

AMETEK TIP (Technical & Industrial Products), 627 Lake St. Kent, OH 44240, Phone: 215-256-6601, Fax: 330-677-3306, www.ametektip.com

Azbil North America, Inc., 9033 N. 24th Ave., Suite 5 Phoenix, AZ 85021, Phone: 888-262-4639, Fax: 602-216-8213, us.azbil.com

Controls and Meters Inc., 7613 Washington Ave. S. Minneapolis, MN 55439, Phone: 952-944-3666, www.controlsandmeters.com

Davis/Inotek, Bustleton Business Center, 2200 Michener St., Suite 23 Philadelphia, PA 19115, Phone: 800-548-9409, Fax: 410-358-0252, www.davis.com

Dwyer Instruments, Inc., Hwy. 212 at 12 P.O. Box 373 Michigan City, IN 46361, Phone: 219-879-8000, 800-872-9141 (toll free), Fax: 219-872-9057, www.dwyer-inst.com

Eastern Controls, Inc., 3866 Providence Rd. Edgemont, PA 19028, Phone: 610-325-4600, Fax: 610-325-2476, www.easterncontrols.com

Emerson Process Management, Rosemount Div., 8200 Market Blvd. Chanhassen, MN 55317, Phone: 952-906-8888, 800-685-8254 (toll free), Fax: 952-906-8889, www2.emersonprocess.com/en-us/brands/ros…

Endress+Hauser, 2350 Endress Place Greenwood, IN 46143, Phone: 888-363-7377, 888-ENDRESS (toll free), Fax: 317-535-8498, www.us.endress.com

Enpro, Inc., 121 S. Lombard Rd. Addison, IL 60101, Phone: 630-629-3504, 800-323-2416 (toll free), Fax: 630-629-3512, www.enproinc.com

Entegris, Inc., 300 Old Greenwood Rd. Decatur, TX 76234, Phone: 940-627-2121, 800-433-5547 (toll free), www.entegris.com

FCX Performance, 3000 E. 14th Ave. Columbus, OH 43219, Phone: 614-253-1996, 800-253-6223 (toll free), Fax: 614-253-2033, www.fcxperformance.com/

FMC Technologies Inc., Measurement Solutions, 1602 Wagner Ave. P.O. Box 10428 Erie, PA 16514, Phone: 814-898-5000, 800-477-6375 (toll free), Fax: 814-899-8927, www.fmctechnologies.com/en/MeasurementSo…

FTI Flow Technology Inc., 8930 S. Beck Ave. Suite 107 Tempe, AZ 85284, Phone: 480-240-3400, Fax: 480-240-3401, www.ftimeters.com

G Instruments, 13240 Evening Creek Dr. Suite 304 San Diego, CA 92128, Phone: 858-668-3088, Fax: 858-876-1963, www.ginstruments.com

Honeywell Sensing and Control, 1985 Douglas Dr. North, MN10-192B Golden Valley, MN 55422, Phone: 763-954-4818, 800-446-6555 (toll free), sensing.honeywell.com/index.cfm/ci_id/15…

Industrial Dynamics, Inc., 405 Gordon Ave. Exton, PA 19341, Phone: 610-363-8100, Fax: 610-363-8101, www.industrialdynamics.com

Intek, Inc., 751 Intek Way Westerville, OH 43082-9057, Phone: 614-895-0301, 888-569-3569 (toll free), Fax: 614-895-0319, www.intekflow.com

Keco Engineered Controls, 1200 River Ave. Bldg. 3A Lakewood, NJ 08701-5657, Phone: 732-901-5900, Fax: 732-901-5904, www.kecocontrols.com

KROHNE, Inc., 7 Dearborn Rd. Peabody, MA 01960, Phone: 978-535-6060, 800-356-9464 (toll free), Fax: 978-535-1720, www.krohne.com/index.php?id=12076

Liquid Measurement & Controls, Inc., 43 W. Third Ave., P.O. Box 26130 Collegeville, PA 19426, Phone: 610-489-0900, Fax: 610-489-1722, www.lmnc.net

Matheson, 166 Keystone Dr. Montgomeryville, PA 18936, Phone: 215-641-2700, 800-416-2505 (toll free), 877-MTG4GAS (toll free), Fax: 215-619-0458, www.mathesongas.com/index.aspx

MSC Industrial Supply Co., 75 Maxess Rd. Melville, NY 11747, Phone: 516-812-2000, 800-753-7937 (toll free), Fax: 516-812-1710, 800-255-5067 (toll free), www.mscdirect.com

MSR Magmeter, P.O. Box 32170 Edmonton, AB T6K4C2, Phone: 780-662-2171, Fax: 780-662-2146, www.mscdirect.com

Omron, STI Safety-Scientific Technologies, Inc., 6550 Dumbarton Circle Fremont, CA 94555, Phone: 510-608-3400, 888-510-4357 (toll free), Fax: 510-744-1442, www.sti.com

RCM Industries, Inc., 110 Mason Circle Suite D Concord, CA 94520-1214, Phone: 925-687-8363, 800-276-7915 (toll free), Fax: 925-671-9636, www.flo-gage.com

Siemens Corp., 527 Madison Ave. 8th Fl., New York, NY 10022-4611, Phone: 800-SIEMENS (toll free), Fax: 212-767-0580, www.usa.siemens.com/entry/en/

Sierra Instruments, 5 Harris Ct., Bldg. L, Monterey, CA 93940, Phone: 831-373-0200, 800-866-0200 (toll free), Fax: 831-373-4402, www.sierrainstruments.com

Steven Engineering, 230 Ryan Way South San Francisco, CA 94080, Phone: 866-974-0170 (toll free), Fax: 800-314-0716, 800-314-0716 (toll free), stevenengineering.rtrk.com/?scid=1975164…

Taco, Inc., 1160 Cranston St. Cranston, RI 02920, Phone: 401-942-8000, Fax: 401-942-2360, www.taco-hvac.com

Toshiba International Corp., 13131 W. Little York Rd. Houston, TX 77041, Phone: 713-466-0277, Fax: 713-466-8773, www.toshiba.com/ind/

V-F Controls, Inc., 8619 Tyler Blvd. Mentor, OH 44060-1008, Phone: 440-974-7757, 800-752-2033 (toll free), Fax: 440-974-6766, www.v-fcontrols.com

Zepeda Instruments, 615-T Aloha St. Seattle, WA 98109, Phone: 206-284-8519.

57

Ultrasonic Flowmeters

Hans-Peter Vaterlaus
Rittmeyer Ltd.

Thomas Hossle
Rittmeyer Ltd.

Paolo Giordano
Rittmeyer Ltd.

Christophe Bruttin
Rittmeyer Ltd.

57.1 Introduction

Flow is one of the most important physical parameters measured in industry and water management. There are various kinds of flowmeters available, depending on the requirements defined by the different market segments. For many years, differential pressure types of flowmeters have been the most widely applied flow measuring device for fluid flows in pipes and open channels that require accurate measurement at reasonable cost. In markets like waterpower, water supply, and irrigation, however, flow must be measured without any head losses or any pressure drop. This means there are no moving parts, no secondary devices, nor any restrictions allowed. Two types of flowmeters presently fulfill this requirement: electromagnetic and ultrasonic flowmeters. Whereas *ultrasonic flowmeters* can be applied in nearly any kind of flowing liquid, *electromagnetic* flowmeters require a minimum electric conductivity of the liquid for operation. In addition, the cost of ultrasonic flowmeters is nearly independent of pipe diameter, whereas the price of electromagnetic flowmeters increases drastically with pipe diameter.

There are various types of ultrasonic flowmeters in use for discharge measurement: (1) *Transit time*: This is today's state-of-the-art technology and most widely used type and will be discussed in this chapter section. This type of ultrasonic flowmeter makes use of the difference in the time for a sonic pulse to travel a fixed distance, first against the flow and then in the direction of flow. Transmit time flowmeters are sensitive to suspended solids or air bubbles in the fluid. (2) *Doppler*: This type is more popular and less expensive, but is not considered as accurate as the transit time flowmeter. It makes use of the Doppler frequency shift caused by sound reflected or scattered from suspensions in the flow path and is therefore more complementary than competitive to transit time flowmeters. (3) *Cross correlation*: Two measuring sections are installed with a certain distance to each other. Both measure the energy absorption of the ultrasonic signal. A cross correlation calculates the flow velocity. (4) *Phase shift*: The phase position of the transmitting and receiving signal is measured in the direction of the flow and against it. The resulting phase shift angle is directly proportional to the flow velocity. (5) *Drift*: The drift of an ultrasonic signal crossing the flow is measured by signal attenuation.

57.2 Transit Time Flowmeter

57.2.1 Principle of Operation

The acoustic method of discharge measurement is based on the fact that the propagation velocity of an acoustic wave and the flow velocity are summed vectorially. This type of flowmeter measures the difference in transit times between two ultrasonic pulses transmitted upstream t_{21} and downstream t_{12} across the flow, as shown in Figure 57.1. If there are no transverse flow components in the conduit, these two transmit times of acoustic pulses are given by

$$t_{12} = \frac{L_w}{c + v_a \cos\phi} \quad \text{and} \quad t_{21} = \frac{L_w}{c - v_a \cos\phi} \tag{57.1}$$

where

L_w is the distance in the fluid between the two transducers
c is the speed of sound at the operating conditions
ϕ is the angle between the axis of the conduit and the acoustic path
$\overline{v}_a$ is the axial low velocity averaged along the distance L_w

Since the transducers are generally used both as transmitters and receivers, the difference in travel time can be determined with the same pair of transducers. Thus, the mean axial velocity $\overline{v}_a$ along the path is given by

$$\overline{v}_a = \frac{L_w}{2\cos\phi}\left(\frac{1}{t_{21}} - \frac{1}{t_{12}}\right) = \frac{D}{2\cos\phi\sin\phi}\left(\frac{1}{t_{21}} - \frac{1}{t_{12}}\right) \tag{57.2}$$

The following example shows the demands on the time measurement technique: assuming a closed conduit with diameter D = 150 mm, angle ϕ = 60°, flow velocity $\overline{v}_a$ = 1 m·s^{-1}, and water temperature = 20 °C. This results in transmit times of about 116 µs and a time difference $\Delta t(\Delta t = t_{12} - t_{21})$ on the order of 78 ns. To achieve an accuracy of 1% of the corresponding full-scale range, Δt has to be measured with a resolution of at least 100 ps (1×10^{-10} s).

Standard time measurement techniques are not able to meet such requirements so that special techniques must be applied. The advantage of the approach of state-of-the-art real digital measurement is to process the measured value directly by a microcomputer. The most difficult problem is to reach the required resolution and to cope with the jitter of digital logic gates. It is well known in the measurement technique that, if signals are sampled multiple times (N_n), the resolution increases with the number of samples ("oversampling") [1]. This knowledge is not only applied for analog signals but also for transit time signals and is used in today's technology of flowmeters. The propagation time $t(t_{12} + t_{21})$, depending

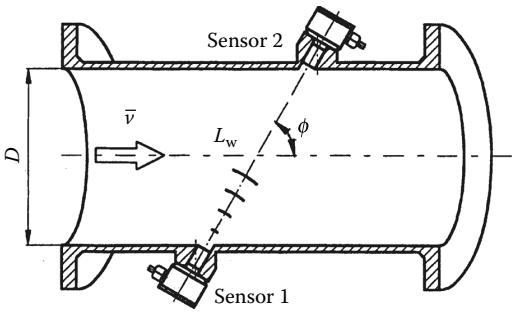

FIGURE 57.1 Principle of transit time flowmeters. Transmitting an ultrasonic pulse upstream and downstream across the flow: the liquid is moving with velocity $\overline{v}_a$ and with angle ϕ to the ultrasonic pulse.

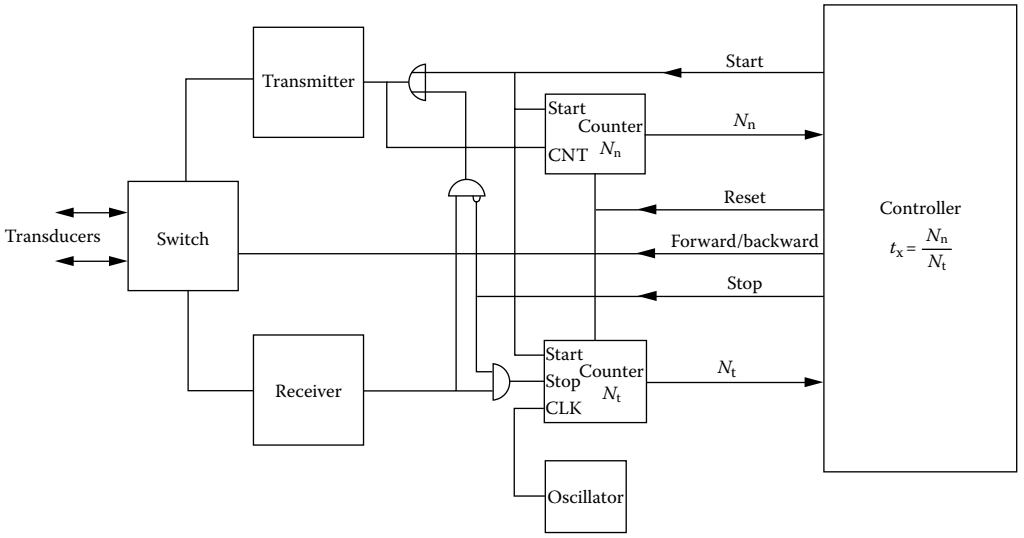

FIGURE 57.2 Block diagram of a transit time ultrasonic flowmeter using oversampling for higher resolution.

on the distance the sound pulse has to travel through the fluid, is measured several times. Due to this fact, one obtains the following relation [2]:

$$t = \frac{1}{N_n} \int_0^{\tau} \frac{1}{f} dt \tag{57.3}$$

where

τ is the integration time
f is the frequency

According to the block diagram in Figure 57.2, two counters are used. One counter, N_t, is clocked during the measuring period by a stable quartz oscillator; the other one counts the number of samples N_n. The measurement stops after a certain period of some milliseconds and after having reached an integer value for N_n. The two counts of N_t and N_n are used to calculate propagation time t_{12} or t_{2l} by dividing N_t by N_n. The resolution r is calculated by

$$r = \frac{1}{N_n \cdot f} \tag{57.4}$$

Advantages of this measurement method for transit time flowmeters are

1. The resolution of the velocity measurement is constant (typical value 0.8 mm s^{-1}).
2. The accuracy depends almost only on the stability and the temperature coefficient of the quartz oscillator.
3. Due to the multiple sampling, the jitter of the digital logic is averaged.

57.2.2 Sensors

The transducer comprises the piezoelectric element that converts electric energy to acoustic energy and the basic structure for supporting the piezoceramic and providing electric connections. Transducer design entails choice of the piezoelectric element, determination of suitable dimensions and resonant

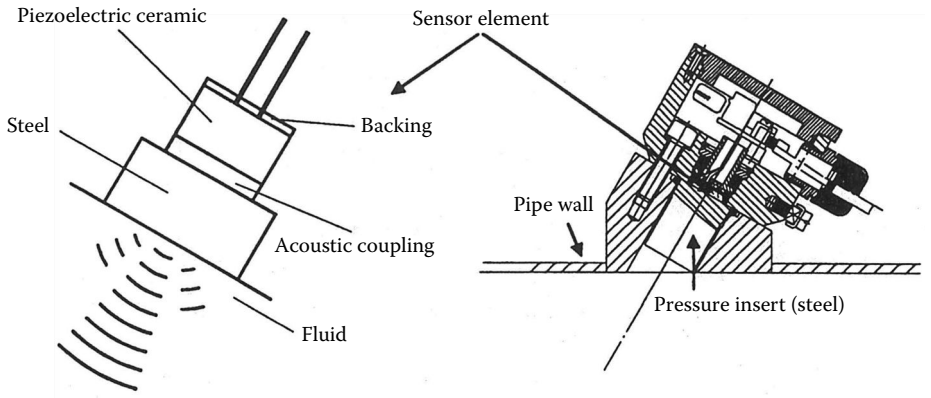

FIGURE 57.3 Ultrasonic transducer in principle and as an example of an existing version. The sensor element can be changed even under pressure.

frequency, and construction to withstand thermal and mechanical stress (see Figure 57.3). Considering the transmission line model [3,4], the optimal electroacoustic response, and the best matching of acoustic impedances $Z = \rho c$ of the different transducer elements is important. Not only must suitable waveforms to be detected by the electronics be obtained but also the energy loss must be minimized when crossing several interface boundaries. Because of the wide versatility of pipe sizes and flow conditions, there are a number of different sensor configurations for transit time flowmeters.

57.2.3 Axial

Due to the small differences in small-diameter pipes, it is necessary to pass the sonic pulse directly down the axis of the pipe to ensure that there is sufficient path length. Figure 57.4 shows an example of an axial sensor pipe section. The upper pipe size limit for this kind of sensor is about 0.075 m [5].

57.2.4 Radial

Many manufacturers supply complete metering sections with built-in sonic transducers on either side of a spool section. Such sensors, shown in Figure 57.5, are generally called "radial" because of the transducer placement. A lower pipe size limit of radial-type sensors is about 100 mm.

57.2.5 Field Mounting

Radial-type sensors are often used to instrument an existing line, where it is desirable to make the installation without cutting out a section of the pipe. To meet this requirement, field-mountable transducers, cemented, drilled, or welded into an existing pipe section, can be used. Metering sections with diameters up to 13 m or more can be achieved in this way.

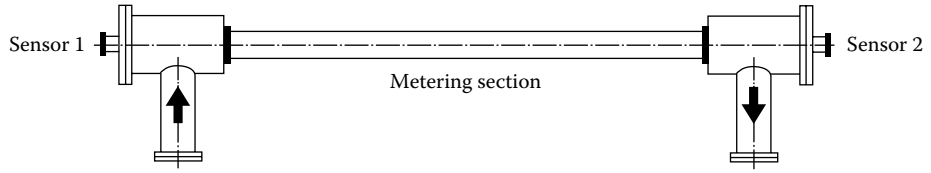

FIGURE 57.4 Axial sensor type. The ultrasonic pulse passes directly down the axis of the pipe.

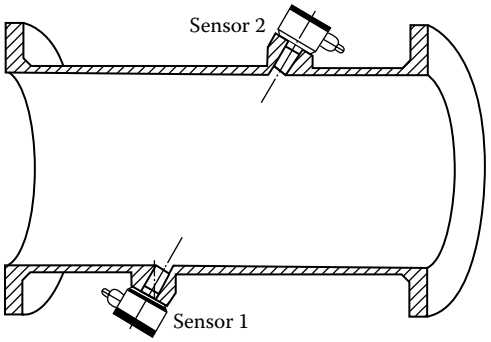

FIGURE 57.5 Radial sensor type. Manufacturers provide them as complete metering sections or as field-mounting sensors for existing conduits.

57.2.6 Clamp on

If there is a need for an installation where the pipe wall is not penetrated by the transducers, clamp-on systems are the right choice. Achieving a lower accuracy and being somewhat more complex to calibrate, clamp-on systems have their entitlement in applications where an easy movement of the metering section is an important requirement or where an existing process cannot be interrupted. The transducers are mounted on a calibration device and acoustically coupled to the pipe wall with grease and/or epoxy.

57.2.7 Open Channels and Special Applications

In open channels, the transducers are normally mounted on or dug into the channel walls. Figure 57.6 shows an example of an open-channel sensor. The piezoceramic element is placed on a sphere to achieve a wide range of mounting possibilities. Sometimes, existing pipe sections are completely enclosed with rock or concrete. In these cases, the transducers can be fixed in the wall of the conduit. For small diameters, the resulting protrusion of the transducers into the metering section must be taken into account.

57.2.8 Measurement of Flow in Closed Conduits

The most important issue in applying ultrasonic flowmeters is the understanding of the effects of the velocity profile of the flowing fluid within the conduit. The flow profile depends on the fluid, the Reynolds number Re, the relative roughness and shape of the conduit, upstream and downstream disturbances, and other factors. Transit time flowmeters give an average flow velocity v along the sonic path. The acoustic flow rate Q_{ADM} is therefore calculated through $Q = \overline{v}A$, with $\overline{v}$ the area-averaged flow velocity

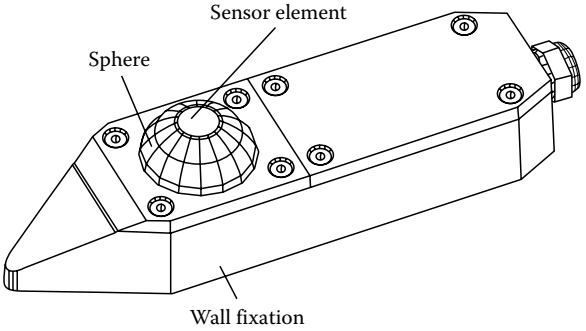

FIGURE 57.6 Open-channel sensor with sensor element placed on a movable sphere. Alignment of two sensors can be executed by laser equipment.

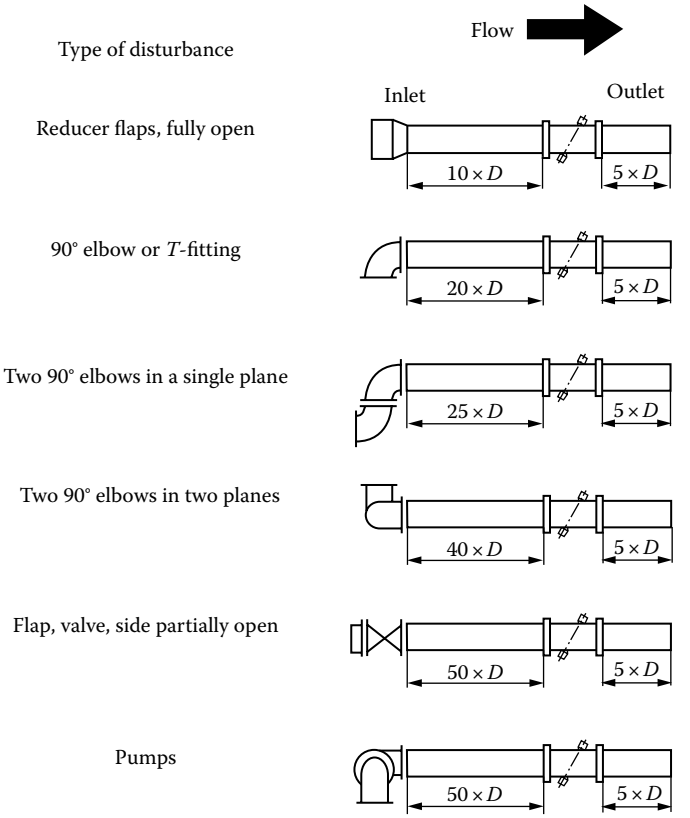

FIGURE 57.7 Minimum straight run requirements for a 1% accuracy of a single-path transit time flowmeter.

and A the cross section of the conduit. In order to obtain the area-averaged flow velocity $\overline{v}$, the measured velocity $\overline{v}_a$ must be corrected by a hydraulic coefficient k_h that depends on the type of the conduit and the Reynolds number. In order to achieve maximum performance and accuracy of ultrasonic flowmeters, one has to keep to sufficient straight run requirements as shown for some examples in Figure 57.7. By doing so, a typical accuracy of 1% of reading or better can be achieved, even when applying a single-path measurement system. Reduced straight runs lead to reduced accuracy. In some applications, this reduced accuracy is acceptable; if not, a multipath ultrasonic flowmeter must be installed. These flowmeters provide averaging of the various error-producing flow components. Accuracy of 0.5% of reading can be achieved even under nonideal conditions or insufficient straight runs. Figure 57.8 shows four examples of possible sonic path arrangements in a closed conduit.

57.2.9 Single Path with Circular and Rectangular Cross Sections

The Reynolds number Re is given by

$$\mathrm{Re} = \frac{\overline{v} \cdot D}{\nu} \tag{57.5}$$

where

$\overline{v}$ is the mean velocity over the cross section [m s^{-1}]
D is the pipe diameter
ν is the temperature-dependent cinematic viscosity

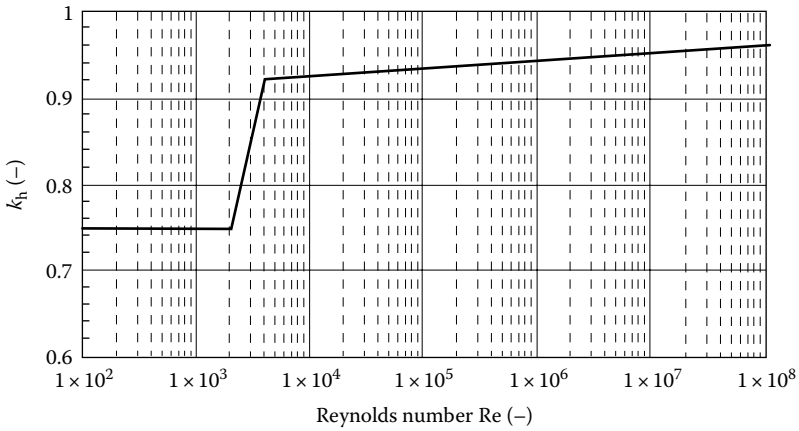

FIGURE 57.8 Dependence of the k_h actor for single-path measurement on the Reynolds number. Between a Reynolds number of 2000 and 4000, the transitional flow regime occurs.

In normal piping, a laminar flow exists as long as the Reynolds number is below about 2600. The shape of the velocity profile conforms to a parabola, and the velocity of a point on the profile is given by

$$v(r) = v_{\max}\left(1 - \left(\frac{r}{R}\right)^2\right) \tag{57.6}$$

where
r is the variable radius
R is the pipe radius

Between a Reynolds number Re of 2600 and 4000, the transitional flow regime with continuous switching between laminar and turbulent velocity profile comes into existence. When the Reynolds number exceeds 4000, the velocity profile enters the turbulent flow regime. Nikuradse [6] showed that the turbulent velocity profile of an axis-symmetrical flow in a closed conduit without swirl and sufficient inlet and outlet sections and smooth walls can be expressed by

$$v(r) = v_{\max}\left(\frac{R-r}{R}\right)^{1/n} \tag{57.7}$$

where, according to Nikuradse, n is a Reynolds number-dependent exponent given by

$$n = \frac{1}{(0.2525 - 0.0229 \times \log(\mathrm{Re}))} \tag{57.8}$$

With the definition of a hydraulic corrective coefficient k_h given by

$$k_h = \frac{\overline{v}}{\overline{v}_a} \tag{57.9}$$

where
$\overline{v}$ is the mean velocity over the cross section
$\overline{v}_a$ is the mean velocity along the sonic path

and integrating over the cross section according to

$$k_h = \frac{1/A\int_0^R \int_0^{2\pi} v(r)r\mathrm{d}\theta}{1/2R\int_{-R}^{R} v(r)\mathrm{d}r} \tag{57.10}$$

one obtains for laminar flow a hydraulic corrective coefficient of $k_h = 0.75$.

In the turbulent flow regime, according to Nikuradse [6], the hydraulic corrective coefficient k_h, dependent on the Reynolds number Re, can be expressed by

$$k_h = \frac{1}{1.125 - 0.011 \times \log(\mathrm{Re})} \tag{57.11}$$

for a circular cross section and

$$k_h = 0.79 + 0.02 \times \log(\mathrm{Re}) \tag{57.12}$$

for a rectangular cross section.

In hydropower applications, the Reynolds number Re generally exceeds the value of 4000. Figure 57.8 shows the dependence of the k_h factor in closed conduits with circular cross section on the Reynolds number. The Reynolds number not only changes its value as a function of the flow velocity v for a given diameter D but also is strongly dependent on the temperature-dependent cinematic viscosity $\nu(T)$. Not taking into account for correct value of Re can easily lead to errors of the k_h factor and thus to the flow rate Q on the order of 2%–3%. Modern transit time meters with microprocessors update the k_h factor at a rate of four times a second and by measuring the temperature T of the fluid at the same rate. A correct k_h factor is obtained and hence a temperature and Reynolds number-compensated flow rate Q.

57.2.10 Multipath Integration in Circular Cross Sections

In reality, however, the straight run requirements as defined in Figure 57.7 cannot always be kept. In addition, cross flow errors occur when nonaxial components of velocity in a pipe alter the transit times of a pulse between the sensors. Nonaxial velocities are caused by such disturbances in closed conduits as bends, asymmetric intake flows, and discontinuities in the pipe wall or pumps. It has become an accepted practice to eliminate the sensitivity of an acoustic flowmeter to velocity distributions by increasing the number of acoustic paths n. Additional paths not only decrease substantially the velocity distribution error but also reduce the numerical integration error as well as errors due to path misalignment. This suggests that for accurate measurements for which a few tenths of a percent error are significant, the cost of installing more sensors for a four-path arrangement according to Figure 57.9

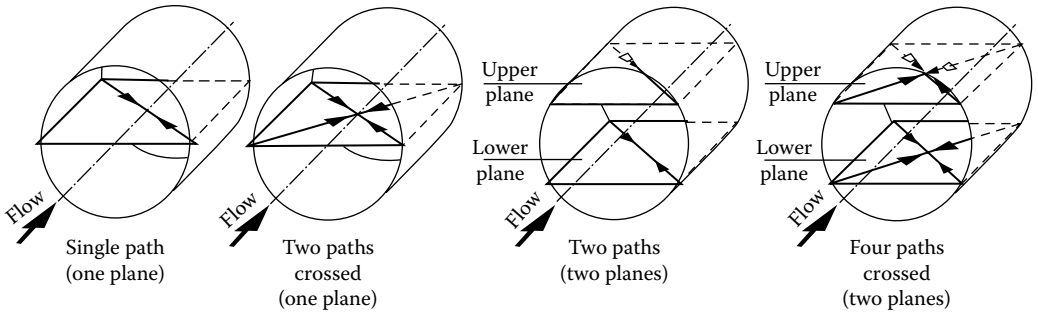

FIGURE 57.9 Possible sonic path arrangements for transit time flowmeters in closed conduits. Using multiple paths leads to reduced straight run requirements.

can be justified. In a multipath measurement system, according to the integration method described by IEC 41, Appendix J1 [7], the flow rate Q_{ADM} can be expressed by

$$Q_{ADM} = k\frac{D}{2}\sum_{i=1}^{n}\overline{v}_{ai}W_iL_i\sin\phi_i \tag{57.13}$$

where

$\overline{v}_{ai}$ is the velocities along the acoustic path i
W_i is the corresponding weighting factor
L_i is the corresponding path length
ϕ_i is the corresponding path angle

The method described in IEC 41 needs a very accurate transducer positioning due to the fact that the weighting factors W_i obtained by mathematical analysis are only valid when the sensors are positioned at the correct locations. Misalignment of the acoustic paths in conjunction with fixed weights can lead to considerable errors.

57.3 Measurement of Flow in Open Channels

Open-channel flow measurement is used in many applications, including water supply networks, hydrography, allocation of water for irrigation and agricultural purposes, and sewage treatment plants. Discharge measurements in rivers and open channels are often computed by means of a rating curve, used to convert records of water level readings into flow rates. The rating curve is developed using a set of discharge measurements and water level in the stream and must be checked periodically to ensure that the level–discharge relationship has remained constant; many phenomena can cause the rating curve to change so that the same recorded water level produces a different discharge. This is the case of open channels under changeable hydraulic conditions due, for example, to backwater effects and gates and where a univocal stage–discharge relationship does not exist. In this context, acoustic flowmeter application is extremely interesting and is currently experiencing wide success in water management. In fact, while different flow rate values can correspond to a given water level in relation to the hydraulic characteristics, there is always univocal relationship between the acoustic wave propagation velocity in a flowing fluid and the flowing fluid itself.

By means of the ultrasonic technique, discharge through open channels can be determined using single- and multipath technology. In a single-path configuration, particular attention must be paid to define the vertical velocity distribution (Figure 57.10) in order to achieve a good level of accuracy by a single "line" velocity reading $\overline{v}_{az}$ at the distance z above the bottom. On the other hand, in a multipath configuration, the mean line velocity profile is well described. In this case, special attention must be paid to the integration method used to determine the flow rate from the acoustic path readings.

57.3.1 Single Path

In single-path measurements, using the area–velocity method, the flow rate Q is calculated through $Q = \overline{v}A$, with $\overline{v}$ (ms^{-1}) the area-averaged flow velocity and A the cross section. To obtain the velocity average $\overline{v}$ over the entire cross section, the mean path velocity $\overline{v}_{az}$, measured by the acoustic flowmeter at a given depth z, must be corrected by a dimensionless hydraulic corrective coefficient k_h according to the h relation $\overline{v} = k_h\overline{v}_{az}$. In general, the coefficient k_h reflects the influence of the horizontal and vertical velocity profile. It mainly depends on the water level, on the cross section shape, and on the boundary

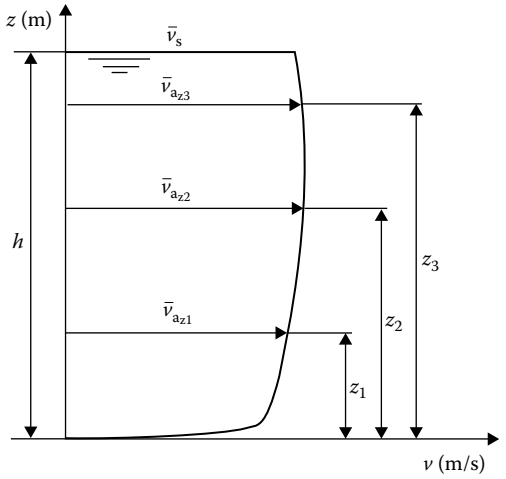

FIGURE 57.10 Open channel: possible vertical velocity distribution.

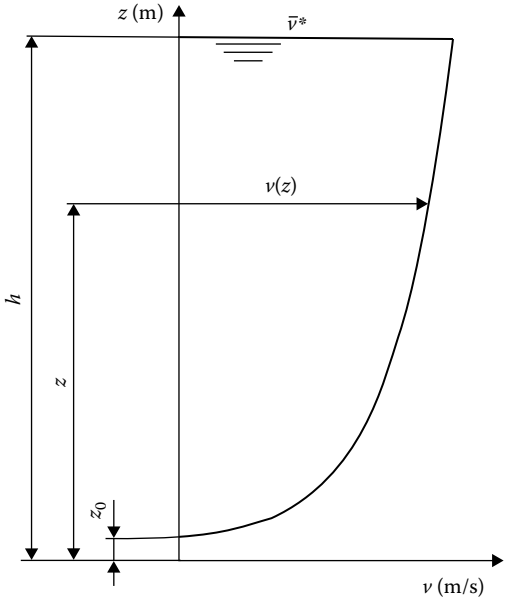

FIGURE 57.11 Logarithmic law describing open-channel velocity profile.

roughness. The mean vertical velocity profile can be described by the well-known logarithmic law (Figure 57.11) given by [8]

$$\bar{v}(z) = \left(\frac{\bar{v}^*}{k}\right) \ln \frac{z}{z_0} \tag{57.14}$$

where

$\bar{v}(z)$ is the mean velocity a distance z above the bottom
k is the von Kàrmàn's turbulence constant
z is the distance above the bottom
$\bar{v}^*$ is the shear velocity
z_0 is the constant of integration, dependent on the boundary roughness

When the boundary surface is hydraulically rough, z_0 has been found to depend solely on the roughness height k_s according to the relation $Z_0 = k_s/30$. Integrating Equation 57.14 over the total water height h and substituting for $\overline{v}$, the following equation is obtained:

$$k_h = \frac{\ln(h/k_s) - 1}{\ln(z/k_s)} \tag{57.15}$$

assuming z_0 is negligible with respect to h.

In Figure 57.12, the logarithmic k_h factor is represented for two different types of bottom roughness. However, in many practical applications, it is often difficult to define correct values for k_s. For this reason, another k_h model has been developed on the basis of the power law [9,10]. In this formula, the exponent $1/m$ is not constant anymore, but depends on the roughness and the hydraulic radius to take into account the influence of the channel shape. The mean vertical velocity profile $\overline{v}(z)$, according to the power law, can be expressed by the following formula (Figure 57.13):

$$\overline{v}(z) = \overline{v}_s \left(\frac{z}{h}\right)^{1/m} \tag{57.16}$$

where

h is the current water level
$\overline{v}$ is the mean line velocity at the free surface (maximum value)
$1/m$ is the exponent

From the integration of Equation 57.16 over the total water depth, one obtains the following expression for the k_h factor:

$$k_h = \frac{m}{m+1}\left(\frac{h}{z}\right)^{1/m} \tag{57.17}$$

The value of m, depending on the roughness, can be expressed using the dimensional friction factor f of the Darcy–Weisbach formula [8], according to

$$m = k\sqrt{\frac{8}{f}} \tag{57.18}$$

where k is the Von Kàrmàn constant, varying from 0.2 to 0.4.

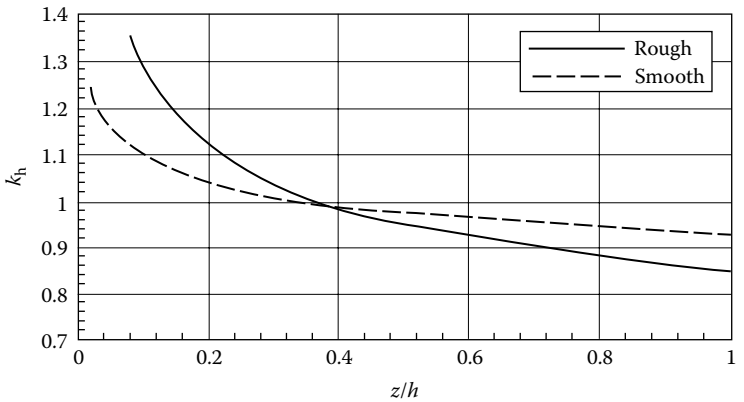

FIGURE 57.12 Logarithmic k_h factor in open channels for two different roughnesses k_s.

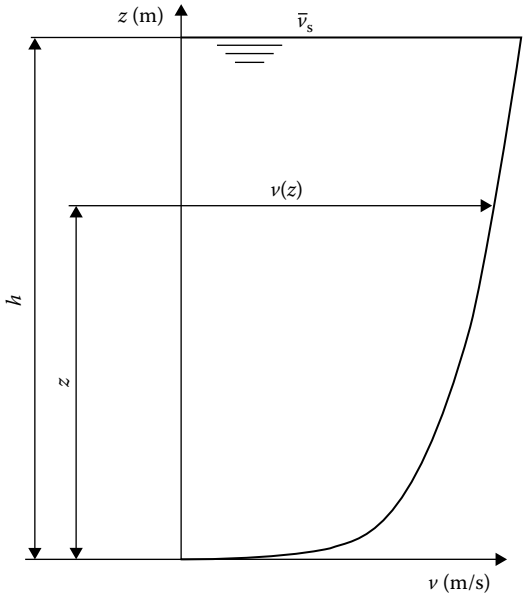

FIGURE 57.13 Power law describing open-channel velocity profile.

k depends on the suspended load (low values for high turbidity) or can be expressed using the Manning formula by the relation [11]

$$m = \left(\frac{k}{\sqrt{g}}\right)\frac{R_h^{1/6}}{n} \tag{57.19}$$

where

g is the gravity acceleration
n is the Manning's roughness coefficient
R_h is the hydraulic radius

In Figure 57.14, the corrective factor is represented for smooth and rough surfaces. By means of this relation, an easier field application has been obtained due to wide familiarity with the Manning formula in open-channel flow computation because of its simplicity of form, high versatility, and satisfactory results.

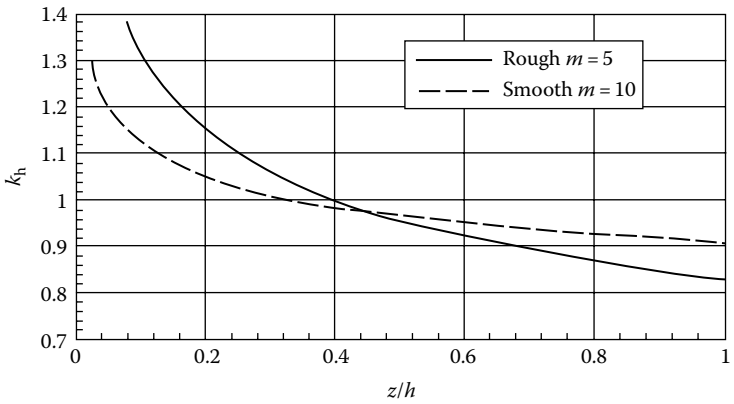

FIGURE 57.14 Power law k_h factor in open channels for two different roughnesses.

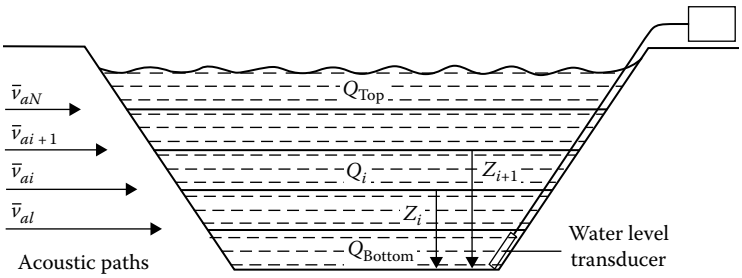

FIGURE 57.15 Multipath measurement in open channels by the mean section method. The flow velocity is measured by several levels.

57.3.2 Multipath

The foregoing equations for the mean vertical velocity profile in open channels predict that the maximum mean velocity occurs at the free surface. Field and laboratory measurements, however, demonstrate that the maximum mean velocity occurs below the free surface, strongly depending on the ratio B/h, with B being the channel width. These observations show that a 1-D velocity distribution law cannot always completely describe flow profiles in open channels. Therefore, to reduce uncertainties in velocity profile description and to achieve high accuracies even under unfavorable hydraulic conditions, a multipath configuration must be used.

In multipath measurement, using the "mean section method," the flow velocity is measured at several levels between the free surface and the channel bottom (Figure 57.15). The total discharge Q_{ADM} is performed by the relation [12]

$$Q_{ADM} = Q_b + Q_t + \sum_{i=1}^{n}\left(\frac{\bar{v}_{ai} + \bar{v}_{ai+1}}{2}[A(z_{i+1}) - A(z_i)]\right) \tag{57.20}$$

where

Q_b is the flow rate in the bottom section with the bottom velocity obtained from the lowest path velocity by correction for bottom friction
Q_t is the flow rate at the highest active section with velocity v_{top}, interpolated from the velocity profile
$\bar{v}_{ai}$ is the mean velocity along the ith acoustic path
$A(z_i)$ is the cross section below the ith path

Modern microprocessor-controlled ultrasonic flowmeters can cope with either single-path or multipath measurement in open channels, using the logarithmic or the power law for single-path measurement. In addition, up-to-date completely modular systems are able to use the major part of the equipment for measuring both in open channels and closed conduits.

57.4 Application: Penstock Leak Detection with Surge Chambers

Penstock leak detection is a typical acoustic flowmeter application [13]. It is used for immediate recognition of pipe rupture and leak losses in penstocks. Two flowmeters are installed at opposite ends of the penstock: one for measuring Q_{up} as near as possible to the intake and the other for measuring Q_{down} at the powerhouse entrance. In this description, the upstream flow is compared to the downstream flow and the flow difference. $\Delta Q = Q_{up} - Q_{down}$ is calculated and supervised. If the difference ΔQ exceeds a given threshold, the system enunciates alarms or valve closure contacts.

In hydropower applications, another problem arises due to the presence of surge chambers (Figure 57.16). This hydraulic structure causes mass oscillations due to load changes of the turbine.

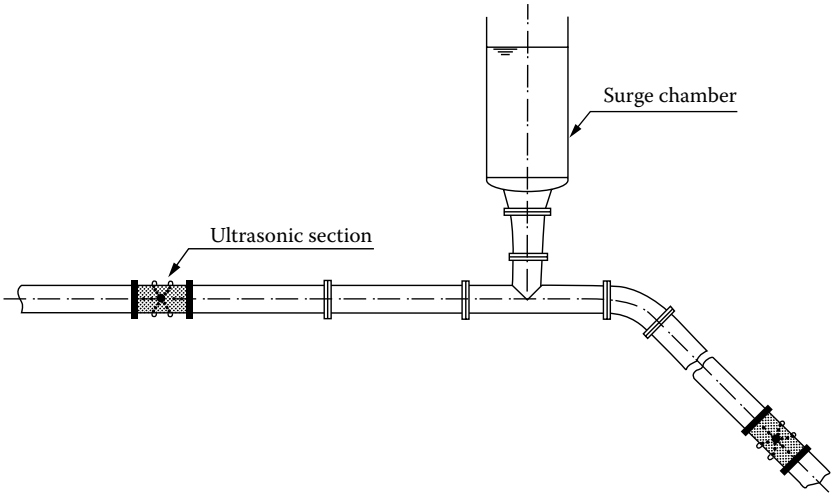

FIGURE 57.16 Penstock leak detection by transit time flowmeter. The penstock contains a surge chamber that causes mass oscillation in case of load changes of the turbine.

Up to now, if there was a surge tank in a penstock, one had two possibilities. On the one hand, one could divide the penstock into two parts, one before the surge chamber and one after it, and protect them separately. This solution is expensive and very often impractical because the surge chamber is built into the rock and inaccessible. On the other hand, one could develop something like a "leak detection algorithm," which includes the oscillatory behavior of a penstock. Such a system, however, needs extensive field tests and the knowledge for exact settings of resonant frequency, damping factor, and thresholds. The new technology in ultrasonic flowmeters, combined with accurate water level sensors, can offer a solution to this problem, by applying the formula

$$\Delta Q = Q_{\text{up}} - Q_{\text{down}} - \frac{\Delta V_{\text{chamber}}}{\Delta t} \tag{57.21}$$

TABLE 57.1 Companies Manufacturing and Distributing Ultrasonic Transit Time Flowmeters

Rittmeyer AG
P.O. Box 2143, CH-6302 Zug,
Switzerland, Tel: (+4141)-767-1000, Fax: (+4141)-767-1075,
instrumentation@rittmeyer.ch, http://www.rittmeyer.com/

Krohne Messtechnik GmbH & Co. KG
Postfach 10 08 62, Ludwig-Krohne-Strasse 5, 4100 Duisburg 1,
Germany, http://www.krohne.com/

Danfoss
A/S DK-6430, Nordborg, Denmark,
Tel: (+45) 74 88 22 22

Panametrics, Inc.
221 Crescent Street,
Waltham, MA 02254, Tel: (617) 899-2719, http://www.
panametrics.com/

Ultraflux le technoparc, 17, rue Charles
Edouard Jeanneret, 78306 Poissy Cedex,
France, Tel: 33(1)39 79 26 40

Accusonic Division, ORE International, Inc.
P.O. Box 709, Falmouth, MA 02541,
Tel: (508) 548-5800, http://www.ore.com/

Fuji Electric Co., Ltd.
12-1 Yurakucho 1-chome, Chiyoda-ku, Tokyo 100, Japan,
Tel: Tokyo 211-7111

Crouzet SA
Division "Aérospatial" 25, rue Jules-Védrines,
26027 Valence Cedex, France. Tel: 75 79 85 11

Nusonics Inc.
11391 E. Tecumseh St., Tulsa, OK 74116-1602,
Tel: (918) 438-1010

Changes of the volume of the surge chamber due to mass oscillations are taken into account, leading to a better and more realistic behavior of penstock leak detection in the presence of surge tanks.

57.4.1 Instrumentation and Manufacturers/Distributors

Table 57.1 gives an overview of some companies manufacturing and distributing transit time flowmeters. Prices of transit time flowmeters have a very wide range due to the wide versatility of different applications and are therefore difficult to list accurately. Generally, ultrasonic flowmeters are seldom sold as a "pre-packed" instrument. For this reason, the price for a metering section, including installation, varies from a few $1,000 to nearly $100,000.

References

1. M. Barmettler and P. Gruber, Anwendung von Oversampling-Verfahren zur Erhöhung der Auflösung digital erfasster Signale, *Technisches Messen*, Oldenbourg Verlag, 1992.
2. D. Hoppe, Kombinierte Zählung und Abstandsbestimmung von Impulssignalen, *Technisches Messen*, Oldenbourg Verlag, 10, 1991.
3. R. Krimholtz, D. Leedom, and G. Matthaei, New equivalent circuits for elementary piezoelectric transducers, *Electron. Lett*., 6, 398, 1970.
4. P. D. Edmonds, *Methods of Experimental Physics, Ultrasonics*, New York: Academic Press, 1981.
5. D. W. Spitzer, *Flow Measurement, Practical Guides for Measurement and Control*, Research Triangle Park, NC: Instrument Society of America, 1991.
6. J. Nikuradse, Gesetzmässigkeiten der turbulenten Strömung in glatten Rohren, *VDI Verlag GmbH*, 1932.
7. F. L. Brand, Akustische Verfahren zur Durchflussmessung, *Messen, Prüfen Automatisieren*, April 1987.
8. *International Standard IEC 41*, 3rd edn., 1991.
9. R. H. French, *Open Channel Hydraulics*, New York: McGraw-Hill, 1985.
10. Chen-Iung Chen, *J. Hydraulic Eng*., 379, 117, 1990.
11. M. F. Karim and J. F. Kennedy, *J. Hydraulic Eng*., 162, 113, 1987.
12. G. Grego, M. Baldin, et al., *Application of an Acoustic Flowmeter for Discharge Measurement in the Po*.
13. G. Grego and M. Baldin, *Energia Elettrica*, 1, 52, 72, 1995.
14. H. P. Vaterlaus and H. Gabler, A new intelligent ultrasonic flowmeter for hydropower applications, *Int. Water Power & Dam Construction*, 46, 84–88, 1994.

Further Reading

Introduction to Ultrasonic Doppler Flowmeters, http://www.omega.com/prodinfo/ultrasonicflowmeters.html, accessed on July 26, 2012.

John Flood, Acoustic/Ultrasound, Ultrasonic Flowmeter Basics, http://www.sensorsmag.com/sensors/acoustic-ultrasound/ultrasonic-flowmeter-basics-842, accessed on July 26, 2012.

Ultrasonic Flowmeter, Portable Flowmeter, Triton Process Technologies, http://www.ultrasonicflowmeter.in/index.html, accessed on July 24, 2012.

58

Vortex-Shedding Flowmeters

Wade M. Mattar
The Foxboro Company

James H. Vignos
The Foxboro Company

58.1 Introduction

The *vortex-shedding flowmeter* first emerged 25–30 years ago and has steadily grown in acceptance since then to be a major flow measurement technique. Its appeal is due, in part, to the fact that it has no moving parts yet produces a frequency output that varies linearly with flow rate over a wide range of Reynolds numbers. The vortex meter has a very simple construction, provides accuracy (1% or better) comparable to higher-priced and/or more maintenance-intensive techniques, and works equally well on liquids and gases. In addition, it is powered primarily by the fluid and lends itself more readily than other linear flow devices to two-wire operation. Comparing the vortex-shedding flowmeter to an orifice plate, the former has higher accuracy and rangeability, does not require complex pressure impulse lines, is less sensitive to wear, and, for volumetric flow measurement, does not require the need to compensate for fluid density.

Industrial vortex-shedding flowmeters are normally available in pipe sizes ranging from 15 to 300 mm (1/2–12 in.), with some manufacturers offering sizes up to 400 mm (16 in.). Flow ranges covered depend on fluid properties and meter design. Typical ranges for a 15 mm meter are

- Water at 21 °C (70 °F), 0.06–2.2 L s^{-1} (1–35 gal min^{-1})
- Air at 16 °C (60 °F) and 101 kPa (14.7 psia), 1.1–15.7 L s^{-1} (140–2000 ft^3 h^{-1})
- Dry saturated steam at 689 kPa (100 psig), 4.5–225 kg h^{-1} (10–500 lb h^{-1})

Typical ranges for a 300 mm (12 in.) meter are

- Water at 21 °C (70 °F), 5.4–5400 L s^{-1} (85–8500 gal min^{-1})
- Air at 16 °C (60 °F) and 101 kPa (14.7 psia), 157–12,500 L s^{-1} (20,000–1,600,000 ft^3 h^{-1})
- Dry saturated steam at 689 kPa (100 psig), 1,240–124,000 kg h^{-1} (2,750–275,000 lb h^{-1})

Temperature capability ranges from cryogenic temperatures up to 427 °C (800 °F). Pressure capability as high as 20.7 MPa (3000 psig) is available.

58.2 Principle of Operation

Probably the first time, ages ago, that anyone placed a blunt obstacle in a flowing fluid, he or she observed the whirlpools or vortices that naturally form and shed downstream. In everyday life, examples of vortex shedding are numerous. The undulation of a flag is due to vortex shedding from the pole, and the singing of telephone wires in a strong wind is due to shedding from the wires. Analysis by Theodore von Karman in 1911 described the stability criterion for the array of shed vortices. Consequently, when stable array of vortices form downstream from an obstacle, it is often referred to as the von Karman vortex street (Figure 58.1).

Very early on, it was noted that, for a large class of obstacles, as the velocity increased, the number of vortices shed in a given time (or frequency of vortex shedding) increased in direct proportion to the velocity. The dimensionless Strouhal number, St, is used to describe the relationship between vortex-shedding frequency and fluid velocity and is given by

$$\mathrm{St} = \frac{f \times d}{U} \tag{58.1}$$

where

f is the vortex-shedding frequency
d is the width of shedding body
U is the fluid velocity

Alternatively,

$$U = \frac{f \times d}{\mathrm{St}} \tag{58.2}$$

Although early studies were conducted in unconfined flow, it was later observed that vortex shedding also occurred in confined flow, such as exists in a pipe (see Figure 58.2). For this case, the average

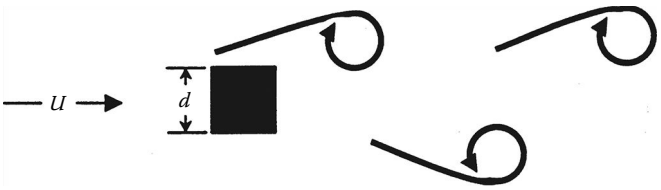

FIGURE 58.1 Von Karman vortex street.

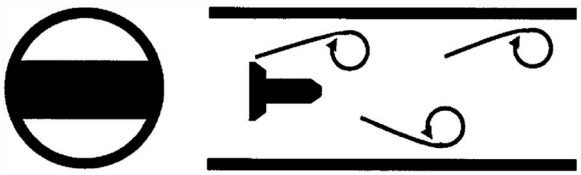

FIGURE 58.2 Vortex shedding in a pipe.

fluid velocity, $\bar{U}$, and the meter Strouhal number, St′, replace the fluid velocity and Strouhal number, respectively, in Equation 58.2 to give

$$\bar{U} = \frac{f \times d}{\text{St}'} \tag{58.3}$$

Since the cross-sectional area, A, of the pipe is fixed, it is possible to define a flowmeter K factor, K, that relates the volumetric flow rate (Q) to the vortex-shedding frequency. Given that

$$Q = A \times \bar{U} \tag{58.4}$$

from Equation 58.3, one obtains

$$Q = \left(\frac{A \times d}{\text{St}'} \right) \times f \tag{58.5}$$

defining

$$K = \frac{\text{St}'}{A \times d} \tag{58.6}$$

resulting in

$$Q = \frac{f}{K} \tag{58.7}$$

Vortex-shedding frequencies range from less than 1 Hz to greater than 3000 Hz, the former being for large meters at low velocities and the latter for small meters at high velocities.

For a vortex-shedding flowmeter, an obstacle is chosen that will produce a constant K factor over a wide range of pipe Reynolds numbers. Thus, simply counting the vortices that are shed in a given amount of time and dividing by the K factor will give a measurement of the total volume of fluid that has passed through the meter. A typical K factor vs. Reynolds number curve is shown in Figure 58.3.

The variation in K factor over a specified Reynolds number range is sometimes referred to as *linearity*. For the example in Figure 58.3, it can be seen that between Reynolds numbers from 15,000 to 2,000,000, the K factor is the most linear. This is referred to as the *linear range* of the shedder. The wider the linear range a shedder exhibits, the more suitable the device is as a flowmeter.

At Reynolds numbers below the linear range, linearization is possible but flowmeter uncertainty can increase.

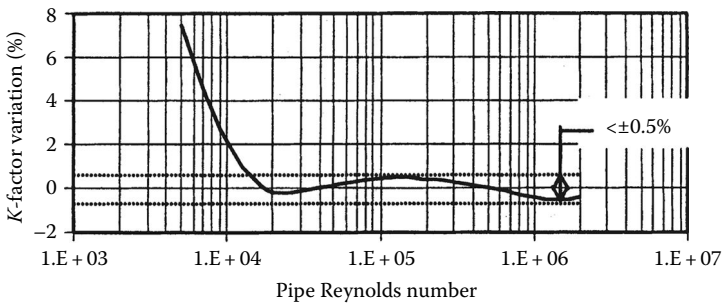

FIGURE 58.3 Typical K factor curve.

58.3 Calculation of Mass Flow and Standard Volume

Although the vortex flowmeter is a volumetric flowmeter, it is often combined with additional measurements to calculate or infer mass flow or standard volume.

To determine mass flow, $\dot{M}$,

$$\dot{M} = \rho_f \times Q = \rho_f \times \frac{f}{K} \tag{58.8}$$

where ρ_f is the fluid density at flowing conditions.

It is often desirable to know what the volumetric flow rate would be at standard process conditions with respect to pressure and temperature. This is referred to as *standard volume*. In different parts of the world and for different industries, the standard temperature and pressure can be different. The fluid density at standard conditions is referred to as the *base density*, ρ_b.

To calculate *standard volume*, Q_v,

$$Q_v = \left(\frac{\rho_f}{\rho_b}\right) \times \frac{f}{K} \tag{58.9}$$

58.4 Flowmeter Construction

The vortex-shedding flowmeter can be described as having two major components: the *flow tube* and the *transmitter*. Both are described as follows.

58.4.1 Flow Tube

The flow tube is composed of three functional parts: the flowmeter *body*, which contains the fluid and acts as housing for the hydraulic components; the *shedder*, which generates the vortices when the fluid passes by; and the *sensor*(*s*), which by some transducing means detects the vortices and produces a usable electric signal.

58.4.1.1 Flowmeter Body

The pressure-containing portion of the vortex flowmeter, sometimes referred to as the *flowmeter body*, is available in two forms: wafer or flanged (see Figure 58.4). The wafer design, which is

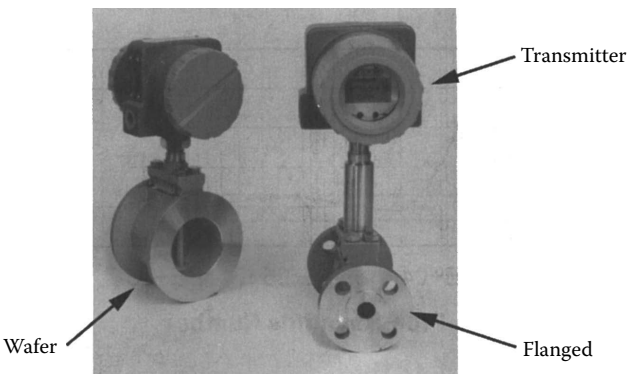

FIGURE 58.4 Vortex flowmeter construction.

FIGURE 58.5 Shedder cross sections.

sandwiched between flanges of adjacent pipe, is generally lower in cost than the flanged design, but often its use is limited by piping codes.

58.4.1.2 Shedder

The *shedder* spans the flowmeter body along the diameter and has a constant cross section along its length. Typical cross sections are shown in Figure 58.5.

58.4.1.3 Sensors

When shedding is present, both the pressure and velocity fields in the vicinity of the shedder will oscillate at the vortex-shedding frequency. *Pressure or velocity sensors* are used to transform the oscillating fields to an electric signal, current, or voltage, from which the vortex-shedding frequency can be extracted.

Figure 58.6 shows an example of a piezoelectric differential pressure sensor located in the upper portion of the shedder, which converts the oscillating differential pressure that exists between the two sides of the shedder into an electric signal. Some other sensing means utilized to detect vortex shedding are capacitive, thermal, and ultrasonic. Often times, the flowmeter electronics are mounted remotely from the flow tube. This might require a local preamplifier to power the sensor or boost its signal strength.

Since the sensor is the most likely mechanical component in a vortex flowmeter to fail, most designs have a provision for replacement of the sensors. In some cases, they can be replaced without removing the flowmeter from the pipeline. An example of an isolation manifold for sensor replacement under process conditions is shown in Figure 58.7.

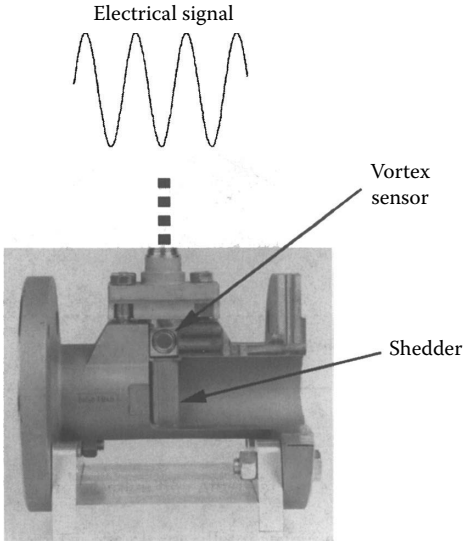

FIGURE 58.6 Example of vortex sensor.

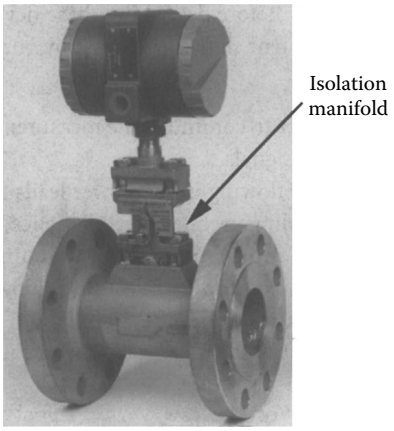

FIGURE 58.7 Isolation manifold for sensor replacement.

58.4.2 Transmitter

Vortex flowmeter *transmitters* can be classified into two broad groups: analog and intelligent (or smart). Communication with the analog transmitter is carried out via local manual means, including switches and jumper wires. Communication with the newer intelligent device is carried out via digital electronic techniques. Both types of transmitters are two-wire devices. One of the more important features of the intelligent transmitter is that it allows application-specific information to be loaded into the transmitter. This information is then used internally to automatically tailor the transmitter to the application, including calibration of the 4–20 mA output. Before describing these devices, it is useful to consider the three most common forms of flow measurement signals provided by vortex transmitters.

58.4.2.1 Measurement Output Signals

The three most common ways for a transmitter to communicate measurement information to the outside world are 4–20 mA, digital, and pulse signals.

The *4–20 mA signal* is the DC current flowing in the power leads to the transmitter. This current is directly proportional to the vortex-shedding frequency and, hence, is also linear with flow (see Figure 58.8). Four milli amperes corresponds to zero flow and 20 mA to the maximum flow rate,

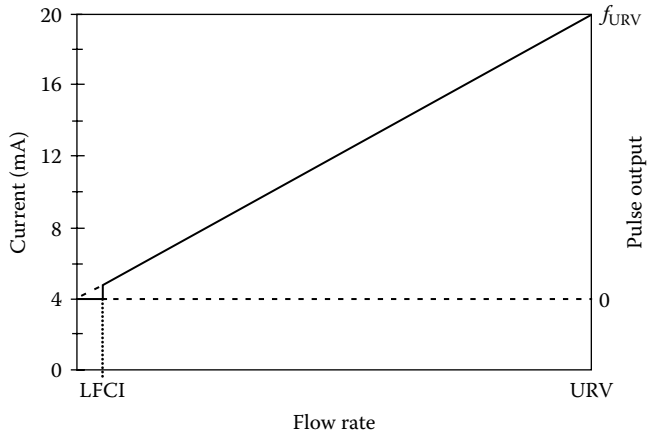

FIGURE 58.8 4–20 mA and pulse outputs.

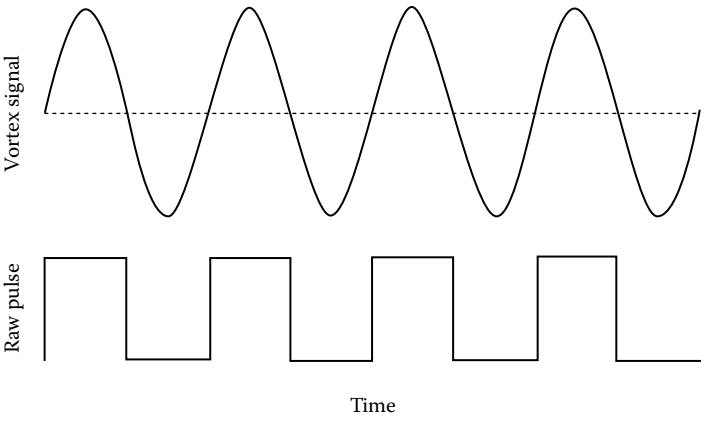

FIGURE 58.9 Raw pulse output.

that is, the upper range value (URV) of the meter. A frequency-to-analog converter in the analog meter and a digital-to-analog converter in the intelligent meter produce this output.

The *digital signal* is a digitized numeric value of the measured flow rate in engineering units transmitted over the two wires powering the meter.

The *pulse signal* is a squared-up version of the raw vortex signal coming from the sensor (see Figure 58.9) and is accessible via a pair of electric terminals inside the transmitter housing. The frequency of the pulse signal is either identical to the vortex-shedding frequency (raw pulse) or some multiple thereof (scaled pulse). As discussed in Section 58.2, in either case, the frequency of the pulse signal is linearly proportional to flow rate, going from zero to the frequency at the URV, f_{URV} (see Figure 58.8).

As shown in Figure 58.8, at a low but nonzero flow rate, the frequency and mA signals drop to 0 Hz and 4 mA, respectively. The flow rate at which this abrupt change takes place is normally referred to as the low-flow cut-in (LFCI) or cutoff. The reason for this forced zero is to avoid erroneous flow measurements at low flow, which result from process noise, including hydrodynamic fluctuations, mechanical vibration, and electrical interference. The digital signal also drops to zero below the LFCI flow rate.

58.4.2.2 Analog Transmitter

Originally, *analog transmitters* were constructed entirely of analog electronic components. Today, they are built around a combination of analog and digital electronic components. In either case, the measurement output is in the form of a raw pulse and/or a 4–20 mA signal. Depending on the particular transmitter, one or more of the following functions are available for tailoring the device via mechanical means to the specific application:

1. Signal output selection: If the transmitter provides both raw pulse and 4–20 mA signals, but not simultaneously, a means is available for selecting the one desired.
2. 4–20 mA calibration: Use of this signal requires that 20 mA corresponds to the desired URV. This is accomplished by inputting, via a signal or pulse generator, a periodic signal whose frequency corresponds to the upper range frequency (URF) and adjusting the output current until it reads 20 mA. The URF, which is the frequency corresponding to the vortex-shedding frequency at the desired URV, is calculated using the equation $\text{URF} = K \times \text{URV}$.

   In order to achieve the accuracy specified by the manufacturer, the K used in the preceding calculation must be corrected for process temperature and piping effects according to the

manufacturer's instructions. The temperature effect is a result of thermal expansion of the flow tube and is described by

$$\Delta K(\%) = -300 \times \alpha \times (T - T_0) \tag{58.10}$$

where

α is the thermal expansion coefficient of the flow tube material
T_0 is the fluid temperature at which the meter was calibrated

If the shedder and meter body materials are different, α must be replaced by $(2\alpha_1 + \alpha_2)/3$, where α_1 is the thermal expansion coefficient of the meter body material and α_2 that of the shedder.

Piping disturbances also affect the *K* factor because they alter the flow profile within the flow tube. This will be discussed in more detail in Section 58.5.2.2.

3. LFCI: For optimum measurement performance, the LFCI should be set to fit the specific application. The goal is to set it as low as possible, while at the same time avoiding an erroneous flow measurement output.
4. Filter settings: To reduce noise present on the signal from the sensor, electronic filters are built into the transmitter. Normally, means are provided for adjusting these filters, that is, setting the frequencies at which they become active. By attenuating frequencies outside the range of the vortex-shedding frequency, which varies from one application to another, better measurement performance is achieved.

58.4.2.3 Intelligent Transmitters

Intelligent transmitters, which are microprocessor-based digital electronic devices, have measurement outputs that usually include two or more of the following: raw pulse, scaled pulse, 4–20 mA, and digital. With regard to the digital output, there is at present no single, universally accepted protocol for digital communication; however, a number of proprietary and nonproprietary protocols exist.

The presence of a microprocessor in the intelligent transmitter allows for improved functionality and features compared to the analog transmitter, including

- Elimination of the need for 4–20 mA calibration
- Automatic setting of LFCI
- Automatic setting of filters
- Adaptive filtering (active filters that track the vortex frequency)
- Digital signal conditioning
- *K* factor correction for temperature and piping disturbances
- Correction for nonlinearity of *K* factor curve, including the pronounced nonlinearity at low Reynolds numbers (see Figure 58.3)
- Integral flow totalization
- Digital measurement output in desired engineering units

Configuring—that is, tailoring the transmitter to a specific application—is carried out by one or more of the following digital communicators:

- Local configurator: a configurator, built into a transmitter, that has a display and keypad
- Handheld terminal: a palm-size digital device programmed for configuration purposes
- PC configurator: a personal computer containing configuration software
- System configurator: a digital measurement and control system with embedded configuration software

Using one of these configurators, the dataset of parameters that defines the configuration can be modified to fit the application in question. The details of this dataset vary, depending on the specific transmitter; however, the general categories of information listed as follows apply:

- Flow-tube parameters (e.g., tube bore, *K* factor, serial no.)
- User identification parameters (e.g., tag no., location)
- Transmitter options (e.g., measurement units, function selections)
- Process fluid parameters (e.g., fluid density and viscosity, process temperature)
- Application parameters (e.g., *K* factor corrections, URV, LFCI level)
- Output options (e.g., measurement output modes, damping, fail-safe state)

58.5 Application Considerations

58.5.1 Meter Selection

From a safety viewpoint, it is essential that the vortex flowmeter satisfies the appropriate electrical safety requirements and be compatible with the process, that is, be able to withstand the temperature, pressure, and chemical nature of the process fluid. From a mechanical viewpoint, it must have the proper end connections and, if required for critical applications, have a sensor that can be replaced without shutting down the process. Meter size and measurement output signal type are also very important selection factors.

58.5.1.1 Size

Contrary to what one might expect, the required *meter size* is not always the same as the nominal size of the piping in which it is to be installed. In some applications, selecting the size based on adjacent piping will not allow the low end of the required flow range to be measured. The appropriate criterion for selecting meter size is that the meter provides a reliable and accurate measurement over the entire required flow range. This could dictate a meter size that is less than the adjacent piping.

Pressure drop is a competing sizing criteria to that described previously. This drop is given by

$$\Delta P = C \times \rho_f \times \frac{Q^2}{D^4} \tag{58.11}$$

where

C is a constant dependent on meter design
D is the bore diameter of the flow tube

The tendency is to pick a flow tube with the same nominal diameter as the adjacent piping to eliminate the extra pressure drop introduced by a smaller-sized meter. However, in the majority of cases, this added drop is of little consequence.

The meter manufacturer can provide the needed information for making the proper selection. In some cases, sizing programs from manufacturers are available on the Internet in either an interactive or downloadable form.

58.5.1.2 Measurement Output Options

As mentioned previously, three types of *measurement outputs* are in current use: a 4–20 mA analog signal, a pulse train, and a digital signal. Some vortex meters will provide all three of these outputs, but not always simultaneously. It is essential that the meter has the output(s) required by the application.

58.5.2 Meter Installation

The performance specifications of a vortex flowmeter are normally established under the following conditions: (1) the flow tube is installed in a pipeline running full with a single-phase fluid; (2) the piping adjacent to the flow tube consists of straight sections of specified schedule pipe (normally schedule 40), typically a minimum of 30 PD (pipe diameters) in length upstream and 5 PD downstream of the flow tube with no flow-disturbing elements located within these sections; and (3) the meter is located in a vibration-free and electrical interference–free environment. As a consequence, certain constraints are placed on where and how the meter is installed in process piping if published performance specifications are to be achieved. These constraints are discussed later. Because meters from different suppliers differ in their sensitivity to the aforementioned influences, the statements made are of a qualitative nature. The specific manufacturer should be consulted for more quantitative information.

58.5.2.1 Location

The flowmeter should be located in a place where vibration and electrical interference levels are low. Both of these influences can decrease the signal-to-noise ratio at the input to the transmitter. This reduction can degrade the ability of the meter to measure low flows.

The meter should not be installed in a vertical line in which the fluid is flowing down because there is a good possibility that the pipe will not be full.

58.5.2.2 Adjacent Piping

Recommended practice is to mount the flowmeter in the process piping according to the manufacturer's stated upstream and downstream minimum straight-length piping requirements. These are typically 15–30 and 5 PD, respectively. Piping elements such as elbows or reducers upstream of the meter normally affect its K factor, but not its linearity. This allows a bias correction to be applied to the K factor. Many manufacturers provide bias factors for common upstream piping arrangements. Some who offer intelligent flowmeters make the corrections internally once the user has selected the appropriate configuration from a pick list. For piping elements and arrangements where the bias correction is not available, an in situ calibration should be run if the manufacturer's specified uncertainty is to be achieved. If this is not possible, calibration in a test facility with an identical configuration should be run.

The same situation as earlier applies if the pipe schedule adjacent to the meter differs from that under which the meter was calibrated.

To avoid disturbance to the flow, flange gaskets should never protrude into the process fluid.

The following recommendations apply if a control valve is to be situated near a vortex flowmeter. In liquid applications, the control valve should be located a minimum of 5 PD downstream of the flowmeter. This not only prevents disturbance to the flow profile in the flow tube but also aids in preventing flashing and cavitation (see as follows). In gas applications, the control valve should be installed upstream of the meter, typically a minimum of 30 PD upstream of the meter to ensure an undisturbed flow profile. Having the pressure drop across the valve upstream of the meter results in a decreased density and subsequent increased velocity at the flowmeter. This helps in achieving good measurements at low flows. For condensable gases, such as steam, it also helps to reduce the amount of condensate that might otherwise be present at the flowmeter.

58.5.2.3 Orientation

In general, meter orientation is not an issue for vortex flowmeters, particularly for vertical pipe installations. However, for meters having electronics at the flow tube, it is recommended in high-temperature horizontal pipe applications that the flow tube be oriented with the electronics beneath the meter. Although vortex flowmeters are not recommended for multiphase applications, they do operate with somewhat degraded performance with dirty fluids (i.e., small amounts of gas bubbles in liquid, solid particles in liquid, or liquid

droplets in gas). The degree of degradation in horizontal pipe applications depends to some extent on the specific meter design. Orienting the flow tube according to manufacturer's recommendations for the dirty fluid in question can help to alleviate this problem.

58.5.2.4 Pressure and Temperature Taps

The placement of pressure and temperature taps for determining gas densities, if required, is also an important consideration. Recommendations for location of these taps vary, depending on the manufacturer. The temperature probe is inserted typically 6 PD downstream of the flow tube. This prevents any flow disturbance in the meter and at the same time gets the probe as close to the meter as possible. The pressure tap is made typically 4 PD downstream of the meter. Although a pressure tap does not significantly affect the flow, its placement is critical for achieving an accurate density measurement.

58.5.2.5 Process Conditions

Flashing and cavitation can occur in a liquid application just downstream of the shedder if the pressure drop across the meter results in the downstream pressure being below the vapor pressure of the liquid. These phenomena lead to undefined measurement errors and possibly to structural damage and hence should be avoided. This is usually accomplished by increasing the inlet pressure or inserting a back-pressure valve downstream of the meter. To avoid flashing and cavitation, the downstream pressure after recovery (approximately 5 PD downstream) must be equal to or greater than P_{dmin}, where

$$P_{dmin} = c_1 \times \Delta P + c_2 \times P_{vap} \tag{58.12}$$

where

P_{dmin} is the minimum absolute downstream pressure after recovery
P_{vap} is the vapor pressure of the liquid at the flowing temperature
ΔP is the overall pressure drop
c_1, c_2 is the empirical constants for a specific meter (normally available from the meter manufacturer)

Pulsating flow can also in some circumstances lead to measurement errors. It is best to avoid placing the meter in process lines where noticeable pulsation exists.

58.5.3 Meter Configuration

It is important when installing an analog or intelligent vortex flowmeter that it be configured for the specific application (see Section 58.4). This is often done by the supplier prior to shipping if the user supplies the relevant information at the time the order is placed. If this is not the case, the user must carry out the configuration procedures provided by the manufacturer.

58.6 Recent Developments

Recent efforts have been made to make the vortex flowmeter into a real-time mass flow measurement device. As was demonstrated in Section 58.2, the output of the meter, based on the frequency of vortex shedding, is related to actual volumetric flow (see Equation 58.7). In intelligent transmitters, the flowing density (the density at flowing conditions) and the base density can be entered into the transmitter's database. Based on these values, mass flow or standard volumetric flow can be computed (see Equations 58.8 and 58.9). This procedure is valid if the flowing density does not vary in time. If this is not the case, an on-line, real-time measure of the density must be provided. Two different approaches have been used. One (multisensor) employs sensors in addition to the vortex sensor; the other (single sensor) relies on additional information being extracted from the vortex-shedding signal.

58.6.1 Multisensor

In this method, temperature and pressure measurements are made in addition to the vortex frequency. This approach is similar to that used in orifice-d/p mass flowmetering, in which case temperature and pressure ports are located in the pipe normally downstream of the orifice plate. However, for the multisensor vortex, the temperature and pressure sensors are incorporated into the flowmeter rather than located in the adjacent piping. Using these two additional measurements, the flowing density is calculated from the equation of state for the process fluid.

58.6.2 Single Sensor

This approach takes advantage of the fact that, in principle, for a force- or pressure-based vortex-shedding sensor, the amplitude of the vortex-shedding signal is directly proportional to the density times the square of the fluid velocity; that is,

$$\text{Signal amplitude} \propto \rho_f \times U^2 \tag{58.13}$$

The fluid velocity can be determined from the vortex frequency; that is,

$$\text{Frequency} \propto U \tag{58.14}$$

Hence,

$$\frac{\text{Signal amplitude}}{\text{Frequency}} \propto \rho_f \times U \propto \text{Mass flow} \tag{58.15}$$

This approach, in principle, is independent of the process fluid and requires no additional sensors.

Further Information

ASME MFC-6M, *Measurement of Fluid Flow in Closed Conduits Using Vortex Flowmeters*, Washington, DC: American Society of Mechanical Engineers, 1998.

DeCarlo, J. P., *Fundamentals of Flow Measurement*, Research Triangle Park, NC: Instrument Society of America, 1984, Chapter 8.

Gotthardt, W. C., Oscillatory flowmeters, in *Practical Guides for Measurement and Control: Flow Measurement*, D. W. Spitzer (ed.), Research Triangle Park, NC: Instrument Society of America, 1991, Chapter 12.

Miller, R. W., *Flow Measurement Engineering Handbook*, 3rd edn., New York: McGraw-Hill, 1996, Chapter 14.

Vortex Flowmeters, http://saba.kntu.ac.ir/eecd/Ecourses/instrumentation/projects/reports/Flowmeter/vortex.htm (accessed on July 12, 2012).

Vortex Shedding Flowmeter, UFM, http://www.flowmeters.com/ufm/index.cfm?task=vortex_fluidic, (accessed on July 11, 2012).

Partial List of Vendors and Manufacturers

BDC, Inc., 436 Anglum Road Hazelwood, MO 63042, Toll Free: 800-432-5810, Phone: 314-993-5810, Fax: 314-993-4107, www.gobdc.com

Ives Instrument Corp., 601 Croton Rd., King of Prussia, PA 19406-3111, Phone: 610-265-3071, 877-768-1600 (toll free), Fax: 610-768-1605, www.ivesequipment.com

Malema Flow Sensors, 1060 S. Rogers Cir., Boca Raton, FL 33487-2815, Phone: 561-702-7273, www.malema.com

Sierra Instruments, 5 Harris Ct., Bldg. L, Monterey, CA 93940, Phone: 831-373-0200, 800-866-0200 (toll free), Fax: 831-373-4402, www.sierrainstruments.com

Vortex Instruments, 8475 W I-25 Frontage Rd., Suite 300, Longmont, CO 80504, Phone: 866-901-4141 (toll free), Fax: 303-682-4368, vortekinst.rtrk.com/?scid=2127745&rl_alt…

Yokogawa Filed Instruments Division, 2 Dart Rd., Newnan, GA 30265, Phone: 770-254-0400, Fax: 770-254-4913, www.yokogawa.com/us/ia/fieldinstruments/…

59

Thermal Anemometry

Jugal K. Agarwal
TSI, Inc.

John G. Olin
Sierra Instruments, Inc.

59.1 General Description

A thermal anemometer measures the velocity at a point in a flowing fluid—a gas or a liquid. Figure 59.1 shows a typical thermal anemometer used to monitor velocity in gas flows. It has two sensors—a velocity sensor and a temperature sensor—which automatically correct for changes in gas temperature. Both sensors are reference-grade platinum resistance temperature detectors (RTDs). The electric resistance of RTDs increases as temperature increases. For this reason, they are one of the most commonly used sensors for accurate temperature measurements. The electronics circuit passes current through the velocity sensor, thereby heating it to a constant-temperature differential ($T_v - T_a$) above the gas temperature T_a, and measures the heat q_c carried away by the cooler gas as it flows past the sensor. Hence, it is called a "constant-temperature thermal anemometer."

Since the heat is carried away by the gas molecules, the heated sensor directly measures gas mass velocity (mass flow rate per unit area), ρU. The mass velocity is typically expressed as U_s in engineering units of standard meters per second, or standard $m \cdot s^{-1}$, referenced to standard conditions of 20°C temperature and 1 atm pressure. If the fluid's temperature and the fluid's pressure are constant, then the anemometer's measurement can be expressed as actual meters per second, or $m \cdot s^{-1}$. When the average mass velocity is multiplied by the cross-sectional area of a flow channel, the mass flow rate through the channel is obtained. Mass flow rate, rather than volumetric flow rate, is the direct quantity of interest in most applications, such as chemical reactions, combustion, heating, cooling, drying, mixing, fluid power, human respiration, meteorology, and natural convection.

The thermal anemometer has some advantages and disadvantages when compared with the two other common point-velocity instruments—Pitot tubes and laser-Doppler anemometers. Compared with Pitot tubes, the thermal anemometer measures lower velocities, has a much wider dynamic range, and has better frequency response (i.e., it responds well to changing flows) but may cost slightly more. When thermal anemometers are compared with laser-Doppler anemometers, they have a much lower cost, do not require seeding the flow with particles, and can have a higher signal-to-noise ratio. On the other hand, laser-Doppler anemometers provide a fundamental measurement of velocity, independent of temperature and fluid properties. For this reason, they are often used to calibrate thermal anemometers.

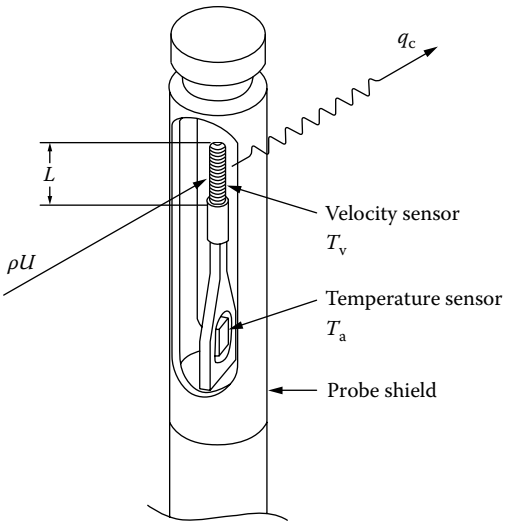

FIGURE 59.1 Principle of operation of a typical thermal anemometer. T_v is the temperature of the heated velocity sensor, T_a is the gas temperature measured by the temperature sensor, ρ is the gas mass density, U is the gas velocity, q_c is the heat carried away by the flowing gas stream, and L is the length of the heated tip of the velocity sensor. (With permission of TSI Incorporated, Shoreview, MN.)

Thermal anemometers are subdivided into three categories: heavy duty for industrial applications, medium-duty battery powered for commercial (building) applications, and research grade (delicate and very small) designed for fluctuating flow applications. Small thermal anemometers are also used in many medical devices. Figure 59.2 shows typical sensors of thermal anemometers. Industrial thermal anemometers are described in Chapter 63. Commercial and research thermal anemometers are discussed in this section.

59.1.1 Commercial Thermal Anemometers

Thermal anemometers are used in many commercial applications to measure point velocity. Total flow through a duct or pipe can be calculated from a single-point sensor located at the center if the flow profile is well defined. When the flow profile is not well defined, multiple single-point sensors located at various points in the cross section are used. In general, thermal anemometers are accurate at very low velocities, have very large dynamic range, have very good frequency response, and maintain their accuracy for many years without the need for any recalibration or adjustments. Due to contamination problems, it is advisable to use thermal anemometers to measure air or gases that are clean enough to breathe. Thermal anemometers are not suitable to measure or monitor dirty unfiltered air.

In modern buildings, conditioned (heated or cooled) filtered air is supplied for human comfort and safety. Because of their ability to measure very low velocity, thermal anemometers have found many applications in the heating, ventilating, and air conditioning (HVAC) industry. Often, multipoint thermal anemometer arrays are used to monitor fresh air that is drawn into a building. Since conditioning the air is expensive, it is economical to bring in only the amount of fresh air that is needed and recirculate the remaining air from the occupied space. The air velocities are typically kept low at the fresh air intake to reduce noise; hence, multipoint thermal anemometer arrays are ideal for this application. Single-point installed thermal anemometers are used to monitor supply air for many processes such as drying of pills in the pharmaceutical industry.

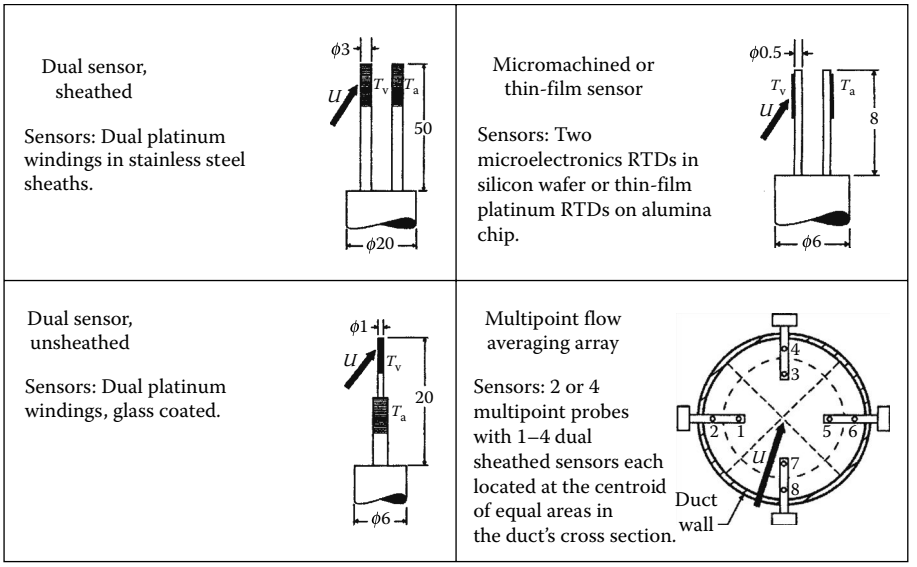

(a)

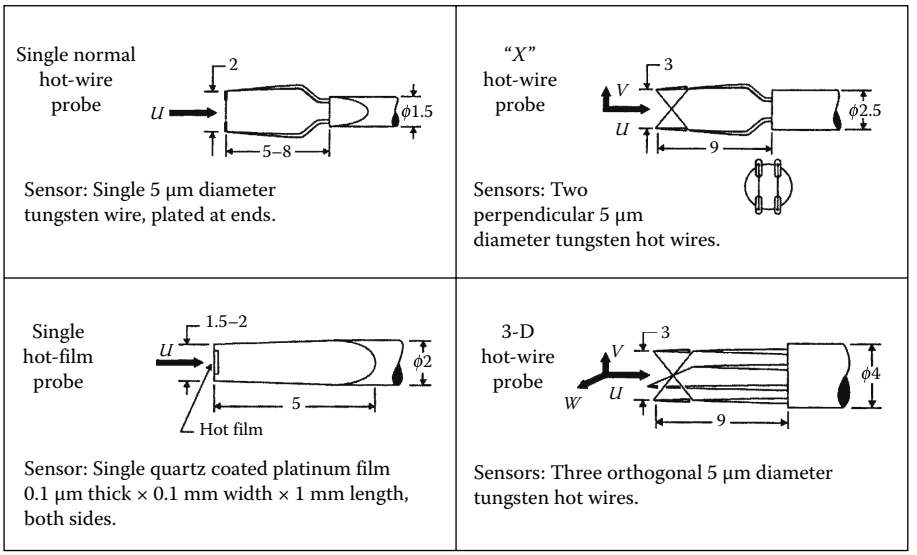

(b)

FIGURE 59.2 (a) Typical commercial and (b) research thermal anemometer sensors. All dimensions are in millimeters. T_v indicates the heated velocity sensor, T_a indicates the temperature sensor, U is the major velocity component in the x direction, V is the transverse velocity component in the y direction, and W is the transverse velocity component in the z direction.

Battery-operated portable thermal anemometers are used to measure face velocities of devices like fume hoods, biological safety cabinets, and HEPA filters. In such applications, the velocity of interest is very low (0.5 $m \cdot s^{-1}$ or 100 fpm). Other point-velocity measurement techniques such as Pitot probe anemometry are not accurate at these low velocities. Sometimes, thermal anemometers are incorporated into flow measuring devices such as capture hoods, which are used to measure the total airflow exiting or entering an HVAC ducting system. Thermal anemometers are also used to measure air velocities inside an HVAC ducting system.

Another interesting application of thermal anemometry is the measurement of the very low differential pressure between two adjacent spaces, such as a hospital room and the corridor. The two adjacent spaces are connected through a tube. The differential pressure between the two spaces creates a flow. A thermal anemometer measures this flow velocity. This velocity is indicative of the differential pressure between the two adjacent spaces. Normally the pressure differential in such applications is too low to be measured by conventional differential pressure transducers.

Because of their good frequency response, thermal anemometers are widely used in medical applications to measure air, oxygen, nitrous oxide, or other gases that may be given to a patient. In particular, thermal anemometers are used to monitor air and oxygen flow inside ventilators that are used to assist the breathing of a patient.

The construction of thermal anemometers depends on their applications. All thermal anemometers consist of a velocity sensor and a temperature sensor. The velocity sensor is heated to several degrees centigrade higher than the fluid temperature. The resulting temperature difference is often referred as "overheat." The temperature sensor is not heated and measures the fluid temperature. Higher overheat is preferred for better temperature compensation. Since higher overheat increases power consumption, it is less desirable for battery-operated instruments.

Heated thermistors have been used for multipoint applications, but platinum RTDs are more common for both velocity and temperature sensors. Typically, the velocity sensors are in the 10–20 Ω range, whereas the temperature sensors are in the 100–1000 Ω range. Portable air velocity meters typically use sensors manufactured by winding a platinum wire around a ceramic mandrel. Such wire-wound sensors are normally covered by a high-temperature glass coating. The sensors used in medical applications are made by depositing a thin film of platinum onto a very small diameter glass cylinder, about 50 μm in diameter and 4 mm long.

59.1.2 Research Thermal Anemometers

Research thermal anemometers are used to measure the point velocity and/or turbulence of clean gases or liquids for fundamental fluid flow and heat-transfer research and related product development. Because of their more fragile nature, they are not suitable for commercial applications. Typically, the gas is ambient air. Constant-temperature, filtered, and degasified water is the primary liquid application, but the technique has also been applied to clean hydrocarbon liquids. As shown in Figure 59.2, the research anemometer's velocity sensor is either a hot wire or a hot film. Hot-wire sensors have a high-frequency response and, therefore, are excellent for turbulence measurements in air and other gases. They are seldom used in liquid flows because they are susceptible to fouling and contamination. Hot-film sensors trade off lower frequency response for increased ruggedness and are used in gas and liquid flows. For liquid flows, hot-film sensors are designed to shed lint and other fouling or contaminating materials. Bruun [1] is an excellent reference source for the theory and applications of hot-wire and hot-film anemometers. Another comprehensive source is Fingerson and Freymuth [2].

Typical applications for hot-wire and hot-film anemometers include 1-D, 2-D, and 3-D flow and turbulence studies; validation of computational fluid dynamics codes; environmental and micrometeorological measurements; turbomachinery; internal combustion engines; biological studies; heat-transfer research; boundary-layer measurements; supersonic flows; two-phase flows; and vorticity measurements. Freymuth [3] describes the 80-year history of research thermal anemometers. Laser-Doppler anemometry and particle image velocimetry are also widely used for these applications.

The typical hot-wire sensor is a fine platinum or tungsten wire welded at each end to miniature prongs designed to minimize their influence on the wire's flow field. A hot-film sensor is made by coating a glass rod with a platinum film. The hot-film sensors are also attached to miniature prongs. A short length at each end of the hot-film sensor is usually gold plated to define an active sensor length away from the two prongs. For work in water, the film is quartz coated to prevent electrolysis or electrical shorting, but in this case, cracking of the coating can occur. A typical tungsten wire has a diameter of 4–5 μm, an active

length of 1–3 mm, and an electrical resistance of 2–6 Ω. Because it oxidizes above 350 °C in air, tungsten hot wires are usually operated at a temperature not exceeding 300 °C. Platinum, 90% platinum + 10% rhodium and 80% platinum + 20% iridium, wires also are used. They can be soldered onto the prongs but are weaker than tungsten. In cases where the fluid temperature T_a changes enough to cause measurement errors, a separate sensor is used to measure T_a and make temperature corrections. The temperature sensor is either a hot-wire- or larger-wire-wound RTD mounted either on a separate probe or integrally on the same probe stem as the velocity sensor. As shown in Figure 59.2, for 2-D or 3-D flow studies, probes with two perpendicular wires in an "X" pattern or three orthogonal wires are used, respectively. Special subminiature probes and probes with the prongs displaced from the probe stem are used for near-wall, boundary-layer work and small flow passages. Gibbings et al. [4,5] describe hot-wire probes for use in near-wall, turbulent boundary-layer studies.

As shown in Figure 59.2, the typical hot-film sensor for water applications is a wedge-tipped or cone-tipped quartz rod with a thin 0.1 μm thick platinum film plated on its tip via cathode sputtering. The platinum film usually is coated with a 1–2 μm layer of quartz for protection and to avoid electrical shorting or electrolysis in water flows. Because hot-film sensors have a much larger mass than hot-wire sensors, their frequency response is not as good as hot wires; hence, they are not quite as applicable to high-frequency turbulence measurements. It also has been observed by Mikulla [6] that the shape of some hot-film sensors can suppress response to the turbulent velocity component normal to its surface. On the other hand, hot-film sensors have less breakage and a more stable geometry than hot-wire sensors. Other configurations of hot-film sensors include cylindrical quartz rods (approximately 50–150 μm in diameter), one or more split-film cylindrical sensors for multidimensional measurements, and flush-mounted sensors for wall heat-transfer measurements.

59.2 Principle of Operation

59.2.1 First Law of Thermodynamics

Figure 59.3 shows the first law of thermodynamics applied to a control volume consisting of the velocity sensor of a thermal anemometer, such as shown in Figure 59.1. The application of the first law to thermal anemometer sensors provides the basis for determining point velocity. Applied to Figure 59.3, the first law states that the energy into the control volume equals the energy out plus the energy stored.

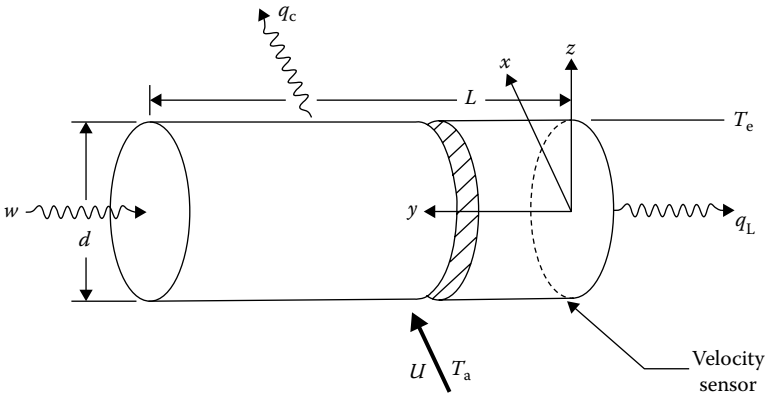

FIGURE 59.3 First law of thermodynamics applied to a thermal anemometer velocity sensor. The term w is the electric power (W) supplied to the sensor, q_c is the heat convected away from the sensor by the flowing fluid having a velocity U and temperature T_a, q_L is the conductive heat lost, T_e is the average surface temperature of the sensor over its length L, and d is the sensor's outside diameter.

Making the practical simplifying assumptions of steady-state operation (i.e., no energy stored) and no heat transfer via radiation, one obtains

$$w = q_c + q_L \tag{59.1}$$

The heat transfer q_c due to natural and forced convection normally is expressed in terms of the heat-transfer coefficient h as

$$q_c = hA_v(T_e - T_a) \tag{59.2}$$

where $A_v = \pi dL$ is the external surface area of the velocity sensor. The electric power w usually is expressed as

$$w = \frac{E_v^2}{R_v} \tag{59.3}$$

where

E_v is the voltage across the sensor
R_v is its electric resistance

For the velocity sensor shown in Figure 59.1, q_L is the heat conducted from the end of the heated velocity sensor of length L to the remainder of the sensor's length. Most of this heat is convected away by the flowing fluid, and a small fraction is conducted to the probe stem. In the case of research hot-wire or cylindrical hot-film sensors, q_L is conducted to the two prongs, of which a major fraction is convected away and a minor fraction enters the probe stem. In well-designed velocity sensors, q_L is at most 10%–15% of w, a fraction that decreases as velocity increases.

For research hot-wire sensors, the surface temperature T_e is identical to the wire temperature T_v. However, the surface temperature T_e of other sensors with some kind of coating is slightly less than the temperature T_v of the platinum because a temperature drop is required to pass the heat q_c through the intervening "skin." This is expressed as

$$T_e = T_v - q_c R_s \tag{59.4}$$

where R_s is the thermal skin resistance in units of kW^{-1}. R_s is a constant for a given sensor and is the sum of the thermal resistances of the coating layers. For research anemometer velocity sensors, $R_s = 0$ and $T_e = T_v$ in Equation 59.4. As evidenced by Equation 59.4, the effect of skin resistance increases as velocity (i.e., q_c) increases. The effect is almost negligible at low velocity; but at high velocity, it is responsible for the characteristic droop in power vs. velocity curves.

Because the flow around cylinders in cross flow is confounded by the boundary-layer separation and vortex shedding, it has defied analytical solution. Therefore, the film coefficient h in Equation 59.2 is found using empirical correlations. Correlations for h are expressed in terms of the following nondimensional parameters:

$$\mathrm{Nu} = \Im(\mathrm{Re}, \mathrm{Pr}, \mathrm{Gr}, \mathrm{M}, \mathrm{Kn}) \tag{59.5}$$

where

Nu = hd/k is the Nusselt number (the heat-transfer parameter)
Re = $\rho Vd/\mu$ is the Reynolds number (the ratio of dynamic to viscous forces)
Pr = $\mu C_p/k$ is the Prandtl number (the fluid properties parameter)
M is the Mach number (the gas compressibility parameter)
Kn is the Knudsen number (the ratio of the gas mean free path to d)

In the aforementioned, d is the outside diameter of the sensor, ρ is the fluid density, V is average velocity, k is the fluid's thermal conductivity, μ is its viscosity, and C_p is its coefficient of specific heat at constant pressure. If one takes the practical case where (1) natural convection is embodied in Re and Pr, (2) the velocity is less than one-third the fluid's speed of sound (i.e., <100 $m \cdot s^{-1}$ in ambient air), and (3) the flow is not in a high vacuum, then one can ignore the effects of Gr, M, and Kn, respectively. Thus,

$$\mathrm{Nu} = \tilde{\mathcal{O}}(\mathrm{Re}, \mathrm{Pr}) \tag{59.6}$$

Over the years, many attempts have been made to find universal correlations for the heat transfer from cylinders in cross flow. For an isothermal fluid at constant pressure, King [7] expresses Equation 59.6 as

$$\mathrm{Nu} = A + B\,\mathrm{Re}^{0.5} \tag{59.7}$$

where A and B are empirical calibration constants that are different for each fluid and each temperature and pressure. Kramers [8] suggests the following correlation:

$$\mathrm{Nu} = 0.42\,\mathrm{Pr}^{0.2} + 0.57\,\mathrm{Pr}^{0.33}\,\mathrm{Re}^{0.50} \tag{59.8}$$

This correlation accounts for the variation in fluid properties (k, μ, and Pr) with temperature. Kramers [8] evaluates these properties at the so-called "film" temperature $(T_v + T_a)/2$, rather than at T_a itself. Another comprehensive correlation is given by Churchill and Bernstein [9]. Several other correlations are similar to Equation 59.8 but have exponents for the Reynolds number ranging from 0.4 to 0.6. Others have 0.36 and 0.38 for the exponent of the Prandtl number. Equations 59.7 and 59.8 are strictly valid only for hot-wire sensors with very high L/d ratios, in which case q_L and R_s are zero. The following universal correlation is suggested for real-world velocity sensors with variable fluid temperature and nonzero q_L and R_s:

$$\mathrm{Nu} = A + B\,\mathrm{Pr}^{0.33}\,\mathrm{Re}^{n} \tag{59.9}$$

where constants A, B, and n are determined via flow calibration. Equation 59.9 is applicable to most commercial, industrial, and research velocity sensors.

Combining Equations 59.1 through 59.3, and 59.9, and recognizing that $h = kNu/d$, one obtains

$$\frac{E_v^2}{R_v} = (Ak + Bk\,\mathrm{Pr}^{0.33}\,\mathrm{Re}^{n})(T_v - T_a) \tag{59.10}$$

where A and B are new constants. A, B, and n are determined via flow calibration and account for all nonidealities, including end conduction and skin resistance. Equation 59.10 is applicable to most commercial, industrial, and research velocity sensors. The manufacturers of industrial thermal anemometers can add other calibration constants to Equation 59.10 to enhance its correlation with flow-calibration data. The presence of end conduction means that the temperature of the velocity sensor varies with the axial coordinate y in Figure 59.3. The temperature T actually sensed by the velocity sensor is the average temperature over length L, or

$$T_v = \left(\frac{1}{L}\right)\int_0^L T_v(y)\,\mathrm{d}y \tag{59.11}$$

Bruun [1] presents an analytical solution for $T_v(y)$ for hot-wire sensors. Equation 59.11 is the correct expression for T_v in Equation 59.10 and is so defined hereafter.

For fluid temperatures less than 200 °C, the electric resistance of the RTD velocity and temperature sensors is usually expressed as

$$R_v = R_{v0}\left[1 + \alpha_v (T_v - T_0)\right] \tag{59.12}$$

$$R_T = R_{T0}\left[1 + \alpha_T (T_T - T_0)\right] \tag{59.13}$$

where R_{v0} and R_{T0} are, respectively, the electric resistances of the velocity sensor and the temperature sensor at temperature T_0 (usually 0 °C or 20 °C), and α_v and α_T are the temperature coefficients of resistivity at temperature T_0. Additional terms are added to Equations 59.12 and 59.13 when fluid temperatures exceed 200 °C. When evaluated at the fluid temperature T_a, the resistance R_a of the velocity sensor is

$$R_a = R_{v0}\left[1 + \alpha_v (T_a - T_0)\right] \tag{59.14}$$

For applications with wide excursions in fluid temperature, additional terms are added to Equations 59.12 through 59.14. At 20 °C, α_v and α_T are approximately 0.0036 °C^{-1} for tungsten wire, 0.0038 °C^{-1} for pure platinum wire, 0.0016 °C^{-1} for 90% platinum + 10% rhodium wire, 0.0024 °C^{-1} for platinum film, and 0.0040 °C^{-1} for tungsten film. R_v and R_a are called the "hot" and "cold" resistances of the velocity sensor, respectively. The ratio R_v/R_a is called the "overheat ratio." For gas flows, commercial thermal velocity sensors are operated at overheat ratios from 1.1 to 1.4 ($T_v - T_a$ = 30 °C–100 °C). For gas flows, the overheat ratio of tungsten hot-wire and hot-film sensors is usually set to approximately 1.8 ($T_v - T_a$ = 200 °C–300 °C) and 1.4 ($T_v - T_a$ = 150 °C–200 °C), respectively. For water flows, the overheat ratio of hot-film sensors is approximately 1.05–1.10 ($T_v - T_a$ = 10 °C–20 °C). Mikulla [6] shows the importance of the effect of overheat ratio on frequency response.

Combining Equations 59.12 and 59.14, one obtains

$$T_v - T_a = \frac{R_v - R_a}{\alpha_v R_{v0}} \tag{59.15}$$

Inserting this into Equation 59.10, one obtains

$$\frac{E_v^2}{R_v (R_v - R_a)} = Ak + Bk\mathrm{Pr}^{0.33}\mathrm{Re}^n \tag{59.16}$$

where new constants A and B have absorbed the constants α_v and R_{v0}.

Figures 59.4 through 59.6 show three typical electronic drives for thermal anemometer sensors. Figure 59.4 shows the commonly used constant-temperature anemometer Wheatstone bridge circuit described by Takagi [10]. Figure 59.5 is similar but is controlled and operated via a personal computer (PC). In the constant-temperature mode, the hot resistance R_v, and hence the velocity sensor's temperature, remains virtually constant, independent of changes in velocity. With the addition of the temperature sensor shown in Figure 59.4, the bridge circuit also compensates for variations in fluid temperature T_a, as described later. Another common analog sensor drive is the constant-current anemometer. In this mode, a constant current is passed through the velocity sensor, and the sensor's temperature decreases as the velocity increases. Because the entire mass of the sensor must participate in this temperature change, the sensor is slower in responding to changes in velocity. Because the constant-temperature anemometer has a flatter frequency response and an excellent signal-to-noise ratio [2] and is easier to use, it is favored over constant-current anemometers by most researchers and manufacturers for velocity and turbulence measurements. The constant-current anemometer with a very low overheat ratio is often used as the temperature sensor. Subsequently, references made herein to sensor electronics will be based on the constant-temperature anemometer.

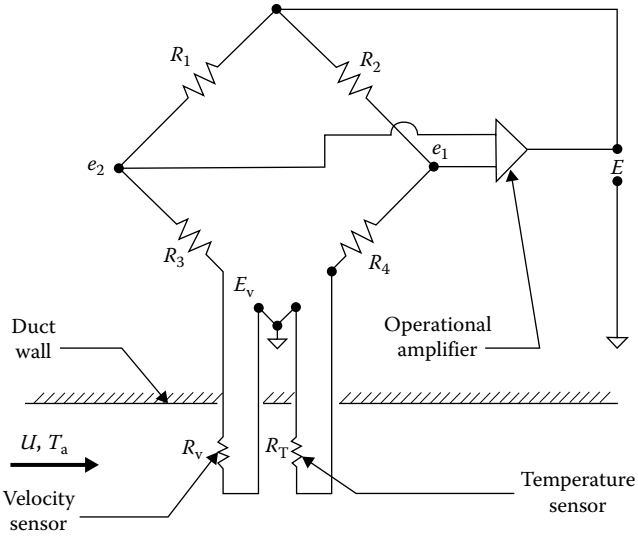

FIGURE 59.4 Constant-temperature thermal anemometer bridge circuit with automatic temperature compensation. R_1, R_2, and R_4 are fixed resistors selected to achieve temperature compensation, R_3 is the probe and cable resistance, R_v is the velocity sensor's resistance, R_T is the temperature sensor's resistance, and E is the bridge voltage output signal. For research anemometers operating in isothermal flows, the temperature sensor is eliminated and replaced with a variable bridge resistor. Some temperature-compensation circuits have an additional resistor in parallel with R_T.

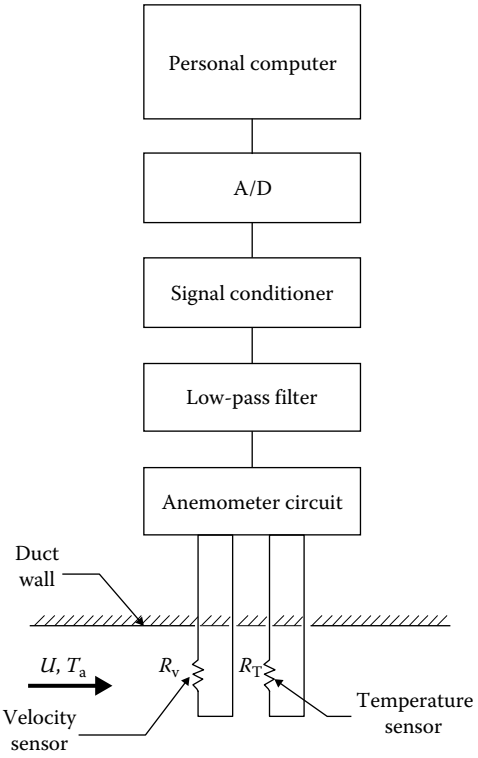

FIGURE 59.5 PC-based digital thermal anemometer system. The signal conditioner matches the anemometer circuit's output to the ADC. For isothermal flows, the temperature sensor is eliminated.

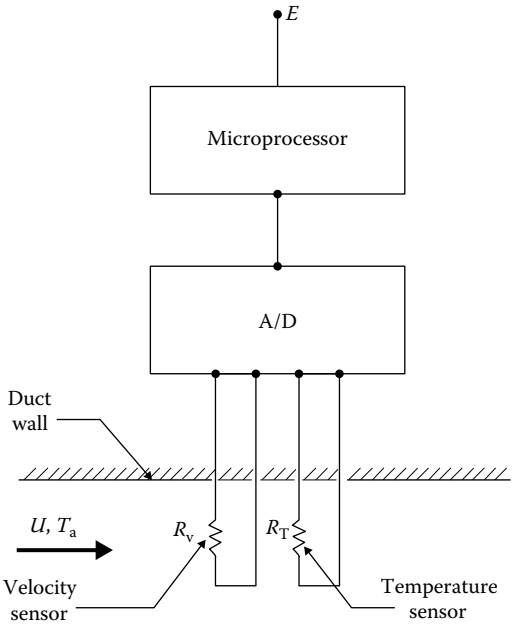

FIGURE 59.6 Microprocessor-based digital thermal anemometer. This system digitally maintains a constant-temperature difference ($T_v - T_T$) and automatically corrects for the variation in fluid properties with temperature. The manufacturer provides a probe-mounted electronics package delivering an analog output signal E and/or a digital RS485 signal linearly proportional to gas mass velocity. (With permission of Sierra Instruments, Inc., Monterey, CA.)

In the constant-temperature anemometer drive shown in Figure 59.4, the resistances R_1 and R_2 are chosen to (1) maximize the current on the velocity-sensor side of the bridge so it becomes self-heated and (2) minimize the current on the temperature-sensor side of the bridge so it is not self-heated and is independent of velocity. Additionally, the temperature sensor must be sufficiently large in size to avoid self-heating. The ratio R_2/R_1 is called the "bridge ratio." A bridge ratio of 5:1–20:1 is normally used, but for optimum frequency response and compensation for long cable length, a bridge ratio of 1:1 can be used. In Figure 59.4, the operational amplifier, in a feedback control loop, senses the error voltage ($e_2 - e_1$,) and feeds the exact amount of current to the top of the bridge necessary to make ($e_2 - e_1$,) approach zero. In this condition, the bridge is balanced; that is,

$$\frac{R_1}{R_v + R_3} = \frac{R_2}{R_T + R_4} \tag{59.17}$$

or

$$R_v = \frac{R_1}{R_2}(R_T + R_4) - R_3 \tag{59.18}$$

From Equation 59.18, one sees that R_v is a linear function of R_T. This relationship forms the basis for analog temperature compensation.

Expressing the voltage E_v across the velocity sensor in terms of the bridge voltage E, one obtains

$$E_v = \frac{ER_v}{R_1 + R_3 + R_v} \tag{59.19}$$

Inserting this into Equation 59.16, one arrives at the generalized expression for the first law of thermodynamics for the thermal anemometer velocity sensor:

$$E^2 = G\left[Ak + Bk\left(\frac{\rho_s}{\mu}\right)^n \mathrm{Pr}^{0.33} U_s^n\right] \tag{59.20}$$

where $G = (R_1 + R_3 + R_v)^2 (R_v - R_a)/R_v$ and where A and B again are new constants. In Equation 59.20, one recognizes that conservation-of-mass considerations require that $\rho U = \rho_s U_s$, where ρ and U are referenced to the actual fluid temperature and pressure and ρ_s and U_s are referenced to standard conditions of 20 °C temperature and 1 atm pressure. To write Equation 59.20 in terms of U, one simply replaces ρ_s by ρ and U_s by U.

59.2.2 Temperature Compensation

The objective of temperature compensation is to make the bridge voltage E in Equation 59.20 independent of changes in the fluid temperature T_a. This is accomplished if (1) the term G in Equation 59.20 is independent of T_a and (2) compensation is made for the change in fluid properties (k, μ, and Pr) with T_a. Since these fluid properties have weaker temperature dependence than G in Equation 59.20, for small temperature changes (less than ±10 °C) in gas flows, only G requires compensation.

The two-temperature method is a typical procedure for compensating for both G and fluid properties. In this method, fixed-bridge resistors R_1, R_2, and R_4 in Figure 59.4 are selected so that E is identical at two different temperatures but at the same mass flow rate. This procedure is accomplished with flow calibration at two different temperatures and has variations among manufacturers.

The two-temperature method adequately compensates for temperature variations less than approximately ±50 °C. In higher temperature gas flow applications, such as the flow of preheated combustion air and stack gas, temperature variations typically are higher. The microprocessor-based digital sensor drive in Figure 59.6 provides temperature compensation for temperature variations ranging from ±50 °C to ±150 °C. This sensor drive has no analog bridge. Instead, it has a virtual digital bridge that maintains $(T_v - T_a)$ constant within 0.1 °C and has algorithms that automatically compensate for temperature variations in k, m, and Pr. For this digital sensor drive, the first law of thermodynamics is found from Equation 59.10 as

$$w = \left[Ak + Bk\left(\frac{\rho_s}{\mu}\right)^n \mathrm{Pr}^{0.33} U_s^n\right]\Delta T \tag{59.21}$$

where $\Delta T = (T_v - T_a)$ is now a known constant.

59.2.3 Flow Calibration

Figure 59.7 shows a typical flow-calibration curve for the digital electronics drive shown in Figure 59.4. The curve is nonlinear in nature. In the past, this inherent nonlinearity was considered a disadvantage because it required linearization circuitry that was expensive to implement using analog circuits. Now, digital circuits are universally used in instrumentation, and the nonlinearity is no longer a disadvantage. The steep curve at low velocities is advantageous because it provides excellent resolution at low velocities. This increases the dynamic range up to 1000:1 for a single sensor. Additionally, the high-level output of several volts provides excellent repeatability and requires no amplification other than that for spanning. Since the critical dimensions of thermal anemometer sensors are small, current manufacturing technology is incapable of maintaining tolerances sufficient to ensure sensor reproducibility.

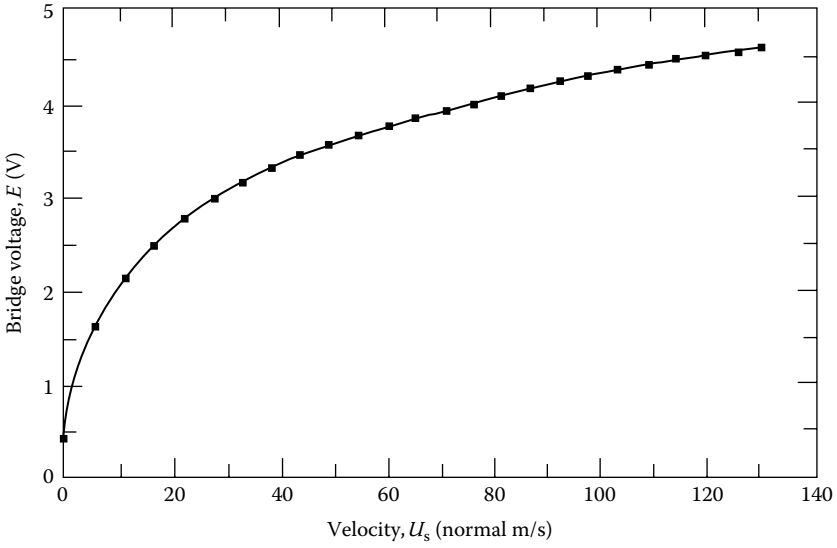

FIGURE 59.7 Typical flow-calibration curve for an industrial thermal anemometer. The electronics drive is that shown in Figure 59.6. The constant-temperature differential ($T_v - T_T$) is 50.0 °C. The cold resistances R_{v0} and R_{T0} of the velocity and temperature sensors at 20 °C are approximately 20 and 200 W, respectively. (With permission of Sierra Instruments, Inc., Monterey, CA.)

Therefore, each thermal anemometer must be calibrated by exposing it to a known flow, for example, as in Figure 59.7, over its entire velocity range, either at the exact fluid temperature of its usage or over the range of temperatures it will encounter if it is to be temperature compensated. A 10–20-point-velocity calibration is required to accurately determine the calibration constants *A*, *B*, and *n* in Equation 59.20. A least-squares curve-fitting procedure usually is applied. Bruun [1] and Gibbings et al. [4] provide more insight into curve fitting.

Proper flow calibration requires two critical elements: (1) a stable, reproducible, flow-generating facility and (2) an accurate velocity transfer standard. A typical flow-calibration facility consists of (1) a flow source such as a fan, pump, elevated tank, or compressed gas supply; (2) a flow-quieting section, such as a plenum with flow straighteners, screens, or other means to reduce swirling, turbulence, or other flow nonuniformities; (3) a nozzle to accelerate the flow and further flatten, or make uniform, the velocity profile; (4) a test section or free jet into which the thermal anemometer probe is inserted; (5) a means for holding and sealing the thermal anemometer probe; and (6) a velocity transfer standard. The test section or free jet must have a velocity profile that is uniform within approximately 0.5%–1.0% in its central portion, turbulence intensity less than about 0.5%, and an area large enough so that the projected area of the velocity probe is less than 5%–10% of the cross-sectional area. In the free-jet type of flow calibrator, the flow velocity is often determined by measuring the pressure drop across the nozzle. In a wind-tunnel type of flow calibrator, the flow velocity is determined by inserting a Pitot tube into the test section. Gibbings [4] describes a water box displacement rig for flow calibration at very low velocities in the range of 0.1–4 m s^{-1}.

Pitot tubes and laser-Doppler anemometers are the two most common velocity transfer standards used to calibrate thermal anemometers. Both have detailed descriptions earlier in this handbook. The Pitot tube usually has the classical "L" shape and an outside diameter of about 3 mm. Its tip is located in the same plane in the test section as the thermal anemometer probe and is no closer than approximately 3 cm from the wall. The measuring volume of the laser-Doppler anemometer is similarly located. The Pitot tube is far less expensive and easier to operate but is difficult to use if air velocities are less than about 3 m·s^{-1}. A Pitot-tube-based flow transfer standard should have its calibration recertified every

6 months by an accredited standards laboratory. On the other hand, the laser-Doppler anemometer is a first-principle standard that accurately measures air velocity from approximately 0.5 to 100 $m \cdot s^{-1}$. Its primary disadvantages are high expense and complications associated with properly seeding the flow with particles.

Small wind tunnels are used for calibrating thermal anemometers in manufacturing facilities and in accreditation laboratories. Such wind tunnels are calibrated using Pitot-tube and/or laser-Doppler anemometry. In operation, the wind-tunnel velocity at the test section is found by measuring the difference between the total pressure and the static pressure with a differential pressure transducer. This method is easier to use than other methods and has an excellent repeatability. Generating a uniform and stable low velocity (lower than 2.5 $m \cdot s^{-1}$) is a challenge. In one commercially available benchtop wind tunnel [11], this is accomplished by using a nozzle plate with multiple equally spaced holes downstream of the test section. The manufacturer claims uniform, stable low velocities down to 0.15 $m \cdot s^{-1}$ in the test section.

59.3 Measurements

59.3.1 Point Velocity

Based on the first law of thermodynamics expressed by Equation 59.20, one now can solve for the desired quantity—either the actual point velocity U ($m \cdot s^{-1}$) or the point mass velocity U_s (standard $m \cdot s^{-1}$). Here, one assumes that the velocity vector is normal to the flow sensor. The 2-D and 3-D velocity measurements are discussed later. In the following, A, B, and n are constants but are different for each case.

The simplest case is isothermal flow with a hot-wire sensor having a very high length-to-diameter ratio (L/d). In this case, the exponent n in Equation 59.20 is 0.5, as shown in Equation 59.7. The applicable first law and velocity expressions are

$$E^2 = A + BU^{0.5} \tag{59.22}$$

and

$$U = \left[\frac{E^2 - A}{B}\right]^2 \tag{59.23}$$

In the case of a real-world sensor in an isothermal flow having either end loss only or both end loss and skin resistance, one obtains

$$E^2 = A + BU^n \tag{59.24}$$

and

$$U = \left[\frac{E^2 - A}{B}\right]^{1/n} \tag{59.25}$$

Often, Equation 59.25 is replaced with a polynomial of the form $U = F(E^2)$, where the function $F(\ )$ is a fourth-order polynomial whose coefficients are determined from flow-calibration data using least-squares curve-fitting algorithms. For the same case as earlier, but with non-isothermal flow, the first law is expressed by (59.20), and the velocity is expressed as

$$U_s = \frac{\mu}{\rho_s}\left[\frac{E^2/G - Ak}{Bk\,\mathrm{Pr}^{0.33}}\right]^{1/n} \tag{59.26}$$

For the digital sensor drive of Figure 59.6, the first law is given by Equation 59.21 and the velocity by

$$U_s = \frac{\mu}{\rho_s}\left[\frac{w/\Delta T - Ak}{Bk\,\mathrm{Pr}^{0.33}}\right]^{1/n} \tag{59.27}$$

Current commercial thermal anemometer systems have temperature-compensation and "linearization" electronics (or lookup table in software) that automatically calculate U_s as a linear function of E or w, based on the foregoing relationships.

59.3.2 Turbulence

Turbulence measurements are the second most common application of research thermal anemometers. This measurement requires the high-frequency response of hot-wire and hot-film research anemometers operated in the constant-temperature mode. The vast majority of fluid flows are turbulent. Only flows with very low Reynolds numbers are nonturbulent, or laminar. Turbulent flows are time variant and usually are separated as follows into time-mean and fluctuating parts:

$$\begin{aligned} U(t) &= \bar{U} + u \\ V(t) &= \bar{V} + v \\ W(t) &= \bar{W} + w \\ T_a(t) &= \bar{T}_a + \theta \\ E &= \bar{E} + e \end{aligned} \tag{59.28}$$

where $U(t)$, $V(t)$, and $W(t)$ are the orthogonal components in the x, y, and z directions, respectively, such as shown in Figure 59.2 for the 3-D hot-wire probe. $T_a(t)$ is the fluid temperature, and $E(t)$ is the bridge voltage. $\bar{U}$, $\bar{W}$, $\bar{V}$, $\bar{T}_a$, and $\bar{E}$ are the time-mean parts, and $u(t)$, $v(t)$. $w(t)$, $\theta(t)$, and $e(t)$ are the time-dependent fluctuating parts. The time-mean parts are averaged sufficiently long to become independent of turbulent fluctuations, yet respond to changes with time in the main flow. In most of this text and for the purpose of simplicity, we have used the symbols U and T_a for the time-mean velocity and the time-mean temperature, respectively. In the study of turbulence, one is primarily interested in the time average of the product of two fluctuating velocity components (turbulence correlations) because these terms appear in the time-averaged Navier–Stokes equation. Two important turbulence correlations are $\overline{u^2}$ and $\overline{uv}$. The correlation $\left(\sqrt{\overline{u^2}}\right)/\bar{U}$ is called the *turbulence intensity*. The manufacturers of research anemometer systems provide electronics for automatically computing turbulence correlations.

For a fluid with changes in temperature sufficiently small that fluid properties are essentially constant, one can write Equation 59.20 in the following form:

$$E^2 = (A + BU^n)(T_v - T_a) \tag{59.29}$$

where A, B, and n are constant and where R_v is virtually constant because the anemometer is in the constant-temperature mode. Elsner [12] shows that the fluctuating voltage e is found by taking the total derivative of Equation 59.29, as follows:

$$e = S_u u + S_\theta \theta \tag{59.30}$$

where

$$S_u = \frac{\delta E}{\delta U} = \frac{nBU^{n-1}}{2}\left[\frac{(T_v - T_a)}{A + BU^n}\right]^{1/2} = \text{Velocity sensitivity} \tag{59.31}$$

$$S_\theta = \frac{\delta E}{\delta T_a} = -\frac{1}{2}\left[\frac{(A+BU)^n}{T_v - T_a}\right]^{1/2} = \text{Temperature sensitivity} \tag{59.32}$$

It is seen from Equations 59.31 and 59.32 that increasing $(T_v - T_a)$, that is, operating the sensor as hot as possible, maximizes the velocity sensitivity and minimizes the sensitivity to temperature fluctuations. This is why tungsten hot wires are operated at high temperatures (typically 200 °C–300 °C).

The fluctuating components of velocity have a broad frequency spectrum, ranging from 10^2 to 10^5 Hz and sometimes even higher. Therefore, it is imperative that the frequency response of constant-temperature research anemometers have a flat frequency response, that is, minimized attenuation and phase shift at higher frequencies. Blackwelder [13] and several other investigators have studied the frequency response of hot-wire anemometers. For turbulence measurements, Borgos [14] describes commercial research anemometer systems with features such as low-pass filters to decrease electronics noise, a sub-circuit for determining and setting overheat ratio, a square-wave generator for frequency response testing, and two or more controls to optimize the frequency response to fast fluctuations. Recent systems have electronics that compensate for frequency attenuation. When used with 5 μm diameter hot-wire sensors in air, commercial systems are capable of nearly flat frequency response and very small phase lag from 0 Hz to approximately 10^4 Hz. As reported by Nelson and Borgos [15], wedge and conical hot-film sensors in water have a relatively flat response from 0 to 10 Hz for velocities above 0.3 m s^{-1}. The compensation for attenuation to get high-frequency response is a more involved process for hot-film sensors than for hot-wire sensors.

Two- and three-component velocity and turbulence measurements are made using hot-wire or hot-film research anemometers, such as shown in Figure 59.2. As described by Müller [16], hot-wire or cylindrical hot-film probes in the "X" configuration are used to measure the *U* and *V* velocity components. In a three-sensor orthogonal array, they measure *U*, *V*, and *W*. Döbbeling et al. [17] and other investigators have developed four-wire arrays for measurement of *U*, *V*, and *W*. Olin and Kiland [18] describe an orthogonal array of three cylindrical split hot-film sensors. Each of the three sensors in this array has two individually operated hot films separated by two axial splits 180° apart along its entire length. The two split films take advantage of the nonuniform heat-transfer distribution around a cylinder in cross flow.

In multisensor arrays, the velocity vector is not necessarily normal to a cylindrical sensor. If the discussion is limited to isothermal flows, the first law expressed by Equation 59.20 becomes

$$E^2 = A + BV_e^n \tag{59.33}$$

where V_e is the effective velocity sensed by a single cylindrical sensor in the array and *A*, *B*, and *n* are constants. Jörgenson [19] describes V_e as follows:

$$V_e^2 = U_N^2 + a^2U_T^2 + b^2U_B^2 \tag{59.34}$$

where

U_N is the velocity component normal to the sensor
U_T is the tangential component
U_B is the component perpendicular to both U_N and U_T (i.e., binormal)

The constants *a* and *b* in Equation 59.34 are referred to as the sensor's yaw and pitch coefficients, respectively, and are determined via flow calibration. Typical values for *a* and *b* for a plated hot-wire sensor are 0.2 and 1.05, respectively. Inserting Equation 59.34 into Equation 59.33, we get the following expression for the output signal of a single sensor in the array:

$$E^2 = A + B\left(U_N^2 + a^2U_T + b^2U_B^2\right)^{n/2} \tag{59.35}$$

Expressions like this, or similar ones such as given by Lekakis et al. [20], are written for all sensors in the array. These expressions and the geometry of the sensor configuration are then used to solve for the components of velocity U, V, and W in the x, y, and z spatially fixed reference frame.

59.3.3 Thermal Anemometer Instruments

Table 59.1 lists examples of typical thermal anemometer instruments offered by manufacturers. Table 59.2 lists the major manufacturers. A typical portable thermal anemometer includes sensor, probe, Wheatstone bridge drive circuits, linearization circuits, memory to store calibration information, battery, and digital display. Sensors and probes have been described in the previous sections. The electronics of a portable meter is enclosed in a small plastic case with a digital display. They are powered by dry cell batteries. In addition to the digital display, they have data storage and recall capabilities.

Research thermal anemometer systems usually are coupled with a PC, as shown in Figure 59.5. The PC provides system setup and control, as well as data display and analysis. Modern systems feature low-noise circuits, together with smart bridge optimization technology that eliminates tuning and automatically provides flat frequency response up to 300,000 Hz. Lower-cost units provide flat response up to 10,000 Hz. A built-in thermocouple circuit simplifies temperature measurement. The PC's windows-based software provides near real-time displays of velocity, probability distribution, and turbulence intensity. Postprocessing gives additional statistics, including mean velocity; turbulence intensity; standard deviation; skewness; flatness; normal stress for one-, two-, and three-component probes; as well as shear stress, correlation coefficients, and flow-direction angle for 2-D and 3-D probes. In addition, power spectrum, autocorrelations, and cross correlations can be displayed. The software automatically handles flow-calibration setup and calculates calibration velocity. Systems are available in 1-, 2-, 8-, and 16-channel versions. A relatively new approach, known as constant-voltage anemometry (CVA), has been aimed at making measurements in supersonic flows. Berson et al. [21] examine the behavior of this technique in high levels of turbulence.

Research thermal anemometer systems were first introduced in the early 1960s. The commercial anemometers were introduced in late 1970s. Nowadays, portable, handheld thermal anemometers are popular with professionals responsible for measuring air velocities in airflow applications. At first, thermal anemometers were not considered sufficiently durable for the rigors of industrial use. With the advent of

TABLE 59.1 Typical Thermal Anemometers

Product Description	Approximate 2010 U.S. Price
Portable battery-operated instruments	
Basic portable air velocity meter	$300–$900
Data-logging multiparameter portable air velocity meter	$700–1,500
Installed duct monitoring systems	
Single-point air velocity probe	$300–$800
Multipoint air-duct flow monitoring system	$2,000–$10,000
Research systems	
Single-channel hot-wire or hot-film anemometer system	$25,000
Three-component hot-wire anemometer system	$35,000

Note: Prices listed are the price range quoted by the manufacturers listed in Table 59.2. All portable air velocity meters include sensor, battery, and display. The multiparameter instruments typically measure air velocity, temperature, humidity, and differential pressure and have data-logging capabilities. The single-point air velocity instruments typically have analog or digital outputs, and the required voltage is supplied by an external power supply. The multipoint systems are typically used with a control system. Research anemometer systems have standard hot-wire probes and electronics and include ambient air calibrations.

TABLE 59.2 Manufacturers of Thermal Anemometer Instruments

Portable battery-operated instruments
TSI Incorporated, 500 Cardigan Road, Shoreview, MN 55164, Tel.: 1 800 874 2811, info@tsi.com
Dwyer Instruments, Inc., P. O. BOX 373, Michigan City, IN 46361, Tel.: 219 879 8000, info@dwyer-inst.com
Extech Instruments Corp., 285 Bear Hill Road, Waltham, MA 02451, Tel.: 781 890 7440, sales@extech.com
Testo, Inc., 40 White Lake Road, Sparta, NJ 07871, Tel.: 1 800 227 0729, info@testo.com
Kanomax USA, Inc., P. O. Box 372, 219 US Hwy. 206, Andover, NJ 07821, Tel.: 1 800 247 8887, info@kanomax-usa.com
TES Electrical Electronic Corp., 7F, No 31, Lane 513, Rui Guang Road, Neihu Dist. Taiwan, Republic of China, Tel.: 866 2 27999 3660, www.tes.com.tw/indexe.htm
Single-point duct monitoring systems
TSI Incorporated, 500 Cardigan Road, Shoreview, MN 55164, Tel.: 800 874 2811, info@tsi.com
Sierra Instruments, Inc., 5 Harris Court, Building L, Monterey, CA 93940, Tel.: 800 866 0200, info@sierrainstruments.com
Dwyer Instruments, Inc., P. O. BOX 373, Michigan City, IN 46361, Tel.: 219 879 8000, info@dwyer-inst.com
E+E Elektronik, Langwiesen 7, A-4209 Engerwitzdorf, Austria, Tel.: 43 7235 605-0, info@epluse.com
Multipoint duct monitoring systems
Ebtron, Inc., 1663 Highway 701 South, Loris, SC 29569, Tel.: 843.756.1828, www.ebtron.com
Air Monitor Corporation, 1050 Hopper Avenue, Santa Rosa, CA 95406, Tel.: 919 491 2127, amcsales@airmonitor.com
Research systems
TSI Incorporated, 500 Cardigan Road, Shoreview, MN 55164, Tel.: 800 874 2811, info@tsi.com
Dantec Dynamics A/S, Tonsbakken 16–18, DK-2740 Skovlunde, Denmark, Tel.: 45 44 57 80 00, www.dantecdynamics.com

stainless-steel sheathed sensors and microprocessor-based electronics, industrial thermal anemometers now enjoy the credibility formerly attributed to only traditional flowmeter approaches (see Chapter 63). Initial research systems required a high level of user knowledge and considerable involvement in operation. In contrast, current research systems have nearly flat frequency response, high accuracy, and easy-to-use controls providing the flexibility researchers require. Research systems based on PCs have graphical user interfaces that enhance both performance and simplicity of operation.

References

1. H. H. Bruun, *Hot-Wire Anemometry: Principles and Signal Analysis*, Oxford, U.K.: Oxford University Press, 1995.
2. L. M. Fingerson and P. Freymuth, Thermal anemometers, in R. J. Goldstein (ed.), *Fluid Mechanics Measurements*, Washington, DC: Hemisphere, 1983.
3. P. Freymuth, History of thermal anemometry, in N. P. Cheremisinoff and R. Gupta (eds.), *Handbook of Fluids in Motion*, Ann Arbor, MI: Ann Arbor Science Publishers, 1983.
4. J. C. Gibbings, J. Madadnia, and A. H. Yousif, The wall correction of the hot-wire anemometer, *Flow Meas. Instrum.*, 6(2), 127–136, 1995.
5. J. C. Gibbings, J. Madadnia, S. Riley, and A. H. Yousif, The proximity hot-wire probe for measuring surface shear in air flows, *Flow Meas. Instrum.*, 6(3), 201–206, 1995.
6. V. Mikulla, The measurement of intensities and stresses of turbulence in incompressible and compressible air flow, PhD Thesis, University of Liverpool, Liverpool, U.K., 1972.
7. L. V. King, On the convection of heat from small cylinders in a stream of fluid: Determination of the convection constants of small platinum wires with application to hot-wire anemometry, *Phil. Trans. Roy. Soc.*, A214, 373–432, 1914.
8. H. Kramers, Heat transfer from spheres to flowing media, *Physica*, 12, 61–80, 1946.
9. S. W. Churchill and M. Bernstein, A correlating equation for forced convection from gases and liquids to a circular cylinder in crossflow, *J. Heat Transfer*, 99, 300–306, 1997.

10. S. Takagi, A hot-wire anemometer compensated for ambient temperature variations, *J. Phys. E.: Sci. Instrum*., 19, 739–743, 1986.
11. Calibration of the CERTIFIER air velocity calibrator using a laser doppler velocimeter (LDV), TSI Incorporated, http://www.tsi.com/uploadedFiles/Product_Information/Literature/Application_Notes/TI-130.pdf (accessed on March 15, 2013).
12. J. W. Elsner, An analysis of hot-wire sensitivity in non-isothermal flow, *Proceedings of the Dynamics Flow Conference*, Marseille, France, 1972.
13. F. Blackwelder, Hot-wire and hot-film anemometers, in R. J. Emrich (ed.), *Methods of Experimental Physics: Fluid Dynamics*, New York: Academic Press, 18A, pp. 259–314, 1981.
14. J. A. Borgos, A review of electrical testing of hot-wire and hot-film anemometers, *TSI Quart*., VI(3), 3–9, 1980.
15. E. W. Nelson and J. A. Borgos, Dynamic response of conical and wedge type hot films: Comparison of experimental and theoretical results, *TSI Quart*., IX(1), 3–10, 1983.
16. U. R. Müller, Comparison of turbulence measurements with single, X and triple hot-wire probes, *Exp. Fluids*, 13, 208–216, 1992.
17. K. Döbbeling, B. Lenze, and W. Leuckel, Four-sensor hot-wire probe measurements of the isothermal flow in a model combustion chamber with different levels of swirl, *Exp. Thermal Fluid Sci*., 5, 381–389, 1992.
18. J. G. Olin and R. B. Kiland, Split-film anemometer sensors for three-dimensional velocity-vector measurement, *Proceedings of the Symposium on Aircraft Wake Turbulence*, Seattle, WA, 1970, pp. 57–79.
19. F. E. Jörgenson, Directional sensitivity of wire and fibre-film probes, *DISA Info*., (11), 31–37, 1971.
20. I. C. Lekakis, R. J. Adrian, and B. G. Jones, Measurement of velocity vectors with orthogonal and non-orthogonal triple-sensor probes, *Exp. Fluids*, 7, 228–240, 1989.
21. A. Berson, P. Blanc-Benon, and G. Comte-Bellot, A strategy to eliminate all nonlinear effects in constant-voltage hot-wire anemometry, *Rev. Sci. Instrum*., 80, 045102, 2009, DOI: 10.1063/1.3103948

60

Coriolis Effect Mass Flowmeters

Jesse Yoder
Flow Research, Inc.
Automation Research Corporation

Coriolis flowmeters were developed in the 1970s to fill the need for a flowmeter that measures mass directly, as opposed to those that only measure velocity or volume. Because they are independent of changing fluid parameters, Coriolis meters have found wide application. Many velocity and volumetric meters are affected by changes in fluid pressure, temperature, viscosity, and density. Coriolis meters, on the other hand, are virtually unaffected by these types of changes. By measuring mass directly as it passes through the meter, Coriolis meters make a highly accurate measurement that is virtually independent of changing process conditions. As a result, Coriolis meters can be used on a variety of process fluids without recalibration and without compensating for parameters specific to a particular type of fluid. Coriolis flowmeters are named after Gaspard G. Coriolis (1792–1843), a French civil engineer and physicist for whom the Coriolis force is named.

Coriolis meters have become widely used in industrial environments because they have the highest accuracy of all types of flowmeters. They measure mass directly, rather than inferentially. Coriolis meters do not have moving parts like turbine and positive displacement meters, which have parts that are subject to wear. Maintenance requirements for Coriolis meters are low, and they do not require frequent calibration. Wetted parts can be made from a variety of materials to make these meters adaptable to many types of fluids. Coriolis meters can handle corrosive fluids and fluids that contain solids or particulate matter. While these meters were used mainly for liquids when they were first introduced, they have since become adaptable for gas applications.

60.1 Theory of Operation

Coriolis meters typically consist of one or two vibrating tubes with an inlet and an outlet. While some are U shaped, most Coriolis meters have some type of complex geometric shape that is proprietary to the manufacturer. Fluid enters the meter in the inlet, and mass flow is determined based on the action of the fluid on the vibrating tubes. Figure 60.1 shows flow tube response to Coriolis acceleration.

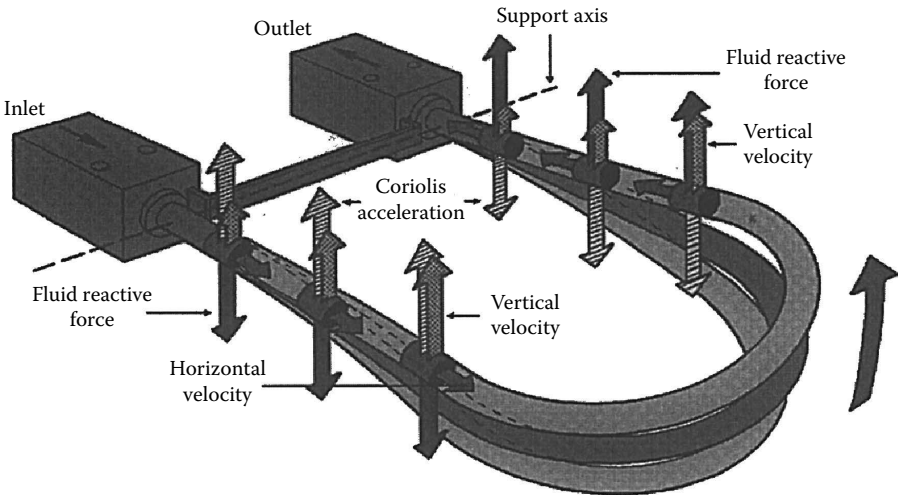

FIGURE 60.1 Flow tube response to Coriolis acceleration.

Common to Coriolis meters is a central point that serves as the axis of rotation. This point is also the peak amplitude of vibration. What is distinctive about this point is that fluid behaves differently, depending on which side of the axis of rotation or point of peak amplitude it is on. As fluid flows toward this central point, the fluid takes on acceleration due to the vibration of the tube. As the fluid flows away from the amplitude of peak vibration, it decelerates as it moves toward the tube outlet. On the inlet side of the tube, the accelerating force of the flowing fluid causes the tube to lag behind its no-flow position. On the outlet side of the tube, the decelerating force of the flowing fluid causes the tube to lead ahead of its no-flow position. As a result of these forces, the tube takes on a twisting motion as it passes through each vibrational cycle; the amount of twist is directly proportional to the mass flow through the tube. Figure 60.2 shows the Coriolis flow tube in a no-flow situation, and Figure 60.3 shows Coriolis tube response to flow.

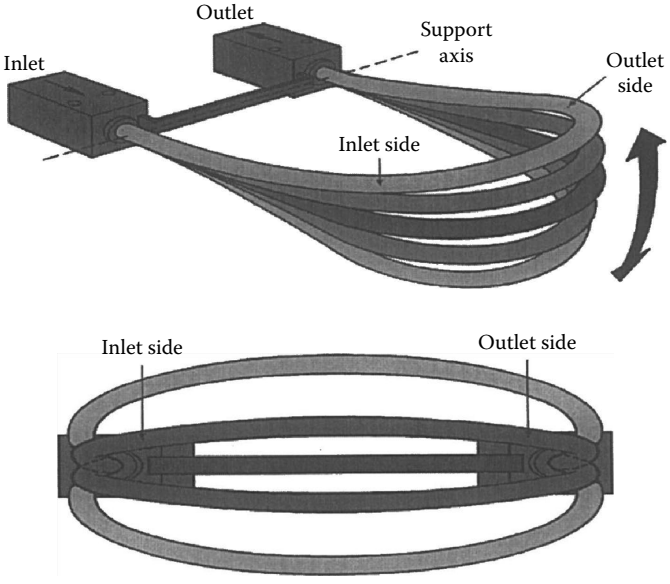

FIGURE 60.2 Two views of an oscillating flow tube with no flow.

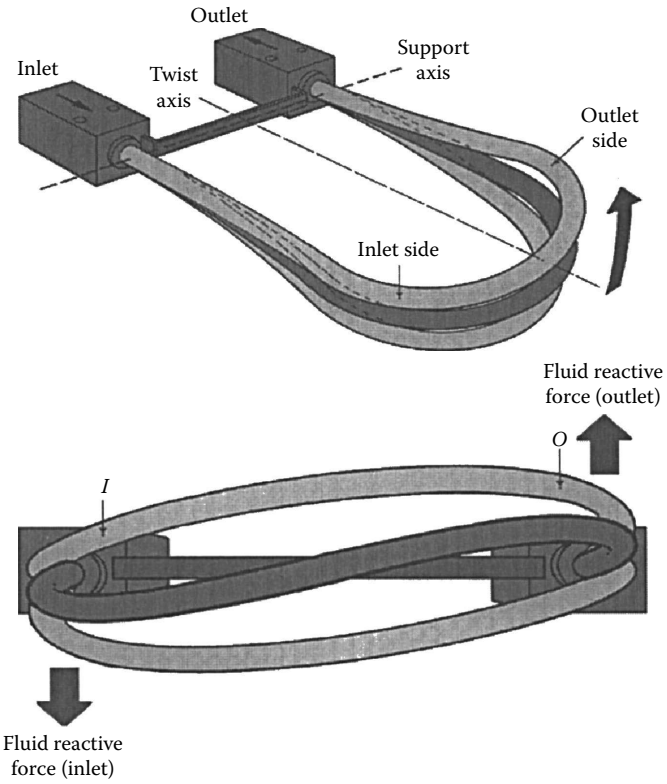

FIGURE 60.3 Two views of an oscillating flow tube in response to flow.

The Coriolis tube (or tubes, for multitube devices) is vibrated through the use of electromagnetic devices. The tube has a drive assembly and has a predictable vibratory profile in the no-flow position. As flow occurs and the tube twists in response to the flow, it departs from this predictable profile. The degree of tube twisting is sensed by the Coriolis meter's detector system. At any point on the tube, tube motion represents a sine wave. As mass flow occurs, there is a phase shift between the inlet side and the outlet side. This is shown in Figure 60.4.

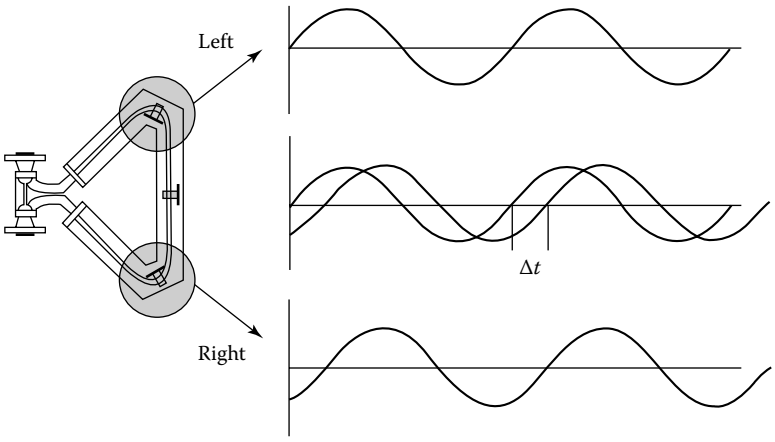

FIGURE 60.4 Phase shift between inlet side and outlet side.

The Coriolis force induced by flow is described by an equation that is equivalent to Newton's second law for rotational motion. This equation is as follows:

$$F = 2m\omega\overline{v} \tag{60.1}$$

where

F is the force
m is the mass to be applied to a known point at a distance L from the axis 0–0
ω is a vector representing angular motion
$\overline{v}$ is a vector that represents average velocity

The Coriolis force is sometime illustrated by likening it to a ball propelled through the air, a long distance in a straight line from the North Pole to a target on the equator. By the time the ball arrives at the equator, it will not land at the apparent target, since the target will have moved due to the rotation of the earth. This makes the path of the ball appear curved from the perspective of the person standing on the North Pole.

A similar example is used with a merry-go-round. If someone throws a ball directly at a horse on the merry-go-round, the ball will miss its target since the horse will have moved by the time the ball arrives at the place where the horse was located at the time the ball was thrown.

If both these examples are intended to illustrate the Coriolis "force," then it should be more appropriately called the Coriolis "effect." There is no force acting to push the ball in a curved direction in either case. Instead, it appears to be curved due to the rotating frame of reference underneath the ball. This Coriolis effect refers to the apparent motion of an object that is passing over a rotating frame of reference when it is viewed from the perspective of the thrown object's frame of reference.

Since Coriolis flowmeters do not have a rotating frame of reference, it is difficult to see in what way they illustrate either the Coriolis force or the Coriolis effect. Instead, they rely on the inertia created by fluid flowing through an oscillating tube, which causes the tubes to twist in proportion to flow rate. While it is unlikely that they will ever be renamed, their name does cause some confusion about their true operating principle.

60.2 Construction

The internal part of the Coriolis tube is the only part of the meter that is wetted. A typical material of construction is stainless steel. Other corrosion-resistant metals such as Hastelloy are used for tube construction. Some meters are lined with Teflon.

Some designs have thin-wall tubes as well as standard tubes. A thin-wall design makes the meter more useful for gas and low-velocity liquid applications, where the amount of twist by the tube is reduced. It is important to be aware of the extent to which the fluid degrades or attacks the tube wall or lining. If the fluid eats away at the wall, this can reduce the accuracy of the meter.

60.3 Advantages

The most significant advantage of Coriolis meters is high accuracy under wide flow ranges and conditions. Because Coriolis meters measure mass flow directly, they have fewer sources of errors. Coriolis meters have a high turndown, which makes them applicable over a wide flow range. This gives them a strong advantage over orifice plate meters, which typically have low turndown. Coriolis meters are also insensitive to swirl effects, making flow conditioning unnecessary. Flow conditioners are placed upstream from some flowmeters to reduce swirl and turbulence for flowmeters whose accuracy or reliability is affected by these factors.

Coriolis meters have a low cost of ownership. Unlike turbine and positive displacement meters, Coriolis meters have no moving parts to wear down over time. The only motion is due to the vibration

of the tube and the motion of the fluid flowing inside the tube. Because Coriolis flowmeters are designed not to be affected by fluid parameters such as viscosity, pressure, temperature, and density, they do not have to be recalibrated for different fluids. Installation is simpler than installation for many other flowmeters, especially orifice plate meters, because Coriolis meters have fewer components.

Coriolis meters can measure more than one process variable. Besides mass flow, they can also measure density, temperature, and viscosity. This makes them especially valuable in process applications where information about these variables reduces costs. It also makes it unnecessary to have a separate instrument to measure these additional variables.

60.4 Disadvantages

The chief disadvantage of Coriolis meters is their initial cost. While some small Coriolis meters have prices as low as $4000, the base price for most Coriolis meters is $6000 and up. The cost of Coriolis meters rises significantly as line sizes increase. The physical size of Coriolis meters increases substantially with the increase in line size. In the past, 150 mm (6 in.) was the upper-line size limit on Coriolis meters today. The large size of some Coriolis meters makes them difficult to handle and can also make installation difficult in some cases.

In the past 5 years, at least four suppliers have begun manufacturing Coriolis flowmeters in sizes from 8 to 16 in. The primary motivation for this change is that Coriolis suppliers want to address the expanding energy markets, especially oil and gas. Many of these large-size meters are designed for custody transfer. While most are targeting liquid applications, mainly hydrocarbon based, some are also being designed for gas applications.

These new meters are 5 ft and more in height, and many cost as much as $75,000. They are also very heavy and bulky. Even so, some end users are ordering them because of the high accuracy of Coriolis meters. While they are still not large enough to handle most pipeline applications, they are beginning to be used in oil production environments.

The lack of an established body of knowledge about Coriolis meters is a substantial disadvantage. Because Coriolis meters were recently invented, not nearly as much data are available about them as are for differential pressure–based flowmeters. This made it more difficult in the past for Coriolis meters to gain approvals from industry associations. However, the American Gas Association and the American Petroleum Institute have now issued standards for the use of Coriolis flowmeters in custody transfer applications.

60.5 Applications

Coriolis meters have no Reynolds number constraints and can be applied to almost any liquid or gas flowing at a sufficient mass flow to affect vibration of the flowmeter. Typical liquid applications include foods, slurries, harsh chemicals, and blending systems. The versatility of Coriolis meters in handling multiple fluids makes them very useful for plants where the flow of multiple fluid types must be measured.

There are an increasing number of gas applications for Coriolis meters. While gas applications are still very much in the minority, the use of this meter to measure gas is likely to increase as more is learned about its use for this purpose.

60.6 A Look Ahead

There are some important areas of research for Coriolis meters. While most Coriolis meters have been bent, several manufacturers have recently introduced straight-tube designs. Manufacturers will continue to fine tune the single-tube design versus double-tube design and to work on tube geometry. As noted earlier, the use of Coriolis meters for gas and also for steam applications is another area for future development.

Bibliography

Coriolis Flowmeter, Coriolis Flowmeter resource Center, http://www.coriolisflowmeter.net/seafloor-spreading/, accessed on August 8, 2012.

Coriolis Mass Flowmeters, UFM, http://www.flowmeters.com/ufm/index.cfm?task=coriolis, accessed August 8, 2012.

Doebelin, E. O., *Measurement Systems: Application and Design*, 4th edn., New York: McGraw-Hill, 1990, pp. 603–605.

Figliola, R. S. and Beasley, D. E., *Theory and Design for Mechanical Measurements*, 2nd edn., New York: John Wiley & Sons, 1995, pp. 475–478.

Plache, K. O., Coriolis/gyroscopic flowmeter, *Mechanical Engineering*, March 1979, 36–41.

Smith, L. and Ruesch, J. R., Mass flowmeters, in D. W. Spitzer (ed.), *Flow Measurement*, Research Triangle Park, NC: Instrument Society of America, 1996, pp. 221–247.

Yoder, J., The Coriolis effect: Unquestionable accuracy, but are Coriolis meters aptly named? *Flow Control*, November 2011, 14–18

Partial List of Vendors and Suppliers

ABB, Inc., 125 E. County Line Rd., Warminster, PA 18974, Phone: 215-674-6580, 800-829-6001 (toll free), Fax: 215-674-7180, www.abb.us/instrumentation

Endress+Hauser, 2350 Endress Place Greenwood, IN 46143, Phone: 888-363-7377, 888-ENDRESS (toll free), Fax: 317-535-8498, www.us.endress.com

FMC Technologies, Inc., Measurement Solutions, 1602 Wagner Ave., P.O. Box 10428, Erie, PA 16514, Phone: 814-898-5000, 800-477-6375 (toll free), Fax: 814-899-8927, www.fmctechnologies.com/en/MeasurementSo…

Keco Engineered Controls, 1200 River Ave., Bldg. 3A, Lakewood, NJ 08701-5657, Phone: 732-901-5900, Fax: 732-901-5904, www.kecocontrols.com

KROHNE, Inc., 7 Dearborn Rd., Peabody, MA 01960, Phone: 978-535-6060, 800-356-9464 (toll free), Fax: 978-535-1720, www.krohne.com/index.php?id=12076

Siemens Corp., 527 Madison Ave., 8th Fl., New York 10022-4611, Phone: 800-SIEMENS (toll free), Fax: 212-767-0580, www.usa.siemens.com/entry/en/

61

Drag Force Flowmeters

Rekha Philip-Chandy
Liverpool John Moores University

Roger Morgan
Liverpool John Moores University

Patricia J. Scully
Liverpool John Moores University

In a *target flowmeter*, a solid object known as a *drag element* is exposed to the flow of fluid that is to be measured. The force exerted by the fluid on the drag element is measured and converted to a value for speed of flow.

The flow-sensing element has no rotating parts, and this makes the instrument suitable for conditions where abrasion, contamination, or corrosion makes more conventional instruments unsuitable. An important application of such flowmeters involves environmental monitoring in areas such as meteorology, hydrology, and maritime studies to measure speeds of air or water flow and turbulence close to the surface. In these applications, the fluid flows are sporadic and multidirectional.

A further advantage of the instrument is that it can be made to generate a measurement of flow *direction* in two dimensions, or even in three dimensions, as well as of flow speed. To implement this feature, the drag element must be symmetrical in the appropriate number of dimensions, and it is necessary to measure the force on it vectorially, again in the appropriate number of dimensions. Provided that the deflecting forces are independent in the sensing directions, the resulting outputs can be added vectorially to generate independent values for flow speed and direction. Target flowmeters using strain gage technology have been used by industry, utilities, aerospace, and research laboratories. They have been used to successfully measure the flow of unidirectional and bidirectional liquids (including cryogenic), gases, and steam (both saturated and superheated) for almost half a century.

Despite these advantages, the target flowmeter appears to have been neglected in favor of more complex and sophisticated devices. The authors have sought to remedy this neglect by developing a sensor suitable for measuring multidirectional flows in two dimensions, instead of measuring only bidirectional flows in a single dimension.

61.1 Design of the Flow Sensor

The sensor described in this section is ideally suited for environmental flow measurement. The operation is based on strain measurement of deformation of an elastic rubber cantilever, to which a force is applied by a spherically symmetrical drag element (Figure 61.1). This sensor has many advantages,

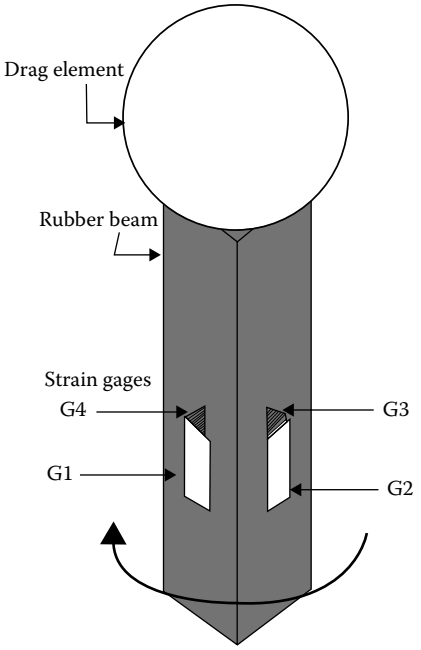

FIGURE 61.1 Schematic of the electric resistance strain gage drag force flow sensor.

including compactness and a simple construction requiring no infrastructure other than a rigid support, and it can cope with fluids containing solid matter such as sludge and slurries, provided that they do not tangle with the drag element or the rubber beam.

According to Clarke [1], the ideal drag element is a flat disk, because this configuration gives a drag coefficient independent of flow rate. Using a spherical drag element, which departs from the ideal of a flat disk [1], the drag coefficient is likely to vary with flow speed, and therefore the gage must be calibrated and optimized for the conditions of intended use. In this discussion, a gage is developed for air flows in the range normally encountered in the natural environment.

The strain measurement can be performed with conventional strain gages, but this limits the applications of the device to conditions where corrosion of the metal-resistive track of the strain gage can be avoided. Therefore, an optical fiber strain gage has been developed as an alternative.

61.2 Principle of Fluid Flow Measurement

The drag force F_D exerted by a fluid on a solid object exposed to it is given by the *drag equation*, which from incompressible fluid dynamics is

$$F_D = \frac{C_D \rho A V^2}{2} \tag{61.1}$$

where

ρ is the fluid density
V is the fluid's velocity at the point of measurement
A is the projected area of the body normal to the flow
C_D is the overall drag coefficient

C_D is a dimensionless factor, whose magnitude depends primarily on the physical shape of the object and its orientation relative to the fluid stream.

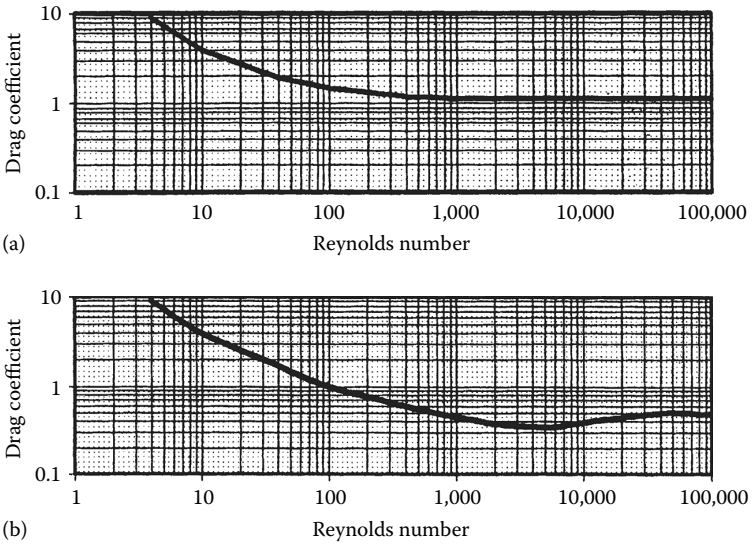

FIGURE 61.2 Graph shows drag coefficient C_D plotted against Reynolds number Re for (a) a flat disk and (b) a sphere.

The drag coefficient C_D for a sphere is related to the Reynolds number (Re), another dimensionless factor, given by

$$\mathrm{Re} = \frac{\rho V A}{\eta} \tag{61.2}$$

where η is the viscosity of the fluid.

A graph of C_D against Reynolds number (derived from Clarke [1]) is shown in Figure 61.2a for a flat disk and Figure 61.2b for a sphere, from which it is evident that the value of C_D, although not constant, is not subject to wide variation over the range of the graph.

Now consider the effect of the force F_D on an elastic beam to which the drag element is attached (as in Figure 61.1). If the mass of the beam can be ignored, the deflection of the beam will only be due to force exerted on the drag element by the fluid. From the theory of elasticity for a cantilever beam of length L with point load at its end [2], the shear force P will be constant along the beam. The bending moment, M, at a point x along the beam will be $P(L - x)$ so that it varies linearly from PL at $x = 0$ to 0 at $x = L$. The distance y is measured from the neutral plane, which for a rectangular section is the mid-plane.

The inverse of the radius of curvature is given by

$$\frac{1}{\rho} = \frac{M}{EI} \tag{61.3}$$

where

E is the modulus of elasticity or Young's modulus

I is the moment of inertia of the cross section where it is assumed that the force is applied perpendicular to the broad face of width b:

$$I = \frac{ba^3}{12} \tag{61.4}$$

Through the thickness a of the beam, the strain is ε_x:

$$\varepsilon_x = \frac{\sigma_x}{E} = \frac{Y}{\rho} \tag{61.5}$$

Substituting Equation 61.3 in Equation 61.5 gives

$$\varepsilon_x = \frac{YM}{EI} \tag{61.6}$$

The strain at the surfaces is

$$\varepsilon_x = \frac{a}{2\rho} = \frac{YM}{2EI} \tag{61.7}$$

Substituting Equation 61.4 and the bending moment into Equation 61.6 gives

$$\varepsilon_x = \frac{6P(L-x)}{Ea^2b} \tag{61.8}$$

or the shear force P is

$$P = \frac{\varepsilon Ea^2b}{6(L-x)} \tag{61.9}$$

Consequently,

$$\frac{C_D \rho A V^2}{2} = \frac{\varepsilon Ea^2b}{6(L-x)} \tag{61.10}$$

Therefore, the strain is

$$\varepsilon = \frac{3C_D \rho A V^2 (L-x)}{Ea^2b} \tag{61.11}$$

From Equation 61.11, the strain is a square law function of fluid speed.

For most fluid flows in the natural environment, a two-dimensional measurement is necessary as the flow in the natural environment is almost always two-dimensional. For a measurement of flow speed and direction, it is necessary to relate wind speed to strain measured in two orthogonal directions, on the assumption (which has been justified by experiment) that the velocity vector has a zero component along (parallel to) the rubber beam support (i.e., $U_z = 0$). The wind speed U has orthogonal components U_x and U_y that are proportional to the strain measured in the x (strain$_x$) and y directions (strain$_y$), respectively. Since U_x is proportional to $\sqrt{\text{strain}_x}$ and U_y is proportional to $\sqrt{\text{strain}_y}$, then the velocity magnitude $|U|$ can be written as

$$|U| = \sqrt{U_x^2 + U_y^2} \tag{61.12}$$

thus,

$$|U| \propto \sqrt{\text{strain}_x + \text{strain}_y} \tag{61.13}$$

Therefore, the magnitude of the velocity, $|U|$, is proportional to the square root of the sum of the orthogonal strain components, strain_x and strain_y. The velocity direction, θ, is calculated using the relation

$$\theta = \tan^{-1}\left[\frac{\sqrt{\text{strain}_y}}{\sqrt{\text{strain}_x}}\right] \tag{61.14}$$

61.3 Implementation Using Resistive Strain Gages

A sensor was constructed for measuring one-dimensional flows by bonding two strain gages onto the opposite sides of a square-sectioned elastic beam, 165 mm long and 13.5 mm square, made from polybutadiene polymer (unfilled vulcanized rubber) supplied by the Malaysian Rubber Products Research Association. The modulus of the beam, at approximately 1.2×10^6 N m^{-2}, was relatively low in order to achieve good sensitivity. The drag element was a table tennis ball of diameter 20 mm, glued to the end of the rubber beam. The strain gages were cupro-nickel alloy on a polyimide film and were bonded to the rubber beam with epoxy resin. The two gage elements were connected in a half-bridge configuration, and the output was taken to a digital strain gage indicator reading directly in microstrain units.

The sensor was mounted in a calibrated wind tunnel, in such a way that one gage underwent compression and the other gage underwent extension. The wind speed was set at different values, and the corresponding strain readings were noted. Results were plotted as wind speed against square root of strain (Figure 61.3). The graph obtained was linear with a correlation coefficient of 0.98. The linearity shows that the strain is a square-law function of speed, which confirms the earlier theory.

In this first prototype of the sensor, the range was limited by beam oscillations at speeds greater than 23 m s^{-1}, causing spurious signals. In principle, however, much greater speeds up to 50 m s^{-1} can be monitored by this sensor, if the construction is suitable.

A second sensor was constructed for measuring two-dimensional flows, in which a square-sectioned rubber beam similar to the previous one was set up with four strain gages attached to the four longitudinal surfaces of the beam. Each opposite pair of strain gage elements was connected in a half-bridge

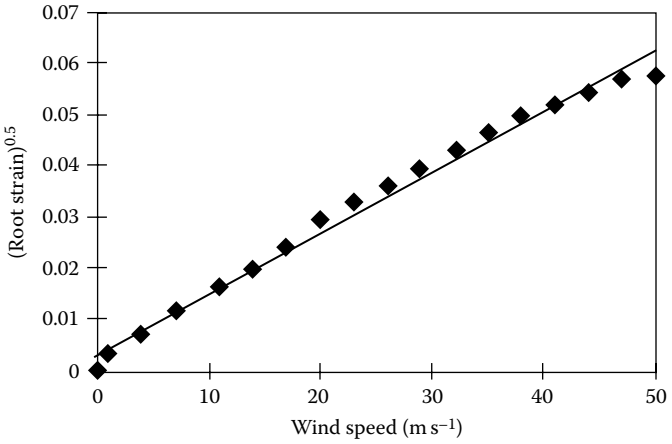

FIGURE 61.3 Root strain versus wind speed for one-dimensional air flow measurement.

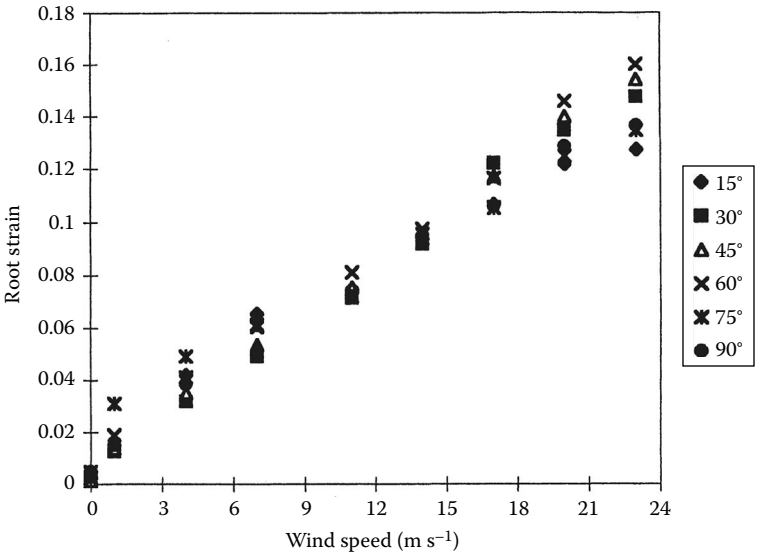

FIGURE 61.4 Root strain plotted against wind speed with the flowmeter oriented at various angles to wind flow.

configuration as before. The two outputs were taken to instrumentation amplifiers and then to a data acquisition board interfaced to the LabVIEW instrumentation software package (National Instruments Corporation). After appropriate signal processing by the software, the values of strain$_x$ and strain$_y$ from both the channels are added and then the square root of the absolute value of this sum is found.

The device was clamped on a turntable, and this was rotated about its longitudinal axis from 0° to 90° at 15° intervals. At each angle, the x and y strain gage outputs were recorded as a function of velocity, over a range from 0 to 23 m s^{-1}. The graph of speed versus (strain$_x$ + strain$_y$)$^{1/2}$ for different angles is shown in Figure 61.4. The data presented in Figure 61.4 can be used to obtain a speed calibration curve for the sensor, which will be valid for multidirectional air flow.

The direction of wind flow was calculated according to Equation 61.14 for the different wind speeds. Figure 61.5 shows the plots of the wind flow direction at different wind speeds for various sensor positions. Several authors have published the inability of calculating the wind direction

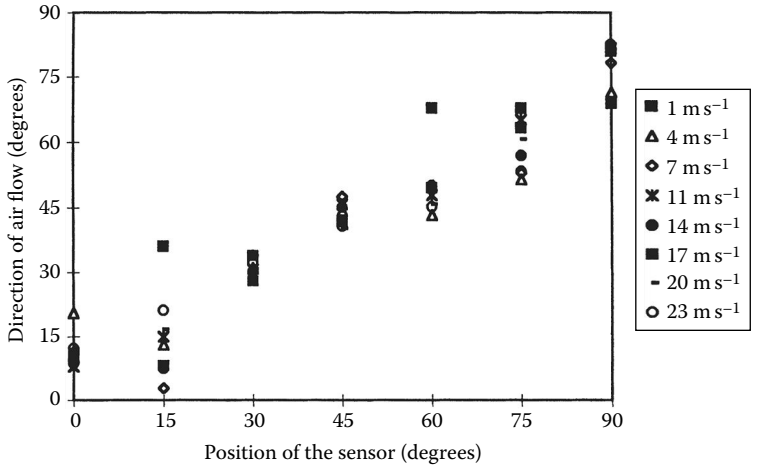

FIGURE 61.5 Calculated direction of wind velocity at different wind speeds.

accurately at low wind speeds. The situation is similar in this case, and the readings get more accurate as the wind speed increases, especially beyond 11 m s^{-1}.

For the measurement of gusts, the time response of the sensor becomes a critical parameter. Experiments were performed to measure the response time by dropping known weights on the free end of the sensor and using a specially written program in Labview to acquire and record the response. The sensor indicated a 95% response time of 50 ms and a time constant of 30 ms.

61.4 Optical Fiber Strain Gage Drag Force Flowmeter

Optical fibers have been applied to measurement of fluid flow, and strain measurement, using interferometric techniques and bending losses [3–5]. The instrument described in the previous sections can be adapted to use optical strain measurement instead of resistive strain gages. In this way, the advantages of the instrument can be preserved; in addition, the flowmeter has the usual benefits of optical fiber sensors such as immunity to electromagnetic interference and intrinsic safety in hazardous environments.

The principle of an optical fiber strain gage is based on the effect of one or more grooves inserted radially into a 1 mm diameter PMMA fiber, which cause a loss in light transmission. As the optical fiber is bent, as in a cantilever, the angle of the grooves varies. These changes of angle cause light to be attenuated at each groove. The intensity variation can be related to the change of the angle of the groove caused by the bending of the cantilever.

To develop an analogy between the optical strain measurement and the resistive strain measurement, the optical strain was calculated using the formula

$$\text{Strain}_{\text{opt}} = \frac{\text{Change in power output}}{\text{Original power output}} = \frac{\Delta P}{P} \tag{61.15}$$

Hence,

$$\text{Strain}_x = \frac{\Delta P_x}{P_x} \quad \text{and} \quad \text{Strain}_y = \frac{\Delta P_y}{P_y} \tag{61.16}$$

Therefore, the magnitude of the velocity, $|U|$ is given by

$$|U| = \sqrt{U_x^2 + U_y^2} = \sqrt{\text{strain}_x + \text{strain}_y}$$

Substituting Equation 61.16 in $|U|$, the optical root strain magnitude is

$$|U| = \sqrt{\left(\frac{\Delta P_x}{P_x} + \frac{\Delta P_y}{P_y}\right)} \tag{61.17}$$

and the direction of wind velocity, θ

$$\theta = \tan^{-1}\left[\frac{U_y}{U_x}\right] = \tan^{-1}\sqrt{\frac{\text{strain}_y}{\text{strain}_x}} \tag{61.18}$$

Substituting Equation 61.16 in θ, the optical strain direction is

$$\theta = \tan^{-1} \frac{\sqrt{\left(\Delta P_y / P_y\right)}}{\sqrt{\left(\Delta P_x / P_x\right)}} \tag{61.19}$$

Two types of the optical fiber flow sensor are described here. In the first type, the rubber beam is used as the deflected device with optical fiber strain gages attached to the deflected beam. The second version of this flow sensor uses an unsupported sensitized 1 mm diameter plastic optical fiber that undergoes deflection in the airflow.

61.4.1 Fiber Optic Flow Sensor with Rubber Beam

The sensor has been built using a rectangular cross-sectioned rubber beam and a spherical drag element with a 1 mm plastic optical fiber glued to the beam with epoxy. The fiber is looped inside the drag element to enhance the sensitivity of the device. Grooves have been made in the fiber surface that extends into the core of the fiber to increase the losses as a function of the bending of the rubber beam (Figure 61.6).

The grooves are normal to the rubber beam on its outside face, and their depths affect only the cladding of the fiber. As the cantilever bends due to the force exerted by the air flow, the angle of the grooves varies. The groove angle increases when the air flow is facing the sensor, and vice versa. These changes of groove angle cause an intensity modulation of the light transmitted through the fiber because light is lost at each groove. Changes in intensity can be related to changes in the angle caused by the force inducing the bending of the cantilever and therefore to the velocity of the fluid.

The orthogonal components of strain were measured by attaching two grooved optical fibers on adjacent sides of the rubber beam, orthogonal to each other, as illustrated in Figure 61.7. These two fibers measured the x and y components of optical strain.

Light from a 1 mW helium–neon laser of peak wavelength 633 nm was split into equal components using a cubic beam splitter and coupled to each fiber. The transmitted intensity through each of the two fibers was monitored using a power meter. The signals from the power meter were sent to a 486 DX2 laptop computer via a data acquisition card to be acquired and processed by Labview. Experiments indicated that this version of the flow sensor could measure wind speeds up to 30 m s^{-1} with a resolution of 1.3 m s^{-1}.

61.4.2 Fiber Optic Flow Sensor without Rubber Beam

This version of the sensor uses 1 mm diameter polymer fiber as the deflection element, with a core diameter of 0.980 mm, and a thin cladding layer of approximately 20 μm [6]. Multiple grooves were etched radially into the fiber surface to a depth of 0.5 mm, extending into the core of the fiber, using a hot scalpel, and a manufactured V-groove template to ensure uniformity of grooves. Six grooves were

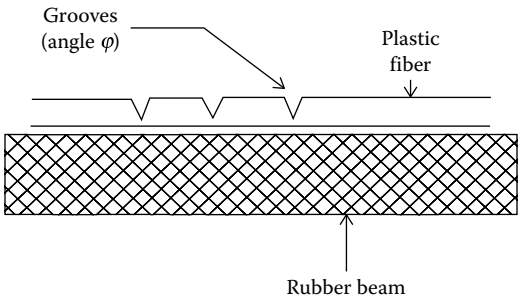

FIGURE 61.6 Principle of operation of the fiber optic drag force flow sensor.

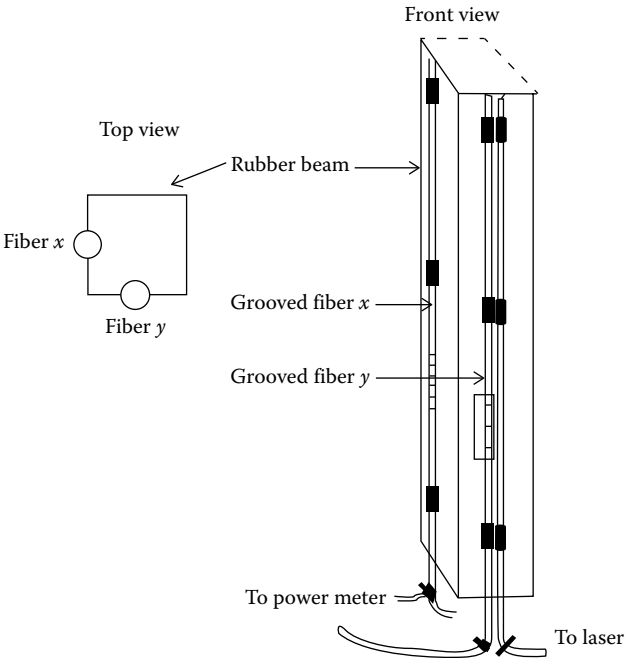

FIGURE 61.7 Front and top views of a section of the fiber optic drag force flow sensor used to measure the two-dimensional fluid flow.

determined as the optimum number to achieve a compromise between insertion losses and strain sensitivity, spaced 0.4 cm apart, over a length of 2.5 cm.

In order to measure strain in two orthogonal directions, perpendicular to the longitudinal axis of the fiber, two fibers were used, as shown in Figure 61.8, with the grooves oriented at 90° to each other. This was achieved by positioning the fibers on two adjacent faces of a beam of square cross section. This beam was short enough to prevent any restriction to the deflection and yet long enough to hold and support the optical fibers. The fibers were looped around so that the looped ends acted as drag elements. The grooved portion of the fiber was unsupported and free to deflect in the air stream. Wind tunnel calibration indicated that the sensor could measure two-dimensional flow up to 35 m s^{-1} with a resolution of 0.96 m s^{-1}.

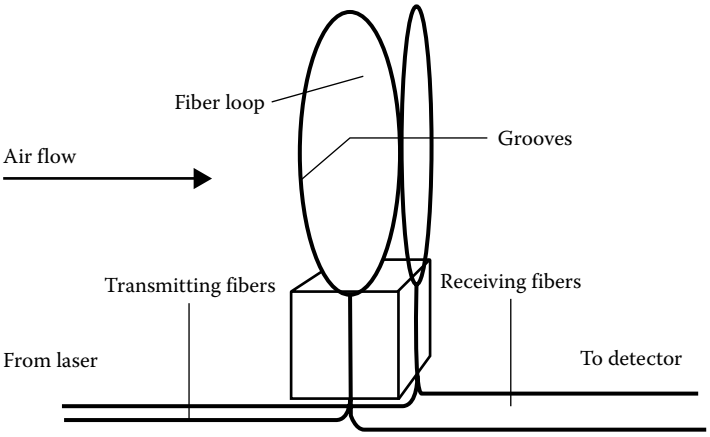

FIGURE 61.8 Optical fiber drag force flow sensor without rubber beam.

61.5 Conclusion

The measurement of one- and two-dimensional fluid velocity, using both optical fiber and conventional strain gages on a deflected beam, for a range of 0–30 m s^{-1}, has been demonstrated experimentally. Although flow visualization and modeling techniques are well advanced in engineering, there is still a need for real measurements, especially in the natural environment. The sensors described in this study are particularly suited for such measurements, which are almost always two-dimensional. The outputs of the sensor representing speed and direction of fluid flow are independent of each other, so the sensor is suitable for environmental applications such as wind measurement or river flow, where the fluid forms gusts and can change direction as well as speed. One noteworthy feature of this sensor is its quick response time of 50 ms, which easily enables the measurement of gusts. The dimensions and materials of the sensor must be chosen to suit the fluid. In terms of sensitivity and resolution, the resistive strain gage sensor is a better option, but replacing the conventional strain gages with optical fiber strain gages ensures electrical noise immunity and intrinsic safety for use in hazardous environments.

References

1. T. Clarke, Design and operation of target flowmeters, in *Encyclopedia of Fluid Mechanics*, Vol. 1, Houston, TX: Gulf Publishing Company, 1986.
2. F. H. Newman and V. H. L. Searle, *The General Properties of Matter*, London, U.K.: Edward Arnold, 1948.
3. S. Webster, R. McBride, J. S. Barton, and J. D. C. Jones, Air flow measurement by vortex shedding from multimode and monomode fibres, *Meas. Sci. Technol.*, 3, 210–216, 1992.
4. J. S. Barton and M. Saudi, A fibre optic vortex flowmeter. *J. Phys. E: Sci. Instrum*. 19, 64–66, 1986.
5. N. Narendran, A. Shukla, and S. Letcher, Optical fibre interferometric strain sensor using a single fibre, *Exp. Tech*. 16(2), 33–36, 1992.
6. R. Philip-Chandy, Fluid flow measurement using electrical and optical fibre strain gauges, PhD thesis, Liverpool John Moores University, Liverpool, U.K., 1997.

Partial List of Vendors and Suppliers

AMETEKTIP (Technical&Industrial Products), 627 Lake St., Kent, OH 44240, Phone: 215-256-6601, Fax: 330-677-3306, www.ametektip.com

Cooper Instruments, 400 Belle Air Lane, P.O. Box 3048, Warrenton, VA 20188, Phone: 540-349-4746, 800-344-3921 (toll free), Fax: 540-347-4755, www.cooperinstruments.com

Kistler North America, 75 John Glenn Dr., Amherst, NY 14228-2119, Phone: 716-691-5100, 888-KISTLER, 888-547-8537 (toll free), Fax: 716-691-5226, www.kistler.com

PCB Piezotronics, Inc., 3425 Walden Ave., Depew, NY 14043-2417, Phone: 716-684-0001, 800-828-8840 (toll free), Fax: 716-684-0987, www.pcb.com

Strainsert Co, 12 Union Hill Rd., West Conshohocken, PA 19428, Phone: 610-825-3310, 800-529-1502 (toll free), Fax: 610-825-1734, www.strainsert.com

Tekscan, 307 W. First St., South Boston, MA 02127, Phone: 617-464-4500, 800-248-3669 (toll free), Fax: 617-464-4266, www.tekscan.com

62

Pitot Probe Anemometer

John A. Kleppe
University of Nevada, Reno

62.1 Theory

It is instructive to review briefly the principles of fluid dynamics in order to understand *Pitot tube theory* and applications. Consider, for example, a constant-density fluid flowing steadily without friction through the simple device shown in Figure 62.1. If it is assumed that there is no heat being added and no shaft work being produced by the fluid, a simple expression can be developed to describe this flow:

$$\frac{p_1}{w} + \frac{v_1^2}{2g} + z_1 = \frac{p_2}{w} + \frac{v_2^2}{2g} + z_2 \tag{62.1}$$

where

p_1, v_1, z_1 are the pressure, velocity, and elevation at the inlet, respectively
p_2, v_2, z_2 are the pressure, velocity, and elevation at the outlet, respectively
$w = \rho g$ is the specific weight of the fluid
ρ is the density
$g = 9.80665\ \text{m s}^{-2}$

Equation 62.1 is the well-known Bernoulli equation. The following example will demonstrate the use of Equation 62.1 and lead to a discussion of the theory of Pitot tubes.

Example 62.1

A manometer [1] is used to measure the dynamic pressure of the tube assembly shown in Figure 62.2 [2]. The manometer fluid is mercury with a density of 13,600 kg m^{-3}. For a measured elevation change, Δh, of 2.5 cm, calculate the flow rate in the tube if the flowing fluid is (a) water, (b) air. Neglect all losses and assume STP conditions for the air flowing in the tube and $g = 9.81\ \text{m s}^{-2}$.

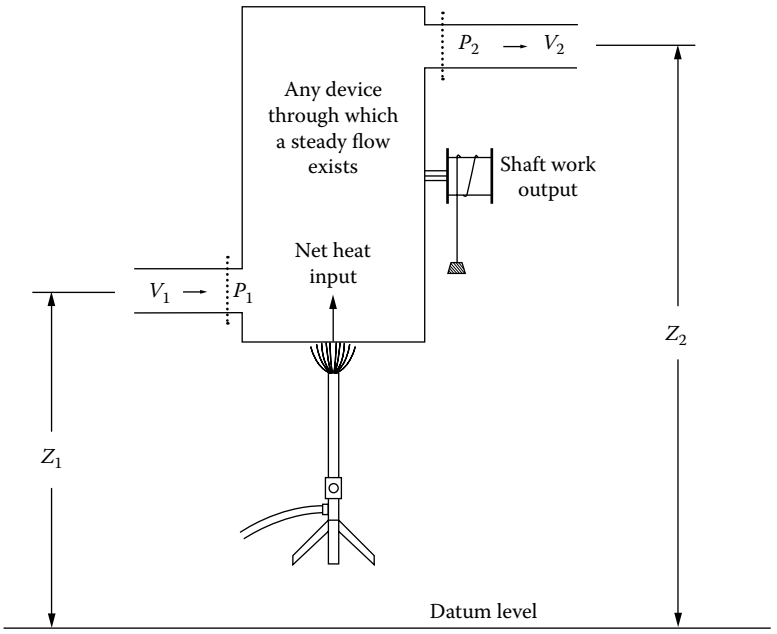

FIGURE 62.1 A device demonstrating Bernoulli's equation for steady flow, neglecting losses. (From Massey, B.S., *Mechanics of Fluids*, Van Nostrand, Princeton, NJ, 1968.)

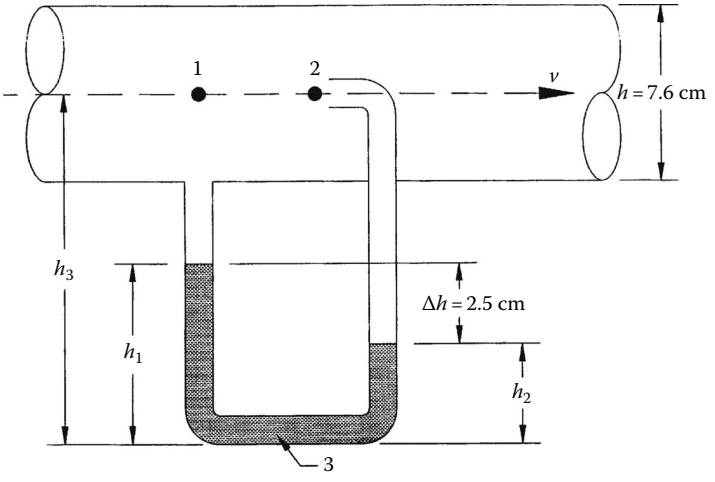

FIGURE 62.2 Using a manometer to measure a Pitot-static tube type assembly—Example 62.1.

Solution 62.1

Begin by writing expressions for the pressure at point 3

$$p_3 = h_1 w_{Hg} + (h_3 - h_1)w + p_1 \tag{62.2}$$

and

$$p_3 = h_2 w_{Hg} + (h_3 - h_2)w + p_2 \tag{62.3}$$

Subtracting these equations and rearrangement yields an expression for the pressure difference

$$p_2 - p_1 = \Delta h(w_{Hg} - w) \tag{62.4}$$

where w is the specific weight for water or air, etc.

Also using Equation 62.1, one can show that for $z_1 = z_2$ and $v_2 = 0$,

$$p_2 - p_1 = \frac{wv_1^2}{2g} \tag{62.5}$$

1. For water,

$$\begin{aligned} p_2 - p_1 &= \Delta h(w_{Hg} - w_{H_2O}) \\ &= 0.025[13{,}600(9.81) - 998(9.81)] \\ &= 3090.6\,\text{Pa} \end{aligned} \tag{62.6}$$

Then,

$$3090.6 = \frac{(998)(9.81)v_1^2}{2(9.81)} \tag{62.7}$$

or

$$v_1 = 2.5\,\text{m s}^{-1} \tag{62.8}$$

The flow Q is then calculated to be

$$Q = A_1 v_1 = \frac{\pi d^2 v_1}{4} = \frac{\pi(0.076)^2(2.5)}{4} = 0.011\,\text{m}^3\,\text{s}^{-1} \tag{62.9}$$

2. For air, one can use these same methods to show that

$$Q = 0.34\,\text{m}^3\,\text{s}^{-1} \tag{62.10}$$

A point in a fluid stream where the velocity is reduced to zero is known as a stagnation point [3]. Any nonrotating object placed in the fluid stream will produce a stagnation point, x, as seen in Figure 62.3. A manometer connected to point x would record the stagnation pressure of the fluid. From Bernoulli's equation (Equation 62.1), the quantity $p + \frac{1}{2}\rho v^2 + \rho gz$ is constant along a streamline for the steady flow of a fluid of constant density. Consequently, if the velocity v

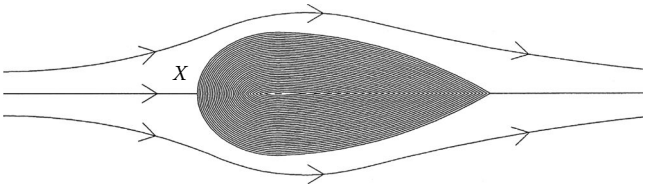

FIGURE 62.3 Flow around a nonrotating solid body. (From Massey, B.S., *Mechanics of Fluids*, Van Nostrand, Princeton, NJ, 1968.)

at a particular point is brought to zero, the pressure there is increased from p to $p + \frac{1}{2}\rho v^2$. For a constant-density fluid, the quantity $p + \frac{1}{2}\rho v^2$ is known as the stagnation pressure p_0 of that streamline, while the term $\frac{1}{2}\rho v^2$—that part of the stagnation pressure due to the motion—is termed the dynamic pressure. A manometer connected to point x would measure the stagnation pressure, and if the static pressure p were also known, then $\frac{1}{2}\rho v^2$ could be obtained. One can show that

$$p_t = p + p_v \tag{62.11}$$

where

p_t is the total pressure, which is the sum of the static and dynamic pressures that can be sensed by a probe that is at rest with respect to the system boundaries when it locally stagnates the fluid isentropically

p is the actual pressure of the fluid whether in motion or at rest and can be sensed by a probe that is at rest with respect to the fluid and does not disturb the fluid in any way

p_v is the dynamic or velocity pressure equivalent of the directed kinetic energy of the fluid

Using Equation 62.11, one can develop an expression that relates to the velocity of the fluid:

$$p_t = p + \frac{1}{2}\rho v^2 \tag{62.12}$$

or solving for v,

$$v = \sqrt{\frac{2(p_t - p)}{\rho}} \tag{62.13}$$

Consider as an example the tube arrangement shown in Figure 62.4. A right-angled tube, large enough to neglect capillary effects, has one end A facing the flow. When equilibrium is attained, the fluid at A is stationary and the pressure in the tube exceeds that of the surrounding stream by $\frac{1}{2}v^2$. The liquid is forced up the vertical part of the tube to a height

$$\Delta h = \frac{\Delta p}{w} = \frac{v^2}{2g} \tag{62.14}$$

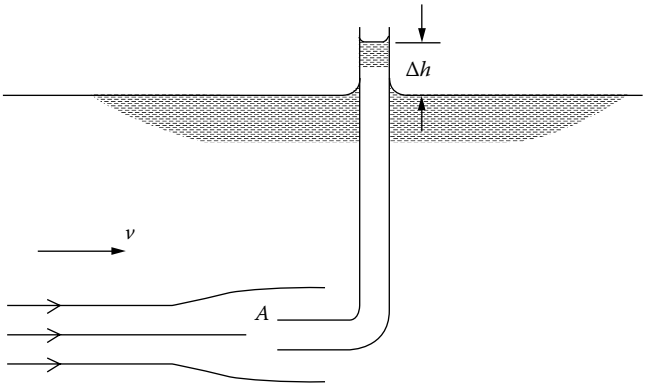

FIGURE 62.4 Right-angle tube in a flow system.

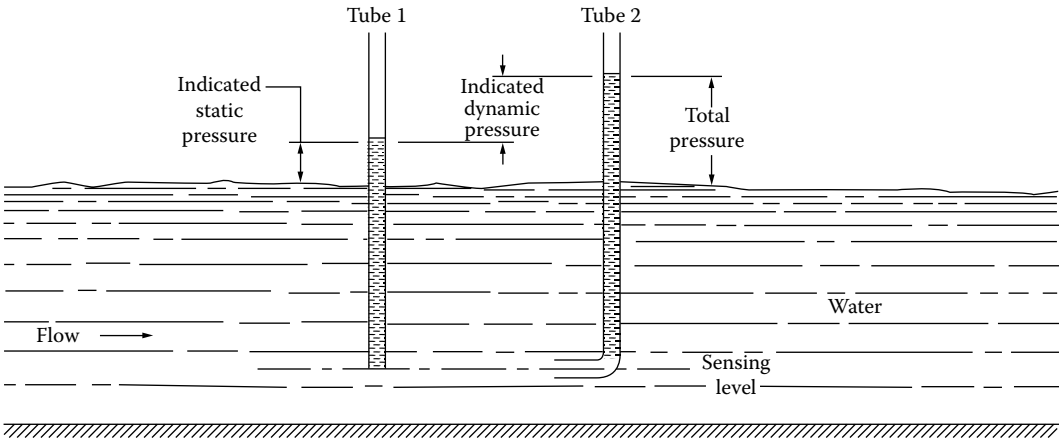

FIGURE 62.5 Basic Pitot tube method of sensing static, dynamic, and total pressure. (From Benedict, R.P., *Fundamentals of Temperature, Pressure and Flow Measurements*, 3rd edn., John Wiley & Sons, New York, 1984. With permission.)

This relationship was used in the example given earlier to solve for *v*. It must be remembered that the total pressure in a fluid can be sensed only by stagnating the flow isentropically, that is, when its entropy is identical at all points in the flow. Such stagnation can be accomplished by a Pitot tube, as first developed by Henri de Pitot in 1732 [4]. In order to obtain a velocity measurement in the River Seine (in France), Pitot made use of two tubes immersed in water. Figure 62.5 shows his basic Pitot tube method. The lower opening in one of the tubes was taken to be a measurement of the static pressure. The rise of fluid in the 90° tube was used as an indication of the velocity of the flow. For reasons to be discussed later, Pitot's method for measuring the static pressure was highly inadequate and would be considered incorrect today [4].

A modern-day Pitot-static tube assembly is shown in Figure 62.6 [5]. The static pressure is measured using "static holes" or pressure taps in the boundary. A pressure tap usually takes the form of a hole drilled in the side of a flow passage and is assumed to sense the "true" static pressure. When the fluid is moving past in the tap, which is usually the case, the tap will

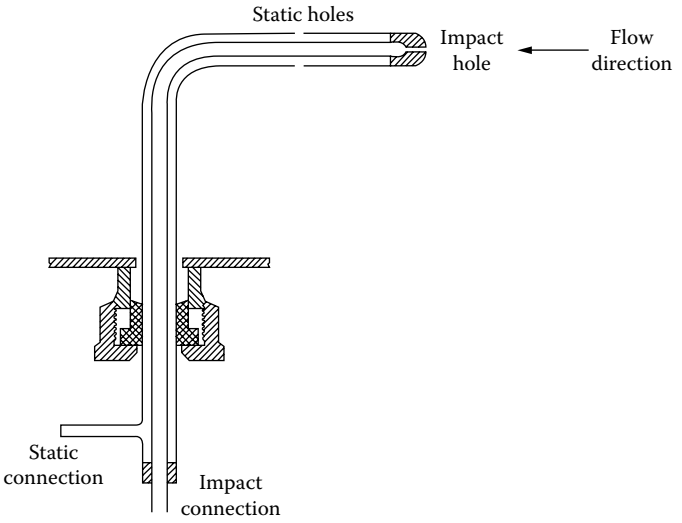

FIGURE 62.6 A modern Pitot-static tube assembly. (From ASME/ANSI PTC 19.2-2010, *Instruments and Apparatus, Part 2, Pressure Measurements*, ASME, Washington, DC, 1987. With permission.)

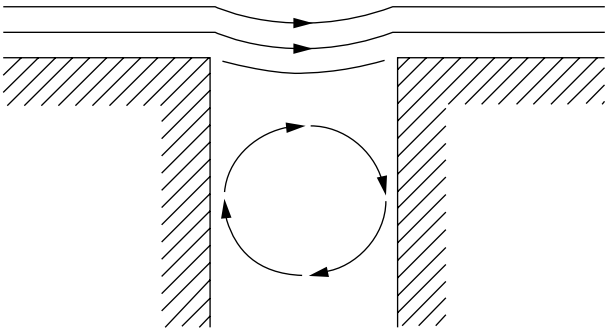

FIGURE 62.7 Pressure tap flow field.

not indicate the true static pressure. The streamlines are deflected into the holes as shown in Figure 62.7, thus setting up a system of eddies. The streamline curvature results in a pressure at the tap "mouth" different from the true fluid pressure. These factors in combination result in a higher pressure at the tap mouth than the true fluid pressure, a positive pressure error. The magnitude of this pressure error is a function of the Reynolds number based on the shear velocity and the tap diameter [5]. Larger tap diameters and high velocities give larger errors [5]. The effect of compressibility on tap errors is not well understood or demonstrated, although correlations for this effect have been suggested [5]. It is possible to reduce tap errors by moving the location of the tap to a nonaccelerating flow location or use pressure taps of smaller diameter. The effect of edge burrs is also noteworthy. All burrs must be removed. There is also an error that results with the angle of attack of the Pitot tube with the flow direction. Figure 62.8

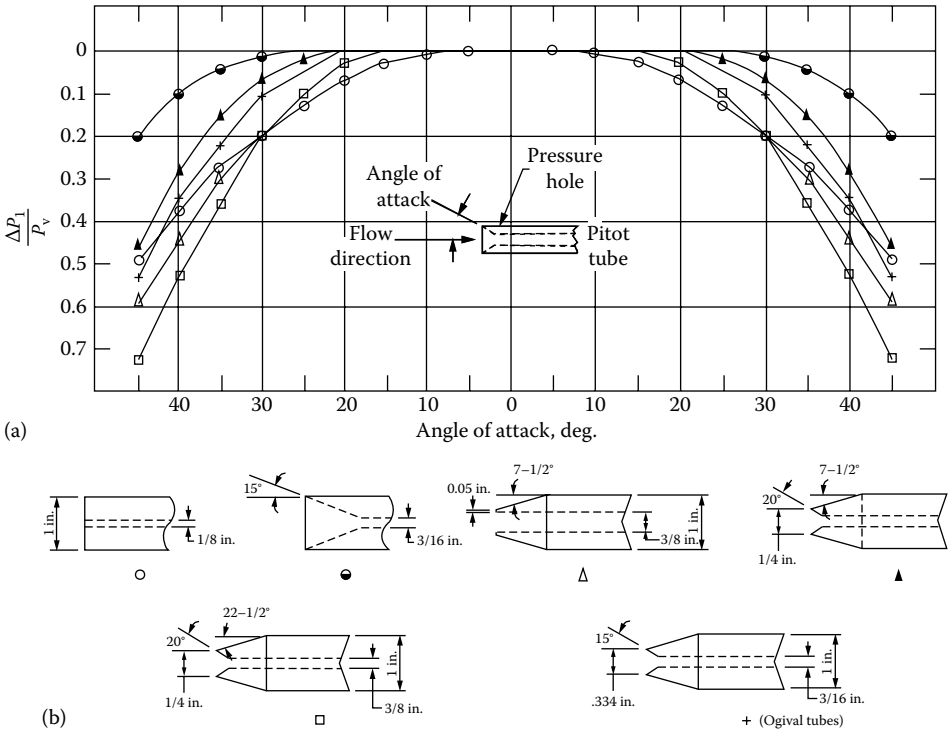

FIGURE 62.8 (a) Variation of total pressure indication with angle of attack and (b) geometry for Pitot tubes. (From ASME/ANSI PTC 19.2-2010, *Instruments and Apparatus, Part 2, Pressure Measurements*, ASME, Washington, DC, 2010. With permission.)

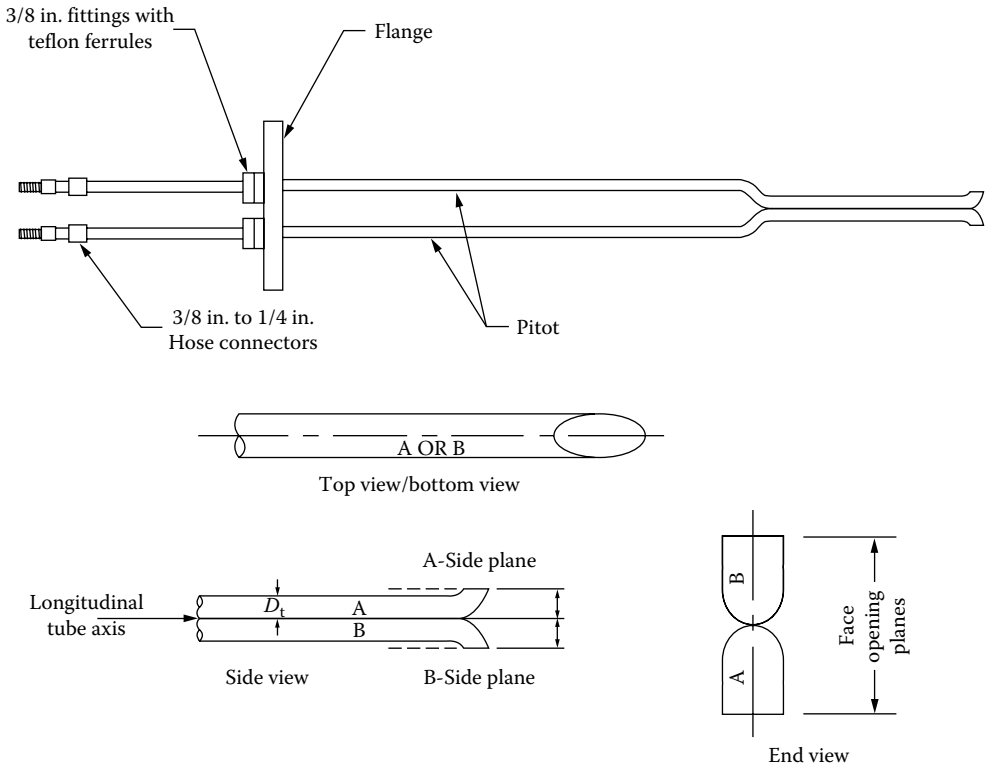

FIGURE 62.9 An S-type Pitot tube for use in gas flow measurement will have specific design parameters. For example, the diameter of the tubing D_t, a gas probe, will be between 0.48 and 0.95 cm. There should be equal distances from the base of each leg of the Pitot tube to its face-opening plane, dimensions d_1, d_2. This distance should be between 1.05 and 1.50 times the external tubing diameter, D_t The face openings of the Pitot tube should be aligned as shown. This configuration of the type S Pitot tube results in a correction coefficient of approximately 0.84. (From EPA, CFR 40 Part 60, Appendix A—Test Methods, September 20, 2011. http://www.epa.gov/ttnemc01/methods/methods2.html.)

shows the variation of total pressure indications as a function of the angle of attack. It can be seen that little error results if the angle of attack is less than ±10°.

A widely used variation of the Pitot-static tube is the type S Pitot tube assembly shown in Figure 62.9. It must be carefully designed and fabricated to ensure that it will properly measure the static pressure. The "static" tube faces backward into the wake behind the probe where the pressure is usually somewhat lower than the undisturbed static pressure. The type S Pitot tube therefore requires the application of a correction factor (usually in the range of 0.84). This correction factor will be valid only over a limited range of velocity measurement. The type S Pitot tube does, however, have the advantage of being compact and relatively inexpensive. A type S Pitot tube can be traversed across a duct or stack to determine the velocity profile and hence total volumetric flow. This is discussed later.

62.2 The Pitot Tube in Flow with Variable Density [3]

When a Pitot-static tube is used to determine the velocity of a constant-density fluid, the stagnation pressure and static pressure need not be separately measured: it is sufficient to measure their difference. A high-velocity gas stream, however, can undergo an appreciable change of density in being brought to rest at the front of the Pitot-static tube; under these circumstances, stagnation and static pressures must

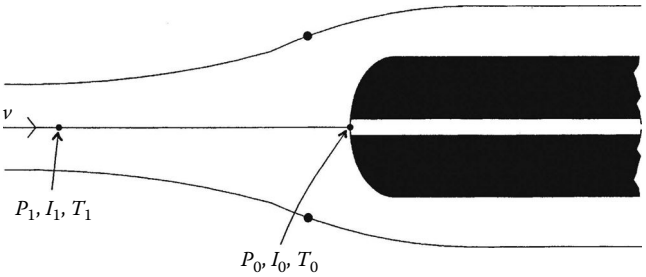

FIGURE 62.10 Pitot static tube in uniform subsonic flow.

be separately measured. Moreover, if the flow is initially supersonic, a shock wave is formed ahead of the tube, and, thus, results for supersonic flow differ essentially from those for subsonic flow. Consider first the Pitot-static tube in uniform subsonic flow, as in Figure 62.10.

The process by which the fluid is brought to rest at the nose of the tube is assumed to be frictionless and adiabatic. From the energy equation for a perfect gas, it can be shown that [3,6].

$$\frac{v^2}{2} = C_p(T_0 - T) = C_p T_0 \left\{1 - \left(\frac{p}{p_0}\right)^{(\gamma-1)/\gamma}\right\} \tag{62.15}$$

where

v is the velocity
C_p is the specific heat at constant pressure
T is the absolute temperature of the gas
T_0 is the absolute temperature at stagnation conditions
p is the total pressure
γ is the ratio of specific heats

For measuring T_0, it is usual to incorporate in the instrument a small thermocouple surrounded by an open-ended jacket. If T_0 and the ratio of static to stagnation pressure are known, the velocity of the stream can then be determined from Equation 62.15.

The influence of compressibility is best illustrated using the Mach number, M. It can be shown that [3]

$$\frac{p_0}{p} = \left(1 + \frac{\gamma - 1}{2} M^2\right)^{\gamma/(\gamma-1)} \tag{62.16}$$

For subsonic flow, $[(\gamma - 1)/2]M^2 < 1$ and so the right side of Equation 62.16 can be expanded by the binomial theorem to give

$$\frac{p_0}{p} = 1 + \frac{\gamma}{2} M^2 + \frac{\gamma}{8} M^4 + \frac{\gamma(2-\gamma)}{48} M^6 + \cdots \tag{62.17}$$

$$p_0 - p = \frac{p\gamma M^2}{2}\left\{1 + \frac{M^2}{4} + \left(\frac{2-\gamma}{24}\right) M^4 + \ldots\right\} \tag{62.18}$$

$$= \frac{1}{2\rho v^2}\left\{1 + \frac{M^2}{4} + \left(\frac{2-\gamma}{24}\right) M^4 + \ldots\right\} \tag{62.19}$$

TABLE 62.1 Variation of "Compressibility Factor" for Air

M	$\frac{p_0 - p}{1/2\rho v^2}$
0.1	1.003
0.2	1.010
0.3	1.023
0.4	1.041
0.5	1.064
0.6	1.093
0.7	1.129
0.8	1.170
0.9	1.219
1.0	1.276

The bracketed quantity is the compressibility factor and represents the effect of compressibility. Table 62.1 indicates the variation of the compressibility factor with M for air with $\gamma = 1.4$.

It is seen that for $M < 0.2$, compressibility affects the pressure difference by less than 1%, and the simple formula for flow at constant density is then sufficiently accurate. For larger values of M, however, the compressibility must be taken into account.

For supersonic flow, Equation 62.16 is not valid because a shock wave forms ahead of the Pitot tube, as shown in Figure 62.11, and, thus, the fluid is not brought to rest isentropically. The nose of the tube must be shaped so that the shock wave is detached, that is, the semiangle must be greater than 45.6° [3].

If the axis of the tube is parallel to the oncoming flow, the wave can be assumed normal to the streamline leading to the stagnation point. The pressure rise across the shock can therefore be given by

$$\frac{p_2}{p_1} = \frac{1+\gamma M_1^2}{1+\gamma M_2^2} \tag{62.20}$$

In the subsonic region downstream of the shock, there is a gradual isentropic pressure rise that can be represented as

$$\frac{p_0}{p_1} = \frac{p_0}{p_2}\frac{p_2}{p_1} = \left(1+\frac{\gamma-1}{2}M_2^2\right)^{\gamma/(\gamma-1)}\frac{1+\gamma M_1^2}{1+\gamma M_2^2} \tag{62.21}$$

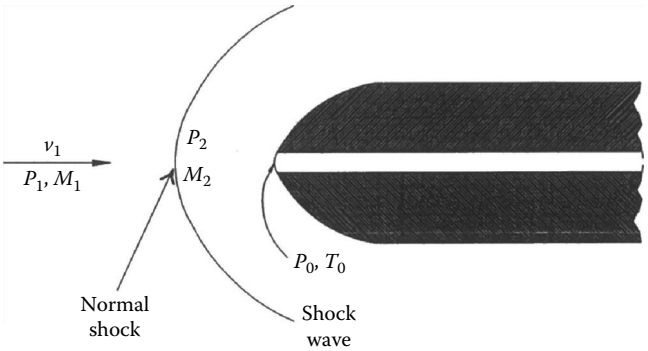

FIGURE 62.11 Pitot tube in supersonic flow switching a shock wave formed ahead of the pitot tube.

Finally, one obtains Rayleigh's formula

$$\frac{p_0}{p_1} = \left\{ \frac{(\gamma+1)^{\gamma+1}}{2\gamma M_1^2 - \gamma + 1} \left(\frac{M_1^2}{2} \right)^{\gamma} \right\}^{1/(\gamma-1)} \tag{62.22}$$

This expression for air reduces to

$$\frac{P_0}{P_1} = \frac{166.9 M_1^7}{(7M_1^2 - 1)^{2.5}} \quad \text{when } \gamma = 1.4 \tag{62.23}$$

Although a conventional Pitot-static tube gives satisfactory results at Mach numbers low enough for no shock waves to form, it is unsuitable in supersonic flow because its "static holes" or "pressure taps," being in the region downstream of the shock, do not then register p_1, nor do they register p_2 since this is found only on the central streamline, immediately behind the normal part of the shock wave. Consequently, p_1 is best determined independently—for example, through an orifice in a boundary wall well upstream of the shock. Where independent measurement of p_1 is not possible, a special Pitot-static tube can be used in which the static holes are much further back (about 10 times the outside diameter of the tube) from the nose. The oblique shock wave on each side of the tube has by then degenerated into a Mach wave across which the pressure rise is very small.

When $M_1 = 1$, the pressure rise across the shock is infinitesimal and, thus, Equations 62.16 and 62.22 both give

$$\frac{p_0}{p_1} = \left\{ \frac{(\gamma+1)}{2} \right\}^{\gamma/(\gamma-1)} = 1.893 \,(\text{for air}) \tag{62.24}$$

A small value of p_0/p therefore indicates subsonic flow and a larger value supersonic flow.

Notice that Equation 62.22 enables the upstream Mach number to be calculated from the ratio of stagnation to static pressure. Since the stagnation temperature does not change across a shock wave,

$$C_p T_0 = C_p T_1 + \frac{v_1^2}{2} = C_p \frac{v_1^2}{\gamma R M_1^2} + \frac{v_1^2}{2} \tag{62.25}$$

Thus, v_1 can also be calculated if T_0 is determined.

62.3 Volumetric Flow Measurements

The currently accepted method for measuring volumetric gas flow in ducts and stacks involves the use of Pitot tubes to obtain the velocity at points of equal area of the cross-sectional areas of the stack [7]. For example, Figure 62.12 shows a case where the circular stack of cross-sectional area A has been divided into 12 equal areas. An estimate of the average volumetric flow velocity is determined using the following relationship:

$$\bar{v}_n \approx \frac{\sum v_n A_n}{A} = \frac{A_i \sum v_n}{N A_i} = \frac{1}{N} \sum v_n \tag{62.26}$$

where

A_i is the one segment of the equal-area segments
N is the number of equal-area segments
v_n is the velocity measured at each point of equal-area segments

This relationship shows that one can estimate the average volumetric flow velocity by taking velocity measurements at each point of equal area and then calculate the arithmetic mean of these measurements.

Traverse Point	Distance % of Diameter
1	4.4
2	14.6
3	29.6
4	70.4
5	85.4
6	95.6

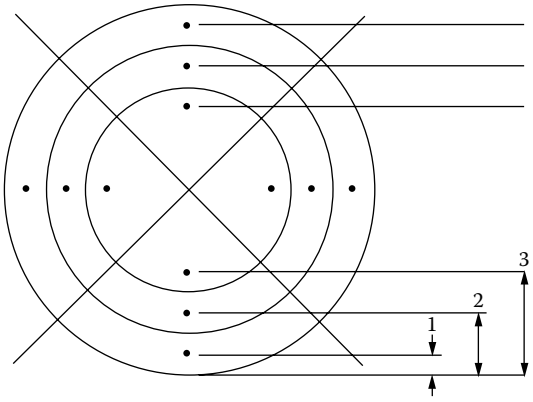

FIGURE 62.12 Example showing circular stack cross section divided into 12 equal areas, with location of traverse points indicated.

It is clearly seen that a different result would be obtained if one were to simply take velocity measurements at equidistant points across the measurement plane and then take the arithmetic mean of these measurements. What would result in this case would be the path-averaged velocity, $\overline{v}_p$, which would be in error.

The sampling site and the number of traverse points designated will affect the quality of the volumetric flow measurement. The acceptability of the sampling procedure is generally determined by the distances from the nearest upstream and downstream disturbances (obstruction or change in direction) to gas flow. The minimum requirements for an acceptable sampling procedure can be found in the literature [7].

An automated system for accomplishing this measurement is shown in Figure 62.13 [8].

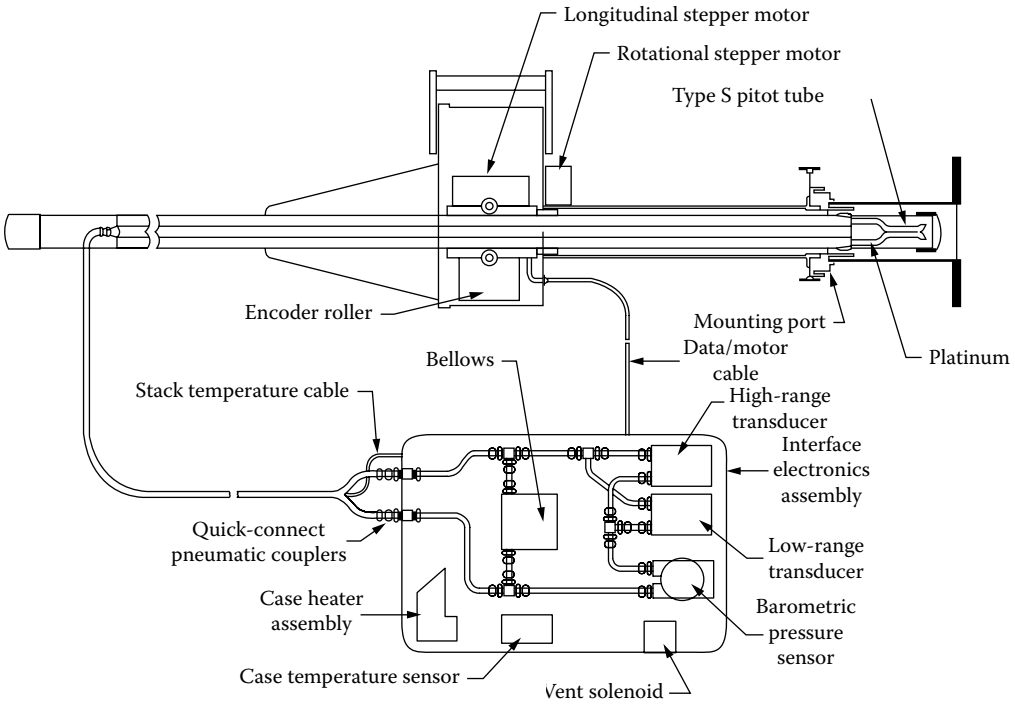

FIGURE 62.13 Automated probe consists of a type S Pitot tube and a platinum RTD mounted onto a type 319 stainless steel probe. (From Elliott, T. C., *Power*, May, 31, 1995. With permission.)

62.4 A Hybrid System

A hybrid system that combines sonic (acoustic) and Pitot tube technology has been developed to measure volumetric flow in large ducts and stacks [9–12]. A block diagram of this system is shown in Figure 62.14. The sensors (Figure 62.15) are mounted on opposite sides of the stack or duct at an angle θ to the flow direction. The acoustic portion of the sensor measures the flight time of the sound waves with and against the gas flow. It can easily be shown [9] that by transmitting and receiving the sound waves in opposite directions, the path average velocity of the gaseous medium can be determined from

$$\overline{v}_p = \frac{d}{2\cos\theta}\left(\frac{\tau_2 - \tau_1}{\tau_1\tau_2}\right) \text{m s}^{-1} \tag{62.27}$$

where

$\overline{v}_p$ is the path average velocity of the gas m s^{-1}
d is the distance between the transceivers (m)
θ is the angle, in degrees, of the path of the transducers with the vertical
τ_1 is the flight time of the sound with the gas flow (s)
τ_2 is the flight time of the sound against gas flow (s)

The result of this part of the total measurement is the area under the velocity curve plotted in Figure 62.16. The Pitot tubes provide differential pressure measurements at two points within the stack. The differential pressure is converted to velocity in a unique manner. The flight times of the

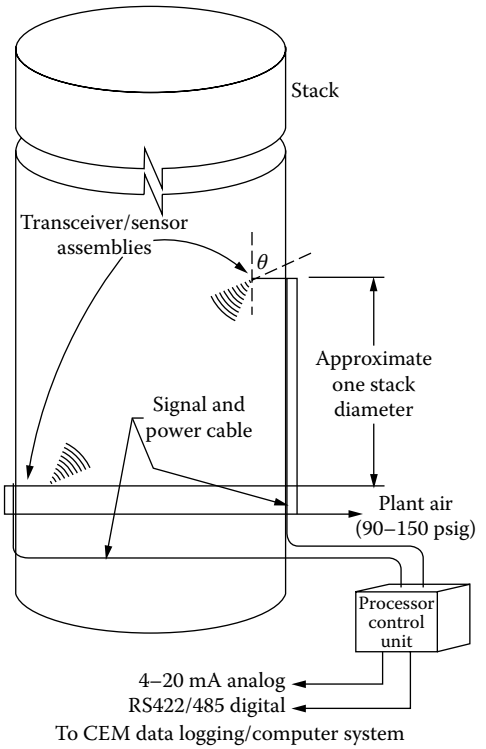

FIGURE 62.14 Block diagram of the hybrid system.

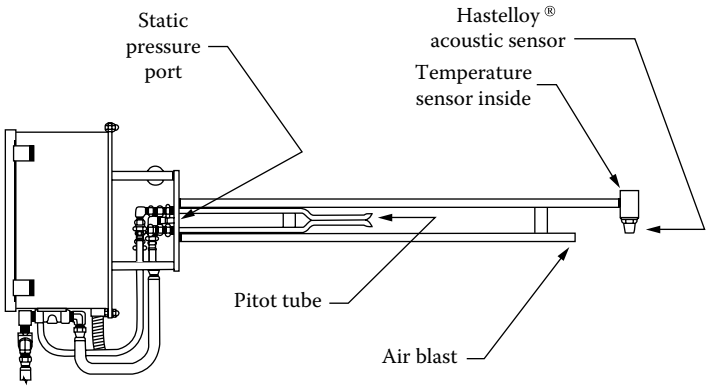

FIGURE 62.15 Acoustic probe contains acoustic, Pitot, and temperature sensors.

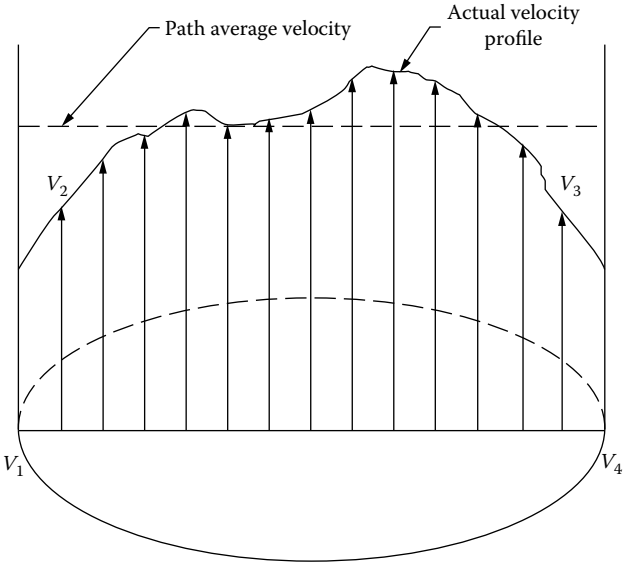

FIGURE 62.16 The velocity profile in a typical large duct or stack can vary greatly, thus changing the total volumetric flow. The hybrid system assumes V_1 and V_4 to be zero, measures V_2 and V_3 using the Pitot tubes, and provides the path average (area under the curve) using the acoustic portions of this sensor. $V_1 = V_4 = 0$ at walls.

acoustic wave, when properly combined with the temperature sensor reading, provide a measurement of the molecular weight of the wet flue gas. This value is then used to obtain the point velocity measurements shown as V_2 and V_3 in Figure 62.16. The actual flow profile curve is then estimated using the values V_1, V_2, V_3, and V_4 and the area under the flow profile curve generated by the acoustic portion of the system. The final part of the measurement involves using the static pressure measurements and the stack temperature measurements to calculate the total standard volumetric flow in scfh (wet).

The vast majority of fossil-fired utility generating units and many industrial sources within the United States have installed and certified continuous emission monitoring systems (CEMS) in accordance with the EPA's 40 CFR Part 75 CEM Rule as required under the Acid Rain Program as well as the NOX Budget Program and Clean Air Rule (CAIR). Under Part 75, sources are required to report emissions data on

a quarterly basis and submit monitoring plan information that identifies the source, power generating units, the emission being monitored, analyzer manufacturer, and sample acquisition methods [13].

Most commercially available flue gas flow monitors operate using one of the following three principles for measuring velocity and volumetric flow: ultrasonic pulse detection, differential pressure, and thermal detection (convective cooling).

The ultrasonic pulse detection system is a form of the hybrid system where corrections to the flow shape are provided from other correlated data such as change in plant loading. It has been reported in Ref. [13] that the ultrasonic flow monitoring technology comprises approximately 67% of the installed base in the United States with differential pressure or Pitot tube based systems having a share of 29%. The remaining 4% of the flow monitoring system are thermal and others.

62.5 Commercial Availability

There is a variety of materials used to construct Pitot tubes. The reasons for this are that Pitot tubes are used to measure a wide range of fluids. For example, to use a type S Pitot tube in a large power plant stack with a wet scrubber where the environment is extremely hostile and corrosive, stainless steel 316 or C276 (Hastelloy®) must be used. This, of course, makes the price of the Pitot tube as varied as its application. Many of the basic type S Pitot tube probes themselves are manufactured by a few small companies who, in turn, supply them on an OEM basis to others.

A typical type S Pitot tube assembly, such as that shown in Figure 62.9, can be purchased from:

EMRC
3730 North Pellegrino Drive
Tucson, AZ 85749
Tel: (520) 749-2167
Fax: (520) 749-3582
www.gasflowmonitors.com

A typical modern Pitot-static assembly, such as that shown in Figure 62.6, can be purchased from:

Dwyer Instruments, Inc.
102 Indiana Highway 212
(P.O. Box 373)
Michigan City, IN 46361
Tel: (219) 879-8000
Fax: (219) 872-9057
www.dwyer-inst.com

More complex, custom-designed and fabricated Pitot-static probes for use on aircraft are available at

Rosemount Aerospace, Inc.
14300 Judicial Road
Burnsville, MN 55306-4898
Tel: (612) 892-4300
Fax: (612) 892-4430
www.goodrich.com/Goodrich/Business/Sensors-and-Integrated Systems

Table 62.2 lists a number of manufactures/vendors that sell Pitot tube and general differential pressure measurement instrumentation.

TABLE 62.2 Sample of Manufacturers/Vendors

Name	Address	Telephone/Fax	Probe Type
EMRC	3730 North Pellegrino Dr. Tucson, AZ 85749	Tel: (520) 749-2167 Fax: (520) 749-3582 www.gasflowmonitors.com	Type S Pitot probe
Dwyer Instruments, Inc.	102 Indiana Hwy. 212 (P.O. Box 373) Michigan City, IN 46361	Tel: (219) 879-8000 Fax: (219) 872-9057 www.dwyer-inst.com	Pitot-static tubes and type S Pitot probe
Rosemount Aerospace, Inc.	14300 Judicial Rd. Burnsville, MN 55306-4898	Tel: (612) 892-4300 Fax: (612) 892-4430 www.goodrich.com	Flow angle sensors, Pitot/Pitot-static tubes, vane angle of attack sensors, temperature sensors, ice detectors, and pressure transducers
Air Monitor Corporation	1050 Hopper Avenue Santa Rosa, CA 95406	Tel: (707) 544-2706 (800) AIRFLOW Fax: (707) 526-9970 www.airmonitor.com	Multipoint, self-averaging
United Sciences, Inc.	201 Commonwealth Drive Warrendale, PA 15086	Tel: 704-778-6934 Fax: 724-778-6959 www.ustirata.com	Auto-PROBE 2000® automated Method 2 Testing
Teledyne Monitor Labs	35 Inverness Drive East Englewood, CO 80113	Tel: 800-422-1499, 303-792-3300 Fax: 303-799-4853 www.teledyne-ml.com	Ultrasonic flow sensor

References

1. W. F. Hughes and J. A. Brighton, *Theory and Problems of Fluid Dynamics*, 3rd edn., New York: McGraw-Hill, 1999.
2. J. B. Evett and C. Liu, *Fluid Mechanics and Hydraulics: 2500 Solved Problems*, New York: McGraw-Hill, 1989.
3. B. S. Massey, *Mechanics of Fluids*, Princeton, NJ: Van Nostrand, 1968.
4. R. P. Benedict, *Fundamentals of Temperature, Pressure and Flow Measurements*, 3rd edn., New York: John Wiley & Sons, 1984.
5. ASME/ANSI PTC 19.2-2010, *Instruments and Apparatus, Part 2, Pressure Measurement*, Washington, DC: ASMW, 2010.
6. S. P. Parker, *Fluid Mechanics Source Book*, New York: McGraw-Hill, 1988.
7. EPA, CFR 40 Part 60, Appendix A—Test methods, Revised September 20, 2011.
8. T. C. Elliott, CEM system: Lynchpin holding CAA compliance together, *Power*, May 1995, 31–40.
9. J. A. Kleppe, Principles and applications of acoustic sensors used for gas temperature and flow measurement, *Proceedings of the SENSOR EXPO*, Boston, MA, May 1995, pp. 337–374.
10. J. A. Kleppe, Method and apppartus for flow rate mesurement, U.S. Patent No. 5,392, CY 5, February 28, 1995.
11. Guidelines for flue gas flow rate monitoring, EPRI TR-104527, Project 1961-13 Final Report, June 1995.
12. A. Mann and J. A. Kleppe, A report on the performance of a hybrid flow monitor used for CEMS and heat rate applications, *Proceedings of the EPRI 1996 Heat Rate Improvement Conference*, Dallas, TX, May 1996, Part 33, pp. 1–13.

63

Thermal Dispersion Mass Flow Meters

John G. Olin
Sierra Instruments, Inc.

63.1 Introduction

Thermal dispersion mass flow meters measure the mass flow rate of fluids, primarily gases, flowing through a closed conduit. Their first-general description is attributed to L. V. King, who, in 1914 [1], published his famous King's Law, revealing how a heated wire immersed in a fluid flow measures the mass velocity at a point in the flow. He called his instrument a "hot-wire anemometer." Since then, hot-wire and hot-film anemometers have seen wide use in fluid mechanics research and as light-duty mass flow meters and handheld air velocity meters. This class of instruments is described in Chapter 59 [2].

It was not until the 1960s and 1970s that we saw the emergence of industrial-grade thermal dispersion mass flow meters that could solve the wide range of general industry's more ruggedized needs for directly measuring the mass flow rate of air, natural gas, and other gases in pipes and ducts. This chapter describes that class of instruments with emphasis on currently available technology. Future advances in the technology of thermal dispersion mass flow meters are described in Refs. [3,4].

Thermal dispersion mass flow meters measure the heat convected into the boundary layer of the gas flowing over the surface of a heated velocity sensor immersed in the flow. Since it is the molecules of the gas, which bear its mass, that carry away the heat, thermal dispersion mass flow meters directly measure mass flow rate. Capillary tube thermal mass flow meters constitute a second type of thermal mass flow technology, but their principle of operation and their applications are sufficiently different that the American Society of Mechanical Engineers has published separate national standards for each type [5,6]. Capillary tube thermal mass flow meters are not covered in this chapter.

Typical gases monitored by industrial thermal dispersion mass flow meters include air, methane, natural gas, carbon dioxide, nitrogen, oxygen, argon, helium, hydrogen, propane, and stack gases, as well as mixtures of these gases and mixtures of hydrocarbon gases. Common applications are combustion air; preheated air; compressed air; boilers; electric power plants; drying of materials; food and beverage industries; natural gas distribution; aeration and digester gas monitoring in waste water treatment plants; cogeneration with biogas; fuel gas; flare gas; semiconductor manufacturing; heating, ventilation, and air conditioning; and single- and multipoint stack gas monitoring.

63.2 Description

Thermal dispersion mass flow meters directly measure the mass flow rate of single-phase pure gases and gas mixtures of known composition flowing through pipes or other flow conduits. They also have limited application to single-phase liquids of known composition. In most of the following text, we shall assume that the fluid is a gas, without the loss of applicability to liquids. Multivariable versions also provide an output for gas temperature.

Thermal dispersion mass flow meters have two primary configurations: in-line and insertion. Figure 63.1a and b, respectively, shows these two configurations and their major components. Figure 63.1c

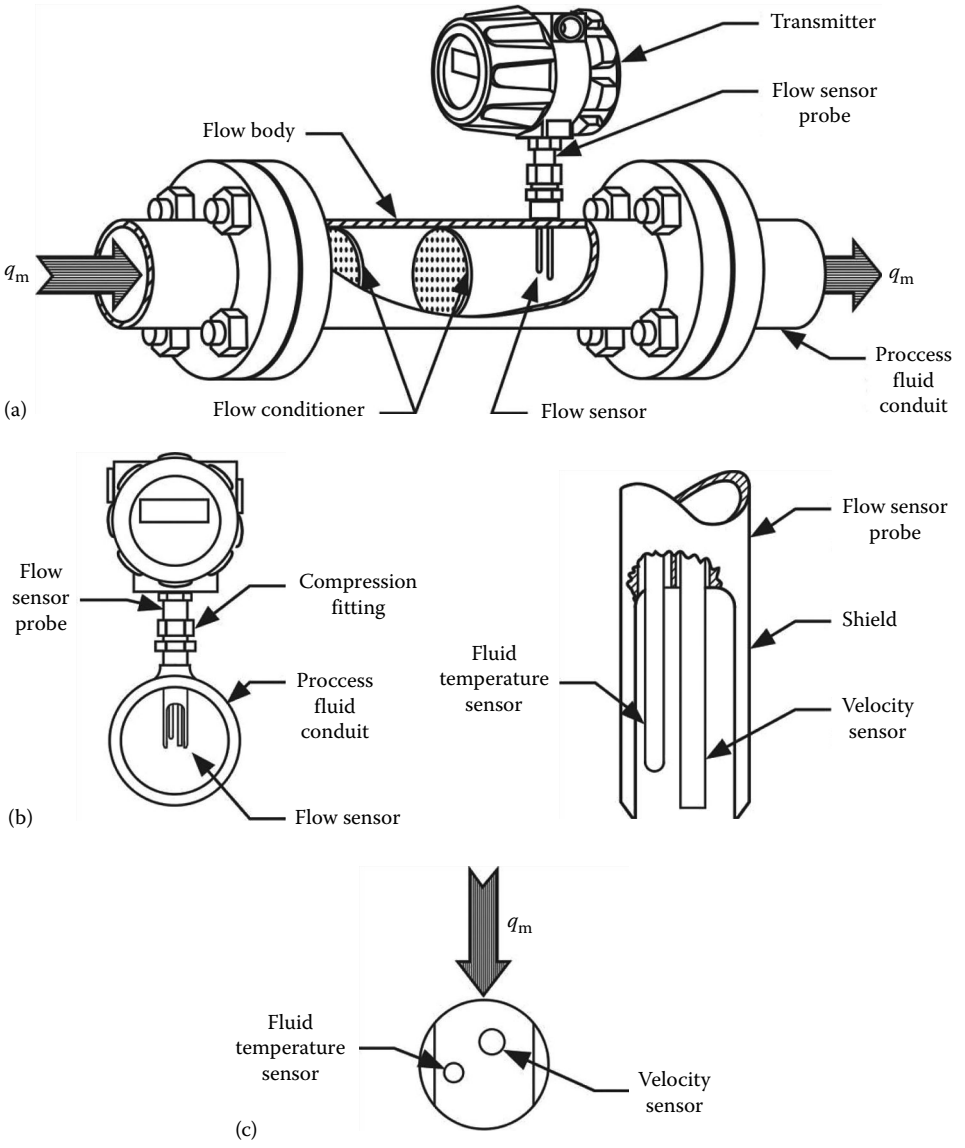

FIGURE 63.1 In-line and insertion meter configurations of thermal dispersion mass flow meters. (a) In-line configuration, (b) insertion configuration, installed, and (c) detail of flow sensor, insertion meter shown. (Adapted from Olin, J.G., Advances in thermal dispersion mass flow meters—Part 1: Principle of operation, Sierra Instruments Technical Report No. SI-JGO-2010-1, 2010. With permission from Sierra Instruments, Inc.)

shows the flow sensor that is common to both configurations, although smaller in-line meters may not have the shield. In-line meters are applied to pipes and ducts with diameters typically ranging from about 10 to 100 mm, but some manufacturers offer sizes up to 300 mm. Process connections include flanges, pipe threads, and compression fittings. A built-in flow conditioner reduces the length of upstream straight pipe required to achieve independence of upstream flow disturbances.

Insertion meters [7] usually are applied to larger pipes, ducts, and other flow conduits having equivalent diameters typically ranging from approximately 75 mm to 5 m. Because insertion meters are more economical than in-line meters, they also have found wide use as flow switches. Compression fittings and flanges are commonly used process connections. Insertion meters measure the mass velocity at a point in the conduit's cross-sectional area, but for applications with smaller conduits, they may be flow calibrated to measure the total mass flow rate through the conduit. Multipoint insertion meters measure the mass velocities at the centroids of equal areas in the cross section of large pipes, ducts, and stacks. The total mass flow rate through the entire conduit is the average mass velocity of the several points multiplied by the total cross-sectional area and the standard mass density of the gas [8].

Figure 63.2a shows a traditional thermal dispersion flow sensor used in in-line and insertion mass flow meters intended for industrial-grade applications. Other kinds of thermal dispersion flow sensors intended for lighter-duty applications are described in Ref. [2]. The flow sensor in Figure 63.2a has a velocity sensor and a separate temperature sensor immersed in the flow stream. For that reason, thermal dispersion mass flow meters are also named "immersible" thermal mass flow meters. The velocity sensor has a single electrically self-heated temperature sensor element located in its tip that both heats the velocity sensor and measures its own average temperature T_1. The gas temperature

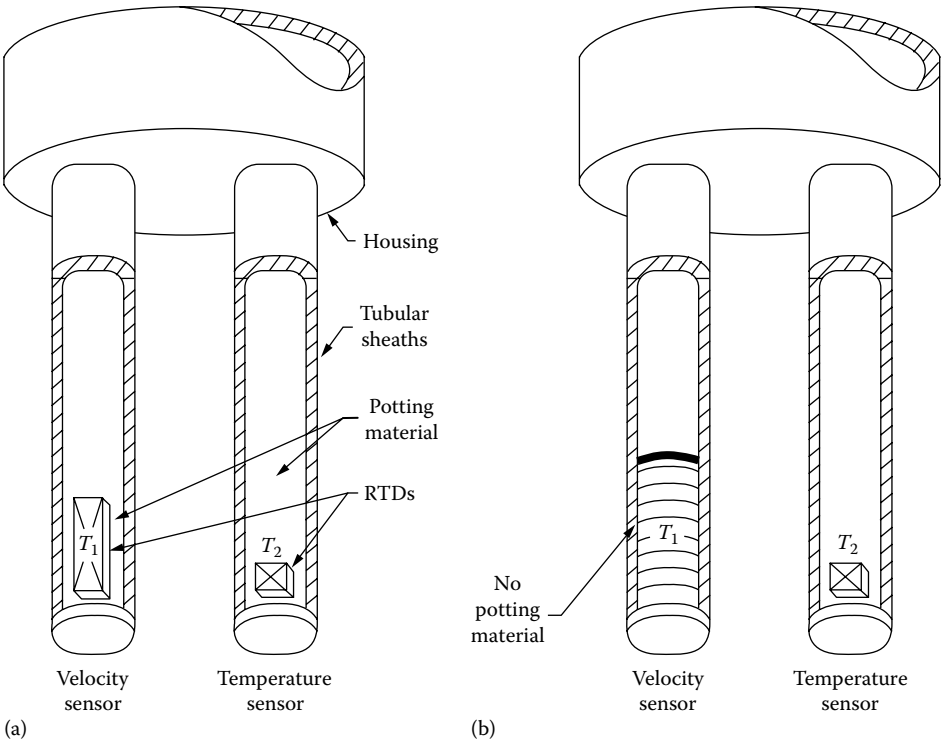

FIGURE 63.2 Two kinds of thermal dispersion mass flow sensors. (a) Flow sensor with potted velocity sensor and (b) flow sensor with dry velocity sensor. (Adapted from Olin, J.G., Advances in thermal dispersion mass flow meters—Part 1: Principle of operation, Sierra Instruments Technical Report No. SI-JGO-2010-1, 2010. With permission from Sierra Instruments, Inc.)

sensor has a single non-self-heated temperature sensor element T_2 located in its tip that measures the gas temperature T. The velocity sensor and the temperature sensor are mounted side by side. Each is enclosed in a rugged, sealed, single-ended, corrosion-resistant metallic tube, usually composed of 316 stainless steel or a nickel alloy. The introduction of this kind of rugged construction in the 1960s and 1970s is responsible for transforming thermal anemometers into industrial-grade instruments. In traditional velocity sensors of the kind shown in Figure 63.2a, the T_1 sensor is potted into the tip of the tubular sheath. Typically, the potting compound, or filler material, is ceramic cement or epoxy. Heat sink grease also has been used for this purpose. In the following text, we shall call this kind of velocity sensor a "potted" one.

For higher-accuracy and higher-stability applications, the temperature sensing elements in the velocity sensor and the temperature sensor in Figure 63.2a and b are either wire-wound or thin-film platinum resistance temperature detectors (RTDs) protected by a thin insulation layer of glass or ceramic. The electrical resistance of RTDs increases as temperature increases, providing the means for transducing their electrical output into temperature. The platinum RTD sensor element in the velocity sensor is called the T_1 element and has a relatively low electrical resistance in the range of about 10–30 **Ω**. The platinum RTD element in the temperature sensor is called the T_2 element and has a relatively high electrical resistance in the range of 300–1000 **Ω**. Other types of temperature sensing elements, such as thermistors, thermocouples, and micro-electronic machined devices, have been used for applications with lower-accuracy requirements. In the following text, we shall assume that the T_1 and T_2 elements are platinum RTDs.

In the field, the outside temperature external to the flow sensor can change and be different from its value at the time of flow calibration. For that reason, heat can be conducted in or out of the stems of the velocity sensor and the temperature sensor. Additionally, heat can be conducted from the hot velocity sensor to the cooler temperature sensor via their stems. Both effects are further complicated because they depend on the mass flow rate. These phenomena are collectively called "stem conduction." Stem conduction is a large fraction of the total heat supplied to the velocity sensor and is an unwanted quantity. Left uncorrected, stem conduction constitutes a major source of error in measuring mass flow rate. Flow sensors with long stems have far less stem conduction than those with short, stubby stems.

The use of the potting material between the T_1 element in Figure 63.2a and the internal surface of the sheath has potential long-term stability problems because the filler material can crack or otherwise degrade due to differences in the thermal expansion coefficients of the potting and the sheath materials when exposed to gas temperatures that cycle, change frequently, or are elevated. Any change in the potting material causes a change in the "skin resistance" of the velocity sensor and thereby its stability. Skin resistance and stem conduction are the two major factors that can degrade measurement accuracy if not managed properly. This will be discussed further in the following text.

The construction and assembly of the T_1 element in the flow sensor in Figure 63.2b eliminate the skin resistance problem by (1) avoiding altogether the use of any potting materials between the T_1 element and the internal surface of the sheath and (2) using mating materials that have the same coefficient of thermal expansion. In this design, the T_1 element is cylindrical wire-wound platinum RTD. Potting materials are avoided altogether by means of tightly fitting, as in swaging or press fitting, the wire-wound T_1 element into the sheath. Such velocity sensors are known as "dry" sensors, in contrast with potted velocity sensors fabricated with cements or epoxies that are wet when mixed. In contrast with the velocity sensor, any degradation of potting materials in the temperature sensor changes only its time response, a relatively minor effect.

In operation, the gas temperature sensor in the thermal dispersion mass flow meter measures the gas temperature T. The sensor drive in the transmitter electronics delivers an electrical current I_1 to the velocity sensor such that it is self-heated to an average temperature T_1 that is elevated above the gas temperature. Since it is the molecules of the gas, which bear its mass, that flow over the heated velocity sensor and carry away its heat, thermal dispersion flow meters directly measure the mass flow rate q_m

of the gas or gas mixture. Heat convected from the velocity sensor in this manner depends on the properties of the gas, and therefore the composition of the gas must be known.

In yet another thermal flow sensor construction for in-line meters, the flow sensor is embedded in the wall of the flow body and is not immersed in the flow. This flow sensor consists of a heater element with adjacent upstream and downstream temperature sensing elements. The difference in the two temperatures increases as flow increases, providing the output. This construction is used primarily for low-flow liquid applications.

The transmitter shown in Figure 63.1 is the electronic system that provides the flow sensor drive and many other functions for the flow meter. It accepts the inputs from the two temperature sensing elements as well as the heating current I_1 input and transforms these independent variables into linear analog outputs of the primary dependent variable, mass flow rate q_m, and, in the case of multivariable versions, the gas temperature T. The transmitter is housed in an enclosure that conforms with relevant codes, such as hazardous area codes or area classifications. Digital transmitters with digital displays in engineering units facilitate additional functions. Later, we shall describe microprocessor-based digital transmitters that also provide automatic correction for changes in gas temperature.

Many transport properties of the gas that are involved in convective heat transfer, such as thermal conductivity, viscosity, and Prandtl number, depend on temperature. Likewise, the thermal conductivity of some of the materials in the flow sensor depends on temperature. For this reason, thermal dispersion mass flow meters must correct for changes in gas temperature. In traditional flow meters, this is done by means of an analog Wheatstone bridge at the front end of the flow sensor drive. The velocity sensor and the temperature sensor are located at opposite legs of the bridge. This provides compensation for changes in fluid temperature by adjusting overheat of the velocity sensor. The bridge voltage is a high-level output signal in the order of several volts that provides a high signal-to-noise ratio. The Wheatstone bridge and its temperature-compensation properties are thoroughly described in the literature [2,8–11]. Advanced flow meters with a microprocessor-based flow sensor drive digitally correct for changes in temperature without requiring a Wheatstone bridge [3].

The flow sensor drive in thermal dispersion mass flow meters has two modes of operation: the constant temperature differential mode and the constant current mode. In the constant temperature differential mode of operation, the flow sensor drive maintains at a constant value the difference $\Delta T = T_1 - T$ between the heated velocity sensor T_1 and the gas temperature T. The output signal is the electrical power W supplied to the heated velocity sensor that is required to keep ΔT constant. In the constant current mode of operation, the flow sensor drive maintains at a constant value the current I_1 supplied to the heated velocity sensor. In this case, the output signal is ΔT. Measuring mass flow rate with constant current operation is slower than constant temperature differential operation because the temperature of the entire mass of the velocity sensor must change when velocity changes and also because the masses of the velocity and temperature sensors may be imbalanced. In the following text, we assume constant temperature differential operation and that therefore ΔT is a constant, usually in the range of 20–100 K.

63.3 Principle of Operation

The purpose of this section is to provide a brief description of some of the important principles involved in finding the two output variables—the mass flow rate q_m and the gas temperature T. Figure 63.3 shows the principle of operation of the industrial-grade thermal dispersion flow sensor with the dry velocity sensor shown in Figure 63.2b. The flow sensor is operated in the constant temperature differential mode. The transmitter is the modern microprocessor-based system shown in Figure 63.4. In the following text, we shall call this flow sensor/transmitter combination the "dry-sensor microprocessor-based system." The fluid is a pure gas or gas mixture of known composition. The following treatment specifically applies to the dry velocity sensor, but has general applicability to potted velocity sensors and liquid flows. Refs. [3,9] are good back-up sources for the principle of operation described here, although Ref. [9] specifically applies to hot-wire anemometers.

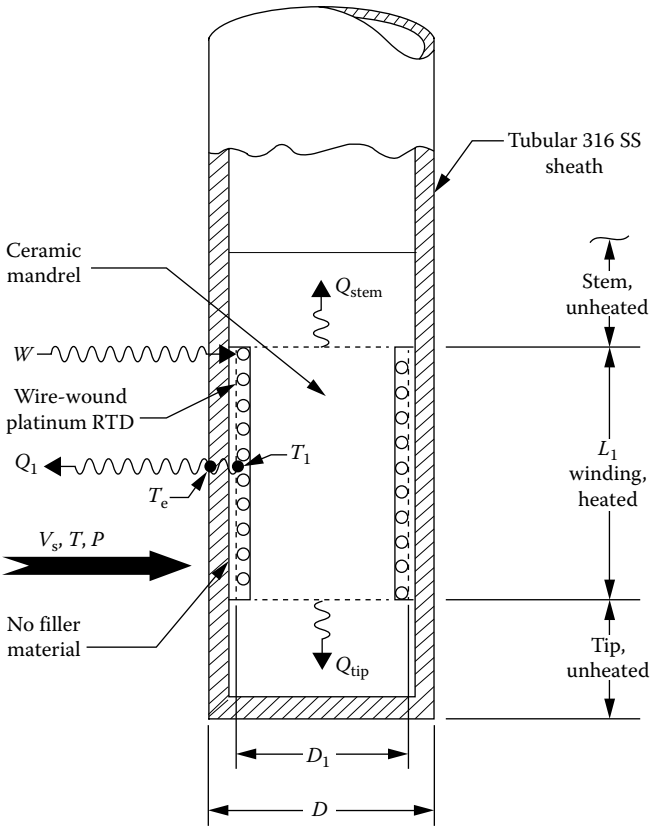

FIGURE 63.3 Principle of operation of the flow sensor with a dry velocity sensor. (Adapted from Olin, J.G., Advances in thermal dispersion mass flow meters—Part 1: Principle of operation, Sierra Instruments Technical Report No. SI-JGO-2010-1, 2010. With permission from Sierra Instruments, Inc.)

The temperatures T_1(K) and T_2(K) are found from the two platinum RTD temperature sensing elements by solving the following equations for temperature using the quadratic formula:

$$R_1 = R_{1,0}\left[1 + A_1\left(T_1 - T_0\right) + A_2\left(T_1 - T_0\right)^2\right] \tag{63.1}$$

$$R_2 = R_{2,0}\left[1 + B_1\left(T_2 - T_0\right) + B_2\left(T_2 - T_0\right)^2\right] \tag{63.2}$$

where

R_1, R_2 are the electrical resistance of temperature sensing elements T_1 and T_2 at temperatures T_1 and T_2, respectively (**Ω**)

$R_{1,0}$, $R_{2,0}$ are the electrical resistance of temperature sensing elements T_1 and T_2 at temperature T_0 (**Ω**)

T_0 is the reference temperature, usually 273.15 (K) [0 (°C)]

A_1, B_1; A_2, B_2 are constants provided by the manufacturer (K^{-1}); (K^{-2})

Equations 63.1 and 63.2 specifically apply if temperatures T_1 and T_2 are above 0 °C. Assuming that stem conduction is negligible for the temperature sensor, we can solve Equation 63.2 for T_2. This results in the following relationship for the desired gas temperature output variable:

$$T = T_2 \tag{63.3}$$

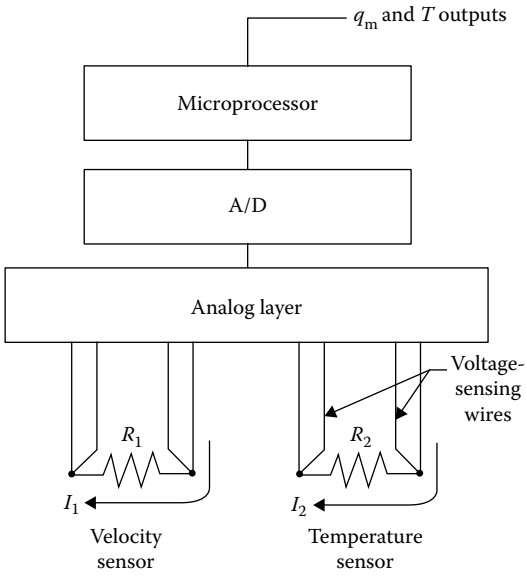

FIGURE 63.4 The dry-sensor microprocessor-based system. The flow meter drives the velocity sensor so that the temperature difference $\Delta T = T_1 - T$ is maintained constant. The system automatically corrects for changes in gas temperature. (Adapted from Olin, J.G., Advances in thermal dispersion mass flow meters—Part 1: Principle of operation, Sierra Instruments Technical Report No. SI-JGO-2010-1, 2010. With permission from Sierra Instruments, Inc.)

The relationship between electrical resistance and temperature for the T_1 sensor sometimes is expressed as

$$R_1 = R_{1,0}\left[1 + \alpha\left(T_1 - T_0\right)\right] \tag{63.4}$$

In Equation 63.4, the term α is the temperature coefficient of resistivity (K^{-1}) and has a value of approximately 0.0039 (K^{-1}) for platinum RTDs. Equation 63.4 is quite accurate for gas temperatures in the range of 0 °C–100 °C.

The dry-sensor microprocessor-based system measures the primary inputs R_1, R_2, and I_1. It then converts them into secondary inputs T_1 and T_2 using Equations 63.1 and 63.2 and computes the electrical power W supplied to the T_1 heated element using the relationship $W = I_1^2 R_1$ (W). The transmitter operates in the constant temperature differential mode and therefore maintains the temperature difference $\Delta T = T_1 - T$ at a constant value. The following text describes some of the important relationships needed to convert these inputs into a linear output of mass flow rate q_m.

In steady state, the first law of thermodynamics states that the energy (or power) flowing into a defined control volume equals the energy flowing out of the control volume. The control volume to which we shall apply this law is the entire heated section of the velocity sensor. As shown in Figure 63.3, this control volume is enclosed in the dotted lines and is defined by length L_1 and diameter D_1. It consists of the cylindrical ceramic mandrel; the R_1 platinum RTD winding around the mandrel that is heated by electrical power W; and a ceramic or high-temperature glass insulating binder for the winding. The first law for this control volume is

$$W = Q_1 + Q_{tip} + Q_{stem} \tag{63.5}$$

In Equation 63.5, Q_{tip} and Q_{stem} are the heat rates (W) conducted from the heated control volume to the tip and stem of the velocity sensor, respectively.

Collectively, they constitute the heat rate lost via the previously mentioned "stem conduction." Q_1 is the heat rate (W) transferred from the heated control volume to the flowing gas by convection and radiation. Q_1 is expressed as

$$Q_1 = h_e(\pi D L_1)\Delta T \tag{63.6}$$

In Equation 63.6, D and L_1 are the outside diameter (m) and the length (m) of the heated section of the cylindrical velocity sensor, respectively. h_e is the effective film coefficient for convection (W/m^2/K), defined as

$$h_e = \frac{h}{1 + h\pi D L_1 R_{skin}} \tag{63.7}$$

where

h is the film coefficient for convection averaged over the surface of the heated section of the velocity sensor (W/m^2/K)

R_{skin} is the skin resistance described in the following text (K/W)

In Equation 63.7, we have ignored radiative heat transfer because it is negligible, except when the gas temperature is very high. The average temperature T_e of the external surface of the velocity sensor over length L_1, shown in Figure 63.3, is less than the average temperature T_1 of the control volume. This is due to the temperature drop that is required to pass the heat rate Q_1 through the intervening layers of material between the control volume and its external surface. These intervening layers are called the "skin." R_{skin}, the average thermal resistance of the skin over length L_1, i.e., the "skin resistance," is defined by

$$Q_1 = \frac{(T_1 - T_e)}{R_{skin}} \tag{63.8}$$

As evidenced by Equation 63.7, at higher flow rates and thus higher values of h, the skin resistance R_{skin} causes a droop in the output signal and consequently a reduction in sensitivity. This is why skin resistance is an unwanted quantity that should be minimized in flow sensor design, should not change over time, and should be taken into account. R_{skin} is the sum of the thermal resistances of the annular layers in the skin of the velocity sensor and is calculated as follows:

$$R_{skin} = \left(\frac{1}{2\pi L_1}\right)\sum_{j=1}^{n}\left[\frac{\ln\left(D_{j+1}/D_j\right)}{k_j}\right] \tag{63.9}$$

where

n is the total number of layers in the skin

$j = 1,\ldots,n$

D_j and D_{j+1} are the inside and outside diameters of layer j, respectively ($D_1 < \cdots < D_{n+1} = D$)

k_j is the thermal conductivity of layer j

The potted velocity sensor shown in Figure 63.2a has three layers in its skin—the thin insulation layer over the platinum RTD, the potting material, and the sheath. The dry velocity sensor in Figure 63.2b also has three layers in its skin—the thin insulation layer over the platinum RTD winding, a thin air gap with an average thickness in the order of 0.005 mm [0.0002 (in.)], and the sheath. The

thin air gap in the dry velocity sensor exists because, although the mating parts are in tight contact via their press fit, slight imperfections in their circularity can cause thin air gaps over a fraction of the mating surface. R_{skin} ranges from 3 to 10 W/K for potted velocity sensors and from 2 to 5 W/K for dry velocity sensors.

h and T are found based on the earlier principles. Given h and T, the next step in finding the mass flow rate q_m is to find the Reynolds number Re using an empirical correlation for convective heat transfer. This correlation has the following two forms, depending upon whether it is solved for the Nusselt number Nu or the Reynolds number Re:

$$\text{Nu} = F_1(\text{Re}, \text{Pr}) \quad \text{or} \quad \text{Re} = F_2(\text{Nu}, \text{Pr}) \tag{63.10}$$

where

Nu = hD/k = Nusselt number, the nondimensional heat-transfer parameter

Re = $\rho VD/\mu$ = Reynolds number, the nondimensional ratio of dynamic forces to viscous forces, based on the outside diameter D of the velocity sensor

Pr = $\mu c_p/k$ = Prandtl number, the nondimensional ratio of the diffusivity of momentum to the diffusivity of heat

k is the thermal conductivity of the gas (W/m/K)

ρ is the mass density of the gas (kg/m^3)

μ is the absolute viscosity of the gas (kg/s/m)

c_p is the coefficient of specific heat of the gas at constant pressure (J/kg/K)

The simplest example of the two forms of the correlation is

$$\text{Nu} = b_1 \text{Pr}^{b_2} \text{Re}^{b_3} \quad \text{or} \quad \text{Re} = \left[\frac{\text{Nu}}{b_1 \text{Pr}^{b_2}} \right]^{1/b_3} \tag{63.11}$$

where b_i is the dimensionless constants, i = 1, 2, or 3.

In Equations 63.10 and 63.11, all properties and dimensions refer to the velocity sensor. In the earlier text, we have assumed that the flow is nonzero, is in the continuum flow regime (i.e., is not in a high vacuum), and is incompressible (i.e., the Mach number is less than approximately 0.3).

The law of conservation of mass (the continuity equation) requires that

$$\rho V = \rho_s V_s \tag{63.12}$$

In Equation 63.12, V is the actual velocity (m/s) measured at the midpoint of the heated section of the velocity sensor, often called the "point velocity." The subscript $()_s$ refers to standard, or base, conditions of standard temperature T_s and absolute pressure P_s. Many applications use standard conditions of T_s = 70 °F = 21.11 °C = 294.26 K and P_s = 1 atm = 101325 Pa = 1.01325 bara. Another class of applications uses standard conditions, often called "normal" conditions, of T_s = 0 °C = 273.15 K and P_s = 1 atm = 1.01325 bara. The constant standard mass density ρ_s (kg/standard m^3) for gases obeying a modified perfect gas law equation of state is calculated as follows:

$$\rho_s = \frac{P_s M}{z_s R T_s} \tag{63.13}$$

where

M is the molecular weight of the pure gas or gas mixture (kg/kg-mole)

R is the universal gas constant (m^3 bara/kg-mole/K)

z_s is the dimensionless compressibility of the gas at standard conditions

In Equation 63.13, P_s and T_s are the standard absolute pressure (bara) and the standard absolute temperature (K) of the gas, respectively.

Based on Equation 63.12, the Reynolds number Re defined in Equation 63.10 also can be expressed as

$$\mathrm{Re} = \frac{\rho_s V_s D}{\mu} \tag{63.14}$$

From Equations 63.10 to 63.14, we arrive at

$$V_s = \left(\frac{\mu}{\rho_s D}\right) F_2(\mathrm{Nu}, \mathrm{Pr}) \tag{63.15}$$

In the earlier text, V_s is called the point "mass velocity" (standard m/s) because when it is multiplied by the constant mass density ρ_s, it yields the mass flow rate per unit area. This is the mathematical reason why thermal dispersion mass flow meters directly measure mass flow rate.

In most insertion meter applications, the desired final output variable is the mass velocity V_s (standard m/s). In this case, V_s is calculated using Equation 63.15. If the desired output is the actual velocity V (m/s), then V is found from $V = (\rho_s/\rho)V_s$. If the desired final output is the total mass flow rate q_m (kg/s) flowing through a pipe or other flow conduit, then the following relationship is used:

$$q_m = \left(F_c A_{pipe}\right) \rho_s V_s \tag{63.16}$$

In Equation 63.16, A_{pipe} is the cross-sectional area (m^2) of the pipe or flow conduit; and the term F_c is defined as $F_c = V_{s,ave}/V_s$, where $V_{s,ave}$ is the average point mass velocity (standard m/s) over the cross-sectional area A_{pipe}. Most insertion meters are inserted such that the midpoint of the heated section of the velocity sensor is at the centerline of the pipe. In this case and with a fully developed velocity profile in the pipe, typical values of F_c are $F_c = 0.5$ for $\mathrm{Re}_{pipe} \leq 2{,}000$, and $F_c = 0.83 \pm 0.03$ for $\mathrm{Re}_{pipe} \geq 40{,}000$, where Re_{pipe} is the Reynolds number based on the *internal* diameter of the pipe [12]. For in-line meters, Equation 63.16 is not used explicitly. Instead, the factor $(F_c A_{pipe})$ becomes a meter factor determined via flow calibration. Tables 63.1 and 63.2 provide a list of the formulas used by the four-temperature microprocessor-based system to calculate the output variables of insertion meters and in-line meters, respectively.

TABLE 63.1 Calculation of Output Variables for Insertion Flow Meters

Variable	Units	Symbol	Formula
Point mass velocity, the primary output	Standard m/s	V_s	V_s from Equation 63.15 or from flow calibration
Actual velocity	m/s	V	$(\rho_s/\rho)V_s$
Mass flow rate	kg/s	q_m	$\rho_s A_{pipe} F_c V_s$
Mass flow rate, expressed as volumetric flow rate referenced to standard conditions $()_s$	Standard m^3/s	$q_{v,s}$	$A_{pipe} F_c V_s$
Volumetric flow rate	m^3/s	q_v	$(\rho_s/\rho) A_{pipe} F_c V_s$
Total mass flow rate for multipoint measurements in N equal areas	kg/s	q_m	$(\rho_s A_{pipe}/N) \sum_{i=1}^{N} V_{s,i}$

TABLE 63.2 Calculation of Output Variables for In-Line Flow Meters

Variable	Units	Symbol	Formula
Mass flow rate, the primary output	kg/s	q_m	q_m from flow calibration
Mass flow rate, expressed as volumetric flow rate referenced to standard conditions $(\ )_s$	Standard m^3/s	$q_{v,s}$	q_m/ρ_s
Volumetric flow rate	m^3/s	q_v	q_m/ρ

63.4 Dry-Sensor Microprocessor-Based System

Figure 63.4 shows a simplified block diagram of the digital microprocessor-based thermal dispersion mass flow meter with the dry flow sensor shown in Figure 63.2b. It is operated in the constant temperature differential mode. As before, we call this configuration the dry-sensor microprocessor-based system. The voltage sensing wires in Figure 63.4 make the measurement of the RTD resistances independent of the length of the flow sensor cable, facilitating remote location of the transmitter. The temperature sensing current I_2 is less than 1 mA to avoid self-heating the T_2 sensor. The analog layer shown in Figure 63.4 includes precision resistors for measuring the currents I_1 and I_2 and may include a bridge circuit.

The dry-sensor microprocessor-based system shown in Figure 63.4 digitally linearizes the q_m output and, optionally, the T output and provides analog outputs for these variables. The system also automatically corrects for changes in gas temperature. The system enables a number of digital functions, such as a multivariable digital readout and user interface; digital RS 232 and RS 485 communications; flow meter diagnostics, validation, calibration adjustment, and reconfiguration; flow totalization; and alarms.

Figure 63.5 shows typical outputs for the dry-sensor microprocessor-based system for air, methane, and argon. These curves are plotted in the conventional manner with the mass velocity V_s shown as

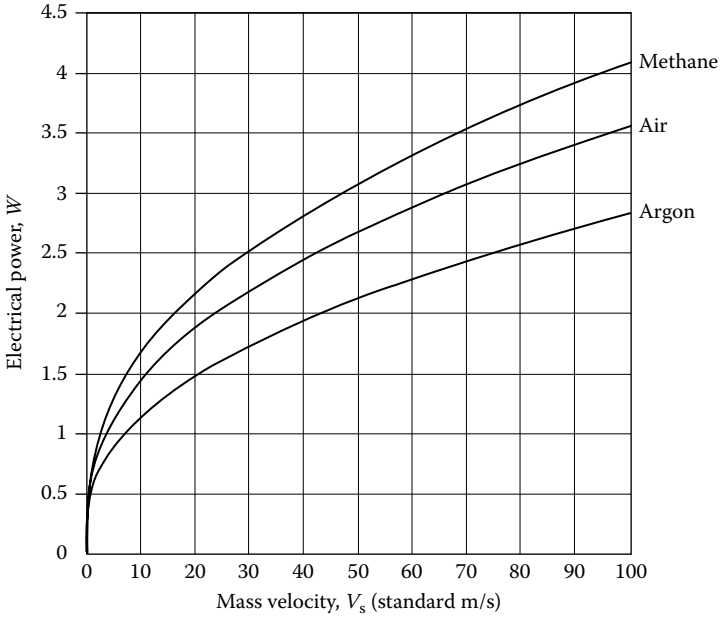

FIGURE 63.5 Typical outputs of the dry-sensor microprocessor-based system for three different gases. $T = 300$ K; $P = 1$ bara; $\Delta T = 50$ K. The "standard" conditions for V_s (standard m/s) are 70 °F and 1 atm. (Adapted from Olin, J.G., Advances in thermal dispersion mass flow meters—Part 1: Principle of operation, Sierra Instruments Technical Report No. SI-JGO-2010-1, 2010. With permission from Sierra Instruments, Inc.)

the independent variable and the electrical power W shown as the dependent variable, whereas in the system they have reversed roles. The three curves reflect the different values of thermal conductivity of the three gases, i.e., $k_{methane} > k_{air} > k_{argon}$.

Figure 63.5 also reveals the nonlinear, logarithmic nature of the output. Log versus Log plots of the three curves will reveal nearly straight lines over approximately 1–150 standard m/s. This logarithmic property is responsible for the exceptional rangeability and low-velocity sensitivity of thermal dispersion mass flow meters. A rangeability as high as 100:1 is common. Even higher rangeabilities are achieved with multirange flow calibration. Detectable minimum point mass velocities as low as approximately 0.1 standard m/s (20 standard ft/min) are reported by some manufacturers. In the early days of analog electronics, it was difficult to linearize the output of thermal dispersion mass flow meters. But now, with microprocessor-based electronics, it is not a problem, and the nonlinear, logarithmic nature of the output bears only advantages.

63.5 Flow Meter Selection, Installation, and Flow Calibration

In all cases, specifications and instructions provided by the manufacturer should be followed in selecting, sizing, and installing in-line and insertion thermal dispersion mass flow meters. Table 63.3 is helpful in the flow meter selection process. The specifications in Table 63.3 are typical of currently available thermal dispersion mass flow meters, but may vary from manufacturer to manufacturer. Accuracy specifications may apply to gas temperatures and gas pressures that lie within bands around their respective values at flow calibration. References [4,5,11] provide additional information regarding flow meter selection, installation, and flow calibration.

The vast majority of applications are gas flow applications because they benefit from the exceptional low-flow sensitivity and wide rangeability of measurement. Thermal dispersion technology is not well suited for liquid flow applications because at the zero-flow condition, a majority of the heat budget is carried away by the liquid via conduction, instead of the desired convection. This is caused

TABLE 63.3 Typical Specifications for Thermal Dispersion Mass Flow Meters

Quantity	Specification
Gases	Most clean gases, including air, methane, Ar, CO_2, He, N_2, O_2, propane, and mixtures of these components
In-line flow body sizes[a]	0.25, 0.5, 1.0, 1.5, 2.0, 4.0 in.; DN6 to DN100
In-line flow meter mass flow rate range for air[b]	0–1.5 kg/s; 0–2,600 scfm
Insertion flow meter mass velocity range for air[c]	0–140 normal m/s; 0–30,000 standard ft/min
Temperature range[d]	−40 °C to 200 °C; −40 °F to 392 °F
Pressure range	0.01–16 bara
Accuracy	±1% of reading plus 0.5% of full scale
Repeatability	±0.2% of full scale
Rangeability	100:1
Time response[e]	3 s (constant power operation); 1.2 s (constant ΔT operation)
Stability	1 year; typical drift 1%–2% per year (potted V-sensor) 10 years; typical drift 0.1% per year (dry V-sensor)

[a] Some manufacturers offer sizes up to 12.0 in. (DN300).

[b] Based on the point mass velocity ranges for insertion flow meters cited later.

[c] "Normal" conditions are 0°C and 1 atm, and "standard" conditions are 70°F and 1 atm.

[d] High-temperature models are available up to approximately 450 °C = 842 °F.

[e] Time response is the time required to reach 63% of the final value (i.e., the 1 sigma value).

by the high thermal conductivity of liquids relative to gases. The result is reduced measurement sensitivity for liquid flows. Additionally, for liquid flows, the temperature differential $\Delta T = T_1 - T$ must not exceed an upper critical limit, or else at higher flow rates, the liquid may flash to the vapor phase and subsequent cavitation may occur, creating unwanted erratic readings. For water flows, this upper critical limit in ΔT is approximately 10 °C–20 °C. The constant differential temperature mode of operation is preferred for liquid flows because ΔT is controlled, whereas in the constant current mode, ΔT varies and may exceed the upper critical limit. Application of thermal dispersion technology to liquid flows has been limited to cases, such as ultra-low flow applications, where it offers advantages over other technologies.

As with most kinds of flow meters, the performance of thermal dispersion mass flow meters can be degraded if the flow meter is installed where flow conditions are different than those for which it was flow calibrated. Improper installation is the single biggest cause of measurement inaccuracy for any kind of flow meter. Components in the piping system upstream and, to a far lesser extent, downstream of the flow meter can create nonuniformities in the flow profile, swirls, and turbulence. All of these phenomena degrade performance. Such flow-disturbing components include single or multiple elbows, expansions, contractions, tees, valves, and pumps. Fortunately, viscous forces in a sufficiently long length of straight pipe upstream and downstream of the flow meter reduce swirl and drive the flow toward a fully developed velocity profile. In-line flow meters with a built-in flow conditioner greatly reduce the need for long runs of straight pipe upstream of the flow meter. For example, the in-line flow meter shown in Figure 63.1a has a built-in flow conditioner upstream of the flow sensor consisting of two separated perforated plates. Flow meters with this built-in flow conditioner require only 1 diameter of straight pipe upstream when located downstream of a single elbow. In contrast, for this same case, an orifice plate flow meter with a 0.7 beta ratio requires 28 diameters of straight pipe upstream.

Because the critical dimensions of the flow sensor of thermal dispersion mass flow meters are so small, manufacturing technology is generally incapable of maintaining sufficiently small tolerances to ensure a high degree of reproducibility from flow sensor to flow sensor. Additionally, the internal diameters of the pipes used in in-line flow bodies have substantial variations. For these reasons, every general-purpose thermal dispersion mass flow meter is flow calibrated by the manufacturer, just like most other kinds of flow meters. Exceptions may include flow switches and low-accuracy flow meters.

The gas flow calibration facilities of manufacturers, flow calibration laboratories, and users should be capable of (1) generating a stable, steady-state, reproducible gas mass flow rate; (2) accommodating the entire mass flow rate range specified; (3) having a flow calibration standard that has an accuracy at least three times better than the flow meter under test; and (4) reproducing the gas composition, temperature, and pressure to be encountered in the actual application. Gas flow calibration facilities are of two types: open loop and closed loop.

Closed-loop facilities are preferred because they allow flow calibration at elevated pressures and temperatures and with gases other than air. A good pressurized closed-loop system has the following major components, listed in flow sequence: (1) a gas charging source, such as a compressed gas tank; (2) a flow source, such as a high pressure axial or centrifugal in-line pump; (3) a flow controller, such as a precision flow control valve; (4) a flow-conditioning section upstream of the flow calibration standard; (5) the in-line flow calibration standard (more than one may be needed to cover the mass flow rate range); (6) a flow-conditioning section upstream of the flow meter under test; and (7) the flow meter under test. Additionally, the facility should have accurate gas temperature and pressure instrumentation at both the flow calibration standard and the flow meter under test, pressure relief and venting components, and a vacuum pump for evacuating the system prior to charging. High-accuracy in-line flow calibration standards include custody-transfer grade multipath ultrasonic flow meters, turbine flow meters, flow nozzles, and positive-displacement flow meters.

63.5.1 Manufacturers

Following is a list of major manufacturers of thermal dispersion mass flow meters for general industrial applications. Details regarding their contact information, products, and current pricing are found in their websites.

- Sierra Instruments, Inc.; Monterey, California
- Endress and Hauser, Inc.; Reinach, Switzerland
- Fluid Components International, LLC; Costa Mesa, California

References

1. King, L. V. 1914. On the convection of heat from small cylinders in a stream of fluid: Determination of the convection constants of small platinum wires with application to hot-wire anemometry. *Phil. Trans. Roy. Soc*. A214: 373–432.
2. Agarwall, J. K. and J. G. Olin, Thermal anemometry, in Webster, J. G. and H. Eren (eds.), *The Measurement, Instrumentation and Sensors Handbook*, 2nd edn., CRC Press, Boca Raton, FL, 2013.
3. Olin, J. G. 2010. Advances in thermal dispersion mass flow meters—Part 1: Principle of operation. Sierra Instruments Technical Report No. SI-JGO-2010-1.
4. Olin, J. G. 2010. Advances in thermal dispersion mass flow meters—Part 2: Installation and flow calibration. Sierra Instruments Technical Report No. SI-JGO-2010-2.
5. ANSI/ASME MFC-21.2-2011. 2011. Measurement of fluid flow by means of thermal dispersion mass flowmeters. Washington, DC: ANSI/ASME.
6. ANSI/ASME MFC-9M, 2008, Measurement of fluid flow by means of capillary tube thermal mass flowmeters and controllers. Washington, DC: ANSI/ASME.
7. ANSI/ASME MFC-15M. 2001, Insertion metering. Washington, DC: ANSI/ASME.
8. Olin, J. G. 1993. A thermal mass flow monitor for continuous emissions monitoring systems (CEMS). *Proceedings of ISA/93 International Conference, Exhibition and Training Program* 93–404: 1635–1653.
9. Bruun, H. H. 1995. *Hot-Wire Anemometry: Principles and Signal Analysis*. Oxford, U.K.: Oxford University Press.
10. Olin, J. G. 1999. Industrial thermal mass flowmeters—Part 1: Principles of operation. *Measurement. Control* 193(February): 83–90.
11. Olin, J. G. 1999. Industrial thermal mass flowmeters—Part 2: Applications. *Measurement. Control* 194(April): 1–6.
12. Miller, R. W. 1996. *Flow Measurement Engineering Handbook*, 3rd edn. New York: McGraw-Hill.

64

Laser Anemometry

Rajan K. Menon
TSI Inc.

Laser anemometry, or *laser velocimetry,* refers to any technique that uses lasers to measure velocity. The most common approach uses the Doppler shift principle to measure the velocity of a flowing fluid at a point and is referred to as Laser Doppler Velocimetry (LDV) or Laser Doppler Anemometry (LDA). This technique (also known as dual beam, differential Doppler, or fringe mode technique), incorporating intersecting (focused) laser beams, is also used to measure the motion of surfaces, for example, in industrial applications [1]. In some special flow situations, another approach using two *nonintersecting,* focused laser beams known as *Laser two focus* (also known as Laser transit velocimetry or L2F) technique is used to measure flow velocity at a point [2]. Laser illumination by light sheets is used to make global flow measurements in a plane and is referred to as *Particle Image Velocimetry* (PIV) [3]. The strength of PIV (including particle tracking velocimetry) lies in its ability to capture instantaneous velocity fields, extract turbulence structures within the flow, observe transient phenomena, and examine unsteady flows. The development of this technique to obtain both spatial and temporal information about flow fields is making this a powerful diagnostic tool in fluid mechanics research [4–6]. More recently, using pulsed-laser volume illumination (in place of light sheet illumination), combined with multi-camera capture of particle images in a volumetric region in the flow, has provided the instantaneous velocity vector field in the three-dimensional domain [7]. Other approaches to measure global flow velocities come under the category of molecular tagging velocimetry [8] or Doppler global velocimetry [9].

The noninvasive nature of the LDV technique and its ability to make accurate velocity measurements with high spatial and temporal resolution, even in highly turbulent flows, have led to the widespread use of LDV for flow measurement. Flow velocities ranging from micrometers per second to hypersonic speeds have been measured using LDV systems. Measurements of flows in rotating machinery, including in the interblade region of rotors, flows in combustors and engines, flows at high temperatures, and flows in small spaces and in other hostile environments have been performed using the LDV technique [10–17].

The versatility and the widespread use of the LDV approach to measure flows accurately have resulted in referring to this technique as *laser velocimetry* or *laser anemometry*. Many details of the technique, including some of the early developments of the hardware, are provided in the book by Durst [18]. A bibliography of the landmark papers in LDV has been compiled by Adrian [19].

For the case of spherical scatterers, the technique has also been extended to measure the size of these particles. In this case, the scattered light signal collected by a suitably placed receiver system is converted into an electrical signal (by a photodetector) and processed to obtain the diameter of the particle, using the phase Doppler technique [20,21].

The first reported fluid flow measurements using LDV principles were by Yeh and Cummins [22]. Although in this case an optical arrangement referred to as the reference beam system was used to measure the Doppler shift, in almost all measurement applications, what is referred to as the dual beam or differential Doppler arrangement is used. This arrangement, also referred to as the "fringe" mode of operation, uses two intersecting laser beams (Figure 64.1) to measure one velocity component.

The advantages of the LDV technique in measuring flows include (1) a small measuring region (i.e., point measurement), (2) high measurement accuracy, (3) the ability to measure any desired velocity component, (4) accurate measurement of high-turbulence intensities, including flow reversals, (5) a large dynamic range, (6) no required velocity calibration, (7) no probe in the flow (does not disturb the flow; measures in hostile environments), and (8) good frequency response.

LDV technique relies on the light scattered by scattering centers in the fluid to measure flow velocity. These scattering centers will also be referred to as *particles,* with the understanding that bubbles or anything else that has a refractive index different from that of the fluid could be the source of scattered light. The particles, whose velocities are measured, must be small enough (generally in the micrometer range) to follow the flow variations and large enough to provide signal strength adequate for the signal processor to give velocity measurements. It should be noted that the signal exists only when a "detectable" particle is in the measuring volume and, hence, is discontinuous. This, along with other properties of the signal, places special requirements on the signal processing and the subsequent data analysis systems. The scattered light signal is processed to obtain the Doppler shift frequency and from that the velocity of

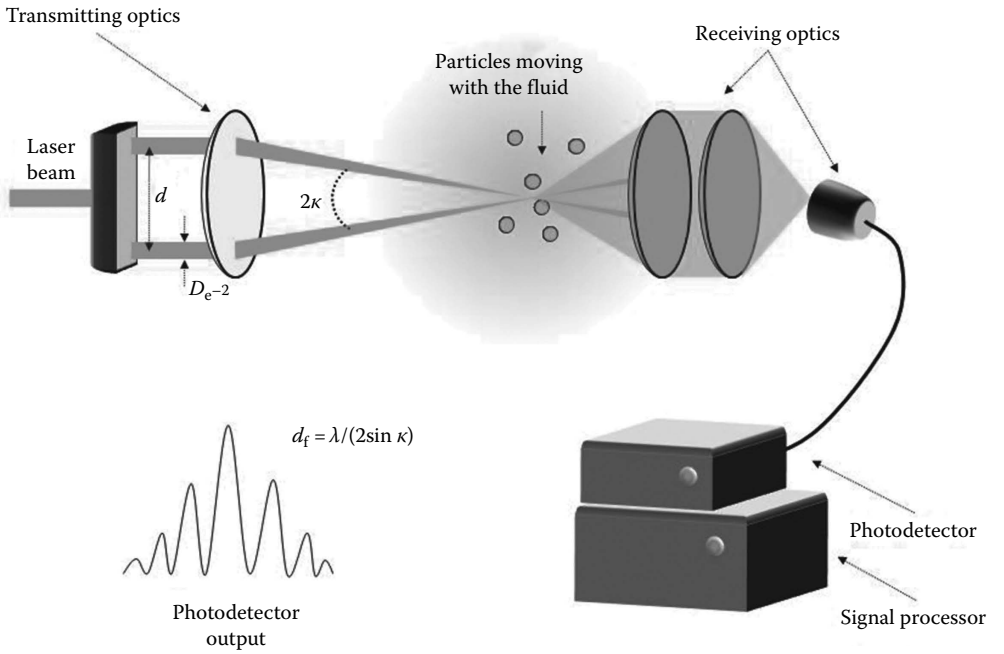

FIGURE 64.1 Schematic of a dual-beam system.

the particle. Hence, the rate at which the velocity measurements are made depends on the rate of particle arrival. It is desirable to have a high particle concentration to obtain a nearly continuous update of velocity. In carefully controlled experiments, the LDV system can provide very high accuracy (0.1% or better in mean velocity) measurements. Thermal anemometer systems are generally able to measure lower turbulence levels compared to that by an LDV system [23]. While the direct measurement of the Doppler-shifted frequency from a single laser beam caused by a moving particle is possible, most LDV systems employ the heterodyne principle to obtain and process only the Doppler shift (difference) frequency.

64.1 Principle of Operation

64.1.1 Dual-Beam Approach

The dual-beam approach is the most common optical arrangement used for LDV systems for flow measurement applications. The schematic (Figure 64.1) shows the basic components of a complete LDV system to measure one component of velocity. The transmitting optics includes an optical element to split the original laser beam into two parallel beams and a lens system to focus and cross the two beams. The intersection region of the two beams becomes the measuring region. The receiving optics (shown to be set up in the forward direction) collects a portion of the light scattered by the particles, in the fluid stream, passing through the beam-crossing region (measuring volume) and direct this light to a photodetector, which converts the scattered light intensity to an analog electrical signal. The frequency of this signal is proportional to the velocity of the particle. A signal processor extracts the frequency information from the photodetector output and provides this as a digital number corresponding to the instantaneous velocity of the particle. The data processing system obtains the detailed flow properties from these instantaneous velocity measurements. The idealized photodetector signal, for a particle passing through the center of the measuring volume, is shown in the lower left side of Figure 64.1. Actual signals will have noise superimposed on them, and the signal shape will vary, depending on the particle trajectory through the measuring volume [21,24].

64.1.1.1 Fringe Model Description

While there are several ways to describe the features of a dual-beam system, the description based on a fringe model is, perhaps, the simplest. For simplicity, the diameter and the intensity of both the beams are assumed to be the same. After the beams pass through the transmitting lens, the diameter of each beam continuously decreases to a minimum value (beam waist) at the focal point of the lens and then increases again. Thus, the beam waists cross where the two laser beams intersect (at the focal point of the lens), and the wavefronts in the beams interfere with each other, creating a fringe pattern [21]. In this pattern, assuming equal-intensity beams and other needed qualities of the beams, the light intensity varies from zero (dark fringe) to a maximum (bright fringe), and the fringes are equally spaced. The particles in the flow passing through the intersection region (measuring region) scatter light in all directions. An optical system, including a receiving lens (to collimate the scattered light collected) and a focusing lens, is used to collect the scattered light and focus it on to the detector. The aperture in front of the receiver is used to block out stray light and reflections and collect only the light scattered from the measuring region.

As a particle in the flow, with velocity u, moves across the fringes, the intensity pattern of the light scattered by the particle resembles that shown in the lower left of Figure 64.1. The velocity component, u_y (perpendicular to the optical axis and in the plane of the incident beams) can be obtained from the ratio of the distance between fringes (or fringe spacing, d_f), and the time t (=$1/f_D$) for the particle to cross one pair of fringes, where f_D is the frequency of the signal. The amplitude variation of the signal reflects the Gaussian intensity distribution across the laser beam. Collection (receiving) optics for the dual-beam system can be placed at any angle, and the resulting signal from the receiving system will still give the same frequency. However, signal quality and intensity will vary greatly with the collection optics angle.

64.1.1.2 Doppler Shift Explanation

The description of the dual-beam system using the Doppler shift principle is as follows. At the receiver, the frequencies of the Doppler-shifted light scattered by a particle from beam one and beam two are given by

$$\nu_{D1} = \nu_{01} + \frac{\vec{u}}{\lambda}\left(\hat{r} - \hat{S}_1\right); \quad \nu_{D2} = \nu_{02} + \frac{\vec{u}}{\lambda}\left(\hat{r} - \hat{S}_2\right) \tag{64.1}$$

where

ν_{01} and ν_{02} are the frequencies of laser beam 1 and laser beam 2, respectively
$\hat{r}$ is the unit vector directed from the measuring volume to the receiving optics
$\hat{S}_1$ and $\hat{S}_2$ are the unit vectors in the direction of incident beam 1 and incident beam 2, respectively
$\vec{u}$ is the velocity vector of the particle (scattering center)
λ is the wavelength of light

The frequency of the net (heterodyne) signal output from the photodetector system is given by the difference between ν_{D1} and ν_{D2}:

$$f_D = f_s + \frac{\vec{u}}{\lambda}\left(\hat{S}_2 - \hat{S}_1\right) \tag{64.2}$$

where $f_s = \nu_{01} - \nu_{02}$ is the difference in frequency between the two incident beams. This difference frequency is often intentionally imposed (see Section 64.1.2) to permit unambiguous measurement of flow direction and high-turbulence intensities. Assuming $f_s = 0$, the frequency detected by the photodetector is

$$f_D = \frac{\dot{u}}{\lambda}\left(\hat{S}_2 - \hat{S}_1\right) = 2u_y \sin k \tag{64.3}$$

Hence,

$$u_y = \frac{f_D \lambda}{2 \sin k} = f_D d_f \tag{64.4}$$

This is the equation for u_y and shows that the signal frequency f_D is directly proportional to the velocity component u_y. The heterodyning of the scattered light from the two laser beams at the photodetector actually gives both the sum and difference frequency. However, the sum frequency is too high to be detected, and so only the difference frequency ($\nu_{D1} - \nu_{D2}$) is output from the photodetector as an electrical signal. The frequency f_D is often referred to as the Doppler frequency of the output signal, and the output signal is referred to as the Doppler signal.

It can be seen from Equation 64.4 that the Doppler frequency is independent of the receiver location ($\hat{r}$). Hence, the receiver system location can be chosen based on considerations such as signal strength, ease of alignment, and clear access to the measuring region. The expressions for the other optical configurations can be reduced similarly [24], giving the identical equation for the Doppler shift frequency f_D. It should be noted that the fringe description does not involve a "Doppler shift" and is, in fact, not always appropriate. The fringe model is convenient and gives the correct expression for the frequency. However, it can be misleading when studying the details of the Doppler signal (e.g., signal-to-noise ratio [SNR]) and other important parameters, for example, modulation depth or visibility ($\overline{V}$) of the signal [21,24].

The time taken by the particle to cross the measuring volume is referred to as *transit time, residence time,* or *total burst time,* τ_B, and corresponds to the duration of the scattered light signal. The number of cycles (N) in the signal (same as the number of fringes the particle crosses) is given by the product of the transit time (τ_B) and the frequency, f_D, of the signal.

It should also be noted that the fringe spacing (d_f) depends only on the wavelength of the laser light (λ) and the angle (2κ) between the two beams. It can be shown that the effect of the fluid refractive index on these two terms tends to cancel out, and hence, the value of fringe spacing is independent of the fluid medium [25]. The values of λ and κ are known for any dual-beam system, and hence, an actual velocity calibration is not needed. In some cases, an actual velocity calibration using the rim of a precisely controlled rotating wheel has been performed to overcome the errors in measuring accurately the angle between the beams.

The intensity distribution in a laser beam operating in the TEM_{00} mode is Gaussian. Using wave theory and assuming diffraction-limited optics, the effective diameter of the laser beam and the size of the measurement region can be defined. The conventional approach to the definition of laser beam diameter and measuring volume dimensions is based on the locations where the light intensity is $1/e^2$ of the maximum intensity (at the center of the beam). This definition of the dimensions is analogous to that of the boundary layer thickness. The dimensions d_m and l_m of the ellipsoidal measuring volume (Figure 64.2) are based on the $1/e^2$ criterion and are given by

$$d_m = \frac{4f\lambda}{\pi D_{e^{-2}}}; \quad l_m = \frac{d_m}{\tan\kappa}; \quad N_{FR} = \frac{d_m}{d_f} \tag{64.5}$$

N_{FR} is the maximum number of fringes in the ellipsoidal measuring region. Note that as the value of $D_{e^{-2}}$ increases, the measuring volume becomes smaller. In flow measurement applications, this relationship is exploited to arrive at the desired size of the measuring volume.

Consider the following sample optical arrangement of wavelength, $\lambda = 514.5$ nm (green line of argon-ion laser), $D_{e^{-2}} = 1.1$ mm, $d = 35$ mm, and $f = 250$ mm. Then, $\kappa = 4°$, and the measuring volume parameters are $d_m = 149$ μm, and $l_m = 2.13$ mm. The fringe spacing, d_f, is 3.67 μm and the maximum number (N_{FR}) of fringes (same as the number of cycles in a signal burst generated by a particle going through the center of the measuring volume in the y-direction) in the measuring volume is 40. Consider a particle

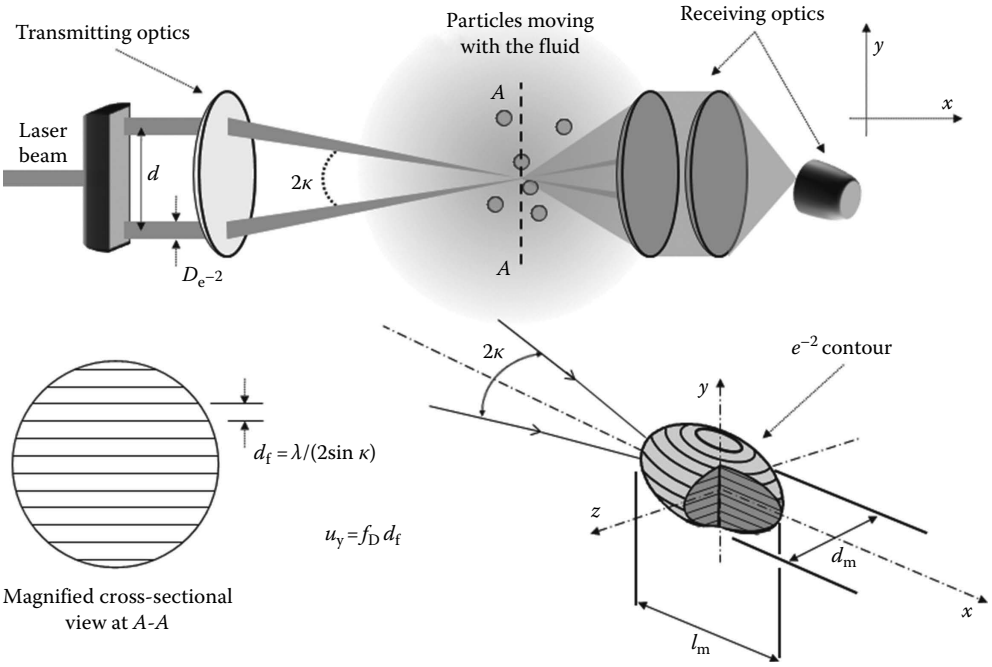

FIGURE 64.2 Details of the beam crossing.

passing through the center of the measuring region with a velocity (normal to the fringes) of 15 m s^{-1}. This would generate a signal with a frequency of 4.087 MHz. The transit time of the particle (same as the duration of the signal) would be approximately 9.93 μs!

64.1.2 Frequency Shifting

The presence of high-turbulence intensity and recirculating or oscillatory flow regions is common in most flow measuring situations. In the fringe model and the Doppler shift (with $f_s = 0$) descriptions of the dual-beam system, the Doppler signal does not indicate the influence of the sign (positive or negative) of the velocity. Further, a particle passing through the measuring volume parallel to the fringes would not cross any fringes and, hence, would not generate a signal having the cyclic pattern, resulting in the inability to measure the zero normal (to the fringes) component of velocity. In addition, signal processing hardware used to extract the frequency information often requires the signals to have a minimum number of cycles. This, as well as the ability to measure flow reversals, is achieved by a method of frequency offsetting referred to as *frequency shifting*. Frequency shifting is also used to measure small velocity components perpendicular to the dominant flow direction and to increase the effective velocity measuring range of the signal processors [25].

By introducing a phase or frequency offset (f_s) to one of the two beams in a dual-beam system, the directional ambiguity can be resolved. From the fringe model standpoint, this situation corresponds to a moving (instead of a stationary) fringe system. A stationary particle in the measuring volume will provide a continuous signal at the photodetector output whose frequency is equal to the difference in frequency, f_s, between the two incident beams. In other words, as shown in Figure 64.3b, the linear curve

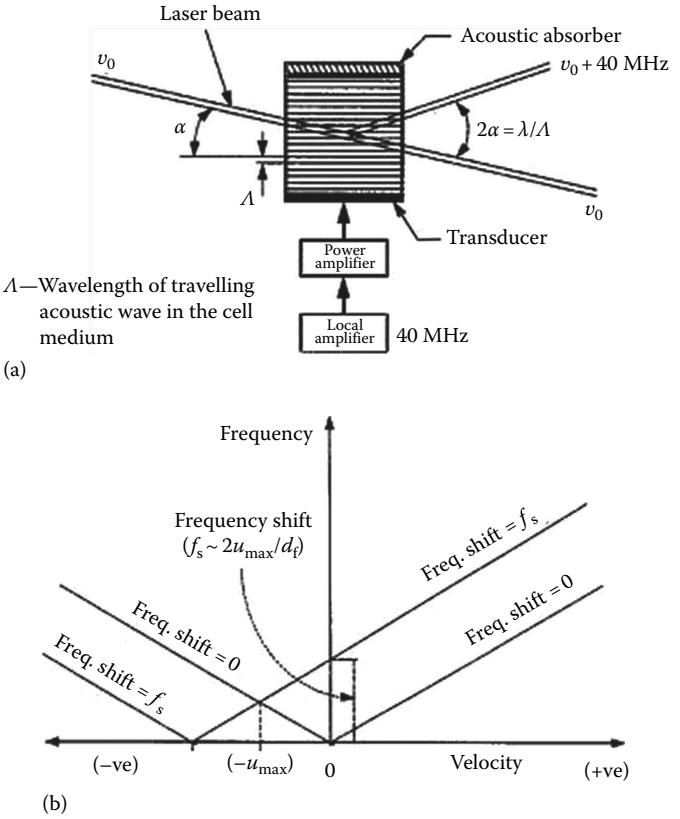

FIGURE 64.3 (a) Bragg cell arrangement; (b) velocity vs. frequency.

between velocity and frequency is offset along the positive frequency direction by an amount equal to the frequency shift, f_s. Motion of a particle in a direction opposite to fringe movement would provide an increase in signal frequency, while particle motion in the direction of fringe motion would provide a decrease in frequency. To create a signal with an adequate number of cycles even while measuring negative velocities (e.g., flow reversals, recirculating flows), a convenient "rule-of-thumb" approach for frequency shifting is often used. The approach is to select the frequency shift ($f_s \sim 2u_{max}/d_f$) to be approximately twice the frequency corresponding to the magnitude of the maximum negative velocity (u_{max}) expected in the flow. This provides approximately equal probability of measurement for all particle trajectories through the measuring volume [21].

Frequency shifting is most commonly achieved by sending the laser beam through a Bragg cell (Figure 64.3a), driven by an external oscillator. Typically, the propagation of the 40 MHz acoustic wave (created by a 40 MHz drive frequency) inside the cell affects the beam passing through the cell to yield a frequency shift of 40 MHz for that beam. By properly adjusting the angle the cell makes with the incoming beam and blocking off the unwanted beams, up to about 80% of input light intensity is recovered in the shifted beam. The Bragg cell approach will provide a 40 MHz frequency shift in the photodetector output signal. To improve the measurement resolution of the signal processor, the resulting photodetector signal is often "downmixed" to have a more appropriate frequency shift (based on the rule-of-thumb shift value) for the flow velocities being measured. Frequency shifting using two Bragg cells (one for each beam of a dual-beam system) operating at different frequencies is attractive to systems where the bandwidth of the photodetector is limited. However, the need to readjust the beam crossing with a change in frequency shift has not made this approach (double Bragg cell technique) attractive for applications where frequency shift needs to be varied [25].

More recently, Bragg cells have been used in a multifunctional mode to split the incoming laser beam into two equal-intensity beams, with one of them having the 40 MHz frequency shift. This is accomplished by adjusting the Bragg cell angle differently. In addition to Bragg cells, rotating diffraction gratings and other mechanical approaches have been used for frequency shifting. However, limits on rotational speed and other mechanical aspects of these systems make them limited in frequency range [18]. Other frequency-shifting techniques also have been suggested for use with LDV [21]. Because so many flow measurement applications involve recirculating regions and high-turbulence intensities, frequency shifting is almost always a part of an LDV system used for flow measurement.

64.1.3 Signal Strength

Understanding the influence of various parameters of an LDV system on the SNR of the photodetector signal provides methods or approaches to enhance signal quality and hence improve the performance of the measuring system. The basic equation for the ratio of signal power to noise power (SNR) of the photodetector signal can be written as [24]

$$\mathrm{SNR} = A_1 \frac{\eta_q P_0}{\Delta f}\left[\frac{D_a}{r_a}\frac{D_{e^{-2}}}{f}\right]^2 d_p^2 \bar{G}\bar{V}^2 \tag{64.6}$$

Equation 64.6 shows that higher laser power (P_0) provides better signal quality. The quantum efficiency of the photodetector, η_q, depends on the type of photodetector used and is generally fixed. The SNR is inversely proportional to the bandwidth, Δf, of the Doppler signal. The term in brackets relates to the optical parameters of the system: the "f-number" of the receiving optics, D_a/r_a, and parameters associated with the transmitting optics, $D_{e^{-2}}/f$. The square dependence of SNR on these parameters makes them the prime choice for improving signal quality and, hence, measurement accuracy. The focal length of the transmitting (f) and receiving (r_a) lenses is generally decided by the size of the flow facility. Using the smallest possible values for these would

increase the signal quality. The first ratio (D_a is the diameter of the receiving lens) determines the amount of the scattered light that is collected, and the second ratio determines the diameter of (and hence the light intensity in) the measuring volume. The last three terms are the diameter, d_p, of the scattering center and the two terms (scattering gain $\overline{G}$, visibility $\overline{V}$) relating to properties of the scattered light. These need to be evaluated using the Mie scattering equations [24] or the generalized Lorenz–Mie theory [21].

64.1.4 Measuring Multiple Components of Velocity

A pair of intersecting laser beams is needed to measure (Figure 64.1) one component of velocity. This concept is extended to measure two components of velocity (perpendicular to the optical axis) by having two pairs of beams that have an overlapping intersection region. In this case, the plane of each pair of beams is set to be orthogonal to that of the other. The most common approach to measure two components of velocity (such a system is referred to as a two-component system) is to use a laser source that can generate multiwavelength beams so that the wavelength of one pair of beams is different from that of the other pair. The Doppler signals corresponding to the two components of velocity are separated by wavelength [21,24].

Historically, LDV systems were assembled by putting together a variety of optical modules. These modules included beam splitters, color separators, polarization rotators, and scattered light collection systems. The size of such a modular system depended on the number of velocity components to be measured.

The use of optical fibers along with multifunctional optical elements has made the systems more compact, flexible, and easier to make measurements. The laser, optics to generate the necessary number of beams (typically, one pair per component of velocity to be measured), photodetectors, and electronics can be isolated from the measurement location. The fibers carrying the laser beams thus generated are arranged in the probe to achieve the desired beam geometry for measuring the velocity components. Hence, flow field mapping is achieved by moving only the fiber-optic probes, while keeping the rest of the system stationary. To achieve maximum power transmission efficiency and beam quality, special single-mode, polarization-preserving optical fibers along with precision couplers are used. In most cases, these fiber probes also have a receiving system and a separate fiber (multimode) to collect (in back scatter) the scattered light and carry that back to the photodetector system [21].

A schematic arrangement of a fiber probe system to measure one component of velocity is shown in Figure 64.4a. In flow measurement applications, LDV systems using these types of fiber-optic probes have largely replaced the earlier modular systems.

The best way to make three-component velocity measurements is to use an arrangement using two probes—a two-component probe and a single-component probe. In this case, the obvious orientation of the optical axis of the system to measure the third component of velocity (u_x) would be perpendicular to that of the two-component system. Unfortunately, access and/or traversing difficulties, often, make this arrangement impractical or less attractive. In most practical situations, the angle between the two probes is selected to be less than 90° [11,16,21].

Another three-component LDV system configuration uses a single fiber-optic probe by effectively combining the laser beams associated with the two-probe arrangement. This system incorporating a single-lens coaxial probe, with five laser beams, is used to make measurements in regions with limited access or map the velocity vector fields in liquid flows in channels and tunnels [25,26].

More recently, the availability of solid-state lasers with reasonable power levels and good beam quality has resulted in configuring compact LDV systems. These compact systems (Figure 64.4b) have the lasers integrated with the required optics to measure one or two components of velocity, simultaneously. Such an arrangement using a diode laser to measure two components of velocity, simultaneously, is shown in Figure 64.5.

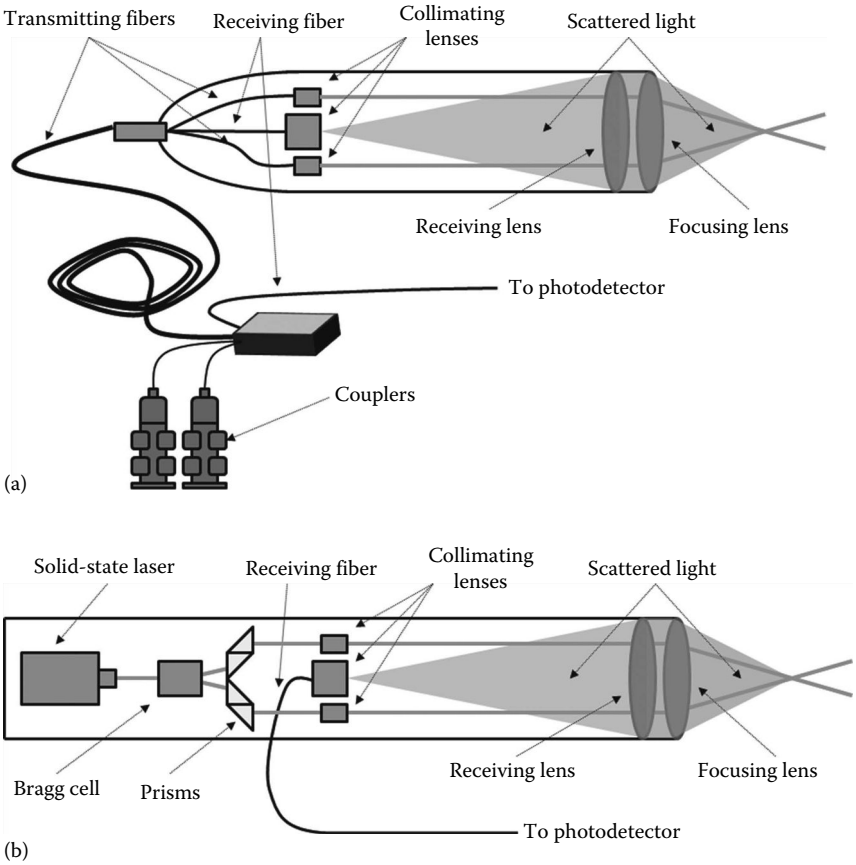

FIGURE 64.4 (a) Schematic arrangement of a fiber-optic system; (b) schematic arrangement of a diode laser-based system.

FIGURE 64.5 Two-component LDV system with diode laser and integrated optics.

64.2 Signal Processing

64.2.1 Nature of the Signal

Every time a particle passes through the measuring region, the scattered light signal level (Figure 64.6) suddenly increases ("burst"). The characteristics of the burst signal are (1) amplitude in the burst not constant, (2) lasts for only a short duration, (3) amplitude varies from burst to burst, (4) presence of noise, (5) high frequency, and (6) random arrival.

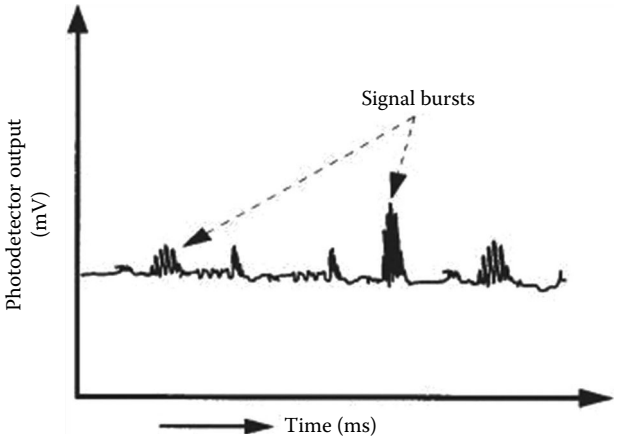

FIGURE 64.6 Time history of the photodetector signal.

The primary task of the LDV signal processor is to extract the frequency information from the burst signal generated by a particle passing through the measuring volume and provide an analog or digital output proportional to the frequency of the signal. The unique nature of the signals demands the use of a special signal processing system to extract the velocity information.

A variety of techniques have been used for processing Doppler signals. Signal processors have been based on spectrum analysis, frequency tracking, photon correlation, frequency counting, Fourier transform, and autocorrelation principles. The evolution of the signal processing techniques shows the improvement in their ability to handle more difficult measuring situations (generally implies noisier signals), give more accurate measurements, and have higher processing speed.

The traditional instrument to measure signal frequency is a spectrum analyzer. The need to measure individual particle velocities, and to obtain the time history and other properties of the flow, has eliminated the use of "standard" spectrum analyzers [24]. The "tracker" can be thought of as a fixed-bandwidth filter that "tracked" the Doppler frequency as the fluid velocity changed. This technique of "tracking flow" worked quite well at modest velocities and where the concentration of scattering centers was high enough to provide an essentially continuous signal. However, too frequently, these conditions could not be met in the flows of most interest.

When the scattered light level is very low, the photodetector output reveals the presence of the individual photon pulses. By correlating the actual photon pulses from a wide bandwidth photodetector, the photon correlator was designed to work in situations where the attainable signal intensity was very low (low SNR). However, as normally used, it could not provide the velocity of individual particles but only the averaged quantities, such as mean velocity and turbulence intensity.

The "counter" type processor was developed next and basically measured the time for a certain number (typically, eight) of cycles of the Doppler signal. Although it measured the velocity of individual particles, its performance depended on the careful setting of amplifier gain and, especially, threshold levels to discriminate burst signals from background noise. Counters were the processors of choice for many years, and excellent measurements were obtained. However, the reliance on user skill, difficulty in handling low SNR signals, possibility of getting erroneous measurements, inclination to ignore signals from small particles, and desire to make measurements close to surfaces and in complex flows led to the need for a better signal processor.

64.2.2 Digital Signal Processing

The latest development in signal processing is in the area of digital signal processors. Developments in high-speed digital signal processing permit the use of these techniques to extract the frequency, from individual Doppler bursts, fast enough to actually follow the flow when the seeding concentration is adequate,

in a wide range of measurement situations. By digitizing the incoming signal and using the Fourier transform or autocorrelation algorithms, these new digital processors can work with lower SNR signals (than counters), while generally avoiding erroneous data outputs [21,27,28]. While instruments using these techniques are certainly not new, standard instruments were not designed to make rapid individual measurements on the noisy, short-duration burst signals with varying amplitudes that are typical of Doppler bursts.

Because the flow velocity and hence the signal frequency vary from one burst to the next, the sampling rate needs to be varied accordingly. And because the signal frequency is not known *a priori,* the ability to optimally sample the signal has been one of the most important challenges in digital signal processing. In one of the digital signal processors, the question of deciding the sample rate is addressed by a burst detector that uses SNR to identify the presence of a signal [28]. In addition, the burst detector provides the duration and an approximate estimate of the frequency of each of the burst signals. This frequency estimate is used to select the output of the sampler (from the many samplers) that had sampled the burst signal at close to the optimum rate. Besides optimizing the sample rate for each burst, the burst detector information is also used to focus on and process the middle portion of the burst where the SNR is maximum. These optimization schemes, followed by digital signal processing, provide an accurate digital output that is proportional to the signal frequency, and hence the fluid velocity and detailed flow statistics [29].

64.3 Seeding and Other Aspects

The performance of an LDV system can be significantly improved by optimizing the source of the signal, the scattering particle. The first reaction of many experimentalists is to rely on the particles naturally present in the flow. There are a few situations (e.g., LDV systems operating in forward scatter to measure water or liquid flow velocities) where the particles naturally present in the flow are sufficient in number and size to provide good signal quality and, hence, good measurements. In most flow measurement situations, particles are added to the flow (generally referred to as seeding the flow) to obtain an adequate number of suitable scatterers. Use of a proper particle can result in orders-of-magnitude increase in signal quality (SNR), and, hence, can have greater impact on signal quality than the modification of any other component in the LDV system. Ideally, the seed particles should be naturally buoyant in the fluid, provide adequate scattered light intensity, have large enough number-concentration, and have uniform properties from particle to particle. While this ideal is difficult to achieve, adequate particle sources and distribution systems have been developed [21,24,30–32].

LDV measurements of internal flows such as in channels, pipes, and combustion chambers result in the laser beams (as well as the scattered light) going through transparent walls or "windows." In many cases, the window is flat and, hence, the effect of light refraction can be a simple displacement of the measuring region. In the case of internal flows with curved walls, each beam can refract by different amounts, and the location of the measuring region needs to be carefully estimated [33]. For internal flows in models with complex geometries, the beam access needs to be carefully selected so that the beams do cross inside. Further, to make measurements close to the wall in an internal flow, the refraction effect of the wall material on the beam path needs to be minimized. One of the approaches is to use a liquid [21,34] that has the same refractive index as that of the wall material.

To make velocity measurements near a boundary or a wall, light reflected from these background surfaces need to be reduced. Fluorescent seed particles [21,30] would generate, as they pass through the measuring region, a signal that is different in wavelength from that of the laser light and, hence, the reflected light. Thus, the impact of reflected light can be minimized by the use of receiver systems with proper optical filters (band pass) that collect the fluoresced wavelength light and filter out other wavelengths. In some cases, surfaces were painted with a fluorescent paint to reduce the influence of reflected light [35].

Properties of the scattered light signal have also been used in discriminate phases (in two-phase flows) to obtain velocity distribution of different phases or distinguish large and small particles. Fluorescent seed particles were used in two-phase flows to discriminate the phases [45], whereas signal amplitude [46] was used to separate gas and particle phases and get the corresponding velocity distributions.

64.4 Data Analysis

The flow velocity is "sampled" by the particle passing through the measuring volume, and the velocity measurement is obtained only when the Doppler signal, created by the particle, is processed and output as a data point by the signal processor. While averaging the measurements to get, for example, mean velocity would seem reasonable, this method may give the wrong answer. This arises from the fact that the number of particles going through the measuring region per unit time is higher at high velocities than at low velocities. In effect, there is a correlation between the measured quantity (velocity) and the sampling process (particle arrival). Hence, a simple average of the data points will bias the mean value (and other statistical parameters) toward the high-velocity end and is referred to as *velocity bias* [36]. The magnitude of the bias error depends on the magnitude of the velocity variations about the mean. If the variations in velocity are sufficiently small, the error might not be significant.

If the actual data rate is so high that the output data are essentially able to characterize the flow (time history), then the output can be sampled at uniform time increments. This is similar to the procedure normally used for sampling a continuous analog signal using an ADC. This will give the proper value for both the mean and the variance when the data rate is sufficiently high compared to the rates based on the Taylor microscale for the temporal variation of velocity. This is referred to as a high data density situation [24].

In many measurement situations, the data rate is not high enough (low data density) to actually characterize the flow. Here, sampling the output of the signal processor at uniform time increments will not work because the probability of getting an updated velocity (new data point) is higher at high velocity than at low velocity. The solution to the velocity bias problem is to weight the individual measurements with a factor inversely proportional to the probability of making the measurement:

$$\bar{U} = \frac{\Sigma u_j \tau_{B_j}}{\Sigma \tau_{B_j}} \tag{64.7}$$

where

u_j is the velocity of particle j

τ_{Bj} is the transit time for particle j

Similar procedures can be used to obtain unbiased estimators for variance and other statistical properties of the flow [24,17]. Modern signal processors provide the residence time and the time between data points along with the velocity data. Comparison of some of the different approaches to do bias correction and other types of biases associated with LDV has been summarized [17,21,37].

A variety of techniques to obtain spectral information of the flow velocity from the random data output of the signal processors have been tried. The goal of all these techniques has been to get accurate and unbiased spectral information to as high a frequency as possible. Direct spectral estimation of the digital output of the processors exhibits the spectrum estimates at high frequency to be less reliable. The "slotting" technique of estimating the autocorrelation of the (random) velocity data followed by Fourier transform continues to be attractive from a computational standpoint. To obtain reliable spectrum estimates at high frequencies, a variety of methods aimed at interpolation of measured velocity values have been attempted. These are generally referred to as *data* or *signal reconstruction* techniques [17,21].

64.4.1 LDV Systems

Tables 64.1 and 64.2 list examples of typical commercial LDV systems. The research systems are generally configured to suit the application requirements, including the need to do flow field mapping. This results in wide variation of possible light sources, signal processors, data analysis packages, and seeding systems. Hence, the system price can vary significantly, and the numbers shown in Table 64.2 are only indicative.

TABLE 64.1 Manufacturers of Laser Doppler Velocimeter Systems

Systems for research and industrial applications
TSI Inc., 500 Cardigan Road, Shoreview, MN 55126, U.S.A., Tel.: 800-874-2811, Fax: 651-490-3824, http://www.tsi.com/Fluid-Mechanic-Systems/
Dantec Dynamics A/S, Tonsbakken 16–18, P.O. Box 121, DK-2740 Skovlunde, Denmark, Tel: +45 44 57 80 00, Fax: +45 44 57 80 01, http://www.dantecdynamics.com/
Miniature LDV systems
Measurement Science Enterprise, Inc., 123 West Bellevue Drive, Suite 1, Pasadena, California 91105-2549, USA, Tel.: 626-577-0566, Fax: 626-577-0565, http://measurementsci.com/index.html

TABLE 64.2 Typical Commercial Laser Doppler Velocimeter Systems

One-velocity-component LDV system	$60,000–90,000
Two-velocity-component LDV system	$100,000–130,000
Three-velocity-component LDV system	$150,000–190,000

Note: The price of the systems varies significantly depending upon the type of lasers, signal processors, and other components of the system.

64.5 Extension to Particle Sizing

In LDV, the frequency of the scattered light signal provides the velocity of the scatterer. Processing the scattered light to get information about the scatterer other than velocity has always been a topic of great interest in flow and particle diagnostics. One of the most promising developments is the extension of the LDV technique to measure the surface curvature and, hence, the diameter of a spherical scatterer [20]. This approach (limited to spherical particles) uses the phase information of the scattered light signal to extract the size information. To obtain a unique and, preferably, monotonic relation between phase of the signal and the size of the particle, the orientation and the geometry (aperture) of the scattered light collection system need to be carefully chosen. In the following, unless otherwise mentioned, the particles are assumed to be spherical.

The light scattered by a particle, generally, contains contributions from the different scattering mechanisms—reflection, refraction, diffraction, and internal reflection(s). It can be shown that, by selecting the position of the scattered light collection set-up, contributions from one scattering mechanism can be made dominant over the others. The aim in phase Doppler measurements is to have the orientation of the receiver system such that the scattered light collected is from one dominant scattering mechanism.

The popularity of the technique is evidenced by its widespread use for measuring particle diameter and velocity in a large number of applications, especially in the field of liquid sprays [21,38,43]. The technique has also been used in diagnosing flow fields associated with combustion, cavitation, manufacturing processes, and other two-phase flows.

64.6 Phase Doppler System: Principle

The phase Doppler approach, outlined as an extension to an LDV system, was first proposed by Durst and Zare [39] to measure velocity and size of spherical particles. The first practical phase Doppler systems using a single receiver were proposed by Bachalo and Houser [20].

A schematic arrangement of a phase Doppler system is shown in Figure 64.7a. This shows a receiver system arrangement that collects, separates, and focuses the scattered light onto multiple photodetectors. In general, the receiving system aperture is divided into three parts, and the scattered light collected through these is focused into three separate photodetectors. For simplicity, in Figure 64.7a, the output of two detectors is shown. The different spatial locations of the detectors (receiving apertures)

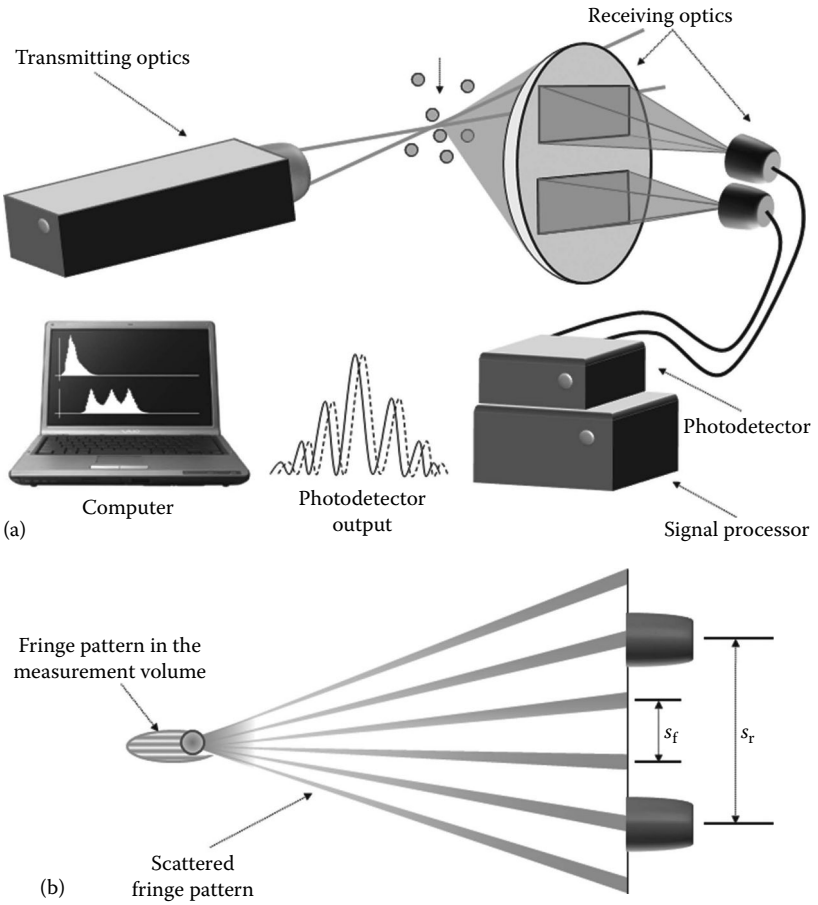

FIGURE 64.7 (a) Phase Doppler system: schematic; (b) phase Doppler system: schematic of the scattered fringes (fringe model).

result in the signals received by each detector having a slightly different phase. In general, the difference in phase between the signals from the detectors is used to obtain the particle diameter, whereas the signal frequency provides the velocity of the particle.

64.6.1 Fringe Model Explanation

The fringe model provides an easy and straightforward approach to arrive at the expressions for Doppler frequency and phase shift created by a particle going through the measuring volume. When the particle moves through fringes in the measuring volume, it "scatters a fringe pattern" (Figure 64.7b). The phase shift in the signals can be arrived at by examining the scattered fringe pattern. If the particle acts like a spherical mirror (dominant reflection) or a spherical lens (dominant refraction), it projects fringes from the measuring volume into space all around as diverging bands of bright and dark light, known as *scattered fringes*. The scattered fringe pattern is collected through the apertures by the receiver system, as shown in Figure 64.7b. The spacing between the scattered fringes at the plane of the receiver is s_f, whereas the spacing between a pair of apertures is denoted by s_r.

The receiver system in Figure 64.7b shows two apertures. The distance between (separation) the centroids of the two receiving apertures is s_r. Scattered fringes move across the apertures in the receiver, as the particle moves through the measuring volume. The scattered fringe pattern thus collected through

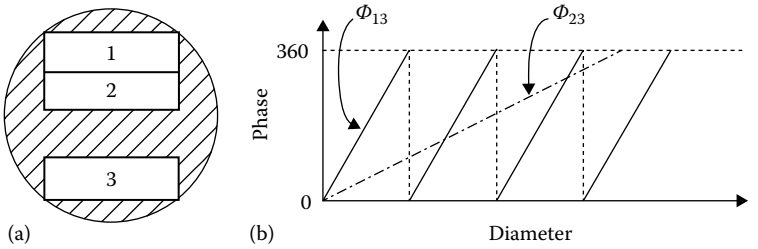

FIGURE 64.8 (a) Three-detector configuration; (b) phase–diameter relationship.

the apertures in the receiver is converted, using photodetectors, into electrical signals. These would be temporally fluctuating signals. The two photodetector output signals are shifted in phase by s_r/s_f times 360° [25]. Large particles create a scattered fringe pattern with a smaller fringe spacing (compared to that for small particles), that is, particle diameter is inversely proportional to s_f, while s_f is inversely proportional to phase difference. Thus, the fringe model shows the particle diameter to be directly proportional to the phase difference. It can also be seen that the sensitivity (degrees of phase difference per micrometer) of the phase Doppler system can be increased by increasing the separation (s_r) between the detectors.

The phase Doppler system shown earlier measures the phase difference between two detectors in the receiver system to obtain particle diameter. This brings in the limitation that the maximum value of phase that could be measured is 2π. A three-detector (using three apertures) arrangement in the receiver system is used to overcome this 2π ambiguity. Figure 64.8 shows the three-detector (aperture) arrangement. Scattered light collected through apertures 1, 2, and 3 is focused into detectors 1, 2, and 3. Φ_{13} is the phase difference between the detectors 1 and 3 and provides the higher phase sensitivity because of their greater separation compared to detectors 2 and 3. As Φ_{13} exceeds 2π, the value of Φ_{23} is below 360° and is used to keep track of Φ_{13}. It should be noted that the simplified approach in terms of geometrical scattering provides a linear relationship between the phase difference and diameter of the particle.

It has been pointed out that significant errors in measured size can occur due to trajectory-dependent scattering [21]. These errors could be minimized by choosing the appropriate optical configuration of the phase Doppler system [21,40]. Intensity-validation technique is a simple processing approach to minimize the errors [41]. Other methods such Dual-mode phase Doppler [21] have also been used to address this problem.

To explore the fundamental physical limits on the applicability of the phase Doppler technique, a rigorous model based on the electromagnetic theory of light has been developed. Computational results based on Mie scattering and comparison with and limitations of the geometric scattering approach have also been outlined [42]. By integrating a phase Doppler velocimeter system with a *rainbow refractometer* system, the velocity, size, and the refractive index of a droplet could be determined [21].

The values of particle velocity and diameter are obtained by processing the photodetector output signals. In general, the signal processing system for velocity measurements is expanded to measure the phase difference between two photodetector signals. The digital signal processing approaches described earlier have been complimented by the addition of accurate phase measurement techniques to get velocity and diameter information, simultaneously, for each particle [38].

Phase Doppler technique has been used to diagnose detailed behavior and characteristics of various different sprays [21,38,43]. This technique has also been used to examine flow and droplet motion in complex flows such as the interaction of an aerated-liquid jet exiting into a cross-stream supersonic flow [44].

Although the phase Doppler technique is limited to the domain of spherical particles, there has always been an interest in extending the technique to size nonspherical particles. In the past, symmetry checks and other similar techniques have been used to ensure the sphericity of particles. Sizing irregular particles is a more complex problem because the local radius of curvature is not a meaningful concept in these cases. Past efforts include going from a single particle approach to using stochastic models for the signals from irregular-shaped and inhomogeneous particles [21].

64.7 Conclusion

LDV has become the preferred technique for measuring flow velocity in a wide range of applications. The ability to measure noninvasively the velocity, without calibration, of any transparent flowing fluid has made it attractive for measuring almost any type of flow. Velocity measurement of moving surfaces by LDV is used to monitor and control industrial processes. Use of laser diodes, fiber optics, and advances in signal processing and data analysis is reducing both the cost and complexity of measuring systems. This noncontact measurement system's (as opposed to mechanical systems) ability to give reliable, repeatable, and accurate measurements has made it attractive for calibrating other devices [47].

The extension of LDV to the phase-Doppler technique provides an attractive, noncontact method for measuring size and velocity of spherical particles. Recent developments in the phase Doppler technique have generated a method to size submicrometer particles as well. These ideas have been extended to examine irregular particles also.

Acknowledgments

The input and comments from Dr. L. M. Fingerson have been valuable in the preparation of this chapter.

References

1. D. Niccum, A new tool for fiber spinning process control and diagnostics, *Int. Fiber J.*, 10(1), 48–57, 1995.
2. Meyers, J. F., Lee, J. W., and Schwartz, R. J., Characterization of measurement error sources in Doppler global velocimetry. *Measure. Sci. Technol.*, 12(4), 357–368, 2001.
3. R. J. Adrian, Particle imaging techniques for experimental fluid mechanics, *Annu. Rev. Fluid Mech.*, 23, 261–304, 1991.
4. I. Grant, *Selected Papers in Particle Image Velocimetry,* SPIE Milestone Series, MS 99, Bellingham, WA: SPIE Optical Engineering Press, 1994.
5. R. J. Adrian, *Bibliography of Particle Velocimetry Using Imaging Methods: 1917–1995,* TAM Report, University of Illinois Urbana-Champaign, Produced and distributed in cooperation with TSI Inc., March 1996, 2009 version is available at http://25-years-piv.dlr.de/wiki/Public/Article/Page/step1.php?sid=ae9f351a9ee34ca47e84f5ed8b10580451434adfc1bc8 (accessed on March 15, 2013).
6. R. J. Adrian and J. Westerweel, *Particle Image Velocimetry*, Cambridge, U.K.: Cambridge University Press, 2010.
7. E. Wolf, C. J. Kähler, D. R. Troolin, C. Kykal, and W. Lai, Time-resolved volumetric particle tracking velocimetry of large-scale vortex structures from the reattachment region of a laminar separation bubble to the wake, *Exp. Fluids*, Online first, September 16, 1–12, 2010, http://www.springerlink.com/content/577833210v421t46/
8. D. G. Bohl and M. M. Koochesfahani, MTV measurements of the vortical field in the wake of an airfoil oscillating at high reduced frequency, *J. Fluid Mech.*, 620, 63–88, 2009.
9. J. F. Meyers, J. W. Lee, and A. A. Cavone, Boundary layer measurements in a supersonic wind tunnel using Doppler global velocimetry, *Proceedings of 15th International Symposium on Applications of Laser Techniques to Fluid Mechanics,* Lisbon, Portugal, July 05–08, 2010.
10. A. Hamed, W. Tabakoff, and R. Wenglarz, Erosion and deposition in turbomachinery, *J. Propulsion Power*, 22(2), 350–360, March–April 2006.
11. P. B. Martin, G. Pugliese, and J. G. Leishman, High resolution trailing vortex measurements in the wake of a hovering rotor, *J. Am. Helicopter Soc.*, 49(1), 39–52, 2004.
12. J. Colby, S. Menon, and J. Jagoda, Flow field measurements in a counter-swirling spray combustor, *AIAA Paper AIAA-2005-4143, 41st AIAA/ASME/SAE/ASEE Joint Propulsion Conference & Exhibit*, Tucson, AZ, July 10–13, 2005.

13. K. Jaffri, H. G. Hascher, M. Novak, K. Lee, H. Schock, M. Bonne, and P. Keller, Tumble and swirl quantification within a four-valve SI engine cylinder based on 3D LDV measurements, *SAE*, Paper No. 970792, February 1997.
14. F. Payri, J. M. Desantes, and J. V. Pastor, LDV measurements of the flow inside the combustion chamber of a 4-valve D.I. diesel engine with axisymmetric piston-bowls, *Exp. Fluids*, 22(2), 118–128, 1996.
15. J. Furukawa, Y. Noguchi, and T. Hirano, Investigation of flame generated turbulence in a large-scale and low-intensity turbulent premixed flame with a 3-element electrostatic probe and a 2-D LDV, *Combust. Sci. Technol*., 154(1), 163–178, 2000.
16. R. Semaan and J. W. Naughton, Three component LDA measurements in the near and far field of swirling jets, *AIAA Paper AIAA 2008-761, 46th AIAA Aerospace Sciences Meeting and Exhibit*, Reno, NV, January 7–10, 2008.
17. Z. Zhang, *LDA Application Methods: Laser Doppler Anemometry for Fluid Dynamics*, Berlin, Germany: Springer, 2010.
18. F. Durst, A. Melling, and J. H. Whitelaw, *Principles and Practice of Laser Doppler Anemometry,* 2nd edn., New York: Academic Press, 1981.
19. R. J. Adrian (ed.), *Selected Papers on Laser Doppler Velocimetry,* SPIE Milestone Series, MS 78, Bellingham, WA: SPIE Optical Engineering Press, 1993.
20. W. D. Bachalo and M. J. Houser, Phase Doppler spray analyzer for simultaneous measurements of drop size and velocity distributions, *Opt. Eng*., 23, 583–590, 1984.
21. H. E. Albrecht, M. Borys, N. Damaschke, and C. Tropea, *Laser Doppler and Phase Doppler Measurement Techniques,* Berlin, Germany: Springer, 2003.
22. Y. Yeh and H. Z. Cummins, Localized fluid flow measurements with an He-Ne laser spectrometer, *Appl. Phys. Lett*., 4, 176–178, 1964.
23. L. M. Fingerson and P. Freymuth, Thermal anemometers, in *Fluid Mechanics Measurements,* 2nd edn., R. J. Goldstein (ed.), Washington, DC: Taylor & Francis Publishing, pp. 115–170, 1996.
24. R. J. Adrian, Laser velocimetry, in *Fluid Mechanics Measurements,* 2nd edn., R. J. Goldstein (ed.), Washington, DC: Taylor & Francis Publishing, pp. 175–300, 1996.
25. L. M. Fingerson, R. J. Adrian, R. K. Menon, S. L. Kaufman, and A. Naqwi, Data analysis, in *Laser Doppler Velocimetry and Particle Image Velocimetry, TSI Short Course Text*, St. Paul, MN: TSI Inc., 1993.
26. P. A. Chevrin, H. L. Petrie, and S. Deutsch, Accuracy of a three-component laser Doppler velocimeter system using a single lens approach, *J. Fluids Eng*., 115, 142–147, 1993.
27. K. M. Ibrahim, G. D. Werthimer, and W. D. Bachalo, Signal processing considerations for laser Doppler and phase Doppler applications, *Proceedings of 5th International Symposium on Applications Laser Techniques Fluid Mechanics,* Lisbon, Portugal, 1990.
28. L. Jenson, LDV digital signal processor based on Autocorrelation, *Proceedings of 6th International Symposium on Applications Laser Techniques Fluid Mechanics,* Lisbon, Portugal, 1992.
29. M. P. Schultz and K. A. Flack, The rough-wall turbulent boundary layer from the hydraulically smooth to the fully rough regime, *J. Fluid Mech*., 580, 381–405, 2007.
30. R. K. Menon and W. T. Lai, Key considerations in the selection of seed particles for LDV measurements, *Proceedings of the 4th International Conference on Laser Anemometry,* Cleveland, OH, August 1991.
31. M. F. Reeder, J. W. Crafton, J. Estevadeordal, J. DeLapp, C. McNiel, D. Peltier, and T. Reynolds, Clean seeding for flow visualization and velocimetry measurements, *Exp. Fluids*, 48(5), 889–900, 2010.
32. Y. Ikeda, M. Nishigaki, M. Ippommatsu, and T. Nakajima, Optimum seeding particles for successful laser Doppler velocimeter measurements, *Part. Part. Syst. Charact*., 11, 127–132, 1994.
33. M. L. Lowe, and P. H. Kutt, Refraction through cylindrical tubes, *Exp. Fluids*, 13, 315–320, 1992.
34. R. Budwig, Refractive index matching methods for liquid flow investigations, *Exp. Fluids,* 17, 350–355, 1994.
35. Q. Tian, Near wall behavior of vortical flow around the tip of an axial pump rotor blade, PhD thesis, Aerospace Engineering, Virginia Polytechnic Institute and State University, Blacksburg, VA, 2006, http://scholar.lib.vt.edu/theses/available/etd-12122006-112751/unrestricted/TianDissertation.pdf

36. D. K. McLaughlin and W. G. Tiederman, Biasing correction for individual realization of laser anemometer measurements in turbulent flows, *Phys. Fluids*, 16, 2082–2088, 1973.
37. R. D. Gould and K. W. Loseke, A comparison of four velocity bias correction techniques in laser Doppler velocimetry, *J. Fluids Eng*., 115, 508–514, 1993.
38. J. D. Schwarzkopf, J. S. Shakal, and C. Bonuccelli, A new method for minimizing volumetric flux errors associated with PDPA measurements in the dilute region of full cone pressure swirl atomizers, *ICLASS 2006*, Kyoto, Japan, Paper ID ICLASS06-163, August 2006.
39. F. Durst and M. Zare, Laser Doppler measurements in two-phase flows, *The Accuracy of Flow Measurements by Laser Doppler Methods,* Skovulunde, Denmark: Dantec Measurement Technology, pp. 480–489, 1976.
40. A. Naqwi, Innovative phase Doppler systems and their applications, *Part. Part. Syst. Charact*., 11, 7–21, 1994.
41. S. V. Sankar, D. A. Robart, and W. D. Bachalo, An adaptive intensity validation technique for minimizing trajectory dependent scattering errors in phase Doppler interferometry, *Proceedings of the 4th International Congress Optical Particle Sizing,* Nuremberg, Germany, March 1995.
42. A. Naqwi and F. Durst, Light scattering applied to LDA and PDA measurements. 2. Computational results and their discussion, *Part. Part. Syst. Charact*., 9, 66–80, 1992.
43. J. Benajes, R. Payri, S. Molina, and V. Soare, Restore desktop view investigation of the influence of injection rate shaping on the spray characteristics in a diesel common rail system equipped with a piston amplifier, *J. Fluids Eng*., 127(6), 1102–1111, 2005.
44. K.-C. Lin, P. J. Kennedy, and T. A. Jackson, Structures of water jets in a Mach 1.94 supersonic crossflow *42nd AIAA Aerospace Sciences Meeting and Exhibit*, AIAA Paper, pp. 12096–12115, 2004.
45. G. Rottenkolber, R. Meier, O. Schafer, S. Wachter, and K. Dullenkopf, Phase discrimination inside a spray: LDV measurements using fluorescent seeding particles (FLDV*)*, *Laser Techniques for Fluid Mechanics*, R. J. Adrian, D. F. G. Durao, F. Durst, M. V. Heitor, M. Maeda, and J. H. Whitelaw (eds.), Berlin, Germany: Springer-Verlag, pp. 511–527, 2002.
46. A. Mychkowsky, D. Rangarajan, and S. Ceccio, LDV Techniques to simultaneously measure gas and particulate phase velocities in a jet plume in a 2D bubbling fluidized bed, *7th International Conference on Multiphase Flows, ICMF 2010*, May 30–June 4, 2010.
47. K. Shirai, L. Buttner, J. Czarske, and C. Kykal, A new calibration method and device for certified flow measurements with laser velocimetry, *Proceedings of the ASME 2012 International Mechanical Engineering Congress & Exposition, IMECE2012-93100*, November 9–15, 2012, Houston, TX.

Further Information

Buchave, P., W. K. George, and J. L. Lumley, The measurement of turbulence with the laser Doppler anemometer, *Annu. Rev. Fluid Mech*., 11, 443–504, 1979.

Drain, L. E., *The Laser Doppler Technique,* New York: John Wiley & Sons, 1980.

Greated, C. A. and T. S. Durrani, *Laser Systems and Flow Measurement*, New York: Plenum, 1977.

Naqwi, A. and F. Durst, Light scattering applied to LDA and PDA measurements. 1. Theory and numerical treatments, *Part. Part. Syst. Characteriz*., 8, 245–258, 1991.

Proceedings, *Proceedings of the International Symposium* (1 to 16) *on Applications of Laser Techniques to Fluid Mechanics*, Lisbon, Portugal, 1982–2012, http://ltces.dem.ist.utl.pt/lxlaser/

Proceedings, *International Conference* (1 to 8) *on Laser Anemometry—Advances and Applications*, 1985–1999.

C. Tropea, Cameron, A. L. Yarin, J. Foss (eds.), *Handbook of Experimental Fluid Mechanics*, Berlin, Germany: Springer, 2007.

VII

Thermal and Temperature Measurement

65

Temperature Measurements, Scales, and Calibrations

Franco Pavese
National Institute of Meterology Research

65.1 Definitions of Temperature

The modern definition of temperature according to classical thermodynamics stems from Carnot's well-known *closed reversible cycle*, which must be formed by alternating isotherms and adiabats. A minimum of *two* temperatures is necessary to construct the cycle.

The Carnot cycle is represented in Figure 65.1, with the p–V coordinates originally used by Carnot. Assume that there are two heat reservoirs able to provide any required amount of heat isothermally, at temperatures θ_1 and $\theta_2 > \theta_1$. The working substance absorbs an amount of heat Q_2 from the hot reservoir in expanding isothermally from A to B; from B to C, it does not exchange heat, but performs mechanical work W_2 until it cools down to θ_1; the working substance then undergoes an isothermal reduction in volume from C to D, releasing an amount of heat Q_1 to the cold reservoir; finally, the working substance is returned to its original state A and temperature θ_2 by reversible compression utilizing mechanical work W_1 without any exchange of heat. If the two isotherms differ by an infinitesimal amount $\mathrm{d}\theta$, and the engine produces a total net work of $\mathrm{d}W$ over the full cycle, the amount of heat Q that is transferred from the higher to the lower reservoir may be shown to be such that

$$\frac{đ\,W}{Q} = \mu(\theta)\mathrm{d}\theta \tag{65.1}$$

where the differential $\mathrm{d}W$ is not exact, since the total work performed along a path depends on the path, and $\mu(\theta)$ is a function of temperature θ *only*—the so-called Carnot function. A Carnot engine does *not* depend on the substance used in performing the work. For a cycle performed between two

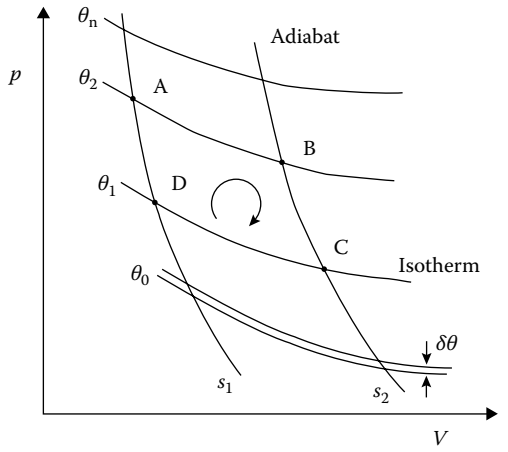

FIGURE 65.1 The Carnot cycle (ABCD), in the p–V representation.

temperatures θ_1 and θ_2 with $\theta_2 > \theta_1$, Equation 65.1 defines the efficiency η equal to W/Q_2 or to $(Q_2 - Q_1)/Q_2$. Then there is a choice of defining the (absolute) temperature in terms of the mechanical work or the thermal effect of heat.

Thomson (Lord Kelvin) made the first recognized attempt to define absolute temperature both ways, based on the theory initiated by Carnot that $\mu(\theta)$ in Equation 65.1 is "universal," as required by an *absolute* temperature. The first of his definitions [1] states that a unit *difference* of absolute temperature precisely equals the maximum *work* that can be obtained from *a unit of heat let down in a cyclic process,* irrespective of the temperature values involved, or

$$W = (\Theta_2^* - \Theta_1^*) \cdot Q \tag{65.2}$$

which is equivalent to setting $\mu(\Theta^*) = 1$ in Equation 65.1. Using this definition, it would be $\theta = \Theta^*$. Thomson assumed a "reference" temperature $\Theta_0^* = 0$. In general, the definition holds for $\mu(\Theta^*) = const$. Therefore, temperature intervals are proportioned to increments of efficiency. For an arbitrary "reference" temperature Θ_0^* and any Θ_n^*, one can write $Q_n/Q_0 = \mu(\Theta^*)^n$, or $\Theta^* = \Theta_0^* + \log(Q/Q_0)/\mu(\Theta^*)$. When $\Theta^* \to \pm\infty$, $\eta \to 1$. In his second definition [2], upon the suggestion of Joule, who found from experiments on compression of air that $\mu(\theta)$ was rather proportional to $1/\theta$, he preferred to change the definition to one that can be derived from Carnot's finite cycle of Figure 65.1:

$$\frac{Q_2}{Q_1} = \frac{\Theta_2}{\Theta_1} \tag{65.3}$$

The use of Θ instead of Θ^* marks the fact that this definition of temperature is different from the one in Equation 65.2. If chosen as the temperature definition, $\theta = \Theta$ would hold. Notice that definition in Equation 65.3 does not place any dimensional constraint on temperature, since only temperature *ratios* are defined, whereas Equation 65.2 does, since it is using temperature *differences*. The relationship between the two definitions is given by $\theta^* = J \log\theta + const$, where J is a constant defined as the *mechanical equivalent of a unit of heat*. Equation 65.3 is the modern definition of thermodynamic temperature, $\Theta = T$, where temperature is assumed proportional to the heat exchanged and where $\Theta \geq 0$. Notice that, instead, Equation 65.2 is equivalent to assuming that temperature increases by the same *proportion* as the corresponding increase in the gas volume, that is, $\Theta^* \propto \ln(V/V_0)$ and the earlier restriction for Θ does not hold. Figure 65.2 pictures the intrinsic logarithmic nature of temperature.

Other definitions of temperature (axiomatic, from statistical thermodynamics, kinetic theory, quantum theory, etc.) can be found in [3].

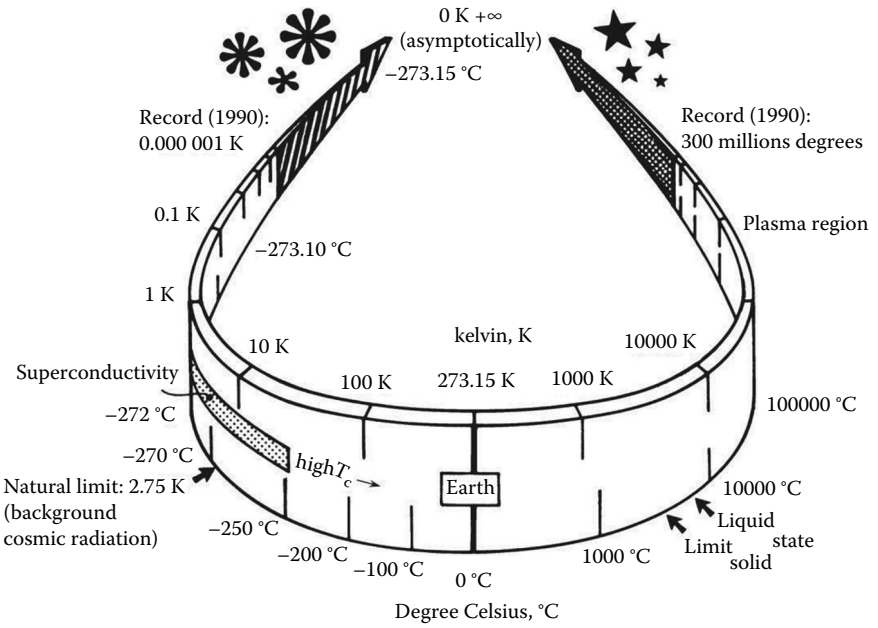

FIGURE 65.2 The logarithmic natural scale of temperatures.

65.2 Temperature Scales

Temperature cannot be measured in the same way as other fundamental quantities, for example, length. The unit size of the degree having been defined, it cannot subsequently be labeled "unit interval" and used to measure temperature in the same way as the meter in length measurements. That is, an additive procedure cannot be used for temperature, by which its value is determined from the number of the "unit intervals" contained in it. Temperature values, instead, can only be determined by comparing two temperatures, one of which is the reference, and by observing whether they are equal—or which one is higher—by observing, in accordance with the zeroth law of thermodynamics, whether there is—or not—a heat flow, and by noting its direction. To assign a numerical value to each temperature, one has to first "order" the measured temperatures, that is, to establish a *scale* in which the heat flows always in the same direction, and then *assign* a sign to the flow. Accordingly, it can be said that $\{\ldots T_1 > T_2 > T_3 \ldots\}$: temperature is a simply ordered manifold. By this procedure, one cannot yet assign a numerical value to different temperatures, but only give them a serial number that will be altered by the arbitrary addition of any new measurement. Nor can one say yet that the value of any T_2 is closer to that of T_1 than to that of T_3 (in fact, one cannot assign a distance between two temperatures), even if he or she should decide to take the interval, say $\{T_1, T_2\}$, as the unit interval, because neither intervals nor ratios can be compared by means of heat flow measurements.

As mentioned before, the definitions of "absolute" temperature are given only as ratios or differences of values. Therefore, normalization constants are required to make the relationship of temperature with another physical quantity determined. These definitions may be said to provide a "blank tape," which is necessary for temperature measurement, but leaves free the choice as regards both the *size* of the graduation in unit intervals and the *position* of the "zero" value on the tape. These are the two degrees of freedom characteristic of any *linear* scale. In the case, for instance, of the unit of length, the *meter*, it is appropriate to define it in such a way as to maintain the additive property in the classical isotropic space. In this respect, in the absolute temperature definition of Equation 65.3, the space of heat—that is, of energy—is used, whereas in his first definition (Equation 65.2), Lord Kelvin used the space of mechanical work equivalent to heat. The transformation between the two definitions is not linear, but logarithmic, as a reflection of the fact that the first defines a temperature ratio and the second a temperature difference.

The definition in the space of heat has been preferred because it closely approximates the numerical values obtained with gaseous substances—already experimentally available at Kelvin's times—and, more specifically, because it matches *exactly* the physical properties of a model state of the matter called "the ideal gas," more or less approximated by real gaseous low-density substances. This limit model has unique characteristics assuming that the "gas" constituents are particles not subjected to any external force field (not even to gravity) and not interacting with each other, but only subjected to perfectly elastic—nondissipative—collisions; the model is independent of the size of the atoms and of the scale. In the classical ideal-gas theory, particles are in fact not characterized by any parameter, namely, mass, but they are identical, so indistinguishable from each other. Starting from the modern generalization of the model of *quantum* ideal gas, they satisfy the equation of state

$$pV = gT \tag{65.4}$$

where g is a constant [4].

In the case of the classical ideal gas, g is defined by Rn, (n being the amount of substance and R is the gas constant) or by kN (N being the number of particles (entities) and k the Boltzmann constant). Equation 65.4 *alone* defines the ideal gas model for absolute temperature. Actually, the plural form "ideal *gases*" is often found. For an empirical temperature θ, on the contrary, the definition of the model requires, in addition to Equation 65.4, the condition $(\delta U/\delta V)\theta = 0$, which is no longer implied. The reason is that other conditions are assumed to be added to the basic model. For example, a common (but *unnecessary*) condition is the definition of a relationship $c(T)$ for the specific heat (e.g., $c(T) = const$). Or, of a "structure," for example, molecular, with an additional kinetic energy associated to each noninteracting particle. Therefore, we may have different *gases*, depending on whether they are monoatomic or polyatomic, have a spin, and so on. In such cases, they can be considered as the limit condition for vanishing intermolecular and external interactions of real gas species. The ideal gas model was fully developed in the second half of the nineteenth century on the basis of the kinetic theory of gases. To summarize, it is because temperature is defined in the heat (energy) space that the absolute lower end of the temperature scale is a zero (only asymptotically approached) and not an (negative) infinity.

65.3 Thermodynamic Temperature Scale

First, let us remark again that only an empirical temperature θ can be measured. The aim of this section is to show how a usable relationship can be established between a scale based on θ and the "thermodynamic" temperature T. Second, it must be pointed out again that none of the definitions of temperature given in the preceding section defines a unique scale. Each only puts constraints on the scale form. An example is given in Equation 65.2, where the values of two constants can be chosen arbitrarily by setting the zero point in the scale (Kelvin first definition) and the size of the degree. As a matter of curiosity, with θ = 273.16 K and with the old value 373.16 K for the boiling point of water, one would have $\theta^*/[\text{unit}] = 738 \cdot \log T/\text{K} - 1798$. On this scale, the value of the tungsten melting point (3673 K) is 833 [units], smaller in absolute value than that of the normal boiling point of ^{4}He (4.2 K), which would be –1336 [units].

Kelvin's second definition Equation 65.3 was used as the basis for the first internationally accepted temperature scale at the first meeting of the Conférence Générale des Poids et Mesures (CGPM) held in 1887 [5]; it was the "normal hydrogen scale" using a hydrogen gas thermometer developed by Chappuis at the BIPM. Temperature $\theta := t$ was defined with the use of *two* fixed points T_1 and T_0, and was assumed to be proportional to the pressure increase (at constant volume), $(p - p_0)/p_0 = \alpha t$. Pressure has a defined value p_0 at the first fixed point T_0, the ice point, which was assumed to be 0 °C (this symbol, and the term "degree Celsius" later adopted in 1948, replaced the *previous*, "degree centigrade"). The second fixed point T_1, necessary to define α, was the normal boiling point of water, defined as 100 °C: $\alpha \approx 0.003661\ ^\circ\text{C}^{-1}$.

The size of the unit was, therefore, so chosen that the interval between the normal melting point of water and its normal boiling point be *exactly* 100 °C. In this way, the *size* of the degree Celsius is exactly that of the historical degree centigrade defined by Celsius in 1742. The temperature is defined, as a consequence, in terms of the "Celsius scale": $T_{emp} = 1/\alpha + t$, with $1/\alpha = 273.15$ °C *exactly*. The coefficient of cubic thermal expansion of the gas α is defined as $\lim_{p_0 \to 0} \alpha_v = \lim_{p_0 \to 0} \alpha_p = \alpha$, where α_v and α_p are obtained by measuring the volumes or the pressures, respectively, of a sample of gas enclosed in a bulb thermostated at 0 °C and then at 100 °C: values of $1/\alpha$ ranging from 273.25 °C to 273.08 °C were actually measured.

Subsequently, however, international preference moved to the use of only *one* fixed point for the definition of temperature. The main objection [6] to the use of a two-point definition was that the definition of the absolute temperature is affected in this case by the experimental uncertainty in the determination of a (0.01–0.02° at the time), while in the Celsius temperature, an empirical scale, it is exact by definition. Celsius temperature, an empirical scale, is exact by definition. The reverse seemed more appropriate. In 1954, the Comité International des Poids et Mesures endorsed the one-point definition, which was included by the next CGPM in 1960 [5] in the revision of the 1948 scale. Temperature T_{48} was defined proportional to gas pressure, at a constant volume, $(p/p_0)_V = T$. The size of the temperature unit was then set by defining the numerical value of a *single* thermodynamic state, which is actually the only definition necessary for a scale that assumes as well $T = 0$ K at zero thermodynamic temperature.

This single state was selected to be the triple point of water: it is today reproducible to within ±50 μK: it was given the value, *exact by definition*, 273.16 K. The term "kelvin" of this symbol was adopted in 1954; subsequently, in 1968, the symbol of the unit was changed to K, *no longer* °K. At that time, this value was consistent, within the uncertainty of its determination, with the Celsius scale (in which the triple point of ice is 0.01 °C) since the temperature value of the normal boiling point of water was still 100 °C. After subsequent measurements performed in 1976–1988, the "0 °C–100 °C" historical interval lost its exactness, when the interval was found shorter by (26 ± 2) mK. However, the CGPM in 1989 [5] decided to maintain the 1954 definition of the Celsius temperature, that is, to maintain the *size* of the degree Celsius equal to that of the kelvin. Therefore, the temperature value of water boiling at 101325 Pa is 99.974 °C, a big change for the more accurate thermodynamic tables. If it had been decided, instead, to maintain *also* the difference between ice point and normal boiling point of water equal to 100 °C (a decision having no physical basis), the temperature of the triple point of water ought to have been redefined as: 273.16 × (100:99.975) = 273.23 K.

The present definition for the unit of the fundamental physical quantity known as thermodynamic temperature, symbol *T*, is the kelvin, symbol K, defined as the fraction 1/273.16 of the thermodynamic temperature of the triple point of water. The CIPM in 2005 [5] clarified the definition of the triple point of water by specifying the isotopic composition of the water to be that of Vienna Standard Mean Ocean Water (V-SMOW). This was the situation until a process started in the scientific community and later within the Conférence Internationale des Poids et Mesures (CGPM), concerning the redefinition of the kelvin by using the Boltzmann constant. In its Resolution 1 of October 2011 [5], the CGPM "takes note of the intention of the International Committee for Weights and Measures to propose a revision of the SI as follows: the International System of Units, the SI, will be the system of units in which:

- The ground state hyperfine splitting frequency of the caesium 133 atom $\Delta\nu(^{133}Cs)_{hfs}$ is exactly 9 192 631 770 Hz.
- The speed of light in vacuum *c* is exactly 299 792 458 m/s.
- The Planck constant *h* is exactly $6.626\,06 \times 10^{-34}$ J/s.
- The elementary charge *e* is exactly $1.602\,17 \times 10^{-19}$ C.
- The Boltzmann constant *k* is exactly $1.380\,6488 \times 10^{-23}$ J/K.
- The Avogadro constant N_A is exactly $6.022\,14 \times 10^{23}$ reciprocal mole.
- The luminous efficacy K_{cd} of monochromatic radiation of frequency 540×10^{12} Hz is exactly 683 lumen per watt.

where

1. The hertz, joule, coulomb, lumen, and watt, with unit symbols Hz, J, C, lm, and W, respectively, are related to the units second, meter, kilogram, ampere, kelvin, mole, and candela, with unit symbols s, m, kg, A, K, mol, and cd, respectively, according to Hz = s^{-1}, J = m^2 kg s^{-2}, C = s A, lm = cd m^2 m^{-2} = cd sr, and W = m^2 kg s^{-3}.
2. The symbol X in this Draft Resolution represents one or more additional digits to be added to the numerical values of h, e, k, and N_A, using values based on the most recent CODATA adjustment, from which it follows that the SI will continue to have the present set of seven base units, in particular the kelvin will continue to be the unit of thermodynamic temperature, but its magnitude will be set by fixing the numerical value of the Boltzmann constant to be equal to exactly $1.380\,6 \times 10^{-23}$ when it is expressed in the SI unit m^2 kg s^{-2} K^{-1}, which is equal to J K^{-1}".

Actually, the CGPM in October 2011 did not yet take any final decision about the earlier provided matter, so no change in the kelvin definition is in force after that meeting at least until the next CGPM meeting would possibly confirm the previous intention. Table 65.1 summarizes chronologically the developments of thermometry. In principle, any thermodynamic law can be used to obtain a thermodynamic scale.

65.4 Empirical Temperature Scales

The determination of thermodynamic temperature from first principles is a difficult experiment. Every measurement is, in fact, only an approximation, because of imperfections in the model used for describing the basic thermodynamic law, of insufficient control of the secondary experimental parameters that are included in the model (the so-called corrections), or of experimental random errors. However, in nature, a temperature-independent phenomenon is rather the exception than the rule. Any temperature-dependent physical quantity can, in principle, be used to measure temperature. An important element to consider for the evaluation of a candidate empirical scale, apart from the trivial necessity for the physical quantity to behave monotonically with temperature (e.g., water density is not), is its being or not a linear transformation of absolute temperature, allowing the experimentalist to assign numerical values sequentially to the thermodynamic states. The relationship between the physical quantity and the thermodynamic temperature must be carefully specified; this specification is often difficult to find in the literature, especially over long periods of time. It is well known that scale-conversion calculations are cumbersome and errors frequently occur. Most of the possible empirical scales are not linear in thermodynamic temperature. All empirical scales require *calibration*.

65.4.1 Semi-Empirical Scales

The only element that makes these scales different from a primary thermodynamic scale is the increased number of conventions stipulated for their definition. The defining equation may be the exact representation of a thermodynamic law, but the value of some of the parameters either cannot be calculated with sufficient accuracy, or accurate calculations are not estimated convenient. For instance, Curie's law for paramagnetic substances is $\chi = \chi_0 + C/(T + A + B/T)$. This equation, which also is nonlinear in T, can be exploited to determine temperature by measuring the magnetic susceptibility χ, but the three constants must be experimentally determined by measuring the susceptibility values (χ_1, …χ_3) at three reference temperatures ($T_{r,1}$, …, $T_{r,3}$), whose values are *defined*. The procedure can then be considered a *calibration* of the experimental setup. The reference points are at least two. Since they are always selected from well-defined thermodynamic states, it is assumed that, when the state is exactly reproduced, the thermodynamic temperature is too, independently of the experimental setup or of the experimentalist. A scale so defined assumes no approximations in the defining thermodynamic equation and no simplifications in the experiment, as would be the case of a primary thermodynamic measurement. Consequently, the

TABLE 65.1 Short History of Thermometry

1600	Thermoscope invented by Galileo Galilei	The thermoscope has no graduated scale; therefore, temperature evaluation is only qualitative
Mid-1600	Liquid-in-glass graduated thermometers are widely spread	Famous are the alcohol thermometers of the Accademia del Cimento in Florence Their graduation marks are made of colored glass bits attached to the stem
1694	Melting ice and boiling water adopted by G. Renaldini as fixed points	Fixed points must be established by reference to natural phenomena, whose temperature is assumed to be intrinsically determined
1724	Modern temperature scale proposed by G. Fahrenheit, defined by a thermometer, a law, and three fixed points	Fahrenheit's thermometer was a mercury-in-glass one. Thermal expansion vs. temperature was assumed linear. Three fixed points were defined: 0 °F: temperature of a mixture of water, ice, and ammonium chloride 32 °F: temperature of melting ice 96 °F: temperature of human body
1742	The temperature interval between melting ice and boiling water subdivided into 100 equal parts by A. Celsius	The degree Celsius was the one eventually adopted
1821	Thermoelectric effect discovered by T.J. Seebeck	The Seebeck effect is the basis for the thermometers designated as thermocouples
1854	The modern absolute temperature definition, suggested by W. Thomson, is based on Carnot cycle	A scale whose definition does not depend on a specific substance is called "absolute"
1871	First electrical resistance thermometer built by C.W. Siemens	The electrical resistance thermometer is still today the best practical thermometer
1879	Blackbody radiation law proposed by J. Stefan; forms the basis for the radiation thermometers, with Planck's law	The radiation law is strongly nonlinear in temperature, since it depends on T^4
1967	The XIII Conférence Générale des Poids et Mesures adopts the kelvin scale with a single fixed point: 273.16 K	The unit of temperature is designated "kelvin"; its symbol is K
1990	The XVIII Conférence Générale des Poids et Mesures adopts the present version of the International Temperature Scale, the ITS-90	The ITS-90 provides the best to-date practical approximation of the thermodynamic scale and offers a reproducibility that is better than the thermodynamic scale
2006	Definition of a "*mise en pratique*" of the kelvin	ITS-90, PLTS-2000, and thermodynamic scale transformed in realizations of the "*mise en pratique*" of the kelvin. A technical annex contains changes in scales definitions
2011	CGPM takes note of the change of the kelvin definition in the frame of "the possible future revision of the International System of Units, the SI"	If the present CCU proposal will stand, the kelvin will be defined by means of the Boltzmann constant set to a stipulated value. This will not have any practical effect on the *mise en pratique* in force since 2006

scale definition need *not* specify any characteristics of the experimental equipment or any measurement procedure. Measurements have to be performed according to state-of-the-art techniques required by the accuracy to be achieved. With respect to primary measurements, the measurement procedure is simplified in that calibration at the fixed points avoids measuring several secondary parameters and performing cumbersome and uncertain correction calculations. The two (minimum) defining points are called *fixed points* of the scale. None need to be the defining point of the kelvin scale. The scale definition assigns them *conventional* temperature values. Though these values are assumed to be *exact* thermodynamic temperature values, they are actually the best up-to-date approximations. The empirical temperature θ defined by these scales is considered to be satisfactory enough as an approximation of the thermodynamic temperature T.

65.4.2 Strictly Empirical Scales

Quite frequently, the thermodynamic relationship between the measured physical quantity and thermodynamic temperature is not known to sufficient accuracy, or this relationship is not convenient for direct use; it might be as well that measurements are executed with instruments that cannot or need not be fully characterized. A temperature scale stemming from situations such as these is substantially different from semi-empirical scales because the defining equation becomes a purely computational model to obtain an approximation of the thermodynamic temperature T. The model must prove to fit T over the whole chosen range between the fixed points within the chosen uncertainty, on the basis of *experimental* $T(y)$ data (actually only an estimate $\theta(y)$ is available, as data are affected by experimental errors). The number p of parameters necessary to fit the model equation to the required accuracy determines the number of the fixed points necessary to *calibrate* the thermometer. The optimum spacing between these fixed points on the temperature scale is determined by the characteristics of the model, that is, by the mathematical function used, but at the same time, it is obviously constrained by the availability of suitable thermodynamic states in nature.

Such a scale requires an *interpolating instrument*. Since the relationship between the chosen physical property (e.g., electrical resistance) and the thermodynamic temperature is not calculated from first principles but is derived from experimental data, the use of that temperature scale is limited to a specific device, or at least to a family of devices. This point will be made clearer by the example of the platinum resistance thermometer. In the first place, the experimental data pertain exclusively to a *specific* substance, platinum, as they cannot be extended, by means of a theory, to be valid for other metals. Other restrictions must be considered as well, for instance, the bulk material must be in well-defined chemical (oxidized…) and physical (strain-free…) states, and the results are valid only for a given range of chemical purity. When some of the characteristics of the interpolating instrument can be specifically quantified, the range of the accepted values for these parameters must be defined as well in the scale, to enable one following this prescription to reproduce the results, that is, the scale. If this is not possible, with, for example, diode thermometers or thermistors, results, *and that scale*, will be valid only for the specific production-lot of devices from which results were obtained. The thermometer used in a scale of these types is known as an "interpolating instrument," because it is not itself required to reproduce a thermodynamic property, but only precisely the smooth selected function that is used to *interpolate* temperature values between the values assigned to the fixed points. To summarize, there are three constitutive elements associated with an empirical scale:

1. An interpolating instrument
2. A mathematical definition
3. A set of *fixed points*

The need of an *interpolating instrument* has already been illustrated. The *mathematical definition* must conveniently be the simplest function (or set of functions) representing, within the stated accuracy, the relationship between the measured quantity and the thermodynamic temperature; it has a number of free parameters, a characteristic of an *empirical* scale, whose numerical values must be obtained from "calibration" of the interpolation instrument at a number of reference points. The number of these *defining fixed points*, called "fixed points," must be equal to the number of free parameters, and their position must be such as to permit the best compromise between mathematical requirements and what is available in nature. The temperature value of the reference point is *defined*, that is, *fixed* by the scale definition. A scale of this type, which is the most common, is affected by a specific shortcoming, which must be kept in mind, called *nonuniqueness*, a *nonstatistical* term expressing the concept that in each particular unit implementing the *interpolating instrument* (i.e., the thermometer), the relationship between the measured quantity and temperature is slightly different. Therefore, the mathematical interpolating procedure defined by the scale *cannot* adequately represent the measurements performed with each individual unit of the thermometer, but can only approximate the physical behavior of these units. In other words, if the scale definition is applied to two specific units of the thermometer placed in an isothermal enclosure, there will be a measurable difference between the temperature values supplied

by their calibration tables and the temperatures actually measured. This is true at every temperature *except* at the fixed points, at which the units have originally been calibrated. Calibration at the fixed points means, by definition, to associate the measured numerical value of the property (e.g., of electrical resistance) to each temperature value of the calibration table (expressed in the scale, e.g., T_{90}). The nonuniqueness effect cannot be reduced, since it is a nonstatistical systematic error intrinsic to thermometer fabrication. Consequently, it must neither be mixed up with errors in the scale realization, nor be ascribed to the limited ability of the mathematical definition to match the physical behavior of each individual thermometer; it is due, instead, to technical limits of the interpolating instrument itself. Still in connection with these scales, another problem, concerning instead their mathematical definition, is the *smoothness* of the selected mathematical model with respect to the physical relationship between the measured quantity and thermodynamic temperature. In order to model this relationship accurately, high-order polynomials are often required, which tend to oscillate between the constraints. A striking example is the difference between the International Temperature Scale of 1990 (ITS-90) and the thermodynamic scale, whose smoothness will be illustrated in Section 65.6.

65.5 International Temperature Scales

The measurement of temperature is a necessity in most laboratories. As a consequence of the accuracy requirements, quite early, an ITS was agreed upon a strictly empirical scale. At its first meeting after the Convention du Mètre, the CGPM (actually a diplomatic body) in 1887 endorsed the "Normal Hydrogen Scale." In 1927, the CGPM adopted the first ITS. Since then, two other such international scales were agreed: in 1948 and 1968. A historical review of this process can be found in many texts, for example [3,7–11]. The present version of the temperature scale (ITS-90) was adopted in 1990 and it is still in charge, but in 2006, a basic change in meaning has been adopted (see next section). The meaning of an "official" scale is not to be considered a bureaucratic one, but scientific and technical. As in all types of measurements, to improve accuracy, not only random errors must be reduced, but the largest possible number of causes of systematic deviations as well has to be eliminated. An international body, within which the recognized specialists in the temperature measurements field meet and discuss their experiences and those of their colleagues, makes it possible to obtain the best approaches for reducing the error limits. The first task of such a body is to collate the best estimates of the thermodynamic temperature and then to assess methods for its measurement to the state-of-the-art accuracy. In carrying out this work, it is often realized that the direct measurement of the thermodynamic temperature is affected by an uncertainty larger than the reproducibility level obtainable in empirical temperature measurements. Consequently, so far, it has proved advantageous to define an empirical scale that can be reproduced more accurately and is internationally agreed upon (the ITS). Another equally important role of this body is to assess the *traceability of lower-level approximations* of the thermodynamic scale to the ITS and to fill a gap of information between the ITS definition and the international codes developed for industry (e.g., by OIML, IEC) or prepared by other international bodies (e.g., IUPAC, IUPAP). At the same time, the body reviews critically the scientific and technical information necessary for code updating. The change in the philosophy of the meaning of the temperature scales that occurred in 2006 has an influence also on these matters, as illustrated in the next section.

65.5.1 *"Mise en Pratique"* for the Definition of the kelvin

In 2005, the CCT approved a document, officially endorsed in 2006, containing a basic change in the meaning of temperature scale "*Mise en pratique* for the definition of the kelvin" [11]. This document provides the information needed to perform a practical measurement of temperature in accord with the SI. This document states: "for temperatures other than the triple point of water, direct measurements of thermodynamic temperature require a primary thermometer based on a well-understood physical system whose temperature may be derived from measurements of other quantities. In practice, primary thermometry is difficult and time consuming and not a practical means of disseminating the kelvin.

As an alternative, the International Temperature Scale provides an internationally accepted recipe for realizing temperature in a practical way." At present, "the ITS-90 and the PLTS-2000 [between 1 K and 0.9 mK] define temperatures T_{90} and T_{2000} that are good approximations to thermodynamic temperature." Concluding, "Recent developments in thermometry have motivated the creation of a broader, more flexible document that incorporates the temperature scales in current use: the *mise en pratique* for the definition of the kelvin. As envisioned by the CCT, the *mise en pratique* will serve as a reference for

- The text of the ITS-90 and PLTS-2000
- A Technical Annex of material deemed essential to realization of the ITS-90 or PLTS-2000, but not included in the scale definitions themselves
- Descriptions of primary thermometers for direct measurement of thermodynamic temperature
- Assessment of the uncertainty of the ITS-90, PLTS-2000, and measurements made by primary thermometry"

The rational of the *mise en pratique* is that, since it was promulgated as the realization of the kelvin, the status of the official temperature scales—and of the thermodynamic scale—is now that of a specific realization of the *mise en pratique*. This basic change has several important implications that should carefully be kept in mind [12,13]. ITS-90 and PLTS-2000 have not changed their regulatory status, but the new method approved by the CIPM has relaxed some of the previous constraints placed on temperature standards:

1. Adjustment to their definitions can now be implemented by simply updating the Technical Annex. In fact, the specifications for the triple point of water and the e-H_2 fixed points of the ITS-90 have recently been refined to account for isotopic effect [11].
2. Addition "in due course" of other methods to the *mise en pratique* is also foreseen, at present with the explicit mention to thermodynamic temperature.

This means that the new method intrinsically does not prevent the acceptance of a multiplicity of methods for the *mise en pratique*, even though they may apply to the same temperature range and have different levels of uncertainty. This simply means the addition to the *mise en pratique* of scales that had previously only the status of "approximations" to the ITS-90, without formal status, showing levels of accuracy—and precision—lower than that of the ITS-90. A summary of the official scale definitions is reported in Table 65.2.

65.6 Differences between the Realized Thermodynamic Temperature Scale and the T_{90}

For the most accurate thermo-physical and chemical–physical data, the differences $T - T_{90}$ are significant. For this reason, the Technical Annex to the *mise en pratique* of the kelvin now includes an official relationship between thermodynamic temperature T and T_{90}.

Interpolating functions were generated by CCT for representing this relationship [14]. The method used was to subdivide the range of the *critically selected 1046 experimental temperature values* available until 2010 in the temperature range from 4.2 K (normal boiling point of ^{4}He) to 1358 K (copper fixed point of the T_{90}) into 42 narrow subranges, and for each of them to obtain a *consensus* mean value and attribute it to the mean temperature value of the subrange; for this purpose, in the ranges 2.0–35 and 77–273.16 K, a weighted mean was used—basically this choice corresponds to keep intact the short-range local behavior of the experimental data. Then, the set of 42 data was fitted using:

- Between 8.0 and 273.16 K, a logarithmic polynomial of degree 7
- Between 273.16 and 1358 K, a rational polynomial of degree 4
- Between 2.0 and 8.0 K, the difference set to zero, exactly
- Between 1.0 and 2.0 K, $T - T_{2000} = T_{2006} - T_{2000}$, where T_{2000} is the PLTS-2000 scale
- Between 0.65 and 1.0 K, $T - T_{2006}$, where T_{2006} is from [15]

TABLE 65.2 International Temperature Standards from 1927 to 2011 and the Future

	ITS-27	IPTS-48 (from 1960)		IPTS-68		ITS-90	PLTS-2000	"*Mise en Pratique*"	Future (Anticipated)
	1927	ITS 1948	1954[a]	1968	1976	1990	2000	2005	≥2014
Unit	Degree centigrade, °C	Degree Celsius, °C	Degree kelvin, °K; degree Celsius, °C	kelvin, K; degree Celsius, °C	kelvin, K; degree Celsius, °C	kelvin, K; degree Celsius, °C	kelvin, K; degree Celsius ,°C	kelvin, K; degree Celsius, °C	kelvin, K; degree Celsius, °C
Reference T	0.000°C and 100.000°C	0° and 100°	273.16 K	273.16 K	273.16 K	273.16 K	273.16 K	273.16 K	None
Range	0.000°C up	90.2 K up	90.2 K up	13.8 K up	13.8 K up	0.65 K up	0.9 mK–1 K	ITS-90, PLTS-2000, thermodynamic scale realizations; Technical Annex with changes of the above included (see text)	0.9 mK up
Interpolating instrument (cryogenic range, K)	None	SPRT	SPRT	SPRT; T_{58} (^{4}He vp) T_{62} (^{3}He vp) recommended	SPRT; T_{58} (^{4}He vp) T_{62} (^{3}He vp) recommended	0.65–3.2 ^{3}He vp 1.25–5 ^{3}He vp 3.0–24.6 ICVGT 13.8 up SPRT	0.9 mK–1 K melting curve ^{3}He		Possible re-definition of the kelvin in terms of Boltzmann constant k Scale major revisions of: ITS-xx, Other implement-ations of the "*mise en pratique*," Technical Annex
Definition fixed points (cryogenic range)	None	nbp O_2	nbp O_2	tp H_2, vp H_2, nbp H_2, nbp Ne, tp O_2, nbp O_2	tp H_2, vp H_2, nbp H_2, nbp Ne, tp O_2, nbp O_2	ICVGT: 3–5 K ^{3}He or ^{3}He vp, tp H_2, tp Ne; SPRT: tp H_2, vp H_2, nbp H_2, tp Ne, tp O_2, tp Ar, tp Hg	None		
Mathematical definition (cryogenic range)	None	Single interpolation polynomial	Single interpolation polynomial	Reference function plus correction polynomial for sub-ranges	Same, but new reference function	vp: polynomials. ICVGT: quadratic polyn. SPRT: New ref. function and corr. polynomials; multiple definitions in some sub-ranges	Polynomial		
Thermodynamic scale	Excluded from defin.[b]	Excluded from defin.	Excluded from defin.	Excluded from defin.	Excluded from defin.	Excluded from defin.	Excluded from defin.	Included "in due time"	Included

[a] In 1964, a provisional definition between 13 K and 90 K was adopted, CCT-64.

[b] Before 1927, the thermodynamic hydrogen "normal scale" (CVGT) was the standard; until 2005, the international scales were only empirical and an approximation of the thermodynamic T. SPRT, standard platinum resistance thermometer; vp, vapor pressure scale; nbp, normal boiling point; tp, triple point.

TABLE 65.3 $T - T_{90}$ Functions

Range (K)	Interpolating Function	Parameters	
0.65–1.0 K	$T - T_{90} \equiv T - T_{2000}$ $(T - T_{90})/\text{mK} = \sum_{i=0\ldots3} d_i\,(T_{90}/\text{K})^i$	$d_0 = -14.0651$ $d_1 = 40.9970$ $d_2 = -44.1079$	$d_3 = 16.5315$
1.0–2.0 K	$T - T_{90} \equiv T_{2006} - T_{2000}$ $(T - T_{90})/\text{mK} = \sum_{i=0\ldots5} a_i\,(T_{90}/\text{K})^i$	$a_0 = 8.7999$ $a_1 = -54.8216$ $a_2 = 101.4590$	$a_3 = -83.5816$ $a_4 = 32.2307$ $a_5 = -4{,}7513$
2.0–8.0 K	$T - T_{90}$: = 0	—	
8.0–273.16 K	$(T - T_{90})/\text{mK} = \sum_{i=0\ldots7} b_i \cdot (\log_{10}(T_{90}/273.16\text{ K}))^{i+1}$	$b_0 = 4.42457 \cdot 10^1$ $b_1 = -1.76311 \cdot 10^2$ $b_2 = -1.53985 \cdot 10^3$ $b_3 = -3.63685 \cdot 10^3$	$b_4 = -4.19898 \cdot 10^3$ $b_5 = -2.61319 \cdot 10^3$ $b_6 = -8.41922 \cdot 10^2$ $b_7 = -1.10322 \cdot 10^2$
273.16–1358 K	$(T - T_{90})/\text{mK} = (T_{90}/\text{K}) \cdot \sum_{i=0\ldots4} c_i\,(273.16\text{ K}/T_{90})^{2i}$	$c_0 = 0.0497$ $c_1 = -0.3032$ $c_2 = 1.0254$	$c_3 = -1.2895$ $c_4 = 0.5176$

Source: Report of Working Group 4, Doc. CCT/08-13rev, 2008, Comité Consultatif de Thermométrie (CCT), Bureau International des Poids et Mesures, Sèvres, France, http://www.bipm.org; Fischer, J. et al., *Int. J. Thermophys.*, 32, 12, 2011.

The functions are reported in Table 65.3. The basic feature of the results is the following:

- The functions fit the 42 data points well within their uncertainty.
- The existing discontinuity of the first derivative $\mathrm{d}(T - T_{90})/\mathrm{d}T$ at 273.16 K arising from the ITS-90 *reference functions is maintained*, whose value, however, depends on each thermometer used, due to ITS-90 nonuniqueness.
- The function set to zero between 4.2 and 8 K produces *another discontinuity* of the first derivative at 8 K.

Since second-order discontinuities in interpolating functions are quite inconvenient outside strict metrological applications, namely, for the correction of thermophysical or physical–chemical data, a different calculation has been published in [16] for correcting the data of these types between 2.3 K (lambda point of ^{4}He) and 1238 K (close to copper fixed point of the T_{90}), having the following characteristics:

- Directly interpolates the whole set of 1046 selected experimental data, without the intermediate step of the 42 local-averages or further assumptions—like weighting
- Covers the full range with a *single function*, continuous up to the first derivative over the full range: the four-knots function is a *cubic spline*, for optimal smoothness (see Table 65.4)
- By providing the function also in the form of its explicit *polynomial representation* between pairs of knots (Cox–de Boor recursion formula), that is, for each of the four subintervals, allows the user to compute the $T - T_{90}$ function only in the temperature subinterval(s) of one's interest (see Table 65.4)
- Removes the discontinuity of the first derivative at 273.16 K and does *not* retain the difference $(T - T_{90})$: = 0 at 273.16 K, though the resulting value is <+0.0005 K—the spline function does not force the function to any specific value at any knot
- Also removes the second-order discontinuity of the official function at 8.0 K

The deviations of the function in Table 65.4 with respect to the official set of functions in Table 65.3 are minor for many users and are limited within one standard deviation of the data, as shown in Figures 65.3 and 65.4 [16] for the full range (with detail below 50 K in the insert), and above 273.16 K, respectively. In Figure 65.4, curve (d), closest to (a), indicates the variability within CCT elaborations referring to a previous one using a different interpolating function—see Doc. CCT/08-13rev, (a) in [14].

TABLE 65.4 $T - T_{90}$ Functions

Four Subintervals Spline		
Spline Function[a] (2.3–1238 K)	Cubic Polynomials[b]	
	Subinterval (T_{knots})	Coefficients a_{ij}
−0.003073048	2.3–90 K a_0	−0.000593965
0.002521906	a_1	0.000084027
−0.007092070	a_2	−0.000003974
−0.007160607	a_3	0.000000052
0.011774420	90–300 K a_0	−0.002642255
0.015114007	a_1	−0.000063857
0.000330789	a_2	0.000000602
0.060097369	a_3	0.000000004
0.042668756	300–450 K a_0	0.003884825
	a_1	0.000157792
	a_2	−0.000001213
	a_3	−0.000000002
	450–1238 K a_0	0.012749953
	a_1	−0.000047281
	a_2	0.000000582
	a_3	−0.000000001

Source: Pavese, F. et al., *J. Chem. Thermodynam.*, 43, 75, 2011; Pavese, F., *J. Chem. Thermodynam.*, 44, 179, 2012.

[a] Spline coefficients b_j.

[b] Coefficients a_{ij} of the corresponding cubic polynomial (Cox–de Boor recursion formula: $p_i = a_{0i} + h(a_{1i} + h/2\,(a_{2i}\,h + 1/3\,a_{3i}\,h^2)$, $h = x - \tau_i$, where τ_i is the x value of the lower knot of the ith subinterval) for each of the four subintervals.

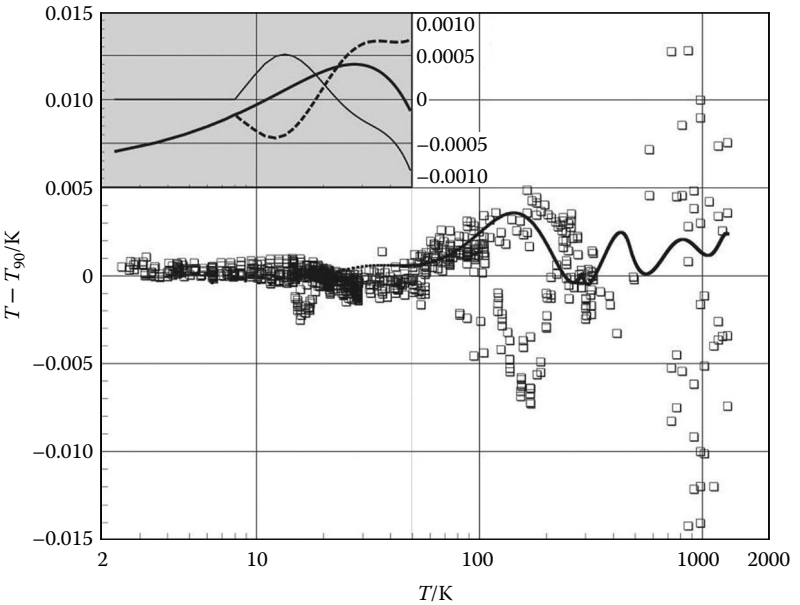

FIGURE 65.3 $T - T_{90}$ as computed by different functions. (From Pavese, F. et al., *J. Chem. Thermodynam.*, 43, 75, 2011; Pavese, F., *J. Chem. Thermodynam.*, 44, 179, 2012.) Full range: using the spline in Table 65.4.

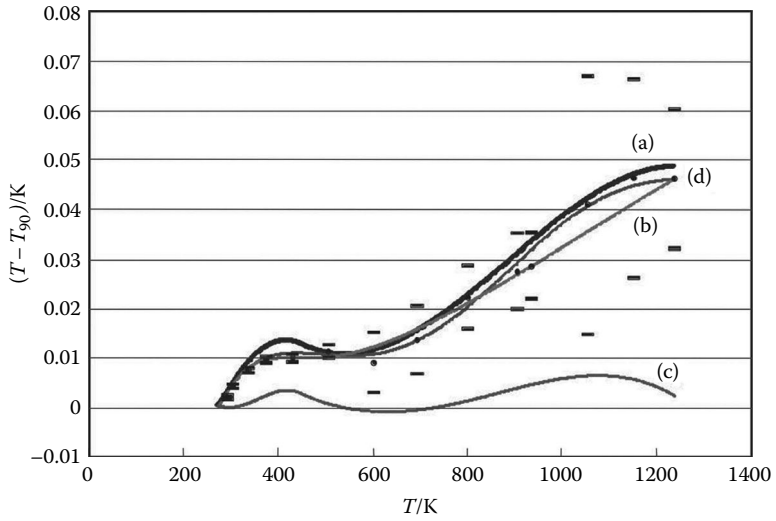

FIGURE 65.4 $T - T_{90}$ as computed by different functions. (Adapted from Pavese, F. et al., *J. Chem. Thermodynam.*, 43, 75, 2011; Pavese, F., *J. Chem. Thermodynam.*, 44, 179, 2012.) Range above 273.16 K: (a) using the spline in Table 65.4; (b) official function in Table 65.3 [14]; (c) difference (a)–(b). The short segments are the uncertainty limits of the standard uncertainty of each of the 42 local averages shown as thick dots. For curve (d), see text.

In the Figure 65.3, note that in this case there is not a first-derivative discontinuity at 8.0 K, nor there is at 273.16 K. The thick line is the difference between the spline function and the official functions in Table 65.3 ($\sigma = 0.9$ mK). The open squares are the residuals of the spline fit, indicating the dispersion of the original 1046 experimental data. *In the insert*, for $T < 50$ K the spline function (thick line), the official functions in Table 65.3 (thin line) and the difference between the two (broken line) are reported.

65.7 Calibration of Thermometers

"Laboratory scales" more or less based on thermodynamic determinations have always proliferated. However, having demonstrated how delicate a matter the temperature definition is, it seems now appropriate to draw attention on the great care that accurate temperature measurements demand. This care should start from the recognition of the need of using *calibrated* thermometers.

This is a general requirement when using any sensor or any transducer for performing quantitative measurements: a non-calibrated device is a gadget, not a measuring instrument.

To allow measurements whose uncertainty can be evaluated, a calibration is mandatory, and the calibration certificate must still be valid at the time the measurements are performed. This is by far less than trivial for thermometers, since all of them are likely to shift their characteristics over time after they are subjected, inherently to their function, to thermal cycling, from room to higher temperatures or to lower temperatures. The higher is the quality of the thermometers in this respect, the more sensitive they are, in general, to mishandling, especially mechanical shocks or stresses. The consequence is that the validity of a calibration within the declared uncertainty is invariably limited in time. The time span of validity depends on the conditions of use and cannot be easily predicted. In conclusion, thermometers should not only carry an initial calibration, but also be recalibrated at convenient intervals of time.

Concerning calibration in itself, it is a highly specialized job. In addition, except in cases when the measured values need only to be compared with the previous ones for an internal check of the "trend" of a process, like it may happen in industrial applications, the calibration must be "traceable" to higher-rank standards pertaining to a metrological chain—national or international. On this subject matter, see [10] and [17].

Each country has a National Metrology Institute heading a National Calibration System (whose name changes from country to country) of laboratories formally accredited to perform calibrations traceable to the national standards, each within a stated uncertainty. The system makes references to Metrology Regional Organizations [18], eventually headed by the Bureau International des Poids et Mesures (BIPM). Official monographs dedicated to methods and equipment for calibrating thermometers on the current official scales, namely, the ITS-90 (see Table 65.2), can be found in [19], most being currently under revision.

TABLE 65.5 Types of Contact Thermometers and Their Typical Precision

Type		Typical Temperature Range (K)	Typical Precision (mK)
1.	Thermocouples[a]		
1.1	Type T	77 to >30	10[b]
1.2	Au + 0.07 at %Fe-KP	<4 to 100	10[b]
1.3	Au + 2.10 at %Co-KP	<4 to 300	10[b]
2.	Resistance		
2.1	Platinum		
	Standard	14 to >300	Better than 0.5
	Industrial	20 to >300	50[c]
2.2	Rhodium–iron		
	Standard	0.5 to >30	Better than 0.3
	Industrial	<4 to >300	10
2.3	Platinum–cobalt		
	Industrial	2 to >300	10
2.4	CLTS	4–300	100
2.5	Germanium	1–100	$DT/T = 0.00024$
2.6	Carbon	0.5–100	200
2.7	Carbon–glass	0.5–100	$DT/T = 0.002$[d]
2.8	Thermistor	77 to >300	100[e]
2.9	Cernox®	0.1–325	25[f]
2.10	Ge on GaAs	0.2–300	10
3.	Capacitance	2–300	100[g]
4.	Diode		
4.1	Gallium arsenide	4 to >300	50
4.2	Silicon	4–300	50
5.	Gas		
5.1	Vapor pressure	0.5–100	1–100
5.2	Gas	2 to >300	1–100
6.	Mechanical (bimetal)		1000

[a] Other types available, suitable only for industrial use: type E and K down to 77 K; type S and R down to 220 K. KP = chromel P.

[b] Best precision for laboratory use in the differential mode and with offset for parasitic e.m.f.'s (up to several microvolts) corrected. Typical precision in the absolute mode (reference junction at refrigerant temperature): 100 mK.

[c] Can improve to 10 mK for selected units above 50 K.

[d] The relative precision in mK/K is preferred for this stable thermometer because of its $R \log(T)$ characteristics. Each unit does not cover the whole temperature range. The same applies for the carbon type.

[e] Can improve to a few millikelvin in narrow ranges above 200 K.

[f] Up to 77 K, 153 mK at 300 K.

[g] Not usable between 40 and 70 K, because of a slope inversion.

TABLE 65.6 Precision Requirements for the Measuring Instrument for Some Contact Thermometers

Sensor	Thermal Parameter (Max.)	Sensitivity	Max. Accuracy (Absolute and Relative) Required for			
			1 K	0.1 K	0.01 K	0.001 K
Thermocouple	emf/mV	($\mu V\ K^{-1}$)	(μV and (% or ppm))			
Type T	6	10–40	10 (0.6)	1 (0.06)	0.1 (60 ppm)	—
Au + 0.07 at %Fe-KP	5	12–22	12 (0.4)	1 (0.04)	0.1 (40 ppm)	—
Au + 2.1 at %Co-KP	14	5–70	5 (0.5)	0.5 (0.05)	0.05 (50 ppm)	—
Resistance	R_0/Ω	(ΩK^{-1})	($m\Omega$ and (% or ppm))			
Platinum	25	0.004–0.1	4 (0.4)	0.4 (0.04)	0.04 (40 ppm)	4 $\mu\Omega$ (4 ppm)
Platinum (industr.)	100	0.08–0.8	80 (8)	8 (0.8)	—	—
Rhodium-05–0.5% iron	100	0.15–0.6	150 (0.4)	15 (0.04)	1.5 (40 ppm)	0.15 (4 ppm)
CLTS	290	0.23	230 (0.1)	23 (0.01)	2.3 (10 ppm)	—
	$R_{4.2\,K}$ (Ω)					
Germanium	1000	0.1–1000	100 (10)	10 (1)	1 (0.1)	0.1 (0.01)
Carbon–glass	1000	0.1–1000	100 (10)	10 (1)	1 (0.1)	—
Diodes	$V_{4.2\,K}$/V	($mV\ K^{-1}$)	(mV and (% or ppm))			
Gallium arsenide	1.5	0.6–3	0.6 (0.05)	0.06 (50 ppm)	6 μV (5 ppm)	—
Silicon	2	2–60	2 (0.2)	0.2 (0.02)	0.02 (20 ppm)	—
Capacitance	$C_{4.2\,K}$/pF	($pF\ K^{-1}$)	(pF and %)			
	15000	(0)–300	150 (1)	15 (0.1)	1.5 (0.01)	—

The direct use of the thermodynamic scale for the calibration of thermometers is not generally advisable. Its correct realization is an extremely specialized job [3], and no official documents for the best practice to follow in its realizations are available so far from the specialized bodies in thermal metrology.

In Table 65.5, the typical precision that can be expected from a number of types of thermometers (generally suitable for the temperature range below room temperature, but some also suitable above; radiation thermometers not included) are reported: obviously any calibration can be expected to exceed these values in accuracy. In addition, when used, they place different requirements to the precision of the measuring equipment, some quite stringent, as shown in Table 65.6. Free consultancy on thermal metrology and specifically on thermometer use and calibration can be obtained by requesting from the nonprofit organization http://www.evitherm.org.

References

1. W. Thompson (1848), On an absolute thermometric scale founded on Carnot's theory of the motive power of heat, and calculated from Regnault's observations, *Phil. Magazine*, 33, 313–317.
2. W. Thomson (1851), On the dynamical theory of heat, with numerical results deduced from Mr Joule's equivalent of a thermal unit, and M. Regnault's observations on steam". *Trans. Royal Soc. Ed*. 20 (part II): 261–268, 289–298.
3. F. Pavese and G. F. Molinar (1992), Modern gas-based temperature and pressure measurements, *International Monograph Series on Cryogenic Engineering*, New York: Plenum Publishing, p. 514, and references therein. Augmented II Edition, 2012, Springer, New York, p. 660, also available as e-Book.
4. P. T. Landsberg (1961), *Thermodynamics*, New York: Interscience Publishers.
5. CIPM (1887), *Procès Verbaux 85*, Bureau International des Poids et Mesures, Sèvres, France; CGPM (1889), *Comptes Rendus des Séances de la I Conférence Générale*, Bureau International des Poids et Mesures, Sèvres, France, 35; CGPM (1960), *Comptes Rendus des Séances de la XI Conférence Générale*, Bureau International des Poids et Mesures, Sèvres, France, 124–133; CGPM (1989), *Comptes Rendus des Séances de la XVIII Conférence Générale*, Bureau International des Poids et Mesures,

Sèvres, France; CIPM (2005), Recommendation 2 (CI-2005): *Clarification of the Definition of the Kelvin, Unit of Thermodynamic Temperature*, International Committee for Weights and Measures, Bureau International des Poids et Mesures, Sèvres, France; CGPM (2011), On the possible future revision of the International System of Units, the SI, *Comptes Rendus des Séances de la XXIV Conférence Générale*, Resolution 1, Bureau International des Poids et Mesures, Sèvres, France, http://www.bipm.org/en/convention/cgpm/resolutions.html (accessed on March 14, 2013).

6. J. De Boer (1965), Temperature as a basic physical quantity, *Metrologia*, 1, 158–169.
7. Supplementary Information for the ITS–90, Monograph, Bureau International des Poids et Mesures, Sèvres, France, http://www.bipm.org/en/publications/mep_kelvin/its-90_supplementary.html (accessed on March 16, 2013).
8. J. F. Schooley (1986), *Thermometry*, Boca Raton, FL: CRC Press Inc.
9. T. J. Quinn (1983), *Temperature*, London, U.K.: Academic Press.
10. J. V. Nicholas and D. R. White (1994), *Traceable Temperatures*, Brisbane, Queensland, Australia: Wiley & Sons
11. *Mise en pratique* for the definition of the Kelvin & Technical annex for the International Temperature Scale of 1990 (ITS-90), 2006, Bureau International des Poids et Mesures, Sèvres, France, http://www.bipm.org/utils/en/pdf/MeP_K.pdf (accessed on March 16, 2013).
12. F. Pavese (2007), Possible implications of the principle of the 'mise en pratique' in its application to the kelvin, *Int. J. Thermophys.*, 28, 1766–1774.
13. D. C. Ripple, R. Davis, B. Fellmuth, J. Fischer, G. Machin, T. J. Quinn, P. P. M. Steur, O. Tamura, and D. R. White (2010), The roles of the mise en pratique for the definition of the kelvin, *Int. J. Thermophys.*, 31, 1795–1808.
14. (a) Report of Working Group 4, Doc. CCT/08-13rev, 2008, Comité Consultatif de Thermométrie (CCT), Bureau International des Poids et Mesures, Sèvres, France, http://www.bipm.org/en/committees/cc/cct/ (accessed on March 16, 2013). (b) J. Fischer, M. de Podesta, K. D. Hill, M. Moldover, L. Pitre, R. L. Rusby, P. P. M. Steur, O. Tamura, R. White, and L. Wolber (2011), Present estimates of the differences between thermodynamic temperatures and the ITS-90, *Int. J. Thermophys.*, 32, 12–25.
15. J. Engert, B. Fellmuth, and K. Jousten (2007), A new ^{3}He vapour–pressure based temperature scale from 0.65 K to 3.2 K consistent with the PLTS-2000, *Metrologia*, 44, 40–52.
16. (a) F. Pavese, P. Ciarlini, and P. P. M. Steur (2011), Thermodynamic temperature differences from the ITS-90 for the correction of thermodynamic property data, *J. Chem. Thermodynam.*, 43, 75–79; (b) F. Pavese (2012), Note on comment on 'Thermodynamic temperature differences from the ITS-90 for the correction of thermodynamic property data' by F. Pavese, P. Ciarlini, and P. P. M. Steur by J. Fischer, Chairman of WG4 of CCT, *J. Chem. Thermodynam.*, 44, 179–180.
17. F. Pavese (2012), Mathematical and statistical tools in metrological measurements, Chapter E6-35-78 on EOLSS, Unesco Encyclopedia of Life Support Systems, http://www.eolss.net (accessed on March 14, 2013).
18. Bureau International des Poids et Mesures, Sèvres, Regional metrology organizations (RMOs), Practical info. http://www.bipm.org/en/practical_info/useful_links/rmo.html (accessed on March 14, 2013).
19. Bureau International des Poids et Mesures, Sèvres, Mise en pratique of the definition of the kelvin (2011). http://www.bipm.org/en/publications/mep_kelvin/ ; Bureau International des Poids et Mesures, Sèvres, Techniques for Approximating the ITS-90 (R.E. Bedford, G. Bonnier, H. Maas and F. Pavese), 1990. http://www.bipm.org/en/publications/mep_kelvin/its-90_techniques.html (accessed on March 14, 2013).

66

Thermal Conductivity Measurement

William A. Wakeham
Imperial College, London

Marc J. Assael
Aristotle University of Thessaloniki

66.1 Introduction

There are three mechanisms whereby energy can be transported from one region of space to another under the influence of a temperature difference. One is by transmission in the form of electromagnetic waves (radiation); the second is the process of convection, in which a bulk or local motion of the material effects the transport; and the final process is that of thermal conduction when energy is transported through a medium. In most practical situations, energy transport is accomplished by all three processes to some extent, but the relative importance of each contribution varies markedly. For example, within an evacuated region, radiation is the sole mechanism of transport, whereas in an opaque solid, conduction is the only mechanism possible.

These processes of heat transfer are often very important in a wide variety of scientific and industrial applications. In the cooling of cast or crystalline materials (e.g., metals, semiconductors, or polymers) from a molten state to a solid state, the heat transfer within the material can have a profound effect on the final properties of the solid. Equally, the heat transfer in a foodstuff is a determinant of its cooking, freezing, or processing time, while the size of equipment needed to heat or cool the liquid or gas stream in a chemical plant depends sensitively on the heat transfer within and between one stream and another.

For these reasons, there has been a great interest in the understanding and description of all three heat transfer processes. Among the three, that of thermal conduction is the simplest to describe in principle, since the empirical law of Fourier simply states that the heat transported by conduction per unit area in a particular direction is proportional to the gradient of the temperature in that direction. The coefficient of proportionality in this law is known as the thermal conductivity and denoted here by the symbol λ. Many important materials, whether made of pure chemical components or mixtures, are of uniform composition throughout, and for them the thermal conductivity is a true physical property of the material, depending often only on the temperature, pressure, and composition of the sample.

However, particularly in the solid state, the thermal conductivity can depend on the direction of the heat flow, for example, in the case of a molecular crystal.

It is also conventional to speak of the thermal conductivity of various types of composite materials such as bricks, glass–fiber insulation, carbon–fiber composites, or polymer blends. In this case, the thermal conductivity is taken to be the empirical constant of proportionality in the linear relationship between a measured heat transport per unit area and the temperature difference over a prescribed distance in the material. The thermal conductivity is not then, strictly, a property of the material, since it can often depend on a large number of parameters, including the history of the material, its method of manufacture, and even the character of its surface. However, this distinction between homogeneous and inhomogeneous materials is often ignored and leads to more than a little confusion, especially where intercomparisons among measurements are concerned.

The fact that in most practical situations all three heat transfer mechanisms are present greatly complicates the process of measurement of the thermal conductivity. Thus, much early work in the field is substantially in error, and it has been really quite difficult to devise methods of measurement that unequivocally determine the thermal conductivity. For that reason, the instruments to be described in the following sections often seem to be rather far removed from the apparent simplicity implied by Fourier's Law.

66.2 Fundamental Equations

The essential constitutive equation for thermal conduction relates the heat flux in a material to the temperature gradient by the equation

$$Q = -\lambda \nabla T \tag{66.1}$$

It is not possible to measure local heat fluxes and gradients; thus, all experimental techniques must make use of an integrated form of the equation, subject to certain conditions at the boundaries of the sample. All experiments are designed so that the mathematical problem of the ideal model is reduced to an integral of the one-dimensional version of Equation 66.1, which yields, in general,

$$Q_a = G\lambda \Delta T \tag{66.2}$$

in which G is constant for a given apparatus and depends on the geometric arrangement of the boundaries of the test sample. Typical arrangements of the apparatus, which have been employed in conjunction with Equation 66.2, are two flat, parallel plates on either side of a sample, concentric cylinders with the sample in the annulus and concentric spheres.

Techniques that make use of Equation 66.2 are known as steady-state techniques and they have found wide application, some of which are discussed later. They are operated usually by measuring the temperature difference ΔT that is generated by the application of a measured heat input Q_a at one of the boundaries. The absolute determination of the thermal conductivity, λ, of the sample contained between the boundaries then requires a knowledge of the geometry of the cell contained in the quanity G. In practice, it is impossible to arrange an exactly one-dimensional heat flow in any finite sample so that great efforts have to be devoted to approaching these circumstances, and then there must always be corrections to Equation 66.2 to account for departures from the ideal situation.

If the application of heat to one region of the test sample is made in some kind of time-dependent fashion, then the temporal response of the temperature in any region of the sample can be used to determine the thermal conductivity of the fluid. In these transient techniques, the fundamental differential equation that is important for the conduction process is

$$\rho C_P \frac{\partial T}{\partial t} = \nabla \cdot (\lambda \nabla T) \tag{66.3}$$

which arises from an elementary energy balance in the absence of any other processes and in which ρ is the density of the material and C_p its isobaric heat capacity. In most, but not all, circumstances, it is acceptable to ignore the temperature dependence of the thermal conductivity in this equation and to write

$$\frac{\partial T}{\partial t} = \frac{\lambda}{\rho C_p} \nabla^2 T = a \nabla^2 T \tag{66.4}$$

in which a is known as the thermal diffusivity.

Experimental techniques for the measurement of the thermal conductivity based on Equation 66.4 generally take the form of the application of heat at one surface of the sample in a known time-dependent manner, followed by detection of the temperature change in the material at the same or a different location. In most applications, every effort is made to ensure that the heat conduction is unidirectional so that the integration of Equation 66.4 is straightforward. This is never accomplished in practice, so some corrections to the integrated form of Equation 66.4 are necessary. The techniques differ among each other by virtue of the method of generating the heating, of measuring the transient temperature rise, and of the geometric configuration. Interestingly, in one geometric configuration only, it is possible to determine the thermal conductivity essentially independent of a knowledge of ρ and C_p, which has evident advantages. More usually, it is the thermal diffusivity, a, that is the quantity measured directly, so that the evaluation of the thermal conductivity requires further, independent measurements.

In the following sections, brief descriptions of the specific applications of these general principles are given. The examples chosen for study are intended to cover the full spectrum of materials and thermodynamic states, and in each case, attention is concentrated on a method that has proved most accurate and is widely used. The steady-state and transient techniques are considered separately.

66.3 Measurement Techniques

66.3.1 Steady-State Methods

The steady-state methods employed for the measurement of the thermal conductivity of fluids and solids have most often employed the geometry of parallel plates so that it is that configuration described here in two variants. Coaxial cylinder equipment has largely been used within the preserve of the research laboratory, with the apparatus of Tufeu and Le Neindre [1] an excellent example of the genre.

66.3.2 Steady-State Methods = Parallel-Plate Instrument

A schematic diagram of a guarded parallel-plate instrument is shown in Figure 66.1. The sample is contained in the gap between two plates (upper and lower) maintained at a distance d apart by spacers. A small amount of heat, Q_a, is generated electrically in the upper plate and is transported through the sample to the lower plate. Around the upper plate, and very close to it, is placed a guard plate. This plate

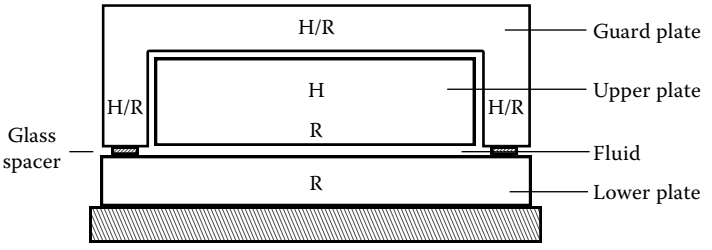

FIGURE 66.1 Schematic diagram of a guarded parallel-plate instrument. H, heater; R, resistance thermometer.

is, in many instruments, maintained automatically at the same temperature as the upper plate so as to reduce heat losses from the upper surface of the upper plate and to most nearly secure a one-dimensional heat flow at the edges of the sample.

The temperatures at the surfaces of the upper and lower plates are measured very precisely, as is the electric input of energy, so that the thermal conductivity can, in principle, be evaluated from the following equation:

$$Q_a = \frac{A\lambda\Delta T}{d} \tag{66.5}$$

where

ΔT is the measured temperature difference
A is the area of the upper plate

Whether the sample is a fluid or a solid, the electric energy generated in the upper plate is not all conducted to the lower plate. Thus, it is necessary in all cases to account for spurious heat losses and for all except opaque materials for the radiative transfer between the two surfaces. When the sample is transparent to radiation, this correction is straightforward and can be reduced by means of surface coating the plates to reduce their emissivity; but when the material adsorbs radiation, the problem is much more complicated and has been the subject of some controversy in the past, which has since been resolved (p. 147 of [2]). In many cases, the effort of performing absolute measurements cannot be justified so that the ratio A/d is determined by calibration with a material of known thermal conductivity.

66.3.3 Measurement on Fluids

Measurements with parallel-plate instruments on fluids have been performed for a considerable period of time. The technique has particular advantages in some special regions of thermodynamic space but requires great attention to detail if accurate results are to be obtained. In the most accurate instruments for fluids, the gap between upper and lower plates is kept as small as possible (perhaps as small as 0.2 mm). This has the benefit of reducing the effect of heat flows that are not normal to the heat surfaces, but more importantly, the small gap contributes to the reduction of the heat transferred by bulk convective motion of the fluid. Indeed, if very small temperature differences are employed by heating the top plate (to have a stable density gradient) *and* considerable care is taken to align the parallel plates normal to the earth's gravitational acceleration, then the effects of convective heat transfer can be rendered negligible (p. 154 of [2]). It is a fact of history that the necessary care with this instrument has been taken by only a few workers so that despite the fact that the instrument has been used in the temperature range from 4 to 800 K, and for pressures up to 250 MPa, only some of the measurements are reliable.

An example of what can be achieved with a parallel-plate instrument is provided by the work of Mostert [3] and Sakonidou [4] at the van der Waals laboratory in Amsterdam. They have used the technique near the critical point of a pure fluid or mixture where the extreme values of the compressibility make the fluid exceedingly prone to convection. In such circumstances, the small vertical extent of the fluid layer required for this technique avoids large density variations in the test layer and, combined with the fact that very small temperature differences (0.3 mK) can be employed, has enabled measurements of the thermal conductivity to be conducted to within 100 mK of the critical temperature at the critical density. Under these circumstances, the thermal conductivity of a pure fluid reveals an enhancement that is, in principle, infinite at the critical point itself.

The unique characteristics of the parallel-plate instrument mean that it is the method of choice for work near the critical region of a material. The arguments given earlier pertaining to the care required for reliable measurements militate against the production of commercial instruments.

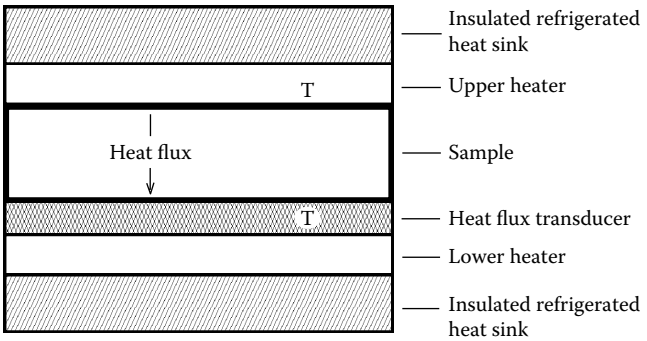

FIGURE 66.2 Schematic diagram of a heat flow meter instrument. T, thermocouple.

66.3.4 Measurements on Solids

A parallel-plate instrument of exactly the same type as has been described for fluids has been employed for solids. However, the spacing of the two plates is normally significantly greater for solids, owing to the difficulty of preparing very thin samples of solids. One essential difficulty with solid samples in this configuration is the contact between the two heater surfaces and those of the sample. Unlike the case for fluids, the contact cannot be made uniform at the molecular level. There is therefore always the possibility of an unaccounted interfacial heat transfer resistance. It seems likely that these considerations contribute to the wide differences between values reported for the same sample by different authors.

A more popular implementation of the parallel-plate configuration for solids is the so-called heat flow meter instrument, also described in the ASTM E1530 test method [5]. When applied to materials such as building insulation, the dimensions of this type of instrument can be very large.

In such instruments (see Figure 66.2), the upper heater plate is set at a higher temperature than the lower one. The hot and cold surface temperatures of the sample are measured with the two thermocouples permanently installed on the adjacent surface plates while a precalibrated heat flow transducer on the lower plate measures the magnitude of the heat flux through the sample. The thermal conductivity is calculated directly from Equation 66.5. In some cases, contact resistances (i.e., insulation) can be characterized and controlled by employing a pressurized gas in the sample chamber or applying a thermally conductive paste to the samples surfaces.

It should also be mentioned that there are many commercial steady-state instruments for measuring the thermal conductivity of solids that operate according to the guarded hot plate method. In the type of instrument, which complies with the ASTM C177 [6] and the ISO 8302 [7] test methods, there are two isothermal cold surface assemblies and a guarded hot plate, which is sandwiched between two identical specimens of the material. Electrically produced heat flux is dissipated through the hot plate and heat flows through both specimens creating a temperature gradient across them. The temperature drop and the heat flow from the hot plate surface are used to calculate the thermal conductivity value. The main difference between the heat flow meter instrument and the hot plate apparatus is that in the first one, the thermal conductivity value depends on the heat flux reference standards while the second one operates in an absolute way. Commercial instruments of both types are included in the listing of Table 66.1.

66.3.5 Transient Methods

There are rather more transient techniques that have achieved popularity than steady-state instruments. This is because transient techniques generally require much less precise alignment and dimensional knowledge and stability. Furthermore, some of the techniques have distinct advantages that arise from the speed of the measurement.

TABLE 66.1 Companies That Make Thermal Conductivity Instruments

Type of Instrument	Temperature Range	Supplier	Approximate Price (U.S. $)
Transient hot disk			
TPS 2500S	290–1,000 K	K-analys AB	25,000
Transient hot bridge	220–480 K	LINSEIS	45,000
Guarded hot plate			
GHP 456 Titan	110–1,000 K	NETZSCH	35,000
Heat flow meter			
HFM 300	290–350 K	LINSEIS	20,000
Hot-wire			
TCT 426	300–1,800 K	NETZSCH	Variable
Needle probe			
MTN01	240–350 K	HUKSEFLUX	8,000
Laser flash			
LFA 1000	290–1,800 K	LINSEIS	130,000
LFA 427	300–3,100 K	NETZSCH	Variable

Note: Prices are only indicative and depend on the operating temperature range and options of accessories.

66.3.6 Transient Hot-Wire Technique

In this technique, the thermal conductivity of a material is determined by observing the temporal evolution of the temperature of a very thin metallic wire (see Figure 66.3) after a step change in voltage has been applied to it. The voltage applied results in the creation of a line source of nearly constant heat flux in the fluid. As the wire is surrounded by the sample material, this produces a temperature field in the material that increases with time. The wire itself acts as the temperature sensor, and from its resistance change, its temperature change is evaluated, and this is related to the thermal conductivity of the surrounding material.

According to the ideal model of this instrument, an infinitely long line source of heat possessing zero heat capacity and infinite thermal conductivity is immersed in an infinite isotropic material, with physical properties independent of temperature and in thermodynamic equilibrium with the line source at time $t = 0$ at a temperature T_0. The heat transferred from the line source to the sample when a stepwise

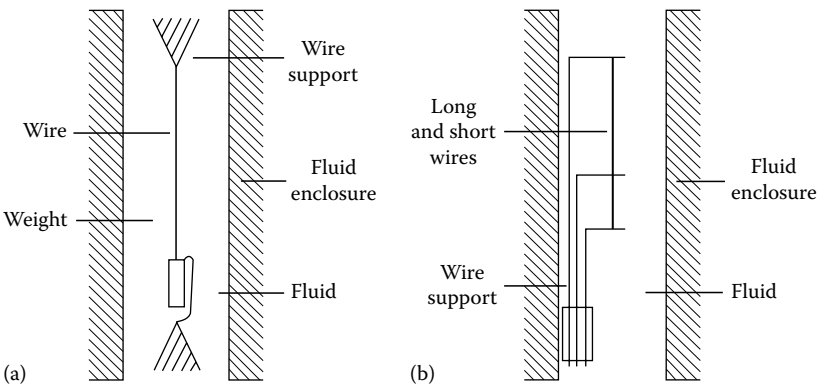

FIGURE 66.3 Schematic diagram of a transient hot-wire instrument for fluids: (a) hot wire is kept under constant tension by a weight; (b) hot wires and supports made of same material.

heat flux, q, per unit length is applied is assumed to be entirely conductive. Then the temperature rise of the material at a radial distance, r_0, which it transpires, is the same as the temperature rise at the surface of a wire of radius r_0, $\Delta T_i(r_0, t)$, which is given by

$$\Delta T_i(r_0,t) = T(r_0,t) - T_0 = \frac{q}{4\pi\lambda}\left[\text{in}\left(\frac{4at}{r_0^2 C}\right) + \frac{r_0^2}{4at} + \cdots\right] \tag{66.6}$$

In this equation, C is a known constant [8]. The equation suggests that, provided the radius of the wire is chosen small enough so that the second term on the right-hand side of Equation 66.6 is negligible, the thermal conductivity of the fluid can be obtained from the slope of the line ΔT_i, vs. ln t. Any practical implementation of this method of measurement inevitably deviates from this ideal model. The success of the technique, however, rests on the fact that by proper design, it is possible to construct an instrument that can operate very closely to the ideal model, while at the same time, small departures can be treated by a first-order analysis [8].

The roots of the transient hot-wire technique extend way back in time to the first heated-wire experiments in 1780. In the 1930s, the technique was used to measure the effective thermal conductivity of powders and solids [9]. However, its application to other materials was somewhat slower until in the late 1960s, the new technology associated with electronics made it possible to measure small, transient resistance changes with high accuracy in a period of less than 1 s. This development, pioneered by Haarman [10], made it possible to complete the transient heating process so quickly that, despite the inevitability of convective motion in the fluid from time zero, the inertia of the fluid ensures that the fluid velocity is sufficiently small so that there is no significant contribution to heat transfer. This fact prompted a rapid development of the measurement technique for fluids—first in gases and then in liquids—that was then followed by further developments in solids. The differences in the technique between solids and fluids are rather small; thus, some aspects of the instrumentation for liquids are briefly discussed, and the differences for solids are just outlined.

In the case of fluids, the instrumentation generally involves a wire some 7–25 μm in diameter (in order to reduce the correction owing to its heat capacity) and some 150 mm long. The wire is mounted vertically in a cylindrical cell containing the test sample. Often, a second wire differing only in length is employed to compensate automatically for effects at the ends of the wires via the electrical measurement system, but this can also be accomplished with potential taps [8]. In the more recent instruments [11], the wire supports are made of the same material so that they expand similarly to the wire when temperature rises, and hence the wire is always kept taut. Moreover, in this design, the wires are much shorter and placed one above the other. Whenever possible, platinum is used for the wire material because its resistance/temperature characteristics are well known and it can be readily obtained in the form of wires with a diameter as small as 5 μm. When the material under test is electrically conducting, it is necessary to insulate electrically the wire from the fluid. Several varieties of technique that enjoy different degrees of success depending on the range of conditions to be studied have been employed for this purpose. Near ambient temperature over a range of pressures, it has been found adequate to use a tantalum wire as the sensor that is electrolytically anodized to cover the wire with an insulating layer of tantalum pentoxide 100 nm thick [12]. Under more aggressive conditions, it has been necessary to employ ion-plating of the wire with a ceramic to secure the isolation [13]. In either case, the theory has been modified by the addition of a small correction.

In the case of solids, the need for the wire to be straight and vertical is removed by virtue of the rigidity of the material. Thus, Bäckström et al. [14] were able to employ a wire embedded as an arc within the compressed solid matrix of the material under study, particularly at very high pressures (up to 4 GPa). It should be noted that there are many standards (ASTM C1113 [15], EN 993-14/15 [16,17], ISO 8894 [18,19], and DIN 51046 [20]) that describe hot-wire test methods. The main problem arising in applying the technique to solids is the inevitable contact resistance between the samples and the wire.

A recent transient hot-wire design employs a silicone paste in order to avoid air gaps. The wires are placed inside a soft silicone layer that is squeezed between the two solids [21]. However, the last device is still available only for research laboratory use owing to difficulties in the sensor preparation. It is worth noting that this idea evolved from a transient hot-wire sensor originally employed for the measurement of the thermal conductivity of molten metals [22,23]. In that case, a 25 μm diameter platinum wire was placed over a sheet of pure green alumina, while its connections were printed on the substrate using platinum ink and a screen printing technique [24]. A second sheet of alumina was placed over them, and everything was hot-pressed in order to guarantee the best contact between the substrate and the platinum wire. Subsequent firing of the assembly produces a sufficiently robust sensor for it to be immersed in the molten metal.

The transient hot-wire technique has a unique advantage among transient methods that the thermal conductivity of the test material can be evaluated directly from the slope of the line relating the temperature rise of the wire to the logarithm of time. The heat capacity and density of the test material are required only to evaluate small corrections. Also advances in computer technology now allowed the use of a finite element method for the simulation of the exact geometry of the experimental setup, and therefore the uncertainty of the results is enhanced [21]. Furthermore, because the exact dimensions of the heating element and the cell are unimportant, the method avoids the intricate alignment problems of the parallel-plate technique while securing absolute measurements of the property. Despite these advantages and its wide application to measurements in gases, solids, and liquids, there has been no significant commercial development of an instrument of this kind, presumably because of the delicacy of the long thin wire in the case of devices for fluids, and the difficulty of sample and sensor preparation for solids. In Table 66.1, one of the few commercial hot-wire instruments is included.

66.3.7 Hot-Disk Instrument

A transient technique for which there is a commercial version suitable for solid materials is the transient hot-disk instrument shown in Figure 66.4.

The sensor in this case comprises a thin metal strip, often of nickel, wound in the form of a double-spiral in a plane. It is printed on, and embedded within, a thin sandwich formed by two layers of a material that is a poor electrical conductor but a good thermal conductor. This disk heater is then, in turn, placed either between two halves of a disk-shaped sample of solid material or affixed to the outside of the sample.

However it is configured, the essential measurement performed is the same as that for the hot-wire technique, and the temperature history of the sensor when subject to known electrical dissipation is inferred from its resistance charge. In the most recent version of the instrument, developed by Gustafsson [25], and also available commercially, the interpretation of the data is accomplished via a numerical solution of the differential equation rather than by some analytical

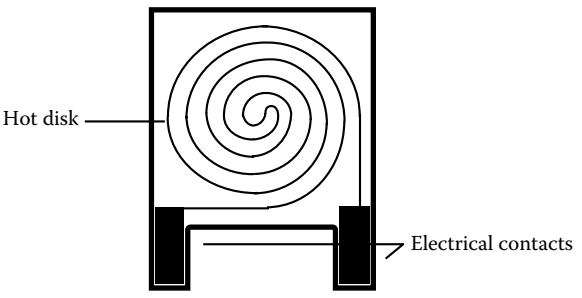

FIGURE 66.4 Schematic diagram of a transient hot-disk instrument.

approximation to it. The technique is used frequently for studies of polymer composites, glasses, superconductors, and insulating materials, and its use is defined by ISO 22007-2 [26].

66.3.8 Transient Hot Bridge

In this technique, which was developed at Physikalisch-Technische Bundesanstalt in Germany, the sensor is realized as a printed circuit foil of nickel between two polyimide sheets [27]. The sensor is itself placed symmetrically between two blocks of the solid material under test. The sensor itself consists of four identical strips arranged parallel to each other on the printed substrate. Each strip is itself composed of an identical short and long segment separated by a very small gap. Two of the strips are placed very close together either side of the central line of the sensor, and two are mounted some distance away from the central line but still symmetrically placed about it. All eight segments of strip are connected into the arms of a Wheatstone bridge so that the bridge is balanced at each and every homogeneous temperature of the sensor. However, when the same current is passed through the eight elements starting at time zero, there is an inhomogeneous heating of the inner and outer strips to an extent determined by the thermal properties of the test material. That differential heating is reflected in an out-of-balance of the bridge, which can be readily detected and related to the thermal conductivity and diffusivity of the test material [27]. The configuration has the advantages over some other techniques of automatically eliminating end effects in the sensor strips, homogeneous temperature drifts of the sample, thermoelectric emfs, and the need for external reference resistors.

66.3.9 Heated-Needle Probe

A further commercial device exists for the measurement of the thermal conductivity of granular materials such as powders and soils, natural materials such as rock and concrete, and, indeed, food. The probe is shown schematically in Figure 66.5, where it is seen that it consists of a thin, hollow, metallic needle (diameter 3 mm) containing an electric heater and a separate thermistor as a probe of the temperature history of the needle following initiation of a heat pulse [28]. The temperature history of the probe is generally interpreted with the aid of the equation appropriate to a transient hot-wire instrument but in a relative manner whereby its response is calibrated against known standards. This rather simplistic approach to the analysis of a somewhat complex cell inevitably restricts the accuracy that can be achieved, but does provide a measurement capability where no other technique is viable. It is often employed for measurements in inhomogeneous samples such as rocks or soils where it is simply the effective thermal conductivity that is required.

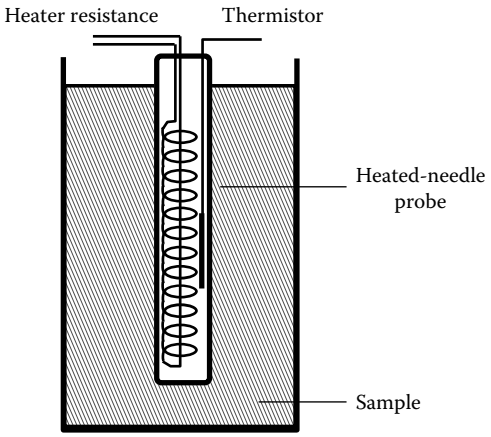

FIGURE 66.5 Schematic diagram of a transient heated-needle probe.

66.3.10 Laser-Flash Instrument

A final transient technique is that which has become known as the laser-flash technique developed originally for measurements in solids but occasionally used on liquids, particularly at high temperatures. The technique has been a standard test method since 1992 under the ASTM designation E1461 [29], and later also under the DIN EN 821 [30] and the ISO 18755 [31] standards.

Figure 66.6 contains a schematic diagram of the instrument as it is available today in a commercial form. The sample is illuminated on one face with a laser pulse of very short duration and high intensity. The absorption of the laser energy on the front face of the sample causes the generation of heat at that front surface, which is subsequently transmitted throughout the sample to the back face of the sample where the temperature rise is detected with an infrared remote sensor. The interpretation of measurements is based on a one-dimensional solution of Equation 66.4 subject to an initial condition of an instantaneous heat pulse at one location.

The temperature rise at the back face of a sample of thickness l and radius r is therefore given by [32]

$$\Delta T(l,t) = \frac{Q}{\rho C_p l \pi r^2}\left[1 + 2\sum_{n=1}^{\infty}(-1)^n \exp\left(-\frac{n^2\pi^2 at}{l^2}\right)\right] \tag{66.7}$$

where Q is the energy absorbed at the front surface at time zero. The thermal diffusivity of the sample, a, is then often deduced from the measurement of the time taken for the back face of the sample to reach one half of its maximum value. The technique has the very distinct advantage that it does not require physical contact between the test sample and the heater or detector. For this reason, it is a particularly appropriate technique for use at high temperatures or in aggressive environments.

However, there are a number of precautions that must be taken to ensure accurate results. First, the theory should be modified to account for non-unidirectional heat flow. Second, care must be taken to ensure that no radiation incident on the front face penetrates to the back face for transparent samples. Due care must also be taken to match the laser power to the system being studied so that there is neither fusion nor ablation at the front face that can distort the results. Finally, when the fluid state is studied, due care should be taken to eliminate convective heat transport. Seldom are all of these precautions adopted in routine work, so that some results obtained with the technique are of dubious validity. Nevertheless, the method has seen widespread application to a wide range of materials, including composites, polymers, glasses, metals, refractory materials, insulating solids, and coatings. Commercially available instruments operating according to this technique are listed in Table 66.1. Finally, the radial heat-flow method should also be mentioned. This is a transient technique in which the sample is heated and cooled continuously [33]. From the recording of the temperature gradient via thermocouples, the thermal diffusivity is obtained and thus the thermal conductivity is calculated. The advantage of the radial heat-flow method is that the measurements are fast and only small temperature gradients are necessary in the sample.

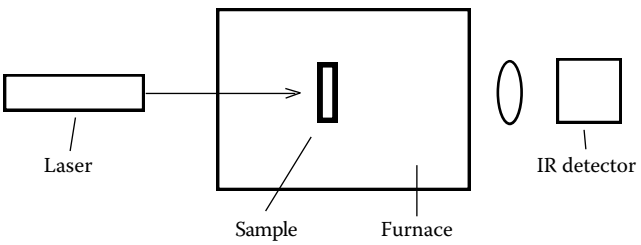

FIGURE 66.6 Schematic diagram of a laser-flash instrument.

TABLE 66.2 Addresses of Companies That Make Thermal Conductivity Instruments

TA Instruments, 159 Lukens Drive, New Castle, DE 19720, USA, Tel.: (302) 427-4000, Fax: (302) 427-4001
HUKSEFLUX Thermal Sensors B.V., Elektronicaweg 25, 2628 XG Delft, The Netherlands, Tel.: (31)-15-2142669, Fax: (31)-15-2574949
K-ANALYS AB, Salagatan 16F, SE-753 30 Uppsala, Sweden, Tel.: (46) 18 59 05 75, Fax: (46) 18 59 05 85
LINSEIS, Messgeraete GmbH, Vielitzerstr. 43, 95100 Selb, Germany, Tel.: (49) (0) 9287/880 0, Fax: (49) (0) 9287/704 88
NETZSCH, Gerätebau GmbH, Wittelsbacherstraβe 42, D-95100 Selb/Bayern, Germany, Tel.: (49) (9287) 88136, Fax: (49) (9287) 88144

66.4 Instrumentation

Table 66.1 lists various instruments for the measurement of the thermal conductivity of solids, while the addresses of the suppliers are shown in Table 66.2. As already mentioned, to our knowledge, there is no company that produces instruments specifically for the measurement of the thermal conductivity of fluids.

66.5 Appraisal

Naturally, the technique to be employed for the measurement of thermal conductivity depends on the type of sample to be studied, the range of conditions to be employed, and the required uncertainty. For fluid samples under most conditions, a variant of the transient hot-wire method must be the preferred technique. Under favorable conditions, an accuracy of ±0.3% can be achieved and a level of ±1% is possible under all but the most aggressive circumstances. Near the critical region of fluids, a parallel-plate instrument is essentially the only viable method. For molten materials at high temperature, while a variant of the hot-wire system has advantages, the laser-flash technique is very attractive, but an accuracy of no better than 10% is then to be expected.

For solids, the hot-disk or laser-flash techniques have many features that recommend them when the sample is amenable to appropriate preparation. In those cases, an accuracy of a few percent should be possible but is rarely attained. For samples such as rocks, the heated-needle probe is undoubtedly the only viable technique.

It should be emphasized again here that when a sample is inhomogeneous, the quantity determined is not the thermal conductivity of any element of it, but rather an effective value suitable for engineering purposes. It is not an intrinsic thermophysical property of the material.

References

1. B. Le Neindre, Contribution à l'étude expérimentale de la conductivité thermique de quelques fluides a haute température et à haute pression, PhD thesis, Université de Paris, Paris, France, 1969.
2. M. Sirota, Steady-state measurements for thermal conductivity, in A. Nagashima, G. V. Sengers, and W. A. Wakeham (eds.), *Experimental Thermodynamics. Vol. III. Measurement of the Transport Properties of Fluids*, London, U.K.: Blackwell Scientific Publications, 1991, Chapter 6.
3. R. Mostert, H. R. van der Berg, and P. S. van der Gulik, The thermal conductivity of ethane in the critical region, *J. Chem. Phys*., 92, 5454–5462, 1990.
4. E. Sakonidou, The thermal conductivity of methane and ethane mixtures around the critical point, PhD thesis, University of Amsterdam, Amsterdam, the Netherlands, 1996.
5. ASTM Standard E1530, 1999 (2006), Standard test method for evaluating the resistance to thermal transmission of materials by the guarded heat flow meter technique, ASTM International, West Conshohocken, PA, 2006.

6. ASTM Standard C177, 1997 (2010), Standard test method for steady-state heat flux measurements and thermal transmission properties by means of the guarded-hot-plate apparatus, ASTM International, West Conshohocken, PA, 2010.
7. ISO 8302, Thermal insulation—Determination of steady-state thermal resistance and related properties—Guarded hot plate apparatus, Beuth Verlag GmbH, Berlin, Germany, 1996; M. J. Assael, K. D. Antoniadis, and W. A. Wakeham, Historical evolution of the transient hot-wire technique, *Int. J. Thermophys*., 31, 1051–1072, 2010.
8. M. J. Assael, C. A. Nieto de Castro, H. M. Roder, and W. A. Wakeham, Transient methods for thermal conductivity, in A. Nagashima, J. V. Sengers, and W. A. Wakeham (eds.), *Experimental Thermodynamics. Vol. III. Measurement of the Transport Properties of Fluids*, London, U.K.: Blackwell Scientific Publications, 1991, Chapter 7.
9. B. Stâlhane and S. Pyk, Ny Metod för Bestämning Av Värmelednings-Koefficienter, *Teknisk Tidskrift*, 61, 389–398, 1931.
10. J. W. Haarman, Thermal conductivity measurements with a transient hot-wire method, PhD thesis, Technische Hogeschool Delft, Delft, the Netherlands, 1969.
11. M. J. Assael, C.-F. Chen, I. Metaxa, and W. A. Wakeham, Thermal conductivity of suspensions of carbon nanotubes in water, *Int. J. Thermophys*., 25, 971–985, 2004.
12. A. Alloush, W. B. Gosney, and W. A. Wakeham, A transient hot-wire instrument for thermal conductivity measurements in electrically conducting liquids at elevated temperatures, *Int. J. Thermophys*., 3, 225–234, 1982.
13. Y. Nagasaka and A. Nagashima, Absolute measurements of the thermal conductivity of electrically conducting liquids by the transient-hot wire method, *J. Phys*., *E*, 14, 1435, 1981.
14. P. Andersson and G. Bäckström, Measurement of the thermal conductivity under high pressures, *Rev. Sci. Instrum*., 47, 205, 1976.
15. ASTM C1113, 1999 (2009) Standard test method for thermal conductivity of refractories by hot wire (platinum resistance thermometer technique), ASTM International, West Conshohocken, PA, 2009.
16. EN 993-14, Methods of test dense shaped refractory products—Determination of thermal conductivity by the hot-wire (parallel) method, European Committee for Standardization, Brussels, Belgium, 2005.
17. EN 993-15, Methods of test dense shaped refractory products—Determination of thermal conductivity by the hot-wire (cross-array) method, European Committee for Standardization, Brussels, Belgium, 1998.
18. ISO 8894-1, Refractory materials—Determination of thermal conductivity—Part 1: Hot-wire methods (cross-array and resistance thermometer), Beuth Verlag GmbH, Berlin, Germany, 2010.
19. ISO 8894-2, Refractory materials—Determination of thermal conductivity—Part 1: Hot-wire methods (parallel), Beuth Verlag GmbH, Berlin, Germany, 2007.
20. DIN 51046, Testing of ceramic materials: Determination of thermal conductivity up to 1600°C by the hot-wire method thermal conductivity up to 2 W/m/K, Deutsches Institut für Normung, Berlin, 1976.
21. M. J. Assael, K. D. Antoniadis, K. E. Kakosimos, and I. N. Metaxa, An improved application of the transient hot-wire technique for the absolute accurate measurement of the thermal conductivity of pyroceram 9606 up to 420 K, *Int. J. Thermophys*., 29, 445–456, 2008.
22. M. V. Peralta-Martinez, M. J. Assael, M. Dix, L. Karagiannidis, and W. A. Wakeham, A novel instrument for the measurement of the thermal conductivity of molten metals. Part I. Instrument's description, *Int. J. Thermophys*., 27, 353–375, 2006.
23. M. V. Peralta-Martinez, M. J. Assael, M. Dix, L. Karagiannidis, and W. A. Wakeham, A novel instrument for the measurement of the thermal conductivity of molten metals. Part II. Measurements, *Int. J. Thermophys*., 27, 681–699, 2006.
24. M. Dix, I. W. Drummond, M. Lesemann, M. V. Peralta-Martinez, W. A. Wakeham, M. J. Assael, L. Karagiannidis, and H. R. van den Berg, The thermal conductivity of liquid metals near ambient conditions, *Proc. 5th Asian Thermophysical Properties Conference*, Seoul, Korea, pp. 133–136, 1998.

25. S. E. Gustafsson, E. Karawacki, and M. N. Khan, Transient hot-strip method for simultaneously measuring thermal conductivity and thermal diffusivity of solids and fluids, *J. Phys. D*: *Appl. Phys*., 12, 1411, 1979.
26. ISO 22207, Plastics—Determination of thermal conductivity and thermal diffusivity—Part 2: Transient plane heat source (hot disc) method, Beuth Verlag GmbH, Berlin, Germany, 2008.
27. U. Hammerschmidt and V. Meier, A new pulse hot strip sensor for measuring thermal conductivity and thermal diffusivity of solids, *Int. J. Thermophys*., 27, 840–865, 2006.
28. J. Nicolas, Ph. André, J. F. Rivez, and V. Debaut, Thermal conductivity measurements in soil using an instrument based on the cylindrical probe method, *Rev. Sci. Instrum*., 64, 774–780, 1993.
29. ASTM Standard E1461, 1992 (2007), Standard test method for thermal diffusivity by the flash method, ASTM International, West Conshohocken, PA, 2007.
30. EN 821-2, Advanced technical ceramics—Monolithic ceramics—Thermo-physical properties—Part 2: Determination of thermal diffusivity by the laser flash (or heat pulse) method, European Committee for Standardization, Brussels, Belgium, 1997.
31. ISO 18755, Refractory fine ceramics (advanced ceramics, advanced technical ceramics)—Determination of thermal diffusivity of monolithic ceramics by laser flash method, Beuth Verlag GmbH, Berlin, Germany, 2005.
32. W. J. Parker, R. J. Jenkins, C. P. Butler, and G. L. Abbott, Flash method for determining thermal diffusivity, heat capacity and thermal conductivity, *J. Appl. Phys*., 32, 1679–1684, 1960.
33. G. S. Sheffield and J. R. Schorr, Comparison of thermal diffusivity and thermal conductivity methods, *Ceram. Bull*., 70, 102, 1991.

67

Heat Flux

Thomas E. Diller
Virginia Tech

Energy use is coming under increasing scrutiny as the effects of carbon dioxide on the environment are being factored into the cost. Consequently, thermal management is becoming a sophisticated science in modern society. It has become accepted that living spaces should be heated and cooled for maximum comfort of the occupants. Many industrial manufacturing processes require tight temperature control of material throughout processing to establish the desired properties and quality control. Examples include control of thermal stresses in ceramics and thin films, plasma deposition, annealing of glass and metals, heat treatment of many materials, fiber spinning of plastics, film drying, growth of electronic films and crystals, and laser surface processing.

Temperature control of materials requires that energy be transferred to or from solids and fluids in a known and controlled manner. Consequently, the optimal control of the heat transfer in equipment such as dryers, heat exchangers, boilers, condensers, and data management centers becomes crucial. The constant drive toward higher power densities in electronic, propulsion, and electric generation equipment continually pushes the limits of the associated cooling systems.

Although the measurement of temperature is common and well accepted, the measurement of heat flux is often given little consideration. Temperature is one of the fundamental properties of a substance. Moreover, because temperature can be felt by human senses, most people are familiar with its meaning. Conversely, heat flux is a derived quantity that is not easily sensed. How and where thermal energy is transferred is often equally or more important than the temperature. For example, the temperature of human skin can indicate the comfort level of the person, but has little connection with the energy being dissipated to the surroundings, particularly if evaporation is occurring simultaneously. Wind chill factor is a common example of the importance of convection heat transfer in addition to air temperature.

Controlling the thermal energy transfer in many systems is crucial to their optimum performance. Consequently, sensors that can be used to directly sense heat flux can be extremely important. It is amazing that heat flux sensors are not more widely used in modern technology. The subsequent material in this chapter is intended to help individuals understand and implement heat flux measurements that are best suited for the required applications.

67.1 Heat Transfer Fundamentals

The movement of thermal energy is known as "heat," and the rate of this transfer is commonly called "heat transfer." It is given the symbol q and has the units of watts. The heat transfer per unit area is termed the "heat flux" and is given the symbol q'' with the units of W m^{-2}. Although in some cases only the overall heat transfer from a system is required, often the spatial and temporal variations of the heat flux are important to performance enhancement. Methods for measuring these distributions of heat flux are identified and discussed in this chapter.

One of the most important principles concerning heat transfer is the first law of thermodynamics, which states that the rate of energy storage is equal to the overall energy transfer to and from a system. It includes all types of energy transfer across the system boundary, including the three modes of heat transfer—conduction, convection, and radiation. For the simple example shown in Figure 67.1, the transient energy balance for a control volume around the surface can be expressed as

$$mC\frac{\partial T}{\partial t} = q_{\text{convection}} + q_{\text{radition}} - q_{\text{conduction}} \tag{67.1}$$

where

m is the mass of the material included
C is the corresponding specific heat

The effect of the thermal capacitance (mC) of the material causes a time lag in the temperature response of the material (T) to a change in heat transfer. A short summary of important heat transfer principles follows, with many engineering textbooks available in the field that give additional details [1].

67.1.1 Conduction

Conduction encompasses heat transfer through stationary materials by electrons and phonons. It is related to the temperature distribution by Fourier's law, which states that the heat flux vector is proportional to and in the opposite direction of the temperature gradient:

$$\overline{q}'' = -k\overline{\nabla} T \tag{67.2}$$

The constant k is the thermal conductivity of the material. Measuring this temperature gradient is one of the basic methods for determining heat flux.

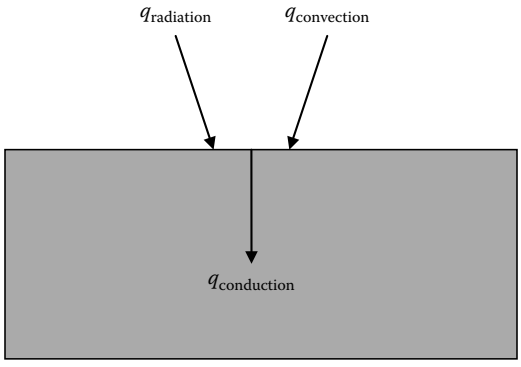

FIGURE 67.1 Illustration of energy balance.

For a homogeneous material in Cartesian coordinates, Equation 67.1 becomes

$$\frac{\partial T}{\partial t} = a\left(\frac{\partial^2 T}{\partial x^2} + \frac{\partial^2 T}{\partial y^2} + \frac{\partial^2 T}{\partial z^2}\right) \tag{67.3}$$

where a is the thermal diffusivity of the material with a density of ρ, $a = k/(\rho C)$. Measuring the transient temperature response of the system according to this equation is the second major method for determining the heat transfer.

As illustrated in Figure 67.1, convection and radiation are the modes of heat transfer at the boundary of a solid with conduction. They are usually the quantities of interest to measure with a heat flux sensor.

67.1.2 Convection

Although heat transfer by convection occurs by the same physical mechanisms as conduction, the fluid is free or forced to move relative to the surface. The fluid motion greatly complicates the analysis by coupling the heat transfer problem with the fluid mechanics. Particularly when the flow is turbulent, the fluid equations are generally impossible to solve exactly. Consequently, the heat transfer and fluid mechanics are commonly isolated by the introduction of a heat transfer coefficient, which encompasses all of the fluid flow effects.

$$q'' = h_{\mathrm{T}}(T_{\mathrm{r}} - T_{\mathrm{s}}) \tag{67.4}$$

The temperature of the fluid is represented by T_{r}, which for low-speed flows is simply the fluid temperature away from the surface. The recovery temperature is used for high-speed flows because it includes the effect of frictional heating in the fluid. The subscript T on the heat transfer coefficient, h_{T}, implies that the boundary condition on the surface is a constant temperature, T_s. Although other surface temperature conditions can be encountered, it is then important to carefully document the surface temperature distribution because it can have a profound effect on the values of h and q'' [2].

67.1.3 Radiation

Heat transfer by radiation occurs by the electromagnetic emission and adsorption of photons. Because this does not rely on a medium for transmission of the energy, radiation is very different from conduction and convection. Radiation has a spectrum of wavelengths dependent on the temperature and characteristics of the emitting surface material. Moreover, the surface properties are often dependent on the wavelength and angular direction of the radiation. Special coatings are sometimes applied to surfaces to control the absorption characteristics. For example, the surface of a radiation sensor is often coated with a high absorptivity paint or graphite.

Because the power emitted from a surface is proportional to the fourth power of the absolute temperature, radiation detectors are usually cooled sufficiently for the power emitted from the detector itself to be negligible. In this case, the temperature distribution of the sensor is not important and the heat flux is equal to the incident radiation:

$$q'' = \sigma T^4 \tag{67.5}$$

where

σ is the Stefan–Boltzmann constant

T is the temperature of the surroundings

This is a big advantage over convection measurements, where the temperature distribution on the surface has a big influence on the measurement.

67.2 Heat Flux Measurement

Most of the methods for measuring heat flux are based on temperature measurements on the surface or in the solid material. Usually this involves insertion of a device either onto or into the surface, which has the potential to cause both a physical disruption and a thermal disruption of the surface. As with any good sensor design, the goal for good measurements must be to minimize the disruption caused by the presence of the sensor. It is particularly important to understand the thermal disruption caused by the sensor because it cannot be readily visualized and because all heat flux sensors have a temperature change associated with the measurement. Consequently, wise selection of the sensor type and operating range is important for good heat flux measurements [2,3]. The following sections emphasize important factors in using the currently available heat flux sensors. They are grouped by the general type of sensor action. The commercially available gages are listed in Table 67.1 with the general characteristics of the system.

TABLE 67.1 Heat Flux Instrumentation

Manufacturer	Sensor	Description	Mounting Method
RdF	Micro-foil	Foil thermopile	Surface
Concept	Heat flow sensor	Wire-wound thermopile	Surface
MesoScribe Technologies	Heat flux transducer	Direct write thermal spray	Surface
ITI	Thermal flux meter	Thermopile	Surface
Vatell	HFM	Microsensor thermopile	Insert
Medtherm, Vatell	Gardon gage	Circular foil design	Insert
Medtherm, Vatell, Hukseflux	Schmidt-Boelter	Wire-wound thermopile	Insert
Medtherm	Coaxial thermocouple	Transient temperature	Insert
Medtherm	Null-point calorimeter	Transient temperature	Insert
Hallcrest	Liquid crystals	Temperature measurement kit	Surface

TABLE 67.2 Companies That Make Sensors for Heat Flux Measurement

Concept Engineering
43 Ragged Rock Road
Old Saybrook, CT 06475
(860) 388–5566
http://conceptengineering2000.com/

International Thermal Instrument Co.
P.O. Box 309
Del Mar, CA 92014
(858) 755–4436
http://www.iticompany.com/

Medtherm Corporation
P.O. Box 412
Huntsville, AL 35804
(205) 837–2000

Hukseflux Thermal Sensors
Elektronicaweg 25
2628 XG Delft
The Netherlands
31-15-2142669
http://www.hukseflux.com/

RdF Corporation
P.O. Box 490
Hudson, NH 03051-9981
(603) 882–5195
www.rdfcorp.com/

Vatell Corporation
P.O. Box 66
Christiansburg, VA 24073
(540) 961–3576
http://vatell.com/

LCR Hallcrest
1911 Pickwick Lane
Glenview, IL 60026
(8472) 998–8580
http://hallcrest.com/

MesoScribe Technologies, Inc.
7 Flowerfield, Suite 28
St. James, NY 11780
631-686-5710
http://www.mesoscribe.com/

Prices have not been included because there are usually many specific variations of gages with different costs. They are usually made individually rather than mass produced. Contact information for the manufacturers is given in Table 67.2. Many also have dealers and representatives located around the world.

67.3 Sensors Based on Spatial Temperature Gradient

The heat flux at the material surface can be found at a location if the temperature gradient can be determined at that position, as indicated in Equation 67.2. Because it is difficult to position temperature sensors with the requisite accuracy inside the material, sensors to measure heat flux are either applied on the surface or mounted in a hole in the material.

67.3.1 One-Dimensional Planar Sensors

A simple heat flux sensor concept for mounting on a surface is illustrated in Figure 67.2. The one-dimensional heat flux perpendicular to the surface is found from Equation 67.3 for steady-state conditions:

$$q'' = \frac{k}{\delta}(T_1 - T_2) \tag{67.6}$$

The thickness of the sensor δ and thermal conductivity k are not known with sufficient accuracy for any particular sensor to preclude direct calibrations of each sensor. An adhesive layer may also be required between the sensor and the surface to securely attach the sensor, which adds an additional thermal resistance and increases the thermal disruption. Temperature measurements on the sensor and on the surrounding undisturbed material are recommended to quantify this disruption. A new ASTM standard [4] gives guidance on the use of these sensors.

Although the temperature difference can be measured by any number of methods, the most commonly used are thermocouples. Thermocouples have the advantage that they generate their own voltage output corresponding to the temperature difference between two junctions. Consequently, they can be connected in series to form a thermopile that amplifies the output from a given temperature difference, as illustrated in Figure 67.3. Most any pair of conductors (e.g., copper–constantan) can be used for the legs of the thermopile, but the output leads should be of the same material so that additional thermocouple junctions are not created. The voltage output, E, is simply

$$E = NS_T(T_1 - T_2) \tag{67.7}$$

where

N represents the number of thermocouple junction pairs

S_T is the Seebeck coefficient or thermoelectric sensitivity of the materials, expressed in volts per degree Centigrade

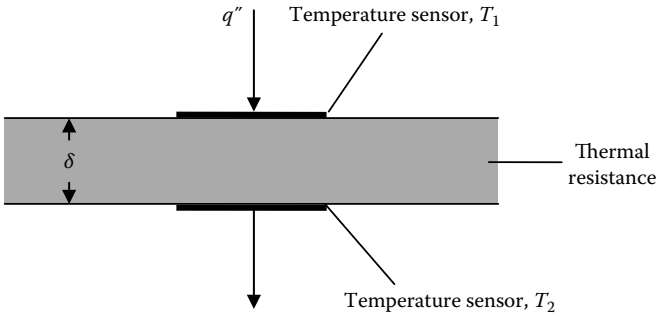

FIGURE 67.2 One-dimensional planar sensor concepts.

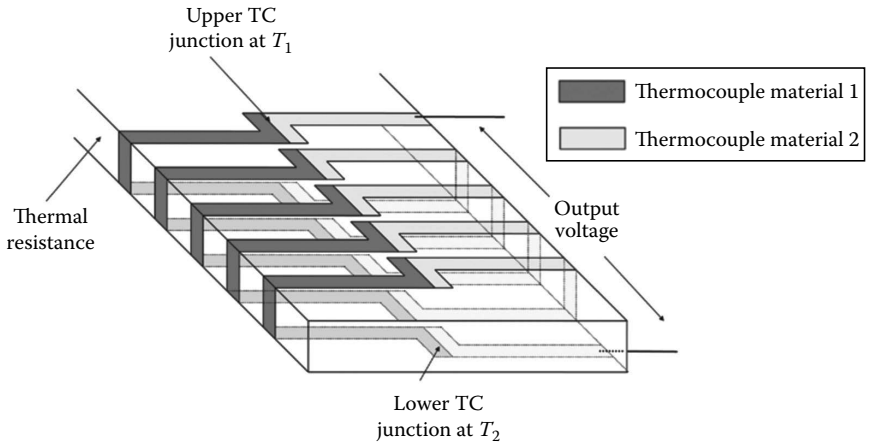

FIGURE 67.3 Thermopile heat flux sensor.

The corresponding sensitivity of the heat flux sensor is

$$S = \frac{E}{q''} = \frac{NS_T\delta}{k} \tag{67.8}$$

Although the sensitivity is determined in practice from a direct calibration, the last part of the equation can be used to determine the effects of different parameters for design purposes.

One successful design using a thermopile is the Micro-Foil HFS currently manufactured by RdF Corp. Thin pieces of two types of metal foil are alternately wrapped around a thin plastic (Kapton) sheet and butt-welded on either side to form thermocouple junctions, as illustrated in Figure 67.3. A separate thermocouple is included to provide a measure of the sensor temperature. The flexible, micro-foil sensors are 75–400 μm thick and can be glued to a variety of surface shapes, but are limited to temperatures below (250°C) and heat fluxes less than 100 kW m^{-2}. This covers many general-purpose industrial and research applications. The time response can be as fast as 20 ms, but transient signals can be attenuated unless the frequency of the disturbance is less than a few hertz. These sensors act much like a first-order system, which has 70% amplitude response to a sinusoidal input with a period six times the exponential time constant.

If the individual legs of the sensor are left in parallel instead of in series, an array of heat flux sensors is created. This was done by Hubble and Diller [5] using copper and constantan for the thermocouple materials. The time constants were between 100 and 200 ms when using a 50 μm thick layer of Kapton for the thermal resistance. The output from the 10-sensor array was arranged to give both the heat flux (from the differential temperature) and surface temperature at each location.

A high-temperature heat flux gage (HTHFS) has been developed by MesoScribe Technologies, Inc., which can be deposited directly onto test surfaces using a Direct Write Thermal Spray process. Up to 80 thermocouple pairs (Type K or N) are scribed around a layer of dielectric serving as the thermal resistance for the heat flux with a separate thermocouple giving the surface temperature. A layer of ceramic dielectric is first deposited on a metal surface to provide electrical isolation and can also be deposited over the gage to encapsulate it for better durability. All of the layers together are less than 0.4 mm thick, which gives the sensor a low profile. The sensor is sufficiently thick, however, for good survivability at high temperatures, and it gives a good output signal. The sensor can also be embedded in existing barrier coatings used for thermal, environmental, or erosion resistance.

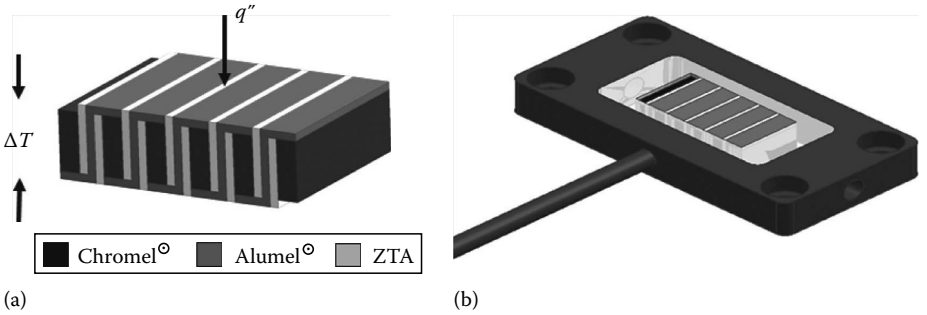

FIGURE 67.4 HTHFS: (a) schematic of the measuring element, (b) complete sensor.

A robust HTHFS is made by welding Chromel and Alumel strips [6] as illustrated in Figure 67.4. The thermal resistance between the top and bottom thermocouples is formed by the elements themselves. Ceramic (ZTA) strips are included to provide electrical insulation between elements. An additional thermocouple wire welded to the top of the gage provides the surface temperature, which is useful for interpreting the heat flux signal. The gage can be operated and cycled to over 1000 °C. The thickness is about 3 mm with a thermal time constant less than 1 s. Because of the all-metal construction, the thermal resistance is small. The measurement chip can also be mounted in an insert type housing that can be air or water cooled for gage temperature control.

A design using welded wire to form the thermopile across the thermal resistance layer is made by International Thermal Instrument Co. The sensors are about 3 mm thick with thermal time constants on the order of 1 s and an upper temperature limit of 300 °C. Typical applications include heat transfer in buildings and physiology. Sensors with higher sensitivity are made with semiconductor thermocouple materials for geothermal applications. Sensors are also available for operating temperatures up to 1000 °C.

Another technique for measuring the temperature difference across the thermal resistance layer is to wrap wire and then plate one side of it with a different metal. A common combination is constantan wire with copper plating. The resulting wire-wound sensor looks similar to the sensor shown in Figure 67.3, except that the constantan wire is continuous all around the sensor. A summary of the theory is given by Hauser [7], and a general review is given by van der Graaf [8]. Concept Engineering offers a range of these types of sensors at moderate cost. Because of the many wire windings around 2 mm thick plastic strips, the sensitivity to heat flux is high. The corresponding thermal resistance is also large and time constants are around 1 s. Temperatures are limited to about 150 °C. Measured heat flux levels are usually less than 1 kW m^{-2}, with applications including building structures, insulation, geothermal, and medicine.

Heat flux gages are normally mounted on a good heat sink to provide a pathway for the thermal energy to flow. Not all real applications provide such an ideal situation, however. Hubble and Diller [9] have shown with a simple modification of the signal how to use heat flux gages on any surface, including thermal insulators. Adding a second term to account for the energy storage in the sensor itself creates what is termed the "hybrid heat flux"

$$q'' = q''_{\text{dif}} + \frac{1}{2} q''_{\text{cal}} \tag{67.9}$$

The first term is the usual differential signal from the sensor, while the second term is the transient response representative of the signal from a calorimeter. This gives the correct heat flux whether the gage is mounted on a good heat sink (high-conductivity material) or a good insulator (low-conductivity material). It also increases the time response of the gage by about an order of magnitude. The differential heat flux is proportional to the usual temperature difference measured across the gage, and the calorimeter heat flux is proportional to the time rate of temperature change of the gage.

67.3.2 Insert Gages

Insert gages are mounted through a hole flush with the surface of the material. Their use is covered by a new ASTM standard [10]. One popular version uses a plated wire wrapped around a small anodized piece of aluminum that is potted into a circular housing, commonly known as a Schmidt-Boelter gage. Kidd and Nelson [11] have analyzed these gages to determine the effect of the plating relative to a true differential thermopile. The sensors are commercially available from Medtherm, Vatell, and Hukseflux in sizes as small as 1.5 mm diameter. There is also some ability to contour the surface of the sensor to match a curved model surface for complex test article shapes.

A thin thermopile sensor called the Heat Flux Microsensor (HFM) is manufactured by Vatell Corp. Because it is made with thin-film sputtering techniques, the entire sensor is less than 2 μm thick. The thermal resistance layer of silicon monoxide and the metal layers are sputtered directly onto the aluminum nitride surface of the gage. The resulting physical and thermal disruption of the surface due to the presence of the sensor is extremely small. They are best suited for heat flux values above 1 kW m^{-2}, with no practical upper limit. Because the sensor is so thin, the thermal response time is less than 10 μs [12], giving a good frequency response well above 1 kHz. A temperature measurement that is integrated into the sensor is very useful for determining the heat transfer coefficient. The high temperature and fast time response capabilities are useful for aerodynamic applications, combusting flows in engines and propulsion systems, and capturing high-speed events such as shock passage.

The circular foil or Gardon gage consists of a hollow cylinder of one thermocouple material with a thin foil of a second thermocouple material attached to one end. A wire of the first material is attached to the center of the foil to complete a differential thermocouple pair between the center and edge of the foil as illustrated in Figure 67.5. The body and wire are commonly made of copper with the foil made of constantan. Heat flux to the gage causes a radial temperature distribution along the foil as measured by this single thermocouple pair. These sensors are covered by an ASTM standard [13]. They are manufactured by two companies at moderate cost (Medtherm and Vatell) and are often used as secondary standards for measurement of radiation. The biggest problems with the circular foil gages arise when they are used with any type of convection heat transfer. It has been shown analytically and experimentally that the output is altered for convective heat transfer because of the distortion of the temperature profile in the foil from the parabolic profile of radiation [14]. Because the amount of error is a function of the gage geometry, the fluid flow, and the heat transfer coefficient, it is difficult to correct reliably. The errors become particularly large when the sensor is used in a flow that has a shear flow component, which encompasses most convection situations. Consequently, great care must be used to keep the temperature difference across the gage small if Gardon gages are used to measure convective heat transfer.

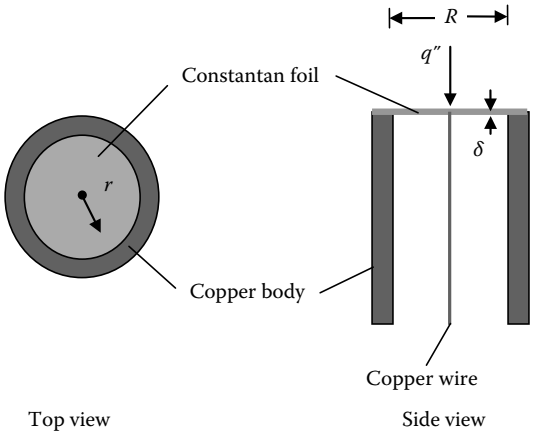

FIGURE 67.5 Circular foil heat flux gage.

When insert heat flux gages are used in high heat flux situations, such as combustors, water cooling is usually supplied through the body of the sensor to keep the temperature from exceeding material limits. Because of the resulting temperature mismatch of the gage and surrounding material in which it is mounted, a water-cooled gage is not recommended for convection heat transfer measurements. It is also important for a water-cooled gage to ensure that condensation does not occur on the sensor face.

Although most heat flux sensors are designed to measure the total heat flux, sensors have been developed to separate convection from radiation. The most common method is to put a transparent window over the sensor to eliminate convection to the sensor face. Because the resulting sensor only measures radiation, it is termed a radiometer. The field of view is limited, however, in these radiometers and must be included in the interpretation of results. In a dirty environment where the transmission of the window could be degraded, air is blown across the face of the window to keep the particles away from the sensor. Applications include use in high-ash boilers and gas turbine combustors.

67.4 Sensors Based on Temperature Change with Time

Equations 67.1 through 67.3 give the form of the relationship between the unsteady response of temperature and surface heat transfer. If the thermal properties of the wall material are known along with sufficient detail about the temperature history and distribution, the heat transfer as a function of time can, in principle, be determined. Although temperature sensors are available from manufacturers, the necessary data manipulation must be done by the user to obtain heat flux. There are two types of solutions used to reduce the temperature history to heat flux. These are discussed separately as the semi-infinite solution and calorimeter methods. In addition, a variety of methods for measuring the required temperature history are discussed.

67.4.1 Semi-Infinite Surface Temperature Methods

An important technique for short-duration heat flux tests is to measure the surface temperature history on a test object with a fast-response temperature sensor. For short enough times and sufficiently thick material, it can be assumed that the transfer is one-dimensional and that the thermal effects do not reach the back surface of the material. Equation 67.3 reduces to a one-dimensional, semi-infinite solution, which is simple to implement for this case. For example, the surface temperature for a step change of heat flux at time zero is

$$T_s - T_i = \frac{2q_o''\sqrt{t}}{\sqrt{\pi k\rho C}} \tag{67.10}$$

The substrate properties are the thermal conductivity, density, and specific heat, represented by the product $k\rho C$. T_i is the uniform initial temperature of the substrate and T_s is the surface temperature as a function of time. The effects of both energy storage in the material and conduction through the material are included.

Data analysis of the measured temperature record to find the corresponding heat flux can be performed by several methods. The simplest is to use the analytical solution with each sampled data point to recreate the heat flux signal. The most popular equation for this conversion is that attributed to Cook and Felderman [15] for uniformly sampled data:

$$q''(t_n) = \frac{2\sqrt{k\rho C}}{\sqrt{\pi\Delta t}} \sum_{j=1}^{n} \frac{T_j - T_{j-1}}{\sqrt{n-j} + \sqrt{n+1-j}} \tag{67.11}$$

This can easily be implemented for digital data with a short computer program to perform the summation for the measured points. Numerical solutions are used to account for changes in property values if there are large temperature changes. One problem is the inherent instability of using a temperature record to infer the heat flux. This is akin to taking the derivative of the temperature signal, which greatly amplifies any noise present in the signal and is particularly important when making detailed measurements of time-resolved heat flux. There are several methods to increase the stability of the signal, such as that reported by Oldfield [16].

A good criterion for the time limit on the test is the time before 1% error occurs in the heat flux:

$$t = 0.3\frac{L^2}{a} \tag{67.12}$$

where

a represents the thermal diffusivity of the substrate material
L is the substrate thickness

For a typical ceramic substrate (MACOR), the corresponding minimum thickness for 1 s of test time is 1.6 mm. High-conductivity materials, such as metals, have much larger required thicknesses.

The required surface temperature can be measured with a number of different techniques. Two broad categories are point measurements using thermocouples or resistance temperature devices (RTDs) and optical methods that allow for simultaneous measurement of temperatures over the entire surface. They all require substantial effort from the user to initiate the test procedure and reduce the data to find the heat flux.

Point temperature measurements for determining convective heat flux are often made with thin-film RTDs. A metallic resistance layer is sputtered, painted and baked, or plated onto the surface. Because the resulting thickness of the sensor is less than 0.1 μm, the response time is a fraction of 1 μs, and there should be no physical or thermal disruption of the measured temperature due to the sensor. Most researchers develop techniques for instrumenting models themselves. An alternative is to deposit RTDs onto a thin plastic sheet and then glue that to the surface [17]. This may require consideration of the different properties of the multiple layers of plastic, adhesive, and model. Transient flow facilities provide an easy method for quickly initiating the flow and heat transfer, as required by this transient method. However, the model can also be injected into the flow or the flow can be quickly diverted to provide the fast initiation of heat flux. The method is used for basic measurements applicable to gas turbine engines, rockets, internal combustion engines, and high-speed aerodynamics [2].

A special type of thermocouple called coaxial thermocouples [18] is specifically made for transient surface temperature measurement. It has one thermocouple wire inside the second thermocouple material with an insulating layer in between. One end is mounted into a metal sheath for press fitting into the surface material for testing. A thin thermocouple is formed by combining the two metals right at the end of the assembly. Response times are typically 1 ms or less, which although slower than the thin-film sensors is sufficient for most applications. The cost per sensor is moderate, and they are available from Medtherm Corp. The average properties of the sensor should be matched with those of the substrate material.

Null-point calorimeters [19] are a further extension of the semi-infinite surface temperature method. They are designed for the measurement of extremely high levels of heat flux (over 1000 kW m^{-2}). To protect the thermocouple and wires, they are mounted in a cavity behind the surface. The geometry of the null-point calorimeter is designed, however, for the thermocouple to measure a temperature that would match the surface temperature of a semi-infinite material so that Equation 67.11 can be used for data reduction [19]. Medtherm is the current supplier of null-point calorimeters.

Optical methods give the opportunity to measure the entire temperature field over the surface of interest. Consequently, much data can be collected over each test, but interpretation to obtain

quantitative heat flux values is more challenging than measurements with point sensors. The visual display of the temperature over the surface is very appealing and can enhance the interpretation of data by seeing the distribution of temperature on a surface in addition to its numerical value.

One popular optical method for measuring temperature is to record the color change using liquid crystals. These are specially prepared molecules that reversibly change their color reflection through several distinct colors as a function of temperature, typically in the range of 25 °C–40 °C. The best for transient measurements are the chiral-nematic form, which has been microencapsulated to stabilize their properties. A variety of types can be obtained from Hallcrest. They can easily be spray-painted onto a blackened surface for testing. Setting the lighting for reproducible color, temperature calibration, image acquisition, and accurately establishing the starting temperature are crucial steps [20]. The basic materials are cheap, but the associated equipment is expensive, including a high-quality video camera, lighting system, calibration system, computer hardware, and software for image processing.

As previously discussed for radiation heat transfer, all surfaces emit radiation with an intensity and wavelength distribution that can be related to the surface temperature. The advent of high-speed infrared scanning radiometers has made it feasible to record the transient temperature field for the determination of the transient heat flux distribution [21]. A coating is usually applied to establish a known high-emissivity surface. To convert the measured radiation emission to surface temperature, the radiation field of the surroundings is also required because reflections can be important.

Thermographic phosphors emit radiation in the visible spectrum when illuminated with ultraviolet light. The intensity of emission at specific wavelengths can be related to the temperature over a wide range of surface temperatures [22]. The potential high-temperature applications are particularly appealing. A CCD camera is required to record the transient optical images, and calibration is challenging.

The temperature-sensitive paint method uses a Europium complex as the luminophore with a mercury-xenon arc lamp for illumination [23]. A CCD camera is used to collect the images as a function of time.

67.4.2 Calorimeter Methods

A *calorimeter* is a device for measuring the amount of absorbed thermal energy. A slug calorimeter [24] uses the rate of temperature change in a known mass of material to determine the heat flux at the surface. It is used as an insert gage mounted flush with the surface of a material and isolated thermally from the material. This is done with a small air gap around the calorimeter and insulation on the back side where the thermocouple for temperature sensing is attached. Although there is a temperature gradient through the material of the slug, after a short transient, the rate of temperature change in the gage is uniform. When exposed to a constant heat flux, the rate of temperature change will be constant and can be related to the heat transfer by

$$q = mC\frac{dT}{dt} + q_{\text{losses}} \tag{67.13}$$

where the product of mass (m) and specific heat (C) is the thermal capacitance of the slug. The heat losses should be kept small unless they can be quantified. One way to determine the losses is to monitor the rate of temperature cooling after the heat source is removed. Although slug calorimeters are rarely used currently, they can provide an important standard in the calibration process.

A similar device is the differential flame thermometer [25], which consists of two inconel plates separated by a layer of insulation with a thermocouple mounted on each plate. Plates are typically 120 mm square and the insulation is 19 mm thick. The resulting time constant for the system is about 90 s. The application is in a radiation-dominated furnace or combustor to measure the heat flux and steady-state temperature. Inverse heat transfer methods are used to convert the two temperature records into heat flux. It should be noted that this device is different from a standard heat flux gage because it is suspended in the furnace or environment rather than mounted on or in a surface.

67.5 Measurements Based on Surface Heating

For research on convective heat transfer, electric heating provides an easy method of controlling and measuring the heat flux from a surface. A combination of guard heaters and insulation allows control of the heat losses to give an accurate knowledge of the heat flux leaving the surface based on the total electrical power supplied once steady-state conditions have been established. The temperatures of the surface and fluid are used in Equation 67.4 to give the heat transfer coefficient for the surface:

$$h = \frac{q''}{T_r - T_s} \tag{67.14}$$

The experimental techniques can be grouped according to the two boundary conditions that normally result: constant heat flux and constant wall temperature. In constant heat flux cases, the experiment usually runs until a steady-state temperature distribution is achieved. For constant wall temperature, manual or active control of the power is required to stabilize the system at the prescribed constant temperature.

For constant heat flux conditions, a thin metal sheet is often used as the heater to provide uniformity of resistance (and heat flux) and to minimize the lateral conduction. Several centimeters of good insulation as the backing material usually insures acceptable heat loss from the back surface. Unfortunately, the response time for this arrangement is typically very long, depending on the surface convection and substrate properties. With a surface heat transfer coefficient of 100 $W/m^2 \cdot K$ and a good substrate insulator, the time from a cold start to reach steady-state conditions (within 2%) is typically over 1 h. The time limitation is the result of transient heat transfer into the insulation backing layer.

Surface temperature measurements are not needed to determine the heat flux, but they are required for the determination of the heat transfer coefficient. Although any of the methods for measuring temperature are possible candidates, only thermocouples, RTDs, infrared cameras, and liquid crystals are commonly used. Thermocouples give point measurements and must be carefully mounted to avoid losses along the wires. Resistance elements can be used to both supply the heating and to measure the average temperature of the element. Infrared radiation measurements can give the entire surface distribution. Liquid crystals can also give the surface distribution and can even measure the transient response under the right conditions [26].

The design and operation of constant surface temperature experiments are substantially different than those for constant heat flux. Instead of measuring the temperature that results from an imposed heat flux, the electrical power that is required to maintain a set temperature is measured. This typically requires a control system to maintain the temperature constant spatially and/or temporally, depending on whether steady or unsteady measurements are desired. Time-averaged measurements of spatial distributions of convection heat transfer are usually made with segmented plates and heaters. If the plates are made of a thick, high-conductivity material, the surface will be nearly isothermal, even if the heat transfer coefficient has large spatial variations. Some thermal isolation is required between segments, often provided by insulation strips. A good set of PID automatic temperature controllers can greatly speed the stabilization process. When combined with thin-film heaters deposited on insulation, time-resolved measurements are even possible.

67.6 Calibration and Problems to Avoid

Calibration of heat flux is a complicated issue because some heat flux sensors respond to different modes and conditions of heat flux differently. For example, a sensor calibrated by radiation can have a substantially different response to the same amount of heat flux in convection.

For the low heat fluxes seen in building applications, the guarded hot-plate method for calibration has been well established [27]. The sensor to be calibrated is placed between a heated plate and a cooled plate.

The electrical power into the heated plate is measured at steady state to provide the known heat flux. The National Institute of Standards and Technology (NIST) maintains calibration devices for this range of conduction heat transfer through one-dimensional planar sensors. Calibrated insulation samples are readily available to check other guarded hot-plate calibrators against their standards.

Most insert gages are calibrated with radiation. There are two basic approaches. The first is to use a system that provides an absolute comparison with a primary standard. The second uses another heat flux sensor as a secondary standard for the comparison. There are three methods for absolute radiation calibration of heat flux sensors as illustrated in the facilities at NIST [28]. They are all designed for water-cooled sensors that are kept at room temperature for the calibration. One uses an electrical substitution radiometer as the primary standard in a narrow-angle facility. The second is a spherical cavity that uses the temperature of the wall as the standard along with the Stefan–Boltzmann law (Equation 67.5) for the blackbody radiation to the sensor. The heat flux sensor should be located at the bottom of the sphere or the sphere should be in a vacuum to minimize the effects of convection. The third method is insertion into a graphite tube blackbody cavity with a pyrometer on the opposite side of the center partition for the primary standard. All of these methods calibrate the sensors based on the incident radiation, q''_{inc}.

$$S_{inc} = E/q''_{inc} \tag{67.15}$$

The voltage output is E and the sensitivity is S in units of voltage per heat flux. The emissivity of the surface ε is required to calculate the radiation that is actually absorbed by the sensor.

$$q''_{abs} = \varepsilon q''_{inc} \tag{67.16}$$

The gage surface is assumed to be gray with the absorptivity equal to the emissivity, ε, and both values constant with angle and wavelength for the conditions of use. Here it is assumed that the radiation emitted from the gage is negligible compared to the incident because the gage is water cooled and kept at a temperature near 300 K.

The manufacturers use secondary standards to calibrate heat flux gages by direct comparison either simultaneously or sequentially with matching radiation fluxes. The same can be done for convection [29]. The resulting sensitivity corresponds to the absorbed radiation. Consequently, the usual incident radiation calibration must be adjusted to correspond to the convection sensitivity by the emissivity of the original surface coating:

$$S_{conv} = S_{inc}/\varepsilon \tag{67.17}$$

As with many other measurements, the major problem with heat flux measurement is the error caused in the heat flux by the disruption of the sensor itself. For sensors based on the spatial temperature gradient methods, a larger signal implies a larger temperature difference and a larger temperature disruption. For the second type of sensors based on the transient temperature change, the surface temperature is changing while the measurement occurs. The larger the temperature change, the easier the determination of the sensor heat flux, but the larger the error from the sensor temperature disruption. In convection, the effect of the surface temperature disruption directly affects the apparent heat flux measured by the gage [29]. Therefore, it is imperative in convection measurements to keep the thermal disruption of the sensor to a minimum.

There are many situations where the heat flux is desired on surfaces with elevated temperatures. As previously discussed, there are several gages that are capable of operating at up to 1000 °C. Because of changes in thermal properties of the gage materials with temperature, calibration at the actual gage temperature is required. One method is to place the sensor on a heated surface and a water-cooled gage

on a cold surface and measure the radiation from the hot surface to the cold surface in enclosure [30]. If the side walls are insulated and adiabatic, the heat leaving the hot surface will match that received by the cold plate. This system allows sensors to be characterized up to 900 °C.

67.7 Summary

There are a large number of heat flux sensors available for use in a wide variety of applications. Those commercially available have been listed in Table 67.1, and the information for contacting the manufacturers is given in Table 67.2. The sensors that have not yet been commercialized are sometimes still available from the labs where they were developed.

The differential temperature devices provide a direct readout of the heat flux over the surface of the sensor. With the proper choice of sensor for the application and care in measurement method, the results are easily interpreted and used. Alternatively, the transient temperature methods can provide more surface details, but the output is a surface temperature history that must be analyzed to obtain the corresponding heat flux. Although certain components of these systems are off-the-shelf, more work is required of the user to interpret the results. Issues of calibration and errors have been addressed briefly here. More detail on all aspects of heat flux measurement can be obtained from the manufacturers and the references listed.

References

1. F. Incropera, D. DeWitt, T. Bergman, and A. Lavine, *Fundamentals of Heat and Mass Transfer*, 7th edn., New York: John Wiley & Sons, 2011.
2. T. E. Diller, Advances in heat flux measurement, in J. P. Hartnett et al. (eds.), *Advances in Heat Transfer*, Vol. 23, Boston, MA: Academic Press, 1993, pp. 279–368.
3. N. R. Keltner, Heat flux measurements: Theory and applications, Chapter 8, in K. Azar (ed.), *Thermal Measurements in Electronics Cooling*, Boca Raton, FL: CRC Press, 1997, pp. 273–320.
4. ASTM E2684-09, Standard test method for measuring heat flux using surface-mounted one-dimensional flat gages, *Ann. Book ASTM Standards*, 15.03, 2009.
5. D. O. Hubble and T. E. Diller, Development and evaluation of the time-resolved heat and temperature array, *Journal of Thermal Science and Engineering Applications*, 2, 2010, 031003, 9.
6. A. R. Gifford, D. O. Hubble, C. A. Pullins, S. T. Huxtable, and T. E. Diller, A durable heat flux sensor for extreme temperature and heat flux environments, *AIAA Journal of Thermophysics and Heat Transfer*, 24, 2010, 69–76.
7. R. L. Hauser, Construction and performance of in situ heat flux transducers, in E. Bales et al. (eds.), *Building Applications of Heat Flux Transducers*, ASTM STP 885, 1985, pp. 172–183.
8. F. Van der Graaf, Heat flux sensors, in W. Gopel et al. (eds.), *Sensors*, Vol. 4, New York: VCH, 1989, pp. 295–322.
9. D. O. Hubble and T. E. Diller, A hybrid method for measuring heat flux, *ASME Journal of Heat Transfer*, 132, 2010, 031602, 8.
10. ASTM E2683-09, Standard test method for measuring heat flux using flush-mounted insert temperature-gradient gages, *Annual Book ASTM Standards*, 15.03, 2009.
11. C. T. Kidd and C. G. Nelson, How the Schmidt-Boelter gage really works, *Proc. 41st Int. Instrum. Symp.*, Research Triangle Park, NC: ISA, 1995, pp. 347–368.
12. D. G. Holmberg and T. E. Diller, High-frequency heat flux sensor calibration and modeling, *ASME J. Fluids Eng.*, 117, 1995, 659–664.
13. ASTM E511-07, Measurement of heat flux using a copper-constantan circular foil heat-flux gage, *Annual Book ASTM Standards*, 15.03, 2009.
14. C. H. Kuo and A. K. Kulkarni, Analysis of heat flux measurement by circular foil gages in a mixed convection/radiation environment, *ASME Journal of Heat Transfer*, 113, 1991, 1037–1040.

15. W. J. Cook and E. M. Felderman, Reduction of data from thin film heat-transfer gages: A concise numerical technique, *AIAA Journal*, 4, 1966, 561–562.
16. M. L. G. Oldfield, Impulse response processing of transient heat transfer gauge signals, *Journal of Turbomachinery*, 130, 2008, 021023.
17. S. M. Guo, C. C. Lai, T. V. Jones, M. L. G. Oldfield, G. D. Lock, and A. J. Rawlinson, The application of thin-film technology to measure turbine-vane heat transfer and effectiveness in a film-cooled, engine-simulated environment, *International Journal of Heat Fluid Flow*, 19, 1998, 594–600.
18. C. T. Kidd, C. G. Nelson, and W. T. Scott, Extraneous thermoelectric EMF effects resulting from the press-fit installation of coaxial thermocouples in metal models, *Proc. 40th Int. Instrum. Symp.*, Research Triangle Park, NC: ISA, 1994, pp. 317–335.
19. ASTM Standard E598-77, Standard method for measuring extreme heat-transfer rates from high-energy environments using a transient null-point calorimeter, *Annual Book of ASTM Standards*, 15.03, 1988, pp. 381–387.
20. G. Wagner, M. Kotulla, P. Ott, B. Wegand, and J. von Wolfersdorf, The transient liquid crystal technique: Influence of surface curvature and finite wall thickness, *Journal of Turbomachinery*, 127, 2005, 175–182.
21. J.-W. Ahn, R. Maingi, D. Mastrovito, and A. L. Roquemore, High speed infrared camera diagnostic for heat flux measurement in NSTX, *Review of Scientific Instruments*, 81, 2010, 023501.
22. A. H. Khalid and K. Kontis, Thermographic phosphors for high temperature measurements: Principles, current state of the art and recent applications, *Sensors*, 8, 2008, 5673–5744.
23. I. Kurits and M. J. Lewis, Global temperature-sensitive paint system for heat transfer measurements in long-duration hypersonic flows, *Journal Thermophysics Heat Transfer*, 23, 2009, 256–266.
24. ASTM Standard E457-72, Standard method for measuring heat-transfer rate using a thermal capacitance (slug) calorimeter, *Annual Book of ASTM Standards*, 15.03, 1988, 299–303.
25. N. R. Keltner, J. V. Beck, and J. T. Nakos, Using directional flame thermometers for measuring thermal exposure, *Journal of ASTM International*, 7, 2010, 102280.
26. T. J. Praisner and C. R. Smith, The dynamics of the horseshoe vortex and associated endwall heat transfer–Part 1: Temporal behavior, *Journal of Turbomachinery*, 128, 2006, 747–754, 2006.
27. M. Bomberg, A workshop on measurement errors and methods of calibration of a heat flow meter apparatus, *Journal of Thermal Insulation and Building Environments*, 18, 1994, 100–114.
28. A. V. Murthy, B. K. Tsai, and R. D. Saunders, Radiative calibration of heat-flux sensors at NIST: Facilities and techniques, *Journal of Research of National Institute of Standards and Technology*, 105, 2000, 293–305.
29. A. Gifford, A. Hoffie, T. Diller, and S. Huxtable, Convection calibration of Schmidt-Boelter heat flux gages in stagnation and shear air flow, *ASME Journal of Heat Transfer*, 132, 2010, 031601, 9.
30. C. A. Pullins and T. E. Diller, In situ high temperature heat flux sensor calibration, *International Journal of Heat and Mass Transfer*, 53, 2010, 3429–3438.

68

Resistive Thermometers

Jim Burns
Burns Engineering, Inc.

68.1 Introduction

Temperature, the most frequently measured process variable on the planet, can be measured in various ways. Many temperature measurement devices incorporate a resistive material that when exposed to an environment, the resistance will change in response to the temperature in a predictable manner. This style of sensor is referred to as a resistance temperature detector (RTD). The resistive materials used are nickel, copper, and most commonly platinum. RTDs designed with platinum provide the most stable resistance versus temperature relationship and therefore can achieve accuracies capable for use as a primary reference standard.

The resistive material is "packaged" in a wide variety of approaches to achieve the performance required and to support the installation constraints of the measurement point in the process of concern. There are many factors that should be considered in the design, selection, installation, integration, and monitoring of an RTD to ensure that the actual measurement meets the needs of the process.

This chapter discusses the principle of operation of an RTD, the general construction methods, common applications, how to select an RTD, interfacing an RTD with measurement instruments, and finally an overview of the types of errors that must be taken into consideration when using an RTD.

68.2 How an RTD Works?

Common RTD sensing elements constructed of platinum copper or nickel have a unique, and repeatable and predictable resistance versus temperature relationship (R versus T) and operating temperature range. The R versus T relationship is defined as the amount of resistance change of the

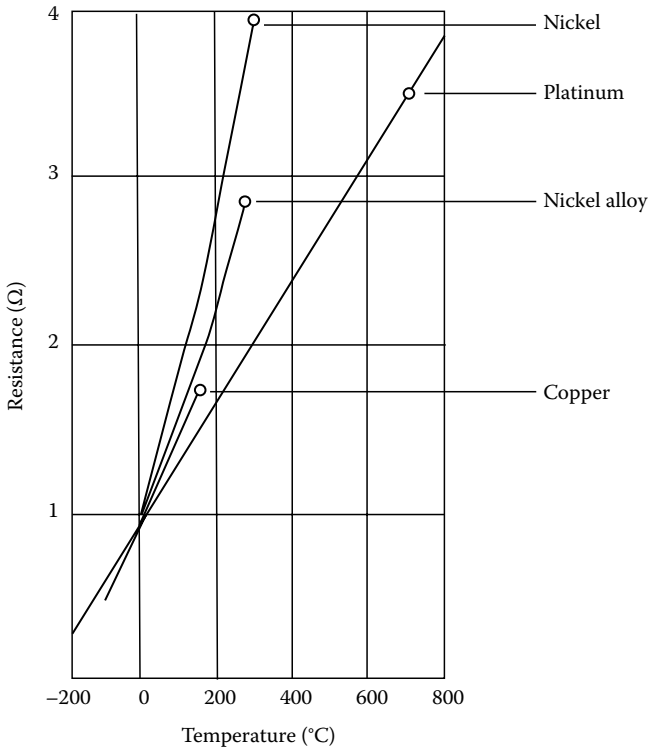

FIGURE 68.1 *R* versus *T* relationship for various metals.

sensor per degree of temperature change. Figure 68.1 shows the resistance relationship for the most common metals used for RTDs and the temperature ranges.

68.2.1 *R* versus *T* Relationship of Various Metals

Platinum is a noble metal and has the most stable resistance to temperature relationship over the largest temperature range. Nickel elements have a limited temperature range because the amount of change in resistance per degree of change in temperature becomes very nonlinear at temperatures over 572 °F (300 °C). Copper has a very linear resistance to temperature relationship; however, copper oxidizes at moderate temperatures and cannot be used over 302 °F (150 °C).

Platinum is the best metal for RTDs because it follows a very linear resistance to temperature relationship and it follows the *R* versus *T* relationship in a highly repeatable manner over a wide temperature range. The unique properties of platinum make it the material of choice for temperature standards over the range of –272.5 °C to 961.78 °C.

The basic differentiator between metals used as resistive elements is the linear approximation of the *R* versus *T* relationship between 0 °C and 100 °C and is referred to as alpha, α. Equation 68.1 defines α; its units are Ω/Ω/°C.

$$\alpha = \frac{R_{100} - R_0}{100 R_0} \tag{68.1}$$

where

R_0 is the resistance of the sensor at 0 °C

R_{100} is the resistance of the sensor at 100 °C

Pure platinum has an alpha of 0.003925 Ω/Ω/°C and is used in the construction of laboratory-grade RTDs. Conversely, two widely recognized standards for industrial RTDs IEC60751 [1] and ASTM E-1137 [2] specify an alpha of 0.00385 Ω/Ω/°C. Before these standards were widely adopted, several different alpha values were used. It is still possible to find older probes that are made with platinum that have alpha values of 0.003916 Ω/Ω/°C and 0.003902 Ω/Ω/°C.

These different alpha values for platinum are achieved by doping, basically carefully introducing impurities into the platinum. The impurities introduced during doping become embedded in the lattice structure of the platinum and result in a different *R* versus *T* curve and hence alpha value. To characterize the *R* versus *T* relationship of any RTD over a temperature range that represents the planned range of use, calibration must be performed at temperatures other than 0 °C and 100 °C. Two common calibration methods are the fixed-point method and the comparison method.

Fixed-point calibration, used for the highest accuracy calibrations, uses the triple point, freezing point, or melting point of pure substances such as water, zinc, tin, and argon to generate a known and repeatable temperature. These cells allow the user to reproduce actual conditions of the ITS-90 temperature scale. Fixed-point calibrations provide extremely accurate calibrations (within ±0.001 °C). A common fixed-point calibration method for industrial-grade probes is the ice bath. The equipment is inexpensive, easy to use, and can accommodate several sensors at once. The ice point is designated as a secondary standard because its accuracy is ±0.005 °C (±0.009 °F), compared to ±0.001 °C (±0.0018 °F) for primary fixed points.

In *comparison calibrations,* commonly used with secondary standard platinum resistance thermometers (SPRTs) and industrial RTDs, the thermometers being calibrated are compared to calibrated thermometers by means of a bath whose temperature is uniformly stable. Unlike fixed-point calibrations, comparisons can be made at any temperature between –100 °C and 500 °C (–148 °F to 932 °F). This method might be more cost-effective since several sensors can be calibrated simultaneously with automated equipment. These electrically heated and well-stirred baths use silicone oils and molten salts as the medium for the various calibration temperatures.

68.2.2 Resistance versus Temperature Relationship of a PRT

After determining the platinum resistance thermometer's (PRT) resistance at various temperature points, the *R* versus *T* curve can be defined. Once this has been done, any temperature can be determined from the measured resistance. These equations are multivariable polynomials, and although complex, the various forms of the equations are typically incorporated into transmitters, handheld readouts, and temperature-related electronic devices to solve this challenge.

The two most common curve-fitting techniques are the ITS-90 [3] and Callendar–Van Dusen equations. On January 1, 1990, the International Temperature Scale of 1990 (ITS-90) became the official international temperature scale. Two reference functions are used to define the temperature coefficient for an ideal SPRT: one for temperatures below 0 °C and the other for temperatures above 0 °C. When a PRT is calibrated on the ITS-90, the coefficients determined in the calibration are used to describe a deviation function that represents the difference between the resistance of the standard PRT and the reference function at all temperatures within the range. Using the calibration coefficients and the deviation functions, the SPRT can be used to determine any temperature from its measured resistance. Because ITS-90 equations are complex, computer software is necessary for accurate calculations.

Not all PRT users need to follow the complex equations and computer programs associated with ITS-90. As a rule of thumb, if the minimum required uncertainty of measurement is less than 0.1 °C, one probably will want to use ITS-90. For uncertainty of measurements greater than 0.1 °C, the effect of the change in scales is relatively small. Callendar–Van Dusen equations are interpolation equations that describe the temperature versus resistance relationship of industrial PRTs. These second- and fourth-order equations can be programmed easily into many electronic controllers.

The equation for an RTD with a 100 Ω R_0:

For the temperature range of 0 °C–850 °C (32 °F–1562 °F) is

$$R(t) = R_0(1 + At + Bt^2) \tag{68.2}$$

For the temperature range –200 °C to 0 °C (–392 °F to 32 °F):

$$R(t) = R_0[1 + At + Bt^2 + C(t - 100)t^3] \tag{68.3}$$

where

$R(t)$ is the resistance of the PRT at temperature t
t is the temperature in °C
R_0 is the nominal resistance of the PRT at 0 °C
A, B, and C are constants based on calibration coefficients: α, δ, β
(These coefficients and constants are generally provided by the calibration laboratory)
Expressions for the constants A, B, and C are

$$\boxed{A = \alpha + \frac{\alpha \cdot \delta}{100}} \quad \boxed{C = -\frac{\alpha \cdot \beta}{100^4}} \quad \boxed{B = -\frac{\alpha \cdot \delta}{100^2}} \tag{68.4}$$

Expressions for the constants α, δ, and β are

$$\boxed{\alpha = \frac{R_{100} - R_0}{100 \cdot R_0}} \quad \boxed{\delta = \frac{t_h - \frac{R_{th} - R_0}{R_0 \cdot \alpha}}{\left(\frac{t_h}{100} - 1\right)\left(\frac{t_h}{100}\right)}}$$

$$\boxed{\beta = \frac{t_l - \left(\frac{R_{tl} - R_0}{R_0 \cdot \alpha} + \delta\left(\frac{t_l}{100} - 1\right)\left(\frac{t_l}{100}\right)\right)}{\left(\frac{t_l}{100} - 1\right)\left(\frac{t_l}{100}\right)^3}} \tag{68.5}$$

where

t_h is the high temperature in the calibration range (e.g., 260 °C)
t_l is the low temperature in the calibration range (e.g., –196 °C)
R_{th} is the resistance of the sensor at the high temperature
R_{tl} is the resistance of the sensor at the low temperature

68.3 RTD Construction

There are many different types of RTDs for different applications. Generally, an RTD consists of three major components:

- Sensing element
- Protective housing
- Lead wires

Figure 68.2 shows the construction of a typical industrial RTD; the tip is cut away to show the position of the sensing element.

The selection of these three components is critical to the performance of the probe, and careful selection is required to ensure that the probe is suitable for the application.

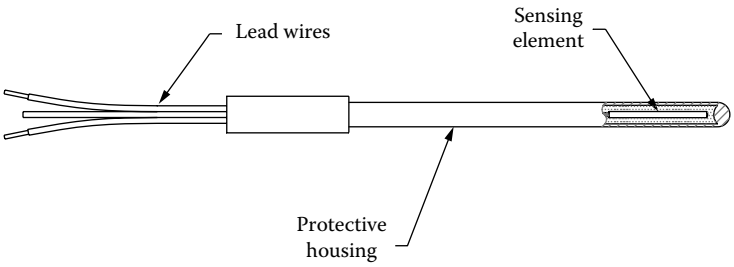

FIGURE 68.2 Construction of a typical industrial RTD.

68.3.1 Sensing Element

All RTD elements are in essence a length of wire (whether coiled, wound, or deposited through vapor deposition as in the case of thin film) that becomes more resistive at higher temperature. But the resistance of these wires can also be affected by physical deformation or strain. The two main causes of strain in RTDs come from thermal expansion of the wire relative to the electrically insulating support structure and from deformation of the wire due to shock or vibration. All element designs attempt to minimize the effect of strain on the wire, but there is a trade-off between strain from thermal expansion versus shock and vibration. This can be understood simplistically as the more firmly the wire is attached to the electrical insulator, the less likely it is able to move under shock and vibration conditions, but it is more likely to be stretched with the thermal expansion and contraction of the insulator.

There are three different categories of elements; each has their own particular characteristics:

Strain Free Elements consist of platinum wire loosely coiled over a support structure so the element is free to expand and contract with temperature, but it is very susceptible to shock and vibration as the loops of platinum can sway back and forth causing deformation (see Figure 68.3).

Wire coil wound elements (or coil-in-the-hole elements) are coils of platinum placed in ceramic tubes that are filled with ceramic powder to support the coils, as in Figure 68.4. The powder supports the coil against some shock and vibration, and allows some movement for thermal expansion and contraction.

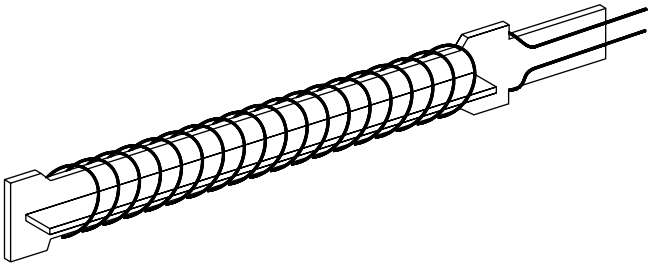

FIGURE 68.3 Strain-free constructions.

FIGURE 68.4 Wire coil wound.

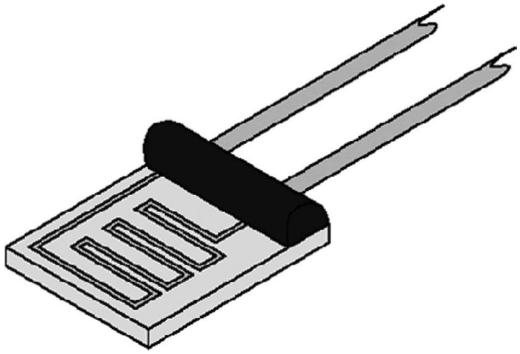

FIGURE 68.5 Thin-film elements.

Thin Film elements are small squares of ceramic that have a thin film of platinum deposited on them, Figure 68.5. Some platinum is removed to form a zigzag patterned electrical path. The thin film of platinum does not move with shock and vibration but due to the small mismatch in coefficient of expansion between the platinum pattern and ceramic, thin films become less accurate over large temperature ranges. This limits their useful range.

A fourth type called externally wire wound is still used, but thin films and wire coil wound elements are generally preferred, and there are few instances where this older design is better than modern thin films or wire coil wound elements.

68.3.2 Protective Housing

The protective housing has to ensure there is adequate thermal connection between the element and the measurement environment of interest, and at the same time protect the element from its soundings. Stainless steel probes are among the most common; a stainless steel tube closed at one end houses the element with the electrical connections coming out the other end. Many types of mounting fittings are available for various uses. Other types of probes use high-temperature plastics such as PTFE to encase the element.

The working temperature range of the probe is one of the criteria that will influence or limit the choices regarding the sheath material. For example, if stainless steel is used at elevated temperatures, the oxides formed can cause contamination of the platinum sensing element adversely affecting the accuracy of the probe.

How the element and lead wires are supported inside the protective housing is also critical. The materials used have to be capable of the temperature range, provide a good thermal path to the element, and isolate the element from the ambient vibrations without putting excessive strain on the element. Materials used include ceramic powder, heat sink compounds, and silicone RTVs.

68.3.3 Lead Wires

When selecting the lead wire materials and the number of lead wires, consideration has to be given to the environment in which the probe will reside as well as the instrumentation to which it is going to interface. The element is basically a length of wire that changes in resistance with temperature. In order to measure the resistance of the element, it must be wired to the measurement equipment in such a way that the resistance of the leads does not adversely affect the measurement. This is done in three ways, using two, three, or four wire connections. See the section on *Common Sources of Error* to understand the considerations that must be taken into account with regard to specifying the number of lead wires.

68.4 Classifications of RTDs

Though many types of element wire can be used to make RTDs, platinum has become the standard in both laboratory and industrial settings. Platinum RTDs are often called platinum resistance thermometers (PRTs). RTDs utilizing other metals for the sensing element are only used in special applications or for measurements outside the PRT temperature range.

The highest accuracy of all PRTs is the SPRTs. This accuracy is achieved at the expense of durability and cost. The SPRT elements are wound from reference-grade platinum wire. Internal lead wires are usually made from platinum while internal supports are made from quartz or fuse silica. The sheaths are usually made from quartz or sometimes Inconel, depending on temperature range. Larger diameter platinum wire is used, which drives up the cost and results in a lower resistance for the probe (typically 25.5 Ω). SPRTs have a wide temperature range (–200 °C to 1,000 °C) and approximately accurate to ±0.001 °C over the temperature range. SPRTs are only appropriate for laboratory use.

Another classification of laboratory PRTs is secondary SPRTs. They are constructed like the SPRT, but the materials are more cost-effective. SPRTs commonly use reference-grade, high–purity, smaller diameter platinum wire, metal sheaths, and ceramic-type insulators. Internal lead wires are usually a nickel-based alloy. Secondary SPRTs are limited in temperature range (–200 °C to 500 °C) and are approximately accurate to ±0.03 °C over the temperature range.

Industrial-grade PRTs are designed to withstand industrial environments. They can be almost as durable as a thermocouple. Depending on the application, industrial PRTs can use thin film elements or coil wound elements. The internal lead wires can range from PTFE insulated stranded nickel-plated copper to silver wire, depending on the sensor size and application. Sheath material is typically stainless steel; higher-temperature applications may demand Inconel. Other materials are used for specialized applications.

68.5 Applications

Sensor assemblies can be categorized into two groups by how they are installed or interface with the process: immersion or surface mounted.

Immersion sensors take the form of an SS tube and some type of process connection fitting (Figures 68.6 and 68.7). They are installed into the process with sufficient immersion length to ensure good contact with the process medium and reduce external influences. A variation of this style includes a separate thermowell that provides additional protection for the sensor. These

FIGURE 68.6 Direct immersion styles.

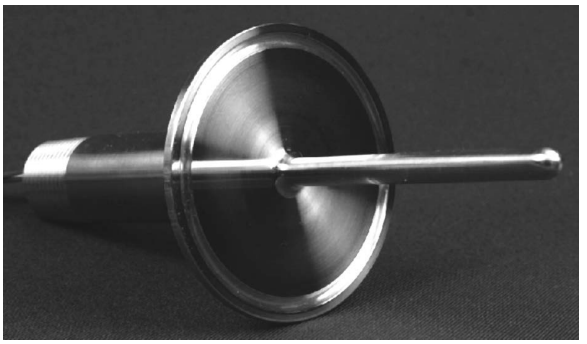

FIGURE 68.7 Direct immersions with sanitary process connection.

styles are used to measure fluid or gas temperatures in pipes and tanks. Most sensors have the sensing element located at the tip of the stainless steel tube. An averaging-style RTD, however, can measure an average temperature of air in a large duct. This style of immersion RTD has the sensing element distributed along the entire probe length and provides an average temperature. Lengths range from 3 to 60 ft.

Surface-mounted sensors (Figure 68.8) are used when immersion into a process fluid is not possible due to configuration of the piping or tank, or the fluid properties may not allow an immersion-style sensor. Configurations range from tiny cylinders to large blocks that are mounted by clamps, adhesives, or bolted into place (Figure 68.9). Most require the addition of insulation to isolate them from cooling or heating effects of the ambient conditions to ensure accuracy.

Other applications may require special water proofing or pressure seals. A heavy-duty underwater temperature sensor is designed for complete submersion under rivers, cooling ponds, or sewers. Steam autoclaves require a sensor that is sealed from intrusion by steam during the vacuum cycle process.

Immersion sensors generally have the best measurement accuracy because they are in direct contact with the process fluid. Surface-mounted sensors are measuring the pipe surface as a close approximation of the internal process fluid.

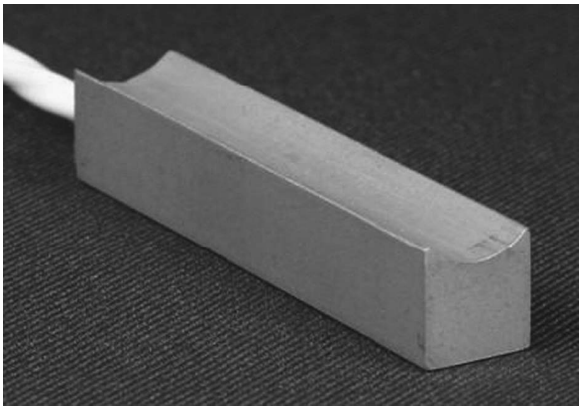

FIGURE 68.8 Surface mount for a pipe.

FIGURE 68.9 Surface mount for flat surfaces.

68.5.1 Selection

Selection of a PRT can be achieved by considering each of five criteria:

- Placement
- Protection
- Performance
- Price
- Service life

Placement refers to how the sensor will be mounted in or on the process. Several factors influence which style is selected to achieve the desired measurement accuracy and longest service life. An immersion-style sensor usually provides the best accuracy but does require cutting a hole in the pipe or tank to allow for installation. A surface-mount sensor is the easiest to install and of lowest cost; however, some accuracy is sacrificed. Placement considerations involve determining where in the piping or tank an entry can be made to accommodate an RTD and provide enough immersion length for an accurate measurement. The ideal immersion length to avoid external thermal influences is equal to 10 sensor or thermowell diameters plus the sensitive length (the element length). For a direct immersion, 1/4 ft diameter RTD with a 1.0 in. element length, the minimum immersion would be 3.5 ft. A 1/4 ft diameter sensor with a thermowell should have at least 4.5 ft of immersion in the process. For pipes less than 4 ft and other situations where sufficient immersion cannot be obtained, there are other solutions. Installing an elbow allows the RTD to be aligned parallel to the flow and extend down the pipe. Other choices may be to use a surface mount RTD, or a modified immersion sensor that mounts flush to the inside of the process vessel.

Protection refers to the items that are used to shield the sensor from the ambient conditions and from the process environment. External to the process, a connection head is commonly used to provide a transition from the RTD leads to the facility wiring. In addition, it can provide protection from explosive atmospheres and keep water and other contaminants away from the sensor. Any of these ambient conditions can, over time, cause sensor failure.

To maintain protection from the process, a thermowell (Figure 68.10) can be used to protect the sensor from corrosive, erosive, high-velocity flow, high pressure, and vibration. Another advantage of using a thermowell is that RTDs that need periodic calibration can be easily removed from the protective thermowell without draining the process.

FIGURE 68.10 RTD and thermowell assembly.

Performance includes factors such as probe accuracy, installation errors, long-term drift, and erosion or corrosion considerations. Accuracy of the sensor and accuracy of the measurement are most times quite different. Sensor accuracy is determined mostly by the manufacturing interchangeability and the style of sensing element. The wire wound style has the widest temperature range and lowest drift, and a thin film element may have the same interchangeability but larger drift characteristics. Temperature range is often restricted by manufacturers to minimize the effect of drift on the sensor accuracy. Measurement accuracy includes the sensor accuracy and the installation affects. In addition, time response can be a large factor in the measurement accuracy. A sensor that does not keep pace with the process temperature change may be several degrees off from the actual temperature during thermal transients.

Price, or from the user's perspective, the cost is always a consideration. For any measurement point, the costs for maintenance, calibration, acquisition, and accuracy must be determined. The initial cost of the RTD can be insignificant if a poor-quality inaccurate device is selected. A poor-quality RTD will waste energy, require frequent replacement, require more frequent calibration, and can reduce product quality. A more expensive high-quality RTD will alleviate all of these problems and related expenses, resulting in the lowest life cycle cost for the measurement point.

Service life of an RTD varies dramatically based on how and where the sensor is used. Two main factors that affect the life span are temperature cycling and vibration. All industrial-grade RTDs will drift over time and require periodic calibration to determine if they are still within tolerance. Vibration and wide temperature cycles can accelerate the drift rate possibly leading to premature failure. Selecting the right RTD and following the selection criteria will ensure accuracy, long service life, and trouble-free temperature measurement.

68.5.2 Common Sources of Error

To fully understand the accuracy of a temperature measurement, it is imperative that all the sources of errors are understood and where possible quantified. Accuracy is not a statement of the correctness of a temperature sensor independent of its system. It is the total accuracy of the sensor system, and process for which one needs to measure temperature. This accuracy value is a summation of the sensors'

interchangeability value, as well as all the errors sources associated with the system, the measurement location, and the installation of the RTD. The method that is used for calculating the accuracy of the system is by calculating the root-sum-square (RSS) of all the sources of error and variation of the probe, and the errors related to the system. Generally, the sensors' interchangeability value is the largest component of the accuracy analysis and can be reduced to near zero by matching the sensor with a transmitter. As the temperature range of use expands, the errors associated with stability, repeatability, and stem conduction will begin to play a larger role in the system accuracy at higher temperatures.

With all measurement devices, there are common sources of error that have to be accounted for. In PRTs, these sources of error are interchangeability, insulation resistance, stability, repeatability, stem conduction, hysteresis, calibration and interpolation, lead wire resistance, self-heating, rime response, and thermal EMF.

68.5.3 Interchangeability

Interchangeability refers to the "closeness of agreement" in the *R* versus *T* relationship of a PRT to a predefined nominal *R* versus *T* relationship. Since it is not possible to manufacture a PRT that exactly replicates a predefined nominal *R* versus *T* relationship, a tolerance band about the relationship must be established, and this is what is called the "interchangeability" of the PRT.

The two most widely used industrial PRT standards in the United States are ASTM E1137 and IEC 60751. Fortunately, both of these standards have the same nominal *R* versus *T* relationship, but they do not have the same interchangeability tolerance. These standards use the term "tolerance" to describe the permissible variation in the *R* versus *T* relationship, define tolerance as a function of temperature in °C, and offer multiple tolerance levels—referring to them by either a tolerance "class" or tolerance "grade." Table 68.1 shows the interchangeability tolerances for these two industry standards while Figure 68.11 shows a comparison of the interchangeability levels graphically.

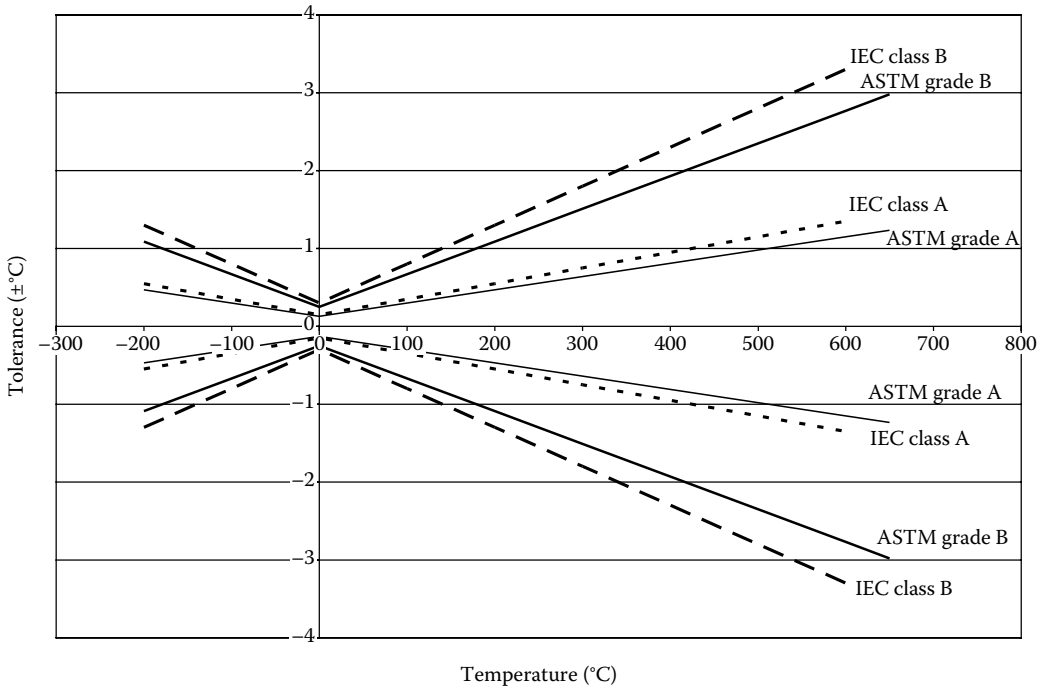

FIGURE 68.11 Standard PRT interchangeability.

TABLE 68.1 Standard PRT Interchangeability Equations

Standard	Tolerance Nomenclature	Defining Equation[1]
ASTM E1137	Grade A	± [0.13 + 0.0017 | *t* |]
ASTM E1137	Grade B	± [0.25 + 0.0042 | *t* |]
IEC 60751	Class A	± [0.15 + 0.002 | *t* |]
IEC 60751	Class B	± [0.3 + 0.005 | *t* |]

Note: \| *t* \| = the value of temperature in °C without regard to sign.

It is worth noting that many times manufacturers will define interchangeability in terms of a percent, such as 0.06%. In these cases, the percent refers to a percent of resistance valid only at 0 °C. For example, 0.06% interchangeability is ±.06 Ω (±.15 °C) for a 100 Ω PRT. This is not enough information to know what the tolerance is at other temperatures. The user should be provided with either a statement that the tolerance meets one of the industry standard classes or grades, or a table showing the tolerances, or an equation similar to the ones shown in Table 68.1 that define the tolerance over the entire rated temperature range of the PRT.

68.5.4 Insulation Resistance

Insulation resistance (IR) refers to the electrical resistance between the sensing circuit and the metallic sheath of a PRT. It is important for the sensing element circuit to be insulated from the sheath because electrical leakage can cause an error when measuring the resistance of the sensing element. Any error in measuring the resistance will translate to an error in the indicated temperature.

Resistance is a parameter that cannot be measured directly. The typical method used to measure the resistance of an industrial PRT is to apply a constant current and measure the voltage drop to determine the resistance. If a portion of the applied current has the opportunity to "leak out" of the circuit, through a low IR, then a false resistance reading will be obtained for the sensing element.

ASTM E1137 and IEC 60751 specify a minimum IR value at ambient temperature (25 °C) as well as at elevated temperatures. Table 68.2 shows the minimum IR values required by these standards and the estimated temperature error values calculated for a 100 Ω PRT. It is easy to see by examining this table that the minimum IR requirement decreases as the temperature increases. This represents the typical behavior of an industrial PRT and is a reason why the ambient temperature IR requirements are generally much higher than necessary for accurate operation at ambient temperature.

TABLE 68.2 PRT Insulation Resistance Requirements

Standard	Rated Temperature (°C)	Minimum IR (MΩ)	Test Voltage (VDC)	Estimated Error for 100 Ω PRT (°C)
ASTM E1137	25	100	10–50	0.0003
ASTM E1137	300	10	10–50	0.013
ASTM E1137	650	2	10–50	0.17
IEC 60751	25	100	10–100	0.0003
IEC 60751	100–300	10	10	0.013
IEC 60751	301–500	2	10	0.12
IEC 60751	501–850	0.5	10	1.0

68.5.5 Stability

Stability refers to the ability of a PRT to maintain its *R* versus *T* relationship over time as a result of thermal exposure. Both ASTM E1137 and IEC 60751 address resistance change due to thermal exposure; however, the criteria are somewhat different. ASTM E1137 essentially states that the PRT must meet the resistance tolerance for a Grade A or Grade B sensor as applicable, after 4 weeks (672 h) of exposure to the maximum rated temperature. IEC 60751 states that the PRT can change at 0 °C by the equivalent of 0.15 °C for a Class A sensor and 0.30 °C for a Class B sensor after 250 h at maximum rated temperature. Many manufacturers state stability specifications more like the IEC 60751 standard, stating a maximum change at 0 °C as a result of exposure to maximum rated temperature for a given period of time. These specifications typically do not require the PRT to remain within the original *R* versus *T* tolerance after the exposure.

Typically three or four temperatures including the maximum rated temperature would be adequate to estimate stability. The graph in Figure 68.12 gives a realistic representation of the stability of a typical industrial PRT at five different exposure temperatures.

By examining Figure 68.12, a few generalizations can be made about the stability of this industrial PRT. These generalizations hold true for the behavior of most industrial PRTs; however, the shape of the curve will be unique based on the specific PRT design. If a better understanding is needed regarding a specific PRT, the manufacturer of that PRT should be consulted.

1. The resistance change due to exposure to room temperature and below can be considered negligible. Test results on several industrial PRTs have shown that the ice point resistance shift following 25,000+ h at 23 °C is less than 0.01 °C. This is a very small change in comparison to other potential error sources.
2. The magnitude of the change increases with increasing exposure temperature and is a maximum at maximum rated temperature. For example, the change after 1,000 h will be larger for an exposure temperature of 500 °C than an exposure temperature of 400 °C.
3. The magnitude of the change is not linear with temperature and cannot be extrapolated beyond the upper temperature limit. For example, the change caused by exposure to 550 °C cannot be reliably predicted based on the changes observed due to 500 °C or 400 °C exposure.
4. The rate of change over time is fairly linear and remains fairly constant. For example, the change after 2,000 h can be conservatively approximated as twice the amount of change as was present after 1,000 h for the same exposure temperature.

Given the earlier generalizations along with the information illustrated in Figure 68.12, a reasonably accurate estimation of stability can be made for the hypothetical example of a PRT at 350 °C for 1 year. The stability can be estimated by looking at the graph and estimating a change after 1,000 h for a 350 °C exposure. According to the graph, this would be approximately 0.1 °C. Multiplying this number

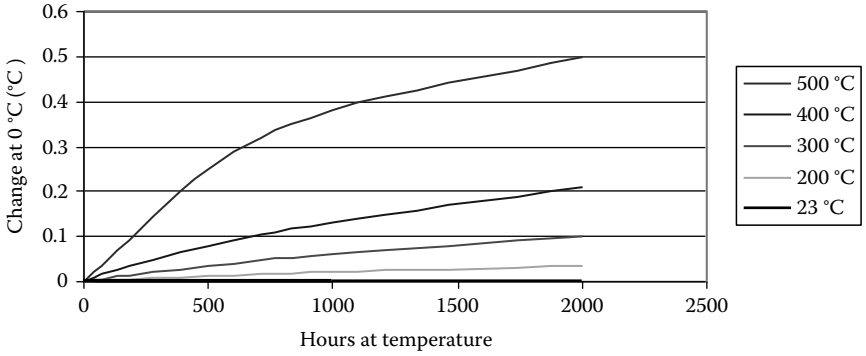

FIGURE 68.12 Example of industrial PRT stability.

by 9 to determine the cumulative effect over 9,000 h gives a result of 0.9 °C maximum change at 0 °C after 1 year of exposure to 350 °C. This is likely to be a more accurate estimate than extrapolating the IEC 60751 requirement of 0.15 °C for Class A (or 0.30 °C for Class B) per 250 h out to 9,000 h, which would result in an estimated value of 5.4 °C for Class A (or 10.8 °C for Class B).

68.5.6 Repeatability

Repeatability refers to the ability of a PRT to maintain its *R* versus *T* relationship when measured under the *same test condition* after experiencing thermal cycling throughout a specified temperature range. Industrial specification IEC 60751 refers to this as "Effect of temperature cycling" and states that the PRT can change at 0 °C by the equivalent of the class tolerance after 10 thermal cycles between the PRT's upper and lower temperature limits. The standard also contains a note to the effect that improved performance may be achieved for certain thermometers when used over narrower temperature ranges, but no specific requirements are given. ASTM E1137 does not contain any requirement for thermal cycling performance other than to state that the PRT must be capable of continuous operation over the specified temperature range. Neither of these industry standards provides substantial information about the performance of a PRT as a result of thermal cycling.

A practical and useful approach to understanding PRT repeatability would be a set of specifications that state the change due to a varying number of cycles over varying temperature ranges. Typically three or four temperature ranges including the maximum rated range and cycles up to 1,000 would be sufficient. The graph in Figure 68.13 gives a realistic representation of the repeatability of a typical industrial PRT that has a temperature rating of 0 °C–500 °C, over four different thermal cycle temperature ranges.

From Figure 68.13, several generalizations can be identified regarding repeatability. The generalizations hold true for the behavior of most industrial PRTs; however, the actual values, maximum temperature ranges, and so on will all be unique based on the specific PRT design. If a better understanding is needed regarding a specific PRT, the manufacturer of that PRT should be consulted.

1. A disproportionate amount of change can occur during the first few thermal cycles. Figure 68.13 starts at 10 thermal cycles, which align with a typical specification such as "0.1 °C maximum change after 10 cycles from 20 °C to 500 °C."
2. There will be some temperature range for which there is virtually no difference in repeatability between 10 cycles and 1,000 cycles. In the case of this example, that temperature range is 20 °C–200 °C.

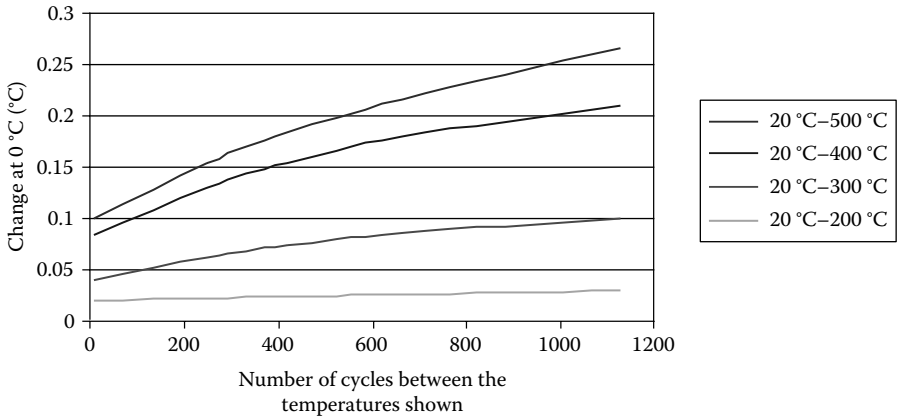

FIGURE 68.13 Example of industrial PRT repeatability.

3. The maximum nonrepeatability will occur due to cycling over the maximum rated temperature range of the PRT. Smaller ranges will result in smaller changes.
4. The change at intermediate temperature ranges and numbers of cycles can be estimated by interpolating between known values. For example, the repeatability after 500 cycles from 20 °C to 350 °C could be estimated as approximately 0.13 °C.
5. The change can be estimated as linear with the number of cycles for any given temperature range. For example, the change after 2,000 cycles can be conservatively estimated as two times the change after 1,000 cycles. This method should result in a conservative estimate for most high-quality PRTs.

Given the information contained in Figure 68.13, a reasonable and useful estimate could be made for the repeatability of the PRT under various conditions. An application example would be the use of a PRT in a process that must heat from room ambient to 350 °C for 1 h and then cool back to room ambient temperature. Assuming this process runs three times per day for an entire year, the error due to repeatability could be estimated from Figure 68.13 as the value shown at 1,095 cycles (3/day × 365 days/year) in the region between the 300 °C line and the 400 °C line. From Figure 68.13, an estimate of 0.16 °C could be made. Keep in mind that this error is separate from the error that would be created due to the 1,095 h of heat soak at 350 °C: that error is considered in the stability component of the overall error.

68.5.7 Hysteresis

In PRTs, thermal hysteresis results in a difference in resistance at a given temperature based on the thermal history to which the PRT was exposed. More specifically, the resistance of the PRT will be different when the temperature is approached from an increasing direction versus a decreasing direction, and the magnitude of the difference will depend on the magnitude of the temperature excursion and the design of the PRT.

Industrial specification IEC 60751 refers to this as "Effect of hysteresis" and states that the PRT resistance shall be measured at the middle temperature after exposure to the lower limit temperature and after exposure to the upper limit temperature. The acceptance criterion that is given is that the resistance at the midpoint cannot change by more than the tolerance value at the test temperature for the respective tolerance class tested. It does not state that both measurements must meet the resistance tolerance; therefore, it is possible that the hysteresis effect could result in the sensor producing an out-of-tolerance measurement. ASTM standard E1137 does not contain any requirement for thermal hysteresis, however; a test method for hysteresis is contained in ASTM standard E644, which would allow testing over ranges less than the maximum rated range of the PRT. While the requirement of the IEC 60751 standard is fairly well defined, it does not provide any information about hysteresis when the range is less than the maximum, and neither of these industrial PRT standards provides information about the hysteresis performance at temperatures other than the midpoint temperature where hysteresis is considered to be at its maximum.

A practical and useful approach to understanding a PRT's hysteresis would be if the hysteresis was specified as a percent of span to which the PRT was exposed.

Figure 68.14 shows a hypothetical representation of what could be considered a very well-behaved hysteresis loop for a typical industrial PRT. The hysteresis is a maximum at the midpoint temperature and a minimum at each end point. While there is still some variability expected in the measurements taken at the end points, this variability is caused by the PRT repeatability, not by hysteresis.

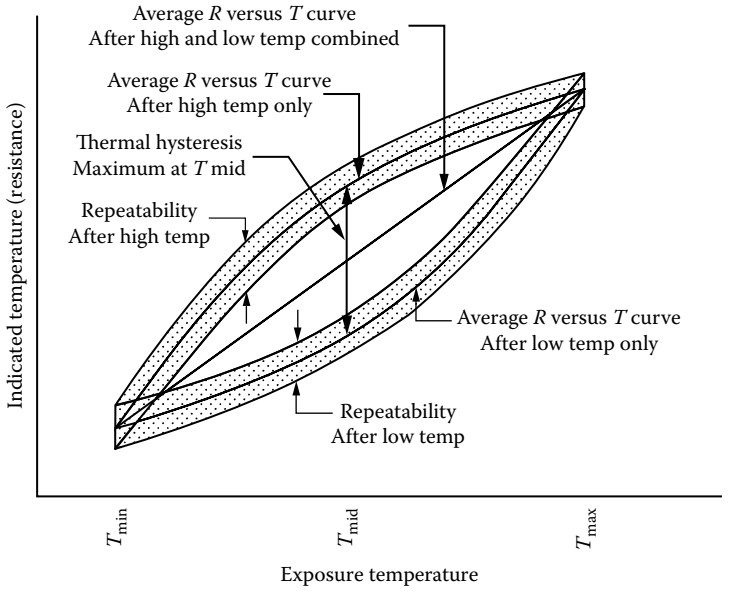

FIGURE 68.14 Hypothetical well-behaved hysteresis loops for industrial PRT.

One simplified method to estimate the hysteresis error at any temperature within the range of use is to perform a linear interpolation between the midpoint temperature and the temperature of interest. Since no known equation exists for this estimate, one is offered here for the purpose of this chapter and it is given as

$$\text{Hysteresis (°C)} = H\left(\frac{T_{\max} - T_{\min}}{100}\right)\left(1 - \left|\frac{\left(T_{\max} + T_{\min} - 2T\right)}{\left(T_{\max} - T_{\min}\right)}\right|\right) \tag{68.6}$$

where

H is the hysteresis error coefficient in % of temperature span
$T_{\max}$ is the maximum temperature of span
$T_{\min}$ is the minimum temperature of span
T is the temperature where hysteresis is being determined
(all temperatures are in °C)

To provide a context for the order of magnitude of the hysteresis error, several examples were created. Table 68.3 shows the estimated hysteresis error in °C calculated using this method for PRTs with varying specifications over several common temperature ranges.

By examining the values in Table 68.3, it is easy to see that the hysteresis error can be nearly negligible or approaching as much as ±1 °C.

68.5.8 Stem Conduction

Stem conduction is the error that results from the PRT sheath conducting heat into or out of the process of interest. ASTM offers a test method to compare PRT performance in the lab, specifying a maximum error of 0.13 Ω (0.25 °C) when the PRT is immersed 2 in. into an ice bath. International Electrotechnical Commission (IEC) defines the "minimum immersion depth" to be that where a 1 °C error is produced in

TABLE 68.3 Hysteresis Error Estimates for Common Temperature Ranges

	Temperature Range: −200 °C–600 °C			Temperature Range: 0 °C–400 °C			Temperature Range: 0 °C–200 °C			
Hysteresis Spec	0.02% of span	0.05% of span	0.10% of span	0.02% of span	0.05% of span	0.10% of span	0.02% of span	0.05% of span	0.10% of span	
	Error (±°C)									
Temperature (°C)	−200	0	0	0	—	—	—	—	—	—
	−100	0.04	0.10	0.20	—	—	—	—	—	—
	0	0.08	0.20	0.40	0	0	0	0	0	0
	100	0.12	0.30	0.60	0.04	0.10	0.20	0.04	0.10	0.20
	200	0.16	0.40	0.80	0.08	0.20	0.40	0	0	0
	300	0.12	0.30	0.60	0.04	0.10	0.20	—	—	—
	400	0.08	0.20	0.40	0	0	0	—	—	—
	500	0.04	0.10	0.20	—	—	—	—	—	—
	600	0	0	0	—	—	—	—	—	—

an 85 °C water bath. The test methods are an effective method to compare sensors, although the thermal dynamics of the installed sensor can produce different stem conduction results than those found from the lab test method. The specific installation, heat transfer conditions, and the temperature difference—process to ambient—can have a significant influence on the stem condition error.

To manage this error,

- Strive to achieve the ideal immersion depth of 10× the sensor diameter plus the element sensitive length. For a 0.25 ft diameter sheath with a 1 ft element length, the ideal immersion depth is 3.4 ft.
- Select a sensor design that is tip sensitive. These are typically smaller diameter, specifically in the element area.
- Insulate the portion of the sensor external to the process.

68.5.9 Calibration/Interpolation

These are errors that occur due to calibration uncertainty at the cal points or between cal points due to propagation of uncertainty, or curve fit errors. The ASTM and IEC standards do not address this error source beyond the requirement of the resistance tolerance limits. For most industrial sensor uses, these errors are less significant. To minimize these errors, select a calibration laboratory with low calibration uncertainties and a PRT with low repeatability and hysteresis error values.

68.5.10 Lead Wire

To provide a practical temperature measuring instrument, it is necessary to attach extension leads to the platinum sensing element. If not properly selected for the application, the number and type of extension leads used can introduce significant errors into the temperature measurement. See Figure 68.15 for the different connection methods.

The two-lead-wire circuit has no mechanism to compensate or eliminate the resistance of the lead wires from the resistance of the element. As the temperature increases, the resistance of the lead wires will also increase. Unlike the platinum element, the resistance in the lead wires increases in a nonlinear manner, which will result in inaccurate measurements. The two-lead-wire designs are only useful where extension lead resistance is insignificant to the sensing element, either short leads or large sensing resistance, and an accurate temperature measurement is not required.

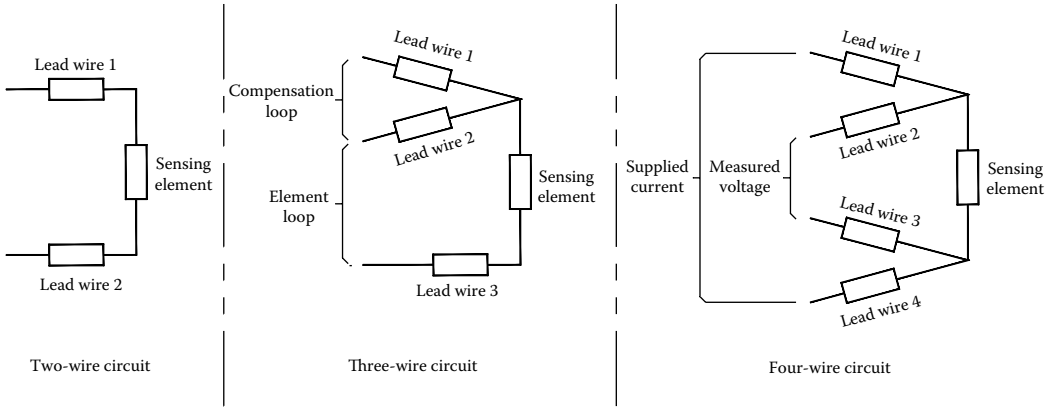

FIGURE 68.15 Temperature sensor lead wire configurations.

The three-wire configuration provides a compensation loop that can be used to subtract the lead wire resistance from the measurement to provide a value for just the element resistance. The resistances of two different electrical paths are used. The first is through the element like a two-wire measurement. The second is to one end of the element and back without going through the element to approximate the lead resistance. The measurement is obtained by subtracting the second electrical path from the first. Complete compensation in this method is predicated on the resistance of each of the leads being exactly equal. Unfortunately, this is seldom the case, and steps in the design and application of a three-wire sensor must be taken to maintain the accuracy of the measurement.

The method that offers the highest accuracy temperature measurement is the four-wire scheme. Having two wires either side of the element allows for a measurement current to be passed across the element via two of the leads and a voltage measurement to be taken through the other two leads. The resistance is simply then calculated using Ohm's law. The impedance of the meter taking the voltage measurement is sufficiently high to prevent any current from flowing through the leads being used for the voltage measurement. The current flowing through the other two leads and the element is the same throughout the circuit. Therefore, by measuring the voltage across the element and dividing it by the known current yields just the resistance of the element.

In applications where the sensor must be at a long distance from the measurement equipment, temperature transmitters are often used. Temperature transmitters are capable of measuring the resistance of the RTD probe and converting the measurement to a signal that can be transmitted longer distances, typically a 4–20 mA signal. It is not uncommon for measurement equipment, even respected brands, to take short cuts when it comes to lead wire connections. Be especially wary if the manual instructs the user to use jumpers to unused terminals. This will almost always cause the resistance of at least one lead to be included in the measurement. Measurement equipment that requires internal settings to be changed specifically for two-, three-, or four-wire measurement is fewer suspects. It is good practice to verify how the measurement is being taken by switching between settings and/or disconnecting a lead to verify that the output is congruent with the connections.

68.5.11 Self-Heating

Self-heating errors are caused by the inability of the element to dissipate the heat generated by the required power applied via the measuring current. The ASTM Standard requires the error to be a maximum of 1 °C when 33 mW is applied in 25 °C water. IEC requires a maximum error of 0.05 °C in 25 °C water when the maximum operating current is applied. These test methods are good laboratory comparison methods. For PRTs installed with proper immersion in a process, the operating current is 1 mA or less,

so the power (I^2R) for a 100 Ω PRT is also small (0.02–0.39 mW). Lager errors can occur in sensors with resistances in the 500–1,000 Ω range, or when the process exhibits poor heat transfer conditions such as still air or low-pressure gases.

68.5.12 Time Response

A time response-related error can be produced during temperature transients if the PRT cannot respond to the change in temperature fast enough. During steady-state or near-steady-state operation, this error is zero. ASTM and IEC do not define this error, although there is a test method to characterize a PRTs' response time for comparison purposes. When it is important to monitor transient conditions, this error can be minimized by selecting a sensor with a faster lab-tested response time and assessing the related rate of change to the process to best match the sensors' time response performance.

68.5.13 Thermal EMF

Thermal EMF errors are also known as the thermocouple effect. This error is caused by various wire compositions, wire connections in homogeneity of materials, and temperature gradients within the PRT. The ASTM and IEC Standards offer guidelines at high sensing currents—although when an EMF influence exists, it will have a greater effect at lower currents near the standard operating current. This error occurs primarily in direct current systems. To minimize thermal EMF errors, select a PRT with a low specified EMF. Also, using alternating current circuitry and appropriately selected transmitters can eliminate EMF influences.

68.6 Calibration and Maintenance

Testing programs such as periodic calibration or performance testing are essential to verify the accuracy and general health of PRTs. Some industrial PRTs are factory-calibrated to a temperature such as at the ice point, but PRT users might want to calibrate them at other temperatures, depending on their application. The periodic calibration results can be compared to prior or original calibration values to help determine if it is necessary to repair or replace the instrument, or if calibration is required more often.

An RTD's stability depends on its working environment. High temperatures can cause drift and contamination of the platinum wire. Shock, vibration, and rough handling will put stress in the platinum wire and change its characteristics, and eventually cause damage that may not be recoverable. Humidity can get into the sensor and reduce the IR. Under extreme operating conditions, a sensor should be calibrated more frequently. If several calibrations are completed without a significant change, then the time between calibrations can be extended based on the user's quality system guidelines; at least once a year is common.

68.7 Conclusion

Measuring temperature using RTDs is extremely common. The sensor design and packaging approaches have evolved over the years, yet the basic technology remains generally unchanged. The user or specifier of RTD-based measurements need to be aware that the values obtained and confidence on those results are very much dependent on the sensors used. Managing the sources of error, establishing a procedure to monitor the health and performance of the sensor, and properly installing the sensor into the system are necessary to ensure that the measurement result will meet the needs of the process control. The process performance characteristics should drive the decisions regarding element design, sensor packaging, sensor capability, calibration, and electronic interface needs.

Defining Terms

Accuracy: The degree of agreement between an actual measurement and its reference standard.

Alpha (α): The temperature coefficient of resistance of a PRT over the range 0 °C–100 °C. For example, α for a standard platinum resistance thermometer (SPRT) is 0.003925 Ω/Ω/°C.

Callendar–Van Dusen: An interpolation equation, which provides resistance/temperature values for PRTs.

Calibrate: To check, adjust, or determine an RTD's accuracy by comparing it to a standard.

Calibration, Calibration: A calibration technique commonly used with industrial PRTs. The PRT and a temperature standard are both measured at a stable temperature, then compared.

Calibration, Fixed Point: A calibration technique that uses the triple point, freezing point, or melting point of pure substances to generate a known and repeatable temperature. The sensor's resistance is measured at one of these points.

Connection Head: A housing that provides a terminal block for a sensor assembly, with threads for attaching it to a protection tube or conduit.

Defining Fixed Points: Specific temperatures that create the basis for the ITS-90.

Fixed Point: A reproducible temperature of equilibrium between the phase changes in a material.

Immersion Error: An error caused by heat conduction or radiation, both between the resistance thermometer element and environment external to the measurement system (also known as stem conduction error).

Interchangeability: The ability to interchange one sensor for another, without affecting the overall accuracy of the system.

Interchangeability Errors: Results from the manufacturing tolerances of the sensing elements and several of the performance characteristics including hysteresis repeatability and calibration errors.

Primary Standard: (Or SPRT) A platinum resistance thermometer that meets the requirements for establishing calibrations according to the ITS-90. This highly accurate instrument is intended for laboratory environments and is accurate to 0.001 °C.

PRT: Platinum resistance thermometer (PRT) is an RTD that uses platinum wire in the sensing element.

Response Time: The time required for the output of the sensor to change by 63.2% of the step change in temperature.

RSS: Root-sum-square. A mathematical method to quantify various errors of a system.

RTD: Resistance temperature detector.

SPRT: A PRT that has its temperature resistance relationship determined by reference to a primary standard of temperature.

Self-Heating Error: Caused because the current that measures sensor resistance also heats the sensor. This causes the temperature reading to be higher than the actual temperature.

Span: The algebraic difference between the upper and lower range values of an instrument.

Stability: The state of being resistant to change or deterioration.

Stem Conduction Error: Heat transfer along the sheath or lead wires of a probe, or along the length of a thermowell. This results in the sensor being at a different temperature than the medium.

Thermowell: Closed sleeve for protecting temperature sensors from the rigors of industrial processes while permitting accurate measurement.

References

1. IEC, *Industrial Platinum Resistance Thermometer Sensors*, IEC 60751:2008 Genéve, Suisse: Bureau Central de la Commission Electrotechnique Internationale, 2008.
2. ASTM Standards, Standard Specification for Industrial Platinum Resistance Thermometers, Standard E 1137/E 1137M-08, 2008.
3. NIST Technical Note 1265, Guidelines for Realizing the International Temperature Scale of 1990 (ITS-90), National Institute of Standards and Technology, 1990.

69

Thermistor Thermometers

Rod White
Measurement Standards Laboratory of New Zealand

Meyer Sapoff
MS Consultants

Thermistors are temperature-sensitive semiconducting devices. There are several types used in a wide variety of temperature measurement, switching, and sensing applications. This section will focus primarily on negative temperature coefficient (NTC) thermistors designed specifically for temperature measurement. While NTC thermistors are used over a very wide range of temperatures, from 1 K to 1000°C, we will focus on the range −80 °C to 300 °C, where they are most commonly used and offer genuine advantages over platinum resistance thermometers for some applications. A brief overview of other types of thermistors and other applications for thermistors is given at the end of the chapter.

NTC thermistors are suited to a number of specialized thermometry applications because they are smaller, faster, and more sensitive than almost all other contact thermometers. However, they are very nonlinear and have a narrow temperature range. Traditionally, thermistors have also had a reputation for instability, but thermistors are now readily available for temperature ranges within −40 °C to 60 °C with stabilities of a few tenths of a millikelvin per year. Their short-term performance approaches that of standard platinum resistance thermometers, but at a much lower cost. Thermistors are also available with selected performance characteristics, including interchangeability to 0.05 °C, aged and selected for stability, as well as qualification for military and space applications.

Reviews of the properties and applications of thermistors can be found in [1,2] and, with simpler overviews, in [3,4].

69.1 Principles of Operation

NTC thermistors are extrinsic semiconductors manufactured from mixtures of metal oxides heated to high temperatures to form a polycrystalline ceramic. Ordinarily, the individual oxides have a large energy gap between the vacant conduction band and the fully occupied valence band, which makes them good electrical insulators. The mixture of oxides, however, has intermediate electronic states that make the ceramic a semiconductor. As the temperature increases, increasing numbers of electrons jump to higher-energy states enabling conduction in the conduction bands, and, by creating holes, enabling

conduction in the valence band. The total number of mobile charge carriers, n, depends on the energies of the electrons as determined by the Boltzmann distribution and on the density of electronic states near the band edges [5]:

$$n \propto T^{3/2} \exp\left(\frac{-E_g}{2kT}\right) \tag{69.1}$$

where
E_g is the excitation energy for the carriers
k is Boltzmann's constant
T is temperature (K)

The leading $T^{3/2}$ term in Equation 69.1 is due to the density of states at the band edges and tends to be compensated by a similar term in the carrier mobilities (due to the density of states for phonons that scatter the carriers). The combination of effects gives an overall resistance–temperature behavior that is roughly approximated by

$$R(T) = R_0 \exp\left(\frac{E_g}{2kT}\right) \tag{69.2}$$

where R_0 is a constant. Usually, this equation is rewritten in the form

$$R(T) = R(T_0)\exp\left[\beta\left(\frac{1}{T} - \frac{1}{T_0}\right)\right], \tag{69.3}$$

where T_0 is some convenient reference temperature, often 298.15 K (25 °C). The parameter β is a characteristic of the thermistor material with typical values in the range 2000–6000 K. Figure 69.1 plots the

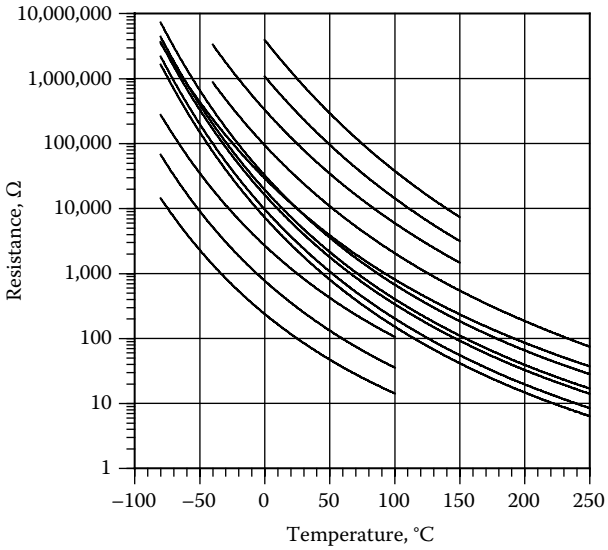

FIGURE 69.1 The resistance–temperature characteristics for a range of thermistors showing the typical resistance and temperature ranges.

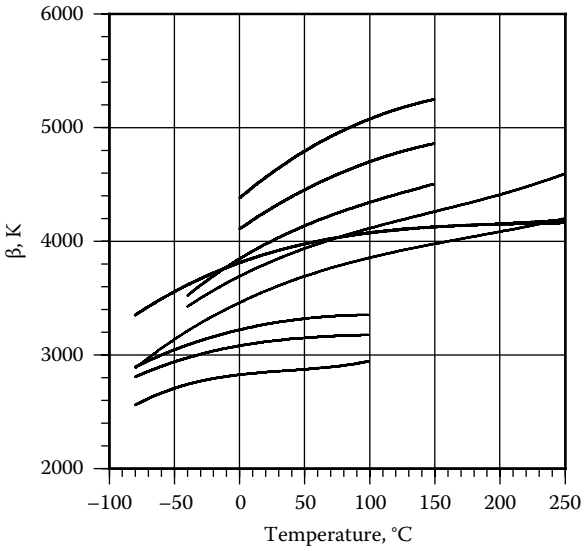

FIGURE 69.2 The β values for the thermistors of Figure 69.1. Some of the thermistors have the same β value.

resistance–temperature characteristic for a range of commercially available thermistors. Figure 69.2 plots the β values for the same set of thermistors and shows the typical variation in β with temperature.

The sensitivity, S, of the thermistor is defined as the relative change in resistance for a change in temperature and is given by

$$S = \frac{1}{R}\frac{dR}{dT} = \frac{d\ln(R)}{dT} = -\frac{\beta}{T^2}. \tag{69.4}$$

This number is useful for evaluating measurement errors, as will be shown later. Figure 69.3 shows the sensitivities for the thermistors of Figure 69.1. At room temperature, they range between about −0.03/°C

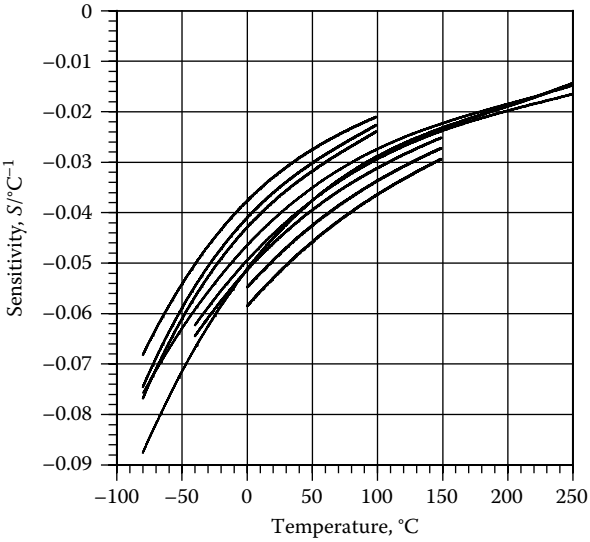

FIGURE 69.3 The sensitivities, the fractional change in resistance per degree Celsius, as a function of temperature for the thermistors of Figure 69.1.

and −0.05/°C. That is, thermistors are about 10 times more sensitive to temperature than platinum resistance thermometers: the sensitivity for platinum resistance thermometers is more nearly constant and approximately equal to the alpha value, $\alpha = 3.85 \times 10^{-3}$/°C.

69.2 Calibration Equations

One of the notable features of Figure 69.2 is that the β value for a thermistor varies with temperature, which is characteristic of extrinsic semiconductors. This means that (3) is only useful as a calibration equation for temperature ranges of no more than 20 °C–30 °C. For high-accuracy or wide temperature ranges, more complex equations are required. Although a wide range of calibration equations have been explored, for example, [6–10], there are two extended series expansions of Equation 69.3 that are most commonly used:

$$\frac{1}{T} = A + B\ln\left(\frac{R}{R_0}\right) + C\left[\ln\left(\frac{R}{R_0}\right)\right]^2 + D\left[\ln\left(\frac{R}{R_0}\right)\right]^3 + \cdots \tag{69.5}$$

and

$$\ln\left(\frac{R}{R_0}\right) = A + \frac{B}{T} + \frac{C}{T^2} + \frac{D}{T^3} + \cdots \tag{69.6}$$

where R_0 is usually a convenient reference resistance, for example, 1 Ω or 1 kΩ, depending on the measurement units. The number of terms in each series, N, is chosen according to the temperature range and the accuracy required, with more terms required as the range or accuracy increases. Most commonly, the equations are used with four terms, but occasionally up to five terms. Equation 69.5 has the advantage of giving temperature directly from the measured resistance and tends to be used more frequently. Both equations are linear in their coefficients so are amenable to least-squares fitting using the linear algorithms found in many spreadsheet and graphing applications. Figure 69.4 summarizes the performance of Equation 69.5 when different numbers of terms are used. Note that the $N = 2$ case corresponds to Equation 69.3.

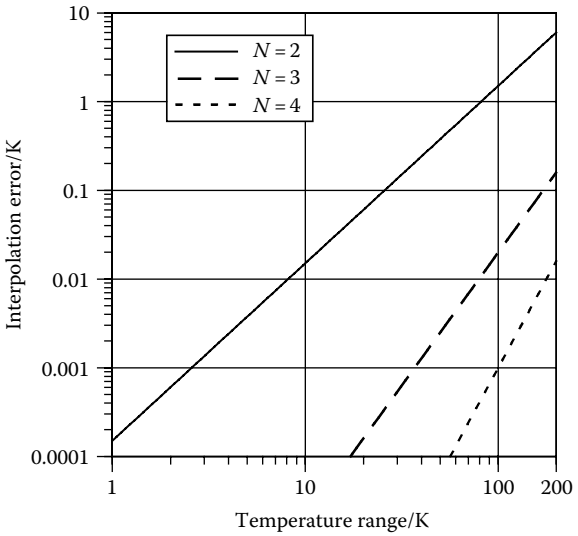

FIGURE 69.4 The typical standard deviation of interpolation errors versus the number of terms used in the calibration equation. The lines are indicative only: the errors tend to be greater for temperatures below 0 °C, and for thermistors with a high β value.

Among a number of equations investigated by Steinhart and Hart [6] is an alternative calibration equation,

$$\frac{1}{T} = A + B\ln\left(\frac{R}{R_0}\right) + D\left[\ln\left(\frac{R}{R_0}\right)\right]^3 \tag{69.7}$$

which is, unfortunately, in common use and recommended by many thermistor manufacturers. The original recommendation for Equation 69.7 was based on a numerical error [7], and use of Equation 69.7 should be discouraged. The equation has some peculiar attributes that make its performance depend on the $R(25\ °C)$ value of the thermistor, the unit of measurement, R_0, and whether thermistors are connected in series or parallel [10,11]. Under very specific conditions, its performance can approach, but never exceed, that of Equation 69.5 with $N = 4$.

69.3 Instrumentation

For the highest accuracy and for temperature ranges of more than a few degrees, the thermistor resistance is best measured directly using a good-quality digital voltmeter in combination with either Equation 69.5 or 69.6, for example, [12]. Care should be taken to account for lead resistance effects and offset voltages and to make sure that the self-heating of the thermistor due to the sensing current is not excessive (see the discussion of errors later). With care in the design of the measurement, selection of the thermistor, use, and calibration, accuracies approaching 0.001 °C are achievable. Thermistor-based thermometers are commercially available with this level of accuracy.

For narrow temperature ranges, and the highest resolution, purpose-built measurement circuits can be advantageous, and an example is shown in Figure 69.5.

The output voltage of the circuit in Figure 69.5 is

$$V_{out} = \frac{R(T)R_{in} - rR_f}{R_{in}\left[r + R(T)\right]}V_{ref}, \tag{69.8}$$

where the resistors are as indicated. The condition for zero output voltage is

$$\frac{R_{in}}{R_f} = \frac{r}{R(T_0)} \tag{69.9}$$

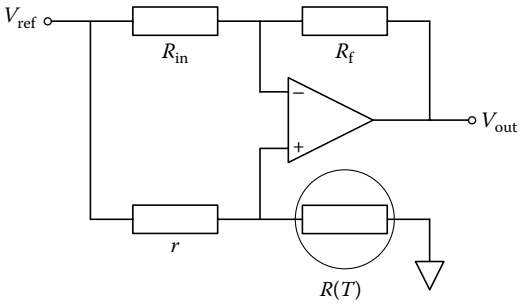

FIGURE 69.5 A simple narrow-range thermistor thermometer using a half-bridge formed by the thermistor, $R(T)$, and the linearizing resistor, r. The operational amplifier with the resistors R_{in} and R_f provides buffering, gain, and offset features.

where T_0 is the nominal operating temperature of the thermometer. The output voltage is a nonlinear function of the thermistor resistance, and this nonlinearity is used to compensate for the thermistor nonlinearity. By replacing $R(T)$ in Equation 69.8 by 69.3, and differentiating with respect to T, it is found that the nonlinearity is largely eliminated if r is chosen so that [13]

$$r = \frac{\beta - 2T_0}{\beta + 2T_0} R(T_0). \tag{69.10}$$

The key feature of the linearization circuit is the resistance r in series with the thermistor (the half-bridge in Figure 69.5). The same scheme can be applied when a single thermistor is used in more complex resistor networks by recognizing that r corresponds to the Norton or Thévenin equivalent resistance seen by the thermistor. Near room temperature, r is often found to be about $0.6 \times R(T_0)$. With the linearizing resistor, r, set according to Equation 69.10 and the gain setting resistors R_{in} and R_f set to the ratio given by Equation 69.9, the output of the thermometer in Figure 69.5 is approximately

$$V_{out}(T_0 + \Delta T) \approx -\frac{\beta + 2T_0}{2T_0^2}\left[\Delta T - \frac{1}{12}\frac{\beta^2}{T_0^4}\Delta T^3\right] V_{ref}. \tag{69.11}$$

The residual nonlinearity is almost purely a cubic function of temperature, as shown in Figure 69.6, with maximum errors of about ±0.1 °C for a 30 °C range. Equation 69.11 shows that the residual nonlinearity scales as cube of the temperature range. Sapoff and Oppenheim [14] describe refinements of this basic linearization technique and give a wide range of examples for different applications.

One of the big advantages of purpose-built circuits like that of Figure 60.5 is, with care and appropriate signal conditioning, a resolution of better than 10 μK can be achieved relatively easily. This enables thermistors to be used for narrow-range high-resolution applications such as differential thermometry, calorimetry, and precision temperature control.

For temperature ranges wider than a couple of tens of degrees, linearization of the thermistor response becomes more difficult. Practical solutions include the use of logarithmic amplifiers [15,16] and oscillators [17], which work well for thermistors with a nearly constant β value. Some commercial thermistor thermometers use this technique and yield accuracies of a few tenths of a degree over a 100 °C range. Another solution is to expand the linearizing scheme of Figure 69.5 to resistance networks in which two or more thermistors are used in combination with linearizing resistors [18] (see Figure 69.7 for example). Commercial thermistor networks optimized for specific temperature ranges are available with linearities as good as ±0.03 °C for a 40 °C temperature range and ±0.2 °C for a 100 °C temperature range.

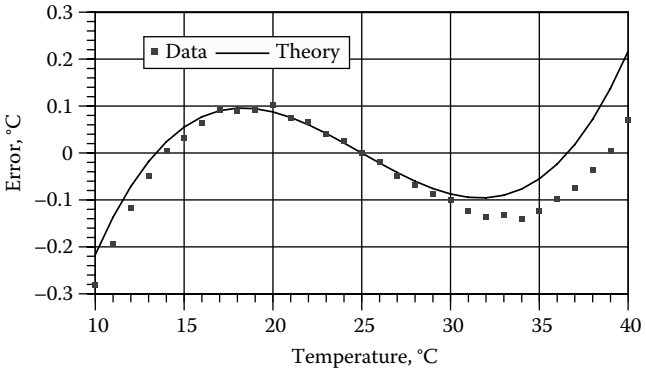

FIGURE 69.6 The nonlinearity for the thermistor thermometer of Figure 69.5.

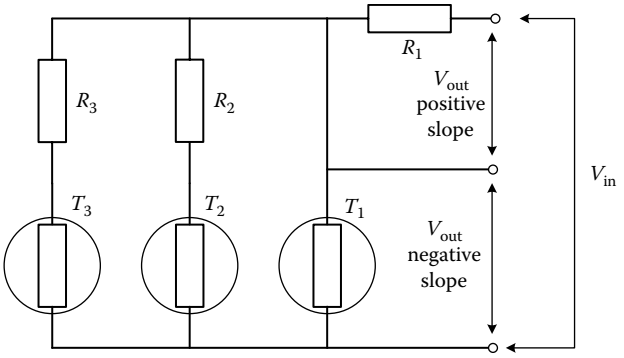

FIGURE 69.7 A three-element linear thermistor network.

A variation on the multithermistor scheme is to sum the outputs from several single-thermistor networks. While superficially the same as the type of network illustrated in Figure 69.7, the approach uses additional resistors and creates extra degrees of freedom in the design, which enables further reduction in the nonlinearities. A three-thermistor network of this design has peak nonlinearities of about 16 mK over a 100 °C range [19], more than 10 times better than the network of Figure 69.7.

69.4 Limitations in Performance

This section describes in detail the most significant errors affecting thermistor thermometers. To illustrate the typical magnitude of the errors, numerical examples are included.

69.4.1 Self-heating

In order to measure a resistance, a current must be passed through the thermistor, which leads to Joule heating and a small temperature increase called the self-heating error. The error, ΔT, is proportional to the power dissipated and the thermal resistance between the thermistor and its environment:

$$\Delta T = \rho I^2 R(T) = \rho \frac{V^2}{R(T)}, \tag{69.12}$$

where

I and V are the sensing current and the voltage across the thermistor, respectively
ρ is the thermal resistance between the thermistor and its surroundings

The thermal resistance depends in part on the dimensions of the thermistor and the material from which it is made, as well as the thermal conductivity and, if fluid, the velocity and viscosity of the medium in which the thermistor is immersed. Self-heating can be a serious problem for measurements made over a wide temperature range. If a constant sensing current is used, the power dissipated (I^2R) at low temperatures becomes large, and if constant voltage excitation is used, the power at high temperatures (V^2/R) becomes a problem.

The thermal resistance is often expressed as the dissipation constant, which is the reciprocal of the thermal resistance. The dissipation constant measures the power required to raise the thermistor temperature 1 °C and is usually reported in units of mW/°C. Typical values of the dissipation constants range from 0.05 to 20 mW/°C in stirred fluids, but are very dependent on the environment so may vary as much as 10–100 times between still air and stirred water. For a 10 kΩ thermistor with a dissipation constant of 10 mW/°C driven with a sensing current of 100 μA, the self-heating error is 0.01 °C.

In many applications, the thermal resistance may fluctuate due to turbulence in the air or stirred fluids. This causes the self-heating error to fluctuate and can limit the resolution of thermistors, when used, for example, in precision temperature controllers or differential thermometers.

69.4.2 Stray Thermal Influences

The generally high thermal resistance between the thermistor and the environment means that thermistors are prone to stray thermal influences from either infrared radiation or heat conducted along the lead wires to the thermistor. This effect may be exacerbated by the poor thermal design of many commercial thermistor probes. The "stem conduction" or "immersion errors" tend to fall exponentially with immersion depth, and a useful rule of thumb is that the error is reduced by a factor of 100 for each 10 diameters of immersion [20]. For example, to measure temperatures near 120 °C (100 °C different from ambient temperature) with accuracy of 0.01 °C, a stainless-steel sheathed probe may need to be immersed as much as 20 diameters.

Stray thermal effects are a particular problem when thermistors, and other contact thermometers, are used to measure air and surface temperatures. For air temperature measurements, the leads should be long and thermally anchored to an object at a temperature as close as practical to that of the air, so that the leads adjacent to the thermistor also come to thermal equilibrium with the air and do not provide a source of heating or cooling. Polished-metal cylinders can be used as radiation shields to reduce the influence of infrared radiation sources such as incandescent lamps, sunlight, warm electronics, heaters, and people [21]. With surface temperatures, a sufficient length of the leads must be thermally anchored to the surface to ensure that the thermistor is at the surface temperature. Radiation shielding is often required.

69.4.3 Settling Time

One of the major advantages of thermistors is their small size and fast response time. The responses times are normally characterized by the 1/*e* time constant, which is the constant, τ in the model of the temperature error, ΔT, due to a step change in temperature:

$$\Delta T = \Delta T_{\text{step}} \exp\left(\frac{-t}{\tau}\right), \tag{69.13}$$

where

t is the time following the step change

ΔT_{step} is the step change to which the thermistor is responding

This model suggests that the error is reduced by a factor of 100 for each five time constants. For example, a thermistor with a time constant of 100 ms will have settled to within 1% of a step change within 500 ms. The time constants for thermistors range from about 20 ms for ultra-small beads to more than 200 s for large disk types and are very strongly correlated with size and thermal resistance.

Bead thermistors with environmental protection such as glass or epoxy coatings, or a stainless steel sheath, typically have time constants in the range of 1–20 s. Often, larger and more complex probes can exhibit settling behavior that is more complex than that suggested by Equation 69.13 and may be characterized by two or more time constants. For these probes, the settling behavior may be more usefully characterized by the 10%–90% settling time, and many industrial and military applications use such specifications.

As with the dissipation constants, the time constants are very strongly dependent on the medium into which the thermistors are immersed. A thermistor in a well-stirred low-viscosity fluid may be 10–100 times faster than the same thermistor in still air.

69.4.4 Thermistor Stability

There are several effects causing instability in thermistors [22], including mechanical cracking of the thermistor body with temperature cycling, drift at high temperatures due to ingress of atmospheric gases, changes in the atomic and crystallographic structure, and changing contact resistance between the leads and the thermistor body. The most stable thermistors are bead thermistors encapsulated in glass, closely followed by epoxy encapsulated beads. Within the range –20 °C to 60 °C, selected and pre-aged thermistors are often stable to better than a few tenths of a millikelvin per year, and thermistors used as high as 120 °C can be stable to a few millikelvin [23,24]. Thermistors with $R(25\ °C)$ resistances in the range 2–10 kΩ appear to be the most stable. For further information on thermistor stability, see Ref. [25–29].

69.4.5 Resistor Stability

A thermistor-based thermometer is only as stable as the other components in the instrument. The effect of the instability of the other resistors in Figure 69.5, for example, can be inferred from the zero-output condition (Equation 69.9), so that the apparent change in the thermistor resistance due to changes in the other three resistors is

$$\frac{\Delta R(T)}{R(T)} = \frac{\Delta r}{r} + \frac{\Delta R_{\mathrm{f}}}{R_{\mathrm{f}}} - \frac{\Delta R_{\mathrm{in}}}{R_{\mathrm{in}}}, \tag{69.14}$$

and hence, from Equation 69.4, the apparent change in measured temperature caused by changes in the resistances is

$$\Delta T = -\frac{T^2}{\beta}\left(\frac{\Delta r}{r} + \frac{\Delta R_{\mathrm{f}}}{R_{\mathrm{f}}} - \frac{\Delta R_{\mathrm{in}}}{R_{\mathrm{in}}}\right). \tag{69.15}$$

The effects of resistor drift on the observed temperature can be estimated using this equation. If the changes in the resistors are due to changes in the ambient temperature, T_a, then the apparent temperature change is

$$\Delta T = -\frac{T^2}{\beta}\left(\alpha_r + \alpha_{R\mathrm{f}} - \alpha_{R\mathrm{in}}\right)\Delta T_a, \tag{69.16}$$

where α_r, $\alpha_{R\mathrm{f}}$, and $\alpha_{R\mathrm{in}}$ are the temperature coefficients of the three resistors.

Equation (69.16) shows that the effects of ambient temperature are reduced by the ratio of the temperature coefficients. Good-quality resistors have temperature coefficients of 0.0005%/°C or less, being about 1/10,000 that of thermistors. Hence a 10 °C change in the temperature of the circuit will cause an apparent change of about 1 mK in the measured temperature.

69.4.6 Lead Resistances

The high sensitivity and high resistance of thermistors mean that for many measurements, a two-wire resistance measurement is satisfactory and provides a useful simplification. However, the lead resistances are often forgotten and can become a problem at higher temperatures when the thermistor resistance is low. The error due to a lead resistance, R_{L}, is

$$\Delta T = -\frac{T^2}{\beta}\frac{R_{\mathrm{L}}}{R(T)}. \tag{69.17}$$

The error increases very rapidly with temperature due to the falling resistance of the thermistor and the T^2 temperature dependence. For a 10 kΩ thermistor with a β value of 3600 K and a 1 Ω lead resistance, the error at 25 °C (~300 K) is 2.5 mK, while at 50 °C, the error increases to 7.4 mK. Where lead resistances are a problem, a four-wire measurement should be used [21].

69.4.7 Offset Voltages

Typically, a thermistor resistance measurement involves a voltage measurement, the accuracy of which may be limited by the resolution of a voltmeter, or the input-offset voltage and input bias currents of an operational amplifier, and/or thermoelectric effects. The error in a temperature measurement due to an error, ΔV, in the voltage measurement is

$$\Delta T = \frac{T^2}{\beta}\frac{\Delta V}{I_0 R(T)}, \tag{69.18}$$

where I_0 is the sensing current. For a 10 kΩ thermistor with a β value of 3600 K, a 100 μV error, and a sensing current of 100 μA, the error at 25 °C (~300 K) is 2.5 mK.

69.4.8 Insulation Resistance

At low temperatures, the thermistor resistance becomes very large, often greater than 10 MΩ. In such applications, care should be given to the insulation on the connecting leads to ensure that the insulation resistance does not shunt the measuring current. Some pigmented plastics can be very poor in this respect. The temperature error due to an insulation resistance R_{ins} shunting the thermistor is

$$\Delta T_{\text{ins}} \approx -\frac{T^2}{\beta}\frac{R(T)}{R_{\text{ins}}}, \tag{69.19}$$

which increases in proportion to the thermistor's resistance (low temperatures). A 10 kΩ thermistor shunted by 10 MΩ will exhibit an error of 25 mK.

69.5 Choice of Thermistor

The temperature range of commercially available thermistors varies from 1 K to 1000 °C with large differences in the R(25 °C) resistance, β values, the metal oxides used, and the encapsulation and sheath assemblies. The most stable thermistors for temperature measurement have a much restricted range: glass-encapsulated thermistors are most useful in the range from about −40 °C to 100 °C, but some are usable from −80 °C to 250 °C. Epoxy-encapsulated thermistors have an upper temperature limit of about 150 °C.

Thermistors are made in many different forms. Bead thermistors are supplied with leads attached during the manufacturing process but may be further encapsulated in glass or epoxy, as well as diode-like forms suitable for automatic insertion into printed circuit boards. Other forms include flakes, disks, surface-mount, and rod types, which may be supplied with or without leads. When supplied without leads, they have metallized surfaces for the contacts.

There are many large companies manufacturing thermistors, and comparing specifications from different suppliers can be very helpful to highlight limitations in the specifications, manufacturing tolerances, and sheath assemblies that might be relevant to any application. Most of the manufacturers also

provide extensive application information. Thermistors are available to meet military specifications, space qualification, and can be selected for long-term stability and interchangeability. Military standard MIL-PRF-23648 [30] not only provides specifications for thermistors, but also gives the measurement conditions for the various electrical and thermal properties of thermistors.

69.6 Thermistors in Other Applications

The term thermistor is applied generically to any semiconducting device with a high temperature coefficient of resistance. While NTC thermistors are the best of the devices for thermometry, once other fields of application are considered, other types of thermistors, including positive temperature coefficient (PTC) ceramic and silicon thermistors, become useful.

69.6.1 NTC Thermistors

When used for thermometry, thermistors are operated with a low current to avoid self-heating errors. However, for many applications, NTC thermistors are deliberately operated at very high currents to exploit the thermal feedback that occurs [31]. If a thermistor is operated at a nominal ambient temperature T_a and with a sensing current I_0, then the thermistor temperature can be written as

$$T = T_a + \rho P + \rho I_0^2 R(T_a) \exp\left[\beta\left(\frac{1}{T} - \frac{1}{T_a}\right)\right], \tag{69.20}$$

where P is any additional power applied to the thermistor (e.g., microwave or optical) and ρ is the thermal resistance between the thermistor and its environment. The essential feature of the model equation is that any power applied to the thermistor, either through Joule heating $I_0^2 R(T)$ or external power P, causes the temperature of the thermistor to rise and, hence, its resistance to fall. Equation 69.20 can be solved numerically for T and then the voltage $I_0 R(T)$ plotted against the current to give a voltage–current characteristic for the thermistor. Example curves are shown in Figure 69.8.

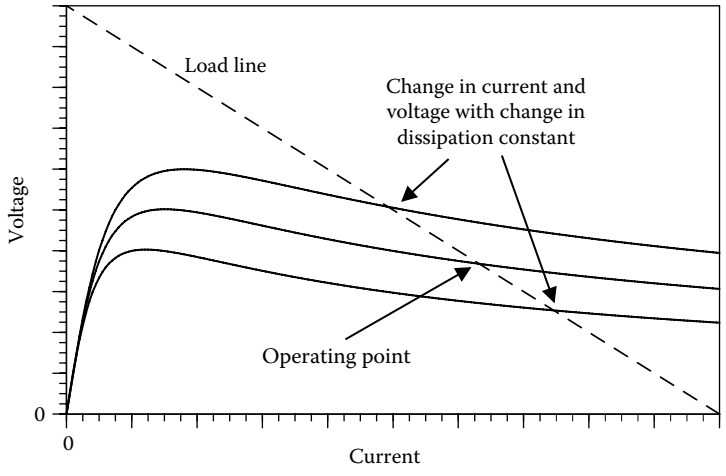

FIGURE 69.8 The voltage–current characteristic for a thermistor operated at high currents and with three different values of the dissipation constant. The load line is the voltage–current characteristic for a Thévenin voltage source. The intersection of the load line with the thermistor curves gives the operating point for the thermistor when driven by the source.

There are three distinct operating regimes in Figure 69.8. At low currents, the power dissipated is small compared with the dissipation constant, and the self-heating effect is negligible. Under these conditions, the thermistor resistance depends only on the temperature, and the voltage across the thermistor is directly proportional to the current. Consequently, at low currents, the ratio of the voltage to the current is equal to the zero-power resistance of the thermistor. This is the regime used for temperature measurement, as described in the previous sections.

As the current increases, the effects of self-heating become more evident, the thermistor temperature rises, its resistance begins to decrease, and the slope of the voltage–current characteristic decreases. This trend continues until the slope of the voltage–current characteristic is zero. The temperature, voltage, and current at the peak of the curve are [31]

$$T_{\text{peak}} = \frac{\beta - \sqrt{\beta^2 - 4\beta T_a}}{2}, \tag{69.21}$$

$$V_{\text{peak}} = \sqrt{R(T_{\text{peak}})\rho\left(T_{\text{peak}} - T_a\right)}, \tag{69.22}$$

and

$$I_{\text{peak}} = \sqrt{\frac{\rho(T_{\text{peak}} - T_a)}{R(T_{\text{peak}})}}. \tag{69.23}$$

Beyond the peak voltage, the slope of the curve continues to decrease, and the thermistor exhibits a negative resistance characteristic, that is, dV/dI_0 is negative.

Also shown in Figure 69.8 is a straight line corresponding to the voltage–current characteristic of a Thévenin voltage source. The characteristic is usually called a "load line" and has the equation

$$V = V_{\text{Thev}} - IR_{\text{Thev}} \tag{69.24}$$

where V_{Thev} and R_{Thev} are the voltage and resistance in the Thévenin equivalent circuit for the circuit around the thermistor. The load line intersects with the thermistor's characteristic at the points indicated. Applications based on self-heated thermistors work by detecting changes in the operating point of the thermistors. For example, Figure 69.8 shows three voltage–current curves for the same thermistor but with different values of the dissipation constant. The changes in voltage and current between the points on the load line indicate the circuit's response to the changes in the dissipation constant. The circuit could be used in a wide variety of applications where, by measuring changes in the dissipation constant, the circuit can be used for leak detection, flow measurement, and level detection.

Once the operating point of the thermistor is chosen, the sensitivity of the circuit in the vicinity of the operating point can be expressed as a partial derivative of the voltage to all of the other variables in the circuit. For example,

$$\Delta V = \mu_{T0}\Delta T_0 + \mu_{I0}\Delta I_0 + \mu_\delta \Delta\rho + \mu_{V0}\Delta V_0 + \mu_P \Delta P \cdots \tag{69.25}$$

where the sensitivity coefficients $\mu_{T0}, \mu_{I0}, \mu_\rho, \mu_{V0}, \mu_P \ldots$, are the respective derivatives of the voltage while all other variables are constant. For example,

$$\mu_{T0} = \left.\frac{\partial V}{\partial T_0}\right|_{\rho,I,P,\ldots=\text{constant}}. \tag{69.26}$$

In some cases, mathematical expressions can be determined for the sensitivity coefficients [31]. The key to using the thermistor as a sensor is to design the circuit so that the sensitivity of the circuit to the variable of interest is as large as practicable while all other sensitivity coefficients are as small as practicable. It is not possible to have all other coefficients equal to zero, so the circuit is often designed as a differential system using two identical thermistor subcircuits with one measuring the variable of interest and the other serving as a reference. In this way, unwanted influences affect both subcircuits equally and the differential output signal does not change. Note too that the load line in Figure 69.8 could be placed to intersect the curve at one, two, or three points. In some cases, the circuit will exhibit switching behavior as it jumps from one operating point to another in response to external changes.

Sapoff [31] cataloged a wide range of applications for thermistors and describes many examples of circuits using different operating principles:

- Variation in dissipation constant and time constant: vacuum manometers, flow meters, velocity meters, thermal conductivity, leak detectors, gas chromatography, liquid level, surge suppression, filament protection, overload protection, and switching.
- Variation in the load line (over a fixed current–voltage curve): oscillator amplitude and/or frequency control, gain control, level stabilization, equalization, voltage regulators, signal limiters, signal expansion and compression, switching.
- Variation in ambient temperature: principally thermometry including measurement, control, and alarm applications.
- Power measurement: bolometry for optical and microwave measurement, ac-to-dc conversion, and true rms measurement.

69.6.2 PTC Thermistors

The PTC thermistor refers to another family of semiconducting ceramic devices with an extremely variable temperature coefficient that is dominated by a temperature region in which the resistance rises extremely rapidly [32]. This makes the thermistors ideally suited to switching applications, and typically they are manufactured in families with specified switching temperatures. Figure 69.9 shows a sample of the resistance–temperature characteristics for a family of PTC thermistors.

At low temperatures, the resistance is low, and the thermistor exhibits a small NTC of resistance on the order of –1%/°C. As the temperature increases, the temperature coefficient of resistance becomes positive and the resistance begins to rise, and then rise rapidly. At the switching or "threshold" temperature,

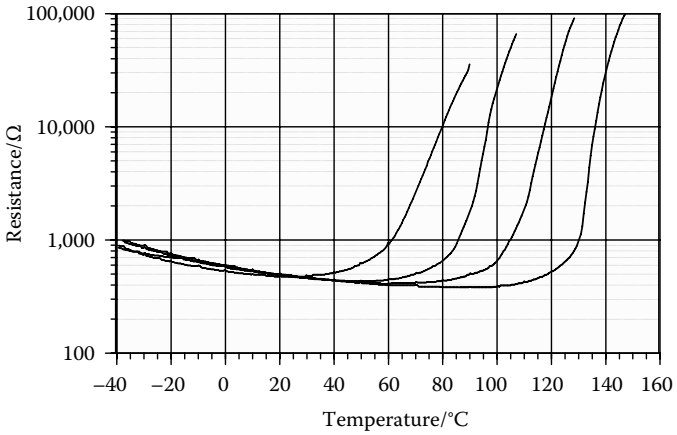

FIGURE 69.9 A sample of the resistance–temperature characteristics for a family of PTC thermistors with nominal switching temperatures of 75 °C, 95 °C, 115 °C, and 135 °C.

the rate of rise becomes very rapid and the resistance–temperature characteristic becomes very steep, sometimes as high as 100%/°C. At temperatures above the switching range, the resistance reaches a maximum value beyond which the temperature coefficient becomes negative again.

The resistance–temperature characteristic of the PTC thermistor can be exploited in a number of ways. A simple application is to use the thermistor as a heating element. The power dissipated is $V^2/R(T)$, and as the temperature rises in response to the heat, the applied power falls so that the thermistor can be used as a temperature controller or simply to limit the current flowing in the circuit. If the joule heating is sufficient to maintain the thermistor temperature when in its high-resistance state, the thermistor may be used for delaying the switching of start-up mechanisms in electronic equipment such as the auxiliary windings in electric motors. When used as a liquid level or flow sensor, the thermistor is forced back into its low-resistance state by changing its dissipation coefficient. These simple examples show that the thermistor can have a wide range of different behaviors, which makes them suitable for heating, current limiting, motor start, overcurrent protection, temperature control, alarm, time delay, level, and flow sensing applications.

PTC thermistors are available in many different forms with the form usually designed for specific applications. The switching temperature can be varied between about 70 °C and 240 °C by altering the chemical composition of the ceramic. As with the NTC thermistors, most manufacturers provide extensive literature supporting their selection and application.

69.6.3 Silicon Thermistors

Silicon PTC thermistors, also known as "silistors" or "sensistors," are typically single-crystal silicon devices that have been heavily doped to give the silicon a resistance–temperature characteristic similar to that of a metal [33]. The resistance–temperature characteristic is predominantly linear with an additional weak quadratic dependence that give the device an almost constant sensitivity of about 0.7%/°C for all temperatures. It is about twice that of platinum resistance thermometers. The main advantages of the silicon thermistors are the higher sensitivity, higher resistance (typically 100 Ω to 5 kΩ, but some up to 40,000 kΩ), and very much lower cost (below US$1 in large numbers). Although less accurate and less stable than NTC thermistors and platinum resistance thermometers, the low cost and ease of use make them the sensor of choice in many low-accuracy high-production applications.

The most common types of silicon PTC have the same package as small glass diodes with diameters of 1.8–2.5 mm and lengths of 3.8–7.5 mm, and the molded epoxy package with diameters of 3.6–6.0 mm and lengths of 10.4–15.0 mm. Such units also have axial leads, so are suited for electronic applications with automated component insertion. Epoxy-coated chips and disks with radial leads are also available, with diameters of approximately 3 mm. Silicon PTC thermistors that comply with MIL-T-23648 have an operating temperature range of −55 °C to 125 °C. Commercial versions can be obtained with a range of −65 °C to 300 °C.

References

1. Sachse, H. B., *Semiconducting Temperature Sensors and Their Applications*, John Wiley & Sons: New York, 1975.
2. Hyde, F. J., *Thermistors*, Iliffe Books: London, U.K., 1971.
3. McGee, T. D., *Principles and Methods of Temperature Measurement*, John Wiley & Sons: New York, 1988.
4. Michalski, L., Eckersdorf, K., and McGhee, J., *Temperature Measurement*, John Wiley & Sons: Chichester, U.K., 1991.
5. Sze, S. M., *Physics of Semiconductor Devices*, 2nd edn., John Wiley & Sons: New York, 1981.
6. Steinhart, J. S. and Hart, S. R., Calibration curves for thermistors, *Deep Sea Research*, **15**, 497–503, 1968.

7. Bennett, A. S., The calibration of thermistors over the range 0–30°C, *Deep Sea Research*, **19,** 157–163, 1971.
8. Sapoff, M., Siwek, W. R., Johnson, H. C., Slepian, J., and Weber, S., The exactness of fit of resistance-temperature data of thermistors with third-degree polynomials, In *Temperature: Its Measurement and Control in Science and Industry*, J. F. Schooley (ed.), Vol. 5 American Institute of Physics: New York, pp. 875–887, 1982.
9. Siwek, W. R., Sapoff, M., Goldberg, A., Johnson, H. C., Botting, M., Lonsdorf, R., and Weber, S., A precision temperature standard based on the exactness of fit of thermistor resistance-temperature data using third degree polynomials, In *Temperature: Its Measurement and Control in Science and Industry*, J. F Schooley (ed.), Vol. 6, American Institute of Physics: New York, pp. 491–496, 1992.
10. Chen, C-C, Evaluation of resistance–temperature calibration equations for NTC thermistors, *Measurement*, **42,** 1103–1111, 2009.
11. White, D. R., Some mathematical properties of the ITS-90, In *Temperature: Its Measurement and Control in Science and Industry*, C. W. Meyer (ed.), Vol. 8, American Institute of Physics: New York, 2012.
12. Mangum, B. W., The triple point of succinonitrile and its use in the calibration of thermistor thermometers, *Review of Scientific Instruments*, **54**, 1687–1692, 1983.
13. Beakley, W. R., The design of thermistor thermometers with linear calibration, *Journal of Scientific Instruments*, **28**, 176–179, 1951.
14. Sapoff, M. and Oppenheim, R. M., The design of linear thermistor networks, *IEEE International Convention Record*, **Part 8**, 12–24, 1964.
15. Patranabis, D., Ghosh, S., and Bakshi, C., Linearizing transducer characteristics, *IEEE Transactions on Instrumentation and Measurement*, **IM-37**, 66–69, 1988.
16. Seingold, D. H., *Non-linear Circuits Handbook*, Analog Devices: Norward, MA, 1976.
17. Natarajan, S., Widely Linear temperature-to-frequency converters, *IEEE Transactions on Instrumentation and Measurement* **IM-24**, 235–239, 1975.
18. Trolander, H. W., Case, D. A., and Harruff, R. W., Reproducibility, stability and linearization of thermistor resistance thermometers, In *Temperature: Its Measurement and Control in Science and Industry*, H. H. Plumb (ed.), Vol. 4, Instrument Society of America: Pittsburgh, PA, pp. 997–1009, 1972.
19. Renneberg, C. and Lehmann, T., Analogue circuits for thermistor linearization with Chebyshev-optimal linearity error, *Proceedings of 18th European Conference on Circuit Theory and Design*, Seville, Spain, pp. 910–913, 2007.
20. White, D. R. and Jongenelen, C. L., The immersion characteristics of industrial PRTs, *International Journal of Thermophysics*, **31**, 1685–1695, 2010.
21. Nicholas, J. V. and White, D. R., *Traceable Temperatures*, John Wiley & Sons: Chichester, U.K., 2001.
22. Zurbuchen, J. M. and Case, D. A., Aging phenomena in nickel-manganese oxide thermistors, In *Temperature: Its Measurement and Control in Science and Industry*, J. F. Schooley (ed.), Vol. 5, American Institute of Physics: New York, pp. 889–896, 1982.
23. Strouse, G. F., Meyer, C. W., and Miller, W. W., Drift study of thermistors used between 90°C and 150°C, In *Temperature Its Measurement and Control*, C. W. Meyer (ed.), Vol. 8, American Institute of Physics: New York, 2012.
24. Vaughn, C. D., Gartenhaus, J., and Strouse, G. F., NIST calibration uncertainties of thermistors thermometers over the range from −50°C to 90°C, *Proceedings of NCSL Workshop and Symposium*, Washington, DC, 2005.
25. Siwek, W. R., Sapoff, M., Goldberg, A., Johnson, H. C., Botting, M., Lonsdorf, R., and Weber, S., Stability of NTC thermistors, In *Temperature: Its Measurement and Control in Science and Industry*, J. F. Schooley (ed.), Vol. 6, American Institute of Physics: New York, pp. 497–502, 1992.
26. Wise, J. A., Stability of glass-encapsulated disc-type thermistors, In *Temperature: Its Measurement and Control in Science and Industry*, J. F. Schooley (ed.), Vol. 6, American Institute of Physics: New York, pp. 481–484, 1992.

27. Edwards, T. J., Observations on the stability of thermistors, *Review of Scientific Instruments*, **54**, 613–617, 1983.
28. LaMers, T. H., Zurbuchen, J. M., and Trolander, H., Enhanced stability in precision interchangeable thermistors, In *Temperature: Its Measurement and Control in Science and Industry*, J. F. Schooley (ed.), American Institute of Physics: New York, pp. 865–873, 1982.
29. Wood, S. D., Mangum, B. W., Filliben, J. J., and Tillet, S. B., An investigation of the stability of thermistors, *Journal of Research of NBS*, **83**, 247–263, 1978.
30. DSCC, General specifications for Resistors, Thermal (thermistors) Insulated, MIL-PRF-23648, Jan 23, 2009.
31. Sapoff, M. and Oppenheim, R. M., Theory and application of self-heated thermistors, *Proceedings of IEEE*, **51**, 1292, 1963.
32. Fabian, J., Heating with PTC thermistors, *EDN Products Edition*, **41**(12A), 10, 1996.
33. Michalski, L., Eckersdorf, K., and McGhee, J., *Temperature Measurement*, John Wiley & Sons: Chichester, U.K., 1986.

70

Thermocouple Thermometry

R.P. Reed
Proteun Services

70.1 Introduction

The self-generating thermocouple is one of the more widely used (but most misunderstood) sensors for routine and specialty thermometry because of its versatility, simplicity, ease of use, and low cost. It employs the Seebeck thermoelectric effect that, unlike the related Peltier and Thomson thermoelectric effects, alone converts heat to emf [1–4]. T.J. Seebeck first recognized the phenomenon in 1821. However, as a very early pioneer of electrical phenomena, he misunderstood the effect that bears his name. Seebeck monitored the magnetic symptom of current rather than voltage. He never applied it to thermometry. Seebeck and other early users could apply the effect only in closed circuits, rather than in modern current-suppressed "open-circuit" mode. Seebeck's discovery enabled George Ohm to use thermocouples as the essential steady current source to develop his law of resistance in 1826. A. C. Becquerel recognized in 1826 that Seebeck's discovery could be used for pyrometry, but C. S. M. Pouillet, in 1836, was the first to use the Seebeck effect for applied thermometry.

70.2 Terminology

Thermocouple: Any pair of electrically conducting thermoelectrically different material legs in Ohmic contact at a junction is a *thermocouple*. The individual legs are *thermoelements*. Thermoelements can be solid or liquid, normal-, semi-, or superconductors. Seebeck emf occurs only in nonisothermal thermoelements, not junctions.

Junction: Any electrically conducting *interface* between dissimilar thermoelements is a thermoelectric *junction*. Junctions provide electrical connectivity. Junctions contribute no Seebeck emf. Therefore, calibration is of thermoelement segments, not of junctions. Junctions define thermoelement endpoint temperatures and thereby "sense" temperature. Electrical connections between like thermocouple legs are *splices*, not junctions.

Sensitivity: The sensitivity, emf versus temperature, of each individual leg material is expressed by an *absolute Seebeck coefficient*. Net emf between thermally paired dissimilar thermoelements is described by the more familiar *relative Seebeck coefficient*.

Thermocouple states: Segments of thermoelements are *isothermal* where they are at uniform temperature. Multiple junctions are *isothermal* for thermometry while they are acceptably near the same temperature. A thermoelement is *thermoelectrically homogeneous* along any segment where its Seebeck coefficient is uniform. It is *inhomogeneous* for thermometry where spatial nonuniformity of the absolute Seebeck coefficient could significantly degrade thermometry. Significant hidden *inhomogeneity* resulting from use is a commonplace and usually unrecognized problem in practical thermometry and calibration.

70.3 Simplest Thermocouple Thermometer

Correctly understood, thermocouple thermometry is simple and its many significant, distinctive, and obscure problems are easily avoidable. However, from simplistic descriptions of circuits and principles and its elementary applications, a need for deeper understanding may not be apparent. Commonplace concealed problems cause unrecognized thermometry error.

Elementary thermocouple thermometry can seem as easy as is the measurement of electrical quantities by a multimeter. A digital multimeter that can be used with a thermocouple probe alternately to monitor temperature as well as voltage, current, resistance, and other variables is shown in Figure 70.1. This meter, complete with a thermocouple probe of Type **K** material, presently sells as a consumer product in the Electrical Department of some neighborhood hardware stores for the price of a gallon of paint.

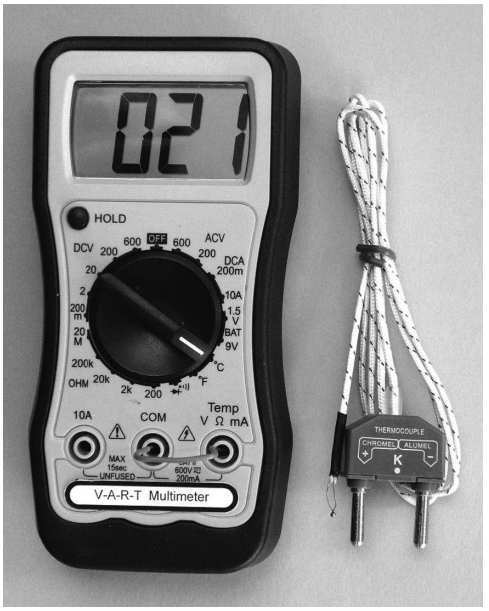

FIGURE 70.1 The simplest thermocouple thermometer. Inexpensive multimeters with a thermocouple temperature sensor obscure the need for detailed understanding of the principles of thermoelectricity for modern thermometry circuits. (Note shorted input and unplugged thermocouple. See Section 70.10.3.6.)

This illusion of ultimate operational simplicity may suggest incorrectly that it is unnecessary to understand the essential principles of the diverse thermoelectric circuits now in use and for thermometry.

Critical applications, modern circuits, and inconsistent international thermocouple conventions make it more important than ever to understand the distinctions between electrical and thermoelectric circuits. Thermometry errors of only a few degrees in energy, process, manufacturing, medical, and research fields annually cost millions of dollars in lost yield, fuel cost, performance bonuses, and so on. Consequence of hidden error also occurs as incorrect interpretation of data, failure of objective, equipment damage, personal injury, or even loss of life.

This chapter explains why for realistic thermometry understanding of the authentic principles and conventions is essential. It offers useful tools for recognizing and avoiding commonplace significant obscure measurement errors that are unique to modern practical thermoelectric thermometry.

70.4 Thermoelectricity

The physical cause of thermoelectric phenomena is complex in detail as applied to real materials. It is explained by modern theory confirmed by experiment [1,2]. Seebeck properties of many materials can be predicted. For reliable thermometry, it is not essential to understand the underlying physics. For application, it is sufficient to understand a few very simple but general thermoelectric principles that are fully consistent with physical theory and experiment.

70.4.1 Absolute Seebeck Effect

The absolute Seebeck thermoelectric effect, the occurrence of a net emf between two points of a conductor because their temperatures are different, results from the temperature-dependent distribution of charge carriers [1–5]. Seebeck emf occurs *without* dissimilar materials. It is *not* a junction phenomenon, nor is it the same as Volta's contact potential. It is related to but is not the result of the associated Peltier or Thomson thermoelectric effects that are insignificant in thermocouple thermometry.

To practice and to fully apply the simple principles, it also is not necessary to understand calculus. Nevertheless, the application principles are developed as follows. The *absolute Seebeck coefficient* expresses the measurement sensitivity (volts per unit of temperature) of the Seebeck effect. It is defined over any *thermoelectrically homogeneous* region, x, along a slender conducting material

$$\sigma(T) = \lim_{\Delta T \to 0} \frac{\Delta E}{\Delta T} = \frac{dE}{dT} \tag{70.1}$$

where

ΔE is the net Seebeck emf across the homogeneous segment
ΔT is the temperature difference between ends of that region

The Seebeck coefficient, $\sigma(T)$, is a physical transport property of *all* individual electrically conducting materials.

From Equation 70.1, the net emf is

$$\Delta E = \int_{T_1}^{T_2} \sigma(T) dT = E(T_2) - E(T_1) \tag{70.2}$$

where ΔE is simply the difference of emf between any pair of points of a *homogeneous* segment, separated by any distance, x, between which the temperature difference is $\Delta T = (T_2 - T_1)$. Note that the net Seebeck emf for such a *homogeneous* segment depends only on the temperatures at the two segment endpoints and *not* on the local values of temperature or temperature gradients, dT/dx, between them, nor on the distance between those two points. An overall inhomogeneous thermoelement is composed of locally homogeneous segments. Nevertheless, for general thermometry, each entire thermoelement must be homogeneous so that only endpoint temperatures, not temperature distribution, matter.

The Seebeck coefficient $\sigma(T)$ is a nonlinear function of temperature. For meaningful thermometry, it must be a function of temperature alone, independent of time or location along a thermoelement. Although it is vulnerable to environmental effects, for accurate thermometry, it must not depend on such environmental variables as strain, pressure, or magnetic field during measurement. The coefficient, $\sigma_M(T)$, is an absolute Seebeck *coefficient* for a particular material, **M**. The corresponding *source* voltage within a single material is an *absolute Seebeck emf*, $E_M(T)$. The absolute Seebeck emf does physically exist, but it is *directly* observable over only a limited cryogenic temperature range near 0 K where it can be related to a superconductive thermoelement reference that has, over the range, a negligible Seebeck coefficient. The absolute Seebeck coefficient at higher temperatures is usually determined indirectly [1–5]. The *Thomson coefficient*, $\tau(T)$, of the individual material is measured. The Seebeck coefficient is determined from a thermodynamic Kelvin relationship as follows:

$$\sigma = \int_0^{T_{abs}} \left(\frac{\tau}{T_{abs}} \right) dT \tag{70.3}$$

70.4.2 Relative Seebeck Characteristics

The difference between the Seebeck emfs of two thermoelements, of materials **A** and **B**, with one end of each at temperature, T_m, and the other ends both at temperature, T_r, is their relative *Seebeck emf*, $E_{AB}(T)$, expressed as

$$E_{AB}(T_m, T_r) = E_A(T_m, T_r) - E_B(T_m, T_r) \tag{70.4}$$

The corresponding relative Seebeck coefficient at T_m for a pair is

$$\sigma_{AB}(T_m) = \sigma_A(T_m) - \sigma_B(T_m) \tag{70.5}$$

Note that these relationships apply whether or not the thermoelements are joined at a junction. The thermally paired segments often are remote in a circuit. It is this relative Seebeck coefficient that has been called by the anachronistic term "*thermopower*." (*Thermoelectric power* appropriately refers to electrical power generated using the Seebeck effect.) It is these *relative* voltage or coefficient values that are directly observable and are used in thermoelectric thermometry. These are the values that are presented in the tables of thermocouple emf vs. measuring junction temperature, T_m, referred to a designated reference temperature, T_r [5]. Standardized thermocouple characteristics, by convention, are referenced to $T_r = 0$ °C.

70.5 Basic Thermocouple Circuits

70.5.1 Thermoelectric Circuit Schematics

Conventional *electric* circuit schematics represent passive conductors that often all are of copper. Distinctively, in *thermoelectric* circuits, paired legs are of very different materials and the "*conductors*" are the emf sources. Much more is involved than circuit connectivity. True thermoelectric schematics must explicitly acknowledge each leg material, all junctions, essential relative junction temperatures, and any complementary voltage sources, as these all affect the Seebeck emf and net thermocouple voltage.

70.5.2 Seebeck's Circuit

Inappropriately, the thermocouple is sometimes defined essentially as a closed circuit of two dissimilar thermoelements joined at two junctions, a "hotter" junction and a "colder" junction, as studied by Seebeck. Based on this unbroken circuit, the Seebeck effect has been wrongly characterized as the occurrence of current in the closed loop, as was electromagnetically observed by Seebeck rather than properly as thermally caused emf. The net Seebeck source emf is indeed proportional to the temperature difference between the two junctions and to a relative coefficient for the paired materials, but that emf results in loop current and IR voltage loss in the typically high-resistance thermocouple circuit. That significantly reduces the net voltage. The Seebeck *emf* for accurate thermometry should be measured in "open-circuit" mode that suppresses current by monitoring with an instrument of relatively large input resistance (e.g., greater than 10 kΩ).

In practical thermometry, no applied thermoelectric circuit has only two dissimilar materials or only two junctions. Typical thermometry circuits have many materials and junctions. Several incidental junctions, if not temperature controlled, can result in significant unrecognized spurious Seebeck emf and error. In each of the two following basic thermocouple circuits, a particular electrical circuit connectivity, but with different materials and temperature distributions, results in very different thermoelectric characteristics and error sources.

70.5.3 Dual-Reference-Junction Circuit

A generalized form of the circuit that is most commonplace in practical thermocouple thermometry (Figure 70.2) involves a single *measuring junction* and one essential pair of isothermal temperature *reference junctions*. Most applied thermocouples also have one or more *optional* extensions. Two are shown. It is this circuit that is used in multimeters like Figure 70.1 and in most thermometry. The primary, *measuring*, thermocouple is a pair of thermoelements, **P** and **N**, that are joined at a single *measuring junction*, **a**. Legs **P** and **N** must have different Seebeck coefficients. The coefficients of either or both can be of either positive or negative polarity.

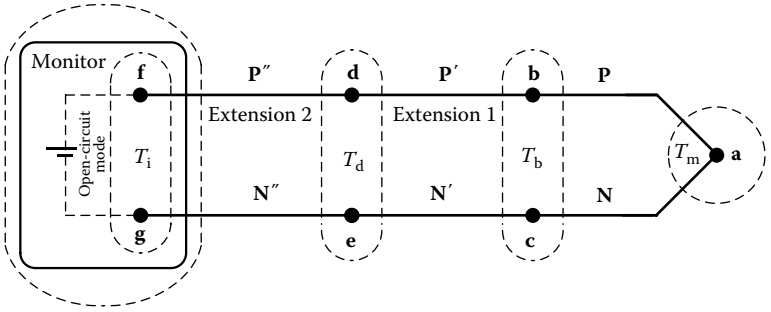

FIGURE 70.2 Dual-reference junction circuit. This most used circuit requires temperature reference to be applied at two junctions at locations in the circuit that depends on the type of optional extensions.

70.5.4 Reference Temperature Compensation

In thermometry, the reference junctions usually are not at the 0 °C reference temperature. Complementary compensation voltage to effect the 0 °C reference temperature is applied internally by the monitor or by an external compensator. (Note that the internal circuitry of the monitoring instrument—and of any compensator—unavoidably is itself a complex thermoelectric network that also contributes an indefinite varying Seebeck voltage unless, after warm-up, it remains stable at sufficiently uniform temperature.)

70.5.5 Types of Optional Extension

In Figure 70.2, pairs **P′N′**, **P″N″** and any additional thermoelement pairs are *optional* circuit extensions. A connector is an extension. Every thermoelement must be homogeneous. Only two junctions may function as the essential reference junctions. Which two depends on the type of extensions? If there are no extensions, **b** and **c** are the reference junctions and are directly connected to the instrument terminals.

In most practical applications, the **PN** measuring thermocouple must be remote from the monitor. In such cases, extension legs **P′** and **N′** (and any additional ones) might be either similar to or very different in Seebeck characteristic from continuous thermoelements **P** and **N** and from each other. Extension leads are of three types: (1) *passive*, (2) *corresponding*, and (3) *compensating*. These types serve different applications. All extension styles are commercially available. Some are proprietary.

70.5.5.1 Passive-Type Extensions

The positive and negative legs of *passive*-type extensions are alike in Seebeck characteristic. As they are alike, they are intended to contribute no significant emf. Usually both legs are of un-plated electrical grade copper, but any conductor could be used. If all extensions are of passive type, reference temperature compensation is applied only at isothermal reference junctions **b** and **c** of thermocouple, **PN**. Compensation must not additionally be applied at the monitor terminals.

As junctions **f** and **g** at the monitor are often remote from junctions **b** and **c** of the measuring thermocouple, they usually are at very different temperatures. With passive extensions, if compensation incorrectly were applied at instrument terminals **f** and **g**, essential Seebeck emf from the temperature interval between T_b and T_i would be missing causing substantial error.

Passive leads often are used with the dual-reference junction circuit in precision calibration. An accurate 0°C reference temperature can be applied to reference junctions **b** and **c** by a fixed-point physical temperature reference such as a precision ice bath. Inappropriate emf contributions of other thermoelements are eliminated. For passive extensions, the temperature value at incidental junctions, such as **d** and **e**, does not matter *if* they are isothermal.

Two other kinds of extension leads are *corresponding* and *compensating* types. They are used where compensating voltage is to be provided by the monitor. For these two styles, the paired extension thermoelements are essential contributing sources of emf. Commercial corresponding- or compensating-style leads, *as a pair*, are of the same nominal thermocouple characteristic as the principal thermocouple but usually they are uncalibrated.

70.5.5.2 Corresponding-Type Extensions

Each leg of *corresponding-type* extensions and connectors for base-metal thermocouples has an absolute Seebeck coefficient of the same nominal type as the corresponding leg of the thermocouple. Corresponding-type extensions contribute emf. They are used with base-metal thermocouples, particularly those many measuring thermocouple assemblies specialized for diverse applications. Extensions can be of thermocouple-grade material. If of extension grade, they might have a broader tolerance and match over a narrower temperature range than the **PN** thermocouple. Corresponding extensions usually are not calibrated. If all extensions are of the *corresponding* type, reference junctions must be at terminals **f** and **g**. They must be isothermal. Extension leads for refractory or precious metal thermocouples are of compensating style rather than corresponding type.

70.5.5.3 Compensating-Type Extensions

The third extension type also is intended to contribute emf. This *compensating* style is used for economy and convenience to extend costly precious or refractory metal thermocouples that are necessary for measuring very high temperatures and for some environments.

Compensating-type extensions can have positive legs that are of different Seebeck coefficient than positive leg **P** and also from other linked positive extension legs. Likewise, negative extension legs are all not like **N**. Rather, each paired *compensating extension* must have the relative coefficient of each extension, as a pair, approximate the σ_{PN} of the **PN** pair.

Usually, only a short length of costly precious or refractory metal measurement thermocouple material has to be exposed to the adverse environment. Extensions can be less costly, insulated differently from the thermocouple, can add bulky shielding and mechanical protection, and can extend a great distance to a recording facility. Often, compensating extensions are made for much higher temperatures than are corresponding-type extensions. However, accuracy is degraded if extensions are used to the higher allowed temperatures because more of the emf is from the compensating extensions than would be from corresponding extensions limited to lower temperature.

70.5.5.4 Extensions of Mixed Type

One or more passive extension pairs and connectors can be used in series with multiple extensions of the corresponding or of compensating types. All emf-supplying extensions and connectors must be nearer the measuring thermocouple than any passive extension. Mixed corresponding and compensating extension pairs can be connected. However, all passive extensions must follow all emf-supplying extensions and must connect to the monitor. The only reference junctions are of the final pair of the emf-contributing corresponding-type or compensating-type extensions. The monitor must not apply additional compensating voltage if the last extension is of passive style. It is essential that the incidental junctions at each end of every extension be isothermal.

70.5.6 Single-Reference-Junction Circuit

Another practical circuit form, Figure 70.3, combines two separate thermocouples and their connectors. The measuring thermocouple is **PN**. The reference thermocouple is **P′N′**. The reference thermocouple often is a commercially fabricated assembly that includes the several components ending with connector terminals, **d** and **e**. The connector of measuring thermocouple **PN** (or any emf-contributing extensions, as **P″N″**) plugs into the reference at **d** and **e**. For calibration, extensions should not be used between the

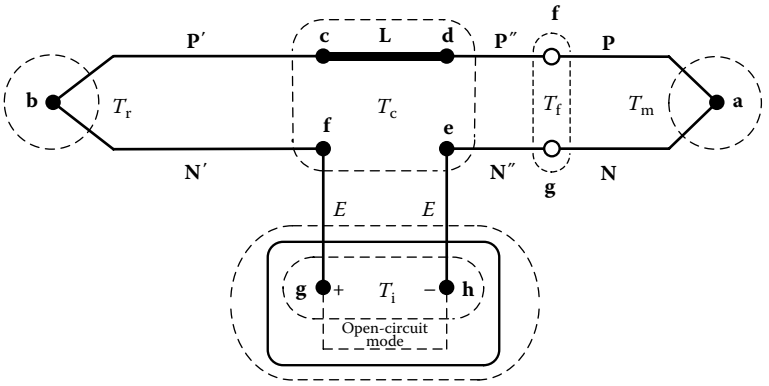

FIGURE 70.3 Single-reference junction circuit. This circuit is often used for convenience in calibration. A reference temperature is physically applied at a single junction.

measuring thermocouple assembly and the reference thermocouple assembly. If extensions are used, they must never be of *passive* type. This circuit is commonly used for convenience in routine calibration laboratories where it is desired to physically impose a controlled and precisely known reference temperature on junction **b**. (For accurate calibration, the circuit of Figure 70.2 with *passive*-style extension is less subject to hidden error, particularly near ambient temperature.)

Typically, in circuits like Figure 70.3, the measuring thermocouple and reference thermocouple are separately acquired thermocouple assemblies. The two thermocouples likely have significantly different Seebeck characteristics even if they are nominally of the same thermocouple type. The calibration of the reference thermocouple initially should be confirmed around room temperature but often it is not. For T_m near ambient temperature, much of the emf is from the reference thermocouple—not from the measuring thermocouple. Therefore, reported calibration of a measuring thermocouple, with contribution from the reference, is misleading at all temperatures. Only if connector link **L** is isothermal, it may be of any material, inhomogeneity, length, or temperature, T_c. The input terminals **g** and **h** of the monitoring instrument may be of any isothermal temperature, T_i. The reference temperature is physically applied and only at **b**. The monitoring instrument *must not* also apply compensation voltage for temperature T_i of the instrument junctions.

70.5.7 Differential Thermocouple Thermometer

The temperature difference between two points often is of interest. The difference emf of a pair of thermocouples of the same type connected in series opposition provides a direct *indication* of temperature difference. However, the difference emf depends nonlinearly on the temperatures. Examples: standard values of emf for the same 100 °C temperature difference of a differential Type *T* thermocouple are

$$T_1 = 20\ °C, \quad T_2 = 120\ °C, \quad \Delta T = 100\ °C, \quad \text{net emf} = 2849.2\ \mu V$$

$$T_1 = 120\ °C, \quad T_2 = 220\ °C, \quad \Delta T = 100\ °C, \quad \text{net emf} = 3204.5\ \mu V$$

$$T_1 = 220\ °C, \quad T_2 = 320\ °C, \quad \Delta T = 100\ °C, \quad \text{net emf} = 3665.3\ \mu V$$

The emfs, therefore the deduced difference temperatures, would significantly disagree. Accurate scaling of emf to temperature would require applying separate nonlinear scaling relations for a known temperature of the thermocouple type. For accuracy, some monitors instead provide dual sets of input

terminals for simultaneous monitoring of a pair of thermocouples of the same type. Either of the measured temperatures is displayed along with the accurate calculated temperature difference.

70.6 Functional Model of Thermoelectric Circuits

The commonplace obscure problems of thermoelectric circuits are difficult to visualize without a graphic tool. Conventional electrical circuit diagrams conceal the actual thermoelectric emf sources, unrecognized thermoelements, incorrect pairings, incidental junctions, and changing functions that often cause significant hidden thermometry error. The spurious "junction-source" model conceals the fact that all thermoelectric problems occur apart from the measuring junction. A general-purpose model of thermoelectric circuits shows what junction temperature structures and relationships must be maintained for reliable thermoelectric thermometry and why.

This nontraditional *Functional Model of Thermoelectric Circuits*, combines (1) a basic thermoelectric circuit element, (2) a single fundamental law that describes the sensitivity of that element, (3) a set of practical corollaries from the law that reveal practical implications, and (4) an informal **T/X** graphic tool for circuit visualization and to aid analysis [2,4,6].

70.6.1 Basic Thermoelectric Circuit Element

A *Seebeck emf cell* (Figure 70.4) is any thermoelectrically homogeneous nonisothermal segment of material **M** of any length within any thermoelement. (An overall inhomogeneous thermoelement is composed of such locally homogeneous segments.) Seebeck emf is dependent on cross section for different metals only if dimensions are less than 50–3500 Å. Each such *homogeneous* segment across which a net temperature difference, ΔT, exists is a *nonideal voltage source* with resistance $R(T)$. (Thermocouple thermometry is rarely of very fast transient temperature change so circuit capacitance and inductance usually are irrelevant.) Therefore, for accurate thermometry, the Seebeck *source emf* must be observed in an "open-circuit" mode (i.e., current effectively nulled by high input resistance.) Any *IR* voltage drop due to current through the resistive thermoelements allowed by too-low input resistance of the voltage monitor lowers the net voltage from the source emf and causes significant error unless compensated.

The emf from each Seebeck Cell was, from Equation 70.2, $\Delta E_M(T) = E_M(T_2) - E_M(T_1)$.

Simply, the net Seebeck emf of the cell can be determined as the difference between the tabulated emf value for the point at $\mathbf{T_2}$ and that value for the point at $\mathbf{T_1}$, both referenced to $\mathbf{T_r}$. Any segments

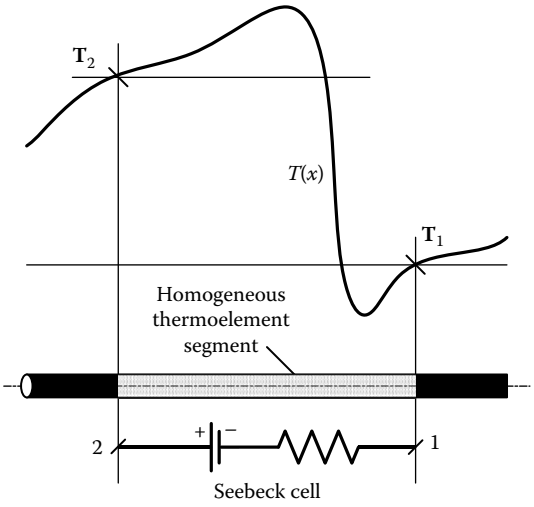

FIGURE 70.4 The Seebeck cell. All thermoelectric emf is produced along thermoelements.

of materials **A** and **B** that happen momentarily to share a pair of endpoint temperatures are *thermally paired*, regardless of their location, proximity, or connectivity in a circuit. The net relative emf for such a pair is $\Delta E_{AB}(T) = E_{AB}(T_2) - E_{AB}(T_1)$ from Equation 70.4. For calculation alone, they need not even be electrically joined.

Either *relative* properties of thermally paired thermoelement segments or *absolute* properties of individuals can be used in analysis. Seebeck properties of a pair, each relative to a third shared reference material, such as standardized Pt-67, also can be used.

Either the Seebeck coefficient, or the sense of the temperature increment across a segment, or both of them, can be either positive or negative. Therefore, unlike an electrochemical cell, the polarity of a Seebeck cell within a circuit depends *momentarily* both on the material and on the sense of temperature difference across the segment. Cell polarity—and even its function—change with temperature distribution.

70.6.2 Law of Seebeck emf

Equation 70.1, $dE = \sigma(T)dT$, is invoked by all quantitative descriptions of the Seebeck effect, whether the description attributes emf to thermoelements or wrongly to junctions. All, in effect, agree that it is the only functional law that governs the Seebeck emf. In this Functional Model, it is named the sole *Law of Seebeck emf*. The Functional Model recognizes that every thermoelectric aspect of circuit behavior follows from this one simple relation.

Note: If this simple relationship does not apply, then accurate thermometry is not possible.

70.6.3 Corollaries from the Seebeck Law

Corollaries express useful and practical truths and implications that may not be obvious from a concisely stated law. Here, they encourage a distinctive way to view real thermoelectric circuits. From the Law of Seebeck emf, five particularly instructive practical corollaries are recognized. The Functional Model corollaries are stated in Table 70.1. These are corollaries of (1) *functional roles*, (2) *functional determinacy*, (3) *temperature determinacy*, (4) *emf determinacy*, and (5) *Seebeck emf*. They are to be comprehended, not memorized. These corollaries relate more directly to practical thermoelectric thermometry than do the commonplace archaic statements of three thermocouple "laws" that actually also are only corollaries of the sole Seebeck Law, not "laws" themselves [2,4]. The significance of the five functional corollaries is illustrated by a nonconventional **T/X** sketch.

70.6.4 T/X Sketch

An informal **T/X** sketch, Figure 70.5, plots one present distribution of *temperatures*, **T**, of all junctions against the *sequence*, **X**, in which those junctions occur in the circuit. (**X** is not a space variable; slopes do not represent temperature gradients.) A **T/X** sketch is not rendered to scale. It is not for graphic calculation. It is only for visualization of momentary functions and consequences.

The **T/X** sketch clearly illustrates how thermoelements, not junctions, function as the physical Seebeck sources. This nontraditional **T/X** sketch is one proper form of thermoelectric schematic that necessarily acknowledges (1) electrical connectivity, (2) junction relative temperatures, (3) leg materials, and (4) any applied reference temperature compensation. The sketch forces attention to problem areas that are not apparent from a conventional electrical schematic nor from alternative traditional **E**(**T**), **E**(**x**), or **T**(**x**) plots. It directs attention to inherently hidden errors so that they can be recognized and avoided.

Note: The practical **T/X** sketch requires no more information than is essential for successful thermometry. If the relative temperatures of incidental junctions are not known and properly controlled, then thermoelectric thermometry is of indefinite accuracy regardless of any perceived calibration.

TABLE 70.1 Corollaries from the Law of Seebeck emf

In any circuit of electrically conducting dissimilar material segments that have absolute Seebeck coefficients $\sigma(T)$, that are each thermoelectrically homogeneous, and each of which follow the Seebeck Law,

$$dE(T) = \sigma(T)dT$$

1. *The corollary of functional roles*

   In a thermoelectric circuit, for any temperature distribution, there are three momentary thermoelectric functional roles: Seebeck emf sources, "conductors," and junctions:

   a. Real thermoelectric *junctions* are interfaces that ohmically connect dissimilar materials
   b. "*Conductors*" are thermoelement segments that, *in effect*, individually or in combination, contribute no net Seebeck emf
   c. All other segments are *sources* of Seebeck emf
2. *The corollary of functional determinacy*

   Thermoelectric roles of segments cannot be *predetermined* by physical construction, material choice, or circuit arrangement alone; they are *determined* by temperature distribution.
3. *The corollary of temperature determinacy*

   In a thermoelectric circuit, only a single junction temperature can be *determined* from the net emf and only if the individual or relative temperatures of all other real junctions are known.
4. *The corollary of emf determinacy*

   Seebeck emf occurs only in thermoelements, but the circuit net Seebeck emf is *determined* by the temperatures of only real junctions.
5. *The corollary of Seebeck emf*

   The Seebeck emf of any thermoelement segment of material, **M**, of any cross-section area,[a] with endpoint temperatures, $\mathbf{T}_1$ and $\mathbf{T}_2$, is independent of *temperature distribution* or of *temperature gradients*, dT/dx, between those endpoints because it is determined only by

$$E_M(T) = \int_{T_1(X_1)}^{T_2(X_2)} \sigma(T)dT = E_M(T_2(X_2)) - E_M(T_1(X_1))$$

[a] Seebeck characteristics of different metals depend on dimension below thresholds of, 30 to −3500 Å.

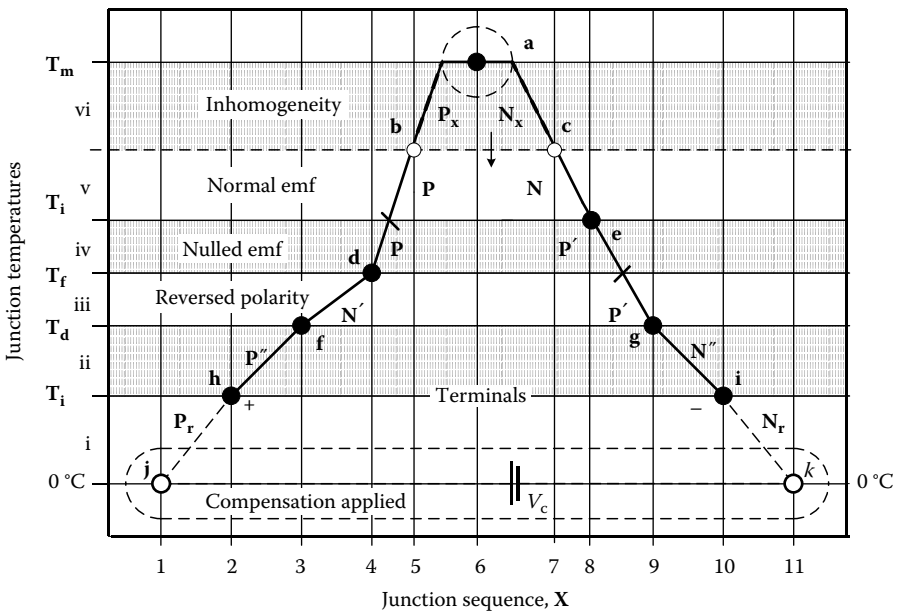

FIGURE 70.5 **T/X** sketch of dual-reference junction circuit. Illustration of sources of error that is due to improper temperature distribution at incidental junctions.

70.6.4.1 Junctions

Filled circles represent real physical junctions between dissimilar thermoelements. *Measuring junctions* are those of which an unknown temperature is to be determined. *Reference junctions* are any of which the temperature must be accurately known and controlled for thermometry. Other real junctions are *incidental junctions*. For incidental junctions, relative temperatures must be controlled to avoid error.

Open circles importantly represent connections only *presumed* to be *splice connections* between identical thermoelements. (Consequentially, these joins, unrecognized, might actually be real junctions between merely *similar* thermoelements or between thermoelements unintentionally misconnected in reversed polarity.) Open circles can also depict indefinite invisible boundaries between initially homogeneous segments and any local segments made inhomogeneous along thermoelements damaged in use. These might not be visible in the physical circuit though effectively they are real junctions.

70.6.4.2 Thermoelements

Thermoelements between the junctions may be shown simply as solid straight lines. Optionally, a conventional electrical cell symbol with indicated polarity and a resistor symbol for segments in each temperature zone may be shown on each leg for clarity, as in some electrical schematics. Usually, these distinctly thermoelectric electrical functions are just understood. Circuit analysis is the same as for regular electrical circuits except that, momentarily, both thermoelectric cell emfs and their polarities are temperature-determined. If numerical estimation of plausible magnitudes of errors is wanted, both the *actual* and *relative* temperatures of incidental junctions must be estimated.

70.6.4.3 Isotherms

Lines are drawn across the sketch at the temperature of every real junction. Isotherms through two adjacent junction temperatures bound a temperature zone that functionally pairs thermoelements. Intercepts of isotherms where they cross thermoelements apart from real junctions may be indicated by *tics* that identify segment ends that can be viewed as nonfunctional *virtual junctions* used only for visualization and calculation.

In a strictly series thermoelectric circuit, all thermoelement segments that span a temperature interval between adjacent isotherms occur in pairs. Each zone contributes to the net Seebeck emf. In such circuits, each temperature zone contributes a specific net *relative* Seebeck emf. Any temperature zone might include paired segments of several different materials. For a temperature zone defined by two temperature-adjacent junctions (e.g., **d** and **e** in Figure 70.5), both the sign and the magnitude of the relative emf as well as which materials are paired depend just on whether the temperature of **d** is greater than or less than that of **e**.

70.6.4.4 Reference Temperature Compensation

Complementary nonthermoelectric voltage sources, $\mathbf{V}_c$, are indicated as dashed equivalent *virtual thermoelements*. Thermocouple monitors or else separate modules might apply such reference junction temperature compensation voltage. It is important to show any compensation voltage source on the **T/X** sketch. Some circuits require that compensation *not* be applied. If applied redundantly or at the wrong junctions, such complementary voltage results in substantial error.

70.6.4.5 Evaluation of emf

Beyond visualization, optionally, the **T/X** sketch can support calculation of zone and circuit emfs. When available, the *relative* Seebeck coefficients of thermally paired materials can be used for direct evaluation of net emf, zone by zone. The values of $E_{AB}(T)$ for each of the thermally paired cells are obtained from the standard thermocouple polynomial defining equations, simpler representations of those equations, tables, or graphs. Alternatively, the emfs of individual standardized thermoelements relative to a particular Pt-67

platinum reference, also tabulated in the NIST defining document, can be used [7]. *Absolute* Seebeck properties for many nonstandardized materials also are known, but are less commonly reported [4].

The relative Seebeck emf from thermoelement segment pairs in all temperature zones is summed from the reference temperature, 0 °C. Like thermoelements that cross the same temperature zone in opposite temperature directions as the circuit is traversed contribute no *net* emf (Corollary 1). They cancel. Any such opposed pairs can immediately be eliminated from analysis by inspection as passive "conductors" that, momentarily, are contributing no net emf. Alternatively, the *absolute* Seebeck emfs could be summed as the **T/X** circuit is traversed on the sketch from one instrument terminal (e.g., the negative), to the other terminal. The two approaches can be intermixed.

70.7 Applications of the Functional Model

A representative **T/X** sketch, Figure 70.5, for a dual-reference junction thermocouple with two extensions, Figure 70.2, illustrates **T/X** application. It shows one deliberately inappropriate yet plausible temperature distribution. It reveals how particular segments of thermoelements, variably, are thermally paired in electrical effect, with different segments that may be remote in the circuit. It also illustrates the commonplace profound effect of unrecognized inhomogeneity in thermometry. The **T/X** sketch, applied here to the two basic thermocouple circuits, depicts the significant circuit elements (the junctions and thermoelements) in a way that focuses on their temperature-determined thermoelectric functions (Corollaries 1 and 2). The **T/X** sketch illustrates realistic, commonplace, yet usually unrecognized, problems of circuits used in thermometry. For illustration, circuits are here depicted with plausible defects or with improperly controlled incidental junction *relative* temperatures. Each kind of error source represented here has been recognized as significant in practical application and even in calibration performed by qualified calibration laboratories. The errors, if not detected, would have significantly degraded thermometry and invalidated costly calibrations. Viewed from the perspective of the spurious junction-source model, the thermal response of such circuits sometimes has been very puzzling.

Note: Though usually hidden, most such commonplace problems are easily recognized, diagnosed, and avoided if thermoelectric principles are understood and applied.

70.7.1 Dual-Reference-Junction Circuit

Figure 70.5 is a **T/X** sketch for an initially homogeneous *then use-degraded* dual-reference junction thermocouple, Figure 70.2, with measuring thermocouple **PN**, junctions **d** and **e**, and two extensions **P′N′** and **P″N″**. This single **T/X** sketch illustrates eight of the commonplace obscure sources of error additional to any calibration, instrument, or thermal coupling error. One or more of these, or other such errors, can occur in any installation. Temperature Zones **i** through **vi** each contribute essential Seebeck emf. Zone **ii** shows the *corresponding*-type extension in appropriate polarity, but Zone **iii** has the extension, **N′P′**, in reversed polarity. (Zone **ii** might have been improperly of a passive-type extension.) Zone **iv** thermally pairs very *similar* segments, **P** and **P′**, inappropriately contributing too little emf. Note that if $\mathbf{T_d}$ is greater than $\mathbf{T_e}$, the emf from Zone **iv** is from a very different thermoelement pair.

70.7.1.1 Inhomogeneous Segments

Troublesome inhomogeneity most often occurs around a severely heated measuring junction. Severe damage, experienced as drift, often is not visible on the thermoelements nor recognized as inhomogeneity in thermometry. Figure 70.5 shows measuring junction, **a**, with adjoining segments of thermoelements appropriately immersed within an isothermal region (as in calibration.) However, heat-damaged segments, $\mathbf{P_x}$ and $\mathbf{N_x}$, extend from junction **a** to phantom real junctions **b** and **c** that bound the damage. This portion of the inhomogeneity, as in calibration, lies partially in the isothermal zone at junction **a**, where it contributes no emf, but it extends to a location of much lower temperature, $\mathbf{T_x}$. (Realistically, the degradation would affect the dissimilar thermoelements differently so **b** and **c** would not likely be isothermal.)

In thermometry, this damage usually spans the highest temperature zone where the effect of its modified emf is greatest in thermometry. (When inhomogeneity is hidden isothermally, recalibration is invalidated.)

70.7.1.2 Electrical Shorting

Note that mechanical damage apart from the junction could incidentally result in a progressive contact short junction between legs, as directly between **b** and **c**. That would result in uninterrupted temperature indication from a different location along the thermoelements and probably at a different local temperature than the perceived measuring junction with no definite warning of serious thermocouple failure.

70.7.1.3 Compensation Scaling Error

This **T/X** sketch illustrates the contribution of reference junction temperature compensation, when needed, by virtual thermoelements $\mathbf{P}_r$ and $\mathbf{N}_r$. The compensation characteristic, which only approximates the standard Seebeck characteristic, is at least slightly different from the one used for scaling the thermocouple emf. Scaling error in this temperature zone can be substantial yet remain unnoticed. That reference affects scaling at all temperatures. Some approximations initially are, or else progressively become, inaccurate.

70.7.1.4 Inappropriate Reference Temperature Compensation

Compensation error is usually unrecognized even if it is significant and variable. It can occur (1) due to lack of needed compensation, (2) as redundant compensation at more than one set of reference junctions, (3) as compensation applied to junctions inappropriate for the extension style, or (4) simply of incorrect value. A similar magnitude of error occurs whether no compensation is applied or whether proper compensation is applied, but redundantly at two sets of reference junctions.

70.7.1.5 Compensation at the Monitor

Typical thermocouple monitors apply compensation voltage at input terminal junctions **h** and **i**. That reference temperature compensation feature should be selectable because compensation sometimes must *not* be applied there. Compensation must be at the monitor terminals for the basic measuring thermocouple **PN** alone or else with complete *corresponding*- or *compensating*-type extensions, **P′N′**, and so on. It must *not* be at the monitor if passive extensions are used.

70.7.1.6 Compensation Apart from the Monitor

If *all* extensions are of the *passive* style, reference temperature compensation must be applied only at terminal junctions **d** and **e** external to the monitor and not also or alternatively at the monitor. If $\mathbf{T}_i$ and $\mathbf{T}_d$ are similar and compensation is improperly applied at the monitor, the error might be small but significant and variable and remain unrecognized. However, if the transition from the measuring thermocouple to extensions is remote from the monitor, those junction temperatures could be very different and the error significant but inconspicuous relative to the indicated temperature.

70.7.1.7 Compensation with Multiple Extensions

Each extension interface risks introduction of thermoelements that might accidentally be of slightly or very different material types, of incorrect style, or else be connected in crossed polarity as by misinterpretation of color codes. Each extension connection introduces incidental junctions. In such instances, the compensation could be misplaced at the measuring thermocouple, at the monitor, between a *corresponding*-style extension and a *passive*-style extension, and so on.

70.7.1.8 Reversed Polarity

Error resulting from polarity reversal of extensions may not be recognized even if it is significant. Misunderstood or contradictory polarity color codes risk accidentally connecting extensions in reversed polarity at **d** and **e** or at **f** and **g** so that the extension, unnoticed, effectively becomes relatively an **N′P′**pairing in the circuit, Zone **iii**. If temperatures of incidental extension junctions are different,

polarity reversal at either end of extension **P′N′** introduces error. Also if an obvious polarity error is noticed in temperature indication and polarity then is merely reversed at the monitor or measuring thermocouple, a different error is introduced. If dissimilar thermoelements are spliced, hidden within insulators or connector shells, along the circuit, the hidden incidental junction can be found with a swept "temperature spike" test (see Section 70.10.2.3.2).

70.7.2 Single-Reference-Junction Circuit

This commonplace circuit, Figure 70.3, is widely used for convenience in routine calibration of a measuring thermocouple, **PN**, as well as for thermometry. Represented by a **T/X** sketch, Figure 70.6, plausible error sources are introduced for illustration. The monitor *must not* apply electronic compensation for this circuit inappropriately as is shown in the sketch.

70.7.2.1 Reference Thermocouple

The reference thermocouple, **P′N′**, of the same nominal type as the measuring thermocouple, usually is separately purchased as an assembly with thermocouple connectors and *passive*-type extension leads, **E**, that contribute no net emf in Zone **iv** as they are of the same type. Except for use in thermocouple type-characterization, they are of a type different from **N**. Usually they are of copper. The measuring thermocouple, **PN**, with optional extension **P″N″**, plugs into the jack of the reference thermocouple assembly at points **d** and **e**.

Reference junction, **b**, should be held accurately at reference temperature, 0°C but is shown at slightly higher temperature. However, as this reference thermocouple is separately fabricated and purchased, reference junction thermocouple, **P′N′**, has a Seebeck characteristic that, even if within tolerance, is different from the **PN** thermocouple. Typically, it is not individually calibrated. As $\mathbf{T_b}$ and $\mathbf{T_f}$ are very different, when the measuring junction temperature is near ambient, all or most of an observed "calibration" emf is from the uncalibrated reference thermocouple even with proper isothermal temperature control of link **L**. Calibration of **PN** is compromised at all temperatures. This systematic reference error source should be acknowledged in a calibration report, but it can neither be eliminated nor corrected.

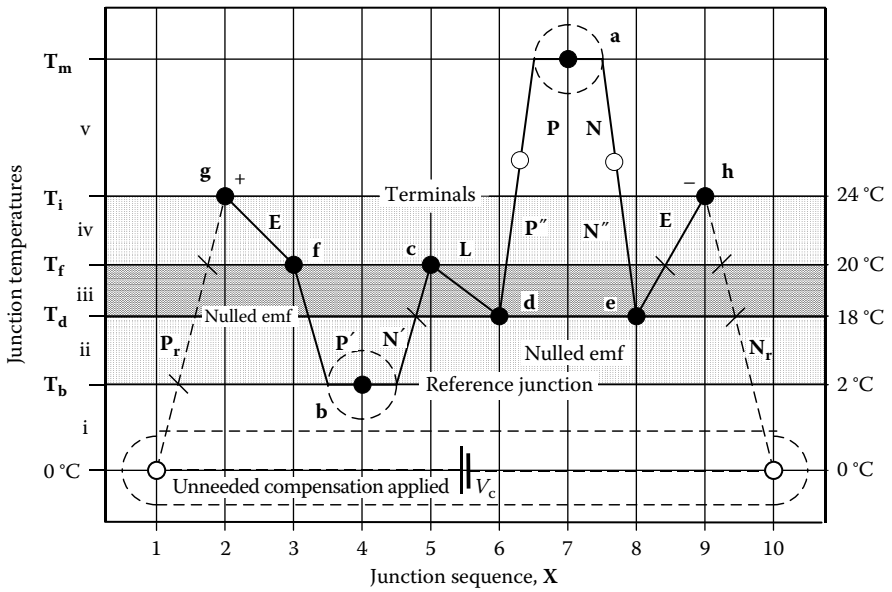

FIGURE 70.6 **T/X** sketch of single-reference junction circuit. Measuring junctions and reference junctions are usually sold as separate assemblies.

70.7.2.2 Incidental Junctions

The connector components, ideally isothermal in Zone **iii**, and the monitor input terminals separately are to be isothermal at temperatures that should both be near ambient temperature. Just as in the dual-reference junction circuit, the temperatures of incidental junctions must be controlled. For illustration of error source, they are shown uncontrolled in the **T/X** sketch (Figure 70.6). Such incidental errors often are not evident in calibration or in temperature indications, even if they are significant.

Fortunately, most of the hidden error sources illustrated in Figures 70.5 and 70.6 are very easily avoided, but only if recognized. Avoidance of most errors by isothermal control of incidental junctions using passive thermal lagging and insulation usually is very easy. A practical significance of the **T/X** schematic is that it forces the attention to specific incidental junctions of which temperatures must be controlled to avoid hidden error. It also guides estimate of plausible error.

70.7.3 Paralleled Thermoelements

In some situations, two or more thermoelements might accidentally be paralleled by electrical contact at widely separate points that are at different temperatures as by multiple shorting of a shield to thermoelements or between multiple thermoelements within a mineral-insulated, metal-sheathed (MIMS) thermocouple. Alternatively, by design, legs of dissimilar paralleled thermoelements have been used as a compound leg, intending to make a leg of customizable relative Seebeck coefficient.

Figure 70.7 shows a circuit with a negative leg paralleled to form a loop by **T/X** sketch. The overall circuit is monitored in the usual "open-circuit" mode, but it includes a closed loop that locally results in current that affects the net voltage. The net loop voltage is affected by temperature-dependent resistance, therefore, by wire diameter and thermoelement lengths. Thus, the effective Seebeck coefficient of the paralleled leg is not a function of junction temperature alone as it must be for thermometry. This is a source of error. The paralleled leg circuit is inappropriate for accurate thermometry but occurs as a defect.

Just for illustration, let thermoelement legs **A** and **B** both be of Type **TP** and leg **C** of Type **TN**. Values for these thermoelements relative to Pt-67 are tabulated by NIST. Resistances of 3 Ft., 22 AWG, legs **A** and **B** are 0.0483 Ω. Leg **C** resistance is, 1.728 Ω. Between junction temperatures 20 and 300 °C, relative to a shared Pt-67 reference, Seebeck emfs for the TP legs would be 3,024.0 μV. Leg **C** alone would contribute 11,048.4 μV. The Seebeck emf would result in a loop current of 4.517 mA reducing the net

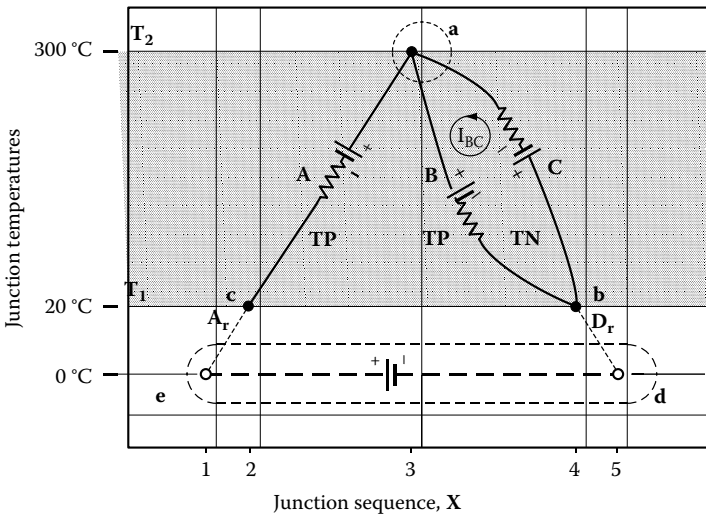

FIGURE 70.7 **T/X** sketch of a paralleled-leg circuit. Thermoelements, paralleled accidentally or by design, are inappropriate for thermometry.

loop voltage to 3242.1 μV. As a normal "open-circuit" **TP/TN** thermocouple, an **AB** pair alone would contribute 14,072.4 μV. Seebeck emf-induced current has reduced the net emf voltage by 10,830.3 μV.

Note: The BC loop is a closed-circuit "thermocouple" as employed by Seebeck.

70.8 Thermocouple Characteristics

70.8.1 Standardized Thermocouple Types

In the United States, nine material combinations presently are letter-designated by the American Society for Testing and Materials (ASTM) as thermocouple types: **B**, **C**, **E**, **J**, **K**, **N**, **R**, **S**, and **T** [7,8]. Representative properties of letter-designated thermocouples are summarized in Table 70.2. They are specialized for use in different temperature ranges and environments. For U.S. standards, Seebeck characteristics are experimentally determined by the National Institute of Standards and Technology (NIST) from samples of the same nominal thermoelement material type provided by several manufacturers. Then, the independent standardizing committee, ASTM, with volunteer members representing manufacturers, calibrators, NIST, and users, prepares a consensus standardizing document based on the NIST data. The standards committee adds commercial tolerances and application recommendations. The standards are only sanctioned by the American National Standards Institute (ANSI).

From measurements at intrinsic standard reference temperatures, NIST defines the Seebeck characteristics, emfs, and coefficients, by $E(T)$ polynomial functions of degrees between 8 and 14, rather than by the tabulated values. NIST then derives the corresponding inverse $T(E)$ values, determined from $E(T)$ by iteration. For application convenience, NIST also presents polynomials of lower degree that approximate the actual characteristics over narrower temperature ranges. Properties of most letter-designated types are published in NIST Monograph 175. The tables are also available at www.nist.gov.

Significantly, it is the relative Seebeck *characteristics* rather than the material *compositions* or alloy *names* that are standardized. The specific alloy composition and metallurgical treatments of actual thermoelements may be varied, as for improved stability, so long as the pair initially conforms to the standard within tolerance. For example, the nominal alloy composition used for **EN** and **TN** legs is slightly different from **JN** thermoelements that share the same alloy name ("Constantan"). Therefore, individual thermoelements should be used as selectively paired for thermocouples by the producer. Randomly paired thermoelements of the same letter-designated type from the same or different manufacturers or batches are not assured to conform to neither standardized paired characteristics nor tolerances. Any thermocouple exposed to excessive high temperature for durations longer than a few weeks might progressively exceed the initial tolerance. (Such thermocouple "drift," incorrectly viewed as global "de-calibration," is from progressing local inhomogeneity.)

The letter designation is complemented by suffixes. A first suffix **P** or **N**, as in thermoelement types **KP** or **KN** of a thermocouple Type **K** pair, distinguishes positive from negative thermoelements. An added final **X** suffix distinguishes *corresponding-type* extension-grade wire material, as in **KPX** for a positive Type **K** extension thermoelement or **KX** for an extension-grade pair. (Some manufacturers distinguish *compensating*-type extensions by a nonstandardized **C** final suffix.) Thermoelement extension-grade wire has the same nominal Seebeck coefficient as the nominal thermocouple type over some temperature range around ambient temperature but has a broader standardized tolerance than thermocouple-grade material.

70.8.2 Color Codes

Both thermocouple letter type and thermoelement polarity should be visually distinguishable. Seebeck *emfs*, *coefficients*, *letter designations*, and *tolerances* of the thermocouple types as standardized in the United States are essentially the same in many international standards [8]. Therefore, it is now functionally possible, *but very inadvisable*, to intermix in a circuit thermoelements of a particular type made to different standards and marked with multiple conflicting color codes. Unfortunately, the *color codes* used to identify these few types in different standards are inconsistent in every possible way. The unfortunate Babel of national color codes that presently exists is displayed in Table 70.3.

TABLE 70.2 Characteristics of the U.S. Letter-Designated Thermocouples

Type	Common Name	Resistivity (mΩ·cm)	MP (°C)	Recommended Range (°C)	emf at 400 °C (mV)	Initial Tolerance (Norm/Special)
B	—	34.4	1810	870–1700	0.787	0.25%
BX	—	—	—	—	—	0.50%
BP	Pt30Rh	18.6	1910	—	—	—
BN	Pt6Rh	15.8	1810	—	—	—
C	W5Re	—	—	0–2315	6.731	4.40%
	W26Re	—	—	—	—	0.11 mV
CPX	—	—	—	—	—	—
CNX	—	—	—	—	—	—
E	—	127	1270	−200 to 870	28.946	1.0 °C or 0.40%
EX	—	—	—	—	—	1.7 °C or 0.50%
EP	Chromel®	80	1430	—	—	—
EN	Constantan	46	1270	—	—	—
J	—	56	1270	0–760	21.848	1.1 °C or 0.40%
JX	—	—	—	—	—	2.2 °C or 0.75%
JP	Iron	10	1536	—	—	—
JN	Constantan	46	1270	—	—	—
K	—	112	1400	−200 to 1260	16.397	1.1 °C or 0.40%
KX	—	—	—	—	—	2.2 °C or 0.75%
KP	Chromel	80	1430	—	—	—
KN	Alumel®	31	1400	—	—	—
N	—	—	—	0–1260	12.974	1.1 °C or 0.40%
NX	—	—	—	—	—	2.2 °C or 0.75%
NP	Nisil	—	—	—	—	—
NN	Nicrosil	—	—	—	—	—
R	—	29	1769	0–1480	3.408	0.6 °C or 0.10%
RX	—	—	—	—	—	1.5 ° C or 0.25%
RP	Pt13Rh	19	1840	—	—	—
RN	Pt	10	1769	—	—	—
S	—	30	1769	0–1480	3.259	0.6 °C or 0.10%
SX	—	—	—	—	—	1.5 °C or 0.25%
SP	Pt10Rh	20	1830	—	—	—
SN	Pt	10	1769	—	—	—
T	—	48	1083	−200 to 370	20.81	0.5 °C or 0.40%
TX	—	—	—	—	—	1.0 °C or 0.75%
TP	Copper	2	1083	—	—	—
TN	Constantan	46	1270	—	—	—

Source: Park, R.M. (ed.), *Manual on the Use of Thermocouples in Temperature Measurement*, 4th edn. or later, MNL12, American Society for Testing and Materials, Philadelphia, PA, 1993; *Annual Book of ASTM Standards, Temperature Measurement*, Vol. 14.03, American Society for Testing and Materials, Philadelphia, PA, 2013.

Chromel and Alumel are trademarks of Hoskins Mfg. Co.

Initial tolerances are for material as manufactured and used within recommended temperature range protected in a benign environment for moderate durations.

TABLE 70.3 International Color Codes for Letter-Designated Thermocouples

Std. No.	ASTM E230-03	IEC 584-3	BS 1843	DIN 43714	JIS 1620	NMI	NFC42 42-323
Letter	United States	Euro	England	Germany	Japan	China	France
B	Brown	—	—	—	—	—	—
BX	Gray	—	—	Gray	Gray	—	—
BP	Gray	—	—	Red	Red	—	—
BN	Red	—	—	Gray	Gray	—	—
C	Brown	—	—	—	—	—	—
CX	Red	—	—	—	—	—	—
CP	Green	—	—	—	—	—	—
CN	Red	—	—	—	—	—	—
E	Brown	—	—	—	—	—	—
EX	Purple	Purple	Brown	Black	Purple		Purple
EP	Purple	Purple	Brown	Red	Red	Red	Yellow
EN	Red	White	Blue	Black	White	Brown	Purple
J	Brown	—	Red	—	—	—	—
JX	Black	Black	Black	Blue	Yellow		Black
JP	White	Black	Yellow	Red	Red	Red	Yellow
JN	Red	White	Blue	Blue	White	Purple	Black
K	Brown	—	—	—	—	—	—
KX	Yellow	Green	Red	Green	Blue	—	Yellow
KP	Yellow	Green	Brown	Red	Red	Red	Yellow
KN	Red	White	Blue	Green	White	Blue	Purple
N	Brown	—	—	—	—	—	—
NX	Orange	—	—	—	—	—	—
NP	Orange	—	—	—	—	—	—
NN	Red	—	—	—	—	—	—
R	Brown	—	—	—	—	—	—
RX	Black	Orange	Green	White	Black	—	Green
RP	Black	Orange	White	Red	Red	Red	Yellow
RN	Red	White	Blue	White	White	Green	Green
S	Brown	—	—	—	—	—	—
SX	Black	Orange	Green	White	Black	—	Green
SP	Black	Orange	White	Red	Red	Red	Yellow
SN	Red	White	Blue	White	White	Green	Green
T	Brown	—	—	—	—	—	—
TX	Blue	Brown	Blue	Brown	Brown	—	Blue
TP	Blue	Brown	White	Red	Red	Red	Yellow
TN	Red	White	Blue	Brown	White	White	Blue

Source: Park, R.M. (ed.), *Manual on the Use of Thermocouples in Temperature Measurement*, 4th edn. or later, MNL12, American Society for Testing and Materials, Philadelphia, PA, 1993; *Annual Book of ASTM Standards, Temperature Measurement*, Vol. 14.03, American Society for Testing and Materials, Philadelphia, PA, 2013.

American-standardized color codes used in the United States and Canada have remained fixed for many decades. Therefore, color code confusion of material types in the United States is mostly due to user error, carelessness, or, infrequently, to flawed coding or labeling in manufacture.

Now, from a single vendor, thermocouple materials are available made to several of the conflicting color codes. The disagreement between color codes could present a costly problem of misidentification, as of polarity. Circuits with multiple extension cables risk crossed-polarity error that may be hidden in thermometry. In the U.S. thermocouple standards, uniquely, the *negative* thermoelement is always coded as *red* (unfortunately, contrary to other common U.S. electrical and instrument practices). This is also contrary to historic national thermocouple color codes of China, Germany, and Japan, in which *red always* designated the *positive* thermoelement. The Japanese standard denotes thermocouple type only by overall jacket color with positive leg always red and negative always white. By U.K. standard, the *negative leg* of all letter-designated types is *blue*. In France, the *positive* thermoelement is always yellow, but both Types **E** and **K** have the same yellow/purple wire in the French code with type distinguished by overall jacket color. In English standards, yellow denotes only the positive Type **JP** material. In the U.S. standards, yellow marks only the **KP** thermoelement and Type **K** thermocouple material. The copper wire leads of some U.S. electric blasting caps use yellow insulated wire with a faint narrow parallel red tracer stripe that, in field use, has been confused with Type **KX** thermocouple extension wire.

The outer jacket of U.S. thermocouples is brown. Extension-grade material is distinguished by a jacket of the color of the positive thermoelement. An IEC standard provides for "intrinsic-safing" of instrumentation that must reside within a hazardous environment but be electrically isolated by electronic barriers from separated monitoring areas. (Intrinsic safety is not addressed in U.S. thermocouple standards.) For uniform distinction of the intrinsic-safe class of application, even the low-voltage thermocouple circuits uniformly must be distinguished by a blue outer jacket. Special materials and electrical parameters may also be specified. Nevertheless, the thermoelectric characteristics of intrinsically safe and regular thermocouples are functionally identical. The user should confirm the material of each leg.

70.8.3 Thermocouple Selection

Thermocouple type selection is based on temperature range, compatibility with environment, sensitivity, wire size, cost, and user access to compatible indicators.

70.8.3.1 Temperature Range

Base-metal thermocouples cover the range from –200 °C to 1260 °C (Table 70.2). Higher temperatures require more expensive precious or refractory materials that extend the available upper limit to 1700 °C.

70.8.3.2 Environmental Compatibility

Potentially harmful environments are classified as oxidizing, oxygen-poor, neutral, vacuum, reducing, radiation, sulfurous, and so on. Thermocouples and sheaths react adversely to some environments depending on temperature range. A thermocouple type is best suited for one or more of these environments but often is very unsuited to the others. An adverse environment locally introduces inhomogeneity into thermoelements and breaches protective sheaths. Merely conditional recommendations are summarized in Table 70.4. Unfortunately, some environments alternate between incompatible conditions or simultaneously combine them. Thermocouple suppliers should be consulted for material recommendations for especially difficult situations that involve harsh chemical or radiation environments or mixed environments. Trial may be required.

70.8.3.3 Sensitivity

Relatively low emf once was a major limitation of thermocouples. Now, commonplace modern thermocouple monitoring instruments, in "open-circuit" (nulled-current) mode, can routinely indicate temperatures to 0.1°C or even 0.01°C resolution and stability with excellent noise rejection for all

TABLE 70.4 Environmental Tolerance of Letter-Designated Thermocouples

Type	Oxygen Rich	Oxygen Poor	Neutral	Reducing	Hydrogen	Humid	Vacuum	Below 0 °C	Sulfurous	Neutrons
B	Good	Good	Fair	Poor	—	Good	Fair	Poor	Poor	Fair
C	Bad	—	Good	Good	Poor	—	Good	—	—	—
E	Good	Poor	Poor	Poor	—	Good	Poor	Good	Poor	Poor
J	Fair	Good	Good	Good	—	Poor	Good	Poor	Fair	Poor
K	Good	Poor	Poor	Poor	—	Good	Poor	Fair	Poor	Good
N	Good	Fair	Fair	Poor	—	Good	Poor	Good	Fair	Good
R, S	Good	Good	Fair	Poor	—	Good	Poor	Fair	Poor	Poor
T	Fair	Fair	Fair	Good	—	Good	Good	Good	Fair	Poor

Source: Park, R.M. (ed.), *Manual on the Use of Thermocouples in Temperature Measurement*, 4th edn. or later, MNL12, American Society for Testing and Materials, Philadelphia, PA, 1993; *Annual Book of ASTM Standards, Temperature Measurement*, Vol. 14.03, American Society for Testing and Materials, Philadelphia, PA, 2013.

letter-designated thermocouple types. Thermocouple tolerances are much larger. As seen in Table 70.2, the sensitivities of various types are very different. Precious and refractory metals have less than a quarter of the emf of the least sensitive Type **N** base-metal thermocouple.

70.8.3.4 Wire Size

Bare thermoelement material is readily available in diameters from 0.13 mm (0.0005 in.) to 3.3 mm (0.128 in.). Thermoelements of all diameters are sold separately or else matched as a thermocouple pair with standard tolerance. The finer wire sizes have less effect on the temperature being measured but degrade more quickly. Upper temperature limits vary with wire size (Table 70.5). Fine wires are favored for transient thermometry, where space is limited, or for fine spatial resolution. Thermoelement resistance is not a factor in nulled-current thermometry. Some special applications favor thin foil or film thermoelements.

70.8.3.5 Cost

Thermoelement and thermocouple wire is available bare or in a wide variety of insulants ranging from vinyl, Kapton®, and Teflon® to glass or ceramic fiber with metal over-braid. The price varies irregularly with material and diameter. Typically, the lowest price is for bare wire of mid-range diameters between 20 and 28 AWG. Price depends more on diameter than on material. The much larger and very fine diameter wires are more costly. Present unit price ranges widely between $0.24 and $5.28/ft over the range of available wire sizes.

TABLE 70.5 Temperature Upper Limits for Different Wire Diameters

Dia., mm	0.025	0.127	0.254	0.330	0.510	0.813	1.600	3.175
Dia., in.	0.001	0.005	0.010	0.013	0.020	0.032	0.063	0.125
AWG	50	35	30	28	24	20	14	8
Type	Temperature Limit, °C							
B	—	—	—	—	—	1,700	—	—
C	—	—	—	—	—	2,315	—	—
E	290	325	370	430	430	540	650	870
J	230	275	320	370	370	480	590	760
K, N	690	730	760	870	870	980	1090	1260
R, S	—	—	—	1480	1480	—	—	—
T	90	110	150	200	200	260	370	—

70.8.4 Standardized Tolerances

ASTM standardized tolerances for as-manufactured thermocouple materials are established by committee formal consensus judgment of many experienced producers, users, and calibration standards laboratories staff [8]. Manufacturers characterize the Seebeck property typical of a production batch by calibration of one or more surrogate samples. Sampled first-cycle calibration is taken to be representative of all other thermoelements of the same batch. No authentic inhomogeneity tests are performed. Inhomogeneity has been shown usually to be well within tolerance for new material. Once conformity to standardized tolerance is affirmed, rather than the specific calibration, the standardized type-characteristic is often attributed to the entire batch. Standardized tolerances include not only overall deviation from the standardized Seebeck properties, but also cover inevitable small uncertainty from tolerable inhomogeneity and, in application, even possible irregular deviations, over small temperature spans, of user-simplified scaling relations from the standardized characteristic.

Tolerances apply only initially and briefly to material as delivered, not exposed to excessive temperature or adverse environments. The initial tolerances for standard letter-designated thermocouple types are presumed to be reliable until the thermocouples are exposed to an aggressive environment or for a few weeks at excessive temperature. Thermocouple tolerances are additional to uncertainties of monitoring instruments and of thermal coupling and mass.

There are separate initial tolerances for *normal-* and for *special-grade* material. Initial percent tolerances of ordinary material may be double or more of that of special-grade material. Yet the different degree uncertainty between *commercial-* and *premium*-grade tolerances is small and the cost premium is large (but less than the cost of individual calibration). In severe use, special-grade materials can quickly degrade to exceed the initial tolerances of normal-grade material. Additionally, ASTM Standard E235-06 specifies special requirements for Types **K** or **N** thermocouples destined for nuclear or high-reliability application.

70.8.5 Other Thermocouple Types

70.8.5.1 Standardized Non-Letter-Designated Thermocouples

Some less used commercial thermocouple pairs are for specialized use in thermometry. Some alloys are proprietary. These have not been formally standardized by letter designation or color code. Though not letter-designated, Seebeck properties of some commercial alloys that have significant use are addressed in ASTM Standard E1751 that presents NIST-defined Seebeck properties. Most are relatively expensive high-temperature alloys that promise benefits of accuracy, stability, and environmental tolerance for special application. These include elemental pairs, Au vs. Pt, Pt vs. Pd, and Platinel®, a proprietary thermocouple alloy of Englehard Industries that has Seebeck characteristics very similar to Type **K** with improved stability and accuracy and with greater sensitivity than other precious metal materials. The very pure precious metal thermocouples initially can be very accurate but are particularly vulnerable to contamination and introduced inhomogeneity in use. Infrequently, as usage broadens, additional commercially popular materials are considered for standardization.

Producers and vendors apply proprietary trade names to letter-designated types. A few apply their own unofficial letter designations and color codes. Informal designations might be inconsistent between sources. Identifiers assigned by individual manufacturers have no universal meaning. Letter Type **U** is ambiguous. German standard DIN EN 60584-1 specified thermocouple Type **U** as Cu vs. CuNi with brown jacket, red positive, Brown negative. However, that letter also has ambiguously been used to denote a Cu/Cu pair used as a passive thermocouple extension or for RDT or thermistor wiring. Seebeck characteristics and informal color codes for nonstandardized materials should be confirmed by the vendor.

70.8.5.2 Unconventional Thermoelement Materials

Any thermoelectrically dissimilar pair of conducting materials can form a thermocouple. The *absolute Seebeck characteristic* of thermocouple platinum, Pt-67, a common thermoelectric reference material, was determined by the Center for Information and Numerical Data Analysis and Synthesis of Purdue University under contract to, but not published by, NIST. Others have published the E(T) absolute characteristic for platinum as well [5,9,10]. Limited information on Seebeck properties and application for a multitude of nonstandard materials used as thermoelements is available in papers or in one useful compendium [10]. Most such combinations have not been used widely and are not appropriate for general thermometry.

70.9 Thermocouple Hardware

70.9.1 Material Sources

Thermoelectric alloys and thermoelements are manufactured by a very few specialized sources. These manufacture bare thermoelement bar stock, wire, and foil, and selectively pair thermoelements for thermocouples. Fewer sources fabricate the MIMS (see Section 70.9.3.5) thermocouple materials that are incorporated by others into finished products. These producers of basic forms and very many other sources fabricate these starting forms into finished specialized thermocouple cables and a multitude of products. Few vendors of thermocouples make the thermoelements. Some vendors do not manufacture thermometry products they offer.

70.9.2 Quality Assurance

Pioneer thermocouple users worked with commercial-grade metals and alloys that were not controlled for thermoelectric sensitivity or homogeneity. Each thermocouple had to be individually calibrated and tested for uniformity. Now, thermoelectric quality assurance is first applied by the thermoelement manufacturer. However, properties might later be modified during additional fabrication. Additional thermoelectric testing could be performed by the provider of the final thermocouple product. Infrequently, through the production chain, materials might be modified or misidentified in type or color code. The prudent user confirms the materials.

70.9.3 Forms of Thermoelements

70.9.3.1 Bar Stock

Some thermoelectric products, such as links, connectors, foil, and so on, require bulk feedstock available in a form not usually seen by consumers. The processed materials may be re-characterized as later fabricated. Circuit components that are short and of high thermal conductivity tend to remain nearly isothermal in application; therefore, they introduce little Seebeck emf.

70.9.3.2 Foil and Film

The Seebeck coefficient of metals is independent of material dimension down to about 3500 Å, or even much less, thickness. Commercial thermoelement foils have thickness down to 0.013 mm (0.0005 in.), leaf to 0.01 in. Vapor-deposited alloy films, properly conditioned, can have Seebeck characteristics like thicker material. That allows fabrication of intricate thermoelectric circuits. Very thin thermoelements are more vulnerable to mechanical damage and degradation than are the wire sizes most used in thermometry. Rolled thin foil, ribbon, or vapor-deposited film thermoelements are used in thermocouples specialized for transient or much localized thermometry.

70.9.3.3 Wire

Thermoelements are most familiar to users as wire or cylindrical rod in diameters from 0.013 to 3.3 mm (0.0005–0.128 in.) or more. Individual or thermocouple-paired bare thermoelement wire is available

to consumers. Such bare materials are not indelibly identified by color code. Identification is by label. Labels are easily separated from the material. It is important to maintain identification of all thermoelectric materials by type, color code, source, and batch throughout their use. Individual thermoelement wire is also available with color-coded insulation. Insulating tubing in all the international coding colors is available for use on bare thermoelements. Casually applied by a user, the color code might be incorrect or misinterpreted.

70.9.3.4 Cable

A very wide variety of measurement and extension-grade thermoelements and thermocouple pairs are available cabled as insulated in thermally and chemically resistant plastics and other materials. Individual pairs in solid or stranded form may be covered with protective insulation and wire braid or shielding foil. For severe duty field and process industry use, they are assembled into cables of many separately color-coded pairs that have mechanically and chemically resistant jackets. Some have rugged steel reinforcement. Special connectors can connect extension cables of 24 or more thermocouple pairs.

70.9.3.5 Mineral-Insulated, Metal-Sheathed Thermocouple Material

Many fabricated thermocouple assemblies have thermoelements tightly drawn within a thin-walled tubular metal sheath. Such bulk material is available drawn to overall diameters of 0.075–6.35 mm (0.003–0.25 in.). Materials are controlled to conform to ASTM E585. The process results in highly compressed mineral insulation that allows bending to a radius as small as a few sheath diameters without harm. Many measuring thermocouples of special design use MIMS thermocouple construction. Needle-sized hypodermic probes must be rigid; lengthy small-diameter material is very flexible.

High isolation resistance between thermoelements is essential. The crushed insulant is very hygroscopic. The resistance is difficult to maintain in very small-diameter MIMS material. Immediate sealing is particularly important for MIMS material of small diameter. Ends opened for fabrication must be quickly sealed to avoid absorption of moisture that decimates resistive isolation of thermoelements. Special epoxy sealants are used for the lower temperature end. Sealants for the exposed measuring junctions of MIMS thermocouples require fused glass or other high-temperature material. Such seals may breach in service.

MIMS material is available in all standardized thermocouple types. Different sheath and insulation materials are adapted to a variety of application environments and to temperatures up to 2315°C. MIMS thermocouple material as seen by most users is as commercially fabricated into the variety of special measuring thermocouple assemblies. Like bare wire, the bulk MIMS material is not color-coded. It is identified by batch or product label.

The sheath of a MIMS thermocouple can contain several thermoelements of the same or different thermocouple types. Additionally, for concurrent longitudinal temperature profile measurement, several individual small-diameter MIMS thermocouples can be enclosed and swaged tightly within an overall metal sheath with measuring junctions longitudinally spaced at intervals.

The thin-walled MIMS thermocouple sheaths appear impervious to external contaminants but unrecognized pinholes and fine cracks can allow penetration of moisture or other contaminants. Some surrounding materials at very high temperature can actually diffuse through intact sheaths. Moreover, constituents of the sheath alloy or of its thermoelements can migrate through intact mineral insulation to locally affect the Seebeck properties of the thermoelements.

An externally similar less costly metal-sheathed form simply encloses insulated thermoelements loosely within a tubular sheath without drawing. This less expensive rigid form cannot be bent. It lacks most benefits of MIMS construction.

70.9.4 Insulation

Formerly, most measuring thermocouples were of bare wire insulated using simple ceramic beads. Beads of nesting fish-spine and many other forms still provide flexible high temperature insulation

for bare thermoelements. The insulators and exposed thermoelement are vulnerable to contamination. Specialized insulators now include lengthy rigid cylindrical forms with one to six holes for thermoelements. Lengths may be up to 5 ft. Some are usable to temperatures up to 1600 °C. Typical materials are alumina or mullite. Diverse applications require a variety of insulating materials of different forms and costs adapted to particular temperature ranges.

Individual thermoelements and thermocouple pairs usually are insulated by flexible insulation. Typical materials are Kapton, Teflon, and glass or ceramic braid. Flexible insulation temperature upper limits range from 230 °C to 1200 °C. Extension pairs are normally exposed to temperatures near room temperature. Insulations of connectors or extensions may be rated to 220 °C or even to 650 °C. However, if used to such high temperatures, a significant part of the emf will be from the uncalibrated extension rather than from the measuring thermocouple.

Special thermally conducting and electrically isolating silicone pastes and epoxies are used for coupling or temporarily bonding thermocouple sensors to the test subject. Typical temperature limits are between −40 °C and 200 °C. Special adhesives for thermal coupling, electrical isolation, and bonding are for use to 260 °C.

70.9.5 Connectors

Quick-connect plug and jack connectors using thermoelement materials as contacts are of full, miniature, and sub-miniature sizes with either two or three pins. For MIMS dual element thermocouples, four-pin styles are used. The largest pin marks negative polarity. Pins can be of cylindrical, flat, or banana-plug form. Other styles include specialty connectors of circuit board or "Sub-D" form and multipin connectors for 25 or more pairs. For thermometry in electrically noisy environments, connectors for shielded cable add shield continuity straps. Some have built-in ferrite core noise filters. Most connector shells are of plastic with temperature limits up to 220 °C or of ceramic rated to 650 °C. Connector shells are color coded like the associated thermocouples. For large installations of multipair cable, special barrier terminals or panel-mounted connectors, maintained isothermal, can be used.

Some thermocouple measurements must be made within high-pressure or vacuum chambers. The circuit must cross an impervious wall. The temperature difference across thermoelectric feedthroughs is likely to be much greater than for connectors used near ambient temperature. Therefore, they are more subject to error than are quick-connects. An alternative penetration method uses a compression-style feedthrough that allows several uninterrupted insulated thermoelements to pass sealed through a wall while maintaining pressure or vacuum integrity. That avoids adding incidental thermoelements.

70.9.6 Thermocouple Junction Styles

Junction designs vary widely for specialized application. Most junctions are very localized. Some, to average surface temperature along a line, have widely extended a junction between foil thermoelements. Measuring and reference junctions are conspicuous. However, the many incidental junctions are inconspicuous and may not be recognized yet, uncontrolled; their temperatures can significantly degrade accuracy.

70.9.6.1 Contact Junctions

The area of contact between thermoelements has no influence on the Seebeck emf *if* thermometry is performed under proper nulled-current conditions. An electrical point contact is as effective as contact over a broad area. A pair of pointed probe tips contacting a conducting subject closely spaced can serve as the measuring junctions to measure local temperature. The characteristic emf difference between a pair of well-spaced thermocouples with contact measuring junctions heated at two different controlled temperatures can be used to identify metals. Temporary measuring junctions can be formed merely by holding or taping together crossed thermoelements. Thermoelements accidentally shorted by contact

apart from the measuring junction monitor temperature where shorted, not at the intended measuring junction. In calibration, ends of thermoelements often are electrically connected to extensions by immersing bare tips into a bridging isothermal pool of mercury in an ice bath.

70.9.6.2 Intrinsic Thermocouples

If the subject of thermometry is an electrically conductive material, tips of the two thermoelements can be fused directly to the test subject as by spot welding. These form junctions of an "intrinsic" thermocouple. Closely spaced fine wires or thin foils spot-welded to the subject allow the fastest possible electro-thermal response and reduce the influence of the thermocouple on the temperature being measured. For fastest response, the two thermoelements should be fused to the subject nearly in contact side-by-side or end-to-end (but not one over the other). As the fused spots are very close together, they tend to be nearly isothermal even in transient thermometry so any bridging conductive subject material has negligible effect on the Seebeck emf. However, if the points of fusion are widely separated, the nonisothermal bridging conductor of indefinite thermoelectric property can contribute spurious emf to the measurement while the two weld spots are at different transient temperatures.

For transient thermometry, the thermoelements at the intrinsic junctions should be short and as fine as feasible to reduce thermal loading. A strain-relieved transition from the fine filaments to more substantial *corresponding-type* extension wires should be made. The effect of circuit capacitance or inductance on electrical response is significant only in transient thermometry. As the intrinsic junction is electrically common to the subject, circuit grounding and isolation must be appropriate.

70.9.6.3 Twisted Junctions

A temporary junction contact can be formed merely by twisting together ends of dissimilar wire thermoelements. Twisted junctions may also be soldered or tip-welded for strength. Such robust elongated connections do not affect the Seebeck emf as the sensing junctions are the dual interfaces where the adjacent thermoelements first contact the twisted section. The mass of the extended twisted section only slows thermal response and thereby can affect the temperatures of the junctions and the subject. Such junctions are not used for transient thermometry.

70.9.6.4 Fused Junctions

The familiar "bead-junction" style of thermocouple is formed by fusion of paired thermoelements. Specialized thermocouple welders perform the melt in a localized inert atmosphere to reduce local oxidation of the thermoelements. The spheroidal bead is neither the "junction" nor an emf source. Its purity is irrelevant. The bead is an indeterminate thermoelement alloyed from the joined thermoelements. It is the *interfaces* between the bead and thermoelements that are junctions. They function as one if the bead is isothermal.

Compact junctions are formed by spot welding of crossed thermoelements. The free ends can be trimmed to leave a small robust junction. A very compact junction can also be formed as a smooth "butt-weld" for thermoelement wires as small as 0.003 in. diameter fused end-to-end.

70.9.6.5 Enclosed Junctions

The metal sheath of a mineral-insulated (MIMS) style thermocouple usually encloses two or more thermoelements. Thermoelements can be of different thermocouple types. Thermoelements may be paired with separate junctions or several legs may share a common junction as a "tip-branched" thermocouple. Junctions usually are enclosed within the sheath and are either isolated from or made electrically common with the closed sheath tip. Isolated "junctions" are fused beads insulated within the enclosed end of the sheath. A form with junctions electrically common to the sheath tip inappropriately is termed a "grounded junction" even though it may not be electrically common with the important circuit "electrical ground" point (i.e., "grounded" junctions might be electrically "isolated" from electrical power reference ground). Alternatively, bead-style junctions, bare or insulated, can extend outside the sheath

for faster response. The sheath end must be sealed immediately and remain sealed. A short span of the MIMS material tip that includes enclosed junctions can be drawn to reduced diameter. Such thermoelements are reduced proportionately in diameter. The reduced tip diameter speeds transient response and localizes temperature measurement.

70.9.7 Specialized Thermocouple Assemblies

70.9.7.1 Measuring Junction Assemblies

The simple Seebeck phenomenon invites more diverse specialty thermometry designs than any other thermal sensing technology. Seebeck would be astonished! Process, industrial, and scientific applications for thermocouples now are specialized to diverse applications. Manufacturer's catalogs present dozens of variations. These fabricated assemblies may conceal the functional measuring junction and adjacent thermoelements and circuit components within housings that are designed for convenient handling and for protection. Thermoelements of these specialty forms might be subjected to degrading mechanical treatment in fabrication. The irregular geometries and size, and the fact that sensitivity is distributed rather than localized to the measuring junction, complicate calibration and homogeneity verification.

Most specialized thermocouple assemblies are of the dual-reference-junction circuit style of Figure 70.2, except that they contain many more inconspicuous incidental junctions and thermoelements. For ease of connection, each packaged measuring junction assembly is fitted with a thermocouple plug connector that mates through a connector jack to extension cables or instruments.

The concealed measuring junction, incidental junctions, thermoelements, and extensions are subject internally to all the problems illustrated by the Functional Model for dual-reference junction circuits. The distributed nature of the Seebeck emf requires an authentic understanding of thermoelectric circuits to recognize sources of significant thermoelectric error concealed within assemblies.

70.9.7.2 Reference Junction Assemblies

Most specialized thermocouple assemblies are for use as measuring junctions. As a convenience, a few thermocouple assemblies are specialized to physically apply the 0 °C temperature references as in Figure 70.3. Such reference junction assemblies form most of the thermoelectric circuit as they combine the reference junction with extension leads and connectors. The separate measuring thermocouple simply plugs into the assembly. Though convenient, that reference system is not best suited for accurate calibration.

Resembling a regular color-coded connector, an optional battery-powered Reference Temperature Compensator can bridge the measuring thermocouple and its passive extension with regular thermocouple plug and jack connectors. Inserted near the measuring thermocouple assembly, the compensator electronically applies reference voltage to place the reference junctions effectively at the conventional 0 °C reference temperature. This component, used only with passive-style extensions, is usually joined directly to the measuring thermocouple or its "active" extensions. If this local reference is used, the remote monitor must *not* redundantly apply additional compensation. The connector-like reference is small so it allows the reference compensation to be individually oven-calibrated over the temperature range near ambient temperature.

70.9.7.3 Wells

Process thermometry may require the measuring junction to be isolated from a chemically damaging or mechanically abrasive environment, sealed from pressure or vacuum, or to isolate a sanitary process from the thermocouple. Thermometry, as of incinerators, thermal reactors, and coal gasifiers, is a severe challenge because vibration and the chemical environment are particularly destructive of refractory thermocouples required for the high temperatures. Thermocouple-specialized metal, ceramic, or plastic

wells extending sealed into a process allow replacement of the sensor without interruption. These rugged thick-walled metal or ceramic wells separate the junction from direct contact with the process so they are used for thermometry of steady or slowly varying temperatures. Special wells can flow protective gases along the thermoelements adjacent to the junction. The wells usually are used with MIMS thermocouples that must be seated and thermally coupled in good thermal contact with the well. These massive protections with lengthy immersion depths also beneficially tend to place the measuring junction in a nearly isothermal region where locally degraded segments near the junction contribute less spurious emf.

70.10 Quality Assurance by Users

Manufacturers routinely apply quality control to their thermocouple products, yet users are responsible locally to assure that no occasional defect, error, or change has occurred in manufacture or installation. Several simple and routine test procedures are available to the user.

70.10.1 Thermoelement Identification

Color codes apply to extension-grade wires, to insulated thermocouple-grade wire, and in principle to bare thermocouple wire. Bare wires are not indelibly color-coded. An installer very skilled in electronics might not be familiar with the distinctive thermocouple codes or their consequence. Thermocouples of the same letter-designated type but of different international standards have different international color codes for both type and polarity. The prudent user, before installation or application, will confirm material-type identification of each thermoelement independent of the color code. Definite type identification must be by a combination of methods. A single identification method may be indefinite. No method fits all materials or circumstances.

70.10.1.1 Visual Identification

Type **TP** thermoelements are of copper. Bare, they are visually distinguished by their distinctive reddish color. **JP** thermoelements are of iron and have a distinctive matte gray cast. Other base-metal alloys and platinum and its alloys, if bare, are not easily distinguished by appearance. Usually they all have a similar bright silvery appearance unless, if heat treatment or if bared from compressed mineral insulation, fabrication has produced a roughened gray matte surface appearance.

70.10.1.2 Magnetic Identification

A type **JP** (iron) leg is strongly magnetic. Type **KN** is only weakly magnetic. All other standard thermoelement materials are nonmagnetic. **JP** and **KN** thermoelements can be distinguished from the others by testing the relative attraction to them of a small magnet.

70.10.1.3 Resistive Identification

Thermocouple assemblies or cables usually have paired thermoelements that are of the same length and wire size. If the temperatures of the ends are about the same, the resistance of each thermoelement and the ratio between leg resistances are diagnostic for identification of the materials. Room temperature resistivities of thermoelements are given in Table 70.2. If the identity of one thermocouple or a thermoelement of a batch of like material, wire size, and length is determined, the others can be confirmed by comparison of loop resistances. Resistance measurement of isolated individual thermoelements requires that both ends be accessible at the same location and temperature. For assembled thermocouples with inaccessible measuring junctions, only the isothermal loop resistance can be measured and compared with calculated loop resistances. This quantitative loop resistance measurement is complicated by Seebeck emf that can affect apparent resistance if the circuit ends are at a substantially different temperature.

70.10.1.4 Thermal Identification

Less conveniently, a pair can be identified by the terminal voltage or indicated temperature for a known temperature of measuring junction and the reference junction. Definite identification does not require the accuracy of formal thermometry. Reference junction temperature may be applied by simple ice bath or compensation by the monitor. An independently known temperature, at least 200 °C, applied to the measuring junction for identification is required. Otherwise, uncertainty of the thermocouple calibration and of the imposed temperature would make the emf distinction of thermocouple pairs unreliable, such as **E** from **J** and **K** from **N** or **T** by using a 100 °C boiling water bath. Very similar types **R** and **S** (that have identical color codes) can be reliably distinguished only at much higher temperatures or by formal calibration.

70.10.2 Active Tests

70.10.2.1 Symptom and Occurrence of Inhomogeneity

Thermoelectric inhomogeneity, though now widely misunderstood, has long been recognized as a very real and commonplace problem of thermocouples applied in damaging circumstances. Modern production of thermoelements now results in only slight, but measurable, irregular longitudinal variation of Seebeck coefficient, $\Delta(T, x)$, distributed along the full length of a thermoelement. Maximum deviations of $\Delta(T)$ typically are a very small fraction of the standard tolerance. The risk of significant inhomogeneity in as-received new wire material is slight.

Inhomogeneity that is significant in thermocouple thermometry occurs as a broad localized distinctive deviation from the initial uniform Seebeck coefficient. Recognizable drift during measurement of a temperature expected to be constant is always a symptom of progressing inhomogeneity. Inhomogeneity rarely is authentically tested in commercial practice or by calibration laboratories.

Profound inhomogeneity very often results from prolonged use at high temperature, in a harsh environment, or during fabrication. Most often, significant inhomogeneity is caused or aggravated by excessive temperature so it usually occurs broadly distributed adjacent to the measuring junction precisely where it has the greatest adverse effect in thermometry when junction temperature varies. Less often, it results from defective insulation, metallurgical interaction between thermoelements or with their insulant, evaporation of alloy constituents, or from exposure to higher temperature regions or chemical attack remote from the measuring junction.

Conventional NIST-traceable precise and costly calibrations might sincerely but incorrectly be certified even if a degraded thermocouple can accurately be measured to be locally *severely* inhomogeneous and of indefinite uncertainty as actually applied in thermometry. Most troublesome inhomogeneity is unrecognized even by experienced thermocouple users. Therefore, inhomogeneity remains a commonplace, very real, but usually discounted problem. Display of the distribution of such inhomogeneity requires a special test.

70.10.2.2 Authentic Inhomogeneity Test Methods

A consequentially inhomogeneous segment has, for a test temperature step, ΔT at $\mathbf{T_a}$, a deviant Seebeck emf, $\Delta E(x)$, which is significant relative to initial tolerance. The objective of inhomogeneity testing is to identify locations, longitudinal distributions, and the relative amount of deviations from the initial Seebeck coefficient along thermoelements. The inhomogeneity test is used only to disqualify for calibration or thermometry. It is not a recalibration. Inhomogeneity identified by scanning a 100°C step above ambient temperature is adequate to disqualify a thermocouple for use or recalibration. While the relative magnitude of excessive inhomogeneity at moderate temperature might be greater or less at higher temperature, inhomogeneity significant at a temperature of use is also apparent at moderate temperature. It is not necessary to test inhomogeneity at the temperature of intended use.

Several authentic thermoelectric inhomogeneity tests, simple to sophisticated, have been developed and extensively demonstrated [9,11,12]. Effective primitive methods were practiced by pioneers.

Valid tests range from methods of many-cm spatial resolution to advanced methods that have accurately resolved inhomogeneity with spatial resolution of a few millimeters [11,12]. Their practical need has been very clearly proved, yet few authentic inhomogeneity tests are now performed.

Consequential inhomogeneity is spatially distributed; therefore, all authentic inhomogeneity tests of thermocouples require moving a very narrow temperature step between two temperature plateaus scanned progressively along the paired thermoelements while spatially monitoring the voltage. This appropriate step temperature pattern is best applied by progressive immersion of a thermocouple from ambient temperature into an isothermal-heated deep liquid bath of high thermal conductivity while recording the voltage as a function of position. This step compares the Seebeck emfs of widely separated segments of nearly equal length. The Seebeck coefficients of the two segments are likely most dissimilar if the segments are well separated. The finest resolution is by stepped-progressive immersion of the thermocouple into a deep isothermal liquid bath of high thermal conductivity, such as of a eutectic alloy of gallium, indium, and tin. That alloy is liquid at room temperature. Heated to near 100°C, the nondamaging bath imposes a narrow step of temperature above ambient temperature at the liquid interface. The bath test is well adapted to MIMS thermocouples. It is applied to other thermocouple forms by enclosing them temporarily in a thin close-fitting insulating plastic sheath. The spatial resolution depends on immersion speed, step duration, and thermal properties of the liquid. Even water-based liquids below their boiling point can be used but with lower spatial resolution. Such advanced tests well-demonstrated by several laboratories have used specialized equipment so they have not been accepted by the thermometry community. However, the Australian National Measurement Laboratory has routinely preceded calibration by one *authentic* inhomogeneity test [9]. The test uses progressive entry of the thermocouple into a lengthy isothermal oven while monitoring the emf. That produces an authentic inhomogeneity test with spatial resolution of several cm. The vertical immersion tests restrict the length of the test subject.

A similar authentic test is performed on individual thermoelements of any length. A thermoelement is run through a heated liquid bath or furnace with widely separated entry and exit points. This imposes two spaced temperature steps of equal width and temperature different from ambient temperature. The effect of such progressive immersions is well visualized by the **T/X** sketch of the Functional Model.

70.10.2.3 False Inhomogeneity Tests

70.10.2.3.1 Comparison Test

Some procedures are misunderstood to be inhomogeneity tests. For example, two or more samples taken from well-separated locations along a batch of thermocouple wire are calibrated. Calibrations are of indefinite local segments of thermoelements. Agreement between two calibrations only suggests that homogeneity is within thermocouple tolerance, but it effectively misunderstands troublesome inhomogeneity to be global rather than localized. It is *not* an authentic inhomogeneity test.

70.10.2.3.2 Temperature Spike Test

Another commonplace quality procedure also is misunderstood to be an inhomogeneity test. This "spike test" is the very opposite of a true inhomogeneity test. The thermocouple pair, of any length, must be electrically joined at the end opposite the thermocouple monitor. That junction is held at any fixed temperature. While monitoring the temperature indication, a symmetric very narrow swept spike of temperature is applied by a narrow-tipped soldering iron, flame, or a transverse heated wire that is slowly scanned along the thermocouple. This commonplace practice inappropriately compares the difference between Seebeck coefficients of two very closely spaced segments that are most likely to be similar even in severely inhomogeneous thermoelements. The narrower the temperature spike, the worse the test as an indicator of consequential inhomogeneity. Its widespread misunderstanding as an inhomogeneity test has misled many to discount inhomogeneity as a practical significant problem in accurate thermoelectric thermometry.

70.10.2.4 Hidden Junction Test

The temperature spike test does serve a very different practical purpose. As the very narrow temperature source scans past a location, a localized spike of temperature indication reveals and locates a real junction. This quick and simple procedure actually is an important test for hidden real junctions. Such defects do infrequently occur where different thermoelements, spliced or connected hidden within a cable assembly, are different though of the same nominal type or even of a different type. Otherwise, concealed, they might be connected in crossed polarity. Such consequential defects, unless discovered by this important test, are very difficult to recognize during setup and thermometry.

70.10.2.5 Thermocouple Instability Test

The most obvious occurrence of thermocouple inhomogeneity is that which, unrecognized, is produced in the traditional thermocouple test of long-term drift of sensitivity. The measuring junction, and adjacent lengths of thermoelements, is fixed deeply immersed (more than 20 probe diameters), within an essentially isothermal zone of a furnace. Oven temperature and environment remain constant. Thermoelectric instability is measured as a sustained progressive change of thermocouple voltage that, with exposure time, drifts toward the tolerance limit and beyond. Costly long-duration thermocouple instability tests, conducted by suppliers rather than by users, are usually performed over durations from weeks to months.

The traditional instability test result is misperceived as if a test of overall rather than localized thermocouple sensitivity. Peculiarly, the emf drift observed is not from those segments that are uniformly degrading within the isothermal furnace. Actually, as understood from the Functional Model and T/X sketch, the material degrading isothermally within the furnace contributes little of the observed voltage. Rather, the observed drift of emf is of thermoelement segments at the oven entry that span the temperature difference between furnace and ambient temperature remote from the measuring junction. Therefore, the uniform change of Seebeck emf of the segments within the furnace actually is much greater than is reported. Likewise, tolerance is exceeded earlier than observed in this test.

70.10.2.6 Inhomogeneity Test Incidental to Instability Test

A simple in-place inhomogeneity test, complementing the instability test, can reveal the actual inhomogeneity pattern and improves the significance of the drift test at little additional cost. Beginning the instability test, voltages $E_1(x)$ are recorded as the measuring junction, and thermoelements are progressively advanced from ambient temperature to dwell at the drift test position. That data document, for new material, the initial temperature profile of the entry temperature step and of the oven. Eventually, at the end of the drift test, the exit profile, $E_2(x)$, is recorded as the measuring junction is first advanced a distance greater than the width of the entry step into the furnace. That documents the final profile of the entry step with undamaged material. Then, the thermocouple is slowly withdrawn until the measuring junction dwells at ambient temperature. The difference between the two profiles, $E_1(x)$ and $E_2(x)$, from each test subject documents the actual test-induced pattern of inhomogeneity and the relative magnitude of the actual change of the degraded material. Unlike the formal inhomogeneity test conducted near room temperature, this complementary test is performed at the elevated test temperature that produced the inhomogeneity that appeared as drift.

A special automated calibration furnace, Model FUR-1200, offered by the Electronic Development Labs, Inc., www.edl.com, is well adapted to such complementary programmed in-place inhomogeneity test as it allows programmed computer-controlled immersion and withdrawal of the test subject. It also is used to document the effect on stability of cyclic rather than fixed temperature. MIMS assemblies are degraded differently by varying rather than constant temperatures.

70.10.3 Thermocouple Calibration

Thermocouple calibration is intended to improve accuracy [9,13]. Conventional calibration might not. Calibration of a sample from a uniform set of as-delivered thermocouples to confirm conformity to

standard tolerance is appropriate. However, despite individual calibration, the approximated standard scaling relation, rather than the actual calibration, usually is used in thermometry regardless of calibration result. Individual calibration of each new thermocouple can reduce uncertainty only if the specific calibrations are used in data analysis.

Recalibration of thermocouples recognized or suspected as "drifting" in sensitivity is rarely beneficial. Some quality assurance programs mandate periodic recalibration of unused thermocouples. Initial calibration applies generally so long as thermometry is restricted always to temperatures well below the upper temperature limit, in benign environments and for moderate duration. Sensitivity of unused thermocouples does not "age." Recalibration of severely used but possibly reusable thermocouples that have been suspected of error from observed drift is appropriate only after the subjects are proved acceptably homogeneous by *authentic* inhomogeneity test. Otherwise, costly recalibration may be counterproductive in certifying a thermocouple that is not recognized to be seriously inhomogeneous by conventional calibration.

70.10.3.1 Option to Calibrate

70.10.3.1.1 Base-Metal Thermocouples

Two ways to address calibration problems presented by possible hidden inhomogeneity are the following: *First*, for inexpensive base-metal thermocouples, it is acceptable to presume that unused thermoelements are homogeneous within standardized tolerances. First-cycle calibration of unused thermocouples with only brief exposure, and to temperatures, not exceeding a damage threshold, can usefully confirm the actual as-received state and allow more precise data analysis. *Second*, used base-metal wire thermocouples that have shown significant "drift" might be damaged only near the measuring junction. From the known circumstance of exposure, a length of segments believed damaged adjacent to the measuring junction could be discarded and the measuring junction re-formed. For relatively inexpensive thermocouples, economy may suggest that they be replaced if drift is suspected.

In-place *recalibration* of degraded thermocouples by comparison with reference thermocouple temporarily placed adjacent is often suggested. That common practice assumes the spurious junction-source model. Calibration is not of the "junction." Such comparison presumes that the temperature distribution remains constant in thermometry. However, the Functional Model clearly illustrates why in-place recalibration of a drifted inhomogeneous thermocouple can be deceptive if temperature distribution along the thermocouple varies in use.

70.10.3.1.2 Precious-Metal Thermocouples

The accuracy of precious-metal alloy thermocouples relies on their purity. They are vulnerable to contamination and inhomogeneity. Damage from the local migration, absorption, or evaporation of alloy constituents or other chemical contamination is not reversible. However, unlike base-metal thermoelements, costly precious metal thermoelement materials sometimes can be reconditioned but only if they are degraded by plastic strain alone. Platinum-based thermocouple wire might be annealed to an original state by electrically heating full length in air. Such annealed thermoelements can be presumed to be free only of reversible *strain-induced* inhomogeneity. Confirming recalibration is justified after annealing, but homogeneity must be verified. Precious metal thermocouples have a significant material salvage value.

70.10.3.2 Calibration Process

Thermocouple calibration of effective $E(T)$ requires immersing the thermoelements at the measuring junction into an isothermal calibration zone to a depth sufficient to assure that longitudinal heat conduction along the thermoelements does not affect the junction temperature [9,13]. A junction immersion depth of 10–20 times the thermocouple probe diameter is usually recommended. Emphasis on avoiding the effect of longitudinal heat conduction on measuring junction temperature is appropriate.

However, the spurious junction-source model has encouraged the false notion that it is the junction that is being calibrated. As illustrated by the Functional Model, the calibration emf is from unidentified segments of thermoelements, remote from the measuring junction where they pass through the temperature transition from calibration to room temperature. Those unidentified segments then are presumed to be representative of the entire thermocouple. This conventional calibration obscures a practical fact. It is those thermoelement segments adjacent to the measuring junction that are most likely to become inhomogeneous in fabrication and application. Significantly, it is those segments made isothermal that are the most likely to be inhomogeneous so they are eliminated from a recalibration.

70.10.3.2.1 Routine Calibration

Commercial benchtop dry-block calibrators simplify routine calibration. Electronic refrigeration or heating applies the selected isothermal calibration temperature. Different units are required to cover a range from –30 °C to 1292 °C. Thermocouples are presumed to be homogeneous. One or more probes of different diameters simultaneously can reside at sufficient depth in isothermal wells to assure that heat conduction along each probe does not affect measuring junction or reference temperature.

70.10.3.2.2 Certified Calibration

It is inefficient for incidental users of thermocouples to set up for formal thermocouple calibration. Calibration is often performed by specialized in-house or commercial calibration laboratories that offer calibration certified to be directly traceable to NIST. In the most accurate calibration, fixed-point temperature cells realize intrinsic melting point temperatures of pure metals or the melting or triple point of water ice. These sophisticated sources are more accurate and reproducible than dry-well calibrators or monitored baths. A set of cells, each of one particular metal and standardized freezing point temperature, imposes one of the few specific standardized temperatures. They are used in the establishment of the temperature scale, for thermocouple type-characterization, and in the most accurate calibration. The sources are extremely accurate but are very costly and inconvenient to operate. They are used in the highest-level calibration and standards laboratories for calibration of homogeneous thermocouples.

The melting point of pure water ice is most widely used to accurately impose the standard 0 °C reference temperature. A Dewar thermal flask is filled with a slush of finely crushed ice just immersed in pure chilled deionized water. The flask is surrounded by crushed ice so the melting point temperature can be maintained for a very long duration. The flask must be deep enough to accommodate electrically insulated junctions to sufficient depth. Such baths, properly established, can maintain the standard 0 °C melting point within 0.01 °C–0.02 °C. Standard procedures for 0 °C reference baths are defined in ASTM standard E563-08. A poorly formed and carelessly maintained bath of sizeable ice chunks in tap water in an un-insulated glass beaker might deviate from 0 °C by several degrees.

70.10.3.3 Calibration of Measuring-Junction Thermocouple Assemblies

Measuring junction thermocouple assemblies are of diverse specialized designs. The complicated geometry of some styles makes meaningful calibration difficult or impossible. The Functional Model forces recognition that immersion of all or most of the thermocouple assembly into an isothermal oven actually eliminates it from the intended calibration.

70.10.3.4 Calibration of Reference-Junction Thermocouple Assemblies

Reference junction thermocouple assemblies are of the single-reference junction circuit style (Figure 70.3). The reference thermocouple is intended never to be exposed to either excessive temperature or to a degrading environment; therefore, its initial sensitivity is not expected to change. However, initial calibration should assure that the thermocouple is well within standard tolerance. Usually, they are not calibrated as sold and often not as used in calibration of measuring thermocouples. Unfavorably, reference-junction-thermocouple assemblies always contribute some of the emf when used in a calibration procedure. With the measuring junction at ambient calibration temperature, all the emf is from

the reference thermocouple; none from the test subject. For calibration temperatures to about 40 °C, up to half the emf is from the reference thermocouple. It provides the portion of net emf from 0 °C to the ambient temperature at all higher calibration temperatures. If the reference is calibrated, the data cannot be used to correct calibrations of measuring junctions for which they were used.

70.10.3.5 Calibration of Monitor Scaling Functions

Usually, the scaling relations within monitors are not directly accessible to the user. Separate electronic calibrators for monitors allow scaling between emf and temperature to be confirmed. Scaling within the calibrator is performed by internal scaling relations that approximate with the standard tables. The user specifies a temperature and a thermocouple type. The calibrator presents to the monitor a corresponding emf compensated for the temperature of its own reference terminals. The calibrator and monitor must be connected by an extension of the *passive* type. Such calibration is jointly of thermocouple and compensation scaling. Stand-alone reference temperature compensators can be calibrated by the same kind of electronic calibrator.

70.10.3.6 Calibration of Reference Temperature Compensators

Over the small span around normal ambient temperature, monitor reference temperature compensation uncertainties often range from 0.25 °C to 0.75 °C. Few monitors have reference temperature compensators that are separable for calibration. Nevertheless, infrequently, both internal and external references have been observed to drift by many degrees. Such drift is usually unnoticed as it is indistinguishable from variation of measuring junction temperature.

Compensation should independently be confirmed. By temporarily shorting the input terminals, the monitor indicates the scaled temperature compensation it actually is applying. The monitor should indicate a plausible ambient temperature of the input terminals. (Note: In Figure 70.1, with terminals shorted at an actual ambient temperature of 32 °C, the meter incorrectly, by design for economy, is applying a fixed compensation for a constant 21 °C, a systematic error of 11 °C at all indicated temperatures.)

70.11 Thermocouple Instrumentation Systems

70.11.1 Signal Transmission

The few elementary thermocouples used in a compact laboratory or classroom setting often have simple circuits without extensions. The measuring junction is near the monitor. However, in commercial application, as in field and process thermometry, indication and recording often are separated from the measuring junction by hundreds of meters. There are many ways to transmit thermocouple information over great distances.

70.11.1.1 Wired Transmission

70.11.1.1.1 Extension Cables

Passive-, *corresponding*-, and *compensating*-type thermoelectric extension cables are available in a wide variety of constructions and insulations. They can be a single, short, twisted, insulated thermoelectric pair, a retractile cord, or a very lengthy ruggedized multipair cable designed for suppression of both electrostatic (ES) and electromagnetic (EM) noise and for environmental protection.

Twisted-pair unplated copper instrumentation cable can serve as *passive-type* extension grade leads. Thermoelectric *corresponding-type* or *compensating-style* extensions are more expensive than ordinary copper instrumentation cable but must be used where reference junctions must be at a remote monitor.

70.11.1.1.2 Thermocouple Transmitters

A less familiar form of thermocouple signal conditioning, the *thermocouple transmitter* also conveys signals to distant locations by wire, *not* by wireless transmission. The cable is twisted shielded pair

instrumentation cable. Instrumentation transmitters convert the Seebeck emf data to an Instrument Society of America (ISA) Standard modulated 4–20 A current signal protocol or else to an alternative 1–5 V dc protocol. The transmitter is powered through the signal pair from the receiving end. It is a small module that, additional to the protocol, local to the thermocouple compensates for reference temperature, scales the thermocouple emf to a temperature, related voltage, or current, and provides circuit isolation. The transmitter may also locally display temperature on alternative scales. Some fit within the conventional connection head of a thermocouple well. A few are integral to thermocouple connectors that mate with the measuring thermocouple. Others are rack mounted or are adapted for use with the DIN rail mounting system. Thermocouple transmitters are suited to monitoring slowly changing temperatures at monitoring sites distant from the measuring junction.

70.11.1.2 Wireless Transmission

70.11.1.2.1 Radio Frequency

Cabled wire systems may be simpler for general technicians to install and to maintain than are more elaborate electronic systems. However, hardware, cable, and setup cost may favor alternative wireless transmission systems rather than extension wiring. In some field or process situations, widely distributed measuring junctions must be very distant from a central monitoring location. Wireless data transmission can be particularly economical where the distance between the measuring junction and recorder is great, when many thermocouples must be recorded, when little setup time is available for field cabling, and where the measuring setup must be moved occasionally.

Several inexpensive radio frequency wireless data acquisition systems are adapted to combine thermocouple signal conditioning, data acquisition, recording, and wireless signal transmission. Inexpensive connector- or palm-sized radio transmitter systems communicate wirelessly over distances up to 300 m under favorable conditions. Radio modems can communicate data from a measuring location to recording sites as far as 5 km away. In the United States, they do not require a communications license.

70.11.1.2.2 Internet

Where transmission distance is even greater, real-time temperature monitoring via the Internet can provide, local or worldwide, control and alarms for remote process monitoring or administration of field experiments.

70.11.2 Thermocouple Instruments

70.11.2.1 Indicators and Monitors

A wide variety of nonrecording instruments is available for merely observing temperature by thermocouple. Some basic thermocouple indicators are handheld and multipurpose like the multimeter in Figure 70.1 with 1 °C resolution and marginal accuracy. Advanced handheld meters can be very accurate and certified with calibration NIST-traceable and resolution to 0.1 °C. A few provide dual thermocouple inputs and allow direct differential temperature measurement. Some accommodate only a single thermocouple and of only a single type. Other benchtop or rack-mounted units accommodate many thermocouple inputs of the same or of intermixed thermocouple and other sensor types.

70.11.2.2 Simple Recorders

Temperature might simply be monitored visually in setup or for control, but most temperatures now are digitally recorded for documentation and detailed analysis. Local portable recording can be on inexpensive SD, USB, or other flash memory. Some specialized multichannel thermocouple data recorders are now battery powered for stand-alone field use. The range of recorders now extends from tiny handheld devices to specialized fieldable data loggers for untended local recording in isolated locations.

70.11.2.3 Data Acquisition Systems

Stand-alone systems specialized to thermocouple thermometry allow a user to focus on the measurement rather than on details of its indication or recording. Larger digital data loggers with multiplex switching that sequentially samples the output from individual thermocouples in fixed order can accommodate up to several hundred inputs and can record a mix of both thermocouple and other signals at sample intervals programmable from a few milliseconds to hours or days without special programming. Microvolt-level signal resolution, stability, noise reduction, nonlinear scaling, reference temperature compensation, and high input resistance are commonplace. Most provide desirable three-wire and balanced switching between thermocouples. Despite the sophistication of the advanced systems, the manufacturer cannot shelter the user from most thermoelectric problems.

70.11.2.4 Computer-Based Systems

Even tiny specialized recording thermocouple thermometers now perform signal processing digitally. Desktop personal computers accommodate inexpensive internal digital data acquisition boards that can add high-resolution temperature recording to complement analysis capability. Laptop computers can accept special palm-sized PCMCIA or USB plug-ins for multiple thermocouple input for field use.

Computer-based systems offer great flexibility. Digital computer-based data acquisition systems with software integrated for data acquisition, analysis, and presentation allow the user to apply special reference temperature compensation, custom linearization of thermocouple scaling functions for either standard or individual calibrations and of special thermocouple types and sampling to arbitrary sequence and intervals. Computer-based thermocouple thermometry systems with suitable commercial data acquisition and other software provide for experiment design, prediction, data acquisition, alarming, information management, analysis, reporting, archiving, and communication within a single compact fieldable laptop computer. Computer-based data acquisition also allows complementary communication via the Internet.

70.11.2.5 Modular Components

The many diverse and economical packaged data acquisition systems satisfy the thermocouple thermometry needs of most users. However, many major electronic component manufacturers offer thermocouple-focused modular integrated circuit components that simplify special application. Small integrated circuit modules, www.analog.com, for thermocouples provide reference junction compensation, linearization, isolation, open input indication, amplification, and set-point control for incorporation of thermoelectric components into special-purpose systems. Outputs may be of temperature-linearized current or voltage or of the ISA protocol.

Individually, the components are capable. They can be integrated into systems that have other principal functions. Some customers, hoping for economy of hardware, have built customized thermocouple thermometry systems using modular components. Some have proved more costly and less accurate because the designer did not understand critical distinctions between thermoelectric circuits and ordinary electric circuits. Related components, apart from modules, like switches, relays, connectors, and printed circuits can introduce troublesome thermoelectric noise emf. When applying modular components into a system, it is particularly important to understand thermoelectric circuit pitfalls and their avoidance.

70.11.2.6 Nonconventional Components

Occasionally, useful special functions do justify the knowledgeable design and application of unconventional system components. One example is a nonconventional *Combinatorial Multiplexing Switch*, a "CoMux" [14]. To efficiently share a single metering device, reference, and scaling, ordinary computer-controlled switches successively multiplex-sample thermoelements by conventional "positive–negative" thermocouple pairs. Instead, the CoMux samples nonconventional multi-thermoelement "Tip-branched" or "Leg-branched" thermocouples. These allow unique complementary validation measures of continuing

thermoelectric circuit integrity. Tip-branched thermocouples have three or more dissimilar thermoelements that share a single "juncture." Such multi-thermoelement circuits have long been commercially available and used but are sampled only as conventional pairs. Uncommon leg-branched thermocouples have three or more thermoelements with junctions along different legs. The programmable CoMux samples arbitrary combinatorial nonconventional pairing of the several circuit-connected thermoelements. These samples allow such critically important independent complementary diagnostic measures as loop resistance, noise voltage, redundant measure of temperature, and with standard and nonstandard thermoelement pairings of thermoelements of these compound thermocouple circuits. These unconventional diagnostic measures unambiguously reveal and document otherwise unrecognizable flawed thermocouple readings as where thermocouple failure in harsh environments is expected [14].

70.12 Thermocouple Thermometry Practice

70.12.1 Temperature Ranges

70.12.1.1 Moderate and High Temperatures

Temperature and duration of exposure are unavoidable environmental variables in thermometry. Other environments can sometimes be controlled. Standard thermocouple tables extend only to the greatest temperature of *recommended* use for benign protected environments, short durations, and for wire materials of 3 mm or greater diameter. Reduced temperature limits apply for materials of smaller cross section (Table 70.5). Degradation of the Seebeck property can occur due to excessive temperature alone, well below the melting point, eventually even well within the range recommended for use. Environmental degradation is accelerated by heat. Frequent cyclic heating and cooling accelerate damage of MIMS thermocouple. Within the recommended temperature range, damage progresses gradually with time at temperature over periods of weeks to months. Calibration should be performed quickly, allowing time only for equilibration, and only to the maximum temperature of intended use. Although thermoelements may not be visibly affected, the Seebeck coefficient of thermoelement segments adjacent to the measuring junction might be substantially degraded.

70.12.1.2 Very High Temperatures

Type **K** thermocouples are limited to temperatures up to 1372 °C. Proprietary Platinell® has a Seebeck characteristic similar to Type K with improved stability and recommended upper limit of 1392 °C. Types **R** and **S** extend the range to 1768 °C, and Type **B** to 1820 °C. Special commercial gold vs. platinum thermocouples of very special design and construction are used for stable precision thermometry to 1000 °C. Damage by chemical exposure is not reversible, but the precious materials can be recycled. Refractory metal thermocouples are of specially treated materials such as tungsten, rhodium, or rhenium alloys.

70.12.1.3 Low Temperatures

The scaling functions for use of normal thermocouple material below 0 °**C** are different than for elevated temperature use of the same thermocouple type. Standardized thermocouple characteristics below 0 °C are based on less data than for higher temperatures. Also materials manufactured for thermometry at elevated temperatures conform less well to the standard characteristics for cryogenic thermometry than do special modified alloys of the same thermocouple letter type especially made for such use. This quality issue should be discussed with the thermocouple supplier.

70.12.1.4 Cryogenic Temperatures

Cryogenic thermometry has been loosely defined as measurement of temperatures below 280 K (7 °C). That range broadly overlaps the measure of atmospheric temperatures below the ice point (down to –50 °C) that, along with higher ambient temperatures, often are measured by a single thermocouple system. A more restrictive definition limits cryogenic thermometry to temperatures below 90 K (–183 °C)

(the boiling point temperature of liquid oxygen at 1 atm). The latter definition characterizes as cryogenic only the extremely low-temperature regime over which thermometry involves distinctive severe problems and very different techniques. The Seebeck properties are degraded at extremely low as well as high temperatures.

Common thermoelement materials progressively decrease in thermoelectric sensitivity below the ice point. The Seebeck coefficient of all conductors is insignificant at 0 K (–273.15 °C). Superconductive materials experience an abrupt drop in Seebeck coefficient to near zero at a characteristic superconducting transition threshold. That threshold is below 10 K for most unalloyed metal superconductors. Special alloys have been developed to raise the atmospheric pressure superconducting threshold to as much as 138 K—well above the strict cryogenic range. Only between 0 K and a superconductive threshold is it possible directly to observe the absolute Seebeck characteristic of a normal thermoelement by pairing it with a superconductive thermoelement.

Standard Seebeck characteristics are defined for Types **E**, **J**, **K**, **N**, and **T** down to –270 °C. The characteristics for Types **R** and **S** extend down only to –50 °C. Type **B** is not characterized below 0 °C. It is not recommended for thermometry below 400 °C because its sensitivity is very small at lower temperatures. Often, simple *passive-type* extensions are used for Type B thermocouples near ambient temperature where the thermocouple emf is very small.

For very low temperatures, the letter-designated thermocouple material, Type **E**, is preferred for use down to –233 °C (40 K) because of its higher relative Seebeck coefficient in that range. The less-sensitive Type **K** and Type **T** materials are also used in this range. Below 40 K, special nonstandardized alloy combinations, such as Type **KP** vs. Au/0.07 Fe, are preferred.

Some thermoelement alloys experience grain growth and incur serious inhomogeneity under prolonged exposure to deep cryogenic temperatures. More sensitively at cryogenic temperatures than at elevated temperatures, the Seebeck coefficient of most thermocouple alloys is very strongly dependent on magnetic field. Strong magnetic fields are often involved in cryogenic experiments, so thermomagnetoelectric effects become significant in studies of superconductivity.

Peltier heating at junctions and Thomson heating along thermoelements are current-dependent thermoelectric effects that rarely affect thermometry. Fortunately, neither effect is significant if thermometry is conducted properly by "open-circuit" measurement. There is no significant thermocouple self-heating as with resistance thermometers.

70.12.2 Thermometry Process

70.12.2.1 Coupling

As any thermal sensor, the temperature of the measuring junction of a thermocouple must approach and track the temperature of the subject [9,13]. Close thermal coupling of the measuring junction to the point of measurement is enhanced by a very thin layer of thermally conducting coupling grease or adhesive, avoiding even thin air gaps. Electrically conducting coupling between junction and subject may be appropriate for noise control. Thermal coupling and loading problems are aggravated in the measurement of subjects of low thermal mass. Heat transfer is more delayed for surface, liquid, and gas measurements than for internal solid measurements. Centering the measurement point in an isothermal region is preferred. Even for steady-state measurement, temperature gradients can cause the measuring junction to be at a significantly different temperature from the intended point of measurement.

70.12.2.2 Transient Thermometry

The very small dimensions possible for the junction and low thermal mass of its adjoining thermoelements well adapt thermocouples to transient thermometry. The Seebeck effect occurs at electronic speed, independent of thermoelement size. Seebeck emf immediately corresponds to the actual temperatures of all junctions in the circuit. An isolated thermocouple alone has no characteristic response.

Thermal response is necessarily a joint property of the thermoelements at the measuring junction, of its subject, and of the monitoring system. Traditionally, thermocouple transient behavior is represented simply as a first-order exponential step rise time with a time-constant reflecting rise time to respond to 63.2% of an instantaneous temperature step. The actual forms of response for different geometries are similar yet more complex. Risetimes are often stated for beaded-junction thermocouples of different wire sizes plunged into an air or water stream. The response of actual thermocouples depends on many factors such as junction dimension, material, and style of the junction and of adjacent thermoelements, the thermal properties of the test subject, and thermal coupling, as well as circuitry and the recording electronics. Butt-welded fine wire and foil thermocouples might respond within 3 ms. Small-diameter MIMS thermocouples with exposed or enclosed junctions in air have response times in the range from fractional seconds to several seconds. Surface contact thermocouples have time constants around 2 or 3 s. Unlike for static thermometry, in fast transient thermometry, the electrical parameters of the thermocouple and associated circuitry and the dynamic response of the recording system might further slow response time.

70.12.3 Distinctive Thermocouple Noise Problems

Thermocouple emfs are small. Fine temperature resolution requires substantial amplification. For quasi-static thermometry, modern noise suppression techniques available to designers of data loggers overcome ordinary coupled electrical noise to routinely achieve as small as 0.1 °C temperature resolution and long-term stability (much smaller than required by thermocouple tolerance). Thermocouple measurement of transient temperatures requires more careful attention to classical noise reduction techniques because thermoelectric circuits present distinctive problems.

70.12.3.1 Electromagnetic Noise

In thermocouple probes of MIMS construction, ceramic-bead-insulated thermocouples, and some paired insulated thermocouple wires, the paired thermoelements are not twisted and are spaced uniformly apart in a plane. Thermocouples are unbalanced lines because the paired legs have very different resistance. Lengthy and larger diameter thermocouple probes present a significant circuit loop area to couple magnetic noise fields. Even though MIMS probes are entirely metal-enclosed, the sheaths are very thin and of low magnetic permeability. They are scarcely effective for EM shielding. These features prevent the use of some classic techniques for the rejection of EM noise. To reduce troublesome EM noise, the measuring thermocouple probe should be of the smallest feasible diameter and of minimum length. In instances where the EM source is localized and identified, the orientation of the probe relative to the source might be arranged to minimize EM coupling. For rejection of EM noise, extension leads should always be of twisted-pair construction, with a pitch small enough to reject high-frequency noise. Some special thermocouple connectors incorporate a ferrite core intended to suppress transient noise.

70.12.3.2 Electrostatic Noise

ES noise is more easily reduced than is EM noise. Shields of low resistance, though thin, can be effective if properly connected. Shields of plated copper braid are commonly used and are effective for noise of moderate frequency. Continuous shields, such as the MIMS sheaths and aluminized Mylar® film, are effective for low-frequency ES noise and are more effective than braid shields for very-high-frequency noise. ES shields must be continuous (without gaps and holes as in braid) for maximum effectiveness. Shield continuity must be maintained across connectors. Optimum benefits from shielding require use with thermocouple monitors that provide three-wire input and multiplexers that, individually for each thermocouple, switch both the signal pair and their separate shield lead.

70.12.3.3 Grounding and Shielding

Dynamic thermocouple thermometry can require monitoring with rapid frequency response in electrically noisy environments. The technically well-founded principles of noise control for electric circuits

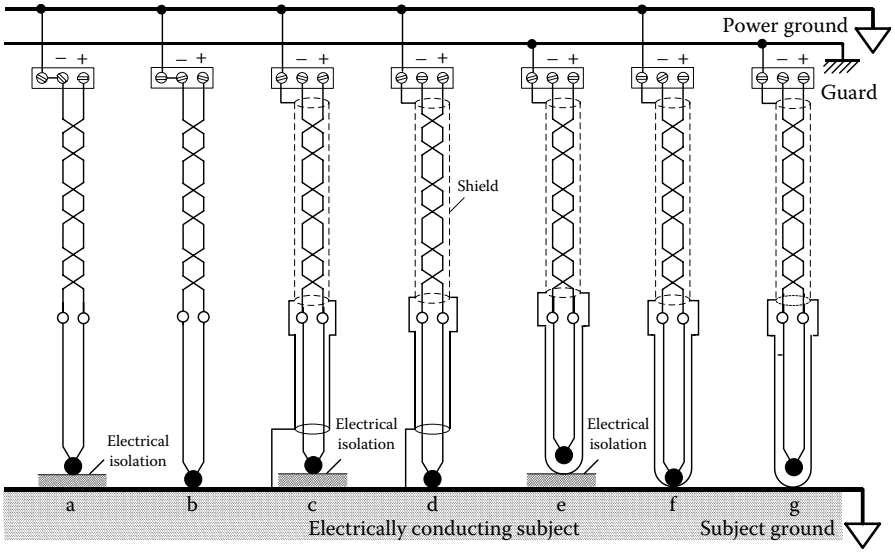

FIGURE 70.8 Preferred thermocouple grounding arrangements. Minimization of electrical noise requires careful attention ion to grounding and shielding.

apply equally to thermoelectric circuits. Well-designed thermocouple instruments carefully isolate the circuitry from other components and control ground reference points. A secondary overall shield, isolated from inner shields and separately grounded, can improve the rejection of EM noise. The circuit grounding of thermocouple is complicated by intimate thermal contact of the measuring junction with an earth-grounded conducting test subject, as for an intrinsic thermocouple, is needed for rapid transient thermometry. Ordinary *coaxial* instrumentation cable must not be used as *passive-type* extension leads because the outer braid and center conductors—as thermoelements—have very different Seebeck coefficients. If not at uniform temperature, such cable can be a significant source of Seebeck dc noise emf.

Figure 70.8 illustrates appropriate grounding for several of the many possible situations. Because the measuring junction is not a localized site of source emf, the point of thermocouple grounding must be carefully considered. Circuit grounding should be at one point only and never at any point of the thermocouple circuit other than at measuring or reference junctions. Electric contact, and particularly shunting or shorting, to a thermoelement at any points at different temperatures between measuring and reference junctions can introduce spurious Seebeck emf from incidental unrecognized thermoelements or ground potential differences.

Feasibility of a grounding method is usually dictated by the internal design of monitors and data loggers. Instrument designers address noise suppression in different ways. Simple and inexpensive line-powered thermocouple thermometers often have only single-ended inputs with the negative lead internally connected to the power ground. This references the sensor grounding also to power ground. In conflict, a "grounded-junction"-style thermocouple might be required for fast transient thermometry. In use, initially isolated thermocouples might short to the protective sheath or test subject. Although this does change the grounding configuration, resulting errors due to thermoelectric effects then usually are predominant.

70.12.3.4 Filtering

Most common thermometry is of static or low-frequency temperature changes. This allows designers to complement the user-provided passive rejection of EM and ES noise by proper grounding and shielding. Internal filtering provided by manufacturers of data acquisition systems can effectively reject high-frequency noise. Some systems provide very effective averaging or "double-slope integration"

techniques for low-frequency thermometry. Routine resolution and stability to 0.1 μV variation over a period of days are achieved by many modern thermocouple data systems. However, these noise rejection methods restrict sampling to intervals no shorter than 10–20 ms that are unsuited to very fast transient thermometry.

70.12.4 Thermocouple Modes of Failure

70.12.4.1 Short or Open Circuit Failure

Thermocouple thermometry has *failed* when its indications are beyond uncertainty limits required for a measurement [14]. Thermocouples sometimes do fail "open" as junctions separate or thermoelements corrode, yield, or melt. Special "open-circuit" indication is a promoted feature of many modern thermocouple indicators. If failure is for other reasons, such indicators encourage unwarranted confidence.

More often thermocouples fail before the circuit opens. The more common but less apparent circuit failures are by insidious shunting, shorting, or progressing inhomogeneity of thermoelements. These common faults are not detected by the "open-circuit" indication [14].

70.12.4.2 Environmental Damage

Corrosive or reactive environments breach protective sheaths and disrupt circuits (Table 70.4). Inhomogeneity is introduced locally in thermoelements. Plastic, ceramic, or fiber insulators are vulnerable to contamination. The compressed granular insulation of MIMS thermocouples, if exposed, rapidly absorbs moisture that can seriously degrade resistive isolation. Electrically conductive fluid or solid shunts can displace the location of measurement without interrupting temperature indication.

70.12.4.3 Metallurgical Change

Alloy thermoelements can locally change composition by evaporation of constituents when exposed to vacuum. Appropriate MIMS construction and material selection usually extend life and increase temperature limits, but damage can occur even within apparently fully sheathed assemblies. Alloy constituents evaporated internally from a sheath or from one thermoelement can migrate and coat adjacent thermoelements even through an insulant. Traces of contaminants can penetrate through pinholes and hairline cracks in metal sheaths and can actually diffuse through intact protective sheaths and affect apparently isolated thermoelements. Minute trace impurities in sheaths or insulants can interact with thermoelements. Alloy components can migrate from one thermoelement to the other through the measuring junction, but the effect is negligible if the junction region is properly maintained isothermal during measurement. Excessive distributed strain can locally modify the Seebeck coefficient of one or both thermoelements resulting in temporary or persistent inhomogeneity. However, very narrowly localized plastic strain as might be introduced by very sharp bends has negligible effect on practical thermometry as is evident from the Functional Model.

70.13 Information Sources for Thermoelectric Theory and Thermometry

70.13.1 Internet

The Internet is a readily accessible and ever-changing source for information on the multitude of thermocouple products. One website, www.temperatures.com, links to more than 300 thermometry and thermocouple-related sites. (These linked sites are not individually screened for accuracy.) Notable is www.omega.com that displays a huge variety of specialty products. Many vendors also provide current tables of Seebeck characteristics, color codes, and properties for standardized as well as for less common materials. Suppliers of nonstandardized specialty thermocouple materials post properties of their products and welcome inquiries.

The definitive NIST tables for seven of the letter-designated types are available on the Internet without charge at www.nist.gov. Site www.hartscientific.com provides values and online conversion between emf and temperature well as Seebeck coefficient, and tolerances for the eight letter-designated types. Another site, www.capco.com provides conversions for the eight U.S. letter-designated and four added non-letter-designated types. A convenient free Apple iPod® thermocouple application presents the full tables and direct conversion between individual temperatures and emfs for the eight U.S. letter-designated types as well as the conflicting color-codes of several international standards.

Unfortunately, very many websites that address thermocouple thermometry contain well-intentioned, but misleading, simplistic or even incorrect information. Most consequential in thermometry is perpetuation of the false thermoelectric junction-source model that obscures most causes of real problems in practical thermocouple thermometry.

70.13.2 Standards, Reports, and Books

A comprehensive, detailed, and authoritative thermocouple application manual is published by the ASTM [4]. That detailed manual addresses applied theory, application, and properties. Closely related standards prepared by the ASTM and sanctioned by ANSI adopt the values and complement the definitive and detailed NIST report 175 [7]. That report is the primary source for Seebeck properties and physical characteristics of most U.S. letter-designated thermocouples. ASTM standards are current as they are reviewed and updated by committee E20 at intervals of 5 years or less. The ASTM also publishes as "gray pages" interim tables of Seebeck emf for a few popular commercial materials that have not been letter-designated. All thermometry-related ASTM standards are collected in a single, annually revised volume [8]. The hardcopy thermocouple tables from these volumes are now available also as functional computer programs that calculate $E(T)$ and $T(E)$ of the NIST 175 document over ranges, at intervals, and in units selected by the user. Many other national and international consensus standards organizations publish thermoelectric test methods and material characterizations.

70.13.3 Technical Papers

Thermocouple thermometry is a mature technology. Progressively, fewer papers now are devoted specifically to thermocouples. Some are distributed across trade magazines and journals of professional societies. Critical details of thermocouple measurements supporting experimental data are most often described only incidentally and inadequately in reports of experimental studies.

The most concentrated and broadest sources of refereed technical papers addressing thermocouple thermometry are the serial proceedings of decennial international symposia on temperature [15]. The seven volumes published to date are a rich, refereed, and mostly reliable source of application data and theory. Other proceedings of annual symposia of the ISA and the National Conference of Standards Laboratories also include papers describing current developments in thermocouple thermometry. Reference 10 has thermoelectric data on the widest variety of nonstandard and ordinary materials.

Fundamental papers addressing the basic science of thermoelectricity are now mostly in the historic literature. Many of the very convincing treatments are directly contradictory. Persons who require historic information must rely on a few specialty technical libraries such as the Linda Hall Technical Library in Kansas City, MO. The online catalog is at www.lindahall.com.

70.13.4 Trade Publications

Abundant, free, extensive commercial catalog literature describes currently available thermocouple hardware and data acquisition products. Catalogs include tables of characteristics. Many manufacturers publish elaborate catalogs of thermocouple-related hardware, software, and books. Notably, the "Omega

Temperature Measurement Handbook," updated and enlarged periodically, presents a supermarket of diverse specialized thermocouple and other components and instruments for thermometry.

70.13.5 Workshops and Symposia

There are occasional workshops and short courses of a few hours' or days' duration devoted to measurement, thermometry, and occasionally even to thermocouple thermometry. Professional societies, such as the ISA, present tutorial workshops in association with special symposia or annual meetings.

70.14 Caveat

At every level, from the promotional to the most esoteric mathematical and physical thermoelectric theory, historic and current, convincing, innocently propagated misconceptions are commonplace concerning thermoelectric effects. More than any other measurement technology, the extensive literature of thermoelectric thermometry, refereed papers, advice from "experts," standards, catalogs, websites, and tutorial articles (*even this one*) all must be approached cautiously with an *authentic* thermoelectric circuit model in mind.

70.15 Summary

The very simple Seebeck thermoelectric effect, the occurrence of an emf in response to a temperature difference along a thermoelement, can be used to measure temperature at modest cost, with finer spatial and time resolution, over a broader temperature range, and in more diverse sensor geometries, than any other class of electric temperature sensors. Properly understood and used within its limitations, the thermocouple is capable of accurate and reliable thermometry. Misunderstood, the thermocouple is subject to inconspicuous, very significant, and sometimes costly errors in thermometry and calibration that too often remain unrecognized. Thermoelectric circuits are distinctly different from ordinary electrical circuits. The practical and useful Functional Model of Thermoelectric Circuits encourages recognition and avoidance of commonplace problems unique to thermocouple thermometry. The principles apply to the most complex generalized thermoelectric circuits, to diverse applications in thermometry, and in the design of low-level electronic circuits.

References

1. D. D. Pollock, *Physics of Engineering Materials*, Englewood Cliffs, NJ, Prentice Hall, 1990.
2. D. D. Pollock, *Thermocouples—Theory and Properties*, Boca Raton, FL, CRC Press, 1991.
3. R. P. Reed, Thermal effects in industrial electronics circuits, in J. D. Irwin (ed.), *The Industrial Electronics Handbook*, Boca Raton, FL, CRC/IEEE Press, pp. 57–70, 1996.
4. R. M. Park (ed.), *Manual on the Use of Thermocouples in Temperature Measurement*, 4th edn. or later, MNL12, Philadelphia, PA, American Society for Testing and Materials, 1993.
5. R. P. Reed, Absolute Seebeck thermoelectric characteristics—Principles, significance, and applications, in J. F. Schooley (ed.), *Temperature, Its Measurement and Control in Science and Industry*, Vol. 6, Part 1, New York, American Institute of Physics, pp. 503–508, 1992.
6. R. P. Reed, Thermoelectric thermometry—A functional model, *Temperature, Its Measurement and Control in Science and Industry*, Vol. 5, Part 2, New York, American Institute of Physics, pp. 915–922, 1982.
7. G. W. Burns et al., Temperature-electromotive force reference functions and tables for the letter-designated thermocouple types based on the ITS-90. Gaithersburg, MD: U.S. Department of Commerce, National Institute of Standards and Technology, Washington, Supt. of Docs., U.S. G.P.O., 1993.

8. ASTM International, *Annual Book of ASTM Standards, Temperature Measurement*, Vol. 14.03, Philadelphia, PA, American Society for Testing and Materials, 2011.
9. R. E. Bentley (ed.), *Handbook of Temperature Measurement, Vol. 3, Theory and Practice of Thermoelectric Thermometry*, Singapore, Springer-Verlag, 1998.
10. P. A. Kinzie, *Thermocouple Temperature Measurement*, New York, John Wiley & Sons, 1973.
11. R. P. Reed, Thermoelectric inhomogeneity testing. Part I: Principles; Part II: Advanced methods, in J. R. Schooley (ed.), *Temperature, Its Measurement and Control in Science and Industry*, Vol. 6, Part 1, New York, American Institute of Physics, pp. 519–530, 1992.
12. R. P. Reed, The effect of interrogating temperature profile in the Seebeck inhomogeneity method of test (SIMOT), in D. C. Ripple (ed.), *Temperature, Its Measurement and Control in Science and Industry*, Vol. 7, Part 1, New York, American Institute of Physics, pp. 491–496, 915–922, 2003.
13. J. V. Nicholas and D. R. White, *Traceable Temperatures—An Introduction to Temperature Measurement and Calibration*, 2nd edn., New York, John Wiley & Sons, 2001.
14. R. P. Reed, Possibilities and limitations of self-validation of thermoelectric thermometry, in D. C. Ripple (ed.), *Temperature, Its Measurement and Control in Science and Industry*, Vol. 7, Part 1, New York, American Institute of Physics, pp. 491–496, 507–512, 2003.
15. *Temperature, Its Measurement and Control in Science and Industry*, Vols. 2–8 (Serial), New York, American Institute of Physics, 1942–2013.

71

Semiconductor Junction Thermometers

Randy Frank
Randy Frank & Associates, Ltd and Motorola, Inc.

Temperature sensors can be easily produced with semiconductor processing technology by using the temperature characteristics of the *pn junction*. The batch processing and well-defined manufacturing processes associated with semiconductor technology can provide low-cost and consistent-quality temperature sensors. The temperature sensitivity of the *pn junction* is part of the transistor's defining equations and is quite predictable over the typical semiconductor operating range of −55 °C to + 150 °C.

Most semiconductor junction temperature sensors use a diode-connected bipolar transistor (short-circuited collector-base junction) [1]. A constant current passed through the base–emitter junction produces a junction voltage between the base and emitter (V_{be}), which is a linear function of the absolute temperature (Figure 71.1). The overall forward voltage drop has a temperature coefficient of approximately 2 mV °C^{-1}.

When compared to a thermocouple or a resistive temperature device (RTD), the temperature coefficient of a semiconductor sensor is larger but still quite small. Also the semiconductor sensor's forward voltage has an offset that varies significantly from unit to unit. However, the semiconductor junction voltage versus temperature is much more linear than that of a thermocouple or RTD. In addition to the temperature-sensing element, circuitry is integrated to produce a monolithic temperature sensor with an output that can be easily interfaced to a microcontroller and to provide features that are useful in specific applications. For example, by using an *embedded temperature sensor* with additional circuitry, protection features can be added to integrated circuits (ICs). A temperature sensor becomes an embedded item in a semiconductor product when it has a secondary or supplemental purpose instead of the primary function.

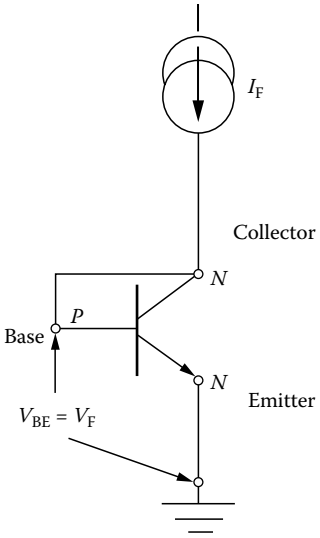

FIGURE 71.1 Bipolar transistor configured as a temperature sensor. The base of the transistor is shorted to the collector. A constant current flowing in the remaining *pn* (base to emitter) junction produces a forward voltage drop V_F proportional to temperature.

71.1 Transistor as a Temperature Sensor

A common semiconductor product for temperature sensing is a small-signal transistor such as 2N2222 or 2N3904. By selecting a narrow portion of the overall distribution of the V_{be} for these devices, a temperature sensor with a lower variation in characteristics can be obtained. The lower variation can provide a part-for-part replacement when a tolerance of only a few percent is acceptable. This device (formerly offered as MTS102 but no longer in production) demonstrates the performance characteristics of the transistor used as a temperature sensor [2].

As shown in Figure 71.2 [2], a silicon temperature sensor has a nominal output of 730 mV at −40 °C and an output of 300 mV at 150 °C. The narrowly specified V_{be} ranges between 580 and 620 mV at 25 °C. The linearity error or variation from a straight line of this device is shown in Figure 71.3 [2]. The total accuracy is within ±3.0 mV including nonlinearity, which is typically within ± 1 °C in the range of −40 °C to 150 °C.

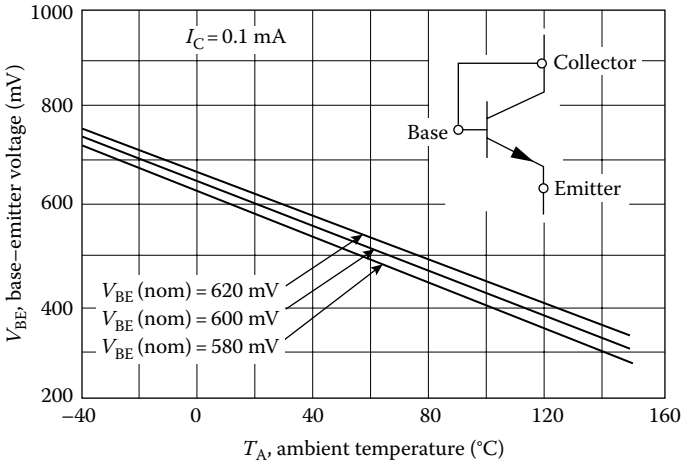

FIGURE 71.2 Base–emitter voltage versus ambient temperature for a silicon temperature sensor.

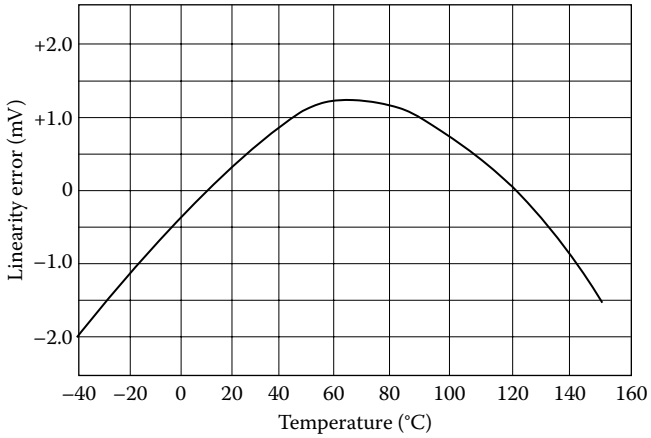

FIGURE 71.3 Linearity error (in mV) versus temperature for a silicon temperature sensor.

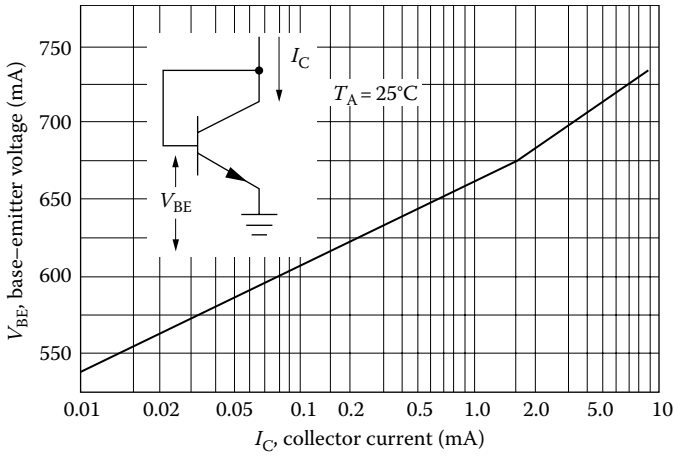

FIGURE 71.4 Base–emitter voltage versus collector–emitter current.

These readings are made with a constant (collector) current of 0.1 mA, passing through the device to minimize the effect of self-heating of the junction. When the constant current applied is larger than 0.1 mA, the effect of self-heating in the device must be taken into account. The variation of the V_{be} with current is shown in Figure 71.4 [2].

71.2 Thermal Properties of Semiconductors: Defining Equations

A constant forward current supplied through an ideal silicon *pn* junction produces a forward voltage drop, V_F [3,4]:

$$V_F = V_{be} = \left(\frac{kT}{q}\right)\ln\left(\frac{I_F}{I_s}\right) \tag{71.1}$$

where

k is the Boltzmann constant (1.38×10^{-23} J K^{-1})
T is the temperature (K)
q is the charge of electron (1.6×10^{-19} C)
I_F is the forward current (A)
I_s is the junction's reverse saturation current (A)

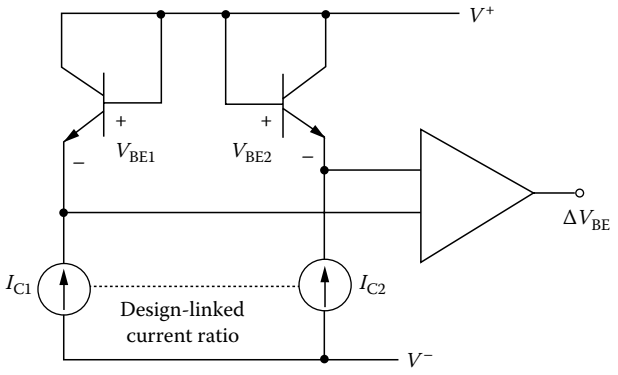

FIGURE 71.5 Differential pair formed by two *pn* junctions. The transistors are diode connected to form a temperature sensor independent of variations in source current.

For constant I_s, the junction voltage (V_{be}) would be directly proportional to absolute temperature. Unfortunately, I_s is temperature dependent and varies with the cube of absolute temperature. As a result, V_F has an overall temperature coefficient of approximately –2 mV °C^{-1}.

To reduce the temperature variation, a *bandgap reference* is formed based on two adjacent and essentially identical-behavior transistors with proportional emitter area designed in an IC process. The two base–emitter junctions are biased with different current densities (*I*/*A*), but the ratio of current densities is essentially constant over the operating temperature range (–55 °C to +150 °C). The following equation shows how the differential voltage (ΔV_{be}) is related to the current (*I*) and emitter area (*A*) of the respective transistors:

$$V_{be1} - V_{be2} = \Delta V_{be} = \left(\frac{kT}{q}\right)\ln\left(\frac{I_1/A_1}{I_2/A_2}\right) \tag{71.2}$$

The differential voltage appearing at the output can be amplified as shown in Figure 71.5 and used as a direct indication of absolute temperature. Additional circuitry can eliminate the offset voltage at 0 °C and provide an output in degrees Celsius or degrees Fahrenheit.

The ability to obtain temperature sensing using semiconductor processing techniques has two significant consequences: (1) semiconductor processing and IC design can be used to improve the temperature sensor's performance for specific applications, and (2) temperature sensors can be integrated within other ICs to obtain additional features. The next two sections explain these approaches.

71.3 Integrated Temperature Sensors

Once a temperature sensor can be manufactured using semiconductor processing techniques, a number of shortcomings of the sensor can be corrected by additional circuitry integrated into the sensor or by using circuit techniques external to the sensor. The linearity improvement, addition of precision voltage references, precision voltage amplifiers, and digital output for direct interface to a microcontroller (MCU) are among the enhancements possible. Furthermore, resistance-measuring circuitry (i.e., RTD sensors) or cold junction compensation (i.e., thermocouple sensors) are not required. Three ICs and one external circuit example are discussed. With any of these temperature-sensing techniques, many system-level circuit designs are produced that use temperature sensing for system monitoring or control. These ICs include fan temperature, battery temperature, computer temperature controls, and more.

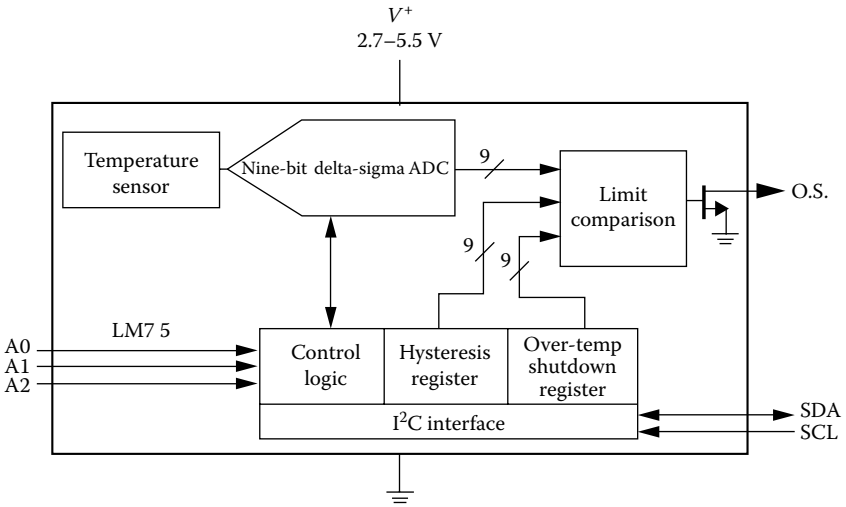

FIGURE 71.6 Block diagram of a monolithic digital-output temperature sensor. (Courtesy of National Semiconductor Corp., Santa Clara, CA.)

71.3.1 Integrated Digital Temperature Sensor

A *monolithic* (one piece of silicon) semiconductor junction temperature sensor (LM75 from National Semiconductor, now part of Texas Instruments) that incorporates several features, including a digital output, is shown in Figure 71.6 [3]. The analog signal of the temperature sensor is converted to digital format by an on-board sigma-delta converter [3]. Digital communication is provided directly to a host microcontroller through a serial two-wire interface. The sensor has a software-programmable set point that can be used to terminate the operation of the controller or implementing protection [5]. To avoid false triggering, a user-programmable number of comparisons (up to six successive over-temperature occurrences) can be implemented.

Eight different sensors can be operated on the bus. Resolution is ±1/2 °C and the accuracy is ±2% from –25 °C to +100 °C. The sensor consumes 250 μA during operation and only 10 μA in sleep mode.

More recent versions can be found at the suppliers' websites as indicated near the end of this section.

71.3.2 Analog-Output Integrated Temperature Sensor

Another approach to integrated temperature sensing is shown in Figure 71.7 [4]. The TMP-1 resistor-programmable temperature controller features a 5 mV °C^{-1} output high and low set points and over- and under-temperature output. A low-drift voltage reference is also included in the 70 mil × 78 mil (2.76 mm × 3.07 mm) design. Figure 71.8 shows a photomicrograph of the silicon die. The TMP-1 is specified for operation between –55 °C and +125 °C, with ±1 °C accuracy over the entire range.

More recently, the DS600 is a ±0.5 °C accuracy analog-output temperature sensor. Other more recent versions can be found at the suppliers' websites as indicated near the end of this section.

71.3.3 Digital-Output Temperature Sensor

A direct-to-digital temperature sensor has been designed for multi-drop temperature-sensing applications [6]. A unique serial number is etched onto each device. The 64-bit read-only memory identifies the temperature of a particular sensor in a measurement system, with several sensors providing readings from different locations. The signal can be transmitted for distances up to 300 m.

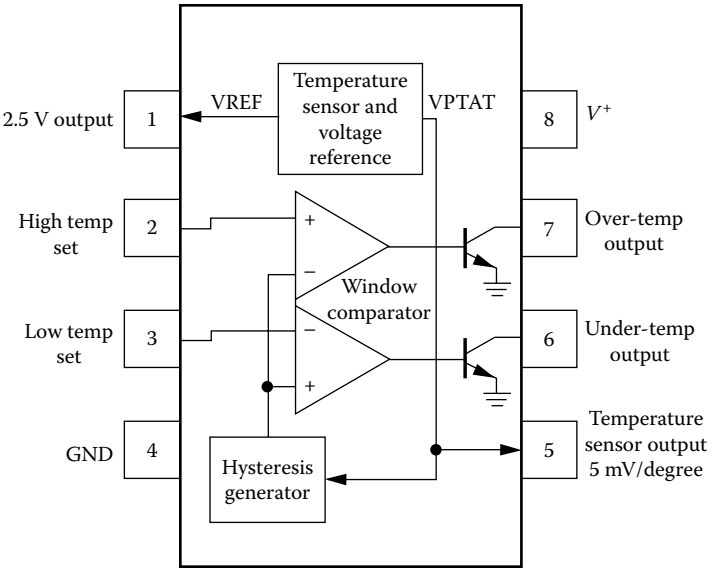

FIGURE 71.7 Block diagram and pinout of TMP-1 monolithic, programmable temperature controller. (Courtesy of Analog Devices, Inc., Norwood, MA.)

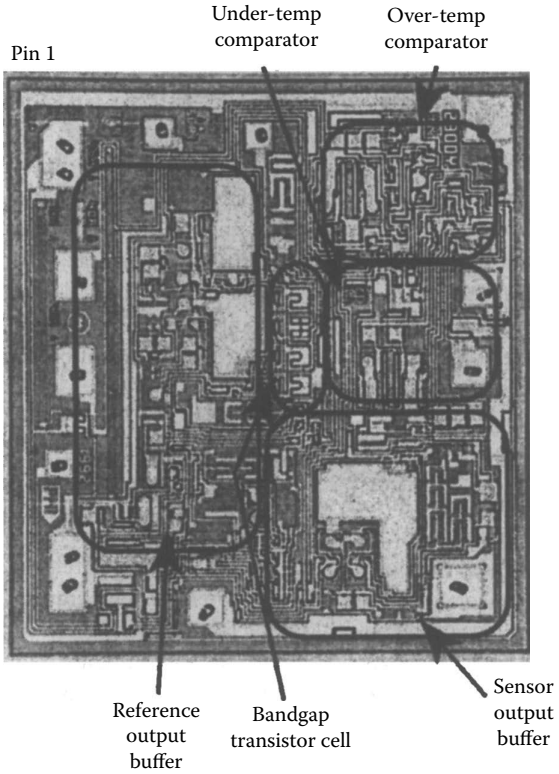

FIGURE 71.8 Detail of TMP-1 die. Note the relative size of the bandgap transistor cell to the other circuitry included in the monolithic device. (Courtesy of Analog Devices, Inc., Norwood, MA.)

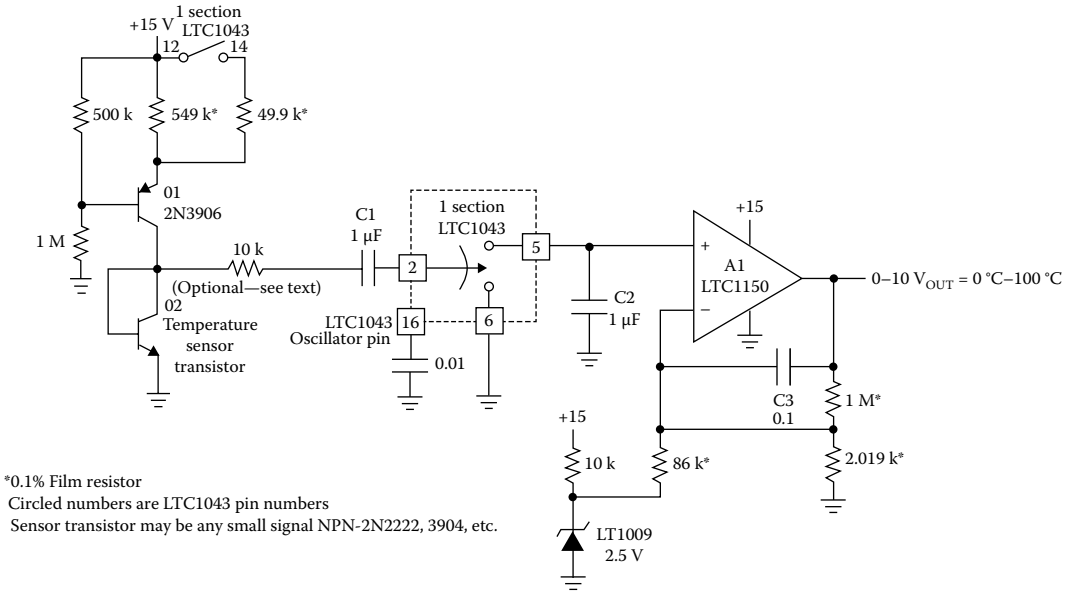

FIGURE 71.9 External circuitry provides ΔV_{be}-based thermometer that does not require calibration. (Courtesy of Linear Technologies Corporation, Milpitas, CA.)

The temperature sensor operates from −55 °C to 125 °C with the power supplied from the data line. The measurement is resolved in 0.5 °C increments as a 9-bit digital value with the conversion occurring within 200 ms. User-definable alarm settings are included in the device.

Digital-output sensors use different communication techniques, including

- 1-Wire
- 2-Wire, I²C, SMBus™
- 3-Wire, SPI™
- PWM
- SMAART wire interface

71.3.4 External Circuitry Eliminates Calibration

External circuitry can be designed to utilize the inherent sensing capability of low-cost transistors without incurring the additional cost of integrated circuitry or the need to calibrate each device. The circuit shown in Figure 71.9 uses an IC (LTC1043 from Linear Technology Corporation) to provide a 0–10 V output from 0 °C to 100 °C, with an accuracy of ±1 °C using any common small signal transistor as the temperature sensor [7]. The circuitry establishes a ΔV_{be} versus current relationship that is constant regardless of the V_{be} diode's absolute value. Substituting different transistors from multiple sources showed a variation of less than 0.4 °C.

71.4 Common Applications of Semiconductor Sensing

Common applications for semiconductor junction thermometers include thus:

- Medical equipment and instrumentation
- Handset and notebook personal computers
- Portable and battery-powered applications

- Power-supply temperature monitoring
- Computer peripheral thermal protection
- Battery management
- Office machines
- Electromechanical device temperatures
- Industrial controls
- Test equipment
- Food processing
- HVAC systems
- System temperature compensation
- Board-level temperature sensing
- Electronic thermostats

71.4.1 Other Applications of Semiconductor Sensing Techniques

Several semiconductor parameters vary linearly over the operating temperature range. Power MOSFETs used to switch high levels of current (typically several amperes) at voltages that can exceed 500 V provide an example of these characteristics. As shown in Figure 71.10 [8], the gate threshold voltage of a power MOSFET changes from 1.17 to 0.65 times its 25 °C value when the temperature increases from −40 °C to 150 °C. Also the breakdown voltage of the power MOSFET varies from 0.9 to 1.18 times its value at 25 °C over the same temperature range (Figure 71.11) [8]. These relationships are frequently used to determine the junction temperature of a semiconductor component in actual circuit operation during the design phase (see Section 71.6). External package level temperature measurements can be many degrees lower than the junction temperature, especially during rapid, high-energy switching events. The actual junction temperature and the resulting effect on semiconductor parameters must be taken into account for the proper application of semiconductor devices.

Polysilicon diodes (and resistors) that are isolated from the power MOSFET can be produced as part of the semiconductor manufacturing process with minor process modifications. The diodes can be used as temperature-sensing elements in an actual application [9]. The thermal sensing that is performed by the polysilicon elements is a significant improvement over power device temperature sensing that is performed by an external temperature-sensing element. By sensing with polysilicon diodes, the sensor can be located close to the center of the power device near the source bond pads where the current density

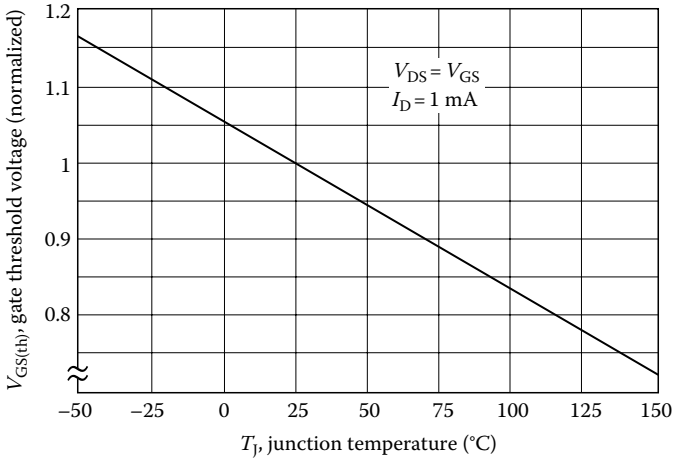

FIGURE 71.10 Power MOSFET's gate threshold variation versus temperature.

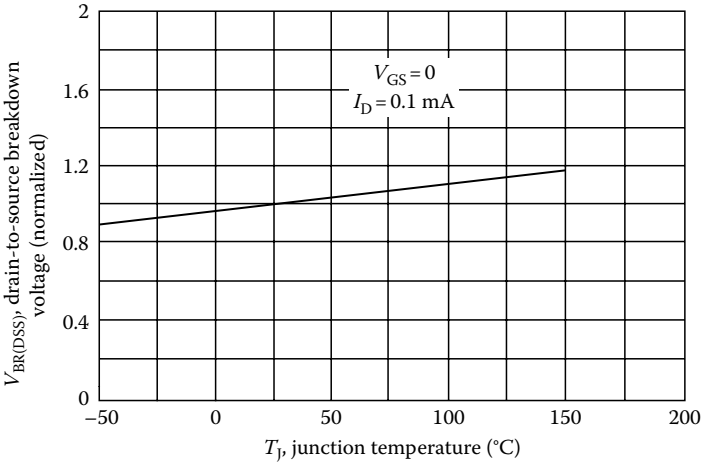

FIGURE 71.11 Power MOSFET's breakdown voltage variation versus temperature.

is the highest, and consequently, the highest die temperature occurs. The thermal conductivity of the oxide that separates the polysilicon diodes from the power device is two orders of magnitude less than that of silicon. However, because the layer is thin, the polysilicon element offers an accurate indication of the actual peak junction temperature.

A power FET that incorporates temperature-sensing diodes is shown in Figure 71.12 [9]. By monitoring the output voltage when a constant current is passed through the integrated polysilicon diode(s), an accurate indication of the maximum die temperature is obtained. A number of diodes are actually provided in the design. A single diode in this design has a temperature coefficient of 1.90 mV °C^{-1}. Two or more can be placed in series if a larger output is desired. For greater accuracy, the diodes can be

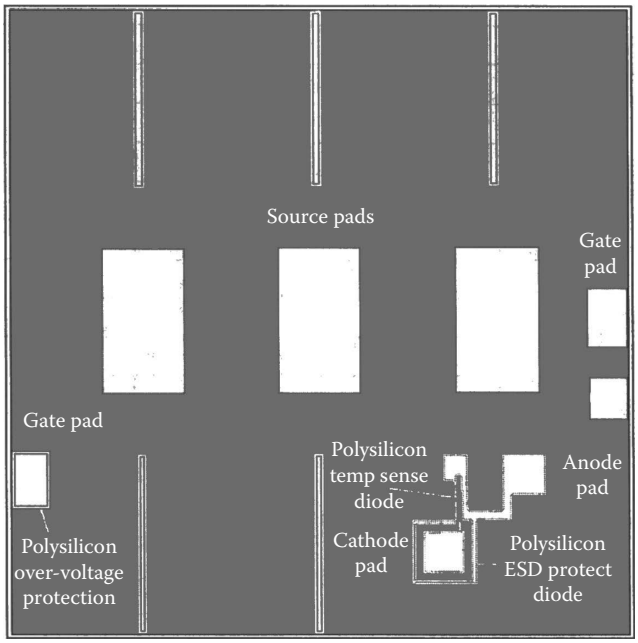

FIGURE 71.12 Photomicrograph of temperature sensor integrated in power MOSFET. Note the relative size of the temperature sensor compared to the total area of the power MOSFET and the source pads that allow attachment of 15 mil (0.60 mm) aluminum wire. (Courtesy of Motorola, Inc., Schaumburg, IL.)

trimmed during wafer-level testing by blowing fusible links made from polysilicon. The response time of the diodes is less than 100 μs, which has allowed the device to withstand a direct connection across an automobile battery with external circuitry providing shutdown prior to device failure. The sensing capability also allows the output device to provide an indication (with additional external circuitry) if the heatsinking is not proper when the unit is installed in a module or if a change occurs in the application that would ultimately cause a failure.

71.5 Temperature Sensing in Power ICs for Fault Protection and Diagnostics

Sensing for fault conditions, such as a short circuit, is an integral part of many smart power (or power) ICs. The ability to obtain temperature sensors in the semiconductor process provides protection and diagnostics as part of the features of these devices. The primary function of the power IC is to provide a microcontroller-to-load interface for a variety of loads. In multiple output devices, sensing the junction temperature of each device allows the status of each device to be provided to the microcontroller (MCU), and, if necessary, the MCU can shut down a particular unit that has a fault condition.

A *smart power IC* can have multiple power drivers integrated on a single monolithic piece of silicon [10]. Each of these drivers can have a temperature sensor integrated to determine the proper operating status and shut off only a specific driver if a fault occurs. Figure 71.13 shows an eight-output driver that independently shuts down the output of a particular driver if its temperature is excessive (i.e., between 155 °C and 185 °C) [10].

The octal serial switch adds independent thermal sensing through over-temperature detection circuitry to the protection features. Faults can be detected for each output device, and individual

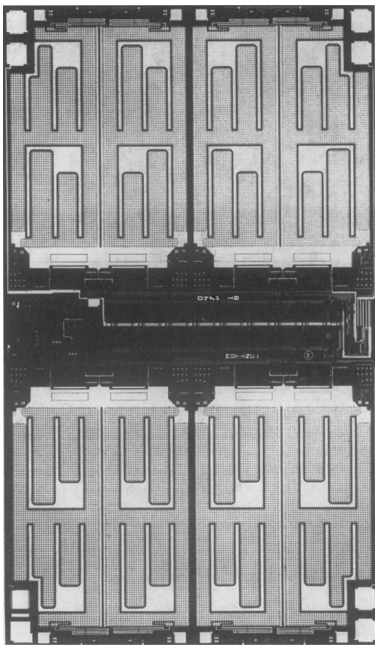

FIGURE 71.13 Photomicrograph of eight-output power IC. Note that the area of the eight-output devices (two located at each corner of the die) are considerably larger than the circuitry in the center, and top, and bottom that provides the temperature sensing, signal conditioning, and other control features. (Courtesy of Motorola, Inc., Schaumburg, IL.)

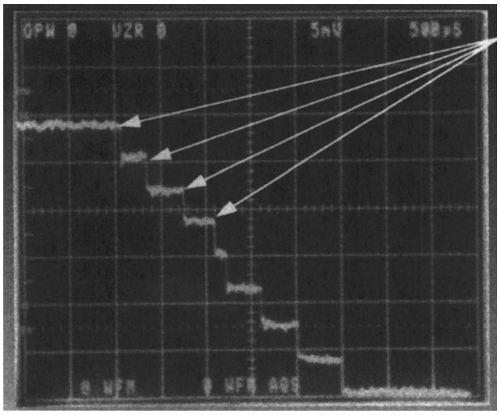

FIGURE 71.14 Independent thermal shutdown of an eight-output power IC. (Courtesy of Motorola, Inc., Schaumburg, IL.)

shutdown can be implemented. In a multiple output power IC, it is highly desirable to shut down only the device that is experiencing a fault condition and not all of the devices that are integrated on the power IC. With outputs in various physical locations on the chip, it is difficult to predict the thermal gradients that could occur in a fault situation. Local temperature sensing at each output, instead of a single global temperature sensor, is required.

As shown in Figure 71.14, the eight outputs of the device with individual temperature sensors can be independently shut down when the thermal limit of 170 °C is exceeded [10]. All of the outputs were connected to a 16 V supply at a room temperature ambient. A total current of almost 30 A initially flowed through the device. Note that each device turns off independently. The hottest device turns off first. Variations can result from differences in current level and thermal resistance. As each device turns off, the total power dissipation in the chip decreases, and the devices that are still on can dissipate heat more effectively.

Connecting directly to the battery is a hard short that could have been detected by current limit circuitry. However, a soft short is below the current limit, but exceeds the power-dissipating capability of the chip, and can be an extremely difficult condition to detect. Soft shorts require over-temperature sensing to protect the IC from destructive temperature levels.

The over-temperature condition sensed by the power IC could mean that the device turns itself off to prevent failure in one case, and in another situation, a fault signal provides a warning to the MCU but no action is taken, depending on the fault circuit design. The remaining portion of the system is allowed to function normally. With the fault conditions supplied to the MCU, an orderly system shutdown can be implemented. Integrated temperature sensing is essential to provide this type of protection in a multiple-output power IC.

71.6 Reliability Implications of Temperature to Electronic Components

The effect of temperature on electronic components and their successful application in electronic systems is one of the issues that must be addressed during the design of the system. Temperature affects the performance and expected life of semiconductor components. Mechanical stress created by different coefficients of thermal expansion can cause failures in thermal cycling tests (air-to-air) or during thermal shock (water-to-water) transitions.

The typical failure rate for semiconductor component can be expressed by the Arrhenius equation [9]:

$$\lambda = Ae^{-\text{ø}/KT} \tag{71.3}$$

where

λ is the failure rate
A is the constant
ø is the activation energy (eV)
K is the Boltzmann constant (8.62×10^{-5} eV K^{-1})
T is the junction temperature (K)

The failure rate of semiconductor components is typically stated to double for every 10°C–15°C increase in operating (i.e., junction) temperature. However, increased testing and design improvements have minimized the failures due to specific failure mechanisms.

One of the temperature-related parameters that must be taken into account during the design phase of a power switch is the transient thermal response, which is designated as $r(t)\ R\text{ø}_{JC}$, where $r(t)$ represents the normalized transient thermal resistance. The value of $r(t)$ is determined from the semiconductor manufacturer's data sheet using duty cycle and pulse duration used in the application. This reduced level of the thermal resistance (see Section 71.6.1), based on the transistor operating in a switching mode and being off for a period of time, approaches the dc level within a second. Excessive temperatures can be generated quickly and must be detected within milliseconds to prevent failure.

71.6.1 Junction Temperature Measurement

In a semiconductor, the change in temperature is directly related to the power dissipated through the thermal resistance. The steady-state dc thermal resistance junction-to-case, $R\text{ø}_{JC}$, is defined as the temperature rise per unit power above an external reference point (typically the case). The relationship is shown in Equation 71.4 [8].

$$R\text{ø}_{JC} = \frac{\Delta T}{P_D} \tag{71.4}$$

where

ΔT is the junction temperature minus the case temperature (°C)
P_D is the power dissipated in the junction (W)

The semiconductor device or silicon die is typically enclosed in a package that prevents a direct measurement of the junction temperature. The junction temperature is measured indirectly by measuring the case temperature, T_C; the heatsink temperature, T_S; for those higher-power applications that require a heatsink; the ambient temperature, T_A; and a temperature-sensitive electrical parameter of the device.

The first step of the process requires calibrating the temperature-sensitive parameter. Using a bipolar power transistor as an example, the base–emitter forward voltage is measured and recorded with a low calibration current (I_M) flowing through the device that is low enough to avoid self-heating (typically between 2 and 10 mA) and yet sufficiently high to be in the linear range of the forward voltage curve. The procedure is performed at room and elevated temperatures, typically 100 °C.

After calibration, a power switching fixture (such as Figure 71.15) is used to alternately apply and interrupt the power to the device under test (DUT) [8]. The on portion is long (typically several milliseconds) and the off portion is short (only a few 100 μs), so the temperature of the case is stabilized and junction cooling is minimal. The transistor is operated in its active region, and the power dissipation is varied by adjusting the I_E and/or V_{CE} until the junction is at the calibration temperature. This point is known by measuring V_{BE} during the time that I_M is the only current flowing.

When the V_{BE} value equals the value on the calibration curve, the junction temperature is at the calibration temperature. Measurements of V_{BE}, T_C, and I_E allow the thermal resistance for the device to

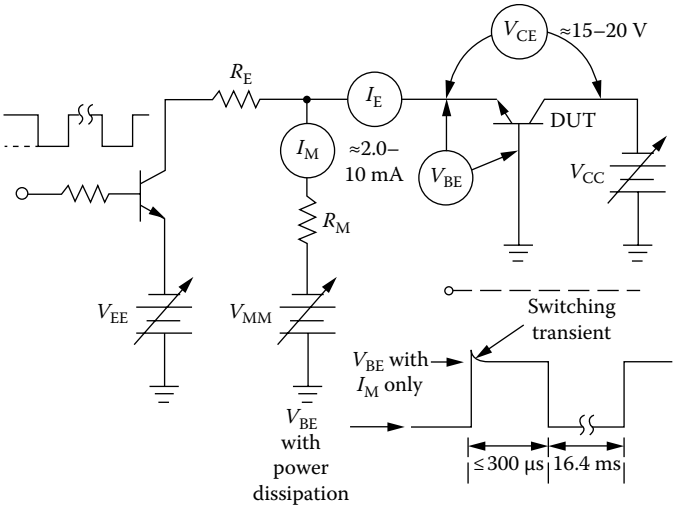

FIGURE 71.15 Example of steady-state thermal resistance test circuit for a bipolar power transistor. Power is applied for 16.4 ms and interrupted for ≤300 μs to measure the V_{BE}.

be calculated using Equation 71.4. Since $R\text{ø}_{JC}$ is a constant, subsequent measurements of T_C, V_{CE}, and I_E under different operating conditions can be used to calculate the junction temperature to keep the device within its safe operating range in the actual application. For devices with different electrical characteristics, such as the power MOSFETs discussed earlier, other parameters that have a linear relationship to temperature are used for calibration and measurement.

71.7 Semiconductor Temperature Sensor Packaging

Temperature sensors that are manufactured using semiconductor technology are typically packaged in packages common to the semiconductor industry. These include metal can (TO-99), ceramic, and more commonly available plastic (SOT-23, 8-lead DIP, TO-92, 8-lead SOIC, etc.) packages. These packages are designed for circuit board solder attachment that can be either through-hole or surface-mount technology. As a result, package form factors can be considerably different from packages for temperature sensors manufactured using other technologies. Figure 71.16 shows examples of five available silicon temperature sensor packages.

More recent packages include SC70, four-ball wafer chip-scale package, micro small outline package, and dual, flat no-lead packages.

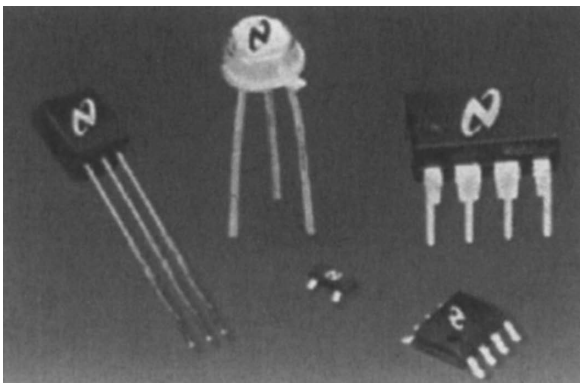

FIGURE 71.16 Plastic TO-92, TO-99 metal can, 8-lead DIP, 8-lead SOIC, and TinyPak™ SOT-23 plastic packages. (Courtesy of National Semiconductor Corp., Santa Clara, CA.)

Defining Terms

Bandgap reference: Forward-biased emitter junction characteristics of adjacent transistors used to provide an output voltage with zero temperature coefficient.

Die: An unpackaged semiconductor chip separated from the wafer.

Embedded temperature sensor: A temperature sensor included within an integrated circuit.

Integrated circuit: A multiplicity of transistors, as well as diodes, resistors, capacitors, and so on, on the same silicon die.

Junction: The interface at which the conductivity type of a material changes from *p* type to *n* type.

Junction voltage: The voltage drop across a forward-biased *pn* interface in a transistor (V_{be}) or diode.

Junction temperature: The temperature of the *pn* interface in a transistor or diode.

Monolithic (integrated circuit): Constructed from a single piece of silicon.

Power IC or smart power IC: Hybrid or monolithic (semiconductor) device that is capable of being conduction-cooled, performs signal conditioning, and includes a power control function such as fault management and/or diagnostics.

Self-heating: Temperature rise within a (semiconductor) device caused by current flowing in the device.

Soft short: An excessive load condition that causes excessive temperature but is below the current limit of a device.

Thermal resistance: The steady-state dc thermal resistance junction-to-case, $R\text{ø}_{JC}$, is the temperature rise per unit power above an external reference point (typically the case).

TinyPak: A trademark of Texas Instruments.

Wafer: A thin slice of semiconductor material, commonly silicon in 400 mm, 300 mm, used to manufacture or fabricate integrated circuits.

Vendors and Suppliers

Analog Devices, Inc.
http://www.analog.com
AD590
AD22100

Maxim Integrated Products
http://www.maxim-ic.com
DS600
DS18S20
MAX31826

Microchip Technology, Inc.
http://www.microchip.com
MCP9808
MCP9701
TC620
TC74A0
TC07
TC6501

Rohm Semiconductor
http://www.rohm.com/products/lsi/sensor/temperature_sensor/174sel2/

STMicroelectronics
http://www.st.com/internet/analog/class/1577.jsp

Texas Instruments, Inc.
http://www.ti.com
http://www.ti.com/lsds/ti/analog/temperature_sensor.page?DCMP=hpa_bestbets&HQS=hpa-sc-bb-temphome
MSP430
TMP275
TMP100

SMSC
http://www.smsc.com/index.php?tid=157

References

1. J. Carr, *Sensors and Circuits*, Englewood Cliffs, NJ, PTR Prentice-Hall, 1993.
2. Pressure sensor device data DL200/D Rev. 1, Phoenix, AZ, Motorola, 1994.
3. K. Lacanette, Using IC temperature sensors to protect electronic systems, Sensors, Peterborough, NH, 14(1), pp. 28–34, January 1997.
4. R. Wegner and H. Hulsemann, New family of monolithic temperature sensor and controller circuits present challenges in maintaining temperature measurement accuracy, *Proceedings of Sensors Expo West*, Anaheim, CA, February 8–10, 1994.
5. W. Schweber, Temperature sensors fill different needs, *EDN*, 41(20), 1996.
6. R. Downs, Digital thermometer IC simplifies distributed sensing, *Electronic Products*, 56, 1995, available at http://www.electronicproducts.com/PrintArticle.aspx?ArticleID=9763 (accessed on December 23, 2012).
7. J. Williams, High performance signal conditioning for transducers, *Proceedings of Sensors Expo West*, San Jose, CA, March 2–4, 1993.
8. TMOS power MOSFET transistor data DL135/D Rev. 4, Phoenix, AZ, Motorola Semiconductor.
9. R. K. Jurgen (ed.), *Automotive Electronics Handbook,* New York, McGraw-Hill, 1999.
10. R. Frank, *Understanding Smart Sensors*, Boston, MA, Artech House, 2013.
11. J. R. Gyorki, Designing with semiconductor temperature sensors, Sensor Tips website: http://www.sensortips.com/temperature/designing-with-semiconductor-temperature-sensors (accessed on March 14, 2013).

72

Noncontact Thermometers

Jacob Fraden
Fraden Corporation

There are two ways of measuring temperature—contact and noncontact. In the former case, a temperature probe is placed into an intimate physical connection with the object, while in the latter case, a temperature probe is nearly disconnected from the object, except one link—the optical. In this chapter, we examine noncontact ways of measuring temperature by exchange of electromagnetic radiation from the visible to far infrared spectral ranges.

72.1 Thermal Radiation (Physical Laws)

In any object, every atom and every molecule exist in a perpetual motion. When an atom moves, it collides with other atoms and transfers to them part of its kinetic energy, thus losing some of its own energy in this perpetual bouncing. On the other hand, an atom that had a smaller kinetic energy, after a collision, gains some. Afterward, the material body consisting of such agitated atoms reaches the energetic equilibrium where all atoms, while not vibrating with exactly the same intensity and frequency, still may be described by an average kinetic energy. Such an average kinetic energy of the agitated particles is represented by the *absolute temperature*, which is measured in degrees kelvin. In other words, what we commonly call temperature is a measure on a macroscale of the microscopic atomic motion.

According to laws of electrodynamics, a moving electric charge (all atoms are made of electric charges) is associated with a variable electric field. An electric field around a charged particle changes while the particle moves. A variable electric field, in turn, produces an alternating magnetic field.

When the magnetic field changes, it results in a coupling with its variable electric field, and so on. Thus, a thermally agitated particle becomes a source of the electromagnetic field that propagates outwardly with the speed of light and is called *thermal radiation*. It is called thermal because it directly depends on the kinetic energy of vibrating particles. Since this radiation is predominantly situated in the optical region, it is governed by the laws of optics—it can be reflected, filtered, focused, and so on. And also, it can be used as a measure of the object's temperature.

Electromagnetic waves originated from the mechanical movement of particles may be characterized by their magnitude and wavelengths (or frequencies). Both of these characteristics relate to temperature, that is, the hotter the object, the shorter the wavelength and the stronger the magnitude. Very hot objects radiate in the visible portion of the spectrum of wavelengths between 0.4 μm (blue) and 0.7 μm (red). For example, a filament in an incandescent lamp is so hot (around 3000 K) that it radiates bright visible light. If the lamp is controlled by a dimmer, the light intensity may be reduced by turning the knob, and one may observe that the dimmed light becomes more yellowish and reddish and finally visibly disappears. This means that the filament cools down and its heat intensity drops and the radiated spectrum shifts toward longer wavelengths. Near the end of the dimmer control, the filament is still quite hot, yet we cannot see it because it emanates light in the invisible infrared spectral range, the wavelengths somewhere longer than 0.8 μm. Cooler objects radiate light in the near, mid, and far infrared spectral ranges that we cannot see. For instance, thermal radiation that is emanated from a human skin primarily is situated at wavelengths between 5 and 15 μm in the mid and far infrared ranges and is not visible to human eyes; otherwise, we all would glow in dark (sick people with fever would look a bit brighter).

If we imagine that all atomic vibrations for some mysterious reason would stop, no electromagnetic radiation will be emanated from the object. Such an imaginable but impossible event is characterized by the infinitely cold temperature, which is called the *absolute zero*.

Since temperature is a measure of the average atomic kinetic energy, it is logical to assume that one may determine the object's temperature by measuring intensity of the emanated thermal radiation or its spectral characteristics. This presumption is the basis for noncontact temperature measurements, which is known by the various names depending on the application: infrared thermometry, optical pyrometry, radiation thermometry, and so on. *Pyrometry* is derived from the Greek word *pyr* (*πυρ*), which means *fire*, and thus is more appropriate for measuring hotter temperatures. For the lower temperatures, the name *infrared thermometry* is used interchangeably with *radiation thermometry*.

72.1.1 Planck's Law

A relationship between the magnitude of radiation at a particular wavelength λ and absolute temperature T is rather complex and governed by Planck's law, which was discovered in 1901. It establishes a radiant flux density W_λ as a power of electromagnetic radiation per unit of wavelength:

$$W_\lambda = \frac{\varepsilon(\lambda) C_1}{\pi \lambda^5 (e^{C_2/\lambda T} - 1)} \tag{72.1}$$

where

$\varepsilon(\lambda)$ is the emissivity of an object
$C_1 = 3.74 \times 10^{-12}$ W cm^2 and $C_2 = 1.44$ cm K are the constants
e is the base of natural logarithms

Spectral densities have clearly pronounced, albeit not sharp maxima at different temperatures (Figure 72.1).

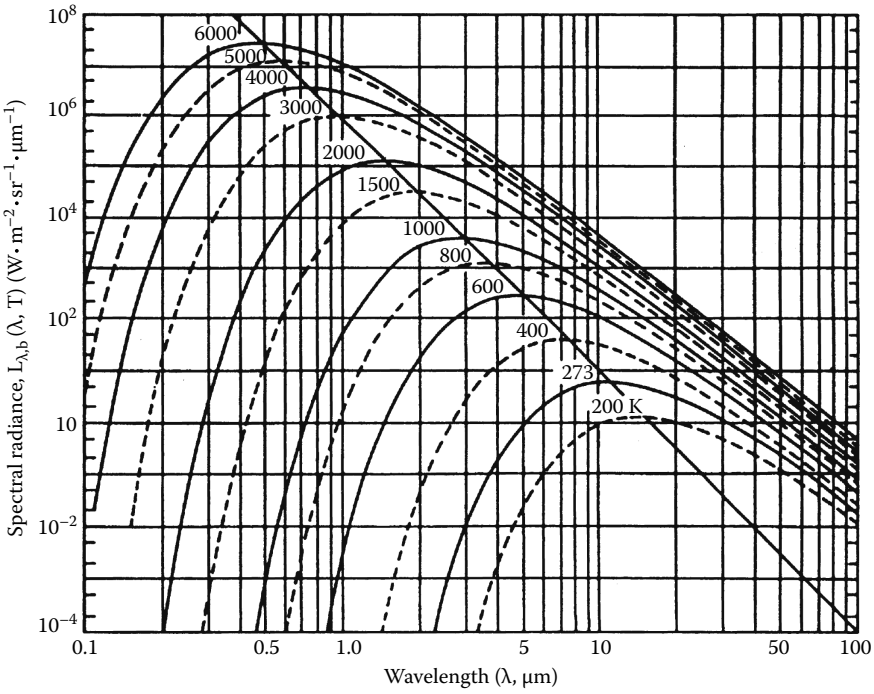

FIGURE 72.1 Spectral densities calculated within solid angle of 1 sr for radiation of a blackbody source.

72.1.2 Wien's Law

Equation 72.1 does not lend itself to a simple mathematical analysis and thus was approximated by a simplified version that is known as Wien's law:

$$W_\lambda = \frac{C_1}{\pi}\varepsilon(\lambda)\lambda^{-5}e^{-\frac{C_2}{\lambda T}} \tag{72.2}$$

Since temperature is a statistical representation of an average kinetic energy, it determines the highest probability for the particles to vibrate with a specific frequency and to have a specific wavelength. This most probable wavelength can be found from Wien's law by equating a first derivative of Equation 72.2 to zero. The result of the calculation is a peak wavelength near which most of the radiant power is concentrated:

$$\lambda_m \approx \frac{2898}{T}, \tag{72.3}$$

where

λ_m is in μm
T in kelvin

Wien's law states that the higher the temperature, the shorter wavelength. This formula also defines the midpoint of the spectral response of a pyrometer or infrared thermometer.

72.1.3 Stefan–Boltzmann Law

Theoretically, a thermal radiation bandwidth is infinitely wide. Yet most of the emanated power is situated within quite a limited bandwidth. Also filtering properties of the real-world windows used in the instruments allow passing only limited wavelengths and thus must be accounted for. In order to

determine the total radiated power (light flux) that is limited within a particular bandwidth, Equation 72.1 or (72.2) has to be integrated within the limits from λ_1 to λ_2:

$$\Phi_b = \frac{1}{\pi}\int_{\lambda_1}^{\lambda_2} \frac{\varepsilon(\lambda)C_1\lambda^{-5}}{e^{C_2/\lambda T}-1}. \tag{72.4}$$

This integral can be resolved only numerically or by approximation. For a narrow bandwidth (λ_1 and λ_2 are close to one another), the solution may be approximated by a high-order parabola:

$$\lambda_b = gT^x, \tag{72.5}$$

where

g is constant
$x \approx (12/\lambda_2)(1200/T)$

For example, in the visible portion of the spectrum at $\lambda_2 \approx 0.7$ μm and for temperatures near 2000 K, the approximation is a 10th order parabola.

For a very broad bandwidth where $\lambda_2 \to \infty$ or practically, when the range between λ_1 and λ_2 embrace well over 50% of the total radiated power, an approximation is a fourth-order parabola, which is known as the *Stefan–Boltzmann law*

$$\Phi_b = A\varepsilon\sigma T^4 \tag{72.6}$$

where

$\sigma = 5.67 \times 10^{-8}$ W/m^{2}K^4 (Stefan–Boltzmann constant)
A is the area from which the radiation is emanated
emissivity, ε, is assumed to be wavelength independent

It is seen that with the increase in temperature, intensity of the thermal radiation Φ_b grows very fast due to the fourth power of T. To improve accuracy and reduce noise, practically all radiation thermometers employ the magnitude of thermal radiation power within a relatively wide bandwidth and seldom, if ever, consider the wavelength shift resulted from changing temperatures.

72.1.4 Kirchhoff's Law

As it follows from Equations 72.5 and 72.6, besides a temperature, the magnitude of the radiation also is a function of the surface property called *emissivity*, ε, that is measured on a scale from 0 to 1. Emissivity is a ratio of the radiant flux that is emanated from a surface to the maximum theoretically possible flux that would be emanated from an ideal emitter (blackbody) having the same temperature. *Reflectivity*, ρ, and *transparency*, γ, also on a scale from 0 to 1, show what portion of the incident light is reflected and passed through, respectively. There is a fundamental equation that connects these three characteristics:

$$\varepsilon + \gamma + \rho = 1 \tag{72.7}$$

All these factors are wavelength dependent. Equation 72.7 that is known as Kirchhoff's Law indicates that any one of the three properties of a material may be changed only on the expense of the others. As a result, if at a particular wavelength the object is opaque ($\gamma = 0$), reflectivity, ρ, and emissivity, ε, are connected by a simple relationship: $\rho = 1 - \varepsilon$. This makes a mirror a good reflector but a poor emitter. That is, an ability to absorb light (not to reflect or transmit) is equal to an ability of emanating thermal radiation.

72.2 Emissivity

The emissivity of a material is a function of its dielectric constant and, subsequently, refractive index n. As it was mentioned earlier, emissivity is generally wavelength dependent (see Figure 72.2). For example, a white sheet of paper is very much reflective in the visible spectral range and emits no visible light. In the mid and

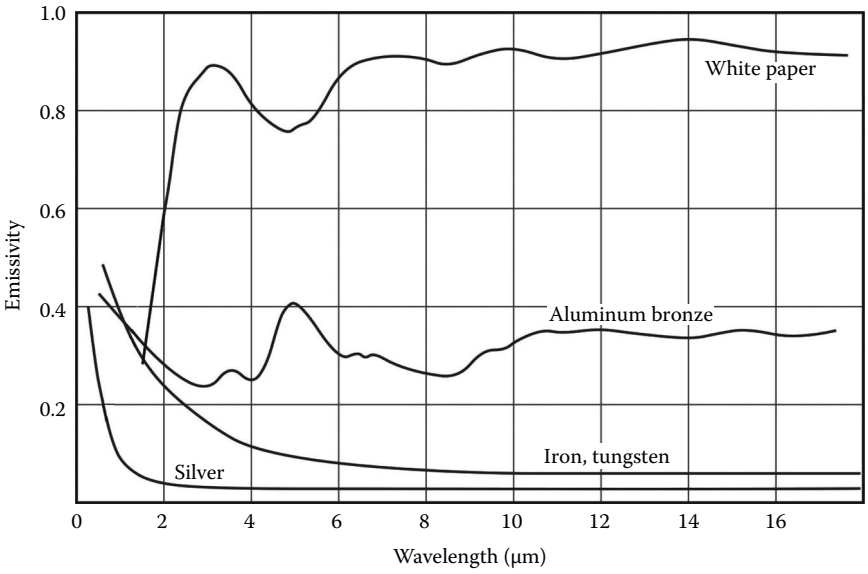

FIGURE 72.2 Wavelength dependence of emissivities of some materials. (Used with permission from Springer Science+Business Media: *Handbook of Modern Sensors*, 4th edn., 2010, Fraden, J., 2010.)

far infrared spectral ranges, its reflectivity is low and emissivity is high (about 0.92), thus making a paper a good emitter of thermal radiation at room temperatures. For many practical purposes, in the infrared thermometry, emissivity may be considered constant but seldom is accurately known. Since emissivity is an ability to emanate electromagnetic radiation, knowing its value for a particular object of measurement is important for the accuracy of a radiation thermometer, unless a special design negates the effects of emissivity on accuracy, as described later.

As a rule, emissivities of dielectrics are high and of bare nonoxidized metals, low. Due to a high emissivity of dielectrics, a dielectric emanates strong thermal radiation and thus lends itself for easy and accurate noncontact temperature measurement. On the other hand, a radiation thermometry of nonoxidized metals is difficult, due to a low level of the emanated thermal radiation flux. Table 72.1 gives typical emissivities of some opaque materials in a temperature range between 0 °C and 100 °C.

Unlike most solid bodies, gases in many cases are transparent to thermal radiation. When they absorb and emit radiation, they usually do so only in certain narrow spectral bands. Some gases, such as N_2, O_2, and others of the nonpolar symmetrical molecular structure, are essentially transparent at low temperatures, while CO_2, H_2O, and various hydrocarbon gases radiate and absorb to an appreciable extent. When thermal radiation light enters a layer of gas, its absorption has an exponential decay profile over the layer's thickness, governed by *Beer's law*

$$\frac{\Phi_x}{\Phi_0} = e^{-\alpha_\lambda x}, \tag{72.8}$$

where

Φ_0 is the incident thermal flux
Φ_x is the flux at thickness x
α_λ is the spectral coefficient of absorption

The ratio given earlier is called a monochromatic transmissivity at a specific wavelength λ. If gas is nonreflecting (usually it is), then from Kirchhoff's law, its emissivity is defined as

$$\varepsilon_\lambda = 1 - \gamma_\lambda = 1 - e^{-\alpha_\lambda x}. \tag{72.9}$$

TABLE 72.1 Typical Emissivities of Different Materials (from 0°C to 100°C)

Material	Emissivity	Material	Emissivity
Blackbody (ideal)	1	Green leaves	0.88
Cavity radiator	0.990–0.999	Ice	0.96
Aluminum (anodized)	0.70	Iron or steel (rusted)	0.70
Aluminum (oxidized)	0.11	Nickel (oxidized)	0.40
Aluminum (polished)	0.05	Nickel (unoxidized)	0.04
Aluminum (rough surface)	0.06–0.07	Nichrome (80Ni–20Cr) (oxidized)	0.97
Asbestos	0.96	Nichrome (80Ni–20Cr) (polished)	0.87
Brass (dull tarnished)	0.61	Oil	0.80
Brass (polished)	0.05	Silicon	0.64
Brick	0.90	Silicone rubber	0.94
Bronze (polished)	0.10	Silver (polished)	0.02
Carbon-filled latex paint	0.96	Skin (human)	0.93–0.96
Carbon lamp black	0.96	Snow	0.85
Chromium (polished)	0.10	Soil	0.90
Copper (oxidized)	0.6–0.7	Stainless steel (buffed)	0.20
Copper (polished)	0.02	Steel (flat rough surface)	0.95–0.98
Cotton cloth	0.80	Steel (ground)	0.56
Epoxy resin	0.95	Tin plate	0.10
Glass	0.95	Water	0.96
Gold	0.01–0.02	White paper	0.92
Gold-black	0.98–0.99	Wood	0.93
Graphite	0.7–0.8	Zinc (polished)	0.04

It should be emphasized that since gases absorb only in narrow bands, emissivity and transmissivity (transparency) must be specified separately for any particular wavelength. For instance, water vapor is highly absorptive (emissive) at wavelengths of 1.4, 1.8, and 2.7 μm while very transparent at 1.6, 2.2, and 4 μm.

All nongaseous nonmetals are good diffusive emitters of thermal radiation with a remarkably constant emissivity within a solid angle of about ±70°. Beyond that angle, emissivity begins to decrease rapidly to zero with the angle approaching 90°. Near angles of 90°, emissivity is very low. A typical calculated graph of the directional emissivity of nonmetals into air is shown in Figure 72.3a.

Metals behave quite differently. Their emissivities greatly depend on surface finish. Generally, polished metals are poor emitters within the solid angle of ±70° while their emissivity increases at larger angles (Figure 72.3b). Oxidized metals start behaving more like dielectrics with the increased thickness of oxides. To increase emissivity of a metal surface for a noncontact temperature measurement, it may be treated, for example, painted, oxidized, or anodized.

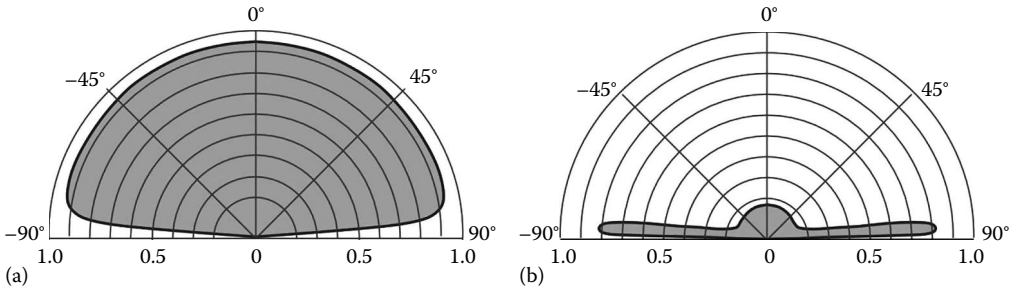

FIGURE 72.3 Spatial emissivities for (a) a nonmetal and (b) a polished metal. (Used with permission from Springer Science+Business Media: *Handbook of Modern Sensors*, 4th edn., 2010, Fraden, J., 2010.)

72.3 Blackbody

By definition, the highest possible emissivity is unity. It is attributed to the so-called *blackbody*—an ideal emitter of electromagnetic radiation. If an object is opaque ($\gamma = 0$) and totally nonreflective ($\rho = 0$), according to Equation 72.7, it becomes an ideal emitter and absorber of electromagnetic radiation. The name blackbody implies its appearance at normal room temperatures—indeed, since absolutely no light is reflected back, it does look very black. In reality, an ideal blackbody does not exist: it is just a fantasy, and any real object with a less-than-unity emissivity sometimes is called a *graybody*.

A practical blackbody (ε is about 0.99 or higher) is an approximation to an ideal blackbody and is an essential tool for calibrating and verifying accuracy of infrared thermometers.

72.3.1 Cavity Effect

To design a high-accuracy blackbody, a "cavity effect" is put to work. This effect appears when electromagnetic radiation escapes via an opening of a cavity [1]. For this purpose, a cavity means a void of a generally irregular shape whose inner wall temperature is uniform over the entire surface. Emissivity of the cavity opening dramatically increases and approaches unity at any wavelength, as compared with a flat surface that typically is much less than unity and is wavelength dependent. The cavity effect is especially pronounced when the cavity inner walls have higher emissivity. To explain the cavity effect, let us consider a cavity with a nonmetal inner surface. All nonmetals are diffuse emitters. Also they are diffuse reflectors. These are the key properties of the cavity wall surface for the cavity effect. We assume that temperature and surface emissivity of the cavity inner surface are homogeneous over an entire inner area. Figure 72.4 illustrates a simple conical cavity. Let us select area a on the cavity wall. In accordance with the Stefan–Boltzmann Law, the ideal emitter (blackbody) would emanate from a, the photon flux being $\Phi_0 = a\sigma T_b^4$. However, the surface is not an ideal emitter and has the actual emissivity ε_b.

The flux that is emitted by other parts of the cavity and incident on area a is also equal to Φ_b (the object is thermally homogeneous and assumes a uniform radiation within a hemisphere). A substantial portion of that incident flux Φ_b is absorbed by the surface of area a, without changing its temperature. The remaining part of the incident flux is diffusely reflected:

$$\Phi_\rho = \rho\Phi_b = (1 - \varepsilon_b)\varepsilon_b\Phi_0 \tag{72.10}$$

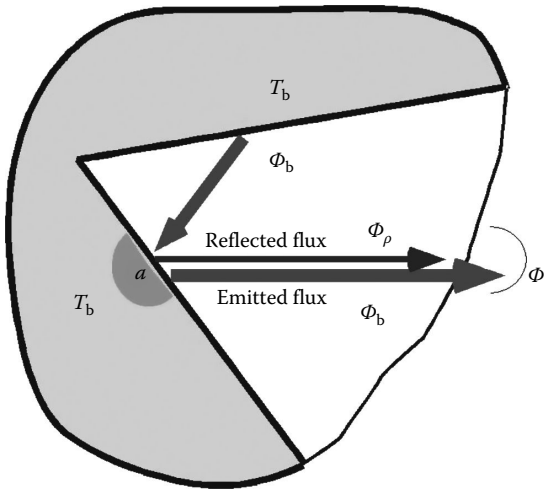

FIGURE 72.4 Cavity effect enhances emissivity by combining the emanated and reflected fluxes.

and a combined flux effusing from the area a is the sum of two fluxes:

$$\Phi = \Phi_b + \Phi_\rho = \varepsilon_b \Phi_0 + (1 - \varepsilon_b)\varepsilon_b \Phi_0 = (2 - \varepsilon_b)\varepsilon_b \Phi_0 \tag{72.11}$$

As a result, the *effective emissivity* may be expressed as

$$\varepsilon_e = \frac{\Phi}{\Phi_0} = (2 - \varepsilon_b)\varepsilon_b \tag{72.12}$$

To illustrate the effective emissivity, we assume that the cavity walls are painted with organic paint (a paint color in the visible spectrum makes no difference) having a surface emissivity $\varepsilon_b = 0.92$ in the mid and far infrared ranges. Then according to Equation 72.12, the effective emissivity at the cavity opening is $\varepsilon_e = 0.9936$. It follows from the earlier text that due to the cavity effect, a perceived (effective) emissivity of a cavity is equal to the wall emissivity magnified by a factor of $(2 - \varepsilon_b)$. For the cavity effect to work, the effective emissivity must be attributed only to the cavity opening (aperture) from which the radiation escapes. If the probe of a radiation thermometer is inserted inside the cavity facing the walls directly (blocking the flux from other walls of the cavity), the cavity effect is substantially diminished and emissivity will drop to that of a wall surface.

72.3.2 Practical Blackbodies

To achieve emissivity well over 0.990, there are four fundamental requirements to a blackbody design:

1. The inner wall temperatures must be uniform within ±0.01 °C all over the cavity surface. Thus, in most practical cases, the blackbody cavity should be fabricated of a metal of high thermal conductivity.
2. Temperature accuracy of the inner walls should be measured with uncertainty no greater than 0.02 °C.
3. A ratio of the inner wall area to the aperture area should be at least 100:1 and preferably much higher.
4. The cavity should have no inner surfaces that are parallel to the aperture. A blackbody serves as a light trap for any light incident on the aperture, thus there must be multiple inner reflections of the light beam arriving from the aperture until it is nearly extinguished. This allows to closely satisfying Kirchhoff's law for a blackbody, that is, no light is reflected back or passing through.

A practical blackbody can be fabricated in several ways. Copper and aluminum are the best choices for the cavity body material—thanks to their high thermal conductivity that helps equalizing temperatures of the cavity walls. Figure 72.5 shows simplified cross-sectional views of two practical blackbodies. One (A) is a solid-state blackbody having thermoelectric elements (heat pumps) that provide either heating or cooling to the cavity body. This solid-state blackbody has a useful temperature range from about –20 °C to +120 °C. To control temperature, the imbedded precision temperature sensor is connected to the heat pump control circuit (not shown). The inner shape of the cavity is partly conical to increase the number of reflections and prevent a direct reflection of light that may come to the aperture from outside, so the light will be trapped inside and not reflected back via the aperture. The entire inner surface is treated for a relatively high surface emissivity, typically over 0.9.

The aperture potentially may act as an entry for undesirable ambient air. Cooler or warmer air may disturb the thermal uniformity inside the cavity resulting in excessively high uncertainty of the radiated flux. To reduce that problem, the cavity has a slightly positive air pressure where air is continuously pumped inside through the air ducts. Before entering the cavity, air passes through the narrow channels inside the cavity walls and acquires temperature near that of the blackbody.

There is another problem with the cavity opening—a temperature of the front aperture plate. Since for the convenience of use the plate is relatively thin, it is very difficult to maintain it at exactly the same

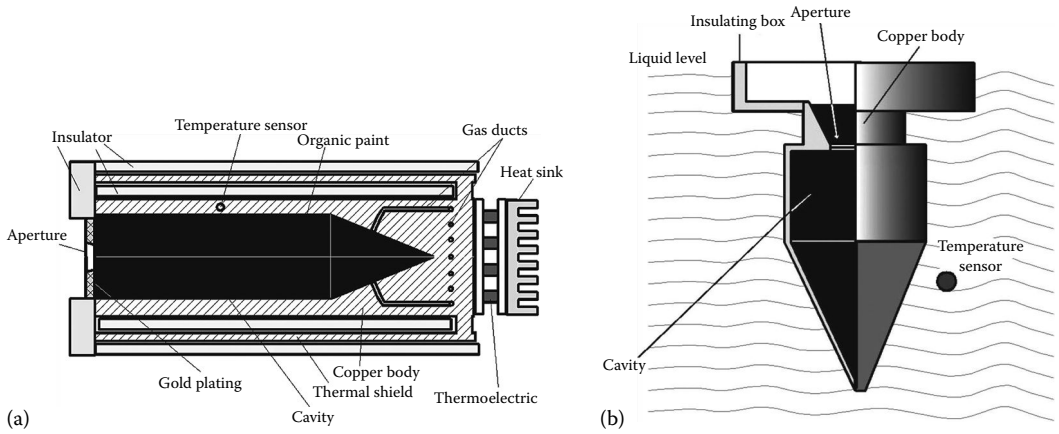

FIGURE 72.5 Solid-state blackbody with (a) thermoelectric elements and (b) water-immersed blackbody. A gold mirror creates a virtual cavity surface.

temperature as the cavity walls, thus violating the fundamental requirement (#1 given earlier)—the cavity temperature uniformity. To resolve this issue, the wall of the aperture plate that faces the cavity is mirror polished and coated with a thin layer of gold—the best reflector of infrared energy [2]. Since gold is an extremely poor emitter, the plate temperature becomes irrelevant. On the other hand, a very high reflectivity ($\sigma \approx 0.99$ for polished gold) bounces back the cavity thermal radiation. Thus, the gold mirror creates an extended virtual cavity that nearly doubles the size of the real cavity (see requirement #3 given earlier), improving the walls/aperture ratio.

To achieve a high temperature uniformity of the cavity walls, an active thermal shield is placed outside of the cavity body (see Figure 72.5a). This blackbody was tested to have an emissivity of at least 0.998.

Another example is an immersed blackbody (Figure 72.5b). The cavity body has relatively thin walls (few millimeters) and is immersed into a stirred liquid bath (often water) whose temperature is precisely controlled by the heating/cooling devices. The liquid assures uniform temperature distribution around the cavity with a typical thermal instability on the order of ±0.02 °C. The inner surface of the cavity is coated with organic paint. The aperture of the cavity is relatively small, just to allow the tested probe insertion, and can be also covered with a gold-coated plate as described earlier.

72.4 Detectors for Thermal Radiation

72.4.1 Classification

Generally speaking, there are two types of sensors (detectors) known for their capabilities of responding to thermal radiation within the spectral range from the visible to near infrared to far infrared, that is, approximately from about 0.4 to 40 μm of wavelengths. The first type is the *quantum* detectors and the second—*thermal* detectors.

72.4.2 Quantum Detectors

Quantum detectors (photovoltaic and photoconductive devices) rely on the interaction of individual photons with a crystalline lattice of semiconductor materials. Photovoltaic devices are the photodiodes and phototransistors, and photoconductive devices are the photoresistors. Their operations are based on the photo effect that was discovered by A. Einstein and brought him the Nobel Prize. In 1905, he made a remarkable assumption about the nature of light that at least under

certain circumstances, its energy was concentrated into localized bundles, later named photons. The energy of a single photon is given by

$$E = h\nu \tag{72.13}$$

where

ν is the frequency of light

$h = 6.63 \cdot 10^{-34}$ J · s (or $4.13 \cdot 10^{-15}$ eV) is Planck's constant derived on the basis of the wave theory of light

When a photon strikes a surface of a conductor, it may result in the generation of a free electron—meaning that the conductor becomes light sensitive.

The periodic lattice of crystalline materials establishes allowed energy bands for electrons that exist within that solid. The energy of any electron within a pure material must be confined to one of these energy bands that may be separated by gaps or ranges of forbidden energies.

In isolators and semiconductors, the electron must first cross the energy band gap in order to reach the conduction band. Hence, conductivities of these materials are therefore many orders of magnitude lower than that in conductors. For isolators, the band gap is usually 5 eV or more, whereas for semiconductors, the gap is considerably less.

When the photon of frequency ν_1 strikes a semiconductive crystal, its energy shall be high enough to separate the electron from its site in the valence band and push it through the band gap into a conduction band at a higher energy level. In that band, the electron is free to serve as a current carrier—that is what is required for the light sensing. The deficiency of an electron in the valence band creates a hole that also serves as a current carrier. This is manifested in the reduction of specific resistivity of the material.

The energy gap serves as a photon energy threshold, below which the material is not light sensitive.

Examples of the quantum detectors operating in the visible and near infrared ranges are the popular and inexpensive photodiodes, phototransistors, and photoresistors. They are quite sensitive because in that spectral range, energies of the photons (2 eV and more) are sufficiently high to cross a relatively wide energy gap. These detectors are used for noncontact measurement of hot objects that emanate photons of higher energies.

For cooler temperatures, that is—for the smaller photon energies (longer wavelengths)—the narrower band gap semiconductors are required, otherwise the "cooler" photons are just too weak to cross the gap. However, even if a special quantum detector has a sufficiently narrow energy band gap, at room temperatures, its own intrinsic noise is much higher than a signal originated by incoming photons. In other words, the detector will generate its own spurious "signal" (noise) and respond to its own temperature that will wash out signals from the external objects. This is the reason why for operation in the mid and far infrared spectral ranges, a quantum detector not only must have a sufficiently narrow energy gap, but its temperature also has to be lowered to the level where its own intrinsic noise is reduced to an acceptable level, that is, it must be cryogenically cooled down. Depending on the required sensitivity and operating wavelength, the following crystals are typically used for the cryogenically cooled photoresistors (see in Figure 72.6 the curves just below the dotted lines): lead sulfide (PbS), indium arsenide (InAs), germanium (G), lead selenide (PbSe), and mercury-cadmium-telluride (HgCdTe).

The sensor cooling allows it to respond to longer wavelengths. However, the response speeds of PbS and PbSe become less with cooling. Methods of cooling include a Dewar cooling using dry ice, liquid nitrogen, liquid helium, or thermoelectric coolers operating on the Peltier effect.

72.4.3 Thermal Detectors

Another class of infrared radiation detectors is called *thermal detectors*. Contrary to quantum detectors that respond to individual photons, thermal detectors respond to heat resulted from the absorption of thermal radiation by the surface of a sensing element that is capable of converting a heat level into an

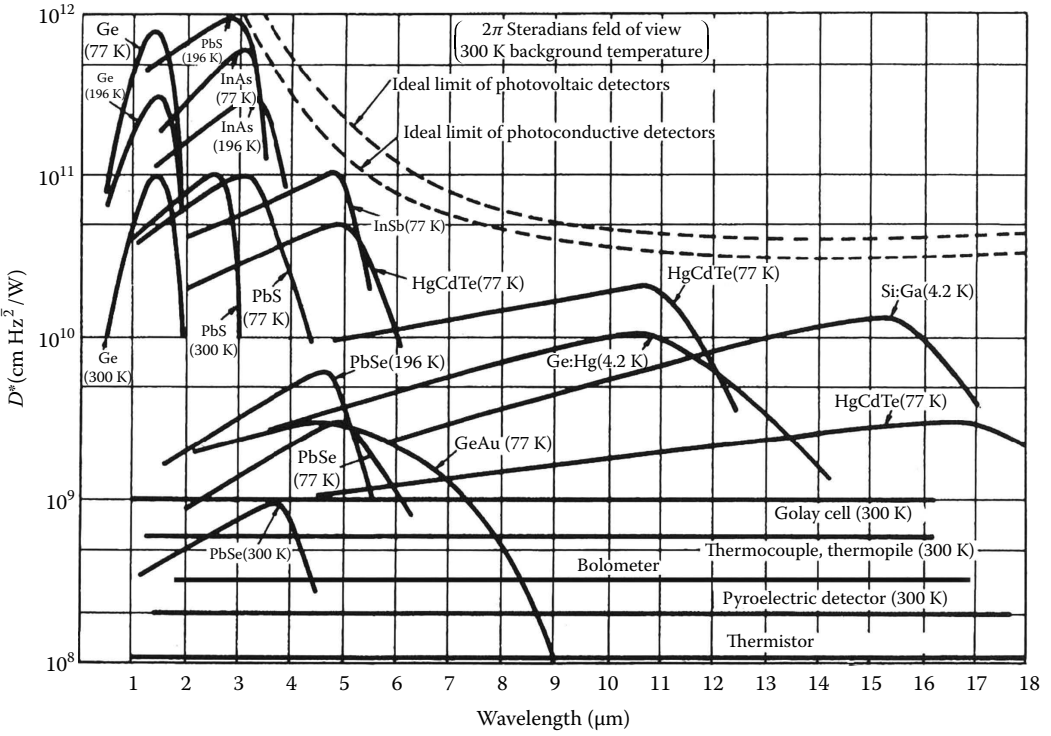

FIGURE 72.6 Operating ranges for the quantum and thermal infrared detectors.

electrical signal. The absorbed heat raises the temperature of the surface, and the resulting temperature increase becomes a measure of the incident thermal radiation. The thermal detectors are much less sensitive than quantum detectors because to elevate temperature of a detector to an appreciable level, a great number of photons is required, while a quantum detector produces an electron (and sometimes many) for a single absorbed photon. The thermal detectors are indicated at the lower portion of Figure 72.6. Note that unlike the quantum detectors, responses of the thermal detectors are flat over all spectral ranges.

Let us analyze the behavior of a thermal radiation detector when it is exposed to an object. Figure 72.7 illustrates an object having a temperature T and an emissivity ε. The object faces a detector having the temperature T_s and the emissivity ε_s. Note that the object radiates thermal flux Φ_{bo} toward the sensor while the sensor radiates its own flux Φ_{so} toward the object. This bidirectional radiation flow goes

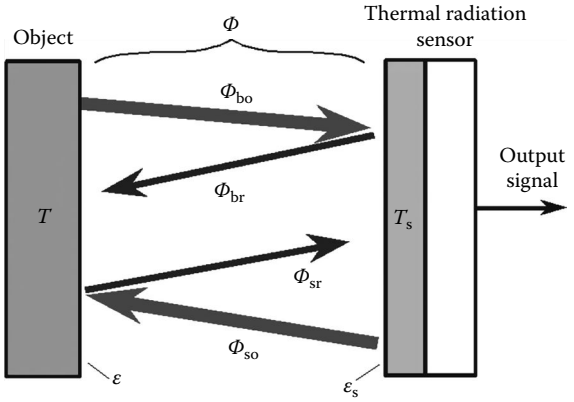

FIGURE 72.7 Radiative heat exchange between an object and a thermal radiation sensor.

through a coupling channel having a cross-sectional area A. According to the Stefan–Boltzmann law (Equation 72.6), these fluxes can be expressed as

$$\begin{aligned} \Phi_{bo} &= A\varepsilon\sigma T^4 \\ \Phi_{so} &= -A\varepsilon_s\sigma T_s^4 \end{aligned} \tag{72.14}$$

A negative sign indicates an opposite direction of flux from the detector Φ_{bo} with respect to flux Φ_{bo} from the object.

A larger part of flux Φ_{bo} is absorbed by the detector having an absorptivity (emissivity) ε_s:

$$\Phi_{bs} = A\varepsilon\varepsilon_s\sigma T^4 \tag{72.15}$$

While the detector absorbs energy from the object, it also loses energy toward the object. Thus, in turn, the object absorbs the detector's flux propagating at the opposite direction:

$$\Phi_{sb} = -A\varepsilon\varepsilon_s\sigma T_s^4 \tag{72.16}$$

These two fluxes combine into the final net flux that is absorbed or liberated by the detector's surface:

$$\Phi = \Phi_{bs} + \Phi_{sb} = A\varepsilon\varepsilon_s\sigma\left(T^4 - T_s^4\right). \tag{72.17}$$

This equation establishes a connection between thermal power, Φ, absorbed or liberated by the sensor, and the absolute temperatures of the object and the sensor, T and T_s, respectively. This net flux causes temperature of the sensing element in the detector to shift accordingly. Depending on which is larger, T or T_s, the sensing element temperature will go up or down. The temperature change can be used to determine the net thermal flux. To measure the temperature shift of the detector, the sensing element has an imbedded temperature sensor that produces the output electric signal proportional to the net flux, Φ, described by Equation 72.17.

The detector's output signal in the form of voltage can be defined as

$$V = g\Phi = Ag\varepsilon\varepsilon_s\sigma\left(T^4 - T_s^4\right), \tag{72.18}$$

where g is the conversion factor of the incident thermal flux to the sensor output voltage. The conversion factor generally is a function of the sensor's temperature T_s, albeit for a well-designed sensor, this dependence is small.

A temperature (in kelvin) of the object can be calculated from the inverted Equation 72.18:

$$T_b = \sqrt[4]{T_{sc}^4 + \frac{V}{Ag\varepsilon\varepsilon_s\sigma}}, \tag{72.19}$$

Note that in a sensor's relatively narrow temperature range, the denominator is a constant whose value is found during the thermometer calibration, while T_{sc} and T_b are the *computed* reference sensor and object's temperatures, respectively. These computed temperatures may somewhat differ from the true temperature T_s and T of Equation 72.18 because of the inevitable measurement uncertainties.

If we consider T being close to T_s, Equation 72.19 can be simplified to

$$T_b \approx T_{sc} + \frac{V}{4Ag\varepsilon\varepsilon_s\sigma T_{sc}^3} \tag{72.20}$$

Thus, to compute the object's temperature, one needs to know two variables—the detector's temperature and the detector's output voltage. The calibration factor (denominator) is found during the thermometer calibration.

There are a number of thermal detectors that can be used for measuring the sensor's temperature change described by the second summand. Such a detector is imbedded into the IR sensor's surface. One example is a thermistor-type sensor known as a *bolometer* [3]. But by far, the most popular is the so-called *thermopile* [4]. A thermopile belongs to a class of passive infrared detectors, that is, it generates electric output in relation to the absorbed thermal flux with no need for any additional source of energy (unlike the bolometers). Its operating principle is the same as that of a thermocouple (see the description of a thermoelectric effect in Chapter 70 in this book or in [1]). A thermopile consists of many serially connected thermocouples. Originally, it was invented by Joule to increase the output signal of a thermoelectric sensor. He connected several thermocouples in a series and thermally joined together all their "hot" and separately all "cold" junctions. Nowadays, a thermopile has a different configuration. Its prime application is a detection of thermal radiation. Note that a thermopile detector produces a signal that is nearly proportional to a temperature gradient between the "hot" and "cold" junctions but, unlike a bolometer, is not responsive to an absolute temperature. That is why a thermopile must be appended by an absolute temperature sensor, for example, a thermistor or a semiconductive temperature sensor. This additional absolute sensor sometimes is called a *reference temperature sensor*. It is essential for monitoring temperature T_s if Equation 72.19 or 72.20 is to be employed for computing temperature T_b of an object.

A cutout view of a thermopile IR sensor is shown in Figure 72.8 [1]. The sensor consists of a frame having a relatively large thermal mass. Typically, it is fabricated of silicon. To further stabilize it thermally, the frame is usually bonded to a metal header. The frame is the place where the "cold" junctions and reference temperature sensor are positioned. The frame supports a thin membrane (on the order of 1 μm) whose thermal capacity and thermal conductivity are small, so its temperature can change quickly and by a sufficient amount. The membrane is the area where all "hot" junctions are positioned. The membrane absorbs incident thermal radiation, thus its temperature shifts from T_s and subsequently is detected by the thermopile junctions. Even though a thermopile is just one part of the thermal IR sensor, the entire sensor is called a "thermopile."

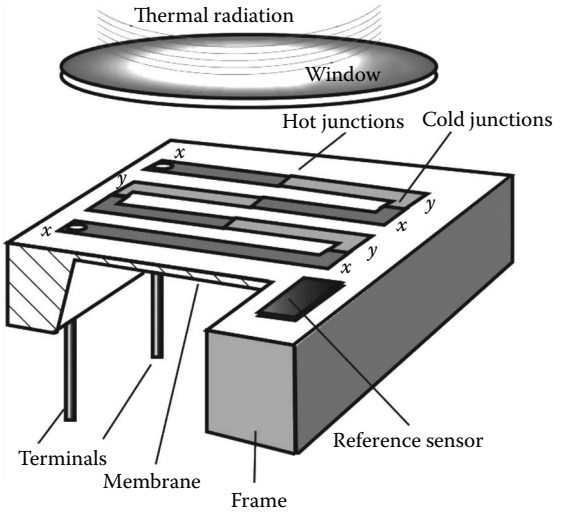

FIGURE 72.8 Thermopile sensor. The "hot" junctions are deposited on the membrane while the "cold" junctions on the frame. (Used with permission from Springer Science+Business Media: *Handbook of Modern Sensors,* 4th edn., 2010, Fraden, J., 2010.)

(a)

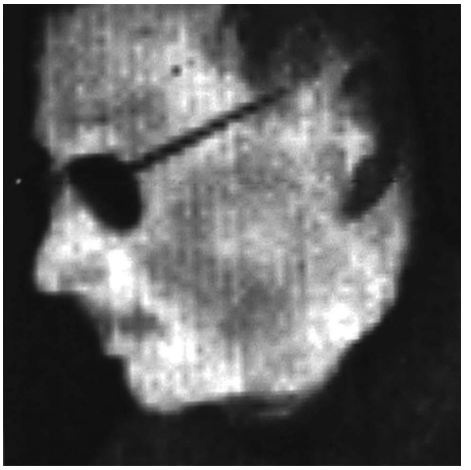

(b)

FIGURE 72.9 (a) Thermal imaging camera from Heimann Sensor GmbH and (b) an example of a thermal image.

The best performance of a thermopile is characterized by a high sensitivity, fast response, and low noise, which may be achieved if the junction materials have high thermoelectric coefficients, low thermal conductivity, and low volume resistivity. Besides, the junction pairs should have the thermoelectric coefficients of the opposite signs. This dictates selection of the materials. Methods of construction of the junctions may differ to some extent, but all incorporate vacuum deposition techniques and evaporation masks to apply the thermoelectric materials on thin membranes [4]. The number of junctions varies from twenty to several hundreds. The membrane is given an additional coat on the top to increase the surface emissivity (absorptivity). The output voltage of a thermopile is nearly proportional to the net thermal flux when the IR flux is absorbed. As opposed to quantum detectors that require a cryogenic cooling, the thermopile sensors can operate at room temperatures. Since thermopiles produce rather small output voltages, the signal become susceptible to external interferences. This is the reason why these sensors often incorporate various interface electronic circuits in the same packaging [5]. The examples are the thermopile modules HID L1x FL5.5 from Heimann Sensor GmbH (Germany) and TMP006 from Texas Instruments (U.S.A.).

A thermopile sensor essentially is a "single-pixel" detector. However, multiple thermopile groups can be deposited onto a single membrane to form a multifaceted sensor array. This allows not only to measure temperature but also to create a thermal image of an object formed on the membrane by a special focusing infrared lens. Each pixel represents temperature of a small area of the object's surface [6]. At the time of this writing, the best thermal imaging sensors having up to 64 × 62-element arrays with the corresponding focusing IR optics and electronics are produced by Heimann Sensor GmbH (Wiesbaden, Germany: www.heimannsensor.de). Figure 72.9 illustrates a small Heimann imaging camera operating at room temperature and an example of a thermal image it produces.

72.5 Pyrometers

72.5.1 Disappearing Filament Pyrometer

The other names for this instrument are the *optical pyrometer* and *monochromatic-brightness radiation thermometer*. It is a rather old technology [7]. This type of a pyrometer is considered the most accurate radiation thermometer for temperatures over 700 °C and efficient to temperatures up to 4200 °C. The lower limit is a result of human eye sensitivity within a specific wavelength range. This limit can be lowered when a human eye is replaced with a light-sensitive detector as explained later.

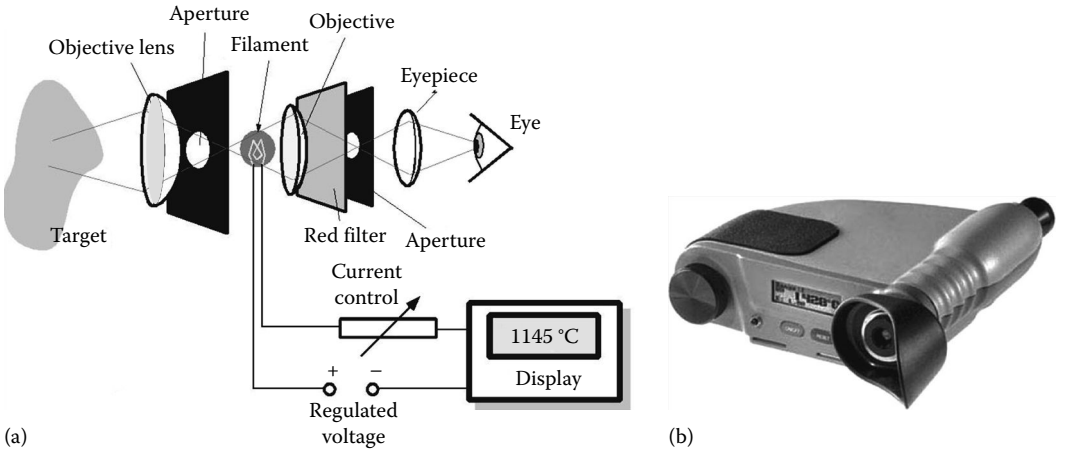

FIGURE 72.10 (a) Simplified block diagram of a disappearing-filament optical pyrometer. (b) A handheld DFP 2000 optical pyrometer. (Courtesy of Spectrodyne, Inc. www.spectrodyne.com.)

The operating principle of this thermometer is based on Planck's law (Equation 72.1 and Figure 72.1), which states that intensity and color of the surface change with temperature. The idea behind the design is to balance a radiation from a hot reference element having a known temperature against unknown radiation from a target. The pyrometer has a lens through which the operator views the target (Figure 72.10a).

An image of a tungsten filament (reference element) is superimposed on the image of a target. The filament is warmed up by electric current to glow. During calibration, the relationship between the heating current and the filament temperature was established by measuring brightness of a blackbody at known temperatures. The operator views the target through the eyepiece (see Figure 72.10b) and manually adjusts the heating current to the level when an image of the glowing filament visible in the foreground disappears, that is, when both the target and the filament have the same brightness and color. A color component complicates the measurement somewhat, so to remove this difficulty, a narrow-band red filter ($\lambda_f \approx 0.65$ μm) is inserted in front of an eyepiece. Therefore, the operator has to balance only the brightness of an image visible in red color. Another advantage of the filter is that emissivity ε_{bf} of the target needs to be known only at λ_f. There are several error sources in the pyrometer. One is difficulty in using it under dusty conditions. The other is known as the target emissivity. Fortunately, this is not a very large error since the error is given by

$$\frac{dT_b}{T_b} = -\frac{\lambda_f T_b}{C_2}\frac{d\varepsilon_{bf}}{\varepsilon_{bf}} \tag{72.21}$$

Thus, for a target at $T_b = 1000$ K, a 10% uncertainty in knowing emissivity of the target at the filter's wavelength results in only 0.45% (4.5 K) uncertainty in measured temperature. And of course the operator's ability to balance the filament brightness against the object may be a significant human factor.

The instrument may be further improved by removing an operator from the measurement process. Figure 72.11 shows an automatic version of the pyrometer where a rotating mirror tilted by 45° has a cutout sector that allows light from a target to pass through to the photo sensor. Such a mirror serves as a chopper that alternatively sends light to a photo sensor either from a target or from the filament. The microprocessor (μP) adjusts current through the filament to bring the optical contrast to zero. The optocoupler provides synchronization between the chopper and the microprocessor. In more advanced devices, instead of a chopper, a CCD receives an image of different portions of the field of view.

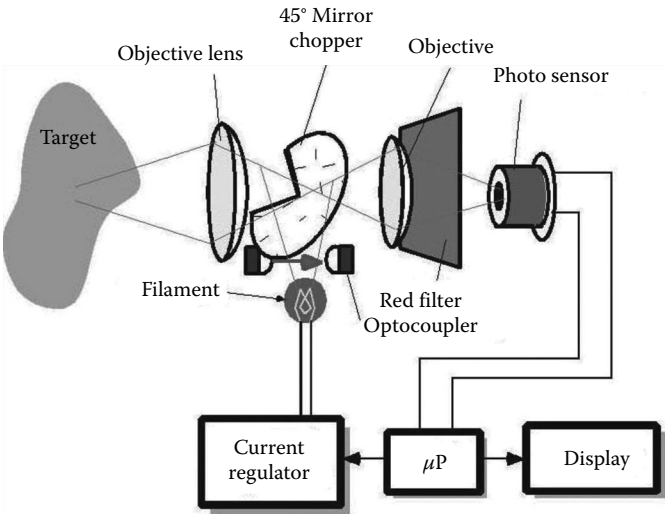

FIGURE 72.11 Block diagram of an automatic disappearing-filament optical pyrometer with a chopper.

72.5.2 Two-Color Pyrometer

Since emissivities of many materials, especially at high temperatures, are not known, measurement of a surface temperature may become impractical due to unacceptably large errors, unless the emissivity is excluded from the calculation. This can be accomplished by the use of a ratiometric technique in the so-called two-color radiation thermometer or *ratio thermometer*. In such a thermometer, the radiation is detected at two separate wavelengths λ_x and λ_y at which emissivities of the surface may be considered nearly the same. If the coefficients of transmission of the optical system at each wavelength respectively are λ_x and λ_y, then the ratio of two fluxes calculated for two wavelengths is

$$\phi = \frac{\Phi_x}{\Phi_y} = \frac{\gamma_x \varepsilon(\lambda_x)\frac{C_1}{\pi}\varepsilon(\lambda_x)\lambda_x^{-5}e^{-\frac{C_2}{\lambda_x T}}}{\gamma_y \varepsilon(\lambda_y)\frac{C_1}{\pi}\varepsilon(\lambda_y)\lambda_y^{-5}e^{-\frac{C_2}{\lambda_y T}}} \tag{72.22}$$

Since the emissivities are the same, $\varepsilon(\lambda_x) \approx \varepsilon(\lambda_y)$, after simple manipulations, Equation 72.22 can be rewritten for the computed temperature T_c, where ϕ represents a ratio of the thermal radiation sensor outputs at two wavelengths

$$T_c \approx C_2\left(\frac{1}{\lambda_y} - \frac{1}{\lambda_x}\right)\left(\ln\phi\frac{\gamma_y}{\gamma_x}\frac{\lambda_x^5}{\lambda_y^5}\right)^{-1} \tag{72.23}$$

It is seen that the equation for calculating temperature no longer depends on emissivity of the surface. Figure 72.12 shows a block diagram of a two-color pyrometer where an optical modulator is designed in the form of a disk with two filters. To eliminate a chopper, a CCD may be used instead of a single light sensor with a more complex signal processing [8].

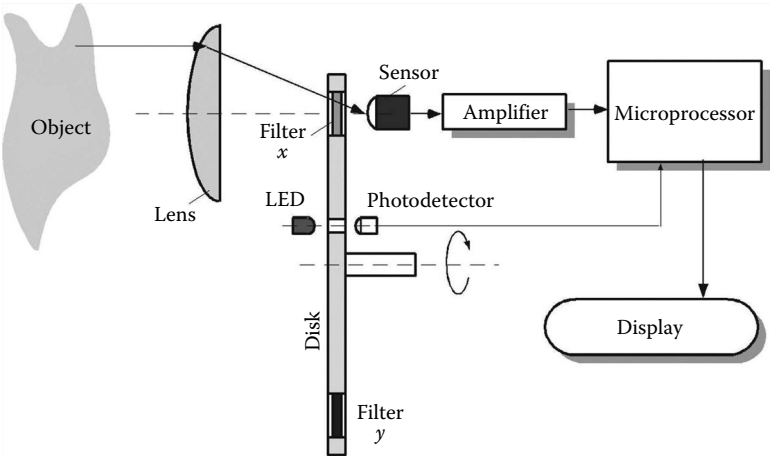

FIGURE 72.12 Block diagram of a two-color noncontact pyrometer.

72.6 IR Thermometry

72.6.1 Errors

To identify sources of errors in a noncontact temperature measurement by a thermal IR sensor, we need to take partial derivatives of Equation 72.20 for all factors that potentially may vary. For example, we take a partial derivative for the conversion factor *g*.

$$\frac{\partial T}{\partial g} \approx \frac{V}{4Ag^2\varepsilon\varepsilon_s\sigma T_{sc}^3} \tag{72.24}$$

It can be seen that the error is proportional to the IR sensor output signal V and it becomes smaller when emissivities of both the sensor and the object approach unity. On the other hand, if ε is small, error grows greatly. Since emissivities of metals are quite low and one never can be sure about their actual values, it is advisable, whenever practical, to coat a measured portion of a metal surface by a dielectric material, such as metal oxide or organic paint having known surface emissivity [9]. Alternatively, temperatures shall be taken not from a flat surface but rather from a hole or cavity in a metal object—taking an advantage of the cavity effect.

Another source of errors is a thermal instability of the IR sensor housing. It increases inaccuracy in measuring T_s, which is in the third power in Equation 72.24—meaning that even small variations in monitoring the sensor temperature will result in sizable errors. To minimize these errors, the IR sensors usually are encapsulated into metal housings having high thermal capacity and being well insulated from the environment (high thermal resistance). This helps stabilizing the temperature of the thermopile frame.

The optical coupling factor A is influenced by numerous variable components, such as transparency of the optical materials in the IR sensor and thermometer, angle of view, dust and scratches on the optical components, and so on.

A source of an error that is not part of the mathematical model of Equation 72.24 is a spurious heat source that may emanate its own thermal radiation either directly into the optical system of the IR thermometer or by means of reflection from the measured surface. Since no object is an ideal emitter (absorber), its reflectivity may have a significant value. For instance, an opaque object with emissivity 0.9 has a reflectivity of 0.1 (Equation 72.7), thus about 10% of radiation from a stray object in the vicinity of a measured surface is spuriously reflected toward the IR thermometer and may greatly disturb the measurement.

72.7 Special Applications

72.7.1 Measuring Semiconductor Materials

Temperature measurement of a semiconductor material during processing, such as growth of epitaxial films in vacuum chambers, always has been a difficult problem. Various process controls require accurate temperature monitoring, often without physical contact with the substrates. As a rule, heating of a substrate is provided by resistive heaters. The substrates are often loaded into the chambers through various locks and rotated during processing. Therefore, it is very difficult to attach a contact sensor, such as a thermocouple, to the wafer. And even if one does so, thermal gradient between the sensor and the substrate may be so large that one should never trust the result. The attractive alternative is the optical pyrometry; however, here we have another set of difficulties. The major problem is that semiconductors are substantially transparent in the spectral region where thermal radiation would be emanated. In other words, emissivity of a semiconductor is small and the amount of thermal radiation from a semiconductor is also not only small, but due to wafer transparency, radiation from the underlying devices (e.g., a heater) will go through to the noncontact thermometer.

One relatively simple method is to coat a small portion of the semiconductor with a material having high and known emissivity in the IR spectral range. Then, the thermal radiation can be measured from that small patch. An example of such a material is *Nichrome* (see Table 72.1).

An attractive method of temperature monitoring when no emissive patch can be deposited is the use of temperature dependence of band gaps of common semiconductors. The band gap is determined from the threshold wavelength at which the radiation from the heaters behind the substrate is transmitted through the substrate. Another method is based on temperature dependence of diffuse reflection of a semiconductor. In effect, this method is similar to the former; however, it relies on reflection, rather than on transmission of the semiconductor. An external lamp is used for the measurement of a threshold wavelength from a front polished and backside textured substrate. The temperature measurement arrangement is shown in Figure 72.13, where the diffused light is detected by cryogenically cooled quantum detector. The monochromator has a resolution of 3 nm and scans through the threshold area at a rate of 100 nm/s.

72.7.2 Medical Thermometers

Medical noncontact (infrared) thermometry covers two distinct types of measurements: *body* and *skin* surface temperature measurements. The skin temperature measurements have specific applications in

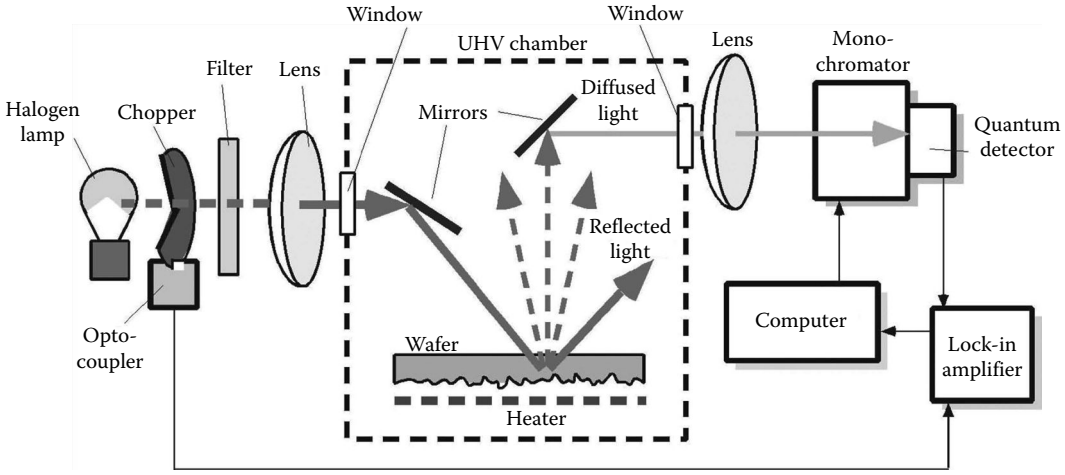

FIGURE 72.13 Diffused-light thermometer for measuring temperature of GaAs wafers.

diagnostics and are also used for estimation of the internal (core) body temperature. The skin temperature greatly depends on both the skin blood perfusion and environmental conditions. Therefore, it can be independently correlated with the temperature of the core only with some appreciable error; however, due to simplicity of use, the surface IR thermometers nowadays are quite popular for detecting fever.

A much more accurate way of measuring the core body temperature is by placing the probe of an IR thermometer into an ear canal and aiming it at a tympanic membrane [10]. The tympanic membrane has a temperature very close (within 0.1 °C) to that of blood, and by a correctly designed IR ear thermometer, it can be measured with high clinical accuracy.

Accuracy of the ear thermometer greatly depends on the accuracy of measuring flux Φ through the sensor's output voltage V, as in Equation 72.20. This is affected by the IR sensor sensitivity and its variations with temperature, optical components and their cleanliness, manufacturer's tolerances of the disposable sanitary probe covers, skill of an operator, and even the patient cooperation. All these often uncontrollable variables can cause an appreciable error that sometimes may be too large for an accurate medical diagnostic. Fortunately, Equation 72.24 suggests a solution that can dramatically improve accuracy in measuring patient's temperature. The error resulted from uncertainty of g is the so-called multiplicative, that is, it is proportional to the sensor's voltage V that, in turn, is proportional to a temperature gradient between the patient and the sensor (see Equation 72.18). Thus, by reducing a difference between T and T_s, one can reduce all multiplicative errors to smaller values and even close to zero. To do that, the sensor's temperature T_s should be artificially forced to come close to the patient temperature T. This was implemented in practice in the Braun-Thermoscan ear thermometer [11]. Figure 72.14 illustrates

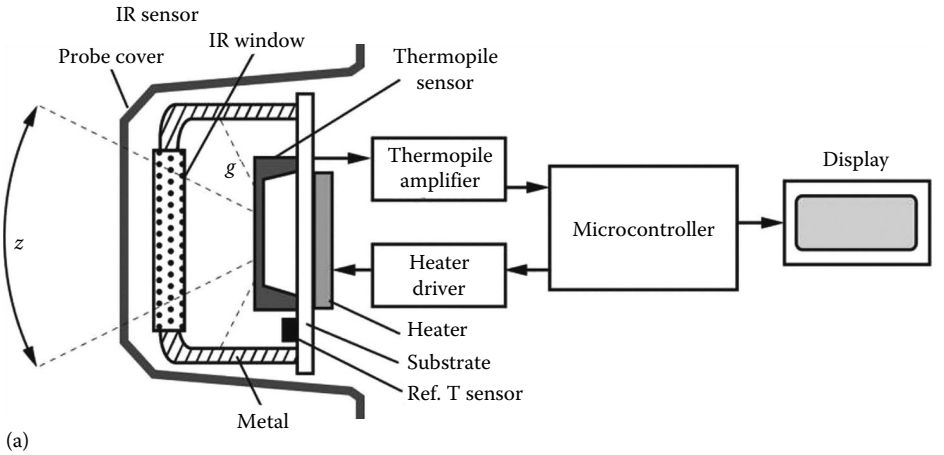

FIGURE 72.14 (a) Heated IR sensor in a medical ear thermometer and (b) the front end of Braun-Thermoscan ear thermometer.

a simplified block diagram of the thermometer. A thermopile IR sensor is encapsulated inside a metal header that is attached to a heater. Before taking temperature from a patient, the heater warms up the IR sensor from room temperature up to $t_{ss} = 37$ °C—a typical normal human body temperature. Thus, for a healthy patient, the thermal gradient between the patient and the sensor is close to zero and so is the measurement error. Even for a patient with fever, the temperature gradient is only 2 °C–4 °C and the error reduction is still very substantial, thus making this type of a medical thermometer highly accurate. Note that if the IR sensor is not warmed up and stays near room temperature, say 20 °C, the temperature gradient will be nearly an order of magnitude larger, and the errors will be larger as much. Since the skin emissivity is also multiplicative with *g*, a prewarmed sensor negates the effect of emissivity on accuracy as well.

A prewarming of the IR sensor to a temperature close to that of the patient is a powerful solution for medical applications since the patient's temperature varies in a narrow range (only from 35 °C to 42 °C) and a prewarming of the IR sensor to that range is not too difficult. Unfortunately, the method is not practical for use in much broader temperature ranges that are typical for nonmedical applications.

References

1. J. Fraden. *Handbook of Modern Sensors*, 4th edn., Springer Verlag, New York, 2010.
2. J. Fraden. Blackbody cavity for calibration of infrared thermometers. U.S. Patent 6447160, 2002.
3. J.L. Tissot, C. Trouilleau, B. Fieque, A. Crastes, and O. Legras. Uncooled microbolometer: Recent development at ULIS. *Opto-Electron. Rev*., 14(1), 25–32, 2006.
4. J. Schieferdecker, R. Quad, E. Holzenkämpfer, and M. Schulze. Infrared thermopile sensors with high sensitivity and very low temperature coefficient. *Sensor Actuat. A,* 46–47, 422–427,1995.
5. J. Schieferdecker, R. Quad, and M. Schulze. Temperature sensing module. U.S. Patent 5826982, 1998.
6. W. Leneke, M. Simon, M. Schulze, K. Storck, and J. Schieferdecker. Thermopile infrared sensor array. US Patent Publication No. 20080216883, 2008.
7. F.A. Cunnold. The optical system of the disappearing filament pyrometer. *Proc. R. Soc. Lond. A*, 152, 64–80, 1935.
8. T. Fu, X. Cheng, and Z. Yang. Theoretical evaluation of measurement uncertainties of two-color pyrometry applied to optical diagnostics. *Appl. Opt.,* 47(32), 6112–6123, November 10, 2008.
9. D.R. White and J.V. Nicholas. Emissivity and reflection error sources in radiation thermometry. In: *Temperature, Its Measurement and Control in Science and Industry*. Vol. 6, Part 2, pp. 917–922, AIP, New York, 1992.
10. J. Fraden. Medical infrared thermometry (review of modern techniques). In: *Temperature, Its Measurement and Control in Science and Industry*. Vol. 6, Part 2, pp. 825–830, AIP, New York, 1992.
11. B. Kraus and A. Klos. Radiation thermometer containing a heated measuring tip. U.S. Patent No. 7014358, 2006.

73

Pyroelectric Detectors

Jacob Fraden
Fraden Corporation

73.1 Pyroelectric Effect

The pyroelectric materials are crystalline substances capable of generating an electric charge in response to heat flow [1]. The pyroelectric effect is very closely related to the piezoelectric effect. The materials belong to a class of ferroelectrics. The name was given in association with ferromagnetics and is rather misleading because most such materials have nothing to do with iron.

A crystal is considered to be pyroelectric if it exhibits a spontaneous temperature-dependent polarization. Of the 32 crystal classes, 21 are noncentrosymmetric, and 10 of these exhibit pyroelectric properties. Besides pyroelectric properties, all these materials exhibit some degree of piezoelectric properties as well—they generate an electric charge in response to mechanical stress.

Pyroelectricity was observed for the first time in tourmaline crystals in the eighteenth century (some claim that the Greeks noticed it 23 centuries ago). Later, in the nineteenth century, Rochelle salt was used to make pyroelectric sensors. A large variety of materials became available after 1915: KDP (KH_2PO_4), ADP ($NH_4H_2PO_4$), $BaTiO_3$, and a composite of $PbTiO_3$ and $PbZrO_3$ known as PZT. Presently, more than 1000 materials with reversible polarization are known. They are called ferroelectric crystals. Most important among them are triglycine sulfate (TGS) and lithium tantalate ($LiTaO_3$).

A pyroelectric material can be considered a composition of a large number of minute crystallites, where each behaves as a small electric dipole. All these dipoles are randomly oriented, however, along a preferred direction. Above a certain temperature, known as the Curie point, the crystallites have no dipole moment.

When temperature of a pyroelectric material changes, the material becomes polarized. In other words, an electric charge appears on its surface. It should be clearly understood that the polarization occurs not as a function of temperature but only as function of a *change in temperature* of the material. There are several mechanisms by which changes in temperature will result in pyroelectricity. Temperature changes can cause shortening or elongation of individual dipoles. It can also affect the randomness of the dipole orientations due to thermal agitation. These phenomena are called *primary pyroelectricity*. There is also *secondary pyroelectricity*, which, in a simplified way, can be described as a result of the piezoelectric effect, that is, a development of strain in the material due to thermal expansion.

The dipole moment, M, of the bulk pyroelectric sensor is

$$M = \mu A h \tag{73.1}$$

where
μ is the dipole moment per unit volume
A is the sensor's area
h is the thickness

The charge, Q_a, which can be picked up by the electrodes, develops the dipole moment across the material:

$$M_0 = Q_a h \tag{73.2}$$

M must be equal to M_0 so that

$$Q_a = \mu A \tag{73.3}$$

As the temperature varies, the dipole moment also changes, resulting in an induced charge.

Thermal absorption can be related to a dipole change so that μ must be considered a function of both temperature, T_a, and an incremental thermal energy, ΔW, absorbed by the material:

$$\Delta Q_a = A\mu(T_a, \Delta W) \tag{73.4}$$

The aforementioned equation shows the magnitude of electric charge resulting from absorption of thermal energy. To pick up the charge, the pyroelectric materials are fabricated in the shapes of a flat capacitor with two electrodes on opposite sides and the pyroelectric material serving as a dielectric.

73.2 Pyroelectric Materials

To select the most appropriate pyroelectric material, energy conversion efficiency should be considered. It is, indeed, the function of the pyroelectric sensor to convert thermal energy into electrical. "How effective is the sensor?" is a key question in the design practice. A measure of efficiency is k_p^2 that is called the pyroelectric coupling coefficient [2,3]. It shows the factor by which the pyroelectric efficiency is lower than the Carnot limiting value $\Delta T/T_a$. Numerical values for k_p^2 are shown in Table 73.1.

Table 73.1 shows that TGS crystals are the most efficient pyroelectric converters. However, for a long time, they were quite impractical for use in sensors because of a low Curie temperature. If the sensor's temperature is elevated above that level, it permanently loses its polarization. In fact, TGS sensors proved to be unstable even below the Curie temperature, with the signal being lost quite spontaneously [4]. It was discovered that doping of TGS crystals with L-alanine (LATGS process patented by Philips) during its growth stabilizes the material below the Curie temperature. The Curie temperature was raised to 60 °C, which allows its use at the upper operating temperature of 55 °C, which is sufficient for many applications.

Other materials, such as lithium tantalate and pyroelectric ceramics, are also used to produce pyroelectric sensors. During recent years, deposition of pyroelectric thin films has been intensively researched. Especially promising is the use of lead titanate ($PbTiO_3$), which is a ferroelectric ceramic

TABLE 73.1 Physical Properties of Pyroelectric Materials

Material	Curie Temperature, °C	Thermal Conductivity, W mK^{-1}	Relative Permittivity, ε_r	Pyroelectric Charge Coeff. C $(m^2K)^{-1}$	Pyroelectric Voltage Coeff. V $(mK)^{-1}$	Coupling k_p^2 (%)
Single crystals						
TGS	49	0.4	30	3.5×10^{-4}	1.3×10^{6}	7.5
$LiTaO_3$	618	4.2	45	2.0×10^{-4}	0.5×10^{6}	1.0
Ceramics						
$BaTiO_3$	120	3.0	1000	4.0×10^{-4}	0.05×10^{6}	0.2
PZT	340	1.2	1600	4.2×10^{-4}	0.03×10^{6}	0.14
Polymers						
PVDF polycrystalline layers	205	0.13	12	0.4×10^{-4}	0.40×10^{6}	0.2
$PbTiO_3$	470	2 (monocrystal)	200	2.3×10^{-4}	0.13×10^{6}	0.39

Source: Meixner, H. et al., *Siemens Forsch. Entwickl. Ber.*, 15(3), 105, 1986.
Note: The above-mentioned figures may vary depending on manufacturing technologies.

having both a high pyroelectric coefficient and a high Curie temperature of about 490 °C. This material can be easily deposited on silicon substrates by the so-called sol–gel spin-casting deposition method [5].

In 1969, Kawai discovered strong piezoelectricity in the plastic materials, polyvinyl fluoride (PVF) and polyvinylidene fluoride (PVDF) [6]. These materials also possess substantial pyroelectric properties. PVDF is a semicrystalline polymer with an approximate degree of crystallinity of 50% [7]. Like other semicrystalline polymers, PVDF consists of a lamellar structure mixed with amorphous regions. The chemical structure contains the repeat unit of doubly fluorinated ethane CF_2–CH_2:

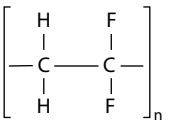

The molecular weight of PVDF is about 10^5, which corresponds to about 2000 repeat units. The film is quite transparent in the visible- and near-IR regions and is absorptive in the far-infrared (IR) portion of the electromagnetic spectrum. The polymer melts at about 170 °C. Its density is about 1780 kg m^{-3}. PVDF is mechanically durable and flexible. In piezoelectric applications, it is usually drawn, uniaxially or biaxially, to several times its length. Elastic constants, for example, Young's modulus, depend on this draw ratio. Thus, if the PVDF film was drawn at 140 °C to the ratio of 4:1, the modulus value is 2.1 GPa, while for the draw ratio of 6.8:1, it was 4.1 GPa. Resistivity of the film also depends on the stretch ratio. For example, at low stretch, it is about 6.3×10^{15} Ω cm, while for the stretch ratio 7:1, it is 2×10^{16} Ω cm.

Since silicon does not possess pyroelectric properties, such properties can be added on by depositing crystalline layers of pyroelectric materials. The three most popular materials are zinc oxide (ZnO), aluminum nitride (AlN), and the so-called solid solution system of lead–zirconite–titanium oxides $Pb(Zr,Ti)O_3$ known as PZT ceramic, which is basically the same material used for fabrication of discrete piezoelectric and pyroelectric sensors. One of the advantages of using zinc oxide is the ease of chemical etching. The zinc oxide thin films are usually deposited on silicon by employing sputtering technology. Note, however, that silicon has a large coefficient of thermal conductivity. That is, its thermal time constant is very small (see as follows), so the pyroelectric sensors made with silicon substrates possess low sensitivity yet are capable of fast response.

73.3 Manufacturing Process

Manufacturing of ceramic PZT elements begins with high-purity metal oxides (lead oxide, zirconium oxide, titanium oxide, etc.) in the form of fine powders having various colors. The powders are milled to a specific fineness and mixed thoroughly in chemically correct proportions. In a process called "calcining," the mixtures are then exposed to an elevated temperature, allowing the ingredients to react to form a powder, each grain of which has a chemical composition close to the desired final composition. At this stage, however, the grain does not yet have the desired crystalline structure.

The next step is to mix the calcined powder with solid and/or liquid organic binders (intended to burn out during firing) and mechanically form the mixture into a "cake" that closely approximates a shape of the final sensing element. To form the "cakes" of desired shapes, several methods can be used. Among them are pressing (under force of a hydraulic-powered piston), casting (pouring viscous liquid into molds and allowing to dry), extrusion (pressing the mixture through a die or a pair of rolls to form thin sheets), and tape casting (pulling viscous liquid onto a smooth moving belt).

After the "cakes" have been formed, they are placed into a kiln and exposed to a very carefully controlled temperature profile. After burning out of organic binders, the material shrinks by about 15%. The "cakes" are heated to a red glow and maintained at that state for some time, which is called the "soak time," during which the final chemical reaction occurs. The crystalline structure is formed when the material is cooled down. Depending on the material, the entire firing may take 24 h.

When the material is cold, contact electrodes are applied to its surface. This can be done by several methods. The most common are fired-on silver (a silk screening of silver–glass mixture and refiring), electroless plating (a chemical deposition in a special bath), and sputtering (an exposure to metal vapor in partial vacuum).

Cristalities (crystal cells) in the material can be considered electric dipoles. In some materials, like quartz, these cells are naturally oriented along the crystal axes, thus giving the material sensitivity to stress. In other materials, the dipoles are randomly oriented, and the materials need to be "poled" to possess piezoelectric properties. To give crystalline material pyroelectric properties, several poling techniques can be used. The most popular poling process is thermal poling, which includes the following steps:

1. A crystalline material (ceramic or polymer film) that has randomly oriented dipoles (Figure 73.1a) is warmed to slightly below its Curie temperature. In some cases (for a PVDF film), the material is stressed. High temperature results in stronger agitation of dipoles and permits one to more easily orient them in a desirable direction.
2. The material is placed in strong electric field, E (Figure 73.1b), where dipoles align along the field lines. The alignment is not total. Many dipoles deviate from the field direction quite strongly; however, statistically predominant orientation of the dipoles is maintained.

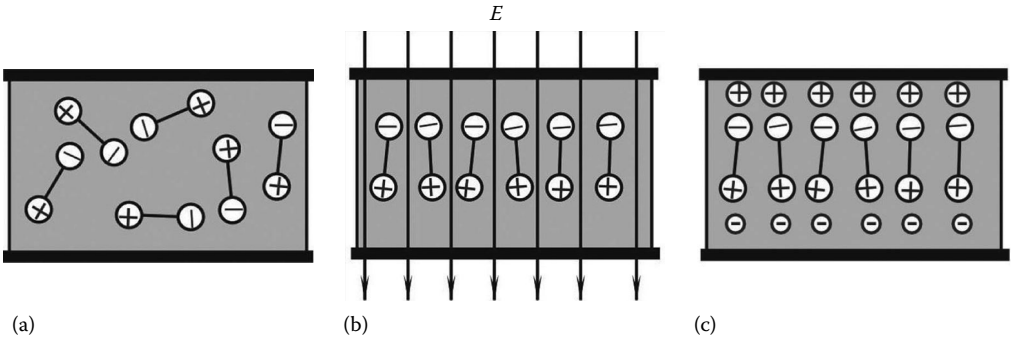

FIGURE 73.1 Poling of a pyroelectric crystal in a strong electric field: (a) randomly oriented dipoles, (b) dipoles aligning with electric field, and (c) dipoles frozen at high temperature without the electric field. The sensor must be stored and operated below the Curie temperature.

3. The material is cooled down, while the electric field across its thickness is maintained.
4. The electric field is removed, and the poling process is complete. As long as the poled material is maintained below the Curie temperature, its polarization remains permanent. The dipoles stay "frozen" in the direction that was given to them by the electric field at high temperature (Figure 73.1c). The aforementioned method is used to manufacture ceramic and plastic pyroelectric materials.

Another method, called a corona discharge poling, can be used to produce polymer piezoelectric/pyroelectric films. The film is subjected to a corona discharge from an electrode at several million volts per centimeter of film thickness for 40–50 s [8,9]. Corona polarization is uncomplicated to perform and can be easily applied before electric breakdown occurs, making this process useful at room temperature.

The final operation in preparing the sensing element is shaping and finishing. This includes cutting, machining, and grinding. After the piezo (pyro) element is prepared, it is installed into a sensor's housing, where its electrodes are bonded to electrical terminals and other electronic components.

After poling, the crystal remains permanently polarized; however, it remains electrically charged for a relatively short time. There is a sufficient amount of free carriers that move in the electric field setup inside the bulk material, and there are plenty of charged ions in the surrounding air. The charge carriers move toward the poled dipoles and neutralize their charges (Figure 73.1c). Hence, after a while, the poled piezoelectric material becomes electrically discharged as long as it remains under steady-state conditions. When temperature changes and thermally induced stress develops, the balanced state is degraded, and the pyroelectric material develops an electric charge. If the stress is maintained for a while, the charges again will be neutralized by the internal leakage. Thus, a pyroelectric material is responsive only to a changing temperature rather than to a steady level of it. In other words, a pyroelectric sensor is an ac device, rather than a dc device. Sometimes, it is called a *dynamic* sensor, which reflects the nature of its response.

73.4 Pyroelectric Sensors

To make sensors, the pyroelectric materials are used in the form of thin slices or films with electrodes deposited on the opposite sides to collect the thermally induced charges (Figure 73.2). The pyroelectric detector is essentially a capacitor that can be charged by an influx of heat. The detector does not require any external electrical bias (excitation signal). It needs only an appropriate electronic interface circuit to measure the charge. Contrary to thermoelectrics (thermocouples), which produce a steady voltage when two dissimilar metal junctions are held at steady but different temperatures, pyroelectrics generate charge in response to a change in temperature. Since a change in temperature essentially requires propagation of heat, a pyroelectric device is a heat flow detector rather than a heat detector. Figure 73.2 shows a pyroelectric detector (pyro-sensor) connected to a resistor R_b that represents either the internal leakage resistance or a combined input resistance of the interface circuit connected to the sensor. The equivalent electrical circuit of the sensor is shown on the right. It consists of three components: (1) the current source generating a heat-induced current, i (remember that a current is a movement of electric charges); (2) the sensor's capacitance, C; and (3) the leakage resistance, R_b. Since the leakage resistance

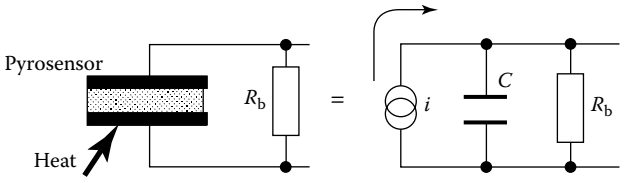

FIGURE 73.2 Pyroelectric sensor and its equivalent circuit.

is very high and often unpredictable, an additional bias resistor is often connected in parallel with the pyroelectric material. The value of that resistor is much smaller than the leakage resistance, yet its typical value is still on the order of 10^{10} Ω (10 GΩ).

The output signal from the pyroelectric sensor can be taken in the form of either charge (current) or voltage, depending on the application. Being a capacitor, the pyroelectric device is discharged when connected to a resistor, R_b (Figure 73.2). Electric current through the resistor and voltage across the resistor represent the heat flow–induced charge. It can be characterized by two pyroelectric coefficients [2]:

$$\begin{aligned} P_Q &= \frac{\mathrm{d}P_s}{\mathrm{d}T} \text{ Pyroelectric charge coefficient} \\ P_V &= \frac{\mathrm{d}E}{\mathrm{d}T} \text{ Pyroelectric voltage coefficient} \end{aligned} \tag{73.5}$$

where

P_s is the spontaneous polarization (which is the other way to say "electric charge")
E is the electric field strength
T is the temperature in K

Both coefficients are related by way of the electric permittivity, ε_r, and dielectric constant, ε_0:

$$\frac{P_Q}{P_V} = \frac{\mathrm{d}P_s}{\mathrm{d}E} = \varepsilon_r \varepsilon_0 \tag{73.6}$$

The polarization is temperature dependent, and, as a result, both pyroelectric coefficients in Equation 73.5 are also functions of temperature.

If a pyroelectric material is exposed to a heat source, its temperature rises by ΔT, and the corresponding charge and voltage changes can be described by the following equations:

$$\Delta Q = P_Q A \Delta T \tag{73.7}$$

$$\Delta V = P_V h \Delta T \tag{73.8}$$

Remembering that the sensor's capacitance can be defined as

$$C_e = \frac{\Delta Q}{\Delta V} = \varepsilon_r \varepsilon_0 \frac{A}{h} \tag{73.9}$$

then, from Equations 73.6, 73.8, and 73.9, it follows that

$$\Delta V = \frac{\Delta Q}{C_e} = P_Q \frac{h}{\varepsilon_r \varepsilon_0} \Delta T \tag{73.10}$$

It is seen that the peak output voltage is proportional to the sensor's temperature rise and pyroelectric charge coefficient.

Figure 73.3 shows a pyroelectric sensor whose temperature, T_0, is homogeneous over its volume. Being electrically polarized, the dipoles are oriented (poled) in such a manner as to make one side of the material positive and the opposite side negative. However, under steady-state conditions, free charge carriers

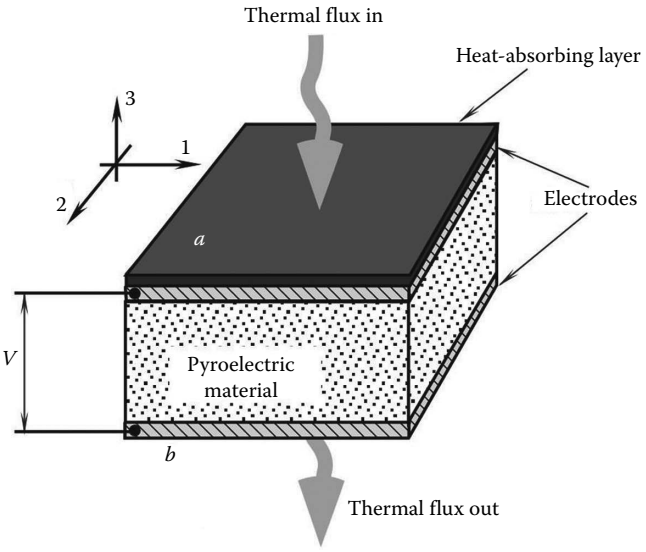

FIGURE 73.3 Pyroelectric sensor has two electrodes at the opposite sides of the crystalline material. Thermal radiation is applied along axis 3.

(electrons and holes) neutralize the polarized charge, and the capacitance between the electrodes does not appear to be charged. That is, the sensor generates zero charge. Now, assume that heat is applied to the top side of the sensor. Heat can enter the sensor in a form of thermal radiation that is absorbed by the top electrode and propagates toward the pyroelectric material via the mechanism of thermal conduction. The top electrode can be given a heat-absorbing coating, such as gold–black or organic paint. As a result of heat absorption, the top side becomes warmer (the new temperature is T_1), which causes the top side of the material to expand. The expansion leads to flexing of the sensor, which, in turn, produces stress and a change in dipole orientation. Being piezoelectric, stressed material generates electric charges of opposite polarities across the electrodes. Hence, one can regard secondary pyroelectricity as a sequence of events: thermal radiation, heat absorption, thermally induced stress, and electric charge.

The temperature of the sensor T_s is a function of time. That function is dependent on the sensing element: its density, specific heat, and thickness. If the input thermal flux has the shape of a step function of time, for the sensor freely mounted in air, the output current can be approximated by an exponential function so that

$$i = i_0 e^{-t/\tau_T} \tag{73.11}$$

where i_0 is the peak current.

Figure 73.4 shows timing diagrams for a pyroelectric sensor when it is exposed to a step function of heat. It is seen that the electric charge reaches its peak value almost instantaneously and then decays with a *thermal time constant,* τ_T. This time constant is a product of the sensor's thermal capacitance, C, and thermal resistance, r, which defines a thermal loss from the sensing element to its surroundings:

$$\tau_T = Cr = cAhr \tag{73.12}$$

where c is the specific heat of the sensing element

The thermal resistance r is a function of all thermal losses to the surroundings through convection, conduction, and thermal radiation. For low-frequency applications, it is desirable to use sensors with τ_T

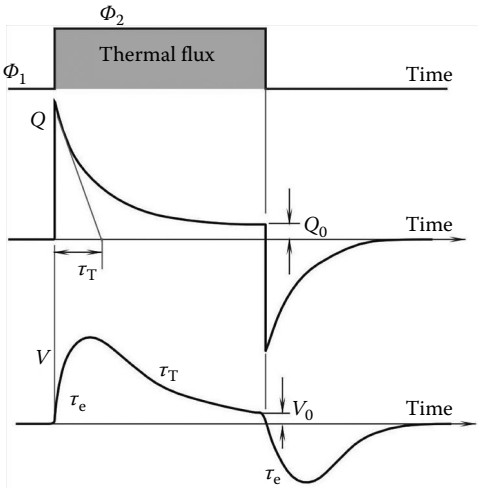

FIGURE 73.4 Response of a pyroelectric sensor to a thermal step function. The magnitudes of charge Q_0 and voltage V_0 are exaggerated for clarity.

as large as practical, while for the high-speed applications (e.g., to measure the power of laser pulses), a thermal time constant should be dramatically reduced. For that purpose, the pyroelectric material can be laminated with a heat sink: a piece of aluminum or copper.

When a heat flow exists inside the pyroelectric crystal, there is an outflow of heat from the opposite side of the crystal, as shown in Figure 73.3. Thermal energy enters the pyroelectric material from side *a*. Since the other side *b* of the sensor faces a cooler environment, part of the thermal energy leaves the sensor and is lost to its surroundings. Because the sides *a* and *b* face objects of different temperatures (one is the temperature of a target and the other is the temperature of the environment), a continuous heat flow exists through the pyroelectric material. As a result, in Figure 73.4, charge Q and voltage V do not completely return to zero no matter how much time has elapsed. Electric current generated by the pyroelectric sensor has the same shape as the thermal current through its material. An accurate measurement can demonstrate that as long as the heat continues to flow, the pyroelectric sensor will generate a constant voltage V_0 whose magnitude is proportional to the heat flow.

73.5 Applications

The pyroelectric sensors are useful whenever changing thermal radiation or heat flow needs to be measured. Examples are motion detectors for security systems and light control switches [1], instant medical IR thermometers, and laser power meters. Depending on the application, a pyroelectric sensor can be used either in *current* or in *voltage* mode. The voltage mode (Figure 73.5a) uses a voltage follower with a very high input resistance. Hence, JFET- and CMOS-input stages are essential. As a rule, in the voltage-mode sensor, the follower is incorporated inside the same package along with the element and bias resistor. Advantages of the voltage mode are simplicity and lower noise. The disadvantages are slower speed response due to high capacitance of the sensor (typically on the order of 30 pF) and other influences of the sensor capacitance on the quality of output voltage. The output voltage of the follower is shown in Figure 73.4 (V). It is seen that it rises slowly with electric time constant τ_e and decays with thermal time constant τ_T.

The current mode uses an electronic circuit having a "virtual ground" as its input (Figure 73.5b). An advantage of this circuit is that the output signal is independent of the sensor's capacitance and, as a result, is much faster. The signal reaches its peak value relatively fast and decays with thermal time

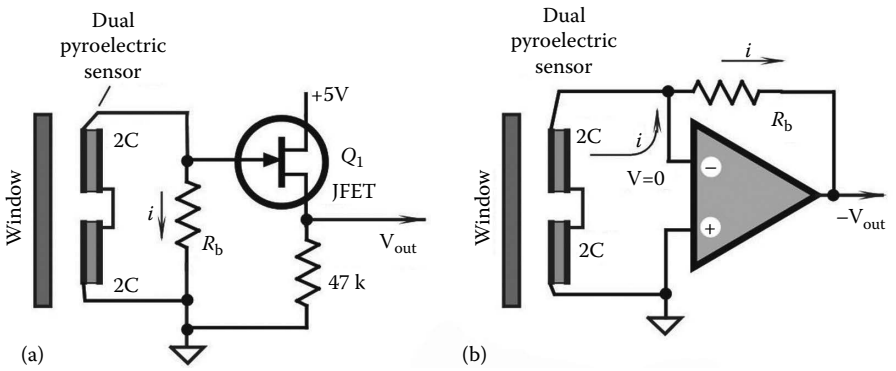

FIGURE 73.5 Interface circuits for pyroelectric sensors operating in (a) voltage and (b) current modes.

constant τ_T. The output voltage V_0 has the same shape of charge Q in Figure 73.4. The disadvantages of the circuit are higher noise (due to wider bandwidth) and higher cost.

Note that Figure 73.5 shows dual pyroelectric sensors, where two sensing elements are formed on the same crystalline plate by depositing two pairs of electrodes. The electrodes are connected in a serial opposite manner. If both sensors are exposed to the same magnitude of far-IR radiation, they will produce nearly identical polarizations, and, due to the opposite connection, the voltage applied to the input of the transistor or the current passing through resistor R_b will be nullified. This feature allows for cancelation of undesirable common-mode input signals in order to improve stability and reduce noise. Signals that arrive only to one of the elements will not be canceled.

References

1. J. Fraden, *Handbook of Modern Sensors*, 4th edn. New York: Springer Verlag, 2010.
2. H. Meixner, G. Mader, and P. Kleinschmidt, Infrared sensors based on the pyroelectric polymer polyvinylidene fluoride (PVDF), *Siemens Forsch. Entwickl. Ber.*, 15(3), 105–114, 1986.
3. P. Kleinschmidt, Piezo-und pyroelektrische Effekte. In: Heywang, W. (Ed.), *Sensorik*, Kap. 6. New York: Springer, 1984.
4. Semiconductor Sensors, *Data Handbook*. Eindhoven, the Netherlands: Philips Export B.V., 1988.
5. C. Ye, T. Tamagawa, and D.L. Polla, Pyroelectric $PbTiO_3$ thin films for microsensor applications. In: *Transducers'91. International Conference on Solid-State Sensors and Actuators*, San Francisco, CA, pp. 904–907, 1991.
6. H. Kawai, The piezoelectricity of poly(vinylidene fluoride), *Jap. J. Appl. Phys.*, 8, 975–976, 1969.
7. A. Okada, Some electrical and optical properties of ferroelectric lead-zirconite-lead-titanate thin films, *J. Appl. Phys.*, N. 48, 2905, 1977.
8. P.F. Radice, Corona discharge poling process, U.S. Patent No. 4,365,283, 1982.
9. P.D. Southgate, Room-temperature poling and morphology changes in pyroelectric polyvinylidene fluoride. *Appl. Phys. Lett.*, 28, 250, 1976.

Further Readings

Allied Industries, Pyroelectric. http://www.alliedelec.com/Emitters-and-Detectors/Pyroelectric (accessed on August 1, 2012).

EOC, Pyroelectric Sensor Detector. http://www.eoc-inc.com/pyroelectric_detectors.htm (accessed on August 4, 2012).

Infratec, How does a Pyroelectric Detector Work. http://www.infratec.de/en/sensor-division/literature/faq.html (accessed on August 4, 2012).

74

Liquid-in-Glass Thermometers

Rod White
Measurement Standards Laboratory of New Zealand

J.V. Nicholas
Measurement Standards Laboratory of New Zealand

Liquid-in-glass (LIG) thermometers are a remarkably long-lived technology. The first sealed LIG thermometers were based on the thermal expansion of wine spirit and developed in 1641 by the then Duke of Tuscany [1,2]. For the next 300 years, the technology gradually improved so that a bewildering variety of LIG thermometers are now available to suit almost every application. They cover temperature ranges from –190 °C to 600 °C, and some achieve accuracies approaching 0.001 °C. The distinctive form, self-contained nature, and apparent simplicity of the LIG thermometer have made it the archetypical thermometer for many generations of technical staff and the general public.

However, LIG thermometers have limitations: they are fragile, potentially toxic, and prone to instability. Nowadays, in practically all but the most specialized applications, LIG thermometers are being replaced by electronic resistance thermometers that outperform them in almost every respect, especially in cost of ownership. Nevertheless, LIG thermometers still have appeal for some general-purpose applications and are required in a wide range of product and materials testing applications covered by documentary standards.

74.1 General Description

The most common form of LIG thermometer is the solid-stem thermometer, similar to that illustrated in Figure 74.1. There are four main parts to the LIG thermometer:

- The thin glass bulb, which contains the bulk of the thermometric liquid, is usually designed for stability with temperature change and must be properly annealed to remove stresses and strains that may cause the bulb to slowly change shape. The bulb must be thin to ensure good thermal contact with the medium being measured, but this means it is susceptible to instabilities due to mechanical or thermal shock. Some low-accuracy, general-purpose thermometers are made with a thicker bulb to lower the risk of breakage.
- The stem is a glass capillary. Again, a suitable glass is necessary, and it may differ from that of the bulb. The volume of the capillary must be significantly smaller than the volume of the bulb for

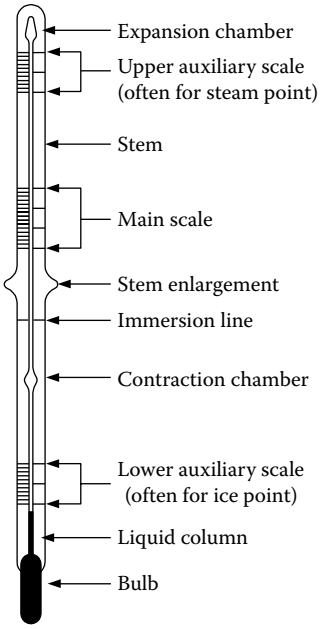

FIGURE 74.1 Main features of a solid-stem LIG thermometer.

good sensitivity, and it must be smooth and have a uniform cross section. The empty part of the capillary above the thermometric fluid can be gas filled or vacuous.

- The thermometric liquid is usually mercury in high-precision thermometers but is commonly an organic liquid in low-cost thermometers and in thermometers used for low temperatures. Mercury–thallium alloy is occasionally used for applications down to −55 °C, below the freezing point of mercury near −38 °C, but is also very toxic.
- The markings may be engraved, etched, or printed onto the stem. The markings include the scale, to allow direct reading of the temperature, as well as other useful information. In enclosed-scale thermometers, the scale is printed onto a separate glass plate and enclosed within the tubular body of the thermometer next to the capillary.

In addition to these basic features, many thermometers will have some of the additional features illustrated in Figure 74.1. The additional features may include

- An expansion chamber, which prevents the mercury from overpressuring the thermometer if it is exposed to temperatures above its maximum indication.
- A contraction chamber accompanied by an auxiliary scale near 0 °C, or sometimes 100 °C, which makes it possible to manufacture high-resolution thermometers that can be checked at the ice point or water boiling point. Good-quality thermometers include a 0 °C indication, either on the main scale or as an auxiliary scale.
- An immersion line or instructions for immersion, typically indicating that the thermometer should be immersed to 75 mm (or 3 in.) or 100 mm (or 4 in.) for partial-immersion thermometers, and the words "total immersion" for total-immersion thermometers.
- A short descriptor indicating whether the thermometer is gas filled or vacuous.
- A light-colored stripe up the back of the stem to aid scale visibility. The color of the stripe also indicates the type of glass [3].
- A stem enlargement, which is typically used to enable mounting of the thermometer in specialized apparatus.

Not all of these features will be found on all LIG thermometers.

TABLE 74.1 Summary of Specifications for ASTM Precision Thermometers

ASTM Thermometer Number	Range (°C)	Maximum Length (mm)	Graduations (°C)	Maximum Error (°C)
62C	−38 to +2	384	0.1	0.1
63C	−8 to +32	384	0.1	0.1
64C	−0.5 to +0.5 and 25 to 55	384	0.1	0.1
65C	−0.5 to +0.5 and 50 to 80	384	0.1	0.1
66C	−0.5 to +0.5 and 75 to 105	384	0.1	0.1
67C	−0.5 to +0.5 and 95 to 155	384	0.2	0.2
68C	−0.5 to +0.5 and 145 to 205	384	0.2	0.2
69C	−0.5 to +0.5 and 195 to 305	384	0.5	0.5
70C	−0.5 to +0.5 and 295 to 405	384	0.5	0.5

74.2 Choice of Thermometers

A large number of different types of LIG thermometer are available, with many of the variations designed with different dimensions and temperature ranges to suit specific applications. For best accuracy, mercury-in-glass thermometers should be used and restricted to operation over the range –38 °C to 250 °C. The purchase should be guided by a specification from a recognized standards body. Such bodies include the International Standards Organization (ISO) [4], the American Society for Testing and Materials (ASTM) [5], the British Standards Institute (BSI) [6], or the Institute for Petroleum (IP). Be aware that the standards bodies may use the same type number for different thermometers. For example, the IP 16C and the ASTM 16C are very different thermometers.

A choice of thermometer will probably be a compromise between the best range, resolution, and dimensions for the application. If good precision is required, then the thermometer range should be constrained to avoid long and unwieldy thermometers. Table 74.1 summarizes the ASTM specifications [5] for precision thermometers for which the smallest scale division is 0.1 °C. BS 1900 reference thermometers are available divided to 0.02 °C. The ASTM thermometers are also specified to be accurate to one scale division. Experience suggests that as many as 15% of all LIG thermometers are in error by more than one scale division at some point on their scales. However, with calibration, the scales on LIG thermometers can usually be interpolated to achieve accuracies of between 0.2 and 0.5 of a scale division, depending on the quality and resolution of the thermometer. The purchase cost of a good reference thermometer depends on the range and would typically be US$100 to US$200 for a good-quality thermometer. However, such costing neglects the cost of calibration that may be US$200 to US$2,000 or more. In general, good-quality electronic platinum resistance thermometers will have a lower cost of ownership and should be the first choice where measurement specifications allow. More information can be found in the references at the end of this chapter for further guidance on LIG thermometers [3,7,8], especially if high accuracy is required.*

74.3 Operation

The operation of LIG thermometers is most obviously based on the expansion of the thermometric liquid. As the volume of the liquid increases with temperature, it occupies a greater fraction of the space within the thermometer and is forced up the capillary where it provides the temperature indication. The flattest part of the liquid meniscus is used as the indicator: for mercury, this is the top of a convex meniscus; for organic liquids, the bottom of a concave meniscus.

* A good treatment of calibration practice for LIG thermometers, with a wider coverage than given here.

Perhaps less obviously, the glass is also a key part of the thermometer and a major source of the errors in LIG thermometry. Glass expands and contracts on heating sufficiently to offset the expansion of mercury by about 10%, and much of the nonlinearity, hysteresis, and possible erratic behavior of mercury-in-glass thermometers is due to the glass. Hysteresis, in particular, limits the basic accuracy of mercury-in-glass thermometers to about 0.1% of the temperature range, and special care and procedures are required to achieve greater accuracies. To avoid stress, mercury-in-glass thermometers should be stored horizontally on trays in cabinets, with care being taken to avoid any weight or pressure on the bulb. Vibration should also be avoided. Corrugated cardboard, or similar material, can be used as a liner for a tray to prevent the thermometers from rolling.

LIG thermometers employing organic fluids or "spirits" suffer less from the effects of the glass because the fluids have a much larger expansion coefficient. However, organic fluids have their own sources of error making spirit thermometers much less accurate and less reliable than mercury-in-glass thermometers. Spirit thermometers are useful below –38 °C, where mercury freezes, in situations where mercury is to be avoided, and in low-cost thermometers.

The sources of error associated with sprit thermometers include the thermal expansion of organic fluids, which is far less linear than for mercury. Secondly, the fluids are more volatile, which may lead to condensation on the upper part of the capillary. Spirit thermometers may also be difficult to read because of the clear liquid and concave meniscus. However, they do have a wider capillary, and, in combination with a suitable dye, they can be more readable than mercury thermometers. The wetting of the capillary by the liquid also means that many minutes may be required for the liquid to drain properly when measuring falling temperatures. Some of the liquids are also prone to polymerization when exposed to UV light.

Perhaps the largest source of error in LIG thermometry is due to the fact that not all of the thermometric fluid is at the measured temperature. Because some part of the liquid column must be visible, that part of the thermometric fluid must be outside the medium of interest and not at the correct temperature. This undesirable situation is made much worse when the operator fails to immerse a thermometer sufficiently and is also a feature of the normal use of partial-immersion thermometers. The same effect means that partial-immersion thermometers are sensitive to the stem temperature. The resulting errors can be large: a total-immersion thermometer partially immersed in boiling water with the entire stem outside the water exhibits an error of about 1 °C.

74.4 Errors in Liquid-in-Glass Thermometry

74.4.1 Scale Markings

During manufacture, the unmarked thermometer is exposed to two or more known temperatures, and "pointing" marks are placed on the stem corresponding to those temperatures, as shown in Figure 74.2. A linear scale is then placed on the stem to interpolate between adjacent pointing marks. In high-precision or wide-range thermometers, the scale may be placed in several segments to reduce nonlinearity errors. In general-purpose thermometers, there may only be two pointing marks, so the whole scale is placed at once. There are several factors that contribute to errors in the placement of the scale markings.

Firstly, in low-quality thermometers, the scale placement is not well controlled and may be up to one division in error. A good indicator of the quality of a thermometer is how close the pointing marks are to the scale markings. Sometimes, pronounced glitches in the scale markings can be seen where two scale segments meet. In high-quality thermometers, the scale will be well aligned with the pointing marks.

Secondly, the quality of the interpolation can vary. In good-quality thermometers, the scale is usually engraved or etched using a ruling machine to interpolate between the pointing marks. The scale markings are typically very fine and easy to interpolate between. In low-quality thermometers, the scale may be screen printed or stenciled. Such scales tend to have coarse scale markings and may be distorted through stretching of the screen or stencil.

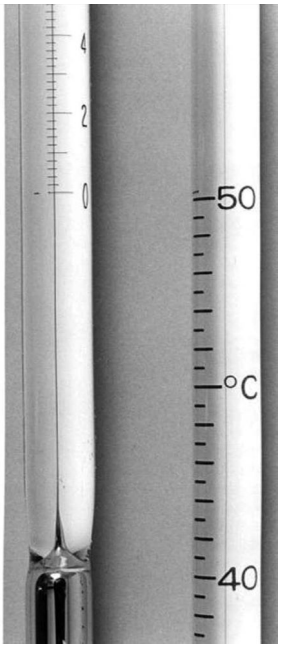

FIGURE 74.2 Good-quality thermometer (left) and general-purpose thermometer (right) showing the difference in the quality of scale markings. In the good-quality thermometer, the 0 °C pointing mark is immediately alongside the corresponding scale mark. In the general-purpose thermometer, the 50 °C pointing mark is about ¼ scale divisions above the scale mark.

Thirdly, as noted earlier, the expansion of both the thermometric liquid and the glass is nonlinear to some degree. This means that most of the scale indications will be in error with the error varying over the entire range of the thermometer, and the scale indication may be correct only near the pointing marks.

Another major contributor to nonlinearity is the capillary. Ideally, the cross section of the capillary should be uniform over the length of the thermometer and, to some degree, uniform between thermometers of the same type so that their dimensions are the same. In high-quality thermometers, the uniformity of the capillary is specified and tested before being used for thermometers.

Collectively, these errors mean that LIG thermometer scales can have a very complicated pattern of errors, and effective calibrations must sample the errors over the anticipated range of use. For the most part, thermometers designed for specific applications will be used over a very narrow range of temperatures, perhaps only within ±0.3 °C of a single temperature. Examples include thermometers used for viscosity testing at 40 °C and 100 °C. General-purpose thermometers, on the other hand, tend to be used almost randomly over their whole range, and the calibration must sample the scale over the whole range.

74.4.2 Immersion Errors and Stem Corrections

If some of the thermometric liquid in a LIG thermometer is at a different temperature from the bulb, then immersion errors occur. In the context of LIG thermometry, they are often called "stem errors." Because LIG thermometers are sometimes used with varying immersion conditions, such errors are common. Indeed, in order to read a thermometer, a small part of the liquid column is normally required to be outside the region of interest. The errors due to immersion effects can be estimated and corrected by the procedures given as follows.

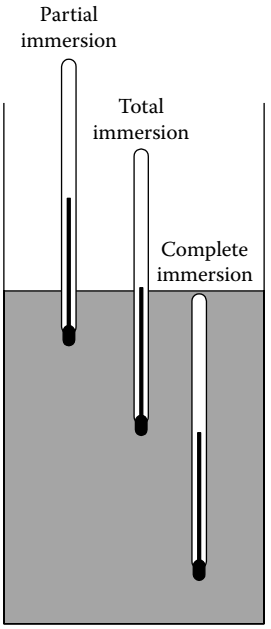

FIGURE 74.3 Immersion conditions used for LIG thermometers.

Three distinct immersion conditions are recognized for LIG thermometers, as illustrated in Figure 74.3:

- *Complete immersion*: By definition, if the bulb and the entire stem are immersed at the same temperature, the thermometer is completely immersed. This condition is not common, except at room temperature. Complete immersion should be avoided, especially at higher temperatures as the excess pressure above the liquid can cause the thermometer to rupture leading to a spread of mercury vapor. DO NOT put a mercury thermometer completely inside an oven to measure the temperature.
- *Total immersion*: This is the most common and most reliable operating condition. The description "total immersion" applies to the thermometric liquid, that is, all the liquid in the bulb, any contraction chambers, and the stem, is at the temperature of interest. The remaining portion of the stem where there is no thermometric liquid will be closer to room temperature. When thermometers are designed, calibrated, and used in total-immersion conditions, the immersion errors are very small, and usually no further corrections are required.
- *Partial immersion*: One way around the problem of scale visibility and the need that mount a thermometer within a complex apparatus is to immerse the thermometer to some fixed depth so that most, but not all, of the fluid is at the temperature of interest. The part of the fluid column not immersed is referred to as the emergent column. Many thermometers are designed and calibrated for partial immersion and are marked accordingly on the stem with an immersion depth or an immersion line (see Figure 74.1). The scale of a partial-immersion thermometer is properly defined only when the average temperature of the emergent column is also specified. Corrections may be required to compensate for the error arising from the emergent column not being at the specified temperature.

When LIG thermometers are used in incorrect immersion conditions, corrections should be made on the basis of the measured temperature of the emergent column. The traditional stem temperature measurement is made with a faden thermometer (the German word for thread thermometer). These are mercury-in-glass thermometers with a very thin long bulb, and a set of faden thermometers includes a wide range of bulb lengths. The bulb of the appropriate faden thermometer is mounted alongside the emergent column with the bottom of the bulb just in the fluid. The faden thermometer then indicates

the average stem temperature. Other ways of measuring the temperature profile are to use other small temperature sensors, such as thermocouples, mounted along the length of the emergent column. The thermometers should be evenly distributed over the length so that the average reading gives the correct length-weighted average stem temperature.

Thermometers are usually calibrated at the immersion conditions for which they have been designed. For partial-immersion thermometers, the stem temperatures during calibration should be measured and reported on the certificate. This ensures that the errors are negligible and can be ignored when the thermometer is used under its proper conditions. In many applications, a thermometer used for a standard test method, such as specified by the ASTM or IP, will have a specified immersion length and a specified stem temperature. Depending on the stem temperature during calibration, measurements reported in a calibration certificate may have to be corrected to meet the immersion conditions of the specification and to confirm that the thermometer meets any specified quality criteria.

When making a stem correction, the true temperature reading t is given by

$$t = t_i + N(t_2 - t_1)k \tag{74.1}$$

where

t_i is the indicated temperature

N is the length of emergent column expressed in degrees, as determined by the thermometer scale

t_2 is the mean temperature of the emergent column as specified or when calibrated (i.e., the stem temperature on a certificate for a partial-immersion thermometer or the reported reading for a total-immersion thermometer)

t_1 is the mean temperature of the emergent column in use, the fluid temperature if used in total immersion, or the measured stem temperature if used in partial immersion

k is the coefficient of apparent expansion of the thermometric liquid used in the glass of which the thermometer is made

See Table 74.2 for suitable values to use for normal temperature ranges and common glasses.

The use of Equation 74.1 with typical values of the liquid expansion coefficients from Table 74.2 is estimated to give about 10% accuracy in the correction. Consequently, a large correction is a major source of uncertainty. If the uncertainty due to the correction is considered too large, an alternative measurement method should be used.

Figure 74.4 shows a chart derived from Equation 74.1 for mercury thermometers. The chart is useful for making estimates of the correction and determining whether the immersion error is significant and therefore needs correction. For example, consider the case of measuring boiling water in a

TABLE 74.2 Working Range of Some Thermometric Liquids and Their Apparent Thermal Expansion Coefficient in Thermometer Glasses around Room Temperature

Liquid	Typical Apparent Expansion Coefficient $(°C)^{-1}$	Possible Temperature Range (°C)
Mercury	0.000 16	−35 to 510
Ethanol	0.001 04	−80 to 60
Pentane	0.001 45	−200 to 30
Toluene	0.001 03	−80 to 100

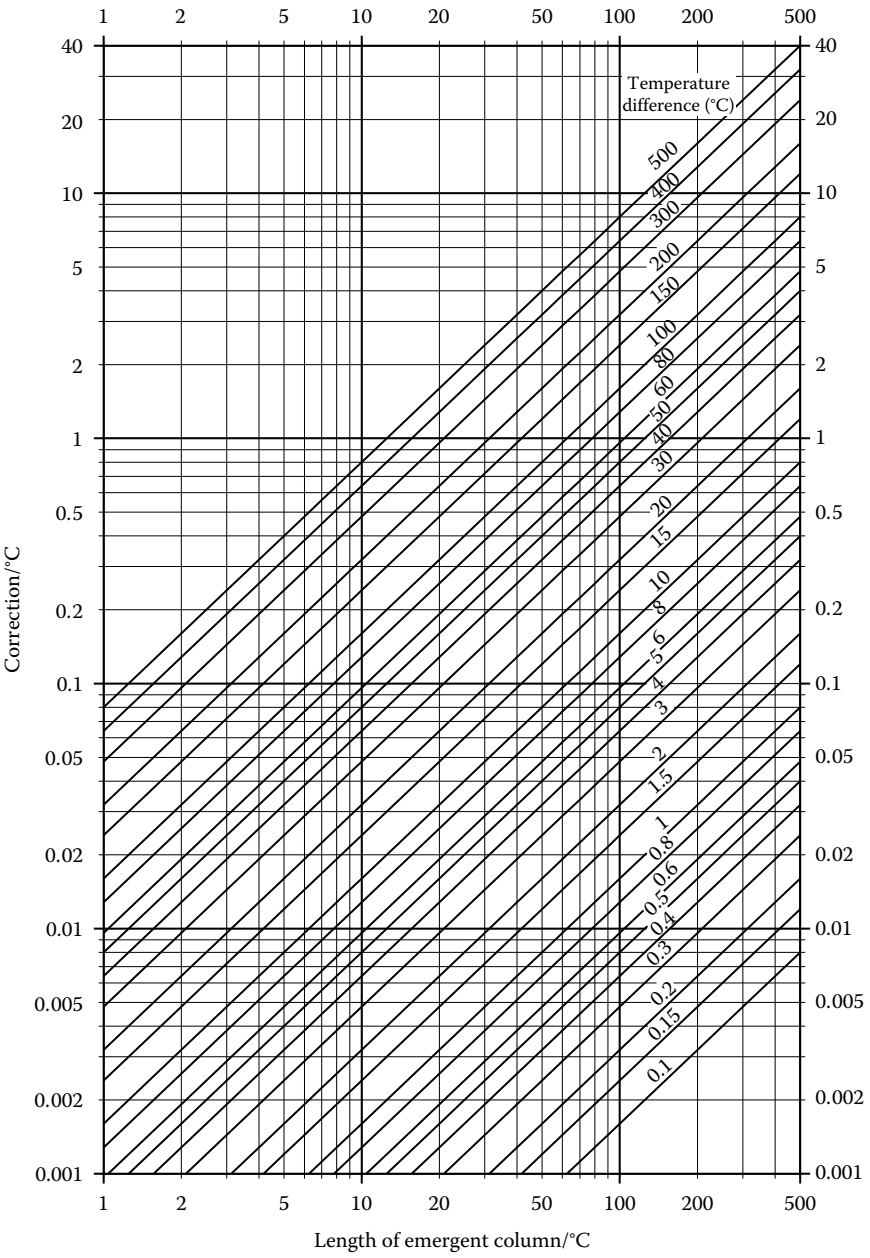

FIGURE 74.4 Stem correction chart for mercury-in-glass thermometers.

beaker with a total-immersion thermometer. The thermometer is immersed in the water to around the 20 °C mark. The emergent column is therefore 80 °C long. For the purpose of this calculation, we assume that the stem is close to the room temperature of 20 °C, resulting in an 80 °C temperature difference in the stem temperature from the calibration conditions. On the chart, the intersection of the line for the 80 °C emergent column length and line for the 80 °C temperature difference indicates a correction of just over 1 °C.

A similar application of the chart, with 1 °C emergent column length and a 5 °C temperature difference, shows that the error in the correct use of a total-immersion thermometer, with 1 °C of the column

visible, is well below 0.001 °C and can therefore be neglected. There are several different permutations of the correction equation depending on the thermometer type and how it is used. More examples can be found in the text of Nicholas and White [3].*

74.4.3 Hysteresis and Stability

Glass is an amorphous solid, which means that it does not have a well-defined atomic structure. A small part of the volume expansion and contraction of the glass that occurs with heating and cooling is due to small atomic rearrangements that occur slowly. If a thermometer is withdrawn from high temperatures and allowed to cool naturally, it will exhibit hysteresis or "temporary depression," the magnitude of which depends on the type of glass and the temperature to which the thermometer was exposed. The effect is easily measured by performing an ice-point check immediately before and after a measurement. The ice point, at 0.000 °C, is the temperature at which ice- and air-saturated water are in thermal equilibrium [9]. Always, after exposure to a higher temperature, the second ice-point reading will be lower than the first because the mercury contracts much faster than the glass. For good-quality mercury-in-glass thermometers, the effect is about 0.1% of the temperature change, that is, about 0.1 °C depression for a 100 °C temperature change in the glass. The thermometer will then relax quite rapidly over a period of days to close to its normal state although a residual effect will be measureable for months.

If accuracies of better than 0.1% are sought using mercury-in-glass thermometers, care must be taken to ensure that the thermal history of the thermometer is well controlled. This involves prescribed heating, cooling, and recovery processes that must be applied identically in use and calibration. With care, the temporary depression can be avoided. The atomic rearrangements responsible for the hysteresis occur more quickly at higher temperatures, and if the thermometer is cooled slowly, at 10 °C/h or slower [10], the effect is almost completely eliminated.

Besides the hysteresis, the glass bulb undergoes a slow contraction known as the secular effect, which causes the thermometer reading to slowly increase with age. Fortunately the effect is very slow, typically much less than a scale division per year, and regular calibration checks at the ice point will indicate the rate of drift. Because the effect originates in the bulb, the measured change in ice-point reading can be used to correct the whole of the thermometer scale.

The tendency for the glass to reorganize itself and seek the most stable amorphous state means that poorly annealed thermometers or thermometers that are subject to thermal or mechanical stress, such as being rested on their bulb, may never fully stabilize. Improperly annealed thermometers, for example, usually appear perfectly stable when received from the manufacturer but may exhibit random upward and downward changes of many scale divisions over periods as short as days or weeks following their first use.

74.4.4 Time-Constant Effects

In well-stirred media, the thermal time constant of an LIG thermometer is determined almost entirely by the diameter of the bulb as heat is conducted through the glass from the outside to the center of the bulb. A typical bulb of 5 mm diameter has a relatively short time constant of a few seconds when in well-stirred fluids. However, when the medium is slow or has a high thermal resistivity, the time constant is dominated by the medium itself and may be as large as many tens or hundreds of seconds. Table 74.3 gives the $1/e$ time constants in various media for a thermometer with a 5 mm diameter bulb. Time constants for other diameters can be estimated by scaling the times in proportion to the diameter.

* The material presented in this chapter section was extracted and adapted from this text. The text explains, for several different thermometer types, how to make traceable measurements and calibrate thermometers to meet international requirements.

TABLE 74.3 Time Constants for a Mercury-in-Glass Thermometer with a 5 mm Diameter Bulb

Medium	Still (s)	0.5 m/s Flow (s)	Infinite Flow Velocity (s)
Water	10	2.4	2.2
Oil	40	4.8	2.2
Air	190	71	2.2

LIG thermometers using organic thermometric fluids have an additional time-constant effect when measuring falling temperatures due to the time required for the fluid wetting the capillary to drain and join the main column. For precision thermometry, about 3 min/cm of wetted capillary is recommended.

74.4.5 Pressure

The thin bulb on most LIG thermometers unfortunately makes them sensitive to pressure. In good-quality mercury thermometers, the effect corresponds to about 0.1 °C for a one atmosphere change in pressure. This may seem like a small effect, but the pressure of a 760 mm high mercury column corresponds to one atmosphere. For this reason, most thermometers will give different readings in vertical and horizontal positions.

Another source of pressure variations is fluid turbulence in calibration or test baths. The pressure fluctuations from turbulence are readily visible as small and rapid variations in the reading. Ideally, fluid baths used with LIG thermometers should be constructed to provide a laminar flow along the axis of the thermometer.

74.4.6 Parallax

Parallax is the difference in the apparent position of an object viewed along two different lines of sight. The effect occurs in solid-stem LIG thermometers because the liquid column and the scale on thermometers are in different planes. Ideally, the thermometer should be set up so that the scale can be easily read while viewing at right angles to the stem. Optical aids can be useful to ensure a repeatable viewing position and to enlarge the image, but paradoxically they also increase the parallax effect, so care is still required.

Enclosed-scale thermometers are designed to minimize parallax by placing the capillary, and the scale markings in the same plane, nevertheless, always viewing at right angles will minimize the effects of any scale misplacement.

74.4.7 Stiction

A mercury thermometer with a fine capillary not only becomes difficult to read but also suffers from stiction: the mercury moving in fits and starts due to the surface tension between the mercury and the capillary walls. The effect can be overcome by lightly tapping the thermometer with a small pencil or paintbrush. The brush is also useful for clearing condensation when doing an ice-point check.

74.4.8 Thermal Capacity Effects

Glass thermometers are bulky and have considerable mass, especially high-precision thermometers with long bulbs. The transient heat flow accompanying the warming or cooling of the thermometer can upset temperature measurements, making high-precision measurements difficult. Preheating or cooling the

thermometer can alleviate the worst of the problem. For higher precision and lower masses, choose a platinum resistance thermometer or thermistor instead. Simple estimates of the heat requirements can be made by measuring the volume of thermometer immersed and assuming that 2 J are required to raise 1 cm^3 of the thermometer volume (glass or mercury) by 1 °C. This is a good rule of thumb for most solids and liquids.

74.4.9 Separated Columns

A common problem with LIG thermometers is for a part of the thermometric liquid to become separated from the main volume. This happens often when thermometers are shipped but may also happen with use at high temperature when the liquid vapor condenses near the cool end of the capillary (Figure 74.5). The effect is readily detectable as an ice-point shift, but the capillary of thermometers should be checked visually before use and especially after shipping.

With organic liquids, the problem can be more difficult to identify because the liquid is often clear and wets the surface of the capillary and may not be as visible. For this reason, spirit thermometers should be stored by suspending them vertically to allow the thermometric liquid to drain. The typical vertical temperature gradient found in most rooms will also warm the top of the thermometer to prevent condensation of vapor high up the capillary.

The main reason for including a gas fill in LIG thermometers is to prevent column separation. The gas not only "holds" a column together but also retards the diffusion of vapor at high temperatures and so prevents condensation. Usually, an inert gas like dry nitrogen is used to prevent oxidation. Note that an expansion chamber must be kept cooler than the bulb to prevent excessive gas-pressure buildup. The high pressure can permanently distort the bulb even if rupture does not occur.

Mechanical separation of the liquid column is, unfortunately, a common occurrence. The gas fill helps prevent separation, but, conversely, the gas makes the column more difficult to rejoin. There is also a risk of trapped gas bubbles in the bulb or contraction chambers, and careful inspection may be needed to locate them. A vacuous capillary will give rise to more breaks, but the column is easily rejoined.

With care, it is usually possible to rejoin the column and still have a viable thermometer. However, it must be realized that attempts to join a broken column may stress a thermometer sufficiently to render it permanently unstable. Column breaks that occur repeatedly when the thermometer is heated indicate the thermometer should be discarded.

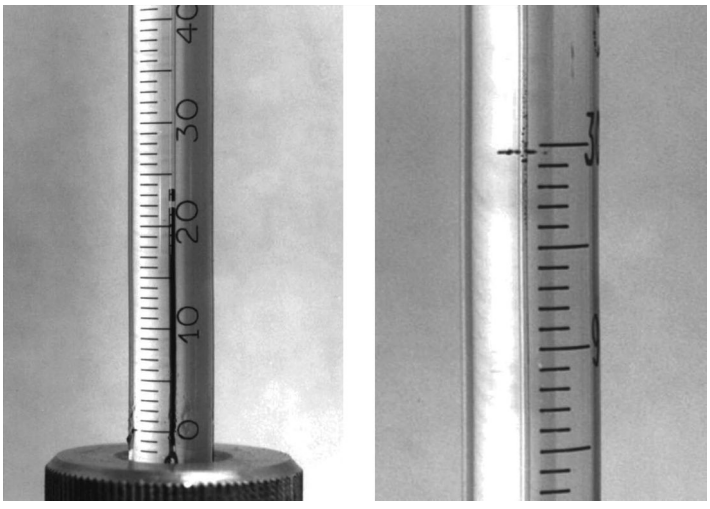

(a) (b)

FIGURE 74.5 Separated columns in mercury-in-glass thermometers, showing (a) a break in the column and (b) condensation—near the pointing mark.

Various procedures for joining a broken column can be tried. The procedures as follows are given in order of preference:

- Lightly tap the thermometer while holding it vertically. This may work for a vacuous thermometer.
- For LIG thermometers using organic fluids, suspend the thermometer vertically for several hours with the upper end of the stem warmed slightly.
- Apply centrifugal force. This is best done by holding the bulb alongside the thumb, protecting it with the fingers, and with the stem along the arm. Raise the unbent arm above the head and bring it down quickly to alongside the leg. This method avoids a flicking action, which will cause breakage, and protects the thermometer from striking other objects.
- If the aforementioned methods are unsuccessful, try cooling the thermometer. This method relies on sufficient cooling for all the fluid to contract into the bulb, leaving none in the stem. The column should be rejoined when it has warmed to room temperature. More than one attempt might be needed. Tapping and centrifugal force might also be needed to assist the movement of the fluid.

Three readily available cooling media can be used:

- Salt, ice, and water (to –18 °C)
- Dry ice, that is, solid CO_2 (–78 °C)
- Liquid nitrogen (–196 °C)

Liquid nitrogen and dry ice require more care as they will freeze the mercury (near –38°C). *Cold burns to the user could also occur.* It pays to cool the thermometer slowly by alternately dipping the thermometer quickly into the media and then watching the mercury column fall. A slow cooling will also prevent excessive stress in the glass.

Heating a thermometer to force a rejoin in the expansion chamber is NOT RECOMMENDED because it exposes the thermometer to temperatures above its annealing temperature, which will cause it to become unstable, and it may cause the bulb to rupture.

If the broken column has been successfully rejoined, then an ice-point check (or other reference check) should be made. If the reading is the same as obtained previously, then the join can be considered completely successful, and the thermometer is ready for use. However, a significant ice-point shift indicates that the join was not successful and that the thermometer should be discarded. If a small ice-point shift has occurred, then the shift might simply be due to hysteresis, so treat the thermometer with suspicion until there is evidence of long-term stability, that is, no further significant ice-point changes occur.

References

1. W. E. K. Middleton, *A History of the Thermometer and Its Uses in Meteorology*, John Hopkins Press, Baltimore, MD, 1966.
2. T. J. Quinn, *Temperature*, 2nd edn., Academic Press, London, U.K., 1990.
3. J. V. Nicholas and D. R. White, *Traceable Temperatures*, 2nd edn., John Wiley & Sons, Chichester, U.K., 2001.
4. ISO issued documentary standards related to the liquid-in-glass thermometer:
   ISO 386-1977 Liquid-in-glass laboratory thermometer—Principles of design, construction and use
   ISO 651-1975 Solid-stem calorimeter thermometers
   ISO 653-1980 Long solid-stem thermometers for precision use
   ISO 654-1980 Short solid-stem thermometers for precision use
   ISO 1770-1981 Solid-stem general purpose thermometer
5. ASTM in their standards on Temperature Measurement, Vol. 14.03, include two standards related to liquid-in-glass thermometers:
   E1-95 Specification for ASTM Thermometers
   E77-92 Test Method for Inspection and Verification of Liquid-in-glass Thermometers

6. BSI published a series of documentary specifications for thermometers, including
   BS 593:1989 Laboratory Thermometers
   BS 791:1990 Thermometers for Bomb Calorimeters
   BS 1704:1985 General Thermometers
   BS 1900:1976 Secondary Reference Thermometers
7. J. A. Wise, *Liquid-in-Glass Thermometer Calibration Service*, National Institute of Standards and Technology Special Publication, 250-23, 1988.
8. E. C. Holligan, Calibration and use of liquid-in-glass thermometers. In: R. E. Bentley (ed.), *Handbook of Temperature Measurement*, Vol. 2, pp. 107–133, Springer, New York, 1998.
9. ASTM International, *ASTM E 563-08 Standard Practice for Preparation and Use of an Ice-Point Bath as a Reference Temperature,* ASTM International, West Conshohocken, PA, 2008.
10. S. J. Van Dijk, J.A. Hall, and V.M. Leaver, The influence of cooling rate on the zeros of mercury-in-glass thermometers, *J. Sci. Instrum*., 35, 334–348, 1958.

Partial List of Vendors and Suppliers

Kimble Chase, 8500 Spruce St., Vineland, NJ 08360-1502, Phone: 856-692-8500, 888-546-2531 (toll free), Fax: 856-794-9762, www.kimble-chase.com/index.html

Palmer Wahl, 234 Old Weaverville Rd., Asheville, NC 28804-1228, Phone: 828-658-3131, 800-421-2853 (toll free), Fax: 828-658-0728, www.palmerwahl.com

Tel-True Mfg. Co., Inc., 408 St. Paul St., Rochester, NY 14605-1734, Phone: 585-232-1440, 800-232-5335 (toll free), Fax: 585-232-3857, www.teltru.com/

ThermoProbe, Inc., 112-A Jetport Dr., Pearl, MS 39208, Phone: 601-939-1831, Fax: 601-355-1831, www.thermoprobe.net

ThermoWorks, 1762 W. 20 S., Suite 100, Lindon, UT 84042, Phone: 801-756-7705, Fax: 801-756-8948, www.thermoworks.com

VEE GEE Scientific, Inc., 13600 N.E. 126th Place, "A", Kirkland, WA 98034-8720, Phone: 425-823-4518, 800-423-8842 (toll free), Fax: 425-820-9826, www.veegee.com

75

Manometric Thermometers

Franco Pavese
National Institute of Meterology Research

Manometric thermometers are defined in this handbook as those thermometers that make use of the pressure of a *gaseous* medium as the physical quantity to obtain temperature. Very seldom are they available from commercial sources; for example, the temperature control of a home freezer is often of this kind. Consequently, instead of simply buying one, every user must build his or her own when this type thermometer is needed. They can be a quite useful choice since, in the era of electronic devices and sensors, it is still possible to make a totally nonelectronic thermometer, though of modest precision, which in addition keeps its calibration indefinitely, as long as the quantity of substance sealed in it remains unchanged. The range of temperatures that can be covered by this kind of thermometer depends on the principle and on the substance used. When the thermodynamic equilibrium between the *condensed* phase of a substance (either liquid or solid) and its vapor is used, one has a "vapor-pressure thermometer," and the temperature range spanned by each substance is generally narrow. In addition, only substances that are gaseous at room temperature (i.e., condensed at temperatures lower than 0 °C) are normally used, confining the working range to below room temperature; however, some substances that are liquid at room temperature and have a high vapor pressure (i.e., which easily evaporate) have been used, but do not result in a sizable extension of the working range much above room temperature. A special case of vapor pressure being used at high temperature is the device called a "heat pipe," which is not used as a thermometer, but instead as an accurate thermostat [1]; using sodium, the working range is pushed up to ~1100 °C. When a pure substance is used only in its gaseous state, one has a "gas thermometer," whose temperature range can be very wide, especially for moderate accuracy, depending mainly on the manometer; on the other hand, its fabrication is somewhat more complex and its use normally much less straightforward.

Both thermometers can be built to satisfy the state-of-the-art accuracy of national standards (uncertainty better than ±0.001 K) or for lower accuracies, down to an uncertainty of ±1% or higher. Both thermometers require the measurement of pressure, in the range from less than 1 Pa up to 100 bar. A complete and specialized treatment on both vapor-pressure and gas thermometers up to room temperature and on pressure measurement instruments and techniques for gaseous media can be found in [2]. Gas thermometry above room temperature is treated in [3,4].

In consideration of the fact that these kinds of thermometers typically must be built by the users, the following will concentrate on the basic guidelines for their design and fabrication.

75.1 Vapor Pressure

Figures 75.1 and 75.2 show the pressure values and the sensitivities in the temperature range allowed for each of the most common gaseous substances, considering also, in addition to the liquid phase, the use of the solid phase (where vapor pressure is lower) below the triple point. The lower end of the range is determined by the manometer uncertainty (for a given accuracy), the upper end by the full-scale pressure of the manometer (or by the full evaporation of the condensed phase).

Table 75.1 reports "certified" vapor-pressure equations, linking the measured pressure p to the unknown temperature T. The reader might prefer them to the plethora of equations found in the

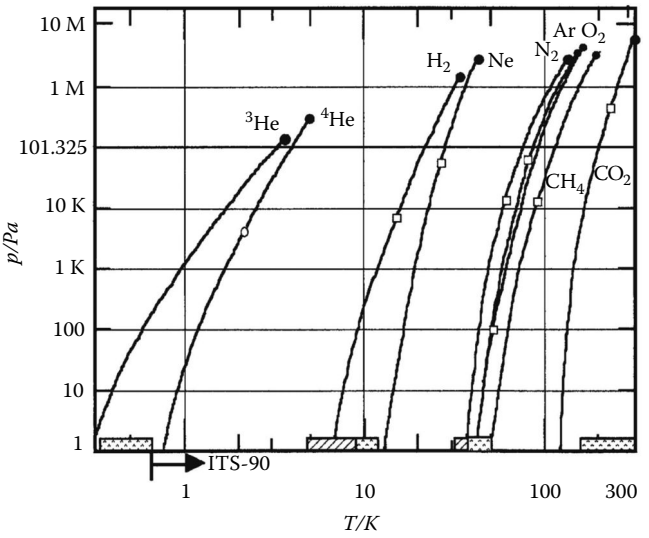

FIGURE 75.1 Range for vapor-pressure thermometry of various gases. The shaded parts indicate regions where it is less common or less accurate. ▨, not available; ▩, lower accuracy; ●, critical point; ○, triple point; 0, lambda point.

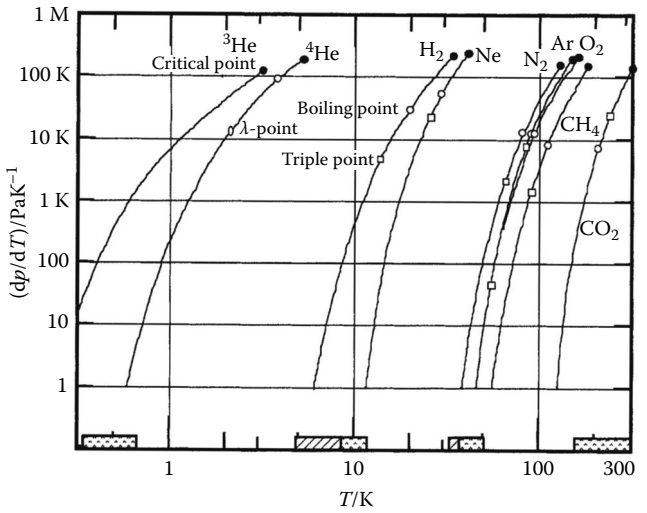

FIGURE 75.2 Sensitivity dp/dT of vapor-pressure thermometry for selected gases. The shaded parts indicate regions where it is less common or less accurate. ▨, not available; ▩, lower accuracy; ●, critical point; ○, triple point; 0, lambda point.

TABLE 75.1 Vapor-Pressure Equations

Equilibrium State	T_{90} (K)	Uncertainty $\pm\delta T$ (mK)	Purity of Material[a] (vol%)
Liquid–vapor phases of helium-4	1.25–2.1768	0.1	99.9999
	$T_{90}/K = A_0 + \sum_{i=1}^{9} A_i \left[\left(\ln(p/Pa) - B \right) / C \right]^i$		
	$A_0 = 1.392408$	$A_1 = 0.527153$	$A_2 = 0.166756$
	$A_3 = 0.050988$	$A_4 = 0.026514$	$A_5 = 0.001975$
	$A_6 = -0.017976$	$A_7 = 0.005409$	$A_8 = 0.013259$
	$B = 5.6$	$C = 2.9$	
	2.1768–5.0	0.1	99.9999
	$A_0 = 3.146631$	$A_1 = 1.357655$	$A_2 = 0.413923$
	$A_3 = 0.091159$	$A_4 = 0.016349$	$A_5 = 0.001826$
	$A_6 = -0.004325$	$A_7 = -0.004973$	$B = 10.3$
	$C = 1.95$		
Liquid–vapor phases of equilibrium hydrogen	13.8–20.3	1[b]	99.99
	$p/Pa = (p_0/Pa)\exp\left[A + B/(T_{90}/K) + C\,T_{90}/K \right] + \sum_{i=0}^{5} b_i (T_{90}/K)^i$		
	$A = 4.037592968$	$B = -101.2775246$	
	$C = 0.0478333313$		
	$b_0 = 1902.885683$	$b_1 = -331.2282212$	$b_2 = 32.25341774$
	$b_3 = -2.106674684$	$b_4 = 0.060293573$	$b_5 = -0.000645154$
Liquid–vapor phases of natural neon[c]	24.6–40	2	99.99
	$\log(p/p_0) = A + B/(T_{90}/K) + C(T_{90}/K) + D(T_{90}/K)^2$		
	$A = 4.61948943$	$B = -160.478268$	
	$C = -0.0369937132$	$D = 0.00004256101$	
Solid–vapor phases of nitrogen	56.0–63.1	2	99.999
	$\log(p/p_0) = A + B/(T_{90}/K) + C(T_{90}/K)$		
	$A = 12.07856655$	$B = -858.0046109$	$C = -0.009224098$
Liquid–vapor phases of nitrogen	63.2–125	5	99.999
	$A = -6.10273365$	$B = 1.153844492$	$C = -1.087106903$
	$D = -1.759094154$	$T_c = 126.2124$ K	$P_c = 3.39997$ MPa
Liquid–vapor phases of oxygen	54–154	2	99.999
	$\mathrm{In}(p/p_c) = T_c/T_{90}\left[A\tau + B\tau^{1.5} + C\tau^3 + D\tau^7 + D\tau^9 \right]$		
	$\tau = 1 - T_{90}/T_c$	$A = -6.044437278$	
	$B = 1.176127337$	$C = -0.994073392$	$D = -3.449554987$
	$E = 3.343141113$	$T_c = 154.5947$ K	$P_c = 5.0430$ MPa
	$\mathrm{In}(p/p_c) = T_c/T_{90}\left[A\tau + B\tau^{1.5} + C\tau^3 + D\tau^6 \right]; \quad \tau = 1 - (T_{90}/T_c)$		

(*continued*)

TABLE 75.1 (continued) Vapor-Pressure Equations

Equilibrium State	T_{90} (K)	Uncertainty $\pm\delta T$ (mK)	Purity of Material[a] (vol%)
Liquid–vapor phases of argon	83.8–150	5	99.999
	$A = -5.906852299$	$B = 1.132416723$	$C = -0.7720072001$
	$D = -1.671235815$	$T_c = 150.7037$ K	$P_c = 4.8653$ MPa
Liquid–vapor phases of methane	90.7–190	5[d]	99.99
	$\ln(p/p_c) = T_c/T_{90}\left[At + B\tau^{1.5} + C\tau^{2.5} + D\tau^5\right];\quad \tau = 1-(T_{90}/T_c)$		
	$A = -6.047641425$	$B = 1.346053934$	$C = -0.660194779$
	$D = -1.304583684$	$T_c = 190.568$ K	$p_c = 4.595$ MPa
Liquid–vapor phases of carbon dioxide	216.6–304	15	99.99
	$\ln(p/p_c) = A_0\left(1-(T_{90}/T_c)\right)^{1.935} + \sum_{i=1}^{4} A_i\left((T_c/T_{90})-1\right)^i$		
	$p_c = 7.3825$	$T_c = 304.2022$ K	$A_0 = 11.37453929$
	$A_1 = -6.886475614$	$A_2 = -9.589976746$	$A_3 = 13.6748941$
	$A_4 = -8.601763027$		

Note: For the relevant references and more gases, see [6]. p_0 = 101325 Pa, except when otherwise indicated.

[a] Minimum purity of the material to which the listed values of temperature and uncertainty apply.

[b] The summation term in the equation adds to the value of p a pressure amounting to the equivalent of 1 mK maximum.

[c] These values are for neon with an isotopic composition close to that specified in the ITS-90 definition.

[d] Above 100 K. It increases to 15 mK at 91 K and to 10 mK near the critical point.

literature, since they have been checked by official bodies and T is expressed as T_{90}, in the ITS-90, the International Temperature Scale [5, text in 2]. More checked equations can be found in [6]. The vapor-pressure equations are generally empirical equations; therefore, the temperature measured with a vapor-pressure thermometer is not the thermodynamic temperature. T_{90} and thermodynamic temperature T must be used (see Section 75.6).

Figure 75.3 shows the general layout of a vapor-pressure thermometer. The fabrication of a vapor-pressure thermometer is not exceedingly difficult if a few guidelines are followed. Table 75.2 summarizes the most critical ones—design criteria and filling information—in a compact form [2]. Much more constructional details can be found in [1,3]. In most cases, the manometer is located at room temperature, and the bulb is connected to it via a small-bore tube (the "capillary tube") without critical drawbacks. The accuracy of these thermometers ranges from ±0.0001 K using very pure substances in calorimeters and precision mercury manometers to ≈ ±1% using dial manometers.

75.2 Gas Thermometry

As indicated in Chapter 65 of this handbook, since 2005, one is allowed to consider the direct use of thermodynamic temperature as an internationally agreed method to measure temperature. Thermodynamic thermometers can be of different kinds. The manometric ones can be of different types. The historically more common is the constant-volume gas thermometer (CVGT), but in recent years also, the acoustical thermometer has greatly improved its accuracy and, to a minor extent, the dielectric-constant gas thermometer.

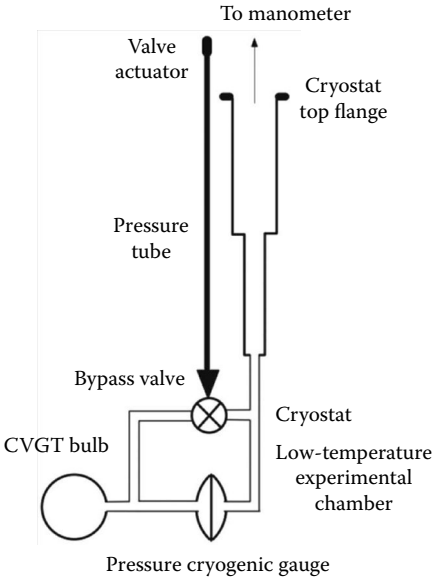

FIGURE 75.3 General layout of a manometric thermometer. It is shown with a cryogenic diaphragm pressure transducer; when the transducer is placed instead at room temperature, the bypass valve is also placed at room temperature. *Vapor-pressure thermometer:* The diameter of the pressure tube increases in steps when pressures lower than ≈0 Pa must be measured, in order to decrease the thermomolecular pressure drop. Gas *thermometer* (constant volume): The diameter of the pipes connecting the bulb to the cryogenic pressure transducer must be small in order to reduce the so-called dead-volume. This requirement is much more stringent when the pressure transducer is moved up to room temperature. In this case, in order to reduce the error due to the "dead volume," the bulb volume must be increased significantly, as shown in Figure 75.4.

75.2.1 Constant-Volume Gas Thermometer

The layout of Figure 75.3 also applies to the design of a CVGT (more common than the constant-pressure type), with the differences indicated in the relevant caption.

For a pressure gauge placed at room temperature, the design becomes that of Figure 75.4. The lower temperature end of the working range of a gas thermometer of this type is stated, well before condensation of the substance takes place, by the increase of the uncertainty due to the increase in the nonideality of the gas—that is, deviation from linearity of the relationship $p(T)$—which takes place when approaching the condensed state or for increasing gas densities or due to excessive absorption of gas on the bulb surface, thereby changing the quantity of the thermometric substance. All these conditions act at the lower end of the range. The upper end is stated by technological reasons or by the manometer full-scale capability. The best substances are, as listed, helium (either isotopes), hydrogen, and nitrogen.

From a design point of view, Table 75.3 summarizes the most critical issues. The major problem, apart from gas purity and ideality, is meeting the constant-volume requirement. Being that the manometer is generally at room temperature, the fraction of gas filling the connecting "capillary" tube is subtracted from the total amount of thermometric substance amount filling the system, and since this fraction is not constant, but depends on temperature and on technical conditions, it tends to increase the measurement uncertainty, which is contrary to the case of the vapor-pressure thermometer; this error is called the *dead-volume error,* which determines the largest contribution to the total uncertainty. In modern realizations, the use of a cryostat based on a close-cycle refrigerator can sensibly reduce this

TABLE 75.2 Summary of Design Criteria for Vapor-Pressure Thermometers

	Example
1. Choice of working substance	$T_{max} = P_c$
Temperature range: Each substance spans only a narrow temperature interval.	T_{min} = 100 Pa K^{-1}
T_{max}/T_{min} < 2–3 (including solid–vapor range), except helium. The limit	
T_{max} set by maximum manometer pressure	$T_{max}/T_{min} = {}^3He \approx 10$
T_{max} set by manometer sensitivity	$^4He \approx 9$
Accuracy	$H_2 \approx 3$
Manometer: No single manometer spans whole range from ≈ 1 Pa ($dp/dT \approx 100$ Pa K^{-1}) and critical point ($p_c > 10^6$ Pa, except helium) with high or constant accuracy or with sufficient sensitivity.	Ne ≈ 3
Substance: Not all substances allow for maximum accuracy, due to purity or to thermal problems related to a low thermal diffusivity value.	$N_2 \approx 2.5$
2. Choice of pressure measuring system	$O_2 \approx 2.5$
Sensitivity and accuracy must be matched to the range of dp/dT and of p, that is, T, to be measured.	Ar ≈ 2.5
Without separating diaphragm: can be used only for low to medium accuracy, as thermometric gas also fills the entire manometric apparatus, with problems of contamination and increases in vapor volume.	$CO_2 \approx 2$ (solid ≈ 1.5)
Dial *manometers*: used only for accuracy > ±1%.	
Metal *diaphragm* or bellows (electronic) manometers: can achieve a ±0.1%–0.03% accuracy.	
Quartz Bourdon gauges: can approach a ±0.01% accuracy, but helium leaks through quartz.	
Cryogenic *pressure* transducers: None is commercially available with accuracy better than ± 0.1% (after cryogenic calibration). Eliminate the need of the connecting tube in sealed thermometers, but transducer must withstand high room-temperature pressure.	
With separation diaphragm: mandatory for high or top accuracy. Only zero reproducibility and a moderate linearity near zero are important.	
Capacitive diaphragms: Several commercial models, when properly used, allow zero sensitivity and reproducibility better than ±0.1 Pa.	
Cryogenic diaphragms: Only laboratory-made diaphragms are available, some with high zero reproducibility. Allow to confine thermometric gas at low temperatures, but the tube connecting the diaphragm to room-temperature manometer is still necessary.	
Room-temperature manometers: When a cryogenic diaphragm is used, only manometers allowing helium as manometric gas can be used.	
3. Choice of sealed versus "open" thermometer	
Sealed: low-accuracy-only (e.g., dial) thermometers.	
Medium-accuracy sealed thermometers are still very simple when using cryogenic manometer and reducing vapor volume, but room-temperature pressure can be higher than 10 MPa. Therefore, only low-sensitivity manometers can be used, and thermometer measures only upper part of vapor-pressure scale.	
High-accuracy sealed thermometers can be made, using ballast room-temperature volume and precision room-temperature diaphragm.	
"Open": Vapor-pressure thermometers using gases are open only since working substance does not stay permanently in working bulb, but (new) samples are condensed in it only during measurements. Requires permanent use of a gas-handling system.	

TABLE 75.2 (continued) Summary of Design Criteria for Vapor-Pressure Thermometers

	Example
4. Gas purity, isotopic composition, and spin equilibrium	
Purity: must be known and possibly checked, for example, by performing a triple-point temperature measurement. Dew boiling point difference measurement must also routinely be performed, before sealing in the case of sealed devices.	Problems only for high-accuracy Kr, Xe (for isotopic composition), H_2, D_2 (for spin-equilibrium composition)
Isotopic composition: Some gases show irreproducibility in results due to sample-to-sample changes in isotopic composition. It is impossible to obtain top accuracy with these substances, unless pure isotopes are used.	
Spin equilibrium: With some gases, showing different spin species, equilibrium must be ensured with use of a suitable catalyst.	
5. Thermometer filling	^{4}He thermometer
Amount of substance n_{max} at $T_{min} \rightarrow V^L \approx V_b$	T_{min} = 2.2 K
$n_{max} \le \frac{p_{max}}{RT_r}\left[\frac{2V_cT_r}{T_f+T_{min}}+V_f\right]+\frac{V_b}{M}\rho_{min}$	p_{min} = 5.263 kPa ρ_{min} = 146 kg m^{-3}
Amount of substance n_{max} at $T_{min} \rightarrow V^L = V_\varepsilon^L; \approx 0$	T_{max} = 5.2 K
$n_{min} \ge \frac{V_\varepsilon^L\rho_{max}}{M}+\frac{\rho_{max}}{RT_t}\left[\frac{2V_cT_t}{T_t+T_{min}}+V_r+\frac{T_r}{T_{max}}(V_{max}-V_\varepsilon^L)\right]$	p_{max} = 227.5 kPa
Bulb volume V_b	p_{max} = 67.5 kg m^{-3}
$V_b\left[\frac{\rho_{min}}{M}-\frac{\rho_{max}}{RT_{max}}\right] \le \frac{V_r}{RT_r}\left[p_{max}-p_{min}\right]+\left[\frac{\boldsymbol{\rho_{max}}}{\boldsymbol{M}}-\frac{\boldsymbol{\rho_{max}}}{\boldsymbol{RT_{max}}}\right]$	T_f = 4.2 K p_f = 100 kPa T_t = 300 K p_t = 200 kPa V_t = 220 cm^3 V_c = 16 cm^3 V_T = 500 cm^3 M = 4 g mol^{-1}
$+\frac{\mathbf{2V_c}}{\boldsymbol{R}}\left[\frac{\boldsymbol{p}_{min}}{\boldsymbol{T_t+T_{max}}}-\frac{\boldsymbol{p}_{max}}{\boldsymbol{T_t\xi V_{min}}}\right]$	
to a first approximation the terms in bold can be omitted.	It follows $V_b \ge \approx 2$ cm^3. Taking the minimum volume $0.074 \ge n$ $n \ge 0.034$
Calculation of the amount of substance n to condense in the thermometer: The gas is stored at P_r in the room-temperature reservoir of volume V_T. When the substance is condensed in the thermometer bulb at a temperature T_f, a residual $n_0 = p_fV_T/R_T$ remains in V_T. Therefore, in order to condense a quantity N, one must have in the system	In order to seal in 0.05 mol, the filling system must contain 0.069 mol.
$n' = \frac{p_rV_T}{RT_r}\left[1-\frac{p_f}{p_r}\right]+\left(V_b+V_c+V_r\right)$	

V^L = volume of the liquid phase; ρ, density; p, pressure; V, volume; subscript r, room temperature; c, capillary; b, bulb.

error, allowing for a shorter total length of the capillary. Also, the bulb volume itself changes with temperature, due to thermal expansion and, to a much smaller extent, to the change in internal pressure. Design and fabrication criteria and measuring procedures are given in great detail in [2]. The case where the gas thermometer is *calibrated* at a number of fixed points is also described in [2], with a discussion of the simplification in the use of the gas thermometer introduced with this instrument (called the *interpolating CVGT* (ICVGT), defined in the ITS-90 for use between 3 K and 26 K), though it is not

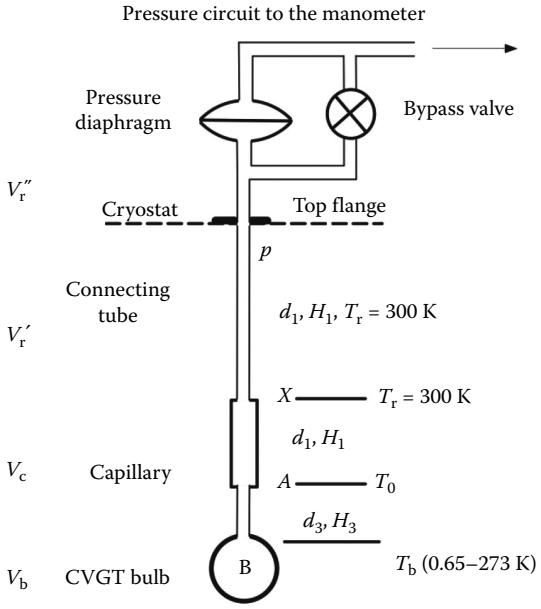

FIGURE 75.4 General layout of a constant-volume gas thermometer with room temperature diaphragm pressure transducer. d and H = pipe diameter and length.The temperature gradient should be concentrated in a short length of capillary tube AX whose diameter must be larger to limit the thermomomecular effect, if placed horizontally, the aerostatic head pressure gradient can also be avoided. In order to reduce the correction due to the "dead-volume" (sum of V_c, V_r', and V_r'') and its uncertainty, the bulb volume must be increased significantly.

more a thermodynamic thermometer, but a semiempirical one, providing only T_{90} values. Tables 75.4 and 75.5 summarize the most important differences between an ICVGT and a CVGT.

75.2.2 Acoustic Gas Thermometer

Figure 75.5 shows the layout of this type of thermometer: only the bulb is shown since all the rest of the gas circuit is much less critical than for the CVGT. For details, see [2].

The main problems to be taken into account in this type of gas thermometer are the following:

Correction of the effect of the acoustic boundary layer: Ideally, the normal component of the particle velocity is expected to vanish at the boundary (wall), and for a viscous fluid (gas) also, the tangential component should vanish. Further, the solid boundary should disturb the temperature field associated with the velocity field. Thus, near the interface, the acoustic propagation would be more isothermal than adiabatic, due to the very high thermal conductivity of the wall with respect to the gas. The calculation of this correction requires the knowledge of the density and heat capacity of the gas as a function of temperature and pressure. These can be obtained by inversion of the second-order virial equation. The importance of the boundary layer correction is indicated by the fact that it leads overall to the largest correction and that it can assume values as high as 5×10^{-4}.

Measurement of the acoustic thermometer volume: The use of a spherical bulb (the resonator) allows the employment of resonances and an improved quantification of the boundary layer effect through an appropriate choice of the available acoustic modes. The volume of the resonator can be measured by filling it with mercury and then weighing it. A much better method is to measure the radius of the resonator and its variation due to thermal expansion, by the application of microwaves. The microwave measurements can be performed separately in vacuum. Using a quasi-spherical resonator, in order to

TABLE 75.3 Summary of Design Criteria for an Absolute CVGT in the Low-Temperature Range ($T < 273.16$ K)

1. Choice of temperature range and of span $T_{min} \leftrightarrow T_{max}$
   This choice is preliminary to the choice of most of the design parameters.

   Below 273.16 K, ^{4}He gas thermometry is limited down to 2.5 K. With ^{3}He, accurate virial corrections available down to 1.5 K.

   Only CVGTs of special design can be used in full span. Being that $p \propto T$, the 2.5–273.16 K range corresponds to $p_{max}/p_{min} > 100$. For top accuracy, $\delta p/p < 0.01\%$, corresponding at p_{min} to $\delta p < 10^{-6}$. p_{max}, generally not achievable.

   Being that $p \propto = n/V$, molar density must generally be changed over the range to optimize accuracy, but n/V must be limited to avoid third virial correction, especially below = 2 K.

   In general, a CVGT is designed for work only below or only above a temperature between 25 K and 100 K.

2. Choice of reference temperature T_0

   Truly absolute thermometer: only one choice possible—273.16 K.

   Two-bulb CVGT: avoids necessity to bring up to T_0 the bulb measuring $T_{min} > T < T_{max}$. Useful with thermometers designed for use at $T \ll T_0$.

   Single-bulb CVGT: Same bulb spans the entire range up to T_0.

   Low-temperature reference temperature T_0^* (≈from 25 K to 90 K)

   Single-bulb CVGT commonly used. T_0^* value assigned by an independent experiment and, therefore, not exact by definition. However, the additional uncertainty is a minor inconvenience with respect to the advantage of limiting bulb temperature within the span $T_{min} \leftrightarrow T_{max}$.

3. Choice of thermometric gas and filling density
   Thermometric gas

   Nitrogen: low-medium accuracy.

   e-Hydrogen: not used for over 50 years but still suitable for low-medium accuracy and temperature range above ≈20 K.

   Helium-4: commonly employed in recent gas thermometers. Use limited to above 2.5 K.

   Helium-3: considered more in modern gas thermometry. Use presently limited to above 1.5 K; potential for use down to <1 K.

   Filling density: $p \propto n/V$ and $\mathrm{d}p/\mathrm{d}T \propto n/V$ (1 kPa K^{-1} ≙ 121 mol m^{-3}). Always advantageous increasing n/V, up to an upper boundary set by need of third virial correction. As a rule, $n/V < 250$ mol m^{-3} above = 2.5 K; $n/V < 160$ mol m^{-3}, down to 1.2 K; and $n/V < 30$ mol m^{-3} at 0.8 K.

4. Choice of the pressure measuring system
   See Table 75.1.

5. CVGT parameter design
   Room-temperature pressure transducer
   Bulb: top accuracy, 1 L volume typical; low accuracy, as low as 50 cm^3

   Dead volume: top accuracy, <10 cm^3; low accuracy, up to 10% of bulb volume

   Cryogenic pressure transducer
   Bulb: minimum volume limited only by its invariance, affected by adsorption and wall deflection. It can reduce to the transducer chamber

   Dead-volume: none (or very small)

6. Bulb design
   Volume may not be constant because of

   Compression modulus: Walls must be thick to limit deflection due to pressure, or bulb must be enclosed in a guard chamber kept at bulb pressure. Stress in bulb material must be relieved by annealing after machining.

   Thermal expansion: Nothing can be done to suppress this effect, except using glass; must be corrected for. Small effect below ≈30 K.

   Amount of "active" gas might not be constant because of

   Gas adsorption: Physicochemical interaction of bulb walls with the gas determines the amount adsorbed. Copper often gold plated to limit adsorption: this prevents heating the bulb above 50°C–70°C.

   Impurity molecules on walls and leaks: clean machining used for metal bulbs, followed by physicochemical cleaning. The bulb sealing gaskets must be stable in shape and leakproof at working temperatures.

(*continued*)

TABLE 75.3 (continued) Summary of Design Criteria for an Absolute CVGT in the Low-Temperature Range ($T < 273.16$ K)

7. Dead-volume design (case of room temperature pressure transducer)
   Dead-volume effect comes from combination of geometrical volume, working pressure, and gas density distribution, that is, from the amount of substance contained in it.

   Room-temperature dead volume: consists of all volumes of the gas measuring system at room temperature. Must be kept at uniform temperature (except diaphragm, often thermostated at ≈40 °C), to be measured within 0.1 °C–1 °C.

   Low-temperature dead volume: (part of) capillary tube between room and bulb temperatures. Temperature and density change from one end to the other. Tube diameter is a trade-off between geometrical volume and thermomolecular pressure effect: typical values between 0.5 mm and 3 mm. Advantageous in keeping the parts of tube where temperature variations occur as short as possible. For medium-high accuracy, temperature distribution must be known accurately.
8. Gas handling and measuring system (for non-sealed CVGTs)
   Handling system: must ensure purity, checked online with a mass spectrometer for the highest accuracy, and include gas recovery with cryogenic pumps and clean storage (or purification).

   Measuring system (case A): Separating diaphragm requires valve system for zero check, including constant-value valves and provisions to avoid (or to restore) thermometric gas losses and contamination from the manometric gas. For this purpose, a second diaphragm separator can be used.

resolve the degenerate microwave resonance triplets TE1n and TM1n, allows a reduction in the uncertainty: In this case, gas helium filling is used or argon; the use of different gases is an important check on the correctness of the corrections. They must also account for the heat exchange between the gas and the wall. Similarly, the use of different metals for the resonator allows a check on the correctness of the term accounting for the penetration of the e.m. field into the walls. Copper was used, as also stainless steel and aluminum, with the thermal conductivities of copper and stainless steel differing by a factor of about 300 at 77 K and of about 50 at the triple point of water. The use of helium has one drawback with respect to argon: it is much more sensitive to impurities. It is therefore advisable in such a case to apply a small flow of the measuring gas for the determination of impurities in a gas chromatograph, passing through a liquid-helium-cooled trap with the drawback, however, that the total amount of gas n is not perfectly constant anymore.

Effects from other acoustic parameters: Some effects include increase in acoustic noise from the bubbling helium bath, perturbation of the acoustic modes by the coil-terminated coaxial cables used for coupling microwaves into the cavity, and the condition of the inner surface of the resonator. It is expected that an electropolished surface, as compared with the as-machined one, would reduce the apparent precondensation of argon at 95 K and of helium at 4 K. High-purity argon is used at high temperatures, while for temperatures below, say, 100 K, the use of helium is more appropriate.

Effect of the amount of gas and of impurities in the gas: The influence of the quantity of gas enclosed in the resonator is by far less critical than in a CVGT, a great advantage that has been used to allow a real-time verification of an important influence factor, the effect of chemical impurities in the gas. These issues can be resolved with the apparatus including continuous (slow) flushing of the gas (3×10^{-5} to 3×10^{-4} mol s^{-1}) through the resonator and the outgoing gas being analyzed by an inline gas chromatograph, able to measure the presence of impurities at a level of 0.3×10^{-6} amount of substance fraction. Impurities affect helium much more than argon (10^{-6} of H_2O causes a shift of -3.93×10^{-6} and 0.12×10^{-6}, respectively). Also isotopic composition affects the measurements when argon is used.

TABLE 75.4 Differences and Simplifications in Design Criteria of an ICVGT with Respect to a CVGT

1. Choice of temperature range and span $T_{min} \ll T_{max}$
   An ICVGT can usefully replace other types of thermometers between 5 K and 30 K.

   ITS-90 defines two types, between 4.2 K and 24.5 K and between 3 K and 24.5 K.

   ICVGT definitions always assume constant molar density n/V in the whole range. According to the CVGT limits, T_{min} is set at ≈2.5 K for $n/V = 250$ mol m^{-3} and at ≈1.2 K for $n/V = 160$ mol m^{-3}. Pushing the definition as follows requires much lower density (i.e., sensitivity) values in *whole* range (e.g., for $T_{min} = 0.8$, K is $n/V = 30$ mol m^{-3}), or lower accuracy must be accepted.
2. Choice of definition range and of reference temperatures $T_{r,i}$
   An ICVGT is always of the single-bulb type. Its definition range can be extended below ≈1.2 K, down to 0.8 K using lower values of n/V, thus with lower accuracy.

   The number, N, of reference temperatures $T_{r,i}$, where the ICVGT has to be *calibrated*, set by the number of free parameters in definition equation. Fixed points are selected among the available (not always choice is possible) to minimize nonuniqueness, allow easiest realization, and allow maximum *extrapolation* interval (in order of importance).

   ITS-90 definitions: $n = 3$. Two triple points (Ne and e-H_2). The lowest is a ^{4}He or ^{3}He vapor-pressure point of ITS-90 definition.

   Other possible definitions (see details in Pavese and Molinar, first edition 1992): $n = 2–4$.

   Three main categories, using

   Only triple points: $n = 2$. Definitions with some stipulated parameters, in the 2–30 K range; only triple points of Ne and e-H_2.

   Only fixed points, not requiring pressure measurements: $n = 3$. Definitions in 2–30 K range; triple points of Ne and e-H_2 and the λ-point of ^{4}He.

   Only triple points and superconducting transitions: $n = 3–4$. Definitions in 0.8–30 K range; triple points of Ne and e-H_2 and superconducting transitions: zinc, aluminum, or indium.
3. Choice of thermometric gas and filling density
   Thermometric gas
   No difference with respect to a CVGT.

   Filling density: can be higher than with a CVGT, as calibration can take into account also the third virial coefficient effect.[a] For the ITS-90 definitions, the same limits of a CVGT apply.
4. Choice of pressure measuring system
   No difference with respect to a CVGT, but ICVGT calibration can also incorporate (re)calibration of some of the pressure transducer parameters.[a]
5. ICVGT parameter design
   Room-temperature pressure transducer
   Bulb: Volume V_b can be smaller than that of a CVGT, even for top accuracy, since calibration takes into account dead-volume effects.[a]
   Dead volume V_d: The ratio V_b/V_d can be smaller.

   Cryogenic pressure transducer
   No difference with respect to a CVGT.
6. Bulb design
   Variations of ICVGT volume V_b: due to wall modulus of elasticity and to thermal expansion, taken into account by calibration[a].

   Change of the quan.tity of "active" gas n_b: due to gas adsorption, taken into account by calibration[a], if reversible and reproducible. As regards to impurity molecules on the walls and to leaks, same problems as a CVGT.
7. Dead-volume design (case A)
   All dead-volume effects fully taken into account by calibration[a].
8. Gas handling and measuring system (for non-sealed CVGT)
   No difference with respect to a CVGT.

[a] Within the validity of the mathematical model used for the definition.

TABLE 75.5 Differences and Simplifications in Measurement Procedures for an ICVGT with Respect to a CVGT

1. Preliminary procedures and measurements
Only gas purity check is necessary. Then the ICVGT filling can be performed.
Realization of the fixed points: One or more thermometers must be calibrated at the fixed points realizing the ICVGT reference temperatures.
2. Measurements of the manometer pressure (p^*)
Measurement at the reference temperatures T_i: The bulb is first stabilized at each T_i. After capillary temperature distribution stabilization, which can take more time than bulb, pressure measurement and all manometric system corrections are performed; a p_i^* value is obtained. No auxiliary measurements need be done.
Measurement at any other temperature θ: same procedure; a p^* value is obtained. With the ICVGT, temperature distributions and, in general, all corrections taken into account by calibration procedure must remain the same in subsequent measurements, at least in between calibrations.
3. Calculation of temperature θ_b
The p_i^* values are *directly* used in the defining equation:
The numerical values of the equation coefficients are obtained by solving the system of equations obtained by substitution of the p_i^* values.
The defining equation (e.g., T_{90}) is then used with each p^* value to compute the corresponding value of θ_b of the bulb where thermometers are fitted.

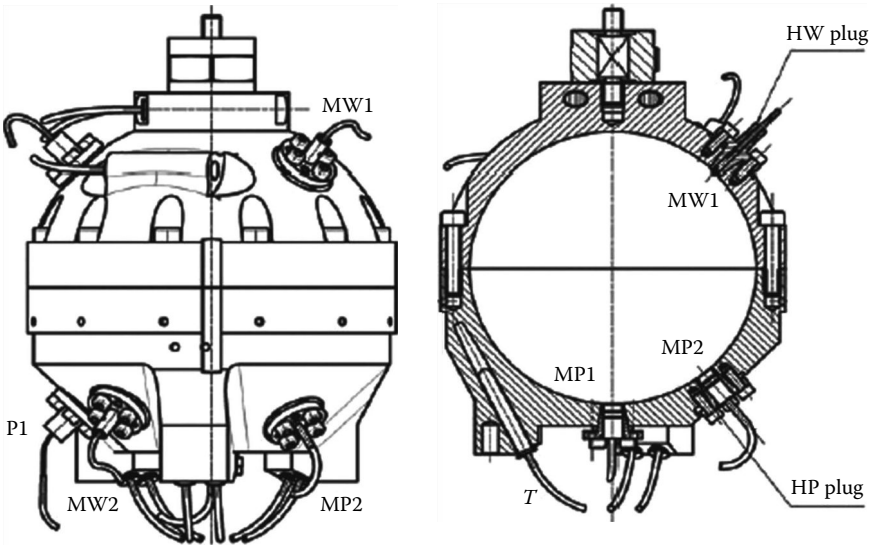

FIGURE 75.5 Layout of acoustic gas thermometers with quasi-spherical (tri-elliptical) resonator type. The symbols indicate the various acoustic, microwave and temperature transducers: MP, microphone; MW, microwave; *T*, thermometer. (After Gavioso, R. M. et al., *Int. J. Thermophys*., 32, 1339, 2011.)

References

1. R. E. Bedford, G. Bonnier, H. Maas, and F. Pavese, Techniques for approximating the ITS-90, Monograph 90/1 of the Bureau International des Poids et Mesures, Sevres: BIPM, 1997. http://www.bipm.org/en/publications/its-90_techniques.html (accessed on March 17, 2013).
2. F. Pavese and G. F. Molinar, *Modern Gas-Based Temperature and Pressure Measurements*, International monograph series on cryogenic engineering, New York: Plenum Publishing, 1992, pp. 514, and references therein; Augmented 2nd edn., 2012, New York: Springer, pp. 660, also available as e-Book.

3. J. F. Schooley, *Thermometry*, Boca Raton, FL: CRC Press, 1986.
4. T. J. Quinn, *Temperature*, 2nd edn., London, U.K.: Academic Press, 1990.
5. R. E. Bedford, G. Bonnier, H. Maas, and F. Pavese, Recommended values of temperature on the ITS-90 for a selected set of secondary reference points, *Metrologia*, 33, 133–154, 1996.
6. F. Pavese, Recalculation on ITS-90 of accurate vapour-pressure equations for e-H_2, Ne, N_2, O_2, Ar, CH_4 and CO_2, *J. Chem. Thermodynam.,* 25, 1351–1361, 1993.
7. R. M. Gavioso, G. Benedetto, D. Madonna Ripa, P. A. Giuliano Albo, C. Guianvarc'h, A. Merlone, L. Pitre, D. Truong, F. Moro, and R. Cuccaro, Progress in INRIM experiment for the determination of the Boltzmann constant with a quasi-spherical Resonator. *Int. J. Thermophys*. 32, 1339–1354, 2011.

76

Temperature Indicators

Jan Stasiek
Technical University of Gdansk

Tolestyn Madaj
Technical University of Gdansk

Jaroslaw Mikielewicz
Institute of Fluid Flow Machinery

Temperature indicators serve for approximate determination of bodies' temperatures and are used to control a variety of temperature treatment processes. The temperatures are determined based on knowledge of characteristic rated temperatures, which are mean critical temperatures of the indicator. However, it should be stressed that the accuracy of these measurements is satisfactory only if the measurement conditions are similar to the standard conditions for which the temperature indicators were calibrated. Otherwise, the critical temperatures of the indicators can be different from their rated temperatures listed in the standards, and the measurements can have considerable errors.

The temperature indicators can be classified into two groups, each group using different physical properties for the determination of the temperature. The indicators belonging to the first group melt at certain temperatures. For some of these indicators, such as pyrometric cones, thermoscope bars, and rings, the process of melting manifests itself as a shape/size deformation for which the temperature is determined by measuring the degree/rate of deformation of the indicator. For others, such as melting pellets, liquids, crayons, and monitors, the melting means turning entirely into a liquid smear. This can also be accompanied by color changing. The second group consists of color-change indicators containing pigments that at different temperatures show different colors by selectively reflecting incident white light. Among this group are reversible and irreversible paints, color-change crayons, and liquid-crystal indicators.

76.1 Melting and Shape/Size Changing Temperature Indicators

The latest British Standard BS 1041, part 7, 1988 [1], lists the following temperature indicators: Seger cones, thermoscope bars, and Bullers rings. Some temperature indicators used in the past—such as Watkin cylinders and Holdcroft bars—are no longer used and are of historical value only. In the United States, melting pellets, crayons, liquids, and monitors are available on the market and widely used.

The rated temperature for Seger cones (pyrometric cones) and thermoscope bars is defined by appropriate shape deformation resulting from the transformation of a certain amount of the indicator substance from solid to liquid state. For chemically pure elements and compounds at a constant pressure, the temperature during the entire process of phase change remains constant. If the pressure changes

within the range of changes for atmospheric pressure, then the temperature changes are insignificant and can be neglected even during precise measurements. The pyrometric cones and thermoscope bars are prepared from complex mixes of frits, fluxes, clays, calcium and magnesium compounds, silica, etc. The melting temperature of the indicators also referred to as the critical or rated temperatures varies with the proportions of the aforementioned compounds. Therefore, a set of indicators differing in the proportions of the compounds is capable of covering a required range of rated temperatures. The melting temperatures can also change, to a degree, with the proportion of phases. For mixes that constitute pyrometric cones and thermoscope bars, the temperature difference between the beginning and the end of the melting process can be as large as 25 °C–40 °C. At the rated temperature, one can assume that the temperature is either at the beginning or at the end of the melting process. In practice, an intermediate value is assumed, referring to an expected shape deformation of the temperature indicator.

For Bullers rings, the rated temperature is determined by a shape deformation that can be described as temperature shrinkage. An indication of the required temperature is a proper contraction of the outer diameter of the ring made of special clay (a mix of appropriate materials) that contracts uniformly with the increase in temperature throughout the operating range.

For melting pellets, crayons, liquids, and monitors, the rated temperature is that of the beginning of the melting process when the indicator turns entirely into a liquid smear. Usually, on cooling, the liquid mark solidifies and becomes glossy transparent or translucent in appearance. The entire process can be accompanied by a change in color—mostly because the color of the workpiece surface or the back of an adhesive label, which enables the contact of the indicator with the surface, will show up from under the transparent mark. However, the moment of melting—not a color change—is the temperature signal.

76.1.1 Seger Cones

The pyrometric cones are typically slender, truncated, trihedral pyramids, about 25–60 mm in height. The base of the pyramid is a regular triangle of side 7–16 mm. One edge of the pyramid is vertical or slightly leaned outward (see Figure 76.1a). The recommended height of the standard cones is 60 mm; the laboratory cones are 30 mm high.

The pyramids are manufactured by pressing a powder mixture of a number of minerals mixed in different proportions throughout the required range of rated temperatures. The main components are silicon oxide (SiO_2), aluminum oxide ($A1_2O_3$) with additives in the form of oxides (MgO, K_2O, Na_2O, CaO, B_2O_3, PbO), and an organic binder. The following equation is an example of chemical constitution of the pyrometric cone for the temperature range of 600 °C–900 °C:

$$X(2SiO_2 + A1_2O_3) + (1 - X)(0.5Na_2O + 0.5PbO + B_2O_3 + 2SiO_2)$$

where X is a mass unit. The pyramids designed for higher rated temperatures are prepared based on similar equations.

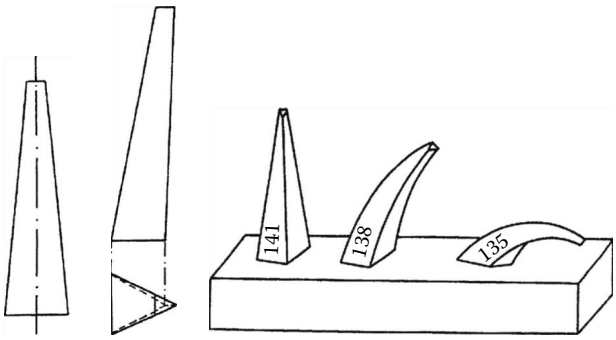

FIGURE 76.1 Pyrometric cones (a) in cross sections and (b) on a plaque during firing.

76.1.1.1 Touchdown Temperatures for Seger Cones

As the heating progresses, the cone used for the measurement begins to soften and bends until its tip touches down on the surface on which it was placed. The rated temperature referring to this deformation is called the *touchdown temperature*. The touchdown temperatures for the Seger cones are determined in an electric kiln with clean atmospheric air at a heating rate of 60 °C h^{-1}.

According to the earlier German standard DIN 51063 [2], the range of touchdown temperatures from 600 °C to 2000 °C at 10 °C–50 °C steps is covered by a series of Seger cones denoted traditionally by numbers from 022 to 42 (see Table 76.1).

According to the latest British Standard BS 1041, part 7, 1988, the touchdown temperatures within the range of 600 °C–1535 °C at temperature intervals of 15 °C–35 °C are realized by a series of Seger cones numbered from 022 to 20 (see Table 76.1).

TABLE 76.1 Approximate Touchdown Temperatures of Pyrometric Cones

Cone No.	Temperature (°C)	Cone No.	Temperature (°C)	Cone No.	Temperature (°C)	Cone No.	Temperature (°C)
DIN 51063							
022	600	07a	960	9	1280	29	1650
021	650	06a	980	10	1300	30	1670
020	670	05a	1000	11	1320	31	1690
019	690	04a	1020	12	1350	32	1710
018	710	03a	1040	13	1380	33	1730
017	730	02a	1060	14	1410	34	1750
016	750	0la	1080	15	1435	35	1770
015a	790	la	1100	16	1460	36	1790
014a	815	2a	1120	17	1480	37	1825
013a	835	3a	1140	18	1500	38	1850
012a	855	4a	1160	19	1520	39	1880
011a	880	5a	1180	20	1530	40	1920
010a	900	6a	1200	26	1580	41	1960
09a	920	7	1230	27	1610	42	2000
08a	940	8	1250	28	1630		
BS 1041							
022	600	011	880	1	1135	11	1310
021	615	010	900	2	1150	12	1330
020	630	09	925	3	1165	13	1350
019	665	08	950	4	1180	14	1380
018	700	07	975	5	1195	15	1410
017	730	06	1000	6	1210	16	1435
016	760	05	1030	7	1230	17	1460
015	790	04	1060	8	1250	18	1485
014	810	03	1085	9	1270	19	1510
013	830	02	1105	10	1290	20	1535
012	860	01	1120				

Notes: (1) Each temperature given in the table is that at which the tip of a cone will bend sufficiently to touch the base in an electric kiln with a heating rate of 60°C h^{-1}. (2) The touchdown temperature depends on the rate of heating: reports on firing behavior should quote the cone number, not the temperature taken from the aforementioned table. (3) Intermediate degrees of bending can be referred to the hands of a clock; e.g., 3 o' clock would represent a cone bent halfway to the stand.

The precision of determination of the touchdown temperatures for the industrial cones should be better than ±15 °C; for the laboratory cones, better than ±10 °C. If the heating rate undergoes change within the range of 20 °C h^{-1} to 150 °C h^{-1}, then the rated temperatures can change by −40 °C for the above lower limiting value of the heating rate up to 60 °C for the upper value. A 0.35% content of SO_2 in the atmosphere increases the rated temperatures by about 35 °C. Also, the presence of soot in the atmosphere slightly raises the rated temperatures.

How to use the materials: While single cones are sometimes used, usually three or four consecutively numbered cones, including a cone whose rated temperature is equal to the required temperature of the heat treatment and two cones of neighboring numbers (one less and one more), are employed for the temperature determination (see Figure 76.1b). They are installed into specially unfired plaques with tapered holes and protrusions that hold the cones firmly. The plaques are mounted to a workpiece surface to allow observations. A cone can be set up in other ways, such as inserting its base into refractory clay. However, it is necessary to assure a correct angle and firm hold of the cones during the firing cycle. Failure in these respects will cause the cone to bend unpredictably and give incorrect assessment of the heat treatment. If the process of heating takes place with a standard heating rate, then the rated temperature is reached when the tip of the central cone touches the base of the plaque. With further prolongation of the firing cycle, the cone will melt completely to form a blob on the plaque. The process of reaching the rated temperature is signaled in advance by the cone of one-less number. The cone of one-more number is there to prove that the required temperature value is not exceeded. Placing a series of cones with lower numbers (lower rated temperatures) provides the opportunity to carry out the process of heating at a required rate.

Typical application: Seger cones are used for the control of firing processes in the ceramics industry and artistry.

76.1.2 Thermoscope Bars

These indicators have the shape of bars of rectangular cross sections. The typical dimensions of the bars are length, 57 mm; width, 8 mm; and height, 6 mm. Bars of consecutive numbers (rated temperatures) are placed horizontally on a refractory stand as in Figure 76.2. The set of thermoscope bars is a more convenient and slightly modified form of Holdcroft bars. The bars are made of the same composites (mineral mixes and organic binder) as the pyrometric cones. The mixed powders are pressed and can be hardened by prefiring at relatively low temperatures, below those at which bending should occur.

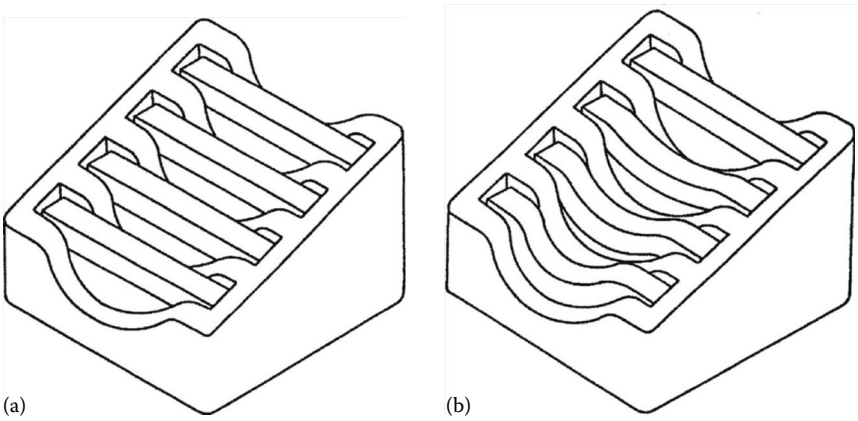

FIGURE 76.2 Thermoscope bars on a stand (a) before and (b) after firing.

TABLE 76.2 Approximate Bending Temperatures of Thermoscope Bars (BS 1041)

Bar No.	Temperature (°C)	Cone No.	Temperature (°C)	Cone No.	Temperature (°C)	Cone No.	Temperature (°C)
1	590	12	870	23	1130	33	1300
2	610	13	890	24	1145	34	1320
3	625	14	915	25	1160	35	1340
4	650	15	940	26	1175	36	1365
5	685	16	965	27	1190	37	1395
6	715	17	990	28	1205	38	1425
7	745	18	1015	29	1220	39	1450
8	775	19	1045	30	1240	40	1475
9	800	20	1075	31	1260	41	1500
10	820	21	1095	32	1280	42	1525
11	845	22	1115				

Notes: (1) Each temperature given in the table is that at which the bar starts to bend in an electric kiln with a heating rate of 60 °C h^{-1}. (2) The bending temperature depends on the rate of heating: reports on firing behavior should quote the bar number, not the temperature taken from the aforementioned table. (3) The bar can be expected to bend sufficiently to touch the stand at a temperature of 10 °C–30 °C higher than the values given in the table, depending on the composition of the bar.

76.1.2.1 Bending Temperatures of Thermoscope Bars

The rated temperatures of thermoscope bars, referred to as the bending temperatures, are found during the calibration in an electric kiln with a heating rate of 60 °C h^{-1} when the bars start to exhibit deformation (i.e., begin to bend).

According to the British Standard BS 1041, the range of rated temperatures from 590 °C to 1525 °C at temperature intervals of 15 °C–35 °C is covered by 42 thermoscope bars (see Table 76.2).

The precision of determination of the bending is about ±15 °C; the other properties of the thermoscope bars referring to changes of the standard conditions are the same as for the pyrometric cones.

How to use the materials: Four thermoscope bars of consecutive numbers—the first two having lower bending temperatures, the third one having the bending temperature equal or close to the required temperature, and the fourth one having a higher bending temperature—are placed in sequence on a special refractory stand as in Figure 76.2a. The set is mounted to the workpiece surface where observations take place. If the process of heating takes place with a standard heating rate, then the beginning of deformation (bending) of the third bar indicates that the required temperature is reached. The process of reaching the rated temperature for the third bar is signaled in advance by the deformation of the proceeding bars whose behavior allows the evaluation of the heating rate. The unbent fourth bar testifies that the required temperature is not exceeded (see Figure 76.2b).

Typical application: The application of the thermoscope bars is identical to that of the Seger cones.

76.1.3 Bullers Rings

These temperature indicators in the form of rings have the following dimensions: outer diameter, 63 mm; inner diameter, 22 mm; and width, 8 mm. The appropriate measuring unit consists of a Bullers ring and a specially prescaled device for measurement of the temperature shrinkage of the ring. This contraction gage measures the outer diameter of the heated ring, based on which the

heating work is assessed. The full measuring range of rated temperatures from 960 °C to 1440 °C is covered by four types of rings manufactured by pressing powders of ceramics mixes, with a binder and without prefiring.

1. Rings denoted as 55 of brown color, suitable for temperatures from 960 °C to 1100 °C, are used in the firing of glost ware and common building bricks where the finishing temperatures are relatively low.
2. Rings numbered 27/84, colored green, suitable for temperatures from 960 °C to 1250 °C, are used for firing earthenware at the medium finishing temperatures, as well as tiles and bricks refractory with respect to low temperatures.
3. Rings numbered 75/84, colored natural, recommended for firing temperatures from 960 °C to 1320 °C, are allowed for higher-finishing temperatures and are used for firing electrical porcelain, china, grinding wheels, and bricks refractory with respect to higher temperatures.
4. Rings numbered 73, colored yellow, recommended for temperatures from 1280 °C to 1440 °C for slow firing conditions, are used in the manufacture of high-temperature ceramics and heavy refractories.

Approximate rated temperatures for the Bullers rings and corresponding readings of the contraction gage according to the British Standard BS 1041 are presented in Table 76.3.

How to use the materials: One or more rings of the same type are placed vertically in a prefired stand and mounted to a workpiece surface. To determine the temperature as the firing progresses, the heated rings are withdrawn from their stands, cooled to the ambient temperature, and then measured for contraction. This measurement is carried out on a gage consisting of a brass baseplate on which a radial arm with a pointer moving over a scale and the two steel dowel pins, against which the ring is pressed by the movable arm, are mounted (see Figure 76.3). A contraction of the ring gives rise to an amplified movement of the pointer over the scale. The divisions on the scale are numbered from –5 to 60. More heavily fired rings contract more and give higher readings on the gage. The divisions below 0 indicate expansion of the ring; above 0 indicates contraction. Rings should be measured across several diameters by turning them around in the gage so as to find the mean value to which the temperature can be assigned with the help of Table 76.3. Placing several rings in the stand in a manner that allows their easy withdrawal gives the possibility of measuring the heating rate. In a similar way, distribution of a number of rings throughout the furnace enables the determination of the temperature field in the furnace.

Usually, one or more test pieces from a series of rings are picked out for the sake of calibration so as to compare the obtained readings with the standard values enclosed in Table 76.3. Intermediate measurements are also carried out to evaluate the effect of the heating rate on the temperature shrinkage of the rings. The accuracy of the temperature determination for the standard heating conditions is ±0.5 of a single division of the scale.

Typical application: The application of the Bullers rings is similar to the Seger cones and thermoscope bars. An inconvenience is the fact that the Bullers rings require gage measurements and the temperature cannot be solely determined based on naked-eye observations.

76.1.4 Temperature-Indicating Pellets, Liquids, and Crayons and Temperature Monitors

76.1.4.1 Temperature-Indicating Pellets

Temperature-indicating pellets are manufactured by pressing powders of mineral mixes of certain melting temperatures and an indifferent binder. Melting pellets are recommended as standard tablets $\phi 7/16 \times 1/8$ and miniature tablets $\phi 1/8 \times 1/8$ (see Figure 76.4). There are 112 different pellets that cover

TABLE 76.3 Approximate Rated Temperatures for Bullers Rings

	Gage Readings			
Temperature (°C)	Ring No. 55	Ring No. 27/84	Ring No. 75/84	Ring No. 73
960	3	0	0	
970	7	1	1	
980	11	2.5	2	
990	15	4	3	
1000	18	5.5	4	
1010	21	7	5	
1020	24	8.5	6	
1030	27	10	7	
1040	30	11.5	8.5	
1050	32	13	10	
1060	34	14	11	
1070	36	15.5	12.5	
1080	37	17	14	
1090	38	18.5	15.5	
1100	39	20	17	
1110		21.5	18	
1120		23	20	
1130		24.5	21	
1140		26	22	
1150		27	23	
1160		28.5	24.5	
1170		30	26	
1180		31.5	27	
1190		33	28	
1200		34.5	29	
1210		36	30	
1220		37.5	31	
1230		38.5	32	
1240		40	33	
1250		41.5	34.5	
1260			36.5	
1270			38.5	
1280			40	29.5
1290			42	30
1300			44	31
1320			46	34
1340				37
1360				40.5
1380				44
1400				48
1420				51
1440				54

Notes: These values should be used with caution because they are dependent on the firing cycle to which the rings are subjected.

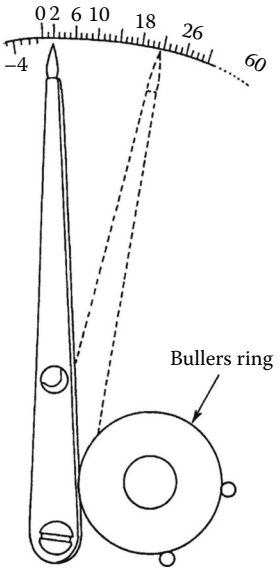

FIGURE 76.3 Contraction gage.

the temperature range from 40 °C (100 °F) to 1650 °C (3000 °F); see Table 76.4. The accuracy of the temperature determination is ±1% of the rated temperature. There are also available pellets for temperature control in strongly reducing atmospheres.

How to use the materials: A pellet of the rated temperature equal to the required temperature of heat treatment is placed on the investigated surface before the heating starts. When the heating progresses, the beginning of melting signals that the rated temperature is reached. Placing more pellets with the rated temperatures lower and higher than the required temperature enables more precise control of the heating process.

Typical application: Typical applications are checking furnace temperatures, control of heat treating of large units, as well as other applications involving long-duration heating.

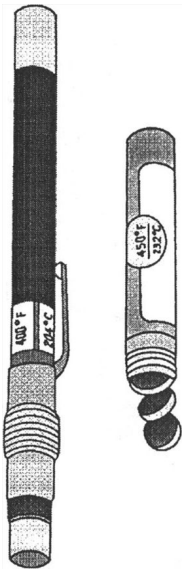

FIGURE 76.4 Temperature-indicating crayon and pellets.

TABLE 76.4 Rated Temperatures for Temperature-Indicating Pellets, Liquids, and Crayons

°F	°C	°F	°C	°F	°C
100	38	325	163	1200[a]	649
103	39	331	166	1250[a]	677
106	41	338	170	1300[a]	704
109	43	344	173	1350[a]	732
113	45	350	177	1400[a]	760
119	48	363	184	1425	774
125	52	375	191	1450[a]	788
131	55	388	198	1480	804
138	59	400	204	1500[a]	816
144	62	413	212	1550	843
150	66	425	218	1600	871
156	69	438	226	1650	899
163	73	450	232	1700	927
169	76	463	239	1750[a]	954
175	79	475	246	1800	982
182	83	488	253	1850	1010
188	87	500	260	1900[a]	1032
194	90	525	274	1950	1066
200	93	550	288	2000	1093
206	97	575	302	2050	1121
213	101	600	316	2100	1149
219	104	625	329	2150[a]	1177
225	107	650’	343	2200[a]	1204
231	111	675	357	2250[a]	1232
238	114	700	371	2300[a]	1260
244	118	725	385	2350[a]	1288
250	121	750[a]	399	2400	1316
256	124	800[a]	427	2450	1343
263	128	850[a]	454	2500[a]	1371
269	132	900	482	2550[b]	1390
275	135	932	500	2600[b]	1427
282	139	950	510	2650[b]	1454
288	142	977	525	2700[b]	1482
294	146	1000	538	2800[b]	1538
300	149	1022	550	2900[b]	1593
306	152	1050[a]	566	3000[b]	1649
313	156	1100	593		
319	159	1150	621		

[a] Series “R” pellets for use in strongly reducing atmospheres.
[b] Available in pellets only.

76.1.4.2 Temperature-Indicating Liquids

Temperature-indicating liquids are solutions of powdered mineral mixes in indifferent highly volatile solvents. They are available for use by brushing or spraying. There are over 100 different liquids with the rated temperatures from 40 °C (100 °F) to 1371 °C (2500 °F); see Table 76.4. The accuracy of the temperature determination is ±1% of the rated temperature.

How to use the materials: A thin coating of the liquid is put on the clean and dry surface by brushing or spraying before the heating starts. It dries almost instantly to a dull opaque mark. When the required temperature is reached, this mark liquefies. The melted coating does not revert to its original opaque appearance but remains glossy transparent on cooling. It should be noted that color changes do not signal the required temperature. The melting, not the color change, is the temperature signal.

Typical application: They are recommended for temperature control on fabrics, rubber, plastics, and smooth surfaces such as glass or polished metals, as well as for monitoring critical temperatures in electronic fields.

76.1.4.3 Temperature-Indicating Crayons

Temperature-indicating crayons are sticks manufactured from powders of mineral mixes of certain melting temperatures and an indifferent binder. The crayons are put in specially made adjustable metal holders with labels saying their rated temperatures; see Figure 76.4. Similar to the temperature-indicating liquids, there are over 100 different crayons that cover the temperature range from 40 °C (100 °F) to 1371 °C (2500 °F); see Table 76.4. The accuracy of the temperature determination is also ±1% of the rated temperature.

How to use the materials: During heating, the workpiece should be struck repeatedly by the crayon. Below its rated temperature, the crayon leaves a dry opaque mark. When the rated temperature is reached, the crayon leaves a liquid smear. On cooling, the liquid mark will solidify with a transparent or translucent appearance. For temperatures below 700 °F, the mark can be put on the workpiece surface before the heating process. The mark will liquefy when the rated temperature is reached. It should be remembered that the moment of melting, not any change in color, is the temperature signal.

Typical application: The crayons can be applied in welding, forging, heat treating and fabrication of metals, and molding of rubber and plastics, wherever the workpiece is accessible during the heating process. Very smooth surfaces are excluded.

76.1.4.4 Temperature Monitors (Labels)

These temperature indicators are adhesive-backed labels with one or more heat-sensitive indicators under transparent circular windows. The indicators turn black (show black paper backing) when the rated temperature is reached. The rated temperatures are from 40 °C (100 °F) to 320 °C (600 °F). They are available as single temperature or multi-temperature indicators with 10°, 25°, or 50° steps. The tolerance of the temperature determination is ±1 °C (±1.8 °F) below 100 °C and ±1% of the rated temperature above 100 °C. Exemplary rated temperatures for a series of 4-temperature (4 dots) indicators are presented in Table 76.5. A 4-dot temperature monitor is displayed in Figure 76.5.

How to use the material: After removing the backing, the label is pressed firmly to the dry and clean workpiece surface. A change in color to black is the temperature signal. Application of multi-temperature-indicating labels allows more precise temperature determination.

Typical application: They are especially applied for monitoring the safe operating temperature of equipment and processes, safeguarding temperature-sensitive materials during storage and transport.

The melting temperature indicators are described in the catalogs of their manufacturers [3,4]. As the melting indicators are widely used in the United States, temperatures in Fahrenheit are also given.

TABLE 76.5 Rated Temperatures for 4-Temperature (4 Dots) Labels

Model No.	°F	°C	°F	°C	°F	°C	°F	°C
4A-100	100	38	110	43	120	49	130	54
4A-110	110	43	120	49	130	54	140	60
4A-120	120	49	130	54	140	60	150	66
4A-130	130	54	140	60	150	66	160	71
4A-140	140	60	150	66	160	71	170	77
4A-150	150	66	160	71	170	77	180	82
4A-160	160	71	170	77	180	82	190	88
4A-170	170	77	180	82	190	88	200	93
4A-180	180	82	190	88	200	93	210	99
4A-190	190	88	200	93	210	99	220	104
4A-200	200	93	210	99	220	104	230	110
4A-210	210	99	220	104	230	110	240	116
4A-220	220	104	230	110	240	116	250	121
4A-230	230	No	240	116	250	121	260	127
4A-240	240	116	250	121	260	127	270	132
4A-250	250	121	260	127	270	132	280	138
4A-260	260	127	270	132	280	138	290	143
4A-270	270	132	280	138	290	143	300	149

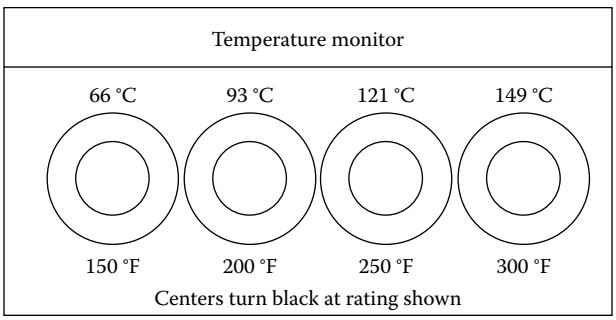

FIGURE 76.5 Four-dot label.

76.2 Color-Change Temperature Indicators

Color-change indicators comprise temperature-indicating paints, crayons, as well as liquid-crystal indicators.

76.2.1 Temperature-Indicating Paints and Crayons

Temperature-indicating paints are basically acrylic lacquers containing finely dispersed temperature-sensitive inorganic pigments. The principle of operation of these indicators draws on the change in color of incident light reflected from the surface of the paint due to chemical reactions that the dispersed pigments undergo and creation of new compounds at specific transition temperatures. The color-change temperatures are also determined by the heating time. According to the British Standard, it is assumed that the rated temperatures of the paints correspond to the change in color at a heating interval of 10 min.

To make the characteristics of temperature-indicating paints complete, the manufacturers also provide, together with the paints, graphs of trigger temperature versus heating-time relationships.

Temperature-indicating paints and crayons can be divided into two groups:

- Irreversible indicators: where the change of color becomes permanent.
- Reversible indicators: after cooling and some time, they revert to previous colors.

Irreversible color-change indicators are complex compounds containing various metals, including cobalt, chromium, molybdenum, nickel, copper, vanadium, or uranium. However, they are lead-free and sulfur-free. They are available on the market in the form of paints and crayons.

76.2.1.1 Irreversible Color-Change Paints

The irreversible paints can change color once or several times during the heating process. Thus, another division can be made on single-change and multichange paints. The range of rated temperatures is from 40 °C to 1350 °C at 10 °C–200 °C steps. At the standard conditions, the tolerance of measurements is ±5 °C for lower temperature values and ±1% for higher temperatures. Exemplary single-change paints with two critical temperatures—the initial trigger temperature for which the paint changes color after 10 min heating and the cutoff temperature being the lowest temperature for which the color change is achieved for long-duration heating—are collected in Table 76.6. Color changes and critical temperatures for some multichange paints (changing color 2, 3, or 6 times throughout the heating cycle) are presented in Table 76.7.

How to use the materials: A thin layer of the paint is applied to a workpiece surface by brushing or spraying like an ordinary paint and allowed to dry before the heating starts. During the heating, when a point of the surface reaches or exceeds the critical temperature, a color change will take place. To determine the distribution of temperature, a multichange paint can be applied. With a nonuniform temperature rise, a number of colored bands separated by isothermal lines will appear on the workpiece surface, allowing the thermal record to be made of the temperature gradient across the surface.

Typical application: The temperature-indicating paints are widely used in industrial applications for observing heat patterns, detecting high- and low-temperature points on surfaces of heat engines, pipelines, and refrigeration fins. They can be also used for controlling temperatures of powered elements and surfaces that are inaccessible or revolve at high speeds.

TABLE 76.6 Single-Change Paints

Original Color	Signal Color	Initial Trigger Temperature[a] (°C)	Cutoff Temperature (°C)
Pink	Blue	48	30
Pink	Blue	135	110
Mauve pink	Blue	148	120
Blue	Dark green	155	46
Yellow	Red	235	180
Blue	Fawn	275	150
Mauve red	Gray	350	220
Mauve	White	386	290
Green	Salmon pink	447	312
Green	White	458	312
Orange	Yellow	555	482
Red	White	630	450

[a] Color-change temperature for 10 min heating.

TABLE 76.7 Multichange Paints

Original Color	Signal Color	Initial Trigger Temperature[a]	Cutoff Temperature °C
Light tan	Bronze green	160	150
Bronze green	Pale Indian red	230	210
Reddish orange	Dark gray	242	193
Dark gray	Medium gray	255	211
Medium gray	Dirty white	338	228
Purple	Pink	395	355
Pink	Fawn	500	386
Fawn	Blue	580	408
Red	Dusty gray	420	310
Dusty gray	Yellow	555	328
Yellow	Orange	610	450
Orange	Green	690	535
Green	Brown	820	621
Brown	Green/gray	1050	945

[a] Color-change temperature for 10 min heating.

76.2.1.2 Color-Change Crayons

Color-change crayons, available in more than 10 distinct colors, similar in shape to regular crayons for drawing, cover the temperature range from 65 °C to 670 °C at 10 °C–100 °C temperature intervals. Exemplary single-change crayons are presented in Table 76.8. The accuracy of the temperature determination is the same as for the temperature-sensitive paints. They can be used for evaluating the temperature on already heated surfaces. They change color 2 min after reaching the rated temperature. Easy to use and inexpensive, they are invaluable for occasional temperature control in auto repairs, soldering, welding, electrical wiring, and enameling and for any operation involving boiling, baking, and other forms of heating.

TABLE 76.8 Single-Change Crayons

Original Color	Signal Color	Initial Trigger Temperature (°C)
Ivory	Light green	65
Yellow and green	Light green	75
Light pink	Blue	100
Gray and white	Light blue	120
Light ivory	Pink	150
Light blue	Black	200
Green	Black	280
Light green	Gray and brown	300
Blue	White	320
Brown	Red orange	350
White	Yellow	410
Light pink	Black	450
Ochre	Black	500
Blue	White	600
Green	White	670

76.2.1.3 Reversible Color-Change Indicators

Reversible color-change indicators are available on the market as paints and in label form. The thermal pigments of these temperature indicators are mercury-based complexes. Therefore, they cannot be applied directly to metal surfaces as this causes decomposition. They also tend to decompose after long exposure to heat, but the decomposition can be retarded by using a clear over-lacquer. The pigments find their most successful application when encapsulated into labels.

The rated temperatures for the reversible color-change paints do not exceed 170 °C. For temperatures up to 70 °C under standard conditions, the tolerance of measurements is ±1 °C; for 70 °C–150 °C, ±2 °C; and for 150 °C–170 °C, ±3 °C.

How to use the materials: A thin layer of a reversible paint is applied to a workpiece surface by brushing or spraying, or a label is pressed to the surface. During the heating, a color change will take place when the temperature of the surface reaches or exceeds the critical temperature.

Typical application: The reversible color-change paints are widely used in the electrical industry, especially on bus bars, live conductors, and connectors in high-current switches and in electronic fault-finding. They also find application as warning and indicating devices of domestic appliances. They are invaluable for controlling lower temperatures when it is necessary to detect undesirable temperature excursions, correct faults, and revert to normal conditions.

76.2.2 Thermochromic Liquid Crystals

Liquid crystals constitute a class of matter unique in exhibiting mechanical properties of liquids (fluidity and surface tension) and optical properties of solids (anisotropy to light, birefringence). Certain liquid crystals are thermochromic and react to changes in temperature by changing color. They can be painted on a surface or suspended in a fluid and used to make the distribution of temperature visible. Normally clear or slightly milky in appearance, liquid crystals change in appearance over a narrow range of temperatures called the color-play bandwidth (the temperature interval between first red and last blue), centered around the nominal event temperature (mid-green temperature). The displayed color is red at the low-temperature margin of the color-play interval and blue at the high end. Within the color-play interval, the colors range smoothly from red to blue as a function of temperature; see Figure 76.6. Liquid crystals or mesophases have been classified as smectic, chiral nematic, cholesteric, and blue. The structure of liquid crystals is shown schematically in Figure 76.7.

76.2.2.1 Temperature-Sensitive and Shear-Sensitive Formulations

Temperature-sensitive liquid crystals show colors by selectively reflecting incident white light. Conventional temperature-sensitive mixtures turn from colorless (or black against a black background) to red at a given temperature and, as the temperature is increased, pass smoothly through the other colors of the visible spectrum in sequence (orange, yellow, green, blue, violet) before turning colorless (or black) again in the ultraviolet at a higher temperature. The color changes are reversible, and on cooling, the color-change sequence is reversed.

Temperature-insensitive (sometimes called shear-sensitive) formulations can also be made. These mixtures show just a single color below a given transition temperature (called the clearing point) and change to colorless (black) above it. The working temperature range is thus below the clearing point. Both reversible and hysteretic (memory) formulations can be made. All liquid-crystal mixtures should be viewed against nonreflecting backgrounds (ideally black, totally absorbing) for best visualization of the colors.

76.2.2.2 Color-Play Properties and Resolution

Temperature-sensitive thermochromic mixtures have a characteristic red-start or mid-green temperature and color-play bandwidth. The bandwidth is defined as the blue-start temperature minus the red-start temperature. The color play is defined by specifying either the red-start or mid-green temperature and the bandwidth. For example, R35C1W describes a liquid crystal with a red start at 35 °C and a

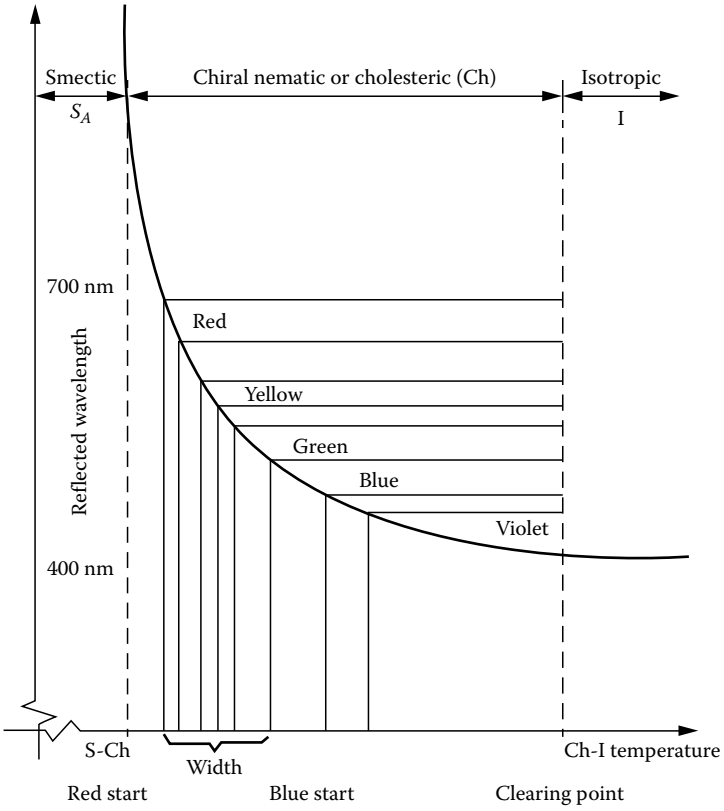

FIGURE 76.6 Typical pitch versus temperature response of thermochromic liquid crystals.

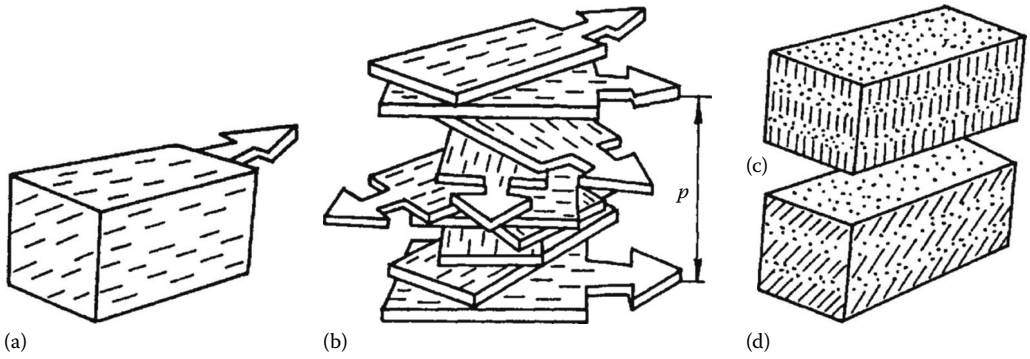

FIGURE 76.7 Structures of liquid crystals (a) nematic, (b) cholesteric, (c) smectic A, and (d) smectic B.

bandwidth of 1 °C, that is, a blue start 1 °C higher, at 36 °C; G100F2W describes a liquid crystal with a mid-green temperature at 100 °F and a bandwidth of 2 °F.

Both the color-play bandwidth and the event temperature of a liquid crystal can be selected by its proper chemical composition. The event temperatures of liquid crystals range from –30 °C to 115 °C with color-play bands from 0.5 °C to 20 °C, although not all combinations of event temperature and color-play bandwidth are available. Liquid crystals with color-play bandwidths of 1 °C or less are called narrowband materials, while those whose bandwidth exceeds 5 °C are referred to as wide band. The type of material to be specified for temperature indicating should depend very much on the type of available image interpretation technique—human observers and intensity-based image-processing or true-color

image-processing systems [5]. The uncertainty associated with direct visual inspection is about 1/3 the color-play bandwidth, given an observer with normal color vision—about ±0.2 °C to 0.5 °C. The uncertainty of true-color image-processing interpreters using wideband liquid crystals is of the same order as the uncertainty assigned to human observers using narrowband materials and depends on the pixel-to-pixel uniformity of the applied paint and the size of the area averaged by the interpreter (about ±0.05 °C can be achieved). Using a multiply filtered, intensity-based system, the resolution is better than ±0.1 °C.

How to use the materials: Liquid-crystal indicators can be used in a number of different forms: as unsealed liquids (also in solutions), in the microencapsulated form (as aqueous slurries or coating formulations), and as coated (printed) sheets. The different forms of the materials have selective advantages and suit different temperatures and flow-visualization applications. Individual products are described in more detail in relevant booklets issued by the manufacturers of liquid crystals [6].

Typical application: Liquid-crystal indicators are ideal for monitoring temperatures of electronic parts, transformers, relays, and motors. They are invaluable for a fast visual indication of temperatures.

References

1. BSI BS 1041-7: Temperature Measurements—Part 7: Guide to Selection and Use of Temperature/Time Indicators, 1988.
2. DIN EN 993-12: 1997-06: Methods of test for dense shaped refractory products—Part 12: determination of pyrometric cone equivalent refractoriness.
3. Temperature Products, Sensors, OMEGA, http://www.omega.com/temperature/tsc.html (accessed on March 14, 2013).
4. Tempil, Data Library, *Technical Data Sheets*, http://www.tempil.com/resources/ (accessed on March 14, 2013).
5. Moffat, R.J., Experimental heat transfer, *Proceedings of the 9th International Heat Transfer Conference,* Jerusalem, Israel, pp. 187–206, 1990.
6. LCR Hallcrest, *Products, Thermometry, Labels*, http://hallcrest.com/cat.cfm?cat_id=67 (accessed on March 14, 2013).

Further Readings

Roger Lindsay Hand, Temperature Indicators, http://www.devileye.net/catalog/laser_facial_rejuvenation/temperature_indicators.html, accessed on July 21, 2012.

Temperature and Humidity Indicators, eHow, http://www.ehow.com/list_7522896_temperature-humidity-indicators.html, accessed on July 26, 2012.

Partial List of Vendors and Suppliers

ISE, Inc., 10100 Royalton Rd., Cleveland, OH 44133, Phone: 440-237-3200, 800-642-1670 (toll free), Fax: 440-237-1744, www.instserv.com

Liberty Industries, 133 Commerce St., East Berlin, CT 06023-1106, Phone: 860-828-6361, 800-828-5656 (toll free), Fax: 860-828-8879, www.liberty-ind.com

Palmer Wahl, 234 Old Weaverville Rd., Asheville, NC 28804-1228, Phone: 828-658-3131, 800-421-2853 (toll free), Fax: 828-658-0728, www.palmerwahl.com

Pyrodynamics, 3522 Ashford Dunwoody Rd., Suite 423, Atlanta, GA 30319-2002, Phone: 657-444-7976, www.pyrodynamics.com

ShockWatch, 5501 LBJ Freeway, Suite 350, Dallas, TX 75240, Phone: 214-630-9625, 800-527-9497 (toll free), Fax: 214-638-4512, www.shockwatch.com/

Watlow, 12001 Lackland Rd., Saint Louis, MO 63146-4001, Phone: 314-878-4600, 800-928-5692 (toll free), www.watlow.com

77

Fiber-Optic Thermometers

Brian Culshaw
University of Strathclyde

77.1 Introduction

Optical fiber sensing is a remarkably versatile approach to measurement. A fiber sensor guides light to and from a measurement zone where the light is modulated by the measurand of interest and returned along the same or a different optical fiber to a detector at which the optical signal is interpreted. The measurement zone can be intrinsic within the fiber that transports the optical signal or can be extrinsic to the optical waveguide. The versatility of the fiber sensing medium arises in part because of the range of optical parameters that can be modulated and in part because of the diversity of physical phenomena that involve environmentally sensitive interactions with light.

For example, highly coherent light from a laser source can be introduced into a fiber and its phase modulated by a parameter of interest. The resulting phase changes can then be detected interferometrically. The phase change is simply a modification to the optical path length within the fiber and can be modulated by shifts in temperature, strain, external pressure field, or inertial rotation. A well-designed interferometer can detect 10^{-7} rad—equivalent to 10^{-14} m!

The laser light could also be Doppler shifted through reflection from a moving object. Its state of polarization can be changed. Its throughput intensity can be modified, or the light can be used to stimulate some secondary emissions, which in turn can be monitored to produce the relevant optical signal. If the light is incoherent, then its wavelength distribution (color) can be modified, in addition, of course, to the possibilities for polarization changes and intensity changes.

The physical phenomena capable of imposing this modulation are again many and varied. They include, for example, periodically bending an optical fiber to introduce a localized loss that depends on the sharpness of the bend (usually referred to as microbend loss); changing the relative refractive indices of the core and the cladding of the optical fiber and thereby changing the guiding properties and again introducing a loss; modifying an optical phase delay by introducing a change in refractive index or a change in physical length; examining changes in birefringence introduced through modifications to physical stress and/or temperature; and using external indicators to color modulate a broadband source and relate the color distribution to temperature, chemical activity, etc. These are all linear effects where

the input optical frequency is the same as the output optical frequency (regarding Doppler shift as a rate of change of phase of an optical carrier) and where, for a given system setting, the output at all frequencies is directly proportional to the input.

Nonlinear effects are also widely exploited. Of these, the most important are fluorescence, observed usually in fluorophores external to the optical fiber, and Raman and Brillouin scattering, usually observed within the fiber itself. In all these phenomena, the light is absorbed within a material and reemitted as a different optical wavelength from the one that was observed. The difference in optical wavelengths depends on the material and usually on strain and temperature fields to which the material is subjected. These major features of optical fiber sensors are encapsulated in Figure 77.1.

Optical fiber sensors have an additional feature that is unique to the medium—namely, the abilities for intrinsic networking in either distributed, quasi-distributed/multiplexed, or discrete (point) configurations. The essential features of these architectures are sketched in Figure 77.2. For intrinsic sensors,

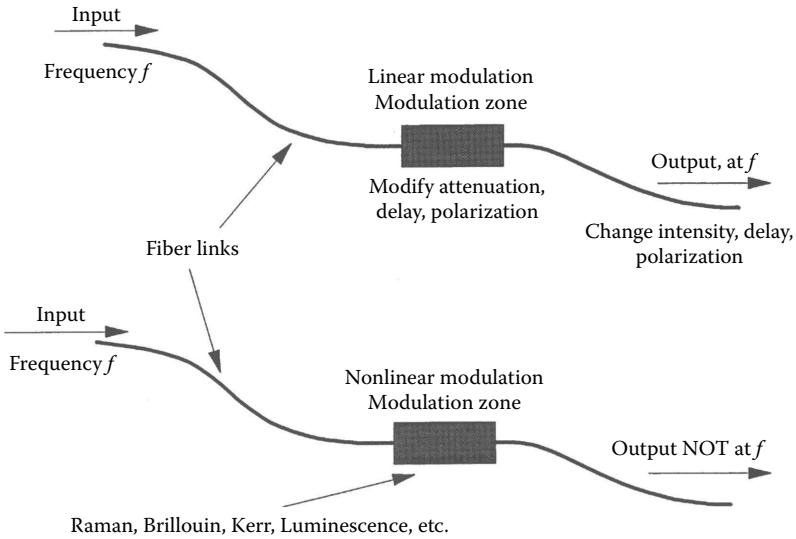

FIGURE 77.1 Linear and nonlinear optical processes for measurement using optical fiber sensors.

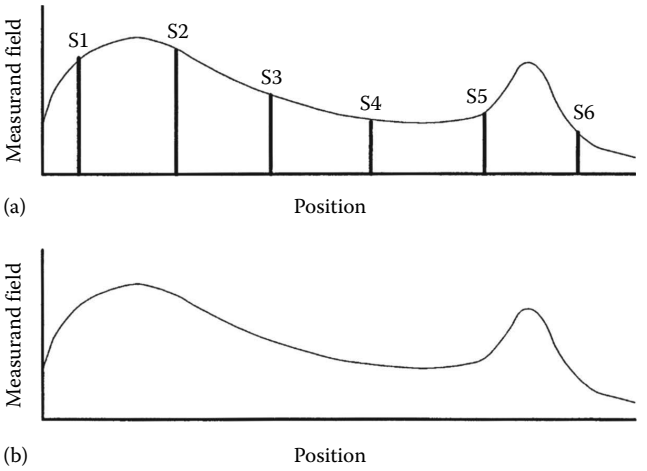

FIGURE 77.2 Sensor system outputs for (a) point array and (b) distributed sensor systems.

the fiber responds to the measurand throughout its length, and the output in transmission is an integral of this linear response. However, using an interrogation scheme in reflection that incorporates a delay proportional to distance along the fiber enables the system to retrieve the measurand as a function of position. These are distributed sensors. The quasi-distributed architecture examines separately identified individual (usually adjacent) lengths of fiber and extracts the integral of the measurand along each of these individual lengths. Distributed and quasi-distributed sensors effectively convolve the measurand field along the interrogation fiber with a window determined by either the time resolution of the interrogating electronics (distributed architectures) or the defined lengths of the individual fiber sections (quasi-distributed systems).

Point and multiplexed systems address the measurement as essentially a point sample located at a specific distance along the interrogating fiber. All these architectures can be realized in all optical fiber form and have been demonstrated to address a very wide range of measurements, often within a single network. The availability of distributed sensing is unique to optical fiber technology, as indeed are optical fiber-addressed passive arrays.

In summary, the optical fiber approach to measurement has the demonstrated capability to address a wide range of physical, chemical, and biological parameters. It must take its place alongside the other competing technologies against which its merits must be assessed. The principal benefits of using fiber optics include:

- Immunity to electromagnetic interference within the sensor system and within the optical feed and return leads
- The capacity for intrinsic distributed measurements
- Chemical passivity within the sensor system itself and inherent immunity to corrosion
- Small size, providing a physically, chemically, and electrically noninvasive measurement system
- Mechanical ruggedness and flexibility, optical fibers are exceptionally strong and elastic—they can withstand strains of several percent
- High temperature capability—silica melts at over 1500 °C

There remain cost and user acceptability deterrents within the exploitation of optical fiber sensor technology. Consequently, the majority of field experience in optical fiber sensors is targeted at addressing the specialized problems where these aforementioned benefits are paramount. Many of these lie in the area of temperature measurement.

77.2 Fiber-Optic Temperature Sensors

The important phenomena that have been exploited in the optical techniques for temperature measurement include:

- Collection and detection of blackbody radiation
- Changes in refractive index of external media with temperature
- Changes in fluorescence spectra and/or fluorescence rise times with temperature
- Changes in Raman or Brillouin scatter with temperature
- Phase transitions in carefully selected materials imposing mechanical modulation on optical fiber transmission properties
- Changes within an optical path length with temperature, either within the fiber or an external interferometer element

Within these phenomena, Brillouin and Raman scatter and mechanical phase transitions have been primarily used in distributed measurement systems. Some distributed measurement/quasi-distributed measurement systems based on modulated to phase delay have also been evaluated, although they have yet to reach commercial reality. The remaining phenomena are almost exclusively used in point sensor systems.

77.3 Fiber-Optic Point Temperature Measurement Systems

One of the first commercial optical fiber sensors was a fluorescence-based temperature probe introduced in the early 1980s by the Luxtron Corporation of Mountain View, CA. Successors to these early sensors are still commercially available and are a very effective, but expensive, approach to solving specific measurement problems. These include monitoring temperature profiles in both domestic and industrial microwave ovens, examining temperatures in power transformer oils, motor/generator windings, and similar areas where (primarily) the issue is the operation of a reasonably precise temperature probe within very high electromagnetic fields. In such circumstances, a metallic probe either distorts the electromagnetic field significantly (e.g., in microwave ovens) or is subjected to very high levels of interference, producing spurious readings. Other applications sectors exploit the small size or chemical passivity of the device, including operation within corrosive solvents or examination of extremely localized phenomena such as laser heating or in determining the selectivity of radiation and diathermy treatments.

The principles of the probe are quite simple and are shown in Figure 77.3. The rare earth phosphor is excited by an ultraviolet light source (which limits the length of the silica-based feed fiber to a few tens of meters), and the return spectrum is divided into "red" and "green" components, the intensity ratios of which are a simple single-valued function of phosphor temperature. For precision measurement, the detectors and feed fiber require calibration, and, especially for the detectors, the calibration is a function of ambient temperature. However, this can be resolved through curve fitting and interrogation of a thermal reference. The instrument, which has now gone through several generations to improve upon the basic concept, is capable of accuracies of about ±0.1 °C within subsecond integration times over a temperature range extending from approximately −50 °C to +200 °C. Since its introduction, this particular probe has accumulated extensive field experience in a wide variety of applications and remains among the most widely exploited fiber-optic sensor concepts.

A number of temperature probes based on fluorescence decay time measurements have also been demonstrated. The level of commercial activity exploiting these concepts has, to date, been very modest, partly because the accurate measurement of decay times can be problematic.

Measuring the temperature response of dyes and other thermally sensitive color-selective materials can afford a very simple approach to temperature measurements. Among the most successful of these has been the temperature probe examining the band edge of gallium arsenide introduced by ASEA (now ABB),

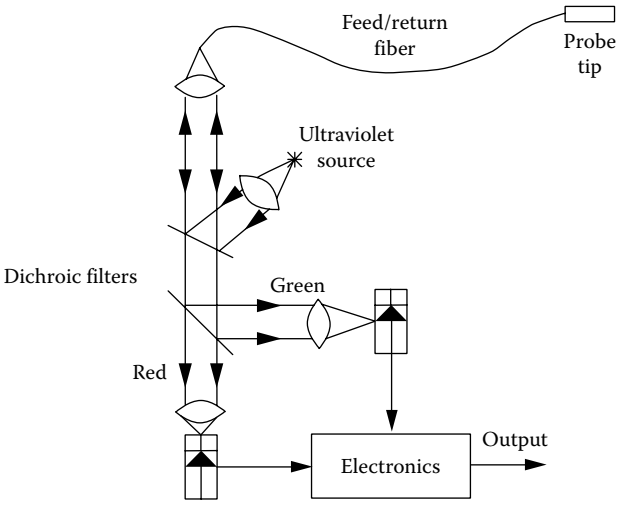

FIGURE 77.3 Optical fiber fluorescent thermometer.

again in the early 1980s and now transferred to Takaoka. The band edge can either be monitored through examining the spectra of induced fluorescence or through interrogating the absorption characteristics of the material when subjected to a constant spectrum excitation. The accuracy and temperature range of this probe are comparable with those of the Luxtron system, and this particular version of the band-edge probe has the additional benefit of operating primarily in the near-infrared range of the spectrum, thereby accessing the best transmission characteristics of the optical fiber medium. The probe was originally conceived to address ASEA's internal needs in monitoring electrical power system components. Similar band edge probes have also been demonstrated based on absorption edge detection in materials such as ruby.

Refractometry and interferometry are potential extremely sensitive thermal probes. Several have been demonstrated, some of which achieve microkelvin resolution. Interferometric detection or exploitation of sensitive mode coupling phenomena is the source of this very high sensitivity, although rarely is such high sensitivity required in practice. The relatively simple Fabry–Perot probe shown in Figure 77.4 has been introduced commercially with simplified spectral analysis and a semiconductor source, although as yet its market penetration has been relatively modest.

Optical pyrometry is a well-established approach to measuring temperatures in the hundreds to thousands of degrees centigrade. The disappearing filament pyrometer has been used in this fashion for over half a century. The optical fiber equivalent has also found a few niche applications. The general form of such a sensor is to place the blackbody at the end of the fiber and place it with the fiber into the hot zone. The consequent radiation within the transmission spectrum of the fiber is then monitored using a semiconductor photodetector that can be based on III–V materials or silicon. The received radiation is then primarily within the red and near infrared from about 600 nm to, depending on the detector, 1.8 μm. Blackbodies radiate significantly in this range at temperatures in the hundreds of degrees centigrade and above. The most significant success of this approach has been in the fabrication of the reference standard temperature probe at NIST for temperatures above 1200 °C. This uses a sapphire rather than silica collection fiber because of its superior optical and thermal properties within the temperature and the wavelength ranges of interest. It defines these high temperatures with subdegree precision.

Optical fibers also have the capacity to make unique nanoprobes—the opposite end of the scale by orders often from the distributed sensors discussed as follows. These (Figure 77.5) are tapered optical fibers with the end reduced in diameter to tens of nanometers. The tapered region is coated with a

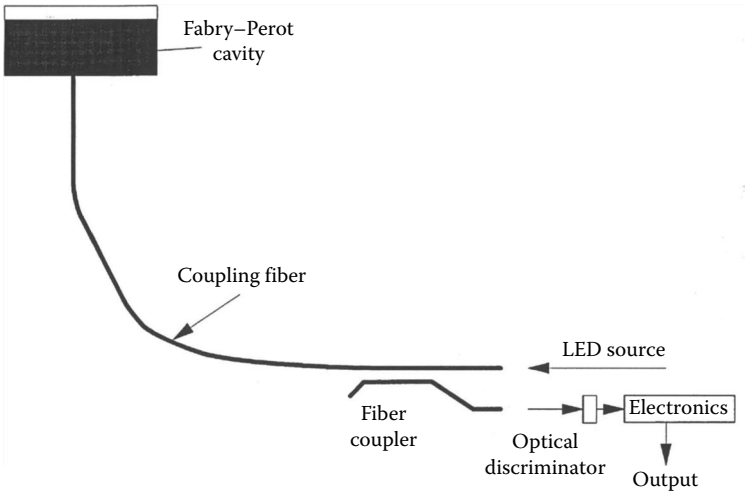

FIGURE 77.4 Optical fiber thermometry using short temperature-sensitive Fabry–Perot cavity.

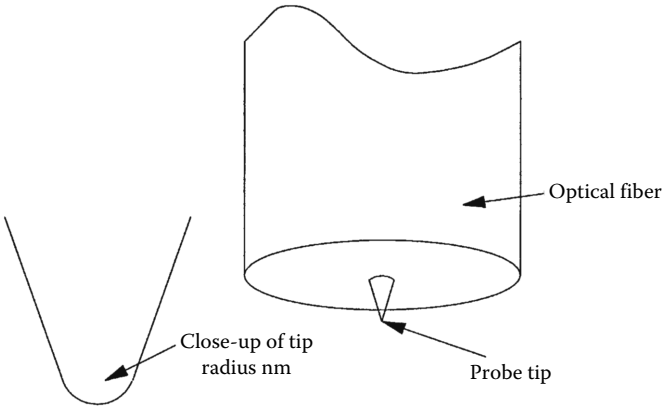

FIGURE 77.5 Probe for photon tunneling microscope and nanooptrode.

metal, often aluminum or silver, to confine the optical field. This produces an intense spot of light at the fiber tip, which irradiates an area in nanometers dimensions. The tip can be coated with the dye or the fluorescent thermally sensitive material and used to monitor temperature over extremely small areas. This enables thermal profiles within cellular dimensions to be assessed. In other formats, the same probe can also be used to address chemical activity and chemical composition.

Fiber-optic temperature sensing can be realized using a wide variety of techniques primarily, but not exclusively, based on the variation of optical properties of materials with temperature. An example of the exceptions is the optically excited vibrating element probe shown in Figure 77.6. This probe has been primarily used for pressure measurement and is now available commercially for pressure assessment downhole in oil wells. It can also be configured to exhibit extremely high temperature sensitivity with accuracies and resolutions in the millikelvin region. It uses the beneficial features of mechanical resonators and the consequential frequency readout in parallel with optomechanical excitation and direct optical interrogation to produce a probe that can be reliably exploited over interrogation lengths of tens of kilometers.

Fiber-optic point sensors for temperature measurement are now a relatively mature technology. Most of the devices mentioned previously were first introduced and characterized 10 or more years ago and have since been refined to address specific applications sectors. They remain expensive, especially when compared to the ubiquitous thermocouple, but their unique capability for noninvasive electrically passive interference immune measurement gives them a very specific market address that cannot be accessed using alternative technologies. Within these market areas, the probes have been extremely successful.

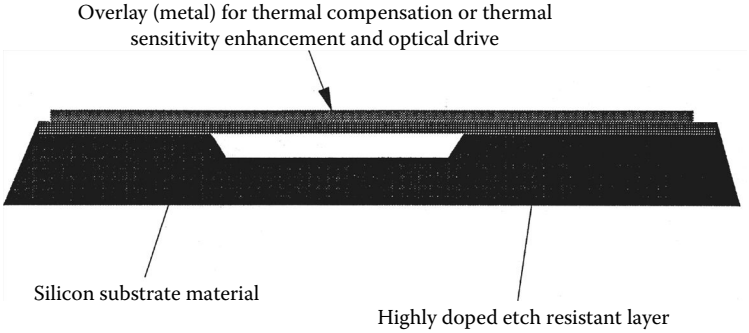

FIGURE 77.6 Longitudinal section of silicon optically excited microresonator.

77.4 Distributed and Quasi-Distributed Optical Fiber Temperature Measurement Systems

These systems all exploit the unique capability for optical fibers to measure and resolve environmental parameters as a function of position along the fiber length. This generic technology is unique to optical fiber systems, and, while there are a few commercial distributed temperature sensor systems available, the research in this sector continues.

The stimulated Raman scatter (SRS) distributed temperature probe is the most well established of these and, in common with many of the point sensors, was originally introduced commercially in the late 1980s. The principle (Figure 77.7) is quite simple. Within the Raman backscatter process (and also within the spontaneous Brillouin backscatter process), the amplitudes of the Stokes and anti-Stokes lines are related to the energy gap between these lines by a simple $\exp(-\Delta E/kT)$ relationship. Therefore, measuring this ratio immediately produces the temperature. Furthermore, this ratio is uniquely related to temperature and cannot be interfered with by the influence of other external parameters. The system block diagram is shown in Figure 77.8. The currently available performance from such systems enables resolutions of around 1 K in integration times of the order of 1 min, with resolution lengths of one to a few meters over total interrogation lengths of kilometers. The interrogation can extend to tens of kilometers if either the interrogation times are increased or the temperature and/or spatial resolutions are relaxed.

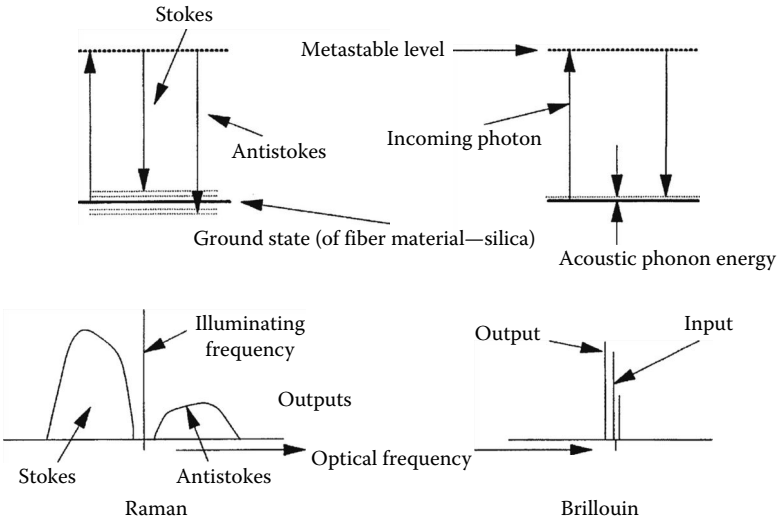

FIGURE 77.7 Thermally sensitive nonlinear scattering processes in optical fibers.

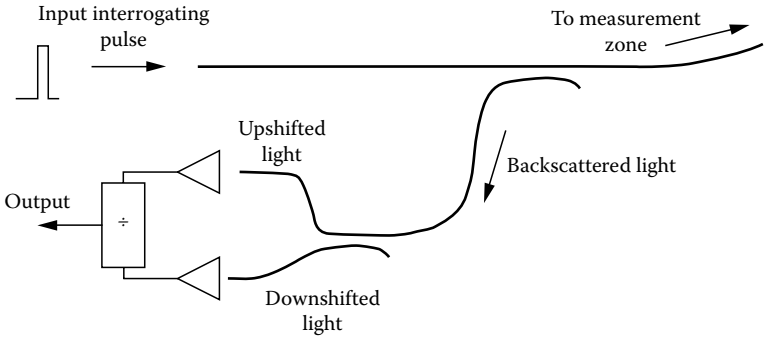

FIGURE 77.8 Raman distributed temperature probe: basic schematic.

The system is available from both European and Japanese manufacturers. The applications are very specific, as indeed they must be to accommodate an instrument price that is typically in tens of thousands of dollars. The instruments have been used in a variety of highly specific areas, ranging from monitoring temperature profiles in long process ovens to observing the thermal characteristics within large volumes of concrete during the curing process.

Distributed temperature alarms triggering on and locating the presence of either hot or cold spots along the fiber can be realized at significantly lower costs and have been modestly successful as commercial systems. The first of these—and probably the simplest—was originally conceived in the 1970s. This uses a simple step index fiber in which the refractive index of the core material has a different temperature coefficient than that of the cladding material. The temperature coefficient is designed such that at a particular threshold temperature, the two indices become equal and thereafter that of the cladding exceeds that of the core. Within this section, light is no longer guided. Simple intensity transmittance measurement is then very sensitive to the occurrence of this threshold temperature at a particular point along the fiber. If used with an optical time domain reflectometer, the position at which this first event occurs can be located. This system is now in use as a temperature alarm on liquefied natural gas storage tanks. Here, the core and cladding indices for a plastic-clad silica fiber cross at a temperature in the region of 50 °C. Such temperatures can only be achieved when a leak occurs. Further, the system has the obvious benefit of intrinsic safety and total compatibility with use within potentially explosive atmospheres.

A heat—as opposed to cold—alarm system that has also been introduced commercially is shown in Figure 77.9. In this system, the central tube is filled with a wax that expands by typically 20% when passing through its melting point. This expansion in turn forces the optical fiber against the helical binding, introducing a periodic microbend and thereby increasing the local loss within the fiber. The wax transition temperatures can be defined over a relatively wide range (say 30 °C–70 °C) and a low-cost OTDR system enables location of the hot spot to within a few meters. This system presents a very cost-effective overheat or fire alarm when such systems are required and are in intrinsically safe areas or in regions of very high electromagnetic interference. Again, it is the unique properties of the optical fiber sensing medium—especially intrinsic safety and electromagnetic immunity—that provide this system with its market address.

Brillouin scatter is very similar in character to Raman scatter except that in Brillouin scatter, the interaction is with an acoustic phonon rather than an optical phonon. The frequency shifts are then correspondingly significantly smaller (typically 10–15 GHz). Additionally, in Brillouin scatter, the frequency of the scattered light depends on the acoustic velocities in the medium within which the light is scattering. Consequently, the Brillouin scatter spectrum is a function of both temperature (through variations of

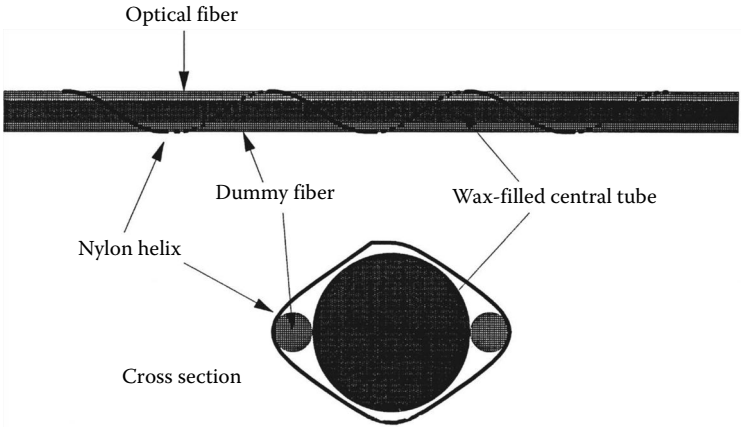

FIGURE 77.9 Fiber-optic distributed heat (fire) alarm.

modulus and density) and strain applied to the optical fiber. Usually this is exploited as a complex but very effective means for measuring strain distributions along an optical fiber. The Brillouin scatter cross section is much higher than that for Raman scatter so that distributed strain distributions can be measured over distances well in excess of 100 km. This measurement is particularly effective when exploiting stimulated Brillouin scatter that guides the scattered light back toward the source. However, since the apparent value of strain depends on temperature through the variation of acoustic velocity with temperature, temperature correction is required in most practical situations, and, in principle, this correction can be implemented by measuring spontaneous Brillouin scatter and specifically the intensity ratio of this in the upper and lower sidebands. This particular correction technique is currently in its infancy, and accuracies in the degree Kelvin range are the current state of the art. The difficulty in temperature measurement is that the energy gap between the two sidebands is very small so that the ratio of the amplitudes is close to unity but must be measured very accurately in order to invert the exponential.

The optical Kerr effect manifests itself as an intensity-dependent refractive index. Consequently, this nonlinearity gives rise to either second harmonic generation or sum and difference frequencies. It has been investigated for distributed temperature sensing using pump/probe configurations and birefringent fiber from which the beat length is a function of temperature and strain. This beat length in turn determines the frequency offset through phase-matching conditions of the mixed pump and probe signal (Figure 77.10). The overall situation is conceptually similar—this offset frequency depends on temperature and strain although in principle, dual measurements and adequate calibration can retrieve both, or alternatively the probe can measure a temperature field in the absence of strain. Again, the actual experimental results that have been achieved remain in the laboratory, and the accuracies and resolutions are modest.

In quasi-distributed sensing and point multiplexed systems, temperature probes have, as yet, been but little exploited. There are many variations on the basic theme of a marked optical fiber within which the optical interrogation system measures the optical path length between the marks. These marks can be introduced using partially reflective gratings, mode coupling Bragg gratings, partially reflective splices or connectors, low reflectivity directional couplers, or a multitude of other arrangements. Similarly, the optical delay between the markings can be measured directly as an optical or subcarrier phase or indirectly through monitoring dispersion between adjacent modes typically in low-mode or birefringent fibers. Yet again, the different delays depend on both temperature and strain so that for temperature measurement, a strain-free mounting is ideal. The context within which most, if not all, of this class of system has been evaluated is that of smart structures, and here the technique does offer some promise as a means for deconvolving strain, mechanical, and thermal effects and assessing structural integrity. It could also function as a temperature measurement probe, but to date has been minimally addressed in this application.

In multiplexed systems, the current fashion, again primarily for combined strain and temperature measurement, is to incorporate arrays of Bragg gratings used here as wavelength filters rather than

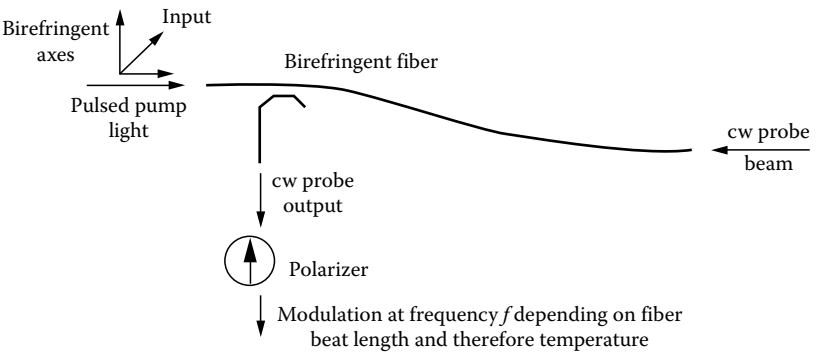

FIGURE 77.10 Distributed Kerr effect probe for temperature or strain field measurements.

as broadband reflectors. In this configuration, the Bragg grating presents a combined temperature/strain field at its location encoded within the reflection wavelength. Multiple addressing schemes can deconvolve temperature and strain sensitivities. There have also been a few demonstrations of discrete temperature-sensitive elements inserted at strategic points along an optical fiber. Of these the use of band-edge shifting in ruby crystals interrogated using a pulsed source observed in reflection has probably been the most successful. In this arrangement, the reflectors are replaced by the crystals and sample the temperature field at these points. The receiver then determines the return to spectrum as a function of time.

77.5 Application for Optical Fiber Temperature Probes

Instrumentation is a very application-specific discipline, and, in particular for sensors, a particular technology is usually only relevant in a limited number of application sectors. As the technology becomes more and more specialized and expensive, these applications niches become much more tightly defined.

For optical fiber sensors and their use in temperature probes, the more conventional approaches (thermocouples, thermistors, platinum resistance thermometers, etc.) are always easier and simpler. The fiber-optic technology must exploit one or more of electromagnetic immunity, small size, noninvasiveness, chemical immunity, or the capacity for distributed measurement.

Point optical sensors are therefore primarily used as measurement probes in regions of very high electromagnetic fields, in zone zero intrinsically safe areas, and as in vivo medical probes.

The distributed capability of fiber sensors is especially relevant in structural monitoring and in other specialized areas such as measuring the temperature distribution along underground power lines, tunnels, or similar structures or in experimental circumstances such as the measurement of curing processes in large volumes of concrete.

Fiber optics then is exactly similar to all other sensing techniques—it is an inappropriate temperature probe for the majority of applications; but for those for which it is appropriate, it offers a unique and effective solution to frequently otherwise intractable measurement challenges. As a technology evolves and becomes both more widely accepted and readily available, the applications address will no doubt expand.

Further Information

Additional information on optical fiber temperature measurements can be obtained from the following:

Culshaw, B., *Optical Fiber Sensing and Signal Processing,* Stevenage, U.K.: IEE/Peter Perigrinus, 1983.

Culshaw, B. and J. P. Dakin, *Optical Fiber Sensors, Vol. I-IV,* Boston, MA: Artech House, Vol. 1, 1988; Vol. II, 1989; Vols. III and IV, 1997.

Grattan, K. T. V. and B. T. Meggitt, *Optical Fiber Sensor Technology*, Kluwer Academic Publisher, Dordrecht, the Netherlands, 2000.

Udd, E. and W. B. Spillman Jr., *Fiber Optic Sensors for Engineers and Scientists.* 2nd edn., John Wiley and Sons, New York, 2011.

Udd, E., *Fiber Optic Smart Structures*, Wiley Interscience Publication, New York, 1995.

Further Reading

Dills, R.R., Optical fiber thermometers, Online, available at, http://www.devileye.net/catalog/position_sensitive_friction_damper/optical_fiber_thermometer.html (accessed on August 2, 2012).

Introduction to fiber optics temperature measurement, Omega Engineering, http://www.omega.com/prodinfo/FiberOpticTemp.html (accessed on August 3, 2012).

Yoder, J., From glass thermometer to fiber optics, Flow Control, http://www.flowcontrolnetwork.com/measurement/temperature/article/from-the-glass-thermometer-to-fiber-optics (accessed on August 2, 2012).

Partial List of Vendors and Suppliers

Grainger Industrial Supply, 100 Grainger Pkwy., Lake Forest, IL 60045, Phone: 847-535-1000, 888-361-8649 (toll free), Fax: 847-535-9123, www.grainger.com/thomasnet

LumaSense Technologies, Inc., 3301 Leonard Ct., Santa Clara, CA 95054, Phone: 408-727-1600, Fax: 408-727-1677, www.lumasenseinc.com/EN/

Neoptic Inc., 1415 Frank-Carrel Ste. 220, Quebec, QC G1N4N7, Phone: 418-687-2500, Fax: 418-948-1173, www.neoptix.com

PICS INC, 81 Lancaster Ave., Suite 202, Malvern, PA 19355, Phone: 610-644-7701, Fax: 610-644-9297, www.picscontrols.com

Process Sensors Corp., 113 Cedar St., Milford, MA 01757, Phone: 508-473-9901, Fax: 508-473-0715, www.processsensors.com

Therm,-X, 1837 Whipple Rd., Hayward, CA 94544, Phone: 510-441-7566, Fax: 510-441-2414, www.therm-x.com

78

Thermal Imaging

Herbert M. Runciman
Pilkington Optronics

All objects at temperatures above absolute zero emit electromagnetic radiation. Radiation thermometry makes use of this fact to estimate the temperatures of objects by measuring the radiated energy from selected regions. Thermal imaging takes the process one stage further and uses the emitted radiation to generate a picture of the object and its surroundings, usually on a TV display or computer monitor, in such a way that the desired temperature information is easily interpreted by the user.

Thermal imagers require no form of illumination to operate, and the military significance of this, together with their ability to penetrate most forms of smoke, has been largely responsible for driving thermal imager development. Although thermal imagers intended for military or security applications can be used for temperature measurement, they are not optimized for this purpose since the aim is to detect, recognize, or identify targets at long ranges by their shape; thus, resolution and sensitivity are favored over radiometric accuracy.

78.1 Essential Components

All thermal imagers must have a detector or array of detectors sensitive to radiation in the required wave band and optics to form an image of the object on the detector. In modern thermal imagers, the detector array might have a sufficient number of sensitive elements to cover the focal plane completely (a "staring array"), in the same way as a CCD television camera. Some of the most recent staring arrays can give good performance without cooling. In other imagers, the detector might take the form of a single row or column of elements, in which case a scanning mechanism is required to sweep the image across the detector array. If a single-element detector, or a very small detector array, is used, a means of

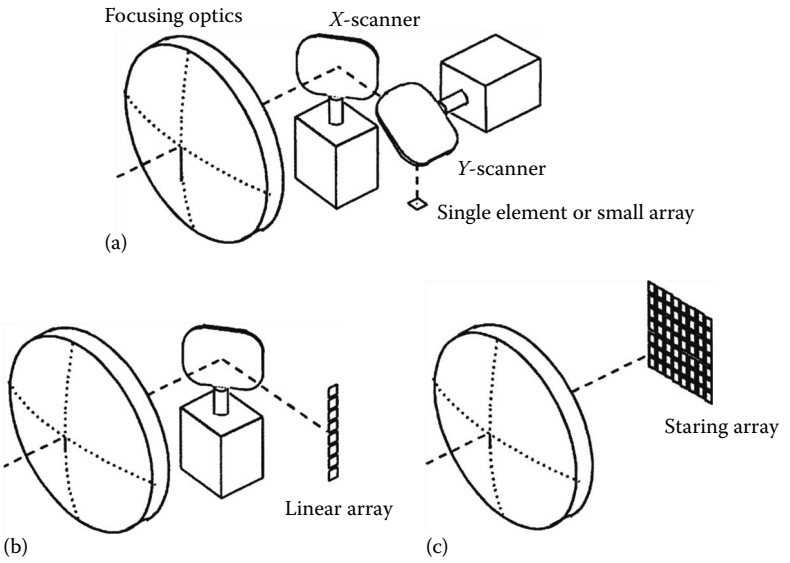

FIGURE 78.1 Thermal imaging options: (a) 2-D scanning for small detector array or single element, (b) 1-D scanning with linear detector array, and (c) staring array without scanning.

providing a 2-D scan is required. (Figure 78.1 shows these options schematically.) For scanning imagers, it is necessary to cool the detectors (usually to about 80–120 K) to achieve adequate performance.

Although in principle it would be possible to deduce target temperature from the absolute value of the detector signal, it is necessary in practice to estimate temperature by comparison with one or more reference bodies of known temperature. The temperature references are usually internal to the equipment and accessed by mechanical movement of the reference (which may take the form of a rotating chopper) or by deflecting the optical path using a mirror.

78.2 Thermal Imaging Wave Bands

The optimum wave band for thermal imaging is determined partly by the wavelength distribution of the emitted radiation, partly by the transmission of the atmosphere, and partly by the chosen detector technology.

The power radiated from a given area of an object depends only on its temperature and the nature of its surface. If the surface absorbs radiation of all wavelengths completely, it is referred to as a "blackbody." It then also emits the maximum amount possible, which can be calculated using the Planck equation (given later). Figure 78.2a shows the way in which blackbody emission varies with wavelength for several temperatures. It will be seen that for objects near normal ambient temperature, maximum output occurs at a wavelength of about 10 μm or about 20 times the wavelength of visible light. At wavelengths below about 3 μm, there is generally insufficient energy emitted to allow thermal imaging of room-temperature objects. The emissivity at any wavelength is defined as the ratio of the energy emitted at that wavelength to the energy that would be emitted by a blackbody at the same wavelength.

It is important that the atmosphere should have sufficient transparency to permit the target to be observed. There are two important "atmospheric windows"—one between 3 and 5 μm (with a notch at 4.2 μm due to carbon dioxide absorption) and one between 7.5 and 14 μm. These are commonly referred to as the medium-wave infrared (MWIR) and long-wave infrared (LWIR) windows, respectively. For thermal measurement over short ranges in the laboratory, it is possible to work outside these bands,

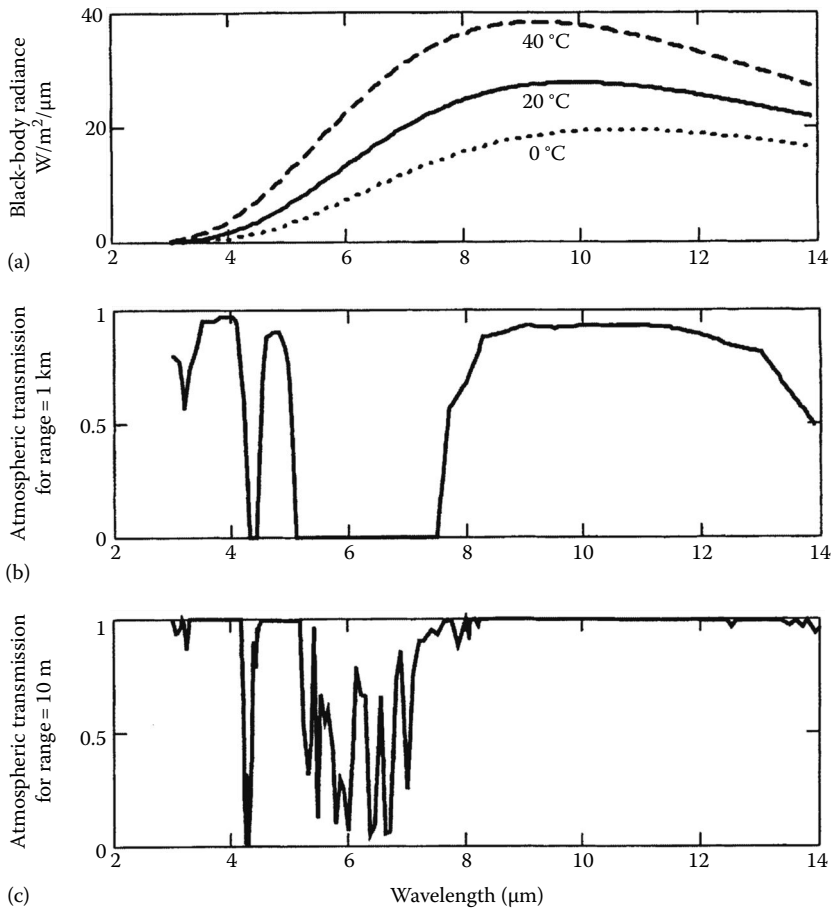

FIGURE 78.2 Factors determining thermal imaging wave bands. Imager must operate in regions where (a) radiance is sufficiently high and (b, c) atmospheric transmission is good.

but most instruments are optimized for either MWIR or LWIR. Typical transmissions through 1 km and 10 m of a clear U.S. Standard Atmosphere are shown in Figure 78.2b and c.

Emissivity for most naturally occurring objects and organic paints is high (>0.8) in the LWIR, but is lower and more variable in the MWIR. Metallic surfaces have low emissivity in both bands. Solar radiation in the MWIR is significant and can cause errors in measurements made outdoors. These considerations favor the LWIR for quantitative imaging, but the band chosen can also be influenced by detector technology, the latter frequently is being determined by its cost. Scanning imagers can be used in either band but are more sensitive for a given detector architecture in the LWIR. Cooled staring arrays give similar sensitivity in either band but are currently more readily available in the MWIR. Uncooled staring arrays work well only in the LWIR band.

For temperature measurement, the electronics can be used to encode signal level as false color, a color scale derived from the thermal references being injected into the display to allow the user to identify the temperature of the object under examination. For general surveillance, a conventional gray-scale image is usually preferred. Imagers for thermography can also include emissivity compensation. If accurate results are required for an object of low emissivity, it is important to ensure that the temperature of anything that might be reflected by the object is known and that the emissivity is accurately known. If the object is accessible, another object placed beside it with the same surface characteristics but known temperature can be used for calibration.

78.3 Emission from Source

The spectral radiance $W(\lambda,T)$ of a blackbody at temperature T and wavelength λ is given by the Planck equation [1]. For temperature differences between the target and the reference of a few degrees, it is frequently sufficiently accurate to assume a linear dependence of radiance on temperature difference, making the temperature derivative of the blackbody equation, $dW(\lambda,T)/dT$, more relevant. In the case of photon detectors, the detector output is proportional to the photon flux, which can be derived from the radiance using the fact that photon energy $E(\lambda) = hc/\lambda$, where h is the Planck constant. The total photon flux $N(\lambda)$ and its derivative with respect to temperature are thus relevant in this case. The equations are as follows:

$$W(\lambda,T) = \frac{c_1}{\lambda^5\left(e^{(c_2/\lambda T)}-1\right)}\ \mathrm{W\,m^{-2}\,\mu^{-1}} \tag{78.1}$$

$$N(\lambda,T) = \frac{c_3}{\lambda^4\left(e^{(c_2/\lambda T)}-1\right)}\ \mathrm{photons\ s^{-1}\,m^{-2}\,\mu m^{-1}} \tag{78.2}$$

$$\frac{dW(\lambda,T)}{dT} = \frac{c_1c_2e^{(c_2/\lambda T)}}{\lambda^6T^2\left(e^{(c_2/\lambda T)}-1\right)},\ \mathrm{W\,m^{-2}\,\mu m^{-1}\,K^{-1}} \tag{78.3}$$

$$\frac{dN(\lambda,T)}{dT} = \frac{c_3c_2e^{(c_2/\lambda T)}}{\lambda^5T^2\left(e^{(c_2/\lambda T)}-1\right)}\ \mathrm{photons\ s^{-1}\,m^{-2}\,\mu m^{-1}\,K^{-1}} \tag{78.4}$$

where

numerical values of the constants are

$c_1 = 3.742 \times 10^8$

$c_2 = 1.439 \times 10^4$

$c_3 = 1.884 \times 10^{27}$

The unit of wavelength is chosen for convenience to be the micrometer (μm).

The aforementioned values are for radiation into a hemisphere. The intensities (watts per steradian, photons per steradian, etc.) are obtained by dividing the aforementioned values by π. The actual radiances for real targets are obtained by multiplying by the spectral emissivity $\varepsilon(\lambda)$, but since target reflectivity $\rho(\lambda) = 1 - \varepsilon(\lambda)$, some caution is required. For example, a target at temperature T surrounded by a background of temperature T_b will appear to emit $W(\lambda,T)\varepsilon(\lambda) + W(\lambda,T_b)\rho(\lambda) = [W(\lambda,T) - W(\lambda,T_b)]\varepsilon(\lambda) + W(\lambda,T_b)$. Provided that the background surrounds the target and that the target is reasonably small, the background acts as an isothermal enclosure, which can be shown [2] to behave as an ideal blackbody (i.e., $\varepsilon(\lambda) = 1$). The differential spectral radiance against background $\Delta W(\lambda)$ is thus $[W(\lambda,T) - W(\lambda,T_b)]\varepsilon(\lambda)$, which for a small temperature difference ΔT is simply

$$\Delta W(\lambda) = \varepsilon(\lambda)\frac{dW(\lambda,T)}{dT}\Delta T \tag{78.5}$$

The spectral emissivity of a wide variety of natural and man-made objects is also given in [2].

A major difference between thermal imaging and visual imaging is the very low contrast. In the MWIR, the contrast calculated from Equation 78.1 due to 1 K at the target is about 4%, falling to about 2% in the LWIR.

78.4 Atmospheric Transmission

Provided that the absorption bands shown in Figure 78.2b and c are avoided, atmospheric transmission can frequently be ignored in the laboratory or industrial context. For longer ranges, an atmospheric transmission model must be used, or calibrating sources must be placed at the target range. The standard atmospheric transmission model is LOWTRAN [3], currently at version 7. The atmospheric transmission $T_a(\lambda)$ reduces the differential signal from the target proportionately, but has no effect on the background flux if the atmosphere is at background temperature. Atmospheric transmission in the LWIR is severely affected by high humidity, making the MWIR the band of choice for long-range operation in the Tropics. (Many gases and vapors such as methane or ammonia have very strong absorptions in the infrared, making thermal imaging a possible means of leak detection and location.)

78.5 Detectors

There are two main types of detector—photon (or quantum) and thermal. A more detailed discussion of photon detectors is given in this handbook, so only aspects unique to thermal imaging are discussed here.

78.5.1 Photon Detectors

In photon detectors, the response is caused by photons of radiation that generate free carriers in a semiconductor, which in turn increase the conductivity (for photoconductive detectors) or generate a potential difference across a junction (for photovoltaic detectors). Photovoltaic devices have the advantage of not requiring a bias current (important to reduce the heat load on the cooling system), and they have 40% lower noise because the electric field at the junction separates the carriers, thereby eliminating recombination noise. Whether or not the lower noise is achieved in practice depends on the readout electronics. The photon energy in the LWIR is only about l/20th of that of a photon in the visible region of the spectrum, so a semiconductor with a much smaller bandgap than silicon must be used. The most widely used material is a compound of mercury, cadmium, and tellurium (MCT or CMT) since not only is the quantum efficiency excellent (70% or more) but also the bandgap can be tuned to the desired wavelength (in either wave band) by altering the composition. Cooling of the detector to about 80 K is desirable for the LWIR, but about 120 K is acceptable for the MWIR. For the MWIR, indium antimonide (InSb) is also an excellent material, and since it is a true stoichiometric compound, it is easier to achieve good uniformity of response, but cooling to 80 K is required.

Detectors for use in scanning systems are frequently arranged so that several elements are scanned over the same part of the scene in rapid succession, the output of each element being delayed and added to the previous one to enhance the signal-to-noise ratio (SNR). This approach (Figure 78.3) is termed serial scanning or "time delay and integrate" (TDI) mode and gives a theoretical gain in the SNR equal to the square root of the number of elements in TDI. It is also possible to perform TDI in the detector material itself. In the signal processing in the element (SPRITE) detector, the sensitive element is an elongated strip of CMT. Photons incident on the device generate carriers that drift toward a readout electrode near one end. If the image is scanned along the detector at the same speed as the carrier drift, the signal builds up along the length of the device. The useful length is limited by carrier recombination, while diffusion of the carriers limits spatial resolution.

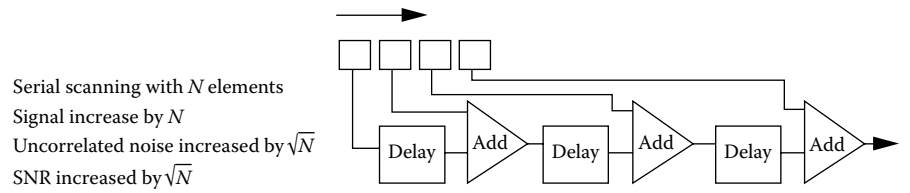

FIGURE 78.3 Use of serial scanning to enhance SNR. The delay times are chosen to match the speed at which the image is swept along the detector array. Serial scanning is usually combined with parallel scanning using a detector matrix.

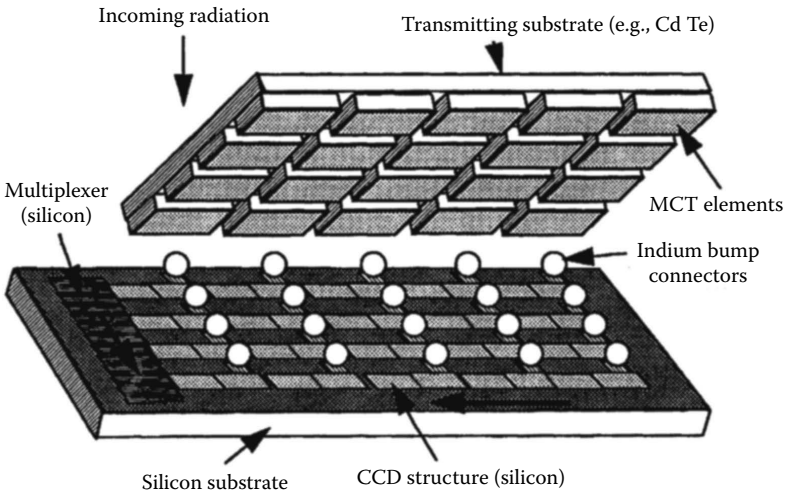

FIGURE 78.4 Typical hybrid detector construction. A typical element size is 30 μm. A large array of this type to match U.S. TV standard would have 640 × 480 elements.

Large arrays of photon detectors are generally of hybrid construction, the sensitive elements being bonded to a silicon CCD or CMOS addressing circuit using indium "bumps" (Figure 78.4). An exception is the Schottky barrier detector (e.g., platinum silicide), which can be manufactured by a monolithic process and thus tends to be lower in cost, but quantum efficiency is much lower, and operation is usually limited to the MWIR band. Detector arrays and readout architectures are discussed in depth in [2] (Vol. 3, p. 246–341) and [4].

The detector assembly is encapsulated in a Dewar as shown in Figure 78.5. In front of the detector is a "cold shield" that limits the acceptance angle of the radiation to match that of the optics.

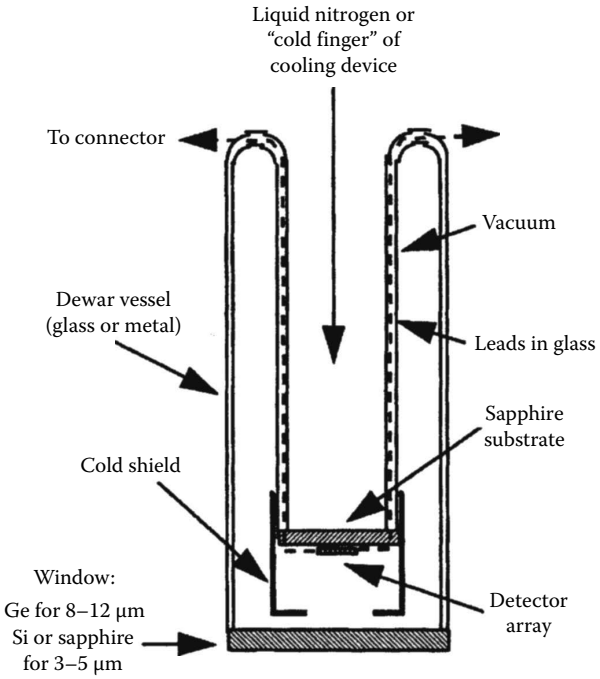

FIGURE 78.5 Construction of typical cooled detector. Cooling can be by liquid nitrogen, Joule–Thomson expansion of compressed gas, or cooling engine.

78.5.2 Thermal Detectors

Thermal detectors rely on the heating effect of the incoming radiation, the change in temperature causing a change in resistance, capacitance, or electrical polarization that might be detected electrically. They are generally fairly slow in response (several milliseconds) but have the advantage that cooling is not essential (although it can be of considerable benefit with some types). The detectivity of uncooled thermal detectors is typically 1/100 that of cooled photon detectors, so real-time imaging requires the use of staring arrays. The essentials of a pyroelectric array are shown in Figure 78.6. Incoming radiation is absorbed by the blackened electrode, and the heat generated is transferred to the pyroelectric layer, which comprises a dielectric material that has been polarized by means of a high electric field during manufacture. The change in electrical polarization with temperature gives the electric signal. One of the most important parameters is the thermal isolation of the sensitive elements, so some kind of insulating support structure is necessary, and for good performance, the device must be evacuated to prevent convection. In a variant of this approach, the dielectric bolometer, the rapid variation of the dielectric constant at temperatures near the Curie point, causes the capacitance of the sensitive element to change and hence the voltage for a constant charge. A detailed description of this approach is given in [5]. In both techniques, the detector responds only to change in temperature, so it is necessary to modulate the incoming radiation using a chopper. In the technique used initially by Wood [6] (now licensed to several manufacturers), the sensitive elements are vanadium dioxide coatings that undergo a large change in resistivity for a small temperature change. The elements are supported by silicon strips that are micromachined from the substrate and give excellent thermal insulation of the element. Changes in resistivity are read out by circuitry on the substrate, and no chopping is required, but the array must be maintained at a precise and uniform temperature.

78.5.3 Detector Performance Measures

The wavelength-dependent power responsivity of a detector $R(\lambda)$ is defined as the output potential or current that would result from 1 W of radiation at wavelength λ, assuming that linearity was maintained at such a high-flux level. The units are VW^{-1} or AW^{-1}. Photon responsivities in V photon^{-1} s^{-1} and A photon^{-1} s^{-1} are similarly defined.

A thermal detector has a power responsivity that is essentially independent of wavelength, the limits of response being determined by the transparency of the window and the absorption spectrum of the element or the material used to blacken it.

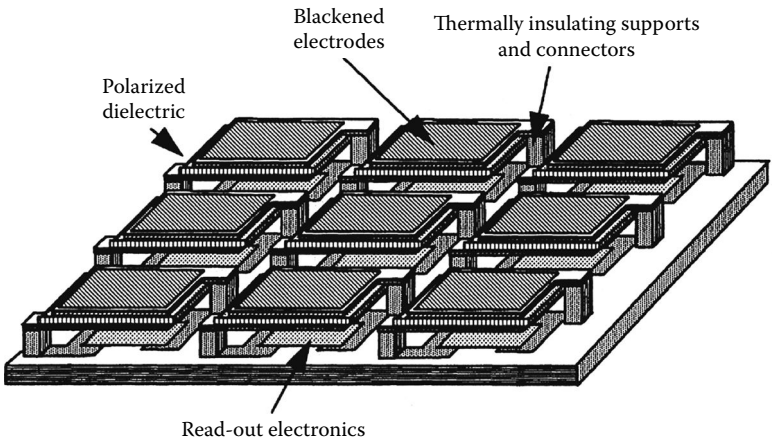

FIGURE 78.6 Essentials of an uncooled thermal detector array. The device is shown as pyroelectric or dielectric bolometer, but the essentials for a resistive bolometer are similar if the capacitors are replaced by resistors.

In an ideal photon detector, the quantum efficiency η (defined as the number of carriers generated per photon) would be constant at all wavelengths for which the photon energy is greater than the bandgap, that is, the photon responsivity is independent of wavelength up to the chosen cutoff wavelength. Since a given number of watts correspond to a number of photons proportional to the wavelength, the power responsivity (VW^{-1} or AW^{-1}) would increase linearly with wavelength until the cutoff. In practice, the cutoff is spread over about 0.5 μm, and the shortwave performance is modified by window transmission and antireflection coatings.

The sensitivity of a detector is limited by noise that may be due to the detector itself or due to the background radiation (as is discussed later). Noise-equivalent power (NEP) (λ) is defined as the power incident on the detector at wavelength λ, which gives a signal equal to the rms noise when the measurement is made with a 1 Hz bandwidth. The NEP depends also on the modulation frequency, the latter effect being large for thermal detectors but frequently negligible for quantum detectors. For many types of detector, the noise is proportional to the square root of the sensitive area A_d and the electrical bandwidth B so that $\sqrt{(A_dB)}/\text{NEP}$ is constant. A performance figure that is proportional to sensitivity can then be defined as specific detectivity $D^*(\lambda) = \sqrt{(A_dB)}/\text{NEP}(\lambda)$. For historical reasons, specific detectivity is usually given in units of $\text{cm}\sqrt{\text{Hz}}\,\text{W}^{-1}$, so it is important to remember to convert this to SI units or to measure detector area in square centimeters. Since noise is an electrical quantity particular to the detector under the conditions for which D^* is defined and is independent of wavelength, NEP(λ) is proportional to $1/R(\lambda)$, so if the value of detectivity D_p^* at the wavelength of peak responsivity R_p is known, for other wavelengths, $D^*(\lambda) = D_p^*(R(\lambda)/R_p)$. Sometimes, "blackbody $D^*(T)$" figures are quoted rather than D_p^*. If the blackbody temperature is T, the value of D_p^* is given by

$$D_p^* = \frac{D^*(T)R_p\int_0^\infty W(\lambda,T)\,\mathrm{d}\lambda}{\int_0^\infty W(\lambda,T)R(\lambda)\,\mathrm{d}\lambda} \tag{78.6}$$

The rms noise voltage V_n is simply the NEP multiplied by the responsivity. Since the ratio $D^*(\lambda)/R(\lambda)$ is independent of wavelength, one obtains

$$V_n = \sqrt{A_dB}\,\frac{R_p}{D_p^*} \tag{78.7}$$

The detector also affects the modulation transfer function (MTF) of the imager, defined as the ratio of the modulation depth of the signal due to a target with sinusoidally varying brightness of spatial frequency f cycles per milliradian to the modulation depth from a similar target at very low frequency. If there are no limitations due to time constant, the MTF of a detector is due to its instantaneous field of view (IFOV), which is given by IFOV = xlF where F is the focal length of the optics. For example, a lens of 500 mm focal length used with a 50 μm square detector would give an IFOV of 0.1 mrad. Then,

$$\text{MTF}_d = \frac{\sin(\pi \times f \times \text{IFOV})}{\pi \times f \times \text{IFOV}} \tag{78.8}$$

For staring arrays, frequencies above 1/2 cycle per element pitch (the Nyquist frequency) give aliasing, and it is undesirable to rely on performance above this frequency.

78.5.4 Detector Cooling

The method with the lowest cost is to use liquid nitrogen poured directly into the detector Dewar, and many detector manufacturers supply detectors in Dewars with sufficient capacity for many hours of use per filling. Outside the laboratory, this technique is seldom practical, and a cooling engine (usually based on the Stirling thermodynamic cycle) is commonly used. The cost of such an engine has now fallen to a level where it no longer dominates the cost of the instrument, and power consumption is only a few watts to give cooling to 80 K. Dimensions vary widely, but a typical low-power cooling engine is about 40 mm × 40 mm × 60 mm excluding the length of the cold finger that lies inside the detector Dewar. A disadvantage is the relatively slow cooldown time (several minutes typically), and where this is critical (as in military or security applications), Joule–Thomson cooling can be used. This method operates by expansion of air or nitrogen compressed to about 15 MPa through a nozzle and can give cooldown times of a few seconds. Thermoelectric cooling (using the Peltier effect) can be used for temperatures down to about 200 K. Some detectors (e.g., lead selenide) have been designed to operate at this temperature in the 3–5 μm band, but thermoelectric cooling is inadequate for most types of photon detectors. A survey of cooling methods and devices is given in [2] (Vol. 3, pp. 345–431).

78.6 Electronics

The electronics architecture depends on the type of detector and the application, but typically electronics are required to provide bias and clocking signals to the detector, to amplify the low-level signals from the detector, to equalize the responses of the outputs from different detector elements, to provide scan conversion to a form suitable for display, and to provide image processing suitable to the application.

In scanning imagers with a small number of detector elements, the output of each detector element can be amplified continuously, the amplifier outputs then being multiplexed to give the required display. The bandwidth (important for estimating sensitivity) must be at least sufficient to accommodate the data rate, but too wide a bandwidth gives excess high-frequency noise. An approach frequently used for the measurement of sensitivity (e.g., [1], p. 167) is to make the electronics response equivalent to that of a single-pole filter with the 3 dB point placed at a frequency corresponding to 1/(2 × dwell time), in which case the bandwidth is

$$B = \frac{\pi \times \mathrm{FOV_h} \times \mathrm{FOV_v} \times f_\mathrm{f}}{4E \times N \times \mathrm{IFOV}^2} \tag{78.9}$$

where

$\mathrm{FOV_h}$ and $\mathrm{FOV_v}$ is the horizontal and vertical fields of view, respectively
f_f is the field rate
E is the ratio of the active scan period to the total period
N is the number of parallel detector channels

Often high-frequency boost filters are used to compensate for optics and detector MTFs, in which case the noise bandwidth can be much increased. A commonly used criterion for the electronic filtering is to make the perceived noise independent of frequency up to the cutoff frequency of the detector.

To maintain good spatial resolution, it is desirable that the detector output be sampled at least twice during the dwell time so that the Nyquist frequency is not a major limitation [7]. Frequencies above the Nyquist frequency are changed by the sampling process into lower frequencies, a process known as aliasing. Thus, the fidelity of the image is affected so that noise that might be expected to be of sufficiently high frequency to be filtered out can appear within the passband. To avoid aliasing, a steep-cut filter is used to eliminate frequencies above the Nyquist frequency before sampling. In staring systems, the Nyquist sampling frequency is 1/2 cycle per element pitch, so a 256 × 256 element array would be limited

to a resolution of 128 cycles per line. This can be overcome by using "microscan" (or μscan), in which the image is collected over a number of fields with an image shift performed optically between each field, the commonest patterns being diagonal (low implementation cost) and 2×2 with four fields per frame.

For large detector arrays, charge is usually accumulated on a capacitor associated with each pixel for an integration time τ (which can often be controlled independently of the frame rate or dwell time to prevent saturation), the capacitor being discharged when the pixel is read out. The effective bandwidth of such an integrator is

$$B = \frac{1}{2\tau} \tag{78.10}$$

With state-of-the-art amplifiers, it is generally possible to make amplifier and readout noise less than the detector noise, the exceptions being systems of small aperture that are "photon-starved" and uncooled systems.

In multichannel systems, a crucial role of the electronics is to provide channel equalization. The importance of this is due to the very low contrast of the target against the background. If the full sensitivity of an imager with a typical noise-equivalent temperature difference (NETD) of 0.1 K is to be realized, the difference in response between adjacent detector channels must be less than 0.4% in the MWIR or 0.2% in the LWIR. In a real-time imager where the eye integrates over several frames, the requirement is 2–3 times more stringent, since nonuniformity, unlike SNR, is not improved by eye integration.

78.7 Optics and Scanning

The materials commonly used for visual optics are opaque in the thermal wave bands. In the LWIR, germanium is by far the most widely used material. It has a refractive index of 4, and chromatic dispersion is sufficiently low that it is frequently unnecessary to use a second material for color correction. These properties allow high performance to be achieved with few optical components, largely offsetting the relatively high cost of the material. In the MWIR, germanium has fairly high dispersion, but silicon/germanium doublets give highly achromatic performance. Zinc selenide and zinc sulfide are commonly used for color correction, some forms of the latter being transparent also in the visible band. The high refractive indices make antireflection coating essential to reduce surface losses—the transmission of a thin piece of uncoated germanium is only 40%, rising to better than 99% when coated. Front-surface mirrors coated with aluminum or gold perform well in the thermal bands, and optics based on parabolic mirrors can be used if the detector array is small. For most applications, it is necessary to seal the imager to prevent ingress of dust or moisture, in which case a window is required, making reflecting optics less attractive than it first appears, since the cost of a mirror and window can be a little less than that of a lens. Plastic materials in general have poor transmission, although a thin polythene or "cling-wrap" window might be acceptable for laboratory use.

For uncooled staring arrays, the sole function of the optics is to focus an image of the scene on the detector. Good performance in the 8–12 μm band can be achieved with a two-element Petzval lens [8] with aspheric surfaces (Figure 78.7a). With a cooled array, it is desirable that the cold shield inside the detector should form the aperture stop of the system, since any radiation from the interior of the instrument will add to the system noise and might give shading effects. If the field of view (FOV) is reasonably small, it is sometimes possible to use the same type of lens in the manner shown in Figure 78.7b, but it can be seen that the beam diameter that can be accepted is now much smaller than the lens diameter; thus, for long-range applications requiring large beam diameters, the lens becomes very costly. The solution is to use reimaging optics as shown in simplified form in Figure 78.7c. The relay stage not only reimages the scene on the detector but also images the cold shield on the objective lens so that the latter need be no larger than the input beam. The intermediate image can be useful to allow insertion of temperature references or microscanning.

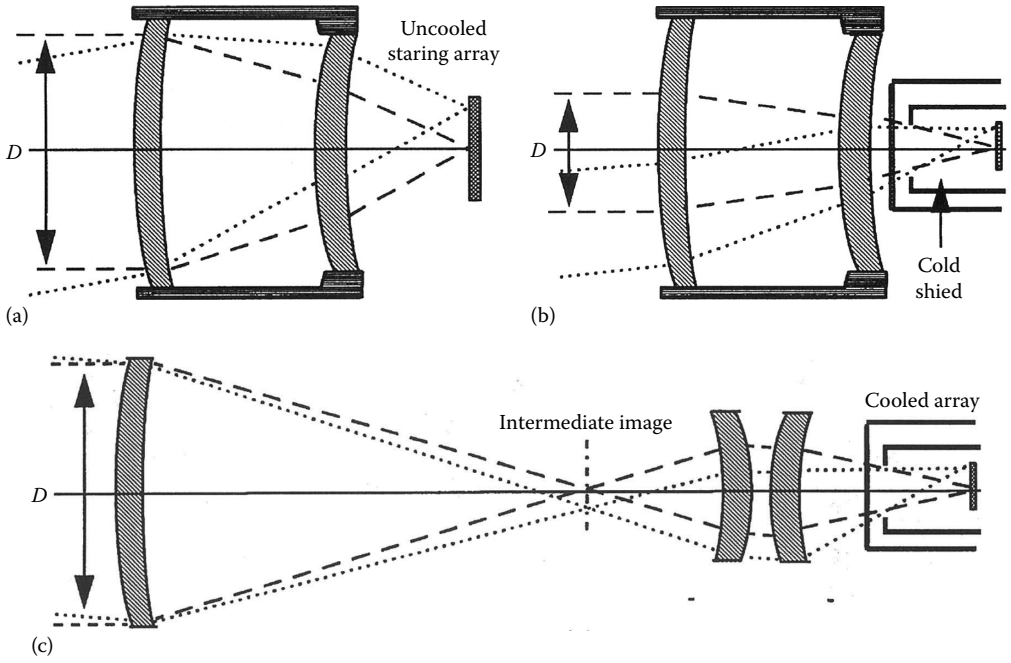

FIGURE 78.7 Optics for staring arrays. The same lens as is used for uncooled operation (a) can be used as in (b) for a cooled device, but reimaging optics (c) is needed for a cooled imager to use the full aperture. In practice, the optics in (c) would usually have more components than shown.

Scanning, when required, is most commonly performed by moving reflective surfaces since electro-optic and acousto-optic techniques either provide insufficient deflection angle or are highly wavelength dependent, causing smearing over the thermal wave bands. Rotating refractive polygons are now less used than previously. For fast line scanners, rotating reflective polygons (sometimes with curved facets) are used, in some cases using gas-bearing motors operating in helium to reduce windage. For frame scanning, a plane mirror driven by a powerful galvanometer is customary. This can give very linear sweeps at 60 Hz with scan efficiencies of about 80% when operated in a closed loop. For microscan or interlace, a small image movement can be achieved by tilting a mirror using piezoelectric actuators or by tilting a refractive plate using a galvanometer. For scanning systems, it is generally necessary to reimage the detector cold shield at each scan mechanism, since otherwise the optics must be enlarged to accommodate pupil movements. Figure 78.8 shows how this is done in a typical imager using a linear array. The movement of the interlace mirror is sufficiently small that pupil reimaging at this mirror is not required.

Figure 78.9 shows a typical arrangement for a 2-D scanner, a high-speed polygon rotor being used to generate the line scan.

The main optical parameters to be specified are transmission T_0, focal length F, and f/number $F_\#$ or numerical aperture (NA). Since IFOV = x/F, the focal length determines the spatial resolution for a given detector. The NA is defined as the sine of the semicone angle of the output beam from the optics. It can be shown that if a diffuse (Lambertian) source emits W W m^{-2} into a hemisphere, the radiance due to the source in the focal plane is $WT_0(\text{NA})^2$. $F_\#$ is defined as the ratio of focal length to diameter and for a distant object NA = $1/(2\ F_\#)$, so the ratio of the irradiance in the focal plane to the source radiance is

$$\frac{\text{Irradiance in focal plane}}{\text{Radiance from extended object}} = \frac{T_0(\lambda)T_a(\lambda)}{4F_\#^2} \tag{78.11}$$

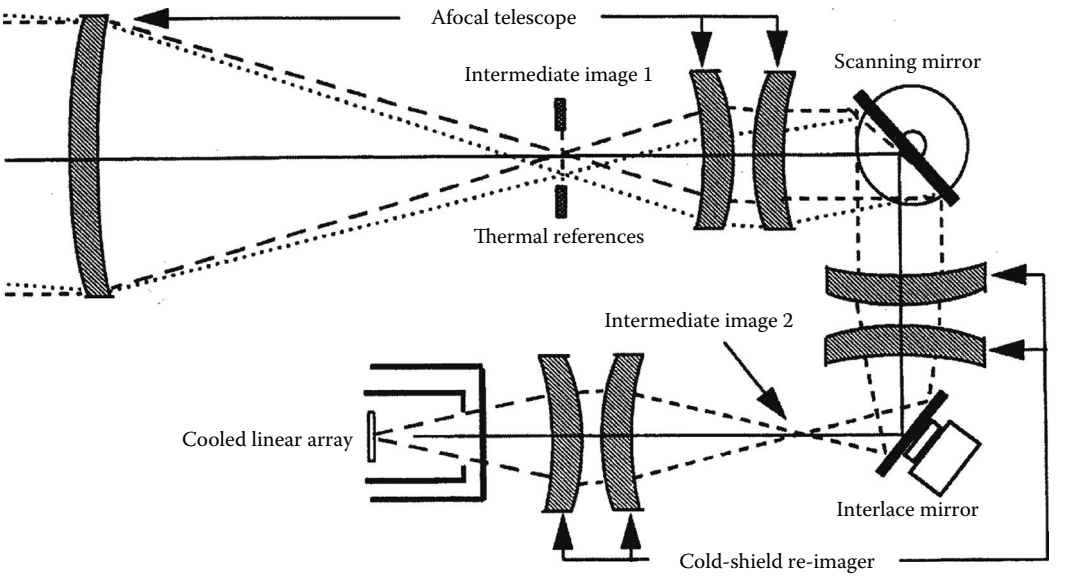

FIGURE 78.8 Optics for a linear array imager. The cold shield is imaged on the scanning mirror, and the scanning mirror is placed at the exit pupil of the telescope.

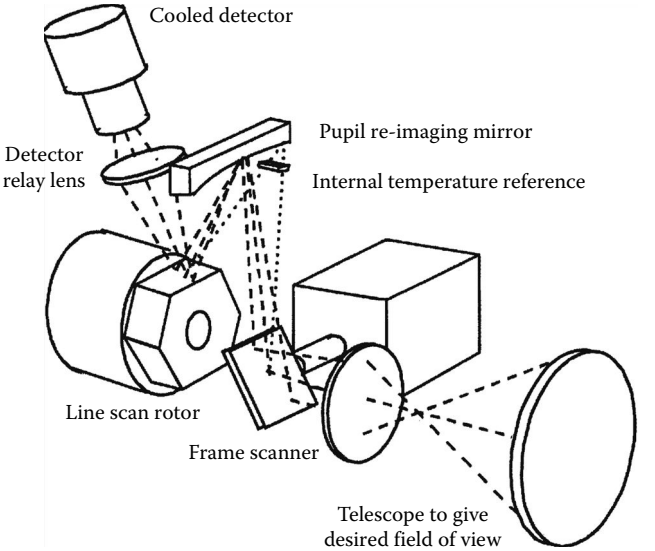

FIGURE 78.9 Simplified layout of imager using 2-D scanning (based on Pilkington Optronics HDTI). The line scan uses a high-speed polygon, and the concave strip mirror images the line scan pupil on the frame scanner.

The transmission of thermal imaging optics is typically 60%–90%, depending on complexity. The transmission of any optics between the temperature reference and the target must be known for quantitative measurement.

The imaging performance of a lens can be indicated by the size of the spot generated in the focal plane by a distant point object, and accurate results can be obtained if the intensity as a function of the angle α from the center of the image (point spread function, PSF) is known. A more usual approach is to use the MTF, defined as the ratio of the contrast of the image of a target with a sinusoidal spatial variation in intensity to the contrast of the target itself. The MTF depends on the spatial frequency f of the target

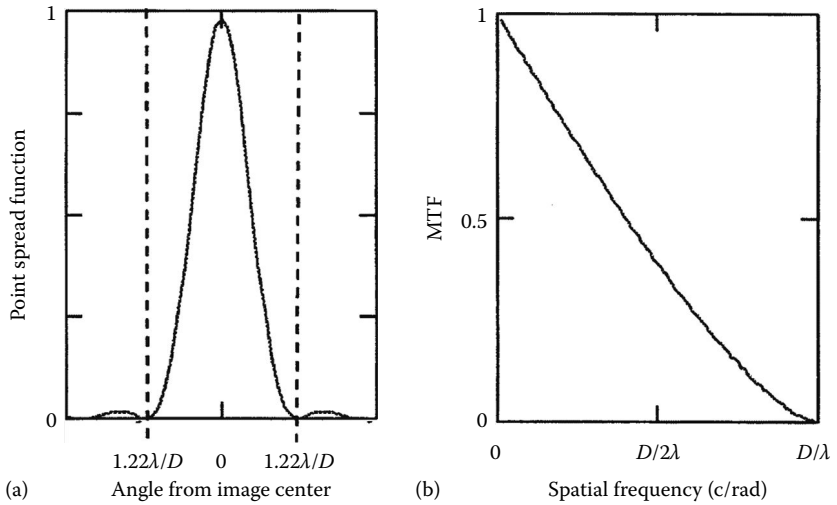

FIGURE 78.10 (a) PSF and (b) MTF for ideal optics of diameter D at wavelength λ. The first dark ring of the PSF has angular diameter $2.44\lambda/D$ and encircles 86% of the total energy. The MTF is zero for all frequencies above D/λ.

(expressed in cycles per radian) and on the wavelength of the radiation. For perfect optics of diameter D, diffraction gives the following values for PSF and MTF, which are also plotted in Figure 78.10:

$$\mathrm{PSF}(a) = 4\left[\left(\frac{\lambda}{\pi D a}\right) J_1\left(\frac{\pi D a}{\lambda}\right)\right]^2 \tag{78.12}$$

where J_1 is the Bessel function, and

$$\mathrm{MTF_o}(f) = \frac{2}{\pi}\left\{\mathrm{a}\cos\left(\frac{\lambda f}{D}\right) - \frac{\lambda f}{D}\sqrt{1-\left(\frac{\lambda f}{D}\right)^2}\right\} \tag{78.13}$$

In practice, optics is frequently far from the diffraction limit, so manufacturers' figures must be used. If a thermal imager is to be used for measurement, correction for MTF will be required unless the IFOV and the PSF are both smaller than the region over which the temperature is to be measured. The signal level for a subresolution point source can be obtained by integrating the PSF over the detector area. For diffraction-limited optics, a rule of thumb for the LWIR band is that the diffraction spot diameter in mrad is the reciprocal of the lens diameter in inches (or $25/D$ when D is in millimeters).

78.8 Temperature References

If a thermal imager is to be used for measurement, it is generally necessary to compare the signal from the target with that from one or more bodies at known temperature. The most precise results are obtained if two bodies at different known temperatures and having the same emissivity as the target (e.g., painted with the same paint type) are placed adjacent to the target and the target temperature is deduced by interpolation. There is then no dependence on emissivity, atmospheric transmission, and optical transmission. Outside the laboratory, this is seldom practical, however, and it is necessary to use thermal references within the imager itself. The fewer optical components there are between the reference and the scene, the better will be the accuracy. If the interior of a cavity of uniform temperature is viewed through a small

hole, the emission from the hole follows the Planck equation accurately, irrespective of the emissivity of the interior surface of the cavity. Although very accurate, such a blackbody cavity is usually inconveniently large, and it is more usual to use a blackened surface with deep grooves or pits to give high emissivity.

Unless the detector has only one element, thermal references are also desirable if not essential to allow the outputs of the different detector elements to be equalized.

78.9 Imager Performance

78.9.1 SNR and NETD

If the target is larger than the IFOV and the PSF, the signal level due to a small temperature difference is found by multiplying the source differential output, the atmospheric and optical transmissions, the geometric attenuation due to the *f*/number, the detector area, and the responsivity as derived or defined in the previous sections and integrating over the imager passband to give

$$V = \frac{A_d \Delta T}{4F_\#^2} \int R(\lambda) T_t(\lambda) T_a(\lambda) \varepsilon(\lambda) \frac{dW(\lambda, T)}{dT} d\lambda \tag{78.14}$$

The noise voltage V_n is given by Equation 78.7, so the SNR is obtained. If the number of serial detector elements is N_s, the signal level is increased by this factor, but since the noise is uncorrelated between the elements, it increases only as $\sqrt{N_s}$, so SNR improves as $\sqrt{N_s}$. The SNR also improves as the square root of the number of parallel channels since the dwell time is increased, giving a reduction in bandwidth B.

The sensitivity of a thermal imager for large targets is normally defined in terms of its NETD—the temperature difference between a large blackbody at zero range and its background—which gives a signal equal to the rms noise. This is given by V_n/V when $\Delta T = 1$, $T_a = 1$, and $\varepsilon(\lambda) = 1$ and is found to be

$$\text{NETD} = \frac{4F_\#^2}{\int_0^\infty D^*(\lambda) T_t(\lambda) (dW(\lambda, T)/dT) d\lambda} \sqrt{\frac{B}{A_d N_s}} \tag{78.15}$$

A good indication of SNR is given if it is assumed that T_a and ε are constant within the imager passband, in which case SNR = $\varepsilon\ T_a\ \Delta T$/NETD.

78.9.2 Minimum Resolvable Temperature Difference

The performance of a thermal imager is frequently defined by its minimum resolvable temperature difference (MRTD). MRTD(f) is the temperature difference between a four-bar square test pattern of frequency f c mrad^{-1} and its background required for an observer to count the imaged bars. The test is subjective but has the advantage of characterizing the complete system and display, including any effects of nonuniformity. MRTD is proportional to NETD and inversely proportional to the MTF and the square root of the number of frames presented within the integration time of the eye τ_e. The constant of proportionality depends on the degree of overlap between the scan lines. Discussion of the full MRTD model is beyond the scope of this chapter, but a simple expression (based on [1], p. 167)—which gives an indication of performance for an imager with square detector elements without overlap and at least two samples per IFOV and in which the electronics bandwidth is the same as that used for NETD calculation—is

$$\text{MRTD}(f) = \frac{3 \cdot \text{NETD} \cdot f \cdot \text{IFOV}}{\text{MTF}_o \text{MTF}_d \sqrt{\tau_e f_f}} \tag{78.16}$$

Calculation of MRTD is best performed using standard models, the most widely adopted being FLIR 92 [9].

78.10 Available Imagers

Recent advances in detector technology are only now beginning to be incorporated in commercially available systems. The result is that product ranges are currently changing rapidly and prices are very unstable. The prices for uncooled systems in particular are likely to drop significantly in the near future as the market size increases. An indication of cost at present is

Military high-performance imagers $100,000–300,000
Medium-performance imagers for measurement $30,000–100,000
Uncooled imagers $10,000–30,000 (but falling rapidly)

Prices reflect not only performance but also ruggedness, environmental survivability, and image processing software. Military imagers in many countries are based on "common modules" that are sometimes multisourced and that must be configured for specific applications. Table 78.1 lists some typical commercial imagers, which were selected to emphasize the wide variety of imager types, and the list must not be taken as a comprehensive survey. Some compact imagers weigh less than 2 kg, while some of the bench systems weigh over 100 kg. Accuracy of temperature measurement is not generally specified, but ±2 K or ±2% is a good figure for a calibrated imager. The information is based on published brochures, and there is a likelihood that improved models will be available by the time this book is published. It is strongly recommended that prospective purchasers should contact as many manufacturers as possible to obtain specifications and prices.

TABLE 78.1 Typical Commercially Available Thermal Imagers

Manufacturer	Model	Data	Description
AGEMA	880 LWB	LWIR, CMT	Thermal measurement system
		NETD = 0.07	175 pixels (50% MTF)
Amber	Radiancel	MWIR, InSb	Compact imager for measurement
		NETD = 0.025	256 × 256 pixels, InSb
Amber	Sentinel	LWIR	Uncooled compact imager
		NETD = 0.07 K	320 × 240 pixels
Cincinnati	IRRIS-160ST	MWIR, InSb	Compact imager
		NETD = 0.025	160 pixels/line
FLIR Systems	2000F	LWIR, CMT	Surveillance imager
		NETD = 0.1 K	>350 pixels/line
GEC Sensors	Sentry	LWIR	Uncooled low-cost imager 100 × 100 pixels
Hamamatsu	THEMOS 50	MWIR	Microscope, 4 μm resolution
		NETD = 0.2 K	256 × 256 pixels
Inframetrics	ThermaCAM	MWIR, PtSi	Thermal measurement system
		NETD < 0.1 K	256 × 256 pixels
Mitsubishi	IR-M600	MWIR, PtSi	High-definition imager
		NETD = 0.08 K	512 × 512 pixels
Nikon	LAIRD-3	MWIR, PtSi	High-definition imager
		NETD = 0.1 K	768 × 576 pixels
Pilkington Optronics	LITE	LWIR	Handheld surveillance imager
		NETD = 0.2 K	350 × 175 pixels
Quest	TAM200	MWIR	Microscope with probe facility
		NETD = 0.05 K	Bench system with 12.5 μm resolution

78.11 Performance Trade-Offs

The expression for NETD presented earlier is appropriate for evaluation of existing systems where D^* is known. To predict performance of future systems based on photon detectors and to carry out design trade-offs, it is important to appreciate that D^* is very dependent on conditions of use and on wave band. One reason is that the photons from an object of given temperature, although having a well-defined average flux, are emitted at random times. Statistical theory shows that if on average, N photons are collected within a given time interval, the standard deviation is $\sqrt{N}$ if N is large enough to make the distribution Gaussian (as is almost always the case in the infrared due to the high background flux). This "photon noise" frequently predominates, in which case the detector is referred to as background-limited photodetector (BLIP). The D^* is then determined more by the conditions of use than by the detector itself. If the efficiency of the cold shield η_c is defined as the ratio of the effective f/number for the background flux to that of the signal, the number of background electrons generated within an integration time τ is given by

$$N_e = \frac{\tau A_d}{4F_\#^2 \eta_c^2} \int_0^\infty N(\lambda,T)\eta(\lambda)d\lambda \tag{78.17}$$

For the reasons discussed earlier, the rms electron noise for a BLIP device within time τ is simply the square root of the aforementioned figure. If the detector also has readout noise of N_n electrons rms, this could be regarded as the noise that would be caused by a background flux that caused the generation of N_n^2 photoelectrons, so the noise can be written as

$$\text{Noise} = \sqrt{N_e + N_n^2} \text{ electrons rms} \tag{78.18}$$

The signal due to a temperature difference of 1 K between target and background expressed in electrons within the integration time is

$$\text{Signal} = \frac{\tau A_d}{4F_\#^2} \int_0^\infty T_t(\lambda)T_a(\lambda)\eta(\lambda)\frac{dN(\lambda,T)}{dT}d\lambda \tag{78.19}$$

Thus, the SNR for $\Delta T = 1$ K is found, NETD being simply 1/SNR when $T_a = 1$.

For staring systems, and some scanning systems, the integration time is limited by saturation. If the maximum number of electrons that can be stored is N_m, we find that the maximum integration time is

$$\tau_m = \frac{4F_\#^2 \eta_c^2 N_m}{A_d \int_0^\infty N(\lambda)\eta(\lambda)d\lambda} \tag{78.20}$$

When the integration time is controlled to restrict the number of electrons generated within the sampling interval to τ_m, the noise is given by letting $N_e = N_m$ in Equation 78.18 so is independent of f/number. If one also substitutes τ_m for τ in Equation 78.19 and divides Equation 78.19 by Equation 78.18, to obtain SNR, one obtains

$$\text{SNR} = \frac{\Delta T \eta_c^2 N_m \int T_o(\lambda)T_a(\lambda)\eta(\lambda)(dN(\lambda,T)/dT)d\lambda}{\sqrt{N_m + N_n^2}\int N(\lambda)\eta(\lambda)d\lambda} \tag{78.21}$$

The ratio of integrals is effectively the contrast of the scene behind the optics, which is further reduced by the inefficiency of the cold shield; thus, performance depends mainly on image contrast at the detector and the number of electrons stored. (Quantum efficiency essentially cancels out, and for a saturated device, $\sqrt{N_m}$ is usually greater than N_n.)

The aforementioned formulae are sufficiently general to allow trade-offs for photon detectors to be carried out against aperture, wave band, range, and frame rate, the main uncertainty being the readout noise. For staring array detectors with processing on the focal plane, a typical figure is $N_n = 1000$, but much better (and worse) values are possible. The SNR and NETD values obtained in this way are for a single pixel. If the samples overlap spatially, the SNR is improved by the square root of the overlap factor. In practice, nonuniformity of the detector array will introduce spatial noise that will affect MRTD, and even after electronic correction, this is frequently the main limitation on performance. Nonuniformity effects are discussed in [10,11].

The resulting trade-offs are discussed at some length in [12]. It is observed that if the integration time is controlled to prevent saturation, NETD is independent of *f*/number and quantum efficiency but depends strongly on image contrast. This tends to favor the MWIR band and makes high cold-shield efficiency crucial. The problem can be overcome in the LWIR by operating at a high frame rate, which has no effect on NETD but improves MRTD due to eye integration. For long-range applications, it is frequently necessary to use long focal lengths, giving large *f*/numbers if the optics diameter is to be kept within reasonable bounds. Under these conditions, saturation is less likely, and the high photon flux in the LWIR is necessary to overwhelm the readout noise. If high spatial resolution rather than sensitivity is required, the MWIR band has a much better diffraction limit. Figure 78.11 indicates the ways in which the various limitations combine to define the combination of IFOV and wave band that gives optimum performance when it is necessary to resolve a given spatial frequency; the positions of the lines on this chart are of course peculiar to the system under investigation.

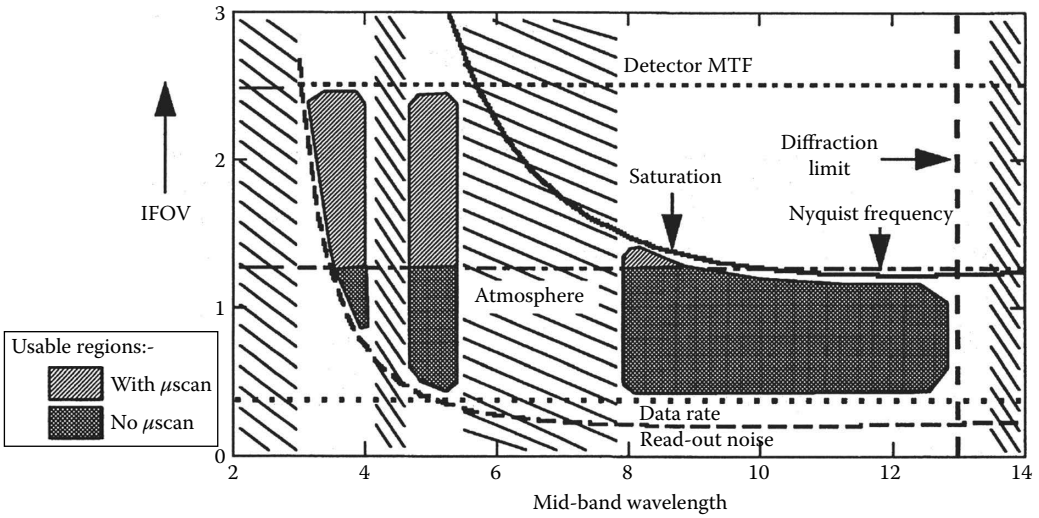

FIGURE 78.11 Physical limitations to thermal imaging when a specified spatial frequency must be resolved. The shaded regions indicate the combinations of wavelength and IFOV for which the task can be achieved. All the lines on the graph depend on system parameters such as aperture, quantum efficiency, readout noise, and electron storage but can be calculated from the equations given in the text.

TABLE 78.2 Companies That Make Commercial Thermal Imagers

AGEMA Infrared Systems Inc., 550 County Avenue, Secaucus, NJ 07094, Tel.: (201) 867-5390
Amber Engineering Inc., 57566 Thornwood Drive, Goleta, CA 93117-3802, Tel.: (800) 232-6237, Fax: (805) 964-2185
Cincinnati Electronics Corporation, Detector and Microcircuit Devices Laboratories, 7500 Innovation Way, Mason, OH 45040-9699, Tel.: (513) 573-6275, Fax: (513) 573-6290
Hamamatsu Photonic Systems, 360 Foothill Rd., Bridgewater, NJ 08807-0910, Tel.: (908) 231-1116, Fax: (908) 231-0852, http://www.hamamatsu.com/
Inframetrics Imaging Radiometer Group, 12 Oak Park Drive, Bedford, MA 01730, Tel.: (617) 275-8990, TWX: (710) 326-0659, www.inframet.pl/
Mitsubishi Electronics America Inc., 5665 Plaza Drive, P.O. Box 6007, Cypress, CA 90630-0007, Tel.: (800) 843-2515, http://www.mitsubishi-imaging.com/
Nikos Corporation (Nikon), 1502 West Campo Bello Drive, Phoenix, AZ 85023, Tel.: (602) 863-6182, http://www.nikon.com/
Pilkington Optronics Inc., 7550 Chapman Ave., Garden Grove, CA 92841, Tel.: (714) 373-6061, Fax: (714) 373-6074, http://www.pilkington.com/
Quest Integrated Inc., 21414-68th Avenue South, Kent, WA 98032, Tel.: (206) 872-9500, Fax: (206) 872-8967, http://www.qi2.com/

78.12 Future Trends in Thermal Imaging

At the high-performance end of the market, the developments are most likely to be driven initially by military requirements. Many countries already have thermal imaging common module programs, and many developments will be aimed at productionizing these modules to reduce cost and enhance performance. Multispectral instruments to aid in camouflage penetration and to broaden the conditions of operability through the atmosphere can be taken out of the laboratory into service. Currently, these are mainly scanning devices using adjacent long linear arrays of LWIR and MWIR detectors. For spectral agility, detector arrays based on multi-quantum-well (MQW) technology can be used, since they can be tuned to some extent by varying the electrical bias. Multispectral refracting optics is complex and has poor transmission, so reflecting optics is generally used. Multispectral systems will allow more accurate compensation for emissivity, but their high cost might limit their use except for high-value applications such as earth resources surveys in aircraft or satellites. Techniques employed include frame-sequential filtering and imaging Fourier transform spectroscopy (Table 78.2).

For commercial thermal imaging, the main thrust is likely to be cost reduction via the use of uncooled imagers and in packaging to provide increased ease of use and functionality using in-built software. Optics cost can be reduced or performance improved by the use of hybrid aspheric components, which are now practical due to improvements in diamond turning. A diffractive surface is generated on one surface of a refracting lens. Because the power of a diffractive component is proportional to wavelength, a very low diffractive power can compensate for the chromatic aberration of the lens. This allows the use of materials such as zinc sulfide, which would otherwise be unacceptable due to chromatic aberration but which have other desirable properties such as low cost or a low thermal coefficient of refractive index.

References

1. J.M. Lloyd, *Thermal Imaging Systems*, New York: Plenum Press, 1975, pp. 20–21.
2. J.S. Acetta and D.L. Shumaker (Eds.), *The Infrared & Electro-Optical Systems Handbook*, Bellingham, WA: SPIE Optical Engineering Press, 1993, Vol. 1, 52, pp. 251–254.
3. F.X. Kneizys, E.P. Shettle, L.W. Abreu, G.P. Anderson, J.H. Chetwynd, W.O. Gallery, J.E.A. Selby, and S.A. Clough, *Users' Guide to LOWTRAN 7*, Report No. AFGL-TR-88–0177 Hanscom, Air Force Geophysics Laboratory, 1988.
4. M. Bass (Ed.), *Handbook of Optics*, New York: McGraw-Hill, 1995, Vol. 1, Chapter 23.

5. C.M. Hanson, Uncooled ferroelectric thermal imaging, *Proc. SPIE 2020*, *Infrared Technology XIX*, 1993.
6. R.A. Wood, Uncooled thermal imaging with monolithic silicon focal plane arrays, *Proceedings of SPIE 2020*, *Infrared Technology XIX*, San Diego, CA, p. 329, 1993.
7. G.C. Holst, *Testing and Evaluation of Infrared Imaging Systems*, Winter Park, FL: JCD Publishing, 1993, pp. 36–42.
8. M.J. Riedl, *Optical Design Fundamentals for Infrared Systems*, Bellingham, WA: SPIE Optical Engineering Press, 1995, p. 55.
9. L. Scott and J. D'Agostino, NVEOD FLIR92 thermal imaging systems performance model, *Proceedings of SPIE*, *Vol. 1689*, *Infrared Imaging*, pp. 194–203, 1992.
10. A.F. Milton, F.R. Barone, and M.R. Kruer, Influence of nonuniformity on infrared focal plane performance, *Opt. Eng.*, 24, 855–862, 1985.
11. H.M. Runciman, Impact of FLIR parameters on waveband selection, *Infrared Phys. Technol.*, 37, 581–593, 1996.

Further Information

Catalina Bixler, *Types of Thermal Sensors, Fiber Optic Transducers*, http://www.ehow.com/list_6767046_types-thermal-sensors.html (accessed on June 21, 2012).

Compix, Thermal imaging: more than just pretty pictures, http://www.compix.com/articles.quality.html (accessed on June 28, 2012).

Gaussorgues, G., *Infrared Thermography*, London, U.K.: Chapman and Hall, 1994.

Grum, F. and Becherer, R.J. (Eds.), *Optical Radiation Measurements*, New York: Academic Press, 1979, Vol. 1.

Holst, G.C., *Electro-optical Imaging System Performance*, Winter Park, FL: JCD Publishing, 1993, pp. 36–42.

Wyatt, C.L., *Radiometric Calibration: Theory and Methods*, New York: Academic Press, 1978.

79

Calorimetry Measurement

Sander van Herwaarden
Xensor Integration

Elina Iervolino
Xensor Integration

79.1 Introduction

This chapter is a revision of the homonymous chapter contained in the previous edition of this book. While the overview of the most important calorimeter showed in the previous chapter has been left, more space is given to the latest innovation in the field of chip calorimeter.

This chapter starts again with a small introduction on thermodynamics. An overview of the most important types of calorimeters and chip calorimeters will then be presented. The typical application of calorimeters and chip calorimeters follows. For those who want to do measurements without having to make their own devices, an overview of the most important calorimeters and their vendors and approximate prices will be given. The chapter concludes with some hints on present and future developments and on further reading, since there is a large amount of literature on calorimeters.

79.1.1 Thermal Energy, Heat, and Temperature

One of the forms in which energy can be present in a system is the random, internal kinetic energy of the particles (molecules or atoms) of a system, which can intuitively be called "thermal energy." Thermal energy is the portion of internal energy U that is responsible for a system temperature and has to be distinguished from the average, external movement of a system of particles as a whole, which can be called the "mechanical energy" of the system. For gases, thermal energy is closely related to the random velocity of the molecules and, in the case of multiatom molecules, the rotations and vibrations of the atoms within the molecules. The thermal energy is an extensive property as it is dependent by the amount of matter the object contains. The temperature is instead an intensive property, and its empirical definition comes out from the zeroth law of thermodynamics. The zeroth law of thermodynamics states that if two systems are each in equilibrium with a third system, they will be in equilibrium with each other. They are said to have the same temperature. For gases, statistical mechanics shows the direct relation between the thermal energy stored in the system and the temperature [1]. This law, however, also applies to liquids and solids, although the quantitative relation between thermal energy (agitation of the particles) and temperature is less straightforward and not so easy to calculate as for gases. Temperature and thermal energy distribution can be viewed as the result of statistical processes, such as diffusion. Diffusion ensures that if ever there is a surplus of thermal energy (i.e., of fast molecules or electrons or a higher density of phonons) in some area, some of it will flow toward areas with a lower thermal energy density until thermal equilibrium has been established. This flow of energy P (in W = J s^{-1}) is called heat flow. Heat flow is therefore the transfer of (thermal) energy from one (part of a) system to another. Note that heat is not conserved, because a change in thermal energy of a system may be achieved by heat exchange with the environment but also by mechanical interaction, and heat can be used to do mechanical work (motor) just as well as heating up a system. Heat can be viewed as "thermal energy on the move." Heat is energy transferred from one body to another due to thermal contact when the systems are at different temperatures, but whether it ends up as thermal, mechanical, or another form of energy depends on the circumstances.

79.1.2 Work and Enthalpy

The first law of thermodynamics is an expression of the principle of the conservation of energy. In a simple form, in the absence of other forms of energy exchange, it states that the change in internal energy ΔU of a system is equal to the heat Q supplied by the ambient to the system minus the work (mechanical energy) $p\Delta V$ done by the system on the ambient:

$$\Delta U = Q - p\Delta V \tag{79.1}$$

This is of importance when measuring the heat capacity C (in J K^{-1}) of a substance, defined as the amount of heat required to change the temperature of the substance by a given amount:

$$C = \frac{\Delta Q}{\Delta T} \tag{79.2}$$

where

ΔQ is the heat exchanged

ΔT is the temperature change of the substance

This measurement can be performed under two conditions: at constant volume V and at constant pressure p. At constant volume, no work will be done by the system, since $p\Delta V = 0$. So, the heat capacity

at constant volume c_v is related to the change in internal energy ($\Delta Q = \Delta U$)0. The specific heat capacity of a system at constant pressure c_p is (usually) higher, since additional energy (heat) is needed to perform work on the ambient: $p\Delta V$. The quantity combining these contributions to the energy at constant pressure is called enthalpy H, and the change in enthalpy versus temperature (in J K^{-1}) at constant pressure is the heat capacity C_p of a sample at constant pressure: $C_p = (dH/dT)_p$.

79.1.3 Signals Measured with Calorimeters

In measurement science, physical quantities can be distinguished by six different so-called signal domains: thermal, electrical, chemical, mechanical, magnetic, and radiant [2]. Signals can be transduced from one domain to the other. For a thermal signal, the change of the ambient temperature can be transduced into an electrical signal thanks to a resistor, reading its temperature-dependent resistance value with a multimeter. All signals in calorimeters are either thermal signals or other signals that are transduced into thermal signals. So, calorimetric measurement of signals can occur from all domains [3]. The thermal signal (e.g., heat) is then transduced into an electrical signal. Calorimeters usually measure the thermal effects of (bio)chemical or mechanical processes, or they measure the thermal effect of temperature changes on matter.

79.2 Calorimeters: Criteria for Their Classification

In essence, a calorimeter performs three functions: It encloses a chamber in which a thermal experiment is carried out; it measures the heat exchange between the sample under test and the calorimeter (and often other quantities are being measured as well, such as temperature and amount of substance); and it thermally separates the experimental chamber from its surroundings. The same three functions are realized also in a chip calorimeter. In silicon (Si) technology, a chip calorimeter usually schematically consists of a heater and a temperature sensor on a thin-film membrane connected to the Si frame that gives mechanical stability to the calorimeter, and it acts as thermal heat sink; see Figure 79.1. For a chip calorimeter, the three aforementioned functions are realized by the hot spot that delimits the sample area where the experiment is performed, the temperature sensor that measures the temperature, and the thin membrane that thermally isolates the sample area from the surrounding. There exist many types of calorimeters. Four essential criteria can be used to classify calorimeters [4,5]:

1. *Heat measurement*. What does the calorimeter do with the heat that is generated (or absorbed) by the experiment?
2. *Relation with surrounding*. How does the calorimeter relate to its surroundings?
3. *Single or twin design*. Does the calorimeter measure a single experimental sample, or is it a twin design with a reference compensating for common-mode errors?

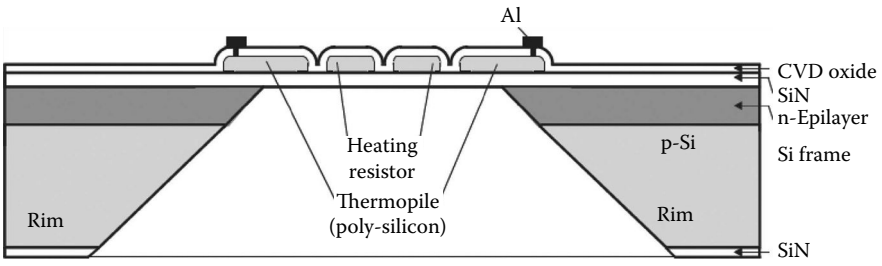

FIGURE 79.1 Schematic of a chip calorimeter: on a thin-film membrane, the heater, which makes up the sample area, and the hot junctions of the thermopile (temperature sensor) are located. The cold junctions of the thermopile are on the Si frame that acts as thermal heat sink, and it gives also mechanical stability to the device. (Picture loaded from the website www.xensor.nl)

TABLE 79.1 Overview of the Classification Criteria for Calorimeters

Relation to Surroundings Heat Measurement	Heat Measurement
Isothermal	Phase-transition compensation of heat Thermoelectric compensation of heat
Adiabatic	Measurement of temporal temperature difference
Isoperibol	Measurement of spatial temperature difference

4. *Fixed temperature or scan of a temperature range*. Does the calorimeter function at a fixed temperature, or can it scan a temperature range?
   a. A fifth criterion can be added to include calorimeters that are based on a calorimeter chip.
5. *Conventional design or chip design*. Is the calorimeter based on a "conventional design," or is it based on a chip calorimeter?

Table 79.1 lists the various possibilities for the relation to the surroundings and for the heat measurement. In principle, almost every combination is possible. In practice, some combinations naturally go together because they compensate for their strengths and weaknesses. For example, calorimeters in which the experimental temperature is scanned often use a twin configuration to eliminate the common-mode errors arising from the continually changing temperature. In the following paragraphs, the main types of calorimeters are described.

79.2.1 Isothermal Calorimeters

In the isothermal calorimeter, the experiment is always kept at a fixed temperature. This is attained by instantly removing (or supplying) any heat that the experiment releases (or absorbs). The isothermal calorimeter was the first to be developed. In 1780, Lavoisier and Laplace made the "ice calorimeter" in which the heat generated by the experiment is used to melt ice into water. If enough ice is available, the calorimeter will remain at 0 °C, regardless of the progress of the experiment. The experimentally generated heat Q (J) is calculated by weighing the mass m (kg) of the melt water and multiplying by the heat of the ice-water transition q_{fus} (J kg^{-1}):

$$Q = m q_{\text{fus}} \tag{79.3}$$

The experiment with the melting ice is enveloped within a thermostat, which consists of a double-walled vessel with melting ice between the walls, which is always at 0 °C as well. Thus, the isothermal calorimeter has a perfect thermal isolation between experiment and surroundings in the form of a second guard vessel that buffers all the heat coming from the surroundings.

79.2.2 Phase-Transition or Thermoelectric Compensation of the Heat

In the isothermal calorimeter, the heat generated by the experiment is immediately absorbed by the calorimeter. This can be accomplished by phase-transition compensation of the heat, for example, by melting of solids or evaporation of liquids. But nowadays, compensation by electrical means is preferred because it can be measured so easily. Thus, heat Q (J) absorbed by the experiment is replaced using Joule heating (dissipation of heat by a current I (A) through an electric heater with resistance R_{h} (**Ω**)), while heat generated by the experiment is absorbed by Peltier coolers:

$$Q = \int I^2 R_{\text{h}} \mathrm{d}t \tag{79.4}$$

79.2.3 Adiabatic Calorimeters Often Measure Time-Dependent Temperature Differences

In the adiabatic calorimeter, no heat exchange with the surroundings is allowed, and all the heat generated by the experiment is used to increase the temperature of the calorimeter. The amount of heat Q (J) generated follows from the temperature increase ΔT (K) divided by the heat capacity of the calorimeter C_c (K J^{-1}):

$$Q = \frac{\Delta T}{C_c} \tag{79.5}$$

The absence of heat exchange with the surroundings of the calorimeter is obtained by immersing the experimental chamber of the adiabatic calorimeter in an outer vessel. The temperature of the outer vessel is kept at the same (increasing) temperature as the experimental chamber by means of electronic feedback, heating the outer vessel to maintain a practically zero temperature difference. In the adiabatic calorimeter, one must wait a few minutes after the experiment has finished to allow the heat to spread itself uniformly over the chamber and to obtain the final temperature. An example of such calorimeter is a so-called calorimetric bomb. In its experimental chamber, fuel is fully burned to measure its heat of reaction. The bomb is immersed in a vessel filled with water—the inner vessel. A stirrer assures fast heat exchange between the bomb and the inner vessel; thermometers measure the temperature of the inner guard vessel and the outer guard vessel. The outer vessel is regulated to the inner-vessel temperature by means of electrical heaters and refrigerator coolers.

79.2.4 Isoperibol and Heat-Flux Calorimeters

The term *isoperibol* was devised to indicate a calorimeter having "uniform surroundings." In this calorimeter, the outer shell provides a reference temperature, and customarily, the experiment starts at the same temperature. The experimental chamber is connected to the outer shell by a well-defined thermal conductance. Any heat generated by the experiment will cause a well-defined temperature difference ΔT (K) across the thermal conductance G_{th} (W K^{-1}), and this temperature difference is subsequently measured as a "local temperature difference." Calorimeters utilizing this way of measuring the heat are referred to as "heat-flux calorimeters" and often measure the power P (J s^{-1} or W) generated by the experiment, rather than the energy:

$$P = \Delta T G_{th} \tag{79.6}$$

Chip calorimeters are an example of isoperibol calorimeters.

79.2.5 Chip Calorimeters

With respect to "conventional calorimeters," chip calorimeters bring in the calorimeter field two important improvements: the scale-down of the sample to nanogram amounts of material [6,7] and the possibility to increase the temperature scan rate to 10^6 K/s (scanning calorimeter is presented in the next paragraph). Ultrafast-scanning calorimeters are commercially available, and extensive characterizations are present in literature [8,9]. Calorimeter chips generally consist of a heater resistor and thermopile (temperature sensor) on a thin-film dielectric material. Different designs of calorimeter chips have been proposed with the intent to come to a device capable of fast temperature scan rates [9–11]. So far, the use of these sensors was restricted to isoperibol operation around room

FIGURE 79.2 Flash DSC 1 of Mettler-Toledo with a close-up of the device UFS 1. The device is made of two identical cells, the reference and the sample cell, respectively. Both cells consist of two heaters covered with an aluminum layer that makes up the sample area, in the center of the membrane; the hot junctions of the eight thermocouples are inside the sample area.

temperature [12], using aluminum heat sinks to provide the reference temperature. The main drawback of the chip calorimeters was the absence of a commercial available apparatus and software for the signal analysis. The problem has been overcome with the recent introduction on the market of the Flash DSC 1 of Mettler-Toledo. Figure 79.2 shows the Flash DSC 1 with a close-up of the chip designed for the instrument. The chip is made of two identical cells, the reference and the sample cell, respectively. Both cells consist of a 1.6×1.6 mm^2 large and about 2 μm thick membranes. The membranes of the two cells are thermally separated by a thick Si frame of 300 μm that acts as heat sink. Two heaters are integrated in the center of the membrane. The main heater, with a resistance of about 5 kΩ, is used for the general temperature scan program. The other heater, of about 4 kΩ, is active only in power compensation mode and has to compensate for temperature differences between the reference and the sample cell. The two heaters, covered by an aluminum (Al) layer, make up a circular area with a diameter of 0.5 mm, where the sample can be loaded. The Al layer is used to get temperature uniformity in the sample area. The temperature of the heated area is measured with an integrated thermopile.

79.3 Scanning Calorimetry Sweeps the Experiment Temperature

In the scanning calorimeter, the experimental chamber is not kept at (approximately) one temperature, but it is swept over a temperature range. The temperature is increased at given rate (e.g., 10 K min^{-1}) by electric heating or decreased by, for example, cooling with liquid nitrogen. To achieve the temperature sweep, the experiment is placed inside a computer-controlled oven. To compensate for common-mode errors (i.e., backlogging or deviation of the sample temperature from the oven temperature and imperfections in the oven temperature profile with respect to time and location), scanning calorimeters are often built with twin experimental sites for which the difference is measured. One site is for the sample under test; the other site serves as reference, which either is left empty or contains material resembling the sample under test as much as possible, except for the phenomena to be measured. Such calorimeters are called differential scanning calorimeters, DSCs (see "Further Information" for a general book on DSC). There are three principal types of DSCs design: heat flux, power compensation, and (the new introduced) dynamic power compensation [13]. In heat-flux measurements, the reference and the sample have a common heating source, or more in general, they are subjected to the same heating/cooling function; see Figure 79.3. The output signal is the temperature difference between the reference and the sample site. In the second type of DSC, the power compensation DSC, sample and reference each have an individual heating source, which is electronically controlled to maintain sample and reference at the same required temperature course. The difference between reference and sample

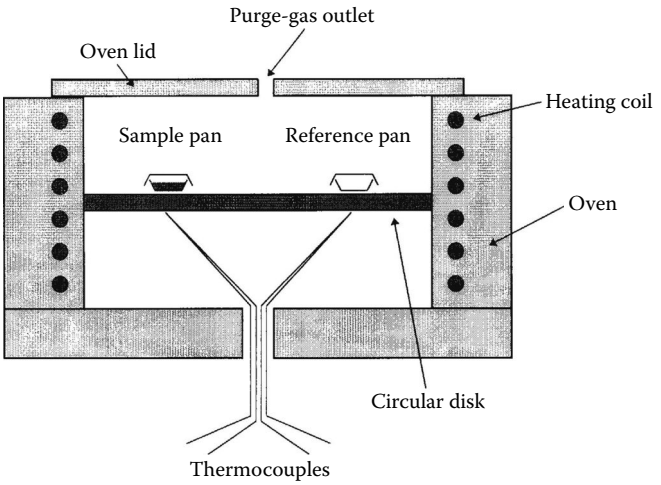

FIGURE 79.3 The heat-flux DSC consists of two experimental sites on a heat-conducting disk. Heat generation in the sample pan results in a temperature increase of the sample with respect to the reference, measured by thermocouple (the disk being one part of the couple).

heating power immediately gives the experimental heat. In dynamic compensation DSC, sample and reference still have each an individual heating source, but the sign of the applied compensation power is always positive. This can be made by dynamic switching the cell to which the excess power is applied. The additive nature of this compensation principle enables implementation by dedicated compensation heating units, physically distinct from the heaters empowering the common temperature program. The separation of compensation power from bulk power offers advantages in terms of noise, signal resolution, and response time.

There is also a fourth (less accurate) type of DSC, where only the temperature at which phenomena occur is registered. This type can be used for bigger samples (2–3 mL against 0.1 mL for the heat-flux DSC) or at very high temperatures up to 2000 °C.

79.3.1 Differential Scanning Calorimeters Techniques

In DSCs, three different techniques have recently become popular: temperature-modulated DSC (TM-DSC), high-sensitivity DSC (HS-DSC), and fast-scan DSC (FS-DSC). Each technique has some advantages, and the choice of one over the other technique has to be done in dependence of the sample to be studied. The TM-DSC and the FS-DSC techniques are treated in more details in the following subparagraph.

79.3.1.1 Temperature-Modulated DSCs Improve Insight into the Measurement

One of the developments in DSC is the use of a nonuniform temperature scan. On the standard linear temperature increase, mostly slow (e.g., 1 K min^{-1}), an alternating temperature change is superimposed, which is fast compared with the linear scan rate. The signal can be a sinusoidal signal, or alternatively, a stepped temperature profile can be used. Here, the temperature is increased during, for example, 0.5 min with 2 °C, and then stabilized for 0.5 min, resulting in an overall scan rate of 2°C min^{-1}. In fact, the scan is now modulated with a block wave of amplitude 2 °C min^{-1}; see Figure 79.4. For an instrument with small time constant, this means that the heat flow for increasing the experiment temperature in the stabilization time will be completely stopped. Any heat flow remaining results from the processes in the sample itself; see Figure 79.4.

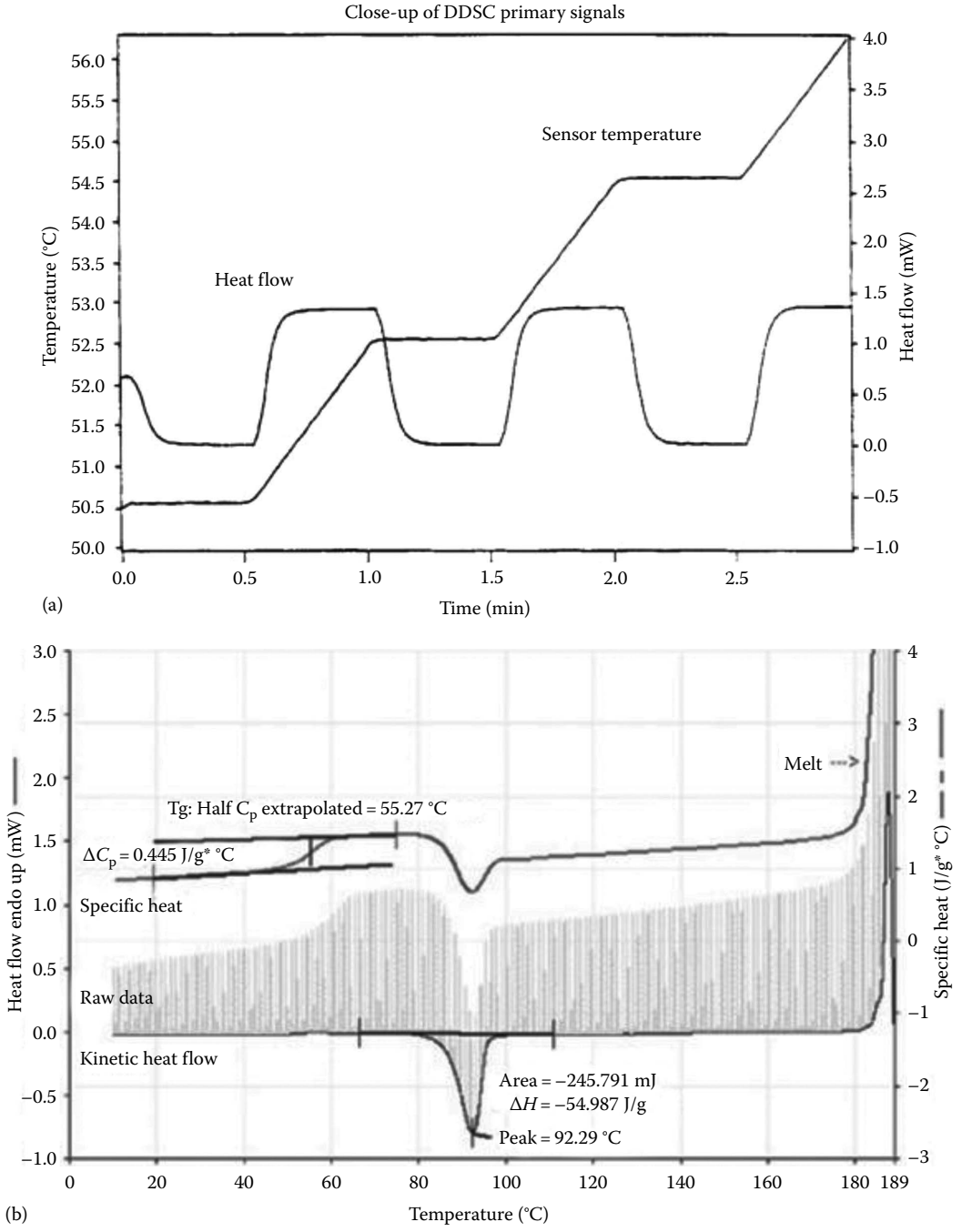

FIGURE 79.4 In modulated or dynamic DSCs, the temperature is not increased at a given rate, but modulated with a sinusoidal or (a) stepwise deviation to separate heat transfer due to temperature increase (specific heat) and heat transfer due to phase changes in the material (glass transition, crystallization, melting). (b) TM-DSC of carbamazepine shock cooled from the melt. This figure shows the absence of heat flow in regions without material change, while the curve indicates the glass transition of the amorphous form and the crystallization into a crystalline polymorphic form, which then melts. (Courtesy of Perkin Elmer, Waltham, MA.)

79.3.1.2 FS-DSCs and FS-DSCs Based on Chip Calorimeter

FS-DSCs gain popularity, thanks to the new possibilities of fast scan rates that brought

1. The study of materials in nonequilibrium states. Fast scan rates prevent reorganization during the scan.
2. The study of microgram–gram samples. Fast scan rates yield to heat flows that can be detected by FS-DSC.
3. Short run time.
4. Higher sensitivity than conventional DSCs with slow scan rates. The gain in sensitivity (the magnitude of each thermal event) corresponds to a loss in resolution (separation between thermal events) [14].

FS-DSCs can be realized either modifying existing machines or using chip calorimeters. In the first case, the drawback is that only a few hundreds of K/s can be realized, while with chip calorimeters, 10^6 K/s have been demonstrated to be possible. The recent introduction on the market of the Flash DSC 1 of Mettler-Toledo combined the advantages of the chip calorimeters with the comfort of a standard DSC.

79.3.2 Converting the Measured Curve to the Actual Progress of the Experiment

Due to the thermal resistance and the heat capacitance inside the experimental chamber of a calorimeter, there is a time constant associated with distributing the experimental heat over the chamber and reaching the final temperature. A heat pulse does not create a temperature pulse but rather a smeared-out curve. In a DSC, this smearing out is usually not significant because of the small time constant (1–3 s). For some other instruments, the so-called curve desmearing has to be carried out using convolution integrals to extract all the information from the measurement curve. With commercially available instruments, software is often supplied that does the job for you, but the accuracy of this software is not satisfactory in all cases, so one might need to do some further study on desmearing [4].

79.4 Calibration of Calorimeters

The inaccuracy of the calorimeter can be reduced by *calibration*. Heat production can easily be simulated electrically. Unfortunately, the thermal leakage of the electric leads reduces the accuracy of this method. More common, therefore, is the use of primary standards with a known heat of transition or reaction for calibration. For bomb calorimeters, the response can be calibrated using the heat of reaction of benzoic acid, which has been carefully determined to be 26,457 J g^{-1} [15]. For a DSC, a range of materials can be used for calibration. This is due to the wide range of applications and also to the wide range of temperatures used. Generally, one or more metals are used for calibration of both the power and the temperature scale, for example, indium, which has a melting point of 156.6 °C, and an enthalpy of melting of 28.6 J g^{-1}. The uncertainty of the value for the heat of fusion (in this case, of melting) is about 0.5%. This is the limit when calibrating in this manner. Basically, DSC inaccuracy is around a few percent. For up-to-date details on calibration and the calibration materials, please consult [16,17], the references given there, and the most recent data published, since calibration procedures for the DSC are still improving. Specific heat capacity measurements are often performed in three steps. First, the baseline offset of the DSC is measured with empty reference and empty sample sites (one measures the difference between sample and reference baseline, i.e., the systematic asymmetry of the instrument). Then, a measurement of a primary standard with accurately determined specific heat capacity is made; for this, sapphire (crystalline Al_2O_3) is often used. Finally, a measurement of the unknown sample is carried out. By correcting for the baseline offset and division of the measurements of the known and the unknown samples, the specific heat capacity of the unknown sample can be determined. Currently, these corrections are all made by the computer controlling the DSC [18].

79.4.1 Calibration of Chip Calorimeters

Chip calorimeters need also to be calibrated. Like for "conventional" calorimeters, different primary standards can be chosen to cover the entire temperature range of interest. The drawback is that for each primary standard, so for each measured temperature, a different chip has to be used [19] since the sample has to be deposited directly on the chip. Moreover, since the chips used for the calibration are contaminated, calorimetric measurements can be performed only with not calibrated devices. In [20], a calibration method that allows the use of calibrated devices for calorimetric measurements is proposed. First, the chip is inserted into an oven and the heater integrated on the calorimeter chip is calibrated in the temperature range of interest. Then, the obtained calibration curve is used for the calibration of the temperature sensor, that is, the thermopile. In order to determine the accuracy of the calibration, the extrapolated onset temperature (T_e) of primary standards is measured with chips having uncalibrated heater resistance.

79.5 Typical Applications of Calorimeters

79.5.1 Specific Heat, Transition Heat, and Temperatures

Specific heat capacity can be measured by accurate point-wise measurements, but measurement with a DSC is much more efficient. With the DSC, one also obtains the temperature and heat of phase transitions by enthalpy measurement at the transition temperature. Many materials also exhibit changes in crystallization at some given temperature (e.g., glass transition points). Also, these are transition points with their specific heat and temperature, and these can be measured with DSC as well.

79.5.2 Analysis of Chemical and Physical Reactions

Calorimetry is very well suited for analysis of chemical reactions. In particular, the heat of exothermic and endothermic reactions can be determined. An important example is the calorific value of fuels. Households and factories buying fuels are primarily interested in the calorimetric value of their purchases. The so-called oxygen bomb calorimeter is indispensable for primary calibration in this application. The oxygen bomb is usually an adiabatic calorimeter, in which a sample of the fuel (such as solid coal, liquid oil, or gaseous methane) is brought together with an excessive amount of oxygen (e.g., at a pressure of 30 bar). Then, the mixture is ignited, and the heat of burning will spread over the bomb, until equilibrium is reached. The temperature increase of the bomb, divided by the heat capacity of the device, gives the heat of reaction. In general, corrections have to be made for volume and pressure changes (work) as liquids or solids are burned and converted to gases and liquids and also for the additional heat capacity and for the transition heat of the reaction products. Of course, chemical reactions other than burning of fuel can be analyzed in this way as well. In a slightly modified version, the adiabatic calorimeter can also serve to analyze, for example, weak bases and weak acids that do not easily respond to other analysis methods. Similarly, the heat of mixing two solutions, of dissolving a solid in a solvent, and of diluting a mixture and even the heat of wetting can be determined in this so-called solution calorimeter.

79.6 Thermal Analysis of Materials and Their Behavior with Temperature

Apart from directly measuring chemical reactions, one can also analyze materials by exposing them to a temperature sweep, either in an inert atmosphere (nitrogen or helium) or in an oxidizing atmosphere. Then, all effects—such as glass transition, crystallization, melting, evaporation, decomposition, and even

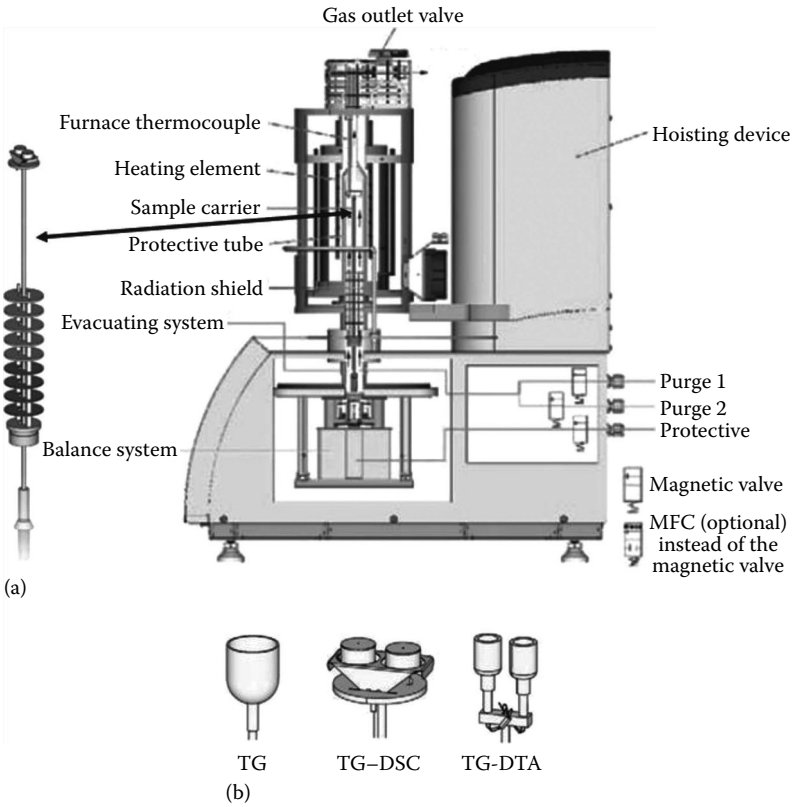

FIGURE 79.5 (a) Schematic diagram of STA 449 Jupiter. In a TG-DSC instrument, heat is transferred to the sample from the oven by the enveloping purge gas, with radiation shields to diminish heat loss by infrared radiation. The entire sample carrier, in (b) showed three different types of sample carriers for the STA 449 Jupiter, is placed on a balance to enable thermogravimetric analysis. (Courtesy of Netzsch GmbH, Selb, Germany.)

oxidation—can be detected. For this, a DSC is again utilized. In the more expensive analysis systems, DSC instruments often offer the possibility of incorporating other techniques. Mass changes due to oxidation and evaporation are detected by thermogravimetry (TG). This is accomplished by placing the entire experimental chamber on a balance that continuously measures the sample mass. These data are available as a function of temperature as well, parallel to the heat data. The DSC inner gas atmosphere is usually refreshed continuously using purge gas. This makes it possible to collect the gases coming from the calorimeter furnace and subject them to further analysis, such as mass spectrometry (MS), gas chromatography (GC), Fourier transform infrared analysis (FTIR), and other analysis methods. With sensitive DSC, it is thus possible to detect almost any structural change in matter as a function of temperature. Figure 79.5 shows a drawing of a combined DSC and TG instrument, capable of analyses up to 2400°C. Radiation shields are required to reduce heat losses by infrared radiation, which is significant at high temperatures.

79.6.1 Biological Analysis from Cells to Entire Human Beings

Calorimetry is not just the measurement of thermal effects in 1 mL samples. Calorimeters receiving entire human beings are available as well. In practice, there is a wide range of application of calorimeters to biology. This is not surprising, since all forms of life produce heat in activity and often also in rest. The

first calorimeters were already used to measure the heat produced by animals. But also, the study of cells (with their heat production of about 1 pW [24]) and the efficiency of enzymatic conversions can be studied using chip calorimetry. Calorimeter chip has also been used for the measurement of thermal conductivity and diffusivity of liquid samples [21–23]; see [24] for an overview and many references. Applications of calorimetry are also found in the food industry, for routine analyses, ecology, plants, etc.

79.6.2 Summary

The applications of thermal analysis are overwhelming in number. In many cases, when wanting to learn more about materials, thermal analysis can add insight. Some applications were mentioned earlier. In Table 79.2, some of the often encountered applications for various disciplines are listed.

TABLE 79.2 Applications of Calorimeters

Area of Interest	Parameter That Can Be Measured with Calorimeters
Material characterization and all other areas listed as follows	Specific heat
	Melting and boiling temperature and behavior
	Fusion and reaction heat and kinetics
	Heat of solution, dilution, mixing, wetting
	Thermal safety
	Glass transition
	Rate and degree of cure
	Crystallization time, temperature, and percentage
	Purity and solid–liquid ratios
	Thermal and oxidative stability
	Identification of multicomponent systems
	Dehydration
Polymers	Effect of the thermomechanical history
	Compatibility tests
	Effects of additives
Pharmaceuticals/cosmetics	Purity and compatibility of active ingredients
	Polymorphism
	Effects of storage and hydrolysis
	Tablet-compression characteristics
	Influence of emulsifiers
	Concentration of medicines in polymers
	Melting and crystallization behavior of waxes
Foods	Melting, solidification behavior, and specific heat of fats and oils
	Polymorphism
	Denaturation of proteins
	Gelatinization of starch
	Freezing–thawing behavior
Biology	Metabolism of cells, organs, animals, and human beings
	Influence of nutrition, toxins, and others on organisms
	Enzymatic efficiency and selectivity
	Concentration of solutions using enzymes or organisms
	Environmental monitoring

79.7 Choosing the Proper Calorimeter for an Application

When faced with a practical analysis problem, one can choose between many instruments. The three main categories are the DSC, the calorimetric bomb or solution calorimeter, and the large reaction or fermentation calorimeter.

79.7.1 What Do You Want to Measure?

If one wants to measure specific heats of reaction, oxidation, solution, etc., at room temperature, a calorimetric bomb or a solution calorimeter might be the first choice. They are accurate and economical. If one wants to optimize a chemical or biological process, reaction calorimeters or fermentation calorimeters might be the choice. In almost all other cases, a DSC will be the most effective instrument. A DSC is especially useful when one wants to obtain the thermal behavior of materials as a function of temperature. In turn, the temperature-dependent behavior of materials can tell a lot about their structure, their properties, and even their thermomechanical history. Important is the scanning range and rate of the DSC. For a sample in the sub-microgram range, chip calorimeters can be used. The chip calorimeters give also new possibilities especially for studying the phase transitions of polymers. Scan rates as fast as 1 kK/s prevent recrystallization of the sample during the scan, and thermal properties of polymers can be studied under the same conditions as during injection molding [25,26]. In some cases, the measurement problem cannot be solved by a standard available calorimeter, and one is forced to either use an experimental calorimeter or develop a special-purpose calorimeter.

79.7.2 Budget and the Need of Pre- and After-Sales Service

A cost-effective DSC will cost about $40,000; the most expensive models can cost up to $150,000 and include thermogravimetric measurement. Calorimetric bombs are somewhat cheaper, starting at $20,000. Finally, one can buy experimental instruments or make one's own system. An adiabatic system consisting of a Dewar in a polystyrene housing, using a commercially available stirrer and platinum resistance (measured with any 5½ digit DMM), will put you in business, although at reduced accuracy. However, the budget for this will not need to exceed much more than about $1000 (excluding the DMM). It is less advisable to make one's own DSC (for cost reasons) or calorimetric bomb (for cost and safety reasons).

79.8 Can the Instrument of Choice Measure the Signals Desired?

Here, various parameters must be considered. Accuracy, the degree to which an instrument reading approaches the true value, lies around a few percent for DSCs and parts of percent for adiabatic calorimeters. Repeatability of the major calorimeter measurement results—such as heat peak area and peak starting temperature—depends, among other things, on such matters as baseline noise/drift, influence of sample preparation, and positioning in the DSC sample site. Resolution should be considered for two parameters: heat and temperature. First, there is the sensitivity of the instrument for generated heat or power, related to its noise. For DSCs, resolution for power is usually around 0.1–10 μW; for bomb calorimeters, resolution for heat is around 0.1–10 J. But there is also the resolution of a DSC for separating two heat pulses at two nearby temperatures. This can be designated as the temperature resolution and depends on time constant and heating rate. Finally, there is the point of linearity and time constant. In case the time constant of the instrument is much larger than that of the process, good linearity is required if one wants to "desmear" the measured curve and obtain the actually produced heat as a function of time. But a current DSC is a very fast instrument, and desmearing is not really necessary anymore. So, linearity is less important for fast DSCs.

79.8.1 Instrument Control and Data Management

Software is becoming more and more important. Since it will control the measurement, its user-friendliness determines how easy and how error-free one can operate the instrument. It also can take care of analysis of the measurement results and graphical and numerical presentation of the results. The software can also take care of quality-control aspects of analysis, such as writing to file all the measurement details (not only what was measured but also how it was measured). Presently, top models of all three types described earlier will perform these functions. With DSC instruments, software can often be used to control all kinds of thermal analysis instruments apart from the DSC, such as TG and DMA, and merge results obtained with DSCs, TG, DMA, and other analysis techniques. This facilitates interpretation of measurements.

TABLE 79.3 Some Commercially Available Calorimeters and Their Specifications

Type	Instrument	Vendor	Cost[a] ($1000)	Range[b] (°C)	Scan Rate[c] (K min^{-1})
Bomb	C 200	IKA	20	25	—
	C 5000	IKA	50	Ambient	—
	C 7000	IKA	46	Ambient	—
Calvet	C 80	Setaram	70	Ambient to 300	2
DSC	Flash DSC	Mettler	75	−95 to 420	2400 000
	DSC 1	Mettler	30	−150 to 700	300
	DSC 200F3	Netzsch	27	−170 to 600	100
	DSC 204F1	Netzsch	40	−180 to 700	200
	DSC 8500	Perkin Elmer	95	−180 to 750	750
	DSC 8000	Perkin Elmer	80	−180 to 750	300
	DSC 6000	Perkin Elmer	45	−180 to 450	100
	DSC 4000	Perkin Elmer	40	−100 to 450	100
	μDSC7evo	Setaram	70	−45 to 120	2
MMC[d]	MMC 274Nexus	Netzsch	55	25 to 500	2

[a] Approximate price of the simplest system without intracooler.
[b] Addition of the widest ranges available.
[c] The highest controlled scan rate (usually for heating).
[d] Multi-module calorimeter.

TABLE 79.4 Companies That Sell Calorimeters

SETARAM Instrumentation, 7, Rue de l'Oratoire, 69300 Caluire, Tel.: +33 (0)4 72 10 25 25, http://www.setaram.com

IKA® Werke GmbH & Co. KG, Janke & Kunkel-Str. 10, D-79219 Staufen, Germany, Tel.: +49 7633 831-0, http://www.ika.net

Mettler-Toledo (Schweiz) GmbH, Im Langacher, Greifensee, CH-8606, Switzerland, Tel.: (41)044 944 45 45, http://www.ch.mt.com

Netzsch Gerätebau GmbH, Wittelsbacherstrasse 42, 95100 Selb, Germany, Tel.: (+49) 9287 881-0, http://www.netzsch-thermal-analysis.com

Parr Instrument Company, 211 53rd St., Moline, IL 61265, Tel.: (309)762-7716, http://www.parrinst.com

Perkin Elmer, 940 Winter Street, Waltham, MA 02451, Tel.: +1 (781) 663-6900, http://www.perkinelmer.com

SII Nano Technology USA Inc., 19865 Nordhoff Street, Northridge, CA 91324, Tel.: +1-818-280-0745, http://www.siint.com

Shimadzu Corp., 1 Nishinokyo-Kuwabaracho, Nakagyo-ku, Kyoto 604-8511, Japan, Tel.: (81)075 823-1111 http://www.shimadzu.co

TA Instruments Inc., 159 Lukens Dr., New Castle, DE 19720, Tel.: (302)427-4005, (302)427-4001 fax, http://www.tainstruments.com

Xensor Integration, 2645 EJ Delfgauw, the Netherlands, Tel.: + 31-15-2578040, http://www.xensor.nl

79.9 Commercially Available Calorimeters

Tables 79.3 and 79.4 describe the different instruments and vendors. Table 79.3 gives an overview of instruments and some characteristics, while Table 79.4 gives vendor information. Tables 79.3 and 79.4 are (necessarily) incomplete since only some of the major vendors have been listed; thus, if looking for a calorimeter, please complete the list with local (and up-to-date) information.

References

1. H.B. Callen, *Thermodynamics and an Introduction to Thermostatistics*, New Delhi, India: Wiley India Pvt. Ltd., 2006.
2. S. Middelhoek and S.A. Audet, *Silicon Sensors*, London, U.K.: Academic Press, 1989.
3. A.W. van Herwaarden, Physical principles of thermal sensors, *Sens. Mater*., 8, 373–387, 1996.
4. W. Hemminger and G.W.H. Höhne, *Calorimetry—Fundamentals and Practice*, Weinheim, Germany: Verlag Chemie, 1984.
5. W. Hemminger, Calorimetric methods. In: V.B.F. Mathot (Ed.), *Calorimetry and Thermal Analysis of Polymers*, Munich, Germany: Hanser Publishers, 1994.
6. K. Allen, F. Hellman, Specific heat of C60 and K3C60 thin films for T = 6–400 K, *Phys. Rev. B* 60, 11765–11772, 1999.
7. K. Allen, F. Hellman, Specific heat of endohedral and higher fullerene thin films, *J. Chem. Phys*. 111, 5291, 1999.
8. A. Minakov, J. Morikawa, T. Hashimoto, H. Huth, C. Schick, Temperature distribution in a thin-film chip utilized for advanced nanocalorimetry, *Meas. Sci. Technol*. 17, 199–207, 2006.
9. A.A. Minakov, S.A. Adamovsky, C. Schick, Non-adiabatic thin-film (chip) nanocalorimetry, *Thermochim. Acta*, 432, 177–185, 2005.
10. S.L. Lai, G. Ramanath, L.H. Allen, P. Infante, and Z. Ma, High-speed (104 OC/S) scanning microcalorimetry with monolayer sensitivity (J/m^2), *Appl. Phys. Lett*., 67, 1229–1231, 1995.
11. S. Zhang, Y. Rabin, Y. Yang, and M. Asheghi, Nanoscale calorimetry using a suspended bridge configuration, *J. Microelectromech. Systems*, 16, 861–871, 2007.
12. A.W. van Herwaarden, P.M. Sarro, J.W. Gardner, and P. Bataillard, Liquid and gas micro-calorimeters for (bio)chemical measurements, *Sens. Actuat.*, A43, 24–30, 1994.
13. E. Van De Kerkhof, Thermoanalytical instrument. Pub. No.: US 2009/0310644 A1, Appl. No.: 12/466,068, Filed: May 14, 2009. Greifensee, CH: Mettler-Toledo AG, December 17, 2009.
14. S. Gaisford, Fast-scan differential scanning calorimetry, *Eur. Pharm. Rev*., 13(4), 2008.
15. K.N. Marsh (Ed.), *Recommended Reference Materials for Realization of Physicochemical Properties*, Oxford, U.K.: Blackwell Scientific, 1987.
16. E. Gmelin and St.M. Sarge, Calibration of differential scanning calorimeters, *Pure Appl. Chem*., 67, 1789–1800, 1995.
17. G.V. Poel, Vincent B.F. Mathot, High-speed/high performance differential scanning calorimetry (HPer DSC): Temperature calibration in the heating and cooling mode and minimization of thermal lag, *Thermochim. Acta* 446, 41–54, 2006.
18. T.M.V.R. de Barros, R.C. Santos, A.C. Fernandes, and M.E. Minas da Piedade, Accuracy and precision of heat capacity measurements using a heat flux differential scanning calorimeter, *Thermochim. Acta*, 269/272, 51–60, 1995.
19. W. Winter, G.W.H. Höhne, Chip-calorimeter for small samples, *Thermochim. Acta*, 403, 43–53, 2003.
20. E. Iervolino, A.W. van Herwaarden, F.G. van Herwaarden, E. van de Kerkhof, P. van Grinsven, A. Leenaers,V.B.F. Mathot, P.M. Sarro, Temperature calibration and electrical characterization of the differential scanning calorimeter chip UFS1 for the Mettler-Toledo Flash DSC 1, *Themochim. Acta*, 512(1), 55–58, 2011.

21. E. Iervolino, A.W. van Herwaarden, P.M. Sarro, Calorimeter chip calibration for thermal characterization of liquid samples, *Thermochim. Acta* 492, 95–100, 2009.
22. T. Adrega, E. Iervolino, A. W. van Herwaarden, P.M. Sarro, Dual-inlet microfluidic calorimeter for thermal characterization of bio-chemical solutions, *Proceedings of the Eurosensors XXIV*, September 5–8, 2010, Linz, Austria.
23. Y. Zhang, S. Tadigadapa, Thermal characterization of liquids and polymer films using a microcalorimeter, *Appl. Phys. Lett*. 86, 034101/1–034101/3, 2005.
24. P. Bataillard, Calorimetric sensing in bioanalytical chemistry: Principles, applications and trends, *Trends Anal. Chem*., 12, 387–394, 1993.
25. V. Brucato, F.G. Crippa, S. Piccarolo, G. Titomanlio, Crystallization of polymer melts under fast cooling I: Nucleated polyamide 6, *Polym. Eng. Sci*., 31(19), 1411–1416, 1991.
26. V. Brucato, F. De Santis, A. Giannattasio, G. Lamberti, G. Titomanlio, Crystallization during fast cooling experiments, a novel apparatus for real time monitoring, *Macromol. Symp*., 185, 181–196, 2002.

Further Information

Much is being published on calorimetry each year. Some very good books to obtain a basic understanding of calorimetry are

Brown, M., *Introduction to Thermal Analysis*, 2nd edn., Dordrecht, the Netherlands: Kluwer, 2001.

Brown, M., Gallagher, P., Handbook of Thermal Analysis and Calorimetry. Vol. 5. Recent Advances, Techniques and Applications, Amsterdam, the Netherlands: Elsevier, 2008.

Haines, P. J., *Principles of Thermal Analysis and Calorimetry*, London, U.K.: Royal Society of Chemistry, 2002.

Hill, J.O. (Ed.), *For Better Thermal Analysis and Calorimetry*, 3rd edn., ICTAC, Vancouver, Canada, 1991.

On DSC, an up-to-date book is: Höhne, G.W.H., Hemminger, W., and Flammersheim, H.-J., *Differential Scanning Calorimetry*, 2nd edn. Berlin, Germany: Springer-Verlag, 2003.

Mathot, V.B.F. (Ed.), *Calorimetry and Thermal Analysis of Polymers*, Munich, Germany: Hanser Publishers, 1994.

Wunderlich, B., *Thermal Analysis of Polymeric Materials*, Berlin, Germany: Springer, 2005.

Apart from these, many relevant papers appear in: *Thermochimica Acta*, Elsevier Science Publishers; *Journal of Thermal Analysis and Calorimetry*, Springer.

Leafing through the latest volumes will bring one up to date on calorimetry research. Regular conferences on calorimetry and thermal analysis are being held, organized by local and global institutes such as ICTAC (International Confederation on Thermal Analysis and Calorimetry), ESTAC (European Symposium on Thermal Analysis and Calorimetry), and NATAS (North American Thermal Analysis Society). Proceedings of these conferences are often published in *Thermochimica Acta* or the *Journal of Thermal Analysis*.

Very interesting is the publication of ICTA from 1991, which contains significant information on nomenclature, literature, suppliers of instrumentation, etc.

VIII

Radiation

80

Radioactivity Measurement

Bert M. Coursey
National Institute of Standards and Technology

80.1 Radioactivity

Radioactivity is the phenomenon of emissions of neutral or charged particles or electromagnetic radiations from unstable atomic nuclei. The more common types of radiations are listed in Table 80.1. Several naturally occurring (primordial) radionuclides and some produced by cosmic rays in the Earth's atmosphere are given in Table 80.2. Methods of producing other unstable nuclei are discussed as follows. Radioactive isotopes from man-made sources and from naturally occurring nuclides are widely used in health sciences, industry, and academic research.

Radioactivity was first discovered by Henri Becquerel in 1896. His student Marie Curie and her husband Pierre Curie were the first to chemically separate the radioactive elements polonium and radium. Becquerel and the Curies received the Nobel Prize in physics in 1903 for their pioneering work in nuclear and radiochemistry. The historical development of the field of radioactivity is covered in a number of standard texts, including *The Atomic Nucleus* [1] and *Radioactivity and Its Measurement* [2] and in *Radioactivity Measurements: Principles and Practice* [3]. Other excellent texts are available for students in nuclear medicine [4], in radiochemistry and nuclear chemistry [5,6], in nuclear and particle physics [7,8], and a popular general textbook *Radiation Detection and Measurement* by Knoll [9] for nuclear engineering and health physics.

Radioactivity is defined by the International Commission on Radiation Units and Measurements [10] in terms of the *activity*, A, of an amount of a radionuclide in a particular energy state at a given time. Mathematically, it is defined as the quotient of dN by dt, where dN is the number of spontaneous nuclear transformations from that energy state in the time interval dt; thus,

$$A = \frac{dN}{dt} \tag{80.1}$$

TABLE 80.1 Characteristics of Nuclear Radiations

Type	Origin	Process	Charge	Mass (MeV)	Spectrum (Energy)
α-Particles	Nucleus	Nuclear decay or reaction	+2	3727.33	Discrete (MeV)
β^--Rays (negatrons)	Nucleus	Nuclear decay	−1	0.511	Continuous (keV-MeV)
β^+-Rays (positrons)	Nuclear	Nuclear decay	+1	0.511	Continuous (keV-MeV)
γ-Rays	Nucleus	Nuclear de-excitation	0	0	Discrete [keV-MeV]
X-rays	Orbital electrons	Atomic de-excitation	0	0	Discrete (eV-keV)
Internal conversion electrons	Orbital electrons	Nuclear de-excitation	−1	0.511	Discrete (high keV)
Auger electrons	Orbital electrons	Atomic de-excitation	−1	0.511	Discrete (eV-keV)
Neutrons	Nucleus	Nuclear reaction	0	939.57	Continuous or discrete (keV-MeV)
Fission fragments	Nucleus	Fission	≅20	80–160	Continuous (bimodal) 30–150 MeV

Source: Leo, W.R., *Techniques for Nuclear and Particle Physics Experiments*, Springer-Verlag, Berlin, Germany, 1992.

TABLE 80.2 Some Cosmogenic and Naturally Occurring Radionuclides

Radionuclide	Half-Life
^{3}H	12.35 years
^{7}Be	53.3 days
^{14}C	5730 years
^{40}K	1.28×10^{9} years
^{232}Th	1.405×10^{10} years
^{235}U	7.04×10^{8} years
^{238}U	4.47×10^{9} years

The unit of activity in the International System (SI) of units is the becquerel (Bq), which is equal to the unit reciprocal second (s^{-1}). In many fields, the older unit, the curie (Ci), is still in use, where 1 Ci = 3.7×10^{10} Bq (exactly).

The activity of an amount of radionuclide is given by the product of the decay constant, λ, and the number of nuclei present at time t; thus,

$$A = \lambda N \tag{80.2}$$

The reciprocal of λ is the mean life of the nuclide. More commonly, one computes the time necessary for one-half of the nuclei to decay, and since this is an exponential process, the half-life is given by

$$T_{1/2} = \frac{\text{In2}}{\lambda} = \frac{0.69315}{\lambda} \tag{80.3}$$

The activity at any time t can be computed using the initial activity A_0 and the decay time t according to

$$A = A_0 \exp\left(-0.69315 \frac{t}{T_{1/2}}\right) \tag{80.4}$$

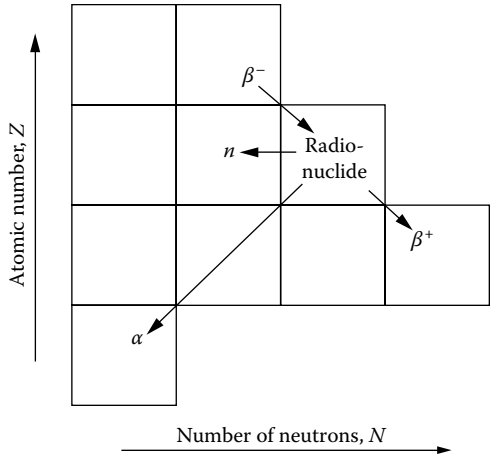

FIGURE 80.1 Characteristics of nuclear radiations. (From Leo, W.R., *Techniques for Nuclear and Particle Physics Experiments*, Springer-Verlag, Berlin, Germany, 1992.)

The term *specific activity* is in use in several applied fields, and one should be careful to look at the units in any particular application. It is normally defined in terms of the amount of activity per unit mass of the element. For example, the nominal activity of ^{14}C in modern carbon (which is found in the biosphere) is 0.3 Bq g^{-1}. In nuclear medicine, however, specific activity is widely used to express the amount of activity per unit quantity of the radioactively labeled compound. For example, one might produce ^{11}C in a cyclotron and oxidize it to carbon monoxide CO with a specific activity of 1 MBq ^{11}C μmol^{-1} (CO) (megabecquerel of activity per micromole of substance).

Stable nuclei are those nuclei in their ground state that have a proper number of neutrons and protons to balance the nuclear forces between constituents and thus do not decay spontaneously. Radioactive nuclei may be divided into three categories:

1. Those that have an excess of neutrons over protons
2. Those that are neutron deficient
3. Those that are in excited nuclear states

A schematic showing the most prominent simple transformations between elements of atomic number Z and neutron number N is given in Figure 80.1. The atomic number Z is the number of protons, and the isotopic mass number A is the total number of nucleons (protons plus neutrons). The notation for an isotope—for example, one of krypton—is ${}^{A}_{Z}\mathrm{Kr}$. In this chapter, isotopes will be identified only by the mass number and the element symbol, for example, ^{241}Am.

80.2 Particle Emission Radioactivity

80.2.1 Alpha Particles

Alpha particles are ^{4}He nuclei (two protons plus two neutrons) and are usually emitted by heavy nuclei ($A > 150$). Alpha particles are monoenergetic and usually have energies between 4 and 6 MeV. Table 80.3 lists several alpha emitters, including some at lower and higher energies that can be used for the energy calibration of instruments. Alpha particles carry a +2 charge, and their detection with a variety of instruments is described in detail in Chapter 82. Alpha-particle pulse-height distributions for several radionuclides of interest in the nuclear fuel cycle are shown in Figure 80.2. The alpha-particle pulse-height distribution for an ^{241}Am source obtained with a high-resolution detector is given in Figure 81.16.

TABLE 80.3 Alpha-Particle-Emitting Radionuclides

Radionuclide	Half-Life	Energies (MeV)
^{148}Gd	90 years	3.183
^{241}Am	432.2 years	5.486, 5.443
^{210}Po	138 days	5.305
^{242}Cm	163 days	6.113, 6.070

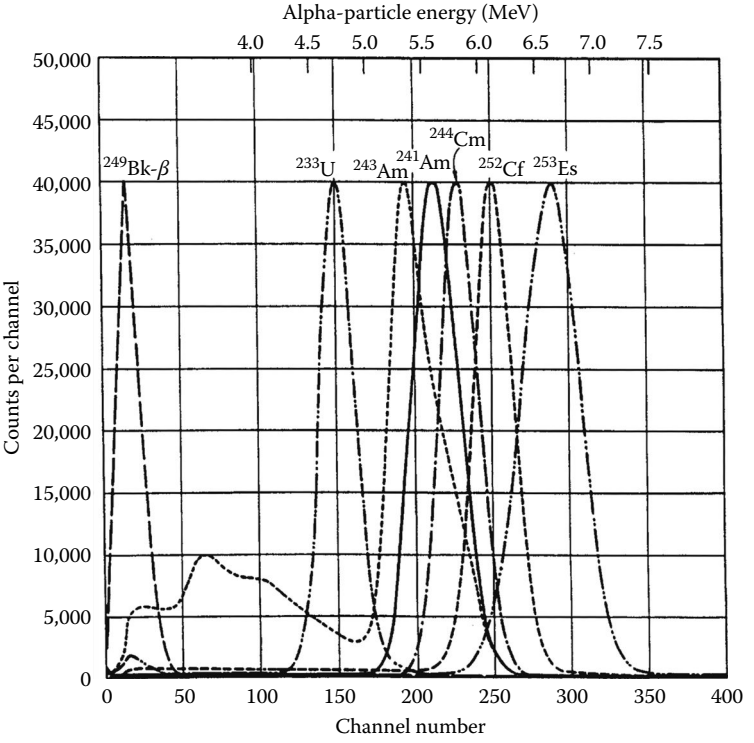

FIGURE 80.2 Liquid-scintillation spectra of selected actinides using a single-phototube detector with the peak channel counts for each major peak preset to 40,000 counts. (From McDowell, W.J., Liquid scintillation counting techniques for the higher actinides, in *Organic Scintillators and Liquid Scintillation Counting*, Horrocks, D.L. and Peng, C.T. (eds.), p. 937, Academic Press, New York, 1971.)

80.2.2 Beta Particles

Beta particles are high-energy electrons emitted by the nucleus as a result of the "weak force" interactions in nuclei that contain too many or too few neutrons. For a system with excess neutrons, the neutron is transformed into a proton, and in the process, an electron and an antineutrino $\overline{\nu}$ are emitted:

$$n \rightarrow p + e^{-} + \overline{\nu} \tag{80.5}$$

The proton remains behind in the nucleus. The antineutrino is required to maintain the conservation of momentum, energy, and "weak-interaction" quantum numbers with respect to the emitted electron [5]. The emitted negatively charged beta particles, usually denoted as β^{-}, have a continuum of energies from zero to a maximum energy denoted by $E_{\beta\max}$. $E_{\beta\max}$ is the total energy available for the kinetic energy of the electron. The antineutrino carries away that portion not transferred to the electron. An example of

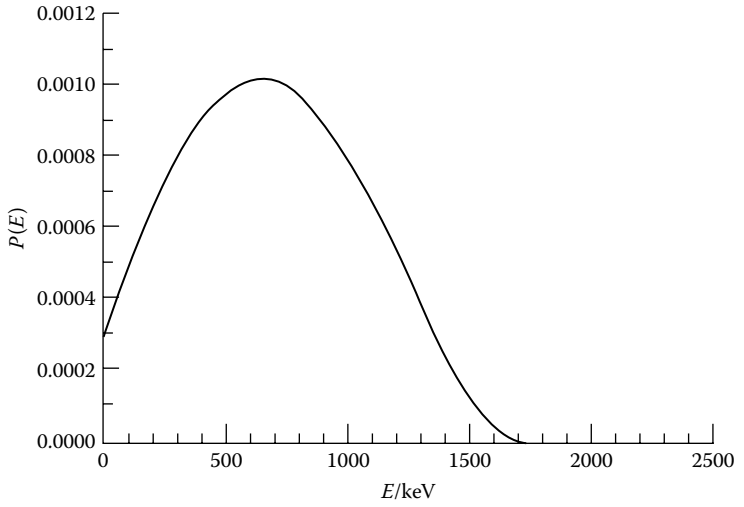

FIGURE 80.3 Theoretical distribution of beta particles as a function of energy for ^{32}P. (From Collé, R., NIST, private communication, 1997.)

an emission spectrum for ^{32}P is given in Figure 80.3. The mode of decay for neutron-deficient nuclei is quite similar, except that the proton is converted to a neutron with the emission of a positive electron or *positron* (β^+) and a neutrino, which may be written as

$$p \rightarrow n + e^+ + \nu \tag{80.6}$$

Although it is unusual, some radioisotopes decay by both negatron β^- and positron β^+ emission. For example, in the decay of the 13 day half-life ^{126}I, one has

$$^{126}\mathrm{I} \rightarrow {}^{126}\mathrm{Te} + \mathrm{e}^+ + \nu \tag{80.7}$$

$$^{126}\mathrm{I} \rightarrow {}^{126}\mathrm{Xe} + \mathrm{e}^- + \bar{\nu} \tag{80.8}$$

Table 80.4 gives a short list of pure-beta-particle emitters.

80.2.3 Neutrons

Neutrons are constituents of the nucleus that have a mass number of unity and carry no charge. In normal radioactive decay processes, neutrons are not emitted from the nucleus. With energies exceeding a few million electron volts (MeVs), however, one can add sufficient energy to cause a neutron to be ejected from the nucleus. These energies can be attained by bombardment with alpha particles from radioactive decay, which is the basis for the common neutron source americium–beryllium (AmBe) in which the alpha particles from the ^{241}Am induce neutron emission from the ^{9}Be nucleus:

$$^{241}\mathrm{Am} \rightarrow {}^{237}\mathrm{Np} + \alpha \tag{80.9}$$

$$\alpha + {}^{9}\mathrm{Be} \rightarrow {}^{13}\mathrm{C}^{*} \text{ (excited state)} \tag{80.10}$$

$$^{13}\mathrm{C}^{*} \rightarrow \begin{cases} {}^{12}\mathrm{C}^{*} + n \\ {}^{8}\mathrm{Be} + \alpha + n \\ 3\alpha + n \end{cases} \tag{80.11}$$

TABLE 80.4 Pure-Beta-Particle-Emitting Radionuclides

Radionuclide	Half-Life	Maximum Energy (keV)	Average Energy (keV)
Negatron (β^-) Emitters			
^{3}H	12.35 years	18.6	5.69
^{14}C	5730.0 years	156.5	49.5
^{32}p	14.29 days	1710	695
^{33}P	25.34 days	249	77
^{35}s	87.44 days	167	49
^{89}Sr	50.5 days	1492	583
^{90}Sr	28.5 years	546	196
^{90}Y	64.0 h	2283	934
Positron (β^+) Emitters[a]			
^{11}C	20.38 min	960	386
^{18}F	109.71 min	633	250
^{22}Na	2.602 years	545	216

[a] These nuclides exhibit a small amount of EC decay.

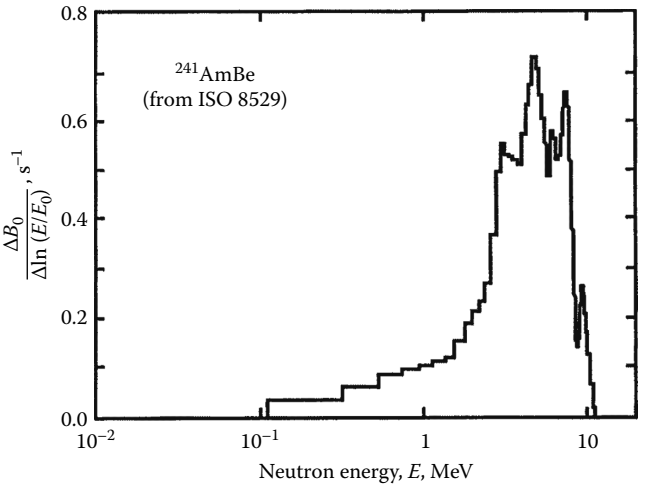

FIGURE 80.4 Neutron spectrum of an ^{241}AmBe radioisotopic source as given in the American National Standard [13] and the International Standard [14]. The units used on the *y*-axis are explained in Ref. [13].

In this case, the ^{13}C nucleus is formed in a highly unstable excited state and rapidly disintegrates by several processes, all of which lead to neutron emission. The neutron spectrum from a ^{241}AmBe source is shown in Figure 80.4. It is very difficult to measure neutron spectra directly because it is necessary to deconvolve a complicated detector response. Figure 80.4 is the "standard" spectral shape recommended in recent national and international standards [13,14]. The units on the *y*-axis are explained in Ref. [13].

Neutrons are also readily produced in high-energy particle accelerators. Various combinations of accelerated particles and target materials are used to produce neutron beams with selected energies (e.g., 2 and 14 MeV). Neutrons from isotopic sources, accelerators, and nuclear reactors can then be used in such applications as boron neutron capture therapy to treat cancer or in metal fatigue analysis. The neutrons can also be used to produce radionuclides for other applications.

80.2.4 Protons

Protons with unit positive charge and unit mass number are simply ^{1}H nuclei stripped of the single orbital electron. Spontaneous emission of protons by nuclei is an exotic decay mode that has been observed in only a few cases involving extremely neutron-deficient nuclei [15]. However, beams of protons can be made in positive-ion, charged particle accelerators by injecting high-purity hydrogen gas, stripping the electrons, and then accelerating the protons to high energies. When these protons are incident on stable target nuclei, a variety of nuclear reactions are possible. The product nuclides are normally radioactive and neutron deficient.

80.2.5 Fission Fragments

Fission fragments are the large-mass debris formed when a high-Z nuclide such as ^{235}U spontaneously (or by absorption of a slow neutron) breaks up into two or more smaller nuclides in a process known as nuclear fission. The best-known fissionable nuclei are ^{235} U and ^{239}Pu. Their fission is a result of capturing neutrons. For a given nucleus, the fission fragments are distributed according to a mass distribution that has two maxima. For ^{235}U fission, the maxima occur at $A = 90$ and 130, resulting in fission-product radionuclides such as ^{90}Sr, ^{95}Zr, ^{131}I, and ^{137}Cs. A small number of high-Z radionuclides decay by spontaneous fission (e.g., ^{248}Cm). This decay process usually competes with alpha-particle decay and is mostly limited to high-Z nuclides.

80.3 Electromagnetic Emission Radioactivity

80.3.1 Gamma Rays

Gamma rays are photons emitted during nuclear de-excitation processes. These gamma-ray transitions may be from a metastable excited state or between levels in a daughter nucleus. Two examples are shown in Figure 80.5 for the 6 h half-life ^{99m}Tc and the 2 day ^{111}In. The large majority of gamma rays from fission products and man-made radionuclides have energies between 20 keV and 2 MeV. A list of gamma-ray emitters used for instrument calibrations is given in Table 80.5. The probability of gamma-ray emission in a particular radionuclide decay (P_γ) is also given in the table. The rate of gamma-ray emission is given by the product $P_\gamma A_0$.

80.3.2 X-Rays

Characteristic x-rays are photons emitted during atomic relaxation processes. X-rays are emitted from radionuclides when electrons are involved in the high-energy processes in the nucleus. In the *electron-capture* (EC) process, for example, the nucleus captures an electron (usually a K-shell electron, since it is closest to the nucleus), and a proton and an electron form a neutron. This process leaves a K-shell vacancy, and a characteristic x-ray from the daughter nucleus can be emitted as orbital electrons from higher shells fill the vacancy. An example is the decay of the 2.6 year half-life ^{55}Fe

$$^{55}\mathrm{Fe} + e^{-} \rightarrow {}^{55}\mathrm{Mn} + \mathrm{X} \tag{80.12}$$

The rate of Mn K x-ray emission from an ^{55}Fe source of activity A_0 is

$$N_{\mathrm{K}} = P_{\mathrm{KX}} A_0 \tag{80.13}$$

where P_{KX} = probability of K x-ray emission.

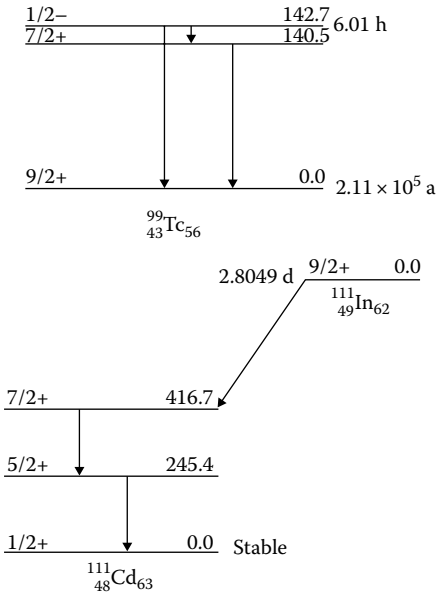

FIGURE 80.5 Simplified nuclear decay schemes for the radionuclides ^{99m}Tc and ^{111}In. The vertical arrows indicate transitions between nuclear excited states. Gamma-ray emission competes with internal conversion processes for each transition. (From Leo, W.R., *Techniques for Nuclear and Particle Physics Experiments*, Springer-Verlag, Berlin, Germany, 1992.)

TABLE 80.5 Gamma-Ray-Emitting Radionuclides Used for Detector Efficiency Calibrations

Radionuclide	Half-Life (Days)	Energy (keV)	Gamma Rays per Decay, P_γ
^{109}Cd	462.6	88	0.0363 ± 0.0002
^{57}Co	271.79	122	0.8593 ± 0.0027
^{139}Ce	137.64	166	0.7987 ± 0.0006
^{203}Hg	46.595	279	0.8148 ± 0.0008
^{113}Sn	115.09	392	0.6489 ± 0.0013
^{85}Sr	64.849	514	0.984 ± 0.004
^{137}Cs	1.102×10^4	662	0.851 ± 0.002
^{88}Y	106.63	898	0.940 ± 0.003
^{60}Co	1925.5	1173	0.9990 ± 0.0002
^{60}Co	1925.5	1332	0.99983 ± 0.00001
^{88}Y	106.63	1836	0.9936 ± 0.0003

80.3.3 Conversion Electrons

Conversion electrons are monoenergetic electrons emitted from the nucleus in isomeric transitions between nuclear levels. Conversion-electron emission competes with gamma-ray emission as a mode of nuclear de-excitation.

80.4 Interactions with Matter

Before examining in detail the manner in which ionizing radiations can interact, consider two sources of photon radiations, annihilation radiation and bremsstrahlung, which are associated with radioactive decay but depend on the material in which the decay process occurs.

80.4.1 Annihilation Radiation

Annihilation radiation is a form of photon radiation associated with a class of radioactive decays. Positrons, since they are the antiparticles of ordinary electrons, cannot survive long in normal matter. Thus, positrons emitted during radioactive decay will slow down in matter until they reach thermal equilibrium. (Depending on the material, they may exist for some microseconds in a state of matter known as positronium.) Ultimately, they combine with an electron in an annihilation event in which their combined mass (1.022 MeV) is converted to energy. This takes the form of two annihilation quanta of 0.511 MeV each, which are oppositely directed (to ensure the conservation of momentum). Depending on the positron energy and the density and thickness of the stopping material, there is a slight but calculable probability of *annihilation in flight* [1]. These decays do not result in characteristic 0.511 keV quanta.

80.4.2 Bremsstrahlung

Bremsstrahlung is the photon radiation emitted by the deceleration of an electron in the Coulomb field of an atom. Thus, bremsstrahlung radiation is present during all beta decay processes as the emitted β-particles (both negatrons and positrons) slow down in matter; it has a continuum of photon energies extending up to the maximum beta-particle energy. The shape of this continuum depends on the nature of the stopping material, as is described in the following section. Bremsstrahlung radiation represents a particular safety hazard for high-energy pure-beta-particle emitters such as ^{32}P (14.4 day, 1.710 MeV β^- max). At higher energies, bremsstrahlung production is almost linear in electron energy and proportional to Z^2 of the stopping material. Thus, to minimize bremsstrahlung, one uses low-Z shielding materials such as plastic.

Now, consider the more general ways in which ionizing radiations from radioactive decay interact with matter. They interact by collisions with the electrons and nuclei along their path. The nature of these interactions is characterized by the charge, mass, and energy of the incident ionizing photon or particle, as well as the charge and mass of the traversed matter. In the energy region of interest, electromagnetic radiation (gamma-ray and x-ray photons) interacts with matter principally by three processes: photoelectric absorption, Compton scattering, and pair production. In the photoelectric process, which dominates at lower energies, the photon transfers its energy to an atomic electron, which is then ejected from the atom with an energy equal to that of the incident photon minus the electron's binding energy. In Compton scattering (incoherent scattering), the photon loses a fraction of its energy to an atomic electron, and the scattered photon emerges generally in a direction different from that of the incident photon. Higher-energy photons will undergo multiple Compton scatter events until the process is finally terminated by a photoelectric absorption. For photons with energies exceeding 1.022 MeV, the process of pair production can occur whereby an electron–positron pair is formed. The positron produced will ultimately annihilate with the production of two 0.511 MeV photons (or in flight). The three interaction processes compete as a function of photon energy, electron density, and nuclear charge of the stopping material. Above 2.044 MeV, triplet production can occur [16], but this is a low-probability process, and few radionuclides emit gamma rays above 2 MeV.

Quantitative measures of the photon interactions in matter are attenuation coefficients based on cross sections for specific interactions [8,9]. The total narrow-beam attenuation coefficient μ is given by the sum

$$\mu = \mu_{\text{photoelectric}} + \mu_{\text{Compton}} + \mu_{\text{pair production}}$$

The attenuation process for a beam of photons traversing a slab of matter is an exponential function of the form

$$I = I_0 \exp(-\mu l) \tag{80.14}$$

where

I and I_0 are the intensities of the transmitted beam and the incident beam, respectively
l is the distance traveled in matter
μ is the linear attenuation coefficient

A useful procedure is to express distances in terms of the mass thickness—the product of density ρ and thickness l. The beam transmission equation can then be rewritten as

$$I = I_0 \exp\left[\frac{-\mu}{\rho}\right](\rho l) \tag{80.15}$$

where μ/ρ is the *mass attenuation coefficient*. The mass attenuation coefficient, in contrast to the linear attenuation coefficient, does not depend on the density of the absorber, but only on its composition. The mass attenuation coefficient as a function of energy for water and lead is shown in Figures 80.6 and 80.7. This discussion of photon interactions has been limited to narrow-beam (or ideal) geometries.

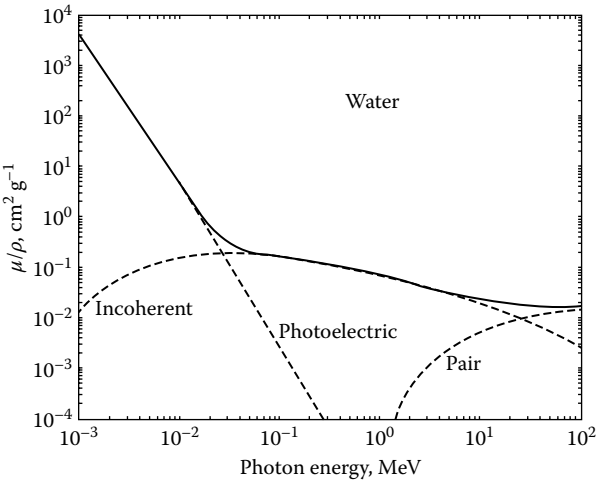

FIGURE 80.6 Narrow-beam mass attenuation coefficients for water as a function of photon energy. (From Seltzer, S.M., *Radiat. Res.*, 136, 147, 1993.)

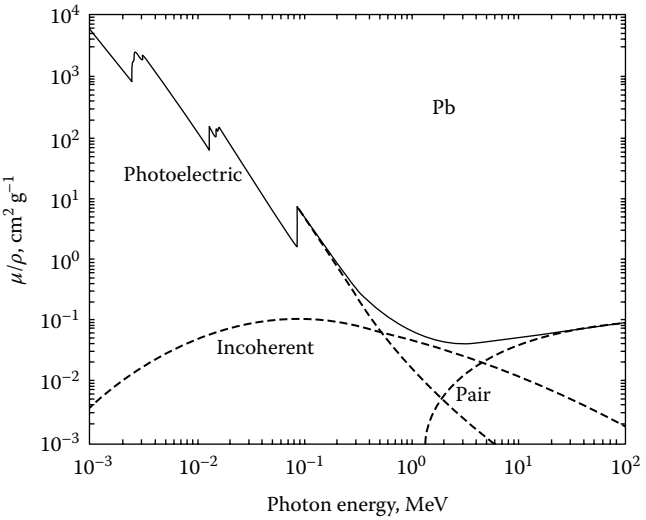

FIGURE 80.7 Narrow-beam mass attenuation coefficients for lead as a function of photon energy. (From Seltzer, S.M., *Radiat. Res.*, 136, 147, 1993.)

In practice, most radioactive sources emit a broad beam of radiation such that the detector registers not only events from the incident beam but also those scattered through large angles, and these effects must be included in computing detector response [9].

Charged particles interact with matter in many different ways. These include

1. Inelastic collisions involving ionization and excitation of atomic electrons of the material
2. Inelastic collisions involving bremsstrahlung production in the field of the atom
3. Elastic scattering in the field of the atom
4. Nuclear reactions
5. Emission of Cherenkov radiation (photons in the visible and ultraviolet regions)

Electrons and positrons, due to their much smaller mass, behave differently from protons, alpha particles, and low-Z charged particles. Two quantitative parameters used to describe inelastic interactions of charged particles as they slow down in matter are *stopping power* and *range*. The total mass stopping power, S/ρ, is defined by the ICRU [10] as the quotient of dE by ρdl, where dE is the energy lost by a charged particle in traversing a distance dl in the material of density ρ. For energies for which the nuclear interactions can be neglected, the total mass stopping power can be represented as the sum of an electronic (ionization and excitation) term and a radiative (bremsstrahlung) term as follows:

$$\frac{S}{\rho} = \frac{1}{\rho}\left(\frac{dE}{dl}\right)_{\text{elec}} + \frac{1}{\rho}\left(\frac{dE}{dl}\right)_{\text{rad}} \tag{80.16}$$

Figure 80.8 illustrates the contributions of the electronic term and the radiative term to the total mass stopping power for electrons in lead and water over the energy range from 10^{-2}–10^{3} MeV. For alpha particles, the radiative term can be neglected, but the nuclear interactions cannot. The nuclear interactions are pronounced at lower energies, while at higher energies, the inelastic collision process dominates. This is illustrated in Figure 80.9 for alpha-particle interactions in lead and water.

The range of a charged particle of a given energy in a material is an important parameter in designing detectors and shielding materials. In general, a charged particle does not travel in a

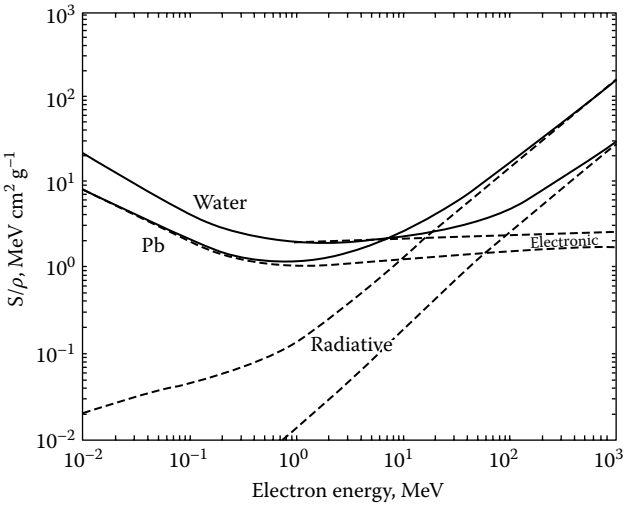

FIGURE 80.8 Stopping power for electrons in water and lead as a function of electron energy. (From ICRU, Stopping powers for electrons and positrons, Report 37, International Commission on Radiation Units and Measurements, ICRU/NCRP Publications, Bethesda, MD, 1984.)

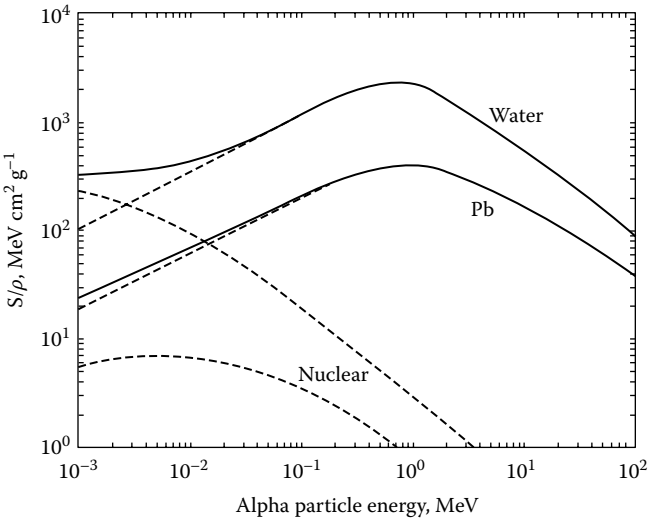

FIGURE 80.9 Stopping power for alpha particles in water and lead as a function of alpha-particle energy. (From ICRU, Stopping powers and ranges for alpha particles and protons, Report 49, International Commission on Radiation Units and Measurements, ICRU/NCRP Publications, Bethesda, MD, 1993.)

straight line as it slows down. However, the total rectified path length traveled by the charged particle, called the mean range, is given by

$$r_0 = \int_0^E \frac{\rho}{S} dE \tag{80.17}$$

where E is the incident electron energy. The range as given in Equation 80.17 has units of g cm^{-2}. Range in water and lead as a function of incident particle energy for electrons and for alpha particles is given in Figures 80.10 and 80.11, respectively.

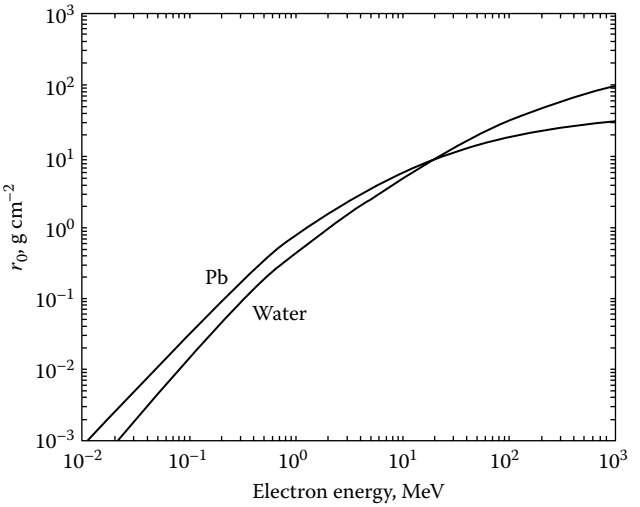

FIGURE 80.10 Range–energy curves for electrons in water and lead. (From ICRU, Stopping powers for electrons and positrons, Report 37, International Commission on Radiation Units and Measurements, ICRU/NCRP Publications, Bethesda, MD, 1984.)

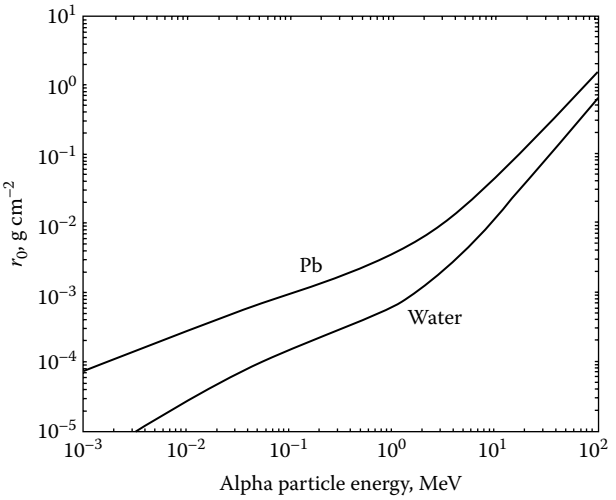

FIGURE 80.11 Range–energy curve for alpha particles in water and lead. (From ICRU, Stopping powers and ranges for alpha particles and protons, Report 49, International Commission on Radiation Units and Measurements, ICRU/NCRP Publications, Bethesda, MD, 1993.)

80.5 Neutron Interactions

Since neutrons are uncharged, they can travel some distance in matter before they interact. This interaction is normally a "nuclear reaction" in which the neutron is absorbed or scattered or produces a nuclear reaction. The probability of each of these interactions occurring is described by the capture, scatter, and nuclear reaction cross sections. Secondary particles produced by neutrons are usually high-energy charged particles that are stopped in short distances in the stopping material. Neutrons from nuclear reactions normally start with energies of a few MeV. They are moderated by collisions with atomic nuclei until they experience a capture process. Capture cross sections for a given elemental stopping material exhibit resonances characteristic of specific nuclear excited states. The total neutron cross section of carbon as a function of neutron energy is shown in Figure 80.12 [20]. The structure in the cross section

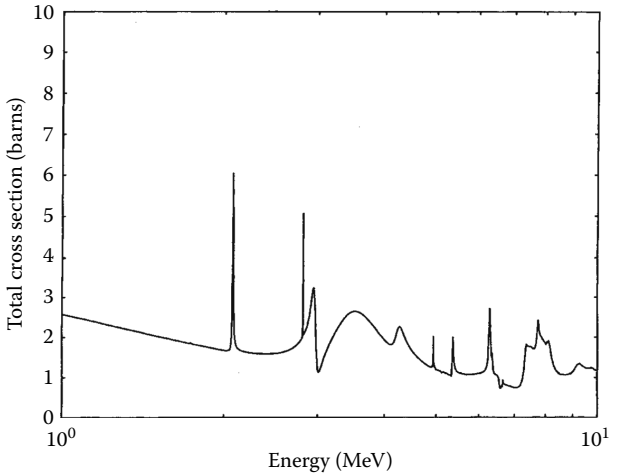

FIGURE 80.12 Total neutron cross section for carbon as a function of neutron energy. The *barn* is the traditional unit of area used to describe neutron cross sections (1 *barn* = 10^{-28}m^2). (From Rose, P.F., ENDF-201, ENDF/B-VI summary documentation, BNL-NCS-17541, 4th edn., Brookhaven National Laboratory, Upton, NY, 1991.)

is the result of resonances in the compound nucleus formed by neutron interaction with ^{12}C. The intensity of a neutron beam in an absorber will decrease exponentially (analogous to a photon beam) with absorber thickness. The attenuation coefficient will include the scatter and capture components.

80.6 Radioactivity Measurements

Measurements of electromagnetic radiations and charged particles are discussed in various chapters, particularly in Chapter 81. However, there are certain classes of instruments that are widely used for the measurement of radioactivity. Three examples will be dealt with here: alpha- and beta-particle liquid-scintillation spectrometers, high-purity germanium (HPGe) gamma-ray spectrometers, and gamma-ray dose calibrators.

Most liquid-scintillation spectrometers operate with two phototubes that view a cylindrical vial containing the radionuclide intimately mixed with an organic liquid scintillator [21,22]. The radiations emitted during radioactive decay interact in the scintillator to produce light pulses that strike the photocathodes of the phototubes. The magnitude of the light pulse depends on the energy deposited by the radiation and on chemical and optical quenching processes [21]. The scintillation yield for high-energy electrons (low dE/dx) for the best organic scintillators does not exceed 5%. That is, 5% of the deposited energy is emitted as photons in the near ultraviolet (~400 nm wavelength), and the remaining 95% is lost to radiationless transitions in the organic molecules. In real samples, this photon yield is reduced further through chemical processes (electron scavengers) and optical losses (colored samples, mismatches at vial interfaces, etc.). The counting efficiency for the two phototubes in coincidence is defined as the ratio of the counting rate to the activity. The counting efficiency approaches unity for beta particles with energies exceeding 20 keV [23]. For alpha particles, the efficiency is essentially unity (although the magnitude of the light pulse for alpha particles is less than that for beta particles due to the nature of the interactions of the particles with the organic scintillator). The counting systems are calibrated using standard solutions of known activity [22]. Since the pulse height is largely proportional to the energy of the incident particle, the signal from the counting system can be sorted according to pulse height in a multichannel analyzer (MCA). The pulse-height spectra for a mixture of alpha-particle emitters are shown in Figure 80.13 [24]. In practice, one obtains the area

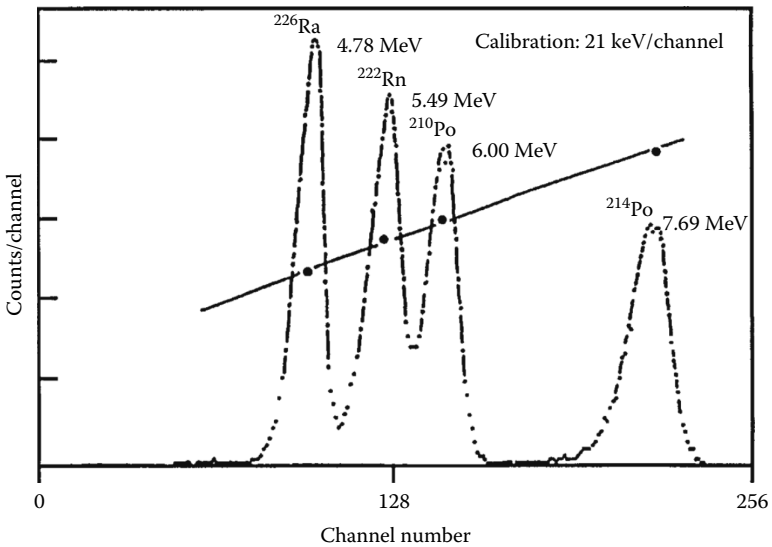

FIGURE 80.13 Liquid-scintillation spectrum of mixture of alpha-particle-emitting radionuclides. (From McDowell, W.J., *Radioact. Radiochem.*, 3(2), 26, 1992.)

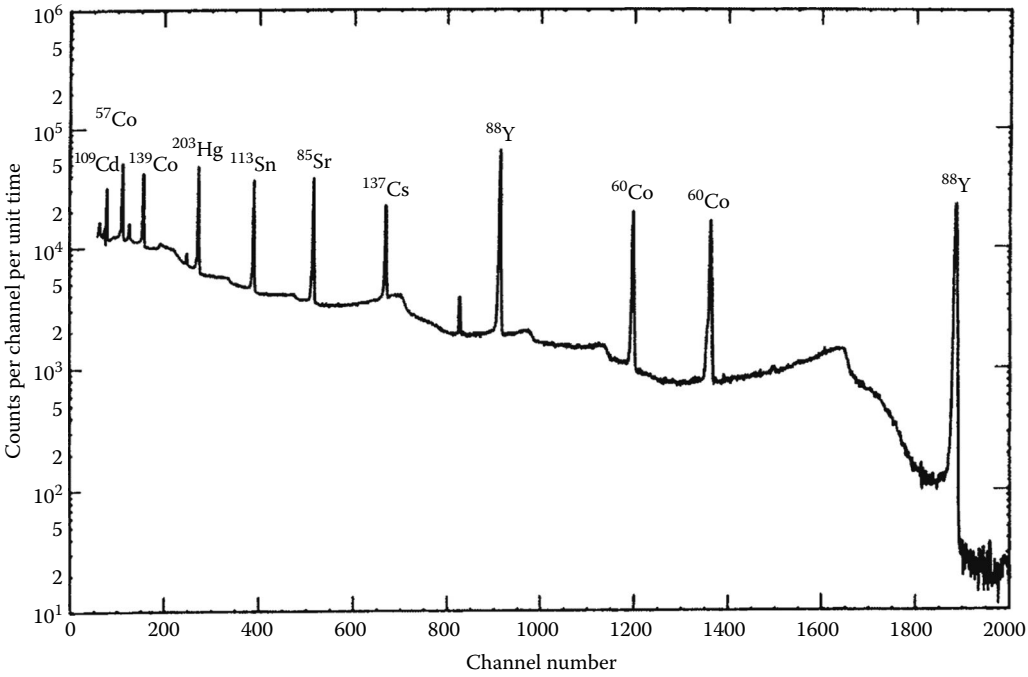

FIGURE 80.14 Gamma-ray spectrum for a solution standard of mixed radionuclides obtained with a Ge(Li) semiconductor detector. (From Mann, W.B. (ed.), *A Handbook of Radioactivity Measurements Procedures*, Report No. 58, 2nd edn., National Council on Radiation Protection and Measurements, NCRP Publications, Bethesda, MD, 1985.)

under the peak for a given radionuclide and divides by time to get the counting rate N_α. The activity A_0 is given by N_α/ε_c, where ε_c is the coincidence counting efficiency.

The activity of mixtures of gamma-ray emitters is needed at many stages in the nuclear fuel cycle. For example, in measurements of environmental radioactivity, a gamma-ray spectrometer allows rapid determination of many fission and activation product nuclides in the presence of naturally occurring radioactivity. Both NaI(Tl) scintillation detectors and HPGe semiconductors are used for this purpose, and their design and operation are covered in Chapter 81. Gamma-ray spectra for a mixture of radionuclides with a semiconductor detector are shown in Figure 80.14 [22]. The detectors are calibrated using radioactivity standard sources prepared by the National Institute of Standards and Technology or one of the commercial secondary standards suppliers. A photopeak efficiency curve for a HPGe detector is shown in Figure 80.15.

Single radionuclides are widely used in many applications in health sciences. In nuclear medicine, most samples are assayed in reentrant dose calibrators, which are essentially ionization chambers. In this counting geometry, the sample is placed inside a well detector that is normally a sealed, pressurized argon gas, ionization chamber (see, e.g., Figure 80.16). The photons emitted from the sample traverse the inner wall of the chamber and cause ionization events in the counting gas. The chambers typically operate at a few atmospheres pressure at a bias voltage of 600–1000 V. The charge created is subsequently collected at the anode. These chambers are designed to assay large amounts of activity such that the current from the device in picoamperes is proportional to the activity in megabecquerels. For a given radionuclide, the manufacturer can establish calibration factors for specific radionuclides in order to convert the current response of the chamber to a unit activity (pA MBq^{-1}). A dose-calibrator response curve for gamma-ray emitters is shown in Figure 80.17 [26].

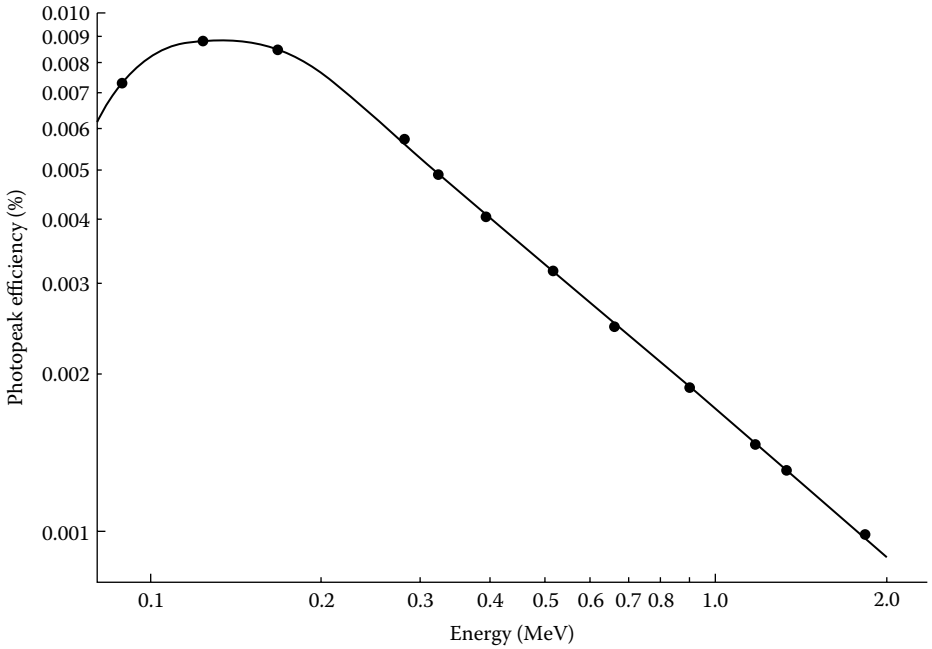

FIGURE 80.15 Photopeak efficiency as a function of energy for a 90 cm^3 HPGe detector for a mixed radionuclide gamma-ray standard of the type listed in Table 80.5. A 5 mL solution source was positioned at 10 cm from the side of a *p*-type semiconductor. (From Cessna, J., NIST, private communication, 1997.)

FIGURE 80.16 A well-type ionization chamber used for the assay of single radionuclides in nuclear medicine. (From Dell, M.A., Capintec, instruments, private communication, 1997.)

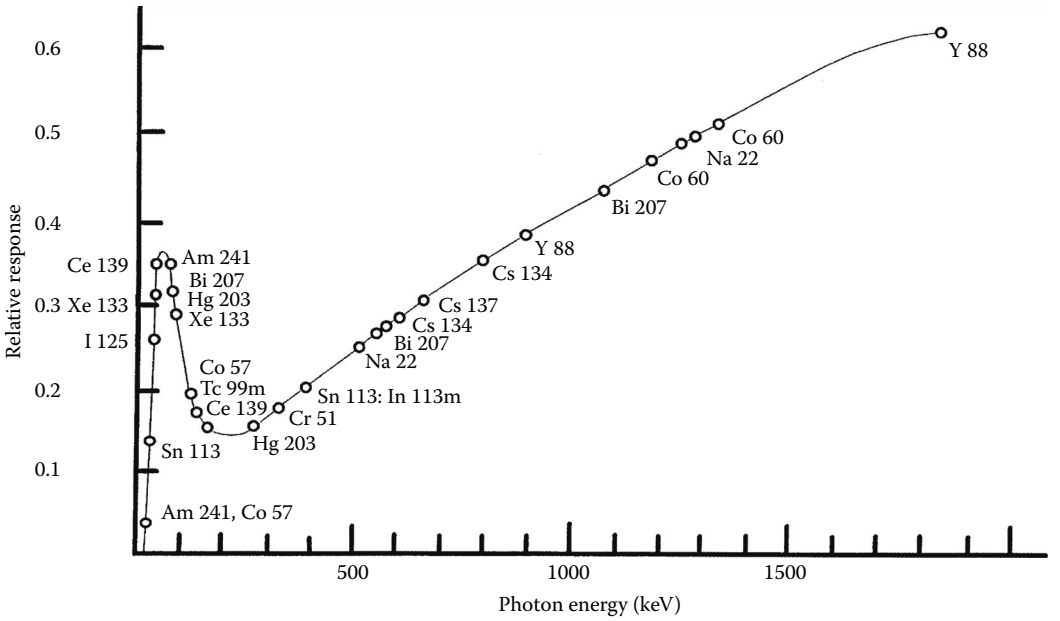

FIGURE 80.17 Photon response as a function of energy for a pressurized reentrant ionization chamber. (From Dell, M.A., Capintec, instruments, private communication, 1997.)

References

1. R.D. Evans, *The Atomic Nucleus*, New York: McGraw-Hill, 1955.
2. W.B. Mann, R.L. Ayres, and S.B. Garfinkel, *Radioactivity and Its Measurement*, Oxford, U.K.: Pergamon Press, 1980.
3. W.B. Mann, A. Rytz, and A. Spernol, *Radioactivity Measurements: Principles and Practice*, Oxford, U.K.: Pergamon Press, 1991.
4. J.C. Harbert, W.C. Eckelman, and R.D. Neumann, *Nuclear Medicine: Diagnosis and Therapy*, New York: Thieme, 1996.
5. G. Friedlander, J.W. Kennedy, E.S. Macias, and J.M. Miller, *Nuclear and Radiochemistry*, New York: Wiley-Interscience, 1981.
6. G. Choppin, J. Rydberg, and J.O. Liljenzin, *Radiochemistry and Nuclear Chemistry*, 2nd edn., Oxford, U.K.: Butterworth-Heinemann, 1995.
7. K.S. Krane, *Introductory Nuclear Physics*, New York: John Wiley & Sons, 1988.
8. W.R. Leo, *Techniques for Nuclear and Particle Physics Experiments*, Berlin, Germany: Springer-Verlag, 1992.
9. G.F. Knoll, *Radiation Detection and Measurement*, 2nd edn., New York: John Wiley & Sons, 1989.
10. ICRU, Radiation quantities and units, Report 33, International Commission on Radiation Units and Measurements, Bethesda, MD: ICRU/NCRP Publications, 1980.
11. W.J. McDowell, Liquid scintillation counting techniques for the higher actinides, in *Organic Scintillators and Liquid Scintillation Counting*, Horrocks, D.L. and Peng, C.T. (eds.), New York: Academic Press, 1971, p. 937.
12. R. Collé (NIST), private communication, 1997.
13. Personnel Performance Criteria for Testing, An American National Standard, HPS N13. 11, Health Physics Society, McLean, VA, 1993.

14. International Standard ISO 8529, Neutron reference radiations for calibrating neutron-measuring devices used for radiation protection purposes and for determining their response as a function of neutron energy, International Organization for Standards, Geneva, Switzerland, 1989.
15. C.N. Davids, P.J. Woods, J.C. Batchelder, C.R. Bingham, D.J. Blumenthal, L.T. Brown, B.C. Busse et al., New proton radioactivities, ^{165,166,167}Ir and ^{171}Au, *Physical Review*, C55, 2255, 1997.
16. J.W. Motz, H.K. Olsen, and H.W. Koch, Pair production by photons, *Reviews of Modern Physics*, 41, 581–639, 1969.
17. S.M. Seltzer, Calculation of photon mass energy-transfer and mass energy-absorption coefficients, *Radiation Research*, 136, 147–170, 1993.
18. ICRU, Stopping powers for electrons and positrons, Report 37, International Commission on Radiation Units and Measurements, Bethesda, MD: ICRU/NCRP Publications, 1984.
19. ICRU, Stopping powers and ranges for alpha particles and protons, Report 49, International Commission on Radiation Units and Measurements, Bethesda, MD: ICRU/NCRP Publications, 1993.
20. P.F. Rose, ENDF-201, ENDF/B-VI summary documentation, Upton, NY: Brookhaven National Laboratory, BNL-NCS-17541, 4th edn., October 1991.
21. D.L. Horrocks, *Applications of Liquid Scintillation Counting*, New York: Academic Press, 1974.
22. W.B. Mann (ed.), *A Handbook of Radioactivity Measurements Procedures*, Report No. 58, 2nd edn., National Council on Radiation Protection and Measurements, Bethesda, MD: NCRP Publications, 1985.
23. B.M. Coursey, W.B. Mann, A. Grau Malonda, E. Garcia-Torano, J.M. Los Arcos, J.A.B. Gibson, and D. Reher, Standardization of carbon-14 by $4\pi\beta$ liquid-scintillation efficiency tracing with hydrogen-3, *International Journal of Applied Radiation and Isotopes*, 37, 403–408, 1986.
24. W.J. McDowell, Photon/electron rejecting alpha liquid scintillation spectrometry, *Radioactivity and Radiochemistry*, 3(2), 26–54, 1992.
25. J. Cessna (NIST), private communication, 1997.
26. M.A. Dell, Capintec, instruments, private communication, 1997.

Further Readings

Frank Herbert Attix, *Introduction to Radiological Physics and Radiation Dosimetry*, Morlenbach, Germany: Wiley-VCH, 2004.

Glenn F. Knoll, *Radiation Detection and Measurement*, 4th edn., New York: Hamilton Printing Company, 2010.

James E. Turner, *Atoms, Radiation and Radiation Protection,* 3rd edn., Weinheim, Germany: Wiley-VCH, 2007.

Partial List of Manufacturers and Suppliers

Global Dosimetry Solutions, 2652 McGaw Ave., Irvine, CA 92614, Phone: 800-251-3331 (toll free), Fax: 949-296-1130, www.mirion.com/index.php?p=dosimetry_div…

Mirion Technologies, 3000 Executive Pkwy., Suite 222, San Ramon, CA 94583, Phone: 925-543-0800, www.mirion.com

MP Biomedical, Inc., 29525 Fountain Pkwy, Solon, OH 44139, Phone: 440-337-1200, 800-848-1163 (toll free), Fax: 714-668-3149, 800-334-6999 (toll free), www.mpbio.com/?country=223

Radiation Detection Company, 8095 Camino Arroyo, Gilroy, CA 95020, Phone: 408-842-2700, Fax: 800-250-3314 (toll free), www.radetco.com/

RAE Systems, Inc., 3775 N. First St., San Jose, CA 95134, Phone: 408-952-8200, 877-723-2878 (toll free), Fax: 408-952-8480, www.raesystems.com

Sierra Radiation Dosimetry Solutions, 2312 Park Ave. # 9b, Tustin, CA 92782, Phone: 949-242-0469, 866-897-8707 (toll free), Fax: 714-249-9001, www.sierradosimetry.com

81

Radioactivity Detectors

Larry A. Franks
Sandia National Laboratories

Ralph B. James
Sandia National Laboratories

Larry S. Darken
Oxford Instruments, Inc.

Radioactivity was first discovered by Henry Becquerel in 1896 when he noticed that photographic plates became fogged after exposure to uranium atoms. In addition to uranium nuclei, many other naturally occurring and man-made isotopes are known to be radioactive and decay by emitting uncharged particles (gamma rays and neutrons) and charged particles (alpha or beta particles) from their nuclei. Over the past few decades, there has been a growing need for monitoring, locating, and imaging radioactive sources in a wide variety of medical, environmental, industrial, space, scientific, and national security applications. Many of the applications rely on the use of commercially available radiation detectors, whereas others require the development of new detectors to meet system requirements related to sensitivity, power, size, portability, ruggedness, maintenance, radiation hardness, and energy resolution.

The signals generated by a radiation-sensing system depend on (1) the mechanisms in which the incident radiation interacts with the detector material and (2) the scheme used to read out the interaction. In general, there are three types of radiation sensors in use today: gas-filled detectors, scintillation devices, and semiconductor detectors. The types of radiation sensor can also be divided into two groups according to whether they can measure the energy of the emitted gamma rays, x-rays, or charged particles. Whenever an energy-resolving capability is desired, a large number of information carriers must be generated for each absorbed pulse to reduce the statistical limit on energy resolution. This is best accomplished by the use of semiconductor detectors, although some spectral information can be achieved through the use of scintillators and gas-filled detectors.

The typical unit of measure of radioactivity is the becquerel (Bq), which is defined as the rate of one disintegration per second of a decaying isotope. Another common measure of radioactivity is the curie, which can be obtained by multiplying the becquerel by 3.7×10^{10}.

This chapter is divided into sections on gaseous, scintillation, and semiconductor detectors. Separate sections describing semiconductor detectors that must be cooled to cryogenic temperatures for operation and those capable of operation at ambient temperatures are presented. There are several texts devoted to the subject of radiation detection [1–7], and the reader is directed to these books for more detailed information on the principles of detector operation, device performance, problems limiting detector performance, areas of current research and development, and applications.

81.1 Gaseous Detectors

Ionization in a gas resulting from the interaction of x-radiation and gamma radiation is the basis for a wide variety of radiation detectors. The versatility of gas-phase detection arises from the great flexibility in detector sizes and shapes that can be produced, their relatively low production cost, and particularly, the ability to perform a multitude of measurement tasks. Gas detectors can be separated into three distinct types: ionization chambers, Geiger–Müller counters (more commonly known as G-M counters or tubes), and proportional counters, with numerous variations in each type. All utilize the ions and electrons created by the interaction of an incident photon with the detector gas, directly or indirectly, to produce an output signal. They differ in the characteristics of the electric field and nature of the output signal.

Ionization chambers can be operated in either a current mode or pulsed mode, although the current mode is more common. They operate by collecting (with an applied electric field) all the charge generated by the original ionizing event and differ in this way from both proportional and G-M counters. The latter, normally operated in a pulsed mode, have output signals that result from amplification of the original ion pairs by gas multiplication processes.

81.1.1 General Operating Principles

Fundamental to the operation of gas detectors is the generation of electron–ion pairs and their movement through the surrounding gas under the influence of an applied electric field. It is convenient to summarize basic features of these processes before turning to specific detector designs.

81.1.2 *W* Values

The energy (W) required for producing an electron–ion pair in a gas depends on the gas and the type of radiation (and its energy). W values for fast electrons in common filling gases range from 26.4 eV per ion pair in argon to 41.3 eV per ion pair in helium. The presence of nonionizing energy loss processes accounts for the W values greatly in excess of the ionization energy. Fluctuations in the number of pairs produced from photons of the same energy are of significance in pulse-mode operation. The variance is generally less than expected based on Poisson statistics and is accounted for by an empirical constant, the Fano factor (typically 0.1–0.2).

81.1.3 Charge Transport

The motion of free electrons and ions in the gas under the influence of the electric field (E) is quite different. The drift velocity (v) of the more massive ions is a linear function of E/p where p is the gas pressure. It can be expressed as

$$v = \frac{\mu E}{p} \tag{81.1}$$

The proportionally constant μ is the mobility, which depends on the type of gas and the charge of the ion. Values are typically in the region of 1000 $cm^2/V \cdot s/mm$ Hg. The electron mobility is normally about 1000 times ion values; the electron drift velocity is not linear in E/p [8].

81.1.4 Electric Field Effects

The amplitude of a pulse resulting from the interaction of a photon with the wall or fill gas depends strongly on the voltage applied to the detector and serves to distinguish the three detector types. A plot of pulse amplitude as a function of applied voltage is shown in Figure 81.1. The plateau following the initial steep segment is the region of ion chamber operation. It is a region where the electric field is sufficient to reduce recombination of the original pairs to an acceptable value and further voltage increases yield no more charge (as it has all been collected) and ion saturation is established. Assuming complete charge collection, the output current accurately represents the rate of ion pairs that are being produced. This is the basis for ionization chamber operation.

The rapidly rising portion following the plateau marks the onset of gas multiplication (the initial electrons can acquire enough energy between collisions to generate further ionization). In the initial segment, the multiplication process is linear; that is, the charge collected is proportional to the number of original ion pairs. This is the defining characteristic of proportional counter operation. The proportionality eventually is ended at higher voltages by space charge effects caused by positive ions.

At yet higher voltages, the space charge becomes sufficient to reduce the electric field below the multiplication threshold, and no further multiplication takes place. Thus, a condition is reached where the same number of positive ions is produced for all initial ion-pair populations, and the pulse amplitude is independent of the initial conditions. This characterizes G-M counter operation.

Further details on the operation of these devices may be found in texts by Knoll [1], Price [9], Attix and Roesch [10], and Tait [11]. The monograph by Rossi and Staub [2] contains a lengthy discussion of ionization chambers together with data on the physics of the transport process.

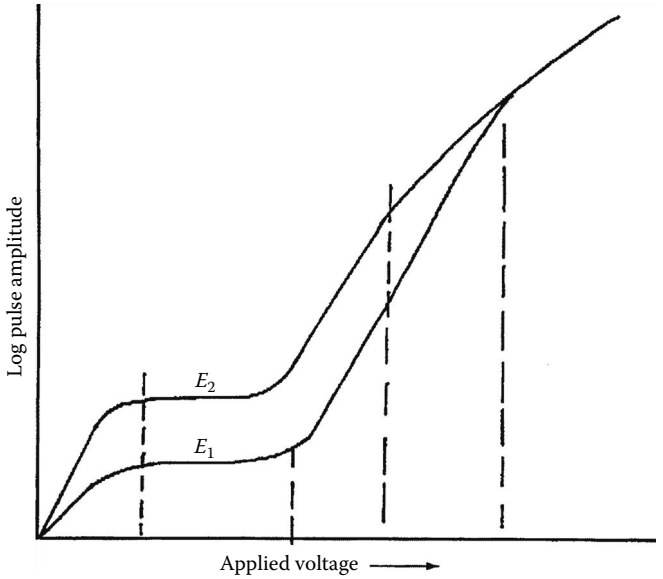

FIGURE 81.1 Distinct operation regions of gas-filled detectors. E_1 and E_2 depict pulses from photons of two energies.

81.1.5 Ionization Chambers

Ionization chambers have been designed for numerous x- and gamma-ray measurement applications. They are frequently employed in radiation survey instruments. They are found in parallel-plate, cylindrical, and spherical geometries. Essential features of their design can be found in the parallel-plate chamber shown schematically in Figure 81.2. The design shown contains an optional guard ring that helps to define the active volume of the chamber. The ring is normally maintained near the collector electrode potential. (Guard rings are also employed in very-low-current designs to reduce leakage current.) Because the current for the ionization chamber is low, typically 1 nA or less, considerable care must be taken with the insulators to minimize leakage currents.

Because of the low output current, special care must be taken with the readout system. Both DC and dynamic-capacitor types are used. Only electrometers of the highest quality should be used. Dynamic-capacitor (or vibrating reed) varieties provide more stable operation. They are normally the choice for very-low-current applications.

Several special-purpose ion chambers are notable. The "free-air" chamber, a parallel-plate variant, is valued for accurate gamma-ray exposure measurements, particularly when absolute measurements are required. This is achieved by collimation of the incoming gamma flux and by an internal design that ensures compensation for ionization produced outside the sensitive volume by secondary electrons. These chambers are limited to energies below about 100 keV, however. Cavity ionization chambers are widely used for dosimetry purpose. To function in this manner, it is necessary that they be designed to meet the requirement of the Bragg–Gray principle [12]. This states that the absorbed dose in a medium can be determined from the ionization produced in a small gas-filled cavity in the medium. The cavity dimension must be small compared to the range of the ionizing particles generated in the material so that the particle flux is essentially unperturbed. Of particular interest for health physics applications are tissue-equivalent chambers where the wall material is a plastic that closely simulates the absorption properties of tissue.

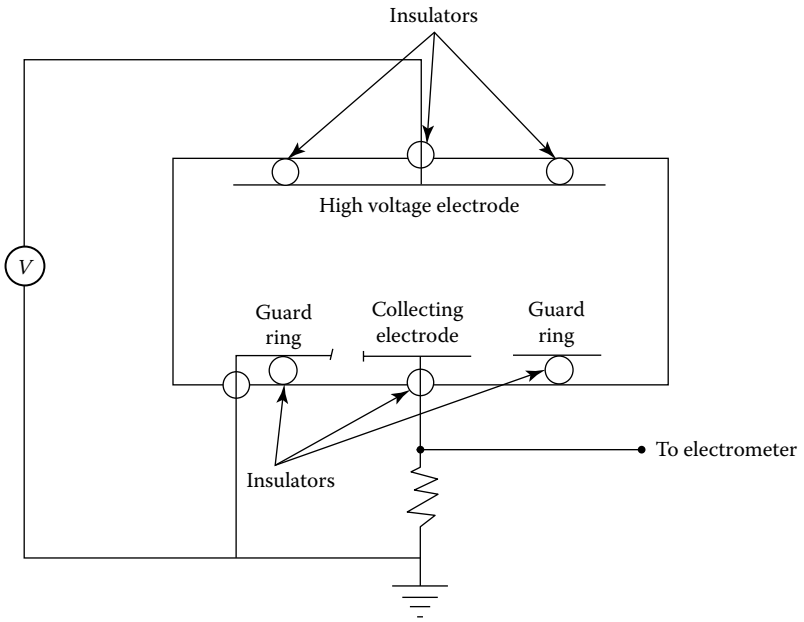

FIGURE 81.2 Schematic diagram of parallel-plate ionization chamber with guard ring defining active volume.

81.1.6 Proportional Counters

Proportional counters utilize gas multiplication to amplify the charge of the initial ion-pair population and have the important characteristic that the charge associated with the amplified pulse is proportional to the ion pairs produced initially. They are normally operated in a pulse mode. They can be operated sealed or in a gas flow mode. The sealed style is most common for x- and gamma-ray applications. While they are found in a number of geometries, cylindrical is the most common shape. A typical cylindrical design is shown in Figure 81.3. This relatively simple design features a central wire that is maintained at high voltage and a surrounding metal container that serves as the cathode. The electric field in this geometry is given by

$$E(r) = \frac{V}{r} \ln\left(\frac{b}{a}\right) \tag{81.2}$$

where

V is the anode–cathode voltage
a is the anode wire radius
b is the inner radius of the cathode

It should be noted that $E(r)$ depends on the diameter of the anode wire, allowing the threshold electric field needed for multiplication to be obtained at relatively modest voltages. The multiplication process is confined to a small volume surrounding the anode where the field exceeds the multiplication threshold. The characteristics of several common counting gases are given in Table 81.1.

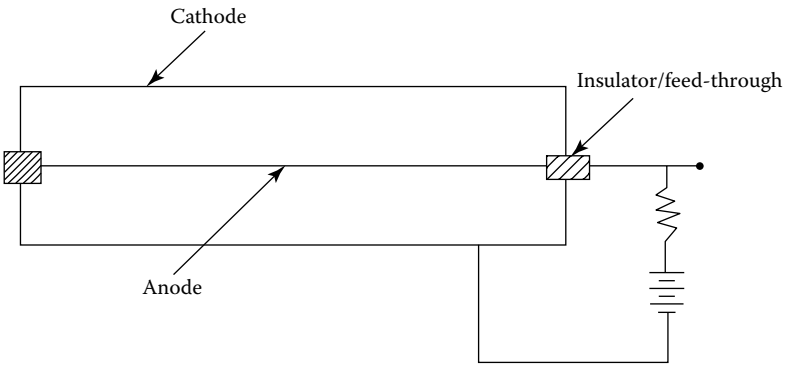

FIGURE 81.3 Schematic diagram of cylindrical proportional counter.

TABLE 81.1 Characteristics of Common Proportional Counter Gases

Gas	W (eV per Ion Pair)	Fano Factor	Resolution (%) at 5.9 keV	
			Calculated	Measured
Ne + 0.5% Ar	25.3	0.05	10.1	11.6
Ar + 0.5% C_2H_2	20.3	0.075	9.8	12.2
Ar + 10% CH_4	26.0		12.8	13.2

Source: Adapted from Knoll, G.F., *Radiation Detection and Measurement*, John Wiley & Sons, New York, 1979.

Proportional counters can be used for both photon and particle measurements. In photon applications, they are particularly valued for spectroscopy in the low-energy x-ray region. Their energy resolution and detection efficiency is generally inferior to semiconductor detectors such as lithium-drifted silicon or mercuric iodide, but they offer large surface areas, reliable operation, and low cost. The energy resolution ΔE for given gas mixture for a specific photon energy can be estimated from the statistical limit given by

$$\Delta E = 2.35\left[W\frac{(F+\beta)}{E}\right]^{1/2} \tag{81.3}$$

where

F is the Fano factor
β is the variance factor (typically about 0.5) [1]
E is the energy in eV
W is the energy in eV required to produce an ion pair

Energy resolution for a proportional counter at 5.9 keV can be expected to be on the order of 10% (Table 81.1).

81.1.7 Geiger–Müller Counters

G-M counters remain among the most widely used means of detecting x-radiation and gamma radiation. They have high sensitivity, are rugged, and offer low cost. Also of importance is the large amplitude of the output pulse (several volts, typically), which greatly simplifies the readout. Because of these factors, they are the detectors of choice for a variety of commercial gamma survey instruments. Like proportional counters, they utilize gas amplification to generate an output pulse, although here the output is independent of the initial number of ion pairs. They are counters only and not applicable to spectroscopy. A G-M counter with typical readout is shown schematically in Figure 81.4.

G-M counters typically use a noble gas filling, most frequently argon or helium. The gas pressure is normally in the region of a few tenths of an atmosphere. At this pressure, a typical counter would require about 1000 V.

The process that terminates multiplication in a G-M counter has important counting implications. The positive ions' space charge and resultant subthreshold electric field (for gas multiplication) persist

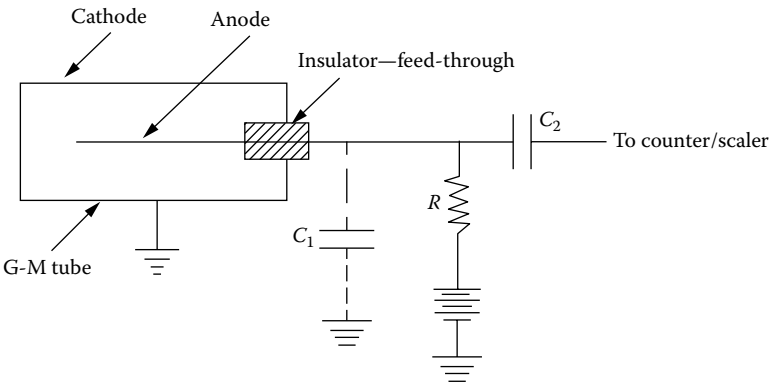

FIGURE 81.4 Typical counting circuit using a G-M tube. C_1 represents the combined tube and wiring capacitance; C_2 is a blocking capacitor that isolates the high voltage from the counter/sealer. The time constant of the circuit is RC_1.

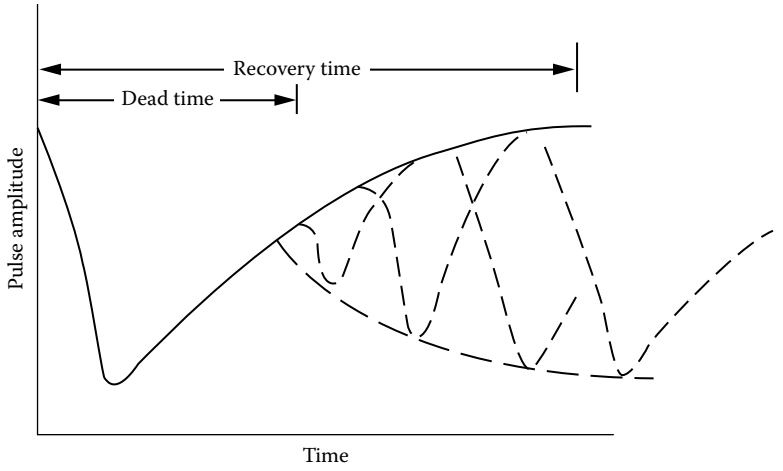

FIGURE 81.5 Illustration of dead time (T_d) in a typical G-M counter.

for some time after the discharge is terminated. As a result, there is an interval following each pulse when pulses from subsequent input gamma rays are not produced or have less than full amplitude. This is illustrated in Figure 81.5. The period between a full-amplitude pulse and the next discharge of any size is the dead time of the G-M counter (T_d). The time from the initial full-amplitude pulse until another full-amplitude pulse produced is the recovery time. Dead times in G-M counters are on the order of 100 μs, with recovery time several times that. If the dead time is known and independent of count rate, the true count rate R_t may be determined in most cases from the observed rate R_o by the expression

$$R_t = \frac{R_o}{1 - R_o R_d} \tag{81.4}$$

81.1.8 Availability

Ionization chambers, proportional counters, and G-M counters are standard commercial products. They are available as stand-alone detectors requiring the user to supply ancillary electronics or as part of an instrument. Custom design devices are also available.

81.1.9 Scintillation Detectors

Scintillators, one of the oldest means of detecting gamma radiation, remain the method of choice for a multitude of counting and spectroscopy applications, particularly when counting efficiency rather than high-energy resolution is the primary objective. They are also widely used to record transient radiation events and in timing applications. While available in solid, liquid, and gas phases, solids and liquids are preferred for gamma-ray applications. Scintillators have the common property of converting energy absorbed from the incident gamma ray into visible or near-visible light. The scintillation detector thus consists of a scintillator element, in which gamma-ray energy is converted to optical photons and some form of a photocell, normally a photomultiplier tube, to convert the optical photons into an electrical signal for processing by ancillary electronics.

The desired properties of a scintillator include high transparency to its own optical emission, efficient conversion of the absorbed gamma energy into optical output, short duration of the output, and output

that is proportional to the amount of energy absorbed. Other useful properties include the ability to be produced in large sizes, ability to be machined, stable output over a wide range of environmental conditions, and efficient gamma-ray absorption.

81.1.10 Scintillation Process

The excess energy contained by the scintillator as a result of the gamma-ray absorption is dissipated largely through nonradiative processes and appears as heat. A small fraction decays radiatively and appears as visible and near-visible light. That fraction of the absorbed energy converted to optical photons is referred to as the scintillation efficiency, which varies from <1% to ≈10% for the more efficient scintillators.

The optical emission originates from electronically excited atomic and molecular states. The emission is broadband, frequently exceeding 50 nm at the half-intensity points. Temporally, it is characterized by a very fast rise, followed by exponential decay. For most purposes, the light pulse can be adequately represented by

$$I(t) \propto N\left[e^{-t/\tau} - e^{-t/\tau_R}\right] \tag{81.5}$$

where

$I(t)$ is intensity at time t
N is related to the total number of scintillation photons
τ_R is the time constant associated with the pulse rise time
τ is the time constant for decay

The time required for the intensity to fall to $1/e$ of the maximum value is the pulse decay time. Optical pulses from organic scintillators are often described by the full width of the pulse at the half maximum of intensity. Further details of the scintillation process can be found in the text by Knoll [1] and, in particular, the treatise by Birks [13].

81.1.11 Scintillator Types

As previously noted, the scintillation process is observed in solid, liquid, and gas phases, but gamma applications are limited mainly to solids and liquids. This brief discussion is confined to the most common solid- and liquid-phase scintillants that are applicable to gamma-ray detection. A number of scintillators, including pure organic crystals and gas scintillators used primarily for charged particles, are not considered. Those remaining ones fall into two groups: inorganic and organic.

81.1.11.1 Inorganics

The most important of this group is the crystals of inorganic salts containing trace quantities of activators to enhance the emission. Because of their high atomic number, high density, and light output, they are valued for gamma spectroscopy. They are available commercially in a variety of standard forms, including right cylinders and parallelepipeds, and are readily machined to custom shapes. Ruggedness varies considerably among crystal types; care in packaging and use is required. Encapsulated crystals are available, but integrated units comprising a scintillator and photomultiplier are also available and often preferable.

The most widely used of this group is sodium iodide activated with thallium, NaI(Tl). NaI(Tl) has high light output and is generally the choice for scintillator-based spectroscopy systems. This material is hydroscopic and must be encapsulated. A typical pulse-height spectrum from a NaI(Tl) photomultiplier combination is shown in Figure 81.6.

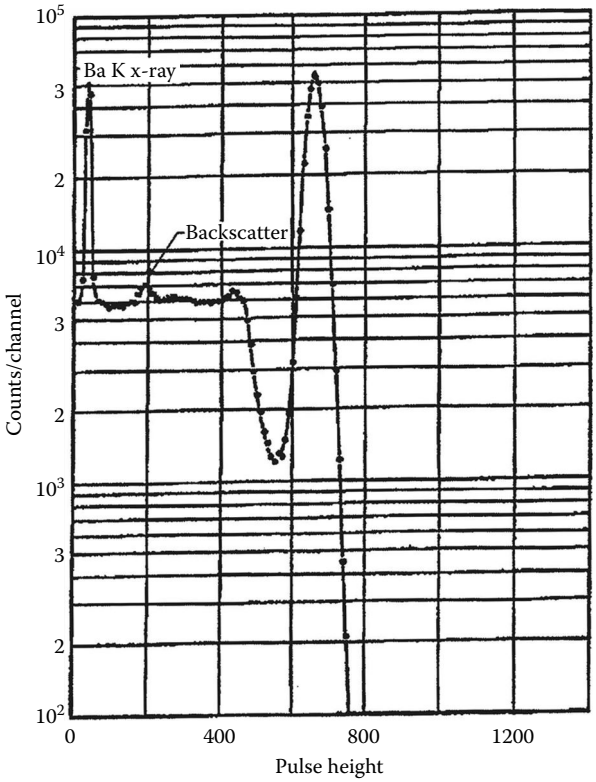

FIGURE 81.6 Typical energy spectrum obtained with a NaI(Tl) scintillator/photomultiplier combination in response to a Cs-137 source (662 keV).

Also useful for spectrographic applications is cesium iodide, which is available with either a thallium or sodium activator. The optical output of CsI(Tl) is at substantially longer wavelengths than either NaI(Tl) or CsI(Na) and is well matched to the spectral response of silicon. This has been successfully exploited to produce small, rugged CsI(Tl)–silicon PIN devices. A spectrum of Cs-137 obtained with a CsI(Tl)/PIN detector combination is shown in Figure 81.7. Exceptional resolution can be obtained when CsI(Tl) is used with a mercuric iodide photocell. With this combination, resolution at 662 keV of better than 5% has been reported [14].

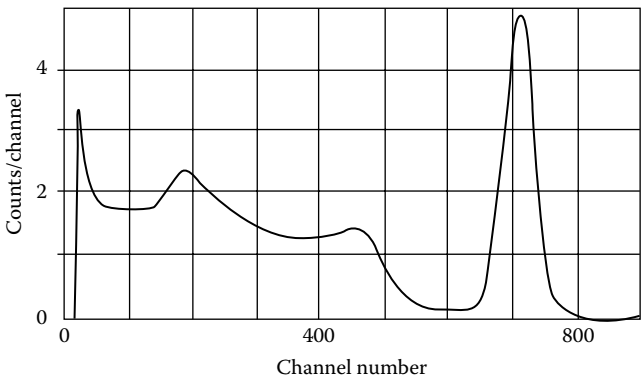

FIGURE 81.7 Energy spectrum of Cs-137 (662 keV) obtained with a CsI(Tl)/PIN combination. Specifications: CsI(Tl) (1 cm × 2 cm × 2 cm) and PIN (1 cm × 2 cm).

TABLE 81.2 Properties of Common Scintillators

Scintillator	Wavelength of Emission Maximum (nm)	Density (g/cm^3)	Principle Decay Constant (ns)
NaI(Tl)	415	3.67	230.0
CsI(Tl)	530	4.51	1000.0
CsI(Na)	430	4.51	630.0
BaF_2	220	4.88	0.6
$Bi_4Ge_3O_{12}$	460	7.13	300.0
BC-505 (liquid)	425	0.88	2.5
BC-400 (plastic)	423	1.032	2.4

Source: Courtesy of Bicron, Newberry, OH.

Two unactivated inorganic crystals, barium fluoride (BaF_2) and bismuth germinate ($Bi_4Ge_3O_{12}$), warrant comment. Barium fluoride has a weak subnanosecond component in the ultraviolet that is useful for the timing and the recording of fast transients. With proper attention to ultraviolet transmission and photocell response requirements, gamma spectra can be obtained. Bismuth germanate has lower light output than either CsI or NaI and inferior energy resolution. However, because of its high density (7.1 g/cm^3) and the high atomic number (83) of bismuth, it is a good choice when high counting efficiency per unit volume rather than energy resolution is required.

81.1.11.2 Organics

Organic scintillators are available in both solid and liquid forms. This group is characterized by very fast rise times (often subnanosecond) and decay times of a few nanoseconds. Their scintillation efficiency is about one-third that of the more efficient inorganics, however. Because of the low atomic number, photoelectric absorption is not significant. As a result, gamma spectra consist mainly of a Compton continuum with, in large samples, a distinct Compton edge. Because of the absence of a photopeak, they are not well suited for spectroscopy applications. (High-*Z* additives such as tin or lead have been shown to enhance the photoelectric response but sometimes at the cost of light output.) They are particularly well suited for counting applications when very large detector volumes are required or for wide bandwidth measurements of fast transients. Because of the large number of available fluorescent organic compounds, organic scintillators are much more easily tailored to meet emission wavelength and decay time requirements than inorganics. The liquids typically consist of one or more fluorescent organic compounds dissolved in an aromatic solvent. A large number of formulations are commercially available. They can be obtained in sealed vessels suitable for mounting on a photomultiplier or as part of integrated scintillator–photomultiplier combination.

Solid organic solutions or plastic scintillator is prepared by dissolving fluorescent compounds in monomers of styrene or vinyl toluene, which then are polymerized. Like liquid organics, several different solutes can be used to achieve the desired wavelength and efficiency. Slabs of plastic scintillator several meters in length can be prepared in this manner. Alternatively, custom shapes can be either cast directly or machined.

The characteristics of several representative scintillators are shown in Table 81.2.

81.2 Germanium Detectors

High-purity germanium (HPGe) detectors are widely used for gamma-ray spectroscopy due to their combination of efficient absorption and high-energy resolution. Figure 81.8 shows the cross sections of germanium and silicon for photoelectric absorption, Compton scattering, and absorption by electron–positron pair production in several materials used for solid-state nuclear radiation detectors. Attenuation is significantly stronger in germanium than in silicon. Over much of the gamma spectrum, the dominant interaction is Compton scattering. However, it is principally the stronger photoelectric absorption in germanium that makes it more

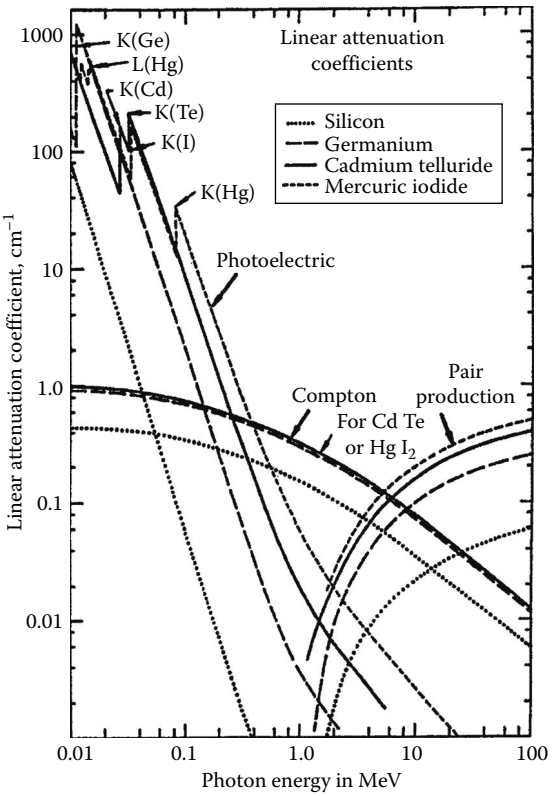

FIGURE 81.8 Attenuation coefficients vs. energy in common semiconductor materials. (From Schlesinger, T. E. and James, R. B. (eds.), *Semiconductors for Room-Temperature Nuclear Detector Applications*, Vol. 43, Semiconductors and Semimetals, Academic Press, San Diego, CA, 1995.)

suitable than silicon for gamma-ray spectroscopy. In the typical-size germanium detector, a gamma ray may be scattered several times before it is photoelectrically absorbed. Thus, the energy of the gamma ray is primarily transmitted directly to a small number of electrons. These energetic electrons in turn interact with electrons in the valence bands to create mobile pairs of electrons and holes. In a detector with sufficiently large volume, the average number of electron–hole pairs N produced by an absorbed gamma ray of energy E becomes independent of the details of the initial reaction path and varies linearly with E as follows:

$$N = \frac{E}{\varepsilon} \tag{81.6}$$

This relationship is more broadly valid and is the foundation of energy spectroscopy of gamma rays using semiconductors, gases, and cryogenic liquids (ε depending on the material). While ε is independent of the gamma-ray energy (and is also virtually the same for energy deposited by charged particles), ε in germanium does increase slightly with decreasing temperature, as does the energy gap. At 77 K, ε is 2.96 eV, and the energy gap is 0.72 eV.

The practical exploitation of Equation 81.6 depends on electronically detecting the motion of the ionized charge in an electric field. The signal-to-noise ratio is improved by reducing current flow in the detector from other mechanisms. In germanium, this is achieved by producing a rectifying and a blocking contact and by cooling to about 100 K. For a planar detector, a slice of HPGe is diffused with the donor lithium on one side, forming a strongly n-type layer. The opposite side is implanted with the

acceptor boron, forming a *p*+ layer. When voltage is properly applied, the electric field direction prevents the majority carriers in the contact regions from being injected across the device. As the voltage is applied, a region depleted of holes will advance into the slice from the *n*+ contact if the slice is *p* type. If the slice is *n* type, a region depleted of electrons will advance from the *p*+ contact. At the depletion voltage V_d, the depletion region reaches the opposite contact. For germanium,

$$V_d = 565\,\text{V} \times \frac{N_e}{10^{10}\,\text{cm}^{-3}} \times \frac{d^2}{\text{cm}^2} \tag{81.7}$$

where

N_e is the net charge density in the depleted or active region of the detector
d is the thickness of this region

This is a key relationship in HPGe technology, as it quantifies the effect of the residual impurity concentration on device size and depletion voltage. Techniques to grow germanium pure enough for gamma detectors were pioneered by Hall [15] and the detector group at Lawrence Berkeley Laboratory [16], based on purification methods of Pfann [17] and crystal-growing techniques developed by Teal and Little [18] to produce crystals for germanium transistors.

81.2.1 Leakage Current

Germanium detectors need to be cooled to reduce leakage current. There are several potential sources of leakage current, including

- Diffusion of minority carriers from either doped contact into the depletion region
- Thermal generation of carriers at either bulk or surface defects in the depletion region
- Electrical breakdown at points where the electric field is concentrated due to irregularities in the contact geometry, large-scale inhomogeneities in the bulk, or surface states

Current will also be generated if the detector is not shielded from room-temperature infrared radiation. Background nuclear radiation from materials near the detector and cosmic radiation also generate leakage current.

Germanium detectors are typically liquid-nitrogen cooled and operated between 85 and 100 K. In this temperature range, leakage current is typically less than 40 pA in "good" detectors and is not a significant contributor to system noise (400–900 eV). Leakage current increases with temperature and eventually becomes the predominant noise component. Pehl et al. [19] reported a leakage current-driven system noise of 2 keV at 150 K and 7 keV at 170 K for an 8 cm^3 planar detector. These authors also reported that, above about 120 K, the leakage current had an activation energy of approximately one-half the bandgap and attributed this to generation at mid-gap surface states. Below 120 K, the temperature dependence was milder.

A typical detector/cryostat configuration is shown in Figure 81.9. The detector resides in an evacuated cryostat and is cooled by means of a copper rod inserted into a liquid-nitrogen dewar. The first stage of amplification is an FET, also cooled, positioned nearby the detector. Mechanical fixturing is designed to stabilize the detector and the mechanisms for contacting it, to provide a cooling path from the detector to liquid nitrogen, and to electrically insulate the high-voltage contact.

A variety of detector geometries are shown in Figure 81.10. These different electrode configurations allow efficiency and energy resolution to be optimized for different gamma-ray energies and applications. For example, the detector in Figure 81.10c minimizes noise by the lower capacitance of its electrode configuration at the expense of the reduced stopping power. Thus, this detector would be more suitable for lower-energy gamma rays.

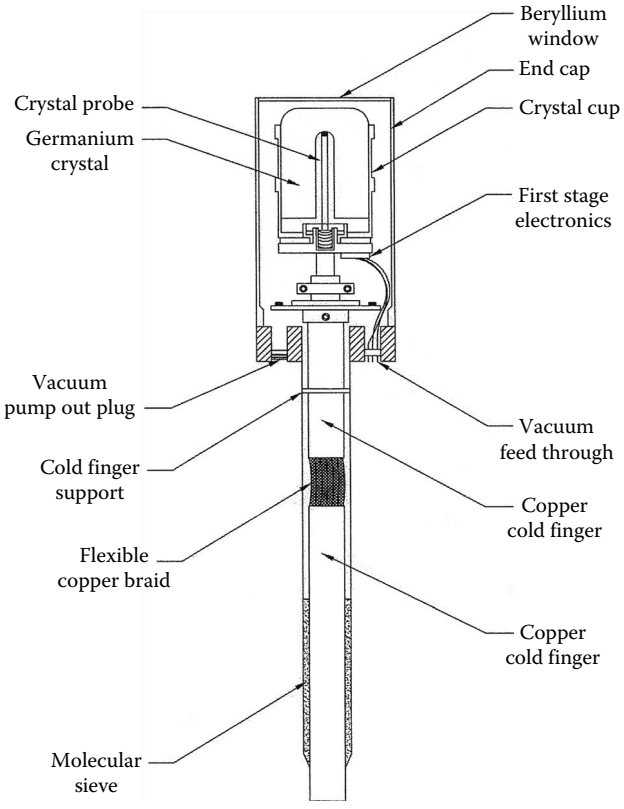

FIGURE 81.9 Schematic cross section of a dipstick cryostat. (From Darken, L. S. and Cox, C. E., in *Semiconductors for Room-Temperature Nuclear Detector Applications*, Academic Press, New York, 1995, reprinted with permission of Oxford Instruments, Inc.)

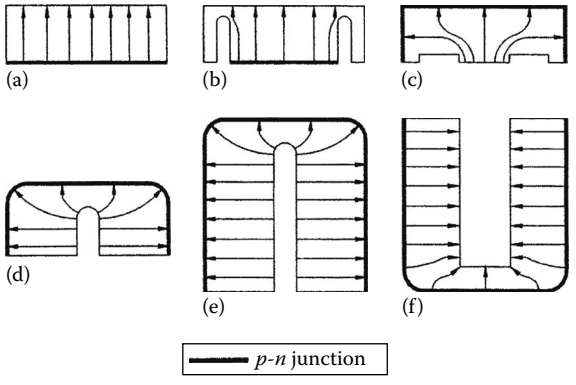

FIGURE 81.10 Schematic cross section and electrostatic field distribution in HPGe detectors. The dark line represents the *p-n* junction: (a) true planar, (b) grooved planar, (c) low-capacity planar, (d) truncated coaxial, (e) closed-end coaxial, and (f) well geometry.

81.2.2 Coaxial Detectors

The detector type shown in Figures 81.9 and 81.10e has a closed-end coaxial geometry. Nearly all of the largest-volume (active volumes of 100–800 cm^3) HPGe detectors are of this type. This electrode geometry reduces both capacitance and depletion voltage with respect to a planar detector of the same volume.

This latter benefit relaxes the constraint on material purity. In addition, charge collection distances are shortened, and the uncontacted surface area, frequently troublesome in processing, is reduced. Also, the HPGe is grown by the Czochralski technique and is therefore nearly cylindrical, even before machining. It is important, however, to note that the reduction in depletion voltage is realized only when the device is contacted so that it depletes from the outer contact to the inner contact. Thus, *p*-type HPGe to be fabricated into a coaxial detector is lithium diffused on the outer diameter, and in the case of *n*-type HPGe, the outer diameter is boron implanted.

The boron-implanted contact (depth approximately 0.2 μm) is thinner than the lithium-diffused contact (depth approximately 750 μm), so the *n*-type coaxial detector can detect lower-energy radiation and is usually built with a beryllium window in the aluminum end cap to take full advantage of this feature. The difference in the range of use is illustrated in Figure 81.11. The geometric asymmetry of the contacting electrodes in the coaxial detector makes charge collection more dependent on the carriers (electrons or holes) traversing to the inner contact. As more gamma rays are absorbed near the outer contact, the carriers traversing to the inner contact must travel on average a longer distance. Also, charge traversal near the inner contact is particularly effective in inducing current in the external circuit [20], Thus, the *p*-type coaxial detector with positive bias on the outer electrode is more sensitive to hole collection, and the *n*-type coaxial detector with negative bias on the outer electrode is more sensitive to electron collection. This is a crucial consideration in applications where the hole collection is going to be degraded during use by exposure to fast neutrons or other damaging radiation. The superior neutron damage resistance of the electrode biasing polarity on *n*-type coaxial detectors was demonstrated by Pehl et al. [21].

A typical gamma-ray spectrum of a Co^{60} source taken with a coaxial HPGe detector is shown in Figure 81.12. The salient features are the full-energy peaks at 1.17 MeV and at 1.33 MeV and the lower-energy plateaus due to incomplete energy absorption of Compton-scattered gamma rays. The peak-to-Compton ratio [22] is generally 40–100, depending on the size and quality of the detector. The 1.33 MeV peak is shown separately in Figure 81.13. The energy resolution measured as the full width at half the peak maximum (FWHM) for typical coaxial germanium detectors is between 1.6 and 2.1 keV for 1.33 MeV gamma rays, again depending on the size and quality of the detector. The variance in the peak L^2 (FWHM = 2.35 × L, L being the standard deviation for a Gaussian distribution) can be divided into three additive components: the electronic noise

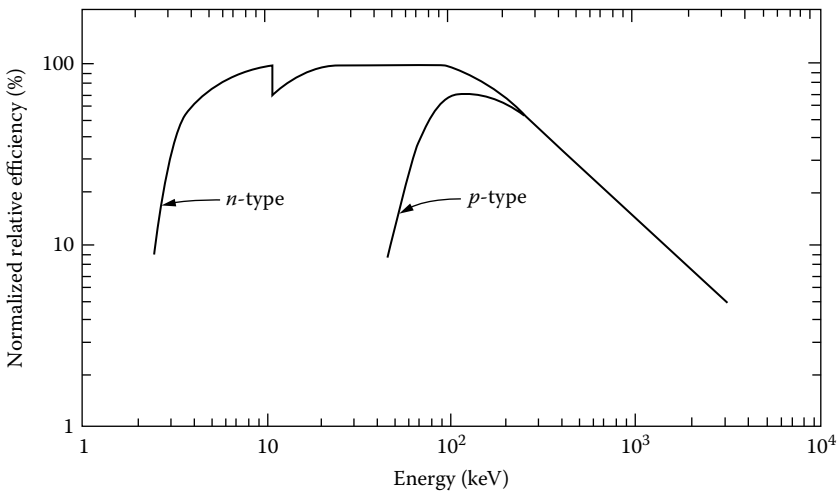

FIGURE 81.11 Relative absorption efficiencies for typical *n*- and *p*-type detectors. (From Darken, L. S. and Cox, C. E., in *Semiconductors for Room-Temperature Nuclear Detector Applications*, Academic Press, New York, 1995, reprinted with permission of Oxford Instruments, Inc.)

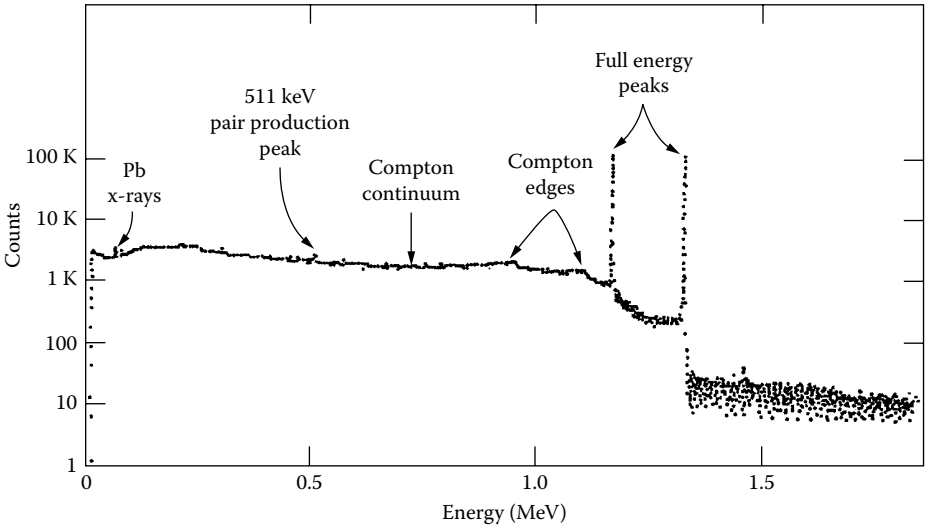

FIGURE 81.12 ^{60}Co spectrum collected with a 15% *p*-type detector showing typical features of germanium detector spectrum.

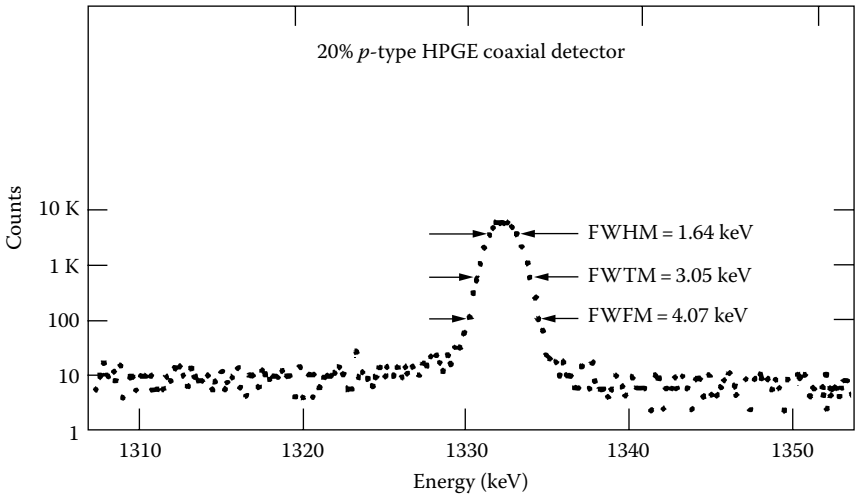

FIGURE 81.13 ^{60}Co spectrum collected with a 22% relative efficiency *p*-type detector. (From Darken, L. S. and Cox, C. E., in *Semiconductors for Room-Temperature Nuclear Detector Applications*, Academic Press, New York, 1995, reprinted with permission of Oxford Instruments, Inc.)

component L_N^2, a component reflecting the variance in the number of electron–hole pairs created L_F^2, and a component due to incomplete charge collection L_T^2:

$$L^2 = L_N^2 + L_F^2 + L_T^2 \tag{81.8}$$

$$L_F^2 = \varepsilon EF \tag{81.9}$$

F is called the Fano factor and has been experimentally determined to be no greater than 0.08 for germanium [23]. $F < 1$ implies that electron–hole pair creation events are not uncorrelated. L_T^2 is usually dominated by the trapping of electrons and holes at defect sites. However, shorter electronic shaping times,

lower electric fields, and larger detectors accentuate ballistic deficit (loss of collected charge in the external electronics due to the finite traversal time of the electrons and holes across the detector). L_N^2 is independent of gamma ray E and is the dominant resolution-limiting factor at low energies. L_F^2 depends linearly on E and, for a coaxial detector, usually dominates L_N^2 for E over a few hundred keV. The energy dependence of L_T^2 is not given simply from first principles for an arbitrary trap distribution, but an E^2 dependence seems to fit under many circumstances. Thus, at high enough E, L_T^2 is expected to be the largest component. For "good" detectors at 1.33 MeV, however, L_T^2 is always smaller than L_F^2. In addition, the magnitude of L_T^2 is variable enough between detectors that it distinguishes between acceptable, very good, and excellent detectors. L_T^2 is usually also the only component of resolution drawn from a non–Gaussian distribution and is thus responsible for any low-energy tailing of the peak.

81.2.3 X-Ray Detection

Both silicon and germanium detectors are used in low-noise systems for the detection of fluorescent x-rays produced by electron beams (usually in an electron microscope) or x-rays (XRF). For both materials, the detector is liquid-nitrogen cooled to reduce leakage current, and small-volume devices (Figure 81.10b, typically 10 mm^2 active area and 3 mm depth) are used to decrease capacitance and therefore to further reduce electronic noise. Lithium-drifted silicon (SiLi) detectors were used first for these applications. Early germanium detectors displayed poor peak shape for x-ray energies just above the L absorption edges (attributed to diffusion against the field to the front contact by some electrons and their resulting loss to the photopeak [24]). However, as was first demonstrated by Cox et al. [25] this is not a fundamental problem but can be solved by the contacting technology. An x-ray spectrum taken with HPGe detector is shown in Figure 81.14. Germanium has the advantages with respect to silicon of a smaller ε (2.96 eV per pair versus 3.96 eV per pair at 77 K) for better energy resolution and a higher Z (32 versus 14) for better photoelectric absorption of higher-energy x-rays.

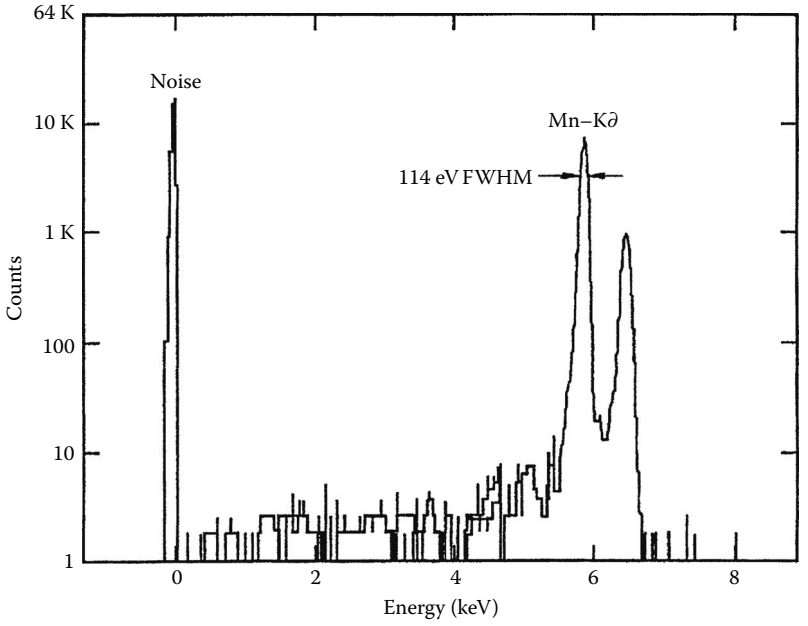

FIGURE 81.14 Manganese x-ray spectrum from ^{55}Fe source collected with an HPGe detector. (From Darken, L. S. and Cox, C. E., in *Semiconductors for Room-Temperature Nuclear Detector Applications*, Academic Press, New York, 1995, reprinted with permission of Oxford Instruments, Inc.)

81.2.4 Current Status of HPGe Detector Technology

HPGe detectors are a mature commercial technology. Process development in crystal growing and diode fabrication has been conducted in private industry where significant advances are proprietary. However, the results of technological advances in these areas are quite evident in the continual improvement in the size, performance, and availability of HPGe detectors. Maximum photopeak efficiency for HPGe gamma-ray detectors is doubling every 6–8 years. Concurrently, energy resolutions are moving toward the theoretical limits of Equation 81.8 as the concentrations of trapping centers are reduced.

The reliability as well as the performance of germanium gamma-ray detectors has also continued to improve, although this is harder to quantify. Cryostats have been redesigned to reduce virtual and direct leaks, reduce microphonics, implement modular design, and improve ruggedness. Detector makers are also making more serious attempts to offer models with reduced backgrounds by judicious design changes and careful selection of materials.

New applications for gamma-ray spectroscopy have emerged. The HPGe detector industry has recently supplied over 100 detectors each to two different experimental facilities (Gammasphere in the United States and Euroball in Europe), where they were arranged spherically in a modular fashion around the target of an ion accelerator to study the decay of nuclei from excited states of high angular momentum.

For users of single-detector systems, developments in the pulse-processing electronics necessary for data acquisition and in the hardware and software for data analysis have resulted in both more compact and more flexible systems. Plug-in cards for a personal computer are available that contain not only the functions of the ADC and multichannel analyzer but the high-voltage power supply and amplifier as well. Software developments also allow for control of many pulse-processing parameters that were previously set manually.

81.3 Silicon Detectors

As with germanium for gamma-ray spectroscopy, the impurity requirements on silicon for nuclear radiation detectors are also stringently low—and difficult to obtain. Such silicon must be grown by the float-zone technique to eliminate contamination from a crucible. Unlike with germanium, little dedicated effort has been expended trying to improve silicon growth techniques to achieve superior detector characteristics. Most progress in material quality has come from technology improvements aimed at other applications. The purest silicon commercially available typically has a net electrically active impurity concentration of a few times 10^{11} cm^{-3} (compared to 10^{10} cm^{-3} for HPGe), which usually limits device thicknesses to less than 1 mm. However, this thickness is sufficient for many applications. Silicon detectors are widely used for heavy-charged-particle (alpha, proton, and ion) spectroscopy. When thicker silicon devices are required (x-ray spectroscopy, beta spectroscopy, or medium-energy protons: $E > 25$ MeV), silicon of higher net purity may be obtained by lithium drifting [26], but such material cannot be subsequently processed above room temperature.

In contrast to germanium detectors, silicon detectors can be operated at room temperature. Compared to gas and scintillation detectors, silicon detectors have good energy resolution and are reasonably compact. They are fabricated from slices of a silicon single crystal and are available in a variety of areas (25–3000 mm^2), and the active thickness is usually a few hundred micrometers. Specialized detectors have been developed for a wide variety of applications.

Energetic heavy-charged particles lose kinetic energy continuously along a linear path in an absorbing material. Energy is transferred primarily to the electrons in the absorbing material but to a lesser extent to the nuclei also, via Rutherford scattering. Although only energy transferred directly to the electronic system generates electron hole pairs, Equation 81.6 (with epsilon = 3.62/pair for silicon at 300 K) is still a good approximation. Energy loss is characterized by two parameters: the specific ionization loss dE/dx, which depends on the incident particle, its energy, and the absorbing material,

and the range R (i.e., the penetration depth of the particle), which determines the detector thickness required for complete energy absorption. The continuous nature of energy loss leads to substantial window effects.

81.3.1 Diffused Junction Detector

Silicon detectors can be generically categorized by the type of rectifying contact employed. The diffused junction detector is fabricated by diffusing phosphorus from the gas phase into *p*-type silicon. This is a high-temperature (900 °C–1200 °C) operation that is prone to introducing faster diffusing metals into the bulk that can act either as generation centers increasing leakage current or as trapping centers degrading charge collection. The thickness of the diffused region, from 0.1 to 2.0 μm, also presents a dead layer to incident particles that are reduced in alternative technologies. Nonetheless, these detectors find use due to their ruggedness and economy.

81.3.2 Surface Barrier Detector

Surface barrier junctions are fabricated by evaporating either gold onto *n*-type silicon or aluminum onto *p*-type silicon. A typical entrance window is equivalent to 80 nm of silicon. The rectification properties depend on the charge density of surface states of the silicon and of the thin oxide layer over the silicon, as well as on the evaporated metal. The wafer is epoxied in an insulating ring before metallization. The finished detector is encapsulated in a can that has a front window for particle entry and a single contact in the back for the combined function of applying bias and for extracting the signal pulse. Devices can be operated either in the partially depleted or totally depleted mode. As fabrication is entirely at room temperature, there is no opportunity for metal contamination by diffusion. Generally, surface barrier detectors have lower leakage current and less system noise than a diffused junction detector of comparable area and depth. However, detectors currently fabricated by ion implantation have still lower leakage current and electronic noise, together with a thinner and more rugged front contact. On the other hand, implanted detectors are not available in the same range of active thicknesses as surface barrier detectors. Below 100 μm and above 500 μm, only surface barrier detectors are currently available. Surface barrier detectors can be made in small quantities with rather simple equipment.

81.3.3 Ion-Implanted Detectors

A simplified representation of ion-implanted detector fabrication is shown in Figure 81.15. The first successful implementation of silicon planar processing to silicon detectors was reported by Kemmer [27]. The procedure starts with the thermal growth of an oxide film on a high-purity, *n*-type silicon wafer. Windows are then opened in the oxide by photolithographic techniques. The front contact area is implanted with boron to form the rectifying contact, and arsenic is implanted into the back side. The wafer is then annealed to activate the implant, and aluminum is evaporated on both sides to reduce sheet resistivity. Typical entrance windows are 50 nm silicon equivalent. Electrical connections are made by wire bonding to the aluminum layers. Finished detectors are canned in a manner similar to surface barrier detectors. More than one detector can be fabricated on the same wafer using the appropriate masks during photolithography. In fact, quite elaborate detector geometries can be achieved via photolithography. The detector in Figure 81.15 is actually a strip type.

This ion implantation planar process technology is well suited for mass production of wafer sizes compatible with the rest of the silicon industry. Minimum wafer diameters are now 4 or 5 in. At this diameter, breakage during fabrication is an issue for thicknesses less than 150 μm. For thicknesses greater than 500 μm, the availability of enough sufficiently pure material to justify the cost of photolithographic masks is an issue. Ion-implanted detectors can be baked at 200 °C to reduce outgassing. This is a

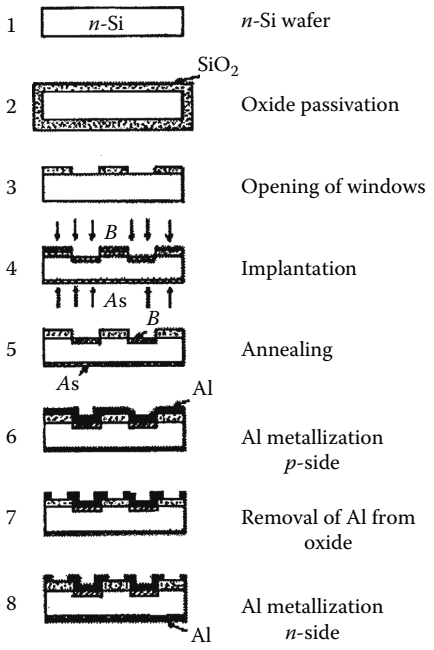

FIGURE 81.15 Steps in the fabrication of passivated-planar silicon diode detectors. (From Kemmer, J. et al., *IEEE Trans. Nucl. Sci.*, NS-29, 733, 1982.)

significant improvement over surface barrier detectors, which irreversibly degrade by device processing above room temperature. This is a useful feature, as most heavy-charged-particle spectroscopy is done in a vacuum.

Leakage currents, at room temperature, are typically 1–10 nA per cm^2 active area and per 100 μm depletion depth. These values represent an order of magnitude reduction in leakage current with respect to surface barrier detectors. Two factors are relevant. Passivation of silicon surfaces by thermal oxidation is extremely effective in reducing leakage current around the rectifying contact. Also, the bulk generation current is reduced by the gettering of metal impurities during the high-temperature oxidation. Float-zone silicon for radiation detectors usually has a minority carrier lifetime longer than 1 ms, and this can be increased to an order of magnitude during detector fabrication [28]. Thus, not only is leakage current reduced, but potential charge collection problems are also eliminated.

81.3.4 Energy Resolution

A typical spectrum of an Am-241 alpha-particle source taken with an ion-implanted detector is shown in Figure 81.16. While the factors considered in Equation 81.8 for germanium gamma-ray spectrometers are still valid, additional considerations also apply. In particular, if the source is moved closer to the detector to improve collection efficiency, larger differences in the angle of incidence will produce peak broadening due to larger variation in effective window thickness. Even when the source is sufficiently distanced from the detector, there will still be spatial variations in window thickness, as well as some variation in energy lost escaping from the source and traversing to the detector.

Another source of peak broadening is the variation in the small amount of particle energy lost during Rutherford scattering. This energy is transmitted directly to the scattering nuclei and does not generate electron–hole pairs, and a small pulse deficit results. These events are relatively few but large and therefore contribute disproportionately to peak variance. The FWHM contribution of this effect on a 6 MeV alpha-particle peak has been estimated to be 3.5 keV [29].

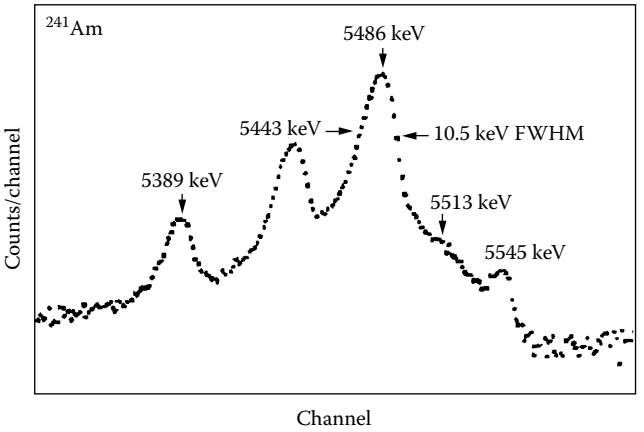

FIGURE 81.16 Spectrum of a ^{241}Am alpha-particle source (log scale) measured with an IP detector (25 mm^2 area, 300 μm thick) at room temperature. Resolution at 5.486 MeV is 10.6 keV (FWHM). (From Kemmer, J. et al., *IEEE Trans. Nucl. Sci.*, NS-29, 733, 1982.)

81.3.5 Spatial Resolution

The uninterrupted progress of the semiconductor silicon industry in achieving both larger wafers and smaller device features has allowed the development of larger and more complex silicon detectors that can provide position information in addition to (or instead of) energy information. Spatial detection can be obtained by fabricating detectors as pixels (2D) or strips (1D) on the same wafer. For penetrating radiation, two strip detectors, one behind the other but with the strip pattern rotated 90°, provide 2D positioning. Frequently, such detectors are individually designed and fabricated for a particular application. Strip detectors, drift detectors, and charge-coupled device (CCD) detectors will be discussed here.

81.3.6 Strip Detectors

Silicon strip detectors are currently fabricated on silicon wafers (typically approximately 300 μm thick) by using photolithographic masking to implant the rectifying contact in strips [30]. The strips usually have a pitch on the order of 100 μm and a width less than half of this size to minimize strip-to-strip capacitance and hence electronic noise [31]. The device is biased past depletion, and the back-blocking contact is continuous. Each strip requires, in principle, its own signal processing electronics; however, charge division readout (capacitive or resistive) can reduce the number of amplifiers by a factor of 10. Detectors are fabricated in rectangular segments from a single wafer and can be ganged together if a larger area is needed.

Strip detectors are well established in high-energy physics experiments for reconstruction on the micron scale of the tracks of ionizing particles. The particles being tracked result from the collision of accelerated particles with a target and are highly energetic (>10^{10} eV). Frequently, experimental interest is focused on short-lived particles created in the collision but which decay before they can be directly detected. The spatial resolution of the decay vertex from the original collision is necessary to detect such a particle and to determine its lifetime.

The requirements of new high-energy experiments and advances in silicon technology have produced much evolution and innovation in the strip detector concept. For example, a double-sided microstrip detector with an oxide–nitride–oxide capacitor dielectric film has been reported [32]. The use of intermediate strips to improve spatial resolution has become common [33], and the biasing network has been integrated onto the detector [34].

81.3.7 Drift Detectors

Silicon drift detectors were first proposed by Gatti and Rehak [35] as an alternative to silicon strip detectors in high-energy physics experiments. The primary motivation was to significantly reduce the number of readout channels. Drift detectors have subsequently been adapted for x-ray spectroscopy. These detectors are usually fabricated on *n*-type silicon wafers with holes collected to either a *p*+ contact on the back side of the detector or a concentric annular *p*+ contacts on the front side. The detector is depleted from both sides. The reverse bias applied to the *p*+ annular rings is varied in such a way that electrons are collected radially in a potential energy trough to an *n*+ anode at the center of the detector on the front side.

A cross section through a circular drift detector is shown in Figure 81.17. The electron collecting anode ring surrounds the integrated FET used for the first stage of signal amplification. Enough negative bias is applied to the back contact (actually the entrance window) to deplete the wafer to the anode, which is near ground potential. At the same time, negative bias, progressively increasing in magnitude, is applied from the ring next to the anode (near ground potential) to the outermost ring, which is maintained at about two times the bias of the back contact. These applied biases deplete the detector in such a way that there is an electrostatic potential minimum for electrons that varies in depth across the detector from right under the front surface at the anode to near the back contact at the last ring. Ionized electrons will drift first to this minimum and then drift radially to the anode as shown in Figure 81.17. A feature of this contacting arrangement is that the anode capacitance, and hence amplifier series noise, is low and nearly independent of the active area of the detector.

Silicon drift detectors have been designed in several different topologies of various sizes for different experimental needs. Spatial resolution for tracking and vertexing of high-energy particles is obtained by segmenting the cathode (for angular position) and analysis of signal rise time (for radial position [36]). Drift detectors with integrated electronics have been demonstrated for high-resolution room-temperature x-ray spectroscopy [37].

81.3.8 CCD Detectors

The design of CCD detectors has similarities to the silicon drift detector [35]. The CCD detector is normally fabricated on an *n*-type silicon wafer depleted both from the back side with a continuous *p*+ contact on the back and from *p*+ CCD registers on the front. Reverse bias voltages are such that the wafer is totally depleted and the electron potential minimum is about 10 μm below the CCD registers.

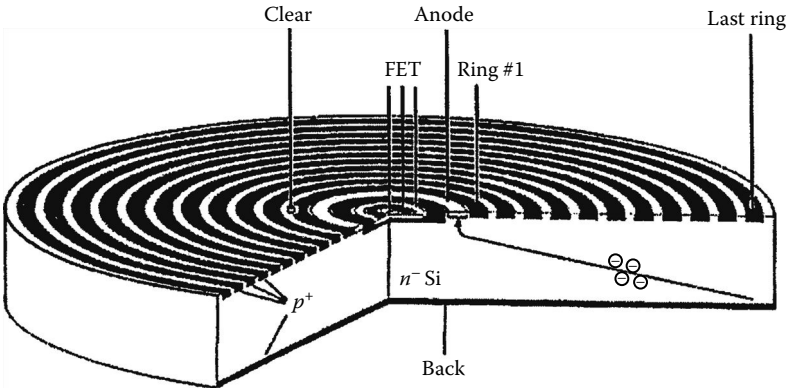

FIGURE 81.17 Cross section of a cylindrical silicon drift detector with integrated *n*-channel JFET. The gate of the transistor is connected to the collecting mode. The radiation entrance window for the ionizing radiation is the nonstructured back side of the device. (From Lechner, P. et al., *Nucl. Instru. Meth.*, A377,346, 1996.)

After an ionizing event, holes are collected to the *p*+ contacts, and electrons are trapped under a nearby register, then transported down a channel of registers by properly clocked voltage pulses to the registers. Each channel has its own readout anode, which can be made small to minimize capacitance, a prerequisite for minimizing noise. The first stage of amplification is frequently integrated onto the same wafer. Spatial resolution is limited to the register (pixel) size. Brauniger et al. [38] described initial results on a 6 × 6 cm CCD array of 150 × 150 μm pixels intended for satellite x-ray imaging. The system also had an energy resolution of 200 eV FWHM for 5.9 keV x-rays at room temperature.

Silicon pixel detectors have also been designed using other highly integrated device structures to optimize particular performance aspects such as timing resolution. Pixel detectors using MOS transistors [39] and using reverse-biased diodes with individual readout circuitry [40] have been described.

81.3.9 Present Status of Silicon Detector Technology

The simple-structured silicon detectors fabricated with parallel contacts on a silicon wafer continue to serve a well-established need for charged-particle spectroscopy. Where economies of scale can be applied, ion-implanted detectors have replaced surface barrier detectors. In x-ray spectroscopy for microanalysis (SEM and XRF), liquid-nitrogen-cooled Si:Li detectors are being challenged by similarly sized HPGe detectors, but Si:Li are still more widely used. In projects of sufficient size to support their development, specialized low-noise silicon drift detectors and CCD-based detectors have been designed and fabricated with promising room-temperature energy resolution: 200 eV FWHM at 5.9 keV. These highly structured detector technologies may find future application in liquid-nitrogen-cooled or room-temperature systems for microanalysis using x-ray spectroscopy.

In high-energy physics, the use of various strip, drift, and pixelated detectors for tracking and vertex determination has flourished. These efforts will intensify as experimental requirements for spatial resolution increase. However, radiation damage to the detector is already an issue in this application, and higher-luminosity beams will only increase the problems. Nevertheless, it appears that the continuing need of the high-energy physics community for a higher number and density of signal paths forecasts continued reliance on the ever-improving integration technology of the semiconductor silicon industry.

81.4 Room-Temperature Semiconductors

Applications arise that require energy resolution beyond the capability of scintillator systems and where cryogenically cooled semiconductors are not suited. Examples include detector probes for monitoring restricted areas, monitoring at remote sites where replenishing the coolant is impractical, spectral imaging, and many portable instrument applications. There is available a class of semiconductor detectors that satisfy many such needs by providing energy resolution substantially better than the best scintillators (although inferior to cooled semiconductors) while operating at ambient temperature. In addition to spectroscopy, these devices are also useful for counting applications where high detection efficiency per unit volume is required. In these applications, the devices are operated in pulse mode wherein the charge associated with single-photon absorption events is recorded. They also can be operated in a current mode in the manner of a solid-state ion chamber. In their current stage of development, room-temperature detectors are limited in size and best suited for the energy region below 1 MeV.

The room-temperature detectors are distinguished from cryogenic semiconductors by the magnitude of the energy gap that separates the normally vacant conduction band from the highest filled band. If this energy gap is small, as is in the case of silicon (1.14 eV) and germanium (0.67 eV), electrons can be thermally stimulated across the bandgap at room temperature. The resultant current competes with the gamma-ray-generated signal precluding room-temperature operation of germanium and high-resolution applications of silicon. Thermally stimulated current is reduced to acceptable levels at

bandgaps energies of about 1.4 eV and above. This phenomenon has been successfully exploited in the development of room-temperature detector materials including cadmium zinc telluride (acronym, CZT), cadmium telluride (CdTe), and mercuric iodide (HgI_2).

81.4.1 Theory of Operation

Operating principles of room-temperature detectors are similar to those governing the more familiar cryogenic semiconductor devices. Gamma radiation is absorbed in the material and generates electron–hole pairs that move under the influence of an applied electric field to contacts and external electronics for processing and production of the familiar pulse-height spectrum. The process is shown schematically in Figure 81.18. Fundamental to the charge transfer process is the carrier mobility (μ) and the carrier life time (τ). The product $\mu\tau E$ defines a drift length (λ) that should be long compared to the inter-contact dimensions. Owing to the substantially higher average atomic number of the room-temperature detector materials in the gamma absorption cross sections, the probability of gamma-ray absorption is much higher than in silicon or germanium (Figure 81.8). As a result, room-temperature detectors provide greater detection efficiency per unit thickness.

The energy required to produce an electron–hole pair (ε) is typically a few times the energy bandgap of the material. In silicon where the bandgap is 1.14 eV, the energy to produce an electron–hole pair (ε) is about 3.5 eV. The absorption of a 1 MeV photon in silicon thus produces about 285,000 pairs. Values of ε for room-temperature materials are in the region 4.2–5.0 eV per e–h pair (see Table 81.3), and consequently, fewer electron–hole pairs are generated per unit of absorbed energy. Complete collection of the

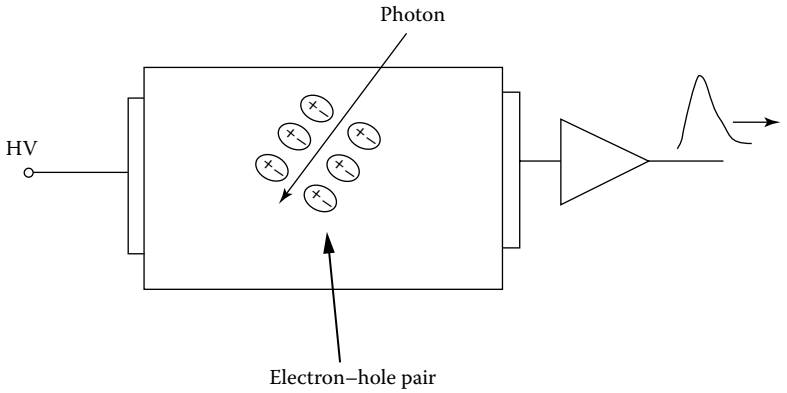

FIGURE 81.18 Schematic illustration of charge generation in a planar detector.

TABLE 81.3 Physical Parameters of Common Room-Temperature Semiconductor Materials

Material	E_g (eV)	1	ε (eV)	ρ (Ω)	$(\mu\tau)_e$ (cm²/V)	$(\mu\tau)_h$ (cm²/V)
CZT	1.65	48	5.0	10^{11}	1×10^{-3}	6×10^{-6}
Cadmium telluride	1.5	50	4.4	10^{9}	3.5×10^{-3}	2.3×10^{-4}
Mercuric iodide	2.13	62	4.2	10^{13}	1×10^{-4}	4×10^{-5}

Source: James, R.B. et al. (eds.), *Semiconductors for Room-Temperature Radiation Detector Applications*, Vol. 32, Materials Research Society, Pittsburgh, PA, 1993.

E_g, bandgap energy; Z, average atomic number; ε, energy to create an electron–hole pair; ρ, resistivity.

[1]Note also that ionizing radiation can cause both permanent and transient resistivity losses in insulating materials and should be considered in high-flux or high-fluence applications.

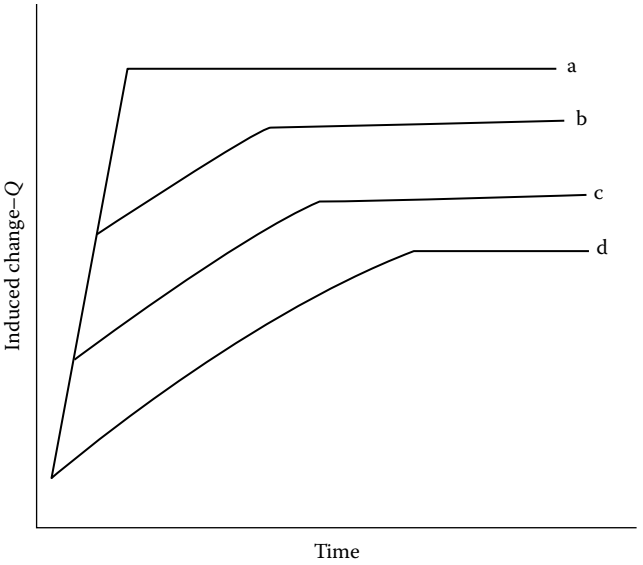

FIGURE 81.19 Charge collections in planar detector for single-photon interaction in a planar detector. Curves a through d depict the charge from photon interactions at increasing depths below the cathode.

charge is desired, although charge trapping, which may not affect the two carrier types equally, prevents this in most cases. The drift length for holes (λ_h) in these materials is often less than the intercontact dimensions and creates a condition where the collection efficiency depends on the photon interaction depth. This phenomenon is illustrated in Figure 81.19, where induced charge from single gamma absorption events originating at various depths in the material is plotted as a function of time. The initial fast-rising segment is due to the more mobile electrons; the slower component is due to holes. In this example, hole trapping is assumed and is manifest in the curvature of the hole segment. The charge collection efficiency (η) can be derived from the Hecht relation [41]. For a photon absorbed at a distance x from the cathode of a planar detector of thickness L operated with a uniform electric, the relationship becomes

$$\eta = \frac{\lambda_e}{L}\left[1 - \exp\frac{(L-x)}{\lambda_e}\right] + \frac{\lambda_h}{L}\left[1 - \exp\frac{-x}{\lambda_h}\right] \tag{81.10}$$

The dependence of the collection efficiency on interaction depth reduces energy resolution and without mitigation would limit high resolution to thin devices. Fortunately, methods have been developed that permit high-energy resolution to be achieved in relatively thick samples. As with cooled semiconductor detectors, the energy resolution of the combined detector-electronics system is normally specified by the full width of a monoenergetic spectral peak at its half amplitude points (ΔE). The FWHM is in turn related to the variance in the peak L^2 (see Equation 81.8). It is useful to note that the energy resolution is related to the reciprocal of the product $\mu\tau$.

81.4.2 Operational Considerations

Important physical parameters for the leading room-temperature detectors are summarized in Table 81.3. Detectors are available with surface area of a few square centimeters and thicknesses up to about 1 cm. The performance of detectors based on the different materials varies considerably, as can the performance for detectors of the same material. The choice of specific detector material is normally dictated by the application. The exceptionally high-resistivity and high-photoelectric cross section in mercuric

iodide permits good resolution and high efficiency in the x-ray region, particularly below 10 keV. For example, ΔE of 4% has been reported [42] with typical values in the region of 10%. For applications in the region of 0.5 MeV, a trade-off between efficient gamma absorption and resolution may be required. If energy resolution is the primary concern, thinner devices that minimize charge trapping are generally required. Considerable progress is being made in achieving both high efficiency and high resolution in the region of 0.5 MeV, particularly with CZT. For example, the resolution of better than 3% has been achieved in 1 cm thick detector at 511 keV and about 5% at 662 keV in a 2.5 cm thick device [4]. Improvements in material quality can be expected that further improve the performance of thick detectors, as the $\mu\tau$ values are further increased.

Procedures have been developed to overcome many of the thickness and surface area limitations of currently available devices. For instance, electronic circuits have been developed that permit the operation of planar arrays that provide spectral resolution approaching that of single units while providing substantially greater area [43]. Similarly, high gamma absorption efficiency with useful spectral resolution has been obtained with stacks of thin spectrometer-quality detectors [44]. Additionally, pulse-processing and single-charge collection procedures have been demonstrated that enhance spectrometer performance. This development can be expected to substantially improve the availability and price of spectrometer grade devices. Further details concerning the performance of these devices, as well as electronic processing and design details, are available in the literature [2,3,45,46].

Detectors based on the materials in Table 81.3 are available commercially. Due to the evolving nature of this technology, it is recommended that buyers' guides be consulted for suppliers and current availability.

81.5 Prices and Availability

The detectors described in this chapter are available commercially. Their prices vary widely, depending on type, size, and performance. Gaseous detectors are normally in the range of a few hundred dollars for standard designs. Scintillator–photomultiplier combinations range from about a thousand to several thousand dollars, depending on size and resolution. Room-temperature semiconductor detectors range from less than one hundred dollars for small, low-resolution devices to over a thousand dollars for large (1 cm^3), high-resolution devices. Pricing of coaxial HPGe detectors is based largely on their gamma-ray efficiency, which is specified relative to a 3 × 3 in. sodium iodide scintillator at 1.33 MeV. Coaxial detectors are available with relative efficiencies up to about 150% with cost in the area of several hundred dollars per percent efficiency. Planar HPGe detectors are normally less expensive than coaxial designs. In either case, the price includes cryostat, dewar, and preamplifier. Cryogenic silicon detectors are available in area up to several tens of square millimeters. Cost ranges to >$10,000, depending on size, performance, and complexity of design.

References

1. G. F. Knoll, *Radiation Detection and Measurement*, New York: John Wiley & Sons, 1979.
2. R. B. Rossi and H. H. Staub, *Ionization Chambers and Counters*, New York: McGraw-Hill, 1949.
3. M. J. Weber, P. Lecoq, R. C. Ruchti, C. Woody, W. M. Yen, and R. Y. Zhu (eds.), *Scintillator and Phosphor Materials*, Vol. 348, Pittsburgh, PA: Materials Research Society, 1994.
4. T. E. Schlesinger and R. B. James (eds.), *Semiconductors for Room-Temperature Nuclear Detector Applications*, Vol. 43, Semiconductors and Semimetals, San Diego, CA: Academic Press, 1995.
5. R. B. James, T. E. Schlesinger, P. Siffert, and L. Franks (eds.), *Semiconductors for Room-Temperature Radiation Detector Applications*, Vol. 302, Pittsburgh, PA: Materials Research Society, 1993.
6. J. Fraden, *AIP Handbook of Modern Sensors*, New York: American Institute of Physics, 1993.
7. M. Cuzin, R. B. James, P. F. Manfredi, and P. Siffert (eds.), *Proceedings of the 9th International Workshop on Room Temperature Semiconductor X- and Gamma-Ray Detectors*, Grenoble, France, September 18–22, 1995, *Nucl. Instru. Meth.*, 380, 1996.

8. T. E. Bortner, G. S. Hurst, and W. G. Stone, Drift velocities of electrons in some commonly used counting gases, *Rev. Sci. Instru.*, 28(2), 103, 1957.
9. W. J. Price, *Nuclear Radiation Detection*, New York: McGraw-Hill, 1958.
10. F. H. Attix and W. C. Roesch, *Radiation Dosimetry*, 2nd edn., New York: Academic Press, 1966.
11. W. H. Tait, *Radiation Detection*, Boston, MA: Butterworth, 1980.
12. G. N. Whyte, *Principles of Radiation Dosimetry*, New York: John Wiley & Sons, 1959.
13. J. B. Birks, *Theory and Practice of Scintillation Counting*, New York: MacMillan, 1964.
14. J. Markakis, High resolution scintillation spectroscopy with HgI_2 as the photodetector, *Nucl. Instru. Meth.*, A263, 499, 1988.
15. R. N. Hall, Chemical impurities and lattice defects in high-purity germanium, *IEEE Trans. Nucl. Sci.*, 260, NS-21, 260–272, 1974.
16. E. E. Haller, W. L. Hansen, and F. S. Goulding, Physics of ultra-pure germanium, *Adv. Phys.,* 30(1), 93–138, 1981.
17. W. G. Pfann, *Zone Melting*, New York: John Wiley & Sons, 1966.
18. G. K. Teal and J. B. Little, Growth of germanium single crystals, *Phys. Rev.*, 78, 647, 1950.
19. R. H. Pehl, E. E. Haller, and R. C. Cordi, Operational characteristics of germanium detectors at higher temperatures, *IEEE Trans. Nucl. Sci.*, NS-20, 494, 1973.
20. L. S. Darken and C. E. Cox, High-purity germanium detector, pp. 23–80, in *Semiconductors for Room-Temperature Nuclear Detector Applications*, New York: Academic Press, 1995.
21. R. H. Pehl, N. W. Madden, J. H. Elliott, T. W. Raudorf, R. C. Trammell, and L. S. Darken, Jr., Radiation damage resistance of reverse electrode GE coaxial detectors, *IEEE Trans. Nucl. Sci.*, NS-26, 321, 1979.
22. ANSI, *IEEE Test Procedures for Germanium Detectors for Ionizing Radiation*, ANSI/IEEE Standard 325–1989.
23. R. H. Pehl and F. S. Goulding, Recent observations on the fano factor in germanium, *Nucl. Instru. Meth.*, 81, 329–330, 1970.
24. J. Lacer, E. E. Haller, and R. C. Cordi, Entrance windows in germanium low-energy x-ray detectors, *IEEE Trans. Nucl. Sci.*, NS-24, 53, 1977.
25. C. E. Cox, B. G. Lowe, and R. Sareen, Small area high purity germanium detectors for use in the energy range 100 eV to 100 keV, *IEEE Trans. Nucl. Sci.*, 35, 28, 1988.
26. E. M. Pell, Ion drift in an *n-p* junction, *J Appl. Phys.*, 31, 291, 1960.
27. J. Kemmer, Fabrication of low noise silicon radiation detectors by the planar process, *Nucl. Instru. Meth.*, 169, 499–502, 1980.
28. J. Kemmer and G. Lutz, New detector concepts, *Nucl. Instru. Meth.*, A235, 365–377, 1987.
29. G. D. Alkhazov, A. P. Komar, and A. Vorob'ev, Ionizing fluctuations and resolution of ionization chambers and semiconductor detectors, *Nucl. Instru. Meth.*, 48, 1–12, 1967.
30. J. Kemmer, P. Burger, R. Henck, and E. Heijne, Performance and applications of passivated ion-implanted silicon detectors, *IEEE Trans. Nucl. Sci.*, NS-29, 733, 1982.
31. T. Dubbs, S. Kashigin, M. Kratzer, W. Kroeger, T. Pulliam, H. E.-W. Sadrozinski et al., Noise determination in silicon micro strips, *IEEE Trans. Nucl. Sci.*, 42, 1119, 1996.
32. Y. Saitoh, T. Akamine, M. Inoue, J. Yamanaka, K. Kadoi, R. Takano, Y. Kojima et al., Fabrication of a double-sided silicon microstrip detector with an ONO capacitor dielectric film, *IEEE Trans. Nucl. Sci.*, 43, 1123, 1996.
33. P. Chochula, V. Cindro, R. Jeraj, S. Macek, D. Zontar, M. Krammer, H. Pernegger, M. Pernicka, and C. Mariotti, Readout of a Si strip detector with 200 μm pitch, *Nucl. Instru. Meth.*, A377, 409–411, 1996.
34. T. I. Westgaard, B. S. Avset, N. N. Ahmed, and L. Eversen, Radiation hardness of punch-through and FET biased silicon microstrip detectors, *Nucl. Instru. Meth.*, A377, 429–434, 1996.
35. E. Gatti and P. Rehak, Semiconductor drift chamber—An application of a novel charge transport scheme, *Nucl. Instru. Meth.*, 225, 608–614, 1984.
36. P. Rehak, J. Walton, E. Gatti, A. Longoni, M. Sampietro, J. Kemmer, H. Dietl et al., Progress in semiconductor drift detectors, *Nucl. Instru. Meth.*, A248, 367–378, 1986.

37. P. Lechner, S. Eckbauer, R. Hartman, S. Krisch, D. Hauff, R. Richter, H. Soltau et al., Silicon drift detectors for high resolution room temperature x-ray spectroscopy, *Nucl. Instru. Meth*., A377, 346–351, 1996.
38. H. Brauninger, R. Danner, D. Hauff, P. Lechner, G. Lutz, N. Meidinger, E. Pinotti, C. Reppin, L. Struder, and J. Trumper, First results with the *pn*-CCD detector system for the XMM satellite mission, *Nucl. Instru. Meth*., 326(1–2), 129–135, 1993.
39. K. Misiakos and S. Kavadias, A pixel segmented silicon strip detector for ultra fast shaping at low noise and low power consumption, *IEEE Trans. Nucl. Sci*., 43, 1102, 1996.
40. E. Beauville, C. Cork, T. Earnest, W. Mar, J. Millaud, D. Nygen, H. Padmore et al., A 2D smart pixel detector for time resolved protein crystallography, *IEEE Trans. Nucl. Sci*., 43(3), 1243, 1996.
41. H. K. Hecht, Zum mechanisms des lichtelektrischen primarstromes in isolierenden kristallen, *Z Phys*., 77, 235–245, 1932.
42. J. S. Iwanczyk, B. E. Patt, Y. J. Wang, and A. K. Khusainov, Comparison of HgI_2, CdTe, and Si (*p-i-n*) x-ray detectors, *Nucl. Instru. Meth*., A380, 186–192, 1996.
43. V. Gerrish, private communication, 1995.
44. R. Olsen, R. B. James, A. Antolak, and C. Wang, *Proceedings of the 1994 International Nuclear Materials Management Conference*, Bruges, Belgium, Vol. 23, p. 589, 1994.
45. B. E. Patt, J. S. Iwanczyk, G. Vikelis, and Y. J. Wang, New gamma-ray detector structures for electron only charge carrier collection utilizing high-Z compound semiconductors, *Nucl. Instr. Meth*., A380, 276–281, 1996.
46. P. N. Luke, Electrode configuration and energy resolution in gamma-ray detectors, *Nucl. Instr. Meth*., A380, 232–237, 1996.

Further Readings

Guerra A. D., *Ionizing Radiation Detectors for Medical Imaging*, World Scientific Publishing, Co. Pte, Ltd, Singapore, 2004

Lutz G., *Semiconductor Radiation Detectors*, 2nd edn., Springer, Berlin, Germany, 2001.

Maas M. C., *Monolithic Scintillator Detectors for High Resolution Positron Emission Tomography*, IOS Press, Amsterdam, the Netherlands, 2008.

Partial List of Vendors and Suppliers

Gamma products, Inc., 7730 W. 114th Pl., Palos Hills, IL 60465, Phone: 708-974-4100, Fax: 708-974-0071, www.gammaproducts.com

Industrial Test Systems, Inc., 1875 Langston Street, Rock Hill, SC 29730, Phone: 803-329-9712, 800-861-9712 (toll free), Fax: 803-329-9743, www.sensafe.com

LPR Global, 720 Bathurst St., 408, Toronto, Ontario M5S2R4, Canada, Phone: 416-423-5590, Fax: 416-406-6141, www.uskoreahotlink.com/

National X-Ray Corp., 595 Old Norcross Rd., Suite G, Lawrenceville, GA 30045, Phone: 866-484-9269 (toll free), Fax: 678-960-0085, www.nationalx-ray.com

Princeton Gamma-Tech, Inc., 303C College Rd. E., Princeton, NJ 08540, Phone: 609-924-7310, Fax: 609-924-1729, www.pgt.com

Radiation Monitoring Devices, 44 Hunt St., Suite 2, Watertown, MA 02472, Phone: 617-668-6800, 800-532-3763 (toll free), 800-LEAD-RMD (toll free), Fax: 617-926-9980, www.rmdinc.com

Rapiscan Systems, 1901 S. Bell St., Suite 325, Arlington, VA 22202, Phone: 703-812-0322, Fax: 703-812-0335, www.rapiscansystems.com/

82

Charged-Particle Measurement

John C. Armitage
Carleton University

Madhu S. Dixit
Carleton University

Jacques Dubeau
Carleton University

Hans Mes
Carleton University

F. Gerald Oakham
Carleton University

82.1 Introduction

82.1.1 Interaction of Charged Particles with Matter

There are a number of subatomic charged particles that can be detected by their interaction with matter. These include protons (hydrogen nuclei), β-particles (fast electrons), α-particles (helium nuclei), light ions, heavy ions, and fission fragments. Some of these particles are emitted by natural radioactivity on Earth or originate from space and reach the Earth in the form of cosmic rays; others are due to human activities (nuclear industry, accelerators). The kinetic energy of charged particles is given in units of electron volts (eV), where $1\ \text{eV} = 1.6 \times 10^{-19}$ J. Naturally occurring α- and β-particles from radioactive decay have energies up to 10 MeV. Ions, such as Cl^+, are accelerated to 35 MeV and higher in beam analysis procedures. Energetic particles that originate from space can have energies up to 10^{12} GeV. Charged particles traversing matter lose kinetic energy until they eventually come to a halt. In the case of electrons, protons, α-particles, or light ions, most of this energy is lost through interactions with the electrons of the target. Heavier ions also lose a significant amount of kinetic energy through direct collisions with the nuclei of the constituent atoms.

However, for all types of charged particles of concern here, ionization of the target atoms is the dominant mode of excitation of the detection medium. This process is also the main source of radiation damage in biological tissue.

82.1.2 Energy Loss of Protons and Ions

The quantity of energy deposited by an incident energetic charged particle in a detection medium is a function of the atomic mass, A_{med}; the atomic number, Z_{med}; and the density of target atoms that it meets along its path. Hence, the unit of dimension used in this field is the mass thickness, and it is measured most often in units of g cm^{-2}. This is equal to the geometric thickness or path length x, multiplied by the density of the detector volume, ρ. It follows that the rate of energy loss of a particle in the detection volume is $dE/(\rho\, dx)$ and it is given in units of keV (g cm^{-2})$^{-1}$ or MeV (g cm^{-2})$^{-1}$. The energy loss due to ionization is characterized by the Bethe–Bloch equation:

$$-\frac{1}{\rho}\frac{dE}{dx_{ion}} = D\frac{z^2 Z_{med}}{A_{med}}\frac{c^2}{v^2}\left[\ln\frac{2m_0v^2}{I_{med}} - \ln\left(1-\frac{v^2}{c^2}\right) - \frac{v^2}{c^2}\right] \quad \text{MeV (g cm}^{-2})^{-1} \tag{82.1}$$

with $D = 0.307$ MeV (g cm^{-2})$^{-1}$ and c is the velocity of light (3.0×10^8 m s^{-1}). The incident ion is described by z and v, its charge and velocity, respectively. The response of the atoms of the target are further defined by $I_{med} \sim 16\, Z_{med}^{0.9}$ eV, their mean ionization energy. The energy loss is characterized by a peak at low energy and a minimum at higher energies where a particle of $z = 1$ is referred to as a minimum ionizing particle (MIP). The energy loss curves of protons in Si, Ar, and Au are shown in Figure 82.1. The energy loss expressed in MeV (g cm^{-2})$^{-1}$ is lower for higher Z_{med} materials, where the ratio Z_{med}/A_{med} becomes less than 0.5 and I_{med} is large. However, when multiplied by the material's density, the energy loss in MeV cm^{-1} shows a reverse trend; it is greater for high Z_{med} materials because they have a high density. The rate of energy loss varies to the second power of the charge z of the incident ion and as the inverse square of its kinetic energy ($1/v^2$ term). Equation 82.1 holds for protons and α-particles of energy above 500 keV and 1 MeV, respectively, in Si where the target is described by an

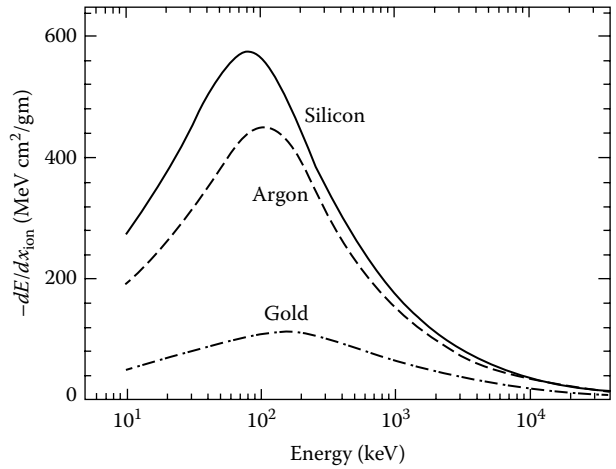

FIGURE 82.1 Electronic energy loss curves for protons in three different absorber elements are shown as a function of kinetic energy. The target element with the lower Z_{med} displays the highest stopping power due to its low average ionizing potential. These curves were obtained using the SRIM computer program. (From Ziegler, J.F., *SRIM: The Stopping and Range of Ions in Matter*, IBM-Research, Yorktown, NY, 1996.)

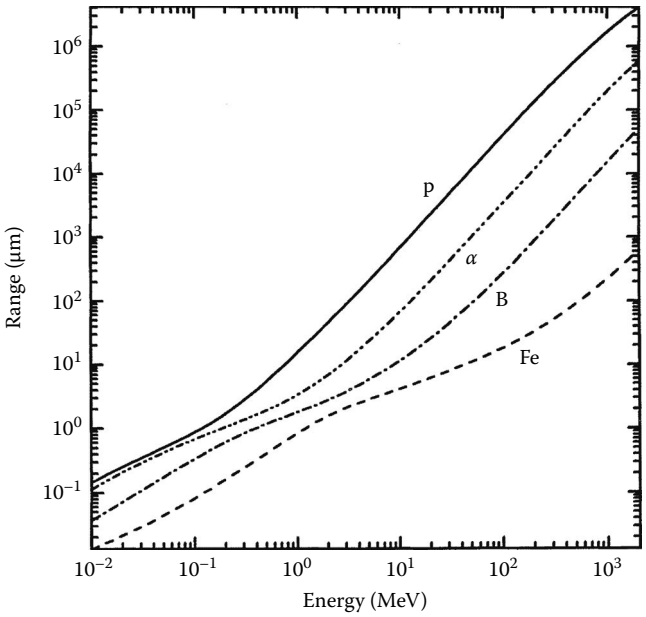

FIGURE 82.2 Ions of widely different masses have widely different ranges in a target element such as silicon. These curves for protons (p), α-particles, boron ions (B), and iron (Fe) were obtained using the SRIM computer program. (From Ziegler, J.F., *SRIM: The Stopping and Range of Ions in Matter*, IBM-Research, Yorktown, NY, 1996.)

average ionization energy. It is not applicable for ions for which $z > 2$, where stripping must be considered. Ziegler et al. [1] give a very useful description of scaling rules that allow the proton energy loss to be scaled to any incident ion and target atoms. They have included these rules in a software package called SRIM [2]. Their empirical relation allows for ion stripping and gives a more exact representation of the energy loss than Equation 82.1 in the case of heavy ions and for low-velocity light ions. Alternatively, one can use published $dE/(\rho\, dx)_{ion}$ plots [3]. The interaction of fast charged particles with the nuclei of the constituent atoms of a target produces an additional contribution to the energy loss, $dE/(\rho\, dx)_{nucl}$, the nuclear stopping power. For protons and α-particles, the electronic stopping power dominates by a factor of 1000 over the nuclear stopping power for most energies of interest. For ions, the nuclear stopping power may dominate at low energies (<1 MeV), with its contribution decreasing at higher energies and becoming negligible. The range of a particle, or its path length, is also a very important parameter in the selection of a detector. It is given by

$$R(E_0) = \int_0^{E_0} \frac{dE}{dE/dx} \tag{82.2}$$

where dE/dx in this case is the total stopping power $dE/dx_{ion} + dE/dx_{nucl}$. Range–energy curves for various ions in silicon are shown in Figure 82.2.

82.1.3 Energy Loss of Electrons

The case of electron propagation through matter is more complicated. The electron collides with bodies having a mass equal to it (other electrons) or much heavier (nuclei). The collisions cause it to undergo many changes in direction. This "random walk" type of behavior is superimposed on the forward motion of the electron. Along its random path, an electron loses energy through ionization in a way similar to ions. At increasing kinetic energy, electrons also lose energy through the emission of x-rays,

called bremsstrahlung radiation. In a target constituted of atoms of charge Z_{med} and below a critical energy E_c, ~817/Z_{med} MeV, electrons lose a greater fraction of their energy through ionization. Above E_c, the energy loss due to bremsstrahlung x-ray emission dominates and is given by

$$-\frac{1}{\rho}\frac{dE}{dx_{rad}} = B\frac{Z_{med}^2 E}{A}\left(\ln\left(\frac{183}{Z_{med}^{1/3}}\right)+\frac{1}{18}\right)\text{MeV (g cm}^{-2})^{-1} \tag{82.3}$$

where $B = 1.40 \times 10^{-3}$ for E in MeV and for the molar weight of the target A in grams. Equation 82.3 applies for specified energy ranges, and the interested reader should consult the available literature [4].

The electron range is defined as the distance separating the point of entry in the detection medium to the point where the electron stops. It is much shorter than its actual path length and can be approximated by $R(E)$ (Equation 82.4) for E ranging from 0.01 to 3 MeV [5]. Ultimately, the problem of electron propagation through materials has to be addressed using Monte Carlo programs (see Refs. [6,7]), which follow the individual electron histories to a specified energy or geometric cutoff:

$$R(E) = 0.2115 Z_{med}^{0.26} E^n (\text{g cm}^{-2}) \tag{82.4}$$

$$n = 1.265 - 0.0954 \ln(E)$$

82.1.4 Technologies

The most appropriate detection technique selected depends on the particle under study, its energy, and the type of information sought, such as source activity, position or energy measurement, or particle identification. For all cases reviewed here, except nuclear emulsions, the detection process is active and accompanied by electronic signal processing. Nuclear emulsions permanently record the ionization tracks left by traversing particles and can only be examined after their development. The active technologies include gas-filled detectors (ionization chambers, proportional counters, Geiger–Müller counters), scintillators, and solid-state detectors. The active volume consists of a radiation-sensitive material that is raised to an excited state through ionization by the passage of charged particles. For active detectors, this ionization is sensed by the external electronics as an induced charge in the case of gas-based and solid-state detectors or as visible or near-visible light in the case of scintillators. The sensors described here are the front ends of complex detection systems.

Nuclear emulsions are a special preparation of photographic emulsion designed to record "tracks" left by ionizing particles as they traverse the emulsion. The emulsion is sensitive up to the time it is processed, and the image is latent for many months or years if the emulsion is cooled. Once processed, the emulsion is a permanent record of the ionizing radiation that traversed it. In a situation where a prompt signal is not required, the nuclear emulsion may be a suitable detector. Its primary advantage is that it is compact, is self-contained, and has high spatial resolution. Since no associated equipment is needed during exposure, it is well suited for remote applications, such as studying cosmic rays and for recording the cumulative exposure to ionizing radiation in space.

Gas-filled detectors were among the first instruments designed for radiation detection. A charged particle passing through a gas-filled container leaves a trail of ionization electrons and ions. With a suitably configured external electric field, the ionization can be used to produce an electric signal for charged-particle detection. Depending on the magnitude of the applied electric field, a variety of ionization phenomena can arise in gases that have been used over the years to develop different types of gaseous charged-particle detectors, for example, ionization chambers, proportional counters, Geiger–Müller counters, and spark chambers. Spark chambers are rarely used these days because of electric

TABLE 82.1 Detection Applications and Suggested Instruments

Detector Type	Typical Applications	Advantages	Shortcomings
Nuclear emulsion	Cosmic ray studies, dosimetry, low statistic (single track) studies	Passive detector, high spatial resolution, unattended operation, particle identification, and energy measurement	No time information, manual scanning, chemical development
Gas-filled counter	Radiation monitoring, dosimetry	Low density, large area at low cost, nuclear and particle physics experiments, real-time particle identification	Needs ultrapure flammable gases, high voltages required, signals need amplification
Scintillation counter	Energy measurement, particle counting, triggering	Large volumes, flexible shapes, fastest timing, high efficiency	Poor spatial resolution, poor energy resolution
Solid-state detector	Energy measurement, particle identification, position measurement, radiation monitoring, beam analysis techniques	High-energy resolution, compact size	High cost per area, signal needs amplification

noise and limited counting rate ability. The other three devices are used primarily as instruments for radiation protection and monitoring. Their advantage is that they are inexpensive, easy to operate, and available commercially. In addition, many variants of gas-filled proportional counters have been developed for use in experimental nuclear physics and elementary particle physics. These, however, need to be specifically designed and fabricated for particular applications.

Scintillation counters consist of a scintillation material, a photodetector, and a light guide to link the two. Charged particles crossing the scintillator material deposit energy in the material, which responds by emitting light isotropically. A large fraction of the light can be trapped in the material by internal reflection and directed toward a photodetector, such as a photomultiplier (PM) tube. This kind of detector can be used at very high counting rates and can achieve efficiencies approaching 100%. Components for scintillation counters are readily available and it is possible to purchase assembled counters.

Solid-state detectors are large semiconductor diodes made of very high-resistivity material and are operated under reverse bias. The small bandgap in these materials ensures that the kinetic energy of the incident charged particle is efficiently converted into an electric signal through the creation of electron–hole pairs. A signal is induced on the metal contacts as the charge carriers drift under the applied electric field present in the depletion region. Their advantages include a fast response, good energy resolution, and compact size.

Table 82.1 presents some radiation-sensing applications, the particles under study, and the suggested sensor–system combination. The following subsections present each sensing technology in more detail.

82.2 Nuclear Emulsions

Nuclear emulsions are a suspension of silver halide grains, primarily AgBr, in a gelatin medium. The silver halide grains are small, on the order of 0.2–0.5 μm, and constitute about half the volume and 80% of the total weight. The "pellicles" of nuclear emulsion range from 25 to 600 μm in thickness and can be as large as 70 cm by 30 cm. The pellicles may be supported on a glass or plastic plate during exposure or stacked to increase the thickness of the emulsion detector, in which case the pellicles will be placed on a supporting plate as part of processing. If pellicles are stacked for an exposure, then a reference grid is usually printed on the bottom surface of each pellicle to assist in following tracks from one pellicle to the next.

The ionizing radiation crossing a grain of silver halide leaves the grain in an excited state. During development, the excited grains are reduced to elemental silver. The undeveloped grains are washed out

during the fixing process. Due to their thickness and to ensure uniform response, a special development process, involving presoaking the emulsions at a reduced temperature, must be used. After development, the nuclear emulsion will have shrunk to about 40% of its original thickness. The thickness is also sensitive to the ambient humidity, and the plates are normally kept in humidity-controlled storage (~50% relative humidity). The shrinkage needs to be taken into account for most measurements.

The track image in the emulsion is viewed with a microscope with magnification in the range of 10 × 10 to 10 × 100. With the aid of a special microscope, having a calibrated micrometer vertical focus adjustment and a special high-precision stage with calibrated micrometer x and y movements, the characteristics of the tracks can be determined and used to identify most particles and to measure their momentum. The dE/dx is measured by determining the grain density along the track. The energy or momentum is determined from the range of the particle or from multiple scattering. Additional information can also be obtained from the density of associated delta rays. These measurements can usually be combined to uniquely determine the charge (but not the sign) and momentum of the particle and the mass in the case of a singly charged particle. The interested reader may find additional information in Refs. [8–10].

Nuclear emulsions are currently produced by Ilford Photographic (Ilford Research Laboratory, Ilford Ltd., London, England) and Fuji Photo Film Co. Ltd. (Tokyo, Japan). Several types of emulsion are available with different sensitivities to ionizing radiation.

82.3 Gas-Filled Charged-Particle Counters

A gas-filled counter detects the ionization electrons and positive ions produced by a charged particle passing through a gas volume. An electrostatic field established between a pair of electrodes in a gas-filled container causes the electrons to move toward the anode and the ions toward the cathode. The charge movement produces an electric pulse that can be detected using suitable electronics. A gas-filled counter can operate as an ionization counter, a proportional counter, or a Geiger–Müller counter. Figure 82.3 shows the three operating regions with characteristics determined by the electric field region in which they operate.

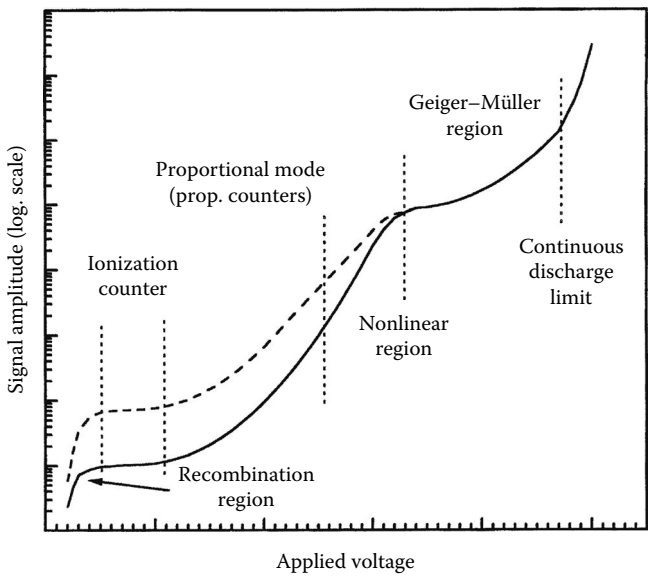

FIGURE 82.3 Typical behavior at atmospheric pressure for a gas-filled counter. Three principal operating regions are identified: ionization region, proportional region, and Geiger–Müller region. The lower curve is for minimum ionizing charged particles and the upper one for heavily ionizing ones. At low operating voltages, the ions and electrons recombine. Continuous discharge occurs at high voltages above the Geiger–Müller region of operation.

Ionization counter/chamber: At low fields, the recombination of electron–ion pairs reduces the detector signal, making it electric field dependent. With increasing field, nearly all the charges can be collected before they recombine. In an ionization counter, the signal-to-noise ratio is quite unfavorable, except when used for the detection of heavily ionizing particles (e.g., alpha particles). For radiation monitoring, the device is generally used in integrating mode as an ionization chamber. The current signal in an ionization chamber is proportional to the rate of ionization produced by charged particles interacting in the detector gas volume.

Proportional counter: At still higher fields, the electrons acquire enough energy between collisions with gas molecules to produce secondary ionization in the gas. The secondary electrons in turn can produce further ionization along their path, leading to an electron avalanche that stops only when all the electrons are collected at the anode. This large increase in the number of primary electrons leads to a detector signal substantially larger than that produced by a pulse ionization counter. The signal amplitude in a proportional counter is directly proportional to the ionization energy deposited in the gas by the ionizing particle. The proportional counter can detect charged particles without loss of gain at incident particle rates approaching 10^4 s^{-1} for each millimeter length of anode wires.

Geiger–Müller counter: Increasing the electric field still further results in increasing loss of proportionality until the counter enters the Geiger–Müller region of operation. In the Geiger–Müller region of operation, a single ionizing event induces an electric discharge along the entire length of the anode wire. The output pulse amplitude is large and independent of the energy deposited by the ionizing particle in the gas. The Geiger–Müller counter has a relatively long dead time of a few hundred microseconds, and the detector saturates at counting rates above a few thousand particles per second.

Proportional counters have many advantages over ionization chambers and Geiger–Müller counters, both of which are now used mainly as radiation monitors in the laboratory. A gas-flow proportional counter is sensitive to the ionization produced in a gas volume by a single charged particle. It can be used for counting charged particles, to measure their energy loss in the gas and to measure their track coordinates. The proportional counter is more sensitive than an ionization counter because of a built-in gas multiplication process that amplifies the initial ionization pulse. Because of its relatively short pulse duration, a proportional counter recovers quickly and can count particles at higher rates than a Geiger–Müller counter with its long dead time.

82.3.1 Gas-Filled Proportional Counters

82.3.1.1 Basic Design and Operating Principle

Figure 82.4 shows the schematic diagram of gas-filled proportional counter and associated readout electronics. An electrically conducting gas-filled tube serves as the proportional counter cathode. A fine wire 20–25 μm in diameter (usually made of gold-plated tungsten) at the center of the tube, supported by insulators on both ends, forms the anode. For reasons of mechanical and electric stability, the anode wire is strung under a tension of several tens of grams, depending on the wire length and operating voltage of the detector. Mylar windows thin enough to allow passage of α- and β-particles close the gas volume. The cathode is usually kept at ground potential and a positive voltage V_0 is applied to the anode. The electrostatic field is radial with magnitude given by

$$E = \frac{V_0}{(r \ln(b/a))} \tag{82.5}$$

where

r is the distance from the central axis
a is the radius of the anode wire
b is the radius of the tube

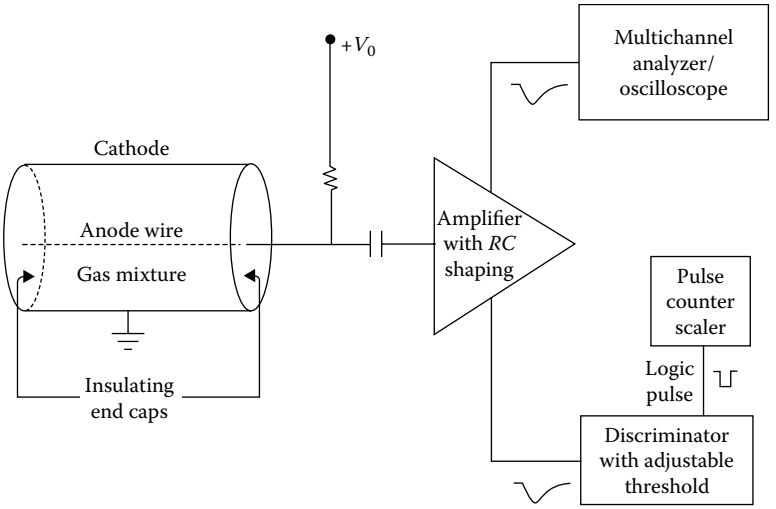

FIGURE 82.4 Schematic diagram of a gas-filled proportional counter and measurement system.

The $1/r$ dependence leads to the existence of an intense electric field near the anode wire; for example, at $r = 20$ μm, the electric field is 25 MV m^{-1} for a 20 μm diameter anode wire held at 1.5 kV within a cathode tube of radius 1 cm. A charged particle passing through the detector ionizes the gas molecules along its path. Under the influence of electric field, the primary ionization electrons start drifting toward the anode. In the strong anode field region a few wire radii from the anode surface, the electrons produce additional ionization along their paths, which leads to the production of an electron avalanche. The large increase in number of primary electrons is called gas multiplication or gas gain, which becomes significant in the high-field region near the anode. The gas gain is related to the mean free path of the electrons in the gas for secondary ionizing collisions. The electron mean free path is a function of the electric field and the gas pressure. Gas gains as high as 10^8 can be achieved by proper choice of gas mixture and mechanical construction before reaching the limit imposed by electric breakdown in the gas. Most commonly used proportional counter systems have gas gains in the range of 10^4–10^6 [4,11,12].

The voltage pulse observed on the anode is the result of a change in the electrostatic potential energy of the system. Most of the potential energy change is due to the movement of positive ions away from the high anode field region. The contribution of electrons to the total signal is quite small since most of the avalanche electrons traverse only a short distance before being collected by the anode. The fast movement of the ions away from the intense electric field region near the anode produces an initial rapid rise of the signal. About 50% of the pulse height is reached in roughly 0.1% of the total time, followed by a slow logarithmic rise lasting a few hundred microseconds. The signal is proportional to the total amount of ionization produced in the gas, that is, the product of the gas gain and the number of primary electron–ion pairs. The proportional counter energy resolution is determined by statistical fluctuations in the number of ions and by the statistical nature of the gas gain process itself. Deviations from proportionality occur when the space charge density of the positive ion sheath around the anode wire becomes large enough to locally reduce the electric field. The space charge effects become appreciable, depending on the gas gain at counting rates above 10^4 s^{-1} mm^{-1} of anode wire length.

82.3.2 Fill Gases for Proportional Counters

The choice of proportional counter fill gases is dictated by practical considerations. If low gas gain is acceptable, such as for the detection of α-particles or heavy ions, both of which produce extremely high specific ionization (initial number of electron–ion pairs produced per cm), almost any gas (even air)

TABLE 82.2 Characteristics of Gases Commonly Used in Proportional Counter Gas Mixtures

Gas	W (eV)	dE/dx_{ion} (keV cm^{-1})	Specific Ionization (Ion Pairs per cm)
Ar	26	2.44	94
Xe	22	6.76	307
CO_2	33	3.01	91
CH_4	28	1.48	53
C_4H_{10}	23	4.50	195

Note: dE/dx_{ion} and specific ionization values are for minimum ionizing charged particles in gas at atmospheric pressure.

can be used. For other particles, one requires a gas that has high specific ionization, high gas gain, low operating voltage, good proportionality, high single-particle counting rate ability, and long operating lifetime. Noble gases such as argon meet the criteria of reasonable gas gain at low operating voltage and high specific ionization. However, the ultraviolet photons produced by excited argon atoms can cause secondary electron emission from cathodes, leading to electric breakdown at higher operating voltages. The problem can be cured by adding a quenching polyatomic gas with rotational and vibrational levels that can readily absorb the ultraviolet photons. The addition of a quenching gas permits stable high-gain operation of proportional chambers. A mixture of 90% argon and 10% methane (CH_4) called P10 is a commonly used proportional counter gas. Several different gas mixtures exist that are capable of achieving proportional gas gains in the neighborhood of 10^6.

The specific ionization for a gas can be calculated from the knowledge of dE/dx_{ion}, the rate of charged-particle energy loss in the gas, and W, the mean energy needed to create a single electron–ion pair. The properties of some common proportional counter gases are shown in Table 82.2. The values of dE/dx_{ion} and the specific ionization shown in the table are for minimum ionizing charged-particle tracks. The specific ionization for a gas mixture is the average specific ionization calculated with partial pressures of the component gases as weights.

The use of organic quenching gases as quenchers in proportional chamber gas mixtures can lead to the formation and deposition of polymers on the electrodes that reduce the operating life of a proportional chamber. To improve chamber lifetime and reduce aging, nonpolymerizing agents such as methylal are frequently added in small quantities to the gas mixture. For proportional counters with sealed gas volumes, the detector performance will degrade due to the contamination of gas in a sealed volume caused by component outgassing. Cleanliness and careful choice of components during fabrication can minimize these effects. The performance of a sealed proportional counter will also degrade with the degradation of the quenching gas component, which can happen when the device is exposed to large fluxes of radiation or after prolonged use. To minimize these problems, proportional counters are often used with external gas supply systems capable of refreshing the gas continuously.

82.3.3 Proportional Counter Operation and Readout

It takes a few hundred microseconds to develop the full voltage pulse in a proportional counter after a leading edge rise time of a few hundred nanoseconds. Even with a gas gain of 10^4–10^5, the pulse amplitude is only a few millivolts. Further amplification and shaping is needed to obtain signals suitable for measurements. Often, low-noise amplifiers with built-in *RC* differentiation to shorten the output pulses to 1 μs or less are used (see Figure 82.4). These improve the ability of proportional counters to measure particles at high counting rates without pulse pileup distortions caused by closely spaced pulses overlapping in time. The energy loss of a charged particle in a gas can be measured by measuring the pulse height of the anode signal with an oscilloscope or a multichannel analyzer (MCA). For charged-particle

counting, a discriminator can be used to produce logic pulses that can be counted with a scaler. For coincidence applications, timing resolution of a few nanoseconds is typical for a proportional counter. Good RF shielding and careful electric grounding are essential to maximize the sensitivity of most proportional counters.

The performance of a proportional counter is determined by operating voltage. At lower operating voltages, the best linearity is achieved at the expense of lower gas gain and, consequently, a low signal-to-noise ratio and low efficiency for particle detection. Increasing the voltage leads to larger gain, better signal-to-noise ratio, reduced linearity, faster aging, and susceptibility to electric sparking and damage. In general, the lowest possible anode voltage consistent with achieving good particle detection efficiency is preferred for the operation of proportional counters. This can be accomplished by choosing the operating voltage roughly in the middle of the high-voltage (HV) plateau for the device. On the HV plateau, the counting efficiency of the device remains constant for any variations of anode HV [12]. Typical proportional counter operating voltage plateaus are reached in the voltage range of 1.5–2.5 kV.

82.3.4 Proportional Counters: Advanced Techniques

Many variants of the simple, single wire design have been developed for nuclear physics and particle physics experiments [4,11,12]. Multiwire proportional counters were invented by George Charpak in 1968. In a multiwire proportional chamber, a parallel equidistant row of anode wires is enclosed between two cathode planes. Each anode acts as an independent proportional counter that is read out using suitable electronics. Segments of charged-particle tracks can be localized in a multiwire proportional counter in the anode wire plane in a direction perpendicular to the anodes with accuracies on the order of 0.5 mm. A second coordinate along the length of the anode can also be obtained by a measurement of induced signals on a cathode that is segmented in strips in a direction normal to the anode wires. Much more precise particle track coordinate measurements with accuracies of tens of micrometers are possible in another variant called the drift chamber. This is achieved from knowledge of drift velocities of electrons in the chamber gas as a function of electric field and by measuring the drift time of the ionization electrons to the anode. Complete 3D determination of particle tracks is possible in a device known as the time projection chamber, which is a combination of a multiwire proportional chamber and a drift chamber. Gas microstrip detectors [13] improve on the high count rate abilities and spatial resolution of a multiwire proportional chamber using closely spaced anode strips that are printed photolithographically on a rigid substrate. Gas microstrip detectors with anode spacings of 200 μm are able to achieve spatial resolution of under 40 μm and count rate abilities in excess of 10^6/(s mm^2).

82.3.5 Geiger–Müller Counters

82.3.5.1 Basic Design and Operation

A Geiger–Müller counter [14] is similar in construction to a proportional counter. Operating at electric fields above the proportional region, it is a controlled discharge counter that produces a large output pulse of a few volts for every ionizing event in the gas independent of the amount of energy deposited in the gas. The ultraviolet photons from the electron avalanche in a Geiger–Müller counter induce an electric discharge along the entire length of the anode wire. Gas mixtures used in Geiger–Müller counters generally contain a noble gas mixed with ethyl alcohol or halogen containing a vapor such as ethyl bromide, which acts as a quencher and eventually stops the discharge. After the discharge, the Geiger–Müller counter has a large dead time on the order of a few hundred microseconds, while the excess ionization is swept out of the chamber, during which it cannot register another pulse. If ethyl alcohol is the quenching agent, the gradual decomposition of molecules causes the counter characteristics to degrade with usage, and the counter eventually ceases to function. Counters with a halogen compound used as a quenching agent do not suffer from this defect; however, because halogens are

TABLE 82.3 List of Manufacturers for Gas-Filled Proportional Counters and Geiger–Müller Tubes

Aptec Engineering Ltd., East 50 B, Caldari Road, Concord, Ontario L4K 4N8, Canada, Phone: +1 (905) 660-5373, Fax: +1 (905) 660-9693
Canberra Industries, Inc., 800 Research Parkway, Meriden, CT 06540, Phone: +1 (203) 238-2351, Fax: +1 (203) 235-1347, http://www.canberra.com/
EG & G Berthold, P.O. Box 100163, D-75312, Bad Wildbad, Germany, Phone:+49 708 1177-140, Fax: +49 708 1177-100, http://www.berthold-us.com/
EG&G Ortec, 100 Midland Road, Oak Ridge, TN 37831, Phone: +1 (615) 482-4411, Fax: +1 (615) 483-0396, http://www.ortec-online.com/
Ludlum Measurements Inc., P.O. Box 810, 501 Oak Street, Sweetwater, TX 79556, Phone: +1 (915) 235-5494, Fax: +1 (915) 235-4672, http://www.ludlums.com/
Oxford Instruments Inc., 601 Oak Ridge Turnpike, P.O. Box 2560, Oak Ridge TN 37831-2560, Phone: +1 (615) 483-8405, Fax: +1 (615) 483-5891, http://www.oxford-instruments.com/Pages/home.aspx
Panasonic, Two Panasonic Way, Secaucus, NJ 07094, Phone: +1 (201) 392-6044, Fax: +1 (201) 392-4315, http://www.panasonic.com/
TGM Detectors Inc., 160 Bear Hill Road, Waltham, MA 02154-1075, Phone: +1 (617) 890-2090, Fax: +1 (617) 890-4711
Cardinal Health (Victoreen Instruments), 6000 Cochran Road, Cleveland, OH 44139, Phone: 800-850-4608, Fax: 440-248-9300, www.cardinal.com/rms

electronegative and capture electrons, such counters suffer from the problem of variable output signal delays. Since the Geiger–Müller counter pulses are several volts high, they require no further amplification for measurement purposes.

82.3.6 Proportional Counter and Geiger–Müller Counter Applications

Proportional counters and Geiger–Müller counters are often used in instruments for radiation protection and monitoring. Depending on the construction, they can be used for the detection of both α- and β-particles. The simple Geiger–Müller counter is perhaps more commonly used as a radiation monitor because it is easier to use and it has high efficiency, close to 100%. However, because of its relatively long dead time, a Geiger–Müller counter becomes less useful as a monitor in high radiation environments where particle rates exceed a few thousand counts per second. Also, a Geiger–Müller counter provides no energy information. For high counting rate applications or when energy discrimination is needed, it is better to use a proportional counter. Unfortunately, they can be cumbersome to use if an external gas supply is required. Geiger–Müller counters and proportional counter systems can be purchased from many different vendors (see Table 82.3). Prices vary from $100 to $500 for Geiger–Müller and proportional tubes and up to $2000 for complete systems and accessories (e.g., survey meters, scalers, rate meters, analyzers).

82.4 Scintillation Counters

82.4.1 Introduction

The use of scintillation light is one of the original methods used to detect charged particles. In 1911, Rutherford used an activated zinc sulfide screen to detect α-particles. The flashes of light produced in the screen were counted by a dark-adapted observer. Today, scintillation counters are usually made of plastic, liquid, or crystal materials, and the resulting signal is detected electronically. The principle of operation of these devices is that the energy deposited by charged particles moving through the scintillator material causes some of the molecules to be raised to an excited state. On returning to the ground state, the molecules emit light. The decay time of the light emitted depends on the fluorescence time of the scintillator. This can be very short, producing signal pulses as short as a few nanoseconds and thus allowing this type of detector to be used at very high counting rates. The light produced by the

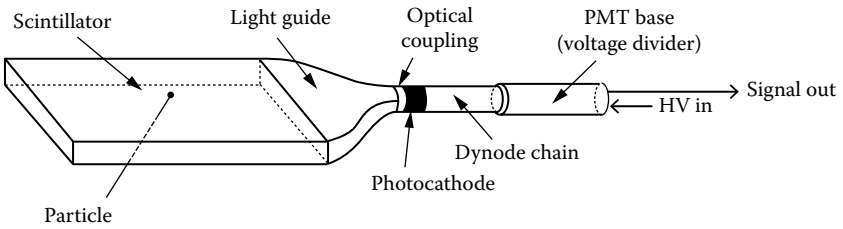

FIGURE 82.5 Typical scintillator system consisting of a scintillation medium, light detector, and light guide.

scintillator is usually detected using a PM. An appropriate choice of scintillation medium and detection method can produce a highly effective charged-particle counter with an efficiency of essentially 100%.

82.4.2 Scintillation Counters: A Detailed Description

A scintillation counter consists of the scintillation medium, a light detector, and a light guide to transfer the light from one to the other (see Figure 82.5). Information on each of the components of a scintillation detector follows [4].

82.4.3 Scintillation Medium

Plastic or liquid scintillators are usually used for the detection of charged particles. Crystal scintillation media such as sodium iodide or bismuth germanate (BGO) are normally used for photon detection or applications in which energy resolution is important. Plastic detectors are inexpensive and have proved to be a reliable way of detecting charged particles. Large areas can be covered using adjacent sheets of plastic scintillator. Such an array of detectors is known as a hodoscope. Primary light output from a plastic scintillator is at short wavelengths, below 400 nm. Light at these wavelengths has a short attenuation length in the plastic, so wave-shifting dyes are employed to convert the light to longer wavelengths. Thus, a plastic scintillator contains two or more additives such as polystyrene doped with *p*-terphenyl and tetraphenyl-butadiene. Proprietary scintillators are available in a large variety of shapes and sizes from companies such as Bicron Corporation. Plastic scintillators will darken upon exposure to radiation in excess of about 10^3 grays, which will lead to inefficiencies. Liquid scintillation materials, such as toluene, are useful for constructing large-volume detectors. Such devices are used in high radiation areas as liquid scintillators are inherently more radiation resistant. It is also possible to replace the liquid if radiation damage occurs. The main problem with this kind of device has been maintaining a leak-proof container and the resulting hazard associated with the toxicity of the liquid.

82.4.4 Light Coupling to Photon Detectors

The light produced in the scintillator is emitted isotropically. A portion of this light is trapped in the scintillator by total internal reflection. For a small detector, it is possible to couple the end of the scintillator directly to a phototube. For larger detectors (exceeding the width of the photodetector), a light guide made of a UV-transparent acrylic plastic is recommended. Acrylic plastic is widely available; Plexiglas by Rohm is one example. Light guides can be made of one piece of shaped plastic, but maximum efficiency can be realized using adiabatic (constant area) light guides that minimize light losses. These light guides are quite artistic (see Figure 82.6) and are made from acrylic strips heated and then bent to the appropriate shape. The cut edges are flame polished to produce a smooth surface for good internal reflection. To match large scintillators to a small area detecting device, a light guide known as a "Winston cone" [15] is used on the light detector. The shape of the Winston cone minimizes light losses.

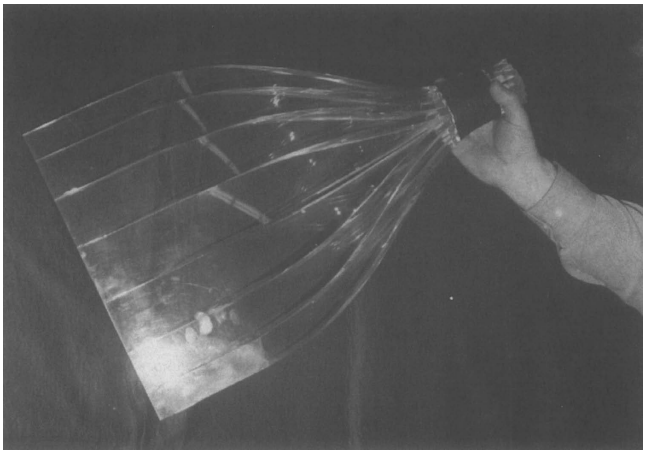

FIGURE 82.6 Photograph of adiabatic Plexiglas light guide. (Courtesy of Science and Technology Centre, Carleton University, Ottawa, Ontario, Canada.)

82.4.5 Light Detection and Readout

The standard method of detecting light from a scintillator is the use of PM tubes. These consist of a light-sensitive photocathode and an amplification stage. The photocathode is a thin layer deposited on the inside of a vacuum tube that has a good probability (>10%) of emitting an electron when struck by a photon. These electrons are electrostatically focused on a secondary electrode (dynode), which is the first element of the amplification structure. The voltage between the photocathode and this first dynode is sufficient to give the electrons enough energy to eject two to four electrons from the dynode. This process is continued through a series of dynodes resulting in a large gain, up to 10^8 in a tube with 14 dynodes. The output pulse is read out from a connection to the anode or the last dynode. The PM has connection pins corresponding to each dynode. Voltages are supplied to these via a resistive divider network contained in a "base" or "divider." The base requires one HV input and provides one or two signal outputs. Details of divider networks are available from PM tube manufacturers. Further information on the operation of phototubes can be found in Ref. [16].

In operation, PM tubes are sensitive to magnetic fields and it is usually necessary to provide magnetic shielding. A tube of a single layer of mu-metal is often sufficient to shield the PM tube from the Earth's magnetic field. For applications where there are higher ambient fields, a shield of layered tubes can be used consisting of two mu-metal shields and up to two soft iron shields. They should extend approximately one tube diameter beyond the PM tube. In applications where an axial field is unavoidable, a bucking coil can be inserted between the two iron layers. A suitable choice of coil current can counteract the axial field.

82.4.6 Scintillator Detector Construction

Assembly of scintillators, light guides, and PM tubes is usually done with optical cement. It is important in the preparation of the adhesive to remove air bubbles that would scatter the light. It is also possible to make demountable joint using optical grease or vacuum grease and a mechanical fixture. Such a joint can be used to simplify the replacement of phototubes. Light levels produced in the scintillator are extremely low; therefore, detector assemblies must be enclosed in light-tight envelopes. For plastic scintillators, this is most easily arranged by wrapping with aluminum foil and protecting the foil with black plastic sheets held in place with black adhesive tape. In large systems of counters, it is useful to install LEDs in each scintillator to monitor the operation of the counter. A system for powering the LED with a short duration pulse allows a test of the counter and readout system.

Components for scintillator systems can be purchased from many manufacturers, some of which are listed at the end of this section. Prices vary widely, depending on both the details of the detector and the quantity of components ordered. Typical prices would be $600 for a piece of scintillator 0.5 cm × 45 cm × 60 cm, $200 for a voltage divider, and $500 to $1200 for a 12-stage, 5 cm diameter phototube. Liquid scintillators are available for $145 per liter. Prices are in U.S. dollars. The cost of custom light guides is dominated by the available labor rate. There are some suppliers (such as Bicron) that will provide complete custom detectors consisting of scintillator, light guide, PM tube, and divider.

82.4.7 Operating Information

A MIP crossing a 1 cm thick scintillator will liberate about 10^4 photons. With typical scintillators and light guides, about 10% of these will reach the photocathode. The efficiency of photocathodes to produce photoelectrons is usually greater than 10%. Given PM tube gains of 10^8, this leads to 10^{10} electrons at the anode, allowing analog pulses of about 1 V produced. The pulses typically have a rise time of about 1 ns and a fall time of 5 ns. The trailing edge of the pulses can be shortened to approximately 2 ns by attaching a short grounded line to the output (clip line). The anode outputs are normally connected to a discriminator that produces a standard digital pulse for all analog pulses exceeding a fixed threshold voltage. More sophisticated circuits, such as constant fraction discriminators, can be used for best timing resolution. Using these devices along with a scintillator geometry that provides good light output, a timing resolution of the order of 300 ps (1σ) can be achieved. The excellent signal characteristics of scintillation counters allow them to count efficiently at rates exceeding 10 MHz.

Background counts in a scintillator are caused by cosmic rays and noise in the tube. An average rate from cosmic rays is 1 min^{-1} cm^{-2} sr^{-1}. Tube noise tends to have a lower amplitude than pulses resulting from the scintillator and will have a rate dependent on the choice of threshold. A counter should be checked to see if its count rate is consistent with cosmic ray backgrounds. High count rates are indicative of a light leak, which can be detected by shining a flashlight on the counter in a darkened room. Diligent use of aluminum foil and black tape will fix the leaks. In applications measuring particles that are energetic enough to pass through a counter, system noise can be reduced by using two layers of scintillator and putting their signals in coincidence. Noise can also be minimized by optimal setting of the tube HV and discriminator threshold. If the discriminator threshold is too low, then a large number of tube noise pulses are picked up.

82.4.8 Advanced Techniques

A plastic scintillation counter hodoscope can also be used to obtain position information. The spatial resolution of such a device is limited by the size of the individual detectors. For example, thin finger-shaped counters can be used for measuring beam profiles. Larger "paddles" 10 or 20 cm wide can be used to cover large areas. It is also possible to measure impact position along counter using phototubes at both ends of a long scintillator and measuring the difference in arrival time of the pulses at the two tubes. Higher-precision spatial resolution is possible using scintillating fibers with diameters of around 1 mm. Such a device has a large number of channels and requires segmented cathode phototubes or solid-state readout devices. One such device is the visible-light photon counter (VLPC), which is a produced by Rockwell International and is a development from a solid-state PM. To keep noise low, VLPCs are used at cryogenic temperatures.

82.4.9 List of Manufacturers

Table 82.4 shows a selection of potential suppliers of components for scintillator systems.

TABLE 82.4 List of Manufacturers for Scintillator System Components

	Scintillator	Bases/Dividers	Phototubes	Systems
Bicron	x	x		x
DEP Scientific	x			
Hamamatsu		x	x	
Philips		x	x	
POL. HI. TECH.	x			
Burle			x	
Thorn EMI		x	x	x
Bicron, 12345 Kinsman Road, Newbury, OH, 44065-9677, Phone:+1 (216) 564-2251, Fax: +1 (216) 564-8047	Hamamatsu Photonics, 325-6, Sunayama-cho, Hamamatsu City, 430, Japan, Phone: +81 53-452-2141, Fax: +81 53-456-7889, http://www.hamamatsu.com/	Thorn EMI, Bury Street, Ruislip, Middlesex, HA4 7TA, U.K., Phone: +44 1895 630771, Fax: +44 1895 635953		
Burle Industries, 100 New Holland Avenue, Lancaster, PA 17601-5688, Phone: +1 (717) 295-6000, Fax: +1 (717) 295-6096	Philips Photonics, 100 Providence Pike, Slatersville, RI 02876, Phone: +1 (401) 762-3800, Fax: +1 (401) 767-4493			
DEP Scientific, P.O. Box 60, 9300 AB Roden, the Netherlands, Phone: 3150-5018808, Fax: 3150-5013510	POL. HI. TECH. SRL KM44,400 S.P. Turanense 67061 Carsoli (AQ)—Italy, Phone: (986) 3997798, Fax: (986) 3995868			

82.5 Solid-State Detectors

Solid-state detectors have proved to be very versatile in the detection of charged particles. They have been particularly useful for energy measurements of α- and β-particles, light and heavy ions, and fission fragments in applications that include nuclear spectroscopy, radionuclide identification in both the environment and the laboratory, dosimetry, radiation level monitoring, and nondestructive testing using particle beam techniques. In high-energy physics, solid-state detectors are used mainly as high-precision tracking detectors in a particle counting mode. Most of the devices used in all these applications are based on silicon technology except for energy measurements of β-particles (>250 keV), where germanium-based detectors are also used.

82.5.1 Signal Generation

A charged particle moving through a semiconductor crystal loses energy according to the stopping processes described previously (Equation 82.1). The energy lost is spent promoting electrons from the valence band to the conduction band of the crystal. This leaves free electrons in the conduction band and free holes in the valence band. Under the action of an electric field, the free electrons and holes drift in opposite directions and give rise to an electric current that can be sensed by external electronics. The amount of charge produced is very small and the semiconductor must be depleted of majority carriers in order for the signal to be measurable. This is accomplished using a diode structure operated with a reverse-bias voltage. A profile of a "typical" diode detector is given in Figure 82.7. The size of the active region of the detector, the depletion region, is determined by the reverse bias applied and the residual fixed charges. In the case where the material has a very high resistivity (~500 Ω cm or more), the built-in field of the junction can be sufficient to generate a useful depletion layer without any reverse bias.

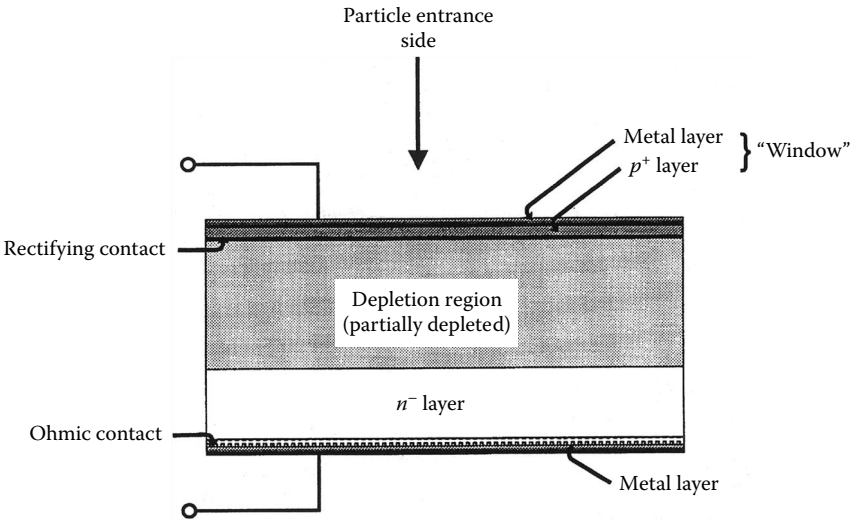

FIGURE 82.7 Solid-state diode detector consists of a thin current blocking layer, a sensitive volume of high-resistivity material, and a back ohmic contact. A near-uniform field may be established in the sensitive volume.

For a quantity of energy E_0 deposited through electronic interactions, the number of free electron–hole pairs created is $N_p = (E_0)/\varepsilon$, where ε is the average energy to produce one pair, a characteristic of the semiconductor, similar to the W value for gas detectors. Typical values of ε are small, 3.62 eV for Si at 300 K and 2.96 eV for Ge at 77 K. The variance of the number of pairs created is FN_p, where F is the Fano factor [17], which is of the order of 0.1 for Ge and Si. Hence, semiconductor materials are very efficient in converting radiation energy to an electric signal, and the pulse-to-pulse variation in the signal size is smaller than predicted by Poisson statistics, where $F = 1$. When all the charge carriers are collected (i.e., the electrons reach the anode side, while the holes reach the cathode side), a total of N_p electrons are available to the front-end electronics for amplification and shaping.

82.5.2 Categories of Detector

82.5.2.1 Device Details

Commercial solid-state detectors (i.e., silicon or germanium devices) are available from a number of manufacturers (see Table 82.5). The following silicon devices are available: silicon surface barrier detectors (SSBD), ion-implanted silicon detectors, diffused junction silicon detectors, *pin* photodiodes, and lithium-drifted silicon detectors (Si(Li)). Some of the manufacturers rename the different types using their own brand names. The first three types actually lend themselves to nearly the same applications: ion detection. Si(Li) detectors are mostly used for soft x-ray detection but can also be used for full-energy measurement of β-particles from 250 keV to 3 MeV. Germanium devices are available as lithium-drifted germanium detectors (Ge(Li)) and high-purity germanium (HPGe) detectors. As with the Si(Li) detector, the primary function of germanium detectors is for photon detection, but they can also be used to detect β-particles. Solid-state detectors are either *pn* or *pin* diodes. Silicon devices fabricated from a starting material of about 500 Ω cm (i.e., ion-implanted Si and diffused junction Si) have the *pn* structure. The SSBD, also made from Si of a few 100 Ω cm, is in fact a hybrid of Schottky junction and *pn* junction due to its gold-on-*n*-type Si interface as well as "*p*-like" surface defects introduced during manufacture. Devices that have a bulk resistivity in excess of 1 kΩ cm, whether it is due to a high-resistivity starting material (such as is used for pin Si and HPGe) or compensated material (Si(Li) and Ge(Li)), are *pin* junctions.

TABLE 82.5 Device Details

Type	Area (mm²)	Sensitive Thickness (μm)	Dead Layers[a] (nm)	Particles Detected	Prices 1996 US$	Manufacturers
SSBD	10–1000	10–5,000	80 225 (back)	p, α, β light and heavy ions	400–6,000	a, b, c, d
Si, ion implanted	Up to 3000	100–1,000	50	p, α, β light and heavy ions	300–3,000	a, b, c, d
Si pin photodiode	1–900	150–400	100	p, α, β light and heavy ions	10–300	e, f, g, h
Si(Li)	25–200	to 5,000	1000 Be +200 Si	β, 0.3–3 MeV	~7,500	a, b, c, d
HPGe	75–800	to 10,000	2500 Be +300 Si	β, 0.3–3 MeV	~9,000	a, b, c, d
Silicon strip	See manufacturer for details					c, d, g, i

Note: (a) EG&G Ortec (Oak Ridge, TN), (b) Oxford Instruments Inc. (United States), (c) Eurisys Mesures (France), (d) Canberra (Australia), (e) EG&G Optoelectronics (Canada), (f) Silonex Inc. (Canada), (g) Hamamatsu Photonics K.K. (Japan), (h) Centronic Inc. (United States), (i) VTT Electronics (Finland).

[a] Values in nm Si unless stated otherwise.

Many aspects dictate the choice of a detector for a given application. To measure the full energy of highly ionizing particles, it is important to keep the surface dead layer of the detector as thin as possible to limit the loss of undetected energy. The dead layer is the combination of the entrance metal electrode and the underlying, radiation insensitive, heavily doped top Si layer (usually *p* type). The required depletion region thickness is determined by the range in Si of the particles of interest. A sufficiently wide depletion region is required for full-energy measurements of ions or to obtain a large signal in the case of energetic particles, such as MIPs, which traverses the whole detector without stopping. Energy measurements of β-particles often require an active volume that is larger than can be achieved with a standard p–n junction, and so Ge(Li), Si(Li), or HPGe detectors are used. Varnish-coated detectors can be obtained to withstand exposures to rugged environments. Bakeable devices, which allow partial recovery from damage, or inexpensive and replaceable photodiodes can be used in situations of heavy radiation damage. For the detection of heavy ions, devices that can be operated at high electric fields (>15 kV cm^{-1}) can be used to overcome recombination effects. One of the most widely used Si detectors is the SSBD. It offers a thin entrance window of less than 100 nm. The diffused junction is the original type of Si detector and it has a rather thick dead layer of 250 nm Si. It is still useful in applications that require a light-insensitive device or for particle physics applications. The implanted junction Si detector results from the implantation of boron ions in an *n*-type Si wafer. It is the most recent addition to commercial Si detectors and it offers a thinner entrance window (less than 50 nm) and a larger surface area than SSBD (see Table 82.5). All these devices can be operated in either partially or fully depleted mode. The thickness of the back dead layer is only relevant to fully depleted, transmission-type detectors for energy loss (ΔE) measurements. Recently, high-quality, inexpensive Si *pin* diodes for visible and UV photon detection have been found to be suitable replacements for SSBD in many applications. The thickness of the dead layer is 100 nm, twice that of ion-implanted Si detectors, and the resistivity is as high as 2–8 kΩ cm for the more expensive versions.

82.5.3 Detector Systems

Three practical systems of increasing sophistication are considered next. The first setup, depicted in Figure 82.8, is used to measure the energy spectrum and the rate of incoming charged particles. One possible application is the measurement of the α-activity from a natural source or from a wipe test sample. This simple count rate measurement requires a *pn* silicon detector or photodiode, a discriminator, and a pulse counter. By adding a pulse analyzer, called an MCA (Figure 82.8), the same system can

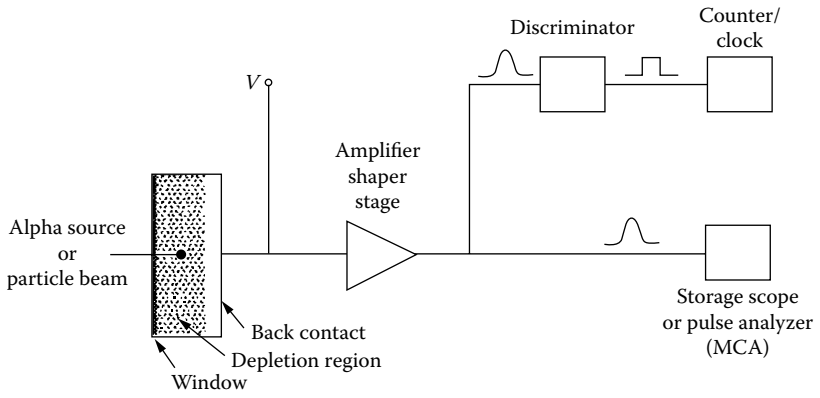

FIGURE 82.8 Using a pulse counter, this simple setup is used to measure the activity of a radioactive sample or the intensity of an accelerator beam. With the addition of a storage oscilloscope or an MCA, the energy deposited in the detector by each incoming charged particle may be measured.

be used to record the energy of the α-particles or the full energy of light ions, such as those encountered at an accelerator site where beam analysis of materials is performed. In this case, the suggested detector is a good quality SSBD or an ion-implanted detector with a thin window and operated at a voltage sufficient to generate a depletion region at least as wide as the range of the ions of interest. The second setup (Figure 82.9) shows a thin transmission-type (ΔE) detector (open front and back), in front of a thick, fully stopping, (E) detector. This configuration is called a ΔE–E telescope and it supplies a simultaneous measure of the energy loss and the full energy of particles going through both devices. This information then uniquely identifies the particle. Finally, Figure 82.10 presents a position-sensitive silicon strip detector for which the localization of a particle hit to better than 5 μm in one dimension is possible [18]. Such a detector is used in particle physics experiments. In many applications, combinations with other detector types, such as scintillators, are also possible.

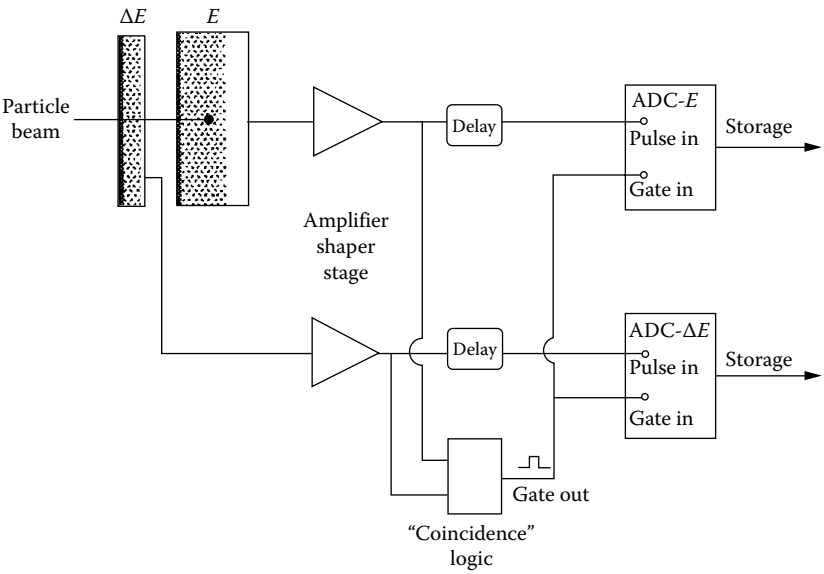

FIGURE 82.9 Knowledge of the amount of energy deposited in a transmission-type detector (ΔE) positioned in line with a full-energy measuring detector (E) allows the identification of a particle due to the unique nature of dE/dx and E combination.

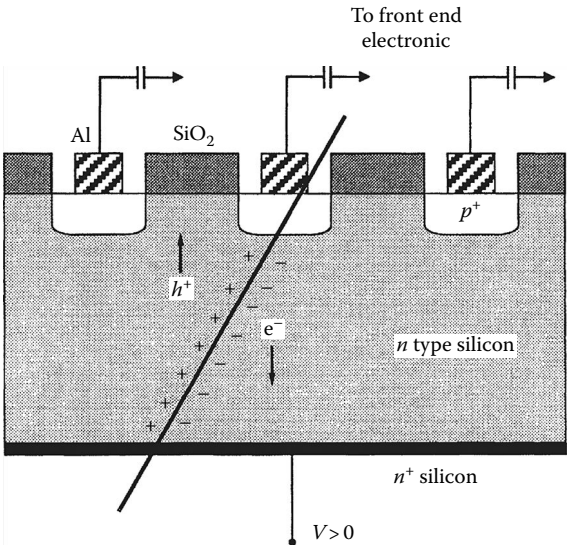

FIGURE 82.10 A silicon strip detector, such as the one depicted here, can be used to localize the hit position of a MIP.

Detectors with sensitive thicknesses of 100–300 μm are used in many nuclear spectroscopy and high-energy physics applications. For typical values of applied voltages, full electron collection occurs in less than 10 ns, while hole collection takes less than 20 ns. The amount of charge in a pulse is very small, of the order of 1.5 (10^6) e for the full energy of an α-particle and 100 e per μm of path in silicon of a MIP. Depending on the application, the signal-processing electronics can be optimized for low noise or fast response. In spectroscopy applications, where precise measurement of the total charge is important, one uses low-noise, charge-integrating preamplifiers, which offer output gains of the order of 1 mV fC^{-1}. The preamplifiers are optimized for specific ranges of detector capacitance. For detectors of 5 pF and smaller, noise values of less than 1 keV (equivalent energy loss signal in Si) can be achieved. In the case of preamplifiers optimized for larger detector capacitances (200–1000 pF), the noise increases with a slope of ~0.02 keV pF^{-1}. Preamplifiers produce a "step" pulse with amplitude proportional to the input signal charge. The rise time of the pulse varies with the detector capacitance, from 5 to 10 ns for <10 pF to 100 ns for 1000 pF. The pulse decay time is determined by internal circuit components and usually falls in the range of 50–300 μs. The signal is further amplified and shaped using an integrating–differentiating amplifier to provide a pulse of Gaussian shape whose width is of the order of 1 μs. This pulse duration limits the counting rate to much less than 10^5 cps before an unreasonably high counting dead time is encountered. In high-energy physics experiments, the signal-processing electronics coupled to position-sensitive detectors are optimized for a high counting rate capability and good timing resolution. Silicon-integrated circuits containing a large number of amplifiers are specially designed for such applications. The individual amplifiers provide large output gain (15 mV fC^{-1}) and output pulses whose width can be as small as 20 ns (baseline to baseline), at the cost of an increase in noise (6 keV Si equivalent). Count rates near 10^6 cps for every detection channel can be achieved with such systems.

82.5.4 Plasma Effects and Pulse Height Defect

Under some conditions, one may observe a loss in proportionality between the energy lost by the particle crossing the detector and the signal. This is called the pulse height deficit (PHD) and it is the sum of three components: E_W, E_N, and E_R, where E_W is the energy lost in the window or dead layer of the detector and E_N is the energy lost to nuclear scattering (nonionizing). The third term, E_R, is harder to define and is

due to a deficit in the charge collection. Ions heavier than the proton create plasma with a charge density as high as 10^{19} e^{-} cm^{-3} that shields the charge from the collecting field and causes charge loss through electron–hole recombination in the plasma to occur. The PHD increases roughly with the particle mass and energy and ranges from 1% to 3% for ions such as oxygen at 20 MeV.

82.5.5 New Structures

Modern silicon processing technologies allow the design of intricate structures that find applications in charged-particle detection, particularly in high-energy physics experiments. These include position-sensitive detectors, with strip electrodes or pixel segmentation, and large-volume silicon drift chambers. Front-end electronics can also be fabricated on the same wafer as the detecting structure itself. Close coupling provides noise reduction. The reader should be aware that new materials, such as GaAs, CVD diamond, natural diamond, cadmium telluride, HgI_2, and hydrogenated amorphous silicon, are being used in prototype detectors. These are beyond the scope of this chapter.

82.5.6 Manufacturers and Prices

A list of typical devices and pricing for each category of solid-state detector is given in Table 82.5. The names of some manufacturers are given, but the interested reader is also encouraged to consider other sources.

References

1. J.F. Ziegler, J.P. Biersack, and U. Littmark, *The Stopping and Range of Ions in Solids*, New York: Pergamon Press, 1985.
2. J.F. Ziegler, *SRIM: The Stopping and Range of Ions in Matter*, Yorktown, NY: IBM-Research, 1996 (computer software).
3. J.F. Ziegler, M.D. Ziegler, and J.P. Biersack, SRIM: The stopping and range of ions in matter, *Nuclear Instruments & Methods in Physics Research, Section B (Beam Interactions with Materials and Atoms)*, 268(11–12), 1818, 2010.
4. R. Fernow, *Introduction to Experimental Particle Physics*, Cambridge, U.K.: Cambridge University Press, 1986.
5. J.E. Bateman, M.W. Waters, and R.E. Jones, Spatial resolution in xenon filled MWPC x-ray imaging detector—A computing physics approach, *Nuclear Instruments and Methods*, A135, 235–239, 1976.
6. W.R. Nelson, H. Hirayama, and D.W.O. Rodgers, *The EGS4 Code System*, SLAC-Report-265, 1985.
7. J.A. Halbleib, R.P. Kensek, T.A. Melhorn, and G.D. Valdez, *ITS Version* 3.0—*The Integrated Tiger Series of Coupled Electron-Photon Transport Codes*, Albuquerque, NM: Sandia National Laboratory, 1992.
8. C.F. Powell, P.H. Fowler, and D.H. Perkins, *The Study of Elementary Particles by the Photographic Method: An Account of the Principal Techniques and Discoveries*, *Illustrated by an Atlas of Photomicrographs*, New York: Pergamon Press, 1959.
9. W.H. Barkas, *Nuclear Research Emulsions*, New York: Academic Press, 1963.
10. C. Plante and J. Hebert, The p/mc dependence of the grain density of tracks in the Fuji ET-7B nuclear emulsion, *Nuclear Instruments and Methods*, B108, 99–113, 1996.
11. W.R. Leo, *Techniques for Nuclear and Particle Physics Experiments*, 2nd edn., New York: Springer-Verlag, 1994.
12. N. Tsoulfanidis, *Measurement and Detection of Radiation*, New York: McGraw Hill, 1981.
13. A. Oed, Position-sensitive detector with microstrip anode for electron multiplication with gases, *Nuclear Instruments and Methods*, A263, 351, 1988.
14. R.W. Williams, Chapter 1.3—Gas filled counters, *Methods of Experimental Physics*, *Nuclear Physics A*, 5, 1961.

15. H. Hinterberger and R. Winston, Efficient light coupler for threshold cerenkov counters, *Review of Scientific Instruments*, 37, 1094, 1966.
16. *Photomultipier Tubes*, *Principle and Applications*, available from Philips Photonics, International Marketing, BP 520, F-19106, France.
17. G.F. Knoll, *Radiation Detection and Measurement*, New York: John Wiley & Sons, 1979.
18. A. Peisert, Silicon microstrip detectors. In: F. Sauli (Ed.), *Instrumentation on High Energy Physics*, Vol. 9, Singapore: World Scientific, 1992.

83

Neutron Measurement

Steven M. Grimes
Ohio University

83.1 Introduction

Neutrons have characteristics that make them of particular importance in technology and research. Since they are uncharged, they are able to enter the nucleus at very low energy. Furthermore, the lack of energy losses through ionization permits deep penetration into materials.

This latter characteristic makes detection of neutrons more complicated than detecting protons or alpha particles. The energy of these charged particles can easily be determined by detecting them in ionization chambers, proportional counters, solid-state detectors, or scintillators, and ultraprecise measurements can also utilize the steering effect of magnetic fields. Detection efficiencies approach 100%. Neutrons, on the other hand, are not directly detected by these detectors, and some means of converting the neutron through a nuclear reaction to a charged particle or gamma ray must be used.

Nuclear reactions occur when neutrons interact with nuclei (including protons). When a neutron interacts with a nucleus, the following processes are possible:

1. Elastic scattering occurs if the neutron simply changes its direction without giving the nucleus any intrinsic excitation energy. The transfer of energy is analogous to that in a collision of two billiard balls and is governed by the laws of mechanics. The cross section for elastic scattering is usually large below 3 MeV and decreases at higher energies, although it is still significant at energies above 100 MeV.
2. Capture reactions are those in which the neutron is absorbed by the nucleus to form a heavier nucleus. In this case, the energy released comes in the form of one or more gamma rays. The capture cross section typically varies with energy E as $1/\sqrt{E}$ at energies below 1 MeV. At energies above 5 MeV, it is usually quite small.
3. Fission occurs in many cases if a heavy nucleus (mass > $A = 230$) is struck by a neutron. The nucleus divides into two smaller nuclei with a huge energy release ($E > 100$ MeV, where 1 MeV = 10^6 eV = 1.6×10^{-13} J).

4. Inelastic scattering occurs if a neutron transfers energy to the target nucleus and leaves it in an excited state. This energy is usually emitted in the form of a gamma ray, although in some cases positron–electron emission occurs and, in many cases, a number of low-energy gamma rays are emitted rather than one higher-energy gamma ray.
5. (n,z) reactions can also occur, where the neutron is absorbed by the nucleus and a charged particle (usually a proton or alpha particle) is emitted.
6. At high enough energies, multiple particles may be emitted. The (n,2n) reaction is particularly strong in the energy range $9 \leq E \leq 16$ MeV.

Each of these processes could, in principle, be used to detect neutrons. Unfortunately, in many cases, one cannot ensure that only one type of reaction occurs, and even when this condition is met, the resulting pulse spectrum does not always allow determination of the energy of the neutron.

83.2 Detector Types

83.2.1 Detectors Based on Elastic Scattering

Detectors based on elastic scattering are attractive because the elastic scattering cross section is large (usually about half of the total interaction cross section). A fundamental problem with elastic scattering is that the recoil energy as a fraction of the incident energy ranges from 0 (at 0° scattering angle) to $4A/(A + 1)^2$ (for 180° scattering angle), where A is the mass number of the target. For $A = 1$ (hydrogen), this recoil energy ranges from 0% to 100%, but for even as light a target as carbon ($A = 12$), the maximum energy of recoil is less than 30%. The fact that a continuous range of energies is produced even from a monoenergetic neutron beam makes the efficiency difficult to calculate, since it depends on accurate knowledge of the cutoff threshold of the electronics. The same feature complicates determining the energy distribution of neutrons when a range of energies is present.

Hydrogen-containing counters are nonetheless frequently used in neutron physics. Below about 500 keV, the pulse height is usually too small to be useful, but above this energy, this type of counter is effective. Proportional counters or ion chambers filled with methane can be used in situations where fast timing is not required. Hydrogen-containing scintillators have poorer energy resolution but better timing information and are available in large volumes. Scintillators are subject to a threshold but can be made highly efficient ($\varepsilon > 50\%$) if the volume is sufficiently large. For either proportional counters or scintillators, gamma rays can produce background pulses through the Compton effect, but some liquid scintillators have the capability of identifying the two types of pulses produced by neutrons and gamma rays, respectively, allowing discrimination against gamma rays. The excellent timing characteristics of scintillators have resulted in extensive use of these detectors for time-of-flight spectrometers. In these spectrometers, the energy of the neutron is deduced by timing the neutron over a measured flight path. For typical flight paths ($L < 10$ m), a precision of a few nanoseconds is required.

The fundamental limitation of counters of this type is that the pulse height in the detector is not uniquely related to the neutron energy. If the detector is not used in a time-of-flight spectrometer, the energy of the neutron is difficult to determine. If a detailed study is done to characterize the pulse height distribution as a function of neutron energy, an estimate of the spectral shape can be obtained [1]. A related problem is that the efficiency is determined by an electronic cutoff, which is difficult to determine accurately. Calculations of the efficiency require a detailed knowledge of the pulse height as described earlier; both calculations and experimental determinations will be described in 83.3. A further complication to calculation of the efficiency is the role of carbon. Above 6 MeV, the (n,α) channel becomes possible, and above 7.6 MeV, the (n,3α) channel opens. Since the (n,p) cross section drops at higher energies, these reactions, plus ^{12}C(n,p) and ^{12}C(n,α), provide significant contributions to the efficiency. The database for

carbon cross sections is not as extensive as that for (n,p). Finally, detectors that include the entire angular distribution do not have directional sensitivity.

All of these drawbacks can be removed if only a limited portion of the angular range is sampled. This is the case in a recoil counter telescope. The spectrometer consists of a polyethylene radiator at one end of an evacuated cylinder. Near the other end are either one or, more typically, two detectors. Neutrons enter the telescope from the end holding the radiator. A small fraction of them produce recoil protons at small angles to the beam. A two-detector system is arranged so that the particles traverse both of the detectors. Requiring a coincidence in pulses reduces backgrounds. These detectors register protons scattered by the neutron beam at angles near 0° to the original beam. The recoil energy of such protons is $E_n \cos^2 \theta$, where E_n is the neutron energy and θ is the angle of recoil. This implies that for a telescope that subtends an angle θ around 0°, the energy range of recoil protons will be E_n to $E_n \cos^2 \theta$. It can be shown that the average energy is simply (1/2) E_n (1 + $\cos^2 \theta$). Obviously, as θ becomes small, the proton energy reflects the neutron energy. The smaller θ becomes, however, the lower the efficiency of the telescope. Typical telescopes of this type have efficiencies of 10^{-5} to 10^{-6}. It is obvious that only neutrons arriving along the axis will give protons of the right energy. Neutrons coming from the backward hemisphere will not be able to produce protons that traverse the spectrometer. The drawback of a low efficiency is partly compensated by the fact that the efficiency can be accurately calculated and the fact that the energy spectrum can be deduced.

A further drawback is that because the (n,p) cross section drops with neutron energy and the proton energy loss drops with proton energy, the optimal radiator thickness varies with neutron energy.

83.2.2 Detectors Based on Capture Reactions

Capture reactions have small cross sections at energies above 1 MeV. At lower energies, the cross section typically varies as $1/\sqrt{E}$, so it can be very large at low energies. Further, the capture process is exoergic, typically yielding about 7 MeV. This energy is usually divided among two to four gamma rays. The efficiency of gamma-ray detectors is usually much less than 100%, and detecting the gamma rays in coincidence requires large solid angles. It is essentially impossible to use the capture process to determine the energy of individual neutrons in a flux of neutrons of varying energies.

An alternative use of the capture process is in a passive detector. A foil of the appropriate material can be placed at the location where the flux is to be determined. The target must be one that produces a radioactive residual nucleus when a neutron is captured. Thus, ^{28}Si would not be appropriate, since ^{29}Si is stable, but ^{27}Al would be a possibility, since ^{28}A1 is radioactive. After the measurement is complete, the foil is removed and placed in a counting area. A detector then counts the beta particles or gamma rays emitted. Of particular importance is the choice of target to ensure an appropriate half-life. A very short half-life would allow the decay of the radioactive nuclei before they could be counted, while a very long half-life (>1 month) might require an excessive length of time to be counted.

The complicated energy dependence of the capture cross section makes use of the capture process mostly useful for relative measurements. If two measurements are made of spectra with the same relative distribution of neutrons with energy, a measurement of the ratio of activities will give the ratio of neutron intensities. An important advantage to this technique is that small foils can be used, allowing the determination of the flux in a small volume. Other radiation, such as gamma rays, usually does not interfere in such a measurement. An important disadvantage is that the flux is not obtained until after the counting is completed; this might be as long as a month after the measurement. An additional disadvantage has already been mentioned. If the relative energy dependence of the two spectra is not the same, the relative ratio of neutrons will not be correct.

Because the cross section for capture typically varies as $1/\sqrt{E}$ at low energy, these detectors are very effective at detecting neutrons below 1 keV, including thermal neutrons.

83.2.3 Detectors Based on Fission

The fission process is relatively unique, since an energy release of over 100 MeV occurs even when the incoming neutron has energy below 1 eV. Fission cross sections for gamma rays are small, so most of the pulses will be due to neutrons. There are two types of fission targets. Those with even proton number (Z) and even neutron number (N) have an energy threshold for fission. The cross section for fission is normally negligible below 2–3 MeV. Other targets for which either N or Z or both are odd have no threshold energy. These isotopes (e.g., ^{235}U) normally have a low-energy cross-sectional dependence of $1/\sqrt{E}$, giving a very large efficiency for neutrons below 100 keV. Fission detectors are designed either for $E_n > 2$ MeV (in which case ^{238}U would be an appropriate choice) or for the entire energy range, in which case the efficiency is highest at low energies.

Fission foils must be fairly thin to allow the escape of the fission fragments into the counting volume. This typically results in low efficiencies ($<10^{-6}$). Fission chambers also require the license to possess radioactive isotopes. The energy release in the fission process is so large that the pulse height in the counter cannot be used to infer the neutron energy. Reasonably good timing information ($\Delta t < 5$ ns) allows the use of fission chambers in time-of-flight spectrometers.

83.2.4 Counters Based on Inelastic Scattering

Inelastic scattering results in a transfer of energy from the neutron to the target nucleus through excitation of an excited energy state. This will then result in the production of one or more gamma rays. Gamma rays can be detected in germanium detectors with good energy resolution. Unfortunately, the efficiency of a spectrometer utilizing a germanium detector and inelastic scattering is quite small. This technique is being examined as a possible approach to identifying contraband materials in luggage, since both the neutrons and the gamma rays they produce are highly penetrating.

Although most gamma-ray decays occur rapidly ($<10^{-6}$ s), some gamma-ray decays are inhibited by angular momentum coupling and have half-lives longer than 1 s. These could be used in a detector based on inelastic scattering just as the capture reaction is used. Two nuclei with such states are ^{89}Y and ^{103}Rh. Unlike the capture reaction, such isomeric transitions will not be effective in detecting low-energy neutrons, since there is a threshold for populating such states (approximately equal to the energy of excitation, ignoring recoil effects).

83.2.5 Detectors Based on (n,p) or (n,α) Reactions

Detectors utilizing (n,p) or (n,α) reactions can be passive, in which a final product nucleus is radioactive, or active, in which a proton or alpha is detected. For a discussion of the passive type, see the section on detectors based on capture reactions (aforementioned text). Direct detection of the charged particle can occur in a proportional counter or a scintillator. As in the case of fission, many (n,p) and (n,α) reactions have an energy threshold, which prevents their occurring until this energy is exceeded. Others have no threshold (they are exoergic) and have low-energy cross sections that vary as $1/\sqrt{E}$. These targets and the reactions that occur are

1. ^{3}He(n,p)^{3}H
2. ^{6}Li(n,α)^{3}H
3. ^{10}B(n,α)^{7}Li

Reaction (1) is often utilized in a proportional counter filled with ^{3}He. The second reaction can be used in a scintillator made of glass that has a loading of up to 9% ^{6}Li. For Reaction (3), the gas BF_3 can be used in a proportional counter.

Each of these reactions is particularly effective in detecting neutrons below 1 MeV and especially thermal neutrons ($E \sim 0.025$ eV). Few charged particles are produced by neutrons at these energies from the counter housing or glass constituents, so the spectra are characterized by minimal interference from other materials. A common problem is that the low-energy neutrons that one seeks to measure are accompanied by a flux of thermal neutrons, which one does not wish to measure. In this case, the counter efficiency will be so high for the thermal neutrons that they may swamp the events one wishes to detect. An obvious solution to this problem is to use a thin layer of cadmium or boron to shield the detector, since these materials have very high thermal absorption cross sections. Each of these reactions is much less effective at energies above 10 MeV, since backgrounds due to charged particles in the housing or in the glass can be comparably large. Although counters utilizing these reactions can be approximately 100% efficient at thermal energies, they are often less than 5% efficient at energies above 3 MeV.

There is an interest in having a counter that can detect neutrons with virtually constant efficiency independent of energy. A counter that approximately meets this characteristic is the long counter. This counter consists of a BF_3-filled proportional counter embedded in a moderating cylinder of polyethylene, paraffin, or similar material. Those neutrons directly incident on the BF_3 chamber with very low energies will be detected with approximately 100% efficiency, while neutrons with $E_n > 1$ MeV will be detected with much smaller efficiency (<10%). By surrounding the BF_3 counter with polyethylene or paraffin, the higher-energy neutrons can be slowed down and the net efficiency increased, although some may be captured in the moderating material. Very low-energy neutrons will be more likely to be captured in the polyethylene or paraffin, so the detection efficiency for these neutron energies is reduced. Study of the detailed energy dependence of the efficiency of such counters has resulted in a design that has certain cavities cut in the shielding on the side from which the neutrons enter. This allows some of the lower-energy neutrons a shorter path to the counter. The fact that neutrons are detected after moderation means that the counter cannot give precise timing information, nor can it be used to determine neutron energy spectra. It also cannot determine the neutron flux over a small cross-sectional area but gives an average over 40–100 cm^2. Further, it will have a slightly different efficiency for neutrons coming from different directions. A sample design is shown in Figure 83.1. Note that since the counting element needs only to have an efficiency that rises sharply at low energy, a long counter can be designed using a ^3He ion chamber instead of a BF_3 tube.

Other (n,z) reactions do not have positive Q values (are not exoergic). These have thresholds and, in fact, usually have small cross sections for a few MeV beyond the threshold. An example is $^{27}Al(n,\alpha)^{24}Na$. This reaction cannot occur for neutrons of less than 3 MeV and has a very small cross section below 4.5 MeV. It does lead to a radioactive final nucleus and can be used as a passive detector. Unlike the detectors based on the (n,γ) reaction, it will not detect low-energy neutrons.

An alternative reaction that can be used in a passive detector is the (n,2n) reaction. This typically has a threshold of about 8 MeV but has a large cross section once the threshold is exceeded. Note that just as is found for (n,γ) or (n,z) reactions, not all nuclei reached in (n,2n) reactions are unstable.

A passive foil can be placed adjacent or behind another foil to obtain more spectral information. If a first foil is counted for the (n,γ) events, a second, which utilizes (n,p) or (n,2n), could provide an estimate of the neutron flux at energies above the region where the (n,γ) reaction is effective.

83.2.6 Standards

The National Institute of Standards and Technology (Gaithersburg, MD) maintains two standard neutron sources [2]. NBS-I is based on ^{226}Ra-Be(γ,n) and NBS-II is a similar backup source. The activities of NBS-I and NBS-II are known to about 0.85%. These can be used with a flowing bath containing ^{55}Mn to compare the production of ^{56}Mn in the $^{55}Mn(n,\gamma)$ reaction between NBS-I or NBS-II and an external source. The estimated error on such a determination of source strength for an external source is about 3.5% (2σ) [2].

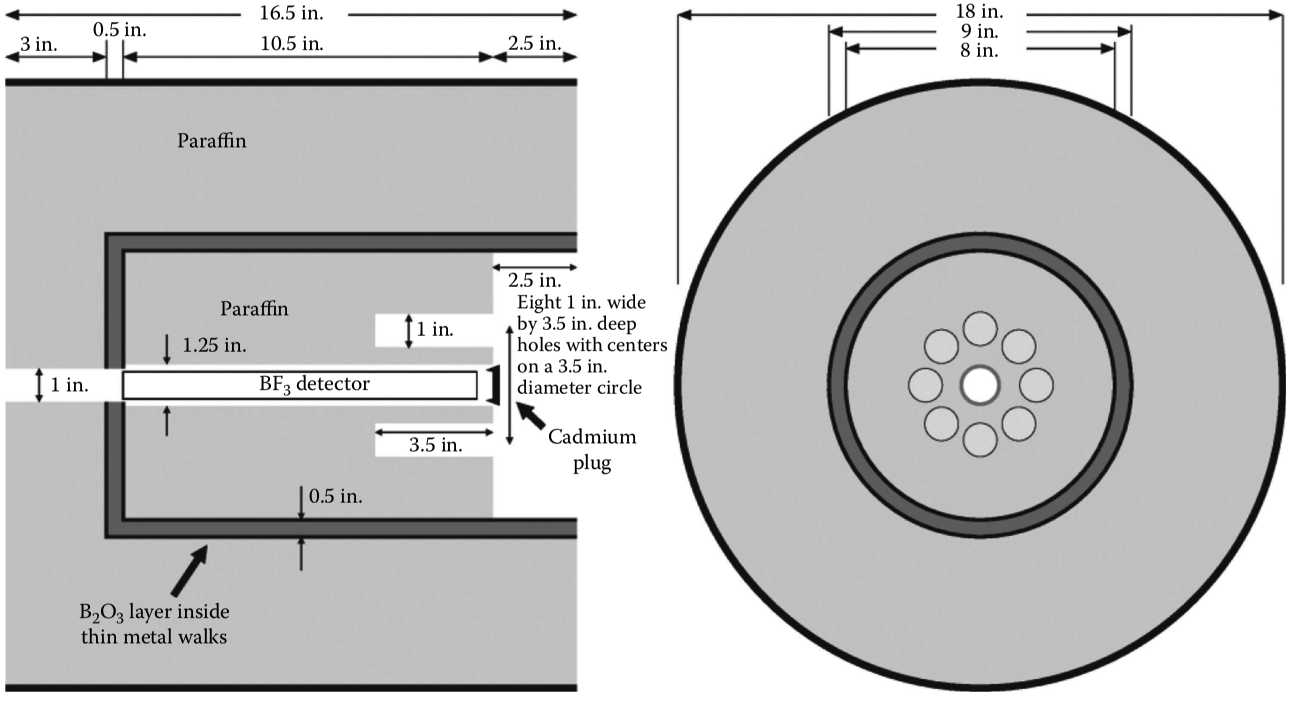

FIGURE 83.1 Cross section of a typical long counter. Neutrons incident from the right are scattered by the paraffin, causing them to lose energy. The BF_3 counter is efficient primarily for neutrons below 1 keV. The holes and the B_2O sections balance the efficiency as a function of energy. Cadmium has a very large $1/E$ capture cross section. Use of the cadmium filter suppresses efficiency for thermal neutrons, while removing it adds the contribution due to thermal neutrons. This counter is at the Edwards Accelerator Laboratory of Ohio University.

83.3 Efficiency Calculations and Measurements

Detectors based on n-p scattering have an efficiency that depends on the n-p elastic cross section. For a proportional counter or scintillator, an approximate expression for the efficiency is

$$\varepsilon = \left(1 - e^{-n\sigma_H L}\right)\left(1 - \frac{B}{E_n}\right) \tag{83.1}$$

This expression involves the parameters n, the number of hydrogen atoms per cm^3; σ_H, the n-p elastic cross section; B, the electronic cutoff (in energy equivalent units); and E_n, the neutron energy. This expression ignores multiple scattering, so it would not include pulses produced by two scattering events in succession. It also does not include carbon interactions. For energies below 4.4 MeV, carbon interactions are almost entirely elastic and do not result in absorption or pulses large enough to detect. Particularly at energies above 10 MeV, carbon interactions not only remove neutrons from the beam but also, through (n,α) or (n,3α) events, can produce pulses that can be detected. Calculating the efficiency in this energy range can be done with Monte Carlo codes, but the efficiency will depend on knowledge of the ^{12}C(n,α) and ^{12}C(n,3α) cross sections as well as the relation between alpha pulse heights and proton pulse heights as a function of energy.

Recoil telescopes have an efficiency that has the form:

$$\varepsilon = \frac{n\sigma(0°)LA}{d^2} \tag{83.2}$$

Here

n is the number of hydrogen atoms per cubic centimeter
$\sigma(0°)$ is the n-p elastic cross section at 0° (in units of cm^2/steradian)
L is the thickness of the radiator
A is the area of the detector
d is the distance between radiator and detector

Note that this assumes that $n\sigma L \ll 1$ and that θ is small. A corrected version based on the assumption that the n-p cross section is isotropic in the center of mass has

$$\sigma(0°) = \frac{\sigma_{np}}{\pi} \tag{83.3}$$

where σ_{np} is the total elastic cross section and, if θ is not sufficiently small, $\sigma(0°)$ is replaced by

$$\frac{\sigma_{np}}{2\pi}(1 + \cos\theta) \tag{83.4}$$

Note that the efficiency can be increased by increasing L or A or reducing d. All of these changes degrade the energy resolution.

Efficiency of passive detectors is a function of many variables. The total activity of a sample after being struck by N_n neutrons will be

$$n\sigma L N_n \frac{\tau}{T}\left[1 - e^{-T/\tau}\right] \tag{83.5}$$

where

n is the number of atoms per cm^3
σ is the appropriate cross section (e.g., for n, γ)
L is the thickness of the foil
T is the time over which the irradiation took place
τ is the average lifetime of the radioactive nuclei produced

This expression assumes that $n\sigma L \ll 1$ and that the source strength was uniform over the time T.

If the counter has an area A, is at a distance d from the activated foil, has an efficiency ε_r, and measures the activity from a time t_1 after the bombardment to a time t_2, the efficiency ε_n will be

$$\varepsilon_n = (n\sigma L)\frac{\tau}{T}\left(1 - e^{-T/\tau}\right)\left(\frac{A\varepsilon_r}{4\pi d^2}\right)\left(e^{-t_1/\tau} - e^{-t_2/\tau}\right) \tag{83.6}$$

Each of the factors in parenthesis is less than one, and the typical efficiency of such a monitor is 10^{-4} to 10^{-6}.

Fission chambers have an efficiency of

$$\varepsilon_n = n\sigma_f L \tag{83.7}$$

where

n is the number of atoms per cm^3 in the foil
σ_f is the fission cross section
L is the thickness of the foil

At low energies, σ_f may be large enough so that the aforementioned expression is greater than 0.1. In that case,

$$\varepsilon_n = \left(1 - e^{-n\sigma L}\right)\frac{\sigma_f}{\sigma} \tag{83.8}$$

where σ is the total cross section for neutrons.

The efficiency for a lithium- or boron-containing scintillator is

$$\varepsilon_n = \left(1 - e^{-(n_1\sigma_1 + n_2\sigma_2)L}\right)\left[\frac{n_1\sigma_1}{n_1\sigma_1 + n_2\sigma_2}\right] \tag{83.9}$$

where

n_1 is the density of lithium or boron atoms per cm^3
σ_1 is the (n,α) cross section
n_2 is the density of atoms other than lithium or boron in the scintillator
σ_2 is the average absorption cross section for these atoms

If $\left(n_1\sigma_1 + n_2\sigma_2\right)L \ll 1$, this becomes

$$\varepsilon_n = n_1\sigma_1 L \tag{83.10}$$

Note that in each case where a term of the form $(1 - e^{-n\sigma L})$ appears, the average of this quantity is not $(1 - e^{-n<\sigma>L})$ if σ has energy fluctuations over an energy bin that are substantial. Here, $<\sigma>$ is the average cross section over the energy bin. This limit is particularly important at low energies, where isolated resonances cause large fluctuations in σ and where the limit of small $n\sigma L$ may not be appropriate. In this case, the expression for the efficiency should be evaluated separately for individual energies in the bin and the resultant efficiencies averaged.

Efficiencies calculated using the aforementioned formulas are likely to be reliable for proton recoil telescopes and fission chambers. This is because the detector as normally used is insensitive to gamma rays. The fission process produces a large pulse, and background pulses from counter constituents are likely much smaller. Further, the thin fission foil makes multiple scattering negligible.

For counters involving the use of (n,p) and (n,α) reactions or elastic scattering, multiple scattering effects may not be negligible. Further, constituent atoms of the counter or support may contribute background.

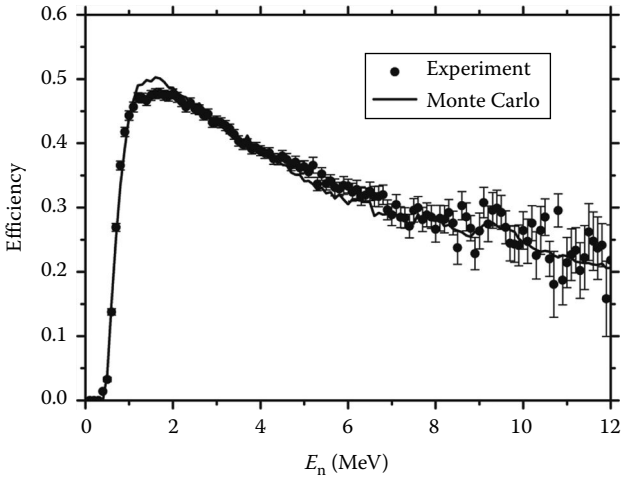

FIGURE 83.2 A calibration of a hydrogenous scintillator using a fission chamber containing ^{252}Cf. The solid line is a calculation based on Monte Carlo. (Reprinted from *Nucl. Instrum. Meth. Phys. Res. A,* 399, Total characterization of neutron detectors with a ^{252}Cf source and a new light output determination, Kornilov, N.V., Fabry, I., Oberstedt, S., and Hambsch, F.J., Copyright 2009, with permission from Elsevier.)

Figure 83.2 shows a calibration [1] of a hydrogenous scintillator using a fission chamber containing ^{252}Cf. This isotope fissions spontaneously. Because its fission spectrum has been previously characterized, the fission chamber in detecting a fission pulse serves as a calibrated neutron source. A detector that is capable of giving an accurate time for a pulse can be used to determine the efficiency as a function of energy. At low energies, the efficiency of the counter is smooth and has the shape expected for

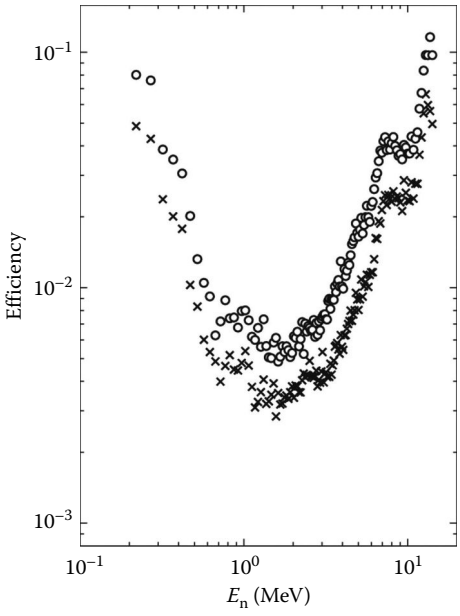

FIGURE 83.3 A calibration for a lithium glass detector using the continuous neutron spectrum produced by deuterons incident on a stopping target of aluminum. At low energy ($E < 1.5$ MeV), the efficiency is largely due to ^{6}Li(n,α) reactions, while above this energy, the observed spectrum and efficiency suggest that the (n,n′ γ) reaction on the constituents of glass provides most of the efficiency.

proton recoil pulse. At energies above 8 MeV, the statistical precision of the measurement gets worse because of the small fission neutron fraction above this energy. It appears that there is some structure in the efficiency. This may be due to carbon-produced pulses or absorption by air between the chamber and detector.

A similar calibration for a lithium glass detector has been carried out [3] using the continuous neutron spectrum produced by deuterons incident on a stopping target of aluminum and is shown in Figure 83.3. This spectrum was measured with a fission chamber. The observed efficiency is striking for two reasons. The different efficiency values are found for detectors that are similar in size and lithium content. Thus, their calculated efficiencies would be identical. Furthermore, the efficiency has the behavior expected for a detector based on the ^{6}Li(n,α) reaction only at energies below 1 MeV. Above this energy, it appears that neutron inelastic scattering from silicon and oxygen in the glass yields gamma rays that are detected and enhance the detection efficiency. This illustrates the value of experimental measurements of detector efficiency.

83.4 Summary

A summary of the features of various counters is presented in Table 83.1. More exhaustive treatment of the subject of neutron detectors can be found in Refs. [4,5]. Table 83.2 lists some suppliers of neutron detectors.

TABLE 83.1 Characteristics of Various Neutron Detectors

Detector Type	Gives Energy Spectrum	Small Size	Directional Information	Insensitive to Gamma Rays	Detects Neutrons below 500 keV	Timing Information[a]	High Efficiency[b]
Hydrogen-containing counters							
Proportional counter	No	Yes	No	Somewhat	No	No	Yes
Scintillator	No[c]	Yes	No	Liquid scintillator can reject gamma rays	No	Yes	Yes
Proton recoil telescope	Yes	Yes	Yes	Yes	No	Yes	No
Non-hydrogen-based counters							
Passive (n,γ) detector	No	Yes (smaller than others)	No	Yes	Yes	No	No
Fission detector	No[c]	Yes	No	Yes	Yes	Yes	No
Passive inelastic-scattering detector	No	Yes	No	Largely	No	No	No
Detectors based on (n,z) reactions							
Passive detector	No	Yes	No	Yes	Yes	No	No
Scintillator (lithium glass)	No[c]	Yes	No	No	Yes	Yes	Yes
Long counter	No	No	No	Yes	Yes	No	Yes

[a] Timing information is considered to be available if the time is determined to within less than 10^{-6} s.

[b] High efficiency means $\geq$1%.

[c] Can give energy information when used in time-of-flight spectrometer.

TABLE 83.2 Commercial Suppliers of Neutron Detectors

Supplier	Product
Saint-Gobain Crystals (Bicron), 17900 Great Lakes Parkway, Hiram, OH 44234-9681, Tel.: (440) 834-5600, Fax: (440) 834-7680, scintillation@saint-gobain.com, www.detectors.saint-gobain.com	Plastic scintillators Liquid scintillators with pulse shape discrimination Assemblies, phototubes
Advanced Measurement Technology, Inc. (ORTEC), 801 South Illinois Avenue, Oak Ridge, TN 37831-0895, Tel: (865) 482-4411, Fax: (865) 483-0396, ortec-info@ametek.com, www.ortec-online.com	He-3 detector and electronics Li-6 detector and electronics
Reuter Stokes, GE Energy, 8499 Darrow Road, Twinsburg, OH 44087, Tel.: (330) 425-3755, www.gepower.com	He-3 proportional counters Fission chambers
REXON, 24500 Highland Point, Beachwood, OH 44122, Tel.: (216) 292-7373, Fax: (216) 292-7714, www.rexon.com	Plastic scintillators Liquid scintillators with pulse shape discrimination Assemblies, phototubes
N. Wood Counter Laboratory, Inc., P.O. Box 509, Chesterton, IN 46304, Tel.: (219) 926-3571, Fax: (219) 926-3571, www.nwooddetectors.com	Boron triflouride (BF_3) gas tubes

Defining Terms

Compton effect: A process by which a gamma ray scatters from an electron on an atom. As a result, the electron is given a recoil velocity, producing ionization and yielding a pulse in an ionization chamber or proportional counter.

Efficiency: The efficiency of a neutron detector is its probability of detecting a neutron incident on the detector. Efficiency is obviously a number between 0 and 1 and generally depends on neutron energy.

Ionization chamber: A detector that collects the charge produced by ionization as a charged particle passes through the chamber.

Isomeric transition: Gamma-ray decay of a nucleus in which the rate of decay is greatly slowed by restriction imposed by angular momentum coupling.

Proportional counter: A detector that collects the charge produced by ionization with linear amplification as a charged particle passes through the chamber.

***Q* value**: A parameter expressing whether a nuclear reaction leads to a final state of higher final mass ($Q < 0$) or of lower final mass ($Q > 0$) than the initial state. Elastic scattering reactions have $Q = 0$.

Scintillator: A detector that converts ionization energy to a short light pulse.

Time-of-flight spectrometer: A detection device for neutrons in which a neutron detector is placed a known distance from the neutron source and the energy of the neutron is deduced from the time the neutron takes to traverse this path.

References

1. N. V. Kornilov, I. Fabry, S. Oberstedt, and F. J. Hambsch, Total characterization of neutron detectors with a ^{252}Cf source and a new light output determination, *Nucl. Instrum. Meth. Phys. Res. A,* **399**, 226 (2009).
2. J. M. Adams, *Nucl. Instr. Meth. B* **213**, 218 (2004).
3. T. N. Massey, S. Al Quraishi, C. E. Brient, J. F. Guillemette, S. M. Grimes, D. Jacobs, J. E. O'Donnell, J. Oldendick, and R. Wheeler, *Nucl. Sci. Eng.* **129**, 175 (1998).
4. J. B. Marion and J. L. Fowler (eds.), *Fast Neutron Physics, Part I,* Interscience Publishers (New York, 1960).
5. G. F. Knoll, *Radiation Detection and Measurement,* John Wiley & Sons (New York, 1979).

84

Dosimetry Measurement

Brian L. Justus
Naval Research Laboratory

Mark A. Miller
Naval Research Laboratory

Alan L. Huston
Naval Research Laboratory

Radiation dosimetry is a field of radiation detection devoted to the quantitative measurement of the physical changes that occur in matter upon exposure to ionizing radiation. Radiation dosimetry is performed on a routine basis to ensure the occupational safety of workers when there exists a risk of radiation exposure. Such routine personal dosimetry is used to monitor and limit the long-term occupational exposure to workers and to assist with the assessment of the dose received in the event of an accidental exposure. Some occupations that have an associated risk of radiation exposure include medical personnel performing clinical x-ray diagnostic and radiotherapy procedures and military and civilian personnel involved in power plant maintenance and operation. Radiation dosimetry is also an important tool in a wide range of environmental monitoring and industrial processing applications. The scope of this chapter is limited to discussion of the most widely used and commercially available technologies for dosimetry of ionizing radiation for personal protection; however, it should be recognized that many of the same technologies are used with equal effectiveness for other dosimetry applications.

84.1 Radiation Dosimetry Quantities and Units

The goal of radiation dosimetry is to quantify the amount of energy that is deposited in matter upon interaction with ionizing radiation. Ionizing radiations fall into three categories: charged particles such as beta and alpha particles, neutral particles such as neutrons, and electromagnetic radiation such as gamma rays and x-rays. The mechanism and the efficiency of the energy deposition depend on the type and the energy of the radiation as well as on the composition of the absorbing material. In particular, the biological consequences to living tissue following radiation exposure are quite dependent on the type of radiation. In order to provide a useful measure of the biological damage that might be expected to occur upon energy deposition in tissue, a system of units and standards has been developed that takes into account the differing biological effectiveness of different types of radiation. Over the years, these units and standards have undergone extensive revision, and this process is still evolving. However, the units and standards in current use have been defined in detail in recent reports [1,2] published by

the International Commission on Radiation Units and Measurements (ICRU) and the International Commission on Radiological Protection (ICRP) and are the subject of a recent review article [3]. A brief summary of the fundamental units is provided as follows.

The quantity of primary interest in radiation dosimetry is the amount of energy that is absorbed per unit mass. The amount of energy imparted to a volume of matter is the difference between the sum of the energies of all the charged and uncharged particles entering the volume and the sum of the energies of all of the charged and uncharged particles leaving the volume, plus any change in the rest mass of the matter. The mean energy imparted per unit mass is defined as the absorbed dose, D, expressed in (SI) units as J kg^{-1}. The special name for the unit of absorbed dose is the gray (Gy). If the mass exposed to radiation is at a point in tissue, knowledge of the amount of absorbed dose alone is not sufficient to judge the biological effectiveness of the charged particles producing the absorbed dose. A quality factor, Q, is used to weight the absorbed dose to provide an estimate of the relative hazard of different energies and types of ionizing radiation. Q is a dimensionless factor that converts absorbed dose to dose equivalent, H, at a point in tissue. The dose equivalent has the same (SI) units, J kg^{-1}, as the absorbed dose, but the special name for the unit of dose equivalent is the sievert (Sv). If the amount of absorbed dose received on average over a specific tissue or organ is of interest, the quality factor is called the radiation weighting factor, w_R [1]. Table 84.1 lists values of w_R for various types and energies of radiation. The equivalent dose, H_T, in a tissue or organ is defined as the average absorbed dose in the given organ due to a particular type of radiation and is scaled by w_R. Thus, the total equivalent dose in a specific organ, T, due to exposure by each radiation type, R, is given by:

$$H_T = \sum_R w_R D_{T,R} \tag{84.1}$$

The equivalent dose also uses the special unit of sievert. For example, if an organ is exposed to neutrons of energy less than 10 keV, and receives an absorbed dose of 10 Gy (10 J kg^{-1}), the equivalent dose is determined, using Table 84.1 and Equation 84.1, to be 50 Sv (50 J kg^{-1}). Since the biological effectiveness of the exposure also depends on the specific organs targeted, dimensionless tissue weighting factors, w_T, have been defined that reflect the probability of damage resulting from a given equivalent dose. The effective dose, E, for an exposed individual is then the sum of the weighted equivalent doses for all tissues and is given by the expression

$$E = \sum_T w_T H_T \tag{84.2}$$

TABLE 84.1 Radiation Weighting Factors for Various Types of Radiation

Type of Radiation	Quality Factor
Photons, all energies	1
Electrons and muons, all energies	1
Neutrons, <10 keV	5
Neutrons, 10–100 keV	10
Neutrons, >100 keV–2 MeV	20
Neutrons, >2–20 MeV	10
Neutrons, >20 MeV	5
Protons, other than recoil protons, >2 MeV	5
Alpha particles, fission fragments, and heavy nuclei	20

Source: From ICRP Publication 60, Ann. ICRP 21(1–3), 1990 *Recommendations of the International Commission on Radiological Protection*, International Commission on Radiological Protection, Pergamon Press, Oxford, U.K., 1991.

The effective dose also uses the special unit of sievert. It should be pointed out that despite the adoption of nomenclature and definitions for equivalent dose and effective dose, for all practical purposes, the quantities measured and reported for dosimetry applications are the dose equivalents defined in terms of the quality factor, Q. A further quantity for reporting purposes is the personal dose equivalent, $H_p(d)$, the dose equivalent in soft tissue, at an appropriate depth, d, below a specified point in the body. For weakly penetrating radiation, such as beta particles, a depth of 0.07 mm, or $H_p(0.07)$, is used. Eye doses are reported for 3 mm depth ($H_p(3)$), and deep doses are reported for 10 mm depth ($H_p(10)$). The personal dose equivalent is typically measured with a dosimeter that is covered with the appropriate thickness of tissue equivalent material. The dosimeter is worn on the surface of the body and is calibrated in a phantom. A phantom is a medium, such as poly(methyl methacrylate), that mimics the attenuating characteristics of the human body.

Another unit for absorbed dose, found in older publications and in current use in the United States, is the rad. One rad equals 100 erg g^{-1}. Similarly, another unit for dose equivalent is the rem. To convert from this system to the international standard (SI) units, the following conversions are used: 1 Gy = 100 rad and 1 Sv = 100 rem.

When an ionization chamber is exposed to x-ray or gamma-ray photons, the amount of ionization produced in the air inside the chamber is called the exposure, X. The (SI) unit of exposure is C kg^{-1} and the special unit is called the roentgen, R. Originally, R was defined as the amount of x-ray or gamma radiation that produces 1 esu of charge of either sign in 0.001293 g of air (the mass of 1 cm^3 of air at STP). The conversion from R to C kg^{-1} is $1\ R = 2.58 \times 10^{-4}$ C kg^{-1}. When air is exposed to radiation, the average energy required to form an ion pair is 33.97 J C^{-1}. For an exposure of 1 R, the absorbed dose in air is 8.77×10^{-3} J kg^{-1}.

84.2 Thermoluminescence Dosimetry

Thermoluminescence (TL) dosimetry is perhaps the most widely used and cost-effective technique for radiation dosimetry. It is for many organizations the technique of choice for routine monitoring of occupational radiation exposure. TL dosimetry is also widely used in medicine to determine patient exposure as a result of x-ray diagnostic procedures and cancer radiotherapy treatments. The dose ranges of interest for these applications can be roughly defined as 0.1–1 mGy for personal dosimetry applications, 1–100 mGy for clinical x-ray diagnostics, and 1–10 Gy for medical radiotherapy applications. TL dosimeter (TLD) phosphors are commercially available that exhibit a linear dose response and are capable of accurately measuring the absorbed dose for all the aforementioned applications and doses. The radiation-sensitive element of a TLD is a small quantity, typically less than 100 mg, of an inorganic crystal doped with metal impurities, called activators. The activators provide the crystal with the energy storage capacity as well as the luminescent properties that are required for the crystal to function as a thermoluminescent phosphor upon exposure to ionizing radiation. The details of the energy storage and TL mechanisms, despite intense research over many decades, are not well understood. Complex, long-range, many-body interactions between activator sites and their immediate environment may be involved. Despite this mechanistic uncertainty, the TL phenomenon has been used reliably by following well-established heuristic procedures and by referring to a simple and intuitive model. This model assumes that the activators provide point defects, known as traps and luminescence centers, in the crystal lattice. Upon exposure to ionizing radiation, electrons and holes are captured in metastable states at the trap centers by local potential minima until such time that the electrons and holes are thermally stimulated to overcome the electric potential. The electrons and holes can then recombine, with the emission of photons, at the luminescence centers. It is apparent from this model that TL dosimetry is a passive, integrating technique. Further, the technique shows no dose rate dependence, and for most applications, the TLD phosphors can be reused many times.

A comprehensive review of the properties and applications of a wide range of TLD phosphors has been published recently [4]. The characteristics of the phosphors that are of most interest for dosimetry applications include the sensitivity and the dynamic range of the TL response, the response to different

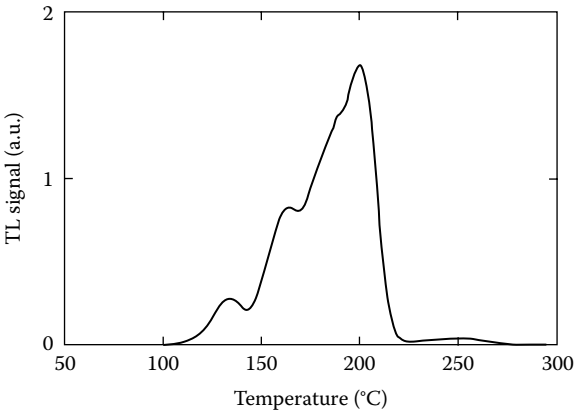

FIGURE 84.1 TL glow curve of LiF phosphor activated with trace amounts of Mg^{2+} and Ti^{4+} (TLD-100). The phosphor was exposed to a 2 Gy dose of ^{60}Co gamma rays and the glow curve was read using a Harshaw 2000 A/B TLD reader.

types of radiation over a broad energy spectrum, and the fading characteristics, reusability, and the reproducibility of the response. The TL response of the phosphor to ionizing radiation is indicated by measurement of the glow curve. A glow curve is a plot of the TL intensity versus temperature, measured as the phosphor is heated. A representative glow curve of a commercially available LiF TLD is shown in Figure 84.1. The glow curve usually exhibits one or more glow peaks that correspond to the release and recombination of electron and hole traps of differing trap depth and stability. TL dosimetry is best accomplished using phosphors having glow peaks in the range 200 °C–250 °C. Peaks in this temperature range are necessary to provide room-temperature trap storage times of several months. Although all traps fade with time, rapid fading of the stored information occurs from traps having glow peak temperatures below 200 °C, effectively precluding practical dosimetry. Glow peaks having temperatures greater than 250 °C require quite high temperatures (>300 °C) to release all the filled traps. In this case, blackbody radiation from the hot phosphor and other ancillary hot matter within the sample readout chamber (sample planchet, hot gas) interferes with and can easily overwhelm the TL signal due to actual trap recombination. The response of TLD phosphors as a function of absorbed dose must be carefully calibrated for all doses of interest. This is necessary because the response deviates from linear above a threshold dose, different for each phosphor, and, ultimately, the TL signal saturates and the phosphors suffer irreversible damage at very high doses. The TL response per absorbed dose as a function of energy, for low-LET electromagnetic radiation (gamma ray and x-ray), is generally fairly uniform. The efficiency for higher LET radiation can vary and should be calibrated as a function of energy. Since personal dosimetry applications require the measurement of doses absorbed by human tissue, tissue equivalent TLDs (effective atomic number closely matches that of tissue) are attractive because the energy dependence of the TL response closely matches that of tissue.

The most commonly used TLD phosphors are lithium fluoride (LiF), calcium fluoride (CaF_2), lithium borate ($Li_2B_4O_7$), calcium sulfate ($CaSO_4$), and aluminum oxide (Al_2O_3) activated with trace quantities of transition metal or rare earth metal ions. TLD phosphors are available in a variety of forms, including powders, compressed chips, Teflon-impregnated disks, single crystals, extruded rods, and thin films. TLD phosphors have been developed that respond primarily to gamma radiation and x-radiation, while others have been developed that, in addition, respond strongly to thermal neutrons. Unfortunately, there are no TLD phosphors having neutron sensitivity without gamma sensitivity. Therefore, in a mixed field of neutrons and gamma rays, TLDs are used in pairs, with one TLD having primarily gamma-ray sensitivity and the other having gamma-ray and thermal neutron sensitivity. The difference in the TL signal between the two TLDs of such a pair is assumed to represent the thermal neutron dose. Neutron sensitivity is enhanced, for example, in LiF phosphors by incorporating a high concentration of ^6Li since ^6Li

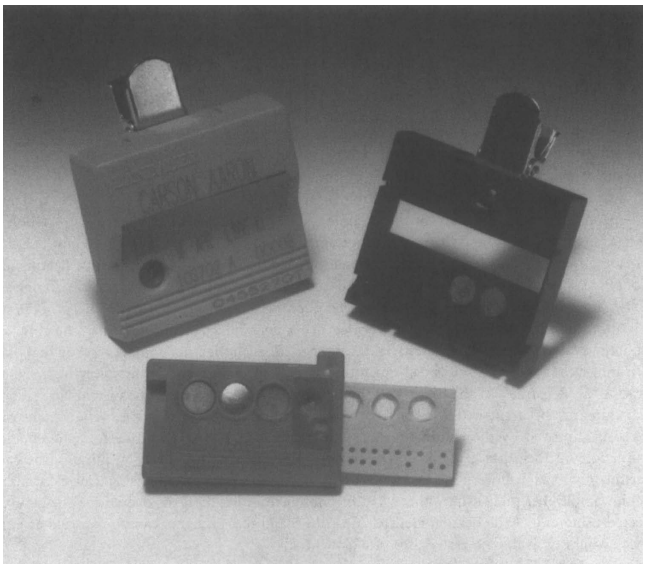

FIGURE 84.2 TLD body badge. A standard TLD badge contains three LiF phosphor chips. A fourth chip and a fast neutron track-etch foil can be added if required. (Courtesy of Landauer, Inc., Glenwood, IL.)

has a much higher thermal neutron cross section than ^{7}Li (TLD-600 contains 96% ^{6}LiF while TLD-700 has essentially no ^{6}Li). The manufacturers of TLDs exert considerable effort to maintain the uniformity of their products from batch to batch, a task of some difficulty since the characteristics of phosphors are a sensitive function of not only the composition but also the details of the manufacturing process. Thus, the properties of TLD phosphors of similar composition can vary considerably, and both the manufacturers of phosphors as well as the dosimetry service industries typically test and sort chips into groups based on their measured parameters. A representative commercially available TLD badge is shown in Figure 84.2. This standard badge contains three LiF TLDs and is capable of measuring gamma- and x-ray doses from 0.1 mGy to 10 Gy and energetic beta radiation doses from 0.4 mGy to 10 Gy. These badges are typically returned to the manufacturer on a monthly or quarterly basis for readout.

The actual practice of TL dosimetry requires some care to achieve accurate and reproducible results. For example, TLD-100 traditionally has been a very widely used phosphor, due to its tissue equivalence, that can yield accurate and fairly sensitive dose information. However, the energetics of the trap population in TLD-100, as well as the trap dynamics and intertrap communication with time, are extremely complex phenomena. Reproducible dosimetry requires that the sensitivity remain unchanged after each use. This is accomplished by careful adherence to a detailed protocol that may include a pre-irradiation anneal (e.g., 400 °C for 1 h followed by 80 °C for 10–24 h), a postirradiation anneal to 125 °C, and finally heating to readout the TL signal. It is common for individual TLD users to develop their own unique protocols for annealing and reading TLD chips. Excellent dose reproducibility (<5%) can be expected with care by following a well-defined protocol and using a set of individually calibrated TLD chips on a single, well-maintained TLD reader.

TLD instrumentation is commercially available from a number of suppliers. The choice of instrumentation depends largely on the form of the dosimeter phosphor chosen (compressed chip, Teflon disk, etc.), the desired sensitivity, and the degree of automation desired. The key element in any TLD reader is the heating method. The heating method should provide for controlled, reproducible heating and, if speed of processing is important, rapid cooling. Contact heating of the TLD on a planchet through which an electric current flows is a widely used heating technique. Because the surface of the TLD is not perfectly smooth, more uniform heating can be performed using noncontact methods, such as heating with a stream of hot gas or heating with infrared light. Laser heating is another noncontact

method that permits rapid heating (>1000 °C s^{-1}) using small quantities of TLD phosphor, yet permits very high signal-to-noise ratios [5]. Regardless of the heating method, blackbody radiation from the metal planchet and/or the TLD chip must be attenuated by colored glass and dielectric coated optical filters. The signal-to-noise ratio is also improved by the elimination of spurious TL signals that arise due to static charges or contamination on the surface of the TLD. Spurious TL signals are reduced by purging the sample compartment with a low flow of inert gas, such as dry nitrogen. Light detection is typically accomplished with a photomultiplier tube, using either a DC or photon-counting mode of operation. The glow curve is collected using any of the heating methods described, and the TL signal can be reported as either a glow peak height or as the integrated area of a glow peak.

The conventional TLD technology described previously requires bulk heating of the TLD to high temperatures (400 °C–600 °C) in order to read the stored dose information. Once the TLD has been read, the dose information is permanently erased. If any malfunction in the equipment occurs during readout, the data cannot be recovered. Alternative TLD technologies have been developed that do not completely erase the dose information and permit additional, successive readouts of the absorbed dose. This characteristic can eliminate accidental loss of dose information and can also provide, if desired, an archival record of exposure. Two such dosimeters, utilizing laser readout methods, are commercially available. These dosimeters function based on optical phenomena known as phototransferred TL (PTTL) [6] and

TABLE 84.2 Vendors of Personal Dosimetry Products and Services

Vendor	Product or Service
Bicron NE, 6801 Cochran Road, Solon, OH 44139, Tel.: (216) 248-7400, http://bicronusa.com/	TLD phosphors, TLD readers
Panasonic Industrial Comp., Applied Technologies Group, 2 Panasonic Way/7E-4, Secaucus, NJ 07094, Tel.: (201) 348-5339, http://www.panasonic.com/	TLD phosphors, optically heated TLD readers, electronic dosimeters
Landauer, Inc., 2 Science Road, Glenwood, IL 60425-1568, Tel.: (708) 755-7000, http://www.landauer.com/	TLD, film, track-etch services, COSL dosimeter
ICN Dosimetry Service, P.O. Box 19536, Irvine, CA 92713, Tel.: (714) 545-0100	TLD, film services
Eberline Dosimetry Service, 5635 Jefferson St, NE, Albuquerque, NM 87109-3412, Tel.: (505) 345-9931, http://www.eberlineservices.com/rad.htm	TLD readers, TLD service
Dosimeter Corporation of America, 5 Eastmans Road, Parsippany, NJ 07054, Tel.: (800) 322-8258	Pocket dosimeters, electronic dosimeters
Toshiba Glass Co., Ltd., 3583-5 Kawashira Yoshida-Cho Haibara-Gun, Shizuoka-Ken, Japan, Tel.: 0548-32-1217, http://www.toshiba.com/	RPL glass dosimeter
Siemens Environmental Systems Limited, Sopers Lane, Poole, Dorset, BH17 7ER, United Kingdom, Tel.: 44 1202 782779, http://www.siemens.com/entry/cc/en/	Electronic dosimeter
SAIC Commercial Products, 4161 Campus Point Court, San Diego, CA 92121, Tel.: (619) 458-3846, https://www.saic.com/	Electronic dosimeters
RADOS Technology, Inc., 6460 Dobbin Road, Columbia, MD 21045, Tel.: (410) 740-1440	TLD dosimeters, electronic dosimeters
SE International, Inc., 436 Farm Road, Summertown, TN 38483-0039, Tel.: (615) 964-3561, http://www.seintl.com/	Pocket dosimeters
Bubble Technology Industries, Hwy. 17, Chalk River, Ontario, Canada, K0J 1J0, Tel.: (613) 589-2456, http://www.bubbletech.ca/	Bubble dosimeters
Apfel Enterprises, 25 Science Park, New Haven, CT 06511, Tel.: (203) 786-5599	Bubble dosimeters

radiophotoluminescence (RPL) [7]. A commercial dosimeter (Landauer, Inc.) based on the phenomenon of PTTL is also known as a cooled optically stimulated luminescence (COSL) dosimeter. In preparation for readout of the dose information, the dosimeter is first cooled to liquid nitrogen temperature. It is then irradiated with ultraviolet laser light to phototransfer electrons from deep traps to shallow traps. The TL that results from the release of electrons from these very shallow traps, as the dosimeter is allowed to warm to room temperature, provides a very sensitive measure of the absorbed dose. Since it is not necessary to heat the dosimeter to high temperatures, the trapped charges are not fully annealed and the process can be repeated several times. A commercial RPL dosimeter, also known as the flat glass dosimeter (Toshiba Glass Co., Ltd.) uses a silver-activated phosphate glass that is read out by a pulsed ultraviolet laser. The manufacturer employs a special luminescence analysis protocol since the glass exhibits a prompt luminescence even in the absence of ionizing radiation exposure. RPL dosimeters are nevertheless capable of performing sensitive and reproducible dose measurements. New optical dosimetry technologies, based on the phenomenon of room-temperature optically stimulated luminescence (OSL), are being developed [8,9] and promise to provide both superior sensitivity and multiple readout capability.

Companies that provide TLD and other personal dosimetry products and services are listed in Table 84.2. This list is not intended to be comprehensive, nor is it intended to represent an endorsement by the U.S. government.

84.3 Ionization Chamber Dosimeters

Ionization chamber-based radiation dosimeters are among the most widely used and the most accurate instruments available for determining radiation exposure and absorbed dose. The operational principle of the ionization chamber is based on the formation and the collection of ion pairs that result from the interaction of energetic charged particles that pass through gases contained in a well-defined volume and electric field. Several types of ionization chambers are available, including real-time radiation field monitors and integrating devices that accumulate dose information for extended periods of time. Real-time devices monitor the radiation-induced currents, while integrating devices record changes in a static electric field. A wide array of ionization chambers, intended for applications in medical physics, equipment calibration, and personal dosimetry, are available. Small volume (<1 mL), precision ionization chambers are used by medical physicists for radiotherapy applications. These chambers are generally tissue or air equivalent and, while very accurate, have low sensitivity. Larger volume (<1000 mL) ionization chambers are used for applications such as field standardization and diagnostic x-ray machine calibration that require high sensitivity in addition to excellent accuracy. For personal dosimetry applications, compact integrating ionization chambers, about the size of a ballpoint pen, termed "pocket chambers" are used. Some pocket chamber dosimeters provide a method for direct visual readout based on the electrostatic deflection of a charged quartz fiber relative to a calibrated scale. Initially, the dosimeter is fully charged, representing the zero dose setting. Exposure to a radiation source causes a loss of charge on the fiber, and spring tension causes the fiber to partially return to its uncharged position. A lens system incorporated into the dosimeter in conjunction with a scale can be used to determine the absorbed dose. A commercially available direct-reading dosimeter is illustrated schematically in Figure 84.3. These instruments can measure gamma- and x-ray doses from a fraction of a milligray up to several gray. Greater accuracy is possible using indirect readout, pocket chambers that utilize precision electrometers to measure the change in the potential between the cathode and anode following exposure to radiation. These dosimeters are particularly useful for measuring low-level (<mGy) exposures. Another type of ionization chamber, used primarily for radon detection, utilizes the voltage drop across an electret element to determine radiation dose (Rad Elec, Inc.). An electret is an electrically poled insulator material, such as Teflon, that retains surface charges for long periods of time. Ion pairs produced by radiation exposure are separated and collected, resulting in a net decrease in the electret charge. Changes in the electret voltage can then be calibrated in terms of radiation exposure.

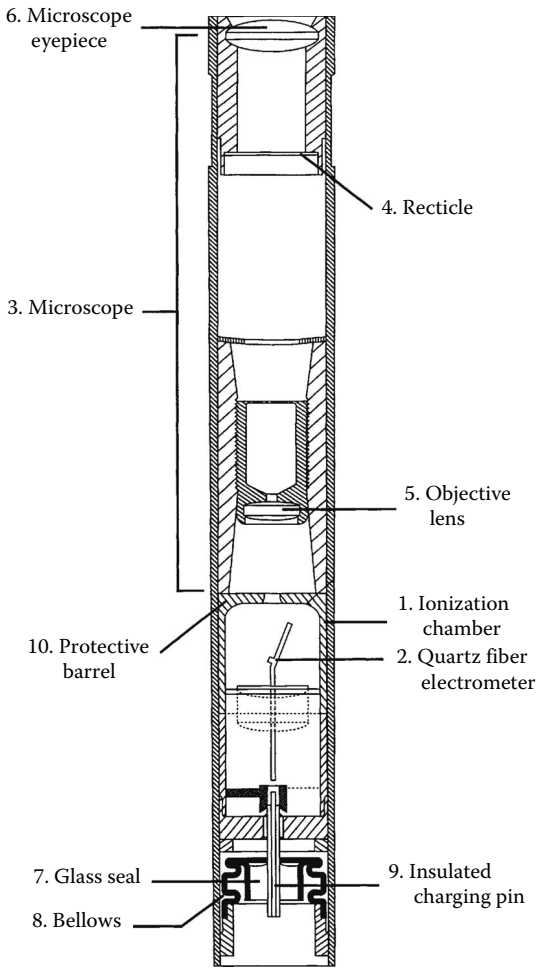

FIGURE 84.3 Schematic of direct-reading pocket ionization chamber. The radiation dose is determined by measuring the deflection of a movable quartz fiber electrode. The deflection of the fiber is determined optically by projecting the image of the fiber onto a reticle using a microscope objective. (Courtesy of Dosimeter Corp. of America , Rolla, ND.)

84.4 Film Dosimetry

Photographic films have been used for many years for radiography and personal dosimetry applications. However, due to the greater convenience, superior sensitivity, faster turnaround, and reusability of TLD personal dosimeters, film emulsion personal dosimeters have in many cases been displaced by TLD dosimeters. A notable example of this trend is the dosimetry program of the U.S. Navy, which has turned exclusively to TLD dosimeters. Despite this, film remains useful for specific applications that require analysis of an image or a charged particle track, and they remain the most convenient dosimetry method available if a permanent record of the exposure is desired. Radiographic films are sensitive to a variety of radiation sources, including photons (x-ray and gamma ray), charged particles (electrons, protons, and alpha particles), and neutrons (slow and fast). A major problem associated with the use of radiographic films for dosimetry purposes is that the energy response is not at all flat. A number of approaches have been used to flatten the response, including the incorporation of a scintillator dye such as *p*-terphenyl in the emulsion [10]. This approach has the effect of flattening

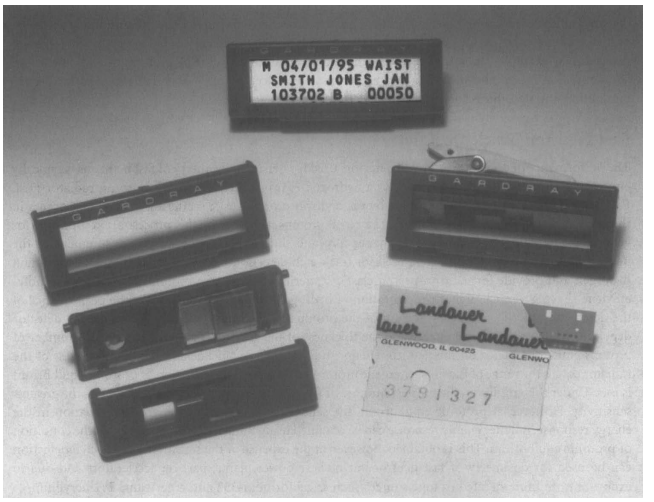

FIGURE 84.4 Film badge for personal dosimetry. (Courtesy of Landauer, Inc., Glenwood, IL.)

the response curve dramatically between 0.1 and 1.0 MeV, as well as increasing the sensitivity of the film. More commonly, in a manner similar to that used in multiple chip TLD badges, a series of metal filters, applied to different portions of the film, is used to provide energy discrimination. The film is then analyzed according to the sensitivity of each film segment for a particular radiation energy range. Figure 84.4 is a photograph of a commercially available film dosimeter badge that incorporates six absorbing filters to discriminate beta, gamma, and x-radiation. The dose range that can be measured is 0.1 mGy–5 Gy for gamma radiation and x-radiation and 0.4 mGy–10 Gy for energetic beta particles. Radiographic films consist of a thin layer of gelatin, approximately 10–20 μm thick, containing silver halide microcrystals, coated onto a polymer or glass substrate. Exposure to a source of radiation sensitizes the microcrystallites, creating a latent image that darkens visibly following development of the film. The radiation dose is determined by measuring the extent of the darkening with a densitometer. The densitometer measures the optical density (OD) of the film by comparing the transmission, T, of light through the exposed film with the transmission, T_0, of an identical film that has not been exposed to radiation. The optical density is a logarithmic function, $\text{OD} = \log(T_0/T)$, and can be measured accurately for values up to approximately 3. Developed film typically has a background OD of about 0.1 due to scattered light. Undeveloped film is quite sensitive to environmental factors such as light, temperature, and, in particular, moisture and must be carefully protected while in use. Film dosimeters are available that can also perform thermal and fast neutron dosimetry. The response of film to thermal neutrons is enhanced by the use of a film converter such as a 0.5–1 mm thick Cd foil. The foil absorbs thermal neutrons, yielding gamma rays that interact with the emulsion. Nuclear track emulsions are films that are used for dosimetry of fast neutrons in a manner quite similar to the track-etch detectors described in the next section. Nuclear track emulsions are generally much thicker than radiographic film emulsions and contain higher concentrations of silver halide microcrystals. Recoil protons transfer energy to the microcrystallites in the emulsion, creating latent images of the tracks of the protons. The range of charged particles in the emulsion is generally quite small, compared to photons, so that practically all of the energy is deposited in the film along the tracks. Nuclear track emulsions are no longer widely used due largely to the extremely high threshold, ~0.7 MeV, required for track visualization. Fast neutron dosimetry with film badges is most often accomplished by using a track-etch detector in conjunction with the radiographic film emulsion.

84.5 Track-Etch Dosimetry

Solid-state track detectors exploit the damage that occurs in dielectric materials upon exposure to ionizing charged particles. Energy is deposited in the material along a track defined by the trajectory of the ionizing particle. The damage is manifested as pits that develop on the surface of the material upon etching by chemical and electrochemical techniques. The pits are clearly evident using a simple optical microscope, and the track density can be estimated using either manual or automated pit counting methods. The track density is a direct measure of the radiation dose (for many particles, there is one track formed per particle), and track-etch detectors are very effective and sensitive dosimeters. At present the most important track-etch dosimetry applications utilize organic polymer films for alpha track detection (radon monitoring) and fast neutron personal dosimetry. The principal attractive features of track-etch detectors are their extreme simplicity and low cost, good sensitivity, near tissue equivalence, small size, passive operation, and insensitivity to fast electrons and gamma rays. Track-etch detection is a favorite dosimetry technique of graduate students worldwide because of its simplicity; however, commercially available track-etch detectors are manufactured with extreme care to provide users with uniform polymer films and reproducible dose response.

84.5.1 Alpha Track Dosimetry

Commonly used solid-state track detectors that possess sensitivity suitable for alpha particle dosimetry include plastics such as cellulose nitrate, polycarbonate, and polyallyl diglycol carbonate [11]. Since track-etch detection is a surface phenomenon, care must be exercised to avoid scratching the surface of the polymer film, as any surface imperfections can result in false-positive signals. The surfaces of the polymer film should also be protected from soiling since dust, dirt, grease, water, or any other foreign material can attenuate the alpha particles and prevent track registration in the detector. Polymer track-etch detectors do not fade significantly at room temperature; however, if the temperature is elevated such that the polymer softens, then the track damage can be annealed and etching will not yield a pit. Typically, radon track dosimeters are allowed to accumulate the alpha dose due to radon and its daughters for extended periods (up to a year) before being returned to the manufacturer for determination of the track density and the corresponding alpha particle activity. Dosimetry of other radioisotopes that emit alpha particles can also be performed; however, the response of the detector is dependent on the isotope detected. For example, alpha track detectors have been used for monitoring plutonium and americium contamination in soil and provide a convenient and cost-effective radiation survey method for decontamination and decommissioning activities [12].

84.5.2 Fast Neutron Track Dosimetry

The performance of polymer track-etch detectors used for personal dosimetry of fast neutrons is typically enhanced by the use of adjacent layers of a hydrogen-rich polymer, known as a proton radiator [13]. Fast neutron dosimetry is made possible by the neutron–proton elastic scattering process that occurs in the track-etch detector and the radiator. The recoil protons produced by this process are responsible for generating the damage tracks in the polymer film and thus provide an indirect measurement of the neutron flux. Although the polymers used for track-etch detection of neutrons, such as CR-39, contain hydrogen and provide for neutron–proton elastic scattering, the use of a proton radiator, such as polyethylene (having a much higher concentration of hydrogen), significantly improves the performance of the dosimeter [14]. The energy spectrum of the protons that leave the radiator and reach the detector depends on both the neutron energy and the thickness of the radiator. In addition, the total number of protons emitted depends on the neutron energy and the radiator thickness. When the thickness of the radiator equals the range of the most energetic proton emitted, then the condition of protonic equilibrium is met. Under this condition, the greatest number of protons are emitted, and the detector has the greatest sensitivity. However, at protonic equilibrium, the sensitivity also displays the greatest variation in the energy response. A flatter energy response can be obtained using thinner radiators that avoid the condition of protonic equilibrium. This is obtained, however, at the expense of the sensitivity. Track-etch detection method can be used

for dosimetry of fast neutrons at nuclear power plants and particle accelerators and due to exposure from unmoderated isotope sources such as californium-252 and americium-241 beryllium.

84.6 Bubble Dosimetry

Another method for fast neutron personal dosimetry is bubble detection. Bubble dosimeters are manufactured using a clear, elastic polymer gel as a host matrix, supporting a dispersion of nanometer-scale superheated droplets of a liquid, such as Freon. Neutrons incident on the polymer gel generate recoil protons in an elastic scattering process, followed by deposition of the proton energy along a track, in a process similar to that described in the discussion of track-etch detectors. However, in the track-etch detectors, the tracks must be visualized by a separate etching procedure. The charged particles in a bubble dosimeter deposit their energy directly into the superheated droplets, causing the droplets to effectively explode into much larger gas bubbles. This process, which can be readily heard, is immediate, generating bubbles that can easily be seen by the naked eye, provided the bubble diameter exceeds a critical diameter required in order for the bubble to persist stably in the gel. The fast neutron dose is determined by counting the total number of bubbles generated. Bubble counting can be performed manually, by visual inspection of the dosimeter, or by automated means. Commercial bubble dosimeters are available that use either optical or acoustic automated counting techniques. Dosimeters have been developed using droplet materials that have differing energy thresholds, thereby providing the dosimeters with limited spectroscopic capabilities. Bubble dosimeters have been developed that are compensated to provide a temperature-independent response. Fast neutron bubble dosimeters have several advantages in common with track-etch detectors, including good sensitivity, near tissue equivalence, passive operation, small size, and insensitivity to thermal neutrons and gamma radiation. Additional advantages include immediate bubble visualization (no need for a separate track developing step), limited reusability, sensitivity adjustability, a flat dose response over a wide energy range, utilization of the entire volume of the dosimeter, and angular response superior to that of track-etch detectors. Bubble dosimeters are more expensive than track-etch dosimeters and are best utilized when the energy of the neutron field is known. Figure 84.5 is a photograph of commercially available bubble dosimeters, before and after exposure to neutrons. A comprehensive review of bubble dosimeters, including new developments, has been published recently [15].

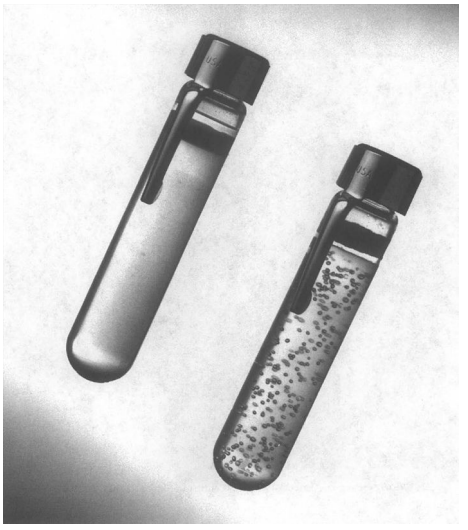

FIGURE 84.5 Bubble dosimeters for personal dosimetry of fast neutrons. The dosimeter on the left is shown before exposure to fast neutrons. For comparison, a dosimeter exposed to fast neutrons is shown on the right. Bubbles are clearly evident throughout the volume of the dosimeter. (Courtesy of Siemens Medical Systems, Inc., Concord, CA.)

FIGURE 84.6 Electronic personal dosimeter. (Courtesy of Siemens Medical Systems, Inc.)

84.7 Electronic Personal Dosimeters

All of the personal dosimeters discussed to this point are passive devices that require no external power source. The radiation dose is determined upon completion of the sampling period by subjecting the dosimeter to a separate processing step. The nature of the processing depends on the dosimeter, but examples include heating of a TLD, chemical etching of a foil, development of an emulsion, or simply counting bubbles. The electronic personal dosimeter (EPD), by contrast, is an active device that uses silicon diode detector technology to provide real-time measurements of radiation dose. The EPD has gained popularity in recent years and has mounted a serious challenge to TL dosimetry as the preferred official dosimeter of record. EPDs can provide extremely sensitive real-time measurements of both the total dose and the dose rate. In addition, the EPD can be designed to provide an audible alarm if the total dose or dose rate exceeds user-defined settings. While the quality and characteristics of EPDs from different manufacturers can vary significantly, some EPDs offer accurate dose measurements over a wide range of doses, dose rates, and energies and perform on a par with TLD dosimeters. A commercially available EPD is shown in Figure 84.6. This unit uses three silicon diodes to provide deep and shallow dose information for a wide range of gamma, beta, and x-radiation energies. EPDs typically have a display for manual readout of dose data but can be used with an automated reader for convenient archiving of data and for rezeroing the dosimeter for repeat use. Personal dosimeters are envisioned that would combine active and passive technologies, providing the accuracy and convenience of real-time dose monitoring in addition to the reliability of passive, cumulative dose measurements.

Defining Terms

Absorbed dose (*D*): The mean energy absorbed per unit mass.

Dose equivalent (*H*): The mean energy absorbed per unit mass, scaled with a quality factor, *Q*, that provides an estimate of the relative biological hazard of the radiation.

Effective dose (*E*): The total mean absorbed dose for an exposed individual. Obtained by summing the equivalent doses for all tissues, each scaled by a tissue weighting factor, w_T.

Equivalent dose (H_T): The mean absorbed dose in an organ, *T*, scaled by a radiation weighting factor, w_R.

Personal dose equivalent $H_p(d)$: The dose equivalent in soft tissue at a depth, d, below a specified point in the body. Commonly reported as shallow dose ($d = 3$ mm) and deep dose ($d = 10$ mm).

Radiation dosimetry: The quantitative measurement of the physical changes that occur in matter upon exposure to ionizing radiation.

References

1. ICRP Publication 60, Ann. ICRP 21(1–3), 1990 *Recommendations of the International Commission on Radiological Protection*, Oxford, U.K.: Pergamon Press; International Commission on Radiological Protection, 1991.
2. ICRU Report 51, *Quantities and Units in Radiation Protection Dosimetry*, Washington, DC: International Commission on Radiation Units and Measurements, 1993.
3. W. K. Sinclair, The present system of quantities and units for radiation protection, *Health Physics*, 70, 781–786, 1996.
4. S. W. S. McKeever, M. Moscovitch, and P. D. Townsend, *Thermoluminescence Dosimetry Materials: Properties and Uses*. Ashford, U.K.: Nuclear Technology Publ., 1995.
5. P. Braunlich, Present state and future of TLD laser heating, *Radiation Protection Dosimetry*, 34, 345–351, 1990.
6. S. D. Miller and P. A. Eschbach, Optimized readout system for cooled optically stimulated luminescence, *Radiation Effects and Defects in Solids*, 119–121, 15–20, 1991.
7. E. Piesch, B. Burgkhardt, and M. Vilgis, Progress in phosphate glass dosimetry: Experiences and routine monitoring with a modern dosimetry system, *Radiation Protection Dosimetry*, 47, 409–414, 1993.
8. S. W. S. McKeever, M. S. Akselrod, and B. G. Markey, Pulsed optically stimulated luminescence dosimetry using α-Al_2O_3:C, *Radiation Protection Dosimetry*, 65, 267–272, 1996.
9. B. L. Justus, S. Rychnovsky, M. A. Miller, K. J. Pawlovich, and A. L. Huston, Optically stimulated luminescence radiation dosimetry using doped silica glass, *Radiation Protection Dosimetry*, 74, 151–154, 1997.
10. R. A. Dudley, Dosimetry with photographic emulsions. In: Frank H. Attix and William C. Roesch (Eds.), *Radiation Dosimetry*, Vol. II, pp. 117–129. New York: Academic Press, 1966.
11. G. Espinosa, R. B. Gammage, and K. E. Meyer, Response of different polyallyl di-glycol carbonate materials to alpha particles, *Radiation Measurements*, 26, 173–177,1996.
12. K. E. Meyer, R. B. Gammage, C. S. Dudney, S. Reed-Walker, P. Kotrappa, R. V. Wheeler, and M. Salasky, Field measurements of plutonium and americium contamination in soils at the nevada test site using passive alpha detectors, *Radioactivity and Radiochemistry*, 5, 26–41, 1994.
13. J. L. Decossas, J. C. Vareille, J. P. Moliton, and J. L. Teyssier, Theoretical study and calculation of the response of a fast neutron dosemeter based on track detection, *Radiation Protection Dosimetry*, 5, 163–170, 1984.
14. S. Sadaka, L. Makovicka, J. C. Vareille, J. L. Decossas, and J. L. Teyssier, Study of a polyethylene and CR 39 fast neutron dosemeter II: Dosimetric efficiency of the device, *Radiation Protection Dosimetry*, 16, 281–287, 1986.
15. H. Ing, R. A. Noulty, and T. D. McLean, Bubble Detectors—A maturing technology, *Radiation Measurements*, 27, 1–11, 1997.

Further Information

Attix, F. H., *Introduction to Radiological Physics and Radiation Dosimetry*. New York: John Wiley & Sons, 1986.

Dosimetry, Radiation, EHS. http://www.ehs.uci.edu/programs/radiation/radfaq.html (accessed on July 27, 2012).

Dosimetry Systems for Radiation Processing, GEX Corporation. http://gexcorporation.com/ProductsType/Dosimetry-Systems.html (accessed on July 28, 2012).

Gad Shani, *Radiation Dosimetry: Instrumentation and Methods*, 2nd edn. Boca Raton, FL: CRC Press, 2000.
Kase, K. R., Bjarngard, B. E., and Attix, F. H. (Eds.), *The Dosimetry of Ionizing Radiation*, Vol. III. New York: Academic Press, 1990.
Kiff, S., *Advanced Ionization Chambers for Radiation Detection: Electrode Design and Performance Analysis of High Pressure Xenon Ionization Chambers*. Saarbrucken, Germany: VDM Verlag, 2008.
Knoll, G. F., *Radiation Detection and Measurement*. New York: John Wiley & Sons, 1989.
Stabin, M.G., *Fundamentals of Nuclear Medicine Dosimetry*. New York: Springer, 2008.

IX

Wireless Instrumentation

85

Wireless Instrumentation

J.P. Carmo
University of Minho

J.H. Correria
University of Minho

85.1 Introduction

Almost anyone knows that a measurement is the process of comparing a quantity with another one of the same type (e.g., length, volume, area) whose result is a number. Such a measurement can be done without ambiguities in a straightforward manner with the help of a measurement system, which requires specific instrumentation for achieving such task [1]. This instrumentation can be a simple instrument for directly measuring a physical quantity (e.g., a voltmeter for measuring an electrical potential difference between two points of a circuit, an ampere meter for measuring a current flowing in a branch of a circuit, a thermometer for measuring temperatures) and can take one of these following forms regarding their internal working and signal processing: analog or digital [2]. The ability to connect and communicate with external devices [3] (using dedicated cables and/or communication networks) as well as the inherent flexibility [4] (their easiness for adding new functions and/or reconfiguration of the existing ones) makes digital instruments have major potential for use in several fields of human activity (heavy industry, medicine, transportation systems, domestic, agriculture, and food industry are some application examples). The next evolutionary step of measurement instruments is integrating functions to provide wireless transfer of data. In this sequence of ideas, the developments of microelectronics and microsystems allowed engineers to successfully develop this new measuring method [5]. This resulted in new possibilities for measuring, acquiring, transferring, storing, and analyzing the physical world: embedded systems [6] and wireless sensors networks [7] are two new possibilities for achieving such a goal, with wireless being the *major attractive technology*. This leads to the wireless instrument concept, which by its nature requires multidisciplinary concepts such as measurement science, electronic circuits design, microelectronics and microsystems fabrication, wireless communication systems, and networking [8]. Figure 85.1 reinforces this idea by showing the different disciplines that must be employed for designing a wireless instrument. The primary focus of this chapter is the presentation and integration of these concepts. This chapter also presents biomedical applications based on wireless instruments and new application concepts.

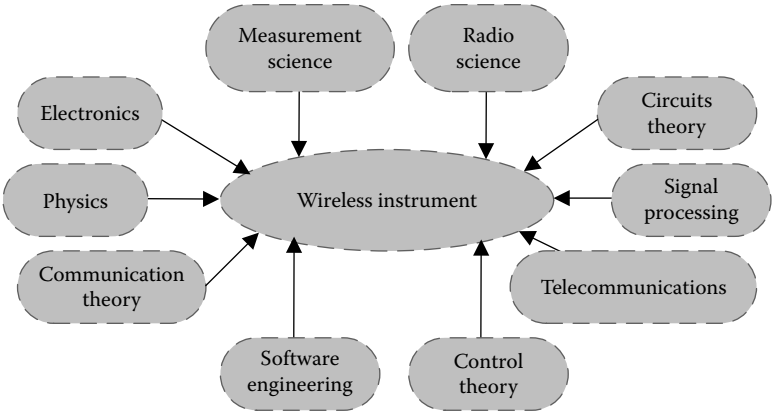

FIGURE 85.1 The multidisciplinary areas to take in account when designing a wireless instrument.

85.2 Instruments and Instrumentation

85.2.1 Measurement Systems

Figure 85.2 shows a block diagram of a generic measurement instrument. The blocks of a measurement system can be grouped into three major types: the real world (representing the physical quantity to be acquired), the interface block (with the sensor), and the core (e.g., the instrumentation itself).

There are situations where the interface block can be part of the core, e.g., a voltmeter doesn't require any external sensor because this one is already embedded inside the measuring instrument, thus the sensing tips can directly touch the electrical potentials. In this context, it must be clarified that a sensor cannot be confused with a transducer, because the transducer can perform the same function as the sensor, but if the sensor is passive (e.g., a physical quantity-dependent resistor mounted in a Wheatstone bridge), then additional circuits must be provided for obtaining the signal from the sensor. This means that the set composed of the sensor and powering system makes a transducer, confirming that certain sensors are simultaneously transducers.

The core blocks can include electronics of control for acquisition from the transducer. The core also provides signal-processing functions for signal conditioning purposes. These last functions include amplification (with the possibility to adjust the gain), filtering (either low-pass or band-pass or even high-pass filtering), and analog-to-digital conversion. Then, the user can read the acquired values in a dedicated display. A more sophisticated core system can interface with the external world either to connect several measurement instruments or to send data to a central unit for further processing. These communications can be done using wired buses (e.g., I^2E bus [9], GPIB [10], RS232 [11,12], parallel ports [13], or even USB [14]) or wirelessly (e.g., IEEE 802.11 [15], ZigBee [16], Bluetooth [17], or using a customized solution [18]).

The core blocks of the measurement instruments can be analog or digital. Analog is the less versatile core because it requires the presence of a person to read the measurements. This type of instrument is very limited

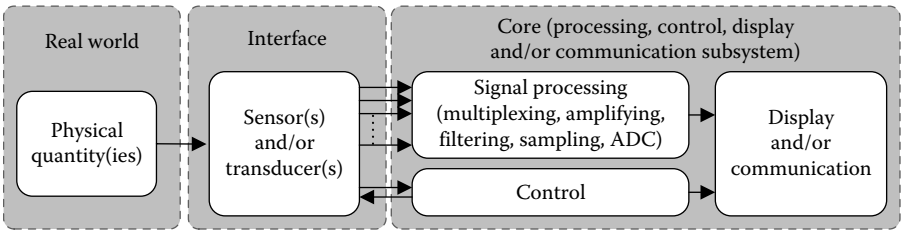

FIGURE 85.2 Block diagram of a generic measurement instrument.

and very difficult to adapt to a wide range of signals to measure. Furthermore, it is not possible to wirelessly send the physical quantities, unless a specific interface with an analog modulation scheme is provided.

A digital core can be used for connecting transducers (whose output can provide signals in the analog or in the digital domain). The difference from their analog counterparts resides in the conversion component used in the final processing stage, e.g., the sampler and the analog-to-digital converter (ADC) block. The inclusion of multiplexers enables the acquisition of multiple channels with a single measurement instrument. This topic will be the focus of discussion in the next section. After the ADC conversion, the acquired measurements can be presented in a numerical display. These cores can also be built with internal memory for storing the ADC-converted samples for rendering in a more complete display system (e.g., a flat screen) or for remote transmission through a communication interface. This core also allows for changing and/or for programming the amplifier's gain, thus allowing adaptation to wide variations of physical quantities. The latest developments of microelectronics make available transducers with digital outputs (e.g., integrated monolithic temperature transducers [19], Hall effect magnetometers [20], and accelerometers [21], among others) it is possible to have full digital and reusable cores.

The judicious selection of transducers and cores can be decisive points for fabricating wireless instruments with low power, reduced sizes, and low prices. This is especially evident on measurement instruments composed by reusable cores (for controlling and displaying/communicating), monolithic transducers (for signal acquisition), and on-chip signal conditioning circuits [22] (for signal processing).

85.2.2 Multiplexing Structures

A multiplexing operation is required in measurement instruments for simultaneously acquiring more than one signal at once. The signal multiplexing is not a simple matter to treat. The first issue concerns the availability of a variety of multiplexing structures and the decision to select the most suitable. This poses tradeoff problems related to implementation costs (e.g., a more complex multiplexing system costs more) and specifications (e.g., a more general purpose instrument will be more complex and cost more). In the second place, it is mandatory to have a clear knowledge of the input characteristics. The most important issues are the input impedance, the dynamic range, the bandwidth, the balancing type of signals (e.g., single-ended or differential), power-supply interference rejection (e.g., 50 Hz in the Europe and 60 Hz in the United States), interference between input channels due to the multiplexer, and noise.

The multiplexing configuration can assume one of the following classifications: either low level or high level for analog or digital multiplexers, respectively.

The structure illustrated in the Figure 85.3 is the most simple. The signals at the outputs of transducers connect to an analog multiplexer (with single-ended or differential inputs). It is important to have a variable gain amplifier when transducers with different signals are used, in order to provide signals within the full dynamic range of inputs of the ADC. This structure poses significant restrictions for solving speed bottlenecks: First, the multiplexer must be fast enough for switching the different analog channels; in the second place, the bandwidth of the ADC and sample-and-hold (S/H) (which is actually a part of the ADC) circuits must be high enough to avoid distortion of the analog signals for conversion.

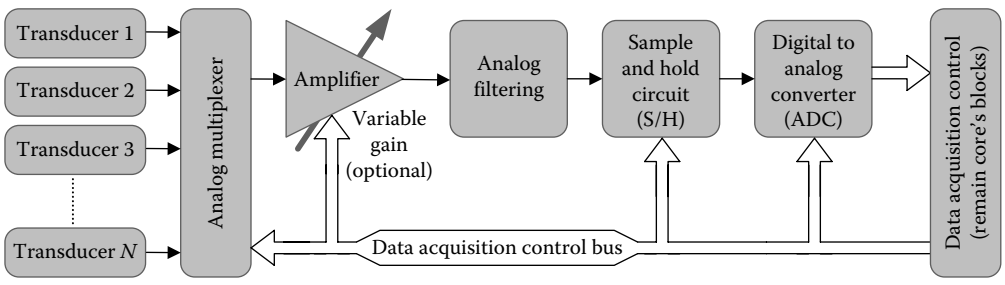

FIGURE 85.3 Low-level multiplexing configurations with shared amplifier.

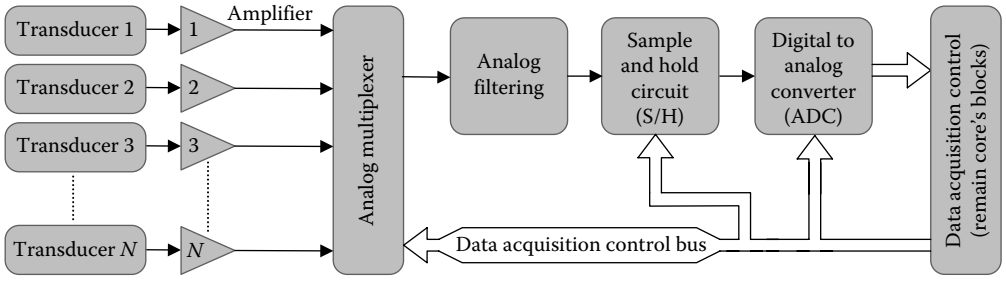

FIGURE 85.4 Low-level multiplexing configurations with dedicated amplifiers.

The low-level shared-amplifier configuration is less flexible in terms of plurality of physical quantities to measure; the ADC must be compatible with the transducer with the highest bandwidth; the direct acquisition of multiple signals can pose shielding problems because the transducers can be located very far away from each other. However, the low-level shared-amplifier configuration is the configuration with the highest potential for fabricating low-size electronic modules with high degree of integration (e.g., one multiplexer, one amplifier, one analog filter, one S/H plus ADC and control electronics).

The structure illustrated in the Figure 85.4 is very similar to that illustrated in Figure 85.3. The only exception is the use of transducers with associated amplifiers. These dedicated amplifiers guarantee signals with equal excursions to use the full dynamic range of the ADC. The bandwidth considerations are the same as those made in the previous multiplexing configuration. A high degree of integration is still possible to achieve with this configuration, but it sacrifices the compactness and low size due to the use of multiple amplifiers. Despite the acquisition of signals with equal amplitudes, the shielding problems remain in applications requiring transducers placed away from each other.

Low-level multiplexing configurations have a high integration potential, allowing the fabrication of wireless instruments with small sizes and low power consumption. However, the shared nature of the analog multiplexer makes them less than ideal. Nonidealities include the finite impedance of unselected analog channels, cross talk between channels, nonzero switching times between channels, and handling of different bandwidths between channels.

Figure 85.5 illustrates a high-level multiplexing configuration, providing a dedicated set of amplifiers, analog filters, S/H circuits, and ADCs for each transducer. After conversion to the digital domain,

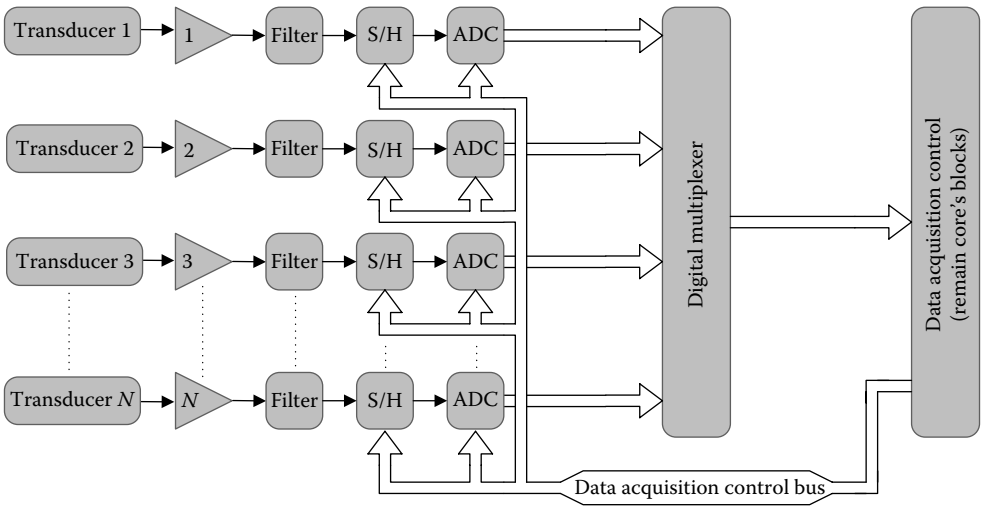

FIGURE 85.5 High-level multiplexing configuration.

the acquired physical measures are digitally multiplexed, avoiding the nonidealities of analog multiplexers. This configuration can pose integration restrictions by requiring circuits with increased sizes because each analog channel requires a dedicated signal-processing chain. However and despite these drawbacks, a high-level configuration is the most flexible of those analyzed because different amplifiers and filters can be provided for an extensive set of transducers. Moreover, this configuration offers the possibility to select the most suitable ADC for the respective analog chain. More important is the ability to accommodate channels with different sampling frequencies, since the switching speed of the analog multiplexer is not exceeded. This configuration also allows a variety of channel-selecting policies for desired channels with desired sampling frequencies.

85.2.3 Wireless Instruments and Communication Protocols

The design of a wireless instrument (as well as a generic measurement instrument) can't be done without taking in account the communication protocol. Table 85.1 shows the layer structure proposed by the OSI (Open Systems Interconnection) model [23].

Layer 1 specifies the modulation in conjunction with the line coding m (*codulation* [24]), the DC balancing, single-ended/differential-ended balancing.

Normally, layer 2 is divided in two sublayers, e.g., the medium access control (MAC) and the logic link control (LLC). The MAC sublayer is on bottom and defines mechanisms (or rules), in which a given transmitter is allowed (or not!) to access the physical medium for signal injection (corresponding to the data intended for the target receiver/s). The top LLC sublayer specifies the types of frames: data or control frames. This sublayer also provides a clear definition of frame formats in terms of their contents (their fields). Basically, the data frames are used to transport useful information in a field known as payload, while the other frames (e.g., the control frames) are used to make the transmitter know if the previous transmissions were received and processed by the receiver with or without errors. The control frames can also be used for performing flow control, in order to avoid data congestion in the receiver or across the network (with possible loss of data).

The network layer specifies a set of procedures for guaranteeing a reliable transmission between consecutive nodes along the network. Examples of procedures include the detection/correction of transmission errors and flow control. This layer also establishes the routing paths for the messages.

The transport layer ensures a reliable communication between terminals, e.g., between end-to-end users. This layer also provides error control procedures to verify the correct reception of all packets that form the messages (e.g., error-free packets). Another important procedure provided by the transport layer is grouping the packets in the correct sequence order to obtain a correct reassembled segment.

The session layer provides mechanisms for allowing the hosts to establish a communication. This layer also provides recovery mechanisms when an interruption occurs during the communication.

TABLE 85.1 Layers in the OSI Model

	Data Unity	Layer	Function
Host layers	Data	Application	Final communicating application
		Presentation	Data formatting and cryptography
		Session	Communication between hosts
	Segments	Transport	End-to-end communication reliability
Medium layers	Packets	Network	Node-to-node routing and communication reliability
	Frames	Data link	Physical identification (MAC and LLC sublayers)
	Bits	Physical	Signal transmission through the communication channel (*codulation*, other physical aspects of signals)

Source: Stallings, W., *Data and Computer Communications*, Prentice Hall, Englewood Cliffs, NJ, 2003.

The definition and conversion between data formats is done in the presentation layer. Normally, it is in this layer that the data are ciphered and/or converted to (and obviously converted from) the format used by the application.

The last layer (e.g., the application layer) provides interfaces between the application itself and between the protocol stack on the bottom.

Figure 85.6 provides a better understanding as how these concepts can be applied when designing a wireless instrument. This example helps to identify the blocks inside the wireless instrument that implement functions defined by the OSI model. This figure shows only the measurement part of the wireless instrument (e.g., the measurement instrument). The system is composed of the core measurement subset including the signal acquisition block, the signal-processing block, the control block, the memory block—a part of the control block—and the display control, which is actually optional in wireless instruments. Additionally and as previously stated, the interface block can be a part of the

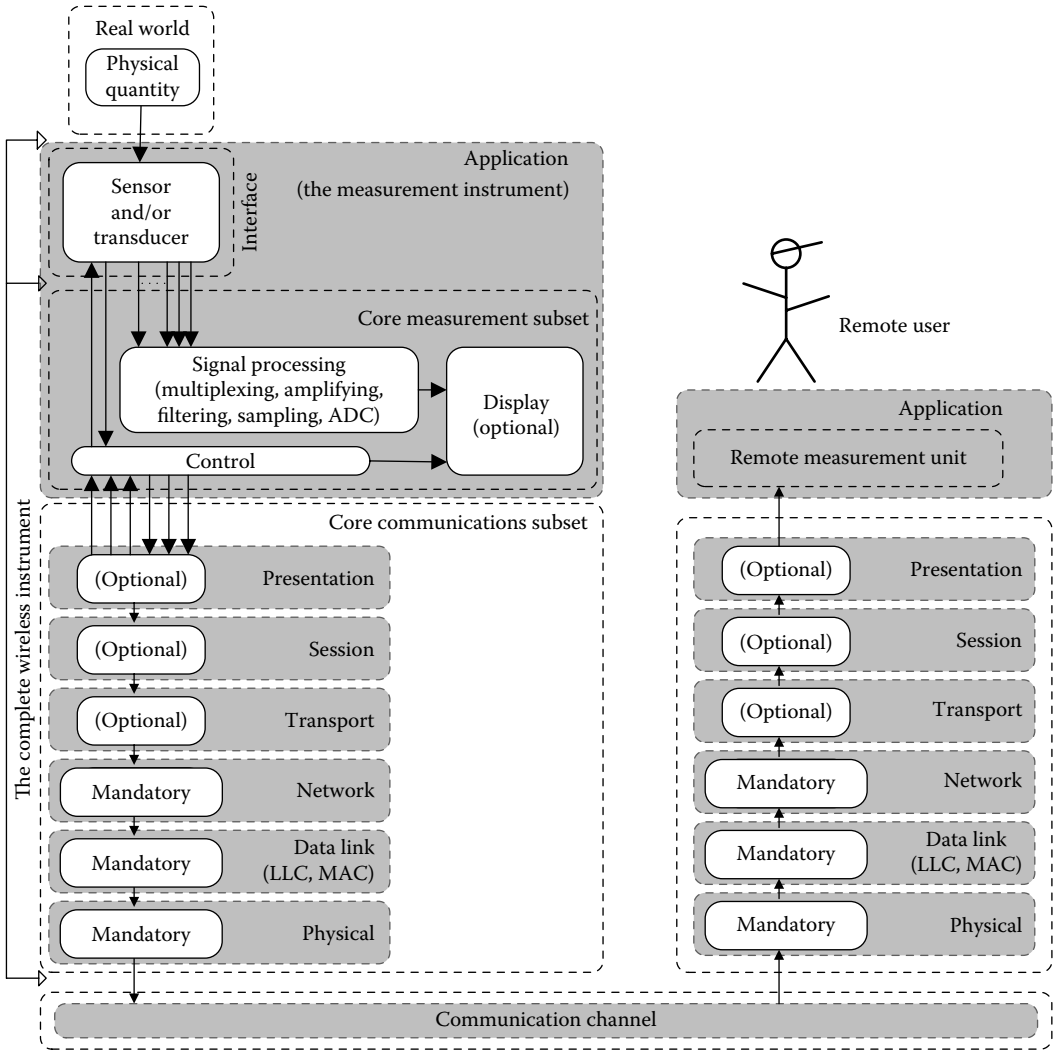

FIGURE 85.6 Relation between wireless instruments with the stacks of the OSI model.

measurement instrument. The remaining part of the wireless instrument is implemented by the core communication subset. This subset is responsible for communicating with external devices (other wireless instruments or with a central processing unit or even a remote measurement unit controlled by a remote user).

Normally and as shown in Figure 85.6, there are three optional functions inside a wireless instrument. This results from the need to simplify the transmission procedures in order to minimize the latencies (this is the case of the IEEE 802.15.4 that supports the low-level layers of the ZigBee protocol stack) and to maximize the data throughput.

The most common function of the network layer is the cyclic redundancy check (CRC) generation (by the wireless instrument on the transmitter side) and decoding (in the receiver side) for detecting transmission errors. It is possible to use forward error correction (FEC) schemes for error correcting but with the cost to send redundant bits for each bit of information (e.g., each bit of acquired data) and larger bit rates. In the case of auto-repeat request (ARQ) schemes, the CRC generation and decoding can be used by the receiver to do a request to the transmitter for retransmission of the erroneous packet.

The LLC sublayer functions can't be bypassed (or at least, a simple implementation must be provided) because at least a frame alignment word (or synchronization character) must be provided in the transmitter in order to allow the receiver to start the bits reception. The LLC implemented by Carmo et al. [18] uses a header composed of an alternate sequence (with a length equal to an integer multiple of eight) 1's and eight 0's for DC balance, while the remaining header contains a synchronization character with 8 bits (this complete header is used by both control and data frames).

The simpler way for implementing MAC sublayer functions is on point-to-point communications with only one transmitter and receiver. In this situation, the transmitter can send data without restrictions because the communication channel is always available and ready for use. Sophisticated MAC protocols are required for managing the medium access when the general scenario (with a multiplicity of transmitters and a multiplicity of receivers) is present. Silva et al. [25] proposes a MAC protocol for transmitting signals from transmitters placed on a multiplicity of paraplegic patients (doing hydrotherapy inside a swimming pool) into a base station, which stores the data for further analysis by a health professional. Note that the most common applications are based on simple point-to-point configurations as it is the case of the work done by Dias et al. [26], where a wireless instrument acquires EEG signals and transmits them to a base station connected to a personal computer for data logging. This solution uses wireless modules based on IEEE 802.15.4, but a solution based on a microcontroller with a simple radio frequency (RF) module could be used for reducing the latencies.

Taking into account the wired case (which can be directly transposed to the wireless case), the physical layer can be implemented by doing a direct connection between the transmitter and the receiver (e.g., connecting the transmitter's output to the receiver's input). A wireless instrument must provide at least one modulation scheme in order to reduce the errors introduced during the communication. A huge set of flexible wireless modules from third-party manufacturers ready for connection into the wireless instrument are available at low cost [27–30]. The modulation is an important issue in wireless instruments, but a coding scheme is recommended either for DC balancing or even for error control and for synchronization. In this context, the RF CMOS receiver at 433 MHz for integration in implantable devices found in [31] was designed taking in account the following *codulation* scheme: simultaneous on/off keying (OOK) modulation and biphase code [31]. Another example of physical layer definition is the RF transmitter proposed by Morais et al. [32] for operation at 433 MHz but with a different codulation scheme: OOK modulation and pulse-width modulation (PWM) code. This RF transmitter is compatible with the commercial receiver unit model LM RXAM2433 (from the manufacturer LPRS Inc.) and was tested with success for soil moisture measurements [33].

85.3 Technology for Wireless Systems

85.3.1 Operational Issues

The selection of the operation frequency is not an easy issue because different factors distinguish between them. In the first place, the dimensions of the antennas are imposed by the frequency. For an acceptable efficiency, the antenna size must be on the order of one-fourth of the wavelength, λ (m), which is given by $\lambda = c/f$ with $c = 3 \times 10^8$ m·s^{-1} being the speed of light in vacuum and f (Hz) the frequency of operation. Decreasing the dimension of an antenna implies the use of high frequencies. This issue can be solved by modulation. The most used modulations in wireless instruments (especially in laboratory environments, e.g., closed and relatively free of common band interference) are *amplitude-shift keying* (ASK), *phase-shift keying* (PSK), and *frequency-shift keying* (FSK). Both ASK and PSK need the same bandwidth given by BW = $2R_b$ (Hz), where R_b (bps) is the bit rate per second. The bandwidth required by FSK modulation is slightly higher and is BW = $2R_b + |f_1 - f_2|$, where $|f_1 - f_2|$ is the frequency shift between the two carriers, f_1 (Hz) and f_2 (Hz). The bit error probability (BEP) of each modulation can be found in Table 85.2, and the plots of their respective values as a function of the ratio E_b/N_0 are shown in Figure 85.7. The ratio E_b/N_0

TABLE 85.2 BEP for the Modulations ASK, PSK, and FSK

Modulation	BEP	
ASK with coherent detection	$Q\left(\sqrt{\frac{E_b}{N_0}}\right)$	$Q\left(\sqrt{\frac{S}{N}}\right)$
ASK with noncoherent detection	$\frac{1}{2}e^{-(1/2)\times(E_b/N_0)}, \left(\frac{E_b}{N_0}\right) > \frac{1}{4}$	$\frac{1}{2}e^{-(S/N)}, \left(\frac{S}{N}\right) > \frac{1}{8}$
PSK	$Q\left(\sqrt{2\times\frac{E_b}{N_0}}\right)$	$Q\left(\sqrt{2}\times\sqrt{\frac{S}{N}}\right)$
FSK	$Q\left(\sqrt{\frac{E_b}{N_0}}\right)$	$Q\left(\sqrt{1+\frac{\lvert f_1 - f_2\rvert}{4r_b}}\times\sqrt{\frac{S}{N}}\right)$

Source: Couch II, L.W., *Digital and Analog Communication Systems*, 5th edn., Prentice Hall, Englewood Cliffs, NJ, 1996.

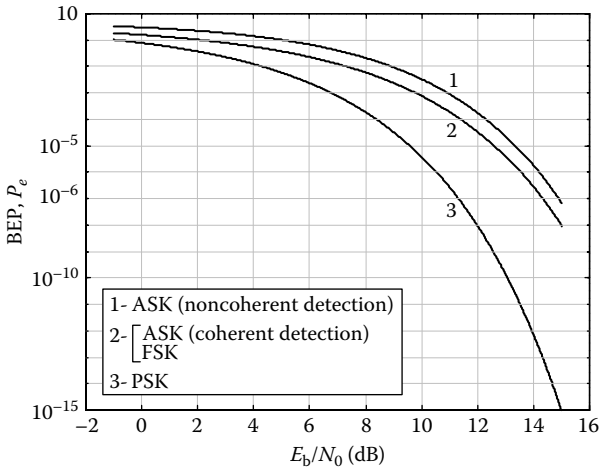

FIGURE 85.7 BEP versus the E_b/N_0 (dB) ratio for the modulations ASK, PSK, and FSK.

is the energy per bit, E_b (J), divided by the spectral density of the noise (additive white Gaussian noise), N_0 (W), which is given by [34]:

$$\frac{E_b}{N_0} = \frac{S/r_b}{N/\mathrm{BW}} = \left(\frac{S}{N}\right) \times \frac{\mathrm{BW}}{r_b} \tag{85.1}$$

where $N = N_0\mathrm{BW}$ (W) is the filtered noise at the output of a band-pass filter BW (Hz).

The selection of the frequency taking only in account the bit rate and antenna size isn't enough because as it is general knowledge, the antenna is perhaps the most critical subsystem in wireless communications. This imposes an antenna small enough for integration with the transmitter but not so small as to compromise this same miniaturization. The size reduction can be a problem because the antenna must be designed for transferring the highest possible power to the receiver. In this context, the size shortening of antennas can introduce additional problems of impedance matching [35] that must be solved. Wafer-level packaging (WLP) techniques can be used for overcoming these problems [36].

The communication range is another issue to take in account when selecting the frequency. This is related to the attenuation of RF signals, whose free-space value increases with transmitter/receiver distance, d (m), and frequency, f (Hz) [37]:

$$L_f(d, f) = -20\log_{10}(d) - 20\log_{10}(f) + K_f(\mathrm{dB}) \tag{85.2}$$

with $K_f = -20\log_{10}[c/(4\pi)]$ (dB). This means that for a simultaneously given transmitted power, P_t (dB), and receiver sensitivity, S_r (dB), the frequency is limited by the range, d_{max} (m):

$$f \le 10^{\frac{(P_t - S_r) - 20\log_{10}(4\pi d_{max})}{20}} (\mathrm{Hz}) \tag{85.3}$$

The free-space model is the most optimistic approach for calculating the link budget because the additional losses due to the surrounding environment (lossy propagation mediums, buildings, terrain conditions, vehicles, persons, shadowing, systemic implementations, among other factors) is not taken in account. Therefore, a general loss model must be used [37]:

$$l(d) = \alpha.c^{-n} + \chi, \quad n \ge 2 \text{ and } \alpha < 1 \tag{85.4}$$

Alternatively, $L(d) = -10n\log_{10}(d) + 10\log_{10}(\alpha) + \chi_{\mathrm{dB}} = A\log_{10}(d) + B + \chi_{\mathrm{dB}}$ (dB). The factor $A = -10n$ is very important to analyze because it justifies why the distance dependence loss is higher than that observed in free space. The signal fluctuations (also known as fading) don't contribute statically to the loss but dynamically. This dynamic behavior can impose severe restrictions when designing a wireless link because a super dimensioned RF receiver must be provided to overcome the temporary losses of signal power. The distance-dependent loss model is normally enough to predict the link budget especially for short distances (typically under 20 m) and closed spaces (laboratories, hospitals, residences, trains, among others). Very good references can be found in [38–40] to deal with the fading.

Figure 85.8 shows the available frequency bands for the different technologies used in wireless communications. Suitable frequencies for possible use in wireless instruments are those belonging to the so-called ISM band (industrial, scientific, and medical), due to its unregulated usage. These frequencies can be freely used without being subject to standardization but keeping the emission power below the maximum levels imposed by regulations. This usage flexibility leads to widespread new applications as will be discussed further.

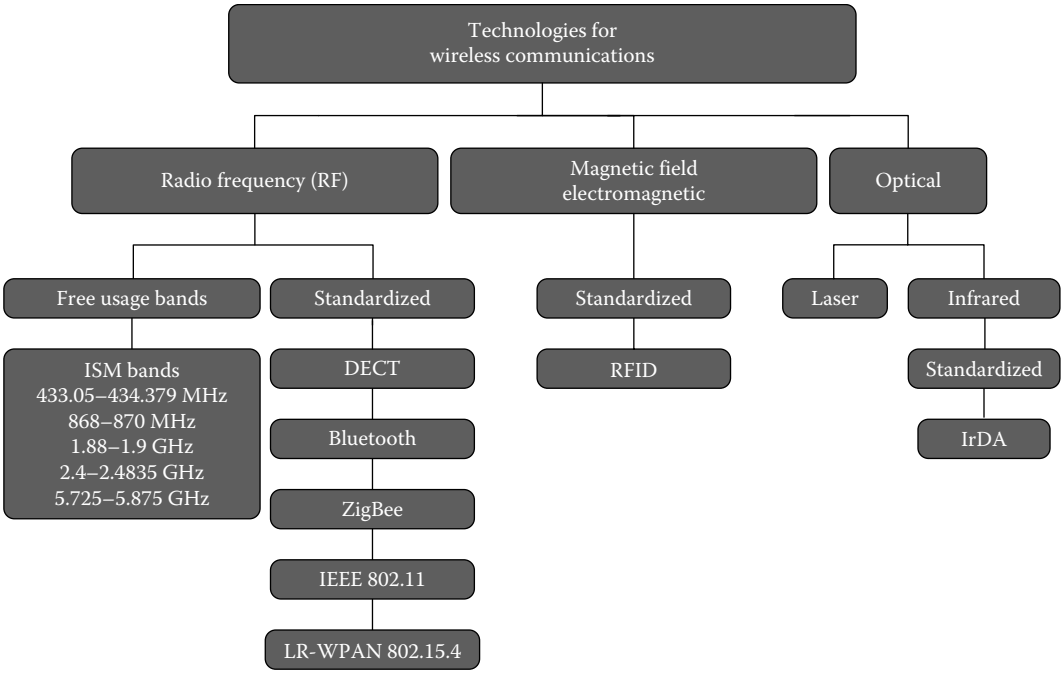

FIGURE 85.8 Currently available frequencies for wireless applications.

85.3.2 RF Interfaces and Examples

A wireless instrument communicates with the external world by RF. Thus, a wireless interface must be provided for allowing RF communications. Figure 85.9 shows a generic schematic block of a wireless microsystem performing functions of a stand-alone wireless instrument. These microsystems are composed of transducers and other electronic components for control and signal processing, by memory and by an RF interface (the RF transceiver) for connecting to an associated antenna. The dimensions of the RF transceiver must be comparable with other elements integrated in the microsystem (e.g., the transducers and remaining electronics). The miniaturization of electronics and the spreading of fabrication processes for integrating heterogeneous technologies (e.g., CMOS, SiGe, III/V technologies, MEMS, among others) will result in the mass production of wireless microsystems at low prices. All these issues combined with the flexibility to select which and the number of transducers for integrating together with the RF transceiver and remaining electronics allow engineers to design a wide number of devices for a wide number of applications. This last goal can be easily achieved with multi-chip module (MCM) techniques applied to a limited number of components (which can be of different technologies). In conclusion, the technology is also a major point to allow the fabrication of

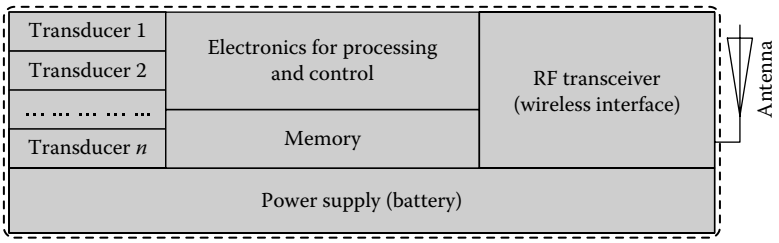

FIGURE 85.9 Generic microsystem architecture connected to an associated antenna.

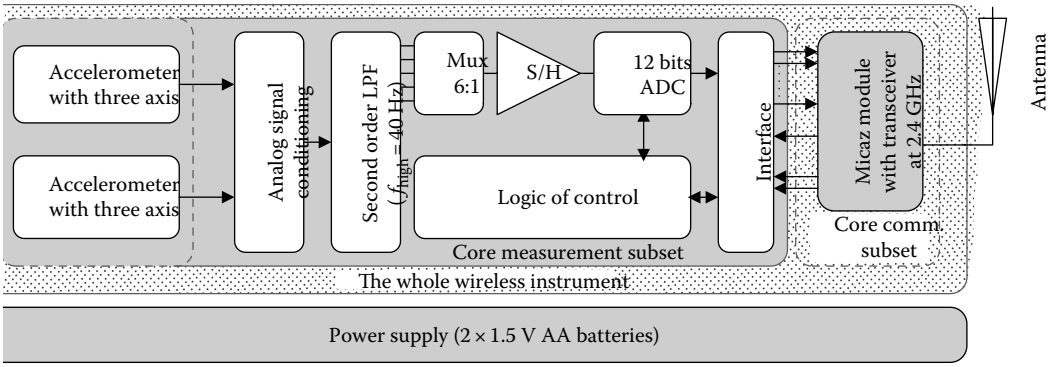

FIGURE 85.10 Block diagram of a wireless instrument at 2.4 GHz ISM band for monitoring the body movements of individuals.

wireless microsystems for use in wireless instruments. In this section, a few examples for each of the ISM bands in Figure 85.8 are presented for a better view of wireless instrument's potential.

85.3.2.1 Monitoring Body Movement

Figure 85.10 shows the block diagram of a wireless instrument for monitoring the body movements of individuals during hydrotherapy [41]. This wireless instrument is modular and is composed of a module with two MEMS accelerometers with three degrees of freedom (with three axes), a module with low-level multiplexing for signal processing and analog-to-digital conversion, and a third-party RF module (with a RF transceiver at 2.4 GHz and control electronics). The analog electronics in the core measurement subset is controlled by the core communications subset. The core communications subset is a Micaz RF module at 2.4 GHz (fabricated by the Crossbow company) for communicating with external devices and for controlling and managing the data acquisition process [42]. The accelerometers module was designed for measuring the movements of the individuals by obtaining information about the instantaneous roll, yaw, and pitch. This wireless instrument was designed for low-power and high-throughput communications using a specific MAC protocol for achieving such goals [43].

85.3.2.2 Connecting to Transducers

Figure 85.11 illustrates the block diagram of a sensor RF interface for operation at 433 MHz [32]. This RF interface has a differential (instrumentation) analog input for interference reduction purposes and allows the connection of other types of transducers. The analog-to-digital conversion is done by $\Sigma\Delta$ modulator for coding the input analog signals, whose result is a bitstream for encapsulation in a frame for RF transmission. As stated by Morais et al. [32], this interface was especially designed for connecting into the soil moisture transducer developed by Valente et al. [33]. The wireless instrument illustrated in Figure 85.11b was developed for measuring the soil moisture of greenhouses and uses the latter RF interface to send the acquired data to an external storing and/or analyzing unit.

85.3.2.3 Implantable Systems

Figure 85.12a shows the block diagram of a receiver for operation in the 433 MHz ISM band that was developed for use in implantable microsystems [31]. The selected architecture explores the superregeneration phenomena to achieve a high sensitivity. This receiver can be supplied with a voltage of only 3 V for demodulating signals with powers in the range (–100, –40) dB. The combination of modulation and coding scheme is OOK modulation combined with a variation of the Manchester code (e.g., a biphase code). The AMIS 0.7 μm CMOS process was selected for targeting the requirement to fabricate a low-cost receiver. Figure 85.12b shows a photograph of the first prototype (shaded area), which was integrated in a die with an area of 5×5 mm^2. An advantage of this receiver is being fully compatible with commercial

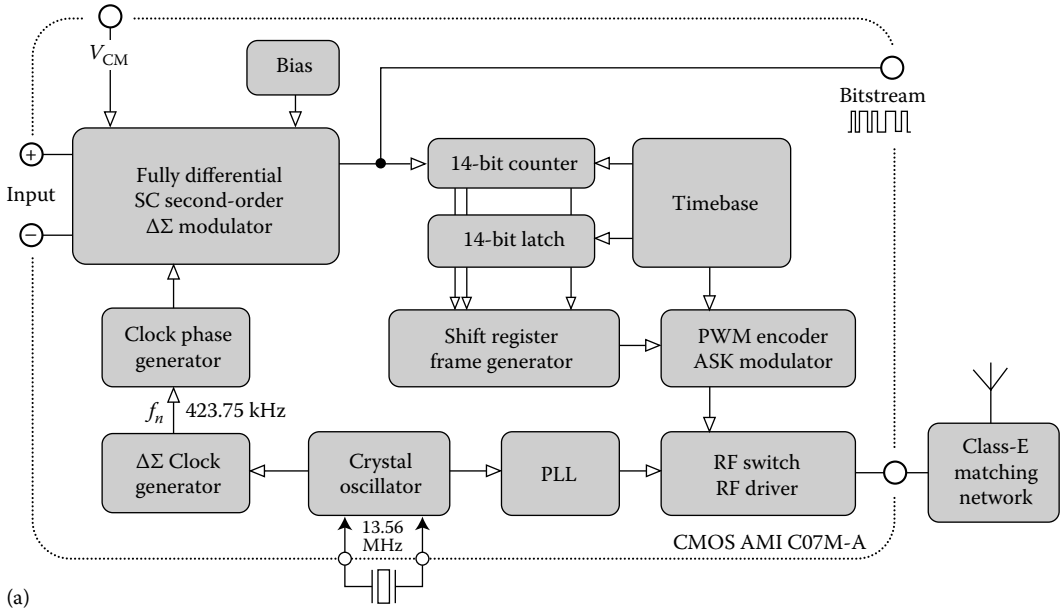

(a)

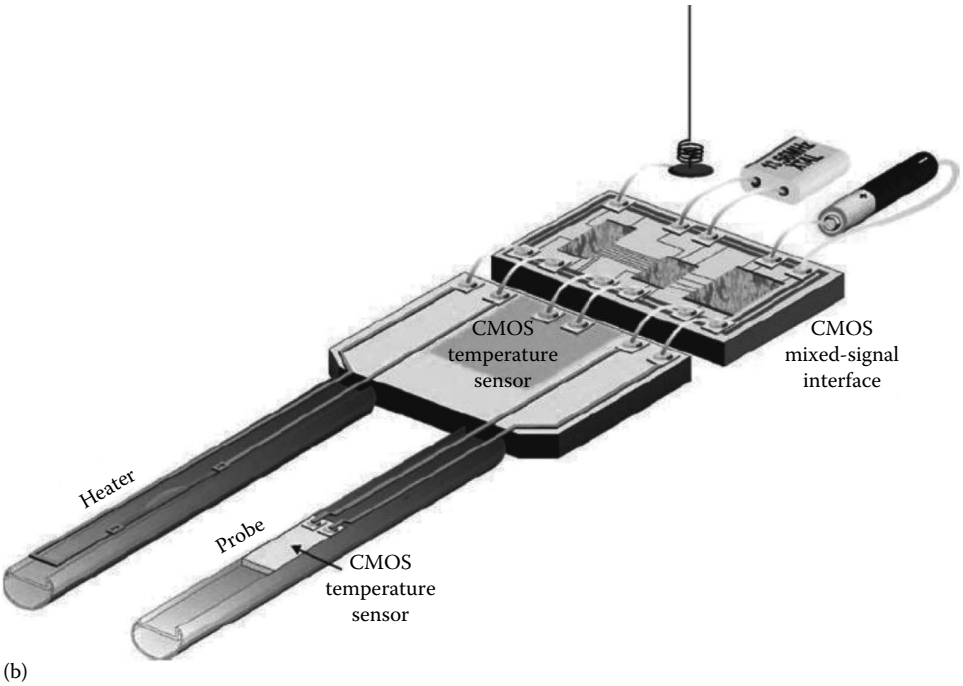

(b)

FIGURE 85.11 (a) The block diagram of a sensor interface for operation in the 433 MHz ISM band. (Reproduced from *J. Sens. Actuat. A*, 115, R. Morais, A. Valente, C. Couto, and J. H. Correia, A wireless RF CMOS mixed-signal interface for soil moisture measurements, 376–384, Copyright (2004), with permission from Elsevier.) and (b) a wireless instrument composed by the latter RF interface mounted in a soil moisture transducer for utilization in greenhouse environments. (Reproduced from *J. Sens. Actuat. A*, 115, A. Valente, R. Morais, C. Couto, and J. H. Correia, Modeling, simulation and testing of a silicon soil moisture sensor based on the dual-probe heat-pulse method, 434–439, Copyright (2004), with permission from Elsevier.)

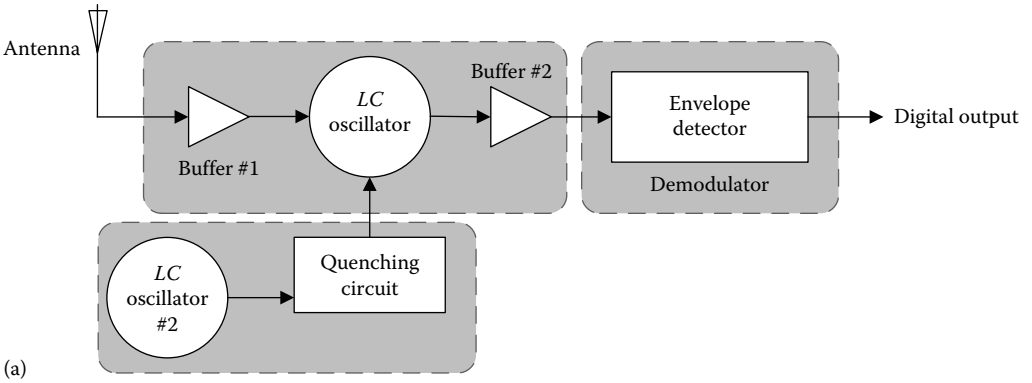

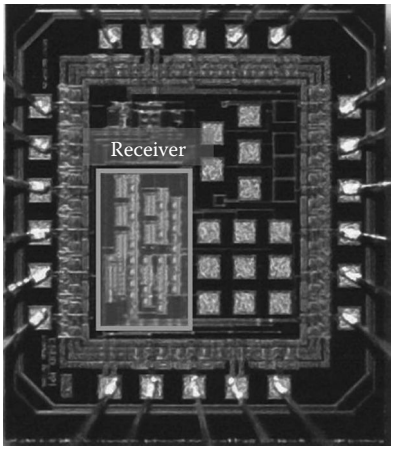

FIGURE 85.12 (a) The block diagram of the superregenerative receiver at 433 MHz and (b) a die photograph containing the first prototype of the superregenerative receiver (the rectangular area under the word Receiver). (Reproduced from *Microelectron. J.*, 42, J. P. Carmo, J. C. Ribeiro, P. M. Mendes, and J. H. Correia, Super regenerative receiver at 433 MHz, 681–687, Copyright (2011), with permission from Elsevier.)

transmitters and the transmitter fabricated by Morais et al. [32], for the same coding scheme (the variation of the Manchester code) in the transmitter.

85.3.3 Power Consumption

The power consumption of a wireless instrument limits its working time, especially when functioning with batteries. In this context, the selection (or even further, the design) of RF transceivers can't neglect this issue because this is the block with major impact for the total power consumption, when compared with the whole electronics in the instrument [44]. Furthermore and despite the spreading of microelectronics fabrication processes with the potential to achieve smaller power consumption, the RF transceiver is irremediably the subsystem of higher power consumption [45,46]. This demands the integrated definition of architectures and methods of control, as well as provides means to predict the power consumption of the RF system. Figure 85.13a shows an RF CMOS transceiver at 2.4 GHz that allows the implementation of control actions for optimizing the power consumption [23,47]. This RF CMOS transceiver was fabricated in a standard 0.18 μm CMOS process for achieving low power consumption with

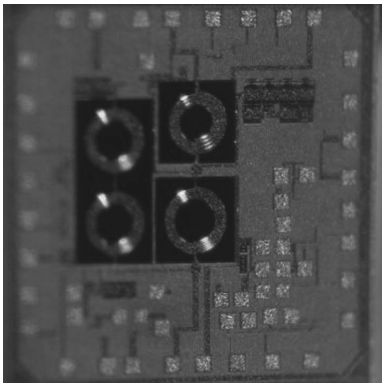

(a)

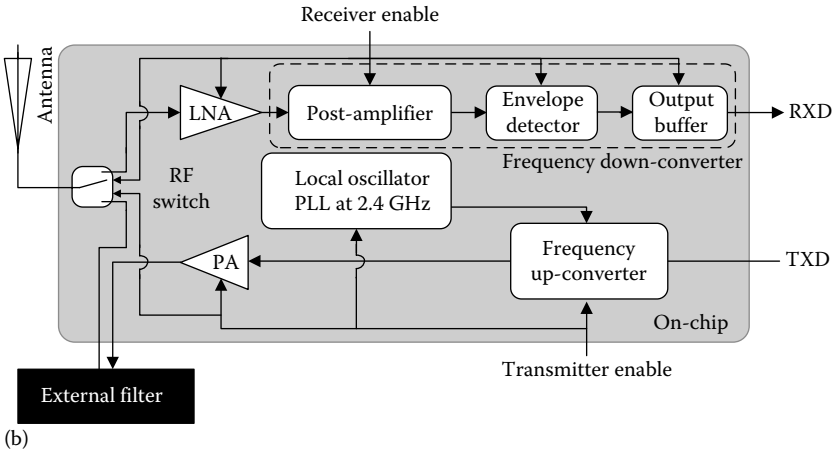

(b)

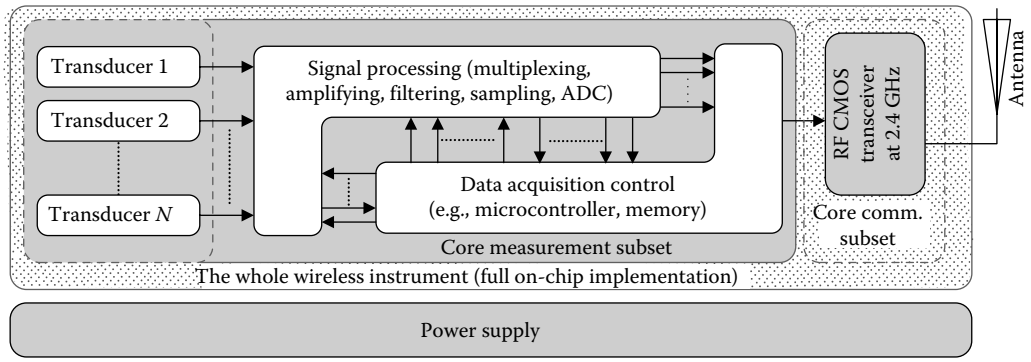

(c)

FIGURE 85.13 (a) Photograph and (b) block schematic of a RF CMOS transceiver at 2.4 GHz especially designed for stand-alone wireless instruments in biomedical applications. (c) A schematic illustrating the integration concept of the RF CMOS transceiver, transducers, and electronics in the same microsystem.

a low-voltage supply. As illustrated in Figure 85.13b, the design of this RF CMOS transceiver predicted the use of a control signal to either select the transmitter or the receiver in order to allow its integration with electronics to perform custom control, Figure 85.13c.

It is possible to explore the band located between the 5.7 and 5.89 GHz for implementing wireless instruments [48]. This band permits the fabrication of antennas, whose small dimensions allows their

integration with the electronics using WLP techniques [36]. The integration of antennas and electronics in the same microsystem results in smaller impedance mismatching problems. Moreover, the antenna and electronics co-integration systematizes the fabrication process and at the same time results in microsystems with a small cost per unit. The work presented in [49] takes all of this into account to provide a low-power/low-voltage wireless interface at 5.7 GHz with dry electrodes for implementing wireless instruments as parts of cognitive networks. Figure 85.14a shows a photograph of the wireless interface measuring of 1.5 × 1.5 mm. The schematic illustrated in the Figure 85.14b shows the block diagram of the RF part at 5.7 GHz. The digital signals $\{S_0, S_1, S_2, S_3\}$ select the target frequency in the range $f_{out} = f_{ref} \times (400 + 2S) = f_{ref} \times [400 + 2(S_0 + 2S_1 + 4S_2 + 8S_3)]$, whose range is located between 5.42 and 5.83 GHz for a reference frequency f_{ref} = 13.56 MHz.

An integrated low-cost solution for wireless instruments based on a microdevice fabricated with low power consumption using a 0.18 μm CMOS process is in [50]. This microdevice is composed of an RF transceiver, a reduced instruction set computer (RISC) microcontroller, a random access memory (RAM),

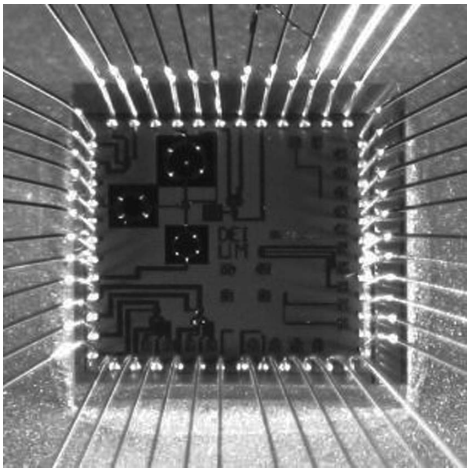

(a)

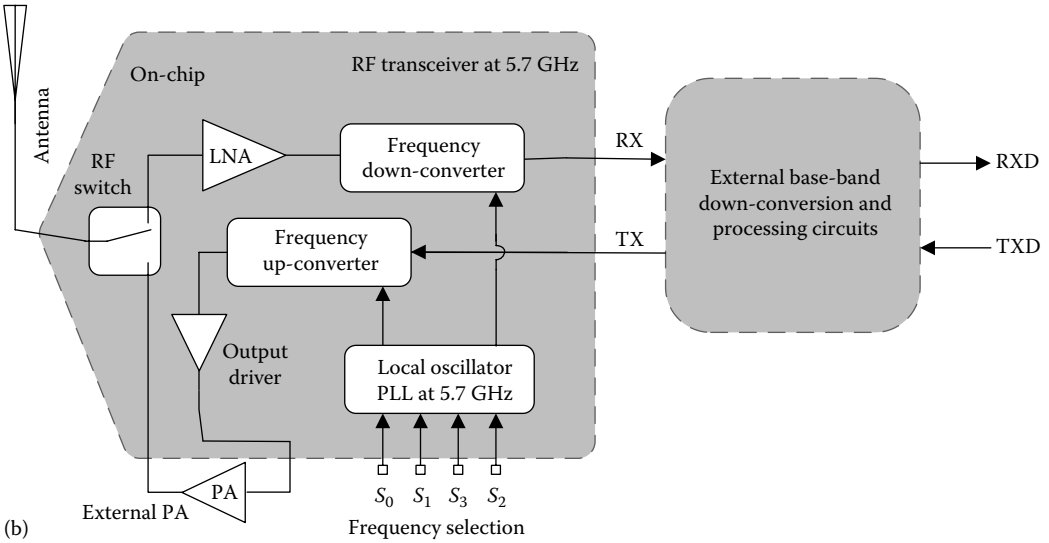

(b)

FIGURE 85.14 For the frequency of 5.7 GHz: (a) photograph and (b) schematic block of the RF part of a wireless interface at 5.7 GHz.

a power-supply management circuit, analog electronics of signal conditioning and analog-to-digital conversion (ADC), and circuits for providing communication based in SPI and I^2C buses. The control electronics was developed for implementing a specific communication protocol for use with multiple wireless instruments and low power consumption, e.g., the WiseMAC protocol. According to the authors, this protocol working together with their RF transceiver achieves power consumptions thirty times smaller than those obtained with the IEEE 802.15.4 (which defines OSI layers 1 and 2 functions). Furthermore, the operation frequency can be selected from 433 to 868 MHz, as well as either with the OOK modulation or the FSK modulation. According to [50], their RF transceiver has a receiver power of 2.5 mW and a transmit power of 39 mW.

85.3.4 Networks of Wireless Instruments

A wireless sensors network can be considered a network of wireless instruments whose sensor nodes are the wireless instruments itself. The stand-alone operation without the need of a human operator for doing maintenance and/or for replacing the batteries (that provide the supply of power) are the main differences of these kind of wireless network compared to conventional networks. In this sequence and as illustrated in Figure 85.15, a wireless sensors network can be considered a distributed sensor network constituted by a high density of nodes. It is expected for each node to run simple protocols and provide low data rates in order to keep power consumption below reasonable levels. These issues are of major interest especially for nodes powered by batteries and without energy-harvesting capabilities because their useful life will be limited by the remaining charge.

In a wireless sensors network, each node acquires the physical data from the sensors and transmits by RF these same data toward a base station for storing and further analysis. The adjacent sensorial nodes can be used for storing the information and relaying into the base station, when the establishment of an RF link between a given sensor node and the base station is not possible. The information of a hidden node (with relation to the base station) is not lost because it can be relayed across the distributed infrastructure that forms the network of wireless sensors. However, their distributed nature and the nonexistence of a central controller imply the development of complex algorithms to deal with the multiplicity of nodes. This is especially true, when the topology of the network changes due to the malfunction of a node and/or when a new node is placed in the network or even when the existent nodes occupy new physical positions [51]. Moreover and contrary to what happens on wired networks, this type of network brings new problems: propagation aspects of RF signals and power-supply issues. The shared nature of the propagation medium is another problem because this makes the signals vulnerable to interference and multiple paths (fading), especially for mobile nodes and when a wide number of surrounding obstacles are present [52]. The shared medium also introduces problems related to the security and confidentiality of the data.

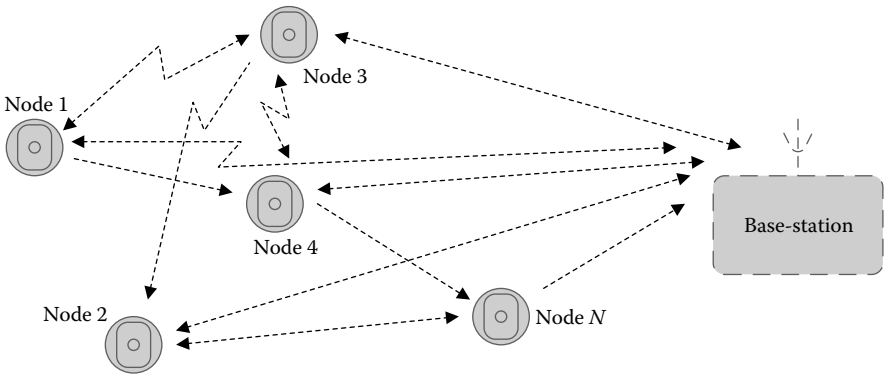

FIGURE 85.15 A schematic illustrating the wireless sensors network concept.

The increased application potential of wireless sensors networks in several fields of the human society (such as industrial, biomedical, transportation, domestic, and energy fields, among others) resulted in the need of their standardization as well as in their wide acceptance. Historically, the first wireless networks were mere technologic extensions of IEEE 802 local networks. Basically, the target of the local wireless networks was the interconnection of computers (as it was a common wired network). With time, other wireless networks appeared such as Bluetooth for connecting computers to their peripherals and IEEE 802.15.4 for wireless sensors networks. The IEEE 802.11 and the Bluetooth protocols are very difficult, complex, and, thus, with the potential to require devices with high power consumption. These are the reasons that made these protocols not suitable for wireless sensors networks but only for point-to-point connections. In this context, the need of protocols with low power consumption and simple procedures resulted in the establishment of the IEEE 802.15 workgroup. The joint actions developed by this workgroup resulted in the proposal of three different classes of wireless operation. The focus of the first class of operation targeted bit rates, whereas the second targeted power consumption, while the third class was more concerned with the quality of service (QoS). The need of protocols for low-power devices resulted in the proposition of the IEEE 802.15.4, as a basic set of rules for application in wireless sensors networks. The IEEE 802.15.4 protocol was developed for low-complexity applications and distances up to 10 m, allowing bit rates up to 250 kbps. Furthermore, the IEEE 802.15.4 protocol was proposed for a wide range of uses, ranging from consumer electronics, industrial and domestic automation, personal healthcare, and interconnection of computer peripherals. The IEEE 802.15.4 protocol defines two lower OSI layer functions. Figure 85.16 shows two versions of the physical layer of the IEEE 802.15.4 protocol [53].

The first version of the physical layer uses 868 MHz in Europe or 915 MHz in the United States. The European version permits only one RF channel for transmitting the maximum bit rate of 20 kbps, whereas the U.S. version allows the use of 10 simultaneous channels spaced by 2 MHz and a maximum bit rate of 40 kbps per channel. The second version of physical layers uses the 2.4 GHz band and supports the use of 16 simultaneous channels spaced by 5 MHz and a maximum bit rate of 250 kbps per channel. Table 85.3 shows that the IEEE 802.15.4 protocol uses spread spectrum techniques for increasing the resilience against a variety of factors that include interference from other radio stations and fading resulting from a multiplicity of radiowave paths. The spread spectrum techniques also ease the clock synchronization task in the receiver. These modulations belong to the constant amplitude modulations group and are very complex to implement because analog products in four quadrants are required. Fortunately, the RF *transceiver* CC2420 from the Chipcon company [54] is commercially available.

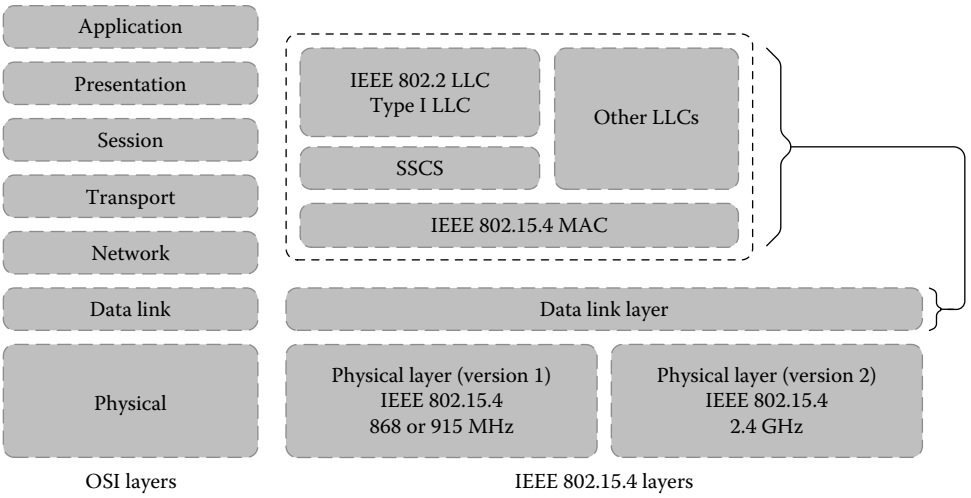

FIGURE 85.16 The OSI layer functions can be found in the IEEE 802.15.4 protocol.

TABLE 85.3 The Main Characteristics of the Physical Layer of the IEEE 802.15.4 Protocol

Band	Frequencies	Bit Rate (kbps)	Symbol Rate (ksymbols/s)	Spreading Parameters	
				Modulation	Chip Rate
868 MHz	868–868.6 MHz	20	20	BPSK	300 kchips/s
915 MHz	902–928 MHz	40	40	BPSK	600 kchips/s
2.4 GHz	2.4–2.4835 GHz	250	62.5	O-QPSK	2 Mchips/s

This RF transceiver contains a core ready for implementing all the IEEE 802.15.4 functions (naturally, the second version of the physical layer) and consumes only 19.7 mW when operating in the receiving mode as well as 17.4 mW when operating in the transmitting mode.

The IEEE 802.15.4 also defines data link layer standardized protocols (e.g., MAC and LLC). In this context, the LLC sublayer of the IEEE 802.15.4 uses the same type I LLC frame formats and procedures specified by the standard IEEE 802.2. The main difference between those used by local area networks and those used by wireless sensors networks is the adopted MAC sublayer. The MAC sublayer adopted by the IEEE 802.15.4 (e.g., the IEEE 802.15.4 MAC) is closer in hardware than the ordinary MACs adopted for local area networks. The service-specific convergence sublayer (SSCS) allows the adoption of other proprietary LLCs as an alternative to this one defined by the IEEE 802.2 (e.g., the type I LLC). The purpose of this model is to allow the IEEE 802.15.4 MAC to implement medium access mechanisms not defined in the IEEE 802.2 [53]. The structure of the MAC sublayer frames is flexible enough to allow the deployment of networks with a wide range of topologies and applications. Typically, an IEEE 802.15.4 MAC frame contains the following fields: a control field to indicate its type, a sequence field to indicate the number of frames for transmission, two fields with receiver and sender addresses information, a field with the information itself (designated as payload), and a field for data integrity check (e.g., the CRC for transmission errors verification).

Figure 85.17 shows that the ZigBee protocol is an extension of the IEEE 802.15.4 protocol. ZigBee uses the IEEE 802.15.4 protocol to implement the physical and data link layer functions. Furthermore, ZigBee supports a wider range of high-level functionalities (not present in the IEEE 802.15.4, which is closer to the hardware) as used in cryptography, management policies in environments with multiple users, as well as error control [53]. CC2430 is another integrated circuit fabricated by the Chipcon company [55] that eases the task of implementing ZigBee networks. CC2430 contains internally an RF transceiver and an additional core for implementing the ZigBee high-level functions. The RF part of CC2430 consumes 21 mW in the receiving mode and 30 mW in the transmitting mode. The CC2430 is at this date the first

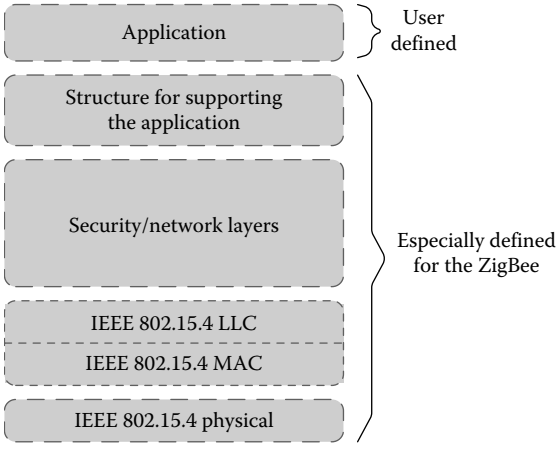

FIGURE 85.17 Adopted layers from the OSI model for use by ZigBee.

integrated circuit to offer a full ZigBee solution for the market. This integrated circuit has flash memory up to 128, 8 kbytes of RAM, an SPI interface, and a few pins for connecting analog and digital signals.

The ZigBee protocol was defined in response to the increased demand for wireless sensors by industry and the need for new personal applications. Thus, ZigBee allows fast prototyping of wireless sensors networks. A wide number of solutions are possible for wireless sensors networks. A few companies (that include Crossbow [42], Dust Networks [56], and Sensicast Systems [57]) offer products such as radios (motes) and sensor interfaces. The motes are battery-powered devices that run specific software. In addition to running the software networking stack, each mote is easily customized and programmed, since it runs open-source operating systems that provide low-level event and task management. Mote processor/radio module families working at 2.4 GHz ISM band that support IEEE 802.15.4 and ZigBee are available from the Crossbow company.

However, despite the inherent ease of the solutions based on motes, they can be very expensive when full custom network prototypes are required. The wireless sensors network solution found in [18] uses microcontrollers PIC from the Microchip company to meet a wide range of small volume applications with a low cost and in a ready to use fashion. Their solution uses a PIC microcontroller to provide the basic services of communication and control. Thanks to the serial connection of ADC chains, this solution is scalable in the sense that is possible to expand the number of attached transducers. The main drawback is that the maximum sampling frequency is limited by the number of transducers: the maximum sampling frequency per transducer is limited to f_S/N (Hz), where f_S (Hz) is the maximum sampling frequency when only one transducer is present and N is the number of transducers. To finish, the reprogramming of the microcontroller increases the functionalities to yield new services of nodes.

85.4 Biomedical Applications

85.4.1 COTS and Customized Applications

Biomedical applications have a high potential for using wireless instruments. An example that confirms this statement is the wireless monitoring systems of human body information as a growing field. A body area network comprises smart sensors able to communicate wirelessly to a base station.

An example of these applications is the wireless electroencephalogram (EEG), which is expected to provide a breakthrough in monitoring, diagnostics, and treatment of patients with neural diseases. Wireless EEG modules composed of the neural electrodes, processing electronics, and a RF transceiver with an associated antenna will be an important breakthrough in EEG diagnostics. Two approaches can be used for implementing wireless EEG systems: commercial off-the-shelf (COTS) and customized solutions. A COTS solution uses discrete integrated circuits and passive components for making wireless instruments, whereas a customized solution is designed from the scratch and further integrated on a single microdevice in order to optimize the size and power consumption and allow a power supply with small batteries (e.g., class AA, coin-sized batteries). The system proposed by Dias et al. [58] is an example of a COTS system for acquiring EEG signals and transmission by RF. This wireless EEG system uses a Micaz module [42] at 2.4 GHz for RF transmission and for controlling and converting the physical data. This system uses two 1.5 V class AA batteries for power supply and achieves maximum bit rates of 120 kbps. Other features of this system include 4 μV resolution, 15 mW power consumption, five single-ended channels, and size of $5.7 \times 4.8 \times 2.0$ cm. Figure 85.18 shows the acquisition part of this wireless EEG system. A reference voltage must be added to the acquired signals before the analog-to-digital conversion because negative potentials are not provided by the power supply (the batteries can provide the following electrical potentials: ground, V_{dd}, and $V_{dd}/2$). Further explanations of this analog circuit (especially for the necessity of neutral and signal ground, SGND, electrodes) can be obtained in [59].

Customized solutions require the development of dedicated microelectronic systems or at least dedicated application-specific integrated circuits (ASICs). The wireless EEG system proposed by Yazicioglu

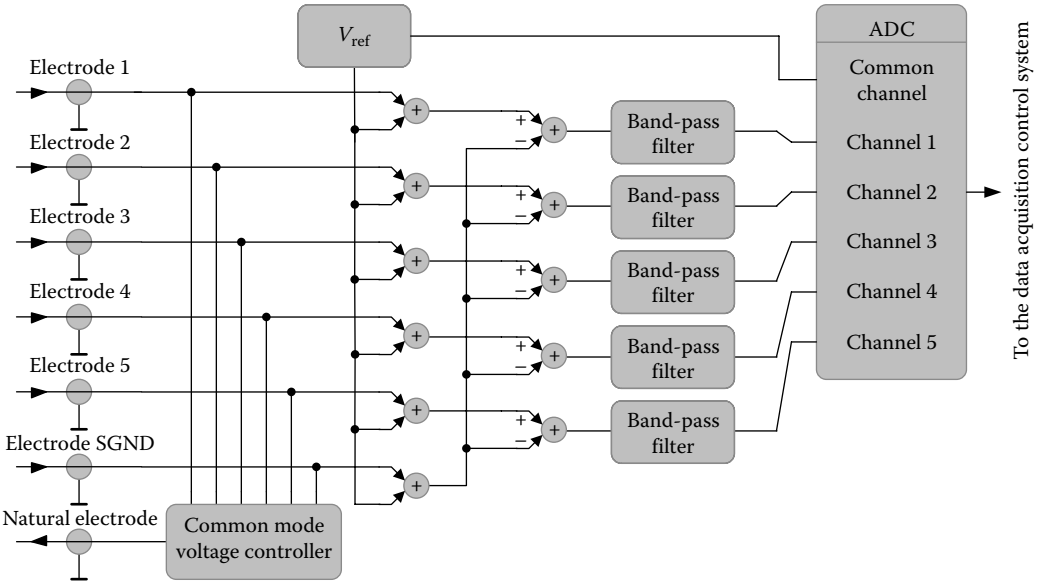

FIGURE 85.18 The analog signal-processing part found in. (From Dias, N.S. et al., A wireless system for biopotential acquisition: An approach for non-invasive brain-computer interface, *Proceedings of IEEE International Symposium on Industrial Electronics—ISIE 2007*, Vigo, Spain, pp. 2709–2712, June 4–7, 2007.)

et al. [60] pushes further the concept of wireless EEG, by using the heat of human body for powering the whole wireless instrument itself. Their wireless EEG system uses a thermoelectric generator to convert the temperature differences between the environment (the coldest side, at temperature T_c [K]) and the forehead of the subject (the hottest side, at temperature T_h [K]) [60]. The output voltage depends on the Seebeck effect [61] temperature difference $\Delta T = T_h - T_c$ (K). This wireless EEG system can acquire signals from eight EEG channels, whose inputs are differential (instrumentation) for noise and interference reduction. Each channel uses a new concept developed by them and known as AC-coupled chopper-stabilized instrumentation amplification (ACCIA) for achieving high common-mode rejection ratio (CMRR) and at the same time eliminating the flicker noise of the transistors as well as for filtering the differential DC voltage generated between two EEG electrodes [60]. A dedicated ASIC was developed for achieving a complete readout front end for the eight EEG channels, and thanks to it, the complete wireless EEG module mounted with the RF front end and with a backup lithium battery occupies a volume of 1 cm^3.

Another example of customized solution is the Sensium TZ1030 sensor interface illustrated in Figure 85.19a [62]. The Sensium TZ1030 sensor interface was developed by Toumaz Technology Limited Company for operation in the following bands: 863–870 MHz in Europe and 902–928 MHz in the United States. Internally, the TZ1030 is composed of analog and digital electronics for interfacing and calibrating the sensors. The sensors are external to the TZ1030 and can attach directly to it. An RF transceiver, an 8051 compatible microcontroller, RAM, and flash memories are also provided and make the TZ1030 a compact solution for an easy placement on the subject's body. The control software contains procedures for local processing of the information, in order to reduce the amount of information and the total transmission times. These features make the TZ1030 a low power consumption solution. Together with an appropriate external sensor, the TZ1030 is ready for acquiring electrocardiograms (ECGs), temperature, glucose levels, and oxygen levels in the blood. Figure 85.19b illustrates a possible architecture for rapid development of wireless body area networks (BANs), offering the possibility.

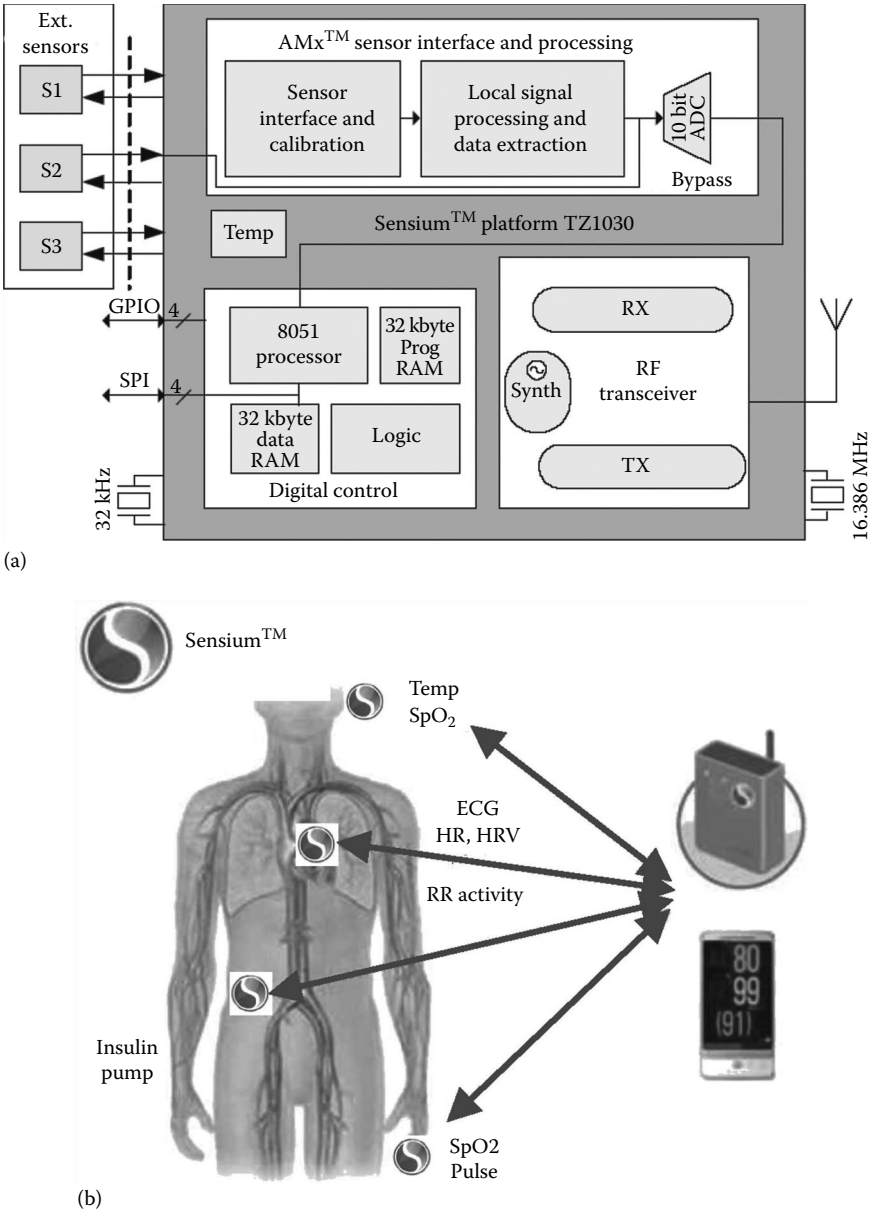

FIGURE 85.19 (a) Sensium TZ1030 sensor interface for transmission at 863–870 MHz, and (b) system architecture for biomedical applications using the TZ1030. (From Sensium TZ1030, Ultra low power smart sensor interface and transceiver platform, Toumaz Technology Limited. Online http://www.toumaz.com, accessed on February 27, 2012.)

85.4.2 New Concepts for Wireless Instruments

New techniques for implementing wireless instruments can be found in the literature. These techniques are extremely innovative due to the breakthrough introduced in the way the measurements are done. The work proposed by Karacolak et al. [63] takes in account the variation of the electric parameters for continuously measuring glucose (the electric parameters vary with the sugar concentration).

Alternatively, the research group of Chow et al. [64] explores an uncommon (but still very innovative) methodology that makes use of cardiovascular stents to receive RF signals inside the human body.

In this work, the stents are used as radiating structures for transmitting the measurements through the tissues of the human body.

Finally, the work proposed by Rodrigues et al. [65] uses a MEMS antenna with a U-shaped cantilever structure. This cantilever is sensitive to the magnetic field component of electromagnetic waves and will oscillate. A piezoelectric material layer of polyvinylidene fluoride (PVDF) is used to convert the magnetic field into a voltage useful enough to be acquired by the reading circuit. The major innovation of this technique allows the integration of antennas with implantable devices by way of WLP techniques for achieving the fabrication of small-sized devices. Their antenna occupies an area of only 1.5×1.5 mm [65].

References

1. D. Buchla and W. McLachlan (eds.), *Applied Electronic Instrumentation and Measurement*, 1st edn., Prentice Hall, Englewood Cliffs, NJ, 1991.
2. W. D. Cooper and A. D. Helfrick, *Electronic Instrumentation and Measurement Techniques*, 3rd edn., Prentice Hall, Englewood Cliffs, NJ, 1985.
3. J. H. Correia, G. de Graaf, M. Bartek, and R. F. Wolffenbuttel, A single-chip CMOS optical microspectrometer with light-to-frequency converter and bus interface, *IEEE Journal Solid-State Circuits*, 37(10), 1344–1347, October 2002.
4. G. R. Tsai and M. C. Lin, FPGA-based reconfigurable measurement instruments with functionality defined by user, *EURASIP Journal on Applied Signal Processing*, Article ID 84340, 1–14, January 2006.
5. I. F. Akyildiz, W. Su, Y. Sankarasubramaniam, and E. Cayirci, Wireless sensor networks: A survey, *Computer Networks*, 38(4), 393–422, March 2002.
6. V. Raghunathan, C. L. Pereira, M. B. Srivastava, and R. K. Gupta, Energy-aware wireless systems with adaptive power—Fidelity tradeoffs, *IEEE Transactions on Very Large Scale Integrated (VLSI) Systems,* 13(2), 211–225, February 2005.
7. W. Wu, M. A. T. Sanduleanu, X. Li, and J. R. Long, 17 GHz RF front-ends for low-power wireless sensor networks, *IEEE Journal of Solid State Circuits*, 43(9), 1909–1919, September 2008.
8. H. Eren, *Wireless Sensors and Instruments: Networks, Design and Applications*, CRC Press, Boca Raton, FL, 2006.
9. J. H. Correia, G. de Graaf, M. Bartek, and R. F. Wolffenbuttel, A CMOS optical microspectrometer with light-to-frequency converter, bus interface and stray-light compensation, *IEEE Transactions on Instrumentation and Measurement*, 50(6), 1530–1537, December 2001.
10. F. J. Naivar, CAMAC to GPIB interface, *IEEE Transactions on Nuclear Science*, 25(1), 515–519, February 1978.
11. L. Korba, S. Elgazzar, and T. Welch, Active infrared sensors for mobile robots, *IEEE Transactions on Instrumentation and Measurement*, 43(2), 283–287, April 1994.
12. R. Mukaro and X. F. Carelse, A microcontroller—Based data acquisition system for solar radiation and environmental monitoring, *IEEE Transactions on Instrumentation and Measurement*, 48(6), 1232–1238, December 1998.
13. D. R. Muñoz, D. M. Pérez, J. S. Moreno, S. C. Berga, and E. C. Montero, Design and experimental verification of a smart sensor to measure the energy and power consumption in a one-phase AC line, *Measurement: Elsevier Science Direct*, 42(3), 412–419, April 2009.
14. A. Depari, A. Flammini, D. Marioli, and A. Taroni, USB sensor network for industrial applications, *IEEE Transactions on Instrumentation and Measurement*, 57(7), 1344–1349, July 2008.
15. G. Bucci, E. Fiorucci, C. Landi, and G. Ocera, Architecture of a digital wireless data communication network for distributed sensor applications, *Measurement: Elsevier Science Direct*, 35(1), 33–45, January 2004.
16. A. Wheeler, Commercial applications of wireless sensor networks using ZigBee, *IEEE Communications Magazine*, 45(4), 70–77, April 2007.

17. L. Ferrigno, V. Paciello, and A. Pietrosanto, Performance characterization of a wireless instrumentation bus, *IEEE Transactions on Instrumentation and Measurement*, 59(12), 3253–3261, December 2010.
18. J. P. Carmo, P. M. Mendes, C. Couto, and J. H. Correia, A low-cost wireless sensor network for industrial applications, *Proceedings of Wireless Telecommunications Symposium 2009*, Praha, Czech Republic, Session D-2, pp. 1–4, 22–24, April 2009.
19. A. Bakker and J. H. Huijsing, Micropower CMOS temperature sensor with digital output, *IEEE Journal of Solid-State Circuits*, 31(7), 933–937, July 1996.
20. M. Motz, D. Draxelmayr, T. Werth, and B. Forster, A chopped hall sensor with small jitter and programmable «true power-on» function, *IEEE Journal of Solid-State Circuits*, 40(7), 1533–1540, July 2005.
21. J. Chae, H. Kulah, and K. Najafi, A monolithic three-axis micro-g micromachined silicon capacitive accelerometer, *IEEE Journal of Microelectromechanical Systems*, 14(2), 235–244, April 2005.
22. A. Arnaud and C. Galup-Montoro, Fully integrated signal conditioning of an accelerometer for implantable pacemakers, *Analog Integrated Circuits and Signal Processing*, 49(3), 313–321, 2006.
23. W. Stallings, *Data and Computer Communications*, Prentice Hall, Englewood Cliffs, NJ, 2003.
24. B. Pattan, *Robust Modulation Methods and Smart Antennas in Wireless Communications*, Prentice Hall, Englewood Cliffs, NJ, 1999.
25. H. R. Silva, L. A. Rocha, J. A. Afonso, P. C. Morim, P. M. Oliveira, and J. H. Correia, Wireless hydrotherapy smart-suit network for posture monitoring, *Proceedings of IEEE International Symposium on Industrial Electronics—ISIE* 2007, Vigo, Spain, pp. 2713–2717, June 2007.
26. N. S. Dias, J. P. Carmo, P. M. Mendes, and J. H. Correia, Wireless instrumentation system based on dry electrodes for acquiring EEG signals, *Medical Engineering & Physics*, 34(7), 1–10, 2012.
27. Taiyo Yuden Functional Modules, Taiyo Yuden Co. Online http://www.yuden.co.jp/ut/product/category/module/, accessed on February 27, 2012.
28. Linx RF modules, Linx Technologies Inc. Online http://www.linxtechnologies.com/, accessed on February 27, 2012.
29. Radiomtrix Wireless Data Transmission, Radiometrix Ltd. Online http://www.radiometrix.com/, accessed on February 27, 2012.
30. Wireless Solutions for a Connected World, Low Power Radio Solutions (LPRS Ltd). Online http://www.lprs.co.uk/, accessed on February 27, 2012.
31. J. P. Carmo, J. C. Ribeiro, P. M. Mendes, and J. H. Correia, Super regenerative receiver at 433 MHz, *Microelectronics Journal*, 42(5), 681–687, May 2011.
32. R. Morais, A. Valente, C. Couto, and J. H. Correia, A wireless RF CMOS mixed-signal interface for soil moisture measurements, *Journal Sensors and Actuators A*, 115, 376–384, September 2004.
33. A. Valente, R. Morais, C. Couto, and J. H. Correia, Modeling, simulation and testing of a silicon soil moisture sensor based on the dual-probe heat-pulse method, *Journal Sensors and Actuators A*, 115, 434–439, September 2004.
34. L. W. Couch II, *Digital and Analog Communication Systems*, 5th edn., Prentice Hall, Englewood Cliffs, NJ, 1996.
35. M. D. Weiss, J. L. Smith, and J. Bach, RF coupling in a 433-MHz biotelemetry system for an artificial hip, *IEEE Antennas and Wireless Propagation Letters*, 8, 916–919, 2009.
36. P. M. Mendes, J. H. Correia, M. Bartek, and J. Burghartz, Analysis of chip—Size antennas on lossy substrates for short-range wireless microsystems, *Proceedings SAFE 2002*, Veldhoven, the Netherlands, pp. 51–54, November 27–28, 2002.
37. J. D. Parsons, *The Mobile Radio Propagation Channel*, Pentech Press, London, U.K., 1992.
38. M. Pätzold, *Mobile Fading Channels*, Wiley–Blackwell, Chichester, U.K., 2002.
39. M. Blaunstein and J. B. Andersen, *Multipath Phenomena in Cellular Networks*, Artech House Publishers, Norwood, MA, 2002.

40. H. L. Bertoni, *Radio Propagation for Modern Wireless Systems*, Prentice Hall, Englewood Cliffs, NJ, 2000.
41. L. A. Rocha, J. A. Afonso, P. M. Mendes, and J. H. Correia, *A Body Sensor Network for E-Textiles Integration*, *Proceedings of Eurosensors XX*, Gothenburg, Sweden, pp. 1–4, September 2006.
42. Crossbow. (2009). Wireless measurement systems, Crossbow Inc. Online http://www.xbow.com, accessed on February 2012.
43. J. A. Afonso, L. A. Rocha, H. R. Silva, and J. H. Correia, MAC protocol for low-power real-time wireless sensing and actuation, *Proceedings of IEEE International Conference on Electronics, Circuits and Systems—ICECS 2006*, Nice, France, pp. 1248–1251, December 2006.
44. J. A. Gutierrez, M. Naeve, E. Callaway, M. Bourgeois, V. Mitter, and B. Heile, IEEE 802.15.4: Developing standards for low-power low-cost wireless personal area networks, *IEEE Network*, 5(15), 12–19, September/October 2001.
45. C. Enz, N. Scolari, and U. Yodprasit, Ultra low-power radio design for wireless sensor networks, *Proceedings of the IEEE International Workshop on Radio Frequency Integration Technology: Integrated Circuits for Wideband Communication and Wireless Sensor Networks*, Singapore, pp. 1–17, December 2005.
46. C. C. Enz, A. El-Hoiydi, J. D. Decotignie, and V. Peiris, WiseNET: An ultralow—Power wireless sensor network solution, *IEEE Computer*, 378, 62–70, August 2004.
47. J. P. Carmo and J. H. Correia, Low-power/low-voltage RF microsystems for wireless sensors networks, *Microelectronics Journal*, 40(12), 1746–1754, December 2009.
48. E. H. Callaway Jr., The physical layer. In: *Wireless Sensor Networks: Architectures and Protocols,* Chapter 3, pp. 41–59, CRC Press, Boca Raton, FL, 2004.
49. N. S. Dias, J. P. Carmo, P. M. Mendes, and J. H. Correis, A low-power/low-voltage CMOS wireless interface at 5.7 GHz with dry electrodes for cognitive networks, *IEEE Sensors Journal*, 11(3), 755–762, March 2011.
50. A. El-Hoiydi, C. Arm, R. Caseiro, S. Cserveny, J. D. Decotignie, C. Enz, F. Giroud et al., The ultra low-power WiseNET system, *Proceedings Design, Automation and Test in Europe, DATE'06*, Munich, Germany, pp. 1–5, March 6–10, 2006.
51. J. A. Afonso, H. D. Silva, P. Macedo, and L. A. Rocha, An enhanced reservation-based MAC protocol for IEEE 802.15.4 networks, *Sensors*, 11(4), 3852–3873, April 2011.
52. W. Y. Lee, *Wireless and Cellular Communications*, 2nd edn., McGraw-Hill, New York, 1998.
53. E. Callaway, P. Gorday, L. Hester, J. A. Gutierrez, M. Naeve, B. Heile, and V. Bahl, Home networking with IEEE 802.15.4: A developing standard for low-rate wireless personal area networks, *IEEE Communications Magazine*, 40(8), 2–9, August 2002.
54. Smart RF CC2420, 2.4 GHz IEEE 802.15.4/ZigBee-ready RF transceiver, Texas Instruments Incorporated. Online http://www.ti.com/, accessed on February 27, 2012.
55. Smart RF CC2430, A true system-on-chip solution for 2.4 GHz IEEE 802.15.4/ZigBee, Texas Instruments Incorporated. Online http://www.ti.com/, accessed on February 27, 2012.
56. Dust, Dust Networks Inc. Online http://www.dust-inc.com/, accessed on February 27, 2012.
57. Sensicast, Sensicast Systems. Online http://www.sensicast.com/, accessed on February 27, 2012.
58. N. S. Dias, J. F. Ferreira, C. P. Figueiredo, and J. H. Correia, A wireless system for biopotential acquisition: An approach for non-invasive brain-computer interface, *Proceedings of IEEE International Symposium on Industrial Electronics—ISIE 2007*, Vigo, Spain, pp. 2709–2712, June 4–7, 2007.
59. A. C. M. van Rijn, A. Peper, and C. A. Grimbergen, High-quality recording of bioelectric events, Part 1: Interference reduction, theory and practice, *Medical & Biological Engineering & Computing*, 28(5), 389–397, September 1990.
60. R. F. Yazicioglu, T. Torfs, P. Merken, J. Penders, V. Leonov, R. Puers, B. Gyselinckx, and C. V. Hoof, Ultra low-power biopotential interfaces and their applications in wearable and implantable systems, *Microelectronics Journal*, 40(9), 1313–1321, September 2009.

61. J. P. Carmo, L. M. Goncalves, and J. H. Correia, Thermoelectric microconverter for energy harvesting systems, *IEEE Transactions on Industrial Electronics*, 57(3), 861–867, March 2010.
62. Sensium TZ1030, Ultra low power smart sensor interface and transceiver platform, Toumaz Technology Limited. Online http://www.toumaz.com, accessed on February 27, 2012.
63. T. Karacolak, A. Z. Hood, and E. Topsakal, Design of a dual band implantable antenna and development of skin mimicking gels for continuous glucose monitoring, *IEEE Transactions on Microwave Theory and Techniques*, 54(4), 1001–1008, April 2008.
64. E. Y. Chow, Y. Ouyang, B. Beier, W. J. Chappell, and P. P. Irazoqui, Evaluation of cardiovascular stents as antennas for implantable wireless applications, *IEEE Transactions on Microwave Theory and Techniques*, 57(10), 2523–2532, October 2009.
65. F. J. O. Rodrigues, J. H. Correia, and P. M. Mendes, Modeling of a neural electrode with MEMS magnetic sensor for telemetry at low frequencies, *Proceedings MicroMechanics Europe, MME 2009*, Toulouse, France, pp. D19/1–D194, September 20–22, 2009.

Partial List of Manufacturers

BWI Eagle, Inc., 105 Bonnie Dr., Butler, PA 16002, Phone: 888-366-7850 (toll free), Fax: 724-283-5939, bwieagle.rtrk.com/?scid=1808652&rl_alt=h…

Cognex Corp., 1 Vision Dr., Natick, MA 01760-2059, Phone: 508-650-3100, 800-677-2646 (toll free), Fax: 508-650-3344, www.cognex.com

Cooper Instruments, 400 Belle Air Lane, P.O. Box 3048, Warrenton, VA 20188, Phone: 540-349-4746, 800-344-3921 (toll free), Fax: 540-347-4755, www.cooperinstruments.com

Micro-Epsilon America, 8120 Brownleigh Dr., Raleigh, NC 27617, Phone: 919-787-9707, Fax: 919-787-9706, www.micro-epsilon.us

Microstrain, Inc., 459 Hurricane Lane, Suite 102, Williston, VT 05495, Phone: 802-862-6629, 800-449-3878 (toll free), Fax: 802-863-4093, www.microstrain.com

Siemens Corp, 300 New Jersey Avenue, N.W., Suite 1000, Washington, DC 20004-2611, Phone: 202-434-4800, 800-SIEMENS (toll free), Fax: 202-347-4015, www.usa.siemens.com/entry/en/

86

Wireless Sensor Node Hardware

Michael Healy
University of Limerick

Thomas Newe
University of Limerick

Elfed Lewis
University of Limerick

86.1 Introduction

The fundamental building blocks of wireless sensor networks (WSNs) are the sensor nodes themselves. For the last 10–12 years, a number of research institutions and companies have been designing and producing nodes. However, the capabilities of the resulting nodes vary widely, but only within certain bounds. All the nodes have a number of features in common, i.e., a low-power microcontroller, a low-power, short-range, radio, a power supply, and either onboard sensors or the capability to attach sensors. However, it is the variance within these bounds that complicates application development.

The resources of conventional computing systems, such as personal computers and mobile phones, increase almost exponentially, and cost is reduced as technology improves. This has not happened with sensor nodes and, indeed, is not expected to happen going forward. WSN deployments are likely to become more widespread, thus allowing economies of scale to come into play at the manufacturing level, driving costs down. Today most sensor nodes consist of a number of components that work together, but there is a move toward system-on-a-chip (SoC) devices that have, at the least, the communication, processing, and sensing subsystems all on a single piece of silicon. This consolidation of component parts will also help to drive down costs.

Table 86.1 lists nodes that have been developed from 1998 to the present day. This list is extensive but perhaps not comprehensive as a large number of universities and research institutions would have created their own nodes from scratch, tailored to their own particular research requirements, and the details of these nodes would not be available.

86.2 Development History of Sensor Node Hardware

Sensor node hardware has always been a very important factor in WSN research and development. The earliest known wireless sensor nodes, from the late 1960s and early 1970s, were the units used in operation Igloo White [1]. These units were used to detect troop movements along the Ho Chi Minh trail,

TABLE 86.1 Selection of Sensor Nodes

Platform	CPU	Clock (MHz)	RAM/Flash/ EEPROM	Radio Transceiver	BW (kbps)	Freq. (MHz)	OS	Year
WeC	Atmel AT90LS8535	4	512/8K/32K	RFM TR1000	10	916.5	TinyOS	1998
Rene 1	Atmel AT90LS8535	4	512/8K/32K	RFM TR1000	10	916.5	TinyOS	1998
AWAIRS 1	Intel StrongARM SA1100	59–206	1M/4M	Conexant RDSSS9M	100	900	MicroC/ OS	1999
μAMPS	Intel StrongARM SA1100	59–206	1M/4M	National LMX3162	1000	2400	μOS	1999
Rene 2	Atmel ATmega 163	8	1K/16K/32K	RFM TR1000	10	916.5	TinyOS	2000
Dot	Atmel ATmega 163	8	1K/16K/32K	RFM TR1000	10	916.5	TinyOS	2000
Mica	Atmel ATmega 128L	4	4K/128K/512K	RFM TR1000	40	916.5	TinyOS	2001
BT node	Atmel ATmega 128L	8	4K/128K/4K	ZV4002 BT/ CC1000	1000	2400	TinyOS	2001
SpotON	Dragonball EZ	16	2M/2M	RFM TR1000	10	916.5		2001
Smart-its	PIC 18F252	8	3K/48K/64K	Radiometrix	64	433	Smart-its	2001
Mica2	Atmel ATmega 128L	8	4K/128K/512K	Chipcon CC1000	38.4	900	TinyOS	2002
Mica2Dot	Atmel ATmega 128L	4	4K/128K/512K	Chipcon CC1000	38.4	900	TinyOS	2002
iBadge	Atmel ATmega 128L	8	4K/128K	Ericsson ROK101007 BT	1000	2400	Palos	2002
CENS Medusa MK2	Atmel ATmega 128L/Atmel AT91FR4081	4/40	4K/32K 136K/1M	RFM TR1000	10	916	Palos	2002
iMote	Zeevo ZV4002 (ARM)	12–48	64K/512K	Zeevo BT	720	2400	TinyOS	2003
U3	PIC 18F452	0.031–8	1K/32K/256	CDC-TR-02B	100	315	Pavenet	2003
Spec	8-bit AVR-like RISC	4–8	3K	FSK Transmitter	100		TinyOS	2003
RFRAIN	Chipcon CC1010 (8051)	3–24	2K/32K	Chipcon CC1010	76.8	0.3–1000	RFRAIN Libraries	2003
Nymph	Atmel ATmega 128L	4	4K/128K/512K	Chipcon CC1000	38.4	900	Mantis	2003
Telos	TI MSP430F149	8	2K/60K/512K	Chipcon CC2420	250	2400	TinyOS	2004
MicaZ	Atmel ATmega 128L	8	4K/128K	Chipcon CC2420	250	2400	TinyOS	2004
CIT sensor node	PIC 16F877	20	368/8K	Nordic nRF903	76.8	868	TinyOS	2004
BSN node	TI MSP430F149	8	2K/60K/512K	Chipcon CC2420	250	2400	TinyOS	2004
MITes	nRF24E1 (8051)	16	4K/512	Nordic nRF24E1	1000	2400	Custom	2004
AquisGrain	Atmel ATmega 128L	4	4K/128K/512K	Chipcon CC2420	250	2400	Custom	2004
RISE	Chipcon CC1010 EM (8051)	3–24	2K/32K	Chipcon CC1010 EM	76.8	0.3–1000	TinyOS	2004
Particle2/29	PIC 18F6720	20	4K/128K/512K	RFM TR1001	125	868.35	Smart-its	2004
Pluto	TI MSP430F149	8	4K/60K/512K	Chipcon CC2420	250	2400	TinyOS	2004
DSYS25	Atmel ATmega 128L	4	4K/128K	Nordic nRF2401	1000	2400	TinyOS	2004

TABLE 86.1 (continued) Selection of Sensor Nodes

Platform	CPU	Clock (MHz)	RAM/Flash/ EEPROM	Radio Transceiver	BW (kbps)	Freq. (MHz)	OS	Year
EnOcean TCM120	PIC 18F452	10	1.5K/32K/256	Infineon TDA 5200	120	868	TinyOS	2005
EyesIFXv2	TI MSP430F1611	8	10K/48K	Infineon TDA 5250	64	868	TinyOS	2005
iMote2	Intel PXA 271	13–104	256K/32M	Chipcon CC2420	250	2400	TinyOS	2005
uPart0140 ilmt	rfPIC 16F675	4	64/1K	rfPIC 16F675	19.2	868	Smart-its	2005
TelosB/Tmote Sky	TI MSP430F1611	4/8	10K/48K/1M	Chipcon CC2420	250	2400	TinyOS	2005
Ember RF module	Atmel ATmega 128L	8	4K/128K	Ember 250	250	2400	EmberNet	2005
XYZ sensor node	OKI ML67Q500x (ARM/ THUMB)	1.8–57.6	4K/256K/512K	Chipcon CC2420	250	2400	SOS	2005
Ant	TI MSP430F1232	8	256/8K	Nordic nRF24AP1	1000	2400	Ant	2005
ProSpeckz II	Cypress CY8C2764	12	256/16K	Chipcon CC2420	250	2400	Speckle net	2005
Fleck	Atmel ATmega 128L	8	4K/2G/512K	Nordic nRF903	76.8	902–928	TinyOS	2005
Sun SPOT	Atmel AT91RM9200	180	512K/4M	Chipcon CC2420	250	2400	Squawk VM (Java)	2005
Tinynode 584 [16]	TI MSP430F1611	8	10K/560K	Semtech XE1205	153	433/ 568/ 915	TinyOS	2005
MSB430 [17]	TI MSP430F1612	8	5K/55K	TI CC1020	153	402–470/ 804/960	Contiki	2005
ECO [18]	nRF24E1 (8051)	16	4K/512/32K	Nordic nRF24E1	1000	2400	Custom	2006
Shimmer [19]	TI MSP430F1611	4/8	10K/2G	WML-C46A BT/ CC2420	250	2400	TinyOS	2006
Firefly [20]	ATmega 32L	8	2K/32K/2G	Chipcon CC2420	250	2400	NanoRK	2006
IRIS [21]	Atmel ATmega 1281	8	8K/640K/4K	Atmel AT86RF230	250	2400	TinyOS	2007
Mulle [22]	Renesas M16C	10	31K/384K	WML-C46A BT	100	2400	TinyOS Contiki	2008
Epic [23]	TI MSP430F1611	4	10K/2M	TI CC2420	250	2400	TinyOS	2008
Ubi-Mote2 [24]	TI MSP430F2618	16	8K/116K	TI CC2520	250	2400	TI ZStack	2009
EZ430-RF2500 [25]	TI MSP430F2274	16	1K/32K	TI CC2500	500	2400	Custom	2009
Zolertia Z1 [26]	TI MSP430F2617	16	8K/2M	TI CC2420	250	2400	TinyOS Contiki	2010
Shimmer2R [27]	TI MSP430F1611	4/8	10K/2G	RN-42 BT/ CC2420	250	2400	TinyOS	2010
G-Node [28]	TI MSP430F2418	16	8K/1M/116K	TI CC1101	500	868	TinyOS	2010
Waspmote [29]	Atmel ATmega 1281	8	8K/2G/4K	Xbee/eUnistone 31308/2 BT/ Hilo GPRS	250	2400/868/ 900/850/ 1800/1900	Custom	2010

Source: Expanded and updated from Healy, M. et al., Wireless sensor node hardware: A review, *The Seventh IEEE Conference on Sensors (IEEE SENSORS 2008)*, Lecce, Italy, October 26–29, pp. 621–624, 2008.

FIGURE 86.1 Smart dust sensor node that includes optical communication, sensors, and power. Approximately the size of a grain of rice.

from North Vietnam through Laos and into South Vietnam. However, the cost of this operation was astronomical, and the project was not continued after the Vietnam War.

The next documented example of wireless sensor node hardware comes from approximately 15 years later, in the mid-1980s, and was part of the DARPA-funded DSN [2,3] project. The wireless node was so large that it needed to be mounted on a truck for mobility purposes. The substantial power requirements were met by a dedicated generator, which was mounted at the rear of the vehicle in an acoustically quieted enclosure.

Progress on wireless sensor node hardware was equally slow for the next 10–15 years. The primary reasons for this were due to the cost and complexity of constructing the nodes from fully custom hardware and software. Examples include the low-power, wireless, integrated, microsensor (LWIM) node from the University of California, Los Angeles (UCLA) [5], constructed circa, 1996, and the smart dust node shown in Figure 86.1 [6]. While these devices were significantly smaller than the previous examples, they were both fully custom affairs, from the silicon level upward.

The revolution in wireless sensor node hardware, which can be seen to have kick-started all current WSN research, was to make use of commercial-off-the-shelf (COTS) components to construct these nodes.

The Hidra node from Rockwell, shown in Figure 86.2, was arguably the first commercially available sensor node, released in 1998. This was 3.5 in. × 3.5 in. × 3 in. in size, but primarily because of the StrongARM 1100 processor running at 133 MHz, either a large external power supply was required to operate it or, if run off battery power, the operating time was measured in minutes [7].

A more significant progression from 1998 was the development of the WeC node, the first entry in Table 86.1. This was developed as part of the proof-of-concept leg of the Smart Dust project [8] at the University of California, Berkeley. This node is significant because it is the arguably the first *low-power* wireless sensor node and is essentially the ancestor of most of the current sensor nodes available today. Approximately 30 units of the WeC mote were constructed, before being superseded by the Rene mote in 1999, of which there are 850+ built. The Rene mote in turn was further improved upon, to give the Dot mote in 2000 and the Mica mote in 2001 [6,9] (Figure 86.3). The next iterations, the Mica2 and Mica2Dot motes, from 2002 onward, were commercialized by Crossbow Technology, Inc. [10]. The Mica2 and its direct descendants, the MicaZ and Iris mote, are still in active use today.

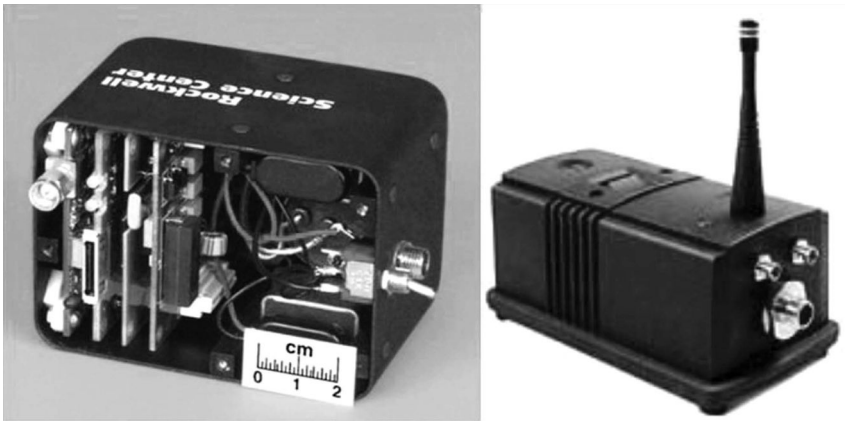

FIGURE 86.2 Rockwell WINS and Hidra nodes.

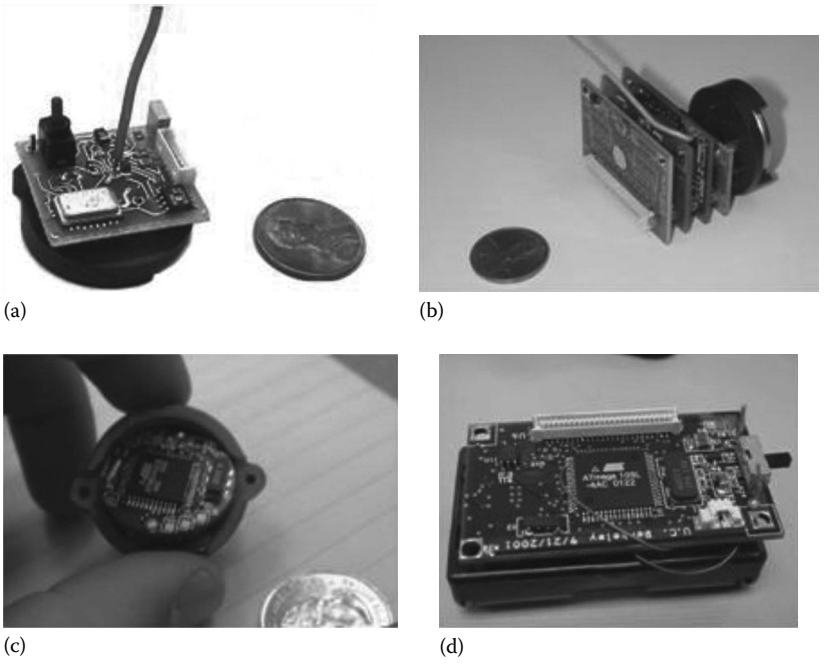

(a) (b)

(c) (d)

FIGURE 86.3 Early Berkeley motes. (a) WeC, (b) Rene, (c) Dot, (d) Mica.

86.3 Sensor Node Components

Despite the variances, almost all sensor nodes are composed of four basic subsystems: a computing subsystem, a communication subsystem, a power subsystem, and a sensing subsystem.

86.3.1 Computing Subsystem

The computing subsystem is responsible for controlling the components of the sensor node and performs any required computations. It consists of two subunits: the processor unit and the storage unit. An important aspect of processors in sensor nodes is the different operational modes, usually active, idle,

and sleep modes as a minimum. This is important so as to preserve power as much as possible without impeding the operation of the processor when it is required.

As can be seen from Table 86.1, the processors used in sensor nodes have, to date, ranged from ultralow-power 8 bit microcontrollers, which can be clocked at speeds as low as 31 kHz, to powerful 32 bit ARM processors that can be clocked at greater than 200 MHz. The price that needs to be paid for using faster and more powerful processors is increased power consumption and purchasing cost. The trend in new generations of sensor nodes is to use low-power processors that focus on very low energy consumption while inactive. As for most WSN applications, the processor is in sleep mode for over 99% of the time. The one major exception to this is the Sun SPOT mote, which uses a powerful processor; the reason for this is to enable the mote to be easily programmed using Java.

An anomaly that can be gleaned from Table 86.1 is that wireless sensor node hardware seems to be very slow to update the processor being used. By far, the most popular processor used in WSN hardware today is the MSP430F1611 from Texas Instruments [11], followed by the Atmel ATmega 128L [12]. While well suited to WSN use, these processors were already well established in the mid-2000s when they were first employed for this purpose. More efficient, faster, cheaper, and lower-power versions of both have been available from their own family of devices for a number of years, but the primary reason they have not been used in this context is due to the lack of open-source compiler support. The WSN operating systems described in the next chapter depend on ports of the GNU C compiler (GCC) [13] tool chains for their build systems, msp430-gcc [14] and avr-gcc [15] to be specific. In recent years, these chip family-specific tool chains have not been updated to support the product line extensions in a timely manner, making it difficult to include the latest and greatest devices on sensor motes. However, this is starting to change, both because of a resurgence of interest from developers who are willing to work on these tool chains, and also, importantly, the manufacturers themselves are starting to recognize the value of these tool chains to their business and as a result are supporting their development.

The storage unit of a node usually consists of both flash memory, containing the program code for the node, and random access memory (RAM), which stores sensed information and any data needed for computations. Some motes also have nonvolatile storage for off-line data capture for later retrieval. Additionally a number of motes have built-in microSD/miniSD/SD card interfaces, or attachable daughter cards to add this functionality, as can be seen in Figure 86.4, allowing up to 2 GB or more of data storage.

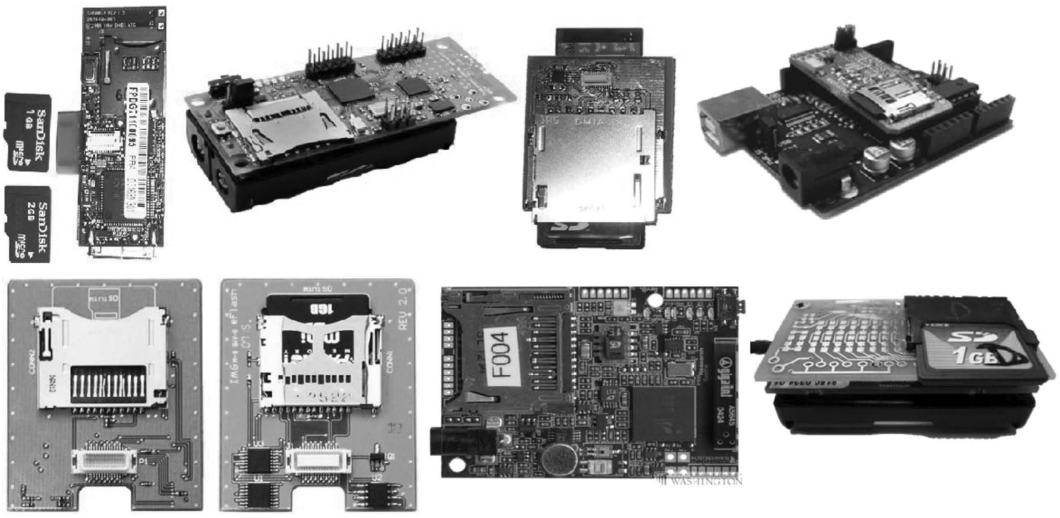

FIGURE 86.4 Selection of motes with SD card support. Top row (L–R): Shimmer, Firefly, Carnivore [30], and SquidBee with expansion board [31]. Bottom row (L–R): expansion board for Sun SPOT (2 miniSD slots, one on top and bottom) [32], expansion board for iMote2 [33], and Luster (MicaZ expansion board) [34].

As a result, there can be anything up to an order of magnitude or more of a disparity between the storage capabilities of different sensor nodes, the choice being made on the basis of the required and desirable storage capacity versus extra cost.

The Carnivore mote shown in Figure 86.4 is tailored to specific application use for wildlife monitoring and is not generally available to developers. It is based on the MSP430 processor and the CC2420 communications platform. The SquidBee mote has generally been preceded by the Waspmote.

86.3.2 Communication Subsystem

The communication subsystem is required to enable the sensor nodes to communicate with each other and with a base station. Generally the communication subsystem is a short-range radio, but the use of infrared communication, ultrasound, and inductive fields has also been explored [35].

While cheap and suitable for implementation with low power consumption, the major drawback with infrared communication is the need for an unobstructed line of sight between the communicating devices. Ultrasound is usually ruled out due to the fact that the network coordinator requires high energy and the form factor of the equipment is also a major problem (i.e., miniaturization). Despite being used extensively for radio-frequency identification (RFID) applications, inductive field communication is also not suitable due to the high-energy requirements of the network coordinator and also because of its very low range. Radio-frequency (RF) communication is ideal for sensor nodes because it is not limited by line of sight and current technology allows implementation of low-power radio transceivers with data rates and ranges scalable according to the application. The RF spectrum is a scarce resource and is regulated by most governments, but there are unlicensed bands, known as the industrial, scientific, and medical (ISM) bands, inside which it is free to operate once the device conforms to the rules that control the band.

Table 86.1 shows a wide variety of radios have been used on sensor nodes. Many current motes use a radio chip that conforms to the IEEE 802.15.4 standard [36], and some nodes use Bluetooth [37] as an alternative. The argument for using Bluetooth is that it allows easy interoperability with a range of existing devices such as mobile phones and laptop computers without the need for additional hardware. The price that needs to be paid for this interoperability is increased energy consumption. Older generations of nodes tended to use radios that conformed to proprietary standards or to no standards at all. Some newer-generation motes are also going in this direction, e.g., those that use the Texas Instruments CC2500 chip [38]. The advantage these nonconforming radios offer is that, because they do not necessarily need to follow ageing standards, they can allow higher throughput or lower power consumption, or both, than the standards-compliant radios. Of course the downside is the lack of interoperability with radios and devices from other manufacturers. Finally, the standards-compliant radios tend to be packet-level devices, whereas the noncompliant radios tend to allow manipulation at the bit level. Bit-level devices allow for more flexibility, but the cost that needs to be paid is that they are usually more difficult to use. However, as the WSN operating systems try to abstract the radio operation so that the application developer does not need to worry about it, this is not a major area for concern. On the other hand, assuming 802.15.4, Bluetooth and other applicable standards are well designed, and there is no reason to date to think otherwise; in the majority of applications, it makes no sense to go to the trouble of creating a communication protocol from scratch, i.e., to reinvent the wheel, especially as the application developer is unlikely to be as experienced or as expert in the field as the committees that developed the standards in the first place, potentially resulting in, to continue the metaphor, a suboptimal wheel design.

An important point to note is that the ISM bands were originally chosen to allow electromagnetic interference (EMI) emissions of products to bleed into without causing problems for other devices. As this is still the case, any device, even ones that use no RF communication, is a potential source of interference. Also humans resonate at 900–1000 MHz, and as the ISM bands are multiples of our fundamental frequency, crowds of people, or even a single person in an inconvenient location, can have a major impact

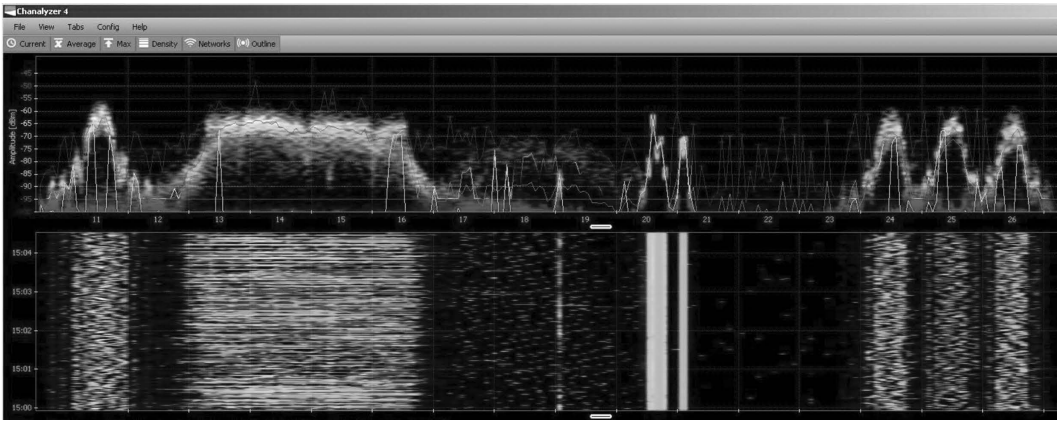

FIGURE 86.5 Density graph and waterfall trace of the 2.4 GHz band.

on the effectiveness of the communications [39]. However, WSNs still tend to operate inside these bands in order to keep costs down. Other problems that should be considered is that the unlicensed bands change from country to country, and there are lots of other devices that also operate in these bands, e.g., wireless local area networks (WLAN), wireless keyboards, home automation systems, wireless surveillance cameras, and digital enhanced cordless telecommunication (DECT) phones, providing additional interference.

Figure 86.5 shows a snapshot of the 2.4 GHz band from a typical industrial environment captured using a Wi-Spy spectrum analyzer [40]. This is the ISM band that the majority of current wireless sensor nodes operate in, a fact that is obvious from looking at Table 86.1. The *x*-axis of both the density graph and the waterfall trace shows the sixteen 802.15.4 channels. When this trace was taken, there was only one WLAN in range, spanning channels 13–16. As a comparison, the activity on channels 11, 24, 25, and 26 is almost entirely from wireless sensor nodes (Shimmer2R devices) transmitting 98 byte 802.15.4 packets at 10 Hz. Eight time-multiplexed nodes were operating in each of channels 11, 24, and 26, and 5 nodes in channel 25, with all 29 nodes being within a meter of the Wi-Spy receiver and all transmitting at their highest power setting. The Wi-Fi router was approximately 20 m away, on the other side of a partition wall. The relatively high-intensity, and very constant, transmissions in channels 20 and 21 were from an unknown source.

This trace shows that even in such close proximity, the 802.15.4 radio can barely match the more distant Wi-Fi radio in intensity level. Also, the amount of data being sent per channel by the 802.15.4 networks would be considered close to the upper bounds of what is realistically achievable even in uncongested channels while maintaining packet reception rates of greater than 90%.

Despite this, the channel bandwidth consumed by the Wi-Fi network is still significantly higher, as can be seen in Table 86.2.

TABLE 86.2 Channel Duty Cycle of 2.4 GHz Band Trace Shown in Figure 86.5

Channel	Duty Cycle (%)	Channel	Duty Cycle (%)
11	21.0	19	1.6
12	0.4	20	20.3
13	29.9	21	13.3
14	38.2	22	0.1
15	37.9	23	0.1
16	21.0	24	15.9
17	0.8	25	10.8
18	2.3	26	15.1

The consequence of this is that when the same 802.15.4 networks were run under these conditions in the channels occupied by the Wi-Fi network, or the unknown transmitters in channels 20 and 21, the packet reception rate dropped from greater than 98% to less than 50% in all cases and less than 10% in some of the channels. This goes to show how great an impact background noise can have on the communication in WSNs and why the RF used is a very important deployment decision.

86.3.3 Power Systems

The power subsystem usually consists of a battery that supplies power to the sensor node.

For many applications of WSNs, the required lifetime of the sensor nodes may be weeks, months, or even years. Battery recharging or replacement is unlikely to be feasible, especially in large-scale deployments with thousands of widely dispersed nodes, or for nodes placed in hazardous environments. For these reasons the developer must ensure every aspect of the network, such as communication algorithms, localization algorithms, and sensing devices, must be as efficient as possible in their power usage.

A power generator may also be included to recharge the battery on site. Photovoltaic, motion/vibration, and thermoelectric energy conversion are all possible sources of power, depending on the location of the node [41].

For a significant subset of WSN applications, the power supply is not a major limiting factor, a category many current deployments fit into. WSNs enable very remote, very-large-scale deployments but are also useful in more mundane situations. For example, for industrial monitoring, while a suitable wired networking infrastructure, or WLAN infrastructure, might not be present in a factory and excessively costly to install, very often a power infrastructure is already present, i.e., the main power supply. Another example is that for many health applications, the sensor nodes are easily accessible, allowing recharging or replacement of batteries at regular intervals. This is a fact that is largely ignored by the research community, primarily as limited energy capacity results in the more difficult and more interesting research problems. However, as most commercially viable sensor networks fall into this category, at least for the moment, suboptimal solutions for the major issues that affect these networks are the only ones currently available, especially along the lines of data aggregation, querying, etc.

That said, in most cases the available power is still the driving factor behind many decisions made about WSN node deployments, including whether or not to include often optional functionality like security, which is why any optional functionality solution needs to be as energy efficient as possible.

86.3.4 Sensing Subsystems

Sensor transducers translate physical phenomena to electrical signals. Therefore, the sensing subsystem of the node is its link to the outside world. The output of the sensors may be digital or analog signals. If the output is analog, the node must also include an analog-to-digital converter (ADC) in order to allow the processor to read the data. Some nodes have sensors built in, such as temperature, humidity, and light sensors, on the Tmote Sky [42] and a three-axis accelerometer on the Shimmer [19], but many do not, instead providing suitable ports and connectors to allow a variety of sensors to be attached for more versatility.

Attaching a sensor with a digital output to a mote is generally a simple exercise, but analog sensors offer some complications. If a node does not have a built-in ADC, one must be included, and without careful design, external ADCs can often send an excessive number of interrupts to the microcontroller unit (MCU), seriously impacting on the other functions of the node. The two most commonly used processors on sensor nodes to date, the Atmel ATmega 128L and the Texas Instruments MSP430, both contain integrated ADCs. However, the resolution and quality of these ADCs can be insufficient for some applications, with the ATmega 128L supplying a 10 bit ADC [12] and the MSP430 offering a 12 bit ADC [11]. Additionally direct memory access (DMA) by the ADC subsystem can be important

for low-jitter, fast-timing accurate sampling, a feature found on the MSP430 processers, but not on the Atmel ATmega devices.

An important feature of sensors that are attached to sensor nodes is the ability to turn on, stabilize, and be read quickly and also power down in a timely manner. When a sensor is switched on, it is consuming power, and as already mentioned, preserving battery life on the nodes is often a prime concern.

A large variety of add-on boards are commercially available for current WSN nodes, capable of measuring a wide variety of phenomena. The following list is a selection of the sensors available from two wireless sensor node vendors, Shimmer Research [43] and Libelium [44], but it is representative of the range available:

- Pressure, acceleration, rotation, vibration, magnetic field, strain, electroencephalography (EEG), electromyography (EMG), electrocardiography (ECG), galvanic skin response (GSR), location (GPS), gas (CO, CO_2, NO_2, etc.), presence (passive infrared), noise, moisture, ultrasound, luminosity, and radiation

This is by no means an exhaustive list as almost any possible sensor could conceivably be connected to a wireless sensor node with the correct interface hardware being available.

86.4 Future Directions

The last few years of the twentieth century and the first five or so years of the twenty-first century saw significant changes in the field of wireless sensor node hardware. However, since then, advancements have been much slower and much more incremental in nature.

For example, the Tinynode 584 from Shockfish [16] was first released in 2005 and is still being sold today in exactly the same form in 2012. The incremental nature of the changes can be seen in the Shimmer family of motes, initially designed at Intel [45], but now developed and sold by Shimmer Research [27]. The current version, the Shimmer2R is the third generation over a 5 year period, but it still uses most of the same parts and has identical functionality and performance as the original Shimmer mote. The entirety of the changes over that period was as follows:

- The accelerometer sensor was changed, but this was only updated because the original chip is at end of life (EOL).
- The Bluetooth radio module employed was changed for the same reason.
- The original Shimmer could not be switched off, but this was a common requirement to preserve battery life when not in use, as the rechargeable battery is soldered directly to the main board and so cannot be easily removed, so power on/off functionally was added.
- Additionally a passive tilt/vibration sensor was added to allow the shimmer to enter the lowest power state possible when idle.
- Power control of the peripherals on the Shimmer was improved, i.e., the ability to power off the Bluetooth radio and the microSD card when not in use.
- Finally, a patented bypass system was added to allow data to be read off the microSD card quickly without having to remove it from the Shimmer device [46].

This trend of slow, incremental changes of existing offerings is likely to continue for the foreseeable future, with the primary aim of making the devices cheaper and more energy efficient, but not necessarily giving them more processing power or more memory capacity.

One of the areas that advancing technology is making an impact with wireless sensor node hardware, and poised to make a much bigger impact, is the components of the power subsystem. This progression is being driven by the power requirements of modern mobile phones, especially the demands of smart phones where higher-capacity batteries are continually being shrunk to fit into smaller packages. Again taking the Shimmer node as an example, when first produced, it was shipped with a rechargeable 280 mAh battery but is now supplied with a 450 mAh battery in the same form factor [47]. Additionally

there have been a number of recent advancements in the field of energy harvesting that should help to extend battery life for WSNs [48–50].

Another trend that is starting to become evident is the emergence of more focused wireless sensor node devices. All the devices listed in Table 86.1 are generic prototyping platforms that allow researchers the flexibility to test new ideas and expand into new application domains. However, this flexibility is expensive, with features and components being present on a mote that are not necessary for a given application. As a result, devices designed specifically, and only, for a particular application domain are starting to become available. For example, the medical domain has offerings from Toumaz [51] and Zepher [52]. The latest example from the Berkeley family of sensor motes, the Epic [23], embodies this specificity by designing each of the sensor node subsystems as stand-alone interchangeable modules. Given that the Epic mote has been released as an open-source hardware (OSHW) platform, anybody can come along and take the required, well-tested, parts and build a custom mote for a particular purpose, including only the required components.

In the general case, there is a need for easy-to-use WSNs as a whole, but in some cases at least, this requirement extends down to the hardware itself. As a result, there are a few recently released hardware platforms that are marketed as easy to set up and use, but this ease of use comes at the cost of the devices being more "locked down," i.e., while the device might be easy to use within certain bounds, it cannot be used outside these bounds even by advanced users. Examples include the WSN hardware from National Instruments, which integrates with their LabVIEW software environment [53]; the very specific targeted wireless sensors from Monnit [54]; and the disposable, self-adhesive wireless sensors from GreenGoose [55]. These types of wireless sensor nodes are going to become more popular as the technology matures and the exact requirements of the different application domains become better understood.

A different approach to making wireless sensor nodes easier to use is to make them programmable using the Java language [56]. The reasoning behind this advancement is that there are many more programmers in the world capable of, and comfortable, using this language than the C [57] or supersets of C, the languages traditionally used to develop applications on wireless sensor nodes. It is also thought that Java would make this application development easier all round, both for experienced software developers and beginners, thus enabling more people to enter the field. This venture was initially driven by Sun Microsystems with their Sun SPOT mote [58] and later by Sentilla Corporation [59] with their JCreate mote. However, despite a lot of excitement in this area between 2005 and 2008, there has been very little news or developments in the area since then. In fact, Sentilla no longer seem to be in the hardware business, instead focusing entirely on application "solutions" [60]. Whether or not Java, or any other higher-level programming language, can be used to program embedded, mote class devices in an efficient and comprehensive manner is still an open question.

Complete SoC wireless sensor nodes have been around for a number of years, such as the original equipment manufacturer (OEM) edition of the Iris node from Memsic [61] and Dust Networks mote-on-chip range [62]. Recently some large processor manufacturers have started producing products that, while not complete SoC wireless sensor nodes, have at least got the computing and communication subsystems on a single chip. An example of this is the CC2531 from Texas Instruments, which includes an 802.15.4 radio transceiver and an 8051 MCU on a single chip [63]. Texas Instruments already have a number of other similar products available, and other manufacturers are likely to follow suit to keep pace with the current movement of adding wireless functionality to any device/product possible.

These same microcontroller manufacturers who also produce low-power, short-range radios are starting to produce node-class devices, both as development kits and also for the hobbyist market. To date these solutions have been much cheaper than any of the dedicated wireless sensor node vendors, albeit not as fully featured or as flexible. These offerings include the EZ430-RFxxxx series from Texas Instruments [25] and the RzRaven from Atmel [64]. This trend is likely to continue as these large companies are recognizing the business opportunities in the "hobbyist" market. Additionally these devices are being targeted toward the education market, which has always been an important segment for these businesses.

Current WSNs sense their environment and report back to the operator. It is envisioned that in the future, WSNs will also be able to influence this environment by having actuators attached to the nodes.

These actuators can then either be controlled by the operator or alternatively the WSN will determine the correct course of action itself using distributed processing, operating as a sort of "hive mind" [65,66].

Additionally, security is going to become much more important in WSNs, and the hardware employed for these networks must be able to support such functionality [67]. As WSNs become more ubiquitous, the collected data will become more valuable to attackers.

86.5 Summary

This chapter gave an overview of the field of WSN hardware. The development kits for sensor nodes available today cost anywhere between 20 U.S. dollars [68] and 900 U.S. dollars [69] and upward. The price of most current sensor motes used for research purposes fall somewhere between these two extremes [70–72]. The vision is for these motes to be truly disposable, with an eventual price point of 1–2 dollars each and a lifetime of at least a year, but this, of course, is totally application dependent. By this reckoning, most commercial sensor nodes will need to drop in price by 50–100 times or more before WSNs become truly ubiquitous. This might seem a massive requirement, but a number of factors need to be remembered:

- Firstly, current commercial products are aimed at being prototyping or development platforms, with costly components and features that are likely to be unnecessary for many deployments.
- As technology improves, causing prices to drop, WSN deployments are likely to become more widespread, thus allowing economies of scale to come into play at the manufacturing level, driving costs down further.

Finally, today most sensor nodes consist of a number of components that work together, but there is a move toward SoC devices that have, at the very least, the communication, processing, and sensing subsystems all on a single piece of silicon. This consolidation of component parts will also help to drive down costs.

References

1. J. T. Correll, Igloo White, *Air Force Magazine*, Vol. 87, November 2004.
2. R. Lacoss and R. Walton, Strawman, Design of a DSN (Distributed Sensors Networks) to Detect and Track Low Flying Aircraft. *Proceedings of the Distributed Sensor Nets Workshop*, Pittsburgh, PA, Department of Computer Science, Carnegie Mellon University, AD-P003791, pp. 41–52, 1978.
3. Distributed sensor networks, MIT Lincoln Laboratory, Lexington, MA, Report number ESD-TR-88-175, 1986.
4. M. Healy, T. Newe, and E. Lewis, Wireless sensor node hardware: A review, *The Seventh IEEE Conference on Sensors (IEEE SENSORS 2008)*, Lecce, Italy, October 26–29, 2008, pp. 621–624. ISBN: 978-1-4244-2581-5, ISSN: 1930-0395, 2008.
5. K. Bult, A. Burstein, D. Chang, M. Dong, M. Fielding, E. Kruglick, J. Ho et al., Low power systems for wireless microsensors, *Proceedings of the International Symposium on Low Power Electronics and Design*, Monterey, CA, 1996, pp. 17–21.
6. B. Warneke, M. Scott, and B. Leibowitz, Ultra-low energy circuits for distributed sensor networks (smart dust), *The EECS Research Summary for 2003*, Berkeley, CA, University of California, 2003.
7. M. Srivastava, Wireless sensor and actuator networks, *Tutorial at 11th Annual International Conference on Mobile Computing and Networking (MobiCom '05)*, Cologne, Germany, 2005.
8. J. M. Kahn, R. H. Katz, and K. S. J. Pister, Mobile networking for smart dust, *Presented at ACM/IEEE International Conference on Mobile Computing and Networking (MobiCom 99)*, Seattle, WA, August 17–19, 1999.
9. J. L. Hill and D. E. Culler, MICA: A wireless platform for deeply embedded networks, *IEEE Micro*, 22, 12–24, 2002.
10. Products, Crossbow Technology, Inc., http://www.xbow.com (accessed on May 1, 2012).

11. Texas Instruments, MSP430F15x, MSP430F16x, MSP430F161x mixed signal microcontroller (Rev. G), http://www.ti.com/lit/ds/symlink/msp430f1611.pdf (accessed on May 1, 2012).
12. Atmel Corporation, 8-bit Atmel microcontroller with 128 Kbytes in-system programmable flash, ATmega128/ATmega128L Datasheet, http://www.atmel.com/Images/doc2467.pdf (accessed on June 5, 2012).
13. Free Software Foundation, Inc., GCC, the GNU compiler collection, http://gcc.gnu.org (accessed on June 5, 2012).
14. Geeknet, Inc., The GCC toolchain for the Texas Instruments MSP430 MCUs, http://mspgcc.sourceforge.net/ (accessed on June 5, 2012).
15. AVR Freaks, AVR GNU toolchain, www.avrfreaks.net/AVRGCC/ (accessed on June 5, 2012).
16. Shockfish SA, Tinynode 584, http://www.tinynode.com/?q=product/tinynode584/tn-584–868 (accessed on June 5, 2012).
17. Freie Universtät Berlin, ScatterWeb: Modular sensor board 430, http://cst.mi.fu-berlin.de/projects/ScatterWeb/mod_MSB-430.html (accessed on June 5, 2012).
18. C. Park, P. H. Chou, Y. Bai, R. Matthews, and A. Hibbs, An ultra-wearable, wireless, low power ECG monitoring system, *Proceedings of the IEEE Biomedical Circuits and Systems Conference (BIOCAS)*, London, U.K., 2006.
19. A. Burns, B. R. Greene, M. J. McGrath, T. J. O'Shea, B. Kuris, S. M. Ayer, F. Stroiescu, and V. Cionca, SHIMMER—A wireless sensor platform for non-invasive biomedical research, *IEEE Sensors Journal*, 10, 1527–1534, 2010.
20. A. Rowe, R. Mangharam, and R. Rajkumar, FireFly: A time synchronized real-time sensor networking platform, in S.-L. Wu and Y.-C. Tseng (Eds.), *Wireless Ad Hoc Networking: Personal-Area, Local-Area, and the Sensory-Area Networks*, Boca Raton, FL: CRC Press, 2006.
21. Memsic Corporation, Iris datasheet, http://www.memsic.com/support/documentation/wireless-sensor-networks/category/7-datasheets.html?download=135%3Airis (accessed on June 5, 2012).
22. J. Eliasson, Low-power design methodologies for embedded internet systems, PhD thesis, EISLAB, Department of Computer Science and Electrical Engineering, Luleå University of Technology, Luleå, Sweden, 2008.
23. P. Dutta, J. Taneja, J. Jeong, X. Jiang, and D. Culler, A building block approach to sensornet systems, in *Proceedings of the 6th ACM Conference on Embedded Network Sensor Systems (SenSys '08)*, Raleigh, NC, pp. 267–280, 2008.
24. Centre for Development of Advanced Computing, Ubiquitous computing, http://www.cdacb.in/html/products_details.aspx (accessed on June 5, 2012).
25. Texas Instruments, MSP430 wireless development tool: EZ430-RF2500, http://www.ti.com/tool/EZ430-RF2500 (accessed on June 5, 2012).
26. Zolertia, Z1 WSN module, http://www.zolertia.com/ti (accessed on June 5, 2012).
27. Realtime Technologies Ltd., Shimmer wireless sensor unit/platform, http://www.shimmer-research.com/p/products/sensor-units-and-modules/shimmer-wireless-sensor-unitplatform (accessed on June 5, 2012).
28. SOWNet Technologies, Introducing the G-Node, http://www.sownet.nl/index.php/products/gnode (accessed on June 5, 2012).
29. Libelium Comunicaciones Distribuidas S.L., Waspmote—Wireless sensor networks 802.15.4 Zigbee mote, http://www.libelium.com/products/waspmote (accessed on June 5, 2012).
30. M. Rutishauser, V. V. Petkov, J. Boice, K. Obraczka, P. Mantey, T. Williams, and C. Wilmers, CARNIVORE: A disruption-tolerant system for studying wildlife, *Proceedings of the 19th International Conference on Computer Communications and Networks (ICCCN '10)*, Zurich, Switzerland, 2010.
31. Wireless Sensor Networks Research Group, Adding a MicroSD flash module to a SquidBee, http://sensor-networks.org/index.php?page=0827727742 (accessed on June 5, 2012).
32. R. Meike, New Sun SPOT hardware open source, http://blogs.oracle.com/roger/entry/new_sun_spot_hardware_open (accessed on June 5, 2012).

33. University of Washington—Ubicomp Research, Sensor boards, http://ubi.cs.washington.edu/wiki/index.php/Sensor_Boards (accessed on June 5, 2012).
34. L. Selavo, A. Wood, Q. Cao, T. Sookoor, H. Liu, A. Srinivasan, Y. Wu et al., LUSTER: Wireless sensor network for environmental research, *Presented at the 5th International ACM Conference on Embedded Networked Sensor System (SenSys'07)*, Sydney, Australia, 2007.
35. S. Roundy, D. Steingart, L. Frechette, P. Wright, and J. Rabaey, Power sources for wireless sensor networks, *Proceedings of First European Workshop on Wireless Sensor Networks (EWSN'04)*, Berlin, Germany, 2004.
36. IEEE, *802.15.4: Wireless Access Control (MAC) and Physical Layer (PHY) Specifications for Low-Rate Wireless Personal Area Networks (LR-WPANs)*, New York: IEEE Standards Association, 2003.
37. The Bluetooth SIG Membership Website, Bluetooth Special Interest Group, http://www.bluetooth.org (accessed on June 5, 2012).
38. Texas Instruments, CC2500, http://www.ti.com/product/cc2500 (accessed on June 5, 2012).
39. K. Lorincz, B. Chen, G. W. Challen, A. R. Chowdhury, S. Patel, P. Bonato, and M. Welsh, Mercury: A wearable sensor network platform for high-fidelity motion analysis, *Presented at the 7th ACM Conference on Embedded Networked Sensor Systems (SenSys'09)*, Berkeley, CA, 2009.
40. Metageek LLC, Wi-Spy, http://www.metageek.net/products/wi-spy/ (accessed on June 5, 2012).
41. S. Roundy, P. K. Wright, and J.M. Rabaey, *Energy Scavenging for Wireless Sensor Networks: With Special Focus on Vibrations*, 1st edn., New York: Springer, 2003.
42. Moteiv Corporation, Tmote Sky, http://www.moteiv.com/products/tmotesky.php (accessed on June 5, 2012).
43. Shimmer Research, Shimmer sensors and modules, http://www.shimmer-research.com/p/sensor-and-modules (accessed on June 5, 2012).
44. Libelium Comunicaciones Distribuidas S.L., Waspmote sensor boards, http://www.libelium.com/products/waspmote/sensors (accessed on June 5, 2012).
45. Products, Topics, Intel Corporation, http://www.intel.com/technology/itj/2009/v13i3/ITJ9.3.7-Research-Platform.htm?wapkw=shimmer (accessed on June 5, 2012).
46. Shimmer Research, Shimmer revisions, http://www.shimmer-research.com/products-2/shimmer-revisions (accessed on June 11, 2012).
47. Shimmer Research, Shimmer Research increase battery capacity by 60% on the Shimmer low power wireless sensing platform, http://www.shimmer-research.com/blog/shimmer-research-increase-battery-capacity-by-60-on-the-shimmer-low-power-wireless-sensing-platform/1805 (accessed on June 11, 2012).
48. M. D. Seeman, S. R. Sanders, and J. M. Rabaey, An ultra-low-power power management IC for energy-scavenged Wireless Sensor Nodes, *Proceedings of the IEEE Power Electronics Specialists Conference (PESC '08)*, Rhodes, Greece, pp. 925–931, 2008.
49. T. Krupenkin and J. A. Taylor, Reverse electrowetting as a new approach to high-power energy harvesting, *Nature Communications*, 2, 23, 2011.
50. K. Bourzac, Power-scavenging batteries, in MIT Technology Review, http://www.technologyreview.com/energy/38434/?mod=chfeatured (accessed on June 11, 2012).
51. Toumaz Healthcare, Toumaz Microsystems, Toumaz UK Ltd., http://www.toumaz.com (accessed on June 11, 2012).
52. Products, Zepher Technology, http://www.zephyr-technology.com/ (accessed on June 11, 2012).
53. National Instruments Corporation, NI wireless sensor networks, http://www.ni.com/wsn/ (accessed on June 11, 2012).
54. Monnit Corporation, Monnit. The leader in low cost wireless sensors, http://www.monnit.com (accessed on June 11, 2012).
55. Green Goose Incorporated, GreenGoose—Play real live, http://www.greengoose.com (accessed on June 11, 2012).
56. J. Gosling, B. Joy, G. Steele, and G. Bracha, *The Java Language Specification*, Santa Clara, CA: Addison-Wesley, 2005.

57. B. W. Kernighan and D. M. Ritchie, *The C Programming Language*, Upper Saddle River, NJ: Prentice Hall, 1988.
58. Sun Microsystems, Inc., Project Sun SPOT: Sun small programmable object technology, http://sunspotworld.com/ (accessed on June 11, 2012).
59. Reuters, World's smallest java-based computers from Sentilla to Debut at JavaOne, http://www.reuters.com/article/2008/05/01/idUS102368+01-May-2008+BW20080501 (accessed on June 11, 2012).
60. Sentilla Corporation, Data center analytics software—Sentilla, http://www.sentilla.com (accessed on June 11, 2012).
61. Memsic Corporation, Iris OEM edition datasheet, http://www.memsic.com/support/documentation/wireless-sensor-networks/category/7-datasheets.html?download=136%3Airis-oem-edition (accessed on June 11, 2012).
62. Dust Networks Incorporated, Motes-on-chip product documentation, http://www.dustnetworks.com/products/list/?field_product_type_value_many_to_one=Mote-on-Chip (accessed on June 11, 2012).
63. Texas Instruments, CC2531: System-on-Chip solution for IEEE 802.15.4 and ZigBee applications, http://www.ti.com/product/cc2531 (accessed on June 11, 2012).
64. Atmel Corporation, RZRAVEN, http://www.atmel.com/tools/RZRAVEN.aspx (accessed on June 11, 2012).
65. K. S. J. Pister, From smart dust to smart plants: The evolution of wireless sensor networking, *Keynote Speaker International Society of Automation (ISA) Exposition*, Houston, TX, 2008.
66. M. Welsh, The next decade of sensor networking, *Keynote Speaker European Conference on Wireless Sensor Networks (EWSN '10)*, Coimbra, Portugal, 2010.
67. G. Press and C. Kane, Smart energy, *ON Magazine*, Issue 1, 2010.
68. Texas Instruments Incorporated TI eStore MSP430 wireless development tool target board, http://www.ti-estore.com/Merchant2/merchant.mvc?Screen=PROD&Product_Code=EZ430-RF2500T (accessed on June 11, 2012).
69. Imote2 development kit from MEMSIC.CH, http://www.memsic.cn/index.php?option=com_phocadownload&view=category&download=168%3Aimote2.builder-q-a&id=7%3Adatasheets&Itemid=86&lang=zh (accessed on June 11, 2012).
70. Shimmer Research, Shimmer, http://www.shimmer-research.com/products_detail.php?cmd=detail&id=SH-SHIM-KIT-001 (accessed on June 11, 2012).
71. TelosB based mote, http://www.advanticsys.com/shop/asxm1000-p-24.html (accessed on June 11, 2012).
72. Eistec AB, Mulle Pricing and availability, http://www.eistec.se/pricing.php (accessed on June 11, 2012).

Partial List of Vendors and Suppliers

Decton, 1 Research Forest Dr., The Woodlands, TX 77381, Phone: 713-559-9333, Fax: 281-292-2860, www.detcon.com

EMRA Controls, Inc., 1502 Pike St. N.W., Suite 4B, Auburn, WA 98001, Phone: 253-351-0292, 800-351-0293 (toll free), Fax: 253-804-2678, www.emracontrols.com

Neal Systems, Inc., 122 Terry Dr., Newtown, PA 18940, Phone: 215-968-7577, Fax: 215-968-6480, www.nealsystems.com/newsite/

PICS INC, 81 Lancaster Ave., Suite 202, Malvern, PA 19355, Phone: 610-644-7701, Fax: 610-644-9297, www.picscontrols.com

Schmitt Industries, Inc., 2765 N.W. Nicolai St., Portland, OR 97210, Phone: 888-425-8020 (toll free), Fax: 503-223-1258, schmittind.rtrk.com/?scid=1407361&rl_alt…

Steven Engineering, 230 Ryan Way, South San Francisco, CA 94080, Phone: 888-790-0022 (toll free), Fax: 800-314-0716, 800-314-0716 (toll free), stevenengineering.rtrk.com/?scid=1975164…

Wireless Cables, Inc., 2880 Zanker Rd., Suite 203, San Jose, CA 95134, Phone: 408-850-1884, Fax: 408-228-0687, www.aircable.net

87

Mobile Instrumentation with Wireless Design and Implementation

Frederick Fortson
Solidica, Inc.

Kenneth Johnson
Solidica, Inc.

Mobile instrumentation has been in use for decades ranging from telemetric navigation systems and aircraft instruments to space shuttles and satellite systems. But today, combined with the communication technologies and microcomputers, it is finding wider proliferation in many consumer products and industrial applications. For instance, the GPS systems, the sensors on board the mobile telephones, coupled together with application software make it possible to employ mobile instrumentation in many areas such as remote health monitoring, personal safety, and many other areas. In this chapter, as an example, the principles and the technology behind the mobile instrumentation of vehicular systems will be explained. Fully automated vehicles are being developed for applications in mining, industrial and personal transportation systems, underground and underwater explorations, and in military. In here, although one example is given in detail, the general principles will apply to many other and diverse ranges of applications. Some examples are also provided in chapters on radiolocation and radio navigation and in the chapter on wireless instruments.

87.1 Introduction

Wireless instruments consist of five main components—sensors and signal conditioners, programmable digital hardware, memory and storage, input/output and communication components, and others, for example, interface with computers, displays, keypads, and power supplies. A typical wireless instrument is illustrated in Figure 87.1. Instruments differ from each other by the way that they transmit, handle, and display information.

Recent developments in technology related to wireless instrumentation and sensor networking have significantly impacted the cost, capabilities, and efficacy of using wireless networks to implement mobile data acquisition, measurement, and control systems. Design engineers architecting wireless sensor and control systems are taking advantage of advances in low power operation, new chip-level system on a chip (SoC) device, and increasingly sophisticated wireless modules that benefit from higher levels of integration. Applications for mobile and remote platforms may now incorporate battery-powered sensor nodes to augment data collection in systems for which mains power may be unavailable and wiring for communications networks is unacceptable.

Previous limitations placed on battery-powered sensor networks involving wireless communications range, power consumption, network topologies, and physical footprint available for mounting have been effectively addressed using newly available devices and protocols. Advances in the state of the art are also mirrored in the embedded processing space, with new microcontroller and microprocessor offerings that also consume less power while offering greater processing speed and improved on-chip peripherals including memory, I/O, and mixed signal capabilities.

Leading practitioners in this field have successfully leveraged recent advances in wireless sensors and enabling technologies to develop novel Vehicle Area Network (VAN) applications that augment and replace existing wired sensor and control networks for mobile asset monitoring in the commercial and military space. These applications take advantage of wireless sensor networks to provide functionality that would not otherwise be possible or practical using traditional wired networks or directly wired sensors. Such applications include distributed tire pressure monitoring system (TPMS), planetary gear temperature sensors for armored vehicles in military applications, aerial platform sensors for "bucket trucks" used in utility service applications, remote digital level sensors to measure and report precise angles of operation for deployment of boom-mounted augers used on "digger derrick" trucks, and precise measurement of drill head position to calculate boring hole depth in mining applications. An example of a commercially available wireless vehicle sensor node that is able to run on battery power for up to 10 years and communicate vibration, temperature, and up to four additional analog inputs via 802.15.4 wireless is shown in Figure 87.2.

Central to mobile asset sensor network efficiency is a sensor or telematics hub, which serves as a bridge to connect wired and wireless data streams and to provide a "central" location for data storage and processing. The wireless sensor hub may also serve as a waypoint prior to moving data off platform to an enterprise application or server. The transport of sensor data off the mobile asset may be performed wirelessly, utilize direct wired connection or what is euphemistically referred to as "sneaker net": using

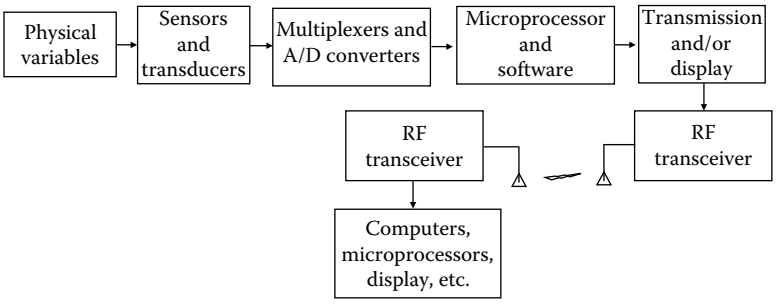

FIGURE 87.1 Components of a wireless instrument.

FIGURE 87.2 Ruggedized wireless wheel vibration and temperature sensor. (Courtesy of Solidica, Inc., Ann Arbor, MI.)

a USB stick or flash memory card as transport mechanism. Telematics and sensor hubs can typically be implemented as either an embedded device in which all processing and I/O are self-contained or by utilizing a ruggedized laptop or other computing resource running a high-level operating systems such as Linux or Microsoft Windows. Both implementations have advantages and disadvantages including cost, size, power consumption, and systems administration overhead. Additionally, the requirements (and constraints) for on-platform sensor networks are typically vastly different than for enterprise networks; a wireless sensor or telematics hub must be able to accommodate both. An overview of a complete system-wide implementation is shown in Figure 87.3.

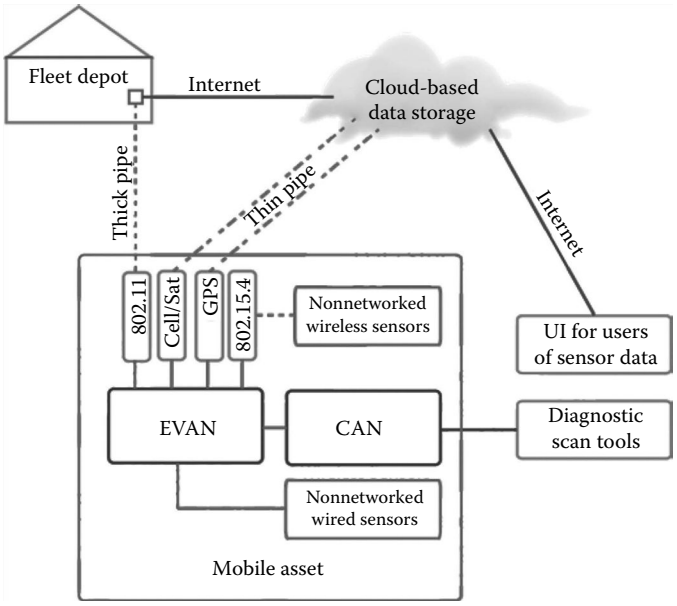

FIGURE 87.3 System-wide EVAN-based architecture.

This chapter provides an overview of the design methodologies for both the wireless sensor hub and the wireless sensor network itself. Advantages and disadvantages of various approaches to constructing wireless sensor networks using dedicated, embedded devices as well as those utilizing generic computing platforms will be discussed. Several real-world examples of VAN implementations will be considered with special attention given to what may be accomplished in commercial and military applications that consist of a multimode telematics hub and a connected sensor network. Considerations and competing requirements such as data security versus computing resources will be examined within the context of establishing wireless sensor networks for various applications and their enterprise requirements.

87.2 Wireless Hub Design Considerations

87.2.1 "PC"-Based Hub Design Approach: PCVAN

Common designs for wireless hubs fall into two broad categories: embedded designs based on microcontrollers or small microprocessors and "PC"-based designs that leverage the x86 architecture and widely available operating systems and expansion hardware. We will refer to this approach as PCVAN.

Designing a PCVAN wireless sensor network hub around an architecture originally used to implement desktop personal computers and industrial control systems has the advantage of being able to incorporate a diverse set of hardware, software, and operating systems available from a wide range of suppliers and OEMs. Development tools are also particularly easy to come by: the same compilers, network protocol stacks, debugging tools, etc., as used for designing PC applications may be leveraged to develop a wireless sensor hub for almost any application.

The development cycle itself for a PCVAN solution may be also significantly shortened using this approach, as applications may be developed, modeled, and test units fielded with readily available, inexpensive hardware designed for operation in a desktop or lab environment, and later refined to use more specialized (and expensive) hardware able to withstand extremes of temperature, shock, vibration, and environmental hazards such as saltwater intrusion.

87.2.2 Form Factor

Choices of platform form factor also exist that must be considered during the design process. Single-board computers (SBCs) that natively run Microsoft Windows, Linux, and real-time operating systems (RTOS) are available in small form factors, rated for industrial temperature and vibration and housed in NEMA-rated enclosures. Although business, residential, and light industrial applications may not require a "hardened" approach to design, and an inexpensive laptop computer is often all that is required, the harsh environment present in mobile and remote asset operation requires that all aspects of the hub be able to withstand daily abuse. Ruggedized laptops, such as the Panasonic Toughbook™, have been successfully employed in commercial, military, fire, police, and other similar telematics applications, although they come with a high initial capital costs.

87.2.3 Network Support

The use of "PC"-related hardware and software also has advantages insofar as wireless network support is concerned. Support for 802.11x (Wi-Fi) as well as Bluetooth wireless networks is commonly provided directly on the system motherboard, with additional sensor network hardware such as 802.15.4 easily added through the use of third-party adapters connected through a USB port or installed internally on an appropriate I/O expansion port.

Any connection to wired networks that may be present on a vehicle or other mobile or marine asset will typically require a protocol converter interface as direct support for mobile and industrial networks such as controller area network (CAN) may not be natively supported on the processor hardware.

For example, support for the J1939 CAN network for large vehicles and trucks might be provided through the use of an internal expansion card, a CF or SD form factor expansion card, or an external protocol converter "box" connected via an RS-232 or USB serial cable. It is important to note that software device drivers available from the manufacturer of the network interface may not be available for a given operating system or may require that additional software protocol stacks be purchased or written in order to support a given vehicle network.

For example, although a generic CAN interface card may be supported by the host hardware and operating system environment, additional drivers are required to support the specific CAN network present on a vehicle or remote asset. SAE-J1979, SAE-J1939, DeviceNet, and CANopen each require a unique protocol stack and may communicate over different network speeds to talk to a supported device on the network, even though the physical CAN network interface hardware is identical for each.

87.2.4 Processor, Memory, and I/O Considerations

The choice of processors for use of an "x86"-based PCVAN architecture typically centers on low cost, lower power microprocessors such as the relatively new Intel Atom family, as well as the well-established advanced micro devices' Geode processor family. Both support Microsoft Windows and Linux operating systems and are available in pre-integrated SBC's and motherboards in a variety of form factors. Memory and mass storage may be sized appropriate to the application and directly connected to the SBC or motherboard through OEM standard interfaces such as SATA and therefore not require special adapter cards for installation.

87.2.5 Power Supply Selection

Most "x86" motherboards, laptops, and SBCs utilize power supply bricks that expect 19 V DC for operation. For systems able to operate from mains power, an external AC adapter provides operating current to the unit. For mobile and portable applications, however, 12 or 24 V DC is more common and will require an appropriately sized DC to DC power converter.

87.3 Implementing I/O for Vehicle and Mobile Assets

Although analog and digital signal I/O is typically not part of the default architecture for SBC's and motherboards, adding connectivity features for PCVAN-based systems is supported by an entire industry dedicated to this task. Connecting thermocouples for measuring temperature, for example, is easily accomplished in much the same was as adding wireless sensors: Attach the needed I/O using externally available serial or network ports or use internal I/O expansion connectors supplied by the OEM to achieve any desired complement of analog, digital, or mixed signal expansion. One important point to note is that such expansion typically defaults to the voltage range most commonly associated with laboratory gear, providing direct connection to sensor signals in a ±5 or 10 V range. Although perfectly acceptable for tabletop or laboratory installations, additional signal conditioning modules will need to be installed between an A/D converter, for example, and a nominal vehicle voltage of 13.8–28 V, depending on the platform for the installation. Note also that most vehicle sensors and actuators operate in "single-ended" mode and may not require much in the way of signal conditioning to "knock down" system voltages for reading by the sensor network hub.

For example, a simple resistor divider network can perform the task to make a 13.8 V alternator output signal readable by an analog-to-digital converter designed to accept up to 5 V. This approach, however, introduces noise on the signal (resistors = noise!) but is generally acceptable in automotive applications, where tolerances are less stringent due to the inherently noisy nature of a vehicle electric subsystem. Using an A/D converter card with buffering provided by an instrumentation amplifier will provide a far less noisy signal and increase the input impedance to several MΩ at the same time.

This may be especially important in situations where it is desirable not to "load" an electric signal present on a vehicle subsystem. Excess loading by devices that present too low input impedance may adversely affect the system under test and measurement, resulting in poor readings and possible system malfunction.

87.3.1 Data Throughput Considerations

Another area of concern for measurement of vehicle systems is related to the sample rate, accuracy, and resolution of the analog data acquisition system being used. Contrary to the "more is better" principle typically applied when measuring and testing electric subsystems, the noise floor present in automotive systems renders as irrelevant extremely fast, high-accuracy data conversion. For example, using a 16 bit A/D converter to measure a source that itself may only be accurate to 10 or 12 bits is a waste of effort and may indeed only increase the perceived noise in the measurement itself, making the task of post-processing data more difficult. Likewise, sample rates must be specified in a manner consistent with the signal under measurement: there is no point in measuring data from a thermocouple attached to a hydraulic subsystem at 100 kHz if the fluid temperature varies slowly, as is usually the case. Samples for this kind of measurement need only be taken at once per minute in most cases. Reducing the data sample rate to values that are reasonable for the system under test generates data sets that are smaller and more manageable and reflect a better understanding of the problem to be solved.

87.3.2 Analog versus Digital I/O Considerations

Sometimes it is required to detect state change in a vehicle electric system, for example, by reading the voltage present on a vehicle switch, dial, or other actuator to determine if a subsystem is energized or otherwise activated. It is common practice to attach an A/D input to a vehicle cab dome light to infer if a driver or passenger side door is open or closed. This type of measurement presents two difficulties: The first difficulty is related to "using up" an A/D input on what is essentially a "digital" (on or off) measurement, and the second difficulty is dealing with this type of "open-switched" signal, which varies from an electric "open" circuit when not used, to a grounded, "logic-zero" state for low-side drive systems or a "logic-one" state at 13.8 V, for systems that switch system electric power to the device under measurement. Thus, inputs being read by an A/D system may only have a defined state when energized and be left floating in an ambiguous logic state when not in use.

Both issues are readily addressed by using a dedicated "digital" input (if available on an I/O adapter) instead of an analog input and by implementing a pull-up or pull-down resistor circuit on the signal line under test. In the previous example of detecting a "door-open" condition, an inexpensive 4.7 kΩ resistor may be connected between the signal line and the ground on the "high side" of the cab dome light: Logic 0 (ground) will be read when the circuit is un-switched an open, and logic 1 (13.8 V) will be present when the door is open and the dome light is switched on.

Of course, the use of any external signal I/O would only be required for signals that are not represented on a vehicle network bus as described earlier in this chapter. The vehicle and the engine OEM have already taken great pains to place their most important state and operational data on the vehicle network, in effect turning the vehicle into its own piece of dedicated test equipment. The manufacturer will also have previously determined and implemented appropriate data sampling rates, accuracy, and resolution for each sensor and subsystem on the vehicle. Taking advantage of this resource reduces overall system complexity and cost while decreasing the development effort and time required for implementation.

87.3.3 Data Acquisition Using Asynchronous Network Sources

Another important difference between wireless vehicular test, measurement, and control applications from more traditional laboratory and industrial applications is the concept of asynchronous data

present on the vehicle network and the more commonly employed synchronous sampling methodologies employed elsewhere. For example, many engineers familiar with traditional analog data acquisition equipment will be familiar with the concept of "aggregate data sample rate" specifications for test equipment. A ten-port analog data acquisition module with an aggregate sample rate capability of 100 kHz would be able to be programmed to concurrently sample data from all ten ports at 10 kHz each, or 5 inputs at 20 kHz, or one input at the full device bandwidth of 100 kHz. This common paradigm of dividing total sampling capacity by the number of inputs may leave an engineer that is not familiar with the asynchronous nature of vehicle network traffic confused by the very nature of how data is presented on a network: Some items may be reported with regularity, such as a temperature being reported once per second. Other items, such as speed, O_2 sensor, throttle position, and fault codes, may be present at varying rates on the network, and values will have to be interpolated or simply thrown away if the engineer tries to fit asynchronous data collection and reporting into methodologies that are designed around synchronous data collection and analysis.

Another area of concern occurs when "request/response" techniques are misused to increase data reporting rates on a vehicle network. If a vehicle network is asked to report vehicle speed many times greater than would otherwise be typical to decrease "granularity" in speed data reporting, other systems might not have network bandwidth left to operate. A common problem encountered when an engineer miscalculates network utilization is such a manner as to overwhelm system messages that may render a vehicle inoperable by dint of preventing system messages from being correctly sourced and delivered: dashboard and lower-priority messages fail first, with unpredictable behavior evident on the affected subsystems. As bus utilization grows further, the vehicle may enter its default "limp-home" mode or fail to operate altogether.

87.3.4 Disadvantages of Using PCVAN-Based Hub Design Approach

Although there are considerable advantages of PCVAN-based designs for implementing a vehicle area wireless test measurement and control network, there are inherent disadvantages of this approach that include high power consumption, physical footprint, large memory footprint, large total code size required for running applications, difficulty ruggedizing and enclosing such systems, large overhead in systems administration, time-stamp "skew," poor real-time performance for data event processing, lack of adaptability/scalability, and expense. Additionally, although using a PC-based architecture is often associated with a large available pool of software developers already familiar with the platform, the developers often struggle with unique challenges posed by automotive and remote application development that is more typical of the challenges faced by those with experience programming for embedded systems.

87.4 Embedded Vehicle Area Network Hub Architectural Overview

A rapidly emerging approach to remote mobile sensor applications that addresses many of the challenges embodied in the PCVAN approach is the Embedded Vehicle Area Network (EVAN) design philosophy. These new breed of low power devices offer a stand-alone, integrated device that incorporates multiple-wired and wireless sensor networks including 802.11b/g, 802.15.4, 2G and 3G cellular, SAE J1979 and SAE J1939 Vehicle CAN, SAE J1708 Vehicle Diagnostic Network, USB, and Ethernet. Also integrated into these new platforms are a variety of analog and digital data acquisition and output capabilities, GPS, real-time clock with battery backup, wide-input voltage-range vehicle power supplies, and water-proof, rugged enclosure with automotive grade connectors. Additionally, module high-value-added sensor subsystems such as TPMS desired for retrofit applications can be provided internally through an expansion connector that mates with the TPMS OEM adapter card. An example of a commercially available EVAN is shown in Figure 87.4.

FIGURE 87.4 Commercially available EVAN device with J1979, J1708, J1939, GPS, cellular, 802.15.4, and 802.11b/g capability. (Courtesy of Solidica, Inc., Ann Arbor, MI.)

87.4.1 Using Microcontrollers

In an EVAN, a dedicated 32-bit microcontroller provides the computational bandwidth required to process and transport multiple data streams to and from various networks simultaneously. The use of an integrated microcontroller offers significant advantages over using a microprocessor as described in the previous examples. Most modern microcontrollers, such as the Freescale ColdFire and ARM core variants, offer deterministic interrupt latencies for true real-time interrupt handling, thereby permitting highly efficient data acquisition, manipulation, and storage algorithms that are not possible when using an "x86"-style processor that was designed originally for desktop computing requirements. Modern microcontrollers also include significant complements of on-chip memory, including single-cycle access RAM, FLASH, and EEPROM (or equivalents) that permit faster interrupt handling and highly efficient data manipulation and buffering on a single die. This also permits the system to run at higher "MIPS per watt" ratios, reducing system power consumption and heat generation. A typical RISC-based microcontroller, using only on-chip memory and peripherals, may consume several orders of magnitude less power to perform essentially the same task set as a larger and faster microprocessor-based approach that would otherwise require significant off-chip memory and I/O resources.

87.4.2 Always Watching!

Significantly, this design approach permits an embedded wireless hub to operate in an "always-on" mode, where the system may operate even when the vehicle is turned off or the remote asset has limited power generation capabilities. Typical configurations will involve having the unit "sleep" when a vehicle engine is off and waking up periodically to check system status and report significant events that would otherwise go unnoticed on PCVAN devices that can operate only when the engine is running. PCVAN solutions that feature low power shutdown or sleep modes are also constrained by what kind of events may be used to "wake up" the device. A hardwired ignition input may be required, as opposed to being able to wake up on a vehicle network or wireless network message. Additionally, current draw for a PCVAN device is too prohibitive for frequent "wake-up" cycles, further limiting their effectiveness. Most newly emerging EVAN systems consume less power when operating than PCVAN approaches consume while "sleeping."

Vehicle electric systems are notoriously difficult to diagnose when there are intermittent failures; the value of an always-on EVAN system is magnified when it is also used to continuously monitor the vehicle during engine starting and shutdown, which places the most demand on the vehicle battery, alternator, and associated electronics. An EVAN system will always able to track electric system behavior,

whereas a PCVAN approach will miss the most taxing part of vehicle operation while it is booting an operating system or recovering from standby.

Data, configuration information, and run-time software may be buffered locally on SD card–based flash memory cards to provide features such as store and forward of vehicle network and sensor data for transmission off platform via Internet and corporate intranet connections. Platform firmware upgrades may also be remotely uploaded in situ while the unit is in service. Another advantage of the code efficiency and use of "lightweight"-embedded RTOS use in the EVAN approach is that large off-line storage and rotating physical media are not required. Booting is usually direct from on-chip flash memory, and system size, complexity, expense, and power are thereby significantly reduced.

The power and flexibility inherent in the EVAN architecture allows the platform to be used in a wide variety of fleet telematics and remotes sensing applications and use cases, from straightforward asset monitoring and remote diagnostics of long-haul trucking fleets to highly specialized applications such as electric utility areal platform work trucks that require wireless monitoring of hydraulic fluid pressures and temperatures in addition to vehicle network sensor awareness.

87.4.3 Additional Design Considerations for EVAN Wireless Vehicle Networks

When designing a wireless sensor network using an EVAN approach for use in a mobile asset, it is often important to take advantage of any features that may be present in an existing network that is "organic" to the platform, such as an existing wired vehicle network. Modern commercial, consumer, and military vehicles incorporate one or more vehicle networks to establish sensor and control communication between electronic body, engine, and transmission modules in place of the direct point to point wiring that dominated the electric systems of legacy vehicles. The use of such networks serves to save space, eliminate costly and failure prone wiring harnesses, improve vehicle safety, and provide operating features that would not be otherwise possible. Servicing a modern vehicle will typically involve the connection of a "scan tool" to one or more on-board diagnostic (OBD) ports to read and reset trouble codes, reprogram or update the firmware of an attached control module, directly query an attached sensor, or read system voltage and current values of interest.

Early designs (OBD 1) would incorporate the majority of functionality in the engine control unit (ECU), where test equipment would be connected to an access point located in the engine compartment for service purposes. Modern vehicles have a more distributed approach to data processing and control, wherein functionality is distributed throughout the vehicle among intelligent nodes connected over a vehicle network such as the SAE-J1939 and SAE-J1979 CAN. This approach lends itself to the combined use of small, simple "body modules" for such functions as door lock and window control and more sophisticated modules for engine and transmission control. Multiple vehicle networks may be also employed where a secondary network is dedicated for high-speed real-time control messages between the ECU and a transmission module, for example. Such systems typically have a diagnostic and debug connector for network access in the passenger compartment of cars and light-duty trucks (J1979 OBD 2) or in the vehicle cab (J1939) for heavy truck, bus, and military vehicle applications. A simple schematic of a modern automotive network configuration is shown in Figure 87.5.

The presence of a vehicle network also presents an opportunity for designers of vehicle sensor and telematics equipment to utilize data available on the network to supplement the data to be used in the wireless network as many data items of interest may be collected without requiring the installation of additional sensors to the vehicle. For example, fuel level, battery voltage, vehicle speed, engine speed, and oil temperature and pressure are all available to be read directly on the vehicle network and may be used in conjunction with other sensor data for whatever use case is desired. Although originally designed to be used for service applications and emissions testing purposes, the use of a vehicle network for other applications such as data acquisition and control has become commonplace. Using EVAN architecture increases the efficiency and reliability of processing and managing this heterogeneous data flow.

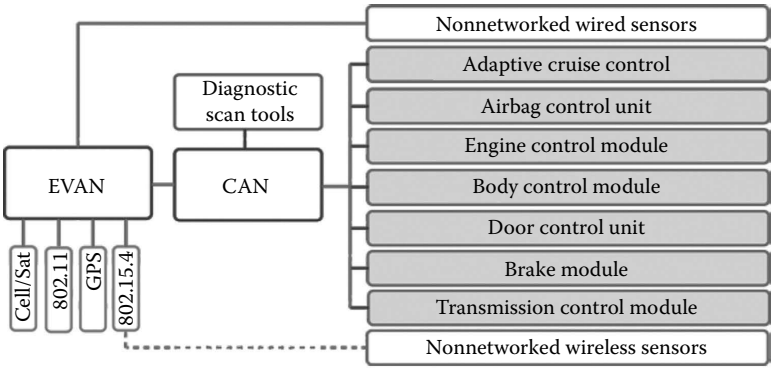

FIGURE 87.5 Modern network schematic with inclusion of EVAN hub.

87.4.4 Peripherals

The microcontroller-based EVAN devices are able to take advantage of on-chip peripherals such as Ethernet, USB, UARTs for legacy serial devices, timers, DMA controllers, and built-in analog and digital I/O that would otherwise need to be added to a PC-based VAN through the use of additional hardware peripherals otherwise not present on the microprocessor itself. This allows the EVAN to be designed using far fewer components, further reducing cost, size, and power consumption and increasing reliability.

87.4.5 Divide and Conquer

Recent advances in microprocessor integration have also revolutionized the off-chip peripheral options as well. For example, in order to implement 802.11x Wi-Fi for a PCVAN, a digital radio subsystem will typically be added to the motherboard, with the Wi-Fi protocol stack and TCP/IP stack left to be implemented on the "x86" microprocessor in addition to all of the other tasks it is expected to perform. An embedded VAN approach, however, may use a highly integrated Wi-Fi module, available from multiple OEMs, which completely encapsulates the Wi-Fi and TCP/IP stacks on its own microcontroller, thereby freeing up the host micro to concentrate on its core mission.

Such highly integrated, microcontroller-based modules are readily available to cover a wide variety of embedded applications including cellular machine to machine modems, GPS, Bluetooth, TPMS, and 802.15.4 support for ZigBee and numerous other wireless network protocols. Such modules leverage the advantages described earlier by encapsulating their functionalities and offering direct, "no glue logic" connection to a host processors serial UART or SPI peripheral complement.

To preserve the advantages in low power operation offered by the highly integrated host microcontroller, most wireless peripherals offer their own internal low power sleep and shutdown modes, enabling an even lower power budget for the system as a whole.

87.5 EVAN Power Supply Design Considerations

To further reduce current consumption, increase reliability, reduce size, and permit remote battery-powered operation in addition to using vehicle power, a large assortment of new, highly efficient power supply modules are available to leverage an EVAN design. Because the total power consumption of an EVAN device is able to be orders of magnitude less than a PCVAN approach, alternate designs may be used to provide power to the system. Wide-input voltage-range switching supply modules with greater than 90% efficiency are now available from many manufacturers. At less than a square

centimeter in area, the modern switching regulator is far smaller than the power supply brick required to operate a PC or laptop. An integrated switching supply module is typically built directly on the EVAN board, as opposed to residing a dedicated off card module. Because the total current needed to be supplied is relatively low, these devices often have an input voltage range of 6–36 VDC, which enables direct connection to 12 or 24 V vehicle electric systems with no external DC to DC converter required.

Another power supply "trick" that may be employed to further reduce current draw and permit always-on operation is the use of a small low-dropout linear regulator to supply power to the host microprocessor when in sleep mode. This permits the host to physically shut down the main switching regulator when not needed, further reducing current consumption.

For supplying power to "hungry" onboard peripherals, such as a Wi-Fi module, the use of a dedicated current switch or switching regulator may also be employed to electrically remove the device from the system when not needed. A well-designed EVAN will thereby only have peripherals in a powered on state when actually required for operation, further reducing the total system power budget. This is in stark contrast to the design choices presented for a PCVAN approach, where many (or all) of the system peripherals will be powered up at the same time.

86.6 Physical and Electric Footprint Advantages

The EVAN approach offers an increase in efficiency and reduced footprint and mounting requirements over the PCVAN approach, thereby allowing applications to exist that would otherwise be impractical to implement. For example, with an EVAN design, it is now possible to place wireless telematics devices in otherwise inaccessible locations, such as the bucket of an aerial platform rig for power line maintenance.

Because the nature of the electric power line service marketplace, which require that the bucket and support arm be free of electric wiring of any kind, a battery-powered EVAN may be placed on board the device to monitor position, vibration, and abuse and determine hours and modes of operation that would not be possible if a large, power-hungry PCVAN were to be used.

Numerous examples of EVAN installations are possible in a diverse range of enterprise applications for which use of a PCVAN is not suitable, such as battery-operated use in a refrigerated cargo container, unpowered trailer asset monitoring, pallets, remote pumping stations, weather and road condition monitoring, factory automation, shipping containers, and large fleet deployments where the expense and the maintenance overhead associated with a PC-based design approach are not workable.

Bibliography

Eren, H., *Electronic Portable Instruments-Design and Applications*, CRC Press, LLC, Boca Raton, FL, 2004.

Eren, H., *Wireless Sensors and Instrument Networks—Networks Design and Applications*, CRC Press, Boca Raton, FL, 2006.

Erl, T., *SOA Design Patterns*, Prentice Hall, Upper Saddle River, NJ, 2009.

Jamsa, J. and Luimula, M., Advanced car navigation: Future vehicle instrumentation for situation-aware services, *12th IEEE International Conference on Mobile Data Management (MDM 2011)*, Lullea, Sweden, pp. 7–10, 2011.

Johnson, K. and Fortson, F., Sense and respond, lessons learned in support of condition-based maintenance programs through data acquisition, analysis and secure transmission, *Ground Vehicle Systems Engineering and Technology Symposium Technical Paper Publication*, Vol. 2, pp. 531–538, August 2010.

Mariusz, M., Zabiegaa, B., and Namiesnic, J., Mobile systems (portable, handheld, transportable) for monitoring air pollution, *Critical Reviews in Analytical Chemistry*, 42(1), 2–15, Taylor & Francis Inc., 2012.

Pecht, M.G., *Prognostics and Health Management of Electronics*, Wiley, Hoboken, New York, 2008.

Zhong, H., Li, P., Hu, Y., Lv, Z., Yin, J., Yu, B., and Wu, J., Solution for the data collection in the field survey based on mobile and wireless GIS, *18th International Conference on Geoinformatics*, Beijing, China, IEEE, Piscataway, NJ, p. 5, 2010.

88

Powering Autonomous Sensors

Manel Gasulla
Universitat Politècnica de Catalunya

Maria Teresa Penella
Urbiotica S.L.

Oscar Lopez-Lapeña
Universitat Politècnica de Catalunya

Wireless sensor networks (WSN) have recently become feasible thanks to reductions in the power consumption of the sensor nodes and to the advent of specific communication standards and commercial transceivers. However, for WSN to thrive, several challenges must first be addressed, including power supply to the nodes.

Primary batteries provide a simple solution to power the sensor nodes. However, batteries have a limited energy, and their replacement can increase the maintenance costs and become unpractical or even unfeasible. Harvesting energy from the ambient is an alternative. This chapter presents both powering alternatives with a higher focus on the second one. First, autonomous sensors are described. Then, the main characteristics and differences between primary batteries and energy harvesters are presented. Finally, a focus is given to some specific parts of energy harvesters such as the ambient energy sources, the related energy transducers, and the energy storage devices.

88.1 Autonomous Sensors

Autonomous sensors are measurement devices in which cables are not used for transmitting data or for the power supply. They serve as the nodes of distributed data acquisition systems and WSNs and are used in numerous fields, including health care [1], aerospace [2], environmental monitoring [3], or Smart Cities [4]. To increase their autonomy, autonomous sensors seek to reduce their average power consumption by working in low-power modes whenever possible. They spend most of the time in *sleep* (standby) mode, and only *wake up* to perform specific actions—namely, measurement, processing, and transmission/reception of data [5].

* Most of the material of this chapter has extracted with kind permission from Springer Science+Business Media: *Powering Autonomous Sensors: An Integral Approach with Focus on Solar and RF Energy Harvesting*, 2011, Penella-López, M.T. and Gasulla-Forner, M.

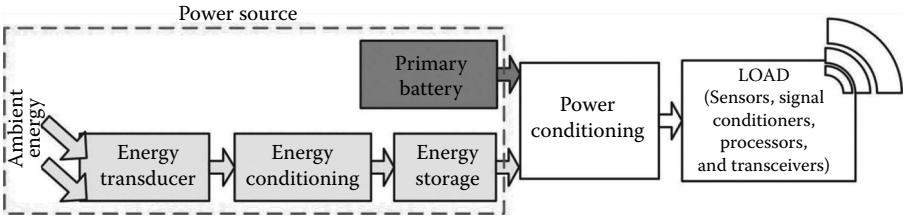

FIGURE 88.1 Block diagram of the power supply of an autonomous sensor. Either a primary battery (dark-gray box) or an energy harvester subsystem (light-gray blocks) can be used.

An autonomous sensor is usually composed of one or more sensors and their corresponding signal conditioners, a processor and a transceiver. Sensors convert a signal from a physical or chemical quantity to a corresponding signal in the electric domain. The sensors to be used depend on the desired application. A signal conditioner (or analog processor) matches a sensor output to the digital processor (usually, a low-cost microcontroller). Commercial transceivers are used for wireless communication. They transmit in the free-licensed ISM bands and can use a proprietary or standard (e.g., IEEE 802.15.4) protocol.

Power needs to be supplied to the autonomous sensor. Figure 88.1 shows a generic block diagram for the power supply. The left-hand rectangle with dashed line shows two options for the power source: either a primary battery (dark-gray box) or an energy harvester (light-gray blocks). Energy harvesting implies more complexity. An optional *power conditioning* stage matches the power source to the power supply requirements of the *load* (sensors, signal conditioners, processor, and transceiver).

88.1.1 Primary Batteries

Primary batteries provide a simple solution yet have several drawbacks, including size, limited energy storage, and poor indication of the remaining capacity. Whenever their replacement is unpractical or unfeasible, batteries with an adequate amount of energy (E_{bat}) for powering the autonomous sensor over its lifetime should be used. Thus, the required E_{bat} for a certain operation lifetime period, T_{op}, can be computed as

$$E_{bat} = \overline{P}_c \cdot T_{op} \tag{88.1}$$

whereby $\overline{P_c}$ is the average power demanded from the power source and includes the power demanded by the load plus the power losses of the different parts, such as that of the power conditioning stage or the battery itself. On the other hand, the peak-power capability of the batteries must be higher than the peak power demanded by the autonomous sensor. Small-size batteries, which are prone to be used with autonomous sensors, present rather high impedances and thus a limited peak-power capability.

88.1.2 Energy Harvesting

Energy harvesting enables autonomous sensors to run in nearly perpetual operation with little or no maintenance; however, it increases circuit complexity and is a fledgling technology that still poses certain challenges. Optical [6], mechanical [7], thermal [8] or even radio frequency (RF) [9] energies have been proposed. The energy harvester comprises a transducer, an energy conditioning stage, and an energy storage unit (Figure 88.1). The transducer converts ambient energy into electric energy with a given efficiency. Typical ambient energy sources operate with a certain degree of variability (e.g., night-to-day variability when harvesting solar energy); thus, an energy storage unit is needed to provide the demanded power flow to the load. An energy conditioning block is used to efficiently charge the storage unit from the output of the transducer. To maintain

sustainable operation of the autonomous sensor when harvesting energy, the average generated power $\left(\overline{P_g}\right)$ must comply with the following:

$$\overline{P}_g \geq \overline{P}_c \tag{88.2}$$

Here

- $\overline{P_c}$ includes the demanded power by the load plus the power losses of the energy and power conditioning blocks and of the storage unit
- $\overline{P_g}$ depends on the ambient conditions at the physical location of the node and on the efficiency of the transducer

The storage unit must supplement the power transferred to the load whenever $P_g < P_c$, whereby P_g and P_c correspond to the instantaneous generated and consumed power, respectively. Then, for any arbitrary long period of time, T, a long-term storage ($E_{storage}$) unit must fulfill the condition

$$E_{storage} \geq \max\left\{\int_T \left(P_c - P_g\right)\cdot dt\right\} \tag{88.3}$$

Both supercapacitors and secondary (rechargeable) batteries can be used as energy storage units and will be reviewed more extensively later on.

88.2 Ambient Energy Sources and Transducers

Thomas et al. [10] extensively described many energy sources for powering small-scale unmanned systems. Based on their initial classification, we have categorized harvested energy for powering autonomous sensors into five types: *radiant, mechanical, thermal, magnetic,* and *biochemical* (Figure 88.2).

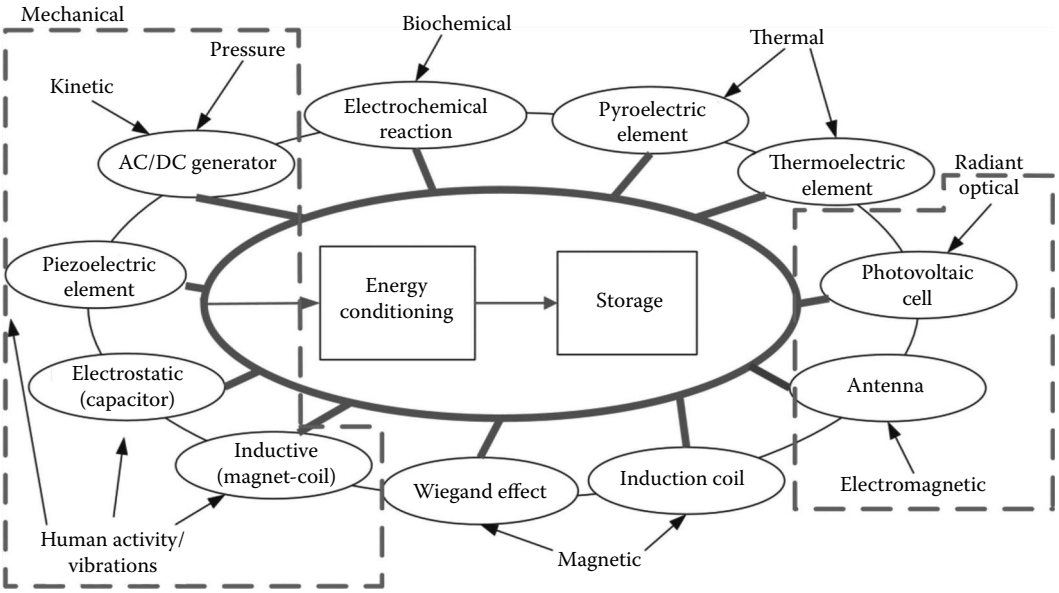

FIGURE 88.2 Energy sources and their respective transducers for powering autonomous sensors. (Adapted from Thomas, J.P. et al., *J. Power Sour.*, 159, 1494, 2006, with additional power sources added.)

Here, we consider energy already present in the environment, although in some cases energy can be expressly distributed, in a process called *remote powering*. Other analyses, more detailed descriptions, and typical power densities of energy sources can be found in the literature, for example, in [11] or [12]. The choice of the ambient energy source strongly depends on the ambient energy density at the autonomous sensor's location and on the load's power needs. On the other hand, energy transducers must be used to convert the ambient energy source into an electric output. Efficiency here is defined as the ratio of the transducer output power to its input power. In this section, we will briefly review different energy sources and associated transducers.

88.2.1 Radiant Energy

Radiant energy is emitted as electromagnetic waves, which includes radioactive, optical, and RF energy. Radioactive materials have extremely high energy densities, and their half-lives span from fractions of a second to millions of years. Radioactive properties can be found in uranium, nickel, or phosphorous isotopes among others. However, because these materials can be extremely dangerous, they must be confined to a closed volume. The energy from radioactive sources that emit alpha and beta particles can be converted by piezoelectric or betavoltaic elements, which determine their efficiency [13]. Commercial tritium batteries based on the betavoltaic effect are already available from City Labs.

Optical energy accounts to the portion of the electromagnetic spectrum spanning from infrared to ultraviolet light. Outdoors, optical energy chiefly comes from the Sun. Part of the energy radiated by the Sun is absorbed by the atmosphere; the rest arrives to the surface of the Earth as both direct and indirect radiations. On cloudy days, indirect radiation predominates. The available power density depends on several factors, including latitude, weather conditions, day of the year, and time of day. For example, at noon on a sunny day, the incident light on the surface of the Earth, in the Equator, can reach a power density of a little more of 1000 W/m^2. Indoor optical energy comes from outdoors (e.g., near windows) and from artificial illumination (e.g., incandescent and fluorescent bulbs). Optical power density, when the lights of a room are on, typically ranges from 100 to 1000 $\mu W/cm^2$. For autonomous sensors, optical energy is harvested via photovoltaic (solar) cells. A solar or photovoltaic cell is basically a semiconductor diode with a large p–n junction in the plane of the cell. A simple model includes a DC current source with a diode in parallel. Most current solar cells are silicon based and fall into one of three categories: monocrystalline, polycrystalline, and amorphous. Their efficiencies at full Sun range from less than 20% for monocrystalline cells down to 5% for commercial amorphous cells. Crystalline cells are better suited for outdoor use, whereas amorphous cells work better indoors. Organic (dye-sensitized solar cells, DSSC) and fourth-generation solar cells are becoming more popular and commercially available (e.g., Solaronix or Dyesol).

RF signals are deliberately radiated by broadcasting station antennas and cellular phone antennas. The RF energy transducer is an antenna, which can be modeled as a voltage AC source in series with output impedance. The generated signals are of low amplitude, so a rectifier and a boosting stage must be used. Except for locations near transmitters, the available ambient power density is in the nW/cm^2 range [14], which is too low to be useful. An alternative to power autonomous sensors is to deliberately transmit RF power on the industrial, scientific, and medical (ISM) frequency bands. Some commercial products are already available (Powercast).

88.2.2 Mechanical Energy

Mechanical energy harvesting [7,15,16] is based on kinetic energy, the sources of which include liquid or gas flow, vibrations, human activity, and pressure variations (e.g., acoustic noise and atmospheric pressure). Available power in flow energy increases cubically with an increase in the speed of the liquid or gas. Low-level vibrations occur in machinery, outdoor windows, and transport vehicles; they produce frequencies between 50 and 200 Hz and acceleration amplitudes between 1 and 10 m/s^2. Human activity can actively or passively generate kinetic energy. Active human power requires deliberate movement,

whereas passive human power exploits common daily activities (e.g., heel strike while walking); indeed, nearly all the energy produced in daily activities stems from when legs are bent and from heel strike.

Mechanical energy can be converted to electric energy by one of the following conversion principles: electrostatic, piezoelectric, and electromagnetic. Electrostatic converters are based on variable capacitors. One plate is fixed, and the other changes with the mechanical force, thereby changing the value of the capacitance. One attractive feature is that they are IC compatible. Reversible electric polarization in response to strain from mechanical stress is called the *piezoelectric effect*. Electromagnetic induction, based on Faraday's law, refers to generation of a voltage in a conductor (typically a coil) located within a magnetic flux, usually generated by a permanent magnet. The generated signals are AC in all three conversion principles and must be rectified in order to power autonomous sensors. The specific energy conditioning stage must be tailored to each transducer type. Based on the electromagnetic principle, some commercial products have appeared that harvest energy from water by using miniature hydroelectric generators (Splashpower), produce energy form vibrations (Perpetuum), or even get enough energy when pressing buttons or switches in order to control lights in buildings (EnOcean). Other products are based on the piezoelectric principle (e.g., Midé, Arveni).

88.2.3 Thermal Energy

Thermal energy can be converted to electric energy by thermoelectric or pyroelectric transducers, among others. The former rely on spatial variations in temperature, whereas the latter rely on temporal variations in temperature. Thermoelectric generators, which exploit the Seebeck effect, comprise several pairs of alternating p- and n-type semiconductor blocks arranged thermally in parallel and connected electrically in series. They can be modeled as a DC voltage source in series with a resistance. Thermoelectric generators are typically built from Bi_2Te_3 or poly-SiGe, and their thermal resistance should be matched to that of the thermal source in order to maximize the harvested power. Optimizing the extracted power requires additional elements—namely, a heat sink for efficient dissipation of heat into the environment and structures, known as *thermal shunts*, which direct the heat that passes between the hot and the cold plates into the thermocouple legs [17]. There are several companies commercializing thermoelectric generators (e.g., EnOcean, Micropelt, Thermolife, Tellurex).

88.2.4 AC Magnetic Energy

AC magnetic energy [10] is available near AC current–carrying conductors (e.g., power grids), magnets, and electric rotating machinery. Electromagnetic induction in a coil can be used to convert AC magnetic energy into electric energy. The transducer (coil) can be modeled as an AC voltage source with inductive series impedance. Wireless nonradiative power transfer through strongly coupled resonant objects (also known as *magnetic resonance*) has been reported in [18]. Coil-to-coil efficiencies of up to 40% over a distance of 2 m were achieved by using coils of 60 cm of diameter. A related company (WiTricity) has been raised. The concept is similar to that already used in low-frequency RFID systems in which energy is transferred via magnetic coupling from a reader in order to power nearby tags. Inductive powering has also been applied in biomedical implants [19]. The same principle is also found in some commercial products (eCoupled), and recently the Wireless Power Consortium has been created in order to set international standards for interoperable wireless charging of mobile devices.

88.2.5 Biochemical Energy

Biochemical energy can be extracted by using fuel cells. In a typical cell, fuel is continuously fed to the anode compartment, and an oxidant (e.g., oxygen from air) is continuously fed to the cathode compartment; electrochemical reactions occur at the electrodes, producing an electric current. For biochemical energy, the fuel is biological material, such as enzymes, microbes, glucose, or marine sediment.

88.3 Energy Storage Units

Both secondary (rechargeable) batteries and supercapacitors can be used as energy storage units in energy harvesters for autonomous sensors. Both of them are electrochemical devices, that is, they consist of two electrodes and an electrolyte. However, in a supercapacitor, in contrast with a battery, no electrochemical reaction takes place [20]. In this section, secondary batteries will be first described. Then, supercapacitors will be presented and compared to secondary batteries. Simple circuit models of batteries and of supercapacitors will be shown. Finally, the combined use of batteries and supercapacitors (*hybrid storage*) and its utility for autonomous sensors will also be addressed.

88.3.1 Batteries

Batteries extract electric power from a chemical reaction. They comprise one or more basic electrochemical units known as *cells*, which are connected in series or parallel, to obtain the desired voltage and capacity. Each cell contains a negative electrode (an *anode*), a positive electrode (a *cathode*), and an ionic conductor (an *electrolyte*). The anode and cathode are physically isolated; the electrolyte provides the medium for charge transfer (via ions) inside the cell, between the anode and the cathode (Figure 88.3a). In practical cells, the anode and the cathode are mechanically separated by a partition material that is permeable to the electrolyte [20]. A battery can be readily modeled with a zero-order electric model similar to that shown in Figure 88.3b, whereby V_B models the open-circuit voltage and R_B models the equivalent series resistance (ESR). The value of V_B decreases with decreasing internal stored charge. The value of R_B depends on the chemistry, battery design, and temperature.

Power density mainly depends on the internal impedance of the battery, which is tightly related to the current collector area and the electrolyte conductivity. Some batteries are specially designed to promote power density through reduced internal impedance by maximizing the current collector area. However, batteries designed to improve power density also present higher self-discharge and lower energy density. Small batteries (e.g., button type) generally exhibit high internal impedance. In addition, battery impedance increases with an increasing *depth of discharge* (DoD) and *number of charging/discharging cycles*.

The rate of chemical reactions increases with increasing temperature. This principle has beneficial consequences (e.g., increased power density because the resistance decreases) as well as detrimental ones (e.g., higher leakage). The lower limit for a battery's operating temperature range is partially determined by the electrolyte's freezing point.

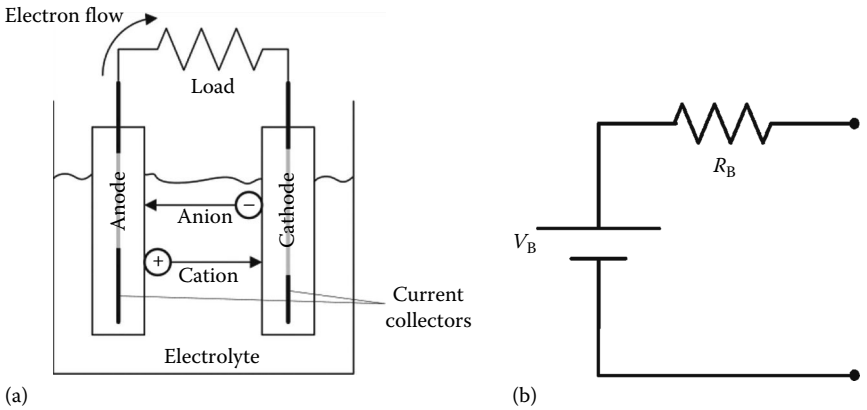

FIGURE 88.3 (a) Electrochemical cell at discharge and (b) a zero-order electric model.

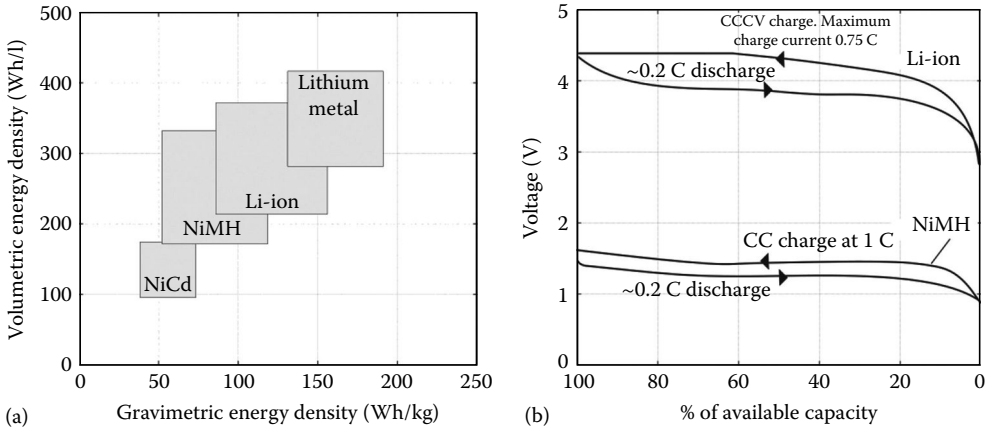

FIGURE 88.4 (a) Volumetric energy density plotted against gravimetric energy density for common secondary battery types. (Adapted from Linden, D. and Reddy, T.B., *Handbook of Batteries*, 3rd edn., McGraw-Hill, New York, 2001.) (b) Charge (at 1 C and 0.75 C) and discharge (at 0.2 C) curves for Li-ion and NiMH batteries.

The most widely used secondary batteries for portable and space-constrained devices are

- Lithium based (Li-ion and Li polymer)
- Nickel metal hydride (NiMH)

Figure 88.4a shows a plot of volumetric versus gravimetric energy density for typical secondary batteries. Metallic-lithium-based batteries offer better energy densities but present more safety risks. Batteries using lithium alloys in the negative electrode (e.g., button $LiAl/MnO_2$ batteries) imply less risks but at the expense of lower energy density and poor cycle life at deep DoD. These batteries are sold in coin configuration and are intended for low rate discharges. Lithium-ion batteries use lithium intercalation compounds as positive and negative materials. Over the past decade, they have become the most popular lithium-based batteries, as they are relatively safe and offer reasonably high energy densities. Lithium polymer batteries are Li-ion batteries that employ polymer-based electrolytes, which enable slimmer, and even flexible, designs. Figure 88.4b shows the charge and discharge curves for Li-ion and NiMH batteries. As observed in the plots, during charge, the battery voltage is higher than during discharge, which can be easily explained by the effect of the internal impedance. Lithium-ion batteries present higher voltage ranges than do NiMH batteries. Table 88.1 shows the principal characteristics of three of

TABLE 88.1 Principal Characteristics of the Three Main Types of Secondary Batteries

Battery Type	Li Ion	Li Polymer	NiMH
Internal impedance Z (mΩ)	30 to thousands	40 to thousands	50 to thousands
Overvoltage tolerance	Explosion risk	Damage risk	Temperature increase
Temperature range (°C)			
Charge	0–40	0–45	0–45[a]
Discharge	−20 to 60	−20 to 60	−20 to 60[a]
Self-discharge (% per month)	2	2.5	15–25
Cycle life (cycles)	500–1000	300–500	300–500
Float or calendar life (years)	>5	>5	4–6

Sources: Linden, D. and Reddy, T.B., *Handbook of Batteries*, 3rd edn., McGraw-Hill, New York, 2001; Woodbank Communications, Electropaedia, Battery and Energy Technologies, Available on: http://www.mpoweruk.com/ (accessed on 2nd August, 2012).

Note: Parameters are specified at 25 °C, otherwise specified.

[a] These are the permissible temperature ranges; however, the cell should operate as closely to room temperature as possible.

the most common types of secondary batteries. As can be seen, NiMH batteries present a higher self-discharge. Furthermore, the number of cycles is higher for Li-ion batteries. The cycle life is defined as the number of cycles at which the battery capacity decreases to 80% of its original capacity. The number of cycles typically increases with a decreasing DoD.

When harvesting energy from the environment, the charging current is usually quite low, thereby minimizing the need for complex charging and protection circuits. Simple over or under voltage protection circuits (e.g., a comparator plus a disconnection switch) can be considered.

Thin-film batteries are solid-state lithium batteries specially designed for integration onto silicon wafers, as they are very thin (micrometers). Both Li-ion and metallic-lithium thin-film batteries have been developed. They can sustain high temperatures (250 °C) for short periods of time and contain no liquid elements; therefore, they can support solder reflow [21]. Cycle lives of several thousands of cycles at room temperature and hundreds of cycles at 150 °C have been demonstrated [23]. These batteries exhibit energy densities of 100–1000 μWh/cm^2, depending on the cathode [24], and power densities (under continuous discharge) of up to 10 mW/cm^2 [23]. Therefore, their internal impedance is quite high compared to traditional Li-ion cells, which they otherwise resemble closely. There are companies that work on and commercialize these types of batteries, for example, Excellatron, Cymbet, and Infinite Power Solutions.

88.3.2 Supercapacitors

Supercapacitors feature activated carbon electrodes that have very large surface areas and that may be separated by distances as short as in the molecular range. These characteristics enable higher capacities per unit area than that of regular capacitors. The electrodes are impregnated with an electrolyte that enables charge transfer via ions. There are two types of electrolytes: *organic* and *aqueous*. Organic electrolytes provide higher voltage per cell and higher energy densities, whereas aqueous electrolytes lead to smaller cell-to-cell voltage differences.

Figure 88.5a shows a simple electric model for a supercapacitor, which is also used for regular capacitors, whereby C is the nominal value of the capacitor, R_C models the ESR, and R_{leak} models the supercapacitor leakage current. There are more complex supercapacitor models, such as one which includes several *RC* branches in parallel. Figure 88.5b shows an example with three *RC* branches and a parallel R_{leak} that models the supercapacitor leakage. The main branch (R_fC_f) is equivalent to CR_C in Figure 88.5a. The other *RC* branches model longer time constants (from seconds or minutes to days). Consequently, fully charging or discharging a supercapacitor may take several hours or days. However, C_f is much larger than the model's remaining capacitors, and consequently, so is its corresponding available energy. The leakage current is the current that passes through R_{leak} once the capacitor has been fully charged or discharged (i.e., the capacitors of all the branches) to some fixed voltage. Other complex models of supercapacitors can be found in [25] and [26].

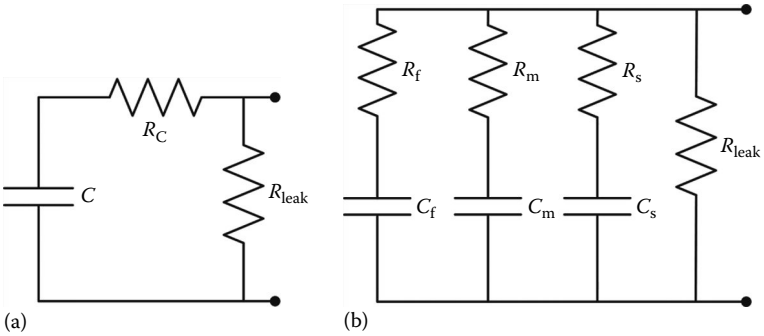

FIGURE 88.5 (a) Simple supercapacitor circuit model and (b) a more complex supercapacitor circuit model.

Supercapacitors designed for backup applications not only have a relatively high R_C (large voltage drop for a step current load) but also have a high R_{leak} (low leakage). Conversely, supercapacitors with very low R_C (tens to hundreds of milliohms) have a relative low R_{leak} (high leakage). Leakage current increases with increasing temperature (similarly to batteries) and with increasing voltage. Several companies offer supercapacitors, for example, Cap-XX, Maxwell, and AVX.

Compared to secondary batteries, supercapacitors feature energy densities of one to two orders of magnitude lower. However, their power densities can be much higher (and conversely, their internal impedances can be much lower) and offer longer lifetimes (in terms of the number of charging/discharging cycles). Additionally, their DoD can be easily obtained by measuring their OCV. However, the voltage decreases linearly with the DoD, which poses more challenges to the preceding energy conditioning stage and to the ensuing power conditioning stage. Moreover, supercapacitors with good power performance can be quite expensive. The advantages of secondary batteries and supercapacitors can be gained through their tandem use in *hybrid-storage units*, as will be reported as follows.

88.3.3 Hybrid Storage

Due to the internal impedance of the battery (Figure 88.3b) and the pulsed current profile of autonomous sensors, a voltage drop across the battery terminals appears at the activation time of the autonomous sensor. This phenomenon, which is more pronounced for high-impedance batteries, can hinder the full extraction of the available energy from the battery. Additionally, some power (and therefore, energy) is lost at the battery impedance. Small batteries are thus greatly affected.

Given that capacitors are complementary to batteries [27,28], they have been harnessed to increase the power capabilities of batteries, even in commercial products [29]. Storage units comprising a battery and a capacitor operating in tandem have been proposed for pulsed loads [30–32]. Whenever the internal impedance of the supercapacitor is much lower than that of the battery, the equivalent impedance of the hybrid-storage unit is dominated by that of the supercapacitor. Thus, when high-impedance batteries are equipped with an appropriate capacitor in parallel, their peak-power capabilities are enhanced, the power losses are reduced, and the amount of energy that can be extracted is increased. In [33], run-time tests using a sensor node as the load and an ML2016 lithium battery with and without a 0.1 F tandem supercapacitor were performed achieving run-time extensions up to 33% when using different power conditioning alternatives.

References

1. M. Zakrzewski, S. Junnila, A. Vehkaoja, H. Kailanto, A. M. Vainio, I. Defee, J. Lekkala, J. Vanhala, and J. Hyttinen, Utilization of wireless sensor network for health monitoring in home environment, in *Proceedings of IEEE International Symposium on Industrial Embedded Systems*, SIES, Lausanne, Switzerland, pp. 132–135, 2009.
2. S. Lintelman, R. Robinson, L. Mingyan, L. Bushnell, R. Poovendran, and K. Sampigethaya, Secure wireless collection and distribution of commercial airplane health data, *IEEE Aerospace and Electronic Systems Magazine*, 24, 14–20, 2009.
3. G. Barrenetxea, F. Ingelrest, G. Schaefer, and M. Vetterli, Wireless sensor networks for environmental monitoring: The SensorScope experience, in *Proceedings of IEEE International Zurich Seminar on Communications*, Zurich, Switzerland, pp. 98–101, 2008.
4. Urbiotica homepage. Available on: www.urbiotica.com (accessed on August 2, 2012).
5. A. Sinha and A. Chandrakasan, Dynamic power management in wireless sensor networks, *IEEE Design & Test of Computers*, 18, 62–74, 2001.
6. V. Raghunathan, A. Kansal, J. Hsu, J. Friedman, and M. Srivastava, Design considerations for solar energy harvesting wireless embedded systems, in *Proceedings of Fourth International Symposium on Information Processing in Sensor Networks*, Los Angeles, CA, pp. 457–462, 2005.

7. P. D. Mitcheson, E. M. Yeatman, G. K. Rao, A. S. Holmes, and T. C. Green, Energy harvesting from human and machine motion for wireless electronic devices, *Proceedings of the IEEE*, 96, 1457–1486, 2008.
8. S. Dalola, M. Ferrari, V. Ferrari, M. Guizzetti, D. Marioli, and A. Taroni, Characterization of thermoelectric modules for powering autonomous sensors, *IEEE Transaction on Instrumentation and Measurement*, 58, 99–107, 2009.
9. T. Le, K. Mayaram, and T. Fiez, Efficient far-field radio frequency energy harvesting for passively powered sensor networks, *IEEE Journal of Solid-State Circuits*, 43, 1287–1302, 2008.
10. J. P. Thomas, M. A. Qidwai, and J. C. Kellogg, Energy scavenging for small-scale unmanned systems, *Journal of Power Sources*, 159, 1494–1509, 2006.
11. S. Roundy, D. Steingart, L. Frechette, P. Wright, and J. Rabaey, Power sources for wireless sensor networks, in *Proceedings of 1st European Workshop on Wireless Sensor Networks*, EWSN, Berlin, Germany, pp. 1–17, 2004.
12. S. F. J. Flipsen, Power sources compared: The ultimate truth? *Journal of Power Sources*, 162, 927–934, 2006.
13. N. Mokhoff. (2006, October 27). IEDM feels the power. Online EETimes Europe. Available: http://www.eetimes.com/electronics-news/4065336/IEDM-feels-the-power (accessed on August 2, 2012).
14. J. A. Hagerty, F. B. Helmbrecht, W. H. McCalpin, R. Zane, and Z. B. Popovic, Recycling ambient microwave energy with broad-band rectenna arrays, *IEEE Transaction on Microwave Theory and Techniques*, 52, 1014–1024, 2004.
15. S. Roundy, J. M. Rabaey, and P. K. Wright, *Energy Scavenging for Wireless Sensor Networks, with Special Focus on Vibrations*, 1st edn., Norwell, MA, Kluiwer Academic Publishers, 2004.
16. S. P. Beeby, M. J. Tudor, and N. M. White, Energy harvesting vibration sources for microsystems applications, *Measurement Science and Technology*, 17, R175, 2006.
17. R. J. M. Vullers, R. van Schaijk, I. Doms, C. Van Hoof, and R. Mertens, Micropower energy harvesting, *Solid-State Electronics*, 53, 684–693, 2009.
18. A. Kurs, A. Karalis, R. Moffatt, J. D. Joannopoulos, P. Fisher, and M. Soljacic, Wireless power transfer via strongly coupled magnetic resonances, *Science*, 317, 83–86, 2007.
19. K. V. Schuylenbergh and R. Puers, *Inductive Powering: Basic Theory and Application to Biomedical Systems*, Analog circuits and signal processing series, Springer, New York, 2009.
20. M. Winter and R. J. Brodd, What are batteries, fuel cells, and supercapacitors? *Chemical Reviews*, 104(10), 4245–4270, 2004.
21. D. Linden and T. B. Reddy, *The Handbook of Batteries*, 3rd edn, McGraw-Hill, New York, 2001.
22. Woodbank Communications, Electropaedia. Battery and Energy Technologies, Available on: http://www.mpoweruk.com/ (accessed on 2nd August, 2012).
23. N. J. Dudney, Thin film batteries for energy harvesting, in *Energy Harvesting Technologies*, S. Priya and D. J. Inman, Eds., New York: Springer Science+Business Media, pp. 355–363, 2009.
24. N. J. Dudney, Solid-state thin-film rechargeable batteries, *Materials Science and Engineering B*, 116, 245–249, 2005.
25. S. Buller, E. Karden, D. Kok, and R. W. De Doncker, Modeling the dynamic behavior of supercapacitors using impedance spectroscopy, *IEEE Transaction on Industry Applications*, 38, 1622–1626, 2002.
26. J. N. Marie-Francoise, H. Gualous, and A. Berthon, Supercapacitor thermal- and electrical-behaviour modelling using ANN, *IEE Proceedings of Electric Power Applications*, 153, 255–262, 2006.
27. G.A. Rincon-Mora and M. Chen. (2006). Squeezing operational life out of a shrinking energy capsule. Power Management Design Line. Available on: http://www.powermanagementdesignline.com/howto/194500129 (accessed on August 3, 2012).
28. T. Christen and M. W. Carlen, Theory of Ragone plots, *Journal of Power Sources*, 91, 210–216, 2000.

29. Tadiran Batteries. PulsesPlus Batteries for High Current Pulse Applications. Available on: http://www.tadiran.com/index.php/pulses-plus-lithium-cells (accessed on August 2, 2012).
30. T. A. Smith, J. P. Mars, and G. A. Turner, Using supercapacitors to improve battery performance, in *Proceedings of 33rd Annual IEEE Power Electronics Specialists Conference*, PESC, Cairns, Queensland, Australia, pp. 124–128, 2002.
31. R. A. Dougal, S. Liu, and R. E. White, Power and life extension of battery-ultracapacitor hybrids, *IEEE Transaction on Components and Packaging Technologies*, 25, 120–131, 2002.
32. C. E. Holland, J. W. Weidner, R. A. Dougal, and R. E. White, Experimental characterization of hybrid power systems under pulse current loads, *Journal of Power Sources*, 109, 32–37, 2002.
33. M. T. Penella and M. Gasulla, Runtime extension of low-power wireless sensor nodes using hybrid-storage units, *IEEE Transaction on Instrumentation and Measurement*, 59, 857–865, 2010.

89

Wireless Sensing Technology

Gregory C. Willden
Southwest Research Institute

Ben A. Abbott
Southwest Research Institute

Ronald T. Green
Southwest Research Institute

89.1 Introduction and General Definition

While specialized wireless technologies have been used to aid the packaging and deployment of sensor systems for decades—particularly in telemetry systems—support has moved to more generalized wireless sensor network (WSN) systems. Commonplace cell and Wi-Fi backbones provide robust options for data delivery, and these mechanisms are further augmented by simpler, lower cost, and lower power delivery technologies such as Bluetooth, IEEE 802.15.4, ZigBee, and 6LoWPAN. Of late, the smartphone and smart-grid markets have accelerated-related technologies. This rapid growth, high competition, and innovative solution space should be considered when designing sensing systems that require small size, low power, and distributed solutions with limited or no interconnection wires. Unfortunately, the lexicon of terminology used within the markets overlaps and lacks precision, so this chapter focuses more on concepts as opposed to definitions. And since there are countless possible uses of the technologies, the chapter utilizes examples of the real systems and the lessons learned to provide a framework for making design decisions.

Much of the genesis of current wireless sensor technology can be attributed to the smart dust and subsequent research directions pioneered by Defense Advanced Research Projects Agency (DARPA) (www.darpa.mil). The work evolved into the creation of the "mote"* (based on the meaning of mote as a small spec or grain of dust). The systems involved low-cost, battery-powered sensors equipped with wireless networking capability. Some formulations included the ability for sensors to transmit data on behalf of other sensors to create a wireless mesh network for increased reliability.

* Use of the word "mote" is based on the meaning as a small spec or grain of dust. Application to wireless sensor nodes can likely be attributed to the Berkeley team performing on the DARPA smart dust project, but subsequently the term was adopted by many organizations.

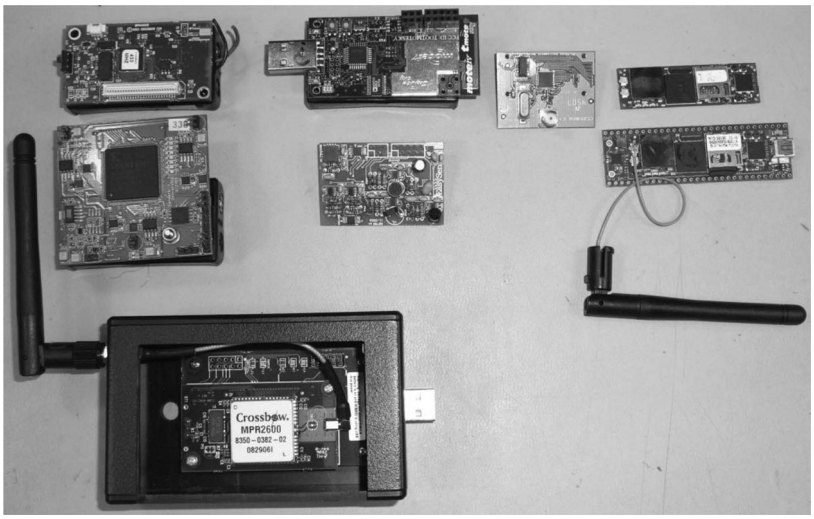

FIGURE 89.1 Example wireless sensor boards and processors (left to right): (upper left) crossbow mote WSN circa 2003, a spin-off of Berkeley mote development; (left middle) Xilinx Spartan-based application-specific mote expansion board; (bottom left) crossbow mote gateway module; (top) TMote Sky Berkeley mote; (middle) EasySen sensor expansion module for TMote Sky; (top) TI Chipcon CC2510 wireless processor evaluation module; (top right) Gumstix Overo computer on module; and (bottom right) Gumstix Pinto-TH Overo expansion module.

Generally speaking, a *wireless sensor node*

- Is battery powered
- Collects measurements
- Communicates wirelessly
- May employ mesh networking

89.2 Wireless Sensor Networks

WSNs are often formed by assembling a collection of wireless sensor nodes with a gateway node that provides data connectivity to the Internet, to the outside systems, or directly to the users in a closed system. A variety of technologies can be used in the design of wireless sensor nodes. Communication technologies vary in complexity, power requirements, maximum data rates, frequency bands of operation, and communication range. Approaches to increase system lifetime and minimize battery requirements are typically employed, and some systems employ energy-harvesting techniques that convert solar, wind, or kinetic energy to extend the life of the nodes. Processors used in wireless sensor systems are frequently highly integrated devices that combine onboard clocks, wireless communication, sensing electronics, and low-power modes into a single electronics chip or compact-printed circuit board. Figure 89.1 shows a few wireless sensor nodes of this class and examples of historical progression.

89.3 Choosing Reasonable Wireless Sensor Technology Solutions

At the height of the smart dust program* at DARPA, there was significant hype regarding the potential of this technology.† Many other research organizations, funding agencies, and universities joined in the race of working with motes as early adopters and applying them to a wide variety of projects.

* The smart dust project started in the late 1980s, and most of the work slowed by 2000.

† During this period of hype, the DARPA program management team commented to one of the authors that they hoped the technology became so ubiquitous that we would soon hear the phrase "Gee, the motes are thick today."

Online searches at the time returned headlines that boasted of how motes and smart dust would change our lives in areas as diverse as military combat, plant life, medical understanding, and pollution control. But today, we do not see the reality mirroring the magnitude of the dream as it had been envisioned. Minimum battery size, system power requirements, and packaging are among the limitations of the dream. While the technology has not lived up to the initial hype, the results of the smart dust program, and other related research, have produced valuable technological advances that should be considered when designing new sensor systems. Taking an objective look at successful wireless sensor designs and deployments will equip the system designer with a useful toolbox of capabilities and a measure of wisdom in how best to employ them to solve real-world sensing problems.

The following WSNs, which the authors developed or contributed to, illustrate design trade-offs and challenges associated with developing and deploying sensors in the real world. Each example concludes with a list of design trade-offs and how well they worked for the particular problem. We learned many things and hope you are able to utilize our lessons to build better systems of your own.

89.4 Example System: Perch and Move

The Perch and Move program [4] was funded by DARPA to demonstrate a remote surveillance and signal intelligence capability deployed on a portable autonomous helicopter. The wireless sensor portion of the program was designed to perform localization of handheld communication devices using radio-frequency (RF) signatures. The device was designed to meet strict size, weight, and power requirements and employed a low-cost Global Positioning Satellite (GPS) unit, a reverse-engineered radio for signal acquisition, and a digital signal processor for signal demodulation and analysis. Node-to-node communication was accomplished using a 9600 bit/s wireless modem. The GPS module provided Universal Time Coordinated (UTC) time and latitude, longitude, and altitude estimates. The module also provided a 1 pulse per second (PPS) signal accurate to approximately 40 ns. A least-mean-square algorithm was used to reduce l PPS jitter and increase the accuracy of time of arrival (TOA) calculations on intercepted signals. The system consisted of a group of homogenous sensors, some deployed on the ground and others on the airborne platform that jointly determined the location of a noncooperative transmitter using a time difference of arrival (TDOA) algorithm.

Radio-wave propagation modeling tools estimated the received signal strength and radio multipath effects for candidate sensor locations by generating city models from existing satellite imagery. Sensor battery life, vehicle flight times, platform stealth, noise, localization accuracy, and RF modeling all factored into a multi-constraint optimization for distributed coordination of sensor locations and flight paths. Design trade-offs and choices related to the development of the Perch and Move system are summarized in Table 89.1.

89.5 Example System: Localization for Landslide Measurements

Although monitoring of certain earth processes (e.g., volcanic eruption, flooding) may call upon very specific measurements (e.g., temperature, atmospheric or soil gas composition, water level), the precise knowledge of the location of sensor nodes is a universal data requirement and for some applications—such as surface displacement associated with a landslide—the only data requirement. According to the U.S. Geological Survey, landslides represent a widespread geologic hazard that results in hundreds of deaths and billions of dollars in property damage throughout the world each year.

WSN designers frequently pursue the ability for individual nodes to determine their own location by estimating node-to-node distances using the round-trip communication times to reference nodes at known locations. However, the primary limitations in this approach to the self-localization problem are the uncertainty created by the small frequency differences between the local oscillators on each node and the bandwidth of the communication signal. Typical localization accuracy for this approach is on the order of meters.

TABLE 89.1 Design Trade-Off Decisions for Perch and Move System

Design Element	Design Selection	Consequences
Power source	Lithium polymer battery	Pros: high power-to-weight ratio was required to extend limited flight distances and short station keeping times of the airborne platform to minimally acceptable levels Cons: cost and availability
Power conservation	Scheduling of sleep modes in an application-specific manner	Pros: fully on when likely to capture events of interest Cons: required application-specific information to design scheduling
Processing	Onboard data reduction	Pros: reduced communication requirements increased mission stealth Cons: increased size, weight, power, and cost; complex algorithm creation required
Networking	Commercial off the shelf (COTS) wireless modem	Pros: extremely reliable Cons: low data rate
Specialized hardware	Customized GPS for clock synchronization	Pros: made it possible to use distributed processing Cons: increased size, weight, power, and cost
Packaging and fabrication	COTS components with wiring interconnects	Pros: overall lower cost for small-volume deployments (<12 units), easily accessible components Cons: reliability suffers due to wiring interconnects, increased size, higher cost for larger volume deployments, and increased assembly time
Deployment	Attach preassembled sensor to existing delivery system	Pros: delivery is independent of sensor node Cons: some duplicate components (GPS)

The authors implemented a sensor network of spatially distributed nodes and deployed it on an active landslide area to measure the continuing motion and settling of the formation over a period of months [1,3]. The sensor nodes were built around the Texas Instruments CC2510 development kit that combined an 8051 microcontroller with a 2.4 GHz radio transceiver employing the 802.15.4 format. With a usable bandwidth of about 750 kHz, the one-way calibrated arrival accuracy is about 1 ms, which yields a range accuracy of about 300 m for any given processed burst. Additional averaging of bursts reduces this uncertainty by the square root of the number. For example, 10 cm accuracy may be achieved using nine million bursts, which is not a problem for stationary objects. However, there is a lower bound on the uncertainty due to (1) the ability to properly calibrate the system for the turnaround time from the responder and (2) the repeatability of the turnaround time. By avoiding baseband processing (perhaps tapping the system at the intermediate frequency), the turnaround repeatability is very good (i.e., picoseconds). For this reason, the developed system used separate RF circuitry to create a cooperative radar-like system that enabled a very accurate measurement of the changes in relative distances between nodes.

Because the primary objective of this effort was to build a network that measures position with about one centimeter accuracy, a simplified flooding-based communication and control program was developed such that all nodes allow control from any other node and flood messages to all of the nodes. This is a classic ad hoc networking approach that results in an extremely reliable and flexible delivery mechanism at the cost of excessive power use. However, under this scenario, the power used by the networking protocol is far less than that of the power required to make a distance measurement. Thus, the focus on optimizing this algorithm was not deemed worthwhile with respect to the research goals. The data collected by the system showed most of the nodes performed as designed and generated

TABLE 89.2 Design Trade-Off Decisions for Landslide Measurement System

Design Element	Design Selection	Consequences
Power source	Commercial-sealed gel cell battery	Pros: rechargeable, reliable, long life, low cost, easily acquired, relatively unaffected by temperature (at least over typical operating ranges) Cons: poor power density (large and heavy), disposal
Power conservation	Extensive use of deep sleep	Pros: current draw on the order of microamperes during sleep Cons: required relays for powering radar electronics, clock drift, no sampling while sleeping
Processing	Wireless processor for coordinating data acquisition and storage. Post-processing for data reduction	Pros: lower battery use, simpler to test and debug Cons: requires larger data storage per sensor node for unreduced sample storage, requires post-processing to verify system is functional; in situ testing requires extensive equipment and greater time than similar lab-based testing
Networking	Brute force network flooding, node locations allow for redundant coverage	Pros: extremely reliable Cons: increased time and power requirements; however, these may be offset by sleep duty cycle
Specialized hardware	Cooperative radar for node localization	Pros: sub-centimeter accuracies not obtainable through processing WSN communication channels Cons: increased size, weight, power, and cost; requires multiple antennas
Packaging and fabrication	Commercial watertight cases and COTS components with wiring interconnects	Pros: overall lower cost for small-volume deployments (<12 units), easily accessible components (some may be acquired near deployment sites) Cons: reliability suffers due to wiring interconnects, increased size, and higher cost for larger volume deployments
Deployment	Final assembly and camouflage performed during deployment	Pros: match the deployment to environmental conditions (vegetation, rock, land features, and color), protect the sensor components during transport to remote site, and adjust antenna height to increase communication reliability. Cons: longer deployment, more extensive in situ checkout needed

radar returns in the sub-centimeter range. Laboratory-based tests measured the units to generate measurements close to 3 mm in accuracy. Design trade-offs and choices related to the development of the landslide measurement system are summarized in Table 89.2.

89.6 Example System: Neutrally Buoyant Sensor Cave Mapping

Many parts of the world rely on karst aquifers, essentially interconnected water-filled caves and passageways, for their water supply needs. Conventional methods for characterizing karst conduits include tracer tests and mapping by cave divers. Dye tracers are useful for determining flow velocities but do not provide sufficient information about the size and complexity of the karst formation. The use of cave divers is very limited to those formations that are large enough to accommodate divers and slow enough to allow them to enter and exit safely and are located at reasonable depths and distances. Since automated sensors do not share those same limitations, the authors developed a sensor technology designed to travel with the flow of water and measure the size and morphology of caves through which it travels.

This patented sensor technology developed at Southwest Research Institute® (SwRI®) is referred to as the neutrally buoyant sensor, or NBS.

The NBSs were assembled using commercially available components such as ultrasound sensors and dual-axis magnetometers and accelerometers. A general-purpose wireless sensor node with onboard processor and memory unit coordinated the overall operation of the data collection components. The magnetometer provided the ability to gauge the orientation relative to magnetic north, and the accelerometer enabled the determination of motion dynamics (furnishing a form of inertial navigation) as the NBS traveled through conduits. Ultrasonic transducers characterized the conduit geometry and, ultimately, velocity. Six pairs of ultrasonic transducers were positioned on each axis around the circular NBS vessel to emit sonar "pings" outward to the conduit walls. Each pair consisted of a transmitter, which sent out ultrasound pulses normal to the sensor node, and a receiver, which recorded the reflected ultrasound pulse. Accurate distances to the surrounding conduit features are determined using the TOA of the first reflected pulse. The time of flight was converted to distance based on the density of water and air. Sonar ranging gives a representative characterization of the conduit geometry. The rate of displacement of distinctive wall features is used in velocity calculations. Post-processing of the data from all components enables the calculation of real-time velocity of the NBS as it travels along the conduit path, as well as calculation of the shape and size of the conduit. The orientation (magnetometer) data are used in combination with the sonar readings to detect features, derive velocity, and ultimately unravel the data into a chain of vectors corresponding to the path taken, velocity profile, and measured conduit shape. Similarly, the floating sonar coordinates are rectified to Cartesian position and distributed to the respective

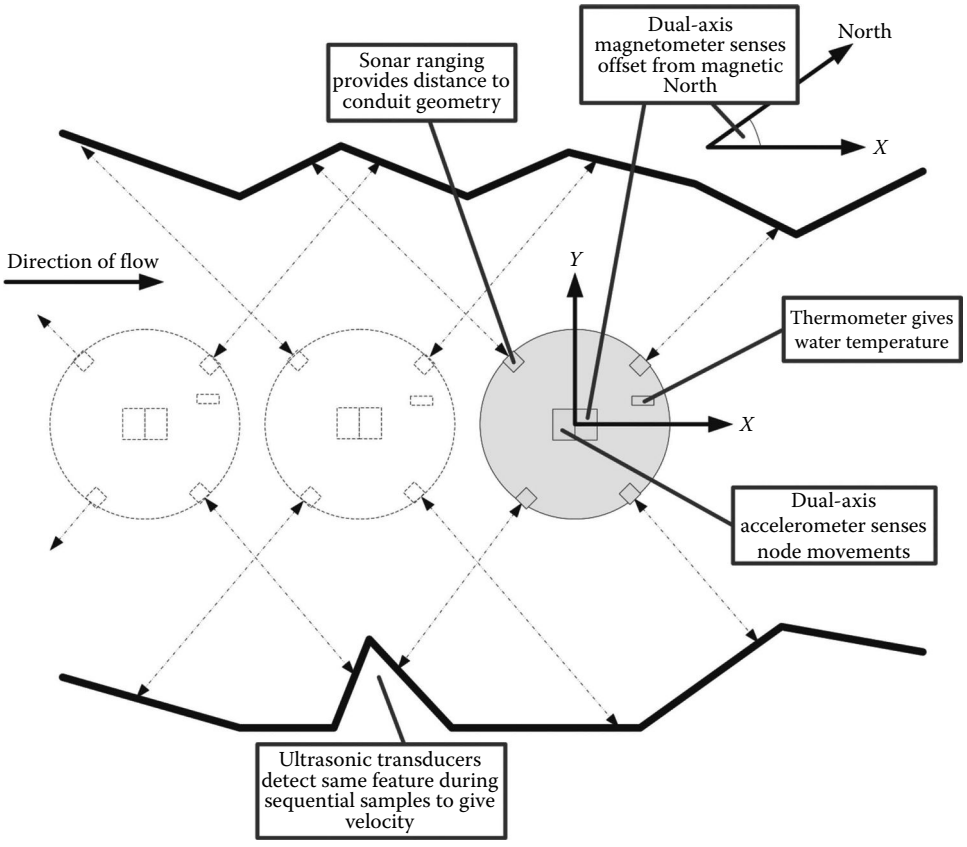

FIGURE 89.2 NBS concept of operations.

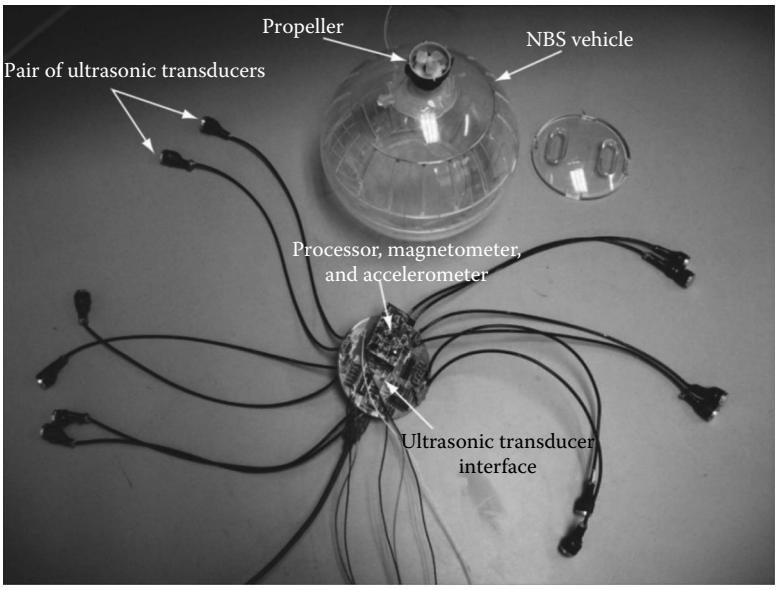

FIGURE 89.3 NBS electronics and housing.

vector segment. Accelerometers are used to detect if any periods of rapid movement occur since these could adversely affect the triangulation used in mapping. The conceptual operation of the NBS is illustrated in Figure 89.2. The prototype circuit assembly with enclosure, built from a "hamster ball" from the local pet store, is shown in Figure 89.3.

A deployment of the NBS in 2008 resulted in a transport trajectory that was sufficiently long and uninterrupted to allow collection of ultrasound, magnetometer, and accelerometer data of a 20 m long stretch of Honey Creek Cave in Texas. The detailed process for data reduction is outlined in [2]. The resulting 3D conduit image is shown in Figure 89.4. Design trade-offs and choices related to the development of the NBS system are summarized in Table 89.3.

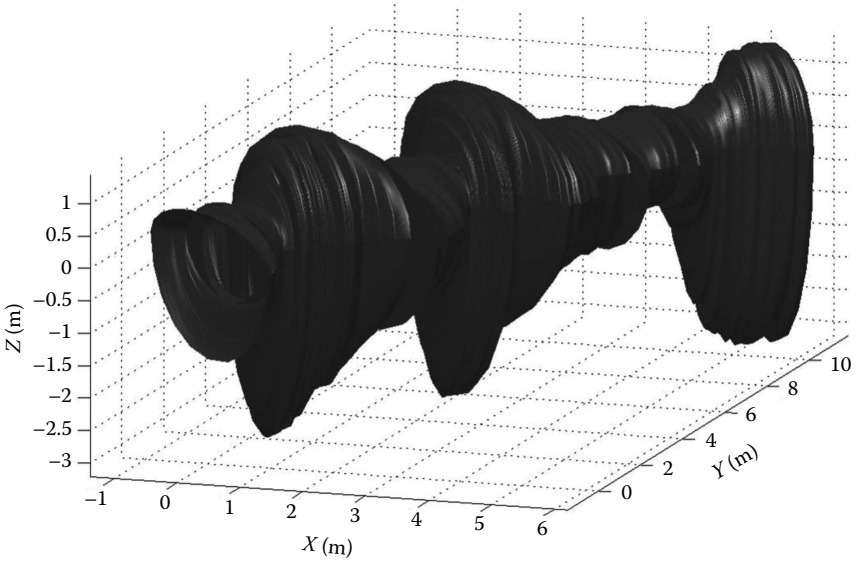

FIGURE 89.4 3D conduit imagery resulting from data collected during cave-mapping deployment.

TABLE 89.3 Design Trade-Offs for NBS

Design Element	Design Selection	Consequences
Power source	Single-use lithium cells	Pros: power density ratio Cons: environmental impact, in situ battery replacement
Power conservation	Low-power processor kept off until use	Pros: continuous data collection and communication Cons: reduced mission lifetime
Processing	Wireless processor for coordinating data acquisition and storage. Post-processing for data reduction	Pros: lower battery use, simpler to test and debug Cons: requires larger data storage per sensor node for unreduced sample storage, requires post-processing to verify system is functional
Networking	Simple point to point and relay	Pros: simple (specialized communications were needed to work in a cave) Cons: lack of robustness, lack of features, low data rate
Specialized hardware	Sonar transmit and receive circuitry-augmented WSN	Pros: required to collect desired measurements, primarily used WSN processor
Packaging and fabrication	Repurposed a commercially available housing, commodity automotive sonar transducers, wiring interconnects, custom waterproofing	Pros: overall lower cost for small-volume deployments (<12 units), tremendous cost savings from commodity sonar transducers Cons: reliability suffers due to wiring interconnects, higher cost for larger volume deployments, and many waterproofing challenges
Deployment	Magnetic relay for waterproof power switch, in situ buoyancy adjustment	Pros: low cost Cons: time to perform sensitive buoyancy adjustment

89.7 Example System: NBS Variant for Borehole-Accessed Caves

The U.S. Army Corps of Engineers (USACE) pursued a project to locate, characterize, and close off karst conduits that divert water around the Center Hill Dam in Tennessee. The project involved drilling regularly spaced boreholes deep into the rock on the south side of the dam with the goal of intersecting the conduits and then filling them with grout. Knowing the size and orientation of the conduits can guide subsequent drilling efforts and provide estimates of the amount of grout required to fill the voids. To that end, the USACE contracted with SwRI to develop a customized version of the NBS technology for mapping borehole-accessed caves.

The original NBS electronics package was redesigned to fit inside a section of two inch PVC tube with ultrasonic transducers oriented at 0°, 90°, 180°, and 270° angles around the tube. This tethered probe transmitted real-time data to the surface via a coaxial cable connected to the wireless radio antenna port. The tether cable was wound onto a cable reel instrumented with rotational encoders for measuring the depth of the probe. An antenna was connected to the top end of the tether cable to provide slip-ring functionality to the cable reel. A conscious design decision was made not to include a means of controlling the rotation of the probe as it descended and ascended through the cavity but to allow it to rotate freely as the cable allowed and measure the orientation with a magnetometer. This decision is in harmony with SwRI's basic low-cost approach to sensors and WSNs, that leveraging inexpensive COTS components enables more ubiquitous and advanced data collection for solving real-world problems. Design trade-offs and choices related to the development of this variant of the NBS system are summarized in Table 89.4.

TABLE 89.4 Design Trade-Offs for NBS Variant for Borehole-Accessed Caves

Design Element	Design Selection	Consequences
Power source	Single-use lithium cells	Pros: power density ratio Cons: in situ battery replacement
Power conservation	Low-power processor kept off until use	Pros: continuous data collection and communication Cons: reduced mission lifetime
Processing	Wireless processor transmitted data to control terminal over commodity coaxial tether cable via RF communications	Pros: continuous live data, ability to use extremely long tethers of commodity cable (RF through air would not work in long boreholes; conventional-wired networking protocols could not support distance requirements), extremely low cost, and memory requirements on WSN
Networking	Simple point to point	Pros: simple, robust networking
Specialized hardware	Sonar transmit and receive circuitry-augmented WSN, commodity 3-axis magnetometer	Pros: required to collect desired measurements, primarily used WSN processor, low cost
Packaging and fabrication	Specialized housing assembled from commodity PVC to match borehole dimensions, commodity coax cable dual purposed for tether and communications	Pros: overall lower cost for small-volume deployments (<12 units), tremendous cost savings from commodity components Cons: reliability suffers due to wiring interconnects, higher cost for larger volume deployments, and many waterproofing challenges; commodity tether strength is lower than classic downhole applications (some sensors were lost due to broken cables)
Deployment	Commodity motorized cable reel with depth measurement	Pros: low-cost expendable sensors and cable allowed measurements in higher-risk locations (competing teams were unwilling to risk loss of higher-cost sensors) Cons: lost probe resulted in minor delays

89.8 Example System: NBS Variant for Culvert Inspection

In its role of ensuring the safety of America's roads, the Federal Highway Administration (FHWA) sought out tools to facilitate and automate the inspection of culvert conduits. The previously described NBS projects offered a compelling alternative to manual inspection or expensive tethered robotic cameras. The FHWA funded development of a specialized version of the NBS system that included a multichannel, a high-speed analog-to-digital converter (ADC) for higher-resolution ultrasonic imagery, a 360° camera and lighting system for visual confirmation of sensor results, and integrated Wi-Fi for live streaming video and data retrieval. The combination of more channels of ultrasonic data, higher sampling rates, and streaming video required the use of more powerful processors and a full embedded Linux operating system. The embedded Linux provided full wireless networking support and digital signal processor (DSP)-accelerated video compression routines including the GStreamer libraries for network streaming video. The user controls the data acquisition and views the live results through a graphical user interface hosted on a ruggedized convertible laptop–tablet. This application is an example of how performance requirements can drive the solution beyond the capabilities of traditional WSN hardware and software environments. Design trade-offs and choices related to the development of the culvert inspection system are summarized in Table 89.5.

TABLE 89.5 Design Trade-Offs for Culvert Inspection System

Design Element	Design Selection	Consequences
Power source	Rechargeable lithium polymer battery	Pros: high power density Cons: cost of battery and charging infrastructure
Power conservation	Increased battery capacity to support compute requirements	Pros: supported high capability processing Cons: increased size and cost
Processing	Primary data reduction and processing is accomplished on the sensor	Pros: dramatically reduced data communication requirements Cons: increased size, weight, power, and cost
Networking	Commodity Wi-Fi	Pros: high throughput, simple, interoperability with commodity ruggedized laptops Cons: increased power requirements
Specialized hardware	360° camera, inertial measurement unit, high-speed ADC, power management	Pros: required to collect desired measurements, provides fusion of sonar and visual imagery Cons: increased size, weight, power, and cost
Packaging and fabrication	Custom circuit boards, custom housing	Pros: reliability Cons: higher per-unit cost for lower volumes means sensors are not expendable unless manufacturing volumes are high
Deployment	Commodity tether with Bluetooth depth/distance measurement	Pros: wireless communication supports broader range of deployment scenarios Cons: wireless may be limited in some scenarios

89.9 Conclusions and General Design Considerations

We have attempted to show the strengths and weaknesses of the WSN approach by examining the trade-offs and design choices from a series of successful deployments. WSN platforms provide a compelling option for low-power applications with straightforward measurement requirements across spatially separated deployment positions. However, as the compute requirements of the system increase, a hybrid approach is often required in which a digital signal processor or conventional processor is employed to augment the processing capability of the wireless platform. Hybrid approaches may also take advantage of the low-power WSN module to wake the expanded system components from extended sleep modes. The highlighted systems also demonstrated a high performance scenario when the WSN hardware should be abandoned in favor of more powerful systems.

In general, the major design factors in the WSN application space, in order of importance, are total power usage, communications rate, system reliability, and communication range. Each of these requirements is in conflict with the others when designing a system. For example, selecting a particular communication technology has far-reaching effects upon many other areas of the system, such as power, antenna size (packaging), algorithms that can be employed, and clock synchronization. In short, every aspect feeds back onto all the other aspects of the system and must be carefully considered.

A general summary of trade-offs and design considerations for wireless sensor systems is given in Table 89.6.

TABLE 89.6 Summary of Trade-offs and Design Considerations

Design Element	Design Considerations
Power source	A variety of battery technologies, capacities, power densities, voltages, rechargeable versus single use, etc. Energy harvesting (solar, wind, kinetic, etc.) may be employed for some applications. Some battery technologies are more sensitive than others to temperature effects.
Power conservation	Reducing the computation and communication duty cycle is not always the whole answer. Often the solution requires application-specific knowledge to balance the conflicting constraints of battery lifetime, communication rate, and system reliability and communication range.
Processing	WSNs that perform a lot of processing shared across nodes are engaging in a form of distributed processing using low-power processors with all the added complexities associated with these techniques, including additional communication requirements to support system coordination. The impact on system performance is analogous to that described by Amdahl's law for multiprocessors and parallel computing.
Networking	Many wireless networking technologies are available across different frequency ranges, power levels, communication ranges, and data throughput capabilities. Some of the technologies that may be considered are Wi-Fi (including low-power implementations), Bluetooth, 802.15.4, ZigBee, 6LoWPAN, ANT, and WirelessHART. The selection of a particular wireless technology is intimately connected with the conflicting design constraints of size, weight, power, cost, and communication requirements.
Specialized hardware	Wireless sensor processors and hardware generally support basic measurements, such as temperature, but solutions to real-world problems almost always require specialized hardware. The inclusion of specialized hardware is entirely dependent on the requirements of the proposed application.
Packaging and fabrication	The featured projects highlight various choices for system packaging, assembly, and fabrication. Solutions have included examples of both disposable and high value sensors, as well as varying levels of time and effort required for assembly. For low volume systems, a higher degree of manual assembly is acceptable, and even desirable, when it leads to lower total cost. Applications featuring higher sensor volumes require additional engineering at the design stage in order to minimize total system cost in the longer term. These opposing choices can also have a direct impact on system reliability since the possibility that a failure will occur increases in direct proportion with the number of interconnects and cables.
Deployment	Employing ultralow-cost components can have huge benefits in scenarios where many nodes can be deployed to provide a measure of redundancy whereby if one node fails, the system still succeeds. In some situations, the nodes are so inexpensive and the resulting data so valuable that individual nodes may be considered disposable and deployments can be designed to accommodate a certain level of loss by attrition. However, some deployments require a more powerful and/or expensive sensor such that individual node loss is deemed unacceptable or, at the very least, undesirable.

References

1. Kenney, J.D., D.R. Poole, G.C. Willden, et al. Precise positioning with wireless sensor nodes: monitoring natural hazards in all terrains, *2009 IEEE International Conference on Systems, Man, and Cybernetics*, San Antonio, TX. October 2009.
2. Kenney, J.D., G.C. Willden, R.N. McGinnis, et al. Development of neutrally buoyant sensors for mapping conduits in karst aquifers, *11th Multidisciplinary Conference on Sinkholes and the Engineering and Environmental Impacts of Karst,* Tallahassee, FL, September 2008.
3. Pilcher, M.E., B.E. Campion, and B.A. Abbott, Wireless system using continuous wave phase measurement for high-precision distance measurement, U.S. Patent No. U.S. 7,504,992, March 2009.
4. Van Rheeden, D.R., B.C. Brown, J.C. Price, et al. Automatic positioning of UAVs to optimize TDOA geolocation performance, *IEEE-AIAA 23rd Digital Avionics Systems Conference,* Salt Lake City, UT, October 2004.

90

Telemetry

Albert Lozano-Nieto
Penn State University

90.1 Introduction

Telemetry is the science of gathering information at some remote location and transmitting the data to a convenient location to be examined and recorded. Telemetry can be done by different methods: optical, mechanical, hydraulic, electric, etc. The mechanical methods, either pneumatic or hydraulic, have acceptable results for short distances and are used in environments that have a high level of electromagnetic interference and in those situations where, for security reasons, it is not possible to use electrical signals, for example, in explosive environments. More recently, use of optical fiber systems allows the measurement of broad bandwidth and high immunity to noise and interference. Other proposed telemetry systems are based on ultrasound, capacitive or magnetic coupling, and infrared radiation, although these methods are not routinely used. The discussion in this chapter will be limited to the most-used systems: telemetry based on electric signals. The main advantage of electric over mechanical methods is that electrically based telemetry does not have practical limits regarding the distance between the measurement and the analysis areas and can be easily adapted and upgraded in already existing infrastructures. Electric telemetry methods are further divided depending on the transmission channel that they use as wire telemetry and wireless (or radio) telemetry. Wire telemetry is technologically the simplest solution. The limitations of wire telemetry are the low bandwidth and low transmission speed that it can support. However, it is used when the transmission wires can use the already existing infrastructure, as in most electric power lines that are also used as wire telemetry carriers. Wireless telemetry is more complex than wire telemetry, as it requires a final radio-frequency (RF) stage. Despite its complexity, it is widely used because it can transmit information over longer distances; thus, it is used in those applications in which the measurement area is not normally accessible. For most applications, the wireless nature of the system is implied when referring to telemetry. The largest area that led to the development of telemetry systems arose from defense and aerospace applications, specifically the development of rockets and ballistic missiles. Designers of these systems needed to monitor a large amount of data, while the rocket was in flight, and this task could only be achieved with sending the data wirelessly.

Figure 90.1 displays a generic telemetry system. It consists of (1) transducers to convert physical variables to be measured into electric signals that can be easily processed; (2) conditioning circuits to amplify the low-level signal from the transducer, limit its bandwidth, and adapt impedance levels;

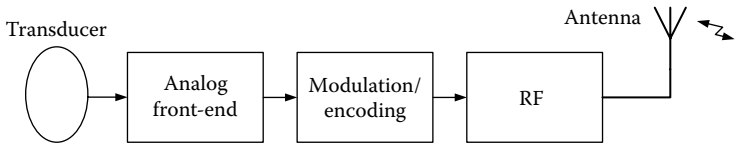

FIGURE 90.1 Block diagram for a basic wireless telemetry system.

(3) a signal-processing circuit that sometimes can be integrated in the previous circuits; (4) a subcarrier oscillator whose signal will be modulated by the output of the different transducers once processed and adapted; (5) a codifier circuit, which can be a digital encoder, an analog modulator, or a digital modulator, that adapts the signal to the characteristics of the transmission channel, which is a wire or an antenna; (6) a radio transmitter, in wireless telemetry, modulated by the composite signal; (7) an impedance line adapter, in case of wire transmission, to adapt the characteristic impedance of the line to the output impedance of the circuits connected to the adapter; and (8) for wireless communication, a transmitting antenna. It is necessary to point out that not all the blocks may be present in a specific system. The receiver end consists of similar modules. For wireless telemetry, these modules are (1) a receiving antenna designed for maximum efficiency in the RF band used, (2) a radio receiver with a demodulation scheme compatible with the modulation scheme, and (3) demodulation circuits for each of the transmitted channels. For wire telemetry, the antenna and the radio receiver are replaced by a generic front end to amplify the signal and adapt the line impedance to the input impedance of the circuits that follow. The transmission in wireless telemetry systems is done by sending a signal whose analog variations in amplitude or frequency are a known function of the variations of the signals from the transducers. The majority of current systems use digital data transmitting a finite set of symbols, each one representing one of the possible finite values of the composite signals at the time that it was sampled. The effective communication distance in a wireless system is limited by the power radiated by the transmitting antenna, the sensitivity of the receiver, and the bandwidth of the RF signal. As the bandwidth increases, the contribution of noise to the total signal also increases, and consequently more transmitted power is needed to maintain the same signal-to-noise ratio (SNR). This is one of the principal limitations of wireless telemetry systems. In some applications, the transmission to the receiver is done on baseband, after the conditioning circuits. The advantage of baseband telemetry systems is their simplicity, although because of the baseband transmission, they are normally limited to only one channel at low speeds.

For most applications, the systems need to acquire either different types of signals or the same type of data at different locations in the process that is being monitored. These different information signals can be transmitted using the same common carrier by multiplexing the data signals. Multiplexing allows different signals to share the same channel. Multiplexing techniques are usually considered either frequency division multiplexing (FDM) or time division multiplexing (TDM). In FDM, different subcarrier frequencies are modulated by the different measurement channel signals that cause the information spectrum to shift from baseband to the subcarrier frequency. Then, the subcarrier frequencies modulate the RF carrier signal, which allows the transmission of all desired measurement channels simultaneously. In TDM, the whole channel is assigned entirely to each of the measurement channels, although only during a fraction of the time. TDM techniques use digital modulation to sample the different measurement channels at different times. Then, these samples are applied sequentially to modulate the RF carrier. Figure 90.2 illustrates these concepts by showing frequency and time graphs for FDM and TDM, respectively.

Current uses of telemetry encompass a large and varied number of applications. Telemetry is widely used in space applications for either telemeasurement of a distant variable or telecommandment of actuators. In most of these types of applications, for example, in space telemetry, it is very important to design the telemetry systems to minimize the consumption of power [1], Some land mobile vehicles, such as trains, also use telemetry systems, either wireless or by using some of the existing power wires to transmit data to the central station and receive its commands [2]. In clinical

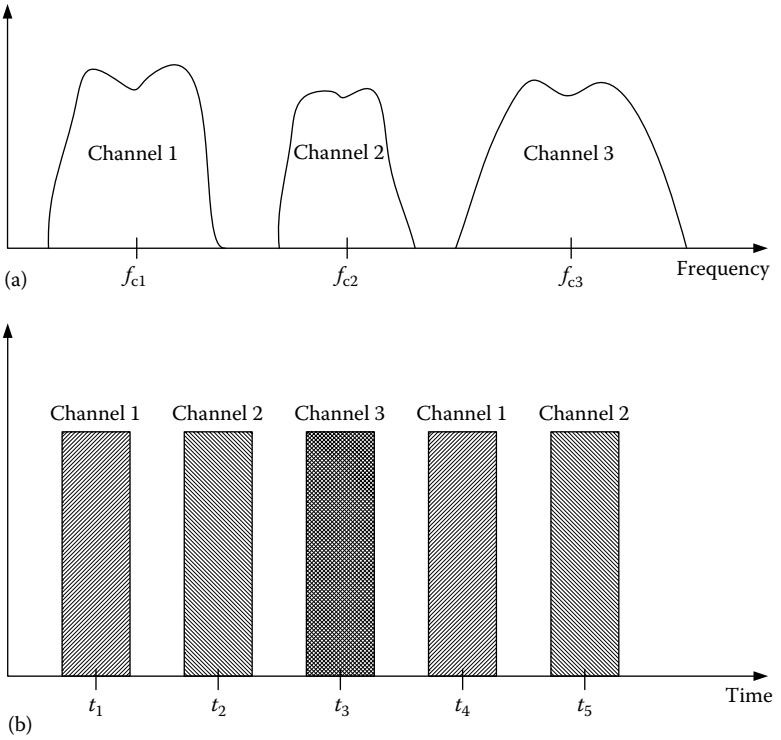

FIGURE 90.2 Basic characteristics of (a) FDM and (b) TDM signals. In FDM different channels are allocated at different subcarrier frequencies (f_{c1}, f_{c2},…) while in TDM, only one channel is transmitted at a given time. The remaining channels are transmitted sequentially.

practice, the telemetry of patients increases their quality of life and their mobility, as patients do not need to be connected to a measurement system to be monitored. Several medical applications are based on implanting a sensor in a patient and transmitting the data to be further analyzed and processed either by radio [3] or by adapted telephone lines [4] from the receiving station. Optical sensors and fiber-optic communications are used in industry to measure in environments where it is not desirable to have electric signals such as explosive atmospheres [5]. The designer of a telemetry system needs also to keep in mind the conditions in which the system will have to operate. In most of the applications, the telemetry systems must operate repeatedly without adjustment and calibration in a wide range of temperatures. Finally, as different telemetry systems are developed, the need to permit tests to be made interchangeable at all ranges increases, which require compatibility of transmitting, receiving, and signal-processing equipment at all ranges. For this reason, the Department of Defense Research and Development Squad created the Guided Missiles Committee, which formed the Working Group on Telemetry. This later became the Inter-Range Instrumentation Group (IRIG) that developed telemetry standards. Today, the IRIG Standard 106-09 is the primary telemetry standard used worldwide by both government and industry.

Wireless telemetry systems need some coordination in order to use the radio spectrum in an efficient manner and more importantly, free of interference. This coordination takes shape in the form of standards, in particular the IRIG Standard 106-09 . While this chapter does not focus on the in-depth discussion of this or other standards, it discusses some of its more relevant and broader points. Most wireless telemetry applications occur in the UHF band. Table 90.1 shows the specific allocation frequencies within this frequency range as well as their unofficial name. The 1435–1535 MHz band is allocated in the United States for aeronautical telemetry including manned and unmanned aircraft, missiles,

TABLE 90.1 Telemetry Frequency Allocations in the UHF Band

Frequency Range (MHz)	Commonly Used Band Designation
1435–1525	Lower L-band
1525–1535	Lower L-band
2200–2290	Lower S-band
2310–2360	Upper S-band
2360–2390	Upper S-band

rocket sleds, and similar systems. The range from 1525 to 1530 MHz telemetry usage is on a secondary service, while the primary service is mobile satellite communications. The range from 1530 to 1535 MHz also supports telemetry as a secondary service, while the primary service is maritime mobile satellite communications. The band ranging from 2200 to 2290 MHz is assigned for space research, space operation, and satellites for Earth exploration including the telemetry systems associated to launch vehicles, research rockets, and space vehicles. The band ranging from 2310 to 2390 MHz is allocated to telemetry in a secondary basis, while the primary user of this band is the wireless communication system. Finally, the service allocation in the 2360–2390 MHz is for aeronautical telemetry similar to the services enumerated in the lower bands. The maximum power allowed for transmitters operating in these bands is 25 watts for both output power and effective isotropic radiated power.

90.2 Multiple-Channel Telemetry

Most of the industrial processes in which telemetry is used require the measurement of different physical variables to control the process, the measurement of only one physical variable at different locations, or normally a combination of both. In these multiple-channel measurements, baseband telemetry is not an option, as it would require building a different system for each channel. Multiple-channel telemetry is achieved by sharing a common resource (transmission channel), as is shown in Figure 90.3. The sharing of the transmission channel by all the measurement channels is designated by multiplexing. There are two basic multiplexing techniques: FDM and TDM. In FDM, different channels are assigned to different spectral bands and the composite signal is transmitted through the communication channel. In TDM, the information for different channels is transmitted sequentially through the communication channel.

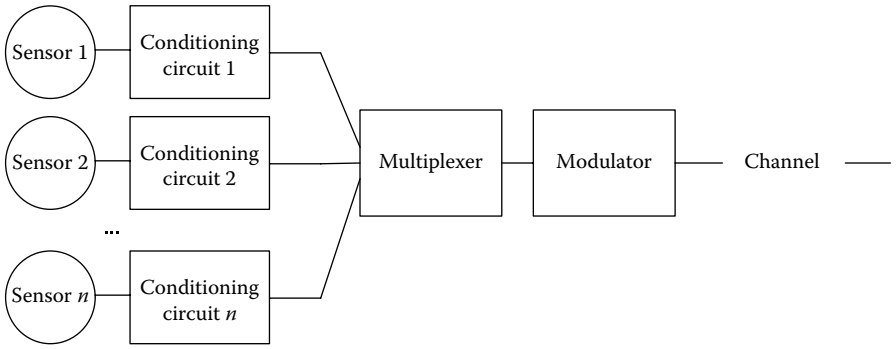

FIGURE 90.3 In multiple-channel telemetry, a common transmission channel is used to transmit the measured signals from different channels using different sharing schemes. The process is reversed at the receiver side.

90.2.1 Frequency Division Multiplexing

In FDM, shown in Figure 90.4a, each measurement channel modulates a sinusoidal signal of different frequency. These sinusoidal signals are called subcarriers. Each of the modulated signals is then low-pass filtered to ensure that the bandwidth limits are observed. After the filtering stage, all the modulated signals are fed into a summing block, producing what is known as a baseband signal. A baseband signal indicates here that the final carrier has not yet been modulated. The spectrum of the baseband signal is shown in Figure 90.4b, where it is possible to see how each measurement channel spectrum signal is allocated its own frequency. This composite signal finally modulates a carrier signal whose frequency depends on the transmission medium that is used. The signal is then fed into a transmission wire (similar to TV-broadcasting systems by cable) or, more commonly, into an antenna in the case of wireless telemetry systems. In wireless telemetry, the frequency of the carrier cannot be chosen arbitrarily, but is chosen in accordance with international agreements on the use of the electromagnetic spectrum. In the United States, the Federal Communications Commission (FCC) is the body that regulates the allocation of frequencies for different communication services. Table 90.2 shows the most common telemetry frequency bands and their intended use. Table 90.2 is for informational purposes only, and it is not a comprehensive guide to telemetry frequencies as these can change often.

At the receiver end, the carrier demodulator detects and recovers the composite baseband signal. The next step is to separate each of the subcarriers, by feeding the signal into a bank of parallel

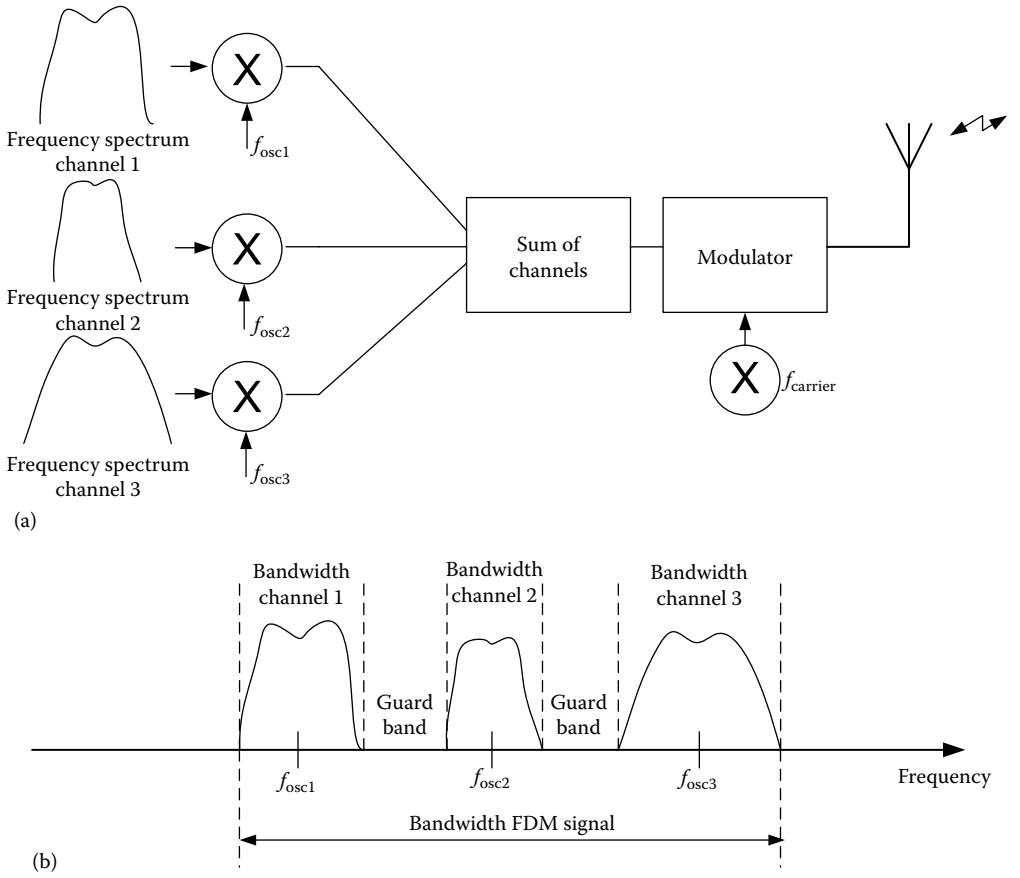

FIGURE 90.4 The different channels in an FDM system (a) are allocated at different subcarrier frequencies producing a composite signal shown in (b) that is later modulated by an RF frequency according to the transmission channel used. The guard bands limit the closeness of contiguous channels to avoid intermodulation and cross talk.

TABLE 90.2 Frequency Bands Allocated for General Telemetry Uses

Frequency Band MHz	Uses	Notes
72–76	Biotelemetry	Low-power devices; restricted by Part 15 of FCC rules
88–108	Educational	Four frequencies in this band; part 90 of FCC rules
154	Industry	Band in TV channels 7–13
174–216	Biotelemetry	Low-power operations restricted to hospitals
216–222	Multiple	BW < 200 kHz
450–470	General	Telemetry as secondary basis; limited to 2 W of RF
467	Industry	Business band; limited to 2 W of RF
458–468	Biotelemetry	Band in TV channels 21–29
512–566	Biotelemetry	Low-power operations restricted to hospitals
1427–1435	Fixed	Uses in land mobile services (telemetering and telecommand)
1435–1535	Aeronautical	
2200–2290	Mobile	

passband filters. Each channel is further demodulated, recovering the information from the transducer. The main practical problem of FDM systems is the cross talk between channels. Cross talk appears due to the nonlinearities of the electronic devices, which originates when the signal for one channel partially modulates another subcarrier in addition to the one assigned to that channel. Cross talk also originates when the spectra for two adjacent channels overlap. To avoid this effect, the subcarriers have to be chosen so that there is a separation (guard band) between the spectra of two contiguous channels. By increasing the guard band, the possibility of cross talk decreases, but the effective bandwidth also increases. The effective bandwidth equals the sum of the bandwidth of all channels, plus the sum of all the guard bands.

There are three alternative methods for each of the two modulation processes: the modulation of the measurement channel signals and the modulation of the composite signal. These methods are amplitude modulation (AM), frequency modulation (FM), and phase modulation (PM). The usual combinations are FM/FM, FM/PM, or AM/FM [6]. This chapter analyzes only the subcarrier modulation schemes, while the modulation for the RF signal is analyzed in *Electromagnetic, Optical, Radiation, Chemical, and Biomedical Measurement*.

90.2.2 Subcarrier Modulation Schemes for FDM

90.2.2.1 Subcarrier Modulation of Amplitude

In an AM subcarrier modulation scheme, the amplitude of a particular subcarrier signal is changed according to the value of the measured channel assigned to that frequency. The resulting AM signal is given by the expression

$$v(t) = A_c[1 + m(t)]\cos(\omega_c t) \tag{90.1}$$

where

A_c is the amplitude of the carrier
$m(t)$ the modulating signal
ω_c the frequency of the carrier

This type subcarrier modulation requires very simple transmitter and receiver circuits. The level of modulation is indicated by a parameter known as the percentage of modulation (P). For simple signals, P can be expressed as

$$P = m \times 100(\%) \tag{90.2}$$

In a more general way, the percentage of modulation (P) can be expressed as

$$P(\%) = \frac{A_{c(\max)} - A_{c(\min)}}{2A_c} \times 100 \tag{90.3}$$

where $A_{c(\max)}$ and $A_{c(\min)}$ are the maximum and minimum values for the carrier signal.

Figure 90.5 shows the spectrum of an amplitude-modulated signal, assuming that the modulating signal is a band-limited, nonperiodic signal of finite energy. The spectrum consists of two sidebands that are symmetrical in reference to the subcarrier. From Figure 90.5, it is also possible to see the main disadvantages of AM schemes. First, the bandwidth of the modulated channel is two times the bandwidth of the modulating signal, due to the two similar sidebands that appear. This results in an inefficient use of the spectrum. Second, the analysis of power for each of the components in Figure 90.5 shows that at least 50% of the transmitted power is used in transmitting the subcarrier, which is independent of the measured signal, as it does not contain any information. The remaining power is split between the two sidebands, which results in a maximum efficiency that it is theoretically possible to achieve of below 25%. The third main problem of AM is the possibility of overmodulation, which occurs when $m > 1$. Once a signal is overmodulated, it is not possible to recover the modulating signal with the simple circuits that are widely used for AM telemetry transmission.

The limitations of AM subcarrier modulation can be overcome using more efficient modulation techniques, such as double sideband (DSB), single sideband (SSB), and compatible single sideband (CSBB), which are also considered AM techniques. However, the complexity of these modulation systems and the cost associated with systems capable of recovering subcarrier signals modulated this way cause them not to be used in most commercial telemetry systems. Most of the available systems that based on AM subcarrier techniques use the traditional AM that has been described here, because its simplicity overcomes the possible problems of its use.

90.2.2.2 Subcarrier Modulation of Frequency

FM (or PM) is by far the most-used subcarrier modulation scheme in FDM telemetry systems. These angle modulations are inherently nonlinear, in contrast to AM. Angle modulation can be expressed as

$$v(t) = A\cos[\omega_c t + \phi(t)] \tag{90.4}$$

where $\phi(t)$ is the modulating signal, that is, the signal from the transducers after conditioning.

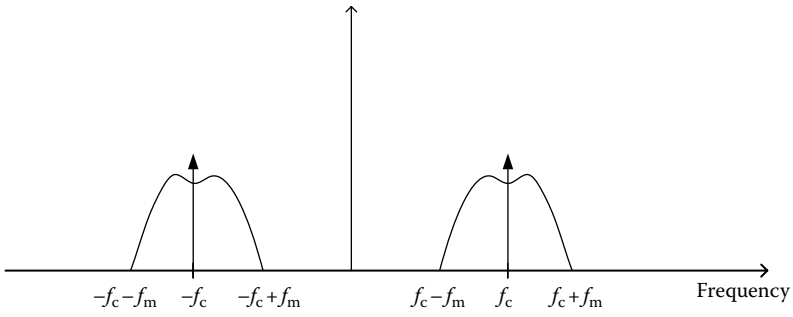

FIGURE 90.5 Resulting spectrum after AM. The spectrum of the baseband signal extends from 0 to f_m Hz. The resulting AM spectrum has doubled the required bandwidth, while only 0.25 of the total power is used in transmitting the desired information.

It is then possible to calculate the value of the instantaneous frequency as

$$f = \frac{1}{2\pi}\frac{d}{dt}[\omega_c t + \phi(t)] = \frac{\omega_c}{2\pi} + \frac{d}{dt}\phi(t) \tag{90.5}$$

This equation shows how the signal $v(t)$ is modulated in frequency. We can analyze two parameters that can be derived from the previous equations: frequency deviation and modulation index. Frequency deviation (f_m) is the maximum departure of the instantaneous frequency from the carrier frequency. The modulation index (β) is the maximum phase deviation. The following equations show how these parameters are related. The value of the instantaneous frequency (f) is [7]

$$f = \frac{\omega_c}{2\pi} + \frac{\beta\omega_m}{2\pi}\cos(\omega_m t) = f_c + \beta f_m \cos(\omega_m t) \tag{90.6}$$

The maximum frequency deviation is Δf and is given by

$$\Delta f = \beta f_m \tag{90.7}$$

Therefore, we can write the equation for the frequency modulated signal as

$$v(t) = A\cos\left[\omega_c t + \frac{\Delta f}{f_m}\sin(\omega_m t)\right] \tag{90.8}$$

The previous equation shows that the instantaneous frequency, f, lies in the range $f_c \pm \Delta f$. However, it does not mean that all the spectral components lie in this range. The spectrum of an angle-modulated waveform cannot be written as a simple equation. In the simplest case, when the modulating signal is a sinusoidal signal, a practical rule states that the bandwidth of an FM signal is twice the sum of the maximum frequency deviation and the modulating frequency. For modulating signals commonly found in measuring systems, the bandwidth is dependent upon the modulation index; that is, as the bandwidth allocated for each channel is limited, the modulation index will also be limited.

90.2.2.3 Frequency Division Multiplexing Telemetry Standards

The standards for telemetry systems using FDM are exclusively based on FM using two different approaches: proportional-bandwidth modulation (PBW) and constant-bandwidth modulation (CBW) as well as their combination.

In PBW, the bandwidth allocated to a channel is proportional to the subcarrier frequency. The standard allows three different subcarrier deviations: 7.5%, 15%, and 30%. Table 90.3 summarizes the most important parameters for the channels used by PBW.

TABLE 90.3 Main Characteristics of the Channels for PBM

Deviation	Number of Channels	Designation	Lowest Channel Center Frequency	Frequency Bandwidth Lowest Channel	Highest Channel Center Frequency	Frequency Bandwidth Highest Channel
7.5%	25	1 … 25	400 Hz	370–430 Hz	560 kHz	518–602 kHz
15%	12	A … L	22 kHz	18.7–25.3 kHz	560 kHz	476–644 kHz
30%	12	AA … LL	22 kHz	15.4–28.6 kHz	560 kHz	392–728 kHz

It is important to note that for the 7.5% deviation, the channels have been chosen so that the ratio between the upper deviation limit for a given channel and the lower deviation limit for the next channel is around 1.2. When using a deviation frequency of 15% (channels A through L), the upper deviation limit of one channel has a frequency higher than the lower deviation limit of the adjacent, higher channel. This results in the need to omit adjacent channels. A similar situation occurs when using a deviation frequency of 30% (channels AA through LL) although in this case, the highest deviation frequency is higher than the lowest deviation frequency of the two adjacent, higher channels, thus requiring the omission of these two channels.

CBW channels keep the bandwidth constant and independent of its carrier frequency. There are eight possible maximum subcarrier frequency deviations labeled A (for 2 kHz deviation) to H (for 256 kHz deviation). The deviation frequency doubles from one group to the next. There are 22 A-channels, whose center frequency range from 8 to 176 kHz. The separation between adjacent channels is a constant of 8 kHz. Table 90.4 shows a summary of the characteristics of CBW channels.

The standard also gives criteria for the use of the FDM standards. It focuses on the limits, most of the time dependent on the hardware used, and performance trade-offs such as data accuracy for data bandwidth that may be required in the implementation of the system. The subcarrier deviation ratio determines the SNR for a channel. As a rule of thumb, the SNR varies as the three-halves power of the subcarrier deviation ratio. On the other hand, the number of subcarrier channels that can be used simultaneously to modulate an RF carrier is limited by the channel bandwidth of the RF carrier as well as considerations of SNR. Given a limited RF bandwidth, as more channels are added to the FDM system, it is necessary to reduce the deviation ratio for each channel, which reduces the SNR for each channel. It is then very important to evaluate the acceptable trade-off between the number of subcarrier channels and the acceptable SNR values. A general equation that might be used to estimate the thermal noise performance of an FM/FM channel is the following [8]:

$$\left(\frac{S}{N}\right)_{\mathrm{d}} = \left(\frac{S}{N}\right)_{\mathrm{c}} \left(\frac{3}{4}\right)^{1/2} \left(\frac{B_{\mathrm{c}}}{F_{\mathrm{ud}}}\right) \left(\frac{f_{\mathrm{dc}}}{f_{\mathrm{s}}}\right) \left(\frac{f_{\mathrm{ds}}}{F_{\mathrm{ud}}}\right) \tag{90.9}$$

where

$(S/N)_{\mathrm{d}}$ represents the SNR at the discriminator output
$(S/N)_{\mathrm{c}}$ represents the SNR of the receiver
B_{c} is the intermediate-frequency (IF) bandwidth of the receiver
F_{ud} is the subcarrier discriminator output filter (at −3 dB)
f_{s} is the subcarrier center frequency
f_{dc} is the carrier peak deviation for the subcarrier considered
f_{ds} is the subcarrier peak deviation

TABLE 90.4 Parameters of CBW Channels in FDM Telemetry

Channel Denomination	Frequency Deviation, kHz	Lowest Channel Center Frequency, kHz	Highest Channel Center Frequency, kHz	No. of Channels	Separation between Channels, kHz
A	±2	8	176	22	8
B	±4	16	352	22	16
C	±8	32	704	22	32
D	±16	64	1408	22	64
E	±32	128	2816	22	128
F	±64	256	3840	15	256
G	±128	512	3584	7	512
H	±256	1024	3072	3	1024

According to the standard, the FM/FM composite FDM signal that is used to modulate an RF carrier can be of PBW format, CBW format, or a combination of both, with the only limitation that the guard bands between the channels used in the mixed format are equal or greater than the guard bands for the same channels in an unmixed format.

90.2.3 Time Division Multiplexing

TDM is a transmission technique that divides the time into different slots and assigns one slot to each measurement channel. In TDM, all the transmission bandwidth is assigned entirely to each of the measurement channels during a fraction of the time. After the signals from the measurement channels have been low-pass filtered, they are sequentially sampled by a digital switch that samples all the measurement channels in a period of time (T) that complies with the Nyquist criteria. Figure 90.6a shows a basic block diagram for an FDM system. The output of the sampler is a train of AM pulses that contains the individual samples for the channels framed periodically, as is shown in Figure 90.6b. Finally, the composite signal modulates an RF carrier. The set of samples from each one of the input channels is called a frame. For M measurement channels, the period between two consecutive pulses is $T_s/M = 1/Mf_s$, where T_s is the sampling period. The period between samples from the same channel is T_s. At the receiver end, by separating the digital signals into different channels by a synchronized demultipler and by low-pass filtering, it is possible to recover the original signal for each measurement channel.

TDM systems have advantages over FDM systems. First, FDM requires subcarrier modulators and demodulators for each channel, whereas in TDM only one multiplexer and one demultiplexer are required. Second, TDM signals are resistant to the error sources that originate cross talk in FDM: nonideal filtering and cross modulation due to nonlinearities. In TDM, the separation between channels depends on the sampling system. However, because it is impossible in practice to produce perfectly square pulses, their rise and fall times are different from zero. It is then necessary to provide guard time between pulses, similar to the band guards in FDM systems. Cross talk in TDM can be easily estimated assuming that the pulse decay is exponential with a time constant (τ) approximately equal to

$$\tau = \frac{1}{2\pi B} \tag{90.10}$$

where B is the –3 dB channel bandwidth. The cross talk (k) between channels can be approximated as

$$k = -54.5T_g \text{ (dB)} \tag{90.11}$$

where T_g is the minimum time separation between channels, called guard time.

A common situation in measurement systems occurs when the M signals that need to be measured have very different speeds. The channel sampling rate is determined by the fastest signal, thus needing an M-input multiplexer capable of handling signals at that sampling frequency. A convenient solution is to feed several slow signals into one multiplexer, then combine its output with the fast signal in a second multiplexer [6].

90.2.3.1 Subcarrier Modulation Schemes for Time Division Multiplexing

In this process, the signal that results after the multiplexing and sampling process modulates a train of pulses. The most common methods for subcarrier modulation are pulse amplitude modulation (PAM), pulse duration modulation (PDM), and pulse position modulation (PPM). Figure 90.7 illustrates these three modulation schemes, where the pulses are shown square for simplicity. The parameter that is modulated (amplitude, duration, or relative position) changes proportionally to the amplitude of the sampled signal. However, in PAM and PDM, the values have an offset, so that when the value of the sample

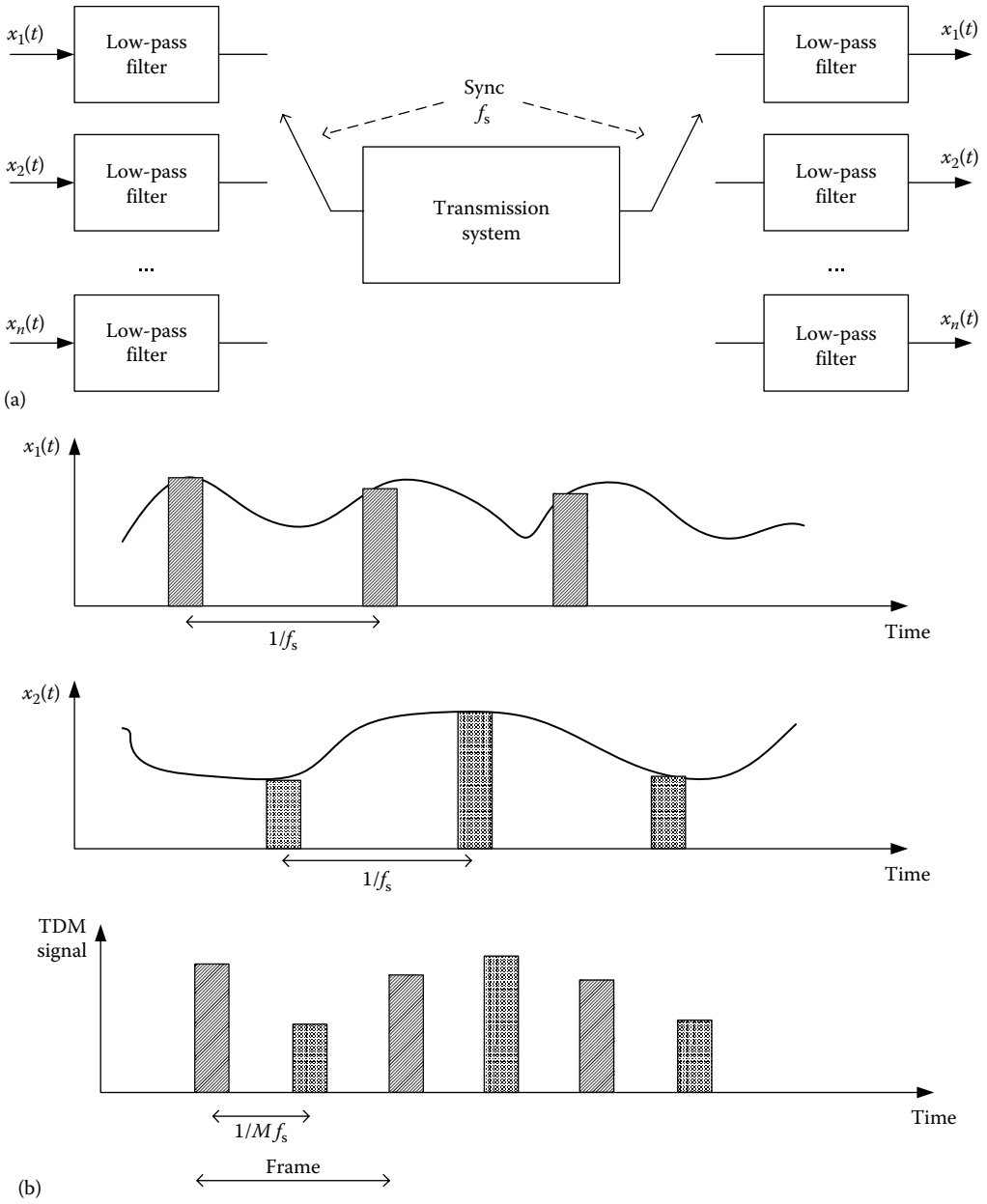

FIGURE 90.6 (a) Block diagram of a TDM system based sequentially sampling M different channels at a sampling frequency f_s and sending the information for each channel sequentially. (b) Time representation of the TDM system.

is zero, the pulse amplitude or the pulse width is different from zero. The reason for these offsets is to maintain the rate of the train of pulses constant, which is very important for synchronization purposes. The common characteristics of the different analog modulation schemes for pulses in TDM are (1) a modulated signal spectrum with a large low-frequency content, especially close to the sampling frequency; (2) the need to avoid overlaying between consecutive pulses in order to conserve the modulation parameters; and (3) the possibility of reconstructing the original samples from the modulated signal through low-pass filtering after demultiplexing. The reduction of noise depends on the bandwidth of the modulated signal, with this being the principal design criterion.

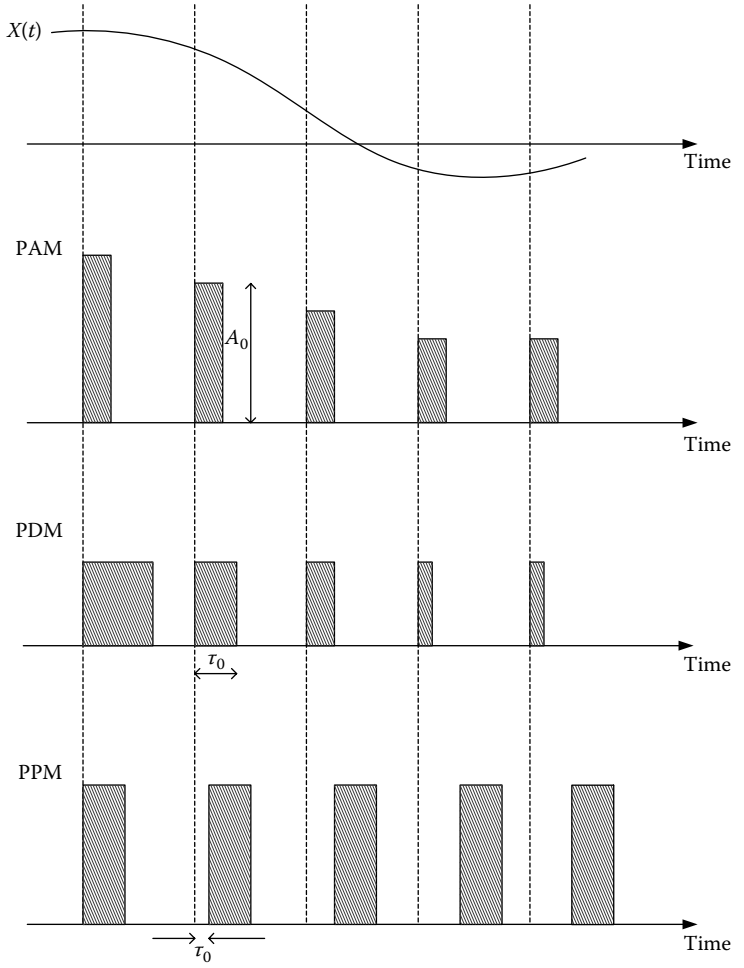

FIGURE 90.7 Different modulation schemes used in TDM. The variations in amplitude of the signal $x(t)$ are transmitted as amplitude variations of pulses (PAM), duration changes of pulses (PDM), or changes in the relative position of the pulses (PPM). In all the cases, level 0 is transmitted by a pulse whose amplitude (A_0), duration (τ_0), or relative position (τ_0) is different from 0.

90.2.3.1.1 Pulse Amplitude Modulation

PAM waveforms are made of unipolar, nonrectangular pulses whose amplitudes are proportional to the values of the samples. It is possible to define the modulation index using similar criteria as in analog AM. Similarly, in PAM the modulation index is limited to values less than 1.

90.2.3.1.2 Pulse Duration Modulation

PDM is made of unipolar, rectangular pulses whose durations or widths depend on the values of the samples. The period between the center of two consecutive pulses is constant. The analysis of the resulting spectrum shows that it is possible to reconstruct the samples by low-pass filtering [9].

90.2.3.1.3 Pulse Position Modulation

PPM is closely related to PDM, as PPM can be generated through PDM. In PPM the information resides on the time location of the pulses rather than in the pulses by themselves. It is then possible to transmit very narrow pulses to reduce the energy needed; this energy reduction is the most important advantage of PPM.

90.2.4 Pulse Code Modulation in Time Division Multiplexing

All the previously analyzed subcarrier modulation schemes in telemetry systems are based on an analog signal that modulates either an analog carrier or a train of pulses. Pulse code modulation (PCM) is different: it is a digital modulation in which the measured signal is represented by a group of codified digital pulses. Two variations of PCM that are also often used are delta modulation (DM) and differential pulse code modulation (DPCM). In analog modulation schemes, the modulating signal from the transducer can take any value between the limits. If noise alters the modulating signal, it is impossible to decide its real value. Instead, if not all the values in the modulating signal are allowed and the separation between the allowed levels is higher than the expected noise values, it is then possible to decide which were the values sent by the transmitter. This immunity against noise makes PCM systems one of the preferred alternatives for telemetry. Figure 90.8 shows the basic elements of a PCM telemetry system. A PCM encoder (or PCM commutator) converts the input data into a serial data format suitable for transmission through lines by wireless techniques. At the receiving end, a PCM decoder (or PCM decommutator) converts the serial data back into individual output data signals. PCM systems transmit data as a serial stream of digital words. The PCM encoder samples the input data and inserts the data words into a PCM frame. Words are assigned specific locations in the PCM frame, so the decoder can recover the data samples corresponding to each input signal. The simplest PCM frame consists of a frame synchronization word followed by a string of data words. The frame repeats continually to provide new data samples as the input data change. Frame synchronization enables the PCM decoder to locate the start of each frame easily.

The IRIG standard also defines the characteristics of PCM transmission for telemetry purposes; in particular, the pulse train structure and system design characteristics. The PCM formats are divided into two classes for standards purposes: class I and class II. The simpler types are class I, whereas the more complex types are class II. Some of the characteristics of class II systems are bit rates greater than 5 Mbit/s, word lengths in excess of 16 bits, fragmented words, unevenly spaced subcommutation, format changes, tagged data formats, asynchronous data transmission, and merger of multiple format types, among others. Table 90.5 provides a brief summary of relevant PCM specifications.

The following PCM codes, shown in Figure 90.9, are recognized by the IRIG standards: NRZ-L (nonreturn-to-zero level), NRZ-M (nonreturn-to-zero mark), NRZ-S (nonreturn-to-zero space), BiØ-L (biphase level), BiØ-M (biphase mark) and BiØ -S (biphase space). The standard also recommends that the transmitted bit stream be continuous and contain sufficient transitions to ensure bit acquisition and continued bit synchronization. Bit rates should be at least 10 bits/s. If the bit rate is above 5 Mbit/s, the PCM system is classified as class II. In reference to the word formats, the standard defines a fixed format as one that does not change during transmissions with regard to the frame structure, word length or location, commutation sequence, sample interval, or measurement list. Individual words may vary in length from 4 bits to not more than 16 bits in class I and not more than 64 bits in class II. Fragmented words, defined as a word divided into not more than eight segments and placed in various locations within a minor frame, are only allowed in class II. All word segments used to form a data word are constrained to the boundaries of a single minor frame.

The frame structure allowed by the standards for PCM telemetry specifies that data are formatted into fixed frame lengths that contain a fixed number of equal-duration bit intervals. A minor frame is defined as the data structure in time sequence from the beginning of a minor frame synchronization

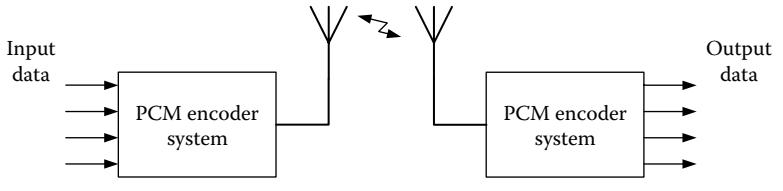

FIGURE 90.8 Block diagram showing a basic PCM link for telemetry.

TABLE 90.5 Summary of Relevant PCM Specifications

Specification	Class I	Class II
Class format support	Class I (simple formats) supported on all ranges	Class II (complex formats) requires concurrence of range involved
Primary bit representation (PCM codes)	NRZ-L, NRZ-M, NRZ-S, RNRZ-L, BiØ-L, BiØ-M, BiØ-S	Same as class II
Bit rate	10 bps–5 Mbps	10 bps to >5 Mbps
Bit rate accuracy and Stability	0.1%	Same as class I
Bit jitter	0.1 bit	Same as class I
Bit numbering	MSB = bit number 1	Same as class I
Word length	4–16 bits	4–64 bits
Fragmented words	Not allowed	Up to 8 segments each; all segments in the same minor frame
Minor frame length	<8192 bits or <1024 words (includes synchro)	<16,384 bits (includes synchro)
Major frame length	<256 minor frames	Same as class I
Minor frame numbering	First minor frames in each major frames number 1	Same as class I
Format change	Not allowed	Frame structure is specified by frame format identification (FFI) word in every minor frame

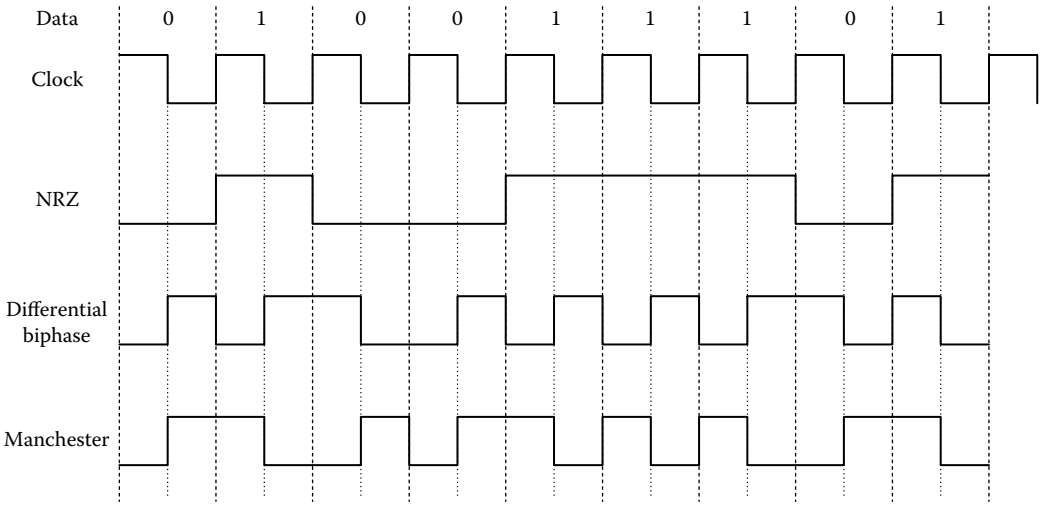

FIGURE 90.9 IRIG standards. *NRZ* (nonreturn to zero): "1" represented by a high logic level and "0" represented by a low logic level. *Differential biphase*: "1" represented by a change in level at the start of the clock period and "0" represented by no change of level at the start of the clock period. There is always a change of level at the middle of the clock period. *Manchester*: "1" represented by a high-to-low transition at the middle of the clock period and "0" represented by a low-to-high transition at the middle of the clock period.

pattern to the beginning of the next minor frame synchronization pattern. The minor frame length is the number of bit intervals from the beginning of the frame synchronization pattern to the beginning of the next synchronization pattern. The maximum length of a minor frame will not exceed 8,192 bits or 1,024 words in class I and will not exceed 16,384 bits in class II. Minor frames consist of the synchronization pattern, data words, and subframe synchronization words if they are used. The standard allows the use of words of different length if they are multiplexed in a single minor frame. Figure 90.10 shows a graphical representation of a PCM frame structure. Major frames contain the number of minor frames

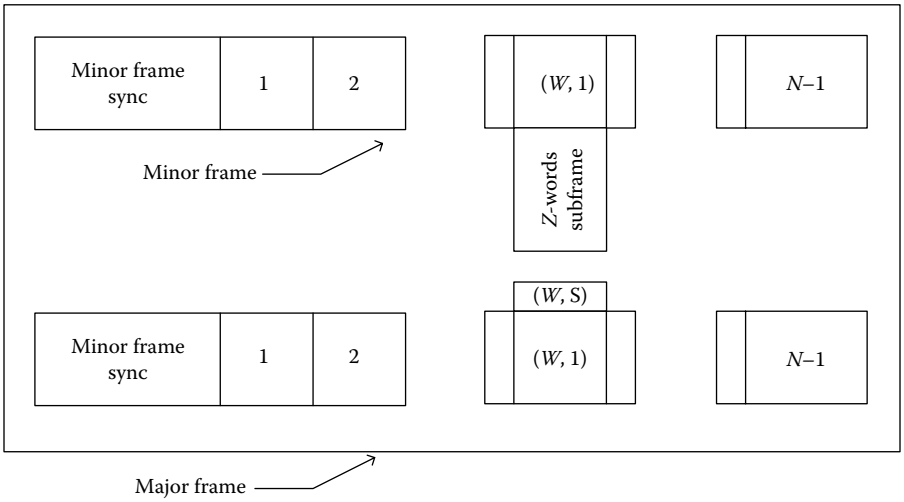

FIGURE 90.10 Structure of a PCM frame. The maximum length of a minor frame is 8192 bits or 512 for class I and 16,284 bits for class II. A major frame contains $N \times Z$ words, where Z is the number of words in the maximum subframe and N is the number of words in the minor frame. Regardless of its length, the minor frame synchronism is considered as one word. W is the word position in the minor frame, while S is the word position in the subframe.

required to include one sample of every parameter in the format. Their length is defined as minor frame length multiplied by the number of minor frames contained in the major frame. The maximum number of minor frames per major frame is limited to 256.

The IRIG standard also gives recommendations for maximal transmission efficiency in PCM telemetry. The IF bandwidth for PCM telemetry data receivers should be selected so that 90%–99% of the transmitted power spectrum is within the receiver 3 dB bandwidth. The IF also has effects on the bit error probability (BEP) according to the following equation for NRZ-L PCM/FM [10]:

$$\text{BEP} = 0.5 * e^{k\,SNR} \tag{90.12}$$

where

$k \approx -0.7$ for IF bandwidth equal to bit rate
$k \approx -0.65$ for IF bandwidth equal to 1.2 times bit rate
$k \approx -0.55$ for IF bandwidth equal to 1.5 times bit rate

Figure 90.11 shows a graphical representation of the bit error rate versus the SNR for these three values of k.

Other data codes and modulation techniques have different BEP versus SNR performance characteristics, but in any case, they will have similar trends.

The standard also specifies the recommended frame synchronization patterns for general use in PCM telemetry. There are different lengths for synchronization patterns, but in all of them, the 111 is the first bit sequence transmitted. The patterns for lengths 16–30 were selected in order to minimize the probability of false synchronization over the entire pattern overlap portion of the ground station frame synchronization [9]. The spectral density (S) for the NRZ and BiØ codes are

$$\text{NRZ Codes} \quad S = \frac{\sin^2(\pi f T)}{(\pi f T)^2} \tag{90.13}$$

$$\text{Biphase Codes} \quad S = \frac{\sin^4(\pi f T/2)}{(\pi f T/2)^4} \tag{90.14}$$

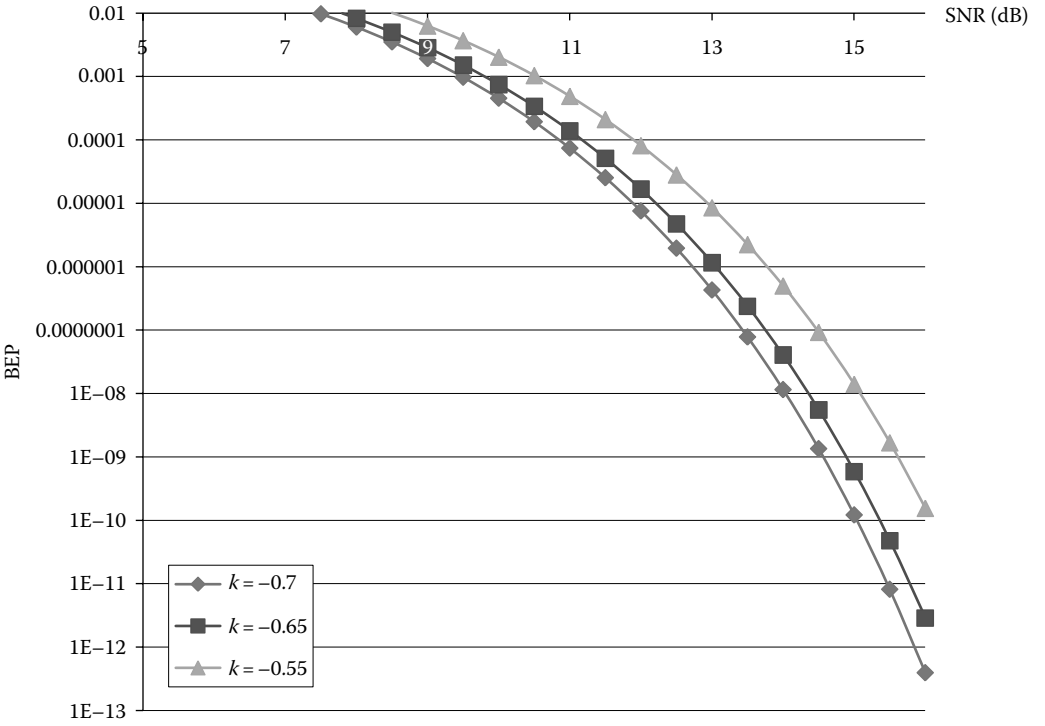

FIGURE 90.11 Bit error rate versus SNR for three values of the parameter k.

The calculation of spectral densities allows the determination of the BEP for the previous type of codes assuming perfect bit synchronization. These calculations show that for the same SNR, the lowest BEP is achieved for NRZ-L and Bi codes, followed by NRZ and BiØ mark and space codes and finally for random NRZ-L codes (RNRZ-L).

Defining Terms

Bandwidth: The range of frequencies occupied by a signal.

Carrier: A frequency that is modulated by a signal containing information.

Channel: A subcarrier that carries information.

Constant-bandwidth (CBW) channel: A channel whose bandwidth is independent of its carrier frequency.

Deviation ratio: The ratio of the maximum carrier frequency deviation to the maximum data frequency deviation.

Frequency deviation: The difference between the center frequency of a carrier and its upper or lower deviation limit.

Frequency division multiplexing (FDM): A composite signal consisting of a group of subcarriers arranged so that their frequencies do not overlap or interfere with each other.

Frequency response: The highest data frequency that can be carried by the channel.

IRIG: Inter-Range Instrumentation Group of the Range Commanders Council (RCC).

Proportional-bandwidth (PBW) channel: A channel whose bandwidth is proportional to its carrier frequency.

Remote switching: Telemetry consisting only of yes/no or on/off orders.

Signaling: Telemetry consisting of binary information.

Subcarrier: A carrier combined with other carriers to create a composite signal.

Subcarrier bandwidth: The difference between the upper and lower frequencies of a modulated carrier.

References

1. B.P. Dagarin, R.K. Taenaka, and E.J. Stofel, Galileo probe battery system, *IEEE Aerospace Electron. Syst. Mag.*, 11 (6): 6–13, 1996.
2. M.W. Pollack, Communications-based signaling: advanced capability for mainline railroads, *IEEE Aerospace Electron. Syst. Mag.*, 11 (11): 13–18, 1996.
3. M.C. Shults, R.K. Rhodes, S.J. Updike, B.J. Gilligan, and W.N. Reining, A telemetry-instrumentation system for monitoring multiple subcutaneously implanted glucose sensors, *IEEE Trans. Biomed. Eng.* 41: 937–942, 1994.
4. M. Rezazadeh and N.E. Evans, Multichannel physiological monitor plus simultaneous full-duplex speech channel using a dial-up telephone line, *IEEE Trans. Biomed. Eng.*, 37: 428–432, 1990.
5. Y.S. Trisno, P. Hsieh, and D. Wobschall, Optical pulses powered signal telemetry system for sensor network application, *IEEE Trans. Instrum. Meas.*, 39: 225–229, 1990.
6. R. Pallás-Areny and J.G. Webster, *Sensors and Signal Conditioning*, 2nd edn., New York: John Wiley & Sons, 486–489, 2001.
7. H. Taub and D.L. Schilling, *Principles of Communication Systems*, 2nd edn., New York: McGraw-Hill, 1986.
8. K.M. Uglow, Noise and bandwidth in FM/FM radio telemetry, *IRE Trans. Telemetry Remote Control*, pp. 19–22, 1957.
9. J.L. Maury and J. Styles, Development of optimum frame synchronization codes for Goddard space flight center PCM telemetry standards, *Proceedings of the National Telemetering Conference*, Houston, TX, 1964.

Relevant Websites about Telemetry

http://www.irig106.org/: IRIG 106 is a comprehensive telemetry standard to ensure interoperability in aeronautical telemetry applications.

http://irig.org/: IRIG ORG is an informational website that is available to all who are interested in quick and easy access to telemetry or IRIG information.

http://www.irig106.org/docs/123-09/IRIG_106-07_Chapter_10_Programming_Handbook.pdf: *IRIG Standard Programming Handbook*.

http://www.telemetry.org: International Telemetry Conference held annually in the United States.

http://www.telemetry-europe.org/: European Society of Telemetry.

X

Control and Human Factors

91

PID Control

F. Greg Shinskey
Process Control Consultant

91.1 Introduction

Process control plays an essential role in the safe manufacture of quality products at market demand while protecting the environment. Flow rates, pressures, and temperatures within pipes and vessels, inventories of liquids and solids, and product quality are all examples of measured variables that must be controlled to meet the above objectives. While there are several means available for controlling these variables, the proportional–integral–derivative (PID) family of controllers has historically carried the major share of this responsibility and, because of their simplicity and reliability, will continue to do so in the future.

The acronym PID stands for the three principal modes of the controller, each of which bears a mathematical relationship between the controlled variable c and the manipulated variable m driven by the controller output. The proportional mode relates changes in m to changes in c through a proportional gain. The integral mode moves the output at a rate related to the deviation of c from its desired value, known as the set point or reference r. Finally, the derivative mode moves the output in response to the time derivative or rate of change of c. Interestingly, the mathematical relationships were actually determined *after* controllers had already been created to solve process-control problems. The integral mode was initially called *automatic reset*, and the derivative mode *hyper-reset* or *pre-act* [1].

91.2 Open and Closed Loops

Figure 91.1 describes the process and controller in functional blocks connected in a loop. Inputs to the process are manipulated m and load q variables, usually rates of flow of material or energy into or out of the process. The load may be a single variable or an aggregate, either independent or

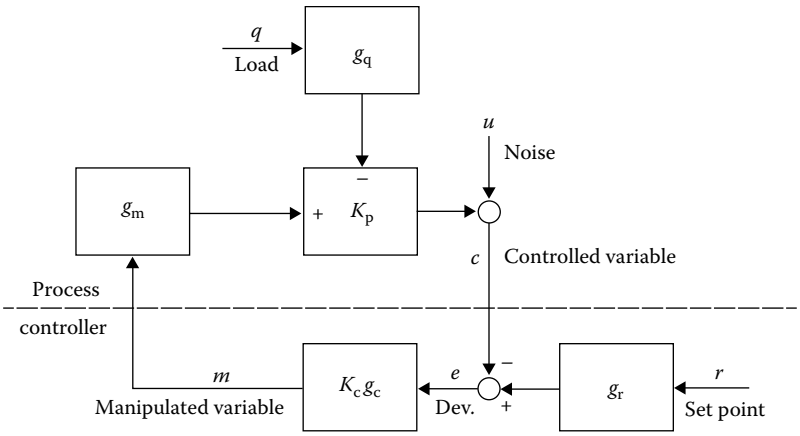

FIGURE 91.1 Process and controller connected in a loop.

manipulated or controlled by another controller. If independent, it is often unmeasured, with its value inferred by the level of controller output required to maintain the controlled variable at set point. Noise u is shown affecting the controlled variable directly, typically caused by local turbulence in flow, pressure, and liquid-level measurements or by nonuniformity of streams whose composition is measured.

91.2.1 Open-Loop Responses

In the absence of automatic control, the controlled variable is subject to variations in the load and to manual adjustments to m intermittently introduced by operators. These cause variations in c following both the steady-state and dynamic functions appearing in Figure 91.1:

$$c = K_p\left(mg_m - qg_q\right) + u \tag{91.1}$$

where

K_p is the steady-state gain
g_m and g_q are the dynamic-gain vectors in the manipulated and load paths, respectively
u is the noise level

The vectors have both magnitude and phase angle that are functions of the frequency or period of the signal passing through. In the *open loop*, variations in m are likely to be steps introduced by operators, but variations in q could take any form—steps, ramps, random variations, or cycles—depending on the source of the disturbance. Steps are easily introduced manually and contain all the frequencies from zero to infinity; consequently, they are useful for evaluating loop response and testing the effectiveness of controllers. Noise is typified by random variations in a frequency range above the bandwidth of the control loop.

The dynamic elements typically consist of dead time and lags. However, liquid level is the *integral* of the difference between inflow and outflow [2], in which case K_p in Figure 91.1 is replaced by an integrator. Any difference between inflow and outflow will then be integrated, causing the liquid level to continue rising or falling until the vessel limit is reached. This process has no self-regulation and therefore cannot be left indefinitely in an open loop.

91.2.2 Closed-Loop Responses

In the *closed loop*, c responds to load and set point as follows:

$$c = \frac{rg_r}{1 + 1/K_p g_m K_c g_c} - \frac{qg_q}{g_m K_c g_c + 1/K_p} + u \tag{91.2}$$

where

K_c is the proportional gain of the controller
g_c is the dynamic gain of its integral and derivative modes
g_r that of its set-point filter

For the typical *self-regulating* process in the open loop, c will take an exponential path following a step change in load as shown by the dashed curve in Figure 91.2. If the loop is closed, the controller can move m to return c to r along the solid curve in Figure 91.2, an optimum trajectory having a minimum integrated absolute error (IAE) between c and r. The leading edge of the curve depends on g_q and the trailing edge depends on g_m and the PID settings. If the PID settings are optimized for load response, they will usually cause c to overshoot a change in set point r, as shown by the dashed curve in Figure 91.3. If the PID settings are then readjusted to reduce set-point overshoot, load response is extended. A preferred solution is to insert a lead–lag filter in the set-point path, which produced the solid curve in Figure 91.3.

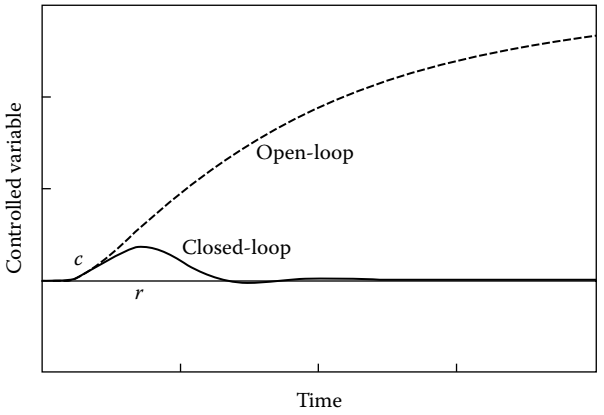

FIGURE 91.2 Closed-loop control minimizes error.

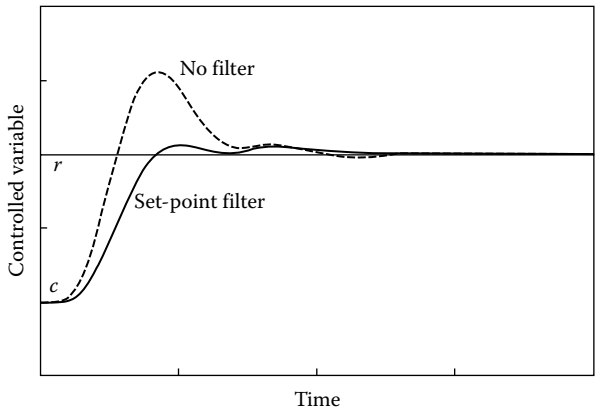

FIGURE 91.3 A lead–lag filter reduces overshoot.

91.3 Mode Selection

The family of PID controllers includes proportional (P), integral (I), proportional–integral (PI), proportional–derivative (PD), and two PID controllers. Each has its own advantages and limitations and therefore its preferred range of applications. Each is outlined along with an application.

91.3.1 Proportional Control

In a *proportional* controller, the deviation between c and r must change for the output to change:

$$m = b \pm K_c(r - c) \tag{91.3}$$

where b is an adjustable bias, also known as "manual reset," and the sign of the deviation is selected to provide negative feedback. Some controllers have proportional gain adjustable as percent proportional band P, where $K_c = 100/P$. If m must move to a different steady-state value because of a change in load or set point, the deviation will also change. Therefore, the proportional controller allows a steady-state offset between c and r whenever m does not equal b, which can only be eliminated by manually resetting b. Proportional control is recommended for liquid level, where K_c can be set quite high without loss of stability and there is no economic penalty for offset.

Proportional control of liquid level is actually preferred when manipulating the flow leaving a tank as the feed to a critical downstream process. Setting K_c slightly above 1.0 will keep the level in the tank for all rates of inflow while minimizing the rate of change of outflow. This application is called averaging level control [2].

91.3.2 Integral Control

The *integral* mode eliminates offset by driving the output at a rate proportional to the deviation:

$$\frac{dm}{dt} = C \pm \frac{r - c}{I} \tag{91.4}$$

where

t is time
d is the differential operator
I is the integral time setting
C is the constant of integration, i.e., the initial value of the controller output when placed on automatic

Some controllers have integral time adjusted as integral gain or "reset rate" $1/I$ in inverse time as "repeats per minute." Integration produces a phase lag of 90° between input and output, which increases the response time and period of oscillation of the loop. The integral controller *cannot be* used for liquid level, because two integrators in series form an unstable closed loop [2]. Its use is limited to optimizing the set points of other closed loops that are already stable [2].

91.3.3 PI Control

The PI controller combines the proportional and integral modes:

$$m = C \pm K_c\left[r - c + \frac{1}{I}\int (r - c)dt\right] \tag{91.5}$$

The deviation and its integral are added vectorially, producing a phase lag falling between 0° and 90°. This combination provides stability with elimination of offset, making it the most common controller used in the fluid-processing industries. It is used almost universally, even in those applications where other controllers are better suited.

91.3.4 PD Control

The addition of derivative action to a proportional controller adds response for the rate of change of the controlled variable:

$$m = b \pm K_c\left(r - c - D\frac{dc}{dt}\right) \tag{91.6}$$

where D is the derivative time setting. Derivative action is preferably applied only to c as indicated and not to the set point, which would only increase set-point overshoot. A pure derivative function has a dynamic gain increasing indefinitely with frequency—to avoid instability within the controller, it is usually limited to about 10 by filtering. This provides an optimum combination of responsiveness and noise rejection. Still, the high-frequency gain amplifies noise in flow and liquid-level measurements enough to prevent the use of the derivative mode on those loops; temperature measurements are usually noise-free, allowing it to be used to advantage there. The phase lead provided by the derivative mode reduces the period of oscillation and settling time of a loop and improves stability.

PD controllers are recommended for batch processes, where operation begins with c away from r and ends ideally with $c = r$ and flows at zero. The PD controller must be biased for this final output state, with D adjusted to eliminate overshoot, which for a zero-load process is permanent [2].

91.3.5 PID Controllers

The phase lead of derivative action more than offsets the phase lag of integral in a properly adjusted PID controller, resulting in a net phase lead and typically half the IAE of a PI controller applied to the same process. There are two types of PID controllers in common use, which differ in the way the modes are combined [3]. Early controllers combined PD and PI action in series, multiplying those functions rather than adding them. These interacting PID controllers remain in common use, even implemented digitally. Noninteracting controllers combine the integral and derivative modes in parallel, producing a more mathematically pure PID expression:

$$m = C \pm K_c\left[r - c - \frac{1}{I}\int(r - c)dt - D\frac{dc}{dt}\right] \tag{91.7}$$

The interacting controller can be described in the same form, but the coefficients of the individual terms are different [3]. The effective integral time of the interacting controller is $I + D$, its effective derivative time is $1/(1/I + 1/D)$, and its proportional gain is augmented by $1 + D/I$. Thus, the principal result of mode interaction is to require different PID settings for the two controllers applied to the same process.

A block diagram of a commercial interacting PID controller appears in Figure 91.4 with transfer functions described in Laplace transforms whose operator s is equivalent to the differential operator d/dt. Integration is achieved by positive feedback of the output through a first-order lag set at the integral time. The feedback signal f is taken downstream of the high and low limits and may be replaced with a constant or other variable to stop integration, in which case, the controller behaves as PD with remote bias. This feature is extremely valuable in preventing reset windup, which occurs whenever a controller with integral action remains in automatic while the loop is open, and results in a large overshoot when the loop is then closed [3]. Most noninteracting controllers lack this feature.

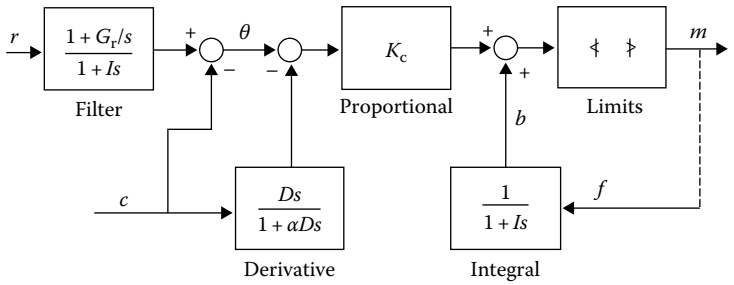

FIGURE 91.4 Commercial interacting PID controller.

Derivative action combines a differentiator Ds with a lag (filter) of time constant αD, where α represents the inverse of the high-frequency gain limit of typically 10. Figure 91.4 also shows a lead–lag set-point filter having a lag time constant of integral time and lead time of $G_r I$, which produces a gain of G_r to a step in set point. This gain is adjustable from 0 to 1, with 1 eliminating the filter and zero imposing a first-order lag. The effect of this lag is equivalent to eliminating proportional action from r in Equations 91.5 and 91.7, an optional feature in some PID controllers. The gain adjustment offers more flexibility in optimizing set-point response as in Figure 91.3; G_r is set around 0.3 for lag-dominant processes such as those described in Figures 91.2 and 91.3 and closer to 1 for dead time–dominant processes [3].

91.4 Controller Hardware

Pneumatic proportional controllers were first used early in this century, with integral and then derivative functions added around 1930. Pneumatic controllers are still in use in hazardous areas, in remote gas fields where they are operated by gas, and for simple tasks such as regulating temperatures in buildings. Electronic analog controllers began to replace pneumatic controllers in the late 1950s, but their functions were implemented using digital microprocessors beginning around 1980. Digital control initially began in mainframes in the 1960s but now is available in programmable logic controllers (PLC), personal computers (PCs), and in distributed control systems (DCS).

91.4.1 Pneumatic Controllers

The simplest pneumatic controllers are proportional units used to control heating, ventilating, and air-conditioning (HVAC) in buildings. However, complete PID controllers with functionality similar to that shown in Figure 91.4 are also available, used for such demanding tasks as temperature control of batch exothermic reactors and regulation of flows and pressures on offshore oil platforms. There are panel-mounted units available as well as weatherproof models used for field installation. Most have automanual transfer stations with bumpless transfer between the two modes of operation. Their principal limitations are a speed of response limited by transmission lines (lengths beyond 30 m are unsuitable for flow and pressure control) and lack of computing capability (required for nonlinear characterization and automatic tuning).

91.4.2 Electronic Controllers

The first electronic controllers mimicked their pneumatic counterparts while eliminating transmission lags. Eventually remote automanual transfer and remote tuning were added, and microprocessors brought these controllers calculation and logic functions, signal conditioning and characterization, and autotuning and self-tuning features as well. Multiple controllers are even available in a single station for implementing cascade and feedforward systems. The bandwidth of electronic *analog* controllers extends

to 10 Hz and in some units even further. *Digital* controllers execute their calculations intermittently rather than continuously; most are limited to 10 Hz operation, which with digital filtering results in an effective dead time of 0.1 s, reducing bandwidth to about 1.3 Hz.

Electronic controllers are used extensively in field locations and dedicated to control of individual units such as pumps, dryers, wastewater-treatment facilities—wherever only a few loops are required. Peer-to-peer communication is available in some controllers for incorporation into networks, and most can communicate with PC where data can be displayed on a graphic interface. Configuration (selection of scales, control modes, alarms, and other functions) can be done either via keys on the controller faceplate or through a PC.

91.4.3 Digital Controllers

While the stand-alone digital controller evolved from electronic analog models, centralized digital controllers originated with digital computers. Mainframe computers were first used for direct digital control (DDC) where valves were manipulated by the computer, and for supervisory control, where the computer positioned set points of analog controllers. Gradually minicomputers and microprocessors replaced the mainframe, with functions becoming *distributed* among field input–output modules, workstations, control modules, etc., in clusters and other configurations such as DCS. PCs are used for some workstations and even for direct control in some plants.

Where many loops are controlled by a single processor, the interval between samples is likely to be 0.5 s or even longer. Users tend to keep expanding the functions demanded of the processor, thereby extending the interval between samples. This reduces the bandwidth of DCS controllers to values too low for combustion and compressor controls. Some digital PID algorithms produce an *incremental* output Δm, requiring an integrator downstream to produce m. These are not available in proportional or PD action because they have no fixed bias b, but only a constant of integration C that is subject to change whenever the controller is operated manually.

The PLC was originally a replacement for relay logic. Eventually PID loops were added, which generally operate much faster (e.g., 100 Hz) than other digital controllers. However, many have nonstandard algorithms and lack the functionality of other PID controllers, such as proportional and PD control, windup protection, derivative filtering, set-point filtering, nonlinear characterization, and autotuning.

91.5 Tuning Controllers

A controller is only as effective as its *tuning*: the adjustment of the PID settings relative to the process parameters to optimize load and set-point response as described in Figures 91.2 and 91.3. Tuning is required when the controller is first commissioned on a loop and may have to be repeated if process parameters change appreciably with time, load, set point, etc. Tuning requires the introduction of a disturbance in either the open or closed loop and interpretation of the resulting response. *Autotuning* essentially automates manual procedures, whereas *self-tuning* can recognize and correct an unsatisfactory response without testing.

91.5.1 Manual Tuning

Ziegler and Nichols [1] developed the first effective tuning methods, and these are still used today. Their open-loop method steps the controller output to produce a response like the broken curve in Figure 91.2. The apparent dead time (delay) in the response and the steepest slope of the curve are then converted into appropriate settings for PI and PID controllers using simple formulas. The open-loop method is most accurate for lag-dominant processes, but the closed-loop method is more broadly applicable. It is based on inducing a uniform cycle by adjusting the gain of a controller with only its

proportional mode effective (D is set to 0 and I at maximum). The period of the cycle and the controller gain are then used to calculate appropriate PID settings.

The open-loop method has been extended to other processes [3] but remains limited to the accuracy of step-test results. Fine-tuning must be done with the loop closed: With the deviation zero, place the controller in manual, step the output, and immediately transfer to automatic—this simulates a closed-loop load change. The resulting response should appear like the solid curve in Figure 91.2, having a first peak, which is symmetrical, followed by a slight overshoot and well-damped cycle. If the overshoot is excessive, I and/or D time should be increased; in the case of undershoot, they should be decreased. (To simplify tuning of PID controllers, I and D can be moved together, keeping the I/D ratio at about 4 for noninteracting controllers and 3 for interacting controllers.) If damping is light, lower the proportional gain; if recovery is slow (producing an unsymmetrical first peak), raise the proportional gain. The set point should *not* be stepped for test purposes unless set-point response is important, as for flow controllers.

91.5.2 Autotuning

Some autotuning controllers use a step test in the open loop, implementing Ziegler–Nichols rules. A single pulse produces more accurate identification, and a doublet pulse is better still [3]. A closed-loop method replaces proportional cycling with relay cycling, where the output switches between high and low limits as c crosses r [3]. The period of the resulting cycle is used to set I and D and its amplitude relative to the distance between output limits to set K_c. The principal limitation of the step and relay autotuning methods is that only two response features are used to identify a complex process. The estimated PID settings may not fit the specific process particularly well, resulting in instability in some loops and sluggishness in others. The autotuning function cannot monitor the effectiveness of its work, as self-tuning does.

91.5.3 Self-Tuning

A self-tuning controller need not test the process, but simply observe its closed-loop response to set-point and load changes with its current PID settings. It then performs fine-tuning as described earlier to bring the overshoot or damping or symmetry of the response curve closer to optimum. This may require several iterations if the PID settings are far from optimum, but can eventually converge on optimum response, and readjust as necessary whenever process parameters change. Without a test disturbance, mischaracterization is possible, especially for a sinusoidal disturbance, where detuning may result when tightening would give better control.

Defining Terms

Averaging level control: Allowing the liquid level in a tank to vary in an effort to minimize changes in its outflow.

Closed-loop response: The response of a controlled variable to changes in set point or load with the controller in the automatic mode.

Derivative action: The change in controller output responding to a rate of change in the controlled variable.

Dynamic gain: The ratio of the change in output from a function to a change in its input that varies with time or with the frequency of the input.

Integral action: The rate of change of controller output responding to a deviation between the controlled variable and set point.

Load: A variable or aggregate of variables that affects the controlled variable.

Manipulated variable: A variable changed by the controller to move the controlled variable.

Noise: A disturbance having a frequency range too high for the controller to affect.

Offset: Steady-state deviation between the controlled variable and set point.

Open-loop response: The response of a controlled variable to process inputs in the absence of control action.

Proportional action: The change in controller output responding directly to a change in the controlled variable.

Proportional band: The percentage change in the controlled variable required to drive the controller output full scale.

Self-regulation: The property of a process through which a change in the controlled variable affects either the flow into or out of a process in such a way as to reduce further changes in the controlled variable.

Tuning: Adjusting the settings of a controller to affect its performance.

Windup: Saturation of the integral model of a controller that results in the controlled variable subsequently overshooting the set point.

References

1. J. G. Ziegler and N. B. Nichols, Optimum settings for automatic controllers, *Trans. ASME*, 64, 759–768, 1942.
2. F. G. Shinskey, *Process Control Systems*, 4th edn., New York: McGraw-Hill, pp. 22–25, 25–28, 192–194, 388–390, 1996.
3. F. G. Shinskey, *Feedback Controllers for the Process Industries*, New York: McGraw-Hill, pp. 68–70, 176–178, 157–164, 148–151, 155–156, 1994.

Further Readings

Astrom, K. J. and T. Hagglund, *Advanced PID Control*, Triangle Park, NC: ISA Publication, 2006.

Finn Peacock, PID loop tuning, http://www.pidtuning.net/ (accessed on July 24, 2012).

PID Algorithm, Straight line control, LLC, http://straightlinecontrol.com/pid_algorithms.html (accessed on July 25, 2012).

Partial List of Suppliers

Applied Processor & Measurement, 8201 Old Post Rd. E., East Amherst, NY 14051, Phone: 716-741-1141, Fax: 716-741-1142, www.appliedprocessor.com

Autonics, 1353 Armour Blvd., Mundelein, IL 60060, Phone: 847-680-8160, 866-862-2602 (toll free), Fax: 847-680-8155, www.autonicsonline.com

Control Warehouse, 356 Cypress Rd., Ocala, FL 34472, Phone: 888-212-5531 (toll free), Fax: 352-687-8925, www.controlswarehouse.com

Divelbiss, 9778 Mt. Gilead Rd., Fredericktown, OH 43019, Phone: 740-694-9015, 800-245-2327 (toll free), Fax: 740-694-9035, www.divelbiss.com

Miller Energy, Inc., 3200 S. Clinton Ave., South Plainfield, NJ 07080, Phone: 908-755-6700, 800-631-5454 (toll free), Fax: 908-755-0312, www.millerenergy.com

WATTCO, 500 S. Federal Hwy., P.O. Box 1811, Hallandale, FL 33009, Phone: 514-488-9124, 800-492-8826 (toll free), Fax: 514-488-9126, www.wattco.com/

92

Optimal Control and the Software

Halit Eren
Curtin University

92.1 Introduction

Optimal control maximizes (or minimizes) the value of a function chosen as the *performance index* or *cost function* from an operational control system. Optimal control theory, on the other hand, is the mathematics of finding parameters that causes the performance index to take an extreme value subject to system constraints.

Optimal control theory is based on calculus variations. It is a mathematical approach for determining control policies in control systems. Some of the first and main contributors of optimal control theory are Lev Pontryagin and his colleagues. The theory made a leap forward by the contribution of Richard Bellman in the United States. Optimal control is applied in many fields, such as satellites and aerospace, aircrafts and spacecrafts, chemical engineering, communications engineering, robots and robotics, power systems, electrical drives, computers and computer systems, management science, finance, and many other areas. In many applications, simple interconnections of control devices and controllers to the processes do not provide the most economical operations. Therefore, optimization is a powerful technique to obtain the best results from a known process. If the process is operating under a steady-state condition, optimization considers the process stationary, and it is only concerned with the operating points. When the process is stationary, the resulting optimum operating point can easily be maintained by setting the predetermined set points and precalculated control parameters. Nevertheless, if the process changes from time to time, new optimum set points for the system need to be determined for each change.

The performance of systems are optimized for many reasons such as improving the quality, increasing production, decreasing waste, obtaining greater efficiency, maximizing the safety, and saving time and energy. In many optimization problems, boundary conditions are imposed by the system for safety in operations, availability of minimum and maximum power, limitations in storage capacity, capability of the operating machinery, temperature, speed, force, acceleration, and indeed any hard physical reasons.

Many different types of mathematical methods may be employed for the solution of optimal control problems depending on the nature of the problem. For example, if the performance index and constraints can be formulated as linear algebraic functions of the controlled variables, then selection of the linear programming may be the best way to go. *Simplex methods* may provide a good way of solving the linear programming problem. If the equations describing the system are nonlinear, then the solution may involve nonlinear techniques or linearization of the problem in some subregions. If the problem involves determination of the largest value of a function with two or more variables, then the *steepest ascent (or descent) methods,* sometimes termed as *hill-climbing* or *gradient methods*, may be used.

Hill-climbing methods still are popular as they are easy to understand and to use. They are briefly discussed here to lay a good background for the sound understanding of optimal control theory.

An illustration of the hill-climbing technique in the region of absolute minima is given in Figure 92.1. This figure also illustrates a common pitfall in control theory, the local maxima and local

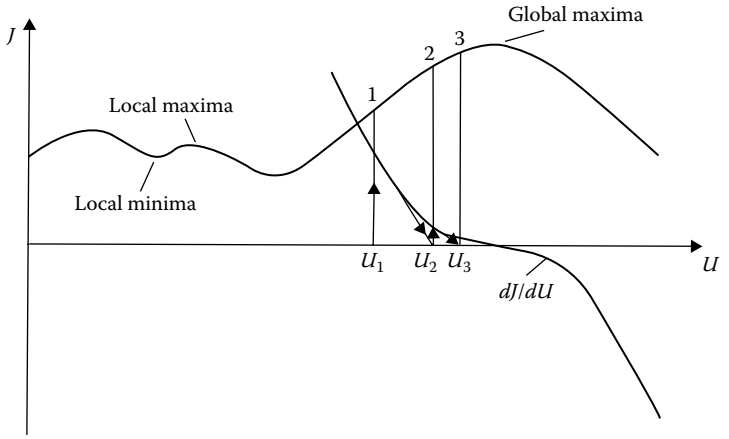

FIGURE 92.1 Hill-climbing technique illustrated in the region of absolute maxima. The sign of the first derivative of the function changes as the derivative passes through the maximum point. This figure shows the local maxima and minima that should be taken care of in optimal control design.

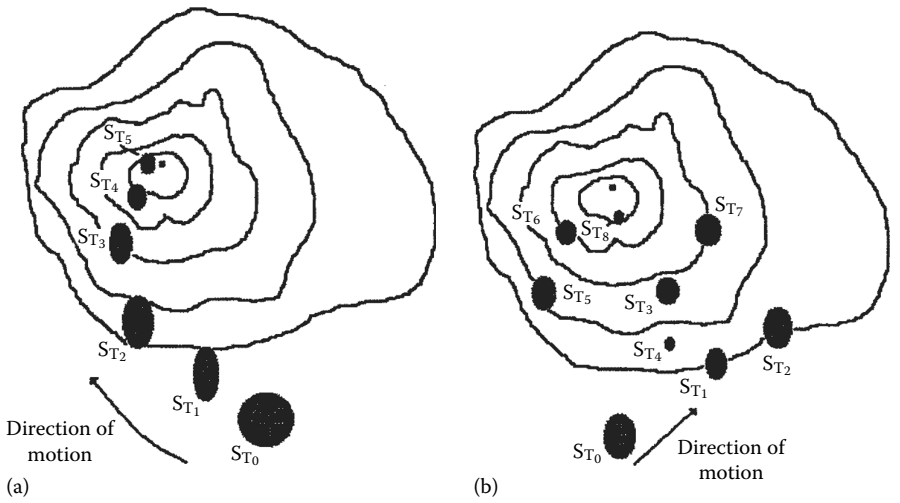

FIGURE 92.2 Examples of hill-climbing method: (a) gradient and (b) random walk. All these methods use an initial estimated point where the first derivative is guessed to be zero. This point is then used, in the direction of steepest ascent or steepest descent as the case may be, for the next point until the absolute maximum or minimum is found.

minima. As it can be seen, in this figure, the sign of the first derivative of the function changes as the derivative passes through the maximum point. This method commonly uses an initial estimated point where the first derivative is considered (guessed) to be zero. This point is then used, in the direction of steepest ascent or descent as the case may be, for the next point until the absolute maxima or minima is found without being trapped in local extreme points. There are many different methods to find maxima or minima by hill-climbing methods, and Figure 92.2 illustrates some examples of implementation.

Apart from hill-climbing techniques, there are many other and relatively new methods available for the solutions of modern optimal control problems. Some of the methods involve complex hyperspaces (many variables) having stringent constraints. If a good mathematical model describing the system is available, then various optimization methods may be used for finding the optimum conditions on the model itself rather than seeking optimum conditions on the actual process. This indicates that availability of the model determines the type of optimization method that can be employed.

92.2 Cost Functions

In designing optimal control systems, rules may be set for determining the control decisions, subject to certain constraints, such that some measure of deviations from an ideal case is minimized. That measure is usually provided by a selected *performance index* or *cost function*. Performance index is a function whose value indicates how well the actual performance of the system matches the desired performance. Appropriate selection of the performance index is important since it determines the nature and complexity of the problem. That is, the optimal control outcome will be dependent on the selected performance index. The choice of the performance index depends on system specifications, physical realizability, and the restrictions on the controls to be used. In general, the choice of an appropriate performance index involves a compromise between a meaningful evaluation of system performance and availability of a feasible mathematical description, which may be linear or nonlinear, or stationary or time varying.

The performance index is often selected by the engineer to make the system behave in a desired fashion. By definition, a system whose design minimizes the selected performance index is optimal. It is important to point out that a system optimal for a performance index may not be optimal under another performance index. In practical systems, due to possible complexities and cost of implementation, it may be better to employ approximate optimal control laws that are not rigidly tied to a single performance index.

Before starting optimization of any system, it is necessary to formulate the system by having information on system parameters and describing equations, constraints, class of allowable control vectors, and the selected performance indexes. Then the solution can be proceeded by determining the optimal *control vector* $\mathbf{u}(k)$ within the class of allowable vectors. The control vector $\mathbf{u}(k)$ will be dependent on factors such as the nature of performance index, constraints, initial values of state, initial outputs, and the desired state as well as the desired outputs. If analytical solutions are impossible or too complicated, then alternative computational solutions may be employed.

In simple cases, errors between the desired and actual responses can be selected as the performance index to be minimized. As an example, different descriptions of error between actual and desired responses are depicted in Figure 92.3. The aim is to keep the errors as small as possible. The time integral of an error gives the severity of the error. However, since the positive and negative errors mathematically cancel each other, absolute values must be used as

$$\text{Integral absolute error IAE} = \int_0^T |e(\tau)|\,d\tau \tag{92.1}$$

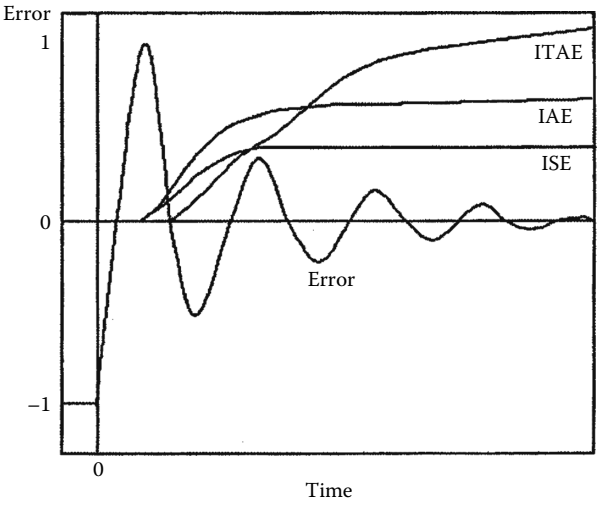

FIGURE 92.3 Description of errors between actual and desired responses. In simple optimal control applications, errors between the desired and actual responses can be selected as the performance indexes. The aim is to keep the errors as small as possible.

In many cases, it is better to use integral squared errors, which take into account large errors rather than regular ones

$$\text{Integral squared error ISE} = \int_0^T e^2(\tau)d\tau \tag{92.2}$$

Time-dependent functions can be implemented to capture errors occurring late in time rather than normal transients:

$$\text{Integral time absolute error ITAE} = \int_0^T |e(\tau)|\tau d\tau \tag{92.3}$$

and

$$\text{Integral time squared error ITSE} = \int_0^T e^2(\tau)\tau d\tau \tag{92.4}$$

The mean square error, MSE, is also commonly used since slight modification leads to inclusion of statistical techniques and analysis of random noise

$$\text{Mean square error MSE} = \lim_{T\to\infty} \frac{1}{T}\int_0^T e^2(\tau)\tau d\tau \tag{92.5}$$

Modern optimal control theory is developed within the *state-space* framework, and performance indexes are more complex and comprehensive, some of which are briefly visited as follows.

Suppose that the control command of a system is expressed in vectorial form as **u** and the state of the system is described by **x** (Oxford English Dictionary describes *state* as a condition with respect to circumstances, attributes, structure, form phase, or the like). Further, suppose that the rate of chance of state $\dot{\mathbf{X}}$ is a function of state **x**, control command **u,** and time *t*:

$$\dot{\mathbf{X}} = f(\mathbf{x}, \mathbf{u}, t) \quad \mathbf{x}(0) = \mathbf{x}_0 \tag{92.6}$$

Then a control law $\mathbf{u}(\mathbf{x}, \mathbf{t})$ or a control history $\mathbf{u}(t)$ can be determined such that a performance index or a scalar functional

$$J(u) = \int_0^T g(\mathbf{x}(\tau), \mathbf{u}(\tau), \tau) d\tau \tag{92.7}$$

This takes a minimum value out of all other possibilities and still holds as in Equation 92.6. A boundary relationship $\mathbf{x}(T) = \mathbf{x}_f$ must also be met as a constraint.

The most common form of the performance index, $J(u)$, is the minimum time control that can be expressed as

$$J(u) = \int_0^T d\tau = T \tag{92.8}$$

Many different criteria are also used, such as minimum fuel consumption, minimum energy consumption, and few other quadratic forms:

$$J(u) = \int_0^T |u(\tau)| d\tau \tag{92.9}$$

$$J(u) = \int_0^T u^2(\tau) d\tau \tag{92.10}$$

$$J(u) = \int_0^T (qx^2(\tau) + ru^2(\tau)) d\tau \tag{92.11}$$

A general term for the continuous time performance index leading to optimal control is expressed as

$$J(u(t)) = \int_0^T g(x(\tau), u(\tau)) d\tau \tag{92.12}$$

The performance indices are minimized for the constraints
$\dot{\mathbf{X}}(t) = f(\mathbf{x}(t), \mathbf{u}(t), t)$, for $t \in (t_0, t_f)$ and $\mathbf{x}(t)$ is an admissible state and $\mathbf{x}(t) \in \mathbf{X}(t)$ and $\forall t \in (t_0, t_f)$ are satisfied.

Slight variations of Equations 92.9 through 92.12 lead to mathematics of the discrete time or digital versions of the optimal control.

92.3 Calculus of Variations

Calculus variations are suitable to solve linear or nonlinear optimization problems with linear or nonlinear boundary conditions. Basically, it is a collection of many different analytical methods, and they are discussed differently from book to book. In here, a typical approach that leads to more general and widely used modern theories is introduced.

Consider a dynamic system operating in a time interval $t_0 < t < t_f$:

$$\dot{\mathbf{X}} = f\left[\mathbf{x}, \mathbf{u}, t\right] \tag{92.13}$$

where the initial state $\mathbf{x}_0$ is given.

The system has n state and m control variables. The scalar function to be optimized is

$$J = k\left[\mathbf{x}_f, t_f\right] + \int \mathbf{L}\left[\mathbf{x}, \mathbf{u}, t\right] dt \tag{92.14}$$

Define a *scalar*, such as Hamiltonian

$$H = H\left[\mathbf{x}, \mathbf{u}, \lambda t\right] = L\left[\mathbf{x}, \mathbf{u}, t\right] + \sum \lambda_i f_i \tag{92.15}$$

λ is known as the *Lagrange multiplier*. Also, we need to define a modified objective function:

$$J = k\left[\mathbf{x}_1, t_1\right] + \int H dt \tag{92.16}$$

The resulting solution is optimal when

$$\lambda = \frac{-\delta H}{\delta x} = \frac{-\delta L}{\delta x} - \sum \frac{-\lambda_i \delta f_i}{\delta x} \tag{92.17}$$

$$\lambda_f = \frac{\delta k}{\delta x} \tag{92.18}$$

and

$$\frac{\delta H}{\delta u} = \frac{\delta L}{\delta u} + \sum \frac{\lambda_i \delta f_i}{\delta u} = 0 \quad \text{for} \quad t_0 < t < t_f \tag{92.19}$$

The solutions of Equations 92.17 and 92.19 in the aforementioned form are difficult to obtain. Nevertheless, based on the these ideas, more general theories can be developed such as Pontryagin's maximum principle.

An advancement over the calculus variations is the Pontryagin's maximum principle, which offers easier solutions and expands the range of applicability to bounded control problems. In simple form, this principle may be explained as follows:

Given the system

$$\mathbf{x}_i = f_i\left[\mathbf{x}, \mathbf{u}, t\right] \tag{92.20}$$

with an objective function

$$J = \sum k_i x_i(t_f) \tag{92.21a}$$

the maximum principle states that if the control vector **u** is optimum, then the Hamiltonian

$$H = \sum p_i f_i \tag{92.21b}$$

is also maximized with respect to the control vector **u** over the set intervals:

$$p_i = \sum p_j \frac{\delta f_j}{\delta x_j} \tag{92.21c}$$

$$p_i(t_f) = k_i \tag{92.21d}$$

where p is the adjoint or costate vector, and

$$\frac{\delta H}{\delta p_i} = f_i\left[\mathbf{x}, \mathbf{u}, t\right] = x_i \tag{92.21e}$$

$$\frac{\delta H}{\delta p_i} = \sum \frac{p_i \delta f_j}{\delta x_j} = -p_i \tag{92.21f}$$

The initial values of state vector **x** provide the remaining constants necessary to solve these equations for determining an optimum control vector. This method is also applicable to systems with complex performance indexes.

Another expansion of calculus variations is the *Kalman filter*. Kalman is essentially a general filtering technique that can be applied to solutions of problems such as optimal estimation, prediction, noise filtering, stochastic optimal control, and designing of optimal controllers. The method has the advantage of providing estimates of variables in the presence of noise for both stationary and nonstationary processes. Most other types of noise can be treated by this method if they can be translated to Gaussian form. The technique can also be employed in systems with forcing disturbances and containing more than one noise source. Generally, systems that have either quadratic objective functions or uncorrelated Gaussian noise as the input are suitable for this technique.

A means of applying the Kalman filter to a nonlinear system is to find a good estimate of the system and then use it to define a new set of linear *state equations* that approximates the system to linear form at a normal operating point. Then the filter can be applied to the new set of linear equations. Applications of Kalman filter are limitless in instrumentation and measurement systems and other optimal control problems. It can easily be programmed on digital computers.

92.4 Riccati Equation

Some of the models in optimization problems resemble the models of traditional control theory and practice. In these models, the process and control variables are vector-valued and constrained by linear plant equations. The cost functions are in the form of quadratic costs. These type of systems are termed as *linear/quadratic* systems or LQ systems. The theory and models of LQ systems are well developed for both deterministic and stochastic cases.

Express a quadratic optimal control problem as

$$\mathbf{x}(k+1) = \mathbf{A}\mathbf{x}(k) + \mathbf{B}\mathbf{u}(k) \quad \mathbf{x}(0) = \mathbf{x}_0 \tag{92.22}$$

where

$\mathbf{x}(k)$ is the state vector (n-vector)
$\mathbf{u}(k)$ is the control vector (r-vector)
$\mathbf{A}$ is the $n \times n$ nonsingular vector
$\mathbf{B}$ is the $n \times r$ matrix

The aim is to find the optimal control sequence $\mathbf{u}(0), \mathbf{u}(1), \ldots, \mathbf{u}(N-1)$ that minimizes a quadratic performance index

$$J = \frac{1}{2}\mathbf{x}^{\star}(N)\mathbf{S}\mathbf{x}(N) + \frac{1}{2}\sum \mathbf{x}^{\star}(k)\mathbf{Q}\mathbf{x}(k) + \mathbf{u}^{\star}(k)\mathbf{R}\mathbf{u}(k) \tag{92.23}$$

where

$\mathbf{x}^{\star}$ and $\mathbf{u}^{\star}$ are transpose of $\mathbf{x}$ and $\mathbf{u}$ matrixes, respectively
$\mathbf{Q} = n \times n$ positive definite or positive semidefinite symmetric matrix
$\mathbf{R} = r \times r$ positive definite or positive semidefinite symmetric matrix
$\mathbf{S} = n \times n$ positive definite or positive semidefinite symmetric matrix

Matrices **Q, S,** and **R** are selected to weight the relative importance of the performance measures caused by the state vectors $\mathbf{x}(k)$, the final state $\mathbf{x}(N)$, and control vectors $\mathbf{u}(k)$, respectively, for $k = 0, 1, 2, \ldots, N-1$.

The initial state of the system is arbitrary but the final state $\mathbf{x}(N)$ may be fixed. If the final state is fixed, then the term 1/2 $\mathbf{x}^{\star}(N)$ $\mathbf{S}\mathbf{x}(N)$ may be removed from the performance index, and the terminal state $\mathbf{x}_f$ may be imposed. If the final state is not fixed, then the term 1/2 $\mathbf{x}^{\star}(N)$ $\mathbf{S}\mathbf{x}(N)$ represents the weight of the performance measure to the final state.

There are many different ways of solving the aforementioned equations, one of which makes use of the concept of Lagrange multipliers. With the aid of Lagrange multipliers, the performance index may be modified as

$$\mathbf{L} = \frac{1}{2}\mathbf{x}^{\star}(N)\mathbf{S}\mathbf{x}(N) + \frac{1}{2}\sum \mathbf{x}^{\star}(k)\mathbf{Q}\mathbf{x}(k) + \mathbf{u}^{\star}(k)\mathbf{R}\mathbf{u}(k) + \lambda^{\star}(k+1)$$
$$\left[\mathbf{A}\mathbf{x}(k) + \mathbf{B}\mathbf{u}(k) - \mathbf{x}(k+1)\right] + \left[\mathbf{A}\mathbf{x}(k) + \mathbf{B}\mathbf{u}(k) - \mathbf{x}(k+1)\right]^{\star} \lambda^{\star}(k+1) \tag{92.24}$$

It is known that minimization of the function **L** is equivalent to minimization of performance index **J** under the same constraints.

In order to minimize, **L** needs to be differentiated with respect to vectors $\mathbf{x}(k)$, $\mathbf{u}(k)$, and $\boldsymbol{\lambda}(k)$, and the results must be set to zero. The partial differentiation of the function **L** with respect to variables gives the following:

$$\frac{\delta \mathbf{L}}{\delta \mathbf{x}(k)} = 0 \quad \mathbf{Q}\mathbf{x}(k) + \mathbf{A}^{*}\lambda(k+1) - \lambda(k) = 0 \tag{92.25}$$

$$\frac{\delta \mathbf{L}}{\delta \mathbf{x}(N)} = 0 \quad \mathbf{S}\mathbf{x}(N) - \lambda(N) = 0 \tag{92.26}$$

$$\frac{\delta \mathbf{L}}{\delta \mathbf{u}(k)} = 0 \quad \mathbf{R}\mathbf{u}(k) + \mathbf{B}^{*}\,\lambda(k+1) = 0 \tag{92.27}$$

and

$$\frac{\delta \mathbf{L}}{\delta \lambda(k)} = 0 \quad \mathbf{A}\mathbf{x}(k-1) + \mathbf{B}\mathbf{u}(k-1) - \mathbf{x}(k) = 0 \tag{92.28}$$

A close inspection of the preceding formulae indicates that the last equation is simply the state equation for $k = 1, 2, 3, \ldots, N$. And also, the value of Lagrange multiplier can be determined by Equation 92.16. The Lagrange multiplier is often termed as *covector* or *adjoint vector.*

Rewriting Equations 92.25 and 92.27,

$$\lambda(k) = \mathbf{Q}\mathbf{x}(k) + \mathbf{A}^{*}\lambda(k+1) \tag{92.29}$$

$$\mathbf{u}(k) = -\mathbf{R}^{-1}\mathbf{B}^{*}\lambda(k+1) \tag{92.30}$$

The state Equation 92.22 can be expressed as

$$\mathbf{x}(k+1) = \mathbf{A}\mathbf{x}(k) - \mathbf{B}\mathbf{R}^{-1}\mathbf{B}^{*}\lambda(k+1) \tag{92.31}$$

In order to obtain the solution to the minimization problem, we need to solve Equations 92.29 and 92.31 simultaneously as a two-point boundary-value problem. The solutions of these two equations in this form, and the optimal values of the state vector and the Lagrange multiplier vector lead to the values of control vector $\mathbf{u}(k)$, which will optimize the open-loop control system. However, for closed-loop control systems, the Riccati transformations must be applied:

$$\mathbf{u}(k) = -\mathbf{K}(k)\mathbf{x}(k) \tag{92.32}$$

where $\mathbf{K}(k)$ is the $r \times n$ feedback matrix. Now the Riccati equation in feedback form can be obtained by assuming that $\boldsymbol{\lambda}(k)$ is written as

$$\lambda(k) = \mathbf{P}(k)\mathbf{x}(k) \tag{92.33}$$

where $\mathbf{P}(k)$ is an $n \times n$ matrix. Substituting Equation 92.33 into 92.29 and 92.31 gives

$$\mathbf{P}(k)\mathbf{x}(k) = \mathbf{Q}\mathbf{x}(k) + \mathbf{A}^* \mathbf{P}(k+1)\mathbf{x}(k+1) \tag{92.34}$$

$$\mathbf{x}(k+1) = \mathbf{A}\mathbf{x}(k) - \mathbf{B}\mathbf{R}^{-1}\mathbf{B}^* \mathbf{P}(k+1)\mathbf{x}(k+1) \tag{92.35}$$

In writing Equations 92.34 and 92.35, the Lagrange multiplier $\boldsymbol{\lambda}(k)$ has been eliminated. This is an important step in solving two-point boundary-value problems. By further manipulations, it is possible to show that

$$\mathbf{P}(k) = \mathbf{Q} + \mathbf{A}^* \mathbf{P}(k+1)\mathbf{A} - \mathbf{A}^* \mathbf{P}(k+1)\mathbf{B}\left[\mathbf{R} + \mathbf{B}^* \mathbf{P}(k+1)\mathbf{B}\right]^{-1} \mathbf{B}^* \mathbf{P}(k+1)\mathbf{A} \tag{92.36}$$

Equation 92.36 is known as the Riccati equation.

From Equations 92.26 and 92.33, writing $\lambda(N) = \mathbf{S}\mathbf{x}(N) = \mathbf{P}(N)\mathbf{x}(N)$ gives

$$\mathbf{P}(N) = \mathbf{S} \tag{92.37}$$

Hence, the Riccati equation can be solved backward from $k = N$ to $k = 0$, starting from the known values of $\mathbf{P}(N)$.

The optimal control vector $\mathbf{u}(k)$ can now be calculated from Equations 92.29, 92.30, and 92.35 as

$$\mathbf{u}(k) = -\mathbf{R}^{-1}\mathbf{B}^* \lambda(k+1) = -\mathbf{R}^{-1}\mathbf{B}^* \left[\mathbf{A}^*\right]^{-1}\left[\mathbf{P}(k) - \mathbf{Q}\right]\mathbf{x}(k) = -\mathbf{K}(k)\mathbf{x}(k) \tag{92.38}$$

where

$$\mathbf{K}(k) = -\mathbf{R}^{-1}\mathbf{B}^* \left[\mathbf{A}^*\right]^{-1}\left[\mathbf{P}(k) - \mathbf{Q}\right] \tag{92.39}$$

It is worth noting that optimal control vector may be obtained in slightly different forms by slightly different manipulations of the aforementioned equations, such as

$$\mathbf{u}(k) = -\mathbf{R}^{-1}\mathbf{B}^* \left[\mathbf{P}^{-1}(k+1) + \mathbf{B}\mathbf{R}^{-1}\mathbf{B}^*\right]^{-1} \mathbf{A}\mathbf{x}(k) \tag{92.40}$$

Equations 92.38 and 92.39 indicate that optimal control law requires feedback of the state vector with time-varying gain $\mathbf{K}(k)$. Figure 92.4 illustrates the optimal control scheme of a system based on the quadratic performance index. In practical applications, the time varying $\mathbf{K}(k)$ is calculated before the process begins. Once the state matrix $\mathbf{A}$, control matrix $\mathbf{B}$, and weighting matrices $\mathbf{Q}$, $\mathbf{R}$, and $\mathbf{S}$ are known, the gain $\mathbf{K}(k)$ may be precomputed off-line to be used later. The control vector $\mathbf{u}(k)$ at each stage can be determined immediately by premultiplying the state vector $\mathbf{x}(k)$ by the known gain $\mathbf{K}(k)$.

From the above equations, the minimum value of the performance index can also be calculated, by using the initial values, as

$$J_{\min} = \frac{1}{2}\mathbf{x}^*(0)\mathbf{P}(0)\mathbf{x}(0) \tag{92.41}$$

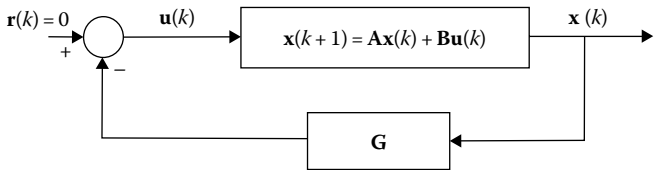

FIGURE 92.4 Optimal control scheme based on the quadratic performance index. The control law requires feedback of the state vector with time-varying gain $\mathbf{K}(k)$. The gain $\mathbf{K}(k)$ is calculated for use later, before the process begins.

The *steady-state* solutions of Riccati equations are necessary when dealing with time-invariant (steady-state) optimal controls. There are many ways of obtaining steady-state Riccati solutions; an example is given as follows:

$$\mathbf{P} = \mathbf{Q} + \mathbf{A}^* \mathbf{PA} - \mathbf{A}^* \mathbf{PB}(\mathbf{R} + \mathbf{B}^* \mathbf{PB})^{-1}\mathbf{B}^* \mathbf{PA} \tag{92.42}$$

The steady-state value of **K** may be found as

$$\mathbf{K} = (\mathbf{R} + \mathbf{B}^* \mathbf{PB})^{-1}\mathbf{B}^* \mathbf{PA} \tag{92.43}$$

Here, the optimal control law for the steady-state operation may be expressed as

$$\mathbf{u}(k) = -(\mathbf{R} + \mathbf{B}^* \mathbf{PB})^{-1}\mathbf{B}^* \mathbf{PAx}(k) \tag{92.44}$$

This section is presented for discrete time optimal control systems rather than continuous systems, due to recent widespread use of computers and microprocessors as online and off-line control tools. Since the principles are the same, solutions can easily be extended for continuous time systems with minor modifications.

92.5 State-Feedback Matrix

The state-feedback method is another design technique that allows the designer to locate the poles of the system wherever they are needed. This type of approach is termed as the *pole-placement method* where the term "pole" refers to the poles of the closed-loop transfer function as in Figure 92.5. In this method, it is assumed that state variables are measurable and are available for feedback. If the state is available, the system is said to be deterministic; it is noise-free and all the parameters are known. If the state is not available, then methods such as measurement feedback laws or state estimators may be selected.

In many applications, instead of state variables, it is more convenient to use state estimates coming from an observer or Kalman filter. In this case, there are three well-known methods available, these being the certainty equivalent, the separation, and the dual control. Certainty equivalence has considerable advantages over others since they lead to deterministic optimal control laws such Pontryagin's principle or the conditional mean of the state such as the Kalman filter. It leads to a practical controller that may be built as a filter and optimal law in cascade.

State-feedback controllers are relatively easy to implement. For example, in the pole-placement method, the relationship of the feedback control **u** to state **x** for *linear systems* is

$$\mathbf{u}(k) = -\mathbf{Kx}(k) \tag{92.45}$$

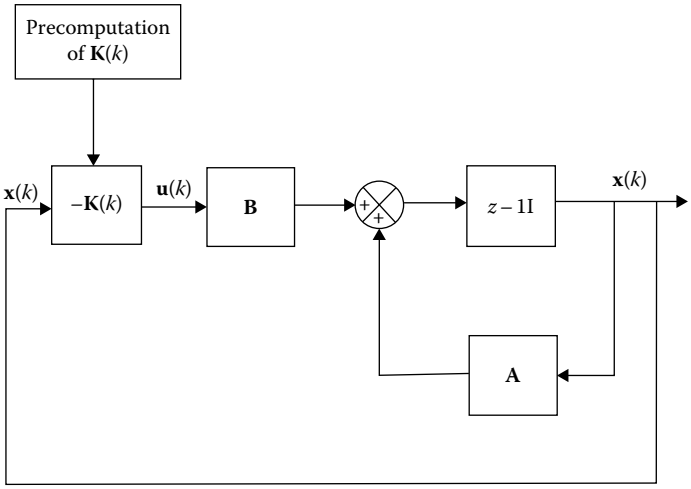

FIGURE 92.5 Pole-placement design of closed-loop transfer function. This method assumes that state variables are measurable and are available for the feedback.

In linear quadratic cases, the gain **K** is time varying:

$$\mathbf{u}(k) = -\mathbf{K}(k)\mathbf{x}(k) \tag{92.46}$$

where **K** is a $(n \times r)$ feedback matrix. This is correct at least in two cases:

1. In linear systems with no noise, pole-placement controllers, and an observer as the state estimator, the control algorithms for

$$\mathbf{x}(k+1) = \mathbf{A}\mathbf{x}(k) + \mathbf{B}\mathbf{u}(k)$$

$$\mathbf{y}(k) = \mathbf{C}\mathbf{x}(k)$$

are

$$\hat{\mathbf{x}}(k+1) = (\mathbf{A} - \mathbf{GC})\hat{\mathbf{x}}(k) + \mathbf{G}\mathbf{y}(k) + \mathbf{B}\mathbf{u}(k) \tag{92.47}$$

$$\mathbf{u}(k) = \mathbf{K}\hat{\mathbf{x}}(k) \tag{92.48}$$

where the eigenvalues of $(\mathbf{A} - \mathbf{GC})$ and $(\mathbf{A} + \mathbf{BK})$ are selected to meet the design specifications.

2. In linear systems, influenced by Gaussian white noise, in which the control is optimal according to a quadratic criterion, the system

$$\mathbf{x}(k+1) = \mathbf{A}\mathbf{x}(k) + \mathbf{B}\mathbf{u}(k) + \mathbf{G}\mathbf{v}(k) \tag{92.49}$$

$$\mathbf{y}(k) = \mathbf{C}\mathbf{x}(k) + \mathbf{w}(k) \tag{92.50}$$

has control law of the form

$$\hat{\mathbf{x}}\left(\frac{k+1}{k}\right) = \mathbf{A}\hat{\mathbf{x}}(k) + \mathbf{B}\hat{\mathbf{u}}(k) \tag{92.51}$$

$$\hat{\mathbf{x}}(k+1) = \mathbf{A}\hat{\mathbf{x}}\left(\frac{k+1}{k}\right) + \mathbf{G}(k+1)\mathbf{y}(k+1) - \mathbf{C}\hat{\mathbf{x}}\left(\frac{k+1}{k}\right) \tag{92.52}$$

$$\hat{\mathbf{u}}(k) = \mathbf{K}(k)\hat{\mathbf{x}}(k) \tag{92.53}$$

where $\mathbf{K}(k)$ and $\mathbf{G}(k)$ are optimal gains for the deterministic optimal controls and the Kalman filters, respectively.

In practice, not all the state variables are easily accessible, and in general only the outputs of the system are measurable. Therefore, when feedback from the state variables is required in a given design, it is necessary to observe the states from information contained in the output as well as the input variables. The subsystem that performs the observation of the state variables based on the information received from the measurements of inputs and outputs is called the state observer. Figure 92.6 shows the block diagram of such a system.

Suppose a state-feedback gain $\mathbf{K}$ has been selected so that the eigenvalues of

$$\mathbf{x}(k+1) = \mathbf{A}\mathbf{x}(k) + \mathbf{B}\mathbf{u}(k) \tag{92.54}$$

$$\mathbf{u}(k) = -\mathbf{K}(k)\mathbf{x}(k) + \mathbf{r}(k) \tag{92.55}$$

are located at $\lambda_1, \lambda_2, \ldots, \lambda_n$. Furthermore, assume that gain $\mathbf{G}$ in the identity observer

$$\hat{\mathbf{x}}(k+1) = (\mathbf{A} - \mathbf{GC})\hat{\mathbf{x}}(k) + \mathbf{G}\mathbf{y}(k) + \mathbf{B}\mathbf{u}(k) + \mathbf{G}\mathbf{y}(k) \tag{92.56}$$

is chosen such that eigenvalues of the observers are $\mu_1, \mu_2, \ldots, \mu_n$.

When the observer state estimate $\mathbf{x}(k)$ is used instead of state $\mathbf{x}(k)$, the resulting system has a state dimension $2n$, modeled by

$$\begin{bmatrix} \mathbf{x}(k+1) \\ \hat{\mathbf{x}}(k+1) \end{bmatrix} = \begin{bmatrix} \mathbf{A} & -\mathbf{BK} \\ \mathbf{GC} & \mathbf{A} - \mathbf{GC} - \mathbf{BK} \end{bmatrix} \begin{bmatrix} \mathbf{x}(k) \\ \hat{\mathbf{x}}(k) \end{bmatrix} + \begin{bmatrix} \mathbf{B} \\ \mathbf{B} \end{bmatrix} \mathbf{r}(k) \tag{92.57}$$

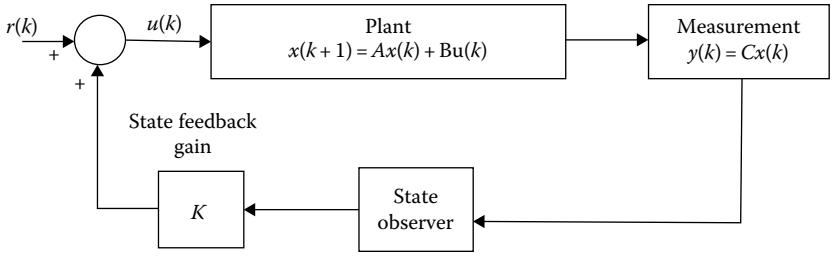

FIGURE 92.6 Use of state observer. When feedback from the state variables are required, it may be possible to observe the states from information contained in the output as well as the input variables based on the information received from the measurements.

A similarity transform

$$\begin{bmatrix} \mathbf{x}(k) \\ \mathbf{e}(k) \end{bmatrix} = \mathbf{P} \begin{bmatrix} \mathbf{x}(k) \\ \hat{\mathbf{x}}(k) \end{bmatrix} \tag{92.58}$$

where

$$\mathbf{P} = \begin{bmatrix} \mathbf{I} & 0 \\ \mathbf{I} & -\mathbf{I} \end{bmatrix} \tag{92.59}$$

corresponds to a change of variables to $\mathbf{x}(k)$ and $\mathbf{e}(k) = \mathbf{x}(k) - \mathbf{x}(k)$ converts this to

$$\begin{bmatrix} \mathbf{x}(k+1) \\ \mathbf{e}(k+1) \end{bmatrix} = \begin{bmatrix} \mathbf{A} - \mathbf{BK} & \mathbf{BK} \\ 0 & \mathbf{A} - \mathbf{GC} \end{bmatrix} \begin{bmatrix} \mathbf{x}(k) \\ \mathbf{e}(k) \end{bmatrix} + \begin{bmatrix} \mathbf{B} \\ 0 \end{bmatrix} \mathbf{r}(k) \tag{92.60}$$

This system has the same eigenvalues as the original because of the nature of the similarity transforms and the eigenvalues are the solution of

$$\det(\lambda \mathbf{I} - (\mathbf{A} - \mathbf{BK}))(\lambda \mathbf{I} - (\mathbf{A} - \mathbf{GC})) = 0 \tag{92.61}$$

This requires that one of

$$\det(\lambda \mathbf{I} - (\mathbf{A} - \mathbf{BK})) = 0 \tag{92.62}$$

$$\det(\lambda \mathbf{I} - (\mathbf{A} - \mathbf{GC})) = 0 \tag{92.63}$$

must hold. These are also the eigenvalues of the design for the pole-placement feedback state controller $\lambda_1, \lambda_2, \ldots, \lambda_n$ and of the design of the state observer $\mu_1, \mu_2, \ldots, \mu_n$, respectively. This indicates that the use of observer does not move the designed poles from the pole-placement algorithm.

The algorithms for pole-placement observer are well known, and they are part of many control design packages. Steady-state Kalman gains and optimal control gains are also commonly available in such programs. Codes for Kalman filters and LQ controllers are also easy to write.

Note: For further readings on this topic, please refer to the sources in the bibliography.

92.6 Software Support and Applications

There are not manufacturers of optimal controllers. Most mathematical packages such as *MATLAB®* Optimization Toolbox, CAD/CAM algorithms, majority of *artificial intelligence and neural network* software tools, and other simulation and design packages offer solutions to optimal control problems. Optimization tools are also part of specialized design packages addressing specific applications, such as FPGA, a language-based design, technology-specific optimizations; OPTCON, optimal control algorithms for linear stochastic models; DISNEL; and MIMO.

MATLAB has additional packages, such as the PROPT, and aims to solve dynamic optimization problems. The problems require mathematical description as a state-space model using ordinary differential

equations or differential algebraic equations. PROPT makes use of Chebyshev or Gauss point collections for solving optimal control problems. Once the initial and final conditions are known, using cost functionals leads to state trajectories.

Another product of MATLAB is an object-oriented software termed DIDO. It has been developed for solving hybrid optimal control problems and based on pseudospectral optimal control theory that mimics control problems in a manner as if being written on a piece of paper. It eliminates the need for solving the costates. Pontryagin's minimum principle is used as a backup tool to check the results.

Sparse Optimal Control Software (SOCS), developed by the Boeing Company, comes in two packages. They can be applied in very large problems, such as trajectory optimization, chemical processes, and machine tools. The software can be implemented on desktop computers and is also capable of solving problems that can contain up to 100,000 variables and constraints. It is capable of solving linear or nonlinear problems.

There are many commercially available and custom-built software packages, some of which are the following: BARON, a global optimization solver; BT, for minimization; CO (constrained optimization); DOC (design optimization control program); DOT (design optimization tool); GENESIS, a structural optimization software; LSNNO, for large-scale optimization; MCS, for global optimization; OPTIMA library, for optimization and sensitivity analysis; TNPACK, for nonlinear unconstrained minimization; TOMLAB, for MATLAB Optimization; and many others. More information can be found in websites, such as NEOS WIKI (http://www.neos-guide.org/NEOS/index.php/Optimization_Software_Guide).

Most of the software packages are used in optimal problem solving in industrial and nonindustrial areas. MATLAB PROPT, for example, finds applications in http://tomdyn.com/matlab_optimal_control_examples.html for the following: aerodynamic trajectory determination, bang-bang control systems, chemical engineering, dynamic systems, flight path tracking, large-scale linear optimal problems, pendulum control, path tracking of robots, mechanical engineering, turbo generators, marine population dynamics, nondifferentiable applications, parameter estimation, radio telescopes, drug displacement, missile intercept, satellite control, space shuttles, and many others.

Bibliography

Cakaj, S. *Modeling, Simulation and Optimization: Tolerance and Optimal Control*, InTech, Vienna, Austria, 2010.

Evans, L.C. *Introduction to Mathematical Optimal Control Theory: Version 0.2*, available at http://math.berkeley.edu/~evans/control.course.pdf (accessed on February 16, 2012).

Grimble, M.J. *Optimal Control Applications and Methods*, Wiley, Chichester, U.K., Online Library. http://onlinelibrary.wiley.com/journal/10.1002/(ISSN)1099-1514, (accessed on February 29, 2012).

Hocking, L.M. *Optimal Control: An Introduction to the Theory and Applications*, Oxford Press, Oxford, U.K., 2001.

Hull, D.J. *Optimal Control Theory for Applications*, Springer, New York, 2003.

Naidu, D.S. *Optimal Control Systems*, CRC Press, Boca Raton, FL, 2003.

Optimization Software Guide, Neos Wiki. http://www.neos-guide.org/NEOS/index.php/Optimization_Software_Guide (accessed on February 20, 2012).

PROPT MATLAB Optimal Control Software. http://tomdyn.com/index.html (accessed on February 28, 2012).

Weber, R. *Optimization and Control*, University of Cambridge, Cambridge, U.K., 2010.

Partial List of Providers

Centurion Controls, 102 Hamilton Industrial Court, Wentzville, MO 63385, Phone: 866-646-4383, Fax: 435-487-9250, www.centurioncontrols.com

Certeon, 4 Van De Graaf Dr., Burlington, MA 01803, Phone: 781-425-5200, Fax: 781-425-5210, www.certeon.com

Innovative Custom Software, Inc., 1323 Bond St., No. 103, Naperville, IL 60563, Phone: 630-892-5022, Fax: 630-748-0153, www.icsinc.net

Managing Automation, 5 Penn Plaza Fl 9, New York, NY 10001, Phone: 212-629-1577, www.managingautomation.com/maonline/

Sterling, 2900 S. 160th St. New Berlin, WI 53151, Phone: 262-641-8610, Fax: 262-641-8653, www.sterlco.com/

Trola Industries, 2360 N. George St., York, PA 17406-3202, Phone: 717-848-3700, Fax: 717-848-6993, www.trolaindustries.com

Zepnick Solution, 1310 Brookfield Ave., Green Bay, WI 54313, Phone: 920-662-1682, Fax: 920-662-1685, www.zepnick.com

93

Electropneumatic and Electrohydraulic Instruments: Modeling

M. Pachter
Air Force Institute of Technology

C.H. Houpis
Air Force Institute of Technology

93.1 Introduction

In control systems, the output of the controller (also of the equalizer or compensator), which operates on the command (and feedback) input signals, is invariably sent to an actuator. The latter is a power element critically positioned at the plant input and, to a large extent, determines the performance of the overall control system. Thus, the importance of the accurate modeling of the actuator element with respect to achieving and maintaining the desired control system performance over its operating range cannot be overemphasized. The impact of items such as the actuator phase-lag characteristics, parameter variations and aging, sensor noise, and operating scenario (e.g., in a flight control context, it is referred to as *flight conditions*) should be explicitly considered in a control system design process. To achieve a robust control system, where these items are taken into account, requires a good understanding and an accurate model of the actuation element. This chapter discusses the actuator modeling process.

93.2 Background

Power-to-weight considerations have driven actuator design to pneumatic, hydraulic, electrohydraulic, and recently, in flight control applications, electrohydrostatic configurations. In this chapter, the point of view is taken that the actuator element constitutes a feedback control system in its own right. Thus, the actuator comprises of an "amplifier" element (the servo valve), a power element (the "ram"), an actuator displacement sensor, and a controller about which more will be said in the sequel. Furthermore, it is

important that the actuator subsystem be considered in the context of the complete control system, e.g., a flight control system. This point of view is promulgated throughout this chapter. First, a relatively simple hydraulic actuator is considered. The focus then shifts to the modern electrohydrostatic actuator (EHA) technology that, in the flight control application, offers a high degree of combat survivability and easier maintainability since its components are collocated with the actuator. Since the EHA does not require long hydraulic lines, required maintenance time and equipment can be reduced. This also substantially reduces the profile exposed to hostile fire. In addition, actuator failures due to various causes and/or aging need to be taken into account in designing the overall control system. The design of a robust control system, utilizing an actuator, requires an accurate actuator model in order to satisfy the system performance specifications. The EHA and its flight control application are used as the "vehicle" for presenting the actuator modeling process.

93.2.1 Actuator Modeling Requirements

When an actuator needs to be replaced in a control system, for reasons cited previously, by one "off the shelf," the robustness of the overall control system must be unaffected by this replacement unit. Thus, the actuator design process entails

1. The derivation of an accurate mathematical model for the actuator.
2. Sensitivity analyses on the actuator control systems. This should include sensitivity to variations in load, component efficiencies, physical plant parameters, and actuator sensor noise.
3. The identification of a reasonable set of plant variations for the actuator, based on the sensitivity analysis, which is required for designing a robust actuator control system that will meet the specifications in the presence of predicted variations.

93.3 Hydraulic Actuator Modeling

The modeling of a purely hydraulic actuator employed in an irreversible flight control system is presented first. Based upon the notation shown in Figure 93.1, the following relationships are obtained:

$$x_1 = \delta_{e_c} a \tag{93.1a}$$

$$\frac{x_v - x_f}{b + c} = \frac{x_v - x_1}{c} \tag{93.1b}$$

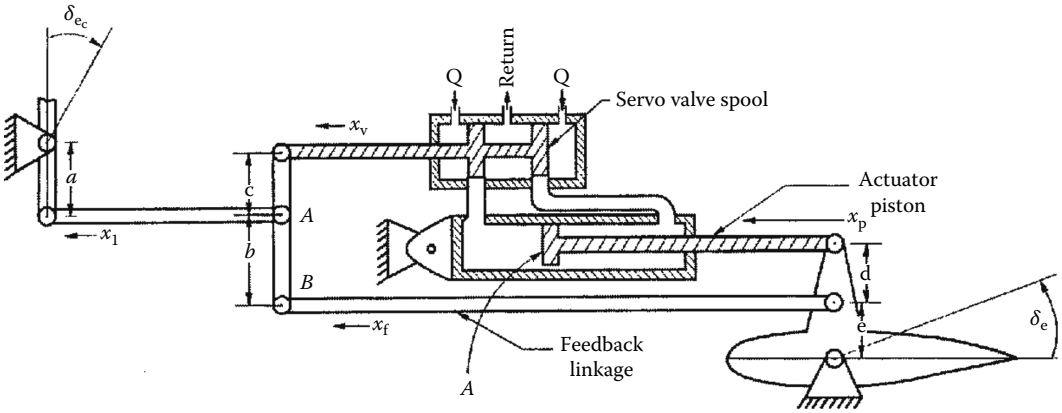

FIGURE 93.1 Irreversible control system.

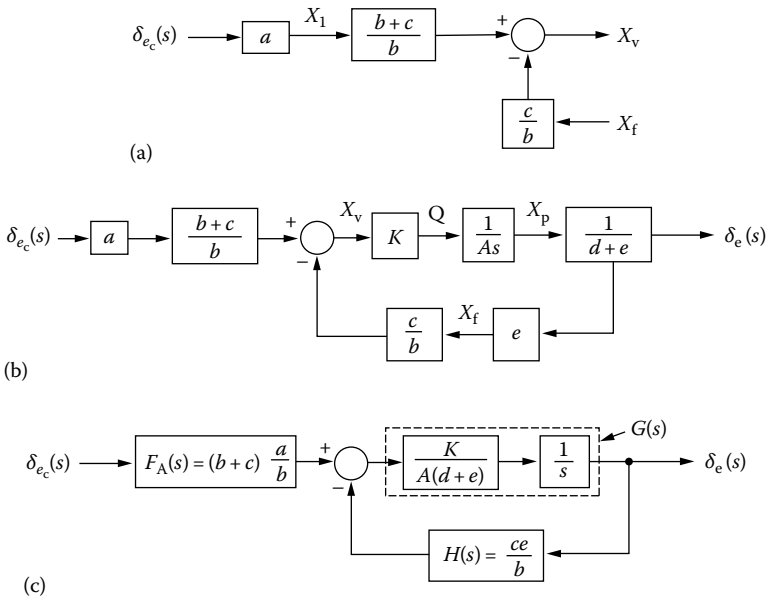

FIGURE 93.2 (a) Actuator block diagram, (b) block diagram of actuator feedback control system, and (c) simplified block diagram.

that yield

$$x_v b + x_f c = x_1(b + c) \tag{93.2}$$

From these equations, Figure 93.2a is obtained. Next, the relationships

$$\frac{dx_p}{dt} = \frac{Q}{A}, \quad Q = Kx_v, \quad \delta_e = \frac{x_p}{d+e}, \quad x_f = e\delta_e \tag{93.3}$$

are utilized to yield the block diagram of a typical feedback control system (shown in Figure 93.2b) that represents the irreversible hydraulic actuator under consideration. This block diagram is simplified to the one shown in Figure 93.2c, which yields the first-order transfer function of the actuator:

$$G(s) = \frac{\delta_e(s)}{\delta_{e_c}(s)} = \frac{K}{\tau s + 1} \tag{93.4}$$

where the gain $K = [a(b + c)]/ce$, the time constant $\tau = [Ab(d + e)]/cKe$ of the actuator, and $0.025 < \tau < 0.1$ s. For a step-input command, a typical actuator time response is shown in Figure 93.3.

The more-detailed dynamic modeling of the valve leads to higher-order hydraulic actuator models. For example, the transfer function of the currently used actuator of the F-16 aircraft is of fourth order [1], and its frequency response is compared with its first-order approximation in Figure 93.4. It is indeed important to use the full-blown high-order actuator dynamic model in robust control system design. As Figure 93.4 shows, the simplified first-order model fits well the high-order model in the low-frequency range. Unfortunately, a significant phase angle difference exists at the higher frequencies where the actuator will be operating, for the higher frequencies are within the bandwidth of modern robust ("high gain") control system compensators.

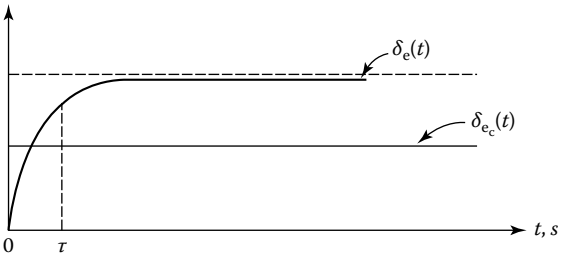

FIGURE 93.3 Time response of an actuator.

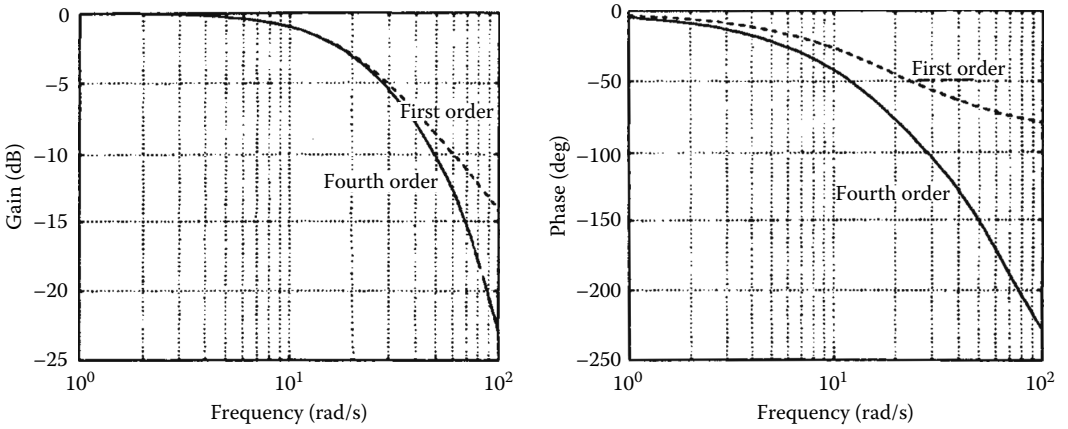

FIGURE 93.4 Comparison of the first- and fourth-order actuator models.

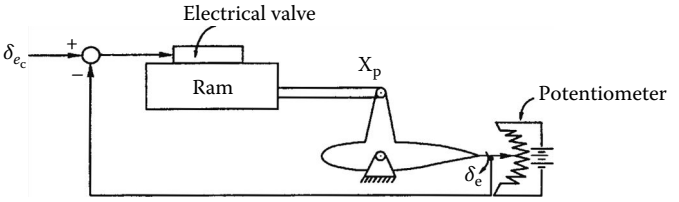

FIGURE 93.5 Electrohydraulic actuator.

The next step in the actuator state of development is then an electronic "fly-by-wire" mechanization of the feedback loop. This is shown in Figure 93.5 where an actuator is shown that employs an electric (solenoid controlled) valve and a potentiometer to measure the control surface deflection (actuator displacement) and where the power element of the actuator, the RAM, is a hydraulic cylinder.

93.4 EHA Actuator Modeling

The novel EHA actuator (see, e.g., Ref. [2]) offers a high degree of maintainability and survivability because all the actuator elements are collocated and a central hydraulic pump with the attendant high-pressure hydraulic plumbing is not needed. The modeling of the modules of the EHA is outlined first.

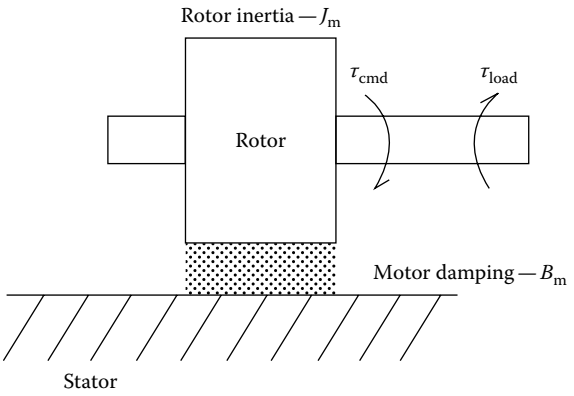

FIGURE 93.6 Motor model.

93.4.1 Motor

Electric motors with the rotor moment of inertia J_m and electromechanical damping B_m (see Figure 93.6) are subject to variations in output torque and subsequent fluctuations in rotor speed ω_m. Since the torque due to the load counteracts the torque generated by the motor, perturbation may also be caused by variations of the load torque. This relationship is expressed as

$$\tau_e(s) = \tau_{cmd}(s) - \tau_{load}(s) \tag{93.5}$$

where τ_{load} is the load torque due to the differential pressure of the fluid in the pump. This results in a first-order transfer function

$$\frac{\Omega_m(s)}{\tau_e(s)} = \frac{1}{J_m s + b_m} \tag{93.6}$$

93.4.2 Pump and Fluid

Electric motors have a limited torque-to-mass ratio, due to the finite and limited magnetic flux density that can be generated [3]. High-pressure hydraulic systems, with the system pressure of 2000–5000 psi, can generate high forces resulting in more compact and higher torque-to-mass ratios than electric motors. Generally, high-pressure hydraulic systems are stiffer against the load than electric motors. Hence, the EHA utilizes a DC motor to pump high-pressure fluid into the piston chamber. The DC motor internal to the EHA converts the electric power into mechanical power. It is the pump that converts this mechanical power into hydraulic power. The hydraulic power, acting against the piston, is converted to mechanical power capable of moving the load, e.g., large flight control surfaces.

The flow rate Q_m generated by the pump is proportional to the motor speed, i.e.,

$$Q_m(s) = \frac{D_m}{2\pi}\Omega_m(s) \tag{93.7}$$

where D_m represents the pump displacement constant. The flow rate of the hydraulic fluid is primarily dependent on two factors: change in chamber volume and change in pressure due to the compressibility of the fluid effect [4]. The chamber volume changes as the piston moves through the chamber at speed dx_p/dt. The flow rate due to the changes in chamber volume is then expressed as $\pm A dx_p/dt$.

Secondary fluid dynamic effects include fluid compressibility, internal leakage flow, and external leakage flow. These secondary effects are modeled by a first-order equation as follows:

$$\delta Q(s) = Q_m(s) - AsX_p = [K_s s + C_t]P(s) \tag{93.8}$$

that results in the transfer function

$$\frac{P(s)}{\delta Q(s)} = \frac{1}{K_s s + C_l} \tag{93.9}$$

93.4.3 Piston and Flight Control Surface

93.4.3.1 Piston and Flight Control Surface Fundamentals

The pressure developed by the pump and fluid acts on the piston surface (see Figure 93.7), causing the RAM to extend or retract. This force then generates a torque through a hinge to deflect the control surface. This torque has to overcome two load components: control surface inertia and aerodynamic loads. The control surface inertia is primarily due to the fact that the control surface has certain size and mass. The aerodynamic load only occurs in flight, when the air pressure over the control surface applies aerodynamic forces to it. The aerodynamic load is determined by three factors: the surface area of the flight control surface, the aerodynamic loading that varies with altitude and airspeed, and the relative angle of the surface to the wind. The surface angle to the wind depends on the angle of surface deflection and on the angle of attack of the aircraft.

93.4.4 Piston and Flight Control Surface Dynamics

93.4.4.1 Flexible Hinge Joint Model

The magnitude of F_A acting on the piston is equal to $\wp A$, where $\wp$ is the differential pressure developed by the pump and fluid and A is the surface area of the piston. Thus, the force created by the pump and fluid can be expressed as

$$F_A = \wp A \tag{93.10}$$

The piston dynamics, with the piston mass M_p and piston damping B_p, can be described by the second-order model:

$$F_A - F_P = [M_P s^2 + B_P s]X_P \tag{93.11}$$

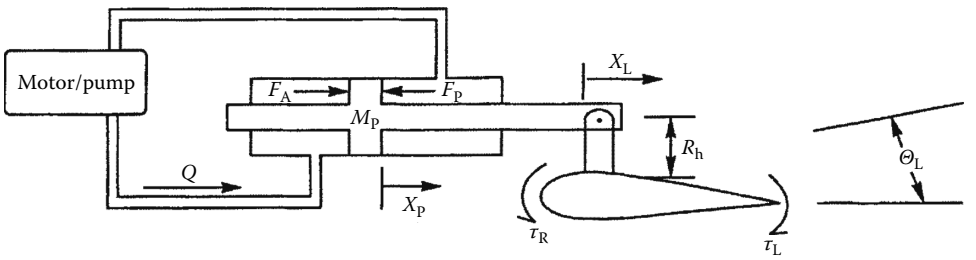

FIGURE 93.7 Simplified actuator control (not drawn to scale).

The resulting torque acting on the flight control surface due to this force imbalance can be described by

$$\tau_R = \frac{K_h}{R_h}(X_P - X_L) \tag{93.12}$$

where
K_h is the hinge stiffness constant
R_h is the hinge length

The stabilator inertia acts against the torque generated by the actuator, such that

$$\tau_R - \tau_L = [J_L s^2 + B_L s]\theta_L \tag{93.13}$$

where
τ_L is the torque created by the aerodynamic load and stabilator inertia
J_L and B_L represent the mass properties of the flight control surface

93.4.4.2 Stiff Hinge Joint Model

Equations 93.11 through 93.13 represent a rather complex model of load dynamics. The complexity of the model can be reduced if the linkage between the actuator and the flight control surface is considered rigid. This is a valid assumption, since the natural frequency of the hinge for a well-designed actuation system is much greater than the actuator bandwidth of concern. Hence, for a rigid linkage, the piston and the load dynamics are still expressed as in Equations 9.11 and 9.13.

$$F_A - F_P = [M_P s^2 + B_P s]X_P \tag{93.14}$$

and

$$\tau_R - \tau_L = [J_L s^2 + B_L s]\theta_L \tag{93.15}$$

Dividing Equation 93.15 by R_h yields

$$F_R - \frac{\tau_L}{R_h} = \left[\frac{J_L s^2 + B_L s}{R_h}\right]\theta_L \tag{93.16}$$

Assuming rigidity of the hinge assembly, $F_R \approx F_P$. Hence, adding Equations 93.14 and 93.16 results in

$$F_A - \frac{\tau_L}{R_h} = [M_P s^2 + B_P s]X_P + \left[\frac{J_L s^2 + B_L s}{R_h}\right]\theta_L \tag{93.17}$$

where τ_L is defined as

$$\tau_L = (\text{Load}_{\text{aero}})\theta_L \tag{93.18}$$

Since rigidity implies that $X_p = X_L$ and $\theta_L = X_p/R_h$, Equation 93.17 is further reduced to

$$F_e = F_A - \frac{\tau_L}{R_h} = \left[\left(M_P + \frac{J_L}{R_h^2}\right)s^2 + \left(B_P \frac{B_L}{R_h^2}\right)s\right]X_P \tag{93.19}$$

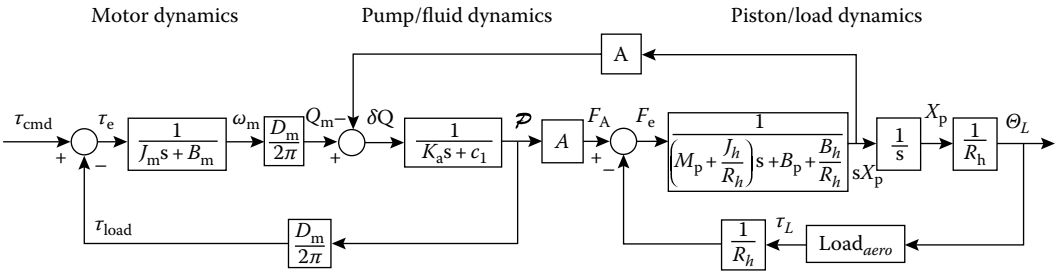

FIGURE 93.8 Bare EHA block diagram.

or expressed in a transfer function form:

$$\frac{X_p(s)}{F_e(s)} = \frac{1}{s\left[\left(M_P + (J_L / R_h^2)\right)s + \left(B_P(B_L / R_h^2)\right)\right]} \tag{93.20}$$

Equation 93.20 represents a simplified model of the load dynamics. A complete simplified design model of the bare EHA, without the controller, is shown in Figure 93.8 using the individual component models.

93.4.4.3 Hinge Moments

The aerodynamic loads mentioned previously describe the torque opposing the piston motion. Thus, load generated by the flow of air above and below the flight control surface applies a torque to the hinge assembly, which in turn adds back pressure to the piston. The hinge moment is modeled as follows:

$$\tau_L = \bar{q} S_t R_h \left(Ch_\alpha \frac{\alpha(s)}{\theta_L(s)} + Ch_\delta \right) \theta_L \tag{93.21}$$

where

S_t denotes the surface area of the control surface
$\bar{q}$ denotes the dynamic pressure
Ch_α and Ch_δ denote the hinge moment coefficients of the control surface with respect to angle of attack and surface deflection δ

The aerodynamic load dynamic pressure $\bar{q}$ is a function of airspeed U_0 and air density [2] ρ, as expressed by

$$\bar{q} = \frac{1}{2} \rho U_0^2 \tag{93.22}$$

The air density in a standard atmosphere drops exponentially with increasing altitude. The dynamic pressure $\bar{q}$ increases as the Mach number gets higher and altitude decreases. The hinge moment for modern fighters with all movable tails, where $Ch_\alpha \approx Ch_\delta$, is modeled by

$$\tau_L = \bar{q} S_t R_h Ch_\delta \left(\frac{\alpha(s)}{\theta_L(s)} + 1 \right) \theta_L \tag{93.23}$$

93.4.4.4 Aircraft Short-Period Approximation

If the aircraft forward speed is assumed constant (i.e., the speed perturbations $u \approx 0$), the X force equation can be neglected since it does not significantly contribute to the short-period oscillation [5]. Thereby, the short-period approximation of the longitudinal channel of the aircraft that is relevant to the actuator dynamics is extracted and is written as

$$\begin{bmatrix} \dot{\alpha} \\ \dot{q} \end{bmatrix} = \begin{bmatrix} z_\alpha & z_q \\ m_\alpha & m_q \end{bmatrix} \begin{bmatrix} \alpha \\ q \end{bmatrix} + \begin{bmatrix} z_\delta \\ M_\delta \end{bmatrix} [\delta_e] \tag{93.24}$$

This yields a second-order minimum-phase transfer function of the form

$$\frac{\alpha(s)}{\delta(s)} = \frac{-K(s+a)}{(s+b)(s+c)} \tag{93.25}$$

For the frequency of interest, the short-period approximation closely resembles the full state model. As seen in Figure 93.9, where the solid lines represent the full state model frequency response of the vehicle and + lines represent the short-period model frequency response of the vehicle, phase and attenuation characteristics are closely matched at high frequency. The approximation, as seen in the figure, is not valid for frequencies below 0.5 rad/s due to the effects from the slow longitudinal mode, which is referred to as the phugoid.

93.4.5 Quantitative Feedback Theory (QFT)

Robust quantitative feedback theory (QFT) [3,6] compensators are ideal for obtaining the desired response from an actuator. The term *robust* in control theory implies that a system under control, in this case the actuator, remains stable throughout its operating envelope, rejects disturbances, and results in minimum degradation in the performance specifications. A QFT-designed feedback system, which uses

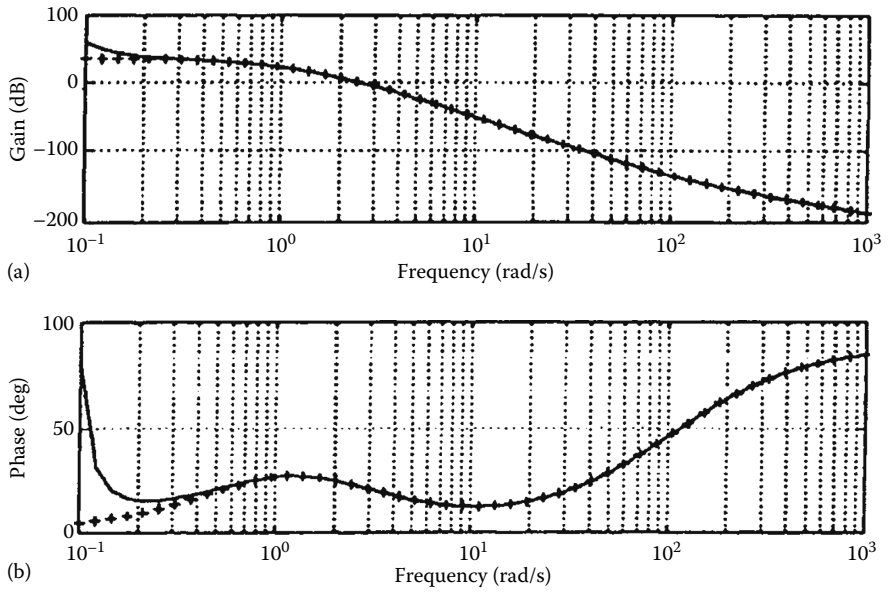

FIGURE 93.9 Comparison of full- and short-period approximation for longitudinal equations of motions: (a) magnitude response and (b) phase response.

output feedback, assures that the output tracks the input values despite parametric uncertainties or disturbances. The output of a unity-gain feedback system with uncertain plant models can vary depending on the plant conditions; however, the output of a robust QFT feedback control system with uncertain plant models will not vary much. The unity-gain system, however, cannot control the tracking response, which necessitates the inclusion of a prefilter.

Plant (specifically, actuator) uncertainties may be caused by manufacturing tolerances. For example, a component A is specified to be 10 ± 0.1 mm long. In a large production run, the length of component A may be anywhere between 9.9 and 10.1 mm. This tolerance range may be substantial enough to produce noticeable variations in the plant model. Plant uncertainties may also be caused by the environment, specifically the system (actuator) operating conditions. For example, the parameters of an aircraft model display large variations depending on altitude and airspeed. Finally, the performances of various components decay over time, introducing an additional element of uncertainty.

The QFT design paradigm accounts for the plant variations in the design procedure. It is a linear design technique for designing a linear robust controller for linear or nonlinear control systems [3,6]—in this case, the actuator control system. As long as all the QFT design requirements are met, the output responses are guaranteed to conform to the specification boundaries. The initial step in the design process is to establish the upper and lower performance tracking boundaries. The maximum allowable disturbance is used to determine the disturbance boundary. The phase margin angle, gain margin, or maximum peak value is used to establish the stability boundary. These combined boundaries establish the limitation of the system performance. The next step is to analyze the system to determine the parameters that will cause noticeable variations to the plant. The system, often modeled only as a single plant transfer function in other design methods, is now modeled more comprehensively as a *set* of plant transfer functions. The variations now form a closed region in the Nichols magnitude and phase chart, called the template; larger template sizes indicate a higher degree of plant uncertainty. Templates at different frequencies differ in size and shape.

The most important aspect of modeling is the thorough analysis of the bare actuator plant, in order to find the sources of plant variation. For an aircraft application, the three largest sources of variations are the fluctuations in aerodynamic load on the flight control surfaces, the motor torque, and the hydraulic pump fluid pressure.

93.5 Actuator Compensator Design

QFT compensators, which are designed in the frequency domain, are ideally suited for the actuator control system. The QFT compensator processes its inputs, which are the commanded actuator displacement and the measured current actuator position, and generates a commanded signal to, e.g., the solenoid valve in a hydraulic actuator or a current for the electric DC motor in the EHA actuator. In order to proceed with the actuator QFT compensator design, the block diagram as shown in Figure 93.7 is transformed to the standard inner and outer QFT loop structures shown in Figure 93.10 [2,3,6]. For this design problem, the external disturbance $d_2(t)$ can be ignored, i.e., $d_2(t) = 0$, whereas the $d_1(t)$ disturbance models a possible measurement bias. The inner loop controls the angular rate of the motor, while

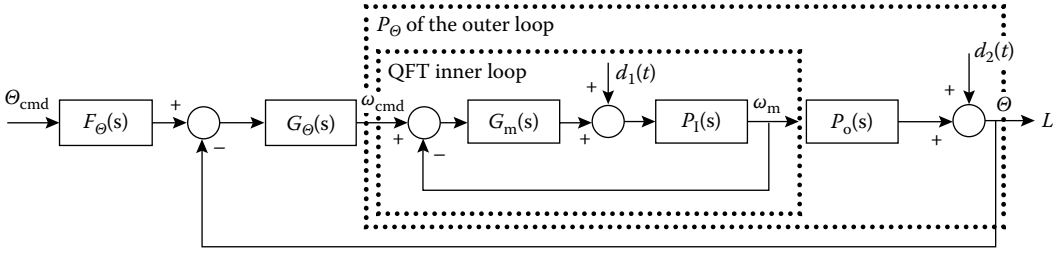

FIGURE 93.10 Two feedback loops in QFT two degrees of freedom structure.

the outer loop controls the surface deflection. Since tracking in the inner loop is less important, for its function is to reduce the uncertainty level of the outer loop, the inner loop prefilter can be set to unity, and the tracking performance enforcement is relegated to the prefilter F_θ of the outer loop.

93.6 Conclusion

The modeling of a hierarchy of hydraulic actuators has been presented. The modeling of modern EHAs is emphasized, and dynamic models of its subcomponents are carefully developed. A systems approach to actuator modeling and design is taken, and the feedback structure is highlighted. In this chapter, it is stressed that because of the complex feedback interactions at work, proper actuator modeling requires consideration of the latter in the full context of the control system in which it is to be employed. Thus, in this presentation, the aerospace application is considered. At the same time, the actuator is being viewed not as a component of a control system but as a control system in its own right. Hence, it is shown that simple mechanical feedback linkages that fulfilled the role of a controlling element for the actuator can be replaced by a more flexible, high-performance, robust, full-blown electronic actuator compensator. Concerning electropneumatic instruments and sensors, these are critical elements in systems where the flow of liquids and/or gases is being controlled, e.g., in the chemical industries. In aerospace, electropneumatic sensors are used to measure airspeed, altitude, and angle of attack and sideslip angles of the aircraft; these functions are collocated in the air data computer (ADC). Currently, modern sensors use feedback action for accuracy enhancement, and as such, the design of modern electropneumatic instruments and sensors is conceptually similar to the design of EHAs. Detailed information on actuators and sensors may be found in Refs. [4,7].

Nomenclature

A	ram cross-sectional area
a,b,c,d,e,R_h	length of linkages
B_p	piston damping
C_h	hinge moment coefficient
D_m	pump displacement constant
F	force
J	moment of inertia
K	gain
K_h	hinge stiffness constant
M_p	mass of piston
M,z,m	aerodynamic stability derivatives
$\wp$	differential pressure developed by the pump
P	pressure
$\overline{q}$	dynamic pressure
q	pitch rate
Q	flow rate
s	Laplace variable
S_t	aerodynamic surface area
U,u	airspeed
x,X	displacement
α	angle of attack of aircraft
δ	deflection angle
Ω, ω	rotor speed
ρ	air density
θ	deflection angle
τ	torque

References

1. O.R. Reynolds, M. Pachter, and C.H. Houpis, Full envelope flight control system design using quantitative feedback theory, *AIAA J. Guidance Control Dyn*., 19, 1023–1029, 1996.
2. K.H. Kang, Electro-hydrostatic actuator controller design using quantitative feedback theory, MS thesis, Graduate School of Engineering, Air Force Institute of Technology, Wright-Patterson AFB, OH, December 1994, AFIT/GE/ENG/94D-18.
3. C.H. Houpis, M. Pachter, S. Rasmussen, and R. Sating, Quantitative feedback theory for the engineer, Wright Laboratory Technical Report, WL-TR-95-3061, Wright Laboratory, Wright-Patterson AFB, OH, June 1995. (Available from the National Technical Information Service, 5285 Port Royal Road, Springfield, VA 22151, document number AD-A297574.)
4. C.W. de Silva, *Control Sensors and Actuators*, Englewood Cliffs, NJ: Prentice-Hall, 1989.
5. J.H. Blakelock, *Automatic Control of Aircraft and Missiles*, New York: John Wiley & Sons, 1991.
6. J.J. D'Azzo and C.H. Houpis, *Linear Control System Analysis and Design—Conventional and Modern*, 4th edn., New York: McGraw-Hill, 1988.
7. E.H.J. Pallet and S. Coyle, *Automatic Flight Control*, Oxford, U.K.: Blackwell, 1993.

Partial List of Vendors and Suppliers

ControlAir, Inc., 8 Columbia Dr., Amherst, NH 03031-2315, Phone: 603-886-9400, 800-216-3636 (toll free), Fax: 603-889-1844, www.controlair.com

Equilibar, 320 Rutledge Rd., Fletcher, NC 28732, Phone: 828-650-6590, Fax: 801-504-4439, www.equilibar.com

Nexen Group, Inc., 560 Oak Grove Pkwy., Vadnais Heights, MN 55127-8509, Phone: 651-484-5900, 800-843-7445 (toll free), Fax: 651-286-1099, www.nexengroup.com/nexen/index.jsp

Ross Controls, 32900 N. Avis Dr., Madison Heights, MI 48071, Phone: 248-397-1958, 800-438-7677 (toll free), commerce.rosscontrols.com

94

Explosion-Proof Instruments

Sam S. Khalilieh
Earth Tech

94.1 Introduction

Where hazardous atmospheres can exist, electricity should be a primary concern of every engineer and system designer. Hazardous atmospheres can exist not only in the more common surroundings of industrial, chemical, and environmental facilities but also in many less obvious environs where dust is present, where gas can accumulate, and where combustible gas-forming reactions occur. To minimize risks in such areas, it is necessary to design specific hazard-reducing electric systems. Most electric equipment is built to specific standards aimed to reduce the incidence of fires and human casualties. The majority of such incidents can be attributed to poor or defective installations, improper use of approved equipment, deteriorated equipment, and accidental applications. In combination with an explosive atmosphere, these factors can result in extremely dangerous conditions. Designing an electric system for a hazardous location requires careful planning, research, engineering, and ingenuity in using proper protection techniques to develop better applications and classifications that reduce hazards.

94.2 Fundamentals of Explosion Protection

The safety of personnel and equipment present in a hazardous area should never be taken for granted. In 1913, a massive methane gas explosion in a coal mine in Glamorganshire, South Wales, claimed the lives of 439 mine workers. After months of research and studies, a group of experts and scientists concluded that the explosion was caused by a small amount of electric energy stored in the circuit. This small amount of energy combined with the presence of an explosive gas and air mixture and the absence of proper protection proved to be fatal for the mine workers.

To understand the dangers associated with electric equipment in hazardous areas, one must first understand the basics. Chemically speaking, oxidation, combustion, and explosions are all exothermic reactions where heat is given off at different reaction speeds. For these reactions to occur, three components must be present simultaneously in certain concentrations. These components are (1) fuel (liquid, gas, or solids), (2) a sufficient amount of oxygen (air), and (3) an ignition source (electric or thermal).

Some of the ignition sources that can be potentially hazardous include (1) hot surfaces (motor windings, heat trace cable, light fixtures), (2) electric sparks and arcs (when circuits are opened and closed, short circuits), (3) mechanical sparks (friction, grinding), (4) electrostatic discharge (separation process in which at least one chargeable substance is present), and (5) radiation, compression, and shock waves.

When dealing with electric equipment in hazardous locations, it is important to understand and to be familiar with the following terms:

1. *Flash point*—the minimum temperature at normal air pressure at which a combustible or flammable material releases sufficient vapors ignitable by an energy source. Depending on the flash point (FP), flammable liquids are divided into four classes of hazard:
   a. AI (FP < 21 °C)
   b. AII (21 °C < FP < 55 °C)
   c. AIII (55 °C < FP < 100 °C)
   d. B (FP < 21 °C at 15 °C dissolving in water)
2. *Ignition temperature*—the minimum temperature under normal operating pressure at which a dangerous mixture ignites independently of the heating or heated element.
3. *Flammable limits*—the upper explosive limit (UEL) or the maximum concentration ratio of vapor to air mixture above which the propagation of flame does not occur when exposed to an ignition source. Here, the mixture is said to be "too rich" to burn. The lower explosive limit (LEL) is the minimum concentration ratio of vapor to air mixture below which the propagation of flame does not occur when exposed to an ignition source. Also, here, the mixture is said to be "too lean" to explode. Significant attention must be given to LEL, since it provides the minimum quantity of gas necessary to create a hazardous mixture. Generally, the flammable limits are indicated in percent by volume, which is abbreviated % vol. Note that the explosion of a mixture in the middle the UEL and the LEL is much more violent than if the mixture were closer to either limit.
4. *Maximum surface temperature*—the maximum temperature generated by a piece of electric equipment under normal or fault conditions. This temperature must be below the minimum ignition temperature of the potentially explosive surrounding atmosphere. Equipment used in hazardous locations must be clearly marked to indicate class, group, and maximum surface temperature or range referenced to 40 °C (104 °F) ambient temperature. Table 94.1 shows that an apparatus with a specific T class can be used in the presence of all gases having an ignition temperature higher than the T temperature class of the device. For added safety, it is recommended that the maximum surface temperature be not more than 80% of the minimum ignition temperature of the surrounding gas. The reader is cautioned not to confuse maximum working (operating) temperature with maximum surface temperature, which is measured under worst-case conditions of the electric apparatus. An electric apparatus designed to operate with a maximum ambient temperature of 70 °C—even in the worst conditions of the expected temperature range—must not have a temperature rise greater than a safety margin of 10 °C to be classified as T6 or 5 °C for classes T3, T4, and T5 (Table 94.1).
5. *Vapor density*—the weight of a volume of pure vapor gas compared with the weight of an equal volume of dry air under the same normal atmospheric pressure and temperature. It is calculated as the ratio of molecular weight of the gas to the average molecular weight of air (28.96). Methane gas (CH_4) with molecular weight of 16 and vapor density of 0.6 tends to rise, while acetone (C_3H_6O) with molecular weight of 58 and vapor density of 2 tends to settle closer to ground levels.

In the United States, the National Electrical Code (NEC) defines a hazardous area as "an area where a potential hazard may exist under normal or abnormal conditions because of the presence of flammable, combustible,

TABLE 94.1 Maximum Surface Temperature under All Operating Conditions

Maximum Temperature		
°C	°F	Identification Number
450	842	T1
300	572	T2
280	536	T2A
260	500	T2B
230	446	T2C
215	419	T2D
200	392	T3
180	356	T3A
165	329	T2B
160	320	T3C
135	275	T4
120	248	T4A
100	212	T5
85	185	T6

Source: Reprinted with permission from NFPA 70-1996, the *National Electrical Code®*, Copyright 1995, NFPA, Quincy, MA 02269. This reprinted material is not the complete and official position of the NFPA, on the referenced subject that is represented only by the standard in its entirety.

Note: Surface temperature of electric apparatus during operation must not exceed limitations of the hazard present.

or ignitable materials" [1]. This general description is divided into different classes, divisions, and groups to assess the extent of the hazard properly and to design and specify safe operating electric systems.

The need for classification is important not only for safety but for economic reasons as well. Proper application, good engineering, and experience can reduce the extent of the most volatile areas (Class I, Division 1) within reasonably safe distances of potential leaks and ignition sources. Under Class I, Division 1, equipment and installation costs can become an economic burden because the equipment is considerably more expensive and must pass stringent tests to ensure proper and safe operation under normal or abnormal conditions. The National Fire Protection Association (NFPA 497 A and B) [2] and the American Petroleum Institute *Recommended Practice for Classification of Locations for Electrical Installations at Petroleum Facilities* (ANSI/API RP 500) [3] are excellent resources for defining hazardous area boundaries.

94.3 Classification of Hazardous Areas

Classification of a hazardous area within a facility is usually determined by highly qualified personnel including chemical engineers, process engineers, and safety officers. Their primary objective is to determine where a potentially hazardous atmosphere exists, under what conditions it exists, and how long it exists. Careful study and design of electric installations, especially in hazardous areas, are crucial for the safe operation of electric equipment and prevention of an accidental ignition of flammable materials. The NEC, which has been adopted by many states, agencies, and companies as the basis for inspections, describes the requirements and procedures for electric installations in hazardous areas. Articles 500–504 contain the requirements of electric equipment and wiring for all voltages in locations where fire or explosion hazards may exist due to flammable gases or vapors, flammable liquids, combustible dust, or ignitable fibers or flyings.

TABLE 94.2 Area Classification Based on NEC

Division 1—Hazard Is Present under Normal Operating Conditions	
Class I	Gases and Vapor
Group A	Acetylene
Group B	Hydrogen
Group C	e.g., ethylene
Group D	e.g., methane
Class II	Combustible Dusts
Group E	Metal dust
Group F	Coal dust
Group G	Grain dust
Class III	Fibers
Division 2—Hazard Is Present Only under Abnormal Operating Conditions	

Table 94.2 describes hazardous locations by class, division, and group. The class defines the physical form of combustible material mixed with oxygen molecules. The division defines the probability of an explosive fuel to air mixture being present. The group indicates the type of vapor or dust present. The NEC gives the following definitions [1]:*

Class I, Division 1 Locations

1. Where ignitable concentrations of flammable gases or vapors can exist under normal operation conditions, may exist frequently because of repair or maintenance operations or because of leakage, and where breakdown or faulty operation of equipment or processes might release ignitable concentrations of flammable gases or vapors and cause simultaneous failure of electric equipment.

Class I, Division 2 Locations

1. Where volatile flammable liquids or flammable gases are handled, processed, or used but where the liquids, vapors, or gases will normally be confined within closed containers or closed systems from which they can escape only in case of accidental rupture or breakdown of such containers or systems or in case of abnormal operation of equipment.
2. Where ignitable concentrations of gases or vapors are normally prevented by positive mechanical ventilation and where they might become hazardous through failure or abnormal operation of the ventilating equipment.
3. Adjacent to Class I, Division 1 locations, and where ignitable concentrations of gases or vapors might occasionally be communicated; unless such communication is prevented by positive-pressure ventilation from a source of clean air, and effective safeguards against ventilation failure are provided.

Class II, Division 1 Locations

1. Where combustible dust is in the air under normal operation conditions in quantities sufficient to produce explosive or ignitable mixtures.
2. Where mechanical failure or abnormal operation of machinery or equipment might cause such explosive or ignitable mixtures to be produced and also might provide a source of ignition through simultaneous failure of electric equipment, operation of protective devices, or from other causes.
3. Where combustible dusts of an electrically conductive nature may be present in hazardous quantities.

* Reprinted with permission from NFPA 70-1996, the *National Electrical Code*®,© 1995, NFPA, Quincy, MA. This reprinted material is not the complete and official position of the NFPA, on the referenced subject that is represented only by the standard in its entirety. *National Electrical Code*® and *NEC*® are registered trademarks of the NFPA, Inc., Quincy, MA.

Class II, Division 2 Locations
Where combustible dust normally is not in the air in quantities sufficient to produce explosive or ignitable mixtures, and dust accumulations normally are insufficient to interfere with the safe dissipation of heat from electric equipment or may be ignitable by abnormal operation or failure of electric equipment.

Class III, Division 1 Locations
Where easily ignitable fibers or materials producing combustible flyings are handled, manufactured, or used.

Class III, Division 2 Locations
Where easily ignitable fibers are stored or handled. Quantities and properties of hazardous materials are the basis upon which the NEC classifies hazardous locations. Each hazardous location must be evaluated carefully to determine the appropriate classification to facilitate the design process and to help specify the correct equipment.

94.4 Enclosure Types and Requirements

Choosing the proper type of enclosure for electric equipment is important for two reasons:

1. Personnel protection against accidental contact with enclosed electric equipment
2. Protection of internal equipment against outside harm

Enclosures are designated by a type number indicating the degree of protection and the condition for which they are suitable. In some applications, enclosures have a dual purpose and therefore are designated by a two-part-type number shown with the smaller number first (i.e., 7/9). The following enclosure types, with their enclosed equipment, have been evaluated in accordance with Underwriters Laboratories, Inc. UL 698, *Industrial Control Equipment for Use in Hazardous Locations*, and are marked to show the class and group letter designations.

Type 7 Enclosures. Type 7 enclosures are nonventilated, intended for indoor applications, and classified for Class I, Group A, B, C, or D, as defined in Table 94.2. The letters A to D sometimes appear as a suffix to the designation Type 7 to give the complete designation. According to UL 698, Type 7 enclosures must be designed to withstand an internal explosion pressure of specific gases and to prevent such an explosion from igniting a hazardous mixture outside the enclosure (explosion test). In addition, Type 7 enclosures fabricated from sheet steel are designed to withstand two times the internal explosion pressure for 1 min without permanent deformation and three times the explosion pressure without rupture. If constructed of cast iron, the enclosure must be capable of withstanding four times the explosion pressure without rupture or deformation. This test may be waived if calculations show a safety factor of five to one for cast metal or four to one for fabricated steel. The enclosed heat-generating devices are specifically designed to prevent external surfaces from reaching temperatures capable of igniting explosive vapor–air mixture outside the enclosure (temperature test).

Type 8 Enclosures. Type 8 enclosures are nonventilated, intended for indoor applications, and intended for Class I, Group A, B, C, or D, as outlined in Table 94.2. The letters A to D appear as a suffix to the designation Type 8 to give the complete designation. According to UL 698, the oil-immersed equipment must be able to operate at rated voltage and most severe current conditions in the presence of flammable gas–air mixtures without igniting these mixtures.

Type 9 Enclosures. Type 9 enclosures are nonventilated, intended for indoor applications, and classified for Class II, Group E, F, or G as outlined in Table 94.2. The letters E, F, or G appear as a suffix to the designation Type 9 to give the complete designation. According to UL 698, the enclosure with its enclosed equipment is evaluated in accordance with UL 698 in effect at the time of manufacture. This evaluation includes a review of dimensional requirements for shaft opening and joints, gaskets material,

and temperature rise under a blanket of dust. The device is operated at full rated load until equilibrium temperatures are reached and then allowed to cool to ambient temperature over a period of at least 30 h while continuously subjected to circulating dust of specified properties. No dust shall enter the enclosure (dust penetration test). Furthermore, Type 9 enclosures must also pass the "temperature test with dust blanket," which is similar to the temperature rise test except the circulating dust is not aimed directly at the device during testing. The dust in contact with the enclosure shall not ignite or discolor from heat, and the exterior surface temperature based on 40 °C (104 °F) shall not exceed specific temperatures under normal or abnormal conditions. Where gasketed enclosures are used, gaskets shall be of a noncombustible, nondeteriorating, vermin-proof material and shall be mechanically attached. Type 9 ventilated enclosures are the same as nonventilated enclosures, except that ventilation is provided by forced air from a source outside the hazardous area to produce positive pressure within the enclosure. The enclosure must also meet the requirements of a temperature design test.

Type 10 Enclosures. Type 10 enclosures are nonventilated and designed to meet the requirements of the U.S. Bureau of Mines that relate to atmospheres containing mixtures of methane and air, with or without coal dust present.

It is important to note that enclosures for hazardous applications are designed for specific applications and must be installed and maintained as recommended by the enclosure manufacturer, since any misapplication or alteration to the enclosure may jeopardize its integrity and may eventually cause catastrophic failure of the system. All enclosures should be solidly grounded and properly labeled with a warning sign reminding the operator of the importance of de-energizing the incoming power to the enclosure prior to its servicing.

94.5 Protection Methodologies

Choosing a protection technique that suits each application can appear complicated because safety, reliability, cost, and maintenance factors must all be considered. Over the years, few hazardous area safety protection methodologies have been used. Although methodologies differ in application and principles of operation, they all have one thing in common: to eliminate one or more components necessary for combustion. Three of the most widely used methodologies are

1. Intrinsic safety (IS)
2. Explosion proof
3. Purging and pressurization

94.5.1 Intrinsic Safety

Simply stated, IS is all about preventing explosions. IS is based on the principle of limiting the thermal and electric energy levels in the hazardous area to levels that cannot cause an ignition of a specific hazardous mixture in its most ignitable concentration. IS pertains to the minimum ignition temperature and the minimum ignition electric energy required to cause a specific group to ignite. The energy level provided by an IS circuit is low (≈1 W) and is used only to power up instruments with a low energy demand. An IS circuit incorporates an intrinsically safe apparatus (field device), an associated apparatus, and an interconnecting wiring system. Designing intrinsically safe systems begins with studying the field device. This will help determine the type of associated apparatus that can be used so that the circuit functions properly under normal operating conditions but still safe under fault conditions. Field devices can be simple, such as *resistance temperature devices* (*RTDs*), thermocouples, mechanical switches, proximity switches, and light-emitting diodes (LEDs), or they can be nonsimple, such as transmitters, solenoid valves, and relays. A field device is considered and recognized as a "simple device" if its energy storing or generating values do not exceed 1.2 V, 0.1 A, and 25 mW (or 20 μJ) in an intrinsically safe system under normal or abnormal conditions.

TABLE 94.3 Comparison of Entity Values of a Field Device and a Safety Barrier

Field Device	Safety Barrier
$V_{max} \geq V_{oc}$	
$I_{max} \geq I_{sc}$	
$C_i \leq C_a$	(Maximum allowed capacitance)
$L_i \leq L_a$	(Maximum allowed inductance)

Source: Reprinted with permission from NFPA 70-1996, the *National Electrical Code*®, Copyright 1995, NFPA, Quincy, MA 02269. This reprinted material is not the complete and official position of the NFPA, on the referenced subject that is represented only by the standard in its entirety. *National Electrical Code*® and *NEC*® are registered trademarks of the National Fire Protection Association, Inc., Quincy, MA 02269.

The simple device may be connected to an intrinsically safe circuit without further certification or approval. The fact that these devices do not have the ability to store or generate high levels of energy does not mean they can be installed in a hazardous area without modification. They must always be used with an associated apparatus to limit the amount of energy in the hazardous area, since a fault outside the hazardous area can cause sufficient high levels of energy to leak into the hazardous area. A nonsimple device (i.e., relay, transmitter) is capable of generating and storing energy levels exceeding the aforementioned values. Such devices require evaluation and approval under the entity concept (described later) to be used in conjunction with an intrinsically safe circuit. Under the entity concept, these devices have the following entity parameters: V_{max} (maximum voltage allowed), I_{max} (maximum current allowed), C_i (internal capacitance), and L_i (internal inductance). Under fault conditions, voltage and current must be kept below the V_{max} and I_{max} of the apparatus to prevent any excess heat or spark, which can be disastrous in hazardous areas. C_i and L_i indicate the ability of a device to store energy in the form of internal capacitance and internal inductance, and their value must be less than C_a and L_a of the associated apparatus (Table 94.3).

An associated apparatus (Figure 94.1), also known as a safety barrier, is an energy-limiting device needed to protect a field device located in a hazardous area from receiving excessive voltage or current. An associated apparatus is normally installed in a dust- and moisture-free enclosure (NEMA 4) located in a nonhazardous area, as close as possible to the hazardous area to minimize the capacitance effect of

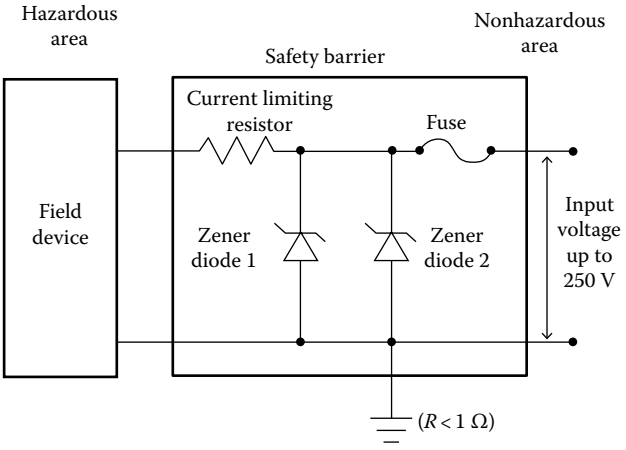

FIGURE 94.1 Major components of barrier circuit.

the cable. If installed in a hazardous area, the associated apparatus must be installed in an explosion-proof enclosure (i.e., NEMA 7D).

Figure 94.1 shows the three major components of a Zener safety barrier. (Note that there are other types of barriers such as isolation and repeater types.) The components are

1. The resistor, which limits the current to a specific value known as short circuit current (I_{sc}).
2. The fuse, which acts as an interrupter or protective device in case of a diode failure (fuse will blow if diode conducts).
3. The *Zener diode*, which limits the voltage to a specific value known as open-circuit voltage (V_{oc}). Zener diodes are unique in their ability to conduct current under reverse bias conditions. When voltage is applied to the Zener diode in the reverse direction, a small amount of current known as leakage current is passed through. This current remains small until the bias voltage exceeds the Zener breakdown voltage. Exceeding the breakdown voltage causes the inherently high resistance of the Zener diode to drop to a very low value, thus allowing the current to increase abruptly. This sudden current increase forces the Zener diode to become a conductor, thereby diverting the excess voltage to ground. If the current continues to flow above and beyond the fuse rating, the fuse will open and the circuit will be completely interrupted. Most safety barriers incorporate at least two diodes in parallel to provide maximum protection in case one diode fails (redundant safety).

In 1988, ANSI/UL 913 [5] allowed the use of IS barriers with replaceable fuses as follows: "if it is accessible for replacement, and the fuse on a fuse protected shunt diode barrier shall not be replaceable by one of higher rating." The fuses are housed in tamper-proof assemblies to prevent confusion or misapplication. The diodes have specific power ratings that must not be exceeded. The Zener diodes and fuses are governed by a very specific set of parameters that allow the fuse to operate at one-third the power rating of the Zener diode and to avoid irreversible damage to the Zener diode. The power rating for the Zener diode can be determined as follows:

$$Z_w = 1.5 \times V_{oc} \times 2 \times I_f$$

where

Z_w is the minimum power rating of the Zener diode
V_{oc} is the maximum Zener diode open-circuit voltage
I_f is the fuse current rating

Selecting the best barrier for the application depends on the field device and requires analysis to ensure proper operation of the intrinsically safe circuit under normal or abnormal conditions. Three of the more important characteristics requiring examination are (1) internal resistance, (2) rated voltage, and (3) circuit polarity. Regardless of the selected barrier, each has an internal resistance (R_i) that limits the short-circuit current under fault conditions. As current passes through R_i, it creates a voltage drop across the barrier that must be accounted for ($V = IR$). The rated voltage of the safety barrier must be equal to or reasonably greater than the supply voltage. The word *reasonably* is significant because excessive supply voltage can cause the diode to conduct, rushing high current through the fuse and blowing it. The use of a regulated power supply can significantly reduce problems associated with excessive supply voltage. To complete an analysis, the circuit polarity must be established. While AC barriers can be connected with either positive or negative power supply, DC barriers can be rated to either positive or negative.

94.5.2 Making Field Devices Intrinsically Safe

RTDs and thermocouples can be made intrinsically safe by using isolated temperature converters (ITCs) that convert a low DC signal from the field device into a proportional 4–20 mA signal. These ITCs require no ground connection for the safe and proper operation of the IS circuit. Because of their ability to store

energy, transmitters are considered nonsimple devices and must be approved as intrinsically safe. If they are third-party approved, their entity parameter must be carefully considered. Transmitters (4–20 mA) convert physical measurements in hazardous areas, such as pressure and flow, into electric signals that can be transmitted to a controller in a safe area. Depending upon the conditions, 4–20 mA signals can be made intrinsically safe by using a repeater barrier that duplicates the output signal to match the input signal. Repeaters can be grounded or ungrounded. Ungrounded repeater barriers are known as "transformer-isolated barriers," since the incoming voltage or signal is completely isolated from the outgoing voltage or signal via a transformer. Digital inputs, such as mechanical and proximity switches, which are simple devices, can be made intrinsically safe by using a switch amplifier. A switch amplifier is simply a relay or an optocoupler (a high-speed relay that uses optical isolation between the input and the output) that transfers a discrete signal (i.e., on/off) from the hazardous area to a safe area. Grounded safety barriers are passive devices designed specifically to prevent excessive energy in a nonhazardous area from reaching a hazardous area. These barriers can be used with most field devices. In order for such barriers to function properly, there is emphatic need for a solid, low-impedance (<1 Ω) connection to ground to prevent ground loops and induced voltages that can hinder operation of the system.

94.5.3 Ignition Curves

All electric circuits possess certain electric characteristics that can be classified under three categories: resistance, inductance, and capacitance. To some extent, all circuits possess these three characteristics. However, some of these characteristics may be so small that their effects are negligible compared with that of the others, thus the terms resistive, inductive, and capacitive circuit. Since the concept of IS is based on the principle that a large electric current can cause an explosion in a hazardous area and the lack of it cannot, it is necessary to identify the ranges of currents that are safe and those that are dangerous.

What is a dangerous amount of electric energy? The answer lies in the ignition curves. Ignition curves are published in most IS standards, such as ANSI/UL 913 [5]. Three of the most referenced curves are shown in Figure 94.2. The curves show the amount of energy required to ignite various hazardous atmospheric mixtures in their most easily ignitable concentration. The most easily ignitable concentration is determined by calculating the percentage of volume to air between UELs and LELs of a specific hazardous atmospheric mixture. In the three referenced curves, the energy levels (voltage and current) below the group curve are not sufficient to cause an ignition of the referenced group.

Since specific ignition temperature is directly related to the amount of voltage and current consumed, both V_{oc} and I_{sc} of the safety barrier must be less than V_{max} and I_{max}. When designing an intrinsically safe system, the cable resistance R (Ω/m), the inductance L (μH/m), and the capacitance C (pF/m), which are inherently distributed over the length of the cable, must be considered. The capacitance and inductance can be readily obtained from the cable manufacturer's literature. If these parameters are not available, certain default values can be used based on NFPA 493/78 (A-4-2). They are $C_c = 200$ pF/m (60 pF/ft), $L_c = 0.66$ μH/m, and (0.2 μH/ft). To determine the maximum wiring distance required to ensure proper operation, the capacitance and inductance must be calculated. One common approach uses "lumped parameters," in which the voltage and current of both the intrinsically safe apparatus and the associated intrinsically safe apparatus are compared and matched according to Equations 94.1 and 94.2. Any deviation from either Equations 94.1 or 94.2 can compromise the integrity of the system and introduce hazardous conditions. The reactive parts of the system must also be considered and verified to demonstrate that C_a and L_a values of the associated apparatus are not be exceeded by the field device and the field wiring values as shown in Equations 94.3 and 94.4. This method, although simple and effective, tends to exaggerate the wiring capacitance and inductance effect, which can be limiting in some applications. Another method takes advantage of the relation between the cable resistance and inductance. This method can be used if the L/R ratio of the associated apparatus is higher than the calculated L/R ratio of the cable. Under these conditions, the lesser D_a (maximum allowed distance) value can be ignored and the cable length can be extended to the

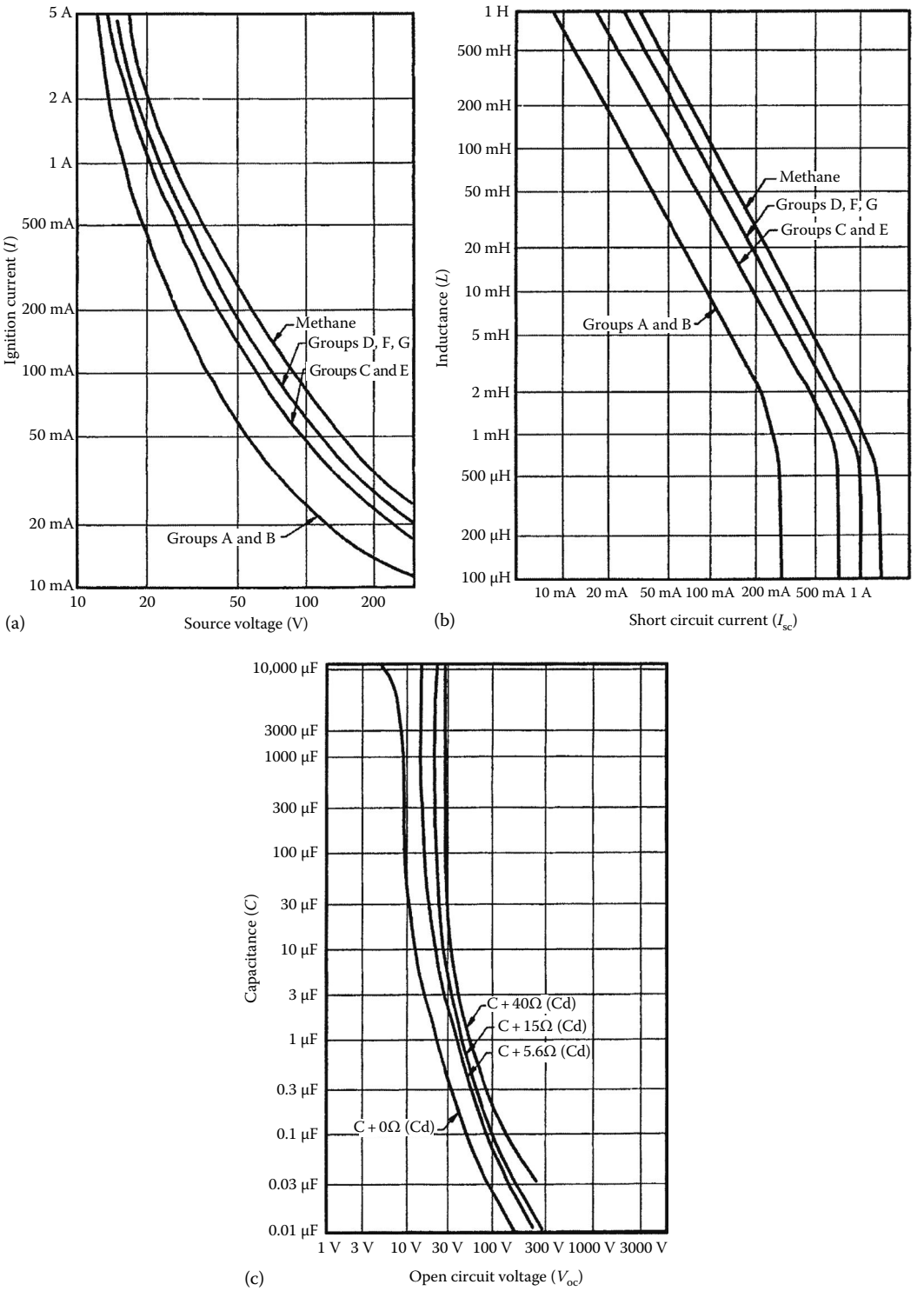

FIGURE 94.2 (a) Resistance circuit ignition curves for all circuit metals, (b) inductance circuit ignition curves at 24 V for all circuit metals, and (c) capacitance circuit ignition curves for Groups A and B for all circuit metals.

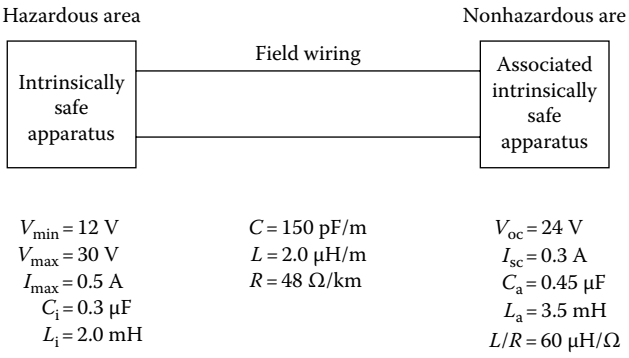

FIGURE 94.3 Analysis of an intrinsically safe system.

higher D_a value. This method is more flexible where cable length is an issue. Figure 94.3 and the following example illustrate these methods.

94.5.3.1 Lumped Parameters Method

$$V_{oc} \leq V_{max} \tag{94.1}$$

$$I_{sc} \leq I_{max} \tag{94.2}$$

$$C_c \leq C_a - C_i \quad 0.45 - 0.30\,\mu F = 0.15\,\mu F \tag{94.3}$$

$$L_c \leq L_a - L_i \quad 3.5 - 2.0\,mH = 1.5\,mH \tag{94.4}$$

The maximum length of the field wiring, referred to its capacitance and inductance, is the lesser value of D_a:

$$D_a = 0.15\,\mu F/150\,pF/m = 1000\,m$$

$$D_a = 1.5\,mH/2.0\,\mu H/m = 750\,m\ (\text{maximum distance of field wiring})$$

94.5.3.2 *L/R* Ratio Method

Since the cable L/R ratio of 41.6 μH/Ω (2 μH/m/48 Ω/km) is less than the given associated apparatus L/R ratio, the inductive effect can be ignored and the maximum distance can be increased to 1000 m.

94.5.4 Certification and Approval

Although approval and certification processes help to provide safety, careful planning, designing, and engineering are still necessary. IS standards, procedures, and tests are recognized worldwide. Testing authorities include Underwriters Laboratories, Inc. (UL), and Factory Mutual Research Corp. (FM) in the United States, Canadian Standards Association (CSA) in Canada, and Physikalisch-Technische Bundesanstalt (PTB) in Europe. Intrinsically safe products are suitable

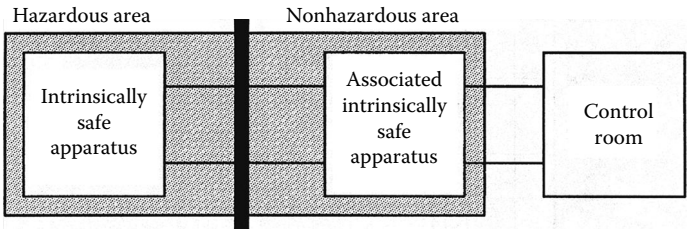

FIGURE 94.4 Loop approval. Intrinsically safe apparatus and associated apparatus are evaluated together. Shaded area indicates evaluated for loop approval.

for all classes, divisions, and groups outlined in Table 94.2. It is necessary to emphasize that the intrinsically safe product must be rated and classified for each specific application (class, division, and group). In the United States, FM adopted two methods for testing and approving equipment to be used in hazardous areas:

1. *Loop* (*system*) *approval*: where an intrinsically safe apparatus is evaluated in combination with a specific associated apparatus and is approved to be installed in this manner. Any changes to the circuit require reevaluation and certification (Figure 94.4).
2. *Entity approval*: where an intrinsically safe apparatus and the associated apparatus are separately evaluated and given their own electric entity parameters (Figure 94.5). The correct application matches the entity parameters shown in Table 94.3. When examining the safety of a circuit, it is crucial to compare the entity values of an intrinsically safe apparatus with an associated apparatus.

Most safety barriers are entity approved for all hazardous locations. Since most field devices have the ability to store energy, they must have loop approval or entity approval for the proper construction and operation of an intrinsically safe system.

IS engineers often advocate the use of intrinsically safe equipment for the following reasons:

1. *Safety*. No explosion can occur in an intrinsically safe system under any operating condition. IS equipment operates on lower power levels and prevents shocks, excess thermal energy, and arcing. In different systems and under various scenarios, shocks, thermal energy, and arcing may cause a hazard.
2. *Reliability*. The components and assemblies of intrinsically safe circuits are tested for reliability before they are labeled and certified. Most intrinsically safe equipment is designed with special circuitry to provide surge suppression and to prevent spikes and transients.
3. *Ease of handling and installation*. Intrinsically safe systems tend to be small and do not require expensive, bulky accessories such as enclosures, seals, and rigid metallic conduits that increase the initial investment.

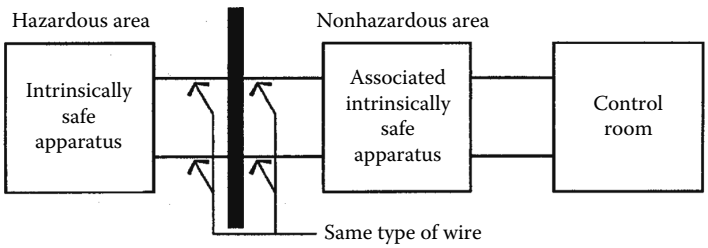

FIGURE 94.5 Entity approval. Intrinsically safe apparatus and associated apparatus are evaluated separately.

4. *Economy.* In some geographic locations, facilities containing hazardous conditions must carry special liability insurance. With the proper installation of intrinsically safe circuits and equipment, the probability of an explosion is 10^{-18} [8], or nearly nonexistent. As a result, insurance rates tend to be lower.
5. *Maintenance.* Equipment may be calibrated and maintained without disconnecting power, thereby resulting in less downtime.

The wiring of intrinsically safe systems is similar to any other application, but to ensure a proper operating system, certain guidelines regarding identification and separation must be strictly followed. All intrinsically safe components including terminal blocks, conductors, and intrinsically safe apparatus must be explicitly marked and labeled. The conventional color used to identify intrinsically safe equipment is blue. In an open wiring installation, intrinsically safe conductors must be physically separated from nonintrinsically safe conductors by at least 50 mm (2 in.), so an induced voltage does not defeat the purpose of IS. Where intrinsically safe conductors occupy a raceway, the raceway should be labeled, "intrinsically safe circuits." Intrinsically safe conductors should not be placed with nonintrinsically safe conductors. Where a cable tray is used, a grounded sheet metal partition may be used as an acceptable means of separation. Where intrinsically safe and nonintrinsically safe conductors occupy the same enclosure, a 50 mm (2 in.) separation must be maintained. In addition, a grounded metal partition shall be in place to prevent contact of any conductors that may come loose. Insulation deterioration of intrinsically safe conductors of different circuits occupying the same raceway or enclosure can be detrimental to the operation of the system. Intrinsically safe conductors must have an insulation grade capable of withstanding an AC test voltage of 550 V root mean square (rms) or twice the operating voltage of the intrinsically safe circuit. Nonintrinsically safe conductors in the same enclosure with intrinsically safe conductors must have an insulation grade capable of withstanding an AC test voltage of $2U + 1000$ V, with a minimum of 1500 V rms, where U is the sum of rms values of the voltages of the intrinsically safe conductors. A commonly used and highly recommended practice utilizes separate compartments for intrinsically safe and nonintrinsically safe conductors. In addition to physical separation of intrinsically safe conductors and nonintrinsically safe conductors, sealing of conduits and raceways housing intrinsically safe conductors is essential to prevent the passage of gases, vapors, and dusts from hazardous to nonhazardous areas. According to the NEC, seal-offs are not required to be explosion proof. Where an associated apparatus is installed in an explosion-proof enclosure in a hazardous area, seal-offs must be explosion proof. Although it is not required by code, it is a good engineering practice to install explosion-proof seal-offs on conduits housing intrinsically safe conductors, as shown in Figure 94.6.

FIGURE 94.6 Explosion-proof seal-off fitting. (Courtesy of Crouse-Hinds Division of Cooper Industries, Inc., Houston, TX.)

94.5.5 Explosion-Proof Fundamentals

Explosion-proof design is a mechanical concept that relies heavily on the mechanical construction of an enclosure and the narrow tolerances between its joints, threads, and flanges to safely contain, cool, and vent any internal explosion that may occur. By definition, explosion-proof enclosures must prevent the ignition of explosive gases or vapors that may surround it (Types 7 and 10 enclosures only). In hazardous areas, Class I, Divisions 1 and 2, arcing devices, such as switches, contactors, and motor starters, must be enclosed in an explosion-proof enclosure specifically rated for that area. Contrary to popular belief, explosion-proof enclosures are not and should not be vapor tight. Succinctly stated, an explosion inside an enclosure must be prevented from starting a larger explosion outside the enclosure. Unlike IS, explosion-proof enclosures address the maximum internal pressure (see NEMA Type 7 enclosures). Figure 94.7 illustrates the rugged construction of a standard explosion-proof panelboard.

In addition to their durability and strength, explosion-proof enclosures must also be "flame tight." The joints or flanges must be held within narrow tolerances to allow cooling of hot gases resulting from internal explosions. In this way, if any gases are released into the outside hazardous atmosphere, they are cool enough not to cause ignition.

Explosion-proof enclosures tend to be bulky (making them easy to identify) and heavy, requiring conduit seals and careful handling. Unlike intrinsically safe equipment, explosion-proof equipment operates on normal power levels that are necessary due to the high power requirements of some circuits and equipment. With the proper equipment, installation, and maintenance, explosion-proof enclosures can safely and effectively distribute high levels of voltage and power into hazardous areas.

Where ignitable amounts of dust are present, enclosures housing electric equipment must be dust-ignition proof. These enclosures must exclude combustible dusts from entering while preventing arcs, sparks, or heat generated internally from igniting dust surrounding the exterior of the enclosure. These enclosures must also efficiently dissipate the heat generated internally, since many types of dust will ignite at relatively low temperatures. Unlike Class I, Division 1 explosion-proof enclosures (Type 7), Class II,

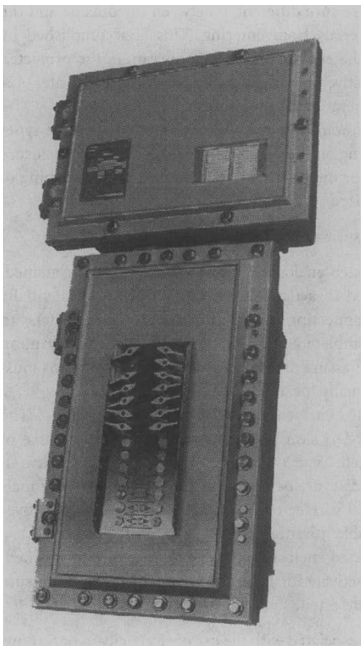

FIGURE 94.7 Explosion-proof lighting panelboard. (Courtesy of Crouse-Hinds Division of Cooper Industries, Inc., Houston, TX.)

Division 1 dust-ignition-proof enclosures (Type 9) are designed to prevent an explosion. Subsequently, dust-ignition-proof enclosures need not be as strong or have walls as thick as explosion-proof enclosures since there will be no internal explosion.

94.5.6 Purging and Pressurization

This methodology allows the safe operation of electric equipment where hazardous conditions exist and where no other methodology is applicable because of the imperative high-energy demands and actual physical dimensions. This is true for large-sized motors and switchgear units where they are not commercially available for Class I, Groups A and B. In addition, this methodology is used where control panels that house the instruments and electric equipment must be located in hazardous areas. Purging and pressurization is a protection method that relies on clean air or inert gas (i.e., nitrogen) to be continuously supplied to the enclosure at sufficient flow to keep the equipment adequately cooled and to provide adequate internal pressure to prevent the influx of combustible atmospheres into the enclosure. Although the enclosures are not explosion proof, they must be relatively vapor tight and must have adequate strength to perform safely and satisfactorily. The system consists of the following:

1. *Clean Air* (*or Inert Gas*) *Supply*: Careful study and analysis is of crucial importance to this process since the air supplied must be reasonably free of contaminants. Finding a safe location for an air intake requires skill and ingenuity. Consulting with an HVAC specialist is recommended. Other factors such as vapor density, location, wind pattern, and surrounding environment should also be considered. Where compressors and blowers are used to supply compressed air, caution must be exercised when selecting the proper compressor or blower size and location in order to meet airflow requirements without compromising the main objective of safety and reliability.
2. *Purging*: A pressurized enclosure that has been out of service for some time tends to collect a combustible mixture. Before energizing, inert gas and positive pressure must provide a sufficient initial clean air volume to minimize the concentration of any combustible mixture that may be present. For typical applications, a flow of four times the internal volume of the enclosure is usually sufficient to minimize the concentration of combustible mixture that may exist. For unusual applications, the flow volume must be carefully calculated to ensure the success of the purging process.
3. *Pressurization*: This process uses the concept of pressure differential between the outside and the inside of the enclosure to keep flammable materials from entering. This is accomplished by maintaining a higher pressure on the inside of the enclosure. For safe operation, the protected enclosure must be constantly maintained at a positive pressure of at least 25 Pa (0.1 in. water) [2] above the surrounding atmosphere during the operation of the protected equipment.
4. *Signals and Alarms:* When positive pressure is lost, warnings and alarms are essential. Three types of pressurization and alarms can be used, depending on the nature of the controls of the enclosure and the degree of hazard outside. In addition, door interlocks are required to prevent opening of the protected enclosure while the circuit is energized.

According to NFPA 496, there are three types of pressurization. They are

Type X—reduces the classification within the protected enclosure from Division 1 to nonclassified. This usually involves a source of ignition housed in a tight enclosure located in a potentially hazardous atmosphere. Type X requires a disconnecting means (flow or pressure switch) to de-energize power to the protected enclosure completely and automatically immediately upon failure of the protective gas supply (loss of either pressure or flow). The disconnecting means must be explosion proof or intrinsically safe, as it is usually located in the hazardous area.

Type Y—reduces the classification within the protected enclosure from Division 1 to Division 2. The protected enclosure houses equipment rated for Division 2 and does not provide a source of ignition. Therefore, no immediate hazard is created. Type Y requires a visual or audible alarm in case of system failure. *Word of caution*: Safeguards must be established to ensure that any malfunction in the system does not raise the external surface temperature of the enclosure to over 80% of the ignition temperature of the combustible mixture present.

Type Z—reduces the classification within the protected enclosure from Division 2 to nonclassified. Type Z requires a visual or audible alarm to be activated if failure to maintain positive pressure or flow within the protected enclosure has been detected.

Recognizing and understanding the potential danger associated with the use of electricity in hazardous areas is a crucial part of selecting the best protection. Techniques for most applications, where the need for different energy demands is required, will likely involve a combination of various methodologies and specialized technologies. Properly performed analysis and investigation may appear to be time consuming and expensive, but for those who are willing to adhere to the established guidelines and solid engineering practices, the process will help ensure the highest level of compliance while yielding tremendous savings and preventing property damage and injuries.

Defining Terms

Inductance: The ability of an electric apparatus to store an electric charge (energy). An inductor will release this energy when the circuit is opened (broken).

Oxidation: The process where negatively charged ions (anions) lose electrons at the anode during electrochemical process. For anions to become neutral, they must lose electrons.

Resistance temperature device (RTD): A device that measures temperature based on change of resistance.

Zener diode: A nonlinear solid-state device that does not conduct current in reverse bias mode until a critical voltage is reached. It is then able to conduct current in reverse bias without damage to the diode. Zener diodes have almost constant voltage characteristics in the reverse bias region (usual operation).

References

1. NFPA 70 (ANCI C1—1996), *National Electrical Code 1996*, Quincy, MA.
2. National Fire Protection Association (NFPA), Articles 493, 496, 497, Quincy, MA.
3. American Petroleum Institute 500 (RP 500), 1st edn., Washington, DC, June 1991. *Recommended Practice for Classification of Location for Electrical Installation at Petroleum Facilities*.
4. Elcon Instruments, Inc., *Introduction to Intrinsic Safety*, 3rd printing, Norcross, GA, 1990.
5. Underwriters Laboratories, Inc., Pub. UL 913, 4th edn., Northbrook, IL, 1988, *Standard for Intrinsically Safe Apparatus & Associated Apparatus for Use in Class I, II, III, Division 1 Hazardous Locations*.
6. UL's Standard Transition for UL 508 (Industrial Control Equipment and UL 508C (Power Conversion Equipment), Publications, Underwriters Laboratories, Inc., http://www.ul.com/global/eng/pages/offerings/industries/powerandcontrols/industrialcontrolequipment/ (accessed on March 15, 2013).
7. Clarence W de Silva, *Sensors and Actuators: Control System Instrumentation*, CRC Press, Boca Raton, FL, 2007.
8. R. Stahl, Inc., RST 49, *Comprehensive Applications and Data Catalog*, Woburn, MA, 1992.
9. Intrinsic Safety, PDF SB, Online, http://pdfsb.com/intrinsic+safety (accessed on March 15, 2013).

Further Readings

Explosion Proof Equipment, North American Industries. http://www.naicranes.com/cranes/explosion_proof.htm (accessed on August 1, 2012).

Explosion Proof motors and Applications Hazardous Location. http://www.reliance.com/mtr/eplprfmn.htm (accessed on August 2, 2012).

Electronic Code of Federal Regulations, Title 30—Mineral resources. http://ecfr.gpoaccess.gov/cgi/t/text/text-idx?c=ecfr&tpl=/ecfrbrowse/Title30/30cfr18_main_02.tpl (accessed on August 9, 2012).

Partial List of Manufacturers and Suppliers

Ashcroft, Inc., 250 E. Main St., Stratford, CT 06614-5145, Phone: 203-378-8281, 800-328-8258 (toll free), Fax: 203-385-0408, www.ashcroft.com

Purge Solutions, 12454 Galveston Rd, Suite C, Webster, TX 77598, Phone: 832-368-7166, Fax: 281-992-5726, www.purgesolutions.com

R. Stahl, Inc., 9001 Knight Rd., Houston, TX 77054, Phone: 713-792-9300, 800-782-4357 (toll free), Fax: 713-797-0162, www.rstahl.com

Stancor, Inc., 515 Fan Hill Rd, Monroe, CT 06468, Phone: 203-268-7513, Fax: 203-268-7958, www.stancorpumps.com/index.html

Unico, Inc., 3725 Nicholson Rd., Franksville, WI 53126, Phone: 262-886-5678, Fax: 262-504-7396, www.unicous.com

Ware, Inc., 4005 Produce Rd., Louisville, KY 40218-3007, Phone: 502-968-2211, 800-228-8861 (toll free), Fax: 502-969-5777, www.wareinc.com/

95

Measurement and Identification of DC Brush and Brushless Stepping Motors

Stuart Schweid
Xerox Corporation

Robert Lofthus
Xerox Corporation

John McInroy
University of Wyoming

95.1 Introduction

There are many systems, such as robots, whose ability to move themselves or other objects is their primary purpose. There is a myriad of other systems, such as xerographic printers, where the motion is not the desired outcome but is required in the performance of the mainline objective. All of these systems require one or more "prime movers," which directly or indirectly create all motion in the system.

All of these applications have differing requirements for both the type and the precision of the motion produced. There are applications, such as children's toys, that can perform well with imprecise motion requirements. Conversely, there are applications, such as printing, that require very precise motion control.

Depending on the type of motion required, a prime mover can be chosen from one of several candidates. The most ubiquitous motor types are DC brush–type motors, DC brushless motors, and hybrid stepping motors. The system, which includes the prime mover, can be controlled simply as a function of time (i.e., open loop) or as a function of both time and system state (i.e., closed loop).

A closed-loop system requires some mechanism of measuring the "state" of the system. For motion systems, this is typically one or more sensors that measure position and/or velocity. In addition, for many of the control techniques, specifically, linear controllers, it is also advantageous to have a model of the system being controlled. The model can be used in conjunction with a plethora of design techniques to improve the dynamic response of the system significantly.

This chapter will describe the major modes of operations for the prime movers listed and will detail a method for measuring the open-loop response of a candidate motion system.

95.2 Hybrid Stepping Motors

Hybrid stepping motors are useful devices that provide fairly accurate positioning in the open loop: their most common mode of operation. They are successful in open-loop operation because they will remain within a commanded position increment or step as long as the motor has sufficient torque to resist any external torque applied by the system.

Since the motor operates in the open loop, it is chosen a priori to ensure it provides the torque necessary to remain within step. The maximum torque needed to operate the system is a function of the inertia of the system, the acceleration profile of the system, the external torque on the system, etc. Once the maximum torque required at every speed is determined, a motor can be chosen from its torque–speed curve. The torque–speed curve describes the maximum torque that can be tolerated at each speed without failing to follow a commanded step (referred to as a "losing step"). A motor whose torque–speed curve exceeds the torque requirements of the system at all speeds will be sufficient for the application. Figure 95.1 shows a typical torque–speed curve.

Hybrid stepping motors have a plurality of coils (almost always two) that, when commutated in a predefined sequence, cause the motor to turn. When the motor is operated in a mode referred to as "full stepping," the current command to each winding is constant in magnitude but varying in polarity (positive or negative). Note that the definition of which direction of current flow is "positive" is purely arbitrary. In this mode, the motor has only four separate energizations of the winding to complete a full revolution, although clever mechanical arrangements allow the number of steps per revolution to be greatly increased: typically 200 but as large as 800.

With two distinct windings (referred to as A and B), the four possible arrangements of winding energizations are A+B+, A+B–, A–B–, and A–B+. If these combinations of winding currents are commanded to the motor in the sequence listed in the previous sentence, the motor will turn.

95.2.1 Chopping Current Amplifiers

As previously stated, the motion of the stepper requires a current of a particular amplitude to be applied. For economic reasons, most systems have a voltage power supply available (V_{ss})—not a current source. A "current chopper" is a low-cost closed-loop switching amplifier that regulates the current to the

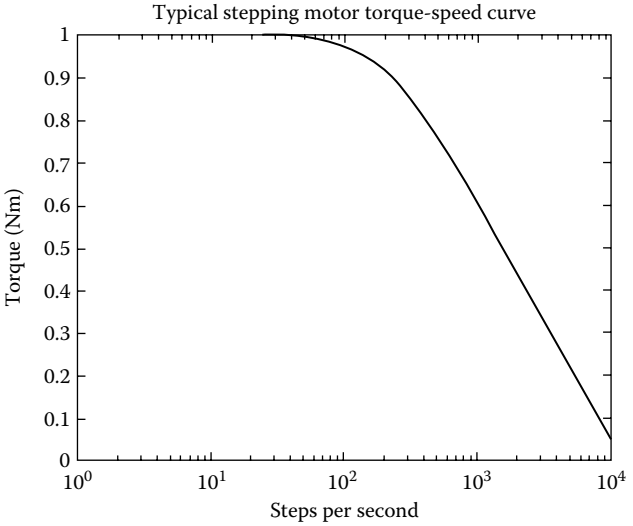

FIGURE 95.1 Typical stepping motor torque–speed curve.

motor winding. It takes advantage of the fact that the motor winding has a significant inductance. The two motor windings have dynamic equations [1]:

$$\frac{dI_A}{dt} = \frac{(V_A - I_A R_A + K_b \omega \sin\theta)}{L_A}$$
$$\frac{dI_B}{dt} = \frac{(V_B - I_B R_B + K_b \omega \cos\theta)}{L_B} \tag{95.1}$$

where

I is the current winding (A)
R is the current resistance (Ω)
L is the current inductance (H)
V is the applied voltage to the winding (V)
K_b is the torque constant of the motor (Nm/A)
ω is the motor velocity (rad/s)
θ is the motor position (electrical rad)

In every t_s (where t_s is very small, i.e., 10 μs), the current chopper applies either V_{ss} or $-V_{ss}$ to the motor winding, depending on whether the desired current (I_M) is greater than or less than the measured (i.e., actual) winding current:

$$\text{if } (I_A > I_M), \quad V_A = -V_{ss} \quad \text{else } V_A = V_{ss}$$
$$\text{if } (I_B > I_M), \quad V_B = -V_{ss} \quad \text{else } V_B = V_{ss} \tag{95.2}$$

The usual requirement is that ($V_{ss}\, t_s/L$) is small in comparison with I_M, resulting in a chopping range that is small when compared with the desired current. Furthermore, the mechanical system that includes the motor is typically low pass in nature, so it will have minimal response to the small-amplitude, very-high-frequency components present in the motor winding current.

95.2.2 Microstepping

Another common open-loop mode for stepper operation is microstepping. In microstepping, the commanded reference positions can be between the "full-step" positions of the motor. The commanded currents for the reference position θ_{ref} are

$$I_A = I_M \cos(\theta_{ref})$$
$$I_B = I_M \sin(\theta_{ref}) \tag{95.3}$$

where θ_{ref} is the desired electrical position of the motor (in four full steps, θ_{ref} traverses one full electrical revolution). For constant-velocity applications,

$$\theta_{ref} = N\omega_d t \tag{95.4}$$

where

N is the number of electrical revolutions per mechanical revolution (one-quarter the number of steps per revolution) of the motor
ω_d is the desired velocity (rad/s)

95.2.3 Closed-Loop Control

In addition to the open-loop uses of hybrid stepping motors, several researchers have recently invented methods of operating these motors in a closed-loop fashion. The principal difficulty arises because hybrid stepping motors are nonlinear devices, so the plethora of design techniques available in linear control theory cannot be directly applied. Hamman [1] uses a fourth-order model to linearize the system about each step. This is useful in altering the undamped response of the stepper motor to a commanded change in position. Schweid [2] suggests a scheme that allows good transient behavior during constant-velocity applications but uses the complete fourth-order model. In systems that use current choppers, a second-order model is sufficient. The following control law can then be applied [3–5]:

$$\begin{aligned} I_A &= I_M \cos(\theta_{ref}) - I_C \sin\theta \\ I_B &= I_M \sin(\theta_{ref}) + I_C \sin\theta \end{aligned} \tag{95.5}$$

The currents of Equation 95.6 linearize the model of the stepper motor, allowing common control techniques such as PID control to be applied [6]. The value I_M is used as an open-loop component to microstep the motor, while I_C is a feedback term that permits an improved dynamic response.

95.2.4 Position Measurement

The implementation of closed-loop control requires a method of measuring the position of the motor. Furthermore, there is the added constraint that this position measurement must be aligned with the motor construction and not have a positional offset with respect to it. This is because the control scheme of Equation 95.5 requires a command current I_C be multiplied by the sine and cosine of the motor position. One way to implement this is to have an incremental encoder with an index pulse attached to the motor. A calibration can then determine the relative position of the index pulse to the motor shaft and use this relationship in all future positional measurement.

Another scheme uses the back emf of the two coil windings to estimate the position. Some motors are constructed with additional sensing coils that allow easy measurement of these values. From Equation 95.2, the back emf of both coils can be found using

$$\begin{aligned} V_{emfA} &= -K_b \omega \sin\theta = V_A - I_A R_A - \frac{L_A dI_A}{dt} \\ V_{emfB} &= -K_b \omega \cos\theta = V_B - I_B R_B - \frac{L_B dI_B}{dt} \end{aligned} \tag{95.6}$$

and the position could be found using

$$\theta = \text{atan}\left(\frac{-V_{emfA}}{V_{emfB}}\right) \tag{95.7}$$

In most motors, however, V_{emfA} and V_{emfB} are not directly measurable. However, it is possible to obtain an excellent estimate of position in the constant-velocity system by approximating the back emf signals through low-pass-filtered measurements of the coil voltages. One method developed at Xerox that has a U.S. patent (U.S. 5378975) is described here. Taking the Laplace transform of Equation 95.6 yields

$$\begin{aligned} V_{emfA}(s) &= V_A(s) - (R_A + sL_A) I_A(s) \\ V_{emfB}(s) &= V_B(s) - (R_B + sL_B) I_B(s) \end{aligned} \tag{95.8}$$

Filtering both sides with low-pass analog filters matched to the dynamics of the coil produces

$$V_{\text{filtA}}(s) = \frac{V_{\text{A}}(s)}{s(L_{\text{A}}/R_{\text{A}})+1} - R_{\text{A}}I_{\text{A}}$$
$$V_{\text{filtB}}(s) = \frac{V_{\text{B}}(s)}{s(\text{L}_{\text{B}}/R_{\text{B}})+1} - R_{\text{B}}I_{\text{B}} \tag{95.9}$$

The quantities V_{filtA} and V_{filtB} are easily obtained by low-pass filtering the coil voltage with a simple *RC* circuit and subtracting the *IR* term. The subtraction is easily implemented because the current is a known input (in fact, it is commanded), and the resistance is easily measured.

Assuming that the coils are matched: $L = L_{\text{A}} = L_{\text{B}}$, $R = R_{\text{A}} = R_{\text{B}}$, and the motor is moving at constant velocity, $\theta = N\omega_{\text{d}}t$, and the back EMF voltages are sinusoidal. The low-pass-filtered versions of these voltages are given by

$$V_{\text{filtA}}(s) = |H(N\omega_{\text{d}})|K_{\text{B}}\sin(\theta+\phi)$$
$$V_{\text{filtB}}(s) = |H(N\omega_{\text{d}})|K_{\text{B}}\cos(\theta+\phi) \tag{95.10}$$

where

$|H(N\omega_{\text{d}})|$ is the magnitude response of the low-pass filter at the input frequency, $N\omega_{\text{d}}$

$\phi = -\text{atan}(N\omega_{\text{d}}\ L/R)$ is the phase shift due to the filtering

Dividing the two Equations 95.10 and taking the inverse tangent yields

$$\theta = \text{atan}\left(\frac{-V_{\text{filtA}}(t)}{V_{\text{filtB}}(t)}\right) + \text{atan}\left(\frac{N\omega_{\text{d}}L}{R}\right) \tag{95.11}$$

The full derivation and analysis are found in Ref. [7]. In addition, Ref. [7] includes a Kalman filtering technique to improve the velocity measurement estimate from the position estimate. This is needed because the derivative or difference of the position measurement is highly sensitive to noise.

95.3 DC Brush and Brushless Motors

The DC servomotor is the oldest and probably the most commonly used actuator for servo systems. The name arises because a constant (or DC) voltage applied to the motor will produce motor movement. Over a linear range, these motors exhibit a torque that is proportional to the current flowing in the winding. The chief disadvantage of the brush DC motor is the brush, which performs the mechanical commutation. These brushes are the first part of the motor to fail, severely limiting the reliability of DC brush motors when compared with other actuators.

Another motor that operates similarly to a DC brush motor is the DC brushless motor (a DC voltage will cause it to rotate). Its method of commutation, however, is much different. Whereas the DC motor accomplishes switching mechanically with brushes, the DC brushless motor contains Hall effect sensors that electronically control the switching. As a result, the DC brushless motors have much greater life and reliability.

95.3.1 Pulse-Width-Modulated Power Amplifier

In many systems where they operate, DC motors are required to have a varying voltage at their input in order to create the position or velocity profiles desired. Many of these systems, however, have only

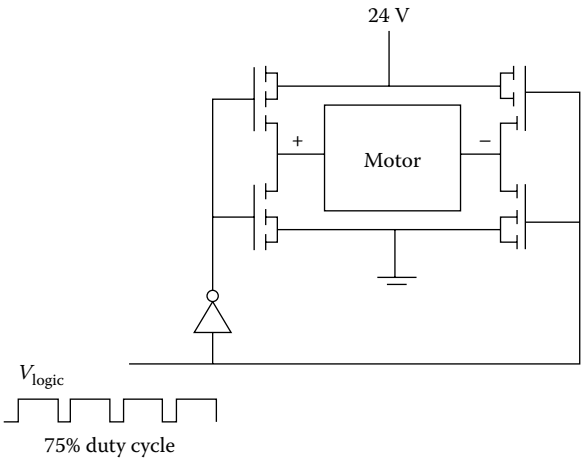

FIGURE 95.2 PWM amplifier set to deliver 12 V to the motor.

a single power supply V_{ss}. Rather than using analog power amplifiers that are both expensive and inefficient, a pulse-width-modulated (PWM) amplifier is used. A pulse-width power amplifier can deliver only V_{ss} or $-V_{ss}$ (or zero in some designs) V to the motor. Different voltages are delivered to the motor by varying the relative percentage that V_{ss} and $-V_{ss}$ are applied to the motor at a high fixed frequency. The mean or average voltage to the motor is a linear function of this relative percentage or duty cycle. The motor also receives the higher harmonics of the switched input that are integer multiples of the base frequency of the square wave. Most motors, however, have at least two poles (an electric and a mechanical) that are significantly slower than the switching frequency and thus greatly attenuate any possible effect they might have on motion. Figure 95.2 shows a PWM amplifier set to deliver 12 V to the motor.

95.3.2 Measuring the System Dynamics

In systems with moderate or stringent motion requirements, the DC brush and brushless motors are operated in a closed-loop fashion. In order to perform in closed loop, some measure of either position or velocity is needed. A tachometer is commonly used to measure rotational speed. It outputs a voltage that is proportional to the speed of a rotating member. If a position measurement is required, an incremental encoder can be used. The incremental encoder produces a digital pulse at equal points in position. For example, a 1000 line/revolution encoder would produce a digital wave with 1000 rising (and falling) edges during one revolution.

Once the full system (including feedback sensors) is determined, a feedback control algorithm can be developed. As part of the design of many compensation algorithms, especially linear compensators such as state feedback or PID, one of the most important tasks is to have a good model of the dynamics of the system.

There are several ways to generate the model. One of the most common methods is to create the state equations of the system from the physical equations. This requires knowledge of all the parameters of the system. Sometimes these parameters are hard to measure and are not provided by the manufacturer. One example of this might be the torsional constant of a hard rubber roll in the system.

Even if all of the parameters are known, it is still desirable to have a method that measures the response of the system. This provides a way to either validate the model or inform the designer that the model is not an accurate representation of the system.

A method is presented that permits the collection of input/output data of a system. These data can then be used to fit a frequency response curve or a transfer function model of the system. Signal analyzers,

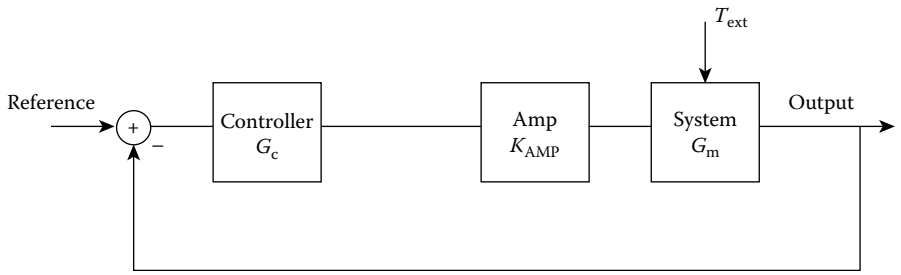

FIGURE 95.3 Typical closed-loop system.

such as the HP3562A, have the ability to perform such curve fitting accurately. In addition, if the data are collected in a discrete fashion, there are commercially available software tools, such as MATLAB®, that can provide model estimation in either a parametric (e.g., state space/transfer function) or a non-parametric (e.g., frequency response) form. Although this procedure is described for motor systems, it is easily implemented in most linear systems.

Assume a typical closed-loop system as shown in Figure 95.3. There are several obstacles that make it difficult to obtain the open- or closed-loop transfer function of this system. These obstacles include the inability to measure some of the outputs and the inability to control/modify certain inputs.

To acquire the frequency response of a system, it is useful to perturb the system with a known input and measure the elicited response. A controllable input—one that can be externally manipulated—is required to accomplish this task. The only controllable inputs of the system in Figure 95.3 are the torque acting upon the motor shaft and the reference command.

Changing the external torque would require mechanically attaching a calibrated brake or another motor. This is not only cumbersome, but it also can alter the system dynamics, as it introduces inertia to the true system under measurement. Within many systems, the reference signal is a digital square wave (since the feedback element is an incremental encoder and produces a similar wave) and therefore requires a voltage-to-frequency converter if the reference is to be directly manipulated. This converter may include dynamics that can corrupt the measured data.

In addition to a controllable input, a measurable output must be available. In many servo systems, the only measurable outputs are the motor armature voltage and the position/velocity. The armature voltage may be a PWM signal that needs to be filtered to create an analog voltage. In the case of an incremental encoder, the output consists of a digital square wave generated by an incremental encoder: a frequency-to-voltage converter is required to produce an analog output. This converter may include dynamics that can corrupt the measured data.

Consider the system described in Figure 95.4. The summing junction placed in the system has the advantage that can be added at any point that is convenient for measurement purposes—it is no longer limited to unaugmented system inputs or outputs.

In the case of analog controllers, the inputs and the outputs of the summing junction are analog voltages, making them easily controlled and measured. The summing node can be easily implemented using a simple op-amp adder circuit. This introduces no appreciable dynamics into the original system and will not, therefore, skew the measured data.

When the system response is to be measured, the time-varying contributions of the other system inputs, the velocity reference and external torque, T_d, acting upon the system must be eliminated. The designer must set the velocity reference as a constant value. There is usually little control of the external torque acting on the system, and this will introduce noise into the measurement technique. To ensure a large signal-to-noise ratio (SNR), the alternative reference input (signal $z(t)$) should be made as large as possible.

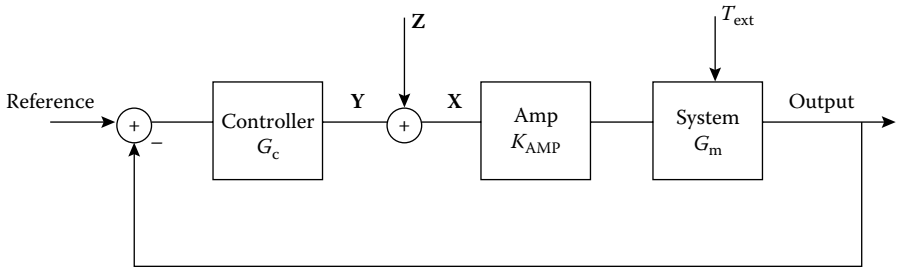

FIGURE 95.4 Instrument-integrated closed-loop system.

The alternative reference input, $z(t)$, can stimulate the system with a swept sine input, a random input, or any other desired signal. During the stimulation, a time record is collected of the other nodes of the summing junction, $y(t)$ and $x(t)$. The transfer function between **Y** and **X** is

$$\frac{\mathbf{Y}(s)}{\mathbf{X}(s)} = -G_c(s)K_{amp}(s)G_m(s), \quad -\frac{\mathbf{Y}(s)}{\mathbf{X}(s)} = G_c(s)K_{amp}(s)G_m(s) \tag{95.12}$$

The second term is, by definition, the open-loop transfer function of the system. As earlier, the MATLAB or a signal analyzer can provide either a parametric or a nonparametric fit of this transfer function from the data record.

Note that this technique requires the system be functioning in a closed-loop mode during data collection. Typically, G_c is set as a proportional controller at a value that will ensure stability of the overall system. For a good data collection, the proportional gain should be made as large as possible.

The case of a digital or microprocessor-controlled system can be handled similarly, with some slight modification. Consider the system of Figure 95.5, where a microprocessor acts as the system controller. In this instance, the summing junction can be implemented internal to the microprocessor by executing an add instruction. The problem here becomes getting the data into and out of the microprocessor. Getting the data into the microprocessor requires the addition of an analog-to-digital converter (ADC). In the block diagram, this ADC process is represented by the block A_f, A_f that allows representation of any dynamics inherent in the ADC design (especially gain). The output of the microprocessor may be a digital PWM signal. This signal may need to be low-pass-filtered to create an analog voltage for the signal analyzer taking the data. The low-pass filter is represented by P_f in Figure 95.5. It is typically a simple *RC* circuit whose cutoff frequency is much lower than the PWM signal frequency.

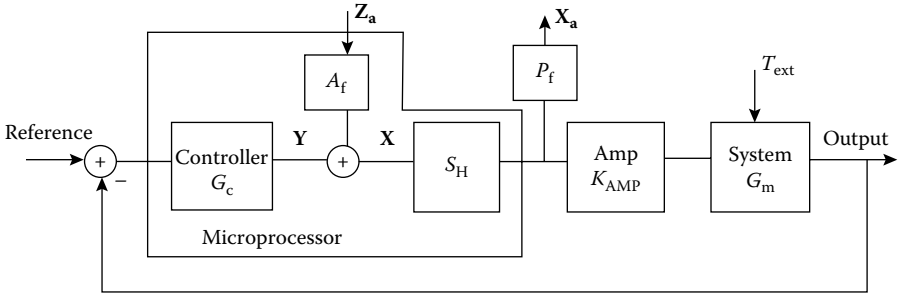

FIGURE 95.5 Microprocessor-controlled closed-loop system.

Given the condition that ω_{ref} is static and external torque, T_d, is minimal, the transfer function between $\mathbf{Z_a}(s)$ and $\mathbf{X_a}(s)$ in Figure 95.5 is

$$\frac{\mathbf{Z}_a(s)}{\mathbf{X}_a(s)} = \frac{1 + G_c(s)S_H(s)K_{amp}(s)G_m(s)}{A_f(s)S_H(s)P_f(s)} \equiv \mathbf{O}(s) \tag{95.13}$$

when $G_c = 0$, $\mathbf{Z_a}(s)/\mathbf{X_a}(s) = 1/(A_f(s)S_H(s)P_f(s)) \equiv \mathbf{C}(s)$, and $(\mathbf{O}(s) - \mathbf{C}(s))/\mathbf{C}(s) = \boldsymbol{G}_c(s)\boldsymbol{S}_H(s)\boldsymbol{K}_{amp}(s)\boldsymbol{G}_m(s)$; this is the system open-loop transfer function.

A more direct approach is possible if a logic analyzer is not used, but a software-based system identification package such as MATLAB is used to fit the data. The stimulus, z, can either be stored as a set of data in a lookup table in the microprocessor memory or can be generated in real time using any random number generator algorithm or other algorithm. The data $\mathbf{Y}$ and $\mathbf{X}$ at the internal summing junction can be captured via a logic analyzer or emulator if the values of $y(k)$ (the value of y at the kth sample period) and $x(k)$ are written to an external bus every sample period. Under this configuration, neither a DAC nor an ADC is necessary, nor is any mathematical combination of two different transfer functions required to produce the desired open-loop transfer function. The transfer function between $\mathbf{Y}(z)$ and $\mathbf{X}(z)$ is

$$\begin{aligned} \frac{\mathbf{Y}(\mathbf{z})}{\mathbf{X}(\mathbf{z})} &= -G_c(z)S_H(z)K_{amp}(z)G_m(z) \\ -\frac{\mathbf{Y}(\mathbf{z})}{\mathbf{X}(\mathbf{z})} &= G_c(z)S_H(z)K_{amp}(z)G_m(z) \end{aligned} \tag{95.14}$$

Again, this is the open-loop transfer function of the system, acquired using only minimal additional software and a logic analyzer. As earlier, the input/output set of data can be sent to any system identification algorithm to fit the transfer function.

References

1. E. Hamman, Closed-loop control of a DC stepping motor using state space techniques, Master's thesis, Rensselaer Polytechnic Institute, Troy, NY, 1983.
2. S. Schweid, Velocity control of DC stepping motors utilizing state space theory, quasilinearization and reduced order estimation/control, Masters thesis, Rensselaer Polytechnic Institute, Troy, NY, 1985.
3. J. Tal, L. Antignini, P. Gandel, and N. Veignat, Damping a two-phase step motor with velocity coils, *Incremental Motion Control Systems and Devices Symposium*, Champaign, IL, pp. 305–309, 1985.
4. D. Reignier, Very accurate positioning system for high speed, high acceleration motion control, *Power Conversion and Intelligent Motion*, 13, 52–62, June 1987.
5. D. Reignier, Damping circuit and rotor encoder cut disc magnet step motor overshoot, settling time and resonances, *Power Conversion and Intelligent Motion*, 14, 64–69, April 1988.
6. S. Schweid, J. McInroy, and R. Lofthus, Closed loop low-velocity regulation of hybrid stepping motors amidst torque disturbances, *IEEE Transactions on Industrial Electronics*, 42, 316–324, 1995.
7. R. Lofthus, S. Schweid, J. Mclnroy, and Y. Ota, Processing back EMF signals of hybrid step motors, *Control Engineering Practice*, 3(10), 1–10, 1995.

Further Readings

Hanselman, D., *Brushless Permanent Magnet Motor Design*, 2nd edn., McGraw-Hill, New York, 2003.

Hughes, A., *Electric Motors and Drives: Fundamental Types and Applications*, 3rd edn., Elsevier, Oxford, U.K., 2006.

Gieras, J.F. and Wing, M., *Permanent Magnet motor Technology: Design and Applications*, 2nd edn., Marcel Dekker, Inc., New York, 2002.

Partial List of Manufacturers and Suppliers

Acme Controls, 6140 W. Higgins Ave., Chicago, IL 60630-1845, Phone: 877-314-2371 (toll free), Fax: 773-774-3737, acmecontrols.rtrk.com/?scid=2216829&rl_a…

Aerotech, Inc., 101 Zeta Dr., Pittsburgh, PA 15238-2811, Phone: 412-963-7470, Fax: 412-963-7459, www.aerotech.com

Dart Controls, 5000 W. 106th St., Zionsville, IN 46077, Phone: 317-873-5211, Fax: 317-873-1105, www.dartcontrols.com

Electric Motor Centre, 3222 Bernice Ave., Russellville, AR 72802, Phone: 479-968-2532, 800-871-3697 (toll free), Fax: 479-968-2052, www.electricmotorcenterinc.com

Unico, Inc., 3725 Nicholson Rd., Franksville, WI 53126, Phone: 262-886-5678, Fax: 262-504-7396, www.unicous.com

Trola Industries, 2360 N. George St., York, PA 17406-3202, Phone: 717-848-3700, Fax: 717-848-6993, www.trolaindustries.com

96

Human Factors in Displays

Jeffrey D. Onken
Purdue University

Barrett S. Caldwell
Purdue University

Steven A. Murray
University of San Diego

96.1 Introduction

The display system is the final information flow link between the electronic system (task automation, measuring process, or other electronic information technology) and the user. If the display is not easy to access, perceive, and understand, then that flow is degraded. The user's sensory capabilities and cognitive characteristics, therefore, must be addressed in defining and improving the system display requirements.

Since the 1990s, there has been a substantial proliferation in the nature and form factors of video- and visually based displays. The range of devices that can be considered "computer displays" has expanded into new classes of mobile and flat-screen device options. Furthermore, display technologies and performance capabilities are easier to evaluate in the context of their intended application. Consideration of

the following issues can narrow the search for candidate systems and can prevent needless frustration during system use:

Environment: Will the display be operated in sunlight or at night or in confined conditions?
Application: Will the display present alphanumeric data, video images, graphics, or some combination?
Task scenario: Is portability, handheld operation, or group viewing required?
System characteristics: Are there critical operational constraints such as weight, volume, power, maintenance, or cost?

This chapter begins with basic treatments of light and vision. It then proceeds to discussions of visual capabilities and the display characteristics that must be matched to them. Rather than elaborating characteristics of specific visual display examples, this chapter will focus on video and visual information presentation technologies and their interactions with human performance.

96.2 Fundamentals of Light Measurement

The foundation metric of light is *luminous flux*, which is the rate at which light energy is emitted from a source and is expressed in lumens (lm). *Luminous intensity* is luminous flux per unit solid angle, and its unit of measurement is the candela (cd). This is distinguished from *illuminance*, or illumination, which is simply luminous flux per unit area, expressed as lux (lx). *Luminance* is a measure of the brightness, that is, the amount of light, per unit area, either emitted by or reflected from a surface. Units of luminance measurement are candelas per square meter (cd/m^2) or nits. Finally, *reflectance* is a unitless ratio of the amount of light striking a surface to the amount of light leaving it:

$$R = \pi \times \frac{\text{Luminance}}{\text{Illuminance}} \tag{96.1}$$

High reflectance can create glare, dramatically reducing visual performance.

96.3 Fundamentals of Vision

The eye functions very much like a conventional camera. Light enters the eye through a transparent *cornea* and is modulated by the *pupil*, a variable aperture opening controlled by muscles of the *iris*. The pupil grows larger in dark surroundings and smaller in bright surroundings to control the range of light intensity to the eye. Light rays are then refracted by an adjustable *lens* and brought into focus on the *retina*, where neural imaging begins. The retina contains both *cones* and *rods*, two distinctly different types of photoreceptors. Cones are concentrated near the *fovea*, or the central 2° of the visual field, and decrease rapidly with distance from this region. In contrast, rods are essentially absent in the fovea and increase in density with distance.

The eye is sensitive to three characteristics of electromagnetic radiation: (1) *brightness* (the intensity of ambient or incident light, measured in lux), (2) *hue* (the wavelength of light, measured in nm), and (3) *saturation* (relative concentration of specific hues in light, measured as a dimensionless ratio from 0 to 1). Cones are differentially sensitive to wavelength, that is, hue, and have greater resolving power than rods because of their one-to-one mapping onto visual nerves. Cones can be further divided into three types, each maximally sensitive to a different portion of the visible light spectrum: (1) red (670 nm peak), (2) green (470 nm peak), and (3) blue (400 nm peak). Rods are more sensitive to light than cones and have many-to-one connections with the nerves that exit the eye, a feature that permits neural summation of low light signals. Human ability to discriminate differences in levels of brightness, saturation, or hue is governed by a psychophysical function known as *Weber's law*:

$$K = \frac{\Delta I}{I} \tag{96.2}$$

where ΔI is the difference, or change, in intensity, I is the initial intensity, and K is the Weber fraction. Values of K have been experimentally determined for brightness (0.079), saturation (0.019 for red), and hue (≈0.02–0.04, depending on the region of the visible spectrum).

Photopic vision occurs at light levels where both rods and cones are sensitive. The minimum light intensity required for photopic vision is approximately 2 lx; colors are seen in this region. As brightness decreases, a transition from photopic to scotopic vision takes place and color perception drops out gradually, a phenomenon that can impact the interpretation of color-coded information in poor light. The perception of blues and reds is lost first, then cyan and yellow orange, and finally green, that is, the wavelengths where the eye is most sensitive. The eye becomes most sensitive to wavelengths of about 550 nm (green) near the limit of photopic vision. *Scotopic vision* occurs at low light levels (2×10^{-7} lx to 2 lx) and primarily involves the rods; only achromatic shades of gray are seen. The transition from photopic to scotopic vision occurs slowly, requiring approximately 30 min for complete adjustment from photopic to scotopic visual sensitivity.

96.4 Visual Performance

Visual acuity is the ability to discriminate detail. The action of the lens, to change focus for objects at different distances, is called *accommodation*. *Minimum separable acuity*, the most common measure of discrimination, is determined by the smallest feature that the eye can detect and is measured in terms of the reciprocal of the visual angle subtended at the eye by that feature. *Visual angle*, in minutes of arc, is calculated as

$$\mathrm{VA} = \frac{3438H}{D} \tag{96.3}$$

where

H is the height of the object
D (in the same units) is the distance from the observer

The ability to distinguish an object from its surroundings is known as *visibility*. The term is related to visual acuity but implicitly combines factors of object size, contrast (i.e., including differences in hue and saturation), and brightness that all interact to determine true visual detection performance. On a more functional level, *readability* or *legibility* describes the ability to distinguish meaningful groups of objects (e.g., words extracted from groups of letters on a display).

Other parameters affecting visual performance include viewing angle and viewing distance. *Viewing angle* at the eye is measured from a line through the visual axis to the point being viewed and determines where an object will register on the retina. The best image resolution occurs at the fovea, directly on the line of gaze, and visual acuity degrades with increasing angle away from this axis. *Viewing angle* at the display is the angle, in degrees, between a line normal to the display surface and the user's visual axis. The best viewing angle is, of course, on the visual axis and normal to the display surface, as luminance falls off for most displays as the angle from normal increases. Luminance reduction with viewing angle can be calculated as

$$E = E_{\mathrm{m}} \cos^4 \theta \tag{96.4}$$

where

E_{m} is the illuminance at the center of the display
θ is the viewing angle

Note that two viewing angles—at the eye and at the display—have been defined. *Viewing distance* is determined primarily by the minimum size requirements (i.e., visual angle) for objects that the user must see. A conventional reading distance is about 71 cm, although VDTs are frequently read at 46 cm. Most design criteria assume a viewing distance of between 50 and 70 cm.

Visual fatigue is an imprecise term but one in common use, referring to the annoyance, irritation, or discomfort associated with visual tasks performed under poor conditions or for extended periods of time. A common cause of visual fatigue is *glare*, which can be due to a combination of high-brightness, high-reflectance, and specular (mirrorlike) reflections causing source light to reflect directly into the eye. Minimizing or eliminating glare is essential for effective display performance and usually involves a thoughtful placement of the display, proper positioning of room lights, control of ambient light (e.g., window shades), or the use of display hoods.

96.5 Display Performance Considerations

96.5.1 Contrast

Contrast is the measure of the luminance difference between an object and its background. While different definitions exist in the literature, luminance contrast as adopted by the International Lighting Commission (CIE) is given as

$$C_R = \frac{\text{Luminance of brighter object} - \text{Luminance of darker object}}{\text{Luminance of brighter object}} \tag{96.5}$$

Lower luminance displays require greater contrast to achieve the same visibility of objects. The *contrast*, or *luminance*, *ratio* between two surfaces in the central field of vision (e.g., a display and the desk on which it rests) should be around 3:1, while the ratio between the central field and the surfaces farther away (e.g., around a room) can be as high as 10:1. Ratios greater than 10:1 can induce glare. The simplest methods for contrast enhancement are the use of hooded shades or displays that can be tilted away from the offending light. Contrast-enhancing *filters*, however, can be more effective. All filters involve reducing the amount of ambient light reflected back to the user while leaving the emitted light from the display content as unchanged as possible. Several strategies for filtering exist, including *etching* or *frosting* the display surface to break up and scatter specular reflections. *Neutral density filters* increase contrast by reducing the amount of light passing through them; ambient light must pass through twice before reaching the user's eye, while display content must only pass through once. Micromesh filters placed on the display surface limit light penetration, so only rays falling perpendicular to the mesh can penetrate; this stops both specular and diffuse reflections and increases contrast. *Circular polarizers* are neutral density filters that polarize incident light, which is then prevented from returning through the filter. *Quarter-wave thin-film coatings* interfere with both specular and diffuse reflections.

In recent years, advertising has distorted the meaning of the term contrast ratio by presenting numbers that display-technology companies calculate using unnatural conditions. In its most basic form, the *contrast ratio of a display* is the ratio of the luminance of a black part to the luminance of a white part, as perceived by an average human eye. The luminance of any light source is the power it emits weighted by the luminosity function, the approximate sensitivity of the human eye to each of the wavelengths of the visible spectrum. The SI unit of measurement of luminance is candela per square meter, cd/m^2. For comparison, a normal candle emits a luminous intensity of roughly one candela.

The problem with the term *contrast ratio* arises when the display specification presents a measurement taken in nonstandard—or even unfair—methods or conditions. In backlit display devices, like liquid-crystal displays (LCDs), the hardware can vary the intensity of the backlight depending on the signal to achieve brighter bright colors and darker dark colors. Thus, the first nonstandard method of measuring contrast ratio is to measure the ratio between a completely black video signals, such that the

device dims the backlight to its lower limit, and a completely white video signal, such that the device increases the backlight to its maximum output. Since normal viewing conditions involve some combination of dark and light parts of the display, the contrast ratio measured in this way will never be seen by viewers because the backlight can only have one output level. An even more unfair measurement technique involves turning the backlight off completely—allowing a ratio of infinity. A ratio measured this way clearly says nothing about normal operating conditions of the display. Some specifications advertise this as a *dynamic contrast ratio* and omit the proper standard—the *static contrast ratio*—since the latter number is so much smaller. Since different display manufacturers can have completely different methods to measuring their dynamic contrast ratio, these numbers are not comparable.

A method for measuring a proper contrast ratio in normal operating conditions involves the following. The display shows a pure-black and pure-white checkerboard test pattern set in a room with typical wall reflectivity. The light from the display that reflects off the walls and back onto the display will reduce the contrast of the display. However, measuring the ratio of black and white in this method provides a useful specification for the display's contrast ratio. Unfortunately, few computer-monitor and television (TV) manufacturers readily provide such specifications.

Despite this misinformation, it is possible to understand the mechanics of displays that can permit higher contrast ratios. For the most part, displays with similar technology will have similar contrast ratios. Display devices that can selectively darken portions of the backlighting or illumination while leaving other portions at full brightness will achieve higher contrast ratios than display devices that have a single backlight. Devices that can achieve this have mechanisms like independent display elements (LED displays), phosphor illumination (CRT displays, plasma displays), or matrix backlighting (like full-array LED-backlit LCDs). Other devices, such as CCFL-backlit or LED-edge-lit LCDs, are unable to darken only portions of the screen and will have a smaller contrast ratio.

96.5.2 Gray Scale

Gray scale refers to the number of luminance levels, or shades of gray, available in a display. The common definition is a luminance ratio of 1.4 between levels, although the eye can discriminate changes as small as 1.03 (a Weber's K value of 0.03). The number of gray shades is useful for evaluating the capability of a display to render pictorial information or the range of luminance levels that can be used for coding. The highest luminance level is determined by display capabilities, but the lowest level is determined by the luminance of the display surface when no signal is present. Bright light incident on the display can elevate this minimum level and reduce the number of usable gray shades.

96.5.3 Pixels

Many display parameters are stated in terms of the *pixel* (the name comes from "picture element"). The pixel is the smallest resolvable information element seen by the user. Pixels in trichromatic displays (composed of red, green, and blue [RGB] components) are themselves composed of three *subpixels*, sometimes referred to as dots that are designed to be so small that the eye only perceives their combined color, the color of the pixel.

96.5.4 Resolution and Aspect Ratio

Resolution is a measure of the size of the smallest resolvable object on a display and is expressed as display lines per centimeter or pixels per square centimeter. Another measurement is *pixel pitch*, which is the distance between adjacent pixels (or between the same points in the recurring pattern of component-color subpixels). The specification of a display's resolution allows the differentiation between, for example, standard-definition (SD) displays and high-definition (HD) displays. HD devices are desirable for their refined display of detailed images and video. In comparison to HD displays, an

TABLE 96.1 Chart Comparing a Few Video Standards

Video Standard	Familiar Ratio	Comparable Resolution	Normalized Ratio
SDTV and standard computer monitors (VGA)	4:3	640 × 480	1.33:1
HDTV	16:9	1920 × 1080	1.78:1
Wide-screen computer monitors (WUXGA)	8:5 or 16:10	1920 × 1200	1.6:1
Wide-screen cinema	2.39:1	2870 × 1200	2.39:1

There is a one-to-one mapping between a *GA standard (like VGA or XGA) and a resolution. There are theoretically infinitely many-to-one mappings between resolutions and aspect ratios; however, manufacturers tend to make large enough gaps in product resolutions to warrant separate marketing, design, advertising, etc. These examples are all very close in size except for VGA, which has been the norm for decades.

image on an SD display of comparable size can appear blurry and lacking, especially when comparing highly detailed imagery such as a dense foliage or a person's head of hair.

Resolution is also useful for describing the size of the display, when considering computer monitors and TVs, which have microscopic, square pixels. This is because resolutions for these and similar devices come in standardized *aspect ratios*. This is to facilitate comparison of similar devices by consumers but mostly due to standardization of data encoding and decoding of computer-graphics and TV media. The aspect ratio is the relationship between the width and the height of the display and is presented in a format similar to "16:9," which is the format of standardized wide-screen high-definition television (HDTV). For comparison, modern digital projection shown on wide screens in cinemas has an aspect ratio of 2.4:1, which is 135% the width of HDTV. Table 96.1 lists a few aspect-ratio standards to demonstrate the differences between the aspect ratios and some associated resolutions.

Traditionally, computer monitors have had aspect ratios of 4:3. Although, recent consumer trends have seen wide-screen versions that match the 16:9 size of HDTV and a 8:5 (also written as 16:10 to be more easily compared with the 16:9 ratio of HDTV), which is slightly taller, allowing for more real estate with which to work on a display of a comparable resolution. The tiers of resolution appear where nontrivial technology and manufacturing differences, or distinct market segment needs, are required to achieve a greater resolution, which translates into major differences in cost to the end user. For example, when selecting a display, devices of roughly comparable prices will have formats of HD 1080, UXGA, WUXGA, or 2 K. The next tier in price will contain displays with formats of QXGA or WQXGA. The next lower tier will contain displays with formats of HD 720, XGA, SXGA, or WXGA. The diagonal sizes are all very similar within these groups, but shifting between the aspect ratios may be important, depending on the intended use of the display. Figure 96.1 compares the sizes of a number of these resolution standards; the tiers are revealed by the gaps around horizontal sizes of 900, 1100, 1500, 1700, and 2300.

These "resolutions" are somewhat misleading since these standards are independent of screen size. An 81.3 cm (32 in.) display at 480i would have fewer phosphors illuminated per inch than a 50.8 cm (20 in.) display, simply because the same number of horizontal lines must cover more space in the larger display. However, current product performance has not generated a need for an intermediate-definition display for larger screen sizes or a different measuring standard.

96.5.5 Sharpness and Legibility

Although *sharpness* and its converse *blur* are normally defined by the subjective reaction of the display user, sharpness has been formally measured as the ratio of the blurred border zone of letters to their stroke width [3]. *Legibility* is related to character quality, or readability, and depends on the sharpness of characters.

The recent proliferation of LCD devices has introduced a large number of display devices with discrete, sharp pixels—in contrast to other display technologies that have some natural blending

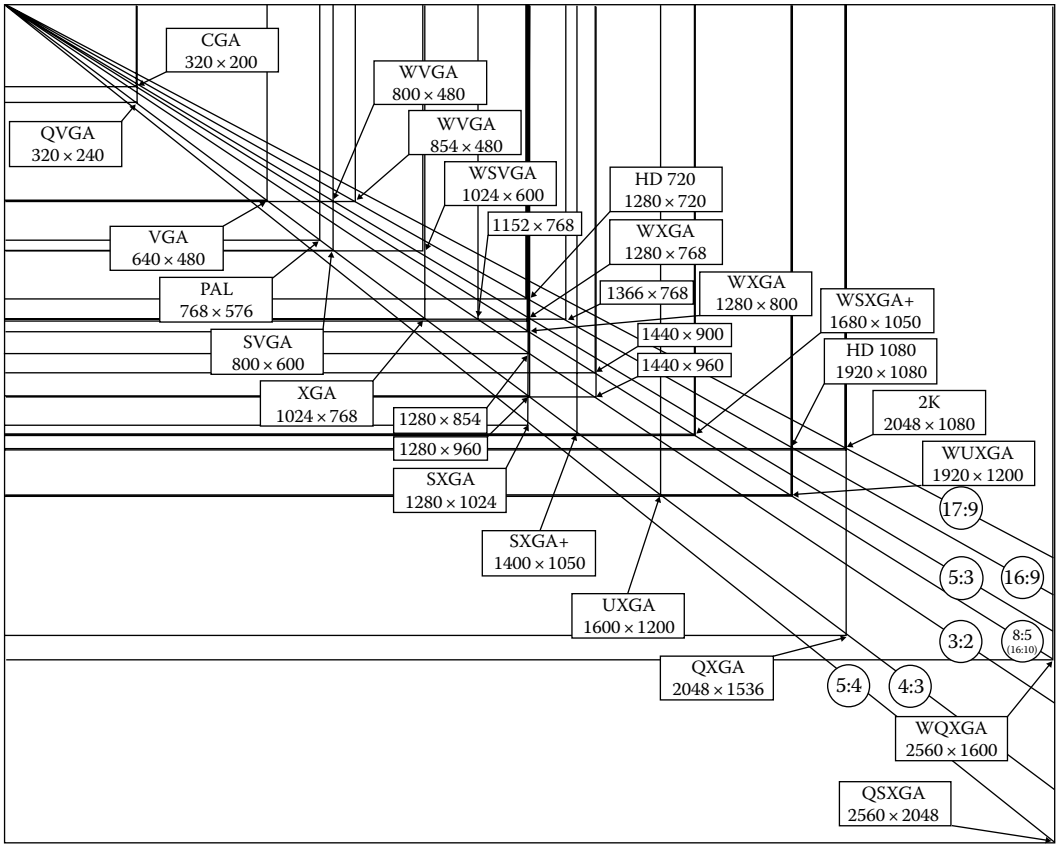

FIGURE 96.1 Variety of aspect ratios and resolutions, showing how they compare in size. The 4:3 aspect ratio has been the historical norm for computer monitors and TVs; however, the popularization of wide-screen formats, especially 16:9 and 8:5, is slowly becoming the new norm. Many dimensions in the variety are used in more than one aspect ratio, such as the vertical dimension of 768—used in 3:2, 4:3, 5:3, and 16:9. This makes it convenient for users when comparing screen resolutions. (Adapted from Steve Pomeroy's similar diagram, retrieved from http://en.wikipedia.org/wiki/File:Vector_Video_Standards2.svg)

between adjacent pixels. LCD devices that display small text (~12 pt fonts) naturally suffer from degraded readability of text, due to the pixels interfering with the shapes of the small letters. The effect causes jagged blocks in the letters where straight lines are not possible due to the pixels in the display. Although this effect is slight, it can degrade the readability of text on the display. One solution is to increase the resolution of the display, although this is usually not cost-effective for improving readability of text alone. Some computer software mitigates this effect by *antialiasing* the text that is displayed. Antialiasing blends pixels together (in effect, creating gray where previously there was only pure black or white) to suggest angled lines and curves that black-and-white pixels cannot display smoothly. Going further, Microsoft's ClearType, Adobe's CoolType, and Apple's Quartz employ *subpixel rendering* to improve type rendering beyond the capabilities of regular antialiasing. Subpixel rendering is not constrained to working with complete pixels and can render any of RGB, GBR, or BRG as white. This allows text to be refined even further than regular antialiasing by using subpixels; the increased resolution is intended to make the readability of text on LCDs approach the readability of printed text on paper [4]. When a discrete-pixel display technology like an LCD is used for extended periods of reading text, subpixel rendering will usually improve readability and reduce fatigue.

96.5.6 Gamut and Color Spaces

Display devices are often discussed in terms of their color reproduction. *Color reproduction* is the similarity between the source color (real-life or high-quality film photograph) and the display color. The *color space* to which humans are sensitive is describable with a convex, smooth mathematical function, called the CIE 1931 XYZ color space. The CIE created this color space in 1931 by combining the visible spectrum (435.8–700 nm) with the photopic luminosity function. The luminosity function is the approximating curve of the human eye's sensitivity to the visible spectrum in normal lighting conditions, with the familiar peak in the green region; the photopic version is for vision in well-lit conditions, as opposed to when the eyes adjust for seeing in the dark (scotopic). The smooth mathematical function is filled to create the color space by mixing adjacent colors, all the way from the curve of the color space (monochromatic light) to the center, white point where all colors mix to form white. In essence, the CIE 1931 color space can describe all combinations of all colors in the visible spectrum.

Decomposing color into a finite (usually small) number of components limits the mixing of colors that can occur. The color *gamut* of a regular trichromatic display device fills a triangle (3 vertices, 1 for each color) that covers some fraction of the CIE 1931 color space. Any given RGB color space completely describes the colors within the triangle but is unable to describe any color outside of the triangle because it requires the mixing of another component of color. The gamuts for SDTV (Rec. 601), HDTV (Rec. 709), and computer graphics (sRGB) are derived from the gamut of CRT displays and cover 35% [5] of the CIE 1931 color space. Color spaces designed especially for professional artists and photographers such as Adobe RGB and Kodak's ProPhoto RGB cover 50% [5] and roughly 80%, respectively, of the CIE 1931 color space. Figure 96.2 illustrates sRGB, Adobe RGB, and ProPhoto as three example color spaces. Most computer monitors follow the sRGB norm, but a few computer monitors are available that display the Adobe RGB color space.

When considering a display device and a color space, it is important to remember that the display device can only display the data given to it. In other words, if you have a digital photograph recorded in the sRGB color space, displaying it on a professional Adobe RGB monitor will not show anything different from displaying the photograph on a household sRGB monitor because its colors have already been clipped—to borrow terminology from audio recording. Similarly, HDTV data are encoded in the same primary colors as sRGB. Adding a yellow component introduces an extra point with which to mix colors and extends the space outside of the HDTV triangle. But if the yellow does not exist in the HDTV specification, then the RYGB display device must extrapolate or not display at all the yellows outside of the sRGB color triangle. Despite sRGB's small coverage of the CIE 1931 color space, it still incorporates most of the colors that exist in the real world. Since natural, real-life colors are not fully saturated and monochromatic, a display gamut that extends to the edges of the CIE 1931 color space is only further capable of displaying unnatural colors. Therefore, given how small the space is between the HDTV/sRGB color space and the CIE 1931 color space, adding yellows (even if extrapolating from HDTV data) does not make colors more lifelike, just oversaturated [6].

96.5.7 Flicker

Flicker is the term for detectable changes in display luminance and occurs when the frequency of those changes is below the integrating capability of the eye. The minimum frequency at which this occurs is the *critical flicker fusion frequency*, or CFF, which depends on the luminance level of the image; that is, displays that do not flicker at high luminance levels may still flicker at low levels. The CFF is calculated as

$$\mathrm{CFF} = a \log L_a + b \tag{96.6}$$

where $a = 12.5$ for high (photopic) ambient light levels and 1.5 for low (scotopic) levels; L_a is the average luminance of the image in cd/m^2, or nits; and $b = 37$. This is an empirical formula, and the values for a

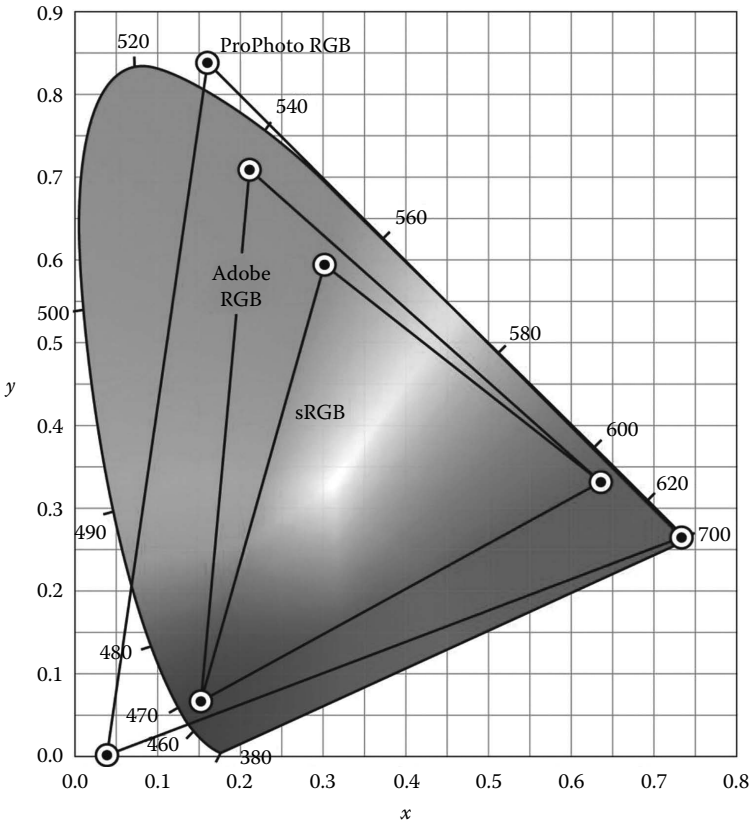

FIGURE 96.2 The ProPhoto, Adobe RGB, and sRGB gamuts overlaid on the CIE 1931 color space. The colors shown in the color space are for representation only. The vertices of the triangles of each of the gamuts represent the locations of the component RGB colors in the CIE 1931 color space. sRGB covers 35% [5], Adobe RGB 50% [5], and ProPhoto roughly 80%, of the CIE 1931 color space. Adobe RGB and sRGB share their red and green components. (Adapted from user "Spigget's" sRGB diagram, user "Juanjfb's" Adobe RGB diagram, and user "Entirety's" ProPhoto diagram, available from http://en.wikipedia.org/wiki/File:Cie_Chart_with_sRGB_gamut_by_spigget.png, http://en.wikipedia.org/wiki/File:CIExy1931_AdobeRGB.png, and http://en.wikipedia.org/wiki/File:CIExy1931_ProPhoto.png)

and *b* are only approximate. Because the eye cannot adapt to flicker fast enough to control the light on the retina, visual irritation usually occurs where flicker is present.

96.5.8 Refresh Rate

Refresh rate is the frequency with which display pixels are re-illuminated. Refresh rates below 50–60 Hz may induce perceptible flicker. The *update rate* is the frequency with which the information content of display is changed and is usually dependent only on the medium through which the content is transmitted to the display and any industry standards for the transmission or medium.

CRT displays are mostly interlaced SD, which for NTSC is 480i (actually 486 scan lines interlaced by two passes of 243 lines each) and for PAL is 576i (two interlaced passes of 288 lines each). HD displays have resolutions of either 720 or 1080 lines, interlaced or progressive. When a display is interlaced, its refresh rate still measures the redrawing time of the entire screen.

Refresh rates become extremely important when one display's content is to be video recorded (and displayed) on a second display. In these situations, the shutter speed (and thus frame rate) of the

recording device may run at a different speed than the refresh rate of the first display. On the second display, the beat frequency may be visible, manifesting somewhere between a brighter band that slowly cycles across the recorded display content and a dramatic, rapid alternating flickering of the bottom and top portions of the screen that makes the recorded display's content difficult and discomforting to view. Since many display refresh rates are not user adjustable, the video recording device needs to have an adjustable shutter speed in this situation.

96.6 Display Content Considerations

Configurable software packages for scientific measurement (e.g., LabView™) allow great flexibility in the design of display formats. Human factors principles for display content, therefore, are as important to effective measurement as the electronic characteristics of the display itself. The following principles are an introduction to the kinds of issues that must be considered when designing display content. The interested reader is referred to Helander (1987) and Grandjean [3] for information on human factors and design guidelines beyond those presented here.

96.6.1 Alphanumeric Displays

The size of a letter is its *pitch*. A general recommendation is that characters should subtend a minimum of about 12 min of arc at common reading distances. Alphanumeric displays are usually constructed of pixel arrays or segmented bars. A 5×7 pixel array is considered the minimum necessary to represent the ASCII character set.

Stroke width is the ratio of the thickness of the stroke to the height of the letter. Recommendations for legibility are 1:6 to 8 or 1:8 to 10 [2]. As illumination is reduced, thick letters are easier to read than thin ones. With low illumination and low contrast, letters should be boldface type with low stroke width–height ratios (e.g., 1:5).

96.6.2 Quantitative and Status Displays

While numeric readout displays are easy to implement in software, analog pointer displays show an advantage when it is important to observe the direction or rate of change of the values presented [7]. If the measurement application involves "more or less" or "up or down" interpretations, a straight-line or thermometer scale is preferred because it shows the measurement in relation to zero. *Moving pointers* are better able to convey minor changes in readings than fixed pointers or numeric readouts. *Scale markings* should reflect the length of the smallest unit to be read. It is desirable to have a marker for each unit, so that no interpolation is required.

Check reading indicators are used to determine whether a condition is "normal." The normal criterion point, therefore, should be clearly coded. If several indicators are grouped together, they should be arranged so that the deviant reading stands out (e.g., by indicating a different column height or dial angle).

Color is an excellent method for organizing information on a display and for locating objects rapidly. Although display users can distinguish between many different colors, they usually cannot remember more than seven to ten of them, so the number should be limited if color is going to be used as a coding dimension.

96.6.3 Summary

The next sections address different display technologies in light of the principles discussed here. While display guidelines are available for essentially any parameter, it is important to remember that visual perception is an integrative process. No single guideline functions alone, and display quality is usually a product of interacting needs and trade-offs.

96.7 Cathode-Ray Tube Displays

The cathode-ray tube (CRT, see Part X of *Electromagnetic, Optical, Radiation, Chemical, and Biomedical Measurement*) in the last decade has seen its ubiquity in electronics stores replaced by the newer solid-state active-matrix LCD and LED display devices and the revisited plasma display. The primary reason for this is size and weight: the traditional CRT displays that were used for every TV and computer monitor require a deep box, often deeper than the screen's diagonal dimension. "Flat" CRT displays have only recently hit the shop floor to catch up to real flat-panel displays: LED, LCD, and plasma displays. However, even "flat" CRT displays are several inches deeper than flat-panel displays and are limited in their diagonal dimension by production costs. Commercial advertising has a major role in shifting consumer preference from CRT to flat-panel TVs and computer monitors. Although a majority of these devices still in use are CRT, device depth and *perceived* technology advancements (some of which are not validated from a technical perspective on human perceptual capabilities) are rapidly influencing the proliferation of flat-panel display technologies.

CRT displays have good contrast ratio, brightness, refresh rate, and product lifetime. The sRGB color space (made ubiquitous by the World Wide Web) was defined based on CRT capabilities, and other display technologies like LCD and plasma follow the sRGB standard, although there are specialized devices that have better gamuts. What sets CRT displays apart from other display technologies is their black levels, which are darker than LCDs and plasma. This is because the CRT can selectively not illuminate the black areas of the screen's content, unlike LCDs, which have a backlight, and plasma displays, which require a small activation charge. For most users, plasma displays will have comparable black levels, although OLED displays that have just recently been made available to consumers promise black levels just as good as CRT displays. On the other hand, CRTs have generally lower luminance compared to other technologies. A typical CRT display may not have a luminance as high as 200 cd/m^2, while LCD and plasma displays easily achieve over that number.

Other than the aforementioned disadvantage of size and weight, CRT screens have also been, in the past, very susceptible to being washed out by ambient light. The ubiquity of smooth glass in CRT displays drove the development of attachable glare filters and the application of antireflective coatings to CRT displays. The former especially can also block a lot of illumination from the display, reducing the contrast ratio and the number of colors that the user can perceive from the display. Finally, the use of CRT displays with continuous exposure to the same screen or user-interface elements (such as on-screen menus, scoreboards, and row or column labels) causes a noticeable "burn-in" of those elements. The phosphors that have displayed those elements for extended time respond poorly to the CRT mechanism, causing colors to be misrepresented in those areas of the screen permanently. Screen burn-in can make a CRT display unusable after hundreds of hours of presentation of a single static image. However, the use of screen savers and multifunction displays has greatly reduced the likelihood of burn-in in modern CRTs compared to early monochrome monitors.

96.7.1 CRT Performance

CRT resolution has plateaued and been standardized to such consistency that the specific measurements are sometimes not even mentioned in product descriptions. CRT displays are mostly interlaced, meaning they require two passes of phosphor illumination to draw a complete screen. This is done at a high enough frequency that the redrawing is invisible to the user, although he or she may perceive a flicker. CRTs used for TVs are SD and interlaced. CRTs used for computer monitors can have resolutions of up to 1200 lines and are interlaced. Historically, CRTs have been manufactured in a very wide spectrum of sizes and resolutions for many different purposes.

A very important parameter of a CRT display is the refresh rate. Because of the mechanics of the phosphors and cathode-ray gun, the refreshing of an interlaced CRT display produces a flicker. On modern screens, the refresh rate is usually one of the standard 60 or 75 Hz. However, because this

measurement refers to the redrawing of the entire screen, due to interlacing, this means alternating halves of the screen is updated 30 or 37 times/s. To many users, CRT displays produce a noticeable flicker that can be fatiguing on the eyes (especially in cases of presenting rapid motion or extremely fine detail). If screen content is to be recorded with a video camera, CRT flicker may make the screen content very difficult to see due to the beat frequency between the video camera's frame rate and the CRT refresh rate.

Contrast ratio is diminished by high ambient light levels, and it is often necessary to compromise between light requirements for work tasks and light levels for optimum CRT visibility. In low ambient lighting conditions, a CRT contrast ratio of 10:1 is usually attainable. Higher ratios of 25:1 or more can be achieved with contrast-enhancing filters but at the expense of brightness and increased power requirements.

96.8 Liquid Crystal Displays

LCDs (see Part X of *Electromagnetic, Optical, Radiation, Chemical, and Biomedical Measurement*) are nonemissive: they do not generate light of their own but control the transmission or reflection of another light source—ambient or built into the same device as the display itself. Many modern LCDs include backlighting, such as cold-cathode fluorescent lamps (CCFLs) or light-emitting diodes (LEDs), to provide ample brightness to the display without the need for often-glare-inducing ambient light. Backlighting also allows the LCD to display color effectively. The simple addition of high-brightness backlighting and an active addressing matrix (rather than passive) allowed LCD technology to go from use in monochrome 7-segment displays to large-screen HDTV capable of displaying one billion colors.

Internally, the liquid-crystal material within an LCD alters the optical path of light when an electric field is placed across it. In a passive-matrix LCD, the material must be stable enough to not require an electric charge to maintain its state. Because of this, passive-matrix LCDs suffer from slow response times. In an active-matrix LCD (AMLCD), an active potential is used to maintain the state of the pixel. An unstable material is desirable so that response times can be as quick as possible.

The principal advantages of LCDs are (1) low power consumption (which is important for battery-operated systems), (2) a flat-panel display package, (3) low cost of the basic materials, and (4) good contrast in high ambient illumination. As mentioned, passive-matrix LCDs can suffer from slow dynamic response for switching display elements on and off: 100–500 ms response times, for example, are visually noticeable and such systems may be unacceptable for many applications. However, for many TVs and computer monitors, AMLCDs have been engineered with response rates sufficient to allow the device to operate with a refresh rate of 120 Hz. Without a backlight, LCDs can be difficult or impossible to read in low light conditions—consider reading a digital watch at night before pressing its light button. Finally, the viewing angle is limited by inherent characteristics with some LCD technologies. Many LCD features, such as switching thresholds and response times, are temperature dependent. Devices with backlights and other electronic components that generate heat (this includes TVs and computer monitors) usually will not suffer from temperature problems in everyday, inside use.

96.8.1 LCD Performance

A full range of resolution capabilities is available, from simple alphanumeric displays to systems with over 5 million pixels and resolutions of 128 pixels per cm (326 ppi) [8]. LCDs have been used in small-display applications, like calculators and watches, all the way through a 274 cm (108 in.) diagonal, full-color HDTV [9]. The difficulty in fabricating the sheet of glass and the TFT matrix useful for an LCD (i.e., with few defects) makes displays of this size remarkable. LCD displays that have been made specifically for signage have a brightness of 700 cd/m^2 [10] for making them clearly visible in locations with bright ambient lighting.

Color in LCDs is achieved by placing a color mosaic over the LCD and switching the cells behind the proper combinations (in RGB) to display color. Modern color displays have colored cells that are small

enough that they cannot actually be resolved. Modern color LCDs are AMLCDs, which employ the use of thin-film transistors (TFTs) as the switching technology, where each red, green, or blue cell is accompanied by a transistor controlling the liquid-crystal material.

96.8.2 TN-Effect LCDs

The matrixes of TFTs that control the LCDs come in several variations. The most common right now utilizes the twisted-nematic (TN) effect, which has been around for many decades for use in calculators, clocks, digital watches, and full-color, high-resolution displays more recently. Backlit displays of this type are easily capable of achieving contrast ratios up to 1000:1 (and luminance commonly between 250 and 300 cd/m^2). In nonbacklit passive-matrix devices, much lower contrast ratios (less than 80:1) are common, but improved capabilities with contrast ratios exceeding 500:1 have been prototyped by late 2010. TN-effect displays suffer from viewing angle limitations, especially in the vertical direction. A large positive viewing angle or a large negative viewing angle results in loss of contrast, distortion of colors, and thus reduced legibility. This makes it very important to install or use TN-effect LCDs at an appropriate viewing angle. The standard ergonomic solution of a downward 15°–20° viewing angle from the user (i.e., measured from the floor horizontal down to the center of the screen), and screen normal tilted to match, works well for TN-effect displays for both user comfort and proper color and contrast display. Aside from viewing angle color shortcomings, TN-effect displays are only capable of 6 bits per color channel, which means they are unable to reproduce the 24 bit color that computer graphics are capable of generating. To accommodate for this shortcoming, TN-effect displays employ dithering (blending colors by using adjacent pixels) to simulate the missing colors. Professional artists and photographers usually avoid TN-effect displays for this reason. TN-effect displays are also insufficient for multiple-user settings because of the aforementioned viewing angle limitations.

96.8.3 IPS LCDs

Designers intended a newer LCD technology, called in-plane switching (IPS), to improve upon the limitations in viewing angle and the poor color reproduction of TN-effect displays. The state of the art in IPS displays achieves 10 bit per color channels, which is capable of over one billion colors. IPS does not suffer from the same color distortion from large horizontal viewing angles that TN-effect displays have. Their superior color reproduction makes IPS displays much more attractive to professionals, artists, and photographers. Originally, IPS displays had poor pixel response times, but recent engineering improvements have made them comparable (around 5 ms) to TN-effect displays. Altogether, IPS displays are superior to TN-effect displays in everything except for their price to the end user. Users who need the excellent color reproduction or viewing angles (e.g., in multiple-user settings) should find the increased price well worth the superior product.

96.8.4 VA LCDs

A third TFT technology is vertical alignment (VA), which comes in multidomain VA (MVA) and patterned VA (PVA). For the most part, VA displays fall in between TN-effect and IPS displays in terms of viewing angles and color reproduction.

96.9 Plasma Displays

Currently, plasma technology (see Part X of *Electromagnetic, Optical, Radiation, Chemical, and Biomedical Measurement*) is used almost exclusively in large-format displays. In the past, monochrome plasma displays were available for portable, laptop, and handheld computers, but advancements in full-color technologies like CRT displays and LCDs dominated the use of plasma displays in these sizes.

Now, plasma displays share the market of TVs of the largest sizes, 100 cm (39 in.) and larger, with LCDs. Cost-effective manufacturing of full-color plasma displays limits the minimum size of the display, so laptop displays and displays in mobile phones—roughly 46.7 cm (18.4 in.) diagonally and smaller—all have LCDs or OLED displays.

The advantages of plasma displays include brightness, luminous efficiency, and dark display of black (as opposed to a washed-out gray). This advantage also allows for excellent contrast ratios in high ambient illumination. However, as discussed earlier, the manufacturer reports of very high contrast ratios should be considered with care, due to the limited human perceptual ability to meaningfully distinguish these ratios in real-world settings. Plasma displays also exhibit long display life and tolerate high shock and vibration environments.

Some disadvantages of plasma displays include higher cost, relative to CRTs, and higher power consumption, relative to LCDs. Similarly sized (107 cm, or 42 in., diagonal) CCFL-backlit LCD and plasma displays can consume 199 W [11] and 327 W [12], respectively.

96.9.1 Plasma Display Performance

The largest plasma display built through 2010 is 386 cm (152 in.) diagonal with a 4 K resolution, 4096 × 2160 [13], which is four times the HDTV standard, almost nine million pixels. Plasma TVs are commercially available in sizes generally greater than 76 cm (30 in.) and up to 275 cm (108 in.). Displays of the largest sizes, advertised for home-theater use, have the best contrast ratios among plasma displays. Advancements in plasma technology have moved plasma into the first place among common display technologies for luminance, with some displays achieving 1300 cd/m^2 [14].

Plasma technology involves similar refresh rates to LCDs, between 60 and 120 Hz. Some advertisements promote plasma displays with "subfield" refresh rates of 480 or even 600 Hz, but this is a misrepresentation [15]. Due to the brief illumination time of subpixels in plasma displays (about 2 ms), maintaining a frame for 1/60s (i.e., displaying a single frame for a full cycle at 60 Hz) requires pulsing the subpixels eight or ten times during the frame, resulting in a misleading 480 or 600 Hz refresh rate, respectively. In fact, the frame is not fully redrawn that quickly—most of the time; the video signal is not even presented to the display this quickly. However, the very short 2 ms duration of the excited states means that plasma displays have nearly no ghosting or blurring when pixels change colors, which is desirable for displaying video containing high movement speeds.

96.10 Electroluminescent Displays

With the exception of LEDs, electroluminescent (EL, see Part X of *Electromagnetic, Optical, Radiation, Chemical, and Biomedical Measurement*) technologies are not as prominent in the commercial arena as other types of display systems. EL materials are complex (i.e., driven and controlled by processes related to solid-state semiconductor physics) and are more difficult to work with than other display materials. Nevertheless, they offer great potential for high brightness and low cost that deserves consideration, especially as new designs become available. Matrix addressing is used for control of information display applications. EL materials are applied in two forms—powders (PEL) and thin-films (TFEL)—and are controlled by both AC and DC voltages, generating four basic design approaches. Some advantages of EL displays are (1) high luminous efficiency (except ACPEL designs); (2) readability in sunlight, (3) color capability, (4) compact, flat-panel designs, and (5) significant potential for low-cost manufacture. A disadvantage of EL displays is that ACPEL systems have low luminance and contrast ratio. In addition, phosphors in powder designs scatter and reflect ambient light, reducing their contrast.

96.10.1 EL Display Performance

Contrast ratios of 50 to 150:1 have been demonstrated with monochrome ACTFEL systems, while 15 to 20:1 have been achieved with DC designs. ACTFEL designs also show excellent brightness, with

demonstrated luminance levels of over 157 cd/m^2 (monochrome) and 26 cd/m^2 (color). DCPEL designs, representing newer technologies, have achieved over 100 cd/m^2 with monochrome designs but may soon meet or exceed AC-based values. The resolution of EL displays is limited by the duty factor of matrix addressing; a finite amount of time is needed to energize each row, and a minimum luminance level is needed for adequate display performance, so the remaining variable becomes the number of addressable lines. A demonstrated ACTFEL display with 640 × 400 elements, with six colors and a resolution of 27 lines/cm, is typical of this technology.

96.11 Light-Emitting Diode Displays

LED displays (see Part X of *Electromagnetic, Optical, Radiation, Chemical, and Biomedical Measurement*) involve single-crystal phosphor materials, which distinguishes them from the polycrystal EL materials discussed in the previous section. The basic physics behind their operation is, however, quite similar. LED displays are highly versatile and well suited to a variety of measurement applications. The advantages of LED displays include high reliability and graceful degrades; individual LED elements can fail without affecting overall display performance. LEDs are rugged, for operation in harsh environments, and they are more tolerant of temperature extremes than other technologies. LEDs demonstrate better viewing angles than LCDs and excellent brightness for visibility in sunlight. Unfortunately, LED displays also have high power consumption when packaged in large, flat-panel displays, and the cost is high for the complex assembly. Optical cross talk between array elements can occur if transparent substrates are used. LEDs are the most-restricted display in terms of color range (e.g., no blue device is commercially available).

96.11.1 LED Display Performance

LED devices have excellent brightness, but because display brightness is also a function of the filters or magnification lenses used over the LED elements, device luminance is not, by itself, a reliable measure of overall system performance. LED displays also show very good luminance contrast. *Chrominance contrast*—the color difference between the LED and its background— however, is a factor in evaluating LED performance that is not found in other technologies. Chrominance contrast is significant because of the high saturation of most LED phosphors. It is affected by display filters and can have significantly more influence on display performance than luminance contrast.

LED displays with resolutions of 20–25 lines/cm have been constructed. Flat-panel displays of 38,400 discrete elements have also been demonstrated with luminance levels of around 137 cd/m^2 (increasing to 240 cd/m^2 with reduced resolution), and at least one aircraft display with 49,000 elements has been built. CRT-equivalent displays with 600 × 400 elements have also been realized with engineering development models.

96.12 Electronic Paper/Electronic Ink

The newest technology to emerge in the past few decades is electronic paper. The researchers currently improving electronic-paper technologies are working to provide a dynamic display that rivals paper in readability and portability (i.e., paper requires no power source). Electronic paper can display content forever with no power required to sustain the image, only change it. Thus, it is possible with electronic paper to provide a single sheet (currently more like a thin tablet) that can display every page of every book, with the proper data connection providing digital versions of the books.

The primary advantage of electronic paper is its readability. The intention is to mimic the way paper is read: a reflective white surface and nonreflective content that provides contrast in almost any lighting (darkness makes electronic paper, like regular paper, unreadable). Currently, electronic paper cannot handle fast-moving images, due to its slow refresh rate.

The technology behind electronic paper is, appropriately enough, electronic ink. There are several different implementations of electronic paper. Either pigment particles are moved to the surface to replace the white background or two-sided particles (one side white and the other black) are rotated in a fluid to display the two colors. Color electronic paper employs either colored inks instead of black or some sort of filtering system. Note that colored inks mean the primaries are subtractive: cyan, magenta, and yellow instead of the additive primaries discussed in the rest of this chapter.

There are other technologies instead of using pigment particles that are also gaining attention, including using microelectromechanical systems to control interference patterns—like the iridescent wings of a butterfly—to display different wavelengths to the viewer, permitting a full-color display [16].

96.12.1 Electronic-Paper Display Performance

Electronic-paper research is diverse, in an attempt to find the best mechanisms for different applications of the technology: tablet computers, electronic books, mobile phones, signage, flexible displays, and others. Currently, the largest set of electronic-paper products is in electronic books, which mostly use the black-and-white mechanism described earlier. A major manufacturer of black-and-white and color electronic paper claims a minimum of 10:1 contrast ratio and viewing angles near 180°, two performance characteristics that make electronic paper so popular. One area in which electronic paper suffers is refresh rate. The mechanism to switch the pigments requires, according to the same manufacturer, between an eighth and a full second [17].

Defining Terms

Decay time: The time required for the peak brightness of a phosphor to drop to a defined fraction of peak luminance; a measure of how long the phosphor remains illuminated after being energized by the electron beam

Duty factor: The time spent addressing each pixel during a refresh cycle; inversely proportional to the number of pixels

Font: Refers to the graphic in which alphanumeric characters and symbols are presented by computers

Spot size: The sizes of the illuminated spot from an electron beam in a CRT; limits the size of the raster line

Wash out: The loss of contrast (i.e., reduction in dynamic range) in an LED as the ambient light reflected off the background of the display surface approaches the light level of the active area

References

1. S. Sherr, *Electronic Displays*, 2nd edn. New York: John Wiley & Sons, 1993.
2. M.S. Sanders and E.J. McCormick, *Human Factors in Engineering and Design*, 6th edn. New York: McGraw-Hill, 1987.
3. E. Grandjean, Design of VDT workstations. In: G. Salvendy (Ed.), *Handbook of Human Factors*, New York: John Wiley & Sons, pp. 1297–1359. 1987.
4. Microsoft Typography. (2002). What is clear type? Retrieved from http://www.microsoft.com/typography/whatiscleartype.mspx (accessed on March 14, 2013).
5. McHugh, S. (n.d.). sRGB vs. Adobe RGB 1998. Retrieved from http://www.cambridgeincolour.com/tutorials/sRGB-AdobeRGB1998.htm (accessed on March 14, 2013).
6. Soneira, R. (2010, July). Display Myths: Shattered. *Maximum PC,* 51. Retrieved from http://dl.maximumpc.com/Archives/MPC0710-web.pdf (accessed on March 14, 2013).
7. D.G. Payne, V.A. Lang, and J.M. Blackwell, Mixed vs. pure display format in integration and nonintegration visual display monitoring tasks, *Human Factors*, 37(3), 507–527, 1995.

8. Apple Inc. (2010). Learn about the high-resolution retina display. Retrieved from http://www.apple.com/iphone/features/retina-display.html (accessed on March 14, 2013).
9. Hanlon, M. (2007). Sharp showcases world's largest LCD TV—108 inches. Retrieved from http://www.gizmag.com/go/6704 (accessed on March 14, 2013).
10. Hewlett-Packard Development Company, L.P. (2011). HP LD4710 47-inch LCD digital signage display specifications. Retrieved from http://h10010.www1.hp.com/wwpc/us/en/sm/WF06a/382087-382087-64283-72270-3915216-5054199.html (accessed on March 14, 2013).
11. Panasonic Corporation. (2010). 2010 Viera U22 Series LCD. Retrieved from http://www2.panasonic.com/match-maker/assets/pdf/viera/2010/VieraU22SeriesLCD.pdf (accessed on March 14, 2013).
12. Panasonic Corporation. (2010). 2010 Viera G25 Series Plasma. Retrieved from http://www2.panasonic.com/match-maker/assets/pdf/viera/2010/VieraG25SeriesPlasmaSpec.pdf (accessed on March 14, 2013).
13. Panasonic Corporation. (2010). Panasonic develops world's largest 1520 inch full-HD 3D plasma display. http://www2.panasonic.com/webapp/wcs/stores/servlet/prModelDetail?storeId=11301&catalogId=13251&itemId=389530&modelNo=Content01062010103949121&surfModel=Content01062010103949121 (accessed on March 14, 2013).
14. SAMSUNG. (2011). 50″ Plasma display specifications. Retrieved from http://www.samsung.com/us/business/commercial-display-solutions/PH50KLPLBF/ZA (accessed on March 14, 2013).
15. Best-3DTVs.com. (2011). What does 600Hz sub-field drive mean? Retrieved from http://www.best-3dtvs.com/guides/what-does-600hz-sub-field-drive-mean/ (accessed on March 14, 2013).
16. Epaper Central. (2010). Spotlight on Mirasol: Qualcomm's full-color e-paper. Retrieved from http://www.epapercentral.com/spotlight-on-mirasol-qualcomms-full-color-epaper.htm (accessed on March 14, 2013).
17. E Ink Corporation. (2010). E Ink Triton Imaging Film. Retrieved from http://www.eink.com/sell_sheets/triton%20sell%20sheet.pdf (accessed on March 14, 2013).

Further Information

Grandjean, E., *Ergonomics in Computerized Offices*, London, U.K.: Taylor & Francis Group, 1987—is an excellent all-around treatise on the principles of effective VDT selection and use. Summarizes a wide range of research literature. If this volume is difficult to obtain, a chapter by the same author is also included in the *Handbook of Human Factors* (Reference 2).

Helander, M.G., Design of visual displays. In: G. Salvendy, (Ed.), *Handbook of Human Factors*, New York: John Wiley & Sons, 1987—is an excellent and concise review of major human factors principles for display design and use. Includes a critical review of the foundation literature in this area.

Sherr, S., *Electronic Displays*, 2nd edn., New York: John Wiley & Sons, 1993—offers clear presentations of all important display technologies, together with a good summary of performance measurement methods for display systems. Well illustrated with a variety of commercial products.

Tannas, L.E., Jr. (Ed.), *Flat-Panel Di splays and CRTs*, New York: Van Nostrand Reinhold, 1985—provides a thorough, yet highly readable examination of the physical principles behind essentially every major display technology. Although the technology capabilities have become dated since publication, this is well worth review.

Appendix: Units and Conversions

B.W. Petley
National Physical Laboratory

This appendix contains several tables that list the SI base units (Table A.1), define the SI base units (Table A.2), list their derived units (Table A.3), list their prefixes (Table A.4), and list their conversion units (Table A.5).

TABLE A.1 SI Base Units

Base Quantity	Name of Base Unit	Symbol
Length	Meter	m
Mass	Kilogram	kg
Time	Second	s
Electric current	Ampere	A
Thermodynamic temperature	Kelvin	K
Amount of substance	Mole	mol
Luminous intensity	Candela	cd

TABLE A.2 International Definitions of the SI Base Units[a]

Unit of length (m)

Meter is the length of the path traveled by light in vacuum during a time interval of 1/299 792 458 of a second (17th CGPM,[b] 1983, Resolution 1).

Note: The original international prototype, made of platinum–iridium, is kept at the BIPM[c] under conditions specified by the 1st CGPM in 1889.

Unit of mass (kg)

Kilogram is the unit of mass: it is equal to the mass of the international prototype of the kilogram (3rd CGPM, 1901).

Unit of time (s)

Second is the duration of 9 192 631 770 periods of the radiation corresponding to the transition between the two hyperfine levels of the ground state of the cesium-133 atom (13th CGPM, 1967, Resolution 1).

Unit of electric current (A)

Ampere is that constant current that, if maintained in two straight parallel conductors of infinite length, of negligible cross section, and placed 1 m apart in vacuum, would produce between these conductors a force equal to 2×10^{-7} N/m of length (CIPM, 1946, Resolution 2 approved by the 9th CGPM, 1948).

Note: The expression "MKS unit of force" that occurs in the original text has been replaced here by "newton," a name adopted for this unit by the 9th CGPM (1948), Resolution 7.

Unit of thermodynamic temperature (K)

Kelvin, unit of thermodynamic temperature, is the fraction 1/273.16 of the thermodynamic temperature of the triple point of water (13th CGPM, 1967, Resolution 4).

The 13th CGPM (1967, Resolution 3) also decided that the unit kelvin and its symbol K should be used to express an interval or a difference in temperature.

Note: In addition to the thermodynamic temperature (symbol T), expressed in kelvin, use is also made of Celsius temperature (symbol t) defined by the equation.

$t = T - T_0$

where $T_0 = 273.15$ K by definition. To express Celsius temperature, the unit "degree Celsius" that is equal to the unit "kelvin" is used; in this case, "degree Celsius" is a special name used in place of "kelvin." An interval or difference of Celsius temperature can, however, be expressed in kelvins as well as degrees Celsius.

Unit of amount of substance (mol)

1. Mole is the amount of substance of a system that contains as many elementary entities as there are atoms in 0.012 kg of carbon-12.
2. When the mole is used, the elementary entities must be specified and may be atoms, molecules, ions, electrons, other particles, or specified groups of such particles.

In the definition of the mole, it is understood that unbound atoms of carbon-12, at rest and in their ground state, are referred to.

Note: This definition specifies at the same time the nature of the quantity whose unit is the mole.

Unit of luminous intensity (cd)

Candela is the luminous intensity, in a given direction, of a source that emits monochromatic radiation of frequency 540×10^{12} Hz and that has a radiant intensity in that direction of (1/683) watt per steradian (16th CGPM, 1979, Resolution 3).

[a] The United States denotes the unit of length by "meter" in place of the international usage of "meter."

[b] CGPM, Conférence Général de Poids et Mesures; CIPM, Comité International des Poids et Mesures.

[c] BIPM: Bureau International des Poids et Mesures.

TABLE A.3 SI-Derived Units with Special Names[a]

Derived Quantity	Name	Symbol	Expressed in Terms of Other Units	Expressed in Terms of SI Base Units
Plane angle	Radian	rad		$m\ m^{-1}$
Solid angle	Steradian	sr		$m^2\ m^{-2}$
Frequency	hertz	Hz		s^{-1}
Force	newton	N		$m\ kg\ s^{-2}$
Pressure, stress	pascal	Pa	$N\ m^{-2}$	$m^{-1}\ kg\ s^{-2}$
Energy, work, quantity of heat	joule	J		$m^2\ kg\ s^{-2}$
Power, radiant flux	watt	W		$m^2\ kg\ s^{-3}$
Electric charge, quantity of electricity	coulomb	C		s A
Electric potential, potential difference, electromotive force	volt	V	W/A	$m^2\ kg\ s^{-3}\ A^{-1}$
Capacitance	farad	F	C/V	$m^{-2}\ kg^{-1}\ s^4\ A^2$
Electric resistance	ohm	Ω	V/A	$m^2\ kg\ s^{-3}\ A^{-2}$
Electric conductance	siemens	S	A/V	$m^{-2}\ kg^{-1}\ s^3\ A^2$
Magnetic flux	weber	Wb	V s	$m^2\ kg\ s^{-2}\ A^{-1}$
Magnetic flux density	tesla	T	Wb/m^2	$kg\ s^{-2}\ A^{-1}$
Inductance	henry	H	Wb/A	$m^2\ kg\ s^{-2}\ A^{-2}$
Celsius temperature	Degree Celsius	°C		K
Luminous flux	Lumen	lm	cd sr	$cd\ m^2\ m^{-2} = cd$
Illuminance	Lux	lx	m^{-2} cd sr	m^{-2} cd
Activity (referred to a radio nuclide)	becquerel	Bq		s^{-1}
Absorbed dose, specific energy imparted, kerma	gray	Gy	J/kg	$m^2\ s^{-2}$
Dose equivalent, ambient dose equivalent, organ equivalent dose	sievert	Sr	J/kg	$m^2\ s^{-2}$

[a] Note that when a unit is named after a person, the *symbol* takes a capital letter and the name takes a lowercase letter.

TABLE A.4 SI Prefixes[a]

Factor	Prefix	Symbol	Factor	Prefix	Symbol
10^{24}	Yotta	Y	10^{-1}	Deci	d
10^{21}	Zetta	Z	10^{-2}	Centi	c
10^{18}	Exa	E	10^{-3}	Milli	m
10^{15}	Peta	P	10^{-6}	Micro	μ
10^{12}	Tera	T	10^{-9}	Nano	n
10^{9}	Giga	G	10^{-12}	Pico	p
10^{6}	Mega	M	10^{-15}	Femto	f
10^{3}	Kilo	k	10^{-18}	Atto	a
10^{2}	Hecto	h	10^{-21}	Zepto	z
10	Deca	da	10^{-24}	Yocto	y

[a] The 11th CGPM (1960, Resolution 12) adopted a first series of prefixes and symbols of prefixes to form the names and symbols of the decimal multiples and submultiples of SI units. Prefixes for 10^{-15} and 10^{-18} were added by the 12th CGPM (1964, Resolution 8), those for 10^{15} and 10^{18} were proposed by the 15th CGPM (1975, Resolution 10), and those for 10^{21}, 10^{24}, 10^{-21}, and 10^{-24} were proposed by the CIPM (1990) for approval by the 19th CGPM (1991).

TABLE A.5 Conversion Factors from English Measures to SI Units[a]

Unit	Equivalent
1. *Acceleration*	
Acceleration of free fall, standard gravity	9.806 65 m s^{-2}
1 ft/s^2	0.304 8 m s^{-2}
1 gal	0.01 m s^{-2}
2. *Angle*	
1 second (″)	$4.484\ 81 \times 10^{-6}$ rad
1 minute (′)	$2.908\ 9 \times 10^{4}$ rad
1 degree (°)	0.0174 532 rad
1 rad	206 264.8″
3. *Area*	
1 barn (b)	10^{-28} m^2
1 $in.^2$	$6.451\ 6 \times 10^{-4}$ m
1 ft^2	0.092 903 04 m^2
1 yd^2	0.836 127 36 m^2
1 are	100 m^2
1 acre [43560 (statute ft)^2]	4046.86 m^2
1 hectare	10,000 m^2
1 mi^2	$2.590\ 0 \times 10^{6}$ m^2
1 square mile (based on U.S. survey foot)	2.589 998 km^2
4. *Concentration, density, mass density*	
1 grain/gal (United States)	0.017 118 kg/m^3
1 lb/ft^3	16.018 46 kg/m^3
1 lb/gal (United States)	119.826 4 kg/m^3
1 short ton/yd^3	1186.6 kg/m^3
1 long ton/yd^3	1328.9 kg/m^3
1 oz (avdp)/$in.^3$	1730.0 kg/m^3
1 oz (avd)/gal (United States)	7.489 152 kg/m^3
1 $lb/in.^3$	27,680 kg/m^3
5. *Energy*	
1 ft lbf	1.355 818 J
1 cal_{th} (thermochemical calorie)	4.184 J
1 cal_{15} (15 °C calorie)	4.185 5 J
1 cal_{IT}[b]	4.186 8 J
1 kilocalorie (nutrition)[c]	4.186.8 J
1 watt second (W s)	1 J
1 watt hour (W h)	3600 J
1 therm (EC)	$1.055\ 06 \times 10^{8}$ J
1 therm (United States)	$1.054\ 804 \times 10^{8}$ J
1 ton TNT (equivalent)	4.184×10^{9} J
1 BT_{th}	1 054.350 J
1 Btu_{15}	1 054.728 J
1 Btu_{ST}	1 055.055 852 62 J
1 quad (=10^{15} Btu)	≈10^{18} J = 1 EJ

TABLE A.5 (continued) Conversion Factors from English Measures to SI Units[a]

Unit	Equivalent
6. *Force*	
1 dyne	10^{-5} N
1 ounce-force	0.278 013 9 N
1 pound-force	4.448 222 N
1 kilogram-force	9.806 65 N
1 kip (1000 lbf)	4448.222 N
1 ton-force (2000 lbf)	8.896 443 N
7. *Fuel consumption*	
1 gallon (United States) per horsepower hour	$1.410\,089 \times 10^{-9}$ m^3/J
1 gallon (United States)/mile	2.352 15 1/km
1 gallon (United Kingdom)/mile	2.824 81 1/km
1 mile/gallon (United States), mpg	0.425 144 km/L
1 mile/gallon (United Kingdom)	0.354 006 km/L
1 pound per horsepower	$1.689\,659 \times 10^{-7}$ kg/J
1 1/(100 km)	235.215/(mpg) (United States)
8. *Length*	
1 fermi	10^{-15} m = 1 fm
1 angstrom (Å)	10^{-10} m
1 microinch	2.54×10^{-8} m
1 mil	2.54×10^{-5} m
1 point (pt) [0.013837 in.][d]	—
1 pica (12 pt)	4.217 5 mm
1 inch (in.)	0.025 4 m
1 hand (4 in.)	0.101 6 m
1 foot (12 in.) (0.999998 statute ft.)	0.304 8 m
1 foot (U.S. survey)	0.304 800 6 m
1 statute foot [(1200/3937) m]	0.304 800 6 m
1 yard (yd)	0.914 4 m
1 fathom (6 ft, U.S. survey)	1.828 8 m
1 rod (16.5 statute ft)	5.029 2 m
1 chain (4 rod)	20.116 8 m
1 furlong (10 chain)	201.168 m
1 mile (8 furlong, 5280 ft)	1609.344 m
1 statute mile (8 furlong, 5280 statute ft)	1609.347 2 m
1 nautical mile (international)[e]	1852 m
1 light-year[f]	$9.640\,73 \times 10^{15}$ m
9. *Light*	
1 foot-candle	10.763 91 lx
1 phot	10,000 lx
1 cd/in.^{2}	1550.003 cd/m^2
1 footlambert	3.426 259 cd/m^2
1 lambert	3183.099 cd/m^2
1 stilb	10,000 cd/m^2

(*continued*)

TABLE A.5 (continued) Conversion Factors from English Measures to SI Units[a]

Unit	Equivalent
10. *Mass*	
1 pound (avdp.) (lb) (7000 g)	0.453 592 37 kg
1 pound (troy) (5760 g)	0.373 241 721 6 kg
1 grain (g)	64.798 91 mg
1 scruple (20 g)	1.296 0 g
1 pennyweight (24 g)	1.555 174 g
1 dram (60 g)	3.887 9 g
1 ounce (avdp) (437.5 g)	28.349 52 g
1 ounce (troy) (480 g)	31.103 48 g
1 carat (metric)	0.2 g
1 stone (14 lb)	6.350 29 kg
1 slug	14.593 9 kg
1 hundredweight (long)	50.802 35 kg
1 ton (short) (2000 lb)	907.184 7 kg
1 ton (long) (2240 lb)	1016.047 kg
	1.016 047 t
Mass per unit length	
1 tex	10^{-6} kg/m
1 denier	$1.111\,111 \times 10^{-7}$ kg/m
1 pound per foot	1.488 164 kg/m
1 pound per inch	17.857 97 kg/m
1 ton/mile	0.631 342 mg/km
1 ton/1000 yd	1.111 6 kg/m
1 lb/ft	1.488 16 kg/m
Mass per unit area	
1 ton/mile^2	3.922 98 kg/ha
1 ton/acre	2510.71 kg/ha
1 oz/yd^2	33.905 7 g/m^2
Mass carried × distance (traffic factor)	
1 ton mile	1635.17 kg km
Mass carried × distance/volume (traffic factor)	
1 ton mile/gal (United States)	431.967 6 mg km/m^3
11. *Power*	
1 erg/s	10^{-7} W
1 ft lbf/h	$3.766\,161 \times 10^{-4}$ W
(1 Btu_{ST})	1.000 669 Btu_{th}
1 metric horsepower (force de cheval)	735.498 8 W
1 horsepower (550 ft lbf/s)	745.70 W
1 electric horsepower	746 W
12. *Pressure, stress*	
1 standard atmosphere	101 325 Pa
1 dyne/cm^2	0.1 Pa
1 torr [(101th 325/760) Pa]	133.322 4 Pa
1 N/cm^2	10,000 Pa
1 bar	100,000 Pa
1 lbf/ft^2	47.880 26 Pa
1 lbf/in.^{2} (psi)	6894.8 Pa

TABLE A.5 (continued) Conversion Factors from English Measures to SI Units[a]

Unit	Equivalent
1 kgf/cm^2	98 066.5 Pa
1 cm water (4 °C)	98.063 7 Pa
1 mm of mercury (0 °C)	133.322 4 Pa
1 in of water (39.2 °F)	249.082 Pa
1 in of mercury (60 °F)	3376.85 Pa
1 ft water (39.2 °F)	2988.98 Pa
13. *Thermal quantities*	
Fixed points	
Triple point of natural water T_{tp}	273.16 K
Zero Celsius (= $T_0 = t_{F,0}$)	273.15 K = 32 °F
Temperature conversions	
Kelvin to Rankine (T_R)	$T = (5/9)\ T_R$
Kelvin to Celsius	$t = T - T_0$
Kelvin to Fahrenheit	$t_F = (9/5)(T - T_0) + t_{F,0}$
Celsius to Fahrenheit	$t_F = (9/5)\ t + t_{F,0}$

[Numerically, $5(\{t_F\} + 40) = 9(\{t\} + 40)$, where $\{t\}$ and $\{t_F\}$ are the numerical values of the Celsius and Fahrenheit temperatures, respectively.]

Temperature interval conversions	
1 degree centigrade	1 degree Celsius, denoted 1 °C
1 °C	1 K
1 °F	(1/1.8) K
1 °R	(1/1.8) K
Other thermal quantities	
1 Btu$_{th}$/h	0.292 875 W
1 Btu$_{IT}$/h	0.293 071th 1 W
1 cal$_{IT}$/s	4.186 8 W
1 cal$_{th}$/s	4.184 W
1 cal$_{IT}$/(g°C)	4186.8 J/(kg K)
1 Btu ft/(ft^2 h°F)	1.730 735 W m^{-1} K^{-1}
1 Btu in./(ft^2 s°F)	519.220 4 W m^{-1} K^{-1}
1 clo	0.155 m^2 K/kW
1 °F h ft^2/Btu	0.176 110 2 K m^2/W
1 °F h ft^2/Btu in	6.933 472 K m/W
1 Btu/lb°F ≡ 1 cal$_{ST}$/g°C	4186.8 J/kg.K
14. *Torque, moment of force*	
1 dyne·cm	10^{-7} N m
1 kgf·m	9.806 65 N m
1 ozf·in.	0.007 061 552 N m
1 lbf·in.	0.112 984 8 N m
1 lbf·ft	1.355 818 N m
15. *Velocity (includes speed)*	
1 foot per hour	8.466 667 × 10^{-5} m/s
1 foot per minute	0.005 08 m/s
1 knot (nautical mile per hour)	0.514 444 m/s
1 mile per hour (mi/h)	0.447 04 m/s

(*continued*)

TABLE A.5 (continued) Conversion Factors from English Measures to SI Units[a]

Unit	Equivalent
16. *Viscosity*	
1 poise	0.1 Pa s
1 ft²/s	0.092 903 04 m²/s
1 lb/(ft s)	1.488 164 Pa s
1 lb/(ft h)	$4.133\,789 \times 10^{-4}$ Pa s
1 lbf s/ft²	47.880 26 Pa s
1 lbf·s/in.²	6894.757 Pa s
1 rhe	10 Pa^{-1} s^{-1}
1 slug/ft s	47.880 26 Pa s
1 stokes, St	1.0×10^{-4} m²/s
17. *Volume (includes capacity)*	
1 stere, st	1 m³
1 liter[g]	0.001 m³
1 ft³	0.028 316 8 m³
1 in.³	$1.638\,7 \times 10^{-5}$ m³
1 board foot	$2.359\,7 \times 10^{-3}$ m³
1 acre-foot	1233.48 m³
1 dram (U.S. fluid)	$3.696\,7 \times 10^{-6}$ m³
1 gill (United States)	$1.182\,941 \times 10^{-4}$ m³
1 ounce (U.S. fluid)	$2.957\,353 \times 10^{-5}$ m³
1 teaspoon (tsp)[h]	$4.9288\,922 \times 10^{-6}$ m³
1 tablespoon (tbsp)	$1.4787\,676 \times 10^{-5}$ m³
1 pint (U.S. fluid)	$4.731\,765 \times 10^{-4}$ m³
1 quart (U.S. fluid)	$9.463\,529 \times 10^{-4}$ m³
1 gallon (U.S. liquid) [231 in.³]	$3.785\,412 \times 10^{-3}$ m³
1 wine barrel (bbl) [31.5 gal (United States)]	0.119 240 m³
1 barrel (petroleum, 42 gal, United States), bbl	0.158 987
1 ounce (U.K. fluid)	$2.841\,3 \times 10^{-5}$ m³
1 gill (Canada and United Kingdom)	$1.420\,6 \times 10^{-4}$ m[q]
1 gallon (Canada and United Kingdom)	$4.546\,09 \times 10^{-3}$ m³
	1.200 950 gal (United States)
1 pint (U.S. dry)	$5.506\,105 \times 10^{-4}$ m³
1 quart (U.S. dry)	$1.101\,221 \times 10^{-3}$ m³
1 gallon (U.S. dry)	$4.404\,884 \times 10^{-3}$ m³
1 peck	$8.809\,768 \times 10^{-3}$ m³
1 bushel (United States) [2150.42 in.³]	$3.523\,907 \times 10^{-2}$ m³

[a] The conversion factor for a compound unit is usually not given here if it may easily be derived from simpler conversions; e.g., the conversion factors for "ft/s" to "m/s" or "ft/s²" to "m/s²" are not given, since they may be obtained from the conversion factor for "ft." Values are given to five or six significant digits except for exact values, which are usually indicated in bold type. A few former cgs measures are also included.

[b] The International Steam Table calorie of 1956.

[c] In practice, the prefix kilo is usually omitted. The kilogram calorie or large calorie is an obsolete term for the kilocalorie that is used to express the energy content of foods.

[d] Typographer's definition, 1886.

[e] Originally, in 1929, the international nautical mile.

[f] Based on 1 day = 86,400 s and 1 Julian century = 36,525 days.

[g] Post-1964 value, SI symbol l or L. Between 1901 and 1964, the liter was defined as 1.000th 028 dm³.

[h] Although often given, it is doubtful whether normal usage justifies this accuracy. In Europe and elsewhere, teaspoon and tablespoon are usually exactly 5 and 15 mL, respectively.

Bibliography

Anderton P. and Bigg P. H., *Changing to the Metric System*, HMSO, London, U.K., 1980.

CIPM, Proces-Verbaux CIPM, 49th Session, 1960, pp. 71–72; *Comptes Rendues, 11th CGPM*, 1960, p. 85.

Cohen E. R., *The Physics Quick Reference Guide*, American Institute of Physics Press, New York, 1995.

Standard for Use of the International System of Units (*SI*): *The Modern Metric System, IEEE/ASTM SI 10–1997*, IEEE Standards Coordinating Committee 14 (Revision and redesignation of ANSI/IEEE Std 268–1992 and ASTM E380), IEEE, New York, 1997.

Taylor B. N., *Interpretation of the SI for the United States and Metric Conversion Policy for Federal Agencies*, Natl. Inst. Stand. Technol., Spec. Publ. 814, U.S. Government Printing Office, Washington, DC, 1991.

Taylor B. N., *Guide for the Use of the International System of Units*, 1995 ed., Natl. Inst. Stand. Technol., Spec. Publ. 811, U.S. Government Printing Office, Washington, DC, 1995.

The International System of Units, 7th edn., BIPM, Sèvres, France, 1998.

The International System of Units (*SI*), Natl. Inst. Stand. Technol., Spec. Publ. 330, 1991 ed., U.S. Government Printing Office, Washington, DC, 1991.

The NIST Guide for the Use of the International System of Units. http://www.nist.gov/pml/pubs/sp811/index.cfm (last accessed August 23, 2013).

Electrical Engineering

SECOND EDITION

Measurement, Instrumentation, and Sensors Handbook

Spatial, Mechanical, Thermal, and Radiation Measurement

The **Second Edition** of the bestselling **Measurement, Instrumentation, and Sensors Handbook** brings together all aspects of the design and implementation of measurement, instrumentation, and sensors. Reflecting the current state of the art, it describes the use of instruments and techniques for performing practical measurements in engineering, physics, chemistry, and the life sciences and discusses processing systems, automatic data acquisition, reduction and analysis, operation characteristics, accuracy, errors, calibrations, and the incorporation of standards for control purposes.

Organized according to measurement problem, the **Spatial, Mechanical, Thermal, and Radiation Measurement** volume of the **Second Edition**:

- Contains contributions from field experts, new chapters, and updates to all 96 existing chapters
- Covers instrumentation and measurement concepts, spatial and mechanical variables, displacement, acoustics, flow and spot velocity, radiation, wireless sensors and instrumentation, and control and human factors

A concise and useful reference for engineers, scientists, academic faculty, students, designers, managers, and industry professionals involved in instrumentation and measurement research and development, **Measurement, Instrumentation, and Sensors Handbook, Second Edition: Spatial, Mechanical, Thermal, and Radiation Measurement** provides readers with a greater understanding of advanced applications.

CRC Press
Taylor & Francis Group
an informa business
www.crcpress.com

6000 Broken Sound Parkway, NW
Suite 300, Boca Raton, FL 33487
711 Third Avenue
New York, NY 10017
2 Park Square, Milton Park
Abingdon, Oxon OX14 4RN, UK

K12208

ISBN: 978-1-4398-4888-3
90000
9 781439 848883